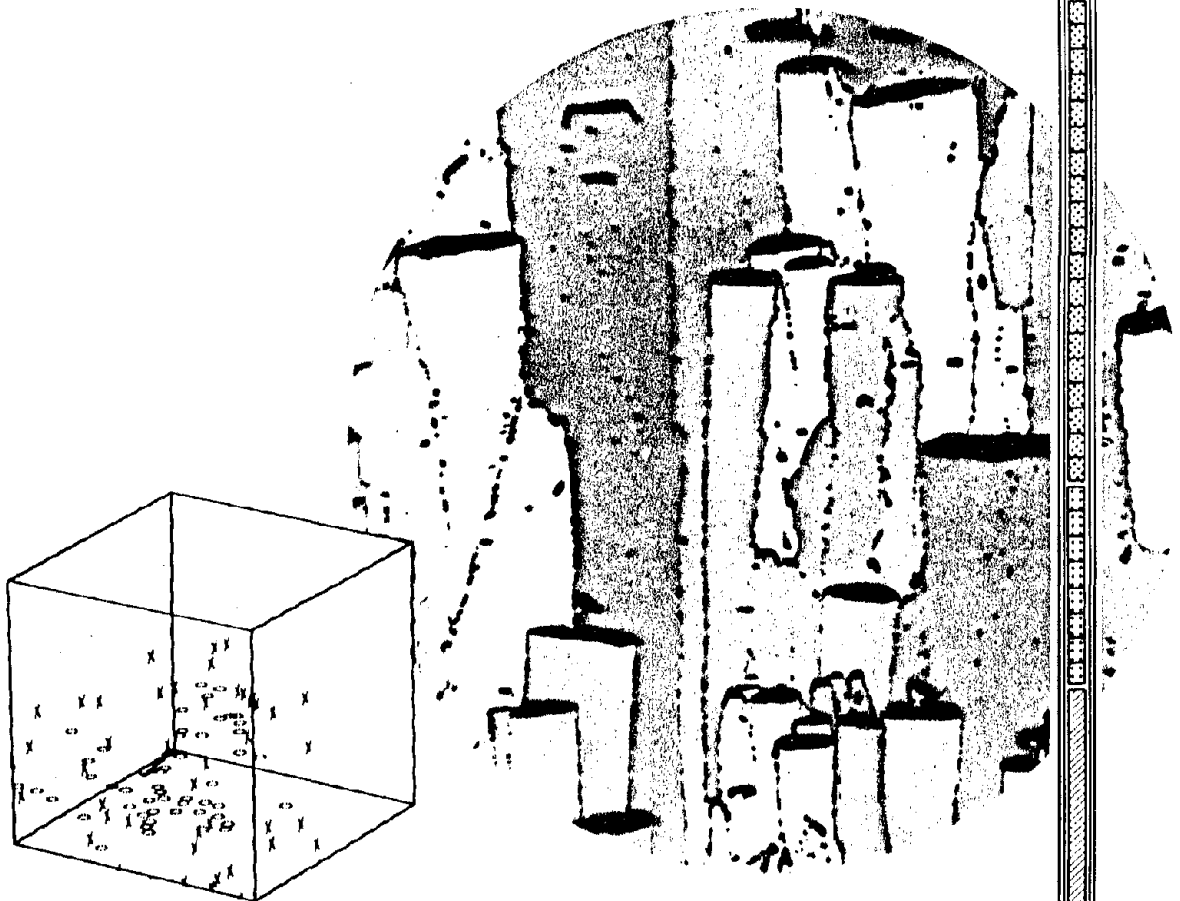


# Fundamental Aspects of Nuclear Reactor Fuel Elements

*Donald R. Olander*



Technical Information Center  
Energy Research and Development Administration



## **ABOUT THE OFFICE OF SCIENTIFIC AND TECHNICAL INFORMATION**

The Office of Scientific and Technical Information (OSTI) in Oak Ridge, Tennessee, has been the national center for scientific and technical information for the Department of Energy (DOE) and its predecessor agencies since 1946. In developing and managing DOE's technical information program, OSTI places under bibliographic control not only DOE-originated information but also worldwide literature on scientific and technical advances in the energy field and announces the source and availability of this information. Whereas the literature of science is emphasized, coverage is extended to DOE programmatic, socioeconomic, environmental, legislative/regulatory, energy analysis, and policy-related areas. To accomplish this mission, OSTI builds and maintains computerized energy-information data bases and disseminates this information via computerized retrieval systems and announcement publications such as abstracting journals, bibliographies, and update journals. Direct access to OSTI's most comprehensive data base, the Energy Data Base, is available to the public through commercial on-line bibliographic retrieval systems. The Energy Data Base and many of OSTI's energy-related data bases are available to DOE offices and contractors and to other government agencies via DOE/RECON, the Department's on-line information retrieval system. The Office of Scientific and Technical Information has developed and maintains systems to record and communicate energy-related research-in-progress information, to maintain a register of DOE public communications publications, to track research report deliverables from DOE contractors, and to test and make available DOE-funded computer software programs with scientific and management applications; OSTI also serves as advisor for special publication needs of the Department. To effectively manage DOE's technical information resources, OSTI's program is one of continual development and evaluation of new information products, systems, and technologies.



## **UNITED STATES DEPARTMENT OF ENERGY**

**John S. Herrington, Secretary**

**Martha Hesse Dolan, Assistant Secretary, Management and Administration**

**William S. Heffelfinger, Director of Administration**

**Joseph G. Coyne, Manager, Office of Scientific and Technical Information**

## **ABOUT BOOKS PUBLISHED BY THE TECHNICAL INFORMATION CENTER**

Books published by the Center include undergraduate, graduate, and workshop textbooks; handbooks and manuals; reference books; monographs; specialized reviews; and DOE-sponsored symposium, workshop, and short-course proceedings.

March 1985

TID26711P1



TID-26711-P1

# Fundamental Aspects of Nuclear Reactor Fuel Elements

**Donald R. Olander**

*Department of Nuclear Engineering  
University of California, Berkeley*

Prepared for the Division of Reactor Development and Demonstration  
Energy Research and Development Administration

1976

Reprinted by the Technical Information Center  
U. S. Department of Energy

Published by  
Technical Information Center  
Energy Research and Development Administration

**Library of Congress Cataloging in Publication Data**

**Olander, Donald R.**

Fundamental aspects of nuclear reactor fuel elements.

"TID-26711-P1"

Includes bibliographies and index.

1. Nuclear fuel elements. I. Title.

TK9207.O4      621.48335      76-6485

ISBN 0-87079-031-5 (v.1)

Available as TID-26711-P1

National Technical Information Service  
U. S. Department of Commerce  
Springfield, Virginia 22161

ERDA Distribution Category UC-79b

1976; latest printing, March 1985

# Preface

Most industrialized nations of the world have accorded high priority to development of nuclear reactors in an effort to stave off an energy crisis. One of the critical areas on which the economic viability of this type of electricity production hinges is the performance of the ceramic fuel and the metallic structural components of the core, which are subject to conditions of high temperature and radiation fields. Research on the behavior of materials under such conditions is relatively recent, and this book represents application of this research to the practical problem of predicting the performance and longevity of reactor fuel elements.

The book is designed to function both as a text for first-year graduate courses in nuclear materials and as a reference for workers involved in the materials design and performance aspects of nuclear reactors for electric power production. It is based on lectures in graduate courses in the Department of Nuclear Engineering, University of California, Berkeley. University students in nuclear engineering come from a variety of undergraduate disciplines, but, by and large, their background in the fundamental physics and chemistry on which much of the applied work treated in the book is based is sketchy. For this reason the first 8 chapters are devoted to reviews of selected aspects of statistical thermodynamics, crystallography, chemical thermodynamics, and physical metallurgy. The remaining 13 chapters constitute the application of these principles to the problems encountered in nuclear fuel elements. Chapters 9 to 16 deal with the properties and irradiation behavior of oxide fuels. Chapters 17 to 20 treat similar problems in the cladding. Chapter 21 incorporates the analyses of materials behavior presented in the earlier chapters into calculations of the performance of the entire fuel element.

The book is primarily concerned with the materials problems uncovered during the development of the liquid-metal fast breeder reactor (LMFBR). Because of the less stringent radiation and thermal conditions in which light-water-reactor (LWR) fuel operates compared to the environment of an LMFBR fuel pin, the fast breeder reactor may be more severely materials-limited than is the water reactor. Except for aqueous corrosion, hydriding, and nonisotropic growth of zircaloy cladding, which are not treated in the book, the basic irradiation effects are common on both LWR and LMFBR fuel elements. Similarly, gas-cooled fast breeder reactors will inherit all the

materials problems of the LMFBR save those arising from the use of liquid-sodium coolant.

Advanced fuels, such as carbides and nitrides, for fast breeder reactors are not specifically discussed in the book. The phenomena responsible for the behavior of oxide fuels in a reactor environment are for the most part found in carbides and nitrides as well. The differences between oxide and advanced ceramic fuels are quantitative rather than qualitative, and some fuel performance analyses in the book are illustrated using  $(U,Pu)C$  instead of  $(U,Pu)O_2$ .

The approach is analytic rather than descriptive. The aim is to make very clear the relation between a model of the performance of some feature of a fuel element and simple, basic physical principles with which the reader is familiar. This philosophy means that a number of standard, classical formulas that constitute the starting point for many fuel-element performance analyses are derived rather than simply presented. The book is intended to be as self-consistent and inclusive in this aspect as possible, and its length is in large part dictated by this approach. The ultimate purpose is to convey an understanding of the physical processes occurring in metals and ceramics which, when taken together, produce the complex irradiation behavior of a nuclear reactor fuel pin. No attempt has been made to provide a method for rational design of a fuel element. Such a recipe does not exist, and, even if it did, its technological lifetime would be very much shorter than that of the fundamental phenomena on which it is based.

As an aid to students, problems are provided at the end of each chapter; solutions to these problems have been published in a separate book, *Solutions to Problems*, available as TID-26711-P2 from the National Technical Information Service, U. S. Department of Commerce, Springfield, Virginia 22161. An attempt was made to maintain a consistent set of symbols throughout the book. This in itself provides a thread of continuity between the many theories of fuel and cladding behavior which have appeared in the technical literature over the past decade. Metric units are used throughout.

It is impossible to be an expert in a field as eclectic as nuclear materials. The disciplines of chemistry, nuclear and solid-state physics, metallurgy, ceramics, applied mechanics, and mathematical analysis are all involved in an accurate description of the fate of an irradiated fuel pin. I am consequently particularly grateful to colleagues who have reviewed sections of the book.

I am indebted to L. Bernath of Atomic International for his detailed review of Chap. 10, to E. A. Aitken and M. G. Adamson for their thoughtful comments on Chaps. 11 and 12, and to P. E. Blackburn and M. G. Chasanov of Argonne National Laboratory for their careful review of Chap. 11. R. Hesketh of the Central Electricity Generating Board placed irradiation creep in metals in its proper perspective. The assistance of T. Kassner on Chap. 20 and R. L. Taylor and J. Stephen on Chap. 21 is acknowledged with thanks. The comments of Professors D. R. O'Boyle of the University of Illinois and T. H. Pigford of the University of California were particularly helpful, since they reflected student reactions to the manuscript. In addition, some of Professor Pigford's problems are included among those appearing at the end of each chapter. The hospitality of Professor J. Kistemaker and the stimulating scientific environment of the FOM—Instituut voor Atoom en Molecuulfysica, Amsterdam, are acknowledged with gratitude.

The largest measure of thanks and my deepest appreciation is due to Mary Wogulis for her extraordinary single-minded determination to type as fast as I could write and for her dogged insistence on a perfect manuscript. The line drawings in the book were prepared with great skill by

E. Grant and G. Pelatowski. J. Doshi, Rosa Yang, and D. Dooley prepared the *Problem Solutions*. They and many other students greatly reduced the seemingly endless supply of errors in the manuscript.

Frank Kerze of the Energy Research and Development Administration meticulously reviewed the entire manuscript. R. F. Pigeon of the Office of Public Affairs, ERDA, and Marian Fox and William Simpson of the Technical Information Center, OPA, ERDA, Oak Ridge, Tennessee, were responsible for shepherding the manuscript to the printed page. The on-site support and help of J. Horak of ORNL is acknowledged with thanks.

Finally, I wish to acknowledge support for preparation of this book from the Energy Research and Development Administration and for its willingness to publish such a specialized tome at a selling price that makes it accessible to students, professionals, and librarians.

This book is dedicated to my parents and wife, who were delighted to see this project finished, but for different reasons.

Donald R. Olander  
University of California, Berkeley

# Contents

Preface . . . . .	iii
<b>Chapter 1 Statistical Thermodynamics . . . . .</b>	<b>1</b>
1.1 Definitions and Terminology . . . . .	1
1.2 Probability Distribution in the Canonical Ensemble . . . . .	2
1.3 Thermodynamic Properties and the Partition Function . . . . .	4
1.4 Ideal Gases . . . . .	6
1.5 Nomenclature . . . . .	12
1.6 Additional Reading . . . . .	12
1.7 Problems . . . . .	12
<b>Chapter 2 Thermal Properties of Solids . . . . .</b>	<b>14</b>
2.1 Vibrational Energy in a Solid . . . . .	14
2.2 Normal Mode Analysis . . . . .	15
2.3 Partition Function for Vibration . . . . .	15
2.4 The Einstein Model . . . . .	17
2.5 The Debye Model . . . . .	17
2.6 Specific Heat According to the Debye Model . . . . .	19
2.7 Debye Equation of State . . . . .	20
2.8 Phonons . . . . .	20
2.9 Nomenclature . . . . .	22
2.10 Additional Reading . . . . .	22
2.11 Problems . . . . .	22
<b>Chapter 3 Crystal Structures . . . . .</b>	<b>24</b>
3.1 The Cubic Crystal System . . . . .	24
3.2 The Diamond Structure . . . . .	25
3.3 The Hexagonal System . . . . .	25
3.4 Other Fundamental Lattice Systems . . . . .	26
3.5 Miller Indices . . . . .	26
3.6 Close-Packed Structures . . . . .	28
3.7 Crystal Structure of Ionic Solids . . . . .	29
3.8 Nomenclature . . . . .	30
3.9 Problems . . . . .	30
<b>Chapter 4 Cohesive Energy of Solids . . . . .</b>	<b>31</b>
4.1 Introduction . . . . .	31
4.2 Cohesion in Metals . . . . .	31
4.3 Bonding of Ionic Solids . . . . .	34
4.4 Covalent Crystals . . . . .	38
4.5 Nomenclature . . . . .	40
4.6 Additional Reading . . . . .	40
4.7 Problems . . . . .	40
<b>Chapter 5 Chemical Equilibrium . . . . .</b>	<b>43</b>
5.1 Multicomponent Systems . . . . .	43
5.2 The Chemical Potential . . . . .	43
5.3 Criteria of Chemical Equilibrium . . . . .	44

5.4	Statistical Mechanical Treatment of Chemical Equilibrium . . . . .	45
5.5	Macroscopic Thermodynamic Treatment of Chemical Equilibrium . . . . .	49
5.6	Nomenclature . . . . .	53
5.7	Problems . . . . .	53
<b>Chapter 6</b>	<b>Point Defects in Solids . . . . .</b>	<b>56</b>
6.1	Types of Lattice Imperfections . . . . .	56
6.2	Point Defects in Elemental Crystals . . . . .	56
6.3	Equilibrium Vacancy Concentration . . . . .	57
6.4	Equilibrium Concentration of Divacancies . . . . .	60
6.5	Equilibrium Concentration of Interstitials . . . . .	61
6.6	Point Defects in Two-Component Ionic Crystals . . . . .	61
6.7	Nomenclature . . . . .	65
6.8	Problems . . . . .	66
<b>Chapter 7</b>	<b>Diffusion in Solids . . . . .</b>	<b>70</b>
7.1	Fick's Laws . . . . .	70
7.2	Atomic Picture of Diffusion . . . . .	71
7.3	Random-Walk Theory . . . . .	72
7.4	Diffusion Mechanisms in Cubic Crystals . . . . .	74
7.5	The Jump Frequency According to Absolute Rate Theory . . . . .	75
7.6	Thermal Diffusion . . . . .	77
7.7	Surface Diffusion . . . . .	79
7.8	Nomenclature . . . . .	80
7.9	Additional Reading . . . . .	80
7.10	Problems . . . . .	80
<b>Chapter 8</b>	<b>Dislocations and Grain Boundaries . . . . .</b>	<b>82</b>
8.1	Slip in Single Crystals . . . . .	82
8.2	Dislocations . . . . .	84
8.3	Strain Energy of Dislocations . . . . .	86
8.4	Force on a Dislocation . . . . .	88
8.5	Miscellaneous Features of Dislocations . . . . .	89
8.6	Interaction Forces Between Nearby Edge Dislocations . . . . .	92
8.7	Grain Boundaries and Grains . . . . .	96
8.8	Creep . . . . .	97
8.9	Nomenclature . . . . .	98
8.10	Additional Reading . . . . .	98
8.11	Problems . . . . .	98
<b>Chapter 9</b>	<b>Equation of State of <math>\text{UO}_2</math> . . . . .</b>	<b>100</b>
9.1	Reactor Meltdown Accident . . . . .	100
9.2	Microscopic Basis of the Theory of Corresponding States . . . . .	100
9.3	Reduced Equation of State . . . . .	102
9.4	Critical Constants of $\text{UO}_2$ . . . . .	103
9.5	$\text{UO}_2$ Equation of State Based on the Theory of Corresponding States . . . . .	106
9.6	Interpretation of the Corresponding-States Plots for $\text{UO}_2$ . . . . .	109
9.7	Nomenclature . . . . .	110
9.8	References . . . . .	111
9.9	Problems . . . . .	111
<b>Chapter 10</b>	<b>Fuel-Element Thermal Performance . . . . .</b>	<b>113</b>
10.1	Comparison of Water Reactors and Fast Oxide Reactors . . . . .	113
10.2	Thermal Properties of Oxide Fuels . . . . .	116
10.3	Thermal Conductivity . . . . .	121
10.4	Temperature Profiles in Cylindrical Fuel Rods . . . . .	127
10.5	Summary . . . . .	139
10.6	Nomenclature . . . . .	141
10.7	References . . . . .	142
10.8	Problems . . . . .	143
<b>Chapter 11</b>	<b>Fuel Chemistry . . . . .</b>	<b>145</b>
11.1	Introduction . . . . .	145
11.2	Phase Diagrams of Uranium and Plutonium Oxides . . . . .	145

11.3	Defect Structure in Nonstoichiometric Oxides . . . . .	146
11.4	Oxygen Potentials of (U,Pu)O <sub>2±x</sub> . . . . .	148
11.5	Thermochemistry of Fuel Vaporization . . . . .	155
11.6	Oxygen Redistribution . . . . .	160
11.7	Actinide Redistribution . . . . .	166
11.8	Nomenclature . . . . .	170
11.9	References . . . . .	170
11.10	Problems . . . . .	171
<b>Chapter 12 Behavior of Solid Fission Products in Oxide Fuel Elements . . . . .</b>		<b>172</b>
12.1	Elemental Yields of Fission Products . . . . .	172
12.2	Physical State of the Fission Products . . . . .	175
12.3	Chemical State of Fission Products in Oxide Fuels . . . . .	177
12.4	Effect of Burnup on the Oxygen Potential of the Fuel . . . . .	180
12.5	Fission-Product Migration . . . . .	184
12.6	Fuel—Cladding Interaction . . . . .	186
12.7	Fuel Swelling Due to Solid Fission Products . . . . .	193
12.8	Nomenclature . . . . .	195
12.9	References . . . . .	196
12.10	Problems . . . . .	196
<b>Chapter 13 Swelling Due to Fission Gases . . . . .</b>		<b>199</b>
13.1	Introduction . . . . .	199
13.2	General Considerations . . . . .	201
13.3	Migration of Atomic-Size Defects . . . . .	204
13.4	Reaction Rates of Atomic-Size Defects . . . . .	206
13.5	Diffusion-Limited Reactions . . . . .	210
13.6	Rate Constants for Bubble Coalescence . . . . .	216
13.7	Re-solution . . . . .	219
13.8	Nucleation of Fission-Gas Bubbles . . . . .	222
13.9	Growth of Stationary Bubbles . . . . .	227
13.10	Migration Mechanisms and Growth of Mobile Bubbles . . . . .	235
13.11	Pinning of Bubbles by Dislocations and Grain Boundaries . . . . .	249
13.12	The BUBL Code . . . . .	251
13.13	Nomenclature . . . . .	260
13.14	References . . . . .	261
13.15	Problems . . . . .	262
<b>Chapter 14 Pore Migration and Fuel Restructuring Kinetics . . . . .</b>		<b>265</b>
14.1	Introduction . . . . .	265
14.2	Pore Migration by the Vapor-Transport Mechanism . . . . .	267
14.3	Porosity Redistribution Kinetics . . . . .	273
14.4	Columnar-Grain Growth . . . . .	275
14.5	Equiaxed-Grain Growth . . . . .	278
14.6	Nomenclature . . . . .	282
14.7	References . . . . .	283
14.8	Problems . . . . .	283
<b>Chapter 15 Fission-Gas Release . . . . .</b>		<b>287</b>
15.1	Introduction . . . . .	287
15.2	Experimental Techniques . . . . .	287
15.3	Recoil and Knockout . . . . .	289
15.4	The Equivalent-Sphere Model of Diffusional Release . . . . .	299
15.5	Simple Diffusion . . . . .	300
15.6	Diffusion with Trapping . . . . .	304
15.7	Gas Accumulation in Grain-Boundary Bubbles . . . . .	314
15.8	Breakaway Gas Release Due to Bubble Interconnection . . . . .	318
15.9	Sweeping of Gas Bubbles by Grain Boundaries . . . . .	320
15.10	Gas-Release Models Based on Bubble Migration . . . . .	322
15.11	Engineering Fission-Gas-Release Calculations . . . . .	324
15.12	Nomenclature . . . . .	328
15.13	References . . . . .	329
15.14	Problems . . . . .	330

<b>Chapter 16 Mechanical Properties of <math>\text{UO}_2</math></b>	<b>333</b>
16.1 Dislocations and Slip Systems in Single-Crystal $\text{UO}_2$	333
16.2 Elastic Moduli of $\text{UO}_2$	335
16.3 Plastic Behavior of $\text{UO}_2$	336
16.4 Theory of Brittle Fracture	338
16.5 Creep Theories	341
16.6 Diffusional Creep	341
16.7 Creep Controlled by Dislocation Climb	346
16.8 Grain-Boundary Sliding	351
16.9 Thermal Creep in Oxide Fuels	353
16.10 Irradiation Creep in Oxide Fuels	357
16.11 Sintering, Densification, and Hot Pressing	362
16.12 Nomenclature	369
16.13 References	370
16.14 Problems	371
<b>Chapter 17 Radiation Damage</b>	<b>373</b>
17.1 Introduction	373
17.2 Binary Elastic-Collision Dynamics	375
17.3 Basic Concepts	377
17.4 Potential Functions and Energy-Transfer Cross Sections	379
17.5 Energy Loss to Electrons	381
17.6 The Displacement Threshold	383
17.7 Displacements Produced by a Primary Knock-On	386
17.8 Focusing and Channeling	390
17.9 Displacements and Damage in a Fast-Neutron Flux	396
17.10 Computer Simulation of Collision Cascades	402
17.11 Fission-Fragment Collision Cascades in Nuclear Fuels	407
17.12 Nomenclature	413
17.13 References	414
17.14 Problems	415
<b>Chapter 18 Radiation Effects in Metals: Hardening, Embrittlement, and Fracture</b>	<b>418</b>
18.1 Structural Metals for Fast Reactors	418
18.2 Evolution of the Microstructure of Steel During Neutron Irradiation	419
18.3 Mechanical-Properties Tests	423
18.4 Theories of Radiation Hardening	429
18.5 Hardening by Depleted Zones	432
18.6 Hardening by Impenetrable Obstacles—Precipitates and Voids	437
18.7 Loop Hardening	439
18.8 Tensile Properties of Irradiated Austenitic Stainless Steel	441
18.9 Creep Rupture	443
18.10 Helium Embrittlement	451
18.11 Summary of Irradiation Embrittlement of Austenitic Stainless Steel	454
18.12 Hardening and Embrittlement of Ferritic Steels	455
18.13 Nomenclature	458
18.14 References	459
18.15 Problems	460
<b>Chapter 19 Radiation Effects in Metals: Void Swelling and Irradiation Creep</b>	<b>463</b>
19.1 Introduction	463
19.2 Observed Characteristics of Voids	465
19.3 Nucleation of Voids	470
19.4 Nucleation of Interstitial Dislocation Loops	480
19.5 Point-Defect Balances and the Void-Growth Law	483
19.6 The Void Continuity Equation and Void Swelling	497
19.7 Irradiation Creep	499
19.8 Nomenclature	512
19.9 References	514
19.10 Problems	514

<b>Chapter 20</b>	<b>Interaction of Sodium and Stainless Steel</b>	<b>518</b>
20.1	Introduction	518
20.2	General Corrosion	520
20.3	Corrosion and Selective Leaching of Stainless Steel	530
20.4	Deposition and Transport of Induced Radioactivity	533
20.5	Sodium-Impurity Chemistry and Monitoring	536
20.6	Carburization and Decarburization of Stainless Steel	544
20.7	Effect of Sodium Exposure on the Mechanical Properties of Stainless Steel	552
20.8	The Sodium—Fuel Interaction	555
20.9	Nomenclature	562
20.10	References	563
20.11	Problems	564
<b>Chapter 21</b>	<b>Modeling of the Structural Behavior of Fuel Elements and Assemblies</b>	<b>566</b>
21.1	Materials Input Functions	566
21.2	Mechanical Modeling of Fuel-Pin Behavior (Uncracked Fuel)	570
21.3	Fuel Cracking	577
21.4	Fuel-Element Deformations During Irradiation	580
21.5	Void Swelling Effects on Other Core Components	583
21.6	Fuel-Assembly Bowing	587
21.7	Solutions to the Swelling Problem	592
21.8	Nomenclature	593
21.9	References	594
21.10	Problems	594
<b>Appendix—Elasticity Theory</b>		<b>597</b>
A.1	Equilibrium Conditions	597
A.2	Displacements	598
A.3	Compatibility Relations	600
A.4	Stress—Strain Relations	600
A.5	Elastic Strain Energy	601
A.6	Cylindrical Coordinates	601
A.7	Nomenclature	602
A.8	Additional Reading	602
<b>Index</b>		<b>603</b>

**Cover:**

*In the circle: Photomicrograph of migrating lenticular pores in  $UO_2$  (courtesy of Dennis M. Rooney, General Electric Company).*

*In the cube: Three-dimensional computer simulation of a displaced spike in a metal (courtesy of Donald G. Doran, Hanford Engineering Development Laboratory).*



# Chapter 1

## Statistical Thermodynamics

### 1.1 DEFINITIONS AND TERMINOLOGY

Many of the phenomena which exert a crucial influence on the performance of nuclear materials, such as fission-gas diffusion, bubble growth and migration, and radiation damage, require an understanding of the behavior of the atomic constituents of the solid. In addition to these primarily kinetic phenomena, the equilibrium properties of a solid, as expressed by the thermodynamic quantities of internal energy, entropy, heat capacity, etc., may be regarded as averages of the properties of the individual particles of which the material is composed.

Statistical thermodynamics provides the link between the energy states that quantum mechanics allocates to individual particles and the observable characteristics of a large assembly of these particles. The large collection of particles which we wish to characterize thermodynamically is called the *system*. It generally contains a fixed number of particles (atoms, molecules, electrons, etc.) and may communicate heat and work with its surroundings via a common boundary.

There are two levels of precision by which the state or condition of the system can be described. In a gross sense, the system can be defined by its composition (if more than one component is present) and by any two of the traditional thermodynamic variables, such as internal energy and volume or temperature and pressure. The state of the system defined by this small number of properties is called a *macrostate*. We can construct systems in a particular macrostate, or by measurement we can know when a system is in a particular macrostate.

A tremendously more detailed description of the system is contained in the specification of the quantum state of each of the constituent particles. The condition of a system described in such precision is called a *microstate*. A system cannot be prepared in a particular microstate, nor is it possible to determine by measurement whether a system is in a particular microstate. However, the concept of the microstate is extremely useful because it provides the connection between the quantum-mechanical description of the individual entities that comprise the system and the gross features that characterize the macrostate.

A very large number of microstates satisfy the few constraints imposed by the specification of the macrostate.

The properties of the macrostate are averages of the properties of the microstates. To picture the averaging process, imagine that a large number of the  $N$ -particle systems are constructed, each one with the same restraints that characterize the macrostate. If the system were macroscopically defined by its temperature and volume, for example, we would prepare many containers of the same size, put  $N$  particles in each, and immerse them all in a constant temperature bath. This collection of systems, each as closely identical to the others as we can make them, is called an *ensemble*. Although all members of the ensemble are in the same macrostate, they are not all in the same microstate at any instant. They can be in any microstate consistent with the few macroscopic properties specified for the system. In fact, each member of the ensemble is continually changing microstates among those which are permitted by the macroscopic restraints.

The ensemble may be labeled by the type of restraints placed upon the systems of which it is comprised. Three ensembles are commonly considered in statistical thermodynamics:

1. If the internal energy,  $U$ , the volume,  $V$ , and the number of particles,  $N$ , are specified, the system is isolated from the surroundings. The ensemble composed of such systems is called the *microcanonical* ensemble.

2. If the temperature,  $T$ , the volume,  $V$ , and the number of particles,  $N$ , are specified, the system can exchange heat with the reservoir that constitutes its surroundings but cannot exchange work or particles. This ensemble is termed the *canonical* ensemble.

3. If the temperature,  $T$ , the volume,  $V$ , and the chemical potential,  $\mu$ , are specified, the system can exchange heat and particles with the reservoir. This ensemble is called the *grand canonical* ensemble.

The microcanonical ensemble is the traditional starting point for developing the framework of statistical thermodynamics. Of the three ensembles, it permits the connection between the dynamic properties of the constituent particles and the thermodynamic properties of the macroscopic system to be made most easily. However, practical computations of thermodynamic properties with this ensemble are difficult.

The canonical ensemble differs from the microcanonical ensemble in that the temperature is specified instead of the

internal energy of the system. Fixing the temperature is equivalent to fixing the average internal energy of the system. Since fluctuations of thermodynamic properties about their mean values are very small in macroscopic systems, there is no difference between the thermodynamic properties developed from the microcanonical and canonical ensembles. However, because of the ease of computation, the canonical ensemble is generally preferred for obtaining thermodynamic properties from models of the microscopic behavior of individual particles.

Just as the temperature represents an average internal energy in the canonical ensemble, so the chemical potential represents an average number of particles in the grand canonical ensemble. This ensemble offers some computational advantages for certain systems (in particular for the ideal quantum gases); however, it is not as commonly used as is the canonical ensemble.

Although the theoretical framework of statistical thermodynamics is formulated in terms of the restraints ( $U, V, N$ ), ( $T, V, N$ ) or ( $T, V, \mu$ ), corresponding to the three ensembles described above, most experimental information on real systems is obtained under conditions of fixed temperature and pressure,  $p$ . An isothermal-isobaric ensemble with restraints summarized by ( $T, p, N$ ) can be constructed and treated theoretically, but it is more convenient to determine thermodynamic parameters from the canonical ensemble and then correct for the fact that a process occurs at constant pressure rather than at constant volume.

## 1.2 PROBABILITY DISTRIBUTION IN THE CANONICAL ENSEMBLE

A macroscopic parameter is the sum of the values of the parameter for a given microstate weighted with the probability that a member of the ensemble is in that particular microstate. This ensemble average requires that the distribution of microstates in the ensemble be known. In the canonical ensemble the only property of the microstate which is needed is its energy.

In weakly interacting systems the quantum state of the entire system is determined by the quantum state of the constituent particles, and the energy of a microstate is the sum of the energies of the individual particles. Each particle may contribute energy in a number of ways: translational (kinetic) energy of the center of mass of the particle and internal forms of energy, such as that stored in vibration, rotation, and the electronic configuration of the particle. According to quantum mechanics, each of these forms of energy is quantized. If the quantum numbers for each mode are specified, the energy of a particle is determined. If the quantum numbers for all particles are specified, the energy of the microstate is fixed. If there are  $b$  quantum numbers associated with each of the  $N$  particles, a total of  $bN$  quantum numbers needs to be specified to determine the microstate of the system. Each combination of the  $bN$  quantum numbers labels one microstate. The energy of the  $i$ th microstate is denoted by  $E_i$ . Since  $N$  is of the order of  $10^{24}$  for macroscopic systems, the number of parameters needed to specify a microstate is very much greater than the number required to determine a macrostate. Because

the quantum numbers are integers or half-integers, the energies of microstates differ by discrete amounts.\*

Because of the very large number of particles in a macroscopic system and because the energy of an individual particle is very much smaller than the internal energy of the system, the change of one quantum number of a single particle alters the system energy by a very small fraction of the total energy. Therefore, the microstates of a large collection of particles may be considered to be distributed in energy according to a continuous function  $\omega$ , called the *density of states*, which represents the number of microstates of the system per unit energy interval.

The manner in which the density of states varies with the energy and the number of particles of the system illustrates some of the unique properties of statistical functions for systems with very large numbers of particles. Consider  $N$  particles with a total energy  $U$ . The average particle energy is  $\bar{\epsilon} = U/N$ . Assume that the energy levels in each particle are spaced by a constant  $\Delta\epsilon$  (this is true only for the simple harmonic oscillator, but the argument given here is equally valid for variable level spacing). There are  $\bar{\epsilon}/\Delta\epsilon$  quantum states between the ground state and the average particle energy. Although individual particles may have any energy between zero and values much greater than  $\bar{\epsilon}$ , significant population of states with energies much different from the average energy would not be expected. The states in which a single particle is likely to be found are those within an energy interval of  $\sim\bar{\epsilon}$  around  $\bar{\epsilon}$  (the argument is not affected if the interval is approximated by  $\bar{\epsilon}/2$  or  $2\bar{\epsilon}$ ). If each particle can be in any one of the  $\bar{\epsilon}/\Delta\epsilon$  states available to it, the number of states in which the  $N$ -particle system might be found is  $(\bar{\epsilon}/\Delta\epsilon)^N$ . Since this number of states is spread over an energy interval of approximately  $\bar{\epsilon}$ , the density of states is

$$\omega \sim \frac{(\bar{\epsilon}/\Delta\epsilon)^N}{\bar{\epsilon}} = \frac{1}{\Delta\epsilon} \left( \frac{\bar{\epsilon}}{\Delta\epsilon} \right)^{N-1}$$

Neglecting unity compared to  $N$ , the density of states increases as either  $\bar{\epsilon}$  or  $N$  increases. Moreover, because of the large value of  $N$  for macroscopic systems, the increase is extremely rapid. Since the total energy  $U$  is  $\bar{\epsilon}N$ , the density of states is also a rapidly increasing function of  $U$ , whether the increase in  $U$  is due to increasing  $\bar{\epsilon}$  or  $N$ .

To determine the probability distribution for the canonical ensemble, we first consider the probability distribution in the microcanonical ensemble. This latter system is subject to the restraints of constant internal energy, volume, and number of particles. The specification of the internal energy of an isolated system, however, must be qualified. A system of precisely specified internal energy cannot be prepared, nor, according to the uncertainty principle, can the energy of a system be known exactly. Therefore, the systems of a microcanonical ensemble must be regarded as possessing an internal energy in the range  $U$

\*In strongly interacting systems, such as liquids, the microstate of  $N$  particles cannot be characterized by the quantum numbers of the individual particles. Nevertheless, the concept of microstates with discrete energies is applicable to such systems as well as to weakly interacting systems.

to  $U + \delta U$ . The energy spread  $\delta U$  is very small compared to  $U$  but very large compared to the energy spacing between adjacent microstates. Since the microstates have discrete energies, the number of them with energies  $E_i$  between  $U$  and  $U + \delta U$  can be counted. If there are  $\omega(U)$  microstates in a unit energy interval about an internal energy  $U$ , the isolated system with an energy spread  $\delta U$  contains  $\omega(U) \delta U$  states. It is the basic postulate of statistical thermodynamics that these states are a priori equally probable; sampling of a microcanonical ensemble will with equal likelihood produce a microstate of any one of the possible energies in the range  $\delta U$  about  $U$ .

Consider an isolated system of energy between  $U$  and  $\delta U$ . As shown in Fig. 1.1(a), the isolated system is divided into two parts by a boundary through which heat can pass. Although the energies at the two subsystems,  $E$  and  $E_r$ , may vary, their sum is a constant. Since the two subsystems comprise an isolated system,

$$U = E + E_r \quad (1.1)$$

Let the density of states in the two subsystems be  $\omega(E)$  and  $\omega(E_r)$ , respectively.

We now ask for the number of states of the composite system under the additional restraint that the energy of one of the subsystems lies between  $E$  and  $E + dE$  (without this restraint, this subsystem could have any energy between zero and  $U$ ). The number of microstates in this subsystem is  $\omega(E) dE$ . Since the rest of the energy is in the remaining part of the isolated system, the number of microstates in the other subsystem is  $\omega_r(U-E) dE_r$ . The restriction that one of the subsystems have an energy in the range  $dE$  about  $E$  does not alter the fact that together the two subsystems still constitute an isolated system to which the postulate of equal a priori probability applies. Hence, all possible combinations of the microstates in the two subsystems are equally probable, or the total number of microstates of the composite system subject to the additional restriction on the energy range of one subsystem is simply the product of the numbers of microstates in each subsystem:

$$[\omega(E) dE][\omega_r(U-E) dE_r] \quad (1.2)$$

Without the restraint on the energy range of one of the subsystems, the total number of states of the composite system is the integral of Eq. 1.2 over  $E$  from zero to  $U$ . The probability that the combined system will be found in a microstate for which one of the subsystems has an energy between  $E$  and  $E + dE$  is proportional to the product of Eq. 1.2, with the normalizing constant being the inverse of the integral of Eq. 1.2. Since the density of states rises sharply with energy,  $\omega(E)$  is a rapidly increasing function of  $E$ , and  $\omega_r(U-E)$  decreases equally rapidly with  $E$ . Consequently, the product of these two functions exhibits a very distinct peak at some particular value of  $E$ . The existence of the sharp maximum in the number of microstates of the composite system as the energy of one of its subsystems is varied means that there is an overwhelming probability that the system will be found in this condition if the ensemble is sampled. The most probable distribution, which describes the condition of thermodynamic equilibrium, occurs at a value of  $E$  for which the product

$\omega(E) \omega_r(U-E)$  is a maximum. Since differentiation of the logarithm of this product yields the same maximum as the derivative of the product itself, the most probable distribution occurs when

$$\frac{\partial \ln \omega(E)}{\partial E} = \frac{\partial \ln \omega_r(E_r)}{\partial E_r} \quad (1.3)$$

where  $U - E$  has been written as  $E_r$ . The two sides of Eq. 1.3 refer to a property of each subsystem. This common property defines the temperature to within a multiplicative constant, which is the Boltzmann constant:

$$\frac{\partial \ln \omega}{\partial E} = \frac{1}{kT} \quad (1.4)$$

Equation 1.3 requires that at equilibrium the temperatures of two systems that can freely communicate heat with each other be equal.

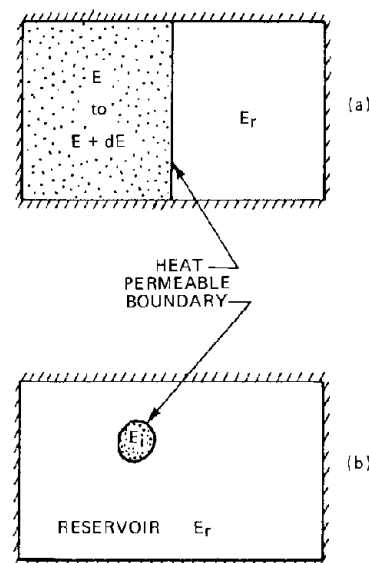


Fig. 1.1 Two subsystems of an isolated system communicating via a heat-permeable divider. (a) Two subsystems in an isolated system. (b) Isolated system divided into a small subsystem and a large reservoir.

In the situation just discussed, the relative sizes of the two subsystems was not specified, and the energy of one of the subsystems was permitted to range over an interval  $dE$ . Although small, the interval  $dE$  was presumed to encompass a large number of microstates. Suppose now that the following, more severe, restraints are imposed: (1) One of the two subsystems is very small compared to the other. The large subsystem is denoted as the reservoir for the small subsystem. (2) Rather than considering states of the combined isolated system for which the small subsystem has an energy between  $E$  and  $E + dE$ , we ask for the probability of finding the combined system in a state such that the small subsystem is in one of its allowable microstates. This situation is depicted in Fig. 1.1(b). If the state of the small subsystem has been precisely fixed at a value  $E - E_i$  (where  $E_i$  is the energy of one of its discrete microstates), the number of states of the combined system is given by Eq. 1.2, the first bracketed term being replaced

by unity and  $E$  in the second bracketed term being replaced by  $E_i$ . This change merely reflects the fact that just one state of the small system is combined with any of the accessible states of the reservoir. The probability of finding the small subsystem in a microstate of energy  $E_i$  is

$$P_i = \frac{\omega_r(U-E_i)}{\sum_i \omega_r(U-E_i)} \quad (1.5)$$

Since the discrete energies of the individual microstates of the small subsystem are involved here, the normalization condition is represented by a sum rather than an integral in Eq. 1.5. Because the subsystem is small compared to the reservoir,  $E_i$  is also much smaller than  $U$ . Therefore the summation in the denominator of Eq. 1.5 can cover all possible microstates of the small subsystem. The restriction that  $E_i$  be less than  $U$  is unnecessary since, even if the particles of the small system possess uncommonly large energies, there are still too few particles in the small system compared to the population of the reservoir to cause  $E_i$  to be comparable to  $U$ .

The fact that  $E_i$  is under all circumstances much smaller than  $U$  permits all properties of the reservoir except its temperature to be eliminated from Eq. 1.5. To this end, the logarithm of  $\omega_r$  is expanded in a Taylor series about  $U$ :

$$\ln [\omega_r(U-E_i)] = \ln [\omega_r(U)] - \left( \frac{\partial \ln \omega_r}{\partial U} \right) E_i + \dots \quad (1.6)$$

Since the reservoir contains essentially all the energy of the combined system,  $U \sim E_r$ , and the coefficient of  $E_i$  in Eq. 1.6 is, by Eq. 1.4, equal to  $1/kT$ . Neglecting higher order terms in the expansion, Eq. 1.6 is equivalent to

$$\omega_r(U-E_i) = \omega_r(U) e^{-E_i/kT} \quad (1.7)$$

Substituting this result into the probability distribution of Eq. 1.5 yields

$$P_i = \frac{e^{-E_i/kT}}{\sum_i e^{-E_i/kT}} \quad (1.8)$$

The small subsystem to which Eq. 1.8 applies is in thermal contact with the large reservoir, which controls the temperature of the small subsystem. The volume and number of particles of the small subsystem are fixed by the nature of the boundary with the reservoir. The small subsystem is identical in all respects to a system in which  $T$ ,  $V$ , and  $N$  have been fixed. Consequently, Eq. 1.8 is indeed the probability distribution of the canonical ensemble.

Equation 1.8 is an extraordinarily useful relation. It forms the essential link between the microscopic behavior of the constituent particles of a system, embodied in the microstate energies  $E_i$ , and the macroscopic thermodynamic properties of the system, which are averages over all microstates with  $P_i$  as the weighting factor.

### 1.3 THERMODYNAMIC PROPERTIES AND THE PARTITION FUNCTION

#### 1.3.1 Ground State and Reference State

Since the microstate energies  $E_i$  are discrete, they can be arranged in order of increasing magnitude,  $E_0, E_1, \dots, E_i$ .

The first term in this sequence is the energy of the entire system when all the particles are in the state with the smallest allowable quantum numbers. This state is commonly called the *ground state* of the system, and  $E_0$  is the ground-state energy. The ground state is approached as the absolute temperature approaches zero. Since all the quantum numbers of all the particles are specified as their lowest values, there is only one possible microstate for the system.\* Consequently, the probability distribution reduces to

$$\begin{aligned} P_0 &= 1 \\ P_i &= 0 \quad (i > 0) \end{aligned} \quad (1.9)$$

and the system energy  $U$  is equal to the ground-state energy  $E_0$ .

Since the energy of a body has no absolute-zero value, the reference state from which  $E_i$  and  $U$  are computed must be specified. The system energy is, by definition, zero in the *reference state*. Choice of the reference state is arbitrary: It is often convenient to consider the ground state to be the reference state, so that  $E_0 = 0$ . Other choices of the reference state are possible and in many cases desirable. For example, the energy of the atoms of a crystalline solid may be referenced to the state in which the solid has been dispersed and all its atoms are at rest infinitely separated from one another.

#### 1.3.2 Internal Energy

The average energy of a microstate in an ensemble is identified with the internal energy of the macroscopic system:

$$U = \sum_i E_i P_i \quad (1.10)$$

Equation 1.10 is valid for any ensemble. It may be applied to the canonical distribution by using  $P_i$  of Eq. 1.8, which is rewritten as

$$P_i = \frac{e^{-E_i/kT}}{Z} \quad (1.11)$$

where

$$Z = \sum_i e^{-E_i/kT} \quad (1.12)$$

and is called the *partition function*. The value of  $Z$  is the sum of Boltzmann factors for all possible microstates of an  $N$ -particle system at a specified temperature and volume.

Substituting Eq. 1.11 into Eq. 1.10, we find the internal energy to be

$$U = \frac{1}{Z} \sum_i E_i e^{-E_i/kT} \quad (1.13)$$

\*There are some situations in which the ground state is not unique. This occurs when the particles have two energetically equivalent spin states (corresponding, for example, to spin quantum numbers of  $\pm 1/2$ ). Changing one of the spin quantum numbers of one or more particles in the system leads to microstates that are distinct but of the same energy. In this case, many microstates have energies equal to  $E_0$ , and the ground state is said to be degenerate.

The sum on the right-hand side of Eq. 1.13 can be evaluated as follows. The temperature derivative of the partition function is

$$\left(\frac{\partial Z}{\partial T}\right)_V = \frac{1}{kT^2} \sum_i E_i e^{-E_i/kT} \quad (1.14)$$

As with any other macroscopic thermodynamic property, the partition function depends on two other thermodynamic parameters. For the canonical distribution, to which Eq. 1.12 applies, these parameters are temperature and volume. As the left-hand side of Eq. 1.14 indicates, the volume is held constant in the derivative. In the case of a multicomponent system, the composition would also remain constant.

Using Eq. 1.14 in Eq. 1.13, we get

$$U = \frac{kT^2}{Z} \left(\frac{\partial Z}{\partial T}\right)_V = kT^2 \left(\frac{\partial \ln Z}{\partial T}\right)_V \quad (1.15)$$

### 1.3.3 The Entropy

While the relation between the probability distribution  $P_i$  and the internal energy expressed by Eq. 1.10 is intuitively obvious, the ensemble average that defines the entropy is not. The entropy of the system is defined by the ensemble average of  $\ln P_i$ :

$$S = -k \sum_i P_i \ln P_i \quad (1.16)$$

In common with Eq. 1.10, Eq. 1.16 is valid for any type of ensemble.\* Substituting the canonical distribution, Eq. 1.11, into Eq. 1.16 yields

$$S = -k \left[ \sum_i \left( \frac{e^{-E_i/kT}}{Z} \right) \left( -\frac{E_i}{kT} \right) - \sum_i \left( \frac{e^{-E_i/kT}}{Z} \right) \ln Z \right]$$

The sum in the first term on the right is given by Eq. 1.14; the sum in the second term on the right is simply  $Z$ . Therefore, the entropy is

$$S = k \ln Z + kT \left(\frac{\partial \ln Z}{\partial T}\right)_V \quad (1.17)$$

In contrast to the internal energy, the entropy is independent of the choice of reference energy. This can be shown by factoring the ground-state energy  $E_0$  out of the partition function, so that Eq. 1.12 becomes

$$Z = e^{E_0/kT} Z' \quad (1.18)$$

where  $Z'$  is the partition function above the ground state:

$$Z' = \sum_i \exp\left(-\frac{E_i - E_0}{kT}\right) \quad (1.19)$$

\*In the microcanonical ensemble, Eq. 1.16 yields  $S = k \ln \Omega$ , where  $\Omega = \omega(U) \delta U$  is the number of microstates of an isolated system in the energy range  $\delta U$  around  $U$ . This formulation, of course, gives the same entropy as the method using the canonical distribution, which is presented here.

Replacing  $Z$  in Eq. 1.15 by Eq. 1.18 yields

$$U - E_0 = kT^2 \left(\frac{\partial \ln Z'}{\partial T}\right)_V \quad (1.20)$$

and the use of Eq. 1.18 in the entropy expression Eq. 1.17 yields

$$S = k \ln Z' + kT \left(\frac{\partial \ln Z'}{\partial T}\right)_V \quad (1.21)$$

The internal energy in Eq. 1.20 is clearly relative to the ground-state energy  $E_0$ . However, the entropy in Eq. 1.21 is identical to Eq. 1.17; hence, the numerical value of  $S$  is independent of the selection of a reference energy.

The ensemble average of  $\ln P_i$  has been identified with the entropy because it possesses all the features of this thermodynamic property: Since  $P_i$  is between zero and unity, Eq. 1.16 shows that the entropy is always zero or positive. At the absolute zero of temperature, when all particles of the system are in their ground states, the probability distribution is given by Eq. 1.9, and the entropy is zero. This characteristic of the entropy, which is called the *third law of thermodynamics*, has been verified experimentally. As a final justification for calling the quantity in Eq. 1.16 the entropy of a macroscopic system, we note that the fundamental thermodynamic relation

$$dU = T dS - p dV \quad (1.22)$$

implies that

$$\left(\frac{\partial U}{\partial T}\right)_V = T \left(\frac{\partial S}{\partial T}\right)_V \quad (1.23)$$

Direct substitution shows that the statistical thermodynamic expressions for  $U$  and  $S$ , Eqs. 1.15 and 1.17, satisfy the above relation, which is a consequence of classical thermodynamics.

One additional characteristic of the entropy, defined by Eq. 1.16 in general or by Eq. 1.17 for the canonical distribution, is that it is an extensive property. That is, for a simple (one component) system,  $S$  is the product of the number of particles in the system and a function that depends upon intensive properties only. This feature will become evident later when the entropy of various simple systems is calculated.

### 1.3.4 Relation of the Partition Function to Other Thermodynamic Parameters

Having related  $U$  and  $S$  to ensemble averages over the canonical distribution, we can express all other thermodynamic quantities in terms of the partition function  $Z$  by standard thermodynamic formulas.

The Helmholtz free energy,  $F$ , is defined by

$$F = U - TS \quad (1.24)$$

Using Eqs. 1.15 and 1.17 yields

$$F = -kT \ln Z \quad (1.25)$$

Applying Eq. 1.22 to the differential of Eq. 1.24 gives

$$dF = dU - T dS - S dT = -p dV - S dT \quad (1.26)$$

from which it follows that

$$p = -\left(\frac{\partial F}{\partial V}\right)_T \quad (1.27)$$

or the pressure is

$$p = kT \left(\frac{\partial \ln Z}{\partial V}\right)_T \quad (1.28)$$

The Gibbs free energy,  $G$ , is

$$G = H - TS = U + pV - TS = F + pV \quad (1.29)$$

where  $H$  is the enthalpy. Using Eq. 1.25 for  $F$  and Eq. 1.28 for  $p$  gives

$$G = -kT \ln Z + V kT \left(\frac{\partial \ln Z}{\partial V}\right)_T \quad (1.30)$$

Finally, the enthalpy is

$$H = U + pV = kT \left[ T \left(\frac{\partial \ln Z}{\partial T}\right)_V + V \left(\frac{\partial \ln Z}{\partial V}\right)_T \right] \quad (1.31)$$

It is important to keep in mind the arbitrary reference energy in the formulas. The reference energy is common to the microstate energies  $E_i$  and to the energy functions  $U$ ,  $H$ ,  $F$ , and  $G$ . None of these quantities has an absolute zero level. The entropy, on the other hand, is zero when all atoms are in a unique ground state.

The connection between the microscopic behavior of a system and its bulk thermodynamic properties is formally complete. We need still to compute the partition function before macroscopic properties, such as internal energy, entropy, and free energy, can be calculated from the preceding relations.

## 1.4 IDEAL GASES

We mean by the term "ideal gas" a system constituted of particles that move freely within the confines of the volume that contains them. A number of seemingly quite different physical systems fit this broad definition. The practical applications of ideal-gas thermodynamics are important, and the partition function for this form of energy is easy to evaluate.

The particles of an ideal gas may collide with each other and thereby exchange energy, as in a molecular gas. They may undergo collisions with other inhabitants of the volume they occupy, as neutrons scatter from the nuclei of the solid medium that contains them or as electrons scatter from defects in the crystal structure of their parent solid. Except for the momentary direct encounters typical of a molecular gas or the indirect communication via collisions with other species in the medium, the particles of an ideal gas do not interact with each other.

The ideal-gas system may consist of particles moving in less than three spatial dimensions. Mobile atoms adsorbed on the surface of a solid can often be very well described by the thermodynamics of a two dimensional ideal gas. At certain points on its migration path, an atom diffusing in a solid may possess characteristics of a one-dimensional ideal gas (see Sec. 7.5).

The ideal gas is a weakly interacting system of particles whose distinguishing feature is the kinetic energy carried by the particles as a result of their free translation. The quantum state of each particle is independent of the quantum states of the other particles, and the total energy of the system is the sum of the energies of the individual particles.

Such a gas may be composed of elementary particles, such as electrons and neutrons, whose only relevant features are mass and intrinsic spin. Or, the gas may be composed of molecules, which possess internal forms of energy in vibration, in rotation, and in the configuration of the atomic electrons. All systems described by the term ideal gas, however, exhibit the common characteristic of energy stored in the motion of the constituent particles.

The macroscopic consequences of the translational motion of the particles of an ideal gas are based upon the premise that the particles are indistinguishable, or that exchange of any two does not produce a new microstate of the system. We may therefore group the particles according to quantum states. Particles in the same quantum state have the same energy. If the number of particles with an energy of  $\epsilon_k$  is denoted by  $n_k$ , the set of occupation numbers ( $n_0, n_1, \dots, n_k, \dots$ ) provides a convenient means of identifying a microstate. The occupation numbers must satisfy restraints reflecting the constancy of the total number of particles and the microstate energy,

$$N = \sum_k n_k \quad (1.32)$$

and

$$E_i = \sum_k n_k \epsilon_k \quad (1.33)$$

In computing the partition function according to Eq. 1.12, our aim is to replace the rather nonspecific sum over the  $i$  microstates by a sum over all allowable sets of occupation numbers. In so doing, however, we must keep two limitations in mind: (1) The exclusion principle of quantum mechanics may restrict the number of particles in an energy state; as an example, for particles with half-integer spins,  $n_k$  may be either zero or unity, but not larger. (2) According to quantum mechanics, and supported by intuition, particles of the same species in an ideal gas are indistinguishable; they cannot be assigned to any particular location in the volume that contains them. They possess no features that would permit distinction of one particle from another.

This last restriction is easily satisfied; it means that a set of occupation numbers uniquely defines a microstate. Therefore, the partition function may be written as a sum over all permissible sets of occupation numbers, and Eq. 1.12 may be written as

$$Z = \sum_{(n_0, n_1, \dots, n_k, \dots)} \exp [-(n_0 \epsilon_0 + n_1 \epsilon_1 + \dots + n_k \epsilon_k + \dots)/kT] \quad (1.34)$$

This sum cannot be simplified directly, primarily because of the restriction imposed by Eq. 1.32. To proceed further, we must employ a calculational method that removes the restriction on the total number of particles in the system.

Since this is exactly what the grand canonical ensemble provides, the partition function for this type of ensemble will be derived and then used to evaluate  $Z$  of Eq. 1.34.

The derivation of the partition function for any ensemble proceeds by way of the probability distribution (the partition function is just the normalizing factor for the probability distribution). In Sec. 1.2, we derived the probability distribution for the canonical ensemble by considering an isolated system that was divided into two subsystems by a boundary through which heat could pass. For the grand canonical ensemble, we begin at exactly the same point, except that in addition the boundary is permitted to pass particles as well as heat freely. In the development of the canonical distribution, we asked for the number of microstates of the composite system when the energy of one subsystem was between  $E$  and  $E + dE$ . To obtain the grand canonical distribution, we ask for the number of microstates of the composite system when the energy of one subsystem is between  $E$  and  $E + dE$  and when the number of particles of the subsystem is between  $N$  and  $N + dN$  (only one component is presumed present). The answer to this question is obtained by a straightforward extension of the arguments that led to Eq. 1.2.

If there are  $N$  particles in one subsystem and  $N_r$  in the other, the total number of particles in the system,  $M$ , is

$$M = N + N_r \quad (1.35)$$

In the previous discussion, the density of states was written as a function of system energy,  $\omega(E)$ . However, it is obvious that this quantity must also depend upon the number of particles as well, even though for simplicity of notation  $N$  was not explicitly listed as a variable. In the present situation, we acknowledge this dependence and designate the density of states of the two subsystems under consideration by  $\omega(E, N)$  and  $\omega_r(E_r, N_r)$ .

Pursuing the argument following Eq. 1.1, with the inclusion of  $N$  as a second variable, we find the number of microstates of the combined system subject to the simultaneous restraints on the ranges of  $E$  and  $N$  in one of the subsystems is, by analogy to Eq. 1.2,

$$[\omega(E, N) dE dN][\omega_r(U-E, M-N) dE_r dN_r] \quad (1.36)$$

As before, maximizing the product of  $\omega$  and  $\omega_r$  with respect to energy yields Eq. 1.3, or the condition of temperature equilibrium of the two systems. If, in addition, the product is maximized with respect to the number of particles, then

$$\frac{\partial \ln \omega(E, N)}{\partial N} = \frac{\partial \ln \omega_r(E_r, N_r)}{\partial N_r} \quad (1.37)$$

Again, a common property is, at equilibrium, equal in the two subsystems. This new property, which is a potential for driving mass just as the temperature is a potential for driving heat, is called the *chemical potential*. It is defined by

$$\frac{\partial \ln \omega}{\partial N} = -\frac{\mu}{kT} \quad (1.38)$$

As in the development of the canonical distribution, we now impose the additional restrictions that one of the subsystems be very much smaller than the first, which implies that  $E \ll U$  and  $N \ll M$ , and that one of the subsystems be in a precisely defined microstate with an energy  $E_i$  and exactly  $N$  particles. These additional restraints are equivalent to replacing the number of microstates represented by the first bracketed term in Eq. 1.36 by unity since a particular microstate is specified. The probability of finding the system in this condition is

$$P_i(N) = \frac{\omega_r(U-E_i, M-N)}{\sum_{N=0}^{\infty} \sum_i \omega_r(U-E_i, M-N)} \quad (1.39)$$

where the upper limit on the outer sum has been approximated by infinity instead of  $M$ , since it is very unlikely that the small system ever accumulates anything approaching the number of particles in the combined system. Expanding  $\omega_r$  in a double Taylor series about  $U$  and  $M$  yields

$$\ln[\omega_r(U-E_i, M-N)] = \ln[\omega_r(U, M)] - \left(\frac{\partial \ln \omega_r}{\partial U}\right) E_i - \left(\frac{\partial \ln \omega_r}{\partial M}\right) N + \dots \quad (1.40)$$

According to Eqs. 1.4 and 1.38, the coefficients of  $E_i$  and  $N$  are related to the temperature and chemical potential, respectively. Combining Eqs. 1.39 and 1.40, we find the probability distribution in the grand canonical ensemble to be

$$P_i(N) = \frac{\exp[-(E_i - \mu N)/kT]}{\sum_{N=0}^{\infty} \sum_i \exp[-(E_i - \mu N)/kT]} \quad (1.41)$$

where  $P_i(N)$  is the probability of finding a system in which the temperature, volume, and chemical potential are specified in a microstate of energy  $E_i$  and in which there are  $N$  particles. The denominator in Eq. 1.41 is the grand canonical partition function:

$$\Xi = \sum_{N=0}^{\infty} \sum_i \exp\left[-\frac{(E_i - \mu N)}{kT}\right] \quad (1.42)$$

There are two methods of simplifying the double sum in this formula. Both must be developed before the goal of determining  $Z$  can be realized.

#### 1.4.1 First Method of Simplifying Eq. 1.42

In performing the inner sum of Eq. 1.42, we must regard the value of  $N$  as a constant corresponding to the current value in the outer sum. Consequently, the term  $e^{\mu N/kT}$  may be removed from the inner sum, and  $\Xi$  written as

$$\Xi = \sum_{N=0}^{\infty} e^{\mu N/kT} \sum_i e^{-E_i/kT}$$

Now, the inner sum is none other than the canonical partition function for a specified number of particles (see Eq. 1.12); hence

$$\Xi = \sum_{N=0}^{\infty} Z(N) e^{\mu N / kT} \quad (1.43)$$

where  $Z$  has been explicitly written as a function of  $N$ .

If each term in the sum of Eq. 1.43 is divided by  $\Xi$ , the quantity

$$P(N) = \frac{Z(N) e^{\mu N / kT}}{\Xi} \quad (1.44)$$

is just the probability that the system contains  $N$  particles, independent of the microstate energy. The average number of particles is given by

$$\bar{N} = \sum_{N=0}^{\infty} N P(N) \quad (1.45)$$

The variation of  $P(N)$  with  $N$  depends upon the partition function  $Z(N)$ , which is the object of the calculation. It will be assumed that  $P(N)$  is so very sharply peaked about the average  $\bar{N}$  that  $P(N) \approx 1$  for  $N = \bar{N}$ , and  $P(N) \approx 0$  for  $N \neq \bar{N}$ . This is equivalent to approximating the sum in Eq. 1.43 by its principal value, which occurs at the average number of particles in the system. With this assumption we can approximate Eq. 1.43 by

$$\Xi \approx Z(\bar{N}) e^{\mu \bar{N} / kT} \quad (1.46)$$

The correctness of this procedure can be assessed by assuming Eq. 1.46 to be valid, calculating  $Z(N)$  (as we shall do), then returning to Eq. 1.44 to demonstrate that  $P(N)$  is in fact sharply peaked about  $\bar{N}$ .

#### 1.4.2 Second Method of Simplifying Eq. 1.42

Recall that the first step in treating the canonical partition function was to write  $E_i$  as  $\sum n_k \epsilon_k$  and to sum over all sets of occupation numbers  $(n_0, \dots, n_k, \dots)$ . Here, the same operation is applied to the inner sum of Eq. 1.42 in conjunction with the replacement of  $\mu N$  by  $\sum \mu n_k$ . The argument of the exponential in Eq. 1.42 is

$$E_i - \mu N = \sum_k n_k \epsilon_k - \sum_k n_k \mu = \sum_k (\epsilon_k - \mu) n_k$$

and the grand partition function may be written as

$$\Xi = \sum_{N=0}^{\infty} \sum_{(n_0, \dots, n_k, \dots)} \exp \left[ -\frac{(\epsilon_0 - \mu) n_0}{kT} - \dots - \frac{(\epsilon_k - \mu) n_k}{kT} - \dots \right] \quad (1.47)$$

The presence of the outer sum over all  $N$  is equivalent to removing the restriction on the sum of the occupation numbers, which was the principal impediment to the calculation of  $Z$  by Eq. 1.34. Each occupation number may range over all values permitted to it, irrespective of the values of the other occupation numbers. Thus, Eq. 1.47 is identical to

$$\Xi = \left\{ \sum_{n=0}^{\infty} \exp \left[ -\frac{(\epsilon_0 - \mu) n}{kT} \right] \right\} \times \dots \times \left\{ \sum_{n=0}^{\infty} \exp \left[ -\frac{(\epsilon_k - \mu) n}{kT} \right] \right\} \dots \quad (1.48)$$

The grand partition function is thereby reduced to the product of sums, each of which is easily evaluated. The sums in Eq. 1.48 are over the number of particles in each single particle energy state. However, the Pauli exclusion principle may place limits on the allowable occupation numbers.

For particles with half-integer spin quantum numbers (such as neutrons and electrons), no more than one particle in the entire system of  $N$  particles may be in a particular quantum state. The upper limit on the sums in Eq. 1.48 is unity, and each sum is of the form

$$\sum_{n=0}^1 e^{-an} = 1 + e^{-a} \quad (1.49)$$

and the grand partition function is

$$\Xi = \prod_k \left[ 1 + \exp \left( -\frac{\epsilon_k - \mu}{kT} \right) \right] \quad (1.50)$$

This form of the grand partition function characterizes particles obeying Fermi-Dirac statistics.\*

#### 1.4.3 Properties of Systems Obeying Fermi-Dirac Statistics

Determination of the canonical partition function is now straightforward; we equate the logarithms of Eqs. 1.46 and 1.50:

$$\ln Z = -\frac{\mu N}{kT} + \sum_k \ln \left[ 1 + \exp \left( -\frac{\epsilon_k - \mu}{kT} \right) \right] \quad (1.51)$$

where the average number of particles in the grand canonical ensemble ( $\bar{N}$  of Eq. 1.45) has been identified with the fixed number of particles  $N$  in the canonical ensemble.

Equation 1.51 contains one parameter that remains to be specified, the chemical potential. This parameter is related to the number of particles in the system. The appropriate relation is obtained by equating the partial derivatives of  $\ln \Xi$  with respect to  $\mu$  obtained from Eqs. 1.46 and 1.50. Since the quantity  $Z(N)$  does not depend explicitly upon  $\mu$ , Eq. 1.46 provides the relation

$$\left( \frac{\partial \ln \Xi}{\partial \mu} \right)_N = \frac{N}{kT}$$

\*For particles characterized by integer spin quantum numbers (such as  $^4\text{He}$ ), there is no limit to the number of particles in each quantum state. In this case, the upper limit on the sums in Eq. 1.48 is infinity, and each sum may be evaluated from the arithmetical formula

$$\sum_{n=0}^{\infty} e^{-an} = (1 - e^{-a})^{-1}$$

Provided that  $a > 0$  or  $\epsilon_k > \mu$ , the grand partition function is

$$\Xi = \prod_k \left[ 1 - \exp \left( -\frac{\epsilon_k - \mu}{kT} \right) \right]^{-1}$$

Systems of particles to which this formula applies are said to obey Bose-Einstein statistics.

while from Eq. 1.50

$$\left(\frac{\partial \ln \bar{z}}{\partial \mu}\right)_N = \frac{1}{kT} \sum_k \left[ \exp\left(\frac{\epsilon_k - \mu}{kT}\right) + 1 \right]^{-1}$$

Equating these two derivatives yields

$$N = \sum_k \left[ \exp\left(\frac{\epsilon_k - \mu}{kT}\right) + 1 \right]^{-1} \quad (1.52)$$

Equation 1.52 may be interpreted in two ways. In the grand canonical ensemble, it shows how the specification of the chemical potential determines the average number of particles in the system. Alternately, in the canonical ensemble, it is a specification of  $\mu$  for a given value of  $N$ . When viewed in the latter sense, Eq. 1.52 provides an auxiliary relation by which the chemical potential can be removed from Eq. 1.51. Taken together, Eqs. 1.51 and 1.52 determine the partition function as a function of the temperature, the number of particles, and a sum over energy states  $\epsilon_k$ . It is not possible to evaluate  $Z$  analytically for any system. Nevertheless, all the essential thermodynamics of an assembly of indistinguishable particles are contained in Eqs. 1.51 and 1.52. All the formulas relating  $Z$  to  $U, S, p, F$ , and  $G$  are valid. Since  $Z$  is so extremely cumbersome, we must be satisfied with two less-general although very important approaches to practical calculations.

If the particle density of the system is sufficiently low,  $Z$  is considerably simplified, and all thermodynamic properties can be calculated. This approach is considered in the next section. When this approximate form of  $Z$  is not applicable, we may still compute the internal energy and any property that can be derived solely from the internal energy without directly confronting Eq. 1.51.

Consider the latter approach. The quantity summed in Eq. 1.52 is the average number of particles in each energy state:

$$\bar{n}_k = \left[ \exp\left(\frac{\epsilon_k - \mu}{kT}\right) + 1 \right]^{-1} \quad (1.53)$$

The internal energy of the  $N$ -particle system may be expressed by

$$U = \sum_k \bar{n}_k \epsilon_k = \sum_k \frac{\epsilon_k}{\exp\left(\frac{\epsilon_k - \mu}{kT}\right) + 1} \quad (1.54)$$

The sum in Eq. 1.54 can be evaluated exactly under certain conditions; we shall consider these conditions in treating the conduction electrons in a metal.

As an example of a thermodynamic quantity that is derivable from the internal energy alone, the pressure at  $0^\circ\text{K}$  is given by

$$p = -\left(\frac{\partial U}{\partial V}\right)_{T=0} \quad (1.55)$$

but pressures at  $T > 0^\circ\text{K}$  require us to use Eq. 1.27 or 1.28, which involves the partition function directly.

#### 1.4.4 The Ideal Gas in the Low-Density Limit

The partition function expression of Eq. 1.51 may be simplified if the number of states over which the particles are distributed is very large compared to the number of particles. This situation generally occurs when the physical density of the particles in the system is low (as in an ideal atomic or molecular gas). To obtain the low-density limit, we first expand Eq. 1.53 using the entire exponential term as the argument:

$$\bar{n}_k = \exp\left(-\frac{\epsilon_k - \mu}{kT}\right) \left[ 1 - \exp\left(-\frac{\epsilon_k - \mu}{kT}\right) + \dots \right] \quad (1.56)$$

By "low density" we mean that the average occupation numbers are very small, or  $\bar{n}_k < 1$ . Since  $\bar{n}_k$  is a function of the exponential term in Eq. 1.56 only, this limit is equivalent to requiring that  $\exp[-(\epsilon_k - \mu)/kT]$  be small. If this is so, all higher order terms in the brackets of Eq. 1.56 can be neglected compared to unity,\* and  $\bar{n}_k$  can be written as

$$\bar{n}_k \approx \exp\left(-\frac{\epsilon_k - \mu}{kT}\right) \quad (1.57)$$

Using this approximation, we find the normalization condition, Eq. 1.52, becomes

$$N = e^{\mu/kT} \sum_k e^{-\epsilon_k/kT} = z e^{\mu/kT} \quad (1.58)$$

where the summation in the middle expression is the *single-particle partition function*,

$$z = \sum_k e^{-\epsilon_k/kT} \quad (1.59)$$

$z$  being the sum over all possible quantum numbers of a single particle. It is analogous to the  $Z$  of Eq. 1.12, which is for  $N$  particles.

Combining Eqs. 1.57 and 1.58, we get

$$\frac{\bar{n}_k}{N} = \frac{e^{-\epsilon_k/kT}}{z} \quad (1.60)$$

This formula gives the fraction of the total number of particles occupying single particle energy state  $k$  in a low-density ideal gas. It is known as the *Maxwell-Boltzmann distribution function*.

We now apply the low-density approximation to Eq. 1.51. Since the exponential term is small compared to unity, the logarithm may be approximated by the formula  $\ln(1+x) = x$ ; thus

$$\begin{aligned} \ln Z &= -\frac{\mu N}{kT} + e^{\mu/kT} \sum_k e^{-\epsilon_k/kT} \\ &= -\frac{\mu N}{kT} + N \end{aligned}$$

\*In the process of discarding the higher order terms in Eq. 1.56, we also lose the distinction between Fermi-Dirac and Bose-Einstein statistics. The latter statistic gives a formula identical to Eq. 1.56 except that the minus sign following the 1 is replaced by a plus sign.

For the second equality in this expression, the last term in the first equality has been replaced by  $N$  according to Eq. 1.58. Again using Eq. 1.58, we find  $\mu/kT$  is

$$\frac{\mu}{kT} = -\ln \frac{z}{N}$$

Combining the preceding two equations yields

$$\ln Z = N \ln z - (N \ln N - N)$$

The term in the parentheses is, by Stirling's formula, simply  $\ln N!$ ; thus the above equation is

$$Z = z^N / N! \quad (1.61)$$

### 1.4.5 Factoring the Partition Function

The quantity  $\epsilon_k$  in Eq. 1.59 refers to the total energy of the particle when it is in its  $k$ th quantum state. If the particles are structureless entities, all the energy is due to translational motion. However, if the particles are atoms or molecules,  $\epsilon_k$  may contain contributions from internal forms of energy as well. In the latter case, the translational and internal energy components are clearly independent; so the total particle energy may be written as

$$\epsilon_k = (\epsilon_{tr})_j + (\epsilon_{int})_l \quad (1.62)$$

If there are  $b$  quantum numbers associated with the quantum state of a single particle, three are reserved for translation and  $(b-3)$  apply to internal quantum states. The subscript  $k$  in Eq. 1.62 denotes one of the quantum states determined by all  $b$  quantum numbers. The subscript  $j$  designates one of the quantum states characterized by the three translational quantum numbers, irrespective of the internal energy of the particle. Similarly, the subscript  $l$  refers to one of the internal quantum states without regard to the particle kinetic energy.

Because of its exponential character, the partition-function sum of Eq. 1.59 can be transformed from a single sum over the set of states labeled by  $k$  to the product of two smaller sums over the states represented by the indices  $j$  and  $l$ :

$$\begin{aligned} z &= \sum_{j,l} \exp \left[ -\frac{(\epsilon_{tr})_j + (\epsilon_{int})_l}{kT} \right] \\ &= \sum_j \exp \left[ -\frac{(\epsilon_{tr})_j}{kT} \right] \sum_l \exp \left[ -\frac{(\epsilon_{int})_l}{kT} \right] \quad (1.63) \end{aligned}$$

Each of the sums in Eq. 1.63 is itself a single-particle partition function but for a smaller number of modes of energy than the original sum of Eq. 1.59:

$$z_{tr} = \sum_j \exp \left[ -\frac{(\epsilon_{tr})_j}{kT} \right] \quad (1.64)$$

$$z_{int} = \sum_l \exp \left[ -\frac{(\epsilon_{int})_l}{kT} \right] \quad (1.65)$$

Thus, the partition function can be factored into components representing translation and internal forms of energy:

$$z = z_{tr} z_{int} \quad (1.66)$$

and the  $N$ -particle partition function for the low-density gas, Eq. 1.61, becomes

$$Z = \frac{(z_{tr} z_{int})^N}{N!} \quad (1.67)$$

### 1.4.6 Electronic Partition Function

In an entirely analogous fashion, the internal partition function of Eq. 1.65 can be further subdivided into components due to vibration, rotation, and electronic excitation. Since we will not be dealing with polyatomic molecules, vibration and rotation are not considered. For a monatomic gas, the only possible form of internal energy is due to excitation of the orbital electrons (we do not consider situations in which nuclear excitation occurs). According to Eq. 1.65, Boltzmann factors of the form  $\exp [-(\epsilon_{e1})_l/kT]$  must be summed over all possible quantum states of the orbital electrons. However, it is more convenient to sum over energy states  $l'$  instead of quantum states  $l$ , each term must be multiplied by the multiplicity of the energy state:

$$\begin{aligned} z_{e1} &= \exp \left[ -\frac{(\epsilon_{e1})_0}{kT} \right] \left\{ g_0 + \dots \right. \\ &\quad \left. + g_{l'} \exp \left[ -\frac{(\epsilon_{l'} - \epsilon_0)_{e1}}{kT} \right] + \dots \right\} \quad (1.68) \end{aligned}$$

where the ground-state electronic energy has been factored out. Since  $(\epsilon_{e1})_0$  is arbitrary, it is usually set equal to zero. The excitation energies  $(\epsilon_{l'} - \epsilon_0)_{e1}$  can be accurately measured spectroscopically. They are usually large enough to render electronic excitation significant only at very high temperatures. However, even at low temperatures, where  $z_{e1} \rightarrow g_0$ , the effect of multiplicity persists. The ground-state multiplicity affects the entropy but not the internal energy. For example,  $g_0 = 2$  in gaseous cesium because of the two possible spin orientations of the single outer  $s$  electron of this atom.

### 1.4.7 Translational Partition Function

Calculation of the single-particle partition function for translation from Eq. 1.64 begins with the quantum-mechanical formula for the discrete values that are allowed for this particular form of energy. For the translational motion of a particle within a cube of side  $L$ , the particle energy is

$$\epsilon = \frac{h^2}{8mL^2} (t_1^2 + t_2^2 + t_3^2) \quad (1.69)$$

where the translational quantum numbers  $t_1$ ,  $t_2$ , and  $t_3$  can assume any positive-integer values (including zero). The

mass of each particle is  $m$ . For simplicity, the energy of a particle at rest has been set equal to zero.

The translational energy levels given by Eq. 1.69 are very closely spaced, which implies that the argument of the exponential terms in Eq. 1.64 changes very little as  $t_1$ ,  $t_2$ , or  $t_3$  change by one. Therefore, the sum in Eq. 1.64 can be approximated to a high degree of accuracy by an integral. For subsequent applications, the integral will be converted to one over energy  $\epsilon$  rather than over quantum numbers  $t_1$ ,  $t_2$ , and  $t_3$ ; so the integral form of Eq. 1.64 is written as

$$z_{tr} = \int_0^{\infty} e^{-\epsilon/kT} \mathcal{D}(\epsilon) d\epsilon \quad (1.70)$$

where  $\mathcal{D}(\epsilon)$  is the *density of states* for the particles of the ideal gas contained in the cube. It represents the number of translational quantum states per unit energy interval about energy  $\epsilon$ . In order to evaluate the density of states for the energy-level formula of Eq. 1.69, we must regard  $\epsilon$  as the square of the magnitude of a vector  $\mathbf{X}$  which has components

$$\begin{aligned} X_1 &= \frac{h}{\sqrt{8m} L} t_1 \\ X_2 &= \frac{h}{\sqrt{8m} L} t_2 \\ X_3 &= \frac{h}{\sqrt{8m} L} t_3 \end{aligned} \quad (1.71)$$

Figure 1.2 shows a Cartesian coordinate system with  $X_1$ ,  $X_2$ , and  $X_3$  as principal axes. Since only positive values of the quantum numbers  $t_1$ ,  $t_2$ , and  $t_3$  are permitted, only one octant of the coordinate system is considered. Specification of the three translational quantum numbers fixes a point in Fig. 1.2. Because these quantum numbers can assume only integer values, there is a countable number of quantum states per unit volume in the coordinate system of Fig. 1.2. The small cube in the drawing is formed by changing each of the quantum numbers by one. According to Eq. 1.71, a unit change of one of the quantum numbers corresponds to a length  $h/\sqrt{8m} L$  in Fig. 1.2. Thus the

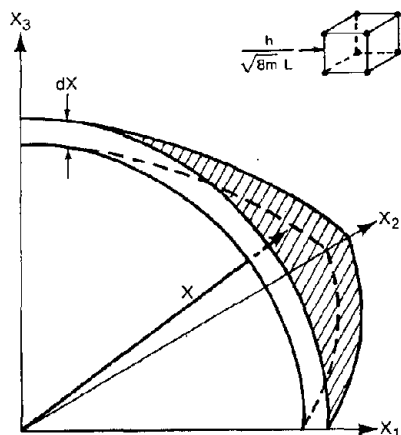


Fig. 1.2 Octant of spherical shell used to determine the number of translational quantum states in a unit energy interval.

volume of the small cube shown in the figure is  $h^3/(8m)^{3/2}L^3$ , or, since the cube contains the equivalent of one quantum state, the number of quantum states per unit volume is  $(8m)^{3/2}L^3/h^3$ .\* The  $1/8$  segment of the spherical shell of thickness  $dX$  in Fig. 1.2 occupies a volume of  $(4\pi X^2/8)dX$  and therefore contains  $(4\pi X^2/8)dX(8m)^{3/2}L^3/h^3$  translational quantum states. Since  $\epsilon = X^2$ , the product  $X^2 dX$  is equal to  $(\sqrt{\epsilon}/2)d\epsilon$ , and so the number of quantum states in the energy interval  $\epsilon$  to  $\epsilon + d\epsilon$  is

$$\mathcal{D}(\epsilon) d\epsilon = \frac{2^{5/2}\pi V m^{3/2}}{h^3} \sqrt{\epsilon} d\epsilon \quad (1.72)$$

where the volume of the container  $V$  has been used in place of  $L^3$ . Equations 1.69 and 1.72 are valid for freely moving particles in a gas of any density, provided the particles do not interact with each other.

Substituting Eq. 1.72 into 1.70 and performing the integration yields the translational partition function:

$$z_{tr} = V \left( \frac{2\pi mkT}{h^2} \right)^{3/2} \quad (1.73)$$

The translational partition function thus depends upon both the volume  $V$  and the temperature  $T$ . The volume dependence arises from the presence of the container dimension  $L$  in Eq. 1.69. Analogous quantum-mechanical formulas describing allowable internal energy levels (vibration, rotation, and electronic excitation) do not depend upon the size of the vessel containing the particles; hence the partition functions for these forms of energy are independent of volume.

#### 1.4.8 Justification of the Low-Density Approximation

At this point, we are in a position to state quantitatively what is meant by a low-density gas. The entire development that led to Eq. 1.61 was based on the premise that the occupation numbers were much less than unity. By Eq. 1.57,

$$\bar{n}_k = e^{\mu/kT} e^{-\epsilon_k/kT}$$

and, by Eq. 1.58,

$$e^{\mu/kT} = N/z_{tr}$$

where both the chemical potential,  $\mu$ , and the partition function have been referred to the ground-state energy  $\epsilon_0$ . Since  $e^{-\epsilon_k/kT}$  is of the order of unity (the average energy of a molecule in an ideal gas, for example, is  $3kT/2$ ), the requirement that  $\bar{n}_k$  be small compared to unity is equivalent to the stipulation that  $N/z_{tr}$  be small, or

$$\frac{N}{V} \ll \left( \frac{2\pi mkT}{h^2} \right)^{3/2} \quad (1.74)$$

\*There is one quantum state at each of the eight corners of the small cube in Fig. 1.2, each of which is shared with eight other identical adjacent cubes. Therefore, each quantum state contributes  $1/8$  of itself to the cube shown in the drawing, or the cube contains one whole quantum state.

where  $N/V$  is the density of the gas and the quantity

$$\lambda = \frac{h}{\sqrt{2\pi mkT}} \quad (1.75)$$

is called the *thermal wavelength* of an ideal gas particle.\*

Equation 1.74 is equivalent to the condition that the thermal wavelength be much smaller than the average distance between particles in the gas, or

$$\lambda \ll (V/N)^{1/3} \quad (1.76)$$

As a typical case for which Eq. 1.76 is satisfied, consider hydrogen gas at 1000°K and 1 atm pressure. At this temperature, the thermal wavelength of  $H_2$  is 0.4Å. Using the ideal gas law, we find the mean intermolecular distance in the gas is 240Å. Equation 1.76 is thus amply fulfilled.

The conduction electrons in a metal can be approximately described as an ideal gas. In this case, however, the density of the gas is of the same order of magnitude as the density of metal atoms in the solid. Because of the high density and small electron mass, the low-density limit of the partition function is not applicable. The electrons in sodium metal at 300°K, for example, have a thermal wavelength of 40Å but a mean separation of only 3.5Å.

### 1.4.9 The Maxwell Distribution

The distribution of kinetic energy in a low-density collection of noninteracting particles is the basis of calculating many useful properties of ordinary dilute gases. This distribution function may be obtained by applying Eq. 1.60 to translational energy and converting from quantum states to energy intervals by using the density of states derived previously. Thus, the number of particles of a dilute gas with energies in the range  $\epsilon$  to  $\epsilon + d\epsilon$  is given by

$$\frac{dn}{N} = \frac{e^{-\epsilon/kT} \mathcal{D}(\epsilon) d\epsilon}{z_{tr}}$$

Using Eqs. 1.72 and 1.73 in this equation yields

$$\frac{dn}{N} = \frac{2}{\sqrt{\pi}} \frac{\sqrt{\epsilon}}{(kT)^{3/2}} e^{-\epsilon/kT} d\epsilon \quad (1.77)$$

which is the Maxwell distribution in the energy variable. For purely translational motion,  $\epsilon = mv^2/2$ , where  $v$  is the particle speed, and Eq. 1.77 is equivalent to

$$\frac{dn}{N} = \left(\frac{2}{\pi}\right)^{1/2} \left(\frac{m}{kT}\right)^{3/2} v^2 e^{-mv^2/2kT} dv \quad (1.78)$$

which is the Maxwell distribution of molecular speeds.

## 1.5 NOMENCLATURE

$b$  = total number of quantum numbers  
 $\mathcal{D}$  = density of states for particles  
 $E$  = energy of a microstate

\*The thermal wavelength is a factor  $2/\pi$  different from the deBroglie wavelength ( $h/mv$ ) if the velocity is taken as the mean speed of the Maxwell-Boltzmann distribution.

$F$  = Helmholtz free energy  
 $g$  = multiplicity of energy state  
 $G$  = Gibbs free energy  
 $h$  = Planck's constant  
 $H$  = enthalpy  
 $k$  = Boltzmann constant  
 $L$  = length of a side of a cube in which a particle is confined  
 $m$  = mass of a particle  
 $M$  = total number of particles in a system  
 $n$  = occupation number of an energy level  
 $N$  = number of particles in a system or a subsystem  
 $\bar{N}$  = average number of particles in a system  
 $p$  = pressure  
 $P$  = probability of a microstate in an ensemble  
 $S$  = entropy  
 $t$  = translational quantum number  
 $T$  = temperature  
 $U$  = internal energy  
 $v$  = particle speed  
 $V$  = volume  
 $z$  = single-particle partition function  
 $Z$  = partition function  
 $Z'$  = partition function above the ground state

### Greek letters

$\mu$  = chemical potential  
 $\omega$  = density of states for system  
 $\epsilon$  = particle energy  
 $\bar{\epsilon}$  = average particle energy  
 $\Xi$  = grand canonical partition function  
 $\lambda$  = thermal wavelength of an ideal gas particle

### Subscripts

$i$  = microstate of a system  
 $j$  = quantum state characterized by translational quantum numbers  
 $k$  = quantum state of a particle  
 $l$  = quantum state characterized by internal quantum numbers  
 $r$  = subsystem of an isolated system  
 $el$  = electronic excitation-energy component  
 $int$  = internal-energy component  
 $tr$  = translational-energy component

## 1.6 ADDITIONAL READING

1. L. M. Grossman, *Thermodynamics and Statistical Thermodynamics*, Chap. 6 and Chap. 7, Secs. 1 and 2, McGraw-Hill Book Company, New York, 1969.
2. F. Reif, *Fundamentals of Statistical and Thermal Physics*, Chap. 2, Secs. 1-5; Chap. 3, Secs. 1-3; Chap. 6, Secs. 1, 2, 5, 6, and 9; and Chap. 9, Secs. 1-11, McGraw-Hill Book Company, New York, 1965.

## 1.7 PROBLEMS

1.1 The average energy of an ideal gas of Fermi-Dirac particles is given by the following expression:

$$E_f = \frac{1}{N} \int_0^\infty \epsilon \bar{n}(\epsilon) \mathcal{D}(\epsilon) d\epsilon$$

where

$$\bar{n}(\epsilon) = \frac{1}{e^{(\epsilon - \mu)/kT} + 1}$$

Show how the above formula for  $E_F$  can also be derived directly from the total partition function of an ideal gas of particles obeying Fermi-Dirac statistics in which the summation is also approximated by an integral.

1.2 Consider a monatomic substance of atomic weight  $M$ . The solid form melts at  $T_f$  with a heat of fusion  $\Delta H_f$  (J/mole). The liquid boils at atmospheric pressure at a temperature  $T_b$  with a heat of vaporization  $\Delta H_v$ . The specific heats of the solid and liquid phases are  $C_{p_s}$  and  $C_{p_l}$  J/mole-°K, respectively, and can be assumed known functions of temperature.

Derive expressions for the entropy of an ideal gas of this substance at a temperature  $T > T_b$  and 1 atm pressure from: (a) the thermodynamic data given above and (b) statistical mechanics, assuming a dilute ideal gas.

1.3 In principle, neutrons are spin  $1/2$  particles and so must obey Fermi-Dirac statistics. [They are, however, commonly treated by Maxwell-Boltzmann statistics.] Derive an expression for the energy spectrum of neutrons of total density  $n_{tot}$  neutrons/cm<sup>3</sup> in thermal equilibrium with a nonabsorbing infinite medium at  $T^\circ\text{K}$ . Start with the two-term approximation to Eq. 1.56.

(a) What is the average neutron energy? What is the deviation of the average energy from the Maxwell-Boltzmann value ( $3kT/2$ ) for a density of  $10^{10}$  neutrons/cm<sup>3</sup> and  $T = 1^\circ\text{K}$ ?

(b) Would you expect the same approximation to be valid for the electron gas consisting of the conduction electrons in copper at room temperature?

1.4 Express the partition function for a system consisting of two Fermi-Dirac particles which can be distributed among three discrete energy states. Be sure to allow for distinct spin orientation.

1.5 The coefficient of thermal expansion is defined by

$$\alpha = \frac{1}{V} \left( \frac{\partial V}{\partial T} \right)_p$$

and the coefficient of compressibility by

$$\beta = -\frac{1}{V} \left( \frac{\partial V}{\partial p} \right)_T$$

(a) Develop expressions for the coefficient of thermal expansion,  $\alpha$ , and the coefficient of compressibility,  $\beta$ , in terms of the partition function,  $Z$ .

(b) For mercury at  $0^\circ\text{C}$ ,  $\alpha = 18 \times 10^{-5} (\text{°C})^{-1}$  and  $\beta = 5.4 \times 10^{-11} (\text{N/m}^2)^{-1}$ . If mercury were heated from  $0^\circ\text{C}$  to  $1^\circ\text{C}$  in a constant-volume system, what pressure would be developed?

(c) Show that the difference in heat capacities at constant pressure and constant volume is

$$C_p - C_v = \frac{\alpha^2}{\beta} VT$$

What is the fractional difference between  $C_p$  and  $C_v$  for mercury at  $0^\circ\text{C}$  and for an ideal monatomic gas?

(d) Prove that

$$\left( \frac{\partial U}{\partial V} \right)_T = T \left( \frac{\partial p}{\partial T} \right)_V - p = \frac{\alpha}{\beta} T - p$$

and

$$\left( \frac{\partial^2 U}{\partial V^2} \right)_T = \frac{1}{\beta V} \left[ 1 + T \frac{\alpha}{\beta^2} \left( \frac{\partial \beta}{\partial p} \right)_T + \frac{T}{\beta} \left( \frac{\partial \beta}{\partial T} \right)_p \right]$$

1.6 Consider an ideal monatomic gas in its ground electronic state (nondegenerate). Starting from the partition function, determine:

(a) The equation of state of the gas (i.e., the ideal gas law).

(b) The entropy of the gas.

(c) The heat capacity at constant pressure of the gas.

(d) Suppose the gas is heated to temperatures high enough to populate the first excited electronic state (also nondegenerate). This state is at an energy  $\Delta\epsilon$  above the ground state, and  $\Delta\epsilon/kT \gg 1$ . How are the results of (a) through (c) above affected?

1.7 Demonstrate the equality of the right-hand sides of Eqs. 1.47 and 1.48 for the restricted case in which there are only two states ( $k = 0$  and  $k = 1$ ).

# Chapter 2

## Thermal Properties of Solids

The statistical interpretation of thermodynamic quantities outlined in Chap. 1 can be applied to the atoms in a perfect crystalline solid. In particular, we will consider the variation of internal energy (or the specific heat) with temperature and the equation of state of the material according to the model of a solid first introduced by Debye.

### 2.1 VIBRATIONAL ENERGY IN A SOLID

The equilibrium positions of the atoms of a solid are determined by the regular geometrical pattern of the crystal structure of the solid. If the atoms of a solid are assembled on their equilibrium positions from a collection of free atoms (which are noninteracting and at rest), a considerable amount of energy is released. The change in energy resulting from the construction of a solid from free atoms (or ions) is termed the *cohesive energy* of the solid.

In addition to the cohesive energy, the crystal also stores energy by the vibration of the atoms about their equilibrium positions. The effect of temperature and pressure upon the cohesive energy and the vibrational energy is responsible for the thermal properties and the equation of state of the solid.

Since the cohesive energy of a crystal is usually quite large, it is apparent that the atoms in the solid phase interact strongly with one another. Yet the statistical analysis of the thermodynamic properties is feasible only for systems whose member particles exhibit a negligible mutual influence. This contradiction is resolved by demonstrating that the strong interactions between the atoms of a solid may be treated as if the solid consisted of independent modes of vibration. Such a transformation depends only upon the rather lenient restriction that the amplitudes of the vibrations of each of the atoms be small enough for Hooke's law to apply.

The total energy of a crystal at any instant consists of the cohesive energy,  $E_{coh}$ , and the kinetic and potential energies of the vibration of each atom:

$$E_{tot} = E_{coh} + E_K + E_P \quad (2.1)$$

The kinetic and potential-energy contributions depend upon the instantaneous positions of each of the atoms of the crystal. However, the energy of the particular configuration

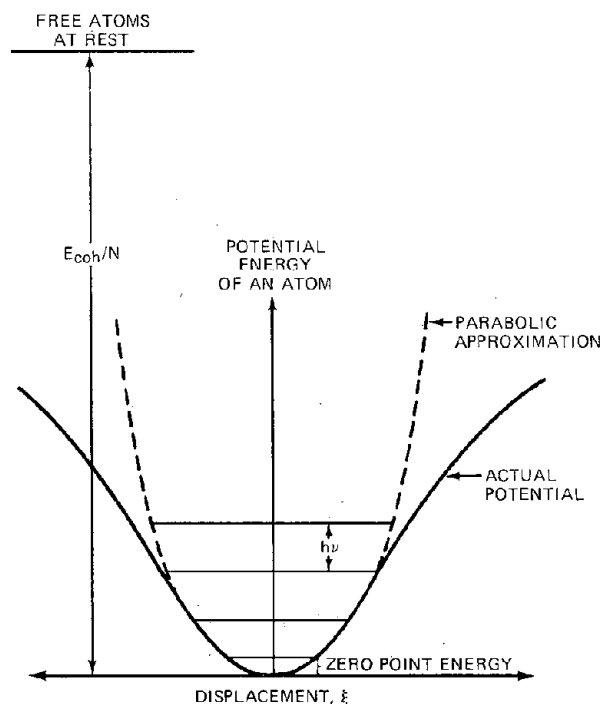


Fig. 2.1 Potential energy of an atom in a crystal.

is denoted by  $E_{tot}$  rather than the usual microstate energy  $E_i$  since the first part of the analysis uses classical mechanics rather than quantum mechanics.

Each atom of a solid is surrounded by a cage consisting of 6 to 12 *nearest-neighbor* atoms which effectively constitute a barrier to free migration of the atom about the crystal. The potential energy of an atom is lowest when it is at the center of this cage, which is its equilibrium position. Movement in any direction causes a sharp increase in potential energy because of the presence of the nearest neighbors. Thus, each atom may be regarded as residing in a potential well created by the interaction of the atom with all other atoms of the crystal. The variation of the potential energy of an atom moving in a particular direction relative to the crystal axes is shown in Fig. 2.1. The minimum in

the potential curve differs from the reference state of free atoms by  $E_{\text{coh}}/N$ , which implies that the sketch has been drawn for the case in which all other atoms are in their equilibrium lattice positions. However, the other atoms are also in constant small-amplitude motion, and the potential curve changes according to the particular location of all other atoms at a given instant.

Since each atom possesses three degrees of vibrational freedom, the entire crystal of  $N$  atoms may be considered as a system with  $3N$  degrees of freedom, all in vibration.

The kinetic-energy term in Eq. 2.1 is

$$E_K = \frac{1}{2} \sum_{i=1}^{3N} m \dot{\xi}_i^2 \quad (2.2)$$

where  $m$  is the mass of the atoms in the monatomic crystal. The displacement of an atom along one of the three coordinate directions is denoted by  $\xi_i$ . The term  $\dot{\xi}_i$  in Eq. 2.2 is the velocity of the vibrational motion for a particular mode.

The potential-energy term in Eq. 2.1 is a function of the displacements of all atoms of the crystal,  $E_p(\xi_1, \dots, \xi_i, \dots, \xi_{3N})$ . Since small-amplitude oscillations are assumed,  $E_p$  may be expanded in a Taylor series:

$$E_p = \sum_{i=1}^{3N} \left( \frac{\partial E_p}{\partial \xi_i} \right)_0 \xi_i + \frac{1}{2} \sum_{i=1}^{3N} \sum_{j=1}^{3N} \left( \frac{\partial^2 E_p}{\partial \xi_i \partial \xi_j} \right)_0 \xi_i \xi_j + \dots \quad (2.3)$$

Inasmuch as the force on each atom is zero in the equilibrium position, the first term on the right of Eq. 2.3 is zero. The second-order derivatives in the double sum are constants, but not zero. They represent the Hooke's law constants that characterize the vibrations:

$$k_{ij} = k_{ji} = \left( \frac{\partial^2 E_p}{\partial \xi_i \partial \xi_j} \right)_0 \quad (2.4)$$

If higher order terms in Eq. 2.3 are neglected, the total energy of the system for a particular set of displacements and velocities can be written as:

$$E_{\text{tot}} = E_{\text{coh}} + \frac{1}{2} \sum_{i=1}^{3N} m \dot{\xi}_i^2 + \frac{1}{2} \sum_{i=1}^{3N} \sum_{j=1}^{3N} k_{ij} \xi_i \xi_j \quad (2.5)$$

Neglecting the higher order terms in Eq. 2.5 is equivalent to representing the potential curve of Fig. 2.1 by a parabola, as shown by the dashed line in the sketch.

Because of the  $i$ - $j$  cross product terms in the double sum, the total energy cannot be represented as the sum of  $i$  independent terms. The strong interactions between atoms of a solid are contained in the cross product terms. Despite the cross product terms in Eq. 2.5, the system energy is still quadratic in the displacements, and the atoms undergo simple harmonic motion. The vibration frequencies can be related to the force constants  $k_{ij}$  by writing an equation of motion for each of the  $3N$  modes of vibration:

$$m \ddot{\xi}_i = - \left( \frac{\partial E_p}{\partial \xi_i} \right)_{\xi_j} = - \sum_j k_{ij} \xi_j \quad (2.6)$$

Solutions of the type  $\xi_i \alpha e^{-2\pi i \nu t}$  (where  $i$  denotes  $\sqrt{-1}$ ) yield the vibration frequencies as roots of the determinant  $|k_{ij} - 4\pi^2 m \nu^2 \delta_{ij}| = 0$ , where  $\delta_{ij}$  is the Kronecker delta. Knowledge of the vibrational frequencies is not equivalent to knowledge of all the force constants. There are fewer frequencies than force constants, and a complete dynamical description of the crystal, in equilibrium as well as nonequilibrium situations, requires all the  $k_{ij}$ . However, the  $3N$  vibrational frequencies are sufficient for determining the thermodynamic properties of the solid, which are due to oscillations about the equilibrium positions.

## 2.2 NORMAL-MODE ANALYSIS

Despite the small-amplitude approximation, we must still devise a scheme to eliminate the cross product terms from the total energy expression before the thermodynamic properties of the crystal can be computed from simple models. Fortunately, the appropriate transformation can be accomplished simply by redefining the spatial coordinate system in which the atoms vibrate. A new coordinate system, in which displacements are denoted by  $q_i$ , is constructed as a linear combination of the actual displacements:

$$q_i = \sum_{j=1}^{3N} C_{ji} \xi_j \quad (2.7)$$

If the coefficients  $C_{ji}$  are chosen according to the prescription:

$$\sum_j C_{ji} C_{j1} = \delta_{i1} \quad (2.8)$$

then Eq. 2.7 may be inverted to give  $\xi_i$  as

$$\xi_i = \sum_{j=1}^{3N} C_{ji} q_j \quad (2.9)$$

If Eq. 2.9 is substituted into Eq. 2.5, the cross product terms disappear, and the total energy becomes

$$E_{\text{tot}} = E_{\text{coh}} + \sum_{i=1}^{3N} \left[ \frac{1}{2} m \dot{q}_i^2 + \frac{1}{2} (4\pi^2 m \nu_i^2) q_i^2 \right] \quad (2.10)$$

The coordinate system  $q_i$ , which converts the vibrational energy of  $3N$  coupled modes to a single sum of terms each depending on a single coordinate, is called the *normal coordinate* system of the assembly. The interatomic forces responsible for the thermodynamic behavior of the crystal, which were contained in the  $k_{ij}$  in Eq. 2.5, reappear as the vibrational frequencies  $\nu_i$  in Eq. 2.10.

## 2.3 PARTITION FUNCTION FOR VIBRATION

We have demonstrated that the strongly interacting system of particles which characterizes a solid can be transformed into a system of weakly interacting modes of vibration for which the total energy is just the sum of the energies of the individual oscillators:

$$E_{\text{tot}} = E_{\text{coh}} + \sum_{i=1}^{3N} \epsilon_i \quad (2.11)$$

Here  $\epsilon_i$  is the energy in the  $i$ th mode of oscillation relative to the reference energy at the minimum of the potential curve in Fig. 2.1. The validity of this simplification depends only upon the assumption that atom displacements are sufficiently small that the potential energy is quadratic in the displacement coordinates.

The energy of vibration of the  $i$ th mode is given by the bracketed term in Eq. 2.10 according to classical mechanics. According to quantum mechanics, however, the energy of each mode can assume only the discrete values given by the formula

$$\epsilon_i = \left( j_i + \frac{1}{2} \right) h\nu_i \quad (2.12)$$

where  $j_i$  is the vibrational quantum number of mode  $i$  and can take on any positive integer value (including zero). The spacing between the vibrational energy levels is constant, as indicated in Fig. 2.1.

In calculating the partition function, and therefore all the thermodynamic quantities of the solid, we use the quantum mechanical energy. The classical analogy has been used only to illustrate the normal-mode analysis, although we could have done this also by quantum mechanical formulation. We need henceforth only the information contained in Eqs. 2.11 and 2.12.

The ground state is taken to be the crystal at  $0^\circ\text{K}$  and a specific volume  $v$ :

$$v = \frac{V}{N} \quad (2.13)$$

The necessity of specifying both these parameters in defining a ground state in the present situation can be explained as follows. Both the cohesive energy and the vibration frequencies depend on the specific volume, or equivalently, on the separation of the atoms in the lattice. Consequently, a completely defined state must fix both  $T$  and  $v$ . Since  $v$  depends on the temperature and pressure, a particular value of  $v$  at  $0^\circ\text{K}$  corresponds to a definite pressure. Hence, either  $v$  or  $p$  may be prescribed.

The reference state has been chosen as the free atoms of the disassembled solid. Relative to this state, the ground-state energy consists of the cohesive energy and the residual vibrational energy when all atoms of the solid are in the lowest quantum state. From Eq. 2.12, with  $j_i = 0$  for all  $i$ , the energy of each mode of oscillation is  $h\nu_i/2$ . This quantity of vibrational energy, which remains with each mode at the absolute zero of temperature, is called the *zero-point energy*. Referred to free atoms at rest, the ground-state energy is:

$$E_0(v) = E_{\text{coh}}(v) + \frac{1}{2} \sum_{i=1}^{3N} h\nu_i(v) \quad (2.14)$$

The energy of a microstate of the system depends upon the quantum numbers  $j_i$  of all  $3N$  modes of vibration:

$$E(j_1 \dots j_i \dots j_{3N}) = E_0(v) + \sum_{i=1}^{3N} j_i h\nu_i \quad (2.15)$$

Although vibration frequencies appearing in Eq. 2.15 are functions of  $v$ , designation of this dependence has been omitted to keep the notation simple.

In evaluating the partition function for the crystal from Eq. 1.12, we replace the sum over microstates by a sum over all quantum numbers:

$$Z = e^{-E_0(v)/kT} \sum_{j_1 \dots j_i \dots j_{3N}} \exp[-(j_1 h\nu_1 + \dots + j_i h\nu_i + \dots + j_{3N} h\nu_{3N})/kT] \quad (2.16)$$

The partition function depends on both temperature and specific volume (or pressure). The specific volume dependence enters in both  $E_0$  and the  $\nu_i$ .

Except for the presence of the ground-state energy term, Eq. 2.16 strongly resembles the partition-function sum for the ideal gas, Eq. 1.34. However, Eq. 2.16 is a sum over quantum numbers, not occupation numbers as in Eq. 1.34. Since each of the quantum numbers  $j_i$  can have any value from zero to infinity, there is no restriction analogous to the requirement that the occupation numbers sum to  $N$ . Consequently the calculational difficulties encountered in evaluating  $Z$  for the ideal gas are not a factor in Eq. 2.16, which may be written as

$$Z = e^{-E_0(v)/kT} \left( \sum_{j=0}^{\infty} e^{-jh\nu_1/kT} \right) \dots \left( \sum_{j=0}^{\infty} e^{-jh\nu_{3N}/kT} \right) \quad (2.17)$$

Each sum in Eq. 2.17 is a single-particle (or mode in this case) partition function for vibration. The sums are evaluated by the formula

$$\sum_{j=0}^{\infty} e^{-jh\nu_i/kT} = (1 - e^{-h\nu_i/kT})^{-1} \quad (2.18)$$

The partition function for a crystal of  $N$  identical atoms is

$$Z = e^{-E_0(v)/kT} \prod_{i=1}^{3N} (1 - e^{-h\nu_i/kT})^{-1} \quad (2.19)$$

In the subsequent discussion, it will be more convenient to deal with the angular frequency,  $\omega_i$ , in place of the usual frequency  $\nu_i$ . We therefore replace  $h\nu_i$  with  $\hbar\omega_i$ , where  $\hbar = h/2\pi$  and  $\omega_i = 2\pi\nu_i$ , and at the same time, take the logarithm of Eq. 2.19:

$$\ln Z = -\frac{E_0(v)}{kT} - \sum_{i=1}^{3N} \ln (1 - e^{-\hbar\omega_i/kT}) \quad (2.20)$$

No conceivable experiment can provide the frequencies of all  $3N$  modes of a macroscopic crystal. Because of the large number of particles, there are many modes in a small frequency span, and the sum in Eq. 2.20 may be very satisfactorily approximated by an integral:

$$\ln Z = -\frac{E_0(v)}{kT} - \int_0^{\infty} \mathcal{G}(\omega) \ln (1 - e^{-\hbar\omega/kT}) d\omega \quad (2.21)$$

where  $\mathcal{G}(\omega)$  is the *frequency spectrum* of the vibrational modes of the solid. It represents the number of modes with angular frequencies between  $\omega$  and  $\omega + d\omega$ . Since there are  $3N$  modes in total,  $\mathcal{G}(\omega)$  must satisfy the normalization condition

$$\int_0^{\infty} \mathcal{G}(\omega) d\omega = 3N \quad (2.22)$$

The thermodynamic properties of the solid can be obtained by the relations of Sec. 1.3 once  $Z$  is known. Computation of  $Z$  rests solely upon determination of the frequency spectrum  $\mathcal{P}(\omega)$ .

## 2.4 THE EINSTEIN MODEL

Einstein's analysis of the frequency spectrum was prompted by the fact that classical thermodynamics fails rather spectacularly to account for the variation of the specific heat of solids as  $T \rightarrow 0^\circ\text{K}$ . According to classical thermodynamics, each of the  $3N$  modes of vibration should contribute  $kT$  to the internal energy. Or, the specific heat per gram atom should be  $3Nk = 3R$  (where  $N$  is Avogadro's number and  $R$  is the gas constant) at all temperatures. Experimentally, however, the specific heat approaches zero as  $T \rightarrow 0^\circ\text{K}$ .

Einstein's approximation to the frequency spectrum was the simplest imaginable, namely, that all modes have the same frequency  $\omega_E$ :

$$\mathcal{P}(\omega) = 3N \delta(\omega - \omega_E) \quad (2.23)$$

where  $\delta$  represents the Dirac delta function.

With the frequency spectrum represented by Eq. 2.23, the partition function can be computed from Eq. 2.21, and the internal energy, from Eq. 1.15. This procedure yields the specific heat at constant volume by the relation

$$C_v = \left( \frac{\partial U}{\partial T} \right)_v = 3R \left( \frac{\hbar\omega_E}{kT} \right)^2 \frac{e^{\hbar\omega_E/kT}}{(e^{\hbar\omega_E/kT} - 1)^2} \quad (2.24)$$

This formula has one adjustable parameter,  $\Theta_E = \hbar\omega_E/k$ , which is called the Einstein temperature. The Einstein formula exhibits the proper limiting behavior, approaching the classical limit of  $3R$  as  $T$  becomes large and going to zero as  $T \rightarrow 0^\circ\text{K}$ . Agreement at intermediate temperatures is optimized by selection of the parameter  $\Theta_E$ . For most solids, accord between the experimental specific heats and the Einstein prediction is fair.

The success of the Einstein theory is not due so much to the accuracy of the assumed frequency spectrum, Eq. 2.23, but rather to the fact that it accepts the quantization of the vibrational energy of the crystal—the development culminating in Eq. 2.21 began with Eq. 2.12. This feature of the theory is absolutely essential if the behavior of the heat capacity at low temperature is to be explained.

## 2.5 THE DEBYE MODEL

The deficiency in the Einstein model lies in the assumption that all modes of vibration have the same frequency. If the atoms of the crystal are regarded as oscillating independently in a potential well created by the surrounding atoms, this assumption is reasonable. However, the vibrational energy of a solid is due to atomic motions of an entirely different nature. Instead of the unrelated jiggling of individual atoms, large groups of atoms move in unison. These correlated motions of the atoms of a solid are

called collective modes of vibration. The vibrational energy stored in collective modes is largely responsible for the thermodynamic behavior of solids.

The correlated atomic motion takes the form of entire planes of atoms performing oscillatory motion, which is a three dimensional analog of a vibrating string. As shown in Fig. 2.2, displacements of successive planes from their equilibrium positions have, at any instant, the shape of a wave. The waves are of the type that are responsible for the transmission of sound in a continuum and are called *elastic waves*. They may be standing or travelling waves. For each direction of wave propagation, there are three modes of vibration, or polarization: if the atomic planes are displaced

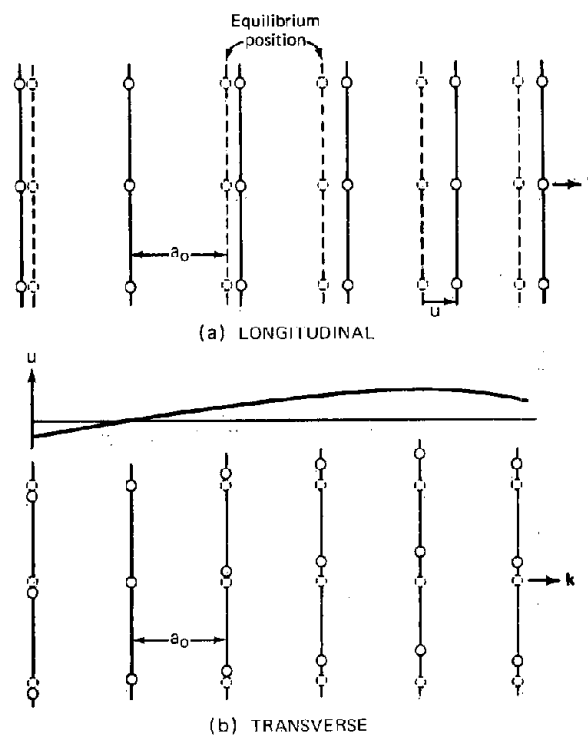


Fig. 2.2 Elastic waves in solids.

back and forth in the direction of propagation, the mode is termed *longitudinal*. If the planes oscillate in a direction perpendicular to the propagation direction, the mode is *transverse*. There are two transverse modes and one longitudinal mode for each wave vector  $k$ .

Since the elastic waves ultimately result from the vibration of the atoms of the solid, the energy carried by the waves must be quantized according to Eq. 2.12. Although this relation was developed with individual atomic oscillations in mind, it is not restricted to the vibrations of a single particle. It merely states that, whatever the entity which is regarded as vibrating, energy can only be stored in integral multiples of  $h\nu$ .

The elastic waves have all the formal properties usually associated with wave motion. They may be characterized by a wave vector  $k$ , whose direction is in the direction of propagation and whose magnitude is

$$k = \frac{2\pi}{\lambda} \quad (2.25)$$

where  $\lambda$  is the wavelength. Wavelengths less than two interplanar spacings have no meaning since they suggest periodic motion between atomic planes where no particles exist. If  $a_0$  is the spacing between atomic planes, waves of length  $\lambda < 2a_0$  can always be represented by a wave of length  $\lambda > 2a_0$  (see Fig. 2.3 for an example). An elastic wave for which  $\lambda_{\min} = 2a_0$  corresponds to a standing wave with nodes at the positions of each atomic plane, and no motion whatsoever occurs. This wave has a wave vector magnitude of  $k_{\max} = \pi/a_0$ .

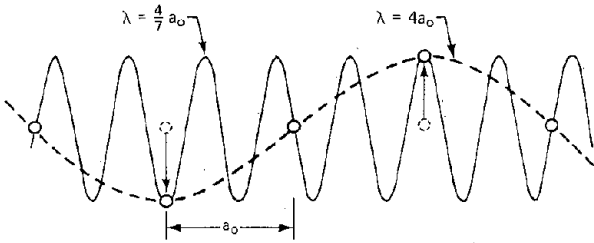


Fig. 2.3 A wavelength less than  $2a_0$  is equivalent to one greater than  $2a_0$ .

In addition to the wavelength, elastic waves have an angular frequency,  $\omega$ . The relation between  $\omega$  and the magnitude of the wave vector  $k$  characterizes the material and is known as the *dispersion relation*. The speed at which a particular wave travels is the *phase velocity* or *propagation speed*

$$c = \frac{\omega}{k} \quad (2.26)$$

Equation 2.26 is a linear dispersion relation if  $c$  is independent of  $\omega$ . If the dispersion relation is nonlinear, the propagation speed is a function of frequency.

For long wavelengths, the displacements of adjacent atomic planes are very nearly equal to each other, and the material behaves as a continuum—the fact that it is constituted of discrete atoms is not important. Long waves all travel at a constant speed, that of the speed of sound in the material. For short wavelengths, however, the atomic nature of the solid becomes significant, and the dispersion relation becomes nonlinear. The approximation due to Debye consists of ignoring this gradual transition from continuum to atomic behavior and assuming that waves of all frequencies propagate with the speed of sound. This is equivalent to assuming a linear dispersion relation  $\omega = ck$ .

The wave equation for a given state of polarization (i.e., longitudinal or transverse) in a three-dimensional isotropic medium is

$$\frac{\partial^2 u}{\partial x^2} + \frac{\partial^2 u}{\partial y^2} + \frac{\partial^2 u}{\partial z^2} = \frac{1}{c^2} \frac{\partial^2 u}{\partial t^2} \quad (2.27)$$

where  $u$  is the displacement of the atomic plane from its equilibrium position and  $c$  is the propagation speed. We seek solution to Eq. 2.27 in the form of standing waves since the displacements vanish at the boundaries of the

crystal. Standing waves in a crystal of dimensions  $L_x$ ,  $L_y$ , and  $L_z$  are of the form

$$u \propto \sin(k_x x) \sin(k_y y) \sin(k_z z) e^{-i\omega t} \quad (2.28)$$

where  $k_x$ ,  $k_y$ , and  $k_z$  are the components of the wave vector  $k$  in the three coordinate directions. Satisfying the condition that the boundaries of the crystal remain stationary requires that

$$\begin{aligned} k_x &= \frac{\pi}{L_x} m_x \\ k_y &= \frac{\pi}{L_y} m_y \\ k_z &= \frac{\pi}{L_z} m_z \end{aligned} \quad (2.29)$$

where  $m_x$ ,  $m_y$ , and  $m_z$  are positive integers.

Because of the restriction on the allowable wave vectors implied by Eq. 2.29, there are a finite number of waves contained within any interval of the wave vector. Since the dispersion relation of the material provides a one-to-one correspondence between the magnitude of the wave vector and the angular frequency, the number of waves in a unit frequency range is calculable. This last quantity is just the frequency spectrum required for determination of the thermodynamic properties of the material. Note that the condition that provides a countable number of elastic waves in a given frequency range is not at all quantum mechanical in nature—it arises simply from the requirement that an integral number of standing waves be contained in the crystal.

To count the number of waves within a small range of the wave vector, consider the elementary volume  $d^3k = dk_x dk_y dk_z$ . According to Eq. 2.29, this volume element contains

$$\left(\frac{L_x}{\pi} dk_x\right) \left(\frac{L_y}{\pi} dk_y\right) \left(\frac{L_z}{\pi} dk_z\right) = \frac{V}{\pi^3} d^3k$$

standing elastic waves. If we write  $d^3k$  in spherical coordinates as  $4\pi k^2 dk$  and divide by 8 to account for the requirement that only positive values of the wave vector components are physically acceptable, the number of waves in the magnitude range  $dk$  is

$$\frac{V}{2\pi^2} k^2 dk$$

Replacing  $k$  in the above expression with the angular frequency by using the linear dispersion relation  $\omega = ck$  of the Debye model, the number of waves in the frequency range from  $\omega$  to  $\omega + d\omega$  is

$$\mathcal{Q}(\omega) d\omega = \frac{V\omega^2}{2\pi^2 c^3} d\omega \quad (2.30)$$

Equation 2.30 can be generalized to include all three states of polarization associated with each wave vector by adding the contributions to  $\mathcal{Q}(\omega)$  from the longitudinal and two transverse modes:

$$\mathcal{L}(\omega) = \frac{V\omega^2}{2\pi^2} \left( \frac{1}{c_l^3} + \frac{2}{c_t^3} \right) \quad (2.31)$$

where  $c_l$  and  $c_t$  represent the propagation speeds of the longitudinal and transverse modes, respectively. The speed of sound in a polycrystalline material is

$$\frac{3}{c^3} = \frac{1}{c_l^3} + \frac{2}{c_t^3} \quad (2.32)$$

We have seen that there is a minimum wavelength determined by the lattice spacing in the solid. Although the Debye model has so far been based solely on consideration of the solid as a continuous medium, the condition  $\lambda_{\min} = 2a_0$  must be recognized. In the Debye model this condition is approximately satisfied by setting an upper limit to the frequency to which Eq. 2.31 is applicable. The maximum frequency  $\omega_D$  replaces  $\infty$  in the upper limit of the normalization condition of Eq. 2.22, which then yields

$$\omega_D = \left( \frac{6\pi^2}{v} \right)^{1/3} \bar{c} \quad (2.33)$$

where the specific volume of the solid (Eq. 2.23) has been used for  $V/N$ .

The maximum frequency,  $\omega_D$ , is called the Debye frequency. It is in the range of  $10^{13}$  to  $10^{14}$   $\text{sec}^{-1}$  and is often used to characterize the vibrational frequency of atoms of a solid. To determine how well the Debye frequency satisfies the condition  $\lambda_{\min} = 2a_0$ , we write

$$\lambda_{\min} = \frac{2\pi}{k_{\max}} = 2\pi \frac{\bar{c}}{\omega_D} = \frac{2\pi}{(6\pi^2)^{1/3}} v^{1/3}$$

where  $v$  is the volume occupied by an atom of the solid and is approximately equal to the cube of the interplanar spacing,  $a_0^3$ . The coefficient of  $v^{1/3}$  is 1.6 compared to the required value of 2. Therefore, the Debye model gives a minimum wavelength reasonably close to that required by the atomistic nature of the solid.

In terms of  $\omega_D$ , the Debye frequency spectrum is

$$\mathcal{L}(\omega) = \begin{cases} 9N\omega^2/\omega_D^3 & \text{for } 0 \leq \omega \leq \omega_D \\ 0 & \text{for } \omega > \omega_D \end{cases} \quad (2.34)$$

The actual frequency spectrum of the lattice vibrations in a solid may be obtained experimentally by X-ray or neutron scattering. These radiations interact with the solid by exchanging discrete quantities of energy, in multiples of  $\hbar\omega$ , with the solid. The frequency spectrum of the solid may be deduced from the spectrum of the scattered radiation. Figure 2.4 compares the Debye frequency spectrum with the experimental spectrum for aluminum. As expected, the Debye spectrum is in good agreement with experiment at low frequencies, where the vibrations closely resemble those of the continuous medium upon which the Debye model is based. The deviations at higher frequencies arise from the fact that the dispersion relation for a real solid is not linear, as assumed in the Debye model, and that the maximum frequency depends upon direction in the crystal, even for isotropic solids. These two effects are responsible for the very rich structure of the experimental spectrum in Fig. 2.4.

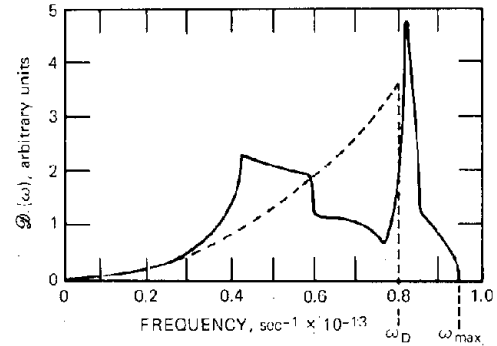


Fig. 2.4 The vibrational-frequency spectrum of aluminum. The solid curve is deduced from X-ray scattering measurements at 300°K. [After C. B. Walker, *Phys. Rev.*, 103: 547 (1956).] The dashed curve represents the Debye approximation with  $\Theta_D = 382^\circ\text{K}$  deduced from the specific heat. (From F. Reif, *Fundamentals of Statistical and Thermal Physics*, McGraw-Hill Book Company, New York, 1965.)

Despite the disagreement evident in Fig. 2.4, the Debye spectrum, in conjunction with Eq. 2.21, provides a reasonably good set of thermodynamic properties. At low temperatures, low-frequency elastic waves predominate, and the Debye spectrum faithfully follows the real spectrum. Thermodynamic properties at low temperatures should be reasonably well explained by the Debye model. At high temperatures, all lattice theories of solid thermodynamic properties (including the Debye model) approach the limits of classical thermodynamics. Even though the frequency spectrum may be in substantial error near the maximum frequency, the thermodynamic properties become increasingly insensitive to  $\mathcal{L}(\omega)$  as the temperature is increased.

Insertion of Eq. 2.34 into Eq. 2.21 yields the partition function of the crystal as a function of temperature and specific volume:

$$\ln Z = -\frac{E_0(v)}{kT} - 9N \left( \frac{T}{\Theta_D} \right)^3 \int_0^{\Theta_D/T} \ln(1 - e^{-x}) x^2 dx \quad (2.35)$$

where  $\Theta_D$  is the Debye temperature

$$\Theta_D = \frac{\hbar\omega_D}{k} \quad (2.36)$$

Since  $\omega_D$  of Eq. 2.33 is a function of solid specific volume, the Debye temperature is dependent on pressure (or specific volume) but not on temperature.

The integral in Eq. 2.35 is a function of its upper limit and must be calculated numerically.

## 2.6 SPECIFIC HEAT ACCORDING TO THE DEBYE MODEL

The specific heat at constant volume is obtained by successive differentiation of Eq. 2.35 with respect to temperature at constant volume. The internal energy is given by Eq. 1.15:

$$U(T, V) = kT^2 \left( \frac{\partial \ln Z}{\partial T} \right)_V$$

$$= E_0(V) + 9RT \left( \frac{T}{\Theta_D} \right)^3 \int_0^{\Theta_D/T} \frac{x^3}{e^x - 1} dx \quad (2.37)$$

where  $Nk$  has been written as  $R$  and  $U$  and  $V$  are for a gram atom of material. The specific heat is obtained from

$$C_v = \left( \frac{\partial U}{\partial T} \right)_V = 3R \left[ 3 \left( \frac{T}{\Theta_D} \right)^3 \int_0^{\Theta_D/T} \frac{x^4 e^x}{(e^x - 1)^2} dx \right] \quad (2.38)$$

The bracketed term in Eq. 2.38 is the Debye function, which is plotted in Fig. 2.5. At high temperatures,  $T/\Theta_D \rightarrow \infty$ , the Debye function approaches unity and the specific heat approaches the classical value of  $3R$  (the law of Dulong and Petit). At low temperatures the Debye function approaches

$$\frac{4}{5} \pi^4 \left( \frac{T}{\Theta_D} \right)^3$$

which leads to the experimentally observed  $T^3$  heat capacity behavior as  $T \rightarrow 0^\circ \text{K}$ . The Debye temperature  $\Theta_D$  is determined from the specific heat variation in this limit.

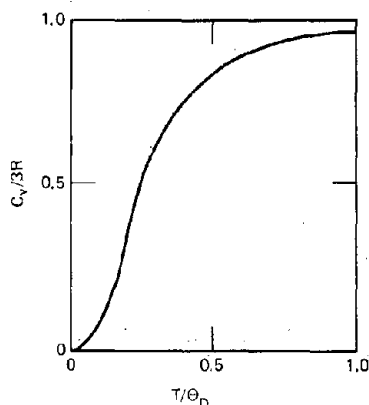


Fig. 2.5 The Debye heat capacity function.

A Debye temperature of  $382^\circ \text{K}$  has been determined for aluminum from specific heat measurements at low temperatures.

## 2.7 DEBYE EQUATION OF STATE

Equation 2.37 shows how the internal energy varies with temperature at a fixed specific volume. The quantities  $E_0$  and  $\Theta_D$  are presumed to be known functions of specific volume only. However, most processes or experiments occur not at constant volume, but at a constant pressure in the neighborhood of 1 atm. The specific volume of a solid is very little affected by moderate changes in pressure or temperature—solids are very nearly incompressible. So it does not matter a great deal whether Eq. 2.37 is applied to temperature changes that occur strictly at constant volume or at a constant pressure in the vicinity of 1 atm (i.e., from

high vacuum to tens of atmospheres)—the major effect on  $U$  is due to the temperature change. However, if pressures of hundreds or thousands of atmospheres are involved, the effect of the compressibility of the solid becomes significant. In such situations, the variations of  $E_0$  and  $\Theta_D$  exert a nonnegligible effect on the internal energy and must be accounted for.

The Debye model provides a relation between the partition function and the Debye temperature  $\Theta_D$ . The pressure is given by Eq. 1.28 in terms of the partition function. Using Eq. 2.35 for  $Z$ , we obtain

$$p = kT \left( \frac{\partial \ln Z}{\partial V} \right)_T = - \frac{dE_0}{dV} + \frac{1}{V} \left( - \frac{V}{\Theta_D} \frac{d\Theta_D}{dV} \right)$$

$$\times \left[ 9RT \left( \frac{T}{\Theta_D} \right)^3 \int_0^{\Theta_D/T} \frac{x^3}{e^x - 1} dx \right] \quad (2.39)$$

According to Eq. 2.37, the bracketed term in Eq. 2.39 is just  $U - E_0$ , and Eq. 2.39 can be expressed as

$$p = - \frac{dE_0}{dV} + \frac{1}{V} \left( - \frac{V}{\Theta_D} \frac{d\Theta_D}{dV} \right) (U - E_0) \quad (2.40)$$

Equation 2.40 is an equation of state of the form  $p(U, v)$ . Because of the presence of the dimensionless parameter  $(V/\Theta_D)(d\Theta_D/dV)$ , this equation of state is peculiar to the Debye model of solids. The derivative of the Debye temperature with specific volume is not an easily obtainable quantity, and the Debye equation of state is rarely used to describe the behavior of solids at high pressures. However, when the dimensionless parameter  $(V/\Theta_D)(d\Theta_D/dV)$  is replaced by an arbitrary function of specific volume, Eq. 2.40 is called the *Grüneisen equation of state*. Equations of state for materials at high pressures and high temperatures will be considered in detail in Chap. 9.

## 2.8 PHONONS

Because of the strong similarity between the wave properties of vibrations in a solid and electromagnetic radiation, it is natural to expect that the particle-like behavior of light waves would find an analogy in the case of elastic waves. The photon is quantized electromagnetic radiation. The quantized elastic wave in a crystal is made up of phonons. Phonons are referred to as quasi-particles to avoid confusion with the real particles of the solid, namely, the constituent atoms.

The quantitative nature of the phonon can be seen by examining Eq. 2.15:

$$E(j_1 \dots j_i \dots j_{3N}) = \sum_{i=1}^{3N} j_i h\nu_i \quad (2.41)$$

from which the reference energy  $E_0(v)$  has been omitted because it is not needed in the present discussion. According to this equation, the energy content of a solid may be regarded as the sum of the energies of a number of particles which are distributed among  $3N$  possible energy states. The particles are phonons, and  $j_i$  represents the number of phonons in state  $i$ . The quantity  $h\nu_i$  is the energy of a phonon in state  $i$ .

Equation 2.41 is identical to the expression for the total energy of an ideal quantum gas, Eq. 1.33. Thus the phonons in a solid possess the following properties:

1. They can be in any one of  $3N$  energy states.
2. There is no limit to their total number.
3. There is no limit to the number of phonons which can occupy a particular energy state;  $j_i$  may be any integer from zero to infinity.
4. They are indistinguishable; a microstate is specified by the numbers  $j_1 \dots j_i \dots j_{3N}$  in each energy state, irrespective of which phonons are in each state.
5. They cannot be assigned to a particular location in space.
6. They are weakly interacting in the sense that the quantum state of each phonon is not affected by the quantum states of the other phonons, and the total energy of the solid is the sum of the individual energies of the phonons present.

Properties 4 through 6 define an ideal quantum gas, which, because of property 3, obeys Bose-Einstein statistics (see footnote, p. 8 of Chap. 1). The fact that the total number of phonons is not limited means that the chemical potential of the phonon gas is zero. The phonons in a solid possess all the attributes of the photon gas that comprises the black-body radiation in equilibrium inside an enclosure.

Properties 1, 2, and 3 differentiate the phonon gas from the ideal gas of conduction electrons in a metal. In the latter, the number of particles is fixed, but the energy states accessible to each particle are unlimited. In the former, just the reverse is true; the number of particles is unlimited but the number of states is fixed. In addition, conduction electrons in a metal obey Fermi-Dirac statistics, whereas phonons obey Bose-Einstein statistics.

Inasmuch as the phonons form an ideal quantum gas, the partition function can be obtained from Eq. 1.34:

$$Z = \sum_{j_1 \dots j_i \dots j_{3N}} \exp \left[ - (j_1 h\nu_1 + \dots + j_i h\nu_i + \dots + j_{3N} h\nu_{3N}) / kT \right] \quad (2.42)$$

which, if the reference energy is neglected, is identical to Eq. 2.16. Thus, the partition function of the phonon gas and hence all its thermodynamic properties are identical to those obtained by regarding the energy of the solid as elastic waves.

The total number of phonons in a crystal at temperature  $T$  can be calculated as follows. The probability of a particular microstate characterized by the set of occupation numbers  $j_1 \dots j_i \dots j_{3N}$  is given by

$$P(j_1 \dots j_i \dots j_{3N}) = \left\{ \exp \left[ - (j_1 h\nu_1 + \dots + j_i h\nu_i + \dots + j_{3N} h\nu_{3N}) / kT \right] \right\} / Z \quad (2.43)$$

The average number of phonons in a particular state  $i$  may be obtained by treating  $P$  as a distribution function:

$$\bar{j}_i = \sum_{j_1 \dots j_i \dots j_{3N}} j_i P(j_1 \dots j_i \dots j_{3N}) \quad (2.44)$$

The sum that results from substituting Eq. 2.43 into 2.44 can be obtained by differentiating  $Z$  of Eq. 2.42 with respect to  $h\nu_i$ . Thus:

$$\bar{j}_i = - \frac{kT}{Z} \frac{\partial Z}{\partial (h\nu_i)} \quad (2.45)$$

Evaluation of  $Z$  given by Eq. 2.42 according to the method described in connection with Eq. 2.16 yields the expression for  $Z$  given by Eq. 2.19. Differentiation of Eq. 2.19 with respect to  $h\nu_i$  and insertion into Eq. 2.45 yields

$$\bar{j}_i = (e^{h\nu_i/kT} - 1)^{-1} \quad (2.46)$$

which is the Planck distribution function, or the distribution function for Bose-Einstein particles with zero chemical potential. It may be compared with the Fermi-Dirac distribution function given by Eq. 1.53, in which the chemical potential is not zero.

The total number of phonons is given by

$$n_p = \sum_{i=1}^{3N} \bar{j}_i \quad (2.47)$$

Approximating the sum by an integral with the use of the frequency spectrum  $\mathcal{D}(\omega)$  and substitution of Eq. 2.46 for  $\bar{j}_i$  yields

$$n_p = \int_0^\infty \frac{\mathcal{D}(\omega) d\omega}{e^{h\omega/kT} - 1} \quad (2.48)$$

Using the Debye frequency spectrum of Eq. 2.34 reduces Eq. 2.48 to

$$\begin{aligned} n_p &= \frac{9N}{\omega_D^3} \int_0^{\omega_D} \frac{\omega^2 d\omega}{e^{h\omega/kT} - 1} \\ &= 9N \left( \frac{T}{\Theta_D} \right)^3 \int_0^{\Theta_D/T} \frac{x^2 dx}{e^x - 1} \end{aligned} \quad (2.49)$$

At low temperatures,  $(\Theta_D/T) \rightarrow \infty$  and  $e^x - 1$  in the integrand can be approximated by  $e^x$ . The phonon density then becomes

$$n_p = 18N \left( \frac{T}{\Theta_D} \right)^3 \quad (2.50)$$

At high temperatures,  $\Theta_D/T$  becomes small, and  $e^x - 1$  can be approximated by  $x$ . Equation 2.49 then reduces to

$$n_p = \frac{9}{2} N \left( \frac{T}{\Theta_D} \right) \quad (2.51)$$

Regarding the thermal energy of a solid as an ideal gas of quasi-particles called phonons leads to exactly the same thermodynamic results as the more straightforward analysis via elastic waves presented in the earlier part of this chapter. However, the phonon description permits a simple explanation for nonequilibrium properties of solids, such as lattice thermal conductivity. Inasmuch as phonons possess the characteristics of an ideal gas, they may be described by the elementary kinetic theory of gases, just as gas molecules. They can be considered to possess properties such as a mean speed, a cross section for collisions with each other or with other objects in the solid, and a mean free path.

## 2.9 NOMENCLATURE

- $a_0$  = spacing between atomic planes  
 $c$  = propagation speed of a wave  
 $C_v$  = specific heat at constant volume  
 $C_{ji}$  = coefficients in normal-mode analysis  
 $\mathcal{Q}$  = frequency spectrum of vibrational modes in a solid  
 $E$  = energy of a crystal  
 $h$  = Planck's constant  
 $\hbar = h/2\pi$   
 $j$  = vibrational quantum numbers; occupation number of phonons  
 $k$  = Hooke's law constant; Boltzmann constant; wave-vector magnitude  
 $L$  = length of a crystal  
 $m$  = mass of an atom  
 $n$  = number of phonons  
 $N$  = number of atoms in a crystal (Avogadro's number)  
 $p$  = pressure  
 $P$  = probability of a microstate  
 $q$  = displacement in normal-mode analysis  
 $R$  = gas constant  
 $T$  = absolute temperature  
 $u$  = displacement of an atomic plane from its equilibrium position  
 $U$  = internal energy  
 $v$  = specific volume (volume per atom)  
 $V$  = total volume of  $N$  atoms  
 $Z$  = partition function

## Greek letters

- $\epsilon$  = energy of a mode of oscillation  
 $\lambda$  = wavelength  
 $\nu$  = vibration frequency  
 $\xi$  = displacement of an atom along a coordinate direction  
 $\Theta$  = characteristic temperature  
 $\omega$  = angular frequency

## Subscripts

- $A$  = particle A  
 $B$  = particle B  
 $\text{Coh}$  = cohesive  
 $D$  = Debye  
 $E$  = Einstein  
 $i$  = microstate; degree of freedom  
 $j$  = degree of freedom  
 $K$  = kinetic  
 $l$  = longitudinal  
 $\text{max}$  = maximum  
 $\text{min}$  = minimum  
 $0$  = ground state; zero point  
 $p$  = phonons  
 $P$  = potential  
 $t$  = transverse  
 $\text{tot}$  = total  
 $x$  =  $x$  direction  
 $y$  =  $y$  direction  
 $z$  =  $z$  direction

## 2.10 ADDITIONAL READING

1. L. M. Grossman, *Thermodynamics and Statistical Thermodynamics*, Chap. 10, Secs. 1-3, McGraw-Hill Book Company, New York, 1969.
2. C. Kittel, *Introduction to Solid State Physics*, 3rd ed., Chaps. 5 and 6, John Wiley & Sons, Inc., New York, 1967.
3. F. Reif, *Fundamentals of Statistical and Thermal Physics*, Chap. 10, Secs. 1-2, McGraw-Hill Book Company, New York, 1965.

## 2.11 PROBLEMS

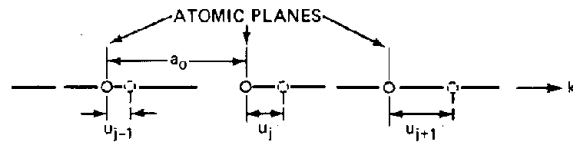
2.1 The vibration of the atoms in a solid often cannot be approximated by simple harmonic motion. The effect of the anharmonicity is taken into account by using in place of Eq. 2.12 the energy-level formula

$$\epsilon_i = \left[ \left( j_i + \frac{1}{2} \right) - x_e \left( j_i + \frac{1}{2} \right)^2 \right] h\nu_i$$

where  $x_e$  is the anharmonicity factor, which is zero for simple harmonic motion.

Derive the vibrational partition function for this energy-level formula. Since  $x_e$  is small, any exponential function that has  $x_e$  in the argument can be approximated by a two-term Taylor series expansion. Sketch the energy-level formula. Show that the partition-function sum must be cut off at  $j < \infty$ .

2.2 Consider a simple cubic lattice. An elastic wave propagating along one of the principal axes of the crystal causes entire planes of atoms to move in phase. Since each plane moves in unison, the restoring forces on the planes due to the displacement of nearby planes can be reduced to those acting on a single atom in the plane. If only nearest-neighbor interactions are considered, the force on an atom in plane  $j$  is caused by the differences between its displacement and the displacements of the atoms in front of and behind it. The restoring forces are assumed to be directly proportional to the differences in the displacements. The force constant is  $\kappa$  and the mass of each atom is  $m$ .



(a) What is the equation of motion for atom (or plane)  $j$ ?

(b) Assuming solutions in the form of standing waves (with  $x = ja_0$ ), what is the dispersion relation for the one-dimensional situation of a propagation vector in the direction of one of the principal axes?

(c) If the displacements are small enough to permit finite differences to be approximated by derivatives, what is the equation of motion?

(d) By comparing the result of part (a) with (c), deduce the finite difference form of the equation of motion for a propagation vector that has components in all three directions. What is the dispersion relation for the three-dimensional case?

(e) What does the three-dimensional dispersion relation reduce to for long wavelengths (small propagation vectors)? What is the velocity of sound in this medium?

2.3 The following simplified model of the structure of graphite (See Fig. 4.5) is assumed for calculating the specific heat by the Einstein model with two characteristic vibration frequencies. The restoring forces parallel to the basal plane are large, and, for the natural frequencies of oscillations in the two directions within this plane,  $\hbar\omega_{\parallel} \gg 300k$ . On the other hand, the restoring forces perpendicular to the basal planes are weak, and  $\hbar\omega_{\perp} < 300k$ .

- (a) What is the molar specific heat of graphite at 300°K in this model?
- (b) Sketch the curve of  $C_v$  as a function of temperature.

2.4 Although the Einstein approximation to the lattice vibration-frequency spectrum provides an adequate match to the specific-heat data and the Debye spectrum provides a still better fit, the best fit is obtained by using a mixture of the Einstein and Debye spectra:

$$\mathcal{L}(\omega) = 3N \left[ \frac{3\omega^2}{\omega_D^3} + \eta\delta(\omega - \omega_E) \right] \quad (\text{for } 0 < \omega < \omega_G)$$

$$\mathcal{L}(\omega) = 0 \quad (\text{for } \omega > \omega_G)$$

where  $\omega_G$  is a cutoff frequency that is less than  $\omega_D$ . The Einstein frequency  $\omega_E$  is also smaller than  $\omega_G$ . The parameter  $\eta$  gives the relative contributions of the Debye and Einstein portions.

- (a) What additional condition relates the four parameters  $\omega_G$ ,  $\omega_D$ ,  $\omega_E$ , and  $\eta$ ? What is the relation between them?
- (b) Derive an expression for the specific heat of the solid with this vibrational-frequency spectrum in terms of the Einstein function\*:

$$E(x) = \frac{x^2 e^x}{(e^x - 1)^2}$$

and the Debye function\*:

$$H(x) = \frac{3}{x^3} \int_0^x \frac{y^4 e^y}{(e^y - 1)^2} dy$$

Express the result in terms of the temperatures  $\Theta_E$ ,  $\Theta_D$ , and  $\Theta_G$ , where  $\Theta_i = \hbar\omega_i/k$ .

2.5 Consider a system consisting of two atoms of mass  $m$  vibrating along a line joining their centers. Assume the force constants of this lattice,  $k_{11}$ ,  $k_{12} = k_{21}$ , and  $k_{22}$ , are known.

- (a) What are the vibration frequencies of the system?
- (b) What are the coefficients  $C_{ij}$  in the normal-mode analysis of this system?
- (c) For this system, show that the total energy in terms of the normal-mode coordinates is given by Eq. 2.10.

2.6 According to the Debye model, what is the zero-point energy of a crystalline solid in terms of the Debye temperature?

2.7 Starting with equations already presented in Chaps. 1 and 2, develop an equation for the entropy of a perfect crystal in which the vibrational modes of the atoms are described by the Einstein model. Assume that the vibrational frequency,  $\nu$ , is such that  $h\nu \ll kT$ .

2.8 The Gruneisen parameter is identified in Debye's theory by

$$\gamma = -\frac{V}{\Theta_D} \frac{d\Theta_D}{dV} = -\frac{d \ln \Theta_D}{d \ln V}$$

where  $\Theta_D$  is a function of specific volume  $v$  and sound velocity  $\bar{c}$  according to the Debye model. From elasticity theory, the velocity of sound in an isotropic solid is related to the density  $\rho$  and the compressibility  $\beta$  by

$$c_l = \left[ \frac{3(1-\nu)}{\beta\rho(1+\nu)} \right]^{1/2}$$

$$c_t = \left[ \frac{3(1-2\nu)}{2\beta\rho(1+\nu)} \right]^{1/2}$$

where  $\nu$  is Poisson's ratio. Neglecting the variation of  $\nu$  with specific volume, show that the Gruneisen constant can be expressed by:

$$\gamma = -\frac{2}{3} - \frac{1}{2} V \frac{(\partial^2 p / \partial V^2)_T}{(\partial p / \partial V)_T}$$

\*The Einstein and Debye functions are such that when the Einstein model alone is applied,  $C_v = 3RE(\Theta_E/T)$ , and when the Debye model alone is applied,  $C_v = 3RH(\Theta_D/T)$ .

# Chapter 3

## Crystal Structures

The periodic three-dimensional array of atoms in a crystalline solid constitutes the **crystal lattice** of the substance. For monatomic solids there are 14 distinct crystal structures, or Bravais lattices. Each of these is defined by a **unit cell**, a block of atoms which displays the crystallographic features of the lattice type and which, by translation alone (no rotation), can reproduce the entire crystal. The parallelepiped representing the unit cell is described by the crystal-axis vectors  $a$ ,  $b$ , and  $c$ , which define its edges.

### 3.1 THE CUBIC CRYSTAL SYSTEM

The most easily visualized of the 14 fundamental lattices is the simple cubic structure (abbreviated *sc*) shown in Fig. 3.1. The crystal axes of the unit cell of this lattice are orthogonal and of equal length.

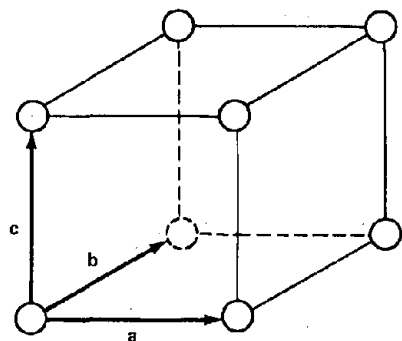


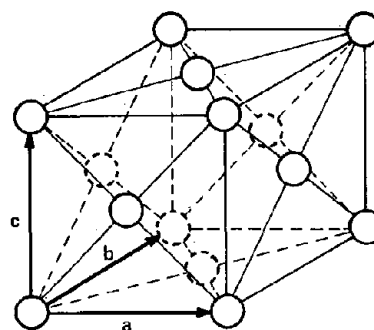
Fig. 3.1 Simple cubic unit cell.

The simple cubic structure shown in Fig. 3.1 is an example of a **primitive unit cell**, since it effectively consists of only one atom. Although eight atoms are shown in the figure, each is shared equally by seven other unit cells adjacent to the one shown. Thus, only  $\frac{1}{8}$  of each atom in Fig. 3.1 belongs to the unit cell shown, or, in total, the unit cell consists of one atom.

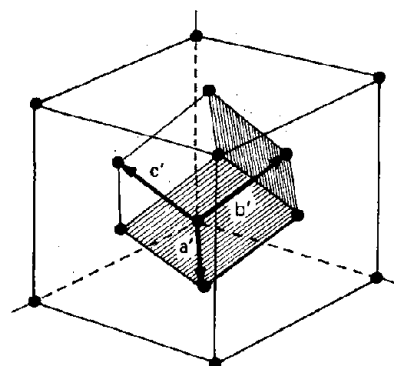
Although the primitive unit cell is the most basic representation of each of the 14 fundamental lattice types, it may not be the most convenient. In many cases, the basic

symmetry of a particular crystal type is obscured by the shape of the primitive cell. The crystal structure may be better displayed by a unit cell containing more than one atom; such unit cells are called **conventional unit cells**. This situation is illustrated by the face-centered cubic (*fcc*) lattice shown in Fig. 3.2.

Figure 3.2 (a) shows the conventional unit cell, a simple cubic lattice with atoms placed on each of the six cube faces. As in the *sc* structure, the eight corner atoms contribute one full atom to the unit cell. Since the six



(a)



(b)

Fig. 3.2 Face-centered cubic unit cells. (a) Conventional. (b) Primitive.

face-centered atoms are shared between two adjoining unit cells, they contribute three atoms to each unit cell. The fcc conventional unit cell contains four atoms and hence is not primitive. The fcc structure is distinct from the sc structure but is related to the latter by the symmetries of the unit cube. Both these lattice types belong to the cubic system. The primitive unit cell characterizing the fcc structure is shown in Fig. 3.2(b). The three edges of the unit cell are equal, but the cell is rhombohedral rather than cubic in shape. Both the conventional and primitive unit cells of Fig. 3.2 are valid representations of the fcc structure, but the primitive version is rarely used in practical applications.

The third member of the cubic system is the body-centered cubic (bcc) lattice. This structure is obtained by inserting a single atom in the center of the sc unit cell. The conventional unit cell of the bcc structure is shown in Fig. 3.3. The bcc primitive unit cell is rhombohedral in shape and similar in general appearance to the fcc primitive unit cell of Fig. 3.2(b).

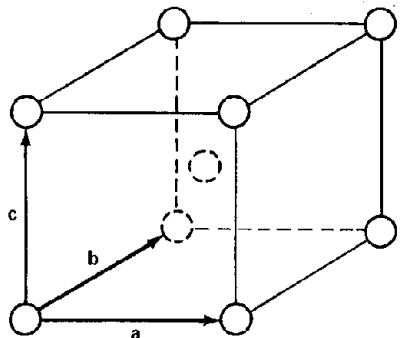


Fig. 3.3 Body-centered cubic conventional unit cell.

In the conventional unit cells of the cubic system, the magnitudes of the crystal axes are all equal and are denoted by the common symbol  $a_0$ , which is called the lattice constant. The distance between nearest neighbors bears a different relation to the lattice constant for the three cubic structures. It is  $a_0$ ,  $a_0/\sqrt{2}$ , and  $\sqrt{3}a_0/2$  for the sc, fcc, and bcc structures, respectively. The magnitude of the lattice constant and the lattice type (sc, fcc, or bcc) determine the structure of monatomic crystals exhibiting cubic symmetry.

### 3.2 THE DIAMOND STRUCTURE

Not all monatomic lattices with cubic symmetry can be described by the structures just discussed. The diamond structure, which characterizes the crystal of the diamond form of carbon and the elements germanium and silicon, is an illustration of a cubic lattice that cannot be reduced to a primitive unit cell with only one atom. As shown in Fig. 3.4, the conventional unit cell of the diamond structure consists of atoms on the corners and face-centered positions of the unit cube in the fcc configuration. In addition, there are four atoms in the interior of the unit cube. The diamond structure may be visualized as stacking the small cubes shown in the top of Fig. 3.4 in only half of the eight available places in the larger conventional unit

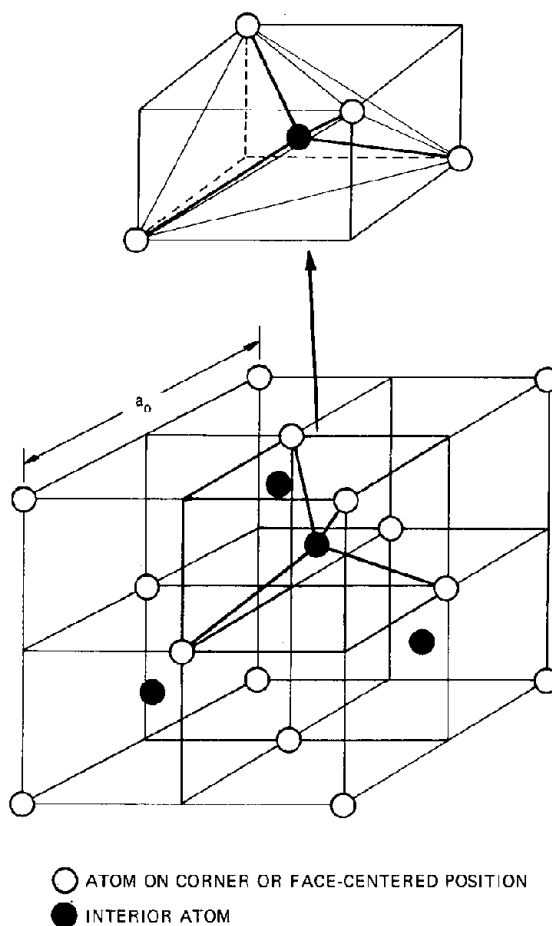


Fig. 3.4 The diamond structure.

cell. Note that the small cubes containing a central atom are not unit cells, since translation of these units about the crystal does not reproduce the structure. The diamond structure may be regarded as fcc with two atoms associated with each lattice point. If the pair of atoms consisting of a corner or face-centered atom and one of the interior atoms located  $1/4$  of a lattice constant away in each direction are regarded as a single entity, the crystal structure is fcc. In this case, the points in space where the atoms reside are not identical with the points that define the crystal structure. The latter is called the space lattice. The number of atoms associated with each space-lattice point is called the basis of the structure. If the basis is unity, each point of the space lattice actually contains an atom. Such is not the case for the diamond structure, which is properly designated as an fcc space lattice with a basis of two. The primitive unit cell of the diamond structure is represented by Fig. 3.2(b) with an additional atom inside the rhombohedral structure. The primitive unit cell also consists of two atoms and hence has a basis of two.

### 3.3 THE HEXAGONAL SYSTEM

Many metals exhibit crystal structures of the type shown in Fig. 3.5. Figure 3.5(a) shows a right-hexagonal

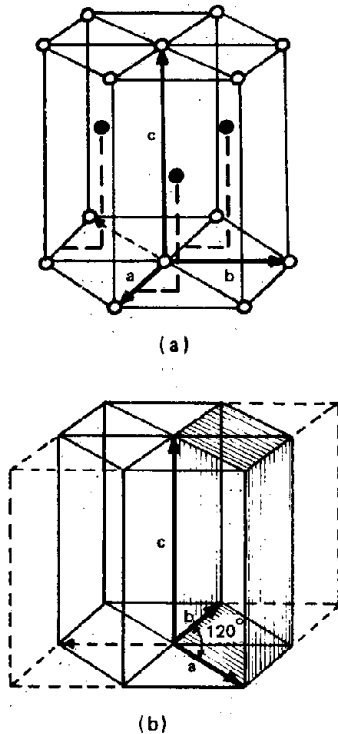


Fig. 3.5 The hexagonal lattice. (a) Common hexagonal structure, basis of two. (b) Space lattice showing primitive unit cell.

prism with atoms at the six corners and at the center of the top and bottom faces. In addition, there are atoms at positions on the midplane inside the structure. The primitive unit cell of the hexagonal structure shown in Fig. 3.5(b) is one-third of the hexagonal prism. It contains eight space lattice points on its corners, each of which is shared among eight primitive unit cells. With atoms positioned as shown in Fig. 3.5(a), the basis is two. Translation of one of the corner atoms and the interior atom of the primitive cell by integral multiples of the crystal axes  $a$ ,  $b$ , and  $c$  of the hexagonal space lattice maps the complete structure. The  $a$  and  $b$  axes are separated by an angle of  $120^\circ$ ; both are perpendicular to the  $c$  axis. The lengths of the  $a$  and  $b$  axes are equal, but neither is equal to the length of the  $c$  axis.

### 3.4 OTHER FUNDAMENTAL LATTICE SYSTEMS

The hexagonal and three cubic lattices described previously possess higher degrees of symmetry than the remaining 10 lattice systems. The symmetries characteristic of each lattice system can be classified as rotational, mirror reflection, or inversion. Alternatively, the relations between the fundamental lattices may be described by operations on the crystal axes which convert a lattice of low symmetry to one of higher symmetry. The hierarchy of symmetries shown in Fig. 3.6 can be constructed to illustrate this process. The least symmetric of the 14 lattice systems is the

triclinic structure, in which the unit cell is a parallelepiped with none of the crystal axes of the same length nor any of the angles between the crystal axes equal. By placing additional restrictions on the lengths and angles of the crystal axes, the triclinic lattice acquires symmetries that lead to systems higher up in the hierarchy. This progression is especially clear for the systems on the left-hand side of Fig. 3.6, which ultimately leads to the cubic system.

Each of the crystal systems illustrated in Fig. 3.6 possesses a primitive lattice, in which the parallelepiped conforms to the restrictions placed on the crystal axes and which contains atoms only on its corners. When used in this sense, the term *primitive* is slightly different from the notion of a primitive unit cell. All the 14 members of the group of fundamental lattices that comprise the seven crystal systems shown in Fig. 3.6 can be reduced to a primitive unit cell. However, only one member of each system has a primitive unit cell that also obeys the symmetry conditions defining the crystal system. The other members of the system, in order to exhibit the same symmetry, must be depicted as conventional, nonprimitive unit cells. Thus in the cubic system the *sc* lattice is the primitive member, and the *fcc* and *bcc* lattices are nonprimitive.

The trigonal and hexagonal lattice types can be viewed as arising directly from the general triclinic lattice by the restrictions on the crystal axes listed in Fig. 3.6. Alternatively, the trigonal system can be considered as a nonprimitive member of the hexagonal system formed by placing two atoms on the long diagonal of the hexagonal primitive cell.

All monatomic crystals can be described by 1 of the 14 fundamental types, although, as in the diamond structure and the hexagonal structure of Fig 3.5, there may be more than one atom associated with each point of the space lattice. The complex crystal structures of substances composed of more than one element can be broken down into intermingling sublattices for each atomic constituent. Each of the sublattices is 1 of the 14 fundamental structures shown in Fig. 3.6. Although no element exhibits a stable phase with the *sc* structure, this structure is frequently found as a sublattice in diatomic crystals.

### 3.5 MILLER INDICES

Each point in the lattice can be reached by a translation vector composed of the sum of multiples of the crystal axis vectors:

$$T = n_a a + n_b b + n_c c \quad (3.1)$$

A particular location in the structure (relative to a preselected origin) can be described by the set of integers  $(n_a, n_b, n_c)$ .

In addition to being described as a collection of points, a crystal can also be represented as a stack of parallel planes. Designation of a plane is somewhat more complex than the specification of a point, which is accomplished by fixing the coefficients of the translation vector of Eq. 3.1. The planes in a crystal differ not only in their orientation in space but also in the arrangement and density of atoms

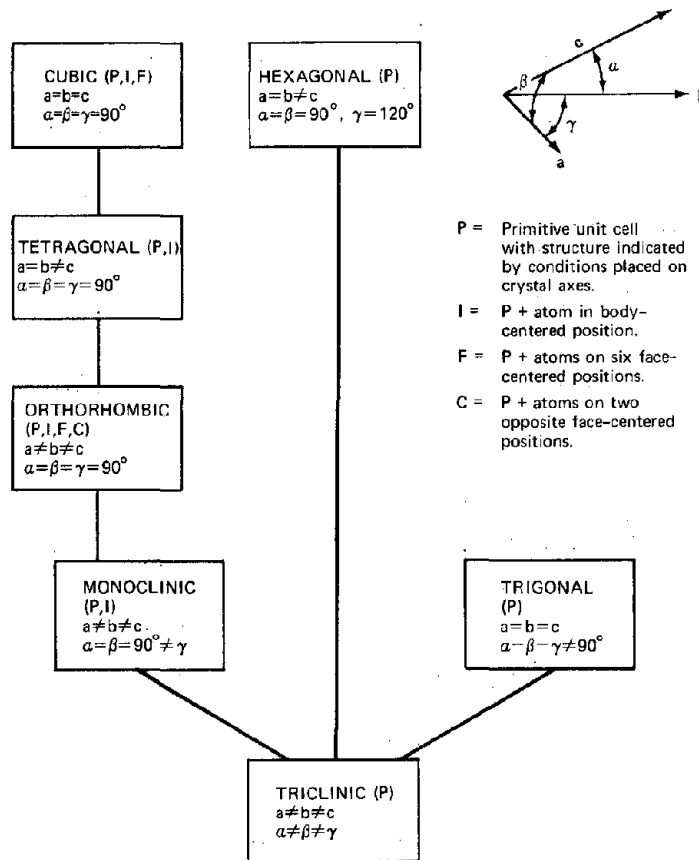


Fig. 3.6 Hierarchy of crystal symmetries.

they contain. Many practical problems require specification of a certain plane in the crystal. A number of techniques can be used for designating a crystal plane. For example, since three points determine a plane and each point can be represented by the coefficients of the crystal axis vectors, as in Eq. 3.1, a plane can be designated by the set  $(n_a, n_b, n_c)_1$ ,  $(n_a, n_b, n_c)_2$ , and  $(n_a, n_b, n_c)_3$ . Such a method requires nine numbers and is quite cumbersome. A more convenient technique is to specify a plane by listing its intersections with the crystal axes.

First, a lattice point that is close to, but not contained in, the plane in question is chosen. The crystal axes  $a$ ,  $b$ , and  $c$  are drawn from this point until they each intersect the plane. The intersection of the  $a$ -axis and the plane is denoted by  $f_a a$ , where  $a$  is the length of the crystal axis  $a$  and  $f_a$  is the number of units of a separating the origin and the intersection. Similarly,  $f_b$  and  $f_c$  are the intersections of the plane and the  $b$ - and  $c$ -axes in units of the crystal axes in the other two directions. The plane is specified by the numbers  $f_a, f_b, f_c$ . As a further simplification, the reciprocals of the  $f$ 's are used instead, and the plane designation becomes  $1/f_a, 1/f_b, 1/f_c$ . Finally, the reciprocals are converted to the smallest set of integers which preserves the relative magnitudes of the  $1/f$  values. The resultant three numbers, say  $h, j, k$ , are known as the Miller indices of the plane (and all planes parallel to it). The indices are

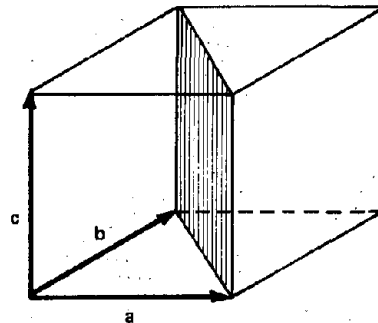


Fig. 3.7 The (110) plane in the cubic unit cell.

enclosed in parentheses and the plane designation becomes  $(hjk)$ .

As an illustration, consider the diagonal plane in the cubic system shown in Fig. 3.7. The intercepts with the crystal axes are 1, 1, and  $\infty$ . The reciprocals are 1, 1, and 0; so the plane is the (110) plane.

In crystal systems whose unit cells exhibit a high degree of symmetry, several planes may differ in orientation in space but not in any other way; that is, they may all have the same arrangement of atoms. Such is the case with the faces of the conventional unit cells of the cubic system

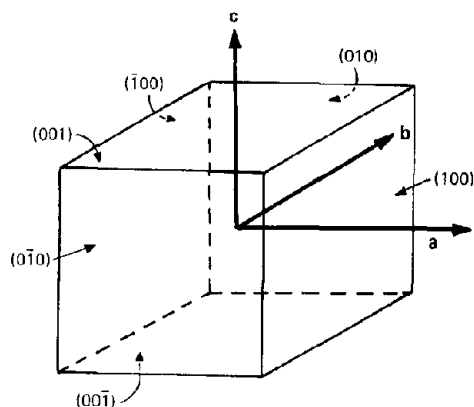


Fig. 3.8 The  $\{100\}$  planes of the cubic unit cell.

shown in Fig. 3.8. With the origin chosen at the center of the unit cell, the top, back, and right-hand faces are portions of planes with Miller indices of (001), (010), and (100), respectively. The remaining three face planes have negative intersections with the crystal axes. According to the procedure for determining Miller indices, the front plane in the diagram would be (0-10). By convention, the minus sign is placed on top of the number; thus the front face is designated (0 $\bar{1}$ 0).

The (010) and (0 $\bar{1}$ 0) planes are parallel to each other and so are identical in all respects. Notation such as (0 $\bar{1}$ 0) is used only when comparison of parallel planes in the unit cell is desired. Most analyses need to distinguish crystallographic planes only if they differ by more than merely spatial orientation; that is, if the planes have different atom configurations. Aside from orientation, the six face planes of the cubic unit cell are equivalent, and one may not care which of the particular face planes is labeled. In this case, braces rather than parentheses are used, and all six face planes may be referred to as the  $\{100\}$  planes.

The specification of a direction in a crystal is more straightforward than the description of a plane. A line is formed by two points, which may be chosen as the origin (0,0,0) and another point with translation-vector coefficients ( $n_a, n_b, n_c$ ). The direction is specified by the latter set of numbers reduced to the smallest integer values and surrounded by brackets. Thus the direction along the  $b$ -axis in Fig. 3.8 is [010]. In the cubic system, directions denoted by  $[hkl]$  are perpendicular to planes with the same Miller indices,  $(hkl)$ . The notation  $\langle hkl \rangle$  is used to designate a set of equivalent directions in the same sense that  $\{hkl\}$  denotes a number of equivalent planes.

The Miller indexing system is slightly modified when applied to the hexagonal crystal system. In addition to the three crystal axes that define the edges of the primitive cell in Fig. 3.5, a fourth axis, in the plane of  $a$  and  $b$  but  $120^\circ$  away from these axes, is included (this axis is shown as the dotted arrow in Fig. 3.5). The method of indexing is the same as previously described, but now four Miller indices ( $hkil$ ) designate a plane. For example, the side of the hexagonal prism parallel to the  $a$ - and  $c$ -axes bears the symbol (01 $\bar{1}$ 0). The extra Miller index arises from the redundant axis. Because of the geometry of the three

equivalent planar axes, the sum of  $h$ ,  $k$ , and  $i$  in the hexagonal indexing method is always zero. The plane in which these three axes lie, the (0001) plane, is called the basal plane of the hexagonal crystal system.

### 3.6 CLOSE-PACKED STRUCTURES

Nearly all metals exhibit fcc, bcc, or hexagonal crystal structures (the nuclear fuels uranium and plutonium, however, do not; see problem 3.1).

The fcc lattice is an example of a close-packed structure; this geometric arrangement of hard spheres produces a solid with less void, or empty space, than any other configuration. The close-packed feature of the fcc structure is not apparent from the unit cell of Fig. 3.2(a). However, if the fcc lattice is viewed as a stack of the (111) planes, close packing can be more easily visualized. Figure 3.9(a) shows the unit cell of the fcc lattice with sections of the (111) planes indicated by numbered atoms. The atoms marked with the symbol  $\oplus$  (atoms 1, 2, 3, 4, and 7) lie in a (111) plane. If we move in the [111] direction (along a body diagonal), the next (111) plane is the one in Fig. 3.9(a) containing the atoms denoted by  $\odot$  (atoms 8, 9, and 10). The next (111) plane along the body diagonal in Fig. 3.9(a) contains only the atom shown at  $\odot$  (atom 11).

The arrangement of these three (111) planes is most easily visualized if the lattice is viewed along the [111] direction, as in Fig. 3.9(b). Here the three (111) planes described above are shown with atoms from adjacent unit cells added for completeness. The bottom (111) plane in Fig. 3.9(b) (atoms 1-7) has been augmented with two additional atoms (numbers 5 and 6) from the next unit cell. The structure of this layer, which consists of a central atom surrounded by six others in a hexagonal configuration, constitutes a close-packed plane. A close-packed three-dimensional lattice consists of successive layers of close-packed planes. Atoms 8, 9, and 10 of the next (111) plane in the figure nestle in the crevices in the layer underneath. The atoms of the third layer [of which number 11 is the only representative in Fig. 3.9(a)] also fit in the triangular crevices formed by the atoms of the second layer. If a fourth layer were added to Fig. 4.9(b), it would have the same arrangement as the first. The stacking sequence of the close-packed (111) planes of the fcc lattice is of the type 123123123. . . .

If we continue to regard close-packed lattices as layers of close-packed planes, we find that there is another distinct way of constructing such a three-dimensional structure. If, instead of placing the third layer as shown in Fig. 3.9(b), we place it so that the atoms in the third layer lie directly above the atoms in the first layer, the lattice so formed would have the stacking sequence 121212. . . . The crystal structure created by this arrangement of close-packed planes is a particular case of the hexagonal lattice [shown in Fig. 3.5(a)] in which the ratio of the  $c$  and  $a$  lattice vector magnitudes is  $\sqrt{8/3}$ . The close-packed (or basal) planes that constitute the hexagonal structure are evident in Fig. 3.5(a). These planes are identical to the (111) planes of the fcc structure, and the two lattice types differ only in the stacking sequence of close-packed planes. The hexagonal structure, which is also

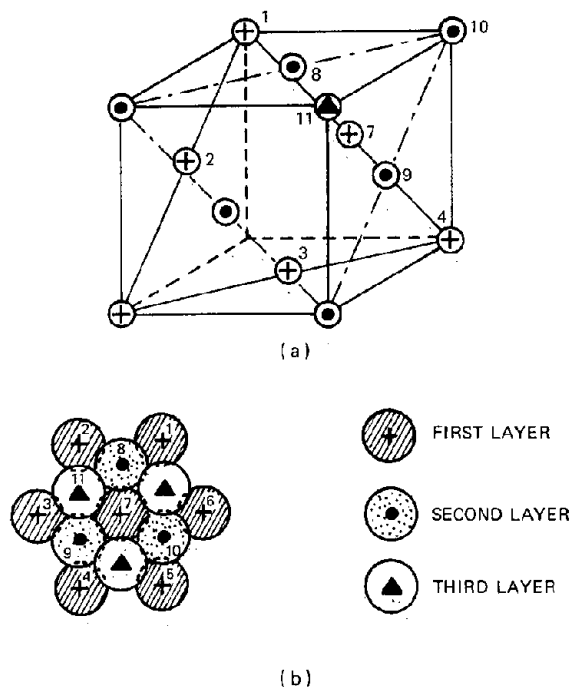


Fig. 3.9 The face-centered cubic structure showing close-packed planes. (a) Unit cell with (111) planes shown. (b) View along [111] (body diagonal) direction.

close packed by virtue of a  $c/a$  ratio of  $\sqrt{8/3}$  is, reasonably enough, termed hexagonal close packed, or hcp.

Each atom of the hcp or fcc lattice is surrounded by 12 nearest neighbors. The distance between centers of nearest-neighbor atoms is the interatomic distance, or twice the atomic radius. No other plane in the fcc or hcp lattice structures contains as dense a packing of atoms as do the close-packed planes. In other structures the atom density varies from one plane to another as well, but no plane is close packed. In the more open lattices, some atoms may be "touching" each other (i.e., separated by twice the atomic radius), but only in the close-packed fcc and hcp structures are there 12 nearest neighbors to a particular atom. Consequently, if a close-packed structure is transformed to any other lattice, the density of the solid decreases (assuming the interatomic distance remains the same).

### 3.7 CRYSTAL STRUCTURE OF IONIC SOLIDS

Cataloging the structures of inorganic solids has occupied crystallographers for many decades. Each of the ionic species in the lattice forms one of the simple lattice types described previously. The structure of the ionic solid may be regarded as the intermingling of two simple lattice types. The lattice structure is restricted by the stoichiometry of the chemical compound (i.e., the  $n$  and  $m$  in the formula  $M_nX_m$ ) and by the fact that the nearest neighbors to a particular ion will be ions of the opposite charge in order to maximize the Coulomb energy of the structure. Even with these restraints, there is a sizeable number of ionic lattice

structures, and we restrict attention to the few most common examples.

Ionic structures are named after a prototype substance; thus the NaCl structure includes not only sodium chloride but also such solids as LiH, KCl, MnO, and the potentially important nuclear fuel UC. The unit cell of the NaCl structure is shown in Fig. 3.10. Nearest neighbors to each ion are six ions of the opposite charge. The NaCl structure is seen to be the interlacing of two equal-sized fcc sublattices of the cations and anions. As in the one-component fcc lattice, the NaCl unit cell contains four ion pairs.

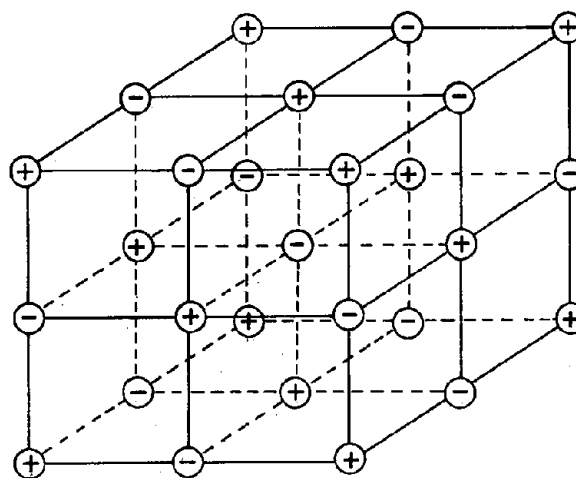


Fig. 3.10 The NaCl structure.

The CsCl structure, shown in Fig. 3.11, can be broken down into two equal-sized sc sublattices of cations and anions. Each ion is surrounded by eight nearest neighbors of opposite charge. There is one ion pair per unit cell.

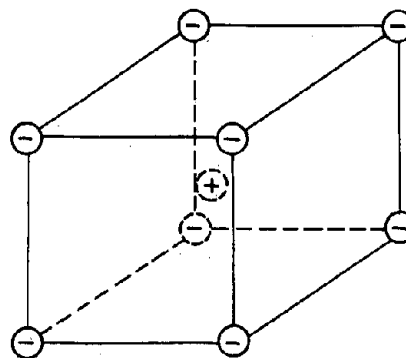


Fig. 3.11 The CsCl structure.

Both the NaCl and CsCl structures are formed by compounds in which the cations and anions have the same magnitude of charge. It is as difficult to theoretically determine which structure is the more stable in any particular case as it is to decide whether a given metal will crystallize in a fcc, bcc, or hcp crystal. In both instances, however, the criterion is the maximization of the cohesive energy.

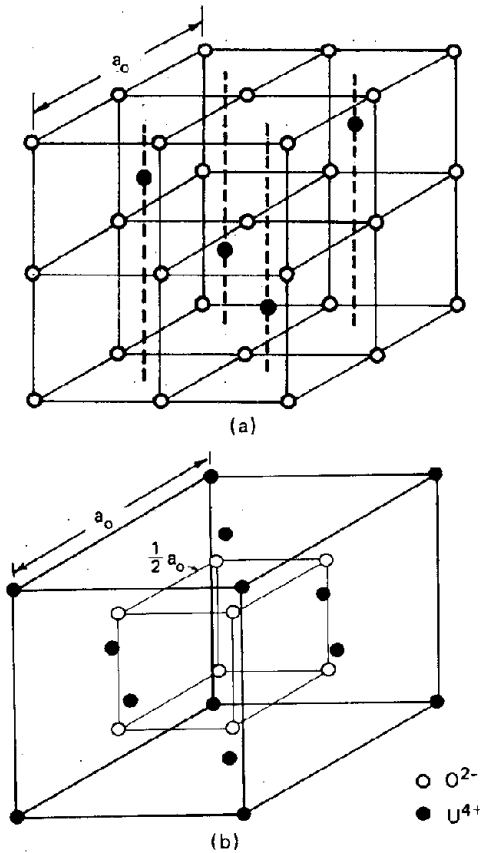


Fig. 3.12 The fluorite structure. (a) The sc structure of the anion sublattice. (b) The fcc structure of the cation sublattice.

The fluorite structure (named after the compound  $\text{CaCl}_2$ ) is important because it is the stable phase of uranium dioxide for all temperatures up to the melting point. Crystalline  $\text{UO}_2$  consists of  $\text{U}^{4+}$  and  $\text{O}^{2-}$  ions. The oxygen ions are arrayed on a simple cubic lattice, and the  $\text{U}^{4+}$  ions form a fcc sublattice. The fluorite structure, shown in Fig. 3.12, contains four  $\text{UO}_2$  molecules. Note the unoccupied interstitial positions in the body centers of the small cubes that do not contain uranium ions. Uranium carbide, which exhibits the NaCl structure, has no such holes in its structure. Uranium carbide has a higher concentration of uranium atoms and from this point of view is preferable to  $\text{UO}_2$  as a nuclear fuel.

### 3.8 NOMENCLATURE

$a_0$  = lattice constant in cubic system  
 a = crystal axis vector  
 b = crystal axis vector  
 c = crystal axis vector  
 f = multiple of crystal axis vector in designating a plane by intersection with crystal axes  
 h = Miller index  
 i = Miller index  
 j = Miller index  
 k = Miller index

l = Miller index  
 n = multiple of crystal axis vector in locating a point to designate a translational vector  
 T = translational vector

#### Greek letters

$\alpha$  = angle between crystal axes  
 $\beta$  = angle between crystal axes  
 $\gamma$  = angle between crystal axes

#### Subscripts

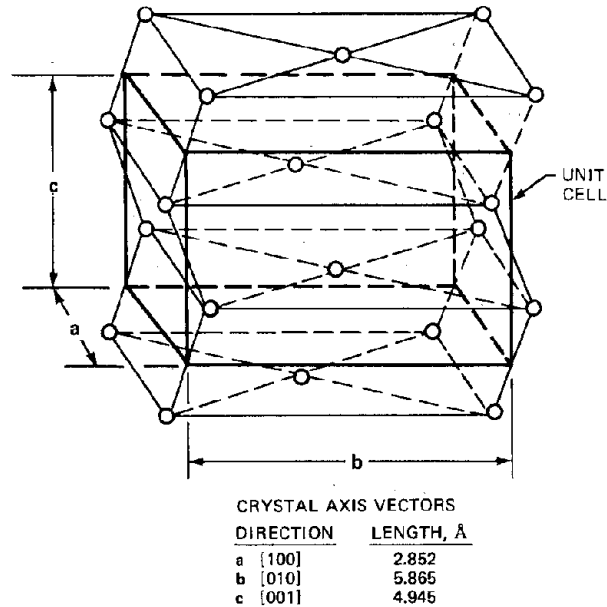
a = direction of crystal axis vector a  
 b = direction of crystal axis vector b  
 c = direction of crystal axis vector c

### 3.9 PROBLEMS

3.1 The crystal structure of  $\alpha$ -uranium is shown in the sketch.

(a) What is the *complete* description of this crystal structure?

(b) One criterion for the suitability of a nuclear fuel is the uranium atom density. Calculate this parameter and the theoretical total density for the three nuclear fuels  $\text{UO}_2$ , UC, and  $\alpha$ -U. The lattice constants of  $\text{UO}_2$  and UC are 5.470 Å and 4.961 Å, respectively.



3.2 What is the close-packed plane of the body-centered cubic lattice? Sketch the configuration of hard-sphere atoms of atomic radius  $d/2$  in this plane. If the lattice constant is  $a_0$ , what is the minimum interatomic distance? What fraction of the total space is occupied by hard-sphere atoms? Is the packing as close as in the (111) plane of an fcc lattice?

3.3 At 910°C iron transforms from bcc to fcc. Each structure consists of hard-sphere atoms that touch the nearest neighbors. Assuming that the diameter of each hard-sphere atom remains constant, what is the percentage change in volume accompanying the transformation?

# Chapter 4

## Cohesive Energy of Solids

### 4.1 INTRODUCTION

When compared to free atoms (or ions) at rest, the assembly of particles in a regular crystalline array constitutes a state of much lower energy. This difference in energy is called the cohesive energy of the solid if it is evaluated at  $0^\circ\text{K}$  and the zero-point vibrations of the particles are excluded. The cohesive energy compares two states of a collection of atoms or ions which differ only in the distance of separation of the particles; the cohesive energy consists of the energy of interaction between particles as they are brought together from infinite separation.

The variation of the energy of the system as the particles are assembled is shown schematically in Fig. 4.1. As this process is begun, the energy at first decreases since the particles initially attract each other. As the particles are brought still closer together, the energy reaches a minimum and then increases sharply at smaller separations.

The magnitude of the minimum in the energy curve of Fig. 4.1 is the cohesive energy. This quantity can be measured indirectly from other thermodynamic properties of the substance. Similarly, the position of the minimum in the curve represents the separation distance in the stable solid, which can be determined by density or X-ray measurements. The curvature of the energy profile at the minimum (which is proportional to the second derivative of the potential energy with respect to separation distance) is related to the compressibility of the solid.

The cohesive energy is a direct reflection of the nature and strength of the forces that bind atoms or ions together in a solid. The magnitude of the cohesive energy is directly responsible for many properties of a solid, such as the melting point and vapor pressure. The state of the particles in the solid determines whether the substance is a conductor or insulator of electricity and heat. If we know (or assume) the state of the particles in the solid (e.g., ionized or not) and are able to describe the forces responsible for the binding (e.g., Coulomb forces), the curve of Fig. 4.1 can be computed. However, in no instance do we have a complete quantitative description of the binding forces. Theory can provide the form of the interatomic potential, and the three experimental parameters related to the energy curve at its minimum can be used to compute adjustable parameters in the theory. The

validity of the model of the solid upon which the calculation is based can be verified by using the theory to predict other experimentally accessible properties of the solid, such as elastic constants other than the compressibility.

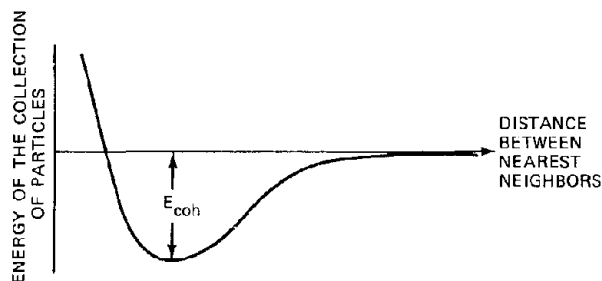


Fig. 4.1 Energy of a collection of particles.

### 4.2 COHESION IN METALS

Most metals tend to crystallize in the high symmetry fcc, bcc, or hcp structures because these configurations maximize the cohesive energy. The forces that bond metal atoms in a solid are spherically symmetric; so there is no preferred orientation of the nearest-neighbor atoms about a central atom which might favor a particular lattice type. All atoms in a pure metal are of the same size; thus the steric restrictions that are important in determining the crystal structure of ionic solids are not present.

Which of the common lattice types a particular metal exhibits is impossible to predict from simple considerations, although one can say that the structure that maximizes the cohesive energy is thermodynamically favored. The cohesive energy of a metal is very large, and the energy difference between the fcc, bcc, and hcp structures is usually quite small by comparison. Hence it is far easier to estimate the cohesive energy than it is to determine theoretically which structure will be formed at a particular temperature. Many metals transform from one lattice type to another at characteristic temperatures, the transformation being accompanied by small energy changes.

In the next section, we explore a simple model that qualitatively accounts for the cohesion of metals, or why a

condensed phase is thermodynamically more stable than a collection of gaseous neutral atoms or ions and electrons.

#### 4.2.1 Free-Electron Model of Metallic Cohesion

The cohesive energy of a solid is the negative of the energy released when the crystalline material is assembled from a collection of gaseous, noninteracting particles at 0°K. The separated particles from which the solid is constructed may be chosen as either neutral atoms or metal ions and electrons, depending upon which most closely resembles the species present in the solid. Thus for ionic solids consisting of cations ( $M^+$ ) and anions ( $X^-$ ), the same ions would be chosen as the free particles. In covalent solids or molecular crystals, the neutral atoms or molecules would be selected as the free particles. There is a vast amount of evidence to indicate that metals consist of ion cores imbedded in a nearly uniform cloud of mobile electrons; so the free-particle state for computing the cohesive energy of metals is taken as the ionized metal atoms and gaseous electrons. The extent of ionization of the metal atoms in the solid phase is not always known. For simple metals, such as the alkali metals and alkaline earths, ionization in the solid usually corresponds to loss of the valence electrons. Thus, sodium always forms ionic compounds as  $Na^+$ , and this is the form of the ion in sodium metal. The single valence electron lost by the sodium atom joins the electron gas moving freely throughout the solid. The remaining atomic electrons in the singly charged ion do not contribute to binding. The  $Na^+$  ion is considered to be an immobile point positive charge called an ion core. The ion cores of the transition metals (e.g., iron, nickel, tungsten, and tantalum) are not inert; these elements contain unfilled d shells that contribute to cohesion of the metal by forming bonds of the covalent type.

The cohesive energy is related to other properties of the metal by a thermodynamic cycle known as the Born-Haber cycle, which is illustrated in Fig. 4.2 for a monovalent metal.

The first step of the cycle is sublimation at 0°K, which requires an energy given by the energy of sublimation at this temperature,  $\Delta E_{sub}(0^\circ K)$ . This quantity is not directly measurable but is related to the heat (or more precisely, the enthalpy) of sublimation measured at some convenient temperature by

$$\Delta E_{sub}(0^\circ K) = \Delta H_{sub}(T^\circ K) - \int_0^T [C_{pv}(T') - C_{ps}(T')]dT' \quad (4.1)$$

where  $\Delta H_{sub}(T^\circ K)$  is the enthalpy of sublimation at temperature  $T$ , and  $C_{pv}$  and  $C_{ps}$  are the heat capacities at constant pressure of the gas and solid phases, respectively. These properties are known for most metals.

The second step of the cycle is ionization of the neutral free metal atom to yield the ion-electron pair. This step requires energy equivalent to the first ionization potential of the metal.

The final step of the cycle reforms the crystal from the gaseous ions and electrons. The energy released in this step is the negative of the cohesive energy. The energetics of the various steps are related by Eq. 4.2.

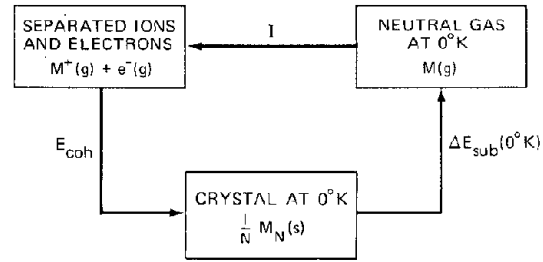


Fig. 4.2 Born-Haber cycle for a monovalent metal. ( $N$  = number of atoms in the crystal.)

$$E_{coh} = - [\Delta E_{sub}(0^\circ K) + I] \quad (4.2)$$

Since the quantities on the right-hand side of Eq. 4.2 can be measured, the left-hand side constitutes an experimental value of the cohesive energy. Inasmuch as both  $\Delta E_{sub}(0^\circ K)$  and  $I$  are positive,  $E_{coh}$  must be negative and larger in magnitude than either the energy of sublimation or the ionization energy.

A theoretical value of the cohesive energy can be computed if a model of the metal crystal is assumed. The agreement between the experimental value of Eq. 4.2 and the computed value provides a test of the validity of the model and of the accuracy of the calculational method used to obtain quantitative results from the physical picture of the metal.

The simplest model for calculating the cohesive energy of a metal is the free electron or jellium model, which pictures the metal as a regular array of ion cores in a medium of uniform electron density. The total energy of such a system consists of the Coulomb energy due to the electrostatic interaction of the electrons and the ions and the kinetic energy of the gas of noninteracting electrons contained within the confines of the metal (even at 0°K, the electron gas possesses kinetic energy). The sum of these contributions is the cohesive energy:

$$E_{coh} = U_c + U_F \quad (4.3)$$

where  $U_c$  is the Coulomb energy and  $U_F$  is the kinetic energy of the electrons.

#### 4.2.2 Coulomb Energy

The many-body electrostatic problem can be reduced to consideration of the energy of interaction of a single ion and a single electron by dividing the solid into  $N$  identical polyhedra which fill the entire space occupied by the crystal. Each polyhedron contains one ion and one electron. For computational ease the polyhedron is approximated by a sphere of the same volume. Since each sphere contains one atom, its radius is related to the electron (or atom) density of the solid by

$$\frac{N}{V} = \frac{1}{4\pi r_0^3/3} \quad (4.4)$$

where  $N$  is the number of electrons (or atoms) and  $V$  is the crystal volume. Since the model assumes a uniform electron

density throughout the crystal, the negative charge density throughout the sphere is also uniform and given by  $e/(4\pi r_0^3/3)$ . There is no interaction between the  $N$  spheres that constitute the entire crystal since each is electrically neutral.

Consider the portion of the sphere up to a radius  $r < r_0$ . The electrostatic energy between a unit point negative charge placed on the surface of the sphere of radius  $r$  and the charges within this sphere is (see problem 4.1):

$$-\frac{e}{r} \left[ 1 - \left( \frac{r}{r_0} \right)^3 \right] \quad (4.5)$$

Therefore, the interaction energy between the sphere and a spherical shell of thickness  $dr$  at  $r$  is

$$dU_c = -4\pi r^2 \left( \frac{e}{4\pi r_0^3/3} \right) dr \frac{e}{r} \left[ 1 - \left( \frac{r}{r_0} \right)^3 \right] \quad (4.6)$$

Integrating from 0 to  $r_0$  gives the Coulomb contribution to the cohesive energy:

$$\begin{aligned} U_c &= -\frac{3e^2}{r_0^3} \int_0^{r_0} r \left[ 1 - \left( \frac{r}{r_0} \right)^3 \right] dr \\ &= -\left( \frac{9e^2}{10} \right) \frac{1}{r_0} \end{aligned} \quad (4.7)$$

The minus sign in Eq. 4.7 indicates that the electronic charge uniformly distributed about the point positive charge is a lower energy configuration than the separated point charges. This term is primarily responsible for the stability of the solid metal.

### 4.2.3 Electron Kinetic Energy

The kinetic energy of the unbound electrons is increased by confining them to the volume of the solid metal. In the separated state the electron density is zero and so is the kinetic energy. In the metallic state the electron density is given by Eq. 4.4 provided that each atom contributes one electron to the population of unattached electrons. The electrons are considered to move freely within the confines of the volume  $V$ , uninhibited by the periodic point charges of the ion cores. The electrons thereby constitute an ideal gas of particles obeying Fermi-Dirac statistics.

Because two spin states are associated with each translational energy state, the total number of quantum states accessible to an electron in a unit energy range about an energy  $\epsilon$  is twice the ideal gas density of states given by Eq. 1.72, or

$$\mathcal{D}(\epsilon) = \left( \frac{V}{2\pi^2} \right) \left( \frac{2m}{\hbar^2} \right)^{3/2} \sqrt{\epsilon} \quad (4.8)$$

The function  $\mathcal{D}(\epsilon)$  is the density of states for the free electrons that constitute the ideal gas within the block of metal. It is quite analogous to the phonon frequency spectrum of Eq. 2.30.

Equation 4.8 only gives the number of allowable states as a function of electron energy. To determine how these states are filled, we use Eq. 1.53 for the average number of

particles in each energy state:

$$\bar{n}_j = \frac{1}{\exp[(\epsilon_j - \mu)/kT] + 1} \quad (4.9)$$

where  $j$  denotes a particular electron state (specified by the three translational quantum numbers and the spin quantum number) and  $\mu$  is the chemical potential of the electron gas. The latter is determined from the condition that the sum of the  $\bar{n}_j$  must be equal to the total number of conduction electrons in the solid (Eq. 1.52):

$$N = \sum_j \bar{n}_j \quad (4.10)$$

At the absolute zero in temperature (which is where the Born-Haber cycle is applied), Eq. 4.9 assumes the simple form

$$\begin{aligned} \bar{n}_j &= 1 & [\text{for } \epsilon_j < \mu(0^\circ\text{K})] \\ &= 0 & [\text{for } \epsilon_j > \mu(0^\circ\text{K})] \end{aligned} \quad (4.11)$$

For this distribution, Eq. 4.10 becomes

$$N = \sum_{j=0}^{j^*} (1) \quad (4.12)$$

where  $j^*$  is the state at which the electron energy is just equal to  $\mu(0^\circ\text{K})$ . The right-hand side of Eq. 4.12 is easily evaluated by replacing the sum over states by the equivalent integral over the density of states. (A similar procedure was employed in Chap. 2, where the partition function sum of Eq. 2.20 was approximated by the integral over the frequency spectrum, leading to Eq. 2.21.) Therefore, Eq. 4.12 can be written as

$$N = \int_0^{\mu(0^\circ\text{K})} \mathcal{D}(\epsilon) d\epsilon \quad (4.13)$$

The upper limit in the integral is the chemical potential of the electron gas at  $0^\circ\text{K}$ , which is called the Fermi energy. Inserting Eq. 4.8 into Eq. 4.13 and performing the integration permits the Fermi energy to be determined as

$$\mu(0^\circ\text{K}) = \epsilon_F = \left( \frac{\hbar^2}{2m} \right) \left( 3\pi^2 \frac{N}{V} \right)^{2/3} \quad (4.14)$$

The quantity  $U_F$  in Eq. 4.3 is the average energy of an electron in the metal. For the  $0^\circ\text{K}$  distribution of Eq. 4.11, it can be obtained from

$$U_F = \frac{1}{N} \sum_{j=0}^{j^*} \epsilon_j = \frac{1}{N} \int_0^{\epsilon_F} \epsilon \mathcal{D}(\epsilon) d\epsilon \quad (4.15)$$

Using Eq. 4.8 for the density of states and expressing the result of the integration in terms of the Fermi energy of Eq. 4.14, we get

$$U_F = \frac{3}{5} \epsilon_F \quad (4.16)$$

Even at  $0^\circ\text{K}$ , the average kinetic energy of an electron in the metal is quite large. For monovalent metals, the electron density  $N/V$  is between  $10^{22}$  and  $10^{23}$  electrons/cm<sup>3</sup>, and the Fermi energy is of the order of 5 eV. The average electron energy in a metal at  $0^\circ\text{K}$  is thus about 3 eV, which is more than a factor of 100 greater than the

average energy of a particle in a Maxwell-Boltzmann ideal gas at 300°K.

The persistence of large kinetic energies in an electron gas at 0°K is due to the very high density of electrons in the metal and to the fact that they must obey Fermi-Dirac statistics. By the Pauli exclusion principle, it is impossible for all the electrons to possess zero kinetic energy, even at 0°K. Instead, they fill up the available energy states according to Eq. 4.11.

#### 4.2.4 The Cohesive Energy

Adding the Coulombic energy of Eq. 4.7 and the electron kinetic energy of Eq. 4.16 gives the total energy of a metal as a function of the sphere radius  $r_0$  (or equivalently, as a function of the separation of the ion cores):

$$U(r_0) = -\left(\frac{9e^2}{10}\right) \frac{1}{r_0} + \left[ \frac{3(9\pi)^{3/2}}{10} \frac{\hbar^2}{m} \right] \frac{1}{r_0^3} \quad (4.17)$$

The  $r_0$ -dependence of Eq. 4.17 is of the same form as that shown in Fig. 4.1. The negative Coulomb term behaves as an attractive force, which dominates the repulsive Fermi contribution at large separations. As the system is further compressed, the energy required to maintain the kinetic energy of the electron gas becomes more important. The minimum energy occurs when  $dU/dr_0 = 0$ , or when  $r_0$  is

$$r_{0eq} = \frac{2(9\pi)^{3/2}}{3} \frac{\hbar^2}{e^2 m} \quad (4.18)$$

If Eq. 4.18 is inserted into Eq. 4.4, the free-electron model predicts an electron (or atom) density in a monovalent metal of

$$\frac{N}{V} = 1.1 \times 10^{23} \text{ electrons (or atoms)/cm}^3$$

This value may be compared with atom densities based upon lattice constants determined from X-ray analysis. For cubic metals, the density is

$$\frac{N}{V} = \frac{\text{atoms/unit cell}}{\text{cm}^3/\text{unit cell}} = \frac{\gamma}{a_0^3} \quad (4.20)$$

where  $\gamma$  is 2 for the bcc structure and 4 for fcc lattices and  $a_0$  is the lattice constant. Experimental values are:

Copper ( $a_0 = 3.61\text{\AA}$ ,  $\gamma = 4$ ),  $N/V = 8.5 \times 10^{22}$  atoms/cm<sup>3</sup>

Sodium ( $a_0 = 4.28\text{\AA}$ ,  $\gamma = 2$ ),  $N/V = 2.5 \times 10^{22}$  atoms/cm<sup>3</sup>

Agreement between the experimental densities for copper and sodium and the free-electron model predictions is rather good for copper but poor for sodium.

The cohesive energy of the metal is obtained by evaluating the total energy at  $r_0 = r_{0eq}$ :

$$E_{coh} = U(r_{0eq}) = -\frac{27(4)}{40(9\pi)^{3/2}} \frac{e^4 m}{\hbar^2} = -5eV \quad (4.21)$$

Experimental values of  $E_{coh}$  from Eq. 4.2 are:

Copper ( $\Delta E_{sub}(0^\circ K) = 3.4 \text{ eV}$ ,  $I = 7.7 \text{ eV}$ )

$$E_{coh} = -11.1 \text{ eV}$$

Sodium ( $\Delta E_{sub}(0^\circ K) = 1.1 \text{ eV}$ ,  $I = 5.1 \text{ eV}$ )

$$E_{coh} = -6.2 \text{ eV}$$

Agreement between the experimental and theoretical values is poor for copper and fair for sodium.

The free-electron model with a uniform electron distribution is a highly simplified picture of the metal, but it expresses in an uncomplicated manner the basic features of metallic binding. Quantitative agreement of theoretical and experimental lattice constants and cohesive energies can be obtained by more sophisticated treatment of the interaction of the ion cores and the electron gas. For example, the electron distribution in the unit spheres is not uniform but tends to be greater in the vicinity of the central ion. This nonuniform distribution increases the stabilizing Coulomb energy (i.e., the coefficient of the  $1/r_0$  term in Eq. 4.17 is larger), thereby decreasing the calculated sphere radius  $r_{0eq}$  and increasing the magnitude of  $E_{coh}$ .

Additional improvement of the theory is obtained by accounting for correlation of electron spins and positions. Neighboring electrons tend to have their spins oriented antiparallel rather than parallel. Such correlation provides a negative contribution to the cohesive energy, leading to closer agreement with experiment. The binding property of opposite electron-spin alignment, which is a correction factor (albeit significant) in metallic cohesion, is the dominant feature of the chemical bonds formed in covalent crystals.

### 4.3 BONDING OF IONIC SOLIDS

Ionic solids are composed of two or more different chemical species that exist in the solid form as ions of different charge. In a two-component ionic solid, the metallic element unequivocally gives up its valence electrons to the nonmetallic element, which acquires a negative charge equal to its ordinary chemical valence. The positively charged metal ions are called cations and the negatively charged nonmetal ions are called anions. In simple ionic substances, the remaining atomic electrons of the cation and the anion form closed shells as in rare-gas atoms.

Ionic crystals would be expected to form most easily from metals of low ionization potential. That is, the energy required for the reaction



(which is the ionization energy,  $I$ ) should be small.

The energy required for the electron attachment reaction of the nonmetal



is called the electron affinity,  $A$ . Adding reactions 4.22 and 4.23 yields



for which energy equal to  $I + A$  is required. Reaction 4.24 does not proceed in the gas phase for any combination of  $M$  and  $X$  (i.e.,  $I + A$  is not negative). However, electron transfer proceeds readily in the solid because of the additional stabilizing effect of the electrostatic attraction of the oppositely charged ions when they are close together.

The cohesive energy of an ionic solid is defined as the energy required to construct the ionic crystal from the gaseous ions. The cohesive energy is related to other thermodynamic properties of the molecule and its component atoms by a Born-Haber cycle of the type shown in Fig. 4.3 for a compound of the type  $MX$ . The relationship is

$$E_{\text{coh}} = -[I + A + D + \Delta E_{\text{sub}}(0^\circ\text{K})] \quad (4.25)$$

Because of the substantially larger positive contribution of the dissociation energy,  $D$ , compared with the generally negative electron affinity, the magnitude of the cohesive energy of most ionic solids is greater than the cohesive energy of the metal that constitutes the cation.

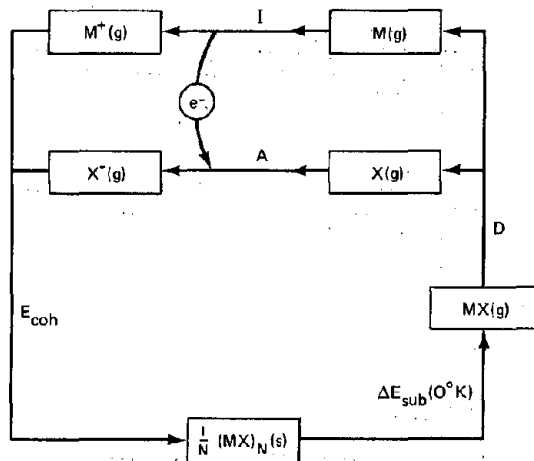


Fig. 4.3 Born-Haber cycle for an ionic solid  $MX$ .

### 4.3.1 Repulsive Potentials

The positive part of the interaction energy in ionic solids is of an entirely different type than that in metals. Contrary to the free-electron picture of metals, ions in ionic solids are not considered as point charges. Rather, they repel each other at separation distances where the closed electron shells begin to overlap. This mode of repulsion performs the function of providing a positive contribution to the cohesive energy, just as the electron kinetic energy did in the case of metals. The overlap repulsive forces would also be important in metal cohesion if the ion cores approached each other as closely as do the anions and cations in an ionic solid. Because they do not and because the repulsion due to ion-ion interaction is very short range, this contribution is negligible compared to the kinetic energy of the free electrons in metals. However, in ionic solids, there is no cloud of free electrons, and the constituent ions are drawn together by electrostatic forces

until the closed electron shells begin to overlap and the energy increases.

The additional energy required to force the electrons of two ions together arises from the Pauli exclusion principle. Overlapping implies that electrons are occupying the same spatial positions. If the outer electronic shells of both ions possess inert-gas configurations, the only way that these electrons can coexist in the same region is for some to be promoted to higher quantum states and hence to larger energies.

The electron density decreases rapidly beyond the average radius of the outer closed shell of a free ion. Accordingly, the increase in potential energy due to the overlapping of electrons of two adjacent ions is a very rapidly changing function of their separation.

There is no single analytical description of the repulsive potential which is valid for all separation distances. For small separations, the nuclei of the two atoms repel each other to the full extent of their nuclear charges, and the interaction is described by the familiar Coulomb potential

$$\phi = \frac{Z_1 Z_2 e^2}{r} \quad (4.26)$$

where  $Z_1$  and  $Z_2$  are the nuclear charges of the two ions. At somewhat greater separations, the atomic electrons partially neutralize or screen the nuclear charge, and the potential energy given by Eq. 4.26 is correspondingly reduced. The resulting screened Coulomb potential is

$$\phi = \frac{Z_1 Z_2 e^2}{r} e^{-r/a} \quad (4.27)$$

where  $a$  is the screening constant.

For the repulsive potentials of Eq. 4.26 or 4.27 to be utilized, the average interaction energy must be quite large in order that the ions approach closely enough to attain the small separations at which these equations are valid. High interaction energies are obtainable by ion bombardment or in the early stages of radiation damage of solids by nuclear particles.

However, in the near-thermal energy environment, which determines the normal thermodynamic properties of solids, neither of these two potential functions is applicable. Unfortunately, there is no theoretical description of the repulsive potential between a pair of ions or atoms in the low-energy range. The potential functions that are commonly used are empirical and have in common only the feature of decreasing very rapidly with increasing distance and of containing unspecified constants (usually two) which must be obtained from experiment. The two most popular are the Born-Mayer potential,

$$\phi = Ae^{-x/\rho} \quad (4.28)$$

and the point center of repulsion (or inverse-power) potential,

$$\phi = b/r^n \quad (4.29)$$

In these potentials,  $A$ ,  $\rho$ ,  $b$ , and  $n$  are empirical constants.

The Born-Mayer potential is most frequently applied to ionic solids and metals (when the separation distance is

small); the inverse-power law is most commonly used to describe the repulsive interaction of neutral atoms.

### 4.3.2 Crystal Energy

The stability (even the very existence) of ionic solids is due to the Coulomb attraction between the interlaced arrays of immobile cations and anions. The primary attractive force between ions of opposite charge in an ionic crystal is due to the Coulomb potential

$$\phi = -\frac{q_1 q_2}{r} \quad (4.30)$$

where  $q_1$  and  $q_2$  are the magnitudes of the charges on the two ions.

In treating the interaction energy in an ionic solid composed of a large number of ions, we make the following two assumptions: (1) The total energy of interaction between any two ions in the crystal may be represented by the sum of the repulsive contribution and the Coulomb interaction. Using the Born-Mayer potential, the total potential is

$$\phi = Ae^{-r/\rho} \pm \frac{q_1 q_2}{r} \quad (4.31)$$

The resulting potential-distance relation for a pair of oppositely charged ions is similar in shape to the curve shown in Fig. 4.1 for a large collection of ions. However, in order to deduce the crystal potential energy-separation relation that Fig. 4.1 actually represents from the potential energy between a pair of ions, we need also to assume that: (2) The interaction energy between a particular ion and all other ions in the crystal is the sum of the interaction energies of the particular ion and the surrounding ions. This assumption of pairwise additivity implies that the energy of interaction between a pair of ions is unaffected if one or both of the partners are simultaneously interacting with other ions. This assumption, which appears quite valid for ionic solids, serves to reduce the many-body problem to a summation of two-body interactions.

Determination of the cohesive energy from the pair potential will be illustrated using a crystal of the NaCl structure (Fig. 3.10) and the pair-potential function of Eq. 4.31. A particular ion (of either type) is chosen, and its interaction with all other ions in the crystal is summed. Since the repulsive potential appears only upon physical contact of adjacent ions, the central ion interacts according to Eq. 4.28 only with its nearest neighbors (six for the NaCl structure).<sup>\*</sup> The Coulomb potential, however, decreases only as  $1/r$ , and the interaction with many equidistant shells of ions (of both signs) surrounding the central ion must be taken into account. If the distance between nearest neighbors of opposite charge is denoted by  $r_0$ , the total interaction energy of the chosen central ion and all other

<sup>\*</sup>Because of the large size of the anions compared to the cations, the anion-anion (second nearest neighbor) repulsive interaction may be comparable to the nearest-neighbor anion-cation repulsion energy. This effect is considered in problem 4.7.

ions in the lattice is:

$$U(r_0) = 6Ae^{-r_0/\rho} - \left( +6\frac{e^2}{r_0} - 12\frac{e^2}{\sqrt{2}r_0} + 8\frac{e^2}{\sqrt{3}r_0} - \dots \right) \quad (4.32)$$

The first term on the right of Eq. 4.32 represents the repulsive interaction with the 6 nearest neighbors. The series in parentheses gives the Coulomb energy between the central ion and the 6 nearest neighbors, the 12 next nearest neighbors (of opposite charge from the nearest neighbors and a factor of  $\sqrt{2}$  further removed from the central ion), and the 8 third nearest neighbors. Upon factoring  $e^2/r_0$  from the term in parentheses in Eq. 4.32, we see that the remaining series of alternating sign obviously does not converge rapidly.

The series can be made to converge by reconstructing it so that the individual terms are nearly neutral rather than due to all positive or all negative charges. To accomplish this, we partition the charge on each ion between adjoining unit cells in the same manner as was used to count the number of atoms in a unit cell (Sec. 4.2). If the calculation is begun from the central ion in Fig. 3.10, the nearest neighbors of opposite charge are located in the face-centered positions of the unit cell. Because face-centered positions are shared with one adjacent unit cell, each of the six nearest neighbors is assigned one-half a charge in the first term of the lattice sum. The next nearest neighbors are the ions on the edges of the unit cell of Fig. 3.10, each of which is shared with four other adjacent unit cells. Similarly, the third nearest neighbors lie on the corner positions of the unit cell of Fig. 3.10 and hence count only  $1/8$  each. In the revised method of summing, the first term in the series consists of the interaction between the central ion and the partial charges assigned to the atoms on the face-centered, edge-centered, and corner positions of the unit cell. Or, the first term in the series becomes

$$\left(\frac{1}{2} \times 6\right) - \frac{1}{\sqrt{2}}\left(\frac{1}{4} \times 12\right) + \frac{1}{\sqrt{3}}\left(\frac{1}{8} \times 8\right) = 1.46$$

instead of 6, as in Eq. 4.32.

The second term in the sum consists of the charges in the region between the cube just considered and the next cube of ions surrounding the central ion (the first cube is  $2r_0$  on a side and the second cube is  $4r_0$  on a side). The fractional charges from the first cube which were not counted in the first term of the series are included in the second term, as are the appropriate fractional charges from ions on surface of the second cube.

Performing the lattice sum in this fashion (which simply amounts to breaking up the terms in the original sum of Eq. 4.32 and rearranging the segments into the terms of the new series) generates a series that converges quite rapidly. The sum of this series is called the Madelung constant,  $M$ . Its numerical value depends upon which characteristic length in the lattice (e.g., the nearest-neighbor distance or the lattice constant, which differ by a factor of 2 in the NaCl structure) was used in preparing the sum such as the one in Eq. 4.32. For the NaCl structure, the Madelung constant based upon nearest-neighbor separation is 1.748.

The sum of the interaction energies of one ion and all other ions in the lattice is thus

$$U(r_0) = -M \frac{e^2}{r_0} + 6Ae^{-r_0/\rho} \quad (4.33)$$

The function  $U(r_0)$  also represents the interaction energy per ion pair in the solid MX, as can be shown by the following argument. Suppose the entire crystal consists of  $N$  ion pairs ( $N$  cations  $M$  and  $N$  anions  $X$ ). Let  $U_M$  denote the interaction energy of one cation with all other ions in the crystal and  $U_X$  be the interaction energy of a single anion and all other ions. If the central ions for which the lattice sums  $U_M$  and  $U_X$  were computed are allowed to range over all ions of the lattice, the quantity  $NU_M + NU_X$  is just twice the desired crystal energy. The factor of 2 arises because each interaction is counted twice in the process of ranging the central ion over the entire lattice. Therefore, the total energy of  $N$  ion pairs is

$$NU = \frac{1}{2} (NU_M + NU_X) \quad (4.33a)$$

For the NaCl lattice (with only nearest-neighbor cation-anion repulsions considered),  $U_M = U_X$ , and both are equal to the right-hand side of Eq. 4.33. Thus, the total energy of the crystal containing  $N$  ion pairs is  $NU$ , or the energy per ion pair (or per molecule MX) is  $U$ .

The lattice summation procedure must properly reflect the anion-to-cation ratio of the solid. In ionic solids of the type  $MX_2$ , for example, the analog of Eq. 4.33a is

$$NU = \frac{1}{2} (2NU_X + NU_M) \quad (4.33b)$$

where  $N$  is the number of molecules of  $MX_2$  in the crystal and  $U$  is the crystal energy per molecule. The quantity in parentheses in Eq. 4.33b represents the sum of lattice sums starting from each of the  $2N$  anions and  $N$  cations of the crystal, and the factor of  $(1/2)$  removes the redundant interactions.

### 4.3.3 Determination of Constants in the Repulsive Potential and the Cohesive Energy

Equation 4.33 is the ionic crystal analog of Eq. 4.17, which applies to metals. Contrary to Eq. 4.17 for free-electron metals, Eq. 4.33 cannot be directly used to predict the cohesive energy and lattice constant of ionic solids. It contains the two empirical constants characterizing the repulsive potential which must be determined from the same type of crystal data the model is designed to predict. Fortunately, there are more types of measurements than there are constants to be determined; so comparison of theory and experiment is possible.

If the equilibrium nearest-neighbor spacing is denoted by  $r_{0eq}$ , Eq. 4.33 and its first and second derivatives evaluated at  $r_{0eq}$  are related to measured properties of the solid. The cohesive energy is

$$U(r_{0eq}) = E_{coh} = -\frac{Me^2}{r_{0eq}} + 6A \exp\left(-\frac{r_{0eq}}{\rho}\right) \quad (4.34)$$

Since the solid is at equilibrium at  $r_0 = r_{0eq}$ :

$$\left(\frac{dU}{dr_0}\right)_{r_{0eq}} = \frac{Me^2}{r_{0eq}^2} - \frac{6A}{\rho} \exp\left(-\frac{r_{0eq}}{\rho}\right) = 0 \quad (4.35)$$

Finally, problem 5 of Chap. 1 shows that the second derivative of the crystal energy with respect to volume is related to the compressibility at  $0^\circ\text{K}$  by

$$\left(\frac{d^2U}{dV^2}\right)_{V_{eq}} = \frac{1}{\beta_0 V_{eq}} \quad (4.36)$$

where  $\beta_0$  is the compressibility at  $0^\circ\text{K}$  and  $V$  is the volume per molecule, which may be expressed in terms of the nearest-neighbor distance by

$$\begin{aligned} V &= \frac{\text{volume/unit cell}}{\text{molecules/unit cell}} \\ &= \frac{(2r_0)^3}{4} \\ &= 2r_0^3 \frac{\text{volume}}{\text{molecule}} \end{aligned} \quad (4.37)$$

Changing variables in Eq. 4.36 from  $V$  to  $r_0$  yields

$$\frac{1}{36r_{0eq}^2} \left[ \frac{1}{r_{0eq}^2} \left(\frac{d^2U}{dr_0^2}\right)_{r_{0eq}} - \frac{2}{r_{0eq}^3} \left(\frac{dU}{dr_0}\right)_{r_{0eq}} \right] = \frac{1}{2\beta_0 r_{0eq}^3}$$

The second term in the brackets is zero according to Eq. 4.35. Therefore, for the NaCl structure,

$$\left(\frac{d^2U}{dr_0^2}\right)_{r_{0eq}} = \frac{18r_{0eq}}{\beta_0} = -\frac{2Me^2}{r_{0eq}^3} + 6 \frac{A}{\rho^2} \exp\left(-\frac{r_{0eq}}{\rho}\right) \quad (4.38)$$

Equations 4.34, 4.35, and 4.38 provide three equations, any two of which may be used to determine the constants  $A$  and  $\rho$ . The unused equation provides an independent comparison of the theoretical model with experiment. Since the first and second derivatives are most sensitive to the constants  $A$  and  $\rho$ , these two parameters are determined from Eqs. 4.35 and 4.38, yielding

$$\rho = \frac{Me^2 \beta_0 r_{0eq}}{2Me^2 \beta_0 + 18r_{0eq}^4} \quad (4.39)$$

and

$$A = \frac{Me^2 \rho}{6r_{0eq}^2} \exp\left(\frac{r_{0eq}}{\rho}\right) \quad (4.40)$$

Using experimental values of  $r_{0eq}$  and  $\beta_0$ , the steepness parameter  $\rho$  is found to be close to  $0.3\text{\AA}$  for all alkali halide crystals. Since  $\rho$  is approximately an order of magnitude smaller than  $r_{0eq}$ , the expectation that the repulsive potential is very short range is confirmed. When the values of  $A$  and  $\rho$  are substituted into Eq. 4.34, cohesive energies that agree to within 1% of the experimental values deduced from the Born-Haber cycle (Eq. 4.25) are obtained. The accord between observed and calculated cohesive energies justifies the assumption of completely ionic binding for this class of solids and implies that no significant components of the interionic forces have been neglected.

#### 4.3.4 Comparison of Metals with Ionic Solids

An ionic substance is generally more refractory than the metal of which it is composed. Typical measures of the refractory nature of a solid are its melting point and vapor pressure. The latter depends upon temperature according to the Clausius-Clapyron equation:

$$P^\circ(T) = \text{constant} \times \exp\left(-\frac{\Delta H_{\text{sub}}}{RT}\right) \quad (4.41)$$

where  $R$  is the gas constant and the heat of sublimation may be approximated by the energy of sublimation (by neglecting the last term in Eq. 4.1). Although the cohesive energy is an important parameter in the theoretical description of a solid, observable thermodynamic properties, such as the vapor pressure, depend upon  $\Delta E_{\text{sub}}(0^\circ\text{K})$  and not upon  $E_{\text{coh}}$ . The reason for this is that the vapor phase is in equilibrium with the solid at all but very high temperatures is the neutral gas,  $M(g)$  or  $MX(g)$ , and not separated ions or electrons.

Sodium metal has a sublimation energy of 1.1 eV, and NaCl has a sublimation energy of 2.2 eV. This pattern is followed by most ionic solids and their parent metals. Assuming that the constants in Eq. 4.41 are approximately the same for the ionic solid and the corresponding metal, the vapor pressure of the ionic solid is considerably lower than the vapor pressure of the metal at the same temperature. The factor of 2 difference in sublimation energy between sodium and sodium chloride is a reflection of the stronger binding of the particles in an ionic lattice compared to a metallic structure. The solid state that results when a neutral atom transfers valence electrons directly to another atom, as in the ionic solid, produces a more stable state than if the valence electrons are simply contributed to the communal electron gas, as in a metal. In addition to the vapor pressure, the tighter binding in an ionic solid is manifest by a higher melting point and smaller ion-ion separation than in the corresponding metal.

#### 4.4 COVALENT CRYSTALS

Solids in which cohesion is due to the sharing of electrons between neighboring atoms are called covalent crystals. Elements preferring this type of bonding often form crystals of the diamond structure (Fig. 3.4). The diamond form of carbon and the semiconductors germanium and silicon crystallize in this configuration. The diamond structure is quite open; hard spheres arranged in this fashion occupy only 34% of the available space compared to 74% occupancy in the close-packed fcc and hcp structures. Each atom has only four nearest neighbors arranged in a regular tetrahedron about the central atom.

The reason for adoption of this crystal form is the type of bonding between atoms. Each atom of carbon, germanium, or silicon can form only four bonds, and these only with nearest neighbors. As isolated atoms, the four outer electrons of these elements occupy  $s^2$  and  $p^2$  orbitals. In forming a solid (or a compound with other elements), the four outer electrons are "hybridized" so that all have the same energy and bonding effectiveness. The four hybridized valence electrons are localized in lobes at angles

of  $109^\circ$  from each other. This directional characteristic is manifest by the tetrahedral bonding configurations in the crystalline phase (see upper portion of Fig. 3.4).

To complete an outer orbital of electrons which would provide the stability of a closed-shell configuration, these elements share electrons with other elements (to form compounds) or with the same species (to form the elemental crystals). If hydrogen is the element with which the four hybridized electrons are shared, the compounds that result are methane ( $\text{CH}_4$ ), germane ( $\text{GeH}_4$ ), or silane ( $\text{SiH}_4$ ). In these compounds, each of the hydrogen atoms provides an electron that is shared with one of the valence electrons of the carbon, germanium, or silicon atoms in the form of a single covalent bond.

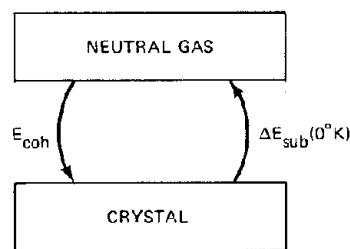


Fig. 4.4 Born-Haber cycle for an elemental covalent crystal.

The covalent bond between carbon atoms is extremely strong and accounts for the refractory nature of the diamond form of this element. The two electrons in each bond (one contributed by each partner) are localized in the region between the bonding atoms. The spins of the electrons in the bond are antiparallel, which results in great stability. A similar stabilizing effect of electron-spin orientation is illustrated by the correlation energy in metals.

The Born-Haber cycle for elemental covalent crystals is shown in Fig. 4.4. The cohesive energy is

$$E_{\text{coh}} = -\Delta E_{\text{sub}}(0^\circ\text{K}) \quad (4.42)$$

The potential energy-distance relation between a pair of covalently bonded atoms may be described by the Morse potential function:

$$\phi(r) = D\{\exp[-2\alpha(r - r_{\text{eq}})] - 2\exp[-\alpha(r - r_{\text{eq}})]\} \quad (4.43)$$

This potential is entirely empirical and contains three parameters:  $r_{\text{eq}}$  is the equilibrium nearest-neighbor distance (in a crystal) or the equilibrium atom separation (as in gaseous  $\text{H}_2$ , in which the two hydrogen atoms are attached by a single covalent bond). The constant  $\alpha$  is a steepness parameter that reflects the rapidity of the potential increase away from the equilibrium separation, and  $D$  is the dissociation energy of the atom pair, or the bond energy. At the equilibrium separation,  $\phi(r_{\text{eq}}) = -D$ . Since each atom in the diamond structure makes four bonds with nearest neighbors, the energy of interaction of a particular

atom with the crystal is  $-4D$ . The total interaction energy of  $N$  atoms with the crystal is  $-(N/2)(4D)$ , where the factor of  $(1/2)$  is introduced to eliminate redundant counting of bonds in performing the lattice sum. The cohesive energy is

$$E_{\text{coh}} = -2D \quad (4.44)$$

The energy of sublimation of diamond is 7.2 eV (170 kcal/mole); so the strength of the carbon-carbon bond in diamond is 3.6 eV.

Although the concept of a localized bond between adjacent atoms in an elemental crystal is, strictly speaking, valid only for covalently bonded substances such as diamond, the simple-bond concept is often applied to metals as a very crude approximation. The bond energy in any elemental crystal can be obtained from the formula

$$\Delta E_{\text{sub}}(0^\circ\text{K}) = \frac{1}{2}\beta D \quad (4.45)$$

where  $\beta$  is the number of nearest neighbors to an atom in the crystal shown in Table 4.1 for various structures.

Table 4.1 Nearest Neighbors in Various Structures

Lattice type	$\beta$
Diamond	4
sc	6
bcc	8
fcc or hcp	12

Not all substances can be categorized as one of the clearly defined bonding types, such as metals, ionic solids, or covalent crystals. Although uranium dioxide ( $\text{UO}_2$ ) is ionic, the properties of uranium carbide (UC) suggest partial metallic character. The compound CdS is partly ionic and partly covalent.

The important nuclear material graphite is a unique example of mixed bonding in a solid. Ordinary graphite is composed of many crystallites with the lattice structure shown in Fig. 4.5. Graphite is a layered structure, the layers consisting of a hexagonal network of carbon atoms. These layers are called basal planes, as are the analogous planes in the hexagonal lattice (Fig. 3.5). The carbon atoms in the basal plane are covalently bonded, but, because each carbon atom has only three nearest neighbors, the bonds are not of the simple shared-electron-pair type as in diamond. The bonding in the basal plane of graphite is shown in Fig. 4.6.

Because each carbon atom has four electrons to share in bonding, a total of four bonds must be made with the three nearest-neighbor carbon atoms in the basal plane. This is accomplished by making one out of every three bonds a double bond, i.e., a covalent bond consisting of two electrons contributed from each partner (the bond contains four electrons in total). Although this mixture of single and double bonds formally satisfies the bonding requirements of the carbon atom, the situation is not static as depicted in Fig. 4.6. Actually, the double bond moves about the hexagonal ring and is not localized at any particular

position. It is more appropriate to describe the bonds in the basal plane of graphite as all equivalent and of  $2/3$  single-bond character and  $1/3$  double-bond character. Because of this partial double-bond character, the carbon-carbon distance in the basal plane ( $1.42 \text{ \AA}$ ) is smaller than in diamond ( $1.54 \text{ \AA}$ ).

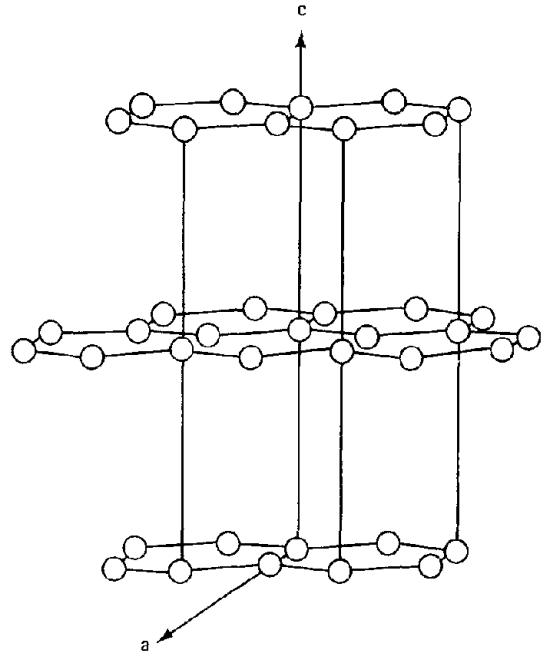


Fig. 4.5 The graphite structure.

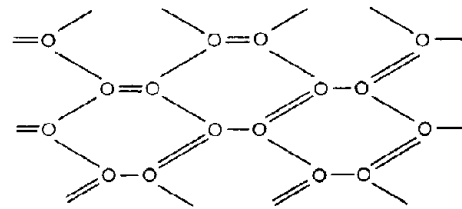


Fig. 4.6 Bonding in the basal plane of graphite.

The basal planes of graphite are held together by a very weak nonchemical type of bond not discussed previously. Since the valence electrons of carbon are all satisfied by the covalent bonds described above and since no electrostatic forces are present to provide binding of the type important in ionic solids or metals, a new type of attraction must be operative. The forces that are responsible for the weak binding of the basal planes of graphite are the same as those which permit rare gases to condense as liquids or solids. Attraction between chemically inactive neutral atoms is due to van der Waals, or dispersion, forces. This force arises from fluctuations in the charge distribution of the atoms which create a momentary dipole moment. The electric field set up by the dipole of one atom creates charge separation in nearby atoms. This random dance of dipole moments among adjacent atoms can be described by a pair potential of the form

$$\phi = \frac{C}{r^6} \quad (4.46)$$

The constant  $C$  in Eq. 4.46 can be estimated theoretically. It depends upon the polarizability of the atoms involved, since this property is a measure of the ease with which a dipole moment can be induced in a neutral atom by an electric field. As in the repulsive potential between ions or atoms, the van der Waals potential energy is pairwise additive.

Because of the dramatic difference in the nature and strength of the binding parallel to and perpendicular to the basal plane, graphite crystals exhibit marked anisotropy. The separation between basal planes is 3.35 Å, but the carbon-carbon distance in the basal plane is 1.42 Å. Such properties as thermal and electrical conductivity are as much as a factor of 1000 smaller in the  $c$  direction than in the  $a$  direction of the structure of Fig. 4.5. Thermal expansion is low in the  $a$  direction and high in the  $c$  direction. This anisotropy can be troublesome in a structural component, and most nuclear graphites are rendered isotropic by fabrication processes that produce a random orientation of graphite crystallites in the product.

## 4.5 NOMENCLATURE

- $a_0$  = lattice constant
- $a$  = screening constant in Coulomb potential
- $A$  = electron affinity; empirical constant in Born-Mayer potential
- $b$  = empirical constant in Born-Mayer potential
- $C$  = specific heat; constant in van der Waal's potential
- $D$  = dissociation energy
- $\mathcal{D}$  = density of states
- $e$  = electronic charge
- $E$  = energy of a collection of particles or a crystal
- $\Delta E$  = energy required in a chemical process
- $\hbar$  = Planck's constant divided by  $2\pi$
- $\Delta H$  = change in enthalpy in a chemical process
- $I$  = ionization energy
- $k$  = Boltzmann constant
- $m$  = mass of a particle
- $M$  = cation; monovalent metal; Madelung constant
- $n$  = empirical constant in Born-Mayer potential
- $n$  = average number of electrons in an energy state
- $N$  = number of atoms or electrons in a crystal
- $P^\circ$  = vapor pressure
- $q$  = magnitude of charge on an ion
- $r$  = separation of nuclei; radius of a sphere surrounding an ion
- $r_0$  = radius of equivalent sphere of the same volume as polyhedron surrounding the metallic ion in a metallic solid; distance between nearest neighbors of opposite charge in an ionic solid
- $R$  = gas constant
- $T$  = temperature
- $\bar{U}$  = average energy of electrons in a metal; energy of a crystal; interaction energy between ions
- $V$  = crystal volume
- $X$  = anion
- $Z$  = nuclear charge

### Greek letters

- $\alpha$  = constant in the Morse potential function
- $\beta$  = number of nearest neighbors to an atom in a solid
- $\beta_0$  = compressibility at 0°K
- $\gamma$  = number of atoms per unit cell
- $\phi$  = repulsive potential; Coulomb potential
- $\epsilon$  = particle energy
- $\mu$  = chemical potential
- $\rho$  = empirical constant in Born-Mayer potential

### Subscripts

- $C$  = Coulomb
- coh = cohesive
- eq = equilibrium
- $F$  = kinetic (due to electrons); Fermi
- $g$  = gas
- $j$  = electron energy state
- $M$  = cation
- $N$  = N-particle solid
- ps = of the solid phase, at constant pressure
- pv = of the gaseous phase, at constant pressure
- $S$  = solid
- sub = sublimation
- $X$  = anion

## 4.6 ADDITIONAL READING

1. C. Kittel, *Introduction to Solid State Physics*, 3rd. ed., Chaps. 1, 3, and 7, John Wiley & Sons, New York, 1967.
2. M. Sachs, *Solid State Theory*, Chaps. 3, 6, and 10, McGraw-Hill Book Company, New York, 1963.
3. L. Pauling, *The Nature of the Chemical Bond*, 3rd ed., Cornell University Press, Ithaca, N. Y., 1960.

## 4.7 PROBLEMS

4.1 The kernel for the Coulomb-energy calculation of Sec. 4.2.2 is the electrostatic energy between a unit point negative charge on the surface of a sphere of radius  $r$  and the charges within the sphere. The sphere contains a uniform negative charge density of  $e/(4\pi r_0^3/3)$  and a unit positive charge at the center. Show that the kernel is given by

$$-\frac{e}{r} \left[ 1 - \left( \frac{r}{r_0} \right)^3 \right]$$

4.2 The free-electron theory of metals includes a Coulomb-energy term that is due to an electronic charge uniformly distributed in a sphere of radius  $r_0$  with a point positive charge at the center. A more realistic model allows a higher charge density toward the center of the sphere than at the outer edge. Suppose the negative-charge distribution in the sphere is given by

$$\rho(r) = \left( \frac{e}{4\pi r_0^3/3} \right) A e^{-(r/r_0)}$$

(a) Compute the Coulomb energy,  $U_c$ , for this distribution.

(b) How are the final values of  $E_{\text{coh}}$  and  $r_{\text{oeq}}$  affected by the nonuniform charge distribution?

4.3 A metal contains  $N$  conduction electrons in a volume  $V$ .

(a) Calculate the compressibility of the electron gas at  $0^\circ\text{K}$ , neglecting all electrostatic interactions.

(b) Set up the equations from which the pressure of the electron gas at  $T > 0^\circ\text{K}$  could be computed. Replace any sums over quantum states by density-of-state integrals, where  $\mathcal{D}(\epsilon)$  is given by Eq. 4.8. Do not attempt to evaluate the integrals.

(c) The Coulomb energy due to the interaction of the electron gas and the ion cores was not considered in (a) and (b). Add this effect (as in the free-electron model) to compute the numerical value of the compressibility at  $0^\circ\text{K}$  for a metal with a simple cubic structure. Compare with the result of (a) and explain the difference.

4.4 The energy of sublimation of the solid  $\text{MX}(\text{s})$  is  $\Delta E_{\text{sub, MX}}^\circ(0^\circ\text{K})$ , and the dissociation energy of  $\text{MX}(\text{g})$  is  $D$ . What additional thermochemical quantity is needed to fix the energy of formation of  $\text{MX}(\text{s})$  from  $\text{M}(\text{s})$  and  $\text{X}(\text{g})$  at  $0^\circ\text{K}$ ? What is the quantitative relation between all these thermochemical quantities?

4.5 Using the method described in Sec. 4.3, evaluate the Madelung constant for the  $\text{CsCl}$  structure (Fig. 3.11). Consider the contributions to the Coulomb energy arising from interactions between a central cesium ion and its primary unit cell (i.e., the eight nearest-neighbor chlorine ions that form a cube of side  $a_0$  around the cesium ion) and between the central cesium ion and the ions in the secondary shell. The latter is the cube of side  $3a_0$  surrounding the primary unit cell. Remember to count appropriate fractional charges.

4.6 The  $\text{UO}_2$  lattice is bound together by the Coulomb forces between the constituent  $\text{U}^{4+}$  and  $\text{O}^{2-}$  ions. The Coulomb energy of the lattice is given by

$$E_{\text{C}} = \frac{Z^2 Me^2}{a_0}$$

where the left-hand side represents the Coulomb energy per  $\text{UO}_2$  molecular unit,  $Z$  is the anion charge,  $a_0$  is the lattice parameter (twice the oxygen-oxygen separation),  $e$  is the electronic charge, and  $M$  is the Madelung constant for the fluorite structure (equal to 11.6365). Attractive potentials due to dispersion forces are neglected. The repulsive forces are due to the separate interactions of oxygen ions with each other, uranium ions with each other, and uranium-oxygen interactions. The repulsive pair potentials between ions are given by expressions of the Born-Mayer type:

$$\phi_{ij}^{\text{rep}} = b_{ij} e^{-r/\rho_{ij}}$$

where  $i$  and  $j$  represent either  $\text{O}^{2-}$  or  $\text{U}^{4+}$  and  $r$  is the interionic separation. The parameters  $b_{ij}$  and  $\rho_{ij}$  are given by

$$b_{ij} = 627.32 (n_i n_j)^{1/2} g_i g_j, \text{ kcal/mole}$$

$$\rho_{ij} = \frac{1.06}{g_i + g_j}, \text{ \AA}$$

where  $n_i$  is the total number of electrons in the ion of type  $i$ ,  $g_{\text{O}} = 1.06$ , and  $g_{\text{U}} = 1.62$ .

(a) Considering the  $\text{O}^{2-}-\text{O}^{2-}$ ,  $\text{U}^{4+}-\text{U}^{4+}$ , and  $\text{U}^{4+}-\text{O}^{2-}$  repulsive interactions separately and assuming nearest-neighbor interactions only, derive an expression for the cohesive energy at  $\text{UO}_2$  in terms of the lattice parameter  $a_0$ .

(b) Derive an expression for the compressibility at  $0^\circ\text{K}$  in terms of the second derivative of the cohesive energy for this crystal type.

(c) Indicate how the cohesive energy, lattice parameter, and compressibility of  $\text{UO}_2$  could be computed from the results of (a) and (b).

(This problem is considered by D. R. Olander in *J. Chem. Phys.*, 43: 779 (1965).)

4.7 Since the anions of an ionic crystal are larger in size than the cations, the anion-anion repulsions (which are second nearest-neighbor interactions) may be comparable to the cation-anion (nearest neighbor) repulsive interactions which are commonly considered.

(a) Derive the expression for the lattice energy of the  $\text{NaCl}$  structure for the case in which anion-anion repulsions are included. Let  $\phi_{\text{XX}}^{\text{r}}(r)$  and  $\phi_{\text{MX}}^{\text{r}}(r)$  represent the repulsive potentials between anions and between anion and cations, respectively. The Madelung constant is  $M$  and the anion-cation separation is  $r_0$ .

(b) So that additional undetermined parameters will not be introduced into the problem, the repulsive potentials are approximated by

$$\text{Anion-anion: } \phi_{\text{XX}}^{\text{r}}(r) = b \exp[(2R_{\text{X}} - r)/\rho]$$

$$\text{Cation-anion: } \phi_{\text{MX}}^{\text{r}}(r) = b \exp[(R_{\text{X}} + R_{\text{M}} - r)/\rho]$$

where  $b$  and  $\rho$  are empirical constants and  $R_{\text{X}}$  and  $R_{\text{M}}$  are the ionic radii of the anion and cation, respectively. For sodium chloride, they are  $R_{\text{Na}^+} = 0.98\text{\AA}$  and  $R_{\text{Cl}^-} = 1.81\text{\AA}$ . The sum of the ionic radii is the cation-anion separation distance in the equilibrium lattice (i.e.,  $r_{\text{oeq}}$ ).

Estimate the error incurred by neglecting anion-anion repulsion in computing the cohesive energy of  $\text{NaCl}$ . Without this contribution, the following parameters were computed:

$$A = 1.05 \times 10^5 \text{ kJ/mole}$$

$$\rho = 0.321\text{\AA}$$

$$E_{\text{coh}} = 750 \text{ kJ/mole}$$

where  $A$  is the coefficient of  $e^{-r/\rho}$  in the  $\text{MX}$  repulsive potential.

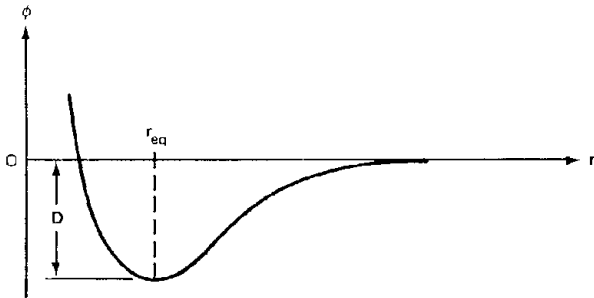
4.8 The atoms in a solid with a simple cubic structure interact only with nearest neighbors according to the potential function of Eq. 4.43. This potential is shown in the accompanying sketch.

(a) Approximate this potential by a parabolic function of the distance from the equilibrium separation. Identify the force constant in terms of parameters of the actual potential function.

(b) What is the cohesive energy of the lattice?

(c) What is the coefficient of compressibility at 0°K?

(d) In the parabolic approximation, what is the Debye frequency of this material? (Each atom is mass  $m$ .) What is its Gruneisen constant?



4.9 The pair potential between carbon atoms in adjacent basal planes of graphite is due to an attractive force of the

van der Waals type and a repulsive Born–Mayer potential term

$$\phi(r) = A e^{-r/\rho} - \frac{C}{r^6}$$

where  $C$ ,  $A$ , and  $\rho$  are known constants.

What is the interlayer separation distance between the basal planes of graphite for this potential? Make the following assumptions: 1. Consider only the interaction of two isolated basal planes. 2. Consider a single atom in one basal plane interacting with another plane of continuous average atom density  $n$ , in atoms/cm<sup>2</sup>.

4.10 Consider a line of  $2N$  monovalent ions of alternating charge. Calculate the cohesive energy in terms of the empirical Born–Mayer constants  $A$  and  $\rho$ . Assume that  $\rho$  is small compared with the equilibrium spacing.

4.11 Suppose  $N$  conduction electrons are confined to a line of length  $L$ .

(a) What is the chemical potential at 0°K?

(b) Assuming that the chemical potential at temperature  $T$  is known, what is the average energy of one of these electrons at temperature  $T$ ?

Assume that sums over discrete states can be replaced by appropriate integrals. Equations already appearing in the text can be used as a starting point.

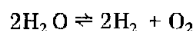
# Chapter 5

## Chemical Equilibrium

### 5.1 MULTICOMPONENT SYSTEMS

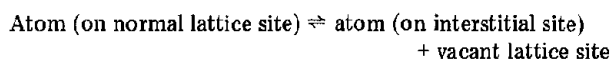
The thermodynamic considerations of Chaps. 1 through 3 involved systems consisting of a single component and a single phase. However, many practical problems require thermodynamic analysis of mixtures. The mixture may consist of two phases of a single species, of several species coexisting in a single phase, or of combinations of these two cases.

For chemical equilibrium to exist among the components of a mixture, it must be possible for some of the components to be converted to other components. For example, at sufficiently high temperatures  $\text{H}_2\text{O}$  can decompose into  $\text{H}_2$  and  $\text{O}_2$ , and, conversely,  $\text{H}_2$  and  $\text{O}_2$  can combine to produce  $\text{H}_2\text{O}$ . Under these conditions, the concentrations of the species  $\text{H}_2\text{O}$ ,  $\text{H}_2$ , and  $\text{O}_2$  in the mixture are not independent but are related by an equilibrium condition. The capability of interconversion is symbolized by the reaction



At low temperatures, on the other hand,  $\text{H}_2$ ,  $\text{O}_2$ , and  $\text{H}_2\text{O}$  may not be capable of such interconversion, and the concentrations of the three species are not related to each other. In this case, the system behaves merely as a mixture of three noninteracting species.

When reaction between the species of a mixture can occur, a situation of chemical equilibrium is possible. The concept of chemical equilibrium can be extended beyond instances of obvious chemical reactions that involve the exchange of atoms between different molecules. For example, some of the atoms in a solid crystal may move from their normal lattice sites to positions in the crystal known as interstitial sites, leaving behind vacant sites in the crystal lattice. Conversely, the atoms of interstitial sites may combine with vacant lattice sites to reform the ordinary lattice structure. By analogy to true chemical processes, the interchange of atom positions between normal lattice sites and interstitial sites may be regarded as a "chemical reaction" described by



The extent to which the process represented by this reaction proceeds may also be described by a condition of chemical equilibrium. Thus, the concept of chemical equilibrium can be applied to any mixture in which the components are capable of interconversion.

Identification of the components of a mixture is not always obvious. If the components are distinct molecular species, such as  $\text{H}_2$ ,  $\text{O}_2$ , and  $\text{H}_2\text{O}$ , labeling of the species is no problem. The defecting reaction in the solid presents a more subtle question of how and when to consider the imperfect crystal as a mixture. When the ordinary thermodynamic properties of real crystals are being considered, such defects as vacancies and interstitial atoms need not be singled out as separate species. We may speak of the heat capacity of metallic uranium at a particular temperature and pressure without specifying the degree to which the uranium crystal is defected. In this case, uranium metal is considered as a one-component system, the single component being uranium. Neglecting defects in describing the thermodynamic properties of uranium, however, implicitly assumes that all samples of metallic uranium under the same conditions contain the same proportion of defects.

Other properties of a solid, such as the mobility of its atoms, may depend much more strongly on the presence of defects than do macroscopic thermodynamic properties. In such cases, we may wish to calculate the concentration of various types of defects in the real crystal. When this degree of detail is desired, defects and atoms on normal lattice sites may be considered as separate species, even though one of the defect components may be nothing but empty space and even though only one chemical element is present.

### 5.2 THE CHEMICAL POTENTIAL

If a system contains more than one component, its thermodynamic state is no longer fixed by just two properties. In a single-component system, the internal energy,  $U$ , is determined by specifying the entropy,  $S$ , and the volume,  $V$ , which implies the following relation between differentials of these variables:

$$dU = \left(\frac{\partial U}{\partial S}\right)_V dS + \left(\frac{\partial U}{\partial V}\right)_S dV = T dS - p dV \quad (5.1)$$

If the system contains more than one component and if the relative proportion of the components changes as  $U$ ,  $S$ , and  $V$  are incremented, then  $U$  depends upon the amount of each component present in addition to  $S$  and  $V$ . The amount of each component in the mixture,  $N_i$ , may be expressed in units of mass, moles, or molecules, but not as a concentration. Since  $U$  is uniquely determined by  $S$ ,  $V$ , and all the  $N_i$  according to a function  $U(S, V, N_i)$ , the differential of  $U$  can be formally written as

$$dU = \left(\frac{\partial U}{\partial S}\right)_{V, N_i} dS + \left(\frac{\partial U}{\partial V}\right)_{S, N_i} dV + \sum_i \left(\frac{\partial U}{\partial N_i}\right)_{S, V, N_j} dN_i \quad (5.2)$$

The coefficients of  $dS$  and  $dV$  have the same meaning as they do in Eq. 5.1, namely  $T$  and  $-p$ , respectively. The other three fundamental thermodynamic relations are similarly modified in multicomponent systems:

$$dH = T dS + V dp + \sum_i \left(\frac{\partial H}{\partial N_i}\right)_{S, p, N_j} dN_i \quad (5.3)$$

$$dF = -S dT - p dV + \sum_i \left(\frac{\partial F}{\partial N_i}\right)_{T, V, N_j} dN_i \quad (5.4)$$

$$dG = -S dT + V dp + \sum_i \left(\frac{\partial G}{\partial N_i}\right)_{T, p, N_j} dN_i \quad (5.5)$$

By virtue of the definitions of  $H$ ,  $F$ , and  $G$  (i.e.,  $H = U + pV$ ,  $F = U - TS$ ,  $G = H - TS$ ), the partial derivatives in the last terms in Eqs. 5.2 through 5.5 are all equal. All four represent equivalent definitions of the chemical potential,\*

$$\begin{aligned} \mu_i &= \left(\frac{\partial U}{\partial N_i}\right)_{S, V, N_j} \\ &= \left(\frac{\partial H}{\partial N_i}\right)_{S, p, N_j} \\ &= \left(\frac{\partial F}{\partial N_i}\right)_{T, V, N_j} \\ &= \left(\frac{\partial G}{\partial N_i}\right)_{T, p, N_j} \end{aligned} \quad (5.6)$$

### 5.3 CRITERIA OF CHEMICAL EQUILIBRIUM

If the components of a mixture can be converted from one to another (as in a true chemical reaction or in a process producing defects in a crystal), the quantities  $N_i$  will in due time attain equilibrium values. In the state of chemical equilibrium, there is no spontaneous tendency for the composition of the mixture to change, just as there is no tendency for the transfer of heat between regions of the same temperature.

\*The chemical potential was previously introduced in Sec. 1.4 in connection with the statistical treatment of ideal gases.

A quantitative description of the condition of chemical equilibrium can be obtained from the second law of thermodynamics. In an isolated system (i.e., one of fixed  $U$  and  $V$ ), the most probable, or equilibrium, state is the one in which the entropy is a maximum. If the system consists of a mixture of species capable of transforming to one another, the entropy attains a maximum at a particular composition. The primary goal of chemical thermodynamics is to determine this equilibrium composition and how it depends upon pressure and temperature.

Consider a reacting mixture constrained as an isolated system. When equilibrium is reached, we may write  $dS = 0$ , meaning that the system is at the maximum of the entropy-composition curve. Inasmuch as the system is isolated,  $dU = dV = 0$  for any changes in composition. Incorporating these restrictions upon the differentials in Eq. 5.2 results in

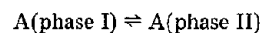
$$\sum_i \mu_i dN_i = 0 \quad (5.7)$$

Equation 5.7 is the starting point for thermodynamic calculations of equilibrium in ordinary chemical systems. It may not, however, be the most convenient basis for analyzing defect equilibria in crystals, partly because of the difficulty of clearly delineating species and reactions in such situations. An alternative statement of chemical equilibrium applicable to crystal thermodynamics can be obtained. Experimental measurements of equilibrium in chemical or crystal systems specify the temperature and pressure rather than the entropy and volume. The equilibrium statement can be conveniently cast in terms of the Gibbs free energy, for which  $T$  and  $p$  are the natural variables. For a system at equilibrium, Eq. 5.7 is valid no matter what restraints are placed on the system. Consequently, Eq. 5.5 shows that for composition changes about the equilibrium composition under conditions of constant temperature and pressure, the Gibbs free-energy variation must be zero, or

$$(dG)_{T, p} = 0 \quad (5.8)$$

Either Eq. 5.7 or Eq. 5.8 can be used as the basis for equilibrium determinations. The choice depends upon whether it is easier to describe the chemical potential of individual species in the mixture or the total free energy of the system. This is not a fundamental difference since  $\mu_i$  and  $G$  are related by the last equality of Eq. 5.6.

When Eq. 5.7 is used, several important relations can be obtained by using the fact that the differentials  $dN_i$  are not all independent. Consider first the equilibrium established between two phases of a single-component system, i.e., the equilibrium



The equilibrium condition, Eq. 5.7, becomes

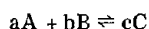
$$\mu_A^I dN_A^I + \mu_A^{II} dN_A^{II} = 0 \quad (5.9)$$

where  $\mu_A^I$  and  $\mu_A^{II}$  are the chemical potentials of substance  $A$  in phases I and II, respectively. Since the system contains a constant total mass of  $A$ , loss of  $A$  from one phase implies

an equivalent gain of A in the other phase, or  $dN_A^I = -dN_A^{II}$ . With this restriction Eq. 5.9 becomes

$$\mu_A^I = \mu_A^{II} \quad (5.10)$$

As a second example, consider the following simple chemical reaction occurring between the components of a single-phase ideal gas mixture:



where A, B, and C denote the molecular species and a, b, and c are the integral coefficients representing the numbers of molecules of each species consumed or produced as the reaction proceeds. The equilibrium condition of Eq. 5.7 is

$$\mu_A dN_A + \mu_B dN_B + \mu_C dN_C = 0 \quad (5.11)$$

Because of the relation between the amounts of A and B consumed and C produced stipulated by the coefficients a, b, and c, the values of dN in Eq. 5.11 are related by

$$dN_B = \frac{b}{a} dN_A$$

$$dN_C = -\frac{c}{a} dN_A$$

which, when used in Eq. 5.11, yields

$$a\mu_A + b\mu_B = c\mu_C \quad (5.12)$$

Results analogous to Eqs. 5.10 and 5.12 can be obtained for a system that simultaneously contains more than one phase and more than one component. In the general case, the condition of chemical equilibrium requires that the chemical potentials of all components be the same in all phases, or

$$\mu_i^I = \mu_i^{II} = \dots \quad (5.13)$$

In addition, for those components which are linked by a chemical reaction (which may occur in either phase):

$$\sum \nu_i \mu_i = 0 \quad (5.14)$$

where  $\nu_i$  denotes the integer coefficients in the reaction as written, taken as positive for reactants and negative for products. It is immaterial whether  $\mu_i$  in Eq. 5.14 represents phase I or phase II since the chemical potential of each species is the same in all coexistent phases.

The ultimate objective of an equilibrium calculation is to determine the equilibrium composition of a mixture. For single-phase systems, the starting point is the equilibrium criterion expressed either by Eq. 5.8 or by Eq. 5.14. If a definite reaction between the components of the mixture can be written, the calculation can be accomplished with Eq. 5.14. In many situations involving defects in solids, however, no such clear-cut reaction exists, and Eq. 5.8 is the more useful equilibrium condition. If the equilibrium is one of distribution of a species between two phases, Eq. 5.13 is the appropriate equilibrium statement.

## 5.4 STATISTICAL MECHANICAL TREATMENT OF CHEMICAL EQUILIBRIUM

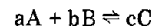
The behavior of a system can often be approximated on a microscopic level. Suppose that by one of the models discussed in Chaps. 1 and 2 (e.g., ideal gases or simple harmonic oscillators) the partition function of the mixture can be calculated directly as a function of T, V, and the number of molecules of each species present. The total Gibbs free energy of the system could then be computed directly with Eq. 1.30 (where all  $N_i$  would be held constant in the derivative term). Alternatively, the chemical potential can be obtained via the intermediary of the Helmholtz free energy, which is related to the partition function by Eq. 1.25 and to the chemical potential by the third equality of Eq. 5.6. Combining these two relations yields

$$\mu_i = -kT \left( \frac{\partial \ln Z}{\partial N_i} \right)_{T, V, N_j} \quad (5.15)$$

Whether Eq. 5.8, 5.13, or 5.14 is selected as the criterion for equilibrium, the partition function of the mixture must be known. The methods of computing this quantity starting from the partition functions of the components are different for ideal gases and solids.

### 5.4.1 Reactions in an Ideal Gas

Consider an ideal-gas mixture consisting of species A, B, and C which participate in the reaction



We wish to find the composition of A, B, and C in the mixture at equilibrium.

In Chap. 1, the partition function of an ideal gas in the pure state was shown to be

$$Z_i = \frac{z_i^{N_i}}{N_i!} \quad (5.16)$$

where  $N_i$  represents the number of molecules of species i contained in a volume V and  $z_i$  is the single-particle partition function of species i, which may be factored into components for translational and internal energy:

$$z_i = (z_i)_{tr} (z_i)_{int} \quad (5.17)$$

The translational partition function is

$$(z_i)_{tr} = V \left( \frac{2\pi m_i kT}{h^2} \right)^{3/2} \quad (5.18)$$

The partition function  $Z_i$  represents the total number of states (each weighted with a Boltzmann factor) accessible to species i in volume V. In an ideal-gas mixture, each component occupies the same volume and is unaffected by the presence of the other components (except of course during molecular collisions when reaction may occur). To determine the total partition function of the mixture, we recognize that each microstate of one component may coexist with any of the possible microstates of each of the other components. The total partition function of the mixture of A, B, and C is thus

$$Z = Z_A Z_B Z_C$$

or

$$Z = \frac{z_A^{N_A} z_B^{N_B} z_C^{N_C}}{N_A! N_B! N_C!} \quad (5.19)$$

The total partition function can be substituted into Eq. 5.15 to determine the chemical potential of each species. For species A

$$\begin{aligned} \mu_A &= -kT \left( \frac{\partial \ln Z}{\partial N_A} \right)_{T, V, N_B, N_C} \\ &= -kT \left( \frac{\partial}{\partial N_A} \right) (N_A \ln z_A - \ln N_A!) \end{aligned}$$

or, using Stirling's approximation ( $\ln N_A! = N_A \ln N_A - N_A$ ),

$$\mu_A = -kT \ln \left( \frac{z_A}{N_A} \right) \quad (5.20)$$

Similar expressions apply to components B and C.

Substituting the chemical potentials into the equilibrium criterion, Eq. 5.12, yields

$$\frac{N_C^c}{N_A^a N_B^b} = \frac{z_C^c}{z_A^a z_B^b} \quad (5.21)$$

Now, substituting Eqs. 5.17 and 5.18 for the single-particle partition functions in Eq. 5.21 yields

$$\begin{aligned} \frac{(N_C/V)^c}{(N_A/V)^a (N_B/V)^b} &= \\ &= \frac{\left( \frac{2\pi m_C kT}{h^2} \right)^{(3/2)c} (z_C^c)_{\text{int}}^c}{\left( \frac{2\pi m_A kT}{h^2} \right)^{(3/2)a} \left( \frac{2\pi m_B kT}{h^2} \right)^{(3/2)b} (z_A^a)_{\text{int}}^a (z_B^b)_{\text{int}}^b} \end{aligned} \quad (5.22)$$

The quantities on the left-hand side of Eq. 5.22 are the molecular concentrations of the species in the mixture

$$n_i = \frac{N_i}{V} \quad (5.23)$$

Although it has not yet been stated explicitly, the partition functions on the right-hand side of Eq. 5.22 must all be reckoned from the same reference energy. Each of the molecular species represented by A, B, and C has its own zero energy level or ground state wherein each of the

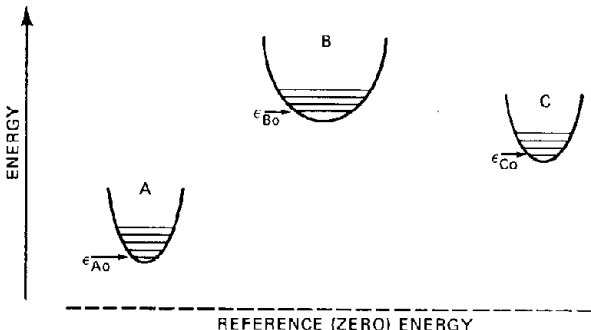


Fig. 5.1 Energy levels in molecules A, B, and C.

quantum numbers associated with vibration, rotation, and electronic excitation takes on its lowest possible values. However, because of the potential energy of the bonds joining the atoms in the three types of molecules, the zero energies in A, B, and C are not the same, as illustrated by Fig. 5.1. The common reference energy has been arbitrarily chosen somewhat below the zero energy level of each of the molecules. The potential wells shown in Fig. 5.1 represent the states accessible to a particular form of energy in each of the molecules, say vibrational energy. The ground-state energies of the three species are denoted by  $\epsilon_{A0}$ ,  $\epsilon_{B0}$ , and  $\epsilon_{C0}$ .

Each of the partition functions in Eq. 5.22 is computed with respect to the common reference energy:

$$\begin{aligned} (z_i)_{\text{int}} &= \exp \left( -\frac{\epsilon_{i0}}{kT} \right) + \exp \left( -\frac{\epsilon_{i1}}{kT} \right) + \dots \\ &= \exp \left( -\frac{\epsilon_{i0}}{kT} \right) \left[ 1 + \exp \left( -\frac{\epsilon_{i1} - \epsilon_{i0}}{kT} \right) + \dots \right] \end{aligned} \quad (5.24)$$

When the quantity  $\exp(-\epsilon_{i0}/kT)$  is factored out, the term in brackets in Eq. 5.24 is seen to represent the single-particle partition function above the ground state of the particular species. It is this quantity, denoted by  $(z_i^0)_{\text{int}}$ , which is calculable by the method of Chaps. 1 and 2. Thus, Eq. 5.24 can be written as

$$(z_i)_{\text{int}} = \exp \left( -\frac{\epsilon_{i0}}{kT} \right) (z_i^0)_{\text{int}} \quad (5.25)$$

Substituting Eqs. 5.23 and 5.25 into the equilibrium condition of Eq. 5.22 yields

$$\begin{aligned} K &= \frac{n_C^c}{n_B^b n_A^a} = \frac{\left( \frac{2\pi m_C kT}{h^2} \right)^{(3/2)c}}{\left( \frac{2\pi m_A kT}{h^2} \right)^{(3/2)a} \left( \frac{2\pi m_B kT}{h^2} \right)^{(3/2)b}} \\ &\quad \times \frac{(z_C^0)_{\text{int}}^c}{(z_A^0)_{\text{int}}^a (z_B^0)_{\text{int}}^b} \exp \left( -\frac{\Delta \epsilon_0}{kT} \right) \end{aligned} \quad (5.26)$$

where  $\Delta \epsilon_0$  is the energy of the reaction at  $0^\circ \text{K}$ :

$$\Delta \epsilon_0 = c\epsilon_{C0} - a\epsilon_{A0} - b\epsilon_{B0} \quad (5.27)$$

and is the energy required to convert a molecules of A and b molecules of B to c molecules of C at absolute zero. If  $\Delta \epsilon_0 > 0$ , the reaction is said to be endothermic. If  $\Delta \epsilon_0 < 0$ , the reaction is exothermic and a release of energy accompanies the reaction.

Equation 5.26 is a form of the law of mass action. It relates the ratio of concentrations at equilibrium to properties of the individual molecules and the temperature. The ratio  $n_C^c/n_A^a n_B^b$  is the equilibrium constant of the reaction in concentration units. It is often convenient to express the equilibrium constant in terms of partial pressures instead of concentrations. Since the mixture is an ideal gas, these units are related by

$$p_i = n_i kT \quad (5.28)$$

and the equilibrium constant in terms of partial pressures is

$$\begin{aligned}
 K_p &= \frac{p_C^c}{p_A^a p_B^b} \\
 &= K(kT)^{c-a-b} \\
 &= \left(\frac{2\pi}{h^2}\right)^{(3/2)(c-a-b)} (kT)^{(5/2)(c-a-b)} \\
 &\quad \times \left(\frac{m_C^c}{m_A^a m_B^b}\right)^{(3/2)} \frac{(z_C^0)^c}{(z_A^0)^a (z_B^0)^b} \exp\left(-\frac{\epsilon_0}{kT}\right) \quad (5.29)
 \end{aligned}$$

The equilibrium constant in terms of  $K_p$  is most commonly used to describe the chemical equilibrium among ideal gases.

### 5.4.2 Reactions in a Crystalline Solid

The equilibrium analysis developed in the preceding section for an ideal gas cannot be applied to the equilibrium between various defect components of a crystalline solid. The reason is that the atoms in a crystal may occupy only definite sites, whereas a particle in an ideal gas may at any instant occupy any position within the container. The question of distinguishability of sites but not atoms again affects the thermodynamics.

Consider the following simple situation. Suppose a region contains  $N_s$  localized sites into which an atom may be placed (see Fig. 5.2). The reference state is taken as free atoms outside the region containing the sites. On entering a

where  $z^0$  is the single-particle partition function referred to the ground vibrational state  $[(1 - e^{-h\nu/kT})^{-3}$  for a three-dimensional oscillator].

When  $N < N_s$ , additional states become available to the system, and these must be included in the partition function. The additional states are due to the number of different ways that  $N$  indistinguishable atoms can be distributed among  $N_s$  distinguishable sites. The partition function of Eq. 5.30 is multiplied by a combinatorial factor that represents the additional states made available when  $N < N_s$ . This additional factor is called the configurational partition function, since it depends only upon the arrangements of particles and not on their energies. The configurational partition function is determined by combinatorial analysis.

For the simple case of distribution of  $N$  atoms among  $N_s$  sites, the configurational partition function is determined as follows. With all sites initially empty,

The first atom may be placed into any of  $N_s$  sites

The second atom may be placed into any of the remaining  $N_s - 1$  sites

⋮

The  $N$ th atom may be placed in any of the remaining  $N_s - (N - 1)$  sites

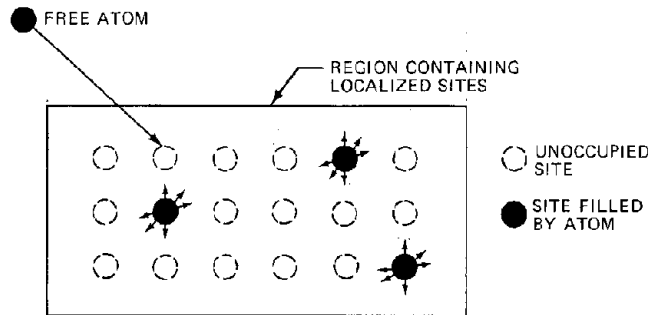


Fig. 5.2 Filling of sites in a crystal lattice.

site, an atom becomes a simple harmonic oscillator in three dimensions. The energy difference between the ground state of the oscillator and the free atom is  $\epsilon_0$ . If  $N$  atoms are introduced into the region containing the localized sites, what is the partition function of the mixture of  $N$  atoms and  $N_s - N$  empty sites?

If every site is filled with an atom ( $N = N_s$ ), we already know the answer; the system represents a perfect crystal corresponding to the Einstein model, and its partition function, denoted by  $Z^*$ , is

$$Z^* = z^N \quad (5.30)$$

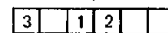
Where, according to Eq. 2.19, the single-particle partition function is

$$z = \exp\left(-\frac{\epsilon_0}{kT}\right) z^0 \quad (5.31)$$

If each atom were distinguishable, the total number of ways that the filling process could be accomplished is

$$N_s(N_s - 1) \dots (N_s - N + 1) = \frac{N_s!}{(N_s - N)!} \quad (5.32)$$

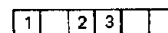
However, the atoms are not distinguishable—only the sites are. For example, for  $N_s = 6$  and  $N = 3$ , the arrangement (numbers represent atoms 1, 2, and 3; the boxes, sites)



is distinct from



but is not distinct from



Therefore, the factor of Eq. 5.32 contains too many states, and we must divide it by the total number of permutations of  $N$  atoms among themselves to obtain the correct factor. The configurational partition function is then

$$W = \frac{N_s!}{(N_s - N)!N!} \quad (5.33)$$

Hence, the total partition function of  $N$  atoms distributed randomly on  $N_s$  sites is

$$Z = \frac{N_s!}{(N_s - N)!N!} z^N \quad (5.34)$$

The combinatorial factor  $W$  may be regarded as providing additional entropy to the system. According to Eqs. 5.33 and 5.34,

$$Z = Wz^N \quad (5.35)$$

and the entropy of the mixture is related to  $Z$  by Eq. 1.17. Since  $W$  is independent of temperature, insertion of Eq. 5.35 into Eq. 1.17 yields

$$S = k \ln W + k \ln Z^* + kT \left( \frac{\partial \ln Z^*}{\partial T} \right)_V \quad (5.36)$$

The last two terms in Eq. 5.36 represent the entropy of the perfect crystal. The first term on the right-hand side is often called the configurational entropy, or the entropy of mixing,

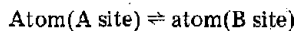
$$S_{\text{mix}} = k \ln W \quad (5.37)$$

When  $W$  has the particular form given by Eq. 5.33, the entropy of mixing is (after using Stirling's approximation)

$$S_{\text{mix}} = -k \left[ N \ln \left( \frac{N}{N_s} \right) + (N_s - N) \ln \left( \frac{N_s - N}{N_s} \right) \right] \quad (5.38)$$

The entropy of mixing given by Eq. 5.38 is valid only for the particular case of  $N$  particles randomly placed on  $N_s$  sites (or equivalently,  $N_A$  and  $N_B$  particles randomly occupying  $N_A + N_B$  sites). In more complex defect equilibria, the form of  $W$  is much more complex than Eq. 5.33, and the configurational entropy of the system is no longer given by Eq. 5.38.

Now suppose that there are two types of sites into which a free atom may be placed. There are  $N_{sA}$  A-type sites and  $N_{sB}$  B-type sites containing  $N_A$  and  $N_B$  atoms, respectively. We wish to determine the equilibrium ratio of  $N_A$  to  $N_B$ , or the equilibrium of the reaction



For this very simple reaction, the condition of chemical equilibrium is that the chemical potential of the atom on the A site be equal to the chemical potential of the atom on the B site, or

$$\mu_A = \mu_B \quad (5.39)$$

The total partition function of the mixture (i.e., atoms on A sites and on B sites) is the product of the partition functions for each site:

$$Z = Z_A Z_B \quad (5.40)$$

where  $Z_A$  and  $Z_B$  denote the partition functions of  $N_A$  atoms on  $N_{sA}$  sites and  $N_B$  atoms on  $N_{sB}$  sites, respectively. Each is given by a formula of the type represented by Eq. 5.34, or

$$Z = \frac{N_{sA}!}{(N_A!)(N_{sA} - N_A)!} z_A^{N_A} \frac{N_{sB}!}{(N_B!)(N_{sB} - N_B)!} z_B^{N_B} \quad (5.41)$$

where  $z_A$  and  $z_B$  are the single-particle partition functions for the atom on sites A and B, respectively.

The chemical potentials are evaluated from Eq. 5.15 with Eq. 5.41. The chemical potential of atoms on the A sites is

$$\begin{aligned} \mu_A &= -kT \left( \frac{\partial \ln Z}{\partial N_A} \right)_{T, V, N_B} \\ &= -kT \left( \frac{\partial \ln Z_A}{\partial N_A} \right)_{T, V} \\ &= -kT \ln \left[ \left( \frac{N_{sA} - N_A}{N_A} \right) z_A \right] \end{aligned} \quad (5.42)$$

A similar equation can be obtained for  $\mu_B$ . Equating  $\mu_A$  and  $\mu_B$  yields

$$\frac{N_A / (N_{sA} - N_A)}{N_B / (N_{sB} - N_B)} = \frac{z_A}{z_B} \quad (5.43)$$

The reference energy for the partition functions  $z_A$  and  $z_B$  is that of the free atom outside the region containing the sites. These partition functions can be converted to partition functions above the ground state of the atoms in each site by Eq. 5.31:

$$\frac{z_A}{z_B} = \left( \frac{z_A^0}{z_B^0} \right) \exp \left( - \frac{\Delta \epsilon_0}{kT} \right) \quad (5.44)$$

where

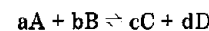
$$\Delta \epsilon_0 = \epsilon_{A0} - \epsilon_{B0} \quad (5.45)$$

If  $N_A \ll N_{sA}$  and  $N_B \ll N_{sB}$ , Eq. 5.43 can be written as a form of the law of mass action:

$$K = \frac{x_A}{x_B} = \left( \frac{z_A^0}{z_B^0} \right) \exp \left( - \frac{\Delta \epsilon_0}{kT} \right) \quad (5.46)$$

where  $x_i = N_i / N_{s_i}$  is the fraction of the sites available to species  $i$  which are occupied by that species. This result is quite similar in form to that obtained for the ideal gas reaction in the preceding section (Eq. 5.26, if the translational and internal partition functions are combined). However, the concentration units in Eq. 5.46 are atom fractions, and atom densities appear in Eq. 5.26.

Equilibrium analysis of defect-producing processes in solids more complex than the simple example considered here invariably results in a law of mass action similar in form to that of Eq. 5.46. A defecting process can be written as the reaction



where the species A, B, C, and D are localized on specified sites in the solid. Subject to the restriction that the number

of defects is much smaller than the number of sites, the general form of the law of mass action can be written as:

$$K = \frac{x_C^c x_D^d}{x_A^a x_B^b} = \alpha \frac{(z_C^0)^c (z_D^0)^d}{(z_A^0)^a (z_B^0)^b} \exp\left(-\frac{\Delta\epsilon_0}{kT}\right) \quad (5.47)$$

The parameters  $z_i^0$  and  $\Delta\epsilon_0$  have the same meaning as before. The quantity  $\alpha$  depends upon the combinatorial factor  $W$ . If  $W$  exhibits the simple random mixing form of Eq. 5.33 (but for four species in this case),  $\alpha$  is unity. If not,  $W$  must be computed by combinatorial analysis of the particular case, which may be very cumbersome.

In most solid-defecting processes, the ratio of the partition functions in Eq. 5.47 is known poorly, if at all. Consequently, this ratio is often set equal to unity. The numerical factor  $\alpha$  usually does not differ appreciably from unity. To avoid extensive combinatorial analysis, we can also set  $\alpha$  equal to unity, since such an approximation is no worse than setting the partition function ratio equal to unity. Thus, if a reaction describing the defecting process can be written, a law of mass action can, to a first approximation, be written as

$$\frac{x_C^c x_D^d}{x_A^a x_B^b} \simeq \exp\left(-\frac{\Delta\epsilon_0}{kT}\right) \quad (5.48)$$

which is probably accurate to within an order of magnitude. Such an approximation should not introduce any more error than is already present in the exact formulation of Eq. 5.47 owing to inaccurate measurement or calculation of the partition function ratio and the energy of the reaction.

### 5.4.3 Hybrid Mixtures

The previous sections considered mixtures either of ideal gases or atoms on localized sites. Free electrons in a metal represent a mixture in which one component (the electrons) behaves as an ideal gas and the other component (the ion cores) as particles on fixed sites. Another simple hybrid mixture is represented by the valence electrons, holes, and conduction electrons in an intrinsic semiconductor. In the case of free electrons in a metal, the total partition function of the metal can be written as

$$Z = Z_e Z_M \quad (5.49)$$

where  $Z_e$  is the partition function of the electrons (given by Eq. 1.51) and  $Z_M$  is the partition function of the metal (given by Eq. 2.19). Calculation of equilibria involving either the metal atoms or the electrons follows the same methods as outlined previously.

### 5.4.4 Two-Phase Equilibria Involving Solids

Important physical phenomena, such as the dissolution of a gas in a solid or the emission of electrons from a metal, involve the thermodynamic equilibrium of a component between a gaseous phase and a solid consisting of a mixture of metal atoms and the distributing species. The criterion for equilibrium is given by Eq. 5.10.

If the distributing species is an atom, the partition function of the solid phase is given by Eq. 5.40, where A is dissolved solute and B is host solid atom. If the distributing

species is an electron, the partition function of the solid phase is given by Eq. 5.49. If the distributing species and the atoms of the solid do not interact with each other, the chemical potential of the distributing species (which depends upon the derivative of the logarithm of  $Z$  with respect to the number of atoms of the solute) will be independent of the properties and number of host atoms. Or, the distributing species behaves as a single component in the solid phase insofar as its two-phase equilibrium behavior is concerned.

## 5.5 MACROSCOPIC THERMODYNAMIC TREATMENT OF CHEMICAL EQUILIBRIUM

Very many chemical systems are too complex to permit reasonable approximation of the total partition function, and so the chemical potential cannot be evaluated by Eq. 5.15. However, the equilibrium criteria expressed by Eqs. 5.13 and 5.14 are still valid and can be used to develop a law of mass action for the reacting system. We realize in advance that, by not knowing enough about the system to construct its partition function, we shall have to be satisfied with an equilibrium statement that contains less information than the equilibrium conditions derived from statistical mechanics.

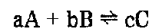
Since chemical potentials are still required, the macroscopic approach determines them from the definition

$$\mu_i = \left(\frac{\partial G}{\partial N_i}\right)_{T,p,N_j} \quad (5.50)$$

We again consider the cases of ideal gases and crystalline solids, but develop the equilibrium conditions without reference to statistical mechanical concepts.

### 5.5.1 Reactions in an Ideal-Gas Mixture

As in Sec. 5.4, the following reaction between ideal-gas components is considered:



The system is allowed to attain equilibrium at a temperature  $T$  and total pressure  $p$ . At equilibrium, the partial pressures of A, B, and C are  $p_A$ ,  $p_B$ , and  $p_C$ , respectively, and the total pressure is

$$p = p_A + p_B + p_C$$

The equilibrium mixture contains  $N_A$  moles of A,  $N_B$  moles of B, and  $N_C$  moles of C. The total number of moles is

$$N = N_A + N_B + N_C$$

Since the mixture is an ideal gas,

$$\frac{p_i}{p} = \frac{N_i}{N} \quad (i = A, B, C) \quad (5.51)$$

To determine the chemical potential by Eq. 5.50, we must obtain the total Gibbs free energy of the equilibrium

mixture. Inasmuch as the free energy is not an absolute quantity, its value is referred to an arbitrary reference state, or standard state. The standard state for an ideal gas is defined as the pure substance (as an ideal gas) at the temperature  $T$  in which we are interested but at a standard pressure  $p_0$  (which is usually taken to be 1 atm). The Gibbs free energy of the equilibrium mixture is computed with reference to the pure components in their standard states.

The method of preparing the equilibrium mixture from the pure components is shown in Fig. 5.3. The top of the sketch shows the components in their standard states, i.e., as pure gases at temperature  $T$  and at the standard pressure  $p_0$ . The Gibbs free energy per mole of the three species in their standard states is denoted by  $G_i^\circ$  ( $i = A, B, C$ ).

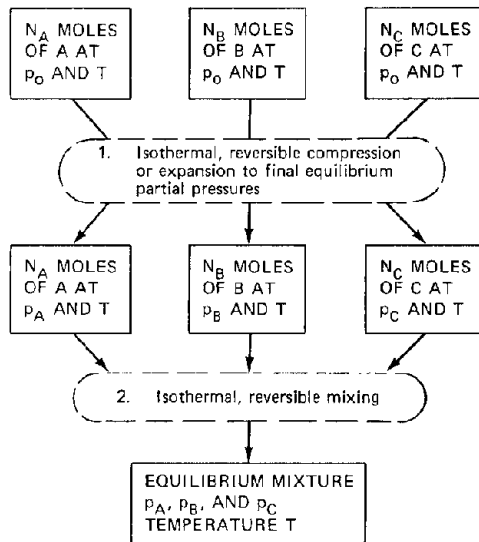


Fig. 5.3 Gibbs free-energy changes in producing the equilibrium mixture from the pure components in their standard states.

The first step in preparing the equilibrium mixture is to isothermally and reversibly compress or expand each of the pure gases to the final partial pressure they will have in the equilibrium mixture. The change in the Gibbs free energy of each component associated with this step is determined from the relationship

$$\left(\frac{\partial G}{\partial p}\right)_T = V = \frac{RT}{p}$$

Or, if the gas pressure is changed from  $p_0$  (in the standard state) to  $p_i$  (the final partial pressure in the equilibrium mixture), the associated change in free energy of component  $i$  is

$$G_i = G_i^\circ + RT \ln \left(\frac{p_i}{p_0}\right) \quad (5.52)$$

The final step is the isothermal, reversible mixing of the three gases. Since the gases are ideal, the mixing step involves no change in enthalpy. Since the gases are mixed in equilibrium proportions, no chemical reaction occurs during the mixing step. The mixing is reversible; so no increase in entropy is involved (just how this can be done is

discussed in the next section). Inasmuch as  $\Delta S$  and  $\Delta H$  are zero, there is no change in the Gibbs free energy as a result of the second (mixing) step.

The free energy of the equilibrium mixture differs from the free energy of the components in their standard states only because of the expansion—compression step. If  $N_A$ ,  $N_B$ , and  $N_C$  moles of each of the species are mixed in the manner just described, the Gibbs free energy of the mixture is

$$G = \sum_{i=A,B,C} N_i \left( G_i^\circ + RT \ln \frac{p_i}{p_0} \right)$$

or, using Eq. 5.51,

$$G = N_A G_A^\circ + N_B G_B^\circ + N_C G_C^\circ + RT \left( N_A \ln N_A + N_B \ln N_B + N_C \ln N_C - N \ln N + N \ln \frac{p}{p_0} \right) \quad (5.53)$$

The chemical potentials of A, B, and C in the mixture are obtained by substituting Eq. 5.53 into Eq. 5.50, which yields

$$\mu_i = G_i^\circ + RT \ln \frac{p_i}{p_0} \quad (i = A, B, C) \quad (5.54)$$

If the chemical potentials of the three species are used in the equilibrium condition of Eq. 5.12,

$$RT \ln \left[ \frac{(p_C/p_0)^c}{(p_A/p_0)^a (p_B/p_0)^b} \right] = -\Delta G^\circ \quad (5.55)$$

where  $\Delta G^\circ$  is the standard-state free-energy change of the reaction

$$\Delta G^\circ = cG_C^\circ - aG_A^\circ - bG_B^\circ \quad (5.56)$$

and is the change in Gibbs free energy when  $a$  moles of pure A and  $b$  moles of pure B are completely converted to  $c$  moles of pure C, all at temperature  $T$  and pressure  $p_0$ . If the pressure in the standard state is taken to be 1 atm, Eq. 5.55 becomes

$$K_p = \frac{p_C^c}{p_A^a p_B^b} = \exp \left( -\frac{\Delta G^\circ}{RT} \right) \quad (5.57)$$

and the partial pressures are in atmospheres. The free-energy change of the reaction can be expressed in terms of the enthalpy (or heat) of the reaction and the entropy change of the reaction:

$$\Delta G^\circ = \Delta H^\circ - T \Delta S^\circ \quad (5.58)$$

where  $\Delta H^\circ$  and  $\Delta S^\circ$  are defined in a manner similar to the definition of  $\Delta G^\circ$  by Eq. 5.56. The entropy of the reaction,  $\Delta S^\circ$ , does not include the entropy of mixing of the three gases since the process to which  $\Delta S^\circ$  refers involves the complete conversion of initially pure reactants to pure product.

The reaction enthalpy is a function of temperature. If  $\Delta H_0^\circ$  denotes the enthalpy change of the reaction at  $0^\circ\text{K}$ ,

$$\Delta H^\circ = \Delta H_0^\circ + \Delta(H^\circ - H_0^\circ)$$

where  $H^\circ - H_0^\circ$  is the enthalpy of a pure ideal gas at temperature  $T$  referred to the enthalpy at  $0^\circ\text{K}$ . The enthalpy\* of the reaction at  $0^\circ\text{K}$  is identical to the energy change of the reaction at  $0^\circ\text{K}$ ,  $\Delta E_0^\circ$ ; so Eq. 5.57 can be written as

$$K_P = \exp \left[ \frac{\Delta S^\circ}{R} - \frac{\Delta(H^\circ - H_0^\circ)}{RT} \right] \exp \left( -\frac{\Delta E_0^\circ}{RT} \right) \quad (5.59)$$

The quantity in the exponential term of Eq. 5.59,  $\Delta E_0^\circ/RT$ , is identical to the quantity in the exponential term of Eq. 5.29,  $\Delta c_0/kT$ . Therefore, the first terms on the right-hand sides of Eqs. 5.29 and 5.59 must also be identical. The statistical thermodynamic approach yields an expression for the equilibrium constant in terms of microscopic properties of the reactant and product molecules, namely, in terms of the single-particle partition functions for translation and internal energy. The macroscopic treatment leading to Eq. 5.59, on the other hand, relates the equilibrium constant to enthalpy and entropy differences between product and reactant species in a standard state. No attempt is made to relate  $\Delta H^\circ$  and  $\Delta S^\circ$  to fundamental properties of the molecules of A, B, and C.

Practical chemical equilibrium calculations (including calculations for systems that contain components other than ideal gases) are accomplished with the aid of extensive tabulations of measured  $\Delta G^\circ$  (or  $\Delta S^\circ$  and  $\Delta H^\circ$ ) values as functions of temperature for a large number of chemical reactions. Such compilations may be graphical (A. Glassner, *Thermochemical Properties of the Oxides, Fluorides, and Chlorides to 2500^\circ\text{K}*, USAEC Report ANL-5750) or in the form of equations (O. Kubaschewski, E. Evans, and C. Alcock, *Metallurgical Thermochemistry*, 4th ed., Pergamon Press, Inc., 1967). The publications of the National Bureau of Standards (NBS Technical Notes Nos. 270-3 to 270-7) provide the most up-to-date information on standard free energies of formation.

### 5.5.2 Reversible and Irreversible Mixing of Ideal Gases

The macroscopic approach to chemical-reaction equilibrium in an ideal-gas mixture relied upon the existence of a method for mixing species without incurring an entropy increase. Such a process requires one of the improbable hypothetical devices for which classical thermodynamics is well-known. The reversible mixing machine is shown in Fig. 5.4. It contains two compartments of equal volume, separated by a fixed semipermeable membrane through which only species A can pass. Semipermeable membranes are presumed to be completely impassable to all but a single species and are supposed to be available for any ideal gas. Two movable pistons are coupled by a connecting rod. One piston is a B-permeable membrane, and the other is impermeable to both A and B. The system is isothermal. It is designed to mix gases A and B, but similar devices can be constructed to prepare ternary mixtures.

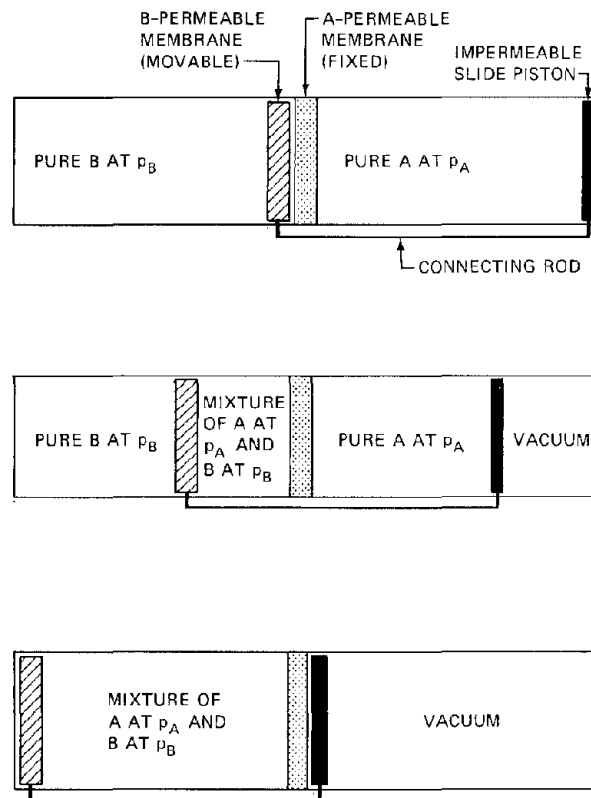


Fig. 5.4 Reversible mixing of two gases.

Suppose the device is loaded with pure A at pressure  $p_A$  in the right-hand compartment and pure B at pressure  $p_B$  in the left-hand compartment, and the connecting rod with its attached pistons is moved very slowly from right to left. There is no friction, and at each instant the partial pressures of A and B are equal on either side of their respective membranes. When the piston has moved as far to the left as possible, mixing is complete, as can be seen by the bottom diagram of Fig. 5.4. During movement from right to left, there is never any net force on the two-piston unit; so the work required to perform the mixing is zero. The internal energy of the two ideal gases is the same whether they are mixed or unmixed. Therefore, by the first law of thermodynamics, no heat is exchanged between the system (the mixing device) and the surroundings during the mixing process. For a reversible process, which this is presumed to be, the entropy change is the heat added divided by the temperature. If no heat is exchanged in the process, the entropy change is also zero. The mixing process of Fig. 5.4 involves no increase in entropy and is therefore reversible.

It is, of course, quite simple to conceive of ways of mixing gases which do increase the entropy of the system. Simply allowing two pure gases, initially at the same pressure and temperature, to mix by opening a valve or partition between them is one such method. The entropy increase in this totally irreversible process is the entropy of mixing, which can be calculated by reference to Fig. 5.5. From the reversible mixing machine of Fig. 5.4, we know that the entropy of pure A and pure B is the same as the entropy of the mixture provided that the partial pressures

\*The enthalpy change and the energy change of the reaction are related by  $\Delta H^\circ = \Delta E^\circ + p_0 \Delta V$ . Since the reactants and products are ideal gases,  $p_0 \Delta V = RT(c - a - b)$ . Therefore at  $T = 0^\circ\text{K}$ ,  $p_0 \Delta V = 0$  and  $\Delta H_0^\circ = \Delta E_0^\circ$ .

of the components in the mixture are the same as in the pure state (this is called Gibbs's theorem). If we start with pure A at pressure  $p_A$  and pure B at pressure  $p_B$  and isothermally compress each gas to the final total pressure of the mixture (i.e.,  $p = p_A + p_B$ ), the entropy decrease due to compression is

$$S_{\text{comp}} = -R \left[ N_A \ln \left( \frac{p_A + p_B}{p_A} \right) + N_B \ln \left( \frac{p_A + p_B}{p_B} \right) \right]$$

(this relation is obtained from Eq. 5.52, since  $\Delta H = 0$  for isothermal compression of an ideal gas and hence  $\Delta S = -\Delta G/T$ ).

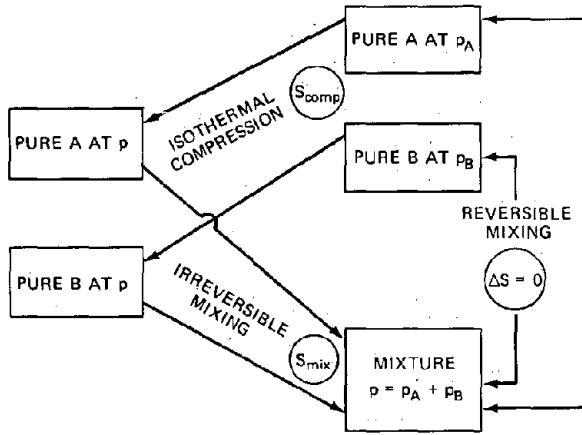


Fig. 5.5 Reversible and irreversible mixing.

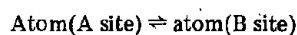
Next, the two gases are allowed to interdiffuse to attain the final mixture. The entropy change in this step is  $S_{\text{mix}}$ . Now, the sum of  $S_{\text{comp}}$  and  $S_{\text{mix}}$  is zero (since the initial and final states of this two-step process are the same as those in Fig. 5.4, for which  $\Delta S = 0$ ). Therefore, the entropy of mixing of two gases initially at the same total pressure is

$$S_{\text{mix}} = -R \left[ N_A \ln \left( \frac{N_A}{N_A + N_B} \right) + N_B \ln \left( \frac{N_B}{N_A + N_B} \right) \right] \quad (5.60)$$

where the partial pressures in the logarithmic terms have been replaced by numbers of moles. Equation 5.60 is identical to Eq. 5.38 if  $N_A$  is identified with  $N$  and  $N_B$  with  $N_s - N$ . Despite the profound differences between the thermodynamics of ideal gases and crystalline solids, the entropy change resulting from random mixing of two components is the same in both instances. Equation 5.60 can also be directly proven by using a statistical mechanical approach and starting with Eq. 5.19.

### 5.5.3 Reactions in a Crystalline Solid

Contrary to the description of reactions in an ideal gas, the macroscopic description of reactions in a crystalline solid requires some help from statistical concepts. The blending of macroscopic and statistical thermodynamic methods can again be illustrated by the simple reaction



for which the equilibrium condition is given by Eq. 5.46. In the present development, the chemical potentials  $\mu_A$  and  $\mu_B$  are obtained from Eq. 5.50 instead of Eq. 5.15. We need, therefore, a method of describing the Gibbs free energy of the mixture containing atoms on A and B sites,  $G(N_A, N_B)$ . Let us select as a reference state the system with all A sites and all B sites empty. If an atom is added to an A site from the pool of free atoms (see Fig. 5.2), the Gibbs free-energy change is denoted by  $g_{0A}$ , where

$$g_{0A} = h_{0A} - T s_{0A} \quad (5.61)$$

and  $h_{0A}$  is the enthalpy difference between an atom in site A and a free atom. The entropy term  $s_{0A}$  is due to the vibrational motion acquired by the atom when it is placed in an A site; it does not include the entropy of mixing, which will be considered separately. A similar free-energy change can be written for atoms placed in B sites.

The total change in system free energy when  $N_A$  free atoms are placed in A sites and  $N_B$  free atoms are placed in B sites is

$$G(N_A, N_B) - G(0, 0) = N_A g_{0A} + N_B g_{0B} - T S_{\text{mix}} \quad (5.62)$$

The last term in Eq. 5.62 represents the stabilizing effect of the many possible ways of placing the atoms in the two types of sites; since  $S_{\text{mix}}$  is always positive, this term leads to a decrease in the free energy. The  $T S_{\text{mix}}$  term represents a Gibbs free energy of mixing since  $G_{\text{mix}} = H_{\text{mix}} - T S_{\text{mix}}$  and  $H_{\text{mix}} = 0$  for the mixing process.

Macroscopic thermodynamics provides no device for calculating  $S_{\text{mix}}$  in solids comparable to the reversible mixing machine for ideal gases (Fig. 5.4). Instead  $S_{\text{mix}}$  is computed from the statistical concepts introduced in Sec. 5.4. In particular,  $S_{\text{mix}}$  is given by Eq. 5.37, which for the reaction considered here becomes

$$S_{\text{mix}} = k \ln \left[ \frac{N_{sA}!}{N_A! (N_{sA} - N_A)!} \frac{N_{sB}!}{N_B! (N_{sB} - N_B)!} \right] \quad (5.63)$$

Equilibrium is determined by using Eq. 5.62 in Eq. 5.50 to obtain the chemical potentials and then equating  $\mu_A$  and  $\mu_B$ . The final expression for the case of low occupancy of available sites is

$$\begin{aligned} K &= \frac{x_A}{x_B} \\ &= \exp \left( -\frac{\Delta g_0}{kT} \right) \\ &= \exp \left( \frac{\Delta s_0}{k} \right) \exp \left( -\frac{\Delta \epsilon_0}{kT} \right) \end{aligned} \quad (5.64)$$

where

$$\begin{aligned} \Delta g_0 &= g_{0A} - g_{0B} \\ &= \Delta h_0 - T \Delta s_0 \\ &\approx \Delta \epsilon_0 - T \Delta s_0 \end{aligned} \quad (5.65)$$

The enthalpy difference between atoms in A and B sites,  $\Delta h_0$ , has been approximated by the energy difference  $\Delta \epsilon_0$ . The difference between  $\Delta h_0$  and  $\Delta \epsilon_0$  is  $p \Delta v_0$ , where

$\Delta v_0$  is the volume change of the system when an atom moves from an A site to a B site. For reactions in the crystalline state, such volume changes are nearly always sufficiently small to permit enthalpy changes to be approximated by energy changes. The  $p \Delta v_0$  needs to be included only when the effect of very large pressures on a solid-state equilibrium is considered.

Comparing the mass action law of Eq. 5.64 and the one developed by purely statistical methods, Eq. 5.46, shows that the partition-function ratio in the latter is identified with the vibrational entropy difference between the atom in site A and in site B:

$$\Delta s_0 = k \ln \left( \frac{z_A^0}{z_B^0} \right) \quad (5.66)$$

The entropy difference  $\Delta s_0$  is often called the excess entropy since it does not include the entropy of mixing. In equilibria in which all species are components of a solid, the excess entropy arises from differences in the vibrational motion of the atom in various sites in the solid. Since this effect is difficult to calculate, the excess entropy is often set equal to zero, which corresponds to setting the partition-function ratio equal to unity. The standard entropy of reaction in an ideal gas ( $\Delta S^\circ$  in Eq. 5.59) is generally much more precisely known than the excess entropy of a solid-state reaction.

### 5.6 NOMENCLATURE

- $\Delta E_0^\circ$  = energy change of reaction at  $0^\circ\text{K}$
- F = Helmholtz free energy
- G = Gibbs free energy
- g = Gibbs free energy per atom
- $\Delta G^\circ$  = standard-state free-energy change of the reaction
- h = Planck's constant
- H = enthalpy
- $\Delta H^\circ$  = standard-state enthalpy change of reaction at temperature T
- $\Delta H_0^\circ$  = enthalpy change of reaction at  $0^\circ\text{K}$
- k = Boltzmann constant
- K = equilibrium constant of a reaction
- $K_p$  = equilibrium constant of a reaction in terms of partial pressures
- m = mass of an atom
- n = molecular concentration of a component in a mixture
- N = number of molecules or moles of a component in a mixture
- $N_s$  = number of sites
- p = pressure
- $p_0$  = standard pressure
- R = gas constant
- S = entropy
- $s_{0i}$  = entropy due to the vibrational motion acquired by the atom when it is placed in site i
- $\Delta s_0$  = excess entropy
- $\Delta S^\circ$  = standard-state entropy change of reaction
- T = temperature
- U = internal energy
- V = volume
- W = configurational partition function

- x = fraction of available sites which are occupied
- z = single-particle partition function
- $z^0$  = single-particle partition function above ground state
- Z = partition function of the mixture
- $Z^*$  = perfect-crystal partition function

#### Greek Letters

- $\epsilon$  = energy level
- $\epsilon_{i0}$  = ground-state energy of species i
- $\Delta \epsilon_0$  = energy of reaction at  $0^\circ\text{K}$ ; energy difference between atom in A site and in B site
- $\mu$  = chemical potential
- $\nu$  = frequency of a three-dimensional oscillator; integer coefficient of components in a chemical reaction

#### Subscripts

- comp = compression
- e = electrons
- i = component in a mixture
- int = internal energy component
- mix = mixing (e.g., entropy)
- M = metal
- tr = translational energy component

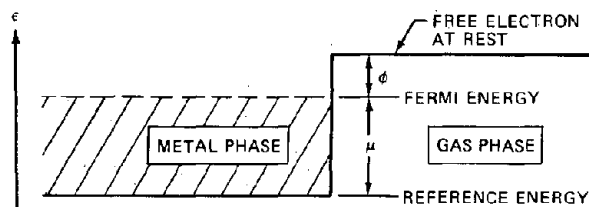
### 5.7 PROBLEMS

5.1 Show that the chemical potential can be expressed as

$$\mu_i = -T \left( \frac{\partial S}{\partial N_i} \right)_{U, V, N_j} = \left( \frac{\partial F}{\partial N_i} \right)_{T, V, N_j} = \left( \frac{\partial G}{\partial N_i} \right)_{T, p, N_j}$$

where S is the entropy, F is the Helmholtz free energy, G is the Gibbs free energy, and  $N_i$  is the number of moles of species i in the mixture.

5.2 The lowest possible energy of a conduction electron in a metal is  $\mu + \phi$  below the energy of a free electron at rest in the gas phase. (See diagram.) Here  $\mu$  is the chemical potential of the conduction electrons and  $\phi$  is the work function of the metal. Consider an electron gas outside the metal in thermal equilibrium with the electrons in the metal at temperature T. The density of the electron gas outside the metal is low enough to permit application of the dilute ideal-gas partition function.

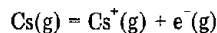


(a) Using equilibrium considerations, find the density of electrons in the gas outside the metal which are at equilibrium with the conduction electrons inside the metal.

(b) The principle of detailed balance states that at equilibrium the rate of an elementary process must be equal to the rate of the reverse elementary step. Use this principle to calculate the number of electrons emitted per second per unit area from the surface of the metal at temperature T. Assume that all electrons striking the metal from the gas phase stick.

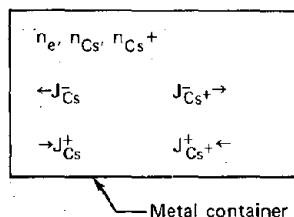
The emission rate so computed is independent of the density of electrons in the gas phase. It applies to highly nonequilibrium situations, such as vacuum outside the metal. The emission rate expression is known as Richardson's equation and is widely used in the analysis of thermionic emission.

5.3 The following equilibrium is established in a gas containing cesium vapor:



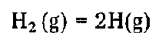
(a) Apply the law of mass action to this equilibrium, and determine the ratio of the atom densities of  $\text{Cs}^+$  to Cs in the gas phase. Express the equilibrium constant in terms of the partition functions of each species and the ionization potential of cesium,  $I$ . Neglect electronic excitation of the cesium species, and consider the electron density in the gas to be specified. (This is a form of Saha's equation, which is important in some plasma problems.)

(b) Suppose the container of cesium vapor is a metal of work function  $\Phi$ . Cesium ions and neutrals strike the metal surface from the gas phase and are adsorbed. The same species are also desorbed from the metal. Apply the principle of detailed balance to determine the ratio of ions to neutrals in the cesium leaving the surface. As in the case of electrons, this ratio is valid whether or not an equilibrium gas phase is present. (This ratio is known as the Saha-Langmuir equation.)



5.4 Using the methods of problem 1.1, show that the chemical potential defined by Eq. 5.15 is identical to that defined by Eq. 1.38. To do this, note that Eq. 1.38 leads to Eqs. 1.51 and 1.52; so it is sufficient to show that these two equations satisfy Eq. 5.15. Also note that the chemical potential of a single-component system is a function of  $T$  and  $N/V$  only.

5.5 (a) Derive the equilibrium constant,  $K_p$ , for the dissociation of gaseous hydrogen:

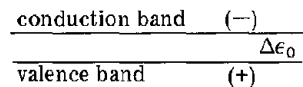


The dissociation energy of  $\text{H}_2$  is  $D$ , and the internal partition function (which is due primarily to rotation of the molecule) is  $(z_2)_{\text{int}}$ .

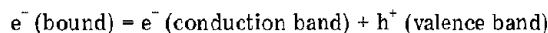
(b) In terms of  $K_p$ , what is the degree of dissociation of hydrogen at a temperature  $T$  and a total pressure  $P$ ?

5.6 Show that the portions of Eqs. 5.29 and 5.59 preceding the exponentials are identical if the definitions of entropy and enthalpy in terms of the partition function are used.

5.7 A semiconductor is a solid in which a few bound electrons from the valence band are excited to the conduction band, leaving an equal number of positive holes behind.



The reaction may be written:



The energy required for this reaction at  $0^\circ\text{K}$  is  $\Delta\epsilon_0$ , which is called the band gap. The system may be regarded as a mixture of  $N_b$  bound electrons,  $N_h$  holes, and  $N_e$  conduction electrons, where  $N_e$  and  $N_h$  are  $\ll N_b$ . The conduction electrons and holes may be treated as components of an ideal gas in the low-density limit, possessing two spin states. The bound electrons may be considered as localized particles with very high vibrational frequency.

- (a) What is the total partition function of the mixture?  
 (b) What is the criterion for equilibrium?  
 (c) What is the chemical potential of each of the species?  
 (d) What is the law of mass action for this system?

5.8 If  $\text{M}(\text{s})$  is a solid metal immiscible with its oxide  $\text{MO}_2(\text{s})$ , show that the standard free-energy change of the reaction  $\text{M}(\text{s}) + \text{O}_2(\text{g}) = \text{MO}_2(\text{s})$  is given by  $\Delta G^0 = RT \ln p_{\text{O}_2}$ , where  $p_{\text{O}_2}$  is the equilibrium oxygen pressure. According to the phase rule, how many degrees of freedom does the system have? What happens if the oxygen pressure is reduced below the value calculated above?

5.9 Gases such as helium and hydrogen dissolve in metals as monatomic species. In the solid the solute atoms behave as simple harmonic oscillators in three dimensions with a vibration frequency  $\nu$ . They are present only on specific sites in the lattice. The gas phase is considered ideal, and monatomic gas atoms possess only translational kinetic energy.

(a) *Helium:* Helium is believed to reside in substitutional positions in the metal lattice. There are  $N_s$  lattice sites per unit volume. The energy difference between free helium atoms and these atoms in their ground vibrational state in the lattice (i.e., the heat of solution) is positive and approximately equal to the energy required to remove a metal atom from a lattice site and place it on the surface. The interaction of dissolved helium atoms with the metal atoms around it is negligible. Consequently, the heat of solution is approximately equal to the energy of vacancy formation of the metal,  $\epsilon_v$ . For helium gas at pressure  $p$  in equilibrium with a metal at temperature  $T$ , derive the expression for the ratio of the equilibrium pressure to  $x$ , the atom fraction of helium in the metal. Assume  $x \ll 1$ . Calculate the equilibrium pressure of helium over nickel containing 1 atomic part per million of dissolved helium at  $500^\circ\text{C}$ . The vacancy-formation energy in nickel is 1.4 eV. The helium atom vibration frequency is  $10^{13} \text{ sec}^{-1}$ .

(b) *Hydrogen:* The solution of hydrogen in metals is treated in a slightly different manner from that of inert

gases, such as helium. First,  $H_2$  dissociates upon entering the metal and, furthermore, dissolves as a proton. Because of the strong interaction of the proton with the conduction electrons in the metal, energy is released when an H atom enters the metal. This heat of solution,  $\epsilon_H$ , is the difference between the energy of a gas-phase H atom and the proton in the solid. Second, hydrogen is located in interstitial sites in the lattice of which there are  $N_{si}$  per unit volume. Generally,  $N_{si} > N_g$ . Finally, hydrogen exists in the gas primarily as  $H_2$ , although at equilibrium some H is present owing to dissociation (see problem 5.5).

Derive the expression for the solubility of hydrogen in a metal when the  $H_2$  pressure in the gas is  $p_2$ . This result is called the Fowler–Smithells equation.

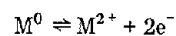
5.10 Indicate which of the following statements are true and which are false for equilibrium between phases I and II, and show the reasons for your answers.

(a) For a single-component system, the Gibbs free energy of phase I,  $g_I$ , equals the Gibbs free energy of phase II,  $g_{II}$ .

(b) For a system containing components A and B in both phases, the Gibbs free energy of phase I,  $g_I$ , equals the Gibbs free energy of phase II,  $g_{II}$ .

(c) For a system containing components A and B in each of the two phases, the Gibbs free energy of component A in phase I,  $g_{IA}$ , equals the Gibbs free energy of component A in phase II,  $g_{IIA}$ .

5.11 A solid material emits electrons thermionically, with a work function  $\phi$ . The solid is in equilibrium with its vapor according to the Clapeyron equation,  $p = A \exp(-\Delta H_s/kT)$ . The vapor is in equilibrium with its ionization products according to the reaction



for which  $I$  = double ionization energy. Calculate the equilibrium concentration of  $M^{2+}$  in the vapor at a specified temperature  $T$ .

# Chapter 6

## Point Defects in Solids

### 6.1 TYPES OF LATTICE IMPERFECTIONS

Chapters 2 and 4 deal with the properties of hypothetical perfect crystals in which every lattice point is occupied by an atom or ion. No faults marred the regularity of the crystal structure. All real crystals, however, no matter how carefully prepared, contain a number of defects, or imperfections, and these defects can be classified according to their dimension.

The zero dimensional defect, or *point defect*, is an imperfection associated with one or perhaps two lattice sites. This class of defects includes vacancies, interstitial atoms, and impurity atoms. The vacancy and the interstitial are intrinsic point defects since they do not depend upon the presence of a foreign substance as does the impurity. In fact, vacancies and interstitials must exist in any crystal. Thermodynamically, a perfect crystal is possible only at 0°K.

Point defects are of interest because their presence controls the mobility of the atoms in the solid. In addition, the primary effect of high-energy radiation in a solid is to create point defects (i.e., vacancy—interstitial pairs) by dislodging atoms from normal lattice sites. The subsequent behavior of the radiation-produced point defects exerts a profound influence on the properties of the irradiated material. The point defects may anneal out, either by vacancy—interstitial annihilation or by migration to sinks, such as free or internal surfaces. Alternatively, vacancies and interstitials may agglomerate into two-dimensional defects (vacancy or interstitial sheets) or three-dimensional imperfections (voids).

All real crystals contain one-dimensional (line) defects called *dislocations*, and two-dimensional defects, of which *grain boundaries* are the most important. The latter may be regarded as internal surfaces. These defects are produced during growth and by stressing of the crystalline solid. Their concentration in the material is not in thermodynamic equilibrium, although prolonged annealing at high temperatures can reduce their numbers. These naturally occurring extended defects are extremely important in influencing the mechanical properties of the material. Dislocations and grain boundaries can interact strongly with

point defects, thereby acting as sinks or traps for vacancies or interstitials.

### 6.2 POINT DEFECTS IN ELEMENTAL CRYSTALS

Figure 6.1 illustrates the point defect known as the vacancy, which is an empty lattice site or a missing atom in the crystal structure. If two adjacent lattice sites are empty, the defect is called a divacancy.

An extra atom in a position that is not part of the normal lattice structure is called an interstitial atom. Certain nonregular positions in a crystal are preferred sites for interstitial atoms. Such sites tend to be those which are relatively open and can accommodate an additional atom without excessive distortion of the neighboring atoms of the regular crystal structure. For example, if atoms are visualized as hard spheres, it would be difficult to place an interstitial atom in the close-packed plane of lattice atoms shown in Fig. 6.1. Instead, the energetically most favorable interstitial sites in the fcc lattice are shown in Fig. 6.2. The site in the upper unit cell is surrounded by four atoms of the regular lattice. This interstitial position, located in the middle of a regular tetrahedron, is called the tetrahedral interstitial site [with the origin at the upper left corner atom of Fig. 6.2, the interstitial site is at position  $(1/4, 1/4, -1/4)$ ].

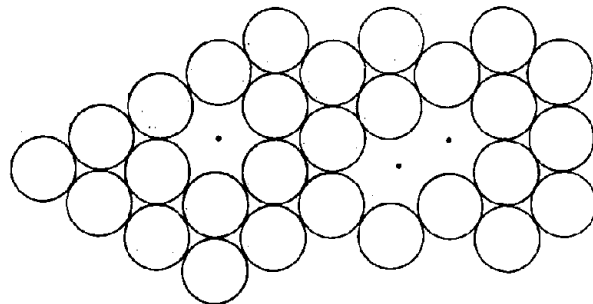


Fig. 6.1 Vacancy and divacancy.

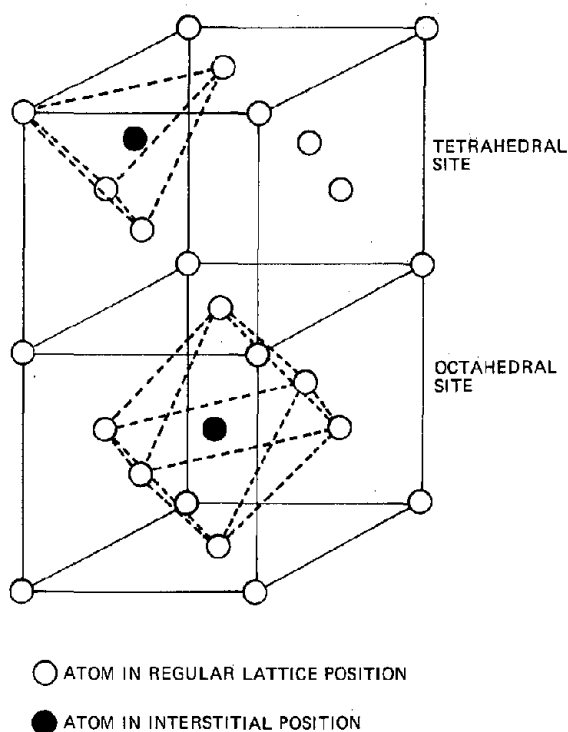


Fig. 6.2 Interstitial positions in the fcc structure.

The bottom unit cell of Fig. 6.2 shows an interstitial atom in the middle of the cube. This location is surrounded by six atoms of the regular lattice in an octahedral configuration. This interstitial position is known as the octahedral site.

The bcc structure also contains tetrahedral and octahedral interstitial sites. These are shown in Fig. 6.3.

The interstitial sites shown in Figs. 6.2 and 6.3 form a sublattice within the ordinary lattice structure of the crystal. The interstitial sublattice may contain more positions than the parent regular lattice. For example, there is one octahedral site on each face of the bcc unit cell (Fig. 6.3). In addition, the centers of the edges of the unit cell are also octahedral sites, since the configuration of atoms surrounding these positions is identical to the configuration of atoms around the face-centered position. The number of octahedral sites per unit cell in the bcc lattice is calculated by adding the 6 sites in the faces (each shared with another unit cell) to the 12 edge-centered sites (each shared between four unit cells). Or, there are  $6 \times \frac{1}{2} + 12 \times \frac{1}{4} = 6$  octahedral interstitial sites per unit cell. Since there are only two lattice atoms per unit cell in the bcc structure, there are three times as many octahedral interstitial sites as there are atoms in the perfect lattice.

Similar sublattices of interstitial positions can be identified in the noncubic crystal systems as well.

The atoms that occupy the interstitial sites shown in Figs. 6.2 and 6.3 may be the same species as the atoms of the parent crystal, or the sites may be occupied by impurity atoms. Small impurity atoms such as hydrogen, carbon, and boron are small enough to fit into these interstitial

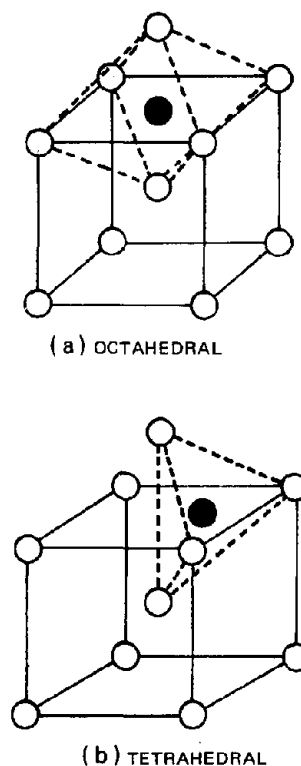


Fig. 6.3 Interstitial positions in the bcc structure.

positions without severe distortion of the host lattice. Larger impurity atoms, such as alloying components in a metal crystal, generally replace a host metal atom on a normal lattice site. Impurities that are present on the interstitial sites, such as those of Figs. 6.2 and 6.3, are called *interstitial impurities*, whereas impurities that replace host atoms on normal lattice sites are called *substitutional impurities*.

When the interstitial is the same species as the remainder of the crystal, configurations other than those shown in Figs. 6.2 and 6.3 are possible. Instead of one in which a tetrahedral or octahedral site is occupied, the stable interstitial configuration may be one in which the added atom displaces a normal atom and the two atoms are symmetrically disposed about the empty lattice site. Two such configurations in the bcc lattice are shown in Fig. 6.4. In Fig. 6.4(a) two atoms lie on an edge diagonal equidistant from the center of the unit cell, which does not contain an atom. The line joining the two atoms is in the  $[110]$  direction; so Fig. 6.4(a) describes a  $[110]$  split interstitial. In Fig. 6.4(b) the line joining the two atoms is along a body diagonal; so the configuration is a  $[111]$  split interstitial.

### 6.3 EQUILIBRIUM VACANCY CONCENTRATION

Consider a system consisting of  $N$  atoms arranged as a crystalline solid. Figure 6.5(a) shows this system as a perfect crystal. Vacancies are introduced into the system

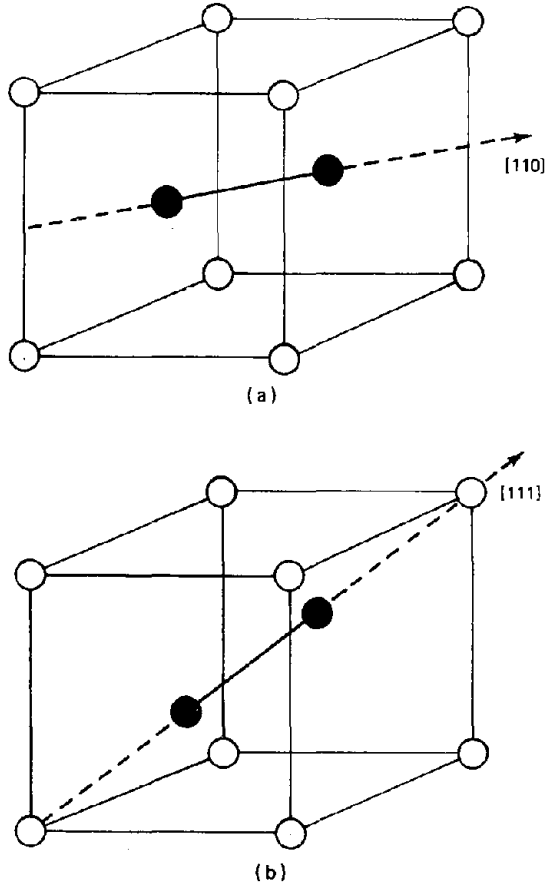


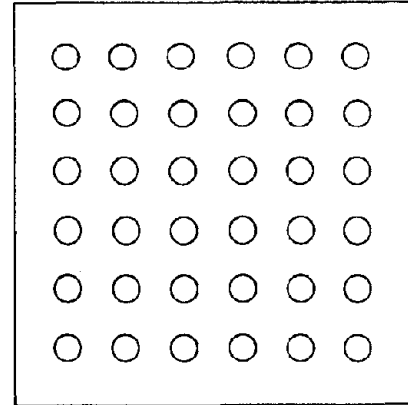
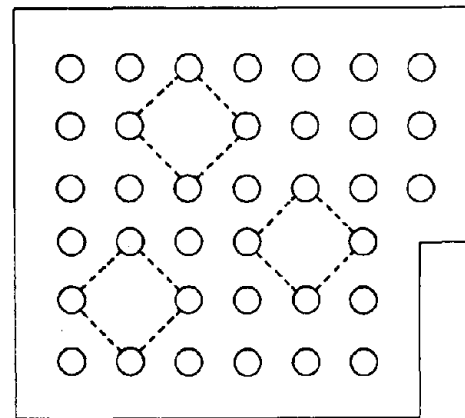
Fig. 6.4 Split interstitials in the bcc lattice.

when atoms move from internal lattice sites to lattice sites on the surface. The system with defects, shown in Fig. 6.5(b), still contains  $N$  atoms but, in addition, contains  $N_v$  vacancies.

The thermodynamic properties of the defected crystal depend on two thermodynamic parameters (e.g., the entropy  $S$  and the volume  $V$ ,  $T$  and  $V$ , or  $T$  and the total pressure  $p$ ) and a single composition variable, the number of vacant lattice sites,  $N_v$ . The system is thermodynamically described by relations of the type  $U(S, V, N_v)$ ,  $F(T, V, N_v)$ , or  $G(T, p, N_v)$ . The fundamental thermodynamic relations for this system are given by Eqs. 5.2 to 5.5 of Chap. 5 except that  $N_i$  is replaced by  $N_v$  and the summation signs are removed. The partial derivatives of the energy parameters with respect to  $N_v$  are related as shown by Eq. 5.6, again with  $N_i$  replaced by  $N_v$ . The arguments of Sec. 5.3 leading to Eq. 5.7 can be applied directly to the system of Fig. 6.5. Since there is only one composition variable, the equilibrium condition can be written

$$\left(\frac{\partial G}{\partial N_v}\right)_{T, p} = 0 \quad (6.1)$$

By virtue of Eq. 5.6, an entirely equivalent equilibrium statement is

(a) PERFECT CRYSTAL  
( $N$  ATOMS, NO VACANCIES)(b) REAL CRYSTAL  
( $N$  ATOMS,  $N_v$  VACANCIES)

--- ALTERED  
VIBRATIONAL  
MODES

Fig. 6.5 Vacancies in a crystalline solid.

$$\left(\frac{\partial F}{\partial N_v}\right)_{T, V} = 0 \quad (6.2)$$

The equilibrium condition can be expressed in terms of the partition function of the system by using Eq. 1.25 in Eq. 6.2:

$$\left(\frac{\partial \ln Z}{\partial N_v}\right)_{T, V} = 0 \quad (6.3)$$

According to the discussion of Sec. 5.4, the partition function of the system, either in the perfect state of Fig. 6.5(a) or in the defected state of Fig. 6.5(b), can be written

$$Z = e^{-E_0/kT} W \prod_{i=1}^{3N} (1 - e^{-h\nu_i/kT})^{-1} \quad (6.4)$$

The quantity  $E_0$  is the energy of the system (containing  $N$  atoms and  $N_v$  vacancies) when all  $N$  atoms are in their ground vibrational states; it is not the energy of the perfect lattice. The energy of  $N$  atoms in their ground vibrational states and arranged as a perfect lattice is  $N\epsilon_0$ , where  $\epsilon_0$  is the energy per atom of the perfect crystal. The defected crystal of Fig. 6.5(b) is obtained from the perfect crystal by moving  $N_v$  atoms from the interior to the surface. If an energy  $\epsilon_v$  is required for each vacancy created at the absolute zero (i.e.,  $\epsilon_v$  is the *formation energy* of a vacancy), the ground-state energy of the real crystal is

$$E_0 = N\epsilon_0 + N_v\epsilon_v \quad (6.5)$$

(Eq. 6.5 may be interpreted as the energy requirement of first assembling a perfect crystal from free atoms, then introducing some defects into it). The configurational partition function  $W$  in Eq. 6.4 is the number of ways of arranging  $N$  atoms on  $N + N_v$  lattice sites, which is given by Eq. 5.33:

$$W = \frac{(N + N_v)!}{N!N_v!} \quad (6.6)$$

The quantity  $(1 - e^{-h\nu_i/kT})^{-1}$  in Eq. 6.4 is the partition function for the  $i$ th mode of vibration in the real crystal. Since the system contains  $N$  atoms, there are  $3N$  modes of vibration. Because vacancies are present, the vibration frequencies of the  $3N$  modes,  $\nu_i$ , are, in general, not the same as those in the perfect crystal (as given, say, by the Einstein or Debye frequency spectra). When a vacancy is created, the atoms surrounding the empty site tend to relax into the hole. The vibrations along the lines joining the nearest-neighbor atoms would be expected to change; the modes of vibration affected by relaxation around the defect are shown as dashed lines in Fig. 6.5(b). Atoms further removed from the vacancy than the nearest neighbors are assumed to retain the vibrational characteristics they possessed in the perfect crystal. The number of vibrational modes that are altered by the introduction of a single vacancy is denoted by  $\alpha$ . (The dashed lines of Fig. 6.5(b) suggest  $\alpha = 4$ ; for a three-dimensional crystal,  $\alpha \approx 6$ .)

Assuming that the perfect crystal can be represented by the Einstein model, all vibrational modes unaffected by the defects have a single frequency  $\nu$ . Assume also that the modes influenced by the presence of the vacancies all have frequency  $\nu'$ . In the defected crystal,  $\alpha N_v$  modes have frequency  $\nu'$ , and  $3N - \alpha N_v$  modes have a frequency  $\nu$ . Assuming that both  $h\nu/kT$  and  $h\nu'/kT$  are much smaller than unity, the last term in Eq. 6.4 can be written

$$\begin{aligned} & \prod_{i=1}^{3N} (1 - e^{-h\nu_i/kT})^{-1} \\ &= (1 - e^{-h\nu/kT})^{-(3N - \alpha N_v)} (1 - e^{-h\nu'/kT})^{-\alpha N_v} \\ &= \left(\frac{kT}{h\nu}\right)^{(3N - \alpha N_v)} \left(\frac{kT}{h\nu'}\right)^{\alpha N_v} \\ &= \left(\frac{kT}{h\nu}\right)^{3N} \left(\frac{\nu}{\nu'}\right)^{\alpha N_v} \quad (6.7) \end{aligned}$$

Inserting Eqs. 6.5, 6.6, and 6.7 into Eq. 6.4 yields

$$Z = Z^* \frac{(N_v + N)!}{N_v!N!} e^{-N_v\epsilon_v/kT} \left(\frac{\nu}{\nu'}\right)^{\alpha N_v} \quad (6.8)$$

where  $Z^*$  is the partition function of the perfect crystal of  $N$  atoms:

$$Z^* = e^{-N\epsilon_0/kT} \left(\frac{kT}{h\nu}\right)^{3N} \quad (6.9)$$

and does not depend on the composition variable,  $N_v$ .

If the last term in Eq. 6.8 is ignored to permit a qualitative explanation, the variation of  $Z$  with  $N_v$  is governed by the product

$$\frac{(N_v + N)!}{N_v!N!} e^{-N_v\epsilon_v/kT}$$

When  $N_v = 0$ , the combinatorial term is unity and so is the exponential term. As  $N_v$  becomes non-zero, the combinatorial term rises more rapidly than the exponential term decreases. At larger  $N_v$  the product again decreases owing to the influence on the exponential term. Physically, the effects of the two terms in the above product represent (1) the entropy of mixing, which favors vacancy formation because of increased randomness, and (2) the energy of formation, which opposes vacancy formation because high-energy states of a constant-temperature system are less probable than low-energy states. One would expect that the equilibrium composition corresponds to the  $N_v$  value that maximizes this product, and this expectation is confirmed by the formal equilibrium criterion of Eq. 6.3. Substitution of Eq. 6.8 into Eq. 6.3 yields the equilibrium vacancy concentration:

$$\frac{N_v}{N + N_v} = \left(\frac{\nu}{\nu'}\right)^{\alpha} e^{-\epsilon_v/kT} \quad (6.10)$$

The equilibrium vacancy concentration can also be deduced by using the macroscopic thermodynamic approach of Sec. 5.5. The difference in the Gibbs free energy of the system when in the two states illustrated by Fig. 6.5 is

$$G(N_v) - G(0) = N_v g_v - TS_{\text{mix}} \quad (6.11)$$

where  $g_v$  is the change in the Gibbs free energy of the system (exclusive of the entropy of mixing contribution) when one atom is moved from the interior to the surface,  $S_{\text{mix}}$  is given by  $k \ln W$ , and  $W$  is given by Eq. 6.6. If we use  $g_v = h_v - TS_v$  and approximate  $h_v$  by  $\epsilon_v$ , when we insert Eq. 6.11 into the equilibrium criterion of Eq. 6.1, we get

$$x_v = \frac{N_v}{N_v + N} = e^{s_v/k} e^{-\epsilon_v/kT} \quad (6.12)$$

where  $x_v$  is the fraction of unoccupied lattice sites. Comparing Eqs. 6.10 and 6.12 shows that the excess entropy of vacancy formation,  $s_v$ , is related to the change in the vibration frequencies of modes characterizing atoms adjacent to the defects:

$$s_v = k \ln \left(\frac{\nu}{\nu'}\right)^{\alpha} \quad (6.13)$$

Since the atoms adjacent to a vacancy are less constricted than they are in a perfect crystal, we expect  $\nu/\nu' > 1$ , i.e., the excess entropy of vacancy formation should be positive. Estimates of the magnitude of  $\exp(s_v/k)$  range from 5 to 50.

In a covalent crystal, where the cohesive energy is due entirely to chemical bonds between nearest-neighbor atoms, the energy of formation of a vacancy can be estimated in a straightforward manner. It consists of two parts.

First, an atom is removed from the interior of the crystal and placed on the surface. If  $\beta$  is the number of nearest neighbors to an interior atom,  $\beta$  bonds are broken in removing an atom from the interior, but  $\beta/2$  bonds are recovered when the atom is placed on the surface. If the energy of a single bond is  $D$ , the energy required for this step is  $\beta D/2$  (which is equal to the energy of sublimation; see Eq. 4.45).

After the atom has been removed from its interior site, a portion of the energy expended is regained by the relaxation of the nearest neighbors into the hole. If the energy term of this second step is denoted by  $\Delta E_{\text{relax}}$ , the vacancy-formation energy is

$$\epsilon_v = \frac{\beta D}{2} - \Delta E_{\text{relax}} \quad (6.14)$$

For germanium,  $\beta = 4$ ,  $D = 1.63$  eV, and the first term of Eq. 6.14 is 3.26 eV. The relaxation energy in germanium has been estimated to be 1.2 eV [R. A. Swalin, *J. Phys. Chem. Solids*, 18: 290 (1961)]. The calculated vacancy-formation energy is 2.1 eV, which is in very good agreement with the measured value of 2.0 eV.

Calculation of the vacancy-formation energy in a metal is far more complex since Eq. 6.14 is not valid even as a first approximation. Metal atoms do not form identifiable bonds with nearest neighbors. The formation energy of a vacancy in a metal is due primarily to the behavior of the free electrons. Crystal volume increases when an atom moves from the interior to the surface. The same number of electrons are now distributed over a larger volume, which, according to Eqs. 4.14 to 4.16, reduces their average kinetic energy. This effect leads to a negative rather than a positive contribution to  $\epsilon_v$ . However, the electron gas in the metal tends to partially fill the vacant lattice site, which leads to an increase in the electrostatic energy of the crystal. Finally, the redistribution of the electron cloud in the vicinity of the vacancy and the relaxation of the ion cores into the hole contribute to the energy of vacancy formation. The energy of vacancy formation is a small number that results from the addition and subtraction of several large terms. Very few calculations of this type have been performed. For copper, Huntington and Seitz [*Phys. Rev.*, 61: 315 (1942)] obtained a value for  $\epsilon_v$  of about 1 eV.

As an illustration of the magnitude of the vacancy concentration in metals, setting  $s_v = 0$ ,  $\epsilon_v = 1$  eV, and  $T = 1000^\circ\text{C}$  in Eq. 6.12 gives a vacancy fraction of  $10^{-4}$ .

## 6.4 EQUILIBRIUM CONCENTRATION OF DIVACANCIES

We consider the thermodynamics of divacancy formation in a crystal for two reasons. First, divacancies may be

the embryos from which macroscopic voids grow by further condensation of vacancies. Second, the calculation illustrates the use of combinatorial analysis somewhat more complex than the standard procedure used to derive the configurational partition function for simple mixing (i.e., Eq. 5.33).

We use the macroscopic thermodynamic approach (similar to that which led to Eq. 6.11), but at the start we neglect the excess entropy and approximate the free energy of divacancy formation by the energy of formation,  $\epsilon_v^{(2)}$ . The superscript 2 indicates that the quantity refers to a divacancy.  $\epsilon_v^{(2)}$  is the energy required to move two adjacent atoms from interior positions in the crystal to the surface. The formation energies of single vacancies and divacancies are related by

$$\epsilon_v^{(2)} = 2\epsilon_v - B \quad (6.15)$$

where  $B$  is the *binding energy* of a divacancy, or the energy required to separate a divacancy into two isolated single vacancies.

The Gibbs free energy of a crystal containing  $N_v^{(2)}$  divacancies compared to the crystal containing no divacancies is

$$G(N_v^{(2)}) - G(0) = N_v^{(2)}\epsilon_v^{(2)} - kT \ln W \quad (6.16)$$

The combinatorial factor  $W$  remains to be computed. Imagine that we have a region containing  $N_s$  sites that are completely filled with atoms. We now start removing pairs of atoms until  $N_v^{(2)}$  divacancies are created.

Consider the withdrawal of the first pair of adjacent atoms from the perfect lattice. The first atom of the pair can be removed from any one of the  $N_s$  sites. The second atom of the pair must be withdrawn from one of the  $\beta$  nearest-neighbor sites to the first atom. This restriction on the second atom is necessary because a pair of adjacent atoms must be withdrawn to create a divacancy. It would appear, therefore, that there are  $\beta N_s$  ways of creating the first divacancy. However, this number must be divided by 2, since it is immaterial which atom was removed first. Thus, there are  $\beta N_s/2$  ways of creating the first divacancy.

Two fewer atoms are available from which to generate the second divacancy, which can be created in  $\beta(N_s - 2)/2$  ways.

Finally, the last of the  $N_v^{(2)}$  divacancies can be created in  $\beta[N_s - 2(N_v^{(2)} - 1)]/2$  ways. The total number of ways of producing the  $N_v^{(2)}$  divacancies is

$$\begin{aligned} & \left(\frac{\beta}{2}\right)^{N_v^{(2)}} N_s(N_s - 2) \dots [N_s - 2(N_v^{(2)} - 1)] \\ &= \beta^{N_v^{(2)}} \left(\frac{N_s}{2}\right) \left(\frac{N_s}{2} - 1\right) \dots \left[\frac{N_s}{2} - (N_v^{(2)} - 1)\right] \\ &= \beta^{N_v^{(2)}} \frac{(N_s/2)!}{[(N_s/2) - N_v^{(2)}]!} \end{aligned}$$

The permutations among the  $N_v^{(2)}$  divacancies are removed by dividing by  $N_v^{(2)}!$ ; thus the combinatorial factor for the divacancy problem is

$$W = \frac{\beta^{N_v^{(2)}} (N_s/2)!}{[(N_s/2) - N_v^{(2)}]! N_v^{(2)}!} \quad (6.17)$$

The equilibrium divacancy concentration is determined by taking the derivative of Eq. 6.16 with respect to  $N_v^{(2)}$  and setting  $dG/dN_v^{(2)} = 0$ . This yields

$$\frac{\epsilon_v^{(2)}}{kT} = \frac{d \ln W}{dN_v^{(2)}}$$

Using Stirling's approximation, we find that the derivative on the right-hand side of this formula is

$$\frac{d \ln W}{dN_v^{(2)}} = \ln \beta - \ln \left[ \frac{N_v^{(2)}}{(N_s/2) - N_v^{(2)}} \right]$$

Neglecting  $N_v^{(2)}$  compared to  $N_s/2$  and combining the preceding equations yields

$$\frac{N_v^{(2)}}{N_s} = \frac{\beta}{2} e^{-\epsilon_v^{(2)}/kT} \quad (6.18)$$

Let the fraction of the total sites occupied by single vacancies be denoted by  $x_v$  and the ratio of divacancies to total sites be denoted by  $x_v^{(2)}$ . Then Eqs. 6.12 (with  $s_v = 0$ ) and 6.18 can be written

$$x_v = e^{-\epsilon_v/kT} \quad (6.19)$$

$$x_v^{(2)} = \frac{\beta}{2} e^{-\epsilon_v^{(2)}/kT} \quad (6.20)$$

Because of the more complicated combinatorial factor in the divacancy case compared to the single-vacancy problem, the factor preceding the exponential in Eq. 6.20 is not unity.

The divacancy concentration can also be approximately calculated by considering the chemical equilibrium between single vacancies and divacancies:



where  $V$  denotes a single vacancy and  $V_2$  a divacancy. The energy change of this reaction is  $B$ , the binding energy of the divacancy. If the complexities of the combinatorial analysis are ignored and the law of mass action is applied to this reaction (according to the discussion leading to Eqs. 5.47 and 5.48), we obtain

$$\frac{x_v^{(2)}}{x_v^2} = e^{B/kT} \quad (6.21)$$

By way of comparison to the exact method, substitution of Eq. 6.15 into Eq. 6.20 shows that

$$x_v^{(2)} = \frac{\beta}{2} e^{-2\epsilon_v/kT} e^{B/kT}$$

Or, identifying  $\exp(-2\epsilon_v/kT)$  with  $x_v^2$  (by Eq. 6.19), the exact result is

$$\frac{x_v^{(2)}}{x_v^2} = \frac{\beta}{2} e^{B/kT} \quad (6.22)$$

Comparison of Eqs. 6.21 and 6.22 shows that the simple law-of-mass-action approach produces a relation between

$x_v^{(2)}$  and  $x_v$ , which is in error by a factor of  $\beta/2$ . However, Eq. 6.21 can be written down by inspection, whereas development of Eq. 6.22 is cumbersome and susceptible to mistakes in the combinatorial analysis. As we argued in Chap. 5, the implication that Eq. 6.22 is an accurate formula is misleading. Although Eq. 6.22 correctly treats the combinatorial problem, it completely neglects excess entropy effects, which are probably of the same magnitude as the combinatorial factor.

## 6.5 EQUILIBRIUM CONCENTRATION OF INTERSTITIALS

The interstitial is regarded as being produced by removing an atom from the surface of the crystal and placing it on an interstitial location in the interior of the solid. The arguments developed for vacancy thermodynamics in Sec. 6.3 are directly applicable to the case of interstitial formation, and the equilibrium concentration is given by

$$\frac{N_i}{N_{si}} = e^{s_i/k} e^{-\epsilon_i/kT} \quad (6.23)$$

where  $N_i$  is the number of atoms on interstitial sites,  $N_{si}$  is the total number of available interstitial sites (which is not necessarily equal to the number of normal lattice sites, see problem 6.4), and  $s_i$  is the excess entropy of interstitial formation and is given by an equation analogous to Eq. 6.13. For interstitials, however, the vibration-frequency ratio  $\nu/\nu'$  is less than unity since the vibration frequency of atoms in the vicinity of an interstitial atom is increased by the congestion caused by the presence of the additional atom. Therefore,  $\exp(s_i/k)$  is less than unity, in contrast to the case of the single vacancy for which this term is larger than unity.

Although only one type of single vacancy is possible, the discussion of Sec. 6.2 indicates that a variety of locations are available to an interstitial atom. It is difficult to determine, either by calculation or experiment, whether an interstitial impurity is located on octahedral or tetrahedral sites or whether an interstitial defect in an elemental crystal is of the normal or split type. Recent calculations for metals favor one of the many possible split interstitial configurations.

The energy of interstitial formation,  $\epsilon_i$ , is probably higher than that of vacancy formation for all solids. Calculations for copper suggest an interstitial-formation energy of approximately 3 eV compared to 1 eV for vacancy formation.

## 6.6 POINT DEFECTS IN TWO-COMPONENT IONIC CRYSTALS

So far in this chapter, we have considered the nature of point defects in elemental crystals. The presence of two species in an ionic solid compared to a single species in an elemental crystal multiplies manifold the variety of possible point defects. However, limitations posed by the requirement of local electrical neutrality severely restrict the number of possibilities; in fact, only two types of point defects are significant.

A perfect ionic crystal is represented in two dimensions in Fig. 6.6(a). In Fig. 6.6(b) a vacancy in the cation sublattice has been formed by moving a cation to a new lattice position on the surface. The loss of a positively charged ion means that the cation vacancy has an effective negative charge, i.e., a small volume of the crystal containing the cation vacancy is short one positive charge, or this volume has a net negative charge with respect to the rest of the crystal. The interior of an ionic crystal tends to be electrically neutral, even on a rather small scale; so the isolated cation-vacancy defect depicted in Fig. 6.6(b) does not occur in real ionic solids. However, if a vacancy on the anion sublattice is created in the vicinity of the cation vacancy, as in Fig. 6.6(c), the defected region of the crystal regains electrical neutrality. Paired anion and cation vacancies in ionic crystals are quite common and are called *Schottky defects*. In a pure crystal of the MX type, Schottky disorder consists of equal numbers of anion and cation vacancies. If the crystal contains impurities of different valence than the host ions or if for some other reason the normal equality of anions and cations in the crystal is disturbed, the numbers of cation vacancies and anion vacancies will not be equal.

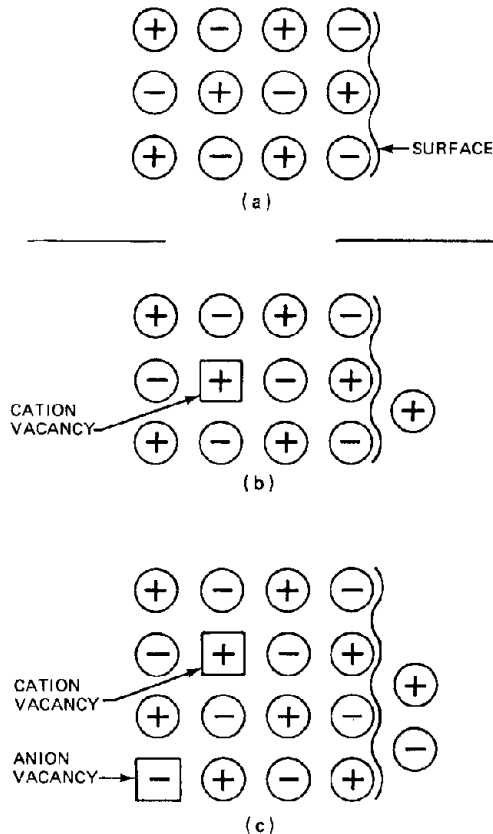


Fig. 6.6 Defects in a type MX ionic crystal. (a) The perfect crystal. (b) The crystal with a cation vacancy. (c) The Schottky defect.

The second type of defect which has been observed in an ionic crystal and which maintains local electrical neutrality is the *Frenkel defect* (Fig. 6.7). Here, an ion (either an anion or a cation, but generally not both simultaneously) moves from a normal lattice site to an interstitial position, leaving behind a vacancy. Frenkel defects can occur either on the cation sublattice or the anion sublattice. The interstitial position that accepts the displaced ion is generally at the center of the elementary cube in the NaCl structure (see Fig. 3.10) or in the body-center position of the simple cubic anion sublattice of the fluorite structure (Fig. 3.12). However, split interstitials similar to those described in elemental crystals in Sec. 6.2 have also been observed in ionic solids.

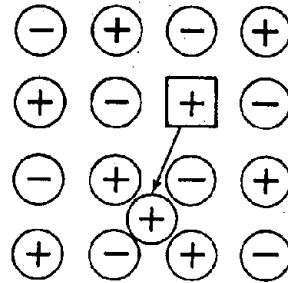


Fig. 6.7 Frenkel defect in an ionic crystal.

It is rare that an ionic solid exhibits Schottky disorder and Frenkel disorder simultaneously. Usually one or the other type predominates. Schottky and Frenkel defects are intrinsic to ionic solids, and, like the vacancy and interstitial defects in elemental crystals, they occur spontaneously and in concentrations controlled by thermodynamics. Since they involve movement of the ions of the lattice to nonregular positions, Schottky and Frenkel defects are often described as *atomic disorder*.

The conduction electrons and holes generated in semiconductor crystals represent a type of defect known as *electronic disorder*. Electronic defects and complex disorder due to association of atomic and electronic defects exert a profound influence on the electrical, optical, and magnetic properties of semiconductor materials. We do not consider electronic defects here since the mechanical properties that are important in reactor fuel element performance are most dependent upon atomic defects.

### 6.6.1 Schottky Defects

Consider a crystal that contains  $N_{VM}$  vacancies and  $N_M$  positive ions on the cation sublattice and  $N_{VX}$  vacancies and  $N_X$  negative ions on the anion sublattice. As with an elemental crystal, a vacancy on either of the sublattices is created by moving an interior ion to the surface. Let  $g_{VM}$  be the difference in the Gibbs free energy of the crystal with one cation vacancy and of the perfect crystal. Let  $g_{VX}$  be the analogous quantity for an anion vacancy. As usual,  $g_v$  can be approximated by

$$g_v = h_v - Ts_v - e_v + pv_v - Ts_v \approx e_v$$

without unacceptable loss of accuracy. Therefore, the Gibbs free energy of a crystal containing both types of vacancies is

$$G(N_{vM}, N_{vX}) - G(0,0) = N_{vM}\epsilon_{vM} + N_{vX}\epsilon_{vX} - kT \ln W \quad (6.24)$$

The combinatorial factor  $W$  is the number of different arrangements of  $N_{vM}$  vacancies and  $N_M$  positive ions on the cation sublattice and  $N_{vX}$  vacancies and  $N_X$  negative ions on the anion sublattice.  $W$  is given by

$$W = \frac{(N_M + N_{vM})! (N_X + N_{vX})!}{N_{vM}! N_M! N_{vX}! N_X!} \quad (6.25)$$

If the crystal is free of impurity atoms, the condition of electrical neutrality requires that the number of cation vacancies be equal to the number of anion vacancies, or

$$N_{vM} = N_{vX} = N_v \quad (6.26)$$

With this restriction, Eqs. 6.24 and 6.25 reduce to

$$G(N_v) - G(0) = N_v \epsilon_s - 2kT \ln \left[ \frac{(N + N_v)!}{N_v! N!} \right] \quad (6.27)$$

where  $N$  represents the number of occupied sites on either the cation or anion sublattices ( $N = N_M = N_X$ ). The term

$$\epsilon_s = \epsilon_{vM} + \epsilon_{vX} \quad (6.28)$$

is the energy required to create a single defect pair consisting of a cation vacancy and an anion vacancy, or the energy of formation of the Schottky defect. Except for the factor of 2 multiplying the last term, Eq. 6.27 is of the same form as the expression for the free energy of an elemental crystal containing vacancies (see Eq. 6.11). If the fraction of the sublattice sites (either the anion or cation sublattice) which is vacant is denoted by  $x_v$ , the equilibrium condition  $dG/dN_v = 0$  yields

$$x_v = x_{vM} = x_{vX} = e^{-\epsilon_s/2kT} \quad (6.29)$$

Let us extend the analysis of Schottky-defect equilibrium to the more general case of a nonstoichiometric crystal. Nonstoichiometry, which in a solid of nominal formula  $MX$  means that the number of cations is not equal to the number of anions, arises for two reasons.

In many ionic compounds, the cation possesses more than one stable valence state, and its crystalline compounds may represent a mixture of two valences. As an example, iron oxide may contain a mixture of  $Fe^{2+}$  and  $Fe^{3+}$  ions yet retain the crystal structure of pure  $FeO$ . For electrical neutrality to be maintained in this case, the oxygen-to-iron ratio must increase in proportion to the quantity of trivalent iron present. The formula  $FeO_{1+x}$  (where  $x > 0$ ) can be used to represent this type of nonstoichiometry. Since the number of anions exceeds the number of cations for  $x > 0$ , yet the number of anion lattice sites is equal to the number of cation lattice sites, vacancies must be present on the cation sublattice in excess of the concentration predicted thermodynamically for the stoichiometric crystal. Alternatively, the excess oxygen may be accommodated as

interstitial ions with the cation sublattice remaining perfect. A similar type of nonstoichiometry occurs in uranium dioxide, and deviations from stoichiometry are very important in the performance of this material in fuel elements for nuclear reactors.

Another common method of creating nonstoichiometry in a crystal is to introduce a different cation into the solid. This process is known as *doping*. As shown in Fig. 6.8, the added cation forms a substitutional impurity on the cation sublattice of the host crystal.\* If the impurity cation has a higher valence than the cation of the parent crystal, neutrality requires that vacancies be created on the cation sublattice. If a lower valence impurity is added, anion vacancies will be generated.†

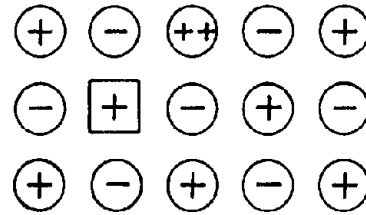


Fig. 6.8 Divalent impurity cation in a crystal of the type  $MX$ .

Thermodynamically, an impurity may be the same chemical species as the cations of the host lattice but of different valence, or it may be a different chemical species. In either event, impurity ions are distinguished from the host cations by a different charge. We consider only the case in which the imbalance in electrical neutrality occasioned by the impurity cations is compensated by vacancy formation, either on the cation or anion sublattices, depending upon the charge of the impurity ion.

As an illustration, consider a crystal of the  $MX$  type with charges  $q_M = q_X$  on the host anions and cations.  $N_{DM}$  impurity ions of charge  $q_D$  are added to the cation sublattice. The solid contains  $N_{sM}$  cation lattice sites upon which are distributed the  $N_{DM}$  impurity ions,  $N_M$  host cations, and  $N_{vM}$  cation vacancies. The  $N_{sX}$  anion lattice sites are shared by  $N_X$  negative ions and  $N_{vX}$  anion vacancies. These quantities are related by

$$N_{sM} = N_{DM} + N_M + N_{vM}$$

$$N_{sX} = N_X + N_{vX}$$

The condition of electrical neutrality requires that, in the region of the crystal considered, there be an equal number of positive and negative charges:

\*It is generally not possible to substitute different anions in an ionic crystal—two phases tend to separate out.

†If the cations of the lattice are capable of forming multiple valence states, impurity cations introduced may be accommodated by oxidation or reduction of the host cations (see Fig. 12.8).

$$q_D N_{DM} + q_M N_M = q_X N_X$$

or

$$q_D N_{DM} + q_M (N_{sM} - N_{DM} - N_{vM}) = q_X (N_{sX} - N_{vX})$$

For a crystal of the MX type

$$q_M = q_X$$

and

$$N_{sM} = N_{sX}$$

so the condition of neutrality becomes

$$\left(\frac{q_D}{q_M} - 1\right) N_{DM} + N_{vX} = N_{vM} \quad (6.30)$$

If the cation impurity has a higher valence than the host cation, Eq. 6.30 shows that the number of vacancies on the cation sublattice must exceed the number of anion vacancies to maintain electrical neutrality. This formula also indicates that anion vacancies behave as positive charges and cation vacancies as negative charges.

The impurity content of the crystal ( $N_{DM}$ ) is presumed fixed; so, when we seek the condition of equilibrium, we regard the Gibbs free energy of the crystal as a function of the vacancy concentrations  $N_{vM}$  and  $N_{vX}$ . Equation 6.24 correctly describes the crystal free energy in this case as well as in the impurity-free situation. However, since the cation sublattice contains an additional species, the combinatorial factor  $W$  is

$$W = W_M W_X = \frac{(N_{vM} + N_M + N_{DM})! (N_{vX} + N_X)!}{N_{vM}! N_M! N_{DM}! N_{vX}! N_X!} \quad (6.31)$$

where  $W_M$  and  $W_X$  are the combinatorial factors for the individual sublattices. Because of the electrical neutrality restriction of Eq. 6.30, the crystal free energy is a function of only one of the variables  $N_{vM}$  and  $N_{vX}$ ; let us use the latter. The condition of equilibrium is

$$\frac{dG}{dN_{vX}} = 0$$

Breaking  $W$  into the components  $W_M$  and  $W_X$ , we can write the derivative of Eq. 6.24 with respect to  $N_{vX}$  as

$$\frac{dG}{dN_{vX}} = \left(\frac{dN_{vM}}{dN_{vX}}\right) \epsilon_{vM} + \epsilon_{vX} - kT \left[ \left(\frac{dN_{vM}}{dN_{vX}}\right) \frac{d \ln W_M}{dN_{vM}} + \frac{d \ln W_X}{dN_{vX}} \right]$$

Since  $N_{vM}$  and  $N_{vX}$  are linearly related by Eq. 6.30, the derivative  $dN_{vM}/dN_{vX}$  is unity.

The derivatives of the combinatorial terms are obtained from Eq. 6.31:

$$\frac{d \ln W_M}{dN_{vM}} = -\ln \left( \frac{N_{vM}}{N_{vM} + N_M + N_{DM}} \right) = -\ln x_{vM}$$

$$\frac{d \ln W_X}{dN_{vX}} = -\ln \left( \frac{N_{vX}}{N_{vX} + N_X} \right) = -\ln x_{vX}$$

The concentrations  $x_{vM}$  and  $x_{vX}$  are the fractions of vacancies on the cation and anion sublattices, respectively. Combining the four preceding equations yields

$$x_{vM} x_{vX} = e^{-\epsilon_s/kT} \quad (6.32)$$

and the condition of electrical neutrality, Eq. 6.30, in terms of the site fractions becomes

$$\left(\frac{q_D}{q_M} - 1\right) x_{DM} + x_{vX} = x_{vM} \quad (6.33)$$

Here  $x_{DM}$  is the fraction the cation sites in the solid which are occupied by impurity ions. Solved simultaneously, Eqs. 6.32 and 6.33 determine  $x_{vM}$  and  $x_{vX}$ . The result for the undoped crystal, Eq. 6.29, is seen to be a special case of the above equations for  $x_{DM} = 0$ .

When different conditions that cause an imbalance in the anion and cation vacancy concentrations are analyzed in a similar fashion, the equilibrium condition is always found to be given by Eq. 6.32, and only the electrical neutrality condition changes. Thus, no matter what else is occurring in the crystal, the vacancy concentrations are always related by Eq. 6.32. This formula embodies all the feature of the law of mass action; if one of the vacancy concentrations is artificially altered by an outside agent, the other vacancy concentration changes in a manner that satisfies Eq. 6.32.

In pure crystal of the type  $MX_2$  (e.g., the fluorite structure), Schottky disorder consists of twice as many anion vacancies as cation vacancies. An analysis similar to that presented for the MX-type solid yields the law of mass action:

$$x_{vM} x_{vX}^2 = e^{-\epsilon_s/kT} \quad (6.34)$$

where  $\epsilon_s$  is the energy of formation of two anion vacancies and one cation vacancy. In the pure crystal electrical neutrality requires that  $N_{vX} = 2N_{vM}$ , or, in terms of site fractions,  $x_{vX} = x_{vM}$ . Equation 6.34 reduces to

$$x_{vM} = x_{vX} = e^{-\epsilon_s/3kT} \quad (6.35)$$

## 6.6.2 Frenkel Defects

The thermodynamics of Frenkel defects can be analyzed in a manner similar to that applied to Schottky disorder in the preceding section. Frenkel disorder may involve either the cations or anions, but generally not both simultaneously. In either case, the concentration of vacancies and interstitials are related by a mass-action law:

$$x_{vM} x_{iM} = e^{-\epsilon_{FM}/kT} \quad (6.36)$$

for the cation sublattice and

$$x_{vX} x_{iX} = e^{-\epsilon_{FX}/kT} \quad (6.37)$$

for the anion sublattice.

The concentrations  $x_{iM}$  and  $x_{iX}$  are the fractional occupancies of the interstitial sites by positive or negative ions, and  $\epsilon_{FM}$  and  $\epsilon_{FX}$  are the formation energies of Frenkel defects on the cation and anion sublattices,

respectively. They represent the energy required to move an ion from its normal lattice position to an interstitial site.

The law of mass action governing Frenkel disorder must also be accompanied by an equation of electrical neutrality. In the simplest case of Frenkel defects in a pure solid that has the same number of interstitial sites as regular lattice sites, the charge balance is  $x_{vM} = x_{iM}$  (or  $x_{vX} = x_{iX}$ ), and the defect concentrations are given by

$$x_{vM} = x_{iM} = e^{-\epsilon_{FM}/2kT} \quad (6.38)$$

for cation Frenkel disorder and by

$$x_{vX} = x_{iX} = e^{-\epsilon_{FX}/2kT} \quad (6.39)$$

for anion Frenkel disorder.

### 6.6.3 General Condition of Electrical Neutrality

For any combination of doping or nonstoichiometry, atomic disorder of the Schottky or Frenkel types can always be analyzed by combining the laws of mass action for the appropriate defecting equilibria with a condition of electrical neutrality. The latter considers the concentration and charges of all species in the crystal and requires that the net charge be zero. The particles involved in the charge balance are given in Table 6.1.

Table 6.1

Species	Concentration	Charge
Normal cations	$N_M$	$q_M$
Cations of same chemical type but different valence	$N'_M$	$q'_M$
Impurity species in the cation lattice	$N_{DM}$	$q_D$
Cations on interstitial sites in the crystal	$N_{iM}$	$q_M$
Normal anions	$N_X$	$q_X$
Anions on interstitial sites in the crystal	$N_{iX}$	$q_X$

Except for electronic disorder in the form of holes or conduction electrons (and complex disorder), Table 6.1 includes all the possible charge-carrying species in ionic solids. The general condition of charge neutrality is

$$q_D N_{DM} + q_M N_M + q'_M N'_M + q_M N_{iM} = q_X N_X + q_X N_{iX} \quad (6.40)$$

In most practical situations, many of the terms in Eq. 6.40 are zero. Vacancies, which are not ponderable species, do not enter directly into the electrical neutrality condition. Rather, they are introduced by equations that show how the anion and cation sublattices are filled. The  $N_{sM}$  available sites in the cation sublattice may be occupied by vacancies (which is to say, unoccupied), by normal cations, by cations of the same species but of different

valence, or by impurity species. These concentrations are related by

$$N_{sM} = N_M + N_{vM} + N'_M + N_{DM} \quad (6.41)$$

For the anion sublattice, only normal anions and vacancies need be considered:

$$N_{sX} = N_X + N_{vX} \quad (6.42)$$

Since the perfect crystal must be electrically neutral, the number of anion and cation lattice sites are related by

$$q_X N_{sX} = q_M N_{sM} \quad (6.43)$$

Combining Eqs. 6.40–6.43 leads to the electrical neutrality restriction involving only adjustable concentrations ( $N_{DM}$  and  $N'_M$ ) or quantities appearing in the laws of mass action associated with the prevalent type of atomic disorder ( $N_{iM}$ ,  $N_{vM}$ ,  $N_{iX}$ , and  $N_{vX}$ ):

$$(q_D - q_M)N_{DM} + (q'_M - q_M)N'_M + q_M(N_{iM} - N_{vM}) = q_X(N_{iX} - N_{vX}) \quad (6.44)$$

## 6.7 NOMENCLATURE

- B = binding energy of a divacancy
- D = energy of a single bond
- $E_0$  = energy of a system when all atoms are in their ground vibrational states
- $\Delta E_{relax}$  = relaxation energy
- F = total Helmholtz energy
- $g_i$  = Gibbs free energy of formation of a single defect *i* (e.g., a vacancy)
- G = total Gibbs free energy
- h = Planck's constant
- $h_i$  = enthalpy of formation of defect *i*
- k = Boltzmann constant
- N = number of atoms or sites in a crystal
- q = electronic charge on an ion
- $s_i$  = entropy change in formation of a single defect *i*
- S = total entropy
- T = temperature
- U = total internal energy
- V = volume of a crystal
- W = combinatorial factor
- $x_i$  = fraction of available sites which contain defect *i*
- Z = total partition function of a crystal
- $Z^*$  = total partition function of a perfect crystal

### Greek letters

- $\alpha$  = number of vibrational modes affected by the presence of a vacancy
- $\beta$  = number of nearest neighbors to an interior atom
- $\epsilon_0$  = energy per atom of the perfect crystal
- $\epsilon_s$  = energy of formation of a Schottky defect
- $\epsilon_v$  = energy of formation of a vacancy
- $\nu$  = frequency of vibration of a mode
- $\nu'$  = frequency of vibration of modes affected by a vacancy

**Subscripts**

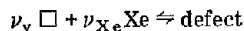
D = impurity ions  
 DM = impurity ions on cation sublattice  
 FM = Frenkel defect on cation sublattice  
 FX = Frenkel defect on anion sublattice  
 i = mode of vibration; interstitial  
 iM = positive ion on an interstitial site  
 iX = negative ion on an interstitial site  
 mix = (entropy of) mixing  
 M = cations or cation sublattice  
 S = lattice sites  
 si = interstitial sites  
 sM = cation lattice sites  
 sX = anion lattice sites  
 v = vacancy or vacant lattice sites  
 vM = vacancy on cation sublattice  
 vX = vacancy on anion sublattice  
 X = anions or anion sublattice

**Superscript**

(2) = divacancy

**6.8 PROBLEMS**

**6.1** The precursors of fission-gas bubbles in metal fuels are defect clusters of xenon atoms and vacancies. Consider a defect that is formed by association of  $\nu_v$  vacancies and  $\nu_{Xe}$  xenon atoms in a particular geometric configuration. The process can be regarded as the reaction



The concentration of defects of this type can be approximated by the law of mass action in which the binding energy of the cluster defect is the difference between the energy of the crystal with isolated vacancies and xenon atoms and the energy in the defect configuration. The binding energy, B, can be approximated by the simple bond theory of interaction between nearest-neighbor point defects:

$$B = [b_{Xe-v} \phi_{Xe-v} + b_{Xe-Xe} \phi_{Xe-Xe} + b_{v-v} \phi_{v-v}]$$

where  $b_{Xe-v}$  represents the number of adjacent xenon atoms and vacancies in the particular defect and  $\phi_{Xe-v}$  is the strength of the Xe-vacancy "bond" (actually, it is the reduction in energy of the crystal when a vacancy and a xenon atom are brought together on adjacent sites). Numerical values for these bond energies in uranium are:

$$\begin{aligned} \phi_{Xe-v} &= 0.6 \text{ eV} \\ \phi_{Xe-Xe} &= -0.7 \text{ eV} \\ \phi_{v-v} &= 0.1 \text{ eV} \end{aligned}$$

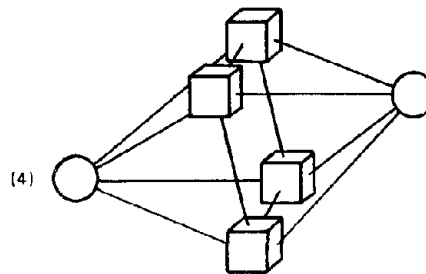
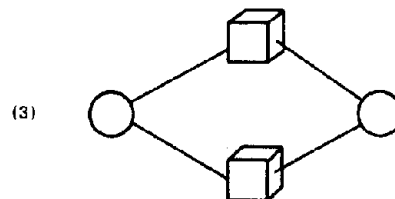
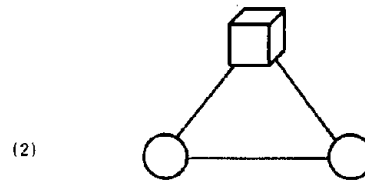
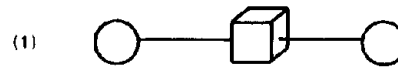
Consider the four defects shown in the diagram (each line represents a nearest-neighbor bond).

(a) Why is  $\phi_{Xe-Xe}$  negative?

(b) Calculate the binding energy of each of these defects.

(c) Assuming the initial concentrations of vacancies and xenon atoms are  $N_v^0$  and  $N_{Xe}^0$  per cubic centimeter,

compute the concentrations of each of the defects at equilibrium from the law of mass action. (Do not attempt combinatorial analysis.)



XENON ATOM

VACANCY

**6.2** From room temperature to 2000°K, the specific heat at constant pressure of  $UO_2$  can be expressed by

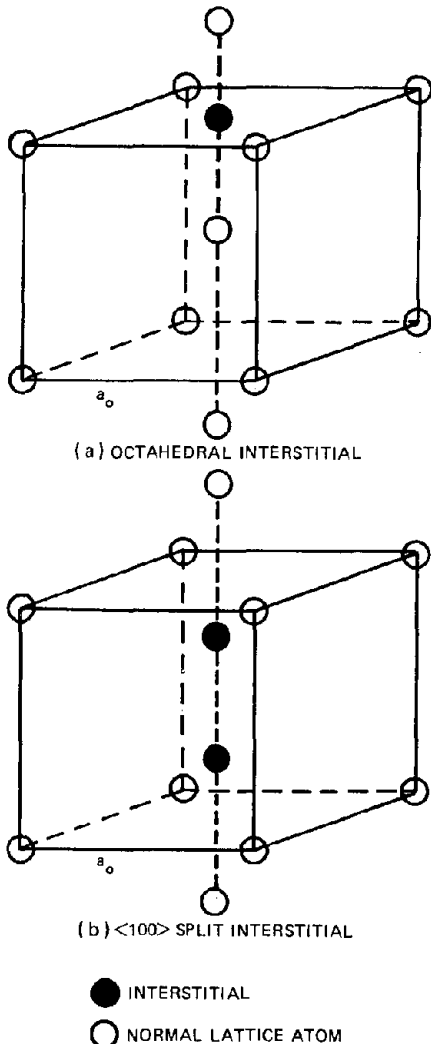
$$C_p = b + cT \quad [J(\text{mole } UO_2)^{-1} \text{ } ^\circ K^{-1}]$$

(a) For ideal crystalline  $UO_2$  well above its Debye temperature, what should be the value of the constant b? Express the constant c in terms of other thermodynamic properties of  $UO_2$ .

(b) At temperatures greater than 2000°K, the measured enthalpy of  $UO_2$  is larger than that predicted by extrapolation of the parabolic behavior suggested by the heat-capacity equation of (a). This difference, which is called the

excess enthalpy, is due to the formation of Frenkel defects resulting from movement of oxygen ions from their normal lattice sites to one of the interstitial sites in the  $\text{UO}_2$  lattice. (The uranium sublattice is not affected; it remains perfect.) If the energy of formation and the excess entropy of the Frenkel defect are  $\epsilon_F$  and  $s_F$ , respectively, derive an expression for the excess enthalpy of  $\text{UO}_2$ . Neglect vacancy–interstitial concentrations compared to the concentrations of lattice sites and interstitial sites. Assume the  $\text{UO}_2$  is stoichiometric. [See R. Swarc, *J. Phys. Chem. Solids*, 30: 705 (1969).]

6.3 Consider a bcc crystal consisting of a single type of atom. When an interstitial of the same species as the host atom is formed in the lattice, two configurations are possible. The *octahedral interstitial* is located on a face-centered position of the unit cell. The  $\langle 100 \rangle$  *split interstitial* consists of the added atom and one that was originally in the lattice lying along the  $\langle 100 \rangle$  direction at equal distances from the body-centered position in the unit cell. The two types of interstitial configurations are shown in the accompanying diagram. Assuming that interactions are



restricted to the 12 atoms shown in the diagram and that pairs of atoms separated by a distance  $r$  have an interaction energy of  $\phi(r)$ , show how to determine which type of interstitial is energetically favored.

6.4 Determine the following two characteristics of the octahedral and tetrahedral interstitial sites in the fcc and bcc lattices:

(a) The maximum diameter of a hard-sphere impurity atom that can fit into the interstitial site if the host atoms are represented by hard spheres of diameter  $d$ .

(b) The chemical formula of the compound formed when all the interstitial positions (of a particular type) are occupied by impurity atoms (i.e., the  $n$  in  $\text{MI}_n$ , where  $M$  = host metal atom and  $I$  = impurity atom).

6.5 Prove that the law of mass action for Schottky disorder in crystals of the type  $\text{MX}_2$  is given by Eq. 6.34.

6.6 An ionic crystal of the type  $\text{MX}$  is simultaneously subject to Schottky disorder and Frenkel disorder on the cation sublattice. If the equilibrium constants for Schottky and Frenkel defects are  $K_S$  and  $K_{FM}$ , respectively, determine the equilibrium concentrations (in units of site fractions) of the pertinent defect species present in the crystal. In the particular crystal structure, there are  $\beta$  interstitial sites for each normal cation lattice site.

6.7 The thermodynamic treatment of the distribution of impurity atoms between two sites in a host crystal in Sec. 5.4 did not allow for alteration of the vibrational modes of the lattice atoms surrounding an impurity atom. That is, the partition function written for the problem (Eq. 5.41) did not contain a component due to host-atom vibrations, which implies that the vibrational spectrum of the lattice is unaffected by the presence of foreign atoms in its A or B interstitial sites. This assumption is, in general, not valid, and the effect of altered lattice vibrations can be incorporated into the analysis by using what was applied to the vacancy equilibrium in the present chapter.

The partition function of a mixture consisting of  $N_1$  lattice atoms,  $N_A$  impurity atoms on the A sites of the lattice, and  $N_B$  impurity atoms on B sites is given by the product of Eq. 5.41 and the partition function of the  $3N_1$  modes of lattice vibration. The latter is

$$\sum_{i=1}^{3N_1} (1 - e^{-h\nu_i/kT})^{-1}$$

It is assumed that the perfect solid (i.e., no impurity atoms present) can be represented as a collection of Einstein oscillators of frequency  $\nu_1$ . Each impurity atom introduced into an A site changes  $\alpha_A$  vibrational modes of the host lattice from frequency  $\nu_1$  to frequency  $\nu_{1A}$ . A similar modification of lattice vibrational frequencies occurs when impurities are introduced into B sites. These vibrations do not include the vibrations of the impurity atoms proper, which are part of the partition functions  $z_A$  and  $z_B$  of Eq. 5.41.

Derive the expression for the partition function of this mixture, and from the partition function obtain the law of mass action governing the distribution of the impurity

atoms between A and B sites. How does this distribution compare with the result assuming a rigid lattice (Eq. 5.46)?

6.8 The dominant type of disorder in uranium dioxide consists of Frenkel defects on the anion sublattice. This type disorder applies to stoichiometric as well as non-stoichiometric material (i.e.,  $\text{UO}_{2+x}$ ). Assume that the uranium sublattice is perfect, except that when  $x > 0$  (hyperstoichiometric) some of the uranium ions are in the 5+ valence state and when  $x < 0$  (hypo-stoichiometric) some of the uranium ions are in the 3+ valence state. The oxygen sublattice, however, contains vacancies, and some oxygen ions occupy interstitial positions in the fluorite structure.

Let:  $N_{sM}$  = cation lattice sites in  $\text{UO}_2$   
 $N_{sX}$  = anion lattice sites in  $\text{UO}_2$   
 $N_{si}$  = interstitial sites in the fluorite structure  
 $N_M^{4+}$  = number of  $\text{U}^{4+}$  ions on cation lattice sites  
 $N_M^{q+}$  = number of  $\text{U}^{q+}$  ions on cation lattice sites ( $q = 3$  or 5)  
 $N_X$  = number of  $\text{O}^{2-}$  ions on anion lattice sites  
 $N_{vX}$  = number of vacancies on the anion sublattice  
 $N_{iX}$  = number of  $\text{O}^{2-}$  interstitials

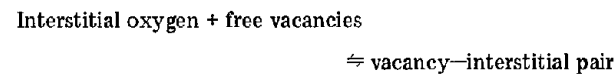
(a) Write all the relationships between the above quantities.

(b) How is the difference between the number of oxygen interstitials and anion vacancies related to the stoichiometry parameter  $x$  in  $\text{UO}_{2+x}$ ?

(c) Determine the fraction of the uranium in the  $q+$  valence state in terms of the stoichiometry parameter  $x$ .

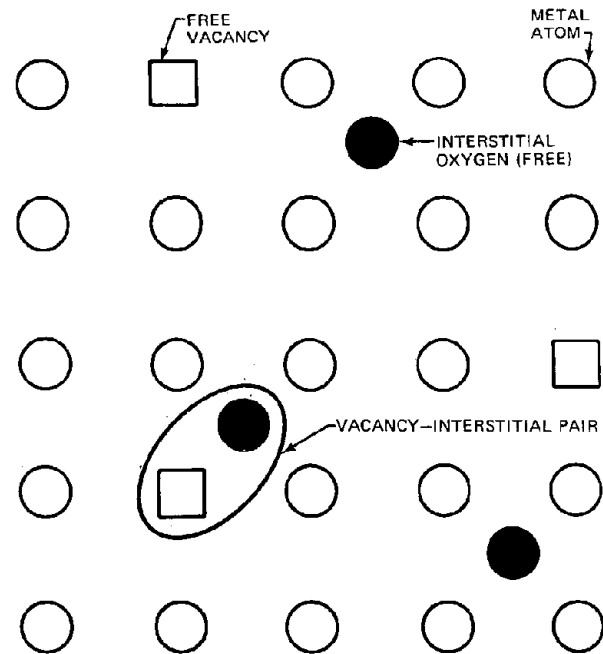
(d) Assuming that the Frenkel defects are in equilibrium with a mass-action constant  $K_{FX}$ , find the fraction of vacancies on the oxygen sublattice as a function of  $x$ .

6.9 When interstitial solutes, such as oxygen, dissolve in a metal, they can cause an increase in the total number of vacancies by the reaction:



The binding energy of the pair,  $B_p$ , is positive; so the above process will occur. As vacancies are removed by the above reaction, the free-vacancy concentration is maintained at nearly the value it would have in the absence of dissolved oxygen. The net result is an increase in the total number of vacancies in the metal (which is the sum of the free vacancies and the vacancies bound in a pair). This effect has been proposed by Kidson (see *Diffusion in bcc Metals*, American Society of Metals, p. 345, 1965) to explain the enhancement of the self-diffusion coefficient when dissolved oxygen is present in otherwise high-purity zirconium. Since self-diffusion in this metal occurs by a vacancy mechanism, additional vacancies created by the dissolved oxygen result in a greater diffusion coefficient. The various defects in the crystal lattice are shown in the accompanying diagram.

In this system there are two defects that attain concentrations governed by equilibrium thermodynamics, namely, the free vacancies,  $N_v^f$ , and the bound pairs,  $N_p$ . The number of unpaired interstitial oxygen atoms is fixed



once  $N_p$  is fixed because the total oxygen content,  $N_b$ , is specified. The numbers of lattice and interstitial sites are  $N_s$  and  $N_{si}$ , respectively.

(a) If the metal has a bcc structure and the oxygen is dissolved in the octahedral interstitial sites, what are the number of interstitial sites per lattice site ( $\alpha$ ), the number of interstitial sites adjacent to a lattice site ( $\beta$ ), and the number of lattice sites adjacent to an interstitial site ( $\beta'$ )?

(b) Write the expression for the total free energy of the defected crystal with respect to the oxygen-free perfect crystal in terms of the following energies:

$\epsilon_v \sim g_v$  = free energy (or energy) to form a single free vacancy

$\epsilon_b \sim g_b$  = free energy (or energy) increase upon adding a single free oxygen atom to an interstitial site in the crystal

$\epsilon_p \sim g_p$  = free energy due to simultaneously creating a vacancy, introducing an oxygen atom, and binding the two into a pair

In writing the total-free-energy expression, let the total configurational entropy be  $k \ln W$ .

(c) How are the three energies defined in (b) and the pair binding energy,  $B_p$ , related?

(d) Calculate the combinatorial factor,  $W$ , in the configurational entropy term by the following method: First split  $W$  into three factors,

$$W = W_p W_b W_v$$

where  $W_p$  = number of ways of arranging  $N_p$  pairs among the available sites

$W_b$  = number of ways of arranging  $N_b - N_p$  free oxygen atoms on the sites available to them

$W_v$  = number of ways of arranging  $N_v^f$  vacancies on the sites available to them

Each of the three factors must be calculated in sequential order. Calculation of  $W_p$  is similar to the divacancy problem discussed in the text.  $W_b$  is calculated on the condition that  $N_p$  of the interstitial sites are already occupied by the oxygen part of a pair.  $W_v$  is calculated under the conditions that  $N_p$  lattice sites are already occupied by the vacancy part of a pair and that the  $\beta'$  lattice sites adjacent to each of the  $N_b - N_p$  free oxygen atoms are also excluded (otherwise a pair would be formed).

(e) Minimize the free-energy expression to obtain the two mass-action laws for this problem.

(f) Compare the result of (e) with the simple approach of writing a law of mass action by inspection of the reaction and assuming that the free-vacancy concentration is the same as in the oxygen-free metal.

6.10 What is the chemical potential of the vacancies in an elemental crystal? What is the chemical potential of the vacancies when the equilibrium concentration of vacancies is attained? Neglect excess entropy effects.

6.11 Irradiation of a metal produces vacancy-interstitial pairs that are called Frenkel pairs. At the temperature of irradiation, the vacancies cannot migrate but the interstitials are mobile. Some of the interstitials annihilate vacancies, but some anneal out at fixed sinks (e.g., dislocations, grain boundaries). The net result is that at the end of irradiation, the metal contains no interstitials but possesses an atomic fraction of vacancies,  $x_v^0$ , which is in excess of the equilibrium value.

After irradiation the temperature of the vacancy-supersaturated sample is raised to a value where the vacancies are mobile. They begin to diffuse about and anneal out at fixed sinks. The annealing process may be followed by measuring the electrical resistivity of the sample, which is proportional to the vacancy concentration.

Let  $x_v$  be the vacancy fraction at any instant. Vacancies are removed by the annealing process at a rate proportional to  $x_v$ , the rate constant being denoted by  $k^-$ . However, vacancies are also generated by thermal processes at a rate designated by  $k^+$ .

Show how the measurement of the vacancy concentration as a function of annealing time can be used to deduce the rate constants  $k^+$  and  $k^-$  and the initial concentration  $x_v^0$ .

The thermodynamic energy of vacancy formation,  $e_v$ , is known. The excess entropy of vacancy formation can be neglected.

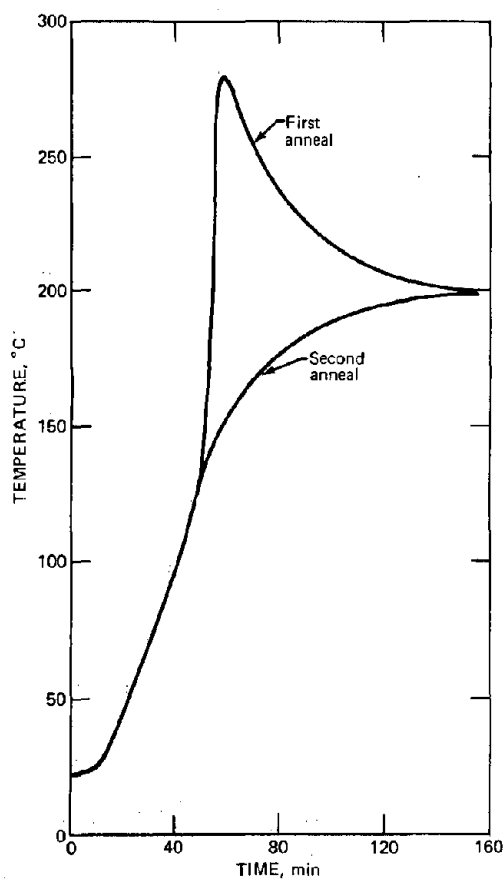
6.12 The energy stored in graphite as displacements (i.e., vacancy-interstitials or Frenkel pairs) produced by low-temperature irradiation can be released if the temperature is raised beyond a critical point. This phenomenon is sometimes called Wigner release. The magnitude of the stored energy,  $Q$  (joules/gram), for irradiation of a graphite specimen to a particular fluence is measured by the following experiment.

Ten grams of the irradiated graphite are placed in a furnace held at  $200^\circ\text{C}$ , and the temperature of the sample is monitored as a function of time. The upper curve on the accompanying graph shows this temperature history. The

sample is then removed from the furnace, cooled to room temperature, and again inserted in the furnace. The lower curve shows the time-temperature behavior of this second anneal. There is no stored energy to be released in the second anneal; so the lower curve represents simple heat exchange between the sample and the furnace. The rate at which heat is added to the sample is proportional to the temperature difference  $(200 - T)$ . The constant of proportionality is  $K = 0.44 \text{ J } ^\circ\text{C}^{-1} \text{ min}^{-1}$ . The temperature at the point where the two curves separate is  $128^\circ\text{C}$ , and the maximum temperature achieved in the first anneal is  $270^\circ\text{C}$ . The area between the two curves is  $4200^\circ\text{C min}$ . The heat capacity of the graphite is  $1.26 \text{ J g}^{-1} ^\circ\text{C}^{-1}$ .

(a) Determine the value of the stored energy per gram of sample. (Hint: The rate of release of stored energy may be written as  $g(T)$ . Use this function in developing the appropriate equations from which  $Q$  can be determined.)

(b) If the stored energy is due to recombination of radiation-produced vacancies and interstitials (Frenkel pairs), what was the atomic fraction of Frenkel pairs prior to annealing? The formation energies of vacancies and interstitials in graphite are  $5.2 \text{ eV}$  and  $13.9 \text{ eV}$ , respectively. The density of graphite is  $2.2 \text{ g/cm}^3$ .



Time vs. temperature plot of graphite placed in a furnace held at  $200^\circ\text{C}$ . Upper curve: sample previously irradiated at  $55^\circ\text{C}$ . Bottom curve: same sample after annealing. (After G. J. Dienes and G. H. Vineyard, *Radiation Effects in Solids*, p. 100, Wiley-Interscience, Inc., New York, 1957)

# Chapter 7

## Diffusion in Solids

Chapter 6 dealt with the thermodynamic properties of point defects. The phenomena that result from the exposure of solid materials to a radiation environment, such as the production and migration of fission products and the creation and annealing of vacancies and interstitials, depend on the kinetic properties of the point defects. Understanding the mechanism of motion of various types of point defects is essential to the development of rational methods for predicting the performance of nuclear reactor fuel elements and other structural components of the reactor core.

On an atomic scale the motion of point defects is best viewed as the uncorrelated hopping of the species from point to point in the solid. The aimless wandering is also exhibited by the molecules of a gas or a liquid and is called *random walk*. If mobile particles are distributed nonuniformly in a medium, the random-walk process tends to make the concentration everywhere uniform, or, on a macroscopic scale, the mobile species exhibit a net flow from regions of high concentration to regions of low concentration. This macroscopic manifestation of the random-walk process in a concentration gradient is called *molecular diffusion*.

### 7.1 FICK'S LAWS

The mobility of a particular species in an isotropic medium is governed by a single parameter, the diffusion coefficient.\* This quantity is defined in terms of the measurable quantities, the net flux of the diffusing species, and the concentration gradient. The defining equation is Fick's first law:

$$\mathbf{J} = -D\nabla C \quad (7.1)$$

\*Throughout this chapter we will restrict attention to solids that are isotropic with respect to diffusion. Anisotropy in diffusional processes occurs in all noncubic crystals, in which case three diffusion coefficients characterize the system. However, irrespective of the crystal structure, the medium may be considered isotropic if it is composed of many small crystallites with no preferred orientation in the polycrystalline compact. In this case any inherent directional properties of individual grains are nulled by the random orientation of the crystallites in the aggregate.

where  $\mathbf{J}$  is the vector flux of the diffusing species in units of atoms (or gram atoms) per unit area per unit time; it is the rate at which the diffusing species passes through a unit area perpendicular to the direction of the flux vector. The concentration of the diffusing species in atoms (or gram atoms) per unit volume is denoted by  $C$ , and  $\nabla C$  is the spatial gradient of the concentration. The diffusion coefficient  $D$  has units of length squared per unit time, usually square centimeters per second. When the diffusing species is present in very low concentrations in the host solid (i.e., as a trace constituent), the diffusion coefficient is independent of concentration. For a particular system,  $D$  is a function of temperature only.†

Equation 7.1 defines the diffusion coefficient. To calculate a concentration distribution or a flux in a particular situation, we must combine Eq. 7.1 with a mathematical statement of conservation of matter for the diffusing species. Figure 7.1 shows a region of the host solid in which a concentration gradient, and consequently a vector flux of the diffusing species, exist. Consider the small element of surface area  $dS$ . The normal to the surface at this point is denoted by the vector  $\mathbf{n}$ . The rate at which

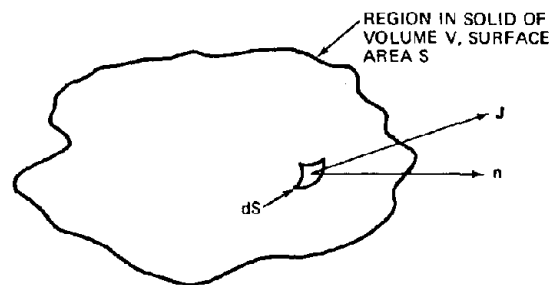


Fig. 7.1 Volume element in a solid containing a diffusing species.

†Here we deal exclusively with the trace diffusion coefficient. In more complex situations involving nonideal solids or driving forces other than a simple concentration gradient, other types of diffusion coefficients are useful. The books on diffusion in solids listed at the end of this chapter describe the many types of diffusion coefficients used.

the diffusing species leaves the region of volume through the small area  $dS$  is the product of  $dS$  and the component of the flux along the normal,  $n \cdot J$ . Integration over the entire surface  $S$  gives the rate at which the diffusing species leaves the region depicted in Fig. 7.1:

$$R_t = \int_S n \cdot J dS \quad (7.2)$$

where  $R_t$  is the rate of transport of the diffusing species across the surface  $S$ .

A differential element of volume  $dV$  inside the region of Fig. 7.1 contains  $C dV$  atoms (or gram atoms) of the diffusing species. The rate of accumulation of the diffusing species in this volume element is  $(\partial/\partial t)(C dV)$  and, over the entire volume  $V$ , it is

$$R_a = \int_V \frac{\partial C}{\partial t} dV \quad (7.3)$$

where  $R_a$  is the rate of accumulation of the diffusing species in the volume  $V$ .

There may be sources or sinks of the diffusing species.\* Let the diffusing species be created at the net rate  $Q$  atoms (or gram atoms) per unit volume per unit time. Hence,

$$R_c = \int_V Q dV \quad (7.4)$$

where  $R_c$  is the rate of creation of diffusing species in the volume  $V$ .

The statement of conservation of the diffusing species is obtained by combining Eqs. 7.2 to 7.4:

$$\int_V \frac{\partial C}{\partial t} dV = - \int_S n \cdot J dS + \int_V Q dV \quad (7.5)$$

By the divergence theorem† the first term on the right-hand side of Eq. 7.5 is equal to the volume integral of the divergence of  $J$ . Thus, Eq. 7.5 becomes

$$\int_V \left( \frac{\partial C}{\partial t} + \nabla \cdot J - Q \right) dV = 0$$

For the integral to be identically zero, the integrand must vanish, or

$$\frac{\partial C}{\partial t} = - \nabla \cdot J + Q \quad (7.6)$$

\*For example, fission-product atoms in a reactor fuel material are created by the act of fission; interstitials and vacancies in a solid are created by radiation and destroyed by annihilating each other; radioactive species disappear by decay.

†For a vector  $F$  defined over a region of volume  $V$  and surface  $S$ , the divergence theorem is

$$\int_S n \cdot F dS = \int_V \nabla \cdot F dV$$

where, for Cartesian coordinates

$$\nabla \cdot F = \frac{\partial F_x}{\partial x} + \frac{\partial F_y}{\partial y} + \frac{\partial F_z}{\partial z}$$

Equation 7.6 is a general condition of material conservation which is independent of the physical phenomena that produce the flux  $J$ . If the flux is due solely to molecular diffusion, Eq. 7.1 may be substituted into Eq. 7.6. In so doing, we assume that the diffusion coefficient is independent of position, so  $D$  can be taken through the divergence operation. Then

$$\frac{\partial C}{\partial t} = D \nabla^2 C + Q \quad (7.7)$$

Equation 7.7 is commonly known as Fick's second law. It is seen to be a combination of a conservation condition on the diffusing species and the definition of the diffusion coefficient. The form of Eq. 7.7 is identical to the heat-conduction equation or the neutron-diffusion equation. When supplied with an initial condition and two boundary conditions for each spatial coordinate represented in the Laplacian  $\nabla^2$ , solution of Eq. 7.7 yields the concentration of the diffusing substance as a function of position and time. There are an enormous number of solutions to Eq. 7.7, depending on the boundary and initial conditions, the coordinate system (Cartesian, cylindrical, or spherical), and the nature of the source term  $Q$ . We make no attempt to review these solutions here. The techniques for solving this type of linear partial differential equation are well known, and practically the world's supply of solutions are given in the book by Carslaw and Jaeger and the book by Crank cited at the end of this chapter. Generally we will simply use solutions to Eq. 7.7 as they are needed without giving the mathematical details of the solution methods.

## 7.2 ATOMIC PICTURE OF DIFFUSION

Migration of one species in a solid occurs by the occasional jump of an atom from one equilibrium site to another. In the hypothetical example shown in Fig. 7.2, the diffusing species is an impurity that most of the time occupies the body-center sites of a simple cubic host crystal. Because of the interaction of the impurity atom with the surrounding atoms of the lattice, the minimum energy (or equilibrium) position of the impurity atom is at the center of the unit cube in Fig. 7.2. As the atom moves from the center in any direction, it experiences an increase

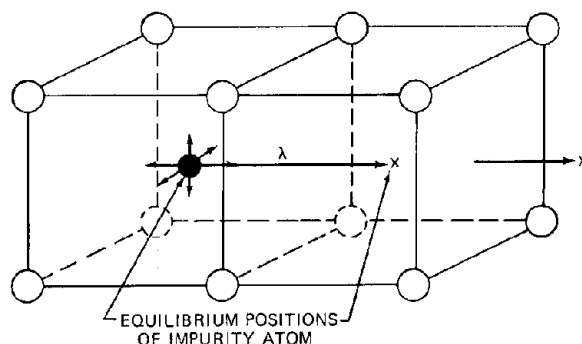


Fig. 7.2 Impurity atom in a crystal of simple cubic structure.

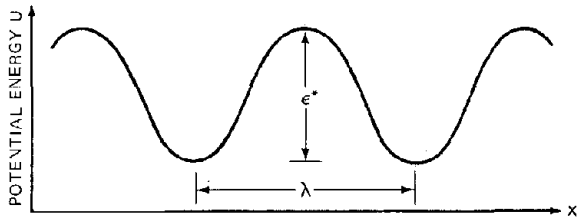


Fig. 7.3 Potential energy of impurity atom—host crystal system as the impurity atom moves through the crystal in the x-direction.

in potential energy. However, there are several directions in which the potential-energy barrier has low points or troughs. The directions normal to the faces of the unit cubes in Fig. 7.2 are such directions. If the impurity atom acquires sufficient energy, it can move out of one unit cube into an adjacent unit cube. This elementary act is the diffusive jump. The jump length  $\lambda$  in this example is one lattice constant.

The magnitude of the energy barrier that the migrating atom must overcome to hop from one position to the next can be determined by computing the potential energy of the system comprising the moving atom and the host crystal as the former occupies various positions along the line of its diffusive jump. A typical potential-energy curve as the impurity atom in Fig. 7.2 moves from the equilibrium position in the left-hand cube to the center of the adjacent cube is illustrated in Fig. 7.3. If the interatomic forces between the impurity atom and the atoms of the crystal are known, the potential-energy contour of Fig. 7.3 can be computed by methods similar to those described in Chap. 4 for determining the cohesive energy of the host atoms of the solid. In particular, if the diffusing atom interacts in a pairwise manner with the surrounding atoms, the potential energy at each point along the line of motion is the sum of the interaction energies between the impurity atom and each of the surrounding atoms of the matrix. In addition, the atoms of the host crystal are permitted to relax to a configuration that minimizes the total potential energy of the system.

The energy is a minimum when the impurity atom is in an equilibrium position and attains a maximum value halfway between equilibrium sites. At the latter position the diffusing atom is in the center of the square of atoms forming the common boundary of the unit cubes in Fig. 7.2. Because of the close approach of the matrix atoms and the diffusing species compared to the separation in the equilibrium position, the system energy is greatest at this point. The difference in potential energy between the equilibrium position and the maximum, or saddle point, is the activation energy for diffusion,  $\epsilon^*$ :

$$\epsilon^* = U(\text{saddle point}) - U(\text{equilibrium site}) \quad (7.8)$$

An atom in the saddle point is also said to be in the activated state.

The impurity atom spends most of its time simply oscillating about the equilibrium position. The vibration frequency  $\nu$  is related to the curvature of the potential energy at the equilibrium position by

$$\nu = \frac{1}{2\pi} \left[ \frac{1}{m} \left( \frac{d^2 U}{dx^2} \right)_{x_{\text{eq}}} \right]^{1/2} \quad (7.9)$$

Very infrequently the vibrating atom acquires an energy equal to or greater than the barrier energy  $\epsilon^*$ , which results in a diffusive jump from one equilibrium position to another.

If the potential-energy curve of Fig. 7.3 is known, the quantities  $\nu$  and  $\epsilon^*$  are thereby determined. Two additional questions must be answered before the mobility of the diffusing species can be fixed:

1. Can the frequency with which an atom jumps from one equilibrium site to another be determined from knowledge of  $\nu$  and  $\epsilon^*$ ?
2. How is the diffusion coefficient related to the jump frequency and the jump distance?

The frequency with which an atom jumps to a particular adjacent site is denoted by  $w$ . This jump frequency can be estimated by absolute-rate theory, which is considered in Sec. 7.5. The frequency with which a diffusing atom jumps into any neighboring equilibrium site (or the total jump frequency) is the product of the jump frequency to a single site,  $w$ , and the number of nearest-neighbor sites,  $\beta$ :

$$\Gamma = \beta w \quad (7.10)$$

where  $\Gamma$  is the total jump frequency. The value of  $\beta$  depends on the crystal structure and the jump path. For the hypothetical example of Fig. 7.2,  $\beta = 6$ .

The total jump frequency and the jump distance can be related to the diffusion coefficient by random-walk theory. This crucial link between the microscopic description of atomic motion embodied in the jump frequency and the jump distance and the purely macroscopic parameter defined by Eq. 7.1 is considered in Sec. 7.3.

### 7.3 RANDOM-WALK THEORY

Suppose at time zero a single impurity atom is placed in a position in a crystal which is designated as the origin. As shown in Fig. 7.4, the atom then proceeds to jump from one equilibrium position to another in a completely random manner. Each jump is of distance  $\lambda$ , but, because the medium is assumed to be isotropic, the direction of each jump is arbitrary and independent of the previous jumps.

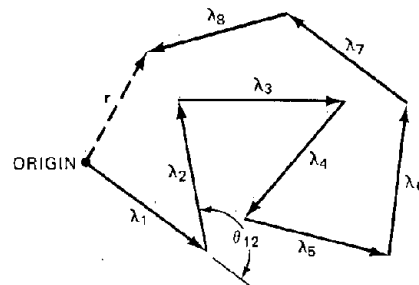


Fig. 7.4 Eight random jumps of equal length  $\lambda$ .

After a time  $t$ , the displacement  $r$  of the particle from the origin is measured. This experiment is repeated many times, and each time the displacement  $r$  for the same time interval  $t$  is measured. Because of the stochastic nature of the process,  $r$  will not be the same for each experiment, even though the time allotted for motion is the same. Rather, the displacements will be distributed according to a function  $p_t(r)$ , where  $p_t(r) d^3r$  is the probability of finding the impurity atom in a volume element  $d^3r$  at a distance  $r$  from the origin after a time  $t$ . The quantity that best describes the extent of migration is the mean square displacement,  $\overline{r^2}$ , which is given by the second moment of the distribution, or

$$\overline{r^2} = \int_{\text{all space}} r^2 p_t(r) d^3r = 4\pi \int_0^\infty r^4 p_t(r) dr \quad (7.11)$$

The mean square displacement can be computed without knowledge of the complete distribution function as follows. Since the atom makes  $\Gamma$  jumps per unit time, the time interval  $t$  corresponds to a number  $n$  of jumps given by

$$n = \Gamma t$$

As indicated in Fig. 7.4, each of the  $n$  jumps can be represented as a vector  $\lambda_i$ . These vectors are all the same length  $\lambda$  but of random direction. The position of the diffusing atom at the end of  $n$  jumps is the vector sum of the  $\lambda_i$ , or

$$r = \lambda_1 + \lambda_2 + \dots + \lambda_n \quad (7.12)$$

For any experiment the magnitude of the square of the displacement is obtained by taking the scalar product of  $r$  with itself, or

$$r^2 = r \cdot r = (\lambda_1 + \lambda_2 + \dots + \lambda_n) \cdot (\lambda_1 + \lambda_2 + \dots + \lambda_n)$$

On performing the scalar product of two sums (which is algebraically equivalent to squaring the sum), we obtain

$$r^2 = \sum_{i=1}^n \lambda_i \cdot \lambda_i + 2 \sum_{i=1}^{n-1} \sum_{j=i+1}^n \lambda_i \cdot \lambda_j \quad (7.13)$$

The double sum in the last term of this formula merely generates all possible combinations of  $i$ - $j$  terms, irrespective of the order of  $i$  and  $j$  in the product and excluding terms for which  $i = j$  (these contributions are included in the first term on the right of Eq. 7.13). For  $n = 3$ , for example, the last term is  $2(\lambda_1 \cdot \lambda_2 + \lambda_1 \cdot \lambda_3 + \lambda_2 \cdot \lambda_3)$ . Since all jumps are of the same magnitude  $\lambda$ , the scalar products in Eq. 7.13 can be written

$$\lambda_i \cdot \lambda_j = \lambda^2 \cos \theta_{ij} \quad (7.14)$$

where  $\theta_{ij}$  is the angle between the  $i$ th and  $j$ th jump vectors ( $j$  need not represent the jump immediately following the  $i$ th jump). For  $i = j$ , the scalar product is  $\lambda^2$ .

Substituting Eq. 7.14 into Eq. 7.13 yields

$$r^2 = \sum_{i=1}^n \lambda^2 + 2\lambda^2 \sum_{i=1}^{n-1} \sum_{j=i+1}^n \cos \theta_{ij}$$

Since  $\lambda^2$  is a constant, the first sum on the right is simply  $n\lambda^2$ , and the preceding formula becomes

$$r^2 = n\lambda^2 \left( 1 + \frac{2}{n} \sum_{i=1}^{n-1} \sum_{j=i+1}^n \cos \theta_{ij} \right) \quad (7.15)$$

Equation 7.15 expresses the square of the distance from the origin attained in a single experiment consisting of  $n$  jumps each of length  $\lambda$ . The mean square displacement is obtained by averaging  $r^2$  of Eq. 7.15 over a large number of identical experiments. The term  $\cos \theta_{ij}$  can take on any value between  $-1$  and  $1$ . By the nature of the random hopping process, the average value of  $\cos \theta_{ij}$  for any  $i$ - $j$  combination is zero.\* Thus, the last term in Eq. 7.15 disappears in the averaging process, and the mean square displacement is

$$\overline{r^2} = n\lambda^2 \quad (7.16)$$

or, replacing  $n$  by  $\Gamma t$ ,

$$\overline{r^2} = \lambda^2 \Gamma t \quad (7.17)$$

Equation 7.17 relates the mean square displacement to the microscopic properties of jump distance and jump frequency. Since the random-walk process on which Eq. 7.17 is based is identical to a diffusion process, the mean square displacement can also be computed from a completely macroscopic viewpoint by application of the appropriate solution of Eq. 7.7 to the random-walk problem just considered: at  $t = 0$ ,  $N$  impurity atoms are introduced to a very restricted region of a host crystal, which shall be taken as the origin. As a consequence of diffusion (or random hopping, which is synonymous), the  $N$  atoms spread out from the origin in a manner described by the concentration distribution  $C(r,t)$ , which is obtained by solving Eq. 7.7. The form of Fick's second law appropriate to this problem is

$$\frac{\partial C}{\partial t} = D \frac{1}{r^2} \frac{\partial}{\partial r} \left( r^2 \frac{\partial C}{\partial r} \right) \quad (7.18)$$

The initial condition is

$$C(r,0) = 0 \quad (\text{for } r \neq 0) \quad (7.19)$$

Since none of the  $N$  atoms introduced into the crystal disappear during the diffusion process, the distribution  $C(r,t)$  is subject to the constraint

$$\int_0^\infty 4\pi r^2 C(r,t) dr = N \quad (7.20)$$

\*There are diffusion mechanisms in which the direction of the  $j$ th jump is related to the direction of the  $i$ th jump, particularly when  $j = i + 1$ . In this case the average value of  $\cos \theta_{ij}$  is not zero, and the term in parentheses in Eq. 7.15 does not reduce to unity as a result of averaging. The net result is that the random-walk formula, Eq. 7.17, is multiplied by a correlation factor  $f$ . Since  $f$  is generally quite close to unity for most diffusion mechanisms involving correlated jumping, it will not be considered here.

The last condition is

$$C(\infty, t) = 0 \quad (7.21)$$

The solution to Eq. 7.18 subject to the conditions of Eqs. 7.19 to 7.21 is

$$C(r, t) = N \frac{e^{-r^2/4Dt}}{(4\pi Dt)^{3/2}} \quad (7.22)$$

In the random-walk problem discussed in the first part of this section, a single impurity atom was placed at the origin at time zero. The probability of finding this atom in the spherical shell between  $r$  and  $r + dr$  after time  $t$  is equivalent, in the macroscopic diffusion description of the same problem, to the fraction of the  $N$  atoms which is located in the same volume element after time  $t$ . Thus, the probability distribution  $p_t(r)$  of the random-walk problem and the concentration distribution  $C(r, t)$  of the diffusion problem are related by

$$p_t(r) = \frac{C(r, t)}{N} = \frac{e^{-r^2/4Dt}}{(4\pi Dt)^{3/2}} \quad (7.23)$$

The mean square displacement is obtained by substituting Eq. 7.23 into Eq. 7.11, which yields

$$\overline{r^2} = \frac{4\pi}{(4\pi Dt)^{3/2}} \int_0^\infty r^4 e^{-r^2/4Dt} dr$$

or

$$\overline{r^2} = 6Dt \quad (7.24)$$

The mean square displacement has been computed by considering (1) the random motion of a single impurity atom and (2) the macroscopic spreading of a large number of impurity atoms in accord with Fick's law. Both methods must yield identical results so that  $\overline{r^2}$  from Eq. 7.24 can be equated to  $\overline{r^2}$  of Eq. 7.17. There follows

$$D = \frac{1}{6} \lambda^2 \Gamma \quad (7.25)$$

which is known as the Einstein formula. It provides the essential link between the atomic properties  $\lambda$  and  $\Gamma$  and the macroscopic quantity  $D$ .

## 7.4 DIFFUSION MECHANISMS IN CUBIC CRYSTALS

To apply Eq. 7.25, we must specify the mechanism by which the diffusive jump occurs. Of the eight or so different diffusion mechanisms that have been proposed, we consider only two of the most important and limit the discussion to elemental cubic crystals. In each mechanism we seek to identify the jump distance  $\lambda$  in terms of the lattice constant  $a_0$  and to ascertain the number of possible jump directions from a particular equilibrium site. This is the quantity  $\beta$  in Eq. 7.10.

### 7.4.1 Interstitial Diffusion of Impurity Atoms in Body-Centered Cubic Crystals

The interstitial mechanism of diffusion in the bcc lattice is illustrated in Fig. 7.5. The equilibrium site of the impurity atom is assumed to be the octahedral interstice [see also Fig. 6.3(a)]. The elementary diffusive jump is in the plane shown in Fig. 7.5 from the center to one of the four adjacent equilibrium sites on the edges of the square. The impurity atom cannot jump in a direction perpendicular to the plane since atoms of the host lattice occupy

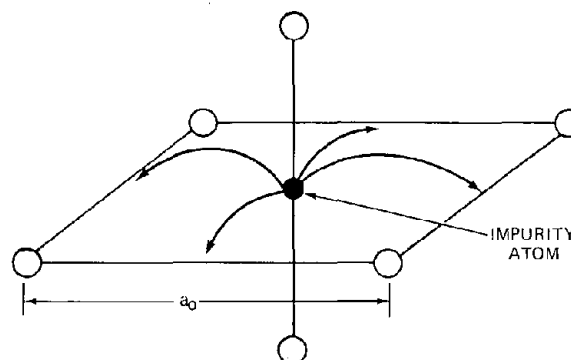


Fig. 7.5 Interstitial diffusion in the bcc structure (octahedral equilibrium site).

these positions. The number of equivalent jumps for this mechanism is  $\beta = 4$ , and the total jump frequency is

$$\Gamma = 4w$$

The diffusive jump is one-half a lattice parameter, or

$$\lambda = \frac{a_0}{2}$$

Inserting these values into Eq. 7.25, we obtain the diffusion coefficient

$$D = \frac{1}{6} \left( \frac{a_0}{2} \right)^2 (4w) = \frac{1}{6} a_0^2 w \quad (7.26)$$

This mechanism is of considerable practical importance since it is the way that carbon migrates in iron. In general, most small impurity atoms (e.g., hydrogen, carbon, and boron) diffuse in metals by an interstitial mechanism of the type described here.

### 7.4.2 Vacancy Mechanism of Self-Diffusion in Face-Centered Cubic Crystals

When the diffusing species and the atoms of the host crystal are one and the same, the migration process is called self-diffusion. Since no net flux of the chemical species occurs and no concentration gradient of the diffusing species exists, the only way that self-diffusion can be observed is by using an isotope of the species. If an imbalance in the isotopic content of a crystal is established (e.g., by placing tagged atoms of the substance on one face of a crystal consisting of the natural isotopic composition), the diffusion process acts to eliminate gradients of isotopic

composition. Since the tracer isotope and the normal isotopic species of the crystal have the same chemical properties, the atomic interactions responsible for mobility involve only one species. Consequently, theoretical interpretation of self-diffusion coefficients is easier than when the diffusing atoms and the matrix atoms are different chemical species. Migration of one species in another is sometimes called mutual diffusion.

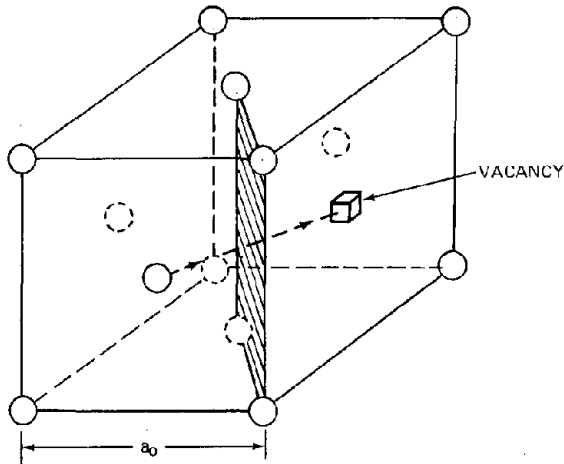


Fig. 7.6 Self-diffusion by a vacancy mechanism in the fcc structure.

Self-diffusion in most metals proceeds by way of diffusive jumps of a lattice atom into an adjacent lattice site that happens to be vacant, as illustrated in Fig. 7.6. The activated state occurs midway in the jump between face-centered positions on adjacent cube sites. For a jump to be possible, the terminal site must be unoccupied. The maximum potential energy in the jump occurs as the diffusing atom squeezes through the rectangle of atoms that has been shaded in Fig. 7.6.

Determination of the jump frequency proceeds as follows. The quantity  $w$  represents the frequency with which a lattice atom jumps to a particular adjacent lattice site, which of course must be vacant. In the close-packed fcc structure, there are  $\beta = 12$  nearest-neighbor sites into which the diffusing atom could jump if the site were vacant. The probability that any particular site in the lattice is vacant is equal to the equilibrium fraction of vacancies in the crystal, given by Eq. 6.12. The total jump frequency is thus

$$\Gamma = 12x_v w = 12e^{s_v/k} e^{-\epsilon_v/kT} w \quad (7.27)$$

The jump distance in Fig. 7.6 is

$$\lambda = \frac{a_0}{\sqrt{2}}$$

Using these values of the jump frequency and jump distance in Eq. 7.25 yields

$$D = a_0^2 x_v w = a_0^2 w e^{s_v/k} e^{-\epsilon_v/kT} \quad (7.28)$$

Equation 7.28 gives the diffusion coefficient of the atomic species of which the crystal is comprised. We will encounter many situations in which the diffusion coefficient of the vacancies, rather than that of the atoms, is of prime interest. It is obvious from Fig. 7.6 that the jump of an atom in one direction is equivalent to the jump of the vacancy in the opposite direction. The diffusion coefficient of the vacancies is obtained by the same arguments used for the atoms, except that the term  $x_v$  representing the probability of a vacancy at any particular site need not be introduced. If we are considering the motion of a vacancy, we obviously do not have to consider the probability of its being there. Thus, the diffusion coefficient for vacancies in an fcc crystal is

$$D_v = a_0^2 w \quad (7.29)$$

where the jump frequency  $w$  is the same as in the atomic diffusion-coefficient formula, Eq. 7.28.

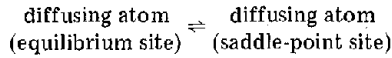
Expressions for the diffusion coefficient based on other atomistic pictures of the jump process and for other crystal structures have been proposed, and some have been experimentally verified. These are treated in detail in the books on solid-state diffusion listed at the end of this chapter.

## 7.5 THE JUMP FREQUENCY ACCORDING TO ABSOLUTE-RATE THEORY

Once a mechanism is chosen, there remains only the problem of estimating the jump frequency  $w$  to calculate a diffusion coefficient by equations such as Eqs. 7.26, 7.28, and 7.29. The jump frequency is best obtained by the theory of absolute reaction rates (sometimes called transition-state theory), first proposed in the 1930s by H. Eyring to explain the kinetics of homogeneous gas-phase reactions. This theory, however, is quite general and has been successfully applied to many other rate processes, of which diffusion in solids is but one example.

The crux of absolute-rate theory is the supposition that in any rate process a barrier must be overcome by the moving species for the elementary step to occur. The atom at the top of its barrier is called an activated complex, and the state of the system with an atom in this metastable position is called the transition state, or the activated state. It is also assumed that the activated state is a true thermodynamic state of the system. This last assumption has far-reaching consequences because it implies that (1) the activated state can be described by a partition function and (2) the distribution of diffusing atoms between normal equilibrium sites in the crystal and the activated sites is governed by a law of mass action. The activated state is treated like any other type of point defect in the crystal, and the concentration of atoms in the activated state can be obtained by the thermodynamic considerations of Chap. 5.

For simplicity, we consider the case of an impurity atom diffusing in a host crystal. The distribution of impurity atoms between normal equilibrium sites and in the locations in the crystal where the saddle point (or activated state) occurs is represented by the reaction:



This reaction is precisely the one considered in Sec. 5.4 and explored in greater detail in problem 6.7. We assume for simplicity that the number of equilibrium interstitial sites in which impurity atoms can reside is equal to the number of saddle-point sites; thus the ratio of site fractions in the law of mass action is the same as the ratio of the number of atoms. The ratio of the number of diffusing atoms in normal interstitial sites,  $N_{eq}$ , to the number of diffusing atoms in the activated state,  $N^*$ , is given by

$$\frac{N^*}{N_{eq}} = \left[ \frac{(\nu_1/\nu_1^*)^{\alpha^*}}{(\nu_1/\nu_{1eq})^{\alpha_{eq}}} \right] \left( \frac{z^*}{z_{eq}} \right) e^{-\epsilon^*/kT} \quad (7.30)$$

This equation is Eq. 5.46 augmented by the first term on the right, which represents the effect of alteration of lattice vibrations on the distribution coefficient (see problem 6.7). The value  $\nu_1$  is the vibration frequency of the atoms in the perfect crystal (represented by the Einstein model). Introducing a diffusing atom in the equilibrium site is assumed to alter nearby  $\alpha_{eq}$  vibrational modes from frequency  $\nu_1$  to frequency  $\nu_{1eq}$ . Similarly, the presence of a diffusing atom in the activated state causes  $\alpha^*$  neighboring vibrational modes to be changed from  $\nu_1$  to  $\nu_1^*$ . These vibrations do not include the contributions of the vibration of the diffusing atom itself, which appears in  $z_{eq}$  and  $z^*$ . These two quantities are the single-particle partition functions of the diffusing atom in the equilibrium and activated states, respectively. They are reckoned with the zero-point energy as the reference energy. The energy  $\epsilon^*$  is therefore the difference in energy between the ground vibrational states of the activated and equilibrium states. If the zero-point vibration energies are assumed to be the same for the two states, the quantity  $\epsilon^*$  also represents the barrier height of Fig. 7.3, which is the potential-energy difference between the two states. Since both the normal interstitial site and the activated site are considered to be equilibrium states of the crystal,  $\epsilon^*$  and all vibration frequencies are computed with the atoms of the host crystal permitted to relax about the impurity atom in both states.

The thermodynamic states of the impurity atom in the equilibrium and activated states are shown schematically in Fig. 7.7. The diffusing atom in the equilibrium interstitial site behaves as a three-dimensional harmonic oscillator. However, the atom on top of its diffusional energy barrier (i.e., the activated state) cannot possibly be a three-dimensional oscillator since, in the direction of the jump, the potential energy is at a maximum rather than a minimum. The potential energy, however, does increase in directions perpendicular to the line of the jump. The potential-energy surface at the top of the energy barrier thus resembles a horse's saddle, whence the name saddle point.

The thermodynamic state of the atom in this peculiar potential is assumed to consist of one degree of translational freedom (in the jump direction) and two degrees of vibrational freedom (perpendicular to the jump direction). The single degree of translational freedom in the activated

state is associated with a length  $\delta$  and an average velocity of a one-dimensional ideal gas:

$$\bar{v}_x = \left( \frac{kT}{2\pi m} \right)^{1/2} \quad (7.31)$$

where  $\bar{v}_x$  is the mean x-component of the Maxwell-Boltzmann distribution of molecular velocities in an ideal gas.

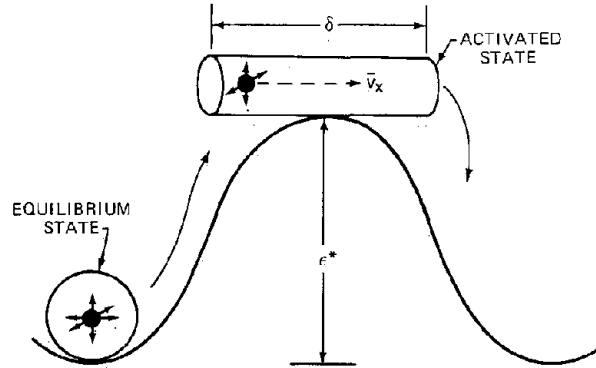


Fig. 7.7 Absolute-rate theory of diffusion.

Once an atom is supplied to the activated state, it is assumed to traverse the length  $\delta$  and fall into the empty equilibrium site on the right of Fig. 7.7 (reflection at the ends of the tube-shaped volume available to the activated atom is not allowed). The mean lifetime of a diffusing atom in the activated state is thus the length of time it takes to traverse the length  $\delta$ , or

$$\text{Mean lifetime of an atom in the saddle point} = \frac{\delta}{\bar{v}_x} \quad (7.32)$$

A steady supply of diffusing atoms to the pipe is maintained by the equilibrium of Eq. 7.30, which fixes the concentration of atoms in the activated state. The rate at which diffusing atoms cross the activated state from one equilibrium site to another can be determined in a fashion similar to the argument applied to radioactive decay. In the latter situation,  $n$  atoms with a decay constant  $\lambda$  disintegrate at a rate  $\lambda n$ . Since the mean lifetime of a radioactive species is  $\tau = 1/\lambda$ , the disintegration rate is  $n/\tau$ . With this analogy, the rate at which atoms cross the saddle point is equal to the number in the activated state,  $N^*$ , divided by their mean lifetime in this state,  $\delta/\bar{v}_x$ :

$$\text{Rate at which atoms cross the saddle point} = \frac{N^*}{\delta/\bar{v}_x}$$

The jump frequency  $w$  is the probability per second that a particular diffusing atom residing in its equilibrium site will execute a successful jump. This quantity is also equal to the fraction of the atoms that make a diffusive jump in 1 sec, which is the preceding rate divided by the number of impurity atoms in normal sites:

$$w = \frac{N^* \bar{v}_x}{N_{eq} \delta} \quad (7.33)$$

If Eq. 7.30 is substituted into this relation, there results

$$w = \left[ \frac{(\nu_1/\nu_1^*)^{\alpha^*}}{(\nu_1/\nu_{1eq})^{\alpha_{eq}}} \right] \left( \frac{z^*}{z_{eq}} \right) \frac{\bar{v}_x}{\delta} e^{-\epsilon^*/kT} \quad (7.34)$$

The partition function of the diffusing atom in the activated state is

$$z^* = z_{tr}^* z_{vib}^* \quad (7.35)$$

where  $z_{tr}^*$  represents the single-particle partition function for translation in one dimension. It is determined by the same methods used for translation in three dimensions (Sec. 1.4). The result is similar to Eq. 1.73, in which the volume is replaced by the length  $\delta$  and the  $\frac{3}{2}$  power becomes the  $\frac{1}{2}$  power. Thus,

$$z_{tr}^* = \delta \left( \frac{2\pi mkT}{h^2} \right)^{\frac{1}{2}} \quad (7.36)$$

The frequency of the two degrees of vibration perpendicular to the jump direction are assumed to be given by  $\nu^*$ . The partition function  $z_{vib}^*$  is given by

$$z_{vib}^* = (1 - e^{-h\nu^*/kT})^{-2} \approx \left( \frac{kT}{h\nu^*} \right)^2 \quad (7.37)$$

The last equality in Eq. 7.37 assumes that the vibration frequency is low, or that  $h\nu^* \ll kT$ .

The partition function for the three vibrational modes of the diffusing atom in its equilibrium site is

$$z_{eq} = \left( 1 - e^{-h\nu/kT} \right)^{-3} \approx \left( \frac{kT}{h\nu} \right)^3 \quad (7.38)$$

where  $\nu$  is the vibration frequency of the impurity atom in the equilibrium site and again the ratio  $h\nu/kT$  has been assumed small compared to unity. When Eqs. 7.31 and 7.35 to 7.38 are substituted into Eq. 7.34, the length  $\delta$  cancels out, and the jump frequency simplifies to

$$w = \nu \left[ \left( \frac{\nu}{\nu^*} \right)^2 \frac{(\nu_1/\nu_1^*)^{\alpha^*}}{(\nu_1/\nu_{1eq})^{\alpha_{eq}}} \right] e^{-\epsilon^*/kT} \quad (7.39)$$

The jump frequency is governed primarily by the vibration frequency of the diffusing atom in the equilibrium site,  $\nu$ , and the activation energy  $\epsilon^*$ . As indicated in Sec. 7.2, both these quantities can be estimated if the interatomic forces between diffusing atoms and the atoms of the lattice are known. The remaining frequency ratios in Eq. 7.39 are more difficult to evaluate. As discussed in Chap. 5, these frequency ratios are related to an excess entropy, which is given by

$$s^* = k \ln \left[ \left( \frac{\nu}{\nu^*} \right)^2 \frac{(\nu_1/\nu_1^*)^{\alpha^*}}{(\nu_1/\nu_{1eq})^{\alpha_{eq}}} \right] \quad (7.40)$$

The jump frequency is then

$$w = \nu e^{s^*/k} e^{-\epsilon^*/kT} \quad (7.41)$$

The quantities  $s^*$  and  $\epsilon^*$  are sometimes called the entropy and energy of motion. As in the case of point defect

thermodynamics, the excess entropy  $s^*$  is often ignored because it does not differ from unity by more than an order of magnitude and because it is difficult to determine theoretically or experimentally.

If the jump frequency is expressed by Eq. 7.41, the diffusion coefficient for interstitial migration in the bcc lattice, Eq. 7.26, becomes

$$D = \frac{1}{6} a_0^2 \nu e^{s^*/k} e^{-\epsilon^*/kT} \quad (7.42)$$

Similarly, use of Eq. 7.41 in Eq. 7.28 yields for the vacancy mechanism

$$D = a_0^2 \nu e^{(s^* + s_v)/k} e^{-(\epsilon^* + \epsilon_v)/kT} \quad (7.43)$$

and for the diffusion coefficient of the vacancies

$$D_v = a_0^2 \nu e^{s^*/k} e^{-\epsilon^*/kT} \quad (7.44)$$

Equations 7.42 to 7.44 illustrate the characteristic exponential variation of the diffusion coefficient with temperature. The diffusion coefficient may quite generally be expressed by

$$D = D_0 e^{-E/kT} \quad (7.45)$$

where  $D_0$  is the preexponential factor and  $E$  is the activation energy. Depending on the mechanism and the diffusing species, the activation energy for diffusion is identified either with the energy of motion of the moving atom or with the sum of the energy of motion and the energy of formation of a vacancy.

Although the activation energy for diffusion is quite difficult to compute, it is readily measured. It ranges from  $\sim 10$  kJ/mole for hydrogen diffusion in metals to  $\sim 500$  kJ/mole for self-diffusion of uranium in  $UO_2$ . The vibration frequency  $\nu$  can be estimated with fair precision. It is usually always within an order of magnitude of  $10^{13}$   $\text{sec}^{-1}$ . For self-diffusion it is often taken to be the Debye frequency of the solid.

## 7.6 THERMAL DIFFUSION

The gradient of a potential represents a force. A force is an agent for effecting motion. For example, an electrical potential gradient drives an electrical current and a temperature gradient results in the flow of heat. In the same spirit, a gradient in the chemical potential can be regarded as a force on diffusing atoms since it results in the transport of matter.\*

The relationship of the fluxes, such as electrical current, heat flow, and mass flow, and the driving forces due to gradients of the potentials of electric field, temperature, and chemical potential is the subject of a branch of

\*Although Fick's first law relates matter flux to a concentration gradient, the chemical potential is the proper driving force for diffusion. In ideal mixtures the gradient of the chemical potential is proportional to the gradient of the concentration; thus the distinction is unimportant.

thermodynamics called irreversible thermodynamics. It is a basic postulate (which is confirmed by experiment) that a particular flux is the result of a combination of all forces present. Or a given type of force can cause more than a single type of flux. In particular, a temperature gradient can cause a mass flux of one component of a mixture even though there is no concentration gradient present. This phenomenon is called thermal diffusion, or the Soret effect. The fuel elements of a nuclear reactor may be subjected to a temperature gradient as large as 4000°C/cm, and the normally insignificant thermal-diffusion effect exerts a profound influence on the performance of the fuel.

Irreversible thermodynamics assumes that the fluxes of various types are related to all forces in a linear manner. In addition, if the forces are expressed in the correct manner, the coefficients of the linear equation are related to each other. For the particular case of fluxes represented by heat and mass transport and forces due to gradients in the chemical potential and the temperature, the flux-force relation in a binary mixture of species A and B is

$$J_A = -L_{11} (\nabla\mu_A)_T - L_{12} \frac{\nabla T}{T} \quad (7.46)$$

$$q = -L_{21} (\nabla\mu_A)_T - L_{22} \frac{\nabla T}{T} \quad (7.47)$$

where  $J_A$  is the mass flux of species A,  $\mu_A$  is the chemical potential of species A, and  $q$  is the heat flux. The coefficients  $L_{11}$  and  $L_{22}$  are related to the diffusion coefficient and the thermal conductivity, respectively. The second term on the right of Eq. 7.46 represents thermal diffusion. The conjugate effect, the creation of a heat flow by a chemical potential gradient (called the Dufour effect), is contained in the first term on the right of Eq. 7.47. When the forces are expressed as the gradient of the chemical potential and the gradient of the logarithm of the temperature (i.e., as  $\nabla T/T$ ), the coefficients of the Soret and Dufour effects are equal, or

$$L_{12} = L_{21} \quad (7.48)$$

In most mixtures of practical significance, the gradient of the chemical potential appearing in Eqs. 7.46 and 7.47 can be related to a concentration gradient. The chemical potential of species A is given by

$$\mu_A = kT \left( \frac{\partial \ln Z}{\partial N_A} \right)_{T, V, N_B}$$

For an ideal mixture of species A and B or one which is so dilute in A that atoms of this species do not interact with each other, the partition function is given by

$$Z = \frac{(N_A + N_B)!}{N_A! N_B!} z_A^{N_A} z_B^{N_B}$$

Combining the preceding two formulas (as in Chap. 5) yields

$$\mu_A = -kT \ln \left( \frac{z_A}{x_A} \right) \quad (7.49)$$

where  $x_A = N_A/(N_A + N_B)$  is the atomic fraction of A in the mixture. The gradient of the chemical potential can be related to the concentration gradient by

$$\nabla\mu_A = \left( \frac{\partial\mu_A}{\partial C_A} \right)_T \nabla C_A \quad (7.50)$$

where  $C_A$  is the volumetric concentration of species A. It is related to the atom fraction of A by

$$x_A = \frac{C_A}{C_{\text{tot}}} \quad (7.51)$$

where  $C_{\text{tot}}$  is the total concentration, or the number of atoms of A and B per unit volume. Using Eq. 7.51 in Eq. 7.49 and assuming constant  $C_{\text{tot}}$ , we find that

$$\left( \frac{\partial\mu_A}{\partial C_A} \right)_T = \frac{kT}{C_A} \quad (7.52)$$

Using Eqs. 7.52 and 7.50 in Eqs. 7.46 and 7.47 permits the linear relations of irreversible thermodynamics to be expressed in terms of the concentration gradient instead of the gradient of the chemical potential. The subscript A is henceforth omitted, but the flux  $J$  and the concentration  $C$  refer to one component of a binary mixture:

$$J = -L_{11} \frac{kT}{C} \left( \nabla C + \frac{L_{12}}{L_{11}} \frac{C}{kT^2} \nabla T \right) \quad (7.53)$$

$$q = -\frac{L_{22}}{T} \left( \frac{L_{21}}{L_{22}} \frac{kT^2}{C} \nabla C + \nabla T \right) \quad (7.54)$$

To conform to Fick's first law for diffusion of matter and to Fourier's law for heat conduction, we identify the coefficients  $L_{11}$  and  $L_{22}$  with the conventional transport properties of molecular diffusivity and thermal conductivity:

$$D = L_{11} \frac{kT}{C} \quad (7.55)$$

$$\kappa = \frac{L_{22}}{T} \quad (7.56)$$

Finally, the coefficients  $L_{21}$  and  $L_{12}$  (which are equal), are expressed in terms of a quantity called the heat of transport:

$$Q^* = \frac{L_{12}}{L_{11}} = \frac{L_{21}}{L_{11}} \quad (7.57)$$

and Eqs. 7.53 and 7.54 become

$$J = -D \nabla C - D \frac{Q^* C}{kT^2} \nabla T \quad (7.58)$$

$$q = -\kappa \nabla T - Q^* D \nabla C \quad (7.59)$$

In the absence of a temperature gradient, Eq. 7.58 is simply Fick's first law, and, in the absence of a concentration gradient, Eq. 7.59 is Fourier's law. The magnitude and direction of the thermal-diffusion effect are governed by  $Q^*$ , which may be either positive or negative. In solids the heat of transport depends on the point along the diffusive path at which the moving atom receives the energy necessary for the jump. Understanding of the nature of atomic motions in crystals is not sufficiently advanced to permit quantitative description of this process. The reason for calling  $Q^*$  the heat of transport can be seen from the last term of Eq. 7.59. The product  $D \nabla C$  is very closely equal to the mass flux  $J$ ; so  $Q^*$  has the physical significance

of the quantity of heat transported by a mole of diffusing material (exclusive of sensible heats).

Although Eq. 7.58 describes the rate of transport of material due to the combined effects of concentration and thermal gradients, one of the more important manifestations of thermal diffusion is the unmixing of a two-component system owing to a temperature gradient. If the flux  $J$  is set equal to zero by not allowing loss of material from the mixture, a temperature gradient  $\nabla T$  induces a concentration gradient given by

$$\frac{\nabla C}{C} = -\left(\frac{Q^*}{kT}\right)\left(\frac{\nabla T}{T}\right) \quad (7.60)$$

If the heat of transport is about 8 kJ/mole at a temperature of, say, 1000°K, Eq. 7.60 shows that the fractional change in composition due to the thermal-diffusion effect is comparable to the fraction change in temperature maintained across the specimen.

In reactor fuel elements a fractional gradient  $\nabla T/T$  of approximately unity is not unusual; thus substantial unmixing is to be expected and, in fact, has been observed. The fuel of a fast reactor is a mixture of 20% PuO<sub>2</sub> and 80% UO<sub>2</sub>. Under the influence of the temperature gradient, plutonium appears to migrate to the hot zone. Such redistribution could affect both the neutronic and the thermal performance of the fuel element.

Hydrogen in the zircaloy cladding of a light-water reactor fuel element readily migrates as a result of even modest temperature gradients. Hydrogen embrittlement of cold spots of the cladding (such as at grid spacers) may result.

## 7.7 SURFACE DIFFUSION

Diffusion in two dimensions on the surface of a solid provides an important mechanism for the migration of bubbles in nuclear fuels. Surface diffusion exhibits many of the features of its three-dimensional counterpart, volume diffusion, and much of the analysis presented in the preceding sections of this chapter is applicable to surface diffusion.

Figure 7.8 shows a simple example of surface diffusion. An impurity substance is deposited as a band on the surface of a substrate material. As a result of surface diffusion, which is a random hopping of impurity atoms over the surface, the deposit tends to become uniformly distributed over the entire available surface area. The spreading may be described by Fick's law:

$$J_s = -D_s \nabla C_s \quad (7.61)$$

where  $J_s$  is the surface flux, which is the number of atoms of the diffusing substance crossing a line of unit length on the surface per unit time. The surface concentration  $C_s$  bears the units of atoms per unit area. The surface diffusion coefficient  $D_s$  has the same units as the volume diffusion coefficient, namely, square centimeters per second.

Consideration of the random walk that a diffusing atom executes in two dimensions on a surface produces the following form of the Einstein equation:

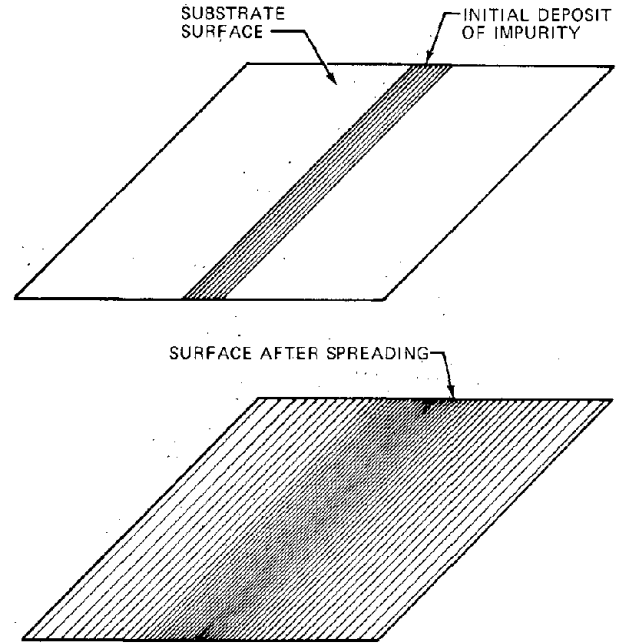


Fig. 7.8 Surface diffusion of impurity species on a crystal surface.

$$D_s = \frac{1}{4} \lambda_s^2 \Gamma_s \quad (7.62)$$

which is of the same form as Eq. 7.25 except that the numerical coefficient is  $\frac{1}{4}$  instead of  $\frac{1}{6}$ . In Eq. 7.62  $\lambda_s$  is the jump distance on the surface, which is of the order of the interatomic spacing, and  $\Gamma_s$  is the surface jump frequency given by

$$\Gamma_s = \beta_s \nu_s e^{\epsilon_s^*/k} e^{-\epsilon_s^\ddagger/kT} \quad (7.63)$$

where  $\beta_s$  is the number of sites on the two-dimensional surface lattice to which an atom may hop (usually about 4) and  $\nu_s$  is the frequency of vibration of the diffusing atom parallel to the surface. As in the case of bulk diffusion, the vibration frequency is approximately  $10^{13} \text{ sec}^{-1}$ . The entropy and energy of motion for the surface jump are  $s_s^\ddagger$  and  $\epsilon_s^\ddagger$ . They have the same meaning as their three-dimensional analogs. The activation energy of surface diffusion,  $\epsilon_s^*$ , has been found to be about two-thirds the heat of vaporization for surface self-diffusion on metals (i.e., the diffusing species and the substrate are one and the same). For adsorbed gases (e.g., hydrogen, oxygen, and nitrogen) on metals, the activation energy for surface migration is approximately  $\frac{1}{5}$  of the binding energy of the adsorbed atom and the surface. That the energy barrier for surface diffusion should be smaller than the energy required to remove an atom completely from the surface is entirely reasonable since a hop on the surface is an atomic motion just short of evaporation.

The phenomenon of surface thermal self-diffusion is important in bubble motion in nuclear fuels. In this sort of diffusive process, atoms of the solid migrate along one of the faces of the crystal under the influence of a tempera-

ture gradient alone. The rate of this process is governed by the two-dimensional counterpart of Eq. 7.58, but, since self-diffusion is involved, no concentration gradient is possible. The surface flux is given by

$$J_s = -D_s Q_s^* \frac{C_s}{kT^2} \nabla T \quad (7.64)$$

where  $Q_s^*$  is the heat of transport for surface thermal diffusion. In contrast to the heat of transport in bulk thermal diffusion,  $Q_s^*$  is always positive; thus thermal diffusion along a surface transfers material from hot to cold regions. The process may be regarded as the result of a high jump frequency in the hot zone which results in greater transport to the cold zone than the return flux from cold to hot.

## 7.8 NOMENCLATURE

- $a_0$  = lattice constant
- $C$  = concentration in atoms per unit volume
- $D$  = diffusion coefficient
- $D_0$  = preexponential factor of diffusion coefficient
- $E$  = activation energy
- $h$  = Planck's constant
- $J$  = vector flux of diffusing species in atoms per unit area per unit time
- $k$  = Boltzmann constant
- $L$  = coefficients connecting mass or heat flux to gradients of chemical potential and temperature
- $m$  = mass of an atom
- $n$  = number of jumps in time  $t$
- $n$  = vector normal to the surface pointing outwards
- $N$  = total number of diffusing atoms or host atoms
- $p_t(r)$  = probability per unit volume of finding an atom at a distance  $r$  from the origin at time  $t$
- $q$  = heat-flux vector
- $Q$  = rate of creation of the diffusing species, atoms per unit volume per unit time
- $Q^*$  = heat of transport
- $r$  = distance from origin after time  $t$
- $s_v$  = entropy of vacancy formation
- $s^*$  = excess entropy of diffusion motion
- $t$  = time
- $T$  = temperature
- $U$  = potential energy of the system
- $\bar{v}_x$  = average  $x$ -component velocity of one-dimensional ideal gas
- $V$  = volume
- $w$  = jump frequency to a single neighboring site
- $x$  = distance along the direction of diffusive jump; site fraction or atomic fraction in a mixture
- $z$  = single-particle partition function
- $Z$  = total partition function of the system

### Greek Letters

- $\alpha$  = number of vibrational modes affected by impurity atom
- $\beta$  = number of nearest neighbors to an equilibrium site
- $\Gamma$  = total jump frequency from an equilibrium site to any neighboring site
- $\delta$  = length of the single degree of translational freedom available to the activated atom

- $\epsilon^*$  = activation energy for diffusion
- $\epsilon_v$  = energy of vacancy formation
- $\kappa$  = thermal conductivity
- $\mu$  = chemical potential of a species
- $\nu$  = frequency of vibration of an atom
- $\theta$  = angle between jump vectors

### Subscripts

- A = diffusing species A
- B = diffusing species B
- eq = equilibrium or equilibrium site
- $i$  =  $i$ th jump
- $l$  = lattice vibrational modes
- $l_{eq}$  = lattice vibrational modes with diffusing atom on equilibrium site
- $l^*$  = lattice vibrational modes with diffusing atom in activated state
- $s$  = surface
- tot = total
- tr = translational
- $v$  = volume (e.g. volume diffusion coefficient); vacancy
- vib = vibrational

### Superscript

- \* = activated state

## 7.9 ADDITIONAL READING

1. L. A. Girifalco, *Atomic Migration in Crystals*, Blaisdell Publishing Co., New York, 1964.
  2. W. Jost, *Diffusion in Solids, Liquids, and Gases*, Academic Press, Inc., New York, 1960.
  3. P. G. Shewmon, *Diffusion in Solids*, McGraw-Hill Book Company, New York, 1963.
  4. J. R. Manning, *Diffusion Kinetics for Atoms in Crystals*, D. Van Nostrand Company, New York, 1968.
- Compilations of solutions to the heat-conduction equation:*
5. H. S. Carslaw and J. C. Jaeger, *Conduction of Heat in Solids*, 2nd ed., Oxford, University Press, Inc., New York, 1959.
  6. J. Crank, *The Mathematics of Diffusion*, Oxford, University Press, Inc., 1956.

## 7.10 PROBLEMS

7.1 Self-diffusion of uranium and oxygen in  $UO_2$  occurs by vacancy mechanisms on the two sublattices (i.e.,  $D_U \sim x_{VM}$  and  $D_O \sim x_{vX}$ ). Even though the predominant mode of disorder in  $UO_2$  consists of Frenkel defects on the oxygen sublattice (see problem 6.8), a very small amount of Schottky disorder occurs at the same time. The cation vacancies responsible for uranium self-diffusion are created by this secondary defecting process. The thermodynamic properties of the two types of defects are

Defect	$s_F$ J mole <sup>-1</sup> °K <sup>-1</sup>	$\epsilon_F$ kJ/mole
Anion Frenkel	63	297
Schottky	~0	544

(a) Assuming that Frenkel defects are dominant (i.e.,  $N_{VM}$  can be neglected in the condition of electrical

neutrality), what are the fractions of vacant sites on the cation and anion sublattices in stoichiometric  $\text{UO}_2$  at  $1400^\circ\text{C}$ ?

(b) If the stoichiometric  $\text{UO}_2$  is doped with  $\text{Nb}_2\text{O}_5$  so that a fraction  $x_{\text{DM}}$  of the total cations are  $\text{Nb}^{5+}$ , compute the fraction of vacant sites on the cation and anion sublattices. Again assume that  $N_{\text{VM}}$  can be neglected in the electrical neutrality condition.

(c) By greatly increasing the concentration of oxygen interstitials, doping decreases the oxygen-vacancy concentration (by the Frenkel equilibrium) and increases the uranium-vacancy concentration (by the Schottky equilibrium). Since self-diffusion in  $\text{UO}_2$  takes place by vacancy mechanisms on both sublattices, doping with  $\text{Nb}_2\text{O}_5$  should increase the uranium self-diffusion coefficient but decrease the oxygen self-diffusion coefficient. For both  $\text{O}^{2-}$  and  $\text{U}^{4+}$ , calculate the ratio of the self-diffusion coefficient in  $\text{UO}_2$  doped with  $x_{\text{DM}} = 0.1$  fraction  $\text{Nb}^{5+}$  to that in pure  $\text{UO}_2$  at  $1400^\circ\text{C}$ .

7.2 The potential energy between equilibrium sites in a lattice is sinusoidal in shape. The saddle point is halfway between sites, which are a distance  $a_0$  apart. The saddle-point energy is  $\epsilon^*$  above the energy of the equilibrium position. What is the jump frequency for this potential curve?

7.3 In treating the diffusive jump frequency by absolute-rate theory, we made two simplifications of the partition functions  $z_{\text{vb}}^*$  and  $z_{\text{eq}}$ .

First, since the energy difference  $\epsilon^*$  represents the difference between the minimums in the potential-energy wells in the activated and equilibrium states, each of the partition functions should be written with the bottom of the potential energy well as the reference energy and not, as in Eqs. 7.37 and 7.38, with the ground vibrational state as the reference energy.

Second, the partition functions should not, in general, be approximated by the high-temperature limits, as in Eqs. 7.37 and 7.38.

(a) These two simplifications can be avoided by writing the partition functions as

$$z_{\text{vb}}^* = [x^* f(x^*)]^{-2}$$

$$z_{\text{eq}} = [x f(x)]^{-3}$$

where  $x = h\nu/kT$ ,  $x^* = h\nu^*/kT$ , and  $f(x)$  is a correction factor that includes the two effects previously discussed. As  $x$  becomes small,  $f(x)$  has the property of approaching unity. What is the function  $f(x)$ ? Express in terms of  $\sinh(x/2)$ .

(b) Ignoring perturbations of the lattice vibrational modes by the diffusing species (i.e., setting the first term on the right of Eq. 7.34 equal to unity), derive the expression for the jump frequency  $w$  which includes the corrected partition functions.

(c) It is customary to express the diffusion coefficient by

$$D = D_0 e^{-E/kT}$$

where  $E$  is the activation energy for diffusion, defined by

$$E = -k \frac{d \ln D}{d(1/T)}$$

If the correction factor  $f$  is unity,  $E = \epsilon^*$ . Derive the complete expression for  $E$  when the correction factors are not equal to unity.

(d) The correction factor  $f$  plays an important role in the theory when  $x$  is large or when  $h\nu$  is comparable to  $kT$ . This occurs for light-mass diffusing species, such as hydrogen. Much can be learned from investigation of the isotope effect on diffusion. When two different isotopes of the diffusing species are studied, all phenomena that depend on the potential energy of interaction between the diffusion atom and the atoms of the host lattice are the same for the two isotopes. The vibrational frequencies of the two isotopes differ only because of their mass difference. Derive an expression for the ratio of the diffusion coefficients of hydrogen and deuterium in an elemental crystal in terms of the parameters  $x$  and  $x^*$ , where the vibration frequencies in these two quantities refer to the light hydrogen isotope.

(e) In an experimental study of the isotope effect on diffusion of hydrogen in nickel, Ebisuzaki et al. [*J. Chem. Phys.*, 46: 1373 (1967)] measured the following values:

$$\frac{h\nu}{k} = 1350^\circ\text{K} \text{ and } \frac{h\nu^*}{k} = 2300^\circ\text{K}$$

What is the ratio of the diffusivity of hydrogen to the diffusivity of deuterium in nickel at  $300^\circ\text{K}$  and at  $1000^\circ\text{K}$ ?

7.4 In terms of the jump frequency to a particular neighboring site ( $w$ ) and the lattice constant ( $a_0$ ), what is the diffusion coefficient for impurity atoms whose equilibrium position is the octahedral interstitial site in the fcc lattice (Fig. 6.2)?

7.5 The conventional method of measuring the diffusion coefficient of one solid in another is by use of a diffusion "couple." A thin layer of the diffusing solute is plated out on a large block of the matrix solid. The couple is raised to the desired temperature, and diffusion is allowed to proceed for a fixed length of time. At the end of the experiment, which may last months, the concentration profile is determined by sectioning or grinding off very small layers of the block ( $\sim 1 \mu\text{m}$ ). The concentration profile of the diffusing solute is determined by analyzing these sections, and the diffusion coefficient is determined from the concentration profile.

(a) If the minimum penetration distance required for reliable measurement of the concentration profile is  $2 \mu\text{m}$  and the minimum time an experiment can be conducted is 1 year, what is the minimum measurable diffusion coefficient?

(b) If the solute diffuses by an interstitial mechanism in the bcc lattice of the matrix, what is the minimum temperature at which diffusion-coefficient measurements can be made? The activation energy for diffusion is  $250 \text{ kJ/mole}$ . Make reasonable estimates of any other parameters you may need.

# Chapter 8

## Dislocations and Grain Boundaries

In addition to the atomic-size point defects discussed in Chap. 6, real crystals are marred by a variety of one-, two-, and three-dimensional defects. In this chapter, we are concerned with the line and plane defects that significantly affect mechanical properties, namely, the dislocation and the grain boundary.

Unlike point defects, dislocations and grain boundaries do not exist in a state of thermodynamic equilibrium—their energies of formation are far too large to be overcome by the configurational entropy they contribute to the free energy. Rather, these faults are produced during formation of the crystal from the melt and, in the case of dislocations, by working or deforming the material. Neither dislocations nor grain boundaries can be completely eliminated from a solid by annealing at high temperatures.

The mechanical response of a solid to external stress can be classified as elastic (or reversible) or plastic (irreversible). If the stresses and strains are small, the deformed solid returns to its original shape on removal of the stress. This mode of deformation is termed elastic. The properties of the solid which govern its mechanical response in the elastic deformation mode are determined by the microscopic atomic properties of the perfect crystal.\* Linear elasticity theory is reviewed in Appendix A.

If the stresses acting on a solid body are sufficiently large, the deformations are permanent. This mode of mechanical behavior is called plastic deformation. The one-dimensional defect known as the dislocation is in large part responsible for the plastic properties of solids.

### 8.1 SLIP IN SINGLE CRYSTALS

The concept of the dislocation was invented nearly two decades before it was observed. It was proposed to explain a many-order-of-magnitude discrepancy between the observed shear strength of a single crystal and the value expected on theoretical grounds.

The strength of single crystals in shear may be measured by the method shown in Fig. 8.1. A cylindrical specimen of

\*One of the elastic constants, the bulk modulus, was shown in Chap. 4 to be determined by the second derivative of the cohesive energy in cubic crystals.

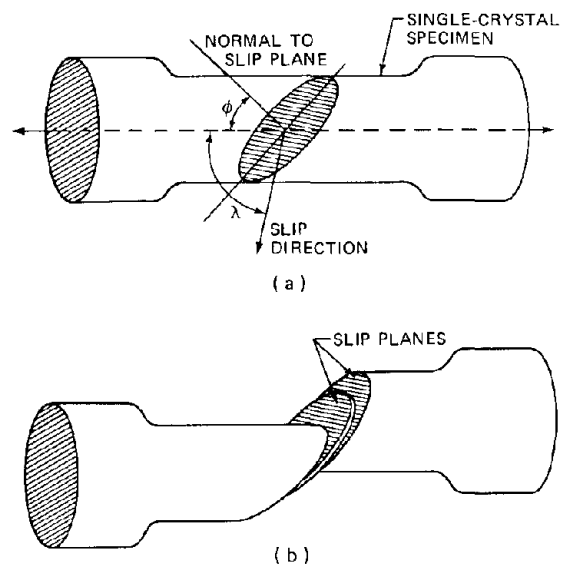


Fig. 8.1 Plastic deformation of a single crystal.

a single crystal is placed in tension. When the applied force attains a critical value, the crystal slips along a particular crystallographic plane called a *slip plane*. The direction in which slip occurs is not in the direction of the maximum shear stress component in the experiment (which would occur for  $\lambda = \pi/2 - \phi$  in Fig. 8.1a). Rather, slip occurs in the direction of the arrow in Fig. 8.1a, which is called the *slip direction*.

The appearance of the specimen after slip has occurred is shown in Fig. 8.1b. Here several parallel planes in the crystal have slipped simultaneously to produce the lamellae. The regions between slipped planes are still perfect. In fact, when examined with X rays, the deformed crystal is often as perfect as the original crystal. This observation suggests that the slip of adjacent planes occurs in a multiple of a minimum lattice distance at which the crystal structure is repeated.

In the experiment depicted in Fig. 8.1, slip suddenly occurs at a force of, say,  $F$ . The force component in the slip direction is  $F \cos \lambda$ . The area of the slip plane in Fig. 8.1a

over which this force is distributed is  $A/\cos \phi$ . Thus, the shear stress at which slip occurs (the critical resolved shear stress) is

$$\sigma_c = \frac{F \cos \lambda}{A/\cos \phi} = \left(\frac{F}{A}\right) \cos \phi \cos \lambda \quad (8.1)$$

Experiments of this type also serve to identify the slip plane and the slip direction. These crystallographic features of slip in fcc and bcc crystals are shown in Fig. 8.2.

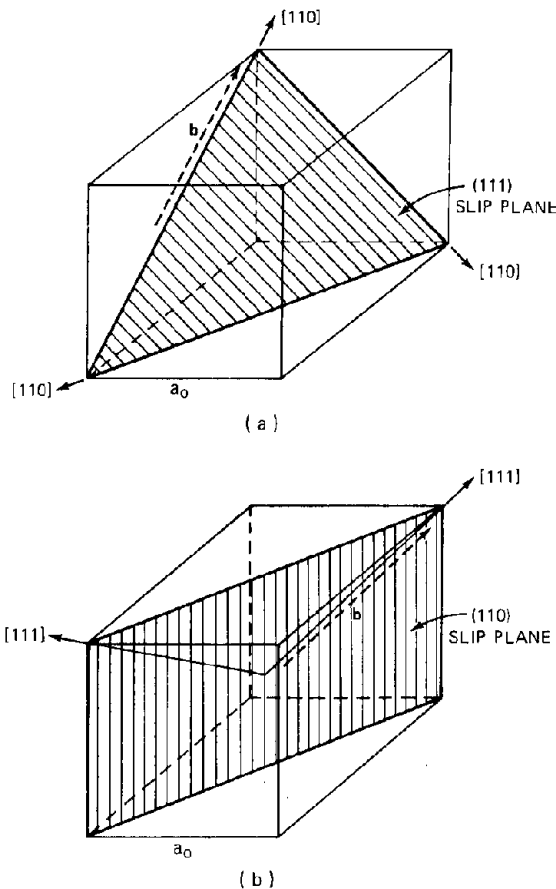


Fig. 8.2 Slip planes and slip directions in cubic crystals. (a) Face-centered cubic. (b) Body-centered cubic.

Slip in fcc crystals occurs on the (111) plane and in a [110] direction. The (111) plane is the close-packed plane, and the [110] direction in the fcc structure is the direction of closest packing. The three equivalent [110] directions are shown by arrows continuing the sides of the triangular portion of the (111) plane in Fig. 8.2a. A view of the (111) plane in the fcc structure is also shown in Chap. 3, Fig. 3.9. The three [110] directions shown by the arrows in Fig. 8.2a correspond to the directions of lines drawn through atoms 1-2, 1-7, and 3-4 in Chap. 3, Fig. 3.9.

The minimum distance that a (111) plane must shift with respect to an adjacent (111) plane in order to reform the perfect lattice is shown as the dotted arrow in Fig. 8.2a.

This shift moves a plane a distance of  $a_0/\sqrt{2}$  in the [110] direction, where  $a_0$  is the lattice constant. The vector represented by the dotted arrow is called the Burgers vector,  $b$ . Referring again to Fig. 3.9b, if the first layer slips with respect to the second and third layers (assumed fixed), the minimum unit of slip requires that atom 3 move to the position of atom 2, atom 4 to the position of atom 7, atom 7 to atom 1, and atom 5 to the location of atom 6. Such a relative translation of the first layer leaves the crystal structure exactly as it was before slip.\*

In bcc crystals slip occurs in the (110), (112), and (123) planes. The first of these is the closest packed plane in the bcc structure. Slip in bcc crystals always occurs in the [111] direction. Figure 8.2b shows the (110) slip plane and the two slip directions in this plane. The magnitude of the Burgers vector in this case is  $\sqrt{3} a_0/2$ .

The Burgers vector defining a dislocation can be represented by the notation

$$b = ca_0 [ijk] \quad (8.2)$$

The direction of the Burgers vector is indicated by the Miller indices in the brackets, and its length is given by

$$b = ca_0 \sqrt{i^2 + j^2 + k^2} \quad (8.3)$$

With the above symbolism, the Burger vectors shown in Fig. 8.2 are  $(a_0/2) [110]$  for the fcc structure and  $(a_0/2) [111]$  for the bcc structure.

A simple calculation permits estimation of the critical shear stress for slip or plastic deformation which then can be compared with the value given by experiments analyzed according to Eq. 8.1. The most obvious microscopic model of the type of motion needed to produce the slip or glide illustrated by Fig. 8.1b is shown in Fig. 8.3, where slip occurs between the two crystallographic planes shown. In this model the entire upper plane of atoms (and all atoms above this plane) is presumed to move as a block in the slip direction over the portion of the crystal below the slip plane, which remains fixed.

The potential energy of the system as the top block moves from one equilibrium position (at displacement  $u = 0$ ) to the next equilibrium position (at  $u = b$ , where  $b$  is the magnitude of the Burgers vector) is also shown in Fig. 8.3. At the displacement  $u = b/2$ , the atoms of the upper plane are in between the atoms in the lower plane, and the potential energy is a maximum. Thereafter, the top plane falls into its next equilibrium position.

The derivative of the potential-energy curve is the force (or in this case the shear stress) required to maintain the relative displacements of the upper and lower blocks of atoms. The variation of the shear stress with displacement is

\*Instead of slip in the [110] direction by the amount  $a_0/\sqrt{2}$ , the first layer of atoms in Fig. 3.9b could slip so that its atoms would appear directly beneath the third layer (i.e., atom 3 moving under atom 11, etc.). This unit of slip would destroy the stacking sequence of the fcc crystal. Instead of the 123123123 sequence of (111) planes, partial slip of this type would yield the sequence 12312|123... The imperfection introduced by the disregistry in the sequence of close-packed planes (at the dotted line) is called a stacking fault.

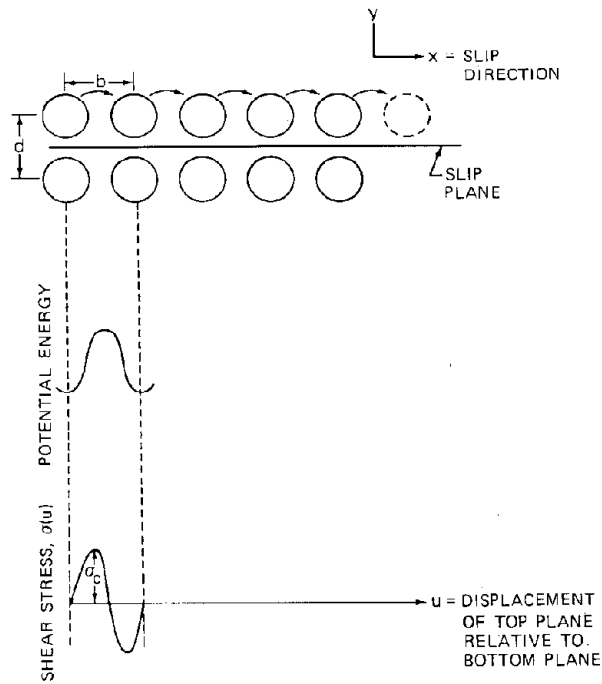


Fig. 8.3 Simultaneous slip of adjacent crystallographic planes in a crystal.

shown in the bottom of Fig. 8.3. The maximum shear stress occurs when the gradient of the potential energy is largest, or at  $u = b/4$ . If the model upon which Fig. 8.3 is based is correct, then the shear stress at this value of the displacement should be the critical resolved shear stress of Eq. 8.1, inasmuch as continued application of shear stress of this magnitude permits continuous translation of the top plane in Fig. 8.3 relative to the bottom plane. To estimate  $\sigma_c$  from this model, we must approximate the shear-stress curve shown at the bottom of Fig. 8.3. The first requirement on the function  $\sigma(u)$  is that it be periodic in the unit of slip,  $b$ . A reasonable approximation to the shape of  $\sigma(u)$  is

$$\sigma(u) \approx \text{constant} \times \sin\left(2\pi \frac{u}{b}\right)$$

The second requirement placed upon the function  $\sigma(u)$  is that, as the displacement becomes very small, the shear stress be related to the strain by linear elasticity theory. The appropriate stress-strain relation for this situation is given by Eq. A.22 of Appendix A:

$$\sigma(u) = 2G\epsilon_{xy} = G\left(\frac{\partial u}{\partial y}\right) = G\left(\frac{u}{d}\right)$$

In this equation,  $u$  is the displacement in the  $x$ -direction of the top plane relative to the bottom plane and  $y$  is the coordinate direction normal to the slip plane. The derivative  $\partial u/\partial y$  may be approximated by  $u/d$ , where  $d$  is the spacing between crystallographic planes in the direction normal to the slip plane. Here  $G$  is the shear modulus of the material.

If the above two formulas for  $\sigma(u)$  are to be equal in the limit of small  $u$ , the constant in the first must be equal to  $(G/2\pi)(b/d)$ . Since the maximum shear stress occurs when the sine function is unity, the constant in this equation represents the critical resolved shear stress predicted by this model of slip in a single crystal. Since  $b/d$  is of order unity (both  $b$  and  $d$  are distances of approximately a lattice constant), we may write

$$\sigma_c \approx \left(\frac{G}{2\pi}\right)\left(\frac{b}{d}\right) \approx 0.1G \quad (8.4)$$

Experiments such as the one depicted in Fig. 8.1 have been performed on single crystals of many materials. The measured critical resolved shear stresses are approximately  $10^{-4}$  to  $10^{-3}$  of the shear modulus; they are not a tenth of  $G$  as predicted by Eq. 8.4. The theoretical estimate of Eq. 8.4 can be refined somewhat, but shear strengths less than  $0.03G$  cannot be obtained by any modification of the model of Fig. 8.3.

## 8.2 DISLOCATIONS

The three-order-of-magnitude discrepancy between theory and experiment means that the model depicted in Fig. 8.3 is an incorrect description of the mechanism by which slip occurs in crystalline solids. The notion that slip occurs simultaneously over the entire slip plane must be dismissed. Instead; slip begins in a particular region of the slip plane and propagates through the crystal, much as a wrinkle in a bedspread is removed by smoothing with the hands instead of pulling the entire spread.

### 8.2.1 Edge Dislocation

Figure 8.4 depicts a model that allows slip propagation to proceed at a much lower shear stress than the mechanism of Fig. 8.3. Instead of the entire top section of the crystal moving as a block from the configuration of Fig. 8.4a to that of Fig. 8.4c, the process occurs by a sequence of stages as shown in Fig. 8.4b. The topography of the crystal in the vicinity of the boundary between slipped and unslipped portions is the same as if an entire half-sheet of atoms had been inserted into the top part of the crystal. The line formed by the termination of the half-sheet of atoms inside the crystal is called an *edge dislocation*. It is a line running perpendicular to the plane of the diagram and lying in the slip plane. The edge dislocation line is denoted by the symbol  $L$ .

The dislocation line marks the boundary between slipped and unslipped portions of the crystal. The columns of atoms to the right of the dislocation line in Fig. 8.4b still have the arrangement of the initial state of Fig. 8.4a (although some strain occurs in the immediate vicinity of the dislocation). The top parts of the columns of atoms to the left of the dislocation, however, have been displaced by a unit of slip (the Burgers vector) with respect to the atoms in the bottom part. Slip propagates from left to right in Fig. 8.4 by the rather minor shifting of the columns of atoms near the dislocation in a manner which is equivalent to motion of the half sheet of atoms to the right; if the bottom five atoms of the third column from the right in

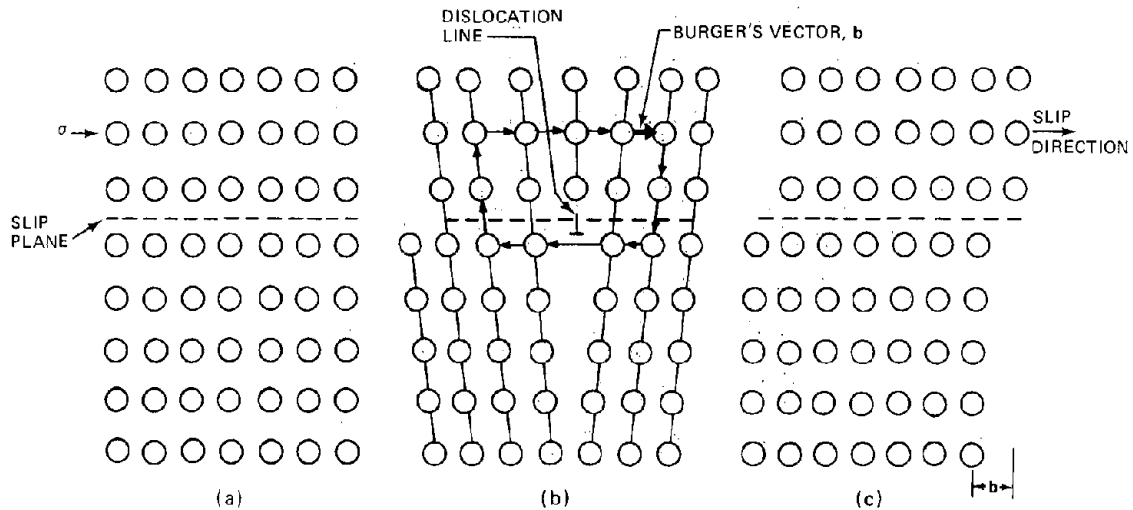


Fig. 8.4 The edge dislocation.

Fig. 8.4b are shifted somewhat to the left and become more or less aligned with the extra half-sheet of atoms, the remaining three atoms of this column would then constitute a new half-sheet. Or, the dislocation line would have moved by one Burgers vector to the right. Because of the relatively modest extent of atom motion required to translate the dislocation line in its slip plane in the fashion just described compared to the simultaneous translation of all atoms along the slip plane, the shear stress required for propagation of the dislocation is far smaller than  $0.1G$ .

The unit of slip required to reform the crystal in its proper periodicity, or the Burgers vector  $b$ , is shown in the lower right-hand corner of Fig. 8.4c. Another method of determining the direction and magnitude of the Burgers vector of a dislocation is illustrated in Fig. 8.4b. A circuit is drawn about the dislocation line, making the same number of up and down and left and right jumps from atom to atom. The circuit in Fig. 8.4b consists of two down, three left, two up and three right jumps. In the perfect crystal, such a circuit would close upon itself. However, when the circuit encompasses a dislocation line, there is a closure failure. The line drawn from the termination of the circuit to the starting point defines the Burgers vector of the dislocation. The Burgers vector is parallel to the slip direction for any dislocation. For the edge dislocation, the Burgers vector is perpendicular to the dislocation line, but both lie in the slip plane.

### 8.2.2 The Screw Dislocation

The result of applying a sufficiently large shear stress to a single-crystal specimen need not be the movement of an edge dislocation through the crystal, as in Fig. 8.4. Rather, slip may propagate by the motion of a fundamentally different type of dislocation line which, in the end, produces exactly the same final slip as passage of the edge dislocation. This other type of dislocation is called a *screw dislocation*; it is depicted in Fig. 8.5. The screw dislocation owes its name to the helical pattern (resembling the ramp

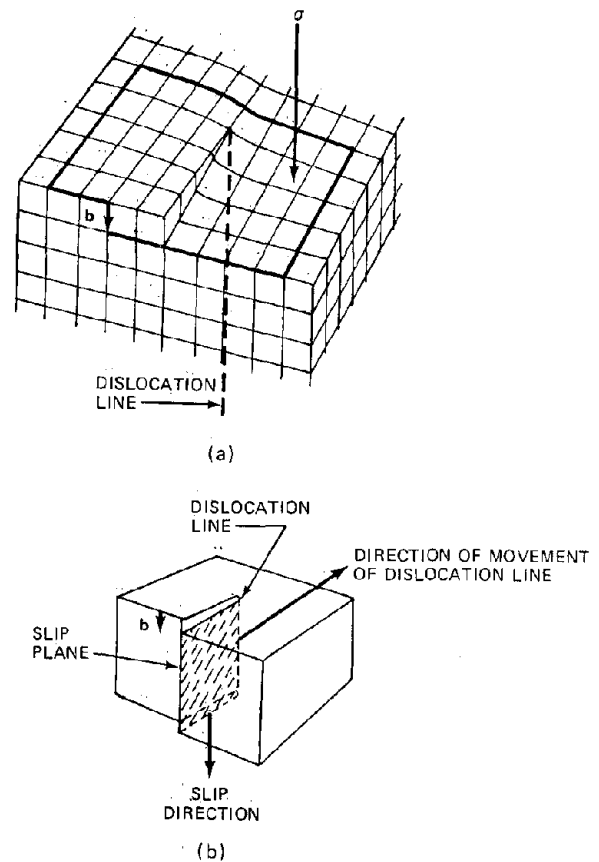


Fig. 8.5 The screw dislocation.

of a multistory parking structure) which is described by continuation of the circuit of Fig. 8.5a into the interior of the crystal.

In a screw dislocation a stepped ledge does not form over the entire length of the crystal surface, as would occur

if the crystal were to yield by propagation of an edge dislocation. Instead, the terracing of the surface starts at one edge and proceeds, like the tearing of a rag, to the opposite edge. As in the case of slip propagation by an edge dislocation, the crystal in the intermediate state of slip exhibits a line separating the region which has slipped from the region which is still in its original configuration. The two views of the screw dislocation shown in Fig. 8.5 are equivalent to the single drawing of the edge dislocation of Fig. 8.4b.

Figure 8.5b shows that the screw dislocation line lies in the slip plane, a feature that it has in common with the edge dislocation. The Burgers vector of the screw dislocation is determined by the circuit about the line, as in Fig. 8.5a. Contrary to the edge dislocation, the Burgers vector of the screw dislocation (or the slip direction) is parallel to the dislocation line. An edge dislocation is perpendicular to its Burgers vector. In both cases, the dislocation line moves in a direction perpendicular to itself and in the slip plane.

Both the edge and the screw dislocations can move in their slip planes under the influence of applied shear stresses far lower than the theoretical strength of a perfect crystal given by Eq. 8.4. Dislocation motion along a slip plane is called *glide*.

Although the edge dislocation is constrained to glide in its slip plane, the screw dislocation can glide in any manner that describes a cylindrical surface having the slip direction as its axis. However, since slip on particular planes is favored, a screw dislocation moves out of a slip plane to another plane of the same Miller index but of different orientation. After travelling a short distance on the new plane, it may move back onto a plane of the original type. This type of motion of a screw dislocation is known as *cross slip*.

### 8.2.3 Dislocation Loops

Dislocation lines in a crystal need not be of pure edge or pure screw character. These two types may be mixed to form *dislocation loops*, which need not be straight and which need not terminate on an external surface of the crystal. Dislocation loops reside completely within the crystal. Figure 8.6 shows a dislocation loop lying in a slip plane (although depicted as a circle in the drawing, dislocation loops may be any closed curve within the

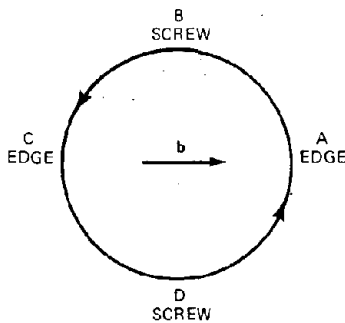


Fig. 8.6 Dislocation loop in a slip plane.

crystal). The portions of the loop of A and C are of pure edge character, although of different sign. The sign of an edge dislocation is changed by inserting the half-sheet of atoms from a direction  $180^\circ$  away from the original direction; the sign of the dislocation of Fig. 8.4b would be changed if the entire half-sheet of atoms were inserted from the bottom instead of the top of the crystal. The portions of the dislocation loop at B and D are composed of screw dislocations, again of opposite sign (one is left-handed and the other right-handed).

Despite the mixture of edge and screw dislocations in the loop of Fig. 8.6, there is but a single Burgers vector describing the entire loop. The circular dislocation delineates the region of slip; the crystal beyond the periphery of the loop is in its unslipped state. Within the loop, the block of atoms above the slip plane has been translated in the direction of the Burgers vector by an amount equal to the magnitude of the Burgers vector with respect to the atoms below the slip plane. However, the atomic fit in the interior of the loop is as good as in the unslipped region; the disregistry of the perfect lattice geometry is concentrated in a toroidal region around the dislocation line.

When the Burgers vector of the loop lies in the slip plane, the loop is called a *shear loop* because it can grow easily in its slip plane under the influence of an applied shear stress. Expansion occurs in the same fashion that pure edge or screw dislocations propagate in a slip plane, namely by glide. When the shear loop grows so large that it leaves the crystal, the final stepped state of the crystal is identical to that produced by the propagation through the crystal of pure straight dislocations of the edge or screw type.

### 8.2.4 Climb

The edge dislocation can move perpendicular to its slip plane only if the length of the extra sheet of atoms in Fig. 8.4b is altered by collecting or shedding vacancies or interstitials from the bulk of the solid. This type of motion of the edge dislocation is known as *climb* and is depicted in Fig. 8.7.

## 8.3 STRAIN ENERGY OF DISLOCATIONS

Consider a long, straight screw dislocation. Let the z-axis of the cylindrical coordinate system be in the direction of the dislocation line. The displacement field for regions sufficiently far removed from the core of the dislocation for Hooke's law to apply can be described by elasticity theory. There is no displacement in the radial or azimuthal directions, or  $u_r = u_\theta = 0$ . (The notation for elasticity calculations is given in Appendix A, Fig. A.4.) The axial displacement is a linear function of the azimuthal angle  $\theta$ . As seen from Fig. 8.5a, with each complete circuit ( $\theta = 2\pi$ ) an axial distance equal to the Burgers vector  $b$  is gained. The axial displacement component of a screw dislocation is given by

$$u_z = \frac{b\theta}{2\pi} \quad (8.5)$$

Referring to the components of the displacement tensor in cylindrical coordinates given by Eqs. A.32 and A.33 of

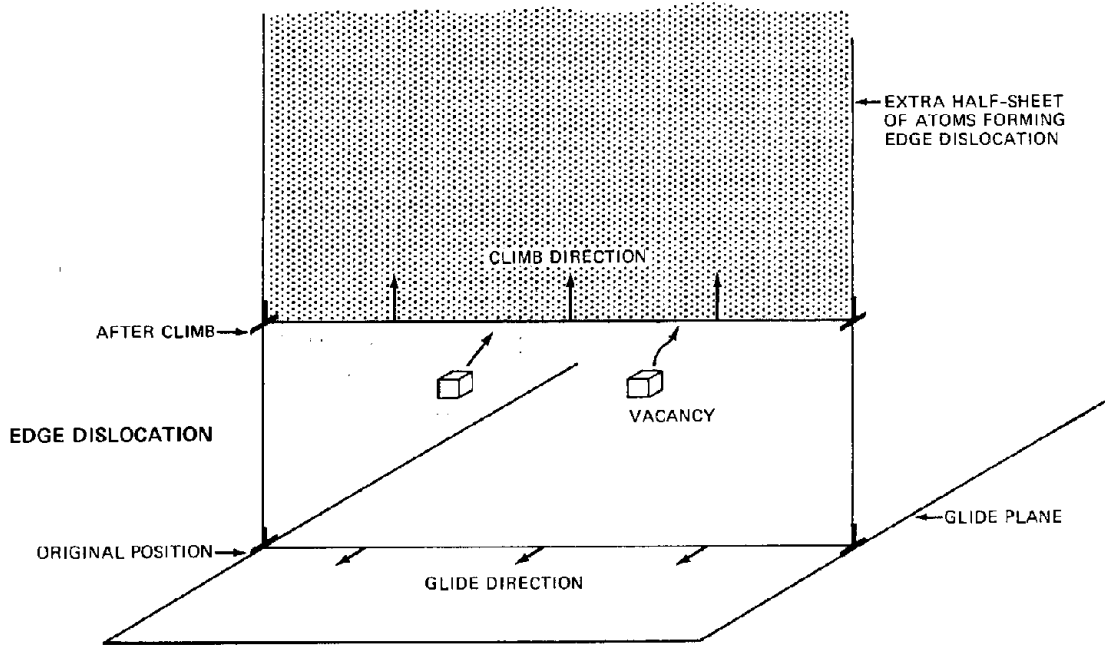


Fig. 8.7 Climb of an edge dislocation due to vacancy absorption.

the Appendix, we see that for the screw dislocation only the  $\epsilon_{z\theta}$  component of the strain is non-zero. It is given by

$$\epsilon_{z\theta} = \frac{1}{2} \frac{1}{r} \frac{\partial u_z}{\partial \theta} = \frac{b}{4\pi r} \quad (8.6)$$

The corresponding stress is

$$\sigma_{z\theta} = 2G\epsilon_{z\theta} = \frac{Gb}{2\pi r} \quad (8.7)$$

The stress field surrounding an edge dislocation is more complex than that of a screw dislocation given by Eq. 8.7. Figure 8.8 shows the  $r$  and  $\theta$  components of the stress field at point P resulting from the presence of an infinitely long edge dislocation which lies along the  $z$ -axis (perpendicular to the plane of the drawing). The glide plane of the dislocation line is represented by the horizontal line at

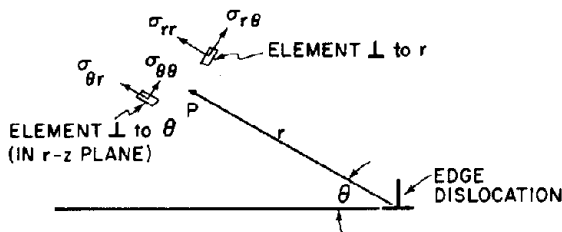
$\theta = 0$ . The extra half-sheet of atoms needed to form the edge dislocation extends vertically upward from the glide plane. When point P lies in the glide plane, the normal stress components are zero, and the solid is placed in pure shear. In directions normal to the glide plane, only normal strains remain. At  $\theta = 90^\circ$ , the solid is in compression, and for  $\theta = -90^\circ$ , the solid is in tension. This asymmetric feature of the stress field about an edge dislocation is responsible for its ability to bind both interstitial atoms and vacancies.

In addition to the stress fields surrounding dislocations, the total strain energy of the solid due to the presence of a dislocation line is of interest. The strain energy is calculated below for a screw dislocation. The comparable result for an edge dislocation differs only by a numerical factor of order unity.

The elastic strain energy per unit volume in the medium surrounding the screw dislocation is obtained from the Appendix, Eq. A.25 (in which  $x$  is replaced by  $r$  and  $y$  by  $\theta$ ):

$$E_{el} = \sigma_{z\theta} \epsilon_{z\theta} = \frac{Gb^2}{8\pi^2 r^2} \quad (8.8)$$

The energy density given by Eq. 8.8 becomes infinite at the dislocation line. However, linear elasticity theory cannot be applied to the large strain field near the dislocation line. Equations 8.6 to 8.8 are valid only for radial positions greater than about five Burgers vectors from the dislocation line. The region within this radius is called the dislocation core. The elastic energy per unit length of dislocation line, or the *line tension*,  $\tau$  is obtained by integrating Eq. 8.8 from the core radius  $r_d$  to a large distance  $R$ , which represents the radius of the grain in which the dislocation resides:



$$\sigma_{rr} = \sigma_{\theta\theta} = \frac{Gb}{2\pi(1-\nu)} \frac{\sin\theta}{r} \text{ (POSITIVE IN COMPRESSION)}$$

$$\sigma_{r\theta} = \sigma_{\theta r} = -\frac{Gb}{2\pi(1-\nu)} \frac{\cos\theta}{r}$$

Fig. 8.8 Stress field in the solid near an edge dislocation.

$$\tau = \int_{r_0}^R 2\pi r E_{e1} dr = \frac{Gb^2}{4\pi} \ln \left( \frac{R}{r_0} \right) \quad (8.9)$$

A similar calculation of the energy of an edge dislocation produces the result of Eq. 8.9 but divided by  $(1 - \nu)$ , where  $\nu$  is Poisson's ratio. Since  $\nu \approx 1/3$  for many materials, and in view of the considerable uncertainty in assigning a precise value to the ratio in the logarithm of Eq. 8.9, the line tension of any dislocation (edge, screw, or mixed) may be expressed by

$$\tau = \alpha Gb^2 \quad (8.10)$$

where  $\alpha$  is taken to be  $1/2$  by some and unity by others. The latter figure will generally be used here.

The line tension of a dislocation possesses many of the features associated with its two-dimensional counterpart, surface tension. A curved dislocation line experiences an inward radial force. Figure 8.9a shows a portion of a dislocation line of length  $S$  with a radius of curvature  $R$ . The radial force on the dislocation line is

$$\frac{\text{Force}}{\text{Unit length}} = \frac{2\tau \sin \theta}{S} \approx \frac{2\tau}{S} \theta = \frac{2\tau}{S} \left( \frac{S}{2R} \right) = \frac{\tau}{R} \quad (8.11)$$

By comparison, Fig. 8.9b shows the radial force on a spherical segment of surface of a material of surface tension  $\gamma$ . The force acting on each unit area of the spherical cap is

$$\frac{\text{Force}}{\text{Unit area}} = \frac{2\pi r \gamma \sin \theta}{A} \approx \frac{2\pi r \gamma}{\pi r^2} \theta = \frac{2\pi r \gamma}{\pi r^2} \left( \frac{r}{R} \right) = \frac{2\gamma}{R} \quad (8.12)$$

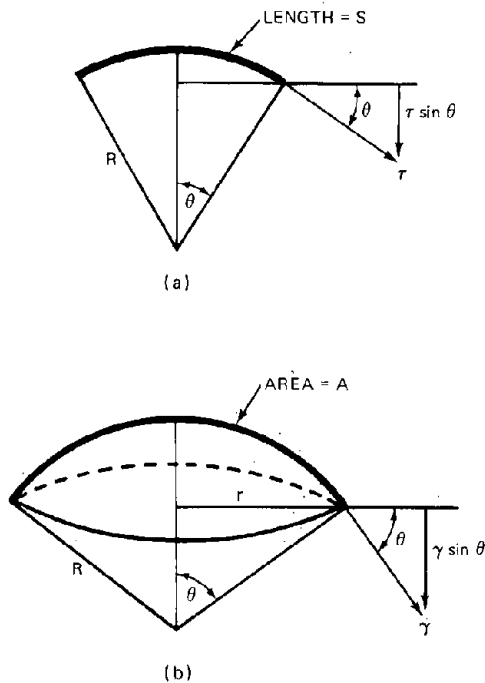


Fig. 8.9 Force (a) on a curved dislocation line and (b) on a curved surface.

### 8.4 FORCE ON A DISLOCATION

Dislocations move or change shape in response to forces acting on them, one of the most important of which is the force due to an applied stress. Figure 8.10a shows a shear stress  $\sigma_{yx}$  applied to a crystal with a slip plane perpendicular to the  $y$ -axis. An edge dislocation line lies along the  $z$ -axis. If the shear stress  $\sigma_{yx}$  is large enough, the dislocation glides in the slip direction. Even if the applied stress is insufficient to move the dislocation, it nevertheless exerts a force on the dislocation line. In Fig. 8.10a, the force is in the slip direction (along the  $x$ -axis).

The magnitude of the force  $F$  per unit length of dislocation line which is generated by the shear stress  $\sigma_{yx}$  on the slip plane can be obtained from the following considerations. Suppose that the applied stress were large enough to move the dislocation line by a distance  $\Delta x$  in the slip direction. This movement of the dislocation line is equivalent to displacement of an area  $S \Delta x$  of the slip plane by a distance of one Burgers vector, or a force  $\sigma_{yx} S \Delta x$  acts

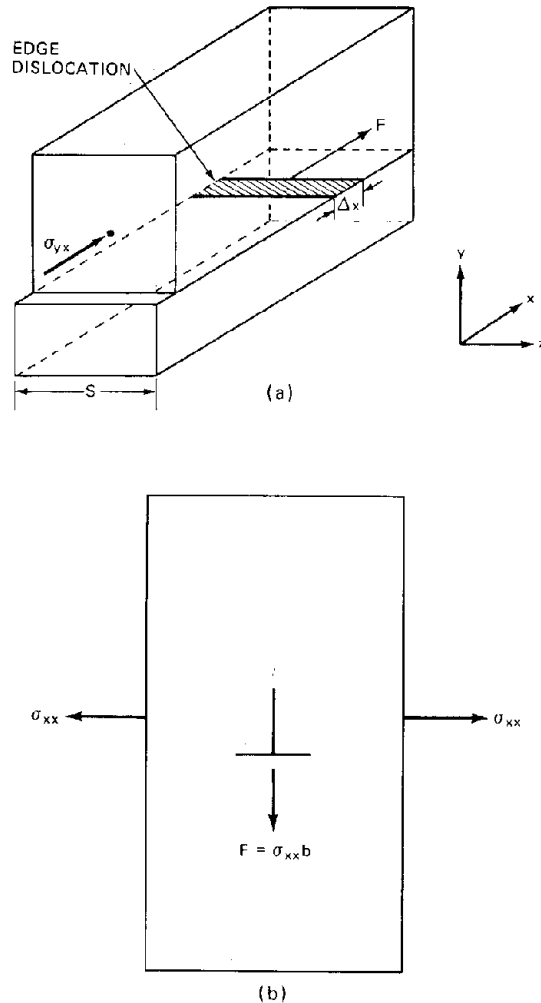


Fig. 8.10 Forces on an edge dislocation due to (a) a shear stress and (b) a normal stress (tension).

over a distance  $b$ . Thus the work required to move the dislocation line is

$$\text{Work} = (\sigma_{yx} S \Delta x) b$$

The work involved is identified with the product of the force  $FS$  on the dislocation line and the distance the line has moved, or the force per unit length on the edge dislocation due to the shear stress is

$$F = \pm \sigma_{yx} b$$

The choice of sign (or direction) of the force depends on whether the extra sheet of atoms forming the dislocation is inserted from above or below the slip plane in Fig. 8.10a.

Figure 8.10b shows the force exerted on an edge dislocation due to an applied tensile stress that acts in a plane parallel to the slip plane and normal to the dislocation line. By arguments similar to that used above for applied shear stresses, the resulting force on the dislocation is found to be  $\pm \sigma_{xx} b$  and in a direction perpendicular to the slip plane. The sign depends on whether the extra sheet of atoms is above or below the slip plane in Fig. 8.10b. The sign also depends on the type of normal stress. If the normal stress is tensile, the force is directed away from the extra sheet of atoms forming the edge dislocation (this case is shown in Fig. 8.10b). A compressive stress tends to drive the dislocation line in the opposite direction.

In a stress field consisting of both normal and shear components, the vector force on a unit length edge dislocation is given by

$$F = \pm [-\sigma_{xy} bi + \sigma_{xx} bj] \quad (8.13)$$

where  $i$  and  $j$  are unit vectors in the  $x$ - and  $y$ -directions, respectively, and the sign depends on the orientation of the extra atomic plane forming the dislocation.

Edge dislocations move easily only in their slip (or glide) plane. Motion perpendicular to the slip plane by climb requires transport of vacancies or interstitials to or from the bulk of the solid to the dislocation line by diffusion. Point defect migration under most conditions is slow because the concentrations of vacancies or interstitials is quite low. However, at temperatures above roughly one-half the melting point ( $^{\circ}\text{K}$ ) or in a radiation field, sufficient point defects are present and their mobility is great enough to permit edge dislocation climb to take place at measurable rates. The climb process is of primary importance in the slow plastic deformation mechanism known as creep, which profoundly affects the performance of reactor fuel elements.

The force causing climb is not restricted to external stresses applied to the solid, as shown in Fig. 8.10b. The internal stress due to the presence of other nearby dislocations or to the creation of high point defect supersaturation by radiation can also induce climb of the edge portions of dislocations (Chap. 16, Sec. 16.7).

A similar analysis can be applied to a screw dislocation. Figure 8.11 shows a screw dislocation of length  $S$  which experiences a force per unit length  $F$  in the slip direction due to an applied shear stress  $\sigma_{yz}$ . The subscripts on the shear stress indicate that it acts in the slip plane (which is perpendicular to the  $y$ -axis) and in the direction of the

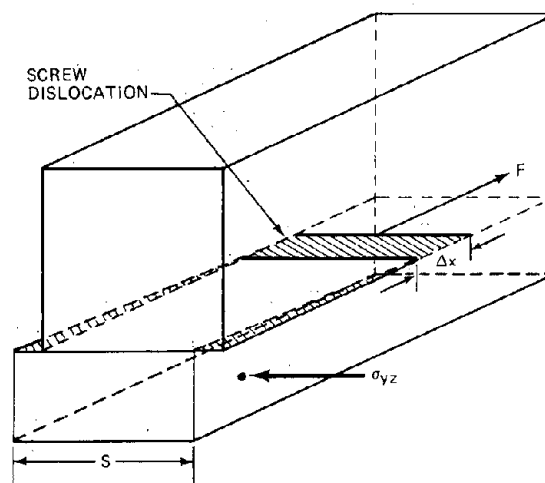


Fig. 8.11 Force on a screw dislocation.

$z$ -axis. Note that in this case the force on the dislocation line is at right angles to the direction of the applied stress that produces the force. If the screw dislocation moves a distance  $\Delta x$  in the  $x$  direction, an area  $S \Delta x$  slips by a distance  $b$  in the slip direction (the  $z$ -direction). The work done by the applied stress is  $(\sigma_{yz} S \Delta x) b$ . Equating this quantity of work to a force on the dislocation line acting in the  $x$ -direction times the distance the line moves, we find the force on a unit length of screw dislocation produced by the shear stress to be

$$F = \pm \sigma_{yz} b \quad (8.14)$$

As in the case of stresses acting on edge dislocations, choice of + or - in Eq. 8.14 depends on the sign of the dislocation (i.e., whether the screw is left-handed or right-handed).

The dependence of the direction of the force exerted by a shear stress on the sign of both edge and screw dislocations implies that the dislocation loop shown in Fig. 8.6 can be made to expand uniformly in the radial direction by a shear force in the direction of the arrow in the drawing. The  $x$ -direction force exerted on the edge component at A is  $+\sigma_{xy} b$ , and the edge component at C is subject to a force  $-\sigma_{xy} b$ . Similarly, the  $y$ -direction forces on the screw components at B and D are  $+\sigma_{xy} b$  and  $-\sigma_{xy} b$ , respectively.

Tensile or compressive stresses produce no force on a screw dislocation, which is incapable of movement by climb.

## 8.5 MISCELLANEOUS FEATURES OF DISLOCATIONS

### 8.5.1 Density of Dislocation Lines

The concentration of dislocation lines in a solid is measured by the number of dislocation lines that penetrate a unit area within the crystal. This quantity, which is known as the *dislocation density*, ranges from  $\sim 10^4$  dislocations/cm<sup>2</sup> in high-purity carefully prepared semiconductor single crystals (germanium or silicon) to  $\sim 10^{11}$

dislocations/cm<sup>2</sup> in severely worked polycrystalline metals. Very fine crystal whiskers about 1  $\mu\text{m}$  ( $10^{-4}$  cm) in diameter have been prepared in a nearly dislocation-free condition. These specimens exhibit the yield strength expected of perfect crystals (i.e.,  $\sigma_c \sim 0.1G$ ).

### 8.5.2 Mechanisms of Hindering Dislocation Motion

Dislocations can move in a slip plane in response to very small applied shear stresses. However, the motion of dislocations, and hence the capacity of the material to deform plastically, is limited by many phenomena.

If there is a high dislocation density in the solid, slip requires that moving dislocations (1) pass by other dislocations in parallel slip planes or (2) cut across other dislocations that intersect the glide plane of the moving dislocation.

When two dislocations intersect while gliding, the character of each is altered in a manner that requires energy and makes further movement of the dislocations more difficult. Figure 8.12a shows two screw dislocations with mutually perpendicular Burgers vectors and slip planes. Dislocation 1 moves toward stationary dislocation 2 (the tree) and passes through it. The situation following the intersection is shown in Fig. 8.12b. Each dislocation has produced a small step or jog in the other. The jog consists of a segment of the dislocation that has acquired the direction of the line that passed through. The Burgers vectors of each line, however, remain unchanged. The portion of the dislocation at the jog is pure edge in character, since at this point the dislocation line is perpendicular to the Burgers vector. (Figure 8.4b shows that this arrangement is characteristic of an edge dislocation.) Any further motion of the dislocation containing the

jog in the same direction as that before intersection requires that the newly created edge portion of the line move in a direction perpendicular to the Burgers vector. According to Fig. 8.4b, such motion is equivalent to climb of the edge portion, which can occur only if vacancies or interstitials are exchanged with the lattice. Consequently, the capability of easy glide of the initially pure screw dislocation has been significantly reduced by the jog.

It can be seen from Fig. 8.12 that the length of each dislocation line has been increased by the jogs. Since energy is required to increase the length of a dislocation line (i.e., by the line tension), passage from (a) to (b) in Fig. 8.12 consumes energy, which is equivalent to a larger force required to maintain slip as the dislocation line becomes increasingly jogged. Or, material that has been heavily deformed and contains a high density of tangled dislocation lines loses plasticity. This phenomenon is known as *strain hardening*.

The glide of dislocations through a crystallite can also be impeded by the presence of impurities. The impurities may be present in the form of small particles of a second phase (i.e., a precipitate) which the dislocation cannot penetrate. On encountering such an obstacle, the moving dislocation line is pinned to the impurity particle.

Edge dislocations can interact with point defects in the lattice (these may be vacancies or impurity atoms) via the interaction of the stress fields surrounding the dislocation and the point defect. It is possible to calculate the interaction energy of such combinations. Point defects, such as an impurity atom, tend to compress the surrounding medium. The expanded region below the extra half-sheet of atoms in the edge dislocation serves to relieve the compression surrounding the impurity atom. The energy of the edge dislocation impurity atom combination is reduced as the two approach each other. Or, the combination has a binding energy that makes it stable. Conversely, vacancies tend to accumulate on the side of the edge dislocation containing the additional half-sheet of atoms.

Point defects move by thermally activated processes, and they are quite immobile at low temperatures. In the course of its glide along a slip plane, a dislocation line may encounter a point defect. Each such encounter lowers the energy of the system by the binding energy of the dislocation and the point defect. To pull the dislocation line away from the immobile point defect, the binding energy of the defect-dislocation combination must be supplied. If the interaction is very strong, the point defect acts to pin the dislocation, or at least to slow down its glide until the bond is broken by thermal fluctuations. Alternatively, the dislocation may continue to travel through the field of point defects, sweeping them along as it moves. The drag due to the cloud of point defects associated with a moving dislocation considerably reduces its mobility.

### 8.5.3 Dislocation Multiplication

Electron microscope observation shows that the number of dislocations in a solid is increased by deformation. The most likely mechanism by which dislocation multiplication occurs is shown in Fig. 8.13. Figure 8.13a shows a portion of a dislocation line ABCD which is pinned at B and C by obstacles of the type described previously. The

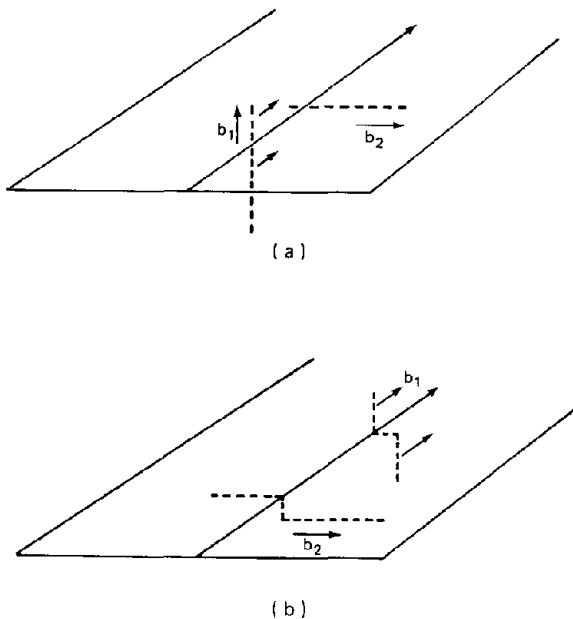


Fig. 8.12 Intersection of two screw dislocations.

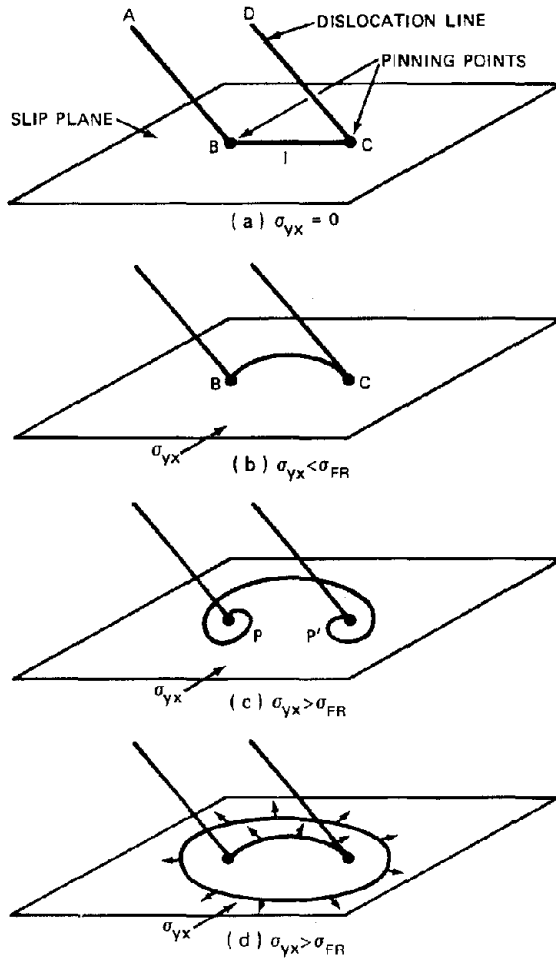


Fig. 8.13 The Frank-Read dislocation source.

length  $l$  of  $BC$  lies in a slip plane, and an applied shear stress acts on this segment. The equilibrium shape of the bowed dislocation is obtained by equating the force per unit length due to the applied stress (Eq. 8.13) to the restoring force due to line tension (Eqs. 8.10 and 8.11). The equilibrium radius of curvature is

$$R = \frac{Gb}{\sigma_{yx}} \quad (8.15)$$

As the applied stress is increased, the radius of curvature decreases from  $R = \infty$  in Fig. 8.13a to a minimum value of  $R = l/2$  for a semicircle (Fig. 8.13b), at which point the applied stress is

$$(\sigma_{yx})_{R=l/2} = \sigma_{FR} = \frac{2Gb}{l} \quad (8.16)$$

If the applied shear stress exceeds  $\sigma_{FR}$  given by the above formula, the bowed segment assumes the shape shown in Fig. 8.13c, which represents an increase in the radius of curvature. Hence this shape continues to grow until the sections at  $P$  and  $P'$  meet. Since these two points represent portions of the dislocation having opposite signs, they annihilate each other when they come into contact. The growing dislocation is pinched off, leaving a dislocation

loop (of the mixed edge-screw type shown in Fig. 8.6) and regenerating the original segment of straight dislocation  $BC$  (Fig. 8.13d). Continued application of an applied shear stress greater than  $\sigma_{FR}$  causes the loop to expand and the segment  $BC$  to repeat the process shown in a through d of Fig. 8.13. As long as the outermost loop (the first one created by the process) does not meet obstacles that halt its expansion, the mechanism depicted in Fig. 8.13 produces dislocation loops indefinitely.

The mechanism of dislocation multiplication described above is named after its discoverers, F. C. Frank and W. C. Read, and the pinned segment of dislocation line in a slip plane is called a Frank-Read source. The critical stress  $\sigma_{FR}$  at which the bowed dislocation becomes unstable is called the unpinning stress of the source, or the stress required to operate or unlock the source. When the outermost loop is stopped by an obstacle, a pileup of loops occurs. This group of stalled loops creates a back stress, which hampers the operation of the Frank-Read source.

In materials containing a high concentration of mobile impurity atoms, the unpinning stress of the source may be determined by the force needed to tear the dislocation line away from the impurity atoms that have collected on it. If the stress required for this process is greater than  $\sigma_{FR}$  of Eq. 8.16, the former determines the critical stress at which dislocations just begin to move.

#### 8.5.4 Shear Strain Due to Dislocation Glide

Because of the obstacles in the slip plane, individual dislocations move through a crystal in a jerky fashion. In the regions between obstacles, they move rapidly under the influence of the applied stress. When obstacles are encountered, the dislocations are temporarily stopped. After a period of time, they may be able to overcome the obstacle, either by thermally activated cutting through or by climbing over it, and resume rapid glide until the next obstacle is met. The motion of a dislocation may be considered as a series of glide events in each of which the dislocation traverses an area  $A$  of the slip plane. The value of  $A$  is determined by the density of obstacles in the slip plane. In general, the loops produced by Frank-Read sources do not expand uniformly as suggested by Fig. 8.13d. Rather, a portion of the loop succeeds in breaking through obstacles and expanding by an area  $A$  and later another segment of the loop may do the same.

The shear strain due to this sort of motion may be determined with the aid of Fig. 8.14, which shows a specimen in the shape of a parallelepiped undergoing slow deformation by an applied shear stress. After some time, the block is deformed from the original shape shown by dashed lines to the configurations shown by the solid lines in Fig. 8.14a. According to Sec. A. 2 of the Appendix, this type deformation is equivalent to the shear strain

$$\epsilon = \frac{\partial u}{\partial y} = \tan \beta$$

Since each individual dislocation climb event displaces the solid above and below the slip plane by an area  $A$  (shown on Fig. 8.14a), a total of  $XZ/A$  elementary glide events are required to displace one entire slip plane. When this number of shear-strain increments has occurred, the whole slip

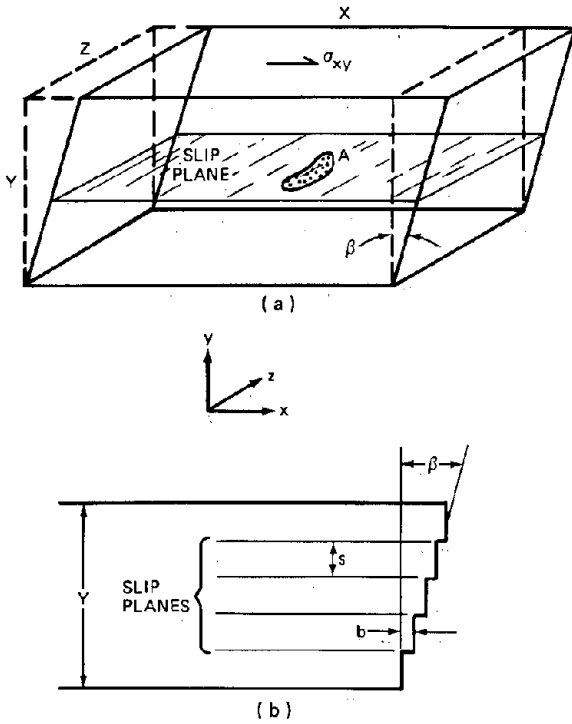


Fig. 8.14 Diagram for calculating the shear strain produced by dislocation glide events which sweep out an area  $A$ .

plane is displaced by a distance equal to one Burgers vector  $b$  (see Fig. 8.4). If the slip planes are separated by a distance  $s$ , Fig. 8.14b shows that  $Y/s$  slip planes must be displaced in order to produce the macroscopic strain characterized by the angle  $\beta$ , or

$$\epsilon = \frac{b}{s} \quad (8.17)$$

The number of individual glide events needed to cause the strain  $\epsilon$  is the product of the  $XZ/A$  glide events to displace one slip plane by a distance  $b$  and the  $Y/s$  slip planes that have to be displaced by  $b$  to produce the strain  $\epsilon$ . Or, the shear strain induced by a single glide event is

$$\begin{aligned} \frac{\text{Shear strain}}{\text{Glide event}} &= \frac{\epsilon}{(XZ/A)(Y/s)} \\ &= \frac{\epsilon Ab}{(XYZ)\epsilon} \\ &= \frac{Ab}{V} \end{aligned} \quad (8.18)$$

where the product  $XYZ$  is the volume  $V$  of the specimen and  $s$  has been eliminated by use of Eq. 8.17.

Suppose that the volume  $V$  contains  $N_1$  mobile dislocations in the form of shear loops of an average radius  $R_1$ . The total length of dislocation line in the volume  $V$  is  $2\pi R_1 N_1$ , or the dislocation density is

$$\rho = \frac{2\pi R_1 N_1}{V} \quad (8.19)$$

If each of the  $N_1$  loops expands by an area  $A$ , the resulting shear strain is, according to Eq. 8.18, equal to

$$\epsilon = N_1 \frac{Ab}{V} = \frac{Ab\rho}{2\pi R_1}$$

The average increase in loop radius,  $\Delta R_1$ , due to expansion by area  $A$  is

$$\Delta R_1 = \frac{A}{2\pi R_1}$$

and the shear strain may be written as

$$\epsilon = \rho b \Delta R_1 \quad (8.20)$$

Since there are very many individual glide events occurring in a stressed crystal in a given time interval, the average result of the jerky expansion increments may be represented as a uniform glide velocity of the dislocation line,

$$v_d = \frac{\Delta R_1}{\Delta t}$$

Or, the shear strain rate is given by

$$\dot{\epsilon} = \rho b v_d \quad (8.21)$$

The velocity of mobile dislocations is controlled by the frictional forces arising from the obstacles that are encountered during slip along the glide plane.

## 8.6 INTERACTION FORCES BETWEEN NEARBY EDGE DISLOCATIONS

### 8.6.1 Movement on Parallel Glide Planes

Edge dislocations can surmount obstacles in their glide plane only by climbing over the obstruction, which frequently is another edge dislocation. Equation 8.13 describes the force on a unit length of an edge dislocation which is placed in a stress field containing both shear and normal components. For two neighboring edge dislocations, the force on one is in part due to the stress field set up by the other, and vice versa. The stress field established by an isolated edge dislocation is shown in Fig. 8.8. The stress components  $\sigma_{rr}$  and  $\sigma_{r\theta}$  in this figure may be converted from cylindrical to rectangular coordinates by the transformation\*

$$\sigma_{xx} = \sigma_{rr} - 2 \sin \theta \cos \theta \sigma_{r\theta} \quad (8.22a)$$

$$\sigma_{xy} = (\cos^2 \theta - \sin^2 \theta) \sigma_{r\theta} \quad (8.22b)$$

Inserting  $\sigma_{rr}$  and  $\sigma_{r\theta}$  from Fig. 8.8 into the above equations and substituting the resulting expressions for  $\sigma_{xx}$  and  $\sigma_{xy}$  into Eq. 8.13 yield the vector interaction force per unit length between two parallel edge dislocations:

\*These formulas are a special case of the cylindrical-rectangular coordinate transformation for  $\sigma_{rr} = \sigma_{\theta\theta}$ . See R. B. Bird, W. E. Stewart, and E. N. Lightfoot, *Transport Phenomena*, p. 742, John Wiley & Sons, New York, 1960.

$$F_i = \pm \frac{Gb^2}{2\pi(1-\nu)r} \left[ \cos \theta (\cos^2 \theta - \sin^2 \theta) i + \sin \theta (1 + 2 \cos^2 \theta) j \right] \quad (8.23)$$

where the choice of the plus or minus sign depends upon the signs of the two edge dislocations. If the slip planes of the two dislocations are separated by a distance  $y = r \sin \theta$ , the x and y components of Eq. 8.23 can be written as

$$F_{ix} = \pm \frac{Gb^2}{2\pi(1-\nu)} \frac{f_x(\theta)}{y} \quad (8.24)$$

$$F_{iy} = \pm \frac{Gb^2}{2\pi(1-\nu)} \frac{f_y(\theta)}{y} \quad (8.25)$$

where

$$f_x(\theta) = \sin \theta \cos \theta (\cos^2 \theta - \sin^2 \theta) \quad (8.26)$$

$$f_y(\theta) = \sin^2 \theta (1 + 2 \cos^2 \theta) \quad (8.27)$$

The angular functions  $f_x$  and  $f_y$  are plotted in Fig. 8.15. The y-direction force is in the same direction for all angles between the two dislocations, but the x-direction force changes sign when the angle between the dislocations is  $45^\circ$ .

Figure 8.16 shows the trajectories of a mobile dislocation that is driven by an applied shear stress  $\sigma_{xy}$  towards an immobile dislocation either of the same or of opposite sign as the mobile dislocation. The slip planes of the two dislocations are parallel and are initially separated by a distance  $y_0$ .

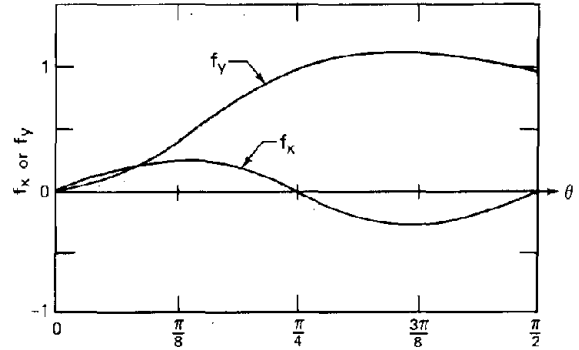


Fig. 8.15 Functions describing the x and y components of the interaction force between two edge dislocations.

Figure 8.16a shows the path of the mobile dislocation when the two interacting dislocations are of the same sign. The applied shear stress pushes the mobile dislocation to the right with a force per unit length of

$$F_m = \sigma_{xy} b \quad (8.28)$$

The x-direction force opposing the motion is given by Eq. 8.24 with the positive sign selected since the two dislocations are of the same sign. They tend to repel each other for angles between  $0$  and  $45^\circ$ , but the interaction becomes attractive for angles between  $45^\circ$  and  $90^\circ$ . The maximum repulsive force occurs at  $22.5^\circ$ . The mobile dislocation glides rapidly toward the immobile dislocation on its original slip plane until the repulsive interaction force just

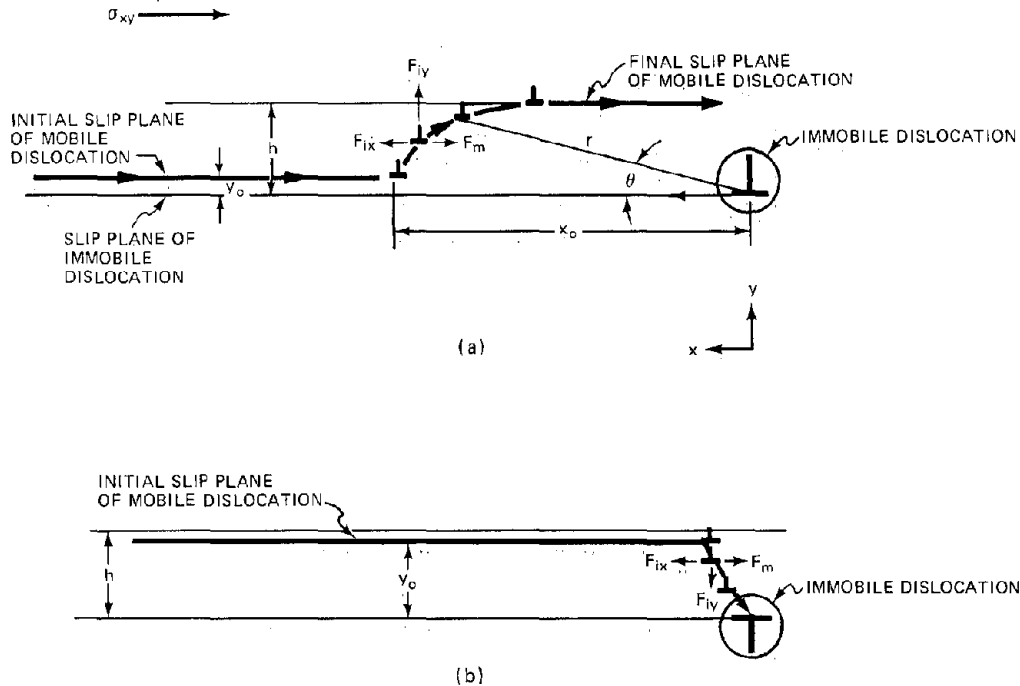


Fig. 8.16 Trajectory of a mobile edge dislocation approaching an immobile one. (a) Both dislocations of the same sign, (b) Dislocations of opposite sign.

balances the driving force due to the applied shear stress, which occurs at some angle  $\theta_o$  between 0 and  $22.5^\circ$ . The mobile dislocation stops when  $F_m = F_{ix}$  or, from Eqs. 8.24 and 8.28, when

$$K f_x(\theta_o) = \sigma_{xy} y_o \quad (8.29)$$

where

$$K = \frac{Gb}{2\pi(1-\nu)} \quad (8.30)$$

The x-distance at which the barrier is first encountered is obtained by eliminating  $\theta_o$  between Eq. 8.29 and the relation

$$x_o = y_o \cot \theta_o \quad (8.31)$$

At this point the mobile dislocation experiences a y-direction force given by Eq. 8.25

$$F_{iy} = \frac{Kb f_y(\theta_o)}{y_o} \quad (8.32)$$

Because of this force, which is in the +y-direction, the mobile dislocation begins to climb by absorbing vacancies. As it does so, its position along the x-axis adjusts in a manner that keeps the net x-direction force on the mobile dislocation just equal to zero. Thus, the trajectory can be described by eliminating  $\theta$  from the equations:

$$K f_x(\theta) = \sigma_{xy} y \quad (8.33)$$

$$x = y \cot \theta \quad (8.34)$$

When  $\theta$  attains a value of  $22.5^\circ$ , the function  $f_x$  reaches a maximum value of  $1/4$  (Fig. 8.15). To reach this angle, the mobile dislocation must have climbed to a height  $h$  determined by setting  $f_x = 1/4$  in Eq. 8.33:

$$h = \frac{K}{4\sigma_{xy}} = \frac{Gb}{8\pi(1-\nu)\sigma_{xy}} \quad (8.35)$$

This distance represents the height of the barrier presented by the immobile dislocation. As soon as the mobile dislocation has climbed to this height above the slip plane of the immobile dislocation, easy glide along the new slip plane can be resumed. If the initial impact parameter  $y_o$  is greater than the climb height given by the above equation (i.e., when  $y_o > h$ ), the immobile dislocation does not impede the glide motion of the mobile dislocation.

Figure 8.16b depicts the fate of a mobile dislocation approaching an immobile dislocation of opposite sign. In this case, the x-direction force between the two dislocations is given by Eq. 8.24 with the negative sign. The two dislocations attract each other until  $\theta = 45^\circ$ , and thereafter the interaction is repulsive. If the initial separation of the approaching dislocations is greater than  $h$  of Eq. 8.35, the mobile one is not stopped by the immobile one. When  $y_o \leq h$ , the mobile dislocation is brought to rest at a position given by

$$-K f_x(\theta_o) = \sigma_{xy} y_o \quad (8.36)$$

from which  $x_o$  can be determined with the aid of Eq. 8.31. When the dislocations are of opposite sign, the y-direction

force on the mobile dislocation is downward in the drawing, and the mobile dislocation climbs toward the immobile obstacle. As climb proceeds, the mobile dislocation moves to the right to keep the net x-direction force on it equal to zero. The trajectory can be computed from Eqs. 8.33 and 8.34 with a negative sign in front of the former. Eventually, the mobile dislocation climbs right into the immobile one, and annihilation of both defects takes place (i.e., the two half-sheets of atoms join and reconstitute a perfect atomic plane).

### 8.6.2 Dislocation Pileup

In Sec. 8.5, the ability of a Frank-Read source to continuously produce dislocation loops (an example of which is shown in Fig. 8.13) was described. The loop continues to expand in the glide plane of the source until it emerges from the crystal and causes deformation. The Frank-Read source operates indefinitely as long as a shear stress is present to generate the dislocations and to sweep the loops. However, if there is an obstacle in the glide plane, the first dislocation produced by the source is stopped, and those produced subsequently pile up on the stalled lead dislocation (Fig. 8.17). The operation of the source ceases, and the configuration remains constant unless the lead dislocation can escape by climbing over the obstacle. The obstacle causing the pileup may be a grain boundary, an immobile dislocation of the type depicted in Fig. 8.16, or the lead dislocation produced by another Frank-Read source in a parallel slip plane no further than a distance  $h$  (Eq. 8.35) from the first source. Both screw and edge dislocations are stopped by a grain boundary, and edge dislocations are blocked by other edge dislocations unless they are able to circumvent the obstacle by climb. Screw dislocations, on the other hand, can glide in any crystallographic plane and therefore do not need to climb (indeed they cannot climb) to surmount the obstacle presented by a nearby dislocation. However, as explained in the preceding section, edge dislocations are at least temporarily delayed when they encounter another edge dislocation.

The pileup shown in Fig. 8.17 represents the edge portions of the dislocation loops generated by the Frank-Read source on the right. The dislocations remain in the positions shown until the lead dislocation (labeled 1) climbs over the obstacle, if it can. When this occurs, dislocation number 2 in the drawing becomes the lead member, and the Frank-Read source produces another dislocation to replenish the pileup. The spacing of the

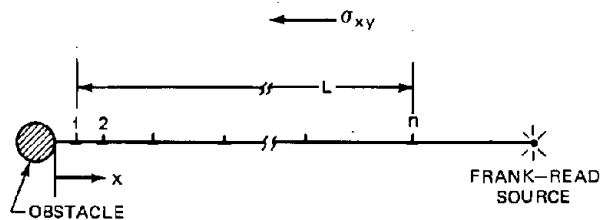


Fig. 8.17 Pileup of the edge portions of dislocation loops generated by a Frank-Read source due to an obstacle in the slip plane.

dislocations and the number between the source and the obstacle can be determined from the condition that the net force acting on each dislocation in the x-direction is zero. If there are n dislocations in the pileup, the condition of mechanical equilibrium of the *i*th member is

$$\sum_{\substack{j=1 \\ j \neq i}}^n F_{x_{i,j}} = F_m \quad (8.37)$$

where  $F_m$  is the force  $\sigma_{xy}b$  acting in the negative x-direction on each dislocation due to the applied shear stress and  $F_{x_{i,j}}$  is the force on the *i*th dislocation arising from interaction with dislocation *j*.  $F_{x_{i,j}}$  is given by the x-component of Eq. 8.23 with *r* replaced by the separation between dislocations *i* and *j*. The force balance can be written as:

$$\frac{Gb^2}{2\pi(1-\nu)} \sum_{\substack{j=1 \\ j \neq i}}^n \frac{1}{x_i - x_j} = \sigma_{xy}b \quad (8.38)$$

which represents  $n - 1$  nonlinear equations in the distances  $x_i$  (Eq. 8.38 does not apply to the lead dislocation). Solution of this set of equations (see problem at end of chapter) shows that the number of dislocations in the pileup is

$$n = \frac{\pi(1-\nu)L\sigma_{xy}}{Gb} \quad (8.39)$$

where *L* is the distance between the first and last dislocations.

The most important feature of the pileup is the stress that this configuration exerts on the nearby solid. Let *r* be the distance in the slip plane from the lead dislocation, taken as positive in the direction to the left in Fig. 8.17.

1. When *r* is small and positive (i.e., just ahead of the lead dislocation), the piled-up group exerts a shear stress that is *n* times larger than the applied shear stress, or

$$\sigma = n\sigma_{xy} = \frac{\pi(1-\nu)L\sigma_{xy}^2}{Gb} \quad (8.40)$$

2. At larger positive values of *r* but less than *L*, the pileup concentrates the stress according to the relation

$$\sigma = \left(\frac{L}{r}\right)^{1/2} \sigma_{xy} \quad (8.41)$$

Equation 8.41 applies to both the shear and the tensile stresses on a plane that contains the lead dislocation. The

tensile stress is given by Eq. 8.41 when the angle between the plane containing the lead dislocation and the slip plane is  $70^\circ$

3. At large distances from the lead dislocation ( $r \gg \pm L$ ), the piled-up group produces the same stress in the medium as a single dislocation of Burgers vector *nb*, or

$$\sigma = \frac{nGb}{2\pi(1-\nu)r} = \left(\frac{L}{2r}\right) \sigma_{xy} \quad (8.42)$$

Setting  $r = -L$  in Eq. 8.42 gives the back stress exerted by the piled-up loops on the Frank-Read source that was responsible for their generation. The back stress is  $\sim 1/2$  of the applied stress, and opposes the latter. The back stress is responsible for stopping operation of the Frank-Read source; when the effective stress (applied stress less the back stress) falls below the stress required to operate the source, no more loops can be produced.

### 8.6.3 Dislocation Dipole Arrays

Figure 8.18 shows another configuration of edge dislocations which is stabilized by the interaction forces between the components. The dislocations of opposite sign created by the two Frank-Read sources on parallel slip planes move toward and pass each other (even when there is no applied stress) and become interlaced in the manner shown in the drawing. The pairs of dislocations of opposite sign in close proximity are called dipoles. By using methods similar to those applied above to the pileup, we can determine the equilibrium spacing of the dipoles ( $\Delta x$ ) as a function of the distance  $y_0$  between the two slip planes and the applied shear stress  $\sigma_{xy}$ . Each dislocation is subject to the force due to the applied stress of magnitude  $\sigma_{xy}b$  directed to the right for the dislocations on the upper plane and to the left for those on the lower plane. In addition, each dislocation experiences an interaction force  $F_{ix}$  due to the other dislocations on its own plane and to the dislocations of opposite sign on the adjacent plane. As in the case of the dislocation pileup on a single plane, contributions to  $F_{ix}$  are determined from Eq. 8.23 with *r* and  $\theta$  values appropriate to each interacting pair. If there are *n* dislocations in each plane, each one of them interacts with  $n(n - 1)$  others. The calculated spacing between dislocations on each plane is found to be nearly independent of the applied shear stress (up to a critical value) and approximately equal to six times the interplanar spacing, or

$$\Delta x \approx 6y_0 \quad (8.43)$$

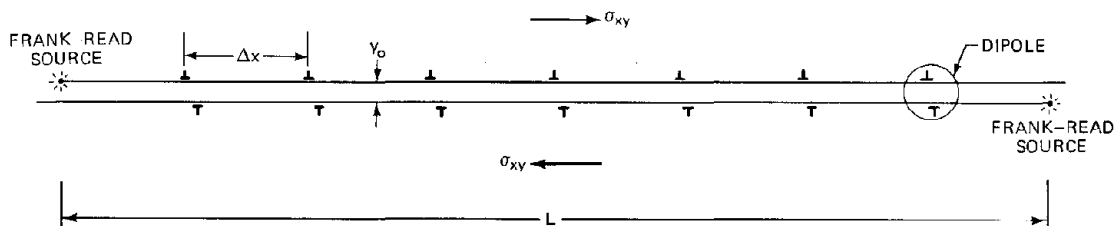


Fig. 8.18 Stable array of dislocation dipoles produced by Frank-Read sources on adjacent slip planes. [After P. M. Hazzledine, *J. Phys. (Paris)*: 27: C3-210 (1966).]

The number of dislocations on each plane (or equivalently, the number of dipoles in the array) between sources separated by a distance  $L$  is therefore

$$n = \frac{L}{\Delta x} \approx \frac{L}{6y_0} \quad (8.44)$$

As the applied shear stress is increased from zero, the two opposite-sign dislocations forming each dipole move slightly closer to each other along their respective slip planes. At a critical value of the applied shear stress, the dipoles move past each other and then continue to glide along the slip planes. Because the distance between dislocations along the slip planes is large compared to the normal distance between the two planes, the critical value of the applied shear stress at which the array decomposes is essentially equal to that required to push two isolated dislocations past each other. The relation between normal separation distance and the critical shear stress for isolated pairs of edge dislocations either of the same or of opposite sign is given by Eq. 8.35, and this equation is applicable to the array shown in Fig. 8.18. The group of dipoles is stable for shear stress up to the value given by

$$(\sigma_{xy})_{\text{crit}} = \frac{Gb}{8\pi(1-\nu)y_0} \quad (8.45)$$

## 8.7 GRAIN BOUNDARIES AND GRAINS

Unless special precautions are taken, solids prepared by solidification of a melt contain a large number of small crystallites, or grains, rather than a single large crystal. Each grain (which is typically of the order of micrometers in size) is a single crystal, containing its complement of point defects and dislocations. The surface separating different grains is termed a *grain boundary*. It is no more than a few atoms thick—just enough to adjust for the misorientation of the lattice structures of neighboring grains. Figure 8.19a shows the atomic arrangement of a large-angle grain boundary. Large-angle grain boundaries are characterized by a liquid-like structure in the  $\sim 10\text{-}\text{\AA}$  wide zone between the adjoining grains.

Grain boundaries in which the lattices of adjacent grains are tilted by only a few degrees from each other are called small-angle grain boundaries. These boundaries are composed of a nearly parallel stack of edge dislocation of the same sign, as shown in Fig. 8.19b. The match between the perfect crystalline regions of adjacent grains is obviously much better than in the large-angle grain boundary. Small-angle grain boundaries require special techniques to render them visible (e.g., chemical etching, which allows the individual edge dislocations composing the grain boundary to be seen). Large-angle grain boundaries can be seen by examining a polished specimen under a microscope of modest magnification. Boundaries composed of aligned dislocations as in Fig. 8.19b are called subgrain boundaries. At sufficiently high temperatures, some of the dislocations in a crystal order themselves into regular geometric patterns consisting of subgrain boundaries inside the larger grains formed by the wide-angle grain boundaries of Fig. 8.19a. This process is called *polygonization*.

In common with dislocation lines and free or external surfaces of a crystal, grain boundaries have a surface

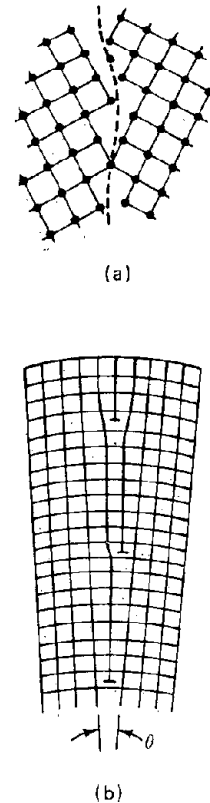


Fig. 8.19 Grain-boundary models. (a) Large-angle grain boundary. (b) Small-angle grain boundary.

tension, or an energy per unit area. The energy a grain boundary brings to a crystal is far too large to expect that such defects would be present in thermal equilibrium. However, because angular mismatches of the type shown in Fig. 8.19a can be eliminated only by collective rearrangement of large numbers of atoms, grain boundaries persist even at high temperatures. Prolonged annealing at elevated temperatures can produce appreciable grain growth, which is a process whereby large grains grow at the expense of smaller ones. The effect of annealing a polycrystalline specimen of uranium carbide on its microstructure is shown in Fig. 8.20.

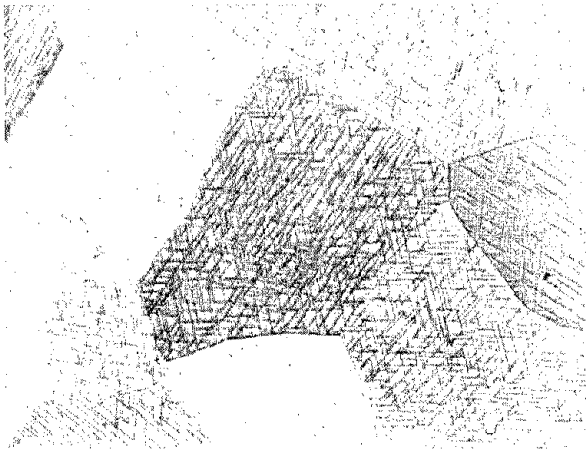
The mechanical response of crystalline material composed of many small grains to applied stresses is of particular importance to the performance of reactor fuel elements.

At low temperatures (below, say, one-third to one-half the melting point in  $^{\circ}\text{K}$ ) ionic solids such as  $\text{UO}_2$  pass directly from elastic deformation at low stresses to fracture at a sufficiently large stress. The material does not deform plastically and is said to be brittle.

Polycrystalline material needs more active slip planes and slip directions than single crystals before plastic deformation is possible. As shown in Fig. 8.21, if only a small number of slip planes are active, the random orientation of grains in a polycrystalline aggregate may permit the critical resolved shear stress to be exceeded in some grains but not in others. The entire body does not



(a)



(b)

Fig. 8.20 Microstructure of uranium carbide. (a) As-cast. (b) After 1-hr anneal at 2000°C.

undergo plastic deformation unless enough slip planes are active that the shear stress component along an active slip plane is likely to exceed the critical value for all orientations relative to the direction of the applied stress.

## 8.8 CREEP

Creep is a type of permanent deformation which occurs over long periods at constant stress. Elastic and plastic deformation occur essentially at the same time that stress is applied. Figure 8.22 shows the strains associated with the phenomenon of creep. On application of stress, instantaneous strain ascribable to elastic and plastic deformation occurs. If the specimen is maintained in a stressed condition and if the temperature is reasonably high (again, about one-third to one-half the melting point in °K), irreversible deformation continues over long periods of time (days or months) until failure occurs. Following a slowing-down

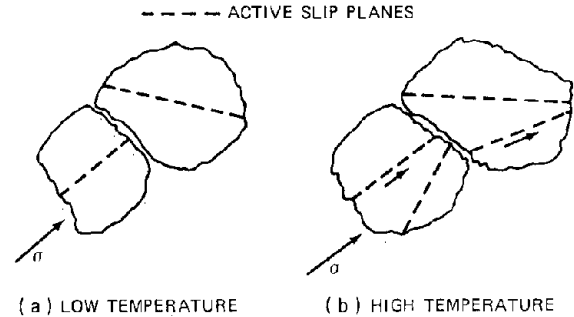


Fig. 8.21 Effect of temperature on slip in polycrystalline materials. Slip does not occur in (a) because the applied stress does not produce a component large enough to initiate slip in the upper grain. In (b) an additional slip plane has become active, and the applied stress is sufficient to cause slip in both grains; hence the material deforms plastically.

period (primary creep), the creep rate becomes essentially constant. This is the region of secondary, or steady-state, creep. This regime ends when the creep rate again speeds up (tertiary creep) shortly before failure, which is called *stress rupture*.

In any material, especially polycrystalline materials, there is nearly a continuous distribution of slip modes which become operable as the stress level is raised. Nearly all the slip mechanisms associated with a particular level of applied stress are exhausted in the instantaneous plastic strain shown in Fig. 8.22. If the stress is maintained constant, several mechanisms are available to permit continuous but very slow deformation.

The additional energy required to move a dislocation along a slip plane not normally active at the particular temperature and applied stress or a dislocation that is pinned by an impurity may be obtained by chance thermal fluctuations. The probability per unit time of supplying the energy  $E$  needed to get a dislocation moving is proportional to the Boltzmann factor  $e^{-E/kT}$ , and hence the creep rate exhibits a very pronounced temperature dependence.

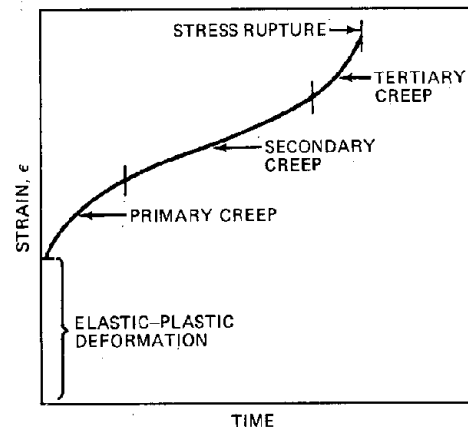


Fig. 8.22 Typical creep curve.

At elevated temperatures, the mobility of point defects increases. Point defects that may have been hindering dislocation motion, such as impurity clouds, are more mobile and hence are more easily dragged by the dislocation line at high temperatures (this mechanism of thermally activated creep is called microcreep).

Finally vacancies and interstitials become mobile at high temperatures and permit dislocation motion by climb.

For all these mechanisms the dependence of the strain rate  $\dot{\epsilon}$  on temperature and stress level in the regime of secondary creep is of the form

$$\dot{\epsilon} = \text{const} \times \sigma^m e^{-E/kT} \quad (8.46)$$

where  $\sigma$  is the applied stress,  $T$  is the absolute temperature, and  $E$  is the activation energy for creep. The exponent on the stress,  $m$ , is about 4 for creep rates governed by dislocation climb.

Creep may also occur by the sliding of adjacent crystallites along grain boundaries or by the diffusion of vacancies from one side of a grain to the other (Nabarro-Herring creep). Creep theories, including the effect of radiation, are discussed in detail in Chaps. 16 and 19.

## 8.9 NOMENCLATURE

- $a_0$  = lattice constant
- $A$  = area of cross section of specimen in which slip occurs on application of force; area of the slip plane; area of spherical cap
- $b$  = Burgers vector
- $c$  = constant proportional to the magnitude of Burgers vector
- $d$  = spacing between crystallographic planes in direction normal to the slip plane
- $E_{el}$  = strain-energy density
- $f_x$  = angular function for the force in the x-direction
- $f_y$  = angular function for the force in the y-direction
- $F$  = force at which slip occurs in a specimen; force per unit length on a dislocation line
- $G$  = shear modulus
- $h$  = height of the barrier presented by an immobile dislocation
- $i, j, k$  = Miller indices indicating the direction of a Burgers vector
- $L$  = length at a dislocation pileup
- $n$  = number of dislocations in a pileup
- $N_l$  = number of dislocation loops
- $r$  = radial distance from a dislocation line; distance in the slip plane from the lead dislocation
- $r_d$  = core radius of a dislocation core in a screw dislocation
- $\mathcal{R}$  = radius of the grain in which dislocation resides
- $R$  = radius of curvature of a dislocation line
- $R_l$  = average radius of dislocation loops
- $\Delta R_l$  = average increase in loop radius
- $s$  = distance between slip planes
- $S$  = length of a dislocation line
- $T$  = temperature
- $u$  = displacement
- $V$  = volume of the specimen
- $v_d$  = glide velocity of dislocation line
- $y$  = distance in the direction normal to the slip plane

- $y_0$  = initial separation of two parallel edge dislocations
- $z$  = distance along a dislocation line

### Greek letters

- $\beta$  = angle of deformation
- $\gamma$  = surface tension
- $\epsilon$  = shear strain
- $\dot{\epsilon}$  = strain rate
- $\phi$  = angle between the normal to the slip plane and the direction of tensile force; angle between the slip direction and the direction of tensile force
- $\nu$  = Poisson's ratio
- $\rho$  = dislocation density
- $\sigma$  = stress
- $\sigma_c$  = critical resolved shear stress
- $\tau$  = line tension (elastic energy per unit length of dislocation line)
- $\theta$  = angle in cylindrical coordinate system

### Subscripts

- crit = critical (shear stress for stability of dislocation dipoles)
- FR = Frank-Read (unpinning stress)
- $i_x$  = (force) in the x-direction on  $i$ th dislocation
- $i_y$  = (force) in the y-direction on  $i$ th dislocation
- $m$  = mobile
- $r$  = in radial direction
- $z$  = in the z-direction
- $\theta$  = in azimuthal direction

## 8.10 ADDITIONAL READING

1. J. Weertman and J. R. Weertman, *Elementary Dislocation Theory*, The Macmillan Company, New York, 1964.
2. J. Friedel, *Dislocations*, Pergamon Press, Inc., New York, 1964.
3. C. Kittel, *Introduction to Solid State Physics*, Chap. 19, John Wiley & Sons, Inc., New York, 1967.
4. L. V. Azaroff, *Introduction to Solids*, Chaps. 5 and 6, McGraw-Hill Book Company, New York, 1960.
5. D. Hull, *Introduction to Dislocations*, Pergamon Press, New York, 1965.

## 8.11 PROBLEMS

8.1 Draw billiard-ball models of the extra half sheet of atoms which constitute the following dislocations:

(a) The  $a_0/2$  [110] edge dislocation in the (111) plane of the fcc lattice.

(b) The  $a_0/2$  [111] edge dislocation on the (110) plane of the bcc lattice.

8.2 The  $r_r$ ,  $\theta\theta$ , and  $r\theta$  components of the stress tensor in the medium around an edge dislocation are given in Fig. 8.8. The axial stress component (not shown on the figure) is

$$\sigma_{zz} = \frac{Gb\nu}{\pi(1-\nu)} \frac{\sin\theta}{r}$$

Determine the line tension of the edge dislocation (i.e., the elastic-strain energy per unit length in the solid from the dislocation core at  $r = r_d$  to some large distance  $r = \mathcal{R}$ ).

8.3 (a) Derive Eq. 8.23.

(b) What is the force per unit length between parallel edge dislocations with perpendicular Burgers vectors?

8.4 In the circular shear loop shown in Fig. 8.6, let the  $x$ -axis be in the direction of the Burgers vector shown in the drawing, the  $z$ -axis be in the plane of the loop but perpendicular to the direction of the Burgers vector, and the  $y$ -axis be perpendicular to the plane of the loop. Let  $\theta$  be the polar angle of the circle measured from point A. At any point  $\theta$  on the loop, the Burgers vector has an edge component  $b_e$  which is perpendicular to the dislocation line at that position and a screw component  $b_s$  which is parallel to the line.

(a) Using the fact that the vector  $\mathbf{b}$  with these components is constant (in magnitude and direction) at all points on the loop, derive expressions for  $b_e$  and  $b_s$  as functions of  $\theta$ .

(b) Suppose a shear stress  $\sigma_{xy}$  is applied to the loop of Fig. 8.6. Show that the resultant force on the dislocation line is always radially directed and has a magnitude  $\sigma_{xy}b$ .

8.5 Consider two special-case solutions of Eq. 8.38.

(a) Solve directly for  $n = 3$ . Compare the length of the pileup determined from the exact solution for this case with the value obtained from Eq. 8.39 with  $n = 3$ .

(b) When the pileup is large (i.e.,  $n$  becomes large), the sum in Eq. 8.38 may be converted to an integral in which the integrand contains the distribution function:

$$f(x) dx = \text{number of dislocations in the range } x \text{ to } x + dx$$

for  $0 < x < L$ .

(1) Convert Eq. 8.38 to integral form.

(2) What is the normalization condition of  $f(x)$ ?

(3) Show that the solution

$$f(x) = \frac{2n}{\pi L} \left( \frac{L-x}{x} \right)^{1/2}$$

where  $L$  is given by Eq. 8.39, satisfies (1) and (2). Hint: Transform the integration variable from  $x$  to  $\theta$ , where  $x = L \sin^2 \theta$ . The integral of (1) is tricky.

8.6 Consider the small-angle grain boundary in Fig. 8.19b.

(a) For a simple cubic lattice in which the lattice constant  $a_0$  is equal to the Burgers vector  $b$  of the edge dislocations forming the grain boundary, what is the distance between dislocations as a function of tilt angle  $\theta$ ?

(b) What is the grain-boundary tension (energy per unit area) for a tilt angle  $\theta$ ? Assume that the extent of the stress field of each dislocation (i.e.,  $\mathcal{R}$  in Eq. 8.9) is equal to the spacing between dislocations and that the core radius of the dislocation is 1 Burgers vector.

# Chapter 9

## Equation of State of $\text{UO}_2$

### 9.1 REACTOR MELTDOWN ACCIDENT

The worst conceivable accident that could befall a fast reactor is a supercritical nuclear excursion that leads to explosive release of a large amount of energy and disassembly of the core. A specific sequence of events culminating in such an accident cannot be clearly defined, but the accident situation is usually assumed to begin with blockage of flow passages for the liquid-sodium coolant. Lacking adequate cooling, the solid fuel heats up to the point where both the fuel material and the cladding melt. Without structural support the entire fuel mass collapses to the bottom of the core. Since a fast reactor does not need a moderator to sustain criticality, the ejection of sodium and compaction of the fuel lead to a supercritical configuration, which results in the release of even more energy into the fuel. The rapid heating of the fuel generates large internal pressures and very high temperatures. The expansion of the fuel mass due to heating and the reduction of nuclear cross sections at high temperatures due to the Doppler effect tend to terminate the transient. However, if the pressure pulse accompanying the heating is large enough, the fuel mass may disassemble explosively. The first analysis of this accident was carried out by Bethe and Tait in 1956.<sup>1</sup> Such analyses have recently become the subject of intense concern.

The starting point of the analysis is a mass of molten  $\text{UO}_2$  at low temperature (i.e., in the neighborhood of the  $\text{UO}_2$  melting point of  $3100^\circ\text{K}$ ) and  $\sim 1$  atm pressure. The molten fuel is considered to contain a small fraction of voids, which may be partially filled with residual sodium coolant or molten structural material. For simplicity in calculation, the void space is assumed to be filled only with  $\text{UO}_2$  vapor at the saturation vapor pressure corresponding to the liquid-phase temperature. As energy is supplied to the fuel mass by fission, the voids close and a single liquid phase is obtained. If subsequent heating were very slow, the molten fuel would simply expand at constant pressure. However, when the heating is as rapid as in a nuclear excursion, the inertia of the material prevents instantaneous adjustment of the fuel-mass geometry to energy input. Sizable internal pressures are generated within the fuel mass, and the motion of the collapsed core is governed by the equations of hydrodynamics.

The internal energy of the system is specified by the fission rate in the liquid fuel. Since very little expansion of the core takes place during the first part of the excursion, the process can be regarded as taking place at constant volume. The specific volume of the material is prescribed by the void fraction in the initially collapsed fuel mass, which must be estimated as part of the basis of the calculation.

The equation of state of the fuel material provides the essential link between the nuclear aspects of the excursion and the dynamic response of the core. In particular, the pressure as a function of internal energy and volume provides a means of determining the variation of the fuel-mass geometry with time by the equations of hydrodynamics. The temperature as a function of the same two independent variables is needed for evaluation of the nuclear cross sections and the Doppler coefficient. Thus, thermodynamic relations of the type  $p(U,v)$  and  $T(U,v)$  are required.

Generally, an equation of state for a one-component system provides a relation between pressure, temperature, and specific volume. Although specification of any two of these variables is sufficient to determine the third, properties such as the internal energy and entropy are not fixed by a  $p$ - $v$ - $T$  equation of state. In addition, the specific heat is required. All thermodynamic properties of the system are determined if both a thermal equation of state, e.g.,  $p(v,T)$ , and a caloric equation of state, e.g.,  $C_v(T)$ , are known. However, an equation of state relating the internal energy to the entropy and specific volume determines all thermodynamic properties. The relation  $U(S,v)$  is a fundamental equation of state since this single function determines parameters such as pressure and temperature by differentiation.

### 9.2 MICROSCOPIC BASIS OF THE THEORY OF CORRESPONDING STATES

The theory of corresponding states demonstrates that the  $p$ - $v$ - $T$  relations of a broad class of fluids are identical if the thermodynamic variables are rendered dimensionless in the appropriate manner.

The p-v-T relationships of nonideal gases and liquids differ from the ideal-gas law because of the potential energy of interaction between all particles in the system. The existence of a universal reduced equation of state is based on the following assumptions concerning the microscopic behavior of the particles of the system:

1. The potential energy of two particles of the system is a function only of their separation; if  $\phi$  is the potential energy of a pair of particles, it is a function only of  $r_{ij}$ , which denotes the distance between particles  $i$  and  $j$ . This requirement in principle eliminates nonspherical molecules, such as water, in which the potential energy of a pair of molecules depends on the orientation of the molecules as well as on the separation. However, because thermal motion even at moderate temperatures smears out asymmetries in the potential function, the theory of corresponding states is applicable to nonspherical molecules as well.

2. The potential energy of the entire N-particle system is the sum of the potential energies of all possible pairs of particles, or

$$E_p(r_1, \dots, r_N) = \sum_{ij} \phi(r_{ij}) \quad (9.1)$$

The sum includes all possible pairs of molecules in the system. The potential energy of the system depends on the positions  $r_i$  of all constituent particles. The atoms of a fluid unlike those of a solid do not have definite positions. Hence, the series expansion of  $E_p$  for crystals (Eq. 2.3) cannot be applied to the potential energy of a collection of particles in a fluid phase.

3. The partition function of the system is evaluated by classical rather than quantum statistical mechanics. Development of classical statistical mechanics is beyond the scope of this exposition. Instead, we use the results of classical statistical mechanics and refer the reader to the references at the end of Chap. 1 for complete development.

If the potential energy of Eq. 9.1 is zero, the system is an ideal gas for which the partition function is given by combining Eqs. 1.61 and 1.73:

$$Z^* = \frac{V^N}{N!} \left( \frac{2\pi mkT}{h^2} \right)^{3N/2} z_{int}^N \quad (9.2)$$

The asterisk denotes an ideal-gas property. The particles of a nonideal gas or liquid possess potential energy  $E_p$  in addition to translational and internal energy. The partition function for these systems is written as

$$Z = \frac{Q_c}{N!} \left( \frac{2\pi mkT}{h^2} \right)^{3N/2} z_{int}^N \quad (9.3)$$

where  $Q_c$  is called the configurational partition function. According to classical statistical mechanics, it is related to the potential energy of the N particles by the 3N-fold integral:

$$Q_c = \int_V \dots \int_V N \dots \int_V \exp \left[ -\frac{E_p(r_1, \dots, r_N)}{kT} \right] \times d^3 r_1 \dots d^3 r_N \quad (9.4)$$

Each of the integrals is over the volume  $V$  of the system. For an ideal gas,  $E_p$  is zero, and the right-hand side of Eq. 9.4 reduces to the product of  $N$  integrals of the integrand unity over the volume of the system. Or,  $Q_c$  reduces to  $V^N$ , and Eq. 9.3 becomes identical to Eq. 9.2.

Evaluation of the configurational partition function forms the basis for much modern work in the theory of liquids. Our aim is not to attempt to evaluate  $Q_c$  but rather to demonstrate that for systems obeying the first two assumptions stated,  $Q_c$  depends only on two dimensionless parameters.

4. The potential energy between a pair of particles,  $\phi(r_{ij})$ , can be written as a universal function provided that the energy is made dimensionless by a characteristic energy  $\epsilon$  and the distance is reduced by a characteristic length  $\sigma$ :

$$\phi(r_{ij}) = \epsilon \psi(r_{ij}/\sigma) \quad (9.5)$$

The reducing parameters  $\epsilon$  and  $\sigma$  are usually chosen as the coordinates of the minimum in the potential-energy function.

The dimensionless energy  $\phi/\epsilon$  is a universal function of the dimensionless distance  $r_{ij}/\sigma$  for all systems whose particles follow the same intermolecular potential law; that is, the shape function  $\psi$  of Eq. 9.5 is the same for all members of the class of systems, and particular systems are distinguished by different numerical values of  $\epsilon$  and  $\sigma$ .

Insertion of Eq. 9.5 and 9.1 into Eq. 9.4 yields

$$Q_c = \sigma^{3N} \int_{V/\sigma^3} \dots \int_{V/\sigma^3} N \dots \int_{V/\sigma^3} \exp \left[ -\frac{\sum \psi(r_{ij}/\sigma)}{(kT/\epsilon)} \right] \times d^3 \left( \frac{r_1}{\sigma} \right) \dots d^3 \left( \frac{r_N}{\sigma} \right) \quad (9.6)$$

Since the universal function  $\psi$  is the same for all fluids in the class to which the corresponding-states argument applies, the integral in Eq. 9.6 is a function only of the group  $kT/\epsilon$  appearing in the integrand, the dimensionless volume  $V/\sigma^3$  over which the integral is carried, and the number of particles in the system  $N$ . In particular,  $Q_c$  is of the form

$$Q_c = \left[ N\sigma^3 f \left( \frac{kT}{\epsilon}, \frac{V}{N\sigma^3} \right) \right]^N = V^N \left[ \frac{f(kT/\epsilon, V/N\sigma^3)}{V/N\sigma^3} \right]^N \quad (9.7)$$

where the function  $f$  approaches  $V/N\sigma^3$  as the intermolecular potential energy disappears, or as  $kT/\epsilon \rightarrow \infty$ .

According to Eq. 1.28, the pressure is

$$\begin{aligned} p &= kT \left( \frac{\partial \ln Z}{\partial V} \right)_{T,N} \\ &= kT \left( \frac{\partial \ln Q_c}{\partial V} \right)_{T,N} \\ &= NkT \left( \frac{\partial \ln f}{\partial V} \right)_{T,N} \end{aligned} \quad (9.8)$$

The dimensionless pressure is

$$\begin{aligned} \frac{p\sigma^3}{\epsilon} &= \left(\frac{kT}{\epsilon}\right) \frac{\partial \ln f(kT/\epsilon, v/\sigma^3)}{\partial (v/\sigma^3)} \\ &= g\left(\frac{kT}{\epsilon}, \frac{v}{\sigma^3}\right) \end{aligned} \quad (9.9)$$

where  $V/N$  has been replaced by the specific volume  $v$ . The function  $g$  is universal and applies to all fluids for which the intermolecular potential has the same shape function  $\psi$ .

Equation 9.9 applies to a single phase, either liquid or vapor. If both phases are present and at equilibrium, the pressure and temperature are connected by the vapor pressure relation:

$$\frac{p_s \sigma^3}{\epsilon} = h\left(\frac{kT}{\epsilon}\right) \quad (9.10)$$

where  $p_s$  is the saturation pressure at temperature  $T$ .

If we follow the vapor-pressure curve to higher and higher temperatures, the distinction between the gaseous and condensed phases becomes less pronounced; the gas density increases because  $p_s$  becomes larger with increasing  $T$ , and the liquid density decreases because of thermal expansion. At a sufficiently high temperature, the densities of the coexistent phases become equal, and the two-phase system merges into a single phase. This state of the fluid is called the critical state and is characterized by unique values of pressure, temperature, and specific volume (or density) for each substance. The critical constants  $p_c$ ,  $T_c$ , and  $v_c$ , when properly reduced by the molecular parameters  $\epsilon$  and  $\sigma$ , should be the same for all substances obeying the law of corresponding states represented by Eq. 9.9. Or, the groups

$$\left(\frac{p_c \sigma^3}{\epsilon}\right), \left(\frac{kT_c}{\epsilon}\right), \text{ and } \left(\frac{v_c}{\sigma^3}\right) \quad (9.11)$$

should be universal constants.

### 9.3 REDUCED EQUATION OF STATE

Since the molecular parameters  $\epsilon$  and  $\sigma$  are generally not known, it is desirable to represent the dimensionless thermodynamic properties in Eq. 9.9 by experimentally accessible macroscopic constants of the fluid. Since the quantities in Eq. 9.11 are supposed to be universal constants, the critical parameters  $p_c$ ,  $T_c$ , and  $v_c$  may be used as reducing factors in Eq. 9.9 instead of  $\epsilon/\sigma^3$ ,  $\epsilon/k$ , and  $\sigma^3$ . Thus, a macroscopic equation of state can be expressed as a universal relation between

$$p_r = \frac{p}{p_c}, \quad T_r = \frac{T}{T_c}, \quad \text{and} \quad v_r = \frac{v}{v_c} \quad (9.12)$$

The terms  $p_r$ ,  $T_r$ , and  $v_r$  are called reduced thermodynamic properties and are related to each other by a reduced equation of state, such as  $v_r(p_r, T_r)$ .

Analytic expressions for a reduced equation of state are generally not available, and the equation of state is expressed in tabular or graphical form (similar to the familiar steam tables). Hougen, Watson, and Ragatz<sup>2</sup> have

combined measurements of  $p$ - $v$ - $T$  behavior with experimentally determined critical constants of a variety of substances to construct reduced equations of state, such as the  $v_r(p_r, T_r)$  plots shown in Fig. 9.1.

In this figure the region in the upper left-hand corner is the normal liquid region, and the curves in the lower left describe the behavior of undersaturated, near-ideal gases.

States within the envelope described by the lines labeled "saturated liquid" and "saturated vapor" consist of two phases in equilibrium. The densities of the liquid and vapor phases in equilibrium are given by the intersection of a vertical line with the saturated-liquid and saturated-vapor curves, respectively. The isotherms and isobars in Fig. 9.1 are continuous curves for values of  $T_r$  and  $p_r$  greater than unity, which implies that the system never separates into two equilibrium phases. For values of reduced temperature or pressure less than unity, the curves are discontinuous at the two-phase envelope. For example, if we follow the  $T_r = 0.8$  isotherm in the left-hand plot of Fig. 9.1 from high temperatures, we find it intersects the saturated liquid curve at a reduced pressure of 0.2. This liquid is in equilibrium with a vapor at the same temperature and pressure but with a density given by the ordinate of the saturated-vapor curve at  $p_r = 0.2$ . The  $T_r = 0.8$  isotherm continues to lower densities at pressures below this intersection, but the curve is not shown on the figure because of the congestion in this region of the drawing.

The critical point is located at values of all reduced parameters equal to unity.

If Fig. 9.1 were truly a universal equation of state, estimation of the thermodynamic properties of unusual liquids, such as  $\text{UO}_2$ , would be simpler than it actually is. However, Fig. 9.1 was constructed from the  $p$ - $v$ - $T$  measurements and critical constants of about 100 ordinary fluids, such as organic compounds, inert gases, and atmospheric gases. The equation of state of polar substances, such as water, or liquid metals, such as mercury, are not well represented by Fig. 9.1. Even accepting that these maverick fluids satisfy the four requirements for the existence of a reduced equation of state (Sec. 9.2), the intermolecular potentials are not represented by the same shape function  $\psi$  of Eq. 9.5 that characterizes the fluids on which Fig. 9.1 was based.

To avoid the inconvenience of proliferating graphs such as Fig. 9.1 and the accompanying tables for each class of fluids, we use the following device.

Since the quantities of Eq. 9.11 are universal constants (for a particular class of fluids, at least), the grouping

$$z_c = \frac{p_c v_c}{RT_c} \quad (9.13)$$

should also be a universal constant. Since we are now dealing with macroscopic parameters, the Boltzmann constant  $k$  in the temperature group of Eq. 9.11 has been replaced by the gas constant  $R$ , and the term  $v_c$  in Eq. 9.13 is interpreted as the molar volume rather than the molecular volume. The quantity  $z_c$  in Eq. 9.13 is the critical compressibility factor, since, in general, the compressibility factor of a nonideal gas or liquid is defined by

$$z = \frac{pv}{RT} \quad (9.14)$$

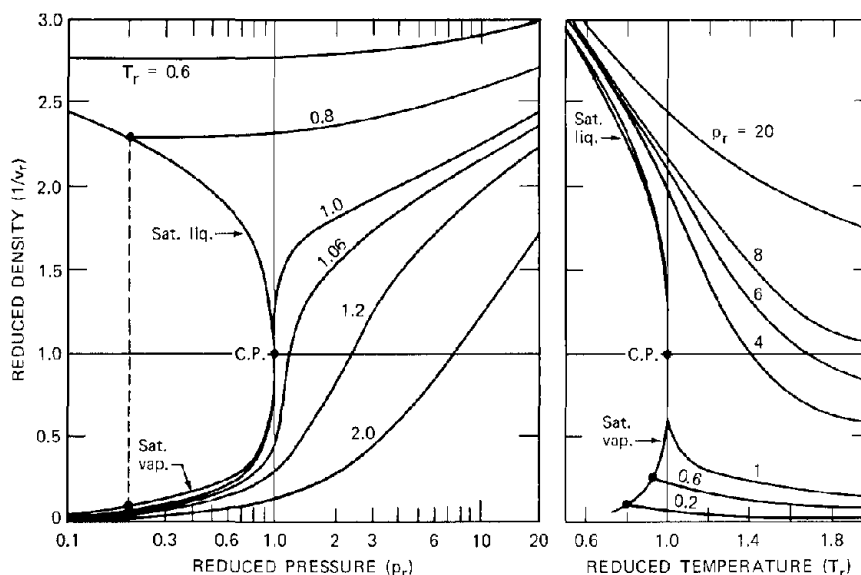


Fig. 9.1 Reduced densities of gases and liquids for  $z_c = 0.27$ . (Based on Ref. 2.)

(An ideal gas is a fluid with a compressibility factor of unity.)

The critical compressibility factor is the same for all substances of a particular class (e.g., hydrocarbons), but different classes of substances may exhibit different critical compressibility factors. So that different classes of substances can be accommodated by a reduced equation of state of manageable proportions, all complicated differences that distinguish one class of fluids from another are lumped into a single factor  $z_c$ . The critical compressibilities of several types of fluids are shown in Table 9.1. Note that the  $z_c$  values for mercury and cesium are vastly different; thus even liquid metals cannot be considered as a single class of fluid from a corresponding-states point of view.

The equations of state are still relations between  $p_r$ ,  $T_r$ , and  $v_r$ , but they are now parametric in the critical compressibility factor  $z_c$ . Figure 9.1 is for those fluids which have a critical compressibility factor of 0.27. A different family of curves would be required for other values of  $z_c$ . Fortunately, the range of  $z_c$  values characteristic of even grossly dissimilar classes of fluids is not great, and the shift in the reduced equation of state with  $z_c$  is also moderate. Consequently, the variation of thermodynamic properties with  $z_c$  can be handled by a simple interpolation scheme. This feature of the corresponding-states equations is discussed in detail in Ref. 2.

Thus, the  $p$ - $v$ - $T$  behavior of a particular fluid, whether as a single liquid phase, a single gas phase, or a two-phase equilibrium mixture, is determined if its three critical constants are known. By Eq. 9.13,  $p_c$ ,  $T_c$ , and  $v_c$  determine  $z_c$ , which in turn determines the reduced equation of state. Since the critical constants are known, the reduced properties read from a graph such as Fig. 9.1 can be converted to the actual  $p$ - $v$ - $T$  behavior of the fluid.

All three critical constants have been measured for a substantial number of ordinary fluids. Some of the critical constants have been measured for a few liquid metals, but only for mercury and cesium has the critical state been

Table 9.1 Critical Compressibility Factors of Various Fluids

Fluid type	$z_c$
Water	0.232
Acetone, ammonia, esters, alcohols	0.25
Hydrocarbons	0.27
Normal gases ( $\text{O}_2$ , $\text{CO}$ , $\text{CH}_4$ , Ar)	0.29
Mercury	0.37
Cesium	0.20

fully established. For an exotic material such as  $\text{UO}_2$ , none of the critical constants have been measured. At the present time, only the density and heat capacity of liquid  $\text{UO}_2$  have been measured, and these only for a few hundred degrees above the melting point of 3100°K. We are therefore forced to explore means of estimating the critical constants from experimental data on other thermodynamic properties obtained at temperatures much lower than either the critical state or the region where practical application of the equation of state is desired.

#### 9.4 CRITICAL CONSTANTS OF $\text{UO}_2$

Lack of experimentally determined critical constants is a severe impediment to development of a reduced equation of state for  $\text{UO}_2$ . Much effort has been expended on estimating the critical constants from empirical laws or from extrapolation of low-temperature properties to high temperatures.

Fortunately, there is one empirical law which appears to apply to a wide variety of substances and which has been used in most attempts to determine the  $\text{UO}_2$  critical constants. We refer to the law of rectilinear diameters, which states that one-half the sum of the liquid and gas densities is a linear function of temperature up to the

critical point. Although this law does not rely on the theory of corresponding states for its validity, it is not in disagreement with the reduced equations of state such as the one shown in Fig. 9.1.

The law of rectilinear diameters is particularly simple to apply to  $\text{UO}_2$ . The density of liquid  $\text{UO}_2$  has been measured from the melting point to a few hundred degrees above the melting point.<sup>3</sup> These measurements were made by placing a weighed amount of  $\text{UO}_2$  in a tungsten crucible, sealing the crucible, and heating it in a furnace to temperatures above the melting point. Gamma radiographs of the molten  $\text{UO}_2$ , such as that shown in Fig. 9.2, were used to determine the volume of the liquid at a particular temperature. From these data the density (or specific volume) of the liquid and the coefficient of thermal expansion

$$\alpha = \frac{1}{v} \left( \frac{\partial v}{\partial T} \right)_p \quad (9.15)$$

were computed. It can be appreciated that the nature of such an experiment does not lead to data of high precision, particularly in the derivative represented by Eq. 9.15.

Since the vapor pressure of  $\text{UO}_2$  is less than 100 torr at the temperatures where the liquid density was measured, the density of the vapor (assuming the ideal-gas law to apply) is negligible compared to the density of the liquid. Consequently the rectilinear diameter can be established from the low-temperature liquid-density data alone. A plot of the  $\text{UO}_2$  density illustrating application of the law of rectilinear diameters is shown in Fig. 9.3. Extending the straight line to the critical point yields the following relation between critical volume and critical temperature:

$$\frac{1}{v_c} = \frac{(1 - \alpha T_c)}{2} \frac{1}{v_l^0} \quad (9.16)$$

where  $v_l^0$  is the specific volume of liquid  $\text{UO}_2$  extrapolated to  $0^\circ\text{K}$ . This formula requires extrapolation of not too reliable data for  $\sim 4000^\circ\text{K}$  above the few hundred degree interval where the measurements were made. Equation 9.16 establishes a relation between the critical volume and the critical temperature to within the precision of the low-temperature liquid-density data. From this point a variety of methods have been used to complete the determination of the critical constants.

The law of corresponding states implicitly contains a universal reduced vapor-pressure relation analogous to Eq. 9.10. The intersection of vertical lines drawn within the two-phase region and the saturated liquid and vapor curves in Fig. 9.1 fit the empirical equation

$$\ln p_{rs} = \delta \ln T_r - 0.0838(\delta - 3.75) \times \left( \frac{36}{T_r} - 35 - T_r^6 - 42 \ln T_r \right) \quad (9.17)$$

where  $p_{rs}$  is the reduced equilibrium vapor pressure corresponding to reduced temperature  $T_r$  and  $\delta$  is related to the critical compressibility factor by

$$z_c = (0.265 + 1.90)^{-1} \quad (9.18)$$

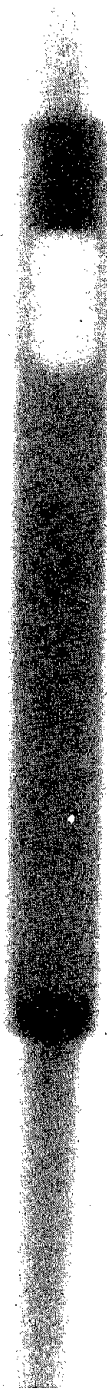


Fig. 9.2 Gamma radiograph of tungsten-encapsulated  $\text{UO}_2$  liquid at  $3000^\circ\text{C}$  [From J. S. Christensen, Thermal Expansion and Change in Volume of Uranium Dioxide on Melting, *J. Amer. Ceram. Soc.*, 46: 607 (1963).]

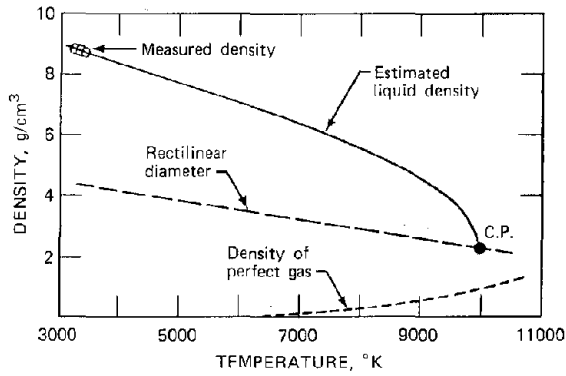


Fig. 9.3 Application of the law of rectilinear diameters to UO<sub>2</sub> for an assumed critical temperature of 10,000°K.

Figure 9.4 shows the results of several sets of measurements of the vapor pressure of solid UO<sub>2</sub> and one of the liquid. The measured vapor pressure of UO<sub>2</sub> can be fit to Eq. 9.17 and  $p_c$ ,  $T_c$ , and  $z_c$  so determined. From Eq. 9.13  $v_c$  can then be calculated. This method of estimating the critical constants of UO<sub>2</sub> has been used by Menzies,<sup>4</sup> although it is subject to the criticism that the entire set of critical constants depends on one type of low-temperature measurement, which in addition was made on solid rather than liquid UO<sub>2</sub>. In addition to requiring extrapolation to pressures six orders of magnitude higher than the highest pressure at which data are available, the slope of the vapor-pressure-temperature curve changes discontinuously at the melting point. If the solid vapor pressures are to be extrapolated to the liquid region, the heat of fusion is needed (see problem 9.3). Early estimates of the critical constants of UO<sub>2</sub> which relied on vapor-pressure extrapolation had guessed values of the heat of fusion ranging from 0 to 85 kJ/mole. The actual figure has been established as 75 kJ/mole.<sup>5</sup>

Instead of relying entirely on Eq. 9.17 to fix the critical constants, we can use the following scheme proposed by Grosse.<sup>6</sup> The fundamental thermodynamic equation

$$dF = -S dT - p dv$$

yields the Maxwell relation

$$\left(\frac{\partial S}{\partial v}\right)_T = \left(\frac{\partial p}{\partial T}\right)_v \quad (9.19)$$

Applying Eq. 9.19 to the vaporization process yields

$$\left(\frac{\partial S}{\partial v}\right)_T = \frac{\Delta S_{vap}}{v_g - v_l} \quad (9.20)$$

where the entropy of vaporization is related to the enthalpy of vaporization (or heat of vaporization) by

$$\Delta S_{vap} = \frac{\Delta H_{vap}}{T} \quad (9.21)$$

Since the system is a two-phase equilibrium mixture, the right-hand side of Eq. 9.19 is given by  $(dp/dT)$ ; so Eq. 9.19 becomes

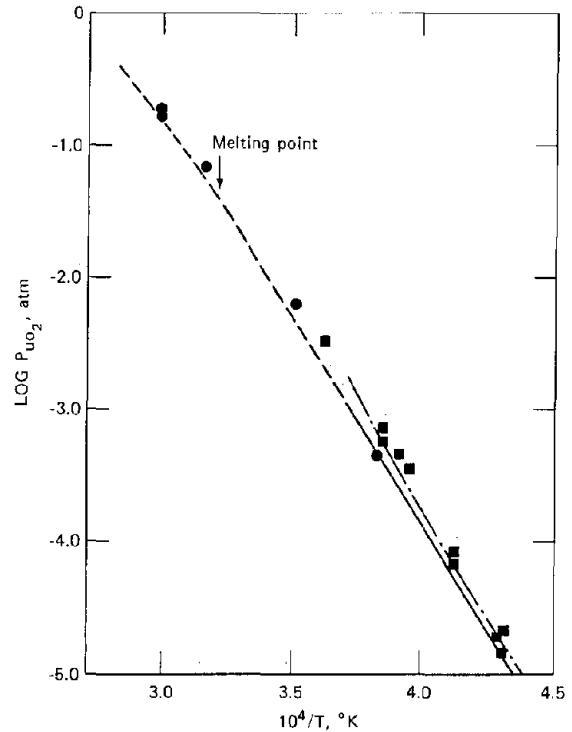


Fig. 9.4 Total pressure of uranium-bearing species over urania. — — —, R. J. Ackermann et al., *J. Chem. Phys.*, 25: 1089 (1956). — — —, M. Tetenbaum and P. D. Hunt, *J. Nucl. Mater.*, 34(1): 86 (1970). — — —, equation of Tetenbaum and Hunt extrapolated to liquid UO<sub>2</sub>. ■, R. W. Ohse, *J. Chem. Phys.*, 44: 1375 (1966). ●, G. T. Reedy and M. G. Chasanov, *J. Nucl. Mater.*, 42: 341 (1972). (Based on Reedy and Chasanov, 1972.)

$$\begin{aligned} \frac{\Delta H_{vap}}{T} &= (v_g - v_l) \left(\frac{dp}{dT}\right)_S \\ &= \frac{R}{z_c} (v_{gr} - v_{lr}) \left(\frac{dp_{rs}}{dT_r}\right) \end{aligned} \quad (9.22)$$

where the second equality has been obtained by using the critical compressibility factor to convert the thermodynamic properties to reduced quantities. The term  $dp_{rs}/dT_r$  is a function of reduced temperature only, since it represents a saturated two-phase mixture. Equation 9.17 is an explicit relation for the reduced saturation curve. The reduced specific volume for gas and liquid phases are, in general, functions of both reduced temperature and pressure. However, when following a saturation line, the latter two are saturation values, and  $v_{gr}$  and  $v_{lr}$  are thereby functions of reduced temperature only. They could be obtained from a plot such as Fig. 9.1 if  $z_c$  were known.

To avoid dependence on the explicit corresponding states relations of Eq. 9.17 or Fig. 9.1, we use only the requirement that the right-hand side of Eq. 9.22 be a function of reduced temperature alone. Therefore, the entropy of vaporization (or  $\Delta H_{vap}/T$ ) for a particular class of substances should all fall on a single universal curve. Such a plot is shown in Fig. 9.5. The various materials fall roughly on curves corresponding to the critical com-

compressibility factors shown in Table 9.1. Thus, if we know the heat of vaporization of the liquid at a single temperature, the ordinate of Fig. 9.5 is fixed. If the critical compressibility factor is assumed, the ordinate  $\Delta H_{\text{vap}}/T$  determines a value of  $T/T_c$  from one of the curves of Fig. 9.5, and hence  $T_c$  follows immediately. This method, in conjunction with the law of rectilinear diameters, has been used by Meyer and Wolfe<sup>7</sup> to determine the critical constants of  $\text{UO}_2$ .

The various approaches to estimating the critical constants of  $\text{UO}_2$  and the rather wide spread in the constants generated by using different types of data and different estimation techniques have been reviewed by Miller.<sup>8</sup> The data and assumptions on which the estimates are based are

1. Coefficient of thermal expansion of the liquid,  $\alpha$ .
2. Critical compressibility factor,  $z_c$ .
3. Vapor-pressure curve,  $p_s(T)$ .
4. Heat of fusion,  $\Delta H_f$ .

The various estimates of the critical constants of  $\text{UO}_2$  are shown in Table 9.2. It can be seen that the range of values is quite large and involves extrapolation of low-temperature measurements by thousands of degrees and many orders of magnitude in pressure. Because of the very extreme conditions represented by these pressures and temperatures, it is unlikely that the critical constants of  $\text{UO}_2$  will be directly measured in the near future.

Table 9.2 Various Estimates of the Critical Constants of  $\text{UO}_2$

Authors	$T_c, ^\circ\text{K}$	$p_c, \text{atm}$	$v_c, \text{cm}^3 / \text{mole}$	$z_c$
Meyer and Wolfe <sup>7</sup>	7,300	1,900	85.5	0.27
Menzies <sup>4</sup>	8,000	2,000	90	0.27
Miller <sup>8</sup>				
High temperature	12,780	493	2,100	0.11
Low temperature	4,910	1,037	78	0.20
Most probable	9,115	1,230	170	0.27

### 9.5 $\text{UO}_2$ EQUATION OF STATE BASED ON THE THEORY OF CORRESPONDING STATES

As developed in Sec. 9.3, the theory of corresponding states leads to a reduced equation of state relating the parameters  $v_r$ ,  $p_r$ , and  $T_r$ . If the critical constants of the substance are known, the  $p$ - $v$ - $T$  relation follows. However, a  $p$ - $v$ - $T$  equation of state is not sufficient for the analysis of the  $\text{UO}_2$  meltdown accident, which requires relations of the type  $p(U, v)$  and  $T(U, v)$ . The  $p$ - $v$ - $T$  equation gives some information on the internal energy which can be used to construct the desired equations of state by the following procedure.

We start from the fundamental formula

$$dU = T dS - p dv \quad (9.23)$$

where the quantities  $U$ ,  $H$ ,  $S$ ,  $F$ , and  $G$  are per mole of substance and are thus intensive parameters. The differ-

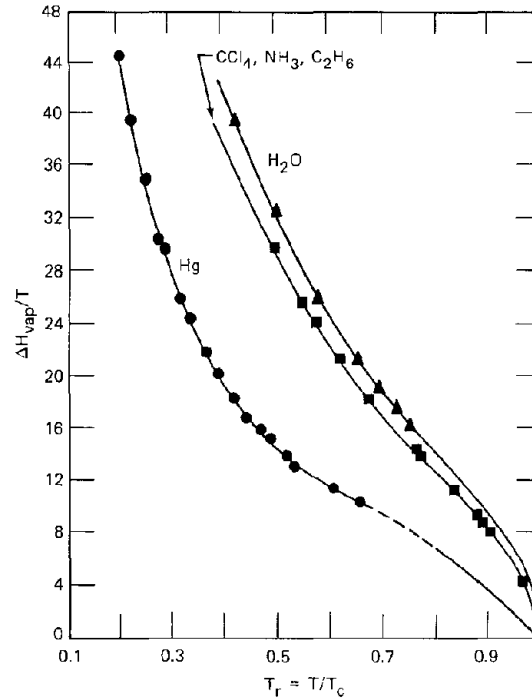


Fig. 9.5 Variation of entropy of vaporization with reduced temperature for different substances. (Based on Ref. 6.)

ential  $dS$  is reformulated in terms of  $dT$  and  $dp$ . Since the entropy is a state function, it can be regarded as a function of temperature and pressure, and its differential can be written as

$$dS = \left(\frac{\partial S}{\partial p}\right)_T dp + \left(\frac{\partial S}{\partial T}\right)_p dT \quad (9.24)$$

The Maxwell relation of the fundamental equation

$$dG = -S dT + v dp$$

is

$$\left(\frac{\partial S}{\partial p}\right)_T = -\left(\frac{\partial v}{\partial T}\right)_p \quad (9.25)$$

The coefficient of  $dT$  in Eq. 9.24 can be written in terms of  $p$ ,  $v$ , and  $T$  by using the specific heat at constant pressure:

$$C_p = \left(\frac{\partial H}{\partial T}\right)_p$$

The fundamental equation

$$dH = T dS + v dp$$

yields

$$\left(\frac{\partial H}{\partial T}\right)_p = T \left(\frac{\partial S}{\partial T}\right)_p$$

Thus

$$\left(\frac{\partial S}{\partial T}\right)_p = \frac{C_p}{T} \quad (9.26)$$

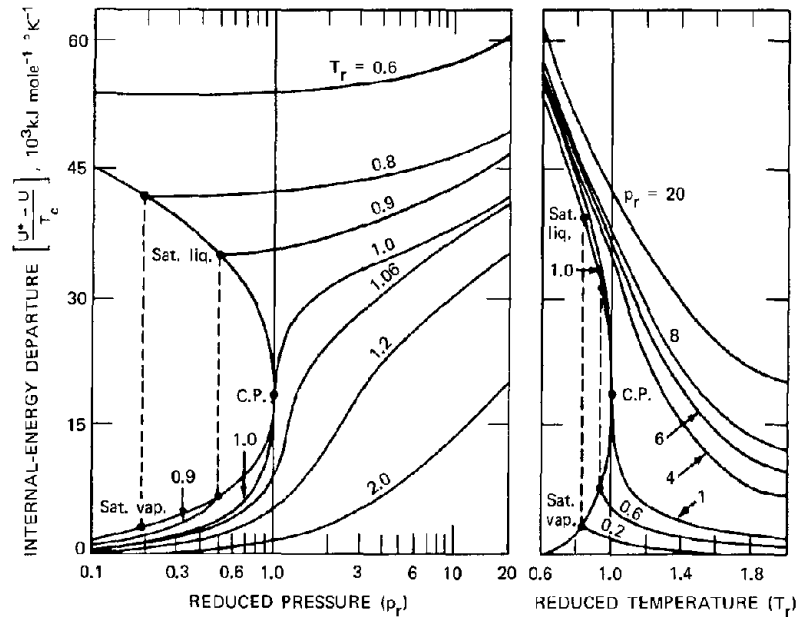


Fig. 9.6 Excess internal energy of gases and liquids for  $z_c = 0.27$ . (From O. A. Hougen, K. M. Watson, and R. A. Ragatz, *Chemical Process Principles*, Part II, 2nd ed., Chap. 14, p. 612, John Wiley & Sons, Inc., New York, 1959.)

Substituting Eqs. 9.25 and 9.26 into 9.24 and using the resulting expression for  $dS$  in Eq. 9.23 yields

$$dU = C_p dT - T \left( \frac{\partial v}{\partial T} \right)_p dp - p dv \quad (9.27)$$

From this equation we obtain

$$\left( \frac{\partial U}{\partial v} \right)_T = -T \left( \frac{\partial v}{\partial T} \right)_p \left( \frac{\partial p}{\partial v} \right)_T - p$$

The product of the derivatives on the right side of this formula is just  $-(\partial p / \partial T)_v$ , as can be shown by considering the differential of  $p(T, v)$ . Thus

$$\left( \frac{\partial U}{\partial v} \right)_T = T \left( \frac{\partial p}{\partial T} \right)_v - p \quad (9.28)$$

The right-hand side of Eq. 9.28 is determined if the  $p$ - $v$ - $T$  equation is known, as we assume it is. Equation 9.28, however, yields only the derivative of the internal energy with respect to specific volume at constant temperature, which must be integrated to obtain  $U$ . We integrate from the actual specific volume at the prevailing pressure and temperature to the specific volume of the hypothetical ideal gas of the substance at the same temperature but at very low pressure. The internal energy of this ideal gas is denoted by  $U^*$ , and its specific volume is very large since the pressure is low. Thus, Eq. 9.28 can be integrated according to

$$U^* - U = \int_v^\infty \left[ T \left( \frac{\partial p}{\partial T} \right)_v - p \right] dv \quad (9.29)$$

where the subscript  $T$  on the integrand indicates that the integration is to be carried out using  $p$  and  $v$  values along an isotherm of specified  $T$ .

Equation 9.29 can be transformed into reduced thermodynamic parameters by multiplying and dividing by the critical compressibility factor of Eq. 9.13, which yields

$$\frac{U^* - U}{T_c} = R z_c \int_{v_r}^\infty \left[ T_r \left( \frac{\partial p_r}{\partial T_r} \right)_{v_r} - p_r \right]_{T_r} dv_r \quad (9.30)$$

The entire right-hand side of Eq. 9.30 can be obtained from the reduced equation of state, such as the one shown in Fig. 9.1. Tables and graphs of  $(U^* - U)/T_c$  vs.  $T_r$  and  $p_r$ , such as the one shown in Fig. 9.6, can be constructed.

Figure 9.6 does not give the internal energy as a function of pressure and temperature even if all critical constants are known. Rather it gives the internal energy excess,  $U^* - U$ . To get  $U$ , we must know the internal energy of the substance if it were an ideal gas at the same temperature. Since the energy is relative to a reference state, we need to choose the latter as well. Suppose we select a reference temperature  $T_0$  where the internal energy of the hypothetical ideal gas is, by definition, zero. In proceeding from  $T_0$  to  $T$ , the internal energy of the ideal gas increases to

$$U^* = C_v(T - T_0) \quad (9.31)$$

If Eq. 9.31 is used for  $U^*$ , the internal energy of the compressed state  $U$  is referred to the same state at  $T_0$ . This simple thermodynamic relationship is shown in Fig. 9.7.

The specific heat of gaseous UO<sub>2</sub> consists of components due to translation, rotation, vibration, and

electronic excitation of the molecule. The last is negligible even at temperatures well above the critical temperature. Classical thermodynamics requires that each degree of freedom that the molecule possesses contributes  $R/2$  to the molar specific heat. The three degrees of translational motion supply  $3R/2$  units of specific heat. Assuming that the spatial configuration of the  $UO_2$  molecule in the ideal gas phase is linear, there is one mode of rotation for each of the principal axes perpendicular to the molecular axis (see Fig. 9.8). Rotation of the linear molecule contributes  $R$  to the specific heat.

Each degree of vibrational freedom provides  $R$  units of specific heat ( $R/2$  from the potential energy and  $R/2$  from the kinetic energy of vibration). For a linear triatomic molecule such as  $UO_2$ , there are four independent modes of vibration. As shown in Fig. 9.8, two represent vibrations of the oxygen-uranium bonds along the molecular axis, and two are bending vibrations of the end oxygen atoms relative

to the central uranium atom. Internal vibration of the three atoms in  $UO_2$  contributes  $4R$  to the specific heat. The total specific heat of an ideal gas of  $UO_2$  (assuming the molecules to be linear) is

$$C_v = \frac{3R}{2} + R + 4R = \frac{13R}{2} \quad (9.32)$$

Having calculated  $C_v$  and hence  $U^*$  by Eq. 9.31, we can determine thermodynamic state from plots such as Fig. 9.6 (appropriate to the assumed value of  $z_c$ ). From this information, graphs of  $T(U,v)$  and  $p(U,v)$ , such as those shown in Figs. 9.9 and 9.10, can be constructed. The vapor regions are not shown on these plots since only the two phase and compressed liquid regions are important in the fuel meltdown analysis. The reference state in these plots is the saturated liquid at  $273^\circ K$ , which differs in energy from the ideal gas at the same temperature by the energy of vaporization.

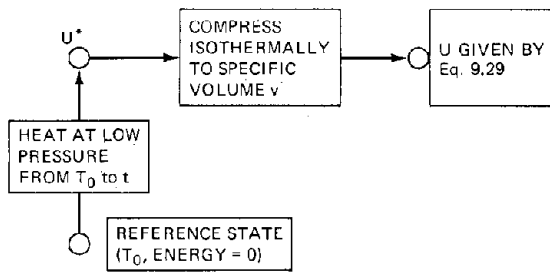


Fig. 9.7 Relationship between the reference, ideal-gas, and actual states.

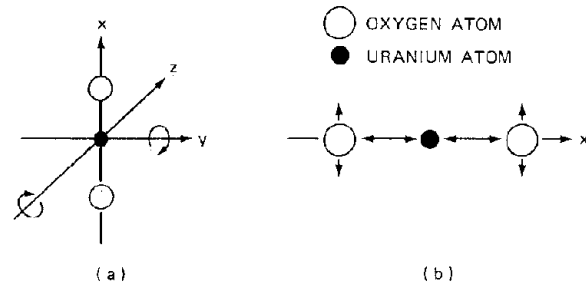


Fig. 9.8 Rotational and vibrational degrees of freedom of the linear  $UO_2$  molecule. (a) Rotation. (b) Vibration.

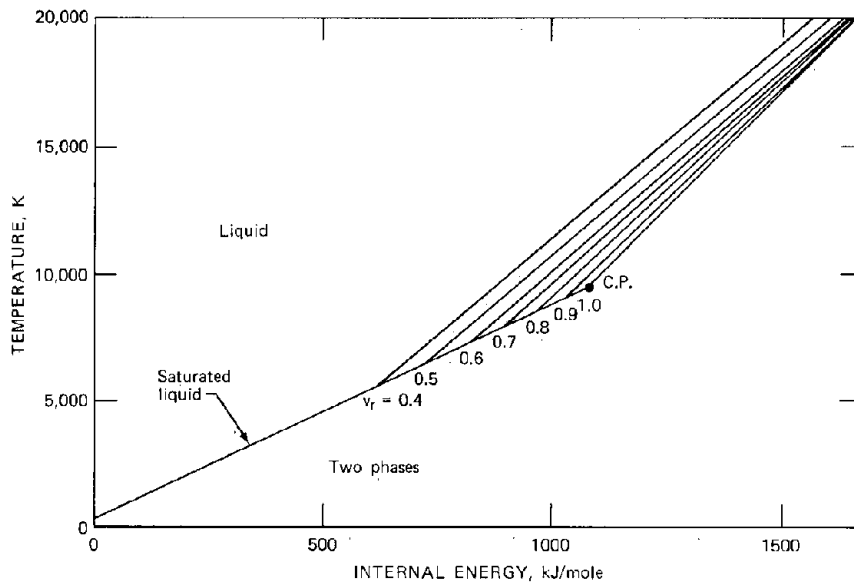


Fig. 9.9 The  $T(U,v)$  plot for  $UO_2$ , based on the theory of corresponding states with  $T_0 = 8000^\circ K$ ,  $p_c = 2000$  atm,  $v_c = 90$   $cm^3/mole$ , and  $C_v = 6.5R$ . Reference state: saturated liquid at  $273^\circ K$ . (Based on Ref. 4.)

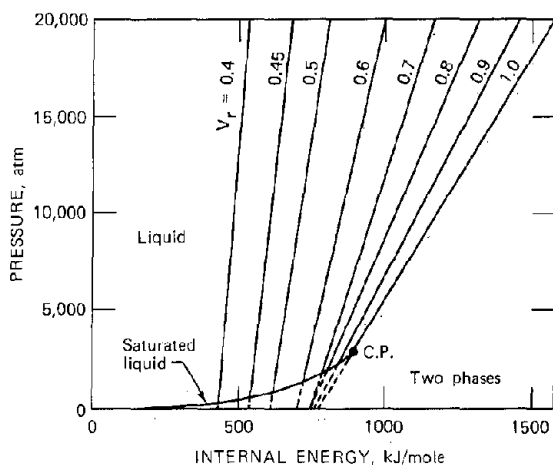


Fig. 9.10 The  $p(U,v)$  plot for  $\text{UO}_2$  based on the theory of corresponding states with  $T_c = 8000^\circ\text{K}$ ,  $p_c = 2000$  atm,  $v_c = 90$  cm<sup>3</sup>/mole, and  $C_v = 6.5R$ . Reference state: saturated liquid at  $273^\circ\text{K}$  (Based on Ref. 4.)

## 9.6 INTERPRETATION OF THE CORRESPONDING-STATES PLOTS FOR $\text{UO}_2$

Figures 9.9 and 9.10 rely entirely on the applicability of the theory of corresponding states to  $\text{UO}_2$ . The only physical properties of  $\text{UO}_2$  required for the construction of these plots are the critical constants and the specific heat at constant volume of gaseous  $\text{UO}_2$ . To assess the reliability of this approach, we examine the corresponding-states plots in light of other methods of predicting partial thermodynamic data. The following comments are based primarily on the discussion presented by Robbins.<sup>9</sup>

### 9.6.1 Two-Phase Region

Each of the members of the family of lines in Figs. 9.9 and 9.10 describes the variation of the temperature or pressure of  $\text{UO}_2$  for a particular specific volume as the internal energy changes. The most striking feature of these two plots is that the constant-volume lines all merge into a single line when two phases are present. This means that the internal energy of a two-phase mixture is independent of the specific volume (or, equivalently, independent of vapor fraction or quality) and that the internal energy of the two-phase mixture is essentially equal to the internal energy of the liquid phase.

To examine this behavior in detail, we consider  $U$  to represent the internal energy of 1 mole of  $\text{UO}_2$ , whether liquid, vapor, or both. In the two-phase region,  $U$  may be expressed as

$$U = x_1 U_1 + (1 - x_1) U_g \quad (9.33)$$

where  $x_1$  is the mole fraction of liquid in the two-phase mixture and  $U_1$  and  $U_g$  are the internal energies per mole of the liquid and vapor phases, respectively. Each of the reduced volumes shown in Figs. 9.9 and 9.10 corresponds to a particular liquid mole fraction (see problem 9.4). Even

though  $U_g$  is larger than  $U_1$ ,  $x_1$  is so close to unity that Eq. 9.33 reduces to

$$U \approx U_1 \quad (9.34)$$

Thus  $U$  does not depend on the specific volume or quality of the two-phase mixture.

The saturated-liquid portion of Fig. 9.9 is a straight line. An estimate of its slope can be obtained by considering Eq. 9.27. According to the previous argument, the quantities  $U$ ,  $C_p$ , and  $v$  in this equation may be considered to represent those of the liquid only. Hence,

$$\begin{aligned} \left(\frac{dU}{dT}\right)_s &\approx \left(\frac{dU_1}{dT}\right)_s \\ &= C_{p1} - T \left(\frac{dv_1}{dT}\right)_p \left(\frac{dp_s}{dT}\right) - p_s \left(\frac{dv_1}{dT}\right)_s \end{aligned} \quad (9.35)$$

where the subscript  $s$  indicates that the properties follow the saturation line. The slope of the saturated-liquid line in Fig. 9.9 is the reciprocal of Eq. 9.35. If the relative magnitudes of the three terms on the right-hand side of this equation are examined, we find that the last two are very much smaller than  $C_{p1}$  over the entire temperature range up to the critical point. Therefore, the slope of the saturated liquid line in Fig. 9.9 should be  $1/C_{p1}$ . The slope corresponds to  $C_{p1} = 120$  kJ mole<sup>-1</sup> °K<sup>-1</sup>, compared to the measured heat capacity at constant pressure<sup>5</sup> of 138 kJ mole<sup>-1</sup> °K<sup>-1</sup>. In this particular aspect the corresponding-states prediction agrees with independent measurements.

The saturated-liquid line in the  $p(U,v)$  plot represented by Fig. 9.10 is obtained from the corresponding line on Fig. 9.9 and the vapor-pressure curve of Fig. 9.4. Here again, agreement is satisfactory (that is, within a factor of about 2).

### 9.6.2 Compressed-Liquid Region

As the internal energy of the two-phase mixture is increased at constant volume, the liquid density decreases and the void space becomes smaller. Consider an initial state at low temperature and of an overall density less than the liquid-density curve in Fig. 9.8. The constant-volume heating of the two-phase mixture moves the system horizontally on Fig. 9.3 until the density of the pure liquid equals that of the initial state. At this point the system becomes a single liquid phase. Further increase of internal energy results in temperature increases given by

$$\left(\frac{\partial T}{\partial U_1}\right)_v = \frac{1}{C_{v1}} \quad (9.36)$$

which is simply the definition of the heat capacity at constant volume of liquid  $\text{UO}_2$ . That the lines in the liquid region of Fig. 9.9 are straight (more or less) indicates that  $C_{v1}$  is almost independent of temperature. The slopes of these lines are greater than the slope of the saturated-liquid line, which implies that  $C_{p1} > C_{v1}$ . The slopes of the single-phase lines approach the slope of the saturated-liquid line as the specific volume is decreased, since under normal conditions  $C_{p1}$  and  $C_{v1}$  differ by very little.

The equation describing the constant-volume lines in the compressed-liquid region of Fig. 9.10 is based on the assumption that the quantity

$$\frac{1}{v} \left( \frac{\partial U}{\partial v} \right)_v = \frac{1}{\gamma} \quad (9.37)$$

is independent of temperature. The Grüneisen constant  $\gamma$ , defined by Eq. 9.37, is in general a function of specific volume. It normally has a value of about 2. In problem 9.5,  $\gamma$  is found to be related to the coefficients of thermal expansion and compressibility by

$$\gamma = \frac{\alpha v}{\beta C_v} \quad (9.38)$$

where  $\alpha$  is the coefficient of thermal expansion (Eq. 9.15) and  $\beta$  is the coefficient of compressibility:

$$\beta = -\frac{1}{v} \left( \frac{\partial v}{\partial p} \right)_T \quad (9.39)$$

Integrating Eq. 9.37 at constant specific volume from a hypothetical liquid at  $0^\circ\text{K}$  yields

$$U - E_0 = \frac{v}{\gamma} (p - p_0) \quad (9.40)$$

where the subscript 0 indicates the state of the liquid at  $0^\circ\text{K}$  and at the specific volume under consideration,  $p_0$  is the pressure required for equilibrium at  $T = 0^\circ\text{K}$  and specific volume  $v$ , and  $E_0$  is the ground-state energy of the system, as used previously for a solid.

The pressure at  $0^\circ\text{K}$  (sometimes called the cohesive pressure) is given by Eq. 1.55; so

$$p_0 = -\left( \frac{\partial U}{\partial v} \right)_{T=0} = -\frac{dE_0}{dv} \quad (9.41)$$

Combining Eqs. 9.40 and 9.41 yields the Grüneisen equation of state:

$$p = -\frac{dE_0}{dv} + \frac{\gamma}{v} (U - E_0) \quad (9.42)$$

Note that the Debye equation of state, Eq. 2.40, is equivalent to the Grüneisen equation of state, Eq. 9.42, if the Grüneisen constant  $\gamma$  is identified with  $-(v/\theta_D)(d\theta_D/dv)$ .

According to Eq. 9.41, the slopes of the constant volume lines in Fig. 9.10 should be

$$\frac{\gamma}{v} = \frac{\alpha}{\beta C_v}$$

Using low-temperature measurements of  $\alpha$  and  $\beta$  on solid  $\text{UO}_2$ ,  $\gamma/v$  is calculated to be  $1200 \text{ atm kJ}^{-1} \text{ mole}^{-1}$ . The slopes of the corresponding-states plots of Fig. 9.10 increase as the reduced volume becomes smaller. At  $v_r = 0.4$ , the slope is  $\sim 240 \text{ atm kJ}^{-1} \text{ mole}^{-1}$ , which is of the correct order of magnitude.

When extrapolated to zero pressure, the constant-volume lines in the compressed-liquid region of Fig. 9.10 intersect the abscissa at an internal energy that we shall

denote by  $Q^*$ . The states in the region where the lines are dashed actually consist of two phases rather than a compressed liquid. However, since the pressures along the saturation line are small compared to those which can be generated in the compressed-liquid region, the pressure can be approximated by zero up to  $U = Q^*$  and

$$p = \frac{\gamma}{v} (U - Q^*) \quad (9.43)$$

for  $U > Q^*$ . A threshold equation of state of this type was used in the original analysis of the meltdown accident by Bethe and Tait.<sup>1</sup>

In view of the substantial uncertainty in the critical constants of  $\text{UO}_2$ , the equation of state of this crucial nuclear fuel is at best of semiquantitative value only. Indeed, the applicability of the theory of corresponding states based on ordinary fluids to a member of a class of exotic fluids (molten oxides) which is not even represented in the original correlation is in the very least an act of faith. Nevertheless, some estimate of the equation of state of  $\text{UO}_2$  at high pressures and high temperatures is essential for assessment of fast reactor safety, and the corresponding-states method does provide a complete set of thermodynamic properties that are generally consistent with other measurements on  $\text{UO}_2$  at much lower temperatures.

## 9.7 NOMENCLATURE

- C = specific heat
- E = internal energy
- $E_p$  = potential energy of N-particle system
- F = Helmholtz free energy
- f,g,h = universal functions for all fluids having the same intermolecular shape function
- h = Planck constant
- H = enthalpy
- $\Delta H$  = change in enthalpy (e.g., on vaporization)
- k = Boltzmann constant
- m = mass of a particle
- N = number of particles in a system
- p = pressure
- $Q_c$  = configurational partition function
- $Q^*$  = internal energy of the hypothetical fluid at very low pressure
- r = distance between particles in an N-particle system
- R = gas constant
- S = entropy
- $\Delta S$  = change in entropy (e.g., on vaporization)
- T = temperature
- U = internal energy
- v = specific volume
- V = volume
- x = mole fraction in a two-phase mixture
- z = (critical) compressibility factor; single-particle partition function
- Z = partition function
- $Z^*$  = ideal-gas partition function

### Greek Letters

- $\alpha$  = coefficient of thermal expansion
- $\beta$  = compressibility

- $\gamma$  = Grüneisen constant  
 $c$  = minimum potential energy between particles  
 $\phi$  = potential energy of a pair of particles  
 $\psi$  = shape function for intermolecular potential  
 $\sigma$  = distance between particles corresponding to minimum potential energy  
 $\theta_D$  = Debye temperature

**Subscripts**

- $c$  = value corresponding to the critical state  
 $f$  = fusion  
 $g$  = gaseous state  
 $gr$  = reduced value of a property (of gaseous state)  
 $i$  = particle  $i$   
 $ij$  = between particles  $i$  and  $j$   
 $int$  = internal-energy component  
 $j$  = particle  $j$   
 $l$  = liquid state  
 $lr$  = reduced value of a property (of liquid state)  
 $p$  = at constant pressure  
 $pl$  = at constant pressure (of liquid phase)  
 $r$  = reduced value  
 $rs$  = reduced value of saturated condition (e.g., vapor pressure)  
 $s$  = saturation or saturated condition  
 $v$  = at constant volume  
 $vap$  = vaporization  
 $vl$  = at constant volume (of liquid phase)  
 $0$  = state of the liquid at  $0^\circ K$  and same specific volume

**Superscripts**

- $0$  = extrapolated to  $0^\circ K$   
 $*$  = hypothetical ideal gas

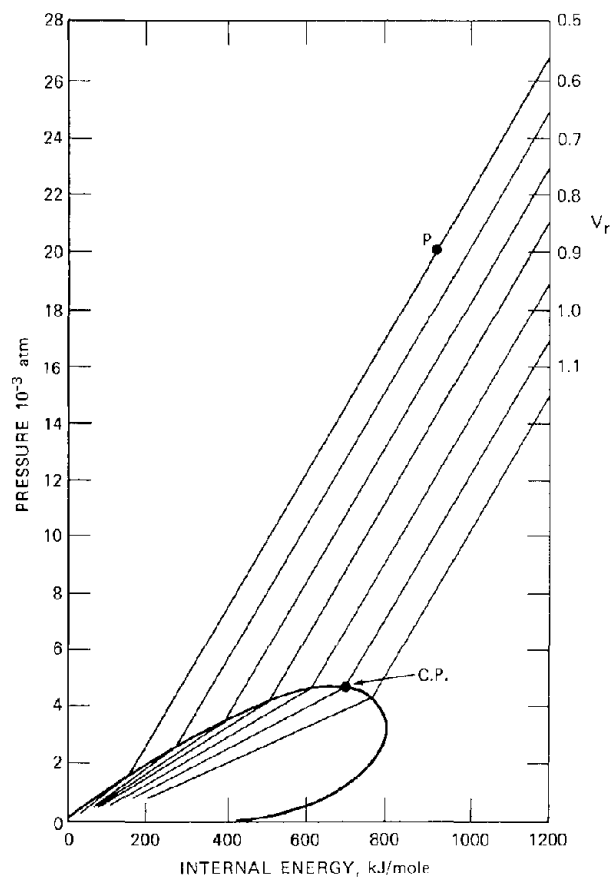
**9.8 REFERENCES**

1. H. A. Bethe and J. H. Tait, An Estimate of the Order of Magnitude of the Explosion When the Core of a Fast Reactor Collapses, British Report RHM(56)/113, 1956.
2. O. A. Hougen, K. M. Watson, and R. A. Ragatz, *Chemical Process Principles*, Part II, 2nd ed., Chap. 14, John Wiley & Sons, Inc., New York, 1959.
3. J. S. Christensen, Thermal Expansion and Change in Volume of Uranium Dioxide on Melting, *J. Amer. Ceram. Soc.*, 46: 607 (1963).
4. D. C. Menzies, The Equation of State of Uranium Dioxide at High Temperatures and Pressures, British TRG-Report-1119, Feb. 7, 1966.
5. R. A. Hein and P. N. Flagella, Enthalpy Measurements of  $UO_2$  and Tungsten to  $3260^\circ K$ , USAEC Report GEMP-578, General Electric Company, Feb. 16, 1968; Chemical Engineering Division Annual Report, 1969, USAEC Report ANL-7675, p. 89, Argonne National Laboratory, April 1970.
6. A. V. Grosse, The Temperature Range of Liquid Metals and an Estimate of Their Critical Constants, *J. Inorg. Nucl. Chem.*, 22: 23 (1961).
7. R. A. Meyer and B. E. Wolfe, High-Temperature Equation of State of Uranium Dioxide, *Trans. Amer. Nucl. Soc.*, 7: 111 (1964).
8. D. Miller, A Critical Review of the Properties of Materials at the High Temperatures and Pressures Significant for Fast Reactor Safety, USAEC Report ANL-7120, p. 641, Argonne National Laboratory, 1965.

9. E. J. Robbins, Limits of the Equation of State of Uranium Dioxide, British TRG-Report-1344 Oct. 6, 1966.

**9.9 PROBLEMS**

9.1 The accompanying illustration is a graph of the equation of state of a nuclear fuel material at high temperature and pressure. The specific volume at the critical temperature and pressure is  $414 \text{ cm}^3/\text{mole}$ . Point P is the termination of a meltdown—reassembly nuclear excursion resulting from the hypothetical loss of coolant of a fast reactor. At point P the fuel has expanded slightly and



the fission heating is discontinued. The next process is expansion of the high-pressure material against the surroundings, resulting in a small explosion. The maximum possible explosive energy results from an isentropic (adiabatic, reversible, and constant-entropy) expansion. The path of the isentropic expansion can be traced on this diagram by using the first law of thermodynamics.

(a) Assume that a change in reduced volume from 0.5 to 0.6 is a good approximation for a differential volume change at a pressure of 20,000 atm. Calculate the isentropic change in internal energy and plot on the diagram.

(b) Use the idea of part a to sketch the path of the expansion down to a pressure of 1000 atm. A qualitative sketch is all that is needed here. Explain departures of the

path from a straight line. Explain any discontinuities in the slope of the path.

(c) Describe the physical state of the fluid at the end of the path at 1000 atm.

9.2 What is the constant-volume molar heat capacity at high temperature for gaseous  $\text{PuO}_2$  if the molecule is linear? What additional contribution results if the molecule is non-linear?

9.3 (a) The vapor pressure of a solid can be expressed by the relation

$$-RT \ln P_s^\circ = \Delta H_s - T \Delta S_s$$

where  $P_s^\circ$  is the vapor pressure of the solid,  $\Delta H_s$  is the heat of sublimation, and  $\Delta S_s$  is the entropy of sublimation. Above the melting point  $T_f$ , the liquid is the stable state, and the vapor pressure  $P_l^\circ$  can be expressed in the same form as that of the solid but with different heat and entropy values. If the heat of fusion is  $\Delta H_f$ , derive an expression for the vapor pressure of the liquid. Assume all enthalpy and entropy differences (i.e.,  $\Delta H_s$ ,  $\Delta S_s$ ,  $\Delta S_l$ , and  $\Delta H_l$ ) are temperature independent.

(b) Although the effect of total pressure on the properties of condensed phases is small, the change in the melting point of a solid when the pressure is increased to hundreds of atmospheres is measurable. If the melting point at 1 atm is  $T_{f1}$  and if the volume increase on melting,  $V_l - V_s = \Delta V_f$ , and the heat of fusion,  $\Delta H_f$ , are known, derive an expression for the change in the melting point with total pressure. Should the melting point increase or decrease with increasing pressure?

9.4 One mole of a saturated two-phase mixture of liquid and vapor  $\text{UO}_2$  at  $3100^\circ\text{K}$  is held in a  $60 \text{ cm}^3$  container.

(a) What are the volume and mole fractions of the liquid phase?

(b) Show that the total energy of the mixture is essentially equal to that of the liquid phase. Take the latent heat of vaporization of  $\text{UO}_2$  to be  $500 \text{ kJ/mole}$ .

(c) Show that  $(dU/dT)_s$  is very closely equal to the heat capacity of the liquid phase.

9.5 Prove that the Grüneisen constant defined by Eq. 9.37 is related to other thermodynamic quantities according to Eq. 9.38. Use the results of problem 1.5 where necessary.

# Chapter 10

## Fuel-Element Thermal Performance

### 10.1 COMPARISON OF WATER REACTORS AND FAST OXIDE REACTORS

A sound understanding of the factors that govern the temperature distribution within a reactor fuel element is essential to successful prediction of fuel performance over long periods of time and in an intense radiation field. The temperature distribution influences fuel performance in two important ways.

1. High temperatures (approaching the melting temperature,  $\sim 2800^\circ\text{C}$ ): Solid-state reactions that would be immeasurably slow at lower temperatures proceed at rates sufficient to produce significant changes in material properties during the lifetime of the fuel in the reactor. Phenomena primarily affected by high operating temperatures include grain growth, densification (sintering), and fission-product diffusion.

2. Steep temperature gradients (approaching  $10^4^\circ\text{C/cm}$ ): A variety of unexpected phenomena are driven by the temperature gradient. Closed pores migrate from low-temperature regions toward the center of the fuel pin; important constituents of the fuel, such as oxygen, plutonium, and fission products, are redistributed from their initial concentration profiles (which are usually uniform); thermal stresses resulting from the temperature gradient cause the fuel to either deform plastically in regions of high temperature or to crack in low-temperature zones.

#### 10.1.1 Oxide Fuels

This chapter deals with those physical properties of uranium dioxide and mixed uranium-plutonium dioxide fuels which are important in determining the temperature distribution under irradiation. Methods of calculating the temperature profile in cylindrical fuel elements are also discussed.

Because of the nearly exclusive use of uranium dioxide in light-water-moderated reactors (LWR) and the commitment to use mixed oxides in the first liquid-metal fast breeder reactors (LMFBR), other potential fuel materials will not be considered here. Ever since the decision to use  $\text{UO}_2$  as the fuel for the Shippingport pressurized-water reactor (PWR) was made in 1955, a vast amount of information on the behavior of this material under reactor

conditions has been obtained. The plutonium produced by irradiation in slightly enriched  $\text{UO}_2$  reactor cores can be mixed with  $\text{UO}_2$  for refueling LWRs. The fuel for the first large LMFBRs will be a mixture of uranium and plutonium oxides. Consequently, the thermal properties of  $(\text{U,Pu})\text{O}_2$  have recently been the subject of intensive study.

Oxide fuels have demonstrated very satisfactory dimensional and radiation stability and chemical compatibility with cladding metals and coolant in light-water reactor service. Under the much more severe conditions in a fast reactor, however, even as inert a material as  $\text{UO}_2$  begins to respond to its environment in a manner that is often detrimental to fuel performance.

Although the fuel used in thermal reactors is pure  $\text{UO}_2$ , mixtures of uranium and plutonium oxides are to be used in the fast reactors. The oxygen-to-metal ratio of the uranium dioxide for thermal reactors is nearly exactly 2.00. The mixed-oxide fuel for fast reactor use, however, will be purposely fabricated with a deficiency of oxygen.

The thermal, chemical, physical, and mechanical properties of the mixed uranium-plutonium oxides depend on two composition variables, which are denoted

$$q = \frac{\text{atoms Pu}}{\text{total heavy-metal atoms}}$$

$$x = \frac{\text{oxygen atom excess or deficiency}}{\text{total heavy-metal atoms}}$$

The chemical formula of the nonstoichiometric mixed oxide is  $(\text{U}_{1-q}\text{Pu}_q)\text{O}_{2\pm x}$ . When the oxygen-to-metal ratio (hereafter denoted O/M) is larger than 2, the plus sign is used in the formula. Such material is said to be hyperstoichiometric. When  $\text{O/M} < 2$ , the minus sign is used in the formula, and the material is hypostoichiometric.

The major disadvantages of oxide fuels that have prompted the investigation of other fuel materials are its low uranium density and low thermal conductivity. The low density of uranium atoms in  $\text{UO}_2$  requires a larger core for a given amount of fissile species than if a fuel of higher uranium density were used. Increase in reactor size with no increase in power raises the capital cost of the reactor.

Poor thermal conductivity means that the center-line temperature of the fuel and the temperature difference between the center and the surface of the rod must be very

large in order that sufficient fission heat be extracted from a unit of fuel to make electric power production economical. On the other hand, central fuel temperatures close to the melting point have a beneficial fission-product scouring effect on the fuel. At temperatures greater than about 1800°C, oxide fuels release practically all the volatile fission products, which then enter the gas phase as rapidly as they are formed. Their removal from the solid greatly alleviates the swelling of the fuel, which in turn reduces the tendency of the fuel element to fail by overstressing the cladding.

Uranium metal, which is far superior to UO<sub>2</sub> in these regards, unfortunately changes its crystallographic state at the rather low temperature of 660°C. This phase change is accompanied by a substantial volume change, which would severely impair the integrity of fuel elements thermally cycled through the transition temperature. Consequently, metallic uranium is not used in current power reactors.

Many refractory compounds of uranium, such as uranium carbide, uranium nitride, uranium sulfide, and uranium phosphide, possess higher thermal conductivity and uranium density than uranium dioxide. However, other characteristics of these fuels, particularly fission-gas retention, compatibility with cladding, or swelling under irradiation, are either inferior to those of the oxide or are not reliably established. These fuels may be employed in later fast reactors.

### 10.1.2 Measures of Fission Rate and Total Fissions

The temperature distribution in a fuel rod is controlled by the rate of heat release by fission. Many properties of the fuel are affected by the cumulative number of fissions that have occurred during the period of time that the fuel element has been in the core.

The fission rate per unit volume is given by

$$\dot{F} = q\sigma_f N_f \Phi \quad \text{fissions cm}^{-3} \text{ sec}^{-1} \quad (10.1)$$

where  $q$  = enrichment, or the ratio of fissile atoms to total heavy-metal atoms (U + Pu)

$\sigma_f$  = effective fission cross section for the fissile species in the appropriate neutron-energy spectrum

$N_f$  = total number of heavy-metal atoms per unit volume

$\Phi$  = neutron flux

The effective fission cross section depends on the average neutron-energy spectrum as well as on the fissile species. The average neutron energy in the LWR spectrum is ~0.03 eV, and that of a LMFBR is ~0.5 MeV. In light-water reactors, <sup>235</sup>U is generally the fissile species. The fission cross section of this nuclide in a thermal-neutron spectrum is ~550 barns. The fissile species <sup>239</sup>Pu has a fission cross section of ~1.8 barns in the harder spectrum of a fast reactor.\*

\*In a fast reactor <sup>238</sup>U may contribute some 10 to 20% of the fissions. The fission cross section of this nuclide exhibits a threshold at 1.5 MeV. From 1.5 to 6 MeV the average fission cross section of <sup>238</sup>U is 1.5 barns.

The density of uranium atoms in UO<sub>2</sub>, which is 90% of theoretical density (TD = 10.98 g/cm<sup>3</sup>), is

$$N_f = \frac{(0.9)(10.98)(6 \times 10^{23})}{270} \\ = 2.2 \times 10^{22} \text{ atoms/cm}^3$$

The total atom density of heavy metals (U + Pu) in fast reactor fuel is approximately the same as the uranium-atom density in pure UO<sub>2</sub>.

In thermal reactors the amount of <sup>235</sup>U decreases as irradiation proceeds, and the fissile species <sup>239</sup>Pu and <sup>241</sup>Pu are produced. Although the total heavy-metal concentration is inexorably reduced by fission and the composition of the heavy elements in the fuel is continually changing, the product  $q\sigma_f N_f$  (which contains contributions from all plutonium isotopes) is not greatly different from the value for fresh fuel.

During irradiation of fast reactor fuel, the concentration of <sup>239</sup>Pu decreases less rapidly than that of <sup>238</sup>U; thus, the plutonium-to-uranium ratio increases. In the core of a fast reactor, <sup>239</sup>Pu is produced by neutron capture in <sup>238</sup>U at nearly the same rate as it is consumed by fission. (If the blanket of a fast reactor is included, more <sup>239</sup>Pu is produced than is consumed; that is, the reactor breeds plutonium.)

There are three common measures of the integrated irradiation to which fuel material has been subjected:

1. The fission density is given by

$$F = \dot{F}t \quad \text{fissions/cm}^3 \quad (10.2)$$

If the neutron flux varies with time,  $F$  is the integral of  $\dot{F}$ .

2. The fractional *burnup* is defined by

$$\beta = \frac{\text{number of fissions}}{\text{initial number of heavy-metal atoms}} \quad (10.3)$$

The quantity  $\beta$  is sometimes referred to as FIMA (fissions per initial metal atom). The atom fraction fissioned can also be expressed by

$$\beta = \frac{F}{N_f^0} \quad (10.4)$$

where  $N_f^0$  is the initial density of heavy-metal atoms in the fuel. If the breeding ratio is unity,  $qN_f$  in Eq. 10.1 can be approximated by  $q_0 N_f^0$ , and Eq. 10.4 can be written

$$\beta = q_0 \sigma_f \Phi t \quad (10.5)$$

The term  $\Phi t$  in Eq. 10.5 is often called the *fluence*. When referred to the fast flux, it is a useful measure of damage-producing exposure in nonfuel components, such as the cladding.

3. Burnup can also be expressed as the number of megawatt days of thermal energy released by fuel containing 1 metric ton (10<sup>6</sup> g) of heavy-metal atoms (MWd/MTU). This unit is often called the exposure. The ~200 MeV of recoverable energy released by a single fission event corresponds to 0.95 MWd per gram fissioned. The exposure is:

$$\frac{0.95 \text{ MWd}}{\text{g fissioned}} \times \frac{\beta \text{ g fissioned}}{\text{g heavy-metal atoms}} \times \frac{10^6 \text{ g}}{\text{metric ton}}$$

$$= 9.5 \times 10^5 \beta \frac{\text{MWd(t)}}{\text{metric ton}} \quad (10.6)$$

As a working rule-of-thumb, 1 at.% burnup is approximately equal to  $10^4$  MWd/MTU.

### 10.1.3 Difference Between Thermal and Fast Reactors

A summary of a few performance characteristics of typical thermal and fast reactors is given in Table 10.1.

Table 10.1 Comparison of Typical 1000-Mw(e) Oxide Reactors

	LWR	LMFBR
Fissile species enrichment	3% $^{235}\text{U}$ in $^{238}\text{U}$	15% $^{239}\text{Pu}$ in $^{238}\text{U}$
$\sigma_f$ , barns	550	1.8
Core-averaged neutron flux, $\text{n cm}^{-2} \text{sec}^{-1}$		
Thermal	$3 \times 10^{13}$	$1 \times 10^{11}$
Fast (>0.2 MeV)	$5 \times 10^{13}$	$8 \times 10^{15}$
Burnup, %	3	10
Fast fluence, $\text{n/cm}^2$	$3 \times 10^{21}$	$3 \times 10^{23}$
Irradiation time (at full power), years	2	1.5

Several differences are evident.

1. The flux in the fast reactor is a factor of 100 larger than that in the thermal reactor. This large increase in neutron flux allows the fuel to produce more power per unit volume despite fission cross sections that differ by a factor of 300.

2. The average burnup is about three times as large in a fast reactor as it is in a thermal reactor. The higher burnup in the fast reactor is economically necessary to keep fuel fabrication, reprocessing, and out-of-reactor inventory charges to a minimum. Damage to the fuel and alteration of its properties are more severe in a fast reactor than in a thermal reactor (damage depends on temperature as well).

3. The fast-neutron fluence in a fast reactor is ~100 times greater than in a thermal reactor. Since the fast fluence is primarily responsible for radiation damage to nonfuel components, it is not surprising that the assurance of the integrity of the core structural members is a much more severe problem in fast reactors than in thermal reactors.

Figures 10.1 and 10.2 show the fuel-pin design of a typical current pressurized-water reactor and the Fast Test Reactor (FTR), respectively. Figures 10.3 and 10.4 show the fuel element assemblies for the pressurized-water reactor and a proposed fast oxide reactor. Table 10.2 gives some of the characteristics of the fuel elements. A

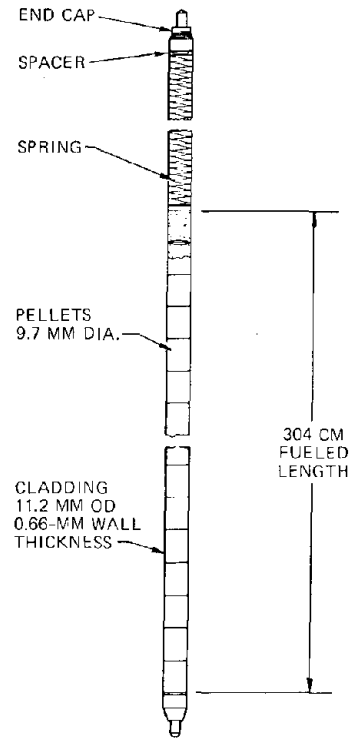


Fig. 10.1 Fuel rod of a pressurized-water reactor.

1000-Mw(e) LMFBR contains about 100,000 fuel elements of the type shown in Fig. 10.2. Several tons of plutonium are contained in the core.

The maximum fuel center-line temperature in a fast reactor is set at the melting point of the fuel. Requiring that the fuel temperature never exceed this value is the limiting factor in the power of a fast reactor. In a water-moderated reactor, the maximum fuel temperature is less than the melting temperature by several hundred degrees. At steady state the power-limiting condition is determined by the change from nucleate to film boiling at the cladding surface.\* Heat transfer through a vapor blanket is considerably poorer than if the fluid adjacent to the cladding were primarily liquid. The occurrence of film boiling means that the fuel-element temperature must abruptly increase to drive the heat flux through the vapor film.

The fuel pins of a fast reactor are smaller in diameter than those of a thermal reactor primarily to provide adequate heat-transfer area per unit mass of fuel to accommodate the higher power density of an LMFBR. Comparison of the fuel assembly cross sections in Figs. 10.3 and 10.4 shows that the fuel pins occupy a larger portion of the available area in a fast reactor than in a thermal reactor. The larger fuel fraction in an LMFBR is a

\*The actual maximum linear power for LWRs is determined by the maximum fuel temperature attained in a loss-of-coolant accident.

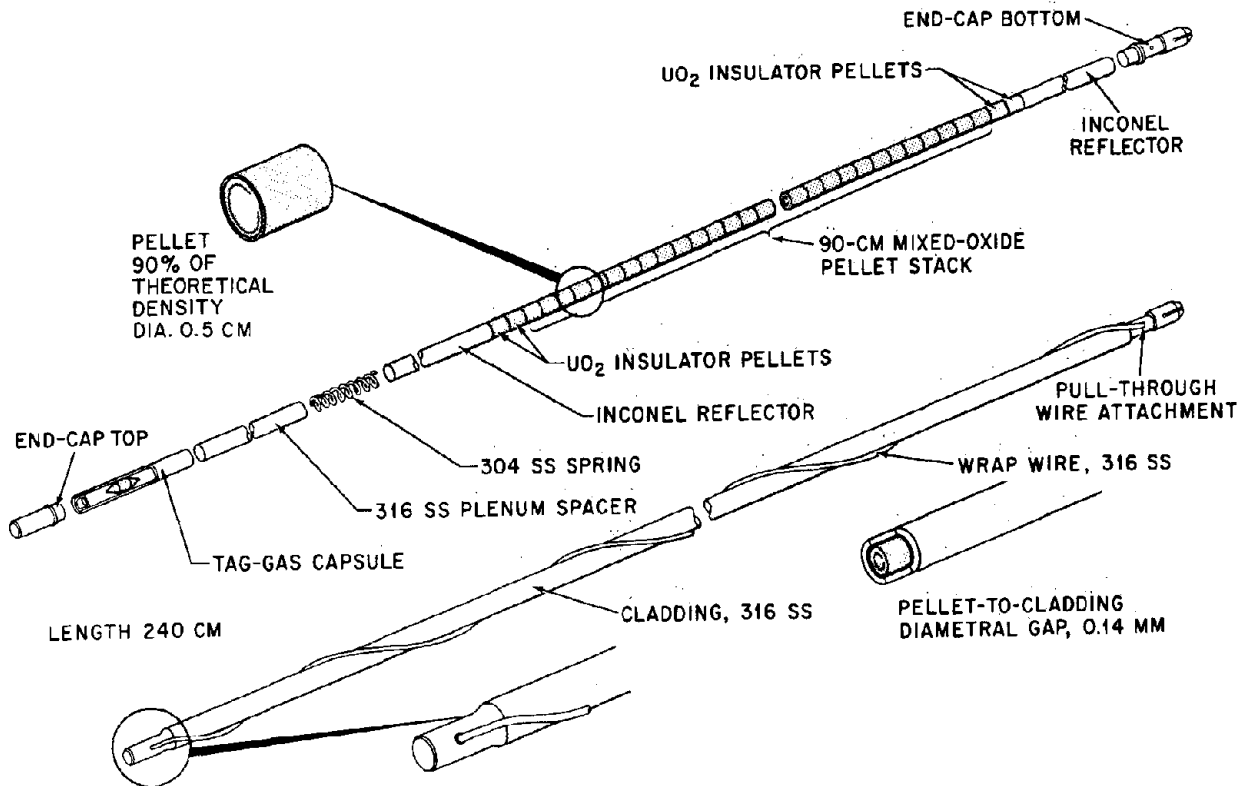


Fig. 10.2 Fuel pin of the Fast Test Reactor. (Courtesy C. Burgess, Hanford Engineering Development Laboratory.)

consequence of eliminating the moderator in fast reactors. In LWRs the water serves both as coolant and as moderator, and the ratio of fuel to water is dictated by the requirements of the latter function. In LMFBRs, on the other hand, the sole purpose of the sodium is to remove heat. In fact, the less sodium, the more efficient is the breeding.

The cladding in a fast reactor is considerably hotter than that in a thermal reactor. As a result, diminished strength and higher thermal creep rates of the thinner cladding in an LMFBR necessitate careful assessment and control of the internal loading of the cladding by fission-gas pressure and contact pressure by the fuel.

Table 10.2 shows that the linear power ratings of the fuel rods of thermal and fast reactors are approximately equal. Because the diameter of a fast reactor fuel pin is smaller than that of a thermal reactor fuel rod, the peak specific power (power per unit mass of fuel) is nearly 2.5 times larger in the fast reactor than in a thermal reactor. The impetus to design reactors of high specific power is to minimize the inventory of expensive enriched fuel and to reduce plant capital costs by making the reactor core as small as possible.

The active length of the fuel-containing portion of the fuel rods is very much smaller in the fast reactor than in a thermal reactor. The LMFBR fuel elements contain pellets of  $^{238}\text{UO}_2$  above and below the mixed-oxide fuel. These axial blanket regions improve overall breeding by capturing

neutrons leaking from the core. Fuel elements for fast reactors incorporate a large plenum region above the blanket for accumulating fission gases (primarily xenon and krypton). Thermal reactor fuel elements do not need such a large free space because the burnup is lower than that of a fast reactor and the lower level of fuel temperature improves the ability of the ceramic matrix to retain fission gases.

An excellent summary of the current status of fast oxide reactor fuel-pin thermal performance is given by Christensen.<sup>1</sup> Additional information concerning the core design of LMFBRs is given in Sec. 21.5.

## 10.2 THERMAL PROPERTIES OF OXIDE FUELS

### 10.2.1 Melting Point

The melting point of oxide fuel material is needed to define the limiting power of a fuel element.

A portion of the uranium-oxygen phase diagram is shown in Fig. 10.5. The melting point of stoichiometric  $\text{UO}_2$  is shown to be  $2865^\circ\text{C}$ , although other investigations have found that  $\text{UO}_2$  melts as low as  $2800^\circ\text{C}$ . Urania of this composition melts congruently (i.e., the liquid and the solid in equilibrium are of the same composition). The transformation temperatures of nonstoichiometric urania are

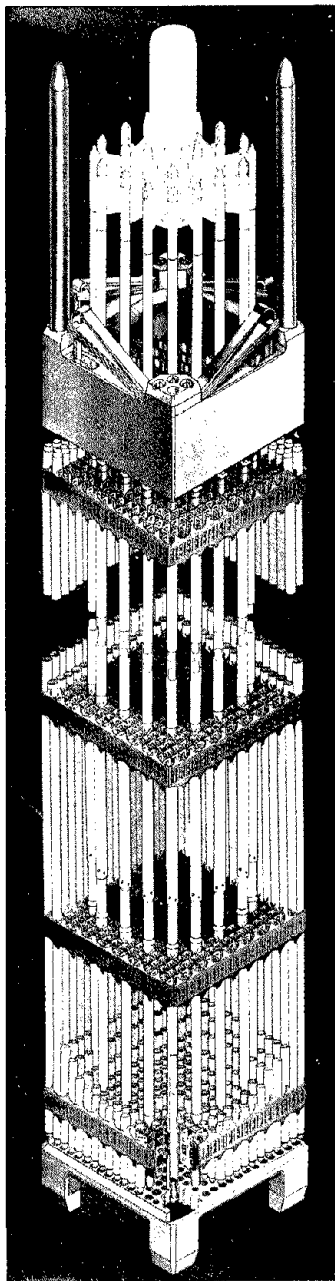


Fig. 10.3 Pressurized-water-reactor fuel assembly. (Courtesy Westinghouse Company.)

lower than that of  $UO_{2.00}$ . The liquidus curve in Fig. 10.5 refers to the temperature at which the first solid appears as the liquid cools. The solidus represents the temperature of the first sign of melting. The latter transformation temperature is loosely referred to as the melting point. It is this temperature which cannot be exceeded in reactor use. Nonstoichiometric urania does not melt congruently. For example, when  $UO_{1.95}$  first melts at  $2800^{\circ}C$ , the liquid phase composition is  $UO_{1.85}$ .

Mixtures of uranium and plutonium oxides melt at lower temperatures than pure urania. Since  $UO_2$  and  $PuO_2$

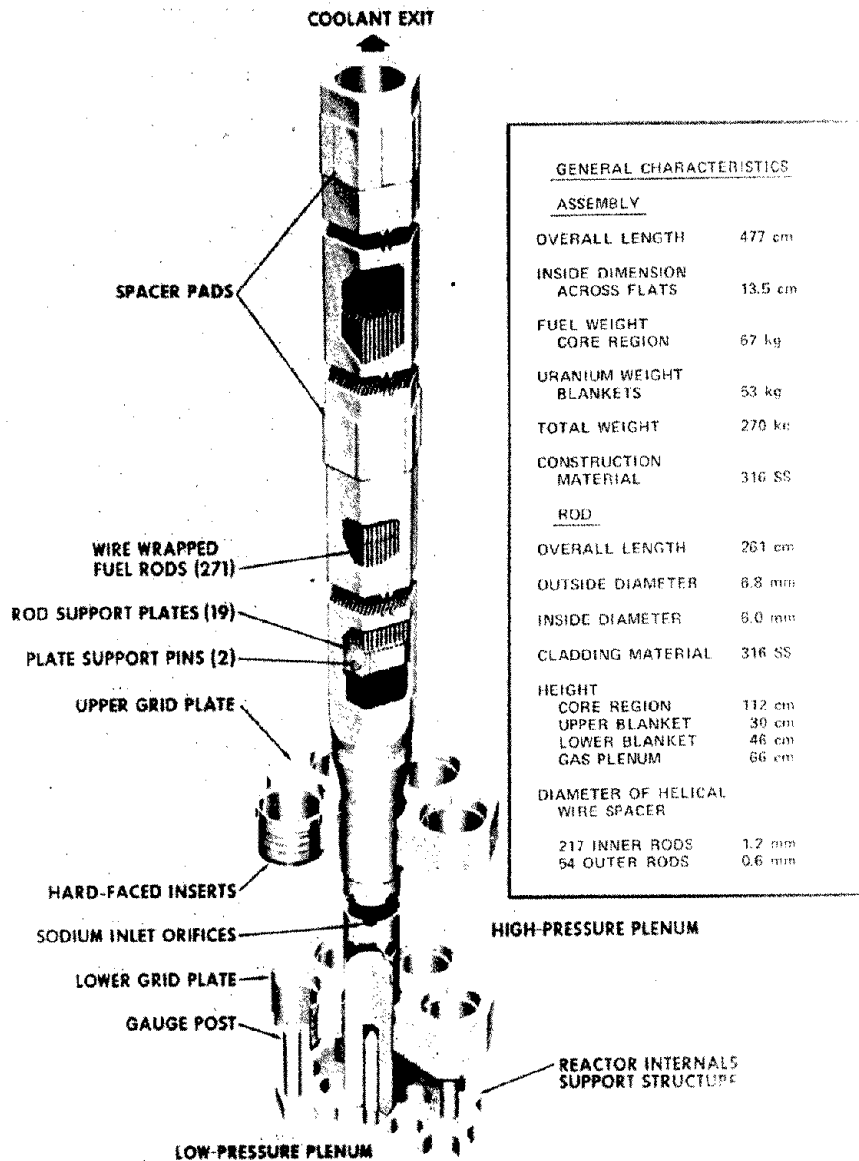


Fig. 10.4 LMFBR fuel assembly. (Courtesy L. Bernath, Atomics International.)

form nearly ideal solid solutions, the melting point of the mixture varies smoothly from that of  $UO_2$  to that of  $PuO_2$ . Figure 10.6 shows the liquidus curve for mixed oxides.

The effect of irradiation (and consequent buildup of fission-product impurities) on the melting point of  $(U,Pu)O_2$  is shown in Fig. 10.7.

### 10.2.2 Thermal Expansion

The difference between the coefficients of thermal expansion of the fuel and the cladding determines whether

Table 10.2 Fuel-Element Characteristics

	Thermal*	Fast
Fuel	UO <sub>2</sub>	(U,Pu)O <sub>1.96</sub>
Fuel-pellet density (% of theoretical)	92	90
Maximum fuel center- line temperature (overpower condi- tion), °C	2450	2800
Cladding	Zircaloy-4	316 stainless steel
Maximum cladding mid-wall temperature, °C	380	660
Coolant temperature rise, °C	H <sub>2</sub> O: 280-320	Na: 470-650
Maximum rod linear power, W/cm	620	550
Fuel assembly wrapper	Square, 20 X 20 cm	Hexagonal, 13 cm across flats
Number of fuel pins in assembly	200	220
Fuel-rod outside diameter, mm	10.7	6.3
Cladding thickness, mm	0.6	0.4
Initial fuel- cladding radial gap, mm	0.08	0.07
Length of fueled portion, cm	365	90

\*Preliminary Safety Analysis Report, Diablo Canyon Pressurized Water Reactor Unit 2, Vol. I, Pacific Gas and Electric Company.

the initial fuel-cladding gap (see Table 10.2) closes or opens when the fuel element is brought to power. If the initial gap is small and the fuel expands more than the cladding, the two come into contact. The resulting pressure at the interface is known as the contact or interfacial pressure. On the other hand, if the cladding expands more than the fuel and the gap is enlarged, heat conduction through the fuel-cladding gap will be low and the fuel temperature will be high because of the thermal resistance of the fuel-cladding gap.

The thermodynamic property of interest is related to the coefficient of thermal expansion, given by

$$\alpha = \frac{1}{V} \left( \frac{\partial V}{\partial T} \right)_p \quad (10.7)$$

Inasmuch as the solid volume  $V$  is very little affected by pressure unless  $p$  is quite large, the constant- $p$  restriction may be dropped. The coefficient of linear thermal expansion is given by

$$\alpha_{lin} = \frac{1}{l} \frac{dl}{dT} = \frac{\alpha}{3} \quad (10.8)$$

where  $l$  is the length of the solid specimen.

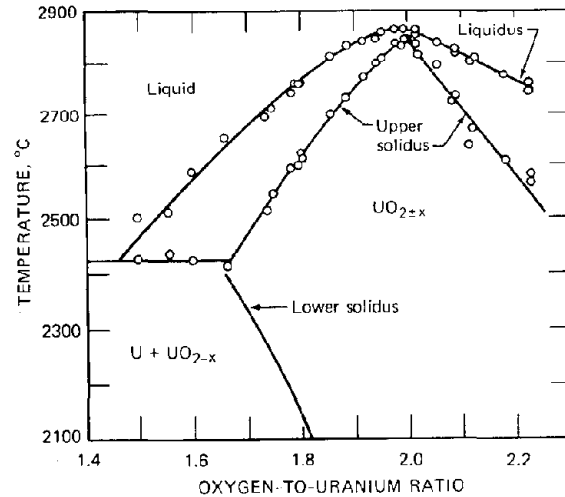


Fig. 10.5 Partial phase diagram for urania from UO<sub>1.5</sub> to UO<sub>2.23</sub>. The separation of the peaks of the liquidus and solidus curves at O/U = 2.0 is undoubtedly due to measurement errors. The UO<sub>2</sub> melts congruently; thus, the curves should coincide for UO<sub>2.0</sub>. Similarly, the lower solidus curve should intersect the corner of the upper solidus and horizontal lines. [From R. E. Latta and R. E. Fryxell, *J. Nucl. Mater.*, 35: 195 (1970).]

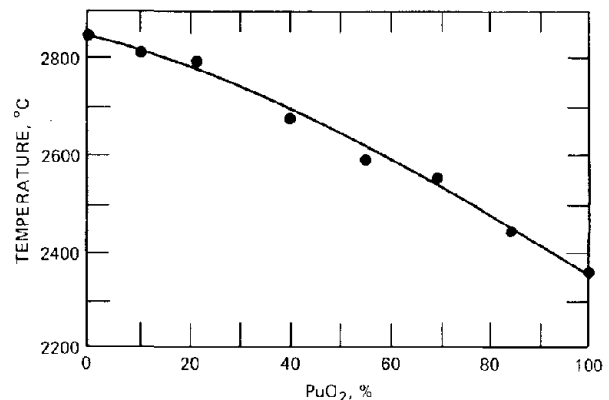


Fig. 10.6 Melting points of mixed uranium-plutonium oxides. (From E. L. Zebroski, W. L. Lyon, and W. E. Bailey, Effect of Stoichiometry on the Properties of Mixed Oxide U-Pu Fuel, in Proceedings of the Conference on Safety, Fuels, and Core Design in Large Fast Power Reactors, Oct. 11-14, 1965, USAEC Report ANL-7120, p. 382, Argonne National Laboratory, 1965.)

Most calculations use the average coefficient of linear expansion from 0°C to the temperature of interest. This quantity is defined as the fractional change in length per degree, or

$$\bar{\alpha}_{lin} = \frac{1}{T} \frac{\Delta l}{l_0} = \frac{1}{T} \int_0^T \alpha_{lin} dT \quad (10.9)$$

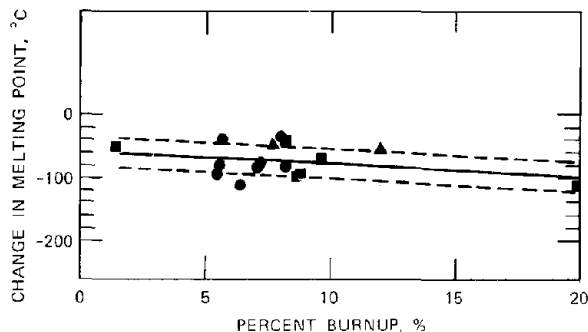


Fig. 10.7 Effect of burnup on the melting point of mixed-oxide fuel material. The dashed lines delineate a band  $\pm$  one standard deviation wide.  $\blacksquare$ , 25%  $\text{PuO}_2$ ,  $\text{O}/\text{M} = 2.00$ .  $\blacktriangle$ , 25%  $\text{PuO}_2$ ,  $\text{O}/\text{M} = 1.96$ .  $\bullet$ , 20%  $\text{PuO}_2$ ,  $\text{O}/\text{M} = 2.00$ . [From A. Biancheria, U. P. Nayak, and M. S. Beck, in *Proceedings of the Conference on Fast Reactor Fuel Element Technology*, R. Farmakes (Ed.), p. 361, American Nuclear Society, Hinsdale, Ill., 1971.]

where  $l_0$  is the length at  $0^\circ\text{C}$  and  $T$  is the temperature in degrees centigrade. For brevity,  $\alpha_{\text{lin}}$  is simply denoted by  $\alpha$  and referred to as the thermal-expansion coefficient.

Figure 10.8 shows the thermal-expansion coefficients for mixed oxides of various compositions. The measurements show that  $\alpha$  increases linearly with temperature, but neither the slope of this variation nor the effect of plutonium content is well established. At the present time, the coefficient of thermal expansion of the fuel is probably not known better than to within a factor of 2.

The effect of the oxygen-to-metal ratio on the thermal expansion coefficient of mixed-oxide fuels has been investigated by Roth et al.<sup>2</sup> They found that  $\alpha$  for  $(\text{U,Pu})\text{O}_{2+x}$  depends on the deviation from stoichiometric composition according to

$$\alpha_{(\text{U,Pu})\text{O}_{2+x}} = \alpha_0(1 - 5.1x) \quad (10.10)$$

where  $\alpha_0$  is the thermal-expansion coefficient of  $(\text{U,Pu})\text{O}_2$  of the same plutonium content. This relation was established for  $-0.06 \leq x \leq 0.01$  (i.e.,  $1.94 \leq \text{O}/\text{M} \leq 2.01$ ) and only for a 20%  $\text{PuO}_2$ - $\text{UO}_2$  mixture.

The thermal expansion of the cladding alloy is a function of temperature only and is relatively well established for zircaloy and stainless steel. Figure 10.9 shows the measured values for stainless steel, for which reasonable correlation is given by

$$\alpha = (16 + 4.62 \times 10^{-3}T) \times 10^{-6} \quad ^\circ\text{C}^{-1} \quad (10.11)$$

### 10.2.3 Specific Heat

Accurate knowledge of the specific heat of the fuel material is needed for assessment of reactor behavior under transient conditions, where the thermal diffusivity,  $k/\rho C_p$ , determines the time dependence of the temperature. In addition, the specific heat is also related to the thermal conductivity of the fuel, as will be shown in this section.

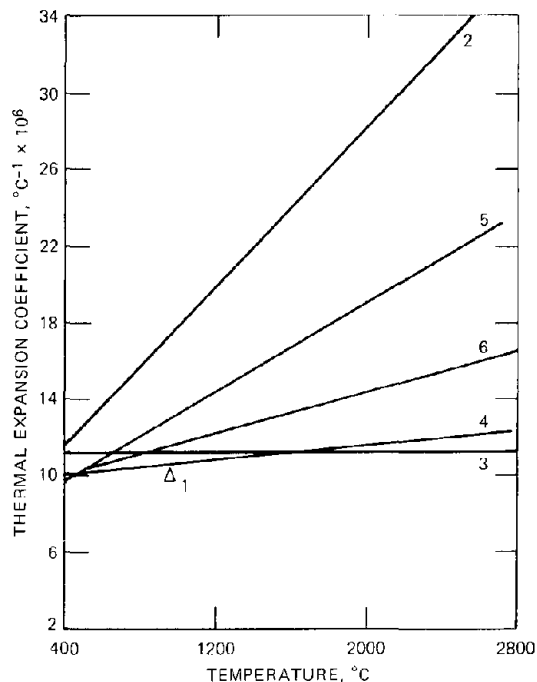


Fig. 10.8 Thermal expansion coefficients of mixed-oxide fuels.

1.  $(\text{U}_{0.8}\text{Pu}_{0.2})\text{O}_2$ , R. P. Nelson, USAEC Report BNWL-473, 1967.
2.  $(\text{U}_{0.8}\text{Pu}_{0.2})\text{O}_{2.10}$ , J. Roth and E. K. Halteman, USAEC Report NUMEC-2389-9, 1965.
3.  $\text{UO}_{2.24}$ , *ibid.*
4.  $\text{UO}_{2.08}$ , *ibid.*
5.  $(\text{U}_{0.95}\text{Pu}_{0.05})\text{O}_{2.11}$ , *ibid.*
6.  $(\text{U}_{0.85}\text{Pu}_{0.15})\text{O}_{2.13}$ , *ibid.*

(From F. J. Homan, Parametric Analysis of Fuel-Cladding Mechanical Interactions, USAEC Report ORNL-TM-3508, p. 13, Oak Ridge National Laboratory, August 1971.)

The specific heats  $C_p$  or  $C_v$  are not directly measured. Instead, the enthalpy of the solid above-room-temperature enthalpy is determined by dropping specimens heated to a known temperature into an adiabatic calorimeter.<sup>3</sup> These experiments on uranium dioxide produce data such as those shown in Fig. 10.10.

Below  $\sim 2100^\circ\text{K}$  the enthalpy can be described by a parabolic equation in temperature, which implies that the heat capacity at constant pressure is a linear function of temperature. As shown in problem 1.5, Chap. 1,  $C_p$  and  $C_v$  for any substance are related by

$$C_p = \left(\frac{\partial H}{\partial T}\right)_p = C_v + \left(\frac{\alpha^2 V}{\beta}\right) T$$

where  $\alpha$  is the coefficient of thermal expansion (Eq. 10.7),  $\beta$  is the coefficient of compressibility, and  $V$  is the molar volume. In the range between the Debye temperature of  $\text{UO}_2$  (which is between 200 and  $300^\circ\text{K}$ ) and the break in the enthalpy-temperature curve of Fig. 10.10 at  $\sim 2100^\circ\text{K}$ ,

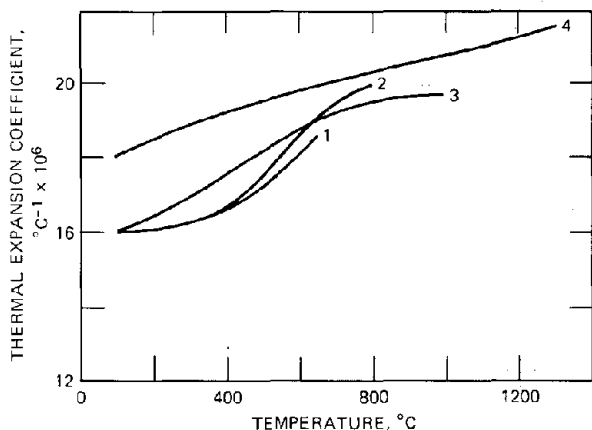


Fig. 10.9 Thermal expansion coefficient vs. temperature for type 316 stainless steel.

1. The Carpenter Steel Company, *Working Data, Carpenter Stainless and Heat Resisting Steels, Selection, Description, Fabrication*, Reading, Pennsylvania, 1962.

2. Properties and Selection of Metals, *Metals Handbook*, Vol. 1, 8th ed., p. 423, American Society for Metals, Metals Park, Ohio, 1962.

3. B. J. Seddon, *Steels Data Manual*, British TRG-Report-840, 1965.

4. I. B. Fieldhouse, J. C. Hedge, and J. I. Lang, USAEC Report WADC-TR-58-274, 1958.

(From F. J. Homan, *Parametric Analysis of Fuel-Cladding Mechanical Interaction*, USAEC Report ORNL-TM-3508, p. 17, Oak Ridge National Laboratory, August 1971.)

the heat capacity at constant volume ( $C_v$ ) is very nearly constant. According to the law of Dulong and Petit, each gram atom in the solid contributes  $3R$  to the specific heat at temperatures well above the Debye temperature. Since a mole of  $\text{UO}_2$  contains 1 gram atom of uranium and 2 gram atoms of oxygen, the molar heat capacity should be given by

$$C_v = 3(3R) = 9R \quad (10.12)$$

which is about 10% less than the constant term obtained from the low-temperature data of Fig. 10.10. Equation 10.12 neglects the contribution of the electronic heat capacity, which is justified because  $\text{UO}_2$  is an ionic solid.

At temperatures greater than  $2100^\circ\text{K}$ , the measured enthalpy of  $\text{UO}_2$  is larger than that predicted by extrapolation of the parabolic behavior suggested by the linear variation of  $C_p$  with  $T$ . This difference, which is called the excess enthalpy, is due to the formation of Frenkel defects resulting from movement of oxygen ions from their normal lattice sites to interstitial sites in the fluorite lattice of  $\text{UO}_2$ . The uranium sublattice is not affected; it remains perfect. The energy required to form the defects is reflected by an increase in the heat capacity, which may be expressed by

$$C_v = C_{v0} + \frac{dH_{\text{ex}}}{dT} \quad (10.13)$$

where  $C_{v0}$  is the constant value of the heat capacity at temperatures below  $2100^\circ\text{K}$  but above the Debye temperature and  $H_{\text{ex}}$  is the energy expended in forming the equilibrium number of point defects at temperature  $T$ . It is found to be (see problem 6.2):

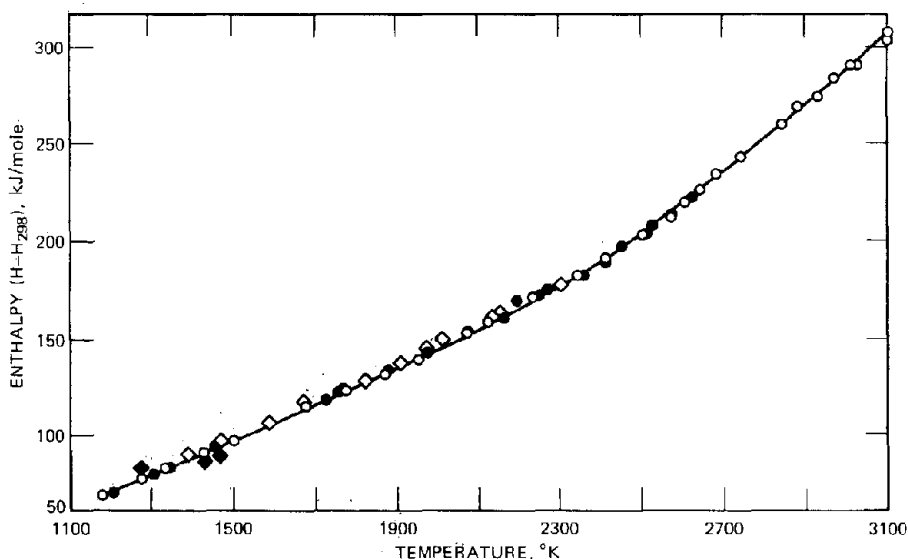


Fig. 10.10 Enthalpy-temperature data for stoichiometric  $\text{UO}_2$ . [From R. A. Hein, L. H. Sjobahl, and R. Szwarc, *J. Nucl. Mater.*, 25: 99 (1968).]

$$H_{ex} = (2)^{1/2} \epsilon_F e^{s_F/2R} e^{-\epsilon_F/2RT} \quad (10.14)$$

where  $\epsilon_F$  and  $s_F$  are the formation energy and excess entropy, respectively, of Frenkel defects in  $UO_2$ . Values of these parameters can be derived from the data shown in Fig. 10.10. According to Szwarc<sup>4</sup> they are  $\epsilon_F = 297$  kJ/mole and  $s_F = 63$  J mole<sup>-1</sup> °K<sup>-1</sup>, respectively.

### 10.3 THERMAL CONDUCTIVITY

#### 10.3.1 Elementary Theory of the Thermal Conductivity of an Ionic Solid

The thermal conductivity of an ionic solid can be derived by assuming the solid to consist of an ideal gas in which the particles are phonons (see Sec. 2.8). The results of the elementary kinetic theory of gases can then be applied directly to the phonon gas. Figure 10.11 depicts the interior of a solid that supports a temperature gradient in the z-direction.

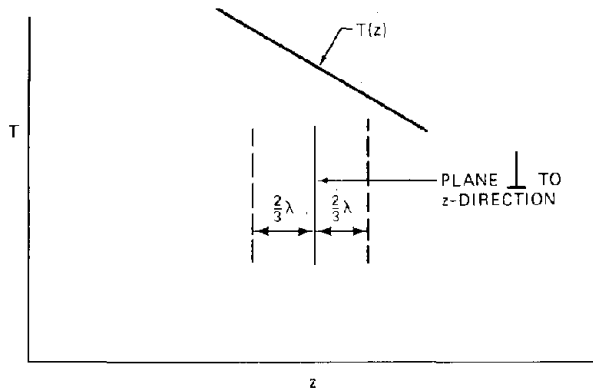


Fig. 10.11 Kinetic theory of thermal conductivity.

Because the phonons are continually colliding with each other or with defects in the solid, the phonon gas is isotropic. It can also be characterized by a density  $n_p$ ; a mean phonon speed  $u$  approximately equal to the speed of sound in the solid; and an average distance between collisions, or mean free path,  $\lambda$ . On the average, the phonons that cross a plane perpendicular to the z-direction underwent their last collision a distance  $2\lambda/3$  from the plane.<sup>5</sup> The rate at which phonons cross a unit area of the plane from either side is  $n_p u/4$ . The energy carried by each phonon is  $cT$ , where  $c$  is the heat capacity of a phonon. The phonons crossing the plane from the hot side carry an energy of

$$c \left( T - \frac{2\lambda}{3} \frac{dT}{dz} \right)$$

and the rate at which energy is transported across the plane from left to right is

$$\left( \frac{n_p u}{4} \right) c \left( T - \frac{2\lambda}{3} \frac{dT}{dz} \right)$$

Similarly, the phonons crossing the plane from the cold side transport energy at a rate given by

$$\left( \frac{n_p u}{4} \right) c \left( T + \frac{2\lambda}{3} \frac{dT}{dz} \right)$$

The net rate of energy transport in the positive z-direction is the z component of the heat flux,  $q_z$

$$q_z = - \left( \frac{n_p u}{4} \right) c \left( \frac{4\lambda}{3} \frac{dT}{dz} \right) \quad (10.15)$$

The thermal conductivity of the solid,  $k_s$ , is defined by Fourier's law:

$$q_z = -k_s \frac{dT}{dz} \quad (10.16)$$

Comparing the coefficients of  $dT/dz$  in Eqs. 10.15 and 10.16 shows that

$$k_s = \frac{1}{3} (c n_p) u \lambda \quad (10.17)$$

The quantity in the parentheses in this equation is the heat capacity per unit volume of the phonon gas. Since the entire energy content of the solid is assumed to be stored in its phonon gas,  $c n_p$  can be replaced by  $\rho C_v$ , where  $\rho$  is the density of the solid and  $C_v$  is the heat capacity at constant volume of a unit mass of the solid. Thus, the thermal conductivity can be expressed by

$$k_s = \frac{1}{3} \rho C_v u \lambda \quad (10.18)$$

Phonon-phonon scattering is due to the anharmonic components of crystal vibrations. Lattice anharmonicity increases with the mass difference between anions and cations in the ionic material, which, of all common oxides, is greatest in  $UO_2$  or  $PuO_2$ . As a result, the thermal conductivity of the oxides of the actinide metals is considerably lower than that of most other crystalline oxides.

The kinetic theory of gases shows that the collision mean free path is given by the reciprocal of the product of the collision cross section  $\sigma_p$  and the density of scatterers:

$$\lambda = \frac{1}{\sigma_p n_p} \quad (10.19)$$

(When both partners of the collision are in motion, as in phonon-phonon scattering, the mean free path is smaller than the value given by Eq. 10.19 by a factor of the square root of 2.)

At temperatures well above the Debye temperature, the phonon density is given by Eq. 2.51. For 1 mole of  $UO_2$ ,  $N$  in Eq. 2.51 is  $3N_{Av}$ ; thus the phonon concentration is

$$n_p = \left( \frac{27N_{Av}}{\theta_D} \right) T \quad (10.20)$$

Combination of Eqs. 10.19 and 10.20 shows that the phonon mean free path should vary as  $1/T$ . However, the presence of point defects in the solid prevents the mean free path from becoming very large at low temperatures, as the  $1/T$  relation would require. If a constant representing the cross section for scattering by entities other than phonons is added to the phonon-phonon cross section in

Eq. 10.19 and if  $n_p$  is assumed to be proportional to the absolute temperature, the phonon mean free path can be expressed by

$$\lambda = \frac{1}{A' + B'T} \quad (10.21)$$

where  $A'$  and  $B'$  are constants. Of course,  $\lambda$  cannot be smaller than the interatomic distance in the  $\text{UO}_2$  crystal structure. Schmidt<sup>6</sup> estimates that Eq. 10.21 is valid up to  $T = 2050^\circ\text{K}$ . Beyond this temperature the mean free path remains constant.

Using Eq. 10.21 in Eq. 10.18 suggests that, if  $\rho$ ,  $C_v$ , and  $u$  are temperature independent, the thermal conductivity of  $\text{UO}_2$  should decrease with temperature until a plateau is reached above  $2000^\circ\text{K}$ . However, numerous experiments have shown that the thermal conductivity of  $\text{UO}_2$  passes through a minimum in the region  $1500$  to  $2000^\circ\text{K}$ . Early studies attributed the increase in  $k_s$  at high temperatures to radiant heat transfer through the translucent solid.<sup>7</sup> This effect is no longer thought to be significant. Recently, Schmidt<sup>6</sup> has shown that the increase of the heat capacity of  $\text{UO}_2$  at high temperatures provides quantitative agreement with measured high-temperature increases in  $k_s$ . Instead of assuming  $C_v$  to be a constant in Eq. 10.18, allowance is made for the generation of point defects according to Eq. 10.13. The temperature dependence of the thermal conductivity is then given by

$$k_s = \frac{1 + (1/C_{vo})(dH_{ex}/dT)}{A + BT} \quad (10.22)$$

where  $H_{ex}$  is given by Eq. 10.14, and, for fully dense  $\text{UO}_2$ ,  $A = 10.8$  cm-deg/W and  $B = 0.022$  cm/W. The numerator of Eq. 10.22 represents the heat-capacity effect, increasing with temperature; the denominator causes  $k_s$  to decrease (up to the cutoff temperature of  $\sim 2050^\circ\text{K}$ ) because of decreasing phonon mean free path. With the constants given previously, Eq. 10.22 predicts a minimum in  $k_s$  at  $T \approx 2000^\circ\text{K}$ .

### 10.3.2 Thermal Conductivity of Nonstoichiometric Mixed Oxides

Although the thermal conductivity of pure stoichiometric uranium dioxide used in thermal reactors has been well established, the thermal conductivity of the fuel to be used in fast oxide reactors has only recently been investigated. In addition to the temperature dependence discussed in the previous section, the thermal conductivity of the mixed uranium-plutonium oxide, in which the O/M is not exactly 2, depends on two composition variables as well. Fortunately, the temperature dependence is found to be the same as that in pure  $\text{UO}_2$ . At temperatures low enough to neglect the contribution of thermal generation of oxygen Frenkel defects, the right-hand term in the numerator of Eq. 10.22 can be omitted,

$$k_s = \frac{1}{\Lambda(x,q) + B(x,q)T} \quad (10.23)$$

where  $x$  and  $q$  are the composition variables denoting the extent of nonstoichiometry and the plutonium content, respectively. Measurements of the thermal conductivity of

mixed oxides have covered the portions of the  $x$ - $q$  plane shown in Fig. 10.12. The horizontal bar in Fig. 10.12 represents a series of experiments by Gibby<sup>8</sup> at  $x = 0$  and  $0 < q < 0.3$ . The vertical bar at  $q = 0.25$  is also due to work by Gibby.<sup>9</sup> The experiments at  $q = 0.20$  have been performed by a number of workers.<sup>10-13</sup> All these studies have shown that nonzero values of  $x$  or  $q$  decrease the thermal conductivity of the oxide. This behavior is expected on physical grounds, since introducing point defects (vacancies or interstitials) into the oxygen ion sublattice or substituting plutonium for uranium on the cation sublattice provides additional centers from which phonon scattering can occur. The observations can be qualitatively analyzed by the classical theory of lattice thermal resistivity.

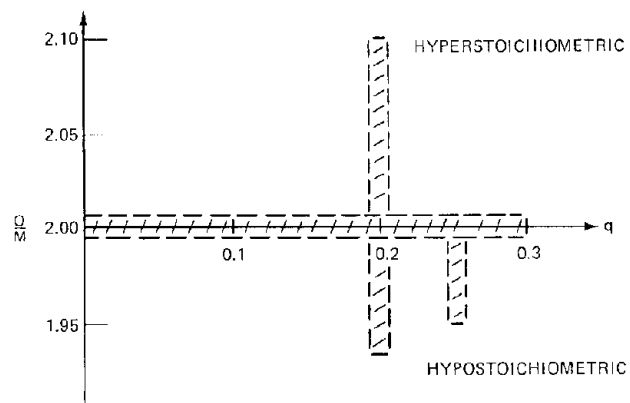


Fig. 10.12 Regions of nonstoichiometry and plutonium content in which the thermal conductivity of mixed-oxide fuel has been measured.

The limited amount of experimental information available suggests that the coefficient  $A$  in Eq. 10.23 depends primarily on the O/M ratio and only very weakly on the plutonium content. Conversely, experiments in which the O/M ratio was held constant and the fraction of plutonium was varied can be explained by considering  $A$  constant and  $B$  variable. Gibby<sup>8,9</sup> has reviewed the theory of the thermal resistivity of dielectric solids, which shows how  $A$  and  $B$  depend on basic properties of the material such as its Debye temperature, molar volume, atomic size, and atomic mass. Because of the numerous approximations in the theory, accurate absolute values of the coefficients  $A$  and  $B$  cannot be determined. However, the theory can be used to predict the effect on the thermal conductivity of introducing small quantities of defects into the crystal.

#### Effect of O/M

The coefficient  $A$  may be written

$$A = A_0 + \Delta A(x) \quad (10.24)$$

where  $A_0$  is the value of  $A$  determined for stoichiometric  $\text{UO}_2$ - $\text{PuO}_2$  mixtures. It is very nearly equal to the  $A$  value of pure  $\text{UO}_2$ . The perturbation  $\Delta A$  arises from interactions

of point defects in the lattice. The magnitude of  $\Delta A$  is proportional to the defect atom fraction (the ratio of the number of defects to the number of heavy metal atoms) and to a measure of the cross section of the defect for phonon scattering. The latter is proportional to the square of the difference between the atomic radius of the defect ( $r_i$ ) and that of the host atom ( $r$ ). The mass difference between the impurity atom and the host atom may also influence  $A$ , but this contribution is not significant in mixed-oxide fuel materials. Thus,  $\Delta A$  may be expressed by

$$\Delta A = A^* \sum_i Y_i \left( \frac{r_i - r}{r} \right)^2 \quad (10.25)$$

where  $A^*$  is a constant (given only to rough approximation by theory) and  $Y_i$  is the concentration of point defects of type  $i$ . The sum is over all defect types. The two defects in hypostoichiometric mixed oxides are oxygen vacancies and trivalent plutonium ions. The atomic fractions of these defects in  $(U,Pu)O_{2-x}$  are  $x$  and  $2x$ , respectively.\* The atomic radius of  $Pu^{3+}$  is  $1.07 \text{ \AA}$ , which is larger than that of either  $Pu^{4+}$  or  $U^{4+}$ , which are  $0.93$  and  $0.97 \text{ \AA}$ , respectively. The fractional radius change in replacing  $Pu^{4+}$  by  $Pu^{3+}$  is  $(1.07 - 0.93)/0.93 = 0.15$ . The lattice distortion may not be this large because the stiffness of the matrix resists expansion of the full 15% suggested by the difference in the atomic radii. However, in view of the qualitative nature of the present application of the theory, this effect is neglected.

The effect of oxygen vacancies, on the other hand, cannot be considered on the same basis as the effect of a foreign ion, since a vacancy has no atomic radius. Contribution to phonon scattering by a vacancy is due entirely to the strain field set up in the matrix surrounding the vacancy by relaxation of the neighboring host atoms. This relaxation is not easy to estimate. In a metal, the nearest-neighbor atoms to a vacancy relax inwards by 2 to 20% of the unperturbed distance from the defect center.<sup>14</sup> In ionic crystals, however, the relaxation is outward. In a perfect fluorite lattice, each oxygen ion is surrounded by four metal ions at the corners of a tetrahedron (see Fig. 3.12). When an oxygen ion is removed to form a vacancy, Coulombic repulsion causes the four metal ions nearest to the vacancy to move outward. Gibby<sup>9</sup> estimates that the fractional increase in the radius of a vacant oxygen site is 0.15.

For hypostoichiometric mixed oxides, therefore, Eq. 10.25 is

$$\begin{aligned} \Delta A &= A^* [2(0.15)^2 + (0.15)^2] x \\ &= 0.068A^*x \end{aligned} \quad (10.26)$$

Gibby<sup>9</sup> found that the  $\Delta A$  values that best fit his measured thermal conductivities were proportional to the nonstoichiometry parameter  $x$ :

$$\frac{\Delta A}{x} = 355$$

\*The defect chemistry of mixed oxides is discussed in Chap. 11.

Similar measurements by Van Craeynest and Weilbacher<sup>11</sup> yielded the values

$$\frac{\Delta A}{x} = 410 \text{ to } 830$$

although proportionality between  $\Delta A$  and  $x$  was not obeyed. Taking the experimental value of  $\Delta A/x$  to be  $\sim 400$ , we can use Eq. 10.26 to show that the constant  $A^* \sim 6000$ . Inserting Eq. 10.26 into Eq. 10.23 shows that the dependence of thermal conductivity on stoichiometry should be

$$k_s = \frac{1}{A_0 + 400x + B(q)T} \quad (10.27)$$

Figure 10.13 shows the measurements of Schmidt and Richter.<sup>10</sup> The curves have the hyperbolic form suggested by Eq. 10.27. As the temperature is increased, the O/M effect becomes less pronounced because the last term in the denominator of Eq. 10.27 dominates the middle term.

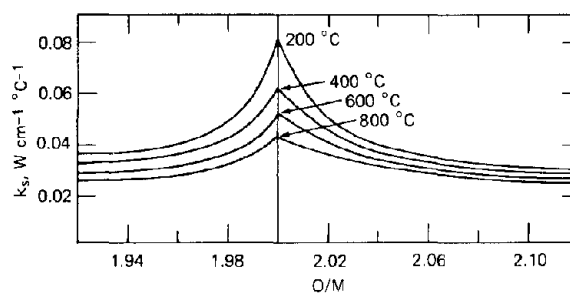


Fig. 10.13 Thermal conductivity of  $U_{0.8}Pu_{0.2}O_{2+x}$  as a function of the O/(U + Pu) ratio. (From H. E. Schmidt and J. Richter, in Symposium on Oxide Fuel Thermal Conductivity, Stockholm, 1967.)

### Effect of Plutonium Content

Gibby<sup>8</sup> measured the thermal conductivity of stoichiometric  $(U,Pu)O_2$  as a function of temperature and plutonium-to-uranium ratio. The data fit Eq. 10.23, and Table 10.3 shows values of the coefficients  $A$  and  $B$  determined from the measurements. There is clearly no systematic variation of  $A$  with plutonium content detectable from the results shown in this table. Absence of such an effect is consistent with Eq. 10.25. The atomic radii of  $U^{4+}$  and  $Pu^{4+}$  are  $0.97 \text{ \AA}$  and  $0.93 \text{ \AA}$ , respectively. Using these values for  $r_i$  and  $r$  in Eq. 10.25 and taking  $A^* = 6000$  yields

$$\Delta A = 5.4q \quad (10.28)$$

The scatter in the experimental values of  $A$  in Table 10.3 is of the same order as the predicted variation according to Eq. 10.28. The values of  $B$ , on the other hand, show a regular increase with plutonium content.

Lattice resistivity theory suggests that the coefficient  $B$  should depend on the molecular volume, the molecular

Table 10.3 Values of A and B Determined from a Least-Squares Fit of (U,Pu)O<sub>2</sub> Thermal Conductivity Data to the Relationship:  $1/k_s = A + BT^{*†}$

% Pu	A, cm <sup>2</sup> -K/W	B, cm/W	
		Exp.	Theory
0	3.08	0.0229	(0.0229)‡
5	3.04	0.0239	0.0232
12	2.20	0.0271	0.0235
20	3.09	0.0261	0.0240
25	3.13	0.0260	0.0242
30	5.30	0.0253	0.0245
100	0.46	0.0283	0.0281

\*From R. L. Gibby, *J. Nucl. Mater.*, 38: 163 (1971).

†Specimens 96 to 98% of theoretical density or corrected to this value.

‡Theory matched to experiment for pure UO<sub>2</sub>.

mass, and the Debye temperature of the solid. The molecular-mass effect is negligible because the atomic weights of uranium and plutonium are so close to each other. The molecular-volume effect is proportional to the lattice constant of the crystal, which may be obtained from X-ray measurements (the lattice constant of mixed oxides varies in a linear manner from 5.47 Å for UO<sub>2</sub> to 5.396 Å for PuO<sub>2</sub>). The Debye temperature can be empirically related to the melting temperature of the solid, which for (U,Pu)O<sub>2</sub> is shown in Fig. 10.7. The parameter B is given by

$$B = B_0 \left\{ \left[ \frac{a_0}{(a_0)_{\text{UO}_2}} \right]^2 \left[ \frac{(T_m)_{\text{UO}_2}}{T_m} \right]^{1/2} \right\} \quad (10.29)$$

where B<sub>0</sub> is the value for pure UO<sub>2</sub>, a<sub>0</sub> is the lattice constant, T<sub>m</sub> is the melting point of the mixed stoichiometric oxide, and (a<sub>0</sub>)<sub>UO<sub>2</sub></sub> and (T<sub>m</sub>)<sub>UO<sub>2</sub></sub> are the same properties for pure UO<sub>2</sub>. The calculated variation of B with q is shown in the last column of Table 10.3. The agreement with experiment is quite good for PuO<sub>2</sub> but less satisfactory for the intermediate compositions. The bracketed term in Eq. 10.29 is very nearly linear in q. The thermal conductivity of (U,Pu)O<sub>2</sub> is given by

$$k_s = \frac{1}{A(1 + 0.8q)B_0 T} \quad (10.30)$$

The data shown in Fig. 10.14 confirm the trends predicted by Eq. 10.30. The thermal conductivity of the oxide decreases by ~15% as the plutonium content is increased from 0 to 25%. This fractional decrease is nearly the same at all temperatures. The magnitude of this decrease in k<sub>s</sub> is small compared to that due to stoichiometry. When the O/M ratio of a mixed oxide is decreased from 2.00 to 1.93, the thermal conductivity at 800°C decreases by ~40%.

### 10.3.3 Effect of Burnup

According to the theory presented in the previous section for mixtures of UO<sub>2</sub> and PuO<sub>2</sub>, the introduction of solid fission products into the oxide lattice should decrease the thermal conductivity slightly. The only attempts to

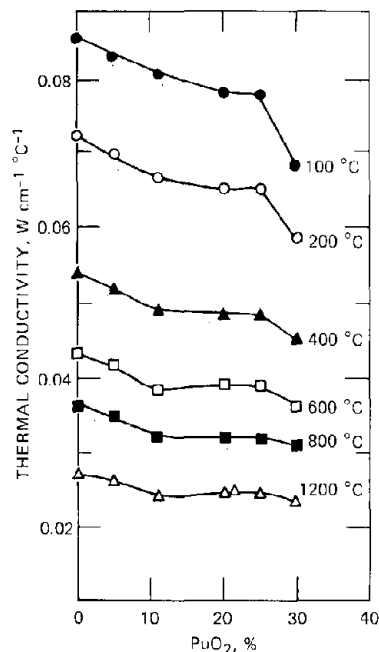


Fig. 10.14 Thermal conductivity of (U,Pu)O<sub>2</sub> solid solutions as a function of PuO<sub>2</sub> content. [From R. L. Gibby, *J. Nucl. Mater.*, 38: 163 (1971).]

measure this effect have been in-pile experiments. These were inconclusive because the burnup effect on the solid conductivity was obscured by the larger effects of restructuring, oxygen redistribution, and porosity generation, which are also consequences of irradiation.<sup>1</sup>

### 10.3.4 The Effect of Porosity

Oxide fuel is generally fabricated by sintering pellets of pressed powdered UO<sub>2</sub> or mixed UO<sub>2</sub>-PuO<sub>2</sub> at high temperatures (typically 1700°C) for a predetermined length of time. By control of the sintering conditions, material of any desired density between 80 and 98% of theoretical density can be produced.

Inasmuch as porosity in a ceramic body invariably reduces its thermal conductivity, it would appear desirable to eliminate all internal pores or voids in the fuel fabrication process. However, a certain amount of as-fabricated porosity is useful in accommodating the fission products that accumulate during irradiation; porosity is a means of minimizing fuel swelling. Table 10.2 shows that the density of both thermal and fast reactor fuels are well below the theoretical value. The porosity of the fast reactor fuel material is purposely made greater than that of the thermal reactor fuel because of the larger burnups required in the former.

Since controlled fuel porosity is a design variable of reactor fuel elements, it is important to be able to predict the effect of porosity on fuel properties, in particular on the thermal conductivity.

Theoretical analysis of the effect of porosity on thermal conductivity has been hampered by the number of variables

that must be considered. The most important variable, and the one that appears in all theoretical models, is the volume porosity, defined by

$$P = \frac{\text{volume of pores}}{\text{volume of pores} + \text{volume of solid}} \quad (10.31)$$

In addition, the geometry and physical properties of the individual pores may also be important. Pore geometry is defined by its size, shape, and orientation with respect to the direction of heat flow. Physical properties that may be significant are the emissivity of the solid and the thermal conductivity of the gas trapped within the pore (if any).

The earliest attempt to treat the thermal conductivity of porous bodies theoretically was by Eucken,<sup>15</sup> who applied equations originally derived by Maxwell for the electrical conductivity of a heterogeneous medium to the closely related problem of the thermal conductivity in the same medium. In 1954 Loeb<sup>16</sup> treated the same problem in a manner that permitted many of the secondary variables mentioned in the preceding paragraph to be properly accounted for. In 1966 Biancheria<sup>17</sup> reexamined the electrical analogue on which the Eucken formula was based and was able to theoretically account for effects of pore shape. Recently, Kampf and Karsten<sup>18</sup> have analyzed the porosity effect in a manner very similar to that employed by Loeb. The analysis of Loeb and of Kampf and Karsten is summarized in the following paragraphs.

The porous body is considered to have a number of closed pores dispersed throughout its interior. All are assumed to be of the same size and shape. If the pores are not isometric (i.e., if they are not either spheres or cubes), all of them are assumed to be oriented with respect to the direction of heat flow in the same way. A single pore and the fully dense solid material associated with it may be regarded as the unit cell of the porous body. As shown in Fig. 10.15, the unit cell may be represented as a cube of the material of sides  $L$  surrounding a pore. For simplicity, the pore is represented as a parallelepiped with sides  $l_x$ ,  $l_y$ , and  $l_z$ . Translation of the unit cell of Fig. 10.15 in space generates the entire porous body. In a real material the

pores are not uniformly arranged like atoms in a crystal lattice; so the amount of solid associated with each pore represents an average value.

Heat is assumed to flow in the  $y$ -direction only. The presence of the pore is assumed not to perturb the temperature profile in the surrounding solid, each point of which possesses the same temperature whether the pore is present or not. Projection of the pore faces on the front and back faces of the unit cell generates a right prism whose axis is parallel to the direction of heat flow. This prism, which contains the pore, is called the pore tube.

The effective thermal conductivity in the  $y$ -direction of the composite body shown in Fig. 10.15 is taken to be the thermal conductivity of the porous fuel material. The conductivity can be evaluated by straightforward means.

Heat flow through the front  $x$ - $z$  face of the unit cell passes through two media in parallel. One medium is the pore tube, which has an apparent thermal conductivity  $k_{(\text{pore tube})}$ . The other medium is the rectangular annulus of fully dense solid, the thermal conductivity of which is  $k_s$ . The effective thermal conductivity of the unit cell in the  $y$ -direction,  $k$ , is given by

$$k = P_c k_{(\text{pore tube})} + (1 - P_c) k_s \quad (10.32)$$

where  $P_c$  is the fraction of the cross-sectional area of the  $x$ - $z$  face of the unit cell which is occupied by the pore tube.

The apparent thermal conductance of the pore tube can be evaluated from the formula for series thermal resistances in the  $y$ -direction. There are two resistances in the pore tube, the pore proper and the solid contained in the pore tube. Thus,

$$\frac{1}{k_{(\text{pore tube})}} = \frac{P_L}{k_p} + \frac{1 - P_L}{k_s} \quad (10.33)$$

where  $P_L$  is the fraction of the length of the pore tube which is occupied by the pore and  $k_p$  is the thermal conductivity of the pore (due to conduction in the contained gas and radiation across the pore). Eliminating  $k_{(\text{pore tube})}$  between Eqs. 10.32 and 10.33 yields

$$\begin{aligned} \frac{k}{k_s} &= 1 - P_c \left\{ \frac{1 - (k_p/k_s)}{1 + [(1 - P_L)/P_L] (k_p/k_s)} \right\} \\ &\approx 1 - P_c \left( 1 - \frac{k_p/k_s}{P_L} \right) \end{aligned} \quad (10.34)$$

Equation 10.34 was obtained by Loeb<sup>16</sup> and Kampf and Karsten.<sup>18</sup> The effect of volume porosity on the thermal conductance is contained in the quantities  $P_c$  and  $P_L$ , which are related to  $P$  of Eq. 10.31 by

$$P = P_c P_L \quad (10.35)$$

The values  $P_c$  and  $P_L$  depend on the shape and orientation of the pores with respect to the direction of heat flow.

For the pore shown in Fig. 10.15, which has sides  $l_x$ ,  $l_y$ , and  $l_z$ ,

$$P = \frac{l_x l_y l_z}{L^3} \quad (10.36)$$

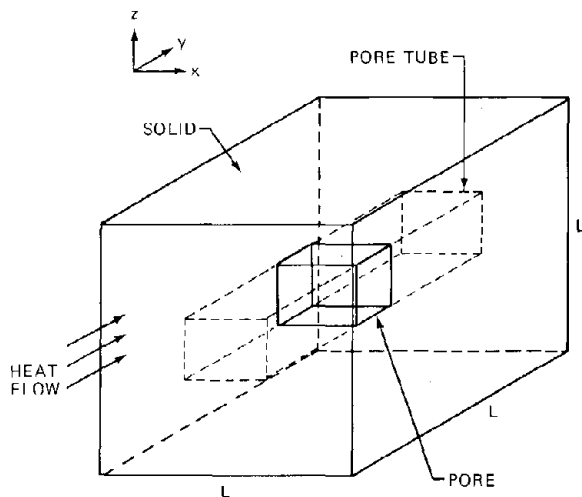


Fig. 10.15 Unit cell of a porous solid.

$$P_c = \frac{l_x l_z}{L^2} \quad (10.37)$$

$$P_L = \frac{l_y}{L} \quad (10.38)$$

Applying Eq. 10.34 to a porous medium requires that the factor  $P_c$  be known. For example, suppose the pores were square holes passing entirely through the specimen. In this case  $l_y$  would be equal to  $L$ , and the longitudinal pore fraction  $P_L$  would be unity. According to Eq. 10.35,  $P_c = P$ . However, if the direction of heat flow was perpendicular to the axis of the through holes (i.e., in the  $x$ - or  $z$ -direction), then  $P_c = P_L = P^{1/2}$ . Francl and Kingery<sup>19</sup> have shown experimentally that Eq. 10.34 describes the porosity effects on the thermal conductivity rather well for these two orientations of cylindrical through holes in an alumina specimen.

The most important special case for reactor fuel material is the isometric pore, for which  $l_x = l_y = l_z$ . In this case Eqs. 10.36 to 10.38 yield

$$\begin{aligned} P_c &= P^{2/3} \\ P_L &= P^{1/3} \end{aligned} \quad (10.39)$$

In addition, if the pore conductivity is small compared to the solid conductivity ( $k_p/k_s \ll 1$ ), Eq. 10.34 reduces to

$$k = k_s(1 - P^{2/3}) \quad (10.40)$$

This result was obtained by Kampf and Karsten.<sup>18</sup>

In treating the isometric pore case, Francl and Kingery<sup>19</sup> have erroneously taken  $P_c = P$ ; thus, in the limit of zero pore conductance, Eq. 10.34 becomes\*

$$k = k_s(1 - P) \quad (10.41)$$

Equation 10.41 has become known as the Loeb equation. It has been found to underestimate the porosity effect on the thermal conductivity of  $UO_2$ . This deficiency has been remedied by inserting an adjustable parameter to yield

$$k = k_s(1 - \alpha P) \quad (10.42)$$

Equation 10.42 is called the modified Loeb equation. Values of the parameter  $\alpha$  from 2 to 3 have been determined by fitting this equation to  $UO_2$  thermal-conductivity measurements.<sup>20</sup> Recent data<sup>21</sup> correspond to

\*What Francl and Kingery evidently had in mind when making this statement is a different type of cross-sectional pore fraction. The quantity  $P_c$  to be used in Eq. 10.34 refers to the fractional cross-sectional area of the pore tube shown in Fig. 10.15. Another type of pore cross-sectional fraction concerns the characteristic of a plane inserted into a solid containing a random distribution of equal-size isometric pores. The fraction of the area of such a plane which is intersected by pores is indeed equal to the pore volume fraction  $P$  (see problem 10.5). However, this particular type of cross-sectional pore fraction is not the one required for Eq. 10.34.

$\alpha = 5$ . Kampf and Karsten<sup>18</sup> show that Eq. 10.40 may be approximated over porosity intervals by a function of the form of Eq. 10.42 with values of  $\alpha$  ranging from 1.7 to 2.5.

The effective pore conductivity required in Eq. 10.34 is obtained by considering the conduction and radiation-heat fluxes across the pore:

$$q = k_g \frac{\Delta T}{l_y} + \epsilon \sigma [(T + \Delta T)^4 - T^4] = k_p \frac{\Delta T}{l_y}$$

where  $\Delta T$  = the temperature drop across the pore

$T$  = the average temperature of the pore walls

$k_g$  = the thermal conductivity of the gas inside the pore

$\epsilon$  = the emissivity of the material

$\sigma$  = the Stefan-Boltzmann constant

For small pores,  $\Delta T/T \ll 1$  and the radiation term can be linearized to  $4\epsilon\sigma T^3 \Delta T$ . The pore conductivity is thus

$$k_p = k_g + 4\epsilon\sigma l_y T^3 \quad (10.43)$$

For pores with curved surfaces, the last term is multiplied by a shape factor of order unity. Figure 10.16 shows  $k_s/k_p$  under various conditions. The radiation contribution to the effective thermal conductivity of the pore can be appreciable for large pores at high temperature, especially if they are helium filled.

Biancheria's<sup>17</sup> analysis of the porosity effect yields the following formula:

$$\frac{k}{k_s} = \frac{1 - P}{1 + (\alpha - 1)P} \quad (10.44)$$

If  $(\alpha - 1)P \ll 1$ , Eq. 10.44 reduces to the unmodified Loeb formula, Eq. 10.41. However, contrary to the purely

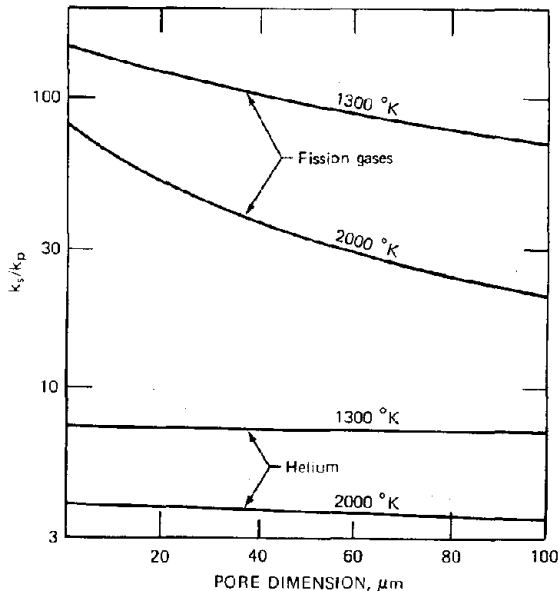


Fig. 10.16 Dependence of the ratio  $k_s/k_p$  on pore dimension for oxide fuels. [From H. Kampf and G. Karsten, *Nucl. Appl. Technol.*, 9: 228 (1970).]

empirical nature of the parameter  $\alpha$  in the latter equation,  $\alpha$  in Eq. 10.44 can be evaluated for equal-size pores of a particular geometry randomly distributed in the solid. For spheres,  $\alpha = 1.5$ , and Eq. 10.44 reduces to the porosity correction factor deduced by Eucken.<sup>15</sup> For axisymmetric shapes, such as ellipsoids of revolution, the shape factor  $\alpha$  is greater than 1.5 by amounts that depend on the ratio of the lengths of the principal axes of the pore. The shape factor is as large as 3 for oblate ellipsoids with an axial ratio of 10. Marino<sup>22</sup> has further extended the Maxwell-Eucken type of porosity analysis by accounting for the conductivity ratio  $k_p/k_s$ .

### 10.3.5 Empirical Thermal Conductivity Formulas

In theory, the thermal conductivity of porous  $\text{UO}_2$  can be determined by using  $k_s$  given by Eq. 10.22 in Eq. 10.40, 10.41, 10.42, or 10.44. However, extensive measurements of  $\text{UO}_2$  thermal conductivity have shown that the theoretical formulas do not agree well enough with experiment to serve as design equations. The trends predicted by theory are by and large observed, but purely empirical formulas are used when reliable numerical values are needed. A typical set of measurements reported by Asamoto, Anselin, and Conti<sup>23</sup> is shown in Fig. 10.17. The data are fit by the equation:

$$k = 0.0130 + \frac{1}{(0.038 + 0.45P)T} \text{ W cm}^{-1} \text{ } ^\circ\text{C}^{-1} \quad (10.45)$$

where  $T$  is in degrees centigrade. The dependence of thermal conductivity on temperature and porosity indicated by Eq. 10.45 is shown in Fig. 10.18. The variation of  $k$  with temperature is plotted for various values of the percentage of theoretical density of the fuel ( $\rho/\rho_s$ ), which is related to the porosity by

$$P = 1 - \frac{\rho}{\rho_s} \quad (10.46)$$

where  $\rho$  is the density of the porous fuel body and  $\rho_s$  is the density of the fully dense solid (also called the theoretical

density). The latter is generally determined from X-ray diffraction measurements of the lattice constants of the crystalline solid. Equation 10.45 does not exhibit the conductivity minimum contained in Eq. 10.22 and confirmed by other data.<sup>6</sup>

Van Craeynest and Stora<sup>24</sup> have found that their measurements of  $\text{UO}_2$  thermal conductivity could be satisfactorily fit by the modified Loeb equation if the coefficient  $\alpha$  were taken to be a function of temperature. Their empirical fit for temperatures from  $50^\circ\text{C}$  to  $1000^\circ\text{C}$  is

$$\frac{k}{k_s} = 1 - (2.58 - 0.58 \times 10^{-3}T)P \quad (10.47)$$

They found that Eq. 10.47 adequately described the porosity effect in both  $\text{UO}_2$  and  $(\text{U}_{0.8}\text{Pu}_{0.2})\text{O}_2$ .

Both these empirical formulas suggest that the theory is incorrect in accounting for variations in  $k$  due to  $T$  and  $P$  by multiplicative terms. Equations 10.45 and 10.47 show that the effects of these two variables cannot be factored into separate terms.

A thermal-conductivity equation commonly used for mixed-oxide fuel of 95% of theoretical density is:<sup>25</sup>

$$k = (3.11 + 0.0272T)^{-1} + 5.39 \times 10^{-13} T^3 \quad (10.48)$$

In this formula the fuel is assumed to be stoichiometric below  $1400^\circ\text{C}$  but to have an O/M of 1.98 at higher temperatures. Equation 10.48 shows a minimum at  $1700^\circ\text{C}$ . It is to be employed with the porosity correction of Eq. 10.44.

## 10.4 TEMPERATURE PROFILES IN CYLINDRICAL FUEL RODS

The steady-state temperature distribution in a cylindrical body in which heat is generated at a volumetric rate  $H$  is governed by the heat-conduction equation:

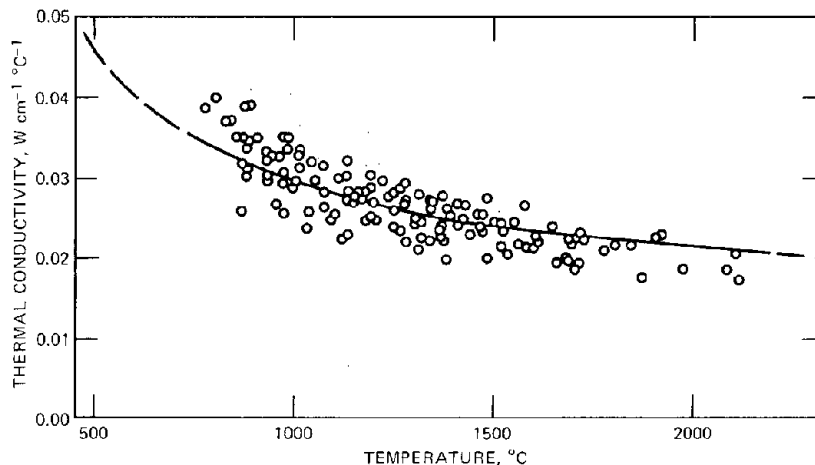


Fig. 10.17 Thermal conductivity of sintered  $\text{UO}_2$  of 95% theoretical density. [From R. R. Asamoto, F. L. Anselin, and A. E. Conti, *J. Nucl. Mater.*, 29: 67 (1969).]

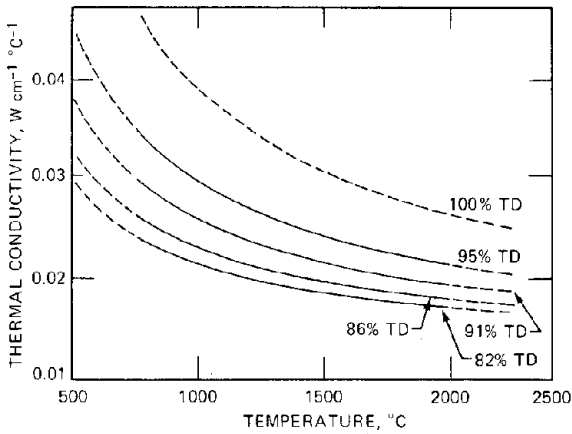


Fig. 10.18 Dependence of the thermal conductivity of  $\text{UO}_2$  on temperature and porosity predicted by Eq. 10.45. TD, theoretical density. ---, extrapolation.

$$\frac{1}{r} \frac{d}{dr} \left( rk \frac{dT}{dr} \right) + H = 0 \quad (10.49)$$

where the thermal conductivity  $k$  is intrinsically a function of temperature and can also depend on position because of radial porosity variations in the fuel. Appropriate local values of  $k$  can be obtained by the methods outlined in the previous section provided that the porosity variation with radius is known. The value  $H$  is the volumetric heat-generation rate, which can be a function of radial position.

Inasmuch as the axial temperature gradient is much smaller than that in the radial direction, the axial conduction term in the heat-conduction equation has been neglected.

Many of the factors that affect both the magnitude and radial variation of  $H$  and  $k$  are time dependent. The removal of porosity due to fuel restructuring occurs in a matter of hours, and fission-gas generation causes changes on a time scale measured in weeks or months. Redistribution of fissile species can have even larger characteristic times. In general, changes in  $k$  and  $H$  due to materials transformations are so gradual that, for fuel-element operation at constant power, the heat-conduction process can be considered to be at steady state.

Solution of Eq. 10.49 requires two boundary conditions. One is the specified temperature at the surface of the fuel ( $r = R$ ):

$$T(R) = T_s \quad (10.50)$$

The fuel rod may have a hole in the center. Fuel pellets can be purposely fabricated in an annular shape to provide room to accommodate fuel swelling. Solid fuel pellets fabricated from low-density material (< 95% of theoretical density) develop a central void by migration of the pores within the fuel body to the center under the influence of the temperature gradient. Irrespective of whether the central hole is purposely manufactured into the fuel pellet or whether it develops as a result of irradiation, the

boundary of the void constitutes an isothermal surface of temperature  $T_0$ . Furthermore, since there is no heat generation in the gas contained in the central void, the heat flux at this surface is zero. The second boundary condition on Eq. 10.49 is

$$\left( \frac{dT}{dr} \right)_{r_0} = 0 \quad (10.51)$$

where  $r_0$  is the radius of the central void.

If  $k$  and  $H$  are constant and the rod is solid, the solution of Eq. 10.49 subject to Eqs. 10.50 and 10.51 is

$$T - T_s = \frac{1}{4} \frac{HR^2}{k} \left( 1 - \frac{r^2}{R^2} \right)$$

or, in terms of the center temperature  $T_0$ ,

$$\frac{T - T_s}{T_0 - T_s} = 1 - \frac{r^2}{R^2} \quad (10.52)$$

Because of the generally unwarranted assumption of constant  $k$  and  $H$ , these solutions are not sufficiently accurate for design purposes. However, the parabolic temperature profile is acceptable for some fuel-property calculations, such as bubble migration rates.

#### 10.4.1 Volumetric Heat-Generation Rate

The thermal rating of a fuel rod is usually described in terms of its linear power, defined by

$$\mathcal{P} = \frac{\text{power}}{\text{unit length of rod}} \quad \text{W/cm} \quad (10.53)$$

The linear power varies with axial position in the fuel rod. With coolant upflow attention is usually centered on the axial location just above the midplane of the core. Here the linear power is somewhat less than its peak value, but the coolant temperature is higher than at the midplane. The fuel temperature is highest at a position slightly above the core center, whereas the cladding temperature peaks near the core outlet.

The linear power is related to the radially averaged volumetric heat-generation rate by

$$\frac{\mathcal{P}}{\pi(R^2 - r_0^2)} = \frac{2}{(R^2 - r_0^2)} \int_{r_0}^R r H(r) dr = \bar{H} \quad (10.54)$$

The local volumetric heat-generation rate is related to the fission density by

$$H = 3.2 \times 10^{-11} \bar{F} \quad \text{W/cm}^3 \quad (10.55)$$

The fission density is given by Eq. 10.1, in which the terms can change with irradiation time and vary with radius in the fuel rod. To isolate these effects, we combine Eq. 10.1 with Eq. 10.55 in the following manner:

$$H(r) = (3.2 \times 10^{-11} q_0 \sigma_f N_{f0} \bar{\Phi}_0) \times \left( \frac{\bar{q}}{q_0} \frac{\bar{N}_f}{N_{f0}} \frac{\bar{\Phi}}{\bar{\Phi}_0} \right) \left[ \frac{q(r) N_f(r) \Phi(r)}{\bar{q} \bar{N}_f \bar{\Phi}} \right] \quad (10.56)$$

where the subscript 0 denotes quantities evaluated at the start of irradiation when the fuel is fresh and the bar over a quantity represents the average over the fuel cross section.

The first term on the right-hand side of Eq. 10.56 is the average volumetric heat-generation rate at startup, which is related to the linear power by Eq. 10.54.

The second term contains the effect of burnup on the heat-generation rate. The product  $\bar{q}\bar{N}_f$  is the average concentration of fissile atoms in the fuel. In a fast reactor,  $\bar{q}/q_0$  can be greater than unity because of conversion of  $^{238}\text{U}$  to  $^{239}\text{Pu}$ . The ratio  $\bar{N}_f/N_{f0}$ , which is one minus the local fractional burnup, is always less than unity. If the local conversion ratio (atoms of fissile material produced from fertile species per atom of fissile species consumed) is close to unity, the product  $\bar{q}\bar{N}_f$  cannot be much smaller than the value for the fresh fuel,  $q_0N_{f0}$ . The ratio of the average flux to that at startup, which appears as the last factor in the second term, is a controllable parameter of the reactor. It is desirable to adjust  $\bar{\Phi}/\Phi_0$  so that the average heat-generation rate (and hence the linear power of the rod) is close to the initial, design-limiting value.

The third term in Eq. 10.56 contains terms describing the radial variation of quantities affecting the heat-generation rate. All are normalized to unity

$$\bar{q} = \frac{2}{(R^2 - r_0^2)} \int_{r_0}^R r q(r) dr \quad (10.57)$$

$$\bar{N}_f = \frac{2}{(R^2 - r_0^2)} \int_{r_0}^R r N_f(r) dr \quad (10.58)$$

$$\bar{\Phi} = \frac{2}{(R^2 - r_0^2)} \int_{r_0}^R r \Phi(r) dr \quad (10.59)$$

In a thermal reactor the enrichment ratio,  $q(r)/\bar{q}$ , can differ from unity because of nonuniform burnout of fissile species due to flux depression in the rod. In a fast reactor the enrichment ratio can change because of the phenomenon of plutonium redistribution under the influence of the temperature gradient.

The nonuniform distribution of total heavy-metal atoms,  $N_f(r)/\bar{N}_f$ , is due primarily to porosity changes in the fuel caused by restructuring (sintering, grain growth), pore and bubble generation, and migration processes. Relatively minor changes in atom density also result from the temperature gradient, which causes nonuniform thermal expansion of the fuel.

The flux ratio  $\Phi(r)/\bar{\Phi}$  is unity in a fast reactor because the mean free path of the neutrons is much larger than the diameter of the fuel rod. In thermal reactors, however, the absorption cross sections are several hundred times larger than in a fast reactor. Neutrons thermalized in the water coolant-moderator must diffuse back into the fuel rods to cause fission. Because absorption occurs during diffusion, the flux is depressed in the center of the fuel rods in a thermal reactor. For solid rods with uniform fissile atom density, neutron-diffusion theory shows that the flux ratio is

$$\frac{\Phi(r)}{\bar{\Phi}} = \left[ \frac{(\kappa R)}{2I_1(\kappa R)} \right] I_0(\kappa r) \quad (10.60)$$

where  $I_0$  and  $I_1$  are modified Bessel functions of the first kind of zeroth and first order, respectively, and  $\kappa$  is the reciprocal of the neutron-diffusion length in the fuel material (typically 2 to 3 cm<sup>-1</sup> in thermal reactor oxide fuel).

The object of solving Eq. 10.49 is twofold. First, the temperature profile in a fuel rod is needed to accurately estimate the extent of materials transformations, such as swelling, gas release, sintering, and mechanical interaction between the fuel and the cladding. Second, it is important to be able to predict the maximum temperature in a fuel rod for specified linear power and fuel conditions to ascertain whether any part of the fuel is close to the melting point. This last reason is especially compelling in fast reactors, where the thermal performance of the reactor is limited by the restriction of fuel melting.

### 10.4.2 The Conductivity Integral

The primary impediment to direct integration of Eq. 10.49 is the radial and temperature variation of the thermal conductivity. Considerable progress in analyzing the thermal characteristics of a fuel rod can be made without confronting the complex behavior of  $k$  by an approach that is generally referred to as the conductivity-integral concept. This notion was first suggested by W. B. Lewis, and its use in treating fuel thermal problems is discussed in detail elsewhere.<sup>2,6,27</sup>

Consider first the case of a solid fuel rod with a constant volumetric heat-generation rate. Equation 10.49 may be integrated once to yield

$$rk \frac{dT}{dr} = -\frac{1}{2} Hr^2 \quad (10.61)$$

The constant of integration is zero by Eq. 10.51 (with  $r_0 = 0$  for a solid rod). Integration of Eq. 10.61 between the center and the surface yields

$$\int_{T_s}^{T_0} k dT = \frac{1}{4} HR^2 \quad (10.62)$$

Or, using the linear power of Eq. 10.53,

$$\int_{T_s}^{T_0} k dT = \frac{\mathcal{P}}{4\pi} \quad (10.63)$$

The integral on the left of Eqs. 10.62 and 10.63 is the conductivity integral. Its utility is due to the following properties:

1. It is directly related to the linear power of the fuel, which is a quantity easily measured by coolant calorimetry (for test capsules) or postirradiation burnup analysis.
2. The central temperature of the rod, which appears as the upper limit of the conductivity integral, is independent of rod diameter.
3. The conductivity integral is a property of the fuel only. It does not depend on the thermal and heat-transfer characteristics of elements outside the fuel proper. However, application of the conductivity integral requires that the surface temperature of the fuel be determined independently.
4. If the upper limit of the conductivity integral is regarded as a variable, differentiation yields the thermal conductivity.
5. By addition the conductivity can be normalized to any temperature as the lower limit of integration. Thus, normalized to 0°C, it is

$$\int_{T_s}^{T_0} k \, dT = \int_0^{T_0} k \, dT - \int_0^{T_s} k \, dT \quad (10.64)$$

6. The conductivity integral can be determined from in-pile experiments for comparison with out-of-pile measurements. The temperatures at which particular fuel transformations, such as melting or grain growth, occur are known. By examining photomicrographs of the fuel cross section after irradiation, we can ascertain the radial location  $r^*$  at which a transformation characterized by temperature  $T^*$  occurred. Figure 10.19 shows the identification of the radius at which melting occurred in a fuel specimen subject to a linear power in excess of that needed to cause fuel melting. With  $r^*$  and  $T^*$  known, the conductivity integral between  $T_s$  and  $T^*$  can be determined by integration of Eq. 10.61:

$$\int_{T_s}^{T^*} k \, dT = \frac{\mathcal{P}}{4\pi} \left[ 1 - \left( \frac{r^*}{R} \right)^2 \right] \quad (10.65)$$

The best values of the conductivity integral obtained from the measurements of several laboratories of unirradiated mixed-oxide fuel are shown in Fig. 10.20. From these data it has been found that melting occurs when the conductivity integral is given by

$$\int_0^{T_m} k \, dT = 93 \pm 4 \text{ W/cm} \quad (10.66)$$

7. The conductivity integral can be used to correlate phenomena such as gas release from the fuel.

8. For design purposes, the conductivity integral can be used to estimate the center-line temperature of the fuel for specified power conditions (see problem 10.2).

The conductivity integral can be applied to situations where  $H$  is a function of  $r$  provided that the form of this dependence can be specified. Two cases are of interest.

In a thermal reactor the heat-generation rate varies with radius because of the depression of the neutron flux in the

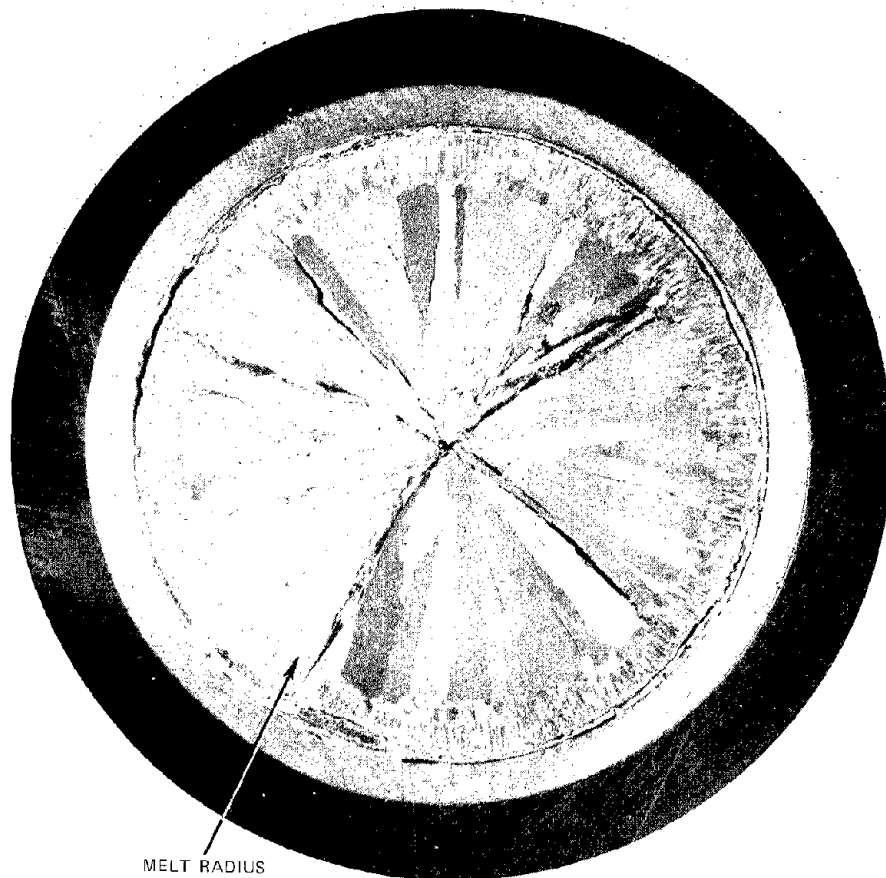


Fig. 10.19 Cross section of a  $\text{UO}_2$  fuel rod operated at a linear power high enough to cause extensive melting. [From M. F. Lyons et al., *Trans. Amer. Nucl. Soc.*, 8: 376 (1965).]

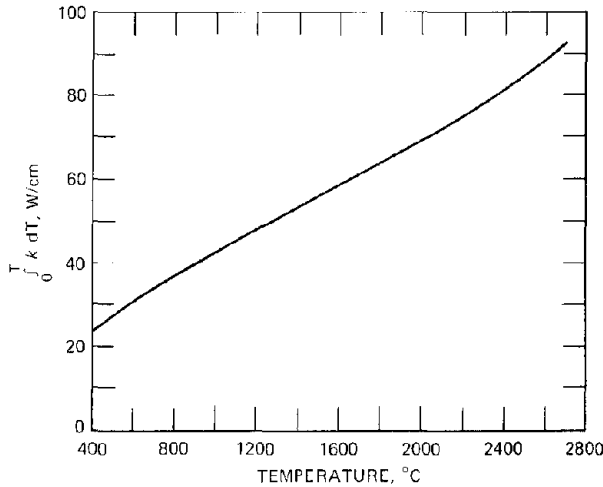


Fig. 10.20 Recommended minimum thermal conductivity integral for  $(U_{0.8}Pu_{0.2})O_2$ . [From M. J. McNelly, Liquid Metal Fast Breeder Reactor Design Study (1000-MWe  $UO_2$ - $PuO_2$  Fueled Plant), 2 vols., USAEC Report GEAP-4418, General Electric Company, January 1963.]

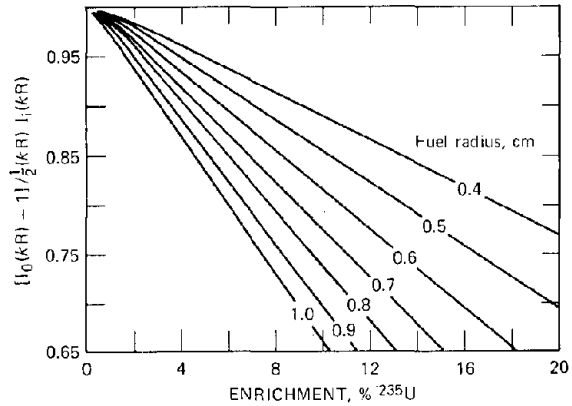


Fig. 10.21 Effect of flux depression of the conductivity integral in thermal reactor fuel rods. (From J. A. L. Robertson,  $\int \kappa d\theta$  in Fuel Irradiations, Canadian Report CRFD-835, 1959.)

center of the rod. The flux ratio is given by Eq. 10.60, and the other two factors in the last term of Eq. 10.54 are assumed to be unity. The heat-generation rate is given by

$$H(r) = \frac{\mathcal{P}}{\pi R^2} \left[ \frac{(\kappa R)}{2I_1(\kappa R)} \right] I_0(\kappa r) \quad (10.67)$$

With Eq. 10.67, Eq. 10.49 can be integrated twice with the aid of the surface and center boundary conditions. For a solid rod the result is

$$\int_{T_s}^{T_o} \kappa dT = \left( \frac{\mathcal{P}}{4\pi} \right) \left[ \frac{I_0(\kappa R) - 1}{\frac{1}{2}(\kappa R) I_1(\kappa R)} \right] \quad (10.68)$$

Figure 10.21 is a graph of the last term in Eq. 10.68. In  $UO_2$  the thermal-diffusion length is governed by the fraction of  $^{235}U$  in the fuel, which has been used instead of  $\kappa R$  as the abscissa in this graph. For the pressurized-water reactor used as an example in Tables 10.1 and 10.2, the factor in Eq. 10.68 due to flux depression is 0.93. In a boiling-water reactor, the fuel rods are larger in diameter than those of a pressurized-water reactor; thus, the effect of flux depression in the fuel rods is more pronounced in the boiling-water reactor.

The effect of the flux depression is to reduce the conductivity integral for a fixed linear power. For a specified fuel surface temperature, the center of the fuel rod is cooler for the case of flux depression compared to a radially uniform flux. From a heat-conduction point of view, it is advantageous to move the heat source to the periphery of the rod, which is effectively what the flux depression does. The effect is general: any phenomenon that decreases heat generation at the center of the rod (at constant average heat-generation rate) reduces the central temperature.

### 10.4.3 Effect of Fuel Restructuring on the Temperature Distribution in Fast Reactors

In fast reactors the flux-depression factor described in the preceding section for fuel elements in thermal reactors is absent. However, because of the higher level of the temperatures and the steeper temperature gradients in fast reactor fuel pins, substantial alterations in the morphology of the fuel material takes place during power operation. Figure 10.22 shows a photograph of the cross section of a mixed-oxide fuel rod that was irradiated at a linear power of 560 W/cm to a burnup of 2.7%. Although the fuel pellet was originally solid, a sizable void has developed in the center. The void is formed by movement of the porosity in the original fuel material (83% in this case) toward the center. The central void in Fig. 10.22 is 1.9 mm in diameter, which is 30% of the fuel-pin diameter.

Immediately adjacent to the void is a solid region characterized by large columnar grains. The boundaries of these grains are delineated by the fine radial streaks terminating at the void. (The large black traces extending from the central void all the way to the cladding are cracks that probably developed during cooling down from the operating temperature. These cracks were probably not part of the fuel structure during most of its lifetime). The radial boundaries of the columnar grains are the trails of the pores present in the as-fabricated fuel material or fission-gas bubbles that migrated up the temperature gradient. The movement of this porosity to the center is responsible for the development of the central void. If fully dense material is irradiated in tight-fitting cladding, neither the columnar-grain structure nor the central void is formed until irradiation swelling of the cladding enlarges the rod.

Moving outward from the columnar-grain region, we find a band of large equiaxed grains. In this region, the temperature rather than the temperature gradient is the significant parameter. In this zone the initial fine grains of

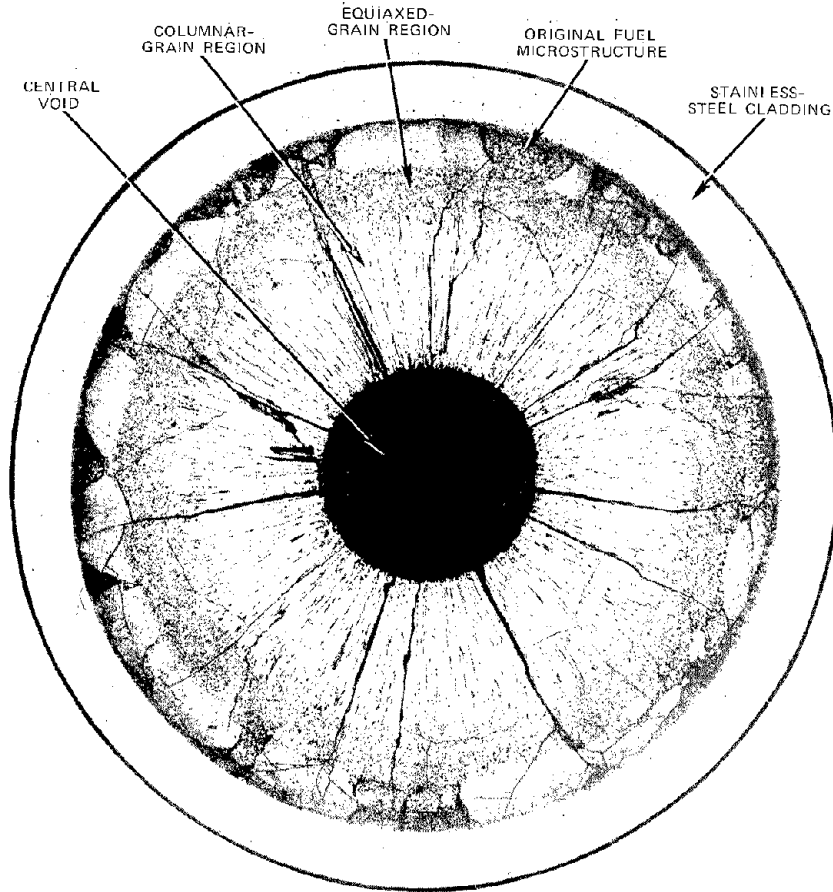


Fig. 10.22 Cross section of mixed-oxide fuel rod irradiated to 2.7% burnup. No melting. [From D. R. O'Boyle et al., *J. Nucl. Mater.*, 29: 27 (1969).]

the as-fabricated oxide have grown to many times their original size. Grain growth is not unique to reactor fuel-element materials nor does it require exposure to nuclear radiation. The phenomenon is observed in many ceramics held at elevated temperatures for appreciable periods of time.

Outside the equiaxed grain region and adjacent to the cladding is an annulus of fuel with the original microstructure. The temperatures in this region are too low to cause any observable restructuring of the fuel material.

For the purposes of thermal analysis of the restructured fuel, the pellet is divided into the three annular regions shown in Fig. 10.23. It is common practice to assign a specific temperature to the boundaries between the restructured regions. Thus, the temperature at  $r = r_1$  is assumed to correspond to a temperature  $T_1$  below which columnar grains do not form. Similarly, equiaxed grains are observed at a radius  $r_2$  because the temperature at this point,  $T_2$ , is just high enough for appreciable grain growth to occur (the growth of equiaxed grains takes place in the region  $r_0 < r < r_1$ , as well, but this effect is masked by the development of the columnar grains). In addition, the columnar- and equiaxed-grain regions (zones 1 and 2) are assigned particular densities that do not depend on the original density of the as-fabricated fuel. Table 10.4 shows

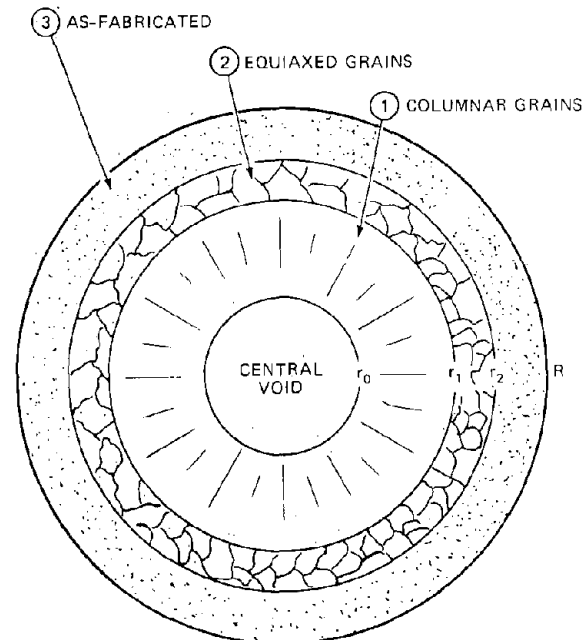


Fig. 10.23 Regions of a restructured fuel rod.

the boundary temperatures and densities assigned to the restructured regions of the fuel by various laboratories.

The density of the columnar-grain region is estimated to be between 95 and 99% of the density of solid fuel at the same temperature. Estimates of the temperature at which this structure forms in an appropriate temperature gradient varies from 1700 to 2150°C. The corresponding densities and temperatures of the equiaxed zone are lower than those of the columnar-grain region. However, it is not certain that any densification occurs in the equiaxed-grain region; the existing pores can simply coalesce or change shape.<sup>1</sup>

Table 10.4 implies that the temperature and hence the radial position of the zone boundaries  $r_1$  and  $r_2$  are independent of irradiation time. Such an assumption is only an approximation, inasmuch as the phenomena involved in structural changes are dynamic rather than static. The question of the rate of growth of the columnar and equiaxed grains is considered in detail in Chap. 14. Similarly, the densities of the restructured regions are functions of irradiation. After the original densification due to removal of the as-fabricated porosity and grain growth (which occurs on a time scale hours after startup), the densities of these regions begin to decrease again because of accumulation of solid fission products and a portion of the fission gases.

$\rho_2$ , and  $\rho_3$  are not constant over an entire zone because of the temperature gradient in the fuel. For example,  $\rho_3$  on the left-hand side of Eq. 10.69 should be evaluated at the average temperature of the entire solid fuel pellet, whereas  $\rho_3$  in the last term on the right is characteristic of the average temperature between  $T_s$  and  $T_2$ . In neglecting this difference, we have considered the density ratios in Eq. 10.70 as arising from porosity differences only. Thus, the coefficient of  $r_1^2$  in Eq. 10.70 is interpreted as

$$\frac{\rho_1 - \rho_2}{\rho_1} = \frac{(\rho_1/\rho_s) - (\rho_2/\rho_s)}{\rho_1/\rho_s}$$

For example, using the densities in the first row of Table 10.4, the above ratio is  $(0.98 - 0.95)/0.98 = 0.031$ . For most calculations this approximation is justified because the effect of porosity changes far outweighs density alterations due to thermal expansion.

The volumetric heat-generation rates in zones 1 and 2 are affected by densification, which increases the density of heavy-metal atoms in a unit volume of fuel. The heat-generation rate in region 3 is the same as that of the original solid pellet at startup. If the fuel is operated with a linear power  $\mathcal{P}$ , Eq. 10.54 shows that the heat-generation rate in the unrestructured region is

Table 10.4 Parameters of the Columnar- and Equiaxed-Grain Regions\*

Laboratory	Columnar grains		Equiaxed grains	
	$T_1, ^\circ\text{C}$	$\rho_1/\rho_s, \%$	$T_2, ^\circ\text{C}$	$\rho_2/\rho_s, \%$
Atomics International	1800	98	1600	95
General Electric	2150	99	1650	97
Kernforschungszentrum Karlsruhe	1700	95	1300	As-fab- ricated
Westinghouse	2000	99	1600	97

\*From W. W. Marr and D. H. Thompson, *Trans. Amer. Nucl. Soc.*, 14: 150 (1971).

However, modeling the fuel restructuring process by the three fixed zones is adequate for estimating the primary consequences of densification on the reduction of the central temperature from the initial value for the solid pellet. Calculations of this effect have been advanced by many investigators.<sup>18,28-30</sup>

The radius of the central void is related to the positions of the boundaries between the restructured regions by a mass balance, which assumes that there has been no axial movement of fuel during the densification process. Thus,

$$\pi R^2 \rho_3 = \pi(r_1^2 - r_0^2)\rho_1 + \pi(r_2^2 - r_1^2)\rho_2 + \pi(R^2 - r_2^2)\rho_3 \quad (10.69)$$

or

$$r_0^2 = \left(\frac{\rho_1 - \rho_2}{\rho_1}\right) r_1^2 + \left(\frac{\rho_2 - \rho_3}{\rho_1}\right) r_2^2 \quad (10.70)$$

Equation 10.70 neglects minor dimensional changes due to thermal expansion of the fuel material. The densities  $\rho_1$ ,

$$H_3 = \frac{\mathcal{P}}{\pi R^2} \quad (10.71)$$

In the equiaxed- and columnar-grain regions, the corresponding volumetric heat rates are

$$H_2 = \left(\frac{\mathcal{P}}{\pi R^2}\right) \frac{\rho_2}{\rho_3} \quad (10.72)$$

$$H_1 = \left(\frac{\mathcal{P}}{\pi R^2}\right) \frac{\rho_1}{\rho_3} \quad (10.73)$$

The density ratios in these equations represent the atom-density ratio  $N_f(r)/N_{f0}$  in Eq. 10.56 for the two regions where fuel sintering has occurred. The enrichment and flux ratios in Eq. 10.56 are assumed to be unity for this calculation.

The heat-conduction equation (Eq. 10.49) for region 3 is

$$\frac{1}{r} \frac{d}{dr} \left( r k_3 \frac{dT}{dr} \right) = -H_3 \quad (10.74)$$

where  $k_3$  is the thermal conductivity of the fuel for temperatures between  $T_s$  and  $T_2$  and for the porosity of the as-fabricated fuel. The latter is given by

$$P_3 = 1 - \frac{\rho_3}{\rho_s} \quad (10.75)$$

If the as-fabricated fuel is specified, for example, as 90% of theoretical density,  $P_3 = 0.1$ .

Integration of Eq. 10.74 once yields

$$k_3 \frac{dT}{dr} = -\frac{1}{2} H_3 r + \frac{C_3}{r} \quad (10.76)$$

A second integration yields

$$\int_{T_s}^{T_2} k_3 dT = \frac{1}{4} H_3 R^2 \left[ 1 - \left( \frac{r_2}{R} \right)^2 \right] - C_3 \ln \left( \frac{R}{r_2} \right) \quad (10.77)$$

Similarly, the first and second integrals of the heat-conduction equation in regions 2 and 1 are

$$k_2 \frac{dT}{dr} = -\frac{1}{2} H_2 r + \frac{C_2}{r} \quad (10.78)$$

$$\int_{T_2}^{T_1} k_2 dT = \frac{1}{4} H_2 r_2^2 \left[ 1 - \left( \frac{r_1}{r_2} \right)^2 \right] - C_2 \ln \left( \frac{r_2}{r_1} \right) \quad (10.79)$$

$$k_1 \frac{dT}{dr} = -\frac{1}{2} H_1 r + \frac{C_1}{r} \quad (10.80)$$

$$\int_{T_1}^{T_0} k_1 dT = \frac{1}{4} H_1 r_1^2 \left[ 1 - \left( \frac{r_0}{r_1} \right)^2 \right] - C_1 \ln \left( \frac{r_1}{r_0} \right) \quad (10.81)$$

The integration constants  $C_1$ ,  $C_2$ , and  $C_3$  are determined by equating the heat fluxes obtained from the solutions in adjacent zones at their common boundary:

$$k_3 \left( \frac{dT}{dr} \right)_3 = k_2 \left( \frac{dT}{dr} \right)_2 \quad \text{at } r = r_2 \quad (10.82)$$

$$k_2 \left( \frac{dT}{dr} \right)_2 = k_1 \left( \frac{dT}{dr} \right)_1 \quad \text{at } r = r_1 \quad (10.83)$$

and applying the adiabatic boundary condition (Eq. 10.50) at the central void:

$$\left( \frac{dT}{dr} \right)_1 = 0 \quad \text{at } r = r_0 \quad (10.84)$$

Equations 10.80 and 10.84 show that

$$C_1 = \frac{1}{2} H_1 r_0^2 = \frac{1}{2} \left( \frac{\mathcal{P}}{\pi R^2} \right) \left( \frac{\rho_1}{\rho_3} \right) r_0^2 \quad (10.85)$$

Similarly,  $C_2$  is found to be

$$C_2 = \frac{1}{2} H_2 r_1^2 - \frac{1}{2} H_1 (r_1^2 - r_0^2) - \frac{1}{2} \left( \frac{\mathcal{P}}{\pi R^2} \right) \left[ \frac{\rho_2}{\rho_3} r_1^2 - \frac{\rho_1}{\rho_3} (r_1^2 - r_0^2) \right] \quad (10.86)$$

Substituting the preceding relations into Eq. 10.82 yields

$$C_3 = \frac{1}{2} \left( \frac{\mathcal{P}}{\pi R^2} \right) \left[ r_2^2 - \frac{\rho_2}{\rho_3} (r_2^2 - r_1^2) - \frac{\rho_1}{\rho_3} (r_1^2 - r_0^2) \right] - 0 \quad (10.87)$$

The bracketed term in Eq. 10.87 vanishes according to Eq. 10.70.

Substitution of these expressions for  $C_1$ ,  $C_2$ , and  $C_3$  into Eqs. 10.77, 10.79, and 10.81 yields the final formulas for the conductivity integrals in the three annular zones:

$$\int_{T_s}^{T_2} k_3 dT = \left( \frac{\mathcal{P}}{4\pi} \right) \left[ 1 - \left( \frac{r_2}{R} \right)^2 \right] \quad (10.88)$$

$$\int_{T_2}^{T_1} k_2 dT = \left( \frac{\mathcal{P}}{4\pi} \right) \left( \frac{\rho_2}{\rho_3} \right) \left( \frac{r_2}{R} \right)^2 \left[ 1 - \left( \frac{r_1}{r_2} \right)^2 + \left( \frac{\rho_3}{\rho_2} - 1 \right) \ln \left( \frac{r_2}{r_1} \right)^2 \right] \quad (10.89)$$

$$\int_{T_1}^{T_0} k_1 dT = \left( \frac{\mathcal{P}}{4\pi} \right) \left( \frac{\rho_1}{\rho_3} \right) \left( \frac{r_1}{R} \right)^2 \left[ 1 - \left( \frac{r_0}{r_1} \right)^2 - \left( \frac{r_0}{r_1} \right)^2 \ln \left( \frac{r_1}{r_0} \right)^2 \right] \quad (10.90)$$

The conductivity integrals on the left-hand sides of Eqs. 10.88 to 10.90 can be obtained in either of two ways. An empirical thermal-conductivity formula, such as Eqs. 10.45 and 10.48, can be integrated directly using  $P_i = 1 - (\rho_i/\rho_s)$ , where  $P_i$  is the porosity of the  $i$ th annular band and  $\rho_i/\rho_s$  is the fraction of theoretical density of the  $i$ th band. Alternatively, a plot of the conductivity integral for a constant porosity (such as Fig. 10.20) can be used directly and corrected for the porosity differences in the three fuel regions. If the conductivity integral is available for 95% dense material, for example, then

$$\int_{T_i}^{T_{i-1}} k_i dT = \left[ \left( \int_0^{T_{i-1}} k dT \right)_{P=0.05} - \left( \int_0^{T_i} k dT \right)_{P=0.05} \right] \frac{f(P_i)}{f(0.05)} \quad (10.91)$$

where  $T_i$  and  $T_{i-1}$  are the temperatures of the outer and inner boundaries of the  $i$ th zone, respectively. The conductivity integrals on the right of Eq. 10.91 can be read directly from a plot such as Fig. 10.20. The function  $f(P)$  is the fractional reduction in thermal conductivity from 100% dense solid due to porosity  $P$ , as given by Eqs. 10.40, 10.42, and 10.44.

The temperature distribution in the rod can be obtained as follows: Assume that the fuel surface temperature  $T_s$ , the linear power  $\mathcal{P}$ , and the density of the fabricated fuel  $\rho_3/\rho_s$  have been specified. The properties of the columnar and equiaxed-grain regions ( $T_1$ ,  $\rho_1/\rho_s$ ,  $T_2$ , and  $\rho_2/\rho_s$ ) are also presumed to be known (as one of the rows in Table 10.4). Equations 10.70, 10.88, 10.89, and 10.90 provide four equations from which the four unknowns  $r_0/R$ ,  $r_1/R$ ,  $r_2/R$ , and  $T_0$  can be determined. The conductivity integrals for the two outer zones are given by Eq. 10.91. First,  $r_2/R$  is determined by solving Eq. 10.88. Equation 10.89 then gives  $r_1/R$ . The radius of the central void is then obtained from Eq. 10.70. Next, the conductivity integral for the inner zone is given by Eq. 10.90. Equation 10.91 is then employed to determine  $(\int_0^{T_0} k dT)_{0.95}$ . Finally, Fig. 10.20 (or the equivalent plot for the appropriate fuel) is used to obtain  $T_0$ .

The method just described fixes the radius and temperature of the central void surface and the locations of the boundaries between the three regions, each of which is associated with a specific temperature. The temperature profile between these anchor points can be obtained from Eqs. 10.88 to 10.90 by replacing the upper limits on the conductivity integral by  $T$  and the corresponding radial position on the right-hand side by  $r$  (except in the coefficient of the logarithmic term in Eq. 10.90). Figure 10.24 shows typical temperature distributions just at startup and after fuel restructuring has occurred. The slopes of the temperature distributions are discontinuous at the boundaries separating the various regions because the thermal conductivities, according to the model, change discontinuously at  $r_1$  and  $r_2$ . As expected, the maximum temperature attained by the fuel decreases substantially as a result of densification and central-void formation. The net effect of these processes is to move the nuclear heat source further toward the periphery of the rod than is the case in the solid rod of as-fabricated fuel. Such a displacement effectively reduces the path length over which heat must be conducted; so a given heat flux can be sustained with a smaller temperature difference. The higher thermal conductivities in regions 1 and 2 which result from densification also act to reduce fuel temperature.

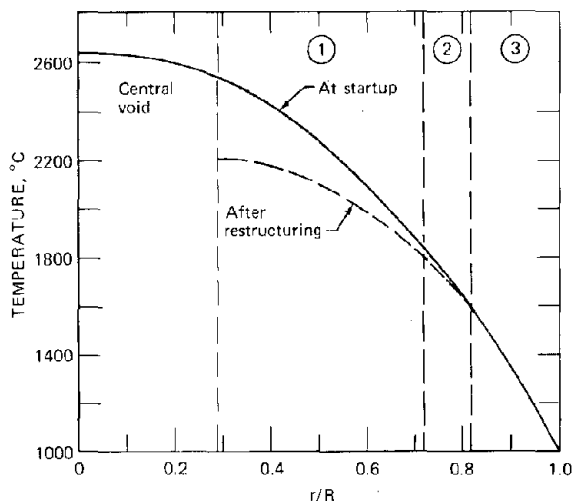


Fig. 10.24 Temperature distribution in a mixed-oxide fuel pin before and after restructuring.  $\mathcal{P} = 500 \text{ W/cm}$ ;  $T_s = 1000^\circ\text{C}$ ; initial density = 85% theoretical density;  $T_1 = 1800^\circ\text{C}$ ,  $\rho_1/\rho_s = 98\% \text{ TD}$ ;  $T_2 = 1600^\circ\text{C}$ ,  $\rho_2/\rho_s = 95\% \text{ TD}$ ;  $f(P) = 1 - P^2$ .

### 10.4.4 Fuel Surface Temperature

Applying the calculations just described requires that the fuel surface temperature  $T_s$  be known at all axial locations of a fuel element.

Design of the reactor core includes specification of the linear power of the fuel rods as a function of axial position. Consider a fuel assembly containing  $N$  fuel rods each of

which has the same axial variation in linear power,  $\mathcal{P}(z)$ . Let  $Q$  be the mass flow rate to the assembly and  $C_{pc}$  the heat capacity of the coolant. An energy balance over the coolant flowing through a differential slice  $dz$  of the assembly cross section yields

$$QC_{pc} \frac{dT_{(\text{coolant})}}{dz} = N\mathcal{P}$$

Integrating from the inlet coolant temperature at  $z = 0$  to axial position  $z$  results in

$$T_{(\text{coolant})} = T_{(\text{inlet coolant})} + \frac{N}{QC_{pc}} \int_0^z \mathcal{P}(z') dz' \quad (10.92)$$

With the coolant temperature at any  $z$  given by Eq. 10.92,  $T_s$  can be estimated as follows:

The heat flux at the surface of the fuel is related to the linear power by

$$q_s = \frac{\mathcal{P}}{2\pi R} \quad (10.93)$$

The overall heat-transfer coefficient between the fuel surface and the bulk coolant temperature is due to the thermal resistance of the fuel-cladding, cladding conduction, and convective heat transfer in the coolant film. These three components act in series to determine the overall heat-transfer coefficient  $U$ . For cladding thicknesses small compared to the fuel radius,  $U$  is given by

$$\frac{1}{U} = \frac{1}{h_{\text{gap}}} + \frac{t_c}{k_c} + \frac{1}{h_{\text{coolant}}} \quad (10.94)$$

where  $h_{\text{gap}}$  = the conductance of the gap between the fuel outer surface and the inner surface of the cladding

$t_c$  = the thickness of cladding

$k_c$  = the thermal conductivity of the cladding

$h_{\text{coolant}}$  = the convective heat-transfer coefficient in the coolant-fuel-rod flow geometry, which can be obtained from correlations as a function of coolant properties and flow rate

Typical conductances and temperature drops for the three resistances between the fuel surface and liquid sodium coolant are shown in Table 10.5. The level of the temperature in the fuel is controlled by the coolant

Table 10.5 Heat-Transfer Resistances Exterior to the Fuel in a Fast Reactor\*

	Typical conductance, $\text{W cm}^{-2} \text{ }^\circ\text{C}^{-1}$	Temperature drop, $^\circ\text{C}$
Fuel-cladding gap	1	290
Cladding	9	32
Coolant film	12	24
Overall	0.84	346

\*Linear power, 550 W/cm; fuel radius, 3 mm; cladding: stainless steel, 0.25 mm thick,  $k_c = 0.22 \text{ W cm}^{-1} \text{ }^\circ\text{C}^{-1}$ ; coolant: sodium.

temperature at the particular axial location and the temperature drop between the coolant and the fuel surface. Assuming that the overall heat-transfer coefficient  $U$  is known, the surface heat flux is

$$q_s = U(T_s - T_{\text{coolant}}) \quad (10.95)$$

Combining Eqs. 10.93 and 10.95 gives

$$T_s = T_{\text{coolant}} + \frac{P}{2\pi R_c U} \quad (10.96)$$

Typical values of  $T_s$  in a fast reactor are 800 to 1000°C. Of the three resistances in series between the coolant and the fuel surface, Table 10.5 shows that the resistance of the fuel-cladding gap is the most significant by an order of magnitude.

#### 10.4.5 Conductance of the Fuel-Cladding Gap

Because of the substantial influence of the thermal resistance of the fuel-cladding gap on fuel temperature, extensive theoretical and experimental investigations have been directed toward methods of predicting  $h_{\text{gap}}$  with sufficient accuracy for design purposes. So far, these efforts have only been marginally successful.

##### Open Gap

If the fuel and the cladding are not in physical contact (i.e., the fuel is free-standing within the cladding), the primary mechanism of heat transfer is by conduction through the filling gas. At reactor startup the gas in the fuel element is helium at approximately atmospheric pressure. After in-pile operation for extended periods, the fission gases krypton and xenon, which are released from the fuel, mix with the helium, and the total gas pressure within the fuel element increases substantially (to perhaps 75 atm at the end of life). The gas that provides the means of thermal communication between the fuel and the cladding is thus a mixture of helium, krypton, and xenon, the composition of which is a function of irradiation time.

If the space between the fuel and the cladding is much larger than the mean free path of the gas atoms at the prevailing temperature and pressure, the gap conductance is simply  $k_g/t_{\text{gap}}$ , where  $k_g$  is the thermal conductivity of the gap mixture and  $t_{\text{gap}}$  is the gap thickness. However, when the two surfaces approach each other closely, a phenomenon analogous to viscous slip in hydrodynamics affects the transfer of heat by conduction through the gas. If a gas sustains a temperature gradient, the gas temperature immediately adjacent to a bounding surface is not equal to the surface temperature. Figure 10.25 shows the temperature profile between two plane surfaces that are at different temperatures. The discontinuity that occurs within a mean free path of the walls is called the temperature jump. Extrapolation of the gradient in the bulk of the gas results in intersections with the solid temperatures at distances  $g_c$  and  $g_f$  inside the solids. These distances, which are termed temperature jump distances, are analogous to the extrapolation lengths of neutron diffusion theory. The conductance of the gap is given by

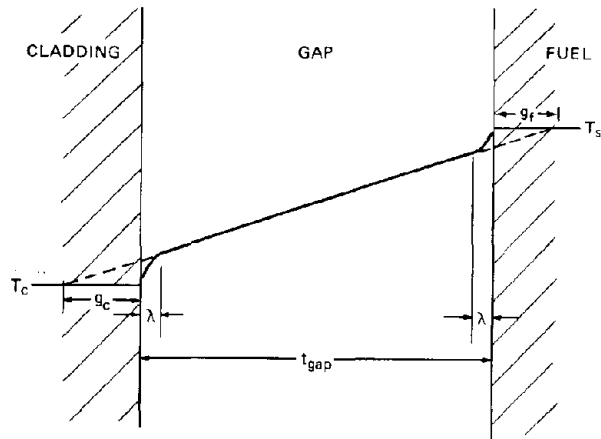


Fig. 10.25 Temperature profile in a gas between two plane surfaces.

$$h_{\text{gap}} = \frac{k_g}{t_{\text{gap}} + g_c + g_f} \quad (10.97)$$

Formulas for  $g$  from the kinetic theory of gases were first worked out by Knudsen in 1911. The derivation reproduced by Kennard<sup>31</sup> gives the temperature jump distance as

$$g = 2 \left( \frac{2-\alpha}{\alpha} \right) \left( \frac{\gamma}{1+\gamma} \right) \left( \frac{k}{\mu C_p} \right)_g \lambda \quad (10.98)$$

where  $\lambda$  is the mean free path in the gas,  $\gamma$  is the ratio  $C_p/C_v$  for the gas, and  $(\mu C_p/k)_g$  is the Prandtl number ( $\mu$  = gas viscosity). Since  $\gamma = 5/3$  for monatomic gases and the Prandtl number is about 0.7 at all temperatures, the product of the two terms containing these quantities in Eq. 10.98 is approximately unity.

The quantity  $\alpha$  in Eq. 10.98 is called the thermal-accommodation coefficient of the gas on the particular surface exposed to the gas. It is the fractional approach of the impinging molecules to complete thermal adjustment to the solid temperature before rebounding. If a stream of molecules of temperature  $T_i$  strikes a solid at  $T_s$  and is reflected with a temperature  $T_r$ , the thermal-accommodation coefficient is defined by

$$\alpha = \frac{T_r - T_i}{T_s - T_i} \quad (10.99)$$

when  $\alpha = 1$ ,  $T_r = T_s$ , and the scattered molecules have been completely equilibrated with the substrate. The simplest theory of thermal accommodation regards the process as an elastic collision between a gas atom and an atom of the solid which is acting as an independent particle (i.e., the bonds connecting the struck surface atom to the remainder of the lattice are ignored).<sup>31</sup> On the basis of this picture, one would expect thermal accommodation to be most complete when the gas and the solid atoms are of equal mass (neutron thermalization in a reactor is most efficient when the moderator is hydrogen for the same reason). Indeed, experiments with metallic surfaces show that  $\alpha$  is smallest for the very light gases hydrogen and helium, for

which the kinematics of energy transfer are least favorable. However, the thermal coefficient is much like the emissivity in its sensitivity to surface conditions, of which cleanliness and roughness are the most significant.

Solid surfaces exposed to environments other than high vacuum adsorb at least a monolayer of impurity gases, such as  $H_2O$ ,  $CO$ , and  $CO_2$ . This adsorbed layer usually contains atoms of lower mass than the substrate solid, thereby forming a softer bed for energy exchange with the gas molecules striking the surface. The thermal-accommodation coefficient on contaminated surfaces is greater than that on substrates that are atomically clean.

Roughness invariably increases thermal accommodation by making possible multiple collisions of an impinging gas atom with the solid before the former escapes from the surface. For example, if incident atoms make on the average three collisions with a rough surface before returning to the gas phase and if at each collision energy is exchanged with the solid according to Eq. 10.99, the apparent coefficient of thermal accommodation,  $\alpha_{app}$ , is related to the single collision value  $\alpha$  by

$$\alpha_{app} = \alpha[1 + (1 - \alpha)(2 - \alpha)]$$

The accommodation coefficients of the rare gases on the fuel outer surface and the cladding inner surface are unknown but are probably close to unity. The fuel surface is undoubtedly roughened by fission recoils and cracking. The cladding surface is also bombarded by fission fragments that recoil across the gap. In addition, the cladding can be subject to corrosion by oxygen transported from the fuel by volatile fission products (e.g., cesium and molybdenum). Finally, the two surfaces defining the gap may both be heavy-metal oxides. Each thermal spike created by a fission-fragment track that intersects the fuel surface is capable of vaporizing many molecules of  $UO_2$  or  $PuO_2$ , which condense on the inner surface of the cladding. Fuel material that is plated on the cladding in such a fashion undoubtedly makes a very intimate thermal contact.

If the thermal-accommodation coefficients are set equal to unity, the coefficient of  $\lambda$  on the right-hand side of Eq. 10.98 is a number of order unity, or the temperature jump distance for use in Eq. 10.97 is approximately equal to the molecular mean free path in the gas. The latter may be obtained from the kinetic theory of gases and expressed by

$$\lambda = \frac{\lambda_0}{p} \left( \frac{T}{273} \right) \quad (10.100)$$

where  $T$  is the temperature in  $^{\circ}K$ ,  $p$  is the gas pressure in atm, and  $\lambda_0$  is a property of the gas that depends on the molecular or atomic diameter. For helium  $\lambda_0 = 1.74 \times 10^{-5}$  atm-cm, and for xenon  $\lambda_0 = 3.6 \times 10^{-6}$  atm-cm. The mean free path in helium at 1 atm pressure and room temperature is  $0.2 \mu m$ . For xenon at 10 atm pressure and  $1000^{\circ}K$  (typical fuel element conditions), the mean free path is  $0.01 \mu m$ . Inasmuch as open gaps at startup are typically  $\sim 80 \mu m$  wide, the temperature jump effect represented by the last two terms in the denominator of Eq. 10.97 is probably not important until the gap closes and the solids make contact.

The conductance of the open gap can be written

$$h_{gap} = \frac{k_g}{t_{gap}} + \frac{4\sigma T^3}{(1/\epsilon_c) + (1/\epsilon_f) - 1} \quad (10.101)$$

The last term on the right is an approximate radiation contribution (analogous to Eq. 10.43 for the effective conductivity of a pore with the addition of the appropriate radiation view factor for cladding and fuel surfaces of emissivities  $\epsilon_c$  and  $\epsilon_f$ , respectively). The temperature in the last term of Eq. 10.101 is the average of the cladding-inner-wall and fuel-surface values. For the small gaps encountered in power operation, the radiation contribution is generally small compared to the conduction term.

Kampf and Karsten<sup>18</sup> describe the thermal conductivity of the rare gases by

$$k_g (\text{pure gas}) = A \times 10^{-6} T^{0.79}, \text{ W cm}^{-1} \text{ } ^{\circ}C^{-1} \quad (10.102)$$

where  $T$  is the average gas temperature in the gap ( $^{\circ}K$ ) and  $A$  is 15.8 for helium, 1.15 for krypton, and 0.72 for xenon. The thermal conductivity of the gas mixtures that develop as a result of release of fission gases from the fuel is approximately given by

$$k_g = (k_{He})^{x_{He}} (k_{Xe})^{1-x_{He}} \quad (10.103)$$

In Eq. 10.103 all the fission gases are taken as xenon, which is the largest component, and the mixture is considered as a binary of helium atom fraction  $x_{He}$ . The thermal conductivities of the pure gases,  $k_{He}$  and  $k_{Xe}$ , are given by Eq. 10.102.

### Closed Gap

As a result of thermal expansion and swelling of both the fuel and the cladding, the fuel-cladding gap may close. When this situation occurs, heat is transported by solid conduction through the regions on the fuel and cladding surfaces that are in physical contact as well as by conduction through the gas film that fills the portion of the interface where contact is not made. Figure 10.26 suggests what the closed gap might look like. Contact between the two solids is made only over a small fraction of the gross interfacial area, but the majority of the heat flux may be through these spots. The thermal contact resistance depends on the pressure or local compressive stress, which acts to increase the area of contact by plastic deformation of the softer material by the harder. The mean thickness of the gas film  $\delta$  is approximately equal to the sum of the mean roughness heights of the two solid surfaces.

Several theories of thermal contact resistance have been advanced.<sup>32-34</sup> Cetinkale and Fishenden<sup>32</sup> represent each contacting spot as a cylinder of radius  $R_1$ . If there are  $N$  contact cylinders per unit area of gross surface arranged on a square lattice, the gross surface area associated with each contact is  $\pi R_2^2 = 1/N$ , where  $R_2$  is the radius of the zone around the contact that forms its unit cell. Analysis of the flow of heat in this idealized geometry yields the following expression for the component of the gap conductance due to the solid-solid contacts:

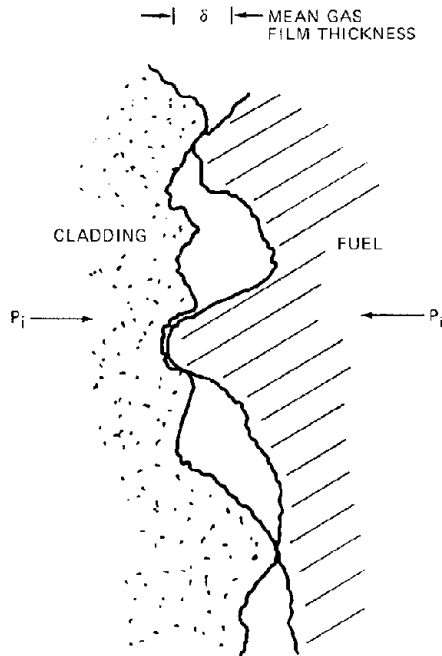


Fig. 10.26 Closed fuel-cladding gap.

$$h_{\text{contact}} = \frac{1}{R_1} \left( \frac{2k_f k_c}{k_f + k_c} \right) \frac{(R_1/R_2)^2}{\tan^{-1} [(R_2/R_1) - 1]} \quad (10.104)$$

where  $k_f$  and  $k_c$  are the thermal conductivities of the fuel and cladding, respectively.

Equation 10.104 neglects heat conduction through the gas film and assumes that the cylinder height (approximately equal to  $\delta$  in Fig. 10.26) is small. The contact area per unit of gross interfacial area,  $(R_1/R_2)^2$ , increases with the interfacial pressure  $P_i$  because of plastic deformation. The effect of loading of the interface on the fractional contact area depends on the yield strength of the softer material, as measured by its Meyer hardness.\* The fraction of the interface that is in solid-solid contact is given by

$$\left( \frac{R_1}{R_2} \right)^2 = \text{constant} \times \frac{P_i}{H} \quad (10.105)$$

where  $H$  is the Meyer hardness of the softer material.

In addition, it has been found<sup>35</sup> that the average radius of the solid-solid contact,  $R_1$ , is proportional to the square root of the mean surface roughness, which is approximately equal to the gas film thickness  $\delta$ :

$$R_1 = \text{constant} \times \delta^{1/2} \quad (10.106)$$

Substituting Eqs. 10.105 and 10.106 into Eq. 10.104 and noting that the arc tangent term can be replaced by  $\pi/2$

for the usual case of  $R_1/R_2 \ll 1$ , the conductance due to solid-solid contact becomes

$$h_{\text{contact}} = C \left( \frac{2k_f k_c}{k_f + k_c} \right) \frac{P_i}{\delta^{1/2} H} \quad (10.107)$$

where  $C$  is a combination of the constants in the preceding equations.

Conduction through the gas film provides a parallel heat-flow path. Heat transfer by this mode is given by Eq. 10.97 with the gap thickness replaced by the mean gas-film thickness:

$$h_{\text{gas}} = \frac{k_g}{\delta + g_c + g_f} \quad (10.108)$$

The total conductance of the closed fuel-cladding gap is the sum of Eqs. 10.107 and 10.108:

$$h_{\text{gap}} = \frac{k_g}{\delta + g_c + g_f} + C \left( \frac{2k_f k_c}{k_f + k_c} \right) \frac{P_i}{\delta^{1/2} H} \quad (10.109)$$

Several investigators have applied Eq. 10.109 to out-of-pile tests on zircaloy- $\text{UO}_2$  systems. Ross and Stoute<sup>36</sup> found that a value for the constant  $C$  of approximately unity gave the best fit to their measurements. The gap conductance depended on the nature of the filling gas, which indicated the importance of the first term in Eq. 10.109. From their data Ross and Stoute obtained  $g_c + g_f$  equal to  $10 \mu\text{m}$  in helium and  $1 \mu\text{m}$  in xenon (both at 1 atm). These values are 10 to 30 times larger than the mean free path of the gases, which suggests either that the thermal-accommodation coefficients were very much smaller than unity (see Eq. 10.98) or that inadequacies in the model that led to Eq. 10.109 were reflected in unrealistic temperature jump distances required to fit the data.

Robertson et al.<sup>27</sup> have compiled Fig. 10.27 from the experiments of Ross and Stoute and others. Bands in which the data lie are plotted for surfaces of three different degrees of roughness (in out-of-pile experiments, the surface roughness can be measured by a profilometer). The data confirm the general features of Eq. 10.109. The gap conductance is greater for helium fill gas than for the other inert gases, in accord with the relative values of the thermal conductivities. The gap conductance increases in a roughly linear fashion with interfacial pressure increases and decreases as the surface roughness increases. Further discussion of gap-conductance theories can be found in Refs. 26, 27, 37, and 38.

Application of Eq. 10.109 to operating fuel pins is hampered by the following difficulties:

1. The thermal conductivity of the fill gas,  $k_g$ , is strongly dependent on its composition. The latter depends on the fraction of the fission gases released from the fuel, which is one of the more difficult fuel performance quantities to predict.

2. The roughness and even the identity of the adjacent surfaces cannot be predicted.

3. The temperature jump distances determined from well-controlled out-of-pile tests may not apply to fuel elements in the reactor.

\*In a hardness test a small cone or sphere is pushed into the material by a fixed force. The depth or diameter of the indentation is a measure of the hardness, which is expressed in units of pressure.

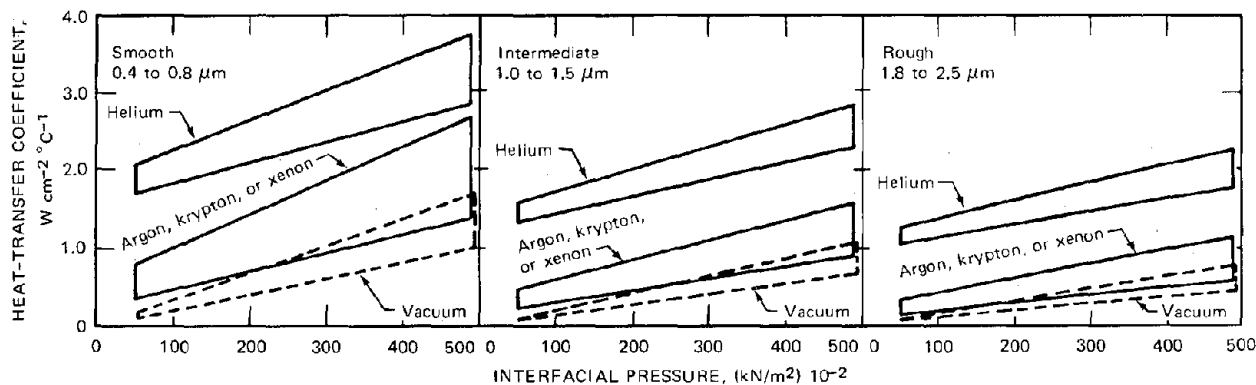


Fig. 10.27 Graphical summary of experimental values for heat-transfer coefficients between  $\text{UO}_2$  and zircaloy either in vacuum or various gases at atmospheric pressure. The values are for the three ranges of arithmetic-mean roughness heights indicated and for an interface temperature of  $350^\circ\text{C}$ . [From J. A. L. Robertson et al., *J. Nucl. Mater.*, 7: 242 (1962).]

4. The interfacial pressure in an operating fuel element is difficult to estimate. Its prediction is one of the primary objectives of the fuel modeling codes described in Chap. 21.

Fuel-element designers either accept the out-of-pile correlations (Eq. 10.109 or variant thereof)<sup>39-42</sup> or assign a constant value to  $h_{\text{gap}}$  for computational purposes.<sup>43-45</sup> The estimate  $h_{\text{gap}} = 1 \text{ W cm}^{-2} \text{ }^\circ\text{C}^{-1}$  is often employed.<sup>43,44</sup>

## 10.5 SUMMARY

The methods described in this chapter for determining the temperature profile in a highly rated fast reactor fuel rod are better than the assumption of a parabolic temperature distribution, but they do not consider many important features of fuel thermal performance. A better calculation should include

1. Differential thermal expansion of the fuel and the consequent displacement of the hot, plastic core regions 1 and 2 toward the center. This effect tends to reduce the size of the central void.

2. Axial fuel displacement (due, for example, to vapor transport of fuel material within the central void).

3. Cracking of the fuel due to thermal stresses. Radial cracks probably do not affect the temperature profile as much as circumferential cracks, which act as gas-filled gaps.

4. The dynamic nature of the fuel restructuring process. The zone boundaries  $r_0$ ,  $r_1$ , and  $r_2$  are in reality functions of irradiation time.

5. The generation of porosity by fission-gas bubbles, expansion due to solid fission products, and reduction in porosity by hydrostatic pressure (hot pressing).

6. The continuous rather than the discrete nature of the porosity variation with radius.

7. The role of thermal expansion, fuel swelling, and cladding swelling in changing the fuel-cladding gap conductance, which causes the fuel surface temperature to vary with irradiation time even though the coolant temperature at the particular axial location is constant.

8. The effects of plutonium redistribution on the volumetric heat generation rate and of oxygen redistribution on the thermal conductivity.

Solutions to the heat-conduction equation, Eq. 10.49, which incorporate many of the previously mentioned features must be accomplished by finite-difference techniques. Computer codes have been written for this purpose.<sup>46-49</sup>

If the coolant temperature at each axial location is known from the specified axial variation in the linear power and the thermal-hydraulic characteristics of the coolant, a complete description of the radial and axial fuel temperature distribution and fuel restructuring can be obtained. Figure 10.28 shows typical results of such a comparison. Note that, although the temperature of the central void is uniform on its circumference, an axial gradient of  $T_0$  is present.

The net effect on the fuel-element thermal performance of the phenomena discussed in this chapter is to reduce the maximum permissible linear power of the rod. Christensen<sup>1</sup> has compared the thermal performance limits of LWRs and LMFBRs by examining the linear power that results in attainment of the melting temperature (Table 10.6). Identifiable components of the difference between the two types of fuel elements are listed separately. All effects involving the fuel melting temperature and the solid thermal conductivity are deleterious to LMFBR performance. Only the restructuring effects that increase the fuel density and form the central void and the thermal expansion-swelling phenomena that result in gap closure are positive contributions. However, although contact between fuel and cladding improves thermal performance, it very probably adversely affects fuel-pin mechanical performance by causing creep deformation of the cladding. Late in fuel-element life, the irradiation-induced swelling of the cladding may cause the gap to reappear. When this occurs, only the pressure of the accumulated fission gas remains to stress the cladding internally. Creep strain is presently proposed as a lifetime-limiting criterion of fast reactor fuel elements, although criteria based on the cumulative effects of all life-consum-

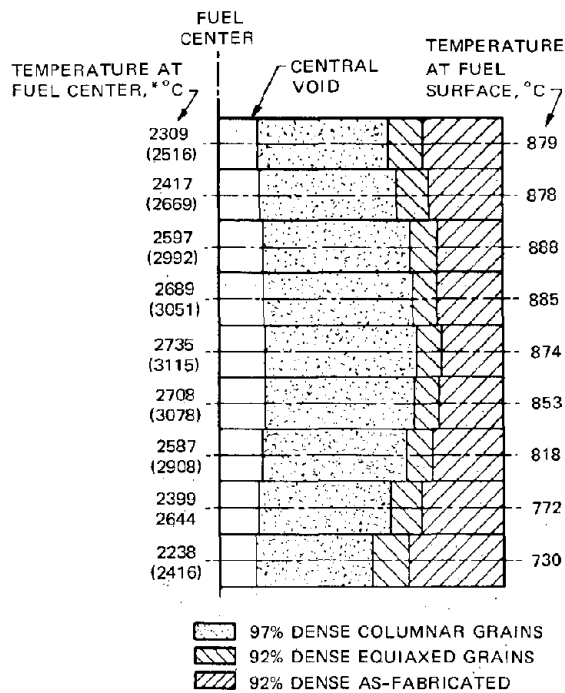
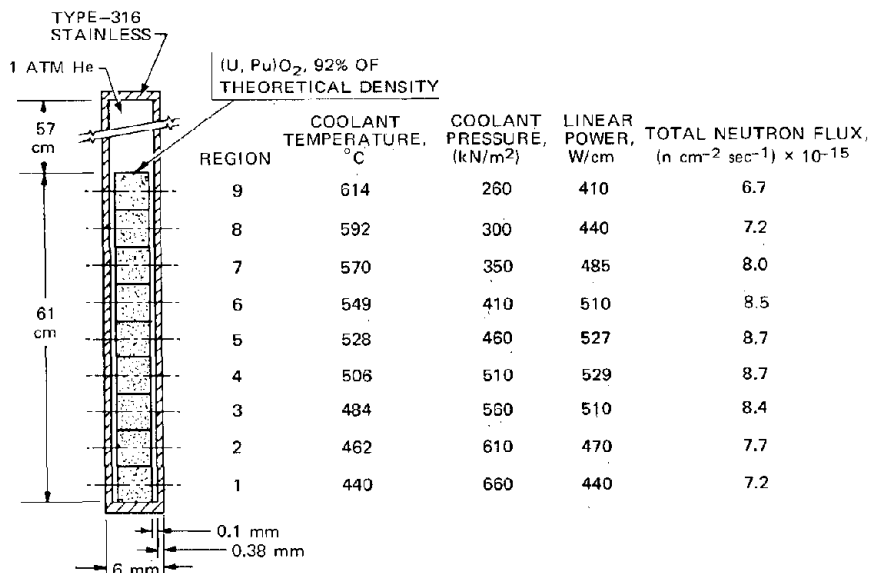


Fig. 10.28 Typical LMFBR fuel element under operating conditions. The pin has been divided axially into 9 zones for thermal analysis. Temperature distribution after restructuring is shown at the bottom.  $T_1 = 1750^\circ\text{C}$ ;  $T_2 = 1450^\circ\text{C}$ . [From C. M. Cox and F. J. Homan, *Nucl. Appl. Tech.*, 9:317 (1970).]

ing phenomena to which the cladding is subjected are being developed.

Table 10.6 Comparison of LWRs and LMFBRs in Terms of Factors That Affect the Linear Power for Fuel Melting\*

Factor	Approximate change in melting linear power, %
Increased coolant temperature in LMFBR	-13
Addition of large fractions of Pu to LMFBR fuels	
Effect on thermal conductivity	-8
Effect on melting temperature	-5
Absence of flux depression in LMFBR fuel rod	-5
Increased porosity for swelling accommodation in LMFBR	
Effect on thermal conductivity	-12
Restructuring effects	+25
Increased fuel-cladding $\Delta T$ because of higher heat fluxes in LMFBR	-10
High burnup effects in LMFBR	
Effect on thermal conductivity and melting temperature	-10
Effect on $h_{gap}$ because of gap closure	+10
Net reduction in allowable heat rating for LMFBR compared to LWR	-28

\*From J. A. Christensen, in *Proceedings of the Conference on Fast Reactor Fuel Element Technology*, p. 371, R. Farnakes (Ed.), American Nuclear Society, Hinsdale, Illinois, 1971.

### 10.6 NOMENCLATURE

- $a_0$  = lattice constant
- A = constant in thermal-conductivity equation for rare gases; coefficient (temperature independent) in the expression for thermal conductivity of solids
- $A_0$  = coefficient (temperature independent) in the expression for thermal conductivity of stoichiometric  $UO_2$ - $PuO_2$
- $\Delta A$  = change in coefficient A due to non-stoichiometry
- $A^*$  = constant in expression for  $\Delta A$
- $A'$  = coefficient (temperature independent) in the expression for mean free path
- B = coefficient (temperature independent) in the expression for thermal conductivity of solids
- $B'$  = coefficient (temperature independent) in the expression for mean free path
- c = heat capacity of a phonon
- C = specific heat
- $f(P)$  = function giving porosity effect on fuel thermal conductivity
- F = fission density in fissions per unit volume

- $\bar{F}$  = fissions per unit volume per unit time
- g = temperature jump distance
- h = heat-transfer coefficient
- H = enthalpy; volumetric heat-generation rate; Meyer hardness of softer material in a contact of two materials
- $H_i$  = volumetric heat-generation rate in zone i (i = 1, 2, 3)
- k = thermal conductivity
- $k_i$  = thermal conductivity in zone i (i = 1, 2, 3)
- l = length of a solid specimen; length of a parallelepiped pore
- $\Delta l$  = change in length of a solid specimen
- L = length of one side of a unit cell in a porous body
- $n_p$  = phonon density
- $N_f$  = total number of heavy-metal atoms per unit volume
- N = number of fuel rods in an assembly; number of contact cylinders per unit area
- p = pressure
- P = volume porosity
- $P_c$  = fraction of cross-sectional area of the x-z face occupied by a pore tube
- $P_i$  = interfacial pressure in a contact of two materials
- $P_L$  = fraction of the length of the pore tube occupied by the pore
- $\mathcal{P}$  = linear power
- q = enrichment, or fissile atoms per total heavy-metal atoms; heat flux
- Q = coolant mass flow rate to a subassembly
- r = atomic radius; radial distance from center line in a fuel rod
- $r_i$  = radius of defect i
- $r_0$  = radius of the central void
- $r_1$  = outer radius of columnar grains
- $r_2$  = outer radius of equiaxed grains
- R = radius of the fuel; gas constant
- $R_c$  = outer radius of cladding
- $R_1$  = radius of contacting spot represented as a cylinder
- $R_2$  = radius of the unit cell around a contact spot
- s = entropy
- t = time; thickness
- T = temperature
- $T_1$  = temperature for columnar-grain formation
- $T_2$  = temperature for equiaxed-grain growth
- $\Delta T$  = temperature drop
- $T_i$  = temperature of a particle incident on a solid surface
- $T_k$  = temperature of the outer boundary of zone k (k = 1, 2)
- $T_r$  = temperature of a particle reflected from a solid surface
- u = average speed of phonons
- U = overall heat-transfer coefficient
- V = volume
- x = oxygen atoms in excess or deficiency per total heavy-metal atom
- $x_{He}$  = helium atom fraction in the gas in fuel-cladding gap

$Y_i$  = concentration of defect  $i$   
 $z$  = distance normal to a plane;  
 distance along fuel-rod axis

\* = radial location or temperature at which fuel transformations take place

### Greek Letters

$\alpha$  = coefficient of thermal expansion; parameter in modified Loeb equation; thermal-accommodation coefficient  
 $\alpha_0$  = coefficient of thermal expansion for stoichiometric (U,Pu)O<sub>2</sub>  
 $\beta$  = fractional burnup; coefficient of compressibility  
 $\gamma$  = ratio of specific heat at constant pressure to that at constant volume  
 $\delta$  = mean gas-film thickness when fuel and cladding make contact  
 $\epsilon$  = emissivity  
 $\epsilon_F$  = energy of formation of the Frenkel defect  
 $\Phi$  = neutron flux  
 $\kappa$  = reciprocal of neutron-diffusion length  
 $\lambda$  = mean free path  
 $\lambda_0$  = constant in the expression for mean free path  
 $\mu$  = gas viscosity  
 $\rho$  = density  
 $\rho_1$  = fuel density in columnar zone  
 $\rho_2$  = fuel density in equiaxed-grain zone  
 $\rho_3$  = fuel density in unstructured zone  
 $\sigma$  = Stefan-Boltzmann constant  
 $\sigma_f$  = fission cross section  
 $\sigma_p$  = collision cross section of phonons  
 $\theta_D$  = Debye temperature

### Subscripts

app = apparent  
 Av = Avogadro  
 c = cladding  
 contact = value at the contact of two materials  
 ex = excess (enthalpy) over perfect crystal value  
 f = fission, fissile, or fissionable; fuel  
 F = Frenkel defects  
 g = gas  
 gap = fuel-cladding gap  
 He = helium  
 i = defect  $i$   
 lin = linear (coefficient of thermal expansion)  
 m = melting point  
 p = at constant pressure; pore tube  
 pc = (heat capacity) at constant pressure of coolant  
 s = solid; surface  
 v = at constant volume  
 vo = refers to heat capacity at constant volume at temperatures below Debye temperature but above 2100°K  
 X, Y, and Z = directions of the parallelepiped pore  
 Z = direction normal to a plane  
 0 = initial value or center-line value

### Superscripts

0 = initial value  
 — = average over fuel cross section

## 10.7 REFERENCES

1. J. A. Christensen, in *Proceedings of the Conference on Fast Reactor Fuel Element Technology*, Apr. 13-15, 1971, New Orleans, La., p. 345, R. Farmakes (Ed.), American Nuclear Society, Hinsdale, Illinois, 1971.
2. J. Roth, M. E. Hybert, J. R. Cherry, and C. S. Caldwell, *Trans. Amer. Nucl. Soc.*, **10**: 457 (1967).
3. R. A. Hein, L. H. Sjodahl, and R. Szwarc, *J. Nucl. Mater.*, **25**: 99 (1968).
4. R. Szwarc, *J. Phys. Chem. Solids*, **30**: 705 (1969).
5. J. F. Lee, F. W. Sears, and D. L. Turcotte, *Statistical Thermodynamics*, p. 80, Addison-Wesley Publishing Company, Inc., Reading, Mass., 1963.
6. H. E. Schmidt, *J. Nucl. Mater.*, **39**: 234 (1971).
7. M. McQuarrie, *J. Amer. Ceram. Soc.*, **37**: 91 (1954); J. L. Bates, *Nucleonics*, **19**(6): 83 (1961).
8. R. L. Gibby, *J. Nucl. Mater.*, **38**: 163 (1971).
9. R. L. Gibby, The Effect of Oxygen Stoichiometry on the Thermal Diffusivity and Conductivity, USAEC Report BNWL-927, Battelle-Northwest, January 1969.
10. H. E. Schmidt and J. Richter, in *Symposium on Oxide Fuel Thermal Conductivity*, Stockholm, 1967.
11. J. C. Van Craeynest and J. C. Weilbacher, *J. Nucl. Mater.*, **26**: 132 (1968).
12. S. K. Evans and P. E. Bohaboy, *Trans. Amer. Nucl. Soc.*, **13**: 571 (1970).
13. F. J. Hetzler, T. E. Lannin, K. J. Perry, and E. L. Zebroski, *Trans. Amer. Nucl. Soc.*, **8**: 36 (1965).
14. A. C. Damask and G. J. Dienes, *Point Defects in Metals*, p. 41, Gordon and Breach, Science Publishers, Inc., New York, 1963.
15. A. Eucken, *Forsch. Geb. Ingenieurw.*, B3, Forschungsheft No. 353, 1932.
16. A. L. Loeb, *J. Amer. Ceram. Soc.*, **37**: 96 (1954).
17. A. Biancheria, *Trans. Amer. Nucl. Soc.*, **9**: 15 (1966).
18. H. Kampf and G. Karsten, *Nucl. Appl. Technol.*, **9**: 288 (1970).
19. J. Franci and W. D. Kingery, *J. Amer. Ceram. Soc.*, **37**: 99 (1954).
20. J. R. MacEwan, R. L. Stoute, and M. J. F. Notley, *J. Nucl. Mater.*, **24**: 109 (1967).
21. J. P. Stora, *Trans. Amer. Nucl. Soc.*, **13**: 137 (1970).
22. G. P. Marino, *J. Nucl. Mater.*, **38**: 178 (1971).
23. R. R. Asamoto, F. L. Anselin, and A. E. Conti, *J. Nucl. Mater.*, **29**: 67 (1969).
24. J. C. Van Craeynest and J. P. Stora, *J. Nucl. Mater.*, **37**: 153 (1970).
25. Westinghouse Electric Corporation, Oxide Fuel Element Development, USAEC Report WARD-4135-1, November 1969.
26. J. Belle (Ed.), *Uranium Dioxide: Properties and Nuclear Applications*, p. 576, Superintendent of Documents, U. S. Government Printing Office, Washington, 1961.
27. J. A. L. Robertson, A. M. Ross, M. J. F. Notley, and J. R. MacEwan, *J. Nucl. Mater.*, **7**: 225 (1962).
28. C. W. Sayles, *Trans. Amer. Nucl. Soc.*, **10**: 458 (1967).
29. E. G. Stevens, *Nucl. Appl.*, **5**: 410 (1968).
30. W. W. Marr and D. H. Thompson, *Nucl. Eng. Des.*, **17**: 361 (1971).
31. E. H. Kennard, *Kinetic Theory of Gases*, 1st ed., pp. 311-325, McGraw-Hill Book Company, New York, 1938.

32. J. N. Cetinkale and M. Fishenden, *Proceedings of the General Discussion on Heat Transfer*, p. 271, The Institution of Mechanical Engineers, London, 1951.
33. M. G. Cooper, B. B. Mikic, and M. M. Yovanovick, *Int. J. Heat Mass Transfer*, 12: 279 (1960).
34. H. Fenech and W.M. Rohsenow, *J. Heat Transfer*, 85(C): 15 (1963).
35. A. Ascoli and E. Germagnoli, *Energ. Nucl. (Milan)*, 3: 113 (1956).
36. A. M. Ross and R. L. Stoute, Heat Transfer Coefficient Between  $\text{UO}_2$  and Zircaloy-2, Canadian Report AECL-1552, 1962.
37. L. S. Tong and J. Weisman, *Thermal Analysis of Pressurized Water Reactors*, pp. 71-81, American Nuclear Society, Hinsdale, Ill., 1970.
38. G. V. Jacobs, M. S. Thesis, Massachusetts Institute of Technology, Cambridge, Mass., 1971.
39. J. H. Scott, M. G. Stevenson, and R. W. Moore, 1000-MWe LMFBR Accident Analysis and Safety System Design Study, Topical Report. Accident Analysis Methods, USAEC Report BAW-1342, Babcock and Wilcox Company, November 1970.
40. M. J. F. Nolley, *Nucl. Appl. Tech.*, 9: 195 (1970).
41. W. K. Anderson and G. L. Lechliter, *Trans. Amer. Nucl. Soc.*, 9: 375 (1966).
42. R. Godesar, M. Guyette, and N. Hoppe, *Nucl. Appl. Tech.*, 9: 205 (1970).
43. V. Z. Jankus and R. W. Weeks, *Nucl. Eng. Des.*, 18: 83 (1972).
44. C. M. Cox and F. J. Homan, *Nucl. Appl. Tech.*, 9: 317 (1970).
45. E. Duncombe, C. M. Friedrich, and W. H. Guilinger, *Nucl. Appl. Tech.*, 12: 194 (1971).
46. C. M. Cox and F. J. Homan, PROFIL: A One-Dimensional FORTRAN-IV Program for Computing Steady-State Temperature Distributions in Cylindrical Ceramic Fuels, USAEC Report ORNL-TM-2443, Oak Ridge National Laboratory, March 1969.
47. K. R. Merckx and G. L. Fox, SINTER: A Program for Calculating Radial Temperature Distributions in Oxide Fuel Pins Undergoing Sintering, USAEC Report BNWL-1241, Battelle-Northwest, January 1969.
48. C. S. Rim and H. Fenech, *Trans. Amer. Nucl. Soc.*, 12: 103 (1969).
49. C. W. Sayles, *Trans. Amer. Nucl. Soc.*, 11: 509 (1968).

## 10.8 PROBLEMS

10.1 It is desired to compute the change in the plutonium fraction of a mixed-oxide fast reactor fuel element as a function of the burnup  $\beta$ . The initial plutonium fraction of the fuel is  $q_0$ . Assume that  $^{239}\text{Pu}$  only undergoes fission but that  $^{238}\text{U}$  both fissions and captures neutrons (to produce  $^{239}\text{Pu}$ ). The ratio of neutron capture to fission in  $^{238}\text{U}$

$$\alpha_U = \frac{\text{rate of neutron capture in } ^{238}\text{U}}{\text{rate of fission in } ^{238}\text{U}}$$

is known and constant.

Obtain an approximate solution to the nuclide balances (on  $^{238}\text{U}$ ,  $^{239}\text{Pu}$ , and fission-product pairs) assuming that the conversion ratio defined by

$$C = \frac{\text{rate of neutron capture in } ^{238}\text{U}}{\text{rate of fission of } ^{239}\text{Pu}}$$

is treated as a constant for the purpose of integrating the differential equation.

10.2 For the fast reactor fuel-pin characteristics listed in Table 10.2, determine the fuel center line and surface temperatures at the midplane of the core (before fuel restructuring). Include the effect of gap closure at power and assume that the gap conductance is due to the thermal conductivity of the helium fill gas. Assume that the axial variation of the linear power is symmetric about the midplane. Use the thermal conductivity integral of Fig. 10.20 and a sodium film heat-transfer coefficient of  $12 \text{ W cm}^{-2} \text{ }^\circ\text{C}^{-1}$ . The thermal conductivity of the cladding is  $0.22 \text{ W cm}^{-1} \text{ }^\circ\text{C}^{-1}$ .

10.3 As a result of plutonium redistribution in a cylindrical fuel rod, the radial distribution of the concentration of this element is given empirically by

$$\frac{q(r)}{q_0} = 1 + D \left\{ \exp \left[ -2\alpha \left( \frac{r-r^*}{R} \right) \right] - 2 \exp \left[ -\alpha \left( \frac{r-r^*}{R} \right) \right] \right\}$$

where  $R$  is the fuel radius;  $D$ ,  $\alpha$ , and  $r^*$  are constants; and  $q_0$  is the initial plutonium distribution (uniform). Neglect restructuring of the fuel (i.e., no central void is formed).

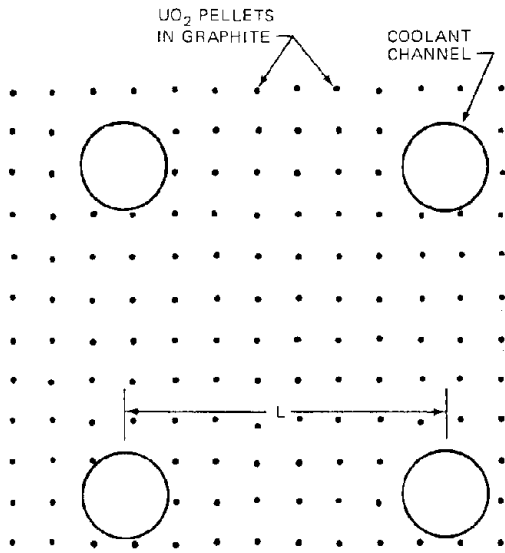
(a) If  $\alpha = 10$ , what is the value of  $r^*/R$  which satisfies the requirement that no plutonium is lost during redistribution?

(b) If  $q_0 = 0.2$  and  $D = 0.01$ , what is the plutonium fraction at the fuel center line? What is the minimum plutonium concentration and where radially does it occur? Sketch the plutonium distribution.

(c) Solve the heat-conduction equation (Eq. 10.49) for the initial uniform plutonium distribution and for the redistributed profile, where  $H(r)/\bar{H}$  is given by the preceding function where  $\bar{H}$  is the average power density. Assume that the thermal conductivity of the fuel is constant.

(d) If the rod linear power is adjusted so that the center-line temperature is just at the melting point of the fuel, by what percentage must the linear power be reduced after redistribution has occurred? Assume the fuel surface temperature,  $T_s$ , remains constant.

10.4 The fuel of the high-temperature gas-cooled reactor (HTGR) consists of small spherical pellets of  $\text{UO}_2$  embedded in a matrix of graphite (see diagram). The fission heat is removed by coolant flowing in channels of radius  $R_0$  penetrating the graphite a distance  $L$  apart. There are  $N_p$  pellets of radius  $R_p$  per unit volume of graphite. The  $\text{UO}_2$  in the pellets is fully enriched in  $^{235}\text{U}$  for which the fission cross section is  $\sigma_f$ . The uranium-atom density in the fuel is  $N_f$ , and the thermal flux  $\phi$  may be assumed to be constant throughout the graphite at a particular location in the core where the surface of the coolant channels is at a temperature  $T_s$ . The thermal conductivities of the  $\text{UO}_2$  and graphite are  $k_p$  and  $k_g$ , respectively. The heat removal from this system is modeled by considering a unit cell consisting of a coolant channel in the center and an annular region of associated graphite.



(a) What is the average heat-generation rate per unit volume of graphite? What is the linear power of a channel?

(b) What is the temperature distribution in the graphite? Assume that the pellets are very small so that the fission heat they produce may be treated as an equivalent homogeneous heat source in the graphite.

(c) Derive the formulas for the temperature distributions in the fuel and in the graphite immediately surrounding a pellet that is at a distance  $r$  from the nearest coolant channel.

10.5 Suppose a porous material contains  $C$  spherical pores per unit volume randomly distributed in the body. Each pore has a radius  $r_p$ . Consider a plane of unit area inserted at random into the material. By considering the volumes of slabs of thickness  $r_p$  on either side of the unit plane, determine:

(a) How many pores intersect the unit plane? What is the average distance between intersections of pores on the plane?

(b) What is the average area of the circles formed by the intersection of the pores with the unit plane?

(c) What fraction of the area of the unit plane is occupied by these intersection circles? Compare this fraction with the volume porosity of the body.

10.6 A fuel element is constructed in the form of a slab of fuel of half-thickness  $L$  sandwiched between two thin plates of cladding. The porosity of the as-fabricated fuel is  $P_0$ . When placed in a reactor, the power density  $H_0$  of the fuel is spatially uniform. The surface temperature is  $T_s$ .

(a) Before restructuring occurs, the power density  $H_0$  is adjusted so that the midplane temperature of the fuel slab is just equal to the melting temperature  $T_m$ . Derive the expression for  $H_0$  which gives this condition. Assume that the thermal conductivity of the 100% dense solid fuel,  $k_s$ , is temperature independent and that the porosity correction is given by Eq. 10.40.

(b) Restructuring of the fuel results in conversion of all original fuel to material with a columnar-grain structure and uniform porosity  $P_1$ . What is the size of the central void formed? Derive the expression for the new power density  $H$  for which the temperature at the central void is equal to the melting temperature. Assume that the fuel surface remains at temperature  $T_s$ .

10.7 Replace part (b) of problem 10.6 with the following:

Restructuring of the fuel is only half complete (i.e., the size of the central void is only half of that computed in problem 10.6) and the total power generated by the fuel element has not been increased to raise the temperature at the central void to the melting temperature.

(a) What is  $x_1/L$ , where  $x_1$  is the distance from the center line to the boundary between the columnar-grain zone and the unstructured material?

(b) Derive the temperature distributions in the columnar-grain zone,  $T_1(x)$ , and in the unstructured zone,  $T_2(x)$ .

(c) What is the ratio of the temperature drop across the fuel,  $T_1(x_0) - T_s$ , to the initial fuel temperature drop,  $T_m - T_s$ ?

10.8 If molecules impinging on a rough solid surface make  $m$  collisions before reentering the gas phase, what is the apparent coefficient of thermal accommodation in terms of the flat surface (i.e., true) value of  $\alpha$ ?

10.9 (a) The conductance of the gas-filled gap between the fuel surface and the inner cladding wall is defined by

$$h_{\text{gap}} = \frac{q}{T_s - T_c}$$

where  $q$  is the heat flux and  $T_s$  and  $T_c$  are the fuel-surface and cladding inside wall temperatures, respectively. Prove that  $h_{\text{gap}}$  is given by Eq. 10.97.

(b) The thermal accommodation coefficients of helium on  $\text{UO}_2$  and stainless steel are 0.1 and 0.2, respectively. Calculate the temperature jumps  $g_f$  and  $g_c$  for a heat flux of  $1200 \text{ W/cm}^2$  through a gap filled with helium at 1 atm pressure and an average temperature of  $1000^\circ \text{K}$ .

10.10 A fast reactor fuel pin operates at a peak linear power of  $800 \text{ W/cm}$ . At the axial location at which this linear power is attained, the sodium-coolant temperature is  $500^\circ \text{C}$ . The conductances of the fuel-cladding gap and the cladding and the heat-transfer coefficient in the sodium are

$$h_{\text{gap}} = 1 \text{ W cm}^{-2} \text{ } ^\circ \text{C}^{-1}$$

$$k_c/t_c = 9 \text{ W cm}^{-2} \text{ } ^\circ \text{C}^{-1}$$

$$h_{\text{coolant}} = 12 \text{ W cm}^{-2} \text{ } ^\circ \text{C}^{-1}$$

The outside diameter of the cladding is 7 mm.

Out to what fractional radius does the fuel melt? Neglect restructuring of the solid portion of the fuel and assume that the conductivity integral of the solid portion is given by Fig. 10.20.

# Chapter 11

## Fuel Chemistry

### 11.1 INTRODUCTION

The most significant chemical property in an oxide fuel pin is the equilibrium pressure of oxygen in the gas phase within the fuel element. The partial pressure of oxygen, or the oxygen potential of the fuel, determines in large part whether the fuel can oxidize the metallic cladding. Corrosion of the cladding of the fuel element reduces the effective load-bearing thickness of the cladding (the phenomenon is called *wastage* or *thinning*). Since the cladding is made as thin as possible to reduce core size and parasitic neutron absorption, use of thick-wall cladding to accommodate extensive oxidation is detrimental to reactor economics.

The chemistry of an operating oxide fuel pin is complicated by two phenomena: (1) the steep temperature gradient and (2) the generation of a host of impurity species (the fission products) as a consequence of irradiation.

The effect of the temperature gradient on the chemical behavior of pure (i.e., fission-product-free) heavy metal oxides, considered in this chapter, is called *fuel chemistry*. The chemical effects resulting primarily from the introduction of fission products into the fuel are termed *fission-product chemistry*. These effects are treated in the next chapter.

The distinction between fuel chemistry and fission-product chemistry is arbitrary, inasmuch as the chemical evolution of oxide reactor fuel material is the result of an intimate mixture of these two phenomena. However, this division permits cleaner analysis of the individual effects, and in some cases the distinction is realistic. For example, oxygen redistribution in the fuel probably occurs shortly after start-up or at least at burnups well below those that result in important fission-product effects.

Much progress in understanding fuel and fission-product chemistry has been made by applying purely thermodynamic analysis to the system. For some problems the application of thermodynamics alone is not unreasonable, since the very high temperatures of fuel operation imply rapid approach to chemical equilibrium. Oxygen redistribution and estimation of the chemical states of fission products are usually treated in this fashion. However, many chemical phenomena occurring in the fuel are intimately connected with some sort of transport process; for such

situations thermodynamic arguments may be necessary but not sufficient. Actinide redistribution by thermal diffusion or vapor migration is an example of a kinetically dominated process.

### 11.2 PHASE DIAGRAMS OF URANIUM AND PLUTONIUM OXIDES

Because uranium and plutonium can exist as ions in a number of different valence states, the phase behavior of the oxides of these metals is more complex than that of other metal oxides. Both uranium and plutonium oxides show broad ranges of nonstoichiometry, where the oxygen-to-metal ratio (O/M) differs substantially from 2, yet the system consists of only a single phase. In addition, these heavy metals form a variety of compounds of the general formula  $M_2O_b$ . Distinction between a true solid solution of oxygen in the oxide, where the O/M ratio is continuously variable within a single phase region, and a two-phase mixture of two compounds of different O/M ratios can be made in two ways: (1) It is often possible to observe two phases metallographically. (2) At constant temperature the equilibrium oxygen pressure over the two-phase mixture is independent of the average O/M (which may be changed by varying the proportion of the two compounds in the mixture), whereas the oxygen pressure over a single-phase solid solution is usually strongly dependent upon O/M. This difference is a consequence of the Gibbs phase rule.

Part of the phase diagram of the uranium-oxygen system is shown in Fig. 11.1. Vertical lines represent compounds, only two of which are shown in the figure. The very stable compound  $UO_2$  appears at O/U = 2.00. At O/U = 2.25, the  $U_4O_9$  oxide is formed. Addition of oxygen to  $U_4O_9$  produces  $U_5O_{13}$  (O/U = 2.6). Other compounds with larger O/U are  $U_3O_8$  and  $UO_3$ . These last two oxides are of no importance in fuel chemistry but are often encountered in fuel reprocessing and feed-material preparation.

The shaded and cross-hatched areas in Fig. 11.1 indicate single-phase regions of the nonstoichiometric oxides  $UO_{2 \pm x}$  and  $U_4O_{9-y}$ . The hypostoichiometric oxide  $UO_{2-x}$  exists only at elevated temperatures. At low temperatures, material with O/U < 2 is a mixture of  $UO_{2.00}$  and metallic uranium. Small particles of uranium metal have been

observed in the grain boundaries of  $\text{UO}_{2-x}$  which had been quenched from high temperature.

Figure 11.2 shows the phase diagram of the plutonium–oxygen system. Four compounds have been observed:  $\text{Pu}_2\text{O}_3$ ,  $\text{PuO}_{1.52}$ ,  $\text{PuO}_{1.61}$ , and  $\text{PuO}_2$ . Below about  $2000^\circ\text{C}$ , no oxide of higher oxidation state than  $\text{PuO}_2$  is found. The shaded areas in the figure show that three of the four compounds exhibit deviations from

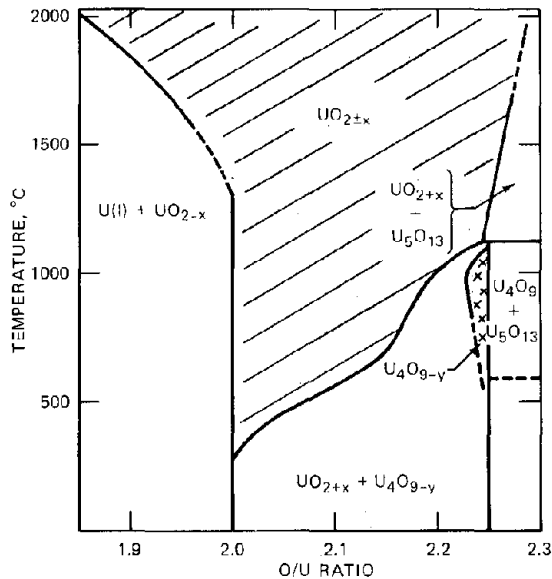


Fig. 11.1 Oxygen–uranium phase-equilibrium system. [After R. K. Edwards and A. E. Martin, in *Thermodynamics*, Symposium Proceedings, July 22-27, 1965, Vienna, International Atomic Energy Agency, Vienna, 1966 (STI/PUB/109).]

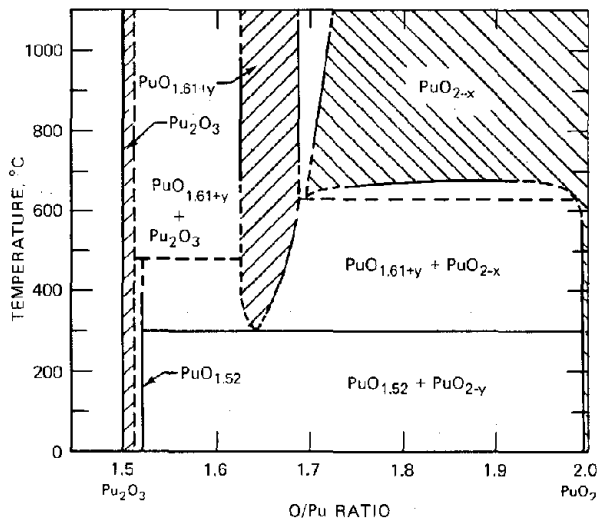


Fig. 11.2 Phase diagram of the plutonium–oxygen system. [From H. M. Mattys, *Actinides Rev.*, 1: 165 (1968).]

stoichiometry. The hypostoichiometric  $\text{PuO}_{2-x}$  region is especially broad.

Much less information is available on the phase equilibria of the ternary system uranium–plutonium–oxygen. A small portion of the phase diagram at  $800^\circ\text{C}$  is shown in Fig. 11.3. For all plutonium-to-uranium ratios, a large single-phase region  $(\text{U,Pu})\text{O}_{2+x}$  exists. The mixed oxide may deviate from stoichiometry in both directions.

### 11.3 DEFECT STRUCTURE IN NONSTOICHIOMETRIC OXIDES

Deviations of uranium and plutonium from exact stoichiometry are permissible because these elements have many valence states. In uranium the  $\text{U}^{4+}$ ,  $\text{U}^{5+}$ , and  $\text{U}^{6+}$  states tend to be the most stable, while in plutonium the  $\text{Pu}^{3+}$  and  $\text{Pu}^{4+}$  states occur most frequently. In the stoichiometric oxides  $\text{UO}_{2.00}$  and  $\text{PuO}_{2.00}$ , the heavy metal ions carry a charge of  $4+$ . To ensure electrical neutrality in the crystal when oxygen ions are removed from or added to exactly stoichiometric material requires that some of the cations change valence. Thus, the uranium ions in  $\text{UO}_{2+x}$  are a mixture of  $\text{U}^{4+}$  and  $\text{U}^{5+}$  (or possibly  $\text{U}^{4+}$  and  $\text{U}^{6+}$ ). Since the addition of one  $\text{O}^{2-}$  ion requires that two  $\text{U}^{4+}$  ions be converted to  $\text{U}^{5+}$  ions, the fraction of the total uranium in the compound  $\text{UO}_{2+x}$  which is in the  $5+$  valence state is  $2x$ . Similarly, electrical neutrality in plutonium oxides is maintained by conversion of some  $\text{Pu}^{4+}$  to  $\text{Pu}^{3+}$ . In  $\text{PuO}_{2-x}$  the fraction of the plutonium in the  $3+$  valence state is  $2x$ . These deviations from perfect stoichiometry are accompanied by the formation of Frenkel defects on the oxygen-ion sublattice of the crystal. The excess oxygen in  $\text{UO}_{2+x}$  is accommodated in interstitial sites in the fluorite structure. The deficiency of oxygen in  $\text{PuO}_{2-x}$  is manifest as vacancies on the oxygen sublattice. The cation sublattice remains perfect even when the O/M deviates from 2. Uranium or plutonium ions are randomly distributed on every available site on the cation sublattice.

The compound  $\text{PuO}_{2+x}$  has not been observed at temperatures below  $2000^\circ\text{C}$ ; so it is unlikely that  $\text{Pu}^{5+}$  or  $\text{Pu}^{6+}$  are present in the hyperstoichiometric mixed oxide  $(\text{U,Pu})\text{O}_{2+x}$  either. The excess charges introduced into the crystal when oxygen is added to the mixed oxide are probably compensated by oxidation of some of the uranium to the  $5+$  or  $6+$  valence states (just as in pure urania) while the plutonium remains as  $\text{Pu}^{4+}$ . The hyperstoichiometric mixed oxide has thermodynamic properties equivalent to an ideal solution of stoichiometric  $\text{PuO}_2$  and hyperstoichiometric urania. Or, the compound  $(\text{U}_{1-q}\text{Pu}_q)\text{O}_{2+x}$  may be represented as a mixture of  $q$  mole fraction  $\text{PuO}_2$  and  $1-q$  mole fraction  $\text{UO}_{2+m}$ , where  $m = x/(1-q)$ .

Although the phase diagram of Fig. 11.1 shows that  $\text{UO}_{2-x}$  exists at high temperatures (and therefore uranium is capable of being reduced to oxidation states such as  $\text{U}^{2+}$ ), the presence of more easily reduced plutonium suggests that hypostoichiometric mixed oxides consist of  $\text{U}^{4+}$  and a mixture of  $\text{Pu}^{3+}$  and  $\text{Pu}^{4+}$ . The compound with the formula  $(\text{U}_{1-q}\text{Pu}_q)\text{O}_{2-x}$  can be treated as an ideal solution of  $1-q$

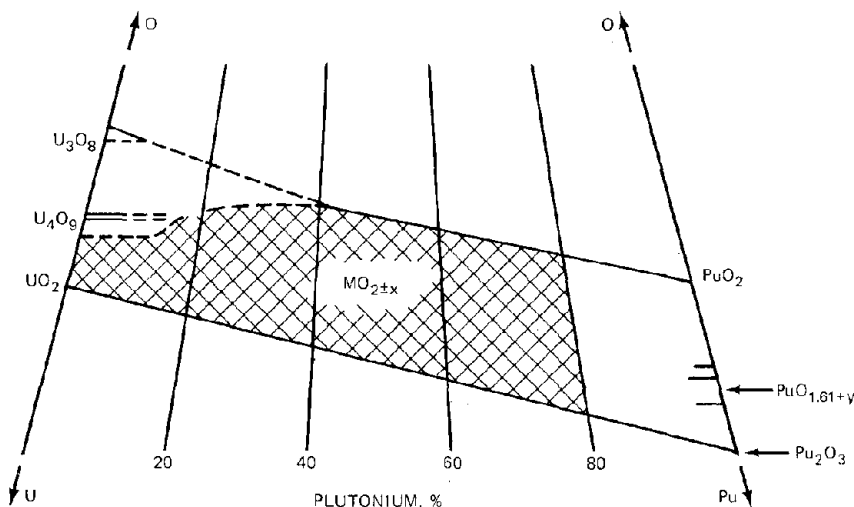


Fig. 11.3 Phase diagram of the uranium-plutonium-oxygen system at 800°C. [From H. M. Mattys, *Actinides Rev.*, 1: 165 (1968).]

mole fraction  $\text{UO}_2$  and  $q$  mole fraction of  $\text{PuO}_{2-m}$ , where  $m = x/q$ .

The extent of nonstoichiometry in the mixed oxide (i.e., the variable  $x$ ) may be limited by the supply of cations whose valence can be altered. Thus, the plutonium component of hypostoichiometric mixtures cannot be reduced to a valence less than  $3+$  (which corresponds to the compound  $\text{Pu}_2\text{O}_3$ ). The maximum value of  $m$  in  $\text{PuO}_{2-m}$  is 0.5, or the maximum value of  $x$  is  $0.5q$ . For 20%  $\text{PuO}_2$  in  $\text{UO}_2$  for example, the most highly reduced oxide obtainable is  $\text{U}_{0.8}\text{Pu}_{0.2}\text{O}_{1.90}$ . Further reduction is hindered by the difficulty of producing the lower oxidation states of uranium (i.e.,  $\text{U}^{2+}$ ).

Knowledge of the atomic structure of the nonstoichiometric phases is important in interpreting the thermodynamic behavior of the material (see next section) and the dependence of transport properties, such as electrical conductivity and diffusivity, upon the O/M ratio. Such properties are critically dependent upon the positions of the excess oxygen atoms in the crystal structure. Information of this sort is difficult to obtain, and only hyperstoichiometric uranium between  $\text{UO}_2$  and  $\text{U}_4\text{O}_9$  has been extensively studied.

Stoichiometric  $\text{UO}_2$  crystallizes in the fluorite structure shown in Fig. 3.12. The largest open spaces in this lattice are the centers of the cubes formed by the eight oxygen ions in the simple cubic sublattice. In  $\text{UO}_2$ , half these cubes are occupied by uranium ions, but the other half are empty. It would be supposed that oxygen added to  $\text{UO}_{2.00}$  to form  $\text{UO}_{2+x}$  would reside in these empty interstices, but such is not the case. Neutron diffraction work<sup>1</sup> has demonstrated the existence of two interstitial sites for oxygen, neither of which is the expected cube center. Figure 11.4 shows the empty cube formed by eight normal oxygen ions (which is  $\frac{1}{8}$  of the fluorite unit cell, see Fig. 3.12a) with the locations of the two types of interstitial sites. The type 1 sites lie along each of the six diagonals

through the edge centers of the cube (i.e., the  $[110]$  directions). The sites are halfway between the cube center and the midpoints of the cube edges. There are 12 type 1 sites in each empty oxygen cube. Because there are four such cubes in the fluorite unit cell (see Fig. 3.12a), the unit cell contains 48 type 1 oxygen interstitial sites, or 12 for each uranium ion.

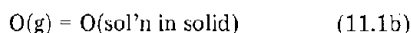
Figure 11.4b shows the type 2 oxygen interstitial sites. One of these is located on each of the four body diagonals (i.e.,  $[111]$  directions) in the empty oxygen cube. The sites are midway from the cube center to the cube corners. There are 16 type 2 sites in each fluorite unit cell, or 4 per uranium ion.

The excess oxygen ions introduced into the fluorite structure are not distributed randomly on the type 1 and type 2 interstitial sites.<sup>2</sup> Rather, the thermodynamic properties of  $\text{UO}_{2+x}$  are best rationalized by ordered substructures or defect complexes of the type shown in Fig. 11.5. This figure shows a complete fluorite unit cell (Fig. 3.12b) with two interstitial oxygen ions placed on type 1 sites. To maintain charge neutrality, four  $\text{U}^{4+}$  ions nearest to the two extra oxygen ions are converted to  $\text{U}^{5+}$  ions. Because of Coulombic repulsion, the two oxygen ions that were on normal lattice sites nearest to the pair of extra oxygen ions relax outward. They do so along  $[111]$  directions and thereby occupy type 2 sites, leaving two normal anion sites vacant. As shown in Fig. 11.4b, a normal oxygen ion can move in any one of four directions to reach a type 2 interstitial location. However, Fig. 11.5 shows that two of these directions would bring the relaxing ion closer to rather than farther away from the interstitials on type 1 sites. The two allowable directions of movement of each of the corner oxygen ions are shown as dashed arrows in Fig. 11.5. The two ions can move to the same side or to opposite sides of the  $(110)$  plane containing the two type 1 interstitials. These possibilities correspond to the *cis* and *trans* isomers encountered in some organic molecules.



Fig. 11.6. Note that the oxygen pressures vary with O/U ratio in the single-phase regions  $UO_{2+x}$  and  $U_4O_{9-y}$  but are independent of overall composition in the two-phase regions, as required by the phase rule.

The situation of thermodynamic equilibrium between gaseous oxygen and the solid oxide is depicted in Fig. 11.7. This equilibrium can be expressed by the reactions



The criterion of chemical equilibrium is the equality of the chemical potentials of atomic oxygen in the gaseous and solid phases and the atomic and molecular forms of oxygen in the gas (see Chap. 5 for a discussion of chemical equilibria):

$$\frac{1}{2} \mu_{O_2(g)} = \mu_{O(g)} \quad (11.2)$$

$$\mu_{O(g)} = \mu_{O(\text{sol'n})}$$

The chemical potential of  $O_2(g)$  is given by Eq. 5.54:

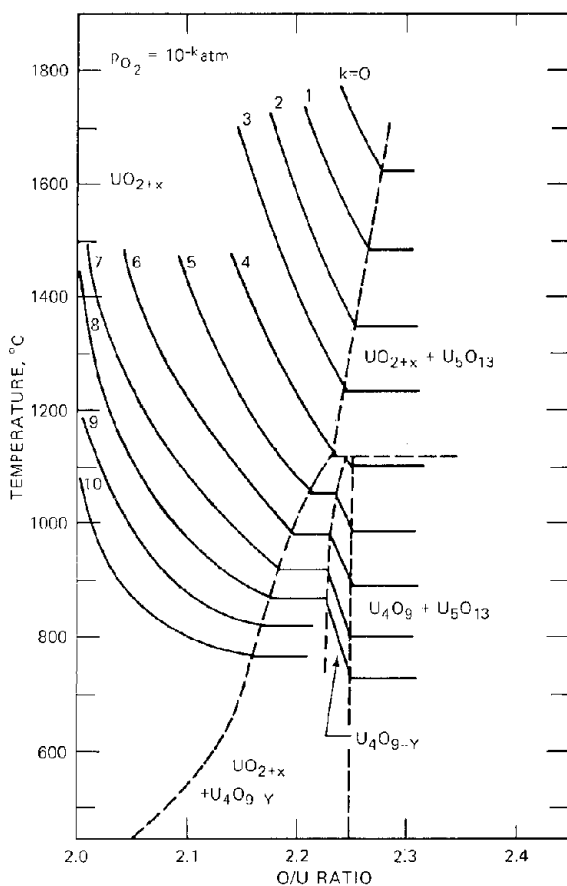


Fig. 11.6 Equilibrium oxygen partial pressure in  $UO_{2+x}$ . ---, phase-equilibrium line. —, isobar of oxygen. [From I. Tamotsu et al., *J. Nucl. Mater.*, 36: 288 (1970).]

$$\mu_{O_2(g)} = G_{O_2}^\circ + RT \ln p_{O_2} \quad (11.3)$$

where  $G_{O_2}^\circ$  is the Gibbs free energy of pure oxygen gas at temperature  $T$  and at the standard-state pressure, which is usually taken to be 1 atm. Combining Eqs. 11.2 and 11.3 yields

$$\Delta G_{O_2} = RT \ln p_{O_2} = 2\mu_{O(\text{sol'n})} - G_{O_2}^\circ \quad (11.4)$$

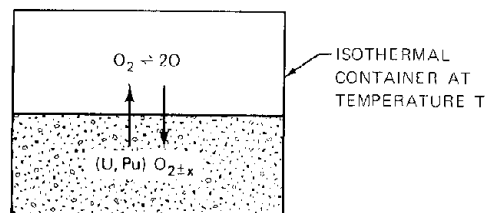


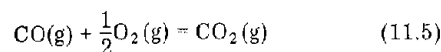
Fig. 11.7 Thermodynamic equilibrium of oxygen gas with uranium—plutonium oxide solids.

The quantity  $RT \ln p_{O_2}$  is denoted by  $\Delta G_{O_2}$ , which is the partial molal free energy of oxygen in the solid per mole of  $O_2$ , or the oxygen potential of the solid. It is the difference between the chemical potential of oxygen in the solid and that of pure gaseous oxygen at the same temperature and at 1 atm pressure. We may regard  $\Delta G_{O_2}$  as simply another way of expressing the equilibrium oxygen pressure over the material, which can be measured by one of the following methods.

### 11.4.1 Gravimetric Measurement of $\Delta G_{O_2}$

The gravimetric method<sup>3</sup> of measuring equilibrium oxygen pressures is based upon weight changes of a sample. The apparatus used is shown in Fig. 11.8. The stoichiometry of the sample held in the furnace is first adjusted to a known value by contacting the solid with a gas phase containing a known partial pressure of  $O_2$ . The oxygen pressure is then changed to a new (but known) value, which causes the O/M ratio of the solid to assume a new equilibrium value. The loss or gain of oxygen by the solid is measured by the change in weight of the sample, which is determined by length changes of the fine quartz helix in the apparatus.

The gravimetric method requires that the oxygen partial pressure in the gas phase be controlled. This may be accomplished by passing a mixture of CO and  $CO_2$  through the furnace. At the high temperature of the experiments, the gas-phase reaction



rapidly attains equilibrium. If  $K_c$  denotes the equilibrium constant of this reaction, the oxygen partial pressure in the gas is given by

$$K_c = \frac{p_{CO_2}}{p_{CO}(p_{O_2})^{1/2}} \quad (11.6)$$

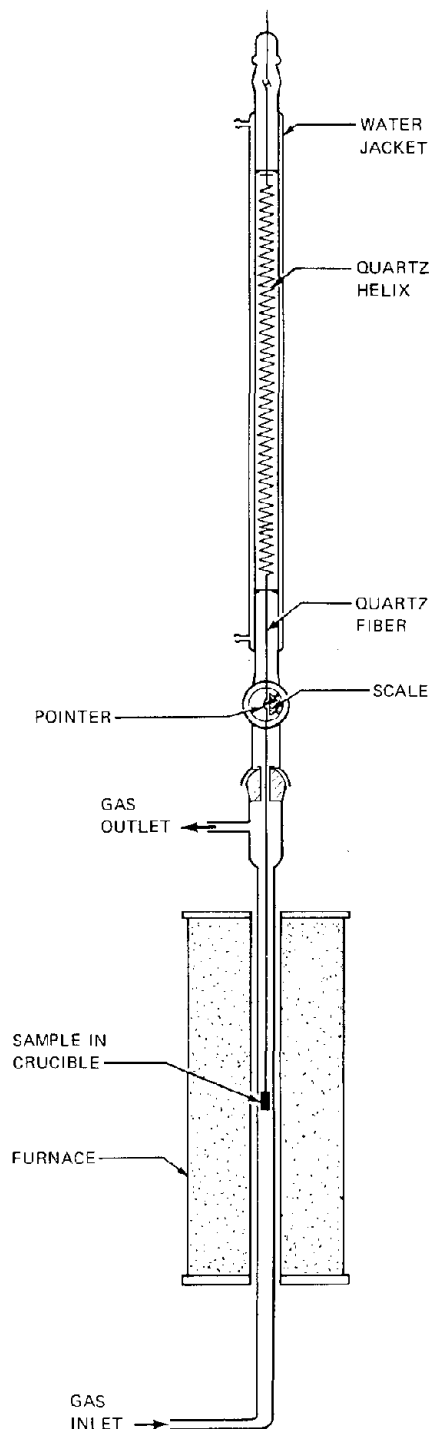


Fig. 11.8 Gravimetric method of measuring oxygen potentials of oxide fuel materials. [From K. Hagemark and M. Broli, *J. Inorg. Nucl. Chem.*, 28: 2837 (1966).]

If the ratio of  $\text{CO}_2$  to  $\text{CO}$  in the inlet gas is fixed,  $p_{\text{O}_2}$  can be determined from Eq. 11.6. The equilibrium constant  $K_c$  is given by Eq. 5.57

$$K_c = \exp\left(-\frac{\Delta G_c^\circ}{RT}\right) \quad (11.7)$$

where  $\Delta G_c^\circ$  is the standard-state free-energy change of reaction 11.5, which can be expressed as

$$\Delta G_c^\circ = \Delta H_c^\circ - \Delta S_c^\circ(T/10^3) \quad (11.8)$$

where  $T$  is the temperature in  $^\circ\text{K}$  and  $\Delta H_c^\circ$  and  $\Delta S_c^\circ$  are the standard enthalpy and entropy changes of reaction 11.5, respectively. They are:

$$\Delta H_c^\circ = -282 \text{ kJ/mole} \quad (11.9)$$

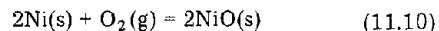
$$\Delta S_c^\circ = -86.8 \text{ J mole}^{-1} \text{ } ^\circ\text{K}^{-1}$$

Thus, by adjustment of the  $\text{CO}_2/\text{CO}$  ratio in the gas phase, oxygen partial pressures in the range from  $10^{-3}$  to  $10^{-4}$  atm can be reliably established. The oxygen pressures easily attained by  $\text{CO}_2$ - $\text{CO}$  mixtures are of the same magnitude as the oxygen pressures in equilibrium with hyperstoichiometric oxides. For hypostoichiometric material (encountered in mixed U-Pu oxides), the equilibrium oxygen pressures over the solid are very low, and the gas phase would have to contain minute quantities of  $\text{CO}_2$  in  $\text{CO}$  to establish the desired oxygen pressure. Control of the  $\text{CO}_2/\text{CO}$  ratio becomes difficult if either component is present in only trace amounts. Consequently, the oxygen partial pressure must be fixed by a reaction other than that of Eq. 11.1.

Tetenbaum<sup>4</sup> has used gases containing known ratios of  $\text{H}_2\text{O}$  in  $\text{H}_2$  to maintain oxygen potentials suitable for study of the hypostoichiometric mixed oxide  $(\text{U}_{0.8}\text{Pu}_{0.2})\text{O}_{2-x}$ . The low  $\text{H}_2\text{O}/\text{H}_2$  ratios required were obtained by controlling the temperature of the inlet gas, and hence the saturation water vapor pressure.

#### 11.4.2 High-Temperature Electrolytic Cell

Other convenient reactions involving  $\text{O}_2$  for which thermochemical properties are well established involve solid metals and their oxides. For example, the pressure of oxygen in equilibrium with the reaction



is given by

$$RT \ln p_{\text{O}_2} = \Delta G_{\text{Ni}}^\circ \quad (11.11)$$

where  $\Delta G_{\text{Ni}}^\circ$  is the standard-state free energy of reaction 11.10. Its numerical value is obtained from

$$\Delta G_{\text{Ni}}^\circ = -489 + 197(T/10^3) \text{ kJ/mole} \quad (11.12)$$

The concentrations of Ni and NiO do not appear in Eq. 11.11 because both these species are in the pure (i.e. standard) states (they are not miscible). Consequently, the oxygen pressure established by reaction 11.10 is a function of temperature only.

The device used to exploit the known oxygen pressure of the Ni-NiO couple to determine the oxygen potential of

mixed oxides is the high-temperature electrolytic cell<sup>5</sup> shown in Fig. 11.9. This apparatus is the solid-state analog of the common electrolytic cell in which aqueous solutions are the working substances. As shown in Fig. 11.9, wafers of the solid oxide and a mixture of Ni and NiO separated by a block of composition 85% ZrO<sub>2</sub>–15% CaO are sandwiched between inert electrodes. The assembly is brought up to the desired temperature in an inert-gas atmosphere or a vacuum and the electromotive force (emf) between the electrodes is measured. The O/M of the hypostoichiometric solid oxide is measured by first reacting the pellet with a measured quantity of pure oxygen which is sufficient to make the oxide hyperstoichiometric. Then the pellet is reduced to exact stoichiometry by adding sufficient CO so that the final CO<sub>2</sub>/CO ratio is 0.1, which at 850°C produces nearly exactly stoichiometric material.

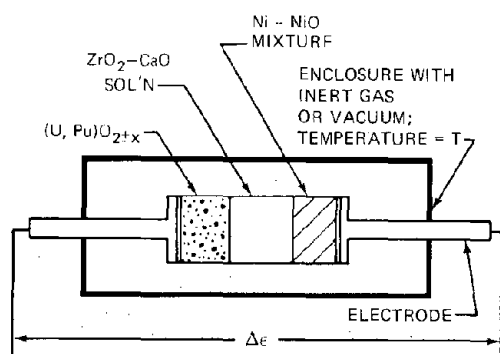


Fig. 11.9 High-temperature galvanic cell using solid electrolytes for the measurement of the oxygen potential of hypostoichiometric mixed-oxide fuels. (From T. L. Markin and E. J. McIver, *Plutonium 1965*, A. E. Kay and M. B. Waldron (Eds.), p. 845, Chapman and Hall, London, 1965.)

The amounts of O<sub>2</sub> and CO used in this two-step procedure determine the initial stoichiometry of the sample.

The ZrO<sub>2</sub>–CaO bridge in the cell provides a means by which oxygen ions can communicate between the sample and the Ni/NiO reference electrode. The ZrO<sub>2</sub>–CaO mixture is a pure ionic conductor in which the current is carried by migration of O<sup>2-</sup> ions in an electric potential gradient. The CaO serves as a phase stabilizer for ZrO<sub>2</sub>. Because of the very low oxygen pressures involved, the sample and the Ni–NiO wafer cannot exchange oxygen with the heavy-metal oxide via the gas phase.

The heavy-metal oxide and the Ni–NiO mixture are in equilibrium if the temperature and stoichiometry (of the former) are such that the oxygen pressures generated by the two are equal. That is, at equilibrium the oxygen potentials  $\Delta\overline{G}_{O_2}$  and  $\Delta\overline{G}_{Ni}$  are the same. Under this condition, the emf of the cell is zero. If the oxygen potentials of the two wafers are not equal, the cell potential is proportional to the difference between the oxygen potentials. According to the theory of ordinary electrolytic cells, the relation is

$$\Delta\overline{G}_{Ni} - \Delta\overline{G}_{O_2} = -4\mathcal{F}\Delta\epsilon \quad (11.13)$$

where  $\Delta\epsilon$  is the emf of the cell and  $\mathcal{F}$  is the Faraday constant (96.48 kJ mole<sup>-1</sup> volt<sup>-1</sup>). The coefficient 4 on the right of Eq. 11.13 arises from the fact that the half-cell reaction, Eq. 11.10, involves transfer of four electrons.

The cell emf is measured by applying a back potential to the cell which is just sufficient to stop all current flow through the circuit. If no back emf were applied, oxygen would slowly transfer through the ZrO<sub>2</sub>–CaO wafer in the direction which would ultimately result in equalizing the oxygen potentials of the sample and the Ni–NiO electrode.

The oxygen potential of the mixed oxide can be determined from the measured emf and Eq. 11.13 as a function of O/M, the Pu/U ratio, and temperature.

### 11.4.3 Measured Oxygen Potentials

If the oxygen potentials determined by the techniques described above are plotted against temperature at constant composition, the resulting variations are often well approximated by straight lines over a modest temperature interval:

$$\Delta\overline{G}_{O_2} = \Delta\overline{H}_{O_2} - \Delta\overline{S}_{O_2} (T/10^3) \quad (11.14)$$

where  $\Delta\overline{H}_{O_2}$  and  $\Delta\overline{S}_{O_2}$  are the partial molar enthalpy and entropy of oxygen in the solid oxide, respectively. To a first approximation, these quantities are independent of temperature and vary only with composition.

### 11.4.4 Urania

Figure 11.10 shows the experimentally determined values of  $\Delta\overline{S}_{O_2}$  and  $\Delta\overline{H}_{O_2}$  of hyperstoichiometric urania. For a specified temperature and oxygen-to-metal ratio, the equilibrium oxygen pressure over UO<sub>2+x</sub> is obtained by first determining  $\Delta\overline{S}_{O_2}$  and  $\Delta\overline{H}_{O_2}$  from these plots for the particular value of x and then obtaining  $\Delta\overline{G}_{O_2}$  at the specified temperature by Eq. 11.14. Finally, p<sub>O<sub>2</sub></sub> can be computed from Eq. 11.4.

The oxygen potentials determined from Fig. 11.10 cannot be extrapolated to stoichiometric or hypostoichiometric urania because of the rapid change in  $\Delta\overline{G}_{O_2}$  with x as stoichiometry is approached. Figure 11.11 depicts the oxygen potentials of urania in the hypo- and slightly hyperstoichiometric range. The lines representing UO<sub>2.000</sub> and UO<sub>2.004</sub> are virtually horizontal, which indicates that  $\Delta\overline{S}_{O_2}$  is approximately zero (see Eq. 11.14). However,  $\Delta\overline{H}_{O_2}$  changes by ~125 kJ/mole between the same two O/U ratios.

The family of curves in Fig. 11.11 labeled according to composition give the oxygen potentials of hypostoichiometric compounds in the high-temperature region (T > 1300°C) where oxygen-deficient urania can exist. The line denoted by U(l) + UO<sub>2-x</sub> represents the oxygen potentials over the two-phase system of liquid metallic uranium and UO<sub>2-x</sub>. The intersections of this line with the family of curves specify the temperature–O/U relationship of the phase boundary. This curve is shown in the upper left hand corner of Fig. 11.1. Thus, as UO<sub>1.94</sub> is cooled, uranium metal precipitates at T ≈ 1700°C.

For T ≤ 1300°C, the oxide in equilibrium with uranium metal is essentially perfectly stoichiometric. The line

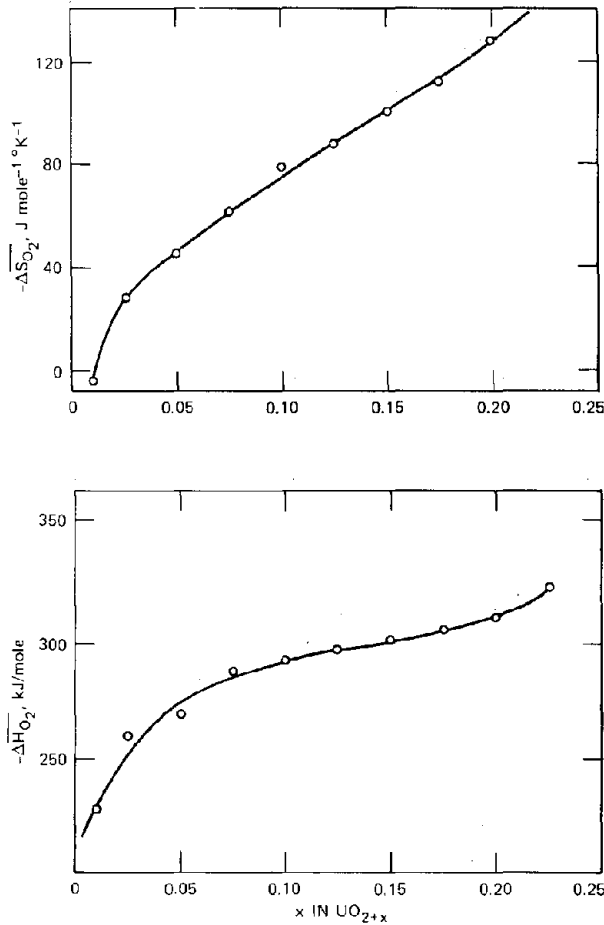
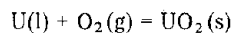


Fig. 11.10 Partial molar entropy and enthalpy of oxygen in  $\text{UO}_{2+x}$ . [From K. Hagemark and M. Broli, *J. Inorg. Nucl. Chem.*, 28: 2837 (1966).]

labeled  $\Delta G_{\text{UO}_2}^{\circ}$  in Fig. 11.11 gives the oxygen potential of the two-phase system, which is equivalent to the standard free energy of the reaction



for which

$$\Delta G_{\text{UO}_2}^{\circ} = -1080 + 167(T/10^3) \quad \text{kJ/mole}$$

For  $T < 1300^{\circ}\text{C}$ , the uranium–oxygen system behaves as an ordinary metal–metal oxide combination in which the metal possesses a fixed valence (e.g., the uranium–oxygen system is analogous to the Ni–NiO couple).

Figure 11.11 demonstrates that below  $1300^{\circ}\text{C}$  the formation of uranium ions with valence less than  $4+$  is essentially impossible;  $\text{UO}_2$  can be reduced only to oxygen and elemental uranium and then only with a very low equilibrium oxygen pressure. Above this temperature, however, uranium ions with a valence less than  $4+$  can exist. The most likely uranium ion in this case is  $\text{U}^{2+}$ .

### 11.4.5 Mixed Oxides

Figure 11.12 shows a set of oxygen potentials measured by the high-temperature electrolytic cell method for a mixed U–Pu oxide. The oxygen potentials of the hyperstoichiometric fuel are quite a bit higher than those of the hypostoichiometric material. The most significant feature of Fig. 11.12 is the very abrupt change in  $\Delta G_{\text{O}_2}$  near exact stoichiometry. This feature has a profound influence upon the chemical behavior of fuel elements in a reactor.

The oxygen potentials for Pu/U ratios other than the ones shown in Fig. 11.12 are similar to the curves for  $q = 0.3$ . For  $\text{UO}_{2+x}$  (i.e.,  $q = 0$ ), oxygen-potential curves have the same general shape as those of the mixed oxides, but only the portion to the right of  $\text{O/M} = 2.00$  is attainable since at temperatures below  $\sim 1300^{\circ}\text{C}$  uranium cannot be rendered hypostoichiometric.

### 11.4.6 The Rand–Markin Model (Ref. 6)

Although the oxygen potentials of the mixed U–Pu oxides follow the linear temperature dependence of Eq. 11.14, the partial molar enthalpy and entropy depend upon two composition variables, the fraction of plutonium in the heavy metal and the O/M ratio (i.e.,  $q$  and  $x$ ). Fortunately, it has been found experimentally that  $\Delta H_{\text{O}_2}$

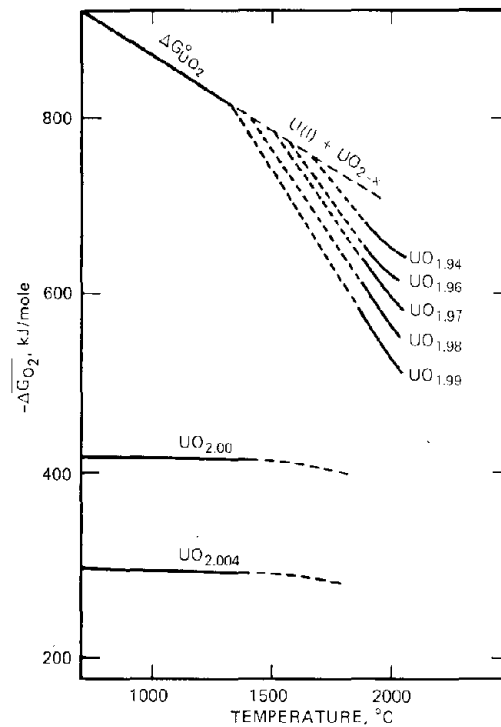


Fig. 11.11 Oxygen potentials of hypostoichiometric and slightly hyperstoichiometric urania. (From T. L. Markin, *Chemical Engineering Progress Symposium Series, Preparation of Nuclear Fuels*, Nuclear Engineering, Part XVIII, Vol. 63, No. 80, p. 43, American Institute of Chemical Engineers, New York, 1967.)

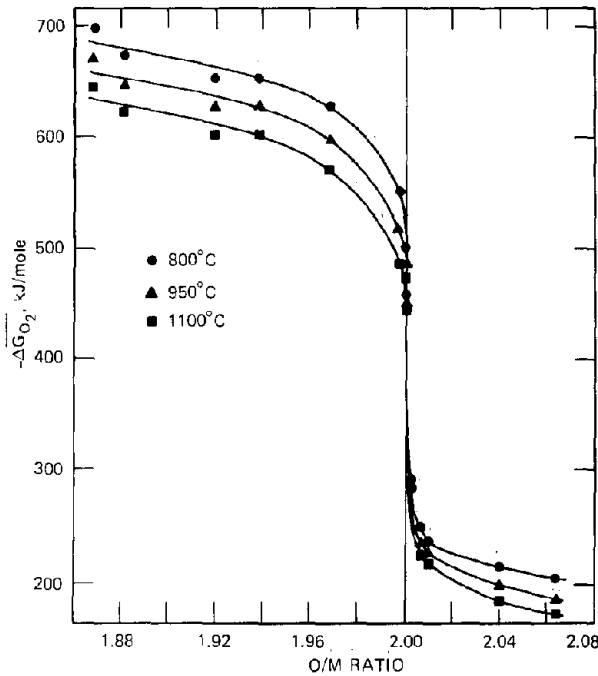


Fig. 11.12  $\Delta G_{O_2}$  vs. O/M ratio for  $U_{0.70}Pu_{0.30}O_{2+x}$ . (From T. L. Markin and E. J. McIver, *Plutonium 1965*, A. E. Kay and M. D. Waldron (Eds.), p. 845, Chapman and Hall, London, 1965.)

and  $\Delta \bar{S}_{O_2}$  depend principally upon the valence (V) of the heavy-metal ions in the oxide. According to the discussion of Sec. 11.3, mixed oxides with  $O/M < 2$  can be regarded as ideal solutions of stoichiometric uranium oxide and hypostoichiometric plutonia. The average valence of the plutonium ions in a crystal of specified  $x$  and  $q$  is easily determined by the requirement of electrical neutrality. Similarly, the average valence of the uranium ions in hyperstoichiometric material can be determined for any composition:

*Hypostoichiometric* ( $U_{1-q}Pu_qO_{2-x}$ )

$$V_U = 4 \quad (11.15)$$

$$V_{Pu} = 4 - \frac{2x}{q}$$

*Hyperstoichiometric* ( $U_{1-q}Pu_qO_{2+x}$ )

$$V_U = 4 + \frac{2x}{(1-q)} \quad (11.16)$$

$$V_{Pu} = 4$$

where  $x$  is considered to be positive in both Eqs. 11.15 and 11.16.

The partial molar thermodynamic properties depend only on  $V_{Pu}$  in hypostoichiometric fuel and only on  $V_U$  in hyperstoichiometric material. Data such as those shown in Fig. 11.12 and additional measurements for other values of the U/Pu ratio have provided a rather complete description

of the oxygen potentials for mixed oxides in the range of interest for fuel-element applications. When plotted as a function of the heavy-metal valence, all these data can be collapsed onto the solid curves shown in Figs. 11.13 and 11.14. The partial molar entropies and enthalpies ( $U_{0.8}Pu_{0.2}$ ) $O_{2-x}$  measured by Tetenbaum<sup>4</sup> using the  $H_2O-H_2$  equilibration technique are also shown on these plots. The substantial discrepancy between the two sets of measurements may be due in part to the different experimental techniques employed by the two groups, but most likely the differences are real and reflect the variations of  $\Delta \bar{H}_{O_2}$  and  $\Delta \bar{S}_{O_2}$  with temperature.

The oxygen pressure in equilibrium with nonstoichiometric mixed-oxide fuel can be determined using the Rand-Markin model,<sup>6</sup> as follows: The O/M ratio of the fuel determines the nonstoichiometry parameter  $x$  by

$$\frac{O}{M} = 2 \pm x \quad (11.17)$$

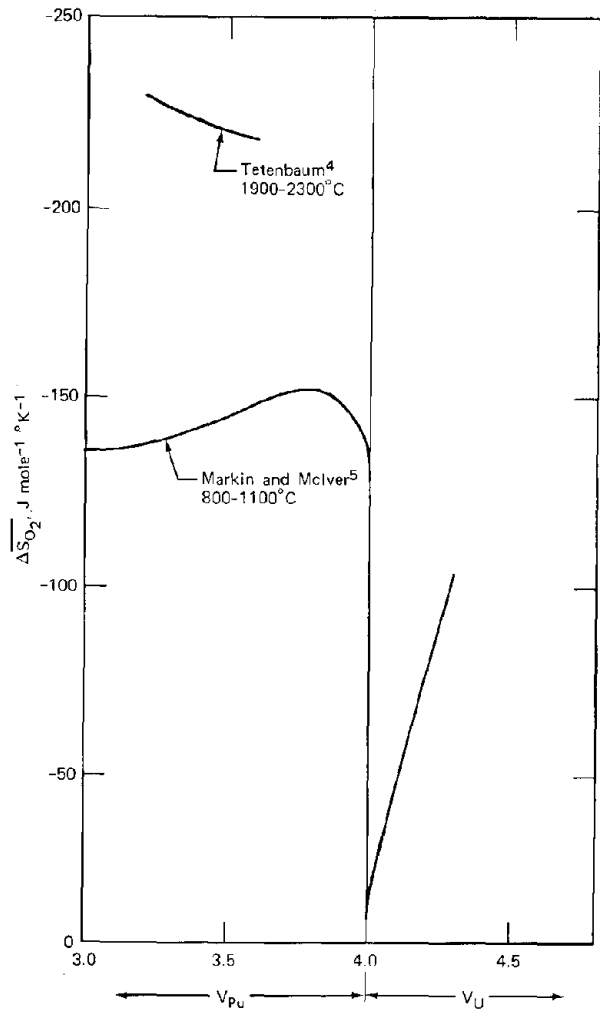


Fig. 11.13 Partial molar entropy of oxygen in mixed uranium-plutonium oxides.

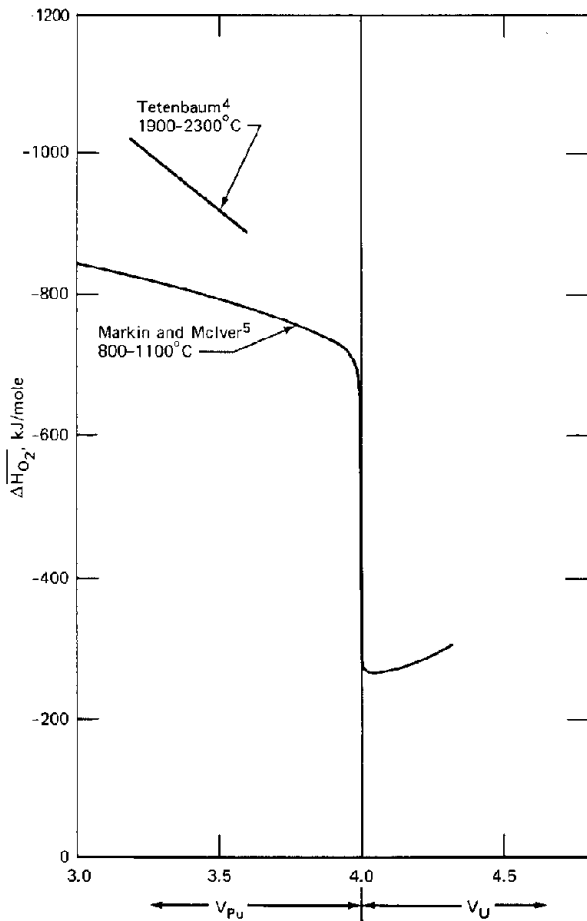


Fig. 11.14 Partial molar enthalpy of oxygen in mixed uranium-plutonium oxides.

where the positive sign is used if  $O/M > 2$ , and the negative sign, when  $O/M < 2$ . The valence of the heavy metal is obtained from  $x$  and  $q$  by use of Eq. 11.15 or 11.16. The partial molar entropy and enthalpy of the solid are then determined from Figs. 11.13 and 11.14. Finally,  $\Delta G_{O_2}$  is obtained from Eq. 11.14 and  $p_{O_2}$  from Eq. 11.4.

#### 11.4.7 Blackburn's Model

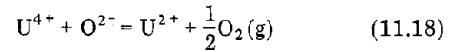
The Rand-Markin thermochemical description of oxygen potentials of mixed-oxide fuels is based upon two conditions:

1. The oxygen potential is a function of uranium valence for hyperstoichiometric material and of plutonium valence for hypostoichiometric fuel.
2. The correlation implied by condition 1 is independent of temperature and Pu/U ratio.

The model proposed by Blackburn<sup>7</sup> is designed to predict oxygen potentials in oxide fuels. Condition 1 is modified slightly for hypostoichiometric urania, but condition 2 is replaced by an analysis based upon thermochemical properties of the pure oxides.

In  $UO_{2-x}$ , the prevailing oxygen partial pressure establishes a definite ratio of  $U^{4+}$  to a lower valence uranium

cation, which is assumed to be  $U^{2+}$ . This equilibrium is governed by the reaction



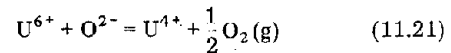
The law of mass action for this equilibrium may be written

$$K_{2,4}^U = \frac{(p_{O_2})^{1/2}[U^{2+}]}{[O^{2-}][U^{4+}]} \quad (11.19)$$

where the concentrations denoted by the bracketed expressions are the number of ions per atom of uranium. Blackburn evaluated the equilibrium constant from the substoichiometric oxide composition at the phase boundary between  $U(l)$  and  $UO_{2-x}$  (Fig. 11.1) and the standard free energy of formation of stoichiometric  $UO_2$ . He finds

$$K_{2,4}^U = -(78.3 \times 10^3/T) + 13.6 \quad (11.20)$$

For  $UO_{2+x}$ , the uranium valence in excess of 4+ is assumed to be due to the presence of  $U^{6+}$  ions. The equilibrium reaction is



for which

$$K_{4,6}^U = \frac{(p_{O_2})^{1/2}[U^{4+}]}{[O^{2-}][U^{6+}]} \quad (11.22)$$

The equilibrium constant  $K_{4,6}^U$  is obtained from the standard free energies of formation of  $UO_2$  and  $U_4O_9$ ,

$$\ln K_{4,6}^U = -(16.4 \times 10^3/T) + 5.0 \quad (11.23)$$

Equations 11.19 and 11.22 apply to any composition in the single-phase region for  $UO_{2 \pm x}$  shown in Fig. 11.1. The oxygen pressure in equilibrium with a particular composition at a specified temperature is obtained by solving Eqs. 11.19 and 11.22 in conjunction with the relation

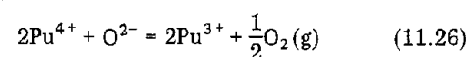
$$[U^{2+}] + [U^{4+}] + [U^{6+}] = 1 \quad (11.24)$$

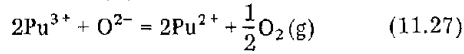
and the condition of electrical neutrality:

$$[O^{2-}] = 2 \pm x = [U^{2+}] + 2[U^{4+}] + 3[U^{6+}] \quad (11.25)$$

The computed oxygen potentials agree very well with measurements of  $p_{O_2}$  over both  $UO_{2-x}$  and  $UO_{2+x}$ . The information used to predict the oxygen potential (Eqs. 11.20 and 11.23) was obtained from thermochemical parameters of the uranium-oxygen system other than the oxygen pressures; that is, the method is not simply data-fitting.

An analysis similar to that applied to the uranium oxides can be used for the hypostoichiometric plutonium oxides,  $PuO_{2-x}$ . In this case, however, it is necessary to consider the cations  $Pu^{2+}$ ,  $Pu^{3+}$ , and  $Pu^{4+}$ , which are related by the reactions





for which the law of mass action requires

$$K_{3,4}^{\text{Pu}} = \frac{(\text{pO}_2)^{1/2}[\text{Pu}^{3+}]^2}{[\text{O}^{2-}][\text{Pu}^{4+}]^2} \quad (11.28)$$

$$K_{2,3}^{\text{Pu}} = \frac{(\text{pO}_2)^{1/2}[\text{Pu}^{2+}]^2}{[\text{O}^{2-}][\text{Pu}^{3+}]^2} \quad (11.29)$$

In this case, the equilibrium constants were determined by fitting the oxygen pressure over  $\text{PuO}_{2-x}$  to Eqs. 11.28 and 11.29 (with equations analogous to Eqs. 11.24 and 11.25 to provide a sufficient number of relations between the ion concentrations in the solid). The results are

$$\ln K_{3,4}^{\text{Pu}} = -(50.9 \times 10^3/T) + 10.3 \quad (11.30)$$

$$\ln K_{2,3}^{\text{Pu}} = -(92.5 \times 10^3/T) + 21.3 \quad (11.31)$$

Higher valence states of plutonium than  $\text{Pu}^{4+}$  are unimportant and are neglected in the analysis.

In order to predict the oxygen potential of mixed U-Pu oxides, all four equilibria, Eqs. 11.19, 11.22, 11.28, and 11.29 are required. The stoichiometric relations become

$$[\text{U}^{2+}] + [\text{U}^{4+}] + [\text{U}^{6+}] = 1 - q \quad (11.32a)$$

$$[\text{Pu}^{2+}] + [\text{Pu}^{3+}] + [\text{Pu}^{4+}] = q \quad (11.32b)$$

and the electroneutrality condition is

$$[\text{O}^{2-}] = 2 \pm x = [\text{U}^{2+}] + [\text{Pu}^{2+}] + \frac{3}{2}[\text{Pu}^{3+}] + 2[\text{U}^{4+}] + 2[\text{Pu}^{4+}] + 3[\text{U}^{6+}] \quad (11.33)$$

The solution proceeds as follows: Eqs. 11.28, 11.29, 11.32b, and the first equality of Eq. 11.33 are solved simultaneously to provide expressions for  $[\text{Pu}^{2+}]$ ,  $[\text{Pu}^{3+}]$ , and  $[\text{Pu}^{4+}]$  in terms of  $K_{2,3}^{\text{Pu}}$ ,  $K_{3,4}^{\text{Pu}}$ ,  $\text{pO}_2$ , and  $x$ . A similar procedure is applied to determine  $[\text{U}^{2+}]$ ,  $[\text{U}^{4+}]$ , and  $[\text{U}^{6+}]$ . The second equality of Eq. 11.33 then determines a unique relation between  $\text{pO}_2$  and  $x$  which depends upon temperature via the four equilibrium constants. The resulting predictions of  $\Delta\bar{G}_{\text{O}_2} = RT \ln \text{pO}_2$  are in good accord with data such as those shown in Fig. 11.12 and other oxygen-potential measurements at higher temperatures. Note that Blackburn's method does not assume that  $\Delta\bar{H}_{\text{O}_2}$  and  $\Delta\bar{S}_{\text{O}_2}$  are temperature independent, as does the empirical method of Rand and Markin. The discrepancies between the data of various investigators shown in Figs. 11.13 and 11.14 are resolved by Blackburn's calculation.

## 11.5 THERMOCHEMISTRY OF FUEL VAPORIZATION

Knowledge of the pressures of volatile species containing uranium or plutonium in a gas phase in contact with the

solid oxide is of great importance in assessing the behavior of operating fuel pins. The thermodynamic problem may be stated as follows: Given a solid oxide of a specified composition and at a particular temperature, what are the species that are present in equilibrium in the gas above the solid and what are their partial pressures? The thermodynamic system for analysis of fuel vaporization is identical to that shown in Fig. 11.7 except that many more species than  $\text{O}_2$  in the gas must be considered. All these species are in equilibrium with the solid oxide and may also be involved in gas-phase equilibria among themselves. Nine gaseous species have been identified in the gas phase which is in equilibrium with solid  $(\text{U,Pu})\text{O}_{2 \pm x}$ . They are  $\text{O}$ ,  $\text{O}_2$ ,  $\text{U}$ ,  $\text{UO}$ ,  $\text{UO}_2$ ,  $\text{UO}_3$ ,  $\text{Pu}$ ,  $\text{PuO}$ , and  $\text{PuO}_2$ . The gaseous species  $\text{PuO}_3$  has not been observed. Complete thermochemical description of this system requires that the gas-solid and gas phase equilibria be known.

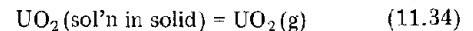
### 11.5.1 Gas-Solid Equilibria (Rand-Markin Model)

Reaction 11.1b represents an important gas-solid equilibrium the properties of which are discussed in Sec. 11.4. Additional reactions must be considered to account for the vaporization of the heavy metals. In Sec. 11.3 it was noted that nonstoichiometric mixed oxides may be considered as two-component ideal solid solutions in which one component is a heavy-metal oxide of exact stoichiometry and the other component is a nonstoichiometric oxide.

#### *Hypostoichiometric Oxides*

The hypostoichiometric mixed oxide  $\text{U}_{1-q}\text{Pu}_q\text{O}_{2-x}$  is a solution of  $\text{UO}_2$  and  $\text{PuO}_{2-m}$ , where  $m = x/q$ . The mole fractions of the two components in this solution are  $1 - q$  and  $q$ , respectively. We consider the gas-solid equilibria in which these two components take part.

Since  $\text{UO}_2$  has an appreciable vapor pressure at high temperatures (see Fig. 9.4), an important gas-solid equilibrium is



Inasmuch as the solid solution in which  $\text{UO}_2$  is one component is very nearly ideal, the partial pressure of  $\text{UO}_2$  in the gas above the solid may be described by Raoult's law:

$$p_{\text{UO}_2} = (1 - q)P_{\text{UO}_2}^\circ \quad (11.35)$$

where  $p_{\text{UO}_2}$  is the partial pressure of  $\text{UO}_2$  in the gas generated by a  $\text{UO}_2$  mole fraction of  $1 - q$  in the solution and  $P_{\text{UO}_2}^\circ$  is the vapor pressure of pure solid  $\text{UO}_2$  at the given temperature. The vaporization of pure solid  $\text{UO}_2$  can be written



where the  $s$  in parentheses on the left denotes a pure solid. The equilibrium constant of this reaction is just the vapor

pressure  $P_{\text{UO}_2}^\circ$ , which is related to the standard free-energy change upon vaporization (or sublimation in this case) by

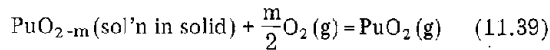
$$P_{\text{UO}_2}^\circ = \exp\left(-\frac{\Delta G_{\text{UO}_2, \text{vap}}^\circ}{RT}\right) \quad (11.37)$$

where

$$\Delta G_{\text{UO}_2, \text{vap}}^\circ = \Delta H_{\text{UO}_2, \text{vap}}^\circ - \Delta S_{\text{UO}_2, \text{vap}}^\circ(T/10^3) \quad (11.38)$$

where  $\Delta H_{\text{UO}_2, \text{vap}}^\circ$  and  $\Delta S_{\text{UO}_2, \text{vap}}^\circ$  are the enthalpy and entropy of vaporization, respectively.

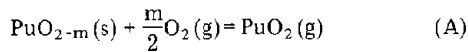
The vaporization of the nonstoichiometric plutonium oxide component of the fuel, on the other hand, cannot be analyzed in as simple a fashion as the  $\text{UO}_2$  component. The compound  $\text{PuO}_{2-m}$  does not exist as a molecular species in the gas; only molecules containing integral numbers of oxygen atoms associated with a plutonium atom are present. From a thermodynamic point of view, gaseous plutonium species may be regarded as being formed by the following gas-solid reaction:



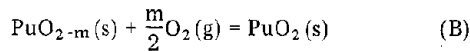
Application of the law of mass action to this reaction gives

$$\frac{P_{\text{PuO}_2}}{qP_{\text{O}_2}^{m/2}} = \exp\left(-\frac{\Delta G_A^\circ}{RT}\right) \quad (11.40)$$

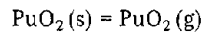
where  $q$  is the mole fraction of  $\text{PuO}_{2-m}$  in the solid and  $\Delta G_A^\circ$  is the standard-state free-energy change of the reaction



The difference between reaction 11.39 and reaction A is that  $\text{PuO}_{2-m}$  is in solution with  $\text{UO}_2$  in the former but is in the pure solid state in the latter. Reaction A may be further broken down into the sum of



and



where the last reaction represents the vaporization of pure solid stoichiometric plutonia. The standard-state free-energy change of reaction A is the sum of the standard-state free energies of the above two reactions:

$$\Delta G_A^\circ = \Delta G_B^\circ + \Delta G_{\text{PuO}_2, \text{vap}}^\circ \quad (11.41)$$

The standard free energy change of reaction B can be obtained by considering a reversible isothermal process that combines 1 mole of pure solid  $\text{PuO}_{2-m}$  with  $m/2$  moles of gaseous oxygen at 1 atm pressure to produce 1 mole of pure solid  $\text{PuO}_2$ . (This is in accord with the definition of the standard-state free energy of a chemical reaction; see Chap. 5.) Figure 11.15 shows a system that accomplishes

this reaction in the desired reversible manner. It consists of a tank of oxygen gas at 1 atm pressure, a reversible isothermal engine that reduces the oxygen from 1 atm to the equilibrium pressure over the oxide, and a box that contains the solid.

Initially, the composition of the oxide is  $\text{PuO}_{2-m}$ . As oxygen is added from the engine, the O/Pu ratio increases until it finally becomes 2. Let this ratio at any intermediate stage in the process be  $2 - m'$ . The free-energy change of the reaction may be identified with the change in the free energy of the oxygen as it passes through the expander. Since the oxygen pressure is reduced from 1 atm to the pressure that is in equilibrium with  $\text{PuO}_{2-m'}$ , there is no change in free energy as oxygen is added to the solid. As

SURROUNDINGS: TEMPERATURE,  $T$ ; PRESSURE, 1 ATM

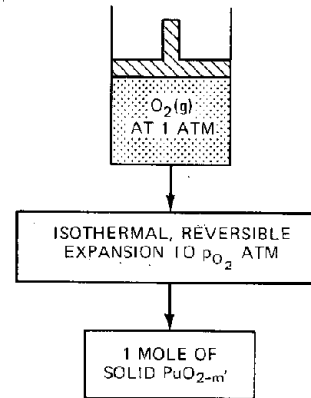
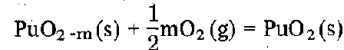


Fig. 11.15 Thermodynamic device for calculating the standard free-energy change of the reaction:



the O/Pu ratio of the solid increases during the transfer of oxygen, the equilibrium oxygen pressure follows a curve of the general shape of those shown in Fig. 11.12 between  $O/M = 2 - mq$  and  $O/M = 2.00$ .

The free-energy change due to expansion of the gas can be obtained as follows: Suppose 1 mole of  $\text{O}_2$  is expanded reversibly and isothermally from 1 atm to  $p_{\text{O}_2}$  atm. Integrating the thermodynamic relation

$$\left(\frac{\partial G}{\partial p}\right)_T = V = \frac{RT}{p}$$

between these pressures shows that the free-energy change per mole is  $RT \ln p_{\text{O}_2}$ . Let  $n$  be the number of moles of oxygen which have been transferred. It is related to the stoichiometric parameter  $m'$  by

$$n = \frac{(m - m')}{2} \quad (11.42)$$

The differential free-energy change due to transfer of  $dn$  moles is  $RT \ln p_{\text{O}_2} dp$ , or, using Eq. 11.42,  $-RT \ln p_{\text{O}_2} dm'/2$ . The total free-energy change for complete conversion of  $\text{PuO}_{2-m}$  to  $\text{PuO}_2$  in the device of Fig. 11.15 is

$$\Delta G_B^\circ = \frac{1}{2} \int_0^m RT \ln p_{O_2} \, dm' \quad (11.43)$$

Since  $RT \ln p_{O_2}$  is the oxygen potential of the fuel, Eq. 11.43 is equivalent to

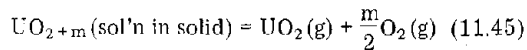
$$\Delta G_B^\circ = \frac{1}{2} \int_0^m \overline{\Delta G_{O_2}} \, dm' \quad (11.44)$$

Thus, the standard free-energy change of reaction B is the integral of the oxygen potential of the fuel from the initial hypostoichiometric composition of the plutonia component to exact stoichiometry. It may be evaluated by graphically integrating curves such as those shown in Fig. 11.12 for the particular temperature ( $O/M$  must first be converted to  $m'$ ).

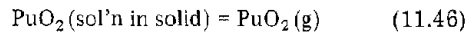
The partial pressures of  $UO_2$  and  $PuO_2$  over hypostoichiometric mixed-oxide fuel are given by Eqs. 11.35 and 11.40, respectively. The vapor pressure of solid  $UO_2$  for use in the former is given by Eq. 11.37, in which the enthalpy and entropy of vaporization have been determined experimentally. The standard free energy of reaction for use in Eq. 11.40 is, according to Eq. 11.41, equal to the sum of the free energy of vaporization of pure solid  $PuO_2$  and the oxygen potential integral of Eq. 11.44. Data are available for estimation of both these quantities.

### Hyperstoichiometric Oxides

For hyperstoichiometric mixed oxides, the analysis is similar to that just presented for hypostoichiometric fuel. In the former, the solid is a mixture of  $PuO_2$  and  $UO_{2+m}$ , where  $m = x/(1-x)$ , and the vaporization process can be written



and



The partial pressure of  $PuO_2$  is given by

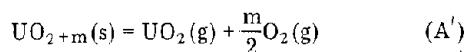
$$p_{PuO_2} = q p_{PuO_2}^\circ \quad (11.47)$$

$$p_{PuO_2}^\circ = \exp\left(-\frac{\Delta G_{PuO_2, \text{vap}}^\circ}{RT}\right) \quad (11.48)$$

while the partial pressure of  $UO_2$  is obtained from the equilibrium of Eq. 11.45:

$$\frac{p_{O_2}^{m/2} p_{UO_2}}{1-q} = \exp\left(-\frac{\Delta G_{A'}^\circ}{RT}\right) \quad (11.49)$$

where  $\Delta G_{A'}^\circ$  is the standard free energy of the reaction



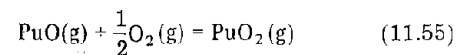
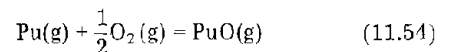
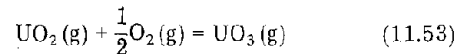
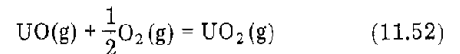
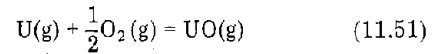
which is

$$\Delta G_{A'}^\circ = -\frac{1}{2} \int_0^m \overline{\Delta G_{O_2}} \, dm' + \Delta G_{UO_2, \text{vap}}^\circ \quad (11.50)$$

The integral of the oxygen potential in Eq. 11.50 can be obtained from curves such as those in Fig. 11.12, except that the range of  $m'$  is to the right of exact stoichiometry.

### 11.5.2 Equilibria in the Gas Phase (Rand-Markin Model)

To the gas-solid equilibria just discussed we must add the requirements of equilibrium of all nine components in the gas phase above the fuel. These are



The equilibrium constants and standard-state free-energy changes of these reactions are

$$\frac{p_O}{(p_{O_2})^{1/2}} = \exp\left(-\frac{\Delta G_{O_2/O}^\circ}{RT}\right) \quad (11.56)$$

$$\frac{p_{UO}}{p_U (p_{O_2})^{1/2}} = \exp\left(-\frac{\Delta G_{UO/UO}^\circ}{RT}\right) \quad (11.57)$$

$$\frac{p_{UO_2}}{p_{UO} (p_{O_2})^{1/2}} = \exp\left(-\frac{\Delta G_{UO_2/UO_2}^\circ}{RT}\right) \quad (11.58)$$

$$\frac{p_{UO_3}}{p_{UO_2} (p_{O_2})^{1/2}} = \exp\left(-\frac{\Delta G_{UO_3/UO_3}^\circ}{RT}\right) \quad (11.59)$$

$$\frac{p_{PuO}}{p_{Pu} (p_{O_2})^{1/2}} = \exp\left(-\frac{\Delta G_{PuO/PuO}^\circ}{RT}\right) \quad (11.60)$$

$$\frac{p_{PuO_2}}{p_{PuO} (p_{O_2})^{1/2}} = \exp\left(-\frac{\Delta G_{PuO_2/PuO_2}^\circ}{RT}\right) \quad (11.61)$$

In each of these equations the standard-state free-energy changes can be written

$$\Delta G_i^\circ = \Delta H_i^\circ - \Delta S_i^\circ (T/10^3) \quad (11.62)$$

where  $\Delta H_i^\circ$  and  $\Delta S_i^\circ$  are independent of temperature. Measurement of these thermochemical parameters is discussed in Sec. 11.5.4.

Once the  $\Delta G_i^\circ$  values for Eqs. 11.56 to 11.61 are known, the composition of the equilibrium vapor over a solid oxide of any composition and temperature can be calculated in the following manner:

1. The pressure of  $O_2$  is determined from the oxygen potential of the fuel, as described in Sec. 11.4. The pressure of atomic oxygen follows from Eq. 11.56.

2. The partial pressures of  $UO_2$  and  $PuO_2$  are obtained by the method described in the first part of this section, using the oxygen potentials of the fuel and the enthalpies and entropies of vaporization of the pure dioxides.

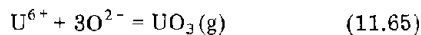
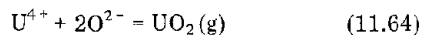
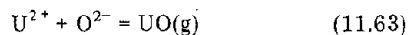
3. The pressures of  $UO$  and  $PuO$  can be determined from Eqs. 11.58 and 11.61, respectively, since the partial pressures of the dioxides are known.

4. The pressures of the metal vapors are obtained from Eqs. 11.57 and 11.60 using the pressures of the monoxides computed in step 3.

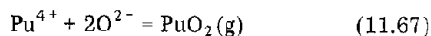
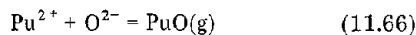
5. The partial pressure of  $UO_3$  is determined from Eq. 11.59 from the known pressure of  $UO_2$ .

### 11.5.3 Heavy-Metal-Oxide Vapor Pressures by the Blackburn Model

Blackburn's thermochemical model of the actinide oxides can be extended to permit computation of the equilibrium pressures of the oxides of uranium and plutonium over fuels of specified composition (i.e., the O/M ratio or  $x$  and the Pu/U ratio or  $q$ ). The vapor pressures of the gaseous oxides are considered to depend upon the concentrations in the solid of the corresponding uranium ions of the same valence. Thus,  $p_{UO}$  depends on  $[U^{2+}]$ ,  $p_{UO_2}$  depends upon  $[U^{4+}]$ , etc. The vaporization reactions are written



Similarly, vaporization of the plutonium oxides proceeds according to the reactions:



The mass-action law corresponding to reaction 11.63 is

$$K_{UO} = \frac{p_{UO}}{[U^{2+}][O^{2-}]} \quad (11.68)$$

According to Eq. 11.33, the concentration of oxygen ions (i.e.,  $O^{2-}$  ions per heavy-metal atom) is  $2 \pm x$ . Inasmuch as the magnitude of  $x$  is less than 0.1, the approximation  $[O^{2-}] \approx 2$  can be employed without introducing appreciable error. Eq. 11.68 then becomes

$$p_{UO} = 2K_{UO} [U^{2+}] \quad (11.69)$$

and the remaining equilibria are

$$p_{UO_2} = 4K_{UO_2} [U^{4+}] \quad (11.70)$$

$$p_{UO_3} = 8K_{UO_3} [U^{6+}] \quad (11.71)$$

$$p_{PuO} = 2K_{PuO} [Pu^{2+}] \quad (11.72)$$

$$p_{PuO_2} = 4K_{PuO_2} [Pu^{4+}] \quad (11.73)$$

The equilibrium constants in Eqs. 11.69 to 11.73 can be expressed in the form

$$\ln K_i = -\frac{A_i}{(T/10^3)} + B_i \quad (i = UO, \dots, PuO_2) \quad (11.74)$$

The constants  $A_i$  and  $B_i$  for each species are shown in Table 11.1. Calculation of the actinide oxide vapor pressures over mixed uranium-plutonium oxide fuels requires knowledge of the solid concentration of the heavy-metal cations. These are obtained in the course of the calculation of the oxygen potential by the method outlined at the end of Sec. 11.4.5. Specifically,  $[U^{2+}]$ ,  $\dots$ ,  $[Pu^{4+}]$  are obtained by simultaneous solution of Eqs. 11.19, 11.22, 11.28, 11.29, 11.32a, 11.32b, and 11.33. Once these concentrations have been determined, the vapor pressures of the actinide oxides follow from Eqs. 11.69 to 11.73, the equilibrium constants being obtained from Eq. 11.74 and Table 11.1.

Table 11.1 Constants in Eq. 11.74 of Blackburn's Model

Species	A	B
UO	49.5	11.9
UO <sub>2</sub>	74.0	19.9
UO <sub>3</sub>	44.0	11.9
PuO	44.1	11.5
PuO <sub>2</sub>	72.5	18.8

Although the thermochemical analysis of Rand and Markin and that of Blackburn are different, prediction of the actinide oxide pressures by either method relies upon measurements of the gas-phase equilibria involving oxygen and these species, as described in the next section.

### 11.5.4 Knudsen Cell-Mass Spectrometer Experiments

The thermochemical parameters of reactions 11.51 to 11.55 for the Rand-Markin model and those listed in Table 11.1 for use in Blackburn's model can be determined by direct measurement of the partial pressures of the species in the vapor phase which are in equilibrium with the solid mixed oxide. The apparatus for such measurements is shown in Fig. 11.16. The solid and the gas-phase in equilibrium with it are contained in a small container called a Knudsen cell, so named because the gas can very slowly escape from a small hole in the top to the cell by effusion (or Knudsen flow) into the vacuum system. The area of the hole must be a small fraction of the internal area of the cell; otherwise equilibrium may not be reached in the enclosure. Only the heavy-metal-containing species are shown in the gas phase in the drawing because the partial pressures of O and  $O_2$  are generally too small to be detected. (The pressure of molecular oxygen,  $p_{O_2}$ , is known, however, as a result of the experiments described in Sec. 11.4 which measure the oxygen potential;  $p_O$  is determined in terms of

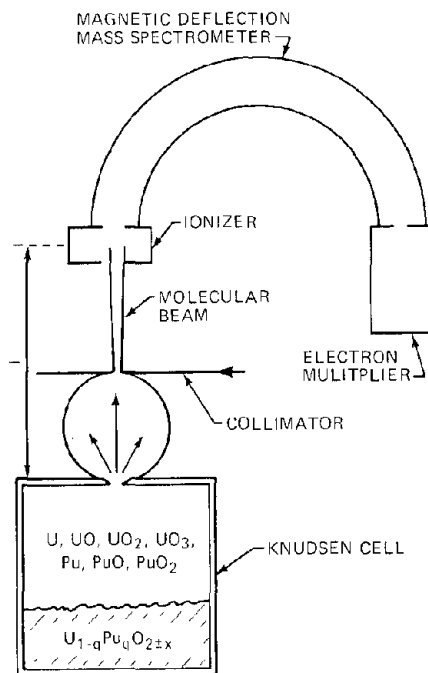


Fig. 11.16 Knudsen cell—mass spectrometer apparatus for determining the composition of the equilibrium vapor over solid uranium—plutonium oxide fuel materials.

$p_{O_2}$  by the dissociation reaction, Eq. 11.1a, for which the equilibrium constant is well known.) The relative quantities of the volatile species can be altered by changing the stoichiometry of the solid; higher oxides are favored by hyperstoichiometric material and lower oxides and metal vapor are enhanced by hypostoichiometric material. The Knudsen cell is heated to high temperatures ( $2500^\circ\text{K}$ ) by electron bombardment, and for this reason it is sometimes referred to as an "oven." Because the material of which the cell is fabricated must be inert to the heavy metals and oxygen at these temperatures, a noble metal, such as iridium or rhenium, is usually used.

According to the classical laws of molecular effusion, each component of the gas flows through the hole independently of the others. The angular distribution of the flux of emitted molecules is cosine-shaped as indicated by the circle above the cell in Fig. 11.16. A small portion of the flux along the axis is permitted to pass through an orifice in a plate above the Knudsen cell. Collimation produces a beam of molecules which passes through the ionizer of a mass spectrometer where some of the neutral particles are ionized by electron impact. The resulting ions are mass analyzed by a magnetic field perpendicular to the plane of the drawing in Fig. 11.16 and detected by an electron multiplier with a first stage made of a substance which emits secondary electrons upon ion impact. Each species in the vapor above the solid is characterized by its mass, and the magnitude of the mass-spectrometer signal when tuned to a particular mass number is a direct measure of the partial pressure of a species in the Knudsen cell.

Consider a cell operating at temperature  $T$  and let  $p_i$  be the partial pressure of species  $i$  in the equilibrium vapor over the solid. If the radius of the hole in the lid is  $r_o$ , the total rate of effusion of species  $i$  is

$$\nu_i = \frac{n_i \bar{v}_i (\pi r_o^2)}{4} \quad (11.75)$$

where  $n_i$  is the molecular density of species  $i$  in the vapor and  $\bar{v}_i$  is the mean speed of these molecules. According to the cosine law of effusion, the intensity of this species in the molecular beam in the ionizer is

$$I_i = \frac{\nu_i}{\pi l^2} \quad (11.76)$$

where  $l$  is the distance between the Knudsen cell lid and the ionizer.

The signal provided by the mass spectrometer is proportional to the number density of species  $i$  in the molecular beam,  $n'_i$ , which is related to the intensity in the beam by

$$S_i = \beta_i n'_i = \frac{\beta_i I_i}{\bar{v}_i} \quad (11.77)$$

Combining Eqs. 11.75 to 11.77, we find the output signal to be

$$S_i = \beta_i \frac{n_i}{4} \left( \frac{r_o}{l} \right)^2 = \beta_i \frac{(r_o/l)^2}{4kT} p_i \quad (11.78)$$

where  $n_i$  has been related to the partial pressure by the perfect gas law. The quantity  $\beta_i$  in Eq. 11.78 is an instrumental constant, which, however, depends upon the species to which the instrument is tuned because each molecular species has a different cross section for ionization by electron impact and the electron multiplier has a different secondary-electron emission coefficient for different species. If these effects are accounted for by estimated corrections or calibration, Eq. 11.78 then provides a means of directly measuring the partial pressures of all species in the equilibrium vapor in the Knudsen cell.

Equations 11.57 to 11.61 show that the standard free-energy changes of the reactions occurring in the gas phase may be determined from the ratios of the partial pressures of the species containing the heavy metals and the oxygen pressure. The former are obtained from the mass-spectrometer measurements just described and the latter from the oxygen potentials corresponding to the temperature and composition of the solid (see Sec. 11.4). Measurement of the standard free-energy changes as functions of temperature permits the standard enthalpies and entropies of the reactions to be computed from Eq. 11.62. The results are shown in Table 11.2 along with the thermochemical parameters of vaporization of the pure dioxides. The thermochemical parameters in Blackburn's model (Table 11.1) were deduced in part from the measurements summarized in Table 11.2.

The composition of the vapor in equilibrium with mixed-oxide fuels can be determined by using either the Rand—Markin or the Blackburn model. The vapor composition depends upon the O/M and Pu/U ratios of the solid and the temperature. Results of a calculation using the

Table 11.2 Thermochemical Parameters of Reactions Among Heavy-Metal Species\*

Gas-phase reaction	$\Delta H^\circ$ , kJ/mole	$\Delta S^\circ$ , J mole <sup>-1</sup> °K <sup>-1</sup>
$\frac{1}{2}\text{O}_2 = \text{O}$	257	68
$\text{U} + \frac{1}{2}\text{O}_2 = \text{UO}$	-528	-62
$\text{UO} + \frac{1}{2}\text{O}_2 = \text{UO}_2$	-471	-71
$\text{UO}_2 + \frac{1}{2}\text{O}_2 = \text{UO}_3$	-404	-90
$\text{Pu} + \frac{1}{2}\text{O}_2 = \text{PuO}$	-498	-46
$\text{PuO} + \frac{1}{2}\text{O}_2 = \text{PuO}_2 \dagger$	-352	-69
Vaporization of dioxides		
$\text{UO}_2(\text{s}) = \text{UO}_2(\text{g})$	567	150
$\text{PuO}_2(\text{s}) = \text{PuO}_2(\text{g})$	571	150

\*After M. H. Rand and T. L. Markin, in *Thermodynamics of Nuclear Materials—1967*, Symposium Proceedings, Vienna, 1967, International Atomic Energy Agency, Vienna, 1968 (STI/PUB/162); more recent data are given by J. E. Battles, W. A. Shinn, P. E. Blackburn, and R. K. Edwards, *Plutonium 1970*, Proceedings of the Fourth International Conference on Plutonium and Other Actinides, Nuclear Metallurgy, Vol. 17, Part II, p. 733, The Metallurgical Society of the AIME, 1970.

†R. W. Ohse and W. M. Olson report  $\Delta H^\circ = -308$  kJ/mole and  $\Delta S^\circ = -37$  J mole<sup>-1</sup> °K<sup>-1</sup> for this reaction, *Plutonium 1970*, Proceedings of the Fourth International Conference on Plutonium and Other Actinides, Nuclear Metallurgy, Vol. 17, Part II, p. 743, The Metallurgical Society of the AIME, 1970.

Rand—Markin approach in which the last two variables are specified are shown in Fig. 11.17.

There are several noteworthy features of this plot: First, the major vapor species over hyperstoichiometric oxide is  $\text{UO}_3$ , not  $\text{UO}_2$ , although the latter is the predominant vapor component over  $\text{UO}_{2.000}$ . The reason is the very much higher oxygen partial pressure over hyperstoichiometric oxide compared with material of exact stoichiometry, which drives reaction 11.53 to the right.

Second, the U/Pu ratio of the vapor in equilibrium with hyperstoichiometric material is larger than that of the solid. Continuous vaporization enriches the solid in plutonium. Conversely, the hypostoichiometric oxide supports an equilibrium vapor which is richer in plutonium than the solid. The O/M ratio at which the proportion of the heavy metals in the vapor is equal to that in the solid is about 1.96. This situation is termed congruent vaporization. The occurrence of congruent vaporization is dependent primarily upon the O/M ratio of the solid but also varies slightly with the Pu/U ratio and temperature.

Third, the vapor generally contains more oxygen per heavy-metal atom than the solid, which therefore becomes more hypostoichiometric as a result of vaporization.

The preferential loss of oxygen or one of the heavy metals due to volatilization has an important bearing upon the behavior of fuel components in a temperature gradient, which is the subject of the remainder of this chapter.

## 11.6 OXYGEN REDISTRIBUTION

The calculation of the identity and concentrations of the components in the gas phase in equilibrium with solid oxides presented in the previous two sections was purely thermodynamic in nature. The solid—vapor system was assumed to be at constant temperature, and no loss of material from it was permitted. The same fuel in a reactor, however, is subject to very large temperature gradients, and it is also very likely that communication between regions of different temperature is made possible by cracks or interconnected porosity within the ceramic body. Introduction of paths for transport via the gas phase means that the components of the fuel present in the vapor can readily move from one region to another. Or, the initially uniform composition of the fuel may become radially unmixed as a result of the imposition of the temperature gradient. This process is generally called *redistribution* of a particular fuel component. Analysis of this process requires combining thermodynamic requirements with a model of the transport mechanism. The latter determines the extent of the redistribution and its kinetics. Transport of fuel constituents is believed to occur principally by diffusion in the gas phase connecting regions of different temperature, although processes based upon migration in the solid phase have been proposed.

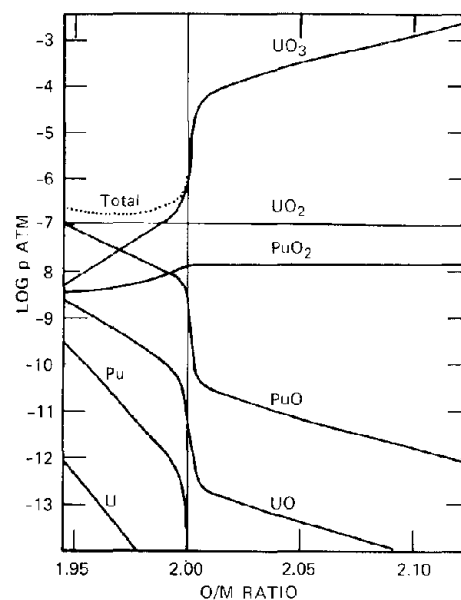


Fig. 11.17 Partial pressures over  $\text{U}_{0.85}\text{Pu}_{0.15}\text{O}_{2\pm x}$  at  $2000^\circ\text{K}$  (calculated). [From M. H. Rand and T. L. Markin, *Thermodynamics of Nuclear Materials—1967*, Symposium Proceedings, Vienna, 1967, International Atomic Energy Agency, Vienna, 1968 (STI/PUB/162).]

Both oxygen and the heavy metals can migrate via the gas-phase transport mechanism, since molecules containing both types of atoms are present in the equilibrium vapor over the solid. Oxygen redistribution will be treated in this section, and heavy-metal migration, in the following section. Knowledge of the extent of oxygen redistribution is important in any overall assessment of fuel performance because many properties of the fuel depend on the O/M ratio. In Chap. 10 a pronounced dependence of the thermal conductivity on O/M was demonstrated; thus, redistribution of oxygen radially will alter the temperature distribution. The O/M ratio strongly influences the oxygen potential of the solid, which determines the ability of the cladding to resist corrosion by the fuel. The O/M ratio affects the creep properties of the oxide, which influences the mechanical performance of the fuel element. Finally, the O/M ratio strongly affects the diffusion coefficients of various species in the solid; so oxygen redistribution indirectly influences the phenomenon of fission-gas bubble formation, which leads either to swelling or to release.

The driving force for oxygen migration can be seen from the relation for the oxygen potential, which can be written

$$\ln p_{O_2} = \frac{\overline{\Delta G_{O_2}}}{RT} = \frac{\overline{\Delta H_{O_2}}}{RT} - \frac{\overline{\Delta S_{O_2}}}{R} \quad (11.79)$$

Since  $\overline{\Delta H_{O_2}}$  and  $\overline{\Delta S_{O_2}}$  are functions of fuel composition but (to first approximation) independent of temperature, Eq. 11.79 shows that a temperature gradient implies a variation in the partial pressure of oxygen in equilibrium with fuel of uniform composition. Or, a gradient of oxygen partial pressure exists in the gas phase as a result of the temperature gradient, and, consequently, oxygen will move along the concentration gradient by gas-phase or solid-state diffusion. Since  $\overline{\Delta H_{O_2}}$  is negative, Eq. 11.79 shows that the highest oxygen pressure is over the hottest part of the fuel. If diffusion of molecular oxygen were the only means of transporting this element, one would expect that in time oxygen would move from the center toward the periphery of the fuel and that the O/M ratio would become larger at the surface than at the center. Experiments have shown that oxygen redistribution does occur but not, however, always in the sense predicted from the above argument.

### 11.6.1 The Markin-Rand-Roberts Model

Markin, Rand, and Roberts<sup>6,8</sup> proposed a mechanism of oxygen transport in the gas phase to explain the observed directions of oxygen redistribution and the magnitude of the effect. They noted that even nuclear-grade  $UO_2$  contains several parts per million of carbon as an impurity. When the fuel is brought to operating temperature, the carbon in the solid may be volatilized as  $CO_2$  or CO, which then mixes with the already present inert gases (helium filling gas or the fission gases xenon and krypton) which occupy all void volumes within the fuel element. By considering the volumes of the plenum region in the fuel element (e.g., Fig. 10.4) and the temperatures of the various parts of the rod, we can show that an impurity content of 1 to 10 ppm will generate from 0.1 to 1 atm of pressure from carbon-bearing gases (see problem at end

of chapter). The mixture of  $CO_2$ , CO, and inert gases presumably fills cracks or interconnected pores within the fuel body as well as the plenum above the fuel.

Oxygen may be transported in such a gas mixture by counterdiffusion of  $CO_2$  and CO. In hyperstoichiometric oxide the process occurs as follows: The  $CO_2$  diffuses from the cold zone to the hot zone where it deposits oxygen in the solid and is simultaneously converted to CO, which then diffuses back to the cold zone. Here the CO picks up oxygen from the fuel to become  $CO_2$ , which again returns to the hot zone. This cyclical movement of CO and  $CO_2$  produces no net transport of carbon, but it does transport oxygen (until a steady state is reached). The reason that the  $CO_2$ -CO mechanism provides a plausible explanation of oxygen transport is that the pressures of  $CO_2$  and CO are usually very much larger than those of other oxygen-bearing species (at least in hyperstoichiometric oxides). The transport role of  $CO_2$  and CO could be played by any pair of gaseous molecules which are connected to each other via an equilibrium reaction involving  $O_2$ . For example,  $H_2O$ - $H_2$  mixtures are equivalent to  $CO_2$ -CO mixtures as far as their ability to transport oxygen is concerned. However, the metallic cladding of reactor fuel elements is quite permeable to hydrogen at operating temperatures, and this impurity, even if present initially in substantial quantities, would soon be lost to the coolant.

The consequences of the  $CO_2$ -CO transport mechanism can be made quantitative by considering the system shown in Fig. 11.18. A block of fuel contains a single pore or crack whose axis is aligned with the temperature gradient. The pore contains the gas mixture described above, namely,  $CO_2$ , CO, and a small amount of  $O_2$  in a large quantity of inert gas. Rectangular coordinates (rather than the cylindrical geometry of a fuel rod) are employed so that the

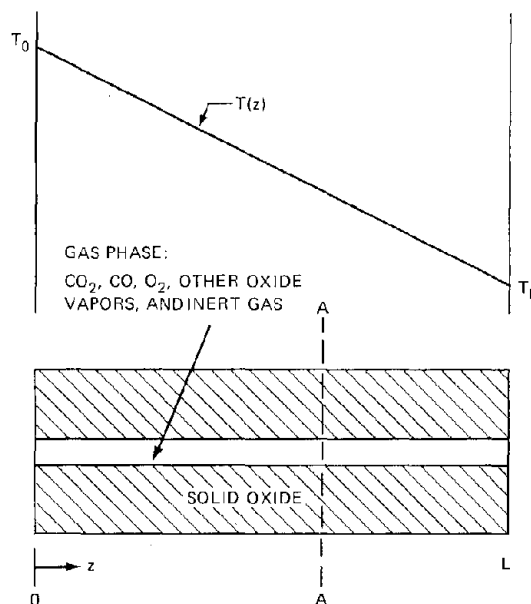


Fig. 11.18 Bar of solid oxide fuel containing a gas-filled pore subject to a temperature gradient. The ends at  $z = 0$  and  $z = L$  are closed.

phenomenon can be illustrated with a minimum of algebra. Experiments in which the oxygen redistribution process have been studied have shown that the average O/M ratio across the temperature gradient is the same as the initial uniform value of the fresh fuel, which implies that no oxygen is lost from the region of fuel which contains the temperature gradient. In keeping with this observation, the ends of the pore in Fig. 11.18 are assumed to be impervious to oxygen (in a fuel element, the cold end faces the cladding and the hot end terminates at the central void, where the gradients of all properties vanish by symmetry). In such a system, gradients of  $\text{CO}_2$ ,  $\text{CO}$ , and other oxygen-containing vapor species may exist along the  $z$ -direction in the gas even at steady state. However, since neither the oxides of carbon nor of oxygen in any form can penetrate the barriers at  $z=0$  and  $z=L$ , the net flux of the elements carbon and oxygen (irrespective of their molecular state) across any plane perpendicular to the axis (such as A-A in the figure) must be zero. Since the active species are diluted by the inert gas, the fluxes of the molecular species can be described by Fick's law. The mass balances on carbon and oxygen assume the forms

$$\text{Carbon: } -D_{\text{CO}} \frac{dp_{\text{CO}}}{dz} - D_{\text{CO}_2} \frac{dp_{\text{CO}_2}}{dz} = 0 \quad (11.80)$$

$$\text{Oxygen: } -D_{\text{CO}} \frac{dp_{\text{CO}}}{dz} - 2D_{\text{CO}_2} \frac{dp_{\text{CO}_2}}{dz} - \sum_i N_i D_i \frac{dp_i}{dz} = 0 \quad (11.81)$$

where  $D_i$  is the diffusion coefficient of species  $i$  in the inert gas,  $p_i$  is the partial pressure of species  $i$  at location  $z$ , and  $N_i$  is the number of oxygen atoms per molecule of the gaseous oxide species. If the reasonable assumption that the diffusion coefficients of  $\text{CO}_2$  and  $\text{CO}$  are equal is made, Eqs. 11.80 and 11.81 can be integrated to yield

$$p_{\text{CO}}(z) + p_{\text{CO}_2}(z) = C_C \quad (11.82)$$

$$p_{\text{CO}}(z) + 2p_{\text{CO}_2}(z) + \sum_i N_i \frac{D_i}{D_{\text{CO}}} p_i(z) = C_O \quad (11.83)$$

where  $C_C$  and  $C_O$  are both constants. Since the model assumes that  $p_{\text{CO}}$  and  $p_{\text{CO}_2}$  are very much larger than any other gaseous oxides, the last term in Eq. 11.83 can be neglected, and we have

$$p_{\text{CO}}(z) + 2p_{\text{CO}_2}(z) = C_O \quad (11.84)$$

The only solution to Eqs. 11.82 and 11.84 is that both  $p_{\text{CO}}$  and  $p_{\text{CO}_2}$  are constant, independent of  $z$ . Thus, consideration of the transport aspects of the problem has led only to the conclusion that the  $\text{CO}_2/\text{CO}$  ratio is everywhere constant, despite the presence of the temperature gradient. However, when coupled to thermodynamic considerations, this restriction is sufficient to completely determine the O/M gradient. The two thermodynamic requirements are that at each point along the temperature gradient:

1. The local oxygen pressure corresponds to the oxygen potential of the fuel (gas-solid equilibrium).

2. The reaction between the gas components  $\text{CO}_2$ ,  $\text{CO}$ , and  $\text{O}_2$  is in thermodynamic equilibrium (gas-phase equilibrium).

Requirement 1 implies that  $p_{\text{O}_2}$  is given by Eq. 11.79, where  $T$  is the temperature at a particular  $z$ , and  $\Delta\overline{H_{\text{O}_2}}$  and  $\Delta\overline{S_{\text{O}_2}}$  are dependent upon the O/M ratio at this location (the oxygen content of the solid will, in general, be different from the value for the fresh fuel).

The gas-phase equilibrium (condition 2) is represented by Eq. 11.5. Its equilibrium is expressed by a combination of Eqs. 11.6 to 11.8 and can be written

$$\ln p_{\text{O}_2} = 2 \frac{\Delta H_{\text{C}}^{\circ}}{RT} - 2 \frac{\Delta S_{\text{C}}^{\circ}}{R} + 2 \ln \left( \frac{p_{\text{CO}_2}}{p_{\text{CO}}} \right) \quad (11.85)$$

Equating the right-hand sides of Eqs. 11.79 and 11.85 yields

$$\frac{\Delta\overline{H_{\text{O}_2}}}{RT} - \frac{\Delta\overline{S_{\text{O}_2}}}{R} = 2 \frac{\Delta H_{\text{C}}^{\circ}}{RT} - 2 \frac{\Delta S_{\text{C}}^{\circ}}{R} + 2 \ln \left( \frac{p_{\text{CO}_2}}{p_{\text{CO}}} \right) \quad (11.86)$$

Now  $\Delta\overline{H_{\text{O}_2}}$  and  $\Delta\overline{S_{\text{O}_2}}$  are known functions of  $T$ ,  $q$ , and  $x$  (Sec. 11.4). Since movement of the heavy metals is not considered in this section,  $q$  is a constant; thus the thermochemical parameters on the left-hand side of Eq. 11.86 are functions of the O/M ratio only. The temperature  $T$  is a known function of  $z$ , and  $p_{\text{CO}_2}/p_{\text{CO}}$  is an unknown constant. Thus, Eq. 11.86 may be regarded as a relation giving  $x$  (or the O/M ratio) as a function of  $z$ , parametric in the ratio  $p_{\text{CO}_2}/p_{\text{CO}}$ . The solution proceeds as follows: Select a value of  $p_{\text{CO}_2}/p_{\text{CO}}$ . Solve Eq. 11.86 for  $x$  as a function of  $z$ . Determine the average value of  $x$  by

$$\bar{x} = \frac{1}{L} \int_0^L x(z) dz \quad (11.87)$$

and compare  $2 \pm \bar{x}$  to the initial O/M ratio (specified). When the two agree, the correct  $p_{\text{CO}_2}/p_{\text{CO}}$  ratio has been guessed, and the problem is solved. The profile of  $x(z)$  represents the redistribution of oxygen due to the temperature gradient.

Experiments that have demonstrated the redistribution of oxygen in a thermal gradient have been reported by a number of investigators.<sup>9-14</sup> The results are summarized in Table 11.3. The measurements of Christensen<sup>9</sup> and Jeffs<sup>12</sup> were conducted on fuel elements irradiated in a reactor (radial geometry); the others were performed on oxide bars held in a longitudinal temperature gradient in out-of-pile experiments (axial geometry).

Table 11.3 shows that application of a temperature gradient to hyperstoichiometric fuel results in an increase of the oxygen content at the hot end with a corresponding deficiency at the cold end. In hypostoichiometric material, redistribution occurs in the opposite direction, the cold end becoming enriched in oxygen and the hot end losing oxygen. These general features are independent of whether the test was performed on a reactor fuel element with a radial temperature distribution established by fission or in an out-of-pile test in which a longitudinal temperature gradient was imposed by external heating. The results for mixed oxides are the same as those for urania.

Table 11.3 Summary of Oxygen Redistribution Experiments

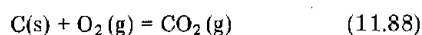
Investigator	Material	Geometry	Redistribution
Christensen <sup>9</sup>	UO <sub>2+x</sub>	Radial	O/U highest at hot zone
Fryxell and Aitken <sup>10</sup>	UO <sub>2-x</sub>	Axial	O/U highest at cold end; no redistribution in UO <sub>2.000</sub>
Evans, Aitken, and Craig <sup>11</sup>	(U,Pu)O <sub>2-x</sub>	Axial	O/M highest at cold end
Jeffs <sup>12</sup>	(U,Pu)O <sub>2+x</sub>	Radial	O/M highest at hot zone; no redistribution in UO <sub>2.000</sub>
Adamson <sup>13</sup>	UO <sub>2+x</sub>	Axial	O/U highest at hot end
Adamson and Carney <sup>14</sup>	(U,Pu)O <sub>2+x</sub>	Axial	O/M highest at hot end

Figure 11.19 compares the data for UO<sub>2+x</sub> with the predictions of the Markin-Rand-Roberts model. The CO<sub>2</sub>/CO ratios listed with each computed curve in Fig. 11.19a are those which yield an O/M distribution with an average value equal to that of the initial fuel. In Fig. 11.19b the H<sub>2</sub> + 1/2 O<sub>2</sub> = H<sub>2</sub>O gas-phase equilibrium was used instead of the reaction CO + 1/2 O<sub>2</sub> = CO<sub>2</sub> since the tests were conducted in a hydrogen atmosphere. In the calculations the thermochemical parameters ΔH<sub>C</sub><sup>o</sup> and ΔS<sub>C</sub><sup>o</sup> in Eq. 11.86 were replaced by analogous values for the H<sub>2</sub>-H<sub>2</sub>O equilibrium. Figure 11.19 shows that the experimental observations of oxygen concentration at the hot end in hyperstoichiometric fuel and at the cold part of hypostoichiometric material are faithfully reproduced by the transport model. (Note that the ordinate in Fig. 11.19b is 2 - O/U and the abscissa is the reciprocal of the absolute temperature instead of position; temperature and location are related by the known temperature distribution.)

Figure 11.20 compares the measurements of Jeffs<sup>12</sup> with the predictions of the Markin-Rand-Roberts model. Agreement with the Markin-Rand-Roberts model is seen to be quite satisfactory.

The model of oxygen redistribution in oxide fuels described above is based on the assumption that the principal carriers of oxygen are gaseous mixtures of CO<sub>2</sub> and CO or H<sub>2</sub>O and H<sub>2</sub>. While this assumption is reasonable for hyperstoichiometric fuels, it may break down when applied to hypostoichiometric oxides. If the CO<sub>2</sub> or H<sub>2</sub>O partial pressure is small, oxygen transfer by this species will require very long times, or, more likely, other oxygen-bearing species in the gas will be present at higher concentrations and dominate the oxygen redistribution process.

Since the activity of carbon in the fuel is largest when free carbon is present, the maximum partial pressure of CO<sub>2</sub> can be obtained from the equilibrium of the reaction



The CO<sub>2</sub> pressure is given by

$$p_{\text{CO}_2}^{\text{max}} = p_{\text{O}_2} \exp\left(-\frac{\Delta G_{\text{CO}_2}^{\circ}}{RT}\right) \quad (11.89)$$

where ΔG<sub>CO<sub>2</sub></sub><sup>o</sup> is the free energy of formation of CO<sub>2</sub>:

$$\Delta G_{\text{CO}_2}^{\circ} = -394 - 0.8(T/10^3) \quad (11.90)$$

Since  $\overline{\Delta G_{\text{O}_2}^{\circ}} = RT \ln p_{\text{O}_2}$ , Eq. 11.89 is equivalent to

$$p_{\text{CO}_2}^{\text{max}} = \exp\left(\frac{\overline{\Delta G_{\text{O}_2}^{\circ}} - \Delta G_{\text{CO}_2}^{\circ}}{RT}\right) \quad (11.91)$$

Consider a mixed-oxide fuel of O/M = 1.96 at 1100°C. Figure 11.12 shows that the oxygen potential of this fuel is -586 kJ/mole. The free energy of formation of CO<sub>2</sub> at 1100°C is -395 kJ/mole. According to Eq. 11.91, the maximum CO<sub>2</sub> pressure above this fuel when free carbon is present is ~5 × 10<sup>-8</sup> atm. (If free carbon is not present, the CO<sub>2</sub> pressure is smaller still.) Although the carbon content of the fuel is large enough to produce CO<sub>2</sub> pressures many orders of magnitude larger than 5 × 10<sup>-8</sup> atm if all carbon were oxidized, the very low oxygen potential of hypostoichiometric fuels does not permit anywhere near complete gasification of the carbon. With the CO<sub>2</sub> pressure limited to such low values, the Markin-Rand-Roberts mechanism, although in principle still possible, would be extremely slow because of the smallness of the CO<sub>2</sub> concentration driving force for gas-phase diffusion. Since oxygen redistribution is observed to occur in hypostoichiometric oxides in times much less than that expected for the maximum allowable CO<sub>2</sub> pressures, it may be concluded that other mechanisms are responsible for moving oxygen along the temperature gradient. At high temperatures (>2000°C), the gaseous oxides of the heavy metals may transport oxygen along with uranium and plutonium as they distill from hot to cold zones.<sup>14</sup> At lower temperatures the oxides of some fission products (e.g., MoO<sub>2</sub> and Cs<sub>2</sub>O or more likely the ternary compound Cs<sub>2</sub>MoO<sub>4</sub>) may be sufficiently volatile to transport significant quantities of oxygen as they migrate down the temperature gradient.

In addition to possible failure of the Markin-Rand-Roberts model due to the presence of oxide vapors with pressures comparable to that of CO<sub>2</sub>, Aitken<sup>15</sup> has suggested that diffusion of oxygen in the solid may be sufficiently rapid to reduce the nonuniform oxygen distribution established in the fuel by the CO<sub>2</sub>-CO gas-phase transport mechanism. Analysis of the redistribution-limiting effect of solid-state diffusion<sup>16</sup> has shown that this mode of transport can be very effective in reducing the extent of oxygen redistribution far below that predicted by the Markin-Rand-Roberts model.

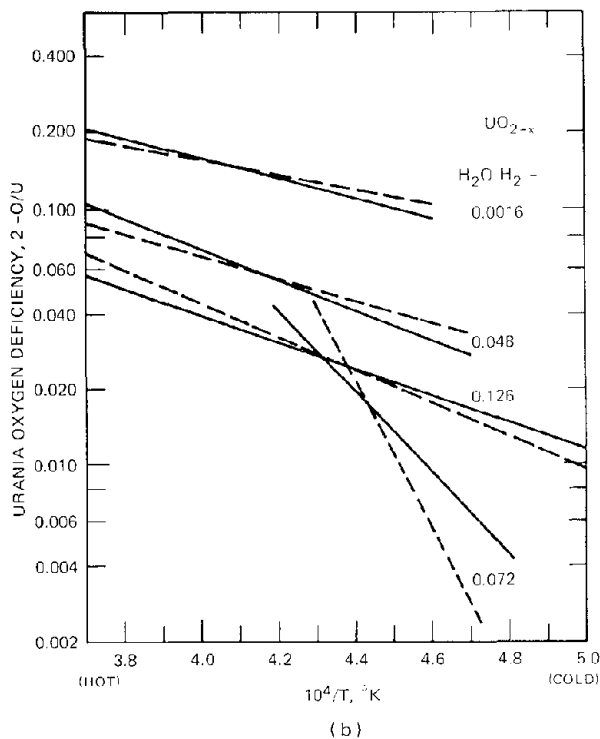
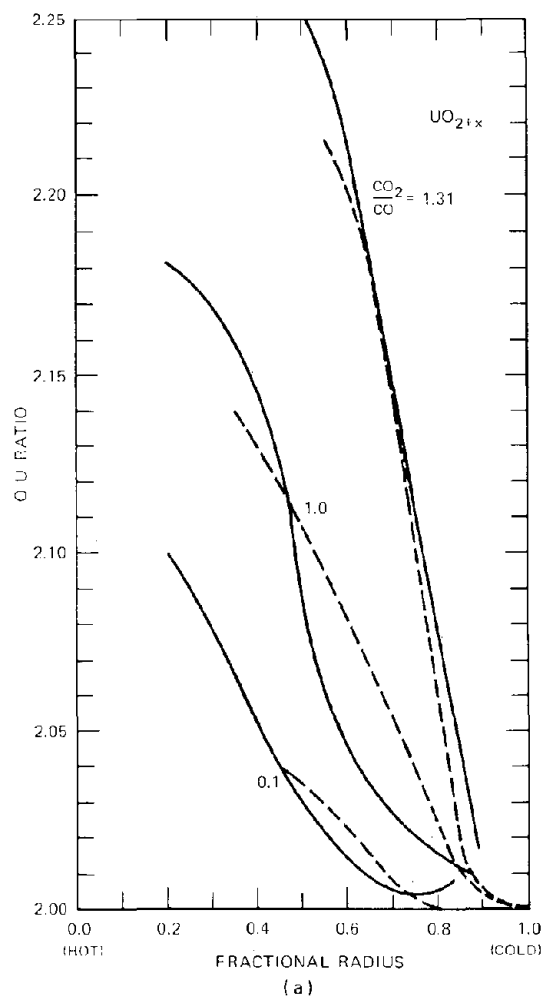


Fig. 11.19 Comparison of calculated and experimental O/U profiles in urania subject to a temperature gradient. [From P. O. Perron, *J. Nucl. Mater.*, 27: 237 (1968).] (a) —, after J. A. Christensen, USAEC Report BNWL-536, 1967. ---, calculated. (b) —, after R. E. Fryxell, USAEC Report GEMP-516, 1967. ---, calculated.

### 11.6.2 Aitken's Model

The difficulty in assigning exact mechanisms for oxygen migration in hypostoichiometric mixed oxides has led Aitken and coworkers<sup>15,17</sup> to develop a phenomenological description of the oxygen redistribution process. Based upon the theory of irreversible thermodynamics, they propose that the stoichiometry parameter  $x$  in  $(U,Pu)O_{2-x}$  should vary with the temperature in a thermal gradient according to

$$\ln x = \frac{Q^+}{RT} + \text{const.} \quad (11.92)$$

where  $Q^+$  is a characteristic heat of transport, the value of which depends upon the mechanism responsible for oxygen migration. The parameter  $Q^+$  is not a true heat of transport which pertains solely to the Soret effect (see Chap. 5); rather,  $Q^+$  represents the combined effect of the solid-state diffusion of oxygen and the vapor migration of all oxygen-bearing species contained in the gas phase filling cracks and fissures in the fuel. If a mechanism is specified (e.g., the Markin-Rand-Roberts  $CO_2/CO$  model), a numerical value of  $Q^+$  can be theoretically determined. In the

absence of an acceptable physical model (as in the case of hypostoichiometric fuels), Eq. 11.92 can be used as a means of correlating experimental results, and the values of  $Q^+$  so obtained can be empirically related to fuel properties and operating conditions. Aitken et al.<sup>18</sup> have shown that the oxygen profiles developed in axial-thermal-gradient experiments in hypostoichiometric mixed oxides are satisfactorily described by an equation of the form of Eq. 11.92. Their results permit a correlation between the average stoichiometry of the fuel,  $\bar{x}$ , and the heat of transport. For  $0 < \bar{x} < 0.02$ , they find that the redistribution measurements are best fitted by a constant value of  $Q^+ = -125$  kJ/mole. For fuel containing less oxygen,

$$Q^+ = -\frac{A}{\bar{x}^2} \quad (\text{for } 0.02 < \bar{x} < 0.1) \quad (11.93)$$

The constant  $A$  varies from 0.059 to 0.096 kJ/mole, depending on whether barriers to oxygen movement (such as cracks perpendicular to the thermal gradient) are present. The latter figure applies to fuel containing a minimum of impedances to transport and represents a larger extent of redistribution than does the smaller value of  $A$ . With the

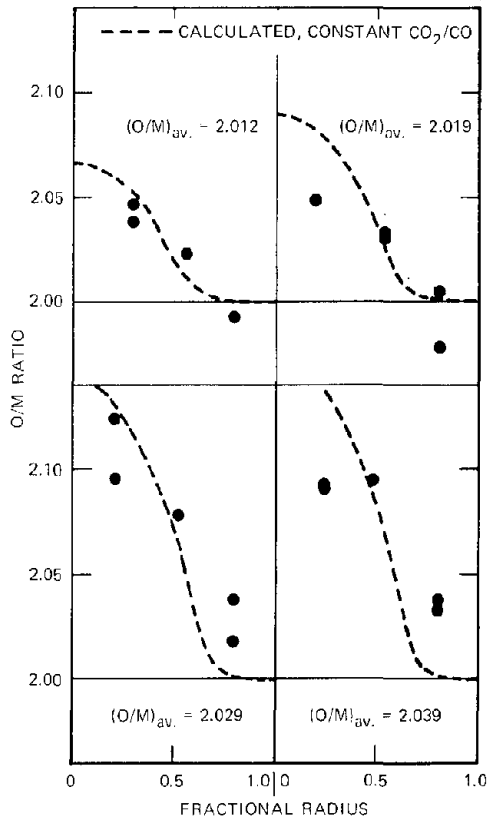


Fig. 11.20 Comparison of experimental oxygen redistribution results and the predictions of the Rand-Markin model for  $(U,Pu)O_{2+x}$ . (From A. T. Jeffs, Canadian Report AECL-3690, 1970.)

experimentally determined values of  $Q^+$  from axial thermal gradient experiments, the radial profiles of the oxygen-to-metal ratio for reactor fuel pins can be calculated with the typical results shown in Fig. 11.21. These curves show the same direction of redistribution as predicted by the Markin-Rand-Roberts model for hypostoichiometric fuel, namely, depletion at the hot center and accumulation at the cold fuel surface. The fuel is very close to exact stoichiometry at the surface (fractional radius of one); in the top curve in Fig. 11.21, for example, the oxygen-to-metal ratio at the surface is 1.999999.

### 11.6.3 The Bober-Schumacher Model

Bober and Schumacher<sup>19</sup> observed that oxygen redistribution occurs in hypostoichiometric mixed-oxide fuels that are fully dense. When no gas pathways along the temperature gradient are available, redistribution by transport in the vapor phase of  $CO_2/CO$  or any other oxide vapors is impossible. They conclude that true thermal diffusion in the solid is responsible for the establishment of a nonuniform oxygen distribution in the hot, plastic region of the fuel characterized by a columnar-grain structure. In their model the diffusing species are assumed to be oxygen

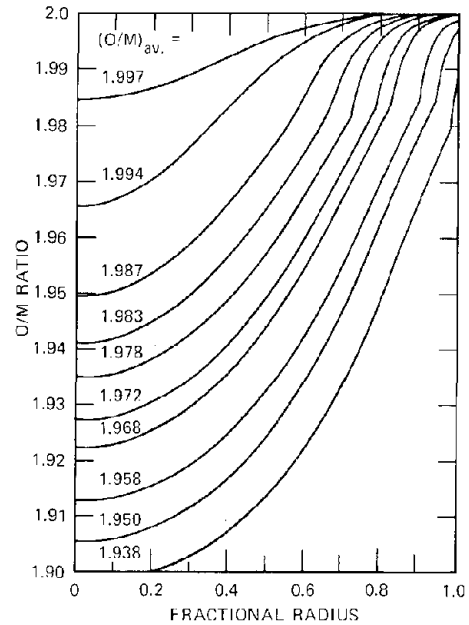


Fig. 11.21 Stoichiometry profiles for irradiation at a linear power of 500 W/cm with 700°C fuel surface temperature using heat of transport from experiments without artificial barriers. (From E. A. Aitken et al., USAEC Report GEAP-12254, General Electric Company, 1971.)

vacancies, which, in  $(U,Pu)O_{2-x}$ , occupy a fraction  $x/2$  of the anion lattice sites. Thermal diffusion acts to drive oxygen vacancies toward the hot region of the fuel, but ordinary diffusion in the solid limits the extent of unmixing. Because the diffusion coefficient of oxygen vacancies is quite large at high temperature, steady state is attained. The dynamic balance of thermal diffusion and ordinary diffusion is described by setting the flux given by Eq. 7.58 equal to zero, which yields

$$\frac{1}{x} \frac{\nabla x}{\nabla T} = - \frac{Q^+}{RT^2} \quad (11.94)$$

in the columnar-grain region. Here  $Q^+$  is the heat of transport of oxygen vacancies in the fuel. Bober and Schumacher find that for hypostoichiometric mixed oxides

$$Q^+ = -125 \pm 62 \text{ kJ/mole}$$

which is in good agreement with the value obtained by Aitken et al.<sup>18</sup> for slightly hypostoichiometric fuel.

Since the heat of transport is negative, Eq. 11.94 shows that the oxygen deficiency,  $x$ , is largest at the high temperature end, or oxygen migrates down the temperature gradient. Cracks in the fuel beyond the columnar-grain zone are considered to be numerous enough to permit oxygen redistribution by the gas-phase transport mechanism of Markin, Rand, and Roberts. For hypostoichiometric oxides the latter mechanism acts in the same direction as does thermal diffusion. The two models are joined at the columnar-grain boundary in order to produce the complete

oxygen distribution in the fuel pin. In strongly hypostoichiometric fuel, the model must be modified to account for the effect of solid-state diffusion in the cool region (see Refs. 15 and 16). Curves similar to those shown in Fig. 11.21 are calculated by Bober and Schumacher's two-zone model.

All the oxygen redistribution models reviewed in this section assume that the average oxygen content of the fuel remains unchanged during migration. While this may be a valid assumption early in the irradiation period, certain fission products accelerate corrosion of the cladding (see Chap. 12, Sec. 12.6). Thus the cladding may become a sink for oxygen, in which case  $\bar{x}$  in Eq. 11.87 decreases with irradiation time.

## 11.7 ACTINIDE REDISTRIBUTION

Actinide redistribution refers to the unmixing of the heavy metals uranium and plutonium in a mixed-oxide fuel rod that supports a radial temperature gradient. The term actinide is used to describe the migration process since the species that actually moves may be uranium, plutonium, or both. Figure 11.22 illustrates the extent of the redistribution phenomenon under irradiation conditions typical of

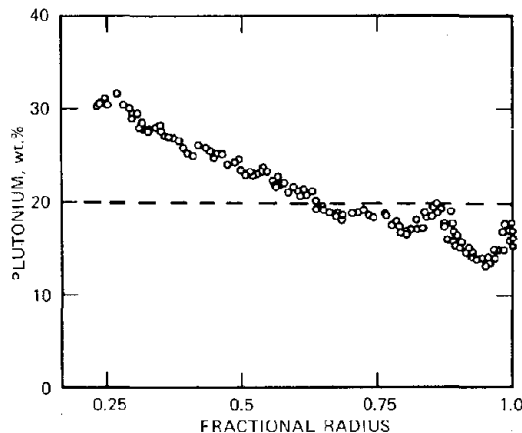


Fig. 11.22 Plutonium redistribution in a fuel element initially containing 20% plutonium uniformly distributed. The element was irradiated to a burnup of 5% at a linear power of 660 W/cm. (From R. Natesh and D. R. O'Boyle, USAEC Report ANL-7669, p. 107, Argonne National Laboratory, 1970.)

those expected in an LMFBR. The heavy metal in the fuel was initially 20% plutonium, uniformly distributed. The redistribution process has caused the plutonium content at the edge of the central void to increase to ~30%, with a corresponding decrease in plutonium at the outer surface. The cross-sectional average of the plutonium content is still 20% since no plutonium or uranium is lost during redistribution.

According to the discussion in Chap. 10, concentration of the fissile species near the center of the fuel pin causes

the temperature at the periphery of the central void to increase at constant linear power because the heat source is displaced further away from the heat sink than it is in a rod with uniform fuel composition. Sha, Huebotter, and Lo<sup>20</sup> estimate that the penalty in thermal performance for actinide redistribution in this case is ~130 W/cm; that is, the linear power must be reduced by this amount in order to keep the temperature of the inside of the central void at the melting temperature. A reduction of 130 W/cm in allowable linear power represents nearly a 25% decrease in fuel thermal performance.

Actinide redistribution has been attributed to two principal mechanisms:<sup>17,19,21</sup>

1. Thermal diffusion of plutonium (the Soret effect).<sup>21-28</sup>

2. Vapor migration of gaseous uranium species (principally UO<sub>3</sub>) from the hot end to the cold end via the gas phase in cracks or in migrating voids.<sup>29-35</sup>

If a portion of the fuel has been molten during operation, another process, analogous to zone refining, may be responsible for redistribution.<sup>22</sup>

### 11.7.1 Thermal Diffusion

According to irreversible thermodynamics, application of a temperature gradient to a mixture of plutonium and uranium oxides creates fluxes of the atomic species Pu, U, and O. Analyses of this process (Refs. 19, 25, 26, 28) assume that only the plutonium component of the fuel is affected and take its flux as given by Eq. 7.58:

$$J_{Pu} = -D_{Pu} \left( \frac{\partial C_{Pu}}{\partial r} + \frac{Q^* C_{Pu}}{RT^2} \frac{\partial T}{\partial r} \right) \quad (11.95)$$

This equation is valid only for low plutonium concentrations. If the atomic fraction of plutonium approaches 1, the atom fraction of uranium, which should appear in the numerator of the last term, must be considered. This term is usually omitted when this process is applied to fuel elements.

In Eq. 11.95,  $J_{Pu}$  is the flux of plutonium ions in the solid,  $C_{Pu}$  is the concentration of plutonium at position  $r$  and time  $t$ ,  $T$  is the specified local temperature of the fuel,  $R$  is the Boltzmann constant, and  $D_{Pu}$  is the diffusion coefficient of plutonium in the solid, which may be expressed in the form given by Eq. 7.45:

$$D_{Pu} = D_0 e^{-E/RT} \quad (11.96)$$

The pre-exponential factor  $D_0$  and the activation energy  $E$  have been reported as:

$$D_0 = 0.046 \text{ cm}^2/\text{sec} \quad E = 418 \text{ kJ/mole (Ref. 36)}$$

$$D_0 = 0.34 \text{ cm}^2/\text{sec} \quad E = 464 \text{ kJ/mole (Ref. 34)}$$

The  $Q^*$  in Eq. 11.95 is the heat of transport of plutonium in the solid. It is not possible to predict this quantity theoretically (even its sign) nor to determine it experimentally in anything but a thermal-gradient experiment. Consequently,  $Q^*$  is obtained by fitting the measured

redistribution in irradiated fuel pins or out-of-pile thermal-gradient tests to the theory. Values of  $-35$  (Ref. 28),  $-146$  (Ref. 34), and  $-240$  (Ref. 25) kJ/mole have been determined in this fashion. Although there is a very wide discrepancy in the magnitude of  $Q^*$  determined by various investigators, all agree that it is negative; that is, plutonium migrates up the thermal gradient and therefore concentrates at the hot part of the fuel.

Alternatively, the Soret effect may be described by the thermal-diffusion factor,  $\alpha$ , which is related to the heat of transport by

$$\alpha = -\frac{Q^*}{kT} \quad (11.97)$$

Because of the lack of precise experimental information, it is immaterial whether  $\alpha$  or  $Q^*$  is considered constant (according to Eq. 11.97, both  $\alpha$  and  $Q^*$  cannot be temperature independent). At temperatures of  $\sim 2400^\circ\text{C}$ , a  $Q^*$  of  $-240$  kJ/mole corresponds to  $\alpha = 11$ .

During the lifetime of a fuel rod in a reactor, the thermal-diffusion process probably does not reach steady state (which would correspond to  $J_{\text{Pu}} = 0$  in Eq. 11.95).<sup>\*</sup> Rather, the evolution of the plutonium-concentration profile is governed by combination of Eq. 11.95 with the mathematical statement of conservation of plutonium, which is given by Eq. 7.6 as:

$$\frac{\partial C_{\text{Pu}}}{\partial t} = -\frac{1}{r} \frac{\partial}{\partial r} (rJ_{\text{Pu}}) \quad (11.98)$$

Substitution of Eq. 11.95 into Eq. 11.98 leads to a second-order partial differential equation which must be solved for the plutonium-concentration profile. The temperature profile  $T(r)$  is assumed to be known (see Chap. 10). The solution is subject to the initial condition

$$C_{\text{Pu}}(r,0) = C_{\text{Pu}0} \quad (11.99)$$

where  $C_{\text{Pu}0}$  is the plutonium concentration in the fabricated fuel. Two boundary conditions are also required. By symmetry considerations (the same as those applied to the temperature-distribution calculation of Sec. 10.4), we have

$$J_{\text{Pu}} = 0 \text{ at } r = r_0$$

where  $r_0$  is the radius of the central void. Since the temperature gradient is zero at  $r = r_0$  (see Eq. 10.51), Eq. 11.95 shows that zero flux at  $r = r_0$  is equivalent to:

$$\left( \frac{\partial C_{\text{Pu}}}{\partial r} \right)_{r_0} = 0 \quad (11.100)$$

<sup>\*</sup>By way of contrast, thermal diffusion of oxygen vacancies in the columnar-grain region of the fuel is assumed to attain steady state rapidly (Bober-Schumacher model in previous section). The reason for this difference is that the diffusion coefficient of oxygen vacancies is many orders of magnitude greater than that of the heavy-metal cations in the solid.

Because there is no loss of plutonium at the fuel-cladding interface either, the second boundary condition is

$$J_{\text{Pu}} = 0 \text{ at } r = R$$

where  $R$  is the radius of the fuel pellet. If we attempted to satisfy this condition by the same method that was applied to the boundary condition at the central void (i.e., setting the quantity in the parentheses of Eq. 11.95 equal to zero), we would find that a large plutonium gradient would be required to counterbalance the temperature gradient, which is not zero at  $r = R$ . However, the condition of vanishing flux is very nearly satisfied because  $D_{\text{Pu}}$  is extremely small at the low fuel-surface temperature (if the central void and the surface temperatures are  $2700^\circ\text{K}$  and  $1000^\circ\text{K}$ , respectively, the plutonium diffusion coefficients at these two positions differ by a factor of  $10^{10}$ ). Thus, the plutonium flux at the fuel surface is essentially zero no matter what plutonium gradient exists at the surface. An appropriate boundary condition for use with Eq. 11.98 is obtained by noting that, since the diffusion coefficient is so low, the plutonium concentration at  $r = R$  does not change at all during the time scale of the exposure to the temperature gradient; inasmuch as the diffusion is frozen well before the outer periphery is reached,  $R$  may be approximated by  $\infty$  and the boundary condition becomes

$$C_{\text{Pu}}(\infty,t) = C_{\text{Pu}0} \quad (11.101)$$

Equations 11.95 and 11.98 can be solved numerically subject to Eqs. 11.99, 11.100, and 11.101.

It should be noted that both the partial differential equation and the boundary conditions just discussed are peculiar to cylindrical symmetry. In the one-dimensional axial geometry characteristic of out-of-pile tests of the thermal-diffusion process, the Cartesian form of the divergence must be used on the right-hand side of Eq. 11.98, and the boundary condition at the hot end is no longer given by Eq. 11.100 (although the argument of zero flux is still valid). The computed concentration profiles are quite different in these two cases.

Figure 11.23(a) shows the experimental results Beisswenger, Bober, and Schumacher<sup>25</sup> obtained in an out-of-pile axial-temperature-gradient experiment on a mixed-oxide fuel material. The solid line through the data points represents the calculated curve in which the heat of transport was adjusted to give the best agreement between theory and experiment. The value of  $Q^* = -240$  kJ/mole so obtained was used to construct the curves shown in Fig. 11.23(b) for the cylindrical geometry of a reactor fuel pin. Note that the variation of the hottest temperature from  $2300^\circ\text{C}$  to  $2600^\circ\text{C}$  greatly accelerates the process but that in either case steady state is not approached even after  $10^4$  hr of operation. The calculated curves of Fig. 11.23(b) bear some resemblance to the measured plutonium distribution in an irradiated fuel pin shown in Fig. 11.22. However, it must be noted that for any process in which plutonium is conserved, the radius-weighted areas of the regions between the theoretical curve and the horizontal line representing the initial uniform concentration must sum to zero. This is

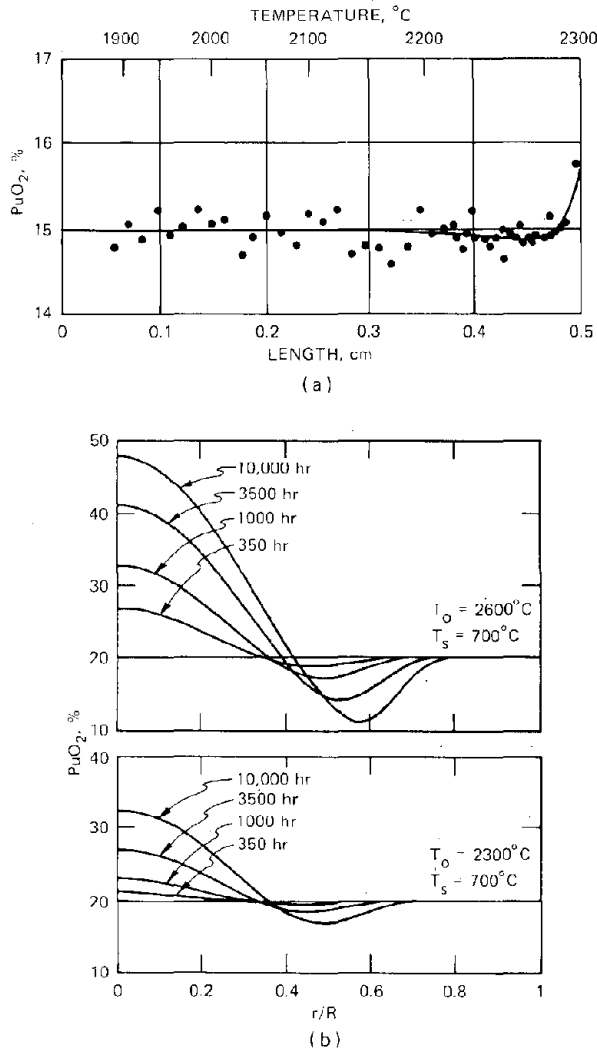


Fig. 11.23 Plutonium redistribution in mixed-oxide fuels due to a thermal gradient. (a) After 110 hr annealing in an axial temperature gradient. (b) Calculated for an LMFBR fuel rod with a parabolic temperature distribution (restructuring not considered). [From H. Beisswenger, M. Bober, and G. Schumacher, *Plutonium as a Reactor Fuel*, Symposium Proceedings, Brussels, 1967, pp. 273-282, International Atomic Energy Agency, Vienna, 1967 (STI/PUB/153).]

a consequence of mass conservation and does not depend upon the mechanism of redistribution.

There is far from unanimous agreement that thermal diffusion of the type described above is in fact the only or even the major process responsible for actinide redistribution. The appeal of this model is due to the relatively clear-cut mathematical description of the process provided by irreversible thermodynamics and to the fact that only a single constant,  $Q^*$ , is needed to completely predict the time behavior of the plutonium-concentration profile in the presence of a temperature gradient.

### 11.7.2 Vapor Transport

At fuel temperatures in excess of  $\sim 2000^\circ\text{C}$ , the partial pressures of the oxides of the heavy metals are large enough to sustain significant fluxes of plutonium and uranium through a gas phase in cracks or voids in the solid. Inasmuch as the Pu/U ratio of the equilibrium vapor is generally quite different from that of the solid, the ratio of the vapor-transport rates of plutonium and uranium is not the same as the ratio of these species in the solid, and unmixing of the heavy metals along the temperature gradient occurs. Figure 11.17 shows that in stoichiometric or hyperstoichiometric mixed oxides the dominant vapor species is  $\text{UO}_3$ , which is present in the gas phase in concentrations 2 to 4 orders of magnitude greater than that of  $\text{PuO}_2$ . In a temperature gradient, the  $\text{UO}_3$  should preferentially evaporate from the hot portion of this type of fuel and condense in the cooler regions, resulting in plutonium enrichment of the solid at the hot zone.

Conversely, in highly hypostoichiometric fuel, Fig. 11.17 shows that  $\text{PuO}$  is the major gaseous heavy-metal oxide. Imposition of a temperature gradient on this fuel should cause plutonium to diffuse via the gas phase down the temperature gradient, and a plutonium deficiency should develop in the hot center of a fuel pin. At an O/M ratio of  $\sim 1.96$ , the Pu/U ratio of the gas is approximately equal to that of the solid (vaporization is said to be congruent when this situation occurs). Even though the vapor pressures of the actinide oxides may be large enough to cause significant vapor transport, no unmixing of the heavy metals occurs if both the gas and solid phases have the same Pu/U ratio.

These general features of actinide redistribution by vapor transport were first outlined by Rand and Markin.<sup>6</sup> The crucial prediction of a change in the direction of redistribution at the fuel O/M ratio corresponding to congruent vaporization has been confirmed by measurements of the radial plutonium distribution in irradiated fuel pins.<sup>37</sup> The sign of the heat of transport,  $Q^*$ , would have to assume negative values for  $\text{O/M} > 1.96$  and positive values for  $\text{O/M} < 1.96$  to explain the change in the direction of plutonium migration at  $\text{O/M} \approx 1.96$  by the thermal-diffusion mechanism.

Because of the temperature dependence of the solid-state diffusion coefficient of the actinide cations, which enters the thermal-diffusion analysis, and because of the temperature variation of the actinide-oxide vapor pressures, which is important in the vapor-transport model, actinide redistribution by either of these mechanisms is restricted to temperatures in excess of  $\sim 2000^\circ\text{C}$ . This temperature roughly corresponds to the outer boundary of the columnar-grain region in a fuel pin. The fuel in the columnar-grain zone is plastic and is generally believed to be free of cracks under operating conditions. However, cooling cracks may open up as a result of reactor power changes, shutdown or startup, and actinide-vapor transport can occur along these cracks until they heal. The gaps between individual pellets in a fuel element also provide gas-filled pathways suitable for actinide-vapor transport until the pellets sinter together. Another form of fissure in the

columnar-grain region is the network of interlinked fission-gas bubbles on grain boundaries (Fig. 15.21).

The other gas-filled spaces commonly found in reactor fuel elements are the pores that have not been removed during the sintering of the material prior to fabrication. The long dimensions of these pores are perpendicular to the temperature gradient, and the pore width in the direction of the temperature gradient is of the order of 10  $\mu\text{m}$ . By way of comparison, the cracks, fissures, or interconnected porosity described in the preceding paragraph can provide gas pathways extending continuously along the temperature gradient for substantial fractions of the columnar-grain radius.

Meyer, Butler, and O'Boyle<sup>33</sup> have proposed a one-dimensional vapor-phase diffusion calculation intended to apply to either radial cracks or migrating pores. However, vapor migration in these two geometries appears to be rather different,<sup>35</sup> and a single calculational model does not apply to both configurations.

Vapor transport of actinide oxides in a crack such as that shown in Fig. 11.18 requires solution of the gas-phase diffusion equation for the actinide oxides in two dimensions because there is a gradient of metal-oxide pressure along the temperature gradient and, owing to the necessity of diffusing uranium and plutonium to and from the crack surface, in the direction transverse to the temperature gradient as well. The time dependence of actinide redistribution depends on the size and number of cracks.

The efficiency with which a migrating pore unmixes uranium and plutonium is easier to analyze than the vapor transport process in a radial crack.<sup>34,35</sup> When a temperature gradient is first applied to a pore in an initially uniform fuel body, the more volatile of the two actinides preferentially evaporates from the hot side of the pore and condenses on the cold side. As a result, the concentration of the less volatile component is depleted on the cold side of the pore and enriched on the hot side. After this initial startup transient, very little additional unmixing occurs as the pore moves up the temperature gradient; the initial spike of the less volatile oxide on the cold side is left behind at the starting point of the pore, and the excess of the more volatile component is pushed ahead of the moving pore. Figure 11.24 shows the plutonium-concentration profiles behind and ahead of a moving pore (the figure refers to hyperstoichiometric fuel, in which uranium is the more volatile of the two heavy metals). The plutonium distribution attached to the moving front face of the pore is:<sup>35</sup>

$$q - q_0 = \Delta q \exp\left(-\frac{v_p}{D_{Pu}}z\right) \quad (11.102)$$

where  $D_{Pu}$  is the diffusion coefficient of plutonium in the solid oxide,  $z$  is the distance measured into the solid from the front face of the pore,  $q_0$  is the Pu/U + Pu ratio in the solid ahead of the pore, and  $\Delta q$  is the plutonium enrichment on the front face. This enrichment is determined by the requirement that the ratio of the plutonium flux to the total heavy-metal flux across the pore be equal to  $q_0$ . The migration velocity of the pore is denoted by  $v_p$  (for a discussion of pore migration in fuels, see Chap. 14).

Each migrating pore carries with it excess plutonium equal to the integral of Eq. 11.102 from the pore front face outward. Redistribution by pore migration consists of a rather uniform depletion of plutonium throughout the columnar-grain region and a large enrichment close to the central void where the pores deposit their charges of excess plutonium. The negative spikes at the starting locations of each pore (Fig. 11.24) are uniformly distributed because the initial porosity is randomly distributed in the fuel.

The extent of actinide redistribution due to pore migration depends upon the ratio  $D_{Pu}/v_p$ . This ratio is rather small (typically  $\sim 1 \mu\text{m}$ ), and the concentration profile in front of each pore extends only a few micrometers into the solid. As a result, the quantity of excess plutonium transported by each pore is small. The extent of actinide redistribution is also proportional to the initial porosity of the fuel, assuming all voidage to exist as closed pores. If the same initial porosity were distributed in the

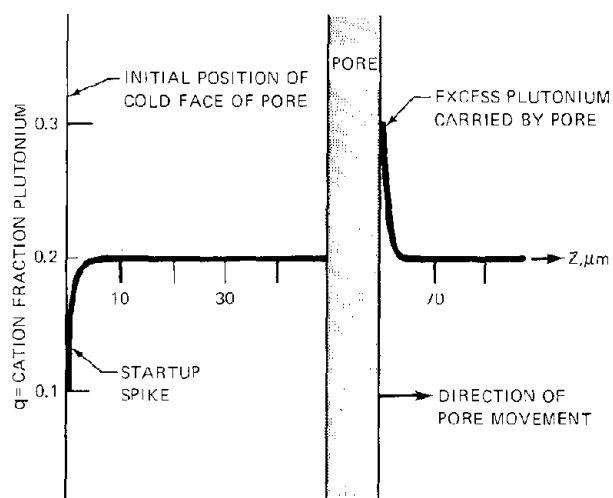


Fig. 11.24 Plutonium-concentration profiles in the vicinity of a migrating pore. [From D. R. Olander, *J. Nucl. Mater.*, 49: 35 (1973/74).]

form of cracks along the temperature gradient, actinide redistribution would proceed more rapidly than if heavy-metal transport occurred in migrating pores. However, lenticular pores may be the only type of gas space available for actinide-vapor migration in the high-temperature columnar-grain zone of the fuel.

Redistribution by pore migration ceases as soon as all pores have reached the central void. For highly rated fuel pins, the restructuring process requires only about 100 hr for completion. Thereafter, any heavy-metal migration must occur either by vapor transport in temporary cracks, which are occasionally opened by power cycling, or by the slower process of thermal diffusion, which does not require a gas-phase pathway to accomplish separation of uranium and plutonium.

## 11.8 NOMENCLATURE

- A = constant in Eq. 11.93  
 $A_i, B_i$  = constants in Eq. 11.74  
 $C_O, C_C$  = constants in Eqs. 11.82 and 11.83  
 $C_{Pu}$  = plutonium concentration in the fuel  
 $D_i$  = gas-phase diffusivity of species i  
 $D_{Pu}$  = diffusion coefficient of plutonium in the solid  
 $D_0$  = pre-exponential factor of the solid-state diffusion coefficient  
E = activation energy for solid-state diffusion  
 $\mathcal{F}$  = Faraday constant  
K = equilibrium constant  
(g) = gas phase  
 $\Delta G^\circ$  = standard-state free-energy change of reaction  
 $\Delta G_{O_2}$  = oxygen potential of the fuel  
 $\Delta H^\circ$  = standard-state enthalpy-change of reaction  
 $\Delta \bar{H}_{O_2}$  = partial molar enthalpy of oxygen in the fuel  
 $J_{Pu}$  = flux of plutonium in the solid  
(l) = liquid phase  
L = length of a crack in the fuel  
m = stoichiometry deviation from two of the oxides of the variable-valence heavy-element in mixed-oxide fuel  
 $N_i$  = atoms of oxygen per molecule of species i  
O/M = oxygen-to-metal ratio in mixed-oxide fuel  
O/U = oxygen-to-uranium ratio in uranium dioxide  
 $P^\circ$  = vapor pressure of pure compound  
 $p_i$  = partial pressure of species i in equilibrium with the fuel  
 $[Pu^{i+}]$  = fraction of plutonium ions in the +i valence state (i = 3, 4) in the solid  
 $Q^+$  = heat of transport of oxygen in the fuel  
 $Q^*$  = heat of transport of plutonium in the fuel  
q = cation fraction of plutonium in mixed-oxide fuel (i.e., the Pu/U + Pu ratio)  
 $q_0$  = plutonium fraction in as-fabricated fuel  
 $\Delta q$  = plutonium enrichment (in excess of  $q_0$ ) on the hot face of a migrating pore  
R = gas constant  
r = radial position in fuel pin  
 $r_0$  = radius of the central void  
(s) = solid phase  
 $\Delta S^\circ$  = standard-state entropy change of reaction  
 $\Delta \bar{S}_{O_2}$  = partial molar entropy of oxygen in the fuel  
t = time  
T = temperature  
 $[U^{i+}]$  = fraction of uranium ions in the +i valence state (i = 2, 4, 5, 6) in the solid  
 $V_{Pu}$  = valence of plutonium in mixed-oxide fuel  
 $V_U$  = valence of uranium in mixed-oxide fuel  
 $v_p$  = pore migration velocity  
x = deviation of the oxygen-to-metal ratio from 2  
z = distance along the temperature gradient, or distance ahead of a migrating pore

## Greek letters

- $\alpha$  = thermal-diffusion factor  
 $\Delta \epsilon$  = emf of electrochemical cell  
 $\mu$  = chemical potential

## Subscripts

- O = atomic oxygen  
 $O_2$  = molecular oxygen  
Pu = plutonium  
U = uranium  
vap = vaporization

## 11.9 REFERENCES

1. B. T. M. Willis, *J. Physiol. (Paris)*, **25**: 431 (1964).
2. L. E. J. Roberts and T. L. Markin, *Proc. Brit. Ceram. Soc.*, **8**: 201 (1967).
3. K. Hagemark and M. Broli, *J. Inorg. Nucl. Chem.*, **28**: 2837 (1966).
4. M. Tetenbaum, in *Thermodynamics of Nuclear Materials*, Symposium Proceedings, Vienna, Oct. 21–25, 1974, International Atomic Energy Agency, Vienna, 1975 (STI/PUB/380).
5. T. L. Markin and E. J. McIver, *Plutonium 1965*, A. E. Kay and M. B. Waldron (Eds.), p. 845, Chapman and Hall, London 1965.
6. M. H. Rand and T. L. Markin, *Thermodynamics of Nuclear Materials—1967*, Symposium Proceedings, Vienna, 1967, p. 637, International Atomic Energy Agency, Vienna, 1968 (STI/PUB/162).
7. P. E. Blackburn, *J. Nucl. Mater.*, **46**: 244 (1973).
8. M. H. Rand and L. E. J. Roberts, in *Thermodynamics*, Symposium Proceedings, Vienna, 1965, Vol. 1, p. 3, International Atomic Energy Agency, Vienna, 1966 (STI/PUB/109).
9. J. A. Christensen, USAEC Report BNWL-536, Battelle-Northwest, December 1967.
10. R. E. Fryxell and E. A. Aitken, *J. Nucl. Mater.*, **30**: 50 (1969).
11. S. K. Evans, E. A. Aitken, and C. N. Craig, *J. Nucl. Mater.*, **30**: 57 (1969).
12. A. T. Jeffs, Canadian Report AECL-3690, August 1970.
13. M. G. Adamson, *J. Nucl. Mater.*, **38**: 213 (1971).
14. M. G. Adamson and R. F. A. Carney, British Reports AERE-R-6830 and AERE-R-6831, 1972.
15. E. A. Aitken, *J. Nucl. Mater.*, **30**: 62 (1969).
16. D. R. Olander, *J. Nucl. Mater.*, **47**: 113 (1973).
17. E. A. Aitken and S. K. Evans, *Plutonium 1970*, Proceedings of the Fourth International Conference on Plutonium and Other Actinides, Nuclear Metallurgy, Vol. 17, Part II, p. 772, The Metallurgical Society of the AIME, 1970.
18. E. A. Aitken, M. G. Adamson, S. K. Evans, and T. E. Ludlow, USAEC Report GEAP-12254, General Electric Company, 1971.
19. M. Bober and G. Schumacher, *Advan. Nucl. Sci. Technol.*, **7**: 121-181 (1973).
20. W. T. Sha, P. R. Huebotter, and R. K. Lo, *Trans. Amer. Nucl. Soc.*, **14**: 183 (1971).
21. P. E. Novak, T. A. Lauritzen, R. Protsik, J. H. Davies, and E. L. Zebroski, in USAEC Report ANL-7120, pp. 392-399, Argonne National Laboratory, 1965.
22. M. G. Chasanov and D. F. Fischer, USAEC Report ANL-7703, Argonne National Laboratory, 1970.
23. M. G. Adamson and E. A. Aitken, *Trans. Amer. Nucl. Soc.*, **14**: 179 (1971).
24. A. A. Bauer, H. Beisswenger, G. Giacchetti, E. Patrassi, G. Schumacher, and R. Theisen, in USAEC Report ANL-7120, pp. 400-401, Argonne National Laboratory, 1965.

25. H. Beisswenger, M. Bober, and G. Schumacher, in *Plutonium as a Reactor Fuel*, Symposium Proceedings, Brussels, 1967, pp. 273-282, International Atomic Energy Agency, Vienna, 1967 (STI/PUB/152).
26. K. Wirtz, *J. Amer. Chem. Soc.*, **90**: 3098 (1968).
27. M. Bober, C. Sari, and G. Schumacher, *Trans. Amer. Nucl. Soc.*, **12**: 603 (1969).
28. N. G. Demas, R. Natesh, and C. W. Maynard, *Trans. Amer. Nucl. Soc.*, **14**: 593 (1971).
29. J. K. Bahl and M. D. Freshley, *Trans. Amer. Nucl. Soc.*, **13**: 599 (1970).
30. W. J. Lackey, A. R. Olsen, J. L. Miller, Jr., and D. K. Bates, *Trans. Amer. Nucl. Soc.*, **14**: 180 (1971).
31. M. Bober, C. Sari, and G. Schumacher, *J. Nucl. Mater.*, **40**: 341 (1971).
32. R. O. Meyer, D. R. O'Boyle, and R. Natesh, *Trans. Amer. Nucl. Soc.*, **14**: 182 (1971).
33. R. O. Meyer, E. M. Butler, and D. R. O'Boyle, *Trans. Amer. Nucl. Soc.*, **15**: 216 (1972); USAEC Report ANL-7929, Argonne National Laboratory, 1972.
34. M. Bober, G. Schumacher, and D. Geilhoff, *J. Nucl. Mater.*, **47**: 187 (1973).
35. D. R. Olander, *J. Nucl. Mater.*, **47**: 251 (1973); *ibid.*, **49**: 21 (1973/74); *ibid.*, **49**: 35 (1973/74).
36. F. Schmitz and R. Lindner, *Radiochim. Acta*, **1**: 218 (1963).
37. R. O. Meyer, D. R. O'Boyle, and E. M. Butler, *J. Nucl. Mater.*, **47**: 265 (1973).

## 11.10 PROBLEMS

11.1 The final step of the sintering process in the fabrication of oxide fuel elements for thermal reactors is the adjustment of the oxygen-to-uranium ratio by heating the element in a controlled atmosphere of hydrogen gas and water vapor.

The stoichiometry of uranium dioxide can be controlled by contacting the solid with a gas mixture containing a well-defined ratio of  $H_2O$  to  $H_2$ . Near perfect stoichiometry, the oxygen potential of  $UO_{2+x}$ , is determined by

$$\begin{aligned}\Delta\overline{H}_{O_2} &= -523 + 6.7 \times 10^4 x && \text{kJ/mole} \\ \Delta\overline{S}_{O_2} &= -121 + 2.8 \times 10^4 x && \text{J mole}^{-1} \text{ } ^\circ\text{K}^{-1}\end{aligned}$$

The standard free energy of formation of water vapor is given by

$$\Delta G_{H_2O(g)}^\circ = -246 + 55 (T/10^3) \quad \text{kJ/mole}$$

If the gas contains equal partial pressures of water vapor and hydrogen, what is the deviation from exact stoichiometry,  $x$ , at  $1500^\circ\text{K}$ ?

11.2 Owing to a processing fault during fuel fabrication, the  $UO_2$  in a Zircaloy-clad fuel rod for a LWR has an O/U

ratio of 2.05. However, the fuel in this rod contains an unusually low level of carbon and hydrogen impurities so that none of the usual gases responsible for oxygen redistribution are present in the hot fuel element. Assume that when the rod is brought to power in the reactor the fuel at a particular axial section has center-line and surface temperatures of  $2500^\circ\text{K}$  and  $1000^\circ\text{K}$ , respectively. The temperature distribution may be approximated as parabolic, and no central void is formed. Oxygen redistribution occurs by virtue of a radially independent oxygen-gas pressure that permeates the fuel element via cracks in the fuel. The partial molar enthalpy and entropy shown in Fig. 11.10 can be approximated by

$$\begin{aligned}\Delta\overline{H}_{O_2} &= -272 \text{ kJ/mole} \\ \Delta\overline{S}_{O_2} &= -1000x \text{ J mole}^{-1} \text{ } ^\circ\text{K}^{-1}\end{aligned}$$

(a) Determine the constant oxygen partial pressure at this particular axial section of the fuel.

(b) Calculate and plot the O/U ratio as a function of fractional radius of the fuel.

(c) Is the oxygen potential at the fuel surface sufficient to oxidize zirconium? Why would the cladding not suffer catastrophic corrosion and early failure under these conditions?

11.3 (a) A mixed oxide fuel contains 5 ppm (by weight) of carbon impurity. If one-half of the carbon is vaporized to form CO and  $CO_2$ , what is the total pressure of these gases in the fuel-element design of Fig. 10.4?

(b) A sample of  $UO_{2.005}$  containing 44 ppm (by weight) of carbon is heated in a closed container to  $1500^\circ\text{K}$ . All the carbon is converted either to CO or  $CO_2$  that is contained in the gas phase contacting the solid. Calculate the stoichiometry of the oxide (i.e.,  $x$  in  $UO_{2+x}$ ) and the  $CO_2/CO$  ratio in the gas phase ( $\gamma$ ) after complete equilibrium of the system is reached. Use the oxygen potential given in problem 11.1.

11.4 Calculate the partial pressure of atomic oxygen in equilibrium with the mixed oxide  $(U_{0.8}Pu_{0.2})O_{1.98}$  at  $2241^\circ\text{K}$ . Use Rand-Markin thermodynamics.

11.5 Consider  $UO_{2.2}$  at  $1600^\circ\text{C}$ .

(a) According to the data of Fig. 11.10, what is the equilibrium partial pressure of oxygen over this fuel? How does this result compare with the value obtained from Fig. 11.6?

(b) Suppose  $UO_{2.2}$  is cooled at constant oxygen partial pressure from  $1600^\circ\text{C}$ . At what temperature does a second phase precipitate out? What are the compositions of the coexisting phases present at this point?

(c) Suppose  $UO_{2.2}$  is cooled down from  $1600^\circ\text{C}$  to  $800^\circ\text{C}$  in a closed container. What phases are present at the lower temperature, and what is the fraction of each phase?

# Chapter 12

## Behavior of Solid Fission Products in Oxide Fuel Elements

Insofar as the materials performance of oxide fuel elements is concerned, the behavior of the fission products is important for the following reasons:

1. The chemical state of the fission products (i.e., element, oxide, or complex compound) influences the availability of oxygen within the fuel rod, which in turn controls the oxygen potential of the fuel. This thermodynamic quantity is of paramount importance in determining whether the fuel can react chemically with the cladding. Such reactions, if they occur, result in corrosion of the metal and consequent weakening of the cladding.

2. The physical state of the fission products, in conjunction with their chemical characteristics, determines the volume occupied by these species. If the volume of the irradiated fuel is greater than that of the fresh fuel that was consumed, the resulting swelling can cause the fuel to exert a contact pressure on the cladding.

3. A portion of the gaseous fission products (xenon and krypton) is not retained in the fuel but escapes to the plenum region of the fuel element. The pressure inside the fuel element produced by the released fission gases contributes to the internal stresses on the cladding. The ratio of the volume of the plenum to that of the solid oxide inside a fuel element is chosen so that the pressure due to the released fission gases does not become large enough to rupture the cladding.

4. Fission products can affect fuel properties, such as its thermal conductivity and melting point, thereby influencing the thermal performance of the fuel rod. Accumulation of xenon and krypton in the fuel-cladding gap reduces the thermal conductance of the gap, which was originally filled with helium.

The magnitude of the potential problems arising from the introduction of fission products into the fuel depends on the expected concentrations of the fission products. The design burnup of LMFBR fuel is 10%. Since each heavy-metal atom that has fissioned produces two fission fragments, the fuel at end-of-life will consist of nearly 20% fission products (excluding oxygen) in a complex mixture of chemical and physical states.

### 12.1 ELEMENTAL YIELDS OF FISSION PRODUCTS

Analysis of the effect of irradiation on fuel performance requires information on the quantities of fission products of various types produced. The probability per fission of directly forming a particular nuclide is defined as the *independent fission yield* of the nuclide. Since the isotopes produced directly from fission are radioactive and generally short-lived, they are transmuted to other elements. Because the predominant mode of fission-product decay is by beta and gamma emission, the decay process does not change the mass number of the species. Thus, fission can be considered to produce decay chains containing many nuclides of the same mass number.

The overall fission yield of a particular nuclide includes the contribution due to beta decay of the precursors in the mass chain in addition to the independent yield of the nuclide. The *cumulative yield* of an isotope  ${}_Z M^A$  is the sum of the independent yields of all members of the mass chain with atomic numbers less than or equal to  $Z$ :

$$(cy)_{Z M^A} = \sum_{Z'}^Z (iy)_{Z' M^A}$$

where (cy) and (iy) denote the cumulative and independent yields, respectively. The cumulative yield of the last member of a chain (i.e., the stable member) is the sum of the independent yields of all nuclides of the chain and is referred to as the *chain yield*  $y_A$ :

$$y_A = (cy)_{Z M_{\text{final}}^A}$$

As an illustration of the modes of the fission-product decay, Fig. 12.1 shows the mass chains at 133, 135, and 137, each of which contains cesium. The figure shows the half-lives of the members of the chain and the measured cumulative yields at various points along the chain. As one proceeds down the chain, the cumulative yield increases primarily because fission produces later chain members as

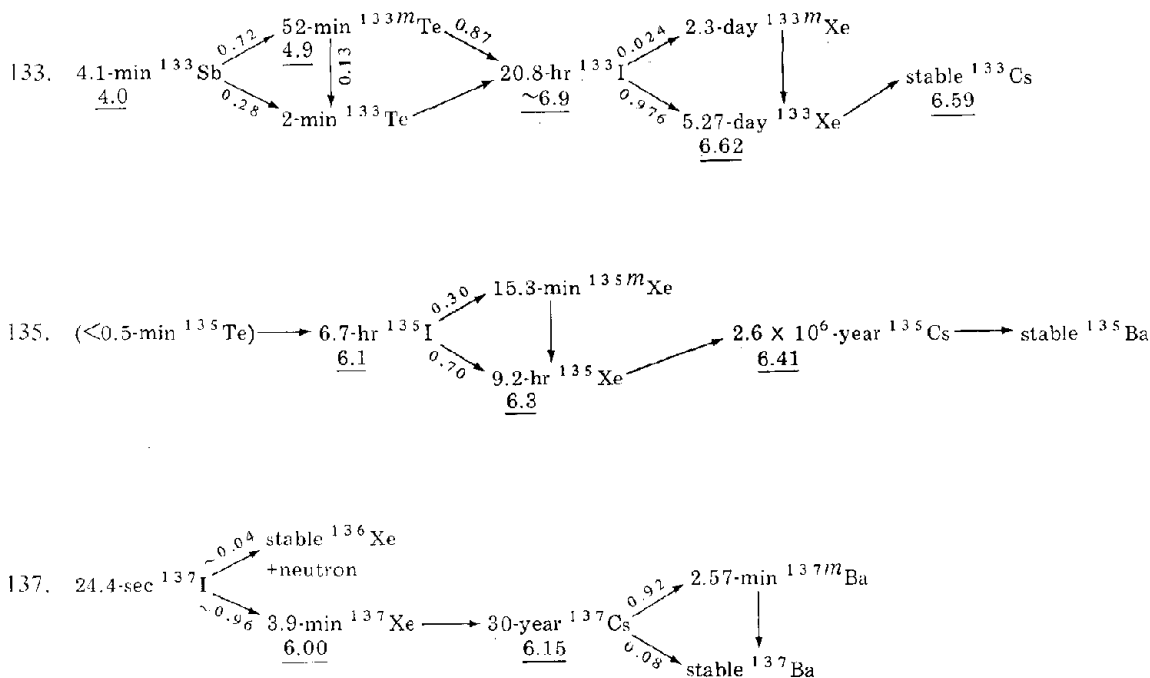


Fig. 12.1 Decay chains containing cesium (mass numbers 133, 135, and 137) from thermal-neutron fission of  $^{235}\text{U}$ . Underlined numbers give the cumulative fission yields. The last yield of the chain represents the chain yield. Lower yields for earlier chain members may be due to (1) direct formation in fission of later chain members, (2) chain branching, or (3) experimental uncertainty. The last reason accounts for instances in which an early chain member has a higher yield than a subsequent member. Where more than one decay mode has been observed, the branching ratios are shown on the arrows. Parentheses indicate that the nuclide probably occurs in fission but has not been observed. [From S. Katkoff, *Nucleonics*, 18: 201 (1960).]

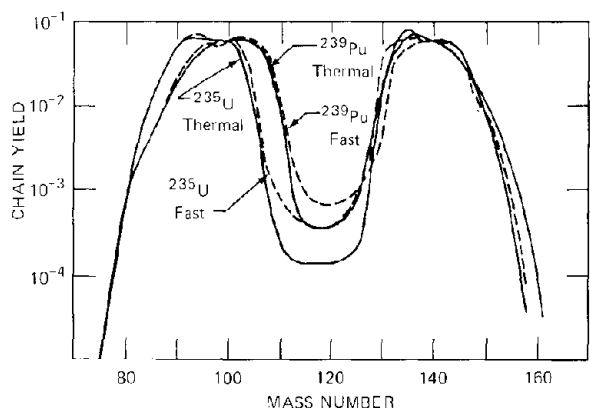


Fig. 12.2 Chain yields as a function of mass number of the chain for fast- and thermal-neutron flux spectra and for  $^{235}\text{U}$  and  $^{239}\text{Pu}$ . [From J. H. Davies and F. T. Ewart, *J. Nucl. Mater.*, 41: 143 (1971).]

well as the first product. Note that the half-lives of the constituent nuclides in each chain generally become larger as the end of the chain is approached. All chains terminate in a stable species.

The chain yields (the last underlined numbers in the decay schemes in Fig. 12.1) are plotted in Fig. 12.2 as a function of the mass number of the chain. The yields of the

abundant chains are seen to depend very slightly on the spectrum of the neutron flux (thermal or fast) but much more significantly on the fissile species (uranium or plutonium). In plutonium fission the low-mass-number peak is shifted to higher mass numbers compared to uranium fission.

The materials aspects of fuel performance are determined by the quantity of a particular chemical element that is released by fission, irrespective of the mass chain in which the element is located. For example, from a chemical or material point of view,  $^{133}\text{Cs}$ ,  $^{135}\text{Cs}$ , and  $^{137}\text{Cs}$  are equivalent.\* We are concerned with the total quantity of a particular element formed after an irradiation time  $t_{\text{irr}}$ . The ratio of the number of atoms of a particular chemical element present at irradiation time  $t_{\text{irr}}$  to the number of heavy-metal atoms that have fissioned is called the *elemental yield* of the species. Because of the different half-lives of

\*The migration of different isotopes of a chemical species can differ because of the mobility of the precursors. The precursor of the cesium isotopes are xenon isotopes (see Fig. 12.1), which can exhibit very high mobilities in the fuel. Thus, because of the 5.3-day half-life of  $^{133}\text{Xe}$ ,  $^{133}\text{Cs}$  may be found far from the location of the fission event that produced the mass-133 chain. Cesium-137, on the other hand, would be expected to be produced very close to the position of the fission because its xenon and iodine precursors are short-lived.

the various nuclides in the decay chains, the elemental yields can be functions of irradiation time. In a thermal flux some fission products have cross sections of sufficient magnitude such that removal of the species by neutron absorption is competitive with radioactive decay ( $^{133}\text{Xe}$  and  $^{135}\text{Xe}$  in the decay schemes of Fig. 12.1 are examples of such fission products). In these cases the concentration of the stable members of the chain depends on the magnitude of the thermal flux as well as the irradiation time.<sup>1</sup> In a fast flux, however, neutron absorption by the fission products is of no consequence.

The number of heavy-metal atoms in a unit volume of fuel which have been fissioned during constant power operation to time  $t_{\text{irr}}$  is  $\dot{F}t_{\text{irr}}$  where  $\dot{F}$  is the fission rate per unit volume. The elemental yield of chemical species is given by

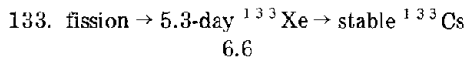
$$Y_i = \frac{1}{\dot{F}t_{\text{irr}}} \sum_A N_{i,A} \quad (12.1)$$

where  $N_{i,A}$  is the concentration of chemical element  $i$  resulting from the decay chain at mass number  $A$ . Because two fission products are produced per fission,

$$\sum_i Y_i = 2$$

Computation of the nuclide concentrations will be illustrated for the case of cesium.

Since irradiation times of the order of months or years are of interest in materials performance, the complex decay chains can be simplified by neglecting species with half-lives shorter than  $\sim 1$  day. Thus the mass-133 decay chain in Fig. 12.1 reduces to



The growth of  $^{133}\text{Xe}$  is governed by

$$\frac{dN_{\text{Xe}}}{dt} = y_{133}\dot{F} - \lambda_{\text{Xe}}N_{\text{Xe}}$$

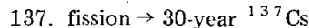
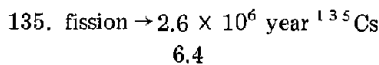
where  $N_{\text{Xe}}$  and  $\lambda_{\text{Xe}}$  are the concentration and decay constant of  $^{133}\text{Xe}$ , respectively, and  $y_{133}$  is the yield of the mass-133 chain. The independent yield of  $^{133}\text{Cs}$  is negligible. This differential equation can be integrated to yield

$$N_{\text{Xe}} = \frac{y_{133}\dot{F}}{\lambda_{\text{Xe}}} (1 - e^{-\lambda_{\text{Xe}}t_{\text{irr}}}) \quad (12.2)$$

The total concentration of both members of this chain is  $y_{133}\dot{F}t_{\text{irr}}$ ; thus the concentration of the last member is  $y_{133}\dot{F}t_{\text{irr}} - N_{\text{Xe}}$ . Or the concentration of cesium due to fission into the mass-133 chain is

$$N_{\text{Cs},133} = y_{133}\dot{F}t_{\text{irr}} \left( 1 - \frac{1 - e^{-\lambda_{\text{Xe}}t_{\text{irr}}}}{\lambda_{\text{Xe}}t_{\text{irr}}} \right) \quad (12.3)$$

Similarly, the mass-135 and -137 decay chains can be simplified to



6.2

Since the half-lives of  $^{135}\text{Cs}$  and  $^{137}\text{Cs}$  are long compared to typical irradiation times, radioactive decay of these isotopes can be neglected, and they can be treated as stable products. Their concentrations after irradiation time  $t_{\text{irr}}$  are

$$N_{\text{Cs},135} = y_{135}\dot{F}t_{\text{irr}} \quad (12.4)$$

and

$$N_{\text{Cs},137} = y_{137}\dot{F}t_{\text{irr}} \quad (12.5)$$

Substitution of Eqs. 12.3 to 12.5 into Eq. 12.1 results in

$$Y_{\text{Cs}} = y_{133} \left( 1 - \frac{1 - e^{-\lambda_{\text{Xe}}t_{\text{irr}}}}{\lambda_{\text{Xe}}t_{\text{irr}}} \right) + y_{135} + y_{137}$$

If the irradiation time is several times longer than the 5.3-day half-life of  $^{133}\text{Xe}$ , the term in parentheses in the preceding equation can be approximated by unity, and the cumulative yield of cesium becomes

$$Y_{\text{Cs}} = y_{133} + y_{135} + y_{137} \quad (12.6)$$

Computations such as those just described can be performed for all chemical elements in the fission-product mixture. Essentially all elemental yield formulas can be approximated by the sums of chain yields as in Eq. 12.6; thus the  $Y_i$  is independent of irradiation time.

Table 12.1 summarizes the elemental yields for the fission of uranium, plutonium, and a typical LMFBR mixed-oxide composition. The elements have been collected into groups that exhibit similar chemical and physical behavior in the irradiated fuel. The yields of the noble metals ruthenium, technetium, rhodium, and palladium are nearly a factor of 2 larger in the case of plutonium fission than the yields of these elements in uranium fission. In compensation the yields of elements such as zirconium, molybdenum, and yttrium are smaller in plutonium fission than in uranium fission. This shift has important ramifications in the chemical behavior

Table 12.1 Elemental Fission-Product Yields in a Fast-Neutron Spectrum

Chemical group	Elemental yield		
	$^{235}\text{U}^*$	$^{239}\text{Pu}^*$	15% $^{239}\text{Pu}^\dagger$ 85% $^{238}\text{U}$
Zr + Nb	0.298	0.204	0.219
Y + rare earths <sup>‡</sup>	0.534	0.471	0.493
Ba + Sr	0.149	0.096	0.109
Mo	0.240	0.203	0.206
Ru + Tc + Rh + Pd	0.263	0.516	0.456
Cs + Rb	0.226	0.189	0.209
I + Te	0.012	0.070	
Xe + Kr	0.251	0.248	

\*All elements with elemental yields greater than 1% are included. The groups shown in the table account for all but about 2% of the fission products. [After L. Burris and J. Dillon, Estimation of Fission Product Spectra in Discharged Fuel from Fast Reactors, USAEC Report ANL-5742, Argonne National Laboratory, June (1957).]

<sup>†</sup>J. H. Davies and F. T. Ewart, *J. Nucl. Mater.*, 41: 143 (1971).

<sup>‡</sup>Lanthanum, cerium, praseodymium, neodymium, promethium, samarium, europium, and gadolinium.

of irradiated fuel, since the noble metals do not combine with oxygen, whereas zirconium, molybdenum, and yttrium can chemically bind oxygen released by the destruction of the fissile heavy metals uranium and plutonium. The elemental yields from fission of the mixed-oxide fuel fall in between the yields for pure uranium and pure plutonium. They are generally closer to the plutonium yields than to the uranium yields because plutonium is the principal fissile species in fast reactor fuel. However, since some fissions occur in the fertile  $^{238}\text{U}$ , the mixed-oxide yields do not correspond exactly to plutonium values.

## 12.2 PHYSICAL STATE OF THE FISSION PRODUCTS

Macroscopic quantities of fission products are created in high burnup fast reactor fuels. Indeed, some solid fission products agglomerate into separate phases large enough to be seen with the unaided eye. Identification of the chemical composition and the accurate location of the fission products along the radius of the fuel element were

made possible by the advent of the electron microprobe, a sketch of which is shown in Fig. 12.3. In this device a very fine beam of high-energy electrons ( $\sim 15\text{ kV}$ ) is focused on a small spot on the surface of a sectioned piece of irradiated fuel or cladding. Typical spot sizes are  $1\ \mu\text{m}$  in diameter. The high-energy electrons induce transitions in the inner electron shells of the atoms on the surface of the sample. Filling of these shells produces the characteristic X rays of the elements. The spectrum of the X rays is obtained by a crystal spectrometer. Identification of the element is accomplished by the  $M\alpha$  or  $M\beta$  lines for uranium and plutonium and by the  $L\alpha$  lines for fission-product elements. Quantitative determination of the concentrations of each of the elements present is made by comparing the intensity of the characteristic X-ray peaks with the intensity of a standard containing a known quantity of the element in question.

Conventional metallographic and electron-microprobe techniques have shown that solid fission products are located principally in the following three phases:<sup>2-8</sup>

1. The oxide matrix of the original fuel, which contains the rare-earth fission products, yttrium, some of

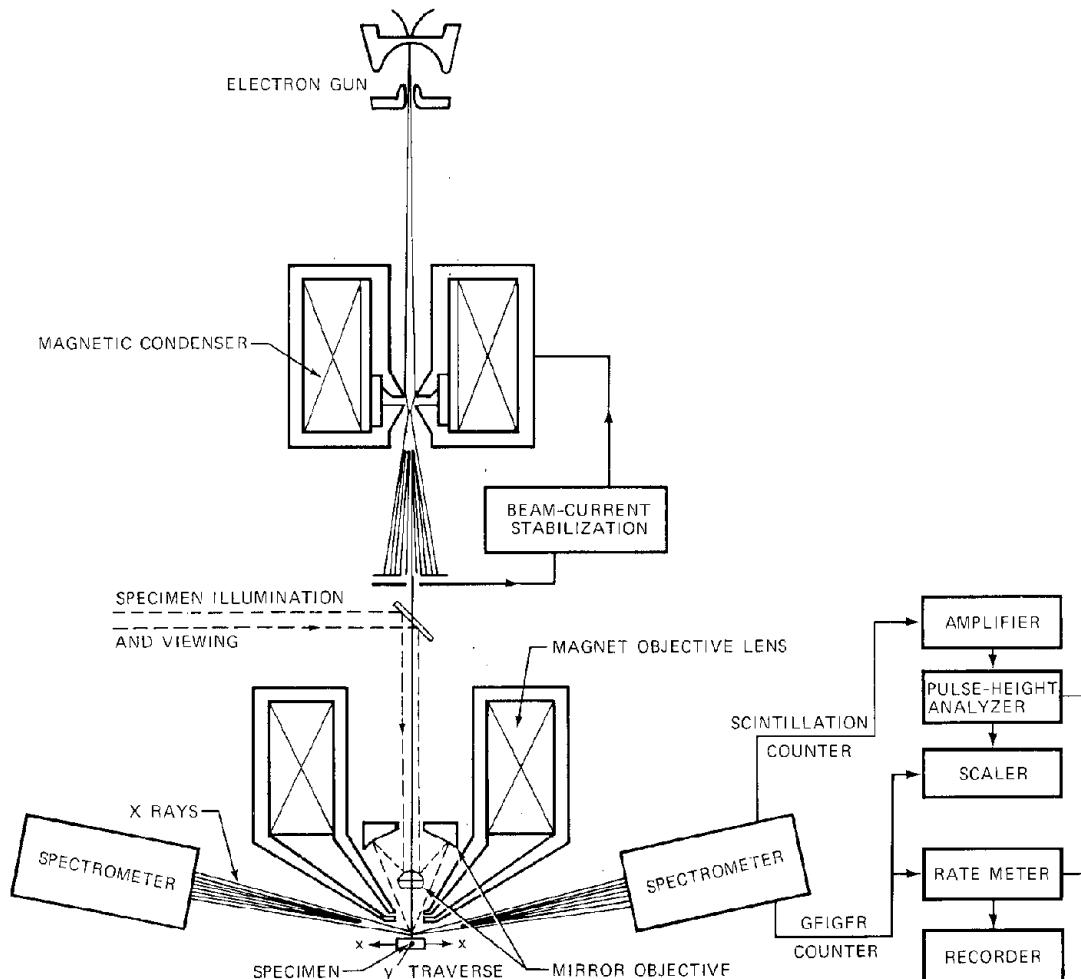


Fig. 12.3 Schematic diagram of the electron microprobe. [After B. T. Bradbury et al., *Proc. Brit. Ceram. Soc.*, 7: 311 (1967).]

the zirconium, niobium, and part of the molybdenum. These fission products are present as oxides which are in solid solution in the uranium and plutonium oxides of the fuel.

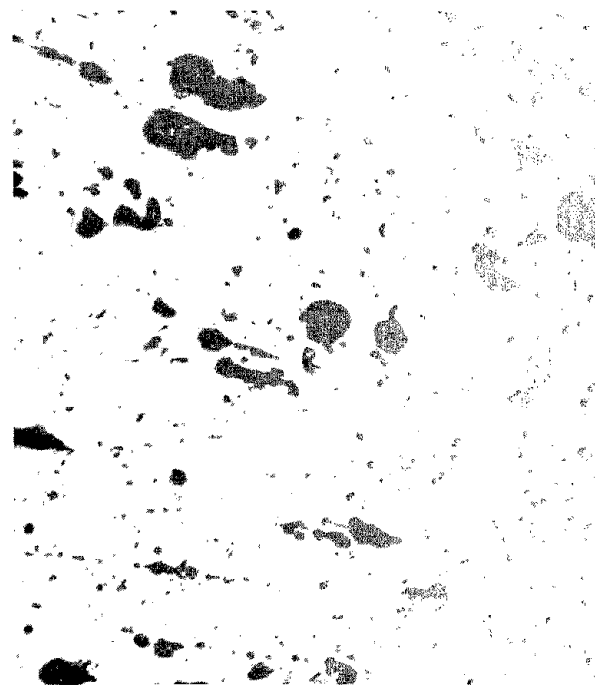
2. *Metallic inclusions* in grain boundaries of the columnar grain region or large metallic ingots within the central void. This phase is a homogeneous alloy of the noble metals ruthenium, technetium, rhodium, and palladium and contains, in addition, the remainder of the molybdenum. The metallic inclusions are shown in Fig. 12.4. This phase has a density of  $\sim 11 \text{ g/cm}^3$ , and a fabricated alloy of the same composition as the inclusions taken from the irradiated fuel was observed to melt at 1800 to 1900°C. The accumulation of the inclusions in the central void suggests that the small metallic particles can migrate up the temperature gradient, although the mechanism by which they do so is unknown.

The composition of the metallic inclusions measured by the electron microprobe is shown in Table 12.2. The first two rows represent analyses of inclusions extracted from  $\text{UO}_2$  fuel. The proportions of the elements in the ingots are approximately equal to those expected from their elemental yields, which suggests that all these fission products have agglomerated into the inclusions. The last two rows of Table 12.2 show the composition of ingots taken from the mixed oxide ( $\text{U}_{0.8}\text{Pu}_{0.2}\text{O}_2$ ). The inclusions contain less molybdenum than was found in ingots extracted from irradiated  $\text{UO}_2$ , in agreement with the reduced molybdenum yield compared to noble-metal yields in fuels containing fissile plutonium. The very low molybdenum content of the inclusion studied by O'Boyle, Brown, and Dwight,<sup>6</sup> however, suggests that not all of this element is contained in the metallic inclusion. The remainder of the molybdenum is in the fuel matrix.

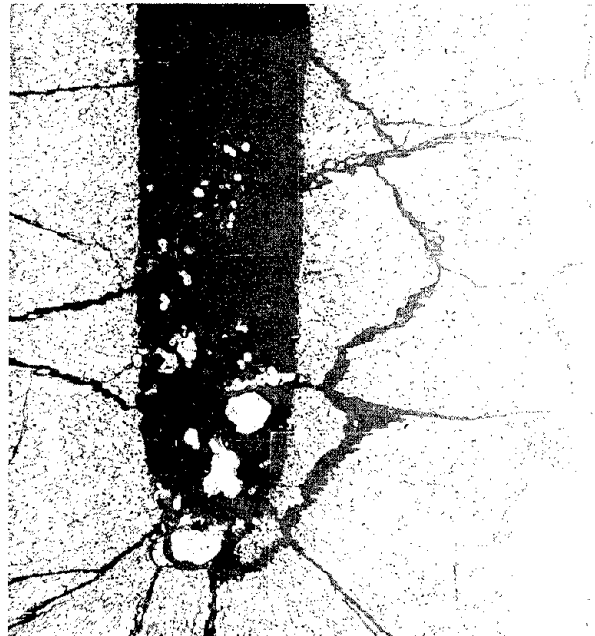
Table 12.2 Composition of the Metallic Inclusions Found in Irradiated Oxide Fuels

Fuel	Composition, at. %					Ref.
	Mo	Ru	Tc	Rh	Pd	
$\text{UO}_2$	60	24	16			2
$\text{UO}_2$	55	22	17	6		3
$(\text{U}_{0.8}\text{Pu}_{0.2})\text{O}_2$	43	32	16	7	2	4
$(\text{U}_{0.8}\text{Pu}_{0.2})\text{O}_2$	21	48	17	12	2	6

3. *A separate oxide phase*, insoluble in the fuel matrix, which contains the alkaline earths barium and strontium, the remainder of the zirconium, and occasionally cerium. The oxides  $\text{BaO}$  and  $\text{SrO}$  are insoluble in the actinide oxides primarily because of the large ionic radius of  $\text{Ba}^{2+}$  and  $\text{Sr}^{2+}$  ions. In the presence of zirconium, however, the stable forms of the oxides are the zirconates  $\text{BaZrO}_3$  and  $\text{SrZrO}_3$ , which account for the presence of zirconium in the alkaline earth oxide phase. Cerium is observed in this phase because it is the stable product of the mass-140 decay chain, which includes 12.6-day  $^{140}\text{Ba}$ . The half-life of this precursor is apparently long enough to permit this element to enter the alkaline earth oxide phase where it eventually transmutes to  $^{140}\text{Ce}$ . The latter tends to move into the fuel matrix where it is thermodynamically most stable. The continual produc-



(a)



(b)

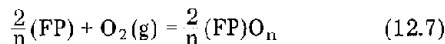
Fig. 12.4 Agglomerates of noble-metal fission products in irradiated mixed-oxide fuel. (a) Metallic inclusions (white). [From J. I. Bramman et al., *J. Nucl. Mater.*, 25: 201 (1968).] (b) Longitudinal section through the bottom end of the fuel element showing the fission-product ingots in the central void. Arrows indicate small ingots attached to the wall of the central void. [From D. R. O'Boyle et al., *J. Nucl. Mater.*, 35: 257 (1970).]

tion and removal processes result in a small steady-state concentration of cerium in the alkaline earth oxide phase. Figure 12.5 shows the locations of this phase. It accumulates at the boundary between the columnar-grain and equiaxed-grain regions of the irradiated fuel, and a solid plug of the material has been observed in the central void.

4. *Other Phases.* In addition to the oxide matrix and the insoluble metallic and oxide inclusions, fission products are located in other phases within the fuel element. The gas spaces within the fuel-cladding gap, cracks, and connected porosity in the fuel and the plenum contain the fission gases xenon and krypton. Another type of metallic inclusion of the general formula  $MN_3$ , where M stands for uranium or plutonium and N denotes rhodium or palladium, has been reported.<sup>4,7</sup> This type of intermetallic compound is thermodynamically stable enough to result in reduction of the  $UO_2$  and  $PuO_2$  to metals. Finally, as a consequence of corrosive attack, some cesium and molybdenum have been found in the grain boundaries of the cladding.

### 12.3 CHEMICAL STATE OF FISSION PRODUCTS IN OXIDE FUELS

The fundamental questions concerning the chemical state of fission products in an oxide fuel element are the following: given the plutonium-to-uranium ratio and the initial oxygen-to-metal ratio of the fuel and the temperature, what chemical compounds are formed by the fission products? and where in the fuel element are they located? The answers to these questions lie principally in the affinity of the fission products for oxygen, which can be expressed by the equilibrium oxygen pressure for the reaction



where the symbols (FP) and  $(\text{FP})\text{O}_n$  denote a fission-product element and its oxide, respectively. The valence of the fission-product cation in the oxide form is  $2n$ . For the purpose of classifying the fission products as oxides or elements, we may take the states of the element and the oxide to be pure single components and disregard for the moment the possibility that either of these two forms might be mixed with the fuel or with other fission products. Such an assumption provides an easily applicable but fairly reliable guide to the chemical state of the fission-product species.

By considering the fission products and their oxides to be pure substances, we have put them in their thermodynamic standard states; so the free energy of reaction (Eq. 12.7) is equal to the tabulated free energy of formation. Furthermore, the oxygen pressure at which both the element and the oxide coexist is given by applying the law of mass action to Eq. 12.7, which yields

$$p_{\text{O}_2} = \exp\left(\frac{\Delta G_{\text{FP}}^\circ}{RT}\right) \quad (12.8)$$

where  $\Delta G_{\text{FP}}^\circ$  is the free energy of formation of the fission-product oxide per mole of oxygen at temperature  $T$ . At  $1500^\circ\text{K}$ , for example, the free energy of formation of the least stable solid fission-product oxide (PdO) is +50

kJ/mole of  $\text{O}_2$ , whereas that of the most stable one ( $\text{La}_2\text{O}_3$ ) is  $-960$  kJ/mole of  $\text{O}_2$ . If Eq. 12.8 is applied, the equilibrium oxygen pressure over a mixture of Pd and PdO at  $1500^\circ\text{K}$  is found to be 50 atm, whereas that over a La-La $_2\text{O}_3$  mixture at the same temperature is 35 orders of magnitude smaller.

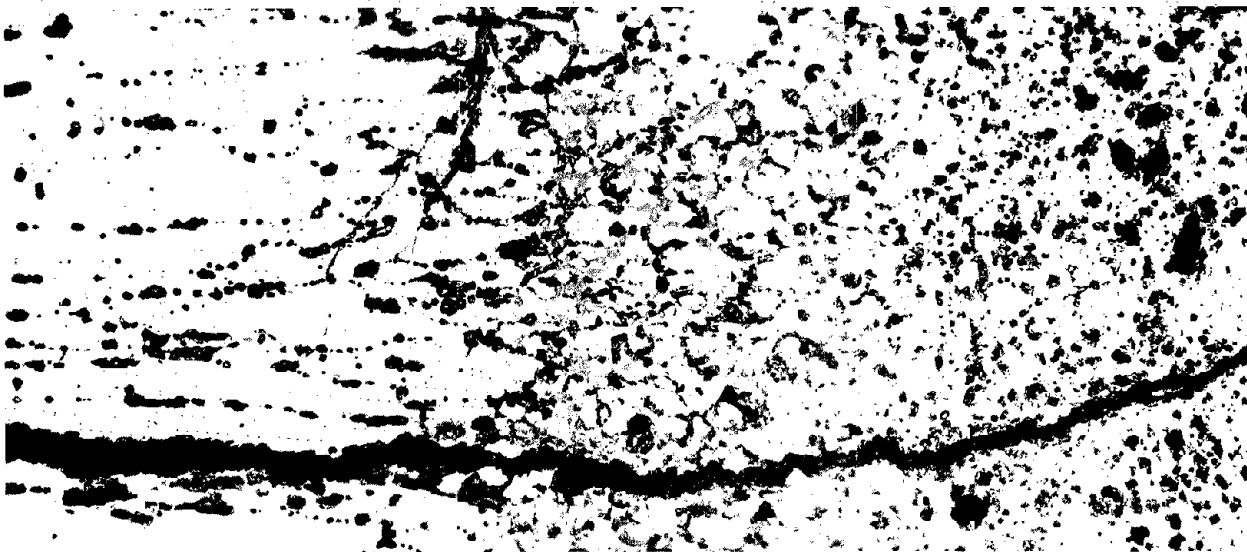
Whether or not a particular fission product is stable as an element or an oxide in the presence of the fuel depends on the difference between the free energy of formation of the fission-product oxide and the oxygen potential of the fuel. Reference to Fig. 11.2 shows that the oxygen potentials of mixed-oxide fuels are roughly bounded by  $-170$  and  $-670$  kJ/mole. If the free energy of formation of the fission-product oxide is smaller than  $-670$  kJ/mole, the element will be capable of removing oxygen from the fuel matrix and forming a stable oxide. On the other hand, fission products for which  $\Delta G_{\text{FP}}^\circ$  is larger than approximately  $-170$  kJ/mole will exist as elements in the fuel under all reactor conditions. According to these qualitative arguments, palladium should always be found as a metal and lanthanum as an oxide.

Comparison of the oxygen potentials of the fuel with the free energies of formation of fission-product oxides is facilitated by use of Figs. 12.6 and 12.7. Figure 12.6 is a graph of the oxygen potential  $\Delta\bar{G}_{\text{O}_2} = RT \ln p_{\text{O}_2}$  for mixed-oxide fuels as a function of temperature for various valences of uranium or plutonium. The lines in the figure were obtained by using the partial molar entropy and enthalpy data of Figs. 11.13 and 11.14 in conjunction with Eq. 11.14. The upper set of lines represents hyperstoichiometric mixed oxide. The uranium valence, which controls the oxygen potential of this type of fuel at a given temperature, is listed next to the lines. Hypostoichiometric fuel, in which the plutonium is reduced to a valence less than 4, is represented by the lines at the bottom.

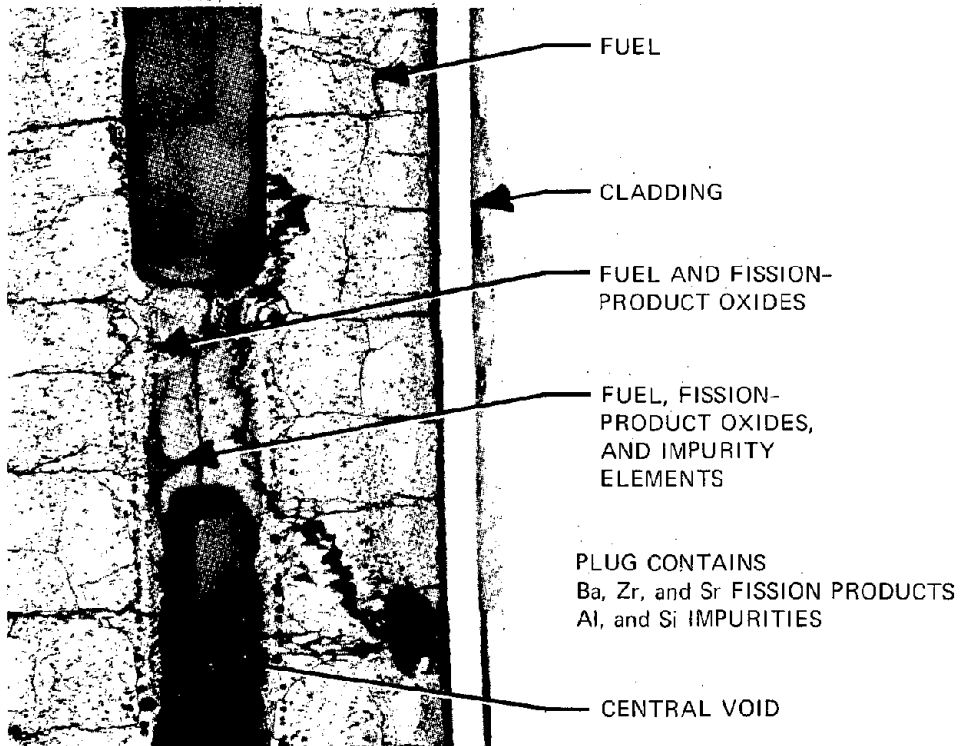
Figure 12.7 shows the free energies of formation of the fission-product oxides on the same scale as that used for the fuel oxygen potential (Fig. 12.6). Some fission products have multiple oxidation states (e.g.,  $\text{Nb}_2\text{O}_5$  and  $\text{NbO}_2$ ,  $\text{Ce}_2\text{O}_3$  and  $\text{CeO}_2$ ), but only one is shown.

Comparison of the two plots permits one to decide whether a particular fission product is stable as an oxide for a particular set of fuel conditions represented by a point on Fig. 12.6. If the free energy of formation of the fission product in question lies below the fuel oxygen potential, the oxide will be formed. If the fission-product point is above the fuel point, the former will be present as an element.

Using arguments of this type, one can examine all the fission products for the stability of their oxides in the presence of the oxides of the fissile species. In most cases the decision is rather clear-cut. There is, however, a good deal of uncertainty in assigning the valence of the important fission-product molybdenum. The free energy of formation of  $\text{MoO}_2$  is very close to that of stoichiometric mixed oxide, and this fission product may be present either as an element or an oxide (or both simultaneously). In hypostoichiometric fuel the oxygen potentials are low enough to reduce  $\text{MoO}_2$  to molybdenum metal, and the high oxygen pressure over hyperstoichiometric fuel favors formation of  $\text{MoO}_2$ . For nearly stoichiometric fuel, molyb-



(a)



(b)

Fig. 12.5 Alkaline earth oxide phase in irradiated  $(U,Pu)O_2$ . (a) As small inclusions (gray spots) at boundary between equiaxed and columnar grains. [From D. R. O'Boyle et al., *J. Nucl. Mater.*, 29: 27 (1969).] (b) As solid plug filling the central void. (From R. N. Duncan et al., in *Proceedings of the Conference on Fast Reactor Fuel Element Technology*, New Orleans, p. 291, American Nuclear Society, Hinsdale, Ill., 1971.)

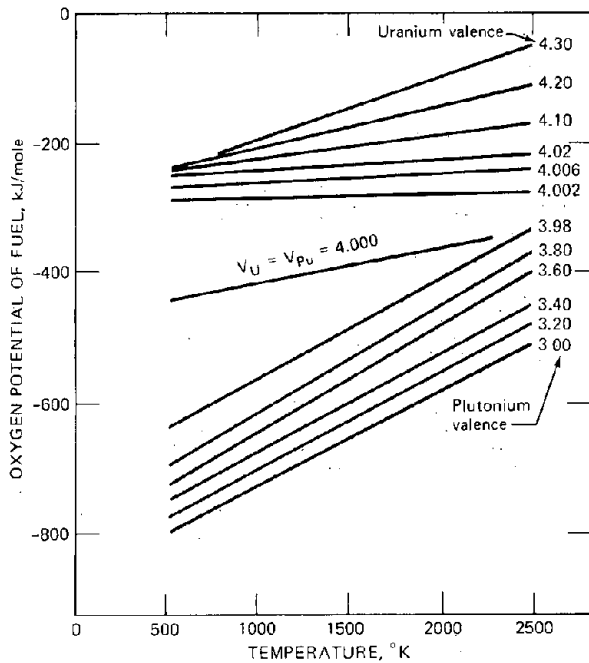


Fig. 12.6 Oxygen potentials of mixed-oxide fuels (taken from Figs. 11.13 and 11.14 and Eq 11.14).

denum is distributed between the fuel matrix (as  $\text{MoO}_2$ ) and the metallic inclusions (as Mo). It thus performs a role similar to that of a buffer in aqueous chemistry; it prevents drastic changes in the oxygen potential of the fuel by converting between element and oxide.

Note that the free energy of formation of cesium oxide becomes comparable to the oxygen potential of near-stoichiometric fuel at temperatures between 500 and 1000°K. It is thus thermodynamically possible for  $\text{Cs}_2\text{O}$  to form in the coolest parts of the fuel rod, particularly in the fuel-cladding gap.

Table 12.3 summarizes the most probable physical and chemical states of the abundant fission products in oxide fuels with oxygen-to-metal ratios not too far from 2.00. It should be emphasized, however, that the assignments in Table 12.3 can be significantly altered if the fuel is either highly hyper- or hypostoichiometric.

The manner by which the soluble fission-product oxides enter the fuel matrix is of some importance. The fission-product cations dissolve in the fluorite structure of the actinide oxides as substitutional ions; that is, they replace a uranium or plutonium on a normal cation lattice site. When a 4+ valence fission product such as  $\text{Zr}^{4+}$  enters the lattice in this manner, no change in the electrical neutrality of the crystal is involved. However, if the charge on the fission-product cation is different from that of the host ions, the lattice must somehow be altered to maintain electrical neutrality.

In their pure states, the rare earths form oxides of the general formula  $\text{M}_2\text{O}_3$  (sesquioxides). Assuming that the rare-earth cations keep a 3+ charge when dissolved substitutionally in the actinide oxide, the crystal can respond to the smaller cationic charge in one of the two ways shown in Fig. 12.8. This figure shows a perfect  $\text{UO}_2$  lattice and

possible crystal configurations after replacement of two  $\text{U}^{4+}$  ions by cations of valence 3+. To maintain the local charge balance, an oxygen ion may be removed from the lattice, thereby creating an anion vacancy [Fig. 12.8(b)]. This is the only manner in which ionic crystals composed of ions of fixed valence can adjust to the introduction of an impurity ion of different charge (see Fig. 6.8). Alternatively, electrical neutrality can be maintained without removal of an oxygen ion by the oxidation of two uranium ions from the 4+ to the 5+ state (or by oxidation of one  $\text{U}^{4+}$  to  $\text{U}^{6+}$ ). This mechanism is shown in Fig. 12.8(c). Whether replacement of  $\text{U}^{4+}$  by a trivalent cation results in an anion vacancy or oxidizes the uranium ion depends on the prevailing oxygen potential. We have seen in Sec. 11.4 that  $\text{U}^{4+}$  can be transformed into  $\text{U}^{5+}$  or  $\text{U}^{6+}$  only when the oxygen potential of the environment is sufficiently large. When  $\Delta\bar{G}_{\text{O}_2}$  is low, all uranium in the solid remains in the 4+ valence state, and the extra negative charges required by the replacement of  $\text{U}^{4+}$  by the trivalent ion (e.g.,  $\text{La}^{3+}$ ) is supplied by the rejection of neutral oxygen to the environment according to

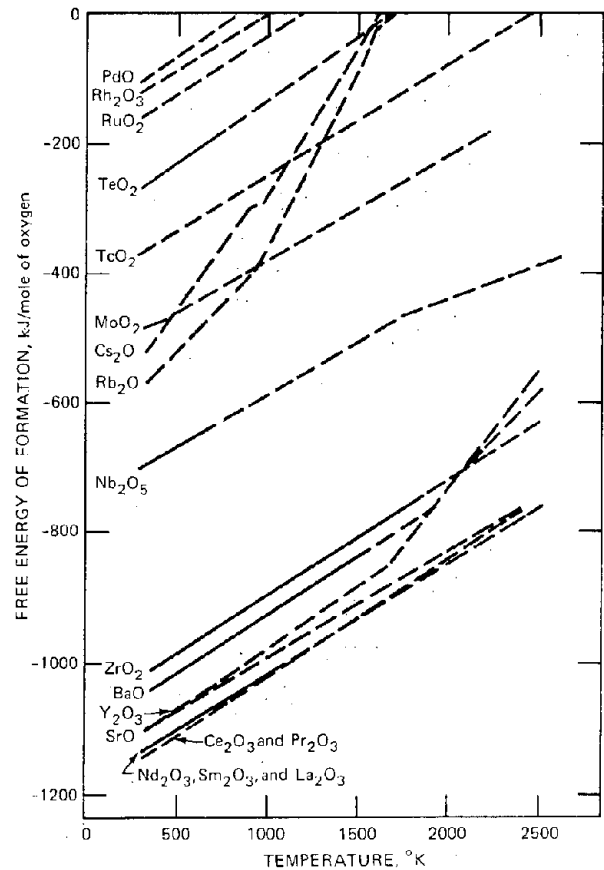
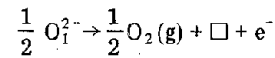


Fig. 12.7 Standard free energies of formation of high-yield fission products. ---, extrapolations of data. [From D. R. O'Boyle et al., *J. Nucl. Mater.*, 29: 27 (1969).]

Table 12.3 Probable Chemical and Physical States of Fission Products in Near-Stoichiometric Mixed-Oxide Fuel

Chemical group	Physical state	Probable valence
Zr and Nb*	Oxide in fuel matrix; some Zr in alkaline earth oxide phase	4+
Y and rare earths†	Oxide in fuel matrix	3+
Ba and Sr	Alkaline earth oxide phase	2+
Mo	Oxide in fuel matrix or element in metallic inclusion	4+ or 0
Ru, Tc, Rh, and Pd	Elements in metallic inclusion	0
Cs and Rb	Elemental vapor or separate oxide phase in cool regions of fuel	1+ or 0
I and Te	Elemental vapor; I may be combined with Cs as CsI	0 or 1-
Xe and Kr	Elemental gas	0

\*Although the most common oxide of niobium is  $Nb_2O_5$ , the dioxide  $NbO_2$  has been assumed to be stable in the fuel. The choice of niobium valence is not critical since its elemental yield is only 4%.

†Cerium has a 4+ valence state and may be stable as  $CeO_2$  in fuels of high oxygen potential. This element has also been found in the alkaline earth oxide phase.

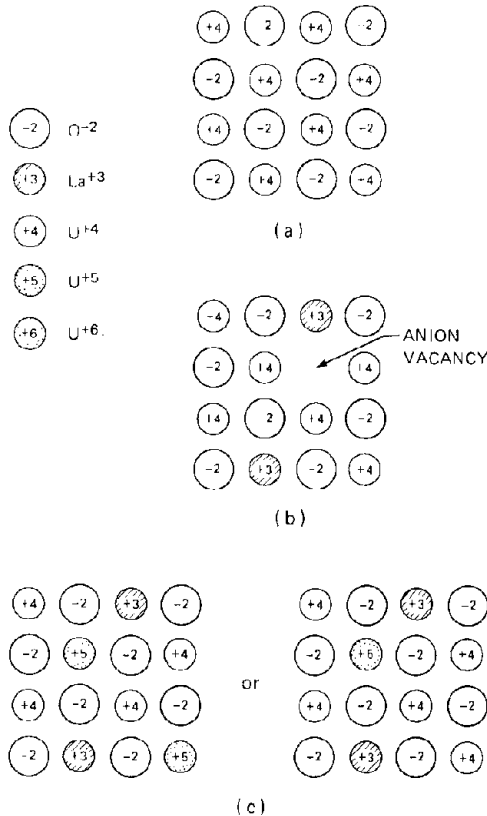
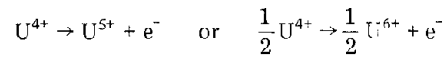


Fig. 12.8 Two-dimensional representation of methods of maintaining electrical neutrality when  $La^{3+}$  is introduced into  $UO_2$ . (a) Perfect  $UO_2$  lattice. (b) Removal of oxygen ions. (c) Oxidation of  $U^{4+}$  to  $U^{5+}$  or  $U^{6+}$ .

where  $O_1^{2-}$  represents a lattice oxygen ion and  $\square$  denotes an anion vacancy. The solid solutions prepared by dissolving  $Y_2O_3$  in  $UO_2$  have been found to increase the concentration of anion vacancies in the manner predicted by this mechanism, which is shown in Fig. 12.8(b).

At high oxygen potentials the extra electronic charge required to accommodate a trivalent ion in place of a  $U^{4+}$  ion is supplied by promotion of a nearby  $U^{4+}$  ion to the 5+ or 6+ valence state:



When trivalent rare-earth ions are created in situ by fission of uranium, electrical neutrality of the lattice appears to be maintained by increasing the valence of the remaining uranium ions in the manner shown in Fig. 12.8(c).

When the system is subject to oxygen potentials that do not clearly favor either of the extreme responses described, a mixture of higher valence uranium ions and oxygen vacancies can result from the replacement of  $U^{4+}$  by trivalent cations.

The alkaline earth cations  $Ba^{2+}$  and  $Sr^{2+}$  do not produce analogous oxidation of the heavy-metal cations since these fission products form a separate phase rather than dissolve in the fuel matrix.

## 12.4 EFFECT OF BURNUP ON THE OXYGEN POTENTIAL OF THE FUEL

The fission process produces twice as many atoms of fission products as the number of uranium and plutonium atoms destroyed. The oxygen atoms in the fuel, however, are not affected by the nuclear processes that are a consequence of neutron irradiation. Thus, as a result of fission, two atoms of oxygen are released for each heavy-metal atom destroyed. Some of the oxygen so liberated may combine with fission products and form the oxides of these elements shown in Table 12.3. Not all the fission products accept oxygen, however, and those that do may form oxides of a lower oxygen-to-metal ratio than that

of the actinide metals (for which the ratio is approximately 2). Even though two fission-product atoms are produced for every actinide atom destroyed, they are on the average not efficient enough in chemically combining with oxygen to use all the oxygen that is released by fission. The excess oxygen dissolves in the fuel matrix, where it increases the valence of the uranium or the plutonium; thus, fission can be regarded as an oxidizing process. The net effect of burnup is to render the fuel more hyperstoichiometric than the fresh fuel or to increase the oxygen potential of the fuel.

The ultimate purpose of analysis of the effect of burnup on the chemical state of the fuel is to permit prediction of the evolution of the spatial distribution of the oxygen potential,  $\Delta\bar{G}_{O_2}$ , during irradiation. To accomplish this goal, we need the following information:

1. The decrease in the concentrations of uranium and plutonium and the increase in the concentrations of the oxygen-consuming fission products as a function of burnup.
2. The chemical and physical states of the fission products, as described in Table 12.3.
3. The extent of redistribution of oxygen, the heavy metals, and the fission products axially and radially in the fuel as a function of burnup.
4. The thermochemistry of the equilibria assumed to be established between the fission-product-contaminated fuel and the gas phase contained in cracks or fissures in the fuel.
5. The extent of chemical attack of the cladding, which, if it occurs, provides a means of removing oxygen and perhaps some fission products from the oxide fuel.

In this section we treat an idealized situation in which migration of the fuel constituents, gas-solid equilibria, and fuel-cladding reaction are neglected. The following section describes the effects of items 3 through 5.

#### 12.4.1 Concentration Changes During Burnup

Figure 12.9 shows a unit volume of unirradiated mixed-oxide fuel material that contains  $N_U^0$  atoms of uranium and  $N_{Pu}^0$  atoms of plutonium. The number of oxygen atoms in the fresh fuel is

$$N_O^0 = \frac{O}{M} (N_U^0 + N_{Pu}^0) \quad (12.9)$$

where  $O/M$  is the oxygen-to-metal ratio of the as-fabricated fuel. The initial cation fraction of plutonium is

$$q_0 = \frac{N_{Pu}^0}{N_U^0 + N_{Pu}^0} \quad (12.10)$$

During irradiation at constant temperature, none of the fuel constituents (oxygen, heavy metals, or fission products) leave or enter the region. Fission-product phases (i.e., the metallic inclusions and the alkaline earth oxide phase) are formed as a result of irradiation. Figure 12.9 also depicts the state of the fuel after burnup,  $\beta$ . The fraction of the initial heavy-metal atoms which remains is given by

$$\frac{N_U + N_{Pu}}{N_U^0 + N_{Pu}^0} = 1 - \beta \quad (12.11)$$

and the ratio of plutonium to total heavy-metal atoms is

$$q = \frac{N_{Pu}}{N_U + N_{Pu}} \quad (12.12)$$

Combining Eqs. 12.11 and 12.12 gives the number of uranium and plutonium atoms remaining after burnup:

$$N_U = (1 - q)(1 - \beta)(N_U^0 + N_{Pu}^0) \quad (12.13)$$

$$N_{Pu} = q(1 - \beta)(N_U^0 + N_{Pu}^0) \quad (12.14)$$

The value of  $q$  depends on the conversion ratio\* and its variation with burnup. The conversion ratio must be obtained from detailed reactor physics calculations. A constant conversion ratio of unity (which means that  $N_{Pu} = N_{Pu}^0$ ) is attained in some core regions of typical fast reactors,<sup>9</sup> in which case  $q$  is given by

$$q = \frac{q_0}{1 - \beta} \quad (12.15)$$

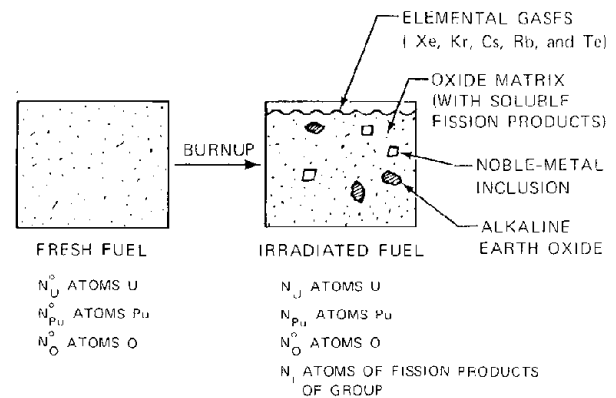


Fig. 12.9 A unit volume of mixed-oxide fuel irradiated as a constant mass system.

Following the classification in Tables 12.1 and 12.3, the fission products are collected into groups characterized by particular chemical states. The concentration of fission product in a particular group present after burnup is

$$N_i = Y_i \beta (N_U^0 + N_{Pu}^0) \quad (12.16)$$

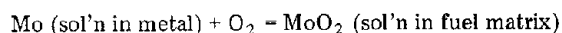
where  $Y_i$  is the sum of the elemental yields of all fission products in group  $i$  and  $N_i$  includes all of group  $i$  that has been formed in the unit volume of fuel depicted in Fig. 12.9 irrespective of the solid phase in which it occurs.

#### 12.4.2 Partitioning of Molybdenum

As pointed out earlier, the free energy of formation of  $MoO_2$  is so close to the oxygen potential of nearly stoichiometric fuel that this fission product cannot be unambiguously assigned to the elemental or the oxide chemical state. Rather, it is distributed between the oxide matrix (as dissolved  $MoO_2$ ) and the metallic inclusions (as

\*The conversion ratio is the ratio of the amount of plutonium produced by neutron capture in fertile  $^{238}U$  to the amount of plutonium consumed by fission.

Mo in the solid solution with the noble metal fission products) in concentrations that satisfy the equilibrium



Application of the law of mass action to this equilibrium results in

$$\frac{a_{\text{Mo}}^f}{a_{\text{Mo}}^m p_{\text{O}_2}} = \exp\left(\frac{-\Delta G_{\text{MoO}_2}^\circ}{RT}\right) \quad (12.17)$$

where  $\Delta G_{\text{MoO}_2}^\circ$  is the free energy of formation of  $\text{MoO}_2$ , which is given by the equation of the straight line for this species in Fig. 12.7 as

$$\Delta G_{\text{MoO}_2}^\circ = -574 + 164(T/10^3) \quad (12.18)$$

The enthalpy and entropy of formation are expressed in kJ/mole and J mole<sup>-1</sup> K<sup>-1</sup>, respectively. The quantities  $a_{\text{Mo}}^f$  and  $a_{\text{Mo}}^m$  are the thermodynamic activities of molybdenum in the fuel matrix and in the metallic inclusions, respectively. For the purpose of the present calculation, we will assume that molybdenum forms ideal solutions in these two phases; thus, the activities can be replaced by the cation fraction of Mo in the fuel matrix ( $y_{\text{Mo}}^f$ ) and by the atom fraction of Mo in the metal phase ( $y_{\text{Mo}}^m$ ).<sup>\*</sup> Equation 12.17 becomes

$$\Delta G_{\text{MoO}_2}^\circ = RT \ln p_{\text{O}_2} - RT \ln \frac{y_{\text{Mo}}^f}{y_{\text{Mo}}^m} \quad (12.19)$$

The oxygen pressure in Eq. 12.19 is governed by the equilibrium of reaction Eq. 11.1, for which the criterion of chemical equilibrium is

$$\Delta \overline{G}_{\text{O}_2} = RT \ln p_{\text{O}_2} \quad (12.20)$$

Attainment of equilibrium within the container depicted in Fig. 12.9 requires that the oxygen partial pressures appearing in Eqs. 12.19 and 12.20 be equal, or

$$\Delta G_{\text{MoO}_2}^\circ = \Delta \overline{G}_{\text{O}_2} - RT \ln \frac{y_{\text{Mo}}^f}{y_{\text{Mo}}^m} \quad (12.21)$$

The partitioning of molybdenum between the fuel matrix and the metallic inclusions can be described by the quantity  $f_{\text{Mo}}$ , which is defined as the fraction of the total molybdenum present which is oxidized to  $\text{MoO}_2$ . In terms of  $f_{\text{Mo}}$  and the concentrations of the other species present, the cation fraction of molybdenum in the oxide matrix is

$$y_{\text{Mo}}^f = \frac{f_{\text{Mo}} N_{\text{Mo}}}{N_{\text{U}} + N_{\text{Pu}} + N_{\text{Y-RE}} + f_{\text{Mo}} N_{\text{Mo}} + N_{\text{Zr-Nb}} - N_{\text{Ba-Sr}}} \quad (12.22)$$

where  $N_{\text{U}}$  and  $N_{\text{Pu}}$  are the concentrations of uranium and plutonium,  $N_{\text{Y-RE}}$  is the sum of the concentrations of yttrium and the rare earths, and  $N_{\text{Mo}}$  is the total concentration of molybdenum, irrespective of whether it is in the fuel matrix or in the inclusions. The difference between  $N_{\text{Zr-Nb}}$  and  $N_{\text{Ba-Sr}}$  represents the amount of zirconium that is dissolved in the fuel matrix. It is the total amount of zirconium less the amount contained in the alkaline earth oxide phase as  $\text{BaZrO}_3$  or  $\text{SrZrO}_3$ .

<sup>\*</sup>The activity coefficients of Mo in the noble metal alloy and of  $\text{MoO}_2$  in urania have been estimated (see Ref. 18).

Similarly, the atom fraction of molybdenum in the metallic inclusions is

$$y_{\text{Mo}}^m = \frac{(1 - f_{\text{Mo}}) N_{\text{Mo}}}{N_{\text{NM}} + (1 - f_{\text{Mo}}) N_{\text{Mo}}} \quad (12.23)$$

where  $N_{\text{NM}}$  stands for the sum of the concentrations of the noble metals ruthenium, technetium, rhodium, and palladium.

The concentrations of uranium and plutonium can be expressed in terms of the burnup,  $\beta$ , and the enrichment,  $q$ , by Eqs. 12.13 and 12.14, and the concentrations of the various fission-product groups are given by Eq. 12.16 in terms of their yields. Substituting these equations and Eqs. 12.22 and 12.23 into Eq. 12.21 gives

$$\Delta G_{\text{MoO}_2}^\circ = \Delta \overline{G}_{\text{O}_2} - RT \ln \left[ \left( \frac{f_{\text{Mo}}}{1 - f_{\text{Mo}}} \right) \times \frac{Y_{\text{NM}} + (1 - f_{\text{Mo}}) Y_{\text{Mo}}}{\frac{1 - \beta}{\beta} + Y_{\text{Y-RE}} + f_{\text{Mo}} Y_{\text{Mo}} + Y_{\text{Zr-Nb}} - Y_{\text{Ba-Sr}}} \right] \quad (12.24)$$

The oxygen potential of the fuel in Eq. 12.24 can be written as

$$\Delta \overline{G}_{\text{O}_2} = \Delta \overline{H}_{\text{O}_2} - T \Delta \overline{S}_{\text{O}_2} \quad (12.25)$$

where  $\Delta \overline{H}_{\text{O}_2}$  and  $\Delta \overline{S}_{\text{O}_2}$  can be obtained as functions of heavy-metal valence from Figs. 11.13 and 11.14. Although the data represented in these graphs were obtained from experiments on unirradiated fuel, they probably apply to mixtures of the heavy metals and soluble fission products, in which the latter act as diluents of fixed charge.

The determination of the thermodynamic state of the irradiated fuel thus reduces to a problem containing two unknowns: the fraction of oxidized molybdenum ( $f_{\text{Mo}}$ ) and the valence of one of the actinides ( $V_{\text{Pu}}$  or  $V_{\text{U}}$ ). Note that  $V_{\text{Pu}}$  and  $V_{\text{U}}$  are not both unknowns; one or the other is exactly 4 (see Sec. 11.4). The heavy-metal valence is needed to compute  $\Delta \overline{G}_{\text{O}_2}$  appearing in Eq. 12.24.

### 12.4.3 Oxygen Balance

Equation 12.24 provides only one relationship between the two unknowns. The second equation needed to completely determine the state of the system is an oxygen balance. Despite the fission process the oxygen concentration in the region of Fig. 12.9 is given by Eq. 12.9. The oxygen can be located in either of the two oxygen-containing phases present in Fig. 12.9(b), and the oxygen balance can be written as

$$N_{\text{O}}^\circ = N_{\text{O}}^{\text{Ba-Sr}} + N_{\text{O}}^f \quad (12.26)$$

where  $N_{\text{O}}^{\text{Ba-Sr}}$  is the amount of oxygen per unit volume of total fuel chemically bound in the alkaline earth oxide phase and  $N_{\text{O}}^f$  is the oxygen contained in the fuel matrix. These quantities are found by charge balances that ensure electrical neutrality of the two oxide phases:

$$N_{\text{O}}^{\text{Ba-Sr}} = 3N_{\text{Ba-Sr}} \quad (12.27)$$

The factor of 3 in this relation is due to the fact that each alkaline earth atom binds three oxygen atoms when zirconates of the type  $\text{BaZrO}_3$  and  $\text{SrZrO}_3$  are present.

If the final state of the fuel matrix is such that  $V_U = 4$  and  $V_{Pu} < 4$ , the charge balance on the fuel oxide phase is

$$2N_O^f = 4N_U + V_{Pu}N_{Pu} + 4(N_{Zr-Nb} - N_{Ba-Sr}) + 3N_{Y-RE} + 4f_{Mo}N_{Mo} \quad (12.28a)$$

The analogous charge balance for the case of  $V_U > 4$ ,  $V_{Pu} = 4$  is

$$2N_O^f = V_U N_U + 4N_{Pu} + 4(N_{Zr-Nb} - N_{Ba-Sr}) + 3N_{Y-RE} + 4f_{Mo}N_{Mo} \quad (12.28b)$$

The fission-product concentrations in these equations can be expressed in terms of the burnup and the elemental yields by Eq. 12.16, and the uranium and plutonium concentrations are given by Eqs. 12.13 and 12.14. Substituting these formulas into Eqs. 12.28a and 12.28b and then into the oxygen balance of Eq. 12.26 yields for  $V_U = 4$ ,  $V_{Pu} < 4$

$$2\left(\frac{O}{M}\right) = 4(1-q)(1-\beta) + V_{Pu}q(1-\beta) + (2Y_{Ba-Sr} + 4Y_{Zr-Nb} + 3Y_{Y-RE} + 4f_{Mo}Y_{Mo})\beta \quad (12.29a)$$

and for  $V_U > 4$ ,  $V_{Pu} = 4$

$$2\left(\frac{O}{M}\right) = V_U(1-q)(1-\beta) + 4q(1-\beta) + (2Y_{Ba-Sr} + 4Y_{Zr-Nb} + 3Y_{Y-RE} + 4f_{Mo}Y_{Mo})\beta \quad (12.29b)$$

Simultaneous solution of Eqs. 12.29a or 12.29b and Eq. 12.24 yields  $f_{Mo}$  and  $V_U$  or  $V_{Pu}$ . To accomplish the solution, we take  $\Delta G_{O_2}$  from Eq. 12.25 and Figs. 11.13 and 11.14 and relate  $q$  to  $q_o$  and  $\beta$  by Eq. 12.15. The fission yields are those given in Table 12.1 (or an equivalent compilation for fuels of initial plutonium enrichments different from 15%). Once the valence of the appropriate actinide element has been determined, the oxygen potential of the fuel can be computed from Figs. 11.13 and 11.14 and Eq. 12.25. Note that the fission products that do not combine with oxygen and are not constituents of the metallic inclusions [i.e., the elemental gases in Fig. 12.9(b)] do not influence the oxygen-potential changes due to burnup.

Figure 12.10 shows the results of applying the preceding calculation to the mixed-oxide fuel of initial composition  $(U_{0.85}Pu_{0.15})O_{1.96}$ . In the early stages of irradiation, the oxygen potential of the fuel increases linearly with burnup, which demonstrates the oxidizing effect of irradiation. Concurrently, the plutonium valence steadily rises from the value in the fresh fuel (given by Eq. 11.15) toward the limiting value of 4. During the low-burnup stage, essentially all the fission-product molybdenum is present as metal.

At a critical burnup of  $\sim 5\%$ , the oxygen potential abruptly increases by nearly 125 kJ/mole. At this burnup all plutonium has been oxidized to  $Pu^{4+}$ , and Fig. 11.10 shows that, at the point of exact stoichiometry, the oxygen potential decreases very rapidly with further oxidation. For  $\beta > 5\%$  the uranium valence may begin to rise slightly above 4, since the plutonium can no longer respond to the excess oxygen released by fission by increasing valence. The

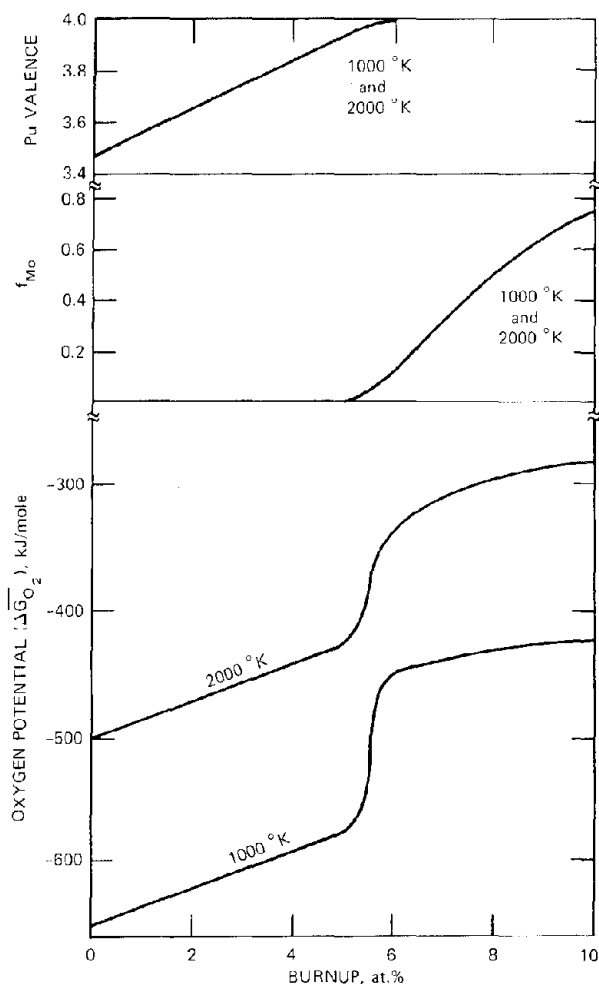


Fig. 12.10 Effect of burnup on the oxygen potential, molybdenum oxidation state, and plutonium valence for fuel of initial composition  $(U_{0.85}Pu_{0.15})O_{1.96}$ . The effects of oxygen, heavy metal, and fission-product migration and oxygen reaction with the cladding are not considered.

middle plot in Fig. 12.10 shows molybdenum gradually transforms from metal to oxide at burnups greater than 5%.

The critical burnup for initially hypostoichiometric fuel can be roughly estimated by setting  $V_{Pu} = 4$  and  $f_{Mo} = 0$  in Eq. 12.29a, which gives

$$\beta_{crit} \approx \frac{1 - (O/M)/2}{1 - [(2Y_{Ba-Sr} + 4Y_{Zr-Nb} + 3Y_{Y-RE})/4]} \quad (12.30)$$

Equation 12.30 predicts a critical burnup of 4.5% for  $(U_{0.85}Pu_{0.15})O_{1.96}$ , which is somewhat lower than the value obtained from Fig. 12.10.

C. E. Johnson, I. Johnson, and Crouthamel<sup>10</sup> have performed similar computations for  $(U_{0.8}Pu_{0.2})O_{2-x}$ . They found that the critical burnups for initial oxygen-to-metal ratios of 1.99, 1.97, and 1.95 were 1.5%, 4.8%, and 6.7%, respectively. As expected, the critical burnup decreases for initial oxygen-to-metal ratios close to 2, since the plutonium in the fresh fuel contains less  $Pu^{3+}$  at the start than fuels that are initially more substoichiometric.

## 12.5 FISSION-PRODUCT MIGRATION

As a result of the steep temperature gradient in the fuel, some fission products can move away from the location of the fission event that produced them. Loss or gain of fission products from the region of fuel where they were created can substantially alter the oxygen-potential profile in the fuel and the swelling due to the solid fission products. Because of the broad range of physical and chemical properties of the fission products, the extent of migration and the mechanism by which it occurs are peculiar to each species. Some can be transported by processes similar to those responsible for oxygen and actinide redistribution, namely, vapor migration and thermal diffusion (Chap. 11). The mobility of a particular fission product may depend on the properties of its precursor in the fission decay chain as well as its own properties. Thus, the migration of cesium is undoubtedly influenced by the fact that the precursors of this species are gaseous xenon isotopes, some of which have appreciable half-lives. The precursors of molybdenum, on the other hand, are zirconium and niobium isotopes, which are not particularly mobile in oxide fuels.

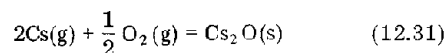
The fission products that form oxides soluble in the fuel matrix (those contained in the first two groups in Table 12.3) show little tendency to migrate in the temperature gradient.<sup>11</sup> Modest redistribution of cerium in a  $\text{CeO}_2\text{-UO}_2$  mixture observed in an out-of-pile thermal gradient test has been attributed to thermal diffusion (Ref. 12 and Sec. 11.7).

The fission products in the last three groups of Table 12.3 are most probably present in gas phases over or in the fuel. After formation as atomic species from fission, they rapidly coalesce into bubbles, which migrate up the temperature gradient to the central void (Chap. 13) or diffuse to grain boundaries, cracks, or interconnected porosity in the matrix from which they escape to the gas spaces in the fuel element. The rapid diffusion in the gas phase permits the volatile elements to distribute uniformly within all open spaces in the fuel element. Except for cesium and the fission gases xenon and krypton, there is little experimental information concerning the movement of the volatile fission products because their low yields make detection difficult.

Cesium is among the least volatile and most chemically active of the volatile class of fission products. The vapor pressure of cesium is 1 atm at 690°C. Because of the high yield of this element, substantial pressures (~1 atm) of cesium may develop, and the vapors may condense in cool regions of the fuel element. Caldwell, Miles, and Ross<sup>13</sup> found cesium on the bottom end cap and in the plenum above the fuel column, which demonstrates appreciable migration followed by condensation. The process by which elemental cesium migrates is simple distillation. Cesium produced in the hot fuel is transported by gas-phase diffusion and/or convection to surfaces cold enough to reduce the cesium vapor pressure below the prevailing partial pressure. Hence, cesium condenses on the cold surface.

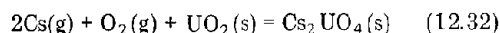
At the interface between the fuel and the cladding, the temperatures are low enough (~700°C) and the oxygen potential of the nearly stoichiometric fuel is high enough

that cesium can react with oxygen to form the oxide by the reaction



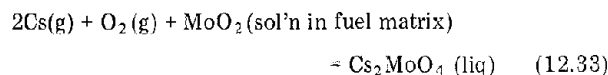
The oxide of cesium is very much less volatile than the element and probably exists as a solid under these conditions.

In addition to  $\text{Cs}_2\text{O}$ , formation of other nonvolatile compounds of cesium near the fuel surface has been proposed. Cesium may react with the oxide fuel to form cesium uranate by the reaction<sup>14,15</sup>

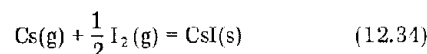


The analogous reaction of sodium with the fuel to form sodium uranate is of importance in assessing the consequences of entry of the coolant of an LMFBR into a defected fuel pin.<sup>16,17</sup>

Cesium can also react with other fission products. With molybdenum the following reaction has been proposed:<sup>18</sup>



Finally, cesium can react with fission-product iodine according to



The free energy of formation of  $\text{CsI}$  is quite negative; thus, this reaction should proceed nearly to completion. Since the elemental yield of cesium from fission is about six times that of iodine, essentially all the iodine should be removed from the gas phase.

The immobilization of cesium as a nonvolatile oxygen-bearing compound is important for several reasons:

1. By providing a sink for cesium at the fuel surface, a radial concentration gradient of this element can be established. Such a gradient causes cesium produced by fission to distill from the hot center of the fuel to the cooler fuel-cladding interface.

2. If the compound contains oxygen, the oxygen balance is altered in a way that reduces the oxygen potential (since  $\text{Cs}^+$  binds some of the oxygen released by fission). The discussion in Sec. 12.4 assumed cesium to be in the elemental form.

3. If cesium is effectively removed from the gas phase by formation of a uranate or a molybdate, there may not be sufficient gaseous cesium remaining to combine all the fission-product iodine by Eq. 12.34.

4. Incorporation of cesium into a solid phase increases the swelling of the fuel.

5. Cesium compounds (particularly  $\text{Cs}_2\text{O}$ ) appear to accelerate corrosion of the stainless-steel cladding.

All investigations of cesium migration have demonstrated that this element accumulates at the fuel-cladding interface. Figure 12.11 shows the radial distribution<sup>19</sup> of <sup>137</sup>Cs in three fuel pins that had been irradiated to burnups ranging from 2.7 to 6.5 at. %. The element designated F2R contained fuel in the form of high-density pellets (>94% of theoretical density). The elements denoted by HOV-15 and SOV-6 were fabricated by vibrationally compacting the

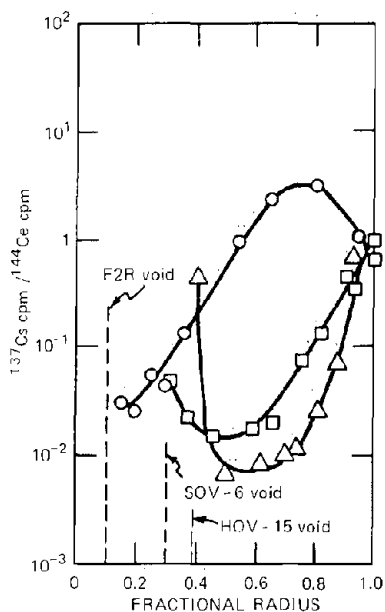


Fig. 12.11 Radial distribution of  $^{137}\text{Cs}$  in irradiated mixed-oxide fuel pins.  $\circ$ , F2R.  $\triangle$ , HOV-15.  $\square$ , SOV-6. (From C. E. Johnson et al., in *Proceedings of the Conference of Fast Reactor Fuel Element Technology*, New Orleans, p. 603, American Nuclear Society, Hinsdale, Ill., 1971.)

oxide powder in the cladding. They were of lower density (80 to 84% of theoretical density) than the pellet fuel. In all three cases the concentration of cesium was greater at the outer fuel surface than anywhere else along the radius of the pin. In the two vibrationally compacted fuel elements, the cesium concentration at the outer surface was approximately two orders of magnitude greater than the minimum value, which occurred at a fractional radius between 0.5 and 0.6. The increase in cesium concentration near the central void in these two elements may be due to pileup of migrating pores that contain gaseous elemental cesium. The denser F2R cesium profile does not show this upswing near the central void because its higher density means that fewer pores are present. In the vibrationally compacted fuel material, the cesium is transported up and down the temperature gradient simultaneously. Movement of closed porosity transports cesium from cold to hot regions, and diffusion in cracks and interconnected porosity moves cesium from hot to cold regions.

The profile of cesium in the pelleted fuel F2R also shows increasing concentration toward the surface but not to as large an extent as in the other two fuel elements. This difference in the cesium migration behavior of the two types of fuel is probably due to the greater amount of open porosity along the temperature gradient in the low-density vibrationally compacted material compared to the dense pellet fuel. The peak in the cesium concentration in the F2R element at a fractional radius of 0.7 coincides with a circumferential crack in the fuel at this location. It appears to be a general feature of cesium migration that such cracks inhibit cesium movement, and they are always associated with high cesium concentrations in postirradiation observations.

The alkaline earth oxide phase also appears to move along the temperature gradient. Figure 12.5(a) shows this oxide phase as small inclusions in the fuel matrix at the boundary between the columnar-grain region and the band of equiaxed grains. The columnar-grain zone on the right of this photograph is devoid of oxide inclusions. Visual evidence such as this suggests either that this phase has migrated down the temperature gradient or that the individual atomic constituents of the inclusion diffused from the columnar-grain regions to the boundary where precipitation occurred. On the other hand, Fig. 12.5(b) shows this same phase present as a massive plug filling the central void, which suggests that the zirconate inclusions or the individual atoms have migrated up the temperature gradient. Mechanisms for the movement of the alkaline earth oxide phase in either direction have not been proposed.

The metallic inclusions containing the noble-metal fission products and some of the molybdenum have been observed only in the columnar-grain region or as large agglomerates in the central void (Fig. 12.4). The latter form suggests migration of the smaller inclusions radially inward. Lambert et al.<sup>15</sup> believe that this process is enhanced by stress on the fuel due to constraint by the cladding. Whatever the cause of the migration, the large size of the ingots in the central void implies that a significant portion of the noble-metal fission products and molybdenum can be removed from the fuel matrix by migration of metallic inclusions.

Neither the alkali metal oxide phase nor the metallic inclusions have been observed in the cool regions of the fuel (i.e., the equiaxed-grain and as-fabricated zones). Most probably the fission products remain trapped in the oxide lattice in atomic form because their solid-state diffusion coefficients are too small to permit coalescence into precipitates of observable size.

Because of its buffering action on the fuel oxygen potential (Sec. 12.4), migration of molybdenum has received the greatest experimental attention of all wandering fission products.<sup>20</sup> Figure 12.12 shows electron microprobe profiles of molybdenum in an irradiated oxide fuel element.<sup>18</sup> The high spatial resolution of the microprobe permitted in situ analysis of the metallic inclusions and the fuel matrix separately. Through the columnar-grain region, the molybdenum concentration in the fuel matrix decreases by about 50% and the concentration in the metallic inclusions increases by approximately the same percentage. The 8 to 12% molybdenum concentration in the inclusions is well below the concentration expected from the relative fission yields of this element and the noble-metal group (Table 12.1). The concentration of molybdenum in the fuel matrix increases by an order of magnitude from the outer edge of the columnar-grain region to the fuel surface. The data in Fig. 12.12 can be interpreted in several ways:

1. The high matrix concentration at the fuel surface is due to migration of molybdenum down the temperature gradient followed by trapping of this element in the surface layers in the form of an immobile compound, i.e., as cesium molybdate according to Eq. 12.33. This argument assumes that  $\text{MoO}_2$  is sufficiently volatile at temperatures below  $\sim 1900^\circ\text{K}$  (the temperature of the outer edge of the columnar grains) to diffuse at an appreciable rate through

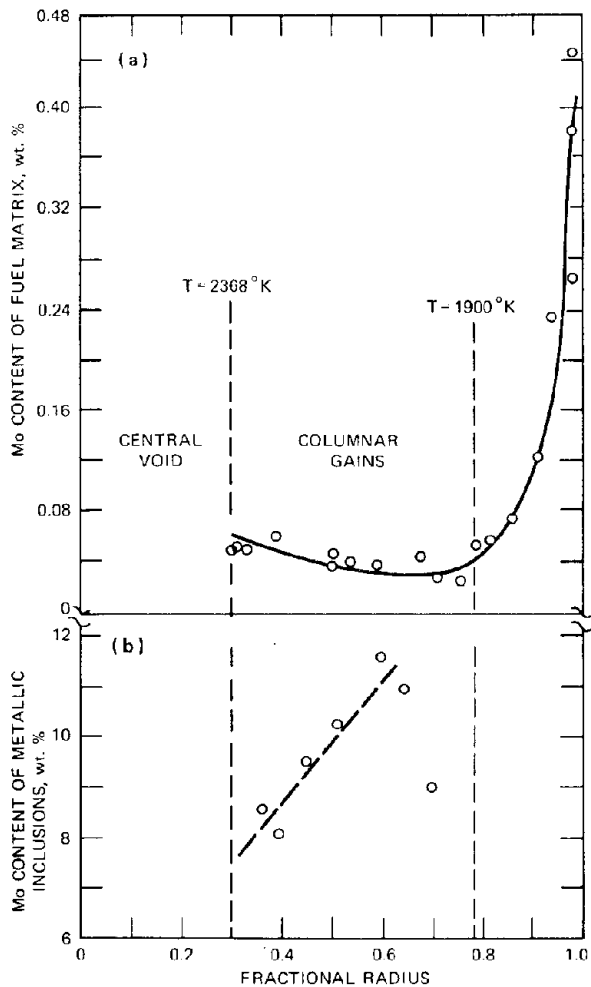


Fig. 12.12 Concentrations of molybdenum in the fuel matrix (a) and in the metallic inclusions (b) of an irradiated mixed-oxide fuel pin. Initial fuel density, 85% of theoretical density; initial oxygen-to-metal ratio, 1.998; burnup, 9.4%; linear power, 425 W/cm. [From I. Johnson et al., *J. Nucl. Mater.*, 48: 21 (1973).]

the gas in cracks or interconnected porosity. However, the partial pressure of  $\text{MoO}_2$  above an oxide containing the concentration of molybdenum shown in Fig. 12.12 is only  $\sim 7 \times 10^{-9}$  atm at  $1900^\circ\text{K}$ . Experience with oxygen and actinide redistribution suggests that a component with such a low partial pressure cannot migrate via the gas phase at a significant rate.

2. Part of the large molybdenum concentration in the equiaxed and as-fabricated regions of the fuel is due to elemental molybdenum that has remained in the matrix as atoms or precipitates too small to be distinguished as metallic inclusions. Note the absence of data on the inclusions for fractional radii greater than 0.7.

3. The molybdenum concentration of the columnar-grain region is low because the inclusions have migrated to the central void carrying molybdenum with them. The high percentage of molybdenum in the fuel matrix near the surface represents the concentrations that would be ex-

pected if no loss of molybdenum from this region had occurred.

## 12.6 FUEL-CLADDING INTERACTION

Corrosive attack of stainless-steel cladding by irradiated fuel may be one of the major performance-limiting phenomena of an LMFBR. Such interaction weakens a portion of the inner wall of the cladding, which is then less able to withstand the internal mechanical stresses from the fuel or from fission gas pressure. Figure 12.13 shows a section of the fuel-cladding interface and the type of thinning attack that occurs during irradiation.

### 12.6.1 Thermodynamics of Stainless-Steel Oxidation

Whether or not chemical reaction between components of irradiated fuel and constituents of the cladding can occur at all is determined by the thermodynamics of the reactions involved. Thermodynamic prediction of fuel-cladding compatibility requires first that the specific chemical reactions responsible for the interaction be identified and second that the thermodynamic properties of the pertinent reactions be known. Table 12.4 lists the oxygen potentials of mixed-oxide fuels of compositions near exact stoichiometry and the free energies of formation of the major alloy components of stainless steel. The values are shown for  $1000^\circ\text{K}$ , which is close to the maximum cladding temperature in an LMFBR (see Table 10.2).

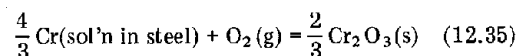
Table 12.4 Thermochemical Properties of Fuel and Cladding at  $1000^\circ\text{K}$

Mixed-oxide fuel*		Stainless-steel components†	
Heavy-metal valence	$\Delta G_{\text{O}_2}$ , kJ/mole	Reaction	$\Delta G^\circ$ , kJ/mole
4.002	-284	$\frac{2}{3}\text{Cr} + \text{O}_2 = \frac{2}{3}\text{Cr}_2\text{O}_3$	-573
4.000	-418		
3.98	-561	$2\text{Fe} + \text{O}_2 = 2\text{FeO}$	-393
3.96	-615	$2\text{Ni} + \text{O}_2 = 2\text{NiO}$	-293

\*Oxygen potentials taken from Fig. 12.6.

†A typical stainless steel used in fast reactor fuel-element cladding contains 74 wt. % Fe, 18 wt. % Cr, and 8 wt. % Ni. Carbon and boron are minor components.

Table 12.4 shows that, of the three constituents of steel, chromium has the greatest affinity for oxygen (i.e., this element forms the most stable oxide). Pure chromium begins to oxidize at  $1000^\circ\text{K}$  when the oxygen pressure reaches a value of  $\exp(-573/\text{RT})$ . However, the chromium is present in steel at a concentration of  $\sim 18$  wt. %, and oxidation is possible when the oxygen partial pressure satisfies the equilibrium of the reaction



When the law of mass action is applied to this reaction, the equilibrium oxygen pressure over stainless steel that contains some chromic oxide is given by

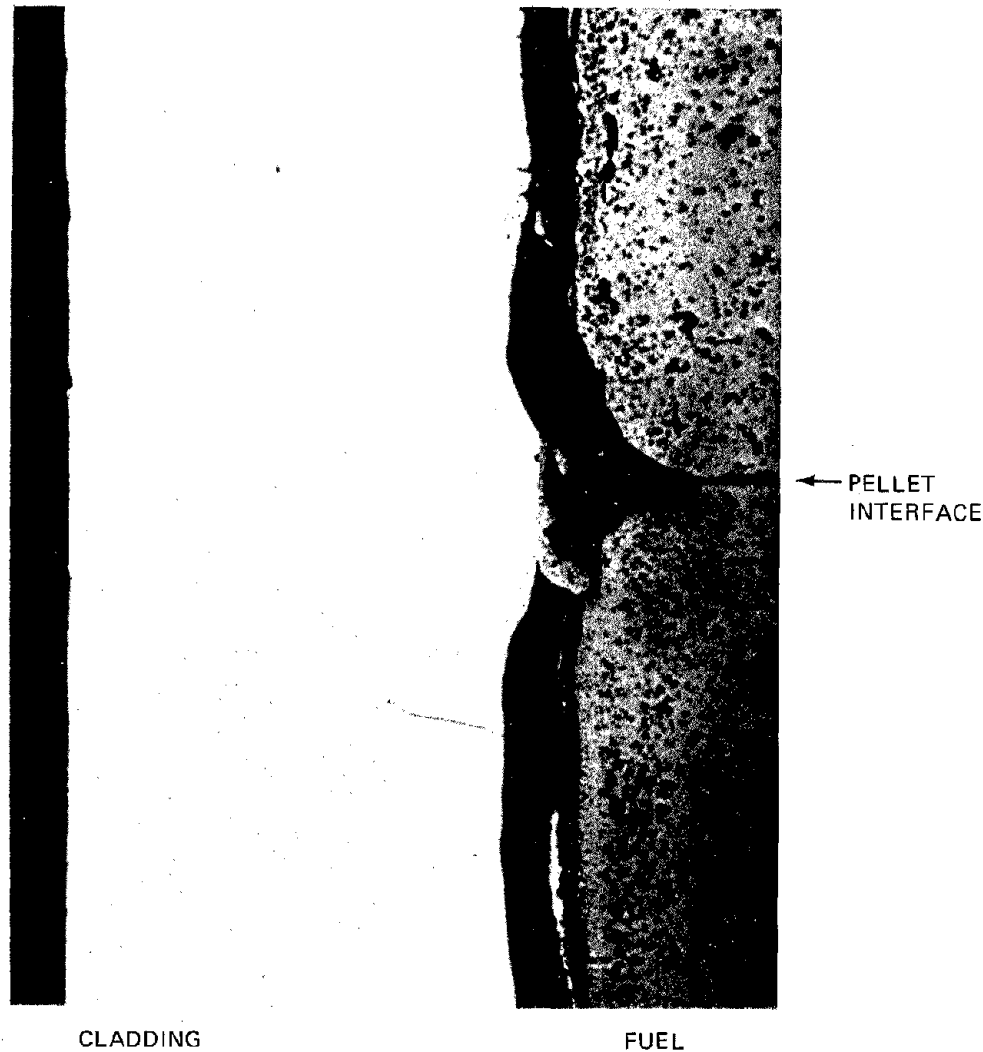


Fig. 12.13 Thinning of the cladding due to attack by irradiated mixed-oxide fuel. Attack directly opposite the pellet interface is less than elsewhere. (From K. J. Perry et al., in *Proceedings of the Conference on Fast Reactor Fuel Element Technology*, New Orleans, p. 411, American Nuclear Society, Hinsdale, Ill., 1971.)

$$RT \ln p_{O_2} = \Delta G_{Cr}^\circ - \frac{4RT}{3} \ln a_{Cr} \quad (12.36)$$

where  $a_{Cr}$  is the activity of chromium in the stainless steel. For equilibrium between the fuel and the cladding, the oxygen pressure in Eq. 12.36 must also be in equilibrium with the fuel; so the left-hand side of the equation can be equated to the oxygen potential of the fuel,  $\Delta \overline{G}_{O_2}$ . For the present purpose we assume that the activity of chromium in the stainless steel is equal to its atom fraction, or  $a_{Cr} \approx 0.18$ . With the free energy of formation listed in Table 12.4 for  $Cr_2O_3$ , Eq. 12.36 becomes

$$\Delta \overline{G}_{O_2} = -573 - \frac{4R}{3} \ln (0.18) = -554 \text{ kJ/mole at } 1000^\circ \text{K}$$

When the oxygen potential of the fuel surface reaches  $-554$  kJ/mole, oxidation of the cladding becomes thermodynamically possible. Table 12.4 shows that this oxygen

potential corresponds to a fuel in which the plutonium valence is 3.98 or, by Eq. 11.15, when the O/M of a fuel containing 20% plutonium is 1.998. If the fuel-surface O/M could be maintained just below exact stoichiometry, oxidation of the cladding could not take place. The fresh fuel for fast reactors is purposely fabricated with an O/M of  $\sim 1.96$  for just this reason. However, even though the as-fabricated fuel is substantially hypostoichiometric, the temperature gradient and irradiation both act to drive the O/M (and hence the oxygen potential) at the fuel surface upward. The discussion in Sec. 11.6 showed that, as a result of oxygen redistribution, the fuel surface approaches exact stoichiometry even though the average fuel O/M is considerably less than 2.00. In addition, the effect of irradiation (Sec. 12.4) is to increase the oxygen potential at all radial positions in the fuel pin. It appears unlikely that the oxygen potential at the fuel-cladding interface can be kept low enough to prevent cladding oxidation throughout the

entire lifetime of the fuel element. Thus, the integrity of the cladding must rely on the kinetics of the chemical attack in an environment where oxidation is thermodynamically possible.

The very name stainless steel implies that this type of alloy is resistant to oxidation. Even though the thermodynamics are unfavorable, metals such as zirconium and alloys such as stainless steel resist oxidation because a protective oxide coating is formed in the initial stage of reaction. In stainless steel, for example, a layer of  $\text{Cr}_2\text{O}_3$  forms on the surface, thereby physically separating the substrate metal from the oxidizing medium. Further growth of this layer requires that chromium ions diffuse from the metal to the outer surface of the coating or that oxygen ions migrate in the opposite direction. The rates of both these processes are very slow at  $1000^\circ\text{K}$  because of the low values of the diffusion coefficients of the ions in the oxide layer. However, if the coating is breached by mechanical forces or is dissolved by a component of the oxidizing environment, the base metal is exposed to rapid attack.

### 12.6.2 Observations of Cladding Corrosion by Irradiated Mixed-Oxide Fuels

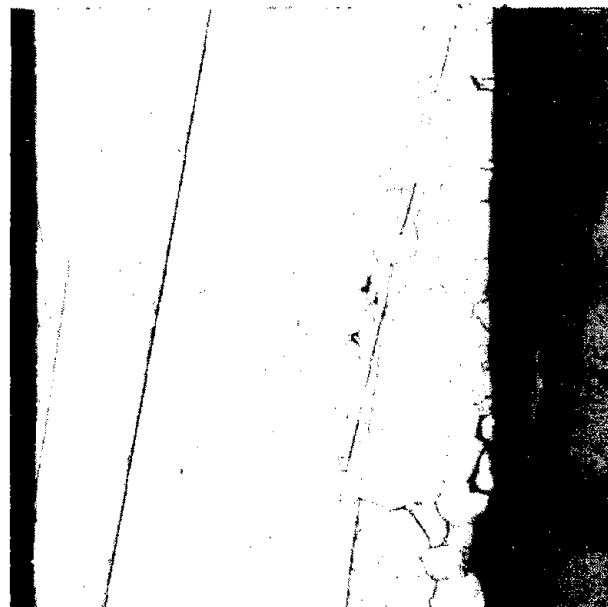
Two types of cladding attack of stainless steel by irradiated fuel have been observed. The first is corrosion of the cladding inner wall and the second is transport of cladding constituents into the fuel.

Figure 12.14 shows that there are two modes of corrosive attack. Figure 12.14(a) depicts the form of corrosion known as matrix attack, in which the entire body of the inner wall of the cladding is converted to a reaction zone containing the oxides of iron, chromium, and nickel. Figure 12.14(b) is an example of intergranular attack. Here, corrosion is restricted to the grain boundaries of the metal; the grains of the alloy are not affected. Figure 12.15 shows an electron microprobe profile of various elements through a fuel-cladding interface in which matrix attack [Fig. 12.14(a)] has occurred. It is interesting to note that the constituents of the cladding are not uniformly distributed in the reaction zone. Instead, the concentrations of iron, nickel, and chromium peak at different positions. The reaction zone appears to act as a chromatographic column that separates the three elements into distinct bands. Similar profiles have been observed by other investigators<sup>2,1</sup> but not necessarily with the iron, chromium, and nickel peaks in the same relative positions as those shown in Fig. 12.15. In addition to the three major components of the cladding, the reaction zone contains the fission products cesium and molybdenum and lesser amounts of iodine, tellurium, and palladium. The reaction zone does not appear to contain the heavy metals uranium and plutonium, and neither does the cladding (the plutonium trace in Fig. 12.15 is essentially the background level of this element in the microprobe).

The depth of the matrix attack depends on temperature and oxygen potential (i.e., fuel stoichiometry). Observable penetration of the cladding begins between  $500^\circ\text{C}$  and  $600^\circ\text{C}$ . Typical depths of attack are 0.05 to 0.1 mm, or 20 to 40% of the cladding thickness (Table 10.2). Figure 12.16 shows that fuel-cladding reaction is enhanced by high temperature and O/M ratios near 2.00. A threshold temper-



(a) MATRIX



(b) INTERGRANULAR

Fig. 12.14 Two types of corrosive attack of type 316 stainless-steel cladding by mixed-oxide fuel irradiated to a burnup of 5%. (From K. J. Perry et al., in *Proceedings of the Conference of Fast Reactor Fuel Element Technology*, New Orleans, p. 411, American Nuclear Society, Hinsdale, Ill., 1971.)

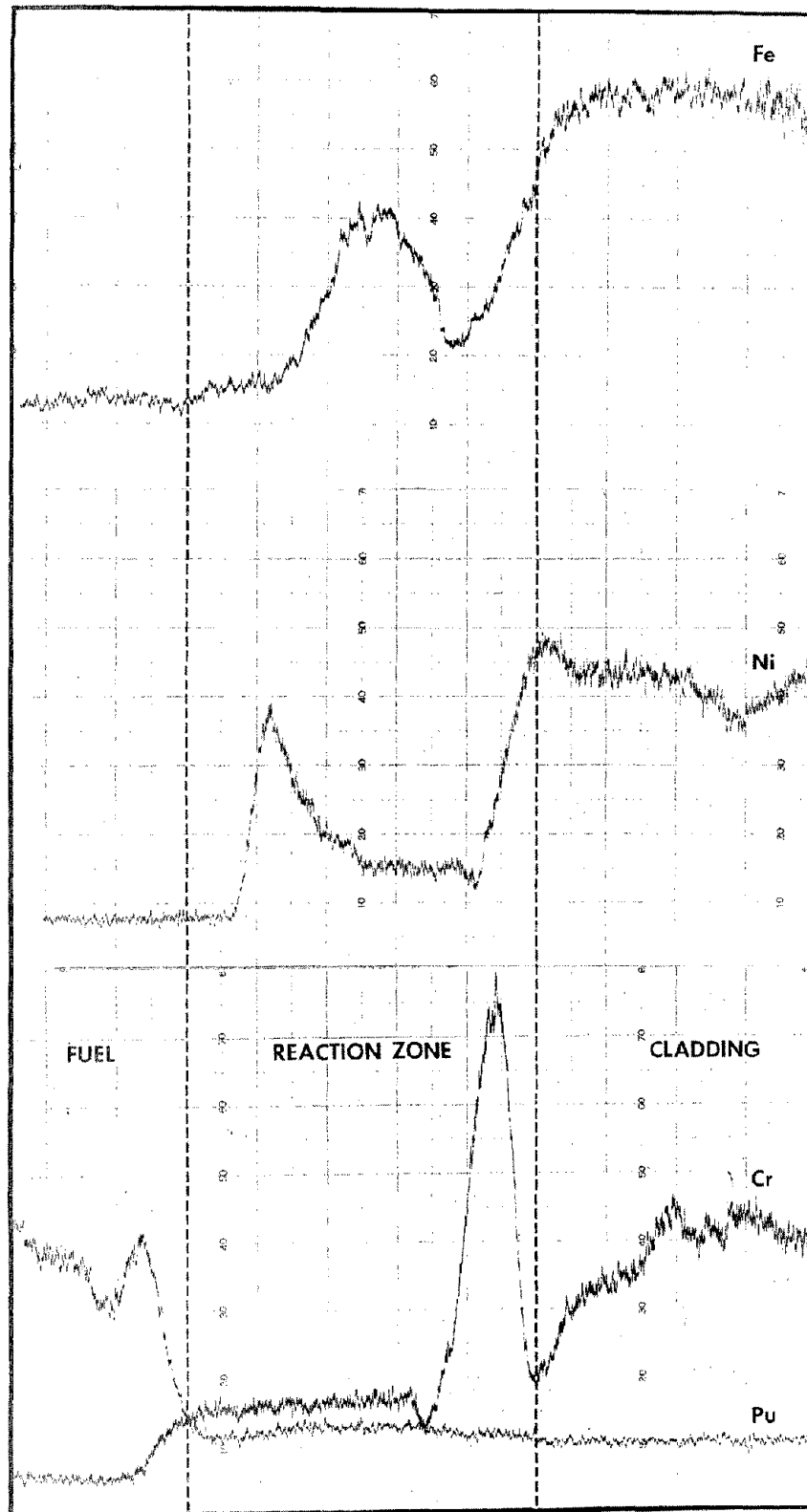


Fig. 12.15 Electron microprobe scans across the fuel-cladding interface. (From R. B. Fitts, E. Long, and J. M. Leitnaker, in *Proceedings of the Conference on Fast Reactor Fuel Element Technology*, New Orleans, p. 431, American Nuclear Society, Hinsdale, Ill., 1971.)

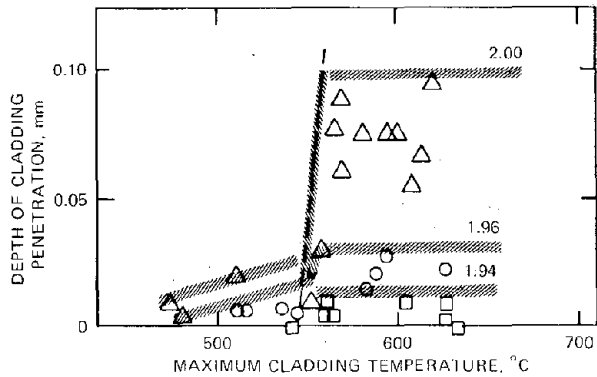


Fig. 12.16 Maximum depth of cladding attack of type 304 stainless-steel cladding by mixed-oxide fuel. The data represent burnups ranging from 7 to 13%. O/M ratios:  $\square$ , 1.94;  $\circ$ , 1.96; and  $\triangle$ , 2.00. [After J. W. Weber and E. D. Jensen, *Trans. Amer. Nucl. Soc.*, 14: 175 (1971).]

ature below which little cladding attack occurs was found to be  $\sim 540^\circ\text{C}$ . This threshold temperature appears to be due to kinetic rather than thermodynamic restrictions. Below this temperature, cladding oxidation is too slow to be observed in typical fuel-element lifetimes, even though corrosion may be thermodynamically possible.

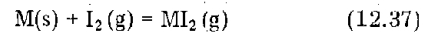
Out-of-pile oxidation tests on stainless steels in which the oxygen potential is established by conventional means (i.e., oxygen gas or water vapor) do not show attack as extensive as that which occurs when the cladding is in contact with irradiated fuel at the same temperature. Neither does unirradiated fuel corrode stainless-steel fuel as much as does irradiated fuel. Such evidence suggests that one or more of the fission products are responsible for accelerated oxidation of stainless-steel cladding in irradiated fuel elements. A search for fission products in the irradiated cladding has revealed that cesium and molybdenum penetrate deep into the cladding along grain boundaries. Figure 12.17 shows electron microprobe images of the fission products in the cladding of an irradiated fuel pin. Molybdenum and cesium are found in the grain boundaries where intergranular attack has occurred. Out-of-pile tests in which a variety of fission-product elements and their compounds were added to simulated fuel pins that were held at temperature for times typical of reactor operation have shown that only  $\text{Cs}_2\text{O}$  accelerates cladding corrosion.<sup>22</sup> It is believed that cesium oxide dissolves the protective oxide coating on the inner wall of the cladding, perhaps by direct reaction between  $\text{Cs}_2\text{O}$  and  $\text{Cr}_2\text{O}_3$  to form cesium chromate.<sup>23</sup> It is possible that molybdenum is necessary to form a low melting liquid electrolyte consisting of  $\text{Cs}_2\text{MoO}_4$  and  $\text{MoO}_3$  which provides a medium for destroying the protective oxide film from the metal and for accelerating oxidation by stabilizing cesium as  $\text{Cs}_2\text{O}$  in oxygen potentials where this compound would thermodynamically tend to dissociate into elemental cesium (which is noncorrosive) and gaseous oxygen.<sup>10</sup>

An important consequence of the oxidation of the cladding (aside from the fact that it adversely affects the structural properties of this member) is that the process is self-regulating. If the stainless steel acts as a sink for

oxygen, the amount available to the fuel and hence the oxygen potential of the latter are reduced. The corrosion process tends to restore thermodynamic equilibrium at the fuel-cladding interface. However, the continual production of excess oxygen by fission and its transport from the hot interior of the fuel pin to the surface by migration of volatile fission-product oxides (particularly  $\text{Cs}_2\text{O}$ ) and perhaps  $\text{CO}_2$  and  $\text{CO}$  means that cladding corrosion probably does not stabilize at large burnups.

### 12.6.3 Transport of Cladding Components to the Fuel

In addition to intergranular and matrix attack of the cladding by the irradiated fuel, migration of the constituents of the cladding into the fuel has been observed.<sup>14,24</sup> Figure 12.18 shows rivers of pure iron filling cracks in the fuel adjacent to the fuel-cladding interface. Johnson and Crouthamel<sup>24</sup> report that metallic inclusions of pure iron have been found as far within the fuel as the boundary between the equiaxed- and columnar-grain regions. Migration of iron over such appreciable distances implies that a form of this species more mobile than the element or the oxide is present in the fuel element. Johnson and Crouthamel<sup>24</sup> have suggested that the transport mechanism is similar to the van Arkel-de Boer process which is commercially used to purify metals such as zirconium and hafnium. According to this mechanism, fission-product iodine provides the means of volatilizing the cladding components according to the reversible reaction



where  $\text{M} = \text{Fe, Cr, or Ni}$  and  $\text{MI}_2$  is the gaseous metal iodide of  $\text{M}$ . Table 12.5 shows the stability and volatility of these compounds at  $1000^\circ\text{K}$ . The equilibrium of Eq. 12.37 is driven to the right at low temperature because the heat of formation of  $\text{MI}_2$  is negative; thus formation of the diiodide is favored at the cooler cladding surface rather than in the hotter regions of the fuel. The temperature drop across the narrow fuel-cladding gap may be large (Table 10.5). Iodine reacts with the cladding to form the metal diiodides, which then diffuse through the gas in the gap to the fuel. Here reaction 12.37 is reversed, and the iodide decomposes to release the metal. The liberated  $\text{I}_2$  then diffuses back to the cladding to pick up more metal. By means of this cyclical process, small quantities of iodine can continually transport cladding material across the fuel-cladding gap. That only iron is found in the fuel is understandable from the information in Table 12.5. The free energy of formation of  $\text{NiI}_2$  is too high (i.e., this compound is not sufficiently stable) to be formed in large enough partial pressures at the prevailing iodine partial pressure to transport the metal in significant quantities. Although quite stable,  $\text{CrI}_2$  is nearly three orders of magnitude less volatile than the other diiodides; thus, the transport of this component would also be limited by low gas-phase partial pressure. The stability and volatility of  $\text{FeI}_2$ , however, appear to be adequate for vapor transport by the proposed mechanism. These arguments are consistent with the observation of only iron in the fuel.

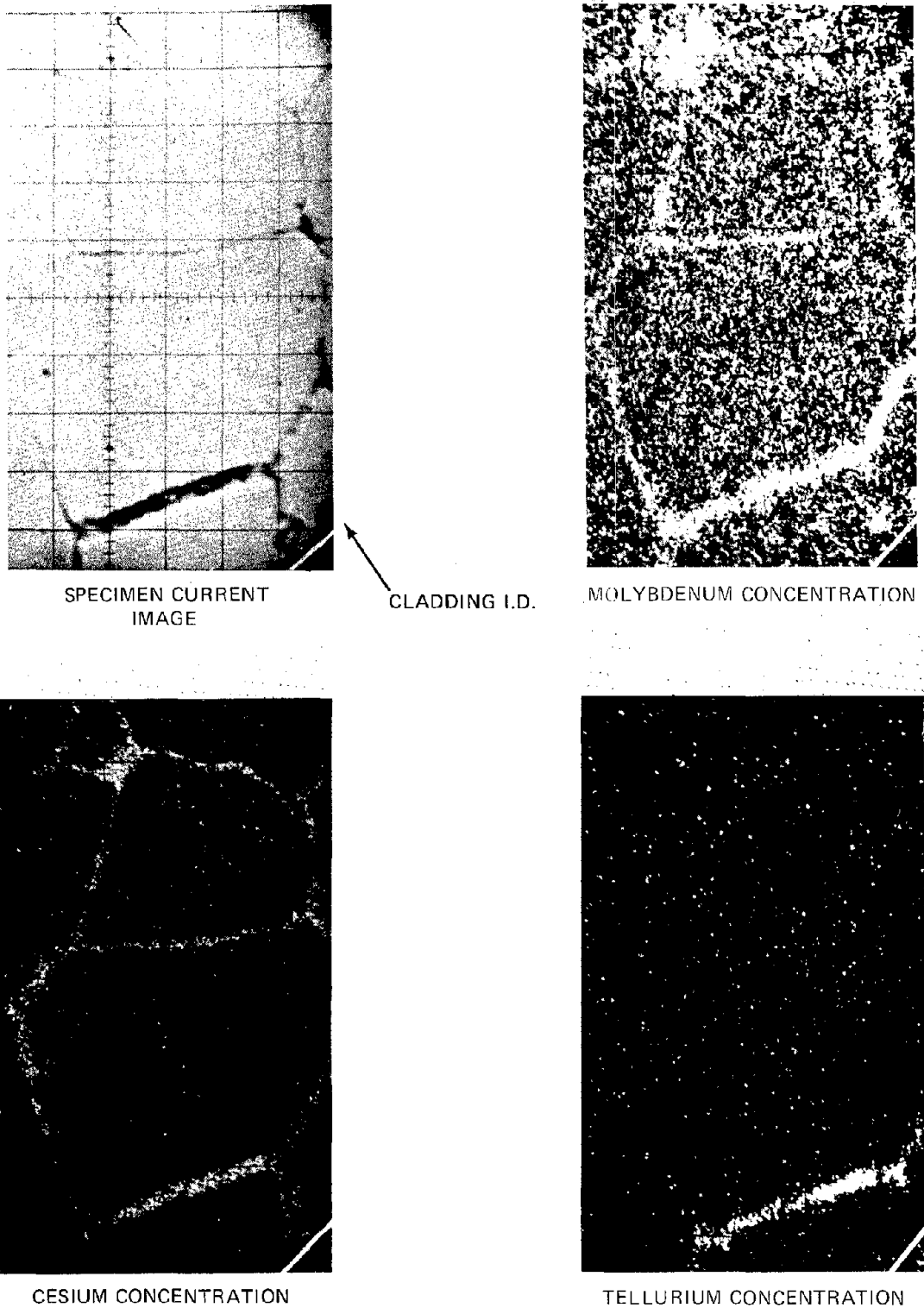


Fig. 12.17 Concentration of fission products between grains in regions of cladding subject to intergranular attack by irradiated fuel. (From K. J. Perry et al., in *Proceedings of the Conference on Fast Reactor Fuel Element Technology*, New Orleans, p. 411, American Nuclear Society, Hinsdale, Ill., 1971.)

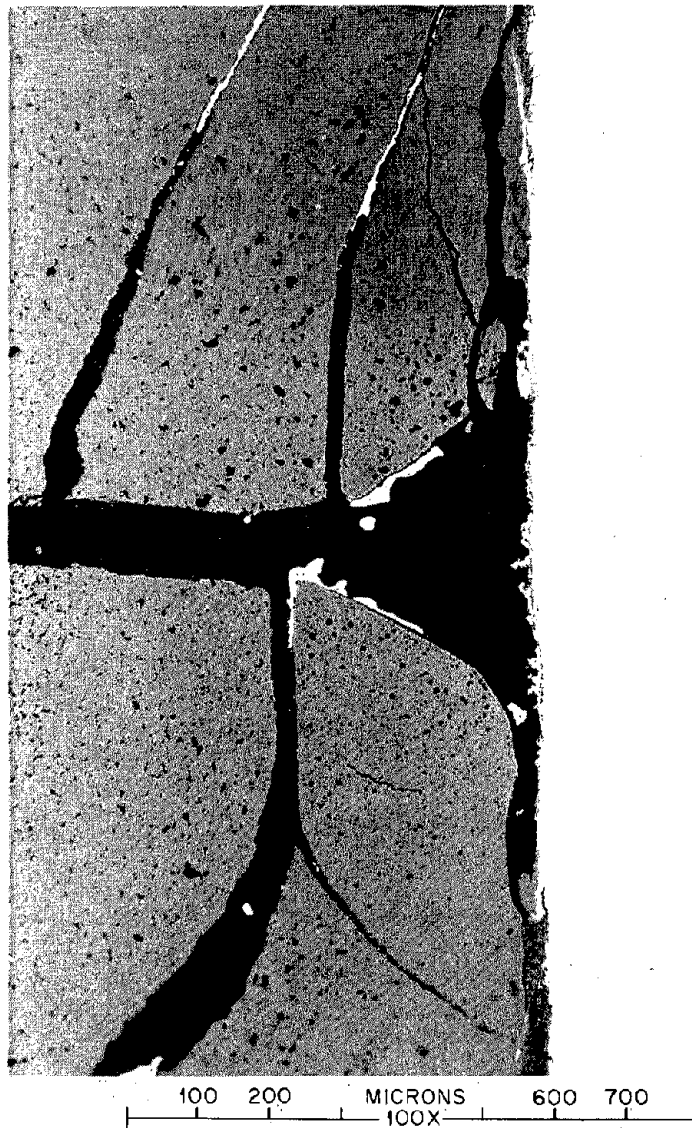


Fig. 12.18 Rivers of pure iron in the fuel adjacent to the fuel-cladding interface. (From R. B. Fitts, E. L. Long, and J. M. Leitnaker, in *Proceedings of the Conference on Fast Reactor Fuel Element Technology*, New Orleans, p. 431, American Nuclear Society, Hinsdale, Ill., 1971.)

The major objection to the iodine transport mechanism is that there may not be enough iodine available to produce the quantities of  $\text{FeI}_2$  necessary to transport iron in amounts comparable to those contained in the rivers<sup>14,21</sup> in Fig. 12.18. Essentially all molecular iodine should be consumed by cesium according to Eq. 12.34, and thus none would be available to volatilize the iron in the cladding. It is possible, however, that  $\text{CsI}$  might not be stable in the high radiation field in which the fuel elements operate; thus its radiation decomposition would release iodine for participation in the iron transport process.<sup>2,4</sup> However, the same arguments could be applied equally well to the radiation stability of  $\text{FeI}_2$ . For iodine to be thermodynamically freed, some other reaction must remove cesium from the gas phase in the fuel-cladding interface. It is possible that

reactions 12.32 and 12.33 form sufficiently stable cesium-metal-oxygen compounds to decompose  $\text{CsI}$  and release free iodine. The experimental work of Keroulas et al.<sup>2,5</sup> supports the hypothesis of iron transport by the iodide process.

Fitts, Long, and Leitnaker<sup>14</sup> have suggested an alternative cyclical process in which cesium ferrate is formed by the reaction



and dissolves in a liquid phase that is presumed to fill the fuel-cladding gap (the presence of such a liquid phase was discussed previously in connection with accelerated oxidation of the cladding). The  $\text{CsFeO}_2$  decomposes at the fuel

Table 12.5 Stability and Volatility of the Diiodides of the Transition Metals at 1000°K

Diiodide	Free energy of formation, kJ/mole	Vapor pressure, atm
CrI <sub>2</sub>	-109	$2.4 \times 10^{-4}$
FeI <sub>2</sub>	-67	$9.1 \times 10^{-2}$
NiI <sub>2</sub>	-8	( $\sim 9 \times 10^{-2}$ )

side of the interface, and the Cs<sub>2</sub>O returns through the liquid to the cladding, where it picks up more iron oxide and completes the cycle. This mechanism has the disadvantage of requiring an additional process to explain why metallic iron is found as deep in the fuel as the observations have shown.

## 12.7 FUEL SWELLING DUE TO SOLID FISSION PRODUCTS

Accurate estimation of the dimensional changes of ceramic fuels during irradiation is of the utmost importance in predicting the mechanical performance of fast reactor fuel elements. Fuel swelling due to replacement of heavy-metal atoms by fission-product atoms is commonly considered as the sum of a contribution due to fission gases and another arising from all other fission products. The former is treated separately because the inert gases xenon and krypton coalesce into bubbles within the fuel, whereas most of the remaining fission products are solids.\* Fission-gas swelling is considered in the next chapter. In this section Anselin's<sup>26</sup> calculation of solid-fission-product swelling is summarized.

Swelling is defined as the fractional increase in the volume of the solid with respect to the initial volume of the as-fabricated fuel, or by

$$\left(\frac{\Delta V}{V}\right)_{\text{solid fp}} = \frac{V - V^{\circ}}{V^{\circ}} \quad (12.39)$$

where  $V^{\circ}$  is the volume of a region of fresh fuel and  $V$  is the volume of this same region after burnup,  $\beta$ . The initial volume  $V^{\circ}$  is that shown in Fig. 12.9. The final volume  $V$  includes all the solid phases shown in Fig. 12.9, namely, the oxide matrix, which contains soluble fission products, the metallic inclusions, and the alkaline earth oxide phase. The gas phase containing the volatile fission products (xenon, krypton, and any other fission products that can be in gaseous form under the irradiation conditions) is not considered to contribute to solid swelling. Since the system is assumed closed to solid fission products and fuel, none of these species is permitted to move into or out of the region during irradiation.

\*At very low temperatures (<1000°C) the fission gases may not be sufficiently mobile in the fuel to permit coalescence into bubbles, in which case the swelling due to these species is treated in the same manner as is that due to the other fission products.

The physicochemical parameter that characterizes solid swelling is the volume associated with each atom of fission products in their expected states in the irradiated fuel. This volume includes the oxygen atoms associated with the fission products (if any) and is referred to as the *partial volume* of the fission product:

$$v_i = \text{partial volume of species } i = \frac{\text{volume}}{\text{atom of } i} \quad (12.40)$$

With reference to Fig. 12.9, we can write

$$V^{\circ} = v_U N_U^{\circ} + v_{P_U} N_{P_U}^{\circ} \approx v_U (N_U^{\circ} + N_{P_U}^{\circ}) \quad (12.41)$$

where  $v_U$  and  $v_{P_U}$  are the volume per molecule of UO<sub>2</sub> and PuO<sub>2</sub>, respectively. Because of the similarity of these two actinide oxides,  $v_{P_U}$  has been assumed equal to  $v_U$ . Note that the partial volume of the heavy metal includes the oxygen normally associated with each atom in the oxide form.

The final volume of the solid phases in Fig. 12.9 is

$$V = v_U (N_U + N_{P_U}) + \sum_{\text{solid fp}} v_i N_i \quad (12.42)$$

If Eqs. 12.13, 12.14, and 12.16 are substituted into Eqs. 12.41, 12.42, and 12.39, the swelling is found to be

$$\left(\frac{\Delta V}{V}\right)_{\text{solid fp}} = \left(\sum_{\text{solid fp}} Y_i \frac{v_i}{v_U} - 1\right) \beta \quad (12.43)$$

The elemental yields  $Y_i$  are those listed in Table 12.1. There remains only to estimate the partial volumes of each solid species in the irradiated fuel.

### 12.7.1 Fuel

The partial volume of uranium (or plutonium) in the fuel can be obtained from the properties of the perfect crystalline form of UO<sub>2</sub> shown in Fig. 3.12. The actinide oxides crystallize in the fluorite structure, which contains four molecules of UO<sub>2</sub> or PuO<sub>2</sub> in the unit cell. The room-temperature lattice constant of uranium dioxide is 5.470 Å; thus, the partial volume of the heavy metals is

$$\begin{aligned} v_U &= \frac{(5.470 \times 10^{-8})^3}{4} \\ &= 40.93 \times 10^{-24} \text{ cm}^3/\text{molecule of UO}_2 \end{aligned}$$

### 12.7.2 Soluble Fission Products

The fission products that form solid solutions with the heavy-metal oxides include yttrium, the rare earths, the portion of the zirconium not contained in the alkaline earth oxide phase as zirconates, niobium, and the fraction of the molybdenum present as oxide. The last three are tetravalent ions that form oxides of the general formula MO<sub>2</sub>, which has the same fluorite structure as the actinide oxides. Although the stable crystallographic form of yttrium and the rare earths in their pure state is the sesquioxide M<sub>2</sub>O<sub>3</sub>, they assume the fluorite structure of the host lattice when dissolved in UO<sub>2</sub>. Figure 12.8 shows that the difference in

cation charge is compensated for by oxidation of the uranium ions or by formation of anion vacancies. In either case the rare-earth (and yttrium) oxides can be represented by the general formula  $REO_2$  when dissolved in  $UO_2$ . Crystallographic studies of the urania-rare-earth oxide binary systems have shown that the fluorite lattice constants of the solution can be either larger or smaller than that of pure  $UO_2$ , depending on the size of the solute cation. Lanthanum is the largest of the rare-earth cations (in terms of its ionic radius or the lattice parameter of the pure sesquioxide phase), and addition of lanthana to urania increases the fluorite lattice constant. At the other extreme, introduction of the smaller yttrium ion into  $UO_2$  reduces the lattice parameter without changing the fluorite structure.

During irradiation the cations of zirconium, niobium, molybdenum, the eight rare earths, and yttrium are produced in the  $UO_2$  lattice in quantities proportional to their elemental yields. Anselin<sup>26</sup> has shown that the particular combination of ionic radii and fission yields of all the soluble fission products results in cancellation of the different size effects. That is, the lattice constant of  $UO_2$  is essentially unchanged as a result of irradiation. This theoretical conclusion is supported by measurements of the lattice constant of  $UO_2$  as a function of irradiation, which show decreases of less than 0.01 Å up to burnups<sup>27</sup> of 15%. Therefore, the partial volume of the soluble fission products is approximately equal to that of pure  $UO_2$ , or

$$v_{\text{soluble fp}} = 40.93 \times 10^{-24} \text{ cm}^3/\text{molecule} \\ \text{of soluble fission-product oxide}$$

### 12.7.3 Metallic Inclusions (Including Molybdenum)

Because of the similar chemical properties of the five major components of the metallic inclusions, they can be assumed to mix in an ideal fashion.\* That is, the volume of the mixture is equal to the sum of the volumes of the pure phases contained in the alloy. The partial volume of the metallic inclusions is given by

$$v_{\text{metallic inclusions}} = \sum_{\substack{i = \text{Mo, Ru} \\ \text{Te, Rh, Pd}}} y_i^m v_i^o \quad (12.44)$$

where  $y_i^m$  is the atom fraction of component  $i$  in the alloy and  $v_i^o$  is the atomic volume of pure metallic species  $i$ . The former is proportional to the elemental fission yield of the metal, and the latter can be obtained from crystallographic data or from the density of single crystals of the pure metals. The atomic volumes of the five constituents of the metallic inclusions (at room temperature) vary from  $15.59 \times 10^{-24} \text{ cm}^3/\text{atom}$  for molybdenum to  $13.57 \times 10^{-24} \text{ cm}^3/\text{atom}$  for palladium. The average atomic volume computed by Eq. 12.44 is not very sensitive to the

\*Although the alloy may be considered ideal from the point of view of volume change upon mixing, it is not ideal in the behavior of other properties (e.g., partial pressures of the components in equilibrium with the alloy do not follow Raoult's law).

elemental yields of the five elements, which differ for uranium and plutonium fission. For uranium fission the partial volume of the inclusions is

$$v_{\text{metallic inclusions}} = 14.73 \times 10^{-24} \text{ cm}^3/\text{atom}$$

### 12.7.4 Alkaline Earth Oxide Inclusions

The alkaline earth oxide phase consists of the zirconates of barium and strontium. The volumes per molecule of  $BaZrO_3$  and  $SrZrO_3$  have been established from crystallographic data as  $72.8 \times 10^{-24} \text{ cm}^3$  and  $69.0 \times 10^{-24} \text{ cm}^3$ , respectively. For a mixture of the two in proportion to their yields from uranium fission, the partial volume is

$$v_{\text{alkaline earth oxide}} = 71.2 \times 10^{-24} \text{ cm}^3/\text{molecule of zirconate oxide}$$

### 12.7.5 Other Fission Products

The remaining fission-product groups in Table 12.1 include the alkali metals cesium and rubidium, the elements iodine and tellurium, and the remaining fission products that were not included in the table because of their low yields. Anselin<sup>26</sup> assumes that all these species are present as ionic solids in the irradiated fuel. Cesium and rubidium is assumed to be a singly charged cation that combines with oxygen or with the anions  $I^-$  and  $Te^{2-}$ , forming  $CsI$  and  $Cs_2Te$  until all iodine and tellurium is consumed and then combining as  $Cs_2O$ . The volumes of these compounds (at room temperature) were calculated from the Pauling ionic radii of the constituent atoms, which yielded a partial volume of

$$v_{\text{other fp}} = 31.1 \times 10^{-24} \text{ cm}^3/\text{fission-product atom}$$

For the purpose of our computation, this figure has been applied to the remaining low-yield fission products not included in Table 12.1. This group includes germanium, arsenic, selenium, bromine, silver, cadmium, indium, tin, and antimony.

### 12.7.6 Swelling

The swelling due to solid fission products can be calculated by using the partial volumes estimated in Eq. 12.43. The results are shown in Table 12.6 for uranium fission, but Anselin<sup>26</sup> has shown that the swelling is essentially the same for mixed uranium-plutonium oxides. The first column in Table 12.6 lists the fission products in groups of the same physical state (i.e., with the same partial volume), the second column gives the elemental yields, and the third column gives the ratio of the partial volume of the group to that of pure  $UO_2$ . Solid-fission-product swelling in oxide fuels is found to be 0.32% per atom percent burnup. This figure, however, is subject to large uncertainties for the following reasons:

1. It is based on the assumption that each region of the fuel acts as a closed system for all fission products (except xenon and krypton) and the heavy metals. The complications introduced by fission-product migration (Sec. 12.5) are not considered. The general tendency for the hotter regions of the fuel to lose fission products by a variety of

mechanisms means that the solid swelling calculated in Table 12.6 is an overestimate near the fuel center. Conversely, swelling in the zone near the fuel surface where some of the volatile fission products condense is underestimated.

2. The assignment of the physical and chemical states of some of the fission products is subject to considerable uncertainty. For example, in Table 12.6 all the molybdenum was assumed to exist as metal, where it contributes a partial volume approximately one-third that of  $\text{UO}_2$ . Had all this element been present in the fuel as soluble  $\text{MoO}_2$ , its partial volume would have been equal to that of  $\text{UO}_2$ . Transfer of molybdenum from the metallic inclusions to the fuel matrix adds  $0.240 \times (1.00 - 0.36) = 0.15$  to the solid swelling, which would then be 0.47% per atom percent burnup instead of 0.32%. Since the analysis of Sec. 12.4 showed that molybdenum transfers from metal to oxide as irradiation proceeds, the solid-fission-product swelling should also increase with irradiation.

Table 12.6 Swelling Due to Solid Fission Products in Pure Uranium Dioxide Fuel\*

Fission-product group	$Y_i^\dagger$	$v_i/v_U$	$Y_i v_i/v_U$
Nb + soluble Zr $^\ddagger$	0.149		
Y + rare earths	0.534		
Total soluble fission products	0.683	1.00	0.683
Mo	0.240		
Ru + Tc + Rh + Pd	0.263		
Total metallic inclusions	0.503	0.36	0.181
Ba + Sr (as zirconates)	0.149	1.74	0.258
Cs + Rb + I + Te	0.238	0.76	0.181
Other fission products	0.027	0.76	0.021
		Total	1.324

\*Solid swelling =  $1.324 - 1 = 0.32\%$  per atom percent burnup.

$^\dagger$ From Table 12.1.

$^\ddagger$ Soluble Zr is the zirconium remaining after fraction in the zirconates in the alkaline earth oxide phase has been removed from the total Zr yield.

In Table 12.6, cesium, rubidium, iodine, and tellurium have been assumed to be solids. Recent evidence on the behavior of these fission products (Secs. 12.5 and 12.6) suggests that they are more likely to be present in gaseous form over most of the fuel and are incorporated into the solid at the fuel surface only if the oxygen potential is sufficiently high. Thus, it would be reasonable to exclude this category of fission product from solid swelling, which would reduce the latter from 0.32% to 0.14%.

The best that available knowledge of the physicochemical states and migration characteristics of the fission products allows is a band of solid-swelling coefficients between 0.15 to 0.45% per atom percent burnup. In initially hypostoichiometric fuel, the lower figure is probably appropriate, but, for hyperstoichiometric fuel or heavily irradiated fuel of any initial stoichiometry, solid swelling is more likely to be close to the larger number.

## 12.8 NOMENCLATURE

- $a_{\text{Mo}}^f$  = thermodynamic activity of molybdenum in the fuel
- $a_{\text{Mo}}^m$  = thermodynamic activity of molybdenum in the metallic inclusions
- $a_{\text{Cr}}$  = thermodynamic activity of chromium in stainless steel
- A = mass number
- (cy) $_{ZMA}$  = cumulative yield of isotope  $ZMA$
- $\bar{F}$  = fissions  $\text{cm}^{-3} \text{sec}^{-1}$
- $f_{\text{Mo}}$  = fraction of total molybdenum present as  $\text{MoO}_2$  in the fuel
- $\Delta G^\circ$  = standard-state free energy change of reaction
- $\overline{\Delta G_{\text{O}_2}}$  = oxygen potential of the fuel
- $\Delta H_{\text{O}_2}$  = partial molar enthalpy of oxygen in the fuel
- (iy) $_{ZMA}$  = independent yield of isotope  $ZMA$
- $N_i$  = concentration of element i in the fuel
- $N_i^0$  = initial concentration of element i in the fuel
- $N_{i,A}$  = concentration of element i due to decay chain of mass number A
- $N_{\text{O}}^{\text{Ba-Sr}}$  = oxygen per unit volume of total fuel chemically bound in the alkaline earth oxide phase
- $N_{\text{O}}^f$  = oxygen concentration in the fuel
- O/M = oxygen-to-metal ratio of the as-fabricated fuel
- $p_{\text{O}_2}$  = oxygen partial pressure, atm
- $q_0$  = initial plutonium fraction in the fuel
- q = plutonium fraction in the fuel after irradiation
- R = gas constant
- $\Delta S_{\text{O}_2}$  = partial molar entropy of oxygen in the fuel
- t = time
- $t_{\text{irr}}$  = irradiation time
- T = temperature,  $^\circ\text{K}$
- $v_i$  = volume per atom of element i in the fuel
- $v_i^0$  = volume per atom of element i in the pure state
- $V_{\text{Pu}}$  = plutonium valence in hypostoichiometric fuel
- $V_{\text{U}}$  = uranium valence in hyperstoichiometric fuel
- $(\Delta V/V)_{\text{solid fp}}$  = fractional increase in fuel volume due to solid fission products
- V = fuel volume
- $V^0$  = initial fuel volume
- $y_{\text{Mo}}^f$  = cation fraction of molybdenum in the fuel
- $y_{\text{Mo}}^m$  = atom fraction of molybdenum in the metallic inclusions
- $y_A$  = yield of mass A chain
- $Y_i$  = yield of element i
- Z = atomic number

Greek letters

$\beta$  = burnup

$\beta_{crit}$  = burnup at which the plutonium valence reaches 4

$\lambda_i$  = decay constant of isotope  $i$

#### Subscripts

Ba—Sr = barium and strontium

Mo = molybdenum

NM = noble metals (technetium, rhodium, palladium, and ruthenium)

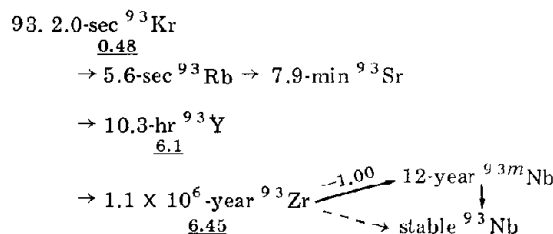
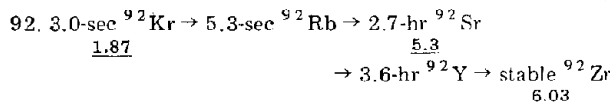
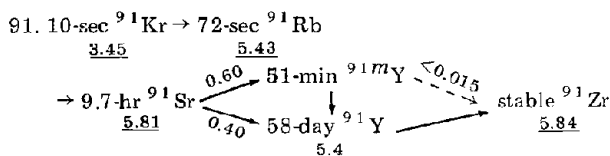
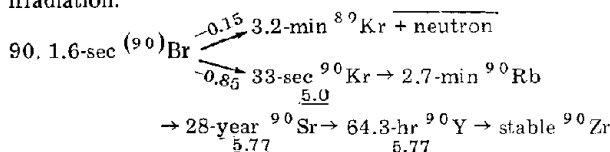
Y—RE = yttrium and rare earths

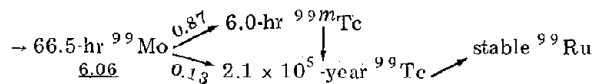
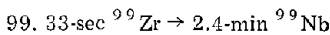
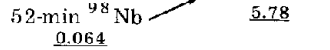
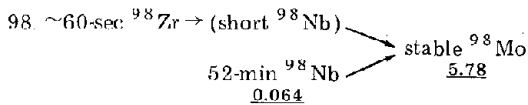
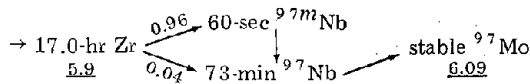
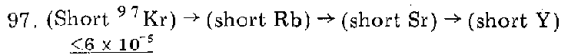
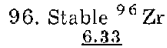
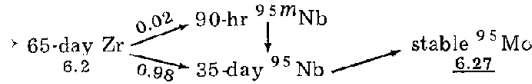
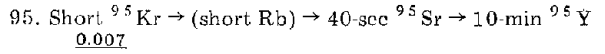
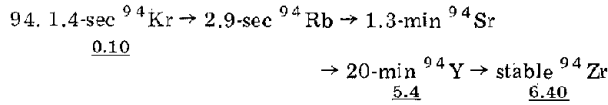
## 12.9 REFERENCES

- J. W. Harrison and L. M. Davies, *J. Nucl. Mater.*, **27**: 239 (1968).
- B. T. Bradbury, J. T. Demant, and P. M. Martin, *Proc. Brit. Ceram. Soc.*, **7**: 311 (1967).
- B. M. Jeffery, *J. Nucl. Mater.*, **22**: 33 (1967).
- J. I. Bramman, R. M. Sharpe, D. Thom, and G. Yates, *J. Nucl. Mater.*, **25**: 201 (1968).
- D. R. O'Boyle, F. L. Brown, and J. E. Sanecki, *J. Nucl. Mater.*, **29**: 27 (1969).
- D. R. O'Boyle, F. L. Brown, and A. E. Dwight, *J. Nucl. Mater.*, **35**: 257 (1970).
- F. Schmitz, G. Dean, M. Housseay, F. de Keroulas, and J. C. Van Craeynest, in *International Meeting on Fast Reactor Fuel and Fuel Elements*, p. 396, Sept. 28–30, 1970, Karlsruhe, Germany, Gesellschaft fuer Kernforschung, Karlsruhe, 1970.
- R. N. Duncan, P. A. Cantley, K. J. Perry, and R. C. Nelson, in *Proceedings of the Conference on Fast Reactor Fuel Element Technology*, p. 291, Apr. 13–15, 1971, New Orleans, American Nuclear Society, Hinsdale, Ill., 1971.
- M. H. Rand and T. L. Markin, in *Thermodynamics of Nuclear Materials*, Symposium Proceedings, Vienna, Sept. 4–8, 1967, pp. 637-650, International Atomic Energy Agency, Vienna, 1968 (STI/PUB/162).
- C. E. Johnson, I. Johnson, and C. E. Crouthamel, in *Proceedings of the Conference on Fast Reactor Fuel Element Technology*, Apr. 13–15, 1971, New Orleans, p. 393, American Nuclear Society, Hinsdale, Ill., 1971.
- T. A. Lauritzen, P. E. Novak, and J. H. Davies, Experimental Studies of Plutonium and Fission Product Redistribution in Fast Reactor Fuels, USAEC Report GEAP-4466, General Electric Company, March 1966.
- A. A. Bauer, H. Beisswenger, G. Giacchetti, E. Patrassi, G. Schumacher, and R. Theisen, Microanalytical Studies of Micro- and Macro-Segregation in Oxide Fuels, USAEC Report ANL-7120, Argonne National Laboratory, 1965.
- C. S. Caldwell, J. F. Miles, and W. J. Ross, *Trans. Amer. Nucl. Soc.*, **12**: 112 (1969).
- R. B. Fitts, E. L. Long, Jr., and J. M. Leitnaker, in *Proceedings of the Conference on Fast Reactor Fuel Element Technology*, Apr. 13–15, 1971, New Orleans, p. 431, American Nuclear Society, Hinsdale, Ill., 1971.
- J. D. B. Lambert et al., in *Proceedings of the Conference on Fast Reactor Fuel Element Technology*, Apr. 13–15, 1971, New Orleans, p. 517, American Nuclear Society, Hinsdale, Ill., 1971.
- E. A. Aitken et al., in *Proceedings of the Conference on Fast Reactor Fuel Element Technology*, Apr. 13–15, 1971, New Orleans, p. 459, American Nuclear Society, Hinsdale, Ill., 1971.
- A. E. Martin et al., in *Proceedings of the Conference on Fast Reactor Fuel Element Technology*, Apr. 13–15, 1971, New Orleans, p. 479, American Nuclear Society, Hinsdale, Ill., 1971.
- I. Johnson et al., *J. Nucl. Mater.*, **48**: 21 (1973).
- C. E. Johnson, D. V. Steidl, and C. E. Crouthamel, in *Proceedings of the Conference on Fast Reactor Fuel Element Technology*, Apr. 13–15, 1971, New Orleans, p. 603, American Nuclear Society, Hinsdale, Ill., 1971.
- L. A. Lawrence and J. A. Christensen, *J. Nucl. Mater.*, **37**: 248 (1970).
- K. J. Perry et al., in *Proceedings of the Conference on Fast Reactor Fuel Element Technology*, Apr. 13–15, 1971, New Orleans, p. 411, American Nuclear Society, Hinsdale, Ill., 1971.
- B. F. Rubin, E. A. Aitken, and S. K. Evans, *Trans. Amer. Nucl. Soc.*, **15**: 218 (1972).
- P. S. Maiya and D. E. Busch, *J. Nucl. Mater.*, **44**: 96 (1972).
- C. E. Johnson and C. E. Crouthamel, *J. Nucl. Mater.*, **34**: 101 (1970).
- F. de Keroulas et al., *J. Nucl. Mater.*, **43**: 313 (1972).
- F. Anselin, The Role of Fission Products in the Swelling of Irradiated  $UO_2$  and  $(U,Pu)O_2$  Fuel, USAEC Report GEAP-5583, General Electric Company, January 1969.
- M. L. Bleiberg, R. M. Berman, and B. Lustman, Effects of High Burnup on Oxide Ceramic Fuels, USAEC Report WAPD-T-1455, Westinghouse Electric Corporation, March 1962.

## 12.10 PROBLEMS

12.1 Using the following fission-product decay chains from  $^{235}U$  for mass numbers 90 to 99, compute the elemental yield of zirconium as a function of time of irradiation.





12.2 The insoluble second oxide phase in irradiated fuel is formed by diffusion of barium and strontium ions from the fuel matrix where they are created by fission to embryos (nuclei) of  $(\text{Ba,Sr})\text{ZrO}_3$ . The growth of these nuclei is modeled by assuming that the oxide particle is a sphere of radius  $R$  surrounded by a spherical annulus of fuel of radius  $\mathcal{R}$ . The latter is calculated from the density of second-phase oxide particles in the fuel. In this unit cell approach, there is no transport of the diffusing species (barium and strontium) across the outer boundary at  $\mathcal{R}$ .

(a) What is the radius  $\mathcal{R}$  if the concentration of second-phase oxide particles in the fuel is  $10^{12}/\text{cm}^3$ ?

(b) The diffusion equation in the annulus for transport of barium and strontium ions to the particle can be taken as the steady-state form of Fick's law, since the concentration changes slowly with time (i.e., the analysis is quasi-stationary). Set up and solve this equation assuming that the second-phase particle in the center acts as a perfect sink for barium and strontium.

(c) Using the solution obtained in (b), derive the growth law (i.e., the equation for  $dR/dt$ ). The volume of the second-phase oxide is  $7 \times 10^{23} \text{ cm}^3$  per molecule of  $(\text{Ba,Sr})\text{ZrO}_3$ . Determine the ratio  $R/\mathcal{R}$  as a function of burnup. By what other reasoning could this result have been arrived at?

(d) Calculate and plot the ratio  $R/\mathcal{R}$  and the atom fraction of Ba—Sr in the fuel as a function of radial position for the following values of the physicochemical constants:

$$\dot{F} = 8 \times 10^{13} \text{ fissions cm}^{-3} \text{ sec}^{-1}$$

$$N_{\text{U+Pu}} = 2.5 \times 10^{22} \text{ atoms/cm}^3$$

$$\beta = 5\%$$

$$Y_{\text{Ba-Sr}} = 0.1$$

$$D_{\text{Ba-Sr}} = 10^{-10} \text{ cm}^2/\text{sec}$$

12.3 (a) The partial molar enthalpy and entropy of oxygen in  $\text{UO}_{2+x}$  are given by

$$\Delta \overline{H}_{\text{O}_2} = -272 \text{ kJ/mole}$$

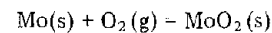
$$\Delta \overline{S}_{\text{O}_2} = -1000x \text{ J mole}^{-1} \text{ } ^\circ\text{K}^{-1}$$

Express these quantities in terms of the uranium valence  $V_{\text{U}}$ .

(b) Suppose that fission of  $^{235}\text{U}$  produced only two fission products, one which assumed a valence of 3+ in the fuel and the other which existed as an element in the fuel. What is the oxygen potential of fuel that was initially of exact stoichiometry after 5% burnup at  $1000^\circ\text{K}$ ?

12.4 During postirradiation examination of a mixed-oxide fuel pin, the molybdenum contents of the fuel matrix and of the metallic inclusions are determined by electron-microprobe analysis. At a point in the fuel pin where the temperature is estimated to have been  $2000^\circ\text{K}$  during irradiation, the fuel matrix contains 0.08 mole %  $\text{MoO}_2$  and the metallic inclusions contain 10 at. % Mo. There is 0.01 g of metallic inclusions per gram of irradiated fuel.

(a) Assuming that molybdenum forms ideal solutions in both the fuel matrix and metallic inclusions, calculate the oxygen potential of the fuel at this position in the fuel pin during operation. The standard free energy of formation of  $\text{MoO}_2$ ,



is

$$\Delta G_{\text{Mo}}^\circ = -574 + 164(T/10^3) \text{ kJ/mole}$$

(b) Assuming that all the noble metals produced by fission are precipitated into the metallic inclusions, calculate the burnup of the fuel. Assume that the atomic weights of all components of the metallic inclusions are 100.

(c) Compute the molybdenum content of the metallic inclusions that should have been found if no molybdenum had been lost from or gained by the unit volume of fuel under consideration.

12.5 It is desired to calculate the effect of removal of oxygen by the cladding on the oxygen potential of irradiated  $\text{UO}_2$ . To simplify the analysis, we neglect oxygen redistribution in the temperature gradient; the oxygen-to-uranium ratio is radially uniform at all times. In addition, the only fission products created are assumed to be the two used in problem 12.3, and the  $\text{UO}_2$  is initially stoichiometric. The rate of oxygen uptake by the cladding is assumed to be proportional to the oxygen partial pressure at the fuel-cladding interface:

$$\frac{\text{Atoms of O removed by cladding}}{\text{Cm}^2\text{-sec}} = k_{\text{corr}} p_{\text{O}_2}$$

where  $p_{O_2}$  is the oxygen partial pressure in atmospheres at the fuel-cladding interface and  $k_{\text{corr}}$  is a temperature-dependent corrosion rate constant. The temperature at the fuel-cladding interface is 1000°K throughout irradiation.

(a) Derive the differential equation for the rate of oxygen uptake by the cladding as a function of burnup. In the calculation appropriately modify the oxygen (charge) balance of problem 12.3 to account for removal of oxygen from the fuel by the corrosion process. Express the final differential equation in terms of the dimensionless quantities:

- $\beta$  = fractional burnup  
 $X(\beta)$  = fraction of oxygen in the fuel that has been absorbed by the cladding at burnup  $\beta$   
 $A = \frac{k_{\text{corr}}}{RF}$  = dimensionless corrosion rate, where  $R$  is the fuel radius and  $F$  is the fission rate per cubic centimeter.

(b) Numerically integrate the differential equation previously derived for  $A = 10^{12}$  to determine  $X(\beta)$ . Use Runge-Kutta or any other numerical method that keeps errors in bounds. Plot this function. From this result, calculate and plot the oxygen potential at the fuel-cladding interface as a function of burnup. Compare the resulting curve with that obtained in problem 12.3.

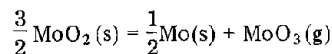
12.6 The possibility of migration of molybdenum from the hot portion of the fuel to the cladding via gas-phase transport in cracks depends on the pressure of the oxides of this element. Consider the fuel shown in Fig. 12.10 which has been irradiated to 8% burnup and in which the oxygen potential is -300 kJ/mole at the radial location where the temperature is 2000°K. At this position ~50% of the molybdenum is oxidized to  $MoO_2$ .

(a) What is the cation fraction of molybdenum in the fuel matrix? and what is the atom fraction of molybdenum in the metallic inclusions?

(b) Assuming that  $MoO_2$  forms an ideal solution in the fuel, what is the pressure of gaseous  $MoO_2$  over the fuel at 2000°K? The free energy of  $MoO_2$  vaporization is\*

$$\Delta G_{\text{vap}, MoO_2}^\circ = 561 - 203(T/10^3) \quad \text{kJ/mole}$$

(c) Another possible vapor species is  $MoO_3$ . If the standard free energy of the reaction

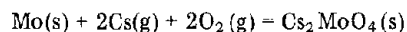


is\*

$$\Delta G^\circ = 510 - 194(T/10^3) \quad \text{kJ/mole}$$

what is the partial pressure of  $MoO_3$  over the fuel at 2000°K?

(d) A third possible molybdenum-bearing gaseous species over the irradiated fuel is  $Cs_2MoO_4$  (cesium molybdate). Assuming that the pressure of gaseous cesium over the fuel is  $10^{-2}$  atm, what is the partial pressure of cesium molybdate at 2000°K as determined from the following thermochemical data:



$$\Delta G^\circ = -1668 + 541(T/10^3) \quad \text{kJ/mole}$$

and the vapor pressure of solid  $Cs_2MoO_4$  is given by

$$\ln P^\circ (\text{atm}) = 15.14 - 32.3/(T/10^3)$$

12.7 In the outer unrestructured region of an LMFBR fuel pin, the fission gases are present as very small bubbles (radius  $< 10 \text{ \AA}$ ). In this form the fission gases can be treated as solid fission products with an atomic volume of  $85 \text{ \AA}^3$  in computing the swelling. Modify the solid fission-product swelling law to include fission gases that are present in the fuel in the form previously described.

12.8 A mixed oxide fuel pin 3 mm in diameter is contained by pure chromium cladding 0.4 mm thick. The oxygen-to-metal ratio of the fuel is initially 2.01. The fuel rod is heated uniformly to 800°C for a time long enough for chemical equilibrium between the fuel and the cladding to be achieved. What fraction of the cladding is converted to  $Cr_2O_3$  at equilibrium?

At 800°C the standard-state free energy of formation of  $Cr_2O_3$  is 560 kJ/mole  $O_2$ , and the oxygen potential of the fuel is shown in Fig. 11.12. The density of the fuel is  $10.9 \text{ g/cm}^3$ , and the density of chromium is  $7.2 \text{ g/cm}^3$ . None of the three phases present at equilibrium ( $Cr$ ,  $Cr_2O_3$ , and fuel) is miscible in the others.

\*R. P. Burns et al., *J. Chem. Phys.*, 32: 1363 (1960).

# Chapter 13

## Swelling Due to Fission Gases

### 13.1 INTRODUCTION

Among the myriad phenomena that occur simultaneously in a nuclear fuel element under irradiation, none has so frustrated the designer, so challenged the experimentalist, or so intrigued the theorist as the behavior of the fission products xenon and krypton. The unique status of these noble gases among the hundreds of other fission products generated in the fuel is due to (1) their virtually complete insolubility in the fuel matrix and (2) the fact that their normal pure state is a gas rather than a solid. Property (1) means that, if at all kinetically possible, xenon and krypton will be rejected from the fuel matrix. The consequence of property (2) is that the rejected gases either are completely released from the fuel and contribute to the gaseous atmosphere within the fuel pin or they are precipitated as small pockets of gas within the fuel body proper. Either route is detrimental to fuel performance; if the gas is released from the fuel, the pressure within the fuel pin is correspondingly increased, and the cladding is subjected to stresses that can ultimately result in failure. In addition, the extent to which the fission gases are freed from the fuel determines in large part the potential hazard of a reactor core in the event of an accidental cladding breach, which can occur either at the reactor site or during transportation of the spent fuel to a reprocessing plant.

On the other hand, if the fission gases are retained in the fuel, they nearly always precipitate as bubbles. Inasmuch as the density of the gas in such bubbles is considerably lower than that of the solid fuel, gas atoms residing in bubbles occupy more volume than either the fissile atoms they replaced or fission-product atoms that segregate as solid phases (e.g., the noble metals). The precipitation of fission gases thus leads to swelling of the fuel to a larger degree than the volume expansion that would occur if the xenon and krypton had remained dispersed on an atomic scale in the fuel matrix (in which case they can be treated as other solid fission products by the methods outlined in Chap. 12). Swelling adversely affects fuel performance because it promotes fuel-cladding contact, and the resultant stress on the cladding can shorten its lifetime. In addition, the bubbles of low-conductivity gas decrease the thermal conductivity of the fuel in the same manner as the fabricated porosity (Chap. 10) and thereby

lead to fuel temperatures higher than exhibited by fully dense fuel at the same heat rating.

Swelling and release are complementary phenomena. A piece of fuel that releases a large portion of its fission gases exhibits low swelling because there is little gas remaining in the fuel to form bubbles. Conversely, complete retention of the fission gases in a section of fuel is usually accompanied by significant swelling. These effects can be illustrated by examining the behavior of the fission gases as a function of radial position in a fuel rod. Near the cool periphery of the fuel, the fission gases are quite immobile in the solid (because of the low temperature), and, consequently, they are not released in large quantities, and the expansion they cause is comparable to that of other solid fission products. In this region both release and swelling are low. At intermediate radial positions in the fuel (corresponding roughly to the region of equiaxed-grain growth), release is appreciable, but large swelling can occur because a significant fraction of the gases is retained in the fuel as bubbles. In the hot inner columnar-grain region, nearly all fission gases are released as soon as they are formed, and the swelling is quite small.

Concern with the fate of fission-produced gases in nuclear fuels dates from the late 1950s. At that time theoretical analyses of fission-gas behavior were quite simple, as befitted a generation of reactors in which fission density, burnup, and fuel temperatures were too low to produce the complex series of phenomena that are now recognized as occurring in modern highly rated fuels. The swelling of uranium metal due to xenon and krypton was simply considered in the same manner as that of all other solid fission products.<sup>1</sup> The release of fission gases from  $\text{UO}_2$  was treated by classical solid diffusion theory, in which the gases diffused as atoms from the fuel matrix to a surface that communicated with the gaseous environment within the fuel pin. It soon became obvious that the diffusion medium could not be considered to be the entire fuel pellet—release rates predicted on this basis were far too low. To account for this discrepancy within the framework of the diffusional release model, the fuel body was regarded as being composed of many small spheres with the spaces between the spheres large enough to permit easy escape of the gas.<sup>2</sup> The size of these *equivalent spheres* was adjusted to produce agreement between diffusion theory and experiment. In many cases the diameters of the

equivalent spheres so determined were comparable to the size of the grains in the polycrystalline fuel compact, which led to the supposition that grain boundaries represented easy escape paths for the fission gases that reached them by atomic diffusion within the grains. Just how easy it is for fission gases to escape from the fuel once they have reached the grain boundaries is still a matter of much dispute, but at least the equivalent-sphere modification of the conventional diffusional release model demonstrated that the microstructure of the fuel is intimately related to the behavior of the fission gases.

Closer examination of the release curves showed significant departures from ordinary diffusion theory, even when the adjustable equivalent-sphere concept was applied. This led to the notion that the migrating fission-gas atoms could be temporarily *trapped* at a variety of natural or radiation-produced defects within the fuel matrix. Quantitative formulation of the diffusion-trapping process introduced a number of parameters characterizing the traps,<sup>3</sup> but the shape of the release curves could be rationalized by this theory.<sup>4</sup>

It is possible to observe small bubbles of xenon and krypton in irradiated fissile materials. Figure 13.1 shows the distribution of bubbles produced in thin wafers of  $\text{UO}_2$  by bombardment with krypton ions produced by an accelerator. The bubbles were produced by annealing the specimens after bombardment for about one-half hour at  $1500^\circ\text{C}$ . Following irradiation and annealing, the specimens were reduced to a thickness between 500 and 2000 Å by electropolishing to permit examination by transmission electron microscopy. Similar evidence of bubble formation in reactor-irradiated nuclear fuels has been obtained.

It was recognized that fission-gas bubbles could act as very efficient traps for the atomically dispersed fission-gas atoms.<sup>5</sup> Once nucleated, the bubbles were thought to simply grow in place by absorbing all the xenon and krypton produced by fission. In 1963, however, Barnes and Mazey<sup>6</sup> observed that bubbles of accelerator-injected helium in copper migrated bodily through the solid. Since it



Fig. 13.1 Inert-gas bubbles in  $\text{UO}_2$ . [From R. M. Cornell and G. H. Bannister, *Proc. Brit. Ceram. Soc.*, 7: 355 (1967).]

was reasonable to expect that the fission gases could do the same thing in  $\text{UO}_2$ , experimental and theoretical studies of the effect of bubble migration and coalescence on swelling and gas release were initiated.<sup>7</sup> It was also realized that, although bubbles in a solid could move about in a random manner (e.g., by a form of Brownian motion), the steep temperature gradient in a fuel rod provided a much more significant driving force for biased bubble migration.<sup>8</sup> The role of the fuel microstructure was demonstrated by the deduction that crystal defects such as dislocations and grain boundaries can effectively pin and immobilize gas bubbles smaller than calculable critical sizes that can be estimated with fair accuracy.<sup>9</sup>

The ability of irradiation to redissolve fission-gas bubbles was demonstrated experimentally by Whapham<sup>10</sup> in 1966. He showed that bubbles produced by irradiation followed by high-temperature annealing could be completely dispersed in the solid by another low-temperature irradiation. Thus, modeling of fission-gas behavior was confronted with another distinct physical process, *resolution* (sometimes called dynamic solubility), which had to be treated in quantitative analyses.

This historical survey is summarized in Table 13.1, which lists the individual phenomena that must be accounted for to quantitatively describe the behavior of fission gases in nuclear fuels. The ultimate goal of analyses of fission-gas behavior is to predict the following quantities as a function of position in the fuel element and irradiation time:

- (1) The concentration of gas atomically dissolved in the fuel matrix.
- (2) The number of bubbles in a particular size range (the bubble-distribution function) in the matrix, on dislocation lines, and on grain boundaries.
- (3) The amount of gas released from the fuel.

The sum of 1 to 3 must be equal to the total amount of gas generated by fission in the unit of fuel under consideration.

The quantitative model should be capable of predicting items 1 to 3 under steady-state, slow transient (power change), and rapid transient (accident) conditions. The variables that govern the rates of the individual processes listed in Table 13.1 are summarized in Table 13.2.

Given the large number of variables that are likely to affect fission-gas behavior and the variety of elementary processes that must be considered simultaneously, it is not surprising that a comprehensive model of fission-gas release and swelling from operating fuel rods has not yet been developed. Even if the analytical tools were fully developed, some of the basic input data to the computation, such as fission-gas diffusivity and the heat of transport for matrix and surface thermal self-diffusion, are simply not known to an accuracy that would permit computational results to be considered quantitative. In view of this state of affairs, the approach of most investigators has been to concentrate on a small portion of the total problem to see how well the results of a modest but tractable analysis agree with experimental data. The tendency has been to consider the problem from two points of view.

One school emphasizes the role of processes dependent on atomic migration of the gas atoms in the fuel. Such calculations are primarily concerned with diffusion to

Table 13.1 Individual Physical Processes  
that Contribute to the Behavior of  
Fission Gases in Nuclear Fuels

1. Production of the gases xenon and krypton by fission. The rate of production and the total amount produced at a particular irradiation time are important.
2. Nucleation of gas bubbles, either homogeneously by chance encounters of wandering gas atoms or heterogeneously on fission-fragment tracks or dislocation lines.
3. Growth of gas bubbles by atomic migration of fission-gas atoms to existing bubbles. Bubble growth can be affected by the availability of vacancies to permit the bubble to expand as gas is accumulated and by the effects of surface tension and the stress state of the surrounding fuel matrix, which determine the stable size of the bubble.
4. Re-resolution of the gas atoms within the bubble.
5. Migration of the bubbles, either as a random-walk process in the absence of directed forces acting on the bubble or as biased motion when such forces are present. The forces that act on gas bubbles in solids are generally believed to be those due to the temperature or stress gradients, or restraining forces due to dislocations and grain boundaries. The former forces always cause the bubble to move in a particular direction. The forces due to crystal defects can act either to pin the bubble if the defects are immobile or to drag the bubbles if the defects are themselves in motion (i.e., dislocations move along glide planes in the crystal in response to mechanical stresses, and grain boundaries move in the process of grain growth). Thus, bubble motion can occur by dislocation-line sweeping or grain-boundary sweeping.
6. Coalescence of bubbles moving either in a random or directional fashion.
7. Interaction of bubbles with the crystal defects (dislocations and grain boundaries).
8. Release of the fission gases, either to external surfaces such as the central void, cracks in the fuel, or the fuel-cladding gap or to internal surfaces such as grain boundaries. When the bubbles on grain boundaries become sufficiently large and numerous, they can link up and release gas to one of the external surfaces.
9. Release of fission gas by direct flight of the energetic fission fragments out of an external surface. This mode of release is small and is significant only at low temperatures.

surfaces from which escape can occur. The processes of trapping during diffusion are treated in detail. Fission-gas bubbles, if they are considered at all, are generally regarded as one of many possible trapping sites for migrating atoms. Such approaches lend themselves to a better description of release rather than of swelling.

The second school concentrates on the role of bubble growth and migration and on the interactions of bubbles between themselves and with structural defects. The results of such analyses tend to produce swelling, rather than release, predictions.

It has been only recently that comprehensive swelling and gas-release calculations have been advanced; yet even the most sophisticated of these do not consider all the

pertinent elementary processes simultaneously. Perhaps because of its relatively recent discovery, the phenomenon of radiation re-resolution has been accorded the least attention in computations aimed at predicting fuel-element performance. Fuel cracking, because of its unpredictability, is also quite difficult to model quantitatively.

The discussion of fission-gas behavior here is divided roughly according to the two schools of thought described. This chapter deals primarily with the phenomena occurring within the fuel body proper and does not consider movement of the fission gases over distances needed for release. The fuel is treated as an infinite medium in the same spirit as many problems in reactor physics are analyzed in the infinite-medium approximation. Chapter 14 describes the kinetics of fuel restructuring, which can be treated by some of the same tools that have been developed to predict fission-gas behavior. Chapter 15 explicitly considers the flow of fission gases to surfaces from which escape from the fuel is possible.

## 13.2 GENERAL CONSIDERATIONS

In this section the formulas common to most fission-gas behavior models are summarized.

### 13.2.1 Rate of Fission-Gas Production

Table 13.3 shows the yields of the isotopes of xenon and krypton resulting from fission of  $^{238}\text{U}$  and  $^{239}\text{Pu}$ . Only the stable or very long lived isotopes (e.g.,  $^{85}\text{Kr}$ ) are important in fuel swelling and gas release that causes a permanent pressure rise in the fuel pin. The short-lived isotopes marked with a dagger in Table 13.3 decay to solid fission products very quickly on the time scale of

Table 13.2 Variables Affecting  
Fission-Gas Behavior

Temperature
Temperature gradient
Matrix stress
Matrix-stress gradient
Fission rate
Irradiation time or burnup
Fuel properties
Vapor pressure
Surface tension
Coefficients of thermal surface and bulk diffusion
Creep strength
Fission-gas properties
Nuclear yields
Equation of state
Diffusion coefficient in the solid fuel
Diffusion coefficient of the gaseous fuel
Fuel microstructure
Dislocation density
Grain size
Restructuring
Crack pattern
The condition of the fuel element, which determines the temperature profile and the state of stress in the fuel

Table 13.3 Isotopes of Xenon and Krypton Released in Fission\*

Isotope	Half-life	Percent yield	
		$^{235}\text{U}$	$^{239}\text{Pu}$
$^{83}\text{Kr}$	Stable	0.4	0.3
$^{84}\text{Kr}$	Stable	0.85	0.5
$^{85}\text{Kr}$	Stable (10.6 years)	0.15	0.13
$^{85\text{m}}\text{Kr}\dagger$	4.4 hr	1.3	
$^{86}\text{Kr}$	Stable	1.4	0.8
$^{87}\text{Kr}\dagger$	78 min	2.5	
$^{88}\text{Kr}\dagger$	2.8 hr	3.5	
Total stable krypton yields		2.8	1.7
$^{131}\text{Xe}$	Stable	3.2	3.8
$^{132}\text{Xe}$	Stable	4.7	5.3
$^{133}\text{Xe}\dagger$	5.3 day	6.6	6.9
$^{134}\text{Xe}$	Stable	6.6	7.5
$^{135}\text{Xe}\dagger$	9.2 hr	5.5	
$^{136}\text{Xe}$	Stable	5.9	6.6
Total stable xenon yields		20.4	23.2

\*From S. Katcoff, *Nucleonics*, 18: 201 (1960). The yields for the stable products represent chain yields; the yields of short-lived isotopes are cumulative yields up to the particular isotope. Plutonium-239 yields are for thermal neutrons, whereas those for  $^{235}\text{U}$  are for fast neutrons.

†Short-lived fission product.

reactor operation. The sum of the yields of the stable xenon and krypton isotopes is between 0.23 and 0.25. The more recent summary of fission-product yields presented by Meek and Rider<sup>11</sup> also shows that the total yield of the stable fission gases is about 0.25 for both uranium and plutonium. Since xenon constitutes the largest part of the fission gas, the total cumulative yield of stable Xe + Kr will be denoted by  $Y_{\text{Xe}}$  and assumed to be independent of irradiation time. The rate of production of fission gases in a unit volume of fuel is then  $Y_{\text{Xe}}\dot{F}$  fission-gas atoms  $\text{sec}^{-1}\text{cm}^{-3}$ , where  $\dot{F}$  is the fission rate density (fissions  $\text{sec}^{-1}\text{cm}^{-3}$ ).

### 13.2.2 Xenon Equation of State

The extent of fuel swelling caused by the fission gases is strongly dependent on the equation of state of the gas in the bubbles. Although the noble gases can be safely considered to be ideal for nearly all applications, the gas pressure within the small bubbles in a nuclear fuel can be very large, and deviations from the perfect-gas law must be considered.

The van der Waals equation of state is most commonly used to describe the thermodynamic state of fission xenon in the bubbles. It can be written as

$$p \left( \frac{1}{\rho_g} - B \right) = kT \quad (13.1)$$

where  $p$  is the pressure of a gas of molecular density  $\rho_g$  at temperature  $T$ . The constant  $B$  can be regarded as expressing the volume occupied by the atoms proper, or, more precisely, it is a reflection of the short-range repulsive forces in the interatomic potential between xenon atoms.

The complete van der Waals equation of state contains another constant arising from the attractive forces. This term is small enough to be neglected for xenon.

Alternatively, the equation of state can be written in terms of the compressibility factor (see Eq. 9.14):

$$\frac{p}{\rho_g kT} = z(p, T) \quad (13.2)$$

Harrison<sup>12</sup> has tabulated the compressibility factor of xenon as a function of temperature and pressure. Combination of Eqs. 13.1 and 13.2 shows that the van der Waals parameter  $B$  is not constant but varies with temperature and pressure according to

$$B(p, T) = \frac{z(p, T) - 1}{(p/kT)} \quad (13.3)$$

In most analyses, however,  $B$  is taken to be a constant equal to  $85 \text{ \AA}^3/\text{atom}$ .

The critical constants for xenon are

$$\begin{aligned} T_{\text{crit}} &= 289.7^\circ\text{K} \\ V_{\text{crit}} &= 200 \text{ \AA}^3/\text{atom} \\ p_{\text{crit}} &= 58 \text{ atm} \end{aligned}$$

### 13.2.3 Mechanical Force Balance on the Bubbles

Figure 13.2 shows a gas-filled bubble of radius  $R$  embedded in a solid medium that is subject to uniform hydrostatic stress  $\sigma$ . If the solid is in tension,  $\sigma$  is taken to be positive. At equilibrium in this system, the gas pressure acting to expand the bubble is just balanced by the hydrostatic stress in the solid and the surface-tension forces that tend to contract the bubble. From the analysis of Chap. 8 [see Eq. 8.12 and Fig. 8.9(b)], the surface-tension force is  $2\gamma/R$ , where  $\gamma$  is the surface tension of the solid. For the equilibrium bubble the force balance takes the form

$$p = \frac{2\gamma}{R} + \sigma \quad (13.4)$$

or, if there is no stress in the solid,

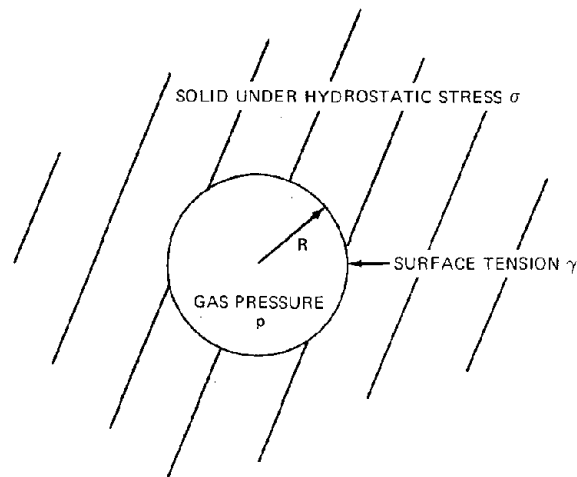


Fig. 13.2 Gas-filled bubble in mechanical equilibrium with a solid under hydrostatic stress.

$$p = \frac{2\gamma}{R} \quad (13.5)$$

Kulcinski et al.<sup>13</sup> have shown that fission-gas bubbles in uranium metal respond to changes in external hydrostatic stress in a manner consistent with Eq. 13.4.

There are important instances, however, in which the equilibrium relations of Eqs. 13.4 and 13.5 are not valid. For example, the bubbles in the fuel may be able to accumulate gas atoms more rapidly than the bubble can expand to satisfy Eq. 13.4 or 13.5. For small bubbles the mechanism by which bubbles expand is by an inflow of atomic vacancies from the bulk of the solid. Vacancies and interstitials are produced copiously in irradiated fissile materials. However, if the flow of vacancies to the bubble is not great enough to provide the volume increase needed to compensate for the increasing number of gas atoms collected by the bubble, an excess pressure can develop. Nonetheless, the forces acting on the interface must always be in mechanical equilibrium or else the bubble surface would accelerate according to Newton's law. The force balance at the interface is maintained by the radial stress component at the interface, which in the case of the nonequilibrium bubble is not equal to the hydrostatic stress far away from the bubble. The mechanical balance that is always satisfied is

$$p = \frac{2\gamma}{R} - \sigma_{rr}(R) \quad (13.6)$$

where  $\sigma_{rr}(R)$  is the radial component of the stress tensor at the bubble surface. The equilibrium bubble is one in which  $\sigma_{rr}(R)$  is equal to the bulk hydrostatic stress. When a pressure excess (or deficit) develops in the bubble, there will be stress gradients in the vicinity of the bubble. The stress field around nonequilibrium bubbles can be calculated by elasticity theory<sup>14</sup> provided that the stresses do not exceed the yield point of the solid. Although any imbalance between the interface and bulk stresses is relieved by vacancy flow for small bubbles, large bubbles can attain mechanical equilibrium with the surrounding solid by plastic deformation.<sup>5,15</sup>

Another important exception to the equilibrium bubble case occurs when there is little or no gas in the enclosure, in which case the bubble is properly termed a void. Mechanical equilibrium at the surface of a void is maintained by a slight contraction of the surface, which places the solid near the interface in tension relative to the stress in the bulk material. The behavior of voids in metals will be treated in detail in Chap. 19.

### 13.2.4 Number of Gas Atoms in a Bubble

All fission-gas swelling models require a relation specifying the number of gas atoms contained in a bubble of a given radius. In most analyses the bubble is assumed to be in mechanical equilibrium with the bulk solid surrounding it; thus, the density of the gas within the bubble can be obtained by replacing the pressure in Eq. 13.1 by the value given by Eq. 13.4, which yields

$$\frac{1}{\rho_g} = B + \left[ \frac{(2\gamma)}{kT} \frac{1}{R} - \frac{\sigma}{kT} \right]^{-1} \quad (13.7)$$

or, if the solid is stress-free,

$$\frac{1}{\rho_g} = B + \left( \frac{kT}{2\gamma} \right) R \quad (13.8)$$

The surface tensions of the common nuclear fuels U,  $UO_2$ , and UC are not well known. Most analyses assume  $\gamma = 1000$  dynes/cm, although recent measurements<sup>16</sup> on  $UO_2$  suggest that  $\gamma$  may be closer to 600 dynes/cm. The temperature dependence of  $\gamma$  is unknown. Using  $\gamma = 1000$  dynes/cm, the group  $(kT/2\gamma)$  in Eqs. 13.7 and 13.8 is  $0.7 \text{ \AA}^2$  at  $1000^\circ\text{K}$  and  $1.4 \text{ \AA}^2$  at  $2000^\circ\text{K}$ . In view of the large uncertainty in  $\gamma$ , we take the following estimate to be valid at all temperatures of interest in reactor fuel operation:

$$\frac{kT}{2\gamma} \approx 1 \text{ \AA}^2 \quad (13.9)$$

Figure 13.3 shows a plot of the gas density according to Eq. 13.8 with the surface-tension term given by Eq. 13.9. For

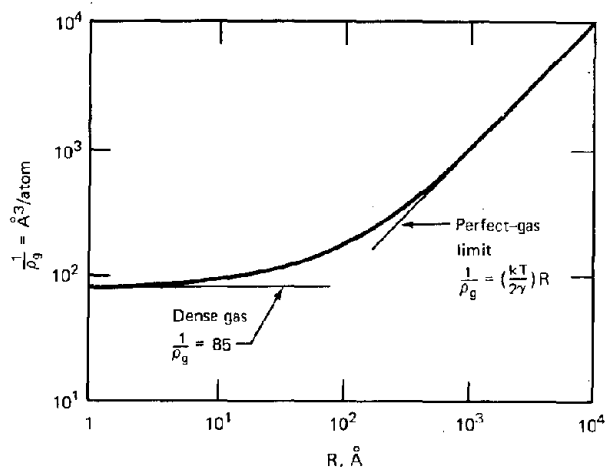


Fig. 13.3 Density of xenon gas in a spherical bubble imbedded in a stress-free solid of surface tension of 1000 dynes/cm.

bubbles with a radius smaller than about  $10 \text{ \AA}$ , the gas behaves as a constant-density condensed phase for which

$$\frac{1}{\rho_g} = 85 \frac{\text{\AA}^3}{\text{atom}} \quad (13.10)$$

For comparison the atomic volume of uranium atoms in the fuel can be computed as follows: In  $UO_2$  the uranium atoms form a face-centered cubic sublattice with a room-temperature lattice parameter of  $5.47 \text{ \AA}$  [see Fig. 3.12(b)]. Since there are four atoms per conventional unit cell of the fcc structure (Chap. 3), the volume per atom of uranium in  $UO_2$  is:

$$\Omega = \frac{(5.47)^3}{4} = 41 \frac{\text{\AA}^3}{\text{U atom}} \quad (13.11)$$

Thus the density of the gas in very small bubbles is nearly half that of the uranium atoms in the fuel matrix.

For bubbles with radii greater than about 1000 Å, the correction for nonideal gas behavior is small, and

$$\frac{1}{\rho_g} = \left( \frac{kT}{2\gamma} \right) R \approx R \frac{\text{Å}^3}{\text{atom}} \quad (13.12)$$

The number of gas atoms contained in a bubble of radius R is

$$m = \left( \frac{4\pi R^3}{3} \right) \rho_g \quad (13.13)$$

or, using  $\rho_g$  given by Eq. 13.8,

$$m = \frac{4\pi R^3 / 3}{B + (kT/2\gamma)R} \quad (13.14)$$

The limiting cases corresponding to Eqs. 13.10 and 13.12 are

$$m = \left( \frac{4\pi R^3 / 3}{B} \right) \quad (\text{for } R < 10 \text{ Å}) \quad (13.15)$$

$$= \left( \frac{4\pi R^3}{3} \right) \left( \frac{2\gamma}{kT} \right) \quad (\text{for } R > 1000 \text{ Å}) \quad (13.16)$$

### 13.2.5 Swelling Due to Gas Bubbles

Consider 1 cm<sup>3</sup> of fresh fuel that contains no bubbles. Now insert  $N'$  bubbles of radius R into this volume of solid, and the final volume is  $1 + (4\pi R^3 / 3)N'$ . The volume increase is  $(4\pi R^3 / 3)N'$ . Measurement of bubble densities determines N, the number of bubbles per unit of total volume (solid plus bubbles), not  $N'$ , which is the number of bubbles per unit volume of solid. The relation between N and  $N'$  is

$$N' = \frac{N}{1 - (4\pi R^3 / 3)N} \quad (13.17)$$

The fractional swelling due to the gas bubbles is defined as the volume increase per unit volume of fresh (i.e., solid) fuel, or

$$\frac{\Delta V}{V} = \left( \frac{4\pi R^3}{3} \right) N' = \frac{(4\pi R^3 / 3)N}{1 - (4\pi R^3 / 3)N} \quad (13.18)$$

If the fractional swelling is small, Eq. 13.18 reduces to

$$\frac{\Delta V}{V} = \left( \frac{4\pi R^3}{3} \right) N \quad (13.19)$$

Equation 13.19 supposes that all bubbles are of the same size. In general, however, the solid contains bubbles of different radii, and the density of bubbles is described by the bubble distribution function:

$$N(R) dR = \text{number of bubbles per unit of total volume with radii in the range } R \text{ to } R + dR$$

We have not distinguished between bubbles in the fuel matrix (intragranular bubbles), bubbles present on dislocation lines, and bubbles located on grain boundaries (intergranular bubbles).

The total bubble density is given by

$$N = \int_0^\infty N(R) dR \quad (13.20)$$

and the volume swelling by

$$\frac{\Delta V}{V} = \frac{4\pi}{3} \int_0^\infty R^3 N(R) dR \quad (13.21)$$

### 13.2.6 Overall Gas Balance

In the infinite-medium approximation, all the fission gas generated in a unit volume of fuel remains there. Assuming a constant rate of gas-atom production by fission, the overall balance can be written as

$$Y_{Xe} \dot{F}t = C + M \quad (13.22)$$

where  $t$  = the irradiation time,  $C$  = gas atoms/cm<sup>3</sup> dispersed atomically in the matrix, and  $M$  = gas atoms/cm<sup>3</sup> contained in bubbles.

In Eq. 13.22 the distinction between a unit of total volume (bubbles + solid) and a unit of solid volume has been neglected. The bubbles are assumed to occupy only a small fraction of the total volume. The quantity  $M$  is given by

$$M = mN \quad (\text{for uniform size bubbles}) \quad (13.23)$$

$$= \int_0^\infty m(R) N(R) dR$$

$$(\text{for a bubble distribution}) \quad (13.24)$$

where  $m(R)$  is the number of gas atoms contained in a bubble of size R, as given by Eq. 13.14, 13.15, or 13.16.

## 13.3 MIGRATION OF ATOMIC-SIZE DEFECTS

In this section and the following two sections, we review the theoretical methods for predicting the rates of those elementary processes which, singly or in various combinations, determine the kinetics of many of the phenomena listed in Table 13.1.

The fission process creates vacancies, interstitials, and fission-gas atoms, which, in the early stages of their lifetimes, exist as entities of atomic size. Understanding the rates at which these species migrate in the solid is crucial to rational prediction of overall fission-gas behavior in nuclear fuels (whether or not the migration of the atomic defects actually controls the kinetics of the more complex processes of which they are a part).

### 13.3.1 Vacancies and Interstitials

Vacancies and interstitial atoms are created by the collision of energetic fission fragments with atoms of the solid crystalline lattice. If the collision transfers sufficient energy to the struck lattice atom, the latter will be knocked far enough from its original site that it will not immediately drop back into its original position. The vacant-site-interstitial-atom pairs created by energetic collisions are known as Frenkel pairs. Although vacancies and interstitials

are constantly being created by thermal processes, radiation produces them in a nonequilibrium fashion.

The lattice atom dislodged by a passing fission fragment is called the primary knock-on. Because the fission-fragment energy is so high, the energy of the primary knock-on is large enough to create additional displacements when it collides with other lattice atoms. In this manner each fission fragment creates a cascade of displaced atoms and vacant lattice sites left behind by the removal of the atoms. We define the efficiency of such a process by the yield of Frenkel pairs:

$$Y_{vi} = \text{number of stable Frenkel pairs per fission event} \quad (13.25)$$

The qualification "stable" means that vacancy-interstitial pairs that are created so close to each other that they immediately recombine are excluded. Theoretical estimation of  $Y_{vi}$  is deferred until Chap. 17. Suffice it here to say that  $Y_{vi}$  is believed<sup>17</sup> to be about  $10^4$  for  $\text{UO}_2$ . This number can be compared to the yield of fission-gas atoms, which is  $\sim 0.25$ . The rate of production of vacancies and interstitials is  $Y_{vi}\bar{F}$  per second per unit volume of fuel.\* Equal numbers of both types of defects are created by irradiation.

The vacancies and interstitials created by fission migrate through the lattice by a random-walk process. They lose their identity as separate species when they encounter other objects with which they can combine (e.g., a dislocation line, a bubble, a free surface, or a grain boundary). They can also recombine with each other, thereby reconstituting the perfect lattice. The rate of migration of vacancies and interstitials can be described by diffusion coefficients (Chap. 7). The relationship between the diffusion coefficient and such atomic parameters as jump frequency and jump distance depends on the lattice structure and, for interstitials, on the type of interstitial site that is occupied (e.g., octahedral, tetrahedral, or split-interstitial sites in the cubic lattice; see Sec. 6.2). In a binary compound, such as  $\text{UO}_2$ , the point-defect diffusion coefficients also depend on whether the defect is on the anion or cation sublattice. In common with most analyses of the mobility of radiation-produced defects in nuclear fuels, we shall ignore these mechanistic details and express the diffusion coefficients for vacancies and interstitials as follows:

For vacancies (see Eq. 7.44),

$$D_v = \lambda_v^2 \nu_v \exp\left(\frac{s_v^*}{R}\right) \exp\left(-\frac{\epsilon_v^*}{RT}\right) \quad (13.26)$$

\*Similar terms can be used to describe the rate of production of vacancy-interstitial pairs in a metal irradiated by fast neutrons. In this situation  $Y_{vi}$  is interpreted as the number of Frenkel pairs generated by each primary knock-on;  $\bar{F}$  denotes the rate at which the latter are created per unit volume. Irradiation effects in metals will be considered in Chap. 17. Defect production by fast neutrons in the fuel, however, is small compared to the production rate due to fission fragments.

and for interstitials,

$$D_i = \lambda_i^2 \nu_i \exp\left(\frac{s_i^*}{R}\right) \exp\left(-\frac{\epsilon_i^*}{RT}\right) \quad (13.27)$$

where  $\lambda$  is the jump distance,  $\nu$  is the vibration frequency of the defect in its equilibrium position, and  $s^*$  and  $\epsilon^*$  are the entropy and energy of motion, respectively. Numerical constants of order unity reflecting the particular lattice structure and the diffusion mechanism in the preceding equations have been set equal to unity. It is common practice to approximate the jump distance by the lattice constant  $a_0$  or a reasonable value such as 3 Å. Similarly, the vibration frequencies are given approximately by

$$\nu_v = \nu_i \approx 10^{13} \text{ sec}^{-1}$$

The entropies and energies of motion for defects in  $\text{UO}_2$  are not known. However, some idea of their relative magnitudes can be obtained by examining the analogous values for copper:<sup>18</sup>

$$\begin{aligned} \epsilon_v^* &= 80 \text{ kJ/mole} & s_v^* &\approx 40 \text{ J mole}^{-1} \text{ }^\circ\text{K}^{-1} \\ \epsilon_i^* &= 20 \text{ kJ/mole} & s_i^* &\approx 0 \end{aligned}$$

The activation energy of interstitial motion is much smaller than that of the vacancy; so the former is considerably more mobile than the latter. The same relative mobilities probably characterize vacancies and interstitials in  $\text{UO}_2$  as well.

### 13.3.2 Xenon in $\text{UO}_2$

According to the classical atomic picture of diffusion reviewed in Chap. 7, atomically dispersed xenon in  $\text{UO}_2$  might be expected to move as an interstitial atom or by a vacancy mechanism on either the oxygen or uranium sublattices. However, it does neither. The neutral xenon atom is much too large to have any significant mobility if it were wedged into any of the interstitial sites in the  $\text{UO}_2$  lattice. If it were to move by a vacancy mechanism, its diffusion coefficient would be given by

$$D_{Xe} = \lambda_{Xe}^2 x_v w \quad (13.28)$$

where  $D_{Xe}$  = the xenon diffusion coefficient

$\lambda_{Xe}$  = the jump distance of a xenon atom in the lattice

$w = \nu_{Xe} \exp(s_{Xe}^*/R) \exp(-\epsilon_{Xe}^*/RT)$ , which is the jump frequency of a xenon atom in a particular direction

$x_v$  = the site fraction of vacancies in the sublattice on which the xenon is assumed to migrate

If xenon diffused by a vacancy mechanism, the diffusion coefficient could be altered simply by controlling the concentration of vacancies on the sublattice by doping the  $\text{UO}_2$  with ions of valence different from 4+. The prevailing type of atomic disorder in  $\text{UO}_2$  consists of vacancies and interstitials on the oxygen sublattice. Thus, the introduction of trivalent cations by doping  $\text{UO}_2$  with a sesquioxide  $\text{M}_2\text{O}_3$  produces oxygen vacancies in excess of the thermo-

dynamic equilibrium value for pure  $\text{UO}_2$  [see Chap. 12 and Fig. 12.8(b)]. Conversely, addition of a soluble compound such as  $\text{Nb}_2\text{O}_5$  should decrease the oxygen vacancy concentration. The site fraction of oxygen vacancies in doped  $\text{UO}_2$  can be computed with the Frenkel equilibrium expression, Eq. 6.37; and from this result the vacancy concentration on the uranium sublattice can be obtained from the Schottky equilibrium, Eq. 6.34. In general, doping of  $\text{UO}_2$  with a trivalent ion should increase the diffusion coefficient of a species that migrates by a vacancy mechanism on the oxygen sublattice but should decrease the diffusion coefficient if migration occurs on the uranium sublattice. Just the opposite should occur when a pentavalent impurity is added to  $\text{UO}_2$ . Matzke<sup>19</sup> has shown that such effects are indeed observed for the self-diffusion of  $\text{U}^{4+}$  in doped  $\text{UO}_2$  ( $\text{U}^{4+}$  diffuses by a vacancy mechanism on the uranium sublattice). However, there was no effect of doping on the xenon diffusion coefficient in the same material. Thus, xenon diffusion in  $\text{UO}_2$  is independent of the concentration of either uranium or oxygen vacancies in the lattice. The only conclusion that can be drawn from these studies is that xenon does not diffuse by a classical single-vacancy mechanism in  $\text{UO}_2$ . By elimination the only mechanism by which single xenon atoms can move about in  $\text{UO}_2$  is as a complex of constant size, the simplest of which is a xenon atom bound to one uranium vacancy and two oxygen vacancies (to maintain electrical neutrality).<sup>20</sup> Similar mechanisms have been offered to explain rare-gas diffusion in other ionic crystals.<sup>21,22</sup>

During fission xenon fission fragments come to rest in a region of the lattice that is especially rich in vacancies. These vacancies (and interstitials) are produced in the fission spike that occurs in the last stages of slowing down of the fission fragment. Consequently, there does not appear to be any difficulty in forming the complex. Once formed, the mobility of the complex is unaffected by the concentration of vacancies in its vicinity. This has been demonstrated experimentally for vacancies produced by doping and should be equally true for vacancies produced by irradiation. For species that diffuse by a true vacancy mechanism (not the complex mechanism proposed for xenon), radiation increases  $x_v$  in Eq. 13.28, and the diffusion coefficient should be enhanced by the presence of radiation-produced vacancies.<sup>18</sup> However, radiation-enhanced diffusion of xenon in  $\text{UO}_2$  would not be expected since the complex carries with it all the vacancies it needs to migrate. Thus, it appears to be incorrect to invoke radiation-enhanced diffusion of fission gases in  $\text{UO}_2$  in developing theories of various processes pertaining to fission-gas behavior, as some investigators have done.<sup>17,23</sup>

Despite the large effort devoted to measuring the diffusion coefficient of the fission gases in  $\text{UO}_2$ , no sound set of values is yet available. Many measurements were made without considering the effect of trapping on the release curves (see Sec. 13.1) or the influence of stoichiometry, and the results range over three orders of magnitude at a particular temperature.<sup>24</sup> The diffusion coefficient of xenon in  $\text{UO}_2$  used in many model calculations of the type described in this chapter is due to Cornell.<sup>25</sup> He measured  $D_{Xe}$  by following the growth of individual gas bubbles in  $\text{UO}_2$  with an electron microscope. His results are

probably freer from the problems associated with trapping than those of other investigations. The diffusion coefficient obtained by Cornell is given by

$$D_{Xe} = 2.1 \times 10^{-4} \exp \left[ -\frac{380}{R(T/10^3)} \right] \text{ cm}^2/\text{sec} \quad (13.29)$$

the activation energy is given in kJ/mole.

### 13.4 REACTION RATES OF ATOMIC-SIZE DEFECTS

In the preceding section it was shown that the motion of crystal defects small enough to be appreciably mobile in the crystal lattice could be described as a random-walk process. When one of these wandering species encounters an object in the crystal to which it is strongly bound, one or both of the partners in this collision can be considered to have disappeared from the solid. This section describes the rates of such processes by analogy to chemical reaction-rate theory. Since the rate is proportional to the concentrations of each of the interacting species, we can write

Rate of reaction between species A and B

$$= k_{AB} C_A C_B \text{ reactions sec}^{-1} \text{ cm}^{-3} \quad (13.30)$$

where  $C_A$  and  $C_B$  are the volumetric concentrations of species A and B in the solid (in units of particles/cm<sup>3</sup>) and  $k_{AB}$  is the rate constant of the reaction with units of cm<sup>3</sup>/sec. Reaction can occur between types of particles that are both mobile (e.g., combination of two vacancies or two fission-gas atoms). Or, in a certain temperature range, one of the particles can be mobile and the other stationary. Such an approximation is commonly applied to recombination of vacancies and interstitials; the mobility of interstitials is generally much greater than that of vacancies; so the latter can be considered fixed in the lattice. Reactions between mobile point defects and stationary line defects (dislocations) can also be treated by reaction-rate formalism.

To determine the rate constant, we assume that there are no macroscopic gradients of the concentrations of either of the reaction partners. If one of the reacting partners is large compared to an atomic-size reactant (e.g., a gas bubble accumulating gas atoms or vacancies) or if one of the species is a strong sink, a concentration gradient on the point defects may be established in the vicinity of the stationary defect. In such cases the rate of the overall process is governed by the rate of diffusion of the mobile species to the stationary sink. Such diffusion-controlled kinetics are considered in the next section. Reactions proceeding in the absence of diffusional limitations are called reaction-rate controlled. The term "rate-controlled jumping" has also been used to describe reaction-rate-limited processes.<sup>26</sup>

#### 13.4.1 Vacancy—Vacancy Reaction

The reaction between two vacancies to form a divacancy can be written



We consider here only the forward reaction. The rate at which divacancies dissociate can be obtained from knowledge of the forward rate constant and the vacancy—divacancy equilibrium (Sec. 6.4) since the ratio of forward and reverse rate constants must equal the thermodynamic equilibrium constant. The rate of divacancy formation has been treated by Damask and Dienes,<sup>2,7</sup> and their analysis is followed here.

The rate of divacancy formation can be written

$$\text{Rate of divacancy formation/cm}^3 = P_{vv} C_v \quad (13.32)$$

where  $C_v$  is the concentration of monovacancies. Since a divacancy is formed when two single vacancies occupy nearest neighbor lattice sites, the coefficient

$P_{vv}$  = probability per second that another vacancy jumps into a site that is nearest neighbor to a particular vacancy

The probability  $P_{vv}$  depends on the crystal structure. The method of calculating it for the fcc lattice is shown in Fig. 13.4. Here, we center attention on a particular vacancy that is located between the upper and lower unit cells on the left of the drawing. The nearest-neighbor sites that result in divacancy formation if they are occupied by another single vacancy are marked with crosses. Since the 12 nearest-neighbor sites on the fcc lattice are all equivalent, we need only calculate the probability

$P_x$  = probability per second that another vacancy jumps into one of the nearest-neighbor positions surrounding the particular vacancy

from which  $P_{vv}$  can be obtained from

$$P_{vv} = 12P_x \quad (13.33)$$

The probability  $P_x$  is proportional to (1) the number of sites surrounding the chosen nearest-neighbor site from which another vacancy could jump, (2) the probability that one of these lattice positions is occupied by a vacancy, and (3) the jump frequency of a vacancy in a particular direction. Figure 13.4 shows that each nearest neighbor to the chosen vacancy has seven nearest neighbors from which a jump could occur. (The other five nearest neighbors are excluded either because they are the original vacancy or one of its nearest neighbors). The arrows in the drawing indicate the seven possible jumps. The probability that any one of these seven sites in fact contains a vacancy is assumed to be equal to the probability that any site in the lattice contains a vacancy, namely, to the vacancy site fraction  $x_v$ . Finally, the rate at which a vacancy jumps to a particular adjacent site is given by the quantity  $w$ , which can be estimated from absolute rate theory (Sec. 7.5). Thus

$$P_x = 7x_v w \quad (13.34)$$

The vacancy-site fraction can be written in terms of the volumetric concentration as

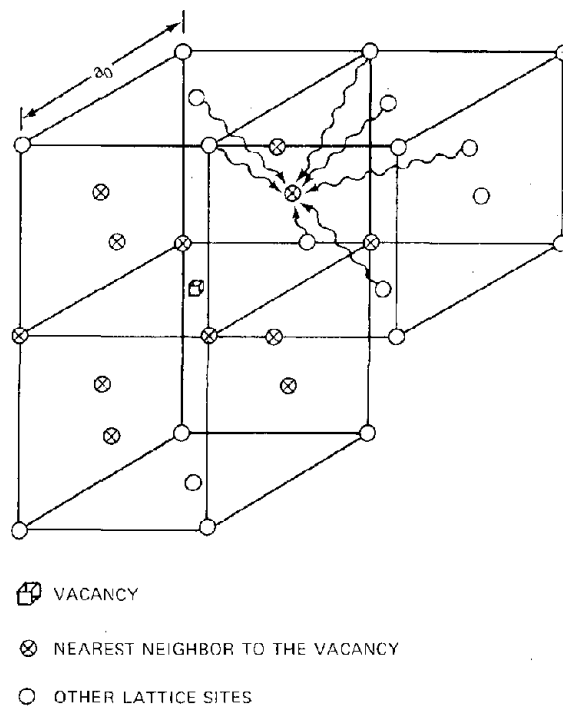


Fig. 13.4 Diagram for computing the rate of divacancy formation in a face-centered cubic lattice.

$$x_v = C_v \Omega \quad (13.35)$$

where  $1/\Omega$  is the number of lattice sites per unit volume. Substituting Eqs. 13.33 through 13.35 into Eq. 13.32 yields the rate:

$$\text{Rate of divacancy formation/cm}^3 = 84w\Omega C_v^2 \quad (13.36)$$

Comparison of this equation with Eq. 13.30 shows that the rate constant for vacancy—vacancy combination is

$$k_{vv} = 84w\Omega \quad (13.37)$$

The jump frequency can be related to the vacancy diffusion coefficient by Eq. 7.29:

$$D_v = a_0^2 w \quad (13.38)$$

where  $a_0$  is the lattice parameter. Combining the two preceding equations yields

$$k_{vv} = \frac{84\Omega D_v}{a_0^2} \quad (13.39)$$

Although Eq. 13.39 has been derived for the interaction of two vacancies, the same formula is obtained for the reaction between any impurity species that occupies a substitutional position in the fcc lattice ( $D_v$  in Eq. 13.39 need only be replaced by the diffusivity of the impurity). Relations similar to Eq. 13.39 can be derived for other lattice types, but the numerical factor on the right-hand side, which is called the combinatorial number, depends on

the crystal structure. Combinatorial numbers represent the solid-state analog of the cross sections that describe reaction rates when nonlocalized particles, such as gas molecules or neutrons, are involved.

As will be seen in Sec. 13.6, the rate of reaction between two mobile species A and B is given by  $(k_{AB} + k_{BA})C_A C_B$ , where  $k_{AB}$  is the rate constant calculated on the assumption that species B is immobile and  $k_{BA}$  is obtained by the same calculation with A immobile. In the case just considered, the vacancy in Fig. 13.4 was assumed to be stationary. When account is taken of its mobility, the rate constant of Eq. 13.39 should be multiplied by a factor of 2.

The derivation of the divacancy formation rate was presented in detail not because the value of this rate constant is of particular importance in analyzing fission-gas behavior in solid nuclear fuels but because it represents one of the few cases in which the geometry and range of the interaction can be accurately specified.

### 13.4.2 Vacancy—Interstitial Recombination

The method described for vacancy—vacancy encounters can be applied to the recombination reaction



where “null” denotes a perfect lattice site. If it is assumed that the vacancy is stationary and the interstitial is mobile and that recombination occurs only when an interstitial atom jumps into an interstitial site that is nearest neighbor to the vacancy, the recombination rate constant for octahedral interstitials in the fcc lattice is

$$k_{vi} = \frac{48\Omega D_i}{a_0^2} \quad (13.41)$$

Such a computation, however, is in error for two reasons. First, the stable interstitial probably does not occupy either an octahedral or tetrahedral interstice in the fcc lattice (Fig. 6.2). Rather, a split interstitial (Fig. 6.4) is believed to be formed. In copper the stable configuration is a [100] split interstitial.<sup>2,8</sup> Second, recombination can spontaneously occur even if the split interstitial is further removed from the vacancy than the nearest-neighbor distance. Surrounding each vacancy is a rather large sphere of influence, which, if entered by an interstitial, inevitably results in spontaneous recombination. Figure 13.5 shows a region on the (100) plane of copper in the center of which a [100] split interstitial resides. Gibson et al.<sup>2,8</sup> have shown that a vacancy on any one of the lattice sites marked with a cross will spontaneously annihilate the split interstitial. The dashed line in the figure delineates the area of the (100) plane surrounding an interstitial in which unstable sites are located. When one expands such a diagram from two to three dimensions, it becomes obvious that there are many more positions surrounding an interstitial (or a vacancy) from which recombination can occur than just the 12 nearest-neighbor sites. The net effect of this large sphere of influence is to replace the combinatorial number 48 in Eq. 13.41 by a much larger number, which leads to the rate constant

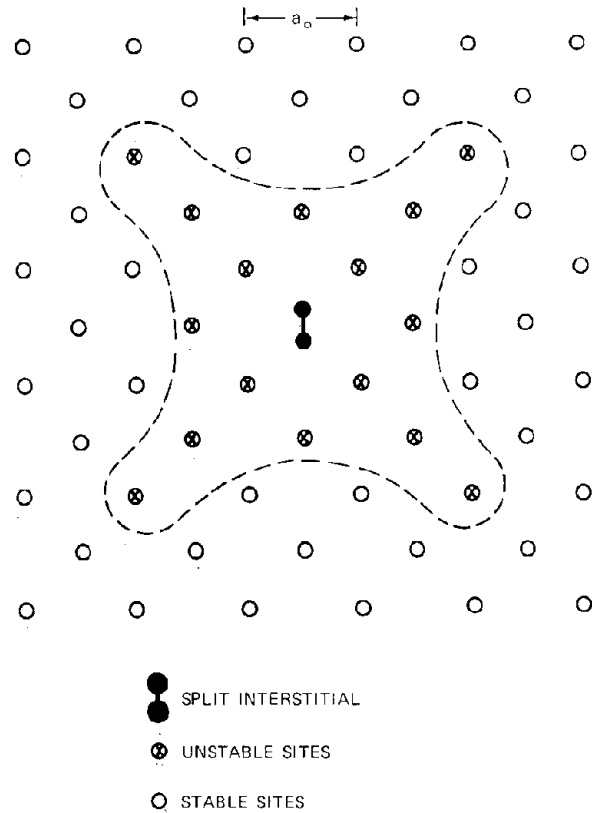


Fig. 13.5 Stability of Frenkel pairs in the (100) plane of copper. The dashed line separates stable from unstable vacancy sites. [After Gibson et al., *Phys. Rev.*, 120: 1229 (1960).]

$$k_{vi} = \frac{z_{iv}\Omega D_i}{a_0^2} \quad (13.42)$$

where the combinatorial number for recombination,  $z_{iv}$ , is of the order of 500.

### 13.4.3 Interaction Between Migrating Fission-Gas Atoms

The rate at which migrating fission-gas atoms encounter each other during their random walk on the lattice is of considerable importance in fission-gas behavior analyses. A pair of adjacent xenon atoms is believed to be a relatively stable entity (see problem 6.1) and is often taken to be the nucleus from which gas bubbles subsequently grow. Thus, it is important to be able to estimate the rate constant for the reaction



where  $g$  represents a mobile fission-gas atom in the solid and  $g_2$  is a diatomic cluster. In most analyses that use this elementary step, dissociation of the di-atom by thermal processes is not considered. However, radiation can reverse this reaction (Eq. 13.43).

Because atomically dispersed xenon migrates as a complex containing the xenon atom and several vacancies, the analysis that was used for vacancies is not applicable (although at least one paper<sup>29</sup> has simply used the vacancy—vacancy analysis and replaced the vacancy concentration by the concentration of matrix xenon atoms and  $D_v$  by  $D_{Xe}$ ). Just as in the case of vacancy—interstitial recombination, the sphere of influence surrounding xenon atoms in the lattice in which a stable diatomic cluster can be formed is probably much larger than the distance between nearest neighbors. The most reasonable approach appears to be to accept the form of the rate constant formula as computed by the vacancy—vacancy interaction problem but allow for a larger combinatorial number. Thus,  $k_{11}$  would be

$$k_{11} = \frac{z_{11} \Omega D_{Xe}}{a_0^2} \quad (13.44)$$

where  $z_{11}$  is a combinatorial number probably much larger than 84. The rate of formation of diatomic gas clusters is then

$$\begin{aligned} \text{Rate of formation of diatomic gas clusters/cm}^3 \\ = k_{11} C^2 \end{aligned} \quad (13.45)$$

#### 13.4.4 Interaction Between Xenon Atoms and Atomic-Size Traps

Theories of the effect of trapping on the mobility of fission gases in ceramic materials often attempt to account for the immobilizing effect of encounters between a migrating gas atom and a structural defect of atomic size, which can be an impurity atom, a small damage area rich in radiation-produced vacancies and interstitials, or another fission-gas atom.<sup>2,6</sup> The rate of gas-atom trapping can be expressed by

$$\begin{aligned} \text{Rate of trapping of fission-gas atoms/cm}^3 \\ = k_{gtr} C_t C \end{aligned} \quad (13.46)$$

where  $C_t$  is the concentration of point traps,  $C$  is the concentration of atomically dispersed fission gas, and  $k_{gtr}$  is the rate constant for the gas-atom—trap interaction. By analogy to Eq. 13.44, the rate constant can be expressed

$$k_{gtr} = \frac{z_{gtr} \Omega D_{Xe}}{a_0^2} \quad (13.47)$$

where  $z_{gtr}$  is a combinatorial number representing the number of trapping sites surrounding each trapping center.

The trapping rate can also be expressed by<sup>2,6</sup>

$$\begin{aligned} \text{Rate of trapping of fission-gas atoms/cm}^3 \\ = \frac{D_{Xe} C}{L^2} \end{aligned} \quad (13.48)$$

The quantity  $L$  is termed the diffusion trapping length for the following reasons. If there are  $C_t$  trapping centers per unit volume of the solid and each offers  $z_{gt}$  sites for

trapping a gas atom, then there are  $z_{gt} C_t$  trapping sites per unit volume. The fraction of all lattice sites on which trapping can occur is therefore  $z_{gt} C_t \Omega$ . Since the jumping of the gas atoms on the lattice is a random-walk process, the probability that an atom lands on a trapping site in any particular jump is also  $z_{gt} C_t \Omega$ . The number of jumps required for a newly created gas atom to reach a trap is just the reciprocal of this probability, or

$$j = (z_{gt} C_t \Omega)^{-1} \quad (13.49)$$

According to random-walk theory (Eq. 7.16), the relation between the mean square distance covered by a diffusing atom in  $j$  jumps is

$$L^2 = ja_0^2 \quad (13.50)$$

where the length of a diffusive jump has been taken as the lattice constant. Combining Eqs. 13.49 and 13.50 yields

$$L^2 = \frac{a_0^2}{z_{gt} C_t \Omega} \quad (13.51)$$

This formula is equivalent to those derived by Kelly and Matzke<sup>30</sup> and Ong and Elleman<sup>31</sup> if the combinatorial number is set equal to 6 and 3, respectively. Equations 13.48 and 13.51 give the same reaction rate as Eqs. 13.46 and 13.47.

#### 13.4.5 Interaction of Migrating Point Defects with Dislocations

Because of the unique nature of the stress fields in the neighborhood of a dislocation line, this type of crystal imperfection is an efficient sink for many atomic defects. The edge dislocation, for example, places the solid beneath the extra sheet of atoms in Fig. 8.4 in tension and creates a region of compression above the glide plane. Vacancies are attracted by the compressive stress field and interstitials by the tensile stress field. A vacancy or interstitial that approaches a dislocation line in the course of a random-walk process can be permanently captured by the line. When capture occurs, the dislocation climbs, in opposite directions for vacancy and interstitial capture. Similarly, any impurity species that acts as a point center of stress in the crystal can be strongly bound to a dislocation line. Thus the dislocation line acts as a nearly perfect sink for vacancies and interstitials\* and as an efficient trap for fission-gas atoms. Following the model of Bullough and Perrin,<sup>32</sup> we derive the rate of reaction of the dislocations and vacancies. The method is applicable to all point defects.

By analogy to the sphere of influence surrounding a vacancy or interstitial in the recombination process, we

\*Dislocations are not quite perfect sinks for vacancies and interstitials in the sense that they never release these species to the bulk crystal. If this were so, the equilibrium concentration of vacancies and interstitials would be zero. One mechanism by which the thermodynamic concentration of these point defects is maintained in a crystal is by a balance between their capture and emission rates from the dislocation network.

visualize a cylinder of influence around each dislocation line. If a vacancy hops onto a lattice site within this volume, capture is certain. The cylinder of influence is considered to be composed of  $z_{vd}$  atomic sites on each of the parallel crystal planes intersected by the dislocation line (Fig. 13.6). The extent of this region is often called the capture radius of the dislocation line. If the spacing between atomic planes in the lattice is approximated by the lattice spacing  $a_0$ , there are  $z_{vd}/a_0$  capture sites per unit length of dislocation line.\* Letting  $\rho_d$  be the density of dislocation lines in the crystal (in units of centimeters of dislocation line per cubic centimeter of solid), we have  $z_{vd}\rho_d/a_0$  capture sites per unit volume. We can now use the analysis developed for the interaction of fission-gas atoms with point traps. In place of the number of trapping sites per unit volume  $z_{gt}C_t$ , the density of capture sites around dislocations is used. Making this replacement in Eq. 13.51 and approximating  $\Omega$  by  $a_0^3$ , we find the diffusion length for vacancy capture by a dislocation to be

$$L^2 = \frac{1}{z_{vd}\rho_d} \quad (13.52)$$

or, the capture rate is

$$\begin{aligned} \text{Rate of vacancy capture by dislocations/cm}^3 \\ = D_v z_{vd} \rho_d C_v \end{aligned} \quad (13.53)$$

The analogous expression for interstitial capture is

$$\begin{aligned} \text{Rate of interstitial capture by dislocations/cm}^3 \\ = D_i z_{id} \rho_d C_i \end{aligned} \quad (13.54)$$

In metals  $z_{vd}$  and  $z_{id}$  are very nearly but not quite equal. The dislocation line has a slightly greater affinity for interstitials than vacancies, perhaps by a few percent. This seemingly minor difference in a calculation full of order-of-magnitude estimates may not at first appear significant, but it will be shown in Chap. 19 that it is just this slight imbalance in capture rates which allows voids to grow in metals. In treating the Frenkel-pair removal by dislocations in the fuel, however,  $z_{vd}$  and  $z_{id}$  are usually assumed to be equal.

For trapping of fission-gas atoms by dislocations, the rate is

$$\begin{aligned} \text{Rate of capture of fission-gas atoms by dislocations/cm}^3 \\ = D_{Xe} z_{gd} \rho_d C \end{aligned} \quad (13.55)$$

where  $z_{gd}$  is the appropriate combinatorial number for the gas-atom—dislocation interaction.

\*This statement does not apply to dislocation loops, which are circular dislocations resulting from the condensation of excess interstitials in the solid. Here, the attachment sites are restricted to jogs on the loop, which can be much less densely spaced than the capture sites on a straight edge dislocation.

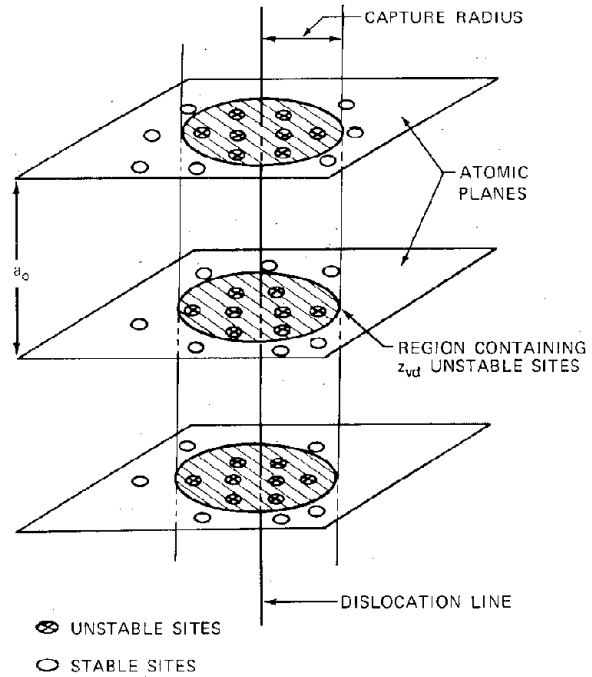


Fig. 13.6 Schematic of the capture sites around a dislocation line.

### 13.5 DIFFUSION-LIMITED REACTIONS

The preceding section described methods of calculating the rates of several elementary processes involving defects in crystals with the supposition that the concentrations of the two reactants were everywhere uniform. This treatment of reaction-rate controlled kinetics is entirely analogous to the way in which the rates of ordinary homogeneous chemical reactions are analyzed. However, interaction between a cloud of point particles and a collection of widely spaced, efficient sinks more closely resembles the fluid—solid systems that occur in the field of heterogeneous chemical kinetics. In particular, if the reaction rate between the point particles and the discrete sinks is very rapid, the surface of the sink can become starved of reactant particles because of kinetic limitations to the rate at which they can be transported from the bulk crystal to the reacting surface. The overall process should therefore be considered as composed of two steps in series: the first is the diffusional process involved in transporting point particles from the bulk to the surface, and the second is the reaction of the particles with the discrete sink.

If reaction occurs on every collision of the two reactants, the question of whether the kinetics are diffusion-limited or reaction-rate-limited depends primarily on the relative sizes of the two interacting species. If both are mobile atomic-size particles, diffusion limitations are not significant. If one particle is small and mobile and the other is large and stationary, the kinetics are likely to be diffusion limited. Between these two limiting situations, there can exist a transition region in which both diffusion and

reaction proceed at comparable rates. The growth of fission-gas bubbles is one example where mixed kinetic control can be significant. The bubble is first formed as a two-atom cluster by the random encounter of two migrating gas atoms. The rate of this process clearly does not involve long-range concentration gradients, or it is free of diffusional limitations in the sense described. However, the two-atom complex eventually reacts with another gas atom to form a tri-atom complex, and so on. At some cluster size, a concentration gradient of gas atoms begins to develop in the vicinity of the growing sphere. As the bubble gets larger and larger, the gas-atom concentration at the surface becomes progressively smaller. Eventually, growth of the bubble is completely dictated by the rate of diffusion of gas atoms down the concentration gradient between the bubble surface, where the concentration is close to zero, and the bulk solid, where the gas-atom concentration is maintained by the fission process. In the course of its growth from a nucleus to a full-fledged bubble, the kinetics of gas-atom absorption by the cluster passes successively through a regime of reaction-rate control, a transition region, and finally to diffusion control. Similar arguments apply to voids in metals that grow by vacancy accumulation.

The rate at which dislocation lines capture vacancies or interstitials can be reaction-rate or diffusion controlled. However, in distinction to gas bubbles or voids, which grow as they accumulate point particles, dislocations do not change size as they capture vacancies or interstitials; they respond by moving by climb. The criterion for determining whether capture kinetics at dislocations is reaction-rate or diffusion controlled is controlled more by the spacing of the dislocations than their size.

### 13.5.1 Diffusion to Spherical Sinks

We consider first the case of  $C_t$  spherical objects per unit volume each of radius  $R$  which are accumulating a particular type of point defect that is present in the solid between the spherical sinks. The rate of transport of the point defects to the spheres by diffusion is most easily treated if only a single sphere is considered. A unit cell, or capture volume, surrounding each sphere is defined as the portion of the solid that can be associated with each sphere. As in the analogous case of electrons in a metal (see Eq. 4.4), the entire volume could be divided into  $C_t$  identical polyhedra each containing one sphere at its center in order to reproduce (on an average basis) the system of solid plus spheres. For ease of computation it is convenient to approximate each polyhedron by a sphere with a radius chosen to satisfy the requirement that the  $C_t$  cells occupy the entire volume. Thus the radius  $\mathcal{R}$  of the capture volume around each sphere is defined by

$$\left(\frac{4\pi\mathcal{R}^3}{3}\right)C_t = 1 \quad (13.56)$$

The idealized geometry is depicted in Fig. 13.7.

The diffusion equation for the point defects is to be solved in the annular spherical shell  $R \leq r \leq \mathcal{R}$ . The concentration of point particles at radial position  $r$  in the capture volume at time  $t$  is denoted by  $C(r,t)$ . The choice of the capture volume implies that there is no net flux of

point defects across the boundary at  $r = \mathcal{R}$ , which supplies the following boundary condition for the diffusion equation

$$\left(\frac{\partial C}{\partial r}\right)_{\mathcal{R}} = 0 \quad (13.57a)$$

The point-defect concentration at the surface of the sphere is specified:

$$C(R,t) = C_R \quad (13.57b)$$

The value of  $C_R$  depends on the particular process. If the spheres represent gas bubbles and the point defects are fission-gas atoms, the complete insolubility of the latter in the solid is equivalent to setting  $C_R = 0$ . If the sphere is a gas bubble or a void and the point defects are vacancies or interstitials,  $C_R$  is the thermodynamic equilibrium concentration of these defects under the stress conditions characteristic of the bubble (or void)—solid interface. For the purpose of this analysis,  $C_R$  is taken to be a specified time-independent quantity.

The particles are assumed to be created uniformly within the capture volume. We further assume that there are no sinks for this particle other than the sphere in the center. The concentration  $C(r,t)$  is determined by solution of the diffusion equation in spherical coordinates with a volumetric source term representing production of the point defects within the capture volume

$$\frac{\partial C}{\partial t} - D \frac{\partial}{\partial r} \left( r^2 \frac{\partial C}{\partial r} \right) + Y\dot{F} \quad (13.58)$$

where  $D$  is the diffusion coefficient of the particles and  $Y\dot{F}$  is the rate of creation per unit volume. In the case of vacancies and interstitials, an additional term representing recombination should be included on the right-hand side of Eq. 13.58. Discussion of this complication is deferred until later. Two special cases of Eq. 13.58 are of interest and are discussed in the next two sections.

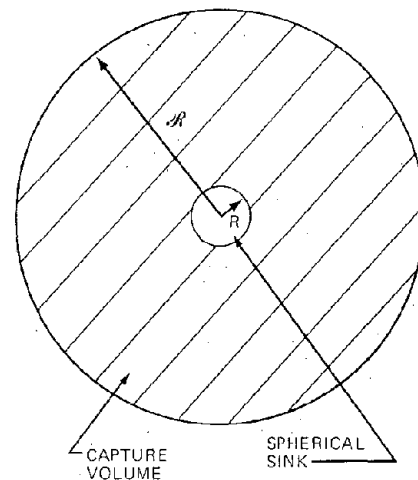


Fig. 13.7 The unit cell for computing the diffusion-controlled rate of point-defect absorption by spherical sinks.

### In-Pile Behavior

When the solid is irradiated at temperatures sufficiently high for appreciable point-defect mobility, loss of particles to the spherical sink is at least partially compensated by production within the capture volume, and the concentration at any point in the capture volume changes rather slowly. In this case we can neglect  $\partial C/\partial t$  on the left of Eq. 13.58 to first approximation. This simplification is called the quasi-stationary approximation, and with it the diffusion equation becomes

$$\frac{D}{r^2} \frac{d}{dr} \left( r^2 \frac{dC}{dr} \right) = -Y\dot{F} \quad (13.59)$$

The solution of Eq. 13.59 subject to the boundary conditions provided by Eqs. 13.57(a) and 13.57(b) is

$$C(r) - C_R + \frac{Y\dot{F}}{6D} \left[ 2\mathcal{R}^3 \frac{(r-R)}{rR} - (r^2 - R^2) \right] \quad (13.60)$$

In many practical cases the radius of the capture volume is much larger than that of the sink, and Eq. 13.60 takes on the general shape shown in Fig. 13.8. The form of the curve suggests an additional approximation. The concentration is changing rapidly only in a region close to the surface of the sphere and approaches a constant value well before the outer radius of the capture volume is reached. This behavior suggests that the capture volume can be divided into the two regions shown in Fig. 13.8. In region 1 diffusion is the most important factor in Eq. 13.59, and the source term can be neglected. In region 2 the relative magnitudes of the two terms are reversed. For region 1 we can write

$$\frac{1}{r^2} \frac{d}{dr} \left( r^2 \frac{dC}{dr} \right) = 0 \quad (13.61)$$

to which the boundary condition of Eq. 13.57(b) still applies but Eq. 13.57(a) is replaced by

$$C(\infty) = C(\mathcal{R}) \quad (13.62)$$

where  $C(\mathcal{R})$  is a concentration to be determined by matching the solutions in regions 1 and 2. Because this concentration is approached at short distances from the surface, the capture volume can be considered to be an infinite medium as far as the diffusion process in region 1 is concerned. The solution to Eq. 13.61 with the appropriate boundary conditions is

$$C(r) = C_R + [C(\mathcal{R}) - C_R] \left[ 1 - \left( \frac{R}{r} \right) \right] \quad (13.63)$$

The flux of particles at the surface of the sphere is

$$J = -D \left( \frac{dC}{dr} \right)_R \quad (13.64)$$

Using Eq. 13.63, the flux is

$$J = - \frac{D[C(\mathcal{R}) - C_R]}{R} \quad (13.65)$$

A minus sign appears in Eq. 13.65 because the flux is positive if in the +r-direction.

The rate at which point defects are absorbed by the sphere is

Rate of absorption by sphere

$$= -(4\pi R^2)J = 4\pi RD [C(\mathcal{R}) - C_R] \quad (13.66)$$

The concentration  $C(\mathcal{R})$  is determined from the production rate of point defects in the capture volume (regions 1 and 2) in conjunction with the condition of no net flow over the boundary at  $r = \mathcal{R}$ . The latter requires that all the point defects produced in the capture volume be absorbed by the sphere, or

$$\frac{4\pi}{3} (\mathcal{R}^3 - R^3) Y\dot{F} = 4\pi RD [C(\mathcal{R}) - C_R] \quad (13.67)$$

If  $R^3$  is negligible compared to  $\mathcal{R}^3$ , the preceding balance yields

$$C(\mathcal{R}) = C_R + \frac{Y\dot{F}\mathcal{R}^3}{3DR} \quad (13.68)$$

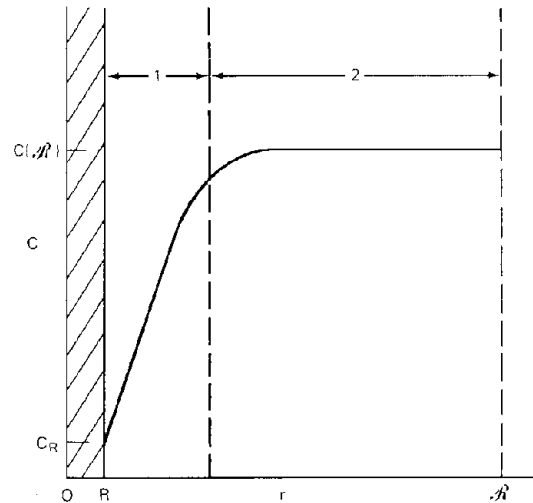


Fig. 13.8 Solution of the diffusion in a spherical shell with a uniform volumetric source.

The agreement between the two-region approximation and the complete solution (both in the quasi-stationary approximation) can be seen by setting  $r = R$  and  $R/R \ll 1$  in Eq. 13.60, which then reduces to Eq. 13.68.

The two-region approximation is not a particularly valuable approximation method in this case because Eq. 13.59 can be solved without difficulty. However, the possibility of decoupling the diffusion phenomena occurring close to absorbing sinks from the source term uniformly distributed in the solid provides a major simplification when the solid contains a variety of sinks of point defects and when nonlinear processes such as recombination occur.

Equation 13.66 can be put into the form of a rate constant so that the diffusion-controlled kinetics can be compared to the reaction-rate-controlled expressions derived in the previous section. We assume for simplicity that  $C(\mathcal{R}) \gg C_R$  in Eq. 13.66 and denote  $C(\mathcal{R})$  by  $C$ , with the understanding that this parameter represents the average concentration of point defects in the medium. To obtain the total rate of diffusion-controlled absorption of point defects by the spherical sink, we multiply Eq. 13.66 by the number of sinks per unit volume,  $C_t$ , which yields

$$\text{Rate of absorption by spherical sinks/cm}^3 = 4\pi R D C_t C \quad (13.69)$$

Or, the rate constant for diffusion-controlled reaction of point particles and a perfect spherical sink of radius  $R$  is

$$k = 4\pi R D \quad (13.70)$$

It should be emphasized that Eq. 13.70 is based on two major simplifications. The first is the quasi-stationary approximation, which permits the time derivative in Eq. 13.58 to be deleted. The second is that the radius of the spherical sink is small compared to the distance separating the sinks, which permits the source-sink terms in the diffusion equation to be decoupled from the concentration gradient term. If the condition  $R/\mathcal{R} \ll 1$  is not satisfied, the complete solution presented by Ham<sup>33</sup> must be used.

The similarity between the two-region approximation and the boundary-layer approximation of fluid mechanics should be noted.

### Postirradiation Annealing

In this application of Eq. 13.58, an initial concentration of fission-gas atoms is generated in the solid by irradiation at low temperature where particle mobility is too low to permit appreciable absorption by sinks. Next, the temperature is increased to a value at which the gas atoms are mobile. Small bubbles are nucleated, and these act as sinks to remove the remainder of the gas in solution. During annealing, the gas-atom concentration in the capture volume surrounding each gas bubble is governed by

$$\frac{\partial C}{\partial t} = \frac{D_{Xe}}{r^2} \frac{\partial}{\partial r} \left( r^2 \frac{\partial C}{\partial r} \right) \quad (13.71)$$

The boundary conditions are given by Eqs. 13.57a and 13.57b. As a result of this initial low-temperature irradiation, a uniform distribution of gas atoms is created, which provides the initial condition for Eq. 13.71:

$$C(r,0) = C_0 = Y_{Xe} \bar{F} t_{irr} \quad (13.72)$$

This set of equations cannot be solved as readily as at first appears because the bubble radius  $R$  is a function of time. The radius  $R$  depends on the number of fission-gas atoms contained by the bubble; so the time rate of change of  $R$  must be coupled to the particle flux at the surface,  $J$ ,

To attack this problem in an analytic manner, we can invoke the two-region approximation. It is assumed that diffusional processes dominate in the region close to the sphere surface, but, because this region is quite thin, the quasi-stationary approximation can be applied to it. The inherent time dependence of the postirradiation anneal is maintained in region 2, but here the diffusional phenomenon is ignored.

Let  $m$  be the number of gas atoms in the bubble at any time during the anneal. The radius of the bubble in terms of  $m$  can be obtained from the discussion of Sec. 13.2. To simplify this analysis, we assume that (1) the bubble is in equilibrium with the bulk solid, (2) the bulk solid is stress-free, and (3) the gas in the bubble behaves ideally. Under these three conditions,  $m$  is given by Eq. 13.16:

$$m = \left( \frac{4\pi R^2}{3} \right) \left( \frac{2\gamma}{kT} \right) \quad (13.16)$$

The rate of change of the number of gas atoms in the bubble is equal to the rate of absorption by the sphere, which in the quasi-stationary, two-region approximation, is given by Eq. 13.66

$$\frac{dm}{dt} = 4\pi R D_{Xe} C \quad (13.73)$$

where the gas concentration at the bubble surface has been set equal to zero and  $C$  is the average concentration of matrix gas atoms at time  $t$ . Since the gas initially in the capture volume either remains there or enters the bubble, an overall gas-atom balance yields

$$\frac{4\pi \mathcal{R}^3}{3} (C_0 - C) = m \quad (13.74)$$

where the bubble radius has been neglected compared to  $\mathcal{R}$ .

Bubble growth ceases when all the gas has precipitated into the bubble, and none remains in the lattice. The final bubble radius can be determined by equating Eqs. 13.16 and 13.74 and setting  $C = 0$  and  $R = R_f$ , which yields

$$R_f^2 = \mathcal{R}^3 C_0 \left( \frac{kT}{2\gamma} \right) \quad (13.75)$$

The time rate of change of the bubble radius is obtained as the simultaneous solution of Eqs. 13.16, 13.73, and 13.74. The solution has been developed by Speight<sup>34</sup> and by Markworth,<sup>35</sup> and the latter treatment is followed here.

First differentiate Eq. 13.16 with respect to  $t$  and equate to Eq. 13.73, which yields

$$\frac{dR}{dt} = \frac{3D_{Xe} C}{2} \left( \frac{kT}{2\gamma} \right) \quad (13.76)$$

Next substitute Eqs. 13.16 and 13.76 into Eq. 13.74 and eliminate  $C_0$  with the aid of Eq. 13.75. The bubble growth rate is then given by

$$\frac{dR}{dt} = \frac{3D_{Xe}}{2\mathcal{R}^3} \left( R_f^2 - R^2 \right) \quad (13.77)$$

which can be integrated with the initial condition  $R = 0$  at  $t = 0$  to give

$$\ln\left(\frac{R_f + R}{R_f - R}\right) = \frac{3D_{Xc}R_f t}{\mathcal{R}^3} \quad (13.78)$$

The major source of inaccuracy in this formula is the assumption of ideal-gas behavior. Equation 13.16 is valid only for large bubbles; yet, at the start of the anneal, the bubbles are very small, and nonideal-gas behavior must be considered. This deficiency can be remedied by using Eq. 13.14 in place of Eq. 13.16 in the calculation. Although an exact solution is no longer possible, Speight<sup>34</sup> has given an approximate solution for the case of the van der Waals equation of state. The modified form of Eq. 13.78 which results from gas nonideality correction has been applied by Cornell<sup>25</sup> to measure the diffusivity of fission gases in  $\text{UO}_2$ . Figure 13.9 shows photomicrographs of an area of a thin film of irradiated  $\text{UO}_2$  during annealing at  $1300^\circ\text{C}$ . The increase in bubble size with time is clearly evident. Use of the radius-time information obtained from such pictures in conjunction with the modified form of Eq. 13.78 yielded the diffusion coefficient given by Eq. 13.29.

### 13.5.2 Diffusion to Dislocations

When deformation-induced dislocations in the crystal are widely spaced (i.e., low dislocation density), they can

be considered as line sinks for vacancies and interstitials that are present in the bulk solid. The diffusion problem governing the rate at which the point defects are captured by the network of dislocations can be solved in the quasi-stationary two-region problem previously applied to spherical sinks. The calculation must be performed in cylindrical rather than spherical symmetry, however. If the diagram of Fig. 13.6 were examined from a direction parallel to the dislocation, a picture similar to that shown in Fig. 13.7 would be seen. However, in the case of dislocations, the radius of the sink is taken as the capture radius of the dislocation,  $R_d$ , and the radius of the spherical capture volume is replaced by the radius of a cylindrical capture volume. If the dislocation density is  $\rho_d$   $\text{cm}/\text{cm}^3$  and we imagine that the dislocations are arranged as parallel lines on a simple square configuration,  $\rho_d$  dislocation lines intersect each unit area perpendicular to the array. Thus, the analog of Eq. 13.56 for the present case is

$$(\pi \mathcal{R}^2) \rho_d = 1 \quad (13.79)$$

which defines the radius of the cylindrical capture volume surrounding each dislocation.

Proceeding as in the analysis of the diffusion of point defects to spherical sinks, we first consider the quasi-

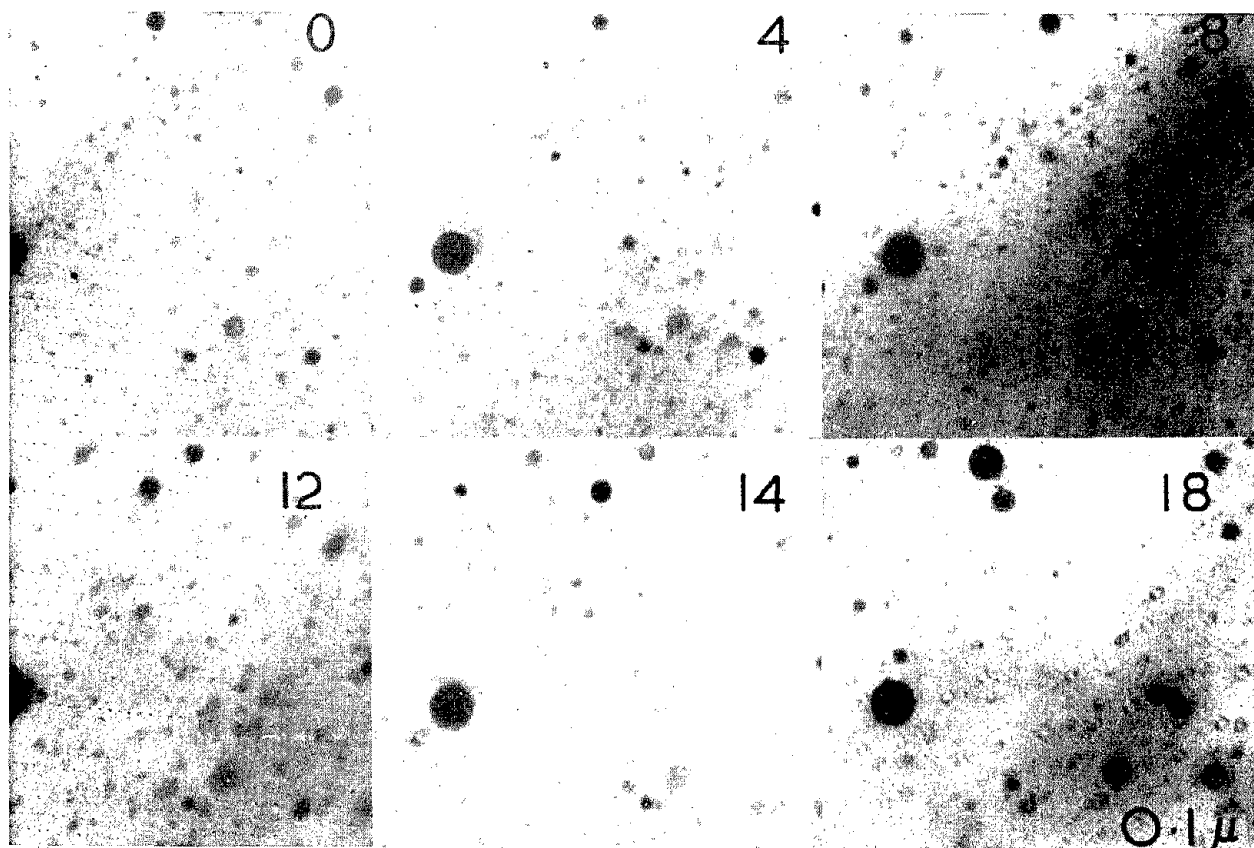


Fig. 13.9 The growth of gas bubbles after annealing for the indicated time in hours at  $1300^\circ\text{C}$ . [From R. M. Cornell, *Phil. Mag.*, 19: 319 (1969).]

stationary diffusion problem with a homogeneous source in the capture volume. The calculation is illustrated for vacancies, for which the diffusion equation is

$$\frac{D_v}{r} \frac{d}{dr} \left( r \frac{dC_v}{dr} \right) = -Y_{vi} \dot{F} + k_{vi} C_v C_i \quad (13.80)$$

The vacancy-interstitial recombination term on the right of Eq. 13.80 requires that the vacancy-diffusion problem be solved simultaneously with that of the interstitials. Because of the recombination term, the coupled equations are nonlinear. For the present purposes the complications caused by recombination can be circumvented by replacing the local value of  $k_{vi} C_v C_i$  by its volume averaged value, which renders the right-hand side of Eq. 13.80 a constant

$$(Y\dot{F})_{\text{eff}} = Y_{vi} \dot{F} - \overline{k_{vi} C_v C_i} \quad (13.81)$$

where the bar over the last term denotes the average value over the capture volume. Using  $(Y\dot{F})_{\text{eff}}$  as the source term in Eq. 13.80 and the boundary conditions

$$C_v(R_d) = C_{R_d} \quad (13.82)$$

and

$$\left( \frac{dC_v}{dr} \right)_{\mathcal{R}} = 0 \quad (13.83)$$

the vacancy-concentration profile around the dislocation is given by

$$C_v(r) = C_{R_d} + \frac{(Y\dot{F})_{\text{eff}} \mathcal{R}^2}{2D_v} \left[ \ln \left( \frac{r}{R_d} \right) - \frac{1}{2} \left( \frac{r^2 - R_d^2}{\mathcal{R}^2} \right) \right] \quad (13.84)$$

We now compare this result with the solution of the source-free diffusion equation:

$$\frac{1}{r} \frac{d}{dr} \left( r \frac{dC_v}{dr} \right) = 0 \quad (13.85)$$

Equation 13.82 provides one boundary condition to Eq. 13.85. However, the outer boundary of the capture volume cannot be approximated by infinity as it could in the case of spherical sinks (Eq. 13.62). This distinction is inherent in the difference between spherical and cylindrical geometry. There is no steady-state solution to the diffusion equation from a line sink of nonzero radius to an infinite medium with a specified concentration at large distances from the sink. A solution to the analogous problem in spherical symmetry, however, does exist and is given by Eq. 13.63. For the dislocation problem, the boundary condition at  $r = \mathcal{R}$  is taken as

$$C_v = C_v(\mathcal{R}) \quad (13.86)$$

The solution of Eq. 13.85 subject to the boundary conditions given by Eqs. 13.82 and 13.86 is

$$C_v(r) = C_{R_d} + \left[ C_v(\mathcal{R}) - C_{R_d} \right] \frac{\ln(r/R_d)}{\ln(\mathcal{R}/R_d)} \quad (13.87)$$

The flux of vacancies to the dislocation line is

$$J = -D_v \left( \frac{dC_v}{dr} \right)_{R_d} = -\frac{D_v [C_v(\mathcal{R}) - C_{R_d}]}{R_d \ln(\mathcal{R}/R_d)} \quad (13.88)$$

The rate of vacancy absorption per unit length of dislocation line is

Rate of capture/cm =  $-(2\pi R_d)J$

$$= \frac{2\pi D_v [C_v(\mathcal{R}) - C_{R_d}]}{\ln(\mathcal{R}/R_d)} \quad (13.89)$$

The rate of production of vacancies (less recombination) within a unit length of dislocation capture volume is

$$\text{Rate of production/cm} = \pi(\mathcal{R}^2 - R_d^2) (Y\dot{F})_{\text{eff}} \quad (13.90)$$

Since all vacancies produced within the capture volume of the dislocation are assumed to be captured by the latter, Eqs. 13.89 and 13.90 can be equated and solved for  $C_v(\mathcal{R})$ , which for  $R_d/\mathcal{R} \ll 1$  yields

$$C_v(\mathcal{R}) = C_{R_d} + \frac{(Y\dot{F})_{\text{eff}} \mathcal{R}^2}{2D_v} \ln \left( \frac{\mathcal{R}}{R_d} \right) \quad (13.91)$$

In comparison, the correct solution for the concentration at the outer boundary of the capture volume is given by Eq. 13.84 at  $r = \mathcal{R}$ :

$$C_v(\mathcal{R}) = C_{R_d} + \frac{(Y\dot{F})_{\text{eff}} \mathcal{R}^2}{2D_v} \left[ \ln \left( \frac{\mathcal{R}}{R_d} \right) - \frac{1}{2} \right] \quad (13.92)$$

In obtaining Eq. 13.92, we have assumed  $\mathcal{R}/R_d$  to be large compared to unity, but we see that, for the solution of the two-region approximation to be identical to the exact solution, the logarithm of  $\mathcal{R}/R_d$  must also be much larger than unity. This is a much more stringent requirement than  $\mathcal{R}/R_d \gg 1$ ; so the analog of the two-region model for dislocations will, in general, not be as accurate as it is for spherical sinks. Nevertheless, the great simplification afforded by use of Eq. 13.89 in analyses involving complex microstructures justifies acceptance of a minor loss of accuracy in the mathematical treatment.

The rate of vacancy capture under diffusion-controlled conditions by all dislocations in a unit volume is obtained by multiplying Eq. 13.89 by the dislocation density, setting  $C_v(\mathcal{R}) = C_v$ , the average vacancy concentration in the matrix, and neglecting  $C_{R_d}$  compared to  $C_v$ :

Rate of vacancy capture by dislocations/cm<sup>3</sup>

$$= \frac{2\pi D_v \rho_d C_v}{\ln(\mathcal{R}/R_d)} \quad (13.93)$$

A similar formula can be derived for interstitial capture by dislocations.

### 13.5.3 Mixed-Rate Control

Equation 13.93 can be compared with the capture rate deduced from the assumption of complete reaction-rate control, namely Eq. 13.53. The mechanism that controls the capture rate depends on the relative magnitudes of  $z_{vd}$

and  $2\pi/\ln(\mathcal{R}/R_d)$ . If both are of comparable size, the overall rate can be obtained in a manner identical to that used to determine the overall heat flux in a heat-transfer problem with series resistances. The rate of capture in the mixed regime is

$$\text{Rate of vacancy capture by dislocations/cm}^3 = \frac{D_v \rho_d C_v}{(1/z_{vd}) + [\ln(\mathcal{R}/R_d)/2\pi]} \quad (13.94)$$

Estimates of the two terms in the denominator of Eq. 13.94 can be obtained by considering  $z_{vd}$  as the area of a circular region of radius  $R_d$  divided by the number of atoms per unit area Fig. 13.6. For the (100) plane of the fcc lattice, for example, the latter is  $2/a_0^2$  atoms per  $\text{cm}^2$ , where  $a_0$  is the lattice constant. Thus

$$z_{vd} \approx \frac{2\pi R_d^2}{a_0^2}$$

If we take  $R_d \approx 6 \text{ \AA}$  and  $a_0 \approx 3 \text{ \AA}$ , we find

$$z_{vd} \approx 24$$

and for a dislocation-line density of  $10^{10} \text{ cm}^{-2}$

$$\frac{2\pi}{\ln(\mathcal{R}/R_d)} \approx 1.4$$

Thus the reaction-rate term  $z_{vd}$  in Eq. 13.94 is an order of magnitude smaller than the diffusion term, and the capture rate of vacancies by dislocations is nearly completely diffusion controlled. Since the dislocation-line density enters only as the logarithm in the denominator of Eq. 13.94, no reasonable values of  $\rho_d$  (i.e.,  $\mathcal{R}$ ) will render the process reaction-rate controlled.

Despite these arguments reaction-rate-controlled capture of vacancies and interstitials by dislocation lines has been used to describe void growth in metals.<sup>3,2,36</sup> There are two cogent reasons for such an application. First, the dislocations in a real crystal are not lined up in neat parallel arrays as assumed in the diffusion model. Rather, the deformed crystal consists of a tangle of dislocations created by stress-induced deformation of the matrix intermingled with dislocation loops produced by condensation of irradiation-produced defects (mainly interstitials).<sup>\*</sup> Second, the very capture process causes the dislocations to move (by climb); thus the line sinks assumed in the diffusion analysis do not even stay in one place. Movement at constant size in the case of dislocations can be compared with the result of gas-atom capture by spherical bubbles, where the sphere remains stationary but increases in size. Movement of the dislocation lines by climb means that they will capture more point defects than if they were stationary and all transport was by diffusion. Under such conditions, it may be reasonable to consider point-defect trapping by disloca-

tions as being due to a homogeneous distribution of trapping sites, which is the basis of the reaction-rate-controlled model of capture.

A series-resistance formula similar to Eq. 13.94 can be derived for spherical sinks. When the capture kinetics are controlled by the rate at which point defects enter the trapping sites around the sink, the rate constant can be expressed by Eq. 13.47. The combinatorial number can be approximated by the number of lattice points on the surface of the sphere. The area occupied by one lattice site is approximately equal to the square of the lattice constant, and the number of trapping sites on the surface of a spherical sink of radius  $R$  is  $4\pi R^2/a_0^2$ . Using this for  $z_{\text{tr}}$  in Eq. 13.47 yields the rate constant

$$k = \frac{4\pi R^2 \Omega D}{a_0^4} = \frac{4\pi R^2 D}{a_0} \quad (13.95)$$

where the atomic volume has been approximated by  $a_0^3$ .

In complete diffusion control, on the other hand, the rate constant is given by Eq. 13.70. The reciprocals of Eqs. 13.70 and 13.95 can be added to give the resistance due to series steps of diffusion and surface attachment. The overall rate constant is

$$k = \frac{4\pi R D}{1 + (a_0/R)} \quad (13.96)$$

For large spheres,  $a_0/R \rightarrow 0$  and the rate constant reduces to that given by considering diffusion only. Equation 13.96 indicates that reaction-rate limitations to the capture kinetics of perfect spherical sinks is appreciable only if the sphere radius approaches the size of the lattice constant.

## 13.6 RATE CONSTANTS FOR BUBBLE COALESCENCE

The significance of coalescence of fission-gas bubbles in nuclear fuels lies in the volume increase that accompanies this phenomenon. The sensitivity of fuel swelling to bubble agglomeration can be appreciated by the following simple calculation. Suppose a section of fuel initially contains  $N$  bubbles with  $m$  gas atoms each. The swelling due to these bubbles is given by Eq. 13.19 where the bubble radius is related to  $m$  by Eq. 13.16 (assuming that the bubbles are large). Now suppose that each of the bubbles collides and coalesces once with another bubble, resulting in  $N/2$  bubbles each containing  $2m$  gas atoms. If  $R_0$  and  $R_f$  denote the initial and final radii of the bubbles, the fractional increase in fuel swelling is

$$\frac{(\Delta V/V)_f}{(\Delta V/V)_0} = \left(\frac{R_f}{R_0}\right)^3 \left(\frac{N/2}{N}\right)$$

Using Eq. 13.16, the initial and final radii are related by

$$\left(\frac{R_f}{R_0}\right)^2 = \frac{2m}{m} = 2$$

from which the increase in swelling due to coalescence is

$$\frac{(\Delta V/V)_f}{(\Delta V/V)_0} = 2^{3/2} \times \frac{1}{2} = 2^{1/2}$$

\*Brailsford and Bullough<sup>37</sup> have analyzed the capture rate of the closed interstitial loops and have developed a transition regime rate expression similar to Eq. 13.94, which applies to straight dislocation lines.

This calculation shows that an approximately 40% increase in swelling results from a single generation of bubble-bubble collisions and coalescence.

In a solid free from gradients of temperature or mechanical stress, gas bubbles move about in a random fashion as do particles in a colloidal suspension. As in any random-walk process, this motion can be characterized by a diffusion coefficient for the bubbles,  $D_b$ . Later we will derive the theoretical expression for  $D_b$  based on various mechanisms of atomic motion on or near the bubble surface. In this section we accept the existence of a bubble-diffusion coefficient and use it to compute bubble collision rates.

If the solid is subject to stress or temperature gradients, random motion of the bubbles is negligible compared to the biased motion due to the potential gradients. The bubbles all migrate in the direction of the gradient but with speeds  $v_b$  that depend on bubble size.

When two bubbles collide, coalescence into a single final bubble invariably occurs because a single bubble has a lower surface energy than that of the two original bubbles. First, the collision must be defined. If two nearby bubbles exert an attractive force on each other before their surfaces actually touch, the collision cross section will be larger than that based on the sum of the bubble radii. Willis and Bullough<sup>38</sup> have shown that a small attractive force does exist between two bubbles provided that at least one of them is not in equilibrium (i.e., Eq. 13.4 is not satisfied). The interaction is due to the elastic stress field established by a bubble with a pressure excess (or deficit). Two bubbles in mechanical equilibrium, however, are not aware of each other's presence until physical contact is made. Hence, a collision is considered to occur when the centers of two bubbles are separated by a distance equal to the sum of the radii.

The sequence of events following the initial collision has been analyzed by Nichols.<sup>39</sup> In the first stage, the two bubbles sinter together into a single bubble having the same volume as that of the original pair. The radius of the coalesced bubble at the end of this stage is

$$(R_f')^3 = R_1^3 + R_2^3$$

where  $R_1$  and  $R_2$  are the radii of the two bubbles before collision. If the two bubbles were in mechanical equilibrium with the solid before collision, it can be seen that the radius  $R_f'$  is less than that required for the single combined bubble to be in mechanical equilibrium. As a result, the bubble at the end of the first stage exhibits a pressure excess, which is relieved by increasing the volume of the bubble by absorption of vacancies from the bulk. This second stage of volume adjustment ceases when mechanical equilibrium is reestablished, or when the final radius satisfies Eq. 13.16:

$$m_1 + m_2 = \left( \frac{4\pi R_f'^2}{3} \right) \frac{2\gamma}{kT}$$

Since the original bubbles were also in mechanical equilibrium,  $m_1$  and  $m_2$  are related to  $R_1$  and  $R_2$  by Eq. 13.16. Thus, the final radius of the coalesced volume adjusted bubble is

$$R_f^2 = R_1^2 + R_2^2 \quad (13.97)$$

which states that the surface area of a bubble population undergoing collision and coalescence but at all times in mechanical equilibrium with the solid remains constant.

To quantitatively describe the rate at which coalescence occurs in a solid containing a distribution of bubbles, we must first determine the rate constants for collisions between bubbles of different sizes. In the absence of biased migration (i.e., for random bubble motion), the collision rate can be described by the theory developed by Chandrasekhar<sup>40</sup> for analysis of coalescence of colloidal particles. Suppose that  $C_m$  is the bubble distribution function, where

$$C_m = \text{number of bubbles containing } m \text{ gas atoms/cm}^3$$

We first calculate the rate of collision of particles of radius  $R'$  with each other as a consequence of their Brownian motion. We pick one bubble and assume it to be fixed in space in an infinite medium initially containing a uniform distribution of similar bubbles in random motion. The stationary bubble is located at the origin of a spherical coordinate system, and the spherical surface at  $r = 2R$  is assumed to be a perfect absorber. Because of the presence of this sink, a concentration gradient of the moving bubbles is established in the vicinity of the fixed bubble. If the concentration of the moving bubbles at time  $t$  and at a distance  $r$  from the fixed bubble is denoted by  $w(r,t)$ , the diffusion equation that must be satisfied is

$$\frac{\partial w}{\partial t} = \frac{D_b}{r^2} \frac{\partial}{\partial r} \left( r^2 \frac{\partial w}{\partial r} \right) \quad (13.98)$$

which is subject to the initial condition:

$$w(r,0) = C_m \quad (\text{for } r > 2R) \quad (13.99)$$

and the boundary conditions:

$$w(2R,t) = 0 \quad (13.100)$$

$$w(\infty,t) = C_m \quad (13.101)$$

The solution to Eqs. 13.98 through 13.101 is

$$w(r,t) = C_m \left\{ 1 - \frac{2R}{r} + \left( \frac{2R}{r} \right) \operatorname{erf} \left[ \frac{r-R}{2(D_b t)^{1/2}} \right] \right\} \quad (13.102)$$

The rate at which bubbles arrive at the surface  $r = 2R$  (i.e., the rate of collision of moving bubbles with the fixed bubble) is given by

Rate of collision of moving bubbles with the fixed bubble

$$\begin{aligned} &= 4\pi(2R)^2 D_b \left( \frac{\partial w}{\partial r} \right)_{2R} \\ &= 4\pi(2R) D_b C_m \left[ 1 + \frac{2R}{(\pi D_b t)^{1/2}} \right] \quad (13.103) \end{aligned}$$

Note the resemblance between Eq. 13.103 and Eq. 13.66, which gives the rate of absorption of atomic defects by a spherical sink of radius  $2R$ . Equation 13.66 is just the steady-state ( $t = \infty$ ) counterpart of Eq. 13.103.

Now we relax the restriction that the particle at the origin be stationary and allow it too to move in random motion as the other bubbles. The fundamental connection between diffusion theory and the random-walk problem is the probability distribution given by Eq. 7.23, which gives the probability that a particle starting from the origin at  $t = 0$  will, after time  $t$ , be located in a volume element  $d^3r$  at a distance  $r$  from starting position. To treat the problem in which the origin of the coordinate system is itself in random motion, we consider the relative displacement at time  $t$  of two particles that started together at time zero. The probability distribution of the relative displacements is given by the following integral of the product of the distributions of the individual particles:

$$p_t(r) = \int_{r_1} p_t(|r_1|) p_t(|r_2|) d^3r_1$$

where  $r$  is the vector relative displacement at time  $t$ ,  $r_1$  is the vector displacement of the first particle, and  $r_2 = r_1 + r$  is the vector displacement of the second particle. The probability distribution function  $p_t$  is given by Eq. 7.23; so the preceding integral becomes

$$p_t(r) = \frac{1}{(4\pi D_b t)^3} \int_{r_1} \exp\left(-\frac{|r_1|^2}{4D_b t}\right) \exp\left(-\frac{|r_1 + r|^2}{4D_b t}\right) d^3r_1$$

The integral in this equation can be evaluated by considering the fixed vector  $r$  as defining a direction in space to which the variable directions of the vector  $r_1$  are referred and with one end as the origin of a spherical coordinate system. The differential volume  $d^3r_1$  is  $2\pi r_1^2 dr_1 d(\cos \theta_1)$ , where  $\theta_1$  is the polar angle between  $r$  and  $r_1$ . The quantity  $|r_1 + r|^2$  can be evaluated in terms of  $r_1$ ,  $r$ , and  $\theta_1$  by the law of cosines and the integration over  $r_1$  and  $\theta_1$  accomplished. The result is

$$p_t(r) = \frac{\exp(-r^2/8D_b t)}{(8\pi D_b t)^{3/2}} \quad (13.104)$$

On comparing this distribution of relative displacements with the corresponding result for displacement of a single particle from a fixed origin (Eq. 7.23), we can see that the relative displacements follow the same distribution law but with an apparent diffusion coefficient twice as large as the particle diffusivity. Therefore the form of Eq. 13.103 appropriate to collisions between a single moving bubble and the other moving bubbles in the medium is

Rate of collision of moving bubbles with a moving bubble

$$= 4\pi(2R)(2D_b)C_m \left\{ 1 + \frac{2R}{[\pi(2D_b)t]^{1/2}} \right\} \quad (13.105)$$

Finally, the collision rate in a unit volume is obtained by multiplying Eq. 13.105 by the density of bubbles of size  $m$ ,  $C_m$ , which yields

Rate of collision between bubbles containing  $m$  atoms/cm<sup>3</sup>

$$= 4\pi(2R)(2D_b) \left\{ 1 + \frac{2R}{[\pi(2D_b)t]^{1/2}} \right\} C_m^2 \quad (13.106)$$

Equation 13.106 can be generalized to give the collision rate between bubbles containing  $i$  and  $j$  atoms. If the concentrations of bubbles of these sizes are  $C_i$  and  $C_j$ , respectively, the collision rate is

Rate of collision between bubbles of size  $i$  and size  $j$ /cm<sup>3</sup>

$$= 4\pi(R_i + R_j)(D_{bi} + D_{bj}) \times \left\{ 1 + \frac{R_i + R_j}{[\pi(D_{bi} + D_{bj})t]^{1/2}} \right\} C_i C_j \quad (13.107)$$

All analyses of bubble coalescence in nuclear fuels (with the exception of that of Ref. 41) omit the second term in the braces on the grounds that the migration distance between collisions is usually large compared to the bubble radii. Omitting this term and expressing the collision rate in terms of the rate constant defined by

Rate of collision between bubbles of size  $i$  and size  $j$ /cm<sup>3</sup>

$$= k_{ij} C_i C_j \quad (13.108)$$

we have

$$k_{ij} = 4\pi(R_i + R_j)(D_{bi} + D_{bj}) \quad (13.109)$$

To derive an expression for the coalescence rate constant when biased migration predominates, we need consider only relative bubble motion in the direction of the potential gradient. Coalescence occurs when a bubble overtakes or is overtaken by one of a different size that has a different velocity. Consider one bubble of size  $j$  moving with velocity  $v_{bj}$  in a particular direction in a medium containing  $C_i$  bubbles of size  $i$  also moving in the same direction as the  $j$  bubble but with speed  $v_{bi}$ . For simplicity, the size- $j$  bubble can be regarded as fixed in position and the size- $i$  bubbles moving with a speed  $v_{bi} - v_{bj}$  (see Fig. 13.10). In a time interval  $\Delta t$ , all size- $i$  bubbles whose centers lie in a cylindrical volume of radius  $R_i + R_j$  and length  $(v_{bi} - v_{bj}) \Delta t$  will collide with the size- $j$  bubble. Hence the rate at which size- $i$  bubbles coalesce with a single size- $j$  bubble is

$$\pi(R_i + R_j)^2 (v_{bi} - v_{bj}) C_i$$

Or, if there are  $C_j$  bubbles of size  $j$  per unit volume, the  $i$ - $j$  collision rate per unit volume is given by Eq. 13.108, where the rate constant is

$$k_{ij} = \pi(R_i + R_j)^2 (v_{bi} - v_{bj}) \quad (13.110)$$

Equation 13.108 and either Eq. 13.109 or 13.110 constitute the basic formulas from which the evolution of the bubble-distribution function due to either random or biased bubble motion can be followed as a function of time. We defer consideration of the bubble conservation relations

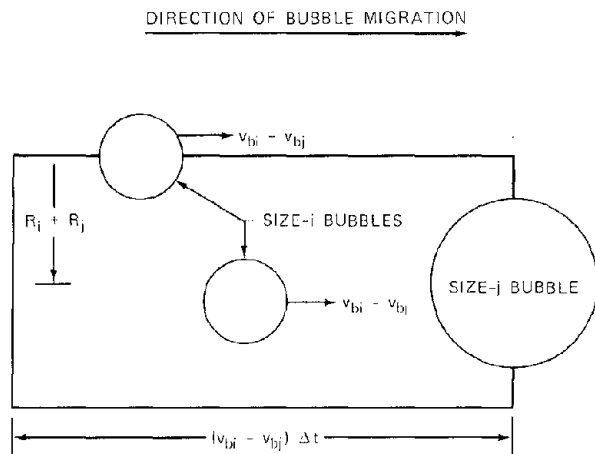


Fig. 13.10 Diagram for computing the coalescence rate for biased bubble motion.

and the fuel-swelling models based on coalescence until the discussion of the mechanisms that govern the bubble diffusion and migration velocity in potential gradients.

### 13.7 BUBBLE RE-SOLUTION

The name re-resolution has been given to the phenomenon by which fission-gas atoms present in bubbles in the fuel are driven back into the matrix by irradiation. By reducing the fraction of the gas held in bubbles and increasing the fraction that is atomically dispersed, re-resolution acts to alleviate swelling but to enhance gas release by mechanisms that involve diffusion of gas atoms from the solid to surfaces from which escape is possible. Because irradiation prevents complete precipitation of fission-gas into bubbles, the gas appears to have a nonzero solubility in the solid. This type of solubility is often called dynamic solubility to distinguish it from the equilibrium thermodynamic solubility of fission gases in fuel materials, which is essentially zero. If the re-resolution phenomenon is to be incorporated into analyses of fission-gas behavior, it is necessary to quantitatively describe the rate at which gas atoms in a bubble are returned to the matrix. This rate depends linearly on the number of fission-gas atoms present and the fission rate and also on the physics of the interaction between energetic particles and the gas atoms in a bubble. In this section we develop the rate equations for the re-resolution process. Coupling of re-resolution with other processes, such as nucleation or bubble growth, will be considered later in this chapter.

A number of physical pictures purporting to represent the re-resolution process have been advanced.<sup>42-46</sup>

The model proposed by Ross<sup>42</sup> attributes re-resolution to the occurrence of a thermal spike in the vicinity of a gas bubble. A thermal spike is an extremely hot region in the track of a fission fragment produced by the intense local heating of the solid during slowing down of the fragment. The thermal disorder created by the spike completely mixes the matrix atoms with the fission-gas atoms in the affected bubble, and, after the temperature transient has decayed,

the gas atoms are considered to be frozen into the solid as atomically dispersed particles.

Whapham<sup>10</sup> proposed a mechanism by which fission fragments passing close by a bubble blast off chunks of fuel from the inner surface and deposit the blown-off material on the opposite surface of the bubble. Some of the gas atoms in the bubble can be trapped beneath the deposited material and thereby returned to the matrix. Blank and Matzke<sup>44</sup> have investigated the properties of the pressure pulse created by the thermal spike of a fission fragment and have deduced the conditions for bubble destruction.

Turnbull<sup>43</sup> believes that a bubble is entirely destroyed (i.e., the gas atoms within it are redissolved) whenever a fission track intersects the bubble. This model can be expressed in analytical form with the aid of Fig. 13.11. The solid is assumed to contain  $C_m$  bubbles/cm<sup>3</sup>, each consisting of  $m$  gas atoms. The bubble radius  $R$  is related to the number of gas atoms by Eq. 13.14 or, for the small bubbles to which the model was intended to apply, by Eq. 13.15. The distance travelled by a fission fragment during slowing down from birth energy is denoted by  $\mu_{ff}$ , which is about  $6 \mu\text{m}$  ( $6000 \text{ \AA}$ ) in most nuclear fuels. Turnbull proposes

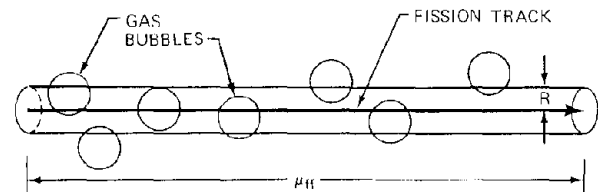


Fig. 13.11 Diagram for calculating the re-resolution parameter by Turnbull's method. [After J. A. Turnbull, *J. Nucl. Mater.*, 38: 203 (1971).]

that all gas bubbles that are touched by the fragment are destroyed. Thus, all bubbles within the volume  $\pi R^2 \mu_{ff}$  are redissolved by the fission fragment. The cylindrical collision volume around the fission track contains  $\pi R^2 \mu_{ff} C_m$  bubbles, and, since  $2\dot{F}$  fission fragments are created per unit volume and per unit time, the re-resolution rate is given by

$$\text{Gas bubbles destroyed cm}^{-3} \text{ sec}^{-1} = b' C_m \quad (13.111)$$

where

$$b' = 2\pi R^2 \mu_{ff} \dot{F} \text{ sec}^{-1} \quad (13.112)$$

is the probability per second that a bubble in the fuel is destroyed. It is also called the re-resolution parameter.

The re-resolution mechanisms proposed by Ross,<sup>42</sup> Whapham,<sup>10</sup> Turnbull,<sup>43</sup> and Blank<sup>44</sup> have in common the feature of partial or complete destruction of a bubble by a single fission fragment. They can be described as macroscopic models. On the other hand, Nelson<sup>17,45</sup> and Manley<sup>46</sup> have proposed models in which re-resolution occurs one gas atom at a time rather than *en bloc*. These are microscopic models of the process. We review Nelson's derivation of re-resolution by fission fragments.

The total flux of fission fragments in the fuel is the number of fragments crossing a sphere of unit cross-sectional area per second (this is the definition of the total flux of any type of particle). Consider a differential volume element  $dV$  a distance  $x$  from the unit sphere ( $x$  must be less than the range of the fission fragments). The rate of generation of fission fragments in  $dV$  is  $2\dot{F}dV$ , and their angular distribution is isotropic. Therefore, the probability that a fission fragment created in  $dV$  crosses the unit sphere is equal to the solid angle subtended by the unit sphere from  $dV$ , or to  $1/4\pi x^2$ . The total flux is obtained by integration over the entire sphere of radius  $\mu_{ff}$  with the unit sphere at its center. Thus,

$$\text{Total fission-fragment flux} = \int_{\text{sphere of radius } \mu_{ff}} \frac{2\dot{F} dV}{4\pi x^2}$$

or, taking  $dV = 4\pi x^2 dx$ , the total fission-fragment flux is  $2\dot{F}\mu_{ff}$ .

Let the energy spectrum of the fission-fragment flux be denoted by  $\phi(E_{ff})$ , where  $E_{ff}$  is the energy of a fission fragment at some point in its slowing-down process. Fission fragments are uniformly distributed in energy between their birth energy ( $E_{ff}^{max} \approx 67$  MeV for the heavier fragment) to zero energy. Therefore the fission-fragment-flux spectrum is

$$\phi(E_{ff}) dE_{ff} = 2\dot{F}\mu_{ff} \frac{dE_{ff}}{E_{ff}^{max}} \quad (13.113)$$

The fission-fragment-gas-atom interaction is assumed to consist of Coulomb collisions. The differential cross section for transferring energy in the range from  $T$  to  $T + dT$  from a fragment of energy  $E_{ff}$  to a stationary gas atom of the same mass and charge number is (see Eq. 17.37)

$$\sigma(E_{ff}, T) dT = \frac{\pi Z^4 e^4}{E_{ff}} \frac{dT}{T^2} \quad (13.114)$$

where  $Z$  is the atomic number of the gas atom (or fission fragment) and  $e$  is the electronic charge. Since the masses of the fission fragments and the gas atoms in the bubble have been assumed equal, the maximum possible energy transferred in a collision is equal to the energy of the fission fragment. Let  $T_{min}$  be the minimum energy which a struck gas atom must acquire to be considered redissolved. The cross section for transferring energy in excess of  $T_{min}$  is given by

$$\sigma(E_{ff}, T_{min}) = \int_{T_{min}}^{E_{ff}} \sigma(E_{ff}, T) dT$$

Or, using Eq. 13.114 and neglecting  $1/E_{ff}$  compared to  $1/T_{min}$ , we obtain the following cross section:

$$\sigma(E_{ff}, T_{min}) = \frac{\pi Z^4 e^4}{E_{ff} T_{min}} \quad (13.115)$$

The minimum energy that a fission fragment must have to redissolve a gas atom in a head-on collision is  $T_{min}$ . The total rate of collisions that transfer energy in excess of  $T_{min}$  to the gas atoms in a bubble is

Collisions  $\text{sec}^{-1} \text{ bubble}^{-1}$

$$= m \int_{T_{min}}^{E_{ff}^{max}} \phi(E_{ff}) \sigma(E_{ff}, T_{min}) dE_{ff}$$

Division of this equation by  $m$  gives  $b$ , the probability per second that a gas atom in a bubble receives an energy greater than  $T_{min}$  by a Coulomb collision with a fission fragment. Using the flux spectrum and cross section given by Eqs. 13.113 and 13.115, respectively, the re-resolution parameter is

$$\begin{aligned} b &= \int_{T_{min}}^{E_{ff}^{max}} \phi(E_{ff}) \sigma(E_{ff}, T_{min}) dE_{ff} \\ &= 2\sigma(E_{ff}^{max}, T_{min}) \ln\left(\frac{E_{ff}^{max}}{T_{min}}\right) \mu_{ff} \dot{F} \quad \text{sec}^{-1} \quad (13.116) \end{aligned}$$

where  $\sigma(E_{ff}^{max}, T_{min})$  is the energy-transfer cross section for a fission fragment of birth energy (given by Eq. 13.115 with  $E_{ff} = E_{ff}^{max}$ ). It can be shown that the result obtained by Manley<sup>4,6</sup> is the same as Eq. 13.116 except that the logarithmic term is missing. This discrepancy arises because Manley did not integrate over the energy spectrum of the fission-fragment flux.

The re-resolution parameter of Eq. 13.116 is independent of the gas density within the bubble but varies nearly inversely with the minimum energy for re-resolution. If we set  $Z = 54$  (xenon),  $E_{ff}^{max} = 67$  MeV, and  $\mu_{ff} = 6 \mu\text{m}$ , Eq. 13.116 yields  $b = 1.1 \times 10^{-19} \dot{F}$  for  $T_{min} = 1$  keV and  $4.1 \times 10^{-19} \dot{F}$  for  $T_{min} = 300$  eV. These values of  $T_{min}$  are considerably larger than the energy that a normal lattice atom needs to receive to be permanently displaced (in most solids,  $T_{min} \approx 25$  eV). The reason for the larger value required to redissolve a gas atom from a bubble is that the gas atom must be driven through gas in the bubble and still have enough energy to be implanted sufficiently deep in the solid so that it has little chance of migrating quickly back into the bubble.

Even for  $E_d = 300$  eV, the calculated re-resolution parameter is at least an order of magnitude smaller than the values inferred from the experiments of Whapham.<sup>10</sup> Consequently, Nelson<sup>4,5</sup> has estimated the re-resolution parameter on the basis of collisions of the gas atoms in the bubbles with the cascade of energetic secondary knock-ons rather than with the fission fragments proper. Because of the detailed knowledge of collision cascades which this calculation requires, we postpone the derivation until the subject of radiation damage is treated (Sec. 17.11). The results of such a calculation, however, predict re-resolution parameters that are an order of magnitude or so larger than the values obtained from collisions between fission fragments and gas atoms, thus putting theory and experiment in qualitative agreement.

According to the microscopic model of re-resolution, the rate at which gas atoms are driven from a bubble containing  $m$  atoms is

$$\text{Gas atoms redissolved } \text{sec}^{-1} \text{ bubble}^{-1} = bm \quad (13.117)$$

Note that Turnbull's  $b'$  (Eq. 13.112) and Nelson's  $b$  (Eq. 13.116) differ only by the cross-section term. In

Turnbull's  $b'$  the cross section is the actual projected area of the bubble,  $\pi R^2$ ; whereas in Nelson's  $b$  it is a true microscopic energy-transfer cross section,  $\sigma(E_{ff}^{max}, T_{min}) \ln(E_{ff}^{max}/T_{min})$ . This difference reflects the physical models of re-resolution on which the parameters  $b'$  and  $b$  are based. Turnbull's model supposes that bubbles are completely destroyed by a single encounter with a fission fragment; whereas in Nelson's model the bubble is gradually consumed by loss of individual gas atoms. This distinction can be illustrated by considering the fate of a group of uniform-size fission-gas bubbles in a solid under irradiation. Suppose that the interior of the solid could be observed while re-resolution is in progress. If Turnbull's model were correct, we would see occasional bubbles disappearing (in the way soap bubbles pop), but those still present would not change size. According to Nelson's mechanism, however, none of the original bubbles would completely disappear during irradiation. They would all gradually shrink in size as gas atoms were driven out of them. Thus,  $1/b'$  is the mean lifetime of a bubble, but  $1/b$  is the mean lifetime of a gas atom in a bubble.

Care must be exercised in applying the re-resolution parameters in fuel-behavior calculations because the form of the term representing re-resolution can depend on whether the macroscopic or microscopic model of the phenomenon is used. However, in the expressions for the rate at which single gas atoms appear in the matrix as a result of re-resolution from all bubbles in a unit volume of fuel, the parameters  $b'$  and  $b$  can be used interchangeably. Consider the case of a solid containing  $N$  bubbles/cm<sup>3</sup> each with  $m$  gas atoms. Using Turnbull's model, the total re-resolution rate is the product of the bubble destruction rate given by Eq. 13.111 and the number of gas atoms per bubble, or

$$\begin{aligned} \text{Gas atoms returned to matrix} \\ \text{from bubbles cm}^{-3} \text{ sec}^{-1} = b' N m \quad (13.118) \end{aligned}$$

Using the microscopic model, the total re-resolution rate is the product of the rate of gas-atom reinjection per bubble (Eq. 13.117) and the number of bubbles per unit volume, or

$$\begin{aligned} \text{Gas atoms returned to matrix} \\ \text{from bubbles cm}^{-3} \text{ sec}^{-1} = b m N \quad (13.119) \end{aligned}$$

Thus, if we are not concerned with the effect of re-resolution on the bubble-distribution function (i.e., the size spectrum), the re-resolution rate can be expressed by

$$\begin{aligned} \text{Re-resolution rate} = bM \text{ or } b'M \text{ gas atoms} \\ \text{redissolved cm}^{-3} \text{ sec}^{-1} \quad (13.120) \end{aligned}$$

where  $M = mN$  is the total number of gas atoms/cm<sup>3</sup> contained in bubbles.

Another case in which the two resolution models are physically identical is that of di-atom cluster destruction. Here, removal of a single atom is equivalent to destruction of the cluster. If there are  $C_2$  di-atom clusters per unit volume, the rate at which they are destroyed is given by

$$\text{Di-atom destruction rate/cm}^3 = b'_2 C_2$$

in Turnbull's model, where  $b'_2$  is the re-resolution parameter for a bubble the size of a di-atomic cluster. In Nelson's model,

$$\text{Di-atom destruction rate/cm}^3 = 2bC_2$$

The factor of 2 appears here because there are  $(2C_2)$  gas atoms/cm<sup>3</sup> in di-atom clusters, and the probability per unit time of redissolving any one of them is  $b$ . Since each displacement of one atom destroys the two-atom cluster, the destruction rate is the product of these two quantities. Numerical values of  $b'_2$  and  $2b$  can be compared. If we set  $m = 2$  and  $B = 85 \text{ \AA}^3$  in Eq. 13.15, the radius of a two-atom cluster is found to be  $3.4 \text{ \AA}$ , and from Eq. 13.112, Turnbull's re-resolution parameter  $b'_2$  is  $4.4 \times 10^{-18} \text{ \AA sec}^{-1}$ . Using  $E_d = 300 \text{ eV}$ , Eq. 13.116 predicts  $2b = 0.8 \times 10^{-18} \text{ \AA sec}^{-1}$ . However, applying Nelson's microscopic re-resolution theory to collision cascades instead of just fission fragments increases the value of the re-resolution parameter by approximately an order of magnitude, which then makes  $2b$  comparable to  $b'_2$ .

The preceding expressions for the re-resolution parameters are valid as they stand only for small bubbles. In Turnbull's model it is unreasonable to expect that a very large bubble can be completely destroyed by a single fission fragment. In Nelson's model a gas atom may not be driven out of a large bubble even if it receives the specified minimum energy by collision with an energetic secondary knock-on or a fission fragment. If the collision occurs near the center of a large bubble, there is a nonnegligible probability that the struck gas atom suffers a large-angle collision with another gas atom before escaping, thereby losing the necessary energy to become implanted firmly in the adjacent solid. Nelson<sup>45</sup> estimates that when the bubble is small enough so that the density of gas within it is equal to the reciprocal of the van der Waals constant (Eq. 13.14), only those gas atoms within a distance  $d$  of about  $15 \text{ \AA}$  from the bubble surface can be redissolved by above-threshold collisions. As the bubble size increases, the gas density decreases, and the escape distance increases according to

$$d = 15 \frac{(1/B)}{\rho_g}$$

Expressing the gas density by Eq. 13.8, the fraction of the bubble radius from which escape is possible is

$$\frac{d}{R} = 15 \left[ \frac{1}{R} + \frac{1}{B} \left( \frac{kT}{2\gamma} \right) \right]$$

The re-resolution efficiency, defined as the fraction of the gas atoms in a bubble which is susceptible to re-resolution, is

$$\eta_{re} = \frac{R^3 - (R - d)^3}{R^3}$$

combining the two preceding equations yields

$$\eta_{re} = 1 - \left\{ 1 - 15 \left[ \frac{1}{R} + \frac{1}{B} \left( \frac{kT}{2\gamma} \right) \right] \right\}^3 \quad (13.121)$$

The re-solution efficiency approaches unity as  $R \rightarrow 15 \text{ \AA}$  and also approaches a limiting value as  $R \rightarrow \infty$ . The latter can be obtained by setting  $B = 85 \text{ \AA}^3$  and  $(kT/2\gamma) = 1 \text{ \AA}^2$  in Eq. 13.121, which gives  $\eta_{re}(R \rightarrow \infty) = 0.44$ . The general form of the re-solution rate in Nelson's model is given by the product of the re-solution efficiency and Eq. 13.117, or by

$$\text{Gas atoms redissolved bubble}^{-1} \text{ sec}^{-1} = \eta_{re}(R) \text{ bm} \quad (13.122)$$

where  $R$  and  $m$  are related by Eq. 13.14.

### 13.8 NUCLEATION OF FISSION-GAS BUBBLES

Sections 13.4 through 13.7 were devoted to developing the rate constants that govern the kinetics of the elementary processes occurring in irradiated fuel materials. These single-step processes can occur simultaneously in the solid to produce more-complex processes that are manifest as observable gas bubbles and fuel swelling. Two of the most important of these complex processes are nucleation and growth of gas bubbles. In reality these are not distinct phenomena but merely different stages in the evolution of the bubble-distribution function during irradiation. In many cases it is possible to examine nucleation and growth as if they were separate events, even though there is no clear demarcation between them. The analysis is considerably simplified by this approach because certain elementary steps are important in nucleation but not in growth and vice versa. Theories of fission-gas-bubble nucleation are reviewed in this section, and subsequent growth is treated in the following section.

Nucleation refers to the formation of clusters of fission-gas atoms that are stable enough to survive and ultimately grow into observable bubbles. Because of the thermodynamic insolubility of xenon and krypton in solid fuels and because of the significant binding energy of small clusters of these species in the solid, a stable cluster probably consists of no more than two to four fission-gas atoms. If clusters of this size form in the fuel by chance encounters of wandering gas atoms, the process is called *homogeneous nucleation*. If gas-atom trapping and cluster formation take place on defects in the crystal which bind individual atoms strongly or which for other reasons are particularly conducive to bubble formation, nucleation is said to be *heterogeneous*. Some of the clusters formed by either of these methods are capable of accumulating more gas atoms before they are destroyed by radiation. The stable clusters of fission-gas atoms are called *bubble nuclei*.

#### 13.8.1 Homogeneous Nucleation

We first consider homogeneous nucleation. It is assumed that the stable nucleus of a bubble consists of a diatomic cluster of gas atoms. Provided that the fuel temperature is sufficiently high for the atomically dispersed fission-gas atoms to be mobile, the nucleation process begins as soon as irradiation starts. During the nucleation

period newly created fission-gas atoms are much more likely to meet another single gas atom and form a new nucleus than they are of joining an existing di-atomic cluster. The concentration of bubble nuclei increases during this period until the density of nuclei is so large that new gas atoms have a higher probability of reaching an existing nucleus and causing it to grow than of forming new nuclei. The time (or burnup) at which this balance point is reached is called the *nucleation time*. It separates the regions of nucleation and growth. Thereafter, the concentration of diatomic clusters decreases with time owing to accumulation of gas atoms. Figure 13.12 shows in a schematic manner how the concentrations of gas atoms and of clusters of two and three gas atoms behave with irradiation time.

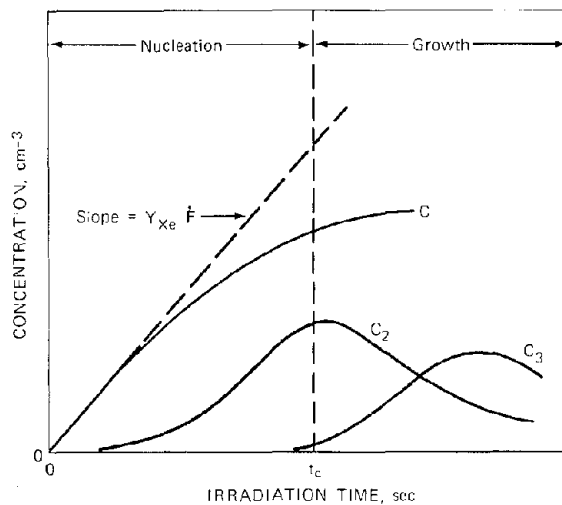


Fig. 13.12 Variation of matrix gas atom and two- and three-atom clusters during irradiation.

The nucleation time  $t_c$  is defined as that time at which the concentration of diatomic clusters,  $C_2$ , passes through a maximum, or

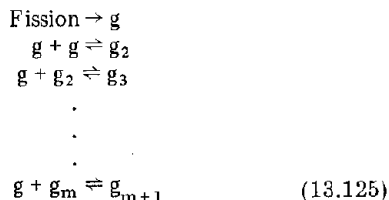
$$\left( \frac{dC_2}{dt} \right)_{t_c} = 0 \quad (13.123)$$

The *nucleation density* is defined as the total concentration of clusters containing two or more gas atoms at time  $t_c$ :

$$N = C_{2c} + C_{3c} + \dots \quad (13.124)$$

where  $C_{ic}$  is the number of clusters containing  $i$  gas atoms present in the solid at time  $t_c$ . For  $t > t_c$  it is assumed that the  $N$  clusters/cm<sup>3</sup> grow and perhaps coalesce but that no new clusters are formed. Although a spectrum of cluster sizes can be present at  $t_c$ , the way in which  $t_c$  is defined means that di-atoms constitute the most abundant size clusters.

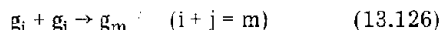
The formation of clusters by collisions between migrating gas atoms with each other or with existing clusters and the re-solution of clusters by radiation can be expressed in the form of the equations:



where  $g_i$  represents a cluster of  $i$  fission-gas atoms and  $m$  is the largest cluster size considered in the calculations.

The forward processes in Eq. 13.125 represent the addition of single gas atoms to existing clusters. The reverse reactions represent the removal of gas atoms from a cluster by microscopic re-resolution. (Re-resolution by complete destruction of a cluster would be written as  $g_i \rightarrow ig$ . Nucleation in the presence of macroscopic re-resolution will be discussed later.)

In most nucleation analyses reaction between clusters,



is not considered. Coalescence reactions are neglected not because they are insignificant but because analysis of nucleation in the presence of coalescence is at present intractable (an approximate treatment will be considered later).

It is assumed that Eq. 13.125 expresses the only elementary processes occurring in the fuel. In addition to coalescence diffusion due to concentration gradients, trapping of gas atoms by defects other than clusters, and migration due to external forces are neglected. The kinetic equations representing the balance on single gas atoms in a unit volume of fuel is

$$\begin{aligned}
 \frac{dC}{dt} = & Y_{Xe} \dot{F} - 2k_{11}C^2 - k_{12}CC_2 - \dots \\
 & - k_{1m}CC_m + 2(2C_2)b + \dots + mC_m b
 \end{aligned}
 \tag{13.127}$$

where  $C$  = concentration of single gas atoms

$Y_{Xe} \dot{F}$  = creation of single gas atoms by fission

$2k_{11}C^2$  = rate at which gas atoms disappear by formation of di-atomic clusters (two atoms are consumed for each di-atomic cluster)

$k_{12}CC_2$  = rate of formation of triatomic clusters from di-atoms and single atoms

$b$  = the probability per unit time that an atom is redissolved

$mC_m$  = the total number of gas atoms contained in  $m$ -size clusters in a unit volume

$mC_m b$  = rate at which single gas atoms are returned to the matrix by re-resolution from size- $m$  clusters

The re-resolution term for  $m = 2$  is multiplied by an additional factor of 2 because collision of an energetic particle with one atom in a diatomic cluster redissolves both partners.

The conservation statement for di-atomic clusters is

$$\frac{dC_2}{dt} = k_{11}C^2 - k_{12}CC_2 - (2C_2)b + (3C_3)b \tag{13.128}$$

and for clusters of  $m$  gas atoms

$$\begin{aligned}
 \frac{dC_m}{dt} = & k_{1,m-1}CC_{m-1} - k_{1m}CC_m \\
 & - (mC_m)b + (m+1)C_{m+1}b
 \end{aligned}
 \tag{13.129}$$

The total balance on all gas generated in a unit volume of fuel yields

$$Y_{Xe} \dot{F} t = C + 2C_2 + \dots + mC_m \tag{13.130}$$

or

$$Y_{Xe} \dot{F} = \frac{dC}{dt} + 2 \frac{dC_2}{dt} + \dots + m \frac{dC_m}{dt} \tag{13.131}$$

Equations 13.127 through 13.129 satisfy Eq. 13.131.

The rate constants for the forward reactions are given by the formulas of Secs. 13.4 and 13.5. Because of the small size of the clusters involved, the rate constants are more likely to be reaction-rate controlled rather than diffusion limited. The rate constant  $k_{11}$  is given by Eq. 13.44. Those representing attachment of single gas atoms to clusters in reaction-rate theory are given by

$$k_{1i} = \frac{z_{1i} \Omega D_{Xe}}{a_0^2} \tag{13.132}$$

where  $z_{1i}$  represents the combinatorial numbers for the particular reactions. They represent the number of sites surrounding a cluster from which a gas atom can attach to the cluster in a single jump.

With the rate constants and the re-resolution parameter  $b$  known, calculation of the growth of clusters to give curves such as those shown in Fig. 13.12 requires numerical solution of Eqs. 13.127 through 13.129 with the initial conditions:

$$C(0) = C_2(0) = \dots = C_m(0) = 0 \tag{13.133}$$

Subject to two rather drastic simplifications, analytical solution is possible. The first approximation consists of neglecting all clusters containing more than two atoms. Setting  $C_3 = \dots = C_m = 0$ , the rate equations reduce to

$$\frac{dC}{dt} = Y_{Xe} \dot{F} - 2k_{11}C^2 - k_{12}CC_2 + 4bC_2 \tag{13.134}$$

$$\frac{dC_2}{dt} = k_{11}C^2 - k_{12}CC_2 - 2bC_2 \tag{13.135}$$

$$\frac{dC_3}{dt} = k_{12}CC_2 \tag{13.136}$$

Equations 13.134 through 13.136 satisfy Eq. 13.131 for  $m = 2$ .

The second simplification is to consider that, in addition to Eq. 13.123, the time rate of change of the single gas-atom concentration is zero at  $t = t_c$ , or

$$\left( \frac{dC}{dt} \right)_{t_c} = 0 \tag{13.137}$$

This simplification is similar to the quasi-stationary approximation used in connection with diffusion-controlled trapping at large sinks. It does not mean that  $dC/dt$  is absolutely zero at the end of nucleation (which it is not), but that this term is small in magnitude compared to the individual terms on the right-hand side of Eq. 13.134. This approximation is similar to the stationary intermediate approximation used in homogeneous chemical kinetics.

Setting the left-hand sides of Eqs. 13.134 and 13.135 equal to zero and appending the subscript "c" onto  $C$  and  $C_2$ , the concentration of single gas atoms and diatomic clusters at the end of the nucleation period ( $t = t_c$ ) is found to be

$$Y_{Xe} \dot{F} = \frac{3k_{11}k_{12}C_c^3}{k_{12}C_c + 2b} \quad (13.138)$$

$$C_{2c} = \frac{k_{11}C_c^2}{k_{12}C_c + 2b} \quad (13.139)$$

The solution to Eq. 13.138 is plotted in Fig. 13.13. Asymptotes occur at large and small values of the parameter

$$\left( \frac{Y_{Xe} \dot{F}}{3k_{11}} \right) \left( \frac{k_{12}}{2b} \right)^2$$

Since  $k_{12}$  and  $k_{11}$  both depend linearly on  $D_{Xe}$ , which increases rapidly with temperature, the preceding group becomes large at high fuel temperatures. The re-resolution parameter  $b$  is directly proportional to  $\dot{F}$  (Eq. 13.116); so the group is large at low fission-rate densities. Both these factors tend to render growth by addition of a gas atom a more important mechanism for removing diatomic clusters than re-resolution. In this limit the ordinate of Fig. 13.13 becomes proportional to the square root of the abscissa, which leads to the solution:

$$C_c = \left( \frac{Y_{Xe} \dot{F}}{3k_{11}} \right)^{1/2} \quad (13.140)$$

The corresponding value of the critical di-atom concentration is

$$C_{2c} = \left( \frac{k_{11} Y_{Xe} \dot{F}}{3k_{12}^2} \right)^{1/2} \quad (13.141)$$

These two formulas were first obtained by Greenwood, Foreman, and Rimmer.<sup>5</sup> These investigators took the rate of addition of single gas atoms to the nuclei to be diffusion controlled, and Eq. 13.70 was used for  $k_{12}$ . Diffusion control does not seem likely if the critical cluster is in fact a di-atom, but Greenwood, Foreman, and Rimmer<sup>5</sup> regarded the nucleus to be a small bubble greater than 10 Å in radius.

The nucleation time is given by applying Eq. 13.130 at  $t = t_c$ :

$$t_c = \frac{C_c + 2C_{2c}}{Y_{Xe} \dot{F}} = \frac{1 + 2k_{11}/k_{12}}{(3k_{11} Y_{Xe} \dot{F})^{1/2}}$$

Harrison<sup>47</sup> has applied Eq. 13.141 to predict swelling in UC and U.

At the opposite limit of low temperature and high fission rate density, re-resolution predominates, and the slope of the curve of Fig. 13.13 approaches  $1/3$ . For this case the solutions are

$$C_c = \left( \frac{2b Y_{Xe} \dot{F}}{3k_{11} k_{12}} \right)^{1/3} \quad (13.142)$$

and

$$C_{2c} = \left( \frac{k_{11}}{2b} \right)^{1/3} \left( \frac{Y_{Xe} \dot{F}}{3k_{12}} \right)^{2/3} \quad (13.143)$$

The nucleation time is again given by  $(C_c + 2C_{2c})/Y_{Xe} \dot{F}$ . Nelson<sup>45</sup> has given a different formula that supposedly represents re-resolution-dominated nucleation. His result,  $C_{2c} = Y_{Xe} \dot{F}/2b$ , does not follow from any rational simplification of Eqs. 13.134 through 13.136.

The only work in which Eqs. 13.127 through 13.129 were solved numerically is that of Eyre and Bullough,<sup>29</sup> who, however, did not include re-resolution in the model. Because the equations were solved without approximations, the auxiliary condition  $(dC/dt)_{t_c} = 0$  was not used. The time dependencies of the concentrations of clusters containing up to five gas atoms were computed until  $C_2$  passed through a maximum, at which point the total number of clusters containing two to five atoms was computed to give the nucleation density. Eyre and Bullough determined the rate constants from Eq. 13.132 in conjunction with the combinatory numbers used by de Jong and Koehler<sup>48</sup> for vacancy-annealing calculations. The values are  $z_{11} = 84$ ,  $z_{12} = 20$ , and  $z_{13} = 12$ . For clusters of four and five atoms, the combinatory numbers were assumed to be proportional to the cluster size and were given by  $z_{14} = 15$  and  $z_{15} = 18$ . We have indicated in Sec. 13.4 that use of the vacancy-vacancy reaction combinatory numbers for determining the rate of collision of fission-gas atoms probably underestimates the rate of this reaction. The derivations of  $z_{12} \dots z_{15}$  is not given either by Eyre and Bullough<sup>29</sup> or by de Jong and Koehler,<sup>48</sup> nor can the source of these numbers be found in the literature.

Eyre and Bullough's calculations were made for uranium carbide, for which a fission-gas diffusion coefficient with an extraordinarily low preexponential factor was employed. To allow for a potentially large underestimate of  $D_{Xe}$ , Eyre and Bullough tested preexponential factors larger than the experimental value by  $10^2$  and  $10^4$  in the computation.

The results of Eyre and Bullough's numerical calculations and the two limiting cases of the approximate analytic solution discussed earlier are shown in Table 13.4 for two temperatures. The calculated nucleation densities drop by some two orders of magnitude as the temperature is increased from 650°C to 1300°C. This prediction is in direct contradiction to the experiments of Cornell,<sup>2,3</sup> in which the bubble concentration was found to decrease by only a factor of about 3 over the same temperature range. The range of nucleation densities shown in the table brackets the experimentally determined value of  $\sim 10^{17}$

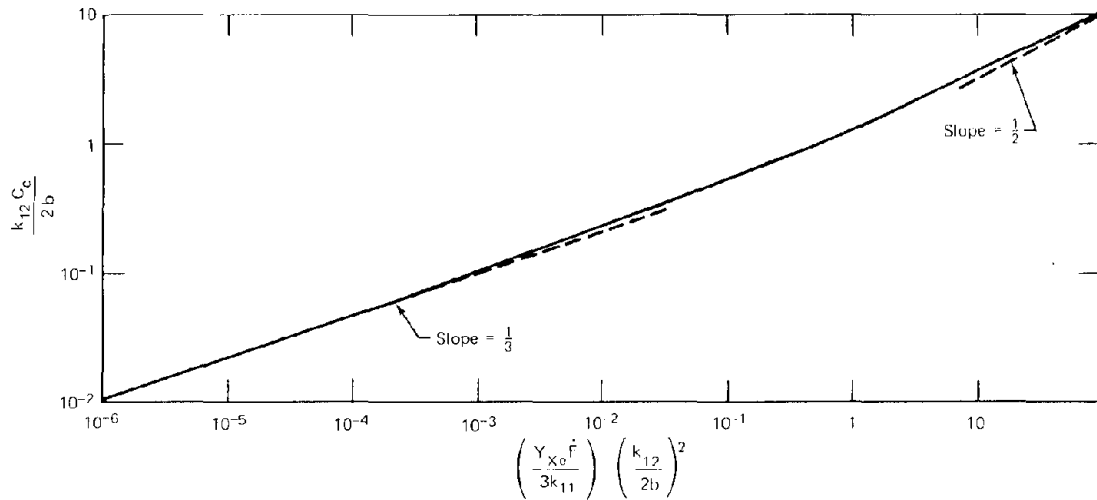


Fig. 13.13 The homogeneous nucleation function (with re-resolution).

Table 13.4 Homogeneous Nucleation in Uranium Carbide\*

Method	650°C			1300°C		
	C <sub>c</sub> , atoms/cm <sup>3</sup>	N, nuclei/cm <sup>3</sup>	t <sub>c</sub> , sec	C <sub>c</sub> , atoms/cm <sup>3</sup>	N, nuclei/cm <sup>3</sup>	t <sub>c</sub> , sec
Numerical† n = 5, b = 0		50 × 10 <sup>18</sup>	80 × 10 <sup>5</sup>		10 × 10 <sup>16</sup>	2 × 10 <sup>3</sup>
Analytic‡ diffusion controlled	1.6 × 10 <sup>18</sup>	6.5 × 10 <sup>18</sup>	2.1 × 10 <sup>5</sup>	1.4 × 10 <sup>16</sup>	5.4 × 10 <sup>16</sup>	1.8 × 10 <sup>3</sup>
Analytic‡ re-resolution controlled	13 × 10 <sup>18</sup>	0.9 × 10 <sup>18</sup>	2.3 × 10 <sup>5</sup>	2.1 × 10 <sup>16</sup>	2.4 × 10 <sup>16</sup>	1.0 × 10 <sup>3</sup>

\*Constants used in the calculations:  
 $Y_{Xe} \bar{F} = 6.6 \times 10^{13}$  gas atoms cm<sup>3</sup> sec<sup>-1</sup>  
 $\Omega = 3.0 \times 10^{23}$  cm<sup>3</sup>/uranium atom  
 $D_{Xe} = 1.7 \times 10^{-7} \exp[-920/R(T/10^3)]$  cm<sup>2</sup>/sec  
 $b = 8 \times 10^{-4}$  sec<sup>-1</sup>

†Results taken from Figs. 1b and 2 of Ref. 29.

‡Analytic solutions: Eqs. 13.140 and 13.141 for diffusion controlled; Eqs. 13.142 and 13.143 for re-resolution controlled.

bubbles/cm<sup>3</sup>. The large nucleation densities obtained by Eyre and Bullough are due to the substantial contribution of clusters containing more than two atoms ( $N/C_{2c} = 25$  at 650°C and 3 at 1300°C). Comparison of the last two rows of Table 13.4 shows that the primary effect of re-resolution is to increase the concentration of single gas atoms and decrease the concentration of nuclei, which reflects the ability of re-resolution to maintain high dynamic gas solubility. Predicted nucleation times are quite short compared to the period over which the fuel is irradiated. At 1300°C nucleation is complete in less than 1 hr.

### 13.8.2 Heterogeneous Nucleation

The nucleation theory proposed by Turnbull<sup>4,3</sup> is based on the observation that all electron microscope studies of fission-gas bubbles in fuel materials that had been irradiated above 700°C have shown that the bubbles lie in straight

lines. Figure 13.14 shows such a micrograph. On the basis of this information, Turnbull<sup>4,3</sup> proposed that the bubbles spontaneously nucleated on the tracks of fission fragments. The nucleation sites are believed to be sections of a fission track that are especially rich in vacancies created by a large energy transfer collision between the fragment and a lattice atom (i.e., a displacement spike). The excess vacancies tend to collect into a void close to the track. If the concentration of fission gas is sufficiently high, these voids will contain a few fission-gas atoms. The voids shed vacancies and shrink until they are in mechanical equilibrium with the gas pressure balanced by the surface tension. Turnbull estimates that each nucleus contains about four gas atoms (and therefore has a radius of approximately 5 Å at mechanical equilibrium). Each fission track nucleates about five gas bubbles, a figure that is consistent with Fig. 13.14. Nucleation occurs only if the matrix gas concentration is greater than about 10<sup>19</sup> gas atoms/cm<sup>3</sup> (which corresponds



Fig. 13.14 Micrographs showing intragranular fission-gas bubbles. Note how many of them lie in straight lines. [From J. A. Turnbull, *J. Nucl. Mater.*, 38: 206 (1971).]

to a burnup of 0.04%). If the gas-atom concentration is less than this value, not enough gas is trapped in the voids resulting from the displacement spikes to stabilize the voids. The nucleation density can be determined from the gas balance:

$$t_c = \frac{10^{19}}{Y_{Xe} \bar{F}}$$

For the same value of the gas-atom production rate used in Table 13.4, the nucleation time in Turnbull's model is

$1.5 \times 10^5$  sec, which is of the same order of magnitude as the values of  $t_c$  predicted by the homogeneous nucleation models at 650°C.

The bubble-density calculation based on Turnbull's model will be considered in the following section, inasmuch as nucleation, re-resolution, and growth must be considered simultaneously.

Heterogeneous nucleation on dislocation lines has not been treated quantitatively in the literature. Qualitative comparisons of this type of nucleation and homogeneous nucleation can be found in Refs. 5 and 29.

### 13.9 GROWTH OF STATIONARY BUBBLES

On completion of the nucleation stage, bubbles grow by absorbing the fission gas that is continually being generated. To analyze the growth process, we neglect for the moment all random or directed motion of the bubbles; increase in bubble size due to coalescence is considered later in this chapter. In this section only growth by the diffusive flow of single gas atoms and single vacancies to the bubble is treated. Neglect of bubble migration and the consequent enlargement by coalescence is probably an acceptable restraint for small bubbles that, although quite mobile in a perfect crystalline lattice, are easily immobilized by binding to a variety of crystal defects.

The nucleation process has supplied the irradiated solid with  $N$  very small bubbles at the end of a period  $t_c$ , which is so short compared to fuel irradiation times that it can be taken to be zero for the purpose of growth calculations. We also assume that the bubbles all have the same initial radius  $R_0$  at the start of the growth stage. As growth proceeds, the number of bubbles per unit volume does not change, but the radius of each increases.

The calculation of the time rate of change of the bubble radii has been performed only under restricted conditions. Current analyses invoke one or more of the following simplifying assumptions:

1. All gas is contained in bubbles, none in the matrix.
2. Re-solution is neglected.
3. All bubbles are of the same size.
4. Bubbles are in mechanical equilibrium with the solid.
5. One of the limiting cases of the gas equation of state (i.e., the dense-gas or the ideal-gas limit) is applicable.

In Sec. 13.5 a simple model of bubble growth during postirradiation annealing was considered. This analysis used assumptions 2 through 5. In this section we are interested in the practical problem of bubble growth under constant fission-gas generation rates (i.e., steady-state in-pile behavior).

#### 13.9.1 The Simplest Growth Model

For illustrative purposes we first discuss the bubble-size-time relationship for the unrealistic case represented by simultaneous observance of all five of the preceding assumptions. According to assumption 1, the overall gas balance of Eq. 13.22 reduces to

$$Y_{Xe} \dot{F}t = mN \quad (13.144)$$

where  $N$  is the constant bubble density and  $m$ , the number of gas atoms in each bubble, is given by

$$m = \frac{4\pi R^3/3}{B + (kT/2\gamma)R} \quad (13.14)$$

For simplicity the solid has been assumed to be unstressed. If Eq. 13.14 is substituted into Eq. 13.144, a cubic equation that can be solved for  $R(t)$  is obtained.<sup>2,9</sup> If we assume that the ideal-gas law applies, the following result is obtained

$$R = \left( \frac{3}{4\pi} \frac{kT}{2\gamma} \frac{Y_{Xe} \dot{F}t}{N} \right)^{1/3} \quad (13.145)$$

and the swelling is given by Eq. 13.19:

$$\frac{\Delta V}{V} = \left( \frac{4\pi R^3}{3} \right) N = \left( \frac{3}{4\pi} \right)^{1/2} \frac{[(kT/2\gamma) Y_{Xe} \dot{F}t]^{3/2}}{N^{1/2}} \quad (13.146)$$

Equation 13.146 predicts that the swelling increases as the  $3/2$  power of the burnup ( $\beta = \dot{F}t\Omega$ ). It also shows that swelling decreases as the nucleation density increases. A given quantity of precipitated gas is held at higher pressures (and consequently smaller volume) if it is dispersed as many small bubbles rather than a few large ones. This behavior arises because surface-tension restraint on bubble size is more effective for small than for large bubbles. For a bubble density of  $10^{17} \text{ cm}^{-3}$  in  $\text{UO}_2$  at 10% burnup, Eq. 13.145 predicts a bubble radius of  $\sim 38 \text{ \AA}$  and Eq. 13.146 gives a fractional swelling of  $\sim 2.3\%$ .

#### 13.9.2 Allowance for Gas Remaining in the Matrix

Markworth<sup>4,9</sup> has treated the bubble-growth problem with assumption 1 relaxed but with 2 through 5 retained. Because the gas is now permitted to partition between the bubble and the solid, the kinetics of gas-atom absorption by the bubble must be included in the analysis. The problem is quite similar to the growth of bubbles during postirradiation annealing (Sec. 13.5). Equations 13.16 and 13.73 of that analysis apply to the present case, but the gas-atom balance is now given by Eq. 13.22. The following equations must be solved simultaneously:

$$m = \left( \frac{4\pi R^2}{3} \right) \left( \frac{2\gamma}{kT} \right) \quad (13.16)$$

$$\frac{dm}{dt} = 4\pi R D_{Xe} C \quad (13.73)$$

$$Y_{Xe} \dot{F}t = C + mN \quad (13.147)$$

These three equations can be combined to yield a non-linear, first-order differential equation for  $R$  as a function of  $t$ . The equation is of the Riccati type, and solutions in terms of Bessel functions are available. The extent to which the relation between  $R$  and  $t$  differs from the simple form given by Eq. 13.145 depends on the dimensionless time (or burnup) parameter:

$$\tau = \left[ \left( \frac{4\pi}{3} \right) N \left( \frac{kT}{2\gamma} \right) \frac{D_{Xe}^2 Y_{Xe}}{\dot{F}^2 \Omega^3} \right]^{1/2} \beta$$

When  $\tau \approx 1$ , the residual gas held in the matrix results in a bubble radius about one-half the value given by Eq. 13.145. If we take the same parameters used in the calculation illustrating use of Eq. 13.145 and assume  $D_{Xe} = 2 \times 10^{-17} \text{ cm}^2/\text{sec}$  (from Eq. 13.29 at  $1500^\circ\text{K}$ ) and  $\dot{F} = 8 \times 10^{13} \text{ fissions cm}^{-3} \text{ sec}^{-1}$ , the computed value of  $\tau$  at 10% burnup is 85. At this value of the dimensionless

time, essentially all the gas is contained in the bubbles, and their radius is accurately given by Eq. 13.145. Thus, simply relaxing assumption 1 does not materially alter the swelling predictions of the stationary bubble model. Markworth<sup>49a</sup> has demonstrated that the existence of a critical temperature of  $\sim 1000^\circ\text{C}$  below which swelling in uranium carbide is not observed experimentally is a natural consequence of the preceding growth model.

### 13.9.3 Bubble Growth with Re-resolution

The next step in bubble growth analysis is to relax assumptions 1 and 2 simultaneously. Since the primary effect of re-resolution is to maintain high matrix gas concentrations, we expect that bubble sizes in the presence of re-resolution will be lower than those predicted by the calculation just described. Growth of stationary bubbles by gas-atom diffusion in the presence of radiation-induced re-resolution has been considered by Nelson,<sup>45</sup> Pati,<sup>50</sup> and Marlowe.<sup>51</sup> In place of the ideal-gas limit used in the preceding analyses, these investigators assume that the bubbles are small enough for the opposite limit, Eq. 13.15, to apply. They also assume that the rate constants describing bubble growth are completely diffusion controlled and take  $k$  as given by Eq. 13.70. The simultaneous use of the dense-gas equation of state and diffusion-limited growth kinetics immediately presents an inconsistency: the former is valid only for small bubbles ( $R < \sim 10 \text{ \AA}$ ), whereas the latter is applicable only when the bubble radius is much larger than the lattice constant (say  $R > \sim 10 \text{ \AA}$ ). This inconsistency could be resolved by using the complete gas equation of state Eq. 13.14 and the rate constant for mixed control Eq. 13.96, but the mathematics would be considerably complicated.

To demonstrate that homogeneous nucleation and growth depend on the same elementary processes, we derive the governing equations for growth from the basic kinetic expressions given by Eqs. 13.127 through 13.131.

Since the bubbles are much larger in the growth stage than during nucleation, the single-atom balance cannot be cut off at some arbitrary upper size, but should be written as

$$\frac{dC}{dt} = Y_{Xe} \dot{F} - 2k_{II} C^2 - \left( \sum_{m=2}^{\infty} k_{Im} C_m \right) C + 2C_2 b + \left( \sum_{m=2}^{\infty} m C_m \right) b \quad (13.148)$$

Because the contribution of growth or re-resolution of diatomic clusters during the growth stage is small, the second and fourth terms on the right-hand side of Eq. 13.148 can be neglected.

The total concentration of bubbles is

$$N = \sum_{m=2}^{\infty} C_m \quad (13.149)$$

and the total number of gas atoms held in bubbles is

$$M = \sum_{m=2}^{\infty} m C_m \quad (13.150)$$

The average rate constant is

$$\bar{k} = \frac{\sum_{m=2}^{\infty} k_{Im} C_m}{\sum_{m=2}^{\infty} C_m} \quad (13.151)$$

Substituting Eqs. 13.149 through 13.151 into Eq. 13.148 yields the following form of the single-atom gas balance:

$$\frac{dC}{dt} = Y_{Xe} \dot{F} - \bar{k} N C + b M \quad (13.152)$$

The rate constant for diffusion-controlled absorption of gas atoms by a bubble of radius  $R$  is given by Eq. 13.70 as

$$k = 4\pi R D_{Xe} \quad (13.153)$$

thus, Eq. 13.151 becomes

$$\bar{k} = \frac{4\pi D_{Xe} \sum_{m=2}^{\infty} R C_m}{\sum_{m=2}^{\infty} C_m} \quad (13.154)$$

The ratio of the sums on the right of Eq. 13.154 is the mean radius of the bubble distribution, and the average rate constant can be expressed by

$$\bar{k} = 4\pi \bar{R} D_{Xe} \quad (13.155)$$

Hereafter, the bar over  $k$  and  $R$  will be omitted.

The total gas balance given by Eq. 13.131 can be treated in the same manner as the single atom gas balance to yield

$$Y_{Xe} \dot{F} = \frac{dC}{dt} + \frac{dM}{dt} \quad (13.156)$$

which, when combined with Eq. 13.152, yields

$$\frac{dM}{dt} = k N C - b M \quad (13.157)$$

As noted in Sec. 13.7, the re-resolution parameter in Eqs. 13.152 and 13.157 can be expressed by either microscopic or macroscopic models.

Because the average bubble radius appears explicitly in the rate constant  $k$  of Eq. 13.155, Eqs. 13.152 and 13.157 contain three dependent variables,  $M$ ,  $C$ , and  $R$ . The matrix gas concentration can be expressed as a function of  $M$  and  $t$  by use of Eq. 13.22. The bubble radius can be expressed in terms of  $M$  by noting that the number of gas atoms in an average bubble is given by

$$\frac{4\pi R^3 / 3}{B} = \frac{M}{N} \quad (13.158)$$

which can be solved to yield

$$R = \left( \frac{3BM}{4\pi N} \right)^{1/3} \quad (13.159)$$

An equation giving the time rate of change of the average bubble radius can be obtained by eliminating  $C$  from Eq. 13.157 by Eq. 13.22 and expressing  $M$  and its time derivative in terms of  $R$  by use of Eq. 13.158. When these substitutions and Eq. 13.155 for  $k$  are used in Eq. 13.157, the growth law is

$$\frac{dR}{dt} = \frac{D_{Xe} B Y_{Xe} \dot{F} t}{R} - \frac{4}{3} \pi D_{Xe} N R^2 - \frac{bR}{3} \quad (13.160)$$

Marlowe<sup>51</sup> has discussed solutions to this equation with the initial condition

$$R(t_c) = 3.4 \text{ \AA} \quad (13.161)$$

where  $R(t_c)$  is the radius of a diatomic cluster and  $t_c$  is the nucleation time. Markworth<sup>51a</sup> has analyzed the effect of re-resolution on the growth rate of bubbles obeying the ideal-gas law instead of the dense-gas limit to which Eq. 13.160 applies.

Alternatively, an equation in the variable  $M$  can be obtained by first substituting Eq. 13.22 into Eq. 13.157, which becomes

$$\frac{dM}{dt} = k N Y_{Xe} \dot{F} t - (kN + b)M \quad (13.162)$$

Instead of attempting to obtain the complete solution to this differential equation, we examine the quasi-stationary solution obtained by setting  $dM/dt$  equal to zero:\*

$$M = (Y_{Xe} \dot{F} t) \left( \frac{kN}{kN + b} \right) \quad (13.163)$$

In terms of the fraction of the gas contained in bubbles,

$$f_b = \frac{M}{Y_{Xe} \dot{F} t} \quad (13.164)$$

Eq. 13.163 is

$$f_b = \frac{kN}{kN + b} \quad (13.165)$$

The product  $kN$  is often denoted by  $g$ , and Eq. 13.165 is written as

$$f_b = \frac{g}{g + b} \quad (13.166)$$

The parameter  $g$  is useful when traps for gas atoms other than gas bubbles are present, in which case it is referred to as the probability per unit time of trapping a gas atom at a crystal defect of any sort.

However, Eq. 13.166 sloughs over the fact that if the gas-atom traps are restricted to gas bubbles,  $k$  is a function

of  $M$ , and hence  $g$  is a function (albeit weak) of  $f_b$ . In this case the trapping probability should be written

$$\begin{aligned} g &= kN \\ &= 4\pi R D_{Xe} N \\ &= 4\pi D_{Xe} N \left( \frac{3BM}{4\pi N} \right)^{1/3} \\ &= (4\pi N)^{2/3} D_{Xe} (3BY_{Xe} \dot{F} t)^{1/3} f_b^{1/3} \end{aligned} \quad (13.167)$$

When this equation is used for  $g$  in Eq. 13.166, the fraction of the total gas trapped in bubbles is the function of time (or burnup) given by

$$\frac{1 - f_b}{f_b^{2/3}} = \frac{b}{(4\pi N)^{2/3} D_{Xe} (3BY_{Xe} \dot{F} t)^{1/3}} \quad (13.168)$$

The influence of irradiation parameters on the fraction of the fission gas held in bubbles can be seen by examining the components of the right-hand side of Eq. 13.168. When this term is large,  $f_b$  is small, and re-resolution effectively maintains the gas in dynamic solution. Since  $b$  increases linearly with  $\dot{F}$ , the right-hand side of Eq. 13.168 varies as  $\dot{F}^{2/3}/D_{Xe}$ , which shows that re-resolution effects are important at high fission rates and low temperatures (where  $D_{Xe}$  is low). These trends are in the same direction as the effects that  $\dot{F}$  and  $T$  have on the way re-resolution influences homogeneous nucleation (Sec. 13.8).

Figure 13.15 shows the solution to Eq. 13.168. The quasi-steady-state fraction of gas contained in the bubbles is plotted against the time-dependent quantity on the right of the equation. Analytical forms for large and small values of the abscissa are shown on the graph. A more illustrative application of the same formula is shown in Fig. 13.16, where  $f_b$  is plotted as a function of burnup for several fuel temperatures. The parameters needed in the computation are listed in the figure caption. The fission-gas diffusion coefficients used in preparing the curves were taken from Cornell (Fig. 9 of Ref. 23). These values of  $D_{Xe}$  were obtained experimentally by measuring the fraction of the gas in the bubbles in irradiated  $UO_2$  and back-calculating  $D_{Xe}$  by a method similar to that used here to proceed in

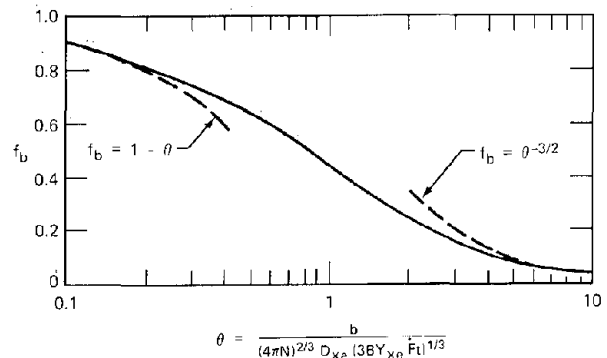


Fig. 13.15 The effect of re-resolution on bubble growth in the quasi-stationary approximation.

\*This condition, called equilibrium trapping, is examined in Chap. 15.

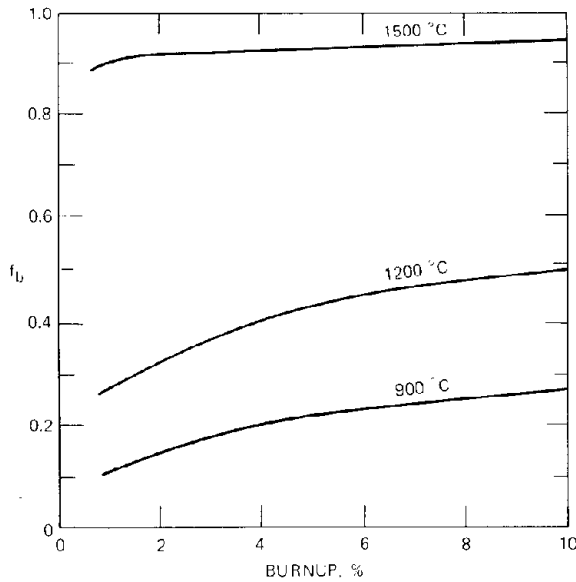


Fig. 13.16 Effect of re-solution on gas precipitation during irradiation:  $\dot{F} = 4 \times 10^{13} \text{ cm}^{-3} \text{ sec}^{-1}$ ;  $b = 5 \times 10^{-5} \text{ sec}^{-1}$ ; and  $N = 2 \times 10^{17} \text{ cm}^{-3}$ .

the other direction (i.e., given  $D_{Xe}$ , find  $f_b$ ). Cornell obtained diffusion coefficients of  $1.0 \times 10^{-17}$ ,  $1.6 \times 10^{-17}$ , and  $1.1 \times 10^{-15} \text{ cm}^2/\text{sec}$  at temperatures of  $900^\circ\text{C}$ ,  $1200^\circ\text{C}$ , and  $1500^\circ\text{C}$ , respectively.\*

The calculations reported by Pati<sup>50</sup> are essentially the same as those shown on Fig. 13.16. The major conclusion drawn from analysis of re-solution effects on bubble growth is that the temperature is the primary variable affecting the fraction of gas which precipitates during irradiation. At high temperatures re-solution is ineffective in maintaining gas in solution because the fission-gas diffusion coefficient is large enough to return gas to the bubble as soon as it is ejected by collision with an energetic fission fragment. At the lower temperatures a much larger fraction of the gas is atomically dispersed in the matrix. This effect is not predicted by the calculations of Markworth reviewed earlier, in which re-solution was not considered. A substantial portion of the fuel in an LMFBR operates at temperatures below  $1200^\circ\text{C}$ , where re-solution can drastically influence gas release and swelling, generally by reducing swelling and enhancing gas release.

\*The apparent lack of an activation energy between the lowest temperature figures was attributed by Cornell to the radiation enhancement of the diffusion coefficient. A theory of this effect due to Speight was cited. This theory,<sup>52</sup> however, is simply that due to Dienes and Damask,<sup>18</sup> which is applicable only when diffusion occurs by a classical vacancy mechanism. Since it was shown in Sec. 13.3 that such a mechanism is highly unlikely in  $\text{UO}_2$ , Cornell's explanation of the non-Arrhenius behavior of the diffusion coefficients deduced from his bubble-growth data is suspect.

### 13.9.4 Growth of Nonequilibrium Bubbles

All analyses of bubble growth discussed in this section have assumed that the bubbles were in mechanical equilibrium with the surrounding solid or that Eq. 13.5 was satisfied at all times. Mechanical equilibrium is usually maintained by flow of vacancies to the bubble to provide the additional volume needed to accommodate the simultaneous influx of gas atoms. Whether or not Eq. 13.5 is satisfied depends on the relative rates at which irradiation-produced point defects and gas atoms are absorbed by the bubble.

A bubble of radius  $R$  can be regarded as the absence of  $(4\pi R^3/3)/\Omega$  matrix atoms, where  $\Omega$  is the volume per atom. Or, since a missing atom is a vacancy, an empty sphere of radius  $R$  can be thought of as consisting of

$$m_v = \frac{4\pi R^3/3}{\Omega} \text{ vacancies} \quad (13.169)$$

It is of interest to determine the number of vacancies that must be acquired by a bubble containing  $m$  gas atoms in order that mechanical equilibrium be established. The number of gas atoms in a sphere of radius  $R$  which is in mechanical equilibrium is given by Eq. 13.14. The number of vacancies per gas atom in an equilibrium bubble is

$$(m_v)_{eq} = \left( \frac{kT}{2\gamma} \right) \frac{R}{\Omega} + \frac{B}{\Omega} \quad (13.170)$$

If we take  $kT/2\gamma = 1 \text{ \AA}^2$ ,  $B = 85 \text{ \AA}^3$ , and  $\Omega = 41 \text{ \AA}^3$  (for  $\text{UO}_2$ ), Eq. 13.170 requires that for equilibrium bubble radii of 10, 100, and 1000  $\text{\AA}$ , there be  $\sim 2$ ,  $\sim 6$ , and 27 vacancies per gas atom, respectively. The vacancy supply problem becomes more acute as the bubble enlarges.

The time rate of change of the volume of a bubble is equal to the difference in the rates at which vacancies and interstitials are absorbed and to the volume carried by each of these point defects. The absorption rates are given by Eq. 13.66, and the volume associated with both vacancies and interstitials is approximately equal to the atomic volume  $\Omega$ . Thus,

$$\frac{d}{dt} \left( \frac{4}{3} \pi R^3 \right) = \Omega [4\pi R D_v (C_v - C_{vR}) - 4\pi R D_i (C_i - C_{iR})]$$

or the growth law is

$$\frac{dR}{dt} = \frac{\Omega}{R} [D_v (C_v - C_{vR}) - D_i (C_i - C_{iR})] \quad (13.171)$$

Here  $C_{vR}$  and  $C_{iR}$  are the concentrations of vacancies and interstitials at the bubble surface, and  $C_v$  and  $C_i$  are the point-defect concentrations in the bulk solid.

It is commonly assumed that the point-defect concentrations at the bubble surface are given by equilibrium thermodynamics. If a bubble were in mechanical equilibrium with an unstressed solid, the vacancy concentration at the bubble surface would be given by Eq. 6.12. This formula was derived with the assumption that there was no pressure on the solid so that the enthalpy of vacancy formation could be replaced by the vacancy formation energy. In the case of a bubble that is not in

mechanical equilibrium, this approximation is no longer correct because a mechanical stress equal to  $p - (2\gamma/R)$  acts on the solid at the bubble surface (see Eq. 13.6).

To account for the effect of stress on the thermodynamic equilibrium of vacancies, consider a solid subject to a uniform pressure  $P$ . The equilibrium vacancy fraction in the solid is given by Eq. 6.12 in which  $h_v$  is retained:

$$x_v^{eq}(P) = \exp\left(\frac{s_v}{k}\right) \exp\left(-\frac{h_v}{kT}\right) \quad (13.172)$$

The thermodynamic relation between enthalpy and energy is

$$h_v = \epsilon_v + Pv_v \quad (13.173)$$

where  $P$  is the system pressure and  $v_v$  is the volume change of the system (the solid body) due to the production of one vacancy by moving an atom from the interior to the surface and is approximately equal to the atomic volume  $\Omega$ . Thus, the equilibrium vacancy fraction in a solid under pressure  $P$  is

$$x_v^{eq}(P) = \exp\left(\frac{s_v}{k}\right) \exp\left(-\frac{\epsilon_v}{kT}\right) \exp\left(-\frac{P\Omega}{kT}\right) \quad (13.174)$$

The product of the first two terms on the right is the equilibrium vacancy fraction for zero pressure; thus, Eq. 13.174 is equivalent to

$$x_v^{eq}(P) = x_v^{eq}(0) \exp\left(-\frac{P\Omega}{kT}\right) \quad (13.175)$$

If we use the relation between volumetric concentration and site fraction ( $C_v = x_v/\Omega$ ) and identify  $P$  with the excess pressure in the bubble, the thermodynamic vacancy concentration at the bubble surface is given by

$$C_{vR} = C_v^{eq} \exp\left[-\frac{\Omega}{kT} \left(p - \frac{2\gamma}{R}\right)\right] \quad (13.176)$$

where  $C_v^{eq}$  is the thermodynamic equilibrium vacancy concentration for a stress-free solid:

$$C_v^{eq} = \frac{\exp(s_v/k) \exp(-\epsilon_v/kT)}{\Omega} \quad (13.177)$$

Similar arguments can be applied to the calculation of the interstitial concentration at the bubble surface, the only difference being a change in the sign of the volume term  $v_v$ . The result is

$$C_{iR} = C_i^{eq} \exp\left[\frac{\Omega}{kT} \left(p - \frac{2\gamma}{R}\right)\right] \quad (13.178)$$

where

$$C_i^{eq} = \frac{\exp(s_i/k) \exp(-\epsilon_i/kT)}{\Omega} \quad (13.179)$$

$s_i$  and  $\epsilon_i$  being the interstitial entropy and energy of formation, respectively.

The bulk concentrations of the point defects,  $C_v$  and  $C_i$ , are determined by balances on these species in the bulk solid. We follow Wiedersich's<sup>53</sup> method slightly simplified for clarity.

Vacancies and interstitials are created by thermal processes (e.g., shedding by dislocations) at rates given by  $G_v^{eq}$  and  $G_i^{eq}$ , respectively, and by radiation at a rate  $Y_{vi}\dot{F}$ . The balance is maintained by the removal of the point defects by recombination and by absorption at sinks. The bubbles proper, free surfaces, grain boundaries, and dislocation lines can act as sinks and sources of point defects, but only dislocation lines are important in most nuclear materials. We will assume that dislocations are the primary sinks for vacancies and interstitials and that only bubbles and dislocations are present in irradiated solid.

In the absence of radiation, the equilibrium concentrations of point defects are determined by equating the rates of production by thermal processes to the rates of removal by recombination and dislocation capture:

$$G_v^{eq} = k_{iv} C_v^{eq} C_i^{eq} + Z_v D_v \rho_d C_v^{eq} \quad (13.180)$$

$$G_i^{eq} = k_{iv} C_v^{eq} C_i^{eq} + Z_i D_i \rho_d C_i^{eq} \quad (13.181)$$

Here  $k_{iv}$  is the rate constant for vacancy-interstitial recombination (Eq. 13.42), and the last term on the right represents the capture of point defects by the dislocation network in the solid. The capture rates are of the form given by Eq. 13.94, where

$$\frac{1}{Z_v} = \frac{1}{z_{vd}} + \frac{\ln(\mathcal{R}/R_{dv})}{2\pi} \quad (13.182)$$

$$\frac{1}{Z_i} = \frac{1}{z_{id}} + \frac{\ln(\mathcal{R}/R_{di})}{2\pi} \quad (13.183)$$

Because of the nature of the stress field surrounding dislocation lines,  $R_{di}$  can be slightly larger than  $R_{dv}$  (see problem at end of chapter). In general,  $Z_i$  exceeds  $Z_v$  by a few percent.

Under irradiation the point-defect balances become

$$Y_{vi}\dot{F} + G_v^{eq} = k_{iv} C_v C_i + Z_v D_v \rho_d C_v \quad (13.184)$$

$$Y_{vi}\dot{F} + G_i^{eq} = k_{iv} C_v C_i + Z_i D_i \rho_d C_i \quad (13.185)$$

We have assumed that the thermal production rates and the dislocation density are unaffected by irradiation. If Eq. 13.180 is subtracted from Eq. 13.184 and Eq. 13.181 from Eq. 13.185, the following equations result:

$$Y_{vi}\dot{F} = k_{iv}(C_v C_i - C_v^{eq} C_i^{eq}) + Z_v D_v \rho_d (C_v - C_v^{eq}) \quad (13.186)$$

$$Y_{vi}\dot{F} = k_{iv}(C_v C_i - C_v^{eq} C_i^{eq}) + Z_i D_i \rho_d (C_i - C_i^{eq}) \quad (13.187)$$

Values for  $Y_{vi}$ ,  $Z_v$ ,  $Z_i$ ,  $D_v$ , and  $D_i$  can be estimated by the methods outlined earlier in this chapter. If the entropy and energy of the point defects are known,  $C_v^{eq}$  and  $C_i^{eq}$  can be obtained from Eqs. 13.177 and 13.179. Equations 13.186 and 13.187 can then be solved for the steady-state vacancy and interstitial concentrations in the irradiated

solid. In the solution the approximation  $Z_v = Z_i$  can be made without affecting the calculated values of  $C_v$  and  $C_i$  appreciably (this approximation cannot be made in the final calculation of the growth rate, however). The general nature of the solution is illustrated by Fig. 13.17, which shows Wiedersich's results for irradiation of nickel. We have retained the original ordinate and abscissa labels but have indicated the values of the other parameters of the solution (defect production rate or  $\dot{F}$  and source efficiency or

matter what the dose rate or the microstructure of the solid. The analogous curves for interstitials [Fig. 13.17(b)] do not show the concentration minimum until very high temperatures because the equilibrium concentration of interstitial atoms in most solid lattices is extremely low owing to the large energy of formation in Eq. 13.179.

The extremely large supersaturation of point defects caused by low-temperature irradiation can lead to enhancement of the diffusion coefficient of species that

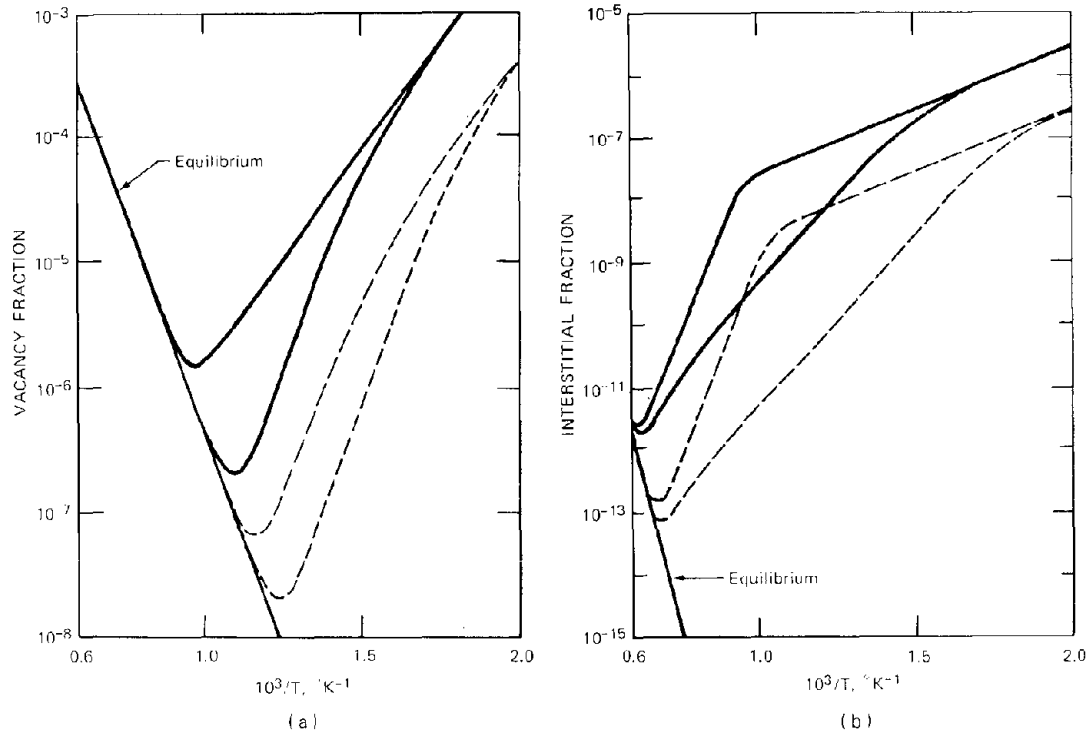


Fig. 13.17 Steady-state point-defect concentrations in an irradiated solid. —, high defect production rate. ----, low defect production rate. The upper and lower curves for each defect production rate represent small and large dislocation densities, respectively. [After H. Wiedersich, *Radial. Eff.*, 12: 111 (1972).]

dislocation density) in qualitative terms. Our aim is to show the general features of the solution, which should be similar for metals and ceramic fuels, such as  $\text{UO}_2$ .

Figure 13.17(a) shows that the radiation-produced vacancy concentration is high at low temperature where the diffusion coefficients are small and the removal processes are therefore slow. As the temperature is increased, recombination and capture by dislocations become more rapid and the concentration of vacancies falls. It begins to rise again at high temperature because of the rapidly increasing rate of thermal production of point defects. The vacancy supersaturation\* is enhanced by high defect production rates and low dislocation-line density (or, in general, low sink efficiencies), but the thermal equilibrium line is approached at sufficiently high temperatures no

migrate by a vacancy mechanism.<sup>18</sup> In a radiation field the diffusion coefficient is still given by the first equality of Eq. 7.28, but the site fraction of vacancies is no longer equal to the equilibrium value. Rather,  $x_v$  is obtained by calculations such as those which produced Fig. 13.17(a). Note that radiation does not alter the diffusion coefficient of the vacancies proper (or of the interstitials); only the diffusivity of atomic species that migrate by the vacancy mechanism (Sec. 7.4) is affected.

Comparison of Eqs. 13.186 and 13.187 shows that the steady-state vacancy and interstitial concentrations in the irradiated solid satisfy the following equation:

$$Z_v D_v (C_v - C_v^{eq}) = Z_i D_i (C_i - C_i^{eq}) \quad (13.188)$$

The surface concentrations  $C_{vR}$  and  $C_{iR}$  given by Eqs. 13.176 and 13.178 and the bulk point-defect balance, Eq. 13.188, can now be used in the growth law,

\*Supersaturation is defined as  $C_v/C_v^{eq}$ .

Eq. 13.171. In using Eqs. 13.176 and 13.178, we can use the approximation  $e^x \approx 1 + x$  because the argument of the exponentials is quite small compared to unity. Thus, Eq. 13.171 becomes

$$\frac{dR}{dt} = \frac{\Omega}{R} \left[ D_v \left( 1 - \frac{Z_v}{Z_i} \right) \left( C_v - C_v^{eq} \right) + \frac{\Omega}{kT} \left( p - \frac{2\gamma}{R} \right) \times \left( D_v C_v^{eq} + D_i C_i^{eq} \right) \right] \quad (13.189)$$

The first term in the brackets represents the effect of the supersaturation of irradiation-produced defects on growth. This effect is often referred to as a chemical stress<sup>5,4</sup> because it produces bubble growth like a mechanical force. Since  $Z_v/Z_i$  is always less than unity, the chemical-stress term always causes bubble growth when the solid is supersaturated with vacancies (i.e.,  $C_v > C_v^{eq}$ ). The difference  $C_v - C_v^{eq}$  can be obtained from such graphs as Fig. 13.17.

The second term in the brackets of Eq. 13.189 is the mechanical component of the growth due to the pressure imbalance  $p - (2\gamma/R)$ .

Equation 13.189 cannot be integrated until the gas pressure  $p$  is related to bubble radius. If the gas density in Eq. 13.1 is expressed in terms of  $m$  and  $R$  by Eq. 13.13 and  $m$  is written as  $M/N$ , where  $N$  is the total bubble concentration, the gas pressure can be written

$$p = \frac{kT}{(4\pi R^3/3)(N/M) - B} \quad (13.190)$$

which, however, simply exchanges the unknown  $p$  for another unknown,  $M$ . The latter is determined by Eq. 13.157, where  $C$  is removed by Eq. 13.22:

$$\frac{dM}{dt} = 4\pi R D_{Xe} N (Y_{Xe} \dot{F}t - M) - bM \quad (13.191)$$

The increase in the bubble radius as a function of time is obtained by solving Eqs. 13.189 through 13.191 simultaneously with appropriate initial conditions for  $R$  and  $M$ . Although the full solution of this problem has not been reported, limiting cases have been examined.

Greenwood, Foreman, and Rimmer<sup>5</sup> assumed  $Z_v = Z_i$  and neglected the interstitial flux term because of the smallness of  $C_i^{eq}$ , whereupon Eq. 13.189 reduces to

$$\frac{dR}{dt} = \left( p - \frac{2\gamma}{R} \right) \frac{\Omega^2}{RkT} D_v C_v^{eq} \quad (13.192)$$

In addition,  $p$  was determined by assuming all gas to be in the bubbles ( $M = Y_{Xe} \dot{F}t$ ), re-solution was not considered, and the gas was assumed to be ideal. These assumptions reduce Eq. 13.190 to the following explicit function of  $R$  and  $t$ :

$$p = \frac{Y_{Xe} \dot{F}kTt}{4\pi R^3 N/3} \quad (13.193)$$

When Eq. 13.193 is substituted into Eq. 13.192, the growth law is

$$\frac{dR}{dt} = \frac{A_1 t}{R^4} - \frac{A_2}{R^2} \quad (13.194)$$

where  $A_1 = 3\Omega^2 D_v C_v^{eq} Y_{Xe} \dot{F}/4\pi N$  and  $A_2 = (2\gamma/kT)\Omega^2 D_v C_v^{eq}$  are constants. Greenwood, Foreman, and Rimmer<sup>5</sup> obtained an approximate solution to Eq. 13.194 with the initial condition  $R(0) = 0$ :

$$R(t) = R_{eq}(t) - \left( \frac{A_1^2}{4A_2^3} \right) t \quad (13.195)$$

where  $R_{eq}(t)$  is the radius that would be obtained at time  $t$  if the bubble had been in mechanical equilibrium throughout its lifetime (Eq. 13.145). The second term in Eq. 13.195 accounts for the reduction in bubble size due to the inability of vacancy diffusion to supply the volume increase required by the bubble to maintain mechanical equilibrium. That is, there is a small but significant pressure excess,  $p - (2\gamma/R) > 0$ , at all times during the growth stage. If the chemical-stress term in Eq. 13.189 had been retained, however, the bubble could grow more rapidly than under conditions of mechanical equilibrium, and a pressure deficit could develop. The chemical-stress term is responsible for the growth of voids in irradiated metals, where  $p \ll 2\gamma/R$ .

A bubble-growth formula similar to Eq. 13.189 has been derived by Gulden and Kaae.<sup>5,5</sup> They included the stress state of the solid in which the bubble is embedded. The net effect of including external stress is, as in Eq. 13.4, to replace  $[p - (2\gamma/R)]$  by  $[p - (2\gamma/R) - \sigma]$  ( $\sigma$  is positive if the solid is in compression). This modification of the growth law follows by noting that, when the bulk solid is subject to a hydrostatic stress, the equilibrium vacancy and interstitial concentrations in Eqs. 13.180 and 13.181 should be written as  $C_v^{eq} \exp(-\Omega\sigma/kT)$  and  $C_i^{eq} \exp(\Omega\sigma/kT)$ , respectively.

Harrison<sup>1,5</sup> has considered the form of the bubble-growth law in the absence of chemical stress. He has shown that, for the case of a general triaxial mechanical stress state of the solid (as opposed to simple hydrostatic stress),  $\sigma$  should be interpreted as the mean normal stress [i.e.,  $(\sigma_{xx} + \sigma_{yy} + \sigma_{zz})/3$ ]. He also shows how the growth rate is affected when the stresses around the bubble are large enough to cause plastic deformation (yielding).

### 13.9.5 Bubble-Size Distribution During Growth

In the bubble-growth analyses discussed up to this point, all restrictive assumptions listed at the beginning of this section have been removed except for the requirement that all bubbles be of the same size. If the nucleation process produces bubbles of the same size, all bubbles will grow at the same rate provided that the only processes operating on the bubbles add or remove one atom at a time. Gas-atom diffusion to the bubble and microscopic re-solution are such processes.\* However, when the bubbles

\*Markworth and Baroody<sup>5,6</sup> have determined the shape of the bubble distribution in the postirradiation annealing situation analyzed by Speight<sup>3,4</sup> (see Sec. 13.5). They show that the variance of the distribution at time  $t$  is proportional to the variance of the initial distribution. If the latter

are subject to processes that change the bubble size in a discontinuous manner, a bubble-size distribution develops during the growth stage. Two important processes in this category are coalescence and macroscopic re-resolution. We analyze here the bubble distribution that occurs when the nucleation and re-resolution models proposed by Turnbull<sup>4,3</sup> are coupled with growth of the bubbles by absorption of matrix gas atoms.

When, as in the present instance, we wish to describe the size distribution of bubbles in the presence of macroscopic re-resolution, the conservation statement for clusters containing  $m$  gas atoms is no longer correctly given by Eq. 13.129, which is valid only if re-resolution removes single atoms of gas from the bubble. If an entire bubble can be destroyed by a single re-resolution event, we must replace Eq. 13.129 by

$$\frac{dC_m}{dt} = k_{l,m-1} C_{m-1} C - k_{lm} C_m C - b' C_m \quad (13.196)$$

Inasmuch as  $m$  can be large, we first convert the bubble distribution function in this equation from discrete to continuous form. The coefficient of  $C$  in the first term on the right can be written as

$$k_{l,m-1} C_{m-1} = k_m C_m - \frac{d}{dm} (k_m C_m) \quad (13.197)$$

Thus Eq. 13.196 becomes a partial differential equation:

$$\frac{\partial C_m}{\partial t} = - \frac{\partial}{\partial m} (k_m C_m) C - b' C_m \quad (13.198)$$

Instead of the function  $C_m$ , we now rewrite Eq. 13.198 in terms of the bubble distribution function  $N(R)$ , where  $N(R) dR$  = number of bubbles per unit volume with radii in the range  $R$  to  $R + dR$ . The relation between the two distributions is

$$N(R) = C_m \frac{dm}{dR} \quad (13.199)$$

For small bubbles,  $m$  is related to  $R$  by Eq. 13.15, and Eq. 13.199 becomes

$$N(R) = \left( \frac{4\pi R^2}{B} \right) C_m \quad (13.200)$$

is zero (i.e., uniform bubbles initially), the bubble distribution function remains a delta function during growth. During in-pile growth with microscopic re-resolution, the variance at time  $t$  is the product of the initial variance of the distribution and a decay term,<sup>5,6a</sup>  $\exp(-bt)$ . Thus, an initially nonuniform distribution becomes narrower because of re-resolution, but an initially uniform distribution (i.e., zero variance) remains uniform during growth.

Substituting Eq. 13.200 into 13.198 and noting that

$$\frac{dm}{dR} = \frac{4\pi R^2}{B}$$

we have

$$\frac{\partial N(R)}{\partial t} = - \frac{\partial}{\partial R} \left[ \frac{kB}{4\pi R^2} N(R) \right] C - b' N(R) \quad (13.201)$$

If we use Eq. 13.112 for the re-resolution parameter and Eq. 13.153 for the rate constant and set the time derivative in Eq. 13.198 equal to zero, the steady-state bubble distribution satisfies the equation

$$\frac{dN(R)}{dR} = - \left[ \left( \frac{2\pi\mu_{ff}\dot{F}}{D_{Xe}BC} \right) R^3 - \frac{1}{R} \right] N(R) \quad (13.202)$$

To provide a boundary condition for Eq. 13.202, we must consider the nucleation process. According to Turnbull's<sup>4,3</sup> model,  $\alpha$  bubbles containing  $m_0$  atoms (and having a radius  $R_0$ ) are heterogeneously nucleated on each fission-fragment track. The steady-state balance on clusters of size  $m_0$  is

$$2\alpha\dot{F} = k_{lm_0} C_{m_0} C + b'_0 C_{m_0} \quad (13.203)$$

where  $k_{lm_0}$  is the rate constant for absorption of single gas atoms by the nuclei and  $b'_0$  is the re-resolution parameter for bubbles of this size. When  $C_{m_0}$  is converted to  $N(R_0)$  by use of Eq. 13.200 and  $k_{lm_0}$  and  $b'_0$  are expressed by the appropriate formulas, the result is

$$N(R_0) = \frac{4\alpha\dot{F}R_0}{2D_{Xe}BC + B\mu_{ff}\dot{F}R_0} \quad (13.204)$$

Speight<sup>5,7</sup> first derived (and integrated) Eq. 13.202, although he neglected to include the second term in the denominator of Eq. 13.204. In addition, Speight set  $R_0 = 0$  in the integration, a deficiency that has been removed by Monti.<sup>5,8</sup> Integration of Eq. 13.202 without either of these simplifications yields

$$N(R) = \left( \frac{4\alpha\dot{F}R_0}{2D_{Xe}CB + B\mu_{ff}\dot{F}R_0} \right) \left( \frac{R}{R_0} \right) \times \exp \left\{ - \left( \frac{\pi\dot{F}\mu_{ff}R_0^4}{2D_{Xe}BC} \right) \left[ \left( \frac{R}{R_0} \right)^4 - 1 \right] \right\} \quad (13.205)$$

The matrix gas concentration required in this equation is given by

$$C = Y_{Xe}\dot{F}t - \int_{R_0}^{\infty} m(R) N(R) dR \quad (13.206)$$

where  $t$  is the irradiation time and  $m(R)$  is given by Eq. 13.15. The total bubble density is the integral of Eq. 13.205:

$$N = \int_{R_0}^{\infty} N(R) dR = \left[ \frac{(\pi)^{1/2} \alpha \dot{F} R_0^2}{2D_{Xe}BC + B\mu_{ff}\dot{F}R_0} \right] \times \frac{e^s \operatorname{erfc}(s)^{1/2}}{(s)^{1/2}} \quad (13.207)$$

where  $s$  is the coefficient in the exponential term of Eq. 13.205,

$$s = \frac{\pi \bar{F} \mu_{ff} R_0^4}{2D_{Xe} BC} \quad (13.208)$$

The bubble distribution function is extraordinarily sensitive to the parameter  $s$ . For  $s < 1/4$ , the distribution function exhibits a maximum at

$$R_{\max} = \frac{R_0}{(4s)^{1/4}}$$

For  $s > 1/4$ ,  $N(R)$  is a monotonically decreasing function of  $R$  for  $R > R_0$ . The width of the distribution is a function of  $s$  alone. If this parameter is small, the distribution is broad, and bubbles of fairly large size are predicted. For  $s = 0.01$ , for example, the maximum of the distribution occurs at  $R = 11 \text{ \AA}$ . For  $s = 1$  and  $R_0 = 5 \text{ \AA}$ ,  $N(R)$  is 10% of  $N(R_0)$  at  $R = 5.4 \text{ \AA}$ .

The irradiation conditions that control the bubble distribution are contained in the grouping of parameters  $\bar{F}D_{Xe}/C$ . This parameter depends on the fission density, temperature, irradiation time, and the fraction of the gas in solution (the last of these can be determined by combining Eqs. 13.205 and 13.206). Let us assign the following values to the constants in Eqs. 13.207 and 13.208:

$$\begin{aligned} \alpha &= 5 \\ R_0 &= 5 \text{ \AA} \\ B &= 85 \text{ \AA}^3 \\ \mu_{ff} &= 6 \text{ \mu m} \end{aligned}$$

The first term on the right of Eq. 13.207 becomes

$$\frac{(\pi)^{1/2} \alpha \bar{F} R_0^2}{2D_{Xe} BC + B\mu_{ff} \bar{F} R_0} = \frac{2.2 \times 10^{-14} (\bar{F}/D_{Xe} C)}{1.7 \times 10^{-22} + 2.6 \times 10^{-33} (\bar{F}/D_{Xe} C)}$$

and the dimensionless coefficient  $s$  is

$$s = 6.9 \times 10^{-11} \left( \frac{\bar{F}}{D_{Xe} C} \right)$$

At small values of  $\bar{F}/D_{Xe} C$  (i.e., less than  $\sim 10^9 \text{ cm}^{-2}$ ), the total bubble density obeys the limiting form

$$N = 1.6 \times 10^{13} \left( \frac{\bar{F}}{D_{Xe} C} \right)^{1/2} \quad (13.209)$$

For  $\bar{F}/D_{Xe} C > 10^{12} \text{ cm}^{-2}$ , Eq. 13.207 reduces to

$$N = \frac{7 \times 10^{28}}{\bar{F}/D_{Xe} C} \quad (13.210)$$

The bubble density passes through a maximum of  $7 \times 10^{17} \text{ cm}^{-3}$  at  $\bar{F}/D_{Xe} C \sim 10^{10} \text{ cm}^{-2}$ .

At low fission densities and high temperatures,  $\bar{F}/D_{Xe} C$  is small and so is the coefficient  $s$ . The bubble distribution is broad and the total bubble density is low because many of the nuclei have escaped re-resolution and have grown to

appreciable size. At the opposite limit of high fission density and low temperature,  $\bar{F}/D_{Xe} C$  and  $s$  are large. The distribution is very narrow and the total bubble density is low because few bubbles survive re-resolution by fission fragments.

The total bubble density  $N$  predicted by Eq. 13.207 is comparable to the nucleation densities determined from homogeneous nucleation models (Table 13.4). Because of the maximum in the total bubble density previously mentioned, however, Eq. 13.207 does not exhibit the extreme temperature sensitivity of the homogeneous nucleation calculations. In addition,  $N$  of Eq. 13.207 is not a nucleation density in the sense that it represents the bubble density developed during a nucleation period which is followed by a growth period. In the Turnbull-Speight model, there is no separation whatsoever between nucleation and growth. Both processes occur simultaneously along with re-resolution.

All characteristics of the bubble distribution (e.g., total density and mean size) vary only slowly with irradiation time as a result of the dependence on  $C$  given by Eq. 13.206. That is, the bubble distribution function of Eq. 13.205 is a quasi-stationary distribution. The mean life of a bubble in the irradiation environment is a good measure of the time required to attain the quasi-steady-state distribution. The mean bubble lifetime is equal to the reciprocal of the re-resolution parameter  $b'$ , or about 4 to 40 hr. Therefore, the irradiation parameters that govern the bubble distribution function (specifically fission density and temperature) are those characteristic of the last day of irradiation.<sup>18</sup>

Swelling due to precipitated gas can be obtained by substituting Eq. 13.205 into 13.21. Unless  $\bar{F}/D_{Xe} C$  is very small, the swelling predicted from this model is extremely low.

### 13.10 MIGRATION MECHANISMS AND GROWTH OF MOBILE BUBBLES

In the previous section, we examined the ways by which stationary bubbles grow by exchanging gas atoms with the solid. In these analyses only the gas atoms were permitted to move, the bubbles being treated as stationary repositories of precipitated gas. In this section we will describe what happens when the bubbles are allowed to move and consequently to collide and coalesce.

There are two types of closed pores found in ceramic nuclear fuels. The pores formed by precipitation of fission gases from solution are usually quite small (radii  $< 5000 \text{ \AA}$ ) and contain a gas consisting mainly of xenon at high pressure. The other type of closed pore results from incomplete densification of the fuel during manufacture. These fabrication pores are usually large (radius  $> 1 \text{ \mu m}$ ) and contain a low-pressure gas that is composed primarily of helium used as a cover gas during fuel-element assembly. Pore migration in solids has been thoroughly reviewed by Nichols.<sup>9,39</sup> In this discussion only those processes affecting fission-gas bubble motion are considered. The behavior of the fabrication porosity will be considered in Chap. 14.

### 13.10.1 Atomic Mechanism of Bubble Mobility Due to Surface Diffusion

Surface diffusion is an important mechanism by which bubbles in nuclear fuels move both randomly and under the influence of a driving force. Molecules of the matrix solid are in constant motion on the inside surface of the bubble. A net displacement of a large number of these surface molecules is manifest as a much smaller displacement of the entire bubble. The motion of the surface molecules can be random or in a particular direction (dictated by the direction of a macroscopic potential gradient applied to the fuel body). When the motion of the surface molecules is random, the resulting bubble motion is also random and is in fact a form of Brownian motion. When the surface molecules move in a particular direction, the bubbles move in the direction of the potential gradient that is acting on individual surface molecules.

### 13.10.2 Random Bubble Motion

In the absence of a driving force, the molecules of the matrix material randomly hop over the inner surface of the bubble. The macroscopic parameter describing this process is the surface self diffusion coefficient,  $D_s$ , which is related to the parameters characterizing the molecular motion by the Einstein equation (Sec. 7.7):

$$D_s = \frac{\lambda_s^2 \Gamma_s}{4} \quad (7.62)$$

where  $\lambda_s$  is the jump distance on the solid surface and  $\Gamma_s$  is the total jump frequency of a molecule on the surface. The bubble, on the other hand, executes random motion in three, not two, dimensions; thus, the Einstein equation describing its average motion is

$$D_b = \frac{\lambda_b^2 \Gamma_b}{6} \quad (13.211)$$

where  $\lambda_b$  and  $\Gamma_b$  are the jump distance and jump frequency of the bubble, respectively.

The jump distance of a bubble is the displacement of the bubble which occurs when one atom on its surface moves a distance  $\lambda_s$ . This quantity has been derived by Nichols,<sup>9</sup> Gruber,<sup>5,9</sup> and Greenwood and Speight<sup>6,0</sup> for spherical bubbles. Figure 13.18 shows how the same result can be obtained by considering a cubical bubble. The original position of the bubble is shown as the dashed figure. If all the matrix molecules in the shaded portion on the right are transported to the shaded area on the left, the bubble is thereby moved by a distance  $\Delta x$  from left to right and occupies the region of the solid square. The number of matrix molecules that have moved from right to left in this process is  $l^2 \Delta x / \Omega$ , where  $\Omega$  is the atomic volume of the matrix. Each atom hopped  $1/\lambda_s$  times to move from the right-hand face to the left-hand face of the cube. Or, to displace the bubble by a distance of  $\Delta x$ , a total of  $l^3 \Delta x / \Omega \lambda_s$  individual molecular jumps on the surface must have occurred. The distance the bubble moves in each jump of a single surface molecule is

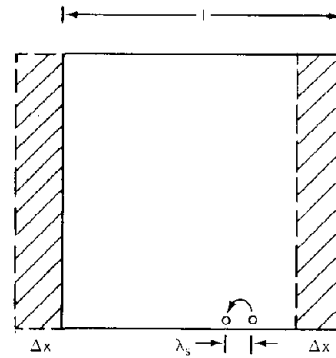


Fig. 13.18 Diagram for determining the jump distance of a bubble due to individual jumps of molecules on its inner surface.

$$\lambda_b = \frac{\Delta x}{l^3 \Delta x / \Omega \lambda_s} = \frac{\Omega \lambda_s}{l^3}$$

where  $l^3$  is the volume of the bubble, which can be replaced by  $4\pi R^3/3$  to convert from a cube to a sphere. The atomic volume can be approximated by the cube of the lattice constant,  $\Omega \approx a_0^3$ , and the bubble jump distance is therefore

$$\lambda_b = \left( \frac{a_0^3}{4\pi R^3/3} \right) \lambda_s \quad (13.212)$$

The bubble jump frequency is the rate at which all molecules on the inner surface of the bubble hop. If the area occupied by a surface molecule is approximated by  $a_0^2$ , the number of molecules on the inner surface of a bubble of radius  $R$  is  $4\pi R^2/a_0^2$ . Since each of these molecules jumps  $\Gamma_s$  times a second, the frequency of the discrete bubble jumps is

$$\Gamma_b = \left( \frac{4\pi R^2}{a_0^2} \right) \Gamma_s \quad (13.213)$$

Substituting Eqs. 13.212 and 13.213 into Eq. 13.211 and using Eq. 7.62 yields

$$D_b = \frac{3a_0^4 D_s}{2\pi R^4} \quad (13.214)$$

Or, expressing the surface-diffusion coefficient in the form of Eq. 7.45,

$$D_b = \frac{3a_0^4 D_{0s} \exp(-E_s/kT)}{2\pi R^4} \quad (13.215)$$

where  $D_{0s}$  is the preexponential factor for surface self-diffusion of the matrix solid and  $E_s$  is the activation energy for this process. Robertson<sup>6,1</sup> and Maiya<sup>1,6</sup> have reviewed the available measurements of surface self-diffusion of  $UO_2$ . Maiya recommends the equation

$$D_s = 4 \times 10^5 \exp \left[ -\frac{450}{R(T/10^3)} \right] \text{ cm}^2/\text{sec} \quad (13.216)$$

The activation energy of 450 kJ/mole is ~80% of that for  $\text{UO}_2$  vaporization (Table 11.1), which is expected since surface migration involves a hop that is just short of vaporization (the elementary steps of surface hopping and vaporization are analogous to excitation and ionization, respectively, of the outer electrons of an atom). The preexponential factor, however, is abnormally large. In Chap. 7 it was shown that the preexponential factor for a normal volume diffusion process should be  $a_0^2 \nu \exp(s^*/k)$ , and the same reasoning can be applied to surface migration. Since  $a_0 \approx 3 \text{ \AA}$  and  $\nu \approx 10^{13} \text{ sec}^{-1}$ , unless the entropy of activation is very large, the preexponential factor  $D_{0s}$  should be  $\sim 0.01$  to  $0.1 \text{ cm}^2/\text{sec}$ . Possible reasons for the six order-of-magnitude discrepancy in the case of surface diffusion on  $\text{UO}_2$  are discussed by Robertson.<sup>61</sup>

Equation 13.214 predicts that small bubbles should be very much more mobile than larger ones. The two studies of bubble migration during isothermal annealing of  $\text{UO}_2$  do not support the  $R^{-4}$  size dependence of the theoretical value of  $D_b$ . Cornell and Bannister<sup>62</sup> find that  $D_b$  is directly proportional to  $R^2$ , or that the larger bubbles are more mobile than the smaller ones. Gulden<sup>63</sup> showed that the mobility varied as  $R^{-3}$ . These results suggest either that surface diffusion is not the mechanism responsible for bubble motion in  $\text{UO}_2$  or that the small bubbles followed in these two studies ( $40 \text{ \AA} < R < 140 \text{ \AA}$ ) were immobilized by interaction with defects in the matrix. We shall analyze the volume-diffusion mechanism of bubble motion later and also show that bubbles of radii less than  $500 \text{ \AA}$  are pinned by dislocation lines. Other crystal defects, too small to be observed by an electron microscope, could very well immobilize bubbles in the  $100\text{-\AA}$  size range.

### 13.10.3 Directed Bubble Migration in a Temperature Gradient

Of the many possible forces that can induce directed motion of bubbles, the large temperature gradient in a fuel element appears to be the most influential. We consider here the case in which the temperature gradient causes preferential motion of the molecules in a particular direction along the inside surface of the bubble by the process of surface thermal self-diffusion described in Sec. 7.7. This form of directed bubble motion was first analyzed by Shewmon.<sup>64</sup> Similar treatments have been given by other investigators.<sup>8,9,60</sup>

We derive the velocity of the cubical bubble shown in Fig. 13.19(a). If the bubble were not present, a temperature gradient  $dT/dx$  would exist in the solid at this point. Because the bubble is small,  $dT/dx$  is approximately constant. The gas in the bubble has a thermal conductivity less than that of the solid, and introduction of the bubble perturbs the temperature profile in the manner shown in Fig. 13.19(b). Let the temperature gradient within the bubble be denoted by  $(dT/dx)_b$  and assume that the four cube faces parallel to the  $x$ -axis experience this gradient. The flux of surface molecules along these faces is given by Eq. 7.64:

$$J_s = -\frac{D_s Q_s^* C_s}{kT^2} \left( \frac{dT}{dx} \right)_b \quad (7.64)$$

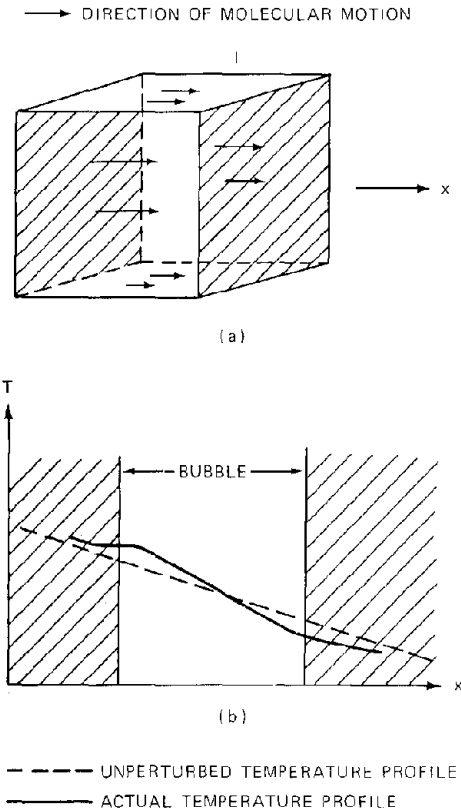


Fig. 13.19 Bubble migration in a temperature gradient. (a) Flow of surface molecules across faces parallel to the temperature gradient. (b) Temperature profiles in the solid and through the bubble.

where  $Q_s^*$  is the heat of transport for surface thermal self-diffusion and  $C_s$  is the density of molecules in the plane of the surface. The units of  $J_s$  are molecules  $\text{sec}^{-1}$  per centimeter of length perpendicular to the direction of flow. Since there are four faces each of width  $l$ , the rate at which molecules are transported from the hot face to the cold face is  $4lJ_s$  molecules/sec. We assume that these molecules are rapidly distributed over the two faces perpendicular to the  $x$ -axis; so the cubical shape is retained during migration. In a time interval  $\Delta t$ ,  $4lJ_s \Delta t$  molecules are transported from the hot face to the cold face, or the displacement of the cube in this time interval is

$$\Delta x = -\frac{(4lJ_s \Delta t)\Omega}{l^2}$$

The minus sign appears in this relation because the cube is displaced in the opposite direction from that of the surface molecules. By combining the two preceding equations, we find a migration velocity given by

$$v_b = \frac{\Delta x}{\Delta t} = -\frac{4J_s \Omega}{l} = \frac{4D_s Q_s^* C_s \Omega}{kT^2} \left( \frac{dT}{dx} \right)_b \quad (13.217)$$

The surface concentration of matrix molecules can be approximated by  $C_s \approx 1/a_0^2$  and  $\Omega$  by  $a_0^3$ . The geometry can

be converted from a cube to a sphere of radius  $R$  by replacing the length of the cube side by the sphere diameter. Finally, the temperature gradient within the bubble can be expressed in terms of the unperturbed temperature gradient in the solid. The latter is equal to the average temperature gradient in the porous body as determined by the methods reviewed in Chap. 10. The relation of  $(dT/dx)_b$  to  $dT/dx$  is obtained by solution of the heat-conduction problem of an inclusion placed in an infinite medium of a different thermal conductivity. For a spherical pore containing a substance of much lower thermal conductivity than that of the surrounding solid, the gradients depicted by the slopes of the solid and dashed lines in Fig. 13.19(b) are related by<sup>6,5</sup>

$$\left(\frac{dT}{dx}\right)_b = \frac{3}{2} \left(\frac{dT}{dx}\right) \quad (13.218)$$

Substituting  $C_s \Omega \approx a_0$ ,  $l = 2R$  and Eq. 13.218 into 13.217 yields the bubble migration velocity:

$$v_b = \frac{3D_s Q_s^* a_0}{kT^2 R} \frac{dT}{dx} \quad (13.219)$$

The heat of transport for surface thermal self-diffusion on  $UO_2$  has not been measured. Its sign must be positive, however, since bubbles migrate up the temperature gradient, as predicted by Eq. 13.219 for  $Q_s^* > 0$ . Estimates of  $Q_s^*$  include assuming it equal to the activation energy for self-diffusion 450 kJ/mole and assuming it to be  $\frac{2}{3}$  of the heat of vaporization ( $Q_s^* = 380$  kJ/mole).

As an example of the magnitude of the bubble migration velocity, consider a 200-Å diameter bubble at 2000°K in a temperature gradient of 4000°K/cm. From Eq. 13.216 the surface diffusion coefficient is  $5 \times 10^{-7}$  cm<sup>2</sup>/sec. Taking  $a_0 = 3$  Å and  $Q_s^* = 415$  kJ/mole, we find the velocity predicted by Eq. 13.219 is  $3 \times 10^{-6}$  cm/sec, or 8 cm/month. At this rate the bubble could traverse the radius of a fast reactor fuel rod in a little more than a day (in applying Eq. 13.219 to actual fuel elements, however, we must take the temperature variation with radius into account).

The inverse dependence of the migration velocity on bubble radius has been qualitatively verified by Cornell and Williamson.<sup>6,6</sup>

The migration velocities of gas bubbles and solid inclusions in mixed-oxide fuel was measured by Michels, Poeppel, and Niemark.<sup>6,7</sup> The bubbles they examined had radii ranging from 1 to 5 μm. Their migration velocities were higher than those predicted from Eq. 13.219 by factors of 2 to 5, and no relationship between bubble radius and velocity was observed. It is possible that the migration process for these large bubbles was not the surface-diffusion mechanism on which Eq. 13.219 is based. It will be shown in Chap. 14 that a mechanism based on transport of matrix molecules by molecular diffusion in the gas from the hot to the cold face of a bubble predicts migration velocities exceeding those computed from the surface-diffusion mechanism when the bubble radius is greater than 1 to 10 μm.

Michels, Poeppel, and Niemark<sup>6,7</sup> also observed that solid inclusions migrated up the temperature gradient with velocities that decreased as the size of the inclusion increased, in accord with the surface-diffusion mechanism. Inclusions cannot migrate by the vapor-transport mechanism because the space inside the cavity in the solid is filled with a solid rather than a gas.

### 13.10.4 General Treatment of Bubble Mobility

Nichols<sup>9,39</sup> has developed a general analysis of bubble mobility that can be applied to any force acting on a bubble or to any microscopic mechanism by which bubble motion occurs. Such a formalism permits  $D_b$  to be obtained if  $v_b$  is known, or vice versa, and thereby makes it unnecessary to calculate each of these parameters in apparently independent ways, as we have done for random and thermal-gradient migration by the surface-diffusion mechanism in the preceding discussion.

Mobility is defined as the velocity attained when a unit force is applied. When applied to a bubble, we have

$$v_b = M_b F_b \quad (13.220)$$

where  $M_b$  is the bubble mobility and  $F_b$  is the force on the bubble. The latter can be directly related to a macroscopic potential gradient, as in the case of the stress gradient discussed later. Alternatively, the force on the entire bubble can be related to the forces on individual molecular species which are actually responsible for bubble motion. The importance of mobility is that it can be related to the bubble diffusion coefficient by the Nernst-Einstein equation:

$$M_b = \frac{D_b}{kT} \quad (13.221)$$

Equation 13.221 can be derived as follows. Consider a species that undergoes ordinary diffusion according to Fick's laws and a diffusivity  $D$ . When placed in a closed system in which a force  $F$  acts upon this species, a stationary state is established in which the tendency to move in one direction due to the external force is just balanced by the motion in the opposite direction due to diffusion. This stationary state is described by the condition of zero net flux

$$J = -D \frac{dC}{dx} + vC = 0$$

where  $v$  is the drift velocity established by the force  $F$  and  $C$  is the concentration of the species as a function of distance  $x$ . Since  $v$  and  $F$  are related by Eq. 13.220, the preceding condition can be written as

$$\frac{dC}{dx} = \frac{MFC}{D} \quad (13.222)$$

The stationary state just described can also be considered as a system in thermodynamic equilibrium. The presence of a force  $F$  in the  $x$  direction means that the potential energy varies with  $x$  according to

$$F = - \frac{dE_p}{dx} \quad (13.223)$$

Because the system is in thermodynamic equilibrium, the concentration  $C$  must vary with position according to the Boltzmann law\*

$$C = \text{constant} \times \exp\left(-\frac{E_p}{kT}\right)$$

Taking the derivative of this equation with respect to  $x$  and using Eq. 13.223 shows that

$$\frac{dC}{dx} = \frac{FC}{kT} \quad (13.224)$$

Equating the right-hand sides of Eqs. 13.222 and 13.224 and appending the subscript  $b$  to the symbols for application to bubble motion results in Eq. 13.221.

If the force on the bubble is known, combination of Eqs. 13.220 and 13.221 provides the following relation between  $v_b$  and  $D_b$ :

$$v_b = \frac{D_b F_b}{kT} \quad (13.225)$$

In some cases, however, a microscopic model provides a prediction of the force  $f$  acting on the individual atomic species that are ultimately the source of bubble mobility. The connection between the microscopic force  $f$  and the macroscopic force  $F_b$  can be obtained with the help of Fig. 13.18. When the bubble moves a distance  $\Delta x$  in one direction,  $l^2 \Delta x / \Omega$  atoms have been transported a distance  $l$  in the opposite direction. If the force acting on each of the moving atoms is  $f$ , the work required to effect this transfer is  $(l^2 \Delta x / \Omega) (l)f = l^3 f \Delta x / \Omega$ . Considering the bubble as an entity, the work required to move it a distance  $-\Delta x$  against a force  $F_b$  is  $-F_b \Delta x$ . (The minus signs are present because the bubble moves in the opposite direction from that of the atoms). The work required is the same whether it is calculated by considering movement of the atomic species or of the bubble proper; so the preceding two expressions for the work can be set equal to each other. Noting that  $l^3$  is the bubble volume, which can be written as  $(4\pi R^3)/3$  for a spherical bubble, and approximating the atomic volume  $\Omega$  by  $a_0^3$ , we arrive at the relation:

$$F_b = - \left( \frac{4\pi R^3 / 3}{a_0^3} \right) f \quad (13.226)$$

If migration is due to surface thermal self-diffusion, the force  $f$  can be obtained by applying the methods of

irreversible thermodynamics (Sec. 7.6). The force  $f$  is identified by writing Eq. 7.46 in the form:

$$J = -L_{11} \nabla \mu - L_{12} \frac{\nabla T}{T} = L_{11} \left( -\nabla \mu - \frac{L_{12}}{L_{11}} \frac{\nabla T}{T} \right)$$

The first term in the parentheses is the force due to the gradient of the chemical potential. The second term is the force due to the temperature gradient. According to Eq. 7.57, the ratio  $L_{12}/L_{11}$  defines the heat of transport; so from the preceding relation we have

$$f = - \frac{Q_s^*}{T} \left( \frac{dT}{dx} \right)_b \quad (13.227)$$

The force on the bubble due to surface diffusion in the temperature gradient is obtained by combining Eqs. 13.226 and 13.227 and using Eq. 13.218 to convert the temperature gradient in the sphere to that in the bulk solid,

$$F_b = \left( \frac{2\pi R^3}{a_0^3} \right) \frac{Q_s^*}{T} \left( \frac{dT}{dx} \right) \quad (13.228)$$

If Eqs. 13.214 and 13.228 are substituted into Eq. 13.225, the migration velocity formula of Eq. 13.219 is recovered.

### 13.10.5 Bubble Migration by Volume Diffusion

A bubble which is in mechanical equilibrium with the surrounding solid and which is not gathering gas atoms from the matrix has no tendency to change size by a net gain or loss of vacancies. However, vacancies present in the adjacent solid continually enter the bubble, and the latter constantly reemits vacancies to the matrix. At equilibrium the vacancy absorption and emission rates are equal. An analogous dynamical balance of particle fluxes occurs when a solid is in contact with its saturated vapor; here the rates of condensation and evaporation are equal, and there is no net flux across the solid-vapor interface.

Just as in the case of the random motion of matrix molecules on the inside surface of the bubble, the exchange of vacancies between the bubble and the nearby solid can cause the entire bubble to undergo Brownian motion. This mode of random bubble migration is termed the volume-diffusion mechanism because it is due to vacancy movement from one position on the bubble surface to another by diffusion in the surrounding matrix. As in all random-walk processes, the bubble diffusion coefficient is expressed by Eq. 13.211, and, as in the case of the surface-diffusion mechanism considered earlier, the jump distance and the jump frequency of the bubble must be obtained by analyzing the motion of the point defects responsible for bubble displacement, namely, vacancies.\*

We first determine  $\Gamma_b$ , the jump frequency of a bubble, for the volume-diffusion mechanism. The bubble undergoes a small displacement every time a vacancy arrives at the

\*Reif<sup>68</sup> applies similar arguments to determine the variation of the density of air as a function of altitude above the earth's surface. In this case the force is  $-mg$  and the potential energy is  $mgz$ , where  $m$  is the mass of a molecule of air,  $g$  is the acceleration of gravity, and  $z$  is the altitude. The density varies according to the law of atmospheres, namely,  $\rho(z) = \rho(0) \exp(-mgz/kT)$ .

\*In principle, interstitials could cause the same random bubble movement as do vacancies. However, the concentration of interstitials in most solids is so low that their influence is negligible compared to that of the vacancies.

surface from the bulk or, conversely, when a surface vacancy jumps back into the solid near the bubble.\* Since these two rates are equal for the equilibrium bubble, we can determine the bubble jump frequency by calculating either of them. The rate at which vacancies enter a bubble is equal to the rate constant for point-defect capture by a perfectly absorbing sphere times the concentration of vacancies in the solid in the vicinity of the surface. Since the bubble is in equilibrium, there is no vacancy concentration gradient near the surface. Consequently, the appropriate rate constant for the vacancy capture process is given by Eq. 13.95, and the vacancy concentration is that at thermodynamic equilibrium, Eq. 13.177. Therefore, the bubble jump frequency is

$$\Gamma_b = \left( \frac{4\pi R^2 D_v}{a_0} \right) C_v^{eq}$$

where  $D_v$  is the vacancy diffusion coefficient. The product  $D_v C_v^{eq}$  can be expressed as  $D_v x_v^{eq} / \Omega \simeq D_v x_v^{eq} / a_0^3$ , where  $x_v^{eq}$  is the equilibrium site fraction of vacancies in the solid. Recalling that  $D_v x_v^{eq}$  is the volume self-diffusion coefficient of the atoms of the solid (compare Eqs. 7.28 and 7.29), we can write

$$D_v C_v^{eq} = \frac{D_{v01}}{a_0^3}$$

where  $D_{v01}$  is the self-diffusion coefficient of the species composing the solid. Combining the above two equations gives

$$\Gamma_b = \frac{4\pi R^2 D_{v01}}{a_0^4} \quad (13.229)$$

The bubble jump distance required in Eq. 13.211 for the volume-diffusion mechanism is somewhat more difficult to obtain than the corresponding quantity in the surface-diffusion model. We follow here the derivation due to Kelly.<sup>6,9</sup>

The argument leading to Eq. 13.212 is valid in the present case; so the bubble jump distance can be expressed by

$$\lambda_b = \left( \frac{a_0^3}{4\pi R^3 / 3} \right) \left( \frac{\lambda_v^2}{3} \right)^{1/2} \quad (13.230)$$

In the case of the volume-diffusion mechanism, the characteristic distance moved by a vacancy each time a displacement of the bubble occurs is not the vacancy jump distance in the normal diffusion process of this species in the solid. Rather, the appropriate distance is that of the following process: a surface vacancy jumps back into the bulk and then, by a random-walk process, hops about in the solid until it is recaptured by the bubble. The characteristic

distance required on the right-hand side of Eq. 13.230 is the root-mean-square distance between the point on the surface where the vacancy enters the solid and the point on the surface where it is recaptured by the bubble. This process is illustrated in Fig. 13.20. The initial hop places the vacancy one jump distance from the bubble surface; from this point it executes random hopping, uninfluenced by the presence of the bubble, until by chance it encounters the bubble. For simplicity, we assume that the initial jump out of the surface and all subsequent vacancy jumps are those characteristic of normal vacancy diffusion in the solid, i.e., of a length equal approximately to a lattice

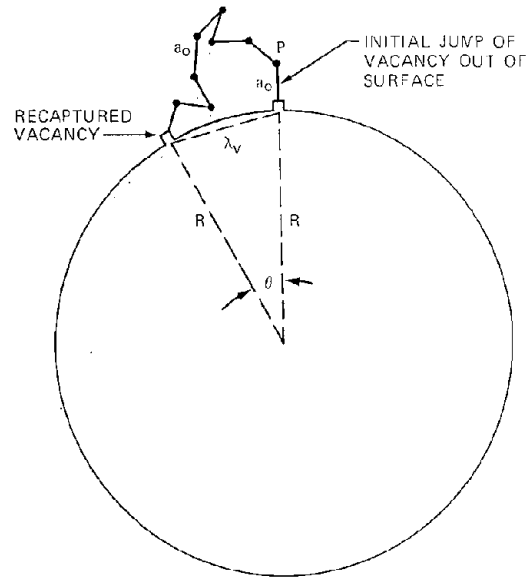


Fig. 13.20 Typical trajectory of a vacancy emitted from, then recaptured by, the bubble. The random walk is assumed to start from point P.

constant,  $a_0$ . We also assume that every vacancy that reaches the bubble surface is captured (i.e., that the vacancy condensation coefficient is unity). The net result of a particular sequence of steps is movement of the vacancy by a chord length  $\lambda_v$  from one point on the surface to another.

To calculate the root-mean-square value of  $\lambda_v$ , we should apply the method of random-walk theory outlined in Sec. 7.3. However, because the present application deals with a particle migrating on a lattice close to a perfectly absorbing spherical surface, the random-walk analysis is much more complicated than in the infinite-medium case considered in Chap. 7. Fortunately, the random walk can be equally well described as a diffusion process (Chap. 7); so a diffusion calculation can be used in place of the statistical analysis of the random walk.

The corresponding diffusion problem is one in which a point source placed a distance  $a_0$  from the surface of a perfect spherical absorber of radius  $R$  continuously emits one vacancy per unit time. Kelly<sup>6,9</sup> has solved this problem, but here we will just indicate the method. The diffusion

\*A surface vacancy refers to an empty lattice site in the crystal plane that forms the bubble surface or to a kink site on an atomic ledge on the surface (see Fig. 5 of Ref. 14).

equation is  $\nabla^2 C_v = 0$ , where  $\nabla^2$  denotes the Laplacian in spherical coordinates  $r$  and  $\theta$  (the system is azimuthally symmetric) and  $C_v(r, \theta)$  is the vacancy concentration at radial position  $r > R$  and polar angle  $\theta$  (Fig. 13.20) due to the continuous unit point source. Solution of steady-state diffusion equation is based on the boundary condition (for a perfect sink)  $C_v(R, \theta) = 0$ . Having found the concentration profile of vacancies outside the sphere, we can determine the vacancy flux to the bubble surface at polar angle  $\theta$  by the usual formula:

$$J_v(\theta) = -D_v \left( \frac{\partial C_v}{\partial r} \right)_R$$

Since the point source emits one vacancy per unit time,  $J_v(\theta)$  is equivalent to the probability that the vacancy emitted at point P in Fig. 13.20 is recaptured within a unit area around a point on the surface at a polar angle  $\theta$  from the source direction. From the geometry of the diagram in Fig. 13.20, the surface displacement of the vacancy after the process is complete is

$$\lambda_v^2(\theta) = 2R^2 (1 - \cos \theta)$$

The mean-square surface displacement follows from

$$\overline{\lambda_v^2} = \int_{\text{sphere}} J_v(\theta) \lambda_v^2(\theta) dA_s$$

where  $dA_s = 2\pi R^2 \sin \theta d\theta$  is the area of an annular strip on the surface between  $\theta$  and  $\theta + d\theta$ . Kelly has evaluated the preceding integral, but a simple limiting result is obtained for the not too restrictive condition  $R/a_0 \gg 1$  (i.e., a reasonably large bubble). Correcting an arithmetical error of a factor of 2 in Kelly's limiting form, the mean surface vacancy displacement is given by

$$\overline{\lambda_v^2} = 2Ra_0 \quad (13.231)$$

Substituting Eq. 13.231 into Eq. 13.230 gives the bubble jump distance; when  $\lambda_b$  and the expression for  $\Gamma_b$  given by Eq. 13.229 are used in Eq. 13.211, we have the desired bubble diffusion coefficient for the volume-diffusion mechanism,

$$D_b = \frac{3a_0^3 D_{v01}}{4\pi R^3} \quad (13.232)$$

The same formula has been given by Nichols,<sup>39</sup> who used different expressions for  $\lambda_b$  and  $\Gamma_b$  than those obtained in this study. Although the formulas presented by Nichols for these two quantities are consistent in the sense that when combined according to Eq. 13.211 they give Eq. 13.232, no physical basis for either the bubble jump distance or frequency is given.

Comparison of Eq. 13.232 with Eq. 13.214 derived for the surface-diffusion mechanism shows that the former depends on bubble size according to  $R^{-3}$  and the latter varies as  $R^4$ . Whereas the surface self-diffusion coefficient of  $\text{UO}_2$  (or whatever the fuel material) is required in the surface-diffusion model, the volume-diffusion mechanism depends on the lattice self-diffusion coefficient of one of

the atomic species in the solid. In a binary compound, such as  $\text{UO}_2$ , the slowest moving species is the  $\text{U}^{4+}$  ion, the self-diffusion coefficient of which is:<sup>70</sup>

$$D_{v01}^{\text{U}^{4+}} = 4 \times 10^{-7} \exp\left(-\frac{290}{RT}\right) \quad (13.233)$$

Having determined  $D_b$  of a bubble rendered mobile by virtue of vacancy motion in the surrounding solid, we can obtain the migration velocity in a thermal gradient from the Nernst-Einstein equation. The force on each vacancy due to the temperature gradient is

$$f = -\frac{Q_v^*}{T} \left( \frac{dT}{dx} \right)_b \quad (13.234)$$

where  $Q_v^*$  is the heat of transport for vacancy diffusion. The force on the bubble is given by inserting this relation into Eq. 13.226. The migration speed in a temperature gradient is then found from the force  $F_b$ , the bubble diffusivity given by Eq. 13.232, and the general relation between these two quantities, Eq. 13.225. The connection between the temperature gradient that should be used in Eq. 13.224 and in the bubble velocity formula and the macroscopic temperature gradient is not as easily obtained as it was in the case of migration by the surface-diffusion mechanism. Nichols<sup>39</sup> shows that for migration by the volume-diffusion mechanism the two are equal provided that the thermal conductivity of the bubble is negligible. The final expression for the migration velocity in a temperature gradient when bubble mobility is due to the volume-diffusion mechanism is

$$v_b = \frac{D_{v01} Q_v^*}{kT^2} \left( \frac{dT}{dx} \right) \quad (13.235)$$

The vacancy heat of transport is often assumed to be equal to the activation energy of uranium-ion self-diffusion.

### 13.10.6 Bubble Migration in a Stress Gradient

Random motion of a bubble in a solid is determined solely by the bubble diffusion coefficient  $D_b$ , which in turn depends on the bubble jump distance and the bubble jump frequency. These two quantities must be determined by considering the jump distance and jump frequency of the atomic species that are assumed to be responsible for bubble mobility. We have previously calculated bubble diffusion coefficients for the mechanisms of surface diffusion and volume diffusion.

Given the bubble diffusivity, we can compute the velocity of a bubble due to an external force  $F_b$  from Eq. 13.225. Calculation of  $F_b$  is independent of the calculation of  $D_b$ . We have shown in the preceding sections how  $D_b$  due to surface and volume diffusion can be coupled with the force due to a thermal gradient to obtain bubble velocities for this particular driving force in combination with bubble diffusivities due to each of the two atomic mechanisms.

In this discussion we calculate the force that is exerted on a bubble when it is present in a solid containing a stress

gradient and compare it to the force due to a temperature gradient. To calculate the force due to temperature gradient, we had to determine the force  $f$  on the individual species first and then obtain  $F_b$  by Eq. 13.226. In the case of a stress gradient, the force on the bubble can be calculated without having to consider the response of the atomic species to the external potential gradient. The force on a bubble in a stress gradient has been determined by Bullough and Perrin,<sup>14</sup> Martin,<sup>71</sup> Eyre and Bullough,<sup>29</sup> and Leiden and Nichols.<sup>72</sup> We summarize the first two analyses.

Consider a bubble placed in an isothermal solid that supports a gradient of hydrostatic stress in the  $x$  direction. The bubble is assumed to be in mechanical equilibrium with the solid at the local hydrostatic stress, and the gas in the bubble is assumed to obey the ideal-gas law. As the bubble moves from position  $x$  to  $x + dx$ , the stress environment changes from  $\sigma$  to  $\sigma + (d\sigma/dx)dx$ . During this displacement the bubble radius changes from  $R$  to  $R + dR$  so as to maintain mechanical equilibrium at all times. The work done by the bubble during the displacement  $dx$  is equal to the negative of the corresponding change in the Gibbs free energy. Since the work can be expressed as the product of the force on the bubble and the displacement  $dx$ ,  $F_b$  is given by

$$F_b = -\frac{dG_b}{dx} \quad (T = \text{constant}) \quad (13.236)$$

where  $dG_b$  is the change in the Gibbs free energy of the entire system (bubble plus solid). It is the sum of three terms:

1. The change in the free energy of the contained gas,  $dG_g$ .
2. The change in the free energy of the system due to a change in the surface area,  $dG_s$ .
3. The change in the strain energy of the solid,  $dE_{\text{solid}}$ .

When a bubble containing a fixed number of gas atoms contracts or expands isothermally, both the volume and pressure change. The free-energy change of the gas is

$$dG_g = V dp = d(pV) - p dV$$

where  $V = 4\pi R^3/3$  is the bubble volume. If the gas is ideal,  $pV$  is a constant, and

$$dG_g = -p dV = -p(4\pi R^2 dR) \quad (13.237)$$

The free-energy change in the system due to the increase or decrease in the surface area of the bubble  $A = 4\pi R^2$  is given by

$$dG_s = \gamma dA = \gamma(8\pi R dR) \quad (13.238)$$

Equation 13.238 is the definition of the surface tension. Adding Eqs. 13.237 and 13.238 yields

$$dG_g + dG_s = -4\pi R^2 \left( p - \frac{2\gamma}{R} \right) dR \quad (13.239)$$

For bubbles in mechanical equilibrium, the local stress, gas pressure, and bubble radius are related by Eq. 13.4:

$$p - \frac{2\gamma}{R} = \sigma$$

Combining this equation with the ideal-gas law yields

$$\left( \sigma + \frac{2\gamma}{R} \right) \left( \frac{4\pi R^3}{3} \right) = mkT \quad (13.240)$$

Since the right-hand side of Eq. 13.240 is constant during bubble migration in the stress gradient, taking the differential of the equation yields

$$\frac{dR}{d\sigma} = -\frac{R^2}{3\sigma R + 4\gamma} \quad (13.241)$$

The differential  $dR$  can be written as

$$dR = \left( \frac{dR}{d\sigma} \right) \left( \frac{d\sigma}{dx} \right) dx$$

or

$$dR = -\frac{R^2}{3\sigma R + 4\gamma} \left( \frac{d\sigma}{dx} \right) dx \quad (13.242)$$

Substituting Eqs. 13.4 and 13.242 into Eq. 13.239 yields

$$\frac{dG_g}{dx} + \frac{dG_s}{dx} = \frac{4\pi R^4 \sigma}{3\sigma R + 4\gamma} \frac{d\sigma}{dx} \quad (13.243)$$

The contribution to  $dG_b$  due to the change in the strain energy of the solid as the bubble moves is computed as follows: The elastic-energy density at a point in the solid subject to a hydrostatic stress  $\sigma$  is given by (see Appendix):

$$E_{\text{el}} = \frac{\sigma^2}{2K} \quad (\text{A.27})$$

where  $K$  is the bulk modulus of the solid. The total strain energy stored in the solid is the integral of  $E_{\text{el}}$  over the entire volume. Assume that the equilibrium bubble is created by moving matrix molecules from the region to be occupied by the bubble to the outer surface of the solid, which is taken to be unstressed. The spherical void is now filled with sufficient gas to produce a pressure that satisfies Eq. 13.4. The change in the stored energy of the solid arises only from the first step. Because material is removed from a region where the stress is  $\sigma$  to the stress-free surface, the elastic energy of the solid containing the bubble is given by

$$E_{\text{solid}} = E_{\text{solid}}^{\circ} - \left( \frac{\sigma^2}{2K} \right) \left( \frac{4\pi R^3}{3} \right) \quad (13.244)$$

where  $E_{\text{solid}}^{\circ}$  is the elastic energy of the solid before the void is introduced. The change  $dE_{\text{solid}}$  is computed by taking the differential of Eq. 13.244, which is

$$dE_{\text{solid}} = -\frac{2\pi\sigma R^3}{3K} \left( 2R + 3\sigma \frac{dR}{d\sigma} \right) d\sigma$$

or, using Eq. 13.241 for  $dR/d\sigma$ , the equation becomes

$$\frac{dE_{\text{solid}}}{dx} = -\frac{2\pi\sigma R^3}{3K} \left( \frac{3\sigma R + 8\gamma}{3\sigma R + 4\gamma} \right) \left( \frac{d\sigma}{dx} \right) \quad (13.245)$$

The force on the bubble is obtained by taking the negative of the sum of Eqs. 13.243 and 13.245:

$$F_b = -\frac{4\pi R^4 \sigma}{3\sigma R + 4\gamma} \left(1 - \frac{3\sigma R + 8\gamma}{6RK}\right) \frac{d\sigma}{dx} \quad (13.246)$$

Because the compressibility of most solids is so low ( $K \approx 10^{12}$  dynes/cm<sup>2</sup>), the last term in parentheses is very small compared to unity even for extremely small bubbles.

Aside from the sign of the last term in the parentheses, Eq. 13.246 was first obtained by Bullough and Perrin.<sup>14</sup> Martin<sup>71</sup> performed the same calculation as described using the van der Waals equation of state (Eq. 13.1) instead of the ideal-gas law. However, he applied Eq. 13.237 to the nonideal gas and used the van der Waals equation only to modify Eq. 13.240. When correctly done, the nonzero term  $d(pV)$  should be included in  $dG_g$ .

Two limiting cases of Eq. 13.246 are of interest. For small bubbles and low stresses,  $3\sigma R \ll 4\gamma$ , and we have

$$F_b = -\frac{\pi R^4 \sigma}{\gamma} \frac{d\sigma}{dx} \quad (13.247)$$

Alternatively, for large bubbles subject to high stress,  $4\gamma \ll 3\sigma R$ , and Eq. 13.246 reduces to

$$F_b = -\left(\frac{4\pi R^3}{3}\right) \frac{d\sigma}{dx} \quad (13.248)$$

Equations 13.246 to 13.248 show that the bubble always moves down the stress gradient, or to regions of lower stress. Equation 13.246 can be applied to tensile-stress fields by setting  $\sigma$  equal to a negative number. The magnitude of the tensile stress must be smaller than the value that renders the denominator of Eq. 13.246 equal to zero. For tensile stresses in excess of this critical value, the bubble cannot be in equilibrium with the solid.

The relative magnitudes of the forces due to stress and temperature gradients can be evaluated by taking the ratio of Eqs. 13.247 and 13.228

$$\frac{(F_b)_{\text{stress}}}{(F_b)_{\text{temp.}}} = \frac{R\sigma^2 a_0^3}{2\gamma kT(Q_s^*/kT)} \frac{(1/\sigma)(d\sigma/dx)}{(1/T)(dT/dx)} \quad (13.249)$$

where  $k$  is the Boltzmann constant. Let us evaluate this ratio for the following values of the variables in Eq. 13.249:

$$\begin{aligned} R &= 100 \text{ \AA} = 10^{-6} \text{ cm} \\ a_0^3 &= \Omega = 4 \times 10^{-23} \text{ cm}^3 \\ \sigma &= 10^4 \text{ kN/m}^2 = 10^8 \text{ dynes/cm}^2 \\ d\sigma/dx &= 10^9 \text{ dynes/cm}^3 \\ T &= 2000^\circ\text{K} \\ dT/dx &= 4000^\circ\text{K/cm} \\ Q_s^* &= 415 \text{ kJ/mole} \quad (Q_s^*/kT = 25) \\ \gamma &= 10^3 \text{ dynes/cm} \end{aligned}$$

Using these values in Eq. 13.249 shows that the stress gradient exerts a force on the bubble that is only  $\sim 1\%$  of that due to the temperature gradient. Stress-gradient migration does not appear to be an important means of causing bubble motion within bulk fuel material, but, in regions of locally high stress gradients, this force can be significant. The large stress gradients of an edge dislocation, for example, can be effective in driving bubbles to the dislocation lines where they are pinned.

### 13.10.7 Bubble Growth by Coalescence

In Sec. 13.9 we considered models of bubble growth in which the only means of enlargement was by diffusion of single gas atoms from the matrix to the bubbles. Another mechanism of growth is by coalescence, which occurs if the bubbles are mobile in the solid and move either in a random fashion or under the influence of a driving force. Since coalescence is an efficient means of making large bubbles from small ones, it can profoundly affect the swelling of nuclear fuels.

The first theory of swelling by coalescence was published by Greenwood and Speight<sup>60</sup> in 1963. Their calculation involved many simplifications to enable analytic expressions for the mean bubble radius and the bubble density as a function of time to be obtained. Gruber<sup>59</sup> extended the work of Greenwood and Speight by solving the relevant conservation equations without approximation on a computer. Both these pioneering studies concentrated on the coalescence phenomenon. Other important processes that undoubtedly occur along with coalescence, such as growth by absorption of single gas atoms and resolution, were neglected. Both calculations also made the following assumptions:

1. The gas in the bubble obeys the ideal-gas law.
2. The bubbles are in mechanical equilibrium with an unstressed solid.
3. The bubbles migrate randomly by the surface-diffusion mechanism or in a biased manner with velocities determined by a combination of the surface-diffusion mechanism with the temperature-gradient external force.

#### The Greenwood-Speight Model

Greenwood and Speight<sup>60</sup> considered only random migration of bubbles. Their analysis can be applied to two situations:

1. Growth by coalescence for a fixed number of gas atoms (postirradiation annealing).
2. Growth by coalescence for constant production rate of gas atoms (in-pile behavior).

In the postirradiation annealing case, the solid at  $t = 0$  contains  $N_0$  bubbles/cm<sup>3</sup> each of radius  $R_0$  and no gas in solution. As time progresses,  $N$  decreases and  $R$  increases due to coalescence. All bubbles are assumed to be characterized by a mean radius. No attempt is made to determine the bubble-distribution function.

The number of gas atoms in each bubble is given by Eq. 13.16:

$$m = \left(\frac{4\pi R^2}{3}\right) \left(\frac{2\gamma}{kT}\right)$$

Because the total quantity of gas is fixed and none is in solution,  $m$  and  $N$  are related by the material balance

$$mN = m_0 N_0 = M = \text{constant} \quad (13.250)$$

Combining Equations 13.16 and 13.250 provides the following relation between bubble radius and bubble density:

$$N = \left( \frac{3MkT}{8\pi\gamma} \right) \frac{1}{R^2} \quad (13.251)$$

The kinetics of coalescence when only random movement occurs is described by Eq. 13.108 in which the rate constant is given by Eq. 13.109. Since all bubbles are assumed to be of the same size, we can set  $C_i = C_j = N$  in the former and  $R_i = R_j = R$  and  $D_{bi} = D_{bj} = D_b$  in the latter. Since two bubbles disappear and one larger bubble is produced at each collision, the time rate of change of the bubble density is equal to the collision rate, or

$$\frac{dN}{dt} = -4\pi(2R)(2D_b)N^2 = -16\pi RD_b N^2 \quad (13.252)$$

If  $D_b$  is eliminated by use of Eq. 13.214 and  $R$  is expressed in terms of  $N$  by Eq. 13.251 the kinetic equation becomes

$$\frac{dN}{dt} = -24a_0^2 D_s \left( \frac{8\pi\gamma}{3MkT} \right)^{3/2} N^{7/2}$$

Integrating this equation with the initial condition  $N(0) = N_0$  yields

$$\frac{1}{N^{5/2}} = \frac{1}{N_0^{5/2}} + 60a_0^2 D_s \left( \frac{8\pi\gamma}{3MkT} \right)^{3/2} t$$

After several generations of coalescence, the condition  $N \ll N_0$  applies, and the first term on the right-hand side of the equation can be neglected. If  $N$  is expressed in terms of  $R$  by Eq. 13.251, the final result is

$$R = 1.48 \left( \frac{a_0^4 D_s MkT}{\gamma} \right)^{1/5} t^{1/5} \quad (13.253)$$

To apply the analysis to the in-pile situation in which gas is created at a constant rate by fission, we replace Eq. 13.250 by the material balance:

$$Y_{Xe} \dot{F}t = mN \quad (13.254)$$

Note that the concentration of dissolved gas ( $C$  in Eq. 13.22) has been neglected. When combined with Eq. 13.16, Eq. 13.254 yields

$$N = \left( \frac{3Y_{Xe} \dot{F}kT}{8\pi\gamma} \right) \frac{t}{R^2} \quad (13.255)$$

Equation 13.255 is based on the assumption that all the fission gas is contained in bubbles of uniform size  $R$ . This restriction is obviously incorrect since newly generated fission gas is injected into the lattice as single atoms and becomes bubbles only after a period of growth by coalescence or absorption by existing bubbles. However, if the simplification of uniform bubble size is accepted, the kinetic equation for the bubble density is

$$\frac{dN}{dt} = \frac{Y_{Xe} \dot{F}}{m} - 16\pi RD_b N^2 \quad (13.256)$$

where the first term on the right represents the rate at which new bubbles are created by fission. According to Eq. 13.254, this term is equal to  $N/t$ . In accord with the uniform-size requirement, the new bubbles must be formed with the same number of atoms as all the other bubbles in the fuel and have the current value of the radius  $R$ . The second term on the right accounts for loss of bubbles by

coalescence. It was the only term in the kinetic equation for the postirradiation annealing situation. Substitution of Eq. 13.214 for  $D_b$  and elimination of  $R$  by use of Eq. 13.255 yield the differential equation

$$\frac{dN}{dt} = \frac{N}{t} - \alpha \frac{N^{7/2}}{t^{3/2}} \quad (13.257)$$

where

$$\alpha = 24a_0^4 D_s \left( \frac{8\pi\gamma}{3Y_{Xe} \dot{F}kT} \right)^{3/2}$$

is a constant.

The initial condition for Eq. 13.257 is  $N(0) = 0$ . The differential equation can be solved by use of a trial solution of the form  $N = At^n$ . The initial condition is automatically satisfied, and the constants  $A$  and  $n$  can be found by substituting the trial solution into the differential equation, which reduces to

$$nAt^{n-1} = At^{n-1} - \alpha A^{3/2} t^{(7n-3)/2}$$

In order for the exponents of  $t$  in all terms to be the same,  $n$  must be equal to  $1/5$ ; for the coefficients of the  $t$  terms to satisfy this equation with this value of  $n$ ,  $A$  must be  $(\frac{4}{5}\alpha)^{2/3}$ . The solution  $N = (\frac{4}{5}\alpha)^{2/3} t^{1/5}$  can be used with Eq. 13.255 to determine the following formula for  $R(t)$ :

$$R = 1.28 \left( \frac{a_0^4 D_s Y_{Xe} \dot{F}kT}{\gamma} \right)^{1/5} t^{3/5} \quad (13.258)$$

which is very close to the result that would have been obtained simply by replacing  $M$  in Eq. 13.253 by  $Y_{Xe} \dot{F}t$ . Greenwood and Speight<sup>60</sup> derived Eq. 13.258 in a different manner from the way it was obtained here, but the only difference in the formulas for  $R(t)$  is that the constant on the right is  $(9Z/16\pi)^{1/5}$  (where  $Z$  is a combinatorial number of order 12) instead of the value of 1.28 in Eq. 13.258.

The volume swelling in all uniform-size bubble models is equal to  $(4\pi R^3/3)N$ , or, with  $N$  given by Eq. 13.255 and  $R$  by Eq. 13.258,

$$\frac{\Delta V}{V} = 1.48(a_0^4 D_s)^{1/5} \left[ Y_{Xe} \dot{F} \left( \frac{kT}{2\gamma} \right) \right]^{2/5} t^{7/5} \quad (13.259)$$

To illustrate the potent effect of coalescence on fuel swelling, let us evaluate  $\Delta V/V$  using the following numerical values for the parameters involved:  $a_0 = 3 \text{ \AA}$ ,  $D_s = 8 \times 10^{-7} \text{ cm}^2/\text{sec}$ ,  $Y_{Xe} \dot{F} = 2 \times 10^{13} \text{ cm}^{-3} \text{ sec}^{-1}$ ,  $(kT/2\gamma) = 1 \text{ \AA}^2$ , and  $t = 3 \times 10^7 \text{ sec}$  (which corresponds to a 10% burnup for the fission density employed). These values lead to a predicted swelling of 165%. Although swelling of this magnitude could not be attained because of gas release from interconnected bubbles, the calculation indicates that coalescence is a major factor influencing swelling in irradiated fuels. By way of comparison, the swelling predicted by the stationary bubble model (Eq. 13.146) at the same burnup is 2.3%. This model employed all the assumptions inherent in Eq. 13.259, the only difference being the phenomenon of coalescence.

### Gruber's Method

The major significance of Gruber's<sup>59</sup> computer calculations of bubble coalescence is that they are exact. In

contrast to the approximate Greenwood—Speight analysis, Gruber does not simplify the conservation equations for tractability. He studied two cases: (1) growth by random migration coalescence for a fixed number of gas atoms and (2) growth by biased-migration coalescence for a fixed number of gas atoms.

Since the first case was also treated by the Greenwood—Speight method, the accuracy of this analysis can be tested. The only difference between cases 1 and 2 in Gruber's work is that the coalescence rate constant in 1 is given by Eq. 13.109, and for case 2 it is given by Eq. 13.110. The bubble conservation equations are the same in both cases.

The time rate of change of the concentration of bubbles containing  $m$  gas atoms is obtained by counting all collisions that produce or destroy bubbles of this size. The loss rate is determined as follows. All collisions between a size- $m$  bubble and any other bubble remove a bubble from the size- $m$  class. The loss rate due to these collisions is

Rate of destruction of size- $m$  bubbles/cm<sup>3</sup>

$$= \sum_{j=1}^{\infty} (1 + \delta_{jm}) k_{mj} C_m C_j \quad (13.260)$$

where  $\delta_{jm}$  is the Kronecker delta ( $\delta_{jm} = 0$  if  $j \neq m$ ,  $\delta_{jm} = 1$  if  $j = m$ ). Its presence in Eq. 13.260 is needed to account for the removal of two bubbles by a single collision between size- $m$  bubbles. The  $k_{mj}$  is the rate constant for coalescence between bubbles containing  $m$  and  $j$  gas atoms (Sec. 13.6).

The rate of production of size- $m$  bubbles arises from all collisions of smaller bubbles in which the number of gas atoms in the product bubble is  $m$ . This rate can be expressed by

Rate of production of size- $m$  bubbles/cm<sup>3</sup>

$$= \frac{1}{2} \sum_{i+j=m} (1 + \delta_{ij}) k_{ij} C_i C_j \quad (13.261)$$

The factor of one-half and the Kronecker delta in this expression are necessary to avoid counting collisions twice. For example, if  $m = 10$ , the collisions that produce bubbles of this size are 1 + 9, 2 + 8, 3 + 7, 4 + 6, and 5 + 5. However, the summation in Eq. 13.261 for  $m = 10$  includes 1 + 9, 2 + 8, 3 + 7, 4 + 6, 5 + 5, 6 + 4, 7 + 3, 8 + 2, and 9 + 1. The Kronecker delta adds another 5 + 5 entry and the factor  $\frac{1}{2}$  removes one of the 5 + 5 terms and the last four combinations in the list, thus resulting in the correct counting.

Alternatively, Eq. 13.261 can be written as

Rate of production of size- $m$  bubbles/cm<sup>3</sup>

$$= \frac{1}{2} \sum_{j=1}^{m-1} (1 + \delta_{j,m/2}) k_{m-j,j} C_{m-j} C_j \quad (13.262)$$

where the Kronecker delta applies only if  $m$  is even.

Combining Eqs. 13.260 and 13.262, the conservation statement for size- $m$  bubbles is

$$\frac{dC_m}{dt} = \frac{1}{2} \sum_{j=1}^{m-1} (1 + \delta_{j,m/2}) k_{m-j,j} C_{m-j} C_j - \sum_{j=1}^{\infty} (1 + \delta_{jm}) k_{mj} C_m C_j \quad (13.263)$$

Equation 13.263 is in reality a set of a large number of coupled nonlinear differential equations. However, the calculation can be cut off at a manageable size if the coalescence time is small enough that very few bubbles have grown to very large sizes. Gruber used the initial conditions:

$$\begin{aligned} C_m(0) &= M & (\text{for } m = 1) \\ C_m(0) &= 0 & (\text{for } m > 1) \end{aligned} \quad (13.264)$$

That is, all gas is initially present as single atoms in the matrix. Solution of Eqs. 13.263 and 13.264 with  $k_{ij}$  a known function of  $i$  and  $j$  (these indices represent the number of gas atoms in the colliding bubbles) determines the time-dependent distribution function  $C_m(t)$ . From these computations the  $k$ th moment of the distribution function, defined by

$$\langle m^k \rangle = \frac{1}{M} \sum_{m=1}^{\infty} m^k C_m(t) \quad (13.265)$$

can be computed as a function of time. The zeroth moment gives the total bubble density:

$$N = \langle m^0 \rangle M = \sum_{m=1}^{\infty} C_m(t) \quad (13.266)$$

The first moment is the total number of gas atoms in the fuel divided by  $M$ , which is unity

$$\langle m^1 \rangle = \frac{1}{M} \sum_{m=1}^{\infty} m C_m(t) = 1 \quad (13.267)$$

Since the ideal-gas law and mechanical equilibrium have been assumed, the radius of a bubble containing  $m$  atoms is given by Eq. 13.16. The mean radius of the bubble distribution function is

$$\bar{R} = \frac{\sum_{m=1}^{\infty} R C_m(t)}{\sum_{m=1}^{\infty} C_m(t)} = \left( \frac{3kT}{8\pi\gamma} \right)^{1/2} \frac{\sum_{m=1}^{\infty} m^{1/2} C_m(t)}{\sum_{m=1}^{\infty} C_m(t)}$$

or

$$\bar{R} = \left( \frac{3kT}{8\pi\gamma} \right)^{1/2} \frac{\langle m^{1/2} \rangle}{\langle m^0 \rangle} \quad (13.268)$$

We first consider Gruber's calculation of coalescence driven by random migration, for which the rate constant is given by Eq. 13.109. Substituting  $D_b$  as a function of  $R$  from Eq. 13.214 and  $R$  in terms of  $i$  and  $j$  from Eq. 13.16 gives the rate constant for use in Eq. 13.263:

$$k_{ij} = 6a_0^2 D_s \left( \frac{8\pi\gamma}{3kT} \right)^{3/2} (i^{1/2} + j^{1/2}) (i^{-2} + j^{-2}) \quad (13.269)$$

The constant term on the right of this equation can be eliminated from the conservation equations by use of a dimensionless time defined by\*

$$\tau = 6Ma_0^4 D_s \left( \frac{8\pi\gamma}{3kT} \right)^{3/2} t \quad (13.270)$$

Incorporating the total concentration of gas M into the definition of  $\tau$  means that the concentrations appearing in Eq. 13.263 are now relative to M, and the solution provides the dimensionless bubble concentration  $C_m/M$  as a function of dimensionless time  $\tau$ . By proceeding in this fashion, we have no parameters in the numerical solution.

Figure 13.21(a) shows the bubble distribution function for three values of the dimensionless time. (The initial distribution is a delta function at  $m = 1$ ). Gruber found (empirically) that for all but short times the curves of Fig. 13.21(a) could all be collapsed onto a single curve if the distribution function is expressed in the form

$$\frac{C_m}{M} = \tau^{-1} C^*(m\tau^{-2/5}) \quad (13.271)$$

where  $C^*$  is a universal distribution curve that is a function of the variable  $m\tau^{-2/5}$  only and not of  $m$  and  $\tau$  separately. The grouping of these variables in the manner shown in Eq. 13.271 is called a similarity transformation and has many parallels in problems of heat conduction and fluid mechanics. Baroody<sup>7,3</sup> has exploited this self-preserving feature of the distribution function to deduce accurate analytical computational methods for the postirradiation annealing coalescence problem. It is not known if similarity solutions could be obtained when continuous gas production (in-pile coalescence) occurs and when other processes in addition to coalescence influence the distribution function.

The universal distribution function for postirradiation annealing by random coalescence is shown in Fig. 13.21(b). It can be used to determine the moments of the distribution function needed to compute properties such as the mean radius. Substituting Eq. 13.271 into Eq. 13.265 yields

$$\langle m^k \rangle = \sum_{m=1}^{\infty} m^k \tau^{-4/5} C^*(m\tau^{-2/5}) \\ = \tau^{-4/5} \sum_{m=1}^{\infty} (m\tau^{-2/5})^k C^*(m\tau^{-2/5})$$

The second sum can be approximated by an integral

$$\sum_{m=1}^{\infty} (m\tau^{-2/5})^k C^*(m\tau^{-2/5}) \simeq \int_0^{\infty} (m\tau^{-2/5})^k C^*(m\tau^{-2/5}) dm \\ = \tau^{2k/5} \int_0^{\infty} u^k C^*(u) du$$

where  $u = m\tau^{-2/5}$ . The integrals can be evaluated numerically from the universal distribution function for any desired value of  $k$ . For example,

\*Gruber's dimensionless time contains a slightly different constant because of the way he described the bubble diffusivity  $D_b$ .

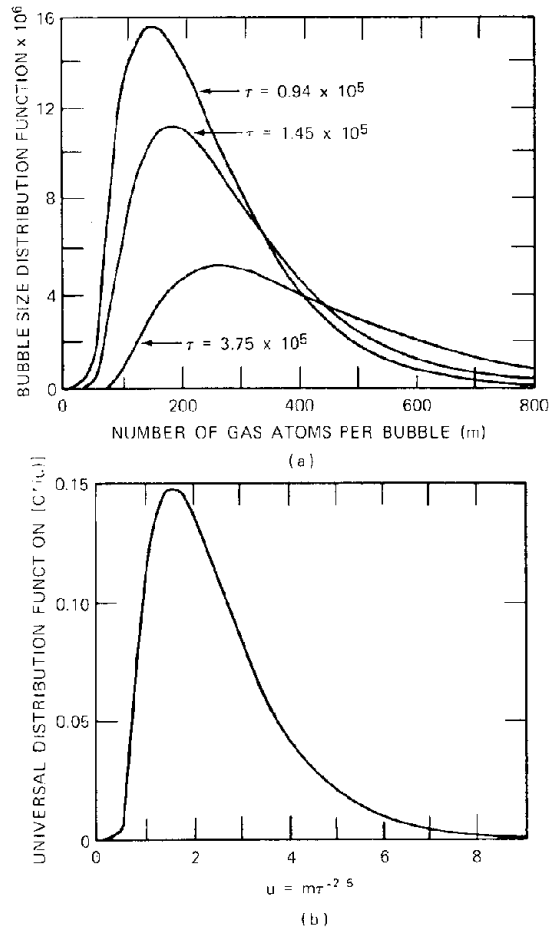


Fig. 13.21 Evolution of the bubble distribution function during postirradiation annealing. Random bubble migration. (a) The dimensionless size distribution for various dimensionless times. (b) The universal distribution function for random coalescence. [After E. E. Gruber, *J. Appl. Phys.*, 38: 243 (1967).]

$$\frac{\langle m^{3/2} \rangle}{\langle m^0 \rangle} = \frac{\tau^{-3/5} \int_0^{\infty} (u)^{3/2} C^*(u) du}{\tau^{-4/5} \int_0^{\infty} C^*(u) du} = 1.53 \tau^{1/5} \quad (13.272)$$

If this equation is now substituted into Eq. 13.268 and  $\tau$  is replaced by use of Eq. 13.270, we arrive at the growth law:

$$\bar{R} = 1.32 \left( \frac{a_0^4 D_s M k T}{\gamma} \right)^{1/5} t^{1/5} \quad (13.273)$$

The analogous formula obtained by the approximate method of Greenwood and Speight, Eq. 13.253, is in remarkably good agreement with Eq. 13.273.

The physical situation to which the preceding analysis applies is identical to that for the growth problem analyzed in Sec. 13.5. Both are cases of postirradiation annealing with the gas initially atomically dispersed. However, the mechanisms of growth are very different in the two models; Speight's analysis<sup>3,4</sup> assumes that the bubbles are immobile and grow only by diffusion-controlled absorption of gas atoms remaining in the matrix. The growth law for this

model is given by Eq. 13.78. In the case just discussed, on the other hand, all growth is attributed to coalescence, and the growth law is given by Eq. 13.273. The two predictions of the mean bubble radius as a function of annealing time are displayed in Fig. 13.22. All parameters in the growth equations are the same except for the diffusion coefficients and the bubble densities. In the single-atom absorption model, the pertinent diffusion coefficient is that of fission-gas atoms in the matrix,  $D_{Xe}$ , whereas in the coalescence model the kinetics of growth are controlled by the surface self-diffusion coefficient of  $UO_2$ ,  $D_s$ . These two diffusivities have been evaluated at 2000°K from Eqs. 13.29 and 13.216, respectively.

The bubble density required for computation of  $\bar{R}(t)$  by Eq. 13.78 has been chosen as  $10^{15} \text{ cm}^{-3}$ , which is rather low compared to the predictions of the nucleation models discussed in Sec. 13.6. However, a larger bubble density would have reduced the limiting bubble radius below the value shown on the plot and increased the discrepancy between the two calculated curves. In the coalescence model, on the other hand, the upper limit to the size of the bubbles is very large. In principle, coalescence continues until all the gas in the entire volume of fuel is contained in one enormous bubble. The initial gas content of the solid was taken to be that generated by a preannealing burnup of ~0.1% in both cases.

Figure 13.22 shows a very large difference between the predictions of the immobile and mobile growth models. The immobile model is probably the more realistic of the two theories, since the quite reasonable fission-gas diffusivity formula given by Eq. 13.29 was obtained from the single-atom absorption model of bubble growth. The reason that the coalescence model does not adequately describe the growth of small bubbles is probably because it overestimates bubble mobility. Small bubbles do not migrate with the ease predicted by the surface-diffusion mechanism because they are immobilized by various defects in the solid. Nonetheless, large bubbles can become detached from common crystal defects by an external driving force; so coalescence in the matrix must be considered at some stage in the lifetime of irradiated fuel. Gruber's work is valuable because it represents a benchmark calculation of the coalescence phenomenon to which other approximate treatments, designed for incorporation into computations dealing with the full range of bubble behavior in irradiated fuels, can be compared for assurance of computational accuracy.

Gruber's calculations represent exact solutions to physical situations that are too idealized to adequately represent actual fuel performance. In addition to assuming a constant total gas content rather than allowing for a constant rate of gas-atom production, phenomena such as nonideal-gas behavior, resolution, and bubble pinning are ignored. In addition, the sums in Eq. 13.263 start from  $j = 1$ , which implies that single atoms and clusters of a few gas atoms behave like gas bubbles. Single-atom reactions with bubbles, however, should be treated by rate constants appropriate to such interactions (Sec. 13.8) and not by coalescence rate constants. Furthermore a di-atom is not a bubble. At what size a group of precipitated gas atoms transforms from a cluster that migrates as an overly large atomic species to a

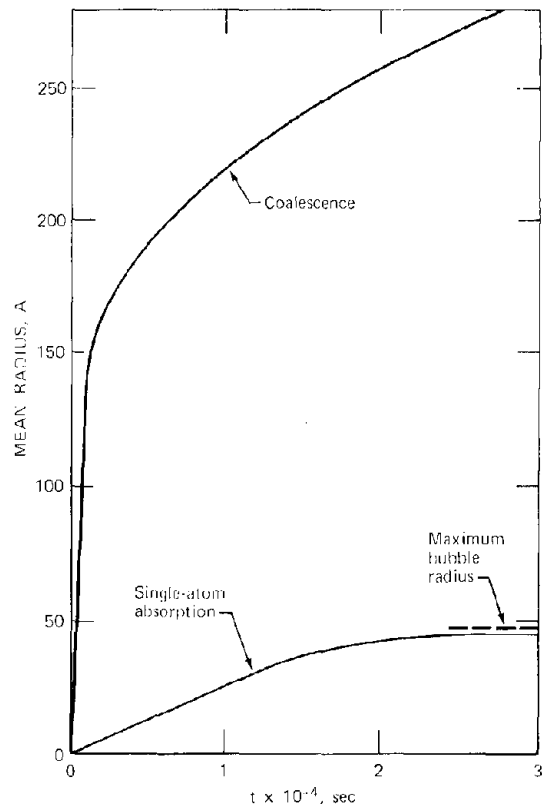


Fig. 13.22 Comparison of bubble growth during postirradiation annealing predicted by the single-atom absorption and coalescence models at 2000°K.  $D_{Xe} = 2.1 \times 10^{-14} \text{ cm}^2/\text{sec}$ ;  $D_s = 5 \times 10^{-7} \text{ cm}^2/\text{sec}$ ;  $N = 10^{15} \text{ cm}^{-3}$ ;  $C_0 - M = 10^{19} \text{ atoms/cm}^3$ ;  $kT/2\gamma = 10^{-16} \text{ cm}^2$ ; and  $a_0^3 = 4.1 \times 10^{-23} \text{ cm}^3$ .

true bubble for which the diffusion coefficient is accurately represented by the surface-diffusion mechanism is not known.

Gruber<sup>5,9</sup> also considered growth during postirradiation annealing in the presence of an external driving force, which he took to be a temperature gradient. The only change from the random-motion calculation previously discussed is the replacement of the rate constant of Eq. 13.109 by that of Eq. 13.110. The migration velocities required by the latter are given by Eq. 13.219. In the biased-migration case, it is essential to start with some spread of bubble sizes. If all bubbles were initially of the same size, all would migrate in the same direction at the same speed, and no overtaking collisions would occur. A distribution of the form shown in Fig. 13.20(a) for a short annealing time during which random migration predominated was used as initial condition for the biased-migration problem. As in the case of random migration, the evolution of the bubble distribution function was calculated, and its moments were used to determine average parameters, such as the mean radius and volume swelling. The volume swelling predicted by the biased-migration model is more than an order of magnitude greater than that computed when only random migration takes place. If Gruber's

method had been applied to in-pile coalescence, it is probable that the swelling would have been correspondingly larger than that predicted by the Greenwood—Speight random-migration analysis (case 2). Since the swelling given by Eq. 13.259 is already unrealistically high, values of  $\Delta V/V$  predicted by biased migration would be unbelievably large. Reasons for the failure of pure coalescence models are connected to pinning by dislocations and neglect of re-resolution.

### Other Coalescence Calculations

Recent studies have set out to remedy the drastic oversimplification of the actual physical situation in a reactor fuel inherent in models based solely on coalescence of freely migrating bubbles. Such attempts involve bubble conservation equations that are much more complex than Eq. 13.263. For example, if single-atom absorption by bubbles and macroscopic re-resolution occur simultaneously with coalescence, the bubble conservation equation is given by a combination of Eqs. 13.130 (wherein the last two terms are replaced by  $b'C_m$ ) and Eq. 13.263:

$$\begin{aligned} \frac{dC_m}{dt} = & k_{1,m-1}^{abs} C C_{m-1} - k_{1m}^{abs} C C_m - b' C_m \\ & + \frac{1}{2} \sum_{j=2}^{m-1} (1 + \delta_{j,m/2}) k_{m-j,j}^{coal} C_{m-j} C_j \\ & - \sum_{j=2}^{\infty} (1 + \delta_{jm}) k_{mj}^{coal} C_m C_j \end{aligned} \quad (13.274)$$

where  $k_{1m}^{abs}$  is the rate constant for single-atom absorption by a bubble of  $m$  atoms (Eq. 13.70) and  $k_{ij}^{coal}$  is the coalescence rate constant (Eq. 13.109 or 13.110). Equation 13.274 assumes that a cluster of two gas atoms migrates as a bubble.

Since Eq. 13.274 contains a term representing return of gas atoms to the matrix (the resolution term), it is no longer permissible to assume that all the gas is contained in the bubble population, as Greenwood and Speight<sup>60</sup> and Gruber<sup>59</sup> have done in their pure coalescence analyses. Rather, the set of bubble equations must be coupled to the total gas balance (Eq. 13.131):

$$Y_{Xe} \dot{F}t = C + \sum_{m=2}^{\infty} m C_m \quad (13.275)$$

As shown by Eq. 13.197, the first term on the right of Eq. 13.274 can be expressed in terms of the derivative of  $k_{1m} C_m$  with respect to  $m$ . The sums in Eqs. 13.274 and 13.275 can be approximated by integrals over the distribution function (see Ref. 73). Consequently, the conservation equations can be reduced to a pair of coupled integro-differential equations, the solution of which presents all the difficulties encountered in solving the Boltzmann equation in gas kinetic theory or in neutron-transport theory.

Although Eqs. 13.274 and 13.275 include single-atom growth, re-resolution, and coalescence, they are missing two important phenomena. They are valid only in the infinite-medium approximation when spatial gradients of the concentrations of single atoms and bubbles are negligible. If

gas release by transport of either of these species to surfaces from which escape can occur is possible, Eq. 13.274 should contain a term representing bubble diffusion in a concentration gradient,  $\nabla \cdot (D_{b,m} \nabla C_m)$ , for random migration and a convective term accounting for transport of bubbles in and out of a unit volume by biased migration,  $\nabla(v_{b,m} C_m)$ . If gas transport out of a unit volume of fuel occurs, the total gas balance given by Eq. 13.275, which is applicable only to an infinite medium, must be replaced by a single-atom balance of the type given by Eq. 13.128. The latter must also be supplemented with a diffusion term of the type  $D_{Xe} \nabla^2 C$ .

The bubble conservation equations should also contain terms representing the rates of capture and release of bubbles by dislocations and grain boundaries. The effect of grain boundaries can be accounted for in boundary conditions that reflect the behavior of these internal surfaces as sources and sinks of bubbles. Dislocations are probably best treated as homogeneous sources or sinks in the solid. A complicating feature of grain boundary and dislocation capture and release of bubbles is that release occurs at a discrete size, thereby introducing a singularity in the  $m$  dependence of the distribution function.

A code GRASS (gas release and swelling subroutine) that purports to account for all these phenomena has been described by Li et al.<sup>74</sup> and Poeppel.<sup>75</sup> These papers deal in quantitative fashion only with the coalescence aspect of the model. Coalescence kinetics are based on Chandrasekhar's rate constants, but, instead of Eq. 13.263, conservation equations are written for ranges of bubble sizes. The attractive feature of this approach is the substantial reduction in the number of interconnected differential equations, which permits application of coalescence theory to practical systems where the bubbles may be large. The procedure resembles the multigroup methods used in neutron slowing-down theory. However, the calculation is still approximate. In contrast to the Greenwood—Speight theory, where approximations were made in the basic bubble conservation equations, Li et al.<sup>74</sup> maintain the correct conservation principles, but the mathematical solution is approximate. The multigroup conservation equations were not derived by averaging Eq. 13.263 over ranges of bubble sizes, and it does not appear that they can be so obtained. Unfortunately, the calculational procedure was not tested on a system (such as the postirradiation annealing situation) for which accurate numerical results are available. The method of treating the other processes in the GRASS code was not quantitatively explained; so it is not possible to tell how the complicated coupling of the bubble and single-atom conservation equations was handled.

Dollins and Ocken<sup>76</sup> have attempted to modify Gruber's results to account for re-resolution during irradiation. To do this, they started from a picture of the life history of a bubble very similar to the one subsequently analyzed quantitatively by Turnbull,<sup>4,3</sup> namely, nucleation by fission fragments, growth, and destruction by fission fragments. In place of growth by single-atom absorption in the Turnbull model, Dollins and Ocken assumed bubble growth to occur solely by coalescence. On the basis of the supposition that re-resolution converts all bubbles in the path of a fission fragment to single gas atoms in the matrix,

Dollins and Ocken argue that Gruber's postirradiation annealing results (which used single gas atoms as the initial condition) could be used. They assumed that, following passage of a fission fragment through a region of fuel, the redissolved gas atoms formed bubbles that grew by coalescence until another fission fragment traversed the same region and destroyed them. The time interval between successive passages of a fission fragment through a particular region of fuel was taken to be the reciprocal of the re-resolution parameter,  $1/b$ . The bubble distribution at the end of one of these periodically repeated growth stages was determined by substituting the mean bubble lifetime  $1/b$  for the annealing time  $t$  in Gruber's results (i.e., in Eq. 13.273 and the corresponding formula for  $\Delta V/V$ ).

Several features of this approach are subject to question. First, the assumption that a region of fuel just after passage of a fission fragment consists of single gas atoms in solution ignores the nucleation aspects of Turnbull's model, according to which fission fragments heterogeneously nucleate about five small bubbles at the same time that existing bubbles are destroyed. The initial condition on the coalescence problem should consist of single gas atoms in solution and  $5\text{-}\text{\AA}$  radius bubble nuclei.

Second, although the model of Dollins and Ocken is based on macroscopic re-resolution (i.e., destruction of entire bubbles by a re-resolution event), they employed the re-resolution parameter based on the microscopic model of this process (which visualizes return of one gas atom at a time to the matrix). Although the magnitudes of the bubble lifetimes  $1/b$  and  $1/b'$  are not very different (4 to 40 hr),  $b'$  is a function of bubble size and not a constant (Eq. 13.112). This feature of macroscopic re-resolution is responsible for the development of a bubble distribution function, as shown at the end of Sec. 13.9.

Finally, the Dollins-Ocken model does not directly confront the conservation equations that govern the process. To account for the combined effect of coalescence and re-resolution to the same accuracy as Gruber has treated the pure coalescence problem, Eqs. 13.274 and 13.275 would have to be solved. Whether grafting of the re-resolution part of Turnbull's model to Gruber's postirradiation calculations produces an accurate description of what actually is occurring is simply not known. Assessment of the validity of the Dollins-Ocken model will be possible only when the exact calculation is performed.

### 13.11 PINNING OF BUBBLES BY DISLOCATIONS AND GRAIN BOUNDARIES

The bubble growth and swelling models based on random or biased migration and coalescence which were discussed earlier assumed that the bubbles moved in a perfect crystalline lattice. However, reactor fuels contain a variety of crystal defects, ranging from clusters of vacancies or interstitial loops produced by fission-fragment damage and precipitates of impurity species (principally solid fission products in highly irradiated fuels) to naturally occurring faults, such as dislocation lines and grain bound-

aries. Our discussion of bubble pinning is restricted to the last two.

There is nearly always a sizable reduction in system energy when a free gas bubble becomes attached to a crystal defect. As the bubble approaches a defect, the interaction energy increases until the two objects are joined together, at which point the strength of the attachment is called the binding energy of the bubble to the defect. For dislocations the physical origin of the interaction energy is the reduction in the elastic energy contained in the stress field of the dislocation line by the bubble. Quantitative estimates of gas-bubble binding energies with precipitate particles have been presented by Nelson,<sup>77</sup> and dislocation-bubble interaction energies have been treated by Weeks et al.<sup>78</sup>

The gradient of the interaction energy when the bubble and the dislocation line are separated a given distance is the force of the attraction at that point. This force is akin to the force on a bubble in a stress field in the matrix discussed in the preceding section. For a bubble to be removed from a dislocation, the maximum value of the restraining force must be overcome by an external driving force acting on the bubble. A driving force such as that due to a temperature gradient increases rapidly with bubble radius at fixed temperature (Eq. 13.218). The restraining forces due to the bubble-defect interaction are generally less sensitive to bubble size than are the driving forces. Thus, the defects in the solid serve to temporarily trap freely migrating bubbles; a small bubble that interacts with a defect remains trapped until it has grown to a size that permits the temperature gradient force to tear it from the defect. Bubble growth while the bubble is pinned takes place by absorption of single gas atoms from the matrix or by coalescence with other gas bubbles which are migrating along the defect or which impinge on the trapped bubble from the matrix. When the critical size for pull-off is reached, the bubble again moves unimpeded through the matrix until it encounters another defect for which the critical size for detachment is larger than that on the defect that the bubble just left. The pinning-growth-detachment-recapture sequence is repeated until no defect in the solid binds the bubble strongly enough to prevent it from migrating right out of the fuel (i.e., to open porosity or cracks within the fuel body or to the central void).

The critical size at which a bubble can pull free from an obstacle occurs when the driving force due to the temperature gradient is equal to the restraining force due to the bubble-defect interaction. The stress-gradient driving force is generally much weaker than the temperature-gradient force, and only the latter will be considered in the following discussion. As previously mentioned, the restraining force can be determined if the interaction-energy-separation-distance relation is known. An easier method, due to Nichols,<sup>9</sup> considers the restraining force to arise from the stretching of the dislocation line or grain boundary as the bubble is pulled away by the thermal-gradient force. Dislocations and grain boundaries are visualized as an elastic string or a membrane characterized by a line tension  $\tau_d$  and a surface tension  $\gamma_{gb}$ , respectively.

Figure 13.23 shows a bubble tugging at a dislocation line and causing the latter to deform so that the ends

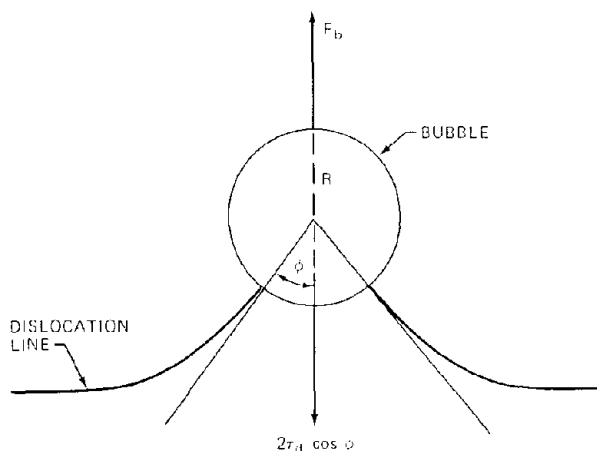


Fig. 13.23 Stretching of a dislocation line by a bubble subject to a force due to the thermal gradient. The dislocation line is assumed to be perpendicular to the force on the bubble.

terminate in the bubble at an angle  $\phi$  (measured from the direction of the temperature driving force). The force balance on the bubble takes the form

$$F_b = 2\tau_d \cos \phi \quad (13.276)$$

The maximum value of the restraining force occurs when the angle  $\phi$  is zero, at which point the line can no longer hold the bubble. The critical bubble radius for detachment is obtained by substituting Eq. 13.228 for  $F_b$  and setting  $\phi = 0$  in Eq. 13.276. Solving the resulting equation for the bubble radius yields

$$R_d = \left[ \frac{a_o^3 \tau_d}{\pi Q_s^* (1/T) (dT/dx)} \right]^{1/2} \quad (13.277)$$

In Sec. 8.3 we showed that the line tension of a dislocation is approximately given by

$$\tau_d = Gb^2 \quad (8.10)$$

where  $G$  is the shear modulus of the solid and  $b$  is the Burgers vector of the dislocation ( $b$  is approximately equal to a lattice constant). For most materials<sup>9</sup>  $\tau_d$  is approximately  $10^{-4}$  dynes. Weeks and Scattergood<sup>79</sup> have analyzed the dislocation stretching model in greater detail using more-accurate line tension expressions for screw and edge dislocations than that given by the preceding formula (e.g., Eq. 8.9 for a screw dislocation); however, since the critical-radius equation contains the line tension to the one-third power, modest changes in  $\tau_d$  do not affect the calculated critical bubble radii significantly. Using  $\tau_d = 10^{-4}$  dynes,  $a_o^3 = \Omega = 4.1 \times 10^{-23}$  cm<sup>3</sup>,  $Q_s^* = 415$  kJ/mole ( $7 \times 10^{-12}$  ergs/molecule),  $T = 2000$  °K, and  $dT/dx = 1000$  °K/cm, Eq. 13.277 gives a critical radius of 700 Å. The critical pull-off radius depends not only on the temperature and temperature gradient but also on the angle that the dislocation line makes with the direction of the temperature gradient. Equation 13.277 assumes that these two are perpendicular.

The restraining force on a bubble due to a stretched grain boundary can be determined with the aid of Fig. 13.24. The force opposing  $F_b$  is the product of the grain-boundary tension  $\gamma_{gb}$ , the circumference of the circle of contact,  $2\pi R \sin \phi$ , and the factor giving the force component in the direction of the temperature gradient,  $\cos \phi$ . The equilibrium condition is

$$F_b = 2\pi R \gamma_{gb} \sin \phi \cos \phi = \pi R \gamma_{gb} \sin 2\phi \quad (13.278)$$

The right-hand side of Eq. 13.278 attains a maximum value at  $\phi = 45^\circ$ . Using this value of the angle and substituting  $F_b$  from Eq. 13.228 yield the critical bubble radius for grain boundary pull-off:

$$R_{gb} = \left[ \frac{a_o^3 \gamma_{gb}}{2Q_s^* (1/T) (dT/dx)} \right]^{1/2} \quad (13.279)$$

Bullington and Leggett<sup>80</sup> have shown experimentally that the average diameter of the gas bubbles found on grain boundaries in irradiated fuel is approximately equal to that predicted by Eq. 13.279.

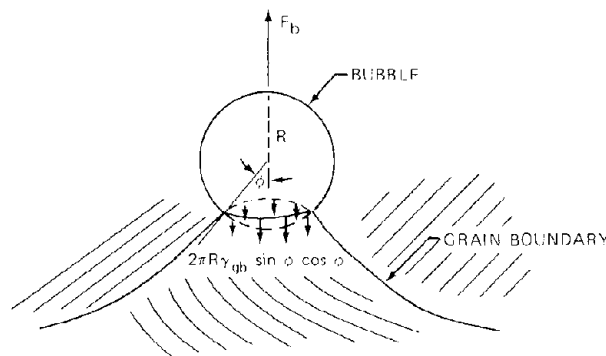


Fig. 13.24 Interaction of a grain boundary and a bubble subject to a force perpendicular to the plane of the grain boundary.

The grain-boundary tensions in  $UO_2$  and  $UC$  are estimated to be  $\sim 300$  dynes/cm. Using this value of  $\gamma_{gb}$  and the same numerical values of the other quantities in Eq. 13.279 as were employed in the illustrative calculation of  $R_d$ , the critical radius for grain-boundary detachment is of the order of 4000 Å.

The preceding formulas for the critical radii for bubble pull-off from dislocations and grain boundaries are based on a thermal-gradient driving force coupled with bubble mobility due to the surface-diffusion mechanism. We can also compute the force on a bubble due to the same driving force but for bubble migration by the volume-diffusion mechanism. In this case  $F_b$  is obtained by using Eq. 13.234 in 13.226, which produces a relation similar to Eq. 13.228 except that the factor 2 is replaced by 4/3 and  $Q_s^*$  is replaced by  $Q_v^*$ .

Figure 13.25 shows graphs of the critical pull-off radii and migration velocities for bubbles in  $UO_2$  and  $UC$  under typical operating conditions.<sup>81</sup> The radii at which detachment occurs were obtained from Eqs. 13.277 and 13.279

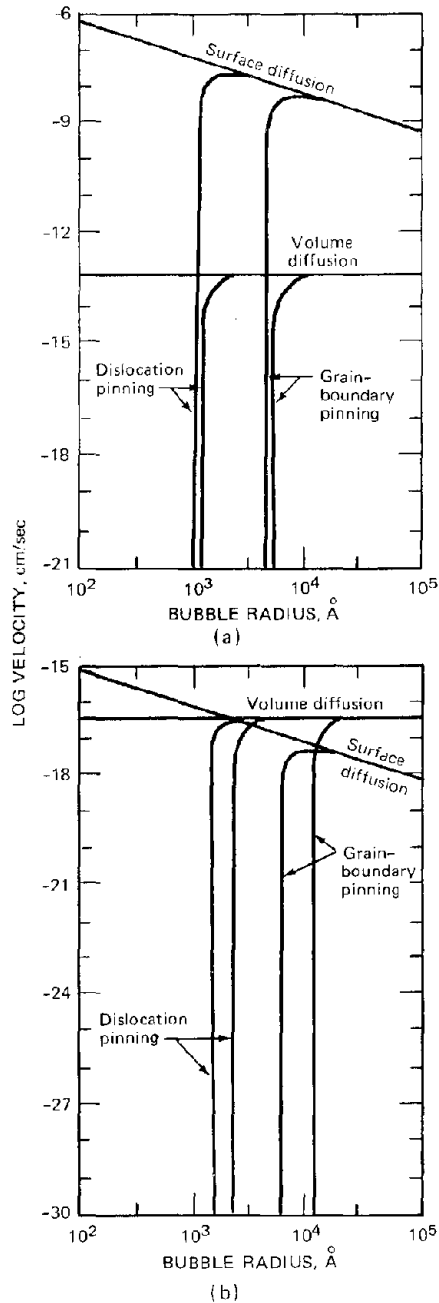


Fig. 13.25 Migration velocity as a function of radius for bubbles in  $UO_2$  and UC for typical temperatures and temperature gradients. (a)  $UO_2$ :  $T = 2000^\circ K$ ,  $dT/dx = 1000^\circ K/cm$ . (b) UC:  $T = 2000^\circ K$ ,  $dT/dx = 200^\circ K/cm$ . [After R. W. Weeks, R. O. Scattergood, and S. R. Pati, *J. Nucl. Mater.*, 36: 223 (1970).]

(with appropriate modifications when based on the volume-diffusion mechanism), and the bubble velocities in free migration in the thermal gradient were calculated by Eqs. 13.219 and 13.235 for the surface and volume-diffusion mechanisms, respectively. The rounded knees on the curves as the critical radii are approached are due to

residual retarding forces on the bubbles when the bubbles are just slightly larger than the size needed for pull-off.<sup>80</sup> Figure 13.25 shows the pinning radii for bubbles on dislocation lines and grain boundaries since these are the most obvious defects in the solid. However, other defects present in irradiated fuel can also temporarily immobilize bubbles smaller than  $1000 \text{ \AA}$ , which is the approximate critical radius for dislocations. Smaller bubbles can be pinned by impurity precipitates and various irradiation-produced clusters in the solid. If these binding sites were included in the graph (they have not yet been analyzed quantitatively in the literature), we would expect to see more vertical lines dropping from the free-migration velocity lines at small radii.

The most interesting aspect of the two plots in Fig. 13.25 is the difference between  $UO_2$  and UC. Bubble detachment for a particular type of defect occurs at approximately the same size for both materials, but the magnitudes of the free-migration velocities are nine orders of magnitude greater in  $UO_2$  than in UC. This large difference is a direct consequence of the higher thermal conductivity of UC compared to  $UO_2$  which, for a specified linear power of the fuel rod, reduces the maximum fuel temperature and temperature gradient in the UC fuel element by comparison with the  $UO_2$  fuel pin. The graphs also show that, whereas volume diffusion is unimportant in free bubble migration in  $UO_2$ , it appears to be the dominant mechanism for bubble mobility in UC.

### 13.12 THE BUBL CODE

So far in this chapter, the first two of three stages required in a model of swelling and gas release applicable to in-reactor fuel performance have been discussed. The first stage, covered in Secs. 13.2 through 13.6, consists of quantitative descriptions of the rates of the elementary steps that ultimately are responsible for gross fission-gas behavior. The second stage combines the elementary steps into distinct processes, such as nucleation, growth, and migration. In the third stage the processes of the second stage are assembled to provide a calculational tool for predicting the fate of the fission gases in a realistic fuel operation situation.\*

By the time the third stage of fission-gas behavior analysis is reached, the calculations are usually too complicated to be written in simple analytical form giving, say, the gas swelling and release from a portion of a fuel pin as a function of all the variables listed in Table 13.2. At the present time, two computer simulations of fission-gas behavior have been reported. These are the GRASS code<sup>74,75</sup> and the BUBL code.<sup>82,83</sup> Neither of these programs is a comprehensive model in the sense that all

\*Fuel modeling is not complete after the third stage. In a fourth stage fission-gas behavior is coupled with the mechanical and chemical behavior of the components of a fuel pin to provide a description of the performance of the entire fuel element. Finally, the large-scale mechanical interaction of the fuel assemblies and of the entire core must be considered.

pertinent parameters and potential processes are accounted for. As mentioned earlier, the GRASS code appears to emphasize bubble coalescence in the fuel matrix, relying principally on the coalescence rate constants described in Sec. 13.6 coupled with the bubble conservation equations derived in Sec. 13.10. The BUBL code, the basic outlines of which were described by Nichols in a 1966 report,<sup>9</sup> is based almost entirely on the biased-migration and bubble-pinning phenomena described in the two preceding sections. Warner and Nichols<sup>8,2</sup> believe that these two processes, when coupled with a realistic description of the microstructure of the fuel, are sufficient to explain much of the available experimental data on gas swelling and release in operational situations. Re-solution, bubble growth by gas-atom absorption, and bubble nucleation are completely ignored. Coalescence is treated, but only as it occurs on dislocations or grain boundaries. Bubble coalescence in the matrix of the solid is neglected. Even with this limited number of basic processes selected for incorporation into the BUBL code, solution of the governing conservation equations (e.g., those discussed at the end of Sec. 13.10) was found to be so complicated that the calculation is performed by Monte Carlo techniques.

A region of fuel is represented by a number of cubical grains, each of which is subdivided into cubical dislocation volumes. The sizes of these two basic units of the microstructure of the solid are determined from actual grain size and dislocation density measurements on uranium dioxide fuels. Fission-gas atoms are produced in the fuel matrix contained in the dislocation volumes. All gas atoms enter the calculation as small bubbles of uniform, prescribed radius at a rate dictated by the assumed size and the fission rate. These bubble nuclei bombard the dislocation lines bounding the dislocation volume at random positions along the lines and with no lag time between generation of gas atoms by fission and impingement on the lines in the form of small bubbles. Because nucleation is assumed to be very rapid compared to other processes, a description of nucleation kinetics is not needed. The small bubbles are pinned to the dislocations because their radius is less than the critical pull-off radius (Eq. 13.277). However, bubbles on dislocation lines grow by coalescence when they are struck directly by a bubble nucleus arriving from the matrix or when an adjacent bubble has grown sufficiently large (by the same mechanism) to overlap its neighbor. When a bubble on the dislocation line attains the critical detachment radius for this defect, it is released and moves in free migration up the temperature gradient until it encounters a grain boundary. During transit from a dislocation line to a grain boundary, the bubble does not change size; in-transit bubbles neither collide with other bubbles nor grow by absorbing gas atoms in the solid through which they move.

The same cycle of bombardment, growth by coalescence, and release when the critical size is attained occurs on the grain boundaries. Bubbles large enough to become detached from grain boundaries again move through the matrix under the influence of the temperature gradient. This time, no defect can stop them; they plow right through dislocations and grain boundaries in their path until they reach a fissure in the fuel where the gas enclosed in the bubble is released to the fuel element. The cracks

that permit escape of the gas are assumed to occur approximately every ten grains.

In the BUBL code the processes outlined in the preceding paragraph are followed as functions of irradiation time. At a particular time the fraction of gas released is determined by the ratio of the amount of gas that has passed through the complete sequence and arrived at the escape cracks to the total quantity of fission gas produced up to that time. The swelling is computed by adding up the volumes of the four classes of gas bubbles in the fuel, namely,

1. Bubbles trapped at dislocations.
2. Bubbles in transit from dislocations to grain boundaries.
3. Bubbles trapped at grain boundaries.
4. Bubbles in transit from grain boundaries to release (i.e., to cracks or interconnected porosity in the fuel).

In the early stages of irradiation, both release and swelling are low because the "pipeline" has not been filled up. As time progresses, the concentration of gas bubbles in each of the four categories listed sequentially attain steady values. When the bubbles in the four categories have achieved constant concentrations, the entire process is at steady state; the gas release approaches 100%, and the swelling becomes constant. Although the time-dependent portion of the history cannot be described analytically, a relatively straightforward calculation permits determination of the limiting value of the swelling when the steady state is reached. This particular aspect of the BUBL code is described as follows.

The model of the fuel microstructure is shown in Figure 13.26. Dislocation lines fill each grain in a regular cubical network. Segments of dislocation line of length  $X_d$  form the edges of the dislocation volumes. Since there are 12 edges to the cube and each edge is shared among 4 adjacent dislocation cubes, the solid contained within each small cube is associated with a length  $3X_d$  of dislocation line. Since the volume of each cube is  $X_d^3$ , the length of a side of a dislocation volume is related to the dislocation density of the matrix by

$$\rho_d = 3X_d \frac{\text{cm of dislocation line}}{\text{dislocation cube}} / X_d^3 \frac{\text{cm}^3 \text{ of solid}}{\text{dislocation cube}}$$

or, the characteristic length is

$$X_d = \left( \frac{3}{\rho_d} \right)^{1/2} \quad (13.280)$$

At 2000°K the dislocation density in UO<sub>2</sub> is  $\sim 10^8$  cm<sup>-2</sup>, and from Eq. 13.280 the length of a side of the dislocation cube is 1.2  $\mu$ m. A typical grain size in UO<sub>2</sub> ( $X_g$ ) is 10  $\mu$ m; so each grain contains about 1000 dislocation cubes. Cracks perpendicular to the temperature gradient are assumed to occur approximately every tenth grain, or with a spacing ( $X_c$ ) of 100  $\mu$ m.

### 13.12.1 Bubbles Trapped on Dislocations

We first compute the rate at which bubble nuclei bombard each segment of dislocation line. Assume that the nuclei contain  $m_1$  gas atoms and have a radius  $R_1$  given by Eq. 13.16. Since there are three dislocation segments of

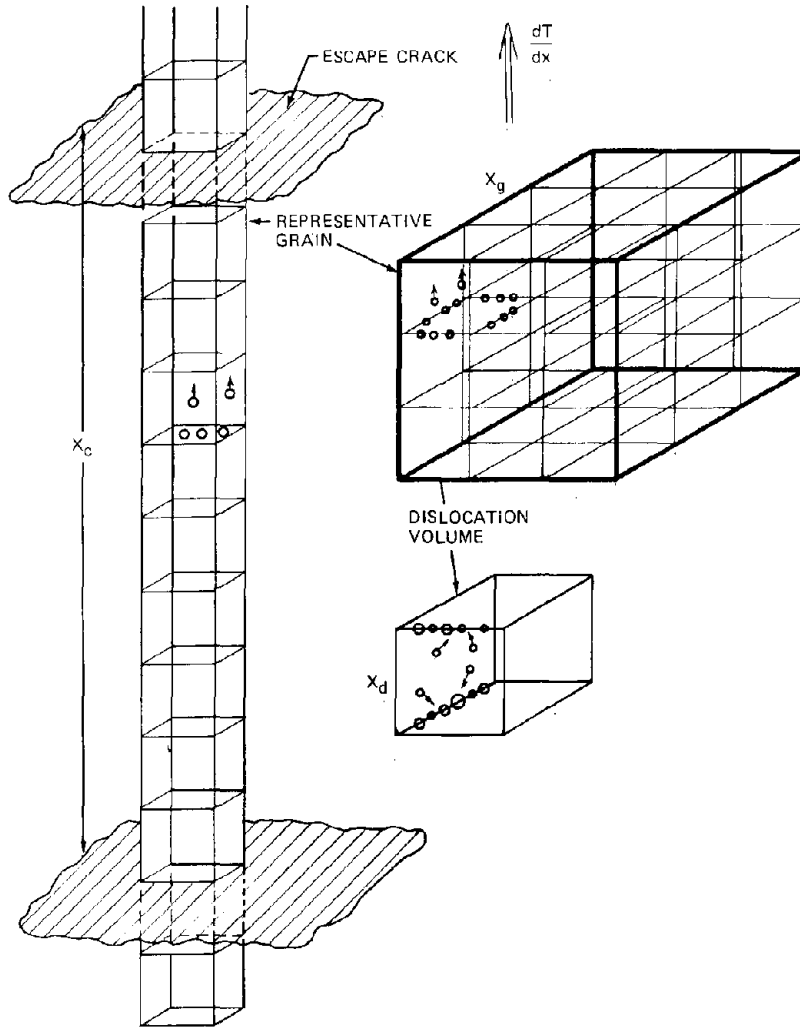


Fig. 13.26 Fuel microstructure model for the BUBL code. [After H. R. Warner and F. A. Nichols, *Nucl. Appl. Technol.*, 9: 148 (1970).]

length  $X_d$  associated with a volume of  $X_d^3$  of fuel, the rate at which bubble nuclei impinge on each segment is  $Y_{X_c} F(X_d^3/3)/m_1$ . The reciprocal of this expression is the average time between collisions of a bubble nucleus with a segment  $X_d$  of dislocation line:

$$t_o = \frac{3m_1}{Y_{X_c} F X_d^3} \quad (13.281)$$

Bubbles are detached from the dislocation line when they have attained a radius  $R_d$  given by Eq. 13.277. The number of gas atoms contained in the released bubbles is given by Eq. 13.14:

$$m_d = \frac{4\pi R_d^3/3}{B + R_d (kT/2\gamma)} \quad (13.282)$$

We now determine the steady-state distribution function of bubbles pinned to the dislocation lines. These bubbles are assumed to grow only by coalescence. Figure 13.27 shows four distinct coalescence sequences that

result from bombardment of the dislocation by bubble nuclei from the matrix. The diagram shows four views of the dislocation line starting from the moment of impingement to the completion of the particular coalescence sequence. The four solid circles on the top of the drawing depict the bubble nuclei about to contact a dislocation line containing a variety of sizes of trapped bubbles. Sequence a on the left illustrates a normal coalescence; the nucleus strikes a bubble on the line, and after coalescence a new, enlarged bubble is formed. Sequence b shows a case in which the impinging nucleus coalesces with a trapped bubble, but, as enlargement of the combined bubble takes place, overlap with a neighboring bubble occurs, and another coalescence event is triggered. This type of interaction is termed secondary coalescence. In c the arriving nucleus simultaneously touches two bubbles on the line, and a large bubble is formed from these three participants in the multiple collision. In d no coalescence occurs, and the bubble nucleus is simply trapped by the dislocation line. The secondary and multiple coalescences represented

- BOMBARDING NUCLEI
- TRAPPED BUBBLE
- ⊙ ENLARGED BUBBLE AFTER COALESCENCE

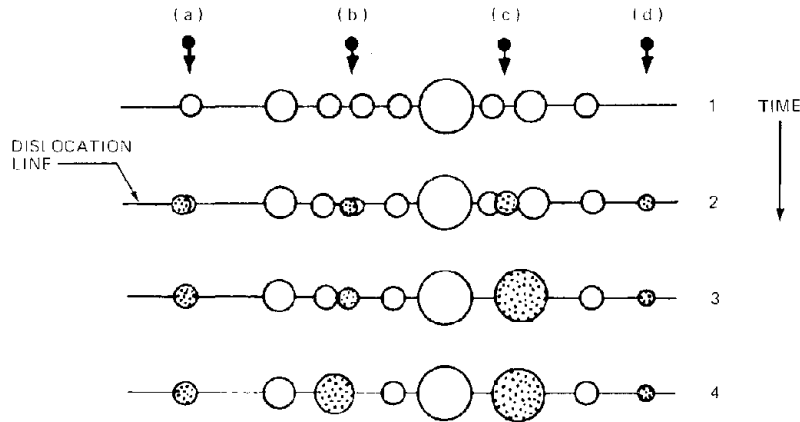


Fig. 13.27 Dislocation bombardment sequences. (a) Normal coalescence. (b) Secondary coalescence. (c) Multiple coalescence. (d) No coalescence.

by sequences b and c in Fig. 13.27 become significant when the bubble density on the dislocation line is high. For simplicity in the subsequent analysis, we will not consider these events and assume that, when a bubble nucleus strikes the dislocation line, either a normal coalescence or no coalescence results.

Since each bubble on the dislocation line grows only by coalescence with bombarding nuclei, the number of gas atoms in any of the trapped bubbles must be an integral multiple of  $m_1$ , the number of gas atoms in a bubble nucleus. Therefore, we can define the size of a trapped bubble by the number of bubble nuclei it contains, which is an integer denoted by  $n$ . The size parameter is restricted to  $1 \leq n \leq n_d$ , where  $n_d = m_d/m_1$  is the number of bubble nuclei contained in the bubble of critical size for pull-off from the dislocation. The distribution function of bubbles trapped on a dislocation segment is

$$f_d(n) = \frac{\text{number of bubbles on a dislocation segment of length } X_d \text{ which contains } n \text{ bubble nuclei}}{\text{segment of length } X_d \text{ which contains } n \text{ bubble nuclei}} \quad (13.283)$$

We will refer to a trapped bubble containing  $n$  bubble nuclei as an  $n$ -type bubble. The radius of an  $n$ -type bubble,  $R_n$ , is given by solution of the cubic equation,

$$nm_1 = \frac{4\pi R_n^3/3}{B + R_n(kT/2\gamma)} \quad (13.284)$$

The distribution function is obtained by formulating the rates of appearance and disappearance of  $n$ -type bubbles by collisions of the trapped bubbles with the incoming nuclei. The rate of removal of  $n$ -type bubbles from a segment  $X_d$  of dislocation is obtained as follows: If

the center of an impinging nucleus is within a distance  $R_n + R_1$  on either side of the center of an  $n$ -type bubble, coalescence occurs. If there are  $f_d(n)$   $n$ -type bubbles on a length  $X_d$  of dislocation line, the fraction of this length on which collisions of nuclei and  $n$ -type bubbles can occur is  $2(R_n + R_1)f_d(n)/X_d$ . Since one bubble nucleus strikes the segment  $X_d$  every  $t_0$  sec, the removal rate of  $n$ -type bubbles is

$$\text{Probability/sec of coalescence of an } n\text{-type bubble with a bombarding nucleus} = \frac{2(R_n + R_1)f_d(n)}{X_d t_0} \quad (13.285)$$

The  $n$ -type bubbles are produced by collisions of bubble nuclei with trapped  $(n-1)$ -type bubbles. The rate of this process is given by Eq. 13.285 with  $n$  replaced by  $n-1$ . At steady state the rates of removal and formation of  $n$ -type bubbles are equal, or

$$(R_n + R_1)f_d(n) = (R_{n-1} + R_1)f_d(n-1) \quad (13.286)$$

Equation 13.286 can be converted to differential form by setting

$$R_{n-1} = R_n - \frac{dR_n}{dn}$$

$$f_d(n-1) = f_d(n) - \frac{df_d}{dn}$$

which, when substituted into Eq. 13.286 yields

$$\frac{df_d}{dn} = - \left[ \frac{dR_n/dn}{R_n + R_1 - (dR_n/dn)} \right] f_d \quad (13.287)$$

the integral of which is

$$f_d(n) = f_d(1) \times \exp \left[ - \int_1^n \frac{dR_n/dn}{R_n + R_1 - (dR_n/dn)} dn \right] \quad (13.288)$$

To streamline the solution, we introduce the dimensionless constant

$$\delta = \frac{B}{R_1} \frac{2\gamma}{kT} \quad (13.289)$$

and the dimensionless bubble size

$$\xi = \frac{R_n}{R_1} \quad (13.290)$$

If Eq. 13.284 is divided by the same equation with  $n = 1$ , we have

$$n = \frac{(\delta + 1)\xi^3}{\delta + \xi} \quad (13.291)$$

The bubbles released from the dislocation by the force due to the temperature gradient contain a large number of nuclei. For a critical pull-off size of 500 Å, for example, the critical-size bubble contains  $\sim 10^6$  gas atoms. If the number of gas atoms in the bombarding nuclei is  $\sim 10$ ,  $n_d \sim 10^5$ . Thus, for most of the bubble size range, the integral in Eq. 13.288 can be approximated by

$$\begin{aligned} \int_1^n \frac{dR_n/dn}{R_n + R_1 - (dR_n/dn)} dn &= \int_1^n \frac{d\xi/dn}{\xi + 1 - (d\xi/dn)} dn \\ &\simeq \int_1^n \frac{1}{\xi} \left( \frac{d\xi}{dn} \right) dn = \int_1^\xi \frac{d\xi}{\xi} = \ln \xi \end{aligned}$$

For  $n = 10^3$  this approximation agrees with the exact integral, using  $\delta = 15$  and Eq. 13.291 to describe  $\xi$  as a function of  $n$ , to within 5%. Equation 13.288 can therefore be satisfactorily represented by

$$f_d(n) = \frac{f_d(1)}{\xi} \quad (13.292)$$

To determine  $f_d(1)$ , the number of bubble nuclei trapped (uncoalesced) on the dislocation segment, we formulate the following balance: The rate of removal of trapped nuclei from the type-1 category to type-2 bubbles by coalescence with impinging nuclei is given by Eq. 13.285 with  $n$  set equal to unity. A trapped bubble nucleus is produced every time a bombarding nucleus does not coalesce with a bubble already on the line. The rate of this process depends on the fraction of the line segment  $X_d$  on which the event depicted by Fig. 13.27(d) can occur, which is

Unoccupied fraction of dislocation line

$$= 1 - \sum_{n=1}^{n_d} 2(R_n + R_1) \frac{f_d(n)}{X_d}$$

Dividing this expression by  $t_o$  gives the rate of formation of trapped bubble nuclei. Approximating the sum in the

preceding expression by an integral, the rate of production of trapped bubble nuclei is

Probability/sec of formation of a type-1 bubble on the dislocation segment of length  $X_d$

$$= \frac{1}{t_o} \left[ 1 - \frac{2}{X_d} \int_1^{n_d} (R_n + R_1) f_d(n) dn \right] \quad (13.293)$$

At steady state Eq. 13.293 can be set equal to Eq. 13.285 wherein  $n = 1$ . This balance can be solved for  $f_d(1)$ , which is

$$f_d(1) = \frac{1}{4} \frac{X_d}{R_1} - \frac{1}{2} \int_1^{n_d} (\xi + 1) f_d(n) dn \quad (13.294)$$

Substituting Eq. 13.292 into the preceding integral and assuming  $\xi \gg 1$ , we obtain  $f_d(1)$ :

$$f_d(1) = \frac{1}{2n_d} \left( \frac{X_d}{R_1} \right) \quad (13.295)$$

The swelling due to bubbles trapped on the dislocation lines is

$$\left( \frac{\Delta V}{V} \right)_d = \frac{\sum_{n=1}^{n_d} (4\pi R_n^3/3) f_d(n)}{X_d^3/3} \simeq \frac{4\pi}{X_d^3} \int_1^{n_d} R_n^3 f_d(n) dn$$

The denominator represents the volume of solid associated with the segment  $X_d$  of dislocation line in terms of which the distribution function is defined. We can change the independent variable from  $n$  to  $\xi$  using Eq. 13.291 and, on substituting Eq. 13.292 for the distribution function and Eq. 13.295 for  $f_d(1)$ , obtain

$$\begin{aligned} \left( \frac{\Delta V}{V} \right)_d &= \frac{2\pi}{n_d} \left( \frac{R_1}{X_d} \right)^2 (\delta + 1) \\ &\quad \times \int_1^{R_d/R_1} \frac{\xi^4 (3\delta + 2\xi)}{(\delta + \xi)^2} d\xi \quad (13.296) \end{aligned}$$

The integral on the right of this equation can be evaluated analytically. Since  $R_d/R_1$  is usually considerably larger than  $\delta$ , the latter can be neglected in the integrand, and Eq. 13.296 reduces to

$$\left( \frac{\Delta V}{V} \right)_d = \frac{\pi R_d \left[ R_d + B \left( \frac{2\gamma}{kT} \right) \right]}{X_d^2} \quad (13.297)$$

where  $n_d$  and  $\delta$  have been replaced by Eqs. 13.291 and 13.289, respectively.

### 13.12.2 Bubbles in Transit from Dislocations to Grain Boundaries

Each dislocation segment of length  $X_d$  releases one critical-size bubble (of radius  $R_d$ ) every  $t_d$  sec, where, by analogy to Eq. 13.281,

$$t_d = \left( \frac{m_d}{m_1} \right) t_o \quad (13.298)$$

Since each dislocation cube contains three dislocation segments, each element of volume  $X_d^3$  emits  $3/t_d$  critical-size bubbles per second. Or, the grains can be considered to contain a uniform volumetric source of these bubbles of strength:

$$S_d = \frac{3}{t_d X_d^3} \frac{\text{bubbles of radius } R_d}{\text{cm}^3 \text{ sec}} \quad (13.299)$$

The concentration of these bubbles as a function of distance along the temperature gradient between grain boundaries (denoted by  $x$ ) is defined by  $f_{d-gb}(x)$  (there is no size distribution of the in-transit bubbles—all have a radius  $R_d$ ).

We formulate the balance on migrating bubbles in an elementary volume within the grain of unit cross-sectional area perpendicular to the temperature gradient and of thickness  $dx$ . The input from the cool side of the volume element due to bubble migration up the temperature gradient is  $f_{d-gb}(x) v_{bd}$ , where  $v_{bd}$  is the migration velocity of bubbles of radius  $R_d$  in the temperature gradient at point  $x$  ( $v_{bd}$  is given by Eq. 13.219 with  $R = R_d$ ). The rate of production of critical-size bubbles within the volume element is  $S_d dx$ . Neglecting the change in bubble velocity over the length  $dx$ , the flux of bubbles out of the volume element is  $[f_{d-gb} + (df_{d-gb}/dx)] v_{bd}$ . At steady state the sum of the first two contributions to the balance equals the outflow, or the bubble conservation equation is

$$v_{bd} \frac{df_{d-gb}}{dx} = S_d \quad (13.300)$$

which, when integrated with the boundary condition  $f_{d-gb}(0) = 0$  ( $x = 0$  represents the cool face of the grain under consideration), yields

$$f_{d-gb}(x) = \frac{S_d x}{v_{bd}} \quad (13.301)$$

The number of critical-size bubbles increases linearly with distance along the temperature gradient within each grain. This profile is repeated at each successively hotter grain because the bubbles arriving at the hot side of a grain are trapped there. The total number of critical-size bubbles within the entire grain is obtained by integrating Eq. 13.301 from  $x = 0$  to  $x = X_g$  and multiplying by the area of a grain,  $X_g^2$

Number of critical-size bubbles per grain

$$= X_g^2 \int_0^{X_g} f_{d-gb}(x) dx = \frac{S_d X_g^4}{2v_{bd}} = \frac{3X_g^4}{2v_{bd} t_d X_d^3} \quad (13.302)$$

The fractional swelling due to this class of in-transit bubbles is obtained by dividing the total volume of bubbles by the volume of a grain, which gives

$$\left(\frac{\Delta V}{V}\right)_{d-gb} = \left(\frac{4\pi R_d^3}{3}\right) \left(\frac{3X_g^4}{2v_{bd} t_d X_d^3}\right) (X_g^3)^{-1} \\ = \frac{2\pi R_d^3 X_g}{t_d X_d^3 v_{bd}} \quad (13.303)$$

### 13.12.3 Bubbles Trapped at Grain Boundaries

The cool side of each grain boundary perpendicular to the temperature gradient is bombarded by bubbles of radius  $R_d$ . The rate of arrival of these bubbles at the grain boundary is given by the flux  $v_{bd} f_{d-gb}(X_g)$  times the area of the grain boundary  $X_g^2$ . The reciprocal of this product is the time between arrivals of the bombarding bubbles

$$t_a = \frac{1}{v_{bd} f_{d-gb}(X_g) X_g^2} = \frac{1}{3} \left(\frac{X_d}{X_g}\right)^3 t_d \quad (13.304)$$

The incoming bubbles coalesce with bubbles already pinned to the grain boundary and cause growth of the latter. Detachment from the grain boundary occurs when the bubbles have attained a radius  $R_{gb}$  given by Eq. 13.279, at which point they contain

$$m_{gb} = \frac{4\pi R_{gb}^2}{3} \left(\frac{2\gamma}{kT}\right) \text{ gas atoms} \quad (13.305)$$

(these bubbles are large enough to justify application of the ideal-gas law).

Coalescence events of the type shown in Fig. 13.27 for the dislocations occur on the grain boundary as well. In the latter case, however, the bombarding bubbles contain  $m_d$  gas atoms each and arrive every  $t_a$  sec. Furthermore, the zone of coalescence is two-dimensional rather than one-dimensional. Secondary and multiple coalescence events are neglected.

The distribution function of grain-boundary bubbles is obtained in a manner analogous to that described by the number of bombarding bubbles it contains. Thus, we let  $n$  be the number of bubbles of the pull-off size from dislocations contained in a bubble on the grain boundary;  $n$  varies from 1 to  $n_{gb}$ , where  $n_{gb} = m_{gb}/m_d$ , and is related to the radius of the trapped bubble by

$$nm_d = \frac{4\pi R_n^2}{3} \left(\frac{2\gamma}{kT}\right) \quad (13.306)$$

The size distribution of bubbles on an area  $X_g^2$  of grain boundary is defined by

$$f_{gb}(n) = \frac{\text{number of bubbles on a grain boundary}}{\text{area } X_g^2 \text{ containing } n \text{ bombarding bubbles}} \quad (13.307)$$

The distribution function at steady state is obtained by equating the rates of formation and removal of type- $n$  bubbles. The two-dimensional analog of Eq. 13.285 is

Probability/sec of coalescence of an  $n$ -type bubble with a bombarding bubble

$$= \frac{\pi(R_n + R_d)^2 f_{gb}(n)}{X_g^2 t_a} \quad (13.308)$$

The rate of formation of  $n$ -type bubbles is given by the same expression with  $n$  replaced by  $n - 1$ . When these two rates are equal, we have

$$(R_n + R_d)^2 f_{gb}(n) = (R_{n-1} + R_d)^2 f_{gb}(n-1) \quad (13.309)$$

which leads to the differential equation

$$\frac{df_{gb}}{dn} = - \left\{ \frac{2(R_n + R_d)(dR_n/dn) - (dR_n/dn)^2}{[R_n + R_d - (dR_n/dn)]^2} \right\} f_{gb} \quad (13.310)$$

or, in integrated form

$$f_{gb}(n) = f_{gb}(1) \times \exp \left\{ - \int_1^n \frac{2(\xi + 1)(d\xi/dn) - (d\xi/dn)^2}{[\xi + 1 - (d\xi/dn)]^2} dn \right\} \quad (13.311)$$

where

$$\xi = \frac{R_n}{R_d} \quad (13.312)$$

Using Eq. 13.306 for all values of  $n$ , the relation between  $\xi$  and  $n$  is

$$n = \xi^2 \quad (13.313)$$

Substitution of Eq. 13.313 into the integral of Eq. 13.311 yields

$$f_{gb}(n) = f_{gb}(1) \times \exp \left\{ - \int_1^n \frac{(n')^{1/2} + 1 - [1/4(n')^{1/2}]}{(n')^{1/2} \{ (n')^{1/2} + 1 - [1/2(n')^{1/2}] \}^2} dn' \right\} \quad (13.314)$$

The integral can be evaluated analytically. The relative distribution function is shown in Fig. 13.28 for  $1 \leq n \leq 10$ . For  $n > 10$  the following asymptotic form is satisfactory:

$$f_{gb}(n) = \frac{2.5f_{gb}(1)}{n^2} \quad (n > 10) \quad (13.315)$$

The value of the distribution function for  $n = 1$  is obtained as in the case of dislocation bubbles. Using Eqs. 13.312 and 13.313 to express  $R_n$  in terms of  $n$ , we have

$$f_{gb}(1) = \frac{1}{4\pi} \left( \frac{X_g}{R_d} \right)^2 - \frac{1}{4} \int_1^{n_{gb}} [(n)^{1/2} + 1]^2 f_{gb}(n) dn \quad (13.316)$$

The integral in the second term is obtained numerically for the range  $1 \leq n \leq 10$  and analytically for  $10 < n \leq n_{gb}$ . The result is

$$\int_1^{n_{gb}} [(n)^{1/2} + 1]^2 f_{gb}(n) dn = f_{gb}(1) \times \left[ 11.9 + 2.5 \ln \left( \frac{n_{gb}}{10} \right) - \frac{10}{(n_{gb})^{1/2}} - \frac{2.5}{n_{gb}} \right] \quad (13.317)$$

Combining Eqs. 13.316 and 13.317 and neglecting the last two terms in Eq. 13.317 yield

$$f_{gb}(1) = \frac{(X_g/R_d)^2}{32.1 + 7.8 \ln(n_{gb})} \quad (13.318)$$

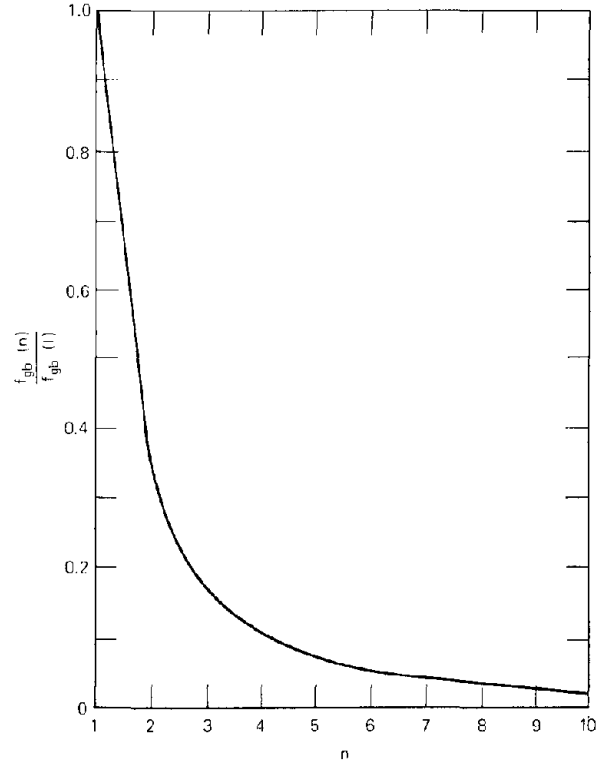


Fig. 13.28 Distribution function of bubbles trapped at a grain boundary.

The distribution of bubble sizes on grain boundaries predicted by the preceding analysis can be compared with the experimental results of Bullington and Leggett.<sup>80</sup> Their measured values of the intergranular bubble density as a function of bubble size are shown on Fig. 13.29. The cut-off at small diameters is due to experimental difficulties in observing small bubbles. If we assume that these data represent the end of the bubble distribution where Eq. 13.315 is valid, the variation of the bubble density with size can be determined theoretically. First, we must change variables from  $n$  to  $\xi$  (which is proportional to bubble diameter) in Eq. 13.315, which is accomplished by the transformation

$$\begin{aligned} f_{gb}(\xi) &= f_{gb}(n(\xi)) \left| \frac{dn}{d\xi} \right| \\ &= \text{constant} \times \xi^{-4} \times 2\xi \\ &= \text{constant} \times \xi^{-3} \end{aligned}$$

The dashed line on Fig. 13.29, which has a slope of -3, shows that the radius dependence of the theoretical model is quite acceptable. No attempt has been made to predict the absolute magnitude of the distribution function; the theoretical line in Fig. 13.29 was matched to the data at one bubble size.

The swelling due to bubbles trapped on the grain boundaries is given by

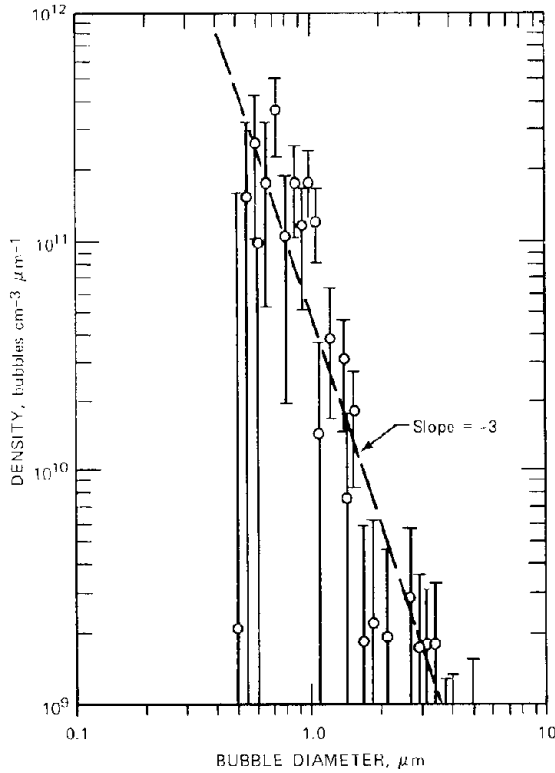


Fig. 13.29 Intergranular bubble density as a function of bubble diameter.  $T = 1600^\circ\text{K}$ .  $dT/dx = 1600^\circ\text{K/cm}$ . (After D. C. Bullington and R. D. Leggett, in *Plutonium 1970*, W. N. Miner (Ed.), p. 545, American Institute of Mining, Metallurgy & Petroleum Engineers, New York, 1971.)

$$\left(\frac{\Delta V}{V}\right)_{gb} = \frac{\sum_{n=1}^{n_{gb}} (4\pi R_n^3/3) f_{gb}(n)}{X_g^3} \approx \frac{4\pi}{3} \left(\frac{R_d}{X_g}\right)^3 \int_1^{n_{gb}} n^{3/2} f_{gb}(n) dn$$

The solid volume associated with one side of the representative grain boundary cube is  $X_g^3$ . Of the six faces only two are perpendicular to the temperature gradient, and each of these shares its bubbles with an adjacent grain. Using Eqs. 13.314 and 13.315 to evaluate the integral and expressing  $f_{gb}(1)$  by Eq. 13.318 yield

$$\left(\frac{\Delta V}{V}\right)_{gb} = \left(\frac{4\pi}{3}\right) \left(\frac{R_d}{X_g}\right) \left[ \frac{5(n_{gb})^{3/2} - 9}{32.1 + 7.8 \ln(n_{gb})} \right] \quad (13.319)$$

#### 13.12.4 Bubbles in Transit from Grain Boundaries to Release

To determine the swelling due to the last type of bubble in the fuel, consider the column of grains between cracks from which escape occurs (Fig. 13.26). Each grain boundary perpendicular to the temperature gradient receives a bubble containing  $m_d$  atoms every  $t_a$  sec (Eq. 13.304). Gas is released from the grain boundary at

the same rate but in bubbles containing  $m_{gb}$  atoms. The time between detachment of successive bubbles of the critical size for pull-off from the grain boundary is thus

$$t_{gb} = \left(\frac{m_{gb}}{m_d}\right) t_a \quad (13.320)$$

The bubbles travel from the point of release to the escape crack at a velocity  $v_{bgb}$  given by Eq. 13.219 with  $R = R_{gb}$ . We wish to determine the number of bubbles in a column of grains between escape cracks. Since each grain boundary emits critical-size bubbles at a rate of  $1/t_{gb}$  per second and the bubbles are not trapped by other grain boundaries they encounter while migrating, the rate at which bubbles flow past a grain boundary is  $M/t_{gb}$ , where  $M$  is an integer denoting the position of the grain boundary relative to the escape crack in the direction opposite to the temperature gradient (starting from the cool end of a column of grains,  $M = 1, 2, \dots, X_c/X_g$ ). The number of critical-size bubbles in grain  $M$  is the flux divided by the migration velocity multiplied by the thickness of the grain in the direction of the temperature gradient, or

$$\text{Number of bubbles in grain } M = \frac{MX_g}{t_{gb} v_{bgb}} \quad (13.321)$$

Summing Eq. 13.321 over all grains between escape cracks gives

Number of critical-size bubbles in column between escape cracks

$$= \frac{X_g}{t_{gb} v_{bgb}} \sum_{M=1}^{X_c/X_g} M \quad (13.322)$$

The volume of each bubble is  $4\pi R_{gb}^3/3$ , and the volume of the solid fuel in the column between release points is  $X_c X_g^2$ . Approximating the sum in Eq. 13.322 by the integral, we obtain the volume swelling due to this category of bubbles:

$$\left(\frac{\Delta V}{V}\right)_{gb-r} = \frac{2\pi R_{gb}^3 X_c}{3X_g^3 t_{gb} v_{bgb}} \quad (13.323)$$

Table 13.5 illustrates the application of the analysis on which the BUBL code is based to a typical LMFBR oxide fuel pin. According to Table 10.4 and Fig. 10.24, the temperature of  $2000^\circ\text{K}$  chosen for the table implies that the location considered in the example is in the middle of the equiaxed-grain region of the fuel. We note, however, that the temperature gradient used in Table 13.5 ( $10^3^\circ\text{K/cm}$ ) is nearly an order of magnitude smaller than that obtained from Fig. 10.24. Most studies of thermal-gradient bubble migration use the smaller figure, which at least gives conservative results for swelling when applied to LMFBR fuel designs. The microstructural parameters are those used by Warner and Nichols,<sup>3,2</sup> and the bubble nuclei that bombard the dislocation lines have been assumed to contain 10 gas atoms. The critical radii and migration velocities of bubbles detached from dislocations and grain boundaries were taken from Fig. 13.25.

Table 13.5 Gas-Swelling Predictions of the BUBL Code

Operating conditions	T = 2000°K dT/dx = 1000°K/cm Y <sub>Xe</sub> F̄ = 2 × 10 <sup>13</sup> gas atoms cm <sup>-2</sup> sec <sup>-1</sup>	
Microstructure	X <sub>d</sub> = 1.7 × 10 <sup>-4</sup> cm (ρ <sub>d</sub> = 10 <sup>8</sup> cm <sup>-2</sup> ) X <sub>g</sub> = 10 <sup>-3</sup> cm X <sub>c</sub> = 10 <sup>-2</sup> cm	
Other constants	kT/2γ = 1 Å <sup>2</sup> B = 85 Å <sup>3</sup>	
Bubble nuclei	m <sub>i</sub> = 10 gas atoms (R <sub>i</sub> = 6 Å)	
Characteristic times	t <sub>a</sub> = 0.3 sec (Eq. 13.281) t <sub>d</sub> = 1.2 × 10 <sup>7</sup> sec (Eq. 13.298) t <sub>gb</sub> = 3.3 × 10 <sup>3</sup> sec (Eqs. 13.304 and 13.320)	
Parameters of critical-size bubbles [from Fig. 13.25(a)]		
Pull-off from dislocations	R <sub>d</sub> = 1000 Å m <sub>d</sub> = 3.9 × 10 <sup>6</sup> v <sub>bd</sub> = 4 × 10 <sup>-8</sup> cm/sec	
Pull-off from grain boundaries	R <sub>gb</sub> = 4000 Å m <sub>gb</sub> = 6.7 × 10 <sup>7</sup> v <sub>gb</sub> = 1 × 10 <sup>-8</sup> cm/sec	
Swelling		
Class of bubble:	Swelling, %	Equation
Trapped on dislocations	1.2	13.297
In-transit, dislocations to grain boundaries	0.03	13.303
Trapped on grain boundaries	0.9	13.319
In-transit, grain boundaries to release	<u>4.1</u>	13.323
Total gas swelling	<u>6.2</u>	

The total swelling at steady state is calculated to be 6.2% for this particular example. The total reflects only swelling due to fission gases. Swelling due solid fission products (Sec. 12.7) should be added to the gas swelling.

The bubbles in-transit from grain boundaries to release constitute two-thirds of the gas swelling. Inasmuch as  $(\Delta V/V)_{gb-r}$  varies inversely as the migration velocity of critical-size bubbles, this contribution to the gas swelling is sensitive to the accuracy of all the parameters that enter into Eq. 13.219, of which the surface diffusivity is the least well established. At temperatures lower than 2000°K, the swelling due to the bubbles in transit to release would increase greatly owing to the rapid reduction of  $v_{bgb}$  due to the large activation energy of surface self-diffusion of UO<sub>2</sub>.

Another parameter that significantly affects the swelling due to large bubbles is the stress state of the solid. The parameter  $(\Delta V/V)_{gb-r}$  is decreased to the extent that  $t_{gb}$  in the denominator of Eq. 13.323 is increased. Combination of Eqs. 13.298, 13.304, and 13.320 shows that  $t_{gb}$  is directly proportional to the number of gas atoms contained in the bubbles released from grain boundaries,  $m_{gb}$ . This quantity was computed from Eq. 13.305, which assumed a stress-free solid. If Eq. 13.4 is used in the ideal-gas law rather than Eq. 13.5,  $m_{gb}$  is increased by the factor  $1 + (R_{gb}\sigma/2\gamma)$ , where  $\sigma$  is the hydrostatic stress in the fuel.

The critical radius  $R_{gb}$  is unaffected by stress (Eq. 13.279). If we take a typical stress level of 15,000 kN/m<sup>2</sup> and  $R_{gb} = 4000$  Å, the number of gas atoms in the bubbles detached from grain boundaries is about four times greater than the number in an unstressed fuel. Thus,  $t_{gb}$  is increased fourfold, and  $(\Delta V/V)_{gb-r}$  is reduced by the same factor.

Nichols and Warner<sup>8,3</sup> have modified the BUBL program to remove the unrealistically high swelling predicted for temperatures in the neighborhood of 1600°K. They added a third trapping site (of unspecified nature) which pins the bubble nuclei and releases bubbles of a size less than the critical radius for dislocation pull-off.

In an attempt to account for cracking and bubble link-up effects, we assume that 25% of the gas bubbles which attain the critical size for detachment from grain boundaries are released at the grain boundary rather than joining the last in-transit class, which contributes most to the swelling. This alteration is comparable to reducing  $X_c$  in Eq. 13.323. Contrary to the dislocation density and grain size, which are reasonably well known in UO<sub>2</sub>, about all that can be ascribed to the crack spacing  $X_c$  is that it must be larger than the grain size and smaller than the fuel radius. For that matter, the very existence of uniformly spaced fissures perpendicular to the temperature gradient

has not been demonstrated experimentally, nor is such proof likely to be forthcoming. The crack pattern created under irradiation is certainly quite different from the fuel morphology seen in postirradiation photomicrographs.

The possibility of substantial gas escape from grain-edge openings and interlinked grain boundaries (and correspondingly lower swelling from bubbles in transit in the grains than predicted by BUBL) has been demonstrated by replica electron microscopy of fracture surfaces of irradiated fuel. Michels et al.<sup>84,85</sup> found that in the transition region between the equiaxed-grain zone and the inner portion of the columnar grains, fission-gas bubbles were present almost exclusively on grain boundaries. Since the smallest bubbles observable by this technique are about 500 Å in radius, bubbles originating from dislocations may have been present but undetected. However, the absence of the large bubbles predicted to pull off grain boundaries is significant. Michels and coworkers believe that the lack of intragranular gas bubbles supports the concept of extensive short-circuiting of gas from interlinked grain boundary bubbles directly to the central void or to fissures from which escape can occur. This mechanism of release eliminates or substantially reduces the number of fourth-category bubbles in the BUBL code, with the result that predicted fuel swelling should be lower and gas release (in the transient period before saturation is achieved) should be enhanced by comparison with calculations that rely solely on thermal-gradient migration for gas movement out of the fuel body.

Finally, to simulate interaction of in-transit bubbles with incoming ones, the BUBL code now requires migration equal to the bubble diameter before a detached bubble is placed in the in-transit category. The more difficult problem of correctly accounting for bubble coalescence in the matrix, however, has not been included in the BUBL code modifications. In its present form BUBL implies a rather unrealistic matrix bubble-distribution function consisting of two delta functions, one at  $R_d$  and the other at  $R_{gb}$ . No observation of irradiated fuel has shown such a bubble distribution. Allowing for coalescence between these two classes of migrating bubbles in the calculation would lead to a more realistic bubble-distribution function, although peaks at the critical radii for pull-off from the various defects in the fuel would probably still be present. However, inclusion of coalescence in the matrix requires an analysis of the type described by Gruber<sup>59</sup> and would greatly complicate the calculation. Moreover, by providing another mechanism for making large bubbles from small ones, the predicted swellings would undoubtedly increase rather than decrease. In addition, one would expect that bubbles trapped on defects would be bombarded by all types of migrating bubbles (and bubble nuclei) and not just those detached from the defect with the next lowest bubble pull-off radius.

It appears certain that re-resolution will eventually have to be included in BUBL to correctly predict low-temperature swelling.

### 13.13 NOMENCLATURE

$a_0$  = lattice constant  
 $b$  = microscopic re-resolution parameter

$b'$  = macroscopic re-resolution parameter  
 $B$  = constant in van der Waals equation of state  
 $C$  = concentration (number per unit volume); when unsubscripted,  $C$  denotes the concentration of gas atoms dispersed in the fuel matrix  
 $C_R$  = point-defect concentration at the surface of a bubble  
 $C_m$  = concentration of bubbles containing  $m$  gas atoms  
 $C_{ic}$  = concentration of bubbles of size  $i$  at end of nucleation period  
 $C_s$  = density of atoms on the surface  
 $d$  = distance from bubble surface at which re-resolution of a gas atom can occur  
 $D$  = volume diffusion coefficient of particle in solid  
 $D_s$  = surface self-diffusion coefficient  
 $D_{0s}$  = preexponential factor for surface self-diffusion  
 $D_b$  = bubble diffusion coefficient  
 $D_{vol}$  = volume self-diffusion coefficient  
 $e$  = electronic charge  
 $E_{ff}$  = fission-fragment energy  
 $E_s$  = activation energy for surface self-diffusion  
 $f$  = force on an atom; distribution function of bubbles pinned to defects in solids  
 $F_b$  = force on a bubble  
 $\bar{F}$  = fissions  $\text{cm}^{-3} \text{sec}^{-1}$   
 $f_b$  = fraction of fission gas contained in intragranular bubbles  
 $g$  = trapping parameter  
 $G$  = Gibbs free energy  
 $G^{eq}$  = production rate of defects by thermal processes  
 $J$  = flux of particles to surface of defect  
 $J_s$  = flux of atoms on a surface  
 $k$  = Boltzmann's constant; rate constant  
 $K$  = bulk modulus  
 $l$  = length of a side of a cubical bubble  
 $L$  = diffusion trapping length  
 $L_{ij}$  = coefficients of forces in irreversible thermodynamic expression of fluxes  
 $m$  = number of gas atoms in bubble  
 $M$  = gas atoms per unit fuel volume which are contained in bubbles; mobility  
 $N$  = total number of bubbles per unit volume of fuel  
 $N(R) dR$  = number of bubbles per unit volume with radii in the range  $R$  to  $R + dR$   
 $n$  = number of bubble nuclei in a bubble trapped on a defect  
 $p$  = gas pressure in a bubble  
 $p_t$  = probability distribution in random walk  
 $P$  = external pressure  
 $Q^*$  = heat of transport  
 $r$  = radial position  
 $R$  = radius of a gas bubble; gas constant  
 $R_d$  = radius of the core of a dislocation; critical radius for bubble pull-off from a dislocation line  
 $R_{gb}$  = critical radius for bubble pull-off from a grain boundary  
 $\mathcal{R}$  = radius of capture volume associated with a bubble or dislocation  
 $s$  = given by Eq. 13.208; entropy of formation  
 $s^*$  = entropy of motion

$S_d$  = rate of bubble pull-off from dislocations  
 $t$  = time  
 $t_{irr}$  = irradiation time  
 $t_c$  = nucleation time  
 $t_a$  = mean time between bubble arrivals on a grain boundary  
 $t_o$  = mean time of bubble nuclei impingement on a dislocation line  
 $t_d$  = mean time between bubble detachments from a dislocation line  
 $t_{gb}$  = mean time between bubble detachments from a grain boundary  
 $T$  = temperature; energy transferred in a collision  
 $T_{min}$  = minimum energy transfer for gas-atom resolution  
 $v_b$  = bubble velocity  
 $V$  = volume  
 $\Delta V$  = volume increase due to gas bubbles  
 $w$  = concentration of moving bubbles; jump frequency  
 $x$  = site fraction; distance  
 $X_d$  = length of side of dislocation cube  
 $X_g$  = length of side of representative grain  
 $X_c$  = distance between cracks along the temperature gradient  
 $Y_{iv}$  = yield of vacancy-interstitial pairs per fission  
 $Y_{Xe}$  = total cumulative yield of stable xenon and krypton per fission  
 $z$  = combinatorial number; compressibility factor  
 $Z$  = atomic number; effective combinatorial number

#### Greek letters

$\alpha$  = number of bubbles nucleated heterogeneously on a fission-fragment track  
 $\beta$  = burnup  
 $\gamma$  = surface tension  
 $\gamma_{gb}$  = grain boundary tension  
 $\delta$  = constant, Eq. 13.289  
 $\delta_{ij}$  = Kronecker delta  
 $\epsilon$  = energy of formation  
 $\epsilon^*$  = energy of motion  
 $\rho_d$  = dislocation density  
 $\rho_g$  = density of gas in a bubble  
 $\Omega$  = atomic volume of uranium atoms in fuel  
 $\phi$  = angle between dislocation line and bubble axis; flux  
 $\theta$  = polar angle in spherical coordinates  
 $\sigma$  = hydrostatic stress (positive in compression)  
 $\sigma_{rr}(R)$  = radial-stress component at bubble surface (surface traction)  
 $\lambda$  = jump distance  
 $\nu$  = vibration frequency  
 $\eta$  = dimensionless bubble size, Eq. 13.290 or 13.312  
 $\eta_{re}$  = re-solution efficiency  
 $\Gamma$  = total jump frequency  
 $\mu$  = chemical potential  
 $\mu_{ff}$  = fission-fragment range  
 $\xi$  = dimensionless bubble radius  
 $\tau$  = dimensionless time, Eq. 13.270  
 $\tau_d$  = line tension of a dislocation

#### Subscripts

$A, B$  = species involved in a reaction in the solid  
 $b$  = bubble  
 $crit$  = critical state  
 $d$  = dislocations  
 $d-gb$  = in transit, dislocation to grain boundary  
 $eq$  = equilibrium bubble  
 $f$  = final  
 $gb$  = grain boundary  
 $gb-r$  = in transit, grain boundary to release  
 $gd$  = reaction between gas atom and dislocation  
 $gt$  = reaction between gas atoms and trap  
 $i$  = interstitial  
 $id$  = reaction between interstitial and dislocation  
 $ij$  = bubble sizes  
 $ll$  = reaction between single gas atoms  
 $n$  = number of bubble nuclei in a bubble trapped on a defect  
 $0$  = initial  
 $s$  = surface  
 $t$  = trap  
 $v$  = vacancy  
 $vd$  = reaction between vacancy and dislocation  
 $Xe$  = xenon and krypton

#### 13.14 REFERENCES

1. J. A. Brinkman, *Nuclear Metallurgy*, Vol. 6, pp. 7-8, American Institute of Mining, Metallurgy & Petroleum Engineers, New York, 1959.
2. A. H. Booth, Canadian Report CRDC-721, 1957.
3. D. G. Hurst, Canadian Report AECL-1550, 1962.
4. J. R. MacEwan and P. A. Morel, *Nucl. Appl.*, 2: 158 (1966).
5. G. W. Greenwood, A. J. E. Foreman, and D. E. Rimmer, *J. Nucl. Mater.*, 4: 305 (1959).
6. R. S. Barnes and D. J. Mazey, *Proc. Roy. Soc. (London) Ser. A*, 275: 47 (1963).
7. G. W. Greenwood and M. V. Speight, *J. Nucl. Mater.*, 10: 140 (1963).
8. R. S. Barnes and R. S. Nelson, in *Symposium on Radiation Effects*, Asheville, N. C., September 1965, W. F. Sheely (Ed.), pp. 225-267, Gordon and Breach, Science Publishers, Inc., New York, 1967.
9. F. A. Nichols, Behavior of Gaseous Fission Products in Oxide Fuel Elements, USAEC WAPD-TM-570, Bettis Atomic Power Laboratory, October 1966.
10. A. R. Whapham, *Nucl. Appl.*, 2: 123 (1966).
11. M. E. Meek and B. F. Rider, Summary of Fission Product Yields for  $^{235}\text{U}$ ,  $^{238}\text{U}$ ,  $^{239}\text{Pu}$ , and  $^{241}\text{Pu}$  at Thermal, Fission Spectrum and 14 MeV Neutron Energies, USAEC Report APED-5398-A (Rev.), General Electric Company, Oct. 1, 1968.
12. J. W. Harrison, *J. Nucl. Mater.*, 31: 99 (1969).
13. G. L. Kulcinski, R. D. Leggett, C. R. Hann, and B. Mastel, *J. Nucl. Mater.*, 30: 303 (1969); G. L. Kulcinski and R. D. Leggett, *J. Nucl. Mater.*, 31: 279 (1969).
14. R. Bullough and R. C. Perrin, in *Radiation Damage in Reactor Materials*, Symposium Proceedings, Vienna, June 2-6, 1969, Vol. 2, pp. 233-251, International Atomic Energy Agency, Vienna, 1969 (STI/PUB/230).
15. J. W. Harrison, *J. Nucl. Mater.*, 23: 139 (1969).
16. P. S. Maiya, *J. Nucl. Mater.*, 40: 57 (1971).

17. R. S. Nelson, *J. Nucl. Mater.*, 25: 227 (1968).
18. C. J. Dienes and A. C. Damask, *J. Appl. Phys.*, 29: 1713 (1958).
19. H. J. Matzke, *Nucl. Appl.*, 2: 131 (1966).
20. H. J. Matzke, *J. Nucl. Mater.*, 21: 190 (1967).
21. H. J. Matzke, *Can. J. Phys.*, 46: 621 (1968).
22. T. S. Elleman, C. H. Fox, Jr., and L. D. Mears, *J. Nucl. Mater.*, 30: 89 (1969).
23. R. M. Cornell, *J. Nucl. Mater.*, 38: 319 (1971).
24. W. Miekeley and F. W. Felix, *J. Nucl. Mater.*, 42: 297 (1972).
25. R. M. Cornell, *Phil. Mag.*, 19: 539 (1969).
26. R. Kelly, *J. Nucl. Mater.*, 30: 122 (1966).
27. A. C. Damask and G. J. Dienes, *Point Defects in Metals*, p. 110, Gordon and Breach, Science Publishers, Inc., Brookhaven National Laboratory, 1972. New York, 1963; A. C. Damask, personal communication.
28. J. B. Gibson et al., *Phys. Rev.*, 120: 1229 (1960).
29. B. L. Eyre and R. Bullough, *J. Nucl. Mater.*, 26: 249 (1968).
30. R. Kelly and H. J. Matzke, *J. Nucl. Mater.*, 20: 171 (1966).
31. A. Sy Ong and T. S. Elleman, *J. Nucl. Mater.*, 42: 191 (1972).
32. R. Bullough and R. C. Perrin, American Society for Testing and Materials, Special Technical Publication 484, p. 317, Philadelphia, 1970.
33. F. S. Ham, *J. Phys. Chem. Solids*, 6: 335 (1958).
34. M. V. Speight, *Metal Sci. J.*, 2: 73 (1968).
35. A. J. Markworth, *Metal Sci. J.*, 3: 39 (1969).
36. J. L. Straaslund and G. L. Guthrie, *Nucl. Technol.*, 16: 36 (1972).
37. A. D. Brailsford and R. Bullough, *J. Nucl. Mater.*, 44: 121 (1972).
38. J. R. Willis and R. Bullough, *J. Nucl. Mater.*, 32: 76 (1969).
39. F. A. Nichols, *J. Nucl. Mater.*, 30: 143 (1969).
40. S. Chandrasekhar, *Rev. Mod. Phys.*, 15: 1 (1943) (the analysis appears on pp. 60 and 61 of this article).
41. E. E. Gruber, in *Radiation Induced Voids in Metals*, J. W. Corbett and L. C. Ianniello (Eds.), ERDA Symposium Series, CONF-710601, p. 663, 1972.
42. A. M. Ross, *J. Nucl. Mater.*, 30: 134 (1969).
43. J. A. Turnbull, *J. Nucl. Mater.*, 38: 203 (1971).
44. H. Blank and H. J. Matzke, *Radiat. Eff.*, 17: 57 (1973).
45. R. S. Nelson, *J. Nucl. Mater.*, 31: 153 (1969).
46. A. J. Manley, British TRG-Report-1681, July 5, 1968.
47. J. W. Harrison, *J. Nucl. Mater.*, 30: 319 (1969); *ibid.*, 31: 327 (1969).
48. M. de Jong and J. S. Koehler, *Phys. Rev.*, 129: 40 (1963).
49. A. J. Markworth, *J. Appl. Phys.*, 40: 1986 (1969).
- 49a. A. J. Markworth, *Nucl. Sci. Eng.*, 49: 506 (1972).
50. S. R. Pati, *Trans. Amer. Nucl. Soc.*, 14: 580 (1971); *ibid.*, 15: 212 (1972).
51. M. O. Marlowe, Fission Gas Re-Resolution Rates: Limitation of Fission Gas Bubble Growth by the Re-Resolution Process, USAEC Report GEAP-12148, General Electric Company, November 1970.
- 51a. A. J. Markworth, *J. Nucl. Mater.*, 43: 341 (1972).
52. M. V. Speight, personal communication, 1973.
53. H. Wiedersich, *Radiat. Eff.*, 12: 111 (1972).
54. H. Wiedersich and K. Herschbach, *Scr. Met.*, 6: 453 (1972).
55. T. D. Gulden and J. L. Kaae, *J. Nucl. Mater.*, 32: 168 (1969).
56. A. J. Markworth and E. M. Baroody, *Met. Sci. J.*, 5: 55 (1971).
- 56a. A. J. Markworth, *J. Mater. Sci.*, 7: 1225 (1972).
57. M. V. Speight, *J. Nucl. Mater.*, 38: 236 (1971).
58. M. A. Monti, *J. Nucl. Mater.*, 44: 102 (1972).
59. E. E. Gruber, *J. Appl. Phys.*, 38: 243 (1967).
60. G. W. Greenwood and M. V. Speight, *J. Nucl. Mater.*, 10: 140 (1963).
61. W. M. Robertson, *J. Nucl. Mater.*, 30: 36 (1969).
62. R. M. Cornell and G. H. Bannister, *Proc. Brit. Ceram. Soc.*, 7: 355 (1967).
63. M. E. Gulden, *J. Nucl. Mater.*, 23: 30 (1967).
64. P. G. Shewmon, *Trans. Amer. Inst. Min. Metall. Pet. Eng.*, 230: 1134 (1964).
65. H. S. Carslaw and J. C. Jaeger, *Conduction of Heat in Solids*, Second Ed., p. 426, Oxford University Press, Inc., New York, 1959.
66. R. M. Cornell and G. K. Williamson, *J. Nucl. Mater.*, 17: 200 (1965).
67. L. C. Michels, R. B. Poeppel, and L. A. Niemark, *Trans. Amer. Nucl. Soc.*, 13: 601 (1970).
68. F. Reif, *Fundamentals of Statistical and Thermal Physics*, pp. 210-211, McGraw-Hill Book Company, New York, 1965.
69. R. Kelly, *Phys. Status Solidi*, 21: 451 (1967).
70. J. Belle, *J. Nucl. Mater.*, 30: 3 (1969).
71. D. G. Martin, *J. Nucl. Mater.*, 33: 23 (1969).
72. S. H. Leiden and F. A. Nichols, *J. Nucl. Mater.*, 38: 309 (1971).
73. E. M. Baroody, *J. Appl. Phys.*, 38: 4893 (1967).
74. C. Y. Li, S. R. Pati, R. B. Poeppel, R. O. Scattergood, and R. W. Weeks, *Nucl. Appl. Technol.*, 9: 188 (1970).
75. R. B. Poeppel, in *Fast Reactor Fuel Element Technology*, New Orleans, Apr. 13-15, 1971, R. Farmakes (Ed.), p. 311, American Nuclear Society, Hinsdale, Ill., 1971.
76. C. C. Dollins and H. Ocken, *Nucl. Appl. Technol.*, 9: 148 (1970).
77. R. S. Nelson, *J. Nucl. Mater.*, 19: 149 (1966).
78. R. W. Weeks, S. R. Pati, M. F. Ashby, and P. Berrand, *Acta Met.*, 17: 1403 (1969).
79. R. W. Weeks and R. O. Scattergood, *J. Nucl. Mater.*, 33: 333 (1969).
80. D. C. Bullington and R. D. Leggett, in *Plutonium 1970*, W. N. Miner (Ed.), p. 545, American Institute of Mining, Metallurgy & Petroleum Engineers, New York, 1971.
81. R. W. Weeks, R. O. Scattergood, and S. R. Pati, *J. Nucl. Mater.*, 36: 223 (1970).
82. H. R. Warner and F. A. Nichols, *Nucl. Appl. Technol.*, 9: 148 (1970).
83. F. A. Nichols and H. R. Warner, in *Fast Reactor Fuel Element and Technology*, New Orleans, Apr. 13-15, 1971, R. Farmakes (Ed.), p. 267, American Nuclear Society, Hinsdale, Ill., 1971.
84. L. C. Michels, R. J. Makenas, and R. B. Poeppel, *Trans. Amer. Nucl. Soc.*, 14: 581 (1971).
85. L. C. Michels and R. B. Poeppel, *Trans. Amer. Nucl. Soc.*, 15: 199 (1972).

### 13.15 PROBLEMS

13.1 As a result of a particular irradiation history, a section of fuel contains  $N$  fission-gas bubbles per cubic centimeter of size  $R_0$ , and the concentration of atomically dispersed gas in the matrix of the fuel is  $C_0$ . This piece of

fuel is now inserted in a reactor. The gas bubbles initially present in the fuel tend to grow by absorption of gas atoms newly created by fission, but re-solution tends to increase the concentration of gas in solution.

(a) Assuming that the bubbles are always in equilibrium with the fuel (stress-free), derive the growth law ( $dR/dt$ ) for this case. Assume that the bubbles are small enough to be approximated by the dense-gas limit of the xenon equation of state and that coalescence or migration of the bubbles does not occur. Neglect gas release from the fuel.

(b) Write the growth law in dimensionless form, with  $\eta = R/R_0$  being the dimensionless bubble radius at dimensionless time  $\tau = bt$ . What dimensionless constants govern the growth process?

(c) Numerically solve the dimensionless differential equation for  $d\eta/d\tau$ . Comment on the shape of the curve. Use the following constants in the solution:

$$\begin{array}{ll} b = 10^{-5} \text{ sec}^{-1} & Y_{Xe} = 0.26 \\ D_{Xe} = 10^{-14} \text{ cm}^2/\text{sec} & F = 10^{13} \text{ fission cm}^{-3} \text{ sec}^{-1} \\ B = 85 \text{ \AA}^3 & N = 1.3 \times 10^{13} \text{ bubbles/cm}^3 \\ R_0 = 20 \text{ \AA} & C_0 = 5.2 \times 10^{17} \text{ gas atoms/cm}^3 \end{array}$$

Plot the swelling ( $\Delta V/V$ ) as a function of time.

13.2 (a) What is the root-mean-square distance travelled in 40 days by a 20- $\text{\AA}$  diameter bubble undergoing Brownian motion in  $\text{UO}_2$  at 1400°C?

(b) Under the same conditions, how far does the bubble migrate up a temperature gradient of 2000°C/cm in 40 days?

In both calculations assume bubble mobility is governed by the surface-diffusion mechanism and take  $Q_s^* = 415 \text{ kJ/mole}$ .

13.3 A common method of developing fission-gas bubbles for viewing in an electron microscope is to irradiate the fuel specimen at low temperature and then anneal at high temperature. During the low-temperature irradiation, the fission-gas atoms are essentially immobile in the fuel, and no bubbles form. A uniform concentration of  $C_0$  gas atoms per cubic centimeter results from the irradiation. During annealing the gas-atom mobility is sufficient for nucleation to occur homogeneously.

(a) Write the equations that, when solved, completely describe the time dependence of the concentration of the atomically dispersed gas remaining in solution and the concentration of di- and triatomic clusters. Make sure that the kinetic equations are consistent with the overall gas balance.

(b) Using the dimensionless concentrations  $\theta_1 = C/C_0$  and  $\theta_2 = C_2/C_0$  and the dimensionless time  $\tau = C_0 k_{11} t$ , numerically solve the system of differential equations. Assume  $k_{12} = k_{11}/2$ .

(c) What is the nucleation time for an initial gas-atom concentration of  $10^{17} \text{ atoms/cm}^3$  and a xenon diffusion coefficient of  $10^{-14} \text{ cm}^2/\text{sec}$ ? What fraction of the initial gas remains in solution and exists as di- and triatom clusters at this time?

13.4 Equal numbers of two groups of fission bubbles are present in a fuel element. The radii of the two groups are  $r_1$  and  $r_2 = 0.5r_1$ , respectively, and the pressures within the

bubbles are the equilibrium values corresponding to zero applied pressure and a solid-gas surface tension of  $\gamma$  dynes/cm. Assume the bubbles are allowed to migrate in a random manner and make one collision with any other bubble. If bubble coalescence occurs at each collision, what is the swelling of the fuel (expressed as  $\Delta V/V$ ) due to this process?

13.5 Self-diffusion in uranium metal occurs by the vacancy mechanism and is given by

$$D_U = x_v a_0^2 \nu \exp\left(-\frac{\epsilon_v^*}{kT}\right)$$

where  $x_v$  is the fraction of vacancies,  $a_0$  is the lattice constant, and  $\epsilon_v^*$  is the migration energy of vacancies in uranium metal.

(a) What is the self-diffusion coefficient of uranium in the absence of radiation? The formation energy of vacancies in uranium metal is  $\epsilon_v$ .

(b) During irradiation vacancy-interstitial pairs are created by fission fragments with a yield  $Y_{vi}$ . The only means of destruction is by recombination. What is the steady-state vacancy fraction  $x_v$  for a fission rate  $\dot{F}$ ? What is the uranium self-diffusion coefficient in this radiation field?

(c) The energy of motion of interstitials is  $\epsilon_i^*$ . Sketch the variation of  $\ln D_U$  vs.  $1/T$  when the fission density is known, and identify significant portions of the curve.

13.6 Consider a region of fuel that contains a uniform distribution of small bubbles. The bubble density is  $N$  bubbles per cubic centimeter, and all bubbles are of radius  $R$ . In addition to the small bubbles, there is one large bubble of radius  $R^*$  in the fuel medium. In both the single large bubble and the small bubbles, mechanical equilibrium is maintained by a balance of gas pressure and surface tension. Assume the ideal-gas law applies to both types of bubbles. If the radius of the large bubble exceeds a critical value, the large bubble can spontaneously and continuously grow by gobbling up the small bubbles in the fuel around it. This phenomenon is known as breakaway swelling. To calculate the critical radius, suppose that the large bubble increases in radius from  $R^*$  to  $R^* + dR^*$  and that in so doing it acquires the gas that was formerly in the small bubbles that occupied the spherical shell of thickness  $dR^*$  outside the large bubble. By comparing the number of gas atoms acquired by the large bubble in the expansion to the number of gas atoms it needs to acquire to maintain mechanical equilibrium at the new radius, determine the critical radius of the large bubble. At what swelling ( $\Delta V/V$ ) does breakaway occur if  $R^* = 10R$ ?

13.7 The preferential bias of dislocations for interstitials compared to vacancies is due to the interaction of the compressive stress field around an interstitial in the lattice with the elastic stress field of the dislocation. A vacancy does not produce a stress field of its own and hence does not interact with the stress fields of dislocation. In the case of interstitials, the interaction of the stress fields produces a nonrandom drift of the point defects toward the dislocation. The interaction energy between the interstitial and the dislocation can be expressed as a function of radial distance from the dislocation core,  $V(r)$ .

(a) Using the Nernst-Einstein equation, what is the drift velocity of the interstitial due to the interaction energy  $V(r)$ ? Use vector notation.

(b) In vector notation what is the interstitial flux due to the simultaneous presence of a concentration gradient and the drift velocity?

(c) In vector notation what is the species conservation (continuity) equation for interstitials near a dislocation?

(d) For the present case, cylindrical coordinates are appropriate and the interaction is given by:  $V(r) = -B/r$ , where  $B$  is a constant. What is the appropriate form of the steady-state continuity equation derived in C? Using the substitution

$$C_i(r) = \exp\left(\frac{B/kT}{r}\right) U(r)$$

show that the differential equation for  $U(r)$  is

$$\frac{d^2 U}{dr^2} + \left(\frac{1}{r} - \frac{A}{r^2}\right) \frac{dU}{dr} = 0$$

where  $A = B/kT$ .

(e) In a stress-free solid, the point-defect concentration at the core of the dislocation ( $r = R_d$ ) is the thermal-equilibrium value, which for interstitials is essentially zero. Assume that the interstitial concentration at the boundary of the capture volume around each dislocation ( $r = \mathcal{R}$ ) is specified as  $C_i$ . Solve the diffusion equation of part d for  $J_i^d$ , the flux of interstitials to a unit length of dislocation line, for the case  $A = 0$ .

(f) Solve the equation of part d for  $A/R_d = 0.1$  and  $A/\mathcal{R} \approx 0$  (i.e., the dislocation-interstitial interaction is restricted to regions close to the dislocation). Comparing this solution with that obtained in e, characterize the drift effect by an increase in the dislocation core radius for interstitials (i.e., calculate the core radius  $R_{di}$  at which the drift-free solution gives the same flux as does the solution with  $A/R_d = 0.1$ ).

(g) How much larger is the  $Z_i$  of Eq. 13.183 than the  $Z_v$  given by Eq. 13.182 if  $z_{id} = z_{vd} = 24$ , the dislocation density of the solid is  $10^{10} \text{ cm}^{-2}$ , and the dislocation core radius is  $6 \text{ \AA}$ ?

13.8 Consider a parallel beam of fission fragments impinging on and passing through a bubble of radius  $R$  in the fuel. From geometrical considerations prove that the average chord length of the fission-fragment paths in the bubble is equal to  $4R/3$ .

13.9 The phenomenon of re-resolution of intragranular fission-gas bubbles was first demonstrated by the following experiment: A piece of fuel was irradiated at low temperature for time  $t_1$ . The sample was then removed from the reactor and given a high-temperature anneal of sufficient duration to precipitate all the fission gas generated in the low-temperature irradiation into bubbles. The density  $N$  and radius  $R_1$  of the bubbles were determined by electron-microscope observation. The specimen was then returned to the reactor for another low-temperature irradiation of duration  $t_2$ , after which the size and density of bubbles were again measured. For the irradiation conditions tabulated at the end of this problem, determine the following:

(a) The concentration of fission gas in solution at the end of  $t_1$  (the irradiation temperature is so low that fission-gas atoms cannot diffuse).

(b) The radius of the bubbles following the anneal. Assume that the bubbles are in mechanical equilibrium with the solid and that the ideal-gas law is applicable.

(c) The swelling of the fuel piece after the anneal.

(d) If the re-resolution parameter is  $b = 2 \times 10^{-19} \dot{F} \text{ sec}^{-1}$ , what is the radius of the bubbles after the second irradiation?

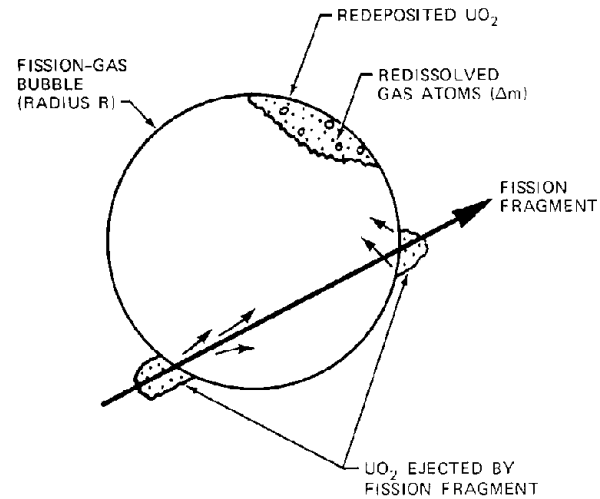
(e) The swelling of the fuel piece after the second irradiation.

(f) The concentration of fission gas in solution at the end of  $t_2$ .

The irradiation conditions are

$$\begin{aligned} \dot{F} &= 5 \times 10^{13} \text{ fissions cm}^{-3} \text{ sec}^{-1} & t_1 &= 10^6 \text{ sec} \\ t_2 &= 10^5 \text{ sec} & N &= 10^{14} \text{ bubbles/cm}^3 \\ & & & \text{(unchanged by the} \\ & & & \text{second irradiation)} \end{aligned}$$

13.10 Each time a fission fragment intersects a gas bubble part of the bubble surface is blasted from one side of the bubble to the other (see attached sketch). The bubble radius is  $R$ , and the range of fission fragments in the solid is  $\mu$ . The fission density in the solid is  $\dot{F}$  fissions  $\text{cm}^{-3} \text{ sec}^{-1}$ .



(a) Derive the equation giving the frequency with which a bubble is pierced by fission fragments. Assume that the bubble density is low enough so that the average distance between bubbles is much larger than the fission-fragment range in the solid.

(b) Each time a fission fragment passes through a bubble,  $\Delta m$  atoms of gas become trapped in the re-deposited solid. This gas is assumed to be returned to the solid as single atoms and is therefore redissolved. Calculate the re-resolution parameter  $b$  (i.e., the probability per second of a gas atom's being returned to the solid) according to this mechanism. Assume that the fission gas in the bubble obeys the ideal-gas law and that the bubble is in equilibrium with a surface tension  $\gamma$ .

# Chapter 14

## Pore Migration and Fuel Restructuring Kinetics

### 14.1 INTRODUCTION

In addition to the fission-gas bubbles discussed in the preceding chapter, ceramic fuels contain another type of gas-filled cavity. This second type of gaseous inclusion is commonly termed a pore, and it differs from the bubble in the following ways.

Whereas bubbles are usually small (less than about  $1\ \mu\text{m}$  in radius), pores are quite large, their smallest dimension generally exceeding  $1\ \mu\text{m}$ . Bubbles are filled almost exclusively with gaseous fission products, but pores contain preponderant quantities of helium, which is used as a cover gas during fuel preparation and fuel-element fabrication. Small amounts of gases arising from impurities in the fuel (e.g., CO and  $\text{CO}_2$  from carbon contamination) can also contribute to the gas phase within a pore. As irradiation proceeds, the pores accumulate fission gases as well, either by diffusion of these species to the pore or by the sweeping action of a pore in motion. Thus, the gas mixture within a pore consists primarily of helium with smaller amounts of  $\text{CO}_2$ , CO, and perhaps  $\text{H}_2\text{O}$  and quantities of xenon and krypton which increase with burnup.

The pressure of the gas within a bubble is large. As described in Chap. 13, the gas pressure is generally sufficient to maintain mechanical equilibrium between the bubble and the surrounding solid. When balanced by the restraint due to surface tension, the gas pressure inside a  $200\text{-\AA}$ -diameter bubble, for example, is  $\sim 300$  atm. For a typical pore of an equivalent diameter of  $20\ \mu\text{m}$ , on the other hand, the gas pressure required to maintain mechanical equilibrium is about 3 atm (in excess of the pressure or hydrostatic stress in the fuel). The pores are initially filled with helium at 1 atm pressure, or zero excess pressure; so, when the fuel is brought to operating temperature, the pores have a tendency to shrink in order to restore mechanical equilibrium. Shrinkage occurs by emission of vacancies to the bulk solid, where they are absorbed by vacancy sinks. Densification of a solid by this mode of pore shrinkage characterizes the last stages of sintering of ceramic materials. However, because of the large temperature gradient in a fuel pin, the pores present in the as-fabricated fuel probably migrate to the center of the rod, where they form the central void before the equilibration

process is complete. Since the pressure deficit in large pores is quite small, the sintering process is not important unless the stress in the fuel is high.\*

The final feature that distinguishes bubbles from pores is the shape of the cavity. Bubbles are usually quite spherical, as expected of a cavity that is able to minimize its surface energy, whereas pores tend to assume the disklike shapes shown in Fig. 14.1 (the question of why pores take on this shape will be considered later). The pores resemble ordinary lenses (which are shaped like the lentil plant), and for this reason are called lenticular pores. As shown in the photomicrograph, they are oriented with their major axis perpendicular to the temperature gradient. As they migrate toward the hot center of the fuel rod, they leave trails from the periphery. These trails are the source of the distinctive radial streaks which characterize the columnar-grain region of the fuel (see Fig. 10.22).

During fuel fabrication,  $\text{UO}_2$  compacts are sintered at high temperatures to produce fuel pellets with a density of  $\sim 90\%$  of the theoretical density of a single crystal. Higher densities could be achieved, but some initial porosity is desirable in the fresh fuel to accommodate fission-product swelling and to permit restructuring to redistribute the fuel into an annular configuration that decreases the central temperature. The 10% void volume in the as-fabricated fuel is homogeneously distributed throughout the solid as pores of irregular shape. The characteristic lenticular shape observed after some time in a temperature gradient is a consequence of the mechanism by which the pores migrate in the hot fuel. Figure 14.2(a) shows how the lenticular pores cluster about the center of an irradiated fuel pin. In Fig. 14.2(b) the pores have reached the center and formed the central void.

It would appear that, once the initial porosity in the fuel has been removed as described (which can take only a

---

\*Sintering under pressure is called *hot pressing* and is an important means of reducing porosity before the central void is fully formed. Since porosity affects the thermal conductivity of the fuel (and therefore the temperature distribution) and the space within the fuel element occupied by the solid fuel, hot pressing is taken into account in many fuel modeling codes.

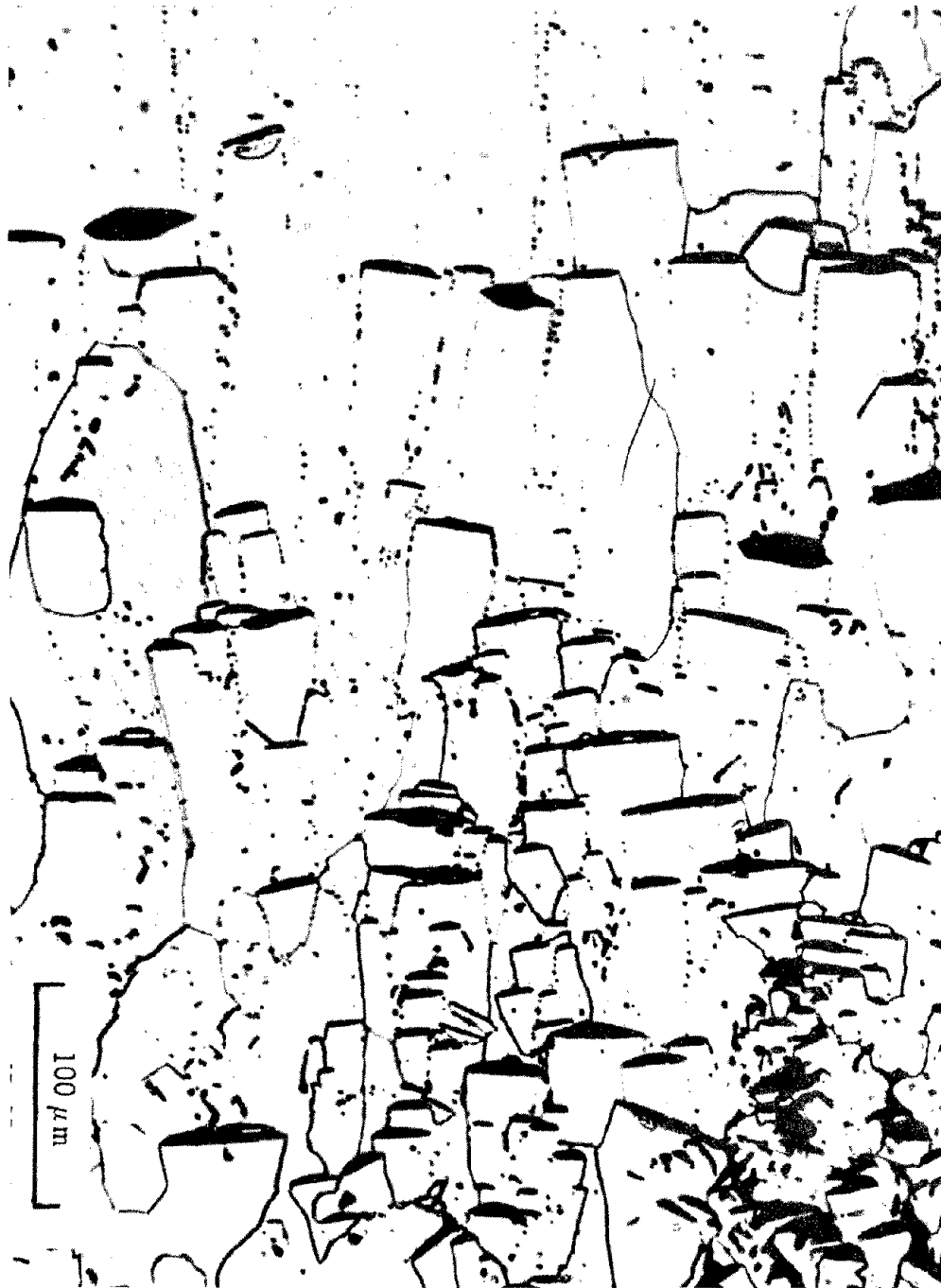


Fig. 14.1 Lenticular pores migrating up the temperature gradient in  $\text{UO}_2$ . The temperature increases from bottom to top. (Courtesy of J. R. MacEwan and V. B. Lawson, Atomic Energy of Canada, Ltd.)

matter of hours in highly rated fuel rods), the question of pore migration would become moot. However, cracks in the fuel that develop as a result of stresses due to thermal cycling of the fuel element or to swelling from fission products can act as continuous sources of pores. Figure 14.3 shows the lenticular pores generated by a crack in

the fuel. The pores spawned by the crack move to the fuel center under the influence of the thermal gradient, thereby creating a mechanism for healing the fissure. In addition, the mobile lenticular pores continually generated during irradiation will sweep up fission gas in their path and deposit it in the central void (or into another large fissure,

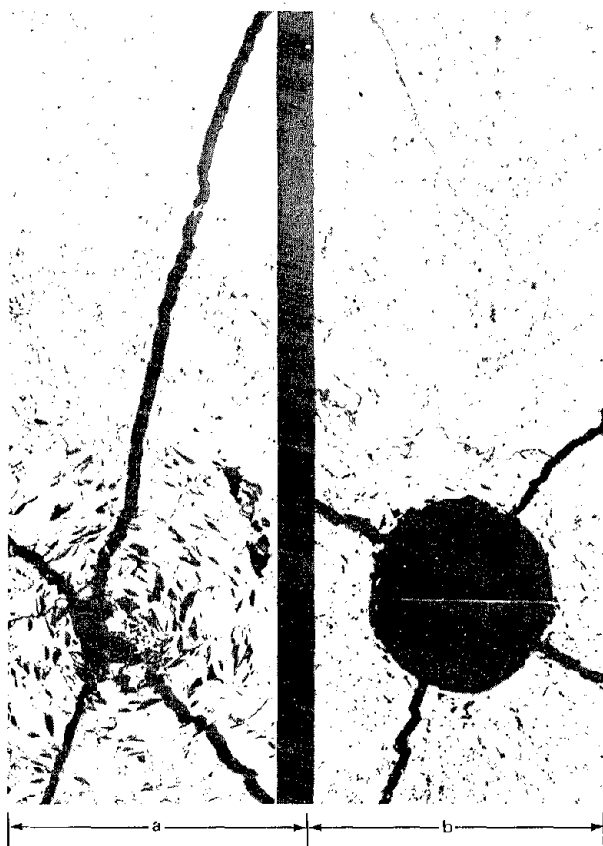


Fig. 14.2 Section through an irradiated fuel pin. (a) Lenticular pores clustering about the fuel center. (b) After agglomeration of the pores to form a central void. [From P. F. Sens, *J. Nucl. Mater.*, 43: 293 (1972).]

if one is encountered before the pore reaches the fuel center). Pore migration thus provides a means of releasing fission gases from the fuel.

Although both fission-gas bubbles and pores migrate up the temperature gradient, the rather large difference in the sizes of these two types of gas-filled cavities results in different mechanisms for motion. Small bubbles move either by the surface-diffusion mechanism (in  $\text{UO}_2$ ) or by the volume-diffusion mechanism (probably in UC). The mobility of large pores, however, is due to molecular diffusion of molecules of the matrix from the hot side of the pore to the cold side through the contained gas. The driving force for this mechanism is the variation of the vapor pressure of the solid with temperature. This process is termed *vapor transport*, or *evaporation-condensation*. In principle, there is no reason why small bubbles could not move by this mechanism or why large pores could not migrate by the surface- or volume-diffusion mechanisms. The controlling mechanism for any cavity is simply a matter of the magnitude of the migration velocity produced by each process, the one yielding the highest speed being the one responsible for motion. Equation 13.219 shows that bubble migration by the surface-diffusion mechanism is inversely proportional to the radius, whereas the volume-diffusion mechanism predicts speeds independent of size

(Eq. 13.235). We shall see in the following section that the migration velocity due to vapor transport is either independent of the cavity radius (if the gas pressure is constant) or proportional to the radius (if the gas pressure is balanced by surface-tension forces). For equilibrium fission-gas bubbles, the velocity due to the vapor-transport mechanism would cross the surface-diffusion-induced velocity shown in Fig. 13.25(a) at a bubble radius of about  $10^{-3}$  cm. Since fission-gas bubbles  $100,000 \text{ \AA}$  in radius rarely survive in the matrix of a fuel body (they would be as large as a typical grain), the vapor-transport mechanism is not likely to be significant in bubble migration. Conversely, the migration velocities of typical pores containing a low-pressure gas are largest for the vapor-transport mechanism, and therefore only this process need be considered in discussing pore migration.

Although the material digested by a moving pore is generally the polycrystalline compact characteristic of the as-fabricated fuel, the solid deposited from the matrix vapor on the cold side of the pore tends to condense into a nearly single-crystal configuration. As in conventional processes in which crystals are grown by deposition from the saturated vapor, the newly formed material exhibits a preference for forming faces consisting of low index crystallographic planes of the solid. Thus, at the boundary of the cylindrical region swept out by the moving pore and the surrounding solid, there is a mismatch of crystal orientation that is manifest as a grain boundary. The characteristic trails left by the periphery of the moving pores (Fig. 14.1) are believed to be in part due to the grain boundary formed in this manner. Because the grains formed by the migrating pores are radially oriented and shaped like a column, the name *columnar grain* is used to describe them.

Closer inspection of the trails behind the lenticular pores in Fig. 14.1 shows that many of them appear to consist of a string of small spheres rather than a straight line separating regions of different crystal orientation as in normal grain boundaries (Fig. 8.17). Figure 14.4 shows this feature of the trails rather clearly. Sens<sup>1</sup> believes that the discrete spots in the peripheral wake of the pore are small spherical pores pinched off from the large disk-shaped parent as the latter migrates. Oldfield and Markworth,<sup>2</sup> on the other hand, ascribe this configuration of the trail to the segregation of impurities (e.g., gaseous fission products) swept up by the moving pore. The impurities are rejected from the pore as a string of small bubbles behind the advancing periphery.

## 14.2 PORE MIGRATION BY THE VAPOR-TRANSPORT MECHANISM

The motion of gas-filled cavities in a solid by the vapor-transport mechanism has been discussed by many authors.<sup>1,3-6</sup> There has been considerable theoretical interest in the question of why an initially irregularly shaped pore should transform to a disklike configuration during migration rather than to a sphere or, as suggested by Nichols,<sup>5</sup> into a cigar-shaped object with its long axis oriented along the thermal gradient. We will not explore this lively academic controversy, inasmuch as the over-

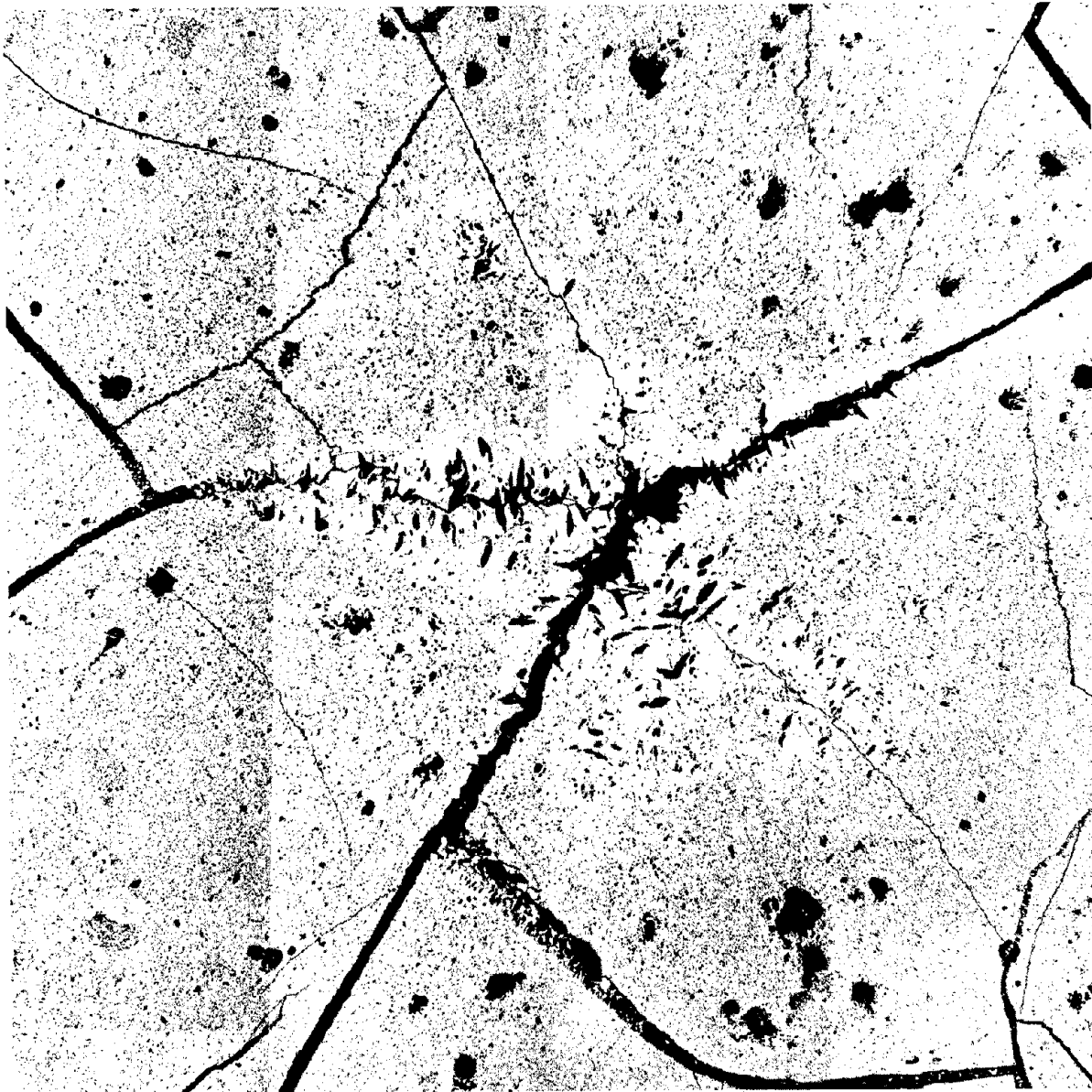


Fig. 14.3 A crack acting as a source of lenticular pores. [From P. F. Sens, *J. Nucl. Mater.*, 43: 293 (1972).]

whelming experimental evidence favors lenticular pores. Moreover, Sens's<sup>1</sup> numerical solution shows that once achieved, this configuration should be stable.

Since lenticular pores are much broader in the direction transverse to the temperature gradient than along this axis, we can treat the migration velocity of an infinite slab of gas embedded in a solid supporting a temperature gradient as a good approximation of a finite disk. Figure 14.5 shows such an idealization of a lenticular pore. The average matrix temperature increases from left to right in the sketch. Because the pore is small compared to fuel-pin dimensions, the macroscopic temperature profile can be approximated by a straight line in the region of the pore. Introduction of

a slab of a second phase into the solid perturbs the temperature profile as shown in the drawing. Since the same quantity of heat flows along the negative  $x$ -direction whether or not the pore is present, we can write for the heat flux at the midplane of the pore

$$k_p \left( \frac{dT}{dx} \right)_p = k_s \left( \frac{dT}{dx} \right) \quad (14.1)$$

where  $k_p$  = thermal conductivity of the gas in the pore

$k_s$  = thermal conductivity of the matrix

$dT/dx$  = unperturbed matrix temperature gradient

$(dT/dx)_p$  = mean temperature gradient in the gas contained in the pore



Fig. 14.4 Lenticular pores moving toward the center of the fuel (top right) leaving behind series of small spherical pores or bubbles. [From F. A. Nichols, *J. Nucl. Mater.*, 27: 137 (1968).]

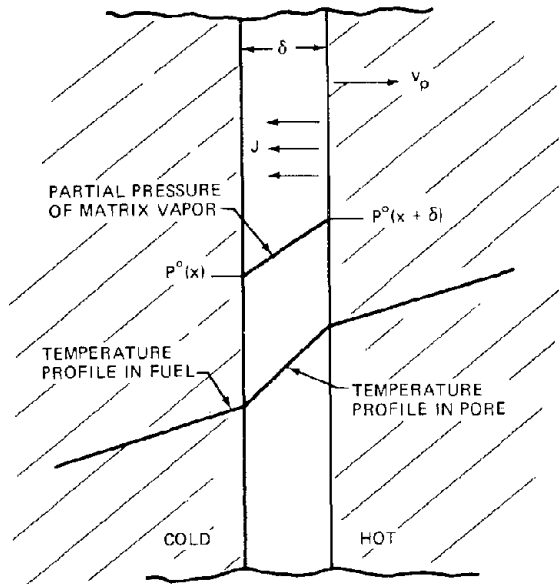


Fig. 14.5 A lenticular pore in a solid containing a temperature gradient. The pore is assumed to be infinite in extent in directions perpendicular to the temperature gradient.

The  $(dT/dx)_p$  is assumed to be constant from the hot to the cold side of the pore. For helium gas in the pore,  $k_s/k_p \sim 5$ , but this ratio increases if impurities such as xenon are added to the gas phase. When the pore is not infinite in lateral extent, some heat flows around the periphery, and the temperature gradient through the center of the pore is less than the gradient in an infinite pore. Determining the temperature profile of a finite pore requires solution of the two-dimensional heat-conduction equation. The numerical results of Sens<sup>1</sup> show that the temperature-gradient ratio  $(dT/dx)_p/(dT/dx)$  is reduced from the value of 5 for an infinite disk to approximately 4 when the disk diameter is five times the pore thickness.

The other symbols in Fig. 14.5 are  $\delta$ , pore thickness;  $v_p$ , pore velocity; and  $J$ , flux of matrix molecules in the negative  $x$  direction.

Since the pore is not considered to be in mechanical equilibrium with the surface-tension forces (if it were, it would be spherical), the gas pressure in the pore does not affect the thickness  $\delta$ . The pore can shrink by pinching off small spherical pores (or gas bubbles) as shown in Fig. 14.4, but then again it can pick up volume by consuming stationary porosity in its path or by being overtaken by more rapidly moving gas bubbles. Pictures such as the one shown in Fig. 14.1 do not indicate a tendency for the pore dimensions to change as the center line is approached; so the thickness  $\delta$  can be considered as a constant.

The velocity of the pore  $v_p$  is related to the flux of matrix molecules according to

$$v_p = J\Omega \quad (14.2)$$

where  $\Omega$  is the volume of a molecule of the matrix solid ( $41 \text{ \AA}^3$  for  $\text{UO}_2$ ). Matrix molecules are transported across the pore by molecular diffusion in the gas. We assume that the partial pressures of the solid in the gas adjacent to the

hot and cold sides are equal to the vapor pressures at the corresponding temperatures. With these two assumptions the flux through the gas is given by the integrated form of Fick's law as

$$J = \frac{D_g}{kT\delta} [P^\circ(x + \delta) - P^\circ(x)] \quad (14.3)$$

where  $D_g$  is the diffusion coefficient of the matrix molecules in the gas and  $P^\circ(x)$  and  $P^\circ(x + \delta)$  represent the vapor pressures of the solid at the cold- and hot-side temperatures, respectively. The vapor pressure can be expressed by the equation (see Sec. 11.5)

$$P^\circ = 10^6 \exp\left(\frac{\Delta S_{\text{vap}}}{k}\right) \exp\left(-\frac{\Delta H_{\text{vap}}}{kT}\right) \quad (14.4)$$

where  $\Delta H_{\text{vap}}$  and  $\Delta S_{\text{vap}}$  are the heat and entropy of vaporization of the solid (Table 11.2) and the factor of  $10^6$  converts atm to dyne/cm<sup>2</sup>. We assume that the equilibrium vapor has the same composition as the solid.\*

Since the pore is thin, the temperature drop and hence the vapor-pressure difference across it are small, and the driving force in Eq. 14.3 is satisfactorily approximated by

$$P^\circ(x + \delta) - P^\circ(x) \approx \frac{dP^\circ}{dx} \delta = \left(\frac{dP^\circ}{dT}\right) \left(\frac{dT}{dx}\right)_p \delta \quad (14.5)$$

Evaluating the derivative of the vapor pressure with respect to temperature from Eq. 14.4 and substituting Eq. 14.5 into 14.3 and thence into Eq. 14.2 yield the pore velocity:

$$v_p = \left[ \frac{1}{(kT)^2} 10^6 D_g \Omega \Delta H_{\text{vap}} \exp(\Delta S_{\text{vap}}/k) \right. \\ \left. \times \exp(-\Delta H_{\text{vap}}/kT) \right] \left[ \frac{1}{T} \left(\frac{dT}{dx}\right)_p \right] \quad (14.6)$$

Equation 14.6 shows that the migration velocity is independent of pore size either along or transverse to the temperature gradient. This implies that overtaking collisions between pores moving by vapor transport do not occur or that pore growth by coalescence can be neglected. Sens's<sup>1</sup> numerical computations show that the leading and trailing edges move at the same speed. Because typical pore sizes are quite large, they cannot be pinned even by grain boundaries that they encounter while migrating.

In Refs. 1 to 6 the diffusion coefficient of the matrix solid in the inert gas in the pore is approximated in the hard-sphere case by application of the elementary kinetic theory of gases. However, the exact theory of the transport properties in dilute gases is well developed, and more accurate values of  $D_g$  can be obtained by this method than by the elementary kinetic theory. The two species in the

\*If the fuel is  $\text{UO}_2$ , the vapor is taken to be  $\text{UO}_2(g)$ ; if the fuel is a mixed oxide, the vapor must also have the same heavy-metal ratio as the solid for the simple analysis presented here to be valid. Problem 14.2 considers pore migration in  $(\text{U,Pu})\text{O}_2$ . Pore migration in UC differs from that of oxide fuels because the equilibrium vapor over UC(s) consists of U(g), not UC(g) [see Hj. Matzke, *J. Nucl. Mater.*, 57: 180 (1975)].

gas are assumed to interact by a Lennard-Jones 6-12 potential, the force constants for which are determined from the viscosities of the pure components if available or estimated from properties at the normal boiling or critical points. The form of the exact theory suitable for numerical work is:<sup>7</sup>

$$D_g = \frac{1.86 \times 10^{-3} T^{3/2}}{\sigma_{12}^2 \Omega_D p} \left( \frac{M_1 + M_2}{M_1 M_2} \right)^{1/2} \quad (14.7)$$

where  $D_g$  is in  $\text{cm}^2/\text{sec}$ ,  $T$  is in  $^\circ\text{K}$ , and  $p$  (the total gas pressure) is in atm. The  $M_1$  and  $M_2$  are the molecular weights of the two species in the gas, and  $\sigma_{12}$  is the collision diameter for the pair of interacting molecules. The quantity  $\Omega_D$  is a collision integral resulting from the theory and is a function of the parameter  $kT/\epsilon_{12}$ . The force constants  $\sigma_{12}$  and  $\epsilon_{12}$  characterize the potential function between the interacting species. They are obtained from the corresponding quantities for the pure substances by the combining rules:

$$\begin{aligned} \epsilon_{12} &= (\epsilon_1 \epsilon_2)^{1/2} \\ \sigma_{12} &= \frac{(\sigma_1 + \sigma_2)}{2} \end{aligned}$$

Table 14.1 lists the force constants for helium, xenon, and  $\text{UO}_2$ . Using these force constants, the combining rules, and the functional dependence of  $\Omega_D$  on  $kT/\epsilon_{12}$  given in Ref. 7 in Eq. 14.7 leads to the following values of the diffusion coefficients for  $\text{UO}_2$  in helium and xenon at 1 atm total pressure and  $2000^\circ\text{K}$ :

$$\begin{aligned} D_g^*(\text{He} - \text{UO}_2) &= 11 \text{ cm}^2/\text{sec} \\ D_g^*(\text{Xe} - \text{UO}_2) &= 0.9 \text{ cm}^2/\text{sec} \end{aligned} \quad (14.8)$$

The asterisks denote the reference conditions of temperature and total pressure.

Table 14.1 Force Constants in the Lennard-Jones Potential Function for He, Xe, and  $\text{UO}_2$ \*

Species	$\sigma, \text{\AA}$	$\epsilon/k, ^\circ\text{K}$
He†	2.55	10
Xe†	4.05	231
$\text{UO}_2$ ‡	3.72	4350
$\text{UO}_2$ §	3.95	6000

\*Based on Ref. 7.

†Obtained from viscosity data.<sup>7</sup>

‡Estimated from normal boiling point (i.e., the temperature at which the vapor pressure equals 1 atm) by  $c/k = 1.21T_b$ . From Fig. 9.4,  $T_b \approx 3600^\circ\text{K}$ . The collision diameter is approximated by  $\sigma = 1.18V_b^{1/3}$ .  $V_b$  is the molar volume of the liquid at the normal boiling point, which has been obtained from the measured liquid density shown on Fig. 9.3.

§Estimated from the critical constants reported by Menzies (Table 9.2) and the rules:  $\sigma = 0.83V_c^{1/3}$  and  $\epsilon/k = 0.75T_c$ .

The diffusion coefficient at total pressures and temperatures other than those for which the preceding values were computed can be obtained from the formula

$$D_g = D_g^* \left( \frac{T}{2000} \right)^{3/2} \left( \frac{1}{p} \right) \quad (14.9)$$

The inverse dependence of  $D_g$  on total pressure<sup>7</sup> is valid up to  $\sim 20$  atm. Since the collision integral  $\Omega_D$  is temperature dependent,  $D_g$  does not vary quite as  $T^{3/2}$ . However, for temperatures close to  $2000^\circ\text{K}$ , Eq. 14.9 is a sufficiently accurate extrapolation formula.

The theory that produced Eq. 14.7 is an exact statistical-mechanical treatment of nonpolar, spherical monatomic dilute gases interacting by a potential function appropriate to this class of substances. How well this theory applies to a species such as  $\text{UO}_2$  is not known, although it works quite well for many polar molecules. However, it is better to use the diffusion coefficient based on a rigorous kinetic theory in conjunction with force constants estimated by rules that have proven to be quite accurate at least for normal substances than to estimate  $D_g$  by the elementary kinetic theory.

The gas pressure inside the lenticular pore depends on the local temperature and the extent to which the pore (1) loses volume by pinching off pores or bubbles and gains volume by digesting cavities moving at a different velocity and (2) loses gas atoms by shedding gas-filled bubbles or by re-solution due to fission fragments and gains gas atoms by diffusion-controlled absorption from the matrix or by sweeping dissolved or precipitated gas from the matrix in front of it. In the special case where none of the processes in item 1 or 2 affects the pore, the volume and gas content are approximately constant during migration. If the pore was sealed off during the final step of the fabrication process conducted at a sintering temperature  $T_{\text{sint}}$  under a helium pressure of 1 atm, the ratio  $p/l$  is constant during pore motion during irradiation at a value  $1/T_{\text{sint}}$ . Or, the pressure in the pore is

$$p = \frac{T}{T_{\text{sint}}} \text{ atm} \quad (14.10)$$

If Eqs. 14.9 and 14.10 are substituted into 14.6 and if the ratio of the temperature gradient inside the pore and that in the solid is assumed to be 4, the final pore velocity formula is

$$\begin{aligned} v_p &= \left( \frac{4 \times 10^6 \Omega}{kT} \right) D_g^* \left( \frac{T}{2000} \right)^{3/2} \left( \frac{T_{\text{sint}}}{T} \right) \left( \frac{\Delta H_{\text{vap}}}{kT} \right) \\ &\times \exp \left( \frac{\Delta S_{\text{vap}}}{k} \right) \exp \left( - \frac{\Delta H_{\text{vap}}}{kT} \right) \left( \frac{1}{T} \frac{dT}{dx} \right) \end{aligned} \quad (14.11)$$

We compute the pore velocity in pure  $\text{UO}_2$  for the following parameters:

$$\begin{aligned} T &= 2000^\circ\text{K} \\ \frac{dT}{dx} &= 1000^\circ\text{K}/\text{cm} \\ D_g^* &= 11 \text{ cm}^2/\text{sec} \quad (\text{Eq. 14.7}) \\ \Delta S_{\text{vap}} &= 150 \text{ J mole}^{-1} \text{ } ^\circ\text{K}^{-1} \quad (\text{Table 11.2}) \\ \Delta H_{\text{vap}} &= 567 \text{ kJ/mole} \quad (\text{Table 11.2}) \\ \Omega &= 41 \text{ \AA}^3 \\ T_{\text{sint}} &= 1800^\circ\text{K} \end{aligned}$$

For these conditions Eq. 14.11 predicts a migration speed of  $0.15 \text{ \AA}/\text{sec}$ .

Finally, we point out two particularly significant approximations implicit in the derivation of Eq. 14.6, both originally identified by Oldfield and Markworth.<sup>2</sup> The first concerns the effect of impurities, and the second has to do with the validity of assuming complete control of the process by gas-phase diffusion. Both these phenomena affect the driving force for diffusion of solid through the gas.

If the pore encounters soluble impurities (e.g., fission-product oxides), the vapor pressure of the matrix solid on the hot side is depressed approximately to the extent predicted by Raoult's law. If the impurity is volatile, it will transfer across the pore along with the matrix molecules. If it is nonvolatile compared to the matrix solid, however, its concentration on the hot side of the pore will continually build up as the pore gathers more and more of it during migration through the solid. If not rejected by some mechanism, accumulation of nonvolatile soluble impurities on the hot face will reduce pore speed and ultimately stop pore motion entirely. If the impurity encountered by the moving pore is not soluble in the solid (e.g., the metallic or alkaline earth fission-product phases), the equilibrium vapor pressure of the lattice solid is not affected. However, if enough contaminant of this type is accumulated, a resistance to transport similar to that produced by oil on water or by scale on a heat-exchanger surface can develop.

If only the matrix material is transported across the vapor in the pore, impurities cannot collect on the cold face. However, the maximum possible rate of condensation of matrix vapor on the nearly single-crystal face of the cold side of the pore can be comparable to the rate of diffusion in the gas in the pore. Such an effect is commonly encountered in crystal growth from a saturated vapor. The net effect of kinetic limitations to vapor condensation at the cold side is to increase the partial pressure of the matrix solid here above the thermodynamic equilibrium value; in effect, the gas phase must be somewhat supersaturated to ensure that the diffusion and surface attachment steps proceed at the same rate (which they must because these two processes occur in series).

The combined effects of soluble impurities in the matrix solid at the hot face and surface attachment limitations on the cold side on pore velocity can be analyzed with the aid of Fig. 14.6. Instead of Eq. 14.3 the flux of molecules of matrix solid across the pore is given by

$$J = \frac{D_g}{kT\delta} [p_M(x+\delta) - p_M(x)] \quad (14.12)$$

where  $p_M$  denotes the partial pressure of the matrix material in the gas adjacent to the solid. If the mole fraction of soluble impurity at the hot side of the pore is  $y_I$  and Raoult's law is obeyed, the hot-side partial pressure  $p_M(x+\delta)$  is given by

$$p_M(x+\delta) = (1 - y_I)P^\circ(x+\delta) \quad (14.13)$$

The cold-side partial pressure  $p_M(x)$  can be determined as follows. Consider the situation of true thermodynamic equilibrium between a solid and its saturated vapor.

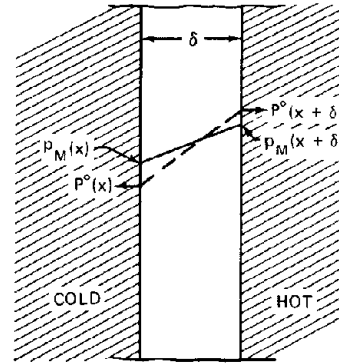


Fig. 14.6 Partial-pressure profiles of matrix solid across a lenticular pore, showing the effects of impurity accumulation on the hot face and condensation rate kinetics on the cold face. ---, partial pressure of matrix material in ideal pore. —, partial pressure of matrix material in actual pore.

Assuming the saturated vapor obeys the perfect-gas law, the rate at which matrix molecules from the gas phase strike a unit area of solid surface is given by the kinetic theory as  $n\bar{v}/4$ , where  $n^\circ = P^\circ/kT$  is the molecular density corresponding to the vapor pressure  $P^\circ$  and  $\bar{v} = (8kT/\pi m)^{1/2}$  is the mean velocity of molecules of mass  $m$  in the gas phase. Although the rate at which molecules from the vapor impinge on the solid is correctly given by the kinetic theory of gases, the rate at which condensation occurs can be smaller than this value. This difference is usually described by the *condensation coefficient*  $\alpha$ , which is defined as the fraction of impinging molecules that stick to the solid surface. The remaining molecules are reflected back into the gas phase. In an equilibrium situation the rates of condensation and evaporation are, by definition, equal; thus:

$$R_{\text{vap}}^{\text{eq}} = R_{\text{cond}}^{\text{eq}} = \frac{\alpha P^\circ}{(2\pi mkT)^{1/2}} \quad (14.14)$$

To treat the nonequilibrium case in which the gas phase above the solid does not contain matrix vapor at the equilibrium pressure, we assume the rate of condensation to be given by Eq. 14.14 with  $P^\circ$  replaced by  $p_M$ , the actual partial pressure of the condensing species in the gas adjacent to the solid:

$$R_{\text{cond}} = \frac{\alpha p_M}{(2\pi mkT)^{1/2}} \quad (14.15)$$

However, since the vaporization process, to a first approximation, is independent of the nature of the gas phase in contact with the solid,  $R_{\text{vap}}$  is assumed equal to  $R_{\text{vap}}^{\text{eq}}$  given by Eq. 14.14. The difference  $R_{\text{cond}} - R_{\text{vap}}$  is the net flux of vapor molecules to the surface or at the cold face of the lenticular pore:

$$J = \frac{\alpha}{(2\pi mkT)^{1/2}} [p_M(x) - P^\circ(x)] \quad (14.16)$$

Hirth and Pound<sup>8</sup> have presented a simple treatment of the condensation coefficient in one-component systems. Their model assumes that the growing solid surface can be represented as a series of terraces separated by ledges of atomic height, a distance  $\lambda_0$  apart (Fig. 14.7). Molecules striking the flat surface are all temporarily trapped and begin to surface diffuse along the terrace as adsorbed atoms. If they reach a ledge, they are considered to be condensed, but, in the course of migrating over the terrace, they can evaporate back to the gas phase. When treated by simple surface-diffusion theory, the condensation coefficient predicted by this model is given by (see problem 14.4)

$$\alpha = \frac{\tanh \beta}{\beta}$$

where

$$\beta^2 = \frac{\nu_1 \exp(-E_b/kT)}{4D_s} \lambda_0^2$$

$D_s$  being the surface self-diffusion coefficient of the matrix solid (Eq. 13.216 for  $\text{UO}_2$ ) and  $\nu_1$  being the frequency of adsorbed atom vibration perpendicular to the surface. As usual, this parameter is estimated to be  $10^{13} \text{ sec}^{-1}$ . The binding energy of an adsorbed atom to the surface,  $E_b$ , is only about 60% of the heat of vaporization  $\Delta H_{\text{vap}}$  because an atom adsorbed on a flat plane is not as strongly bound as the average surface atom. There does not appear to be a reliable way of estimating the ledge spacing  $\lambda_0$ . If we take it to be 4000 lattice spacings ( $\sim 1 \mu\text{m}$ ), the preceding formulas predict  $\alpha = 0.9$ .

We can eliminate  $p_M(x + \delta)$  from Eq. 14.12 by Eq. 14.13. Equating the right-hand sides of Eqs. 14.12 and 14.16 permits  $p_M(x)$  to be eliminated, and the flux can be expressed as

$$J = \frac{1}{[(2\pi mkT)^{1/2} \alpha] + (kT\delta/D_g)} \times [(1 - y_1)P^\circ(x + \delta) - P^\circ(x)] \quad (14.17)$$

The reduction of the pore velocity due to the combined effects of impurity accumulation on the hot face and condensation rate limitations on the cold face is given by the ratio of Eqs. 14.17 and 14.3, which is

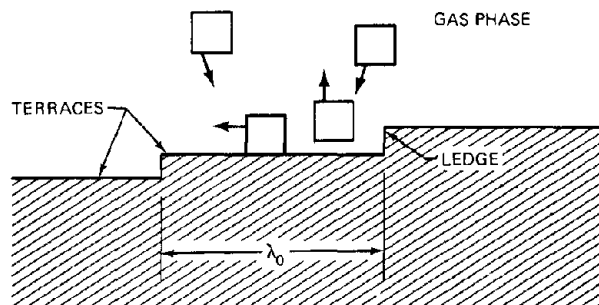


Fig. 14.7 A model of the condensation process. (Based on Ref. 8.)

$$\frac{v_p}{v_p^*} = \frac{1 - y_1}{1 + [D_g(2\pi mkT)^{1/2} / \alpha kT\delta]} \left[ \frac{1 + \{(\Delta H_{\text{vap}}/kT) [(1/T)(dT/dx)]_p \delta\}^{-1}}{1 + [D_g(2\pi mkT)^{1/2} / \alpha kT\delta]} \right]^{-1} \quad (14.18)$$

where  $v_p^*$  is given by Eq. 14.11. The right-hand side of the numerator of Eq. 14.18 represents the hot-side impurity effect, and the last term in the denominator accounts for condensation kinetics on the cold face. (We have neglected the comparable surface kinetic limitation on the hot face.) Both these terms become increasingly significant as the pore thickness  $\delta$  decreases. We evaluate the ratio of Eq. 14.18 for the same parameters used in the previous illustrative calculation of  $v_p^*$  and in addition take

$$\begin{aligned} y_1 &= 0.01 \\ \delta &= 10 \mu\text{m} \\ \alpha &= 0.9 \end{aligned}$$

Using these numbers, we arrive at

$$\frac{v_p}{v_p^*} = \frac{1 - 0.1}{1 + 1.2} = 0.41$$

The pore velocity is very sensitive to a slight accumulation of soluble impurities on the hot face and to condensation rate limitations even when nearly every molecule that strikes the cold surface condenses. The pore thickness is an important parameter in both these effects since this quantity determines the rate of the diffusional step compared to the rate of cold face condensation, which is independent of pore size. For a 20- $\mu\text{m}$ -thick lenticular pore, for example, the ratio  $v_p/v_p^*$  is 0.59. These calculations suggest that small pores are easily immobilized and that only pores thick enough to render the above secondary influences negligible are able to migrate through the solid.

### 14.3 POROSITY REDISTRIBUTION KINETICS

The fuel charged to a nuclear reactor usually consists of pellets of ceramic oxides or carbides of uranium and plutonium which contain approximately 10% void volume. The empty space within the fuel material is mostly small cavities about 10  $\mu\text{m}$  in diameter which were sealed off during the sintering operation of fuel fabrication. When the fuel element is brought to power in the reactor, the steep temperature gradient causes the as-fabricated porosity in the hot region of the fuel to start to migrate toward the center line. The direct effect of this process is relocation of solid fuel closer to the periphery than in the fresh fuel and the development of a central void as a consequence of pores reaching the axis of the fuel rod. The displacement of the nuclear heat source closer to the heat sink (the coolant) and the densification of the zone swept free of pores markedly reduce the temperature in the inner region of the fuel. This restructuring process requires times on the order of hours for fuel rods with center-line temperatures near the melting point but may never attain a steady state during the lifetime of low-rated fuel rods (i.e., central temperatures less than 2000°K in oxide fuels). The difference in the temperature profiles in as-fabricated and completely restructured fuel calculated by the three-region model is

shown in Fig. 10.24. In this model the temperature distribution is computed by assigning constant (but different) porosity values to each of the three zones into which the fuel is subdivided and characteristic temperatures to the two boundaries between the columnar-grain, equiaxed-grain, and unstructured regions (Sec. 10.4). This approach has the advantage of computational ease but is incapable of describing the evolution of the temperature and porosity distribution during restructuring.

If this transient situation is to be treated accurately, the kinetics of the restructuring process must be known and coupled with the quasi-steady-state temperature calculation by means of the dependence of the thermal conductivity on pore fraction and the geometrical effect of a growing central void. Numerical computations of this type have been described by several authors.<sup>1,9,10</sup>

The following analysis is applied to pure stoichiometric  $\text{UO}_2$  and is based on the following assumptions:

1. The pores are closed and migrate only in the radial direction under the influence of the temperature gradient. The pore velocity is given by Eq. 14.11 in which  $dT/dx$  is replaced by the radial temperature gradient to conform to the cylindrical geometry of the fuel rod.

2. All pores are of the same size, and their volume is independent of radial position and time. Collisions between migrating pores and the resulting coalescence to form larger pores is not considered.

We wish to determine the porosity distribution function,  $N_p(r,t)$ , which gives the number of pores per unit volume at radial position  $r$  in the fuel rod at time  $t$  since the temperature gradient was applied. The conservation statement applicable to the moving but noncolliding pores in cylindrical geometry is

$$\frac{\partial N_p}{\partial t} = -\frac{1}{r} \frac{\partial}{\partial r} (r J_p) \quad (14.19)$$

where  $J_p$  is the flux of pores in the  $+r$ -direction (in units of pores  $\text{cm}^{-2} \text{sec}^{-1}$ ). Since the pores move exclusively in the radial direction,  $J_p$  is given by

$$J_p = -v_p N_p \quad (14.20)$$

Inasmuch as the pore velocity  $v_p$  is a known function of  $T$  and  $dT/dr$ , it can be considered as a specified function of radial position and time,  $v_p(r,t)$ , determined from the solution for the temperature distribution. Substitution of Eq. 14.20 into 14.19 gives

$$\frac{\partial N_p}{\partial t} = \frac{1}{r} \frac{\partial}{\partial r} (r v_p N_p) \quad (14.21)$$

which has an initial condition

$$N_p(r,0) = N_{p0} \quad (14.22)$$

where  $N_{p0}$  is the pore concentration in the as-fabricated fuel.

Equation 14.21 requires a boundary condition. The one that prevents motion of the pores through the fuel-cladding interface is

$$J_p = 0 \quad (\text{at } r = R) \quad (14.23)$$

However, because of the low temperatures near the periphery of the fuel rod, pore motion ceases well before  $r = R$ . By using arguments analogous to those advanced in discussing actinide redistribution by thermal diffusion (Sec. 11.7), we replace Eq. 14.23 by the boundary condition:

$$N_p(\infty, t) = N_{p0} \quad (14.24)$$

If the pore concentration is multiplied by the volume per pore, the pore conservation equation can be written in terms of the porosity (defined by Eq. 10.31) as

$$\frac{\partial P}{\partial t} = \frac{1}{r} \frac{\partial}{\partial r} (r v_p P) \quad (14.25)$$

The initial and boundary conditions become

$$\begin{aligned} P(r, 0) &= P_0 \\ P(\infty, t) &= P_0 \end{aligned} \quad (14.26)$$

where  $P_0$  is the as-fabricated porosity of the fuel.

The temperature distribution at any time during restructuring is obtained by solution of the quasi-steady-state heat-conduction equation

$$\frac{1}{r} \frac{d}{dr} \left[ k(T, P) \frac{dT}{dr} \right] + \left( \frac{\mathcal{P}}{\pi R^2} \right) \left( \frac{1-P}{1-P_0} \right) = 0 \quad (14.27)$$

where  $\mathcal{P}$  is the linear power of the fuel rod at the axial position for which the calculation is performed. Equation 14.27 is subject to the boundary conditions

$$T(R) = T_s$$

$$\left( \frac{dT}{dr} \right)_{r_0} = 0 \quad (14.28)$$

The coupling between the temperature distribution and the porosity distribution in Eqs. 14.25 and 14.27 is clear; the porosity appears in the thermal conductivity and in the volumetric heat source term of Eq. 14.27 and indirectly in the location  $r_0$  at which the temperature gradient vanishes (the last boundary condition). The temperature distribution determines  $v_p$  in Eq. 14.25.

Equations 14.25 and 14.27 are valid only over the region  $r > r_0$ , where  $r_0$  is the radius of the central void developed as a consequence of pore migration. It can be determined by equating the volumes of solid per unit fuel length before and after pore migration (assuming that no axial movement of the fuel occurs). The volume of solid per unit length of fresh fuel is  $(1 - P_0)\pi R^2$ ; when a central void and nonuniform porosity distribution have been developed, the total volume of solid fuel per unit length of rod is

$$\pi R^2 - \int_{r_0}^R P 2\pi r dr - \pi r_0^2$$

Equating solid volumes before and after pore redistribution yields

$$\frac{1}{2} r_0^2 \left( \frac{1 - P_0}{P_0} \right) = \int_{r_0}^{\infty} r \left( 1 - \frac{P}{P_0} \right) dr \quad (14.29)$$

where the upper limit on the integral has been approximated by infinity.

Simultaneous solution of Eqs. 14.25 to 14.29 provides a complete description of the evolution of the fuel structure for radii less than that at which the columnar grains form. The change in the temperature distribution as a consequence of restructuring is obtained at the same time from Eq. 14.27.

Figure 14.8 shows the result of the calculations described for a highly rated fuel rod. Significant restructuring occurs even in as little as 1/4 hr; after 2 hr the central void extends to about 10% of the fuel radius. The maximum fuel temperature has dropped by nearly 150°K during the period covered by the calculations. Had the plots of Fig. 14.8 been continued to longer times, the rate of restructuring would have been found to decelerate appreciably; after a few days (for the linear power for which Fig. 14.8 applies), a steady situation would appear to have

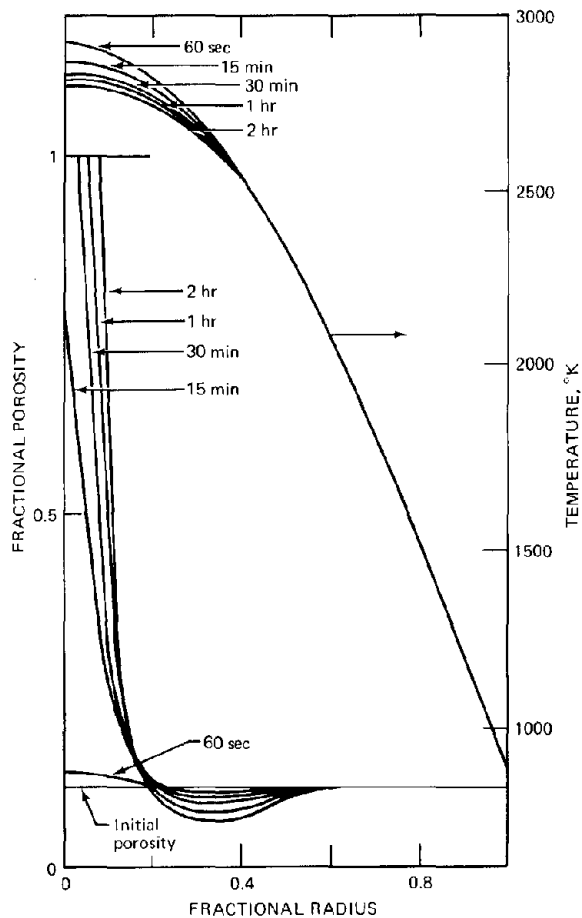


Fig. 14.8 Calculated temperature and porosity distributions at different times from the start of irradiation. Fuel radius = 0.5 cm. Linear power = 600 W/cm. (Based on Ref. 1.)

been reached. Theoretically, however, the system of equations (14.25 to 14.29) never reaches a steady state.

Figure 14.9 compares the theoretical porosity distributions with a measured profile. The good agreement supports the validity of the pore migration velocity formula developed in the preceding section and incorporated into the pore-conservation equation. Neither the experimental nor the theoretical results support the assignment of a constant value of the porosity for the columnar-grain regions, which is the zone in which the porosity differs significantly from the as-fabricated value (out to fractional radii of about 0.7). Figure 14.9 shows that a minimum of 3% porosity is attained in this zone, but, near the central void and at the outer edge of the columnar-grain region, the porosity approaches 8%. The three-region model for calculating the temperature distribution, however, assumes a constant value of the porosity ranging from 1 to 5% for the columnar-grain region (Table 10.4).

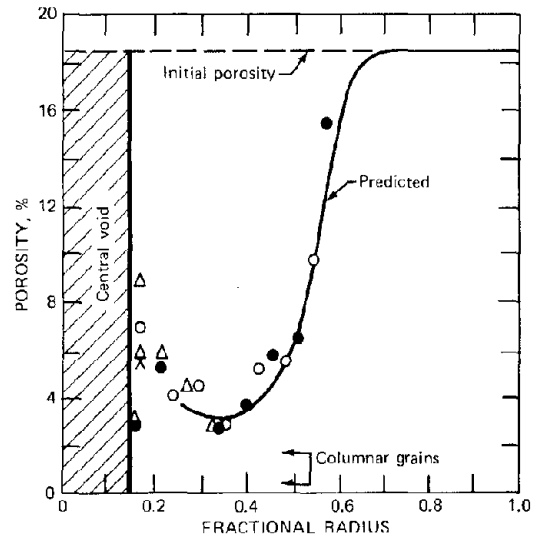


Fig. 14.9 Comparison of experimental and predicted porosity distributions in a fuel rod operated at a linear power of 450 W/cm at a burnup of 0.7%. The fuel rod was fabricated by vibratory compaction of (U,Pu)O<sub>2</sub> microspheres. [After W. J. Lackey, F. J. Homan, and A. R. Olsen, *Nucl. Technol.*, 16: 120 (1972).]

#### 14.4 COLUMNAR-GRAIN GROWTH

The rigorous method of determining the kinetics of fuel restructuring due to migration of the initial porosity on the fuel was presented in the previous section. However, this analysis is mathematically unwieldy and does not yield a clearly definable outer boundary of the columnar-grain region. The latter is important because visual inspection of irradiated fuel (e.g., Fig. 10.22) shows that the extent of columnar-grain growth can be readily identified. Moreover, the rudimentary but widely employed temperature distribu-

tion calculation described in Sec. 10.4 is based on the assumption that the observed microstructural changes in the fuel can be correlated with a fixed temperature (e.g., the temperature at which columnar-grain structure gives way to the equiaxed grains). Although the development of columnar grains is due to the migration of porosity in the fuel, the porosity distribution computed by means of the calculation described in the preceding section does not permit unambiguous identification of the extent of restructuring, by providing either a characteristic temperature or a characteristic extent of densification. In Fig. 14.9, for example, densification commences at a fractional radius of  $\sim 0.65$ , whereas the columnar-grain structure was observed at a fractional radius of  $\sim 0.53$ .

Nichols<sup>5</sup> has suggested a simple means of predicting the outer radius of the columnar-grain zone and the temperature at this location as functions of irradiation time. He assumes that a columnar-grain structure becomes visible only if lenticular pores have moved a minimum distance  $d$  during the time of irradiation. He takes  $\frac{1}{3}$  of the fuel-rod radius ( $d \approx 1$  mm) for this extent of "significant pore motion," but we shall show that the magnitude of  $d$  is, fortunately, not important in the model so long as it is of the order of magnitude suggested by Nichols.

The reason that this seemingly crude notion works rather well is the extraordinarily rapid variation of pore velocity and temperature with radial position near the location where the columnar-grains start. Figure 14.10 shows a plot of the pore velocity according to Eq. 14.11 in which a simple parabolic temperature profile (Eq. 10.52) has been used. The velocity drops to zero at the center line

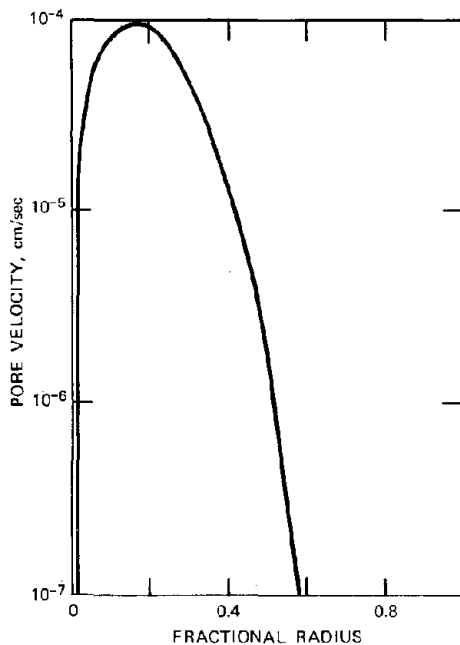


Fig. 14.10 Migration velocity of the lenticular pores at the start of irradiation in the fuel rod described in Fig. 14.8. No restructuring has occurred yet.

because the temperature gradient approaches zero here. At fractional radii  $> 0.6$ , the pore velocity becomes very low because the temperature is low, and hence the fuel vapor pressure becomes extremely small. For fractional radii between 0.2 and 0.6, the pore velocity is a very rapidly changing function of position, increasing by as much as a factor of 10 in a fraction of a millimeter.

Suppose that the outer radius of the columnar-grain zone is located at  $r = r_1$  after irradiation time  $t$ . According to Nichols' concept, a lenticular pore initially at  $r_1$  would have moved to radial position  $r_1 - d$  during time  $t$ . If it had moved a smaller distance, a columnar grain would not have been formed, and the boundary would have been at some radial position less than  $r_1$ . Conversely, if the pore initially at  $r_1$  had moved a distance greater than  $d$  in time  $t$ , there would be another radial position greater than  $r_1$  from which a pore would have moved just the distance  $d$  in time  $t$ , and thus this point would be the columnar-grain boundary. If the temperature profile is assumed constant and known between startup and time  $t$ , the pore velocity can be thought of as a known function of radius  $r$ . The relation between irradiation time  $t$ , outer columnar-grain boundary  $r_1$ , and minimum migration distance  $d$  is given by

$$t = - \int_{r_1}^{r_1 - d} \frac{dr}{v_p(r)} \quad (14.30)$$

The minus sign appears in front of this equation because  $v_p$  is considered positive if in the negative  $r$ -direction.

If  $T(r)$  and hence  $v_p(r)$  are given, Eq. 14.30 can in principle be solved for  $r_1$  as a function of time  $t$  and the assumed distance  $d$ . Solution is most easily accomplished by converting the integration variable in Eq. 14.30 from position to temperature

$$t = - \int_{T_1}^{T_1^d} \frac{dT}{v_p(dT/dr)} \quad (14.31)$$

where  $T_1$  is the temperature at  $r_1$  and  $T_1^d$  is the temperature at a radial distance  $r_1 - d$ .

Let  $v_p^+$  be the velocity of a lenticular pore at reference conditions  $T = 2000^\circ\text{K}$  and  $dT/dr = 1000^\circ\text{K/cm}$  as calculated from Eq. 14.11 for the fuel and gas in the pore under consideration. For a lenticular pore that can be approximated as a constant-volume constant-mass system, the migration velocity varies with temperature according to  $T^{-5/2} \exp(-\Delta H_{vap}/kT)$ . The pore velocity varies directly as the temperature gradient. Therefore,  $v_p$  can be written as

$$v_p = -v_p^+ \left( \frac{T}{2000} \right)^{-5/2} \times \exp \left[ - \left( \frac{\Delta H_{vap}}{2000k} \right) \left( \frac{2000}{T} - 1 \right) \right] \frac{dT/dr}{1000} \quad (14.32)$$

Defining the dimensionless temperature

$$\theta = \frac{T}{2000} \quad (14.33)$$

the fractional radius

$$\xi = \frac{r}{R} \tag{14.34}$$

and the dimensionless heat of vaporization

$$C = \frac{\Delta H_{vap}}{2000k} \tag{14.35}$$

Eq. 14.31 becomes

$$t = \left( \frac{R^2}{2v_p^+} \right) \int_{\theta_1}^{\theta_1^d} \frac{\theta^{3/2} \exp \left[ C \left( \frac{1}{\theta} - 1 \right) \right]}{(d\theta/d\xi)^2} d\theta \tag{14.36}$$

We now assume that the temperature at all times during irradiation is given by the simple parabolic form of Eq. 10.52

$$\frac{\theta - \theta_s}{\theta_0 - \theta_s} = 1 - \xi^2 \tag{14.37}$$

where  $\theta_0$  and  $\theta_s$  are the center-line and surface temperatures divided by 2000. No allowance is made for the drop in  $\theta_0$  during irradiation, which is a principal consequence of restructuring. Eliminating the gradient in the denominator of Eq. 14.36 by use of 14.37 yields

$$t = \frac{R^2 e^{-C}}{8(\theta_0 - \theta_s)^2 v_p^+} \times \int_{\theta_1}^{\theta_1^d} \frac{\theta^{3/2} \exp(C/\theta)}{1 - [(\theta - \theta_s)/(\theta_0 - \theta_s)]} d\theta \tag{14.38}$$

As long as the columnar-grain boundary is at a fractional radius where the pore velocity (Fig. 14.10) and the temperature (Fig. 14.8) are rapidly changing with radius, the principal  $\theta$  dependence in the integral is in the exponential term. Thus, the  $\theta^{3/2}$  term and the denominator of the integrand can be removed from the integral and evaluated at  $\theta = \theta_1$ , and we are reduced to evaluating the integral

$$\int_{\theta_1}^{\theta_1^d} \exp\left(\frac{C}{\theta}\right) d\theta = C \int_{C/\theta_1^d}^{C/\theta_1} \left(\frac{e^u}{u^2}\right) du$$

The integrand  $e^u/u^2$  passes through a minimum at  $u = 2$  and rises to infinity as  $u$  becomes large. Since the parameter  $C$  is 34.2 for  $UO_2$  and  $\theta_1$  and  $\theta_1^d$  are both of order unity, the limits in the integral are far to the right of the minimum, where the variation of the integrand is due mainly to the exponential term. Thus we make the further approximation:

$$\begin{aligned} \int_{C/\theta_1^d}^{C/\theta_1} \left(\frac{e^u}{u^2}\right) du &\sim \left(\frac{\theta_1}{C}\right)^2 \int_{C/\theta_1^d}^{C/\theta_1} e^u du \\ &= \left(\frac{\theta_1}{C}\right)^2 \left[ \exp\left(\frac{C}{\theta_1}\right) - \exp\left(\frac{C}{\theta_1^d}\right) \right] \end{aligned}$$

If the distance of significant motion,  $d$ , is reasonably large, the very steep temperature gradient in the vicinity of the columnar-grain boundary assures that  $\theta_1^d$  exceeds  $\theta_1$  by an

amount sufficient to permit the second exponential term in the brackets in the preceding equation to be neglected compared to the first exponential term. Thus, the parameter  $d$  is entirely eliminated from the model, and Eq. 14.38 becomes

$$t = \left( \frac{R^2 e^{-C}}{8v_p^+ C} \right) \left( \frac{\theta_1^{3/2}}{(\theta_0 - \theta_s)^2 \{1 - [(\theta_1 - \theta_s)/(\theta_0 - \theta_s)]\}} \right) \times \exp\left(\frac{C}{\theta_1}\right) \tag{14.39}$$

The first term on the right of Eq. 14.39 is a constant for a particular fuel material, rod radius, and gas in the pore. For a pure  $UO_2$  fuel rod 0.3 cm in radius filled with 1 atm of helium,  $C = 34.2$  and  $v_p^+ = 1.5 \text{ \AA}/\text{sec}$  (see illustrative calculation in previous section). The first term on the right in Eq. 14.39 is equal to  $3 \times 10^{-10} \text{ sec.}^*$

Equation 14.39 can be solved for  $\theta_1$  as a function of  $t$ ,  $\theta_0$ , and  $\theta_s$ . Again, however, the dominant term is the exponential on the right; so convenient typical values of  $\theta_1$ ,  $\theta_0$ , and  $\theta_s$  can be used in the middle term for all applications of this formula. For this purpose, we take

$$\begin{aligned} \theta_0 &= 1.25 \text{ (} T_0 = 2500^\circ \text{K)} \\ \theta_1 &= 1.0 \text{ (} T_1 = 2000^\circ \text{K)} \\ \theta_s &= 0.5 \text{ (} T_s = 1000^\circ \text{K)} \end{aligned}$$

Solving Eq. 14.39 with the appropriate numerical values of the first two terms on the right and converting  $t$  from seconds to hours yield

$$\theta_1 = \frac{34.2}{2.3 \log t(\text{hr}) + 28} \tag{14.40}$$

or

$$\frac{1}{T_1} = 3.4 \times 10^{-5} \log t(\text{hr}) + 4.2 \times 10^{-4} \tag{14.41}$$

Christensen<sup>11</sup> has found that the measured temperatures at the outer radius of the columnar-grain zone can be correlated with irradiation time by an equation of the same form as Eq. 14.41 but with somewhat different constants. Equation 14.41 yields values of  $T_1$  that are  $\sim 200^\circ \text{K}$  higher than those found by Christensen.

Although the columnar-grain temperature is to a first approximation independent of fuel center-line temperature (i.e., of linear power), the location of the columnar-grain boundary is not. The latter can be obtained by eliminating  $\theta_1$  between Eq. 14.40 and the assumed parabolic temperature distribution of Eq. 14.37, which at  $r = r_1$  can be written as

$$\left(\frac{r_1}{R}\right)^2 = 1 - \frac{\theta_1 - 0.5}{\theta_0 - 0.5} \tag{14.42}$$

\*This group appears to have units of cm-sec, but the standard temperature gradient used in defining  $v_p^+$  and which appears as the number 1000 in Eq. 14.32 supplies a dimension of  $\text{cm}^{-1}$ , which is not attached to a symbol in the equation.

The surface temperature has been assumed equal to  $1000^{\circ}\text{K}$  in Eq. 14.42. According to Nichols,<sup>5</sup> choice of  $T_s$  is not critical.

Figure 14.11 shows the outer radius and temperature of the columnar-grain region predicted by Eqs. 14.40 and 14.42 for three center-line temperatures. The columnar-grain temperature slowly decreases from  $\sim 2400^{\circ}\text{K}$  to  $\sim 1800^{\circ}\text{K}$  over a time span from 1 hr to more than a year. The analogous temperatures listed in Table 10.4 for the three-region model of the fuel fall into the range of the present calculation. The outer boundary of the columnar-grain region moves outward with irradiation time. The rate of advance, however, decreases with time. At a center-line temperature of  $3000^{\circ}\text{K}$ , the microstructure is essentially completely transformed after  $\sim 100$  hr, whereas for  $T_0 = 2000^{\circ}\text{K}$ , significant movement of the columnar-grain boundary is occurring even after a year of irradiation. It should be noted that this analysis assumes a time-independent parabolic temperature distribution extending to the rod axis at all times. Had the readjustment of the temperature profile during restructuring been taken into account, the rate of progression of the columnar-grain boundary would have been lower than that shown on Fig. 14.11 because the fuel temperature calculated with restructuring included is lower than the parabolic profile obtained at startup.

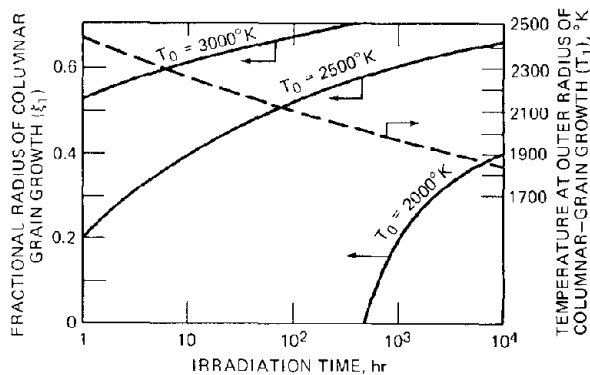


Fig. 14.11 Location and temperature of the outer boundary of the columnar-grain region in pure  $\text{UO}_2$  as a function of irradiation time.

The columnar-grain boundaries calculated by Nichols<sup>5</sup> are displaced to the right of those shown in Fig. 14.11, or, for a given irradiation time,  $r_1$  is smaller and  $T_1$  is larger than the values shown on the graph. Thus, the columnar-grain temperatures calculated in this section fall in between Nichols' original predictions and Christensen's observed values. The variation with irradiation time, however, is very similar in all three cases.

## 14.5 EQUIAXED-GRAIN GROWTH

Although a steep temperature gradient is present in a fuel rod at fractional radii  $>0.7$ , the temperature level here

is too low to permit thermal-gradient migration of the closed pores during typical irradiation times. However, temperatures above  $\sim 1900^{\circ}\text{K}$  are sufficient to cause the grains of the as-fabricated fuel compact to enlarge at rates that are observable in times on the order of days. Thus the annular ring bounded by fractional radii from approximately 0.7 to 0.8 [which roughly corresponds to temperatures from  $2100$  to  $1900^{\circ}\text{K}$  (Fig. 10.24)] defines the zone of equiaxed-grain growth. The question of when the morphology of the as-fabricated fuel has transformed into equiaxed grains can only be answered qualitatively. The grain size in freshly prepared  $\text{UO}_2$  fuel pellets is typically  $5 \mu\text{m}$ . The lower limit of discernible equiaxed-grain growth is  $\sim 25 \mu\text{m}$ . However, the demarcation between the unstructured region and the equiaxed-grain region is rather sharp (Fig. 10.22) because the grain growth process is strongly temperature dependent and the temperature is rapidly varying in the neighborhood of the boundary between the two zones.

### 14.5.1 Grain Growth Kinetics

During grain growth large grains spontaneously grow at the expense of smaller ones (Fig. 8.17). On a microscopic scale the process involves movement of matrix atoms from the convex to the concave side of a curved grain boundary. (A perfectly plane grain boundary has no tendency to move since atoms cross from one side to the other at the same rate in both directions.) The reason that atoms prefer the concave side of the boundary is that they are surrounded by a somewhat larger number of neighboring atoms than when they are part of the crystal on a convex surface. Consequently, the grain boundary, which moves in the direction opposite the net flow of atoms, is displaced toward the center of curvature of the grain on the convex side of the boundary. As illustrated in Fig. 14.12, the net

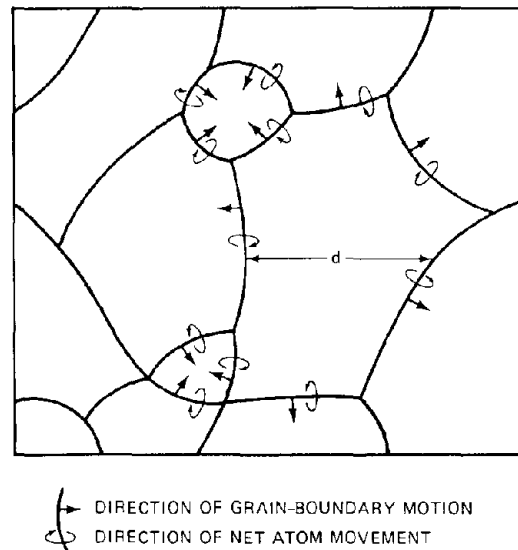


Fig. 14.12 Grain-boundary motion during grain growth ( $d$  = grain size).

result of this atomic motion is shrinkage of small grains with predominantly convex surfaces and growth of large grains with concave surfaces.

From a macroscopic point of view, the driving force for grain growth is the reduction of the energy of the solid that accompanies the decrease of the area of the grain boundaries it contains. The energy per unit grain boundary area is equal to  $\gamma_{gb}$ , the grain-boundary tension. According to Eq. 8.12, a curved grain boundary experiences a force towards the center of curvature equal to  $2\gamma_{gb}/R_c$ , where  $R_c$  is the local radius of curvature. If  $R_c$  is assumed to be proportional to the grain size  $d$ , the driving force for grain-boundary motion is

$$F_{gb} \sim \frac{\gamma_{gb}}{d} \quad (14.43)$$

The presence of a force acting on a curved grain boundary causes motion of the boundary in the direction of the force. The rate of boundary motion is proportional to the force  $F_{gb}$ , the constant of proportionality being the mobility of the grain boundary. In fully dense, very high purity materials, the mobility is an intrinsic property of the solid and presumably reflects the maximum rate that atoms can hop back and forth across the boundary. In this case the velocity of the grain boundaries, which is equal to the rate of grain growth, is given by

$$v_{gb} = \frac{d(d)}{dt} = M_{gb} F_{gb} \quad (14.44)$$

Combining these two equations and integrating with the initial condition  $d = d_0$  (the initial grain size) at  $t = 0$  yields

$$d^2 - d_0^2 = kt \quad (14.45)$$

where  $k = 2M_{gb}\gamma_{gb}$  is called the *grain growth constant*. In high-purity materials where Eq. 14.45 is found to apply,  $k$  is proportional to the mobility of the grain boundaries, which in turn depends on the rate at which atoms cross the boundary. Since this transfer requires that atoms be removed from lattice positions in the crystal structure of a grain, the process is thermally activated, and  $k$  varies with temperature according to the Arrhenius function  $k_0 \exp(-Q/kT)$ , where  $k_0$  is a constant and  $Q$  is the activation energy of grain growth. In pure materials,  $Q$  is much smaller than either the heat of vaporization or the activation energy of volume self-diffusion.

In most materials, however, grain growth kinetics are not well described by the ideal law given by Eq. 14.45. Most data must be fitted with growth laws that contain another adjustable constant

$$d^m - d_0^m = k_0 t \exp\left(-\frac{Q}{kT}\right) \quad (14.46)$$

where  $m$  is a constant  $>2$ , or

$$d^2 - d_0^2 = k_0 t^a \exp\left(-\frac{Q'}{kT}\right) \quad (14.47)$$

where  $a$  is a constant  $<1$ . MacEwan and Hayashi,<sup>12</sup> for example, find that grain growth in  $UO_2$  can be correlated by Eq. 14.46 with  $m = 2.5$  and  $Q = 460$  kJ/mole or, with equal precision, by Eq. 14.47 with  $a = 0.8$  and  $Q' = 360$  kJ/mole.

Figure 14.13(a) shows MacEwan's<sup>12</sup> data plotted using  $m = 3$ . The slope of the lines (which fit the data about as well as Eq. 14.46 with  $m = 2.5$  or Eq. 14.47 with  $a = 0.8$ ) gives the grain growth constant  $k$  as a function of temperature. These are plotted in Arrhenius fashion in Fig. 14.13(b), from which an activation energy of 520 kJ/mole is obtained.

Deviations from the ideal grain growth law of Eq. 14.45 are usually explained by the presence of dissolved impurities or inclusions in the solid that impede the progress of a moving grain boundary. Dissolved impurities that are strongly attracted to grain boundaries, for example, must be pulled along by the moving boundary. The magnitude of this solute drag effect depends on the concentration of the impurity and its volume-diffusion coefficient in the matrix. Addition of less than 1 mole % of CaO to  $UO_2$ , for

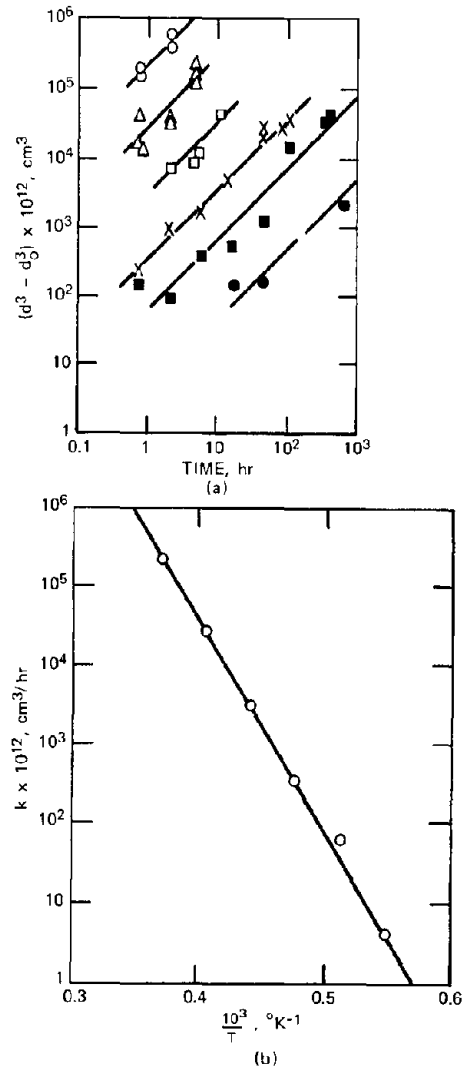


Fig. 14.13 Grain growth in  $UO_2$  compacts. (a) Data of Ref. 12 plotted according to the cubic growth law. (b) Arrhenius plot of grain growth constants [After F. A. Nichols, *J. Appl. Phys.*, 37: 4599 (1966)].

instance, reduces the grain growth constant at 2100°K by a factor of 2 and increases the activation energy<sup>12</sup> (based on  $m = 2.5$ ) from 460 to 570 kJ/mole.

Large obstacles, such as solid precipitates or gas-filled cavities, can also reduce the rate of grain-boundary growth well below the rate in the defect-free solid. Figure 14.14 shows the grain structure of a UO<sub>2</sub> specimen containing a distribution of closed pores. Several grain boundaries are decorated with small pores. The string of pores on the horizontal grain boundary in the middle of the photograph appears to be inhibiting motion of the boundary, which would normally be moving upward (which is the direction of the center of curvature of this particular grain boundary).

Nichols<sup>13,14</sup> has proposed a model whereby the residual closed porosity in UO<sub>2</sub> compacts controls the rate of grain growth during irradiation. The model assumes that the intrinsic mobility of the grain boundaries in pore-free

material is very large and that the grain growth rate is determined solely by how readily the grain boundaries can drag the pores along with them. Thus, instead of Eq. 14.44, the grain-boundary velocity is given by

$$v_{gb} = M_p F_p \quad (14.48)$$

where  $M_p$  is the mobility of the pores in the solid and  $F_p$  is the force exerted on the pores by the grain boundary on which the pores lie.

The mobilities (i.e., the diffusion coefficients) of gas-filled bubbles due to the surface and volume-diffusion mechanisms were derived in Sec. 13.10. However, the most likely migration mechanism for the large, as-fabricated pores is vapor transport. According to the Nernst-Einstein equation (Eq. 13.220), the mobility is the velocity per unit force. In Sec. 14.2 we determined the velocity of lenticular pores for a particular type of force, namely, that due to a temperature gradient. The mobility can be determined by



Fig. 14.14 Grain structure in UO<sub>2</sub> in which some grain growth has occurred. The grain in the center is 50  $\mu\text{m}$  in size. [From J. R. MacEwan and J. Hayashi, *Proc. Brit. Ceram. Soc.*, 7: 245 (1967).]

dividing the velocity by the force on the pore due to vapor transport in a thermal gradient. By analogy to Eqs. 13.227 and 13.234, the force on a single matrix molecule due to the thermal gradient for the vapor-transport mechanism is

$$f = -\frac{\Delta H_{\text{vap}}}{T} \left( \frac{dT}{dx} \right)_p \quad (14.49)$$

The force on the entire pore (spherical and of radius  $R$  in the present case) is given by Eq. 13.226, which, when combined with Eq. 14.49, yields

$$F_p = \left( \frac{4\pi R^3/3}{\Omega} \right) \frac{\Delta H_{\text{vap}}}{T} \left( \frac{dT}{dx} \right)_p \quad (14.50)$$

Dividing Eq. 14.50 into 14.6 and expressing  $D_g$  by Eq. 14.9 yields the pore mobility\*

$$M_p = \frac{3 \times 10^6 \Omega^2 D_g^*}{4\pi R^3 (kT)^2} \left( \frac{T}{2000} \right)^{3/2} \frac{1}{p} \times \exp \left( \frac{\Delta S_{\text{vap}}}{k} \right) \exp \left( -\frac{\Delta H_{\text{vap}}}{kT} \right) \quad (14.51)$$

Although the mobility was derived for the special case of pore motion in a thermal gradient, it is valid for any force acting on the pore, in particular the force due to the movement of a grain boundary on which the pore is located.

In the case of migration in a thermal gradient,  $p$  in Eq. 14.51 was assumed to be given by Eq. 14.10 on the grounds that the mechanical balance of internal gas pressure and surface-tension forces was not attained in thermal-gradient transport by this mechanism. In the present application, on the other hand, it is more likely that mechanical equilibrium is attained. First of all, the pores in the equiaxed region of the fuel are more nearly spherical than lenticular (see Fig. 14.14), which suggests that surface-tension forces are important. Second, the pores in the equiaxed-grain region are not swept out of this zone; they remain more or less in place and shrink by a continuation of the normal sintering process begun during fuel fabrication (see Sec. 16.11). That is, they shed vacancies until the initial pressure deficit is removed and mechanical equilibrium with the solid is approached. Therefore,  $p$  in Eq. 14.51 is replaced by  $2\gamma/R$ , and the pore mobility becomes

$$M_p \sim \frac{\exp(-\Delta H_{\text{vap}}/kT)}{R^2} \quad (14.52)$$

where the terms omitted can be considered as constants that ultimately appear in the grain growth constant.

The force on the pore due to the grain boundary is given by Eq. 13.228 as

$$F_p = \pi R \gamma_{\text{gb}} \sin 2\phi \quad (14.53)$$

\*Equation 14.51 can also be derived from a physical model of the evaporation-condensation processes within the pore instead of invoking Eq. 14.49, which arises from irreversible thermodynamics. The former method, presented by Kelly [*Phys. Status Solidi*, 21: 451 (1967)] is analogous to the derivation of bubble mobility by the volume-diffusion mechanism in Sec. 13.10.

In the application of this formula in Sec. 13.11, the bubbles pulled on a stationary grain boundary and caused the boundary to deform to produce the nonzero contact angle  $\phi$ . In the present case the roles of driver and driven are reversed. The pore is the immobile partner and is tugged on by the moving grain boundary, which is subject to the force due to grain-boundary tension. In attempting to drag the pore along, the grain boundary is distorted so that around a trapped pore it takes on the shape shown by Fig. 13.24. If the grain boundary were not driven to move by the force  $F_{\text{gb}}$  of Eq. 14.43, the angle  $\phi$  would be zero. Since  $\phi$  is  $90^\circ$  when  $F_{\text{gb}} = 0$  but less than  $90^\circ$  when  $F_{\text{gb}} > 0$ , Nichols<sup>1,3</sup> assumes that to a very rough approximation  $\sin 2\phi$  is proportional to  $F_{\text{gb}}$ . Replacing  $\sin 2\phi$  by a quantity proportional to  $F_{\text{gb}}$  and using Eq. 14.43 for  $F_{\text{gb}}$  yield

$$F_p \sim \frac{R}{d} \quad (14.54)$$

Multiplication of Eq. 14.52 and 14.54 gives the grain-boundary velocity (Eq. 14.48) under conditions where pore dragging is controlling

$$v_{\text{gb}} \sim \frac{\exp(-\Delta H_{\text{vap}}/kT)}{Rd} \quad (14.55)$$

To obtain the grain growth law for this model, we must relate the average pore size  $R$  to the average grain size  $d$ . Nichols takes the relation

$$R \sim d \quad (14.56)$$

for the following reasons:

1. As the boundary moves during grain growth, the pores being dragged along will collide and coalesce with pores in the solid contacted by the moving grain boundary. According to MacEwan and Hayashi,<sup>1,2</sup> each point in the matrix is, on the average, swept several times by a moving boundary during a twofold increase in grain size. Coalescence between pores causes the average pore size on the boundaries to increase as grain growth proceeds. Lacking a more detailed theory of this aspect of the process, Eq. 14.56 is the simplest relation consistent with the preceding qualitative picture.

2. Experiments have shown that a maximum in  $\text{UO}_2$  density occurs during sintering, which is interpreted as follows: before the maximum density is attained, grain growth is negligible and the pores shrink until their internal gas pressure balances the surface-tension forces. At the point of maximum density, grain growth begins and the resulting pore coalescence causes the average pore radius to increase in exactly the same manner that coalescence of fusion-gas bubbles in the matrix causes the fuel to swell.

The grain growth law according to this model can be obtained by combining Eqs. 14.55 and 14.56,

$$v_{\text{gb}} = \frac{d(d)}{dt} \sim \frac{\exp(-\Delta H_{\text{vap}}/kT)}{d^2}$$

which, when integrated, yields the cubic growth law:

$$d^3 - d_0^3 = k_0 \exp \left( -\frac{\Delta H_{\text{vap}}}{kT} \right) t \quad (14.57)$$

The model predicts the exponent on  $d$  and the value of the activation energy, but not the preexponential term  $k_0$ . The

data shown in Fig. 14.13(a) are at least consistent with the grain size variation predicted by Eq. 14.57. Stronger support for Nichols' theory is found in the relatively good agreement between the measured activation energy of grain growth (520 kJ/mole) and the predicted value ( $\Delta H_{vap} = 570$  kJ/mole). A theory similar to the one presented here concerning the sweeping of gas bubbles by moving grain boundaries is reviewed in Sec. 15.9.

Ainscough, Oldfield, and Ware<sup>15</sup> have developed an analytical expression for grain growth in  $UO_2$  which is more empirical than the model of Nichols just described. They analyze grain growth by the rate equation obtained by combination of Eqs. 14.43 and 14.44 with an additional term intended to account for the retarding force arising from interaction of the moving grain boundary with pores

$$\frac{d(d)}{dt} = \frac{k}{d} - k' \quad (14.58)$$

where  $k = 2\gamma_{gb}M_{gb}$  is the grain growth constant and  $k'$  is a constant representing the growth-inhibiting effect of the pores in the medium. Noting that Eq. 14.58 shows that grain growth ceases when a maximum grain size  $d_m = k/k'$  is attained, the growth law can be written as

$$\frac{d(d)}{dt} = k \left( \frac{1}{d} - \frac{1}{d_m} \right) \quad (14.59)$$

which can be integrated to give

$$d_m^2 \ln \left( \frac{d_m - d_0}{d_m - d} \right) - d_m(d - d_0) = kt \quad (14.60)$$

Ainscough, Oldfield, and Ware<sup>15</sup> fitted their out-of-pile grain growth data to Eq. 14.60 and obtained the constants

$$k = 5.2 \times 10^7 \exp \left[ -\frac{270}{R(T/10^3)} \right] \frac{\mu m^2}{hr} \quad (14.61)$$

$$d_m = 2200 \exp \left[ -\frac{63}{R(T/10^3)} \right] \mu m \quad (14.62)$$

The existence of a maximum grain size is thought to arise from the ability of the array of pores in the solid to completely stop grain-boundary movement when the grain size becomes sufficiently large (i.e., as  $d$  becomes large, Eq. 14.43 shows that the driving force for continued grain growth diminishes). A limiting grain size is not predicted by Nichols' model. The increase in  $d_m$  with temperature implicit in Eq. 14.62 is believed to be due to the increasing rate of pore shrinkage (sintering) due to vacancy emission as the temperature is increased. This process is discussed in Sec. 16.11. As the pores are reduced in size, their ability to impede grain-boundary migration diminishes, and consequently  $k'$  (or  $d_m$ ) increases. At 2000°K Eq. 14.62 predicts a limiting grain size of  $\sim 50 \mu m$ .

Under irradiation the fabricated porosity is assisted in retarding grain growth by solid fission-product precipitates (see Sec. 12.2) and fission-gas bubbles. On the other hand, irradiation can act to accelerate grain growth by removing porosity (see the subject of densification in Sec. 16.11). Ainscough, Oldfield, and Ware<sup>15</sup> have determined empirically that the net burnup effect can be described by modifying Eq. 14.59 to

$$\frac{d(d)}{dt} = k \left( \frac{1}{d} - \frac{1 + 2000\Omega\dot{F}t}{d_m^0} \right) \quad (14.63)$$

where  $d_m^0$  represents the limiting grain size in the absence of irradiation (given by Eq. 14.62),  $\dot{F}$  is the fission density, and  $\Omega = 41 \text{ \AA}^3$  is the volume per uranium atom in  $UO_2$ . The grain growth constant  $k$  is not affected by irradiation.

## 14.5.2 Characteristic Temperature of the Equiaxed Zone

The temperature characteristic of the boundary between the unstructured and equiaxed-grain zones in a fuel pin can be computed by methods entirely analogous to those employed to determine the temperature at the boundary between the equiaxed and columnar-grain regions (preceding section). To do so, we assume that to be visually identified as "equiaxed," a grain must have grown to a specified diameter  $d_{crit}$ . The temperature  $T_2$  at which this size is attained in irradiation time  $t$  is the point at which the equiaxed grains are just discernible. Setting  $d = d_{crit} = 25 \mu m$  and  $T = T_2$  in Eq. 14.57 and taking the grain growth constant  $k_0$  and the experimental value of the activation energy (instead of  $\Delta H_{vap}$ ) from Fig. 14.13(b), we have

$$\theta_2 = \frac{T_2}{2000} = \frac{31}{2.3 \log t(\text{hr}) + 26} \quad (14.64)$$

which is identical in form and very nearly in absolute value as well to the analogous formula for  $\theta_1$ , Eq. 14.40. Equation 14.64 predicts values of  $T_2$  ranging from 2190°K to 1760°K as the irradiation time increases from 10 to 10,000 hr. These values are only  $\sim 100^\circ K$  lower than the comparable columnar-grain temperatures (dashed curve of Fig. 14.11). The temperatures selected for defining the outer limit of the equiaxed grains in the three-region model for calculating the temperature distribution in the fuel is  $\sim 1900^\circ K$ . The theory on which Eq. 14.64 is based is consistent with the experimental observations from which the  $T_2$  values of Table 10.4 were obtained.

## 14.6 NOMENCLATURE

- C = constant defined by Eq. 14.35
- d = maximum distance a pore must move to form an identifiable columnar grain; grain size
- $d_0$  = initial grain size
- $d_m$  = maximum grain size
- $D_g$  = diffusion coefficient of heavy-metal oxide in inert gas
- $D_g^*$  = gas-phase diffusivity of  $UO_2$  in inert gas at 1 atm pressure and 2000°K
- $D_s$  = surface self-diffusion coefficient of fuel atoms
- $E_b$  = binding energy of adsorbed atom
- f = force on matrix molecule
- $F_{gb}$  = force acting to shrink a grain boundary
- $F_p$  = force on a pore
- $\Delta H_{vap}$  = heat of vaporization
- J = flux of matrix molecules across a pore
- $J_p$  = flux of pores in the radial direction in a fuel pin
- k = grain growth constant; Boltzmann's constant; thermal conductivity of fuel

- $k_p$  = thermal conductivity of gas in a pore  
 $k_s$  = thermal conductivity of solid fuel  
 $k$  = constant reflecting the inhibiting effect of pores on grain growth  
 $m$  = molecular mass  
 $M$  = molecular weight  
 $M_{gb}$  = mobility of grain boundary  
 $M_p$  = mobility of pore  
 $N_p$  = pore concentration (number of pores per unit volume of fuel)  
 $N_{p0}$  = initial concentration of pores in fuel  
 $\mathcal{P}$  = linear power  
 $p$  = total gas pressure in a pore  
 $P_M$  = partial pressure of condensing species in gas adjacent to face of a pore  
 $P^\circ$  = vapor pressure  
 $Q$  = activation energy for grain growth  
 $R$  = fuel pin radius; radius of a spherical pore; gas constant  
 $R_{cond}$  = rate of condensation  
 $R_{cond}^{eq}$  = rate of condensation in equilibrium conditions  
 $R_{vap}^{eq}$  = rate of vaporization in equilibrium conditions  
 $r$  = radial position in fuel pin  
 $r_0$  = radius of central void  
 $r_1$  = outside radius of columnar-grain zone in fuel  
 $\Delta S_{vap}$  = entropy of vaporization  
 $T$  = temperature, °K  
 $T_s$  = surface temperature of fuel  
 $T_0$  = temperature at edge of central void  
 $T_1$  = temperature at outer radius of columnar-grain zone  
 $T_2$  = temperature at outer boundary of equiaxed-grain zone  
 $v_p$  = pore velocity  
 $v_p^*$  = pore velocity at 2000°K and in a temperature gradient of 1000°K/cm  
 $v_{gb}$  = velocity of grain boundary  
 $x$  = direction of pore migration (up the temperature gradient)  
 $y_1$  = mole fraction of solid impurities in the fuel at the hot face of a pore

Greek letters

- $\alpha$  = condensation coefficient  
 $\epsilon_{12}$  = force constant between particles 1 and 2  
 $\sigma_{12}$  = collision diameter for particles 1 and 2  
 $\delta$  = thickness of a lenticular pore  
 $\theta$  = dimensionless temperature,  $T/2000$   
 $\lambda_0$  = ledge spacing on a solid surface  
 $\xi$  = dimensionless radial position,  $r/R$   
 $\Omega$  = atomic volume  
 $\Omega_D$  = collision integral in kinetic theory of gas diffusivity  
 $\gamma_{gb}$  = grain-boundary tension  
 $\nu_1$  = frequency of vibration of adsorbed atom perpendicular to surface  
 $\phi$  = contact angle between pore and grain boundary

Subscripts

- $p$  = pore  
 $sint$  = sintering conditions during fuel fabrication

14.7 REFERENCES

1. P. F. Sens, *J. Nucl. Mater.*, **43**: 293 (1972).
2. W. Oldfield and A. J. Markworth, *Mater. Sci. Eng.*, **4**: 353 (1969).
3. D. R. De Halas and G. R. Horn, *J. Nucl. Mater.*, **8**: 207 (1963).
4. M. V. Speight, *J. Nucl. Mater.*, **13**: 207 (1964).
5. F. A. Nichols, *J. Nucl. Mater.*, **22**: 214 (1967).
6. F. A. Nichols, *J. Nucl. Mater.*, **27**: 137 (1968).
7. R. C. Reid and T. K. Sherwood, *The Properties of Gases and Liquids*, 2nd ed., pp. 523-525, McGraw-Hill Book Company, New York, 1960.
8. J. P. Hirth and G. M. Pound, *J. Chem. Phys.*, **26**: 1216 (1957).
9. W. J. Lackey, F. J. Homan, and A. R. Olsen, *Nucl. Technol.*, **16**: 120 (1972).
10. C. S. Rim and H. Fenech, *Trans. Amer. Nucl. Soc.*, **12**: 103 (1969).
11. J. A. Christensen, *Trans. Amer. Nucl. Soc.*, **15**: 214 (1972).
12. J. R. MacEwan and J. Hayashi, *Proc. Brit. Ceram. Soc.*, **7**: 245 (1967).
13. F. A. Nichols, *J. Appl. Phys.*, **37**: 4599 (1966).
14. F. A. Nichols, *J. Amer. Ceram. Soc.*, **51**: 468 (1968).
15. J. B. Ainscough, B. W. Oldfield, and J. O. Ware, *J. Nucl. Mater.*, **49**: 117 (1973/74).

14.8 PROBLEMS

14.1 The central void in a highly rated UO<sub>2</sub> fuel pin arises from the migration of the pores trapped in the fuel during fabrication. When under power, the temperature gradient in the fuel pin causes these pores to migrate toward the center by a vapor-transport mechanism. As soon as the fuel element is placed in the reactor and the power is raised, the pores within a radius of 0.8R (R = fuel-pin radius) begin to migrate toward the center. After the migration process is complete, the region 0 < r < 0.8R has been swept clean of pores and has become a fully dense columnar-grain region. In this process a central void is formed.

(a) Assuming that all the porosity in the region 0 ≤ r ≤ 0.8R contributes to the central void, calculate the radius of the central void after restructuring is complete (r<sub>of</sub>). The initial porosity of the fuel is P<sub>0</sub>.

(b) Using the heat-conduction equation, determine the temperature distribution in the columnar-grain region (0.8R ≥ r ≥ r<sub>0</sub>) for any central-void radius. Assume that the thermal conductivity in the columnar-grain and unrestructured regions of the fuel are equal and independent of both porosity and of temperature. Assume that the power density in the columnar-grain region is independent of position and equal to the average value appropriate to the central-void radius r<sub>0</sub> at any time during restructuring.

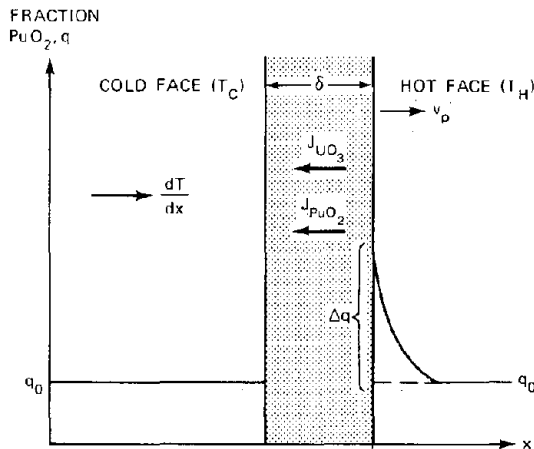
(c) Suppose that the pore migration velocity is known to be a function v<sub>p</sub>(T) of local fuel temperature. Explain how the time required for attainment of the final central-void radius of part a can be calculated.

(d) The pore velocity of part c is determined by the vapor-transport mechanism. The only quantity in this model that must be specified is the gas pressure in the pore,

p. In the usual pore-velocity analysis, the volume of the pore is assumed constant during migration. In this problem we wish to compute the pore velocity under the assumption that the pore becomes spherical and adjusts its radius to the value required for mechanical equilibrium between the internal gas pressure and surface tension. The porosity in the as-fabricated fuel is assumed to be in the form of a uniform distribution of pores of radius  $r_{p0}$ . When cold, each of these pores is filled with helium gas at pressure  $p_0$  and ambient temperature  $T_a$ . During the migration process none of the helium initially in the pore escapes. Calculate  $v_p$  as a function of  $T$  and hence the migration velocity  $v_p(T)$ .

14.2 The velocity of lenticular pores migrating by the vapor-transport mechanism is important in determining the rate at which fuel restructuring occurs when the temperature gradient is applied. Calculations of the migration velocity usually assume a fuel consisting of pure  $UO_2$ . Although this restriction is adequate for thermal reactor fuels, the fuel in fast reactors is a mixture of uranium and plutonium oxide. It is desired to compute the pore velocity  $v_p$  in a mixed oxide with a plutonium-cation fraction of  $q_0$  in a temperature gradient of  $dT/dx$ .

The lenticular pore is modeled as a slab of thickness  $\delta$  in the direction of the temperature gradient and of infinite extent in the directions transverse to the temperature gradient (see sketch). As the pore moves up the tempera-



ture gradient, it consumes fuel of composition  $q_0$  that is transported across the pore by vapor fluxes of  $UO_3$  and  $PuO_2$ , denoted by  $J_{UO_3}$  and  $J_{PuO_2}$ . Material balances over the pore show that

1. The composition of the fuel deposited on the cold face of the pore is equal to that of the fresh fuel (i.e.,  $q_0$ ).
2. The ratio of the vapor fluxes within the gas filling the pore is related to  $q_0$  by

$$q_0 = \frac{J_{PuO_2}}{J_{UO_3} + J_{PuO_2}} \quad (1)$$

However, because  $PuO_2$  and  $UO_3$  do not have the same vapor pressures, the fuel composition just at the hot face of the pore is different from  $q_0$ . That is, if  $PuO_2$  is less volatile

than  $UO_3$ , the plutonium content at the front face of the pore must rise above  $q_0$  to ensure that the ratio of the vapor fluxes satisfies Eq. 1. The profile of the plutonium fraction in the vicinity of the pore is shown in the sketch.

As in the case of vapor transport in pure  $UO_2$ , the diffusive flux of  $UO_3$  and  $PuO_2$  through the gas in the pore is given by Fick's law as

$$J_i = \frac{D_g}{kT\delta} (p_i^H - p_i^C) \quad (i = UO_3, PuO_2) \quad (2)$$

where  $D_g$  is the diffusion coefficient of  $UO_3$  and  $PuO_2$  in the gas and  $p_i^H$  and  $p_i^C$  are the partial pressures of species  $i$  at the hot and cold faces of the pore, respectively.

It is assumed that Raoult's law applies to the binary solid; so the partial pressures are related to the vapor pressures by

$$p_{PuO_2} = q P_{PuO_2}^0 \quad (3)$$

$$p_{UO_3} = (1 - q) f_{UO_3}(T) \quad (4)$$

where the vapor pressures of the pure plutonium dioxides are given by the Clausius-Clapeyron relation

$$P_{PuO_2}^0 = \Lambda_{PuO_2} \exp\left(-\frac{\Delta H_{PuO_2}}{kT}\right) \quad (5)$$

and the function  $f(T)$  governing  $UO_3$  volatility is given by

$$f_{UO_3}(T) = A_{UO_3} \exp\left(-\frac{\Delta H_{UO_3}}{kT}\right) \quad (6)$$

where  $A_i$  and  $\Delta H_i$  are constants for each species and  $k$  is Boltzmann's constant (or the gas constant).

As in the case of pore migration in pure  $UO_2$ , the pore is assumed to be so thin that the functions  $P_{PuO_2}^0$  and  $f_{UO_3}$  at the hot face can be related to those at the cold face by one-term Taylor series expansions.

(a) Derive the expression for the  $PuO_2$  enrichment at the hot face,  $\Delta q$ , in terms of the thermochemical properties in Eqs. 5 and 6 and the composition of the fresh fuel  $q_0$ , the pore thickness  $\delta$ , and the temperature gradient  $dT/dx$ .

(b) Calculate the ratio of the pore velocity in the mixed oxide to that in pure  $UO_2$  (i.e.,  $v_p/(v_p)_{UO_2}$ ).

(c) Solve the plutonium diffusion equation in front of the moving pore, and obtain the equation for the plutonium distribution in the solid in front of the pore.

14.3 A mixed-oxide fuel initially contains disk-shaped pores of thickness  $\delta$  and volume  $V_p$ . The number of these pores per unit volume of fuel,  $N_{p0}$ , is such as to result in an initial porosity  $P_0$  which is uniformly distributed over the fuel cross section. When the fuel element is brought up to power, the pores begin to move at a velocity  $v_p$  given by

$$v_p = (v_p)_{UO_2} X$$

where

$$(v_p)_{UO_2} = \frac{D_g \Delta H_U P_U^0 \Omega}{k^2 T^3} \frac{dT}{dr}$$

is the velocity of a pore in pure  $UO_2$  and  $X$  is the correction factor for the mixed-oxide fuel (Eqs. 18 and 19 of solution to problem 14.2). This factor is assumed to be

independent of temperature. After a time  $t$  in the temperature gradient, the migration of the pores results in porosity redistribution such as that shown in Fig. 14.8. Assume that the porosity profile  $P(r,t)$  is known as a result of having solved the pore conservation equations. During redistribution the pores do not change size or shape; so the concentration of pores,  $N_p(r,t)$  is proportional to  $P(r,t)$ .

We wish to use the pore distribution function  $N_p(r,t)$  in conjunction with the plutonium distribution in front of each pore [problem 14.2(c) or Eq. 11.102] to determine the gross plutonium redistribution in the fuel element. Consider a unit volume of fuel at a radius  $r$ . Initially, this volume element contains  $N_{p0}$  pores. As a result of migration, these pores leave the volume element, leaving behind a plutonium deficit in the solid due to the startup spikes (Fig. 11.24). At time  $t$  during redistribution, the volume element contains  $N_p(r,t)$  pores, each of which contributes an excess of plutonium owing to the profile that is pushed ahead of the pore.

(a) Calculate the amount of excess plutonium (i.e., above the initial enrichment  $q_0$ ) which is transported by each migrating pore.

(b) Calculate the average plutonium fraction in the solid in the volume element at the time and position where the pore concentration is  $N_p(r,t)$  [or, when the porosity is  $P(r,t)$ ].

14.4 Derive the condensation coefficient  $\alpha$  according to the Hirth-Pound model. Note that the quantity  $\nu_1 \exp(-E_b/kT)$  is the reciprocal of the mean desorption lifetime of an atom on a perfect crystal plane.

14.5 Consider a slab of fuel of initial porosity  $P_0$  and thickness  $L_0$ . At  $t = 0$  a fixed temperature gradient  $dT/dx$  is applied across the slab. During the subsequent porosity removal process, the temperature gradient is fixed by

$$T(x) = T_s + \left(\frac{dT}{dx}\right) x$$

where  $x$  is the distance from the cold face of the slab and  $T_s$  is the temperature at  $x = 0$ .

(a) Assume that the velocity of each pore is given by

$$v_p = v_p^+ \exp\left(-\frac{\Delta H_{vap}}{kT}\right) \left(\frac{dT}{dx}\right)$$

where  $v_p^+$  is a constant. Derive the expression for the time required for a pore to move from a position where the temperature is  $T$  to the position where the temperature is  $T'$  ( $T' > T$ ). Use the approximate method described in the text following Eq. 14.38.

(b) Using the solution to a, determine the thickness of the slab at time  $t$  after imposition of the temperature gradient.

14.6 Compute and plot the grain size-time curves for grain growth in  $UO_2$  compacts of initial grain size  $d_0 = 9 \mu m$  when annealed in the absence of neutron irradiation and when annealed in-pile at a fission density of  $6.1 \times 10^{12}$  fissions  $cm^{-3} sec^{-1}$ . The temperature is  $1600^\circ K$ .

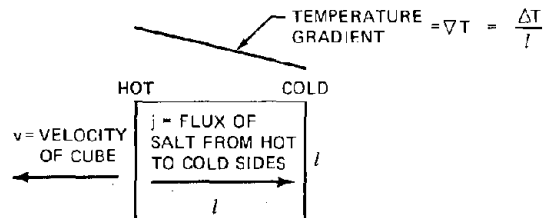
14.7 An experiment is conducted to study the migration of simulated metallic fission-product inclusions in  $UO_2$ . Metal particles are sandwiched between two blocks of  $UO_2$ , and the composite is placed in a furnace that establishes a linear temperature distribution (i.e.,  $dT/dx$  is a constant) perpendicular to the plane of the initial deposit of metal particles. The temperature at the position of the initial deposit is  $T_0$ . Under the influence of the temperature gradient, the particles move to the hot part of the  $UO_2$  by the surface diffusion mechanism (the same mechanism responsible for driving fission-gas bubbles up a temperature gradient). Assume the temperature distribution along the inclusion-matrix interface is the same as in the case of a bubble embedded in the solid.

(a) How far from the initial position ( $x = 0$ ) does a single metal particle of radius  $R$  move in time  $t$ ? Use the approximate method following Eq. 14.38.

(b) The distribution of particle sizes in the metal powder is given by  $f(R)dR =$  number of particles with radii between  $R$  and  $R + dR$ . At time  $t$ , what is the distribution of particles in distance,  $g(x)dx =$  number of particles in the slice  $x$  to  $x + dx$ ?

14.8 *Motion of Brine Cubes in Salt.* The salt deposit in which solidified wastes from fuel reprocessing plants are to be buried contains small cubical cavities filled with brine. Under the influence of the temperature gradient established by the hot-waste-filled canister, the brine cubes migrate towards the canister. The motion of brine cubes embedded in salt may be treated in a manner similar to that applied to pores in solid fuel.

(a) *Motion of a Single Brine Cube.* Suppose a brine cube  $l$  cm on a side is in a temperature gradient  $\nabla T$  as shown below:



The flux of salt from the hot to the cold wall ( $j$  in  $g\ cm^{-2}\ sec^{-1}$ ) is governed by Fick's law, with the diffusion coefficient of the salt in brine given by  $D$ . The solubility of the salt in the brine is given by

$$c = A \exp\left(-\frac{\Delta H}{RT}\right) \quad g/cm^3$$

where  $A$  and  $\Delta H$  are known constants. The density of the salt is  $\rho_s$ . Derive the formula giving the velocity of the brine cube  $v$  in terms of the constants already given, the local temperature  $T$ , and the temperature gradient  $\nabla T$ .

Since the dimension  $l$  of the brine cube is small ( $\sim 1$  mm), the temperature difference  $\Delta T$  and the concentration difference  $\Delta c$  across the cube are also small.

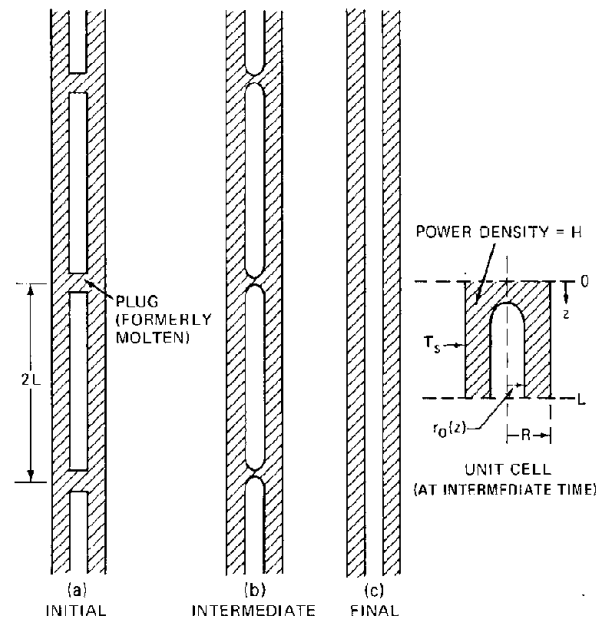
(b) *Rate of Brine Flow to the Pot.* Assume a single spherical canister of radius  $R$  containing solid wastes is inserted in an infinite field of salt containing  $N_0$  brine

cubes/cm<sup>3</sup>. Each cube has a volume  $l^3$ . Assume the steady-state temperature profile around the canister is rapidly established so that the brine cubes move in the steady temperature field at all times. Since the temperature profile is specified, the inward migration velocity of the individual brine cubes is known as a function of  $r$ . Let it be  $v(r)$ .

Neglecting collisions between brine cubes as they move towards the canister, set up the partial differential equation (the conservation equation) which determines the concentration of brine cubes at position  $r$  and time  $t$ ,  $N(r,t)$ . What are the initial and boundary conditions? What is the rate at which brine reaches the canister (expressed as a volumetric rate) in terms of  $N$  and  $v$ ?

14.9 Consider a single lenticular pore of thickness  $\delta$  in a piece of  $\text{UO}_2$  which supports a linear temperature distribution ( $dT/dx = \text{constant}$ ) perpendicular to the face of the pore. The temperature at the initial pore location is  $T_0$ , and the initial inert gas pressure in the pore is  $p_0$ . As a result of the temperature gradient, the pore moves toward the hot region of the fuel. The fuel contains a uniform concentration  $C_0$  fission-gas atoms/cc. As the pore migrates, the gas atoms originally trapped in the fuel become part of the gas contained in the pore. Assuming that the pore moves by the vapor-transport mechanism, derive the formula for the pore velocity. Assume all necessary constants are known. The pore thickness does not change during migration, and the gas in the pore behaves ideally.

14.10 Recent experiments in which oxide fuel pins were irradiated at linear powers sufficient to cause some central melting have shown that the molten fuel collects in plugs separated by a distance  $2L$  along the central void [(a) in sketch]. When the fuel in the (a) configuration is reirradiated at a linear power less than that required for melting, the plugs gradually disappear and a perfect central void is eventually produced [(c) in sketch]. In the sketch (b) shows the geometry at an intermediate time, and the right-hand drawing is an enlargement of the repeating unit (unit cell) of the evolving structure. The restructuring process is believed to be caused by vapor transport of  $\text{UO}_2$ .



(a) Explain qualitatively why vapor transport converts the fuel from configuration (a) to configuration (c).

(b) Set up the appropriate heat and mass-transport equations that describe quantitatively the restoration process. Include the necessary boundary conditions to the differential equations. Make the following assumptions:

1. The fuel surface temperature,  $T_s$ , is independent of axial position.
2. The power density of the solid fuel,  $H \text{ W/cm}^3$ , is everywhere constant.
3. The fuel thermal conductivity,  $k$ , is constant.
4. The fuel behaves as pure  $\text{UO}_2$ , for which the vapor-pressure-temperature relation,  $P(T)$ , is known.
5. The diffusion coefficient of  $\text{UO}_2$  in the inert gas contained in the central void,  $D_g$ , is known.

# Chapter 15

## Fission-Gas Release

### 15.1 INTRODUCTION

Fission gases are considered to be released from the fuel when they reach any space that is connected to the free volume within the fuel pin. Gas collection zones include the fuel-cladding gap (if there is one), the central void, and porosity within the fuel which communicates directly with the fuel-pin gas space. Cracks or interlinked gas bubbles or pores are the most important type of open porosity. The following major differences exist between the gas in closed, gas-filled cavities in the fuel and that in the empty spaces:

1. Once the gas is released, the probability of its reentering the solid from the free volume is virtually nil.
2. The gas pressure in open porosity is equal to that in the free volume of the fuel pin. Because of the insolubility of xenon and krypton in solids, there is no direct influence of plenum fission-gas pressure on the rate of gas escape from the fuel.
3. While the fission gas contained by the fuel tends to cause swelling, fission gas that has been released promotes shrinkage by pressurizing the solid and thereby encouraging collapse of internal porosity and bubbles.

A summary of gas-release theories and the relationship of release and swelling was presented in Sec. 13.1. Regimes of gas release can be classified according to the extent to which they depend on fuel temperature and temperature gradient.

At low temperatures (less than about 1300°K), the mobility of fission-gas atoms is too low to permit appreciable gas-atom movement, either to release surfaces or even to sites where bubbles can form. The fission gases are frozen into the matrix of the solid, and only the gas formed very close to an external surface can escape. Release occurs both by direct flight from the fuel while the gas atom is still an energetic fission fragment (recoil) or by interaction of a fission fragment, a collision cascade, or a fission spike with a stationary gas atom near the surface (knockout). These release mechanisms are independent of both temperature and temperature gradient. Since they affect only the outer layer of the fuel (within  $\sim 10 \mu\text{m}$  of the surface), the fraction of the total fission gas released by recoil or knockout is quite small.

At temperatures between 1300 and  $\sim 1900^\circ\text{K}$  (in  $\text{UO}_2$ ), atomic motion of the gas atoms in the solid becomes important, and release by diffusion to escape surfaces can

occur. Release by atom migration is described by the equivalent-sphere model or variants that include immobilization of gas atoms by natural or radiation-produced defects within the solid coupled with resolution of gas from the traps. In this temperature range bubbles can form, but they are not sufficiently mobile to migrate appreciable distances under the influence of the temperature gradient. Gas that collects at grain boundaries can be released if the intergranular bubble density is large enough to cause interlinkage that provides pathways to open porosity or to sufficiently weaken the grain boundaries so that stress in the fuel causes cracking.

At temperatures greater than 1900°K, gas bubbles and closed pores are sufficiently mobile to be driven by the thermal gradient over distances comparable to grain sizes in periods of days or months. Fission gas is released when either of these types of cavities reach a crack or other surface that communicates directly with the free volume in the fuel element.

### 15.2 EXPERIMENTAL TECHNIQUES

The quantities of xenon and krypton released from irradiated fuels are measured either by postirradiation annealing experiments or in-pile tests.

#### 15.2.1 Postirradiation Annealing

In postirradiation annealing experiments, a sample is subjected to light irradiation at low temperature to provide an initial concentration of gas atoms in the solid and then is transferred to an apparatus where it can be held at high temperatures. The amount of gas released is monitored as a function of time. When fissile material such as  $\text{UO}_2$  is studied, the initial irradiation is usually conducted in a nuclear reactor. The specimen may consist of a fuel pellet, powder, or small chips of fused material. The surface area for release is measured either by standard sieving techniques or by gas-adsorption methods. Evolution of one or more of the radioactive fission gases marked with an asterisk in Table 13.3 is followed in the anneal step.

Alternatively, radioactive gas may be injected into the solid by bombardment in the form of  $\sim 10 \text{ keV}$  ions produced by an accelerator. The solid to be studied need not contain a fissile species and is usually in the form of

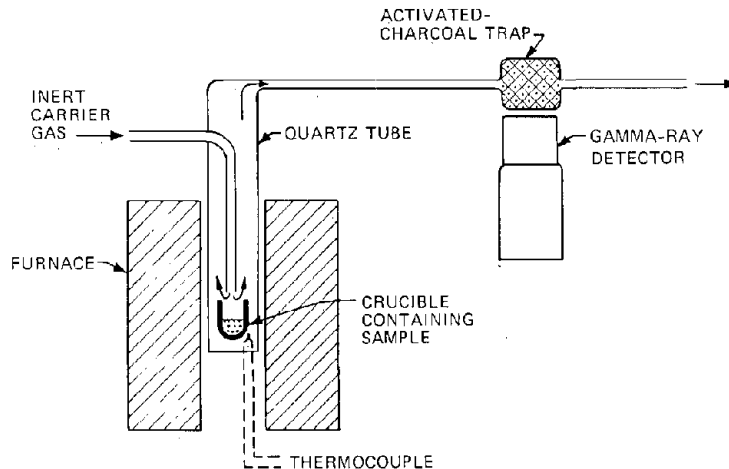


Fig. 15.1 Apparatus for measuring fission-gas release in postirradiation annealing experiments.

single-crystal disks. The disadvantage of this method is that the distribution of embedded gas is very nonuniform, being concentrated in a relatively thin layer near the surface. Reactor irradiation, on the other hand, produces a nearly uniform distribution of fission gas in the sample.\*

Analysis of the radioactive gases emanating from the irradiated samples is the same for both methods of gas introduction. As shown in Fig. 15.1, the sample is placed in a furnace, and the released gases are transported to a gamma-ray detector by a stream of inert sweep gas. The detection system can be augmented by a charcoal trap to concentrate the radioactivity and thereby improve counting statistics. Alternatively, the activity remaining in the sample following each anneal can be measured. The total gas content of the sample is obtained by melting or dissolving the solid after the experiment has been concluded and adding the activity collected in this step to cumulative activity released during the anneals.

The postirradiation annealing technique using reactor-irradiated fuel samples, of which the work of Matzke and Springer<sup>1</sup> and Miekeley and Felix<sup>2</sup> are representative, is the most widely employed method of determining the fission-gas-release characteristics of fissile ceramics. It does not require complex equipment (except for the reactor) and can be applied to shapes and microstructure of actual fuel material. Ion bombardment experiments, which are directed more at probing the nature of the diffusional processes than at determining gas-release parameters, are typified by the work of Matzke and MacEwan,<sup>3</sup> Jech and Kelly,<sup>4</sup> and Ong and Ellman.<sup>5</sup> In the last of these studies, radioactive gas is introduced into the specimen by fission recoil from a surrounding enriched-uranium metal foil.

### 15.2.2 In-Pile Release

Measurement of the rates of release of fission gases from fuels during irradiation provides a more realistic

\*The surface layer of reactor-irradiated fissile specimens, however, is depleted of fission gas owing to recoil or knockout.

understanding of gas migration than can be obtained by the postirradiation annealing method. The main advantage of the in-pile studies is that production and release of the gases occur at the same temperature and in the same irradiation environment. In the postirradiation annealing studies, on the other hand, production occurs at ambient temperature in a low irradiation field, whereas release takes place at high temperature in the absence of a neutron flux. The main disadvantage of in-pile release experiments is their complexity and expense. A sample of fuel material is loaded into a test capsule for insertion into a reactor (Fig. 15.2). The specimen is heated by its own fission power, temperature control being achieved by varying the supply of cooling air flowing around the capsule. The fission gases are continually removed by a sweep gas passing over the sample and discharged into a gamma-ray detection system similar to that employed in postirradiation annealing studies (Fig. 15.1). A detailed view of a test capsule for in-pile investigation of gas release from single-crystal  $\text{UO}_2$  specimens is shown in Fig. 15.3.

Less sophisticated measurements of fission-gas release can be obtained simply by puncturing an ordinary fuel element that has been in the reactor for a known length of time and by measuring the total pressure and composition of the gases inside the element. Information on the total release as a function of irradiation history is obtained often by using instrumented fuel elements equipped with a pressure sensor and thermocouples (Fig. 15.4). The disadvantage of measuring gas release from an entire fuel element is that the data represent averages over the axial temperature and fission-rate distributions in the fuel element.

The types of gas-release information provided by the post-irradiation anneal and in-pile methods are somewhat different. Postirradiation anneal experiments give the fractional release, which is the fraction of the initial quantity of gas in the specimen released during an anneal of time  $t$ . That is, the gas release is studied in an inherently transient manner. In-pile experiments using the apparatus shown in Fig. 15.2, on the other hand, generally analyze the activity of a short-lived fission product, such as  $^{85}\text{Kr}$ . Because of

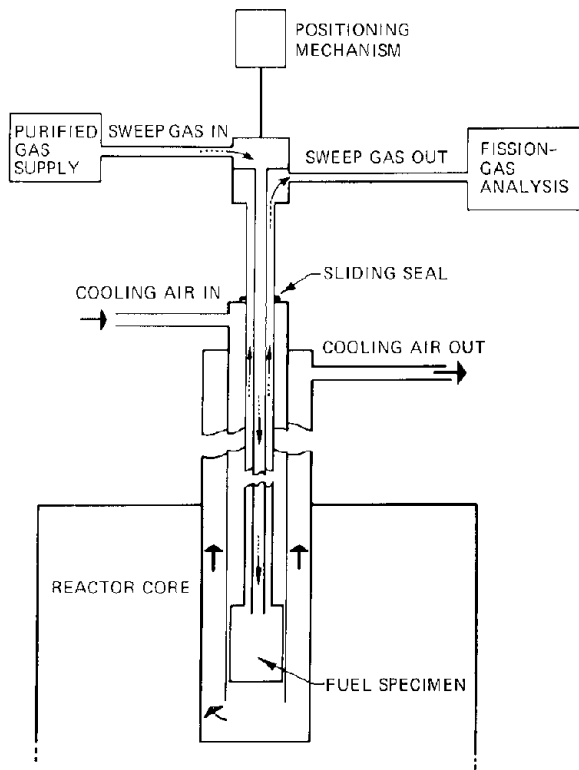


Fig. 15.2 Schematic flow diagram of an irradiation facility for continuous in-pile fission-gas release measurements. [After R. M. Carroll et al., *Nucl. Sci. Eng.*, 38: 143 (1969).]

the short half-life, these experiments attain a true steady state. The fractional release is defined for this experiment as the ratio of the rate of gas release to the rate of production from fission. This quantity is often called the release-to-birth rate ratio instead of the fractional release. Fuel-element puncture tests or continuous pressure measurements are usually reported as a fractional gas release, equal to the quantity of gas in the free volume within the fuel element divided by the total quantity of fission gases produced up to the time that the measurement was made.

### 15.3 RECOIL AND KNOCKOUT

Evidence for a temperature-independent mechanism of fission-gas release comes from data such as those shown on Fig. 15.5, in which the steady-state release rate of 2.8-hr  $^{85}\text{Kr}$  measured in the apparatus of Fig. 15.3 is plotted as a function of temperature. Below about  $625^\circ\text{C}$  ( $900^\circ\text{K}$ ) the emission rate is independent of temperature. Two distinct mechanisms are believed to be involved in the low-temperature portion of the release curve.

The first is direct recoil of fission fragments from within a layer equal to the range of the fission fragments in the fuel ( $\sim 10\ \mu\text{m}$ ). To a good approximation, the fragments of a fission event travel through the solid in straight lines, losing energy en route primarily by interaction with the

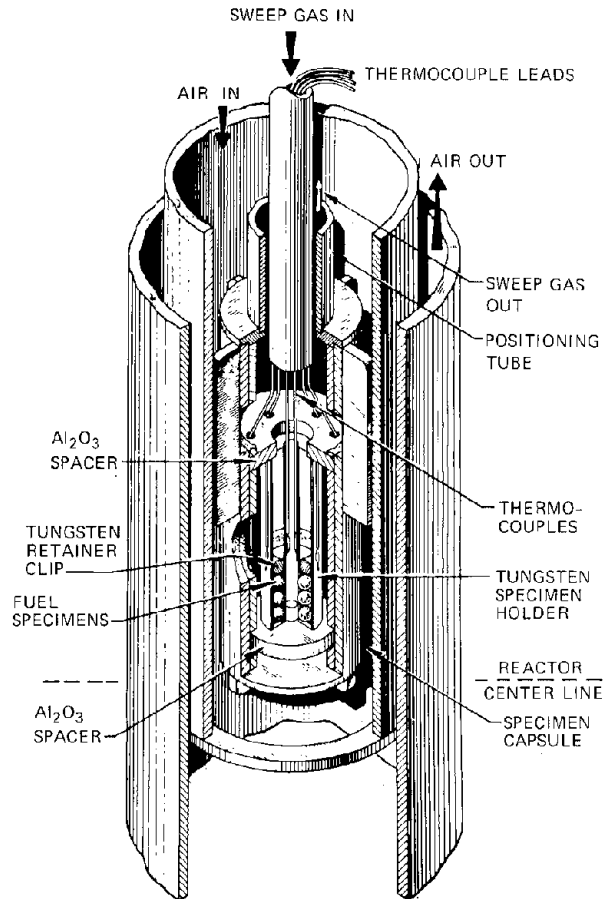


Fig. 15.3 Detail of capsule for in-pile fission-gas release investigation of fused crystal spheres of  $\text{UO}_2$ . [From R. M. Carroll et al., *Nucl. Sci. Eng.*, 38: 143 (1969).]

electrons of the material. When the initial kinetic energy has been expended by the stopping power of the medium, the fragment comes to rest as a fission product.\* However, if the fragment intersects a surface of the solid before its kinetic energy is depleted, it is released. Figure 15.6 shows fission-fragment tracks in a thin film of irradiated  $\text{UO}_2$  which had been suitably etched to reveal the lattice distortion caused by the passage of the high-energy fragment. The track starting in the upper left corner of the electron micrograph and terminating in the lower right is  $6.5\ \mu\text{m}$  in length and  $\sim 150\ \text{\AA}$  in width.†

\*Fission fragments are distinguished from fission products by their kinetic energy. Fission fragments possess all or part of the  $\sim 80\ \text{MeV}$  received from the fission event, whereas fission products are stationary.

†Fission tracks are visible only in thin films of  $\text{UO}_2$ , which have grain sizes less than  $\sim 100\ \text{\AA}$ . These fine grains trap the heat liberated by slowing down of the fragment. As a result of the very high local temperature, considerable disruption (essentially vaporization) of the lattice occurs. In large-grain material, on the other hand, the thermal spike is rapidly quenched and tracks are not visible.<sup>6</sup>

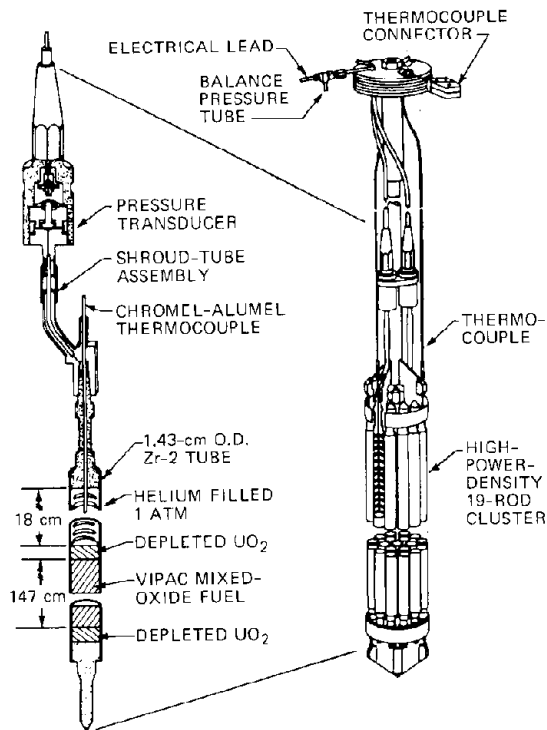


Fig. 15.4 Instrumented fuel element for measuring pressure buildup during irradiation. [After T. B. Burley and M. D. Freshley, *Nucl. Appl. Tech.*, 9: 233 (1970).]

The second mechanism of fission-gas ejection is called the knockout process. In passing through the solid, fission fragments occasionally make elastic collisions with the nuclei of atoms of the lattice, which become energetic particles in their own right. The fission track in Fig. 15.6 shows a slight change in direction near the middle of its path, which is probably due to such a collision. The atom struck by the fission fragment, which is called a primary knock-on, acquires energy of the order<sup>7</sup> of  $\sim 100$  keV. It too travels through the solid in a nearly straight line for a distance of  $\sim 200$  Å before coming to rest. If the primary

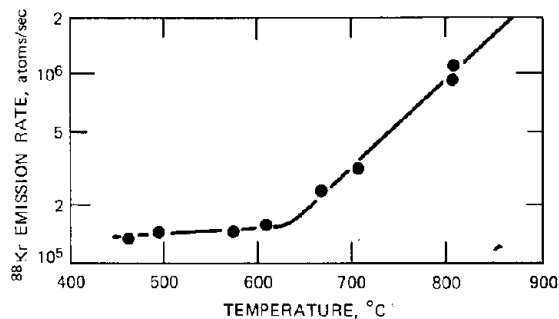


Fig. 15.5 Steady-state release rate of <sup>88</sup>Kr from single-crystal UO<sub>2</sub> for  $\bar{F} \approx 2 \times 10^{12}$  fissions cm<sup>-3</sup> sec<sup>-1</sup>. [After R. M. Carroll and O. Sisman, *Nucl. Sci. Eng.*, 21: 147 (1965).]

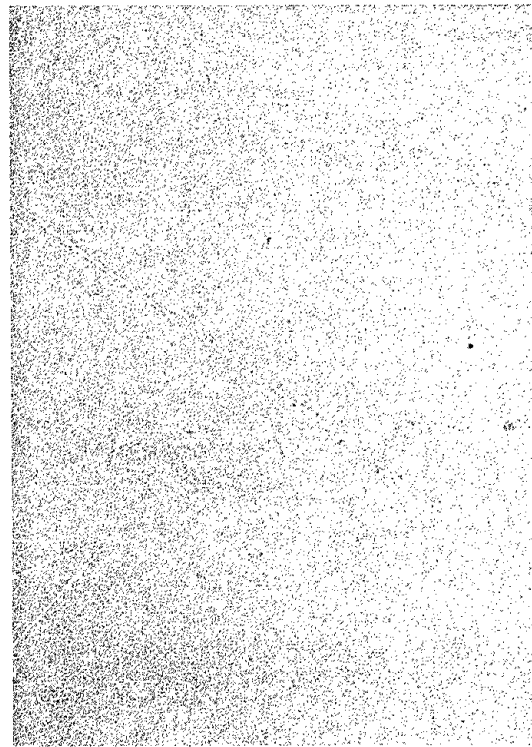


Fig. 15.6 Fission-fragment tracks in a 150-Å-thick film of vacuum-deposited UO<sub>2</sub>. [From M. D. Rogers, *J. Nucl. Mater.*, 16: 298 (1965).]

knock-on is created within this distance of the surface, it may be ejected. The primary knock-on is most likely to be a uranium or oxygen atom of the fuel, but occasionally a fission-gas atom lodged in the lattice may be struck by a passing fission fragment (of any kind) and become a primary knock-on that may have sufficient energy to escape from the surface before coming to rest.

Even if the primary knock-on does not emerge from the solid via a nearby surface, it can transfer its energy to other atoms in the solid by elastic collisions. The atoms struck by the primary knock-on are called secondary knock-ons. These in turn can strike other atoms to create a collision cascade whose members are generally referred to as higher order knock-ons. The mean energy and range of the higher order knock-ons are much less than those of the primary knock-on, but there are many more of the former than of the latter. The primary or higher order knock-on atoms that escape from the surface are said to be knocked out. To escape, the knock-ons must be produced no farther from the surface than their mean range.

The direct recoil and knockout mechanisms of release are illustrated in Fig. 15.7. The knockout process can remove any type of atom from the solid, either as a primary or a higher order knock-on. The energy for creating the collision cascade arises from a fission fragment, which need not escape from the fuel nor be one of the noble-gas fission products. Of course, only fission fragments can be released from the fuel by the direct recoil mechanism since the

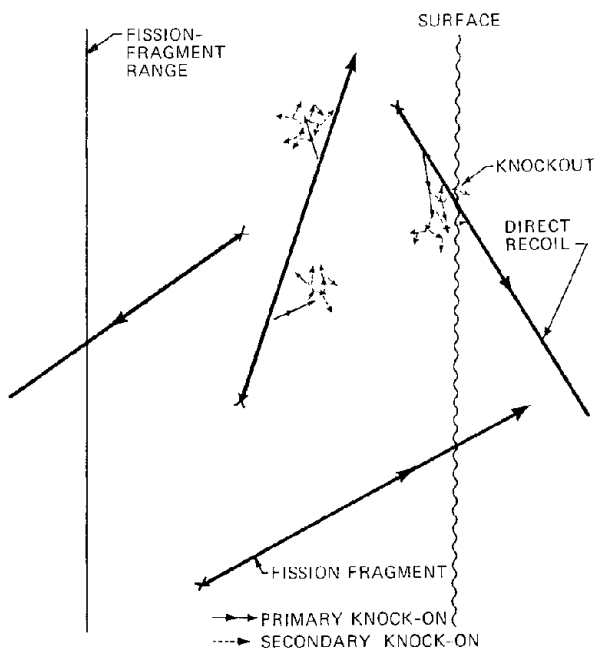


Fig. 15.7 Fission-gas release by direct recoil and knockout.

atoms of the fuel matrix do not directly receive any of the energy of fission. Table 15.1 summarizes the numbers, mean energies, and ranges of the energetic particles of importance in the direct recoil and knockout release mechanisms. The calculated parameters of the knock-ons refer to the uranium atoms of the  $UO_2$  lattice. Analogous numbers can be obtained for the oxygen knock-ons.

In both the direct recoil and knockout mechanisms of fission-gas release, we must analyze a direct-flight particle transport problem near a free surface. Two quantities are of interest: the concentration profile of a particular fission-product species near the surface and the rate at which this species recoils out of the surface. To calculate the concentration distribution, we can balance the production and removal of fission products (not fission fragments) in a unit volume of solid. The method is similar to that applied to thermal neutrons in a reactor, in which fast neutrons are excluded from the thermal neutron balance and contribute to the latter as a slowing down source. In analogous fashion

Table 15.1 Characteristics of Fission Fragments and Knock-ons in  $UO_2$ \*

Particle	Number created per fission fragment	Mean energy, keV	Range, A
Fission fragment	1	80,000	100,000
Primary uranium knock-ons	28	100	220
Higher order uranium knock-ons	21,000	0.2	44

\*Based on Ref. 7.

we calculate the rate at which energetic particles of a certain type slow down and stop in a volume element of the solid. This process provides a source of particles to the balance. Similarly, particles struck by other high-energy species are lost from the stationary class.

Because the ranges of the energetic particles are small compared to the dimensions of the solid, all concentrations and generation rates can be considered as functions of the distance  $x$  from the solid surface. The rate of production of recoils of species  $i$  is defined by

$$P_i(x) = \frac{\text{rate of generation of recoils of species } i \text{ per unit volume at a distance } x \text{ from the surface}}$$

The term "recoil" is used to denote fission fragments or knock-ons of any species in the solid.

We first compute the source term in the balance equation on a stationary species due to stopping of recoils in the solid. This quantity is defined by

$$q_i(x) = \frac{\text{rate at which particles of species } i \text{ are stopped in a unit volume of solid at a distance } x \text{ from the surface}}$$

where  $q_i$  is analogous to the slowing-down density of neutrons at thermal energies treated in reactor physics calculations.

To determine  $q_i$ , consider a spherical volume element of radius  $\rho$  at a distance  $x$  from the surface, as shown in Fig. 15.8. The particles that come to rest in this volume element originated in a spherical shell a distance equal to the recoil range  $\mu$  from the small sphere. The chord length through the small sphere intersected by a parallel line ranges from  $2\rho$  if the particle passes through the center of the sphere to zero if the particle just grazes the sphere. The mean chord length can be obtained from elementary

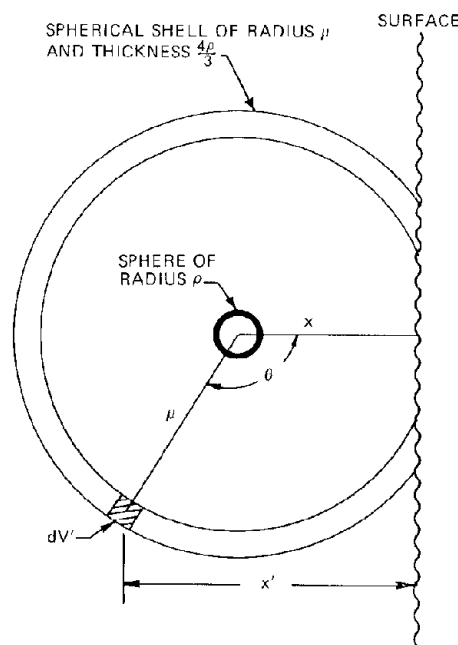


Fig. 15.8 Diagram for determining the rate at which recoils stop in a unit volume of solid.

geometry as  $4\rho/3$ , which is therefore the thickness of the spherical shell surrounding the small sphere. All recoils generated in a volume element  $dV' = 2\pi\mu^2(4\rho/3)d\cos\theta$  in the spherical shell and directed into the solid angle subtended by the small sphere are stopped in the sphere. The rate at which recoils are generated in  $dV'$  is  $P_i(x')dV'$ , where  $x'$  is the distance of the volume element  $dV'$  from the surface. Assuming that the recoils are isotropically distributed, the fraction of them which intersects (and stops in) the small sphere is  $\pi\rho^2/4\pi\mu^2$ . Thus, the recoil stopping source in the small sphere is

Rate of stopping in a sphere of radius  $\rho$

$$= 2\pi \int_{\cos\pi}^{\cos\theta_{\min}} P_i(x') \left(\frac{\pi\rho^2}{4\pi\mu^2}\right)\mu^2 \left(\frac{4\rho}{3}\right) d\cos\theta \quad (15.1)$$

If the point  $x$  is less than the range of the recoils, the minimum angle is

$$\cos\theta_{\min} = \frac{x}{\mu} \quad (15.2)$$

and if  $x > \mu$ ,

$$\cos\theta_{\min} = 1 \quad (15.3)$$

The distances  $x$  and  $x'$  are related by

$$x' = x - \mu \cos\theta \quad (15.4)$$

Division of Eq. 15.1 by the volume of the small sphere,  $4\pi\rho^3/3$ , gives  $q_i(x)$ . Transforming the integration variable from  $\cos\theta$  to  $x'$  and dividing by  $4\pi\rho^3/3$  reduces Eq. 15.1 to

$$q_i(x) = \frac{1}{2\mu} \int_0^{x+\mu} P_i(x') dx' \quad (\text{for } 0 \leq x \leq \mu) \quad (15.5)$$

$$= \frac{1}{2\mu} \int_{x-\mu}^{x+\mu} P_i(x') dx' \quad (\text{for } x > \mu) \quad (15.6)$$

For the special case in which  $P_i$  is independent of distance from the surface,  $q_i$  becomes

$$q_i = \frac{1}{2} (1 + x/\mu) P_i \quad (\text{for } 0 \leq x \leq \mu) \quad (15.7)$$

$$= P_i \quad (\text{for } x > \mu) \quad (15.8)$$

The second quantity of interest is the recoil current at  $x = 0$ , defined by

$I_i$  = rate at which recoils of species  $i$   
cross a unit area of surface

The recoil current at the surface can be determined with the aid of Fig. 15.9. Recoils within a hemisphere of radius  $\mu$  from a point on the surface can escape if they have the appropriate initial direction. Consider a spherical ring of volume  $dV = 2\pi r^2 dr d\cos\theta$ . The rate of production of recoils in this volume element is  $P_i(x) dV$ . The solid angle subtended by the unit area on the surface from a point on the spherical ring is  $\cos\theta/4\pi r^2$ . The contribution to the recoil current at  $x = 0$  from the spherical ring element is

$$dI_i = \frac{1}{2} P_i(x) \cos\theta dr d\cos\theta \quad (15.9)$$

The distance from the surface,  $x$ , is related to  $r$  and  $\theta$  by

$$r = \frac{x}{\cos\theta} \quad (15.10)$$

Integration of Eq. 15.9 is simplified if the  $r$  integral is replaced by an integral over  $x$ . The contribution to  $I_i$  due to recoils originating in a slab of thickness  $dx$  at a distance  $x$  from the surface is obtained from Fig. 15.10, where Eq. 15.10 has been plotted for two constant values of  $x$ , namely  $x$  and  $x + dx$ . The contribution to  $I_i$  from recoils coming from the slab  $dx$  is obtained by integrating over the

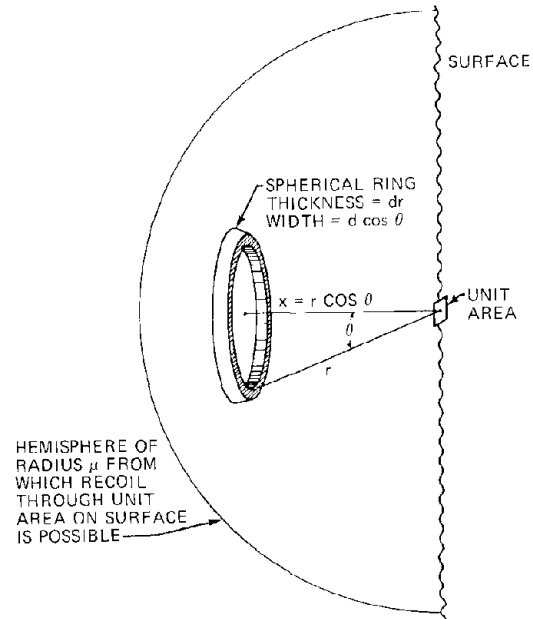


Fig. 15.9 Diagram for calculating the current of recoils through the solid surface.

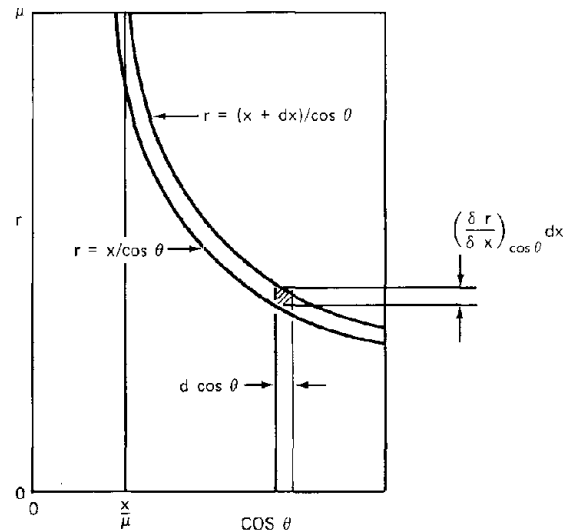


Fig. 15.10 Transformation from  $r$ - $\theta$  to  $x$ - $\theta$  coordinates.

area between the two curves shown in the drawing from  $\cos \theta = x/\mu$  to  $\cos \theta = 1$ . The area element indicated on Fig. 15.10 has a width  $d\cos \theta$  and a height that is equal to the difference between the value of  $r$  on the lower curve and the value of  $r$  on the upper curve, both at the value of  $\cos \theta$  under consideration. The value of  $r$  on the upper curve is

$$r + \left(\frac{\partial r}{\partial x}\right)_{\cos \theta} dx$$

Thus, the area element  $dr d\cos \theta$  in Eq. 15.9 can be replaced by

$$\begin{aligned} dr d\cos \theta &= \left(\frac{\partial r}{\partial x}\right)_{\cos \theta} dx d\cos \theta \\ &= \frac{dx d\cos \theta}{\cos \theta} \end{aligned}$$

where Eq. 15.10 was used to evaluate the partial derivative. Equation 15.9 becomes

$$dI_i = \frac{1}{2} P_i(x) d\cos \theta dx$$

and the recoil current is obtained by integrating over the appropriate range of  $\cos \theta$  and then integrating over  $x$ :

$$I_i = \frac{1}{2} \int_0^\mu P_i(x) \left(1 - \frac{x}{\mu}\right) dx \quad (15.11)$$

For the special case in which  $P_i$  is independent of  $x$ ,  $I_i$  becomes

$$I_i = \frac{P_i \mu}{4} \quad (15.12)$$

### 15.3.1 Direct Recoil

We consider the balance over a unit volume of the solid on fission product  $i$ , which is created directly from fission with an independent fission yield  $y_i$ . This fission product is removed from the unit volume by radioactive decay at a rate  $\lambda_i C_i$ , where  $\lambda_i$  is the decay constant and  $C_i$  is the concentration of the fission product. The input of the fission product to a unit volume is due to stopping of fission fragments of this species. This source is given by Eqs. 15.7 and 15.8 in which  $P_i$  is set equal to  $y_i \dot{F}$  and  $\mu$  is the range of the fission fragment,  $\mu_{ff}$  (all fission fragments are assumed to have the same range). The balance equations are

$$\frac{dC_i}{dt} = \frac{1}{2} (y_i \dot{F}) (1 + x/\mu_{ff}) - \lambda_i C_i \quad (\text{for } 0 \leq x \leq \mu_{ff}) \quad (15.13)$$

$$= y_i \dot{F} - \lambda_i C_i \quad (\text{for } x > \mu_{ff}) \quad (15.14)$$

Integrating these equations yields the profile

$$\frac{C_i(x,t)}{C_i^\infty} = \frac{(1 + x/\mu_{ff})}{2} \quad (\text{for } 0 \leq x \leq \mu_{ff}) \quad (15.15)$$

$$= 1 \quad (\text{for } x > \mu_{ff}) \quad (15.16)$$

where

$$C_i^\infty = \frac{y_i \dot{F}}{\lambda_i} (1 - e^{-\lambda_i t}) \quad (15.17)$$

is the concentration of the fission product in the bulk solid at time  $t$ . The concentration distribution near the surface is plotted in Fig. 15.11. The profile changes slope discontinuously at  $x = \mu_{ff}$ , and the concentration at the surface is one-half the bulk value. The concentration in the surface layer has the same time dependence as that in the bulk.

The fission-fragment current at the surface due to direct recoil is obtained from Eq. 15.12 as

$$I_i^{rec} = \frac{1}{4} y_i \dot{F} \mu_{ff} \quad (15.18)$$

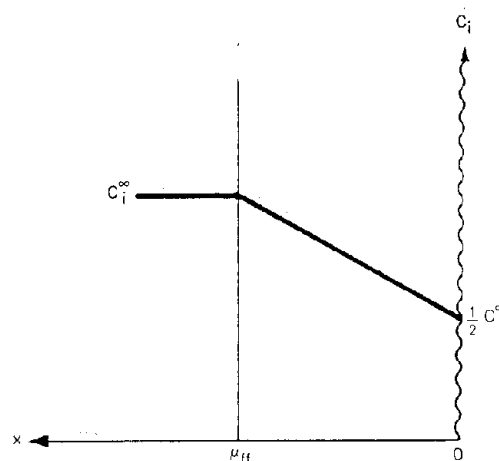


Fig. 15.11 Concentration of fission product  $i$  near the surface.

### 15.3.2 Knockout of Matrix Atoms

Rutherford collisions between a fission fragment and an atom of the lattice generate primary knock-on matrix atoms. If these collisions occur sufficiently close to the surface and if the recoil atom is directed out of the surface, it may be ejected from the solid. Even if it does not escape, the primary knock-on can collide with other matrix atoms to produce secondary and higher order knock-ons. Some of these may escape from the surface of the solid. The yield of escaping knock-ons per fission fragment can be measured by placing a collector plate close to the surface of a piece of fuel, irradiating the assembly under vacuum, and measuring the amount of fuel transferred to the collector plate. From such data the knock-on ejection yield of uranium can be determined by the formula

$$\alpha_U = \frac{I_U^{ko}}{I_{ff}^{rec}} \quad (15.19)$$

where  $I_U^{ko}$  is the measured current of uranium atoms leaving the surface and  $I_{ff}^{rec}$  is the current of all fission fragments leaving the surface. The latter is obtained from Eq. 15.18 by summing over all fission products:

$$\begin{aligned} I_{ff}^{rec} &= \sum_{\text{all } fp} \frac{1}{4} y_i \dot{F} \mu_{ff} \\ &= \frac{1}{4} (2\dot{F}) \mu_{ff} \end{aligned} \quad (15.20)$$

The sum of the independent yields in fission is 2. The values of  $\alpha_U$  measured by Nilsson<sup>7</sup> and by Rogers<sup>8</sup> for sintered  $UO_2$  are both  $\sim 5$ . The value of  $I_U^{k_0}$  can be calculated by using Eq. 15.12 with the knock-on source term given by

$$P_{U1} = 2n_1^{k_0} \dot{F} \quad (\text{for primary knock-ons}) \quad (15.21)$$

$$P_{U2} = 2n_2^{k_0} \dot{F} \quad (\text{for higher order knock-ons}) \quad (15.22)$$

In these equations  $n_1^{k_0}$  is the number of primary uranium knock-ons created by a single fission fragment over its entire range, and  $n_2^{k_0}$  is the corresponding number of higher order knock-ons. The knock-on ejection current is

$$I_U^{k_0} = \frac{1}{4}(2\dot{F}) (n_1^{k_0} \mu_1^{k_0} + n_2^{k_0} \mu_2^{k_0}) = \frac{1}{4}(2\dot{F}) n_U^{k_0} \mu_U^{k_0} \quad (15.23)$$

where  $\mu_1^{k_0}$  and  $\mu_2^{k_0}$  are the ranges of the primary and higher order uranium knock-ons, respectively. The numbers and ranges of uranium knock-ons in  $UO_2$  computed by Nilsson<sup>7</sup> are listed in Table 15.1. The term  $n_U^{k_0} \mu_U^{k_0}$  in Eq. 15.23 is the sum of the corresponding number-range products for the two types of knock-ons. Table 15.1 shows that the higher order knock-ons, despite their very small range in the solid, dominate the ejection current because of the large number of them created per fission fragment. Thus,  $n_U^{k_0}$  is approximately  $2 \times 10^4$ , and  $\mu_U^{k_0}$  is  $\sim 50$  Å. The theoretical value of  $\alpha_U$  is obtained by dividing Eq. 15.23 by 15.20, which yields

$$\alpha_U = \frac{n_U^{k_0} \mu_U^{k_0}}{\mu_{ff}} \approx 10 \quad (15.24)$$

The calculated value of  $\alpha_U$  is in rather good agreement with the measured value of  $\sim 5$ , which justifies the validity of the original theoretical premise that ejection is the result of knock-ons from the collision cascade created by a passing fission fragment.

### 15.3.3 Fission-Product Release by the Knockout Mechanism

The success of the knock-on theory to explain the observed yield of uranium atoms ejected from  $UO_2$  suggests that similar theory should be applicable to the fission-product atoms residing in the lattice close to the surface. If the fission-product atoms had the same mass and charge as the uranium atoms, they would be indistinguishable from the uranium atoms, and the source of fission-product knock-ons would be equal to the uranium-atom knock-on rate times the fraction of the lattice sites occupied by fission-product atoms. The mass and charge of the fission-product atoms, however, are  $\sim 1/2$  those of uranium. These differences mean that the range of the fission-product knock-ons is somewhat larger than that of the uranium knock-ons, but the Rutherford scattering cross section of the fission-product knock-ons is somewhat smaller than that of the uranium knock-ons. Since these two effects compensate each other, we can, to a first approximation, take the source of knock-ons of fission-product species  $i$  as

$$P_i = (2n_U^{k_0} \dot{F}) \frac{C_i}{N_U} \quad (15.25)$$

where  $N_U$  is the density of uranium atoms in the solid. The range of the fission-product knock-ons is also assumed to be

equal to that of the uranium knock-ons. Contrary to the cases of direct recoil of fission fragment and knockout of uranium atoms, the volumetric source of fission-product knock-ons is not constant but depends on distance from the surface according to the concentration profile  $C_i(x)$ . Therefore, to calculate the knockout current of fission products by Eq. 15.11, we must first compute the distribution of fission product  $i$  within a range  $\mu_U^{k_0}$  of the surface.

### 15.3.4 Short-Lived Fission Products

We first set up and solve the balance equations for short-lived fission products, under the assumption that the concentrations are not changing with time. This calculation is applicable to the in-pile fission-gas release experiments described in Sec. 15.2.

Consider a unit volume of fuel in which the concentration of fission product  $i$  at distance  $x$  from the surface is  $C_i(x)$ . The rates at which this species appears and disappears from the unit volume are equated. The output is due to radioactive decay at a rate  $\lambda_i C_i$  and to knock-on by a collision cascade at a rate  $P_i$ . The input to the unit volume includes stopping of fission fragments of species  $i$  at a rate  $q_i^{ff}$  and stopping of knock-ons of the same species at a rate  $q_i^{k_0}$ . At steady state the balance on fission product  $i$  takes the form

$$q_i^{ff} + q_i^{k_0} = P_i + \lambda_i C_i \quad (15.26)$$

Since only positions very close to the surface contribute to knockout, the first term on the left is given by Eq. 15.7 with the source of fission recoils equal to  $y_i \dot{F}$ , or

$$q_i^{ff} = \frac{1}{2}(y_i \dot{F}) (1 + x/\mu_{ff}) \quad (15.27)$$

The first term on the right of Eq. 15.26 is given by Eq. 15.25. The knock-on source in the balance,  $q_i^{k_0}$ , is given by Eqs. 15.5 and 15.6 with  $\mu = \mu_U^{k_0}$  and  $P_i$  of Eq. 15.25. Inserting these quantities into Eq. 15.26 yields

$$\begin{aligned} & \frac{1}{2}(y_i \dot{F}) \left(1 + \frac{x}{\mu_{ff}}\right) \\ & + \frac{1}{2\mu_U^{k_0}} \left(\frac{2n_U^{k_0} \dot{F}}{N_U}\right) \int_0^{x+\mu_U^{k_0}} C_i(x') dx' \\ & = \left(\lambda_i + \frac{2n_U^{k_0} \dot{F}}{N_U}\right) C_i \quad (\text{for } 0 \leq x \leq \mu_U^{k_0}) \end{aligned} \quad (15.28)$$

$$\begin{aligned} & \frac{1}{2}(y_i \dot{F}) \left(1 + \frac{x}{\mu_{ff}}\right) \\ & + \frac{1}{2\mu_U^{k_0}} \left(\frac{2n_U^{k_0} \dot{F}}{N_U}\right) \int_{x-\mu_U^{k_0}}^{x+\mu_U^{k_0}} C_i(x') dx' \\ & = \left(\lambda_i + \frac{2n_U^{k_0} \dot{F}}{N_U}\right) C_i \quad (\text{for } x > \mu_U^{k_0}) \end{aligned} \quad (15.29)$$

The concentration profile  $C_i(x)$  differs from that due to fission-fragment recoil (Fig. 15.11) only in a region within a few multiples of  $\mu_U^{k_0}$  from the surface. According to Table 15.1,  $\mu_U^{k_0}/\mu_{ff} < 10^{-3}$  (for the higher order knock-ons that

are most important in release); so the term  $x/\mu_{ff}$  on the left of Eqs. 15.28 and 15.29 can be neglected compared to unity, and the fission-fragment stopping source term reduces\* to  $y_i \bar{F}/2$ . For the steady situation envisaged for short-lived fission products, Eq. 15.17 shows that  $y_i \bar{F} = \lambda_i C_i^{\infty}$ , and so the first term on the left in Eqs. 15.28 and 15.29 is equal to  $\lambda_i C_i^{\infty}/2$ . The balance equations can be written as

$$\frac{1}{2} + \frac{H}{2} \int_0^{\eta+1} Y(\eta') d\eta' = (1+H)Y \quad (\text{for } 0 \leq \eta \leq 1) \quad (15.30)$$

and

$$\frac{1}{2} + \frac{H}{2} \int_{\eta-1}^{\eta+1} Y(\eta') d\eta' = (1+H)Y \quad (\text{for } \eta > 1) \quad (15.31)$$

where

$$\eta = \frac{x}{\mu_{ff}^{\text{ko}}} \quad (15.32)$$

$$Y = \frac{C_i}{C_i^{\infty}} \quad (15.33)$$

and  $H$  is a dimensionless constant representing the ratio of the rate of removal of fission product  $i$  by the knock-on process to that by radioactive decay:

$$H = \frac{2n_{\text{U}}^{\text{ko}} \bar{F}}{\lambda_i N_{\text{U}}} \quad (15.34)$$

The boundary condition for Eqs. 15.30 and 15.31 requires that the concentration approach  $C_i^{\infty}/2$  at distances from the surface large compared to  $\mu_{\text{U}}^{\text{ko}}$  but small compared to  $\mu_{ff}$ , or

$$Y(\eta) \rightarrow \frac{1}{2} \text{ as } \eta \gg 1 \quad (15.35)$$

This condition is automatically obtained by setting  $Y = \text{constant}$  in Eq. 15.31. Solution of Eqs. 15.30 and 15.31 yields the concentration profile  $Y(\eta)$  parametric in the quantity  $H$ . For  $H = 0$ , the solution is

$$Y(\eta) = \frac{1}{2} \quad (\text{for } H = 0) \quad (15.36)$$

The condition  $H = 0$  applies to fission products that decay so rapidly that their distribution near the surface is not affected by the knock-on process. For  $H > 0$ , however,  $Y$  differs from  $1/2$  over distances of several knock-on ranges from the surface. Moreover, the function  $Y(\eta)$  is discontinuous in slope (but not in value) at the points  $\eta = 1, 2, 3, \dots$ . For Eqs. 15.30 and 15.31 to be solved, different functional forms must be considered in the ranges of  $\eta$  separated by the discontinuities at integer values of  $\eta$ .

\*This simplification can also be obtained from the following argument. In the bulk of the solid, the source of fission products due to slowing down of fission fragments is equal to the rate of creation of the latter,  $y_i \bar{F}$ . Very close to the surface, a unit volume is exposed to fragments only from a semi-infinite solid; the other half of space is empty. Therefore, the stopping source is just one-half what it is in an infinite medium, or  $y_i \bar{F}/2$ .

Thus, the function  $Y_1(\eta)$  is applicable to the range  $0 \leq \eta \leq 1$ ,  $Y_2(\eta)$  to the interval  $1 \leq \eta \leq 2$ , etc. The integrals must be subdivided accordingly. Therefore Eqs. 15.30 and 15.31 can be written

$$\frac{1}{2} + \frac{H}{2} \left[ \int_0^1 Y_1(\eta) d\eta + \int_1^{\eta+1} Y_2(\eta') d\eta' \right] = (1+H)Y_1(\eta) \quad (\text{for } 0 \leq \eta \leq 1) \quad (15.37a)$$

$$\frac{1}{2} + \frac{H}{2} \times \left[ \int_{\eta-1}^1 Y_1(\eta') d\eta' + \int_1^2 Y_2(\eta) d\eta + \int_2^{\eta+1} Y_3(\eta') d\eta' \right] = (1+H)Y_2(\eta) \quad (\text{for } 1 \leq \eta \leq 2) \quad (15.37b)$$

$$\frac{1}{2} + \frac{H}{2} \left[ \int_{\eta-1}^2 Y_2(\eta') d\eta' + \int_2^3 Y_3(\eta) d\eta + \int_3^{\eta+1} Y_4(\eta') d\eta' \right] = (1+H)Y_3(\eta) \quad (\text{for } 2 \leq \eta \leq 3) \quad (15.37c)$$

Equations 15.37a, b, and c can be solved for small values of  $H$  by assuming  $Y_j(\eta)$  to be represented by a power series expansion in  $H$ , the first term of which is the solution for  $H = 0$ , namely,  $1/2$ ,

$$Y_j(\eta) = \frac{1}{2} + f_j(\eta) H + g_j(\eta) H^2 + h_j(\eta) H^3 + \dots \quad (15.38)$$

where  $j = 1, 2, 3, \dots$ . The functions  $Y_j(\eta)$  must be continuous at their common points, which leads to the restrictions,

$$\begin{aligned} f_1(1) &= f_2(1); g_1(1) = g_2(1); h_1(1) = h_2(1); \dots \\ f_2(2) &= f_3(2); g_2(2) = g_3(2); h_2(2) = h_3(2); \dots \\ f_3(3) &= f_4(3); g_3(3) = g_4(3); h_3(3) = h_4(3); \dots \end{aligned}$$

By substituting the series expressions for  $Y_1(\eta)$ ,  $Y_2(\eta)$ , ... of the form shown by Eq. 15.38 into Eqs. 15.37 and setting the coefficients of each power of  $H$  equal to zero, we can determine the functions  $f_j(\eta)$ ,  $g_j(\eta)$ ,  $h_j(\eta)$ , ... explicitly. Proceeding in this fashion with the series terminated after the  $h_j(\eta)H^3$  terms leads to the results shown in Table 15.2, from which the concentration profile can be reconstructed. The cubic expansion gives reliable results for  $H < 0.5$ . The dimensionless concentration profiles for  $H = 0.5$  and  $H = \infty$  (described later) are shown in Fig. 15.12.

The knockout current of fission product  $i$  is given by Eq. 15.11 where  $\mu = \mu_{\text{U}}^{\text{ko}}$  and  $P_i$  is given by Eq. 15.25:

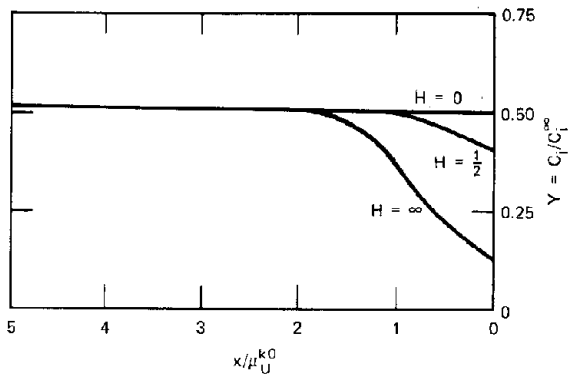
$$I_i^{\text{ko}} = \frac{1}{2} \left( \frac{2n_{\text{U}}^{\text{ko}} \bar{F}}{N_{\text{U}}} \right) \int_0^{\mu_{\text{U}}^{\text{ko}}} C_i(x) \left( 1 - \frac{x}{\mu_{\text{U}}^{\text{ko}}} \right) dx \quad (15.39)$$

or, in terms of the dimensionless parameters used in determining the concentration profile,

$$I_i^{\text{ko}} = \frac{1}{8} (y_i \bar{F}) \mu_{\text{U}}^{\text{ko}} H \left[ 4 \int_0^1 Y_1(\eta) (1-\eta) d\eta \right] \quad (15.40)$$

Table 15.2 Coefficients in Eq. 15.33 for the Cubic-Power-Series Solution for the Concentration Profile Due to the Knockout Process

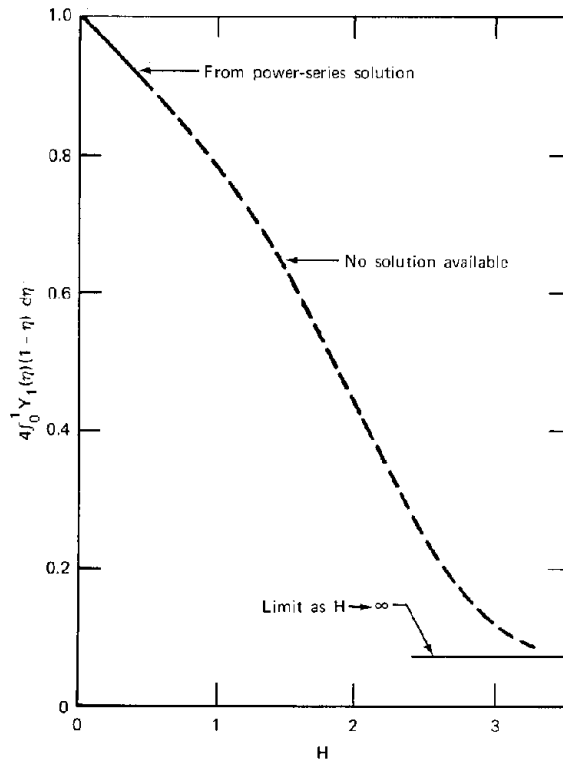
j	Range	$f_j(\eta)$	$g_j(\eta)$	$h_j(\eta)$
1	$0 \leq \eta \leq 1$	$-\frac{1}{4}(1-\eta)$	$\frac{3}{16} - \frac{1}{4}\eta$	$-\frac{5}{32} + \frac{7}{32}\eta + \frac{1}{32}\eta^2 - \frac{1}{96}\eta^3$
2	$1 \leq \eta \leq 2$	0	$-\frac{1}{4} + \frac{1}{4}\eta - \frac{1}{16}\eta^2$	$\frac{41}{96} - \frac{15}{32}\eta + \frac{1}{8}\eta^2$
3	$2 \leq \eta \leq 3$	0	0	$-\frac{27}{96} + \frac{9}{32}\eta - \frac{3}{32}\eta^2 + \frac{1}{96}\eta^3$
4	$3 \leq \eta \leq 4$	0	0	0

Fig. 15.12 Dimensionless fission-product concentration profiles within the knockout zone for several values of the parameter  $H$ .

Using the solutions for  $Y_i(\eta)$  shown in Fig. 15.12, the integral in the brackets in Eq. 15.40 can be determined as a function of the parameter  $H$ . The results are shown on Fig. 15.13. For values of  $H < 0.1$ , the term in the brackets in Eq. 15.40 is very close to unity, and the current is given by

$$I_i^{k0} = \frac{1}{8}(y_i \dot{F}) \mu_U^{k0} H = \left( \frac{y_i \alpha_U \mu_{ff}}{4N_U \lambda_i} \right) \dot{F}^2 \quad (15.41)$$

where the second equality has been obtained by using Eqs. 15.34 and 15.24. Equation 15.41 shows that the knockout current for short-lived isotopes at low power is inversely proportional to the decay constant and directly proportional to the square of the fission density. This latter characteristic of the knockout release was first suggested by Carroll and Sisman.<sup>9</sup> The physical basis of the  $F^2$  dependence is that both the concentration of the fission product in the knockout zone and the recoil rate of fission fragments that initiate the knockout are proportional to the fission rate. Using the apparatus shown in Figs. 15.2 and 15.3, Carroll et al.<sup>10</sup> have tested the implications of the knockout release model. They measured the rates of release of 2.8-hr  $^{88}\text{Kr}$  at low temperatures from fine-grained pellets of natural  $\text{UO}_2$  and from fused crystal spheres of enriched  $\text{UO}_2$ . On the basis of the geometrical surface area

Fig. 15.13 Integral used in the calculation of the knockout release rate as a function of the parameter  $H$ .

of the specimens, the release rates from the pellets were found to be correlated by the equation

$$(I_{88})_{\text{exp}} = 5.3 \times 10^{-20} \dot{F}^2 \text{ atoms cm}^{-2} \text{ sec}^{-1} \quad (15.42)$$

for fission rates between  $7 \times 10^{11}$  and  $1.7 \times 10^{12}$  fissions  $\text{cm}^{-3} \text{ sec}^{-1}$ . The theoretical value of the release rate can be computed from Eq. 15.41 using the following values of the constants:

$$\begin{aligned} y_{88} &= 0.035 \\ \lambda_{88} &= 7 \times 10^{-5} \text{ sec}^{-1} \\ \alpha_U &= 5 \\ \mu_{ff} &= 10^{-3} \text{ cm} \\ N_U &= 2.5 \times 10^{22} \text{ cm}^{-3} \end{aligned}$$

For these conditions the calculated value of  $H$  is  $<0.05$ , which means that Eq. 15.41 should be valid. The predicted knockout rate is

$$I_{88}^{k0} = 2 \times 10^{-23} \bar{F}^2 \text{ atoms cm}^{-2} \text{ sec}^{-1} \quad (15.43)$$

The factor of 2500 discrepancy between the coefficients of  $\bar{F}^2$  in Eqs. 15.42 and 15.43 can be rationalized by one of the following:

1. *The theory is incorrect.* Although this possibility cannot be rejected, the fact that the theory predicts the correct dependence of the release rate on fission rate suggests that the basic assumptions of the model are correct. The values of some of the parameters in Eq. 15.41 may be in error, however. Rogers<sup>6</sup> has observed values of  $\alpha_U$  as large as 50,000 for vacuum-deposited thin films of  $UO_2$  in which the grain size was 50 Å, but this value decreased during irradiation due to grain growth. (The very large value of  $\alpha_U$  is explained by a vaporization mechanism from fission-fragment tracks intersecting the surface, not by knockout due to collision cascades.<sup>6</sup>) If for some reason the pellets used by Carroll et al.<sup>10</sup> contained an extremely fine-grained surface structure, a value of  $\alpha_U$  larger than 5 would be expected.

2. *Additional release mechanisms were operative in the experiment.* This is unlikely, since no other release mechanism predicts a rate that varies as the square of the fission density.

3. *The experimental rates given by Eq. 15.42 are based on the assumption that knockout occurs only from the geometric surface area of the specimen.* The pellet samples contained considerable internal surface area and external surface roughness. Fission products released by knockout emerge from the surface with very low energies (the initial energy of the higher order knock-ons that are responsible for release is only  $\sim 200$  eV), and they would be easily stopped in the gas in even very fine cracks. For a proper comparison of theory with experiment, the data should be referenced to the total specimen surface area, not to the geometrical surface area. Or Eq. 15.43 should be multiplied by the ratio of the total to the geometrical surface areas. Although such a correction places theory closer to observation, it is difficult to account for a factor of 2500 by this explanation.

For the crystal spheres of enriched  $UO_2$ , the  $^{88}\text{Kr}$  release rates measured by Carroll et al.<sup>10</sup> were correlated by

$$(I_{88})_{\text{exp}} = 1.5 \times 10^{-8} \bar{F} \text{ atoms cm}^{-2} \text{ sec}^{-1} \quad (15.44)$$

The fission densities in these experiments were about an order of magnitude larger than in the pellet irradiations, but the calculated values of  $H$  still indicate that Eq. 15.41 should be applicable. Carroll et al.<sup>10</sup> believe that the knockout mechanism is responsible for the release in the crystal sphere experiments and argue that the surfaces of the spheres were saturated with  $^{88}\text{Kr}$ ; so an increase in  $\bar{F}$  increased the recoil rate driving knockout, but not the concentration of this species at the surface. The theoretical model described does not indicate any such saturation phenomenon; Fig. 15.13 shows that the bracketed term in Eq. 15.40 approaches a constant as  $H \rightarrow \infty$ . In this limit the knockout current is a constant fraction of the right-hand side of Eq. 15.41.

An alternate explanation of the linear dependence of the release rate on fission density is that direct recoil rather than knockout is the dominant mechanism for the single-crystal spheres. Fission fragments recoiling directly from the solid emerge from the surface with sufficiently large energies to pass through substantial thicknesses of surrounding gas and become embedded in adjacent surfaces. Thus only the geometrical area of the specimen is available for measurable release by the recoil mechanism. Switching from relatively porous pellets to single-crystal pieces brings the ratio of total area to geometrical area close to unity, which does not affect the release by recoil but reduces the release due to knockout. If it is assumed that direct recoil is responsible for release from the single-crystal spheres, the theoretical rate is given by Eq. 15.18, which for  $^{88}\text{Kr}$  is

$$I_{88}^{\text{ec}} = 9 \times 10^{-6} \bar{F} \text{ atoms cm}^{-2} \text{ sec}^{-1} \quad (15.45)$$

which has the correct dependence on  $\bar{F}$  but is too large in magnitude by a factor of  $\sim 600$ . However, the spheres used in the experiment were 1 mm in diameter, and 36 of them were loaded into the sample holder in the manner shown in Fig. 15.3. The close proximity of the spheres to each other and to the surface of the container means that a significant portion of the recoiling fission fragments from one sphere may have become implanted in an adjacent sphere or in container surfaces. The fraction of the recoils that stop in the gas phase and are measured depends on the geometry of the packing of the spheres and on the gas pressure, and a recoverable fraction of  $1/600$  may not be unreasonable.

### 15.3.5 Release of Short-Lived Isotopes Due to Surface Fissions

A general formula for the fractional release rates of short-lived fission gases applicable to in-pile tests wherein steady state is reached can be obtained by combining the contributions from direct recoil and knockout. The fractional release rate, or release-to-birth rate ratio, can be written

$$f_i = \frac{R_i}{B_i} = \frac{\eta_{\text{rec}} S_g I_i^{\text{ec}} + S_T I_i^{k0}}{y_i \bar{F} V} \quad (15.46)$$

where  $\eta_{\text{rec}}$  = the fraction of the direct recoils that are not embedded in other surfaces after ejection from the solid

$S_g$  = the geometrical area of the specimens

$S_T$  = the total surface area of the specimens

$V$  = the sample volume

Using Eq. 15.18 for  $I_i^{\text{ec}}$  and Eq. 15.41 for  $I_i^{k0}$ , we can obtain the fractional release rate,

$$f_i = \frac{1}{4} \eta_{\text{rec}} \left( \frac{S_g}{V} \right) \mu_{\text{ff}} \left( 1 + \frac{1}{\eta_{\text{rec}}} \frac{S_T}{S_g} \frac{\alpha_U \bar{F}}{N_U \lambda_i} \right) \quad (15.47)$$

This formula shows that several factors affect the relative magnitudes of the fission-gas release rates by the two mechanisms. The efficiency of collection of direct recoils,  $\eta_{\text{rec}}$ , depends on the proximity of the fuel specimens to each other and to container surfaces and to the pressure of the sweep gas. These experimental conditions should not affect the gas released by the knockout process. The ratio of total surface area to geometrical

surface area,  $S_T/S_g$ , can be controlled by the microstructure of the solid and by surface roughness. The knockout yield,  $\alpha_U$ , depends on the grain structure on the surface of the samples; both  $S_T$  and  $\alpha_U$  can decrease during irradiation due to surface smoothing caused by plating out of  $UO_2$  ejected from adjacent fuel surfaces. The fission density  $F$  is controlled by irradiation conditions. As shown by Eq. 15.47, changing any of the listed factors alters the relative magnitudes of the direct recoil and knockout terms.

The variable that has been most systematically exploited in experiments designed to sort out the contributions of direct recoil and knockout in low-temperature gas release is the decay constant  $\lambda$ . By studying the release of  $^{87}Kr$ ,  $^{88}Kr$ ,  $^{85m}Kr$ ,  $^{135}Xe$ , and  $^{133}Xe$ , we see from Table 13.3 that a two order-of-magnitude range of decay constant is readily attainable. Equation 15.47 shows that if the predominant release mode is direct recoil,  $f_i$  should be independent of nuclide half-life, whereas, if knockout is the primary mechanism,  $f_i$  should vary\* as  $\lambda_i^{-1}$ . When both mechanisms are of comparable magnitude, the fractional release rate should vary inversely as the decay constant raised to some power between 0 and 1.

Carroll and Sisman<sup>9</sup> and Souhier<sup>11</sup> have measured the steady-state fractional release rates of several fission-gas isotopes. Souhier's results are shown in Fig. 15.14. Three types of specimens were tested in this investigation: single-crystal spheres  $\sim 3$  mm in diameter, large cylindrical pellets of sintered  $UO_2$ , and small cylindrical specimens of sintered  $UO_2$ . The single-crystal samples showed fractional release rates that varied as the  $-0.1$  power of the decay constant, and the pellets showed a  $-0.2$  to  $-0.3$  power dependence of  $f$  upon  $\lambda$ . According to Eq. 15.47 these results suggest that direct recoil was the dominant release mechanism for the single-crystal spheres. The ratio  $S_T/S_g$  was larger than unity in the polycrystalline sinters, which should increase the knockout contribution in these specimens by comparison to the single crystals. As a result the fractional release decreases more rapidly with decay constant in the pellet tests than in the experiments with single crystals.

The magnitudes of the fractional release rates for the single crystals were only 2 to 3% of that predicted by the formula  $f_i = \frac{1}{4}(S_g/V)\mu_{ff}$ , which indicates that the efficiency of direct recoil collection by the sweep gas,  $\eta_{rec}$ , was also of this order of magnitude. Within the group of large-pellet specimens, both the magnitude of the fractional release and its  $\lambda$  dependence increased with decreasing solid density, which is consistent with larger internal surface areas available for knockout release in high porosity specimens than in solids close to theoretical density. The small pellets exhibited a greater fractional release rate than did the large ones because  $S_g/V$  was five times greater in the small pellets than in the large ones. If the 95% TD (small) points are divided by a factor of 5, they fall quite near the line drawn through the data for the large pellets of the same density.

\*The  $\lambda$  dependence of the knockout mechanism used in Eq. 15.47 is valid only when Eq. 15.41 holds, or for  $H < 0.1$  or  $H \rightarrow \infty$ . This restriction is easily satisfied for the short half-life krypton isotopes but may be violated for the xenon isotopes. In the latter case, the knockout current is less strongly dependent upon decay constant than  $\lambda^{-1}$ .

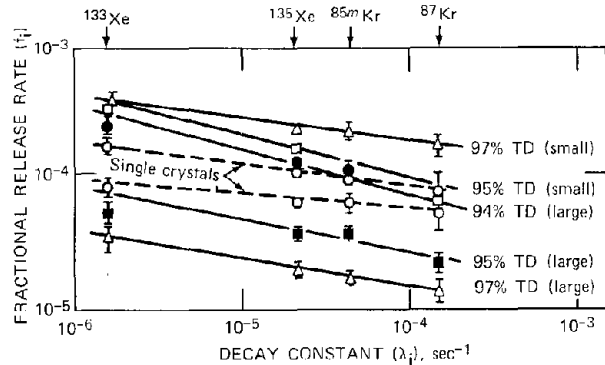


Fig. 15.14 Steady-state fractional release rates of radioactive fission gases from  $UO_2$  irradiated at low temperature. The figures to the right of the lines indicate the percent of theoretical density of the sintered pellet specimens. The samples labeled "small" were  $\frac{1}{10}$  of the mass but five times the geometrical surface-to-volume ratio of the samples labeled "large." [From R. Souhier, *Nucl. Appl.*, 2: 133 (1966).]

The data for the 97% TD small pellet are anomalously high, although the slope of the line through these data is the same as the slope of the line through the 97% TD large pellets.

The data accumulated from in-pile experiments of low-temperature fission-gas release qualitatively support a model that ascribes release to a combination of direct recoil and knockout. Quantitative agreement with theory is difficult to obtain, however, because of the sensitivity of the release rates to the geometry of the samples and the holder and to the microstructure of the fuel specimens.

### 15.3.6 Stable Fission Products

The direct recoil release formula, Eq. 15.18, is applicable to stable as well as to radioactive fission products.

Although the steady-state analysis of the knockout mechanism of radioactive fission gases is useful in interpreting the results of in-pile gas-release experiments, it is of little significance in reactor operation. The fission gases responsible for fuel swelling and internal pressurization of the fuel element are the stable isotopes listed in Table 13.3. The radioactive fission gases decay to solid fission products and are generally included in the cumulative yields of these fission products.

Analysis of the knockout of stable fission products begins with a balance equation similar to Eq. 15.26, except that the radioactive decay term is deleted and the unsteady-state nature of the process is accounted for. Thus,

$$\frac{dC_i}{dt} = q_i^{ff} + q_i^{ko} - P_i \quad (15.48)$$

As in the case of radioactive species,  $q_i^{ff}$  can be approximated by  $y_i \dot{F}/2$  (although the subsequent step of equating  $y_i \dot{F}$  to  $\lambda_i C_i^{ff}$  is not valid), and Eq. 15.48 becomes

$$\frac{dC_i}{dt} = \frac{1}{2} y_i \dot{F} + q_i^{ko} - P_i \quad (15.49)$$

The balance equation for positions far from surfaces is

$$\frac{dC_i}{dt} = y_i \dot{F} \quad (\text{for } x > \mu_{ff}) \quad (15.50)$$

The concentration of fission product  $i$  just inside the knockout zone (i.e., a few knock-on recoil ranges from the surface) is governed by the direct recoil mechanism, for which the appropriate balance is given by Eq. 15.13 (without the decay term),

$$\frac{dC_i}{dt} = \frac{1}{2} y_i \dot{F} \quad (\text{for } x \ll \mu_{ff} \text{ but } > \mu_U^{k_o})$$

We approximate the time dependence of  $C_i$  within the knockout zone by this formula as well, which reduces Eq. 15.49 to

$$q_i^{k_o} = P_i \quad (15.51)$$

Or the knock-on process is in quasi-equilibrium.

As in the previous steady-state analysis,  $q_i^{k_o}$  is given by Eqs. 15.5 and 15.6, and  $P_i$  is given by Eq. 15.25. With the dimensionless variables  $\eta$  and  $Y$  of Eqs. 15.32 and 15.33, Eq. 15.51 becomes

$$\frac{1}{2} \int_0^{\eta+1} Y(\eta') d\eta' = Y(\eta) \quad (0 \leq \eta \leq 1) \quad (15.52a)$$

$$\frac{1}{2} \int_{\eta-1}^{\eta+1} Y(\eta') d\eta' = Y(\eta) \quad (\eta > 1) \quad (15.52b)$$

These integral equations represent the  $H \rightarrow \infty$  limit of Eqs. 15.30 and 15.31. They can be solved approximately by assuming power series solutions in  $\eta$  for the ranges of  $\eta$  separated by the discontinuities in slope. To reduce the algebraic labor, we consider only the first two ranges and approximate the concentrations by

$$Y_1(\eta) = a_1 + b_1 \eta + c_1 \eta^2 \quad (\text{for } 0 \leq \eta \leq 1) \quad (15.53)$$

$$Y_2(\eta) = a_2 + b_2 \eta + c_2 \eta^2 \quad (\text{for } 1 \leq \eta \leq 2) \quad (15.54)$$

$$Y_3 = Y_4 = \dots = \frac{1}{2} \quad (\text{for } \eta > 2) \quad (15.55)$$

These functions are subject to the conditions

$$Y_1(1) = Y_2(1) \quad (15.56)$$

$$Y_2(2) = \frac{1}{2} \quad (15.57)$$

$$\left( \frac{dY_2}{d\eta} \right)_2 = 0 \quad (15.58)$$

Substituting Eqs. 15.53 and 15.54 into 15.52a and setting the coefficients of the zeroth, first, and second powers of  $\eta$  equal to zero provide three equations among the coefficients  $a_1 \dots c_2$  which, with the additional relations supplied by Eqs. 15.56, 15.57, and 15.58, allows us to determine all the coefficients in Eqs. 15.53 and 15.54. Proceeding in this manner, we find

$$a_1 = 5/44; \quad b_1 = 2/11; \quad c_1 = 3/44 \quad (15.59)$$

$$a_2 = -1/22; \quad b_2 = 6/11; \quad c_2 = -3/22$$

The dimensionless concentration profile is plotted as the lower curve in Fig. 15.12.

The knockout current of stable fission gases is given by Eq. 15.39, which, in terms of the dimensionless variables  $\eta$  and  $Y$ , is

$$I_i^{k_o} = \frac{n_U^{k_o} \mu_U^{k_o} \dot{F} C_i^\infty}{N_U} \int_0^1 Y_1(\eta) (1 - \eta) d\eta$$

Using Eq. 15.53 and the preceding values of  $a_1$ ,  $b_1$ , and  $c_1$ , we find the integral in this equation to be 0.017. According to Eq. 15.24,  $n_U^{k_o} \mu_U^{k_o} = \alpha_U \mu_{ff}$ . Integration of Eq. 15.50 shows that  $C_i^\infty = y_i \dot{F} t$ , and  $\dot{F} t / N_U$  is the burnup,  $\beta$ . The knockout release rate is

$$I_i^{k_o} = (0.017 \alpha_U \beta) y_i \dot{F} \mu_{ff} \quad (15.60)$$

The knockout current is of the same form as the recoil current of Eq. 15.18 except that the coefficient  $1/4$  in the recoil current is replaced by the parenthetical expression in Eq. 15.60.

Application of Eq. 15.60 to calculate release rates of stable fission gases during irradiation of a fuel element is hampered by the lack of knowledge of the total fuel surface area available for knockout release and by the fact that much of the fuel is at temperatures high enough so that knockout and recoil are not the only modes of release. In this case the bulk concentration is not correctly described by Eq. 15.50, and  $y_i \beta$  in Eq. 15.60 should be left as  $C_i^\infty / N_U$ . The concentration at the edge of the recoil zone,  $C_i^\infty$ , is controlled by the other release mechanisms. Even if Eq. 15.60 were accepted without modification, the fractional release due to knockout from a fuel rod 6 mm in diameter with total surface area  $10^3$  times the geometrical area is only 6% after a 10% burnup. This is approximately an order of magnitude lower than the observed release fractions from highly rated fuel rods; so release of stable fission gases by direct recoil and knockout is of little importance in reactor fuel-element performance.

## 15.4 THE EQUIVALENT-SPHERE MODEL OF DIFFUSIONAL RELEASE

The simplest explanation for the temperature-dependent release of fission gases which is observed above  $\sim 1000^\circ\text{K}$  is that such escape represents lattice diffusion of gas atoms to surfaces that communicate directly with the surroundings. A polycrystalline sinter is treated as a collection of spheres of uniform size characterized by a single equivalent radius,  $a$ , defined by

$$\frac{S_T}{V} = \frac{3}{a} \quad (15.61)$$

The total surface area for gas escape by diffusional processes is the same as that available for release by knockout. The  $S_T$  can be measured by gas-adsorption techniques; so the equivalent radius is an experimentally accessible parameter.

Having characterized the geometry of a fuel specimen by the particle radius (the actual particle size of crushed and sieved single-crystal specimens or the equivalent radius for a sintered sample is employed), we can use the results of gas-release experiments to determine the diffusion coefficient of the fission-gas in the solid fuel.

Three variations of the equivalent-sphere model have been reported. The first considers gas-atom migration in the sphere to proceed by classical volume diffusion, without allowing for complicating factors, such as trapping or re-solution. This theory is treated in the following section. The effect of trapping of gas atoms by crystal defects in postirradiation anneal and in-pile experiments is reviewed in Sec. 15.6. Finally, the effect of fission-induced re-solution of grain-boundary bubbles on diffusional release during irradiation is considered in Sec. 15.7. All three of these theories assume that the geometry in which diffusion occurs can be described by a sphere of radius  $a$ . They are therefore all equivalent-sphere models and differ only in the detail in which the diffusion process within the sphere is described.

## 15.5 SIMPLE DIFFUSION

The application of classical diffusion theory to fission-gas release from a fuel sphere of radius  $a$  was first described by Booth.<sup>12,13</sup> The sphere is treated as a homogeneous medium, with no account taken of bubbles, pores, dislocations, grain boundaries, or radiation-produced defects that may serve to impede gas-atom migration. The effect of these trapping centers is buried in the quantity  $D$ , which is therefore an *apparent diffusivity* for the heterogeneous medium.

### 15.5.1 Postirradiation Annealing

The postirradiation annealing experiment using the apparatus shown in Fig. 15.1 was described in Sec. 15.2. The fission gas analyzed must be radioactive if gamma-ray detection is to be used. On the other hand, isotopes with very short half-lives lose considerable activity before and during the anneal and thus pose counting precision difficulties. It has proven convenient to work with the long-lived radioactive fission gases, principally  $^{133}\text{Xe}$ , in postirradiation anneal experiments. Where experiments have been capable of distinguishing between xenon and krypton diffusion (as in steady-state sweep-gas experiments conducted in-pile), only minor differences have been observed. It is common to consider the noble-gas fission products as a single species.

If radioactive decay during annealing is neglected, Fick's law for the postirradiation annealing experiment when volume diffusion is the only process occurring is

$$\frac{\partial C}{\partial t} = D \frac{1}{r^2} \frac{\partial}{\partial r} \left( r^2 \frac{\partial C}{\partial r} \right) \quad (15.62)$$

where  $D$  is the apparent diffusion coefficient of the noble gases in the bulk solid. The initial and boundary conditions for Eq. 15.62 are

$$C(r,0) = C_0 \quad (15.63)$$

$$C(0,t) = \text{finite} \quad (15.64)$$

$$C(a,t) = 0 \quad (15.65)$$

The constant  $C_0$  represents the gas concentration generated by the light low-temperature irradiation prior to annealing. Uniform initial distribution of the gas has been assumed,

although the depletion very close to the surface due to recoil should be accounted for in principle. This perturbation, however, has a significant effect only very early in the anneal and is neglected in the following treatment.

The flux of gas atoms for the surface of the equivalent sphere into the surrounding gas space is given by

$$J = -D \left( \frac{\partial C}{\partial r} \right)_a \quad (15.66)$$

and the fraction of the total amount of gas released from the equivalent sphere after anneal time  $t$  is

$$f = \frac{4\pi a^2 \int_0^t J dt'}{4\pi a^3 C_0 / 3} = \frac{3}{a C_0} \int_0^t J dt' \quad (15.67)$$

The solution to Eq. 15.62 and its associated conditions can be obtained either by the method of separation of variables or by the Laplace transform method. Separation of variables is convenient for long times ( $f \rightarrow 1$ ), whereas the Laplace transform provides a simple analytical expression for short times ( $f \rightarrow 0$ ). Since the short-time approximation is accurate over a very wide range of annealing times and is almost exclusively used in data interpretation, we describe here only the Laplace transform solution.

The dimensionless radial position and the dimensionless time are defined by

$$\eta = \frac{r}{a} \quad (15.68)$$

$$\tau = \frac{Dt}{a^2} \quad (15.69)$$

and a dimensionless concentration by

$$u = \frac{r}{a} \frac{C}{C_0} = \eta \frac{C}{C_0} \quad (15.70)$$

Equations 15.62 to 15.65 become

$$\frac{\partial u}{\partial \tau} = \frac{\partial^2 u}{\partial \eta^2} \quad (15.71)$$

$$u(\eta,0) = \eta \quad (15.72)$$

$$u(0,\tau) = 0 \quad (15.73)$$

$$u(1,\tau) = 0 \quad (15.74)$$

Taking the Laplace transform of Eq. 15.71 and using Eq. 15.72 yield

$$p\tilde{u} - \eta = \frac{d^2 \tilde{u}}{d\eta^2} \quad (15.75)$$

where  $p$  is the transform variable and  $\tilde{u}(\eta)$  is the Laplace transform of  $u(\eta,\tau)$ . The boundary conditions are

$$\tilde{u}(0) = 0 \quad (15.76)$$

$$\tilde{u}(1) = 0 \quad (15.77)$$

The solution of Eq. 15.75 and the preceding boundary conditions is

$$\tilde{u}(\eta) = -\frac{e^{p^{1/2}\eta} - e^{-p^{1/2}\eta}}{p(e^{p^{1/2}} - e^{-p^{1/2}})} + \frac{\eta}{p} \quad (15.78)$$

In terms of these dimensionless variables, the Laplace transform of the flux given by Eq. 15.66 is

$$\tilde{J} = -\frac{DC_0}{a} \left[ \left( \frac{d\tilde{u}}{d\eta} \right)_1 - \tilde{u}(1) \right] \quad (15.79)$$

or, with  $\tilde{u}(\eta)$  given by Eq. 15.78,

$$\tilde{J} = \frac{DC_0}{a} \left[ \frac{1}{p^{1/2}} \left( \frac{e^{p^{1/2}} + e^{-p^{1/2}}}{e^{p^{1/2}} - e^{-p^{1/2}}} \right) - \frac{1}{p} \right] \quad (15.80)$$

When the dimensionless time  $\tau$  is small, the Laplace transform variable  $p$  is large; so the term in the parentheses of Eq. 15.80 (which is  $\tanh p^{1/2}$ ) can be set equal to unity. This is the short-time approximation. Taking the inverse transform of Eq. 15.80 with this simplification yields

$$J = \frac{DC_0}{a} \left[ \frac{1}{(\pi\tau)^{1/2}} - 1 \right] \quad (15.81)$$

Substitution of Eq. 15.81 into the integral of Eq. 15.67 gives the fractional release,

$$f = \frac{6}{\pi^{1/2}} \tau^{1/2} - 3\tau \quad (15.82)$$

Although Eq. 15.82 is in principle a short-time approximation, it is remarkably accurate over a large range of fractional releases. At the value of  $\tau$  required for 90% release, for example,  $f$  given by Eq. 15.82 is within 0.2% of the value given by the exact solution. Even using only the first term on the right of Eq. 15.82 gives reasonably accurate results for short times, being 10% too high at  $\tau = 10^{-2}$  ( $f = 0.31$ ). Most analyses of postirradiation annealing experiments disregard the last term in Eq. 15.82 and express the fractional release by

$$f = \frac{6}{\pi^{1/2}} \left( \frac{Dt}{a^2} \right)^{1/2} \quad (15.83)$$

This fractional release formula is valid for shapes other than spheres as long as the actual surface-to-volume ratio is used to determine the equivalent radius  $a$ . The insensitivity to specimen shape is due to the fact that, at the short times to which Eq. 15.83 applies, the surface flux of gas originates from a layer close to the surface while the interior of the specimen is not yet depleted. The diffusion medium is essentially semi-infinite in extent as long as the radius of curvature of the release surface is large compared with the depth over which the concentration departs significantly from the initial value  $C_0$ . This zone must be large compared to the fission-fragment range, however, or else the depletion of the initial distribution due to recoil near the surface must be considered in the analysis.

Very often the appropriate equivalent radius  $a$  of a sintered compact may not be known. It has become common practice to characterize such solids by an *empirical diffusion coefficient* that includes the unknown radius

$$D' = \frac{D}{a^2} \quad \text{sec}^{-1} \quad (15.84)$$

which depends both on temperature by means of the temperature dependence of  $D$  and on fuel open porosity

through the equivalent radius  $a$ . In terms of  $D'$ , the fractional release in a postirradiation annealing experiment can be expressed by

$$f = \frac{6}{\pi^{1/2}} (D't)^{1/2} \quad (15.85)$$

According to Eq. 15.85, the cumulative amount of gas collected in the anneal should increase as the square root of the anneal time. However, in many experiments the initial release is found to be very much more rapid than expected from ideal release kinetics. After this initial burst has subsided,  $f$  increases as  $t^{1/2}$  up to releases of ~30%. The slope of the straight-line portion of a plot of  $f$  vs.  $t^{1/2}$  can be used in conjunction with Eq. 15.85 to determine the empirical diffusion coefficient  $D'$  for the temperature at which the experiment was conducted. Experiments at different temperatures permit the activation energy of  $D'$  to be measured.

### 15.5.2 In-Pile Gas Release

The equivalent-sphere concept can be applied to in-pile gas release, either to interpret the results of steady-state experiments or to predict the release of gas from the fuel during reactor operation.

The form of Fick's second law which must be solved for the in-pile case is

$$\frac{\partial C}{\partial t} = y\dot{F} + D \frac{1}{r^2} \frac{\partial}{\partial r} \left( r^2 \frac{\partial C}{\partial r} \right) - \lambda C \quad (15.86)$$

where  $y$  is the chain yield leading to a particular fission product and  $\lambda$  is its decay constant. The boundary conditions of Eqs. 15.64 and 15.65 apply to the in-pile situation, but the initial condition is

$$C(r,0) = 0 \quad (15.87)$$

The general solution to Eq. 15.86 can be obtained, but particularly simple release formulas are available for the special cases of stable gases in the short-time approximation and radioactive gases in the steady-state limit.

When applied to stable fission products, the last term on the right of Eq. 15.86 is deleted. With the Laplace transform method, the short-time approximation to the gas-atom flux at the surface of the sphere is

$$J = y\dot{F} \left[ 2 \left( \frac{Dt}{\pi} \right)^{1/2} - \frac{Dt}{a} \right] \quad (15.88)$$

and, using Eq. 15.67 with  $C_0$  replaced by  $y\dot{F}t$ , the fractional release is

$$f = \frac{4}{\pi^{1/2}} \left( \frac{Dt}{a^2} \right)^{1/2} - \frac{3}{2} \left( \frac{Dt}{a} \right)$$

which differs from Eq. 15.82 only slightly in the numerical constants, although the physical situations to which each formula applies are quite different. As with the postirradiation anneal, the last term in Eq. 15.88 can be neglected for fractional releases less than ~0.3, and we have

$$f = \frac{4}{\pi^{1/2}} \left( \frac{Dt}{a^2} \right)^{1/2} = \frac{4}{\pi^{1/2}} (D't)^{1/2} \quad (15.89)$$

The fractional release given by Eq. 15.89 is equal to the ratio of the total quantity of fission product released by the fuel at time  $t$  to the total amount of the species produced by irradiation up to time  $t$ . It is not a ratio of release-to-birth rates at time  $t$ .

The diffusion equation for radioactive species that have attained a steady-state concentration profile in the fuel is

$$0 = y\dot{F} + D \frac{1}{r^2} \frac{d}{dr} \left( r^2 \frac{dC}{dr} \right) - \lambda C \quad (15.90)$$

which can be readily solved with the boundary conditions of Eqs. 15.64 and 15.65. The fractional release (defined in this case as the ratio of the release-to-birth rates) is given by

$$f = \frac{3D}{\lambda a^2} \left[ \left( \frac{\lambda a^2}{D} \right)^{1/2} \coth \left( \frac{\lambda a^2}{D} \right)^{1/2} - 1 \right] \quad (15.91)$$

In the limit as  $(a^2 \lambda / D)^{1/2} \gg 1$ , the hyperbolic cotangent term reduces to unity, and the number 1 in the brackets is negligible. The fractional release rate is

$$f = 3 \left( \frac{D}{\lambda a^2} \right)^{1/2} = 3 \left( \frac{D'}{\lambda} \right)^{1/2} \quad (15.92)$$

(The opposite limit is  $f \rightarrow 1$ .) Equation 15.91 has been used to determine empirical diffusion coefficients of  $^{133}\text{Xe}$  in fuel pellets and in crushed oxide of known surface area.<sup>14</sup> In both cases, the in-pile sweep-gas method described in Sec. 15.2 was employed. Although the short-lived isotopes of the noble gases do not contribute significantly to pressure buildup within the fuel element, knowledge of the quantity of these species present during irradiation is important in accident analyses. Equation 15.92 can be used for this computation.

Figure 15.15 summarizes the results of gas-release tests on various types of oxide fuel compacts. Curve A was determined by in-pile experiments on mixed oxide fuel. Curve B represents postirradiation annealing results for  $\text{UO}_2$ . Curve C was obtained by determining the unreleased gas contained in small samples of mixed oxide. Microsamples were drilled from various radial positions in an irradiated fuel pin, and the quantity of fission gas retained by the fuel was measured. These data gave  $1 - f$ , and hence  $D'$ , by Eq. 15.85. Knowledge of the temperature at the sampling location determines a point on Fig. 15.15.

The substantial discrepancies among the three sets of results in Fig. 15.15 are due in part to the different types of experimental techniques employed to determine  $D'$  and to the undoubtedly different microstructures of the specimens studied. Even if the diffusion coefficients of the fission gases in defect-free  $\text{UO}_2$  and  $(\text{U,Pu})\text{O}_2$  were the same (which they probably are, to the accuracy of such measurements), the microstructure developed by the fabrication process and during release at high temperature influences both the equivalent radius (by means of the open porosity) and the diffusion coefficient  $D$  (by the type and quantity of trapping centers) and hence the empirical diffusion coefficient. The activation energies of  $D'$  from the lines of Fig. 15.15 range from 200 to 300 kJ/mole, which is significantly lower than the activation energy given by Eq. 13.29. The experiment on which this formula is based

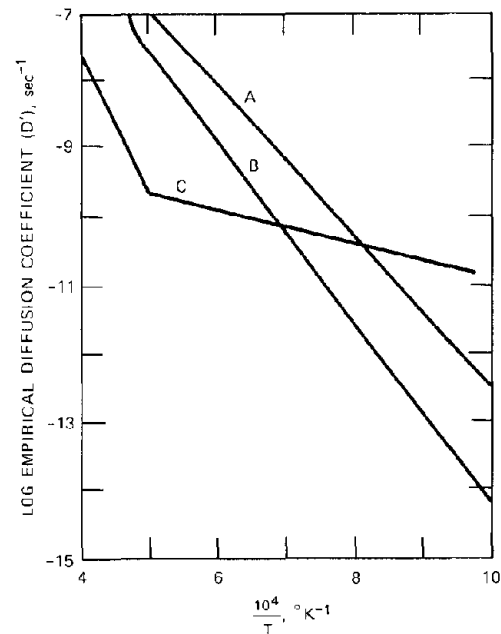


Fig. 15.15 Empirical diffusion coefficients of xenon in sintered oxide fuels. (A) Mixed oxide. (From B. T. R. Frost, in *International Symposium on Ceramic Nuclear Fuels*, p. 225, American Ceramic Society., (1969). (B)  $\text{UO}_2$ . (From G. W. Parker et al., USAEC Report ORNL-3981 Oak Ridge National Laboratory, July 1967). (C) Mixed oxides. [From R. Godesar et al., *Nucl. Appl. Technol.*, 9: 205 (1970)].

probably represents a more reliable measure of true gas diffusion in  $\text{UO}_2$  than any of the experiments that are based solely on classical volume diffusion in the entire fuel body. The latter formulation undoubtedly represents too drastic a simplification of the physical processes occurring during gas release to permit the equivalent-sphere concept to be considered as anything more than a convenient empirical characterization of the gas-release properties of a particular type of fuel. Nevertheless, the simplicity of the mathematical formulas involved in the application of the equivalent-sphere model has led to widespread use of data such as those shown in Fig. 15.15 to predict fission-gas release in operating fuel elements, particularly in thermal reactors.

### 15.5.3 Fission-Gas Release in a Fuel Element

The formulas derived for the fractional release with continuous gas generation can be applied to an entire fuel element.

Consider an annular volume element in a fuel rod of thickness  $dr$  and unit height. This element is characterized by a single value of  $D'$ . The quantity of fission gas generated in the volume  $2\pi r dr$  by irradiation of duration  $t$  is  $yFt(2\pi r dr)$ , and the amount of gas released from the same element is the fractional release times the quantity of gas produced. The gas release from a slice of fuel of unit height extending over the entire cross section of the pin is

obtained by integration over  $r$ . For stable fission gases,  $f$  is given by Eq. 15.89, and we have

$$\text{Gas released from slice of fuel of unit height up to time } t = 8\pi^{1/2} y \dot{F} t^{3/2} \int_0^R (D')^{1/2} r \, dr$$

where  $R$  is the fuel radius.

The empirical diffusion coefficient  $D'$  is a function of fuel temperature only and can be related to radial position for the case of a simple parabolic temperature distribution:

$$\frac{T - T_s}{T_0 - T_s} = 1 - \left(\frac{r}{R}\right)^2 \quad (15.93)$$

where  $T_0$  and  $T_s$  are the temperatures at the center line and the outer edge of the fuel rod, respectively. The empirical diffusion coefficients plotted on Fig. 15.15 can be expressed in Arrhenius form by

$$D' = D'_0 \exp\left(-\frac{E'}{kT}\right) \quad (15.94)$$

where  $D'_0$  is the preexponential factor,  $E'$  is the apparent activation energy, and  $k$  is Boltzman's constant. Using Eq. 15.94 and converting the integration variable from  $r$  to  $T$  by use of Eq. 15.93 yield

Gas release from slice of fuel at unit height up to time  $t$

$$= \frac{4\pi^{1/2} y \dot{F} R^2 t^{3/2} (D'_0)^{1/2}}{T_0 - T_s} \int_{T_s}^{T_0} e^{-T^*/T} \, dT \quad (15.95)$$

where

$$T^* = \frac{E'}{2k} \quad (15.96)$$

is a characteristic temperature between 15,000 and 20,000°K.

The integral on the right of Eq. 15.95 can be written as

$$\begin{aligned} \int_{T_s}^{T_0} e^{-T^*/T} \, dT &= T^* \int_{T^*/T_0}^{T^*/T_s} \frac{e^{-u}}{u^2} \, du \\ &= \frac{1}{2} \left[ \left(\frac{e^{-u}}{u}\right)_{T^*/T_0}^{T^*/T_s} - \int_{T^*/T_0}^{T^*/T_s} \frac{e^{-u}}{u} \, du \right] \end{aligned} \quad (15.97)$$

The last term in the brackets is a form of the exponential integral,<sup>15</sup> which for large values of  $T^*/T$  can be approximated by

$$\int_x^\infty \frac{e^{-u}}{u} \, du \approx \frac{e^{-x}}{x+1} \quad (15.98)$$

Since both  $T^*/T_0$  and  $T^*/T_s$  are large and  $T_s$  is generally a factor of 2 smaller than  $T_0$ , the upper limit in the integrals in the brackets of Eq. 15.97 can be set equal to infinity, and the result is

$$\int_{T_s}^{T_0} e^{-T^*/T} \, dT \approx \frac{T^*}{2} \frac{e^{-T^*/T_0}}{(T^*/T_0)[(T^*/T_0) + 1]} \quad (15.99)$$

Substitution of Eq. 15.99 into 15.95 and division by the total amount of gas generated in the cross-sectional slice of unit height yield the radially averaged fraction released:

$$\bar{f} = \frac{4}{\pi^{1/2}} (\bar{D}'t)^{1/2} \quad (15.100)$$

where  $\bar{D}'$  is the average value of the empirical diffusion coefficient over the fuel cross section,

$$(\bar{D}')^{1/2} = (D'_0)^{1/2} \left[ \frac{T^*}{2(T_0 - T_s)} \frac{e^{-T^*/T_0}}{(T^*/T_0)[(T^*/T_0) + 1]} \right] \quad (15.101)$$

The value of  $\bar{D}'$  depends only on the center-line and surface temperatures of the fuel. For a constant thermal conductivity, Eq. 10.63 shows that  $T_0$  and  $T_s$  are related to the linear power of the rod at the particular axial location of the slice by

$$T_0 - T_s = \frac{\bar{\mathcal{P}}}{4\pi k} \quad (15.102)$$

where  $\bar{k}$  is the average thermal conductivity of the fuel obtained from the slope of the best straight-line fit through the thermal-conductivity integral plot of Fig. 10.20. The radial average of the empirical diffusion coefficient is thus a function of the local rod linear power and, to a lesser extent, of the fuel surface temperature. The fuel surface temperature can be taken at a fixed value between 800 and 1000°K for all applications without appreciably affecting the calculated fractional releases.

Proceeding in analogous fashion over the length of the fuel rod, the average fractional release from the entire fuel element is found to be

$$\bar{f} = \frac{4}{\pi^{1/2}} (\bar{\bar{D}}'t)^{1/2} \quad (15.103)$$

where  $\bar{\bar{D}}'$  is the average value of the empirical diffusion coefficient for the fuel element

$$(\bar{\bar{D}}')^{1/2} = \frac{\int_{-Z/2}^{Z/2} (\bar{D}')^{1/2} [\mathcal{P}(z)/\mathcal{P}(0)] \, dz}{\int_{-Z/2}^{Z/2} [\mathcal{P}(z)/\mathcal{P}(0)] \, dz} \quad (15.104)$$

where  $Z$  is the length of the fuel pin,  $\mathcal{P}(0)$  is the peak linear power in the fuel rod, and  $\mathcal{P}(z)/\mathcal{P}(0)$  is the axial power distribution in the fuel element, which can be represented by a truncated cosine function.

The rod-averaged empirical diffusion coefficient can be determined from the data obtained in fuel-element puncture tests. The total production of fission gas for irradiation time  $t$  is

Total gas produced in the fuel pin in time  $t$

$$= \frac{yt}{3.2 \times 10^{-11}} \int_{-Z/2}^{Z/2} \mathcal{P}(z) \, dz \quad (15.105)$$

where the numerical factor converts watts to fissions per second. Dividing the amount of fission gas collected from the rod by Eq. 15.105 gives the average fractional release,  $\bar{f}$ , from which  $\bar{\bar{D}}'$  can be computed by use of Eq. 15.103. Parker et al.<sup>16</sup> have performed such calculations using the extensive data provided by the AECL fuel irradiation program. The results of their analysis of these data are shown in Fig. 15.16, along with a best-fit line. The value of

$\bar{D}'$  is expressed as a function of the average linear power of the fuel rod. The rod-averaged diffusion coefficients from Fig. 15.16 were then used in Eq. 15.103 to estimate the fractional release of stable fission gases in the Browns Ferry reactor.

Parker also calculated fractional releases for fuel elements in this reactor starting from the empirical diffusion coefficient given by curve B in Fig. 15.15. The value of  $\bar{D}'$  was computed by Eq. 15.101 in which  $T_0$  was related to linear power by Eq. 15.102. The rod-averaged empirical diffusion coefficient was determined from these results and the axial power profile of the particular fuel element by Eq. 15.104. Finally, the fractional release from the rod was computed from Eq. 15.103.

For radioactive fission gases, the same values of  $\bar{D}'$  used for the stable gases were employed, and the fractional release rates were determined from Eq. 15.92

$$\bar{f} = 3 \left( \frac{\bar{D}'}{\lambda} \right)^{1/2}$$

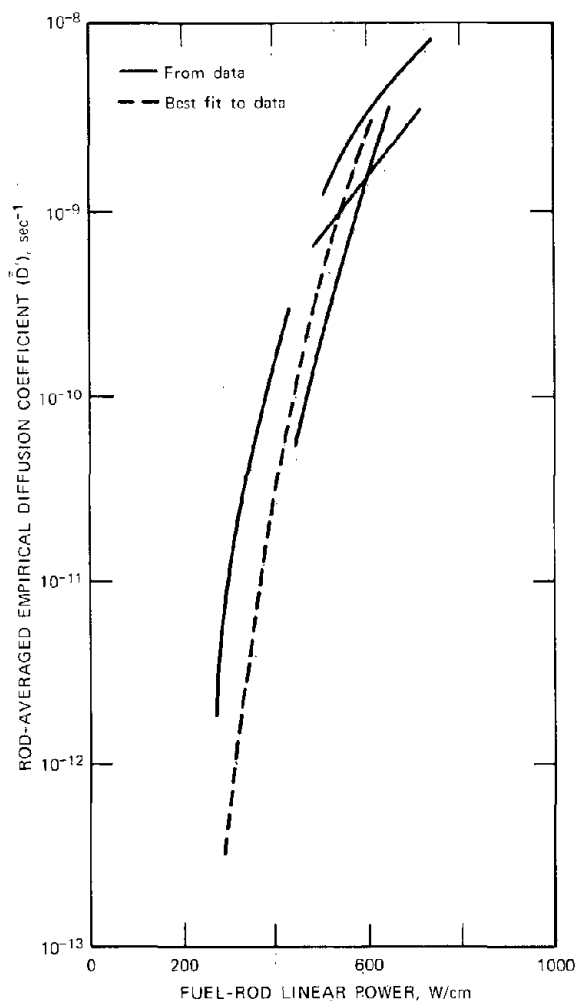


Fig. 15.16 Rod-averaged empirical diffusion coefficients obtained from AECL (Atomic Energy of Canada, Ltd.) rod-puncture data. (From Ref. 16.)

Comparison of the estimated fractional releases from the  $\bar{D}'$  values based on rod-puncture data and those predicted from the results of postirradiation anneal experiments are shown in Table 15.3. The disagreement between the two methods is discouragingly large. Part of the discrepancy can be attributed to the different types of experimental data from which the predictions were made. Since the entire model on which both calculations are based is predominantly empirical, extrapolation to conditions substantially different from those on which the correlating factor  $\bar{D}'$  is based leads to poor prediction of gas release.

## 15.6 DIFFUSION WITH TRAPPING

The large discrepancies in empirical diffusion coefficients measured under ostensibly identical conditions and the poor predictive ability of release calculations based on the equivalent-sphere model suggest that gas-atom migration in nuclear fuels involves more than simple lattice diffusion. In addition, close examination of the release kinetics shows numerous features that are totally inconsistent with purely diffusional motion.

The first anomaly is the burst phenomenon mentioned previously. Nearly every postirradiation anneal experiment has exhibited an initially large release rate before the expected  $t^{1/2}$  behavior becomes established. It was once thought that this effect was due to a physical difference between the surface of the specimen and the bulk caused either by corrosion due to impurities in the atmosphere or by some form of radiation damage that affected the surface layers more than it affected the interior. If the diffusion coefficient were larger in the region close to the surface than in the bulk, rapid initial release of the type observed would be expected. However, it has been found that chemical attack of the surface is not responsible for the burst in  $\text{UO}_2$  postirradiation anneals (although it can be important in the more chemically active  $^1\text{UC}$ ) and that it is unnecessary to attribute special properties to the surface layer as a result of preferential radiation damage.

Ellman, Fox, and Mears<sup>17</sup> have measured the release of  $^{133}\text{Xe}$  from single crystals of  $\text{CsI}$ . Classical release curves (i.e.,  $f \sim t^{1/2}$ ) could be obtained only when the  $^{133}\text{Xe}$  was produced by growing crystals containing radioactive  $^{133}\text{I}$  which decayed in situ to provide the  $^{133}\text{Xe}$  or when fission-product  $^{133}\text{Xe}$  was introduced into the crystal by recoil from a nearby uranium foil. When defects were purposely introduced into the crystal by growing at high rates or by agitating the melt during growth, the  $t^{1/2}$  law was not obeyed. Similarly, when single crystals were irradiated to produce  $^{133}\text{Xe}$  by the (n,p) reaction on  $^{133}\text{Cs}$ , nonideal kinetics were observed. Thus, either natural or radiation-produced imperfections in the solid depress the release rate by temporarily or permanently trapping the migrating gas atoms. Trapping is due to the strong binding of gas atoms to nearly any kind of flaw in the solid. In addition, Ellman, Fox, and Mears<sup>17</sup> and Matzke<sup>18</sup> have shown that high gas concentrations promote trapping of migrating gas. High gas concentrations may stabilize certain types of defects (thus preventing the defect from thermally annealing and disappearing). Or, if the trap is a fission-gas bubble, higher gas

Table 15.3 Comparison of Fission-Gas Releases for the Browns Ferry Reactor Calculated by the Equivalent-Sphere Method Using Empirical Diffusion Coefficients Obtained from Rod-Puncture Experiments and Postirradiation Annealing Data\*

	Fractional release rate, %				Fractional release of stable gases in $10^8$ sec, %	
	$^{133}\text{Xe}$		$^{131}\text{I}^\dagger$		Rod puncture	Annealing
	Rod puncture	Annealing	Rod puncture	Annealing		
Average rod	0.16	0.97	0.40	2.4	1.5	9
Peak rod $^\ddagger$	6	27	14	35	39	50

\*Based on Ref. 16.

$^\dagger$ The diffusion coefficient of iodine is estimated to be four times that of xenon.

$^\ddagger$ The full formulas, Eqs. 15.88 and 15.91, must be used for large release fractions.

contents imply greater bubble densities and hence a greater trapping rate of the free gas atoms. The gas bubbles are much less mobile in the solid than free gas atoms and generally do not contribute to gas release in typical diffusion experiments.

The second observation that is completely inconsistent with simple lattice diffusion is the effect on the release rate of the length of irradiation prior to the high-temperature anneal. Figure 15.17 shows that large low-temperature irradiations can depress the apparent diffusion coefficient by three orders of magnitude. In application of the simple diffusion model to postirradiation annealing experiments, the only function of the low-temperature irradiation is to establish the initial gas content of the solid ( $C_0$  in Eq. 15.63), but this quantity has no effect on the predicted fractional release. MacEwan and Stevens<sup>19</sup> attributed this effect shown in Fig. 15.17 to the defects in the solid produced by the low-temperature irradiation. The larger the exposure in the reactor, the more defects produced and the greater the probability of gas-atom trapping by these defects.

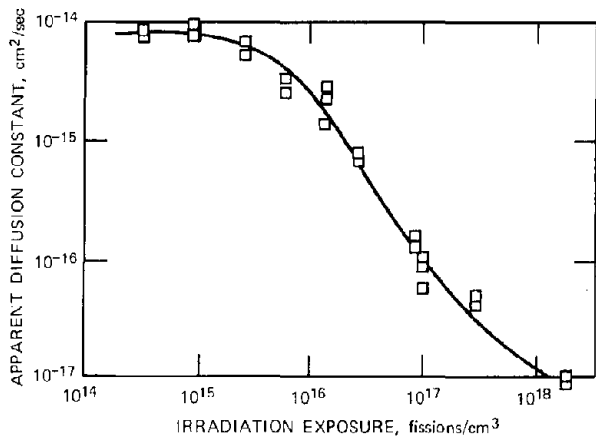


Fig. 15.17 Variation of the apparent diffusion coefficient of fission gases in single-crystal  $\text{UO}_2$  with prior irradiation exposure (at low temperature). Postirradiation annealing conducted at  $1400^\circ\text{C}$ . [From J. R. MacEwan and W. H. Stevens, *J. Nucl. Mater.*, 11: 77 (1964).]

A third contradictory source of evidence was obtained in steady-state in-pile release experiments. The fractional release rate in this case is given by Eq. 15.92 according to the simple diffusion model. However, Fig. 15.18 shows that  $f$  is influenced by fission rate in a rather complex manner. Carroll, Sisman, and Perez<sup>20</sup> suggest that the release rate is normal at low fission rates but that, as  $\dot{F}$  increases, the damage produced in the solid cannot anneal out rapidly enough and extensive gas trapping occurs. At fission rates greater than  $\sim 2 \times 10^{13}$  fissions  $\text{cm}^{-3} \text{sec}^{-1}$ , the defects created by irradiation are destroyed by fission fragments, and the release rate begins to rise.

The final observation strongly suggesting the importance of trapping on gas release is the difference in the measured emanation rates from single-crystal and sintered  $\text{UO}_2$  specimens of the same surface area. At low temperatures [Fig. 15.19(a)], the fine-grained polycrystalline specimen released more gas than did the single-crystal sample, as is expected from the knockout mechanism. The situation is just reversed at high temperatures [Fig. 15.19(b)]. Here the single crystal releases more gas than the polycrystalline specimen does. This observation is most reasonably at-

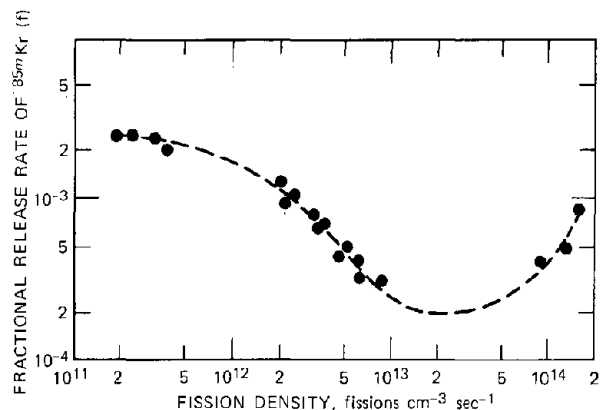
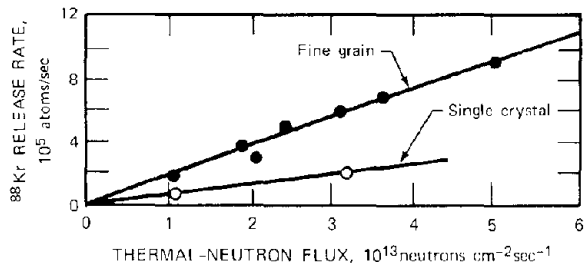
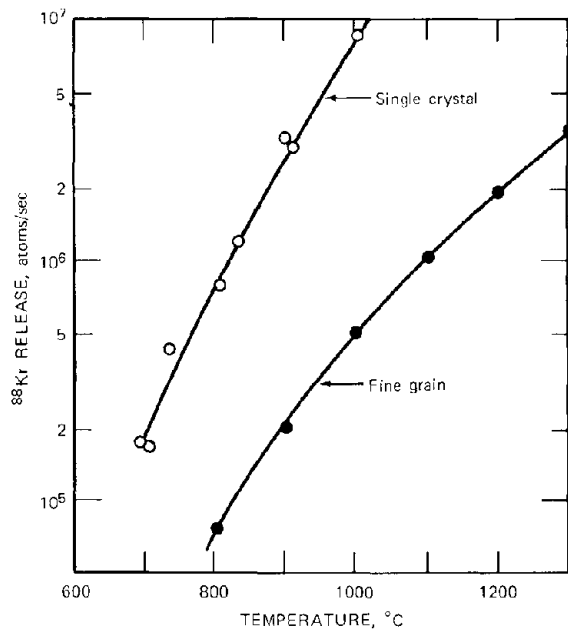


Fig. 15.18 Fractional release rate of  $^{85m}\text{Kr}$  from high-density  $\text{UO}_2$  during irradiation at  $1400^\circ\text{C}$ . [From R. M. Carroll, O. Sisman, and R. B. Perez, *Nucl. Sci. Eng.*, 32: 430 (1968).]



(a)



(b)

Fig. 15.19 Comparison of  $^{88}\text{Kr}$  release rates from single-crystal and polycrystalline  $\text{UO}_2$  at (a) low temperature and (b) high temperature. The specimens in (a) had the same geometric surface area, and the release rates in (b) were normalized to the same geometric surface area. [After R. M. Carroll and O. Sisman, *Nucl. Appl.*, 2: 142 (1966).]

tributed to the fact that the grain boundaries in the sintered specimen act as trapping centers for fission-gas atoms and thus significantly reduce the release rate. The grain boundaries in a polycrystalline solid should not be confused with open porosity within the fuel body. The latter is part of the total surface area from which release occurs. The grain boundaries apparently do not provide pathways for rapid release until large quantities of fission gases are accumulated. Then, stresses due to the gas pressure in intergranular bubbles can assist in fracturing the specimen, or the grain-boundary bubble population may be large enough to cause bubble interlinkage that establishes a pathway to a surface from which rapid escape is possible.

The defects in a solid that can act as trapping centers for fission-gas atoms can be divided into two broad categories:

1. Natural defects:
  - (a) Grain boundaries.
  - (b) Dislocation lines.
  - (c) Closed pores in the as-fabricated fuel.
  - (d) Impurities in the solid.
2. Radiation-produced defects:
  - (a) Vacancy clusters (perhaps stabilized by a few gas atoms). A fission track is especially rich in this type of trap.
  - (b) Dislocation loops formed by condensation of excess interstitial atoms.
  - (c) Fission-gas bubble.
  - (d) Solid fission-product precipitates (e.g., the noble metal and alkaline earth oxide phases).

In addition to distinguishing between natural and radiation-produced defects, the various traps can be characterized by the ease with which they can be destroyed either by natural thermal annealing processes or by fission fragments. Closed pores containing little gas and with a pressure deficit, for example, will shrink until the gas pressure balances the surface-tension forces. Grain boundaries may be removed by the grain growth process described in Sec. 14.5. Small gas bubbles may be obliterated by a passing fission fragment.

The defects can also be distinguished by the tenacity with which they retain the trapped fission gas. Grain boundaries, for example, are deep traps from which gas escape by thermal processes is improbable. In the absence of a radiation field, the gas contained in closed pores or bubbles is usually considered permanently trapped. However, postirradiation anneal experiments suggest that a very slow thermal re-solution of fission gas from closed pores is needed to explain the release kinetics. Gas trapped on smaller defects, such as clusters of just a few vacancies or interstitials or an impurity atom, may not be as tightly bound as the gas in deep traps. Gas in a shallow trap has a higher re-solution probability than that in a deep trap. The re-solution probability, of course, is dramatically enhanced in an irradiation environment.

The rate of trapping of gas atoms has been discussed in Sec. 13.4. The capture rate can be expressed by

$$\begin{aligned} \text{Rate of trapping of fission-gas atoms/cm}^3 \\ = k_{gt} C_t C \quad (15.106) \end{aligned}$$

where  $k_{gt}$  is the rate constant for trapping,  $C_t$  is the concentration of traps in the solid, and  $C$  is the concentration of free gas atoms. Alternatively, the trapping rate can be expressed in terms of the diffusion trapping length  $L$ :

$$\begin{aligned} \text{Rate of trapping of fission-gas atoms/cm}^3 \\ = \frac{D_{Xe}}{L^2} C \quad (15.107) \end{aligned}$$

It is convenient to describe the trapping rate as a probability per unit time,

$$g = k_{gt} C_t = \frac{D_{Xe}}{L^2} \quad \text{sec}^{-1} \quad (15.108)$$

If  $M$  denotes the total number of gas atoms per unit volume held in traps at any time, the rate at which these are returned to the solid as single gas atoms is given by Eq. 13.120:

$$\text{Rate of re-solution/cm}^3 = bM \quad (15.109)$$

When only radiation re-solution is considered,  $b$  is independent of temperature but linearly dependent on fission rate. In the absence of radiation, only much less effective thermal re-solution contributes to the re-solution parameter. In this case,  $b$  is temperature dependent.

Each type of trap is completely characterized by values of  $g$  and  $b$  and the dependence of these quantities on  $T$  and  $\dot{F}$  and, in transient circumstances, on time.

### 15.6.1 Postirradiation Annealing Experiments

Since the bulk of the data on fission-gas release from nuclear fuels has been obtained from postirradiation annealing experiments of the type described in Sec. 15.2, we first analyze this situation when diffusion occurs in a medium containing a stable array of trapping sites.

As in the simple volume-diffusion description of this process, we consider diffusion of the untrapped portion of the gas in a solid that has the shape of a sphere of radius  $a$ . In place of Eq. 15.61, the diffusion equation that explicitly accounts for trapping and release from traps is

$$\frac{\partial C}{\partial t} = D_{Xe} \frac{1}{r^2} \frac{\partial}{\partial r} \left( r^2 \frac{\partial C}{\partial r} \right) - gC + bM \quad (15.110)$$

The subscript  $Xe$  has been appended to the diffusion coefficient to distinguish the true diffusivity of the fission gases,  $D_{Xe}$ , from the apparent diffusivity  $D$  used in the simple diffusion model. The balance for the trapped gas is

$$\frac{\partial M}{\partial t} = gC - bM \quad (15.111)$$

For simplicity, only a single type of trapping center has been assumed. If more than one type of trap were active, the parameters  $g$  and  $b$  and the trapped concentration  $M$  would have to be broken down into separate terms for each trap. There would be one balance equation like Eq. 15.111 for each distinguishable type of trap.

The parameters  $g$  and  $b$  are assumed independent of  $t$  and  $r$ . That is, the traps change neither position nor effectiveness during the anneal. Were they moving in the solid, a convective term would have to be added to the balance.

At the beginning of the anneal, the gas is assumed to be partitioned between the matrix and the traps by the initial trapped fraction  $y$ :

$$y = \text{fraction of gas in traps at } t = 0$$

If  $C_0$  is the total amount of gas in the solid at the start of the anneal (i.e., the sum of the initial values of  $C$  and  $M$ ), the initial conditions of Eq. 15.63 are replaced by

$$C(r,0) = (1-y)C_0 \quad (15.112a)$$

$$M(0) = yC_0 \quad (15.112b)$$

The boundary conditions for Eq. 15.110 are given by Eqs. 15.64 and 15.65.

To elucidate the minimum number of parameters on which the fractional release depends, we can make Eq. 15.110 dimensionless with the time, position, and matrix-gas-concentration variables given by Eqs. 15.68 to 15.70. In addition, we need to define the dimensionless trapped gas concentration:

$$w = \eta \frac{M}{C_0} \quad (15.113)$$

and the dimensionless trapping and re-solution probabilities:

$$G = \frac{ga^2}{D_{Xe}} \quad (15.114)$$

$$B = \frac{ba^2}{D_{Xe}} \quad (15.115)$$

The dimensionless form of the balance equations are

$$\frac{\partial u}{\partial \tau} = \frac{\partial^2 u}{\partial \eta^2} - Gu + Bw \quad (15.116)$$

$$\frac{\partial w}{\partial \tau} = Gu - Bw \quad (15.117)$$

the initial conditions become

$$w(0) = y\eta \quad (15.118a)$$

$$u(\eta,0) = (1-y)\eta \quad (15.118b)$$

and the boundary conditions are

$$u(0,\tau) = 0 \quad (15.119)$$

$$u(1,\tau) = 0$$

The fractional release is obtained by using the solution of Eqs. 15.116 to 15.119 in Eqs. 15.66 and 15.67.

Several limiting cases that do not require detailed analysis are of interest:

1. *No Trapping.* When  $G \rightarrow 0$  and  $y = 0$  (or alternatively,  $B \rightarrow \infty$ ), trapping is so weak that the problem reduces to the simple diffusion situation treated in the previous section.

2. *Equilibrium Trapping.* When  $G$  and  $B$  are both very large, the trapping and re-solution process is in quasi-equilibrium, and

$$w = \frac{G}{B} u \quad (15.120)$$

at all times and positions. Adding Eqs. 15.116 and 15.117 gives

$$\frac{\partial(u+w)}{\partial \tau} = \frac{\partial^2 u}{\partial \eta^2} = \left( \frac{B}{B+G} \right) \frac{\partial^2}{\partial \eta^2} (u+w) \quad (15.121)$$

with the initial condition

$$u+w = \eta \quad (\text{at } t = 0) \quad (15.122)$$

and the boundary conditions  $u+w = 0$  at  $\eta = 0$  and  $\eta = 1$ . These equations are identical to those obtained in the

simple diffusion model of postirradiation annealing if the matrix gas concentration in the latter is replaced by the total gas concentration (matrix plus traps) and dimensionless time is taken as

$$\tau = \left( \frac{b}{b+g} \right) \frac{D_{Xe} t}{a^2} \quad (15.123)$$

The fraction released obeys the normal law (Eq. 15.83) with an apparent diffusion coefficient of

$$D = \left( \frac{b}{b+g} \right) D_{Xe} \quad (15.124)$$

Although equilibrium trapping has not been observed in postirradiation annealing studies of fission gases in nuclear fuels, it appears to satisfactorily describe the trapping of ion-implanted rare gases in some alkali halides.<sup>21</sup> In the following section a model of gas release that assumes equilibrium trapping to apply to fuel under irradiation is described.

3. *Initial Trapping.* If all trapping occurs during the low-temperature irradiation or during warm-up of the sample prior to the start of the high-temperature anneal and none occurs during the period that release of gas is followed, we can set both  $G$  and  $B$  equal to zero. In this limit, the fractional release is obtained from the equations for diffusion without trapping (Eqs. 15.71, 15.73, and 15.74) but with the initial condition given by Eq. 15.118b. The fractional release is a factor  $(1-y)$  smaller than what it would have been had all the gas been in solution at the start of the anneal. Since the diffusivity varies as the square of  $f$ , the apparent diffusion coefficient is

$$D = (1-y)^2 D_{Xe} \quad (15.125)$$

The release curves for the cases analyzed are all "normal" in the sense that  $f$  varies linearly with  $t^{1/2}$  during the entire anneal and no initial burst is predicted. MacEwan and Stevens<sup>19</sup> interpreted the data of Fig. 15.17 in this manner, suggesting that the initial trapped fraction,  $y$ , increased with the extent of prior irradiation. A similar interpretation of xenon release from UC was advanced by Matzke and Springer.<sup>1</sup> There is not, however, any way of quantitatively relating  $y$  to the exposure during low-temperature irradiation.

4. *Irreversible Trapping.* An analytical solution can be obtained for short annealing times if trapping is permanent, or  $B = 0$ . In this case the result (derived later) is

$$f = 3(1-y)G^{-1/2} \operatorname{erf}(G\tau)^{1/2} \quad (15.126)$$

For  $G\tau > 5$ , the following limiting value of  $f$  is obtained:

$$f_{\infty} = \frac{3(1-y)}{G^{1/2}} \quad (15.127)$$

where  $1-f_{\infty}$  represents the fraction of the gas that is permanently retained in the specimen at the annealing temperature. Permanent trapping is indicated experimentally by cessation of gas release before all the initial gas in the specimen has been removed.

Since very few release curves show the normal  $f \sim t^{1/2}$  behavior of the simple diffusion model and the special cases

of trapping described in items 2 and 3, it is necessary to compare most data obtained in postirradiation annealing experiments with the complete solution of the diffusion-trapping equations.

In addition to the dimensionless time  $\tau$ ,  $f$  is a function of the trapping and release parameters,  $G$  and  $B$ , and the initial disposition of the gas,  $y$ . The last of these quantities can be eliminated from the system of equations by noting that the complete solution is a linear combination of the solutions for  $y = 0$  and  $y = 1$ . Thus

$$f(\tau, G, B, y) = (1-y) f_{(0)}(\tau, G, B) + y f_{(1)}(\tau, G, B) \quad (15.128)$$

where  $f_{(0)}$  and  $f_{(1)}$  are the solutions with all the gas initially in the matrix and in the traps, respectively. Hurst<sup>22</sup> has provided numerical solutions giving  $f_{(0)}$  and  $f_{(1)}$  as functions\* of  $\tau$ ,  $B$ , and  $G$ .

An approximate analytical solution for the fractional release can be obtained by the Laplace transform method applied previously to the same situation treated by the simple diffusion model. Taking the Laplace transform of Eqs. 15.116 and 15.117 and using the initial conditions given by Eqs. 15.118 leads to an ordinary differential equation in  $\tilde{u}$  (which contains  $\tilde{w}$ ) and an algebraic relation between  $\tilde{u}$  and  $\tilde{w}$ . Eliminating  $\tilde{w}$  between these two equations provides a single differential equation for  $\tilde{u}$  that is subject to the boundary conditions given by Eqs. 15.76 and 15.77. Solving as in the case of simple diffusion, we obtain the analog of Eq. 15.83

$$\tilde{J} = \frac{D_{Xe} C_0}{a} \left[ \frac{1}{\gamma} \left( 1 - \frac{p}{p+B} y \right) \left( \frac{e^{\gamma} + e^{-\gamma}}{e^{\gamma} - e^{-\gamma}} \right) - \frac{1}{\gamma^2} \left( 1 - \frac{p}{p+B} y \right) \right] \quad (15.129)$$

where

$$\gamma^2 = p + \frac{pG}{p+B} \quad (15.130)$$

Invoking the short-time approximation, we assume that  $\gamma$  is sufficiently large to set the parenthetical expression involving  $e^{\gamma}$  in Eq. 15.129 equal to unity and to neglect the last term entirely, thus leaving

$$\tilde{J} = \left( \frac{D_{Xe} C_0}{a} \right) \frac{1}{\gamma} \left( 1 - \frac{p}{p+B} y \right) \quad (15.131)$$

To simplify the inversion, we write

$$\tilde{J} = (1-y)\tilde{J}_{(0)} + y\tilde{J}_{(1)} \quad (15.132)$$

where

$$\tilde{J}_{(0)} = \left( \frac{D_{Xe} C_0}{a} \right) \frac{1}{\gamma} \quad (15.133)$$

$$\tilde{J}_{(1)} = \left( \frac{D_{Xe} C_0}{a} \right) \frac{1}{\gamma} \frac{B}{p+B} \quad (15.134)$$

\*Hurst used parameters  $\beta^2$  and  $\gamma$  in place of  $G$  and  $B$ . The former should be multiplied by  $\pi^2$  to give the latter.

We first find an approximate inversion of  $1/\gamma$  by writing

$$\frac{1}{\gamma} = \frac{[1 + (B/p)]^{1/2}}{(p + B + G)^{1/2}} \\ = \frac{1 + (B/2p) + \dots}{\{p + G[1 + (B/G)]\}^{1/2}} \approx \frac{1 + (B/2p)}{(p + G)^{1/2}} \quad (15.135)$$

To obtain the last equality, we have terminated the power-series expansion of the numerator after the second term and have neglected  $B/G$  compared to unity in the denominator. This approximate form of  $1/\gamma$  can be inverted directly, and  $J_{(0)}$  is found to be

$$J_{(0)} = \left( \frac{D_{Xe} C_0}{a} \right) \left[ \frac{e^{-G\tau}}{(\pi\tau)^{1/2}} + \frac{B}{2G^{1/2}} \operatorname{erf}(G\tau)^{1/2} \right] \quad (15.136)$$

Similarly, Eq. 15.134 can be inverted by writing

$$\frac{1}{\gamma} \frac{B}{B+p} = \frac{B}{p(p+G)^{1/2}} \quad (15.137)$$

which leads to

$$J_{(1)} = \left( \frac{D_{Xe} C_0}{a} \right) \frac{B}{G^{1/2}} \operatorname{erf}(G\tau)^{1/2} \quad (15.138)$$

Multiplying Eq. 15.136 by  $(1-y)$  and Eq. 15.138 by  $y$  and summing gives  $J$ , which is then integrated according to Eq. 15.67 to yield the fractional release. The result of these manipulations is:<sup>\*</sup>

$$f = \frac{3(1-y)}{G^{1/2}} \operatorname{erf}(G\tau)^{1/2} \\ + \frac{3B}{2G^{3/2}} (1+y) \left[ (G\tau) \operatorname{erf}(G\tau)^{1/2} - \frac{1}{2} \right] \quad (15.139)$$

The first term on the right is valid for any  $G$  in the short-time approximation ( $\tau < \sim 0.01$ ). The formula, however, is less accurate in predicting  $f$  when the re-resolution parameter  $B$  differs from zero. The second term in Eq. 15.139 is a good approximation to Hurst's<sup>22</sup> numerical solution as long as the following restrictions are satisfied: (1)  $\tau < \sim 10^{-3}$ , (2)  $G\tau > \sim 2$ , and (3)  $B/G \ll 1$ .

Fortunately, all these restrictions are satisfied in most postirradiation annealing experiments. Restriction 1 is a short-time limitation which is more severe than in the case of the simple diffusion model. For restrictions 1 and 2 to be simultaneously satisfied,  $G$  must be greater than  $\sim 2000$ . To ascertain if  $G$  values of this magnitude would be expected, we can combine Eqs. 15.108 and 15.114, which gives:

$$G = \left( \frac{a}{L} \right)^2 \quad (15.140)$$

The analysis is valid provided the equivalent radius of the particles is about 50 times larger than the trapping diffusion length. For solids with a normal complement of

<sup>\*</sup>In the process of integrating  $\operatorname{erf}(G\tau)^{1/2}$  by parts, another integral of the form  $\int_0^{(G\tau)^{1/2}} x^2 e^{-x^2} dx$  arises. The upper limit of this integral has been approximated by infinity to arrive at the factor of  $1/2$  in Eq. 15.139.

pores, grain boundaries, and any radiation-produced defects, this ratio is usually attained.

Equation 15.139 is essentially the first two terms of a power-series solution for  $f$  in the re-resolution parameter  $B$ . Restriction 3 requires that the re-resolution probability be much smaller than the trapping probability. This is realistic in postirradiation annealing studies, wherein only thermal re-resolution occurs, but the approximation would not be acceptable in an irradiation environment, where fission-fragment re-resolution increases  $B$  by a factor of 10 to 100 over that due to thermal processes acting alone.

Equation 15.139 reduces to all the limiting cases considered earlier except that of equilibrium trapping, which can be deduced by neglecting  $p$  in the denominator of the second term in Eq. 15.130.

Figure 15.20 shows the release curves measured by MacEwan and Morel<sup>23</sup> in postirradiation annealing studies of xenon release from crushed particles of  $UO_2$ . Each particle behaved as a single spherical diffusion medium with no internal surface area. Figure 15.20(a) shows the data obtained with particles of an equivalent radius of  $31 \mu m$

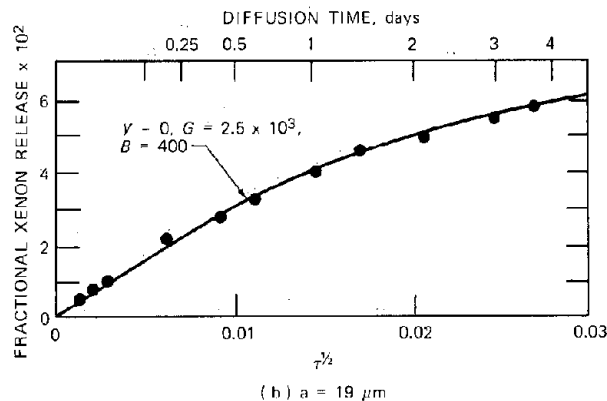
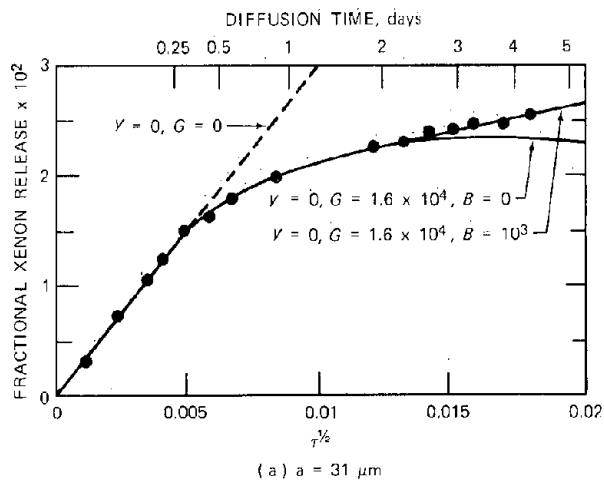


Fig. 15.20 Fractional xenon release from  $UO_2$  single-crystal particles at  $1400^\circ C$ . Preannealing irradiation exposure was less than  $10^{15}$  fissions/cm<sup>3</sup>. Curves are from the solutions to the diffusion-trapping equations for the values of the parameters indicated. [From J. R. MacEwan and P. A. Morel, *Nucl. Appl.*, 2: 158 (1966).]

which had been charged with fission gas by a light low-temperature irradiation. The data points were fit to the numerical solution of the diffusion-trapping equations (Eq. 15.139 could equally well have been employed). The values of the parameters which provided the best agreement between the data and the predictions of the model are shown on the graph. Also shown are lines that ignore trapping entirely ( $y = 0$ ,  $G = 0$ ) and neglect release from the traps ( $y = 0$ ,  $G = 1.6 \times 10^4$ ,  $B = 0$ ).

The best fit is obtained with  $y = 0$ , which justifies the belief that the prior radiation exposure was small enough to prevent production of sufficient radiation defects to measurably impede diffusion in the high-temperature anneal. The most prominent feature of the release curves is the rapid initial rate followed by a nearly linear (with  $\tau^{1/2}$ ), slower rise. This is precisely the burst character which cannot be explained by the simple diffusion model. The diffusion-trapping model shows that the initial slope of the  $f$  vs.  $\tau^{1/2}$  plot is identical to that for simple diffusion in the absence of trapping; early release is due to gas so near to the surface that the probability of encountering a trap before reaching the surface of the specimen and escaping is very small. Trapping is evident in the release kinetics only later when the surface flux arises from gas drawn from deep within the particle. This gas has a substantial probability of being trapped while migrating. Thus, the initial rapid rise in the release rate from  $\text{UO}_2$  is a natural consequence of the trapping-diffusion model; it is representative of true volume diffusion and not, as had been thought earlier, of some unexplained degradation of the surface of the specimen by contamination or other causes.

Figure 15.20 shows that the fraction released continues to increase even at long anneal times. The absence of a saturation value in the release curves (as evidenced by the departure of the data from the irreversible trapping curve for  $\tau^{1/2} > 0.01$ ) suggests that slow release from the traps is occurring, which is reflected by the value of  $B = 10^3$  needed to fit the data.

Figure 15.20(b) shows the results of an experiment performed under identical conditions as those of Fig. 15.20(a) but with  $\text{UO}_2$  particles  $19 \mu\text{m}$  in radius rather than  $31 \mu\text{m}$ . The best fit is obtained with  $y = 0$  (because the initial irradiation was light) and  $G = 2500$  and  $B = 400$ . If the trapping and re-solution probabilities were the same for the two different particle sizes (and there is no reason to expect that they should not be), Eqs. 15.114 and 15.115 show that  $G$  and  $B$  should have decreased by a factor of  $(19/31)^2 = 0.38$  when the small particles replaced the larger ones. On the bases of the values of these parameters obtained from the  $31\text{-}\mu\text{m}$  particle release curve, the predicted values for the small particles are  $G = 6000$  and  $B = 380$ . The observed changes are in the right direction and agree adequately with the predicted magnitudes. Using the average value of the trapping probability  $g$  obtained from the two experiments and Eq. 15.108 shows that the trapping length is  $0.3 \mu\text{m}$ . The re-solution parameter evaluated from the  $B$  value and Eq. 15.115 gives a mean delay time of gas in the traps,  $1/b$ , of about 13 days. This figure can be compared to the mean re-solution lifetime under reactor irradiation, which is 4 to 40 hr (Sec. 13.7). The true diffusion coefficient obtained from the initial slopes of the

release curves in Figs. 15.20(a) and 15.20(b) in conjunction with Eq. 15.83 (which, as explained, applies to early times even when trapping occurs) is  $8 \times 10^{-15} \text{ cm}^2/\text{sec}$  at  $1400^\circ\text{C}$ .

The data from an experiment at  $1500^\circ\text{C}$  with the large ( $31\text{-}\mu\text{m}$  radius) particles and a low initial irradiation dose were best fit to theory with  $y = 0$ ,  $G = 1.2 \times 10^4$ , and  $B = 1.5 \times 10^3$ . The initial linear portion of the  $f$  vs.  $\tau^{1/2}$  curve yielded a diffusion coefficient at this temperature of  $4 \times 10^{-14} \text{ cm}^2/\text{sec}$ . The activation energy for volume diffusion of xenon in  $\text{UO}_2$  computed from the  $D_{\text{Xe}}$  values at  $1400^\circ\text{C}$  and  $1500^\circ\text{C}$  is about 90 kcal/mole, which is in very good agreement with the value obtained by the bubble-growth experiment (Eq. 13.29). The re-solution time calculated from the preceding value of  $B$  is 10 days, compared with 13 days in the experiment at  $1400^\circ\text{C}$ . This decrease in  $b^{-1}$  is an indication of a thermally activated escape process, although the activation energy is rather low.

The value of  $G$  for the  $1500^\circ\text{C}$  experiment was nearly the same as that for the  $1400^\circ\text{C}$  experiment, showing that the anneal temperature did not affect the diffusion trapping length (which remained at  $0.3 \mu\text{m}$ ). The most obvious defect for trapping migrating gas atoms during the annealing stage is the preexisting closed porosity in the particles. MacEwan and Morel assumed that the gas-atom capture rate by the pores is reaction-rate controlled; so  $L^2$  is given by Eq. 13.51 in which the trap concentration is the number of pores per cubic centimeter. The combinatorial number for large spherical traps such as pores is best estimated as the number of atomic sites on the pore surface, or  $4\pi R_t^2/a_0^2$ , where  $R_t$  is the pore radius and  $a_0$  is the lattice constant. Inserting this expression for  $z_{gt}$  into Eq. 13.51 and assuming the atomic volume  $\Omega = a_0^3$ , we have

$$L^2 = \frac{a_0}{4\pi R_t^2 C_t} \quad (15.141)$$

The measured pore concentration and size in the  $\text{UO}_2$  specimens used by MacEwan and Morel were  $R_t = 150 \text{ \AA}$  and  $C_t \approx 2 \times 10^{13} \text{ pores/cm}^3$ . Using these values and  $a_0 = 3.5 \text{ \AA}$  in the preceding formula yields  $L = 0.08 \mu\text{m}$ . This value does not include the effect of other types of traps (e.g., subgrain boundaries or dislocation lines), inclusion of which would have rendered the computed value of  $L$  even smaller than  $0.08 \mu\text{m}$ . The theoretical value of  $L$  is too small because in the derivation of Eq. 15.141 the capture rate of gas atoms by the pores has been assumed to be reaction-rate controlled. Diffusion control of the absorption rate is much more likely for spherical sinks  $150 \text{ \AA}$  in radius. The predicted trapping length for diffusion-controlled absorption can be obtained by using Eq. 13.70 in Eq. 15.108, which results in

$$L^2 = \frac{1}{4\pi R_t C_t} \quad (15.142)$$

The diffusion trapping length predicted by Eq. 15.142 for the pores in the  $\text{UO}_2$  particles used by MacEwan and Morel is  $0.6 \mu\text{m}$ , which is in better accord with the measured value of  $0.3 \mu\text{m}$  than the value computed, assuming reaction-rate control. Inclusion of other natural defects, such as dislocations, in the computation would have brought the diffusion-controlled prediction closer to the measurement.

The data shown in Fig. 15.20 pertain to low initial exposures, which did not produce any defects that survived long enough at the annealing temperatures to contribute to gas-atom trapping. However, when the particles were given long initial irradiations, the release curves showed substantially larger  $G$  values and required that the initial fraction trapped,  $y$ , be other than zero. MacEwan and Morel<sup>2,3</sup> found that, for a particular sphere size, the trapping parameter could be correlated by

$$G = G_0 + K\bar{F}t_{\text{irr}} \quad (15.143)$$

where  $t_{\text{irr}}$  is the length of the low-temperature irradiation,  $G_0$  is the dimensionless trapping parameter arising from the preexisting porosity, and  $K$  is an empirical constant. At a burnup ( $\bar{F}t_{\text{irr}}/N_U$ ) of only  $10^{-4}$ ,  $G$  was found to be 25 times larger than  $G_0$ . Thus, copious quantities of defects must have been produced by irradiation which, moreover, were stable at temperatures of  $1400^\circ\text{C}$ . MacEwan and Morel<sup>2,3</sup> considered that bubbles produced by nucleation of the fission gas during the early stages of the anneal were responsible for the large increase of the trapping probability above that ascribable to the natural porosity of the material. However, even the assumption that all the fission gas precipitated into equilibrium bubbles produced a theoretical value of the constant  $K$  in Eq. 15.143 far lower than the measured value.

MacEwan and Morel<sup>2,3</sup> suggested that the bubbles may not have contained sufficient gas to be at mechanical equilibrium, which would then make them larger than equilibrium bubbles containing the same quantity of gas. However, the assumption of equilibrium bubbles appears to work well in most swelling models (see Chap. 13); so the source of the discrepancy probably lies elsewhere. Other possibilities include dislocation loops formed by interstitial condensation or solid fission products, either dissolved in the matrix as impurities or precipitated as second phases. Whatever the cause of the discrepancy between the estimated and observed effects of preirradiation exposure on the trapping probability, the experiments clearly show that for burnups characteristic in power reactors, gas-atom trapping due to fission-produced defects should be very much more important than trapping at natural defects in the as-fabricated fuel.

### 15.6.2 Steady-State In-Pile Release

When release of radioactive gases takes place under the combined effects of volume diffusion and trapping and a steady state has been attained, the concentration profile of untrapped gas in the spherical specimen is governed by

$$0 = y\bar{F} + D_{Xe} \frac{1}{r^2} \frac{d}{dr} \left( r^2 \frac{dC}{dr} \right) - \lambda C - \sum_j g_j C + \sum_j b_j M_j \quad (15.144)$$

where  $g_j$  and  $b_j$  are the trapping and re-resolution probabilities characterizing the  $j$ th type of trap and  $M_j$  is the amount of gas per unit volume contained in the  $j$ th type of

trap. More than one trapping site has been included in the analysis because of the presence of irradiation. The balances on the trapped gas are given by

$$0 = g_j C - \lambda M_j - b_j M_j \quad (15.145)$$

One balance of this form is required for each distinguishable type of trap assumed to be present in the irradiated solid. The concentration of trapped gas can be eliminated from Eq. 15.144 by use of Eq. 15.145, and the differential equation for migrating gas becomes

$$0 = y\bar{F} + D_{Xe} \frac{1}{r^2} \frac{d}{dr} \left( r^2 \frac{dC}{dr} \right) - \lambda \left[ 1 + \sum_j \left( \frac{g_j}{\lambda + b_j} \right) \right] C \quad (15.146)$$

which is identical in form to the analogous balance in the simple diffusion model (Eq. 15.90) if the decay constant in the latter is modified by the bracketed term in the preceding equation. If  $g_j$  and  $b_j$  are independent of  $C$ , the solution to Eq. 15.146 can be obtained in the same way as in the purely volume-diffusion analysis. Expressing the trapping and re-resolution probabilities in dimensionless terms by use of Eqs. 15.114 and 15.115, we obtain the fractional release at steady state:

$$f = \frac{3\Gamma^{1/2}}{(1 + \sum_j \{G_j / [(1/\Gamma) + B_j]\})^{1/2}} \quad (15.147)$$

where

$$\Gamma = \frac{D_{Xe}}{\lambda a^2} \quad (15.148)$$

is the dimensionless constant of the fission product under consideration. Equation 15.147 reduces to Eq. 15.92 if all  $G_j \rightarrow 0$  (no trapping) or all  $B_j \rightarrow \infty$  (short residence times in the traps). A release formula similar to Eq. 15.147 was first derived by Carroll et al.<sup>24</sup>

Interpretation of fractional release data, such as those shown in Fig. 15.18, in terms of the diffusion-trapping model requires quantitative characterization of the capture and re-resolution probabilities for each type of trap present. On the basis of the observations of MacEwan and Morel,<sup>2,3</sup> trapping due to preexisting defects in the solid can be neglected when release occurs during irradiation. In addition, we assume that only two types of radiation-produced traps are present, shallow ones and deep ones. The distinction between these types of traps is that the shallow traps can be annealed by thermal processes and destroyed by fission fragments but the deep traps are not susceptible to removal by thermal annealing. In addition, we would expect that the re-resolution probability from shallow traps would be larger than that from deep traps, but this is a matter of degree only. According to all models of gas re-resolution from bubbles,  $b$  is directly proportional to the fission rate (Eq. 13.112 or 13.116); so we can write

$$B_j = \alpha_j \bar{F} \quad (15.149)$$

where  $\alpha_j$  is independent of temperature. Thermal re-resolution is neglected.

Consider now the dimensionless trapping probability  $G_j$ . It depends on the trapping length according to Eq. 15.140 where, depending on whether gas-atom capture kinetics are reaction-rate or diffusion controlled,  $L$  is expressed in terms of the defect size and concentration by Eq. 13.51 or Eq. 15.142. The shallow traps are presumably the entities represented by items 2(a) and (b) in the classification given at the beginning of this section. These trapping sites are quite small, and for simplicity we assume that the reaction-rate-controlled expression for  $L$  is applicable to them. On the other hand, the deep radiation-produced traps belonging to categories 2(c) and (d) are probably large objects best characterized by diffusion-controlled gas-atom capture rates. Thus we write

$$G_1 = (z_{gt} z_o a^2) C_1 \quad (15.150)$$

for the shallow traps, and

$$G_2 = (4\pi R_t a^2) C_2 \quad (15.151)$$

for the deep traps. In these equations  $R_t$  is the radius of the large spherical deep traps, and  $z_{gt}$  is the combinatorial number for the atomic-size shallow traps.

At steady state the concentration of shallow traps is obtained by equating the rate of production by fission to the sum of the rates of destruction by thermal annealing and fission

$$Y_1^{tr} \dot{F} = \lambda_1^{tr} C_1 + K_1^{tr} C_1 \dot{F} \quad (15.152)$$

where  $Y_1^{tr}$  is the number of shallow traps created per fission event (the yield of the traps) and  $K_1^{tr}$  is a measure of the ease with which the traps are destroyed by fission fragments.\* The value of  $\lambda_1^{tr}$  is the decay constant for thermal annealing of the shallow traps. We assume that this process is first order in trap concentration, although it need not be (i.e., vacancy-interstitial recombination) and that the decay constant is of the Arrhenius form

$$\lambda_1^{tr} = \lambda_{1o}^{tr} \exp\left(-\frac{E_1^{tr}}{kT}\right) \quad (15.153)$$

where  $E_1^{tr}$  is the activation energy for thermal annealing of the shallow traps and  $\lambda_{1o}^{tr}$  is a constant. Solving Eq. 15.152 for  $C_1$  and substituting the result into Eq. 15.150 yields the dimensionless capture probability for the shallow traps:

$$G_1 = \frac{z_{gt} z_o a^2 Y_1^{tr} \dot{F}}{\lambda_{1o}^{tr} \exp(-E_1^{tr}/kT) + K_1^{tr} \dot{F}} \quad (15.154)$$

The preceding analysis of the dynamic behavior of shallow traps ignores several important details of the overall process. First, the quantity  $b_1 M_1$  represents the rate at

\*If the rate of destruction of shallow traps were analogous to the rate of bubble destruction in Turnbull's model (Chap. 13, Ref. 43),  $K_1^{tr}$  would be equal to  $2\pi R_t^2 \mu_{ff}$ , where  $R_t$  is the radius of the trap and  $\mu_{ff}$  is the fission fragment range. See Fig. 13.11 and Eq. 13.112.

which gas atoms are returned to the matrix from shallow traps, but it is implicitly assumed that in this process, the traps themselves remain intact (otherwise,  $b_1 M_1$  should appear as a trap removal term on the right-hand side of Eq. 15.152). Second, the trap destruction rates in Eq. 15.152 are not included in the gas balances of Eqs. 15.144 and 15.145, although destruction of a trapping site surely releases the gas it had contained. Third, the trap annealing rate described by the first term on the right-hand side of Eq. 15.152 is assumed to be independent of the amount of gas held by the trap. However, it is probable that traps which contain gas atoms are not as easily removed by thermal annealing as are gas-free traps (i.e., the presence of bound fission-gas stabilizes the trap). This effect could be taken into account by allowing  $\lambda_1^{tr}$  to be a function of  $M_1$ , with  $\lambda_1^{tr}$  decreasing as  $M_1$  increases.

If the deep traps were solid fission products, their concentration, like their contribution to fuel swelling, would increase linearly with burnup (or  $\dot{F}t$ ). Were this the case, the free gas-atom balance of Eq. 15.144 would represent a quasi-steady-state situation for the current values of the trapping and re-solution probabilities due to this type of defect.

The most likely deep trap, however, is the population of fission-gas bubbles; Table 13.4 shows that the nucleation period required for establishment of the bubbles ranges from burnups of  $10^{-5}$  to  $10^{-3}$ , depending on the model for this phenomenon and the temperature. Thereafter, the concentration of bubbles can remain fixed if bubble migration does not occur and moving grain boundaries and dislocations do not sweep up bubbles in their path. For such bubbles growth occurs by gas-atom absorption. The constant bubble density, which is denoted by  $C_2$  in Eq. 15.151, is given by Eq. 13.141 or Eq. 13.143 in the homogeneous nucleation models; it is independent of burnup and varies with the fission rate raised to some power between  $1/2$  and  $2/3$ . Although the bubble density may not change with time after nucleation, the radius  $R_2$  continually increases due to growth of the bubbles by gas-atom absorption. If coalescence occurs, both  $C_2$  and  $R_2$  are functions of burnup. In Turnbull's heterogeneous nucleation model, both the bubble size and concentration are functions of the parameter  $(\dot{F}/DC)$  (see Eq. 13.207 et seq.).

Whatever model governs the evolution of the bubble population,  $G_2$  is a complex function of fission rate  $\dot{F}$ , temperature, and matrix gas-atom concentration  $C$ . Because of the dependence on the last of these variables, Eq. 15.146 cannot be integrated to give Eq. 15.147; when  $G_2$  is a function of  $C$ , the equation becomes nonlinear, and the gas-release calculation becomes intimately coupled to the bubble-growth calculation.

Because of the complexities involved in estimating the trapping probability when the deep traps are gas bubbles, we will illustrate application of the trapping-diffusion model to the steady-state in-pile release experiment under the assumption that only shallow traps are important. Such an analysis should be applicable to release experiments at burnups below the critical value for bubble nucleation. Assuming  $G_2 = 0$ , substitution of Eqs. 15.149 and 15.154 for  $B_1$  and  $G_1$  into Eq. 15.147 yields

$$f = 3 \Gamma^{1/2}$$

$$\left\{ 1 + \frac{Z_{\text{eff}} a_0 a^2 Y_1^{\text{tr}} \bar{F}}{[\lambda_{10}^{\text{tr}} \exp(-E_1^{\text{tr}}/kT) + K_1^{\text{tr}} \bar{F}] (1/\Gamma + \alpha_1 \bar{F})} \right\}^{-1/2} \quad (15.155)$$

Let us examine the fission-rate dependence of Eq. 15.155. As  $\bar{F} \rightarrow 0$ , the right-hand term in the braces approaches zero, and  $f$  reduces to the function of  $\Gamma$  given by the simple diffusion formula of Eq. 15.92. As  $\bar{F}$  becomes very large, the right-hand term in the braces again approaches zero, and the normal release law is recovered. If, in between these limits, the last term in the braces becomes comparable to or greater than unity, a minimum in the  $f$  vs.  $\bar{F}$  curve should occur. This predicted behavior is consistent with the shape of the curve shown in Fig. 15.18. The low fission rate asymptote is due to rapid thermal annealing of the shallow traps. At high fission rates the destruction of traps and the re-solution of gas atoms from the surviving traps become large. Together, these effects result in maintenance of essentially all the gas in dynamic solution. At high temperatures Eq. 15.155 predicts that the minimum in the fractional release curve with fission rate should be less pronounced because the large values of the trap annealing constant  $\lambda_1^{\text{tr}}$  and the diffusion coefficient (in  $1/\Gamma$ ) at elevated temperatures act to reduce the trap concentration, all other conditions being held constant.

### 15.6.3 Application to Gas Release from Fuel Elements

The obvious practical utility of clearly distinguishing volume diffusion from trapping effects is the potential of improving on the simple diffusion model in calculating gas release from reactor fuel elements. In such an application, the polycrystalline fuel pin would still have to be considered as an assembly of equivalent spheres; the only difference between the simple volume-diffusion and the trapping-diffusion variants is that the fractional release in the trapping-diffusion model would be a function of the trapping parameters as well as of the gas-diffusion coefficient. A number of assumptions are implicit in such an extension of the trapping-diffusion model:

1. The analysis of gas-release experiments employing single crystal specimens of known size by the methods described earlier has correctly separated the effects of volume diffusion and trapping on gas release. In particular, the quantity  $D$  obtained from the gas-release experiments is supposed to be the true diffusion coefficient of fission gases in  $\text{UO}_2$ , not the admittedly apparent diffusion coefficient provided by the simple diffusion model.

2. The mathematical apparatus required to extend the trapping-diffusion model to fuel elements in which the temperature and fission rate are functions of two position variables is available.

3. The trapping and re-solution probabilities needed for quantitative application of the model can be estimated for reactor conditions and burnups.

4. Gas release due to gross bubble motion (which is not accounted for in the trapping-diffusion model) can be neglected. Bubble motion can occur either by biased migration or by grain-boundary or dislocation sweeping.

Consider the first assumption. Application of the trapping-diffusion model to the postirradiation anneal experiments of MacEwan and Morel<sup>23</sup> resulted in trapping lengths that were in reasonable accord with values expected from diffusion-controlled absorption of gas atoms by the preexisting porosity in the specimens. Although it is surprising to find that the noble gases can escape from closed pores in the absence of radiation (all other experimental evidence strongly suggests that xenon and krypton are totally insoluble in  $\text{UO}_2$ ), the mean residence times of the gas in the pores was at least very much larger than the re-solution lifetimes in a fission-fragment flux.

The one quantity that can be compared to other experiments is the gas diffusion coefficient  $D_{Xe}$ . This parameter is provided directly by the initial slope of the release curve in the postirradiation annealing experiment (Fig. 15.20). The release rates measured by in-pile experiments at low fission densities should also be free of trapping effects; so the limiting value of  $f$  as  $\bar{F} \rightarrow 0$  in Fig. 15.18 should be directly related to the true diffusion coefficient by Eq. 15.92. Finally, Cornell's bubble growth study, which should also have avoided the confounding effects of trapping, provided the diffusion coefficients given by Eq. 13.29. Table 15.4 summarizes the values of  $D_{Xe}$  ( $1400^\circ\text{C}$ ) determined by these three independent experiments. A discouraging three order-of-magnitude discrepancy still exists despite all the effort of eliminating unwanted side effects.

Now let us consider what is required to apply the trapping-diffusion model to an entire fuel element (assumption 2). For the analysis presented at the end of Sec. 15.5 to be modified to account for trapping and re-solution, the fractional release of stable fission gases from a volume element of fuel at a particular temperature and fission rate must be calculated as a function of irradiation time. In the simple diffusion model, the necessary fractional release is given by Eq. 15.89. The analogous formula in the trapping-diffusion model has not been obtained. To do so would require replacing Eq. 15.86 by the equivalent conservation equations for free gas and trapped gas obtained from trapping-diffusion theory, then solving these equations to give  $f$  as a function of  $\tau$ ,  $G$ , and  $B$ . Since the radius  $a$  is not known a priori when the equivalent-sphere concept is applied to fuel bodies, we would, as in the application of the simple diffusion model to the same calculation, have to use an empirical diffusion coefficient whenever the ratio  $D_{Xe}/a^2$  appeared ( $D$  or  $D_{Xe}$  and  $a$  always appear in this combination in both the simple diffusion and trapping-diffusion theories). Armed with the functional dependence of  $f$  on  $D'$ ,  $b$ , and  $g$  (hopefully in analytical rather than

Table 15.4 True Diffusion Coefficient of Fission Gases in  $\text{UO}_2$  at  $1400^\circ\text{C}$

Method	$D_{Xe}$ ( $1400^\circ\text{C}$ ), $\text{cm}^2/\text{sec}$	Reference
Postirradiation anneal	$8 \times 10^{-15}$	23
In-pile release	$5 \times 10^{-13}$	11
In situ bubble growth	$3 \times 10^{-16}$	Ref. 25 of Chap. 13

numerical form), we could in principle perform the appropriate integrations to yield the average fractional release from the fuel element,  $f$ .

Regarding requirement 3, the preceding discussion of the steady-state in-pile release experiments using short-lived radioactive fission gases has shown that a sizeable number of parameters are needed to permit evaluation of  $g$  and  $b$  for each trap present in the irradiated solid. In most cases the prediction of these parameters is not possible, and even the nature of the radiation-produced traps is not well-established. When trapping is due to gas bubbles, the trapping probability  $g$  depends on the bubble size and concentration, and there is no general agreement on how to calculate these quantities even when gas release is ignored (Chap. 13).

Assumption 4 is certainly not correct at high burnup and in a steep temperature gradient.

Thus, not one of the four basic prerequisites for extending the trapping-diffusion model to gas release from reactor fuel elements has been satisfied. It is not surprising that available gas-release theories either totally ignore bubble motion while treating gas-atom migration as a purely volume-diffusion process or disregard all diffusional processes and ascribe release only to bubble migration in a temperature gradient.

### 15.7 GAS ACCUMULATION IN GRAIN-BOUNDARY BUBBLES

Most models of gas release recognize that grain boundaries in the fuel act as efficient traps for fission gas. That substantial quantities of fission gas collect at grain boundaries during irradiation is demonstrated by Fig. 15.21. Bubbles from 1000 Å to well over 10,000 Å in diameter are visible, and large areas of the grain boundary appear to be completely covered by bubbles that have become interconnected. By contrast, the intragranular gas bubbles shown in Figs. 13.1 and 13.14 range in diameter from 10 to 30 Å. Analytical gas-release models involving intergranular gas bubbles differ profoundly on (1) how the gas reached the grain boundary and (2) the fate of the grain-boundary bubbles.

The BURL analysis presented in Sec. 13.12 assumed that gas reached the grain boundaries by migration as bubbles along the temperature gradient within the grain, with periodic stops as a result of trapping by other crystal defects. In this model, bubbles are released from the grain boundary when the critical size is attained, growth having occurred by coalescence with bubbles arriving from within the grain. After detachment, the large grain-boundary bubbles again migrate up the temperature gradient. This time, however, they are unstoppable, and the gas they contain is released to the fuel-element free volume when a crack or the central void is reached.

The model presented by Speight and coworkers<sup>25,26</sup> assumes that the grain boundaries accumulate gas by absorption of single atoms diffusing from the matrix. Neither the intra- nor intergranular gas bubbles are permitted to move. For diffusion of gas within the grain to the grain boundary, not all the gas can be contained in intragranular



Fig. 15.21 Replica fractograph of a grain-boundary surface in  $\text{UO}_2$  irradiated at  $F = 3 \times 10^{12}$  fissions  $\text{cm}^{-3} \text{sec}^{-1}$  and a temperature of  $\sim 1400^\circ\text{K}$  to a burnup of 1%. Both discrete fission-gas bubbles (B) and interlinked bubbles (D) are visible. Large fissures (A) are believed to result from complete bubble interconnection in this area of the grain boundary. An adjacent grain boundary is shown at (C). [From R. M. Cornell, M. V. Speight, and B. C. Masters, *J. Nucl. Mater.*, 30: 169 (1969).]

bubbles. Fission-induced re-solution from intragranular bubbles is postulated as the mechanism by which gas in atomic form is maintained in the solid, thus permitting establishment of a macroscopic concentration gradient in the grain by which gas atoms diffuse to the grain-boundary sinks. Contrary to the BURL model, grain-boundary bubbles are not removed by the thermal-gradient force. Instead, release to the fuel-element free volume occurs in one of two ways: (1) If extensive bubble interlinkage occurs, a pathway to a crack or other fissure communicating with the gas space in the fuel element will eventually be opened. The grain-boundary gas then simply flows out along this leakage path. (2) As a result of stresses in the fuel set up by power cycling, thermal expansion, or cladding restraint, the fuel may crack. Such cracking will most likely take place along the grain boundaries because the reduced contact area due to the presence of bubbles on these internal surfaces renders them the weakest points in the fuel body. However,

the theory presented in Refs. 25 and 26, which is reviewed in this section, does not explicitly account for gas release by either of the two mechanisms cited; it merely determines how much gas is in the intergranular bubbles as a function of irradiation time, thereby providing an estimate of the reservoir of gas available for release.

The model combines aspects of the trapping-release concept described in the preceding section. The intergranular bubbles are assumed to be the sole traps for the gas held in the matrix, and release from these traps is described by the fission-induced re-resolution parameter  $b$ . The grain boundaries are assumed to be perfect sinks in the thermodynamic sense that the concentration of dissolved gas in the solid adjacent to an intergranular bubble is taken to be zero. However, there is no reason why the gas in the grain-boundary bubbles should not be subject to the same re-resolution process as the gas in the intragranular bubbles, and the model allows for return of gas trapped on grain boundaries to the matrix by this mechanism.

The calculation invokes the equivalent-sphere concept to model the diffusion process. However, the radius of the equivalent sphere is not the empirical quantity defined by Eq. 15.61 in terms of the total surface-to-volume ratio of the fuel compact. Rather, it represents the radius of the average grain in the fuel.

The model presented by Speight and coworkers can also be viewed as an extension of the infinite-medium calculation of the growth of fixed intragranular bubbles when re-resolution is important (end of Sec. 13.9). This calculation determined the fraction of the fission gas contained in intragranular bubbles as a function of irradiation time when the bubbles act as traps and release is due to re-resolution. The Speight model retains this picture of the processes affecting the gas inside a grain (with the sole exception that the trapping probability  $g$  of Eq. 13.167 is not taken to be dependent on the gas content  $M$ ) but adds to the infinite-medium model the diffusion of gas to the grain boundaries. Thus, the model provides a means of calculating the fraction  $f_b$  of fission gas contained in intragranular bubbles and the fraction  $f_{gb}$  of gas in intergranular bubbles as functions of irradiation conditions and time. However, it assumes that all the gas generated within a particular grain is contained either in the matrix of the grain or in one of the two classes of bubbles associated with the grain. Periodic gas release from the grain boundaries due to cracking or flushing of the gas collected by a grain boundary due to bubble linkage to a fissure is not taken into account.

Figure 15.22(a) illustrates the configuration of the inter- and intragranular gas bubbles in a section of fuel. The idealized model of the grain analyzed by Speight et al. is shown in Fig. 15.22(b). There are  $N$  intragranular gas bubbles per unit volume of fuel, each of radius  $R$ . Neither  $N$  nor  $R$  is permitted to change during irradiation. The grain boundary in Fig. 15.22(b) is surrounded by a spherical shell blanket of gas representing the grain-boundary bubbles. Each actual grain boundary separates two adjacent grains. If the grain boundaries in Fig. 15.22(a) contain  $M_{gb}$  gas atoms per unit area, the smeared blanket in Fig. 15.22(b) contains  $M_{gb}/2$  gas atoms per unit area. The total quantity of fission gas produced in a unit volume of fuel within the grain is

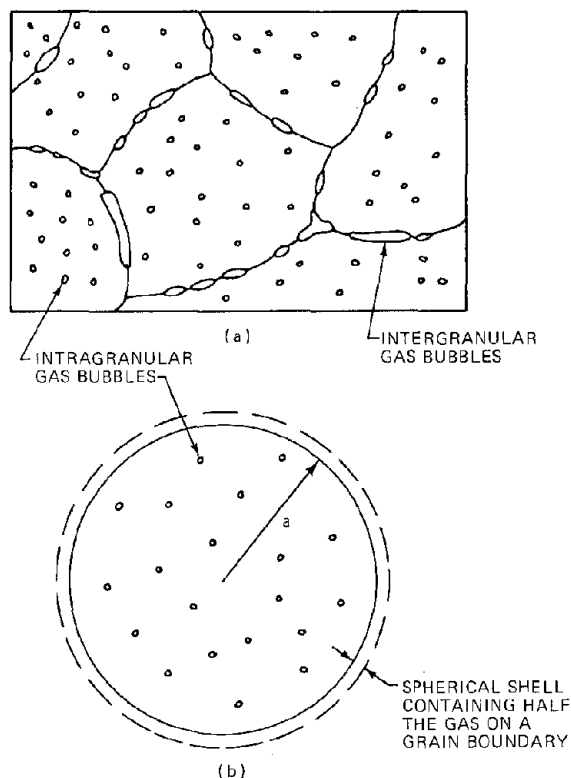


Fig. 15.22 Gas bubbles in grains and on grain boundaries. (a) Actual configuration. (b) Idealized grain used in the model of Speight et al.<sup>25,26</sup>

$Y_{Xe} \bar{F} t$ , where the cumulative yield of all stable fission gases,  $Y_{Xe} \approx 0.25$ , is used instead of the instantaneous yield of a particular species employed in the previous section. In the present analysis, all the fission gas must be accounted for. No net flow of gas occurs across the dashed outer boundary of Fig. 15.22(b); loss by fission-fragment knock-on is just balanced by gain from outside the dashed line.

The fraction of the total amount of gas generated up to time  $t$  which is not in the grain-boundary bubbles is contained within the grain, either in solution or in intragranular bubbles. Partitioning of the gas in the grain between these two locations is assumed to be governed by the condition of equilibrium trapping. This limiting case occurs when the trapping and re-resolution probabilities are large enough to neglect the time derivative of  $M$  in the balance equation for the quantity of trapped gas (i.e., Eq. 15.111 simplifies to  $gC = bM$ ). According to the discussion of equilibrium trapping in the preceding section, diffusional processes in such a medium can be described by Fick's law in which the concentration is interpreted as the sum of the concentrations of dissolved and trapped gas, and the apparent diffusion coefficient is equal to the true gas diffusion coefficient in the matrix multiplied by the ratio of the re-resolution parameter  $b$  to the sum of the re-resolution and trapping parameters,  $b + g$ . Thus, the diffusion equation in the sphere depicted in Fig. 15.22(b) is

$$\frac{\partial V}{\partial t} = Y_{Xe} \dot{F} + D \frac{1}{r^2} \frac{\partial}{\partial r} \left( r^2 \frac{\partial V}{\partial r} \right) \quad (15.156)$$

where  $V = C + M$  is the number of gas atoms per unit volume within the grain, irrespective of whether the gas is in solution or in intragranular bubbles, and  $D$  is the apparent diffusion coefficient given by Eq. 15.124. Speight<sup>2,6</sup> has shown that equilibrium trapping is a good assumption when  $bt > 5$ . The treatment assumes that the apparent diffusion coefficient,  $D$ , is independent of time. However,  $D$  depends on  $b$  and  $g$  as well as the true fission-gas diffusion coefficient  $D_{Xe}$ . Whereas  $b$  and  $D_{Xe}$  are time independent, the trapping probability  $g$  is given by

$$g = 4\pi R D_{Xe} N \quad (15.157)$$

Although the intragranular bubble density  $N$  can be considered as constant once the nucleation period is over, the bubble radius  $R$  can very well increase as irradiation proceeds. In fact, the infinite-medium analysis of bubble growth with re-solution attempts to determine just this variation (e.g., Eq. 13.160). Nonetheless, Speight's model assumes  $g$  to be a constant, at least for the purpose of integrating Eq. 15.156.

If the grain boundaries did nothing more than act as perfect sinks for fission gas, the boundary condition given by Eqs. 15.64 and 15.65 (with  $C$  replaced by  $V$ ) would apply, and the initial condition would be  $V(r,0) = 0$ . The flux of gas to the grain boundary would be given by the original no-trapping formula, Eq. 15.88, with  $D$  interpreted by Eq. 15.124. The fraction of fission gas accumulated by the grain boundaries,  $f_{gb}$ , would be given by Eq. 15.89 in the short-time approximation.

The principal modification of the simple model introduced by Speight et al. is to include re-solution of the gas in the grain boundaries in the analysis. This step essentially provides a source of fission-gas atoms within the matrix which should be added to Eq. 15.156 as a source term. The re-solution source arises because the gas atoms in the grain boundaries are periodically struck by fission fragments or energetic knock-ons. If they acquire an energy in excess of  $\sim 300$  eV in such a collision, they can plow back into the solid. This is the microscopic model of the re-solution process (Sec. 13.7). All knock-on fission-gas atoms do not have the same energy as they begin to penetrate the solid. The source of thermalized gas atoms due to slowing down of the knock-ons from the intergranular bubbles should be spread over all distances from the grain boundary up to the range of the maximum energy knock-on. Rather than deal with such a distributed source of gas atoms, Speight et al. assume that all knock-ons enter with the same energy and consequently have the same range,  $\mu_{Xe}^{k_0}$ , in the lattice. If the mean energy of the knock-ons is a few hundred electron volts, Table 15.1 shows that the depth of penetration into the solid should be several tens of angstroms. Diffusion of gas atoms in the presence of this discrete plane source is treated by dividing the grain into two regions, the interior of the sphere and the outer layer. The boundary between these two regions is the spherical surface a distance  $\mu_{Xe}^{k_0}$  from the actual grain boundary.

The outer region is thin compared to the sphere radius ( $\mu_{Xe}^{k_0}/a < 10^{-2}$ ); so slab geometry with  $x = a - r$  can be employed, and for the same reason quasi-stationary diffusion can be assumed. Thus, the concentration of total gas in the outer region,  $V_2$ , is governed by the equation

$$\frac{\partial V_2}{\partial t} = 0 = Y_{Xe} \dot{F} + D \frac{\partial^2 V_2}{\partial x^2} \quad 0 \leq x \leq \mu_{Xe}^{k_0} \quad (15.158)$$

with boundary conditions

$$V_2(0) = 0 \quad (15.159)$$

$$V_2(\mu_{Xe}^{k_0}) = V^*(t) \quad (15.160)$$

Equation 15.159 assumes total thermodynamic insolubility of the gas in the solid. The concentration at the boundary between the inner and outer regions is a slowly varying function of time  $V^*(t)$  which is to be determined. Equation 15.158 can be integrated directly and the flux in the  $+r$ -direction is found to be

$$J_2(x) = D \frac{dV_2}{dx} = Y_{Xe} \dot{F} \left( \frac{1}{2} \mu_{Xe}^{k_0} - x \right) + \frac{DV^*}{\mu_{Xe}^{k_0}} \quad (15.161)$$

In the interior of the grain, the total gas concentration is denoted by  $V_1$  and satisfies the equation

$$\frac{\partial V_1}{\partial t} - Y_{Xe} \dot{F} + D \frac{1}{r^2} \frac{\partial}{\partial r} \left( r^2 \frac{\partial V_1}{\partial r} \right) = 0 \quad 0 \leq r \leq a - \mu_{Xe}^{k_0} \quad (15.162)$$

with

$$V_1(r,0) = 0 \quad (15.163)$$

$$V_1(0,t) = \text{finite} \quad (15.164)$$

$$V_1(a - \mu_{Xe}^{k_0}, t) = V^*(t) \quad (15.165)$$

Equations 15.162 to 15.165 can be solved by the Laplace transform method. The transformed differential equation is

$$D \frac{d^2 \tilde{u}_1}{dr^2} - p \tilde{u}_1 = \frac{Y_{Xe} \dot{F} r}{p} \quad (15.166)$$

where  $u_1 = rV_1$ ,  $\tilde{u}_1$  is the Laplace transform of  $u_1$ , and  $p$  is the transform variable. The boundary conditions are

$$\tilde{u}_1(0) = 0 \quad (15.167)$$

$$\tilde{u}_1(a - \mu_{Xe}^{k_0}) = (a - \mu_{Xe}^{k_0}) \tilde{V}^* \approx a \tilde{V}^* \quad (15.168)$$

where  $\tilde{V}^*$  is the Laplace transform of  $V^*(t)$ .

Following the method used in solving the related problem involving postirradiation annealing in the equivalent-sphere model (Sec. 15.5), we can solve Eqs. 15.166 to 15.168 for the Laplace transform of the gas-atom diffusive flux at the boundary of the inner region

$$\tilde{J}_1(a - \mu_{Xe}^{k_0}) = \frac{Y_{Xe} \dot{F} D}{ap^2} \left[ \left( \frac{pa^2}{D} \right)^{\frac{1}{2}} - 1 \right] \times \left( 1 - p^2 \frac{\tilde{V}^*}{Y_{Xe} \dot{F}} \right) \quad (15.169)$$

where, in common with previous short-time approximations to the diffusion problem, the hyperbolic tangent of  $(pa^2/D)^{1/2}$  has been approximated by unity.

The unknown concentration at  $r = a - \mu_{Xe}^{k_0}$  is eliminated by a flux-matching condition at this position and an overall material balance on all gas created in the grain up to time  $t$ .

The flux-matching condition states that the difference between the diffusive fluxes  $J_1$  and  $J_2$  at the boundary between the two regions is equal to the slowing-down source of knock-ons arising from the gas in the grain boundary. There are  $M_{gb}$  gas atoms per unit grain-boundary area, and half of this quantity is associated with one grain. The probability per second that one of these atoms is ejected from the intergranular bubble into the solid is  $b$ . Thus, the matching condition becomes

$$J_2(\mu_{Xe}^{k_0}) - J_1(a - \mu_{Xe}^{k_0}) = \frac{1}{2} b M_{gb} = Y_{Xe} \dot{F} Q \quad (15.170)$$

where  $Q$  is the dimensionless quantity of gas in the grain boundary:

$$Q = \frac{b M_{gb}}{2 Y_{Xe} \dot{F} a} \quad (15.171)$$

The overall material balance requires that the time rate of change of the gas within the intergranular bubbles be equal to the net flux of gas atoms across the grain boundary

$$\frac{1}{2} \frac{dM_{gb}}{dt} = J_2(0) - \frac{1}{2} b M_{gb}$$

or

$$J_2(0) - Y_{Xe} \dot{F} Q = \frac{Y_{Xe} \dot{F}}{b} \frac{dQ}{dt} \quad (15.172)$$

Taking the Laplace transform of Eqs. 15.170 and 15.172 yields:

$$\frac{\tilde{J}_2(\mu_{Xe}^{k_0}) - \tilde{J}_1(a - \mu_{Xe}^{k_0})}{Y_{Xe} \dot{F}} = \tilde{Q} \quad (15.173)$$

and

$$\frac{\tilde{J}_2(0)}{Y_{Xe} \dot{F}} = \left(1 + \frac{p}{b}\right) \tilde{Q} \quad (15.174)$$

where  $\tilde{Q}$  is the Laplace transform of  $Q$ .

Equation 15.169 and the Laplace transform of Eq. 15.161 can be substituted into Eqs. 15.173 and 15.174. Then  $\tilde{V}^*$  can be eliminated from the resulting pair of equations, and  $\tilde{Q}$  can be determined as

$$\tilde{Q} = \frac{(\eta/p) + (\mathcal{L}/p^{3/2}) [1 + (p/2\mathcal{L}^2)\eta^2]}{(p/b) + (p^{1/2}/\mathcal{L})\eta} \quad (15.175)$$

In obtaining this result, we assumed  $p/b \ll 1$  (which is equivalent to  $bt \gg 1$ ) and  $(pa^2/D)^{1/2} \gg 1$  (which is equivalent to  $Dt/a^2 \ll 1$ ). The parameters in Eq. 15.175 are

$$\mathcal{L} = \left(\frac{D}{a^2}\right)^{1/2} \quad (15.176)$$

$$\eta = \frac{\mu_{Xe}^{k_0}}{a} \quad (15.177)$$

Equation 15.175 can be inverted with the aid of tables of inverse Laplace transforms. The desired result of the calculation is the fraction of the gas generated in the grain up to time  $t$  which is contained in the intergranular bubbles associated with the grain, or

$$f_{gb} = \frac{[(4\pi a^2)M_{gb}]/2}{(4\pi a^3/3)(Y_{Xe}\dot{F}t)} = \frac{3Q}{bt} \quad (15.178)$$

Substituting the inversion of Eq. 15.175 into 15.178 yields

$$f_{gb} = 3 \left(\frac{\mathcal{L}^2}{b\eta}\right) \frac{1}{\tau} \left(1 - \frac{2}{\pi^{1/2}} \tau^{1/2} + \tau - e^{-\tau} \operatorname{erfc} \tau^{1/2}\right) - 3\eta \frac{1}{\tau} \left(1 - \frac{2}{\pi^{1/2}} \tau^{1/2} - e^{-\tau} \operatorname{erfc} \tau^{1/2}\right) + 3 \left(\frac{b\eta^3}{2\mathcal{L}^2}\right) \frac{1}{\tau} (1 - e^{-\tau} \operatorname{erfc} \tau^{1/2}) \quad (15.179)$$

where

$$\tau = \left(\frac{b\eta}{\mathcal{L}}\right)^2 t = \frac{(bt)^2}{(Dt/a^2)} \left(\frac{\mu_{Xe}^{k_0}}{a}\right)^2 \quad (15.180)$$

The last term in Eq. 15.179 varies as the cube of the parameter  $\eta$  and can be neglected.

The magnitude of the dimensionless time  $\tau$  is set primarily by the fission-gas knock-on range to grain radius ratio, which appears on the right-hand side of Eq. 15.180. For a specified value of this ratio, the range of  $\tau$  is determined by the time-dependent terms, the values of which must satisfy certain restrictions imposed by the approximate mathematical treatment. The lower limit is imposed by the requirement that  $bt > 5$ , which is necessary for the equilibrium trapping approximation to apply to the gas within the grain. The upper time limit is set by the validity of the short-time approximation to the solution of the diffusion equation in the inner region, which requires that  $Dt/a^2 \ll 1$ . For typical values of the parameters involved, the lower and upper bounds represent irradiation times of about 1 month and several years, respectively. This interval is sufficiently broad to render the results applicable to irradiations of practical interest.

The importance of re-resolution from intergranular bubbles on the accumulation of fission gas by grain boundaries is governed by the ratio  $(\mu_{Xe}^{k_0}/a)$ . By means of this parameter,  $\tau$  can become very large or very small without violating the previously mentioned restrictions on the time. The limiting case of Eq. 15.179 for weak grain-boundary trapping is obtained as  $\tau \rightarrow 0$ .\*

$$f_{gb} = \frac{4}{\pi^{1/2}} \left(\frac{Dt}{a^2}\right)^{1/2} - \frac{3}{2}(bt - 2) \left(\frac{\mu_{Xe}^{k_0}}{a}\right) \quad (15.181)$$

As  $(\mu_{Xe}^{k_0}/a) \rightarrow 0$ , the last term disappears, and  $f_{gb}$  reduces to the fractional release formula obtained in the simple diffusion model, Eq. 15.89.

When grain-boundary re-resolution is substantial,  $\tau \rightarrow \infty$  and Eq. 15.179 reduces to

\*If Eq. 15 of Ref. 26 is integrated and then converted to the fraction of the gas in the grain-boundary bubbles,  $f_{gb}$  is found to be of the same form as Eq. 15.181 except that the coefficient of  $(\mu_{Xe}^{k_0}/a)$  is  $2(bt)/\pi$ .

$$f_{gb} = 3 \left( \frac{D}{a^2 b} \right) \left( \frac{a}{\mu_{Xe}^{k_o}} \right) \quad (15.182)$$

or the fraction of fission gas residing in grain-boundary bubbles attains a saturation value.

The disposition of the remainder of the gas can be easily determined. The fraction of the gas in the grain is  $1 - f_{gb}$ , of which the intragranular bubbles contain the fraction  $g/(g+b)$ . Thus, the fraction  $f_b$  of the gas in bubbles within the grain is

$$f_b = \left( \frac{g}{b+g} \right) (1 - f_{gb}) \quad (15.183)$$

which, if  $f_{gb} \rightarrow 0$ , reduces to the result of the infinite medium case in which  $g$  is assumed constant (Eq. 13.166) but not to the result when the growth of the intragranular bubbles during irradiation is taken into account (Eq. 13.168).

Use of Eqs. 15.179 to 15.183 requires a considerable amount of information, most of which is not available. According to Sec. 13.7, the re-solution parameter  $b$  is of the order of  $10^{-6}$  to  $10^{-5}$  sec $^{-1}$ , but the very large size of grain-boundary bubbles can considerably reduce this estimate, as indicated at the end of Sec. 13.7. Grain sizes of 10  $\mu$ m are typical. The fission-gas knock-on range in the fuel,  $\mu_{Xe}^{k_o}$ , is not known with any precision but it is probably  $<100$  Å. The apparent diffusion coefficient  $D$ , according to Eq. 15.124, depends on the trapping probability  $g$ , which, by Eq. 15.157 depends on the size and density of the intragranular bubbles. According to Table 15.4, the fission-gas diffusion coefficient is not well established.

The model proposed by Speight et al. has not been used to predict gas release from fuel elements, partly because of the many parameters required for its quantitative application but also because it gives only the quantity of gas accumulated at intact grain boundaries. An additional model is needed to predict the actual release of the gas from the intergranular bubbles to the free space in the fuel element.

## 15.8 BREAKAWAY GAS RELEASE DUE TO BUBBLE INTERCONNECTION

When the bubble density, either in the grains or on grain boundaries, is sufficiently high and the bubbles are sufficiently large, extensive interconnection of the bubbles can occur. When this situation develops, the fuel resembles a Swiss cheese, and, when one point of the network of interlinked bubbles touches a crack or other easy escape route, all the gas in the now open porosity is vented to the fuel-element interior. Since bubble size and concentration determine fuel swelling (Eq. 13.17), breakaway gas release due to bubble interconnection commences when  $\Delta V/V$  reaches a critical value between 50 and 150%.

### 15.8.1 Intragranular Bubbles

Let us first treat the case in which the gas generated in the fuel is partitioned between intragranular bubbles and the solid matrix but no grain-boundary bubbles are formed

( $f_{gb} = 0$ ). At irradiation time  $t$ , let there be  $N$  intragranular bubbles of radius  $R$  per unit volume of fuel. Since the volume of gas is comparable to that of the solid, the term "fuel" is used to denote solid plus gas. The fuel can be divided into spherical unit cells, each of radius  $\mathcal{R}$  and containing one bubble at the center. This cell is depicted in Fig. 13.7, and the relation between the cell radius and the bubble density is given by

$$\left( \frac{4}{3} \pi \mathcal{R}^3 \right) N = 1 \quad (15.184)$$

Consider a unit volume of fuel at time  $t$ . The volume of solid in the unit volume of fuel is  $1 - (R/\mathcal{R})^3$ . During an irradiation of duration  $t$ ,  $[1 - (R/\mathcal{R})^3] Y_{Xe} \bar{F} t$  fission-gas atoms are produced in the unit volume of fuel ( $\bar{F}$  is the fission rate per unit solid volume). If at time  $t$  the fraction of the fission gas precipitated into bubbles is  $f_b$ , the number of gas atoms in intragranular bubbles is

$$\left[ 1 - \left( \frac{R}{\mathcal{R}} \right)^3 \right] f_b Y_{Xe} \bar{F} t = \text{gas atoms in}$$

intragranular bubbles per unit fuel volume (15.185)

Assume that the bubbles are large enough so that the ideal gas law is applicable. The number of gas atoms in each bubble is given by Eq. 13.16, and the number of gas atoms per unit volume of fuel is this quantity times the number of bubbles per unit volume of fuel

$$\left( \frac{4}{3} \pi R^2 \right) \left( \frac{2\gamma}{kT} \right) N = \frac{1}{R} \left( \frac{2\gamma}{kT} \right) \left( \frac{R}{\mathcal{R}} \right)^3 = \text{gas atoms}$$

in intragranular bubbles per unit fuel volume (15.186)

where the last equality was obtained by eliminating  $N$  through the use of Eq. 15.184. If Eqs. 15.185 and 15.186 are set equal to each other, the porosity of the fuel due to the intragranular bubbles can be determined to be

$$\left( \frac{R}{\mathcal{R}} \right)^3 = \frac{R(kT/2\gamma) f_b Y_{Xe} \bar{F} t}{1 + R(kT/2\gamma) f_b Y_{Xe} \bar{F} t} \quad (15.187)$$

Using Eqs. 13.17 and 15.184, the fractional swelling is related to the porosity by

$$\frac{\Delta V}{V} = \frac{(R/\mathcal{R})^3}{1 - (R/\mathcal{R})^3} \quad (15.188)$$

Swelling as a function of time can be determined by combining Eqs. 15.187 and 15.188, provided that (1) no gas release has occurred up to time  $t$ , (2) the bubbles are all of the same size, and (3) grain-boundary bubbles are absent. Equation 15.187 indicates that the porosity approaches unity as the numerator becomes large compared to 1. However, well before unit porosity is attained, the bubbles become interconnected, and breakaway gas release occurs.

For the extent of bubble linkage to be related to the porosity, the geometrical configuration of the two-phase fuel must be specified. Suppose the bubbles were arranged on a simple cubic lattice with one bubble on each of the eight cube corners. When the bubbles had grown to the extent that they just touched each other, the length of the cube side would be equal to twice the bubble radius. Since

each cube corner is shared among eight adjacent cubes, one whole bubble is associated with each cube. The porosity of a solid containing touching bubbles arranged on a simple cubic lattice is

$$\left(\frac{R}{\mathcal{R}}\right)_{\text{crit}}^3 = \frac{(4\pi R^3/3)}{(2R)^3} = \frac{\pi}{6} \quad (52\%)$$

In this highly idealized geometry, all bubbles become interlinked simultaneously when the porosity attains the definite value of  $\pi/6$ . In place of the regular spacing assumed in the preceding calculation, it would be more realistic to consider that small bubbles were originally nucleated in a random three-dimensional array. As they grow by accretion of gas atoms, pairs of bubbles that were initially formed close to each other would touch first. As growth proceeded, triplets of overlapping bubbles would appear. In this manner the extent of bubble interlinkage increases smoothly with increasing porosity and asymptotically approaches unity as the fuel approaches total porosity. In contrast, the calculation based on the simple cubic lattice shows no interconnection until the critical porosity  $\pi/6$  is reached, when all bubbles simultaneously come into contact. Since 100% interconnection is probably not needed to produce gas release large enough to be termed "breakaway," random rather than regular deployment of the bubbles would result in gas release by this mechanism at porosities considerably less than that calculated from the cubic-lattice model. Ritzman et al.<sup>27</sup> have considered the effect of random bubble arrangement on interlinking and have presented a graphical relation between the fraction of interconnected porosity as a function of the total porosity. Unfortunately, however, the derivation of the curve was not given.

Once the critical porosity for breakaway gas release is determined, the fuel swelling at this point is given by Eq. 15.188. For the simple cubic-lattice model treated previously, the critical swelling at which extensive gas release due to venting of interlinked gas bubbles in the grains first occurs is 110%.

### 15.8.2 Grain-Boundary Bubbles

Interconnection of intergranular bubbles can be analyzed in a manner similar to that applied to intragranular bubbles. In the present case, we assume that the gas is either in solution or in grain-boundary bubbles and that the concentration of intragranular bubbles is small (i.e.,  $f_b \approx 0$ ). Suppose that there are  $N_{gb}$  spherical gas bubbles of radius  $R_{gb}$  per unit area of grain boundary. The grain boundary can be divided into circular unit cells of radius  $\mathcal{R}_{gb}$  each of which contains one bubble at its center. The analog of Eq. 15.184 for this two-dimensional case is

$$(\pi \mathcal{R}_{gb}^2) N_{gb} = 1 \quad (15.189)$$

The grain-boundary content of the fuel is:

$$\frac{[(4\pi a^2)/2]}{4\pi a^3/3} = \frac{3}{2a} = \text{grain-boundary area per unit volume of fuel} \quad (15.190)$$

where  $a$  is the grain radius. The factor of  $1/2$  in Eq. 15.190 arises because each grain boundary is supplied with gas

from two adjacent grains. Multiplication of Eq. 15.190 by  $N_{gb}$  yields the number of grain-boundary bubbles per unit volume of fuel. The porosity of the fuel due to these bubbles is

$$\begin{aligned} \text{Porosity} &= \frac{\text{Volume of grain-boundary bubbles}}{\text{Total fuel volume}} \\ &= \frac{3}{2a} N_{gb} \left( \frac{4}{3} \pi R_{gb}^3 \right) \end{aligned} \quad (15.191)$$

The volume of solid associated with a unit of fuel volume is 1 minus the porosity. In time  $t$ ,  $Y_{Xe} \dot{F} t$  gas atoms are created per unit volume of solid, and a fraction  $f_{gb}$  of them have precipitated into intergranular bubbles. Thus,

$$f_{gb} Y_{Xe} \dot{F} t \left[ 1 - \frac{3}{2a} N_{gb} \left( \frac{4}{3} \pi R_{gb}^3 \right) \right] = \text{gas atoms in grain-boundary bubbles per unit volume of fuel} \quad (15.192)$$

This quantity can also be expressed as the product of the number of gas atoms per bubble (given by Eq. 13.16 if the bubbles are large and in mechanical equilibrium) and the number of bubbles per unit volume of fuel. Thus,

$$\frac{4}{3} \pi R_{gb}^2 \left( \frac{2\gamma}{kT} \right) \frac{3}{2a} N_{gb} = \text{gas atoms in grain-boundary bubbles per unit volume of fuel} \quad (15.193)$$

Equating the right-hand sides of the preceding two formulas and expressing  $N_{gb}$  in terms of  $\mathcal{R}_{gb}$  by use of Eq. 15.189 yields

$$\left( \frac{R_{gb}}{\mathcal{R}_{gb}} \right)^2 = \frac{(a/2) (kT/2\gamma) f_{gb} Y_{Xe} \dot{F} t}{1 + R_{gb} (kT/2\gamma) f_{gb} Y_{Xe} \dot{F} t} \quad (15.194)$$

which is the fraction of the grain-boundary area occupied by bubbles. Using Eqs. 15.189 and 15.191, we can express the fractional swelling due to grain-boundary bubbles

$$\frac{\Delta V}{V} = \frac{2(R_{gb}/a) (R_{gb}/\mathcal{R}_{gb})^2}{1 - 2(R_{gb}/a) (R_{gb}/\mathcal{R}_{gb})^2} \quad (15.195)$$

Based on a simple cubic structure in two dimensions, the critical fraction of the grain-boundary area occupied by bubbles when interlinking first occurs is

$$\left( \frac{R_{gb}}{\mathcal{R}_{gb}} \right)_{\text{crit}}^2 = \frac{\pi R_{gb}^2}{(2R_{gb})^2} = \frac{\pi}{4} \quad (15.196)$$

Fuel swelling when interlinking of grain-boundary bubbles first occurs depends on the ratio  $R_{gb}/a$  as well as on  $(R_{gb}/\mathcal{R}_{gb})_{\text{crit}}$ . Taking  $R_{gb} = 1 \mu\text{m}$  and  $a = 5 \mu\text{m}$  and using Eq. 15.196, we find the swelling at which breakaway gas release occurs is 46%. This value can be compared to the critical swelling of 110% required for interconnection of intragranular gas bubbles with the same lattice structure in three dimensions. Irrespective of the geometry of bubble placement, gas release from interconnection of grain-boundary bubbles occurs at a lower fuel swelling than that required if the same quantity of bubbles were distributed within the grains. The irradiation time at which interconnection of the grain-boundary bubbles occurs can be

estimated by setting the left-hand side of Eq. 15.194 equal to  $\pi/4$  and determining  $f_{gb}$  from Eq. 15.181 of the previous section.

### 15.9 SWEEPING OF GAS BUBBLES BY GRAIN BOUNDARIES

In the theory presented in Sec. 15.7 describing how fission gas was collected at grain boundaries by diffusion from the matrix, the boundaries were assumed to be stationary. However, we know that at temperatures of approximately 2000°K (in  $UO_2$ ) grain boundaries move and grain growth occurs. Small gas bubbles in the path of a moving grain boundary are swept along with the boundary, but they retard the speed of the boundary. However, a moving grain boundary can pass right through large bubbles. Grain-boundary sweeping provides another mechanism for the collection of fission gas at these internal surfaces from which release can occur by cracking or bubble linkage.

A theory of grain-boundary sweeping of gas bubbles has been advanced by Speight and Greenwood.<sup>28</sup> It is similar to the theory of pore dragging during equiaxed-grain growth reviewed in Sec. 14.5, except that in the present instance small fission-gas bubbles rather than the large fabrication pores are involved. Speight and Greenwood's calculation provides a means of determining whether gas bubbles are caught up and moved along by a moving grain boundary or whether the grain boundary is only temporarily retarded by the bubbles and then breaks away.

We have seen in Sec. 13.11 that a bubble located on a grain boundary exerts a force on the latter, either because the bubble is driven to move by an external force (e.g., the temperature gradient) or because the grain boundary has a tendency to move in response to the tension contained in its curved surface. The magnitude of the force exerted by the bubble on the boundary or vice versa depends on bubble radius and angle of contact according to Eq. 13.278:

$$F_b = \pi R_{gb} \gamma_{gb} \sin 2\phi \quad (15.197)$$

We first calculate the velocity that a bubble of radius  $R_{gb}$  achieves when subject to the force exerted by the grain boundary to which the bubble is attached. The bubble velocity is given by combination of Eqs. 13.220 and 13.221:

$$v_b = \frac{D_b}{kT} F_b \quad (15.198)$$

The bubble diffusivity depends on the mechanism by which bubble motion is made possible. For the large natural pores considered in Sec. 14.5, mobility was due to the vapor-transport mechanism. For the smaller fission-gas bubbles, however, surface diffusion is the most probable source of bubble mobility, and  $D_b$  is given by Eq. 13.214. Inserting this expression for  $D_b$  and the force given by Eq. 15.197 into Eq. 15.198, we have

$$v_b = \frac{3 a_o^4 D_{os}}{4 R_{gb}^3} \left( \frac{2\gamma_{gb}}{kT} \right) \sin 2\phi \exp \left( -\frac{E_s}{kT} \right) \quad (15.199)$$

where  $a_o$  is the lattice constant of the solid and  $D_{os}$  and  $E_s$  are the preexponential factor and activation energy, respectively, for surface self-diffusion of the fuel material.

In order to determine the contact angle  $\phi$ , we must evaluate the velocity of the grain boundary on which the bubble is located. The velocity can be obtained by considering the kinetics of the motion of the atoms in the surfaces of the grains which meet at the grain boundary. As explained in Sec. 14.5, a net flux of atoms across a curved grain boundary is established because the binding energy of the atoms in the matrix is somewhat higher on the concave than on the convex side of the boundary. Figure 15.23 depicts schematically the potential energy of an atom as it

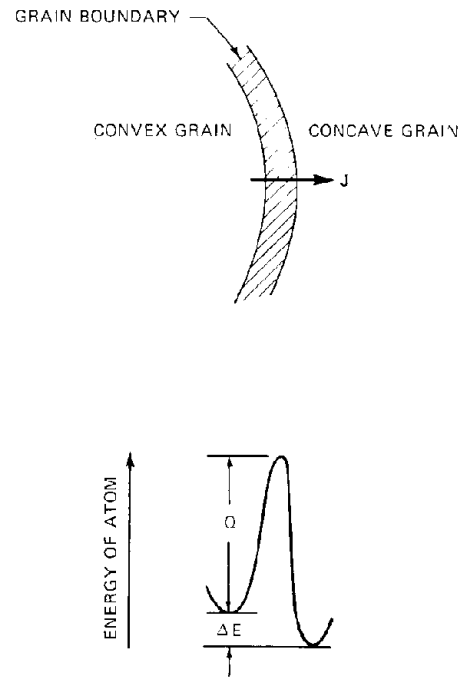


Fig. 15.23 Potential energy of an atom moving through a grain boundary.

moves from one side of a grain boundary to the other. The energy of the atom on the concave side is lower than on the convex side by an amount  $\Delta E$ . To pass from the convex to the concave side, the atom must surmount an energy barrier  $Q$ , which is the activation energy for grain-boundary motion. For movement in the opposite direction, however, the energy barrier is  $Q + \Delta E$ .

The rates at which atoms cross the grain boundary in the two directions can be formulated from absolute rate theory (Chap. 7), which predicts that the frequency of atom jumping from left to right over the barrier in Fig. 15.23 is

$$w_+ = \nu \exp \left( -\frac{Q}{kT} \right) \quad (15.200)$$

where  $\nu$  is the vibration frequency of an atom in the potential well in the solid lattice. The jump frequency in the opposite direction is

$$w_- = \nu \exp\left(-\frac{Q + \Delta E}{kT}\right) \quad (15.201)$$

Because of the asymmetry in the potential barrier introduced by the small perturbation  $\Delta E$ ,  $w_+$  is slightly greater than  $w_-$ ; so there is a net flow of atoms from left to right. The number of atoms on one side of a unit area of grain boundary is approximately equal to the reciprocal of the square of the lattice constant; so the net flux of atoms across the barrier is

$$J = \frac{w_+ - w_-}{a_0^2} = \frac{\nu}{a_0^2} \left[ \exp\left(-\frac{Q}{kT}\right) - \exp\left(-\frac{Q + \Delta E}{kT}\right) \right]$$

Inasmuch as  $\Delta E/kT$  is generally much less than unity, the exponential can be expanded in a power series and truncated after the second term. Thus,

$$J = \frac{\nu}{a_0^2} \frac{\Delta E}{kT} \exp\left(-\frac{Q}{kT}\right) \quad (15.202)$$

The velocity of the grain boundary is the product of the flux  $J$  and the atomic volume, which is approximately equal to the cube of the lattice constant:

$$v_{gb} = J a_0^3 = \nu a_0 \frac{\Delta E}{kT} \exp\left(-\frac{Q}{kT}\right) \quad (15.203)$$

The energy difference  $\Delta E$  can be related to the intrinsic properties of a curved grain boundary and to the size and number of gas bubbles attached to the boundary. Figure 15.24 shows bubbles of radius  $R_{gb}$  uniformly distributed over the boundary with a spacing dictated by the unit cell radius  $\mathcal{R}_{gb}$  (which is related to the bubble density by Eq. 15.189). The forces acting on the portion of the grain boundary of radius  $\mathcal{R}_{gb}$  and containing one bubble at the center of this region are shown on the left of the drawing. The intrinsic grain-boundary tension force acts to move the boundary toward the center of curvature of the convex grain.\* The bubble exerts a drag force in the opposite direction. If the section of grain boundary  $\pi \mathcal{R}_{gb}^2$  in area moves by a distance  $dx$ , the change in energy is

$$\left[ \left( \frac{2\gamma_{gb}}{R_c} \right) \left( \pi \mathcal{R}_{gb}^2 \right) - F_b \right] dx$$

and the number of atoms displaced from one side of the boundary to the other is

$$\pi \mathcal{R}_{gb}^2 dx / a_0^3$$

Dividing this expression by the preceding one gives the energy change per atom transferred across the boundary,

\*The force acting on a grain boundary (excluding that due to attached bubbles) may be much larger than the grain-boundary tension force if there is differential strain between adjacent grains. Such internal strain is highly likely in uranium metal, in which irradiation growth occurs in specific crystallographic directions.<sup>28</sup> Ceramic fuels with cubic crystal structures, however, do not exhibit anisotropic growth, and approximation of the forces on the grain boundaries by the intrinsic force due to the grain-boundary tension and the radius of curvature is probably acceptable for these materials.

which is the desired quantity  $\Delta E$ . Using Eq. 15.197 for  $F_b$ , there results

$$\Delta E = \frac{2a_0^3 \gamma_{gb}}{R_c} \left( 1 - \frac{R_{gb} R_c \sin 2\phi}{2\mathcal{R}_{gb}^2} \right) \quad (15.204)$$

Inserting Eq. 15.204 into 15.203 yields the grain-boundary velocity

$$v_{gb} = \frac{\nu a_0^4}{R_c} \frac{2\gamma_{gb}}{kT} \left[ 1 - \frac{1}{2} \left( \frac{R_{gb}}{\mathcal{R}_{gb}} \right)^2 \times \left( \frac{R_c}{R_{gb}} \right) \sin 2\phi \right] \exp\left(-\frac{Q}{kT}\right) \quad (15.205)$$

When the bubbles are widely spaced ( $\mathcal{R}_{gb} \rightarrow \infty$ ) or small ( $R_{gb} \rightarrow 0$ ), the second term in the brackets of the preceding formula is negligible compared to unity, and  $v_{gb}$  reduces to the intrinsic velocity of the curved grain boundary. The second term in the brackets accounts for the retarding effect of the bubbles on grain-boundary motion.

When the bubbles are swept along with the moving grain boundary, the bubble velocity of Eq. 15.199 is equal to the grain-boundary velocity given by Eq. 15.205. Setting  $v_b = v_{gb}$  and solving for the angle of contact yields

$$\sin 2\phi = \left[ \frac{1}{2} \left( \frac{R_{gb}}{\mathcal{R}_{gb}} \right)^2 \left( \frac{R_c}{R_{gb}} \right) + \frac{3}{4} \frac{D_{os} R_c}{R_{gb}^3 \nu} \exp\left(-\frac{E_s - Q}{kT}\right) \right]^{-1} \quad (15.206)$$

The ratio  $(R_{gb}/\mathcal{R}_{gb})^2$  is the fraction of the grain-boundary area occupied by bubbles. The contact angle can be computed from Eq. 15.206 and used in either Eq. 15.199 or 15.205 to determine the bubble-grain-boundary velocity.

Since  $\sin 2\phi$  cannot exceed unity, the condition for bubble detachment is obtained by setting the right-hand side of Eq. 15.206 equal to 1:

$$1 = \frac{(R_{gb}/\mathcal{R}_{gb})^2}{2 (R_{gb}/R_c)} + \frac{K}{(R_{gb}/R_c)^3} \quad (15.207)$$

where:

$$K = \frac{3}{4} \left( \frac{D_{os}}{R_c^2 \nu} \right) \exp\left(-\frac{E_s - Q}{kT}\right) \quad (15.208)$$

When the right-hand side of Eq. 15.207 exceeds unity, the bubbles are swept along with the grain boundary. When the right-hand side is less than unity, the bubbles are left behind as the grain boundary moves. Equation 15.207 provides a relation between the dimensionless bubble size,  $R_{gb}/R_c$ , and the fraction of the grain-boundary area occupied by bubbles,  $(R_{gb}/\mathcal{R}_{gb})^2$ , which separates regions of bubble sweeping and bubble detachment. This curve is parametric in  $K$ , which depends on temperature and the grain size (which roughly determines the radius of curvature  $R_c$ ). Figure 15.25 shows a plot of Eq. 15.207 for a range of values of the parameter  $K$ . For a specified coverage of the grain boundary by bubbles and a known value of  $K$ , bubbles smaller than the appropriate point on the plot are

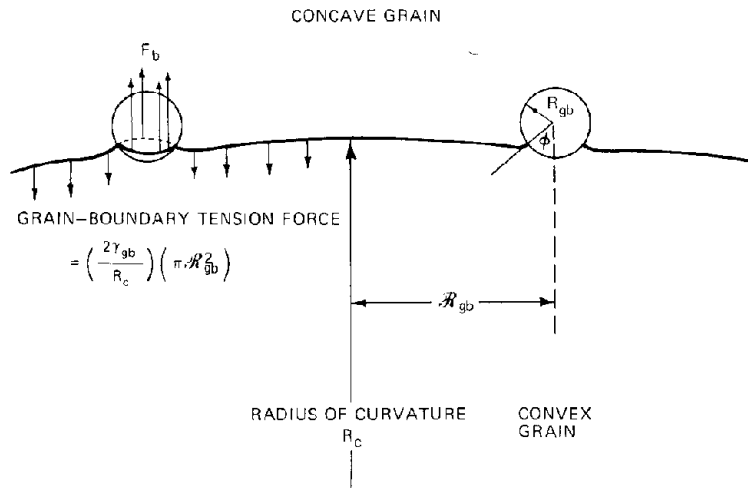


Fig. 15.24 Forces acting on a unit cell of grain boundary containing one bubble.

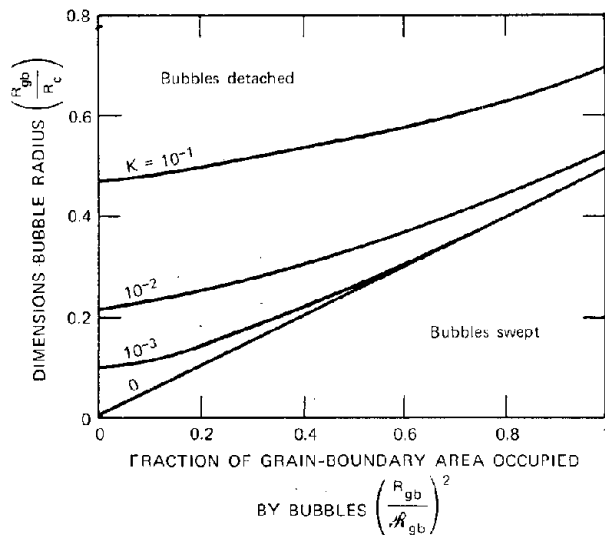


Fig. 15.25 Bubble-grain-boundary stability plot.

swept by the grain boundary, whereas larger bubbles are detached from it. Sweeping of small bubbles and detachment of large ones are shown in Fig. 15.26. The observed sizes of the swept and detached bubbles are in qualitative agreement with the predictions<sup>29</sup> of Eq. 15.207 and Fig. 15.25. Figure 15.26 dramatically illustrates the efficiency with which moving grain boundaries collect fission-gas bubbles from the matrix and thus enhance the potential for gross gas release by cracking along these now weakened internal surfaces or by bubble interconnection due to the high local bubble density. Bellamy and Rich<sup>30</sup> have attributed the marked increase in gas release above 3% burnup to the onset of these phenomena.

The closely related problem of bubble sweeping by moving dislocations has been treated by Speight and Greenwood.<sup>31</sup>

## 15.10 GAS-RELEASE MODELS BASED ON BUBBLE MIGRATION

Gas-release models using the concept of the equivalent sphere all depend on atomic diffusion in the matrix to transport fission gas to interconnected grain boundaries or other open porosity from which escape to the interior of the fuel element is possible. The simple diffusion treatment of this mode of release assumed classical volume diffusion to be the only migration mechanism (Sec. 15.5). Introduction of trapping centers within the fuel delays but does not permanently halt atomic migration as long as some resolution process is operative (Sec. 15.6). Grain boundaries that are not vented to open porosity can act as intermediate storage zones for fission gas collected by diffusion from the grains (Sec. 15.7).

Two gas-release models that completely ignore even the existence of atomically dispersed fission gas have been proposed. These models rely exclusively on the ability of large fission-gas bubbles to migrate along the temperature gradient to accomplish gas release.

In its complete form, the BUBL code described in Section 13.12 is capable of predicting the fraction of fission gas released from the fuel as a function of irradiation time, temperature, fission rate, and the microstructural characteristics of the solid. The treatment of this model in Sec. 13.12 was restricted to times long enough to achieve steady-state distributions of all four classes of bubbles that are supposed to be present. In this steady-state situation, gas is released at the same rate as it is produced; so the fractional release is unity. However, before the steady state is attained, the fission gas produced is absorbed by buildup of the densities of the various classes of bubbles. No release occurs until the first bubbles detached from grain boundaries reach cracks. From this time on, the fractional gas release increases smoothly with time, asymptotically approaching the 100% release situation analyzed in Sec. 13.12. The unsteady state form of the BUBL code is

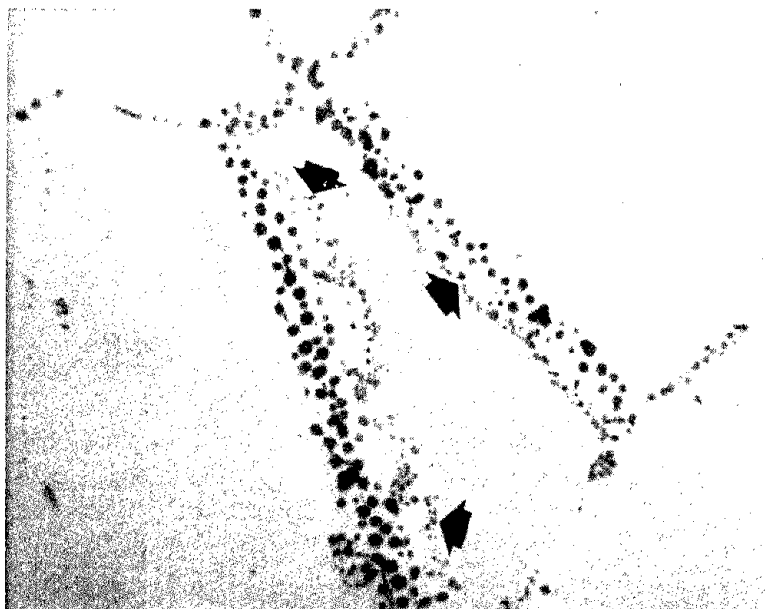


Fig. 15.26 Photomicrograph of a specimen of  $\text{UO}_2$  irradiated at  $835^\circ\text{C}$ . The small bubbles in the string of bubbles outlining the present position of the grain boundary (arrows) are approximately  $0.6\ \mu\text{m}$  in radius. The larger bubbles of about  $1.4\ \mu\text{m}$  in radius mark the earlier positions of the boundary. The bubble spacing is  $\sim 4\ \mu\text{m}$ . [From R. D. MacDonald, *J. Nucl. Mater.*, 22: 109 (1967).]

too complex to be treated analytically, and the entire process is handled by Monte Carlo techniques.

A group at the Battelle Columbus Laboratories has proposed a gas-release-swelling model that also neglects atomic processes and attributes fission-gas behavior entirely to migration of large gas bubbles.<sup>2,7,32,33</sup> A sequence of five stages in the history of a piece of fuel undergoing irradiation is depicted in Fig. 15.27. The hot end of the fuel piece is at the top of the drawing, and the cold end is at the bottom. According to this model, lenticular cavities periodically sweep through each section of fuel and cleanse it of small fission-gas bubbles that have accumulated since the previous passage of such a cavity. The lenticular cavities, which move under the influence of the temperature gradient as described in Sec. 14.2, can be one of the following types: (1) the lenticular pores representing the original porosity of the as-fabricated fuel, (2) lenticular pores spawned by cracks in the fuel (Fig. 14.3), or (3) fission-gas bubbles that have grown large enough to become detached from the many defects in the solid that trap small bubbles. If the bubble moves rapidly enough, the Battelle group believes that it will acquire the characteristic lenticular shape usually associated with as-fabricated porosity, despite the tendency of the internal gas pressure in the bubble to maintain a spherical cavity shape.

Between stages 1 and 2 in Fig. 15.27, the piece of fuel accumulates fission gas in the form of small bubbles that are nucleated from the fission gas and immobilized on a fine scale in the solid. During this period the fuel piece swells but does not release any gas. If swelling produces displacement of the fuel piece toward the cool end, the

cladding can be permanently deformed by creep. After some time of quiescent swelling, a lenticular cavity traverses the region, collecting all fission-gas bubbles in its path and leaving behind a fully dense columnar grain. Observations of sections of irradiated fuel indicate that the columnar grains formed by such a process maintain the same diameter along the temperature gradient, which suggests that the moving cavity loses gas as rapidly as it absorbs it from the small bubbles it encounters. If the absorbed gas were not somehow rejected from the cavity, the columnar grain should become enlarged as the growing cavity moves toward the hot end, owing to the progressively larger amount of gas it contains. Inasmuch as the columnar grains are observed to be of constant width, the model proposes that the accumulated gas is continuously rejected as a string of small bubbles along the periphery of the columnar grain (as in Fig. 14.4). When these bubbles are sufficiently numerous, they interlink and form a channel that leads directly to gas release.

Stage 4 of Fig. 15.27 shows the same section of fuel after a lenticular cavity has swept through it. Stage 5 depicts the fuel again swollen by small gas bubbles. The sequence represented by stages 1 through 3 is periodically repeated throughout the irradiation. Each sweeping event removes small gas bubbles generated since the last passage of a cavity and, in so doing, releases the collected gas to the columnar-grain boundary and redensifies the fuel.

Although the sweeping process is periodic, the gross displacement of the fuel piece can be cumulative in one direction. Figure 15.27 shows the fuel piece moving toward the cold end with each cycle, although it could also move

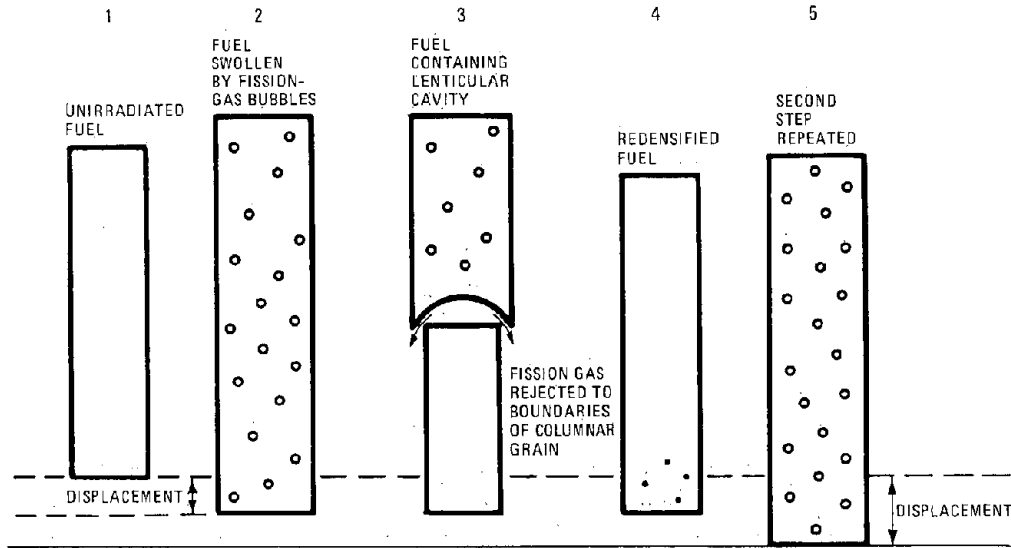


Fig. 15.27 Schematic diagram of the swelling-gas release process due to sweeping by lenticular cavities. (From Ref. 32.)

toward the hot end and close the central void. Hilbert et al.<sup>32</sup> believe movement toward the cold end is responsible for the linear increase with burnup of the diametral strain of the cladding of the specimens they investigated. However, they did notice a tendency for the radius of the central void to decrease at high burnup.

The essential feature of the proposed model is the availability of lenticular cavities throughout irradiation. If these sweeping agents were restricted to the fabrication porosity, the mechanism would cease as soon as restructuring had been completed, which can be only a matter of hours from startup at high temperatures. However, type 2 and 3 cavities can be generated as long as irradiation proceeds, thereby providing the means by which periodic swelling and redensification but cumulative gas release and fuel displacement can occur.

The model described here and in Refs. 32 and 33 is purely descriptive; so no quantitative prediction of gas release or swelling can be made with it.

### 15.11 ENGINEERING FISSION-GAS-RELEASE CALCULATIONS

In view of the rather rudimentary state of the theoretical models of fission-gas migration described in this chapter, it is not surprising that design estimates of gas release from proposed or operating reactors are based on empirical correlations. The only theoretical models simple enough to be applicable to an actual fuel pin are the equivalent-sphere concept using simple volume diffusion (Sec. 15.5) and the BUBL model (Secs. 13.12 and 15.10). However, the most common approach to gas-release estimation is to divide a fuel pin into concentric annuli with known temperatures at each radial boundary and to assign a value of the fractional release of the stable fission gases to

the fuel in each annulus. As an example, Cox and Homan<sup>34</sup> use the following scheme:

$$\begin{aligned} f &= 0.98 & T > 1800^\circ\text{C} \\ f &= 0.50 & 1400 < T < 1800^\circ\text{C} \\ f &= 0.30 & T < 1400^\circ\text{C} \end{aligned}$$

Note that these release fractions are independent of irradiation time (or, equivalently, of burnup  $\beta = Ft\Omega$ ). In the diffusional release models, the temperature dependence of the fractional release is due to the variation of the apparent diffusion coefficient  $D'$  with temperature. Even the very simplest diffusional model predicts fractional releases that increase as the square root of the irradiation time (Eq. 15.85). The data on which empirical gas-release correlations are based exhibit so much scatter that any time or burnup dependence is obscured by the strong dependence of release on temperature, and most correlations simply neglect the time variable. However, the correlation proposed by Dutt et al.<sup>35</sup> includes burnup-dependent release. The best fit of mixed-oxide irradiation gas-release data in a fast-neutron flux was obtained with the assignments

$$\begin{aligned} f &= 1.0 & (\text{for } T > T_2) \\ f &= 1 - \frac{A}{\beta} (1 - e^{-a\beta}) e^{-b\mathcal{P}} & (\text{for } T < T_2) \end{aligned}$$

where  $A$ ,  $a$ , and  $b$  = empirical constants

$\beta$  = burnup

$\mathcal{P}$  = linear power

$T_2$  = the temperature at the radial location separating the unstructured portion of the fuel from the equiaxed-grain growth zone

This formula has no theoretical foundation.

Notley and coworkers<sup>36-40</sup> are responsible for the most detailed analytical and experimental efforts intended

to provide a reliable method of estimating fission-gas release from operating thermal reactor fuel pins. One experiment designed for this purpose involves simultaneous measurement of the internal gas pressure of an instrumented fuel element (see Fig. 15.4) along with the power history during irradiation. The fuel-element internal gas pressure depends on the quantity of free gas and the volumes and temperatures of the various open spaces in the fuel element. The gas phase consists of the filling gas used in fuel-element fabrication, gases desorbed from the fuel at high temperature (principally water vapor), and fission gases that have been released from the fuel. The void spaces in the fuel element include the plenum chamber, the gap between the fuel and the cladding, open porosity and cracks, and any gross voidage arising from the shape of the original fuel (e.g., that introduced by end-face dishing of the pellets or by the use of annular pellets). Each of these void volumes occupies a particular position within the fuel element, and, when the fuel rod is operated at a known power level, the temperature of each can be determined by thermal analysis of the fuel element.<sup>38</sup> The ideal gas law can be applied to the gas contained in each void region

$$p_g V_i = n_i R T_i$$

where  $V_i$  = volume of the  $i$ th void region

$T_i$  = temperature of the  $i$ th void region

$n_i$  = number of moles of gas contained in the  $i$ th region

$p_g$  = gas pressure within the fuel rod, which is the same for all void regions since they are all connected to each other

If the preceding equation is solved for  $n_i$  and then summed over all void regions, there results

$$p_g = \frac{n_{\text{total}} R}{\sum (V_i / T_i)} \quad (15.209)$$

where  $n_{\text{total}}$  is the total number of moles of gas contained in all free space within the fuel element. The sum in Eq. 15.209 is carried out over all void regions within the fuel rod and is a function of rod power only. The calculation of  $\sum (V_i / T_i)$  is independent of the amount of gas released and does not consider the amount of gas trapped in closed pores or bubbles within the fuel proper.

One of the most interesting results of the internal-gas-pressure measurements during irradiation is the observation that gas release from fuel operating at high temperature does not occur continuously, but only during reactor power changes (e.g., shutdown, startup, or a change in power level). Figure 15.28 shows the trace of the gas pressure inside an instrumented fuel element as a function of irradiation time. Each test capsule was sufficiently short so that the linear power was constant over the length of the fuel pin. The lower part of the plot shows the reactor power variation during irradiation. The two sets of histograms in the upper portion of the plot represent fuel elements placed in different parts of the reactor so as to exhibit different linear powers. The vertical lines following each period of steady operation correspond with rapid pressure decreases and are coincident with reactor shutdowns. They result from cooling down of the fuel elements, which reduces each of the  $T_i$  in the sum of Eq. 15.209 and therefore decreases  $p_g$ . On the subsequent reactor restart to the same linear power, however, the gas pressure does not return to the plateau attained during the preceding cycle but rather to a somewhat higher value. The difference in the gas pressures between successive power cycles represents fission-gas release from the fuel, either during the shutdown or during startup between cycles. At high power operation (upper set of data in Fig. 15.28), essentially no gas is released during the period that the fuel is held at steady power. Elements irradiated at the lower linear power occasionally exhibit a gradual increase in gas pressure during steady power operation. The overall linear increase

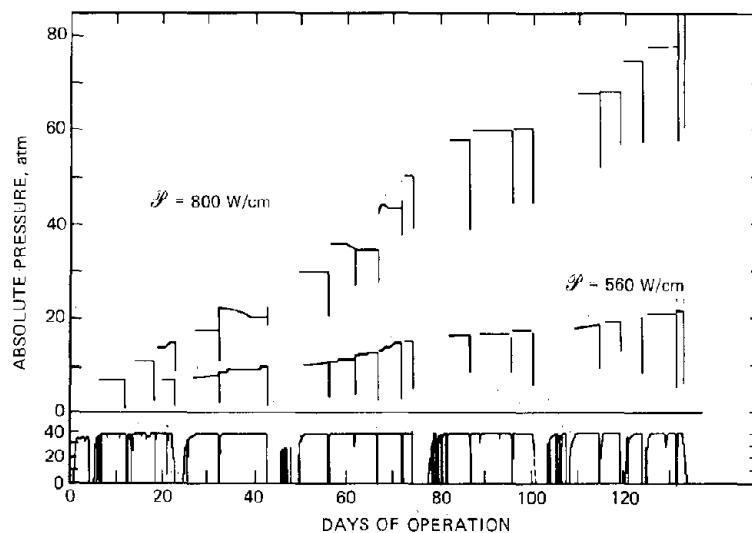


Fig. 15.28 Pressures inside an instrumented  $\text{UO}_2$  fuel element as a function of irradiation time for two linear powers. The reactor power history is also shown. (From Ref. 37.)

in gas pressure with irradiation time is due to the small but discrete puffs of gas released with each power change. Additional data presented in Ref. 37 indicate that release occurs primarily during shutdown from steady power rather than during the startup that begins the next steady power period.

The fission gas released at shutdown is believed to have been stored in the hot central portion of the fuel rod when operated at steady power. This region (at  $T > \sim 1400^\circ\text{C}$ ) is thought to be plastic and uncracked; so escape routes to the free void spaces in the fuel element are not present during operation. Gas is released from the fuel matrix in the form of bubbles that are trapped on grain boundaries or collected in portions of the central void that are sealed off from the free volume within the fuel pin. When the fuel is rapidly cooled at shutdown (or perhaps when fuel temperatures are suddenly altered by any sizable power change in either direction), thermal stresses cause the once plastic central region to crack along bubble-decorated grain boundaries, which are the weakest internal surfaces in the fuel. Closed portions of the central void are probably also opened up by radial cooling cracks extending from the fuel-cladding gap to the axis (see Fig. 10.22). By means of these cracks, the trapped fission gas is released to the void spaces in the fuel element, and this release is manifest as an increase in internal gas pressure during the next return to power.

Similar internal-gas-pressure measurements have been performed by Burley and Freshley.<sup>41</sup> Their results confirm the findings of Notley and MacEwan.<sup>37</sup>

Notley<sup>40</sup> has used the data shown in Fig. 15.29 to develop an empirical gas-release formula. The points on this graph show the fraction of the fission gas recovered from small cores of  $\text{UO}_2$  drilled from a fuel pellet after irradiation. Essentially all the gas generated in regions of the fuel which were at temperatures lower than  $\sim 1400^\circ\text{C}$  during irradiation was recovered from the matrix. With what appears to be great courage, Notley drew the histogram through the points in Fig. 15.29 to provide an analytical expression for the fraction of the gas retained (which is 1 minus the fraction released). The region from

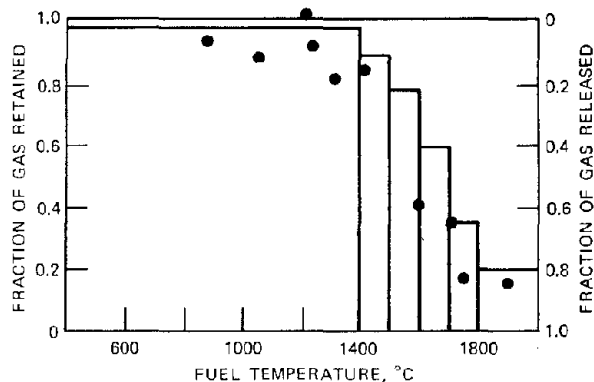


Fig. 15.29 Fission-product gas retention—release in  $\text{UO}_2$  as a function of irradiation temperature; points represent measured gas contents of small samples; the histogram is the analytical gas—release function used in the computations. (From Ref. 40.)

1400 to  $1800^\circ\text{C}$  was divided into four  $100^\circ\text{C}$  intervals each characterized by a fixed gas-release value. A constant 80% release was assumed to apply to all temperatures beyond  $1800^\circ\text{C}$ . The term “release” used in connection with Fig. 15.29 does not mean release to the free voidage of the fuel element. Rather, the gas that does not remain in the fuel matrix is assumed to have collected in the closed spaces in the hot inner regions of the fuel as described. True release occurs only when a power transient takes place. Note that in common with the other correlations presented at the beginning of this section, the release fraction is independent of irradiation time or burnup.

The average fractional release from the entire cross section of a fuel pellet at an axial position characterized by linear power  $\mathcal{P}$  can be obtained by integrating the histogram of Fig. 15.29 over the fuel-rod radius, appropriately weighted with the temperature distribution. Thus, if the histogram in Fig. 15.29 is denoted by the (discontinuous) function  $f(T)$ , the average fractional release from the fuel cross section is

$$\bar{f} = \frac{1}{\pi R^2} \int_0^R f(T) 2\pi r dr \quad (15.210)$$

where  $R$  is the radius of the fuel.

To perform this integration, we assume that the simple parabolic temperature distribution given by Eq. 10.53 can be used, which implies that the thermal conductivity is constant. Transforming the integration variable in Eq. 15.210 by use of Eq. 10.52 and taking  $f(T)$  from Fig. 15.29 yield

$$\begin{aligned} \bar{f} &= \frac{1}{T_0 - T_s} \int_{T_s}^{T_0} f(T) dT \\ &= \frac{1}{T_0 - T_s} \left[ 0.01(1400 - T_s) + 0.1(1500 - 1400) \right. \\ &\quad + 0.22(1600 - 1500) \\ &\quad + 0.4(1700 - 1600) + 0.65(1800 - 1700) \\ &\quad \left. + 0.8(T_0 - 1800) \right] \quad (15.211) \end{aligned}$$

The radially averaged fractional release in the equivalent-sphere model (Eq. 15.100) was obtained by a similar integration over the fuel cross section. To arrive at a numerical result for  $\bar{f}$ , we must know  $T_0$  and  $T_s$ . We assume  $T_s$  to be  $400^\circ\text{C}$  because the gas-release correlation is meant to apply to water reactors. The value of  $T_0$  can be obtained in terms of the surface temperature and the linear power by integrating Eq. 10.63, with the thermal conductivity taken as constant:

$$T_0 = T_s + \frac{\mathcal{P}}{4\pi k} \quad (15.212)$$

The average thermal conductivity in this equation can be obtained from the slope of the best straight line drawn through the conductivity integral shown in Fig. 10.20, which yields  $\bar{k} = 0.028 \text{ W cm}^{-1}\text{C}^{-1}$ . Using these numerical values of  $T_s$  and  $\bar{k}$  in Eq. 15.212,  $\bar{f}$  of Eq. 15.211 is the

explicit function of linear power shown by the curve in Fig. 15.30. Some gas-release data are shown for comparison. The main difference between Notley's correlation and the ones described earlier in this section is that release in Notley's means collection of fission gases in closed pores in the center of the fuel at steady power, from which escape to the fuel-element voidage occurs only during a power transient. In the correlations presented earlier, on the other hand, release is synonymous with an increase in internal gas pressure.

Soulhier and Notley<sup>39</sup> have studied the effect of power changes (as opposed to complete shutdown or startup from zero power) on fission-gas release. They examined the quantity of gas obtained from fuel elements subjected to three different power histories, each of approximately the same total duration. In one set of fuel elements, a constant high power was maintained for the entire experiment. In a second set, the first portion of the irradiation was conducted at low power and the final portion at high power. In the third set, an initial high-power period was followed by a low-power period. After shutdown the gas released from

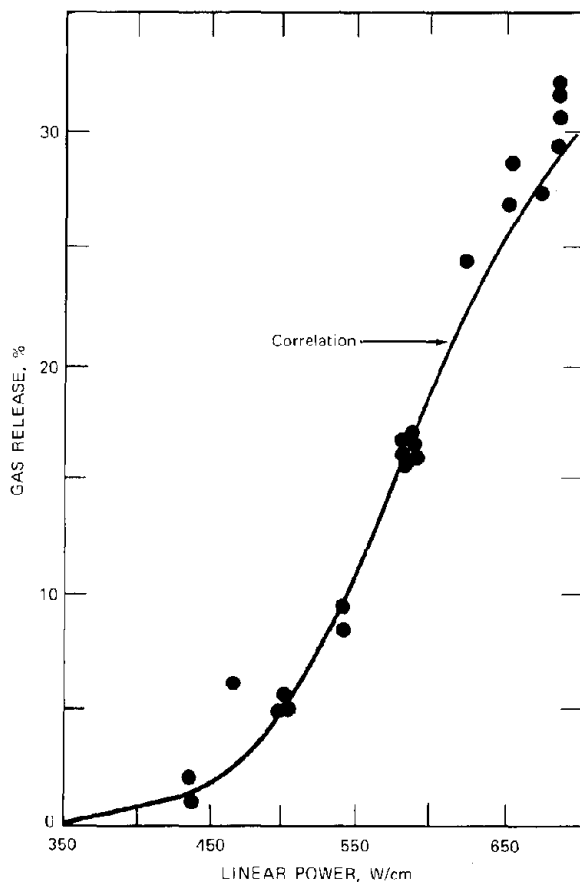


Fig. 15.30 The AECL fission-gas release correlation for thermal (water) reactors. (From J. R. MacEwan et al., in *Proceedings of the Fourth International Conference on the Peaceful Uses of Atomic Energy*, Vol. 10, p. 245, United Nations, New York, 1971.)

each of the test fuel elements was recovered and measured. The results of the experiments can be summarized as follows:

1. The same fraction of fission gases was released from the low-power and high-power cycle as was obtained from the capsules irradiated at constant high power.
2. Initial high-power operation did not enhance gas release during the subsequent low-power irradiation.

These conclusions are applied to predict gas release in the three-stage power cycle shown in Fig. 15.31, which is typical of the power histories of many reactors used for electricity generation. The graph refers to a particular axial location of a fuel element; although the linear power varies as a function of axial position, the fractional changes in power shown in the drawing are the same all along the length of the fuel pin.

A section of fuel is operated at linear power  $\mathcal{P}_1$  to burnup  $\beta_1$ , at which point the power is raised to  $\mathcal{P}_2$ . After burnup to  $\beta_2$  at the new power level, the power is reduced to  $\mathcal{P}_3$ . The number of moles of gas released from a unit length fuel element during irradiation is shown as the dashed line at the top of Fig. 15.31. Note that the gas is not released to the fuel element during the constant power stages; it is stored in the hot regions of the fuel until the power change takes place. The  $n_0$  moles of gas present at the beginning of irradiation consist of the filling gas (usually helium) and any gases that desorb from the fuel when the element is first brought to power. At the end of

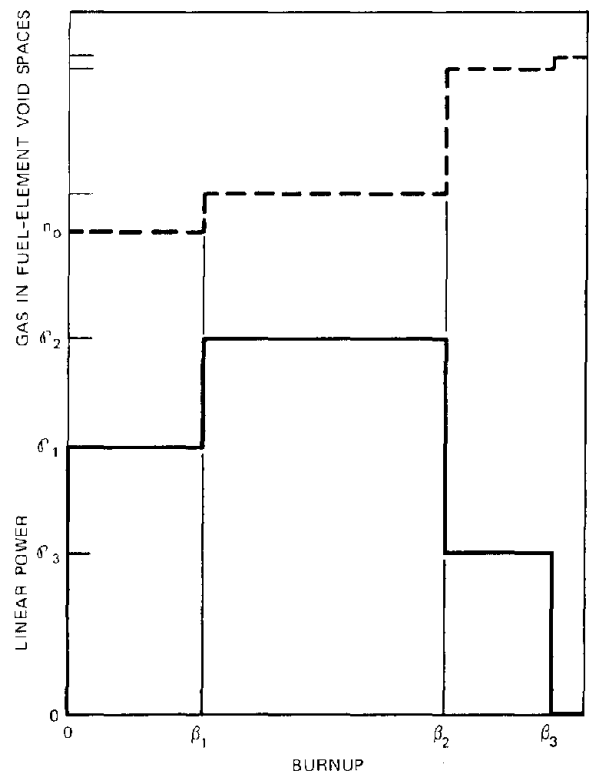


Fig. 15.31 Effect of power changes on gas release. (From Ref. 39.)

stage 1, the quantity of gas released per unit length of fuel at the particular axial location where the linear power is  $\mathcal{P}_1$  is equal to

$$Y_{Xe}(\dot{F}t)_1 \pi R^2 \bar{f}(\mathcal{P}_1)$$

where  $\bar{f}(\mathcal{P}_1)$  is the fractional release at linear power  $\mathcal{P}_1$  taken from Fig. 15.30 and  $(\dot{F}t)_1$  is the total number of fissions per unit fuel volume at the end of this period. The amount of gas in the free volume of the fuel element at burnup  $\beta_1$  from the section of fuel under consideration is

$$n_g(\beta_1) = n_o + \frac{Y_{Xe} \pi R^2}{\Omega} \beta_1 \bar{f}(\mathcal{P}_1) \quad (15.213)$$

where  $\Omega$  is the atomic volume of uranium in the fuel.

According to observation 1 above, the quantity of gas released at the end of the second stage should be the same as the release that would have occurred if the fuel had been operated at linear power  $\mathcal{P}_2$  for the entire burnup  $\beta_2$ , or

$$n_g(\beta_2) = n_o + \frac{Y_{Xe} \pi R^2}{\Omega} \beta_2 \bar{f}(\mathcal{P}_2) \quad (15.214)$$

According to observation 2 above, the gas released by the final low-power stage should be the same as the release that would have taken place if the previous higher power irradiation had not occurred; so

$$n_g(\beta_3) = n_g(\beta_2) + \frac{Y_{Xe} \pi R^2}{\Omega} (\beta_3 - \beta_2) \bar{f}(\mathcal{P}_3) \quad (15.215)$$

The axial variation of the linear power is presumed known. At the burnup corresponding to the end of each steady-power period, values of  $n_g$  calculated by one of the preceding three formulas for each axial section of the fuel element are summed over the fuel length to give the total moles of gas release,  $n_{tot}$ , for use in Eq. 15.209.

The calculational method and the gas-release correlation described by Notley can be readily incorporated into a fuel modeling code designed to predict the complete behavior of a fuel pin undergoing irradiation.

## 15.12 NOMENCLATURE

- $a$  = radius of grain; radius of equivalent sphere, Eq. 15.61
- $a_o$  = lattice constant
- $b$  = re-solution parameter
- $B$  = dimensionless re-solution parameter, Eq. 15.115
- $C$  = concentration in matrix
- $C_t$  = concentration of gas-atom traps in solid
- $D$  = apparent diffusion coefficient
- $D'$  = empirical diffusion coefficient, Eq. 15.84
- $D'_o$  = preexponential factor of empirical diffusion coefficient
- $D_{Xe}$  = true diffusion coefficient of fission gas in fuel
- $\mathcal{D}$  = defined by Eq. 15.176
- $D_b$  = diffusion coefficient of bubble
- $D_{os}$  = preexponential factor for surface-diffusion coefficient

- $E$  = difference in energy of atom on opposite sides of grain boundary
- $E'$  = activation energy of the empirical diffusion coefficient
- $E_{tr}$  = activation energy for thermal destruction of shallow traps
- $E_s$  = activation energy for surface diffusion
- $f$  = fractional release rate (ratio of release to birth rate) for radioactive species; fractional release for stable species
- $f, g, h$  = coefficients in Eq. 15.38
- $\dot{F}$  = fissions  $\text{cm}^{-3} \text{sec}^{-1}$
- $F_b$  = force on bubble
- $g$  = trapping probability per unit time, Eq. 15.108
- $G$  = dimensionless trapping probability, Eq. 15.114
- $H$  = ratio of fission-product removal from a unit volume by the knock-on process to removal by radioactive decay, Eq. 15.34
- $I$  = current across surface
- $J$  = flux of gas atoms to surface
- $k$  = Boltzmann's constant
- $\bar{k}$  = average thermal conductivity of fuel
- $k_{gt}$  = gas trapping rate constant
- $K$  = defined by Eq. 15.208
- $K_{tr}$  = coefficient in rate of trap destruction by fission fragments
- $L$  = diffusion trapping length
- $M$  = number of trapped gas atoms per unit fuel volume
- $n$  = number of moles of released fission gases; number of knock-ons per fission fragment (Table 15.1)
- $N$  = atom density; bubble density
- $p$  = Laplace transform variable
- $p_g$  = gas pressure
- $P$  = rate of production
- $\mathcal{P}$  = linear power
- $q$  = rate of stopping of particle in unit volume of solid
- $Q$  = barrier height across a grain boundary; dimensionless quantity of gas on grain boundaries, Eq. 15.171
- $r$  = radial position
- $\mathcal{R}$  = capture radius around bubble or dislocation
- $\mathcal{R}_{gb}$  = capture radius on a grain boundary
- $R$  = bubble radius; gas constant
- $R_t$  = radius of trapping center
- $R_c$  = radius of curvature of a grain boundary
- $S$  = surface area
- $t$  = time
- $t_{irr}$  = irradiation time
- $T$  = temperature
- $T_o$  = center-line temperature of fuel pin
- $T_s$  = fuel surface temperature
- $T^*$  = temperature defined by Eq. 15.96
- $u$  = dimensionless concentration, Eq. 15.70
- $V$  = volume of solid; total gas per unit volume of fuel ( $C + M$ )
- $\Delta V$  = volume increase (swelling)
- $v_b$  = bubble velocity
- $v_{gb}$  = grain-boundary velocity
- $w$  = jump frequency; dimensionless trapped-gas concentration, Eq. 15.113

$x$  = distance from surface  
 $y_A$  = yield of mass A chain  
 $y$  = fraction of fission gas initially in traps  
 $Y$  = dimensionless concentration, Eq. 15.33  
 $Y_{Xc}$  = total yield of fission gases  
 $Z_{gt}$  = capture sites around a trap  
 $Z$  = length of a fuel pin

#### Greek Letters

$\alpha$  = knock-on ejection yield, Eq. 15.19  
 $\alpha_j$  = ratio of the dimensionless re-solution parameter to the fission rate  
 $\beta$  = burnup  
 $\gamma$  = surface tension; defined by Eq. 15.130  
 $\gamma_{gb}$  = grain-boundary tension  
 $\Gamma$  = dimensionless constant, Eq. 15.148  
 $\Omega$  = atomic volume  
 $\phi$  = contact angle between grain boundary and bubble  
 $\theta$  = angle  
 $\lambda$  = decay constant  
 $\lambda_{i0}^r$  = preexponential factor of thermal decay constant of shallow traps  
 $\eta$  = dimensionless radial position, Eq. 15.68; dimensionless depth in solid, Eq. 15.32; dimensionless recoil range, Eq. 15.177  
 $\eta_{rec}$  = efficiency of recoil-atom collection  
 $\mu$  = range  
 $\nu$  = vibration frequency  
 $\tau$  = dimensionless time, Eq. 15.69 and Eq. 15.180

#### Subscripts and Superscripts

**b** = intragranular bubble  
**ff** = fission fragment  
**g** = geometric  
**gb** = grain-boundary bubble  
**i** = species i; region of fuel element  
**j** = type of trap  
**ko** = knockout  
**rec** = recoil  
**T** = total  
**U** = uranium  
**0** = initial value  
**1** = primary knock-ons  
**2** = secondary knock-ons  
 $\infty$  = far from surface  
 $\bar{\quad}$  = radial average over fuel pin  
 $\overline{\quad}$  = fuel-element average  
 $\sim$  = Laplace transform

### 15.13 REFERENCES

- Hj. Matzke and F. Springer, *Radiat. Eff.*, **2**: 11 (1969).
- W. Miekeley and F. W. Felix, *J. Nucl. Mater.*, **42**: 297 (1972).
- Hj. Matzke and J. R. MacEwan, *J. Nucl. Mater.*, **28**: 316 (1968).
- C. Jech and R. Kelly, *J. Phys. Chem. Solids*, **30**: 465 (1969).
- A. Sy. Ong and T. S. Ellman, *J. Nucl. Mater.*, **42**: 191 (1972).
- M. D. Rogers, *J. Nucl. Mater.*, **16**: 298 (1965).
- G. Nilsson, *J. Nucl. Mater.*, **20**: 215 (1966).
- M. D. Rogers, *J. Nucl. Mater.*, **22**: 103 (1967).
- R. M. Carroll and O. Sisman, *Nucl. Sci. Eng.*, **21**: 147 (1965).
- R. M. Carroll, J. G. Morgan, R. B. Perez, and O. Sisman, *Nucl. Sci. Eng.*, **38**: 143 (1969).
- R. Soulhier, *Nucl. Appl.*, **2**: 138 (1966).
- A. H. Booth, A Method of Calculating Fission Gas Diffusion from UO<sub>2</sub> Fuel and Its Application to the X-2-f Loop Test, Canadian Report CRDC-721, September 1957.
- A. H. Booth and G. T. Rymer, Determination of the Diffusion Constant of Fission Xenon in UO<sub>2</sub> Crystals and Sintered Compacts, Canadian Report AECL-692, August 1958.
- J. R. Findlay et al., *J. Nucl. Mater.*, **35**: 24 (1970).
- E. Jahnke and F. Emde, *Tables of Functions*, 4th ed., pp. 1-9, Dover Publications, Inc., New York, 1945.
- G. W. Parker et al., Nuclear Safety Program Annual Progress Report for Period Ending December 31, 1967, USAEC Report ORNL-4228, Oak Ridge National Laboratory, April 1968.
- T. S. Ellman, C. H. Fox, and L. D. Mears, *J. Nucl. Mater.*, **30**: 89 (1969).
- Hj. Matzke, *J. Nucl. Mater.*, **30**: 107 (1969).
- J. R. MacEwan and W. H. Stevens, *J. Nucl. Mater.*, **11**: 77 (1964).
- R. M. Carroll, O. Sisman, and R. B. Perez, *Nucl. Sci. Eng.*, **32**: 430 (1968).
- P. P. Pronko and R. Kelly, *Appl. Phys. Lett.*, **18**: 335 (1971).
- D. G. Hurst, Diffusion of Fission Gas. Calculated Diffusion from a Sphere Taking into Account Trapping and Return from the Traps, Canadian Report 1550, Nov. 15, 1962.
- J. R. MacEwan and P. A. Morel, *Nucl. Appl.*, **2**: 158 (1966).
- R. M. Carroll, O. Sisman, and R. B. Perez, *J. Amer. Ceram. Soc.*, **48**: 55 (1965).
- R. M. Cornell, M. V. Speight, and B. C. Masters, *J. Nucl. Mater.*, **30**: 169 (1969).
- M. V. Speight, *Nucl. Sci. Eng.*, **37**: 180 (1969).
- R. L. Ritzman, A. J. Markworth, W. Oldfield, and W. Chubb, *Nucl. Appl. Tech.*, **9**: 167 (1970).
- M. V. Speight and G. W. Greenwood, *Phil. Mag.*, **9**: 683 (1964).
- R. D. MacDonald, *J. Nucl. Mater.*, **22**: 109 (1967).
- R. G. Bellamy and J. B. Rich, *J. Nucl. Mater.*, **33**: 64 (1969).
- M. V. Speight and G. W. Greenwood, *J. Nucl. Mater.*, **16**: 327 (1965).
- R. F. Hilbert, V. W. Storhok, W. Chubb, and D. L. Keller, *J. Nucl. Mater.*, **38**: 26 (1971).
- W. Chubb, V. W. Storhok, and D. L. Keller, *J. Nucl. Mater.*, **44**: 138 (1972).
- C. M. Cox and F. J. Homan, *Nucl. Appl. Technol.*, **9**: 317 (1970).
- D. S. Dutt et al., *Trans. Amer. Nucl. Soc.*, **15**: 198 (1972).
- M. J. F. Notley and J. R. MacEwan, *Nucl. Appl.*, **2**: 117 (1966).
- M. J. F. Notley and J. R. MacEwan, *Nucl. Appl.*, **2**: 477 (1966).
- M. J. F. Notley, *Nucl. Appl.*, **3**: 334 (1967).

39. R. Soulhier and M. J. F. Notley, *Nucl. Appl.*, 5: 296 (1968).  
 40. M. J. F. Notley, *Nucl. Appl. Tech.*, 9: 195 (1970).  
 41. T. B. Burley and M. D. Freshley, *Nucl. Appl. Tech.*, 9: 233 (1970).

### 15.14 PROBLEMS

15.1 In addition to the direct recoil and knock-on mechanisms of low-temperature fission-product release, a mechanism based on vaporization of surface layers of the fuel by passing fission fragments has been proposed. In this thermal-spike mechanism, each fission fragment leaving vaporizes a volume of fuel in the form of a right cylinder having the radius  $R_{sp}$  of the thermal spike and a height  $l_{sp}$ . All fission products associated with this volume of fuel are also released.

The vaporized fuel is replaced by fresh fuel deposited from adjacent fuel surfaces, and the fission-product concentration in the surface layer is continually replenished by fission fragments originating in the interior of the rod. Neglecting radioactive decay and assuming steady state in the surface layer  $0 \leq x \leq l_{sp}$ , calculate the release rate due to this mechanism. How important is this mode of release compared to direct recoil if  $R_{sp} = 20 \text{ \AA}$  and  $l_{sp} = 70 \text{ \AA}$ ? In this case how many  $\text{UO}_2$  molecules are vaporized for each fission fragment leaving the surface? For the purposes of the computation, assume all fission fragments leave at right angles to the surface.

15.2 The direct-recoil fractional release calculated in the text represents the fraction of the released fission fragments that remain in the fuel-cladding gap only if all the fission fragments are stopped in the gas phase. If the gap thickness  $t_g$  is greater than the range of fragments of birth energy  $\mu_g^0$  in the gas, all the emerging fragments are stopped in the gas. On the other hand, if  $t_g/\mu_g^0 < 1$ , some of the fission fragments will pass through the gas and become implanted in the cladding.

The energy of a fission fragment decreases approximately linearly with the fraction of the range covered. Thus, a fission fragment that has traversed a path of length  $r$  in the fuel emerges from the surface with an energy given by  $E_s = E_0 [1 - (r/\mu_{ff})]$ , where  $E_0$  is the birth energy of the fission fragments. Because the fission-fragment energy entering the gas is less than the birth energy, its range in the gas is reduced according to  $\mu_g = \mu_g^0 E_s/E_0$ . If the remaining path length of the fission fragment in the gas is less than the range  $\mu_g$ , the fragment remains in the gas; otherwise it is imbedded in the cladding and not available for release.

Assuming that the fuel-rod radius  $\gg \mu_{ff}$  and  $t_g$ , calculate  $\eta_{rec}$ , the fraction of the escaping recoils that are stopped in the gas in the fuel-cladding gap. The range of fission fragments in a gas at 1 atm is  $\sim 2 \text{ cm}$ . Compute  $\eta_{rec}$  for a typical fuel-cladding gap of 0.08 mm. (Hint: Calculate the angular distribution of the fission-fragment current leaving the surface from a particular differential volume element inside the solid. Evaluate the energy of the emerging fragment and determine the spread of distances within the solid for which it will be stopped in the gas. Pay close attention to integration limits.)

15.3 Consider a section of a cylindrical fuel rod of uranium carbide of radius  $R$  operated at a linear power of  $\mathcal{P}$  W/cm. A particular stable metallic fission product is generated with an elemental yield  $Y$ . The rod temperature is high enough so that diffusion of the fission product to the outer edge of the rod occurs. The diffusion coefficient is  $D \text{ cm}^2/\text{sec}$ . The concentration of the fission product at  $r = R$  can be taken as zero.

(a) Express the volumetric rate of production of the fission products in terms of the linear power.

(b) Write the diffusion equation in terms of dimensionless radial distance, concentration, and time.

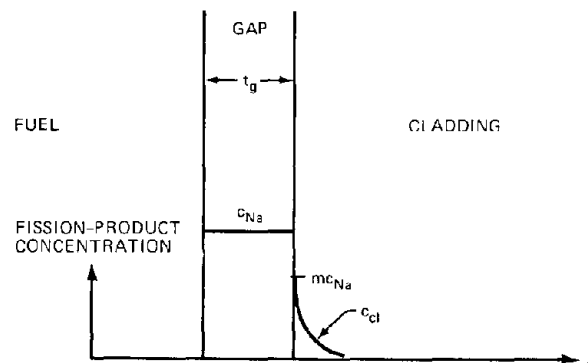
(c) Derive an expression for the rate of release of the fission product per unit surface area of rod. Use the Laplace transform method for solving the transient diffusion equation. Solve for the transform of the fission-product flux per unit surface area. Invert for the steady-state ( $t \rightarrow \infty$ ) and short-time ( $t \rightarrow 0$ ) cases. Useful properties of Bessel functions and Laplace transforms are found in H. S. Carslaw and J. C. Jaeger, *Conduction of Heat in Solids*, 2nd ed., appendixes III and V, Oxford University Press, Inc., New York, 1959.

15.4 The fuel rod considered in the previous problem is clad with stainless steel, and the fuel-cladding gap is sodium bonded. During operation the gap is  $t_g \text{ cm}$  in width, and the sodium is liquid.

Under reactor irradiation the fission product considered in the previous problem is released from the UC rod to the sodium, in which it dissolves. The fission product is insoluble in the UC but thermodynamically distributes between the liquid sodium and the inner surface of the cladding, according to the distribution law

$$c_{cl}(0, t) = mc_{Na}(t)$$

where  $c_{cl}$  is the concentration of the fission product in the cladding material,  $m$  is the distribution coefficient, and  $c_{Na}$  is the concentration of the fission product in the sodium.



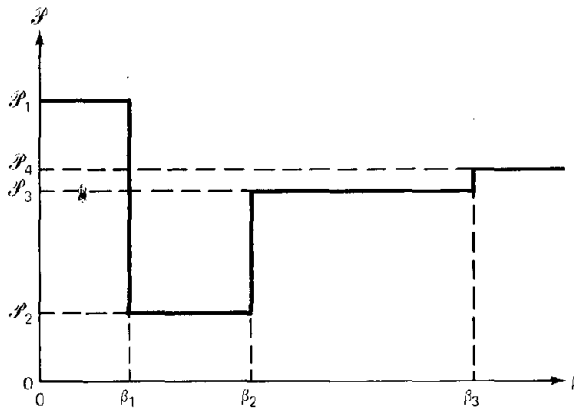
The fission product diffuses into the cladding with a diffusion coefficient  $D_{cl}$ . Assume the sodium gap is small compared to the fuel-rod radius so that plane geometry can be used. Assume the cladding thickness is much greater than the diffusional penetration depth so that the cladding

behaves as a semiinfinite medium. Neglect decay of the fission product. Assume the rate of release of the fission product from the rod is given by the steady-state rate  $J$  atoms  $\text{cm}^{-2} \text{sec}^{-1}$  from  $t = 0$ . At  $t = 0$  there is no fission product in the cladding. The  $x = 0$  boundary condition on the diffusion equation in the cladding is obtained by taking a balance on the fission product in the liquid sodium.

(a) What is the diffusion equation in the cladding and its associated boundary and initial conditions expressed in appropriate dimensionless time, distance, and concentration variables?

(b) Solve this equation by the Laplace transform method to obtain the concentration profile of the fission product in the cladding as a function of time.

15.5 A reactor fuel element is operated with the following power history:



(a) Using the AECL method, estimate the amount of fission gas released as a function of burnup. Assume the linear power is independent of axial position in the rod.

(b) When operating at linear power  $\mathcal{P}_1$ , the outlet sodium temperature is  $T_1$ . Assuming that only the plenum region above the fuel column contributes to open voidage in the element, derive equations for the pressure within the fuel element during each of the constant power segments shown in the graph. Assume that the sodium inlet temperature,  $T_{in}$ , is constant and that the volume of fuel and volume of plenum are known.

(c) The fuel element fails when the cladding ruptures as a result of the pressure-loading history calculated in part b. The basic mechanical-property data needed for the failure analysis is the rupture time,  $t_R$ , of the alloy from which the cladding is fabricated. The time  $t_R$  is the time required for an internally pressurized tube to rupture when the hoop stress and the temperature are specified. (In irradiated metals the rupture time also depends on the fast-neutron fluence, but this effect will be neglected here.) To simplify matters, the effect of cladding temperature on  $t_R$  is neglected, and the hoop stress is taken to be proportional to the internal gas pressure  $p_g$ . Thus, if the cladding were subject to a constant internal gas pressure  $p_g$ , failure would occur at a time given by

$$t_R(p_g) = \frac{k}{p_g^n}$$

where  $k$  and  $n$  are constants ( $n$  is about 4 or 5).

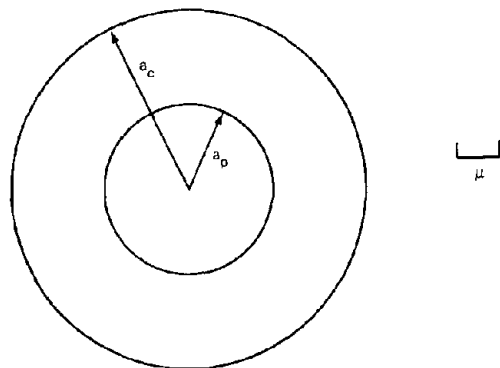
In cases in which the pressure is not constant, failure is determined by the "life fraction rule." Operation for a time interval  $\Delta t_i$  at an internal pressure  $p_{gi}$  consumes a fraction  $\Delta t_i/t_R(p_{gi})$  of the life of the tube. When the sum of the life fractions is equal to unity, failure is assumed to occur.

Assuming that the linear power for  $\beta > \beta_3$  is maintained at  $\mathcal{P}_4$ , at what burnup will the fuel pin fail?

15.6 Solve the steady-state diffusion equation for a sphere of radius  $a$  in which fission products are created at a rate  $y\bar{F}$  atoms  $\text{cm}^{-3} \text{sec}^{-1}$ , decay with a decay constant  $\lambda \text{sec}^{-1}$ , and diffuse with a diffusion constant  $D \text{cm}^2/\text{sec}$ . Derive the expression for the fractional release rate at steady state, defined as the ratio of the rate of release from the sphere to the rate of production in the sphere. What are the limiting expressions for the fractional release when the radioactive half-life is much greater and much smaller than the diffusion half-life,  $a^2/D$ ?

15.7 The high-temperature gas-cooled reactor (HTGR) uses fuel elements consisting of small spherical pellets of uranium carbide fuel embedded in a matrix of graphite. Since the graphite is porous and is not clad, fission-gas release is reduced by coating the fuel pellets with a layer of pyrolytic graphite.

The small fission-gas release that does occur comes about by recoil of fission fragments from the pellet into the coating and subsequent diffusional release to the outside of the coating. The range of fission fragments is the same in the pellet as in the coating and is denoted by  $\mu$ . A sketch of the coated particle sphere is shown, along with a scale of the fission-fragment range in the material. The fission density in the pellet is  $\bar{F}$  fissions  $\text{cm}^{-3} \text{sec}^{-1}$ , and the yield of the fission product of interest is  $y$ .



(a) The rate of deposition of a particular fission fragment at radial position  $r$  in the coating by direct recoil from the pellet is known and given by  $S(r)$  atoms  $\text{cm}^{-3} \text{sec}^{-1}$ . The decay constant of the fission product nuclide is  $\lambda$ . Derive an expression for the steady fractional release of this fission product from the pellet (i.e., the ratio of the rate of release from the surface of the coating to the rate of production in the pellet). Assume that fission products deposited in the coating by recoil from the pellet cannot diffuse through the pellet-coating interface.

(b) Derive an expression for  $S(r)$  by the following method:

1. Compute  $J(r)$ , the rate at which fission fragments cross a unit area of the spherical surface at a radial location  $r$  in the coating by direct recoil (not diffusion). Note that there are three radial zones in the coating, each with different expressions for  $J(r)$ .

2. Assuming  $J(r)$  is known, calculate the source term  $S(r)$ , which is the rate at which fission fragments come to rest in a unit volume at radial location  $r$ . Sketch  $S(r)$ .

Do not attempt to perform the integrations that are obtained in the course of this derivation.

15.8 Consider a hypothetical fission gas that consists of a stable isotope of yield  $y$  and a radioactive isotope of yield  $y^*$  and decay constant  $\lambda$ . Using the empirical diffusion-coefficient concept of gas release, what is the ratio of the

two isotopes in the released gas in the fuel-element plenum at a time  $t$  after startup? Assume that the radioactive isotope is in equilibrium in the fuel element.

15.9 Consider a light-water reactor fuel pin of Table 10.2 operating at a linear power of 500 W/cm with a fuel surface temperature of 400°C. The fuel occupies  $\frac{4}{5}$  of the fuel-element length. The remaining  $\frac{1}{5}$  is plenum space. The gas in the plenum is assumed to be at the outlet coolant temperature. Calculate the pressure of released fission gases in this fuel element after 3 years of operation at 100% power by

(a) The empirical diffusion-coefficient method.

(b) The engineering fission-gas-release method.

Neglect axial variation of the linear power in the rod and assume the fuel thermal conductivity to be  $0.03 \text{ W cm}^{-1} \text{ } ^\circ\text{C}^{-1}$ .

# Chapter 16

## Mechanical Properties of $\text{UO}_2$

### 16.1 DISLOCATIONS AND SLIP SYSTEMS IN SINGLE-CRYSTAL $\text{UO}_2$

Investigation of the deformation behavior of single crystals permits the characteristics of the dislocations and the crystallographic planes on which slip occurs most easily to be determined. Such information provides a fundamental understanding of the mechanical properties of polycrystalline compacts of the ceramic oxides of the heavy metals which are used as reactor fuel elements. The general features of slip in single crystals have been summarized in Sec. 8.1, but ionic solids such as  $\text{UO}_2$  exhibit special deformation properties that warrant a more detailed examination.

The geometry of slip in a single crystal is fully defined by the *slip system*, which designates (1) the crystallographic plane on which slip occurs and (2) the Burgers vector of the dislocation responsible for slip. The dislocation is generally a mixture of screw and edge components in the shape of a loop of the type shown in Fig. 8.6. Mixed dislocations are characterized by a single Burgers vector. Important deformation properties, such as the creep rate and the yield stress (or, as it is usually called in single crystals, the critical resolved shear stress), are controlled primarily by the edge components of the dislocation. Consequently, the nature of edge dislocations in  $\text{UO}_2$  has received the most attention in the literature.

The slip plane is denoted by  $\{ijk\}$ , where the braces indicate that slip occurs with equal probability on any of the equivalent crystallographic planes designated by the Miller indices  $i$ ,  $j$ , and  $k$  (Sec. 3.5). The Burgers vector of a dislocation is defined by the symbolism (Eqs. 8.2 and 8.3):

$$\mathbf{b} = ca_0 \langle i'j'k' \rangle$$

where the directions of the set of equivalent Burgers vectors are designated by the Miller indices  $i'$ ,  $j'$ , and  $k'$ ;  $a_0$  is the lattice constant; and  $c$  is a constant.

The slip system is conveniently designated by combining the Miller indices of the slip plane with those of the Burgers vector of the dislocation, or as  $\{ijk\} \langle i'j'k' \rangle$ . Slip on a particular slip plane due to a particular dislocation is designated by  $(ijk) [i'j'k']$ .

All investigations of the deformation properties of  $\text{UO}_2$  single crystals<sup>1-7</sup> have demonstrated that the Burgers vector of the easy glide dislocation in  $\text{UO}_2$  is

$$\mathbf{b} = \frac{1}{2}a_0 \langle 110 \rangle$$

This Burgers vector is illustrated in Fig. 8.2(a) lying in a  $\{111\}$  slip plane.

The  $\{110\}$  and  $\{100\}$  slip planes are the most active in  $\text{UO}_2$ . Therefore, the slip systems in  $\text{UO}_2$  which are responsible for plastic deformation are

$$\begin{aligned} &\{110\} \langle 110 \rangle \\ &\{100\} \langle 110 \rangle \end{aligned}$$

The deformation properties of a particular slip system can be studied in uniaxial load tests of the type shown in Fig. 8.1. For example, if a single crystal is oriented and tested in uniaxial compression along a  $\langle 100 \rangle$  direction, Fig. 16.1 shows that only the  $\{110\}$  slip planes can be activated. The resolved shear stress on the  $\{100\}$  planes is zero, as can be shown by applying Eq. 8.1 to the  $\{100\}$  planes in Fig. 16.1. On the  $\{100\}$  planes perpendicular to the applied force,  $\phi = 0$  but  $\lambda = 90^\circ$ ; so the resolved shear stress on these planes is zero. On the  $\{100\}$  planes parallel to the applied force,  $\phi = 90^\circ$  and  $\lambda = 0$ ; so again the resolved shear stress is zero. The shear stress on the four symmetric  $\{110\}$  planes in Fig. 16.1 is not zero, however; so the slip on these planes can be initiated by the applied stress.

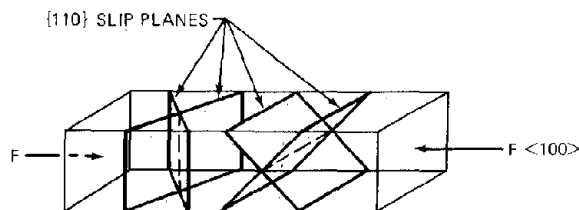


Fig. 16.1 Activation of  $\{110\}$  slip planes by application of a uniaxial load in a  $\langle 100 \rangle$  direction.

The configurations of the  $\text{UO}_2$  lattice (or generally, the fluorite crystal structure) in the neighborhood of a  $\frac{1}{2}a_0$   $\langle 110 \rangle$  edge dislocation on the two principal slip planes  $\{110\}$  and  $\{100\}$  are shown in Figs. 16.2(a) and 16.2(b), respectively. Simplified views of the geometry of each dislocation are shown below each atom model. The cubes in the lower drawings represent the fluorite unit cell of Fig. 3.12(b). Each edge dislocation is formed by insertion of two extra half sheets of atoms into the perfect lattice instead of the usual single half plane that comprises the edge dislocation in metals or covalent crystals. Two half sheets are required in some ionic crystals to maintain the electrical neutrality of the solid near the line defect.

When the dislocation line in Fig. 16.2(a) is viewed along the  $\langle 100 \rangle$  direction, the lattice is seen to consist of alternating layers of uranium and oxygen atoms. The layer sequence is most easily seen in Fig. 3.12(b). Proceeding in the  $\langle 100 \rangle$  direction, we first find a plane of uranium atoms, followed by a plane of oxygen atoms a distance  $a_0/4$  back, then another plane of uranium atoms (shifted with respect to the first plane of uranium atoms, however), then another plane of oxygen atoms, etc. The stacking sequence is denoted by  $ABA'BABA' \dots$ .

A similar view along the  $\langle 110 \rangle$  dislocation-line direction in Fig. 16.2(b) reveals a stacking sequence  $ABAB \dots$ , where each plane contains both types of ions.

Because of the perturbation of the perfect lattice structure near the core of the dislocation line, the dislocation can possess an effective electrical charge, which can be determined by counting the bonds between neighboring atoms that must be broken to form the defect.<sup>5</sup> Using this method, we find that the  $\{110\} \langle 110 \rangle$  edge dislocations of Fig. 16.2(a) are neutral, but the  $\{100\} \langle 110 \rangle$  dislocations of

Fig. 16.2(b) are either positively or negatively charged [the sign depends on whether or not one of the extra half sheets of atoms terminates in the row of uranium atoms marked by A in Fig. 16.2(b)]. A charged dislocation line is harder to move under an applied shear stress than is a neutral one because the charged dislocation line collects impurity ions or vacancies of the opposite charge. The dislocation line must tear itself away from this charge cloud or drag it along in order to glide on the slip plane. Yust and McHargue<sup>3</sup> have presented evidence for charge-related influences on the critical resolved shear stress and dislocation velocity in the  $\{100\} \langle 110 \rangle$  slip system. Similar effects on the creep rate of  $\text{UO}_2$  single crystals on the  $\{110\} \langle 110 \rangle$  slip system, where the dislocations are neutral, were not found.<sup>7</sup>

Dislocation substructures in deformed single-crystal  $\text{UO}_2$  have been observed by transmission electron microscopy of slices cut from the deformed single crystal parallel to the slip plane. The slices are thinned chemically to thicknesses of  $\sim 2500 \text{ \AA}$  and are then transparent to the electron beam of the microscope. Views of the  $\{100\}$  slip planes following compressive deformation of specimens that have been oriented to produce slip only on the  $\{100\} \langle 110 \rangle$  system are shown in Fig. 16.3. At low strain (1%), isolated dislocation lines of the  $\frac{1}{2}a_0 \langle 110 \rangle$  type are observed. Structural features of note include dislocation loops (which expand under the influence of the resolved shear stress), pinning points indicating dislocation-impurity interaction or cutting of dislocations that intersect each other while moving on nonparallel glide planes, and dislocation dipoles. Dipoles represent pairs of edge dislocations of opposite sign that have oriented themselves in their respective glide planes to form a parallel pair; the formation of the pair is accompanied by a reduction in energy. As will

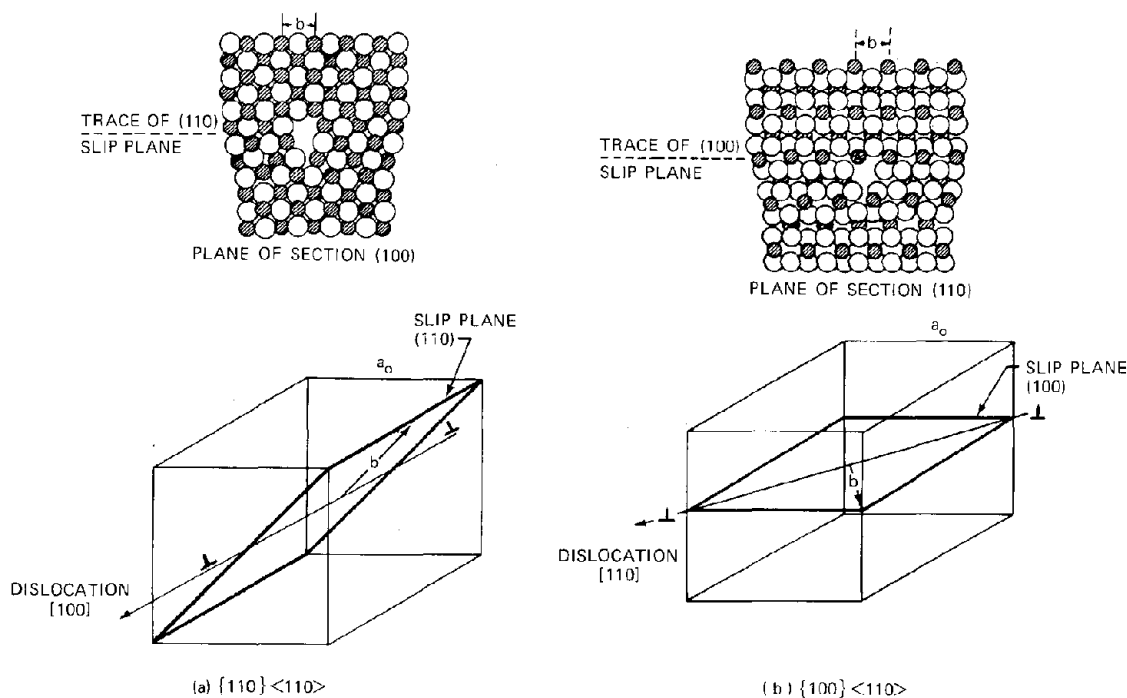
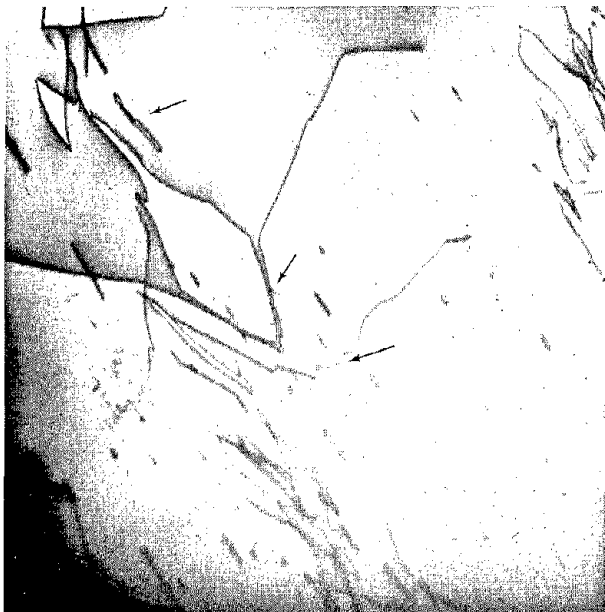


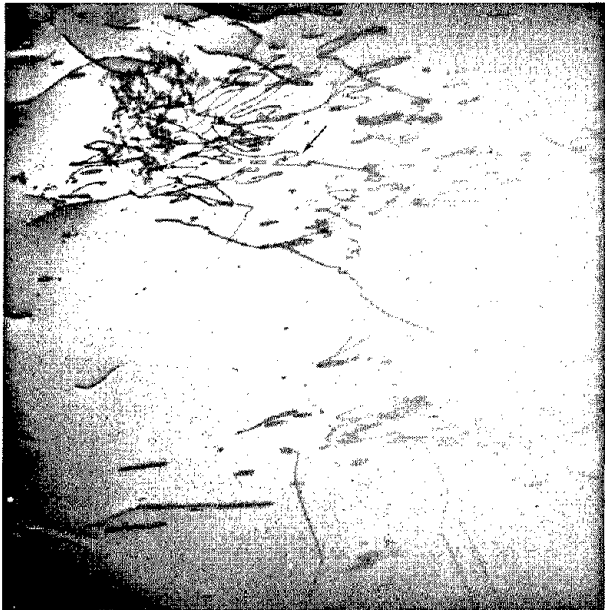
Fig. 16.2 Atomic configurations around edge dislocations in  $\text{UO}_2$ . (From Ref. 5.)

be shown in Sec. 16.7, dislocation dipoles are important in determining the creep properties of the solid.

Figure 16.3(b) shows the dislocation substructure at 5% deformation. A complicated dislocation tangle, formed by the interaction of dislocations moving on intersecting slip planes, is observed.



(a)



(b)

Fig. 16.3 Transmission electron micrographs of the (100) slip plane of  $UO_2$  single crystals deformed in uniaxial compressing at  $1150^\circ C$ . The A, B, and C indicate dislocation loops. (a) 1% deformation. (b) 5% deformation. [From C. S. Yust and C. J. McHargue, *J. Nucl. Mater.*, 31: 121 (1969).]

## 16.2 ELASTIC MODULI OF $UO_2$

Although the elastic properties of solids can be measured by mechanical tests such as uniaxial tension or bending, the sonic resonant frequency technique is simpler to apply at high temperatures and moreover permits both elastic constants to be determined simultaneously.<sup>8</sup> In this method a bar-shaped specimen is excited by vibrations of approximately sonic frequency. At particular frequencies the bar is in mechanical resonance with the driving frequency. The frequency at which resonance in flexure occurs determines the Young's modulus,  $E$ . The torsional resonant frequency is related to the shear modulus,  $G$ . These tests measure the adiabatic elastic moduli since the stresses due to sound waves are applied over a period too short for any portion of the mechanical energy to be converted into heat. The adiabatic elastic moduli can be converted into isothermal moduli, which apply to the practical cases in which the stresses are varying slowly with time.<sup>9</sup> The isothermal elastic moduli of polycrystalline stoichiometric  $UO_2$  at  $25^\circ C$  are

$$\begin{aligned} E &= 2.19 \times 10^8 \text{ kN/m}^2 && \text{(Young's modulus)} \\ G &= 8.14 \times 10^7 \text{ kN/m}^2 && \text{(shear modulus)} \end{aligned}$$

The effect of temperature on the elastic moduli is shown in Fig. 16.4. Lines representing measurements on pure  $UO_2$  and on  $UO_2$  containing 1 wt.%  $Gd_2O_3$  (simulating a soluble fission product) are shown. The elastic moduli are little affected by doping with this type of impurity, but the presence of the solute extends the temperature range over which elastic behavior prevails. Above  $1300^\circ C$  in pure  $UO_2$ , a rapid rise in internal friction (which is a form of plastic deformation due to dislocation or grain-boundary motion) prevented measurement of sample resonances. The more extensive temperature range of elastic behavior in the  $Gd_2O_3$ -doped specimens is attributed to the segregation of the impurity at grain boundaries, where it helps to delay the onset of plastic deformation by slipping of grains past each other (grain-boundary sliding). Figure 16.4 shows that the elastic moduli of  $UO_2$  at the melting point are estimated to be  $\sim 30\%$  of the room-temperature values.

Marlowe and Kaznoff<sup>8</sup> have also determined the effect of porosity on the room-temperature elastic moduli of  $UO_2$ . Their data are correlated by the equations

$$E = 2.23 \times 10^8 (1 - 1.92P) \text{ kN/m}^2 \quad (16.1a)$$

$$G = 8.42 \times 10^7 (1 - 1.66P) \text{ kN/m}^2 \quad (16.1b)$$

where  $P$  is the fractional porosity.

The temperature and porosity dependences of Poisson's ratio can be obtained from the relation between  $E$ ,  $G$ , and  $\nu$  (Eq. A.20 of the Appendix):

$$G = \frac{E}{2(1 + \nu)}$$

Using Eqs. 16.1 a and b, Poisson's ratio at room temperature decreases with fuel porosity according to

$$\nu = 1.32 (1 - 0.26P) - 1 \quad (16.2)$$

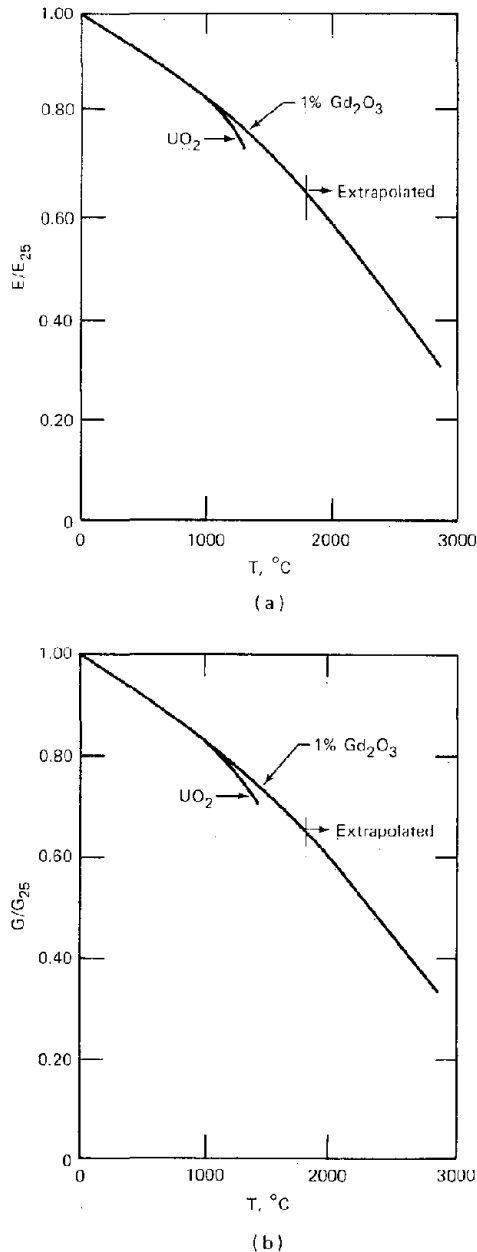


Fig. 16.4 Temperature dependence of the elastic moduli of  $\text{UO}_2$ . (a) Young's modulus. (b) Shear modulus. (From Ref. 9.)

At room temperature fully dense  $\text{UO}_2$  has a Poisson's ratio of 0.32. As the temperature increases,  $G$  and  $E$  decrease in a manner such that  $\nu$  approaches  $1/2$ , which is characteristic of a completely plastic substance.

### 16.3 PLASTIC BEHAVIOR OF $\text{UO}_2$

In common with most other ceramics, polycrystalline  $\text{UO}_2$  is a brittle material under normal conditions. By

"normal" we mean at temperatures less than about one-half the melting point (i.e., for  $T < \sim 1300^\circ\text{C}$ ) and in the absence of radiation. A brittle substance has no capacity for plastic deformation; as stress is applied, the elastic straining that occurs conforms to Hooke's law (see Appendix, Sec. A.4). The strain vanishes when the stress is removed. If the stress exceeds a critical value, the body is torn apart. This mode of failure is known as brittle fracture, and the critical stress at which it occurs is called the fracture stress.

At sufficiently high temperatures, however, even normally brittle materials such as  $\text{UO}_2$  exhibit measurable amounts of unrecoverable or plastic deformation before failure occurs. Substances that respond to loading in this manner are said to be ductile. Typical stress-strain curves illustrating these two modes of mechanical behavior are shown in Fig. 16.5. The regions of elastic behavior are represented by the linear portions of the two curves. The slopes of the straight-line segments in a simple uniaxial tensile test are equal to the Young's modulus of the material. As shown in the drawing, this property decreases with increasing temperature, probably because elastic deformation is made easier by the increased amplitude of thermal fluctuation of the atoms about their equilibrium positions in the lattice which accompanies an increase in temperature. Point C on the high-temperature curve of Fig. 16.5, which is called the proportional limit or yield point, separates regions of elastic deformation and plastic deformation. The strains beyond point C are not recovered when the load is removed.

Transition from brittle to ductile behavior occurs at a temperature characteristic of the material and, to a lesser extent, of the way in which the test is performed. This

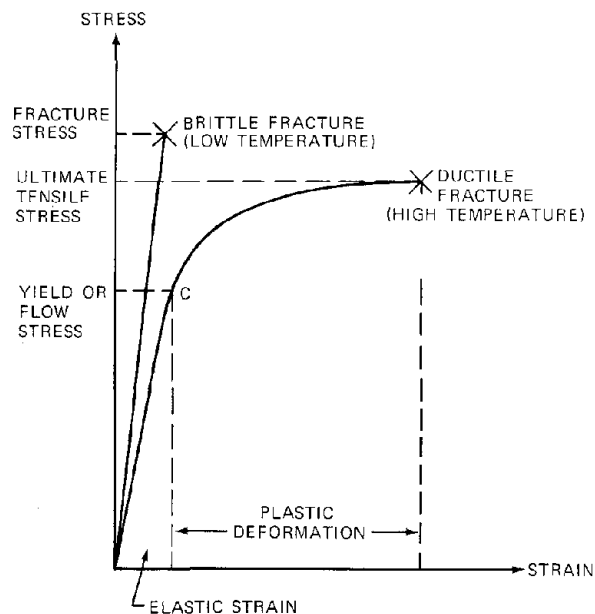


Fig. 16.5 Typical stress-strain curves at temperatures above and below the brittle-ductile transition temperature.

temperature is called the ductile—brittle transition or nil ductility temperature. It is defined as the temperature at which measurable plastic deformation prior to failure first occurs.

The mode of fracture can be characterized by the morphology of the fracture surface. Transgranular fracture occurs along crystallographic planes (sometimes called cleavage planes) within the grains; when the fracture surface runs along grain boundaries, the fracture mode is called intergranular. The transgranular mode is often associated with brittle fracture and the intergranular mode with ductile fracture, although there are many exceptions to this tendency. Fracture in  $\text{UO}_2$ , for example, occurs with fracture surfaces exhibiting a mixture of intergranular and transgranular features, even though the material is distinctly brittle or ductile.<sup>10-12</sup> In large-grained specimens at low temperatures, predominantly transgranular fracture occurs. At high temperatures, on the other hand, completely intergranular ductile fracture is observed. Figure 16.6 shows scanning-electron-microscope pictures of the fracture surface of  $\text{UO}_2$  illustrating the two fracture modes.

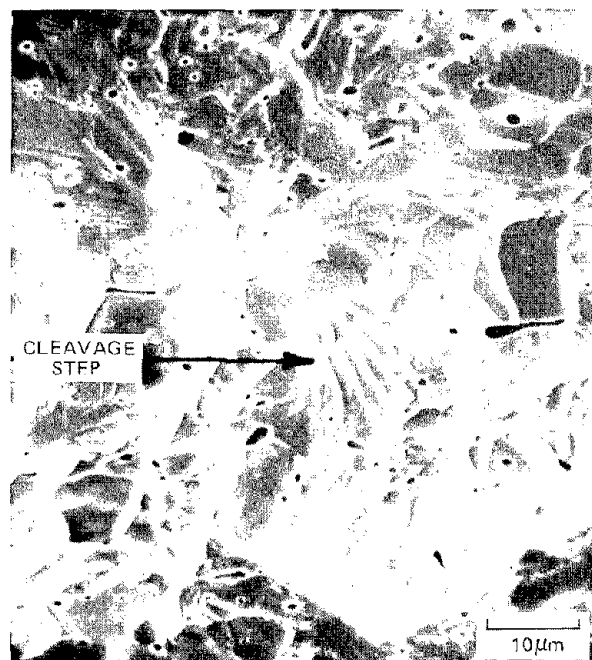
The deformation properties of stoichiometric  $\text{UO}_2$  have been investigated as functions of temperature by Evans and Davidge<sup>10</sup> and by Roberts et al.<sup>11,12</sup> Typical results of the latter studies are shown in Fig. 16.7 in which three regions of temperature can be identified.

1. The first, or brittle, region occupies the range from room temperature to the temperature at which plastic deformation first occurs. This point, which defines the brittle-to-ductile transition temperature, occurs at  $1200^\circ\text{C}$  in Fig. 16.7 but is dependent on the strain rate imposed on the specimen during the test. At higher strain rates than the rate at which the data in Fig. 16.7 were obtained, the transition from brittle to ductile behavior occurs at higher temperatures. In this region of completely elastic behavior, the ultimate tensile stress shown on the plot represents the fracture stress, which increases with temperature in the brittle region.

2. The temperature range from  $1200^\circ\text{C}$  to  $\sim 1400^\circ\text{C}$ , characterizes the semibrittle region. Measurable plastic strain occurs before rupture, and a proportional limit (flow or yield stress) can be determined. The ultimate strength of the material remains high. This region represents the transition from completely brittle to purely ductile behavior.

If the elastic limit yield-stress curve is extrapolated to lower temperatures, it would intersect the ultimate-strength curve at about the ductile-to-brittle transition temperature. Such behavior has led to the notion that the fracture stress and the yield stress are independent temperature-dependent properties of the material. At temperatures where the fracture stress is lower than the yield stress, failure occurs in a brittle fashion, with no plastic flow prior to failure. Conversely, when the yield stress is lower than the fracture stress, yielding and plastic flow occur at a lower stress than that required to produce brittle fracture, and as a result the material behaves in a ductile fashion.

3. Temperatures above  $\sim 1400^\circ\text{C}$  constitute the region of complete ductility. The ultimate strength decreases rapidly with temperature, and appreciable plastic deformation



(a)



(b)

Fig. 16.6 Fracture surfaces of  $\text{UO}_2$ . (a) Transgranular fracture at  $500^\circ\text{C}$  for a specimen of 95% of theoretical density. (b) Intergranular fracture at  $1600^\circ\text{C}$  of a specimen of 84% of theoretical density. The large holes are pores that were on the grain boundaries. [From J. T. A. Roberts and Y. Ueda, *J. Amer. Ceram. Soc.*, 55: 117 (1972).]

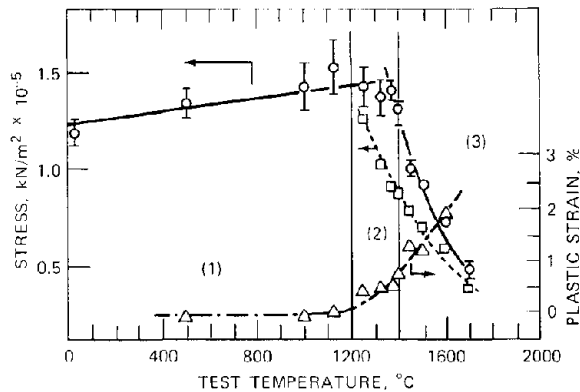


Fig. 16.7 Fracture and flow characteristics of  $\text{UO}_2$  as a function of temperature. —○, ultimate tensile stress . . . □, elastic (proportional) limit. - -△, total plastic strain. The strain rate in the tests was  $\sim 0.1 \text{ hr}^{-1}$ , and the grain size of the specimen was  $\sim 15 \mu\text{m}$ . (From Ref. 11.)

occurs before ductile fracture.\* The drastic decrease in strength at high temperature is attributed to increasing weakness of the grain boundaries; so plastic deformation and ultimate failure occur by grain-boundary sliding.

The pronounced decrease in strength in region 3 has often been exploited in simple models of the mechanical behavior of  $\text{UO}_2$  in a fuel element. Those portions of a fuel pin at temperatures in excess of  $\sim 1400^\circ\text{C}$  are assumed to be completely plastic and to possess no strength, whereas the outer regions of the rod which are cooler than  $1200^\circ\text{C}$  are regarded as completely brittle. In the narrow zone between these two extremes, the material is still strong but is capable of plastic deformation. In this model region 1 is believed to be cracked by thermal stresses set up by the temperature gradient in the fuel pin. Region 3, however, flows very easily under low stress and is therefore not cracked, but neither can it sustain a stress field (except, like a liquid, pure compression). Only region 2, which is strong and moderately ductile, can support the stresses imposed on the fuel by the restraint of the cladding. The interfacial stress at the fuel-cladding gap is transmitted to the thin annular ring containing fuel in the semibrittle state through the cracked outer annulus. Figure 16.8 shows this model. Region 2 is called the bridging annulus. Gittus, Howl, and Hughes<sup>13a</sup> and Notley<sup>13b</sup> have used this simple mechanical model of  $\text{UO}_2$  to calculate the stress and strain distributions developed in a fuel pin during irradiation. More complex treatments of fuel and cladding stress-strain behavior, however, are incorporated in the fuel modeling codes that are reviewed in Chap. 21.

\*In tensile tests ductile fracture is often preceded by considerable "necking" (i.e., area reduction) of the specimen. Part of the rapid decrease in ultimate strength in region 3 can be ascribed to application of the load to an area smaller than the initial cross-sectional area of the specimen. The initial cross-sectional area is used to compute the stress from knowledge of the applied load.

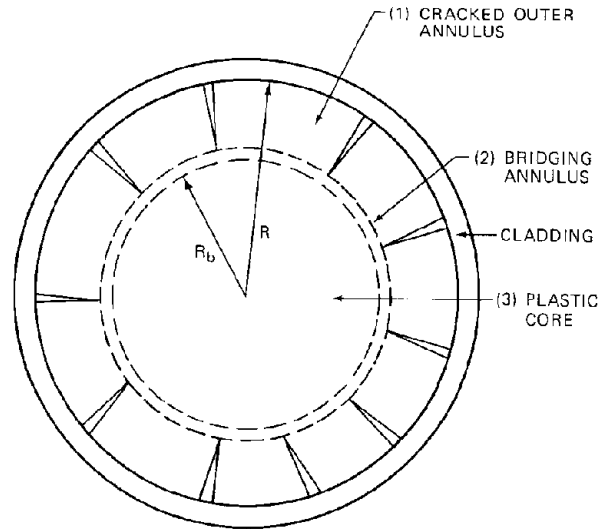


Fig. 16.8 Model of the mechanical state of a fuel pin under irradiation. The fuel is divided radially into zones corresponding to brittle, semibrittle, and plastic regions of temperature observed in mechanical property tests. (From Ref. 13a.)

The fracture and flow properties summarized in Fig. 16.7 were obtained in tests in which a rod of  $\text{UO}_2$  was bent by application of loads to four unequally spaced pins holding the specimen.<sup>11</sup> Failure occurs when the tensile stress established by the test apparatus exceeds the fracture stress in tension (i.e., the ultimate tensile strength). When subjected to purely compressive loads, however, ceramics such as  $\text{UO}_2$  are found to be far stronger than they are in tension. The compressive fracture strength of  $\text{UO}_2$ , for example, is nearly an order of magnitude greater than the ultimate tensile strength obtained from bending tests.<sup>14</sup> For application to fuel-rod analysis (Chap. 21), the tensile fracture strength shown in Fig. 16.7 is the important one.

Tensile fracture occurs by rapid growth of minute cracks in the material, which are opened up by tension (see following section). Failure in a compressive test, on the other hand, occurs by propagation of an avalanche of dislocations that penetrate the entire specimen. Section 18.12 presents the theory of brittle fracture by this mechanism. According to this theory the strength of the material should increase as the grain size is reduced (Eq. 18.109). Figure 16.9 shows that this behavior is faithfully exhibited by compressively loaded  $\text{UO}_2$ .

## 16.4 THEORY OF BRITTLE FRACTURE

Brittle fracture in the transgranular mode (cleavage) occurs by separation of adjacent atomic planes in the crystal. Calculation of the theoretical fracture stress is analogous to estimation of the theoretical shear stress of a perfect crystal (Sec. 8.1). Figure 16.10 shows how the potential energy of a crystal varies as the lattice is separated between atomic planes. (The potential energy varies with

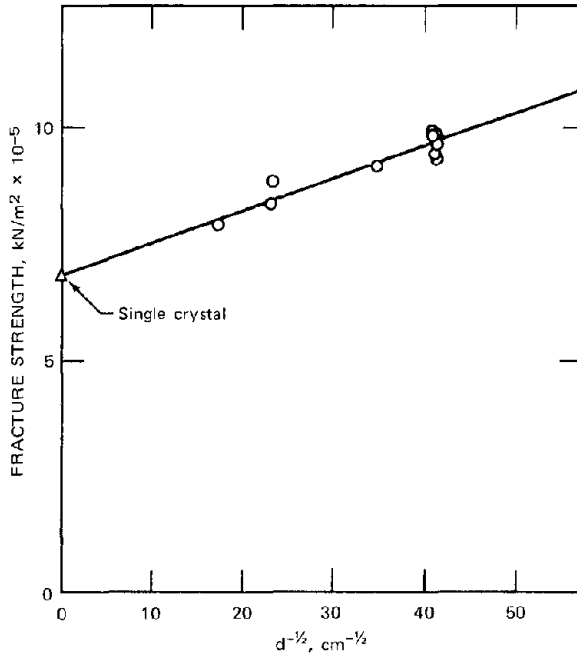


Fig. 16.9 Fracture strength of  $UO_2$  in compression as a function of grain size ( $d$ ). (From Ref. 4.)

distance in a manner similar to the curve shown in Fig. 4.1, which pertains to uniform expansion or contraction of the lattice.) When the two parts of the crystal are widely separated, the interaction energy is zero. As the two halves approach each other, the cohesive forces between the atoms of the solid reduce the energy. The minimum potential energy is attained at the equilibrium lattice spacing,  $a_0$ , and further reduction in separation causes the repulsive forces between atoms on each face to increase the system energy.

The energy required to cleave a perfect crystal is equal to the work required to separate the two parts from a distance  $a_0$  to infinity. Since the potential-energy curve discussed in the preceding paragraph is not known and since its exact shape is not important in the present calculation, the true potential curve can be approximated by the dashed sinusoidal curve shown in Fig. 16.10, which is described by the function:

$$\psi(x) = -\frac{1}{2}\psi_0 \left[ 1 + \cos \frac{2\pi(x - a_0)}{\lambda} \right]$$

This approximate potential is valid only for  $a_0 \leq x \leq a_0 + (\lambda/2)$ , where  $\lambda$  is the wavelength of the sine curve. Complete separation of the two parts of the crystal is considered to occur when  $x = a_0 + (\lambda/2)$ . Figure 16.10 shows the force per unit area, or tensile stress, which is obtained from the potential-energy curve:

$$\begin{aligned} \sigma(x) &\propto \frac{d\psi}{dx} = \frac{\psi_0 \pi}{\lambda} \sin \left[ \frac{2\pi(x - a_0)}{\lambda} \right] \\ &= \sigma_f \sin \left[ \frac{2\pi(x - a_0)}{\lambda} \right] \end{aligned}$$

where the constant  $\psi_0 \pi / \lambda$  represents the maximum stress, which is the desired fracture stress  $\sigma_f$ . For  $x$  very close to  $a_0$ , the sine term in the preceding formula can be replaced by its argument, and the stress can be related to the strain  $(x - a_0)/a_0$  by Hooke's law

$$\sigma(x) = \sigma_f \left( \frac{2\pi}{\lambda} \right) (x - a_0) = E \left( \frac{x - a_0}{a_0} \right)$$

where  $E$  is Young's modulus. From this equation the fracture stress is

$$\sigma_f = \left( \frac{\lambda}{2\pi} \right) \frac{E}{a_0}$$

The unknown parameter  $\lambda$  can be related to a macroscopic material property, the surface energy, by an energy balance. The work done in creating the two fresh surfaces of unit area by cleaving the crystal is twice the surface energy, or  $2\gamma_s$ . The work of cleavage can also be calculated by integrating the sinusoidal stress function from  $x = a_0$  to  $x = a_0 + (\lambda/2)$ , which yields

$$\begin{aligned} \text{Work of cleavage} &= 2\gamma_s \\ &= \int_{a_0}^{a_0 + (\lambda/2)} \sigma \, dx \\ &= \sigma_f \int_{a_0}^{a_0 + (\lambda/2)} \sin \left[ \frac{2\pi(x - a_0)}{\lambda} \right] dx \\ &= \frac{\sigma_f \lambda}{\pi} \end{aligned}$$

From the work expression we find that the quantity  $(\lambda/2\pi)$  is equal to  $\gamma_s/\sigma_f$ , which, when inserted into the previous expression, yields the theoretical normal stress required to fracture the solid:

$$\sigma_f = \left( \frac{E\gamma_s}{a_0} \right)^{1/2} \quad (16.3)$$

For  $UO_2$ ,  $E = 2 \times 10^8$  kN/m $^2$  ( $2 \times 10^{12}$  dynes/cm $^2$ ),  $\gamma_s = 10^3$  dynes/cm, and  $a_0 = 3 \times 10^{-8}$  cm. Equation 16.3 predicts a fracture stress of  $3 \times 10^7$  kN/m $^2$ , which is about 0.1E. However, Fig. 16.7 shows that brittle fracture occurs at stresses of  $\sim 1.4 \times 10^5$  kN/m $^2$ , which is a factor of 200 smaller than the theoretical value.

It is now well established that this large discrepancy is due to the presence of small flaws in the bulk or on the surface of the test specimens. Figure 16.11 shows a section of a solid containing a single crack of elliptical cross section and of infinite extent in the direction perpendicular to the drawing. It was first shown by Griffith<sup>15</sup> that the stress around the tips of the crack,  $\sigma_c$ , can be very much greater than the applied tensile stress  $\sigma$  that acts in the unflawed solid. For a crack with a major axis  $2C$  and a radius of curvature of the tips  $r_c$ , the stress concentration factor  $\sigma_c/\sigma$  is given by

$$\frac{\sigma_c}{\sigma} \sim \left( \frac{C}{r_c} \right)^{1/2}$$

The stress at the crack tips can attain the theoretical maximum value even though the specimen fails at a much

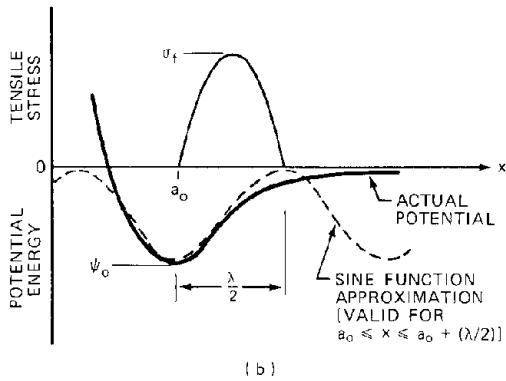
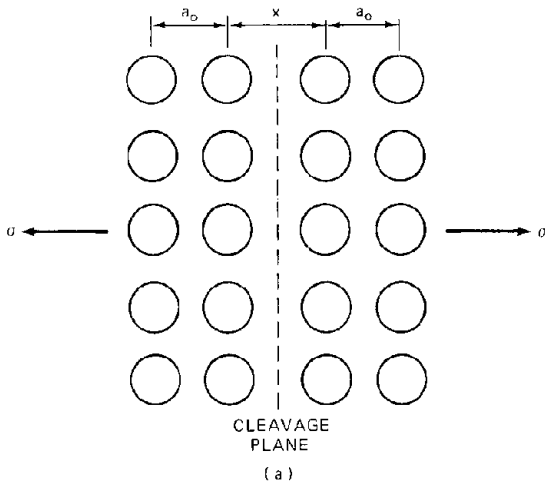


Fig. 16.10 Cleavage fracture.

lower applied stress. The observation of failure at stresses a factor of 50 lower than the theoretical strength can be rationalized by the preceding formula if the crack tips have a radius of curvature approaching atomic size ( $r_c \sim 10 \text{ \AA}$ ) and the flaw dimension is  $\sim 1 \mu\text{m}$ . The larger the crack size, the lower the stress at which fracture can occur.

Another approach to estimating fracture strength from the Griffith model is to balance the increase in surface energy that occurs when a crack grows with the decrease in elastic strain energy in the solid surrounding the crack. The surface energy per unit length of the crack depicted in Fig. 16.11 is

$$E_{\text{surf}} = 4C\gamma_s$$

where the periphery of the very thin ellipse has been approximated by  $4C$  and  $\gamma_s$  is the surface tension of the solid.

Even though the solid in Fig. 16.11 is subject to uniform tension  $\sigma$ , all stresses must vanish at the free surface of the crack. According to Eq. A.26 of the Appendix, the elastic energy per unit volume of solid in pure unidirectional tension is  $\sigma_{xx}^2/2E$ . In a crack-free specimen,  $\sigma_{xx} = \sigma$  at all points. When a crack is present, the normal stresses drop to zero at the crack surface, and the

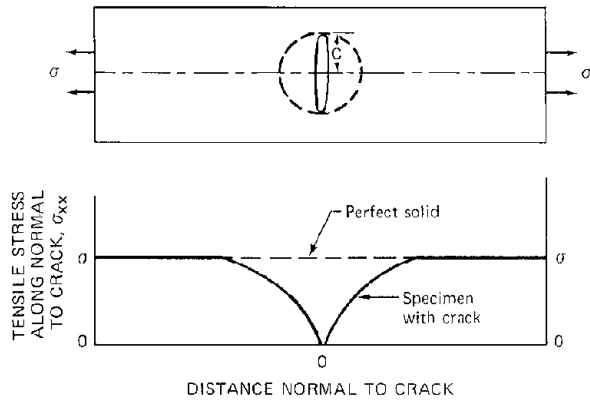


Fig. 16.11 The Griffith model of brittle fracture by crack propagation.

distribution of  $\sigma_{xx}$  along the perpendicular to the crack surface is sketched in the lower part of Fig. 16.11. The elastic energy of the cracked solid is given by

$$E_{e1} = \frac{1}{2E} \int_V \sigma_{xx}^2 dV$$

where  $V$  is the volume of the solid per unit of length perpendicular to the drawing and  $\sigma_{xx}$  is a function of distance from the crack surface. A very crude estimate of the strain energy reduction due to the crack can be obtained by assuming that  $\sigma_{xx}$  is equal to zero in the cylindrical region of radius  $C$  around the crack (dashed line on the top drawing of Fig. 16.11) and equal to  $\sigma$  outside this region. The very high stress in the immediate vicinity of the crack is ignored because it acts over such a small volume that it does not contribute appreciably to the total elastic energy of the solid. The elastic energy per unit length is thus

$$E_{e1} = \frac{\sigma^2}{2E} (V - \pi C^2) = E_{e1}^0 - \frac{\pi C^2 \sigma^2}{2E}$$

where  $E_{e1}^0 = V\sigma^2/2E$  is the elastic energy per unit length in the perfect solid. The total energy of the cracked solid is

$$E_{\text{tot}} = E_{\text{surf}} + E_{e1} = E_{e1}^0 - \frac{\pi C^2 \sigma^2}{2E} + 4C\gamma_s$$

The total energy passes through a maximum at a value of  $C$  given by setting  $dE_{\text{tot}}/dC = 0$ , or when

$$-\frac{\pi C \sigma^2}{E} + 4\gamma_s = 0 \tag{16.4}$$

This formula can be regarded as determining the minimum size of the crack that will spontaneously grow when a tensile stress  $\sigma$  is applied, or alternatively, as giving the minimum stress for which propagation of cracks of size  $C$  is energetically favorable. When viewed in the latter sense, the formula can be solved for the fracture strength:

$$\sigma_f = 2 \left( \frac{E\gamma_s}{\pi C} \right)^{1/2}$$

Using the correct stress distribution around the crack shown in Fig. 16.11, the fracture strength is:

$$\sigma_f = \left( \frac{2E\gamma_s}{\pi(1-\nu^2)C} \right)^{1/2} \quad (16.5)$$

The fracture strength can be estimated from Eq. 16.5 if the long dimension of the largest crack oriented perpendicular to the applied tensile load is known. If we set  $E = 2 \times 10^8$  kN/m<sup>2</sup> ( $2 \times 10^{12}$  dynes/cm<sup>2</sup>) and  $\gamma_s = 10^3$  dynes/cm for  $UO_2$  and assume a typical pore size  $C = 40$   $\mu$ m, Eq. 16.5 yields a fracture stress of  $\sim 10^5$  kN/m<sup>2</sup>, which is in reasonable agreement with the data shown in Fig. 16.7.

Equation 16.5 was derived for a crack geometry (an infinitely long right elliptical cylinder) which is hardly realistic. However, a similar analysis for a disk-shaped pore results in a formula differing from Eq. 16.5 by an inconsequential modification of the constants.<sup>16</sup>

The preceding theory of brittle fracture suggests that the strength of a ceramic such as  $UO_2$  at low temperature should decrease as the porosity of the material becomes greater. The more pores there are, the greater is the likelihood of one of them being oriented in a position that results in fracture at a given stress level. The experiments of Roberts and Ueda<sup>12</sup> confirm this expectation; increasing the porosity of  $UO_2$  from 5 to 16% caused a 70% reduction in fracture strength.

In the semibrittle region of Fig. 16.7, however, increasing porosity increased the yield strength but decreased the ductility (as measured by the onset of yielding). As shown in Fig. 16.12, this combination of effects results in an increase in the ductile-to-brittle transition temperature with increasing porosity. The increase was nearly 150°C on going from 5 to 16% porosity. The reason for the reduced ductility of low-density fuel is probably the presence of fine-scale porosity acting as obstacles to dislocation motion, which is the source of plastic yielding. Porosity did not significantly alter the strength characteristics in the completely ductile region ( $T > 1400^\circ\text{C}$ ). The increase in the ductile-to-brittle transition temperature may have an important influence on the performance of reactor fuel rods. The greater the fractional volume of the fuel which is brittle, the further in toward the center line the cracks penetrate. Since cracking is believed to be a primary

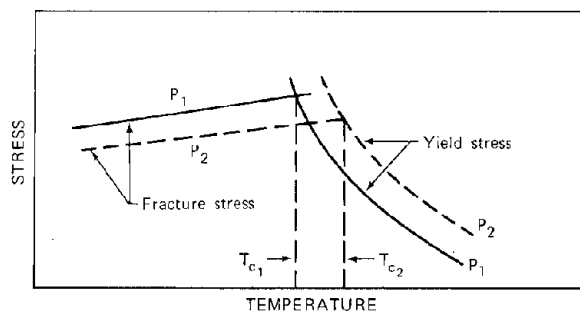


Fig. 16.12 Effect of porosity on the ductile-to-brittle transition temperature ( $T_c$ ) of  $UO_2$ . —, the fracture and yield stresses of material of porosity  $P_1$ . ---, the fracture and yield stresses of material of higher porosity  $P_2$ . (From Ref. 12.)

mechanism for releasing fission gases trapped in the fuel, high-porosity fuels are less likely to be able to retain gaseous fission products than high-density fuels that maintain plasticity to lower temperatures.

## 16.5 CREEP THEORIES

Creep is slow-motion plastic deformation. We saw in Sec. 16.3 that the ductile-to-brittle transition temperature of  $UO_2$  decreased as the strain rate imposed on the specimen during the test was reduced. The strain rates prevailing in creep tests or actual operational situations are usually much lower than those used in fracture or plastic-deformation experiments. Consequently, creep would be expected at stresses and temperatures much lower than those required for plastic flow at high strain rates. In fact, there is no distinct temperature below which a solid does not exhibit creep deformation. Rather, creep is found to be an activated process, with a temperature dependence of the Arrhenius type [i.e.,  $\exp(-E_{vol}/kT)$ ]. Because  $E_{vol}$  is generally rather large (it is approximately equal to the activation energy of atomic self-diffusion), creep effectively ceases at temperatures less than approximately one-third the melting point ( $^\circ\text{K}$ ) of the solid.

Because of the large variety of mobile defects in a solid, the motion of which is potentially responsible for deformation, literally dozens of creep mechanisms have been proposed.<sup>17,18</sup> In the following two sections, we consider creep caused by stress-induced vacancy migration (diffusional creep) and climb-controlled dislocation motion. These two mechanisms result in deformation of the grains of the solid. Creep can occur (i.e., the solid can deform) even if the constituent grains of the solid retain their original shape, however, by the grains' sliding past each other along the grain boundaries. This mode of creep is called grain-boundary sliding and is discussed in Sec. 16.8.

## 16.6 DIFFUSIONAL CREEP

We have seen in Sec. 13.9 that normal stresses (of which hydrostatic pressure is a special case) alter the thermodynamic concentration of vacancies in a solid. Nabarro<sup>19</sup> and Herring<sup>20</sup> were the first to suggest that normal stresses applied in a particular direction to a grain could cause the grain boundary to act as a nonuniform source or sink of vacancies. The diffusional transport of vacancies through the grain which seeks to eliminate the concentration differences established on the boundary of the grain is equivalent to transport of atoms from one point of the grain to another. Such material displacement elongates the grain and hence can be described as a form of creep.

Two variations of diffusional creep have been used in interpreting  $UO_2$  creep data. The first assumes that vacancy migration occurs within the grain proper. The second considers vacancy diffusion to take place in the grain boundary rather than in the interior of the grain.

### 16.6.1 Nabarro-Herring Creep

Following Herring,<sup>20</sup> we consider a spherical grain subject to a uniaxial tensile (or compressive) stress directed

along a particular diameter of the sphere [Fig. 16.13(a)]. In order to fill all available space, grains are polyhedral rather than spherical in shape, but spherical grains are easy to work with analytically, and the results are a good approximation to the behavior of many-sided grains. The positions of the maximum normal stress are called the poles. At the equator of the grain, the normal component of the tensile stress is zero. Between the poles and the equator, the normal stress at the boundary surface varies as  $\sigma \cos \theta$ , where  $\theta$  is the angle measured from the pole [see Fig. 16.13(b)]. Because of this stress distribution, the

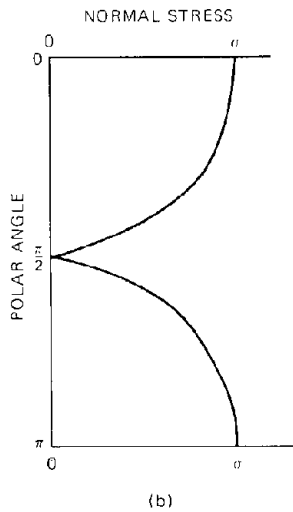
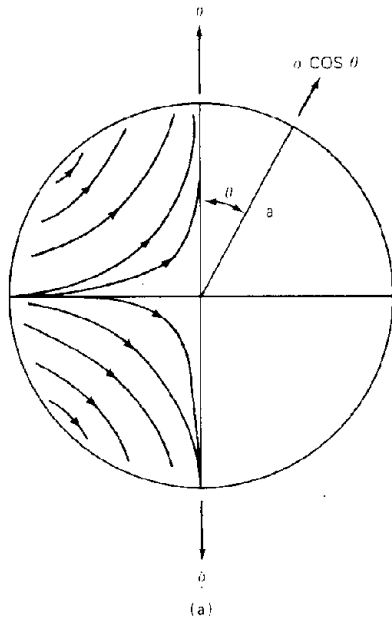


Fig. 16.13 Nabarro—Herring creep. (a) Atom currents set up by nonuniform normal stress on the grain boundary are shown in the left hemisphere. (b) Variation of the normal component of the stress on the grain boundary with polar angle.

vacancy concentration at the poles is larger than at the equator, and vacancies flow from the poles to the equator. Atoms of the matrix flow in the opposite direction from the sense of vacancy movement, or from the equator to the poles. Atom diffusion currents are sketched in the left-hand hemisphere of Fig. 16.13(a).

Equation 13.175 expresses the dependence of the equilibrium vacancy concentration on pressure. This relation is generally valid if the pressure is replaced by the normal stress on a solid surface. The formula then gives the equilibrium concentration of vacancies in the solid just at the surface where the normal stress acts. If the normal stress (tensile) is  $\sigma_n$ , the surface vacancy concentration is

$$C_v = C_v^{eq} \exp\left(\frac{\sigma_n \Omega}{kT}\right) \approx C_v^{eq} \left(1 + \frac{\sigma_n \Omega}{kT}\right)$$

where  $C_v^{eq}$  is the equilibrium vacancy concentration in a stress-free solid and  $\Omega$  is the atomic volume. Since the argument of the exponential is small for the stress levels usually associated with creep, the one-term power series expansion adequately represents the stress effect on the vacancy concentration.

Vacancy transport takes place within the grain. The steady-state vacancy concentration distribution is governed by the solution to the diffusion equation (Fick's second law) written in axisymmetric spherical coordinates appropriate to the spherical grain:

$$\frac{1}{r^2} \frac{\partial}{\partial r} \left( r^2 \frac{\partial C_v}{\partial r} \right) + \frac{1}{r^2 \sin \theta} \frac{\partial}{\partial \theta} \left( \sin \theta \frac{\partial C_v}{\partial \theta} \right) = 0 \quad (16.6)$$

With the normal stress distribution shown in Fig. 16.13(b), the vacancy concentration at the boundary  $r = a$  is

$$\frac{C_v(a, \theta)}{C_v^{eq}} = \begin{cases} 1 + K \cos \theta & (\text{for } 0 \leq \theta \leq \pi/2) \\ 1 - K \cos \theta & (\text{for } \pi/2 \leq \theta \leq \pi) \end{cases} \quad (16.7)$$

where

$$K = \frac{\sigma \Omega}{kT} \quad (16.8)$$

The other boundary conditions are

$$C_v(r, 0) = C_v(r, \pi) = \text{finite} \quad (16.9a)$$

$$C_v(0, \theta) = \text{finite} \quad (16.9b)$$

The general solution of Eq. 16.6 which satisfies Eqs. 16.9 a and b can be obtained by the method of separation of variables. The result is<sup>21</sup>

$$\frac{C_v(r, \theta)}{C_v^{eq}} = \sum_{n=0}^{\infty} A_n \left(\frac{r}{a}\right)^n P_n(\mu) \quad (16.10)$$

where

$$\mu = \cos \theta \quad (16.11)$$

and  $P_n(\mu)$  signifies the Legendre polynomials. The coefficients  $A_n$  are determined by expanding the remaining boundary condition, Eq. 16.7, in a series of Legendre polynomials. Thus we write

$$1 \pm K\mu = \sum_{n=0}^{\infty} A_n P_n(\mu) \quad (16.12)$$

where the positive sign applies for  $0 \leq \mu \leq 1$  and the negative sign for  $-1 \leq \mu \leq 0$ . Since the left-hand side of Eq. 16.12 is an even function of  $\mu$ , the  $A_n$  is zero for odd values of  $n$ , and, for even values of  $n$ , the coefficients are (Ref. 21, p. 257)

$$A_n = (2n + 1) \left[ \int_0^1 P_n(\mu) d\mu + K \int_0^1 \mu P_n(\mu) d\mu \right] \quad (16.13)$$

The first term on the right of Eq. 16.13 is zero except for  $n = 0$  [ $P_0(\mu) = 1$ ], for which

$$A_0 = 1 + \frac{1}{2}K \quad (16.14)$$

For all nonzero even values of  $n$ ,  $A_n$  can be expressed by

$$A_n = \alpha_n K \quad (16.15)$$

where

$$\alpha_n = (2n + 1) \int_0^1 \mu P_n(\mu) d\mu \quad (n = 2, 4, \dots) \quad (16.16)$$

The integral in Eq. 16.16 can be expressed as a function<sup>22</sup> of  $n$ , and we find

$$\alpha_n = \frac{(2n + 1)(n - 2)!}{(-1)^{(n+2)/2} 2^n [(n/2) + 1]! [(n/2) - 1]!} \quad (16.17)$$

For large values of  $n$ , application of Stirling's formula to Eq. 16.17 shows that

$$\alpha_n \rightarrow \frac{2}{n} \quad (16.18)$$

The change in grain shape is governed by the radial flux of vacancies at the grain boundary, which is given by

$$J_r(a, \theta) = -D_v \left( \frac{\partial C_v}{\partial r} \right)_a \quad (16.19)$$

where  $D_v$  is the vacancy diffusion coefficient in the solid.

Substituting Eq. 16.15 into Eq. 16.10, expressing  $K$  by Eq. 16.8, and taking the required derivative with respect to  $r$  yields

$$J_r(a, \mu) = -\frac{C_v^{eq} D_v \Omega \sigma}{akT} \sum_{n=2, 4, \dots}^{\infty} n \alpha_n P_n(\mu) \quad (16.20)$$

(the  $n = 0$  term has been omitted from the sum because of the factor  $n$  in the summand). The strain rate of the spherical grain is given by

$$\dot{\epsilon}(\mu) = \frac{1}{a} \frac{da}{dt} \quad (16.21)$$

where the rate of change of the grain radius is related to the radial flux of vacancies by

$$\frac{da}{dt} = -J_r(a, \mu) \Omega \quad (16.22)$$

Combining the three preceding equations and noting that the volume self-diffusion coefficient of the atoms of the solid is related to the vacancy diffusion coefficient by

$$D_{v01} = D_v C_v^{eq} \Omega \quad (16.23)$$

yields

$$\dot{\epsilon}(\mu) = \frac{4D_{v01}\sigma\Omega}{d^2 kT} \sum_{n=2, 4, \dots}^{\infty} n \alpha_n P_n(\mu) \quad (16.24)$$

where  $d = 2a$  is the grain diameter. Table 16.1 shows the first four terms of the series on the right of Eq. 16.24 for  $\mu = 0$  (the equator) and  $\mu = 1$  (the poles).

Table 16.1 Series Solution to The Nabarro—Herring Creep Equation

n	$\alpha_n$	Equator		Poles	
		$P_n(0)$	$n\alpha_n P_n(0)$	$P_n(1)$	$n\alpha_n P_n(1)$
2	5/8	-1/2	-0.625	1	1.25
4	-3/16	3/8	-0.280	1	-0.75
6	13/128	-5/16	-0.190	1	0.61
8	-17/256	35/128	-0.145	1	-0.53
Total			-1.24		0.58

The sums are only slowly convergent, and many more terms than the four shown in the table would be required for accurate evaluation of  $\dot{\epsilon}(\mu)$ . However, if we estimate the sums to be twice the values shown in the last row of Table 16.1, the creep rates at the poles and at the equator are

$$\dot{\epsilon}(0) \approx -\frac{10D_{v01}\sigma\Omega}{d^2 kT} \quad (\text{equator}) \quad (16.25a)$$

$$\dot{\epsilon}(1) \approx \frac{5D_{v01}\sigma\Omega}{d^2 kT} \quad (\text{poles}) \quad (16.25b)$$

The sign of the creep rate at the equator is negative because this region is a vacancy sink (if  $\sigma$  is a tensile load). Vacancies emitted from the polar regions are absorbed near the equator. Conversely, the creep rate at the poles is positive because vacancies flow away from this zone (and hence atoms are absorbed here). The grain thus elongates in the direction of the applied tensile stress. At some polar angle between 0 and  $\pi/2$ , the creep rate vanishes. An average creep rate for the entire grain can be defined as the integral of the absolute value of  $\dot{\epsilon}(\mu)$  over the hemisphere [the average of  $\dot{\epsilon}(\mu)$  over the hemisphere is zero since volume is conserved in the diffusion process]. Thus,

$$\dot{\epsilon} = \int_0^1 |\dot{\epsilon}(\mu)| d\mu \quad (16.26)$$

The average creep rate defined by Eq. 16.26 is of the same form as Eq. 16.25, but the numerical constant is positive and less than 10 (and possibly less than 5).

Irrespective of the value of the numerical constant, the creep rate can be written in the general form

$$\dot{\epsilon} = B_{v01} \frac{\sigma}{d^2} \exp\left(-\frac{E_{v01}}{kT}\right) \quad (16.27)$$

where  $B_{v01}$  is a constant and  $D_{v01}$  has been written in Arrhenius form where  $E_{v01}$  is the activation energy of atom self-diffusion in the solid. Thus, the Nabarro—Herring mechanism prescribes the temperature dependence of the creep rate and predicts a first-power dependence on applied stress and an inverse-square variation with grain size.

### 16.6.2 Diffusional Creep Due to Vacancy Transport in the Grain Boundary

Coble<sup>2,3</sup> proposed a creep mechanism that differs from Nabarro—Herring creep in that vacancy diffusion from the poles toward the equator occurs within the grain boundary rather than in the grain proper. Despite the small cross section of the transport path offered by the grain boundary compared to that afforded by the entire grain interior, the grain-boundary diffusion coefficient can be much larger than the volume-diffusion coefficient, thereby making up for the reduced transport area. As shown in Fig. 16.14, vacancy diffusion takes place in a spherical shell of thickness  $w$  (the grain-boundary thickness), which is small compared to the grain radius ( $w/a \ll 1$ ). Equation 16.6 governs vacancy transport in the grain boundary, but, because this zone is very thin,  $r^2$  can be replaced by  $a^2$ . Setting

$$x = r - a \quad (0 \leq x \leq w) \quad (16.28)$$

Eq. 16.6 becomes

$$a^2 \frac{\partial^2 C_v}{\partial x^2} + \frac{1}{\sin \theta} \frac{\partial}{\partial \theta} \left( \sin \theta \frac{\partial C_v}{\partial \theta} \right) = 0 \quad (16.29)$$

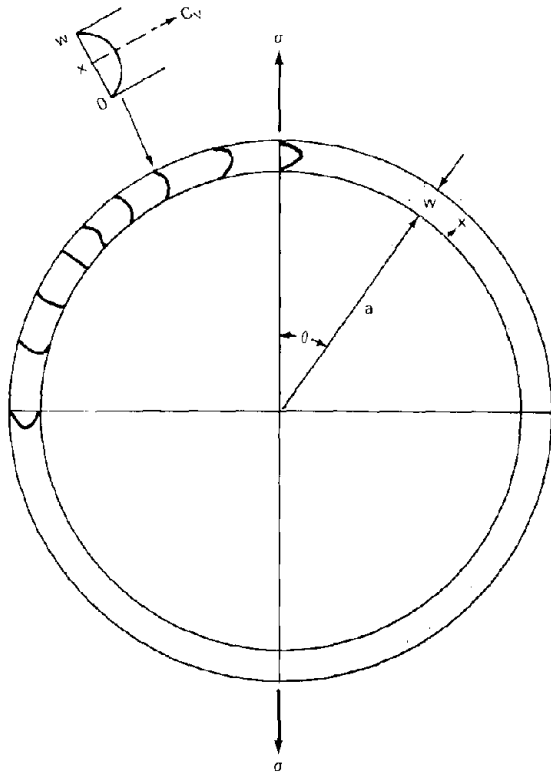


Fig. 16.14 Model of grain-boundary diffusional creep proposed by Coble.<sup>2,3</sup> Vacancy diffusion occurs in the spherical shell around the grain. Vacancy concentration profiles  $C_v(x, \theta)$  are sketched for several values of the polar angle.

In terms of  $x$ , the boundary condition at the grain surface given by Eq. 16.7 is

$$\frac{C_v(0, \theta)}{C_v^{eq}} = \begin{cases} 1 + K \cos \theta & (\text{for } 0 \leq \theta \leq \pi/2) \\ 1 - K \cos \theta & (\text{for } \pi/2 \leq \theta \leq \pi) \end{cases} \quad (16.30)$$

and the boundary condition of Eq. 16.9a becomes

$$C_v(x, 0) = \text{finite} \quad (16.31)$$

Equation 16.9b is replaced by a condition requiring that the vacancy concentration profile in the grain boundary be symmetric about the midplane (Fig. 16.14):

$$\left( \frac{\partial C_v}{\partial x} \right)_{x=w/2} = 0 \quad (16.32)$$

Assuming separable solutions of the form

$$\frac{C_v}{C_v^{eq}} = X(x) \Phi(\theta) \quad (16.33)$$

Substitution into Eq. 16.29 again leads to the angular solutions in terms of Legendre polynomials<sup>2,1</sup>

$$\Phi(\theta) = A_n P_n(\mu) \quad (16.34)$$

and radial solutions obtained by solving the ordinary differential equation:

$$a^2 \frac{d^2 X}{dx^2} - n(n+1) X = 0 \quad (16.35)$$

The particular form of the separation constant [i.e.,  $[n(n+1)]^{1/2}$ ] is dictated by the boundary condition of Eq. 16.31. Solutions of Eq. 16.35 that satisfy Eq. 16.32 are

$$X = B_0 \quad (\text{for } n = 0)$$

and

$$X = B_n \left( \sinh \left\{ [n(n+1)]^{1/2} \left( \frac{x}{a} \right) \right\} - \coth \left\{ [n(n+1)]^{1/2} \left( \frac{w}{2a} \right) \right\} \times \cosh \left\{ [n(n+1)]^{1/2} \left( \frac{x}{a} \right) \right\} \right) \quad (\text{for } n > 0) \quad (16.36)$$

Using Eqs. 16.34 and 16.36 in Eq. 16.33 yields the solution

$$\begin{aligned} \frac{C_v(x, \mu)}{C_v^{eq}} = & A_0 + \sum_{n=1}^{\infty} \left( A'_n \sinh \left\{ [n(n+1)]^{1/2} \left( \frac{x}{a} \right) \right\} \right. \\ & \left. - \coth \left\{ [n(n+1)]^{1/2} \left( \frac{w}{2a} \right) \right\} \right. \\ & \left. \times \cosh \left\{ [n(n+1)]^{1/2} \left( \frac{x}{a} \right) \right\} \right) P_n(\mu) \quad (16.37) \end{aligned}$$

where  $A'_n = A_n B_n$ . At  $x = 0$ , Eq. 16.37 reduces to

$$\frac{C_v(0, \mu)}{C_v^{eq}} = A'_0 - \sum_{n=1}^{\infty} A'_n \times \coth \left\{ [n(n+1)]^{1/2} \left( \frac{w}{2a} \right) \right\} P_n(\mu) \quad (16.38)$$

Expansion of the remaining boundary condition, Eq. 16.30, in Legendre polynomials leads to the same coefficients found for the previous case of diffusion within the grains, namely,

$$\frac{C_v(0, \mu)}{C_v^{eq}} = 1 + K\mu = 1 + \frac{1}{2}K + K \sum_{n=2,4,\dots}^{\infty} \alpha_n P_n(\mu) \quad (16.39)$$

Identification of the coefficients of  $P_n(\mu)$  in Eqs. 16.38 and 16.39 results in the following:

$$\begin{aligned} A'_0 &= 1 + \frac{1}{2}K \\ A'_n &= -\alpha_n \tanh \left\{ [n(n+1)]^{1/2} \left( \frac{w}{2a} \right) \right\} K \\ &\quad (\text{for } n = 2, 4, \dots) \\ A'_n &= 0 \quad (\text{for } n \text{ odd}) \end{aligned} \quad (16.40)$$

where  $\alpha_n$  is given by Eq. 16.17.

To evaluate the creep rate, we first determine the radial flux of vacancies at the grain-boundary surface

$$\begin{aligned} J_r(0, \mu) &= -D_{v_{gb}} \left( \frac{\partial C_v}{\partial x} \right)_{x=0} \\ &= -D_{v_{gb}} C_v^{eq} \left[ \frac{\partial (C_v/C_v^{eq})}{\partial x} \right]_{x=0} \end{aligned} \quad (16.41)$$

where  $D_{v_{gb}}$  is the diffusion coefficient of vacancies in the grain boundary. In the present case the diffusion medium is the exterior of the grain surface, whereas in Nabarro-Herring creep vacancies flow between the boundary and the interior. Hence, Eq. 16.22 must be replaced by

$$\frac{da}{dt} = J_r(0, \mu) \Omega \quad (16.42)$$

The creep rate as a function of polar angle is obtained by combining Eqs. 16.21 and 16.42 and substituting Eq. 16.41 for the flux:

$$\dot{\epsilon}(\mu) = -\frac{D_{v_{gb}} C_v^{eq} \Omega}{a} \left[ \frac{\partial (C_v/C_v^{eq})}{\partial x} \right]_{x=0} \quad (16.43)$$

The grain-boundary self-diffusion coefficient  $D_{gb}$  represents the diffusivity of atoms in the grain boundary. It is related to the vacancy diffusion coefficient in the grain boundary by

$$D_{gb} = D_{v_{gb}} C_v^{eq} \Omega \quad (16.44)$$

Evaluating the derivative in Eq. 16.43 from the solution given by Eq. 16.37 and expressing the  $A'_n$  by Eq. 16.40 yields

$$\begin{aligned} \dot{\epsilon}(\mu) &= \frac{4D_{gb} \sigma \Omega}{d^3 kT} \sum_{n=2,4,\dots}^{\infty} \alpha_n [n(n+1)]^{1/2} \\ &\quad \times \tanh \left\{ [n(n+1)]^{1/2} \left( \frac{w}{2a} \right) \right\} P_n(\mu) \end{aligned} \quad (16.45)$$

This formula can be put into the form obtained by Coble<sup>2,3</sup> by multiplying and dividing by  $[n(n+1)]^{1/2} (w/2a)$ :

$$\begin{aligned} \dot{\epsilon}(\mu) &= \frac{4D_{gb} w \sigma \Omega}{d^3 kT} \sum_{n=2,4,\dots}^{\infty} n(n+1) \alpha_n \\ &\quad \times \left( \frac{\tanh \{ [n(n+1)]^{1/2} (w/2a) \}}{[n(n+1)]^{1/2} (w/2a)} \right) P_n(\mu) \end{aligned} \quad (16.46)$$

In his approximate solution of the diffusion problem, Coble obtained the constant 15 in place of the sum appearing on the right-hand side of Eq. 16.46.\* We see, however, that, as in the case of diffusion within the grain, the creep rate varies with polar angle and is not quite proportional to the grain-boundary thickness because of the term in the large parentheses in the summand. If  $w/2a \ll 1$ , this term is nearly unity for small values of  $n$ . However, this approximation cannot be made in evaluating all terms of the sum, no matter how small  $(w/2a)$  is. If the term in the parentheses were to be replaced by unity for all values of  $n$ , the creep rate at the pole [where  $P_n(1) = 1$ ] would contain the infinite sum  $\sum n(n+1) \alpha_n$ . According to Eq. 16.18, the terms of this sum eventually reduce to  $2(n+1)$ , and the sum diverges. Approximating the term in parentheses in Eq. 16.46 by unity is better at the equator since  $P_n(0)$  decreases as  $n$  increases. The values of  $n(n+1) \alpha_n P_n(0)$  for  $n = 2, 4, 6$ , and  $8$  are  $-1.88$ ,  $-1.00$ ,  $-1.34$ , and  $-1.31$ , respectively, and the sum of the first four terms is  $-5.53$ . Convergence is very slow, however, and the exact value of  $\sum n(n+1) \alpha_n P_n(0)$  may very well be three times as large as the value after the first four terms, which would give an equatorial creep rate very close to the value determined by Coble for the entire sphere.

If the magnitude of the angle-dependent creep rate given by Eq. 16.46 is integrated over the grain surface with Eq. 16.20 and  $D_{gb}$  is expressed in Arrhenius form, the average creep rate is given by

$$\dot{\epsilon} = B_{gb} \frac{\sigma}{d^3} \exp \left( -\frac{E_{gb}}{kT} \right) \quad (16.47)$$

where  $B_{gb}$  is a slowly varying function of the ratio of the grain-boundary thickness to the grain diameter. Equation 16.47 shows that the creep rate for this model is linear in the stress, has a temperature dependence controlled by the activation energy for grain-boundary diffusion  $E_{gb}$ , and, except for the dependence of the factor  $B_{gb}$  on  $d$ , varies inversely as the cube of the grain diameter. Grain-boundary diffusional creep differs from Nabarro-Herring creep in the dependence on temperature and grain size but shows the same linear variation with applied stress.

\*An extra factor of  $1/2$  was introduced by Coble<sup>2,3</sup> to account for "enhancement of the creep rate by shear stress relaxation at the grain boundary."

## 16.7 CREEP CONTROLLED BY DISLOCATION CLIMB

The distinguishing features of the diffusional creep models presented in the previous section are the linear dependence on applied stress and the inverse dependence on grain size raised to some power greater than 1. High-temperature creep behavior consistent with this model is observed in many fine-grained materials. However, creep rates with a much stronger stress dependence ( $\sigma^4$  is typical) but insensitive to grain size are found at somewhat lower temperatures and higher stresses than the region characterized by diffusional creep. The temperature dependence is also of the Arrhenius form with an activation energy of the same order of magnitude as that of atomic self-diffusion. Although a different mechanism is clearly responsible for the second type of creep behavior, the temperature dependence suggests that in this mechanism, as in diffusional creep, vacancy migration is the ultimate rate-controlling step.

In this case it is believed that motion of dislocations in the crystal governs the creep rate, but, in turn, the dislocation velocity is determined by vacancy diffusion. It is well known that glide of dislocations on slip planes is responsible for plastic deformation (Chap. 8). Under conditions where creep is an important deformation mode, the stresses are considerably lower than those which are required to produce essentially instantaneous plastic flow. Because of the low stress levels characteristic of creep, dislocations can be blocked by obstacles in the slip plane that could easily be surmounted or cut through if the dislocations were driven by high applied stresses. When blockage occurs, the only way that deformation can continue is for the mobile dislocation to move around the obstacle or, if the obstruction is another dislocation of opposite sign, to move toward and annihilate the obstacle. In either case, the mobile dislocation must move out of its slip plane, which, in the case of an edge dislocation, is the process of climb requiring emission or absorption of vacancies.

### 16.7.1 Climb Velocity of Edge Dislocations

In order for an edge dislocation to move in a direction perpendicular to its slip plane, the extra half sheet forming this type of line defect must either lose or gain atoms. Since removal of atoms is equivalent to absorption of vacancies and since addition of atoms is the same as emission of vacancies, edge-dislocation climb can be analyzed in terms of the flow of vacancies between the dislocation line and the bulk of the solid. Although an edge dislocation is usually depicted as a perfectly straight knife-edge, it is in actuality quite ragged owing to the presence of jogs (Fig. 16.15). A jog represents a step of one lattice spacing height in the extra half sheet of atoms forming the edge dislocation. The Burgers vector of a dislocation is approximately equal to the lattice constant (Chap. 8); so the height of a jog is  $\sim b$ . The volume of an atom or a vacancy is approximately given by

$$\Omega \approx a_0^3 \approx b^3 \quad (16.48)$$

The number of jogs per unit length of dislocation line is denoted by  $n_j$ .

Figure 8.10(a) shows that a shear stress applied to the slip plane of an edge dislocation produces a force in the slip plane which induces glide of the dislocation. However, the shear stress does not produce a climb force on the dislocation. The normal applied stress shown in Fig. 8.10(b), on the other hand, results in a force on the dislocation that is perpendicular to the slip plane. Thus, only normal stresses induce climb of edge dislocations. The climb force arises from the change in the equilibrium vacancy concentration at the dislocation line caused by application of the normal stress in the same way that the vacancy concentration near a free surface of a grain boundary responds to applied normal stresses. The jogs on the dislocation line are the ultimate sources or sinks of vacancies. The vacancy concentration in the stress-free solid is everywhere uniform and equal to  $C_v^{eq}$ . When a normal stress is applied to the solid, the vacancy concentration in the immediate vicinity of the jogs assumes the new equilibrium value

$$C_v^{jog} = C_v^{eq} \exp\left(\frac{\sigma\Omega}{kT}\right) \quad (16.49)$$

where  $\sigma$  is the applied normal stress [actually  $\sigma_{xx}$  for the coordinate system shown in Fig. 8.10(b), but the subscripts are omitted for simplicity]. Tensile stresses are considered positive. When the stress is applied, the jogs begin to emit vacancies, which flow from the jog to the bulk of the solid until the concentration throughout the medium has reached the value given by Eq. 16.49. In the following analysis, we neglect this approach to saturation and assume that the vacancy concentration of the bulk solid is fixed at the stress-free equilibrium value  $C_v^{eq}$ . On this basis, we compute

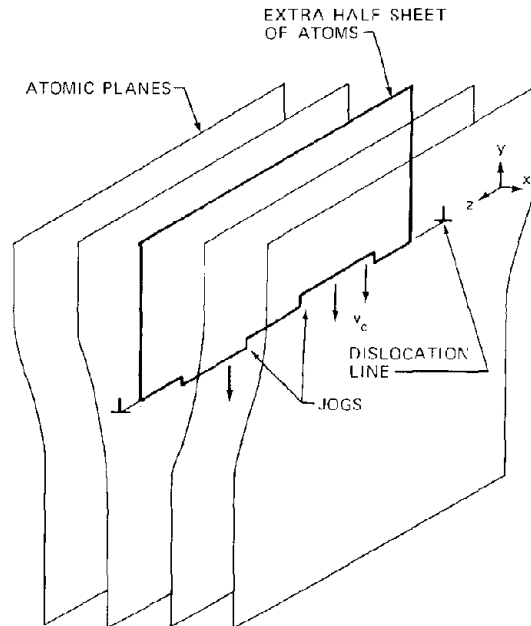


Fig. 16.15 A jogged edge dislocation.

the net rate of vacancy flow from a jog under tensile stress  $\sigma$  to a bulk medium in which the vacancy concentration is  $C_v$ . This flux is the difference between the vacancy emission rate from the jog,  $R_e(\sigma)$ , and the vacancy capture rate by the jog,  $R_c(C_v)$ :

$$R = R_e(\sigma) - R_c(C_v) \quad (16.50)$$

If the vacancy concentration in the bulk were equal to the value given by Eq. 16.49, the net rate of vacancy flow from the jog would be zero, or

$$R_e(\sigma) = R_c(C_v^{jog}) \quad (16.51)$$

The net vacancy flow from the jog in the nonequilibrium case is equal to the difference between the rates at which a perfect sink (the jog) captures vacancies when the bulk concentrations are  $C_v^{jog}$  and  $C_v^{eq}$ , respectively:

$$R = R_c(C_v^{jog}) - R_c(C_v^{eq}) \quad (16.52)$$

[This argument is based on the principle of detailed balancing. It is also employed to calculate the rate of vaporization of a solid into a gas phase in which the partial pressure of the solid species is less than the vapor pressure.] Since the jog is an entity of atomic dimensions, it is unlikely that the rate at which it captures vacancies is diffusion controlled in the sense that the kinetics are limited by vacancy diffusion down the concentration gradient in the vicinity of the jog. As indicated in Secs. 13.4 and 13.5, the kinetics of processes involving atomic-size species are best described as reaction-rate controlled. The rate at which an atomic-size trap captures mobile point defects from the bulk has previously been determined for fission-gas atoms. Combining Eqs. 13.46 and 13.47 and using properties appropriate to vacancies yields

$$R_c(C_v) = \frac{\text{vacancies captured}}{\text{sec} - \text{jog}} = \frac{zD_v\Omega C_v}{a_0^2} \quad (16.53)$$

Using this formula in Eq. 16.52 and expressing  $C_v^{jog}$  by Eq. 16.49 results in a net vacancy flow given by

$$R = \frac{zD_v\Omega C_v^{eq}}{a_0^2} \left[ \exp\left(\frac{\sigma\Omega}{kT}\right) - 1 \right] \approx \frac{zD_{v01}\sigma b}{kT} \quad (16.54)$$

where the exponential has been approximated by a two-term power-series expansion, the vacancy diffusion coefficient has been expressed in terms of the volume self-diffusion coefficient by Eq. 16.23, and Eq. 16.48 has been employed to eliminate  $a_0$  and  $\Omega$  in terms of  $b$ . In the preceding formulas,  $z$  represents the number of atomic sites surrounding a jog from which capture of a vacancy by the jog is certain.

Emission of vacancies by a jog causes the jog to move in the  $\pm z$ -directions shown in Fig. 16.15. The net result of jog motion is the downward growth of the bottom of the extra half sheet of atoms in the drawing. Or, the edge-dislocation climbs in the  $-y$ -direction with a velocity  $v_c$ . If there are  $n_j$  jogs per centimeter of dislocation line,  $n_j R$  vacancies are

lost from each centimeter of line per second. Since each vacancy is equivalent to volume  $\Omega$ , the rate at which the entire half sheet of atoms gains volume is  $n_j R \Omega$  cm<sup>3</sup> sec<sup>-1</sup> cm<sup>-1</sup> of line. In  $\Delta t$  sec, each centimeter of the line grows by  $n_j R \Omega \Delta t$  cm<sup>3</sup>. This volume is equivalent to the product of the width of the extra half sheet of atoms,  $b$ ; the length of dislocation line involved, 1 cm; and the distance climbed in  $\Delta t$ ,  $\Delta y$ . Or the climb velocity is

$$v_c = \frac{\Delta y}{\Delta t} = \frac{n_j R \Omega}{b}$$

Using Eq. 16.54 for  $R$ ,

$$v_c = \frac{zn_j\Omega D_{v01}\sigma}{kT} \quad \text{cm/sec} \quad (16.55)$$

To completely determine the climb velocity, we must estimate the density of jogs on the line,  $n_j$ .

If the jog density is assumed to be in thermodynamic equilibrium at the temperature of the solid, the fraction of the atom sites along the dislocation line which contain jogs is approximately given by the Boltzmann factor  $\exp(-E_j/kT)$ , where  $E_j$  is the energy of formation of a jog. [This formula can be obtained by the same methods used to compute the equilibrium vacancy concentration in a solid (Sec. 6.3), which led to the vacancy fraction given by Eq. 6.12. The entropy of jog formation is assumed to be zero.] Since there are  $1/a_0 \approx 1/b$  atoms sites per unit length of dislocation line, the equilibrium jog density is

$$n_j^{eq} = \frac{1}{b} \exp\left(-\frac{E_j}{kT}\right) \quad (16.56)$$

and the climb velocity is

$$v_c^{eq} = \frac{zb^2 D_{v01} \exp(-E_j/kT)\sigma}{kT} \quad (16.57)$$

where the superscript eq indicates that the quantity is based on the assumption of an equilibrium concentration of jogs. This notation has nothing to do with the ability of a jog to maintain an equilibrium concentration of vacancies in its vicinity. This latter equilibrium assumption (which allows Eq. 16.49 to be written) is accepted whether or not the density of jogs is given by the equilibrium value of Eq. 16.56.

The energy of formation of a jog is not at all well known but can be estimated as follows. Insertion of a jog into an otherwise straight segment of edge dislocation increases the length of the dislocation by the height of the jog,  $b$ . The energy required to create this additional length is the line tension of the dislocation,  $\tau_d$ , times the jog length,  $b$ . Since  $\tau_d \approx 10^{-4}$  dynes and  $b \approx 3 \times 10^{-8}$  cm, the energy of jog formation is approximately given by

$$E_j \approx \tau_d b \approx 3 \times 10^{-12} \text{ ergs} = 2 \text{ eV}$$

More-detailed estimates arrive at values of  $E_j$  between 0.5 and 1 eV. In any case, the energy of jog formation is not negligible compared to the energy of atomic self-diffusion which governs the temperature dependence of the self-diffusion coefficient (for  $U^{4+}$  in UO<sub>2</sub>, for example,  $E_{v01} \approx 3 \text{ eV}$ ).

Jog densities greatly in excess of the equilibrium value given by Eq. 16.56 can be generated when dislocation lines are cut by dislocations moving on other slip planes. This process is illustrated for screw dislocations in Fig. 8.12, but the behavior of edge dislocations is analogous.

When the jogs are very closely spaced, they can no longer be treated as isolated point sinks or sources for vacancies. Instead, the entire length of the dislocation line maintains a vacancy concentration given by Eq. 16.49. The net flux of vacancies from the dislocation to the bulk is best handled as a problem of diffusion from a uniform line source using the techniques developed in Sec. 13.5 for capture of point defects by a dislocation line. In common with this analysis, the vacancy flux and hence the climb velocity depend on the radius of the capture volume surrounding each dislocation, denoted by  $\mathcal{R}$ , and the climb velocity is found to be (see problem 16.1):

$$v_c^{\text{sat}} = \frac{2\pi b^2 D_{v01} \sigma}{kT \ln(\mathcal{R}/R_d)} \quad (16.58)$$

where  $R_d$  is the radius of the dislocation core and the superscript sat indicates that the climb velocity assumes that the entire length of the dislocation line maintains the equilibrium concentration of vacancies characteristic of the applied stress. Equation 16.58 also applies when the jogs on the dislocation line are widely spaced provided that the core of the dislocation offers a rapid artery for vacancy migration (called "pipe diffusion"). In this case, the isolated jogs can supply vacancies to the rest of the dislocation line without the necessity of transport through the bulk solid, where the vacancy diffusion coefficient is much lower than in the dislocation core.

## 16.7.2 Creep Rates

Weertman<sup>24,25</sup> has proposed two closely related models of creep due to dislocation climb. The first is based on Figs. 8.16(a) and 8.17 and the second on Figs. 8.16(b) and 8.18.

### The Climb-Controlled Glide Model

In this model<sup>24</sup> the unit increment of creep deformation is associated with the climb of the lead dislocation of a pile-up over an immobile obstacle, which is assumed to be a pinned edge dislocation. The mobile dislocations are generated by a Frank-Read source located to the left of Fig. 8.16(a). According to Eq. 8.40, the lead dislocation of the pile-up [located at  $x_0$  in Fig. 8.16(a)] is pushed toward the pinned dislocation by an effective shear stress that is larger than the applied shear stress by a factor equal to the number of dislocations in the pile-up. The pile-up extends from the Frank-Read source to the nearest pinned dislocation on a slip plane within a normal distance  $h$  of the plane containing the source. Immobile dislocations on planes further removed from the plane of the source cannot block dislocations produced by the source.

Suppose there are  $M$  Frank-Read sources in a specimen of volume  $V$ , each blocked by a pinned dislocation. Let  $p$  be the probability per second that a particular lead dislocation frees itself from the pinned dislocation by climb. After surmounting the obstacle, the dislocation slips

by an area  $\Lambda$  on its new glide plane before it encounters another obstacle. Since  $Mp$  climb/glide events occur in the specimen per second, Eq. 8.18 gives the strain rate

$$\begin{aligned} \dot{\epsilon} &= \frac{\text{shear strain}}{\text{climb/glide event}} \times \frac{\text{climb/glide events}}{\text{sec}} \\ &= \left( \frac{Ab}{V} \right) Mp = Ab\rho_s p \quad (16.59) \end{aligned}$$

where  $\rho_s = M/V$  is the density of Frank-Read sources in the solid.

We next calculate the climb probability per second,  $p$ . This quantity is identified with the reciprocal of the average time required for a mobile dislocation to climb over the pinned dislocation. Since all impact parameters  $y_0$  between 0 and  $h$  [Fig. 8.16(a)] are equally probable, we first compute the time  $t_c$  for a mobile dislocation to climb over the pinned dislocation as a function of the initial distance  $y_0$  and then average over all possible values of  $y_0$ .

Using Eq. 16.55, the climb velocity of the lead dislocation of a pile-up can be written as

$$v_c = \frac{dy}{dt} = \frac{zn_j D_{v01} \Omega \sigma^+}{kT} \quad (16.60)$$

where  $\sigma^+$  is the hypothetical tensile stress required to produce the force  $F_{iy}$ . The latter is actually due to interaction of the two dislocations in Fig. 8.16(a).<sup>\*</sup> As shown in Chap. 8,  $\sigma^+$  is given by

$$F_{iy} = \sigma^+ b \quad (16.61)$$

But  $F_{iy}$  can also be expressed by Eq. 8.25:

$$F_{iy} = \frac{Kb f_y(\theta)}{y} \quad (16.62)$$

Combining Eqs. 16.61 and 16.62 shows that the hypothetical normal stress driving climb of the mobile dislocation is

$$\sigma^+ = \frac{K f_y(\theta)}{y} \quad (16.63)$$

The value  $y$  can be eliminated by use of Eq. 8.33 in which  $\sigma_{xy}$  is multiplied by  $n$  because the climbing mobile dislocation is the lead member of a pile-up. Therefore,

$$\sigma^+ = \frac{f_y(\theta)}{f_x(\theta)} n \sigma_{xy} \quad (16.64)$$

<sup>\*</sup>Equation 16.55 was derived with the assumption that the vacancy concentration in the bulk solid is equal to the equilibrium value  $C_v^{\text{eq}}$ . This requirement is satisfied when the specimen is subject to a pure shear stress because on the average only half the mobile-immobile dislocation interactions occur between dislocations of the same sign. The other half involve dislocations of opposite sign, for which the hypothetical normal stress  $\sigma^+$  is compressive (i.e., the mobile dislocation tends to emit vacancies as a result of interaction with the immobile dislocation). Since the mobile dislocations are equally divided between vacancy sources and sinks, the average vacancy concentration in the solid is unaffected by a shear stress.

It is convenient to transform the climb rate into a rate of change of angle  $\theta$  with time by using Eq. 8.33, which yields

$$\frac{dy}{dt} = \frac{dy}{d\theta} \frac{d\theta}{dt} = \frac{Kf'_x}{n\sigma_{xy}} \frac{d\theta}{dt} \quad (16.65)$$

where  $f'_x = df'_x/d\theta$  and the total stress on the lead dislocation has been used. Substituting Eqs. 16.64 and 16.65 into Eq. 16.60 yields

$$\frac{d\theta}{dt} = \left( \frac{zn_j D_{vol} \Omega n^2 \sigma_{xy}^2}{KkT} \right) \frac{f_y}{f_x f'_x} \quad (16.66)$$

The group of parameters in the parentheses in Eq. 16.66 has the units of reciprocal time and can be used to define a characteristic time for dislocation climb:

$$\tau_c = \frac{KkT}{zn_j D_{vol} \Omega n^2 \sigma_{xy}^2} \quad (16.67)$$

The time required for a mobile lead dislocation impinging on the pinned dislocation at an impact parameter  $y_0$  to climb over the pinned dislocation is given by the integral of Eq. 16.66:

$$t_c(\theta_0) = \tau_c \int_{\theta_0}^{\pi/8} \frac{f_x f'_x}{f_y} d\theta \quad (16.68)$$

where  $\theta_0$  is the initial polar angle at which the lead dislocation approaches the obstacle. The mean climb time is obtained by averaging  $t_c$  over all impact parameters  $y_0$  or, equivalently, over all initial angles  $\theta_0$ . The distribution of  $y_0$  is assumed uniform over the interval  $0 \leq y_0 \leq h$ , or

$$q_1(y_0) dy_0 = \text{probability of } y_0 \text{ in the range } y_0 \text{ to } y_0 + dy_0 = \frac{dy_0}{h}$$

and the distribution of initial angles can be found from  $q_1(y_0)$  by

$$q_2(\theta_0) d\theta_0 = q_1(y_0) dy_0$$

or

$$q_2(\theta_0) = q_1(y_0) \frac{dy_0}{d\theta_0} = \frac{1}{h} \frac{K}{n\sigma_{xy}} f'_x(\theta_0) \quad (16.69)$$

where the derivative  $dy_0/d\theta_0$  is obtained from Eq. 8.29. However,  $h$  is given by Eq. 8.35; so the distribution of initial angles is governed by

$$q_2(\theta) = 4f'_x(\theta_0) \quad (16.70)$$

We now integrate  $t_c$  of Eq. 16.68 over all initial angles  $\theta_0$  using Eq. 16.70 as the weighting function,

$$\bar{t}_c = \int_0^{\pi/8} t_c(\theta_0) q_2(\theta_0) d\theta_0 \quad (16.71)$$

Substituting Eqs. 16.68 and 16.70 into Eq. 16.71 yields

$$\frac{\bar{t}_c}{\tau_c} = 4 \int_0^{\pi/8} f'_x(\theta_0) \left( \int_{\theta_0}^{\pi/8} \frac{f_x f'_x}{f_y} d\theta \right) d\theta_0 \quad (16.72)$$

The right-hand side of Eq. 16.72 is a pure number, of order unity, which can be calculated by Eqs. 16.26 and 16.27. We

denote it by  $C$ . Therefore, the probability that a particular dislocation in the specimen climbs over a pinned dislocation in unit time is

$$p = \frac{1}{t_c} = \frac{1}{C\tau_c} \quad (16.73)$$

and from Eq. 16.59, the strain rate is

$$\dot{\epsilon} = \frac{Ab\rho_s}{C\tau_c} \quad (16.74)$$

Substituting equations for  $\tau_c$ ,  $K$ , and  $n$  given by Eqs. 16.67, 8.30, and 8.39, respectively, the strain rate assumes the form

$$\dot{\epsilon} = \frac{2\pi^3 (1-\nu)^3}{C} \frac{AL^2 \rho_s zn_j b D_{vol} \sigma_{xy}^4}{G^3 kT} \quad (16.75)$$

Weertman<sup>24</sup> argues that the combination  $AL^2 \rho_s$  is nearly independent of applied stress in single crystals and varies as  $\sigma^{-1}$  in polycrystalline specimens. If the jog concentration,  $n_j$ , is assumed to be in thermodynamic equilibrium, Eq. 16.56 can be used. When the activation energy for self-diffusion is separated from  $D_{vol}$ , the creep rate in polycrystalline material is given by

$$\dot{\epsilon} (\text{equilibrium jogs}) = B\sigma^3 \exp\left[-\frac{(E_j + E_{vol})}{kT}\right] \quad (16.76)$$

where  $B$  is a constant for a particular material. The shear stress  $\sigma_{xy}$  has been replaced by a general applied stress  $\sigma$  which is sure to have shear components along the slip-prone crystallographic planes in the grains of the specimen.

If the climb velocity appropriate to a dislocation line that is saturated with vacancies along its entire length (Eq. 16.58) were used in the preceding derivation, the result would be that given by Eq. 16.75 with  $zn_j$  replaced by  $[2\pi/\ln(\mathcal{R}/R_d)]/b$ , and Eq. 16.76 would be altered to:

$$\dot{\epsilon} (\text{saturated dislocations}) = B'\sigma^3 \exp\left(-\frac{E_{vol}}{kT}\right) \quad (16.77)$$

Both Eqs. 16.76 and 16.77 exhibit the characteristic strong stress dependence often observed in high-strain-rate creep tests. The activation energy for creep, according to this model, is equal to or greater than that of volume self-diffusion. This prediction is also in accord with many experiments. Neither creep formula exhibits a dependence on the grain size of the specimen.

### The Climb-to-Annihilation Model

Weertman's<sup>25</sup> second mechanism assumes that creep occurs as a result of climb and mutual annihilation of pairs of dislocations (the dipoles) of the array produced by interweaving of dislocation loops originating from Frank-Read sources on neighboring slip planes. Figure 16.16 is a schematic diagram of this model. The diagram of Fig. 8.18 represents a cross section along the diagonal between two of the Frank-Read sources in Fig. 16.16. Since the pairs of dislocations forming the dipoles of the array are of opposite sign, they attract each other. This attraction is reflected in a force-induced climb of each partner of the dipole toward its mate, which results in mutual annihilation. Figure 8.16(b) shows the path followed by the two dislocations in the

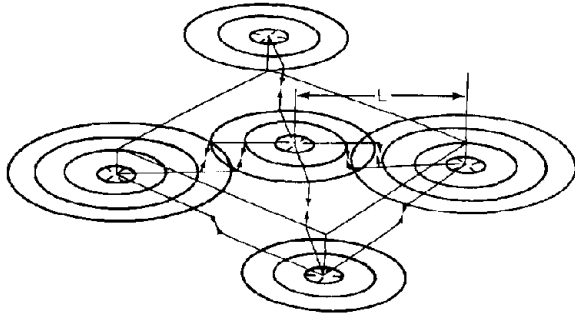


Fig. 16.16 Model of creep resulting from creation and subsequent annihilation through climb of dislocation loops. (From Ref. 25.)

dipole during the climb process (in the present case, however, both dislocations move). As each annihilation event occurs, the sources on the two slip planes each produce another loop to replace the two that have disappeared. The creep rate according to this mechanism is given by Eq. 16.59; yet the parameters  $A$  and  $p$  remain to be determined.

The quantity  $A$  is the area on the slip plane swept out each time a climb-annihilation event takes place. Suppose the dipole on the right of Fig. 8.18 is destroyed by mutual annihilation of the two dislocations. The source on the lower plane produces a new loop that expands radially by a distance  $\Delta x$  to replace the dislocation missing from the lower plane. The area swept out by glide of the new dislocation is  $\pi(\Delta x)^2$ . The remaining dislocations on the lower plane are not affected. To replace the dislocation that disappeared from the upper plane, however, each of the dislocations in this plane moves to the right by a distance  $\Delta x$ , and the source on the left creates a new dislocation loop. The area swept out by the simultaneous shift of dislocations is  $\pi(L - \Delta x)^2$ . Since  $L$  is usually considerably larger than  $\Delta x$ , the total swept out in the process of replacing the destroyed dipole is  $\pi L^2$ . On the other hand, if the dipole halfway between the two sources is annihilated, an area  $\pi(L/2)^2$  in each plane is swept out by the replacement process, and the total area covered during dislocation readjustment by glide is  $2\pi(L/2)^2 = \pi L^2/2$ . To a good approximation, we can take for the typical dipole in Fig. 8.18 a slip plane area swept out during replacement given approximately by

$$A \approx \pi L^2 \quad (16.78)$$

Consider next the relation among the distance between sources along the slip planes ( $L$ ), the normal spacing of the slip planes ( $y_0$ ), and the density of Frank-Read sources in the solid ( $\rho_s$ ). Assume that the sources are arranged in a square array on each slip plane, the side of the unit cell being the separation distance  $L$ . There are thus  $1/L^2$  sources per unit area of slip plane. If the slip planes are separated by a normal distance  $y_0$ , there are  $1/(y_0 L^2)$  sources per unit volume. Equating this expression to the density of Frank-Read sources in the solid and solving for  $L$  yields

$$L = \frac{1}{(y_0 \rho_s)^{1/2}} \quad (16.79)$$

To determine the spacing of slip planes, consider a specified value of the applied shear stress  $\sigma_{xy}$ . If the spacing  $y_0$  were such that  $\sigma_{xy}$  was greater than the critical value for decomposition of the dipole [ $(\sigma_{xy})_{crit}$  given by Eq. 8.45], dislocation loops produced by a source could not be stopped by loops of opposite sign arising from sources on slip planes a normal distance  $y_0$  away. In this situation strain occurs by the unimpeded glide of dislocations through the entire specimen. Climb is not required for deformation. As a result of the deformation, expanding dislocation loops on nonparallel slip planes intersect each other, and many dislocations become pinned in the ensuing dislocation tangle. This is the process of work hardening, and the result is an increase in the density of Frank-Read sources (which are nothing more than segments of pinned dislocation lines in a slip plane), accompanied by a decrease in the average separation distance between slip planes containing the sources. Thus, when the stage of secondary or steady-state creep is attained, the normal separation of planes containing Frank-Read sources just satisfies Eq. 8.45 for the specified applied shear stress. At this point,  $y_0$  is given by:\*

$$y_0 = \frac{Gb}{8\pi(1-\nu)\sigma_{xy}} = \frac{K}{4\sigma_{xy}} \quad (16.80)$$

where  $K$  is given by Eq. 8.30.

Consider now the climb frequency  $p$ . The two dislocations in a dipole attract each other with a force given by Eq. 8.25 with the minus sign chosen because the dislocations are of opposite sign. The polar angle  $\theta$  between the two dislocations in the dipole is between  $45^\circ$  and  $90^\circ$ , and Fig. 8.15 shows that  $f_y$  can be satisfactorily approximated by unity over this range of angles. Therefore, the attractive interaction is expressed by

$$F_{iy} \approx -\frac{Kb}{y} \quad (16.81)$$

The hypothetical normal stress defined by Eq. 16.61 is compressive in the present case and is given by

$$\sigma^* = \frac{F_{iy}}{b} = -\frac{K}{y} \quad (16.82)$$

The time rate of change of the normal distance between the two dislocations in the dipole is given by substitution of Eq. 16.82 into a climb velocity formula, for which we choose Eq. 16.58, and multiplication by a factor of 2 to

\*Weertman<sup>25</sup> explains that the uniform distribution of slip planes used in the creep model can reduce  $y_0$  by as much as an order of magnitude from the value given by Eq. 16.80, which is based on the analysis of dipole arrays produced by two isolated sources. However, we retain Eq. 16.80 for consistency since the dipole spacing  $n$  (Eq. 8.44), which is also used in the creep model, is also strictly valid only for two isolated dislocation sources. In any case, the numerical change indicated by Weertman does not affect the stress or temperature dependence of the creep rate predicted by the model.

account for the fact that both dislocations are moving toward each other:

$$\frac{dy}{dt} = 2v_c = -2 \left( \frac{2\pi b^2 D_{v01} K}{kT \ln(\mathcal{R}/R_d)} \right) \frac{1}{y} \quad (16.83)$$

By using Eq. 16.58 to express the velocity of climb, we have assumed that both dislocations sustain equilibrium vacancy concentrations along their entire lengths.

The time  $t_c$  required for the two dislocations to climb from a separation distance  $y = y_0$  to  $y = 0$  is obtained by integration of Eq. 16.83:

$$t_c = \frac{kT \ln(\mathcal{R}/R_d) y_0^2}{8\pi b^2 D_{v01} K} \quad (16.84)$$

Each Frank-Read source provides  $n$  dislocations, each of which has a probability per unit time equal to  $1/t_c$  of climbing and annihilating its partner in the dipole. Thus, the probability per unit time that one of the dislocations associated with each Frank-Read source in the specimen participates in a climb-annihilation event is  $n/t_c$ , or, using Eq. 8.44 for  $n$  and Eq. 16.84 for  $t_c$ ,

$$p = \frac{4\pi b^2 D_{v01} K L}{3kT \ln(\mathcal{R}/R_d) y_0^2} \quad (16.85)$$

We can now substitute Eqs. 16.85 and 16.78 into Eq. 16.59, eliminate  $L$  with Eq. 16.79, and eliminate  $y_0$  with Eq. 16.80. Finally,  $K$  is replaced by Eq. 8.30, and the creep-rate formula is

$$\dot{\epsilon} = B' \frac{D_{v01} \sigma^{4.5}}{G^{3.5} \rho_s^{1/2} b^{1/2} kT \ln(\mathcal{R}/R_d)} \quad (16.86)$$

where  $B'$  is a collection of numerical constants and  $\sigma_{xy}$  has been replaced by the general applied stress  $\sigma$ . If all but the important stress and temperature variables are collected in the constant, the creep-rate formula reduces to

$$\dot{\epsilon} = B'' \sigma^{4.5} \exp\left(-\frac{E_{v01}}{kT}\right) \quad (16.87)$$

This equation has the same temperature dependence as the dislocation-climb model of creep derived earlier, but the exponent on the stress is 4.5 instead of 3 (Eqs. 16.76 and 16.77). The stronger stress dependence of Eq. 16.87 is in very good agreement with the observations of creep rates in many materials.

## 16.8 GRAIN-BOUNDARY SLIDING

The analyses presented in Secs. 16.6 and 16.7 assumed that the macroscopic strain of a polycrystalline specimen is reflected in comparable deformation of each grain. For small strains, however, a polycrystalline body can deform merely by the relative motion of the grains, without any change in the grain shape. Changes in the shape of the specimen and of the grains of which it is composed as a result of a compressive creep test are illustrated in Fig. 16.17. The specimen is assumed to be a right-circular cylinder of initial diameter  $D_0$  and length  $L_0$ . After deformation the change in these dimensions defines the total creep strain:

$$\epsilon_T = \frac{L_0 - L}{L_0} = 2 \frac{D_0 - D}{D_0} \quad (16.88)$$

Provided that porosity introduced by grain separation is negligible, the volume of the specimen is unchanged.

Assume that the grains are initially equiaxed with an average diameter  $d_0$ . After deformation the average grain dimension parallel to the axis of compression is reduced from  $d_0$  to  $d_{\parallel}$ , and, transverse to the applied stress, the grain size is increased from  $d_0$  to  $d_{\perp}$ . The deformation of the grain is described by the grain strain:

$$\epsilon_g = \frac{d_0 - d_{\parallel}}{d_0} - 2 \frac{d_{\perp} - d_0}{d_0} \quad (16.89)$$

The change in grain shape in a creep experiment can be measured, so that both  $\epsilon_T$  and  $\epsilon_g$  are available. If  $\epsilon_g/\epsilon_T = 1$ , specimen deformation is due only to strain of the grain, and no relative movement of one grain relative to another has occurred. In this case, the creep rate is given by one of the models described in Secs. 16.6 and 16.7. At the other extreme of  $\epsilon_g/\epsilon_T \approx 0$ , no change in grain shape has occurred, and all the creep strain is due to sliding of grains past each other along the grain boundaries of the material. The strain due to grain-boundary sliding

$$\epsilon_{gbs} = \epsilon_T - \epsilon_g \quad (16.90)$$

is a measure of the fraction of the total strain of a polycrystalline specimen resulting from the relative movements of rigid grains. The limiting case  $\epsilon_T \approx \epsilon_{gbs}$  cannot be maintained to large deformations, however, because some grain strain ( $\epsilon_g > 0$ ) is necessary to maintain geometrical continuity between grains of the specimen. If the grains slide past each other easily, yet do not deform, voids

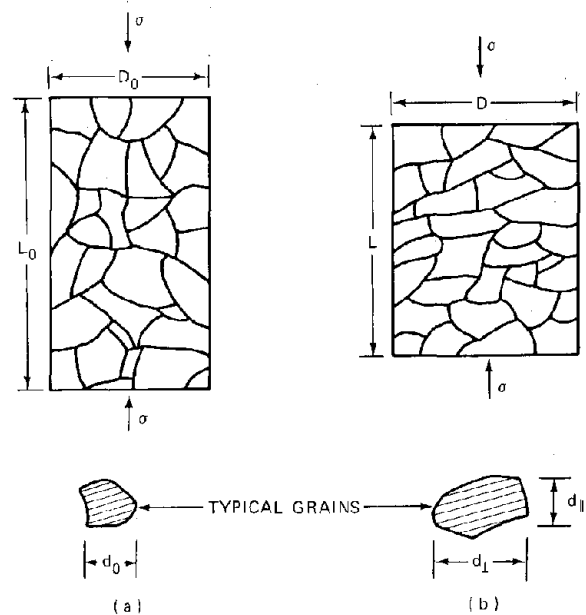


Fig. 16.17 Deformation of specimen and grains during compressive creep test. (a) Initial microstructure. (b) After deformation.

eventually develop on the grain boundaries as the specimen deforms.

In this section we review mechanisms of relative grain motion from which the creep rate due to grain-boundary sliding,  $\dot{\epsilon}_{gbs}$ , can be estimated. By comparing  $\dot{\epsilon}_{gbs}$  with the theoretical estimates of the creep rate due to grain strain,  $\dot{\epsilon}_g$  (as computed by the models presented in the two preceding sections), we can assess the relative importance of the two creep mechanisms. If  $\dot{\epsilon}_{gbs} \gg \dot{\epsilon}_g$ , the grains can slide easily over one another, and no deformation of the grains is needed for creep to occur. Conversely, if the calculated value of  $\dot{\epsilon}_{gbs}$  is much less than the calculated value of  $\dot{\epsilon}_g$ , we expect that the grains would remain locked together at the grain boundaries and the rate of deformation of both the specimen and its constituent grains would be controlled by one of the grain strain theories reviewed earlier.

Although grain boundaries are often represented as smooth plane surfaces, they are in reality covered with nonuniformities of the same sort that is found on external surfaces of solids. Internal surface roughness acts as an impediment to the relative motion of two adjacent grains. An idealized type of grain-boundary roughness that is amenable to analytic description of creep controlled by grain-boundary sliding is shown in Fig. 16.18. The specimen is subject to an applied shear stress that tends to move grain 1 to the left and grain 2 to the right. The imperfection preventing the sliding of the two grains is the ledge shown in cross section in the figure. The applied stress places the right-hand vertical step of the ledge in compression and the opposite side in tension. The vacancy concentration is higher on the tensile side than on the compressive side; so vacancies flow from the tensile side to the compressive side. Consequently, the protrusion moves from right to left under the influence of the applied stress, and this motion controls the rate at which grains 1 and 2 can slide past each other.

The movement of vacancies from one part of a grain to another in response to differences in normal stress along the

boundary has been encountered in theories of diffusional creep (Sec. 16.6). As in this case, vacancy transport can occur either through the lattice separating the affected surfaces or along the grain boundary. Figure 16.18 illustrates the grain-boundary migration variant of the grain-boundary sliding model proposed by Gifkins and co-workers.<sup>26-28</sup> The driving force for diffusion along the grain boundary is the difference in vacancy concentration between the two sides of the ledge normal to the grain boundary. The vacancy concentration along the tensile side is

$$C_v(\text{tensile}) = C_v^{eq} \left( 1 + \frac{\sigma\Omega}{kT} \right) \quad (16.91)$$

and on the compressive side

$$C_v(\text{compressive}) = C_v^{eq} \left( 1 - \frac{\sigma\Omega}{kT} \right) \quad (16.92)$$

The diffusive flow of vacancies per unit ledge length perpendicular to the drawing from left to right is:

$$\text{Vacancy flow rate} = \frac{2D_{vgb}wC_v^{eq}\sigma\Omega}{LkT} \quad (16.93)$$

where  $w$  is the grain-boundary thickness and  $L$  is the width of the ledge. Multiplication of Eq. 16.93 by  $\Omega\Delta t$  gives the volume transferred from one side of the ledge to the other in  $\Delta t$  sec. If  $\Delta x$  is the distance the ledge moves in  $\Delta t$  sec, the volume transferred is also equal to  $\Delta xH$ , where  $H$  is the height of the ledge. The ledge velocity is:

$$v_l = \frac{\Delta x}{\Delta t} = \frac{2D_{gb}w\sigma\Omega}{HLkT} \quad (16.94)$$

where  $D_{gb}$  is the grain-boundary self-diffusion coefficient (Eq. 16.44). The ledge velocity is equal to the relative speed of grain 1 with respect to grain 2. The shear strain rate due to the movement of the ledge can be determined from Fig. 8.14(b) in which  $s$  is replaced by the grain size  $d$ , and

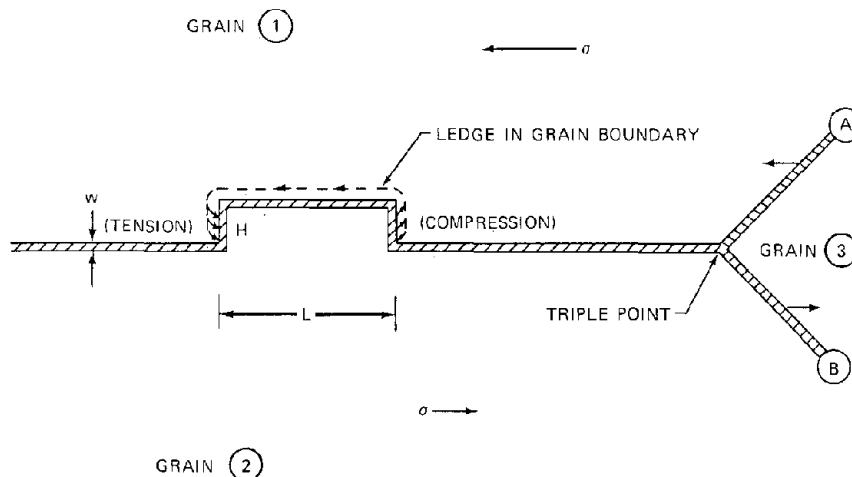


Fig. 16.18 Creep controlled by grain-boundary sliding which is in turn controlled either by movement of ledges or diffusion around triple points. Arrows indicate the direction of atom flow in the grain boundary around the ledge.

the amount of slip occurring in  $\Delta t$  sec is  $v_1 \Delta t$  instead of  $b$ . Therefore, the creep rate due to grain-boundary sliding is

$$\dot{\epsilon}_{gbs} = \frac{\tan \beta}{\Delta t} - \frac{1}{\Delta t} \left( \frac{v_1 \Delta t}{d} \right) = \frac{v_1}{d}$$

or, using Eq. 16.94,

$$\dot{\epsilon}_{gbs} = \frac{2D_{gb}\Omega w\sigma}{dHLkT} \quad (16.95)$$

In common with other diffusional creep models, Gifkins' model predicts a creep rate that is directly proportional to the applied stress. However, the grain-size dependence is weaker than that of Nabarro—Herring creep.

The model must also explain how grains 1 and 2 slide by one another when a third grain, labeled number 3 in Fig. 16.18, intersects the other two grains at the junction called a triple point. For sliding to occur, the boundary A must move to the left and boundary B to the right. If the process of accommodation of sliding by diffusion around triple points is slower than that of ledge migration, the creep rate is controlled by sliding, not ledge migration. As a result of the applied stress, boundary A is placed in tension and boundary B in compression. Distortion of grain 3 occurs by vacancy flow from boundary A to boundary B. Transport can occur either through the interior of grain 3 or along boundary A to boundary B. In either case the analysis of the diffusional process is identical to the analyses discussed in Sec. 16.6. Gifkins' equation for the rate of grain-boundary sliding controlled by diffusion around triple points<sup>29</sup> is identical to Eq. 16.47 except for a minor difference in the numerical constant.

Langdon<sup>30</sup> has developed a grain-boundary sliding model of creep in which slippage of adjacent grains occurs by a combination of climb and glide of dislocations adjacent to the boundary. This model bears the same resemblance to the dislocation-climb creep models of Sec. 16.7 that Gifkins' grain-boundary sliding model does to the diffusional creep models reviewed in Sec. 16.6.

Assuming that the grain strain and grain-boundary creep mechanisms operate independently of each other, the total creep rate can be expressed as the sum of the rates due to each mode. Thus,

$$\dot{\epsilon} = \dot{\epsilon}_g + \dot{\epsilon}_{gbs} = \dot{\epsilon}_{diff} + \dot{\epsilon}_{dc} + \dot{\epsilon}_{gbs} \quad (16.96)$$

where the subscripts diff and dc denote diffusional creep and dislocation-climb creep, respectively. The validity of the assumption of the additivity of creep rates is discussed by Langdon.<sup>30</sup>

## 16.9 THERMAL CREEP IN OXIDE FUELS

The creep-rate data for the oxide nuclear fuels  $UO_{2+x}$  and  $(U,Pu)O_{2-x}$  are summarized in this section. The data were obtained primarily by compression creep tests on polycrystalline specimens. Only creep in the absence of radiation (thermal creep) is considered. Radiation-enhanced creep is discussed in the following section.

### 16.9.1 $UO_{2+x}$

The creep characteristics of hyperstoichiometric uranium dioxide have been studied more thoroughly than those of any other ceramic oxide. The creep rate depends on the applied stress, temperature, grain size, and the oxygen-to-uranium ratio. Since  $UO_{2-x}$  is thermodynamically stable only at temperatures above 1300°C (Chap. 11), only the effect of positive deviations from exact stoichiometry have been investigated in deformation tests. The influences of porosity and of the impurity content on the creep rate have been less extensively explored. The following summary is based largely on a recent review of this topic by Seltzer et al.<sup>31</sup> Figure 16.19 shows the stress dependence of the creep rate in stoichiometric polycrystalline  $UO_2$  obtained from three different investigations. The main feature of the creep curves is the rather clear separation between a region in which the strain rate is linearly dependent on applied stress to one characterized by power-law creep, wherein the stress exponent is between 4 and 5. The data are well represented by the discontinuous function:

$$\dot{\epsilon} = \dot{\epsilon}_{diff} = B \frac{\sigma}{d^2} \exp\left(-\frac{E_c}{kT}\right) \quad (\text{for } \sigma < \sigma_{tr}) \quad (16.97)$$

$$= \dot{\epsilon}_{dc} = B' \sigma^n \exp\left(-\frac{E_c}{kT}\right) \quad (\text{for } \sigma > \sigma_{tr}) \quad (16.98)$$

Equation 16.97 represents Nabarro—Herring diffusional creep (Eq. 16.27). The observed linear stress dependence is also exhibited by Coble's grain-boundary creep formula (Eq. 16.47) or Gifkins' grain-boundary sliding model (Eq. 16.95), but the grain-size dependence of the latter two mechanisms are  $d^{-3}$  and  $d^{-1}$ , respectively. Beyond the transition stress,  $\sigma_{tr}$ , the creep rate becomes independent of grain size and increases as the 4th or 5th power of the applied stress. These features of the creep rate are consistent with the dislocation climb—annihilation model of creep (Sec. 16.7).

In principle, the total creep rate should be expressed as the sum of  $\dot{\epsilon}_{diff}$  and  $\dot{\epsilon}_{dc}$ , but the difference in the exponents of the stress in the two models is so large that the transition region where both modes contribute more or less equally to the total creep rate is quite narrow. It is sufficient to assume that the transition occurs discontinuously at a stress  $\sigma_{tr}$ . Assuming that the activation energy for creep is the same for both the high- and low-stress mechanism, Eqs. 16.97 and 16.98 can be equated at  $\sigma_{tr}$

$$B \frac{\sigma_{tr}}{d^2} = B' \sigma_{tr}^n$$

or

$$\sigma_{tr} \propto d^{-[2/(n-1)]} \quad (16.99)$$

This formula predicts that the transition stress should be temperature independent and vary with the grain size according to a power between  $-0.67$  and  $-0.5$ , which correspond to  $n$  values of 4 and 5, respectively. The creep data in the last two panels of Fig. 16.19 confirm the expected absence of a temperature dependence of the transition stress. The slight variation of  $\sigma_{tr}$  with tempera-

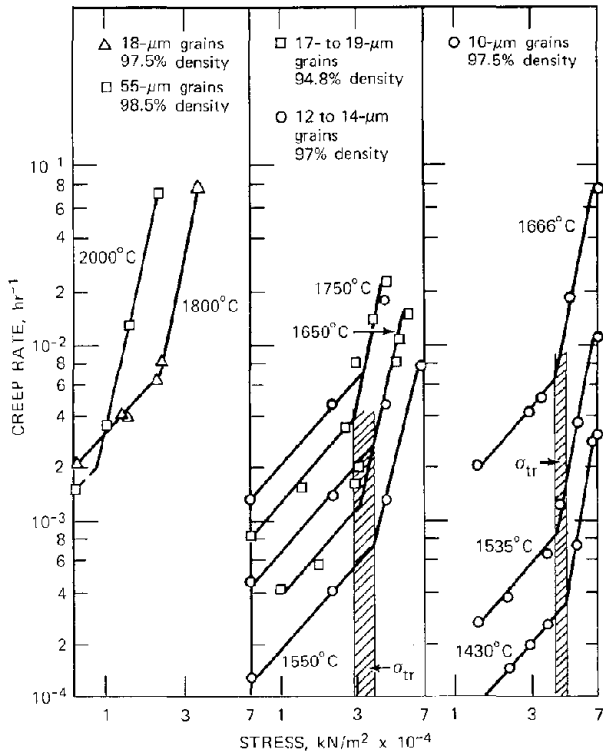


Fig. 16.19 Creep rate vs. stress for stoichiometric  $\text{UO}_2$  tested in compression. The shaded areas in the second and third panels show the range of transition stresses for the range of temperatures at which the tests were conducted. (From Ref. 31.)

ture seen in the data can be due to the temperature dependence of the shear modulus  $G$ , which appears raised to the 3.5 power in the dislocation climb-annihilation creep model. Hence  $B'$  of Eq. 16.98 contains this additional temperature-dependent factor.<sup>32</sup> Figure 16.20 shows the experimental transition stress plotted as a function of grain size. The slope of the line is  $-0.61$ , which is in very good agreement with the value expected for Nabarro-Herring and dislocation climb-annihilation creep in the low- and high-stress regions, respectively. The identification of the low-stress creep mechanism is further substantiated by the

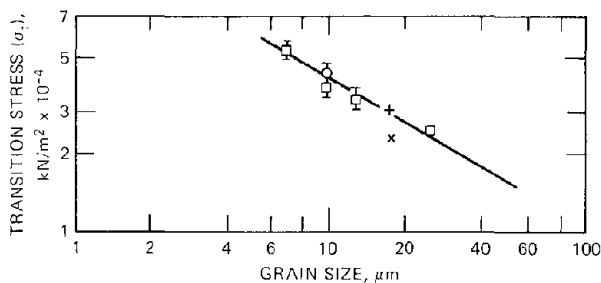


Fig. 16.20 Stresses at which a change in creep mechanism occurs for compressive creep of  $\text{UO}_2$  specimens of various grain sizes. (From Ref. 31.)

grain-size dependence of the creep rate shown in Fig. 16.21. The variation of  $\dot{\epsilon}$  with the inverse square of the grain size supports the assignment of Nabarro-Herring creep as the predominant deformation mode for  $\sigma < \sigma_{tr}$ .

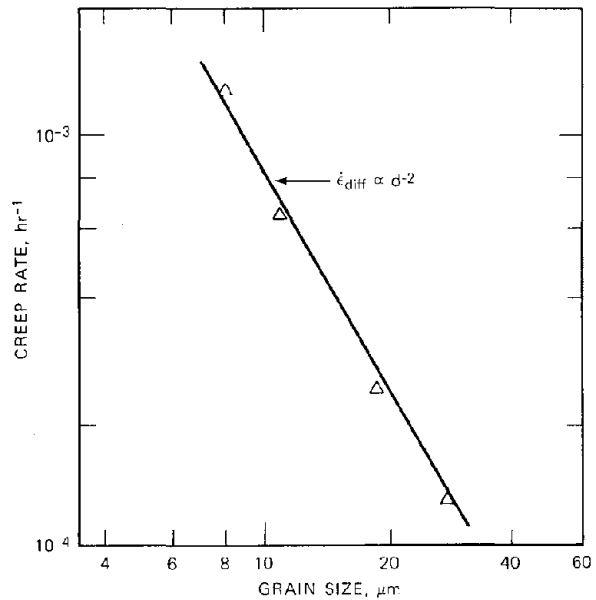


Fig. 16.21 Creep rate as a function of grain size for  $\text{UO}_2$  tested in low stress compression,  $1650^\circ\text{C}$ ,  $7000 \text{ kN/m}^2$ . (After Ref. 31.)

The effect of the composition variable oxygen/metal ratio (O/M) on the creep rate is shown in Fig. 16.22. Regions of diffusional and dislocation-climb creep are still evident at high and low stresses, but the transition is not as sharp as in the data obtained using stoichiometric  $\text{UO}_2$  (Fig. 16.19). Increasing the oxygen-to-metal ratio dramatically increases the creep rate at a fixed temperature and stress level. Stoichiometry changes are reflected in both the coefficients  $B$  and  $B'$  of Eqs. 16.97 and 16.98 and in the activation energy  $E_c$ . At low stresses the composition dependence of the creep rate is given by

$$\dot{\epsilon}_{\text{diff}} \propto \frac{\sigma x}{d^2} \exp\left[-\frac{E_c(x)}{kT}\right] \quad (\sigma < \sigma_{tr}) \quad (16.100)$$

and at high stresses by

$$\dot{\epsilon}_{\text{d.c.}} \propto \sigma^n x^2 \exp\left[-\frac{E_c(x)}{kT}\right] \quad (\sigma > \sigma_{tr}) \quad (16.101)$$

where  $x$  is the stoichiometry parameter in  $\text{UO}_{2+x}$ .

Figure 16.23 shows the composition dependence of the creep activation energy  $E_c(x)$ . In the high-stress region, the activation energy decreases from 565 kJ/mole for nearly stoichiometric  $\text{UO}_2$  to  $\sim 230$  kJ/mole for highly hyperstoichiometric material. In the low-stress region, the corresponding decrease is from 380 kJ/mole to  $\sim 210$  kJ/mole. The  $E_c$  appears to have attained limiting values for  $x \rightarrow 0$  and  $x \rightarrow \text{large}$ . The curves of Fig. 16.23 can be qualitatively explained by considering the composition dependence of

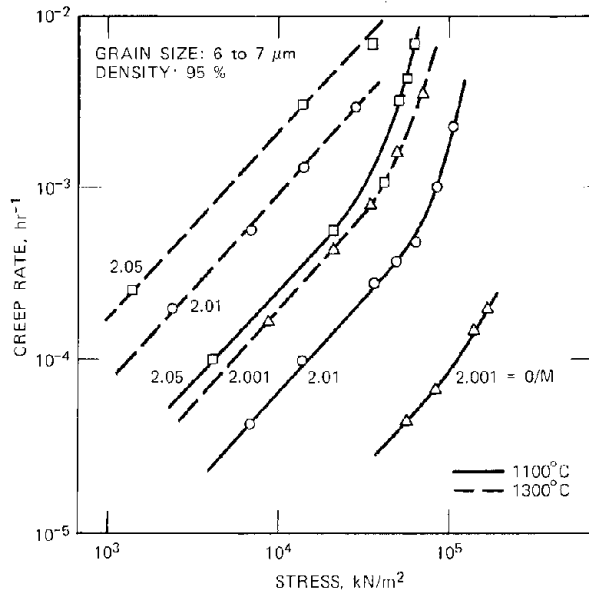


Fig. 16.22 Steady-state creep rate vs. applied stress for polycrystalline  $UO_{2+x}$  tested in compression at 1100 and 1300°C. —, 1100°C. ---, 1300°C. (From Ref. 31.)

the volume self-diffusion coefficient, which appears in both diffusional-creep and dislocation-climb creep models.

In a monatomic solid, there is no ambiguity in the meaning of this transport property, but, in a binary ionic crystal, the two species generally exhibit different self-diffusivities. Since creep results solely in distortion of the solid but does not produce a separation of the constituent atoms, we conclude that the two species are transported in the same ratio as the bulk composition. That is, for every atom of uranium that moves from one point of a grain to another during deformation of  $UO_{2+x}$ ,  $2+x$  atoms of oxygen follow the same path. The rate of deformation, however, is governed by the slowest moving species, which in the case of uranium oxide is the  $U^{4+}$  ion. The  $O^{2-}$  ions merely tag along with each diffusing  $U^{4+}$  ion but do not affect the kinetics of the process. Therefore,  $D_{vO1}$  is to be interpreted as the self-diffusion coefficient of the  $U^{4+}$  in the solid.

The dependence of the uranium self-diffusion coefficient on the oxygen-to-uranium ratio has been considered by Lidiard<sup>33</sup> and Matzke,<sup>34</sup> whose analyses are summarized here (see also problem 6.8 of Chap. 6 and problem 7.1 of Chap. 7 for related calculations). The right-hand side of Eq. 16.23, which relates the volume self-diffusion coefficient to the concentration and diffusion coefficient of vacancies in the crystal, pertains to the  $U^{4+}$  ion. For uranium oxides, then, the volume self-diffusion coefficient appropriate to creep is

$$D_{vO1} = D_{vU} x_{vU} \quad (16.102)$$

where  $D_{vU}$  is the diffusion coefficient of vacancies on the uranium sublattice of the fluorite structure and  $x_{vU}$  is the fraction of the sites on the uranium sublattice which are unoccupied. The cation sublattice in the fluorite structure is face-centered cubic [Fig. 3.12(b)], and the vacancy

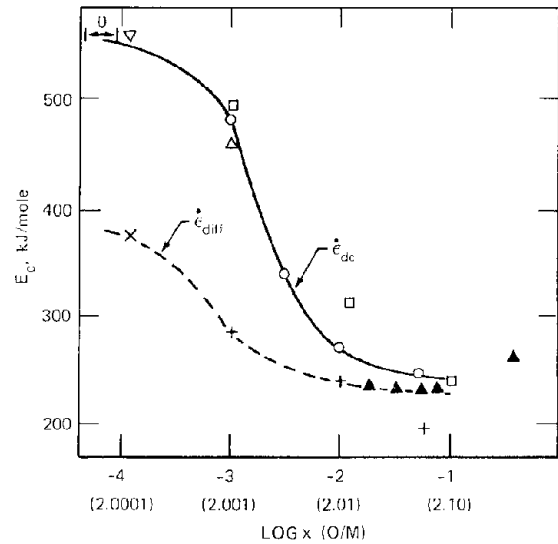


Fig. 16.23 Activation energies for compression creep of  $UO_{2+x}$  ○, single crystals. □, polycrystals, 27- $\mu$ m grains, enriched. +,  $\Delta$ , polycrystals, 7- $\mu$ m grains. ×,  $\nabla$ , polycrystals, 4- to 35- $\mu$ m grains.  $\blacktriangle$ , polycrystals, 6- $\mu$ m grains, in bending.

diffusion coefficient for this lattice type is given by Eq. 7.29, wherein the jump frequency is given by Eq. 7.41. Therefore,

$$D_{vU} = \nu_U a_o^2 \exp\left(\frac{s_U^*}{k}\right) \exp\left(-\frac{\epsilon_U^*}{kT}\right) \quad (16.103)$$

where  $a_o$  = lattice constant

$\nu_U$  = vibration frequency of a uranium ion in its lattice site

$s_U^*$  = entropy of motion of a uranium ion for jumping into an adjacent vacancy on the cation sublattice

$\epsilon_U^*$  = entropy of motion of a uranium ion for jumping into an adjacent vacancy on the cation sublattice

The uranium vacancy fraction  $x_{vU}$  is related to the fraction of the vacant sites on the oxygen sublattice  $x_{vO}$  by the law of mass action governing the Schottky equilibrium (Eq. 6.34):

$$x_{vU} = \frac{K_s}{x_{vO}^2} \quad (16.104)$$

where  $K_s = \exp(-\epsilon_s/kT)$  is the equilibrium constant for Schottky defects in  $UO_2$  and  $\epsilon_s$  is the formation energy of the Schottky defect. Although vacancies on the uranium sublattice are generated by the Schottky equilibrium, the predominant point-defect disorder in  $UO_2$  consists of oxygen-ion vacancies and interstitials. The concentrations of these defects are governed by the Frenkel defect equilibrium constant (Eq. 6.37):

$$K_{FO} = \exp\left(-\frac{\epsilon_{FO}}{kT}\right) = x_{vO} x_{iO} \quad (16.105)$$

where  $\epsilon_{FO}$  is the energy of formation of an anion Frenkel defect pair,  $x_{vO}$  is the fraction of the anion sites that are

vacant, and  $x_{iO}$  is the fraction of the oxygen interstitial sites in the fluorite structure which are occupied by interstitial oxygen ions.

An additional relation between  $x_{vO}$  and  $x_{iO}$  can be obtained from the requirement of electroneutrality of the crystal (Sec. 6.6). However, because  $K_S$  is small compared to  $K_{FO}$  in  $UO_2$ , the uranium sublattice can be considered to be completely filled, and the uranium interstitials can be neglected in the charge balance. The additional relation between  $x_{vO}$  and  $x_{iO}$  can be obtained directly in terms of the stoichiometric parameter  $x$  in  $UO_{2+x}$  by the following method. Consider a volume of crystal that contains  $N_U$  uranium atoms, some of which are in valence states higher than 4+ because of the oxygen excess (Chap. 11). Because the uranium sublattice is nearly perfect,  $N_U$  is equal to  $N_{sO}/2$ , where  $N_{sO}$  is the number of anion sublattice sites in the region of crystal under consideration. Not all the anion lattice sites need be filled, however. Let  $N_O$  and  $N_{iO}$  be the numbers of oxygen ions on normal lattice sites and in interstitial positions, respectively. The oxygen-to-uranium ratio can be written as

$$\frac{O}{U} = \frac{N_O + N_{iO}}{N_U} = 2 \left( \frac{N_O + N_{iO}}{N_{sO}} \right) = 2 + x \quad (16.106)$$

Assuming that the number of interstitial sites available for oxygen interstitials is equal to the number of normal anion sites ( $N_{sO}$ ), the oxygen defect fractions are

$$\begin{aligned} x_{vO} &= \frac{N_{sO} - N_O}{N_{sO}} \\ x_{iO} &= \frac{N_{iO}}{N_{sO}} \end{aligned} \quad (16.107)$$

and Eq. 16.106 becomes

$$x = 2(x_{iO} - x_{vO}) \quad (16.108)$$

Eliminating  $x_{iO}$  between Eqs. 16.105 and 16.108 yields

$$x_{vO} = \frac{1}{4} x \left[ \left( 1 + \frac{16K_{FO}}{x^2} \right)^{1/2} - 1 \right] \quad (16.109)$$

As exact stoichiometry is approached, Eq. 16.109 reduces to

$$x_{vO} \rightarrow (K_{FO})^{1/2} \quad (\text{as } x \rightarrow 0) \quad (16.110)$$

In the opposite limit approximated by highly hyperstoichiometric urania

$$x_{vO} \rightarrow \frac{2K_{FO}}{x} \quad (\text{as } x \rightarrow \text{large}) \quad (16.111)$$

For the same limiting situations, the uranium vacancy concentration is found from Eq. 16.104 to be

$$x_{vU} \rightarrow \frac{K_S}{K_{FO}} \quad (\text{as } x \rightarrow 0) \quad (16.112)$$

$$x_{vU} \rightarrow \frac{1}{4} \frac{K_S}{K_{FO}^2} x^2 \quad (\text{as } x \rightarrow \text{large}) \quad (16.113)$$

Substituting Eqs. 16.112 and 16.113 into Eq. 16.102 and expressing the vacancy diffusion coefficient by Eq. 16.103

yields the theoretical variation of  $D_{vO1}$  with solid composition. Since the creep rate in the linear stress region is proportional to  $D_{vO1}$ , we have

$$\dot{\epsilon}_{diff} \propto \frac{\sigma}{d^2} \exp \left( - \frac{\epsilon_U^* + \epsilon_S - \epsilon_{FO}}{kT} \right) \quad (\text{for } x \rightarrow 0) \quad (16.114)$$

and

$$\dot{\epsilon}_{diff} \propto \frac{\sigma x^2}{d^2} \exp \left( - \frac{\epsilon_U^* + \epsilon_S - 2\epsilon_{FO}}{kT} \right) \quad (\text{for } x \rightarrow \text{large}) \quad (16.115)$$

According to these equations, the difference between the limiting values of the activation energies on the dashed curve of Fig. 16.23 should represent the formation energy of oxygen-ion Frenkel defects. The observed difference ( $\sim 170$  kJ/mole) is quite a bit less than the value of  $\epsilon_{FO}$  deduced from measurements of the heat capacity of  $UO_2$  (about 290 kJ/mole, Ref. 34a), but the trend of  $E_c$  with  $x$  is correctly predicted by the vacancy diffusion theory.

The experimental creep rates at low stresses (Eq. 16.100) were best fitted by a linear dependence on  $x$ , which is intermediate between the limiting cases shown in the preceding formulas. The creep experiments on which Eq. 16.100 is based may have been conducted at stoichiometries that were between the limiting cases treated theoretically, or diffusional creep may be due to a mixture of the Nabarro-Herring and Coble's mechanisms. Coble's mechanism contains the grain-boundary self-diffusion coefficient, which would not be expected to respond to composition changes in the same manner as does the volume self-diffusion coefficient. However, were this the case, the grain-size dependence would be expected to be somewhat larger than  $d^2$ .

The theoretical effect of composition on creep in the power-law stress regions is

$$\dot{\epsilon}_{dc} \propto \sigma^n \exp \left( - \frac{\epsilon_U^* + \epsilon_S - \epsilon_{FO} + E_{jog}}{kT} \right) \quad (\text{for } x \rightarrow 0) \quad (16.116)$$

and

$$\dot{\epsilon}_{dc} \propto \sigma^n x^2 \exp \left( - \frac{\epsilon_U^* + \epsilon_S - 2\epsilon_{FO} + E_{jog}}{kT} \right) \quad (\text{for } x \rightarrow \text{large}) \quad (16.117)$$

where it has been assumed that the climb velocity is controlled by the equilibrium concentration of jogs. Comparison of Eqs. 16.114 and 16.116 with the data on Fig. 16.23 suggests that the difference between the creep-activation energies in the low- and high-stress regions for nearly exact stoichiometry represents the energy of formation of jogs on edge dislocations in  $UO_2$ . The observed difference of  $\sim 190$  kJ/mole ( $\sim 1.6$  eV) is in reasonable agreement with the estimated jog formation energies determined in Sec. 16.7, but the difference can also be due to the presence of other creep mechanisms at high stresses. The activation energy for power-law creep approaches that of low-stress creep as  $x$  becomes large (Fig. 16.23). This

behavior can be due to saturation of the vacancy concentration along the entire length of the climbing dislocations, which removes  $E_{jog}$  from the creep-activation energy (Sec. 16.7). The preexponential factor for high-strain creep, however, follows the  $x^2$  variation predicted by the theory for highly hyperstoichiometric material.

### 16.9.2 Mixed Oxides

Quantitative knowledge of the creep properties of the mixed uranium-plutonium oxides  $(U,Pu)O_{2-x}$  is of considerable practical importance in predicting the mechanical behavior of fast reactor fuel pins. Although investigation of the mechanical properties of this material has only recently begun, preliminary creep data have been reported by several laboratories.<sup>35-37</sup>

In common with the results of the more extensive studies of  $UO_2$ , creep in the mixed oxide is satisfactorily represented by a diffusional creep regime at low stress which gives way to power-law creep at high stress. The creep-activation energies are of the same order of magnitude as those in  $UO_{2+x}$  although the variation of  $E_c$  with stoichiometry (hypostoichiometry in this case) has not been thoroughly explored for the mixed oxides.

The stoichiometric mixed oxides are weaker (i.e., they exhibit higher creep rates) than  $UO_{2.00}$  under the same conditions of applied stress, temperature, grain size, and porosity. However, the creep strength of the mixed oxide is significantly improved as the oxygen-to-metal ratio is reduced; the creep rate of  $(U,Pu)O_{2.00}$  is about an order of magnitude larger than that of  $(U,Pu)O_{1.95}$ .

The effect of porosity on the creep properties of the mixed oxide is of importance since the design specifications of fast reactor fuel call for material of less than 90% of theoretical density. The creep rate is reduced by about a factor of 5 as the density is decreased from 96% of the theoretical value to ~88% of the theoretical value.

## 16.10 IRRADIATION CREEP IN OXIDE FUELS

In thermal creep, deformation is due to the flow of vacancies between sources and sinks (grain boundaries or climbing dislocations) where the equilibrium vacancy concentration  $C_v^{eq}$  is perturbed by application of a stress by a factor  $\exp(\pm\sigma\Omega/kT)$ . In both diffusional creep and dislocation-climb creep, interstitials are neglected because their equilibrium concentration is many orders of magnitude lower than that of the vacancies (Fig. 13.17), and no point defects are produced in the matrix of the solid between the sources and sinks. In a radiation field, neither of these restrictions is valid; in fuel materials vacancies and interstitials are produced equally at a rate  $Y_{vi}\bar{F}$ , where  $Y_{vi}$  is the number of Frenkel pairs created by a single fission event.\*

\*Although vacancies and interstitials are produced in equal numbers by fission, the number of each type of defect available for migration to sinks, such as grain boundaries, dislocations, or (in metals) voids, may not be equal. Vacancies can be immobilized in a depleted zone close to the fission track whereas interstitials can be shot far from the fission track in the form of "dynamic crowdions" (Chap. 17).

Point defects are created by radiation uniformly throughout the solid; so the diffusion equation must contain a volumetric source term to account for this additional entry in the statement of vacancy conservation. Moreover, since interstitials are also present in significant quantities, a recombination term also needs to be added. Since radiation produces both types of point defects at equal rates and leads to concentrations far in excess of thermal equilibrium values, the contribution of interstitial migration to the sinks can no longer be neglected.

The effect of radiation-produced point defects on the rate of diffusion-controlled creep processes (which includes both Nabarro-Herring and dislocation-climb creep) has generated a roaring controversy in the literature. The dispute began with Schoeck's statement<sup>38</sup> that, since all diffusional-creep models contain the volume self-diffusion coefficient and since this property is directly proportional to the vacancy concentration (Eq. 7.28), the creep rate should be enhanced by the increased vacancy concentration resulting from irradiation. Mosedale<sup>39</sup> and Hesketh<sup>40</sup> have insisted that Schoeck and his successors are wrong, claiming that it is the diffusion coefficient of the vacancies, not the volume self-diffusion coefficient, which governs the creep rate. In the final creep formula,  $D_v$  appears multiplied by  $C_v^{eq}$ , and, although the product  $D_v C_v^{eq} \Omega$  is the volume self-diffusion coefficient, the term  $C_v^{eq}$  arises from the boundary conditions to the vacancy diffusion equation, which are of the form  $C_v^{eq} \exp(\pm\sigma\Omega/kT)$ . The  $C_v^{eq}$  term does not represent a bulk vacancy concentration in the stressed solid. Since the boundary conditions that are responsible for injecting  $C_v^{eq}$  into the creep formulas are not affected by radiation (assuming that dislocations and grain boundaries are perfect sources or sinks that always maintain the equilibrium point-defect concentration appropriate to the applied stress whether or not the solid is irradiated), there is no justification for simply replacing  $C_v^{eq}$  in the creep formulas by the bulk concentration of vacancies generated by irradiation.

This argument appears quite convincing, and indeed it is when applied to Nabarro-Herring creep, but Piercy,<sup>41</sup> Lewthwaite,<sup>42</sup> and Nichols<sup>43</sup> have shown that dislocation-climb creep can be accelerated by irradiation provided that the climbing dislocations absorb more interstitials than vacancies. The preference of dislocations for interstitials is well established in metals (see Sec. 13.9); the phenomenon of void growth in neutron-irradiated metals is a manifestation of the need to find a sink for the excess vacancies resulting from the dislocation preference for interstitials. In fuel materials which are ceramic rather than metallic and in which point defects are produced by fission fragments instead of fast neutrons, void growth of the type observed in metals has not been observed; either the voids are unstable in the highly disruptive environment of a fission fragment flux (we have seen that gas-filled bubbles have a difficult time surviving), or else the myriad of other phenomena affecting the fuel mask any void formation. Nevertheless, the arguments suggesting a preference of dislocations for interstitials are rather general, and it is not unreasonable to assume that the effect of radiation on dislocation-climb creep applies to fissile ceramics as well as to metals.

In this section we restrict attention to the effect of radiation on diffusional creep, specifically Nabarro—Herring creep. The few in-pile creep experiments using  $\text{UO}_2$  or  $(\text{U,Pu})\text{O}_2$  have been performed at low stresses where the creep rate is linearly dependent on applied stress. The effect of radiation on dislocation-climb-controlled creep (power-law creep), which is the subject of Refs. 38 to 43, will be discussed in Chap. 19.

### 16.10.1 The Effect of Radiation on Nabarro—Herring Creep

To demonstrate the existence or nonexistence of a radiation effect on creep which occurs by virtue of different normal stresses acting on various parts of a grain boundary, we adopt the hypothetical one-dimensional geometry shown in Fig. 16.24. The upper face of the grain

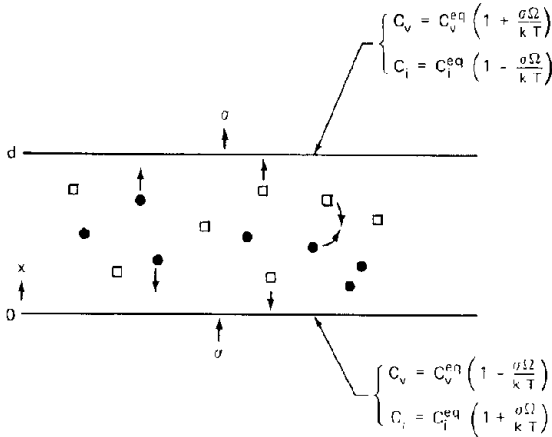


Fig. 16.24 Nabarro—Herring creep in the presence of point defects produced by radiation. □, radiation-produced vacancy. ●, radiation-produced interstitials.

is subject to a tensile stress and the lower face to a compressive stress of the same magnitude as the tensile stress. Although the slab as drawn in the figure is subject to a net force and is therefore not mechanically stable, the mathematics of the problem is very much simpler than that for a spherical grain (Sec. 16.6), and the results are not significantly different.

In common with the thermal-creep analysis of the Nabarro—Herring model, we assume that the grain boundaries are the only source or sink for vacancies, or that there are no dislocations within the grain. The diffusion equation for vacancies in the grain is

$$D_v \frac{d^2 C_v}{dx^2} = -Y_{v1} \dot{\epsilon} + k_{v1} C_v C_i \quad (16.118)$$

and for the interstitials

$$D_i \frac{d^2 C_i}{dx^2} = -Y_{i1} \dot{\epsilon} + k_{i1} C_v C_i \quad (16.119)$$

The last term in each of these equations represents loss due to vacancy—interstitial recombination, for which  $k_{vi}$  is the rate constant. Subtraction of Eq. 16.119 from 16.118 removes the source and sink terms and leaves the equation

$$\frac{d^2}{dx^2} (D_v C_v - D_i C_i) = 0$$

which can be integrated to yield

$$D_v C_v - D_i C_i = Ax + B \quad (16.120)$$

The integration constants A and B can be obtained by using the boundary conditions shown on Fig. 16.24, which assume that the equilibrium point-defect concentrations are maintained at  $x = 0$  and  $x = d$ .

The creep rate is given by

$$\dot{\epsilon} = -\frac{J\Omega}{d} \quad (16.121)$$

where J is the difference between the flux of vacancies and interstitials at either boundary,

$$J = -D_v \frac{dC_v}{dx} + D_i \frac{dC_i}{dx}$$

Using Eq. 16.120, we see that  $J = -A$ , which can be obtained by application of the boundary conditions. Insertion of J into the creep rate of Eq. 16.121 yields

$$\dot{\epsilon} = \frac{2\Omega(D_v C_v^{eq} + D_i C_i^{eq})}{d^2} \frac{\sigma\Omega}{kT} \quad (16.122)$$

In most systems  $D_i$  is larger than  $D_v$  (Sec. 13.3), but  $C_i^{eq}$  is very much smaller than  $C_v^{eq}$  (Fig. 13.7); so  $D_v C_v^{eq} \gg D_i C_i^{eq}$ , and Eq. 16.122 becomes

$$\dot{\epsilon} = \frac{2(D_v C_v^{eq} \Omega)}{d^2} \frac{\sigma\Omega}{kT} \quad (16.123)$$

The term in the parentheses in this formula is the volume self-diffusion coefficient in the absence of radiation; so, except for the numerical constant, Eq. 16.123 is identical to Eq. 16.25. Radiation, therefore, has no effect on the creep rate in the Nabarro—Herring model. The physical reason for this negative result is that the excess point defects produced in the grain by radiation are either annihilated there or flow equally to the grain boundaries. When the flux of vacancies and the flux of interstitials are equal, the boundary does not move. Only the small difference between the equilibrium concentrations of vacancies at the boundary causes creep.

### 16.10.2 Creep Enhancement by Thermal Spikes Due to Fission Fragments

Although the additional defects produced by radiation do not enhance the Nabarro—Herring creep rate, Brucklacher, Dienst, and Thummler<sup>4,4</sup> have proposed a mech-

anism whereby the transient pulses of heat liberated by the slowing down of fission fragments accelerate creep. The transient heating of the lattice in the immediate vicinity of a fission track is known as a *thermal spike*. It extends roughly the length of the fission track. The temperature profile created by the heat released as the fission fragment loses energy is symmetric about the axis of the spike. The temperature transient can be calculated from the known energy per unit track length deposited by the fragment and the heat-transport properties of the solid. Although the duration of the spike is very short ( $\sim 10^{-10}$  sec) and use of ordinary macroscopic properties of the solid (such as its thermal conductivity) may not be quite adequate to describe energy transport, treatment of the problem as one of transient-heat conduction provides at least a qualitative description of the phenomenon.

If the initial energy of the fission fragment is  $Q_{fiss}$  and the track length is  $\mu_{ff}$ , the energy released (as heat) per unit length of track is  $Q_{fiss}/\mu_{ff}$ . Solution of the heat-conduction equation for an instantaneous line source of heat of this magnitude yields the following temperature profile:<sup>45</sup>

$$T(r,t) = \frac{Q_{fiss}/\mu_{ff}}{4\pi k_s t} \exp\left(-\frac{r^2}{4\alpha t}\right) \quad (16.124)$$

The initial solid temperature and the temperature far from the spike are assumed to be zero. The quantity  $k_s$  is the thermal conductivity of the solid and  $\alpha = k_s/\rho_s C_p$  is the thermal diffusivity, where  $\rho_s$  and  $C_p$  are the density and heat capacity of the solid, respectively. Temperatures at various times and positions during a thermal spike are shown in Fig. 16.25. Although the thermal transient is quickly quenched by conduction to the bulk solid, if enough thermal spikes occur, the resulting temperature pulses can appreciably affect the vacancy diffusion coefficient, which varies exponentially with temperature.

The effect of spherical thermal spikes on the rates of activated processes in the solid has been considered by Seitz

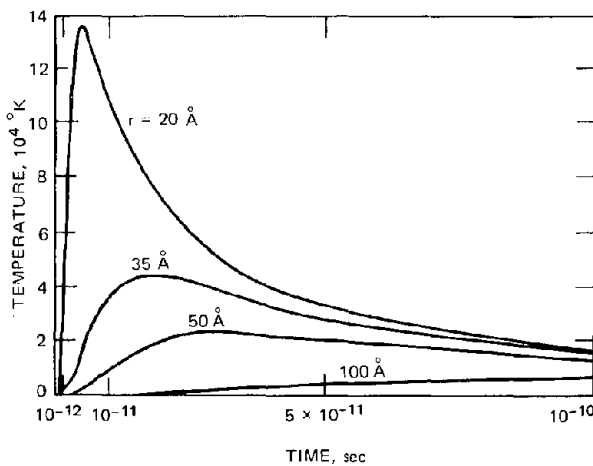


Fig. 16.25 Typical temperatures in a cylindrical thermal spike. (From L. T. Chadderton, *Radiation Damage in Crystals*, Methuen & Company, Ltd., London, 1965.)

and Koehler.<sup>46</sup> Here we extend their analysis to cylindrical geometry.

The vacancy diffusion coefficient is approximately given by

$$D_v = a_o^2 w \quad (16.125)$$

where  $a_o$  is the lattice constant and

$$w = \nu_v \exp\left(-\frac{\epsilon_v^*}{kT}\right) \quad (16.126)$$

is the jump frequency of a vacancy in particular direction. The term  $\nu_v$  is the vacancy vibration frequency, and  $\epsilon_v^*$  is the energy of motion of a vacancy.

Consider a volume  $V$  of the crystal in which the vacancy concentration is  $C_v$ . If the jump frequency at the ambient solid temperature  $T_0$  is denoted by  $w_0$ , the number of vacancy jumps occurring in the volume  $V$  in a time interval  $\Delta t$  is  $VC_v w_0 \Delta t$ . Now consider the incremental number of vacancy jumps that occur when one fission fragment slows down within the volume  $V$  in the time interval  $\Delta t$ . The number of vacancy jumps that occur in this case is

$$C_v \int_V dV \int_0^{\Delta t} dt w(r,t)$$

where  $w(r,t)$  is the jump frequency during the temperature transient, obtained by substitution of Eq. 16.124 into 16.126. The additional jumps produced by a single fission track are obtained by subtracting  $VC_v w_0 \Delta t$  from the preceding expression, or

$$\Delta j_{sp} = C_v \int_V dV \int_0^{\Delta t} dt [w(r,t) - w_0]$$

If the volume  $V$  is large compared to the volume of the fission track and  $\Delta t$  is long compared to the duration of the temperature transient, the upper limits on the spatial and time integrals can be replaced by infinity since  $w$  returns to  $w_0$  well before the actual boundaries are reached. Thus the additional vacancy jumps per spike are

$$\Delta j_{sp} = 2\pi C_v \nu_v \mu_{ff} \int_0^\infty r dr \int_0^\infty dt \times \left\{ \exp\left[-\frac{\epsilon_v^*}{kT(r,t)}\right] - \exp\left(-\frac{\epsilon_v^*}{kT_0}\right) \right\} \quad (16.127)$$

If the fission rate is  $\dot{F}$  fissions  $\text{cm}^{-3} \text{sec}^{-1}$ , the number of thermal spikes occurring in the volume  $V$  in time  $\Delta t$  is  $V(2\dot{F}) \Delta t$ . Multiplying the number of spikes by the incremental vacancy jumps per spike and adding this quantity to the number of vacancy jumps that would have occurred by thermal fluctuations alone gives the total number of jumps,

$$\text{Total jumps} = V \Delta t (C_v w_0 + 2\dot{F} \Delta j_{sp})$$

or, the average vacancy-jump frequency is

$$w = \frac{\text{total jumps}}{VC_v \Delta t} = w_0 + \frac{2\dot{F} \Delta j_{sp}}{C_v}$$

Multiplying the preceding jump frequency by  $a_0^2$  gives the vacancy diffusion coefficient (Eq. 16.125),

$$D_v^* = D_v + 4\pi \dot{F} \nu_v \mu_{ff} a_0^2 \int_0^\infty r dr \int_0^\infty dt \exp\left(-\frac{e_v^*}{kT}\right) \quad (16.128)$$

where the last term in Eq. 16.127 has been neglected on the grounds that  $T_0$  is much less than the temperature attained during the spike.

The thermal-spike enhancement of the vacancy diffusion coefficient can be computed by integration of Eq. 16.128 using the temperature function given by Eq. 16.124. Following Seitz and Koehler<sup>46</sup> this formula is simplified to

$$T(r,t) = \frac{Q_{fiss}/\mu_{ff}}{4\pi k_s t} \quad (\text{for } t > r^2/4\alpha) \\ = 0 \quad (\text{for } t < r^2/4\alpha) \quad (16.129)$$

The double integral of Eq. 16.128 is readily performed when the temperature is described by Eq. 16.129. The spike-enhanced vacancy diffusion coefficient is

$$D_v^* = D_v + \frac{\dot{F} \nu_v a_0^2 k^2}{2\pi k_s \rho_s C_p \mu_{ff}} \frac{Q_{fiss}}{e_v^*} \quad (16.130)$$

For a solid well above its Debye temperature,  $\rho_s C_p = 3k/a_0^3$  where  $a_0^3$  is the atomic volume. Finally, the spike-enhanced diffusion coefficient becomes

$$D_v^* = D_v \left[ 1 + \frac{\dot{F} a_0^3 k}{6\pi k_s \mu_{ff}} \left( \frac{Q_{fiss}}{e_v^*} \right)^2 \exp\left(\frac{e_v^*}{kT}\right) \right] \quad (16.131)$$

The enhancement of the vacancy diffusion coefficient, and hence of the Nabarro-Herring creep rate, is given by the second term in the brackets, which we evaluate for the following numerical values:

$$\begin{aligned} \dot{F} &= 10^{13} \text{ fissions cm}^{-3} \text{ sec}^{-1} \\ a_0^3 &= 4.1 \times 10^{-23} \text{ cm}^3 \\ k &= 1.38 \times 10^{-23} \text{ W-sec/}^\circ\text{C} \\ k_s &= 0.028 \text{ W cm}^{-1} \text{ }^\circ\text{C}^{-1} \\ \mu_{ff} &= 10^{-3} \text{ cm} \\ Q_{fiss} &= 70 \text{ MeV} \\ e_v^* &= 1 \text{ eV} \\ T_0 &= 1000^\circ\text{K} \end{aligned}$$

Using the preceding values, the second term in the brackets of Eq. 16.131 is  $\sim 10^{-8}$ , which is totally negligible compared to unity. Thus, the thermal-spike mechanism as treated by Seitz and Koehler<sup>46</sup> is unable to enhance the vacancy diffusion coefficient by an amount sufficient to affect the creep rate. Brucklacher, Dienst, and Thummler<sup>44</sup> obtain a much higher enhancement by assuming the cylindrical region affected by the thermal spike to be transformed into a liquid with a much larger diffusion coefficient than that of the solid at the average temperature.

### 16.10.3 Creep of Fissile Oxides Under Irradiation

The creep of  $\text{UO}_2$  under reactor irradiation has been measured by three-point bend tests, compression of disks of fuel, and compressive and tensile tests of helical springs of the ceramic. The apparatus suitable for the last two types of creep tests is shown in Fig. 16.26. The capsule is designed to permit insertion into a reactor. Creep testing of  $\text{UO}_2$  in devices of this sort has been limited to stresses lower than the transition stress between diffusional and dislocation-climb creep (Fig. 16.19); so only the effect of radiation on the linear creep rate region has been explored.

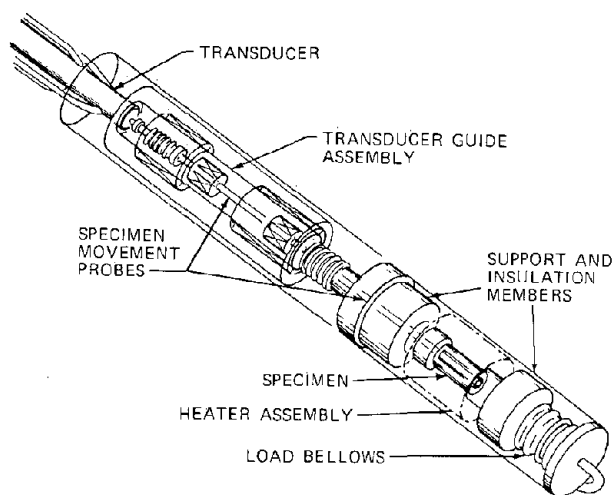


Fig. 16.26 Schematic diagram of an in-pile creep apparatus for use with oxide fuel specimens. (From J. S. Perrin and W. R. D. Wilson, *Effect of Irradiation on the Creep of Uranium Dioxide*, USAEC Report BMI-1899, Battelle Memorial Institute, 1971.)

The creep rates were found to be proportional to both the applied stress and to the fission rate. Figure 16.27 summarizes the data of various investigators, whose results have been normalized to standard stress and radiation conditions using the linear behavior mentioned previously. The effect of radiation on the creep rate is twofold.<sup>47</sup> At high temperatures the creep rate is greater than that observed in the absence of radiation but exhibits the same temperature dependence. This phenomenon is termed *fission-enhanced creep*. As shown in the beginning of this section, it is difficult to rationalize radiation acceleration as diffusional creep, but the thermal-spike model of Brucklacher, Dienst, and Thummler<sup>44</sup> is an attempt at such an explanation. Nonetheless, the effect of radiation on high-temperature low-stress creep is to increase the creep rate by approximately a factor of 4.

At low temperatures, where thermal creep is negligible, a temperature-independent (or "athermal") component of creep is observed. This form of creep, which is solely due to the radiation field, is called *fission-induced creep*. Fission-induced creep is represented by the broad band at low

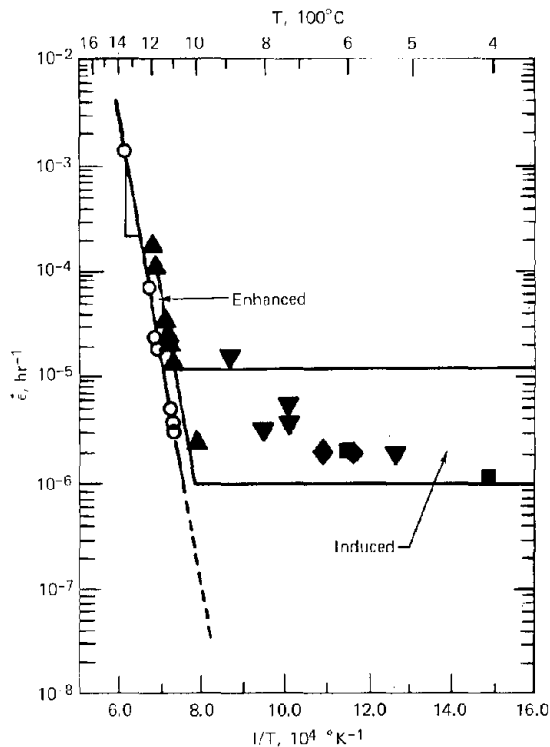


Fig. 16.27 Composite in-pile creep for  $\text{UO}_2$  normalized to  $\sigma = 2.4 \times 10^4 \text{ kN/m}^2$  and  $\dot{F} = 1.2 \times 10^{13} \text{ fissions cm}^{-3} \text{ sec}^{-1}$ . (From Ref. 47.)

temperatures in Fig. 16.27. Because of the scatter of the data, the rate of fission-induced creep is known only to within an order of magnitude. No model of fission-induced creep in ceramics has been proposed, although several explanations of the analogous phenomenon in metals have been offered.

Results similar to those shown for  $\text{UO}_2$  in Fig. 16.27 have been reported for mixed-oxide fuel.<sup>4,8</sup> Creep in fissile ceramic oxides can be represented by

$$\dot{\epsilon} = K(1 + B\dot{F}) \frac{\sigma}{d^2} \exp\left(-\frac{E}{kT}\right) + K'\sigma\dot{F} \quad (16.132)$$

where  $K$ ,  $K'$ , and  $B$  are experimentally determined constants and  $E$  is the activation energy for Nabarro-Herring thermal creep. At stresses above the transition stress, an additional term representing power-law creep would have to be added to Eq. 16.132 (or, such a term would replace the diffusional-creep term). It is not known whether high-stress thermal creep is enhanced by fission, although it probably is because power-law creep in metals is accelerated by fast-neutron irradiation.

The effect of radiation creep in the fissile oxide on fuel element performance has been investigated analytically by using Eq. 16.132 in the LIFE-I fuel modeling code.<sup>47</sup> In the absence of radial cracks caused by thermal stresses (cracking is not included in LIFE-I), the entire cool outer region of the fuel acts as a strong shell that restrains the

expansion of the fuel pellet induced by fission-gas swelling in the hot low-strength inner region. Creep of the peripheral zone of the fuel (the unstructured zone shown in Figs. 10.22 and 10.23) reduces the ability of this annular shell to prevent gross radial expansion of the fuel. When the fuel expands faster than the cladding, the fuel-cladding gap closes, and the resulting interaction between the two components of the fuel element causes cladding deformation. This deformation is manifest as a diametral strain of the fuel element, which can be measured on irradiated fuel pins and which fuel modeling codes such as LIFE-I attempt to predict. Figure 16.28 shows the predicted fractional change in the cladding outer diameter as a function of burnup. The lower curve represents the diametral strain of the cladding that occurs in the absence of interfacial pressure due to fuel-cladding interaction. This strain is due only to swelling of the metal (stainless steel) by formation of voids under fast-neutron irradiation. The middle curve shows that cladding strain is increased when fuel-cladding contact occurs and only thermal creep of the fuel is allowed. The upper band in Fig. 16.28 shows that the diametral strain of the cladding is dramatically increased when fission-induced creep of the fuel is introduced into the calculation. The decreased creep strength of the outer region of the fuel permits the entire fuel mass to be pushed against the cladding by the swollen inner core of hot fuel. The upper band in Fig. 16.28 encompasses the computed results for a range of a factor of 100 of  $\dot{F}$  in Eq. 16.132. Once the tangential stresses in the outer fuel annulus are relieved by even a small amount of fission-induced creep, additional acceleration of the creep rate by higher fission

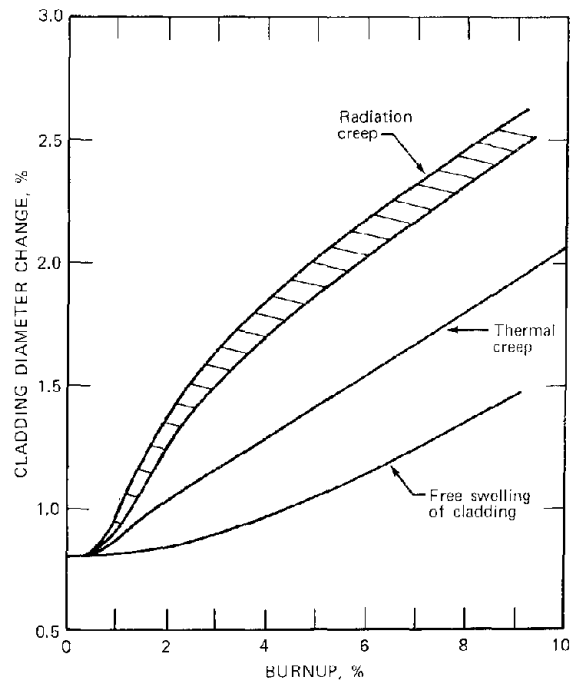


Fig. 16.28 Effect of fission-induced creep on fuel-element diametral strain as computed by the LIFE-I fuel-modeling code. (From Ref. 47.)

rates does not produce greater interfacial pressures on the cladding; the entire fuel pellet is effectively transformed into an incompressible mass with the consistency of tough jelly by the combination of thermal creep in the hot inner core and radiation creep in the peripheral zones. The drastically decreased creep strength of the outer region of the fuel permits the fuel to be pushed against the cladding by fission-product swelling (both solid and gaseous), which increases linearly with burnup. The stresses that were once sustained by the outer annulus of fuel are now transmitted to the cladding, which responds by deforming radially outward.

The effect of fission creep is most marked in the cool outer annulus, which operates at temperatures  $<1300^{\circ}\text{K}$ . According to Fig. 16.27, induced rather than enhanced fission creep is responsible for the impaired creep strength in this region. Enhanced thermal creep becomes important only in the hot core of the fuel, which has little creep strength (owing to the high temperature) even in the absence of radiation. Therefore, radiation-induced creep of the fuel appears to be a more significant phenomenon than fission-enhanced creep in oxide fuel-element performance.

In addition to decreasing the creep strength of the fuel, thereby permitting greater fuel-cladding interaction, fission creep heals cracks in the fuel faster than could be accomplished by thermal creep alone. Closure of pathways from the fuel interior to the fuel-cladding gap should impede the migration of potentially corrosive fission products (Chap. 12) to the cladding and thereby assist in maintaining fuel-element integrity.

## 16.11 SINTERING, DENSIFICATION, AND HOT PRESSING

In sintering, a process that eliminates porosity from a ceramic material, the compacted powder is held at elevated temperatures (usually greater than one-half the melting point in  $^{\circ}\text{K}$ ) for long periods of time. In the initial stages of the process, the particles fuse together at contact points and form necks or bridges with their neighbors. The intermediate stage of the remaining porosity exists in the form of more or less cylindrical tubes lying along the junctures of three or more grains, the grains having been formed from the original particles. Eventually, this tubular network is pinched off and converted into a population of roughly spherical pores (or voids) situated on the corners of the grains. Given sufficient time at elevated temperature, these pores disappear entirely (provided no insoluble gas is trapped in them), and a fully dense ceramic body is produced. Removal of isolated pores, which is called the final stage of sintering, begins when the residual void fraction or porosity is  $\sim 5\%$ . The sintering process constitutes the final step in the production of  $\text{UO}_2$  or mixed-oxide fuel pellets; the green pellets are held at  $\sim 1600^{\circ}\text{C}$  in an atmosphere of hydrogen gas (for control of fuel stoichiometry) for a length of time dictated by the desired end porosity. Some residual porosity is desirable in nuclear fuels to accommodate swelling due to fission products.

The mechanism of final-stage sintering is believed to be associated with the migration of lattice vacancies from the

pores (each of which can be likened to a bubble of vacancies) to vacancy sinks in the solid, which are generally assumed to be the grain boundaries.\* The driving force necessary to transport vacancies through the solid is provided by the surface tension of the solid, which generates a vacancy concentration at the pore surface of  $C_v^{\text{eq}} \exp(2\gamma\Omega/R_p kT)$ , where  $R_p$  is the pore radius. The equilibrium vacancy concentration  $C_v^{\text{eq}}$  is maintained at the grain boundary.

Because normal sintering operations are conducted at elevated temperatures, grain growth (Sec. 14.5) can proceed in parallel with the sintering process. The pores, which were initially located on grain corners or on grain boundaries, can be left behind by moving grain boundaries, and the void space in the solid is transformed to intragranular pores. The kinetics of the final-stage sintering process depends on the location of the pores (which are the vacancy sources) relative to the grain boundaries (which are the vacancy sinks). If the pores are distributed throughout the grain, the vacancies must diffuse through the bulk solid to escape. If the pores lie on grain boundaries or on grain corners, vacancy migration can occur either along the grain boundaries or through the adjacent solid. In either case, porosity close to the grain boundaries is more rapidly eliminated than porosity in the middle of a grain.

The rate of shrinkage of a porous solid is governed by the flux of vacancies reaching the grain boundary from the pores. Each grain must preserve its shape while decreasing in volume, or else stresses on grain boundaries would build up and destroy the driving force for vacancy diffusion. In order that the grains remain congruent to their original three-dimensional shape, the vacancy flux must be the same everywhere on the bounding surfaces of all grains in the solid. For example, a portion of grain boundary that receives vacancies faster than adjacent areas shrinks more rapidly than the latter. The adjacent grains at this local high-flux area attempt to pull away from each other and in so doing place the solid in tension, which increases the vacancy concentration and reduces the driving force for transport from the pores. The flux at this point temporarily subsides until the adjacent areas reach the same level and the tension in the original area of high vacancy flux is relieved. The system has a built-in governor that assures compliance with the stringent requirement of equal vacancy flux to all grain boundaries.

Kinetic analysis of the final-stage vacancy-diffusion-controlled sintering process must begin with an assumed distribution of pores (intra- or intergranular, size, and number density) and, if the porosity is intergranular, an assumption as to whether vacancy transport occurs through the solid (volume diffusion) or along the internal surface (grain-boundary diffusion).

The simplest sintering model is due to Coble,<sup>49</sup> who assumed that, at the start of the final stage of sintering,

\*For no obvious reason dislocations are not considered as strong vacancy sinks. In void swelling in metals (Chap. 19), grain boundaries are insignificant sinks compared to dislocations.

spherical pores were located at each of the corners of an idealized grain. The grains were represented by the 14-sided space-filling polyhedron called the tetrakaidecahedron. This solid is a regular-sided octahedron truncated at each of the six apexes in a manner that produces 36 edges all of the same length,  $l$ . The volume of the tetrakaidecahedron is  $8(2)^{1/2}l^3$ , and it has 24 corners. The pores on each of these corners are shared by four contiguous grains; so each grain contains  $24/4 = 6$  pores. The density of pores in such a model of the porous solid is

$$N_p = \frac{3}{4(2)^{1/2}l^3} \quad (16.133)$$

Coble's model makes no use of the grain boundaries or the grain shape other than to fix the pore density of the solid by the preceding formula. The grain boundaries are not the diffusive path for vacancies. Rather, they serve only as sinks that maintain the equilibrium vacancy concentration  $C_v^{eq}$  in the solid surrounding each pore. The rate of vacancy emission from a pore is then obtained from the formula for the rate of flow of point defects to and from spherical sinks and an infinite medium in which the sinks are embedded (see Sec. 13.5 and Eq. 13.70). The pore loses vacancies at a rate given by

$$J_p = 4\pi R_p D_v \left[ C_v^{eq} \exp\left(\frac{2\gamma}{R_p} \frac{\Omega}{kT}\right) - C_v^{eq} \right] \quad \text{vacancies/sec} \quad (16.134)$$

where  $D_v$  is the vacancy diffusion coefficient and  $\gamma$  is the surface tension of the solid. Multiplication of this equation by the volume per vacancy  $\Omega$  gives the rate of change of the pore volume,

$$\frac{dV_p}{dt} = -\Omega J_p \quad (16.135)$$

The porosity of the body is the ratio of the pore volume to the total volume, or

$$P = N_p V_p \quad (16.136)$$

Thus, the shrinkage rate is given by

$$\dot{P} = \frac{d}{dt} (V_p N_p) = -N_p \Omega J_p = -\frac{6\pi}{2^{1/2}} \frac{(D_v C_v^{eq} \Omega) \gamma}{kTl^3}$$

Inasmuch as  $C_v^{eq}$  is the fraction of vacant sites in the solid, the product in the parentheses in the preceding formula is the volume self-diffusion coefficient

$$D_{vol} = D_v C_v^{eq} \Omega \quad (16.137)$$

In UO<sub>2</sub>,  $D_{vol}$  applies to the U<sup>4+</sup> ion, which is slower moving than the O<sup>2-</sup> ion.

The equivalent diameter  $d$  of the polyhedral grains in Coble's model can be defined by

$$\frac{4}{3} \pi \left(\frac{d}{2}\right)^3 = 8(2)^{1/2}l^3$$

Combining the preceding three formulas yields

$$\dot{P} = -288 \frac{D_{vol} \gamma \Omega}{kT d^3} \quad (16.138)$$

The important features of Coble's sintering formula are

1. The value  $\dot{P}$  is inversely proportional to the cube of the grain size.
2. The sintering rate is proportional to the volume self-diffusion coefficient and shares the usually large activation energy of the latter.
3. The value  $\dot{P}$  is independent of pore size.
4. Complete densification ( $P = 0$ ) is achieved at a time given by

$$t_f = \frac{kT d^3 P_0}{288 D_{vol} \gamma \Omega} \quad (16.139)$$

Sintering calculations that deal more explicitly with the location of the pores in the solid vis-à-vis the grain boundaries have been presented by Rosolowski and Greskovich<sup>50</sup> and Markworth.<sup>51</sup> Markworth shows that correct treatment of diffusion of vacancies from a pore lying in the plane of a grain boundary to the latter (but with vacancy migration still through the bulk solid) produces a vacancy flux approximately twice that given by Eq. 16.134. Rosolowski and Greskovich determined the effect of the location of an intragranular pore on the vacancy emission rate. A spherical grain is assumed to contain a single pore whose center is varied over the range of radial positions from zero to  $(d/2) - R_p$ . The flux  $J_p$  was calculated for the pore at each location. As expected intuitively, the closer the vacancy source (the pore) is to the vacancy sink (the grain boundary), the larger the flux becomes. The effect of pore position, however, does not dramatically affect pore shrinkage until the pore is quite close to the grain boundary. However, if many small pores occupy a grain, the effect of position can be much more pronounced, as shall be seen presently.

Burton and Reynolds<sup>52</sup> have presented a model of final-stage sintering based on pores located on and losing vacancies through grain boundaries. This situation differs from the analyses discussed above, which all assumed vacancy transport by lattice diffusion, even when the pore lay on a grain boundary. The model used by Burton and Reynolds is an adaptation of an earlier calculation designed to explain the opposite effect from sintering, namely, swelling of grain-boundary voids under stress (Sec. 18.9). Specifically, the shrinkage law used by Burton and Reynolds is given by Eq. 18.85 with the applied stress set equal to zero. Using this model, they were able to account for the change in the size distribution of the pores during sintering (the smaller pores disappear before the larger ones), which the Coble model (Eq. 16.138) cannot do. Comparison of the sintering model with data revealed that good accord was possible with a very reasonable choice of the grain-boundary diffusivity, a quantity that has been measured by other methods.

### 16.11.1 An Illustrative Model of Porosity Removal from Ceramic Bodies by Vacancy Diffusion to Grain Boundaries

In the models just described, the only means by which vacancies left a pore and entered the adjacent solid was by diffusion. In fuel undergoing irradiation, however, vacancies can be ejected into the solid by the disruptive action of fission fragments passing through or near a pore. Accelerated sintering in an irradiated fuel is called *irradiation sintering* or *densification*, the latter name being chosen because of the rather dramatic axial shortening of fuel stacks which has been observed in some light-water reactor fuel pins.

If the solid is subject to compressive hydrostatic stress during the final stage of sintering, the process is called *pressure sintering* or *hot pressing*. This phenomenon is accounted for in fuel-modeling calculations (Chap. 21) because of the sensitivity of the fuel-cladding interfacial pressure in liquid-metal fast breeder reactor fuel pins to fuel volume changes.

We now discuss a simple mechanism of porosity elimination from ceramic fuels which includes the three limiting cases of sintering, densification, and hot pressing. The model is too simplified to be of practical use, but it serves to identify the driving forces important in each case and to provide some very simple formulas (on the level of Coble's sintering model) for the rates of densification of an irradiated fuel and hot pressing of fuel under hydrostatic compression.

In the model the porous solid is represented by an assembly of spherical grains of diameter  $d$  which contain a density  $N_p$  of spherical pores of radius  $R_p$  uniformly distributed throughout the solid. Grain growth and intergranular porosity are not considered in the calculation. In addition, the pores are assumed to be very small compared to the grain size and small compared to interpore spacing within the grain, or  $R_p \ll d/2$  and  $R_p \ll N_p^{-1/3}$ .

These two restrictions are the principal reasons for the impracticality of the model, but they permit a clear and illustrative analysis of the general problem of porosity removal by vacancy diffusion from internal porosity to grain-boundary sinks. This general process is accepted as the basic mechanism for sintering, densification, and hot pressing.

Figure 16.29 shows the geometry of the idealized grain and the contained porosity. Initially, all the pores are of the same radius  $R_{p0}$ , but at a later time the pores near the grain boundary have shrunk more than the pores near the center of the grain. The vacancy diffusion equation within the grain is solved with appropriate source functions describing the ways that pores release vacancies to the solid. These vacancy sources are treated as though they were homogeneously distributed throughout the medium, which is precisely the same way that fission-gas diffusion with trapping (Sec. 15.6) and void growth in irradiated metals (Sec. 19.5) are treated.

Diffusion of vacancies from the interior of the grain to the boundary establishes a vacancy concentration distribution whose gradient at  $r = d/2$  is directly proportional to the volume shrinkage rate. The vacancy diffusion equation

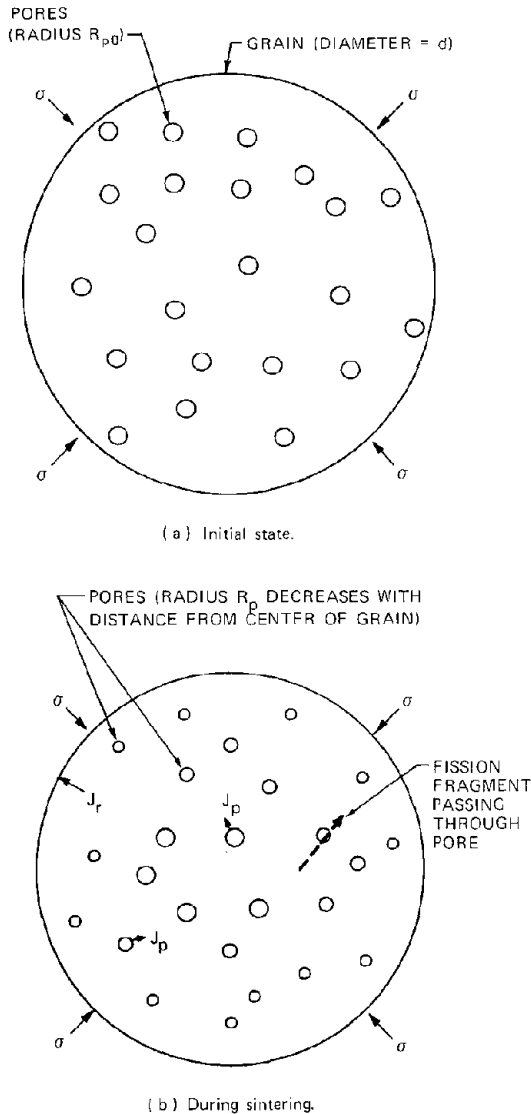


Fig. 16.29 Model of porosity removal.

in the sphere contains terms representing the homogenized sources due to the pores, but the explicit time derivative in Fick's second law is neglected (i.e., the quasi-stationary assumption is adopted). This simplification requires that the decrease in the strength of the internal vacancy sources with time (due to pore shrinkage) is slow compared with the rate at which the vacancy concentration profile in the grain can adjust to the changing conditions. The diffusion equation is

$$\frac{\partial C_v}{\partial t} \cong 0 = D_v \frac{1}{r^2} \frac{\partial}{\partial r} \left( r^2 \frac{\partial C_v}{\partial r} \right) + Q_v^{\text{surf.ten.}} + Q_v^{\text{re-sol.}} \quad (16.140)$$

The boundary conditions for this equation are

$$C_v \left( \frac{d}{2}, t \right) = C_v^{eq} \exp \left( - \frac{\sigma \Omega}{kT} \right) \quad (16.141)$$

where  $\sigma$  is the hydrostatic compressive stress acting on the grain boundary. The remaining boundary condition

$$C_v(0, t) = \text{bounded} \quad (16.142)$$

is equivalent to a symmetry condition at the center of the spherical grain.

Equation 16.140 is coupled to a pore shrinkage law, which is given by

$$\begin{aligned} \frac{dV_p}{dt} &= 4\pi R_p^2 \frac{dR_p}{dt} \\ &= - \frac{Q_v^{surf.ten.} + Q_v^{re-sol.}}{N_p} \Omega \end{aligned} \quad (16.143)$$

where  $V_p$  is the volume of a pore at radial position  $r$  at time  $t$  and  $R_p$  is also a function of  $r$  and  $t$ . The required initial condition for Eq. 16.143 is

$$R_p(r, 0) = R_{p0} \quad (16.144)$$

where  $R_{p0}$  is the initial pore size.

The source term  $Q_v^{surf.ten.}$  designates vacancy emission from the pore due to diffusion from the pore surface to the solid. The driving force for vacancy transport near the pore is the difference between the vacancy concentration at the pore surface (which is increased by surface tension) and that in the bulk solid at the location of the pore within the grain. The source term is given by

$$Q_v^{surf.ten.} = 4\pi R_p D_v N_p \left[ C_v^{eq} \exp \left( \frac{2\gamma \Omega}{R_p kT} \right) - C_v \right] \quad (16.145)$$

This formula is obtained by multiplying Eq. 16.134 by  $N_p$  to convert flux from a single pore to a volumetric source in the solid and by replacing  $C_v^{eq}$  in Eq. 16.134 by  $C_v$ , which is the local concentration of vacancies in the solid.

Vacancies are also introduced into the solid near a pore by a type of re-resolution process that we have previously discussed in connection with fission-gas bubbles (Sec. 13.7). It is obvious that the microscopic re-resolution model cannot be applied to pores directly. Although a pore can be thought of as consisting of  $\frac{4}{3} \pi R_p^3 / \Omega$  vacancies, the vacancies are not ponderable particles that can acquire kinetic energy by collision with a high-speed particle (e.g., a fission fragment or a lattice knock-on). Therefore, pore shrinkage by fission fragments must be described by a form of macroscopic re-resolution, in which a passing fragment blasts solid from one side of a pore to the other, trapping some vacancies in the deposited side in the process. The buried vacancies are considered to be redissolved and to acquire the mobility of single vacancies in the lattice. They are indistinguishable from vacancies emitted from the pore surface by thermal means (which are included in the  $Q_v^{surf.ten.}$  source term). Because the pores in ceramic fuels are considerably larger than fission-gas bubbles, it is unlikely that a pore can be completely converted to

vacancies by a single re-resolution event. Hence, re-resolution is considered to reduce the size of the pores but not to change the total pore concentration  $N_p$ . Therefore, we can define a vacancy re-resolution parameter by

$b$  = probability/sec that a vacancy in a pore will be ejected into the lattice

For fission-gas atoms,  $b$  is typically  $10^{-4}$  to  $10^{-5}$  sec<sup>-1</sup>, and similar values should apply to vacancy re-resolution from pores if the macroscopic mechanism of this process applies in both cases. The source term in the diffusion equation due to re-resolution is therefore given by

$$Q_v^{re-sol.} = b \left[ \frac{(4\pi/3) R_p^3}{\Omega} \right] N_p \quad (16.146)$$

To streamline the notation, we collect the various parameters of the problem in the following dimensionless quantities:

#### Vacancy Concentration

$$\theta = \frac{C_v^{eq} \exp [(2\gamma/R_p)(\Omega/kT)] - C_v}{C_v^{eq} \exp [(2\gamma/R_p)(\Omega/kT)] - C_v^{eq} \exp (-\sigma\Omega/kT)} \quad (16.147)$$

#### Pore Size

$$y = \frac{R_p}{R_{p0}} \quad (16.148)$$

#### Radial Location

$$\eta = \frac{r}{d/2} \quad (16.149)$$

#### Time

$$\tau = \frac{D_v t}{(d/2)^2} \quad (16.150)$$

#### Geometric Parameters

$$q^2 = 4\pi R_{p0} \left( \frac{d}{2} \right)^2 N_p \quad (16.151)$$

$$s = \frac{\Omega C_v^{eq} (d/2)^2}{R_{p0}^2} \quad (16.152)$$

#### Re-resolution Parameter

$$B = \frac{b [(4\pi/3) R_{p0}^3] N_p (d/2)^2}{D_v C_v^{eq} \Omega} \quad (16.153)$$

#### Surface-Tension Parameter

$$\Gamma = \frac{2\gamma \Omega}{R_{p0} kT} \quad (16.154)$$

#### Applied-Stress Parameter

$$\Sigma = \frac{\sigma \Omega}{kT} \quad (16.155)$$

When Eqs. 16.145 and 16.146 are substituted into Eq. 16.140 and the dimensionless groups are used, the result is the diffusion equation

$$\frac{1}{\eta^2} \frac{d}{d\eta} \left( \eta^2 \frac{d\theta}{d\eta} \right) - q^2 y \theta = \frac{By^3}{(\Gamma/y) + \Sigma} \quad (16.156)$$

with the boundary conditions

$$\theta(1, \tau) = 1 \quad (16.157)$$

$$\theta(0, \tau) = \text{bounded} \quad (16.158)$$

The pore shrinkage law, Eq. 16.143, becomes

$$\frac{dy}{d\tau} = -s \left( \frac{\Gamma}{y} + \Sigma \right) \frac{\theta}{y} \frac{Bs}{q^2} y \quad (16.159)$$

with the initial condition

$$y(\eta, 0) = 1 \quad (16.160)$$

Although the time derivative  $\partial\theta/\partial\tau$  has been suppressed from Eq. 16.156, the dimensionless vacancy concentration  $\theta$  is a function of both  $\eta$  and  $\tau$ . The  $\tau$  dependence arises from the variation of the pore size  $y$  with time. Hence, Eq. 16.156 can be treated as an ordinary differential equation and not as a partial differential equation. Similarly, derivatives of  $y$  with respect to  $\eta$  do not appear in Eq. 16.159 because the pores are considered to be immobile.

A computational scheme for solving the preceding equations is as follows:

1. Initially, Eq. 16.156 is solved with  $y = 1$  to give  $\theta(\eta, 0)$ .
2. This result is employed in Eq. 16.159 to determine  $y(\eta, \Delta\tau)$ , where  $\Delta\tau$  is the length of a time step.
3. The new distribution of  $y$  is used in Eq. 16.156 to give  $\theta(\eta, \Delta\tau)$ .
4. The cycle continues in this manner. If the solution of Eq. 16.159 yields  $y < 0$  at any radial location,  $y$  is set equal to zero at this and all larger values of  $\eta$ . An outer shell of pore-free solid gradually penetrates toward the center of the grain.

Several simplified solutions to the complete set of equations, which represent the limiting cases of sintering, densification, and hot pressing, can be obtained without recourse to numerical analysis.

### 16.11.2 Sintering

In the absence of radiation and applied stress,  $B = 0$  and  $\Sigma = 0$ . If, in addition,  $\theta$  is set equal to unity throughout the grain [i.e.,  $C_v(r, t) = C_v^{\text{eq}}$ ] and  $N_p$  is expressed by Eq. 16.133, Coble's simple sintering model is recovered.

### 16.11.3 Densification

Since external stress does not appear to affect radiation sintering, we set  $\Sigma = 0$ . In addition, we let  $\Gamma$  be very small, which physically means that re-resolution is more important in shrinking pores than is surface-tension-driven vacancy

diffusion from the pore surface to the bulk solid. For this case, Eqs. 16.156 and 16.159 reduce to

$$\frac{1}{\eta^2} \frac{d}{d\eta} \left( \eta^2 \frac{d\theta}{d\eta} \right) = \frac{By^4}{1} \quad (16.161)$$

and

$$\frac{dy}{d\tau} = - \left( \frac{Bs}{q^2} \right) y \quad (16.162)$$

Since Eq. 16.162 does not depend on  $\theta$ ,  $y$  is independent of  $\eta$ , or the pores shrink at the same rate throughout the grains. With the right-hand side of Eq. 16.161 constant in space, the diffusion equation can be solved to yield the vacancy concentration profile in the grain:

$$\theta(\eta) = 1 - \frac{1}{6} \frac{B}{\Gamma} y^4 (1 - \eta^2) \quad (16.163)$$

The vacancy flux to the grain boundary is given by

$$J_r = -D_v \left( \frac{dC_v}{dr} \right)_{r=d/2} = \frac{D_v C_v^{\text{eq}} \Gamma}{(d/2) y} \left( \frac{d\theta}{d\eta} \right)_1 \quad (16.164)$$

The shrinkage rate of the solid is the time rate of change of the volume of the spherical grain occasioned by the flow of vacancies to its surface divided by the initial grain volume:

$$\dot{P} = - \frac{4\pi(d/2)^2 J_r \Omega}{(4\pi/3)(d/2)^3} = - \frac{3\Omega J_r}{(d/2)} \quad (16.165)$$

Using Eq. 16.163 in Eq. 16.164 and the resulting equation for  $J_{gb}$  in Eq. 16.165, we find

$$\dot{P} = -b \left( \frac{4}{3} \pi R_p^3 \right) N_p y^3 = -b P_0 y^3 \quad (16.166)$$

where  $P_0$  is the initial porosity of the solid. Equation 16.166 states that the densification rate is controlled entirely by the rate at which vacancies are injected into the solid by re-resolution and that diffusional transport of vacancies through the solid is not important.

Equation 16.162 can be integrated directly to yield

$$y = \exp \left( - \frac{Bs}{q^2} \tau \right) = \exp \left( - \frac{1}{3} b t \right) \quad (16.167)$$

Substituting Eq. 16.167 into Eq. 16.166 and integrating with respect to time gives

$$P_0 - P = P_0 (1 - e^{-bt}) \quad (16.168)$$

A formula comparable to Eq. 16.168 has been obtained by Assman and Stehle<sup>53</sup> using the same set of assumptions that we have used for describing re-resolution-controlled densification (see problem 16.4). The analysis leading to Eq. 16.168 can be faulted for its cavalier treatment of diffusion in the solid; neglect of the  $q^2 y \theta$  term in Eq. 16.156 and the  $s[(\Gamma/y) + \Sigma] \theta/y$  term in Eq. 16.159 is tantamount to shutting off all diffusional communication

between a pore and the solid in the immediate environment. All the while, however, the same diffusional process is retained as a means of transporting vacancies injected into the solid by re-resolution to the grain boundary where shrinkage is manifest. If  $B/\Gamma$  is sufficiently large, Eq. 16.163 shows that  $\theta$  can be negative in the interior of the grain. A negative value of  $\theta$  means that the bulk vacancy concentration is larger than that at the pore surface or, were vacancy diffusion between the pore and the bulk not neglected, the pores would tend to absorb some of the vacancies released by re-resolution.

Despite this fault in the simple model, it is clear that radiation is an essential ingredient in fuel densification; it has been demonstrated<sup>54</sup> that UO<sub>2</sub> pellets heated out of pile for 6 months at 900°C show no signs of sintering, whereas, under the same conditions in-pile, extensive porosity removal occurs in a few hundred days. Yet it is equally clear that diffusion is required to transport the vacancies released from the pore by re-resolution to the grain boundaries where they are absorbed. The conceptual difficulties inherent in the analysis which led to Eq. 16.168 can be avoided by solving Eqs. 16.156 and 16.159 in their entirety. Even then, the model contains important and probably unrealistic assumptions concerning the distribution of the pores, their initial size, and the neglect of grain growth concomitant with densification.

In pointing out the importance of vacancy diffusion in fuel densification, Marlowe<sup>55</sup> suggests that, in addition to re-resolution, radiation also increases the diffusion coefficient proper. However, although the volume self-diffusion coefficient is subject to radiation enhancement, the diffusivity of vacancies is not,\* and, since the transport of vacancies is ultimately responsible for sintering, either in a radiation field or out of pile, the radiation effect must be due only to re-resolution.

The very substantial vacancy production rate due to collision cascades and fission spikes in the irradiated solid was not explicitly included as a source term in the vacancy diffusion equation because of the strong analogy between the densification process and Nabarro–Herring creep. In Nabarro–Herring creep, vacancies move from one point on the grain boundary to another, whereas, in the densification process, vacancies are transported from internal surfaces to grain boundaries. In Sec. 16.10 it was shown that radiation does not affect Nabarro–Herring creep because the vacancies and interstitials produced by radiation either annihilate each other or flow in equal numbers to available sinks. In densification models neither of the vacancy sinks in the solid (pores or grain boundaries) exhibits a preference for interstitials over vacancies; so an excess of one type of point defect in the solid cannot be built up. Only dislocations are biased sinks, and they are not considered in densification models. If they were, swelling rather than shrinkage would probably occur, for this is the prime effect of the presence of dislocation sinks in void swelling in metals.

Densification of light-water-reactor (LWR) fuels appears as decreases in the length of the fuel column in a rod and in the radius of the fuel.

\*Except for the negligible enhancement due to local heating from thermal spikes (Sec. 16.10).

When the length of the fuel is shortened but the quantity of fuel remains the same, there is an increase in linear power, which increases the heat flux through the cladding. When the fuel shrinks axially, the entire stack of pellets need not move as a unit. Rather, gaps as large as 4 to 8 cm appear in the fuel column, the cladding collapses into the empty interior, and water fills in the space outside the fuel pin resulting from cladding flattening. The extra water causes a local neutron flux peak that in turn produces a local power spike.

Radial shrinkage of the fuel alleviates the deleterious effects of fuel–cladding interfacial pressure but at the same time increases the heat-transfer resistance of the fuel–cladding gap, thereby causing the fuel center-line temperature to rise.

Although fuel densification was first identified as a technological problem in LWRs, there is no reason why the same process should not occur in liquid-metal fast breeder reactor (LMFBR) fuel rods as well. However, fuel temperatures are generally higher in LMFBRs than in LWRs, and deformation processes can proceed more readily without radiation assistance in LMFBRs than in LWRs. Closure of porosity is an important aspect of fast reactor fuel performance, although it is generally considered to be a process of sintering under pressure rather than one arising directly from irradiation.

#### 16.11.4 Hot Pressing

To analyze pressure sintering, we disregard radiation re-resolution ( $B = 0$ ) and assume the surface-tension driving-force parameter to be small compared to the effect of applied hydrostatic stress ( $\Gamma = 0$ ). Under these restrictions, Eq. 16.156 becomes

$$\frac{1}{\eta^2} \frac{d}{d\eta} \left( \eta^2 \frac{d\theta}{d\eta} \right) - q^2 y \theta = 0 \quad (16.169)$$

and the pore-shrinkage law, Eq. 16.159, is

$$\frac{dy}{dr} = -s \Sigma \frac{\theta}{y} \quad (16.170)$$

These two equations are coupled, since the dependent variables  $\theta$  and  $y$  appear in each. To obtain an analytical solution that still retains the essential features of the hot-pressing phenomenon, we set  $y$  equal to a constant in Eq. 16.169 and disregard Eq. 16.170 entirely. The solution to Eq. 16.169 which satisfies the boundary conditions given by Eqs. 16.157 and 16.158 is

$$\theta(\eta) = \frac{1}{\eta} \frac{\exp(qy^{1/2}\eta) - \exp(-qy^{1/2}\eta)}{\exp(qy^{1/2}) - \exp(-qy^{1/2})} \quad (16.171)$$

The flux of vacancies to the grain boundary is given by Eq. 16.164 with  $\Gamma/y$  replaced by  $\Sigma$ :

$$J_r = \frac{D_v C_v^e q}{d/2} \Sigma \left( \frac{d\theta}{d\eta} \right)_1 \\ = \frac{D_v C_v^e q}{d/2} \left( \frac{\sigma \Omega}{kT} \right) \left[ qy^{1/2} \operatorname{ctnh}(qy^{1/2}) - 1 \right] \quad (16.172)$$

Taking limiting cases of large and small  $q$ , we find

$$J_r = \frac{D_v C_v^{e q}}{d/2} \left( \frac{\sigma \Omega}{kT} \right) q y^{1/2} \quad \text{for large } q \quad (16.173a)$$

$$J_r = \frac{D_v C_v^{e q}}{d/2} \left( \frac{\sigma \Omega}{kT} \right) \frac{q^2 y}{3} \quad \text{for } q \rightarrow 0 \quad (16.173b)$$

From Eq. 16.151, the product of  $q^2$  and  $y$  is

$$q^2 y = 4\pi \left( \frac{d}{2} \right)^2 R_p N_p \quad (16.174)$$

From which the product  $R_p N_p$  can be eliminated by the definition of the porosity:

$$P = \left( \frac{4}{3} \pi R_p^3 \right) N_p = \frac{4\pi}{3N_p^2} (R_p N_p)^3 \quad (16.175)$$

Using Eqs. 16.174 and 16.175 in Eq. 16.173 and employing Eq. 16.165, which relates the flux of vacancies to the grain boundary and the rate of porosity reduction, yields

$$\dot{P} = -3^{1/2} (4\pi)^{3/2} \left( \frac{\Omega D_{v01}}{kT} \right) (N_p^{3/2} P^{1/2}) \sigma \quad (16.176a)$$

for large  $q$  values, and

$$\dot{P} = -3^{3/2} (32\pi)^{3/2} \left( \frac{\Omega D_{v01}}{kT} \right) \left[ \frac{N_p^{1/2} P^{1/2}}{d} \right] \sigma \quad (16.176b)$$

for small  $q$  values.

The hot-pressing rate is proportional to the applied stress, as is the deformation rate in Nabarro-Herring creep. The grain-size dependence of the hot-pressing rate from this model varies from  $d^0$  to  $d^{-1}$ , and the presence of the terms  $P^{1/2}$  or  $P^{3/2}$  on the right-hand sides of the preceding equations means that complete removal of porosity is not possible.

This model of hot pressing is based on physical premises quite similar to those which underlie diffusional creep; in both cases the solid deforms as a result of applied stress by vacancy migration between surfaces of different vacancy concentrations. Vasilos and Spriggs<sup>56</sup> and Rossi and Fulrath<sup>57</sup> have carried this analogy to the extreme by employing the Nabarro-Herring creep formula (Eq. 16.25) directly and fitting hot-pressing data to the relation

$$\dot{P} = -K \left( \frac{\Omega D_{v01}}{kT} \right) \frac{P}{d^2} \sigma \quad (16.177)$$

The porosity is introduced into the Nabarro-Herring formula when the uniaxial stress in creep model is converted to hydrostatic stress for application in hot pressing. The  $K$  in the preceding formula is a numerical constant. The strong similarity between Eqs. 16.176 and 16.177 is evident.

### 16.11.5 Hot Pressing by Plastic Flow

Equations 16.176 and 16.177 represent hot-pressing models based on vacancy diffusion in the solid. Both closely resemble Nabarro-Herring diffusional creep. It is natural to inquire as to the hot-pressing analogs of dislocation-climb creep or any of the other models of creep.

Hot-pressing theories based on continuum mechanics provide such a general connection between creep and hot pressing without having to specify in advance the atomistic model of the process responsible for both macroscopic phenomena.

In the continuum model of hot pressing, the porous solid is divided into unit cells each containing a pore of volume  $V_p$  at its center. The pore is surrounded by a spherical shell of solid. The total volume of the unit cell, which includes pore and solid, is related to the density of pores in the material by

$$\mathcal{V} = \frac{1}{N_p} \quad (16.178)$$

Under application of a hydrostatic stress to the outside of the unit cell, the solid in the annular shell deforms in a way that causes the pore volume  $V_p$  to decrease. In the spherical-coordinate system centered in the unit cell, the angular components of the strain rate are

$$\dot{\epsilon}_\theta = \dot{\epsilon}_\phi = \frac{\dot{R}}{R} \quad (16.179)$$

where  $\theta$  and  $\phi$  are the polar and azimuthal angles in the spherical coordinate system and  $R$  is a radial location within the solid annulus. The solid is assumed to be incompressible during deformation; so the radial component of the strain rate is

$$\dot{\epsilon}_r = -\dot{\epsilon}_\theta - \dot{\epsilon}_\phi = -\frac{2\dot{R}}{R} \quad (16.180)$$

To relate deformation in the stressed hollow sphere to the uniaxial tests in which creep is commonly measured, we introduce the equivalent strain or strain deviator.\* For spherical geometry and in terms of strain rates rather than strains, Eq. 18.17 is

$$\dot{\epsilon}^* = \frac{2^{1/2}}{3} [(\dot{\epsilon}_\theta - \dot{\epsilon}_\phi)^2 + (\dot{\epsilon}_\theta - \dot{\epsilon}_r)^2 + (\dot{\epsilon}_\phi - \dot{\epsilon}_r)^2]^{1/2} \quad (16.181)$$

Substituting Eqs. 16.179 and 16.180 into Eq. 16.181 and noting that the radial strain rate  $\dot{R}/R$  is one-third the volume dilatation rate  $\dot{V}/V$ , we have

$$\dot{\epsilon}^* = 2 \frac{|\dot{R}|}{R} - \frac{2}{3} \frac{|\dot{V}|}{V} \quad (16.182)$$

The equivalent strain rate is always positive. The rate at which the external stress performs work on the unit cell is

$$\dot{W} = -\sigma \dot{V} \quad (16.183)$$

In Eqs 16.182 and 16.183,  $-\dot{V}$  is the shrinkage rate of the solid. The rate of performing work can also be expressed as the integral of the equivalent stress-equivalent strain product over the volume of the solid in the unit cell

$$\dot{W} = \int_{V_p} \sigma^* \dot{\epsilon}^* dV \quad (16.184)$$

where  $\sigma^*$  is the equivalent stress. Equating the right-hand sides of Eqs. 16.183 and 16.184 and eliminating  $\dot{\epsilon}^*$  by Eq. 16.182 yields

\*An explanation of equivalent stress and equivalent strain is given in Sec. 18.3.

$$-\sigma \dot{V} = \frac{2}{3} \int_{V_p}^{\mathcal{V}} \sigma^* |\dot{V}| \frac{dV}{V}$$

The shrinkage rate is independent of position in the solid spherical shell; so  $|\dot{V}|$  can be removed from the integral on the right of the preceding equation, and there remains

$$-\sigma \dot{V} = \frac{2}{3} |\dot{V}| \int_{V_p}^{\mathcal{V}} \sigma^* \frac{dV}{V} \quad (16.185)$$

The equivalent stress and equivalent strain are related by the creep law, which can be generally written as

$$\dot{\epsilon}^* = \alpha (\sigma^*)^n \quad (16.186)$$

where  $\alpha$  is a constant (which can be temperature dependent) and  $n$  is the creep exponent. Equation 16.186 applies to power-law creep, such as that due to dislocation climb ( $n \approx 4.5$ ), as well as to Nabarro-Herring creep, for which  $n = 1$ . Irradiation creep is also encompassed by the creep law of Eq. 16.186.

For illustration in what follows, we assume  $n = 1$ . Combination of Eqs. 16.182 and 16.186 gives the equivalent stress as

$$\sigma^* = \frac{2}{3\alpha} \frac{|\dot{V}|}{V} \quad (16.187)$$

The shrinkage rate of the unit cell is due to collapse of the empty pore at its center; so  $\dot{V}$  can be set equal to  $\dot{V}_p$ . The porosity of the body is

$$P = \frac{V_p}{\mathcal{V}} = \frac{V_p}{V_p + V_s} \quad (16.188)$$

where  $V_s = \mathcal{V} - V_p$  is the solid volume in the unit cell. From Eq. 16.188 we find that the shrinkage rate can be expressed by

$$\dot{V} = \dot{V}_p = \frac{\dot{P}}{1-P} \mathcal{V} \quad (16.189)$$

Substituting Eq. 16.189 into 16.187 and the expression for  $\sigma^*$  that results into Eq. 16.185 yields

$$\begin{aligned} \dot{P} \sigma &= -\frac{4}{9} \frac{1}{\alpha} |\dot{P}| \int_{V_p}^{\mathcal{V}} \frac{\dot{P}}{V} \frac{1}{1-P} \frac{dV}{V} \\ &= -\frac{4}{9} \frac{1}{\alpha} \frac{(\dot{P})^2}{1-P} \int_p^1 \frac{dX}{X^2} \\ &= -\frac{4}{9} \frac{1}{\alpha} \frac{(\dot{P})^2}{P} \end{aligned}$$

The rate of hot pressing is obtained by multiplying the preceding equation by  $\dot{P}$  and rearranging:

$$\dot{P} = -\frac{9}{4} \alpha \sigma P \quad (16.190)$$

A somewhat more complex formula arises for a generalized power-law creep (see problem 16.3). Equation 16.190

exhibits the same stress and porosity dependence as does Eq. 16.177.

## 16.12 NOMENCLATURE

- a = radius of a spherical grain (equal to  $d/2$ )
- $a_o$  = lattice constant
- $A_n, B_n$  = coefficients in series solutions of diffusional-creep equations
- A = area of glide plane traversed by dislocation
- b = Burgers vector
- b = vacancy re-solution parameter
- B = dimensionless vacancy re-solution parameter
- $B, B', B''$  = constants in creep formulas
- c = constant giving the length of a Burgers vector (see Eq. 8.3)
- C = constant given by the right-hand side of Eq. 16.72; one-half the major axis of an elliptical crack
- $C_i$  = interstitial concentration
- $C_p$  = heat capacity at constant pressure
- $C_v$  = vacancy concentration; heat capacity at constant volume
- $C_v^{\text{eq}}$  = equilibrium vacancy concentration
- d = grain diameter
- D = diameter of polycrystalline sample
- $D_v$  = vacancy diffusion coefficient in solid
- $D_{gb}$  = grain boundary self-diffusion coefficient
- $D_v$  = vacancy diffusion coefficient in solid
- $D_v^*$  = radiation-enhanced vacancy diffusion coefficient
- $D_{vgb}$  = vacancy diffusion coefficient in grain boundary
- $D_{vol}$  = volume self-diffusion coefficient
- E = Young's modulus
- $E_c$  = activation energy for creep
- $E_{el}$  = elastic energy in a cracked solid
- $E_{gb}$  = activation energy for grain-boundary diffusion
- $E_j$  = energy of formation of a jog
- $E_{surf}$  = surface energy of a crack
- $E_{vol}$  = activation energy for volume self-diffusion
- $f_x, f_y$  = angular functions of force between parallel edge dislocations
- $F_{ly}$  = climb force on a dislocation
- $\dot{F}$  = fissions  $\text{cm}^{-3} \text{sec}^{-1}$
- G = shear modulus
- h = climb height necessary for a dislocation to overcome an obstacle
- H = height of a grain-boundary ledge
- J = difference between the vacancy and interstitial fluxes to a grain boundary
- $J_p$  = rate of loss of vacancies by a pore
- $J_r$  = radial flux of vacancies at grain boundary
- k = Boltzmann's constant
- $k_s$  = thermal conductivity of solid
- $k_{vi}$  = vacancy-interstitial recombination rate constant
- K = constant given by Eq. 16.8
- $K_F$  = equilibrium constant for Frenkel defects
- $K_s$  = equilibrium constant for Schottky defects
- l = length of the side of a tetrakaidecahedron
- L = width of a grain-boundary ledge; distance between Frank-Read sources in the glide plane; length of a polycrystalline specimen

$n$  = number of dislocations in a pile-up; exponent in power-law creep  
 $n_j$  = number of jogs per unit length of dislocation line  
 $N$  = number of atoms on normal lattice sites  
 $N_i$  = number of atoms on interstitial sites  
 $N_p$  = density of pores in a grain  
 $N_s$  = number of sites  
 $p$  = probability per unit time that a dislocation surmounts a barrier  
 $P$  = porosity  
 $P_0$  = initial porosity  
 $P_n(\mu)$  =  $n$ th Legendre polynomial of  $\mu$   
 $q$  = defined by Eq. 16.151  
 $q_1, q_2$  = functions describing the distributions of initial separation or angle of parallel edge dislocations  
 $Q_{\text{fiss}}$  = initial energy of a fission fragment  
 $Q_v$  = vacancy source strength in a solid  
 $r$  = radial position  
 $r_c$  = radius of a crack tip  
 $R$  = flux of vacancies to jog; radial location in solid  
 $R_c$  = rate of vacancy capture by a jog  
 $R_d$  = radius of a dislocation core  
 $R_e$  = rate of vacancy emission from a jog  
 $R_p$  = pore radius  
 $\mathcal{R}$  = capture radius of a dislocation  
 $s$  = defined by Eq. 16.152  
 $s_{\text{U}}^{\ddagger}$  = entropy of motion of a uranium ion  
 $t$  = time  
 $t_c$  = time for a dislocation to surmount an obstacle  
 $t_f$  = time to complete densification  
 $T$  = temperature  
 $v_c$  = climb velocity of an edge dislocation  
 $v_l$  = velocity of a grain-boundary ledge  
 $V$  = volume  
 $V_p$  = volume of a pore  
 $\mathcal{V}$  = defined by Eq. 16.178  
 $w$  = jump frequency; grain-boundary thickness  
 $\dot{W}$  = rate at which external stress performs work on solid  
 $x$  = stoichiometric parameter in  $\text{UO}_{2+x}$ ; distance along glide plane; separation of cleaved faces of a crystal; position within grain boundary  
 $x_i$  = site fraction of interstitials  
 $x_v$  = site fraction of vacancies  
 $y$  = climb distance of a dislocation; dimensionless pore size, Eq. 16.148  
 $Y_{vi}$  = yield of vacancy-interstitial pairs per fission  
 $z$  = number of capture sites surrounding a dislocation

#### Greek Letters

$\alpha$  = thermal diffusivity  
 $\alpha_n$  = defined by Eq. 16.16  
 $\gamma$  = surface tension of solid  
 $\gamma_s$  = surface energy of solid (includes energy of plastic deformation)  
 $\Gamma$  = dimensionless surface-tension parameter  
 $\dot{\epsilon}$  = strain rate (or creep rate)  
 $\epsilon^*$  = generalized strain  
 $\dot{\epsilon}_c$  = creep rate due to dislocation climb  
 $\dot{\epsilon}_{\text{diff}}$  = diffusional-creep rate

$\epsilon_F$  = energy of formation of Frenkel defect  
 $\epsilon_g$  = strain in grain  
 $\epsilon_{\text{gbs}}$  = strain due to grain-boundary sliding  
 $\dot{\epsilon}_{\text{gbs}}$  = creep rate due to grain-boundary sliding  
 $\epsilon_s$  = energy of formation of Schottky defect  
 $\epsilon_T$  = total strain  
 $\epsilon_{\text{U}}^{\ddagger}$  = energy of motion of a uranium ion  
 $\epsilon_v^{\ddagger}$  = energy of motion of a vacancy  
 $\eta$  = dimensionless radial position in pore, Eq. 16.149  
 $\theta$  = dimensionless vacancy concentration, Eq. 16.147; polar angle in spherical grain; azimuthal angle between parallel dislocations  
 $\lambda$  = wavelength in sinusoidal approximation to potential energy function  
 $\mu$  = cosine of polar angle  
 $\mu_{\text{ff}}$  = range of fission fragment  
 $\nu$  = Poisson's ratio  
 $\nu_{\text{U}}$  = vibration frequency of uranium ion in  $\text{UO}_2$   
 $\nu_v$  = vibration frequency of a vacancy  
 $\rho$  = density of Frank-Read sources in solid; solid density  
 $\sigma$  = normal stress (positive in tension)  
 $\sigma^*$  = generalized stress  
 $\sigma^*$  = stress needed to produce climb force  $F_{iy}$  on dislocation  
 $\sigma_c$  = stress at crack tip  
 $\sigma_f$  = fracture stress  
 $\sigma_n$  = normal stress on surface  
 $\sigma_{\text{tr}}$  = stress for transition for diffusional creep to dislocation-climb creep  
 $\sigma_{xy}$  = shear stress  
 $\Sigma$  = dimensionless stress parameter  
 $\tau$  = dimensionless time, Eq. 16.150  
 $\tau_c$  = characteristic time for dislocation climb  
 $\tau_d$  = line tension of a dislocation  
 $\psi$  = potential energy between two cleaved crystal surfaces  
 $\Omega$  = atomic volume

#### Subscripts

$O$  = oxygen  
 $U$  = uranium

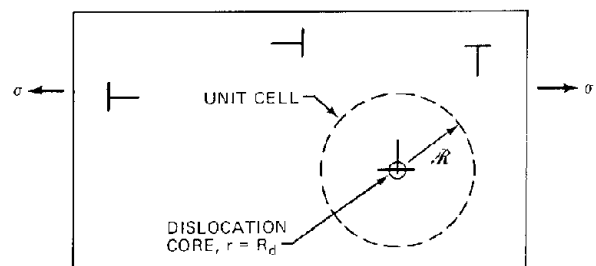
### 16.13 REFERENCES

1. J. F. Byrom, *J. Nucl. Mater.*, **27**: 48 (1968).
2. H. Blank and C. Ronchi, *J. Nucl. Mater.*, **31**: 1 (1969).
3. C. S. Yust and C. J. McHargue, *J. Nucl. Mater.*, **31**: 121 (1969).
4. C. Ronchi and H. Blank, in *Fourth International Conference on Plutonium and Other Actinides*, Santa Fe, N. Mex., Oct. 5-9, 1970, W. H. Miner (Ed.), p. 179, Metallurgical Society of the American Institute of Mining, Metallurgical, and Petroleum Engineers, Inc., New York, 1970.
5. P. T. Sawbridge and E. C. Sykes, *J. Nucl. Mater.*, **35**: 122 (1970).
6. P. T. Sawbridge and E. C. Sykes, *Phil. Mag.*, **24**: 33 (1971).
7. M. S. Seltzer, A. H. Clauer, and B. A. Wilcox, *J. Nucl. Mater.*, **44**: 43 (1972).
8. M. O. Marlowe and A. I. Kaznoff, *Proceedings of the*

- International Symposium on Ceramic Nuclear Fuels*, p. 90, American Ceramic Society, Washington, D. C., 1969.
9. M. O. Marlowe, *J. Nucl. Mater.*, **33**: 242 (1968).
  10. A. G. Evans and R. W. Davidge, *J. Nucl. Mater.*, **33**: 249 (1969).
  11. R. F. Canon, J. T. A. Roberts, and R. J. Beals, *J. Amer. Ceram. Soc.*, **54**: 105 (1971).
  12. J. T. A. Roberts and Y. Ueda, *J. Amer. Ceram. Soc.*, **55**: 117 (1972).
  - 13a. J. H. Gittus, D. A. Howl, and H. Hughes, *Nucl. Appl. Technol.*, **9**: 40 (1970).
  - 13b. M. J. F. Notley, *Nucl. Appl. Technol.*, **9**: 195 (1970).
  14. N. Igata and K. Domoto, *J. Nucl. Mater.*, **45**: 317 (1972/1973).
  15. A. A. Griffith, *Phil. Trans. Roy. Soc. (London)*, Ser. A, **221**: 168 (1921).
  16. R. A. Sack, *Proc. Phys. Soc. (London)*, **58**: 729 (1946).
  17. G. Garofalo, *Fundamentals of Creep and Creep Rupture in Metals*, The MacMillan Company, New York, 1965.
  18. T. G. Langdon, D. R. Cropper, and J. A. Pask, in *Ceramics in Severe Environments*, Proceedings of the Sixth University Conference on Ceramic Science, North Carolina State University at Raleigh, Dec. 7-9, 1970, p. 297, W. Wurth Kriegel and Hayne Palmour III (Eds.), Plenum Publishing Corporation, New York, 1971.
  19. F. R. N. Nabarro, in *Report of a Conference on the Strength of Solids*, p. 75, Physical Society, London, 1948.
  20. C. Herring, *J. Appl. Phys.*, **21**: 437 (1950).
  21. F. B. Hildebrand, *Advanced Calculus for Engineers*, p. 429, Prentice-Hall, Inc., Englewood Cliffs, N. J., 1949.
  22. T. M. MacRobert, *Spherical Harmonics*, p. 95, Pergamon Press, Inc., New York, 1967.
  23. R. L. Coble, *J. Appl. Phys.*, **34**: 1679 (1963).
  24. J. Weertman, *J. Appl. Phys.*, **26**: 1213 (1955).
  25. J. Weertman, *ASM (Amer. Soc. Metals), Trans. Quart.*, **61**: 681 (1968).
  26. R. C. Gifkins and K. V. Snowden, *Nature*, **212**: 916 (1966).
  27. R. C. Gifkins, *J. Amer. Ceram. Soc.*, **51**: 69 (1968).
  28. M. F. Ashby, R. Raj, and R. C. Gifkins, *Ser. Met.*, **4**: 737 (1970).
  29. R. C. Gifkins, *J. Inst. Metals*, **95**: 373 (1967).
  30. T. G. Langdon, *Phil. Mag.*, **22**: 689 (1970).
  31. M. S. Seltzer, J. S. Perrin, A. H. Clauer, and B. A. Wilcox, Review of Out-of-Pile and In-Pile Creep of Ceramic Nuclear Fuels, USAEC Report BMI-1906, Battelle Memorial Institute, July 1971.
  32. T. G. Langdon, *J. Nucl. Mater.*, **38**: 88 (1971).
  33. A. B. Lidiard, *J. Nucl. Mater.*, **19**: 106 (1966).
  34. H. J. Matzke, *J. Nucl. Mater.*, **30**: 26 (1969).
  - 34a. R. Szwarc, *J. Phys. Chem. Solids*, **30**: 705 (1969).
  35. P. E. Bohaboy and S. K. Evans, in *Fourth International Conference on Plutonium and Other Actinides*, Santa Fe, N. Mex., Oct. 5-9, 1970, W. N. Miner (Ed.), p. 478, Metallurgical Society of the American Institute of Mining, Metallurgical, and Petroleum Engineers, Inc., New York, 1970.
  36. M. P. Houston, O. L. Kruger, and W. M. Pardue, in *Fourth International Conference on Plutonium and Other Actinides*, Santa Fe, N. Mex., Oct. 5-9, 1970, W. N. Miner (Ed.), p. 488, Metallurgical Society of the American Institute of Mining, Metallurgical, and Petroleum Engineers, Inc., New York, 1970.
  37. J. A. C. Marples and A. Hough, in *Fourth International Conference on Plutonium and Other Actinides*, Santa Fe, N. Mex., Oct. 5-9, 1970, W. N. Miner (Ed.), p. 497, Metallurgical Society of the American Institute of Mining, Metallurgical, and Petroleum Engineers, Inc., New York, 1970.
  38. G. Schoeck, *J. Appl. Phys.*, **29**: 112 (1958).
  39. D. Mosedale, *J. Appl. Phys.*, **33**: 3142 (1962); *J. Nucl. Mater.*, **35**: 250 (1970).
  40. R. V. Hesketh, *J. Nucl. Mater.*, **26**: 77 (1969); **29**: 217 (1969); **35**: 253 (1970).
  41. G. P. Piercy, *J. Nucl. Mater.*, **26**: 18 (1968).
  42. G. W. Lewthwaite, *J. Nucl. Mater.*, **38**: 118 (1971).
  43. F. A. Nichols, *J. Nucl. Mater.*, **30**: 249 (1969); **35**: 251 (1970); **37**: 59 (1970); W. J. Duffin and F. A. Nichols, *J. Nucl. Mater.*, **45**: 302 (1973).
  44. D. Brucklacher, W. Dienst, and F. Thummler, *International Symposium on Ceramic Nuclear Fuels*, p. 100, American Ceramic Society, Washington, 1969.
  45. H. S. Carslaw and J. C. Jaeger, *Conduction of Heat in Solids*, 2nd ed., Chap. XIV, Oxford Book Company, Inc., New York, 1959.
  46. F. Seitz and J. S. Koehler, *Solid State Phys.*, **2**: 305 (1956).
  47. A. A. Solomon, J. L. Routhert, and J. C. Voglewede, Fission-Induced Creep of  $UO_2$  and Its Significance to Fuel Element Performance, USAEC Report ANL-7857, Argonne National Laboratory, September 1971.
  48. J. S. Perrin, *J. Nucl. Mater.*, **42**: 101 (1972).
  49. R. L. Coble, *J. Appl. Phys.*, **32**: 787 (1961).
  50. J. H. Rosolowski and C. Greskovich, *J. Appl. Phys.*, **44**: 1441 (1973).
  51. A. J. Markworth, *J. Appl. Phys.*, **44**: 1890 (1973).
  52. B. Burton and G. L. Reynolds, *J. Nucl. Mater.*, **45**: 10 (1972/1973).
  53. H. Assman and H. Stehle, Verdichtungseffekte in Gesintertem  $UO_2$ , *Reaktor Tagung*, Karlsruhe, 1973; *J. Nucl. Mater.*, **52**: 303 (1974).
  54. D. H. Locke, *Nucl. Eng. Int.*, **17**(199): 1015 (December 1972).
  55. M. O. Marlowe, Report NEDO-12440, General Electric Company, 1973.
  56. Y. Vasilos and R. M. Spriggs, *J. Amer. Ceram. Soc.*, **46**: 438 (1963).
  57. R. C. Rossi and R. M. Fulrath, *J. Amer. Ceram. Soc.*, **48**: 588 (1965).

## 16.14 PROBLEMS

16.1 A block of solid contains edge dislocations oriented as shown in the sketch.



(a) Which dislocations move by climb when a tensile stress,  $\sigma$ , is applied to the vertical faces of the block? Indicate the climb direction with an arrow.

The climb velocity of the dislocations affected by the applied stress is calculated as follows: A unit cell is chosen to consist of a cylindrical annulus of solid with the core of the dislocation (radius  $R_d$ ) on the axis. At the cores of dislocations properly oriented for climb, the vacancy concentration is equal to that of an equilibrium solid subject to a pressure  $-\sigma$ . The outer radius,  $R$ , is chosen so that the entire solid is filled with cylinders of the type shown in the sketch. The vacancy concentration at the outer radius of the cylinder is assumed to be equal to that in equilibrium in a stress-free solid,  $C_v^0$ .

(b) What is the vacancy concentration at the core of the dislocation in terms of the stress-free equilibrium value  $C_v^0$  and the applied tensile stress,  $\sigma$ ?

(c) If the density of dislocations in the solid is  $\rho_d$  cm of line/cm<sup>3</sup> solid and all are aligned parallel to each other, what is the unit cell radius,  $R$ ?

(d) Set up and solve the steady-state vacancy diffusion equation in the unit cell. Calculate the flux of vacancies from each unit length of dislocation line.

(e) What is the relation between the flux of vacancies from the edge dislocation and the climb velocity? Combine with the answer to (d) and obtain the climb velocity.

(f) Suppose the climbing dislocations meet no obstacles to their motion. What is the creep rate in the direction of the applied stress, which is pure tension? Compare the result with Eq. 8.21.

16.2 We wish to use the ideas behind the continuum analysis of hot pressing (Sec. 16.11) to determine a swelling law for fission-gas bubbles. To do this, we must add a work-rate term

$$\dot{W}_b = \left[ p - \left( \frac{2\gamma}{R_b} \right) \right] \dot{V}_b$$

to the right-hand side by Eq. 16.183. This term represents the work done on the solid by the expanding bubble, which contains fission gas at pressure  $p$  and has a radius  $R_b$ . According to Eq. 13.6,  $p - (2\gamma/R_b)$  is the radial stress in the solid which maintains the bubble surface in mechanical equilibrium. The value  $\dot{V}_b$  is the rate of increase of the volume of the bubble in the center of the unit cell used in the analysis. The gas in the bubble is assumed to obey the ideal-gas law.

Assume that the bubble density is  $N_b$  and that all fission gas produced in the solid part of the unit cell of volume  $V = 1/N_b$  immediately goes to the bubble at the center of the cell. The fission rate is  $\dot{F}$ , and the yield of fission gas is  $Y_{Xe}$ . Let  $s$  be the swelling due to fission gases [i.e.,  $(\Delta V/V)_g$ ] and use the linear creep law (Eq. 16.186 with  $n = 1$ ).

(a) Derive the differential equation giving  $\dot{s}$  = gas swelling rate as an explicit function of irradiation time  $t$  and swelling  $s$ .

(b) Show that, when the fuel has a very low creep strength (i.e., when  $\alpha$  of Eq. 16.186 is very large) and the applied stress is low, the result of part (a) reduces to Eq. 13.146.

16.3 Derive the hot-pressing rate (the generalization of Eq. 16.190) for the creep law of Eq. 16.186 in which  $n > 1$ .

16.4 In their analysis of densification by re-resolution, Assmann and Stehle<sup>53</sup> assume that  $\Delta m_v$  vacancies are returned to the solid each time a fission fragment passes through a pore. The number of fission fragments per second penetrating a pore is given by the result of problem 13.10, in which the limiting case for  $\mu/R \rightarrow 0$  can be used.

(a) What is the vacancy re-resolution parameter  $b$  for this model?

(b) Starting from Eqs. 16.143 and 16.146, derive the analog of Eq. 16.168 for this particular re-resolution parameter expression.

16.5 The presence of a temperature distribution in a cylindrical fuel pin produces thermal stresses in the solid. For a parabolic temperature profile, the tangential, or hoop, stress is given by

$$\sigma_\theta = \frac{\alpha E (T_o - T_s)}{4(1 - \nu)} \left( 1 - 3 \frac{r^2}{R^2} \right)$$

where the stress is positive in compression,  $\alpha$  is the coefficient of linear expansion of the fuel,  $E$  and  $\nu$  are its Young's modulus and Poisson's ratio, respectively, and  $R$  is the fuel radius.

Cracking of the fuel at the outer surface is first observed at a linear power of 100 W/cm. At what fractional radius do the cracks start when the linear power is 500 W/cm? What is the temperature at the root of the crack? Assume a fuel surface temperature,  $T_s$ , of 700°C.

# Chapter 17

## Radiation Damage

### 17.1 INTRODUCTION

The preceding chapters have dealt with some of the observable consequences of fission-fragment irradiation of ceramic fuel materials; succeeding chapters will be concerned with changes in the properties of cladding metals resulting from fast-neutron bombardment. These macroscopic, observable, and often technologically crucial results of exposure of solids to energetic particles are collectively known as *radiation effects*. The primary, microscopic events that precede the appearance of gross changes in the solid are termed *radiation damage*. This branch of physics attempts to predict the number and configuration of the point defects (vacancies and interstitial atoms) produced by the bombarding particles. Radiation-damage analyses are not concerned with what the defects go on to do in the solid—such processes are properly categorized as radiation effects. Radiation damage and radiation effects can also be distinguished by their characteristic time scales; the primary events produced by nuclear irradiation are over in less than  $10^{-11}$  sec after the bombarding particle has interacted with the solid. Subsequent processes require much longer times; the diffusion of radiation-produced point defects to sinks in the solid can take milliseconds. The time scale of the nucleation and growth of voids in metals by agglomeration of radiation-produced vacancies is of the order of months.

The primitive damage-producing processes involve the interaction of lattice atoms with particles possessing energies far in excess of thermal energy ( $\sim kT$ ). Consequently, the temperature of the solid is of no importance in the analysis of radiation damage. The processes included under radiation effects, however, are concerned with point defects, or clusters thereof, which are in thermal equilibrium with the host crystal. The kinetics of such processes are therefore highly dependent on solid temperature, which invariably appears as a Boltzmann factor,  $\exp(-E/kT)$ , where  $E$  is the characteristic energy of a thermodynamic process or a migratory event.

The energy transferred to a stationary lattice atom in a collision with a high-energy bombarding particle is of the order of tens to hundreds of kiloelectron volts. This quantity of energy is so much larger than the energy binding the atom in its lattice site that displacement of the struck atom is virtually certain. The lattice atom first struck

and displaced by the bombarding particle is called the *primary knock-on atom*, or PKA. Because a PKA possesses substantial kinetic energy, it becomes an energetic particle in its own right and is capable of creating additional lattice displacements. These subsequent generations of displaced lattice atoms are known as *higher order knock-ons*, or *recoil atoms*. An atom is considered to have been displaced if it comes to rest sufficiently far from its original lattice site that it cannot return spontaneously. It must also be outside the recombination region of any other vacancy created in the process. The displaced atom ultimately appears in the lattice as an interstitial atom. The empty lattice sites left behind by the displaced atoms (equal in number to the displaced atoms) are indistinguishable from ordinary thermally produced vacancies. The ensemble of point defects created by a single primary knock-on atom is known as a *displacement cascade*.

The earliest and simplest theory of radiation damage treated the cascade as a collection of isolated vacancies and interstitials and gave no consideration to the spatial distribution of the point defects. In the crudest approximation the number of displaced atoms is computed by approximating the collision partners as hard spheres; the only physical property of the solid needed in this model is the energy that a lattice atom must acquire in a collision in order to be displaced. Many improvements on this simple collision model have been made, but the idea of a cascade consisting of isolated point defects has been retained. Hard-sphere scattering can be replaced by energy-transfer cross sections based on realistic interatomic potentials. The loss of energy of a moving atom by interaction with the electrons of the medium, in addition to elastic collisions between atoms, can be added to simple cascade theory. Finally, the simple model can be improved by considering energy-loss mechanisms peculiar to the periodicity of the crystalline lattice, the most important of which are focusing and channeling.

Radiation damage is not restricted to the isolated point defects produced by the bombarding particles. Indeed, vacancies and interstitials can be produced so close to each other that clustering of the point defects occurs spontaneously within the short time required for completion of the primary event. When the distance between successive collisions of a recoil atom and the stationary lattice atoms approaches the interatomic spacing of the crystal structure,

it is clearly inappropriate to model the cascade as a collection of isolated vacancies and interstitials. Instead, a dense cluster of point defects called a *displacement spike* or *depleted zone* is formed. Because of the proximity of the point defects in a displacement spike, the probability of near-instantaneous annihilation of many of the vacancies and interstitials produced by the high-energy collisions becomes large. In fact, the number of point defects that actually survive a cascade and are capable of producing observable radiation effects can be as low as 1% of the number predicted by simple cascade theory.

The cascade is initiated by a primary knock-on atom. The cascade therefore consists of many interactions between moving and stationary atoms of the same kind. The primary knock-on atom, on the other hand, is produced by a bombarding particle arising directly from some nuclear event, principally the fission process. In terms of damage-producing capabilities, the most important nuclear particles are the fission fragments (in fuel materials) and fast neutrons (in the cladding and structural materials). Other energetic subatomic particles, such as electrons, protons, alpha particles, and gamma rays, can also initiate displacement cascades. However, these particles are either far less damaging than fission fragments ( $e^-$  and  $\gamma$ ) or are produced in such small quantities in reactor fuel elements that their contribution to the total damage is negligible ( $p$  and  $\alpha$ ). Only fast neutrons and fission fragments are considered as bombarding particles in this chapter, and only the theoretical treatment of radiation damage in monatomic solids will be reviewed. For practical purposes of estimating damage in reactor materials, the calculations for elemental solids are usually simply applied without modification to multielement systems, such as the fuel  $(U,Pu)O_2$  or the alloy stainless steel.

To calculate the displacement rate, we must know the total flux and the energy spectrum of the bombarding particles. For fast neutrons the differential flux,  $\phi(E_n)$ , is obtained from reactor-physics calculations. The equivalent quantity for fission fragments can be obtained from the fission density,  $\bar{F}$ , and a reasonable assumption concerning the energy loss of the fragments in the fuel. If the energy spectrum of the flux of bombarding particles and the energy-transfer cross section for collisions between these particles and atoms of the lattice are known, the number of primary knock-on atoms in a differential energy range can be computed. The final step is to use this source spectrum of the primary knock-on atoms to determine the total number of recoils, or displaced atoms, using cascade theory. Such a computation provides the best available estimate of the damage inflicted on a solid by irradiation for those properties which depend primarily on the presence of isolated point defects (e.g., irradiation creep and void growth). On the other hand, when such forms of damage as irradiation hardening or embrittlement are of interest, the size and number density of displacement spikes are more important than the concentration of isolated vacancies and interstitials that have escaped from the spike. In this instance, analytic cascade theories that predict only the number of displaced atoms, no matter how sophisticated from the point of view of atomic collisions, are not germane. The characteristics of the clusters of defects

created by a PKA can best be ascertained by computer simulation of the radiation-damage process.

To predict either the number of displaced atoms by an analytical isolated point-defect cascade model or to compute the configuration of a displacement spike by a computer experiment requires that the interatomic potential between atoms of the solid be known. A great deal of information on atomic interaction potentials has been obtained by analysis of the equilibrium properties of a solid (Chap. 4). Unfortunately, these potential functions represent the interaction at separation distances of the order of a lattice constant, whereas the potential at much smaller separations is relevant in radiation-damage calculations, which involve much higher particle energies. For very high energies the colliding atoms approach each other so closely that the bare nuclei interact in a manner prescribed by a Coulomb potential. In the energy range characterizing most of the collisions responsible for cascade production, however, the nuclear charges are partially screened by the atomic electrons, and no completely satisfactory interatomic potential describes the interaction. The screened Coulomb potential (sometimes called the Bohr potential), the inverse power law potential, and the Born-Mayer potential are frequently used. Because of the computational difficulties involved in dealing with potential functions that lead to nonisotropic scattering in the center-of-mass system, these potentials are often used only to compute the radius of the equivalent hard sphere characterizing the collision, but the collision dynamics are determined from the hard-sphere model (which gives isotropic scattering in center-of-mass coordinates). In radiation-damage calculations only the repulsive portion of the interatomic potential function is needed. The attractive forces between lattice atoms, which are important in the equilibrium properties of the solid, play no part in the events associated with radiation damage.

The interaction between a moving atom and the lattice atoms is almost universally treated as a sequence of two-body elastic collisions. The binary-collision assumption is quite satisfactory at high interaction energies because the approach distances giving substantial energy transfer are very much smaller than the distances between lattice atoms; thus the collisions can be considered to occur between isolated pairs of atoms. At energies approaching the threshold energy for displacement, however, the cross section for atom-atom interaction is large, and the incoming atom can interact with more than one atom at the same time.

The collision between a recoil and a lattice atom is often assumed to be elastic, which means that kinetic energy is conserved in the event. Inelasticity can arise from excitation or ionization of the orbital electrons of the atoms involved in the collision. Indeed, interaction of moving atoms or ions with the electrons of the solid constitute the major energy-loss process at high energies. Transfer of energy from the moving atom to electrons does not lead to displacement, only to heat; the low electron mass means that they carry little momentum even though they may be quite energetic. Consequently, it is important to be able to estimate the degree to which the energy of a recoil atom is partitioned between electronic excitation and

elastic atom-atom collisions. Only the energy transferred in the latter process is available for causing displacements. Energy is transferred to the electrons in small increments so closely spaced that the process can be regarded as a continuous loss of energy by the moving atom. The atom continues to travel in a straight line but slows down as if it were passing through a viscous medium. The atom-atom interactions, on the other hand, occur at widely spaced intervals, transfer a significant portion of the initial kinetic energy of the moving atom in an essentially instantaneous collision, and produce substantial deflections of the original energetic atom. Consequently, the total energy loss of a moving atom can be accurately separated into two parts: (1) discrete elastic atom-atom encounters which both reduce the energy of the incident atom and produce lattice displacements and (2) a continuous process of electronic excitation which contributes to energy loss but not to displacements.

Not all the energy transferred to a stationary lattice atom by a recoil atom by process 1 is used to displace the former. A substantial portion of the initial energy of the PKA is degraded to heat by atom-atom collisions that do not deliver the requisite displacement energy to the struck atom. In this event the struck atom simply rattles about in its lattice site, ultimately degrading the energy it received in the collision to heat.

There are several excellent books dealing with the subject of radiation damage in a comprehensive and detailed manner.<sup>1-6</sup> In this chapter only those aspects of the theory pertinent to the performance of nuclear fuel elements are considered. Details of some derivations have been omitted when they can be found in one of the books devoted solely to the field of radiation damage.

## 17.2 BINARY ELASTIC-COLLISION DYNAMICS

### 17.2.1 Scattering Angles and Energy Transfer

Many useful aspects of binary collisions can be obtained without knowledge of the interatomic potential by application of the laws of momentum and energy conservation. Only nonrelativistic elastic collisions are considered. The masses of the interacting particles are denoted by  $M_1$  and  $M_2$ . Particle 1 (the projectile) approaches stationary particle 2 (the target) with speed  $v_{10}$ . Figure 17.1(a) shows the speeds and directions of the particles before and after the collision in the laboratory frame of reference, which is at rest with respect to the observer. The analysis is simplified by transforming the coordinates from the laboratory system to one that moves with the velocity of the center of mass of the two-particle system. The speed of the center of mass is given by

$$v_{cm} = \left( \frac{M_1}{M_1 + M_2} \right) v_{10} \quad (17.1)$$

Since the center-of-mass velocity is unchanged by the collision, the event appears in the new coordinate system as shown in Fig. 17.1(b). The initial speeds of the particles in

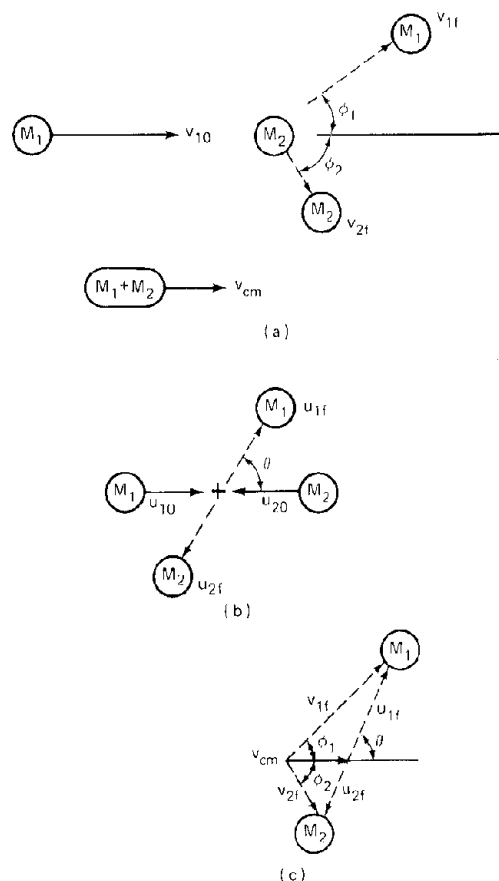


Fig. 17.1 Binary collision between a projectile of mass  $M_1$  and a target particle of mass  $M_2$ . (a) Laboratory frame of reference. (b) Center-of-mass coordinates. (c) Vector diagram relating the velocities in the two coordinate systems.

the center-of-mass system are related to those in the laboratory system by

$$u_{10} = v_{10} - v_{cm} \quad (17.2a)$$

$$u_{20} = v_{cm} \quad (17.2b)$$

The direction of  $u_{20}$  is opposite to that of  $u_{10}$ . The scattering angle in the center-of-mass system is  $\theta$ .

When the collision is viewed in the center-of-mass system, the recoiling particles appear to move away from each other in opposite directions. Momentum conservation along the axes of approach and departure yield

$$M_1 u_{10} + M_2 u_{20} = M_1 u_{1f} + M_2 u_{2f} \quad (17.3)$$

and conservation of kinetic energy requires that

$$\frac{1}{2} M_1 u_{10}^2 + \frac{1}{2} M_2 u_{20}^2 = \frac{1}{2} M_1 u_{1f}^2 + \frac{1}{2} M_2 u_{2f}^2 \quad (17.4)$$

Equations 17.3 and 17.4 are satisfied only if

$$u_{1f} = u_{10} = v_{10} - v_{cm} \quad (17.5a)$$

$$u_{2f} = u_{20} = v_{cm} \quad (17.5b)$$

The particle velocities in the laboratory system after the collision are determined by vectorially adding the center-of-mass velocity to  $u_{1f}$  and  $u_{2f}$ , or

$$v_{1f} = u_{1f} + v_{cm} \quad (17.6a)$$

$$v_{2f} = u_{2f} + v_{cm} \quad (17.6b)$$

The magnitudes of  $v_{1f}$  and  $v_{2f}$  can be obtained from the vector diagrams shown in Fig. 17.1(c). Application of the law of cosines to the lower diagram yields

$$\begin{aligned} v_{2f}^2 &= v_{cm}^2 + u_{2f}^2 - 2v_{cm}u_{2f} \cos \theta \\ &= 2v_{cm}^2 (1 - \cos \theta) \end{aligned} \quad (17.7)$$

where  $u_{2f}$  was expressed by Eq. 17.5b in order to arrive at the second equality in the above equation. We can eliminate  $v_{cm}$  from Eq. 17.7 by using Eq. 17.1, which produces

$$v_{2f}^2 = \frac{2M_1^2 v_{10}^2}{(M_1 + M_2)^2} (1 - \cos \theta)$$

Noting that  $E_{10} = M_1 v_{10}^2 / 2$  is the kinetic energy of the projectile and  $E_{2f} = M_2 v_{2f}^2 / 2$  is the kinetic energy of the recoil particle, we can write the above formula

$$E_{2f} = \frac{2M_1 M_2}{(M_1 + M_2)^2} E_{10} (1 - \cos \theta)$$

To simplify this notation for subsequent use, we replace  $E_{10}$  by  $E$  and denote  $E_{2f}$  by  $T$ , the energy transferred to the struck particle by the collision. The group containing the mass numbers is given a special symbol:

$$\Lambda = \frac{4M_1 M_2}{(M_1 + M_2)^2} \quad (17.8)$$

and the energy-transfer equation becomes

$$T = \frac{1}{2} \Lambda E (1 - \cos \theta) \quad (17.9)$$

The maximum possible energy transferred from the moving particle to the stationary one occurs in a head-on collision, for which  $\theta = \pi$  and

$$T_m = \Lambda E \quad (17.10)$$

If the particles are identical,  $\Lambda = 1$ , and any energy between 0 and  $E$  can be transferred in the collision.

The scattering angle in the laboratory system,  $\phi_1$ , and the direction of the struck atom after the collision,  $\phi_2$ , can be related to the scattering angle in the center-of-mass system with the aid of the vector diagram of Fig. 17.1(c). Applying the law of sines to the triangle representing the scattered projectile yields

$$\frac{v_{1f}}{\sin(\pi - \theta)} = \frac{u_{1f}}{\sin \phi_1}$$

where  $u_{1f}$  is given by Eq. 17.5(a), from which  $v_{cm}$  can be eliminated by Eq. 17.1, giving

$$u_{1f} = v_{cm} \left( \frac{v_{10}}{v_{cm}} - 1 \right) = v_{cm} \frac{M_2}{M_1}$$

Applying the law of cosines to the same triangle yields

$$v_{1f}^2 = u_{1f}^2 + v_{cm}^2 - 2v_{cm}u_{1f} \cos(\pi - \theta)$$

Combining these three equations and rearranging yields

$$\tan \phi_1 = \frac{(M_2/M_1) \sin \theta}{1 + (M_2/M_1) \cos \theta} \quad (17.11a)$$

Similarly, the law of sines for the vector diagram for the recoil particle yields

$$\frac{u_{2f}}{\sin \phi_2} = \frac{v_{2f}}{\sin \theta}$$

which, when combined with Eqs. 17.5b and 17.7, results in the relation

$$\tan \phi_2 = \frac{\sin \theta}{1 - \cos \theta} \quad (17.11b)$$

## 17.2.2 Some Properties of the Head-On Collision

The preceding analysis is valid for any nonrelativistic elastic collision for any center-of-mass scattering angle  $\theta$  provided the collision partners in the initial and final states are sufficiently far apart that the interaction energy between them is negligible compared to their kinetic energies. During the collision event, however, the separation distance is small, and the conversion of kinetic energy to potential energy is important. In particular, for a head-on collision ( $\theta = \pi$ ), the kinetic energy (exclusive of the kinetic energy of the center of mass) becomes zero at the point where the particles turn around and begin to retrace their paths. During a head-on collision, momentum conservation can be expressed by

$$v_{cm} = \left( \frac{M_1}{M_1 + M_2} \right) v_1 + \left( \frac{M_2}{M_1 + M_2} \right) v_2$$

where  $v_1$  and  $v_2$  are the laboratory-system speeds of the two particles at some point during the collision. The relative speed of the two particles is defined by\*

$$g = v_1 - v_2 \quad (17.12)$$

Rearrangement of the above two formulas permits  $v_1$  and  $v_2$  to be expressed as functions of  $v_{cm}$  and  $g$ :

$$v_1 = v_{cm} + \left( \frac{M_2}{M_1 + M_2} \right) g \quad (17.13a)$$

$$v_2 = v_{cm} - \left( \frac{M_1}{M_1 + M_2} \right) g \quad (17.13b)$$

The total kinetic energy of the two particles is given by

$$KE = \frac{1}{2} M_1 v_1^2 + \frac{1}{2} M_2 v_2^2$$

or, when expressed in terms of  $v_{cm}$  and  $g$ , by

$$KE = \frac{1}{2} (M_1 + M_2) v_{cm}^2 + \frac{1}{2} \mu g^2$$

\*In the general elastic collision treated in Sec. 17.2.1, the initial and final relative speeds  $g_0$  and  $g_f$  are represented by the distances separating the two particles in the diagram of Fig. 17.1(b) before and after the collision. The values of  $g_0$  and  $g_f$  have the same magnitude; the collision simply rotates the relative velocity vector by an angle  $\theta$ .

where

$$\mu = \frac{M_1 M_2}{M_1 + M_2} \quad (17.14)$$

is the reduced mass of the system. Thus, the total kinetic energy can be divided into two parts, one due to the motion of the system as a whole described by  $v_{cm}$  and the other arising from the relative kinetic energy of the two particles. The latter is

$$E_r = \frac{1}{2} \mu g^2 \quad (17.15)$$

During the collision the kinetic energy of the center of mass is unchanged, but the relative kinetic energy decreases as the potential energy becomes significant, which occurs at close separation distances. Conservation of total energy at any point in the collision requires that

$$E_r + V(x) = E_{r0} \quad (17.16)$$

where  $V(x)$  is the potential energy of interaction at a head-on separation distance  $x$  and  $E_{r0}$  is the relative kinetic energy in the initial state, which is taken to be at infinite separation. An important special case of Eq. 17.16 occurs at the distance of closest approach,  $x_m$ , where the relative kinetic energy is zero. If the collision partners are of the same mass,  $\mu = M/2$ , and if the target atom is initially at rest,  $g_0 = v_{10}$ , Eq. 17.16 then reduces to

$$V(x_m) = \frac{E}{2} \quad (17.17)$$

where  $E = M_1 v_{10}^2 / 2$  is the kinetic energy of the projectile. This formula will be used to deduce equivalent hard-sphere radii as a function of energy for particular types of interatomic potential functions.

### 17.3 BASIC CONCEPTS

The terminology pertinent to the collision and energy-loss processes involving large numbers of energetic atoms in a solid is reviewed in this section.

#### 17.3.1 Cross Section

The primitive idea of a cross section is shown in Fig. 17.2. Consider a single projectile (or bombarding particle) passing through a medium consisting of  $N$  target particles per unit volume. Target species are assumed to be distributed randomly. We wish to formulate the probability that the projectile collides with a target particle while traversing a path length  $dx$  in the medium. If the incident particle strikes the front face of the  $dx$ -thick slice within any one of the projected areas,  $\sigma$ , characterizing the target particles, a collision occurs. The volume element in the drawing contains  $N dx$  particles whose projected areas occupy a fraction  $\sigma N dx$  of the front face of the volume element. The chance of an interaction is therefore:

$$N \sigma(E) dx = \text{Probability of the collision of an incident particle with a target particle in } dx \quad (17.18)$$

Equation 17.18 defines the *total collision cross section* between the incident and target species when the energy of the former is  $E$ . The total cross section is a measure of the probability of occurrence of any type of collision between the two particles. Cross sections of more restricted types of interactions can be similarly defined. For example, we may require that the collision transfer energy between  $T$  and  $T + dT$  to the target particle during the collision and define the *differential energy-transfer cross section* by:

$$N \sigma(E, T) dT dx = \text{Probability of a collision in the distance } dx \text{ which transfers energy in the range } (T, dT) \text{ to the target particle} \quad (17.19)$$

The differential and total cross sections are related by

$$\sigma(E) = \int_0^{T_m} \sigma(E, T) dT \quad (17.20)$$

where  $T_m$  is the maximum energy transferable in a collision. For elastic collisions,  $T_m$  is given by Eq. 17.10.

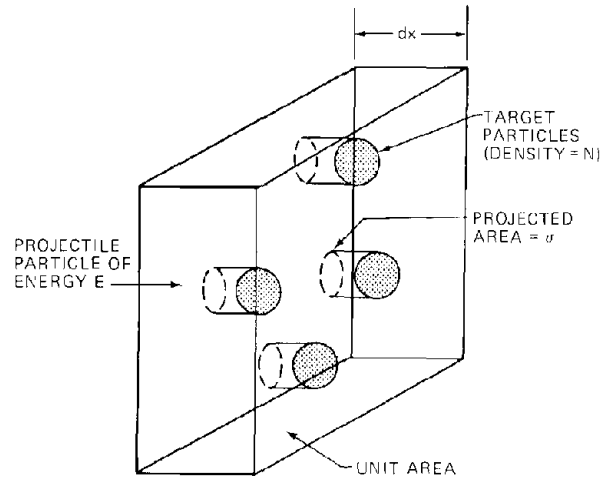


Fig. 17.2 The collision cross section.

The *differential angular cross section* describes the probability of an interaction that results in deflection of the incident particle by an angle  $\theta$  in the center-of-mass system:

$$N \sigma(E, \theta) d\Omega dx = \text{Probability of a collision in } dx \text{ which scatters the incident particle into a center-of-mass angle in the range } (\theta, d\Omega) \quad (17.21)$$

where  $d\Omega$  is an element of solid angle about the scattering direction  $\theta$ . Inasmuch as scattering is azimuthally symmetric (i.e., equally probable in any direction in the plane perpendicular to the  $x$ -direction in Fig. 17.2), the solid-angle increment is

$$d\Omega = 2\pi d(\cos \theta)$$

For elastic scattering, Eq. 17.9 provides a unique relation between  $T$  and  $\theta$ ; thus the angular and energy-transfer differential cross sections are connected by

$$2\pi \sigma(E, \theta) d(\cos \theta) = \sigma(E, T) dT$$

or

$$\begin{aligned} \sigma(E,T) &= 2\pi \sigma[E,\theta(T)] \left| \frac{d(\cos \theta)}{dT} \right| \\ &= \left( \frac{4\pi}{\Lambda E} \right) \sigma[E,\theta(T)] \end{aligned} \quad (17.22)$$

The ratio of the differential elements  $d(\cos \theta)$  and  $dT$  is obtained from Eq. 17.9. The second equality in Eq. 17.22 contains this transformation. The notation  $\theta(T)$  means that  $\theta$  is expressed as a function of  $T$  using the same equation. Equation 17.22 permits the differential energy-transfer cross section to be determined if the differential angular cross section is known. When scattering is isotropic in the center-of-mass system,  $\sigma[E,\theta(T)] = \sigma(E)/4\pi$ .

### 17.3.2 Mean Free Path

The *mean free path* is the average distance travelled by an incident particle between collisions. Equation 17.18 shows that the number of collisions per unit path length is  $N \sigma(E)$ . The reciprocal of this quantity is the average path length per collision, or

$$l(E) = \frac{1}{N \sigma(E)} = \text{Mean free path of a particle of energy } E \quad (17.23)$$

### 17.3.3 Current and Flux

The *current* describes the rate of transport of particles if they are all travelling in one direction, and the *flux* is the analogous measure for particles that are moving in many different directions.

The total current is defined by

$$I = \text{Number of particles crossing a plane of unit area perpendicular to the particle direction per second} \quad (17.24)$$

When the particles are not moving in a single direction, the flux is defined in terms of the unit sphere:

$$\Phi = \text{Number of particles crossing a sphere of unit projected area per second} \quad (17.25)$$

The flux can be restricted to those particles within the energy range from  $E$  to  $E + dE$ :

$$\phi(E) dE = \text{Number of particles with energies in the range } (E,dE) \text{ crossing the unit sphere per second} \quad (17.26)$$

where  $\phi(E)$  is the differential energy flux, or simply the differential flux or the energy flux and is related to the total flux by

$$\Phi = \int_0^\infty \phi(E) dE \quad (17.27)$$

### 17.3.4 Collision Density

If the current of incident particles entering the volume element in Fig. 17.2 is  $I$  and if each particle has a probability given by Eq. 17.18 of interacting, the number of collisions per unit volume per second is  $NI\sigma$ . This expression can be generalized to describe the collision rate

in a flux spectrum for interactions that transfer energy in a particular range. Thus

$$\begin{aligned} F(E,T) dE dT &= \text{Collisions per unit volume per unit time between target particles and incident particles in the range } (E,dE) \text{ which result in energy transfer to the target particle in the range } (T,dT) \\ &= N \phi(E) \sigma(E,T) dE dT \end{aligned} \quad (17.28)$$

Equation 17.28 can also be regarded as a source term expressing the volumetric rate of production of the recoils in the energy range  $(T,dT)$ :

$$N \left[ \int_0^\infty \phi(E) \sigma(E,T) dE \right] dT = \text{Number of recoil atoms produced per unit volume per unit time with energies in the range } (T,dT)$$

### 17.3.5 Stopping Power and Range

The *stopping power* is the energy lost by a moving particle per unit of length travelled in the medium. Equation 17.19 gives the probability of a collision in path length  $dx$  which results in energy loss between  $T$  and  $T + dT$ . The average energy loss in  $dx$  is obtained by multiplying Eq. 17.19 by the energy transfer  $T$  and integrating over all possible values of  $T$ :

$$\begin{aligned} \langle dE \rangle &= N \int_{T_0}^{T_m} T \sigma(E,T) dT dx \\ &= \text{Average energy loss of a particle of energy } E \text{ in moving a distance } dx \end{aligned}$$

Dividing this equation by  $dx$  and omitting the averaging symbol on  $dE$  gives the stopping power:

$$\frac{dE}{dx} = N \int_{T_0}^{T_m} T \sigma(E,T) dT \quad (17.29)$$

The minimum energy transferred,  $T_0$ , need not be zero. The stopping cross section is defined as

$$\frac{1}{N} \frac{dE}{dx} = \int_{T_0}^{T_m} T \sigma(E,T) dT \quad (17.29a)$$

The *range* is a measure of the path length in the solid traversed by a particle from the point of its birth in or entry into the solid to the point at which it no longer possesses kinetic energy. Two ranges can be defined: one easy to calculate and the other easy to measure. Figure 17.3 shows a typical history of a particle that makes a number of collisions before it is stopped. The arrows indicate the path length between successive collisions. They are approxi-

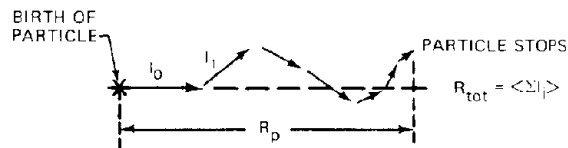


Fig. 17.3 Path of a typical particle slowing down in a solid showing the mean and projected ranges.

mately equal to the mean free path. The total range is defined as the mean value of the sum of the linear segments between collisions between birth and stopping of the particle:

$$R_{tot} = \langle \sum l_i \rangle$$

The total range is related to the stopping power by

$$R_{tot}(E) = \int_0^{R_{tot}(E)} dx = \int_0^E \frac{dE'}{(dE'/dx)} \quad (17.30)$$

The total range can be computed if the dependence of the stopping power on energy is known. According to Eq. 17.29 the differential energy-transfer cross section is needed for this calculation.

The projected range,  $R_p$ , is the component of the total range along the initial direction of the particle. For an interatomic potential that varies as the inverse square of the separation distance, the two ranges are related by:<sup>7</sup>

$$\frac{R_{tot}}{R_p} = 1 + \frac{1}{3} \left( \frac{M_2}{M_1} \right) \quad (17.31)$$

where  $M_2$  and  $M_1$  are the masses of the target and projectile species, respectively. Although  $R_p$  is always less than  $R_{tot}$ , the difference between the two ranges is reduced as the average energy transferred per collision becomes smaller (i.e., for  $M_2/M_1 \ll 1$ ).

The concepts of stopping power and range are most useful when many small-energy-transfer collisions occur during particle slowing down. In this case the energy loss process is nearly continuous, and the deflection per collision is also small. The interaction of atomic particles with the electrons of a solid is an example of this type of slowing down. The maximum energy transferred to an electron by a particle of mass  $M$  is a fraction,  $4m_e/M \approx 0.002/M$ , of the kinetic energy of the moving atom, and, according to Eq. 17.11a, the deflection angle per collision is  $m_e/M \approx 10^{-5}$  radians.

## 17.4 POTENTIAL FUNCTIONS AND ENERGY-TRANSFER CROSS SECTIONS

The manner in which the potential energy of a two-particle system varies with the distance separating the two centers determines both the equilibrium properties of an assembly of atoms and the way that energetic particles interact with a lattice of stationary atoms. The relation between the interatomic potential function and the equilibrium properties of the solid is discussed in Chap. 4. The potential function appears in radiation-damage theory via the differential energy-transfer cross section,  $\sigma(E,T)$ , which determines the energy loss rates, the collision density, the mean free path, and other properties of the slowing-down process. The differential energy-transfer cross section is uniquely determined by the potential function, although the connection between  $V(r)$  and  $\sigma(E,T)$  is rather complex. Only a few simple potential functions can be converted to analytical expressions for the differential cross section.

### 17.4.1 Potential Functions

Because no single potential function applies over the entire range of separation distances between atoms or ions, it is useful to consider the limiting cases of very-high-energy collisions (small distances of approach) and near-thermal energies (i.e., tens of electron volts) where the electronic clouds of the two species just begin to overlap. There are two principal contributions to the repulsive potential between two atoms which correspond to these extremes: (1) the electrostatic repulsion between the positively charged nuclei and (2) the increase in energy required to maintain the electrons of nearby atoms in the same region of space without violating the Pauli exclusion principle. Since no two electrons can occupy the same position, overlapping of electrons from two atoms must be accompanied by promotion of some of the electrons to higher, unoccupied levels of the atomic structure. The energy required for this process increases as the atoms approach each other because a larger number of the orbital electrons become affected.

At separations somewhat smaller than the equilibrium spacing of the atoms in the crystal lattice, which is of the order of a lattice constant, the nuclear repulsion is small because the positive nuclear charges are nearly completely shielded by the intervening electrons [Fig. 17.4(c)]. In this region the potential energy of interaction is adequately represented by the Born-Mayer potential:

$$V(r) = A \exp\left(-\frac{r}{\rho}\right) \quad (17.32)$$

Although the constants  $A$  and  $\rho$  in this formula cannot be determined from theory, they can be obtained from the equilibrium properties of the solid (Chap. 4).

As the separation distance between the two atoms decreases, the closed-shell repulsion described by Eq. 17.32 increases but, since there are fewer electrons between the two nuclei to shield the positive charges from each other, so does the electrostatic repulsion contribution to the potential energy. When the interaction energy is so large that the two nuclei are separated by distances smaller than the radius of the inner electron shells (the K-shells), the principal contribution to the total potential energy of the system is due to the electrostatic force between the two positively charged nuclei [Fig. 17.4(a)]. In this limit the interaction is satisfactorily described by the Coulomb potential:

$$V(r) = \frac{Z_1 Z_2 e^2}{r} \quad (17.33)$$

where  $Z_1$  and  $Z_2$  are the atomic numbers of the two atoms or ions and  $e$  is the electronic charge ( $e^2 = 14.4 \text{ eV}\cdot\text{\AA}$ ).

The intermediate region where both Coulombic repulsion and closed-shell repulsion are of comparable magnitudes is the most difficult to describe accurately. Unfortunately, these separation distances are just those most likely to occur in radiation-damage situations. This region, which is depicted in Fig. 17.4(b), is often represented by the screened Coulomb potential, which reflects the diminution of the pure Coulomb repulsion between the nuclei due to the electrostatic screening of the positive charges by the intervening inner-shell electrons. This potential is given by

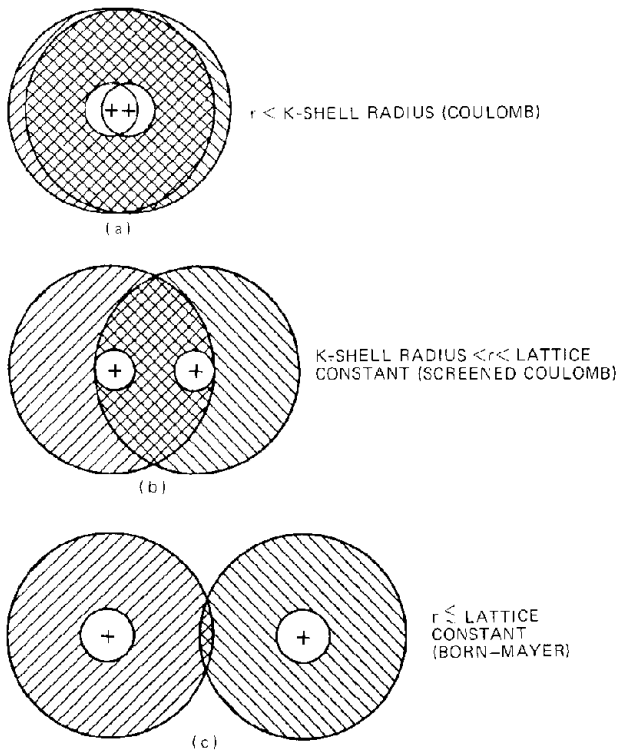


Fig. 17.4 Regions of applicability of various interatomic potential functions. The + sign represents the nuclear charge, and the shaded annular zones depict the radii between the innermost electronic shells and the ionic radius, where most of the atomic electrons are located. The cross-hatched areas denote the regions of overlap of the electron clouds of the two atoms.

$$V(r) = \frac{Z_1 Z_2 e^2}{r} \exp\left(-\frac{r}{a}\right) \quad (17.34)$$

where  $a$  is the screening radius, given by

$$a = \frac{2^{1/2} \lambda a_B}{(Z_1^{2/3} + Z_2^{2/3})^{1/2}} \quad (17.35)$$

where  $a_B$  is the Bohr radius and  $\lambda$  is a constant of order unity (values from 0.707 to 2.09 have been used in various calculations). The screening radius decreases as the atomic numbers of the atomic species increase because the number of electrons with orbital radii less than a specified value  $r$  increases with the charge of the nucleus. As  $r \ll a$ , the screened Coulomb potential reduces smoothly to the Coulomb potential function.

Equation 17.34 does not account for the potential energy due to closed-shell repulsion, which decreases less rapidly than the potential arising from screened repulsion of the nuclear charges. Although Eq. 17.34 extends the range of the Coulomb potential somewhat, it falls off much more rapidly than the Born-Mayer potential. Hence, the screened Coulomb potential cannot be used to bridge the entire gap between the Coulomb and Born-Mayer potential

functions. A number of theoretical and empirical potentials for describing this region have been proposed (Ref. 1, pp. 95-105; Ref. 2, Chap. 6, and Refs. 8 and 9).

Inverse power potentials of the form

$$V(r) = \frac{A}{r^s} \quad (s = 2, 3) \quad (17.36)$$

have also been used extensively. The constants  $A$  and  $s$  are obtained by fitting Eq. 17.36 to the screened Coulomb potential at small  $r$  or to the Born-Mayer potential function at large  $r$ . In this manner the entire interatomic potential can be spliced together by a series of functions of different form (Fig. 17.5).

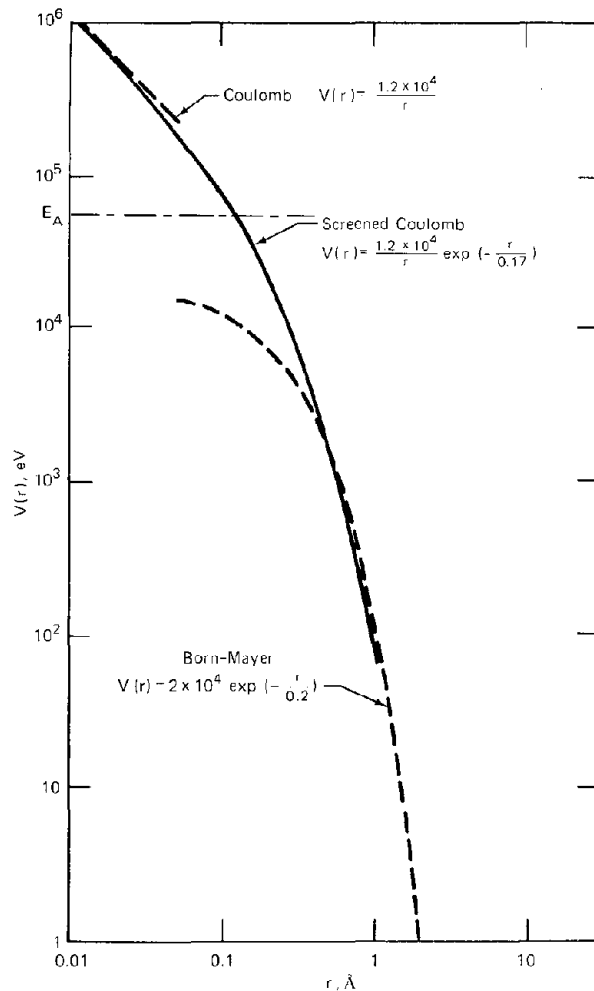


Fig. 17.5 Composite potential function for interaction between copper atoms.

### 17.4.2 Energy-Transfer Cross Sections

It is in principle possible to transform any of the potentials described in the preceding section into a differential angular cross section  $\sigma(E, \theta)$  and then to a differential energy-transfer cross section (see Ref. 1, pp. 105-107). However, only the Coulomb and inverse power potentials yield analytical formulas for  $\sigma(E, T)$ . The Coulomb poten-

tial leads to the familiar Rutherford scattering cross section:

$$\sigma(E,T) = \pi Z_1^2 Z_2^2 e^4 \left( \frac{M_1}{M_2} \right) \frac{1}{ET^2} \quad (17.37)$$

The inverse power potential of Eq. 17.36 yields the differential cross section:

$$\sigma(E,T) = \text{Constant} \frac{1}{E^{1/s}} \frac{1}{T^{1+(1/s)}} \quad (17.38)$$

A form of the differential energy-transfer cross section which is particularly convenient for radiation-damage problems is based on the billiard-ball dynamics of hard spheres. This potential is  $V = \infty$  for  $r < 2r_0$  and  $V = 0$  for  $r > 2r_0$ , where  $r_0$  is the radius of the colliding hard spheres. It is well known that the angular cross section for hard-sphere scattering is isotropic in the center-of-mass system, or  $\sigma(E,\theta) = \pi(2r_0)^2/4\pi$ . Introducing this expression into Eq. 17.22 yields the energy-transfer cross section:

$$\sigma(E,T) = \frac{4\pi r_0^2}{\Delta E} = \frac{\sigma(E)}{\Delta E} \quad (17.39)$$

The major computational advantage of Eq. 17.39 is its lack of dependence on  $T$ , which considerably simplifies the integrals required to determine energy loss and collisional properties of radiation damage. The prime disadvantage of this formula, of course, is that it is based on an unrealistic interatomic potential function.

The utility of the hard-sphere model can be retained and yet some flavor of the correct interatomic potential can be introduced by allowing the hard-sphere radius  $r_0$  to vary with particle energy. This so-called equivalent or energy-dependent hard-sphere model can be applied to any interatomic potential function. The recipe for determining  $r_0$  is to equate  $2r_0$  to the distance of closest approach in a head-on collision. The latter is determined from the actual potential function  $V(r)$ . For identical atoms,  $V(2r_0) = E/2$  (Eq. 17.17), which serves to fix  $r_0$  as a function of  $E$ . For the screened Coulomb potential, this procedure yields

$$\frac{Z^2 e^2}{E} = r_0(E) \exp \left[ \frac{2r_0(E)}{a} \right] \quad (17.40)$$

where  $Z_1 = Z_2$  for collisions between like atoms.

For the Born-Mayer potential of Eq. 17.32, the equivalent hard-sphere radius is

$$r_0(E) = \frac{1}{2} \rho \ln \left( \frac{2A}{E} \right) \quad (17.41)$$

The energy-transfer cross section is given when Eq. 17.39 is combined with either Eq. 17.40 or 17.41.

Collisions become more hard-sphere-like as the potential function steepens. Figure 17.5 shows that  $V(r)$  is changing most rapidly with  $r$  at low energies, where the inverse power or Born-Mayer potentials are applicable. The Coulomb potential, which varies as  $r^{-1}$ , cannot be adequately approximated by an equivalent hard sphere. The crudest approach to delineating the energy below which the equivalent hard-sphere model can be employed is to equate the screening radius with the distance of closest approach in a head-on collision in pure screened Coulomb scattering.

The latter can be obtained from Eqs. 17.17 and 17.34 as a solution of

$$\frac{Z^2 e^2 \exp(-x_m/a)}{x_m} = \frac{E}{2}$$

Setting  $x_m = a$  and determining  $a$  from Eq. 17.35 for  $Z_1 = Z_2$  and  $\lambda = 1$  yields the critical energy separating Rutherford and hard-sphere scattering when projectile and target atoms are the same kind:

$$E_A = \frac{2Z^3 e^2 \exp(-1)}{a_B} \quad (17.42)$$

Figure 17.5 shows the transition for copper at  $\sim 50$  keV. Although the hard-sphere model is to be used for projectile energies less than the value given by Eq. 17.42, the total cross section can vary with energy according to  $r_0$  formulas, such as Eqs. 17.40 and 17.41, or the equivalent expression for an inverse power potential.

The principal difference between the energy-transfer cross sections derived from realistic potentials, such as the Coulomb and inverse power functions, and from the hard-sphere model is the dependence upon  $T$ . Equation 17.39 shows that all energy transfers between 0 and  $T_m = \Delta E$  are equally probable, whereas Eqs. 17.37 and 17.38 strongly favor forward scattering, in which the energy transfer is small. Despite the shortcomings of the hard-sphere model, the fact that it considerably simplifies the analysis makes it valuable for qualitatively demonstrating the salient features of radiation-damage processes.

## 17.5 ENERGY LOSS TO ELECTRONS

The rate at which high-velocity heavy particles lose energy to the electrons of the medium through which they are travelling is important in many radiation-damage calculations; the range of a charged particle in matter is primarily determined by  $(dE/dx)_e$  (Eq. 17.30). The ability of a primary knock-on atom to create displacements in the lattice is in part determined by the fraction of the initial energy of the PKA which is dissipated in electronic interactions during slowing down.

The complexity of accurately accounting for electronic energy losses in cascade theory can be avoided by the simple expedient of determining an energy  $E_c$  below which the moving atom cannot transfer enough energy to an electron of the medium to remove the latter from whatever bound state it may be in. Let  $I$  be the binding energy of an electron to an atom of the solid. For an electron to acquire energy  $I$  in a head-on collision with a moving atom of mass  $M_1$ , the energy of the atom must be (Eqs. 17.8 and 17.10 with  $\tilde{E} = E_c$  and  $M_2 = m_e$ , the electron mass):

$$E_c = \frac{M_1}{4m_e} I$$

For ionic or covalent solids, the most reasonable choice for  $I$  is the energy needed to bridge the forbidden zone between the valence and conduction bands, which is several electron volts. In metals, electrons very near the top of the Fermi sea can be excited by any amount of energy, no

matter how small. However, the bulk of the conduction electrons in a metal lie well below the Fermi level, and excitation by arbitrarily small additions of kinetic energy is precluded by the fact that higher levels are occupied (Chap. 4). The average electron in metal, therefore, needs to receive about one-half the Fermi energy in order to become excited and thereby remove energy from the moving atom. Setting  $m_e = 1/2000$  amu and  $I = 2$  eV, we find the critical energy for all substances to be roughly equal to the mass number of the moving atom in kiloelectron volts:

$$E_c \simeq 10^3 M_1 \text{ (eV)} = M_1 \text{ (keV)} \quad (17.43)$$

When the kinetic energy of the moving atoms or ions falls below this value, energy losses to the electrons of the solid rapidly become small compared to the energy that the moving atom can transfer to stationary atoms of the lattice by elastic collisions. As a corollary, energy transfer by atomic collisions for  $E > E_c$  is presumed to be negligible compared to the electronic stopping of the moving particle.

It will be shown later that electronic energy loss in metals continues for energies below the value given by Eq. 17.43 and that this loss mode is important in assessing the amount of damage that can be inflicted by nuclear radiations. It is therefore useful to analyze energy transfer to the electrons of a solid on a more realistic basis than that described above. Two calculations of  $(dE/dx)_e$  are reviewed below.

### 17.5.1 Electronic Stopping at High Energies

When a heavy particle at high energy (i.e., more than several million electron volts) penetrates a solid, the great velocity strips off its outer orbital electrons. As a consequence, it moves through the solid as an ion whose charge is denoted as  $Z_1$  (this is not the atomic number of the moving atom). The moving ion transfers energy to the electrons of the medium by Coulombic interaction. The energy-transfer cross section for the process is given by Eq. 17.37 in which the second particle is an electron ( $Z_2 = 1, M_2 = m_e$ ). Thus,

$$\sigma(E, T_e) = \frac{\pi Z_1^2 e^4 (M_1/m_e)}{E T_e^2} \quad (17.44)$$

where  $E$  is the energy of the moving ion and  $T_e$  is the energy transferred to the electron during the binary encounter. If the ion energy is sufficiently high, all the electrons in the solid can be excited, and the density of electrons is  $ZN$ , where  $N$  is the atom density of the solid and  $Z$  is the atomic number of the atoms of the solid. The electronic stopping power is given by Eq. 17.29 in which  $T_m = 4(m_e/M_1)E$  and  $T_0 = \bar{I}$ , the average ionization energy of the target atoms. The energy-transfer cross section is given by Eq. 17.44 so the electronic stopping power can be expressed by

$$\left(\frac{dE}{dx}\right)_e = ZN \int_{\bar{I}}^{4(m_e/M_1)E} T_e \left[ \frac{\pi Z_1^2 e^4 (M_1/m_e)}{E T_e^2} \right] dT_e$$

Performing the integration yields

$$\left(\frac{dE}{dx}\right)_e = \frac{\pi N Z_1^2 Z e^4 (M_1/m_e)}{E} \ln \left[ \frac{4E}{(M_1/m_e)\bar{I}} \right] \quad (17.45)$$

When multiplied by a factor of 2 (which arises when the correct quantum-mechanical calculation is performed instead of the above classical analysis), Eq. 17.45 is known as Bethe's formula.

As the ion loses energy, the probability of capturing an electron from the medium increases. Or, the charge  $Z_1$  is dependent on the energy of the ion. Bohr<sup>10</sup> has calculated an effective charge (so called because it need not be an integer) by assuming that the ion retains in its outer shell only those electrons with orbital velocities that exceed the velocity of the moving ion. The Thomas-Fermi distribution of the velocities of electrons in atoms permits the number of electrons in the atom with velocities less than the ion velocity  $(2E/M_1)^{1/2}$  to be computed. These electrons are assumed to be stripped from the ion. The effective charge of the moving ion is given by

$$(Z_1)_{\text{eff}} = \frac{Z_1^{1/2} \hbar}{e^2} \left( \frac{2E}{M_1} \right)^{1/2} \quad (17.46)$$

where  $\hbar$  is Planck's constant divided by  $2\pi$  and  $Z_1$  now denotes the atomic number of the moving ion. Electron capture and loss from an atom or ion moving in a solid are dynamic processes, and noninteger charges should be interpreted as a result of weighting integer charge states (including the neutral atom) with the fraction of the time that is spent in each charge state. The effective charge cannot exceed the atomic number of the moving ion, of course, but Eq. 17.46 indicates that the ion will retain some charge no matter how low its kinetic energy. Actually, there is a lower energy,  $E_{\text{neut}}$ , at which a neutralized moving atom cannot be reionized by impact with a stationary electron in the solid. Consider the collision of the most weakly bound electron in the moving atom with a stationary electron in the medium. Instead of the atom traversing a sea of stationary electrons with a velocity  $v_1 = (2E/M_1)^{1/2}$ , consider the atom to be stationary and let the lattice electrons move with velocity  $v_1$  (i.e., change the frame of reference from the laboratory to the moving atom). If one of the lattice electrons makes a head-on collision with an electron in the atom, energy equal to  $m_e v_1^2/2$  is transferred from the former to the latter. If this quantity of energy is less than the minimum ionization energy of the moving atom,  $I$ , reionization cannot occur and the atom remains neutral for the remainder of the slowing-down process. The condition

$$\frac{1}{2} m_e v_1^2 = E_{\text{neut}} \frac{m_e}{M_1} = I$$

leads to numerical values of  $E_{\text{neut}}$  very similar to those determined for the opposite process (ionization of a lattice atom by a moving atom). Within the framework of this simple treatment, the minimum energy that a moving particle needs in order to maintain some positive charge is approximately given by its mass number in kiloelectron volts:

$$E_{\text{neut}} = M_1 \text{ (keV)} \quad (17.47)$$

Below this energy,  $(Z_1)_{\text{eff}}$  is zero and Eq. 17.46 does not apply.

Actually, Eq. 17.45 ceases to be valid at much greater energies than the tens of kiloelectron volts suggested by simple consideration of charge neutralization. The Bethe formula is in fact valid only on the portion of the stopping power curve where  $(dE/dx)_e$  is decreasing with energy. For heavy ions this occurs at energies<sup>8</sup> as high as 100 meV. The PKA created by fast neutrons scattering from the atoms of a metal are generally not energetic enough to fall in the range of applicability of Eq. 17.45; so a different mechanism is needed to explain the electronic stopping of predominantly neutral atoms passing through a lattice consisting of the same species.

### 17.5.2 Electronic Stopping at Low Energies

In order to compute  $(dE/dx)_e$  for atoms or ions moving in a metal of the same type, we compute the energy transfer to the conduction electrons very near the Fermi surface. As noted previously, these electrons can become excited by collisions that transfer considerably less energy than the energy needed to excite the average conduction electron (which requires  $\sim \epsilon_F/2$ ). Consider an atom of mass  $M_1$  and velocity  $v_{10}$  which makes a head-on collision with a conduction electron moving in the opposite direction with a velocity  $v_e$ . According to Eq. 17.12, with  $v_1 = v_{10}$  and  $v_2 = -v_e$ , the initial relative speed of the two particles is  $g_0 = v_{10} + v_e$ . In a head-on collision, the relative velocity vector changes sign but not magnitude; thus  $g_f = -(v_{10} + v_e)$ . The speed of the atom following the collision with the electron is given by Eq. 17.13a:

$$\begin{aligned} v_{1f} &= v_{cm} + \left( \frac{m_e}{M_1 + m_e} \right) g_f \\ &= \frac{M_1 v_{10} - m_e v_e}{M_1 + m_e} - \left( \frac{m_e}{M_1 + m_e} \right) (v_{10} + v_e) \\ &= v_{10} - \frac{2m_e v_e}{M_1} \end{aligned}$$

where  $m_e$  has been neglected compared to  $M_1$ . The energy loss suffered by the atom in the collision is

$$\begin{aligned} \Delta E &= \Delta \left( \frac{1}{2} M_1 v_1^2 \right) \simeq M_1 v_{10} (v_{10} - v_{1f}) \\ &= 2m_e v_e v_{10} \end{aligned} \quad (17.48)$$

Similarly, the electron velocity after the collision is given by Eq. 17.13b:

$$\begin{aligned} v_{ef} &= v_{cm} - \left( \frac{M_1}{M_1 + m_e} \right) g_f \\ &= \frac{M_1 v_{10} - m_e v_e}{M_1 + m_e} + \left( \frac{M_1}{M_1 + m_e} \right) (v_{10} + v_e) \\ &= 2v_{10} + v_e \end{aligned}$$

Or, the increase in the velocity of the electron is

$$\Delta v_e = v_{ef} - v_e = 2v_{10} \quad (17.49)$$

In a monovalent metal the number of conduction electrons is approximately equal to the atom density  $N$ . However, only those electrons with velocities lying in the range  $\Delta v_e$

of the Fermi velocity  $v_F$  are able to participate in the slowing-down process. Or, the density of effective electrons in the metal is

$$n_e \simeq N \left( \frac{\Delta v_e/2}{v_F} \right) = \left( \frac{v_{10}}{v_F} \right) N \quad (17.50)$$

Now consider a reference frame attached to the moving atom. The current of effective electrons impinging on the atom is

$$I_e = n_e g_0 = n_e (v_{10} + v_e) \simeq n_e v_e \quad (17.51)$$

and the number of collisions of the effective electrons per second with a single moving atom is  $\sigma_e I_e$ , where  $\sigma_e$  is the cross section for the interaction of the moving atom with the conduction electrons. The rate at which a moving atom loses energy to the effective electrons is  $\sigma_e I_e \Delta E$ , which, when divided by the distance moved by the atom in 1 sec ( $v_{10}$ ), gives the stopping power:

$$\left( \frac{dE}{dx} \right)_e = \frac{\text{Energy loss/sec-atom}}{\text{Distance travelled/sec-atom}} = \frac{\sigma_e I_e \Delta E}{v_{10}}$$

Substituting Eqs. 17.48, 17.50, and 17.51 into the above formula and expressing  $v_e$  and  $v_{10}$  as  $2\epsilon_F/m_e$  and  $(2E/M_1)^{1/2}$ , respectively, yields

$$\left( \frac{dE}{dx} \right)_e = 8\sigma_e N \left( \frac{m_e}{M_1} \right)^{1/2} E^{1/2}$$

Or, writing the coefficient of  $E^{1/2}$  as a constant  $k$ , the stopping power becomes

$$\left( \frac{dE}{dx} \right)_e = k E^{1/2} \quad (17.52)$$

More accurate analyses of this stopping mechanism than the simple model described above produce different values for the constant  $k$ , but the dependence upon  $E^{1/2}$  remains (see Ref. 9 for a review of this subject). For like atoms the  $k$ -value derived by Lindhard is

$$k = 0.3NZ^{3/2}, eV^{1/2}/\text{\AA} \quad (17.53a)$$

where  $N$  is the atomic density of the metal in units of  $\text{\AA}^{-3}$  and  $Z$  is the atomic number of the atoms of the metal. Equations 17.52 and 17.53 are valid for the energy range

$$0 < E(\text{keV}) < 37Z^{2/3} \quad (17.53b)$$

In this formula and in Eq. 17.53a, use has been made of the fact that  $Z/M = 0.43 \pm 0.03$  for all elements except hydrogen.

## 17.6 THE DISPLACEMENT THRESHOLD

All analytical cascade theories are based on the assumption that a lattice atom struck by a PKA or a higher order recoil must receive a minimum amount of energy in the collision in order to be displaced from its lattice site. This quantity of energy is called the displacement energy or the displacement threshold and is denoted by  $E_d$ . If the energy transfer,  $T$ , is less than  $E_d$ , the struck atom undergoes large amplitude vibrations without leaving the potential well forming its stable lattice position. The vibrational energy is

quickly communicated to the nearest neighbors of the struck atom and appears as a localized source of heat. On the other hand, if  $T > E_d$ , the struck atom is able to pass over the potential barrier and move off into the lattice as a displaced atom.

Because of the crystallographic structure of the solid, the potential barrier surrounding a lattice atom in its equilibrium position is not uniform in all directions. If the struck atom moves off in a direction where its nearest neighbors are favorably disposed to remove energy from the struck atom before it escapes, the barrier is high. However, the potential barrier in a direction of high lattice symmetry resembles a mountain pass. These "saddle points" where the displacement threshold is low may be along either relatively open direction, such as the  $\langle 111 \rangle$  directions in the fcc lattice, or along close-packed directions, such as the  $\langle 110 \rangle$  directions in the same structure. The direction acquired by the recoil is dictated by the dynamics of the collision and hence is random in the sphere surrounding the equilibrium site. The single value of the displacement energy used in radiation-damage theory is in reality a spherical average of the saddle points in the potential barrier surrounding the equilibrium lattice site.

The displacement energy can in principle be computed if the interaction potential between atoms of the lattice is known. The procedure is to move the atom from its equilibrium position in a chosen direction and sum the interaction energies between the moving atoms and all the nearest neighbors for each position along the line (or curve) representing the trajectory of the struck atom. When the total potential energy reaches a maximum, the position corresponds to a saddle point, and the difference between the energy of the atom at the saddle point,  $e^*$ , and its energy in the equilibrium position,  $e_{eq}$ , represents the displacement threshold for the particular direction. Such calculations are usually carried out by computer<sup>1,12</sup> using a Born-Mayer potential to represent the repulsive forces between the struck atom and the nearest neighbors it encounters during motion. Because the interaction energies involved in these threshold calculations are only tens of electron volts, the Born-Mayer potential is the correct one to use.

In this section we illustrate the basic features of such calculations by using a simpler (but unrealistic) description of the interaction between neighboring atoms.

The atom in the lower left-hand corner of Fig. 17.6(a) is assumed to receive energy by collision with an energetic recoil and to start to move in a direction in the octant of the sphere represented by the unit cell in the drawing. We calculate the potential energy of the struck atom, which is moving in the  $[111]$  direction. The saddle point for this direction is the center of the triangle formed by the three nearest neighbors to the struck atom, which are connected by the wavy lines in Fig. 17.6(a). The energy of the struck atom as a function of position along the  $[111]$  direction is shown schematically in Fig. 17.6(b).

To describe the interaction energies, we describe the solid by the simple bond theory used primarily for covalent substances. In this theory, cohesion of the solid is the result of bonds of strength  $D$  acting in pairs between nearest neighbors. In an fcc lattice, each atom is surrounded by 12

nearest neighbors; thus the energy of a single atom in a normal lattice site is

$$e_{eq} = -12D \quad (17.54)$$

The zero in energy is taken as the isolated atom. In the bond theory of solids, the bond energy may be computed from the energy of sublimation (Eq. 4.45 and Table 4.1).

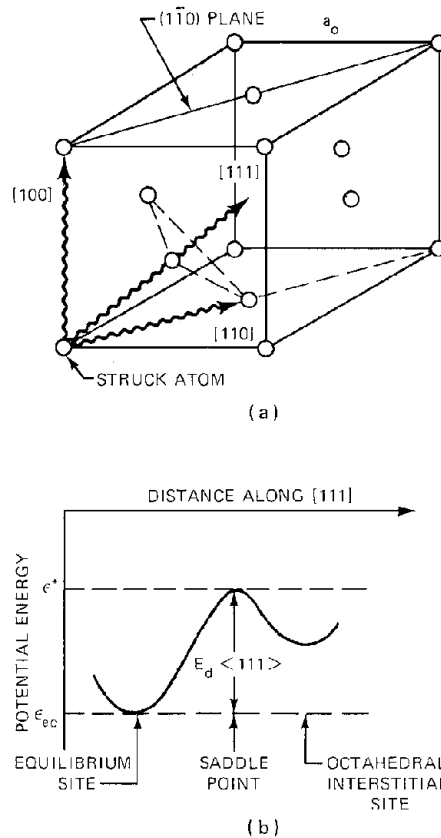


Fig. 17.6 Displacement of a lattice atom recoiling from a collision with an energetic atom.

This quantity is just half the energy of an interior atom since sublimation represents removal of an atom from the surface, a process that involves breaking only half as many bonds as is necessary for removing an atom from the inside of the solid. Thus, for the fcc lattice

$$\Delta E_{sub}^0(0^\circ\text{K}) = 6D \quad (17.55)$$

Since the sublimation energy of metals in the transition region of the periodic table is 5 to 6 eV, the bond energy in the fcc lattice is  $D \approx 1$  eV. When atoms of the lattice are pushed closer to each other than the equilibrium nearest-neighbor distance,  $r_{eq}$ , the potential energy increases. Instead of using a Born-Mayer potential to describe this repulsion, we use a simple parabolic repulsion. The interaction potential between two lattice atoms is represented by

$$V(r) = -D + \frac{1}{2} k(r_{eq} - r)^2 \quad (\text{for } r < r_{eq})$$

$$V(r) = 0 \quad (\text{for } r > r_{eq}) \quad (17.56)$$

where the force constant  $k$  characterizing the repulsive portion of the potential can be computed as follows. Atoms in the crystal can be made to approach each other more closely than  $r_{eq}$  either by the movement of an energetic atom in the crystal (which is pertinent to the displacement threshold computation) or in a uniform manner by exerting external pressure to compress the entire crystal. The resistance of the solid to compression is measured by the compressibility,  $\beta$ . In Chap. 4 we showed that compressibility is related to the second derivative of the crystal energy by

$$\frac{1}{\beta} = v_{eq} \left( \frac{d^2 U}{dv^2} \right)_{eq}$$

where  $U$  is the energy per atom of the crystal when the specific volume is  $v$ . For the fcc lattice,  $v = a_0^3/4$ , where  $a_0$  is the lattice constant. The nearest-neighbor separation distance is  $r = a_0/2^{1/2}$ ; thus  $v = r^3/2^{1/2}$ . The above formula can therefore be written in terms of  $r$  as

$$\frac{1}{\beta} = \frac{2^{1/2}}{9} \frac{1}{r_{eq}} \left( \frac{d^2 U}{dr^2} \right)_{eq}$$

In the bond model of the fcc solid, the crystal energy  $U(r)$  is equal to  $12V(r)/2 = 6V(r)$ , and the compressibility is given by

$$\frac{1}{\beta} = \frac{6(2)^{1/2}}{9r_{eq}} \left( \frac{d^2 V}{dr^2} \right)_{eq} = \frac{2(2)^{1/2}k}{3r_{eq}} = \frac{4k}{3a_0} = \frac{ka_0^2}{3v_{eq}}$$

Thus the force constant of the repulsive portion of the interaction potential is

$$ka_0^2 = \frac{3v_{eq}}{\beta}$$

Typical values of  $v_{eq}$  and  $\beta$  for metals are  $\sim 15 \text{ \AA}^3$  and  $\sim 5 \times 10^{-13} \text{ cm}^2/\text{dyne}$ , respectively, which yield  $ka_0^2 \simeq 60 \text{ eV}$ . We assume that the potential function of Eq. 17.56, in which the constants were obtained from the equilibrium properties of heat of sublimation and compressibility, is applicable to the interaction of the moving atom in the lattice.

When the atom is at the center of the triangle shown in Fig. 17.6(a), it interacts with the three atoms at the corners a distance  $a_0/6^{1/2}$  away. The energy at the saddle point is

$$\epsilon^* = 3V\left(\frac{a_0}{6^{1/2}}\right) = 3\left[-D + \frac{1}{2}(ka_0^2)\left(\frac{1}{2^{1/2}} - \frac{1}{6^{1/2}}\right)^2\right]$$

The displacement energy in the  $[111]$  direction is thus

$$E_d \langle 111 \rangle = \epsilon^* - \epsilon_{eq} = 9D + \frac{3}{2}(ka_0^2)\left(\frac{1}{2^{1/2}} - \frac{1}{6^{1/2}}\right)^2$$

Using the values of  $D$  and  $ka_0^2$  computed above, this equation gives  $E_d \langle 111 \rangle = 15.6 \text{ eV}$ . Displacement thresholds calculated by computer for copper are shown in Table 17.1. The figures shown in the last two columns of the table indicate that displacement is considerably easier when the direction of the struck atom is along a line of atoms in the crystal (i.e., the  $\langle 100 \rangle$  and  $\langle 110 \rangle$  directions) than it is in the open  $\langle 111 \rangle$  directions. The ease of displacement in the former directions is explained by the phenomenon of focusing whereby replacement of the next atom in the line

by the struck atom is followed by replacement of the third atom by the second, etc.

Displacement thresholds corresponding to initial directions other than the three illustrated in Fig. 17.6(a) and Table 17.1 can be obtained by similar computational techniques. A schematic representation of the results for all directions in the plane formed by the  $[100]$ ,  $[111]$ , and  $[110]$  directions in Fig. 17.6(a) [i.e., directions lying in the  $(\bar{1}10)$  plane] is shown in Fig. 17.7. Local minimums in the displacement energies are found in the  $[110]$ ,  $[111]$ , and  $[100]$  directions. Similar calculations out of the  $(110)$  plane show that the minimums along these crystallographic directions are true troughs, not saddle points. The single threshold energy used in most radiation-damage calculations represents the average of results such as those shown in Fig. 17.7 and comparable out-of-plane profiles over all polar and azimuthal angles in the octant delineated by the unit cell with the struck atom at one corner.

The directional dependence of  $E_d$ , coupled with the randomness of the initial directions of the struck atom, implies that the notion of a sharp displacement threshold is

Table 17.1 Displacement Threshold Energies in Copper

Direction	Displacement energy, eV		
	Ref. 11*	Ref. 12	Ref. 13†
$E_d \langle 100 \rangle$	18, 34	24	15, 34
$E_d \langle 111 \rangle$	19, 43	80	70, 52
$E_d \langle 110 \rangle$		25	31, 15

\*The two values were obtained by two sets of the constants  $A$  and  $\rho$  in the Born-Mayer potential function of Eq. 17.32.

†These constants were determined by fitting radiation-damage data. The two sets of threshold energies listed fit the data equally well.

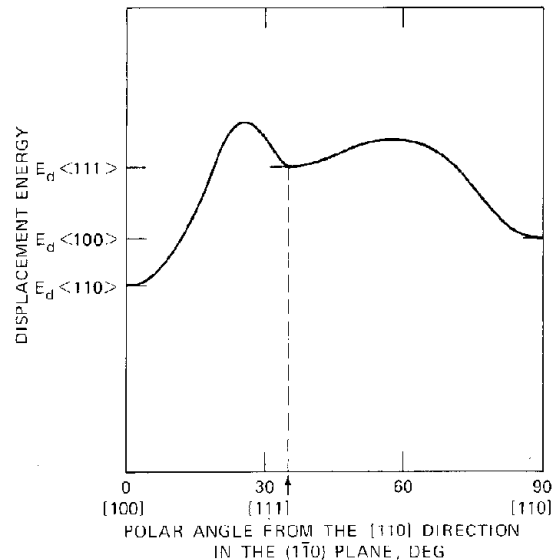


Fig. 17.7 Directional dependence of the displacement threshold.

oversimplified. Rather, there is a range of displacement energies, from  $E_{d(\min)}$  to  $E_{d(\max)}$ , for which displacement may occur. For example, in Fig. 17.7,  $E_{d(\min)}$  corresponds to  $E_d(100)$  and  $E_{d(\max)}$  to an  $\sim 30^\circ$  polar angle. This smearing out of the displacement threshold due to crystallographic direction of the struck atom is commonly incorporated into radiation-damage calculations by defining a displacement probability,  $P_d(T)$ , which gives the probability that a struck atom is displaced upon receipt of energy  $T$ . This probability  $P_d(T)$  is taken to be of the form

$$\begin{aligned} P_d(T) &= 0 & [\text{for } T < E_{d(\min)}] \\ &= f(T) & [\text{for } E_{d(\min)} < T < E_{d(\max)}] \\ &= 1 & [\text{for } T > E_{d(\max)}] \end{aligned} \quad (17.57)$$

Sosin<sup>14</sup> lists seven different functions  $f(T)$  which have been used to generate displacement probability curves. The single displacement energy concept most commonly used in damage analyses corresponds to a step-function displacement probability in which  $E_{d(\min)} = E_{d(\max)} = E_d$ :

$$\begin{aligned} P_d(T) &= 0 & (\text{for } T < E_d) \\ &= 1 & (\text{for } T > E_d) \end{aligned} \quad (17.58)$$

In this model,  $E_d$  is fixed at a value between 25 and 50 eV, the lower figure being the one most commonly used.

## 17.7 DISPLACEMENTS PRODUCED BY A PRIMARY KNOCK-ON

The crux of the damage-producing effect of fast neutrons and fission fragments is the production of displaced atoms by the primary knock-ons. In this section the theoretical basis for calculating the total number of displaced atoms resulting from a single PKA of energy  $E$  is reviewed. The number of displaced atoms is denoted by  $\nu(E)$ .

### 17.7.1 Elementary Theory

The simplest theory of the displacement cascade is that due to Kinchin and Pease.<sup>15</sup> Their analysis is based on the following assumptions:

1. The cascade is created by a sequence of two-body elastic collisions between atoms.
2. The displacement probability is given by Eq. 17.58.
3. The energy  $E_d$  consumed in displacing an atom is neglected in the energy balance of the binary collision that transfers kinetic energy to the struck atom.
4. Energy loss by electron stopping is treated by the cutoff energy of Eq. 17.43. If the PKA energy is greater than  $E_c$ , no displacements occur until electronic energy losses reduce the PKA energy to  $E_c$ . For all energies less than  $E_c$ , electronic stopping is ignored, and only atomic collisions take place.
5. The energy-transfer cross section is given by the hard-sphere model.
6. The arrangement of the atoms in the solid is random; effects due to the crystal structure are neglected.

Later on in this section, we will relax restrictions (3), (4), and (5). In the subsequent section, assumption (6) will be removed from the analysis. Assumption (1) is fundamental to all theories of a cascade consisting of isolated point defects. When this restriction is eliminated, the cascade resembles a displacement spike, which is treated at the end of this chapter.

The cascade is initiated by a single PKA of energy  $E$ , which eventually produces  $\nu(E)$  displaced atoms. At some time during the development of the cascade, the number of energetic, moving atoms is larger than 1 but less than  $\nu(E)$ , and the average kinetic energy of the moving atoms is less than  $E$  but still not zero. However, the population of moving atoms at any intermediate stage will ultimately produce the same number of stationary displaced atoms as the original PKA, namely,  $\nu(E)$ . Therefore, the quantity  $\nu(E)$  is conserved in the sense that it can be determined by starting with the energy distribution of the moving atoms at any time after birth of the PKA but before the final displaced configuration is achieved. In particular,  $\nu(E)$  can be determined by considering the two moving atoms that are created when the PKA first strikes a stationary lattice atom (Fig. 17.8). Thus, if the PKA of energy  $E$  transfers energy  $T$  to the struck atom and leaves the collision with energy  $E - T$ , we can say that

$$\nu(E) = \nu(E - T) + \nu(T) \quad (17.59)$$

Note that the energy  $E_d$  required to displace the struck atom has not been deducted from the energy of the recoil [assumption (3)]. Had this energy loss been included, the last term in Eq. 17.59 would be written as  $\nu(T - E_d)$ .

Equation 17.59 does not suffice to determine  $\nu(E)$  because the energy transfer  $T$  is not specified. Since the PKA and the lattice atoms are identical,  $T$  can be anywhere from 0 to  $E$ . However, if we know the probability of transferring energy between  $T$  and  $T + dT$  in a collision, we can multiply Eq. 17.59 by this probability and integrate over all permissible values of  $T$ . Invoking the hard-sphere assumption (5), the energy-transfer cross section is given by Eq. 17.39, and the probability that a PKA of energy  $E$  transfers energy in the range  $(T, dT)$  to the struck atom is

$$\frac{\sigma(E, T) dT}{\sigma(E)} = \frac{dT}{E} \quad (\text{for } \Lambda = 1) \quad (17.60)$$

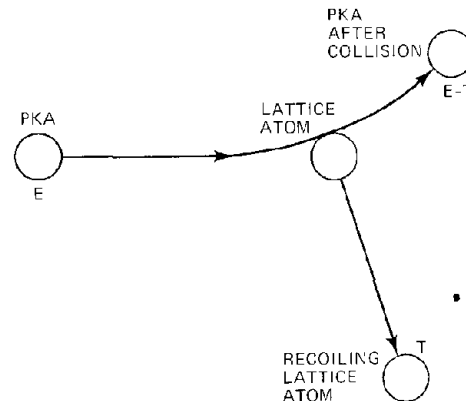


Fig. 17.8 Before and after the first collision of a cascade.

Multiplying the right-hand side of Eq. 17.59 by  $dT/E$  and integrating from 0 to  $E$  yields

$$\nu(E) = \frac{1}{E} \int_0^E [\nu(E-T) + \nu(T)] dT \quad (17.61)$$

The right side of this equation consists of two integrals, which may be shown to be identical by changing the variable of integration in the first from  $T$  to  $T' = E - T$ , and Eq. 17.61 reduces to

$$\nu(E) = \frac{2}{E} \int_0^E \nu(T) dT \quad (17.62)$$

Before attempting to solve this integral equation, we first consider the behavior of  $\nu(E)$  near the threshold energy  $E_d$ . Clearly when  $E < E_d$ , not even the PKA is displaced, and

$$\nu(E) = 0 \quad (\text{for } 0 < E < E_d) \quad (17.63)$$

When the PKA is born with an energy between  $E_d$  and  $2E_d$ , the first collision with a lattice atom has one of two possible results: If energy in excess of  $E_d$ , but necessarily less than  $2E_d$ , is transferred to the lattice atom, the latter is displaced, but the initial PKA is left with energy less than  $E_d$ . The struck atom moves off its lattice site, but the PKA falls into the vacated site, dissipating its remaining kinetic energy as heat. Conversely, if the original PKA transfers less than  $E_d$ , the struck atom is not displaced. In either of the above two possibilities, the first PKA collision results in only one moving atom, which has an energy less than the original PKA. The same arguments advanced above can be applied to the second-generation moving atom, and the conclusion is that it too is incapable of creating any additional displacements. Therefore, a PKA with kinetic energy between  $E_d$  and  $2E_d$  produces only one displaced atom, or

$$\nu(E) = 1 \quad (\text{for } E_d < E < 2E_d) \quad (17.64)$$

We may split the integral in Eq. 17.62 into ranges from 0 to  $E_d$ ,  $E_d$  to  $2E_d$ , and  $2E_d$  to  $E$  and evaluate the first two using Eqs. 17.63 and 17.64. Thus we arrive at

$$\nu(E) = \frac{2E_d}{E} + \frac{2}{E} \int_{2E_d}^E \nu(T) dT \quad (17.65)$$

This equation can be solved by multiplying by  $E$  and differentiating with respect to  $E$ , which yields the differential equation

$$E \frac{d\nu}{dE} = \nu \quad (17.66)$$

the solution of which is

$$\nu = CE \quad (17.67)$$

The constant  $C$  is obtained by substitution of Eq. 17.67 into Eq. 17.65, which shows  $C = (2E_d)^{-1}$ . Therefore the number of displacements is

$$\nu(E) = \frac{E}{2E_d} \quad (\text{for } 2E_d < E < E_c) \quad (17.68)$$

The upper limit on the validity of Eq. 17.68 has been set equal to  $E_c$  since, by assumption (4), only electronic energy loss occurs for higher energies. When the PKA is born with an energy greater than  $E_c$ , the number of displacements is

$$\nu(E) = \frac{E_c}{2E_d} \quad (\text{for } E > E_c) \quad (17.69)$$

The Kinchin—Pease displacement function, which consists of Eqs. 17.63, 17.64, 17.68, and 17.69, is shown in Fig. 17.9. The scale is distorted to illustrate the four regions predicted by the model. If drawn to scale, the ionization cutoff  $E_c$  would be 10 to 20 times further out along the abscissa than shown in the drawing.

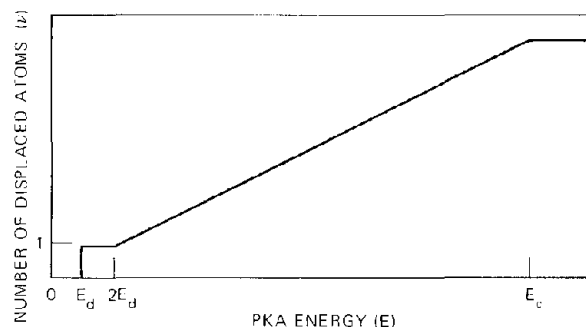


Fig. 17.9 The number of displaced atoms in the cascade as a function of PKA energy according to the model of Kinchin and Pease. (After Ref. 15.)

### 17.7.2 Use of a Realistic Energy-Transfer Cross Section

The hard-sphere assumption (5) can be removed by introducing Eq. 17.60 into the analysis. In this case Eq. 17.61 should be written as

$$\nu(E) = \frac{1}{\sigma(E)} \int_0^E \sigma(E,T) [\nu(E-T) + \nu(T)] dT \quad (17.70)$$

The arguments leading to Eqs. 17.63 and 17.64 are still valid (inasmuch as they depend only on energy conservation and not on the nature of the energy-transfer cross section), and the appropriate integral equation is

$$\nu(E) = \frac{2}{\sigma(E)} \int_{E_d}^{2E_d} \sigma(E,T) dT + \frac{1}{\sigma(E)} \int_{2E_d}^E \sigma(E,T) [\nu(E-T) + \nu(T)] dT \quad (17.71)$$

This equation has been solved by Sanders<sup>16</sup> for the energy-transfer cross section based on the inverse power potential (Eq. 17.38). The result is

$$\nu(E) = s [2^{1/(1+s)} - 1] \left( \frac{E}{2E_d} \right) \quad (\text{for } E_d < E < E_c) \quad (17.72)$$

which, for  $s = 2$ , reduces the Kinchin—Pease result by a factor of  $\sim 2$ . Robinson<sup>8</sup> summarizes the extensive efforts that have been devoted to relieving cascade analysis of the hard-sphere assumption.

### 17.7.3 Energy Loss from the Cascade by Electronic Excitation

Relaxation of assumption (4) of cascade theory requires reformulation of the conservation principle for  $\nu(E)$ . In this case, collisions of the PKA with electrons compete

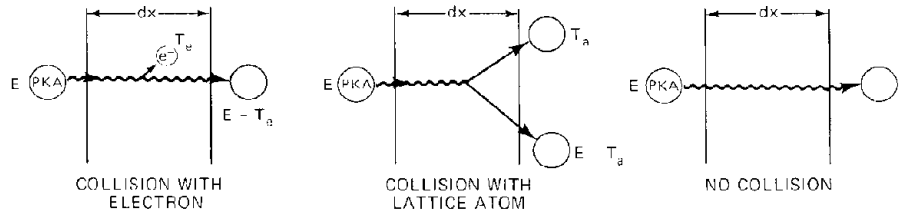


Fig. 17.10 Possible fates of a PKA on passing through a thickness  $dx$  of solid.

with atomic collisions with lattice atoms. As discussed in Sec. 17.1, these two processes can be treated independently, and each can be represented by separate energy-transfer cross sections. We formulate the basic integral equation in the manner originally presented by Lindhard et al.<sup>17</sup> by considering what happens to the PKA as it traverses a small distance  $dx$  of solid (Fig. 17.10). According to the basic definition of the differential energy-transfer cross section (Eq. 17.21), the probability  $p_e dT_e$  that a collision between the PKA and an electron in the interval  $dx$  which transfers energy in the range  $(T_e, dT_e)$  to the electron is

$$p_e dT_e = N \sigma_e(E, T_e) dT_e dx \quad (17.73)$$

where  $\sigma_e(E, T_e)$  is the energy-transfer cross section from the PKA to an electron. Similarly, the probability of a collision in  $dx$  which transfers energy  $(T_a, dT_a)$  to a lattice atom is

$$p_a dT_a = N \sigma_a(E, T_a) dT_a dx \quad (17.74)$$

In these equations,  $N$  is the density of atoms in the solid. The probability that nothing happens in  $dx$  is given by

$$p_0 = 1 - \int_0^{T_{em}} p_e dT_e - \int_0^E p_a dT_a$$

$$= 1 - N dx \left[ \int_0^{T_{em}} \sigma_e(E, T_e) dT_e + \int_0^E \sigma_a(E, T_a) dT_a \right]$$

or

$$p_0 = 1 - N dx [\sigma_e(E) + \sigma_a(E)] \quad (17.75)$$

where  $T_{em}$  is the maximum energy transferrable to an electron by a PKA of energy  $E$  and  $\sigma_e(E)$  and  $\sigma_a(E)$  are the total cross sections for collisions of the PKA with electrons and lattice atoms, respectively.\*

We now apply the principle of conservation of  $\nu(E)$  by requiring that this quantity be the same whether computed from the original PKA at its birth energy or whether it is determined by the products of the possible collisions that occur in  $dx$ . The  $\nu$ -value associated with each of the recoil atoms in Fig. 17.10 is weighted with the appropriate probability for the process by which it is created and is integrated over the permissible ranges of the energy transfers. Thus

$$\nu(E) = \int_0^E [\nu(E - T_a) + \nu(T_a)] p_a dT_a$$

$$+ \int_0^{T_{em}} \nu(E - T_e) p_e dT_e + p_0 \nu(E) \quad (17.76)$$

Substituting Eqs. 17.73 and 17.74 for  $p_e$  and  $p_a$  and Eq. 17.75 for  $p_0$  yields

$$[\sigma_a(E) + \sigma_e(E)] \nu(E) = \int_0^E [\nu(E - T_a) + \nu(T_a)]$$

$$\times \sigma_a(E, T_a) dT_a$$

$$+ \int_0^{T_{em}} \nu(E - T_e) \sigma_e(E, T_e) dT_e \quad (17.77)$$

We now note that the maximum energy transferrable to an electron is very small compared to  $E$ ; thus  $\nu(E - T_e)$  can be expanded in a Taylor series and truncated after the second term:

$$\nu(E - T_e) - \nu(E) - \frac{d\nu}{dE} T_e \quad (17.78)$$

The last term in Eq. 17.77 can therefore be written as

$$\int_0^{T_{em}} \nu(E - T_e) \sigma_e(E, T_e) dT_e = \nu(E) \int_0^{T_{em}}$$

$$\times \sigma_e(E, T_e) dT_e - \frac{d\nu}{dE} \int_0^{T_{em}} T_e \sigma_e(E, T_e) dT_e \quad (17.79)$$

The first integral on the right of Eq. 17.79 is the total cross section for collisions of the PKA with the electron. This term cancels the corresponding term on the left of Eq. 17.77. The second integral on the right of Eq. 17.79 is, according to Eq. 17.29, the electronic stopping power of the medium divided by the atom density, or  $(dE/dx)_e/N$ . When Eq. 17.79 is substituted into Eq. 17.77, the result is

$$\nu(E) + \left[ \frac{(dE/dx)_e}{N \sigma(E)} \right] \frac{d\nu}{dE} = \int_0^E [\nu(E - T) + \nu(T)]$$

$$\times \left[ \frac{\sigma(E, T)}{\sigma(E)} \right] dT \quad (17.80)$$

The subscript "a" on  $T$  and  $\sigma$  has been deleted with the understanding that these two quantities refer to atomic collisions. When  $(dE/dx)_e$  is neglected, Eq. 17.80 reduces to Eq. 17.70, and, when, in addition, the hard-sphere model is used to fix the energy-transfer probability on the right side of the above equation, the original Kinchin—Pease formula, Eq. 17.61, is recovered.

To show the effect of electronic stopping on the number of displaced atoms, we solve Eq. 17.80 with the hard-sphere assumption retained but with  $(dE/dx)_e$  given by the square-root law (Eq. 17.52). With this simplification, Eq. 17.80 reduces to

\*The analysis is not affected by the fact that the total cross section for energy transfer to electrons is infinite.

$$\nu(E) = \frac{2E_d}{E} + \frac{2}{E} \int_{2E_d}^E \nu(T) dT - \frac{k E^{1/2}}{\sigma N} \frac{d\nu}{dE} \quad (17.81)$$

where Eqs. 17.63 and 17.64 have been used to split up the integral over T. We will also assume that the hard-sphere collision cross section  $\sigma$  is energy-independent; thus  $k/\sigma N$  is a constant. To simplify the analysis, we introduce the following dimensionless energy variable:

$$y = \frac{E}{2E_d} \quad (17.82)$$

and Eq. 17.81 is transformed to

$$\nu = \frac{1}{y} + \frac{2}{y} \int_1^y \nu(y') dy' - A y^{1/2} \frac{d\nu}{dy} \quad (17.83)$$

where

$$A = \frac{k}{\sigma N (2E_d)^{1/2}} \quad (17.84)$$

is a dimensionless constant. If  $A = 0$ , the Kinchin—Pease solution  $\nu = y$  (see Eq. 17.68) is recovered. If  $A$  is small compared to unity, electronic stopping only slightly perturbs the basic Kinchin—Pease result. Assuming this to be the case, the number of displacements can be written as a power series in the perturbation parameter  $A$ :

$$\nu = y + f(y) A \dots \quad (17.85)$$

where the first term on the right is the solution for  $A = 0$ , and  $f(y)$  is a function to be determined by insertion of Eq. 17.85 into the integral equation, Eq. 17.83, which yields

$$f(y) = \frac{2}{y} \int_1^y f(y') dy' - y^{1/2} \quad (17.86)$$

The solution of this equation can be obtained by differentiating, solving the differential equation, and determining the constant of integration by substitution into Eq. 17.86. In this way we find

$$f(y) = -4y + 3 y^{1/2} \quad (17.87)$$

If we restrict attention to high PKA energies ( $E \gg E_d$ ), then  $y \gg 1$ , and the second term on the right in Eq. 17.87 can be dropped. Substituting  $-4y$  for  $f(y)$  in Eq. 17.85 gives

$$\nu = y(1 - 4A) \quad (17.88)$$

or

$$\nu(E) = \left[ 1 - \frac{4k}{\sigma N (2E_d)^{1/2}} \right] \left( \frac{E}{2E_d} \right) \quad (\text{for } E \gg E_d) \quad (17.89)$$

Note that the validity of Eq. 17.89 is not subject to an upper limit on  $E$ , as is the case for Eq. 17.68. When electronic stopping is properly accounted for in the basic integral equation, the entire concept of a definite energy  $E_c$  separating regimes of electronic energy loss from atomic collisions can be jettisoned.

To assess the importance of electronic stopping on displacement production by energetic primary knock-ons, consider iron ( $Z = 26$ ), for which  $k = 0.21 \text{ eV}^{1/2} \cdot \text{\AA}$  (Eq. 17.53) and  $N = 0.085 \text{ \AA}^{-3}$ . We take  $E_d = 25 \text{ eV}$ , and, for illustrative purposes, set  $\sigma = 2\text{\AA}^2$ . With these values the

coefficient of  $E/2E_d$  in Eq. 17.89 is 0.3, or electronic energy losses have reduced the displacement efficiency of the PKA by 70%.

The sensitivity of the above calculation to the choice of the hard-sphere cross section suggests that the model should be entirely purged of hard-sphere characteristics and that realistic energy-transfer cross sections must be employed if reliable predictions are to be obtained. The complete calculation of Lindhard<sup>17</sup>, as a matter of fact, used  $\sigma_a(E, T_a)$  based on the Thomas—Fermi potential function rather than on the hard-sphere result.

Lindhard noted that the parameter  $\nu(E)$  in Eq. 17.80 need not be interpreted solely as the number of displacements produced by a PKA. Rather, the integral equation is valid for a number of other radiation-damage effects, such as the number of ion pairs in a gas or the number of electron—hole pairs in a semiconductor. In the original analysis,<sup>17</sup>  $\nu(E)$  was actually taken to be that part of the original PKA energy which is transferred to the atoms of the lattice (rather than to the electrons) during slowing down. The ratio of Lindhard's  $\nu(E)$  to  $E$  is the fraction of the cascade energy transformed into atomic motion, which may be denoted by  $\xi(E)$ . Strictly speaking, Lindhard's application of Eq. 17.80 is not a displacement theory because it does not incorporate the displacement threshold restrictions at low energies, which are contained in Eqs. 17.63 and 17.64.\* Lindhard's analysis has become known as the *energy-partitioning theory*.

Lindhard's energy-partitioning results can be used to predict displacements, however. For sufficiently high PKA energies, the number of displaced atoms is proportional to the original PKA energy (e.g., see Eq. 17.68 for an example of this proportionality in the simple Kinchin—Pease theory). Therefore, Lindhard's  $\xi(E)$  can be used as a correction factor to the simple theory, and the number of displaced atoms is given by

$$\nu(E) = \xi(E) \left( \frac{E}{2E_d} \right) \quad (17.90)$$

Lindhard's numerical solution of Eq. 17.80, using  $(dE/dx)_e$  given by Eq. 17.52 and  $\sigma_a(E, T_a)$  determined from an interaction potential based on the Thomas—Fermi model of the atom, can be expressed in the analytical form by

$$\xi(E) = \frac{1}{1 + 0.13(3.4\epsilon^{1/2} + 0.4\epsilon^{3/4} + \epsilon)} \quad (17.91)$$

where  $\epsilon$  is a reduced PKA energy:

$$\epsilon = \frac{E}{(2Z^2 e^2/a)} \quad (17.92)$$

and  $a$  is the screening radius of Eq. 17.35 with  $\lambda = 0.88$  and  $Z_1 = Z_2$ :

$$a = \frac{0.88a_B}{Z^{1/2}} \quad (17.93)$$

\*When only energy transfer to, and not displacement of, lattice atoms is considered, the notion of a displacement energy  $E_d$  does not enter the calculation at all. Hence  $\nu(E)$  increases continuously from  $E = 0$ , and the lower limit on the integral in Eq. 17.80 is kept as it is written.

Figure 17.11 shows the damage efficiency function  $\xi$  for various elements (i.e., for different values of  $Z$ ). The dashed line represents the locus of the step-function ionization cutoff energies ( $E_c$ ) employed in the Kinchin–Pease theory.

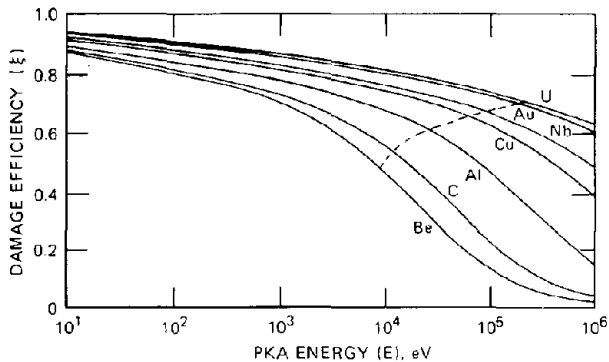


Fig. 17.11 Fraction of PKA energy deposited in the solid in the form of atomic collisions with lattice atoms (also used as the damage efficiency of the PKA). Solid lines are based on Lindhard's energy partitioning theory.<sup>17</sup> The dashed line gives the ionization cutoff for use in the Kinchin–Pease model. ( $E_c$  is read from the abscissa below the point at which the dashed line intersects the solid line for the particular elements.) (After Ref. 8.)

## 17.8 FOCUSING AND CHANNELING

The simple cascade analysis, even when modified to account for a realistic energy-transfer cross section or for electron excitation losses during slowing down, implicitly assumes that the solid consists of a random array of atoms. However, when the cascade is considered to occur in the ordered structure of a crystalline solid, two important phenomena appear: *Focusing* refers to the transfer of energy and atoms by nearly head-on collisions along a row of atoms and *channeling* is the complementary process whereby atoms move long distances in the solid along open directions in the crystal structure. In this case the moving atom is kept in its channel by glancing collisions with the atomic rows that serve as walls. Focusing and channeling affect both the number and configuration of displaced atoms in a cascade. First, atoms moving along the crystallographic direction favorable to either focusing or channeling lose energy only by glancing collisions with the atoms ringing the axis of motion. The energy transfer in these collisions is well below  $E_d$ , with the result that more energy is dissipated in subthreshold collisions than is predicted by the cascade theory reviewed in the preceding section [i.e., the number  $\nu(E)$  is smaller when the crystal effects are considered than when the PKA enters a random array of atoms]. Second, the focused or channeled atoms are able to move much larger distances before coming to rest than ordinary knock-ons. In fact, the former may constitute the lion's share of the displaced atoms that escape recombination with the vacancies which are also produced in the

cascade. As such, displaced atoms that have been created by focusing or channeling mechanisms contribute disproportionately to the radiation-produced interstitials that control radiation effects, such as diffusion-enhanced creep and void growth.

### 17.8.1 Focusing

The phenomenon of focusing can be seen in the calculations of the displacement threshold energies discussed in Sec. 17.6. When such calculations are made for various initial knock-on directions in the lattice (Fig. 17.7), we find that  $E_d$  is particularly small for certain low index directions in the crystal. For the fcc structure, for example, Fig. 17.7 shows that the  $\langle 100 \rangle$  and  $\langle 110 \rangle$  directions permit displacement to take place at the lowest energy transfer of any other lattice direction. This result at first seems somewhat unexpected, since in these directions the knock-on encounters a densely packed row of atoms rather than an open space with an interstitial site following it. The open configuration would be expected to permit displacement most easily. When directed along the  $\langle 100 \rangle$  or  $\langle 110 \rangle$  atomic rows in the fcc structure, the mechanism of knock-on penetration in the solid is very different from the way in which knock-ons initially headed in a more or less random direction achieve displacement. Along the closely packed directions, the knock-on hits a line of atoms head-on, and displacement can occur by the knock-on striking and replacing the nearest lattice atom along the row. The latter then collides with the next atom in a similar manner and replaces it. In this manner the well-known billiard-ball phenomenon in which a direct hit on the lead ball transfers the impact to the last ball in the line takes place. The last ball goes off with essentially the same energy with which the lead ball was hit. Such a linear collision chain can occur easily along the  $\langle 100 \rangle$  and  $\langle 110 \rangle$  directions in the fcc lattice (Fig. 17.6).

If a precise head-on collision were required to produce a linear collision chain, the phenomenon would be of no significance since the probability of its occurrence would be very small. The direction of a primary knock-on is random; so focusing must be possible for a sizable range of polar angles off the exact close-packed direction. Under certain circumstances the angle between the knock-on and the axis of the row of atoms is reduced in each successive collision. This property of the linear collision is responsible for the name "focused collision sequence."

Focusing along an atomic row can be analyzed readily in the hard-sphere approximation. The distance between atoms along a particular crystallographic row is denoted by  $D$ . Figure 17.12 shows the first three members of such a row in which a sequence of collisions is initiated by the atom which was initially centered at point  $A_0$ . This atom receives energy  $E$  and moves off at an angle  $\theta_0$  to the atomic row. The dashed circle shows the position of the initial atom  $A'_0$  as it strikes the next atom in the line. The radius of the colliding hard spheres,  $r_{01}$ , is obtained from Eq. 17.41 using the initial atom energy  $E$ . The impact transfers some of the initial energy  $E$  to the next atom in the row, which moves off in the direction of the line joining  $A'_0$  and  $A_1$ . The recoil angle  $\theta_1$  of atom  $A_1$  can be related

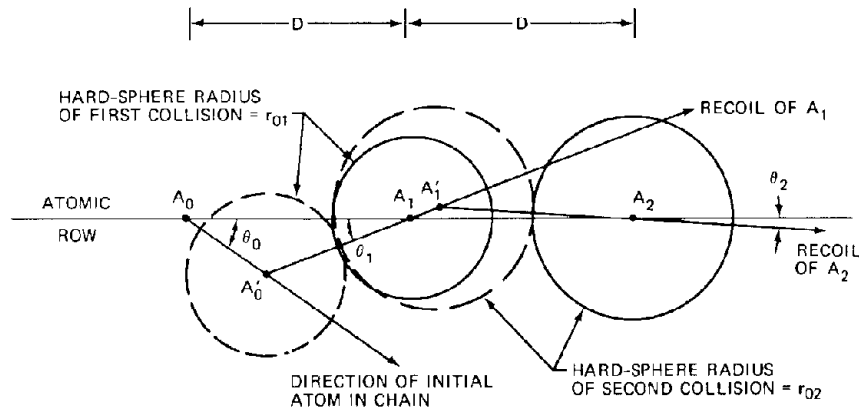


Fig. 17.12 The focused-collision sequence.

to the initial direction of atom  $A_0$  by applying the law of sines to the triangle  $(A_0, A'_0, A_1)$ , which gives

$$\frac{\sin(\pi - \theta_0 - \theta_1)}{\sin \theta_0} = \frac{D}{2r_{01}}$$

The condition for focusing is  $\theta_1 \leq \theta_0$ , focusing just occurs, and the preceding equation shows that the maximum initial angle for this situation is

$$\cos \theta_0^f = \frac{D}{4r_{01}} \quad (17.94)$$

When  $\theta_0 < \theta_0^f$ , calculations based upon the preceding two equations show that  $\theta_1$  is less than  $\theta_0$ .

The larger dashed and solid circles in Fig. 17.12 represent the second collision in the chain. Because the energy transferred to  $A_1$  is less than the initial energy of  $A_0$  (which is  $E$ ), Eq. 17.41 shows that the hard-sphere radius of the second collision,  $r_{02}$ , is larger than  $r_{01}$ . Hence the recoil angle  $\theta_2$  is smaller than  $\theta_1$ . Because  $r_0$  increases as the collision energy decreases, the sequence of collisions rapidly attains a head-on character, and the efficiency of energy transfer along the chain approaches 100%.

The maximum possible energy of the initial atom of the chain for focusing to occur is that value which renders the right-hand side of Eq. 17.94 equal to unity. Under this condition, only a direct head-on collision ( $\theta_0 = 0$ ) results in focusing. The maximum allowable energy of the initial atom can therefore be obtained from the condition  $D = 4r_{01}$ , which, when combined with Eq. 17.41, yields

$$E_f = 2A \exp(-D/2\rho) \quad (17.95)$$

If the energy received by the initial atom is greater than  $E_f$ , the slightest deviation from a head-on collision with the next atom in the chain causes defocusing.

In the fcc structure,  $D$  is  $2^{1/2} a_0$ ,  $a_0$ , and  $a_0/2^{1/2}$  for the  $\{111\}$ ,  $\{100\}$ , and  $\{110\}$  directions, respectively ( $a_0$  is the lattice parameter). Thus focusing should occur most easily

(i.e.,  $E_f$  is the largest) along the close-packed  $\{110\}$  direction in metals with this crystal form. The focusing energy,  $E_f$ , also depends on the parameters  $A$  and  $\rho$  of the Born-Mayer potential. When these parameters are estimated for a variety of metals,  $E_f$  for any direction increases rapidly with the mass of the element. For example,  $E_f$   $\{110\}$  is about 80 eV in copper (using Eq. 17.95 and the Born-Mayer function shown in Fig. 17.5). For gold, it is about 600 eV. In both cases, however, the maximum energy at which focusing can occur ( $E_f$ ) is small compared to typical PKA energies; thus focusing is important only in low-energy cascades or at the very end of a high-energy cascade.

Equation 17.94 can also be used to determine the maximum angle that an initiating atom with energy less than  $E_f$  can have and still produce a focused collision sequence. Using Eq. 17.41 for eliminating  $r_{01}$  in favor of  $E$  and Eq. 17.96 for replacing  $D$  by  $E_f$ , Eq. 17.94 becomes

$$\cos \theta_0^f = \frac{\ln(2A/E_f)}{\ln(2A/E)} \quad (17.96)$$

The condition for focusing can be expressed by either of two quantities: (1) Eq. 17.95 gives the energy  $E_f$  for which focusing occurs for a head-on PKA collision ( $\theta_0 = 0$ ) and (2) Eq. 17.96 gives the maximum angular deviation from a head-on collision,  $\theta_0^f$ , at which a PKA of energy  $E$  can initiate a focused collision sequence. In this case  $E$  must be less than  $E_f$ .

Equation 17.96 can be used to obtain an important parameter that governs the reduction in the number of displaced atoms produced in a cascade owing to focused collisions. If any member of the cascade is produced in a collision that sends the struck atom within an angle  $\theta_0^f$  to an atomic row, a focused collision sequence results, and the energy of the recoil is dissipated without making additional displacements. In an ordinary displacement collision, the struck atom moves off its lattice site in a random direction. The probability that the initial direction of the struck atom is within a cone of apex angle  $\theta_0^f$  about an atomic row is, in

spherical geometry, equal to  $\frac{1}{2}(1 - \cos \theta_0^s)$ . The probability that a struck atom of energy  $E$  starts a focused collision sequence along any of the  $n$  equivalent crystallographic directions emanating from the struck atom is:

$$\begin{aligned} &= \frac{n}{2} \left[ 1 - \frac{\ln(2A/E_f)}{\ln(2A/E)} \right] \\ &= \frac{n}{2} \frac{\ln(E/E_f)}{\ln(E_f/2A) + \ln(E/E_f)} \end{aligned}$$

Since  $E_f/2A \gg 1$  but  $E/E_f$  is of order unity (unless  $E$  becomes very small), the second term in the denominator can be neglected, and we obtain

$$\begin{aligned} P_f(E) &= \frac{n}{2} \frac{\ln(E/E_f)}{\ln(E_f/2A)} \quad (\text{for } E < E_f) \\ &= 0 \quad (\text{for } E > E_f) \end{aligned} \quad (17.97)$$

### 17.8.2 Dynamic Crowdions

Successive head-on collisions along a line of hard-sphere atoms transport the initial kinetic energy of the initiating atom down the row. In addition, the entire row of atoms can be displaced by one lattice site in the direction of the travelling energy pulse provided the following condition is met: With reference to Fig. 17.12, if the  $A'_n$  is beyond the midpoint of the initial separation between  $A_n$  and  $A_{n+1}$ , then  $A_n$  will fall into the site vacated by the recoiling  $A_{n+1}$ . This replacement event is repeated along the line of atoms, with the net result that a vacant site appears at the starting location of the collision sequence and an interstitial is lodged in the solid somewhere far down the line of atoms where, by some other mechanism, the chain of head-on collisions is terminated. This long-range transport of a single atom is known as a *focused replacement* or a *dynamic crowdion*.\*

If we adhere to the hard-sphere model that was used previously to calculate the energy focusing criteria  $E_f$  or  $P_f(E)$ , we would find that the focused replacement is impossible; focusing (with or without replacement) occurs only when  $D < 4r_0$ ; yet in a head-on collision with this restriction, the center of the first atom at the point of impact ( $A'_n$  in Fig. 17.12) is always closer to  $A_n$  than to  $A_{n+1}$ . Consequently, if we are to describe the focused replacement process, the hard-sphere assumption must be modified earlier in the analysis than it was in the argument leading to prediction of the focusing criterion. In the latter case the possibility of focusing was decided by purely geometric arguments based on the relative magnitudes of  $D$  and  $r_0$ , and the real interatomic potential was introduced only at the end by allowing  $r_0$  to depend on  $E$  according to the equivalent hard-sphere model. In the present case, however, we must permit the interaction to begin before

\*The term crowdion refers to an extra atom squeezed into a line of atoms. It is a type of interstitial similar to the split interstitials shown in Fig. 6.4. The dynamic crowdion is a crowdion in motion.

the distance of closest approach is reached and the relative velocity of the colliding particles vanishes. In this way atom  $A_{n+1}$  is induced to move as soon as atom  $A_n$  starts to move, and, consequently,  $A_{n+1}$  is to the right of its initial position when the turnaround occurs.

It is sufficient to analyze the focused replacement process in terms of the head-on collision shown in Fig. 17.13(a). As the collision proceeds, the distance  $x$  between  $A_n$  and  $A_{n+1}$  decreases continuously as shown in Fig. 17.13(b). At any point during the collision, the relative speed of the two atoms,  $g$ , is related to the interaction energy  $V(x)$  according to Eqs. 17.15 and 17.16:

$$\frac{1}{2} \mu g^2 + V(x) = \frac{1}{2} \mu g_0^2 \quad (17.98)$$

where the reduced mass  $\mu$  is equal to  $M/2$  since the colliding atoms are identical and the initial relative speed,  $g_0$ , is equal to the initial speed of atom  $A_n$ ,  $v_{10}$ . Equation 17.98 also assumes that the interaction energy at the initial separation,  $V(D)$ , is small compared with the initial relative kinetic energy,  $\mu g_0^2/2$ . The time rate of change of the separation is equal to the relative speed

$$\frac{dx}{dt} = -g \quad (17.99)$$

Since the curve shown in Fig. 17.13(b) is symmetric about the midpoint, the collision time  $t_c$  is twice the time needed to reach the distance of closest approach, or

$$t_c = -2 \int_D^{x_m} \frac{dx}{g} = -2 \int_{V(D)}^{V(x_m)} \frac{dV}{g(dV/dx)}$$

where  $x_m$  is the distance of closest approach in the head-on collision. Note that  $V(D)$  is not set equal to zero in the above integral. If we evaluate  $dV/dx$  from the Born-Mayer potential function of Eq. 17.32 and solve Eq. 17.98 for  $g$  as a function of  $V$  (using the conditions  $\mu = M/2$  and  $\mu g_0^2/2 = E/2$ , where  $E$  is the kinetic energy received by atom  $A_n$  in its previous collision),  $t_c$  becomes

$$\begin{aligned} t_c &= \rho \left( \frac{2M}{E} \right)^{1/2} \int_{V(D)}^{E/2} \frac{dV}{V(1-2V/E)^{1/2}} = 2\rho \left( \frac{2M}{E} \right)^{1/2} \\ &\quad \times \tanh^{-1} \left[ 1 - \frac{2V(D)}{E} \right]^{1/2} \end{aligned}$$

where the definition of the equivalent hard-sphere radius given by Eq. 17.17 has been used for the upper integration limit. For  $V(D)/E \ll 1$ , the above formula can be simplified to yield

$$t_c = \rho \left( \frac{2M}{E} \right)^{1/2} \ln \left[ \frac{2E}{V(D)} \right] \quad (17.100)$$

The speed of the center of mass of the two-particle system is  $v_{10}/2 = (E/2M)^{1/2}$ . The distance moved by the center of mass during the collision time  $t_c$  is  $t_c (E/2M)^{1/2}$ . If this distance is larger than one-half the initial separation,  $D/2$ , then atom  $A_n$  will end up to the right of the halfway point between the atoms before collision. When this situation occurs, atom  $A_n$  enters the lattice site vacated by atom

$A_{n+1}$  instead of returning to its own lattice position. Replacement has occurred. According to the above arguments, focused replacement is possible when the energy being transported in the collision chain satisfies

$$E > E_r = \frac{1}{2} A \exp\left(\frac{D}{-2\rho}\right) = \frac{1}{4} E_f \quad (17.101)$$

Regardless of whether or not replacement occurs, no focusing is possible if the energy is larger than  $E_f$ . Thus, dynamic crowdions can be created by a knock-on with energy between  $E_f/4$  and  $E_f$  but not with energies outside this range. In metals of interest in reactor technology (primarily iron), the focusing energy  $E_f$  in the close-packed direction is  $\sim 100$  eV. Therefore, the replacement energy  $E_r = E_f/4$  is probably somewhat smaller than the displacement energy  $E_d$ , and the formation of a dynamic crowdion has a slightly lower threshold than the production of a random displaced atom. This conclusion is consistent with the displacement thresholds shown in Fig. 17.7, which indicate that the  $\langle 100 \rangle$  direction, for which  $D = a_0$ , has a smaller replacement threshold than does the  $\langle 110 \rangle$  direction, where  $D = a_0/2^{1/2}$ . On the basis of Eq. 17.101, one would expect that the replacement threshold in the  $\langle 111 \rangle$  direction should be even smaller since here  $D = 2^{1/2} a_0$ . In this case, however, displacement is governed by the energy required to force the struck atom through the triangle of atoms along the  $\langle 111 \rangle$  direction and not by the energy needed to generate a dynamic crowdion. Hence, Eq. 17.101 does not apply to the  $\langle 111 \rangle$  direction in the fcc structure.

Thus far the analysis of the dynamic crowdion has been restricted to the behavior of the atomic row along which both energy and atoms are transported. In this idealized model the collision sequence continues indefinitely since

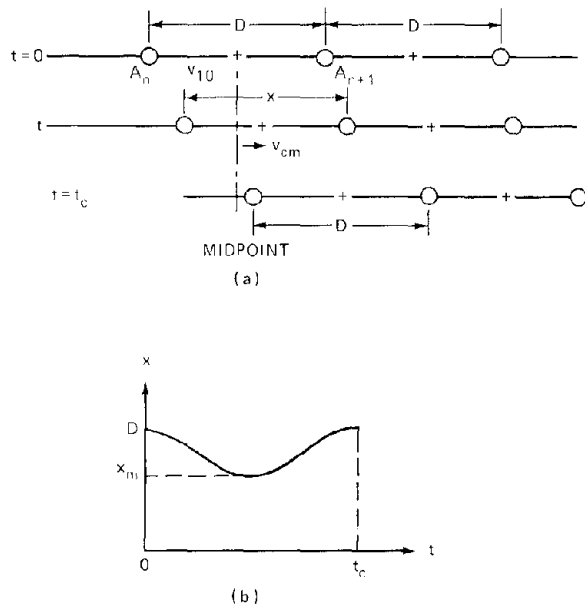


Fig. 17.13 Head-on collisions in a focused chain when the interaction potential acts continuously during the collision. (a) Atom positions during the collision initiated by the atom on the left. (b) Separation of atoms  $A_n$  and  $A_{n+1}$  during the collision.

there is no mechanism for removing energy from the chain. Two effects appear when the interaction of the neighboring rows of atoms with the row along which a focused collision is occurring is taken into account.

First, the neighboring atoms, by their repulsion of a moving atom that approaches more closely than the equilibrium separation, act as a lens and aid in the focusing process (i.e., they tend to reduce the angle  $\theta_n$  on successive collisions to a greater extent than predicted by simple hard-sphere mechanics along the chain). The net result of this process, which is called *assisted focusing*, is to increase the critical energy  $E_f$  at which a focused collision sequence is possible. Focusing is rendered more probable by the presence of the surrounding atomic rows (see Ref. 1 for a detailed discussion of assisted focusing).

Second, in addition to aiding the focusing process, the rings of atoms surrounding a focusing axis in the crystal provide the only means by which the energy of the collision sequence is dissipated. The energy loss results from glancing collisions between the atoms moving in the linear collision sequence and the atoms ringing this chain. This energy transfer occurs as a result of the decrease in the separation distance between an atom in the focused collision chain and its transverse nearest neighbors as the former moves off of its equilibrium position along the focusing axis. The increment of potential energy which results from the smaller separation between the moving atom in the chain and the neighboring atoms ringing the chain is lost to the energy pulse moving along the line (see problem 17.5 at the end of this chapter). This effect is augmented by vibration of the surrounding atoms transverse to the focusing direction, which increases with the temperature of the solid.

Figure 17.14 shows the number of collisions in a focused chain of initial energy  $E$  in room-temperature copper. The transport of energy along the focusing axis ends when interaction with the neighboring atoms has removed the entire initial energy of the knock-on that started the sequence. Focused replacement ceases when the energy left in the chain is reduced to  $E_f/4$ . Thus the length of the dynamic crowdion for initial knock-on energy  $E$  is the difference between the ordinate value corresponding to

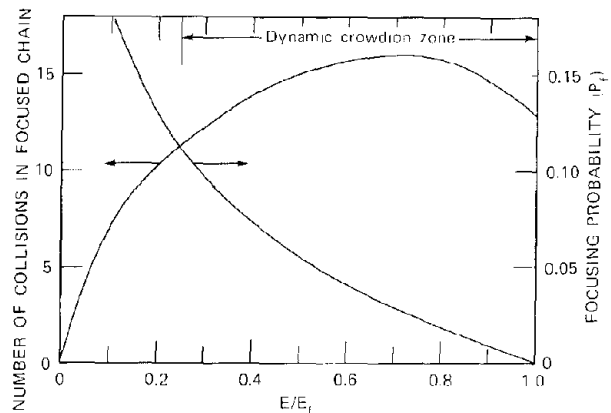


Fig. 17.14 Length and probability of the collision chain in a  $\langle 110 \rangle$  collision sequence in copper at room temperature. (After Ref. 1.)

$E/E_f$  and the ordinate value for  $E/E_f = 1/4$ . The length of the chain or of the dynamic crowdion decreases as the temperature increases due to the greater interference of displaced neighboring atoms with the collision sequence as the thermal vibration amplitude increases. The probability of forming a correlated collision sequence according to Eq. 17.97 is also shown in Fig. 17.14.

The presence of atoms of unequal mass in the atomic row also serves to dissipate energy from the collision chain. Consider a light atom sandwiched between two heavy atoms along the focusing axis. When struck, the light atom not only collides with the downstream heavy atom but may also rebound rapidly enough to re-collide with the upstream heavy atom from which it received the original impact. Such multiple collision events destroy the unidirectional nature of the energy pulse and result in substantial energy loss. This dissipation mechanism may be important in stainless steel, which contains substantial quantities of low-mass additives such as carbon and boron in addition to the transition metals iron, nickel, and chromium, which have not too different masses. A similar effect would be expected if a focusing axis intersected a lattice defect, such as a vacancy.

Extended lattice defects, such as a dislocation or a stacking fault (i.e., an interruption of the stacking sequence of the planes of a crystal), represent such large distortions of the crystal symmetry that they probably terminate the dynamic crowdion, which then becomes lodged in the solid as an interstitial atom. For a heavily deformed matrix with a dislocation density of  $10^{12} \text{ cm}^{-2}$ , for example, the average distance between dislocation lines is about  $100 \text{ \AA}$ , or 40 atom separation distances in the  $\langle 110 \rangle$  direction of the fcc lattice. This chain length is three times longer than the average number of collisions along the focusing axis when interaction with the atoms surrounding the focusing axis is responsible for energy dissipation (Fig. 17.14). Limitation of the length of a dynamic crowdion is most probably controlled by this intrinsic dissipation mechanism

rather than by interaction with dislocations, especially at high temperature.

### 17.8.3 Channeling

Channeling refers to the long-distance displacement of an energetic knock-on down an open direction in the lattice. The walls of the passageway or channel consist of atomic rows. Figure 17.15 shows the  $\langle 110 \rangle$  channel in the fcc structure, which is bounded by four close-packed  $\langle 110 \rangle$  atomic rows. Atoms moving by the focusing or channeling mechanisms both prefer to do so in close-packed directions in the lattice. However, dynamic crowdions move in the close-packed rows, whereas channeled atoms move in between the close-packed rows.

The moving atom is kept in a channel by glancing collisions with the bordering atoms. If the atomic rows surrounding the channel are close packed, the discrete repulsive force between atoms, which is responsible for the channeling action, is smeared out, and the atom appears to be travelling in a long cylindrical tube. The equivalent radius of the channel,  $R_{ch}$ , can be determined by equating  $\pi R_{ch}^2$  with the actual area of the open region between the surrounding atomic rows. The cross-sectional area of the  $\langle 110 \rangle$  channel shown in Fig. 17.15, for example, is  $a_0^2/8^{1/2}$ ; so  $R_{ch} = 0.34a_0 \approx 0.85 \text{ \AA}$ .

If the amplitude of the lateral oscillations of the moving atom in the channel is small compared to  $R_{ch}$ , the effective potential well provided by the channel wall is approximately parabolic in the direction transverse to the channel axis. The interaction of the moving atom with the channel walls can be described by a harmonic channel potential of the form

$$V_{ch}(r) = \kappa r^2 \quad (17.102)$$

where  $r$  is the lateral distance from the axis. The force constant,  $\kappa$ , depends on the potential function describing atom-atom repulsion and the channel dimensions  $R_{ch}$ . An

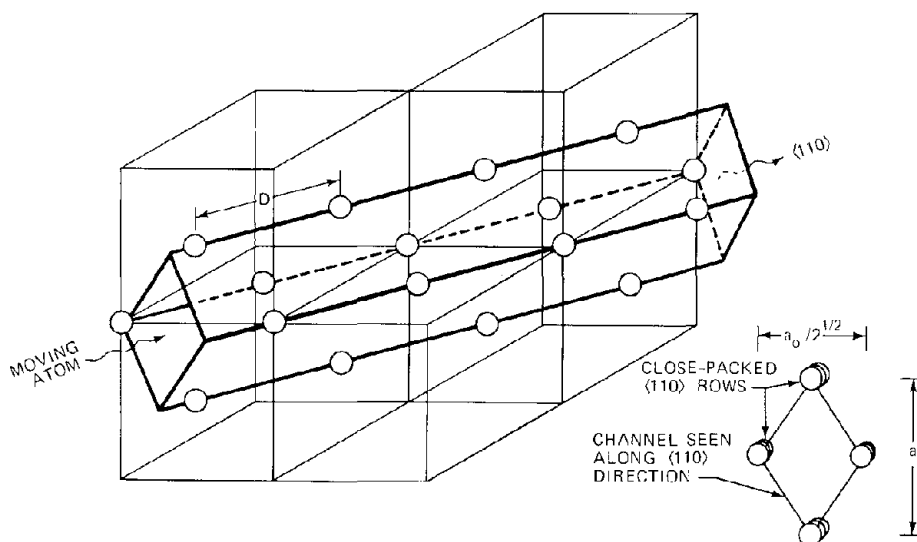


Fig. 17.15 The  $\langle 110 \rangle$  channel in the fcc lattice.

approximate derivation of the force constant is given in Ref. 1. For the Born-Mayer function, for example, it is

$$\kappa = \frac{A}{D\rho} \left( \frac{2\pi R_{ch}}{\rho} \right) \exp \left( -\frac{R_{ch}}{\rho} \right) \quad (17.103)$$

where  $D$  is the atomic spacing of the atoms in the rows forming the channel walls.

Analysis of the trajectory of the channeled atoms with the aid of the parabolic channel potential of Eq. 17.102 is straightforward. The moving atom enters into the channel with a velocity component along the axis (the  $z$ -direction) given by

$$v_{z0} = (2E/M)^{1/2} \cos \theta_0 \quad (17.104)$$

where  $\theta_0$  is the off-axis angle at which the knock-on of energy  $E$  is injected into the channel. The axial velocity is gradually reduced by electron stopping.

The moving atom undergoes simple harmonic motion in the  $r$ -direction with a period  $\tau$  given by

$$\tau = 2\pi \left( \frac{M}{2\kappa} \right)^{1/2} \quad (17.105)$$

The initial wavelength of the oscillation is equal to  $v_{z0}\tau$  for  $\theta_0 = 0$ , or to

$$\lambda = 2\pi \left( \frac{E}{\kappa} \right)^{1/2} \quad (17.106)$$

The amplitude of the lateral oscillation is determined by the injection angle,  $\theta_0$ , and the kinetic energy of the injected atom,  $E$ . The  $r$ -component of the atom velocity as it enters the channel is  $(2E/M)^{1/2} \sin \theta_0 \approx (2E/M)^{1/2} \theta_0$ . Or, the radial component of the entrance kinetic energy is  $E\theta_0^2$ , which is equal to the potential energy at the transverse amplitude,  $\kappa r_{max}^2$ . Solving for  $r_{max}$  yields

$$r_{max} = \left( \frac{E}{\kappa} \right)^{1/2} \theta_0 \quad (17.107)$$

and the trajectory of the channeled atom is

$$r = \theta_0 \left( \frac{E}{\kappa} \right)^{1/2} \sin \left[ \left( \frac{\kappa}{E} \right)^{1/2} z \right] \quad (17.108)$$

A typical trajectory is shown in Fig. 17.16.

Just as in the case of focusing, there is a critical angle beyond which channeling cannot occur. In the harmonic approximation,  $\theta_0^{max}$  is obtained by requiring that the transverse amplitude  $r_{max}$  be less than  $R_{ch}$ , which leads to

$$\theta_0^{max} = \left( \frac{\kappa R_{ch}^2}{E} \right)^{1/2} \quad (17.109)$$

Equation 17.109 is the analog of the critical-angle formula derived for focusing (Eq. 17.96). However, the former cannot be used to determine a channeling probability,  $P_{ch}$ , in the way that the focusing probability,  $P_f$ , given by Eq. 17.97 was obtained from Eq. 17.96. The reason is that for channeling to begin an energetic knock-on must be driven into the open space offered by the channel. For the very reason that a channel is open, there are no normal lattice atoms near the channel axis to act as the channeled atom. Instead, channeling probably starts with an impact on one of the atoms in the row forming the channel walls.

If this atom leaves its lattice position at a small angle with respect to the axis, it may begin to channel. Equation 17.109 was derived for an atom entering the channel at  $r = 0$  and cannot be applied to a knock-on entering at  $r = R_{ch}$ . Although no analytical expression for the channeling probability is available, computer simulations of radiation damage indicate that  $P_{ch}$  is between 1 and 10%. It is usually assumed to be independent of knock-on energy.

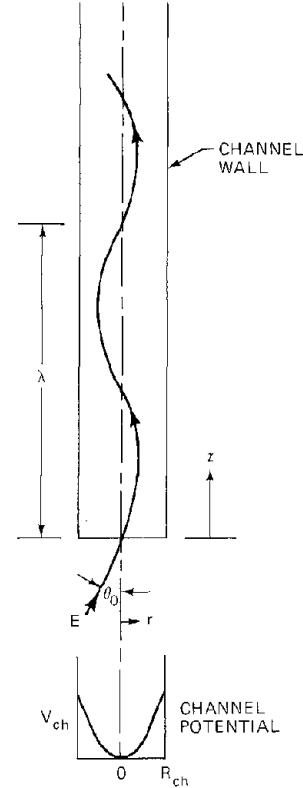


Fig. 17.16 Typical trajectory of channeled atom.

Contrary to the phenomenon of focusing, there is no upper limit to the knock-on energy at which channeling is possible; the maximum allowable injection angle simply becomes smaller as the energy increases. However, there is a minimum energy below which the oscillatory motion is terminated by a violent collision with the channel wall. Equation 17.106 shows that the wavelength decreases as the energy of the channeled atom decreases. When  $\lambda$  is of the order of a few atom spacings along the bounding rows, a large-angle collision becomes probable. The minimum channeling energy,  $E_{ch}$ , can be estimated by setting  $\lambda$  in Eq. 17.106 equal to  $2D$ , which yields

$$E_{ch} = 0.1\kappa D^2 \quad (17.110)$$

For copper,  $E_{ch} = 300$  eV. The energy  $E_{ch}$  increases directly as  $\kappa$ . When available Born-Mayer parameters are used in Eq. 17.103,  $\kappa$ , and hence  $E_{ch}$ , are found to be larger for heavy elements than for light ones. Thus, channeling is a high-energy phenomenon of most significance in low-atomic-weight metals. Conversely, focusing is possible only at low energies and is more important in heavy elements than in light ones.

### 17.8.4 Effect of Focusing and Channeling on the Number of Displaced Atoms

If in the course of formation of a cascade a recoil becomes channeled or develops into a dynamic crowdion, the kinetic energy of the recoil is lost to the cascade; i.e., its energy is transformed to heat through electronic stopping or subthreshold atomic collisions. The probability of the occurrence of a crystal effect is a function of recoil energy. The notation  $P(E)$  is used for either of the probabilities  $P_f$  or  $P_{ch}$ . However, the effect of focused collision sequences on the displacement cascade is quite small owing to the upper energy limit  $E_f$  of  $\sim 100$  eV in the focusing process.

The basic integral equation governing cascade formation can be modified to account for crystal effects by amending Eq. 17.65 to

$$\nu(E) = P(E) + [1 - P(E)] \left[ \frac{2E_d}{E} + \frac{2}{E} \int_{2E_d}^E \nu(T) dT \right] \quad (17.111)$$

The first term on the right represents the lone displaced atom (i.e., the PKA itself) which results if the PKA is channeled or focused on its first collision. The second term, which is weighted with the probability  $1 - P(E)$ , gives the number of displacements created by a PKA that makes an ordinary displacing first collision. This equation can be solved by the method used in the previous section if the probability  $P$  is assumed to be independent of energy. Taking the derivative of Eq. 17.111 with respect to  $E$  then yields

$$E \frac{d\nu}{dE} = (1 - 2P)\nu + P$$

which can be integrated to give

$$\nu = \frac{CE^{(1-2P)} - P}{1 - 2P}$$

The integration constant  $C$  can be found by substituting this solution into Eq. 17.111:

$$C = \frac{1 - P}{(2E_d)^{(1-2P)}}$$

The complete solution is therefore

$$\nu(E) = \frac{1 - P}{1 - 2P} \left( \frac{E}{2E_d} \right)^{(1-2P)} - \frac{P}{1 - 2P} \quad (17.112)$$

Equation 17.112 was first obtained by Oen and Robinson.<sup>18</sup> Equation 17.112 reduces to the Kinchin-Pease result (Eq. 17.68) when  $P = 0$ . The crystal effect (principally channeling) is most important for large PKA energies, which simply reflects the greater number of recoils susceptible to loss from the cascade by this means. For  $P = 7\%$ , for example, a 10-keV PKA in iron produces 100 displaced atoms according to Eq. 17.112. When channeling is neglected, twice this number is generated.

## 17.9 DISPLACEMENTS AND DAMAGE IN A FAST-NEUTRON FLUX

Up until this point we have been concerned with the methods of calculating  $\nu(E)$ , the number of displaced atoms

produced by a single PKA that receives energy  $E$  from a collision with the bombarding particle. In this section the supply of energy to the atoms of a metal from fast neutrons is coupled with cascade theory to permit calculation of the rate at which vacancies and interstitials are produced in a specified neutron flux spectrum. No account is taken of the reduction in the number of displacements due to recombination within the volume of the cascade.

Let  $\sigma_n(E_n, E) dE$  be the differential energy-transfer cross section for the production of PKAs with energies in  $(E, dE)$  due to neutrons of energy  $E_n$ . Each PKA goes on to produce  $\nu(E)$  displaced atoms. If the differential neutron flux is  $\phi(E_n)$ , the rate at which atoms are displaced is

$$R_d = N \int_{E_d/\Lambda}^{\infty} dE_n \phi(E_n) \int_{E_d}^{\Lambda E_n} \sigma_n(E_n, E) \nu(E) dE \quad \frac{\text{displaced atoms}}{\text{cm}^3/\text{sec}} \quad (17.113)$$

The energy-transfer parameter,  $\Lambda$ , is given by Eq. 17.8, which, for the case of neutrons, can be written

$$\Lambda = \frac{4A}{(1 + A)^2} \quad (17.114)$$

where  $A$  is the mass number of the lattice atom in atomic mass units. The upper limit on the inner integral of Eq. 17.113 is the maximum-energy PKA that can be produced by a neutron of energy  $E_n$ , and the lower limit on the outer integral is the minimum neutron energy that produces a PKA of energy  $E_d$ . Neutrons of energies less than  $E_d/\Lambda$  (which is about 200 eV for the major constituents of stainless steel) create no displacements by elastic collisions with the nuclei of lattice atoms.

Therefore, thermal neutrons (mean energy  $\sim 0.1$  eV) are incapable of causing damage to structural or cladding metals by direct collision energy transfer. However, thermal neutrons can cause displacements by becoming absorbed in a nucleus and producing a radioactive species that decays by emission of a high-energy gamma ray. The decay-product atom recoils from this event with sufficient energy to displace itself and perhaps a few other lattice atoms. We do not treat this process here, inasmuch as the scattering collisions between lattice atoms and energetic neutrons are far more important in fast reactors than is the damage caused by capture reactions involving slow neutrons. Problem 17.7 at the end of the chapter deals with the recoil energy of lattice atoms that become radioactive by virtue of neutron capture.

### 17.9.1 Displacement Cross Section

Equation 17.113 can be written in terms of the displacement cross section:

$$R_d = N \int_{E_d/\Lambda}^{\infty} \sigma_d(E_n) \phi(E_n) dE_n \quad (17.115)$$

where  $\sigma_d$  is

$$\sigma_d(E_n) = \int_{E_d}^{\Lambda E_n} \sigma_n(E_n, E) \nu(E) dE \quad (17.116)$$

The displacement cross section can be computed if the nuclear scattering cross section for neutrons with the

element comprising the lattice is known. As mentioned above,  $\nu(E)$  must be known as well. Graphs giving  $\sigma_d$  as a function of neutron energy can then be constructed for each nuclide (isotopes included) contained in an alloy such as steel or zircaloy. This graphical information can then be combined with the neutron-flux spectrum characteristic of the particular location in the reactor in which irradiation occurs in the same manner prescribed by Eq. 17.115. In this way the results of experiments conducted in one flux spectrum can be used to estimate material behavior in a reactor with a different neutron-flux spectrum.

The scattering of fast neutrons by the nucleus of a lattice atom can be elastic or inelastic. In elastic scattering the nucleus of the struck atom is not excited to a higher energy state as a result of the collision; kinetic energy is conserved in the scattering event. In inelastic scattering the nucleus recoils from the collision in an excited state. The excitation energy,  $Q$ , is provided at the expense of the kinetic energies of the scattered neutron and the recoiling nucleus; total energy rather than kinetic energy is conserved in the collision. Inelastic scattering becomes important when the neutron energy becomes just a bit larger than the excitation energy,  $Q$ . When  $E_n < Q$ , inelastic scattering is energetically impossible. The lowest excited state of the nucleus generally has an energy of  $\sim 1$  MeV above the ground-state energy.

In inelastic scattering, one neutron is ejected from the nucleus for each neutron absorbed. At higher neutron energies the nucleus may be left in such a highly excited state as a result of momentarily absorbing the bombarding neutron that two neutrons are emitted in the decay of the compound nucleus. This interaction is the  $(n,2n)$  reaction. Because the flux of fast reactors is low at the threshold energies of the  $(n,2n)$  reaction, the contribution of this reaction to damage is smaller than elastic or inelastic neutron scattering.

Neutron scattering can also be characterized as isotropic or anisotropic. In inelastic scattering the incident neutron is first absorbed by the nucleus, and the scattered neutron is in reality emitted a very short time later from the compound nucleus. Because absorption precedes reemission of the neutron, the angular distribution of the inelastically scattered neutrons is to a very good approximation isotropic in the center-of-mass system.

Below about 0.1 MeV, elastic neutron scattering is also isotropic in the center-of-mass system. At higher energies, however, the elastically scattered neutrons have a distinct forward bias. This phenomenon is known as p-wave scattering.

To explicitly account for elastic and inelastic neutron scattering, we can write Eq. 17.116 as

$$\sigma_d(E_n) = \int_{E_c}^{\Delta E_n} \sigma_{e1}(E_n, E) \nu(E) dE + \int_{E_{\min}}^{E_{\max}} \sigma_{in}(E_n, E) \nu(E) dE \quad (17.117)$$

where  $\sigma_{e1}(E_n, E)$  and  $\sigma_{in}(E_n, E)$  are the differential energy-transfer cross sections for elastic and inelastic neutron scattering, respectively, and  $E_{\min}$  and  $E_{\max}$  are the limiting recoil energies in the inelastic-scattering process. Equation 17.117 can also be written in terms of

the differential angular cross sections for the scattering reactions by use of the first equality in Eq. 17.22:

$$\sigma_d(E_n) = 2\pi \int_{E_c}^{\Delta E_n} \sigma_{e1}(E_n, \theta) \left| \frac{d(\cos \theta)}{dE} \right|_{e1} \nu(E) dE + 2\pi \int_{E_{\min}}^{E_{\max}} \sigma_{in}(E_n, \theta) \left| \frac{d(\cos \theta)}{dE} \right|_{in} \nu(E) dE \quad (17.118)$$

The angular dependence of the elastic-scattering cross section can be written in a series of Legendre polynomials:

$$\sigma_{e1}(E_n, \theta) = \frac{\sigma_{e1}(E_n)}{4\pi} \sum_{l=0}^{\infty} a_l(E_n) P_l(\cos \theta) \quad (17.119)$$

where  $\sigma_{e1}(E_n)$  is the total elastic-scattering cross section for a neutron energy  $E_n$ ,  $P_l$  is the  $l$ th Legendre polynomial, and values of  $a_l$  are the energy-dependent coefficients of the cross-section expansion. At the neutron energies encountered in fast reactors, it is sufficient to retain only the  $l=0$  and  $l=1$  terms in the series expansion of Eq. 17.119. Since  $P_0 = 1$  and  $P_1 = \cos \theta$ , we can write

$$\sigma_{e1}(E_n, \theta) = \frac{\sigma_{e1}(E_n)}{4\pi} [1 + a_1(E_n) \cos \theta] \quad (17.120)$$

where  $a_0$  has been set equal to unity for normalization and  $a_1(E_n)$  represents the degree of anisotropy of the elastic-scattering reaction. If  $a_1 = 0$ , the differential cross section for isotropic elastic scattering is recovered.

When scattering is elastic, the angle-energy transformation derivative is given by Eq. 17.9 with  $T$  and  $E$  replaced by  $E$  and  $E_n$ , respectively:

$$\left| \frac{d(\cos \theta)}{dE} \right|_{e1} = \frac{2}{\Delta E_n} \quad (17.121)$$

Equation 17.121 is valid for both isotropic and anisotropic elastic scattering.

Since inelastic scattering is isotropic in the center-of-mass system,  $\sigma_{in}(E_n, \theta)$  simplifies to

$$\sigma_{in}(E_n, \theta) = \frac{\sigma_{in}(E_n)}{4\pi} \quad (17.122)$$

where  $\sigma_{in}(E_n)$  is the total inelastic-scattering cross section.

The inelastic-scattering process can excite the struck nucleus to a number of discrete levels having energies  $Q_i$  above the ground state or to a continuum of levels at high energies. For simplicity, we treat here the case in which only a single discrete state with excitation energy  $Q$  is produced.

Because the recoiling nucleus has absorbed energy in the collision, the elastic-scattering formula relating energy transferred to scattering angle, Eq. 17.9, is no longer valid. Instead, the collision kinematics must be based on conservation of total (rather than kinetic) energy, which results in addition of a term  $Q$  to the right-hand side of Eq. 17.4. The analog of Eq. 17.9 for an inelastic collision wherein the struck nucleus retains an energy  $Q$  is

$$E = \frac{1}{2} \Lambda E_n \left[ 1 - \frac{1+A}{2A} \frac{Q}{E_n} - \left( 1 - \frac{1+A}{A} \frac{Q}{E_n} \right)^{1/2} \cos \theta \right] \quad (17.123)$$

which reduces to Eq. 17.9 if  $Q = 0$ . The maximum and minimum recoil energies are obtained by setting  $\cos \theta$  equal to  $-1$  and  $1$ , respectively:

$$E_{\max} = \frac{1}{2} \Lambda E_n \left[ 1 - \frac{1+A}{2A} \frac{Q}{E_n} + \left( 1 - \frac{1+A}{A} \frac{Q}{E_n} \right)^{1/2} \right] \quad (17.124)$$

$$E_{\min} = \frac{1}{2} \Lambda E_n \left[ 1 - \frac{1+A}{2A} \frac{Q}{E_n} - \left( 1 - \frac{1+A}{A} \frac{Q}{E_n} \right)^{1/2} \right] \quad (17.125)$$

The threshold energy for production of the excited state is given by the requirement that the term under the square-root sign be greater than zero, or

$$(E_n)_{\min} = \frac{1+A}{A} Q \quad (17.126)$$

where  $\sigma_{in}(E_n)$  is zero for  $E_n < (E_n)_{\min}$ .

The transformation from scattering angle to energy transfer is

$$\left| \frac{d(\cos \theta)}{dE} \right|_{in} = \frac{2}{\Lambda E_n} \left[ 1 - \frac{1+A}{A} \frac{Q}{E_n} \right]^{-1/2} \quad (17.127)$$

Substituting Eqs. 17.120, 17.121, 17.122, and 17.127 into 17.118 yields

$$\begin{aligned} \sigma_d(E_n) = & \left( \frac{1}{\Lambda E_n} \right) \left\{ \sigma_{e1}(E_n) \int_{E_d}^{\Lambda E_n} \left[ 1 + a_1(E_n) \right. \right. \\ & \times \left. \left. \left( 1 - \frac{2E}{\Lambda E_n} \right) \right] \nu(E) dE + \frac{\sigma_{in}(E_n)}{\left( 1 - \frac{1+A}{A} \frac{Q}{E_n} \right)^{1/2}} \right. \\ & \left. \times \int_{E_{\min}}^{E_{\max}} \nu(E) dE \right\} \quad (17.128) \end{aligned}$$

If more than one excited state contributes to the inelastic scattering process, the last term in Eq. 17.128 is replaced by a sum over the excited states, each with its particular  $\sigma_{in}$ ,  $Q$ ,  $E_{\max}$ , and  $E_{\min}$ .

To proceed further, we must specify  $\nu(E)$ . A simple result can be obtained by using the Kinchin-Pease expression for  $\nu(E)$ . Substituting Eq. 17.68 into Eq. 17.128 and neglecting  $E_d$  compared to  $\Lambda E_n$  in the first integral results in

$$\begin{aligned} \sigma_d(E_n) = & \left( \frac{\Lambda E_n}{4E_d} \right) \left\{ \sigma_{e1}(E_n) \left[ 1 - \frac{1}{3} a_1(E_n) \right] \right. \\ & \left. + \sigma_{in}(E_n) \left[ 1 - \frac{1+A}{2A} \frac{Q}{E_n} \right] \right\} \quad (17.129) \end{aligned}$$

We have assumed for illustrative purposes that the maximum PKA energy  $\Lambda E_n$  is less than the ionization limit given by Eq. 17.43.

Except for resonances, the elastic-scattering cross section,  $\sigma_{e1}(E_n)$ , is more or less constant with neutron energy. The inelastic-scattering cross section, however, sharply increases with energy above the threshold  $(E_n)_{\min}$ . The anisotropy factor  $a_1(E_n)$  tends to decrease the displacement cross section because forward scattering transfers less energy, on the average, than does isotropic scattering. If both inelastic scattering and anisotropic elastic scattering are neglected and the elastic-scattering cross section is assumed to be energy independent, Eq. 17.129 reduces to

$$\sigma_d(E_n) = \left( \frac{\Lambda E_n}{4E_d} \right) \sigma_{e1} \quad (17.130)$$

In this simplest of cases, the displacement cross section increases linearly with neutron energy.

Inasmuch as  $\Lambda E_n/2$  is the average energy transferred to the lattice atom by a neutron of energy  $E_n$ , the coefficient  $\Lambda E_n/4E_d$  is the average number of displacements produced by a neutron of energy  $E_n$ . For 0.5-MeV neutrons in iron ( $A = 56$ ), the displacement cross section is  $\sim 350$  times larger than the nuclear scattering cross section. The total displacement rate for this case can be obtained by inserting Eq. 17.130 into Eq. 17.115:

$$\begin{aligned} R_d = & \frac{N \Lambda \sigma_{e1}}{4E_d} \int_{E_d/\Lambda}^{\infty} E_n \phi(E_n) dE_n \\ = & N \sigma_{e1} \left( \frac{\Lambda \bar{E}_n}{4E_d} \right) \Phi \quad (17.131) \end{aligned}$$

where  $\bar{E}_n$  is the average neutron energy and  $\Phi$  is the total neutron flux (with energies above  $E_d/\Lambda$ ). For the conditions

$$N = 0.85 \times 10^{23} \text{ atoms/cm}^3$$

$$\sigma_{e1} = 3 \text{ barns}$$

$$\Phi = 10^{15} \text{ neutrons cm}^{-2} \text{ sec}^{-1}$$

$$\frac{\Lambda \bar{E}_n}{4E_d} = 350 \text{ displaced atoms/neutron collision}$$

we find that  $R_d$  is  $9 \times 10^{16}$  displaced atoms  $\text{cm}^{-3} \text{ sec}^{-1}$ . Or, dividing by  $N$ , the displacement rate per atom (dpa/sec) is  $\sim 10^{-6}$ ; each atom in the metal is displaced from a normal lattice site once every 12 days.

Although Eq. 17.130 is useful for illustrating the order of magnitude of the displacement cross section, it is not sufficiently accurate for predicting mechanical-property behavior under irradiation. Doran<sup>19</sup> and Piercy<sup>20</sup> have calculated displacement cross sections for stainless steel and zirconium, respectively, using the Lindhard model for  $\nu(E)$  (Eqs. 17.90 to 17.93) and available data on the energy dependence of the elastic and inelastic-scattering cross sections and the anisotropy parameter  $a_1(E_n)$ . Figure 17.17 shows the displacement cross section for stainless steel. The jagged appearance of the curves is due to resonances in the elastic scattering cross section.

Figure 17.18 shows the differential neutron-flux spectra in two fast reactors and one thermal reactor. The average neutron energy in the all-metal Experimental Breeder Reactor II (EBR-II) core is 0.85 MeV. In the mixed-oxide Fast Test Reactor (FTR) core, the average neutron energy

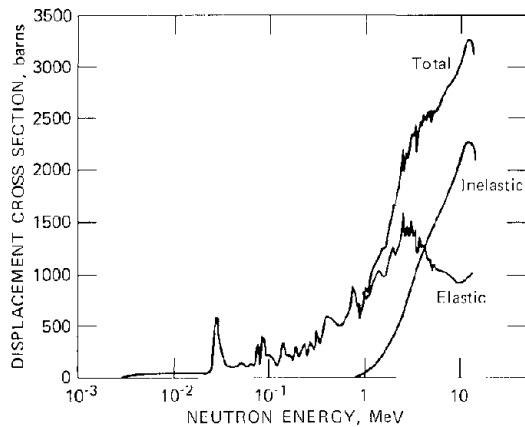


Fig. 17.17 Displacement cross section for stainless steel. (After Ref. 19.)

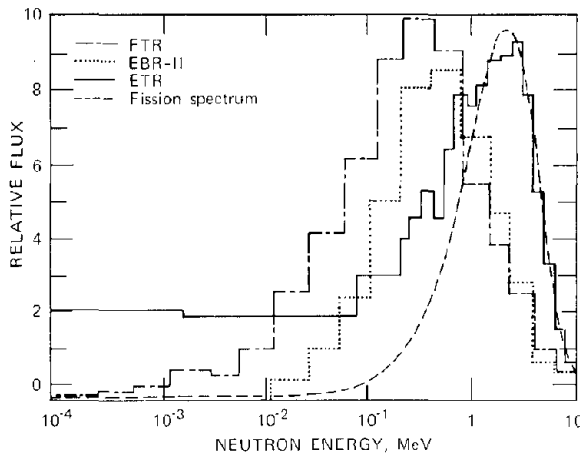


Fig. 17.18 Comparison of neutron-flux spectra for three reactors (FTR, Fast Test Reactor; EBR-II, Experimental Breeder Reactor II; ETR, Engineering Test Reactor). The FTR and EBR-II are fast reactors; the ETR is a thermal reactor. The fission-neutron-energy spectrum is shown for comparison. (After W. N. McElroy and R. E. Dahl, Jr., ASTM Special Technical Publication No. 484, p. 375, American Society for Testing and Materials, 1970.)

is 0.45 MeV. The fission neutron spectrum (average energy = 1 MeV) is shown for comparison. To compute the displacement rate in stainless steel, we multiply the curve of Fig. 17.17 by one of the spectra in Fig. 17.18 and integrate the product according to Eq. 17.115.

### 17.9.2 Damage Functions

The ultimate objective of calculating  $R_d$  is to permit prediction of the extent of a particular mechanical-property change in a fast reactor from the results of experiments conducted in irradiation facilities that have considerably different neutron-flux spectra. Typical mechanical-property changes induced by fast-neutron irradiation are the yield strength, the ductile-to-brittle transition temperature, and swelling. It is by no means generally true that the change in any of these properties is proportional to the number of

displaced atoms produced by an irradiation of known duration. Although the extent of void formation in metals appears to depend primarily on the number of vacancy-interstitial pairs created by irradiation, mechanical properties such as yield strength are determined by the clusters of vacancies and interstitial loops that remain after the nascent cascade has annealed and the isolated vacancies and interstitials have disappeared at the various sinks in the solid. The proper theoretical approach in the latter case is to compute the production of stable point-defect clusters resulting from radiation, not the total number of displaced atoms. This can be accomplished by replacing  $\nu(E)$  in Eq. 17.116 with the number of clusters that are produced by a PKA of energy  $E$ , which may be estimated from computer simulations of radiation damage. The resulting rate of cluster formation,  $R_{\text{cluster}}$ , should be a better measure of the damage (i.e., the yield-strength change) than is the rate of formation of total displaced atoms,  $R_d$ . Calculations of this sort have been performed by Russcher and Dahl.<sup>21</sup>

These completely theoretical attempts to predict some microscopic property of radiation damage (e.g., rate of formation of displaced atoms or rate of formation of clusters) are not sufficient to correlate macroscopic property changes in reactors of different flux spectra primarily because other consequences of irradiation besides the number of displacements or clusters affect the macroscopic property in question. Thus, although void formation certainly depends on the rate of production of vacancies and interstitial atoms by radiation, it is also a function of the quantity of helium gas generated by  $(n, \alpha)$  reactions in the metal because helium appears to be necessary to stabilize embryo voids. Calculation of the displacement rate  $R_d$ , no matter how accurate, provides no information on the helium-production rate.

Because of the inability of displacement calculations to cope with the complexity of most macroscopic radiation effects, a semiempirical method, known as the *damage function method*, has evolved.<sup>22</sup> In this method the rate of displaced-atom production appearing on the left-hand side of Eq. 17.115 is replaced by the change in a particular macroscopic property in a time  $t$  of irradiation, and the displacement cross section on the right is eliminated in favor of a function  $G(E_n)$ , which is to be determined. The damage function for the particular mechanical property is  $G(E_n)$ . Thus, Eq. 17.115 is replaced by

$$\Delta P_i = \Phi t \frac{\int_0^\infty G_i(E_n) \phi(E_n) dE_n}{\int_0^\infty \phi(E_n) dE_n} \quad (17.132)$$

In this equation,  $\Delta P_i$  represents the change in the property labeled by the index  $i$  during an irradiation of time  $t$  in a neutron flux  $\Phi$ . The spectrum of the flux in the irradiation facility is  $\phi(E_n)$ . The equation has been multiplied and divided by the total neutron flux

$$\Phi = \int_0^\infty \phi(E_n) dE_n \quad (17.133)$$

so the ratio  $\phi(E_n)/\int \phi(E_n) dE_n$  is a normalized flux spectrum. The product  $\Phi t$  is the total neutron fluence.

The term  $G_i(E_n)$  is the damage function for property  $i$  for neutrons of energy  $E_n$ . The conditions under which the

property  $P_i$  is measured after irradiation and the conditions (exclusive of the neutron flux) during irradiation must be carefully specified. The damage function depends on these nonneutronic conditions. For instance, if  $P_i$  is the yield strength of a particular metal, the temperature at which the irradiation and the subsequent mechanical test are carried out must be known. The derived damage function may change if either of these two auxiliary conditions is altered.

The technique for obtaining  $G_i(E_n)$  is to measure  $\Delta P_i$  in as many different (but known) neutron-flux spectra as possible. One then attempts to deduce a single function  $G_i(E_n)$  from the data obtained in each irradiation by using equations of the form given by Eq. 17.132. This process is called damage-function unfolding. Deduction of  $G_i(E_n)$  from a set of measured  $\Delta P_i$  values in different neutron-flux spectra is analogous to the determination of the flux spectrum of a reactor by activation of foils of a number of neutron absorbers of different energy-dependent capture cross sections. The damage function is determined by iterative solution of the set of equations given by Eq. 17.132; a first guess of  $G_i(E_n)$  is inserted into the set of integrals, and the calculated property changes  $\Delta P_i$  are compared with the measured values. The function  $G_i(E_n)$  is then adjusted, and the calculation is repeated until the measured property changes are reproduced as closely as possible by the integrals on the right of Eq. 17.132.

In this process both the number of iterations required and even the accuracy of the damage function ultimately obtained depend on the availability of a good first guess of the damage function. The best initial estimate of  $G_i(E_n)$  is the displacement cross section  $\sigma_d(E_n)$  on the assumption that the damage (i.e., the change in the mechanical property in question) should be roughly proportional to the number of displaced atoms.

Figure 17.19(a) shows the damage functions for the yield strength and swelling of stainless steel determined by the method described above. The units of the damage functions are those of the property [yield strength in kilo Newtons per square meter ( $\text{kN/m}^2$ ), swelling in percent (%)] divided by the total neutron fluence (units of neutrons/ $\text{cm}^2$ ). Each damage function was determined from tests conducted in several different reactors with different flux spectra. The dashed lines in the graphs are the displacement cross section of Fig. 17.17 extended to lower energies than in Fig. 17.17. The increase of  $\sigma_d(E_n)$  and  $G_i(E_n)$  at neutron energies below  $\sim 10^{-4}$  MeV is due to damage produced by recoil atoms activated by  $(n,\gamma)$  reactions with slow neutrons (the cross sections for capture reactions are proportional to the inverse of the neutron speed). Although the damage function is appreciable at very low neutron energies, the property change  $\Delta P_i$  is not greatly affected by this low-energy tail of  $G_i(E_n)$  because the flux spectrum of fast reactors contains relatively few low-energy neutrons (Fig. 17.18). The insensitivity of damage to low-energy neutrons is reflected by the breadth of the error band for  $E_n < 10^{-4}$  MeV in Fig. 17.19(a).

The yield-strength damage function is very close to the displacement cross section used as the input first guess of  $G_i(E_n)$ . This accord implies that whatever features of the displacement cascade are responsible for an increase in the strength of irradiated steel are at least proportional to the number of displaced atoms. The damage function deduced

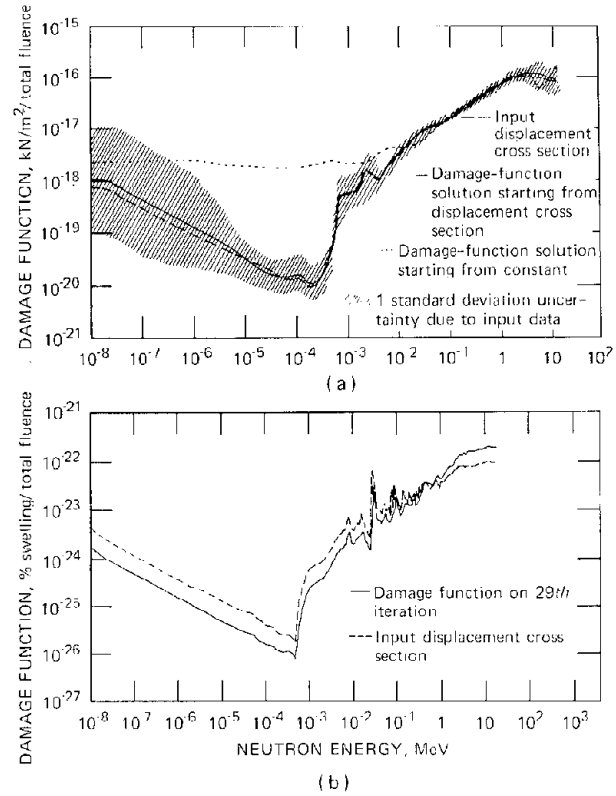


Fig. 17.19 Damage functions for two radiation effects in 304 stainless steel. (a) Yield strength for irradiation and test temperatures of  $480^\circ\text{C}$ . [From R. L. Simmons et al., *Nucl. Technol.*, 16: 14 (1972).] (b) Swelling at  $450^\circ\text{C}$  [From R. L. Simmons et al., *Trans. Amer. Nucl. Soc.*, 15: 249 (1972).]

from the initial guess  $G_i(E_n) = \text{constant}$  is shown as the dotted curve in Fig. 17.19(a). This curve is vastly different from the damage function obtained with the aid of an input displacement function, for which the initial guess is  $G_i(E_n) \propto \sigma_d(E_n)$ . The dotted curve is incorrect and reflects the stringent requirement of a good first guess if the iterative method is to converge to the correct damage function.

Figure 17.19(b) shows the damage function obtained for stainless-steel swelling due to void formation. The damage function for this property change is similar to, but not identical to, that for the yield strength.

### 17.9.3 Damage Production by Ion Bombardment

The extent of radiation damage produced by exposure of a structural metal to a fast-neutron flux depends on the duration of irradiation. The damage increases with the duration of irradiation. The damage increases with the fast-neutron fluence, which is the product of the fast-neutron flux,  $\Phi$ , and the irradiation time,  $t$ . The economics of nuclear power requires that the fuel of commercial fast breeder reactors remain in service for a fluence in excess of  $10^{23}$  neutrons/ $\text{cm}^2$  (i.e., for a year at a flux approaching  $10^{16}$  neutrons  $\text{cm}^{-2} \text{sec}^{-1}$ ). Accurate assessment of the durability of structural metals for use in LMFBR cores requires that the radiation effects produced at these

fluences either be measured directly in an irradiation facility where the expected fluences can be obtained or be extrapolated from tests at much lower fluences by recourse to an appropriate theoretical model. Acceptable theoretical models are often not available for particular radiation effects, and sound fuel-element design can be achieved only by testing to the expected service fluences. This situation applies to swelling of the cladding due to void formation; no accurate theory is available for prediction of void production, and extrapolation of low-fluence swelling data is risky because the phenomenon is not linear with fluence.

Even if adequate irradiation facilities with a fast-neutron flux of  $10^{15}$  neutrons  $\text{cm}^{-2} \text{sec}^{-1}$  were available, 3-year-duration tests would be required to attain the design fluences of an LMFBR core. In a test facility with a flux of  $10^{14}$  neutrons  $\text{cm}^{-2} \text{sec}^{-1}$ , 30 years would be necessary. There is therefore a great incentive to devise irradiation tests that can simulate fast-neutron damage at fluences of  $10^{23}$  neutrons/ $\text{cm}^2$  in a reasonable amount of time (say of the order of days).

Bombardment of metals by energetic heavy ions has proven to be a useful tool for compressing the time scale of irradiation tests by many orders of magnitude. Reasonable currents of  $\text{H}^+$ ,  $\text{C}^+$ , and metal-ion beams of energies from 1 to 10 MeV can be obtained from accelerators. Because the range of heavy ions in solids is quite small (typically 10  $\mu\text{m}$ ), all the initial energy of the ion can be dissipated in a small volume of the specimen. Since the number of displaced atoms in an irradiation experiment is a reasonable measure of the extent of radiation damage, we calculate the rate at which a beam of energetic heavy ions causes lattice displacements and compare this figure with that attainable in fast-neutron irradiations.

Figure 17.20 shows some features of ion stopping in solids. In Fig. 17.20(a) a beam of ions enters a solid with energy  $E_{i0}$ . The ions slow down in the solid and come to rest at a depth given by the projected range. Figure 17.20(b) shows the energy-loss characteristics of the ions while traversing the solid. Because the incident energies are in the million electron volt range, electronic excitation is the principal energy-loss mechanism over most of the range. Figure 17.20(c) shows schematic plots of the electronic and atomic stopping powers as functions of ion energy. The electronic stopping power is based on Eq. 17.52, and the atomic stopping power is obtained by inserting the appropriate cross section for energy transfer from the ion to the lattice atoms into Eq. 17.29. The ion energy at depth  $x$  can be obtained by integrating the electronic stopping-power formula of Eq. 17.52:

$$E_i(x) = \left[ (E_{i0})^{1/2} - \frac{1}{2} kx \right]^2 \quad (17.134)$$

The number of atomic collisions between the ions and the lattice atoms at depth  $x$  can be calculated from the following considerations. Let  $\sigma(E_i, E) dE$  be the differential cross section for transferring energy in the range  $(E, dE)$  to lattice atoms by an ion of energy  $E_i$ . The probability of a collision between an ion and a lattice atom in  $dx$  which transfers energy in the range  $(E, dE)$  is  $N \sigma(E_i, E) dE dx$  (see Eq. 17.19). Since  $I$  ions/ $\text{cm}^2$  pass depth  $x$  per second, the number of collisions per second in the volume element of

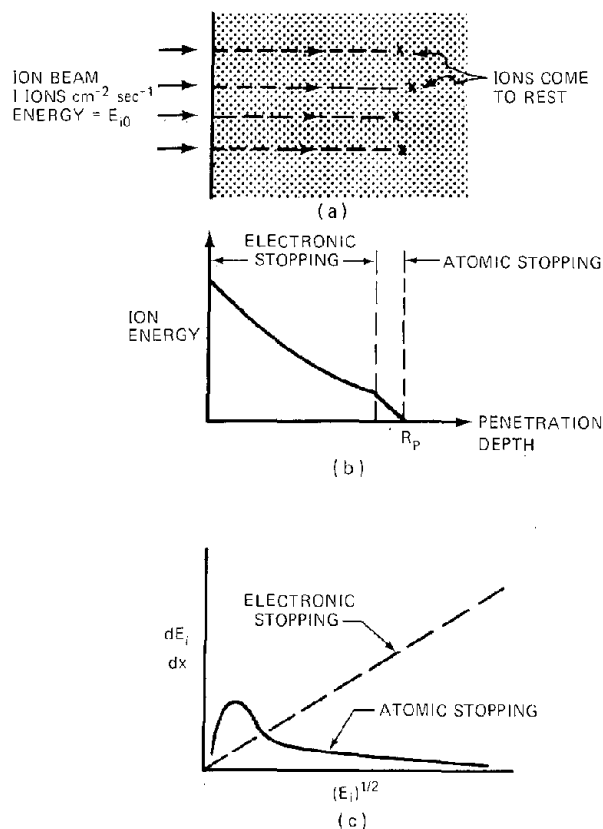


Fig. 17.20 Paths and energy losses of ions penetrating solids.

unit cross-sectional area and thickness  $dx$  which transfer energy in  $(E, dE)$  to the atoms in this element is  $NI \sigma(E_i, E) dE dx$ . Or, the number of collisions per unit volume per unit time which transfer energy in  $(E, dE)$  at depth  $x$  is  $NI \sigma(E_i, E) dE$ . Now the number of displaced atoms for each collision that produces a PKA of energy  $E$  is  $\nu(E)$ . Therefore, the rate of production of displaced atoms at depth  $x$  is

$$R_d(x) = NI \int_{E_d}^{\Lambda E_i} \sigma(E_i, E) \nu(E) dE \quad (17.135)$$

displaced atoms  
 $\text{cm}^3 \cdot \text{sec}$

where  $E_i$  is given in terms of  $x$  by Eq. 17.134 and  $\Lambda$  is given by Eq. 17.8. Multiplication of the above equation by the irradiation time  $t$  and division by the lattice atom density  $N$  gives the number of displacements per lattice atom in irradiation of fluence  $It$ :

$$\text{dpa} = \frac{\text{displacements}}{\text{atom}} = It \int_{E_d}^{\Lambda E_i} \sigma(E_i, E) \nu(E) dE \quad (17.136)$$

Division of Eq. 17.136 by the fluence yields

$$\frac{\text{dpa}}{(\text{ions}/\text{cm}^2)} \text{ at depth } x = \int_{E_d}^{\Lambda E_i} \sigma(E_i, E) \nu(E) dE \quad (17.137)$$

A simple illustrative integration of the right-hand side of Eq. 17.137 can be obtained if the cross section  $\sigma(E_i, E)$  is

assumed to be given by the Rutherford formula and if the Lindhard model is used for  $\nu(E)$ . Substituting Eqs. 17.37 and 17.90 into Eq. 17.137 and assuming the coefficient  $\xi(E)$  in Eq. 17.90 to be a constant equal to  $\sim 0.5$ , we obtain

$$\frac{\text{dpa}}{(\text{ions/cm}^2)} = \frac{\pi Z_i^2 Z^2 e^4}{4E_d E_i} \left( \frac{M_i}{M} \right) \ln \left( \frac{\Delta E_i}{E_d} \right) \quad (17.138)$$

where the subscript  $i$  denotes the incident ion and the unsubscripted properties refer to the lattice atom. Evaluating the right-hand side of Eq. 17.138 for bombardment of nickel by 20 MeV  $\text{C}^+$  ions gives a damage rate at the target surface ( $E_i = E_{i0}$ ) of  $\sim 3 \times 10^{-18}$  dpa/(ions/cm<sup>2</sup>).

Inasmuch as  $E_d$  decreases with  $x$ , Eq. 17.138 shows that the damage efficiency should increase until just before the ion stops. Kulcinski et al.<sup>2,3</sup> have used Eq. 17.137 to determine the efficiency of displacement production by various ion beams. Figure 17.21 shows graphs of the displacement-damage effectiveness for various ions impinging on nickel.

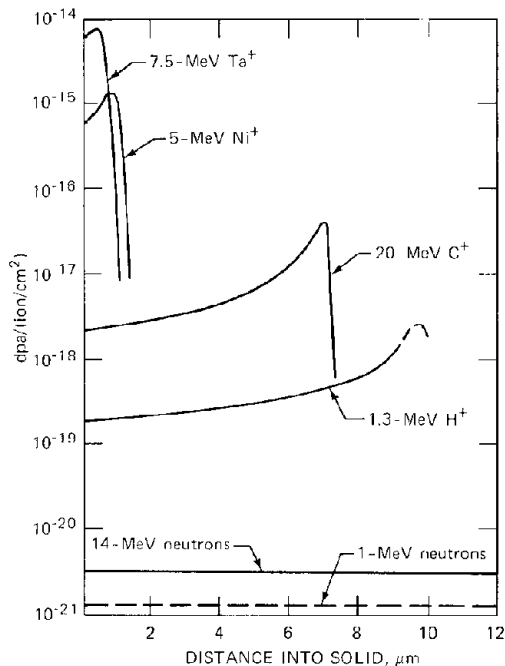


Fig. 17.21 Displacement-damage effectiveness as a function of penetration depth for ions impinging on nickel. (From Ref. 23.)

The amount of damage produced in a given time depends on the intensity of the ion beam. For medium-weight particles, such as  $\text{H}^+$  and  $\text{C}^+$ , intensities of the order of  $10^{14}$  ions  $\text{cm}^{-2} \text{sec}^{-1}$  can be obtained from accelerators. The maximum intensities of heavy-ion beams, such as  $\text{Ni}^+$  and  $\text{Ta}^+$ , are roughly an order of magnitude smaller. Using the maximum displacement rate for 20-MeV  $\text{C}^+$  ions from Fig. 17.21 and a  $\text{C}^+$  beam intensity of  $10^{14}$  ions  $\text{cm}^{-2} \text{sec}^{-1}$  shows that up to  $\sim 4 \times 10^{-3}$  dpa/sec can be achieved. By way of comparison, the calculated figure for a fast-neutron flux of  $10^{15}$  neutrons  $\text{cm}^{-2} \text{sec}^{-1}$  based on Eq. 17.131 gives a displacement rate of  $\sim 10^{-6}$  dpa/sec. The ion bom-

bardment is  $\sim 4000$  times as effective as neutron bombardment; the same number of displaced atoms are produced by a 6-hr ion bombardment as are produced by a 3-year neutron irradiation.

Ion bombardment is not simply a matter of telescoping the time scale of damage production. Figure 17.21 shows that the damage is contained within a very thin layer of the specimen close to the surface and moreover varies by an order of magnitude with depth. Fast-neutron damage, on the other hand, occurs rather uniformly throughout the entire volume of the metal. Such a variation in displacement efficiency over the damaged zone in an ion-bombarded metal is equivalent to a comparable variation in fluence in neutron irradiation. Damage effects in ion bombardment are contained in a narrow band between a free surface and undamaged bulk solid at depths greater than the ion range. The influence of the nearby free surface and the close proximity of the highly damaged zone to undamaged metal on radiation effects involving migration of the point defects created by the collision cascades is difficult to assess.

## 17.10 COMPUTER SIMULATION OF COLLISION CASCADES

Sections 17.7 and 17.8 of this chapter reviewed the analytical methods of predicting the principal feature of a collision cascade, namely, the number  $\nu(E)$  of displaced atoms (and hence the number of vacancies) created by a PKA of energy  $E$ . The simplest model due to Kinchin and Pease was modified to account for

1. A realistic energy-transfer cross section.
2. Continuous electronic energy loss during cascade formation.
3. Channeling of recoils.

Each of these factors reduces the predicted value of  $\nu(E)$  by some 10 to 50%, depending on the PKA energy. All analytical cascade theories, however, deal with the mechanics by which a collection of isolated Frenkel pairs is created by an energetic atom. That is, no interaction between the vacancies and the interstitials or between point defects of the same type was permitted. The former process leads to mutual annihilation of Frenkel pairs and is accompanied by a marked reduction in  $\nu(E)$ . The latter process accounts for the clustering of like point defects; these clusters are the precursors of interstitial dislocation loops or embryonic voids. Both of these entities exert a powerful influence on the mechanical behavior of the irradiated metal.

Within the last decade the advent of large computers has made possible the direct solution of the equations of motion of a large enough collection of atoms (a crystallite) to accurately simulate a macroscopic crystalline specimen undergoing irradiation.<sup>2,4-2,6</sup> In these computer experiments, one atom in a static assembly of several hundred to several thousand atoms arranged in one of the cubic structures (fcc or bcc) is given an initial pulse of kinetic energy in a particular direction. This initial state simulates a lattice atom struck by a fast neutron and thereby transformed into a PKA. The PKA goes on to strike one of the neighboring atoms, which is set in motion (and displaced if the energy transfer is great enough). The entire sequence of collisions between atoms in the crystallite is followed as a

function of time. The positions of all atoms in the crystallite during the cascade is governed by a set of several hundred equations of motion of the type

$$M \frac{d^2 x_i}{dt^2} = F_i(x_1, x_2, \dots, x_n) \quad (\text{for } i = 1, 2, \dots, n) \quad (17.139)$$

where  $F_i$  is the force on the  $i$ th atom due to the repulsive interaction of its neighbors. These forces may be represented as the sum of the pair-interaction potentials between the  $i$ th atom and the surrounding atoms:

$$F_i = \sum_{j \neq i} \frac{\partial V}{\partial r_{ij}}$$

where  $r_{ij} = |x_i - x_j|$  is the distance between the  $i$ th and  $j$ th atom of time  $t$ . Since the repulsive force represented by the gradient of the interaction potential  $V$  is short range, only atoms in the immediate vicinity of the  $i$ th atom (nearest and next-nearest neighbors) need be included in the above sum. The potential-energy function is of the form shown in Fig. 17.5. Since typical kinetic energies of moving atoms in the cascade are  $\sim 10$  keV, potential functions of the Born-Mayer type are most frequently used. As in analytical cascade theory, displacement is assumed to occur if a struck atom receives energy in excess of a step threshold  $E_d$  (usually taken as 25 eV).

We first examine the results of computer simulations for PKA energies close to the displacement threshold. Figure 17.22 shows the atom trajectories created by a 40-eV knock-on in a small crystallite (about 500 atoms) of copper. According to Eq. 17.64, only one Frenkel pair is

created by a 40-eV PKA. The atom labelled A in the figure is the PKA. The diagram represents a section through the (100) plane, in which the atom positions are denoted by large circles. The small dots represent the centers of the atoms. The initial direction of the PKA in Fig. 17.22(a) lies in the (100) plane at an angle of  $15^\circ$  to the [010] direction. Atom A strikes atom B with sufficient energy transfer to displace B. After the collision, A falls into the site vacated by B. This is called a *replacement collision*. Atom B then goes on to dislodge C which, however, does not have sufficient energy left to displace D. The final positions of the atoms along the [010] direction are marked with primes; a vacant site is left at the original PKA position, atoms A and B occupy the former sites of B and C, respectively, and atom C becomes an interstitial. These movements constitute a miniature focused replacement sequence of the type described in Sec. 17.8. The remaining atoms in the crystallite receive subthreshold increments of energy and simply oscillate about their equilibrium positions. The wriggles about the initial atom centers in the diagram show the motion of the atoms during the cascade. Focused energy propagation is apparent in the [011] direction, as expected, and to a lesser extent along the [001] direction from atom A.

Figure 17.22(b) shows the same event with a change in the takeoff direction of the PKA, which is  $22.5^\circ$  with respect to the [010] direction. In this case the [011] focused replacement chain is activated, and a dynamic crowdion propagates in this direction. The displaced atom appears at  $E'$  at the end of the period of cascade formation. Only focused energy transfer occurs in the [010] direction, which in the previous case provided a displaced atom as well. The vacancy is produced at A.

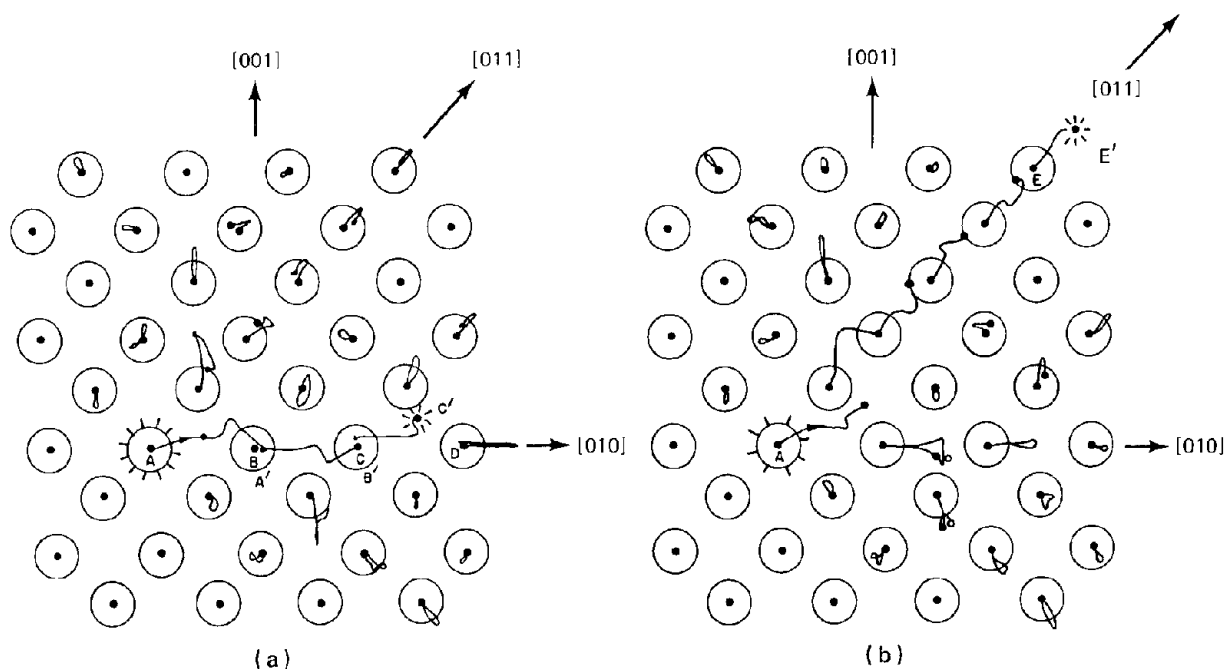


Fig. 17.22 Atom trajectories and displacements due to a 0.04-keV (40 eV) PKA in the (100) plane of copper. The PKA was created at A. For two PKA takeoff directions: (a)  $15^\circ$  to [010]. (b)  $22.5^\circ$  to [010]. [After Gibson et al., *Phys. Rev.*, 120: 1229 (1960).]

### 17.10.1 Displacement Spikes

In the preceding discussion of a near-threshold collision cascade, the question of the spatial configuration of the displaced atoms was trivial; only one Frenkel pair was created, and, thanks to focusing, the vacancy and interstitial were sufficiently separated to prevent annihilation by spontaneous recombination. In collision cascades produced by high-energy PKAs, however, many Frenkel pairs are created, and their relative positions are crucial in determining the number of them that survive annihilation or immobilization by clustering.

The question of the configuration of the displaced atoms and vacancies in a collision cascade was investigated analytically by Brinkman<sup>27</sup> before large computers were available to describe the cascade in atomic detail. Brinkman calculated the mean free path of an energetic recoil in the lattice and found that when  $E$  was of the order of several tens of kiloelectron volts the spacing between successive collisions approached atomic separation distances. This means that every atom in the path of the primary is displaced and the cascade cannot be thought of as a collection of isolated Frenkel pairs. The essence of Brinkman's analysis can be conveyed in the following simple (but not very accurate) calculation. The mean free path for any type of collision is defined by Eq. 17.23. The particular type of collision of interest here is the one that causes atomic displacement, i.e., which transfers energy in excess of  $E_d$ . The cross section for this process is given in terms of the differential energy-transfer cross section between lattice atoms by

$$\sigma'_d(E) = \int_{E_d}^E \sigma(E,T) dT \quad (17.140)$$

Note that  $\sigma'_d(E)$  is not the same as the displacement cross section of Eq. 17.116, which refers to the number of displaced atoms created by a neutron of a particular energy. Equation 17.140 has nothing to do with neutrons. In order to evaluate  $\sigma'_d(E)$ , we use the equivalent hard-sphere model, for which  $\sigma(E,T)$  is given by Eq. 17.39 (with  $\Lambda = 1$  in the present case since identical atoms are involved in the collision). Insertion of Eq. 17.39 into Eq. 17.140 and integration yield

$$\sigma'_d(E) = \sigma(E) \left( 1 - \frac{E_d}{E} \right) \quad (17.141)$$

where  $\sigma(E) = 4\pi r_o^2(E)$  is the total collision cross section between lattice atoms, one of which is moving with energy  $E$ . The term  $r_o(E)$  is the equivalent hard-sphere radius, which we take to be given by Eq. 17.41. Thus we have for  $\sigma(E)$

$$\sigma(E) = \pi \rho^2 \left[ \ln \left( \frac{2A}{E} \right) \right]^2 \quad (17.142)$$

Finally, the mean free path for displacement collisions is given by

$$l_d(E) = \frac{1}{N \sigma'_d(E)} = \frac{1}{N \sigma(E) [1 - (E_d/E)]} \quad (17.143)$$

Equations 17.142 and 17.143 are plotted in Fig. 17.23. The Born-Mayer constants for copper shown in Fig. 17.5 have

been used. The onset of closely spaced displacement collisions (i.e., when  $l_d$  is of the order of 3 to 10 Å) is seen to lie between a few tenths of a kiloelectron volt and several kiloelectron volts. Because the reduction in  $l_d$  with PKA energy is rather gradual at low energy, assignment of a specific energy at which a displacement spike is generated is impossible. We also do not know whether collisions must be separated by one, two, or three interatomic distances to generate a displacement spike. Finally, the  $l_d(E)$  curves are very sensitive to the interaction potential used in the calculation and to the method used to estimate energy transfer. However, all calculations of this sort suggest that the displacements caused by a recoil with an energy between 1 to 10 keV are separated by only one or two lattice parameters. Now the average energy of the PKA produced by a neutron flux in which the average neutron energy is  $\bar{E}_n$  is given by

$$(E_{PKA})_{av.} = \frac{1}{2} \Lambda \bar{E}_n \approx \frac{2\bar{E}_n}{A} \quad (17.144)$$

For stainless steel ( $A = 60$ ) in a typical LMFBR core ( $\bar{E}_n = 0.5$  MeV), the above formula shows that the average PKA energy is about 15 keV, which is just about the energy at which the displacement collisions become separated by distances of the order of a lattice parameter. Thus the bulk of the PKAs generated in the cladding of a fast reactor should create collision cascades that consist of displacement of every atom in the path of the PKA.

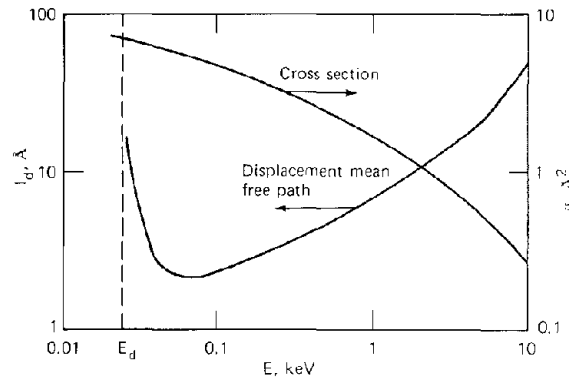


Fig. 17.23 Displacement mean free path and total collision cross section for copper atoms moving in copper.

What does such a collision cascade look like? It most certainly does not resemble the collection of isolated Frenkel pairs envisaged in analytical cascade theory. Figure 17.24 shows Brinkman's conception of the collision cascade created by a typical 5- to 20-keV PKA. The high density of collisions along the path of the primary ejects atoms outward. These atoms appear as a shell of interstitial atoms surrounding a hollow core of vacancies. Brinkman called this collision cascade a *displacement spike*. It would seem that the configuration shown in Fig. 17.24 is unstable, and indeed it probably is. The collapse of the structure, however, need not result in annihilation of all the vacancies and interstitials that were formed, although it is likely that a large fraction of the point defects will be eliminated very soon after the energetic event is over.

Brinkman proposed the displacement spike before the phenomenon of focusing was discovered. Seeger<sup>28</sup> modified Brinkman's picture of the displacement spike to account for the long-range transport of the atoms struck by the PKA by focused collision sequences. Seeger's schematic of the closely spaced collision cascade is shown in Fig. 17.25. The main difference between the configurations shown in Figs. 17.24 and 17.25 is the greater separation of the annular shell of interstitials from the central core of vacancies in the latter. This difference is due to the transport of displaced atoms as dynamic crowdions. Seeger called the nearly empty hole a *depleted zone*.

The displacement spike of Fig. 17.24 or the depleted zone of Fig. 17.25 must be regarded as educated guesses of the configuration of a collision cascade. Quantitative description of the displacement spike was made possible only by computer simulation of crystallites large enough to contain the secondaries and higher order recoils of PKAs with energies in the range from 5 to 100 keV.

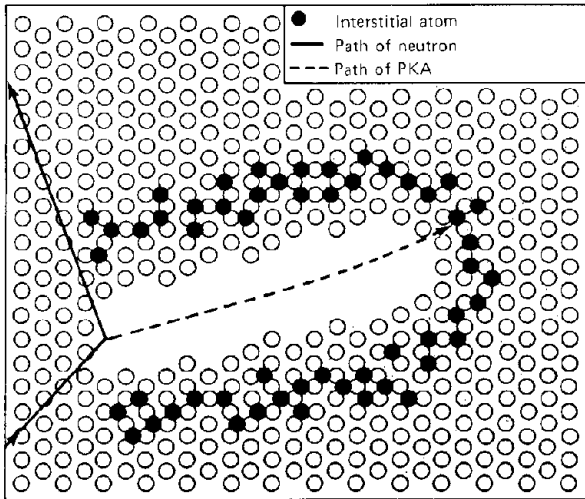


Fig. 17.24 Original version of the displacement spike. [After J. A. Brinkman, *Amer. J. Phys.*, 24: 251 (1956).]

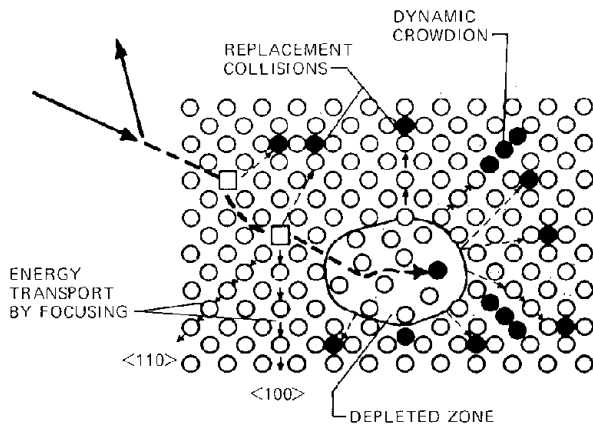
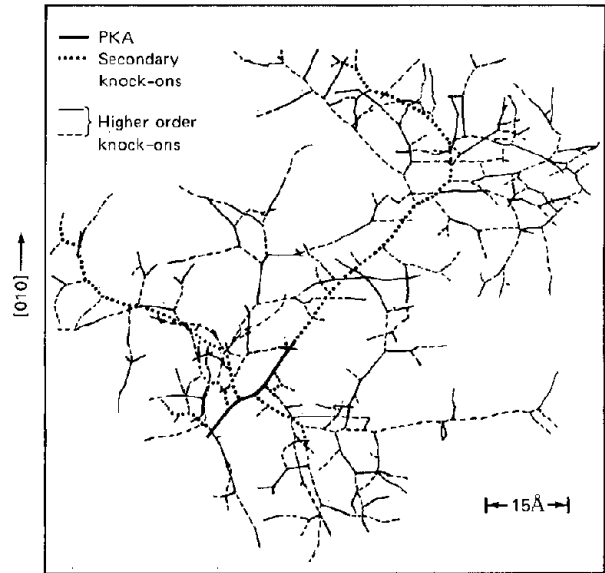
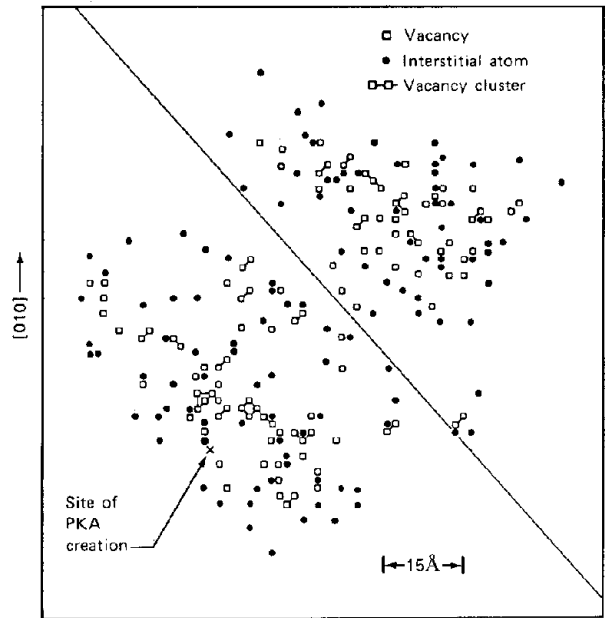


Fig. 17.25 Later version (still qualitative) of the displacement spike. □, vacancy. ●, interstitial atom. —, path of neutron. - - -, path of PKA. (After Ref. 28.)



(a)



(b)

Fig. 17.26 Computer simulation of displacement spike due to a 5-keV PKA in iron. All out-of-plane damage has been projected onto the (001) plane shown in the figure. (a) Recoil trajectories. (b) Vacancies and interstitial atoms at end of the collision cascade (0°K). The diagonal line in (b) shows the effect of channeling (see text). (After Ref. 26.)

The cascade shown in Fig. 17.26 represents the final configuration of the displaced atoms and vacancies in bcc iron resulting from interaction with a 5-keV PKA. The temperature of 0°K is assigned to the calculation because no motion of the point defects which requires thermal activation (i.e., processes with a rate governed by a

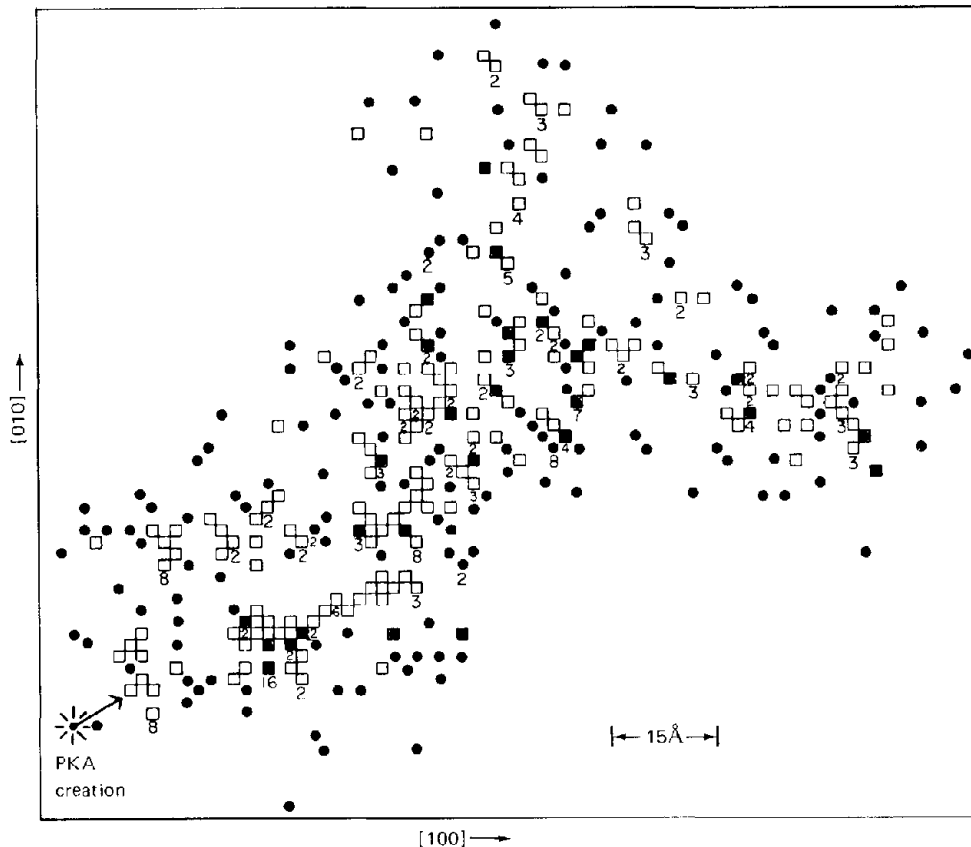


Fig. 17.27 Displacement spike due to a 20-keV PKA in iron projected onto the (001) plane ( $0^\circ\text{K}$ ). [After J. R. Beeler, Jr., *Phys. Rev.*, 150: 470 (1966).]

Boltzmann factor) is allowed. Spontaneous recombination of vacancies and interstitials has been included by simply removing from the calculation any vacancy that is within a sphere containing  $\sim 30$  lattice sites around an interstitial and vice versa. The size of this spontaneous recombination volume is not well established (see Sec. 13.4). Lines joining adjacent vacancies indicate stable vacancy clusters, which are formed by chance during cascade generation.

Figure 17.26(a) shows the trajectories of all the displaced atoms projected onto the (001) plane. The short thick track is that of the PKA, and the paths of the secondary knock-ons are represented by heavy dotted tracks. The thin dashed or solid tracks are those of the higher order recoils. Figure 17.26(b) shows the damage pattern created by the trajectories of Fig. 17.26(a). Again the three-dimensional configuration has been projected onto the (001) plane for illustrative purposes. The qualitative concepts of Brinkman and Seeger are confirmed by the computer experiment. The interstitials appear in a shell around a vacancy-rich core [lower left-hand corner of Fig. 17.26(b)]. Focused collision chains were responsible for removing the interstitials from the core. In addition, the importance of channeling is dramatically illustrated; all damage above the diagonal line in Fig. 17.26(b) disappears when a very slight change is made in the initial PKA direction to permit the head-on secondary in Fig. 17.26(a)

to channel. In this case it loses essentially all its energy by electronic stopping while moving down a [110] channel.

Figure 17.27 shows a displacement spike created by a 20-keV PKA in iron. The numbers on the plot indicate clusters of point defects. The cascade is slightly larger than the 5-keV cascade and is elongated in the direction of the initial PKA. The Kinchin—Pease formula (Eq. 17.68) predicts that  $20,000/(2 \times 25) = 400$  Frenkel pairs should have been created by the 20-keV PKA. There are 198 vacancies and 198 interstitials in Fig. 17.27. The reduction in displacement efficiency is due primarily to spontaneous annihilation of defects of opposite type which happened to have been created within the 30-site recombination volume.

### 17.10.2 Annealing of Displacement Spikes

When a collision cascade is produced in a metal at a temperature greater than absolute zero, thermal motion of the point defects produces recombination and clustering beyond that which occurred in the nascent cascade. The lifetime of cascade formation can be considered to be the interval between the initial energizing of the PKA and the stopping of the last higher order recoil. Cascade lifetimes, including spontaneous recombination of unstable Frenkel pairs, are  $\sim 10^{-13}$  sec. The annealing period during which the spike matures into a more or less stable entity requires

from  $10^{-7}$  to  $10^{-6}$  sec (which is the time required for each point defect to make several hundred to several thousand jumps). At the end of the annealing period, most of the very mobile components of the spike, such as mono- and divacancies and mono- and diinterstitials, have escaped from the spike center (which is roughly where the PKA was born) and have joined the general point-defect population in the bulk of the metal. What remains of the initial collision cascade is a collection of practically immobile clusters of interstitial atoms and vacancies and a few sluggish monovacancies. The clusters may either very slowly atrophy by thermally shedding point defects or grow by accretion of mobile point defects from the environment.

Doran<sup>29</sup> has developed a computer simulation of displacement spike annealing. The calculation uses as input information  $0^\circ\text{K}$  cascade configurations such as those shown in Figs. 17.26 and 17.27. The point defects are permitted to commence random walks in the damaged solid. A Monte Carlo technique is used to determine the jump directions of each point defect. Since the interstitials are quite a bit more mobile than the vacancies, the interstitials are permitted to jump more frequently than the vacancies. The jump frequencies of these two point defects are related by (Chap. 7):

$$\frac{w_i}{w_v} = \exp\left(\frac{s_i - s_v}{k}\right) \exp\left(-\frac{\epsilon_i - \epsilon_v}{kT}\right)$$

The migration energy of a vacancy,  $\epsilon_v$ , is quite a bit larger than that of an interstitial,  $\epsilon_i$ ; so  $w_i/w_v$  is greater than unity and is temperature dependent. At low temperature (i.e.,  $300^\circ\text{K}$ ),  $w_i/w_v$  is several thousand, and, at temperatures of about  $800^\circ\text{K}$ , the ratio is  $\sim 100$ . Real time during the anneal is not computed accurately (there is no need to do so)—the point-defect jump rate serves as a clock during annealing. The ratio of the jump rates is chosen to be consistent with the same annealing time. For example, 6000 interstitial jumps and 60 vacancy jumps at  $800^\circ\text{K}$  both correspond to a real time of  $\sim 10^{-6}$  sec.

If a point defect jumps into the prescribed recombination volume around a point defect of opposite sign, the two are annihilated. A point defect moving into a lattice site adjacent to a cluster composed of the same type of defect increases the cluster size by one.\* If a point defect joins a cluster of opposite type, the cluster shrinks by one.

The computation is continued until a stable state is attained, which usually occurs after most of the mobile interstitials that have not been annihilated or incorporated into clusters early in the anneal escape from the spike. At the end of the anneal, up to 80% of the defects in the nascent cascade have been annihilated (this figure is in addition to the losses that occurred by athermal point-defect recombination during cascade formation). The annihilation loss increases as the temperature becomes higher.

The final state of the 20-keV cascade shown in Fig. 17.27 after annealing at  $800^\circ\text{K}$  is depicted in Fig. 17.28. Twelve interstitials that have escaped from the confines of the region covered by the diagram are not shown. The annealed displacement spike consists mostly of clusters,

some of which contain a sizable number of point defects. Figure 17.29 shows the effect of the short annealing period on the distribution of clusters in the spike. Although 93% of the interstitial atoms were present as isolated point defects at the start of the anneal [Fig. 17.29(a)], the number of mono- and diinterstitials remaining after annealing is just about equal to the number of interstitials contained in clusters of three or more members. Vacancy clustering during the anneal is even more nonuniform [Fig. 17.29(b)]. Only about 7% of the vacancies present in the nascent cascade (whether clustered or not) survive the annealing as monovacancies. The rest ( $\sim 13\%$  of the initial quantity) are contained in clusters of four or more vacancies.

### 17.10.3 Cascade Overlap

The final state of the annealed cascade typified by Fig. 17.28 is stable for relatively long times. In a prolonged irradiation, it is likely that a second or even a third displacement spike will be created in the same region of solid as the first one. Beeler<sup>30</sup> has examined the consequences of cascade overlap by computer simulation techniques. The result of three collision cascades similar to the one shown in Fig. 17.26 at nearly the same location is shown in Fig. 17.30. Spike annealing was not considered. Nonetheless, a 25-vacancy cluster was found in the particular experiment shown in Fig. 17.30. Whether a cluster grows or shrinks as a result of the interaction of cascades depends on a large number of factors, including the separation and directions of the PKAs initiating the successive spikes and the relative size of the spikes (i.e., initial PKA energies). In particular, the vacancy clusters in a spike can be destroyed by the long-range dynamic crowdions from a nearby (not necessarily overlapping) collision cascade. One is led to expect that vacancy clusters in an irradiated metal will reach a saturation concentration at large fast-neutron fluences.

## 17.11 FISSION-FRAGMENT COLLISION CASCADES IN NUCLEAR FUELS

So far, the theoretical analysis of radiation damage has been restricted to monatomic substances. Although computer simulation of collision cascades in metals is rather advanced, very little comparable work on binary inorganic compounds has been reported. Reference 3 describes low-energy PKA computer simulations of displacement cascades in lead iodide, and Beeler and Besco have studied radiation damage in beryllium oxide.<sup>31</sup> No computer simulation of damage in heavy-metal oxides has been published. Most of the analytical studies intended to elucidate the damaging effect of fission fragments on reactor fuels have been confined to uranium metal. To apply these results to mixed-oxide fuels, we must consider the collisional properties of oxygen. The simplest approach to this problem is to consider the interaction of the fission fragment with two monatomic substances, one consisting of uranium atoms and the other composed of oxygen atoms. The radiation-damage parameter for the compound  $\text{UO}_2$  is assumed to be the average of the values for the two elemental calculations.

\*Next-nearest-neighbor vacancies also form stable clusters.

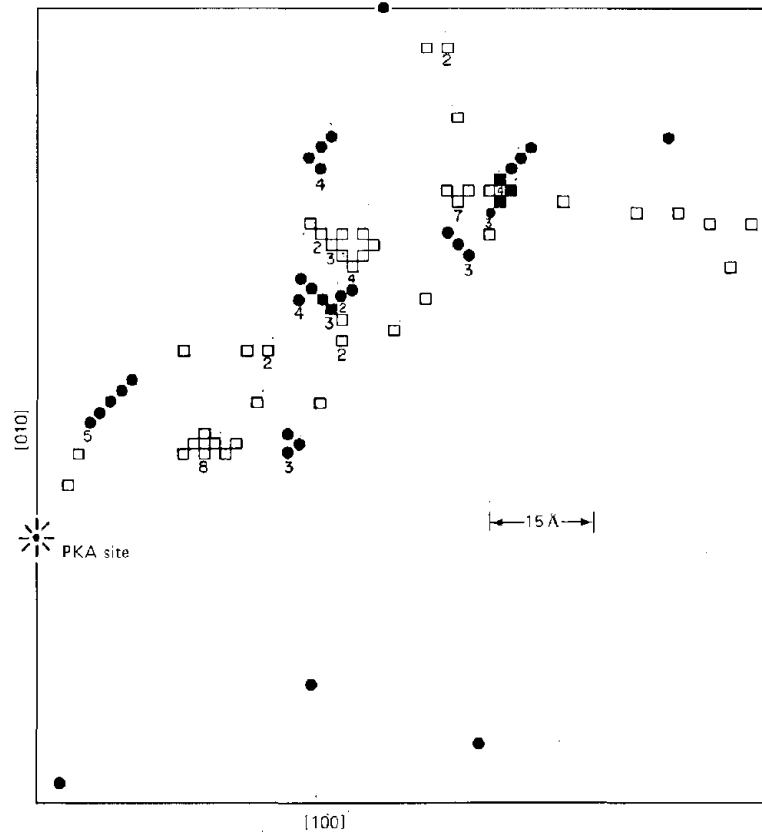


Fig. 17.28 Displacement spike [projected onto the (001) plane] due to a 20-keV PKA in iron after annealing at 800°K (6000 interstitial jumps and 60 vacancy jumps). The preannealed spike is shown in Fig. 17.27. Numbers on the diagram denote cluster sizes. Twelve interstitials have migrated outside the range of the diagram and are not shown. (After Ref. 29.)

There is some justification for this approach. Because the energy-transfer parameter  $\Lambda$  (Eq. 17.8) is unity for U-U and O-O collisions but only 0.23 for O-U collisions, a uranium PKA transfers energy more efficiently to the cation sublattice than to the anion sublattice. Similarly, a collision cascade begun by an oxygen PKA tends to remain on the oxygen sublattice. Considering radiation damage in a binary fuel as the sum of two independent elemental damage problems is at least preferable to simply assuming that  $\text{UO}_2$  behaves as uranium metal.

In this section, we use the above approach to calculate two quantities that were used in Chap. 13 to describe different features of fission-fragment interaction in oxide fuels, namely, the Frenkel-pair yield per fission  $Y_{\text{vi}}$  and the microscopic fission-gas re-solution parameter  $b$ . To treat these problems in a concise, yet tolerably accurate, manner, we introduce a number of simplifying assumptions, the most significant of which is the independence of the total stopping power of the fission fragment (electronic plus atomic) on energy. Because of the large initial energy of the fission fragments, ~90% of the energy loss is due to electronic stopping, which is better approximated by the square-root stopping law (Ref. 3, p. 219 and Ref. 32) than by a constant stopping power. However, the constant stopping-power simplification is often applied to describe fission-fragment slowing down and will be employed here.

### 17.11.1 Frenkel-Pair Yield from Fission Fragments

A general relation between the energy spectrum of the fission-fragment flux (assuming all fragments to be born at a specific energy  $E_{\text{ff}}^{\text{max}}$ ) can be obtained as follows. We do not yet invoke the constant stopping-power assumption. Consider a sphere of unit cross-sectional area at some point within the fuel and set  $\phi(E_{\text{ff}}) dE_{\text{ff}}$  as the number of fission fragments with energies in the range  $(E_{\text{ff}}, dE_{\text{ff}})$  crossing this unit sphere per second. Since the stopping power vs. energy formula provides, by integration, a unique relation between fragment energy and penetration distance, all fragments in the energy range  $(E_{\text{ff}}, dE_{\text{ff}})$  which cross the unit sphere must have come from a spherical shell of thickness  $dx$  at a radial distance  $x$  from the unit sphere. The volume of this shell is  $4\pi x^2 dx$ . The rate at which fission fragments are produced per unit volume of fuel is  $2\dot{F}$ , where  $\dot{F}$  is the fission density. Of those fragments born at a distance  $x$  from the unit sphere, a fraction  $1/(4\pi x^2)$  crosses the latter (the angular distribution of the fission fragments being isotropic). Thus the energy spectrum of the fission-fragment flux is

$$\phi(E_{\text{ff}}) dE_{\text{ff}} = 2\dot{F}(4\pi x^2 dx) \frac{1}{4\pi x^2} = 2\dot{F} dx$$

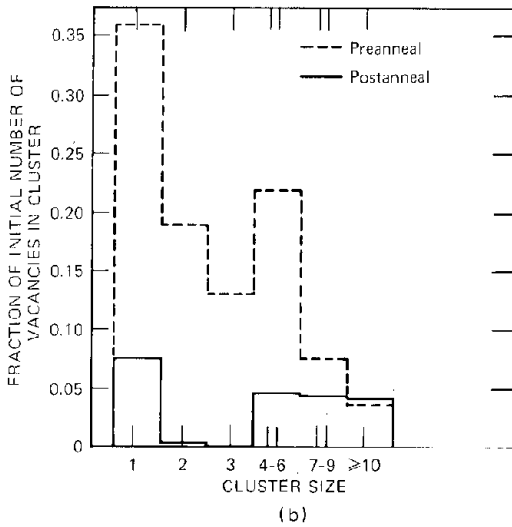
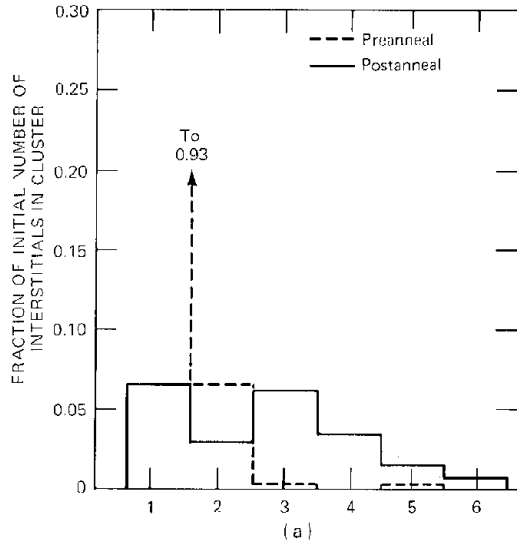


Fig. 17.29 Cluster distributions following a 20-keV PKA collision cascade in iron. The nascent cascade (preannealed state) contained about 200 of each type of point defect. Annealing at 800°K. (a) Interstitials. (b) Vacancies. (After Ref. 29.)

Now the distance interval  $dx$  can be related to the energy range  $dE_{ff}$  by the definition of the stopping power:

$$dx = \frac{dE_{ff}}{(dE_{ff}/dx)_{tot}}$$

where  $(dE_{ff}/dx)_{tot}$  is the sum of the electronic and atomic stopping powers for both oxygen and uranium (taken together). The energy spectrum of the fission-fragment flux is

$$\phi(E_{ff}) = \frac{2\dot{F}}{(dE_{ff}/dx)_{tot}} \quad (17.145)$$

If we now introduce the constant stopping-power assumption,  $(dE_{ff}/dx)_{tot}$  can be replaced by  $E_{ff}^{max}/\mu_{ff}$ , where  $\mu_{ff}$  is the range of fission fragments in the fuel. Equation 17.145 reduces to

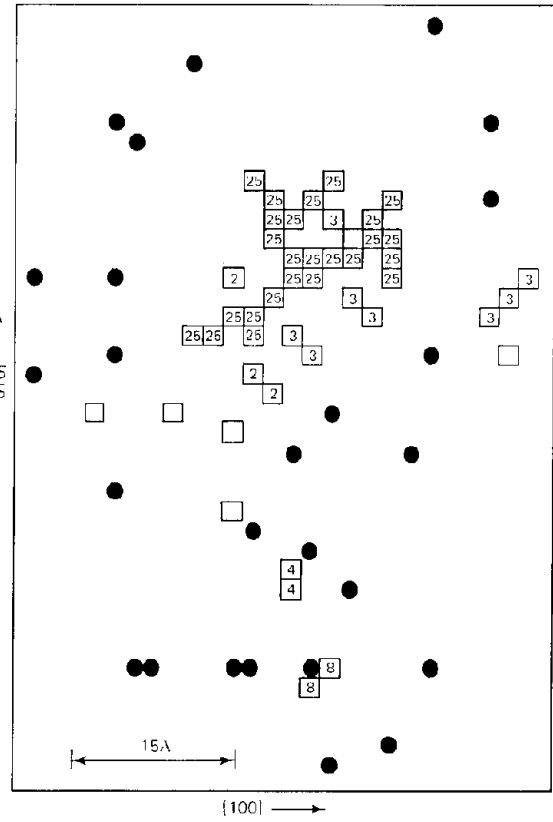


Fig. 17.30 A 25-vacancy cluster formed by the overlap of three successive 5-keV displacement spikes in copper (0°K). (After Ref. 30.)

$$\phi(E_{ff}) = \frac{2\dot{F}\mu_{ff}}{E_{ff}^{max}} \quad (17.146)$$

The rate at which displaced atoms are produced by fission fragments is obtained by the same arguments that led to Eq. 17.113 for fast neutrons. Division of the displacement rate per unit volume by the fission density yields the Frenkel-pair yield per fission on the uranium sublattice:

$$(Y_{vi})_U = \frac{R_{dU}}{\dot{F}} = \frac{N_U}{\dot{F}} \int_{E_d/\Lambda'}^{E_{ff}^{max}} dE_{ff} \phi(E_{ff}) \times \int_{E_d}^{\Lambda' E_{ff}} \sigma_{ff-U}(E_{ff}, E) \nu(E) dE \quad (17.147)$$

where  $N_U$  is the density of uranium atoms and  $\Lambda'$  is the energy-transfer parameter for collisions between fission fragments and lattice uranium atoms. Assuming the fission-fragment mass to be one-half the uranium atom mass,

$$\Lambda' = \frac{4M_{ff}M_U}{(M_{ff} + M_U)^2} = \frac{8}{9} \quad (17.148)$$

To evaluate the integral in Eq. 17.147, we take  $\nu(E) = E/(2E_d)$  and  $\sigma_{ff-U}(E_{ff}, E)$  as the Rutherford cross section between fission fragments and lattice atoms (Eq. 17.37):

$$\sigma_{ff-U}(E_{ff}, E) = \pi Z_{ff}^2 Z_U^2 e^4 \left( \frac{M_{ff}}{M_U} \right) \frac{1}{E_{ff} E^2} \quad (17.149)$$

Subject to the above simplifications, the Frenkel-pair yield per fission in uranium is

$$(Y_{vi})_U = \frac{\pi Z_{ff}^2 Z_U^2 e^4 N_U \mu_{ff}}{4 E_d E_{ff}^{\max}} \left( \frac{M_{ff}}{M_U} \right) \times \left[ \ln \left( \frac{\Lambda' E_{ff}^{\max}}{E_d} \right) \right]^2 \quad (17.150)$$

When evaluated for the heavy fission fragment ( $E_{ff}^{\max} = 67$  MeV, range in  $UO_2 \approx 6 \mu m$ ) on the uranium sublattice in  $UO_2$  ( $N_U = 0.025$  U atoms/ $\text{\AA}^3$ ), the above formula gives  $(Y_{vi})_U = 2.8 \times 10^5$ . For the same fission fragment interacting with the oxygen sublattice of  $UO_2$  ( $N_O = 0.049$  O atoms/ $\text{\AA}^3$ ), the Frenkel-pair yield is  $(Y_{vi})_O = 5.5 \times 10^4$ . We weight these yields with the probability that the fission fragment collides with an oxygen or uranium atom. The weighting function is

Probability of a ff collision with a U atom

$$= \frac{\sigma_{ff-U} N_U}{\sigma_{ff-U} N_U + \sigma_{ff-O} N_O} = \frac{Z_U^2 / M_U}{Z_U^2 / M_U + 2Z_O^2 / M_O} = 0.82$$

which yields a Frenkel-pair yield in  $UO_2$  of  $2.4 \times 10^5$ . This figure can be reduced by nearly an order of magnitude if the collision cascades on each sublattice are not isolated from each other, as has been assumed.

### 17.11.2 The Microscopic Re-resolution Parameter

In Sec. 13.7 the parameter  $b$  governing the probability per second of ejection of a gas atom from a bubble into the fuel matrix was derived on the assumption that direct encounters of the gas atoms and fission fragments controlled the process. Here we analyze the dynamics of fission-gas re-resolution when the collision cascades generated by fission fragments passing near the bubble cause energy transfer to gas atoms. That is, instead of transferring energy directly from the fission fragment to the gas atom, the former first energizes the lattice atoms, which then transmit their energy to the gas atoms. We follow the treatment of Nelson (Ref. 45 of Chap. 13) who only considered the collision cascades on the uranium sublattice; the oxygen sublattice was ignored.

The collision cascades created by energetic fission fragments in a region of fuel containing bubbles set up a flux spectrum,  $\phi(E_r)$ , of recoil atoms (which, following Nelson, are taken to be uranium atoms). The term  $E_r$  is the energy of a recoil atom, which may vary from zero to  $\Lambda' E_{ff}^{\max}$ . Consider a fission-gas bubble containing  $m$  gas atoms immersed in a spatially uniform flux of recoil atoms. The recoil flux in the fuel is assumed to be the same as the recoil flux in the gas bubble. Let  $R_{dg}$  be the rate of collisions between recoils and gas atoms in the bubble which result in transfer of energy to the latter in excess of the minimum required for re-resolution ( $T_{\min}$ ). Let the differential energy-transfer cross section between uranium recoils and gas atoms be  $\sigma_{U-g}(E_r, T)$ , where  $T$  is the energy

imparted to the gas atom by collision with a recoil of energy  $E_r$ . The re-resolution parameter is given by  $R_{dg}/m$ , or, on formulating  $R_{dg}$  in an analogous fashion to the displacement rate in Eq. 17.147, by

$$b = \frac{R_{dg}}{m} = \int_{T_{\min}/\Lambda'}^{\Lambda' E_{ff}^{\max}} dE_r \phi(E_r) \times \int_{T_{\min}}^{\Lambda' E_r} \sigma_{U-g}(E_r, T) dT \quad (17.151)$$

Note that Nelson does not account for multiplication of the collision cascade within the bubble;  $\nu(T)$  is set equal to unity.

To evaluate  $b$  we must derive expressions for the recoil-flux spectrum,  $\phi(E_r)$ , and the differential cross section for scattering of gas atoms by recoils,  $\sigma_{U-g}(E_r, T)$ . Let us consider the latter quantity first. Nelson argues that since the recoils have energies below  $\sim 100$  keV the equivalent hard-sphere approximation can be used to determine the cross section. Thus we may write (Eq. 17.39):

$$\sigma_{U-g}(E_r, T) = \frac{4\pi r_o^2}{\Lambda' E_r} \quad (17.152)$$

where  $2r_o$  is the distance of closest approach between a recoil of energy  $E_r$  and a stationary gas atom. This quantity is obtained from the interatomic potential between these two species,  $V_{U-g}(r)$ , and the criterion relating the distance of closest approach and the relative kinetic energy of the collision. The latter is given for equal mass collision partners by Eq. 17.17. For the present case the relative kinetic energy of the collision is  $M_g E_r / (M_g + M_U)$ , where the recoil-atom mass is that of uranium. If we assume the gas-atom mass to be the same as that of the fission fragments (the gas atoms were once fission fragments), we find the unequal mass analog of Eq. 17.17 is

$$V_{U-g}(2r_o) = \left( \frac{M_{ff}}{M_U + M_{ff}} \right) E_r \quad (17.153)$$

We now need an expression for the potential function  $V_{U-g}(r)$ . Nelson takes the inverse-square potential (Eq. 17.36 with  $s = 2$ ):

$$V_{U-g}(r) = \frac{A}{r^2} \quad (17.154)$$

in which the constant  $A$  is determined by matching the above potential to the screened Coulomb potential, Eq. 17.34, at  $r = a$ , where  $a$  is the screening radius given by Eq. 17.35. From this we deduce

$$A = Z_U Z_{ff} a e^2 \exp(-1) \quad (17.155)$$

where we have taken  $Z_g = Z_{ff}$ .

Combining Eqs. 17.153 to 17.155 gives the equivalent hard-sphere radius, from which the desired cross section follows from Eq. 17.152

$$\sigma_{U-g}(E_r, T) = \frac{K}{E_r^2} \quad (17.156)$$

where, using the screening radius formula given by Eq. 17.35 with  $\lambda = 1$ , the constant  $K$  is\*

$$K = \frac{2^{3/2} \pi Z_U Z_{ff} a_B e^2 \exp(-1)}{\Lambda' (Z_U^{3/2} + Z_{ff}^{3/2})^{1/2}} \left( \frac{M_U + M_{ff}}{M_{ff}} \right) \quad (17.157)$$

Inserting numerical values for the quantities in Eq. 17.157, we find  $K = 2.1 \times 10^{-12}$  eV-cm<sup>2</sup>.

We now approach the more difficult task of calculating the recoil-flux spectrum,  $\phi(E_r)$ . The analysis involves only moving lattice atoms and is not affected by the presence of gas atoms in bubbles. The energy of the PKA produced by collision of a fission fragment with a lattice atom is denoted by  $E$ . The energy of the higher order recoils in the collision cascade is designated by  $E_r$ . Consider first the case in which one PKA of energy  $E$  is produced in the lattice per unit volume per unit time (i.e., the distribution of PKA energies is not yet considered). We wish to calculate the slowing-down density of recoils due to this monoenergetic unit source:  $q_1(E, E_r)$  = recoils slowing down past energy  $E_r$  per cubic centimeter per second due to a source of one PKA of energy  $E$  per cubic centimeter per second. The recoil slowing-down density defined above is entirely analogous to the neutron slowing-down density commonly encountered in reactor physics analyses.

The first collision of the PKA produces one secondary of energy  $T$  while the PKA energy is degraded to  $E - T$  (Fig. 17.8). Just as in the analysis of the number of displaced atoms in Sec. 17.7, the slowing-down density due to the PKA is equal to the sum of the slowing-down densities of the two moving atoms arising from the first collision:

$$q_1(E, E_r) = q_1(T, E_r) + q_1(E - T, E_r) \quad (17.158)$$

We now invoke the hard-sphere scattering assumption and take the probability of an energy transfer in the range  $(T, dT)$  to be  $dT/E$ . The right side of Eq. 17.158 is weighted with this probability and integrated over all possible recoil energies. We must, however, carefully consider the contributions to the slowing down density from the five regions of energy transfer  $T$  shown in Fig. 17.31.

*Region I:*  $0 < T < E_d$ ;  $(E - E_d) < (E - T) < E$ . When the secondary receives an energy less than  $E_d$ , it is not displaced and so contributes nothing to the slowing-down density. The scattered PKA, however, contributes to  $q_1$ . The contribution to  $q_1$  from region I is

$$\begin{aligned} q_1^{(I)} &= 0 + \frac{1}{E} \int_{E-E_d}^E q_1(E - T, E_r) d(E - T) \\ &= \frac{1}{E} \int_{E-E_d}^E q_1(T, E_r) dT \end{aligned}$$

\*Nelson's cross section differs from the value given by combining Eqs. 17.156 and 17.157 by a factor of  $2^{1/2}/(Z_U^{3/2} + Z_{ff}^{3/2})^{1/2} = 0.25$ . One of the Bohr radii in Nelson's Eq. 10 should have been the screening radius. Other than this error, his formulation reduces to the present one if it is noted that the Rydberg energy is equal to  $e^2/2a_B$ .

*Region II:*  $E_d < T < (E - E_r)$ ;  $E_r < (E - T) < (E - E_d)$ . In this region the secondary contributes only 1 atom (itself) to  $q_1$ , and

$$q_1^{(II)} = \frac{1}{E} \int_{E_d}^{E-E_r} (1) dT + \frac{1}{E} \int_{E_r}^{E-E_d} q_1(E - T, E_r) d(E - T)$$

or

$$\begin{aligned} q_1^{(II)} &= \frac{E - E_r - E_d}{E} + \frac{1}{E} \int_{E_r}^E q_1(T, E) dT \\ &\quad - \frac{1}{E} \int_{E-E_d}^E q_1(T, E_r) dT \end{aligned}$$

*Region III:*  $(E - E_r) < T < E_r$ ;  $(E - E_r) < (E - T) < E_r$ . In this type collision, both the scattered PKA and the secondary are reduced in energy below  $E_r$  and thus contribute 1 atom each to  $q_1$ . However, they cannot cause any more displacements that contribute to  $q_1$ .

$$\begin{aligned} q_1^{(III)} &= \frac{1}{E} \int_{E-E_r}^{E_r} (1) dT + \frac{1}{E} \int_{E-E_r}^{E_r} (1) d(E - T) \\ &= 2 \left( \frac{2E_r - E}{E} \right) \end{aligned}$$

*Region IV:*  $E_r < T < (E - E_d)$ ;  $E_d < (E - T) < (E - E_r)$ . Region IV is equivalent to region II (by symmetry of the diagram of Fig. 17.31), and we have

$$\begin{aligned} q_1^{(IV)} &= \frac{1}{E} \int_{E_r}^E q_1(T, E_r) dT \\ &\quad - \frac{1}{E} \int_{E-E_d}^E q_1(T, E_r) dT + \frac{E - E_r - E_d}{E} \end{aligned}$$

*Region V:*  $(E - E_d) < T < E$ ;  $0 < (E - T) < E_d$ . Region V is equivalent to region I:

$$q_1^{(V)} = \frac{1}{E} \int_{E-E_d}^E q_1(T, E_r) dT$$

Adding the preceding five components of the slowing-down density yields

$$q_1(E, E_r) = \frac{2(E_r - E_d)}{E} + \frac{2}{E} \int_{E_r}^E q_1(T, E_r) dT \quad (17.159)$$

A similar analysis for  $E_r < E/2$  produces the same result. Converting this integral equation to a differential equation and solving the latter by the same methods applied to Eq. 17.65 (i.e., differentiation with respect to  $E$ ) yields the solution

$$q_1(E, E_r) = E f(E_r)$$

The function  $f(E_r)$  can be obtained by inserting the above solution for  $q_1$  into the integral equation, which results in

$$q_1(E, E_r) = 2 \left( \frac{E_r - E_d}{E_r^2} \right) E \quad (\text{for } E_r < E) \quad (17.160)$$

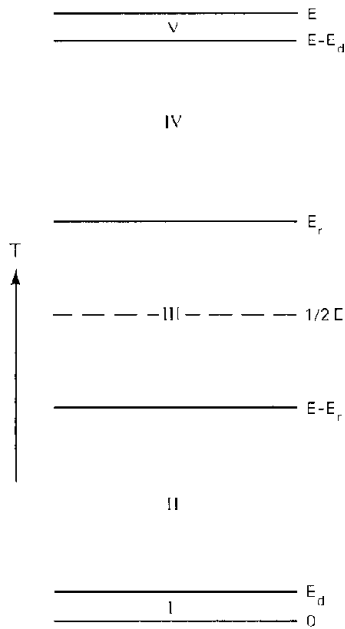


Fig. 17.31 Diagram for calculating the recoil slowing-down density due to contributions from five regions of energy of the secondary.

Note that

$$q_1(E, 2E_d) = \nu(E) = \frac{E}{2E_d}$$

in accord with the Kinchin—Pease result for the number of displaced atoms; the latter are just recoils that have slowed down to energies less than  $2E_d$ .

Since we are generally interested in recoil energies far above the displacement threshold  $E_d$ , Eq. 17.160 can be simplified to

$$q_1(E, E_r) = \frac{2E}{E_r} \quad (\text{for } E_r < E) \quad (17.161)$$

When the PKA energy is less than  $E_r$ , the slowing-down density is

$$q_1(E, E_r) = 0 \quad (\text{for } E_r > E) \quad (17.162)$$

Equation 17.162 applies to a unit volumetric source of PKAs all of energy  $E$ . Fission-fragment bombardment of the lattice, however, creates a PKA source with a distribution of energies. Let  $F(E_{ff}, E) dE dE_{ff}$  be the rate at which PKAs in the energy range  $(E, dE)$  are created per unit volume and per unit time by fission fragments in the energy range  $(E_{ff}, dE_{ff})$ . The slowing-down density to this distributed source is given by

$$q(E_r) = \int_0^{E_{ff}^{max}} dE_{ff} \int_0^{\Lambda' E_{ff}} q_1(E, E_r) F(E_{ff}, E) dE$$

where  $\Lambda' E_{ff}$  is the maximum possible PKA energy due to collision of a lattice atom with a fission fragment of energy

$E_{ff}$ . Using Eqs. 17.161 and 17.162 for  $q_1(E, E_r)$ , we find that the slowing-down density is

$$q(E_r) = \frac{2}{E_r} \int_{E_r/\Lambda'}^{E_{ff}^{max}} dE_{ff} \int_{E_r}^{\Lambda' E_{ff}} EF(E_{ff}, E) dE \quad (17.163)$$

The slowing-down density can be converted to the recoil-flux spectrum using the continuous slowing-down model commonly applied to similar problems in neutron thermalization.<sup>3,5</sup> For hard-sphere collisions between like atoms, one of which is moving with energy  $E_r$ , the average energy loss per collision is  $E_r/2$ . Therefore, in order to pass through an energy range  $dE_r$ ,  $dE_r/(E_r/2)$  collisions per atom are needed. If  $q(E_r)$  recoils  $\text{cm}^{-3} \text{sec}^{-1}$  are passing through  $dE_r$ , the number of collisions per cubic centimeter per second which occurs due to the recoils in the energy range  $(E_r, dE_r)$  is  $2q(E_r) dE_r/E_r$ . On the other hand, the total collision density is also given by  $\sigma_{U-U}(E_r) N_U \phi(E_r) dE_r$ , where  $\sigma_{U-U}(E_r)$  is the total cross section for scattering of stationary lattice atoms by lattice atoms moving with energy  $E_r$ . Equating these two expressions for the collision density yields

$$\phi(E_r) = \frac{2q(E_r)}{E_r \sigma_{U-U}(E_r) N_U} \quad (17.164)$$

The source term in Eq. 17.163 is given by Eq. 17.28:

$$F(E_{ff}, E) = N_U \phi(E_{ff}) \sigma_{ff-U}(E_{ff}, E) \quad (17.165)$$

where the fission-fragment flux is given by Eq. 17.146 and the fission-fragment—uranium atom scattering cross section is of the Rutherford type given by Eq. 17.149.

Substituting Eqs. 17.164 and 17.165 into 17.163 yields

$$q(E_r) = \frac{4}{E_r^2 \sigma_{U-U}(E_r)} \int_{E_r/\Lambda'}^{E_{ff}^{max}} dE_{ff} \phi(E_{ff}) \times \int_{E_r}^{\Lambda' E_{ff}} E \sigma_{ff-U}(E_{ff}, E) dE \quad (17.166)$$

Inserting the appropriate expressions for  $\phi(E_{ff})$  and  $\sigma_{ff-U}(E_{ff}, E)$  and integrating give

$$q(E_r) = \frac{4\pi \bar{F} \mu_{ff} Z_{ff}^2 Z_U^2 e^4}{E_{ff}^{max} E_r^2 \sigma_{U-U}(E_r)} \left( \frac{M_{ff}}{M_U} \right) \times \left[ \ln \left( \frac{\Lambda' E_{ff}^{max}}{E_r} \right) \right]^2 \quad (17.167)$$

Nelson takes a very rough approximation to the cross section  $\sigma_{U-U}(E_r)$ . He assumes that it is equal to the square of the lattice parameter of  $\text{UO}_2$  ( $a_0 = 5.47 \text{ \AA}$ ):

$$\sigma_{U-U}(E_r) = a_0^2 = \frac{4}{N_U a_0} \quad (17.168)$$

The last equality in the above formula is derived from the relation between atom density and the fcc structure of the cation sublattice of  $\text{UO}_2$  (i.e.,  $N_U = 4/a_0^3$ ). Using Eq. 17.168 in 17.167, we find the recoil flux to be

$$\phi(E_r) = \frac{B\dot{F}}{E_r^2} \left[ \ln \left( \frac{\Lambda' E_{ff}^{max}}{E_r} \right) \right]^2 \quad (17.169)$$

where B is a constant:\*

$$B = \frac{\pi\mu_{ff} N_U a_o Z_{ff}^2 Z_U^2 e^4}{E_{ff}^{max}} \left( \frac{M_{ff}}{M_U} \right) \quad (17.170)$$

Inserting numerical values into Eq. 17.170, we find  $B = 0.73 \times 10^{-2}$  eV-cm.

Substituting Eqs. 17.156 and 17.169 into Eq. 17.151 and neglecting  $T_{min}$  compared with  $\Lambda' E_r$ , we find the microscopic re-resolution parameter to be

$$b = \frac{KB(\Lambda')^3}{2T_{min}^2} \left\{ \ln \left[ \frac{(\Lambda')^2 E_{ff}^{max}}{T_{min}} \right] \right\}^2 \dot{F} \quad (17.171)$$

Using the values of the constants K and B found in Eqs. 17.157 and 17.170 and assuming  $T_{min} = 300$  eV, we find that the above formula gives  $b = 1.7 \times 10^{-17}$   $\dot{F}$  sec<sup>-1</sup>. This value is ~40 times larger than the re-resolution parameter based on direct encounters between fission fragments and gas atoms in a bubble (Eq. 13.116). Note that the re-resolution parameter given by Eq. 17.171 is very sensitive to the value of  $T_{min}$  (which was just guessed by Nelson), does not consider the role of the oxygen sublattice in UO<sub>2</sub> at all, incorporates what appears to be a rather large cross section between uranium atoms in the cascade, and assumes a constant electronic stopping power.

## 17.12 NOMENCLATURE

a = screening radius  
 a<sub>B</sub> = Bohr radius of the hydrogen atom  
 a<sub>o</sub> = lattice constant  
 a<sub>1</sub> = coefficients representing degree of nonisotropy of elastic neutron-scattering cross section  
 A = constant given by Eq. 17.84; constant in potential function; mass number  
 b = re-resolution parameter  
 B = constant given by Eq. 17.170  
 dpa = displacements per atom  
 D = bond energy; distance between atoms in a particular direction  
 e = electronic charge  
 E = kinetic energy of a particle  
 E<sub>A</sub> = energy below which the hard-sphere model is valid  
 E<sub>c</sub> = energy below which ionization does not take place  
 E<sub>ch</sub> = channeling energy  
 E<sub>d</sub> = displacement energy  
 E<sub>f</sub> = focusing energy

E<sub>i</sub> = energy of bombarding ion  
 E<sub>n</sub> = neutron energy  
 E<sub>neut</sub> = energy below which a moving atom cannot be ionized by collision with electrons in the solid  
 E<sub>r</sub> = relative kinetic energy of two particles in a head-on collision; energy of a recoil atom; maximum energy for replacement during a focused collision chain  
 dE/dx = stopping power  
 ΔE<sub>sub</sub><sup>o</sup> = energy of sublimation  
 F = collision density  
 $\dot{F}$  = fissions cm<sup>-3</sup> sec<sup>-1</sup>  
 F<sub>i</sub> = force on lattice atom i  
 g = relative speed of two particles in head-on collision  
 G<sub>i</sub> = damage function for property i  
 ħ = Planck's constant divided by 2π  
 I = particle current; binding energy of an electron in the solid  
 k = force constant in a parabolic potential; Boltzmann's constant; constant in Lindhard's stopping power formula, Eq. 17.53a  
 K = constant given by Eq. 17.157  
 KE = total kinetic energy of two particles  
 l = average path length between collisions  
 l<sub>D</sub> = average path length between displacement collisions  
 M = particle mass  
 m<sub>e</sub> = electronic mass  
 N = density of target particles  
 n<sub>e</sub> = density of electrons in a solid capable of absorbing energy from a moving particle  
 p = probability of energy transfer  
 P = probability of channeling or focusing  
 P<sub>d</sub> = displacement probability  
 P<sub>f</sub> = focusing probability  
 P<sub>l</sub> = Legendre polynomial  
 P<sub>1</sub> = mechanical or dimensional property of a solid  
 PKA = primary knock-on atom  
 q = slowing-down density  
 Q = excitation energy of nucleus  
 r = separation distance  
 r<sub>o</sub> = hard-sphere radius  
 R<sub>ch</sub> = radius of a channel  
 R<sub>d</sub> = displacement rate per unit volume in a neutron flux  
 R<sub>dg</sub> = rate of collisions between recoils and gas atoms in bubble which result in re-resolution  
 R<sub>p</sub> = projected range of particle  
 R<sub>tot</sub> = total range of particle  
 s = exponent in the inverse-power potential; entropy of motion  
 t = time  
 t<sub>c</sub> = collision time  
 T = temperature, °K; kinetic energy transferred to struck particle  
 T<sub>m</sub> = maximum kinetic energy transferable to a struck particle  
 u = particle velocity in center-of-mass coordinates  
 U = energy per atom in a solid  
 v = volume per atom in a solid; particle speed in laboratory conditions

\*Equations 17.169 and 17.170. can be transformed into Nelson's Eq. 9 by making the substitutions  $E_{Ryd} = e^2/(2a_B)$  and  $\phi_f = 2\dot{F}\mu_{ff}$ . The latter is obtained by integrating Eq. 17.146 over  $0 < E_{ff} < E_{ff}^{max}$ .

$v_{cm}$  = speed of the center of mass of a two-particle system  
 $v_z$  = velocity of channeled particle along the channel axis  
 $V(r)$  = potential energy between two particles that are a distance  $r$  apart  
 $V_{ch}(r)$  = channel potential  
 $w$  = jump frequency  
 $x$  = path length  
 $x_m$  = distance of closest approach in a head-on collision  
 $y$  = dimensionless energy variable, Eq. 17.82  
 $Y_{iv}$  = yield of Frenkel pairs per fission  
 $z$  = channel axis  
 $Z$  = atomic number

#### Greek letters

$\beta$  = compressibility  
 $\epsilon$  = migration energy; reduced energy in Lindhard's model  
 $\epsilon^*$  = energy of atom at saddle point  
 $\epsilon_{eq}$  = energy of atom in equilibrium position in lattice  
 $\kappa$  = force constant of the channel potential  
 $\lambda$  = wavelength of particle trajectory in channel; parameter in the screening radius formula, Eq. 17.35  
 $\Lambda$  = mass-number group, Eq. 17.8  
 $\mu$  = reduced mass, Eq. 17.14  
 $\mu_{ff}$  = fission-fragment range in a solid  
 $\nu$  = number of displaced atoms per PKA  
 $d\Omega$  = differential solid-angle element  
 $\phi(E)$  = differential energy flux  
 $\phi_1, \phi_2$  = scattering angles in laboratory coordinates  
 $\Phi$  = total particle flux  
 $\rho$  = constant in the Born-Mayer potential function  
 $\sigma(E)$  = total atomic collision cross section  
 $\sigma(E, T)$  = differential energy-transfer cross section  
 $\sigma(E, \theta)$  = differential angular cross section  
 $\sigma_d(E_n)$  = displacement cross section for neutrons of energy  $E_n$   
 $\sigma'_d(E)$  = cross section for energy transfers between  $E_d$  and  $E$   
 $\sigma_n(E_n, E)$  = differential energy-transfer cross section for neutron scattering  
 $\theta$  = scattering angle in center-of-mass coordinates  
 $\theta_u$  = recoil angle in focused collision chain  
 $\theta_0^f$  = maximum angle for which focusing is possible  
 $\theta_0^{max}$  = maximum injection angle into a channel  
 $\xi$  = fraction of PKA energy lost by electronic excitation during slowing down

#### Subscripts

$a$  = lattice atom  
 $e$  = electron  
 $el$  = elastic scattering  
 $eq$  = at equilibrium  
 $f$  = final state (after collision)  
 $ff$  = fission fragment  
 $g$  = fission gas  
 $i$  = interstitial  
 $in$  = inelastic scattering  
 $O$  = oxygen

$U$  = uranium  
 $v$  = vacancy  
 $1$  = particle one  
 $2$  = particle two  
 $0$  = initial state (before collision)

#### 17.13 REFERENCES

1. M. W. Thompson, *Defects and Radiation Damage in Metals*, Cambridge University Press, Cambridge, 1969.
2. L. T. Chadderton, *Radiation Damage in Crystals*, Methuen & Co., Ltd., London, 1965.
3. L. T. Chadderton and I. McC. Torrens, *Fission Damage in Crystals*, Methuen & Co., Ltd., London, 1969.
4. B. T. Kelly, *Irradiation Damage to Solids*, Pergamon Press, Inc., New York, 1966.
5. G. Carter and J. S. Colligon, *Ion Bombardment of Solids*, Heinemann Educational Books, London, 1968.
6. R. S. Nelson, *The Observation of Atomic Collisions in Crystalline Solids*, North-Holland Publishing Company, Amsterdam, 1968.
7. J. Lindhard and M. Scharff, *Phys. Rev.*, **124**: 128 (1961).
8. M. T. Robinson, The Dependence of Radiation Effects on the Primary Recoil Energy, in *Radiation-Induced Voids in Metals*, Albany, N. Y., June 9–11, 1971, J. W. Corbett and L. C. Ianniello (Eds.), AEC Symposium Series, No. 26 (CONF-710601), p. 397, 1972.
9. P. T. Wedepohl, *Radiat. Eff.*, **1**: 77 (1969).
10. N. Bohr, *Dan. Vidensk. Selsk., Math-Fys. Medd.*, **18**: 8 (1948).
11. H. B. Huntington, *Phys. Rev.*, **93**: 1414 (1954).
12. J. B. Gibson, A. N. Goland, M. Milgram, and G. H. Vineyard, *Phys. Rev.*, **120**: 1229 (1960).
13. R. V. Jan and A. Seeger, *Phys. Status Solidi*, **3**: 465 (1963).
14. A. Sosin, in Proceedings of the International Conference on Solid State Research and Accelerators, A. N. Goland (Ed.), USAEC Report BNL-50083, p. 204, 1967.
15. G. H. Kinchin and R. S. Pease, *Rep. Progr. Phys.*, **18**: 1 (1955).
16. J. B. Sanders, Thesis, University of Leiden, 1967.
17. J. Lindhard, V. Nielsen, M. Scharff, and P. V. Thomsen, *Mat.-Fys. Medd., Dan. Vidensk. Selsk.*, **33**(10): 1-42 (1963).
18. O. S. Oen and M. T. Robinson, *Appl. Phys. Lett.*, **2**: 83 (1963).
19. D. G. Doran, Displacement Cross Sections for Stainless Steel and Tantalum Based on a Lindhard Model, USAEC Report HEDL-TME-71-42, WADCO Corporation, Hanford Engineering Development Laboratory, April 1971.
20. G. R. Piercy, *J. Nucl. Mater.*, **29**: 267 (1969).
21. G. E. Russcher and R. E. Dahl, *Trans. Amer. Nucl. Soc.*, **11**: 499 (1968).
22. W. N. McElroy, R. E. Dahl, Jr., and C. Z. Serpan, Jr., *Nucl. Appl. Technol.*, **7**: 561 (1969).
23. G. L. Kulcinski, J. L. Brimhall, and H. E. Kissinger, Production of Voids in Pure Metals by High-Energy Heavy-Ion Bombardment, in *Radiation Induced Voids in Metals*, Albany, N. Y., June 9–11, 1971, J. W. Corbett and L. C. Ianniello (Eds.), AEC Symposium Series, No. 26 (CONF-710601), p. 449, 1972.
24. C. Erginsoy, C. H. Vineyard, and A. Englebert, *Phys. Rev.*, **133**: A595 (1964).

25. M. T. Robinson and O. S. Oen, *Phys. Rev.*, **132**: 1385 (1963).
26. J. R. Beeler, Jr., *Phys. Rev.*, **150**: 470 (1966).
27. J. A. Brinkman, *J. Appl. Phys.*, **25**: 961 (1954).
28. A. Seeger, On the Theory of Radiation Damage and Radiation Hardening, in *Proceedings of the Second United Nations International Conference on the Peaceful Uses of Atomic Energy, Geneva, 1958*, Vol. 6, p. 250, United Nations, New York, 1958.
29. D. G. Doran, *Radiat. Eff.*, **2**: 249 (1970).
30. J. R. Beeler, Jr., Computer Simulation of Radiation-Induced Void Nucleation and Growth in Metals, in *Radiation-Induced Voids in Metals*, Albany, N. Y., June 9–11, 1971, J. W. Corbett and L. C. Ianniello (Eds.), AEC Symposium Series, No. 26 (CONF-710601), p. 684, 1972.
31. J. R. Beeler, Jr. and D. G. Besco, in *Radiation Damage in Solids*, Symposium Proceedings, Venice, 1962, p. 44, International Atomic Energy Agency, Vienna, 1962 (STI/PUB/56).
32. H. Blank, *Phys. Status Solidi*, **10**: 465 (1972).
33. R. V. Meghreblian and D. K. Holmes, *Reactor Analysis*, p. 89, McGraw-Hill Book Company, New York, 1960.

17.14 PROBLEMS

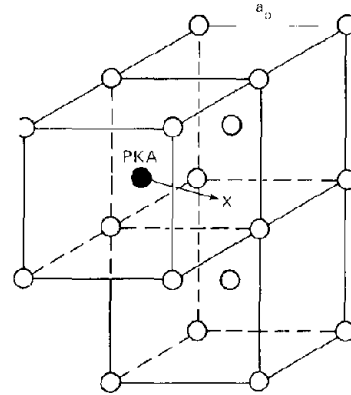
17.1 Figure 15.6 shows a portion of a fission-fragment track in UO<sub>2</sub>. At one point, the track changes direction slightly, which indicates that the fragment has made a Rutherford collision with a lattice atom at this point. The fragment, which may be assumed to have a birth energy of 100 MeV, an atomic number of 42, and a mass number of 100, has travelled 2 μm before undergoing the collision.

- (a) What is the effective charge of the fragment at birth?
- (b) Prior to the Rutherford collision, the fission fragment loses energy by electronic excitation according to the Bethe formula. Calculate the fragment energy at the point of the Rutherford collision. Assume the mean excitation energy in the Bethe formula is  $\bar{I} = 8.8Z$  (eV).
- (c) If the scattering angle on the photograph is 5°, calculate the energy transferred to the struck lattice atom (1) if the latter is oxygen and (2) if the latter is uranium.

17.2 Derive the differential angular cross section for Rutherford scattering from the differential energy-transfer cross section (Eq. 17.37).

17.3 It is desired to join the screened Coulomb potential to the inverse power potential in which the constants A and s are known. The matching point (i.e., the energy E\* above which the screened Coulomb potential is used and below which the inverse power potential is applicable) is determined by the criterion that the distance of closest approach in a head-on collision is the same when computed by both potential functions. Derive the equation from which E\* can be calculated.

17.4 The simple bond theory of lattice cohesion is used to calculate the displacement threshold in tantalum for a knock-on moving in the direction shown in the sketch. The repulsive potential between lattice atoms is approximated by the harmonic-force law.



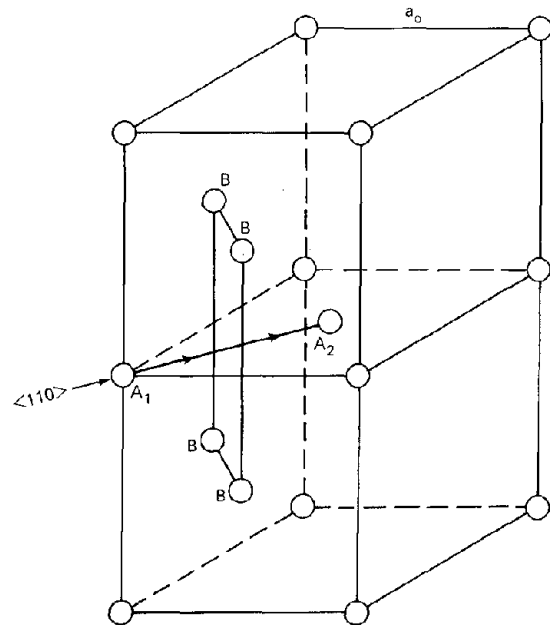
- (a) If the energy of sublimation of tantalum is 8.1 eV, what is the bond strength D?
- (b) If the coefficient of compressibility of tantalum is  $0.53 \times 10^{-12}$  cm<sup>2</sup>/dyne and the density of tantalum is 16.6 g/cm<sup>3</sup>, what is the product of the force constant k and the square of the lattice parameter?

- (c) What are the Miller indices of the PKA direction shown in the sketch?
- (d) At what point along this direction is the PKA potential energy a maximum? Calculate the difference between the PKA energy at this saddle point and the energy in the equilibrium (lattice) site. This potential-energy difference is identified with the displacement energy E<sub>d</sub> for this direction.

(e) The location marked with an X in the sketch is an octahedral interstitial site in the bcc lattice. What is the energy of the PKA when it reaches this position?

(f) Sketch (but do not compute) the variation of the PKA potential energy as it moves along the specified direction.

17.5 Energy losses to the ring of atoms surrounding the focusing direction provide a mechanism for terminating a



focused collision sequence. Consider a  $\langle 110 \rangle$  focusing sequence in the fcc lattice. In the sketch the atom  $A_1$  is struck and moves off in the direction of  $A_2$ . Along this path it must pass through the ring of atoms labeled B.

(a) Calculate the B- $A_1$  distance when collision of  $A_1$  and  $A_2$  occurs. Note that  $A_1$ ,  $A_2$ , and a B atom lie on a close-packed (111) plane. Assume that the equivalent hard-sphere diameter based on the Born-Mayer potential ( $2r_0$ ) is smaller than the interatomic distance along the chain (D). Express  $r_0$  in terms of the energy of  $A_1$  (denoted by E) and D in terms of the focusing energy  $E_f$ .

(b) Calculate the increase in the four  $A_1$ -B interaction energies as  $A_1$  moves from its initial position to the collision point.

(c) The total of  $A_1$ -B interaction energy calculated in (b) is lost to the focused collision sequence (this energy appears as thermal energy in the lattice when the four B atoms and  $A_1$  relax and then oscillate about their equilibrium positions). How many collisions can a dynamic crowdion of initial energy  $E_1 \leq E_f$  encounter along the  $\langle 110 \rangle$  direction before it stops?

17.6 A 30-kV ion enters a channel in a copper lattice and loses energy only by electronic excitation. Using the Lindhard stopping-power formula, determine the distance travelled by the ion before it is dechanneled. The minimum channeling energy is equal to 300 eV.

17.7 The  $(n, \gamma)$  reaction in  $^{56}\text{Fe}$  releases a prompt gamma ray of  $E_\gamma = 7$  MeV.

(a) What is the recoil energy of the  $^{57}\text{Fe}$  product nucleus?

(b) Use the Lindhard model to determine the number of displaced atoms per  $^{57}\text{Fe}$  recoil. Compare this result with that obtained by the Kinchin-Pease formula. Assume  $E_d = 25$  eV.

(c) If the thermal component of the neutron flux in a fast reactor is  $10^{13}$  neutrons  $\text{cm}^{-2} \text{sec}^{-1}$ , what is the damage production rate (i.e., displacements  $\text{cm}^{-3} \text{sec}^{-1}$ ) due to the  $(n, \gamma)$  reaction in  $^{56}\text{Fe}$ ?

(d) If the fast flux is given by

$$\phi_f(E_n) = 10^{15} \delta(E_n - 0.5) \quad (E_n \text{ in MeV})$$

what is the damage production rate due to the fast flux in iron? Assume that scattering of 0.5-MeV neutrons from iron is elastic and isotropic in the center-of-mass system.

Use the Kinchin-Pease displacement formula in (c) and (d). The scattering cross section for 0.5 MeV neutrons is 3 b.

17.8 For a monoenergetic fast-neutron flux of energy 0.5 MeV, calculate the number of displacements per atom (dpa) in iron at a fast-neutron fluence of  $10^{22}$  neutrons/ $\text{cm}^2$ .

17.9 Calculate the average iron PKA energy in a fission-neutron spectrum:

$$\phi(E_n) = \text{constant} \times \exp(-E_n) \sinh(2E_n)^{1/2}$$

where  $E_n$  is the neutron energy in MeV. How does this value compare with the approximation of calculating the

average PKA energy due to collision with the neutron of average energy? Assume isotropic, elastic scattering and an energy-independent scattering cross section.

17.10 Calculate the number of atoms displaced by a 14-MeV neutron incident on the stainless-steel first wall of a fusion reactor. Compare this result with the number of displacements produced by a 0.5-MeV neutron, which is the average neutron energy in an LMFBR. Obtain displacement cross sections from Fig. 17.17.

17.11 Only relatively energetic electrons are capable of causing atomic displacements in metals. For electrons in the million electron volt range, relativistic kinematics of the collision process must be employed. The energy transferred to a stationary atom of mass M and atomic number Z by an electron of energy  $E_e$  is

$$T = \frac{1}{2} \left( \frac{4m_e}{M} \right) E_e (1 + E_e)(1 - \cos \theta)$$

where  $m_e$  is the mass of the electron,  $\theta$  is the center-of-mass scattering angle and all energies are expressed in MeV.

The interaction leading to displacement is nuclear Rutherford scattering between the electron and the unscreened nucleus of the atom. The differential energy-transfer cross section for this process is given by

$$\sigma(E_e, T) = 4\pi Z^2 e^4 \frac{1 - \beta^2}{\beta^4} \frac{T_m}{T^2} \left\{ 1 - \beta^2 \left( \frac{T}{T_m} \right) + \pi \left( \frac{Z}{137} \right) \beta \left[ \left( \frac{T}{T_m} \right)^{1/2} - \left( \frac{T}{T_m} \right) \right] \right\} \text{ MeV}$$

where  $\beta$  is the ratio of the electron speed to the speed of light and the electron energy is

$$E_e = \frac{1}{2} \left[ \frac{1}{(1 - \beta^2)^{1/2}} - 1 \right]$$

(In all the above formulas, the electron rest mass is taken as 0.5 MeV instead of the accurate value of 0.51 MeV).

(a) Determine the minimum electron energy,  $E_e^{\text{min}}$ , required to produce displacements in a metal for which the displacement threshold is  $E_d$ .

(b) If an electron of energy  $E_e^0 > E_e^{\text{min}}$  is injected into or is born in the metal and deposits all its energy there, determine the total number of displacements per electron  $n(E_e)$ . Consider the process as one of occasional electron-atom collisions between which the electron loses energy by radiation (bremsstrahlung) and by interaction with the other electrons of the medium. The total stopping power  $(dE_e/dx)_e$  due to these two processes is nearly energy independent for  $0.2 \leq E_e \leq 3$  MeV (Ref. 2, p. 161). To determine the number of displaced atoms, begin by formulating the probability  $p_d(E_e, T) dT$  = average number of displacement collisions per unit energy loss which produces PKAs in  $(T, dT)$ .

(c) For the limiting case of  $E_e^0$  just slightly larger than  $E_e^{\text{min}}$ , obtain an analytical solution to (b).

17.12 It is desired to calculate the rate of atom displacements in a medium that is subject to a gamma-ray flux of

known spectrum. All damage can be assumed due to the Compton electrons produced by the interaction of the gamma rays with the electrons in the solid. The Compton electrons are produced with a spectrum of energies; assume that the number of displaced atoms produced by a single Compton electron of energy  $E_e$  is known.

The following quantities can be considered known:

$N$  = the total atom density of the solid

$M$  = the mass of an atom in the solid

$E_d$  = the minimum energy that an atom must receive to be displaced, eV

$\phi(E_\gamma)$  = the energy spectrum of the gamma-ray flux in the medium; the maximum photon energy of the spectrum is  $E_\gamma^0$

$\sigma_c(E_\gamma, E_e) dE_e$  = the differential cross section for production of Compton electrons with energy in the range  $E$  to  $E_e + dE_e$  by photons of energy  $E_\gamma$  (i.e., the Klein-Nishina formula)

$n(E_e)$  = the number of displaced atoms produced by an electron of energy  $E_e$ .

(a) Derive an integral expression for  $R_d$ , the number of displaced atoms  $\text{cm}^{-3} \text{sec}^{-1}$ ; pay careful attention to the limits of integration.

(b) What is the minimum value of  $E_\gamma^0$  at which damage can occur?

17.13 In the fuel, fast neutrons, as well as fission fragments and recoils, can cause re-solution of fission-gas bubbles. What is the re-solution parameter  $b$  for a known fast-neutron-flux spectrum,  $\phi(E_n)$ ?

Determine  $b$  for a monoenergetic fast flux of  $10^{15}$  neutrons  $\text{cm}^{-2} \text{sec}^{-1}$  at  $E_n = 0.5$  MeV and an elastic scattering cross section that is isotropic and equal to 10 barns. For this fast flux, calculate the fission density in a mixed-oxide fuel containing 15% plutonium (see Chap. 10). It is shown in Sec. 17.11 that  $b$  for fission-fragment recoils is  $1.7 \times 10^{-7}$  F. Compare re-solution by fast neutrons with that by fission-fragment recoils.

17.14 Helium atoms contained in helium bubbles that have precipitated in stainless-steel cladding can be re-solved by energetic collisions with fast neutrons or with recoil metal atoms. Calculate the re-solution parameter  $b$  for the processes due to:

(a) Direct collisions of fast neutrons with helium atoms.

(b) Collisions of helium atoms in the bubble with recoil atoms (assumed to be iron) produced in the collision cascade.

Use the following property values. Elastic-neutron-scattering cross sections: helium, 1 barn; iron, 3 barns. Iron-iron atomic cross section,  $5 \text{ \AA}^2$ . Fast-neutron flux (assume monoenergetic with  $E_n = 0.5$  MeV,  $\Phi = 10^{15}$  neutrons  $\text{cm}^{-2} \text{sec}^{-1}$ ). Minimum helium-atom energy for re-solution, 200 eV.

# Chapter 18

## Radiation Effects in Metals: Hardening, Embrittlement, and Fracture

### 18.1 STRUCTURAL METALS FOR FAST REACTORS

The neutron economy of a fast reactor is not so significantly affected by neutron capture in the structural materials in the core as is that of a thermal reactor. First, most neutron-capture cross sections increase with decreasing neutron energy, and the neutron population of the liquid-metal fast breeder reactor (LMFBR) contains a far lower percentage of thermal neutrons than does that of a light-water reactor (LWR). Second, the ratio of the mass of structural metal to the mass of fissile materials is much smaller in a fast reactor than in a thermal reactor. Consequently, metals that in a thermal reactor would severely impair neutron economy are acceptable in a fast reactor, and the selection of core structural materials for the LMFBR can be based primarily on cost and mechanical and chemical properties. The downgrading of neutron-absorption characteristics from the selection criteria for core structural metals means that the costly zirconium alloys used in thermal reactors need not be employed in fast reactors. However, parasitic neutron absorption by nonfuel components is important enough to cause LMFBR core designers to be quite sparing in using certain structural metals. The irradiation properties of high-nickel alloys, for example, are generally superior to those of conventional stainless steel, but nickel has a seriously large cross section for absorption of fast neutrons.

The most important metallic component of a reactor core is the fuel cladding; this member provides structural integrity to the fuel element, prevents fission products from escaping to the primary coolant system, and separates the sodium coolant from the ceramic oxide fuel (with which it reacts). The cladding must be thin-walled tubing that can remain intact in a fast reactor environment for periods of up to 3 years at temperatures to 800°C, diametral strains of 3%, and fluences up to  $3 \times 10^{23}$  neutrons  $\text{cm}^{-2} \text{sec}^{-1}$ . The cladding alloy selected for the LMFBR is the austenitic stainless steel described as type 316. This material has an fcc crystal structure. (Austenite is the fcc modification of

iron. It is the stable form of pure iron between 910 and 1400°C. The addition of nickel stabilizes this structure above room temperature.) It has good high-temperature creep strength and resists corrosion by liquid-sodium and hypostoichiometric mixed-oxide fuels. Moreover, it is cheaper than more exotic metals, available in sufficient quantities for the fast reactor program, and is easy to fabricate. The compositions of two austenitic stainless steels are given in Table 18.1.

The austenitic stainless steels, however, are highly susceptible to swelling owing to void formation and to high-temperature embrittlement by the helium produced in neutron reactions with constituents of the alloy. Commercial nickel alloys (e.g., Inconel and Incoloy) are backup materials for core structural components in the liquid-metal fast breeder reactor. These alloys appear to be less prone to void swelling, but their neutron-absorption cross section is higher than that of steel. Vanadium-based and refractory-metal alloys are long-range candidates for LMFBR fuel-element cladding. These two classes of metals both possess bcc lattice structures and are more resistant to helium embrittlement than are the austenitic stainless steels or nickel alloys. In addition, the refractory metals (e.g., molybdenum) do not form voids under large fast-neutron fluences at the cladding service temperatures of the LMFBR. However, both vanadium alloys and the refractory metals are much more costly than stainless steel, and their use as cladding would significantly increase the capital cost of a fast reactor.

Although the generally favorable high-temperature properties of the austenitic stainless steel are utilized in the fast reactor core compounds (e.g., in cladding and assembly wrappers), the lower flux, lower temperature environment outside the core permits less expensive steels to be used for the reactor pressure vessel. In both LMFBR and LWR systems, ordinary ferritic or alloy steel is used for this component. (Ferrite is a bcc modification of iron.) Typical alloy-steel compositions are shown in Table 18.2. This material does not possess, nor does it need to possess, the high-temperature strength and corrosion resistance of stain-

Table 18.1 Composition of Austenitic Stainless Steels

Element	Type 304, wt. %	Type 316, wt. %	
Fe	70	65	} Major constituents
Cr	19	17	
Ni	9	13	
C	0.06	0.06	} Interstitial impurities
Mn	0.8	1.8	
P	0.02	0.02	
S	0.02	0.02	
Si	0.5	0.3	
B	0.0005	0.0005	
N		0.03	} Substitutional impurities
Mo	0.2	2.2	
Co		0.3	

Table 18.2 Composition of Pressure-Vessel Steels

Element	A302-B, wt. %	A212-B, wt. %	
Fe	97	98	
C	0.2	0.3	} Interstitial impurities
Mn	1.3	0.8	
P	0.01	0.01	
Si	0.3	0.3	
S	0.02	0.03	
Cr	0.2	0.2	} Substitutional impurities
Ni	0.2	0.2	
Mo	0.5	0.02	

less steel, but it is much cheaper. In common with most bcc metals, ferritic steel exhibits one potentially serious radiation effect. Below a certain temperature known as the ductile-brittle transition temperature (DBTT), or nil-ductility temperature (NDT), the metal is susceptible to brittle fracture. As long as the lowest operating temperature is greater than the nil-ductility temperature, the metal is ductile. However, the nil-ductility temperature increases dramatically with neutron exposure, and, toward the end of a 30-year lifetime, a pressure vessel can be subject to brittle failure. Such catastrophic failures have occasionally occurred in bridges, large storage tanks, and ships. Usually the entire structure breaks apart when brittle fracture occurs.

Four broad categories of mechanical behavior are pertinent to reactor performance:

1. Radiation hardening.
2. Embrittlement and fracture.
3. Swelling.
4. Irradiation creep.

This chapter deals with the first two of these features. Swelling and irradiation creep are considered in the following chapter.

Radiation hardening usually means the increase in the yield stress and the ultimate tensile stress as a function of fast-neutron fluence and temperature. The yield strength and ultimate strength are measured in tests in which

deformation occurs at high stresses and rather quickly. However, the strength of fuel-element cladding is most accurately represented by the resistance of the metal to slow deformation by creep, since the internal loading on the cladding never reaches the yield stress. The creep strength of a metal is usually determined by the time required for failure under a fixed applied stress (i.e., a stress rupture test).

Embrittlement of a metal is measured by the amount of plastic or creep deformation that occurs before fracture. Fast-neutron irradiation invariably renders a metal less ductile than the unirradiated material. Fracture can be of the brittle type in which a small crack swiftly propagates across an entire piece, or it can occur only after long times at stress and after appreciable deformation. Failure by stress rupture takes place by linkup of small intergranular cracks or cavities that have developed throughout the interior of the metal.

## 18.2 EVOLUTION OF THE MICROSTRUCTURE OF STEEL DURING NEUTRON IRRADIATION

The radiation-produced entities responsible for changes in the mechanical properties of neutron-bombarded metals can be identified, counted, and sized with the aid of the electron microscope. When an electron beam of several-hundred kiloelectron volts energy passes through a thin metal specimen, some of the electrons are transmitted through the foil, and others are diffracted in much the same way that X rays are diffracted by parallel atomic planes near the surface of a crystal. The foil is sufficiently thin (1000 to 5000 Å) and the incident electron beam sufficiently well collimated (spot size of several micrometers) that only a part of a single grain is probed. Within this single-crystal region of the material, some atomic planes are properly oriented to diffract the incident electron beam. The angle of the diffracted beam relative to the incident electron beam is determined by the Bragg condition based on the de Broglie wavelength of the incident electrons and the spacing of the atomic planes of the solid. The intensity of the transmitted beam is reduced to the extent that the intervening solid satisfies the Bragg condition and produces strong diffraction. Figure 18.1 is a sketch of the setup for bright-field transmission-electron microscopy. The transmitted electrons are brought into focus at an aperture by means of an electrostatic lens. The position of the aperture is adjusted so that only transmitted electrons are permitted to pass; the diffracted beams are stopped. Any defect that locally destroys the perfection of the crystal lattice also alters the diffraction conditions at this point. When the orientation and/or spacing of the atomic planes around the defect more closely satisfy the Bragg condition than do the planes in the perfect crystal, the diffraction phenomenon is stronger for the planes around the defect than for those in the perfect crystal. With reference to Fig. 18.1, if  $I_D > I_T$ , then the transmitted beam from the vicinity of the defect is weaker than that from the perfect crystal. The defect appears on the photographic plate behind the aperture as a dark image on a bright background. The contrast of the image is proportional to  $I_T - I_D$ . Such photographs repre-

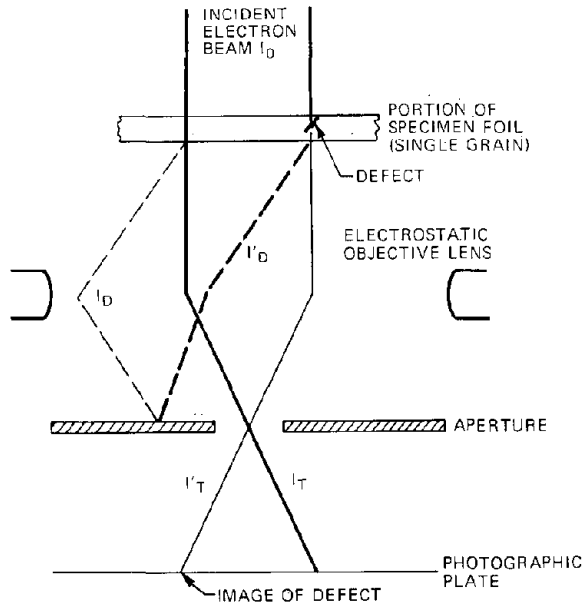


Fig. 18.1 Illustration of image formation in bright-field electron microscopy. The values  $I_T$  and  $I_D$  denote the intensities of the transmitted and diffracted beams for incident electrons passing through a region of perfect crystal. The primed quantities denote the analogous intensities from the region of the defect.

sent the projected image of the three-dimensional crystal defect. Atomic planes that are out of register (as those near a grain boundary or a stacking fault) or zones of the crystal that are distorted by a strain field (as around dislocations) produce interference patterns and can therefore be imaged.

Gas-filled bubbles at equilibrium (i.e., gas pressure balanced by surface tension) do not strain the surrounding solid, which therefore behaves as undistorted crystal. Even when the cavity contains no gas (a void), the strain field in the vicinity of the defect is negligible. Bubbles and voids are detectable by virtue of the smaller absorption of the electron beam passing through the cavity compared with the electrons that pass through a section of the foil consisting entirely of solid.

Figure 18.2 shows the microstructure of a typical unirradiated austenitic stainless steel used for fast reactor fuel-element cladding. Figure 18.2(a) shows an ordinary photomicrograph of a polished specimen. The grains are clearly visible and average  $25 \mu\text{m}$  in size. The transmission-electron micrograph of Fig. 18.2(b) contains only segments of the dislocation network of the as-fabricated metal.

### 18.2.1 Black-Dot Structure

Figure 18.3 shows the microstructure of a specimen irradiated at  $\sim 100^\circ\text{C}$  by a fast-neutron fluence of  $\sim 10^{21}$  neutrons/cm<sup>2</sup>. The defects produced at these conditions appear as black dots in the electron micrograph. The defects are too small to permit their structure to be revealed by the electron microscope, but they are believed

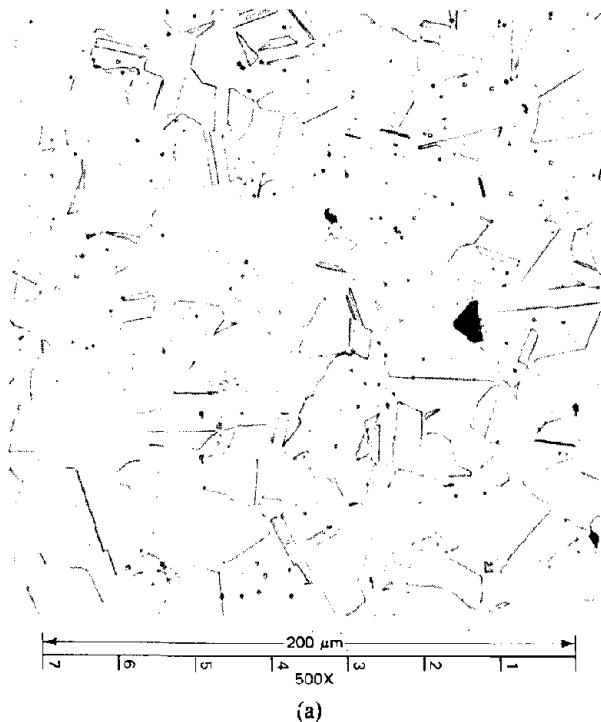


Fig. 18.2 Microstructure of unirradiated type 304 stainless steel (a) Photomicrograph showing grain structure. (b) Electron micrograph showing dislocation structure. (From E. E. Bloom, An Investigation of Fast Neutron Radiation Damage in An Austenitic Stainless Steel, USAEC Report ORNL-4580, Oak Ridge National Laboratory, 1970.)

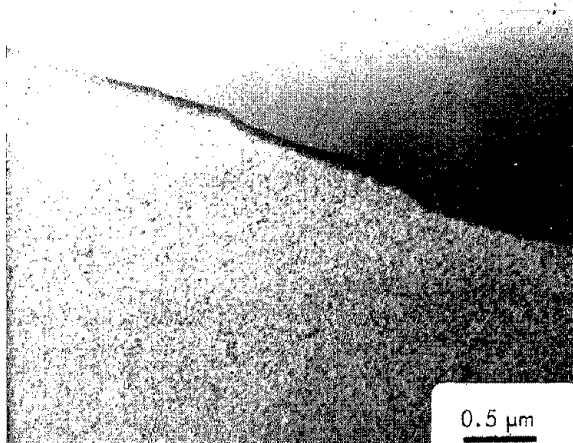


Fig. 18.3 Type 304 stainless steel irradiated at 93°C. [From E. E. Bloom, W. R. Martin, J. O. Stiegler, and J. R. Weir, *J. Nucl. Mater.*, 22: 68 (1967).]

to represent the depleted zones or vacancy clusters predicted by radiation-damage theory (Figs. 17.25 and 17.30). As long as the irradiation temperature is below  $\sim 350^\circ\text{C}$ , increasing fluence simply increases the density of the black-dot damage.

When irradiation is carried out at temperatures greater than  $\sim 350^\circ\text{C}$ , the nature of the microstructure is entirely different from the black-dot pattern characteristic of low-temperature irradiation. In stainless steel irradiated above  $350^\circ\text{C}$ , the point defects created by the collision cascades are sufficiently mobile to move about in the solid and agglomerate into larger defect clusters. The damage structure consists of dislocation loops and voids.

### 18.2.2 Loops

The defect agglomeration commonly called a loop is formed by condensation of radiation-produced vacancies or interstitials into roughly circular disks followed by collapse of the atomic planes adjacent to the platelet. Vacancy-loop formation is shown in Figs. 18.4(a) and 18.4(b), and the corresponding process for interstitials is depicted in Figs. 18.4(c) and 18.4(d). The end result of the condensation/collapse process is a region delineated by a circular edge dislocation. In the fcc structure, loops invariably form on  $\{111\}$  planes. When a  $\{111\}$  plane is added to or removed from the lattice by agglomeration of a disk of interstitials or vacancies, the stacking sequence of the perfect close-packed structure (Sec. 3.6) is disturbed. The circular edge dislocation thus encloses a *stacking fault*.

The dislocation loops shown in Figs. 18.4(b) and 18.4(d) are called *Frank sessile* dislocations or simply Frank loops. The term *sessile* means immobile. Because the dislocation encloses a stacking fault, Frank loops are also called *faulted loops*. The Burgers vector of a Frank dislocation is perpendicular to the plane of the loop, and its magnitude is equal to the separation of the  $\{111\}$  planes. This Burgers vector is denoted symbolically by

$$\mathbf{b} = \pm \frac{a_0}{3} [111] \quad (18.1)$$

The direction is indicated by the Miller indices in the brackets. The sign depends on whether the loop was formed from vacancies or interstitials. The length of the Burgers vector is given by the square root of the sum of the squares of the Miller indices times the coefficient  $a_0/3$ , or  $(a_0/3)3^{1/2} = a_0/3^{1/2}$ .

Edge dislocations can slip only in the direction of their Burgers vector. The cylinder normal to the loop on which the dislocation can move is not a  $\langle 110 \rangle$  glide direction for fcc slip [Fig. 8.2(a)]. Therefore, the Frank dislocation loop cannot move in the direction of its Burgers vector and hence is immobile, or sessile. The loop can change diameter by absorbing or emitting point defects (i.e., by climb). Net addition of the same type of point defect causes the loop to grow, whereas absorption of the opposite type of point defect causes shrinkage. The stacking fault can be eliminated by moving the crystal above the loop relative to the solid below it. This shearing action is accomplished by passage of another type of dislocation, called a Shockley dislocation, across the faulted area. The Shockley dislocation and the Frank dislocation react to form a dislocation loop at the same position as the original Frank loop but with the interior of the loop now in perfect stacking registry with the neighboring  $\{111\}$  planes. The loop unfaultering process occurs spontaneously in stainless steel at about  $600^\circ\text{C}$ . The Burgers vector of the unfaulted loop is

$$\mathbf{b} = \pm \frac{a_0}{2} [110] \quad (18.2)$$

This Burgers vector is properly oriented for glide in the fcc lattice [Fig. 8.2(a)], and the loop is therefore mobile. As it moves by slip, it sweeps out a cylindrical surface tilted at an

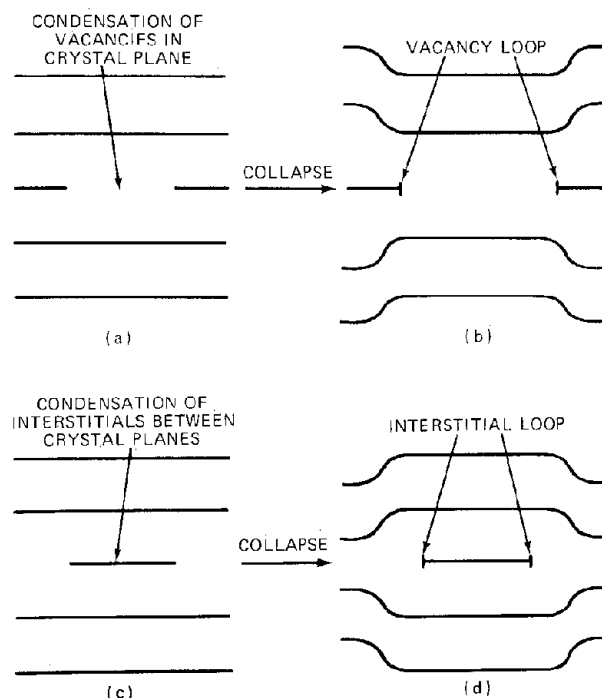


Fig. 18.4 Formation of vacancy loops and interstitial loops.

angle to the (111) plane. Because of the shape of slip pattern, the unfaulted loop is often called a *prismatic* loop. It is distinguished from the shear loop shown in Fig. 8.6 by the direction of the Burgers vector with respect to the plane of the loop. The Burgers vector of a shear loop lies in the plane of the loop, whereas the Burgers vector of a prismatic loop lies outside the plane of the loop. The dislocation of the unfaulted loop given by Eq. 18.2 is perfect in the sense that movement along the slip plane leaves the atoms in positions equivalent to those previously occupied. The dislocation characterizing the Frank sessile loop (Eq. 18.1) does not satisfy this criterion, and the Frank loop is said to be imperfect.

Faulted and unfaulted dislocation loops are shown in Figs. 18.5(a) and 18.5(b), respectively. Because of the stacking fault they enclose, the faulted loops in Fig. 18.5(a) appear in the electron microscope as opaque circles. Removal of the faulted region renders the interior of the loop identical to the rest of the solid, and only the outline of the loop remains [Fig. 18.5(b)]. Since the unfaulted dislocation loops are mobile, they easily lose their distinctive circular shape by gliding under an applied stress and

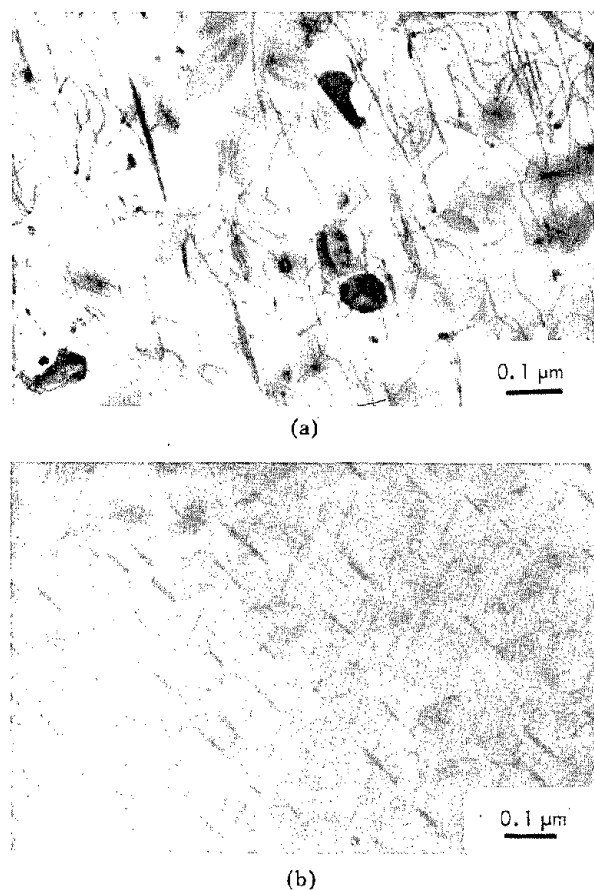


Fig. 18.5 Dislocation loops in type 304 stainless steel. (a) Faulted. (b) Unfaulted. (From E. E. Bloom and J. O. Stiegler, in ASTM Special Technical Publication 484, p. 451, American Society for Testing and Materials, Philadelphia, 1970.)

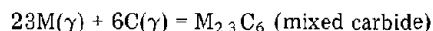
becoming tangled with the natural or deformation-produced dislocation network of the solid. Loops disappear from the irradiated solid at about 600 to 650°C.

### 18.2.3 Voids

Under some conditions the embryo collection of vacancies of Fig. 18.4(a) can begin to grow in a three-dimensional manner rather than collapse into a dislocation loop. This route leads to the formation of voids in metals and consequent swelling of the structure (Chap. 19). Voids produced in stainless steel by high-fluence fast-neutron bombardment at 525°C are shown in Fig. 18.6. The voids are not spherical. Rather, they assume the shape of a regular octahedron with {111} planes as surfaces. The ends of the octahedron, however, are truncated by {100} planes. Voids are annealed out of the microstructure at about 750°C.

### 18.2.4 Carbide Precipitates

In pure metals, only voids and dislocation loops are produced by intermediate-temperature irradiation. In a material as complex as stainless steel, however, neutron irradiation also causes different solid phases to precipitate. Carbon is added to steel in the molten state, where the solubility of carbon is high. Carbon solubility, whether in the solid or in the liquid forms of steel, decreases rapidly as the temperature is reduced. However, when the steel is rapidly quenched from the melt, the kinetics of carbon precipitation are too slow to keep up with the rapid decrease in the mobility of the atomic species in the solid. Consequently, the 0.06 wt.% carbon in steel (Table 18.1) is maintained in atomic form as a supersaturated solution. When the steel is heated to temperatures at which supersaturation persists but atomic mobility is appreciable, the carbon can be expelled from solution and form a second phase in the metal. When steel is aged (i.e., heated for long periods of time at elevated temperatures), dissolved carbon reacts with the matrix elements iron and chromium to form a compound  $M_{23}C_6$  ( $M = Cr$  and  $Fe$ ) which is insoluble in the austenite or gamma phase. These carbides are formed by the reaction



where  $\gamma$  denotes the austenitic phase. The carbide formed is a mixture of  $Fe_{23}C_6$  and  $Cr_{23}C_6$ . Since chromium is a strong carbide-former, the mixed carbide consists primarily of  $Cr_{23}C_6$ . The nickel constituent of stainless steel does not form stable carbides.

Neutron irradiation accelerates the diffusional processes that control the mobilities of the atomic species in the lattice and hence the kinetics of the preceding precipitation reaction. Carbide precipitation occurs at much lower temperatures and shorter times than those required for aging in the absence of irradiation. Radiation accelerates the rates of precipitation reactions when such processes are thermodynamically favorable. If the irradiation temperature is above that at which the solubility limit of carbon is equal to the carbon content of the steel, irradiation cannot cause precipitation. For type 316 stainless steel containing 0.06%



Fig. 18.6 Type 316 stainless-steel specimen irradiated at 525°C to  $7.1 \times 10^{22}$  neutrons/cm<sup>2</sup> ( $E > 0.1$  MeV). Mean void diameter, 640 Å; void number density,  $4.4 \times 10^{14}$  voids/cm<sup>3</sup>. [From W. K. Appleby et al., in *Radiation-Induced Voids in Metals*, Albany, N. Y., James W. Corbett and Louis C. Ianniello (Eds.), USAEC Symposium Series, CONF-710601, p. 166, 1971.]

carbon, for example, carbide precipitation is thermodynamically unfavorable at temperatures greater than ~900°C. At temperatures lower than ~400°C, diffusional processes are too slow (even when enhanced by irradiation) to cause observable precipitation in reasonable irradiation times. Between 400 and 900°C, however, exposure of austenitic stainless steel to fast-neutron fluences between  $10^{21}$  and  $10^{22}$  neutrons/cm<sup>2</sup> produces carbide precipitation. Figure 18.7 shows an electron micrograph of carbide precipitation in type 316 stainless steel. Carbide particles are found both within the grains of the  $\gamma$  phase (austenite) and on the grain boundaries. The presence of precipitates on the grain boundaries affects the creep strength of the alloy.

### 18.2.5 Helium Bubbles

At temperatures above ~800°C, dislocation loops and voids are not found in irradiated steel. In addition to grain boundaries, dislocations (augmented by the unfaulted loops that have joined the original dislocation network), and carbide precipitates, the microstructure contains small helium-filled bubbles. Helium is generated by ( $n,\alpha$ ) reactions with the boron impurity in the steel and

with the major constituents, principally nickel. At temperatures below ~650°C, the helium atoms produced by stopping the alpha particles in the material are not mobile enough to migrate and nucleate bubbles. Consequently, helium remains in solution and is invisible to the electron microscope. At high temperatures helium bubbles form in the metal in the same way that fission-gas bubbles form in ceramic oxide fuel material (Chap. 13). The helium bubbles in the metal are nearly spherical, which suggests that the internal gas pressure is very nearly balanced by surface-tension forces. Figure 18.8 shows the helium bubbles in stainless steel at 800°C. In this instance, the helium was injected into the specimen by a cyclotron. The bubbles on the grain boundaries are larger than those in the matrix. The intergranular helium plays an important role in the high-temperature embrittlement of stainless steel. Short of melting, helium bubbles cannot be removed from the metal by annealing.

## 18.3 MECHANICAL-PROPERTIES TESTS

Much of the mechanical testing designed to elucidate the effects of neutron irradiation on structural metals is performed after irradiation with conventional metallurgical testing machines. Usually the specimens are irradiated in a neutron flux of known energy spectrum for a fixed period of time and then removed for testing. The effects of large neutron fluences (i.e., very long irradiations) can be



Fig. 18.7 Nearly continuous  $M_{23}C_6$  precipitation along grain boundary of solution-treated type 316 irradiated at 850°C to  $5.1 \times 10^{22}$  neutrons/cm<sup>2</sup>. [From H. R. Brager and J. L. Straalsund, *J. Nucl. Mater.*, 46: 134 (1973).]

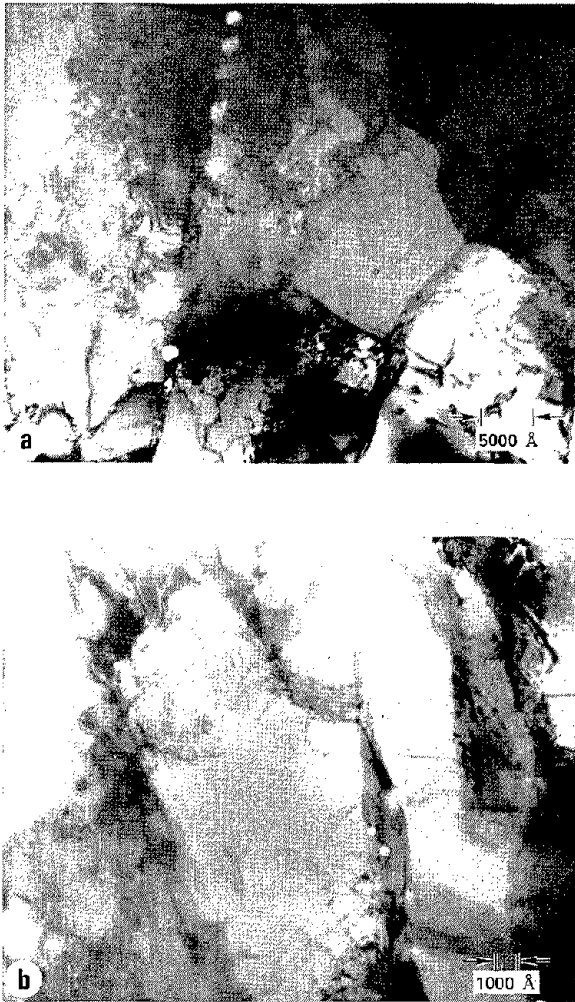


Fig. 18.8 Transmission electron micrographs of stainless steel injected with  $5 \times 10^{-5}$  atom fraction helium, tested at  $800^\circ\text{C}$ . Large helium bubbles are seen in (a) the grain boundary and (b) in the grain boundary, with smaller bubbles in the matrix. (From D. Kramer et al., in ASTM Special Technical Publication 484, p. 509, American Society for Testing and Materials, Philadelphia, 1970.)

determined by the simple expedient of removing core components of a reactor and fabricating test samples from them. Aside from the problems associated with handling and shielding radioactive samples, post-irradiation testing is a routine operation, and a large amount of mechanical-properties data can be accumulated quickly and inexpensively.

The mechanical properties of irradiated structural steels depend on the irradiation temperature. When testing is done after removal from the reactor, the testing temperature is unavoidably introduced as an additional parameter. This additional degree of flexibility is often valuable; tensile tests over a range of test temperatures on specimens

irradiated at a fixed temperature provide information on the thermal stability of defects that are responsible for the change in strength brought about by irradiation. For some properties, however, out-of-pile testing, even at a test temperature equal to the irradiation temperature, does not adequately represent the behavior of the metal in the reactor environment. This complication can be eliminated by performing mechanical tests during irradiation; such experiments, however, are difficult and costly. In-pile testing is usually restricted to measurement of mechanical properties that depend critically on the neutron flux as well as on the neutron fluence (e.g., irradiation creep).

This section reviews some of the conventional mechanical-property tests that are applied to irradiated structural steels.

### 18.3.1 Tensile Test

The tensile test provides a means of uniaxially loading a rod or bar-shaped specimen and of measuring the elongation for various applied loads (Fig. 18.9). When a specimen of initial length  $l_0$  and cross sectional area  $A_0$  is subjected to an applied load in tension  $P$ , the length increases to  $l$ , and the cross-sectional area is reduced to  $A$ . The *engineering stress* in the test is defined as the ratio of the load to the initial cross sectional area, or  $P/A_0$ . The *true tensile stress*, however, is based on the actual specimen area, or

$$\sigma = \frac{P}{A} \quad (18.3)$$

The *engineering strain* is the elongation divided by the initial specimen length, or  $(l - l_0)/l_0$ . The *true strain*, on the other hand, is the integral of the increments of strain over the specimen length:

$$\epsilon = \int_{l_0}^l \frac{dl}{l} = \ln\left(\frac{l}{l_0}\right) \quad (18.4)$$

The true strain is always somewhat less than the engineering strain. The true strain defined by Eq. 18.4 is

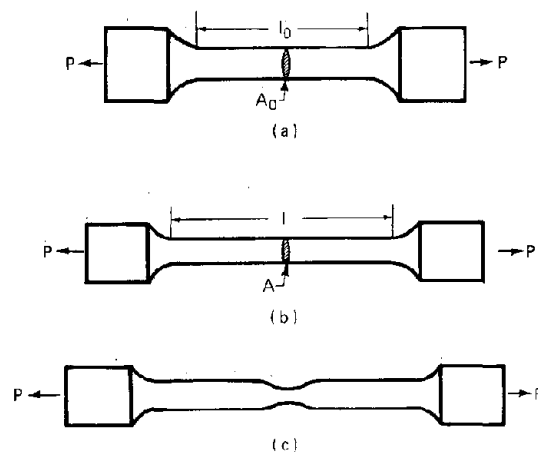


Fig. 18.9 The tensile test. (a) Test specimen. (b) Uniform elongation. (c) Necking.

not equivalent to the strain components commonly employed in elasticity theory (i.e., Eq. A.10 of the Appendix). The relation between the infinitesimal strain components and displacement is determined by Taylor series expansions, which neglect products of strain components. The strain of Eq. 18.4 is applicable to finite deformations encountered in tensile tests far into the plastic region. It is also called the logarithmic strain.

In the elastic stress region, the true stress-strain curve obeys Hooke's law, which for the uniaxial tensile test is  $\sigma = E\epsilon$ . However, tensile tests are generally intended to investigate the behavior of the metal at much larger stresses than those for which Hooke's law is followed. The large, irreversible plastic strains in most tensile tests take place at essentially constant volume because deformation occurs primarily by shear. With the specimen volume constant, area reduction is related to elongation by

$$Al = A_0 l_0$$

or

$$\frac{dl}{l} = -\frac{dA}{A} \quad (18.5)$$

Thus, the true strain can also be expressed by

$$\epsilon = \int_{A_0}^A \left( -\frac{dA}{A} \right) = \ln \left( \frac{A_0}{A} \right) \quad (18.6)$$

The preceding equations apply without qualification to the portion of the deformation in which the cross-sectional area of the specimen is reduced by the same amount over the entire length of the specimen. This mode of deformation is called *uniform elongation* [Fig. 18.9(b)]. At a certain load the cross-sectional area of a localized section of the specimen begins to decrease more rapidly than the remainder of the bar [Fig. 18.9(c)]. This phenomenon is called *necking*, and the stress or strain at which it begins is the point of *plastic instability*.

The stress-strain curves for a typical (unirradiated) low-alloy steel are shown in Fig. 18.10. The general shapes of these curves are characteristic of most metals that crystallize in the bcc lattice structure. The solid line depicts the engineering stress-strain curve, which is a plot of  $P/A_0$  vs.  $(l - l_0)/l_0$ . The material deforms elastically according to Hooke's law up to the point U, where the specimen appears to give way or to *yield*. The load then drops with increasing elongation to the point L. The points U and L are called the upper and lower yield points, respectively. The reported yield strength of a material is usually the stress at the lower yield point. For a short strain interval following point L, plastic deformation proceeds with no increase in load. This interval is called the *Lüders strain*. The stress level characterizing the Lüders strain region is essentially the same as the lower yield point, although it is sometimes called the *flow stress* of the material.

Following the Lüders strain is a region where the stress required to produce further strain increases. This portion of the stress-strain curve is called the *strain-hardening* or *work-hardening* region because the material becomes

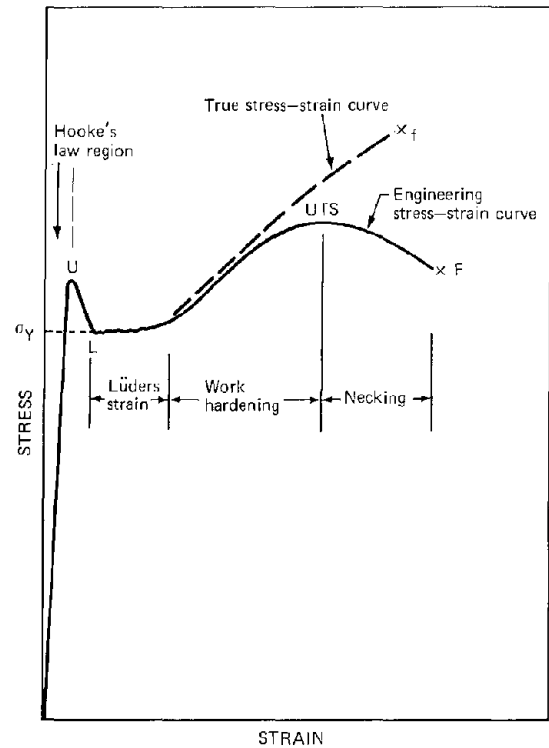


Fig. 18.10 Stress-strain curve for ferritic steel.

stronger as a result of the deformation process. Plastic instability terminates the work-hardening portion of the stress-strain curve at the point labeled UTS, which stands for *ultimate tensile stress*. This point represents the maximum load-bearing capacity of the specimen. At all times during deformation, the load is equal to the product of the actual cross-sectional area and the true stress, or  $P = \sigma A$ . At the UTS,  $dP = 0$ , or

$$\frac{d\sigma}{\sigma} = -\frac{dA}{A}$$

According to Eq. 18.6,  $-dA/A = d\epsilon$ ; so the onset of necking, which occurs at the UTS, is located on the true stress-strain curve at the point at which

$$\frac{d\sigma}{d\epsilon} = \sigma \quad (18.7)$$

Up to plastic instability, the true stress-strain curve (the dashed curve in Fig. 18.10) can be constructed using Eqs. 18.3 and 18.4. During necking, Eq. 18.4 does not apply if the gauge length  $l$  is interpreted as the total specimen length. However, nowhere has it been specified that  $l$  must be the entire specimen length; it could very well have been chosen as a very short segment right in the necking region. Over this small segment, elongation is uniform. It is experimentally difficult to measure length changes in a very tiny gauge length. However, Eq. 18.6 applies to the necked region provided that the area  $A$  is the cross-sectional area at the most severely necked part of the specimen. Therefore, application of Eqs. 18.3 and 18.6

with the necked area taken for A permits the true stress-strain curve to be extended from the UTS to fracture (point F). At fracture, the true strain is always less than and the true stress is larger than those based on the engineering stress-strain curve. At small strains, however, the difference between the two stress-strain curves is negligible. The yield stress, for example, can be represented by either curve with no appreciable error.

Figure 18.11 shows the tensile behavior of a typical austenitic steel. The primary difference between the stress-strain curves in Figs. 18.10 and 18.11 is the absence of a well-defined yield point in Fig. 18.11. For most metals with an fcc structure, the stress-strain curve continuously

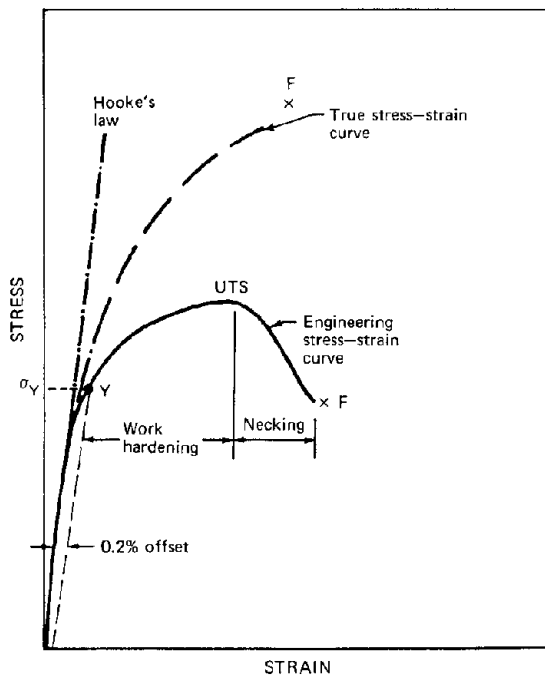


Fig. 18.11 Stress-strain curve for austenitic steel.

deviates from Hooke's law as the stress is increased, and it is impossible to assign a definite stress at which plastic deformation begins. That is, the metal does not yield in an unequivocal manner. Hence, yielding (or the onset of plastic flow) in such metals is arbitrarily considered to occur when the permanent strain in the tensile test is 0.2%. This stress, denoted by  $\sigma_Y$  in Fig. 18.11, is called the *0.2% offset yield strength* of the metal.

*Ductility* is measured either by the amount of strain between the true fracture stress and the yield stress ( $\epsilon_F - \epsilon_Y$ ) or more commonly by the total uniform elongation up to necking. *Embrittlement* means a reduction in either of these two measures of ductility. A brittle material fails when yield occurs or, in the case of a material having no sharp yield point, when failure occurs before 0.2% offset strain.

The rate at which deformation is imposed in the tensile test, or the strain rate, affects the stress-strain curves of

Figs. 18.10 and 18.11. The yield stress is reduced at low strain rates because the slow motion of dislocations at low stress levels becomes sufficient to become manifest as plastic deformation. In unirradiated steels, ductility is not significantly affected by strain rate.

Strain rates of  $0.01 \text{ min}^{-1}$  are characteristic of conventional tensile tests. This figure is also approximately equal to the strain rates induced in cladding by typical reactor power transients (shutdown, startup, and power cycling). When the strain rate in the test is reduced to  $10^{-4} \text{ min}^{-1}$  and the temperature is high, the test is called a creep-rupture test. This strain rate is typical of that imposed on cladding by fuel swelling in the reactor.

### 18.3.2 Tube-Burst Tests—Biaxial Stress State

The tensile test described above is an experimentally convenient way of measuring the mechanical properties of a metal. In addition, theoretical interpretation of the stress-strain curves is simplified by the fact that there is only one nonzero component of the stress tensor, namely, the normal stress in the direction of the applied load. However, the stress state of fuel-element cladding loaded internally by fission-gas pressure and fuel swelling more closely resembles that in a long thin-walled cylindrical tube closed at both ends and pressurized by a gas. Since cladding fails by creep rupture after long periods of being subjected to stresses well below the yield stress, considerable creep-rupture testing of unirradiated and irradiated steel tubing has been performed by pressurizing closed tubing with an inert gas. These tests are called tube-burst tests.

According to elasticity theory, the normal stresses in thin-wall tubes loaded by an internal gas pressure  $p$  are given by (see problem 18.6)

$$\sigma_\theta = \frac{pD}{2t} \quad (18.8a)$$

$$\sigma_z = \frac{pD}{4t} \quad (18.8b)$$

$$\sigma_x \cong 0 \quad (18.8c)$$

where  $D$  is the tube diameter and  $t$  is the wall thickness ( $t \ll D$ ). The infinitesimal radial and tangential strains appropriate to conventional elasticity theory are  $(t - t_0)/t_0$  and  $(D - D_0)/D_0$ , respectively. The logarithmic strains should be used when appreciable deformation occurs. The true (logarithmic) strains are

$$\epsilon_r = \ln\left(\frac{t}{t_0}\right) \quad (18.9a)$$

$$\epsilon_\theta = \ln\left(\frac{D}{D_0}\right) \quad (18.9b)$$

$$\epsilon_z = 0 \quad (18.9c)$$

where  $D_0$  and  $t_0$  are the initial tube diameter and wall thickness, respectively. By varying the gas pressure,  $p$ , plastic deformation of the tube can be induced. Because the tube wall is subject to two stress components of com-

parable magnitude, the stress state is *biaxial*. To interpret the results of tube-burst tests, one needs to know the correspondence between the states of plastic stress and plastic strain for the uniaxial and biaxial situations. For example, if yield occurs in the tensile test at a true stress of  $\sigma_Y$ , at what gas pressure should the tube yield?

More generally, the criterion for yielding in multiaxial stress states is needed. In the tensile and tube-burst tests, no shear stresses are involved. In these cases the coordinates  $(x, y, z)$  and  $(r, \theta, z)$  are called the principal axes, and the normal stresses acting on planes perpendicular to these axes are the principal stresses. In situations where the shear strains are not zero, it is always possible to rotate the conventional coordinate system (cartesian, cylindrical, and spherical) into another set of coordinates, called 1, 2, and 3, for which the shear stresses vanish. The normal stresses acting along these axes,  $\sigma_1$ ,  $\sigma_2$ , and  $\sigma_3$ , are the principal stresses of the system. Although no coordinate rotation is necessary in the tensile and tube-burst tests, the multiaxial yield criterion will be developed in terms of the principal stresses,  $\sigma_1$ ,  $\sigma_2$ , and  $\sigma_3$ , and then specialized to the two cases of interest.

In the absence of a shear stress, the elastic strain energy density of a deformed solid is given by Eq. A.26 of the Appendix as

$$E_{el} = \frac{1}{2E} (\sigma_1^2 + \sigma_2^2 + \sigma_3^2) - \frac{\nu}{E} (\sigma_1 \sigma_2 + \sigma_1 \sigma_3 + \sigma_2 \sigma_3) \quad (18.10)$$

A general yielding criterion could be based on the hypothesis that yielding occurs when the strain energy,  $E_{el}$ , reaches a critical value. However, this criterion is not enough, because it is well known that large amounts of strain energy can be stored by the action of purely hydrostatic stresses without causing the material to deform permanently. Von Mises proposed that the appropriate strain energy is the difference between the total energy density of Eq. 18.10 and the energy density that the solid would acquire had it been subject to the mean of the three principal stresses. The mean normal stress is

$$\sigma_h = \frac{1}{3} (\sigma_1 + \sigma_2 + \sigma_3) \quad (18.11)$$

and the elastic-energy density arising from the hydrostatic stress is obtained by substituting  $\sigma_h$  for  $\sigma_1$ ,  $\sigma_2$ , and  $\sigma_3$  in Eq. 18.10,

$$\begin{aligned} (E_{el})_h &= \frac{3}{2} \left( \frac{1-2\nu}{E} \right) \sigma_h^2 \\ &= \frac{1-2\nu}{6E} (\sigma_1 + \sigma_2 + \sigma_3)^2 \end{aligned} \quad (18.12)$$

According to von Mises, yielding occurs when the distortion energy,  $E_{el} - (E_{el})_h$ , exceeds a critical value. This energy density is obtained from Eqs. 18.10 and 18.12 as

$$\begin{aligned} (E_{el})_d &= E_{el} - (E_{el})_h \\ &= \left( \frac{1+\nu}{6E} \right) [(\sigma_1 - \sigma_2)^2 \\ &\quad + (\sigma_1 - \sigma_3)^2 + (\sigma_2 - \sigma_3)^2] \end{aligned} \quad (18.13)$$

In the uniaxial tensile test,  $\sigma_1 = \sigma_x$ ,  $\sigma_2 = \sigma_y = 0$ , and  $\sigma_3 = \sigma_z = 0$ . Equation 18.13 reduces to

$$(E_{el})_d = 2 \left( \frac{1+\nu}{6E} \right) \sigma_x^2 \quad (18.14)$$

When the right-hand sides of Eqs. 18.13 and 18.14 are equated, the stress  $\sigma_x$  is interpreted as the true stress in a uniaxial tensile test, which is equivalent to the multiaxial stress state characterized by the principal stresses,  $\sigma_1$ ,  $\sigma_2$ , and  $\sigma_3$ . The *equivalent stress* is then

$$\begin{aligned} \sigma_x = \sigma^* &= \frac{1}{2^{1/2}} [(\sigma_1 - \sigma_2)^2 \\ &\quad + (\sigma_1 - \sigma_3)^2 + (\sigma_2 - \sigma_3)^2]^{1/2} \end{aligned} \quad (18.15)$$

To emphasize the concept of equivalent stress, we replace the uniaxial stress  $\sigma_x$  with the notation  $\sigma^*$ . This quantity is also called the stress deviator because it pertains only to that portion of the stress system which leads to distortion in specimen shape but does not include the stresses that contribute to volume dilatation.

For the tube-burst test,  $\sigma_1 = \sigma_\theta$ ,  $\sigma_2 = \sigma_z = \sigma_\theta/2$ , and  $\sigma_3 = \sigma_r = 0$ . Substituting these stresses into the right-hand side of Eq. 18.15 gives

$$\sigma^* = \frac{3^{1/2}}{2} \sigma_\theta \quad (18.16)$$

Equations 18.15 and 18.16 apply from the yield point to fracture. To determine the internal gas pressure that should cause yielding of a closed tube, we set  $\sigma^*$  equal to  $\sigma_Y$ , the measured yield stress in a tensile test;  $\sigma_\theta$  is given by Eq. 18.8a. Equation 18.16 then gives the pressure to cause yielding of the tube

$$p(\text{yielding}) = \frac{4}{3^{1/2}} \frac{t}{D} \sigma_Y$$

The strain deviator analogous to the stress deviator of Eq. 18.15 is defined as

$$\epsilon^* = \frac{2^{1/2}}{3} [(\epsilon_1 - \epsilon_2)^2 + (\epsilon_1 - \epsilon_3)^2 + (\epsilon_2 - \epsilon_3)^2]^{1/2} \quad (18.17)$$

The strain deviator,  $\epsilon^*$ , is also called the equivalent strain. The coefficient  $2^{1/2}/3$  arises because we want  $\epsilon^*$  to reduce to  $\epsilon_1 = \epsilon_x$  in a tensile test. Although the stress is uniaxial in the tensile test, the plastic strains are not. The transverse strains are equal to each other, but, because the material is incompressible in plastic flow, we have

$$\epsilon_1 + \epsilon_2 + \epsilon_3 = 0 \quad (18.18)$$

or, with  $\epsilon_2 = \epsilon_3$

$$\epsilon_2 = \epsilon_3 = -\frac{1}{2} \epsilon_1$$

and Eq. 18.17 shows that  $\epsilon^* = \epsilon_1 = \epsilon_x$ , as desired.

For a pressurized tube,  $\epsilon_r = -\epsilon_\theta$  (since  $\epsilon_z = 0$ ), and the equivalent strain is given by

$$\epsilon^* = \frac{2}{3^{1/2}} \epsilon_\theta \quad (18.19)$$

where  $\epsilon_\theta$  is given by Eq. 18.9b. The radial strain is difficult to measure during plastic deformation of a tube, but  $\epsilon_\theta$ , which is called the *diametral strain*, is more accessible.

Although pressurized-tube-deformation measurements can be used to generate stress-strain curves, tensile tests are much more suitable for this purpose. The principal use of the tube pressurization experiments is to measure the time required to burst the tube under a fixed gas pressure. Since these rupture times are generally rather long (ranging from  $\sim 1$  to 10,000 hr), the phenomenon is called *creep rupture*. The diametral strain can also be measured at rupture. This quantity is a qualitative indication of the ductility of the specimen. Similarly, the time derivative of the diametral strain is a measure of the creep rate. If steady-state creep (Fig. 8.22) prevails for most of the test, the *rupture time*,  $t_R$ , is given by

$$t_R = \frac{\epsilon_F}{\dot{\epsilon}} \quad (18.20)$$

where  $\epsilon_F$  is the diametral strain at failure and  $\dot{\epsilon}$  is the creep rate, which is assumed to be constant for  $0 < t < t_R$ .

Figure 18.12 shows typical stress-rupture curves for type 316 stainless steel at various temperatures. The stress

of the two testing methods are indeed collapsed into single curves when plotted according to Eq. 18.21.

### 18.3.3 Impact Testing and Transition Temperatures

One of the major differences between the mechanical behavior of austenitic and ferritic steels is that ferritic steels tend to become brittle at low temperatures, whereas austenitic steels remain ductile to as low temperatures as it is possible to reach in tensile tests. The degree of ductility or brittleness is related to the strain at fracture (the point F in Fig. 18.10). As the temperature at which a tensile test is conducted is reduced, the fracture stress becomes smaller and eventually coincides with the onset of yielding. Another measure of the ability of a metal to deform plastically before fracture is the energy per unit volume required for fracture. This quantity, which is called *toughness*, is the area under the stress-strain curve up to point F in Fig. 18.10. Determining the energy of fracture by measuring and then integrating a complete stress-strain curve is tedious, and quicker methods, known as impact tests, have been devised. These tests are not intended to

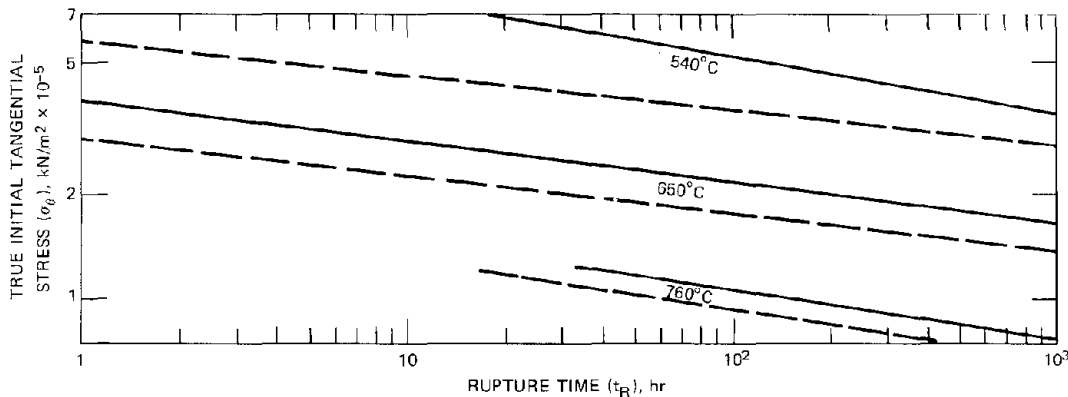


Fig. 18.12 Rupture life of unirradiated type 316 stainless steel. —, uniaxial. ---, biaxial. (After A. J. Lovell and R. W. Barker, in ASTM Special Technical Publication 484, p. 468, American Society for Testing and Materials, Philadelphia, 1970.)

dependence of the rupture time can be obtained by substituting Eq. 8.46 for  $\dot{\epsilon}$  into Eq. 18.20. If the diametral rupture strain is considered constant for tests at different stresses and temperatures, we obtain

$$\sigma_\theta \propto \left[ t_R \exp\left(-\frac{E}{kT}\right) \right]^{-1/m} \quad (18.21)$$

In this equation,  $E$  is the activation energy for steady-state creep.

For dislocation climb creep (Sec. 16.7), the exponent  $m$  is  $\sim 4$ , so the slope of the creep-rupture line on a log-log plot should be 0.2–0.3. Figure 18.12 confirms this expectation. Equation 18.21 also suggests that the temperature dependence of the stress-rupture plot can be removed by plotting the stress as a function of the product  $t_R \exp(-E/kT)$  rather than simply  $t_R$ . The compound variable is called the Dorn theta parameter. The curves in Fig. 18.12 for each

provide an accurate measure of the true energy of fracture; rather they can quickly and reproducibly indicate the effect of such variables as temperature and radiation on the change in the brittle characteristics of ferritic steels. Impact tests are generally referred to as comparative tests as opposed to tensile and tube-burst tests, which are designed to measure one or more well-defined mechanical properties of the metal.

The most commonly used impact test for mild steels is the Charpy V-notch test illustrated in Fig. 18.13(a). A notched specimen of standard size and shape (1 by 1 by 6 cm<sup>3</sup>) is end-mounted in a holder (shown as the solid triangles in the drawing). A hammer attached to the end of a pendulum is raised to an initial height  $h_1$  above the specimen which corresponds to an energy of 325 J at the moment of contact with the specimen. The difference between the initial and final heights of the hammer

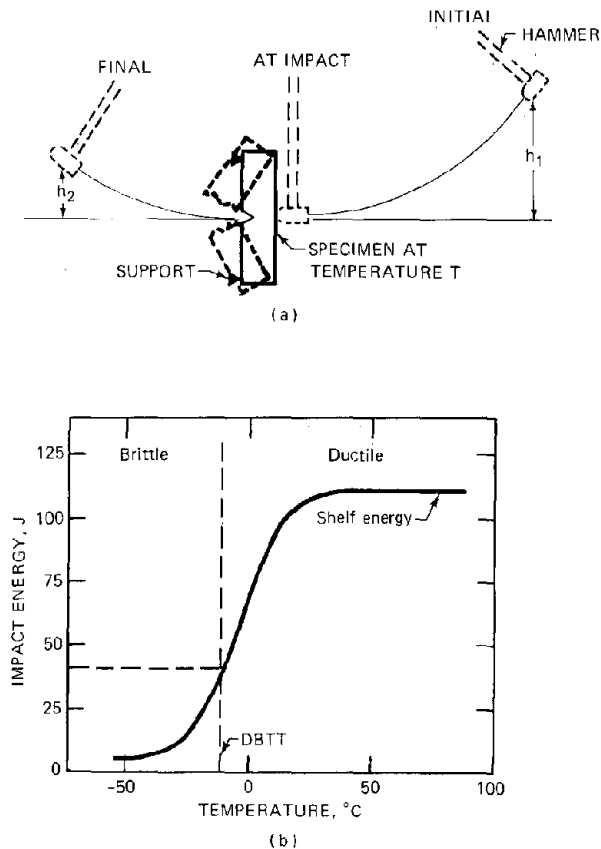


Fig. 18.13 The Charpy V-notch test. (a) Test setup. (b) Variation of absorbed energy with temperature.

$(h_1 - h_2)$  gives the energy absorbed by the specimen in the fracture process. When Charpy tests are performed on specimens at different temperatures, the absorbed energy (called the impact energy) varies as shown in Fig. 18.13(b). The impact energy increases from  $<15$  J at low temperatures to a high-temperature plateau known as the shelf energy, which is typically 100 to 150 J. The transition occurs over a rather narrow temperature range, and the temperature at which the impact energy is 40.7 J is arbitrarily used to separate the ductile and brittle regimes. This temperature is called the *ductile-brittle transition temperature* (DBTT). For unirradiated mild steels, the DBTT is between  $-50$  and  $20^\circ\text{C}$ .

The drop weight test illustrated in Fig. 18.14 is perhaps the simplest of the impact class of tests designed to assess the susceptibility of a metal to brittle fracture. In this test a bead of weld material is deposited on the bottom of a test plate (9 by 35 by  $2.5\text{ cm}^3$ ), and a small crack or notch is made in the weld. The test consists of dropping a weight from a fixed height on top of the plate directly over the bead. The height of the end supports for the plate is fixed so that the maximum deformation of the specimen corresponds to  $5^\circ$  of bend. At low temperatures the specimen fractures in the test. As the test temperature is increased, a temperature is reached at which the fracture does not extend through the entire thickness of the plate. This

temperature is called the *nil ductility temperature* (NDT). At temperatures above the NDT, the specimen bends under impact but does not break. The NDT is approximately equal to the DBTT obtained from the Charpy test. Because the small size of the Charpy test specimens make them easier to load into capsules for irradiation, most irradiation embrittlement studies are made with the Charpy test. However, the NDT correlates well with the DBTT, and the two terms are used interchangeably.

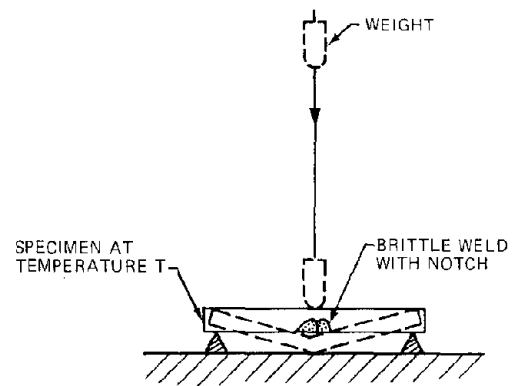


Fig. 18.14 The drop-weight impact test.

Because of the empirical nature of the impact tests, neither transition temperature has a well-defined theoretical significance. However, changes in the DBTT or the NDT due to neutron irradiation can be related to fracture theory.

## 18.4 THEORIES OF RADIATION HARDENING

Over 20 years of intensive experimental effort has established that exposure of all metals to fast-neutron irradiation results in an increase in the yield strength. In ferritic steels this radiation hardening appears as an increase in the lower yield point. Irradiation causes an increase in the 0.2% offset yield strength of austenitic steels and may even result in the development of a stress-strain curve that exhibits a definite yield point (i.e., the curve resembles that shown in Fig. 18.10 rather than that of Fig. 18.11).

Typical engineering stress-strain curves for the two types of steels are shown in Fig. 18.15. In addition to increasing yield strength with irradiation, the ductility (as measured either by total elongation or by uniform elongation) is reduced. The curves shown for the two types of steels apply only when the testing temperature is low [less than one-half or two-thirds the melting point ( $^\circ\text{K}$ ), depending on the neutron fluence]. Austenitic steels irradiated and tested at high temperatures show no increase in either yield or ultimate strength; only the ductility reduction persists [bottom curve of Fig. 18.15(a)]. When bcc metals are irradiated and tested at high temperatures, the stress-strain curve of the unirradiated material is completely recovered. Whatever radiation-produced defects are responsible for strengthening and the loss of ductility are removed by annealing processes at high temperatures.

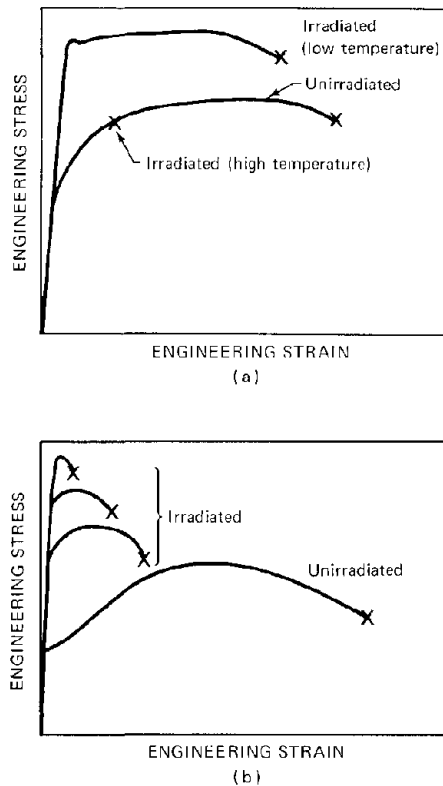


Fig. 18.15 Effect of fast-neutron irradiation on the tensile properties of reactor steels. (a) Face-centered cubic structure. (b) Body-centered cubic structure.

For both the austenitic and ferritic steels, irradiation increases the yield strength much more than it does the ultimate tensile strength. The approach of the yield strength to the UTS as a result of irradiation is responsible for the ductility loss. The upper curve in Fig. 18.15(b) shows a case in which the yield and ultimate strengths coincide. When this occurs, there is no uniform elongation, and necking begins as soon as the specimen departs from the line representing elastic straining. In the bcc metals, when the testing temperature is low enough and the irradiation exposure large enough, there may not even be a region of necking deformation; the specimen can fracture while still on the elastic line. Such specimens are totally brittle.

Radiation hardening in both fcc and bcc metals is attributed to the production by radiation of various defects within the grains. Defects produced by neutron irradiation of metals include

1. Point defects (vacancies and interstitials).
2. Impurity atoms (atomically dispersed transmutation products).
3. Small vacancy clusters (depleted zones).
4. Dislocation loops (faulted or unfaulted, vacancy or interstitial type).
5. Dislocation lines (unfaulted loops that have joined the dislocation network of the original microstructure).

6. Cavities (voids and helium bubbles).

7. Precipitates (in the case of stainless steel,  $M_{23}C_6$  carbides or intermetallic phases).

In this section theories that predict the increase in strength due to defects 3 through 7 in the list are presented. Point defects and impurity atoms are believed to contribute negligibly to hardening compared to the effect of the larger defect clusters.

Radiation strengthens a metal in two different ways: (1) It can increase the stress required to start a dislocation moving on its glide plane. Resistance to dislocation startup is called *source hardening*. The applied stress required to release a dislocation into its slip plane is called the *unpinning* or *unlocking* stress. (2) Once moving, dislocation can be impeded by natural or radiation-produced obstacles close to or lying in the slip plane. This is called *friction hardening*.

#### 18.4.1 Source Hardening

In unirradiated fcc metals, the stress required to initiate dislocation motion can be identified with the unpinning stress of the Frank-Read sources in the metal (Eq. 8.16), which is inversely proportional to the distance between pinning points.<sup>1</sup> The gradual onset of yielding characteristic of this class of metals can be explained by the distribution of stresses required to operate the sources. At low applied stress, the sources easiest to operate (i.e., those with large separation between pinning points) generate dislocations. Plastic strain ceases when pileups produce a back stress on the sources which stops their operation. As the stress is increased, more dislocation sources operate and the strain increases. The multiplication of dislocations in the crystal causes tangling of the moving dislocations, and additional applied stress is necessary for parallel dislocations to move past each other or for nonparallel dislocations to cut through each other. This process of work hardening causes the smooth increase in stress as a function of strain illustrated in Fig. 18.11.

Although source hardening is not found in unirradiated fcc metals and alloys, this phenomenon is common in bcc metals in the unirradiated state. Source hardening is manifest by upper and lower yield points in the stress-strain curve. Unirradiated ferritic steels show this effect quite clearly [Figs. 18.10 and 18.15(b)]. In fcc metals the yield drop that indicates the presence of source hardening is observed only after irradiation [Fig. 18.15(a)]. The development of source hardening in irradiated fcc metals is probably due to the irradiation-produced defect clusters in the vicinity of Frank-Read sources. These obstacles raise the stress required to expand the loops and to permit multiplication to continue, which is tantamount to increasing the stress required to operate the source. Once the stress level is sufficient to release the source, the moving dislocations can destroy the small defect clusters (loops) and thus reduce the stress needed to continue deformation. Therefore, a yield drop similar to that observed in unirradiated ferritic steel is found in irradiated austenitic steel but for a quite different reason. (The origin of source hardening in unirradiated ferritic steels is discussed in Sec. 18.12.)

### 18.4.2 Friction Hardening

The forces responsible for resisting the motion of a dislocation through the crystal can be characterized as long range or short range. The total applied shear stress necessary to move the dislocation is the sum of the long-range and short-range stresses:

$$\sigma_i = \sigma_{LR} + \sigma_s \quad (18.22)$$

where  $\sigma_i$  is the friction stress and the subscripts LR and s represent the long-range and short-range contributions, respectively. An increase in  $\sigma_i$  due to irradiation, to work hardening, or to aging is termed friction hardening. The friction stress is roughly equal to the true stress at any point in the plastic deformation region of the stress-strain plot.

#### Long-Range Stresses

The long-range forces<sup>2</sup> arise from the repulsive interaction between the moving dislocation and the components of the dislocation network of the solid. Although the dislocation network of a metal does not resemble a regular array, it is often represented as a series of cubes the edges of which are formed of dislocation lines. Figure 18.16 shows such an idealized dislocation network with a loop on a glide plane parallel to the top and bottom faces of the cube. The long-range forces are due to the interaction of the stress fields of the dislocation forming the loop and of the network dislocations that make up the edges of the top and bottom planes of the cube, which are parallel to the loop. For simplicity, assume that the interaction forces between the loop and the network dislocations parallel to it can be approximated by the force between parallel edge dislocations (Eq. 8.24). Setting  $f_x(\theta)$  equal to its maximum value of  $1/4$ , taking  $1 - \nu \approx 1/2$ , and approximating the distance between the loop and the nearest parallel network dislocation as one-half the cube side ( $y \approx 1/2$ ), we obtain the long-range force on the moving dislocation,

$$F_{LR} \approx \frac{Gb^2/4}{(2\pi)(1/2)(1/2)} = \frac{Gb^2}{2\pi}$$

The stress needed to overcome this force is  $F_{LR}/b$ ; thus,

$$\sigma_{LR} = \frac{Gb}{2\pi} \quad (18.23)$$

The dislocation network depicted in Fig. 18.16 is the same as that employed in the BUBL swelling code (Sec. 13.12). From Eq. 13.280, the length  $l$  is related to the dislocation density  $\rho_d$  by

$$l = \left( \frac{3}{\rho_d} \right)^{1/2} \quad (18.24)$$

Any process that increases the dislocation density of the material (e.g., cold working, unfauling of radiation-produced prismatic loops, or work hardening) decreases  $l$  and increases the long-range stress on mobile dislocations.

In addition to dislocations in the network, pileups of dislocations on slip planes parallel to the slip plane of an expanding loop can exert long-range forces capable of resisting and even stopping motion of the mobile dislocation (Fig. 8.18).

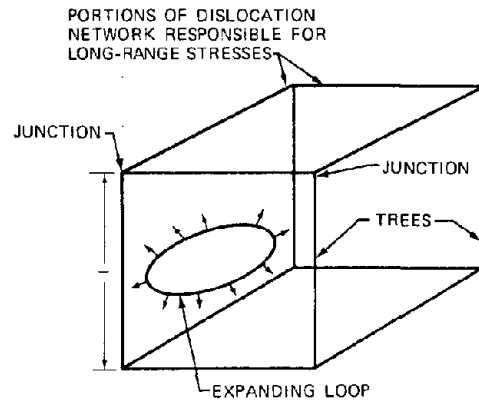


Fig. 18.16 Model of the dislocation network in a solid.

#### Short-Range Stresses

Short-range forces are due to obstacles that lie in the slip plane of the moving dislocation (these represent what are called *planar barriers*). The short-range forces are active only when the moving dislocation comes very close to or contacts the obstacle. Such obstacles exert a force on the moving dislocation only at the point of contact. Short-range forces can be further subdivided into athermal and thermally activated components. An athermal stress component is one whose magnitude is independent of temperature. Athermal mechanisms normally involve bowing of a dislocation around an impenetrable obstacle. In a thermally activated process, overcoming the obstacle usually requires that the moving dislocation cut through or climb over the barrier in its path. Inasmuch as passage of a dislocation line through or over an obstacle requires energy that can be partly supplied by thermal fluctuations, the thermally activated component of the short-range stresses decreases with increasing temperature.

The friction stress due to a dispersion of barriers depends on the average separation between the obstacles in the slip plane of the moving dislocation (not the average separation between obstacles in three dimensions). Figure 18.17 shows a unit area of a slip plane that is intersected by portions of spherical objects of radius  $r$  which are randomly

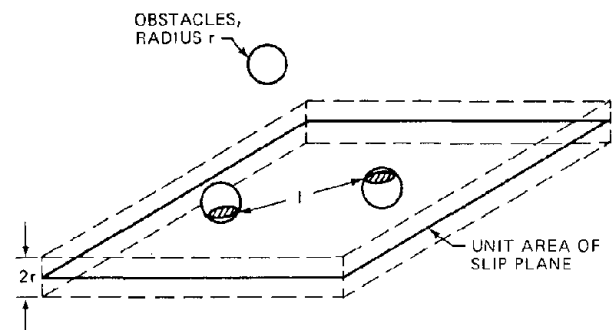


Fig. 18.17 The intersection of spherical obstacles with a slip plane to form an array of planar barriers.

distributed throughout the solid at a concentration  $N \text{ cm}^{-3}$ . Any sphere that has its center within the slab of volume  $2r$  centered on the slip plane intersects the slip plane. The number of obstacles in this volume element is  $2rN$ , which is also the number of intersections per unit area on the slip plane. Since the inverse square of the average obstacle spacing along the slip plane ( $l^2$ ) is equal to the density of intersections on the plane, we have

$$l^2 = \frac{1}{(2rN)^2} \quad (18.25)$$

### 18.5 HARDENING BY DEPLETED ZONES

At low temperatures and low fluences, the main microstructural effect of the neutron irradiation of steel is the production of depleted zones. The irradiation conditions that result in depleted-zone damage exclusively are most likely to be found in the region of the reactor pressure vessel. Core components are subject to high-temperature and high-fluence conditions that produce the larger defects listed at the beginning of Sec. 18.4. However, hardening due to depleted zones has been observed in both austenitic and ferritic steels at low temperature and low fast-neutron fluence. The effect of the depleted zones on mechanical properties can be classified as friction hardening of the short-range thermally activated type. A theory proposed by Seeger<sup>3</sup> for the radiation strengthening of metals due to the formation of depleted zones is reviewed in this section.

A dislocation line wending its way through a metal containing a uniform distribution of depleted zones is pressed against a number of these obstacles at all times. The plane of the drawing in Fig. 18.18(a) represents the slip plane of the dislocation, which is shown as the solid line pressed against the obstacles A, B, and C under the influence of the applied shear stress. According to Eq. 18.22, the net stress available for moving the dislocation through the metal is the difference between the applied stress ( $\sigma_i$ ) and the stress necessary to move the dislocation against the long-range forces of the dislocation network naturally present in the solid ( $\sigma_{LR}$ ). Thus, the dislocation segments between obstacles A, B, and C are acted on by a shear stress  $\sigma_s = \sigma_i - \sigma_{LR}$ . Because of this applied stress, dislocations move through the field of obstacles and thereby produce a macroscopic strain rate  $\dot{\epsilon}$  in the solid. However, the motion of each dislocation line is jerky rather than smooth, and the entire dislocation line does not move at the same time. The line progresses from the left to the right in Fig. 18.18(a) as points on the dislocation line cut through obstacles one at a time. Thus, the line is held up at points A, B, and C; but, with the help of thermal fluctuations, enough energy can be supplied for the line to penetrate the obstacle at B. When this event occurs, the line quickly moves to the position shown by the dashed line, where it is pressed against obstacles A, D, and C. The area of the slip plane sheared by this elementary step is shown as the dotted zone.

In general, the distance  $l_0$  between pinning points is greater than the average separation of obstacles in the slip plane ( $l$  given by Eq. 18.25). The distance that the dislocation advances when the obstacle B is cut is denoted

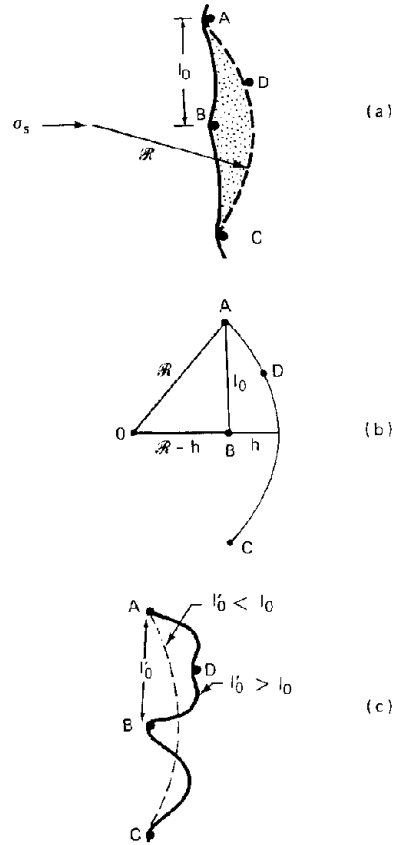


Fig. 18.18 A dislocation line pressed against depleted zones in its slip plane. A, B, C, and D are pinning points.

by  $h$  in Fig. 18.18(b). In any array of points on a plane, the larger  $l_0$  is, the smaller  $h$  is. In fact, the distances  $l$ ,  $l_0$ , and  $h$  are related by (see problem 18.3):

$$l^2 = hl_0 \quad (18.26)$$

The value of  $l_0$  is determined by the requirement that the curvature of each segment of the dislocation line between pinning points is at all times fixed by the balance between line tension of the dislocation and the net applied stress. Equation 8.15 shows that the radius of curvature of the line under applied shear stress  $\sigma_{xy} = \sigma_s$  is

$$R = \frac{Gb}{\sigma_s}$$

The geometry of Fig. 18.18(b) shows that

$$R^2 = l_0^2 + (R - h)^2$$

Combining the preceding three equations and assuming  $h/2R \ll 1$ , we obtain

$$l_0 = \left( \frac{2Gb l^2}{\sigma_s} \right)^{1/2} \quad (18.27)$$

According to this formula, the dislocation line adjusts its orientation in the slip plane according to the applied stress;

it selects positions where the separation between pinning points satisfies Eq. 18.27. The means by which this spacing is attained is illustrated in Fig. 18.18(c), which shows the shapes assumed by the line when the actual pinning point spacing  $l'_0$  does not satisfy Eq. 18.27.

When  $l'_0 < l_0$ , the equilibrium bowing of the line after it cuts the obstacle B is shown as the dashed line in Fig. 18.18(c). In this case, the next obstacle, D, is not reached. Because the line remains between the points B and D, the value of  $l'_0$  effectively has been doubled, a change that is in the proper direction for rectifying the inequality  $l'_0 < l_0$ .

When  $l'_0 > l_0$ , the dislocation line bows out and touches obstacle D before cutting obstacle B. Therefore, ADBC, not ABC, is the stable configuration of the line before any obstacle is cut. In the solid curve shown in the figure,  $l'_0$  is approximately equal to the distances AD or BD, both of which are smaller than the original  $l'_0 = AB$ . Again, the line rearranges its position in a manner that tends to drive the interobstacle distance toward the value expressed by Eq. 18.27.

There is a stress above which Eq. 18.27 is no longer valid. When  $\sigma_s$  is large enough for  $l_0 = l$ , Eq. 18.27 shows that  $\sigma_s = 2Gb/l$ . We shall see later that this stress is the critical stress at which a dislocation line can move through an array of obstacles solely by bowing around them. Cutting through the obstacle is no longer a prerequisite to motion.

We next compute the shear strain rate due to the type of dislocation motion described above. The strain rate is given by Eq. 8.21:

$$\dot{\epsilon} = \rho b v_d \quad (18.28)$$

where  $\rho$  is the density of mobile dislocations (total dislocation density less the density of dislocations comprising the immobile network) and  $v_d$  is the velocity of the moving dislocations. This velocity is

$$v_d = h\Gamma \simeq l\Gamma \quad (18.29)$$

where  $\Gamma$  is the probability per unit time that one segment cuts through an obstacle against which it is pressed. For the purpose of computing the dislocation velocity, the distinction between  $l$  and  $l_0$  has been neglected. If  $l \simeq l_0$ , Eq. 18.26 shows that  $h \simeq 1$ .

The cutting frequency  $\Gamma$  is calculated by analogy to the jump frequency of an atom jumping from one equilibrium site to another over the saddle-point energy barrier. To penetrate an obstacle, the segment of the dislocation line in contact with the obstacle must acquire an activation energy  $U^*$ , which is supplied by thermal fluctuations. The dislocation line at the obstacle can be imagined to be vibrating with a frequency  $\nu$ , striking the obstacle at each vibration. The fraction of the vibrations sufficiently strong to penetrate the obstacle is, by analogy to the atomic jump-frequency formula (Eq. 7.41), given by

$$\Gamma = \nu \exp\left(-\frac{U^*}{kT}\right) \quad (18.30)$$

Substituting Eqs. 18.29 and 18.30 into Eq. 18.28 gives the strain rate:

$$\dot{\epsilon} = \rho l b \nu \exp\left(-\frac{U^*}{kT}\right) \quad (18.31)$$

The depleted zones are modeled as spheres each of radius  $r$  (equal to  $\sim 10 \text{ \AA}$ ). The energy  $U^*$  is the energy required for the dislocation to cut through the approximately circular region on the slip plane which is intersected by the spherical depleted zone. The shaded circles in Fig. 18.17 depict these intersections. In the absence of applied stress, the variation of the energy with the distance of penetration of the line through the zone resembles the sketch shown in Fig. 18.19(a). The energy rises by an amount  $U_0$  from the point of contact of the line and the zone to the point at which cutting is complete. The average radius of the circle of intersection of the depleted zone and the slip plane is smaller than the radius of the spherical zone proper because the slip plane in general does not pass through the center of the depleted zone (Fig. 18.17). The average radius of the circle of intersection of the zone and the slip plane is (see problem 10.5)

$$r' = \left(\frac{2}{3}\right)^{1/2} r \quad (18.32)$$

At any point  $-r' \leq x \leq r'$ , the force resisting dislocation motion is  $-dU/dx$ .

When an applied stress acts on the slip plane, the energy profile is altered as shown in Fig. 18.19(b). The shear stress exerts a force of magnitude  $\sigma_s b$  per unit length of dislocation line in the  $+x$ -direction. Since the obstacles are

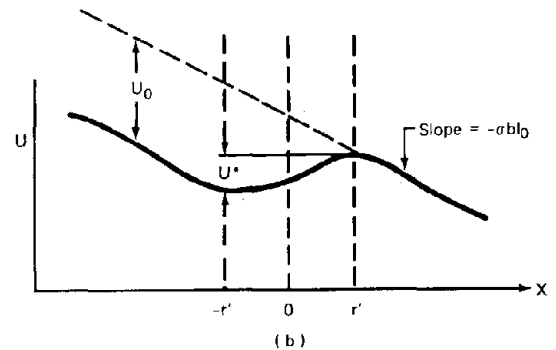
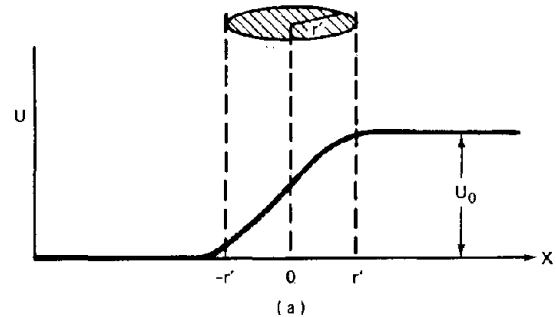


Fig. 18.19 Energy profiles of a dislocation line cutting through a depleted zone. (a) No stress. (b) Shear stress in the  $x$ -direction. (From Ref. 3.)

separated by a distance  $l_0$ , the force exerted by the applied stress on each obstacle is  $\sigma_s b l_0$ . Let  $U(x, \sigma_s)$  be the shape of the energy profile in Fig. 18.19(b) and  $U(x, 0)$  be the shape in the absence of applied stress. When a stress is applied, the force at every point during penetration is given by

$$-\frac{d}{dx} U(x, \sigma_s) = -\frac{d}{dx} U(x, 0) + \sigma_s b l_0$$

That is, the force in the absence of the stress (the first term on the right-hand side) is reduced by the contribution of the applied stress (the last term). Integrating this equation gives

$$U(x, \sigma_s) = U(x, 0) - \sigma_s b l_0 x + \text{constant} \quad (18.33)$$

Inspection of Fig. 18.19(b) shows that the energy barrier to penetration with an applied stress is reduced from  $U_0$  to

$$U^* = U(r', \sigma_s) - U(-r', \sigma_s) \quad (18.34)$$

To calculate  $U^*$ , we must know the energy profile of Fig. 18.19(a). Seeger assumes it to be of the form

$$U(x, 0) = U_0 \left[ 1 - \frac{1}{1 + \exp(x/r')} \right] \quad (18.35)$$

The exact functional form of  $U(x, 0)$  is not important; it simply must have the approximate shape of the curve shown in Fig. 18.19(a), which Eq. 18.35 has. Substituting Eq. 18.35 into 18.33 and forming the difference on the right of Eq. 18.34 yields the following expression for  $U^*$  (see problem 18.3 for details):

$$U^* = U_0 \left( 1 - \frac{4\sigma_s b l_0 r'}{U_0} \right)^{3/2} \quad (18.36)$$

When  $\sigma_s$  is large enough to render the right-hand term in the parentheses of this formula larger than unity, the dislocation can cut through the depleted zone without any assistance from thermal fluctuations. The stress  $\sigma_s^0$  at which the term on the right in the parentheses is equal to unity reduces the barrier height  $U^*$  to zero. Thus,  $\sigma_s^0$  represents the stress required to move dislocations through the obstacles at 0°K. Using Eq. 18.27 for  $l_0$ , Eq. 18.32 for  $r'$ , and Eq. 18.25 for  $l$ , we find

$$\sigma_s^0 = \left[ \frac{U_0}{4 \left( \frac{2}{3} \right)^{3/2}} \right]^{1/2} \frac{1}{b^2 G^{1/2}} \frac{N^{1/2}}{r} \quad (18.37)$$

where  $\sigma_s^0$  is the maximum frictional hardening due to depleted zones of radius  $r$  present in the solid at a volumetric concentration  $N$ .

The effect of temperature on depleted-zone hardening can be obtained by solving Eq. 18.31 for  $U^*$  and equating the result to the right-hand side of Eq. 18.36. Eliminating  $l_0$ ,  $r'$ , and  $l$  as before, we obtain

$$\sigma_s = \sigma_s^0 \left[ 1 - \left( \frac{T}{T_c} \right)^{3/2} \right]^{1/2} \quad (18.38)$$

where  $\sigma_s^0$  is given by Eq. 18.37 and  $T_c$  is a characteristic temperature given by

$$T_c = \frac{U_0}{k \ln [\rho b \nu / \dot{\epsilon} (2rN)^{1/2}]} \quad (18.39)$$

and is not truly constant because it depends on the strain rate  $\dot{\epsilon}$  at which the metal is deforming and on the concentration of depleted zones,  $N$ , which increases with irradiation time. However, these quantities appear in a logarithmic term, and the effect of their variation on  $T_c$  is small enough to be neglected.

The stress  $\sigma_s$  of Eqs. 18.37 to 18.39 represents the radiation hardening due to depleted zones. At temperatures below  $\sim 350^\circ\text{C}$  in steel,  $\sigma_s$  is manifest experimentally as the increase in the yield point due to irradiation on the stress-strain curves shown in Fig. 18.15. The hardening effect given by Eq. 18.38 decreases with increasing temperature and disappears entirely for  $T > T_c$ . At temperatures around  $350^\circ\text{C}$  in steel, depleted-zone hardening decreases even more rapidly with increasing temperature than the prediction of Eq. 18.38. In the postirradiation tensile tests that are usually used to measure hardening, high testing temperatures cause annealing (i.e., destruction) of the depleted zones, which results in a decrease in  $N$  with increasing temperature.

Seeger's theory has been verified experimentally.<sup>4</sup> Figure 18.20 shows the frictional hardening effect of low-fluence low-temperature neutron irradiation on copper and nickel. Both sets of data are plotted on coordinates suggested by Eq. 18.38. The predicted linear relationship between  $(\sigma_s)^{2/3}$  and  $T^{2/3}$  is exhibited with high precision by copper. The curve for nickel, however, shows two distinct

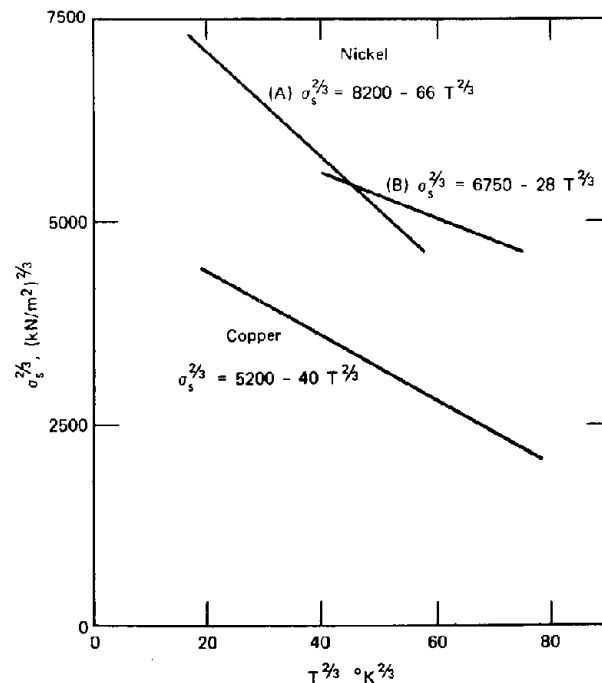


Fig. 18.20 Irradiation hardening of copper and nickel plotted according to Seeger's theory. Fluence,  $7 \times 10^{19}$  neutrons/cm<sup>2</sup>; irradiation temperature,  $100^\circ\text{C}$ ; test temperatures,  $-200$  to  $200^\circ\text{C}$ . (From Ref. 4.)

linear segments, which suggests that two types of depleted zones are created by irradiation. The type that predominates at low temperature (type A) apparently has a lower  $U_0$ , and hence lower  $T_c$ , than does type B (see Eq. 18.39). To a first approximation,  $U_0$  can be considered to be proportional to the area of the circle of intersection of the depleted zone with the slip plane, or  $U_0 \propto r^2$ . However, type A zones must be created more frequently by neutron collisions with the metal lattice than type B zones, since the hardening at 0°K is greater for type A than type B. In general, a spectrum of zones with continuous distributions of size  $r$  and energy barrier  $U_0$  is probably formed by irradiation.

Additional support for Seeger's theory has been obtained by comparing hardening due to neutrons and 4-MeV electrons.<sup>5</sup> The irradiation temperature and the range of tensile-test temperatures were identical for both types of radiation, and the doses were adjusted to produce the same number of Frenkel pairs as calculated by simple cascade theory (Chap. 17). The hardening due to electrons was found to be very small compared to that from neutrons. Using the two-body kinematics appropriate to relativistic electrons, we can show that each 4-MeV electron can transfer a maximum of 66 eV to a copper knock-on. According to the Kinchin—Pease model, this energy transfer produces a cascade consisting of only two or three members. Thus displacement spikes (or depleted zones) cannot be formed by electron irradiation, and the damage consists of isolated vacancies and interstitials. These defects anneal out at very low temperatures (interstitials are mobile at a few tens of °K). By way of contrast, the depleted zones are thermally stable up to ~350°K. In addition, isolated point defects are not as efficient strengtheners as is a vacancy cluster. The virtual absence of radiation hardening due to electron irradiation supports the hypothesis that the depleted zones are real and are responsible for strengthening of metals at low temperatures.

### 18.5.1 Saturation of Radiation Hardening

According to Eq. 18.37,  $\sigma_s$  should increase as  $(N)^{1/2}$ . In the absence of mechanisms of destruction of the depleted zones,  $N$  is proportional to the total neutron fluence, and the theory at this stage predicts that

$$\sigma_s \propto (\Phi t)^{1/2} \quad (18.40)$$

Two models have been proposed to explain the observation that hardening does not follow this formula at high fluence. Both of these theories introduce processes that remove depleted zones and thereby permit a steady-state value of  $N$  to be attained at large fluence.

### 18.5.2 Makin's Theory

Makin and Minter<sup>4</sup> postulate the existence of a volume  $v$  around each depleted zone within which no new zone can be formed. This notion appears to be contrary to the computer experiments simulating radiation damage, which showed that cascade overlap causes the zone to grow (Fig. 17.30). However, a single large zone created by, say,  $n$

displacement spikes in a localized region can be a less effective hardener than  $n$  smaller, isolated zones.

To predict the increase of the depleted-zone concentration with fluence, the rate of production of zones must be estimated. There are  $\Sigma_s \Phi$  neutron collisions  $\text{cm}^{-3} \text{sec}^{-1}$  with lattice atoms, where  $\Sigma_s$  is the macroscopic scattering cross section and  $\Phi$  is the total fast flux. If the average fast-neutron energy is 0.5 MeV (typical of FBR spectra) and  $A = 56$  (iron), Eq. 17.114 shows that the average energy of the knock-ons is ~20 keV. The depleted zone responsible for radiation hardening is believed to be restricted to clusters containing 10 or more vacancies. The distribution of vacancy-cluster sizes resulting from knock-ons of 20 keV is shown in Fig. 17.29(b). The number of point defects included in the cluster distribution shown in this figure is ~200, of which ~5%, or ~10 vacancies, are contained in a cluster of >10 members. Therefore, one cluster containing more than 10 vacancies is formed by the average fast-neutron collision in iron. The time rate of change of the density of clusters of this size is given by

$$\frac{dN}{dt} = \alpha \Sigma_s \Phi (1 - vN)$$

where  $\alpha$  is the number of clusters (zones) created per neutron collision. It is approximately unity. The term in parentheses represents the fraction of the solid volume which, according to Makin's theory, is available for the creation of new depleted zones. The fraction  $vN$  of the volume is inactivated by the presence of the depleted zones. Integration of the preceding differential equation yields

$$N = \frac{1}{v} [1 - \exp(-\alpha v \Sigma_s \Phi t)] \quad (18.41)$$

which, when used in Eq. 18.37, predicts

$$\sigma_s \propto [1 - \exp(-\alpha v \Sigma_s \Phi t)]^{1/2} \quad (18.42)$$

The capture volume  $v$  has been estimated from radiation-hardening data to be between 50 and 80 Å equivalent spherical diameter.<sup>6</sup> This size can be compared with the estimated 20-Å diameter of the depleted zone proper, which occupies the center of the capture volume.

### 18.5.3 Thermal Annealing of Depleted Zones

We have mentioned that thermal annealing is a potential mechanism for destroying depleted zones. Dollins<sup>7</sup> has presented an analysis of depleted-zone dynamics which includes thermal annealing. The object is to predict the concentration of depleted zones as a function of neutron fluence and temperature. It is assumed that one depleted zone of radius  $R_0$  is formed per neutron collision with a lattice atom. Once formed, the zone serves as a sink for free vacancies and interstitial atoms that are created along with the depleted zones in the collision cascade. Because the zone can absorb point defects that reach it by diffusion, there will be a size distribution of zones,  $N(R,t)$ , at any time  $t$  during irradiation. The conservation of depleted zones can be formulated in a manner similar to that applied to determine the size distribution of fission-gas bubbles in the fuel, which grow by absorption of atomically dispersed xenon and krypton (Sec. 13.9). This type of conservation

statement, which focuses on a fixed particle-size interval and equates the difference in fluxes across the boundaries of the interval to the time derivative of the particle concentration, is appropriately termed *Eulerian*. In many cases an equally acceptable conservation principle can be formulated in a *Lagrangian* manner by following a small group of particles from the time they are created up to current time. The size of the particle as it ages is determined by a growth law,  $dR/dt$ , which is appropriate to the particular system. For example, the growth law for a cavity in a solid supersaturated with point defects is given by Eq. 13.171. This growth law can be applied to the depleted zones:\*

$$\dot{R} = \frac{dR}{dt} = -\frac{\Omega}{R} [D_i C_i - D_v (C_v - C_{vR})]$$

The very low equilibrium interstitial concentration permits  $C_{iR}$  to be neglected. The vacancy concentration at the surface is obtained by treating the zone as a small void, for which the  $C_{vR}$  is obtained from Eq. 13.176 with the internal-gas-pressure term neglected:†

$$C_{vR} = C_v^{eq} \exp\left(\frac{2\gamma\Omega}{RkT}\right)$$

Combining these equations yields

$$\dot{R} = -\frac{\Omega}{R} \left\{ D_i C_i - D_v \left[ C_v - C_v^{eq} \exp\left(\frac{2\gamma\Omega}{RkT}\right) \right] \right\} \quad (18.43)$$

The steady-state point-defect balances that serve to fix  $C_v$  and  $C_i$  are similar to Eqs. 13.186 and 13.187. For this calculation the defect production rates are determined in the following manner. Because some of the vacancies produced in the collision cascade initiated by a fast neutron are contained in the depleted zone formed at the same time as the free point defects, the yield  $Y_{vi}$  is replaced by  $\nu_i$  interstitials and  $\nu_v$  free vacancies per primary knock-on atom (PKA). These quantities are related to the size of the nascent depleted zone (only one is assumed formed per neutron collision) by

$$\nu_i = \nu_v + \frac{4\pi R_0^3/3}{\Omega} \quad (18.44)$$

\*In the growth law used by Dollins,<sup>7</sup> the second term in the brackets appears multiplied by  $R/a_0$ , where  $a_0$  is the lattice constant. This difference arises from the assumption of reaction-rate-controlled vacancy capture by the depleted zone instead of the diffusion-limited capture assumed in this equation. Comparison of Eqs. 13.70 and 13.95 shows that these two limiting rates differ by a factor of  $R/a_0$ . The interstitial capture rate by the zone (the first term in the growth law), on the other hand, is taken by Dollins to be diffusion controlled. For consistency, we will assume diffusion-limited kinetics for both types of point-defect capture by the depleted zones. The mixed control formula, Eq. 13.96, is probably most appropriate because of the small zone radii but, for simplicity, will not be employed.

†The argument of the exponential term of  $C_{vR}$  in Dollins' analysis<sup>7</sup> is the difference between the vacancy-formation energy and the binding energy of a vacancy to the depleted zone. If the zone is large enough to be treated as a macroscopic cavity, the capillarity formulation used above is applicable.

where  $\nu_i$  is computed from isolated cascade theory (e.g., the Kinchin—Pease model) and reduced by the vacancy—interstitial annihilation that takes place during cascade formation. In Dollins' analysis  $\nu_i$  is estimated to be 10% of the Kinchin—Pease value.

The PKA production rate on the left in Eqs. 13.186 and 13.187 (i.e., what has been termed  $\dot{F}$  when the bombarding particles are fission fragments) is written as  $\Sigma_s \Phi$ , the fast-neutron collision density.

The numbers  $Z_i$  and  $Z_v$  in Eqs. 13.186 and 13.187 are given by the last terms of Eqs. 13.182 and 13.183. Neglecting the first terms on the right-hand sides of these formulas is equivalent to assuming that point-defect absorption by dislocations is purely diffusion controlled. The dislocation-core radius is assumed to be the same for vacancies and interstitials (i.e.,  $Z_i = Z_v = Z$ ).

The interstitial supersaturation is assumed large enough to neglect  $C_i^{eq}$  compared to  $C_i$ .

Finally, Eqs. 13.186 and 13.187 are supplemented by additional terms representing the absorption of point defects by the depleted zones, and the point-defect balances become

$$\nu_i \Sigma_s \Phi = Z \rho_d D_i C_i + k_{iv} C_i C_v + \int_0^{R_0} 4\pi D_i R C_i N(R,t) dR \quad (18.45a)$$

$$\nu_v \Sigma_s \Phi = Z \rho_d D_v (C_v - C_v^{eq}) + k_{iv} C_i C_v + \int_0^{R_0} 4\pi D_v R \times \left[ C_v - C_v^{eq} \exp\left(\frac{2\gamma\Omega}{RkT}\right) \right] N(R,t) dR \quad (18.45b)$$

The integrals are terminated at  $R = R_0$  because the zones shrink rather than grow; so the newly created zones are the largest in the distribution.

The size distribution of depleted zones can be determined as follows. The zones in the size range  $R$  to  $R + dR$  at time  $t$  are those which were created (at size  $R_0$ ) in a previous time interval  $d\tau$  at  $\tau$ , or

$$N(R,t) dR = \Sigma_s \Phi d\tau \quad (18.46)$$

This conservation statement is equivalent to conserving depleted zones in a fixed size range (e.g., by adapting Eq. 13.196 to depleted zones). Using the preceding reaction, we obtain the distribution function:

$$N(R,t) = \Sigma_s \Phi \left| \frac{\partial \tau}{\partial R} \right|_t$$

The shrinkage law is employed to determine the ratio of the intervals  $d\tau$  and  $dR$  (i.e., the Jacobian of the transformation between  $R$  and  $\tau$ ). The value  $R$ , which is the radius at time  $t$  of a zone created at time  $\tau$ , can be obtained by integrating Eq. 18.43 provided that only the steady-state situation is considered. In this case  $C_i$  and  $C_v$  are constants and  $\dot{R}$  is a function of  $R$  alone. Integration yields

$$\int_{R_0}^R \frac{dR'}{\dot{R}} = \int_{\tau}^t dt' = t - \tau \quad (18.47)$$

Differentiating with respect to  $R$  yields

$$\left| \frac{\partial \tau}{\partial R} \right|_t = -\frac{1}{R}$$

and the distribution function of zones at steady state is

$$\begin{aligned} N(R) &= \frac{\Sigma_s \Phi}{R} \\ &= \frac{\Sigma_s \Phi}{\Omega} \frac{R}{D_i C_i - D_v \left[ C_v - C_v^{eq} \exp\left(\frac{2\gamma \Omega}{R kT}\right) \right]} \end{aligned} \quad (18.48)$$

Note that analytic integration of the shrinkage law cannot be performed in the unsteady state when  $C_i$  and  $C_v$  are time dependent.

Subtracting Eq. 18.45b from Eq. 18.45a and using Eq. 18.44 yields

$$\begin{aligned} \left( \frac{4}{3} \pi R_0^3 \right) \frac{\Sigma_s \Phi}{\Omega} &= Z \rho_d [D_i C_i - D_v (C_v - C_v^{eq})] \\ &+ 4\pi \int_0^{R_0} \left\{ D_i C_i - D_v \left[ C_v \right. \right. \\ &\left. \left. - C_v^{eq} \exp\left(\frac{2\gamma \Omega}{R kT}\right) \right] \right\} R N(R) dR \end{aligned}$$

Substituting Eq. 18.48 into this equation, we find that the left-hand side is identical to the second term on the right, which leads to the following relation between  $C_i$  and  $C_v$ :

$$D_i C_i - D_v (C_v - C_v^{eq}) = 0 \quad (18.49)$$

and Eq. 18.48, after the exponential term is expanded in a two-term Taylor series, simplifies to

$$N(R) = \frac{\Sigma_s \Phi R^2}{D_v C_v^{eq} \Omega^2 (2\gamma/kT)} \quad (18.50)$$

The total density of depleted zones at steady state is obtained by integrating the distribution  $N(R)$ ,

$$N = \int_0^{R_0} N(R) dR = \frac{\Sigma_s \Phi R_0^3}{3 D_v C_v^{eq} \Omega^2 (2\gamma/kT)} \quad (18.51)$$

If desired, the concentrations  $C_i$  and  $C_v$  can be determined by inserting Eqs. 18.49 and 18.50 into either of the point-defect balances (Eq. 18.45a or Eq. 18.45b) and solving for one of the point-defect concentrations. Equation 18.49 then determines the other.

Dollins<sup>7</sup> treated the unsteady-state case of depleted-zone formation and annealing, of which the preceding analysis represents the limit as  $t \rightarrow \infty$  (saturation). The variation of the depleted-zone concentration according to Dollins' thermal-annealing model is compared with Makin's capture-volume mechanism (Eq. 18.41 with a capture volume equivalent to a 75-Å diameter sphere) in Fig. 18.21. The agreement between the saturation-zone densities predicted by the two methods is somewhat fortuitous, inasmuch as the  $N(\infty)$  predicted by Makin's theory is inversely proportional to the cube of the capture-volume radius. Even with  $v$  taken to give approximately equal saturation concentrations from the two models, the

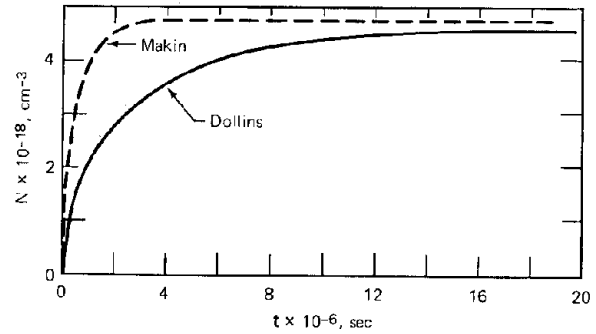


Fig. 18.21 Approach to saturation of the concentration of depleted zones in an irradiated metal. For Makin's model the capture volume has been assumed to be 75 Å in diameter. The following parameters were used in Dollins' computation:  $D_v = 0.38 \exp(-117,000/RT)$  cm<sup>2</sup>/sec;  $D_i = 7.5 \times 10^{-4} \exp(-29,000/RT)$  cm<sup>2</sup>/sec;  $r_d = 3.23$  Å;  $\Omega = 24$  Å<sup>3</sup>;  $\Sigma_s = 0.16$  cm<sup>-1</sup>;  $C_v^{eq} = \exp(-117,000/RT)/\Omega$  cm<sup>-3</sup>;  $R_0 = 7.95$  Å;  $\Phi = 10^{14}$  neutrons cm<sup>-2</sup> sec<sup>-1</sup>;  $T = 573^\circ\text{K}$ ;  $\rho_d = 5 \times 10^{10}$  cm<sup>-2</sup>;  $\gamma = 250$  dynes/cm; and  $\nu_i = 90$ . Activation energies in J/mole.

thermal-annealing analysis predicts a much slower approach to saturation than does Makin's simpler model. The reason for this is the built-in time lag in the annealing calculation due to the necessity of diffusing point defects to the zones to make the zones shrink. Makin's capture-volume calculation, on the other hand, provides a mechanism for instantaneous reduction in the rate of zone formation.

The thermal-annealing computation is extremely sensitive to the value of  $R_0$  selected. The  $N(\infty)$  is temperature insensitive in Makin's analysis but is very sensitive to temperature if thermal annealing is responsible for depleted-zone destruction. A drastic drop in the steady-state concentration of zones is calculated to occur between 300 and 450°C, although this result is also highly dependent on input parameters in the annealing analysis.

## 18.6 HARDENING BY IMPENETRABLE OBSTACLES—PRECIPITATES AND VOIDS

Often the barriers that lie in the glide plane of a moving dislocation cannot be cut by the dislocation as could the depleted zones. A dislocation line moves through a field of impenetrable obstacles by bowing around them. The increased strength produced by obstacles of this sort is often exploited in the metal treatment called precipitation hardening. Neutron irradiation can precipitate  $M_{23}C_6$  carbides or hard intermetallic phases consisting of the major components of steel (e.g., the sigma phase).

There is usually a misfit between the precipitate particle and the matrix in which the particle is lodged. If the precipitate volume is larger than the metal it replaced, the particle acts as a point center of compression and creates a stress field in the surrounding solid. A dislocation "feels" the presence of such a particle (which is called a *coherent*

precipitate) via the stress field before actual contact is made. On the other hand, if the precipitate occupies a smaller volume than the material that has been replaced, there are no internal stresses in the solid around the foreign particle. For these *incoherent* precipitates, the dislocation must physically contact the particle before the interaction force is appreciable.

Figure 18.22(a) illustrates a mechanism by which a moving dislocation line (or a portion of an expanding

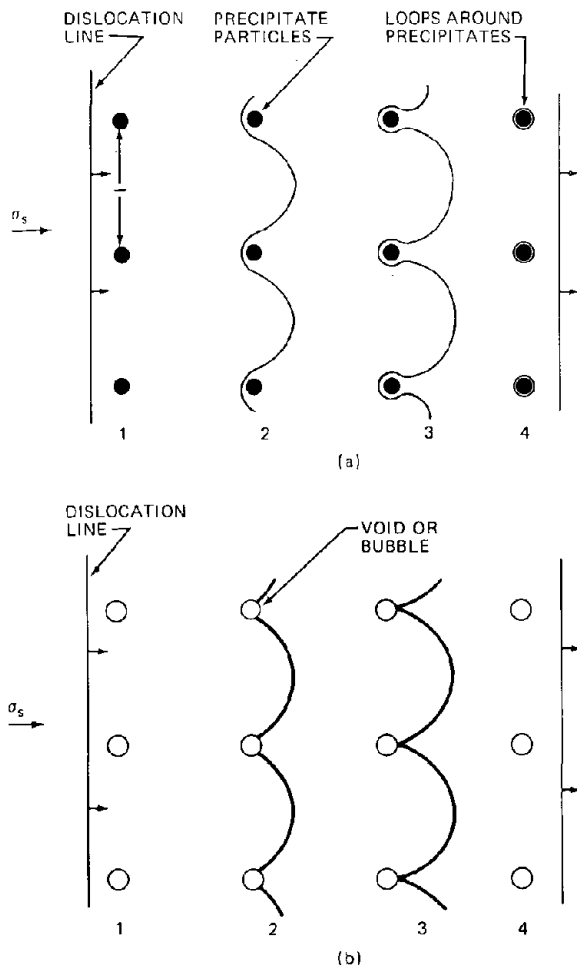


Fig. 18.22 Passage of a dislocation through an array of barriers intersecting the glide plane of the dislocation. (a) Precipitate particles. (b) Cavities (voids or helium bubbles).

dislocation loop) negotiates an array of precipitate particles in its glide plane. Four stages of the process are shown in the drawing. Having been stopped by the particles (1), the line bows out between contact points because of the effective stress, which is the applied shear stress less the internal stresses due to long-range forces (2). When the applied stress is high enough to result in a radius of curvature of the bowed segments which is equal to one-half the interparticle spacing, the semicircular sections on either side of a particle meet (3) and pinch off, in much the same

manner as a Frank-Read dislocation source operates (Fig. 8.13). The final state (4) is a free dislocation line and precipitate particles surrounded by small dislocation rings left as debris of the interaction.

At the pinch-off point,  $R$  in Eq. 8.15 is  $l/2$ , and the stress needed to force passage of a dislocation line through the obstacle array is:

$$\sigma_s = \frac{2Gb}{l} \quad (18.52)$$

The factor of 2 arises because the line tension of the dislocation has been taken as  $Gb^2$ . Had the line tension been given by  $Gb^2/2$ , the factor of 2 would not appear. The particle-separation distance on the glide plane,  $l$ , is given by Eq. 18.25, in which  $N$  is the volumetric concentration of precipitate particles and  $r$  is their radius.

Equation 18.52, which is called the Orowan stress, is the largest possible resistance to dislocation motion for an array of barriers of planar spacing  $l$ . It has been derived assuming a regular pattern of obstacle intersections with the glide plane. If the array were random (as it actually is), the Orowan stress would be reduced by  $\sim 20\%$ . This reduction, however, is less than the factor of 2 uncertainty in the numerical coefficient of Eq. 18.52.

Passage of a mobile dislocation line through solid containing cavities (voids or helium bubbles) that intersect the glide plane is shown in Fig. 18.22(b). The only difference between the precipitate particles and the cavities as obstacles is that the bowed arcs of the dislocation line meet the surface of the cavity at right angles. The critical stress required to move the dislocation is identical to that derived for the coherent precipitate. Unlike the precipitate, no dislocation rings decorate the cavity after the process is complete. A more detailed account of void hardening is given by Coulomb.<sup>8</sup>

In addition to bowing and pinching off, a dislocation may be able to cut through a cavity as it does through a depleted zone.<sup>9</sup> If the dislocation is capable of cutting through the cavity, the structure of the dislocation and the void are the same after the event as before. Therefore, the interaction energy between these two objects as a function of their separation is symmetric about the overlapping position, instead of having the shape shown in Fig. 18.19(a) for dislocations cutting through depleted zones. Aside from this distinction, the stress required to force a dislocation through a void can be obtained by the method applied in Sec. 18.5 to analyze cutting of a depleted zone (see problem 18.3). If the maximum interaction energy between the dislocation and the void is  $U_0$ , the stress to cut through is

$$\sigma_s = \frac{U_0}{blR}$$

where  $R$  is the radius of the cavity. The interaction energy  $U_0$  can be approximated as the elastic strain energy contained in the volume of solid equal to the cavity volume and centered on the line. This strain energy is released when the cavity attaches to the line and must be supplied to separate the two. The elastic-energy density around a screw dislocation is given by Eq. 8.8. Instead of integrating this expression over the volume of a sphere centered on the

dislocation, we replace the sphere with a cylinder of radius  $R$  and length  $2R$ . The total elastic energy contained in this volume (which is the void-dislocation interaction energy) is

$$U_0 = 2R \int_{r_d}^R 2\pi r E_{e1} dr = \frac{R G b^2}{2\pi} \ln\left(\frac{R}{r_d}\right)$$

Combining the preceding two formulas gives the stress required for a dislocation to cut through a void or bubble:

$$\sigma_s = \frac{G b \ln(R/r_d)}{1} \frac{1}{2\pi} \quad (18.53)$$

which differs from the Orowan stress (Eq. 18.52) by a factor of  $\ln(R/r_d)/4\pi$ . It appears that it should be easier for dislocations to cut rather than bypass small cavities, but the stress requirements for the two mechanisms are so close and the analyses so approximate that use of the Orowan stress is the more prudent approach.

## 18.7 LOOP HARDENING

The dislocation loops formed by condensation of irradiation-produced interstitial atoms are either of the pure-edge type if the loop is faulted or of mixed-edge and screw character if the loop is unfaulted. If the glide plane of a mobile dislocation passes close to or intersects a loop, dislocations on the plane will experience a resistance to motion. To exert a significant retarding force on the mobile dislocation, the center of the loop must lie close to the glide plane (say within a loop diameter). Since the loop diameter is generally much less than the distance between loops on the slip plane, each loop is viewed as exerting a force on the dislocation line only at the point at which contact is made. The applied shear stress needed to overcome the loop resistance corresponds to the maximum force,  $F_{max}$ , between the loop and the dislocation line. If the spacing of the loops on the glide plane is  $l$ , the retarding force per unit length experienced by the line is  $F_{max}/l$ . The oppositely directed force on the line due to the applied shear stress is  $\sigma_s b_e$ , where  $b_e$  is the Burgers vector of the mobile dislocation. If all loops exerted the same maximum force on the mobile dislocations in the solid, a sharp yield point would be expected when  $\sigma_s b_e$  equalled or exceeded  $F_{max}/l$ . More precisely, the increase in the yield stress of the metal due to the presence of the loops (loop hardening) is given by

$$\sigma_s = \frac{F_{max}}{b_e l} \quad (18.54)$$

The calculation of  $\sigma_s$  can be performed in two steps:

1. Calculation of  $F_{max}$ , which characterizes the interaction of a single loop and the dislocation line.
2. Calculation of the distance  $l$  between loop intersections with the glide plane.

Calculation of  $F_{max}$  is of necessity approximate owing to the large number of orientations of a circular loop with respect to a particular glide plane and the different possible Burgers vectors of both the loop and the mobile dislocation. Since the loop is a circular dislocation, classical

elasticity theory is often used to describe the loop-dislocation-line interaction. This procedure, however, is of dubious validity when the line actually cuts the loop. Calculation of the purely elastic interaction between a straight, rigid dislocation line that passes near to, but does not intersect, an immobile circular loop is presented in this section as an example of the type of analysis needed to provide  $F_{max}$ . The results for intersecting loops and lines are of the same general form as those obtained from long-range elastic interactions.

Figure 18.23 shows a long, straight edge dislocation whose slip plane lies a distance  $y$  from the plane of a circular loop of pure-edge character. We wish to compute the force  $F_x$  between the two entities as a function of the distance  $x$ . To do so, we first calculate the work required to grow the loop from zero size to radius  $R_1$ . We then differentiate this work with respect to  $x$  to obtain  $F_x$ . Calculations of this sort have been performed for a variety of loop/line combinations.<sup>10</sup>

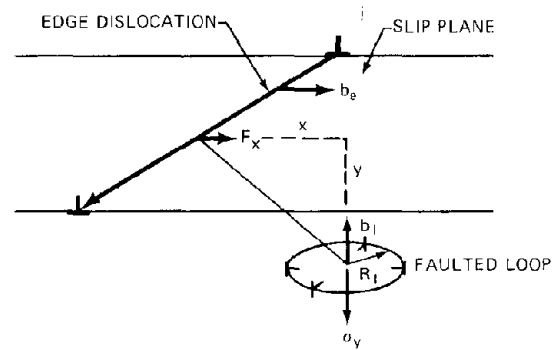


Fig. 18.23 Straight-edge dislocation passing by a faulted dislocation loop. The slip plane of the dislocation is parallel to the plane containing the stacking fault of the loop.

The stress field in the solid adjacent to a straight edge dislocation consists of a shear component and normal components  $\sigma_x$ ,  $\sigma_y$ , and  $\sigma_z$ . The shear component acts in the plane of the loop shown in Fig. 18.23 but in a direction perpendicular to the Burgers vector  $b_1$  of the loop. Hence, this stress component exerts no force on the loop (i.e., the  $b$  component in the first term of Eq. 8.13 is zero). Similarly, the normal stress components  $\sigma_x$  and  $\sigma_z$  do not exert forces on the loop which act to retard its growth. The normal stress  $\sigma_y$ , on the other hand, tends to pull apart or push together the stacking fault, which is surrounded by the loop. Therefore, this stress component exerts a radial force on the loop. Figure 8.10(b) is equivalent to the situation depicted in Fig. 18.23. The total force on the loop due to the stress component  $\sigma_y$  is  $(2\pi R_1)\sigma_y b_1$ . The work done as the loop expands from  $R_1$  to  $R_1 + dR_1$  is

$$dW = (2\pi R_1)\sigma_y b_1 dR_1$$

or the total work for the loop to expand against the stress from the nearby straight edge dislocation is

$$W = \pi R_1^2 \sigma_y b_1 \quad (18.55)$$

The stress  $\sigma_y$  is

$$\sigma_y = \frac{Gb_c}{2\pi(1-\nu)} \frac{y(x^2 - y^2)}{(x^2 + y^2)^2} \quad (18.56)$$

Equation 18.56 was obtained from the stress components in cylindrical components shown in Fig. 8.8 in the manner indicated at the beginning of Sec. 8.6 for obtaining other components in Cartesian coordinates. Inserting Eq. 18.56 into Eq. 18.55 and taking the derivative of W with respect to x yields

$$F_x = -\frac{\partial W}{\partial x} = -\frac{Gb_e b_1 R_1^2}{1-\nu} \frac{xy(3y^2 - x^2)}{(x^2 + y^2)^3} \quad (18.57)$$

In deriving Eq. 18.55, we have assumed that the stress  $\sigma_y$  does not vary appreciably over the area of the loop. This simplification is acceptable only when the line is far from the loop (i.e.,  $x^2 + y^2 > R_1^2$ ). For close approach of the line to the loop, the variation of  $\sigma_y$  over the loop area must be taken into account, and the  $F_x$  formula is considerably more complicated than Eq. 18.57. The results of the complete calculation for  $y = R_1$  and  $y = 0.1R_1$  are shown in Fig. 18.24. The maximum force occurs at  $x \approx R_1$  and increases as y decreases. For  $y > R_1$  the approximate treatment discussed above gives the maximum force as

$$(F_x)_{\max} = F_{\max} = \frac{\alpha Gb_e b_1}{2(1-\nu)} \left(\frac{R_1}{y}\right)^2 \quad (18.58)$$

where the numerical coefficient  $\alpha$  (which is of order unity) depends on the relative orientations and the Burgers vector of the loop and the dislocation line. Averaging over all orientations and Burgers vector combinations, Kroupa and Hirsch<sup>11</sup> find that the average of the maximum forces due

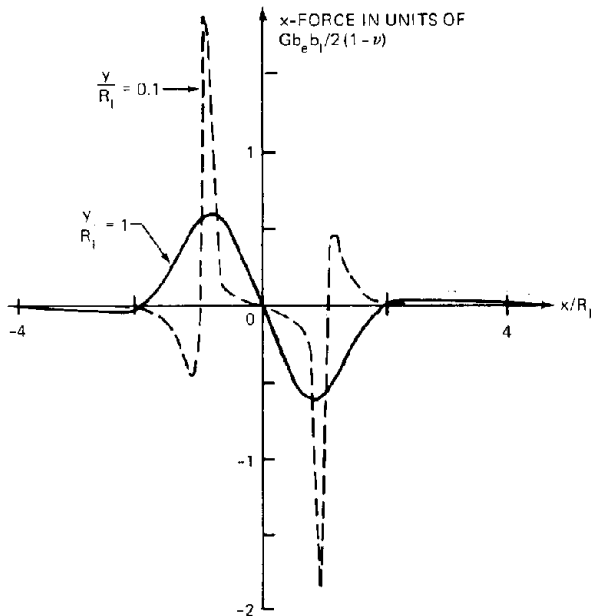


Fig. 18.24 The x-force on the dislocation line for the orientation of Fig. 18.23. (From Ref. 11.)

to loops distributed uniformly in a slab of thickness  $2R_1$  about the slip plane is

$$F_{\max} \approx \frac{1}{8} Gb_e b_1 \quad (18.59)$$

Interaction forces due to loops outside of this slab are negligible because of the  $y^{-2}$  dependence of  $F_{\max}$  (Eq. 18.58). Using Eq. 18.59 in 18.54 shows that the hardening effect of the loops is

$$\sigma_s = \frac{Gb_1}{8l} \quad (18.60)$$

Foreman<sup>12</sup> has performed computer calculations of loop hardening in which the elastic interaction forces of the model presented above are neglected. Instead, the critical stress for tearing the line away from the loop is based on the stability of the junctions formed when the loop and the line intersect. In the calculations a shear stress drives a dislocation line into a solid containing an array of loops of specified size and spacing. At stresses below the value needed to move the line entirely through the array of loops, the dislocation reaches an equilibrium position. As the stress is increased in small steps, the line moves forward to new equilibrium positions. Figure 18.25 shows the equilibrium configurations of a dislocation line (initially of pure screw character) in a cloud of loops whose diameter is  $1/10$

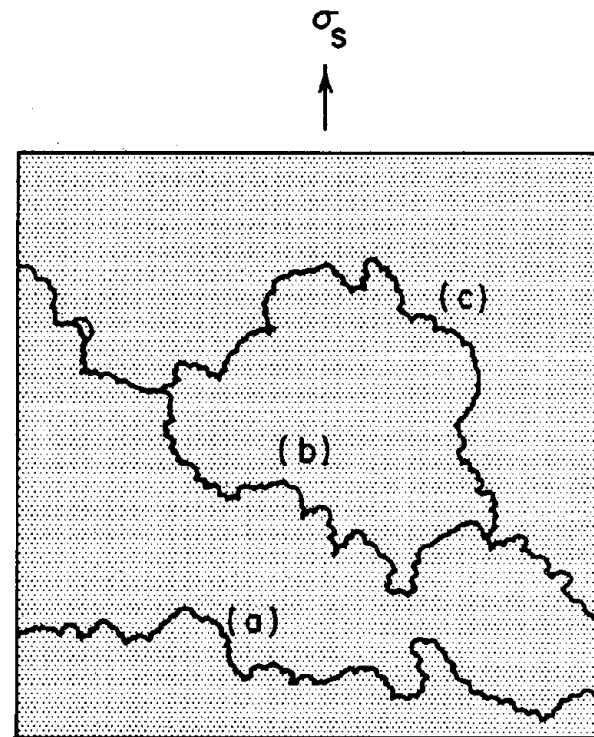


Fig. 18.25 Three stages of the movement of a dislocation (initially screw) upward through an array of loops. The applied stresses corresponding to each position are (a) 0.544 Gb/l, (b) 0.550 Gb/l; and (c) 0.556 Gb/l. (From Ref. 12.)

of the loop spacing in the glide plane. Each dot on the drawing corresponds to a loop cutting the glide plane of the dislocation. The three positions of the line correspond to three different values of the applied shear stress, which acts upward in the diagram. When the applied stress exceeds the value corresponding to the equilibrium position (c), the array of loops can no longer prevent motion of the dislocation. That is, the array of loops exhibits a well-defined yield point at a certain critical stress. When averaged over all dislocation and loop orientations, Foreman's computer simulation gives a critical stress of

$$\sigma_s = \frac{Gb}{4l} \quad (18.61)$$

Foreman's results differ from those of Kroupa and Hirsch (Eq. 18.60) not only in the numerical factor in the denominator but in the interpretation of the spacing  $l$  as well. In Foreman's analysis  $l$  is given by Eq. 18.25. In Kroupa and Hirsch's analysis,  $l$  is larger than this value because of zigzagging of the dislocation through the array of loops. This difference further increases the discrepancy between Eqs. 18.60 and 18.61. The bulk of experimental evidence on loop hardening favors relations of the type of Eq. 18.61 with  $l$  given by Eq. 18.25:

$$\sigma_s = \frac{Gb(2R_1N_1)^{1/2}}{\beta} \quad (18.62)$$

where  $N_1$  is the concentration of loops in the solid and  $\beta$  is a numerical factor between 2 and 4. With either of these constants, the increased strength due to loops is only ~20% of the full Orowan stress (Eq. 18.53) which results from an array of impenetrable obstacles.

## 18.8 TENSILE PROPERTIES OF IRRADIATED AUSTENITIC STAINLESS STEEL

Two features dominate the effects of fast-neutron irradiation on the austenitic stainless steels—hardening, or an increase in the stress needed to initiate plastic deformation (the yield stress, the proportional elastic limit, or the flow stress), and embrittlement, or the reduction in specimen elongation prior to fracture.

### 18.8.1 Radiation Hardening

The strengthening effect of fast-neutron irradiation depends on the fluence and the temperature (both irradiation and test temperatures). High temperatures act to remove damage inflicted by fast-neutron collisions with lattice atoms. During irradiation, creation and thermal annealing of defects proceed simultaneously. During testing at sufficiently high temperatures, only thermal annealing continues, and this process tends to mitigate the hardening effect of the neutron irradiation. Damage effects can be roughly classified by regions of fluence and temperature. The fluence regions above and below  $\sim 10^{21}$  neutrons/cm<sup>2</sup> (fast) correspond approximately to the dosages received by in-core structural components in fast and thermal reactors, respectively.

### 18.8.2 Low Fluence

In this regime ( $\Phi t < 10^{21}$  neutrons/cm<sup>2</sup>), the primary form of radiation damage consists of the depleted zones described in Sec. 18.5. Because of the low fluence, sizable quantities of dislocation loops and voids have not formed. Temperature subdivisions in the low-fluence regime are approximately divided by one-half the melting point in degrees Kelvin, which for stainless steel is 550 to 600°C. (The melting point of steel is 1650 to 1700°K.) For  $T < T_m/2$ , sufficient displacement damage survives annealing during irradiation and testing to cause an increase in the yield strength of the steel. This form of hardening decreases with test temperature according to Eq. 18.38. A typical stress-strain curve following a low-temperature low-fluence irradiation is shown at the top of Fig. 18.15(a). At temperatures greater than  $T_m/2$ , the depleted zones and embryonic interstitial loops anneal so rapidly during irradiation and/or testing that no hardening is observed in tensile tests. The stress-strain curve coincides with that of the unirradiated material [lower curve of Fig. 18.15(a)].

### 18.8.3 High Fluence

At high fast-neutron fluences ( $\Phi t > 10^{21}$  neutrons/cm<sup>2</sup>), dislocation loops and voids grow to large sizes. These large defects require appreciable time to anneal out even in elevated-temperature mechanical tests; so their effect on mechanical properties persists to higher temperatures than does the effect of the depleted zones. Complete recovery of the radiation hardening does not take place until temperatures in excess of 800°C ( $\sim 2T_m/3$ ). Figure 18.26 shows the postirradiation yield stress of type 304 stainless steel as a function of the test temperature. The specimens were irradiated at a temperature equal to one-half the melting point in a fast fluence in excess of  $10^{22}$  neutrons/cm<sup>2</sup>. At testing temperatures up to about 400°C, the hardening is due to a combination of depleted zones, dislocation loops, and voids. The displacement damage (i.e., hardening due to the depleted zones) becomes negligible at about 400°C owing both to thermally activated cutting of the zones by mobile dislocations and to removal of depleted zones by thermal annealing during the test. Between 400 and 550°C,

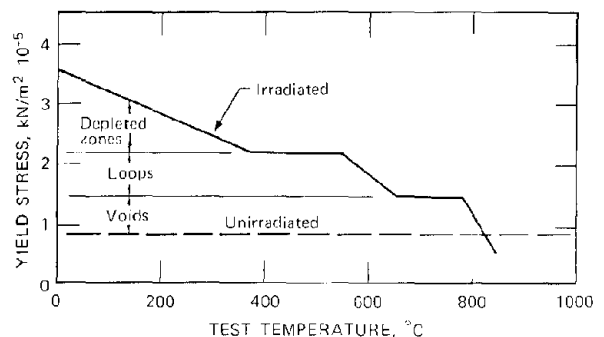


Fig. 18.26 Yield strength of type 304 stainless steel before and after irradiation at  $T \sim T_m/2$  to a fluence of  $1.7 \times 10^{22}$  neutrons/cm<sup>2</sup>. [After J. J. Holmes et al., *Acta Met.*, 16: 955 (1968).]

the hardening is temperature independent (athermal). At temperatures between 550 and 650°C, the loops are either unfaulted or annealed out during the test. Radiation hardening diminishes until at 650°C only hardening due to voids remains. The voids are not completely eliminated until temperatures above 800°C. The rather distinct regions of radiation hardening determined by tensile testing correspond to electron-microscope evidence of depleted zones (black dots), loops, or voids in the microstructure of the specimens. The measured hardening due to loops and voids shown in Fig. 18.26 is somewhat lower than the values predicted by the theories outlined in the previous section, although the athermal nature of strengthening due to these defects is in agreement with theoretical expectations. The discrepancy in the magnitudes of the experimental and predicted hardening can be due to undercounting the concentration of defects from electron micrographs, which do not reveal defects less than a few tens of angstroms in diameter. With Eq. 18.25 the defect concentration can be used to determine the obstacle spacing on the glide plane. This latter quantity enters the void-hardening expression (Eq. 18.53) and the loop-hardening formulas (Eqs. 18.61 and 18.62).

The only radiation-produced defects that can be seen in the electron microscope for  $T > 800^\circ\text{C}$  are helium bubbles, and these are not numerous enough to cause appreciable hardening. They do, however, dramatically reduce ductility at temperatures up to the melting point.

#### 18.8.4 Plastic Instability

The sizable increase in the yield strength of austenitic stainless steel resulting from low-temperature irradiation is not matched by a corresponding increase in the ultimate tensile strength of the metal. Figure 18.15 shows that the percentage increase in the yield strength is much larger than the percentage increase in the ultimate tensile strength (which is the stress at the maximum of the engineering stress-strain curve). The radiation-produced defects are more effective in impeding the motion of dislocations than they are in preventing the theoretical fracture stress from being exceeded in the specimen. The former ability is responsible for the large yield strength increase, and the latter function accounts for the modest increase in ultimate strength. Thus, the net effect of radiation is to decrease the difference between the ultimate and yield strengths of the steel, or to decrease the work-hardening rate,  $d\sigma/d\varepsilon$ .

Work hardening of an unirradiated metal arises from the creation of obstacles to dislocation motion as mobile dislocations become tangled with each other and with the preexisting dislocation network of the solid. In an irradiated metal there are already so many radiation-produced obstacles to dislocation motion that the additional hardening effect of dislocation tangling (normal work hardening) is a small increment to the frictional stress.

According to Eq. 18.7, when the work-hardening rate  $d\sigma/d\varepsilon$  is reduced, the stress at which necking or plastic instability occurs is correspondingly lowered. If the stress for necking is lower, so is the strain at this point. Therefore, the reduction in ductility which occurs in conjunction with hardening (i.e., at low temperatures) is simply a consequence of the early onset of plastic instability.

#### 18.8.5 Dislocation Channeling

In some highly irradiated metals, the onset of necking can coincide with yielding. That is, there may be no uniform elongation at all during a tensile test. An example of the stress-strain curve for a specimen exhibiting this sort of instability is shown as the upper curve in Fig. 18.15(b). This unusual macroscopic behavior during deformation is believed to be associated with the microscopic phenomenon of dislocation channeling.<sup>13</sup> In this process defects impeding dislocation motion in a metal are destroyed as the dislocation moves through them. Succeeding mobile dislocations therefore experience a smaller resistance to motion than their predecessors and thus move along the partially denuded glide plane more easily than the dislocations that first cleared the way. The stress required to move dislocations over slip planes that have been cleared of radiation-produced obstacles is far lower than the stress required to start the first dislocation moving. Thus an avalanche of dislocations can be released along the planar channels that have been cleared of obstacles. The strain due to this type of dislocation motion is highly localized. A group of closely spaced parallel slip planes that have been stripped of defects by moving dislocations is called a dislocation channel. Dislocations continue to be generated in and move along a cleared channel until normal work-hardening processes (intersection of glide dislocations with the dislocation network of the metal) increase the stresses required to maintain dislocation motion. Many channels can become activated during deformation. Evidence of deformation by dislocation channeling is seen in Fig. 18.27. The dark bands, which are called slip traces, represent

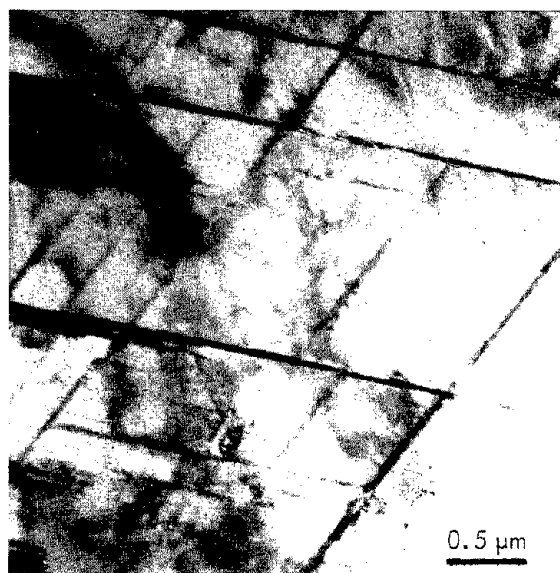


Fig. 18.27 Type 304 stainless steel deformed 10% after irradiation at 121°C. The slip traces (dark bands) represent the intersection of  $\{111\}$  planes with the surface of the specimen. [From E. E. Bloom et al., *J. Nucl. Mater.*, 22: 68 (1967).]

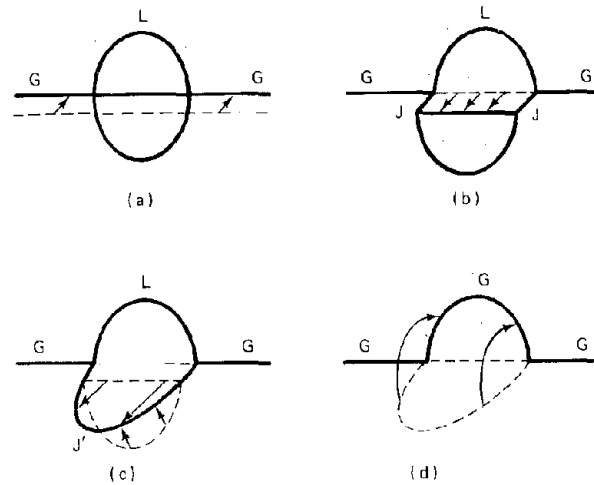


Fig. 18.28 A mechanism of loop destruction by a moving dislocation. The glide dislocation  $G$  cuts (a) into the loop  $L$  to form stable junctions  $J$  at the points of interaction (b). Glide of both parts of the loop causes the junctions to lengthen until they join at  $J'$  in (c) to extend around half the loop. The two halves of the loop then glide together (d) along their glide cylinders owing to mutual attraction and coalesce. [After A. J. E. Foreman and J. V. Sharp, *Phil. Mag.*, 19: 931 (1969).]

dislocation channels where large localized deformation has occurred. The material between the slip bands is not deformed. Each of the slip bands in the photograph corresponds to the intersection of a group of  $\{111\}$  planes with the surface. The  $\{111\}$  planes are the preferred glide planes in the fcc structure [Fig. 8.2(a)].

The radiation-produced defect most likely destroyed by moving glide dislocations is the dislocation loop. Figure 18.28 shows how an immobile loop can be transformed into a part of the moving dislocation as a result of the intersection of these two species. After passage of the glide dislocation, the loop completely disappears. Other models of loop destruction by moving dislocations involve chopping the loop into smaller bits, some of which can be incorporated into the moving dislocation.

## 18.9 CREEP RUPTURE

Creep rupture refers to the failure of a specimen that has been subject to stresses well below the yield stress for long periods of time. Deformation of the metal occurs by creep rather than by the nearly instantaneous plastic deformation characteristic of a tensile test. Creep-rupture tests can be conducted either in equipment similar to that employed for tensile tests or by tube-burst tests, in which a closed tubular specimen is loaded by internal gas pressure. In both types of tests, the time to failure, or the *rupture life*,  $t_R$ , and the *elongation at failure*,  $\epsilon_F$ , are measured. Provided that steady-state creep prevails for the major portion of the test, these two quantities are related to the creep rate by Eq. 18.20. The creep-rupture properties depend on the extent of irradiation, the irradiation and testing temperatures, and on the degree of cold work of the specimens. These variables directly control the creep rate,  $\dot{\epsilon}$ , and the elongation at fracture,  $\epsilon_F$ . The rupture life,  $t_R$ , is

indirectly affected by the same variables because it is the ratio of  $\epsilon_F$  to  $\dot{\epsilon}$ .

Figure 18.29 shows typical results of large fast-neutron fluences on the creep-rupture properties of an austenitic stainless steel. In this particular set of experiments, the specimens were annealed (i.e., not cold worked), and the neutron exposure, testing temperature, and the applied stress were fixed. Only the irradiation temperature was varied. The data indicate that the creep rate,  $\dot{\epsilon}$ , is lower in the irradiated specimens than in the unirradiated metal. The reduction is greatest at the lowest irradiation temperature. This trend is consistent with the effect of temperature on the tensile strength of irradiated steel (see previous section). The decreased creep rate is attributed to the depleted zones, Frank loops, and voids produced by the fast-neutron bombardment, all of which impede the motion of dislocations through the solid. As the irradiation temperature is raised, these obstacles to dislocation motion are progressively removed from the specimen by annealing, and the creep rate increases. At  $780^\circ\text{C}$  the creep rate is practically equal to that of the unirradiated material.

Not all investigations have confirmed the observation of reduced steady-state creep rate in neutron-irradiated steel. The opposite effect, occasionally found, is attributed to the removal of atomically dispersed carbon from the matrix by the formation of large carbide particles ( $M_{2.3}C_6$ ) by the process of radiation-induced precipitation. The dissolved carbon apparently acts as a stronger barrier to dislocation motion than the larger but more widely spaced carbide particles.

Figure 18.29 also demonstrates that radiation reduces the elongation to fracture. As in the case of the creep rate, the strain at rupture is smallest for the specimen irradiated at the lowest temperature. This reduction in  $\epsilon_F$  is most probably due to the loss of work hardenability accompany-

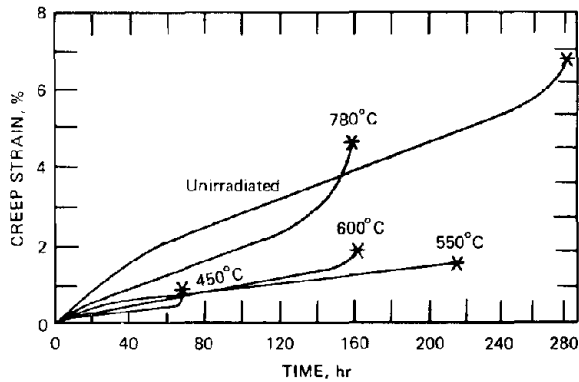


Fig. 18.29 Effect of irradiation temperature on the creep rupture of annealed type 304 stainless steel irradiated to  $1.9 \times 10^{22}$  neutrons/cm<sup>2</sup> ( $>0.1$  MeV) and tested at 550°C under a stress of  $3 \times 10^5$  kN/m<sup>2</sup>. [After E. E. Bloom and J. R. Weir, Jr., *Nucl. Technol.*, 16: 45 (1972).]

ing the radiation strengthening of the metal and leads to premature plastic instability (Sec. 18.8.4). As the irradiation temperature is increased, the elongation to fracture begins to return to the value characteristic of the unirradiated material. Work hardenability is recovered as the radiation-induced increase in yield strength is removed by thermal annealing. However, even at 780°C, where radiation strengthening should have completely annealed out, the creep test shows a significant loss in ductility. In fact, as the irradiation temperature is increased to values greater than those shown in Fig. 18.29, the elongation to fracture again decreases. This high-temperature loss of ductility is associated with the helium produced by  $(n,\alpha)$  reactions in the metal (see following section).

The effect of fast-neutron fluence on the elongation to fracture with all other variables held fixed is shown in Fig. 18.30. The ductility (strain at fracture) is reduced from a value of  $\sim 20\%$  for the unirradiated material to  $\sim 0.1\%$  at fluences expected in LMFBR service. For this particular set of conditions, radiation causes a 200% reduction in the ductility of the specimen.

The combined effects of fluence and temperature on the creep-rupture properties can also be demonstrated by rupture life graphs of the type shown in Fig. 18.12, which illustrated that, for unirradiated steel, increasing the test temperature markedly reduced the rupture life. This effect is a manifestation of the rapid increase in the steady-state creep rate,  $\dot{\epsilon}$ , with test temperature (i.e., in an Arrhenius fashion, Eq. 8.46). Figure 18.31 shows that at fixed stress and fixed test temperature radiation reduces the rupture life, often by as much as an order of magnitude. Reduction of  $t_R$  is due predominantly to the severe loss in ductility induced by radiation. The effect of test temperature (which should not be confused with the influence of the irradiation temperature indicated by Fig. 18.29) is similar to that found in unirradiated specimens (Fig. 18.12).

The effect of neutron fluence on  $t_R$  is exhibited in Fig. 18.32. The rupture life decreases drastically with increased fluence primarily because of the loss in ductility illustrated by Fig. 18.30.

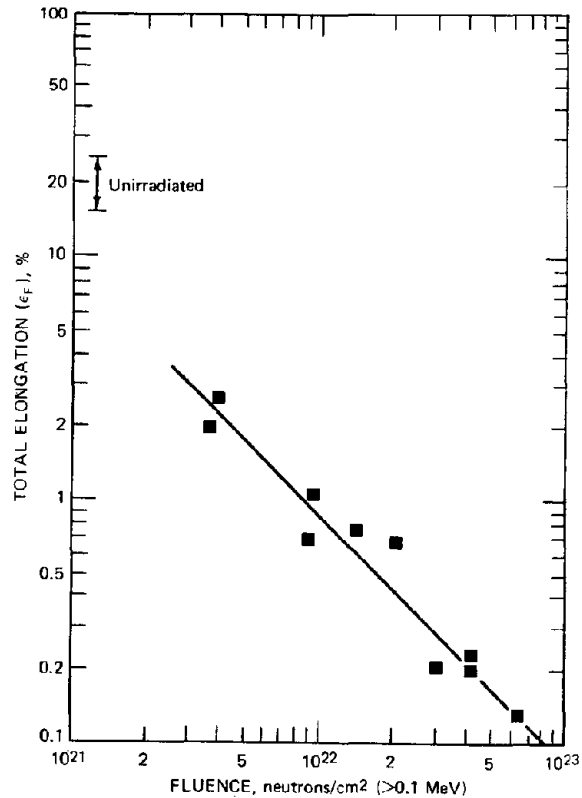


Fig. 18.30 Postirradiation ductility of type 304 stainless steel irradiated at various temperatures between 370 and 470°C and tested at 600°C and  $1.9 \times 10^5$  kN/m<sup>2</sup>. (After E. E. Bloom and J. O. Stiegler, in ASTM Special Technical Publication 484, p. 451, American Society for Testing and Materials, Philadelphia, 1970.)

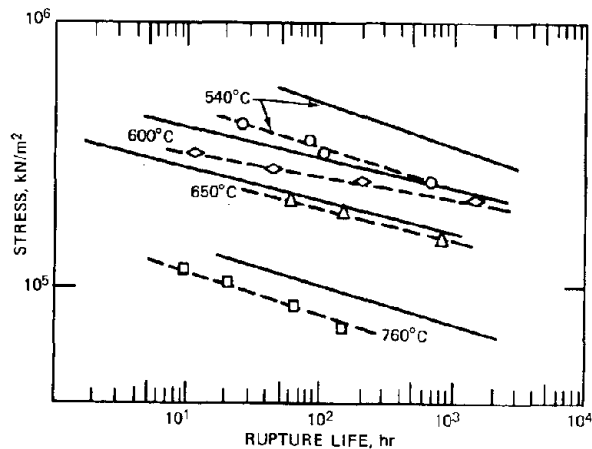


Fig. 18.31 Rupture life of type 316 stainless steel irradiated to a total neutron fluence of  $1.2 \times 10^{22}$  neutrons/cm<sup>2</sup> at an irradiation temperature of 440°C. Tested at various temperatures in uniaxial tension.—, unirradiated; - - -, irradiated. (After A. J. Lovell and R. W. Barker, in ASTM Special Technical Publication 484, p. 468, American Society for Testing and Materials, Philadelphia, 1970.)

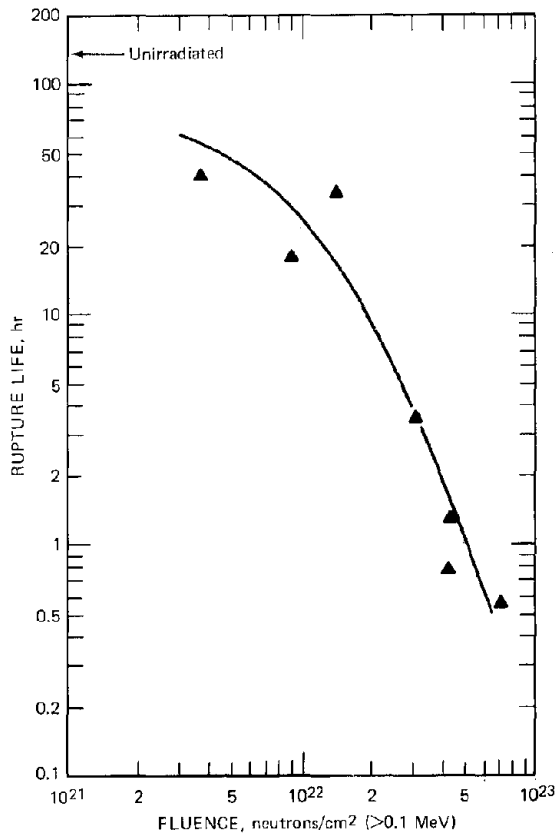


Fig. 18.32 Effect of neutron fluence on the postirradiation rupture life of type 304 stainless steel. The irradiation temperatures were between 370 and 430°C. The tests were performed at 600°C at a stress of  $1.9 \times 10^5$  kN/m<sup>2</sup>. (After E. E. Bloom and J. O. Steigler, ASTM Special Technical Publication 484, p. 451, American Society for Testing and Materials, Philadelphia, 1970.)

The degree of cold work of the tubing used in the fuel elements is a controllable fabrication variable that can be used to optimize the in-pile performance of the cladding. Cold working is measured by the percentage reduction in cross-sectional area resulting from drawing the tubing at room temperature. Microstructurally, the degree of cold work appears as a higher dislocation density than in the annealed metal. Cold working increases the strength of the metal by mechanisms similar to those responsible for radiation hardening, but, in common with this phenomenon, the effects of cold work diminish greatly at elevated temperatures owing to the removal of the mechanically produced dislocation tangles by thermal processes (recovery). The effect of cold work on the stress rupture properties of stainless steel is shown in Fig. 18.33. Moderate cold working (10 to 30%) enhances the short-term stress rupture strength, but the long-term strength eventually becomes poorer than that of the fully annealed material. If a long rupture life at low stress was the sole criterion for choosing a cladding material, the fully annealed metal would be superior to all grades of cold-worked metal. However, the principal value of cold working of the

cladding is that void formation and swelling are suppressed (see Chap. 19). Consequently, a 10% cold-worked material appears to represent the best compromise between improvement of swelling resistance at the expense of some degradation of the creep rupture properties.

### 18.9.1 High-Temperature Fracture

The nature of the fractures that terminate the high-temperature creep process is quite different from the mode of fracture exhibited by metals and alloys following tensile tests at low temperatures. At low temperatures fracture tends to result from shearing through grains of the metal (i.e., the transgranular mode) and often occurs only after appreciable deformation. The fracture mode that terminates the third stage of high-temperature creep or the deformation in a high-temperature tensile test is usually of the intergranular type. In addition, high-temperature fracture is often accompanied by the observation of minute cracks or cavities in the metal adjacent to the fracture surface.

The nature of the metal after fracture in a relatively high-stress tensile test is shown in Fig. 18.34. In the unirradiated specimen [Fig. 18.34(a)], the metal in the vicinity of the fracture is full of wedge-shaped cracks. The actual fracture surface probably followed grain boundaries along a path that had a high density of such cracks. The grains are deformed in the direction of the applied stress. In the irradiated specimen [Fig. 18.34(b)], the small internal

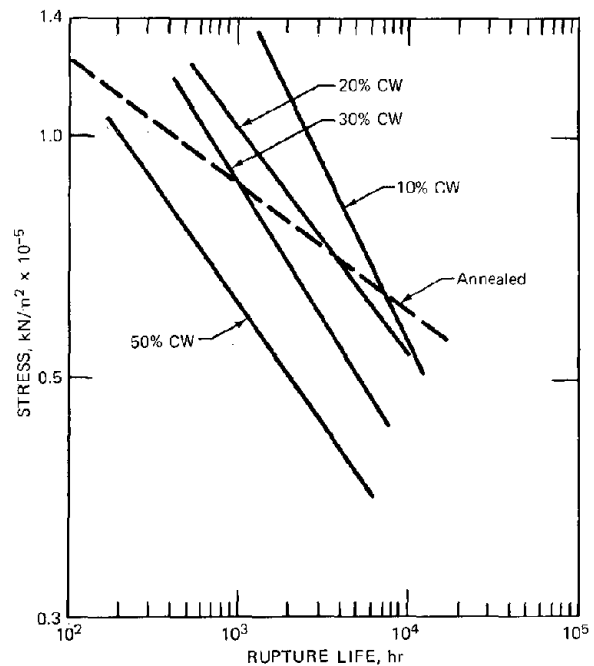


Fig. 18.33 The effect of cold working on the rupture life of type 316 stainless steel. Tested at 700°C. (From T. Lauritzen, Stress-Rupture Behavior of Austenitic Steel Tubing. Influence of Cold Work and Effect of Surface Defects, USAEC Report GEAP-13897, General Electric Company, 1972.)

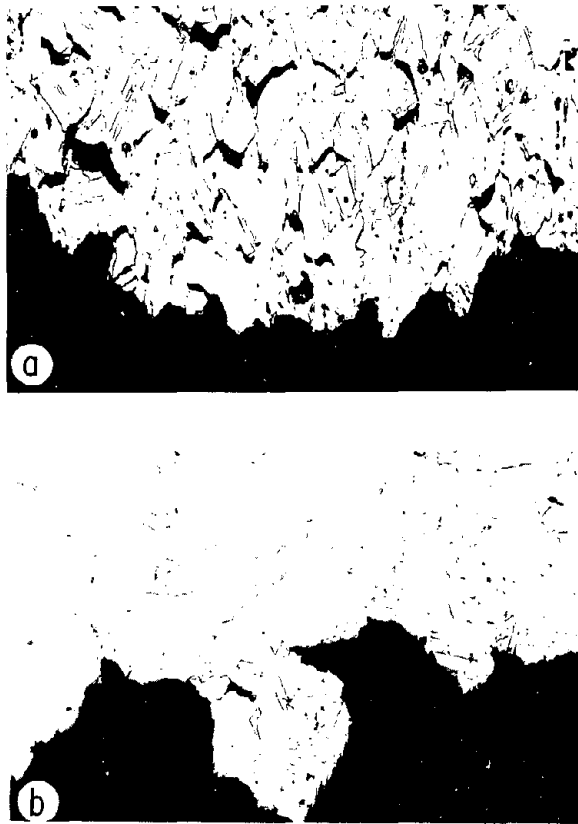


Fig. 18.34 Fractures of type 347 stainless steel after a tensile test at 600°C. (a) Unirradiated,  $\epsilon_F = 18\%$ . (b) Irradiated to a fast fluence of  $2 \times 10^{22}$  neutrons/cm<sup>2</sup>,  $\epsilon_F = 3\%$ . (From M. Kangilaski et al., ASTM Special Technical Publication 457, p. 67, American Society for Testing and Materials, Philadelphia, 1969.)

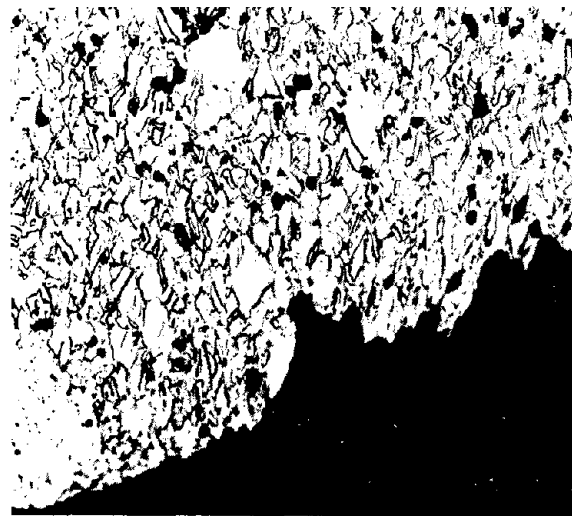
cracks are absent, and the grains do not appear to have been deformed.

Figure 18.35 shows similar photomicrographs of the fracture surface produced in a creep-rupture test. The metal near the fracture in the unirradiated specimen contains many small cavities on the grain boundaries rather than the wedge-shaped cracks that appeared in the high-stress tensile fracture [Fig. 18.34(a)]. Grain deformation perpendicular to the fracture surface is evident in the failed unirradiated specimen. The general appearance of the fracture surface following the creep-rupture test of neutron-irradiated steel [Fig. 18.35(b)] is practically indistinguishable from that observed after a tensile test [Fig. 18.34(b)]. In both cases, intergranular cracking apparently occurred rapidly as soon as a few grain-boundary cracks or cavities were formed. The absence of internal cracks or cavities near the crack surface and the lack of grain deformation are both due to the radiation hardening of the matrix of the grains, which forces failure in a nearly brittle manner along grain boundaries. In contrast to the rapid failure of irradiated specimens as soon as a small number of cracks or cavities

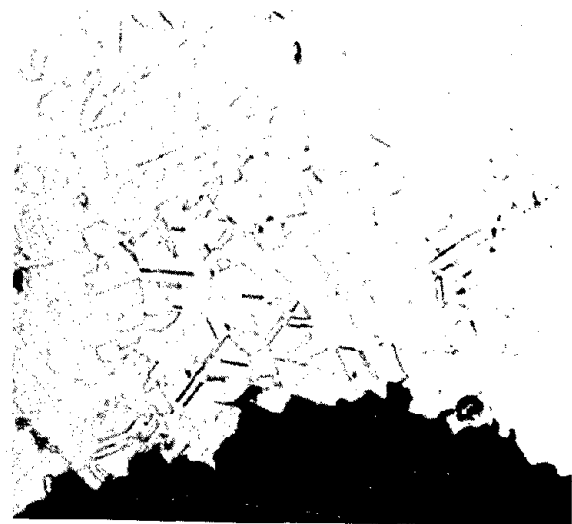
are created, fracture of the unirradiated metal is a result of the slow growth of cracks or cavities by grain-boundary sliding diffusional processes.

### 18.9.2 Wedge Cracks

The high-temperature fracture process can be divided into nucleation and growth regimes. Small wedge cracks are spontaneously formed at grain-boundary triple points when



(a)



(b)

Fig. 18.35 Fractures of type 347 stainless steel after a stress-rupture test at 650°C. (a) Unirradiated; stress =  $2.4 \times 10^5$  kN/m<sup>2</sup>;  $t_R = 32$  hr;  $\epsilon_F = 23\%$ . (b) Irradiated to a fluence of  $2 \times 10^{22}$  neutrons/cm<sup>2</sup>; stress =  $2 \times 10^5$  kN/m<sup>2</sup>;  $t_R = 21$  hr;  $\epsilon_F < 0.2\%$ . [From M. Kangilaski et al., *Trans. Amer. Nucl. Soc.*, 12: 574 (1969).]

the applied stress exceeds a critical value. Stroh<sup>14</sup> calculated the critical stress for the nucleation of wedge cracks on the assumption that dislocation pileups in a slip band provided the necessary stress concentration. Figure 18.36 shows a grain containing a dislocation source that has emitted dislocations into a slip plane under the action of the applied shear stress  $\sigma_{xy}$ . The dislocations are stopped by a grain boundary, and a pileup ensues. As noted in Sec. 8.6, the pileup develops a tensile stress  $\sigma$  that tends to open up a crack at the head of the slip band. The tensile

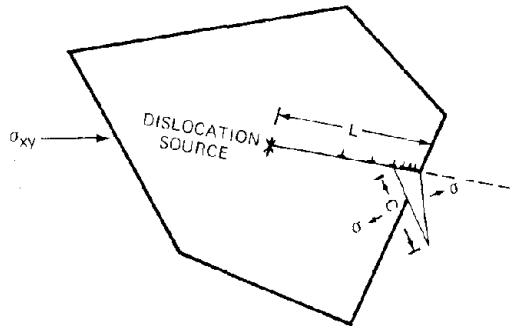


Fig. 18.36 Crack nucleation by the pileup of dislocations against a grain boundary. (From Stroh, Ref. 14.)

stress is greatest at an angle of  $70^\circ$  to the slip plane containing the pileup; so the crack develops in the orientation shown in the drawing. The stress concentration is given by Eq. 8.41 in which the distance from the tip to the pileup is taken as the crack length, or

$$\sigma^2 C = L\sigma_{xy}^2 \quad (18.63)$$

where  $C$  is the length of the crack and  $L$  is the length of the pileup. The stability of the crack is determined by the Griffith energy criterion, which balances the loss of elastic energy of the solid with the gain of surface energy of the crack. When the exact stress distribution in the vicinity of the crack is employed to compute the elastic-energy term, the work required to form the crack is

$$W = E_{tot} - E_{el}^0 = -\frac{\pi(1-\nu)C^2\sigma^2}{8G} + 2C\gamma \quad (18.64)$$

where  $E_{el}^0$  is the elastic energy of the perfect solid and  $\gamma$  is the energy required to produce a unit area of crack surface.

If we eliminate  $\sigma$  from Eq. 18.64 by use of Eq. 18.63, the work of crack formation is found to be a linear function of crack length:

$$W = \left[ -\frac{\pi(1-\nu)L\sigma_{xy}^2}{8G} + 2\gamma \right] C \quad (18.65)$$

The shear stress for which  $dW/dC = 0$  is the critical stress for nucleation of a crack,  $\sigma_{nuc1}$ . Using the approximation  $\nu \approx 1/3$ , crack nucleation occurs when:

$$\sigma_{nuc1} = \left( \frac{24\gamma G}{\pi L} \right)^{1/2} \quad (18.66)$$

A method of estimating  $L$  and of accommodating Stroh's analysis to the observation that the wedge-shaped cracks almost always occur at grain corners (i.e., triple points, see Fig. 16.18) has been proposed by McLean.<sup>15</sup> He argues that the slip planes within the grains on which the pileups occur in Stroh's theory can be replaced by sliding grain boundaries. The cracks formed by this process are shown in Fig. 18.37. In applying Eq. 18.66 to the triple-point crack, we assume that  $L$  is the length of the sliding interface, which is approximately equal to the grain size.

When precipitates (e.g., helium bubbles or  $M_{23}C_6$  particles) have collected on the grain boundary, sliding is impeded. Consequently, Weaver<sup>16</sup> suggests that the length  $L$  should be taken as the average distance between particles on the grain boundary.

If no plastic deformation occurs around the tip of the crack,  $\gamma$  in Eq. 18.66 is best approximated by the difference between the energy of two free surfaces which were formed and the one grain boundary which was eliminated at the time the crack appeared:

$$\gamma = \gamma_s - \frac{1}{2} \gamma_{gb} \quad (18.67)$$

Modifiers of stainless steel (e.g., titanium) affect the creep-rupture properties by increasing the effective surface energy either by segregating on grain boundaries or by removing impurities such as oxygen and nitrogen from the grain boundaries.<sup>17</sup> In either case, one or the other of the terms on the right of Eq. 18.67 is altered.

When the grains of the metal are capable of deforming plastically, the stress concentration at the tip of the crack can be partially relieved by plastic flow. The net effect of grain deformation is to increase the energy required to form

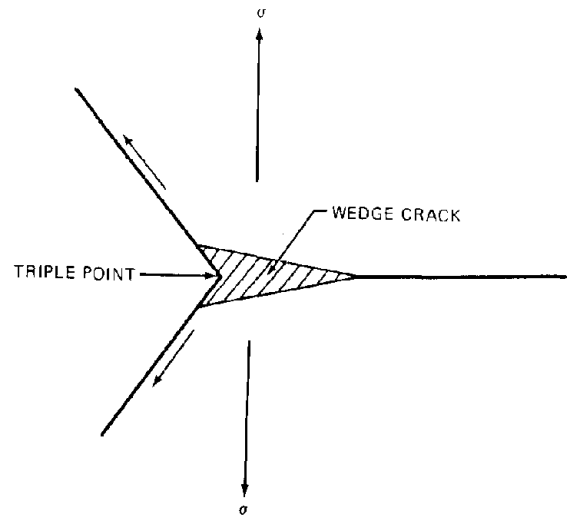


Fig. 18.37 A wedge crack forming on a grain-boundary triple point as a result of an applied stress normal to one of the boundaries.

a unit area of fresh crack surface, or to increase  $\gamma$  above the value predicted by Eq. 18.67. In fairly soft metals, crack nucleation occurs only at stresses that correspond to  $\gamma \approx 100\gamma_s$ . Thus, any process that strengthens the grains and prevents their deformation decreases the stress required to nucleate cracks and thus makes the metal less ductile. Matrix strengthening by irradiation-produced defects is probably one mechanism of the loss of ductility in neutron-bombarded steel.

The nucleation condition given by Eq. 18.66 is applicable only to small cracks. As the crack grows, contributions to the energy balance which depend on the crack width become important. Inclusion of these terms leads to a new critical stress for unstable crack growth and, for stresses below the critical value, to an equilibrium crack size. The width of the crack is assumed to be equal to the product of the number of dislocations in the pileup,  $n$ , and the width of each dislocation, which is approximately equal to the magnitude of the Burgers vector,  $b$ . That is, the crack is visualized as a condensation of  $n$  single dislocations into a superdislocation of Burgers vector  $nb$ .

The work per unit length required to form the crack is given by

$$W = -\frac{\pi(1-\nu)C^2\sigma^2}{8G} + 2C\gamma + \frac{G(nb)^2}{4\pi(1-\nu)} \ln\left(\frac{4\mathcal{R}}{C}\right) - \sigma V_c \quad (18.68)$$

The first two terms are contained in the energy balance for small cracks. They represent the elastic energy of the crack in the applied stress field and the surface energy of the crack. The third term is the elastic energy per unit length (i.e., the line tension) of the superdislocation. This quantity has been calculated for a single dislocation in Sec. 8.3. Equation 8.9 gives the energy per unit length of a screw dislocation of Burgers vector  $b$ , and the corresponding result for a single-edge dislocation is obtained by division by  $1-\nu$ . With the crack modeled as an edge superdislocation, the Burgers vector is  $nb$ , and the core radius is replaced by  $C/4$ . The cutoff radius of the stress field of the superdislocation,  $\mathcal{R}$ , need not be known, because only the derivative of  $W$  with respect to  $C$  is needed.

The last term in Eq. 18.68 represents the work done by the applied stress in opening the crack to a finite volume  $V_c$ . The crack has the shape of a triangle of base  $nb$  and height  $C$ ; so

$$V_c = \frac{1}{2}(nb)C \quad (18.69)$$

Equation 18.69 is substituted into Eq. 18.68, and  $dW/dC$  is set equal to zero, thereby yielding the following quadratic equation for the stable values of the crack length:

$$C^2 - B\left[1 - 2\left(\frac{A}{B}\right)^{1/2}\right]C + AB = 0 \quad (18.70)$$

where

$$A = \frac{G(nb)^2}{8\pi\gamma(1-\nu)} \quad (18.71)$$

$$B = \frac{8\gamma G}{\pi(1-\nu)\sigma^2} \quad (18.72)$$

Inspection of Eq. 18.70 shows that the roots  $C$  are real if  $B > 16A$  and imaginary if  $B < 16A$ . If  $B > 16A$ , the smaller of the two roots represents the stable crack length, and, if  $B < 16A$ , the cracks are unstable and fracture occurs. The condition of neutral stability is given by  $B = 16A$ , or

$$\sigma(nb) = 2\gamma \quad (18.73)$$

The crack width  $nb$  in this formula is obtained from the theory of the dislocation pileup discussed in Sec. 8.6. In applying Eq. 8.39 to determine  $nb$ , we assume that the pileup length (i.e., the distance from the dislocation source to the crack) is approximately equal to one-half the grain size  $d$ . The crack growth criterion on which the preceding analysis was based assumed that the metal was subject to a tensile stress  $\sigma$  normal to the grain boundary in which cracks appeared. The dislocation pileup responsible for development of the crack, however, is produced by a shear stress along the slip band (or grain boundary in this case). The dislocations that move along the grain boundary and condense into the crack are impeded by the frictional stress  $\sigma_i$  due to obstacles in the matrix (Sec. 18.5). In estimating  $nb$ , the shear stress in Eq. 8.39 is reduced by this amount, and we have

$$nb = \frac{\pi(1-\nu)L(\sigma_{xy} - \sigma_i)}{G} \approx (\sigma_{xy} - \sigma_i) \frac{d}{G} \quad (18.74)$$

where the length of the pileup has been taken as one-half the grain size.

Substituting Eq. 18.74 into 18.73 yields the critical tensile stress:

$$\sigma_{crit}(\sigma_{xy} - \sigma_i) = \frac{2G\gamma}{d} \quad (18.75)$$

In Fig. 18.37 the component of the applied stress that produces shear along the grain boundary  $\sigma_{xy}$  is approximately equal to  $\sigma/2$ . If, in addition,  $\sigma_i$  is small, the critical tensile stress for unstable triple-point crack growth given by Eq. 18.75 is very nearly equal to the critical shear stress for crack nucleation in Stroh's theory (Eq. 18.66). Because the internal stress  $\sigma_i$  is generally appreciable,  $\sigma_{crit}$  given by Eq. 18.75 is larger than the value given by Eq. 18.66, which means that fracture is controlled by crack growth rather than by crack nucleation. Thus,  $\sigma_{crit}$  of Eq. 18.75 represents the ultimate strength of a metal when failure occurs by the formation and extension of grain-boundary cracks.

The foregoing analysis of crack stability can be applied to estimate the elongation at fracture when failure is due to grain-boundary triple-point cracks. Elongation (or creep strain) of a grain occurs because  $n$  dislocations have traversed the grain and coalesced into a crack. Each of the  $n$  dislocations causes a displacement  $b$ ; so the displacement due to a crack of width  $nb$  is equal to  $nb$ . The elongation, or fractional displacement, of the grain is  $nb/d$ . Equation 18.73 can be regarded as the condition giving the critical crack width (at which fracture occurs) for a specified applied stress. At the point of fracture,  $nb$  is the

product of the grain diameter and the elongation at fracture; elongation can be found from Eq. 18.73:

$$\epsilon_F = \frac{2\gamma}{\sigma d} \quad (18.76)$$

Equation 18.76, which was first proposed by Williams,<sup>18</sup> has been applied to the embrittlement of neutron-irradiated Inconel (a nickel-based alloy).<sup>19</sup>

The prediction that grain refinement (i.e., reduction in  $d$ ) reduces embrittlement is borne out by experiment. Equation 18.76 also predicts that ductility is improved by increasing the surface energy  $\gamma$ . This parameter is the energy required to form a unit area of fresh surface at the crack tip. If the metal is hard and brittle,  $\gamma$  approaches its minimum value given by Eq. 18.67. On the other hand, soft metals permit plastic flow at the crack tip, thereby requiring more energy to create fresh surface than just the surface energy. In this case,  $\gamma$  can be very much larger than  $\gamma_s$ . By hardening the matrix, irradiation acts to reduce the extent of plastic flow around the crack tip during creep, thereby decreasing  $\gamma$ . In general, any phenomenon that hardens the matrix of the grains without increasing the strength of the grain boundaries makes the metal more brittle.

The inverse dependence of  $\epsilon_F$  on the applied stress indicated by Eq. 18.76 does not appear to have been verified experimentally.

### 18.9.3 Grain-Boundary Voids

Creep in metals at high temperature can be accompanied by the growth of voids (or cavities) lying on grain boundaries that are transverse to the applied tensile stress. These grain-boundary voids can grow at stresses well below the critical stress required for unstable growth of wedge cracks (Eq. 18.75).

The condition of mechanical equilibrium of a gas-free spherical cavity in a solid subject to tensile stress  $\sigma$  is given by Eq. 13.4 (in this relation, however,  $\sigma$  represents a compressive stress). A cavity will tend to grow if its radius is greater than the critical radius given by

$$\sigma = \frac{2\gamma}{R_{\text{crit}}} \quad (18.77)$$

To describe creep rupture by growth of such voids, we must inquire as to the mechanism of the creation of void nuclei with radii large enough to satisfy the above stability criterion and then determine the rate at which these voids grow.

Voids are most easily nucleated on grain boundaries where stress concentrations occur. The triple-point wedge cracks shown in Fig. 18.37 can have equivalent radii large enough for the right-hand side of Eq. 18.77 to be smaller than the applied stress, even though the applied stress does not exceed the critical stress for wedge-crack growth. However, voids in creep specimens are observed all over the grain boundaries and not just at triple points. Defects in the grain boundary that can lead to void nucleation include precipitate particles or small ledges, both of which are effective stress concentrators.

Once nucleated, voids are believed to grow by absorbing vacancies from the bulk until they are large enough to interlink and cause fracture. Vacancies probably flow to the voids via the grain boundary since, at modest temperatures, grain-boundary diffusion is more rapid than lattice diffusion. The description of a quantitative model of the growth of grain-boundary voids under stress, proposed by Hull and Rimmer<sup>20</sup> and lauded by Speight and Harris,<sup>21</sup> follows.

Assume that  $N_{gb}$  voids of radius  $R_0$  have been nucleated per unit area of grain boundary transverse to the tensile stress by one or a combination of the mechanisms listed in the preceding paragraph. The  $R_0$  is assumed to be greater than  $R_{\text{crit}}$  of Eq. 18.77. Figure 18.38 shows such a void at some stage of the growth process when the radius has increased to  $R$ . The analysis neglects nucleation of new voids during growth of the batch nucleated at the time the

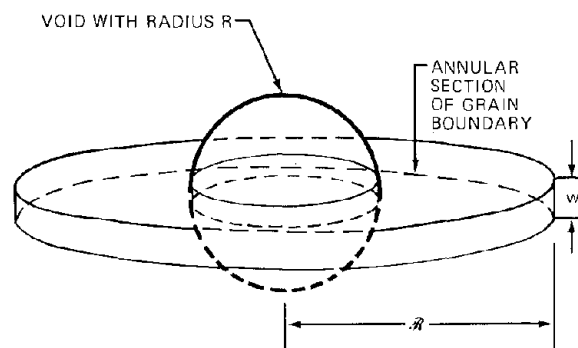


Fig. 18.38 A model for the growth of voids on grain boundaries during creep by diffusion of vacancies in the grain boundary.

tensile stress was applied. By analogy to the treatment of the three-dimensional growth of gas bubbles in the fuel (Chap. 13), the void population is divided into a series of identical unit cells, each with a central void surrounded by the associated grain-boundary area. The extent of grain boundary from which the void draws its vacancies is determined by

$$(\pi R^2) N_{gb} = 1 \quad (18.78)$$

Vacancies are assumed to be created at a uniform rate in the annular disk  $R < r < R$  surrounding each void. The thickness of the disk is taken to be the grain-boundary thickness,  $w$ . The vacancies created in the annulus diffuse to and are absorbed by the void at the center, causing the latter to grow. Because of the unit cell approximation embodied in Eq. 18.78, the void and its associated grain-boundary area are treated as an isolated entity; so the vacancy flux at  $r = R$  is zero. The vacancy-diffusion equation in the wheel-shaped region surrounding each void is

$$D_{v_{gb}} \frac{1}{r} \frac{d}{dr} \left( r \frac{dC_v}{dr} \right) + G_v = 0 \quad (18.79)$$

where  $D_{v_{gb}}$  is the diffusion coefficient of vacancies in the grain boundary,  $C_v$  is the volumetric concentration of

vacancies, and  $G_v$  is the uniform volumetric source of vacancies in the diffusion zone. The vacancy concentration at the void surface\* ( $r = R$ ) is given by Eq. 13.176 with  $p = 0$ :

$$C_v(R) = C_v^{eq} \exp\left(\frac{2\gamma \Omega}{R kT}\right) \quad (18.80)$$

which means that because of surface tension the solid in the vicinity of the void surface is placed in traction, thereby increasing the equilibrium vacancy concentration above the value in the stress-free solid. The boundary condition at  $r = \mathcal{R}$  is

$$\left(\frac{dC_v}{dR}\right)_{\mathcal{R}} = 0 \quad (18.81)$$

The solution of Eq. 18.79 with the above boundary conditions is

$$C_v(r) = C_v^{eq} \exp\left(\frac{2\gamma \Omega}{R kT}\right) + \frac{G_v \mathcal{R}^2}{2D_{vgb}} \left[ \ln\left(\frac{r}{\mathcal{R}}\right) - \left(\frac{1}{2} \frac{r^2 - R^2}{\mathcal{R}^2}\right) \right] \quad (18.82)$$

The vacancy-concentration profile in the grain boundary around the pore depends on the rate of vacancy creation in the grain boundary,  $G_v$ . This quantity is not known a priori, and Speight and Harris invoke the arbitrary condition that  $G_v$  is just sufficient to render the vacancy concentration midway between voids (i.e., at  $r = \mathcal{R}$ ) equal to the thermodynamic equilibrium value appropriate to the solid under the applied tensile stress (see Chap. 13). Or  $G_v$  is determined by applying the auxiliary condition

$$C_v(\mathcal{R}) = C_v^{eq} \exp\left(\frac{\sigma \Omega}{kT}\right) \quad (18.83)$$

to Eq. 18.82.

Having solved the diffusion problem, we obtain the flux of vacancies to the void by

$$(2\pi R w) D_{vgb} \left(\frac{dC_v}{dr}\right)_R$$

Assuming that the void remains spherical despite the fact that its vacancy supply is restricted to a belt of width  $w \ll R$  at its middle, we find the time rate of change of the volume of the void to be

$$\frac{d}{dt} \left( \frac{4}{3} \pi R^3 \right) = (2\pi R w) D_{vgb} \left(\frac{dC_v}{dr}\right)_R \Omega \quad (18.84)$$

The gradient at the void surface is obtained using Eq. 18.82, and  $G_v$  is eliminated by use of Eq. 18.83. The product  $D_{vgb} C_v^{eq} \Omega$  is identified with the grain-boundary self-diffusion coefficient (see Eq. 16.44). Because the arguments of the exponentials in Eqs. 18.80 and 18.83 are small,  $e^x$  is approximated by  $1 + x$ . Equation 18.84 yields

\*We assume that the void radius  $R$  is much larger than the grain-boundary thickness  $w$ . The void surface within the grain boundary is approximated by a cylinder of radius  $R$ .

$$\frac{dR}{dt} = \frac{w D_{vgb} \Omega}{\mathcal{R}^2 kT} \left( \sigma - \frac{2\gamma}{R} \right) \frac{(\mathcal{R}/R)^2 - 1}{2 \ln(\mathcal{R}/R) - 1 + (R/\mathcal{R})^2} \quad (18.85)$$

This equation shows that the growth rate becomes positive when the void size exceeds the critical value given by Eq. 18.77. Cavities smaller in radius than  $R_{crit}$  sinter at a rate given by Eq. 18.85 and eventually disappear. Voids for which  $R_0 > R_{crit}$  grow at an ever-increasing rate.

The fraction of the grain-boundary area occupied by voids is

$$f = \left(\frac{R}{\mathcal{R}}\right)^2 \quad (18.86)$$

Fracture (or creep rupture) is assumed to occur when the voids touch. If the spherical voids are disposed on a regular square array, linkage occurs when the fractional area occupied by the voids is  $\pi R_F^2 / (2R_F)^2 = \pi/4$ , where  $R_F$  is the void radius at fracture. Setting  $f = \pi/4$  in Eq. 18.86 yields

$$R_F = \left(\frac{\pi}{4}\right)^{1/2} \mathcal{R} \quad (18.87)$$

The time to rupture is obtained by integration of the growth law from  $R = R_0$  to  $R = R_F$ , or

$$t_R = \int_{R_0}^{R_F} \frac{dR}{(dR/dt)} \quad (18.88)$$

The elongation (creep strain) at fracture can be estimated as follows. Imagine the solid to be divided into right-square prisms oriented parallel to the applied stress. The height of each prism is the grain size  $d$ , and the base of the prism is a square with sides equal to  $2R_F$ . A void nucleus is located at the center of the top and bottom bases. The volume of solid contained in each prism is  $(2R_F)^2 d$ . At fracture the top and bottom bases of each prism have been transformed into hemispheres of radius  $R_F$ , representing the voids that developed from the nuclei. The centers of the hemispheres at either end of the prism are separated by a distance  $d + 2\delta$ , where  $\delta$  is chosen so that the volume of solid in the original and in the final prisms is the same. Thus,

$$(2R_F)^2 d = (2R_F)^2 (d + 2\delta) - \frac{4}{3} \pi R_F^3$$

where the last term on the right represents the volume of the two hemispherical cavities at either end of the prism. The fractional elongation of the grain at fracture is  $2\delta/d$ , which from the preceding formula is found to be

$$\epsilon_F = \frac{2\delta}{d} = \frac{\pi R_F}{3 d}$$

Substituting Eq. 18.87 for  $R_F$  yields

$$\epsilon_F = \frac{\pi^{3/2}}{6} \frac{\mathcal{R}}{d} = \frac{\pi}{6d(N_{gb})^{1/2}} \quad (18.89)$$

According to this formula, ductility in materials that fail by cavitation is improved by grain refinement and by decreasing the density of void nuclei on grain boundaries.

The theory of void nucleation in the grain boundaries (as opposed to the growth theory just presented) is not sufficiently well developed to permit prediction of the void spacing  $\mathcal{R}$ . However, this quantity can be determined by measuring the void density on grain boundaries from micrographs of the fracture surface and employing Eq. 18.78. Estimates of the time to rupture based on the preceding analysis are in reasonable agreement with the results of creep-rupture tests for many metals. Except for the arbitrariness of the condition of Eq. 18.83, the Hull-Rimmer theory provides a physically acceptable explanation of creep rupture by grain-boundary voids at stresses below that required for wedge-crack propagation. An alternative analysis of the growth process is considered in problem 18.10.

## 18.10 HELIUM EMBRITTLEMENT

Helium gas produced by transmutation of the components of stainless steel causes embrittlement (loss of ductility), which cannot be eliminated by high-temperature annealing. Like fission gases produced in the fuel, helium is thermodynamically insoluble in metals and tends to precipitate into bubbles if the temperature is high enough for the helium atoms to migrate. If the helium bubbles are formed in the matrix, they can contribute to radiation hardening of the metal in the same manner as voids (i.e., by Eq. 18.53). However, when the temperature is low enough for stable dislocation loops and voids (i.e.,  $T < 700$  to  $800^\circ\text{C}$ ), the increment of strength provided by the helium bubbles is small compared with the contributions of the other radiation-produced defects. At temperatures that result in elimination of voids and dislocations by annealing, the strength of the steel returns to its unirradiated value (see Fig. 18.26). The helium bubbles may have coarsened by coalescence to the point that not enough bubbles are present to cause appreciable hardening.

At elevated temperatures, however, helium causes severe embrittlement of the steel. The elongation to fracture never recovers at high temperatures as does the yield strength. Fracture in the unirradiated metal occurs in a transgranular or combination transgranular-intergranular mode, whereas fracture of irradiated steel occurs invariably along grain boundaries. The extent of helium embrittlement depends on fast-neutron fluence, steel composition, and temperature.

Various mechanisms for explaining helium embrittlement have been suggested. Woodford, Smith, and Moteff<sup>2</sup> proposed that the helium bubbles remain in the matrix where they impede the motion of dislocation lines. The increased strength of the matrix prevents relaxation of stress concentrations at grain-boundary triple points and thereby enhances failure by propagation of wedge cracks.

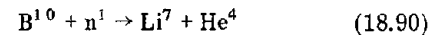
Kramer et al.<sup>2,3</sup> observed that helium bubbles are nucleated mainly on grain-boundary carbide particles (i.e.,  $\text{M}_{23}\text{C}_6$ ), thereby allowing cracks to form without the necessity of satisfying Stroh's nucleation stress criterion of Eq. 18.66. Reiff<sup>2,4</sup> has shown that the presence of helium in triple-point cracks permits unstable growth of these cracks at stresses lower than that required for a gas-free crack (Eq. 18.75).

However, the majority of the workers in this field attribute embrittlement to the stress-induced growth of helium bubbles on grain boundaries which eventually link up and cause intergranular failure.<sup>2,5-27</sup>

### 18.10.1 Helium Production Rates

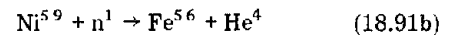
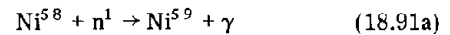
Before discussing the embrittlement mechanism in detail, we first determine the amount of helium produced by the neutron flux. The transmutations that produce an alpha particle (which is the nucleus of a helium atom) can be divided into reactions which occur preferentially in a thermal-neutron flux and those which require a fast-neutron flux.

In a thermal flux spectrum, the primary source of helium in steel is due to the reaction



which has an effective cross section in excess of 3000 barns in a Maxwellian (i.e., thermal) flux spectrum. Thus, even the small quantities of boron in stainless steel (Table 18.1) produce substantial quantities of helium. Moreover, the boron in steel is often associated with grain-boundary carbides, which have the generic formula  $\text{M}_{23}(\text{CB})_6$ . Here M denotes iron or chromium, and (CB) means that boron and carbon are interchangeable in the compound. Thus, the helium produced from the boron reaction is strategically available close to grain boundaries, where it can do the most damage.

Natural boron contains only 20%  $\text{B}^{10}$ , and, in view of the small concentrations of this impurity in most steels, the available  $\text{B}^{10}$  is burned out of the cladding by reaction 18.90 early in the life of the fuel element. However, the amount of helium found in the cladding continues to increase, partly because of the following two-step reaction involving thermal neutrons and nickel:<sup>2,8-30</sup>



The effective thermal-neutron cross sections for these reactions are 4.4 and 13 barns, respectively. Because the supply of nickel in austenitic stainless steel is inexhaustible (from a nuclear reaction point of view), the helium produced by the two-step reaction of neutrons and nickel continues throughout the life of the fuel element.

In the fast breeder reactors the fast-neutron flux is some four orders of magnitude greater than the thermal neutron flux. By comparison the fast and thermal components of the neutron flux in the so-called thermal reactors are about equal (see Table 10.1). Thus, although reactions 18.90 and 18.91 produce helium in the cladding of an LMFBFR, the fast flux induces (n,α) reactions in all components of the metal. [Fast-neutron irradiation also produces (n,p) reactions on nearly all nuclides. However, the hydrogen produced by these reactions does not cause embrittlement because of rapid diffusion of this element in steel, which leads to escape from the cladding.] Birss<sup>31</sup> has reviewed the reactions that produce helium in reactor materials. The most important helium producers in the steel are the nickel

and iron. The other major constituent of steel (chromium) also produces significant quantities of helium. The impurities nitrogen and boron also release helium as a result of  $(n,\alpha)$  reactions induced by fast neutrons. The  $(n,\alpha)$  reactions in the metals and the light impurity elements in steel are of the threshold type, which means that the cross section is zero for all energies below a minimum or threshold value. The threshold energy occurs because the reactions are endothermic and hence require the kinetic energy supplied by the neutron to proceed. By contrast, reactions 18.90 and 18.91 are exothermic with cross sections that increase as  $E^{-1/2}$ . Figure 18.39 shows the energy dependence of the cross sections for a typical  $(n,\alpha)$

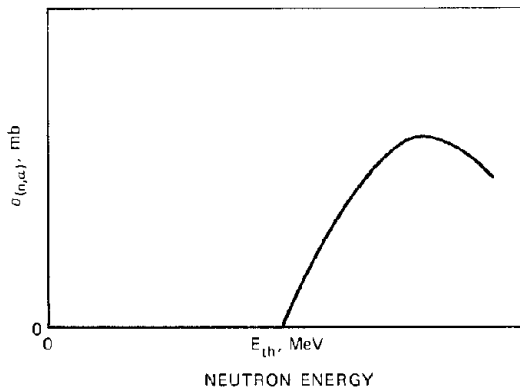


Fig. 18.39 Energy dependence of a typical  $(n,\alpha)$  cross section.

reaction. The threshold energy is of the order of 1 to 5 MeV. When multiplied by the energy spectrum of the flux (Fig. 17.18) and by the density of the particular nuclide, the rate of production of helium is given by

$$N \int_{E_{th}}^{\infty} \phi(E) \sigma_{(n,\alpha)}(E) dE = \text{rate of He production} \\ \text{per unit volume of metal} \quad (18.92)$$

where  $N$  is the density of the nuclide in question and  $\phi(E)$  is the flux spectrum. An effective cross section in a particular flux spectrum can be defined by

$$\sigma_{(n,\alpha)eff} = \frac{\int_{E_{th}}^{\infty} \phi(E) \sigma_{(n,\alpha)}(E) dE}{\int_{0.1}^{\infty} \phi(E) dE} \quad (18.93)$$

The denominator of Eq. 18.93 is the total fast-neutron flux ( $E > 0.1$  MeV). The effective  $(n,\alpha)$  cross section for the major constituents and two impurities in stainless steel in a fission spectrum are listed in Table 18.3. The cross sections represent the values for each stable isotope of the element in the list weighted with the natural abundance and summed.

Note that the cross sections for the metals are of the order of millibarns, whereas the thermal cross sections of reactions 18.90 and 18.91 are three to four orders of magnitude larger. The nitrogen and boron fast flux  $(n,\alpha)$  cross sections are much larger than those of the major constituents of the steel; so these impurity elements are

Table 18.3 Effective  $(n,\alpha)$  Cross Sections in a Fission-Neutron Spectrum

Element	$\sigma_{(n,\alpha)eff}$ , mb
Cr	0.2
Fe	0.23
Ni	4.2
N	41
B	623

significant contributors of helium in fast reactor fuel-element cladding. The effective  $(n,\alpha)$  cross sections in the flux spectrum of a typical LMFBR are about equal to those given for the fission-neutron spectrum in Table 18.3.

Figure 18.40 shows the helium concentrations produced in fast and thermal reactor cladding. The discontinuity in the helium production rate in the thermal reactor is due to burnout of  $B^{10}$ . The continued rise in helium concentration is due to threshold  $(n,\alpha)$  reactions in the fast component of the neutron flux. The two-step nickel reaction of Eq. 18.91 is not considered in the plot. The helium concentration in the fast reactor cladding becomes larger than that in the thermal reactor after  $\sim 100$  days. Despite the small cross sections, the fluxes in the fast reactor are larger than in the thermal reactor. After approximately a 2-year irradiation period, the helium concentration in the cladding approaches 100 ppm.

### 18.10.2 Stress-Induced Growth of Helium Bubbles on Grain Boundaries

The analysis of the rate of growth of helium bubbles lying on grain boundaries perpendicular to the direction of the applied tensile stress is based on the Hull-Rimmer void calculation presented in the previous section. Only two aspects of the void analysis need to be changed: the stability criterion and the vacancy concentration at the bubble surface during growth.

The stability criterion for voids is given by Eq. 18.77. The analogous criterion for gas-filled bubbles in mechanical equilibrium with the solid was deduced by Hyam and

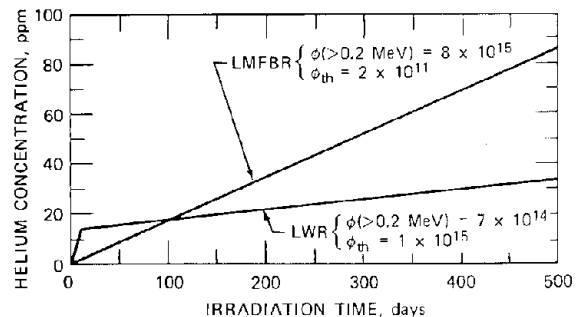


Fig. 18.40 Helium concentration in type 304 stainless steel exposed to LMFBR and LWR flux spectra. [After A. DePino, Jr., *Trans. Amer. Nucl. Soc.*, 9: 386 (1966).]

Sumner.<sup>32</sup> Consider a bubble that contains  $m$  helium atoms. In the absence of stress in the surrounding solid, the radius of the bubble is given by Eq. 13.16; we have assumed that the bubble is large enough to permit application of the perfect gas law, a condition which is less restrictive for helium than it is for xenon. Thus,

$$m = \left(\frac{4}{3} \pi R_0^2\right) \left(\frac{2\gamma}{kT}\right) \quad (18.94)$$

When a tensile stress  $\sigma$  is applied, the new equilibrium radius of the bubble is given by Eq. 13.4:

$$p + \sigma = \frac{2\gamma}{R} \quad (18.95)$$

and the ideal-gas law:

$$p \left(\frac{4}{3} \pi R^3\right) = mkT \quad (18.96)$$

Eliminating  $m$  and  $p$  from Eqs. 18.94 to 18.96 yields the relation

$$\sigma = \frac{2\gamma}{R} \left(1 - \frac{R_0^2}{R^2}\right) \quad (18.97)$$

Equation 18.97 is plotted in Fig. 18.41 for three values of  $R_0$ , which, according to Eq. 18.94, is a measure of the number of helium atoms in the bubble. The function has a maximum when  $R = 3^{1/2}R_0$ , at which size the stress and the initial radius are related by

$$\sigma = \frac{4}{3(3)^{1/2}} \frac{\gamma}{R_0} = 0.77 \frac{\gamma}{R_0} \quad (18.98)$$

This formula can be interpreted in either of two ways. For a given applied tensile stress, it gives the critical initial bubble radius,  $R_{0crit}$ , for stability. If  $R_0 < R_{0crit}$ , application of the stress causes the bubble to enlarge to the size that satisfies Eq. 18.97. Alternatively, if the initial bubble radius is specified, the formula gives the critical stress  $\sigma_{crit}$  for stability. If either  $\sigma$  or  $R_0$  is such that the left-hand side

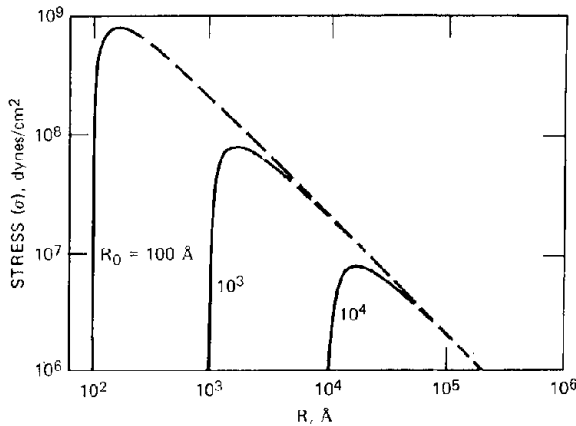


Fig. 18.41 Critical stress for unlimited stress-induced growth of equilibrium bubbles as a function of initial bubble size. Dashed portions of the curves have no physical meaning. (From Ref. 32)

of Eq. 18.98 is greater than the right-hand side, there is no stable bubble radius, and unlimited growth occurs. Equation 18.98 is the bubble analog of Eq. 18.77 for voids. For a given size of cavity, the critical stress is seen to be a factor of  $\sim 3$  smaller for equilibrium gas-filled bubbles than it is for voids. This result reflects the fact that the gas pressure,  $p$ , in Eq. 18.95 assists the applied stress,  $\sigma$ , in enlarging the bubble.

The growth law for the gas-filled bubble is formulated in a manner similar to that applied by Hull and Rimmer to grain-boundary voids (previous section). The density of grain-boundary bubbles defines the unit cell radius according to Eq. 18.78. If it is assumed that all the helium produced in the matrix is in the form of bubbles and all the bubbles are attached to grain boundaries, an estimate of  $N_{gb}$  can be made. Let  $M$  be the total concentration of helium in the metal, as determined from Fig. 18.40. If  $R_0$  is the size of the bubbles in the absence of stress, the number of gas atoms per bubble is given by Eq. 18.94. The bubble density (number of bubbles per unit volume) is

$$N = \frac{M}{m} = \frac{M}{(4\pi R_0^2/3)(2\gamma/kT)} \quad (18.99)$$

If the grain diameter in the specimen is  $d$ , there are  $Nd^3$  bubbles per grain. Assuming that the grains are cubical in shape and that the  $Nd^3$  bubbles are uniformly disposed over the six faces of the cube, there are  $Nd/6$  bubbles per unit area of grain boundary from one grain. However, each grain boundary is supplied with bubbles from two adjacent grains; so

$$N_{gb} = \frac{Nd}{3} \text{ bubbles/unit grain-boundary area} \quad (18.100)$$

Unfortunately, Eqs. 18.99 and 18.100 do not uniquely determine  $N_{gb}$ . In addition, we must either specify the bubble size,  $R_0$ , or the bubble density,  $N$ . Knowledge of either of these two quantities depends on the bubble nucleation, migration, and coalescence properties, none of which is well established.

Nevertheless, assuming that the bubble density on the grain boundaries,  $N_{gb}$ , can be estimated, the Hull-Rimmer analysis is identical to that presented for voids provided that the boundary condition giving the vacancy concentration at the bubble surface, Eq. 18.80, is modified to account for the effect of the internal gas pressure. To do this, we use Eq. 13.176:

$$C_v(R) = C_v^{eq} \exp \left[ \left( \frac{2\gamma}{R} - p \right) \right] \frac{\Omega}{kT} \quad (18.101)$$

Following the lines of the Hull-Rimmer derivation, the growth law for the helium bubbles is found to be

$$\frac{dR}{dt} = \frac{wD_{gb}\Omega}{R^2 kT} \left( \sigma - \frac{2\gamma}{R} + p \right) \times \frac{(\mathcal{R}/R)^2 - 1}{2\ln(\mathcal{R}/R) - 1 + (R/\mathcal{R})^2} \quad (18.102)$$

The gas pressure  $p$  in this formula is expressed in terms of  $m$  and  $R$  by Eq. 18.96, and integration according to Eq. 18.88 can be accomplished if  $m$  is a constant or a known function of time. Equation 18.102 reduces to the

case for voids (Eq. 18.85) if the cavity contains no gas (i.e., when  $p = 0$ ).

If the applied stress is less than the critical value given by Eq. 18.98 for the particular initial bubble size  $R_0$ , the bubbles enlarge from radius  $R_0$  to a final value that satisfies Eq. 18.97 at a rate given by Eq. 18.102. However, if the applied stress is greater than  $0.77\gamma/R_0$ , growth proceeds at the rate prescribed by Eq. 18.102 but with no upper limit to  $R$ . In this case, growth is terminated when the bubbles touch, which occurs at a radius given by Eq. 18.87. The time to rupture is given by Eq. 18.88, and the elongation at fracture, by Eq. 18.89. Using Eq. 18.100 in Eq. 18.89 gives

$$\epsilon_F = \left( \frac{\pi^2}{12Nd^3} \right)^{1/2} \quad (18.103)$$

Equation 18.103 shows that the greater the density of bubbles, the more severe the embrittlement due to helium. Owing to bubble growth by diffusion and coalescence at the expense of nucleation of new bubbles,  $N$  increases linearly with neutron fluence and probably decreases with increasing temperature. This phenomenon is commonly called *overaging*.

### 18.11 SUMMARY OF IRRADIATION EMBRITTLEMENT OF AUSTENITIC STAINLESS STEEL

Mechanical properties are commonly measured in either tensile (high strain rate) or creep-rupture (low strain rate) tests. In these two types of tests, the radiation effects on yield strength,  $\sigma_Y$ , and elongation at fracture,  $\epsilon_F$ , are most pronounced. As a result of irradiation,  $\sigma_Y$  is increased and  $\epsilon_F$  is decreased. The radiation-induced loss of ductility is more significant in fuel-element design than is the increase in yield strength; radiation hardening enhances service performance, whereas ductility losses decrease service life. Of these two factors, service life is by far the more important in limiting the design of a reactor fuel element. Embrittlement will probably be the lifetime limiting factor in the first wall of fusion reactors as well.

Embrittlement increases monotonically with neutron fluence in both tensile and creep-rupture tests (Fig. 18.30). The effect of irradiation temperature, however, is quite complex (irradiation temperature should not be confused with testing temperature, the effect of which is shown in Fig. 18.31). Figure 18.42 shows the effect of irradiation temperature on the elongation at fracture in low-temperature postirradiation tensile tests of specimens that have all been irradiated to the same fast-neutron fluence. At low temperatures reduced ductility is due to plastic instability (Secs. 18.3 and 18.9), which in turn is due to the large increase in yield stress without a comparable increase in ultimate strength. As the temperature approaches  $500^\circ\text{C}$ , barriers to dislocation motion (e.g., loops) responsible for hardening begin to be removed, and the metal recovers its work hardenability. As a consequence of this recovery, ductility increases. At approximately the same temperature that point defects in the metal become sufficiently mobile to anneal out the defect clusters that cause hardening, helium atoms in the matrix also become capable of

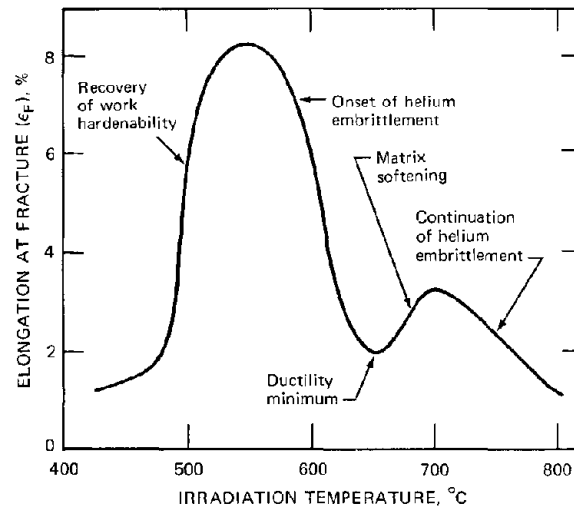


Fig. 18.42 Effect of irradiation temperature on the ductility of irradiated stainless steel. Tensile tests at  $50^\circ\text{C}$ ; fast-neutron fluence  $> 10^{22}$  neutrons  $\text{cm}^{-2} \text{sec}^{-1}$ . [After R. L. Fish and J. J. Holmes, *J. Nucl. Mater.*, 46: (1973).]

migrating and precipitating into bubbles that segregate at the grain boundaries. Consequently, ductility falls because of helium embrittlement. As the temperature reaches  $\sim 650^\circ\text{C}$ , removal of voids becomes appreciable, and the matrix softens some more. The softer matrix permits plastic flow in the neighborhood of wedge cracks and thereby tends to counteract the embrittlement due to helium. The resulting ductility minimum has often been observed in tensile testing of irradiated steels. Eventually, however, helium embrittlement overwhelms all other effects, and the ductility drops to very low values at high temperatures.

Design of fuel elements is usually based on one or more creep-rupture properties of the irradiated metal. For example, if cladding is to operate in a reactor for a specified irradiation time  $t_{\text{irr}}$ , the allowable stress to which it may be subjected by internal pressure from released fission gases and/or fuel-cladding mechanical interaction can be required to be the smaller of the following two values: (1) 67% of the stress for rupture in time  $t_{\text{irr}}$  or (2) 100% of the stress to produce 1% total strain (elastic, plastic, and creep) in time  $t_{\text{irr}}$ .

For irradiated metal the allowable stresses under condition (1) can be obtained from out-of-pile test results such as those shown in Fig. 18.31. The data in Fig. 18.29 permit estimation of the minimum allowable stress under condition (2).

These conditions assume that the stress applied to the cladding is constant over the lifetime  $t_{\text{irr}}$ . When this is not so, the technique known as the *summation of life fractions* is often employed. Neglect for the moment the effect of irradiation, and suppose that the cladding is subject to stress  $\sigma_1$  for time  $t_1$ ,  $\sigma_2$  for time  $t_2$ , etc. The sum of the time increments  $t_1 + t_2 + \dots = t_{\text{irr}}$ . Corresponding to each stress level is a rupture life  $t_{R1}, t_{R2}, \dots$ . The allowable combination of times and stresses is given by

$$\frac{t_1}{t_{R1}} + \frac{t_2}{t_{R2}} + \dots = 1 \quad (18.104)$$

where it is assumed that the temperature is constant and the stress dependence of the rupture life is known. Equation 18.104 does not include the factor of safety in condition (1).

Similarly, condition (2) is modified in the case of different stresses during cladding lifetime to

$$\frac{t_1}{t_{e1}} + \frac{t_2}{t_{e2}} + \dots = 1 \quad (18.105)$$

where  $t_{ei}$  is the time required to produce 1% strain at stress  $\sigma_i$ .

In a radiation field, the time to rupture,  $t_{Ri}$  in Eq. 18.104, and the time to achieve 1% strain,  $t_{ei}$  in Eq. 18.105, depend on the stress  $\sigma_i$ , the temperature  $T_i$ , and the accumulated fluence  $\sum_{j=1}^i \Phi_j t_j$  for the interval  $t_i$  that the cladding has been in the condition denoted by the subscript  $i$ . Thus, stress-rupture failure occurs when<sup>3,3</sup>

$$\sum_{i=1}^n \frac{t_i}{t_{R}(\sigma_i, T_i, \sum_{j=1}^i \Phi_j t_j)} = 1 \quad (18.106)$$

In-pile irradiation creep (Sec. 19.7) is not included in this analysis.

## 18.12 HARDENING AND EMBRITTLEMENT OF FERRITIC STEELS

The theories of radiation hardening reviewed in Secs. 18.4 through 18.7 apply equally well to bcc and fcc metals and alloys. However, there are several important differences in the ways that these two types of metals respond to radiation, all of which can be traced to the greater mobility of atoms or point defects in the more open bcc lattice compared to the close-packed fcc crystal structure.

### 18.12.1 Yield Drop

One of the most important differences in the mechanical properties of austenitic and ferritic steels in the unirradiated condition is the absence of a yield drop in the stress-strain behavior of austenitic steel. The existence of a sharp yield point in unirradiated ferritic steels (the upper yield point in Fig. 18.10) is attributed to the pinning of dislocation lines by impurity atoms (principally carbon) strung out along the line. Before a Frank-Read source can be operated by the applied stress, the dislocation line in the source (BC in Fig. 8.13) has to be unpinned from the impurity atoms that have become attached to it as a result of migration from the matrix. The stress field around dislocation lines can attract impurity atoms. Interstitial carbon atoms, for example, are thermodynamically more comfortable in the tensile region below the extra half-plane of atoms of an edge dislocation than they are in the perfect matrix. The stress required to release the dislocation from a row of carbon atoms can be estimated.<sup>1</sup> Once free from the pinning action of the solute atoms, the dislocation can move at a lower stress, which causes the drop in the yield stress from U to L in Fig. 18.10. Yield then propagates at a

nearly constant flow stress until the beginning of normal work-hardening processes arising from interaction between moving and stationary dislocations.

The carbon-dislocation locking mechanism is not important in austenitic steels because the diffusion coefficient of carbon in the close-packed fcc lattice is lower than it is in the more open bcc structure of ferritic steel. Under normal quenching procedures, the carbon atoms in austenitic steel cannot move rapidly enough to the dislocation line to provide a concentration of atoms along the line which is sufficient to strongly lock the dislocation. As indicated in Sec. 18.5, fcc metals develop a yield drop under irradiation because point defects can take the place of impurity atoms in locking dislocations.

### 18.12.2 Radiation Anneal Hardening

The high mobility of impurity atoms in bcc metals is manifest by the phenomenon of *radiation anneal hardening*, which is not observed in fcc materials. If, following a low-temperature irradiation, specimens of an fcc metal are annealed for several hours before testing, the radiation-produced increase in the yield stress decreases uniformly with annealing temperature. With bcc metals, on the other hand, the yield stress first increases with annealing temperature, then passes through a maximum before returning to the value observed for the unirradiated metal. The increased hardening arising from the annealing process is due to the migration of interstitial impurity atoms (oxygen, nitrogen, and carbon) to radiation-produced defect clusters, such as the depleted zones or dislocation loops.<sup>3,4</sup> Impurity-defect cluster complexes form more effective obstacles to dislocation motion than do impurities and defect clusters when they exist separately in the matrix. The high interstitial-atom diffusivities permit migration of the small impurity atoms to the defect clusters at temperatures lower than those at which the clusters are destroyed by annealing. However, at sufficiently high temperatures, both the complexes and the defect clusters are removed, and hardening diminishes with temperature as in fcc metals.

### 18.12.3 Creep Strength

The high diffusion rate of the intrinsic components of the bcc metals (the vacancies and matrix atoms) in the more open bcc structure is responsible for the poorer creep-rupture strength of the ferritic steels compared with austenitic steels. Creep by growth of grain-boundary cavities, for example, occurs by vacancy diffusion (Sec. 18.9), which is greater in bcc metals than in fcc metals. For this reason, austenitic steels are used in high-temperature core components rather than ferritic alloys.

### 18.12.4 High-Temperature Embrittlement

One of the most striking differences between bcc and fcc metals is the absence of helium embrittlement in bcc metals. That is, bcc metals and alloys are not subject to the drastic loss in ductility when irradiated at high temperature. One would expect that the higher diffusion coefficients in the bcc materials would accelerate creep rupture by the growth of intergranular voids that are stabilized by helium,

which is believed to be the principal mechanism of helium embrittlement in fcc metals. The virtual absence of helium embrittlement in bcc metals indicates that creep failure in these materials does not occur by the stress-enhanced cavity growth mechanism. Rather, it is believed that the large self-diffusion coefficients in bcc metals permit efficient reduction of stress concentrations at grain boundaries, thereby reducing the tendency for triple-point or wedge cracking.<sup>3,5</sup> The high point-defect mobility assists in the processes of recrystallization (growth of new grains) and recovery (softening of the matrix due to annealing of the dislocation network). Both processes act to reduce stress concentrations and thereby inhibit intergranular failure.

### 18.12.5 Brittle Fracture—The Cottrell—Petch Theory

On the basis of an earlier theory of Petch, Cottrell<sup>3,6</sup> has proposed a theory of yielding in metals exhibiting a distinct yield point which can be applied to determine the fracture stress. Knowledge of both the yield and fracture stresses permits the conditions for brittle fracture to be deduced.

The lower yield point in bcc metals or in irradiated fcc metals contains contributions due to source hardening and friction hardening (Sec. 18.5). Friction hardening is the stress experienced by dislocations moving through the metal. Source hardening represents the applied stress needed to unlock pinned dislocations and set them into motion. Cottrell assumes that dislocations in a few isolated grains have been unlocked either because the orientation of these grains relative to the load is such as to produce the maximum resolved shear stress on active slip planes or because a few sources in these grains have particularly low unpinning stresses. In either case, the dislocations produced in the prematurely yielded grains pile up against the grain boundary. The enhanced shear stress in the neighborhood of the pileup triggers the sources in the adjacent grain. Like a row of dominoes, yielding propagates across the entire specimen, or the material flows.

The shear stress exerted on the slip plane in a grain next to one that has yielded and released an avalanche of dislocations which are stopped by the grain boundary is shown in Fig. 18.43. The shear stress acting on the sources in grain 2 consists of two components, the applied shear stress  $\sigma_{xy}$  and the shear stress due to the proximity of the pileup in grain 1. The latter is given by Eq. 8.41 wherein  $\sigma_{xy}$  is reduced by  $\sigma_i$  to account for the frictional stress experienced by dislocations in the pileup in grain 1. Thus, the sources in grain 2 are subject to the shear stress

$$\sigma_2 = \sigma_{xy} + (\sigma_{xy} - \sigma_i) \left( \frac{d}{L'} \right)^{\frac{1}{2}} \quad (18.107)$$

where  $d$  (the grain size) is taken to be the length of the pileup in grain 1 and  $L'$  is the distance from the grain boundary to the nearest dislocation source in grain 2. The ratio  $d/L'$  is generally much greater than unity. The stress required to operate the sources in the material is denoted by  $\sigma_d$ . In high-purity unirradiated metals,  $\sigma_d$  is the stress needed to activate Frank—Read sources (Eq. 8.16), but, in ordinary bcc metals or in irradiated fcc metals,  $\sigma_d > \sigma_{FR}$

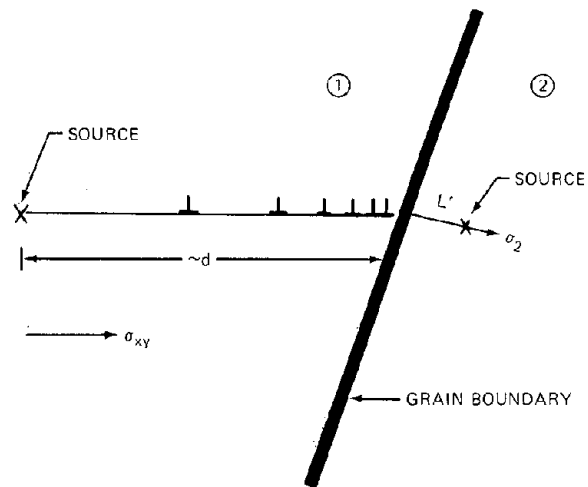


Fig. 18.43 Shear stress on source in unyielded grain due to pileup in adjacent yielded grain.

because of locking of the source dislocations by impurities or point defects produced by radiation.

At the instant yielding is triggered by the mechanism of Fig. 18.43,  $\sigma_{xy}$  is equal to the yield stress  $\sigma_Y$  and  $\sigma_2$  is equal to  $\sigma_d$ . Making these substitutions in Eq. 18.107 gives

$$\sigma_d = \sigma_Y + (\sigma_Y - \sigma_i) \left( \frac{d}{L'} \right)^{\frac{1}{2}}$$

or, solving for the yield stress,

$$\sigma_Y = \frac{\sigma_i + \sigma_d (L'/d)^{\frac{1}{2}}}{1 + (L'/d)^{\frac{1}{2}}} \approx \sigma_i + \sigma_d \left( \frac{L'}{d} \right)^{\frac{1}{2}} \quad (18.108)$$

If the product  $\sigma_d (L')^{\frac{1}{2}}$  is denoted by a constant  $k_y$ , the yield stress becomes

$$\sigma_Y = \sigma_i + k_y d^{-\frac{1}{2}} \quad (18.109)$$

The second term on the right gives the source-hardening contribution to the yield stress. The two components of  $\sigma_Y$  can be determined experimentally by one of two means:

1. By extrapolating the work-hardening portion of the stress—strain curve in Fig. 18.10 to the elastic line. The intercept is interpreted as  $\sigma_i$ , and the difference between the lower yield point and the intercept is the source-hardening contribution  $k_y d^{-\frac{1}{2}}$ . This procedure has been employed by Makin and Minter<sup>4</sup> to determine the effect of neutron irradiation on the friction and source-hardening components of copper.

2. By measuring the yield stress for specimens of different grain size and plotting  $\sigma_Y$  vs.  $d^{-\frac{1}{2}}$ . The intercept of such a plot is  $\sigma_i$ , and the slope gives  $k_y$ .<sup>3,5</sup> Most metals obey a plot of this sort quite well.

With  $k_y$  determined from yield-stress measurements, Cottrell calculates the critical tensile stress for fracture by substituting Eq. 18.109 into Eq. 18.75. At the yield stress,  $\sigma_{xy}$  is identified with  $\sigma_Y$ , and the term in the parentheses of Eq. 18.75 is given by  $k_y d^{-\frac{1}{2}}$ . Thus, the fracture stress is

$$\sigma_{crit} = \sigma_F = \frac{2G\gamma}{k_y} d^{-1/2} \quad (18.110)$$

The effect of grain size on the fracture stress (or ultimate tensile stress) and the yield stress of a low-carbon steel is shown in Fig. 18.44. The two lines cross at the ductile-brittle transition. To the right of this point, the material is ductile, since it yields before fracturing. The incremental stress  $\sigma_F - \sigma_Y$  needed to cause fracture is supplied by work-hardening processes, which means that the metal must deform plastically. As shown by the lower curve in this figure, appreciable elongation occurs before fracture. To the left of the transition, yielding and fracture occur simultaneously. Fracture takes place along the yield stress line since yielding is a prerequisite to fracture. In this region the metal is totally brittle.

The Cottrell-Petch theory can be employed to explain the effect of radiation on the yield and ultimate tensile strengths of steels. The frictional component to the yield stress,  $\sigma_i$ , is quite sensitive to radiation owing to the defect clusters produced by fast-neutron bombardment (Sec. 18.5). The parameter  $k_y$ , on the other hand, depends on the stress to operate dislocation sources in the metal,  $\sigma_d$ . In fcc metals and alloys, this stress is slightly increased by radiation because the point defects assist in pinning the sources. In bcc metals, however, the sources are strongly pinned by impurity atoms in the absence of neutron-produced point defects; so radiation has a negligible effect on  $k_y$  for metals of this crystallographic structure. Conse-

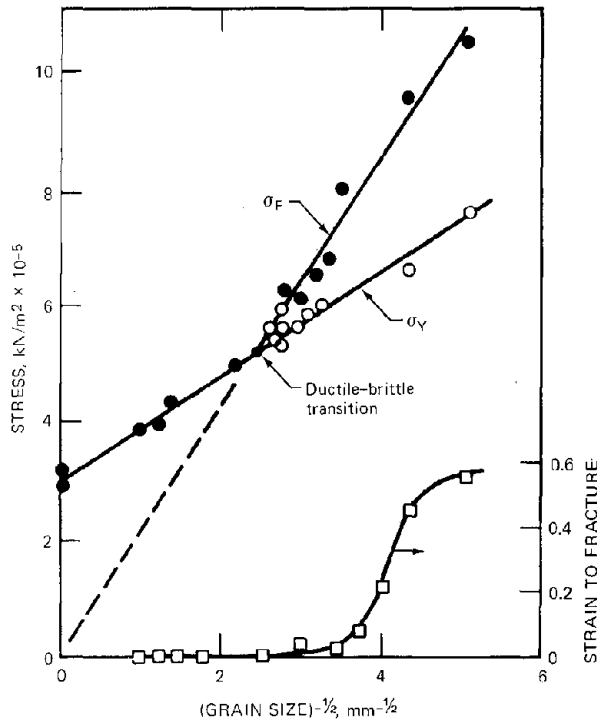


Fig. 18.44 Effect of grain size on yield and fracture stresses of a low-carbon steel tested at low temperature. ●, fracture. ○, yield. □, strain. (After Ref. 36.)

quently, the theory suggests that the yield stress should increase more than the ultimate stress as a result of irradiation. This prediction is borne out by experiments. The drastic loss in ductility at low temperature results from the different sensitivities of  $\sigma_Y$  and  $\sigma_F$  to neutron damage.

Figure 18.45 shows the Cottrell-Petch theory displayed on a temperature plot for different values of the frictional stress. The increase in  $\sigma_i$  is assumed to be due to neutron irradiation. The ductile-brittle transition temperature (DBTT) or the nil-ductility temperature (NDT) is defined by the condition that  $\sigma_F = \sigma_Y$ , or from Eq. 18.110 by the formula:

$$\sigma_Y k_y = 2G\gamma d^{-1/2} \quad (18.111)$$

Although this equation could in principle be solved for the transition temperature (using the temperature dependencies of  $\sigma_Y$  and  $k_y$ ), it is most commonly employed to estimate the effect of neutron exposure on the temperature at which ferritic steels become brittle. The graphic illustration of the increase in the transition temperature shown in Fig. 18.45 can be expressed quantitatively by using Eq. 18.111 and noting that the right-hand side is essentially constant during irradiation and temperature variation. Thus,

$$d(\sigma_Y k_y) = \sigma_Y dk_y + k_y d\sigma_Y = 0$$

The changes in  $k_y$  and  $\sigma_Y$  due to the variables T and neutron fluence (neutron fluence is manifest by radiation hardening or an increase in the frictional stress  $\sigma_i$ ) are

$$dk_y = \left(\frac{\partial k_y}{\partial T}\right) dT + \left(\frac{\partial k_y}{\partial \sigma_i}\right) d\sigma_i$$

$$d\sigma_Y = \left(\frac{\partial \sigma_Y}{\partial T}\right) dT + \left(\frac{\partial \sigma_Y}{\partial \sigma_i}\right) d\sigma_i$$

Combining these expressions and neglecting the effect of radiation on source hardening (i.e.,  $\partial k_y / \partial \sigma_i = 0$  and hence,

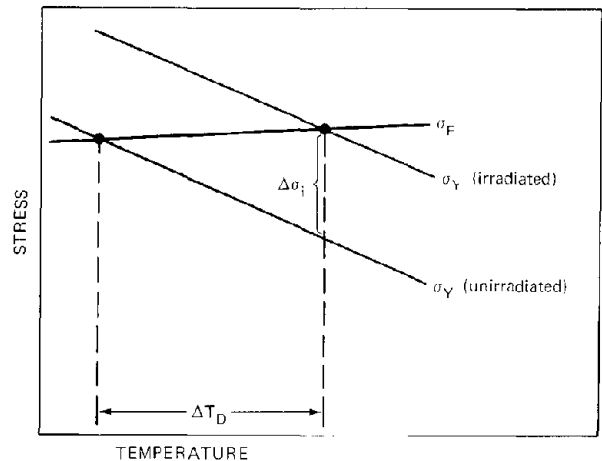


Fig. 18.45 Effect of temperature on the yield and fracture stresses of unirradiated and irradiated ferritic steel.

according to Eq. 18.109,  $\partial\sigma_Y/\partial\sigma_i = 1$ ), we obtain the increase in the transition temperature:

$$\frac{dT}{d\sigma_i} = \frac{\Delta T_D}{\Delta\sigma_i} = - \left( \frac{\sigma_Y}{k_Y} \frac{\partial k_Y}{\partial T} + \frac{\partial\sigma_Y}{\partial T} \right)^{-1} \quad (18.112)$$

The temperature dependence of  $k_Y$  is slight, but, since it is multiplied by a large number in Eq. 18.112, it is retained in the analysis. The yield stress, the source-hardening coefficient, and their temperature derivatives can be obtained from out-of-pile tests. Inserting numerical values shows that

$$\frac{\Delta T_D}{\Delta\sigma_i} = 3 \text{ to } 5^\circ\text{C per } 10^4 \text{ kN/m}^2 \quad (18.113)$$

for typical pressure-vessel steels. As discussed in Sec. 18.3, the DBTT or NDT can be measured by impact tests. Figure 18.13(b) shows that the DBTT of unirradiated low-carbon steel is about  $0^\circ\text{C}$ . The corresponding curve for an irradiated specimen is translated to much higher temperatures than the data for unirradiated material shown in this graph. When the radiation hardening ( $\Delta\sigma_i$ ) is measured as well, observed values of  $\Delta T_D$  are in good agreement with the predictions of the Cottrell-Petch theory, expressed by Eq. 18.113.

The increase in the frictional stress  $\Delta\sigma_i$  is due almost exclusively to the production of obstacles in the slip planes of moving dislocations. At the low temperatures at which pressure vessels in LWRs operate,  $\Delta\sigma_i$  can be identified with the hardening due to depleted zones (Eqs. 18.38 and 18.42). Figure 18.46 summarizes data on the increase in the

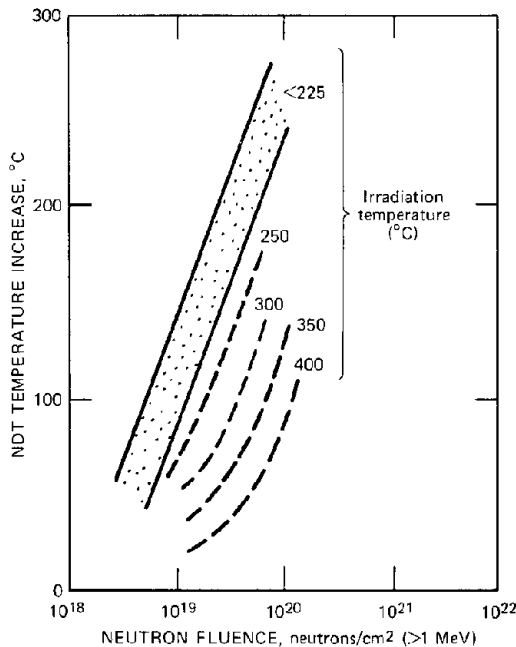


Fig. 18.46 Effect of fast neutron fluence on the increase in the nil-ductility temperature of low carbon steels irradiated at various temperatures. (After L. E. Steele and J. R. Hawthorne, in ASTM Special Technical Publication 380, p. 283, American Society for Testing and Materials, Philadelphia, 1965.)

nil-ductility temperature of various pressure-vessel steels with neutron fluence. If the component operates at temperatures below  $\sim 250^\circ\text{C}$  for long irradiation periods, a considerable increase in the NDT is observed. As shown by the graph, the NDT can approach the operating temperature of the pressure vessel (approximately equal to the inlet coolant temperature in a PWR) after long periods of irradiation. Periodic annealing of ferritic steel components of the reactor core may be necessary to eliminate accumulated radiation damage. As part of a surveillance program, coupons of the metal can be inserted in the core and periodically withdrawn for impact testing.

Additional information on the effects of neutron exposure on ferritic steels can be found in Refs. 6, 37, and 38.

### 18.13 NOMENCLATURE

- $a_0$  = lattice constant
- $A$  = cross-sectional area of a tensile test specimen; mass number
- $b$  = Burgers vector
- $C$  = point-defect concentration (particles per unit volume); crack length
- $d$  = grain size
- $D$  = point-defect diffusion coefficient; tube diameter
- $D_{gb}$  = grain-boundary self-diffusion coefficient
- $D_{vgb}$  = diffusivity of vacancies in grain boundary
- DBTT = ductile-to-brittle transition temperature
- $E$  = neutron energy; activation energy for steady-state creep; Young's modulus
- $E_{e1}$  = elastic-energy density
- $E_{th}$  = threshold energy for  $(n,\alpha)$  reaction
- $f$  = fraction of grain-boundary area occupied by voids
- $f_x, f_y$  = angular functions of the force between edge dislocations in the  $x$  and  $y$  directions, respectively
- $F$  = force on a unit length of dislocation
- $G$  = shear modulus
- $G_v$  = vacancy production rate in a grain boundary
- $k$  = Boltzmann's constant
- $k_{iv}$  = vacancy-interstitial recombination rate constant
- $k_Y$  = constant in the Cottrell-Petch theory, Eq. 18.109
- $l$  = gauge length of tensile test specimen; spacing of obstacles in a glide plane, Eq. 18.25
- $l_0$  = length of dislocation segment between pinning points
- $L$  = length of dislocation pileup
- $L'$  = distance from grain boundary to nearest dislocation source
- $m$  = helium atoms per bubble
- $n$  = number of dislocations in a pileup
- $N$  = concentration of obstacles, depleted zones, loops, or bubbles
- $N_{gb}$  = number of voids or helium bubbles per unit grain-boundary area
- $p$  = gas pressure
- $P$  = load on tensile test specimen
- $r$  = radius of obstacle to dislocation motion

$r_d$  = radius of dislocation core  
 $R$  = radius of depleted zone, dislocation loop, or helium bubble  
 $\mathcal{R}$  = radius of unit cell surrounding a void or bubble on a grain boundary; radius of curvature of a dislocation line; radius of the stress field around a dislocation  
 $t$  = time; wall thickness  
 $t_R$  = rupture time  
 $T$  = temperature  
 $T_c$  = characteristic temperature, Eq. 18.39  
 $T_D$  = ductile-to-brittle transition temperature  
 $T_m$  = melting point, °K  
 $U^*$  = activation energy for dislocation cutting of an obstacle  
 $U_0$  = energy increase when dislocation cuts an obstacle  
 $v$  = capture volume around a depleted zone  
 $v_d$  = velocity of a glide dislocation  
 $V_c$  = crack volume  
 $w$  = thickness of grain boundary  
 $W$  = work  
 $x$  = distance along glide plane  
 $y$  = distance perpendicular to glide plane  
 $Z$  = capture sites around a dislocation

## Greek Letters

$\alpha$  = number of defect clusters per neutron collision  
 $\beta$  = numerical constant, Eq. 18.62  
 $\gamma$  = surface energy (including plastic deformation)  
 $\gamma_{gb}$  = grain-boundary tension  
 $\gamma_s$  = surface tension of solid (used when plastic deformation at crack tip is important)  
 $\Gamma$  = probability per unit time that a dislocation cuts an obstacle  
 $\epsilon$  = strain  
 $\epsilon_F$  = strain at rupture  
 $\epsilon_1, \epsilon_2, \epsilon_3$  = principal strains  
 $\epsilon^*$  = equivalent strain (strain deviator), Eq. 18.17  
 $\dot{\epsilon}$  = strain rate  
 $\nu$  = Poisson's ratio; vibration frequency of dislocation against an obstacle; number of displacements per primary knock-on atom  
 $\rho$  = density of mobile dislocations  
 $\rho_d$  = total density of dislocations in a solid  
 $\sigma$  = stress (positive in tension)  
 $\sigma^*$  = equivalent stress (stress deviator), Eq. 18.15  
 $\sigma_i$  = friction stress  
 $\sigma_{(n,\alpha)}$  = cross section for  $n, \alpha$  reaction  
 $\sigma_{xy}$  = shear stress  
 $\tau$  = time  
 $\phi(E)$  = neutron flux spectrum  
 $\Phi$  = total fast-neutron flux  
 $\Omega$  = atomic volume  
 $\Sigma_s$  = macroscopic neutron-scattering cross section

## Subscripts and Superscripts

crit = critical value  
 e = edge dislocation  
 eq = equilibrium  
 F = at fracture  
 h = hydrostatic

i = interstitial  
 l = dislocation loop  
 LR = long range  
 max = maximum  
 R = at the surface of a defect  
 s = short range  
 v = vacancy  
 Y = at yield point

## 18.14 REFERENCES

1. D. Hull, *Introduction to Dislocations*, Sec. 10.4, Pergamon Press, Inc., New York, 1965.
2. J. Friedel, *Dislocations*, p. 220, Pergamon Press, Inc., New York, 1964.
3. A. Seeger, in *Proceedings of the Second United Nations International Conference on the Peaceful Uses of Atomic Energy*, Geneva, 1958, Vol. 6, p. 250, United Nations, New York, 1958.
4. M. J. Makin and F. J. Minter, *Acta Met.*, **8**: 691 (1960).
5. M. J. Makin and T. H. Blewitt, *Acta Met.*, **10**: 241 (1962).
6. F. A. Nichols, *Phil. Mag.*, **14**: 335 (1966).
7. C. C. Dollins, *Radiat. Eff.*, **11**: 33 (1971).
8. P. Coulomb, *Acta Met.*, **7**: 556 (1959).
9. R. W. Weeks et al., *Acta Met.*, **17**: 1403 (1969).
10. M. J. Makin, *Phil. Mag.*, **10**: 695 (1964); see also F. Kroupa, *Phil. Mag.*, **7**: 783 (1962).
11. F. Kroupa and P. B. Hirsch, *Discuss. Faraday Soc.*, **38**: 49 (1964).
12. A. J. E. Foreman, *Phil. Mag.*, **17**: 353 (1968).
13. F. R. Smidt, Jr., *Dislocation Channeling in Irradiated Metals*, Report NRL-7078, Naval Research Laboratory, 1970.
14. A. N. Stroh, *Proc. Roy. Soc. (London)*, Ser. A, **223**: 404 (1954).
15. D. McLean, *J. Inst. Metals*, **85**: 468 (1956-57).
16. C. W. Weaver, *Acta Met.*, **8**: 343 (1960).
17. E. E. Bloom and J. R. Weir, Jr., in *Irradiation Effects in Structural Alloys for Thermal and Fast Reactors*, Symposium Proceedings, San Francisco, Calif., p. 261, American Society for Testing and Materials, Philadelphia, Pa., 1969.
18. J. A. Williams, *Acta Met.*, **15**: 1559 (1967).
19. F. Garzarolli et al., *J. Nucl. Mater.*, **30**: 242 (1969).
20. D. Hull and D. E. Rimmer, *Phil. Mag.*, **4**: 673 (1959).
21. M. V. Speight and J. E. Harris, *Metal Sci. J.*, **1**: 83 (1967).
22. D. A. Woodford, J. P. Smith, and J. Motteff, *J. Nucl. Mater.*, **29**: 103 (1969).
23. D. Kramer, H. R. Brager, C. G. Rhodes, and A. G. Pard, *J. Nucl. Mater.*, **25**: 121 (1968).
24. K. H. Reiff, *J. Nucl. Mater.*, **33**: 129 (1969).
25. R. S. Barnes, *Nature*, **206**: 1307 (1965).
26. D. R. Harries, *J. Brit. Nucl. Energy Soc.*, **5**: 74 (1966).
27. G. J. C. Carpenter and R. B. Nicholson, in *Radiation Damage in Reactor Materials 1969*, Symposium Proceedings, Vienna, June 2-6, 1969, Vol. 2, p. 383, International Atomic Energy Agency, Vienna, 1969 (STI/PUB/230).
28. J. Weitman et al., *Trans. Amer. Nucl. Soc.*, **13**: 557 (1970).
29. I. R. Birss and W. E. Ellis, in *Voids Formed by Irradiation of Reactor Materials Conference*, p. 339, British Nuclear Energy Society, London, 1971.

30. A. A. Bauer and M. Kangalaski, *J. Nucl. Mater.*, **42**: 91 (1972).
31. I. R. Birss, *J. Nucl. Mater.*, **34**: 241 (1971).
32. E. D. Hyam and G. Sumner, in *Radiation Damage in Solids*, Symposium Proceedings, Venice, May 1962, Vol. 1, p. 323, International Atomic Energy Agency, Vienna, 1962 (STI/PUB/56).
33. A. J. Lovell and J. J. Holmes, *Trans. Amer. Nucl. Soc.*, **15**: 735 (1972).
34. S. M. Ohr et al., in *Second International Conference on Strength of Metals and Alloys*, Vol. 2, Paper 9.3, p. 742, American Society for Metals, Metals Park, Ohio, 1970.
35. H. Bohm and H. Hauck, *J. Nucl. Mater.*, **29**: 184 (1969).
36. A. H. Cottrell, *Trans. AIME*, **212**: 192 (1958).
37. L. P. Trudeau, *Radiation Effects on Toughness of Ferritic Steels for Reactor Vessels*, American Society for Metals—U.S. Atomic Energy Commission Monograph, Rowman and Littlefield, Inc., New York, 1964.
38. N. Igata and R. R. Hasiguti, *J. Nucl. Mater.*, **30**: 234 (1969).

## 18.15 PROBLEMS

18.1 As a result of irradiation, a specimen of metal contains voids. The specimen is annealed out of pile at temperature  $T$ . Voids grow or shrink only by vacancy capture or emission. The bulk solid contains the thermal-equilibrium vacancy concentration.

(a) How does the radius of a void with initial radius  $R_0$  change with annealing time?

(b) If the void sizes after irradiation are distributed according to the function  $N_0(R_0) dR_0 =$  number of voids with radii between  $R_0$  and  $R_0 + dR_0$ , what is the void distribution function at a time  $t$  in the anneal? Assume the vacancy-diffusion coefficient  $D_v$ , the equilibrium vacancy concentration  $C_v^e$ , the surface tension of the metal  $\gamma$ , and the atomic volume  $\Omega$  are specified. Use a calculational method like the one applied to thermal annealing of depleted zones (Sec. 18.5).

(c) Suppose the initial distribution  $N(R_0)$  is Gaussian with an average void radius of 400 Å and a standard deviation of 50 Å. The initial void concentration,  $N_T^0$ , is  $10^{15} \text{ cm}^{-3}$ . During annealing, the voids of average size disappear in 3 hr. Compute and plot the void distributions at  $t = 0$  and  $t = 2$  hr.

18.2 The work-hardening region of the stress-strain curve can be represented by the formula  $\sigma = k\epsilon^n$ , where  $n$  is the work-hardening coefficient. By increasing the yield stress more than the ultimate tensile stress, irradiation effectively reduces the work-hardening coefficient. Using the criterion for plastic instability, calculate the reduction in uniform elongation due to an irradiation that decreases  $n$  by an amount  $\Delta n$ .

18.3 (a) Show that Eq. 18.26 is valid for a regular planar array of dislocation pinning points [e.g., the (100) plane of the fcc structure].

(b) The potential energy of a dislocation cutting through an obstacle in Seeger's treatment of radiation hardening is of the form

$$Y = 1 - \frac{1}{1 + e^\eta} - A\eta + \text{constant}$$

where

$$Y = \frac{U(x, \sigma_s)}{U_0} \quad \eta = \frac{x}{r'} \quad A = \frac{\sigma b l_0 r'}{U_0}$$

Demonstrate the following properties of the function  $Y(\eta)$ :

1. The barrier height disappears if  $A \geq \frac{1}{4}$ .
2. Expand the location of the maximum and minimum in a Taylor's series in the parameter  $\epsilon = 1 - 4A$ , which is presumed to be small and positive. Show that the extrema are given by

$$\eta_{\pm} = \pm 2\epsilon^{1/2}$$

3. Show that the barrier height is given by Eq. 18.36, or

$$Y(\eta_+) - Y(\eta_-) = \epsilon^{3/2}$$

18.4 The data for depleted-zone hardening by nickel (Fig. 18.20) suggest that two types of zones are created by irradiation. From the curves on this figure, compute the ratio of the radii and of the numbers of the zones represented by lines A and B.

18.5 Consider a dislocation line in a solid containing  $N$  bubbles of radius  $R$  per cubic centimeter. A shear stress  $\sigma_{xy}$  is applied to the solid which causes the dislocation to glide along its slip plane.

(a) Under what conditions will the bubbles be swept along by the dislocation line rather than be bypassed by it?

(b) Under conditions permitting bubble sweeping, what is the initial velocity of the dislocation line? Assume that the bubbles move by the surface-diffusion mechanism.

(c) As the dislocation line moves, it collects all the bubbles in its path, which reduces the bubble spacing along the line and slows it down. Neglecting coalescence of the bubbles attached to the dislocation line, find the velocity of the dislocation line after it has moved a distance  $x$  in the direction of the applied shear stress.

18.6 Consider a thin-walled cylinder of radius  $R$  and thickness  $t_c$  which is subject to internal pressure  $p$  but zero external pressure. The top and bottom of the cylinder are closed; so there is an axial stress on the cylinder wall.

(a) Use simple force balances to determine the axial stress  $\sigma_z$  and the hoop stress  $\sigma_\theta$ .

Use linear elasticity theory (see the Appendix) and the assumption of plane strain (i.e.,  $\epsilon_z$  independent of  $r$  and  $z$ , but not necessarily zero) to determine the following:

(b) The differential equations and boundary conditions for the radial stress,  $\sigma_r$ . Without the thin wall assumption, obtain the solutions for  $\sigma_r$  and  $\sigma_\theta$  as functions of radial position. Show that  $\sigma_\theta$  reduces to the result obtained in (a) for the special case of a thin wall.

(c) The strain components  $\epsilon_z$ ,  $\epsilon_r$ , and  $\epsilon_\theta$ .

(d) The differential equation (and its general solution) for the radial displacement,  $u_r$ .

(e) Show that the radial strain,  $\epsilon_r$ , is related to the fractional decrease in wall thickness:

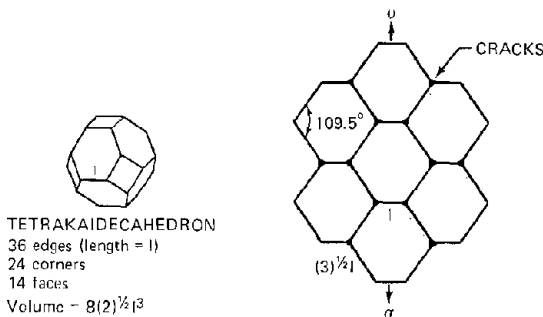
$$\epsilon_r = \frac{\Delta t_c}{t_c}$$

18.7 An irradiated metal contains a network-dislocation density of  $\rho_d$  and  $N_l$  dislocation loops per unit volume of radius  $R_l$ . The yield stress of the irradiated specimen is measured at temperatures just below and just above the temperature at which the loops unfault. What is the difference in the yield stress between these two measurements? Assume that the unfaulted loops become part of the dislocation network of the solid.

18.8 Derive the expression for the force between a straight edge dislocation line and a dislocation loop whose plane is perpendicular to the slip plane of the edge dislocation and parallel to the edge dislocation itself. Prepare a plot similar to Fig. 18.24 for this case when the distance between the slip plane of the straight dislocation and the center of the loop is three loop radii.

18.9 Equation 18.75 gives the critical tensile stress for stability of gas-free wedge-shaped cracks on grain-boundary triple points. Suppose, however, that the cracks form from pores on the triple points which are initially of volume  $V_0$  and contain  $m$  helium atoms. Under the influence of an applied stress  $\sigma$ , the pores grow to wedge cracks of length  $C$  and width  $nb$ .

(a) The grains in the metal are modeled as tetrakaidecahedrons of size  $l$  (see sketch). At a particular time during irradiation,  $M$  atoms of helium have been produced per unit volume of metal. Assume that all the helium has been collected in the triple-point cracks. What is  $m$ , the number of helium atoms per crack?



(b) What is the energy required to form the crack? The effective stress is the sum of the internal gas pressure and the tensile stress  $\sigma$ . In forming the crack, the contained gas does work.

(c) What is the critical stress for unstable growth of those cracks favorably oriented with respect to the applied stress? Assume low gas pressure to simplify your result.

This problem has been analyzed by K. Reiff, *J. Nucl. Mater.*, 33: 129 (1969).

18.10 The stress-induced growth of grain-boundary voids is to be analyzed by a grain-boundary vacancy-diffusion model similar to the one applied by Coble to grain-boundary diffusional creep (Sec. 16.6). Steady-state vacancy diffusion takes place in the annular region  $R < r < R'$  of thickness  $w$  illustrated in Fig. 18.38. The present analysis is two-dimensional, with  $z$  measured from the midplane of the grain-boundary slab. Since the system is symmetric about the midplane, only the region  $0 \leq z < w/2$  need be

considered. The radial boundary conditions on  $C_v$  are given by Eqs. 18.80 and 18.81. One of the two required  $z$  boundary conditions reflects symmetry about  $z = 0$ ,  $(\partial C_v / \partial z)_{z=0} = 0$  for all  $r$ . Following Coble's treatment, the boundary condition at the interface between the matrix and the grain-boundary zone is  $C_v(r, w/2) = C_v^{eq} \exp(\sigma\Omega / kT)$ ; that is, the applied stress affects the equilibrium vacancy concentration only at the boundary of the diffusion zone, not, as in Speight and Harris' treatment, within this zone.

(a) Write the diffusion equation and the boundary conditions in terms of the dimensionless vacancy concentration:

$$\theta = \frac{C_v(r, z) - C_v(R, z)}{C_v(r, w/2) - C_v(R, z)}$$

(b) Obtain a solution for  $\theta(r, z)$  by the method of separation of variables.

(c) What is the total rate of vacancy diffusion to the void and the growth law  $dR/dt$ ?

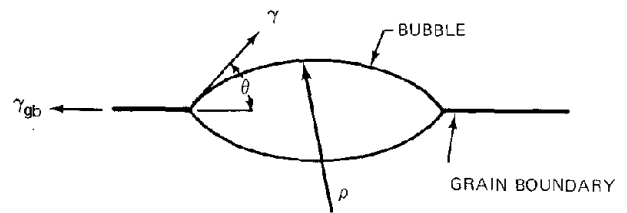
18.11 In the Hull-Rimmer analysis that produced the grain-boundary growth law given by Eq. 18.85, the vacancy concentration midway between voids is assumed to be equal to the thermodynamic equilibrium value under the applied tensile stress. However, the stress in this analysis is determined by dividing the applied load to the specimen by the cross-sectional area. When voids form on grain boundaries perpendicular to the load direction, the load-bearing area on the grain boundaries is reduced by the presence of the voids. How should the growth law be modified to take this effect into account?

18.12 Calculate the helium content (in atomic ppm) in type 304 stainless steel (Table 18.1) irradiated for 1 year in a flux with a thermal component of  $10^{13}$  neutrons  $\text{cm}^{-2} \text{sec}^{-1}$  and a fast component of  $10^{15}$  neutrons  $\text{cm}^{-2} \text{sec}^{-1}$ .

18.13 Consider helium bubbles 1000 Å in radius. To what size do the bubbles grow under the influence of a tensile stress one-half the critical value for instability?

Two of the bubbles coalesce. What is the equilibrium size of the new bubble?

18.14 Equation 18.98 gives the critical stress for spherical helium bubbles on a grain boundary. However, the equilibrium shape of bubbles on grain boundaries is lenticular rather than spherical (see sketch).



(a) If the grain-boundary tension is  $\gamma_{gb}$  and the surface tension of the metal is  $\gamma$ , what is the equilibrium geometry

(i.e., the relation between the angle  $\theta$  and the radius of curvature  $\rho$ ) of a lenticular bubble containing  $m$  gas atoms when the solid is unstressed?

(b) How does the result of (a) change when the solid is subjected to a hydrostatic tensile stress  $\sigma$ ?

(c) What is the critical stress for unstable growth of the lenticular bubble? Express the answer as the ratio of the critical stress for a lenticular bubble to that for a spherical bubble containing the same number of helium atoms. If  $\gamma_{gb}/\gamma = 0.4$ , what is this ratio?

18.15 A specimen of irradiated austenitic stainless steel under an applied stress of  $2 \times 10^5$  kN/m<sup>2</sup> fails owing to helium embrittlement at a strain of 1%. What concentration (in atomic ppm) of helium in the metal is necessary to cause fracture at this value of the strain? The grain size in the metal is 15  $\mu$ m and the surface tension is 1500 dynes/cm. The irradiation temperature is 1000°C.

18.16 Helium is produced in an irradiated metal at a rate of  $G$  atoms cm<sup>-3</sup> sec<sup>-1</sup>. All this helium is trapped in bubbles on grain boundaries as soon as it is formed. There are  $N_{gb}$  bubble sites per unit grain-boundary area, and the grain size is  $d$ .

(a) What is the rate of helium-atom capture at each bubble site?

(b) What is the time  $t_c$  at which the growing grain-boundary bubbles become unstable with respect to an applied tensile stress  $\sigma$ ? What is the bubble radius  $R_c$  at this time? For  $t < t_c$ , bubble growth rate is determined by the helium influx (i.e., the bubble is always at equilibrium).

(c) For  $t > t_c$ , the bubble is unstable, and its rate of expansion is controlled (and limited) by the rate at which vacancies reach it. Gas atoms are assumed to reach the bubble at the rate determined in (a). Accounting for the continued increase in the number of gas atoms in the bubble during the unstable growth period, set up the equations needed to determine the rupture time  $t_R$ .

(d) What is the elongation at rupture  $\epsilon_F$ ?

18.17 The life-fraction approach is to be applied to estimate the most probable service lifetime of a fuel element subject to creep rupture. Steady-state creep is assumed at all times; so the rupture life for fixed conditions is given by  $t_R = \epsilon_F/\dot{\epsilon}$ . Neglect irradiation creep and assume that the creep rate is not affected by fluence but depends on stress and temperature according to Eq. 8.46. Assume that the fracture strain decreases with fluence as shown in Fig. 18.30. The fission-gas pressure within the cladding increases linearly with irradiation time at a known rate. Derive the expression from which the service life could be estimated if all the constants involved were specified. The temperature is constant throughout irradiation.

# Chapter 19

## Radiation Effects in Metals: Void Swelling and Irradiation Creep

### 19.1 INTRODUCTION

Until about 1967 the most detrimental radiation effect expected to be suffered by the stainless-steel cladding of the fuel elements of the projected liquid-metal-cooled fast breeder reactor (LMFBR) was embrittlement due to excessive hardening at low temperatures or helium agglomeration at grain boundaries at high temperatures. These problems, however, were at least qualitatively understood, and sufficient experimental data had been amassed to permit embrittlement to be circumvented by careful design. Since that time a number of unexpected phenomena have been uncovered by microscopic examination of fuel elements and structural components that had been irradiated in a fast reactor environment for long periods. In addition to the chemical attack of the inside of the cladding by the fuel (Chap. 12), steels irradiated to large fast-neutron fluences exhibited dramatic density decreases. Using transmission electron microscopy, Cawthorne and Fulton<sup>1</sup> demonstrated that this swelling was due to the formation of small cavities within the grains of the metal. These voids, which did not contain sufficient gas (if any) to be classed as bubbles, ranged in size from the smallest observable to greater than 1000 Å. Further research has shown that voids form in stainless steel only at temperatures between ~350 to 600°C. Unfortunately, this range falls squarely within the temperature zone in which the cladding of LMFBR fuel pins is designed to operate (Table 10.2).

Void formation is not unique to stainless steel; in fact, steel is one of the alloys most resistant to this phenomenon. Nearly all metals swell by this mechanism over a temperature band from 0.3 to 0.55 of the absolute melting temperature.

The severity of metal swelling under irradiation also depends on the fast-neutron exposure (and to a much smaller extent on the fast-neutron flux). There appears to be an incubation period up to a fast fluence of  $\sim 10^{22}$  neutrons/cm<sup>2</sup> in which no observable swelling of steel occurs. Thereafter swelling (measured, as in the case of fuel swelling by fission gases, as  $\Delta V/V$ ) increases as  $(\Phi t)^n$ , where the exponent  $n$  is greater than unity. Very few data at fluences above  $10^{23}$  neutrons/cm<sup>2</sup> exist, and, because of

the many variables controlling swelling, extrapolation of the dose dependence to the design fluence of the LMFBR ( $\sim 3 \times 10^{23}$  neutrons/cm<sup>2</sup>) is very insecure. Consequently, there has been intense activity in developing theoretical models that can accurately predict swelling at large fluences and in devising experimental techniques other than neutron irradiation to produce voids in metals in short times. Of special interest is the fluence to which the power law  $\Delta V/V \sim (\Phi t)^n$  extends and if and at what fluence the swelling saturates. Leveling off of the swelling curve has not yet been observed in reactor-irradiated steel, but high-energy ion bombardment (Sec. 17.9) has shown<sup>2</sup> that swelling of stainless steel saturates at fluences approaching  $10^{24}$  neutrons/cm<sup>2</sup>. The high equivalent neutron-fluence ion-irradiation studies, taken with extrapolation of low-fluence neutron-irradiation data, suggest that type 316 stainless steel, which is the most likely LMFBR cladding, will swell by 5 to 10% in a commercial reactor. The ramifications of volume increases of this magnitude on fuel-element design are profound, and the remedies are costly. Some of the undesirable side effects of swelling can be alleviated by the related phenomenon of irradiation creep. The effects of swelling and irradiation creep on core design are discussed in Chap. 21.

The origins of void swelling of metals are qualitatively understood. Collision of fast neutrons with lattice atoms produces large numbers of vacancy—interstitial pairs (see Chap. 17). Most of these point defects eventually recombine with each other or migrate to sinks in the solid where the point defects lose their identity. The most effective sinks are dislocations, either those which are part of the natural dislocation network of the metal or dislocation loops created by condensation of radiation-produced interstitials. Precipitates and grain boundaries also act to remove point defects from the medium. The dynamic balance between the point-defect creation and removal processes during irradiation sustains concentrations of vacancies and interstitials far in excess of thermal equilibrium (see Fig. 13.17).

Nucleation of segregated clusters of interstitials and vacancies can take place provided that the temperature is high enough so that both interstitials and vacancies are

mobile in the solid, but not so high that the point defects are removed by recombination or migration to sinks so quickly that high supersaturation cannot be maintained. The type of cluster formed by interstitials is invariably a dislocation loop. Vacancies, however, can agglomerate either into platelets, which collapse into dislocation loops, or into three-dimensional clusters, which are termed voids. The atomic structures of interstitial and vacancy loops are shown in Fig. 18.4.

The collection of interstitial atoms as extra planes in the lattice causes the solid to swell. If the vacancies condensed into analogous vacancy loops, the lattice contraction around these loops would cause shrinkage of the surrounding solid by an amount that just counterbalances the swelling due to interstitial loops. However, when the vacancies agglomerate into voids, no lattice contraction is available to cancel the dilatation due to the interstitial loops, and a net volume increase of the solid ensues. In irradiated zirconium, for example, large vacancy loops, but no voids and hence no swelling, are observed.

The relative stability of voids and vacancy loops can be assessed by comparing the energy difference between the particular cluster containing  $m$  vacancies and the perfect lattice. For the void this difference is just the energy required to form the surface of the void:

$$E_{\text{void}} = 4\pi R^2 \gamma \quad (19.1)$$

where  $\gamma$  is the surface tension of the solid (approximately 500 dynes/cm for stainless steel) and  $R$  is the radius of the void, which is related to the number of vacancies in the cavity by

$$m = \frac{4\pi R^3}{3\Omega} \quad (19.2)$$

where  $\Omega$  is the atomic volume, or the volume contributed by each vacancy to the void. The energy of the void is thus

$$E_{\text{void}} = 4\pi\gamma \left( \frac{3\Omega m}{4\pi} \right)^{2/3} \quad (19.3)$$

The energy of a faulted dislocation loop composed of  $m$  vacancies in a disk of radius  $R_1$  is

$$E_{\text{loop}} = (2\pi R_1)\tau_d + \pi R_1^2 \gamma_{\text{sf}} \quad (19.4)$$

where  $\tau_d$  is the energy per unit length (i.e., the line tension) of the dislocation comprising the periphery of the loop. According to Eq. 8.10  $\tau_d$  is  $\sim Gb^2$ , where  $b$  is the Burgers vector of the faulted loop.

The term  $\gamma_{\text{sf}}$  is the energy per unit area of the stacking fault enclosed by the loop. As shown in Sec. 3.6, the sequence of close-packed (111) planes in the fcc structure is ordered 123123... When part of one of these planes is removed or a section of another (111) plane is inserted, the stacking sequence is disturbed, but the atoms surrounding the stacking fault are surrounded by the same number (12) of nearest neighbors as in the perfect lattice. However, the configuration of the next-nearest neighbors is slightly altered, and the stacking-fault configuration is somewhat more energetic than the perfect lattice. This energy difference is manifest as the stacking-fault energy. Because the energy difference is due to second-order atomic

arrangements,  $\gamma_{\text{sf}}$  is small, typical values being  $\sim 10$  dynes/cm.

In fcc metals dislocation loops form on the close-packed (111) planes in which the area per atom is  $3^{1/2} a_0^2/4$ , where  $a_0$  is the lattice constant. The radius of a vacancy loop created by removal of  $m$  atoms from (or the condensation of  $m$  vacancies on) a (111) plane is

$$R_1 = \left( \frac{3^{1/2} \Omega m}{\pi a_0} \right)^{1/2} \quad (19.5)$$

where  $\Omega = a_0^3/4$  is the atomic volume in the fcc structure. The energy of the faulted vacancy loop is therefore

$$E_{\text{loop}} = 2\pi Gb^2 \left( \frac{3^{1/2} \Omega m}{\pi a_0} \right)^{1/2} + \frac{3^{1/2} \Omega \gamma_{\text{sf}} m}{a_0} \quad (19.6)$$

If the loop is unfaulted (i.e., the stacking fault is removed), the second term on the right of Eq. 19.6 is absent, but the resulting reduction in energy is partially compensated by the larger Burgers vector of the perfect loop compared to that of the faulted loop.

The void and loop energies given by Eqs. 19.3 and 19.6 are rather close to each other, and conclusions concerning the relative stability of the two types of vacancy clusters are uncertain because important parameters, such as the dislocation line tension, are not accurately known. It appears that the void is the stable form for small clusters (small  $m$ ), but, as  $m$  increases, the loop becomes the energetically favored configuration. If the presence of the stacking-fault term in Eq. 19.6 is ignored temporarily, the energy of the void increases more rapidly with  $m$  than that of the loop, and the energy balance tips in favor of the loop at void radii of several tens of angstroms. However, collapse of the embryo void into a vacancy loop is probably impeded by the presence of small quantities of helium gas in the void, and thus voids may survive and grow. Equation 19.6 also indicates that loops rather than voids are favored in metals in which the stacking-fault energy is low. Gold, for example, has a very low stacking-fault energy, and irradiation-produced voids have not been observed in this metal. On the other hand, voids are easily produced in nickel, for which  $\gamma_{\text{sf}}$  is large. The stacking-fault energy in stainless steel lies between these two extremes, and voids can be produced in this alloy but only at much higher fluences than that required for void formation in nickel. This observation is consistent with the preceding discussion of the effect of stacking-fault energy on the relative stability of voids and vacancy loops, but many other factors influence the relative resistances to void formation of a complex alloy, such as steel, and of pure metals, such as gold or nickel.

Granted that, given a choice between forming loops or voids, vacancies will condense as the latter, there remains the question of why the irradiation-produced point defects form separate interstitial loops and voids in the first place. Since vacancies and interstitials are formed in equal numbers by fast-neutron bombardment, one would expect that point defects of both types would diffuse to voids at equal rates and hence produce no net growth of the voids. Inasmuch as the voids represent accumulated excess vacancies, the interstitials must be preferentially absorbed elsewhere in the solid. The preferential interstitial sink is

undoubtedly the dislocations, either those belonging to the original network in the metal or the interstitial loops. It was noted in Sec. 13.9 that dislocations exhibit a slightly larger capture radius for interstitials than for vacancies, and it is this fact which fundamentally provides the mechanism for void formation. The preference of dislocations for interstitials is due to the interaction of the strain field around the dislocation with the strain field established by the misfit of an interstitial atom in the lattice (the strain field around a vacancy is much smaller than that around an interstitial). This strain-field interaction causes an attraction of interstitials for dislocations when the two are in proximity. Ham<sup>3</sup> has shown that the directed drift of interstitials toward dislocations can be incorporated into a diffusional model of the transport process if the dislocation line is assigned a somewhat larger capture radius for interstitials than for vacancies (see problem 13.7). The preferred migration of interstitials to dislocations leaves the matrix of the metal slightly depleted in interstitials relative to vacancies; so nonpreferential sinks, such as voids, absorb vacancies at a somewhat greater rate than interstitials and growth results.

In summary, the conditions necessary for void swelling are:

1. Both interstitials and vacancies must be mobile in the solid. This requirement is easily met by interstitials, which can migrate in metals at very low temperatures. If the vacancies are not mobile as well, they will simply be annihilated by the cloud of moving interstitials.

2. Point defects must be capable of being removed at sinks provided by structural defects in the solid in addition to being destroyed by recombination. Moreover, one of the sinks must have a preference for the interstitials in order to permit establishment of the excess vacancy population necessary for voids to form.

3. The supersaturation of vacancies must be large enough to permit voids and dislocation loops to be nucleated, either homogeneously or heterogeneously, and to grow. At temperatures sufficiently high that the thermal equilibrium concentration of vacancies at the void surface is comparable to that sustained in the matrix by irradiation, void nucleation and growth cease. At high temperatures voids thermally emit vacancies as fast as the irradiation-produced vacancies arrive from the bulk of the solid.

4. Trace quantities of insoluble gases must be present to stabilize the embryo voids and prevent collapse to vacancy loops. Transmutation helium provides the necessary gas content in neutron-irradiated metals, although other gaseous impurities (oxygen, nitrogen, and hydrogen) present in most metals can perform the same function. Although some helium gas is undoubtedly present in voids, there is definitely not enough to class these cavities as equilibrium bubbles.

## 19.2 OBSERVED CHARACTERISTICS OF VOIDS

Excellent summaries of the experimental observations of voids in metals have been presented by Bement<sup>4</sup> and by Norris.<sup>5</sup> In addition, the papers in two conferences devoted

to voids<sup>6,7</sup> contain much detailed information pertinent to the experimental and theoretical status of the subject. Emphasis here is placed on voids formed in neutron-irradiated stainless steel. Void formation in the potential cladding materials nickel and its alloys vanadium and molybdenum will not be considered in detail. In addition to fast-neutron irradiation, voids may be formed by bombarding metals with heavy ions (e.g., protons, carbon, and self-ions) or with electrons. The results of these investigations are summarized in Refs. 4 and 5.

The bulk of the information on void formation in metals has been obtained by transmission electron microscopy (Sec. 18.1). This technique permits the *void distribution function*,  $N(R) dR$  = number of voids/cm<sup>3</sup> with radii between  $R$  and  $R + dR$ , to be measured. Often, only the total void number density,

$$N = \int_0^{\infty} N(R) dR \quad (19.7)$$

the average void size,

$$\bar{R} = \frac{1}{N} \int_0^{\infty} R N(R) dR \quad (19.8)$$

or the void swelling,

$$\frac{\Delta V}{V} = \frac{4}{3} \pi \int_0^{\infty} R^3 N(R) dR \quad (19.9)$$

are reported. If the void distribution is narrow, the swelling may be expressed by

$$\frac{\Delta V}{V} = \left( \frac{4}{3} \pi \bar{R}^3 N \right) \quad (19.10)$$

Most theoretical treatments are content to predict the average void size, assuming that the void density is a specified number rather than the complete void distribution function.

Swelling can also be experimentally determined by immersing a sample of known weight in a fluid to measure the solid volume. However, only the electron microscope can provide data on void size and density. In addition, this tool can provide information on the evolution of the dislocation structure of the irradiated metal. This information consists of:

1. The density of network dislocations (i.e., dislocations other than those comprising the loops).

2. The total dislocation line length of the loops, which is determined by the average diameter of the loops and the number density of the loops.

### 19.2.1 The Void Distribution Function

Figure 19.1 shows the void-size distributions for stainless steel irradiated at different temperatures but to the same fluence. The distributions at low temperatures are approximately Gaussian, with the peak shifted to the larger void sizes as the temperature is increased. The very narrow distributions at low temperatures indicate that, although void nucleation has occurred, the low growth rate prevents voids from attaining large sizes in the allotted irradiation time. At high temperatures the distribution function is very broad and contains some very large voids and a small proportion of little ones. This type of distribution suggests

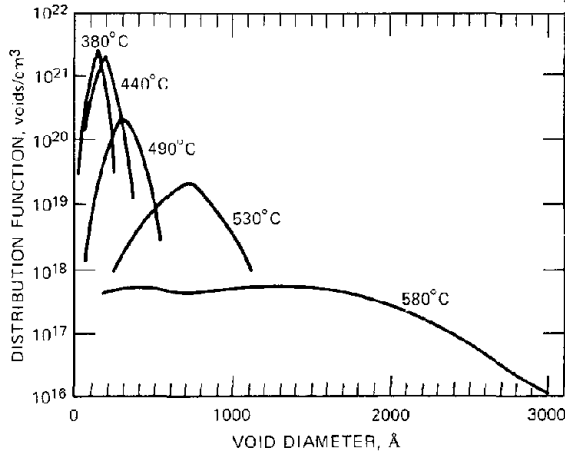


Fig. 19.1 Void-size distribution  $N(R)$  in type 316 stainless steel irradiated to a fluence of  $6 \times 10^{22}$  neutrons/cm<sup>2</sup> at various temperatures. (After J. I. Bramman et al., p. 125, Ref. 6.)

that nucleation has ceased and a constant density of voids is in the process of growing.

19.2.2 Void Size and Density

The zeroth and first moments of the void distribution function, which represent the void number density and average void size, respectively, are shown in the three-dimensional representations of Fig. 19.2. Figure 19.2(a)

indicates a rapid increase in void size at low temperatures and a smaller rate of increase at high temperatures. Similar nonlinear behavior is seen along the fluence axis. Figure 19.2(b) shows that the void number density decreases with increasing temperature and increases with fluence. Observed void densities range from  $10^{13}$  to  $10^{16}$  voids/cm<sup>3</sup>.

19.2.3 Void Swelling

According to Eq. 19.10, the dependence of volume swelling on temperature and fluence could be constructed by multiplying the cube of the surface heights of Fig. 19.2(a) by the surface heights in Fig. 19.2(b). Cuts through this three-dimensional representation of volume swelling are shown in Figs. 19.3 and 19.4. Figure 19.3 shows the restriction of swelling to the temperature band 350 to 600°C with peak swelling occurring at ~500°C. Figure 19.4 indicates a power-law increase of void swelling with neutron fluence. The fluence dependence is of the form

$$\frac{\Delta V}{V} \propto (\Phi t)^n \tag{19.11}$$

where the exponent  $n$  is about unity at 400°C and increases to about 2 at high temperatures. Other functional forms have been suggested for the fluence dependence of swelling. Because of the scatter of the data, swelling can equally well be fitted to a linear equation with an incubation period during which voids are absent:<sup>8</sup>

$$\frac{\Delta V}{V} \propto \Phi t - (\Phi t)_0 \tag{19.12}$$

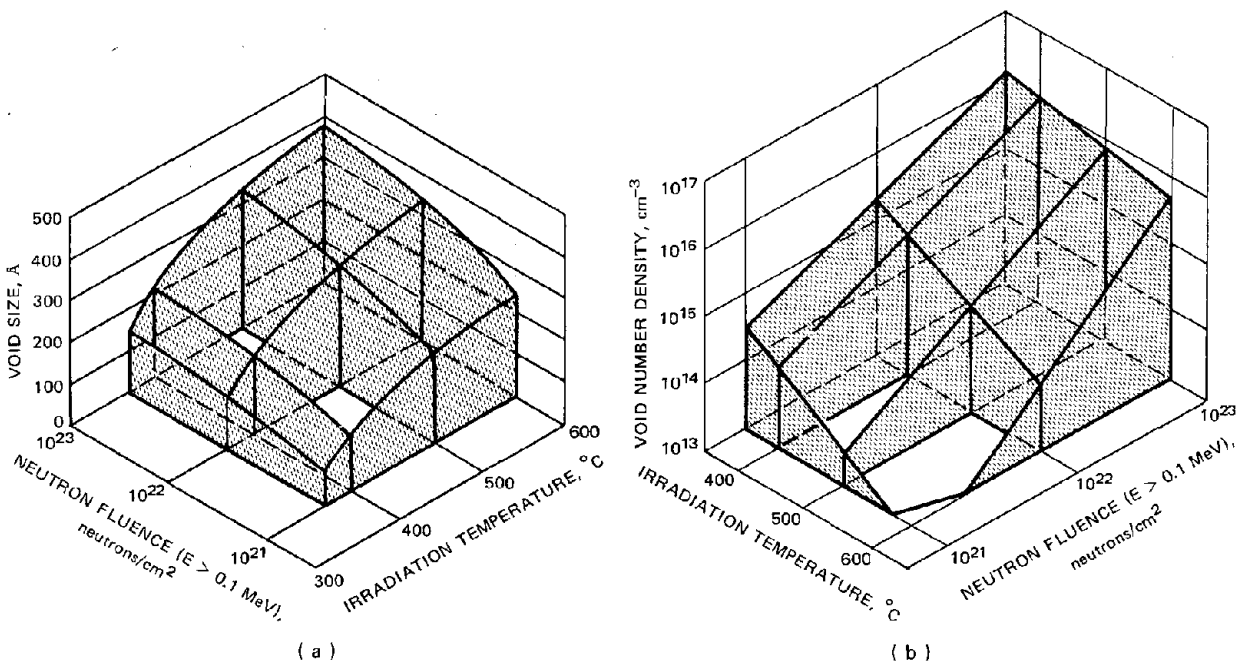


Fig. 19.2 Void size (a) and number density (b) in fast reactor irradiated austenitic stainless steel as a function of fast-neutron fluence and irradiation temperature. [After T. T. Claudson, R. W. Barker, and R. L. Fish, *Nucl. Appl. Technol.*, 9: 10(1970).]

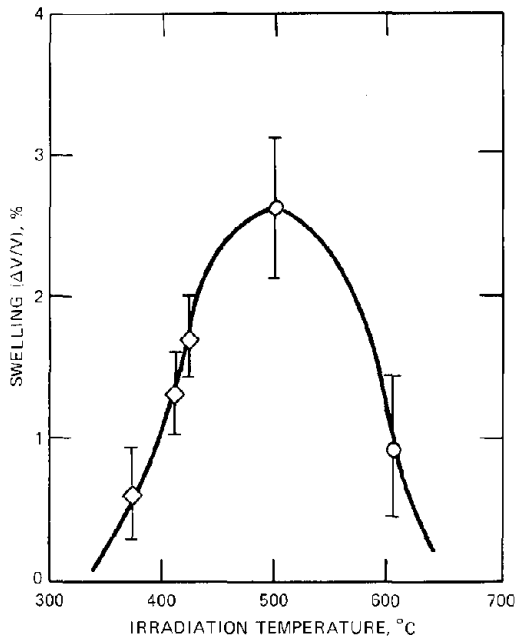


Fig. 19.3 Effect of irradiation temperature on swelling of type 304 stainless steel at a fluence of  $5 \times 10^{22}$  neutrons/cm<sup>2</sup>. ○, transmission electron microscopy. ◇, immersion density. [After S. D. Harkness and Che-Yu Li, *Met. Trans.*, 2: 1457 (1971).]

The incubation period,  $(\Phi t)_0$ , is of the order of  $10^{22}$  neutrons/cm<sup>2</sup> and is believed to represent the neutron dose needed to produce enough helium to permit void nucleation to proceed. The induction period may also be required to build up a sufficient density of interstitial loops to allow the preferential absorption of interstitials by dislocations to sufficiently bias the point-defect population in the metal in favor of vacancies so as to permit vacancy agglomeration into voids.

Neither of the above empirical formulations of the fluence dependence of void swelling indicates saturation (i.e., leveling off) of this phenomenon.

#### 19.2.4 The Effect of Cold Work

Cold work, which increases the density of network dislocations, has a significant effect on the swelling characteristics of austenitic steels. Up to a point, cold working improves the resistance of steel to swelling, as is shown by the smaller swelling of 20% cold worked type 316 stainless steel compared with the solution-treated (i.e., annealed) material (Fig. 19.5). Excessive cold work may not be beneficial, as indicated by the curve for type 304 stainless steel in Fig. 19.5. For this steel, two swelling peaks are observed. The low-temperature hump is associated with normal void formation in a metal of constant microstructure. The high-temperature peak is probably due to the instability of the dislocation network introduced by cold work. Above 600°C extensive recovery and recrystallization occur in the steel, and large segments of the microstructure

are free from dislocations. Voids easily form in these zones and are responsible for the second hump in the swelling curve for type 304 stainless steel. The dislocation structure introduced by cold working of type 316 stainless steel appears to be more stable. The major difference between these two steels is the 2 to 3% molybdenum addition to type 316 stainless steel. This alloying element can sufficiently reduce the mobility of dislocations (by pinning) to diminish the recovery process.

#### 19.2.5 Effect of Precipitates

The effect of alloy composition is even more dramatically exhibited in the swelling behavior of nickel and the high-nickel-content alloy Inconel (Fig. 19.6). Nickel with 0.4% impurities swells considerably less than high-purity nickel, and Inconel actually densifies during irradiation. The excellent swelling resistance of Inconel is probably due to the fine Ni<sub>3</sub>Nb precipitate that is present in this material. This precipitate particle is coherent, which means that its lattice constant is close to that of the matrix, and the precipitate-matrix interface is continuously bonded. It will be shown later that coherent precipitates act as

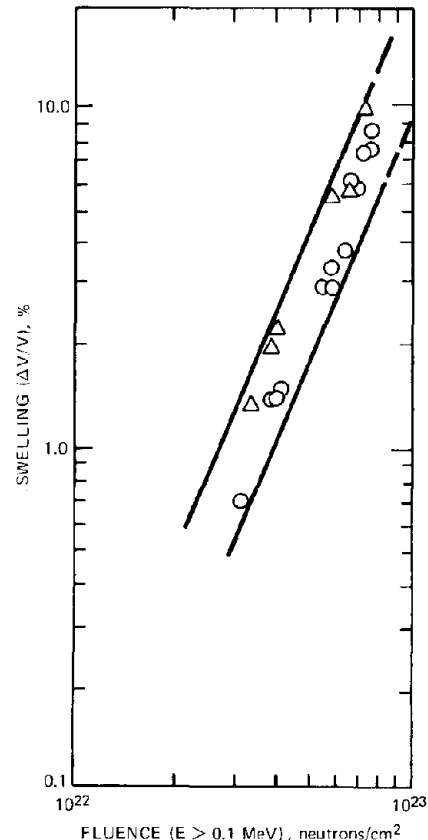


Fig. 19.4 Effect of fast-neutron fluence on swelling in type 316 (○) and in type 347 (△) stainless steels. Irradiation temperatures were between 470 and 540°C. (After W. K. Appleby et al., p. 156, Ref. 6.)

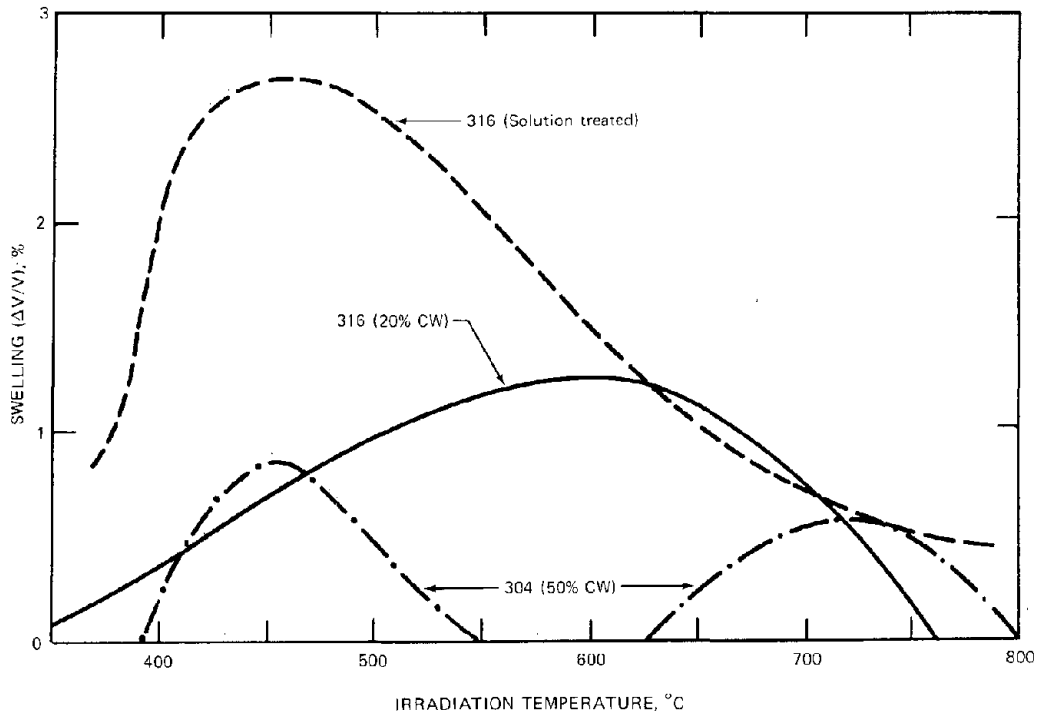


Fig. 19.5 Effect of cold work (CW) on the swelling behavior of austenitic stainless steels. The curves for type 316 stainless steel are plots of Eqs. 19.12a and 19.12b for a fluence of  $5 \times 10^{22}$  neutrons/cm<sup>2</sup>. The curve for 50% CW type 304 stainless steel is for a fluence of  $4 \times 10^{22}$  neutrons/cm<sup>2</sup>. (After Straalsund et al., p. 142, Ref. 6.)

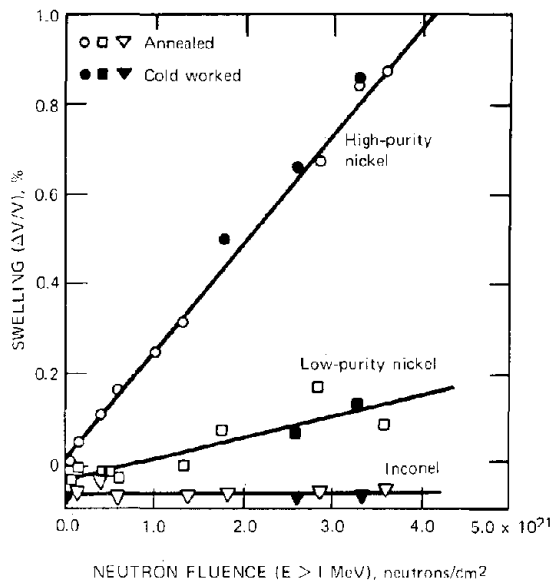


Fig. 19.6 Swelling of high-purity nickel, nickel of 99.6% purity, and Inconel (73% Ni-17% Cr-8% Fe) at 425°C. [After J. J. Holmes, *Trans. Amer. Nucl. Soc.*, 12: 117 (1969).]

recombination sites for vacancies and interstitials and thus contribute to reducing swelling. Another way that a dispersion of fine precipitate particles in an alloy reduces swelling is by impeding dislocation climb (i.e., they act in a manner similar to molybdenum in type 316 stainless steel). Another nickel-based alloy whose microstructure contains a fine dispersion of coherent precipitates is Nimonic PE16. Titanium and aluminum are added in equal amounts to this alloy, and the precipitates have the composition Ni<sub>3</sub>(TiAl). This alloy shows less swelling than does type 316 stainless steel at high fluences.

19.2.6 Empirical Void Swelling Formulas

In view of the rudimentary state of the theory of void formation in alloys, empirical equations are used to account for the effects of void swelling in fuel-element performance estimates. The equations used in current core-design studies reflect the influence of the primary variables of temperature and fluence and the degree of cold work of the alloy. For type 316 stainless steel,<sup>9</sup> the swelling equation for solution-treated steel is

$$\frac{\Delta V}{V} (\%) = (\Phi t \times 10^{-22})^{(2.05 - 2.7/\theta + 7.8/\theta^2)} [(T - 40)10^{-10}] \exp(32.6 - 5100/T - 0.015T) \quad (19.12a)$$

and for 20% cold-worked steel is

$$\frac{\Delta V}{V} (\%) = 9.0 + 10^{-3.5} (\phi t)^{1.5} [4.028 - 3.712 \times 10^{-2} \times (T - 273) + 1.0145 \times 10^{-4} (T - 273)^2 - 7.879 \times 10^{-8} (T - 273)^3] \quad (19.12b)$$

where  $\theta = T - 623^\circ\text{K}$ .

### 19.2.7 Interstitial Loops

The qualitative model of swelling described earlier in this section, the quantitative theories discussed later in this chapter, and electron-microscope observations of irradiated steels all indicate that the nucleation and growth of interstitial dislocation loops accompanies and may even precede void formation. In the fcc structure of austenitic stainless steel, the loops that form first are faulted and lie on  $\{111\}$  planes in the lattice [Figs. 18.4(c) and (d) and Fig. 18.5(a)]. Unfaulting occurs when the faulted loop grows to a size at which it is unstable with respect to a perfect loop (the critical loop size for unfaulting is given by equating Eq. 19.6 for faulted loops with  $b = a_0/3^{1/2}$  to the similar equation for perfect loops, wherein  $b = a_0/2^{1/2}$  and  $\gamma_{sf} = 0$ ). Unfaulting is very slow at temperatures below  $\sim 550^\circ\text{C}$  but may be assisted by the passage of glide dislocations over the fault or by interaction of the growing faulted loops with each other. The unfaulted loops [shown in Fig. 18.5(b)] are capable of conservative motion along their glide cylinders and soon become indistinguishable from (and augment the density of) the original dislocation network of the alloy. At low temperatures ( $\sim 500^\circ\text{C}$ ), loop densities are approximately ten times greater than void densities, and the loop diameters are about two to five times the average void diameter.

For type 316 stainless steel, Brager and Straalsund<sup>10</sup> give the empirical formulas:

$$\rho_1 + \rho_N = 10^9 (\Phi t \times 10^{-22})^{F(T)} \exp [G(T)] \quad (19.13)$$

where

$$F(T) = 31.07 - 0.0145T - \frac{13750}{T} \quad (19.14a)$$

$$G(T) = -47.7 + 0.0193T + \frac{25970}{T} \quad (19.14b)$$

The fraction of the total dislocation density which consists of network dislocations is

$$\frac{\rho_N}{\rho_1 + \rho_N} = \{1 + \exp [0.11(715 - T)]\}^{-1} \quad (19.15)$$

In these formulas,  $\rho_1$  and  $\rho_N$  denote the dislocation densities (in centimeters of dislocation line per cubic centimeter of solid) as faulted loops and network dislocations, respectively;  $\rho_N$  includes the contribution of perfect loops, and  $T$  is the temperature in  $^\circ\text{K}$ .

Equations 19.13 and 19.15 are plotted in Fig. 19.7. For  $T < 500^\circ\text{C}$  the dislocation population is dominated by faulted loops, but above  $500^\circ\text{C}$  the faulted loops rapidly disappear and only network dislocations remain. The network dislocation density decreases with increasing tem-

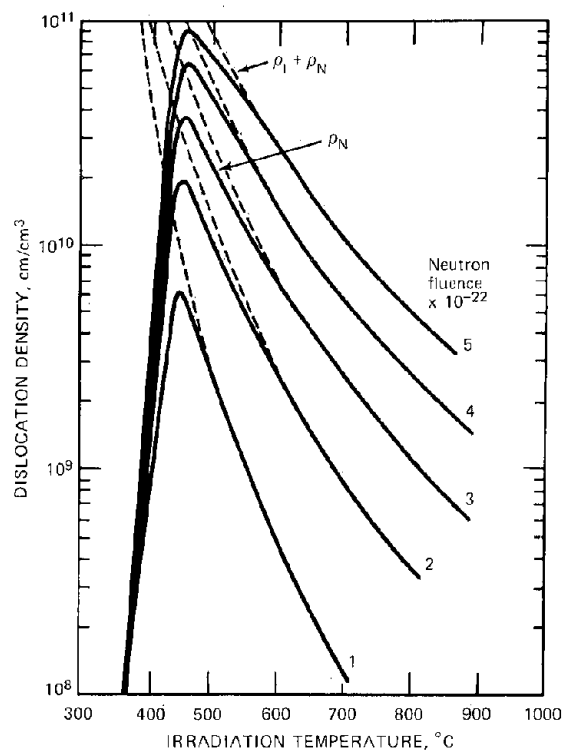


Fig. 19.7 Dislocation density in solution-treated type 316 stainless steel. [After Ref. 10.]

perature because of recovery of the dislocation structure (i.e., mutual annihilation of dislocations of opposite sign or glide out of the specimen).

The average diameter of the faulted loops is correlated by

$$\bar{R}_1 = \frac{1}{2} (\Phi t \times 10^{-22})^{H(T)} \exp [J(T)] \quad \text{\AA} \quad (19.16)$$

where

$$H(T) = -6.31 + 0.00262T + \frac{3060}{T} \quad (19.17a)$$

$$J(T) = 23.89 - 0.0071T - \frac{9040}{T} \quad (19.17b)$$

The faulted-loop number density is given by

$$N_1 = 10^{1.5} (\Phi t \times 10^{-22})^{0.53} \exp [L(T)] \quad (19.18)$$

where

$$L(T) = -203.5 + 0.116T + \frac{85900}{T} \quad (19.19)$$

The loop characteristics according to Eqs. 19.16 and 19.18 are shown in Fig. 19.8.

The preceding recitation of the experimental observations pertaining to void and loop formation in stainless steel illustrates the many different and often poorly defined factors affecting the void-swelling process. It is entirely possible that not all of the variables have been discovered. Consequently, it is unlikely that an accurate and comprehensive theoretical model of this process will be developed,

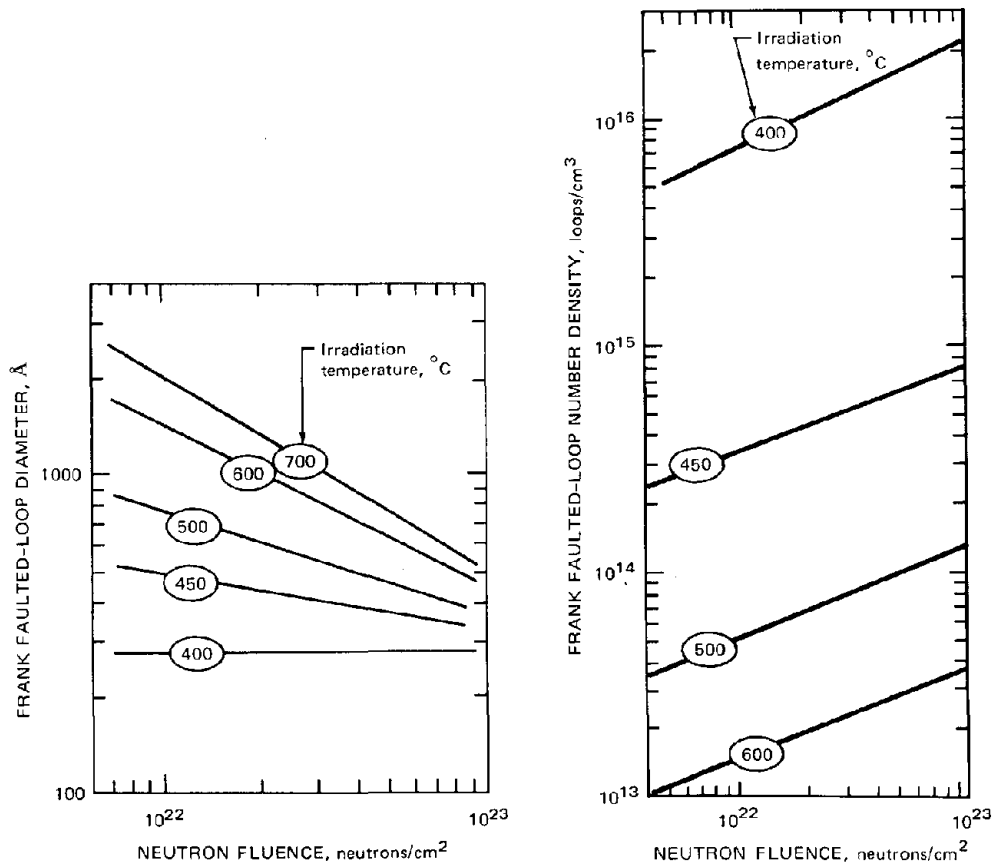


Fig. 19.8 Graphs of equations correlating the size and density of the faulted interstitial loops in type 316 stainless steel for various temperatures and neutron fluences. (After Ref. 10.)

and fuel-element performance predictions will be forced to rely on empirical correlations for LMFBR design. However, theoretical models of the process are valuable because they offer guidance for experiments and elucidate the factors that may prevent or at least retard void growth in cladding materials.

Void-formation theories usually divide the overall process into distinct nucleation and growth phases, models for which are presented in the following two sections. Prediction of the evolution of the loop and void distribution functions with irradiation time requires coupling the basic nucleation and growth laws into point defect, loop, and void conservation statements. Progress in this aspect of void swelling theory is reviewed in Sec. 19.6.

### 19.3 NUCLEATION OF VOIDS

Nucleation of voids refers to the rate at which tiny embryos of these defect clusters appear in the solid. Once nucleated, the embryos tend to grow and are safe from destruction. Nucleation and growth are often treated as sequential steps in the overall process of void formation. Supersaturation of the solid with point defects is a prerequisite to both nucleation and growth, but a higher

supersaturation is required to force nucleation than to continue growth of existing embryos.

The most common example of nucleation is the condensation of water vapor in air. If the partial pressure of water in dust-free air is slowly increased beyond the equilibrium vapor pressure, nothing happens until the supersaturation (i.e., the ratio of the partial pressure to the vapor pressure) attains a value of about 5 to 6. At this point a fog, which corresponds to nucleation of small liquid droplets, appears. The supersaturation of the gas phase falls abruptly at the onset of nucleation, and the newly born droplets consume the remaining excess water vapor at a purely diffusion-limited rate until the equilibrium vapor pressure in the gas phase is attained. Formation of voids and loops in solids may not be as clearly divisible into nucleation and growth phases because in this case generation of point defects acts to maintain the supersaturation. Nucleation of new voids and loops may proceed in parallel with the growth of existing ones.

Nonetheless, nucleation and growth processes can be analyzed as individual phenomena, the rates of which are functions of the point-defect supersaturations, the helium content of the solid, and the temperature. After the basic rate equations have been derived, simultaneous operation of

the growth and nucleation processes can be treated by use of the appropriate conservation statements for voids, loops, and point defects in the solid. When nucleation precedes growth, the conservation equations are considerably simplified, and most theories of void formation in metals have adopted the nucleation-followed-by-growth approach.

As with the condensation of water, nucleation of voids and loops in metals can be classed either as homogeneous or heterogeneous. Homogeneous nucleation refers to the buildup of small clusters by chance encounters of individual point defects executing random walks in the solid. The stability of these clusters relative to the individual point defects of which they are composed (i.e., voids contain vacancies and perhaps gas atoms whereas loops contain interstitials) is the driving force for nucleation. None of the structural features of the solid are needed to cause agglomeration of the point defects.

Heterogeneous nucleation refers to the appearance of voids on distinct structural features of the solid. In water condensation, for example, dust particles provide heterogeneous nucleation sites. In metals the heterogeneities that may accelerate void nucleation include preexisting gas bubbles (containing either impurity gases in the as-fabricated metal or irradiation-produced helium or hydrogen which has precipitated into equilibrium bubbles prior to nucleation of voids), incoherent precipitate particles, and dislocations. The depleted zones created in the collision cascades (Sec. 17.10) can also act as heterogeneous nucleation sites for void formation.

There is no general consensus on the predominant void nucleation mechanism. The importance of homogeneous nucleation vis-a-vis heterogeneous nucleation has been debated since irradiation-produced voids in metals were first discovered (Refs. 4, 5, 11, and 12).

Nucleation of voids in the depleted zones formed in the collision cascade is unlikely because of the rapid thermal annealing (and resulting low concentration) of these zones at the peak swelling temperatures in stainless steel (see Sec. 18.5). Furthermore, irradiation of metals by electrons results in copious void formation, even though depleted zones are not formed by this type of bombarding particle (Sec. 18.5).

It has not been possible to unequivocally determine the conditions under which heterogeneous nucleation of voids on second-phase particles is important. Bloom<sup>11</sup> has found that when the void concentration is low (either by combination of low fluence at low temperature or high fluence at high temperature) the voids are often associated with dislocations or precipitates. At constant fluence Brager and Straalsund<sup>10</sup> observed what appears to be homogeneous nucleation at low temperatures, whereas at high temperatures the voids were fewer in number and attached to precipitates. Nevertheless, the idea that a fixed number of heterogeneous sites is responsible for all void nucleation is unacceptable on two counts. The concept predicts that the void concentration should be (1) limited by the number density of nucleation sites in the metal and (2) independent of irradiation temperature. Neither of these expectations is satisfied by void formation in stainless steel.

All studies of void nucleation in irradiated metals agree that the presence of helium in the solid profoundly affects

the nucleation process, although helium is not a prerequisite for nucleation. Neutron-irradiation and ion-bombardment experiments in which helium gas is expressly preinjected into the sample show a larger density of voids than experiments in which helium is totally absent (ion bombardment) or builds up continuously during irradiation (neutron irradiation). The incubation fluence of  $\sim 10^{22}$  neutrons  $\text{cm}^{-2}$  (Eq. 19.12) may be the time needed for sufficient transmutation helium to be produced by irradiation to cause void nucleation. Although the void density is markedly increased by the presence of helium, the total swelling of the metal is unaffected.<sup>13</sup> Typically,  $\sim 0.1\%$  of the free vacancies produced by the displacement process in a fast-neutron flux end up in voids (see problem 19.1 at the end of this chapter). The remaining 99.9% either recombine or are removed at sinks. The presence of helium does not alter this partitioning of the vacancies. According to Eq. 19.10, if  $\Delta V/V$  is to remain constant even though  $N$  increases, the average void size must decrease. The explanation for this observation is that the high void densities in experiments with preinjected helium provide more effective traps for vacancy capture, thereby reducing the vacancy supersaturation and slowing down the rate of growth of the embryos.

In neutron irradiation there is no way of turning off the helium production as a means of controlling void formation. One can at best hope to understand the mechanism by which helium influences void nucleation in order to be able to predict void behavior at fluences as yet unattainable by neutron-irradiation tests.

The details of the processes by which helium affects void nucleation are not known. The mechanism may simply be a matter of stabilizing embryo voids that have nucleated without the aid of gas atoms and preventing collapse of the embryos to vacancy loops. If such collapse occurs, the fate of the loop is determined—because of the preferential bias of dislocations of any sort for interstitials, the vacancy loop will collect more interstitials than vacancies and will be destroyed. However, it is more likely that helium is intimately involved in the nucleation process, probably by precipitating simultaneously with vacancies and interstitials to form embryo voids that are partially gas filled. Whether or not this role of helium converts a homogeneous nucleation process to a heterogeneous one is a matter of semantics. If, however, the helium first migrates to and is trapped by imperfections in the solid (e.g., precipitates) and then small voids form by accretion of vacancies to these bubbles, the nucleation process is clearly heterogeneous.

Although void nucleation probably occurs by a mixture of homogeneous or heterogeneous processes, each assisted by helium, only homogeneous nucleation has been treated quantitatively. Homogeneous nucleation of voids in metals is not simply a matter of applying classical nucleation theory to a new system. Classical theory, which was developed to explain liquid-droplet formation from supersaturated vapor of condensible gases, has been applied to many precipitation processes occurring in solids. However, in all nucleation problems that have been treated by classical theory, growth or shrinkage of small clusters occurs by exchange of a single species between the embryos and the supersaturated medium. Void nucleation, however,

involves the exchange of at least two species, namely, the vacancy and its antiparticle the interstitial, between the clusters and the lattice. A void can grow either by adding a vacancy or by releasing an interstitial; it can shrink by adding an interstitial or by emitting a vacancy. Moreover, if helium is involved in the nucleation process, three species must be considered in the shrinkage and enlargement processes which contribute to homogeneous nucleation.

In the remainder of this section, homogeneous nucleation of voids from a matrix containing arbitrary supersaturations of both vacancies and interstitials is described. Progress in incorporating helium into the nucleation process is considered briefly; nucleation of interstitial loops is treated in Sec. 19.4. The bulk concentration of vacancies and interstitials, which drives the nucleation processes, is assumed to be determined by point-defect balances that consider all sources and sinks of point defects in the solid, as shown in Sec. 19.5.

### 19.3.1 Homogeneous Nucleation of Voids

Homogeneous nucleation theory begins by deducing the equilibrium void distribution function,  $N^{eq}(m)$  (where  $m$  is the number of vacancies in a void), which is developed by a supersaturation  $S_v = C_v/C_v^{eq}$  of vacancies in the solid. The theory then considers the nonequilibrium situation of arbitrary vacancy and interstitial supersaturations in which there is a net flux,  $I$ , of voids from one size to the next larger size. The resulting equation for  $I$  (which is the desired nucleation rate) is solved with the aid of the equilibrium distribution, from which certain coefficients appearing in the nonequilibrium equation are obtained. The theory of homogeneous nucleation of voids in the absence of gas atoms was developed simultaneously and independently by Katz and Wiedersich<sup>1,4</sup> and by Russell.<sup>1,5</sup>

### 19.3.2 The Equilibrium Void Distribution Function

When there is no vacancy supersaturation ( $S_v = 1$ ), the equilibrium concentration of vacancies in the solid is given by

$$C_v^{eq} = N_s \exp\left(-\frac{\epsilon_v}{kT}\right) \quad (19.20)$$

where  $N_s = 1/\Omega$  and is the number of atom sites in a unit volume of solid and  $\epsilon_v$  is the energy of formation of a vacancy. Even in this situation there are some small voids (i.e., clusters containing more than one vacancy). The equilibrium fraction of divacancies, for example, was derived in Sec. 6.4 and is given by Eq. 6.22. Similar calculations can be used to determine the concentrations of voids containing three or more vacancies. For the particular case of unit supersaturation, the equilibrium concentration of clusters decreases rapidly as the cluster size increases; i.e., for  $S_v = 1$ ,  $N^{eq}(m)$  is a rapidly decreasing function of  $m$ .

When the vacancy concentration is maintained at a value greater than  $C_v^{eq}$  (e.g., by irradiation), it is also possible to compute an equilibrium void distribution function. For  $S_v > 1$ , however,  $N^{eq}(m)$  is not a monotonically decreasing function of  $m$ . Rather, it passes through a

minimum at some cluster size and thereafter increases rapidly with  $m$ . This equilibrium distribution cannot be attained in practice because it implies large concentrations of large voids. In spite of this practical difficulty, the equilibrium distribution is useful because it permits estimation of certain properties of void growth and shrinkage which are needed for analysis of the actual nonequilibrium case.

We therefore determine the hypothetical void distribution function  $N^{eq}(m)$  arising from a supersaturation  $S_v$  of vacancies. The vacancies are in equilibrium with the entire void population, or in the language of chemical thermodynamics, the reaction



is at equilibrium for all values of  $m$ . Here  $v$  denotes a vacancy and  $v_m$  is a void composed of  $m$  vacancies.

Since a situation of total thermodynamic equilibrium is envisaged, the interstitials present in the solid must also be in equilibrium with the vacancies according to the reaction



where  $i$  denotes an interstitial and null means an atom on a normal lattice site. The equilibrium concentration of interstitials in a solid wherein the vacancies are also at equilibrium is

$$C_i^{eq} = N_s \exp\left(-\frac{\epsilon_i}{kT}\right) \quad (19.23)$$

where  $\epsilon_i$  is the energy of formation of an interstitial. Equation 19.22 requires that the product  $C_v C_i$  be a constant, and this constant must be equal to  $C_v^{eq} C_i^{eq}$ . Or, the concentration of interstitials in equilibrium with a supersaturated solution of vacancies is given by

$$C_i = \frac{C_v^{eq} C_i^{eq}}{C_v} = \frac{N_s}{S_v} \exp\left(-\frac{\epsilon_i}{kT}\right) \quad (19.24)$$

The interstitials are undersaturated by an amount equal to the vacancy supersaturation  $S_v$ . Because of this fact and because of the high formation energy of interstitials, the interstitial concentration in the matrix containing a supersaturation of vacancies is negligibly small.

The distribution function  $N^{eq}(m)$  is obtained by applying the criterion of chemical equilibrium to reaction 19.21. Specifically, Eq. 5.14 becomes

$$m\mu_v = \mu_m \quad (19.25)$$

where  $\mu_v$  is the chemical potential of a vacancy and  $\mu_m$  is the chemical potential of a void of size  $m$ . The chemical potentials are related to the total Gibbs free energy of the system by Eq. 5.50:

$$\mu_m = \frac{\partial G}{\partial N^{eq}(m)} \quad (19.26)$$

where the partial derivative is taken with temperature, total pressure, and concentration of clusters of sizes different from  $m$  held constant. By analogy to the cases of monovacancies (Eq. 6.11) or divacancies (Eq. 6.16), the total Gibbs free energy of a system containing a distribution  $N^{eq}(m)$  of clusters is given by

$$G = G_0 + \sum_m N^{eq}(m) g_m - kT \sum_m \ln W_m \quad (19.27)$$

where  $G_0$  is the free energy of the perfect lattice and  $g_m$  is the Gibbs free energy, or reversible work, required to form a void of size  $m$ , which is

$$g_m = h_m - Ts_m = \epsilon_m + pv_m - Ts_m$$

Here  $\epsilon_m$  is the energy required to form a void of  $m$  vacancies,  $s_m$  is the excess entropy associated with this process, and  $v_m$  is the volume change due to introduction of a void in the solid ( $v_m = m\Omega$  if local contraction around an isolated vacancy in the lattice is neglected);  $p$  is the hydrostatic stress in the solid. Following the usual simplifications in dealing with point-defect equilibria, the last two terms on the right are neglected, and  $g_m$  reduces to  $\epsilon_m$ . However, it should be noted that the presence of the term  $pv_m$  in the above expression provides a means whereby the state of stress of the solid can influence the nucleation rate.

For large  $m$ , the energy of the void is assumed to be adequately represented by the surface energy, which may be obtained by combining Eqs. 19.1 and 19.2:

$$g_m \simeq \epsilon_m \simeq (36\pi\Omega^2)^{1/2} \gamma m^{2/3} \quad (19.28)$$

Equation 19.28 represents the capillarity model of homogeneous nucleation, in which the energy of a cluster is related to a macroscopic parameter, namely, the surface tension. Equation 19.28 has no meaning for clusters of one or two vacancies. The energy required to create a monovacancy, is the vacancy formation energy  $c_v$ , and not the right side of Eq. 19.28 with  $m = 1$ . This inability to accurately describe the energy of clusters too small to be treated as droplike entities but too large to be considered in atomic terms is common to all applications of nucleation theory, including the present one.

The last term in Eq. 19.27 is the temperature times the configurational entropy (or entropy of mixing). It can be obtained by calculating the number of ways in which voids can be distributed in a crystal containing  $N_s$  lattice sites per unit volume. To perform this computation, we make the assumption that the solution is dilute in voids and vacancies, so the combinatorial numbers  $W_m$  can be calculated independently of each other. This problem has already been treated in Sec. 6.4 for the particular case of divancies ( $m = 2$ ), and similar methods are applied here. However, the problem is simplified by requiring that the clusters be spherical, which eliminates the orientation factors that entered into the divacancy calculation. We begin with a unit volume of perfect lattice and withdraw voids of size  $m$  sequentially until there are  $N^{eq}(m)$  of these holes in the solid. The size  $m$  is fixed during this process. The center of the first void can be removed from any of the  $N_s$  available sites, which leaves  $N_s - m$  sites from which the second void may be withdrawn. The third void is removed from the  $N_s - 2m$  remaining sites, etc. The product of each of these factors gives the number of different ways of removing  $N^{eq}(m)$  voids of size  $m$  from the solid, or

$$W_m = \frac{N_s(N_s - m)(N_s - 2m) \dots \{N_s - [N^{eq}(m) - 1]m\}}{[N^{eq}(m)]!}$$

where the denominator serves to eliminate permutations among the identical voids (changing the order in which

particular voids are removed does not produce a distinguishable state). The quantity  $m^{N^{eq}(m)}$  is factored from the numerator of the above equation, and the top and bottom are multiplied by  $[(N_s/m) - N^{eq}(m)]!$ ,

$$W_m = \frac{m^{N^{eq}(m)} (N_s/m)!}{[(N_s/m) - N^{eq}(m)]! [N^{eq}(m)]!} \quad (19.29)$$

Substituting Eq. 19.29 into Eq. 19.27, using Stirling's formula for the factorial term, and taking the derivative as required by Eq. 19.26 yields

$$\mu_m = \epsilon_m + kT \ln \left[ \frac{N^{eq}(m)}{N_s} \right] \quad (19.30)$$

In obtaining this result, we have neglected  $m^{N^{eq}(m)}$  compared to  $N_s$  because the void concentration is low. For monovacancies ( $m = 1$ ), Eq. 19.30 reduces to

$$\mu_v = \epsilon_v + kT \ln \left( \frac{C_v}{N_s} \right) \quad (19.31)$$

The vacancy-formation energy is eliminated from Eq. 19.31 by Eq. 19.20. This procedure leads to

$$\mu_v = kT \ln \left( \frac{C_v}{C_v^{eq}} \right) = kT \ln S_v \quad (19.32)$$

Having determined  $\mu_m$  and  $\mu_v$  in terms of the distribution function  $N^{eq}(m)$  and the vacancy supersaturation  $S_v$ , we determine  $N^{eq}(m)$  by substituting Eqs. 19.30 and 19.32 into the criterion of chemical equilibrium, Eq. 19.25, and relating  $\epsilon_m$  to  $m$  by Eq. 19.28. The equilibrium void distribution function is found to be

$$N^{eq}(m) = N_s \exp(m \ln S_v - \xi m^{2/3}) \quad (19.33)$$

where

$$\xi = (36\pi\Omega^2)^{1/2} \frac{\gamma}{kT} \quad (19.34)$$

is dimensionless and of magnitude between 10 and 30.

Equation 19.33 is the result of purely thermodynamic arguments and is independent of the mechanism by which the equilibrium void distribution is established. Mechanistic information of the nucleation process can be extracted from Eq. 19.33 if the distribution is regarded as a dynamic balance of the rates of vacancy capture by a cluster and vacancy emission from the cluster. At equilibrium the rates of these two processes are equal, and, since the rate constant for the forward (capture) process is known, the rate constant of the reverse process can be determined from Eq. 19.33.\* Equilibrium is attained if the rate at which clusters of  $m$  vacancies capture single vacancies is equal to the rate at which clusters of size  $m + 1$  emit vacancies, or

$$\beta_v(m) N^{eq}(m) = \alpha_v(m+1) N^{eq}(m+1) \quad (19.35)$$

\*This procedure is an example of the application of the principle of detailed balancing, which has previously been invoked to determine the climb velocity of an edge dislocation (Eqs. 16.51 and 16.52) and to calculate the rate of condensation of  $UO_2$  on the cold side of a pore (Eqs. 14.14 and 14.15).

where  $\beta_v(m)$  is the rate of vacancy capture by a size  $m$  cluster and  $\alpha_v(m)$  is the rate of vacancy emission from a size  $m$  cluster.

A formula similar to Eq. 19.35 applies to interstitial capture and emission from a cluster, but, because of the very small interstitial concentration at equilibrium, this relation is unnecessary. The ratio  $N^{eq}(m)/N^{eq}(m+1)$  is obtained from Eq. 19.33:

$$\frac{N^{eq}(m)}{N^{eq}(m+1)} = \frac{1}{S_v} \exp\left(\frac{2}{3} \xi m^{-1/2}\right) \quad (19.36)$$

In deriving Eq. 19.36, the approximation  $[1 + (1/m)]^{1/2} \sim 1 + (1/2m)$  has been made.

If the clusters are assumed to be spherical, the vacancy-capture rate is expressed by the rate constant for point-defect absorption by spherical sinks derived in Secs. 13.4 and 13.5. Specifically,  $\beta_v(m)$  is given by the product of the rate constant  $k$  of Eq. 13.96 and the bulk vacancy concentration  $C_v$ . In the present application the void embryos are so small that the capture rate is of the mixed control type in which both diffusion and reaction-rate limitations are of comparable magnitude. Thus

$$\beta_v(m) = \frac{4\pi R D_v C_v}{1 + (a_0/R)} \quad (19.37)$$

where  $a_0$  is the lattice constant and  $D_v$  is the vacancy diffusion coefficient. If unity in the denominator is neglected (which corresponds to complete reaction-rate control of the capture kinetics), Eq. 19.37 reduces to the formulas used in Refs. 14 and 15. However, Eq. 19.37 is preferable to the reaction-rate-limited form since  $a_0/R$  is never larger than unity. In either case,  $R$  in Eq. 19.37 is related to the cluster size  $m$  by Eq. 19.2, and an approximate expression for  $\beta_v(m)$  for  $a_0/R < 1$  is

$$\beta_v(m) \cong a_0 D_v C_v m^{1/2} \quad (19.38)$$

Using Eqs. 19.36 and 19.38 in Eq. 19.35 gives the emission rate constant

$$\alpha_v(m+1) \cong a_0 D_v C_v^{eq} m^{1/2} \exp\left(\frac{2}{3} \xi m^{-1/2}\right) \quad (19.39)$$

The preceding formulas show that the vacancy-capture rate increases with cluster size, whereas the vacancy-emission rate decreases with  $m$ . Once a cluster has managed to reach a certain minimum size, its propensity to grow outweighs its tendency to shrink, and continued existence and development of the embryo into a full-fledged void is assured. Determination of the critical size beyond which growth is favored is the next task for homogeneous nucleation theory.

### 19.3.3 The Nonequilibrium Void Distribution Function, the Nucleation Rate, and the Critical Cluster Size

The nucleation current  $I$  represents a rate of flow of voids in the phase space of cluster size (as opposed to real space, wherein the flux would be denoted by  $J$ ). The current  $I$  is the net rate at which clusters of size  $m$  grow to clusters of size  $m+1$  per unit volume. It is analogous to the slowing-down density in nuclear reactor analysis, which

represents the rate at which neutrons pass a particular energy (i.e., the flux of neutrons in energy space). Since small void clusters grow by capturing vacancies and shrink either by capturing interstitials or emitting vacancies, the nucleation current is the difference between the rate at which clusters pass from size  $m$  to size  $m+1$  and the rate at which clusters of size  $m+1$  are reduced to size  $m$ :

$$I = \beta_v(m) N(m) - \alpha_v(m+1) N(m+1) - \beta_i(m+1) N(m+1) \quad (19.40)$$

where  $N(m)$  is the void distribution function for the nonequilibrium but steady-state case. The vacancies and interstitials are supersaturated to arbitrary extents; thus  $C_v$  and  $C_i$  are not related by a mass action formula such as Eq. 19.24. In addition, the void population represented by the distribution  $N(m)$  is not in equilibrium with either the vacancies or the interstitials in the solid. Therefore,  $N(m)$  can only be determined by kinetic arguments.

Equation 19.40 is applied to the case in which the same number of voids pass from size  $m$  to size  $m+1$  per unit volume no matter how large  $m$  is. To maintain the situation implied by this requirement, one imagines that some mechanism is available for destroying large voids and returning their component vacancies to the metal lattice. In practice, we need not worry about the artificiality of this device for maintaining the steady state; nucleation theory is used solely to determine the ratio at which voids pass the critical size that assures their continued existence. Thereafter, the fate of the voids is determined by growth models, which are formulated independently of the nucleation model and provide the sources and sinks necessary to establish the vacancy and interstitial supersaturations used in the nucleation analysis.

The capture rates are assumed to be the same as those used in determining the equilibrium distribution;  $\beta_v(m)$  is given by Eq. 19.37 or 19.38. The rate at which a void absorbs interstitials,  $\beta_i(m)$ , is given by either of these equations with the subscript  $v$  replaced by  $i$ . The nucleation rate depends on the ratio of the capture rates of interstitials and vacancies by the voids, or by

$$\frac{\beta_i}{\beta_v} = \frac{D_i C_i}{D_v C_v} \quad (19.41)$$

The above ratio is called the *arrival-rate ratio* and is independent of void size. It depends on the rates of point-defect production and removal in the bulk solid. These balances are considered in the section on growth. For the moment, we assume that  $\beta_i/\beta_v$  is a specified constant that is just a bit smaller than unity.

The vacancy-emission rate constant  $\alpha_v$  is assumed to be the same as the one deduced for the equilibrium void population, Eq. 19.39. The term in Eq. 19.40 representing interstitial emission from a void has been neglected owing to the very large formation energy of interstitials, which renders  $C_i^{eq}$  very small. Therefore, a formula of the type given by Eq. 19.39 for interstitials would show  $\alpha_i \cong 0$ .

Elimination of  $\alpha_v(m+1)$  from Eq. 19.40 by use of Eq. 19.35 yields

$$I = \beta_v(m) \left\{ N(m) - N(m+1) \left[ \frac{N^{eq}(m)}{N^{eq}(m+1)} + \frac{\beta_i}{\beta_v} \right] \right\} \quad (19.42)$$

where the ratio  $\beta_i(m+1)/\beta_v(m)$  has been approximated by  $\beta_i(m)/\beta_v(m)$ , which is a constant. We now define a function  $h(m)$  by

$$\frac{h(m)}{h(m+1)} = \frac{N^{eq}(m)}{N^{eq}(m+1)} + \frac{\beta_i}{\beta_v} \quad (19.43)$$

which is determined by Eq. 19.36 in conjunction with the specified constant value of the arrival-rate ratio. The solution of Eq. 19.43 is (see problem 19.2 at the end of this chapter)

$$\ln \left[ \frac{h(m)}{N_s} \right] = - \sum_{m'=0}^{m-1} \ln \left[ \frac{N^{eq}(m')}{N^{eq}(m'+1)} + \frac{\beta_i}{\beta_v} \right] \quad (19.44)$$

Equation 19.44 is plotted in Fig. 19.9 for various arrival-rate ratios and for irradiation conditions appropriate to fast reactor cladding. The properties of nickel were used in

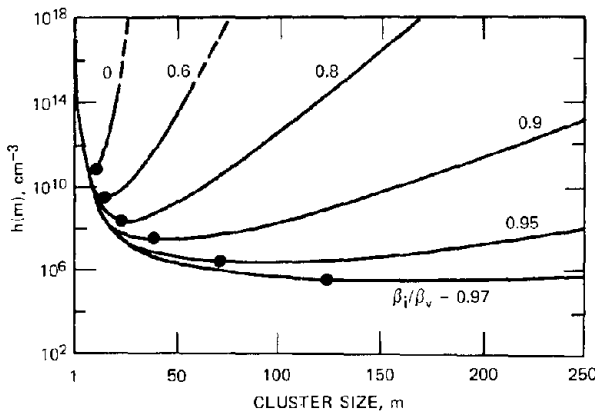


Fig. 19.9 The function  $h(m)$  calculated from Eqs. 19.44 and 19.36 for various values of the arrival-rate ratio  $\beta_i/\beta_v$ . Physical properties for determining  $\xi$  from Eq. 19.34 are for nickel at 900°K. The vacancy supersaturation  $S_v$  is 430. The dots indicate the location of the minima of  $h(m)$ . (After Ref. 14.)

preparing the plots, on the grounds that this pure metal resembles stainless steel. The curve for  $\beta_i/\beta_v = 0$  corresponds to the equilibrium distribution given by Eq. 19.33.

Using Eq. 19.43, we find that Eq. 19.42 becomes

$$I = \beta_v(m) h(m) \left[ \frac{N(m)}{h(m)} - \frac{N(m+1)}{h(m+1)} \right]$$

For sufficiently large values of  $m$  (i.e.,  $m > 2$  is sufficient), the difference in the brackets of the above formula can be approximated by a derivative, and

$$I = -\beta_v h \frac{d(N/h)}{dm} \quad (19.45)$$

Solution of Eq. 19.45 requires one boundary condition, but an additional condition is needed if the heretofore unknown nucleation rate  $I$  is to be determined as well as the distribution function  $N(m)$ .

The first requirement on the distribution function is that it approach the equilibrium distribution function

$N^{eq}(m)$  at small  $m$ . This condition is based on the supposition that very tiny voids capture and shed vacancies so rapidly that they remain in equilibrium with the vacancy supersaturation despite the net drain caused by the nucleation current  $I$ . Since it can be shown from Eq. 19.44 that  $h \rightarrow N^{eq}$  as  $m \rightarrow 1$ , the first condition is

$$\frac{N}{h} \rightarrow 1 \text{ as } m \rightarrow 1 \quad (19.46a)$$

The second condition requires that there be no very large voids in the system or that

$$\frac{N}{h} \rightarrow 0 \text{ as } m \rightarrow \infty \quad (19.46b)$$

Integration of Eq. 19.45 between these limits yields

$$-I \int_1^\infty \frac{dm}{\beta_v h} = \int_{(N/h)_1}^{(N/h)_\infty} d\left(\frac{N}{h}\right) = -1$$

or

$$I = \left[ \int_1^\infty \frac{dm}{\beta_v(m) h(m)} \right]^{-1} \quad (19.47)$$

This equation can be simplified by noting that the function  $h(m)$  has a very sharp minimum at a cluster size  $m_c$  (shown as dots in Fig. 19.9). The minimum becomes broader as  $\beta_i/\beta_v \rightarrow 1$ , but, in view of the 16 order-of-magnitude range of the ordinate of Fig. 19.9, the minimum is still quite distinct. The integral in Eq. 19.45 is determined primarily by the behavior of  $h(m)$  near this minimum. Consequently,  $\beta_v(m)$ , which is a slowly varying function of  $m$ , is evaluated at  $m_c$  and removed from the integral and  $\ln h(m)$  is expanded in a Taylor series about the minimum:

$$\ln [h(m)] = \ln [h(m_c)] + \frac{1}{2} \left( \frac{d^2 \ln h}{dm^2} \right)_{m_c} (m - m_c)^2$$

where  $m_c$  is defined by

$$\left( \frac{d \ln h}{dm} \right)_{m_c} = 0$$

Substituting the series into Eq. 19.47 and integrating yields

$$I = \left[ \frac{1}{2\pi} \left( \frac{d^2 \ln h}{dm^2} \right)_{m_c} \right]^{1/2} \beta_v(m_c) h(m_c) \quad (19.48)$$

The first factor on the right of Eq. 19.48 is called the Zeldovich factor.

The void-nucleation rate is therefore determined by the vacancy-capture rate of a critical-size void and the properties of the function  $h(m)$  near its minimum. The complete void distribution function  $N(m)$  can be determined, but it is of no utility since only the nucleation rate is desired.

Nucleation rates calculated from Eq. 19.48 are plotted in Fig. 19.10. The curves for  $\beta_i/\beta_v = 0$  correspond to classical nucleation theory applied to a single-component system. It can be seen that inclusion of interstitials

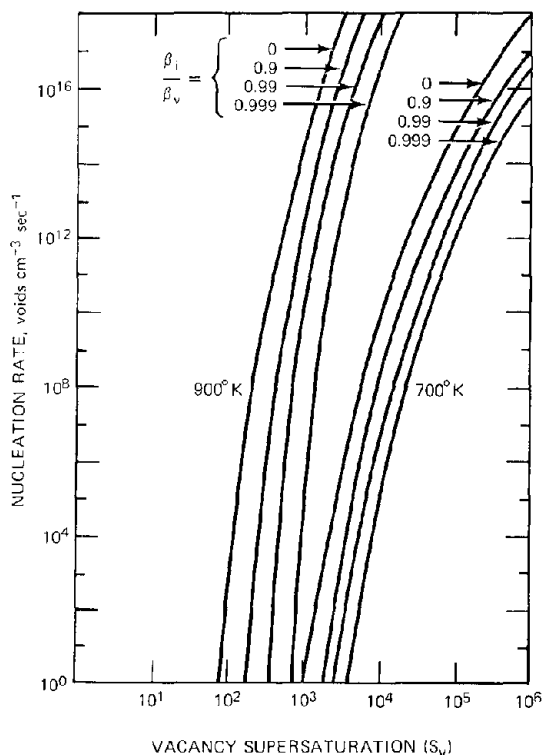


Fig. 19.10 Nucleation rate as a function of vacancy supersaturation for various arrival-rate ratios. (After Ref. 14.)

drastically reduces the nucleation rate. Increasing the arrival-rate ratio from 0 to 0.98 reduces the nucleation rate by six orders of magnitude. If  $\beta_i/\beta_v = 1$ , nucleation is impossible because interstitials arrive at a void embryo as fast as vacancies. The supersaturations on the abscissa of Fig. 19.10 are obtained from the point-defect balances, which will be considered in Sec. 19.5. An example of the vacancy and interstitial concentrations expected in fast reactor cladding is shown in Fig. 13.17. Although at a fixed  $S_v$  the nucleation rate increases with temperature, the supersaturation at high temperature is greatly reduced from what can be maintained at low temperature. At  $T = 700^\circ\text{K}$ , which is somewhat below the peak swelling temperature of stainless steel, Fig. 13.17(a) shows that it is quite possible to sustain a vacancy supersaturation of  $10^4$ , and Fig. 19.10 gives for this condition a nucleation rate of  $10^8$  voids  $\text{cm}^{-3} \text{sec}^{-1}$ . Cladding examined after a year ( $10^7$  sec) in-pile would be expected to show a void density of  $\sim 10^{15} \text{cm}^{-3}$ , which is of the correct order of magnitude. However, the nucleation computation is highly sensitive to poorly known parameters, such as the arrival-rate ratio  $\beta_i/\beta_v$ , and properties, such as the surface tension of the solid. In addition, the supersaturation is determined by the densities and efficiencies of point-defect sinks, which are difficult to estimate and in any case change during irradiation. In general, homogeneous nucleation theory as outlined does not predict as many voids as are in fact observed in irradiated cladding, nor is it able to account for the cluster

incubation period that is also observed experimentally.\* In fact, the theory would suggest that voids should be nucleated early in irradiation while the supersaturation is high. The vacancy concentration decreases during irradiation because of the growth of interstitial loops (loop nucleation appears to precede void nucleation). The loops augment the number of point-defect sinks in the solid and, in so doing, reduce the supersaturation of both vacancies and interstitials (i.e., during irradiation, the vacancy concentration drops from one of the solid curves in Fig. 13.17(a) to the corresponding dashed curve). It is believed that the reason for the incubation period observed in swelling experiments is associated with the time required to build up sufficient helium in the matrix.

### 19.3.4 Nucleation in the Presence of Helium

The preceding theory of void nucleation in a solid supersaturated with vacancies and interstitials was based on the assumption that point defects were capable of readily moving between voids and the bulk solid. Extensions of void nucleation theory to account for helium in the metal have been advanced by Katz and Wiedersich<sup>1,6</sup> and by Russell.<sup>1,7</sup>

Helium generated in the solid is much less mobile than vacancies and interstitials at the temperatures where void formation is important. Moreover, once a helium atom has been trapped by a void embryo, return to the matrix is very difficult. Consequently, nucleation in the presence of helium need not involve the simultaneous equilibration of all three species (vacancies, interstitials, and helium atoms) between the void embryos and the bulk solid. A simpler analysis of the effect of helium on void nucleation may be constructed by regarding the helium atoms as immobile nucleation sites to which vacancies and interstitials can migrate to form void clusters. We visualize point defects quickly moving to and from a distribution of embryo voids which contains a fixed number of gas atoms.

The solid is also supposed to contain a distribution of gas-atom clusters,  $M_j$ , which is the number of gas-atom clusters per unit volume composed of  $j$  helium atoms. The total helium concentration in the solid

$$M = \sum_{j=1} jM_j \quad (19.49)$$

at any time during irradiation is determined by the helium production rates discussed in Sec. 18.10. It is assumed that nucleation of voids proceeds independently and concurrently on each of the gas-atom cluster populations characterized by  $M_j$  nucleation sites per unit volume. All these parallel nucleation processes are driven by the prevailing vacancy and interstitial supersaturations. In addition to the heterogeneous nucleation paths provided by the helium clusters in the metal, the homogeneous nucleation mechanism described earlier in this section still occurs on the  $N_s$  lattice sites in the solid. The total nucleation rate is the sum of the contributions of the

\*There is an incubation period inherent in the theory, but it is not as long as the incubation time for observed void swelling in stainless steel (see Ref. 15).

parallel processes of homogeneous and heterogeneous nucleation:

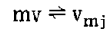
$$I = I_{\text{homo}} + \sum_{j=1} I_j \quad (19.50)$$

where  $I_{\text{homo}}$  is given by Eq. 19.48 with  $h(m)$  given by Eq. 19.44 and  $N_j^{\text{eq}}(m)$  by Eq. 19.33. Thus, we need only to determine the heterogeneous nucleation rate  $I_j$  on the  $M_j$  helium-atom clusters (each containing  $j$  helium atoms) per unit volume. Each of the voids formed on these  $M_j$  sites contains the fixed number  $j$  of gas atoms but a variable number  $m$  of vacancies. The void embryos that form on the gas-atom clusters are described by the equilibrium distribution functions:

$N_j^{\text{eq}}(m)$  = number of embryos per unit volume that contain  $m$  vacancies and  $j$  gas atoms

Equation 19.33 gives the equilibrium distribution of voids that contain no gas atoms ( $j = 0$ ).

The equilibrium reactions that establish the distribution  $N_j^{\text{eq}}(m)$  are



where  $v_{mj}$  denotes a void consisting of  $m$  vacancies and  $j$  gas atoms. In accord with the assumption that the helium is immobile, no chemical reaction expressing equilibration of gas atoms between the voids and the bulk is written. The criterion of chemical equilibrium for the above reactions is

$$m\mu_v = \mu_{mj} \quad (19.51)$$

where  $\mu_v$  is the chemical potential of a vacancy (Eq. 19.32) and  $\mu_{mj}$  is the chemical potential of a void with  $m$  vacancies and  $j$  gas atoms. The latter is given by

$$\mu_{mj} = \frac{\partial G}{\partial N_j^{\text{eq}}(m)} \quad (19.52)$$

where the total Gibbs free energy depends on both the vacancy and helium-atom content of the voids:

$$G = G_0 + \sum_j \sum_m [N_j^{\text{eq}}(m) g_{mj} - kT \ln W_{mj}] \quad (19.53)$$

where  $g_{mj}$  is the reversible work required to form a cluster containing  $m$  vacancies and  $j$  helium atoms and  $k \ln W_{mj}$  is the configuration entropy due to this class of clusters. The effect of helium on the nucleation rate is entirely contained in these two terms.

Following arguments similar to those applied to homogeneous nucleation on all lattice sites, the number of ways of arranging  $N_j^{\text{eq}}(m)$  voids on  $M_j$  sites is found to be

$$W_{mj} = \frac{M_j (M_j - 1) \dots \{M_j - [N_j^{\text{eq}}(m) - 1]\}}{[N_j^{\text{eq}}(m)]!} \\ = \frac{M_j!}{[M_j - N_j^{\text{eq}}(m)]! [N_j^{\text{eq}}(m)]!}$$

Expressing  $W_{mj}$  by the above equation and using Eq. 19.53 in Eq. 19.52 yields:

$$\mu_{mj} = g_{mj} + kT \ln \left[ \frac{N_j^{\text{eq}}(m)}{M_j} \right] \quad (19.54)$$

Next we determine  $g_{mj}$ , the reversible work of forming the vacancy gas-atom cluster from a solid which has no vacancies but contains the  $j$  gas-atom clusters embedded in the otherwise perfect lattice. The term  $g_{mj}$  consists of two terms. The first is the work required to create a gas-free void in the solid, which is given by Eq. 19.28. The second represents the work required to move the helium from the solid to the space inside the void. Since helium is nearly insoluble in the metal, it has a natural tendency to escape from the solid to the gas space of the void. Thus, we expect that work can be recovered by reversibly transferring helium from the solid to the void, or that this step reduces the work requirement of void formation and consequently facilitates nucleation. The helium transfer operation is performed in three stages to determine the free-energy change:

1. Helium is withdrawn from solution to a gas container at the equilibrium helium pressure corresponding to the temperature and the total helium concentration of the solid. This pressure is denoted by  $p_{\text{eq}}$ .
2. The gas is expanded isothermally and reversibly to the pressure at which the helium exists in the void.
3. The helium is transferred to the void.

Consider the free-energy changes that accompany each of the above steps.

The first step, which is analogous to vaporization of a liquid at its vapor pressure, involves no change in free energy. Isothermal, reversible expansion of  $j$  atoms of an ideal gas from pressure  $p_{\text{eq}}$  to pressure  $p$  provides a release of free energy of the amount

$$jkT \ln \left( \frac{p_{\text{eq}}}{p} \right)$$

The third step involves no work and hence contributes nothing to the free-energy change.

Assuming that the helium in the void obeys the ideal gas law, we find the pressure  $p$  is given by

$$p (m\Omega) = jkT \quad (19.55)$$

where  $m\Omega$  is the volume of a void made up of  $m$  vacancies each of which contributes a volume  $\Omega$ .

Determination of the equilibrium helium pressure,  $p_{\text{eq}}$ , requires more information. Although helium is nearly insoluble in metals, it is not completely so. The solubility of a gas in a metal can be analyzed by statistical mechanical methods, as shown in Chap. 5 (see problem 5.9). Briefly, the chemical potential of gas-phase helium is equated to the chemical potential of dissolved helium (which is assumed to be monatomically dispersed in the lattice). The partition of gas-phase helium needed to compute the chemical potential in the gas is due to translation only. The partition function of dissolved helium is obtained by assuming that helium in the lattice behaves as a three-dimensional oscillator. This procedure yields

$$p_{\text{eq}} = M \frac{kT}{N_s} \left( \frac{h\nu}{kT} \right)^3 \left( \frac{2\pi m_{\text{He}} kT}{h^3} \right)^{3/2} \exp \left( \frac{\epsilon_g}{kT} \right) \quad (19.56)$$

where  $M/N_s$  is the total atom fraction of helium in the metal and  $\epsilon_g$  is the energy difference between an atom of gaseous helium and one in the lattice (i.e., the heat of solution). If it is assumed that helium occupies

substitutional positions in the metal lattice,  $\epsilon_g$  very closely represents the energy required to remove a metal atom from a lattice and place it on the surface. This step provides the opening into which a helium atom can fit. The bonding between helium and the surrounding metal atoms is quite small; so the entire energy requirement in the process is consumed in removing the metal atom. Consequently,  $\epsilon_g$  should be approximately equal to the formation energy of a vacancy in the metal, or  $\epsilon_g \approx \epsilon_v$ . The vibration frequency  $\nu$  in Eq. 19.56 is that of a helium atom on a lattice site and is approximately  $10^{13} \text{ sec}^{-1}$ ,  $m_{\text{He}}$  is the mass of a helium atom, and  $h$  is Planck's constant.

Because  $\epsilon_g$  is positive and large compared to  $kT$ , the ratio  $p_{\text{eq}}/M$  is also large. For the parts-per-million helium concentrations encountered in LMFBR fuel-element cladding,  $p_{\text{eq}}$  may be as large as  $10^9$  atm. It should be emphasized that the helium in the cladding never exists as a gas at the pressure  $p_{\text{eq}}$ ; it is either in the metal at concentration  $M$  or in the void at pressure  $p$ . The equilibrium pressure given by Eq. 19.56 appears solely as a result of computing the work that could be extracted from the process of transferring helium from the lattice to the void if it were done reversibly.

Accounting for the stabilizing effect of helium, the reversible work to form a void embryo of  $m$  vacancies and  $j$  gas atoms is

$$g_{mj} = 4\pi \left( \frac{3\Omega}{4\pi} \right)^{2/3} \gamma m^{2/3} - jkT \ln \left( \frac{HMm\Omega}{jkT} \right) \quad (19.57)$$

where  $H$  is the coefficient of  $M$  in Eq. 19.56 (i.e.,  $H$  is the Henry's law constant for the dissolution of helium in the metal). It is a function of temperature only.

We now substitute Eq. 19.57 into Eq. 19.54 to determine  $\mu_{mj}$  and use the resulting equation and Eq. 19.32 for  $\mu_v$  in Eq. 19.51. Solving for the equilibrium distribution, we find

$$N_j^{\text{eq}}(m) = M_j \exp \left[ m \ln S_v - \xi m^{2/3} + j \ln \left( \frac{HMm\Omega}{jkT} \right) \right] \quad (19.58)$$

where  $\xi$  is given by Eq. 19.34. When  $j = 0$ ,  $M_j = N_s$  and Eq. 19.58 reduces to the equilibrium distribution for gas-free voids, given by Eq. 19.33. Figure 19.11 shows the negative of the argument of the exponential in Eq. 19.58

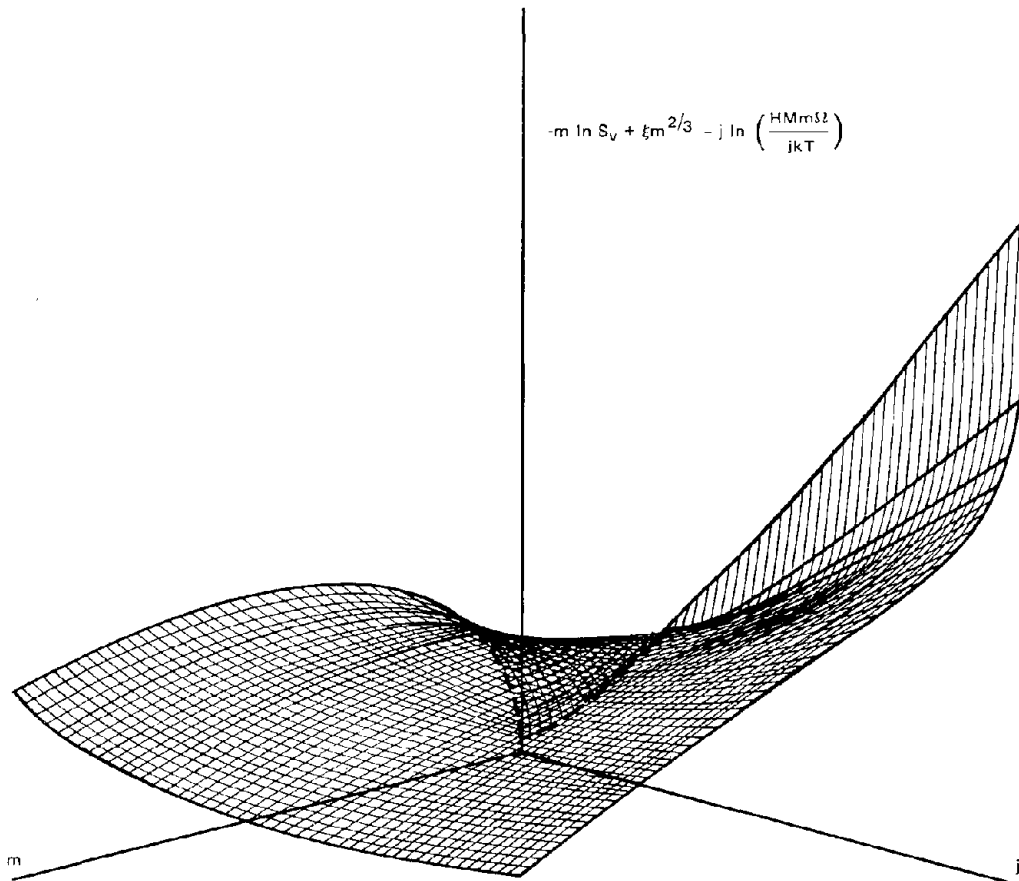


Fig. 19.11 Plot of the free energy of void formation as a function of the number of vacancies ( $m$ ) and the number of gas atoms ( $j$ ) in the void. Conditions:  $S_v = 600$ ,  $p_{\text{eq}} = 5000$  atm,  $T = 500^\circ\text{C}$ ,  $\gamma = 1000$  dynes/cm. (After Ref. 17.)

(which is sometimes called the free energy of void formation) plotted as a function of  $m$  and  $j$ . The intercept of this surface at  $j = 0$  (no gas) corresponds to the  $\beta_i/\beta_v = 0$  curve in Fig. 19.9. Gas atoms in the void reduce the energy barrier for nucleation below the value characteristic of gas-free voids. The saddle point on the surface shown in Fig. 19.11 occurs at  $m = 11$  and  $j = 6$ . This plot, however, does not consider interstitials, which are included in the analysis in exactly the same manner as in the case of homogeneous nucleation in the absence of gas.

The remaining analysis is straightforward. The arrival rates  $\beta_v$  and  $\beta_i$  and the vacancy emission rate  $\alpha_v$  are independent of the presence of gas atoms in the void. As long as the helium is immobile and does not move among the voids, Eq. 19.40 is valid if the subscript  $j$  is appended to both  $I$  and  $N$  in this formula. Only the function  $h(m)$ , which depends on the equilibrium void distribution function, changes explicitly. In place of Eq. 19.43, we write for gas-containing voids

$$\ln \left[ \frac{h_j(m)}{M_j} \right] = - \sum_{m'=0}^{m-1} \ln \left[ \frac{N_j^{eq}(m')}{N_j^{eq}(m'+1)} + \frac{\beta_i}{\beta_v} \right] \quad (19.59)$$

For a specified value of  $j$ , the minimum of the function  $h_j(m)$  occurs at  $m_{cj}$  vacancies, and the nucleation rate on the population of  $j$  helium-atom clusters is given by the analog of Eq. 19.48:

$$I_j = \left[ \frac{1}{2\pi} \left( \frac{d^2 \ln h_j}{dm^2} \right)_{m_{cj}} \right]^{1/2} \beta_v(m_{cj}) h_j(m_{cj}) \quad (19.60)$$

To evaluate the nucleation rate on the gas-atom clusters in the metal, we must estimate the distribution of the available gas ( $M$  atoms/cm<sup>3</sup>) among the various cluster sizes. In principle, the distribution  $M_j$  could be obtained by considering independently the problem of helium-atom agglomeration in the cladding in much the same way that fission-gas precipitation into bubbles in the fuel was analyzed in Chap. 13. However, for simplicity, the distribution

$$M_j = M_1^{(j+1)/2}$$

is assumed. The distribution must also satisfy Eq. 19.49. Figure 19.12 shows the results of calculations based on Eqs. 19.60 and 19.61 for  $M$  equivalent to 10 ppm helium (which is the concentration that would be formed in stainless-steel cladding following irradiation to a fluence of  $\sim 5 \times 10^{22}$  neutrons/cm<sup>2</sup>). The vacancy supersaturation scale is divided into regimes expected in a reactor and in an ion-bombardment experiment. It can be seen from the graph that, for all supersaturations expected in-pile, heterogeneous nucleation on helium-atom clusters far outweighs homogeneous nucleation. This behavior constitutes theoretical confirmation of the often observed enhancement of void nucleation by helium. The relative importance of homogeneous and heterogeneous nucleation shifts according to the helium concentration because  $h_{homom}(m)$  is proportional to  $N_s$ , whereas  $h_j(m)$  is proportional to  $M_j$ . At low fluence homogeneous nucleation is dominant because there is not enough helium

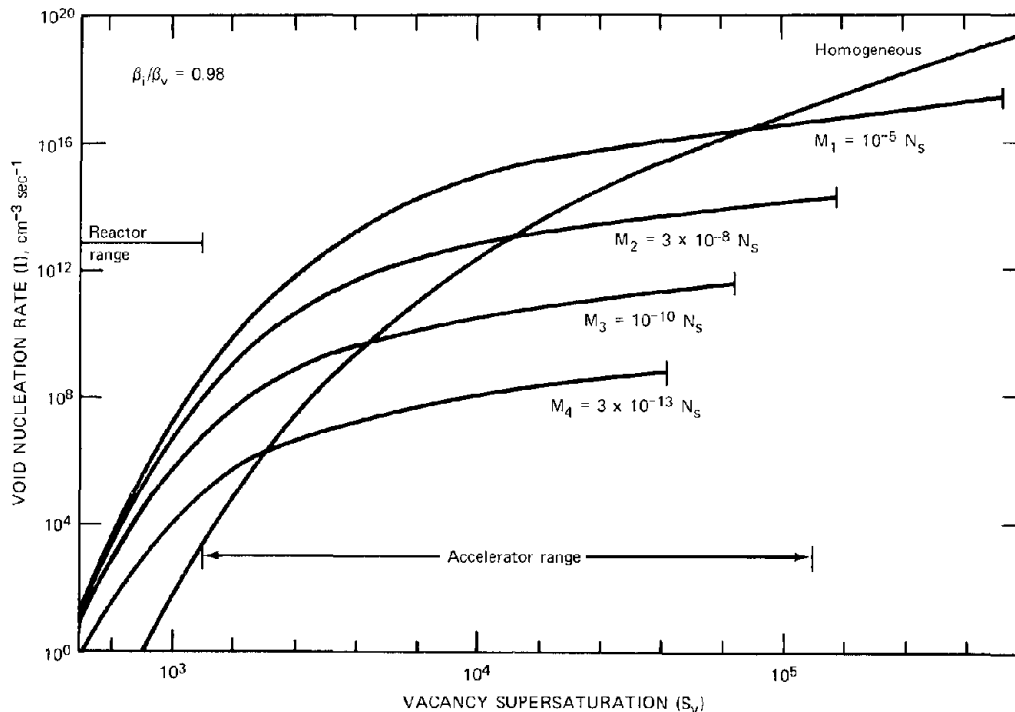


Fig. 19.12 Void-nucleation rates ( $I_j$ ) on helium-atom clusters and the homogeneous nucleation rate ( $I_{homom}$ ) as functions of vacancy supersaturation at 500°C. Total helium content of 10 ppm. (After Ref. 16.)

to drive heterogeneous nucleation. However, since  $I_{homo}$  is quite low, no voids are observed until sufficient helium has been generated by transmutation reactions to give the high heterogeneous nucleation rates shown in Fig. 19.12. This incubation period is equivalent to a fluence of  $\sim 10^{22}$  neutrons/cm<sup>2</sup> for stainless steel.

## 19.4 NUCLEATION OF INTERSTITIAL DISLOCATION LOOPS

The microstructure of irradiated steel is found to contain a high concentration of interstitial dislocation loops in addition to voids. In Sec. 19.3, it was shown that void nucleation is driven by the supersaturation  $S_v$  of vacancies aided by a slightly greater rate of vacancy than interstitial absorption by the voids, which is expressed as  $(\beta_i/\beta_v)_{voids} < 1$ . Nucleation of loops because of interstitial supersaturation  $S_i$  is possible because more interstitials than vacancies arrive at all dislocations in the solid, or  $(\beta_v/\beta_i)_{loops} < 1$ . The fact that the relative vacancy and interstitial arrival rates are inverted for voids and loops is a consequence of the small but extremely important preference of dislocations for interstitials. Formally, interstitial loop nucleation can be treated in precisely the same manner as void nucleation, but the very large formation energy of interstitials ( $\epsilon_i \approx 4$  eV) compared to that for vacancies ( $\epsilon_v \approx 1$  eV) profoundly alters the quantitative aspects of the nucleation process. Another important difference between void and loop nucleation is that the latter is not subject to enhancement by helium in the solid. Growing loops are not sinks for inert gas atoms, as are voids.

### 19.4.1 Loop Nucleation by Classical Theory

The methods applied to predict void-nucleation rates in the preceding section can be utilized in toto for loop nucleation simply by exchanging the subscripts  $i$  and  $v$  in all of the formulas and by replacing the void energy given by Eq. 19.3 by the energy of a faulted loop, Eq. 19.6. Such a calculation has been performed by Russell and Powell.<sup>18</sup> They found that the critical cluster for loop nucleation contains only two or three interstitials, even in the presence of vacancies. The reason for this result can be explained as follows. The equilibrium cluster distribution (i.e., the distribution for which clusters, vacancies, and interstitials are all in equilibrium) is given by the analog of Eq. 19.33:

$$N^{eq}(m) = N_s \exp\left(m \ln S_i - \frac{\epsilon_m}{kT}\right) \quad (19.61)$$

where  $N^{eq}(m)$  is the number of loops per unit volume comprised of  $m$  interstitials;  $S_i$  is the interstitial supersaturation

$$S_i = \frac{C_i}{C_i^{eq}} = \Omega C_i \exp\left(\frac{\epsilon_i}{kT}\right) \quad (19.62)$$

and  $\epsilon_m$  is the work required to form a loop of size  $m$  from a perfect solid. Application of the principle of detailed balancing to the interstitial-capture and -emission rates for a loop leads to a formula similar to Eq. 19.35:

$$\beta_i(m) N^{eq}(m) = \alpha_i(m+1) N^{eq}(m+1) \quad (19.63)$$

where  $\beta_i(m)$  is the rate at which a loop of size  $m$  captures interstitials and  $\alpha_i(m)$  is the rate at which the loop emits interstitials. With the aid of Eq. 19.61, 19.63 can be solved for the interstitial-emission rate

$$\alpha_i(m+1) = \frac{\beta_i(m)}{S_i} \exp\left(\frac{\epsilon_{m+1} - \epsilon_m}{kT}\right) \quad (19.64)$$

The interstitial-capture rate  $\beta_i(m)$  is a slowly varying function of  $m$ , and the primary size dependence of the emission rate is contained in the exponential term in Eq. 19.64. In estimating  $\epsilon_m$ , Russell and Powell<sup>18</sup> neglect the stacking-fault energy in Eq. 19.6 and use a slightly different formula for the strain energy of the loop (i.e., the first term on the right of Eq. 19.6). The loop energy they used is given by

$$\epsilon_m = 500 m^{3/2} \text{ kJ/mole} \quad (19.65)$$

for  $m > 1$  and  $\epsilon_1 = \epsilon_i = 420$  kJ/mole for the formation energy of a single interstitial. Using this energy formula and a typical interstitial supersaturation of  $10^{17}$ , we find the emission rates from di- and tri-interstitials to be

$$\alpha_i(2) \approx 3 \times 10^4 \beta_i(1)$$

$$\alpha_i(3) \approx 6 \times 10^5 \beta_i(2)$$

Since  $\beta_i(1) \approx \beta_i(2)$ ,  $\alpha_i(2)$  is some 9 orders of magnitude larger than  $\alpha_i(3)$ . In other words, the triinterstitial has virtually no tendency to shed interstitials and is therefore the critical cluster for loop nucleation.

Application of classical nucleation theory (even when modified to account for point defects of the opposite sign) is of dubious validity when the critical cluster contains only two or three particles. First, the use of a cluster energy formula based on the strain energy of a circular dislocation loop as calculated from elasticity theory hardly seems appropriate for di- and triinterstitials. Second, approximation of finite differences by differentials, as is required to obtain Eq. 19.45 from the preceding formula, and the subsequent manipulation of the integrals is of questionable accuracy when the sums involved contain only two or three terms. Consequently, loop nucleation is best analyzed by a method that views the nucleation process as the result of homogeneous reactions between the point defects and small clusters.

### 19.4.2 Loop Nucleation by Chemical Reaction-Rate Theory

The kinetics of point-defect annealing are commonly treated by methods analogous to those employed in homogeneous chemical kinetics.<sup>19</sup> This method has been used in Sec. 13.8 to calculate nucleation rates of fission-gas bubbles in fuel. Hayns<sup>20</sup> has treated interstitial loop nucleation in a similar manner.

1. The vacancy and interstitial supersaturations are independent of the loop-nucleation process. For void nucleation,  $S_v$  and  $S_i$  are assumed to be specified by point-defect balances that consider all sinks in the solid.

2. Vacancies and interstitials are mobile.

3. Di- and triinterstitials are immobile.

4. Destruction of the clusters by radiation (i.e., by dynamic resolution due to the energetic recoils in the irradiated metal) is neglected.

Conditions 1 and 2 are quite appropriate for cladding under fast reactor conditions. The third assumption is probably not valid, but inasmuch as interstitial cluster migration is not considered either in void-nucleation theory (Sec. 19.3) or in void- and loop-growth theory (Sec. 19.5), we shall not introduce it at this point. The effect of re-resolution on loop nucleation rates is treated in problem 19.7 at the end of this chapter.

To visualize the process of loop nucleation in an irradiated solid clearly, we first examine the simpler situation in which the metal contains a supersaturation of interstitials  $S_i$  but no vacancies. Interstitial cluster nucleation is assumed to be governed by the reactions



The physical justification for this mechanism is that the rates of formation and decomposition of diinterstitials according to reaction 1 are very rapid compared to the rate of formation of triinterstitials; so the small drain on the diinterstitial population caused by reaction 2 does not appreciably disturb the equilibrium of reaction 1. The triinterstitials do not decompose, because of the very low value of  $\alpha_i(3)$ .

In Sec. 13.4 the forward rate of reaction 1 has been determined for the case of vacancies. For interstitials, the rate  $R_{1f}$  is expressed by

$$R_{1f} = k_{1f} C_i^2 \quad (19.66)$$

where, by analogy to Eq. 13.39,

$$k_{1f} = \frac{z_{1i} \Omega D_i}{a_0^2} \quad (19.67)$$

where  $z_{1i}$  is the combinatorial number that includes the number of sites from which a diinterstitial can be formed in a single jump of one interstitial atom to an adjacent one. For the vacancy-vacancy reaction in fcc metals, this coefficient was found to be 84, but the rate must be multiplied by a factor of 2 to account for the mobility of both partners of the reaction. Thus the combinatorial number  $z_{1i}$  is probably between 100 and 200. Instead of the rate constants  $k$ , nucleation theory uses arrival rates  $\beta$ ; thus the forward rate of reaction 1 can also be written as

$$R_{1f} = \beta_i(1) C_i \quad (19.68)$$

where

$$\beta_i(1) = k_{1f} C_i = \frac{z_{1i} \Omega D_i C_i}{a_0^2} \quad (19.69)$$

and is the arrival rate of interstitials at a cluster of size 1 (i.e., another interstitial).

The rate of the reverse of reaction 1 is

$$R_{1r} = \alpha_i(2) N_2 \quad (19.70)$$

where  $N_2$  is the volumetric concentration of diinterstitials and  $\alpha_i(2)$  is given by Eq. 19.64 with  $m = 1$ . In chemical rate theory, the formation energy of a diinterstitial is not approximated by the strain energy of a dislocation loop of two interstitials as it is in classical nucleation theory. Instead,  $\epsilon_2$  is related to the binding energy of the diinterstitial by the analog of Eq. 6.15:

$$\epsilon_2 = 2\epsilon_1 - B \quad (19.71)$$

where  $B$  is the energy required to separate a diinterstitial into two isolated interstitials. If  $B$  were 125 kJ/mole in stainless steel,  $\epsilon_2$  calculated from Eq. 19.71 would be identical to the value obtained by setting  $m = 2$  in Eq. 19.65. Substituting Eqs. 19.69 and 19.71 into Eq. 19.64, setting  $\epsilon_1 = \epsilon_i$ , and replacing  $C_i$  with  $S_i$  by use of Eq. 19.62 produces the result

$$\alpha_i(2) = \frac{z_{1i} D_i}{a_0^2} \exp\left(-\frac{B}{kT}\right) \quad (19.72)$$

Because reaction 1 is assumed to be at equilibrium, we can set  $R_{1f} = R_{1r}$ , or  $\beta_i(1) C_i = \alpha_i(2) N_2$ . Using Eq. 19.69 for  $\beta_i(1)$  and Eq. 19.72 for  $\alpha_i(2)$  yields

$$N_2 = \Omega \exp\left(\frac{B}{kT}\right) C_i^2 \quad (19.73)$$

The rate of reaction 2 is

$$R_2 = \beta_i(2) N_2 \quad (19.74)$$

Assuming the diinterstitial to be immobile, we find the arrival rate of interstitials at diinterstitials to be given by

$$\beta_i(2) = \frac{z_{2i} \Omega D_i C_i}{a_0^2} \quad (19.75)$$

where  $z_{2i}$  is the number of sites surrounding a diinterstitial from which a single interstitial can jump to form a triinterstitial. Once the latter is formed, it cannot be destroyed; so the rate of nucleation of interstitial loops is equal to the rate of formation of triinterstitials:

$$I_{i0op}^* = R_2 = \beta_i(2) N_2 \quad (19.76)$$

where the asterisk denotes nucleation in the absence of vacancies. Substitution of Eqs. 19.73 and 19.75 into Eq. 19.76 yields the nucleation rate:

$$I_{i0op}^* = \frac{z_{2i} \Omega^2 D_i C_i^3}{a_0^2} \exp\left(\frac{B}{kT}\right) \quad (19.77)$$

or, in terms of the interstitial supersaturation expressed by Eq. 19.62,

$$I_{i0op}^* = \frac{z_{2i} D_i}{a_0^2 \Omega} S_i^3 \exp\left[-\frac{(3\epsilon_i - B)}{kT}\right] \quad (19.78)$$

To apply loop-nucleation theory to irradiated metals, we must consider the role of vacancies. To do so, the preceding analysis is modified to include reactions between vacancies and di- and trinterstitials in addition to reactions 1 and 2. The additional reactions are



for which the rates are

$$R_3 = \beta_v(2) N_2 \quad (19.79)$$

$$R_4 = \beta_v(3) N_3 \quad (19.80)$$

where  $\beta_v(m)$  denotes the rate at which an interstitial cluster of size  $m$  captures vacancies:

$$\beta_v(m) = \frac{z_{vm} \Omega D_v C_v}{a_0^2} \quad (19.81)$$

$z_{vm}$  being the number of locations surrounding a size  $m$  interstitial cluster from which a vacancy can jump and reduce the cluster size by one.

Reactions 1 to 4 are depicted schematically in Fig. 19.13. The nucleation current  $I_m$  is the net rate at which clusters of size  $m$  grow to clusters of size  $m + 1$ . Balances on di- and trinterstitials can be expressed in terms of the nucleation currents by

$$\frac{dN_2}{dt} = I_1 - I_2 \quad (19.82)$$

$$\frac{dN_3}{dt} = I_2 - I_3 \quad (19.83)$$

As indicated in Fig. 19.13, the nucleation currents are related to the reaction rates by

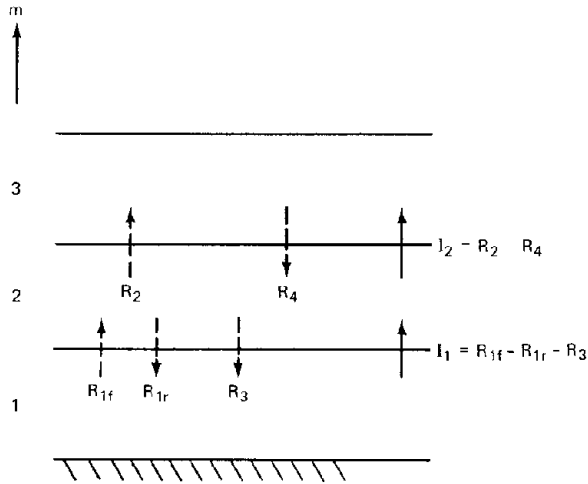


Fig. 19.13 Relations between nucleation currents and the rates of elementary reactions between point defects and interstitial clusters.

$$I_1 = R_{1f} - R_{1r} - R_3 = \beta_i(1) C_i - \alpha_i(2) N_2 - \beta_v(2) N_2 \quad (19.84)$$

$$I_2 = R_2 - R_4 = \beta_i(2) N_2 - \beta_v(3) N_3 \quad (19.85)$$

It will be recalled that steady-state nucleation refers to the condition in which  $I_1 = I_2 = I_3 = \dots = I_{\text{loop}}$ . Application of this constraint to Eq. 19.82 and use of Eqs. 19.84 and 19.85 show that

$$\beta_i C_i = [\alpha_i(2) + \beta_i + \beta_v] N_2 - \beta_v N_3 \quad (19.86)$$

Because the arrival rates  $\beta_i(m)$  and  $\beta_v(m)$  are very weakly dependent on  $m$ , the arguments denoting the cluster-size dependence of these coefficients have been deleted in Eq. 19.86;  $\beta_i$  and  $\beta_v$  are considered as known constants which depend only on the vacancy and interstitial supersaturations.

Under irradiation, the ratio  $\beta_v/\beta_i$  at loops is just slightly less than unity; thus  $\beta_i$  and  $\beta_v$  are of comparable magnitudes. However, it was shown earlier in this section that  $\alpha_i(2)$  is  $\sim 10^4$  times larger than  $\beta_i$  (or  $\beta_v$ ). Consequently, the last two terms in the brackets of Eq. 19.86 can be neglected. By the same token, since  $N_3$  is no greater than  $N_2$ , the last term on the right is also negligibly small. Therefore, when steady-state nucleation has been attained,  $\beta_i C_i = \alpha_i(2) N_2$ , or the equilibrium of reaction 1 is not significantly perturbed by the introduction of vacancies into the system. Therefore,  $N_2$  is given by Eq. 19.73, whether or not vacancies are present along with interstitials.

At steady state, Eq. 19.83 and analogous balances for  $m = 4, \dots$  reduce to

$$(\beta_i + \beta_v) N_3 = \beta_i N_2 + \beta_v N_4$$

$$(\beta_i + \beta_v) N_4 = \beta_i N_3 + \beta_v N_5 \quad (19.87)$$

⋮  
⋮  
⋮

Since the vacancy and interstitial arrival rates are approximately equal, the above equations are satisfied by

$$N_2 \simeq N_3 \simeq N_4 \simeq \dots \quad (19.88)$$

The nucleation rate is equal to any of the  $I_m$ . Using  $m = 2$ ,

$$I_{\text{loop}} = I_2 = R_2 - R_4 = \beta_i N_2 - \beta_v N_3 \quad (19.89)$$

or, taking into account the equality of  $N_2$  and  $N_3$ ,

$$I_{\text{loop}} = (\beta_i - \beta_v) N_2 = \left(1 - \frac{\beta_v}{\beta_i}\right) \beta_i N_2 = \left(1 - \frac{\beta_v}{\beta_i}\right) I_{\text{loop}}^* \quad (19.90)$$

Inasmuch as  $N_2$  is given by Eq. 19.73, the product  $\beta_i N_2$  in the above expression for  $I_{\text{loop}}$  is the nucleation rate in the absence of vacancies. The vacancy supersaturation of

the metal under irradiation reduces the loop-nucleation rate by the factor  $[1 - (\beta_v/\beta_i)]$ . The point-defect balances developed in Sec. 19.5 suggest that  $0.99 < \beta_v/\beta_i < 0.999$  at loops; so loop nucleation under irradiation is reduced by factors ranging from  $10^{-2}$  to  $10^{-3}$  owing to vacancy arrival at the critical nucleus (the triinterstitial).

In the fcc lattice,  $z_{2i} \simeq 20$  (the same combinatorial number was assumed for fission-gas-atom capture on two-atom clusters in the bubble-nucleation calculation of Sec. 13.8). The interstitial diffusion coefficient can be approximated by

$$D_i = a_0^2 \nu \exp\left(-\frac{\epsilon_i^*}{kT}\right) \quad (19.91)$$

where  $\epsilon_i^*$  is the activation energy for interstitial migration. In stainless steel,  $\epsilon_i^*$  is believed to be about 13 kJ/mole. The other parameters in the nucleation rate are

$$\Omega = 12 \text{ \AA}^3$$

$$\epsilon_i = 420 \text{ kJ/mole}$$

The binding energy of a diinterstitial in stainless steel is not known, but the value obtained by the loop strain-energy approximation of Eq. 19.65 is 125 kJ/mole. Taking  $\nu \simeq 10^{13} \text{ sec}^{-1}$ , Eqs. 19.78 and 19.90 together yield

$$I_{\text{loop}} \simeq 2 \times 10^{37} \left(1 - \frac{\beta_v}{\beta_i}\right) S_i^3 \exp\left[-\frac{1150}{R(T/10^3)}\right] \quad (19.92)$$

For a typical LMFBR fuel cladding  $S_i = 10^{18}$ ,  $\beta_v/\beta_i = 0.98$ , and  $T = 500^\circ\text{C}$ . Using these values in Eq. 19.92 gives  $I_{\text{loop}} = 10^{12} \text{ cm}^{-3} \text{ sec}^{-1}$ . Thus, a loop concentration of  $10^{16} \text{ cm}^{-3}$  is established after about 3 hr of irradiation. This time is considerably shorter than the incubation time needed for void nucleation, which is about 1 year. The observation that loop nucleation precedes void nucleation is thus theoretically justifiable. However, the substantial uncertainty in properties such as the binding energy of the diinterstitial in stainless steel renders the accuracy of the calculated nucleation rates no better than a factor of 100.

## 19.5 POINT-DEFECT BALANCES AND THE VOID-GROWTH LAW

Having determined the rate at which embryo voids and dislocation loops are introduced into the solid by nucleation, we next develop the theory for calculating the rates at which these defect clusters grow. Point-defect balances provide the means of computing the vacancy and void supersaturations ( $S_v$  and  $S_i$ , or, equivalently,  $C_v$  and  $C_i$ ) which drive both the nucleation and growth processes. The effects of applied stress and internal gas pressure on the growth law are considered later in this section. The present analysis is restricted to gas-free voids and unstressed solids.

The concentrations of vacancies and interstitials in the irradiated solid are determined by equating the rate of production of point defects to the rate of removal by all mechanisms. The treatment is quasi-stationary because the time derivatives  $dC_v/dt$  and  $dC_i/dt$  are neglected. This approximation is justifiable on the grounds that changes in

the sink strengths (and hence the rates of point-defect removal) due to the evolution of the microstructure of the metal during irradiation are very slow compared with the time required for the point-defect population to respond to such changes.

The spatial gradients in the point-defect population are also neglected because both the rates of production and removal are assumed to be uniform throughout the metal. The calculations are thus of the infinite-medium type. Very strong concentration gradients do exist in the immediate vicinity of the microstructural features of the solid which are responsible for point-defect absorption. This complication is removed from the point-defect balances by homogenizing the sinks. That is, the discrete sinks in the solid are replaced by spatially uniform absorbers of point defects. The strength of the homogenized sinks, however, must be determined by solving the point-defect diffusion equations in the immediate vicinity of the discrete sinks. These calculations have been reviewed in Sec. 13.5. The approach is similar to that applied to nuclear reactor analysis before the advent of extensive computer facilities; properties such as resonance capture or thermal utilization were determined by analysis of the spatial distribution of neutrons in a cell containing representative quantities of fuel and moderator in a geometry appropriate to the actual fuel-element configuration. This analysis provided the infinite multiplication factor, which could then be used (without further reference to the inhomogeneities in the internal configuration of the core) to compute the critical size of the reactor from neutron diffusion theory in which the system was regarded as homogeneous.

Point-defect balance equations have been developed by Harkness, Tesk, and Li;<sup>21</sup> Wiedersich;<sup>22</sup> and Brailsford and Bullough.<sup>23</sup> These three analyses are equivalent in approach but differ in detail. Wiedersich's method was developed in Sec. 13.10 for use in determining the growth rate of nonequilibrium gas bubbles in the fuel. In this section the theory of Brailsford and Bullough is used, since their treatment of vacancy emission from the vacancy sinks in the metal is superior to that used in the earlier theories.

### 19.5.1 Point-Defect Production Rates

Vacancies and interstitials are created in the collision cascade caused by the scattering of fast neutrons from lattice atoms. Each collision creates a primary knock-on atom (PKA), which in turn produces free interstitials, free vacancies, and clusters of interstitials and vacancies which are the debris of the displacement spike (Sec. 17.10). If the defect clusters are thermally stable, the number of free vacancies and free interstitials created by a PKA need not be equal, although the total number of vacancies (free plus in clusters) must be the same as the total number of interstitials. Section 18.5 treats a case in which more free interstitials than free vacancies are formed, the remainder of the latter appearing as a depleted zone. This calculation showed that the depleted zones were not thermally stable (i.e., they tended to evaporate) at temperatures above  $\sim 350^\circ\text{C}$ , which is the lower temperature limit for void formation. For  $T > 350^\circ\text{C}$ , the defect clusters formed in the collision cascade proper are very quickly destroyed, either by dissociation into their component point defects

by thermal evaporation or by annihilation by point defects of the opposite kind. For the purposes of void-growth analysis, we may assume that equal numbers,  $\nu$ , of vacancies and interstitials are produced by each fast-neutron scattering collision with a lattice atom. The volumetric production rate of point defects is

$$\begin{aligned} & \text{Rate of production of vacancies} \\ & = \text{rate of production of interstitials} \\ & = \nu \Sigma_s \Phi \text{ cm}^{-3} \text{ sec}^{-1} \end{aligned} \quad (19.93)$$

The number of displacements per PKA,  $\nu$ , is considerably smaller than that predicted by isolated cascade theory (Sec. 17.7), owing primarily to recombination during cascade formation or shortly thereafter as the point defects move away from the spike. For stainless steel, the best estimate of  $\nu$  in a fast-neutron spectrum is

$$\nu = 30 \text{ Frenkel pairs per neutron collision} \quad (19.94)$$

This number may not be applicable below  $\sim 350^\circ\text{C}$  (Ref. 21).

The macroscopic scattering cross section for the metal is  $\Sigma_s$ . It is the product of the microscopic scattering cross section and the density of metal atoms. For stainless steel,  $\Sigma_s \approx 0.2 \text{ cm}^{-1}$ ;  $\Phi$  is the total fast-neutron flux (with neutron energies  $> 0.1 \text{ MeV}$ ).

### 19.5.2 Bulk Recombination

Recombination of vacancies and interstitials to reform an atom on a normal lattice site occurs in the bulk of the metal at a rate equal to  $k_{vi} C_v C_i \text{ cm}^{-3} \text{ sec}^{-1}$ , where  $k_{vi}$  is the rate constant for recombination (Eq. 13.42).

### 19.5.3 Removal at Microstructural Sinks

Natural and radiation-produced microstructural features in the metal capture point defects of both types. These sinks can be divided into three categories:<sup>2,3</sup>

1. Unbiased (neutral) sinks. This type of sink shows no preference for capturing one type of defect over the other type. The rate of absorption is proportional to the product of the diffusion coefficient of the point defect and the difference in the concentrations of the point defect in the bulk metal and at the sink surface. Included in this category are (1) voids, (2) incoherent precipitates, and (3) grain boundaries.

2. Biased sinks. Any dislocation in the solid exhibits a preferential attraction for interstitials compared with vacancies. This bias is due to the nonrandom drift of interstitials down the stress gradient near the dislocation core. Vacancies do not exhibit stress-induced migration when near the dislocation. The effect may be incorporated into ordinary diffusion calculations by making the effective radius of the dislocation core slightly larger for interstitials than for vacancies. Dislocations are unsaturable sinks for point defects because they can climb as a result of absorbing a vacancy or an interstitial (provided that climb is not impeded by pinning of the line). The dislocations in the solid are divided into two classes: (1) network dislocations

present in the unirradiated metal and augmented by unfauling of the Frank dislocation loops and (2) dislocation loops formed by agglomeration of interstitials.

The only difference between loops and network dislocations is the concentration of vacancies which is maintained at the core. Both types of dislocations exhibit the same bias toward interstitial absorption.

3. Coherent precipitates. If a point defect is captured by a sink but does not lose its identity on absorption, it can only wait at the sink surface to be annihilated by point defects of the opposite type. Such sinks act as recombination centers of limited capacity. The most important example of this type of sink is the coherent precipitate.

### 19.5.4 Point-Defect Absorption by Voids

The diffusion-controlled rate of absorption of vacancies by all of the voids in a unit volume of solid is given by

$$Q_v^{\text{void}} = 4\pi R N D_v \left[ C_v - C_v^{\text{eq}} \exp\left(\frac{2\gamma\Omega}{RkT}\right) \right] \quad (19.95)$$

where  $R$  is the average radius of the void population and  $N$  is the total concentration of voids in the solid. The vacancy concentration at the void surface (the second term in the brackets of Eq. 19.95) has been taken as that corresponding to thermodynamic equilibrium in a solid under a negative hydrostatic stress  $2\gamma/R$ . This tensile stress arises from the surface tension of the solid, which pulls the surface inward.

The analogous formula for interstitial absorption by voids is

$$Q_i^{\text{void}} = 4\pi R N D_i C_i \quad (19.96)$$

The interstitial concentration at the void surface is effectively zero.

### 19.5.5 Incoherent Precipitates

Equations 19.95 and 19.96 apply to incoherent precipitates if  $R$  and  $N$  are interpreted as the average radius and concentration, respectively, of the precipitate particles.

### 19.5.6 Grain Boundaries

For simplicity, grain-boundary absorption of point defects is not included in the analysis presented here. It is, however, covered in problem 19.9 at the end of this chapter. The strength of grain-boundary sinks has been estimated in Refs. 21 and 24. The latter study showed that for grain sizes larger than  $\sim 10 \mu\text{m}$ , grain-boundary absorption of point defects is small compared to the effects of the other sinks in the metal.

### 19.5.7 Network Dislocations

Network dislocations maintain the equilibrium vacancy concentration at the core radius. The rate of diffusion-controlled absorption of vacancies by the  $\rho_N \text{ cm}$  of network dislocations per  $\text{cm}^3$  of solid is given by

$$Q_v^N = \frac{2\pi}{\ln(\mathcal{R}/R_{dv})} D_v \rho_N (C_v - C_v^{\text{eq}}) \quad (19.97)$$

where  $\mathcal{R}$  is approximately one-half the distance between dislocations (Eq. 13.79) and  $R_{dv}$  is the radius of the dislocation core for vacancies.

For interstitials the absorption rate by network dislocations is

$$Q_i^N = \frac{2\pi}{\ln(\mathcal{R}/R_{di})} D_i \rho_N C_i \quad (19.98)$$

where  $R_{di}$  is the core radius for interstitials. Setting

$$Z_v = \frac{2\pi}{\ln(\mathcal{R}/R_{dv})} \quad (19.99)$$

and

$$Z_i = \frac{2\pi}{\ln(\mathcal{R}/R_{di})} \quad (19.100)$$

Eqs. 19.97 and 19.98 can be written as

$$Q_v^N = Z_v D_v \rho_N (C_v - C_v^{eq}) \quad (19.101)$$

and

$$Q_i^N = Z_i D_i \rho_N C_i \quad (19.102)$$

Inasmuch as  $R_{di} > R_{dv}$ ,  $Z_i > Z_v$ . The ratio  $(Z_i - Z_v)/Z_v$  is estimated to be between 0.01 and 0.02.

### 19.5.8 Dislocation Loops

The only difference between network dislocations and interstitial dislocation loops is the equilibrium vacancy concentration at the core. When a dislocation loop emits a vacancy or absorbs an interstitial atom, the area of the stacking fault enclosed by the loop and the perimeter of the loop increase. According to Eq. 19.6, energy is required for this expansion to occur, and so vacancy emission or interstitial absorption by interstitial loops is less favorable than network dislocations. The latter, if unpinned, are free to climb without changing their length and so are not subject to the energy restraint that affects loop expansion. This phenomenon is taken into account by expressing the rates at which loops absorb vacancies and interstitials by the equations

$$Q_v^l = Z_v D_v \rho_l (C_v - C_v^l) \quad (19.103)$$

$$Q_i^l = Z_i D_i \rho_l (C_i - C_i^l) \quad (19.104)$$

The coefficients  $Z_v$  and  $Z_i$  are the same as they are for network dislocations since the stress fields around a dislocation are the same for the two types. The point-defect concentrations at the dislocation core, however, are different for network dislocations and loops;  $C_v^l$  and  $C_i^l$  are determined by thermodynamic arguments.

In a solid containing equilibrium concentrations of vacancies and interstitials, interstitial loops cannot (thermodynamically) exist; the system could reduce its Gibbs free energy by dissolving the loops. However, if the point-defect concentrations are altered in such a way that the vacancies and interstitials are always in equilibrium (i.e.,  $C_i C_v = C_i^{eq} C_v^{eq}$ ), it is possible for an interstitial loop of a particular

size to exist in equilibrium with the point-defect environment provided that  $C_i > C_i^{eq}$ . Conversely, a stable vacancy loop could form in a solid in which  $C_v > C_v^{eq}$ . Here we compute the size of an interstitial loop which exists in equilibrium with a specified vacancy concentration  $C_v^l$  and the corresponding equilibrium interstitial concentration  $C_i^l$ .

The Gibbs free energy of a piece of metal containing  $n_v$  vacancies,  $n_i$  interstitials (at concentrations  $C_v^l$  and  $C_i^l$ , respectively), and one interstitial dislocation loop containing  $m_i$  interstitials is

$$G = G_0 + \epsilon(m_i) + n_v \mu_v + n_i \mu_i \quad (19.105)$$

where  $\mu_v$  and  $\mu_i$  are the chemical potentials of the vacancies and the interstitials, respectively,  $\epsilon(m_i)$  is the energy of the loop, and  $G_0$  is the reference free energy of the piece of metal without the loop and with point-defect concentrations  $C_v^{eq}$  and  $C_i^{eq}$ .

We now perturb the system by transferring point defects between the bulk solid and the loop. The criterion of chemical equilibrium states that for the system at equilibrium the free-energy change,  $\delta G$ , for this process is zero. Thus, taking the differential of Eq. 19.105,

$$\delta G = \left( \frac{d\epsilon}{dm_i} \right) \delta m_i + \mu_v \delta n_v + \mu_i \delta n_i = 0$$

The number of interstitial atoms in the loop can be changed only at the expense of the point defects in the bulk, so the perturbations are related by

$$\delta m_i = \delta n_v - \delta n_i$$

Eliminating  $\delta m_i$  from the preceding equations yields

$$\left( \frac{d\epsilon}{dm_i} \right) \delta n_v - \left( \frac{d\epsilon}{dm_i} \right) \delta n_i + \mu_v \delta n_v + \mu_i \delta n_i = 0$$

The changes  $\delta n_v$  and  $\delta n_i$  are arbitrary and independent of each other; thus the coefficients of both these perturbations must independently be set equal to zero. This requirement leads to two relations:

$$\frac{d\epsilon}{dm_i} + \mu_v = 0 \quad (19.106a)$$

and

$$\frac{d\epsilon}{dm_i} - \mu_i = 0 \quad (19.106b)$$

The chemical potential of vacancies in a solid with a concentration  $C_v^l$  of this species is given by Eq. 19.32:

$$\mu_v = kT \ln \left( \frac{C_v^l}{C_v^{eq}} \right) \quad (19.107a)$$

For interstitials the formula is

$$\mu_i = kT \ln \left( \frac{C_i^l}{C_i^{eq}} \right) \quad (19.107b)$$

When the vacancies and interstitials are in equilibrium with each other,  $C_i^l C_v^l = C_i^{eq} C_v^{eq}$ , which is equivalent to

$$\mu_i = -\mu_v \quad (19.108)$$

applies. Therefore, Eqs. 19.106a and 19.106b are equivalent. Using the former in conjunction with Eq. 19.107a gives

$$C_v^l = C_v^{eq} \exp\left(-\frac{d\epsilon/dm_i}{kT}\right)$$

The loop energy  $\epsilon(m_i)$  is given by Eq. 19.6. If the coefficient of  $m_i^{1/2}$  in this formula is symbolized by  $K$  and the stacking-fault term is neglected (because it is small compared to the line-tension term),  $d\epsilon/dm_i$  can be computed, and the above equation can be written

$$C_v^l = C_v^{eq} \exp\left(-\frac{K}{2(m_i)^{1/2} kT}\right) \quad (19.109)$$

Had Eqs. 19.106b and 19.107b been used, the result would be

$$C_i^l = C_i^{eq} \exp\left(\frac{K}{2(m_i)^{1/2} kT}\right) \quad (19.110)$$

According to Eq. 19.65,  $K = 500$  kJ/mole in stainless steel.

Equation 19.109 shows that the vacancy concentration in equilibrium with an interstitial dislocation loop is less than the equilibrium concentration in the loop-free solid. Simultaneously,  $C_i^l$  is greater than  $C_i^{eq}$  in order to maintain the loop.

Although the above analysis applies to a strictly thermodynamic situation, the results can be employed in the nonequilibrium environment created by irradiation of the solid. To do so, it is assumed that the concentrations of point defects in the solid immediately adjacent to the core of the dislocation line comprising the interstitial loop are given by Eqs. 19.109 and 19.110. The concentrations in the bulk of the solid far from the loop are  $C_v$  and  $C_i$ , which are not in equilibrium with the loop (nor with each other). The assumption of interfacial equilibrium is commonly used in analyses of many chemical engineering mass-transfer operations. With this assumption the rates of vacancy and interstitial absorption by the loops in the solid are determined using Eq. 19.109 in Eq. 19.103 and Eq. 19.110 in Eq. 19.104. For application in the point-defect balance equations,  $m_i$  in Eqs. 19.109 and 19.110 can be approximated by the size of the average loop in the solid, and the point-defect absorption rates by loops become

$$Q_v^l = Z_v D_v \rho_l \left[ C_v - C_v^{eq} \exp\left(-\frac{K}{2(\bar{m}_i)^{1/2} RT}\right) \right] \quad (19.111)$$

and

$$Q_i^l = Z_i D_i \rho_l \left[ C_i - C_i^{eq} \exp\left(\frac{K}{2(\bar{m}_i)^{1/2} RT}\right) \right] \quad (19.112)$$

Thus the loop components of the total dislocation density of the solid do not exhibit quite so large a bias for interstitials as do the network dislocations, for which  $Q_v^N$  and  $Q_i^N$  are given by Eqs. 19.101 and 19.102. The alterations in the driving forces due to the last terms in the brackets of the above formulas tend to reduce the bias toward interstitials introduced by the inequality of the coefficients  $Z_i > Z_v$ . However, if the loops are large and/or

the temperature is high, the exponential terms in Eqs. 19.111 and 19.112 approach unity, and the dislocation network and the dislocation loops behave in an identical manner toward the point defects in the solid.

## 19.5.9 Coherent Precipitates

Brailsford and Bullough<sup>23</sup> assign the recombination function of coherent precipitates to the plane of matrix atoms adjacent to the second-phase particle. This plane, or interface, is endowed with the capacity to strongly bind or trap point defects that hop into it from the adjacent matrix. Figure 19.14 shows a cross section through the precipitate-matrix interface. Vacancies and interstitials that are trapped at the interface are assumed to be unable to escape; removal of trapped point defects occurs only by annihilation with point defects of the opposite type which impinge on the interface or by recombination of trapped vacancies and interstitials. The coherent precipitate is distinguished from the other microstructural defects in the solid by the absence of thermal emission of point defects (which appears in the terms involving  $C_v^{eq}$  in Eq. 19.95 for voids, in Eq. 19.97 for network dislocations, and in Eq. 19.111 for loops).\* We will summarize the function of these sinks in the manner visualized in Ref. 23.

Although the interface between a coherent precipitate particle and the matrix does not release point defects, the fact that it is of limited capacity means that the concentrations of vacancies and interstitials at the surface of the particle are not reduced to zero as they would be at the surface of a totally black sink. Figure 19.15 shows schematically the concentration profiles of point defects near a coherent precipitate-matrix interface. The rates at which vacancies and interstitials flow to the interface can be divided into two steps, which proceed in series. Between the bulk of the solid and the interface, the flow of point defects is governed by ordinary diffusion to a spherical sink. The driving force for this step is the concentration difference  $C_v - C_v^*$  for vacancies and  $C_i - C_i^*$  for interstitials. For diffusion-controlled absorption by a spherical

\*This unique property means that coherent precipitates are capable of removing point defects from a solid in which the point-defect concentrations are at the equilibrium values  $C_v^{eq}$  and  $C_i^{eq}$ . Or these supposedly thermodynamic quantities are determined by Eqs. 19.20 and 19.23 only in solids that contain no coherent precipitates. If coherent precipitate particles are added to a solid that initially contained its equilibrium complement of point defects, the precipitates would augment the homogeneous recombination process and thereby depress the concentrations of vacancies and interstitials below the equilibrium value. The extent of the decrease would depend on the number of precipitate particles and the density of network dislocations in the solid. The latter are the principal suppliers or removers of point defects when the equilibrium concentrations are perturbed by the introduction of sources (e.g., by irradiation) or sinks (in the case of coherent precipitates). Despite the unpalatable theoretical consequences of the lack of thermal emission of point defects from coherent precipitates in a solid, the practical effect on  $C_v^{eq}$  is negligible (see problem 19.11 at the end of this chapter).

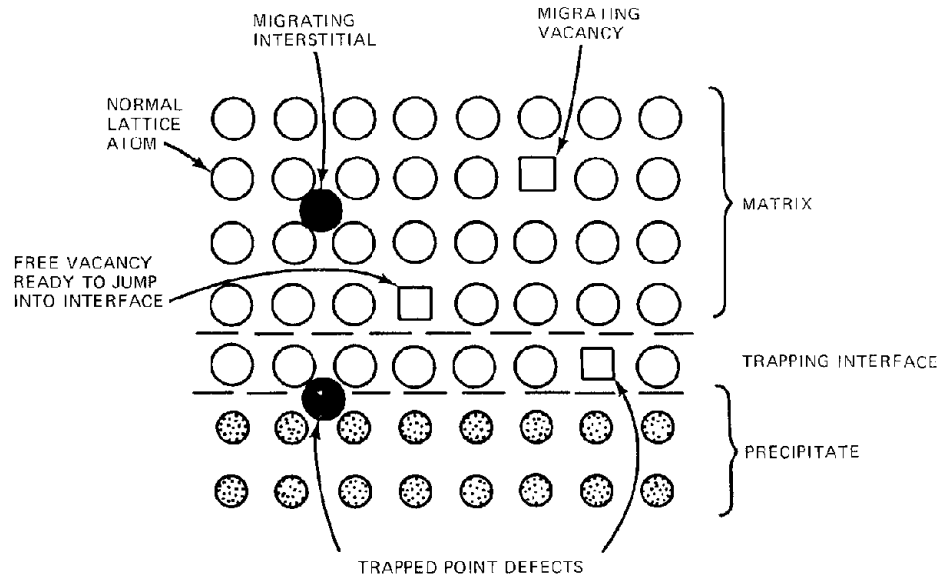


Fig. 19.14 Schematic diagram of the interface between a coherent precipitate particle and the host matrix. (After Ref. 23.)

body in which the concentrations at  $r = R_p$  (the particle radius) and  $r = \infty$  (the bulk solid) are specified, the fluxes are given by Eq. 13.65:

$$J_v = \frac{D_v}{R_p} (C_v - C_v^*) \quad (19.113)$$

and

$$J_i = \frac{D_i}{R_p} (C_i - C_i^*) \quad (19.114)$$

where  $J_v$  and  $J_i$  are the number of point defects reaching a unit area of precipitate per unit time. Because there is no net accumulation of either type of point defect at the interface, the fluxes must obey

$$J_v = J_i \quad (19.115)$$

The concentrations  $C_v^*$  and  $C_i^*$  refer to the matrix adjacent to the trapping interface. In order to evaluate these concentrations, we must consider the second step in the series, that of point-defect attachment to the interface. We first determine the rate at which point defects impinge on the trapping interface from the adjacent matrix when the vacancy and interstitial concentrations here are  $C_v^*$  and  $C_i^*$ , respectively. Consider the case of vacancies. The plane of matrix atoms above the interface plane contains  $1/a_0^2$  lattice sites per unit area from which a vacancy can hop toward the interface. The fraction of lattice sites that are occupied by vacancies in the matrix at this point is  $C_v^* \Omega = C_v^* a_0^3$ , where  $\Omega$  is the atomic volume and  $a_0$  is the lattice parameter. Therefore, a total of  $(a_0^{-2})(C_v^* a_0^3) = a_0 C_v^*$  vacancies per unit area can potentially reach the trapping interface in one jump. The frequency with which a vacancy jumps in any one direction in the matrix is  $w_v$  (Sec. 7.2). For the fcc lattice,  $w_v$  is related to the vacancy diffusion

coefficient by Eq. 7.29. Thus the rate at which vacancies impinge on a unit area of trapping surface is given by

$$\begin{aligned} \text{Vacancy impingement rate} \\ = (a_0 C_v^*) w_v = (a_0 C_v^*) \left( \frac{D_v}{a_0^2} \right) = \frac{D_v C_v^*}{a_0} \end{aligned}$$

Similarly, the interstitial impingement rate on the interface from the adjacent matrix is  $D_i C_i^* / a_0$ . These impingement rates can be regarded as the solid-state analogs of the rate at which molecules from a gas strike a unit area of surface. To determine whether the impinging vacancies and interstitials stick or are reflected back to the matrix, we need to calculate the fraction of the available sites on the trapping interface which are occupied by the two types of point defects. To do this, imagine the trapping interface to be a simple square grid that binds vacancies at the mesh points and interstitials in the open spaces. The mesh-point sites may either be occupied by a trapped vacancy or empty (i.e., occupied by an atom). Similarly, the interstitial trapping sites may either be occupied by a trapped interstitial atom or empty. Let  $\theta_v$  = fraction of vacancy trapping sites on the interface occupied by vacancies and  $\theta_i$  = fraction of interstitial trapping sites on the interface occupied by interstitials. A vacancy is trapped only if it jumps into an unoccupied site; the probability of so doing is  $1 - \theta_v$ . The rate at which vacancies are trapped on the interface is the product of the impingement rate and the fraction of unoccupied sites. Since the process of diffusion from the bulk to the interface is in series with the process of attachment to the interface, we equate the rates of diffusion and trapping,\* or

\*Equating the rates of sequential processes is also used in analyzing series resistances in heat-transfer processes.

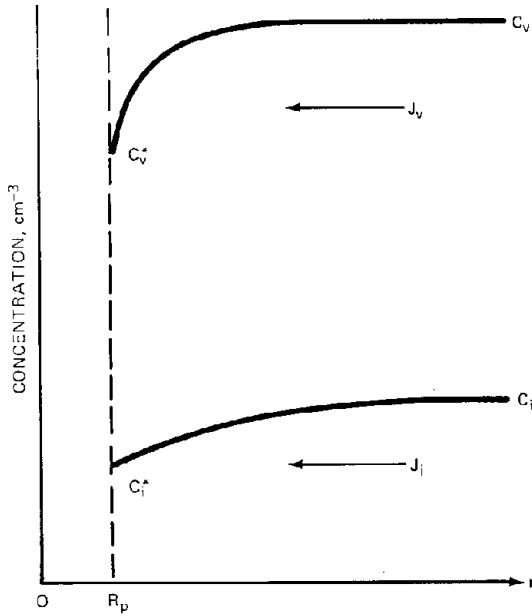


Fig. 19.15 Vacancy- and interstitial-concentration profiles next to a coherent precipitate particle.

$$J_v = \frac{D_v}{R_p} (C_v - C_v^*) = \frac{D_v C_v^*}{a_o} (1 - \theta_v) \quad (19.116)$$

For interstitials, the analogous formula is

$$J_i = \frac{D_i}{R_p} (C_i - C_i^*) = \frac{D_i C_i^*}{a_o} (1 - \theta_i) \quad (19.117)$$

To deduce the connection between the point-defect occupation of the trapping interface (the  $\theta$ 's) and the point-defect concentration in the matrix adjacent to the trapping interface (the  $C^*$ 's), we must specify the details of the interaction between the free point defects and the trapped ones. Many models of this interaction can be constructed; here we will investigate a primitive model similar to that invoked by Brailsford and Bullough<sup>2,3</sup> in their analysis of the same phenomenon (the present model differs from theirs in that recombination reactions between trapped point defects are not considered here). Three possible fates of a vacancy impinging on the trapping interface are depicted in Fig. 19.16. The impinging vacancy may:

(a) Strike a site already occupied by a vacancy, in which case the impinging vacancy is returned to the matrix.

(b) Enter an unoccupied site that is adjacent to a trapped interstitial. The probability of this event is  $z\theta_i$ , where  $z$  is the number of vacancy sites surrounding a trapped interstitial which result in certain recombination when jointly occupied (for the simple square interfacial structure,  $z = 4$ ).

(c) Enter an unoccupied site that is not adjacent to a trapped interstitial. The probability of such a jump is  $1 - \theta_v - z\theta_i$ .

The consequences of interstitial atom impingement on the interface are obtained from processes (a) to (c) by interchanging the subscripts  $i$  and  $v$ .

We now construct a balance equation for the trapped vacancies and interstitials. Because the system is at steady state,  $\theta_v$  and  $\theta_i$  are time independent, or the rate at which point defects become incorporated into the interface by process (c) must be equal to the rate at which they are removed by process (b). Note that process (b) removes a point defect of the opposite type from that which process (c) adds to the interface. Conservation of trapped vacancies is expressed by

$$\frac{D_v C_v^*}{a_o} (1 - \theta_v - z\theta_i) = \frac{D_i C_i^*}{a_o} \theta_v \quad (19.118)$$

where the left side is the input due to the fraction of impinging vacancies that strike an unoccupied site that is not adjacent to a trapped interstitial and the right side is the rate of removal of trapped vacancies by impinging interstitials from the nearby matrix. The balance on trapped interstitials yields

$$\frac{D_i C_i^*}{a_o} (1 - \theta_i - z\theta_v) = \frac{D_v C_v^*}{a_o} \theta_i \quad (19.119)$$

Subtracting Eq. 19.119 from Eq. 19.118 yields

$$D_i C_i^* (1 - \theta_i) = D_v C_v^* (1 - \theta_v)$$

which, when compared with Eqs. 19.116 and 19.117, simply confirms the fact that the fluxes of the two types of point defects from the bulk to the coherent precipitate are equal no matter which step of the two back-to-back processes is considered.

Equations 19.118 and 19.119 can be solved for  $\theta_v$  and  $\theta_i$  to yield

$$\theta_v = \frac{\gamma^* [1 + (\gamma^* - 1)z]}{\gamma^{*2} z + \gamma^* + z} \quad (19.120)$$

$$\theta_i = \frac{\gamma^* + z - \gamma^* z}{\gamma^{*2} z + \gamma^* + z} \quad (19.121)$$

where

$$\gamma^* = \frac{D_v C_v^*}{D_i C_i^*} \quad (19.122)$$

In Fig. 19.17  $\theta_v$  and  $\theta_i$  are shown as functions of the parameter  $\gamma^*$  for a fixed value of  $z$  (e.g.,  $z = 4$ ). Equations 19.120 and 19.121 apply only in the range

$$\frac{z-1}{z} \leq \gamma^* \leq \frac{z}{z-1} \quad (19.123)$$

Beyond this range, either  $\theta_i$  or  $\theta_v$  is zero, and the other is given by the formulas shown on the graph. When  $\gamma^* = 1$ ,  $\theta_i$  and  $\theta_v$  are both equal to  $(1 + 2z)^{-1}$ .

The trapping and recombination efficiency of the interface has been analyzed with the aid of a particular model of what goes on at the boundary separating the precipitate particle and the host matrix. Other models of these interactions are certainly possible, but they will all lead to relations between the  $\theta$ 's and  $\gamma$ 's of the type shown



however, the biasing coefficients  $Y_v$  and  $Y_i$  depend on  $D_v C_v / D_i C_i$ , which is in turn established by the strengths of the other point defects in the system. Thus, the biased absorption properties of coherent precipitates depend on the environment in which the precipitates are situated, which is not the case for the fixed-bias dislocations. The manner in which the coherent precipitates function can be illustrated qualitatively as follows. Because  $Z_i > Z_v$  by a percent or so,  $D_v C_v / D_i C_i$  is greater than unity by a comparable amount (otherwise voids would not nucleate or grow). Since  $D_v C_v / D_i C_i > 1$ , Eq. 19.126 shows that  $\theta_v > \theta_i$  or, according to Eqs. 19.129 and 19.130,  $Y_i > Y_v$ . The requirement that there be no net accumulation of point defects at the coherent precipitates (as expressed by Eq. 19.126) leads to

$$Y_i = \left( \frac{D_v C_v}{D_i C_i} \right) Y_v \quad (19.131)$$

so the problem is reduced to one of finding the magnitude of  $Y_v$  (or of  $Y_i$ ). If the precipitate radius,  $R_p$ , is reasonably large (say several hundreds of angstroms), the ratio  $a_0 / R_p$  is small ( $\sim 10^{-2}$ ). If, in addition, the ratio  $D_v C_v / D_i C_i$  is close to unity, then the parameter  $\gamma^*$  will also be close to unity, and Fig. 19.17 shows that  $\theta_v$  and  $\theta_i$  are equal to  $\sim (2z + 1)^{-1} \sim 10^{-1}$ . For this situation, Eqs. 19.129 and 19.130 show that  $Y_v$  and  $Y_i$  are both close to unity. We may make the approximation

$$Y_v \approx 1 \quad (19.132)$$

$$Y_i = \frac{D_v C_v}{D_i C_i}$$

and Eqs. 19.127 and 19.128 reduce to

$$Q_v^p = Q_i^p = 4\pi R_p N_p D_v C_v \quad (19.133)$$

This equation adequately describes the strength of coherent precipitate sinks in irradiated metals.

### 19.5.10 Point-Defect Balances

Having determined the rate of production of vacancies and interstitials from fast-neutron collisions with lattice atoms and the rates at which the point defects are consumed by various processes involving the large defects in the solid, we can write the steady-state point-defect balances as

$$\nu \Sigma_s \Phi = Q_v^{\text{void}} + Q_v^N + Q_v^I + Q_v^p + \text{homo. recomb.} \quad (19.134)$$

for vacancies, and

$$\nu \Sigma_s \Phi = Q_i^{\text{void}} + Q_i^N + Q_i^I + Q_i^p + \text{homo. recomb.} \quad (19.135)$$

for interstitials.

The vacancy-removal rates per unit volume of solid,  $Q_v^{\text{void}}$ ,  $Q_v^N$ , and  $Q_v^I$ , are given by Eqs. 19.95, 19.101, and 19.111. The corresponding terms for interstitial removal are given by Eqs. 19.96, 19.102, and 19.112 (the thermal emission term in the last of these formulas can be neglected). The rate of absorption of both types of point

defects by coherent precipitates is given by Eq. 19.133. The rate of homogeneous recombination is  $k_{iv} C_v C_i$ , where  $k_{iv}$  is given by Eq. 13.42. With these sink strengths, Eqs. 19.134 and 19.135 become

$$\begin{aligned} \nu \Sigma_s \Phi = & 4\pi R N D_v \left[ C_v - C_v^{\text{eq}} \exp \left( \frac{2\gamma\Omega}{RkT} \right) \right] \\ & + Z_v \rho_N D_v (C_v - C_v^{\text{eq}}) \\ & + Z_v \rho_I D_v \left[ C_v - C_v^{\text{eq}} \exp \left( - \frac{K}{2(\bar{m}_i)^{1/2} kT} \right) \right] \\ & + 4\pi R_p N_p D_v C_v + k_{iv} C_i C_v \end{aligned} \quad (19.136)$$

and

$$\begin{aligned} \nu \Sigma_s \Phi = & 4\pi R N D_i C_i + Z_i (\rho_N + \rho_I) D_i C_i \\ & + 4\pi R_p N_p D_v C_v + k_{iv} C_i C_v \end{aligned} \quad (19.137)$$

Equations 19.136 and 19.137 can be solved for  $C_v$  and  $C_i$  (analytical solutions are reported in Ref. 23). For  $N$ ,  $\rho_I$ , and  $N_p = 0$ , the point-defect balances given above reduce to those obtained earlier for treating fission-gas bubble growth in the fuel (Eqs. 13.186 and 13.187, in which  $C_i^{\text{eq}} = 0$ ). The general shape of plots of  $C_v$  and  $C_i$  as functions of temperature are shown in Fig. 13.17. Such solutions are needed for fixing the supersaturations  $S_v$  and  $S_i$  in nucleation theory and for void growth.

### 19.5.11 The Void-Growth Law

The void-growth law is the time rate of change of the void radius  $R$  at any instant during irradiation. The void is assumed to be spherical, and its growth is controlled by diffusion of vacancies and interstitials from the bulk of the solid to the void surface. The growth law under these circumstances was derived in Sec. 13.9 for the case of a cavity that contained some gas (i.e., a bubble). The same growth law is valid for the gas-free cavity (the void) provided that the internal gas pressure is set equal to zero wherever it appears. The void-growth law is obtained from Eqs. 13.171 and 13.176, with  $p = 0$  in the latter,

$$\begin{aligned} \dot{R} = & \frac{dR}{dt} \\ = & \frac{\Omega}{R} \left\{ D_v \left[ C_v - C_v^{\text{eq}} \exp \left( \frac{2\gamma\Omega}{RkT} \right) \right] - D_i C_i \right\} \end{aligned} \quad (19.138)$$

The concentration of interstitials at the void surface (Eq. 13.179) has been neglected because of the large energy of formation of this point defect.

Brailsford and Bullough<sup>23</sup> have inserted the solutions of Eqs. 19.136 and 19.137 into Eq. 19.138 and expressed the void-growth rate in the following form:

$$\dot{R} = \dot{R}_0 F(\eta) + \dot{R}_e \quad (19.139)$$

where  $\dot{R}_0$  is the void-growth rate in the absence of both homogeneous recombination ( $k_{iv} = 0$ ) and thermal emission ( $C_v^{\text{eq}} = 0$ ),

$$\dot{R}_0 = \frac{\nu \Sigma_s \Phi \rho_d (Z_i - Z_v) \Omega}{R(Z_v \rho_d + 4\pi R N) (Z_i \rho_d + 4\pi R N + 4\pi R_p N_p)} \quad (19.140)$$

where

$$\rho_d = \rho_N + \rho_1 \quad (19.141)$$

is the total dislocation density in the solid. This growth contribution is independent of temperature and depends on the dislocation bias for interstitials  $Z_i - Z_v$  and the morphology of the solid (i.e., the number and size of voids, precipitates, and the dislocation density). It is also directly proportional to the defect-production rate, or the fast-neutron flux.

The effect of homogeneous recombination on void growth is contained in the factor  $F$  in Eq. 19.139, which is\*

$$F(\eta) = \frac{2}{\eta} [(1 + \eta)^{1/2} - 1] \quad (19.142)$$

where  $\eta$  is the dimensionless parameter

$$\eta = 4k_{iv} \nu \Sigma_s \Phi [D_v D_i (Z_v \rho_d + 4\pi R N + 4\pi R_p N_p) \times (Z_i \rho_d + 4\pi R N + 4\pi R_p N_p)]^{-1} \quad (19.143a)$$

or, eliminating  $k_{iv}$  by use of Eq. 13.42 and setting  $Z_i = Z_v$ ,

$$\eta = \frac{4Z_{iv} \nu \Sigma_s \Phi \Omega}{D_v a_0^2 (Z_v \rho_d + 4\pi R N + 4\pi R_p N_p)^2} \quad (19.143b)$$

When homogeneous recombination is negligible ( $k_{iv} \rightarrow 0$  or  $\eta \rightarrow 0$ ), the factor  $F$  reduces to unity.

The effect of thermal emission from the various sinks is contained in the void-shrinkage term  $\dot{R}_e$ :

$$\begin{aligned} \dot{R}_e = & -D_v C_v^{eq} \Omega \left\{ 4\pi R_p N_p \exp\left(\frac{2\gamma \Omega}{R kT}\right) \right. \\ & + Z_v \rho_N \left(\frac{2\gamma \Omega}{R kT}\right) \\ & \left. + Z_v \rho_1 \left(\frac{2\gamma \Omega}{R kT} + [K/2(\bar{m}_1)^{1/2} kT]\right) \right\} \\ & \times [R(Z_v \rho_d + 4\pi R N + 4\pi R_p N_p)]^{-1} \quad (19.144) \end{aligned}$$

In the terms in the second and third lines of Eq. 19.144, differences in exponentials have been approximated by differences in the arguments. The value of  $\dot{R}_e$  is independent of the defect-production rate and approaches zero at temperatures sufficiently low to render thermal emission negligible (i.e.,  $C_v^{eq} \rightarrow 0$ ).

### 19.5.12 The Factor $\dot{R}_0$

When no coherent precipitates are present,  $\dot{R}_0$  can be written as

$$\dot{R}_0 = \frac{\nu \Sigma_s \Phi \Omega}{4\pi R^2 N} \left(\frac{Z_i - Z_v}{Z_v}\right) \frac{x}{(1+x)^2} \quad (19.145)$$

where

$$x = \frac{4\pi R N}{Z_v \rho_d} \quad (19.146)$$

Equation 19.145 demonstrates that both a biased sink (with  $Z_i - Z_v$  greater than zero) and a neutral sink (which for voids provides the term  $4\pi R N$ ) are necessary for void growth. The balance between the strengths of the neutral and biased sinks, as exemplified by the dimensionless quantity  $x$ , is crucial to void growth. The void-growth rate is a maximum when  $x = 1$ . If  $x$  is less than unity (as it would be at the beginning of irradiation), decreasing  $x$  by increasing the dislocation density reduces the rate of void growth. This behavior explains the ability of heavily cold-worked metals to resist void swelling at low fluences. If, however,  $x > 1$  because of the development of a sizable void population, the primary role of the dislocations is to provide a preferential sink for interstitials, thereby permitting the excess vacancies to flow to the voids. In this case, highly cold-worked material promotes rather than deters void growth.

When coherent precipitates are present in the alloy and voids are not strong sinks for vacancies,  $\dot{R}_0$  becomes

$$\dot{R}_0 = \frac{\nu \Sigma_s \Phi \Omega}{R} \left(\frac{Z_i - Z_v}{Z_v}\right) \frac{1}{Z_i \rho_d + 4\pi R_p N_p} \quad (19.147)$$

In this case the dislocations and the precipitate particles combine to reduce void growth. This theoretical prediction is in accord with the very low irradiation swelling of precipitate-containing alloys, such as Inconel and the steel PE-16.

### 19.5.13 Temperature Dependence of Void Growth

The two highly temperature sensitive parameters in the void-growth law are the vacancy diffusion coefficient  $D_v$  and the equilibrium vacancy concentration  $C_v^{eq}$ . The temperature dependence of the parameter  $\eta$  is controlled by  $D_v$  and the product  $D_v C_v^{eq}$  appears in  $\dot{R}_e$ . At low temperatures,  $D_v$  becomes small and Eq. 19.143b shows that  $\eta$  becomes large. In this limit the factor  $F$  becomes small. As the temperature is reduced, Eq. 19.144 indicates that  $\dot{R}_e$  approaches zero. Since both  $F(\eta)$  and  $\dot{R}_e$  become small at low temperature, Eq. 19.139 shows that void growth ceases in this limit.

At the opposite extreme of high temperature,  $\eta$  becomes small and  $F$  approaches unity;  $\dot{R}_e$  then becomes increasingly negative. Thus the theory predicts a temperature at which the void-growth rate is a maximum, which corresponds to the observed peak swelling temperature. Beyond this temperature, void growth should rapidly decrease and eventually become negative since the voids tend to evaporate rather than grow. Figure 19.18 shows how the growth rate changes with temperature for typical fast reactor conditions. The characteristic bell-shaped swelling-temperature plot (Fig. 19.3) is quite well reproduced by the theory. The temperature limits of observable swelling

\*A quantity denoted by  $\mu$  in Ref. 23 has been omitted in Eq. 19.142. This simplification has no significant effect on the numerical values of the void-growth rate.

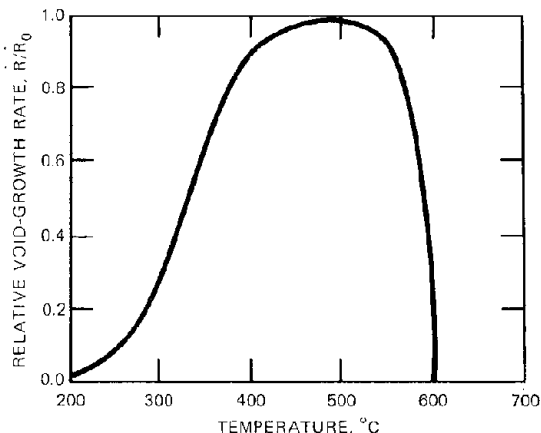


Fig. 19.18 Temperature dependence of the void-growth rate in stainless steel under fast-neutron irradiation. (After Ref. 23.)

and the peak swelling temperature are in accord with observations.

Brailsford and Bullough<sup>23</sup> have deduced an approximate analytical swelling law by simplification of the foregoing equations. However, in view of the change of the void density  $N$  and the dislocation density  $\rho_d$  during irradiation, the void-growth law should be incorporated into a more general analysis that includes the evolution of the microstructural features of the solid with irradiation time. Such a computation would require a loop-growth law in addition to a void-growth law. The loop size and concentration couple back into the void (and loop) growth laws via  $\rho_N$ ,  $\rho_1$ , and the average loop size  $\bar{m}$ .

#### 19.5.14 Stress-Enhanced Void Growth

The growth law developed above is valid only if the void contains no gas and if the metal is not under stress. However, in the temperature range for void growth, helium atoms produced by  $(n, \alpha)$  reactions in the metal are sufficiently mobile to form gas-atom clusters in the lattice. As shown in Sec. 19.3, voids readily nucleate on these clusters; thus some gas must be contained in the voids as they enter their growth stage. In addition, the cladding of a fuel pin is always stressed, either by contact with swelling fuel or by internal pressure in the fuel pin arising from released fission gases. The state of stress in an internally loaded cylindrical tube is biaxial, but, to simplify matters, we consider here a metal subject to uniform hydrostatic tension. The theory of void growth needs modification to account for these two complications. We present the analysis of Brailsford and Bullough.<sup>25</sup>

Equation 19.139 shows that the void-growth rate consists of two components;  $\dot{R}_e$  contains the thermal emission terms and hence is the only part affected by the state of stress or by internal gas pressure. Consequently, it follows that internal gas pressure and stress begin to influence the growth rate only when  $\dot{R}_e$  becomes significant; i.e., for temperatures greater than the peak swelling temperature. Thus, we need only be concerned with  $\dot{R}_e$ , and, in particular, with how internal pressure and stress

affect the equilibrium vacancy concentrations at the voids and the dislocations. Because stress- and gas-assisted growth are important only at high temperatures, we may neglect the presence of interstitial loops. These will have virtually disappeared by vacancy capture by  $\sim 600^\circ\text{C}$  (see Fig. 19.7). The vacancy balances (with the deletion of the above-mentioned terms) are given by Eq. 19.136 if the vacancy concentration at the void surface is replaced by

$$C_v^{eq} \exp \left[ \left( \frac{2\gamma}{R} - p \right) \left( \frac{\Omega}{kT} \right) \right]$$

The vacancy concentration at the void surface depends only on the normal stress at this point, which by a force balance is equal to  $(2\gamma/R) - p$  (see Eq. 13.6). The stress in the medium does not affect the vacancy concentration at the void provided that the volume of a vacancy in the solid is equal to the atomic volume or that there is no lattice contraction around a vacancy. If this is not so (and, in general, it is not), the above expression for the vacancy concentration at the void surface must be modified.<sup>26,27</sup> We neglect this effect here but consider it in problem 19.8 at the end of this chapter.

The other term in the vacancy balance equation which needs to be altered is the equilibrium concentration of vacancies at the network dislocations, which depends on stress according to

$$C_v^{eq} \exp \left( \frac{\sigma\Omega}{kT} \right)$$

where  $\sigma$  is the hydrostatic tension in the solid.

If the modified vacancy balance and the unchanged interstitial balance given by Eq. 19.137 are substituted into the void-growth rate formula (Eq. 19.138 in which the vacancy concentration at the void surface altered to account for internal gas pressure as indicated above),  $\dot{R}_0$  and  $F(\eta)$  are found to be unchanged. However,  $\dot{R}_e$ , which was formerly given by Eq. 19.144, becomes (with  $N_p$  and  $\rho_1 = 0$ )

$$\dot{R}_e = \frac{D_v C_v^{eq} \Omega^2 Z_v \rho_d \left( \sigma + p - \frac{2\gamma}{R} \right)}{RkT(Z_v \rho_d + 4\pi RN)} \quad (19.148)$$

In the gas- and stress-free case, the parenthetical term in the numerator is always negative, and  $\dot{R}_e$  represents a shrinkage. However, the sign of  $\dot{R}_e$  can change when the void contains gas and the solid is in tension. Shrinkage due to thermal emission changes to stress-enhanced growth\* when

$$\sigma + p = \frac{2\gamma}{R} \quad (19.149)$$

The critical stress for unlimited void growth, which depends on the gas content of the cavity, can be obtained in the same manner as that employed in deriving the analogous condition for void growth of helium bubbles on grain boundaries (Sec. 18.10). Suppose that the void contains  $j$  helium atoms. The internal pressure is given by the perfect gas law (Eq. 18.96), and Eq. 19.149 becomes

\*Stress-enhanced swelling is also called volume creep.

$$\sigma = \frac{2\gamma}{R} - \frac{3jkT}{4\pi R^3}$$

The critical void radius occurs when  $d\sigma/dR = 0$  and the stress at this void size is the critical stress for unlimited void growth:

$$\sigma_{crit} = \left( \frac{128\pi\gamma^3}{81jkT} \right)^{1/2} \quad (19.150)$$

which, if  $j$  is expressed in terms of the radius of the stress-free equilibrium bubble containing  $j$  helium atoms (by Eq. 18.94), reduces to the Hyam—Sumner relationship (Eq. 18.98).\* The only difference between helium bubbles on a grain boundary and helium-containing voids in the grains of the solid is the growth law, which is given by Eq. 18.102 for grain-boundary helium bubbles and by Eq. 19.148 for helium-containing voids within the grain.

Whether unbounded stress-enhanced void growth will occur for a specified hydrostatic tension depends on the number of gas atoms in the void. The total quantity of helium gas produced in the metal was discussed in Sec. 18.10. The helium content of stainless steel increases linearly with time (Fig. 18.40). If there are  $M$  atoms of helium per unit volume of the metal and if all the gas is equally distributed among  $N$  equal-size voids,  $j$  would be fixed as  $M/N$ . However, the available helium is, in general, partitioned among the matrix, the voids, and the grain-boundary bubbles. Determination of the fraction of the gas which is in the voids requires calculations similar to those presented in Secs. 13.9 and 15.7 for obtaining the distribution of fission-gas atoms in the same three locations in the fuel. We saw in Sec. 19.3 that void nucleation requires only a few helium atoms per void embryo. Unless much more helium is collected by the voids during the growth period,  $j$  in Eq. 19.150 may be quite small, and the critical stress may always be much larger than the applied stress (when  $\sigma < \sigma_{crit}$ , the void shrinks rather than expands).

Brailsford and Bullough have integrated the void-growth law (Eq. 19.139) with  $R_e$  given by Eq. 19.148.† The computations were performed for applied uniaxial tension, which requires that  $\sigma$  in Eq. 19.148 be replaced by  $\sigma/3$ . Helium was generated at a rate appropriate to fast reactor conditions; so  $j$  increased linearly with time. Since nucleation theory was not incorporated into the calculation, the void and loop densities had to be arbitrarily specified. Typical results of these computations are shown in Fig. 19.19, in which the ordinate is the volume swelling for a population of uniform size voids. Stress-assisted growth becomes dramatic at high temperature because  $D_v C_v^{eq}$  in Eq. 19.148 becomes large. The rather sudden onset of swelling in the high-stress 700 and 800°C curves is

\*Equation 40 of Ref. 25 (when divided by 3 to convert from uniaxial to hydrostatic stress) appears to be in error by a factor of 2.

†Actually, the complete theory, with loops and grain boundaries included as sinks in  $\dot{R}$ , was employed, and loop growth laws were used to determine the change in the dislocation population. The simplified form given by Eq. 19.148 is accurate at high temperatures.

due to the delay time required for sufficient helium to have trickled into the voids to render  $\sigma_{crit}$  of Eq. 19.150 equal to the specified stress. The 600°C results are insensitive to stress because the first term in Eq. 19.139 is the primary contributor to void growth at this temperature.

Figure 19.20 shows similar theoretical results as a function of temperature. The double hump in the swelling curve has not been confirmed by reactor irradiations of steel, but this unexpected shape has been found in ion-bombarded metals at a higher dose than obtainable with fast neutrons.

Restriction of the stress enhancement of void growth to temperatures in excess of 600°C suggests that the assump-

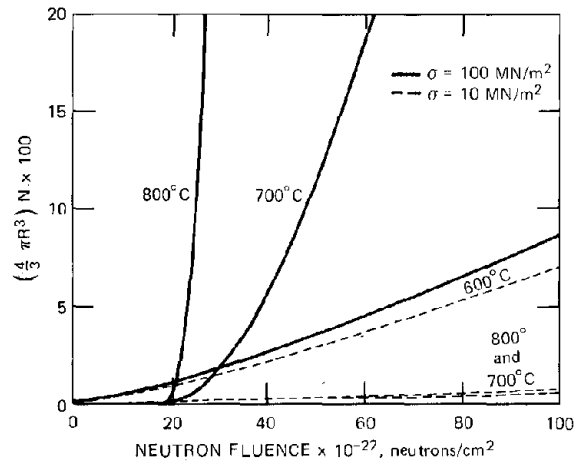


Fig. 19.19 Stress-enhanced swelling for various stress levels and temperatures as a function of fluence. (After Ref. 25.)

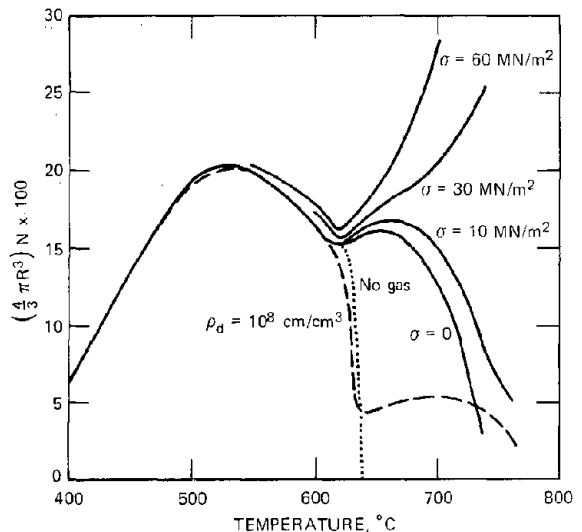


Fig. 19.20 Temperature dependence of stress-enhanced void growth in steel. The solid curves apply to a dislocation density of  $10^9 \text{ cm}^{-2}$  and a helium production rate of  $10^{-6} \text{ ppm/sec}$ . (From A. D. Brailsford and R. Bullough, British Report AERE-TP-542, 1973.)

tion inherent in the analysis that all helium is in the voids may be unrealistic. If most of the gas agglomerates on grain boundaries, the growth law is that of Eq. 18.102, not Eq. 19.148.

### 19.5.15 Saturation of Void Growth

The theory just developed predicts that voids continue to grow indefinitely in an irradiated metal; no mechanism for saturation of growth is provided. Equation 19.145 shows that as the void size  $R$  increases the growth rate decreases but never ceases entirely. The only way that void growth can be completely halted is to remove the preferential bias of the dislocations for interstitials or, equivalently, to imbue the voids with the same preferential attraction for interstitials as the dislocations.

Harkness and Li<sup>28</sup> have proposed a mechanism of terminating void growth which is based on the first of these two possibilities. They seek to determine the conditions under which all the dislocations become interconnected with the voids in a stable manner. If the dislocations are securely pinned to voids, they (the dislocations) can no longer climb freely, and hence their ability to absorb more interstitials than vacancies is eliminated. Here we reanalyze their proposal by extension of the method used previously to determine the equilibrium concentration of point defects at an interstitial dislocation loop.

Consider a single void and the curved length of dislocation line between voids. The associated solid contains  $n_v$  vacancies and  $n_i$  interstitials at concentrations  $C_v$  and  $C_i$ , respectively. We calculate the void radius  $R$  and the dislocation-line length  $\mathcal{L}$  for which the system is stationary in the specified point-defect environment. The void-dislocation segment configuration is depicted in Fig. 19.21(b), where the two halves of the void at the termination of the dislocation-line segment are shown in place of a single void. The remainder of the solid is assumed to be a repetition of the basic unit shown in Fig. 19.21(b), which means that the microstructure appears as sketched in Fig. 18.22(b). The case in which the vacancies and interstitials are in equilibrium (i.e.,  $C_i C_v = C_i^0 C_v^0$ ) is treated first. The derivation is then extended to arbitrary point-defect concentrations. The general method of calculations of this type have been outlined by Straalsund<sup>29</sup> and by Wiedersich and Herschbach.<sup>30</sup>

The Gibbs free energy of the system shown in Fig. 19.21(b) is given by

$$G = G_0 + \epsilon(m_v, m_i) + n_v \mu_v + n_i \mu_i \quad (19.151)$$

where  $\mu_v$  and  $\mu_i$  are the chemical potentials of the vacancies and interstitials (for the first portion of the analysis,  $\mu_v = -\mu_i$ , indicating equilibrium between the two types of point defects); and  $G_0$  is the free energy of the system containing the length  $l$  of dislocation line, but no void, in a solid wherein the point-defect concentrations are  $C_v^0$  and  $C_i^0$ , respectively [Fig. 19.21(a)]. As with the interstitial loop, a void is not thermodynamically stable under these conditions. Dislocation lines, however, can exist in a solid containing equilibrium point-defect concentrations. When the point-defect concentrations are changed from  $C_v^0$  and  $C_i^0$ ,  $\mu_v$  and  $\mu_i$  are no longer zero, and the void-dislocation

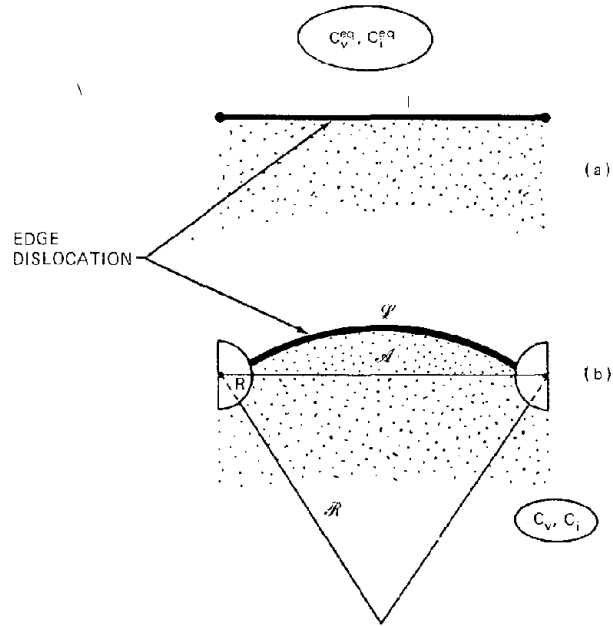


Fig. 19.21 Unit of a system of interconnected voids and dislocations. The shaded area below the dislocation-line segment denotes the extra half-sheet of atoms comprising the edge dislocation.

line segment shown in Fig. 19.21(b) is created from the  $n_v$  vacancies and  $n_i$  interstitials in the piece of solid under examination. The energy of the entity shown in Fig. 19.21(b) is denoted by  $\epsilon(m_v, m_i)$ , where  $m_v$  is the number of vacancies needed to form the void and  $m_i$  is the number of interstitials required for the dislocation line to climb from its original location in Fig. 19.21(a) to the equilibrium position in Fig. 19.21(b). If  $C_i$  and  $C_v$  are such that climb occurs in the opposite direction from that shown in Fig. 19.21(b),  $m_i$  is negative, which means that vacancies rather than interstitials have been absorbed by the pinned segment of dislocation line. The energy  $\epsilon(m_v, m_i)$  is given by the sum of the energies of the void and the associated length of dislocation line:

$$\epsilon(m_v, m_i) = 4\pi R^2 \gamma + (\mathcal{L} - l) \tau_d \quad (19.152)$$

where  $\gamma$  is the surface tension of the solid and  $\tau_d$  is the line tension of the dislocation. The change in the length of line in going from the configuration of Fig. 19.21(a) to that of Fig. 19.21(b) is  $\mathcal{L} - l$ . The first term on the right of Eq. 19.152 depends only on the number of vacancies in the void because  $m_v$  and  $R$  are related by

$$m_v = \frac{4\pi R^3}{3\Omega} \quad (19.153)$$

Similarly, the second term on the right is a function of  $m_i$ , which is related to the area of the circular segment added to the half-sheet of atoms comprising the edge dislocation:

$$m_i = \frac{b\mathcal{A}}{\Omega} \quad (19.154)$$

If the system shown in Fig. 19.21(b) is at equilibrium, the criterion of chemical equilibrium requires that the Gibbs free energy given by Eq. 19.151 be invariant when small perturbations  $\delta m_v$ ,  $\delta m_i$ ,  $\delta n_v$ , and  $\delta n_i$  are applied,

$$\delta G = \left( \frac{\partial \epsilon}{\partial m_v} \right) \delta m_v + \left( \frac{\partial \epsilon}{\partial m_i} \right) \delta m_i + \mu_v \delta n_v + \mu_i \delta n_i = 0$$

The perturbations in the numbers of point defects in each location are related by the balance:

$$\delta m_i - \delta m_v - \delta n_v - \delta n_i$$

The perturbation  $\delta m_v$  can be eliminated by combining the preceding two equations. The resulting equation contains  $\delta m_i$ ,  $\delta n_v$ , and  $\delta n_i$ . Since each of these three perturbations is independent and arbitrary, the coefficients of all three must be individually equated to zero to attain the minimum Gibbs free energy of the system, which leads to three equations:

$$\left( \frac{\partial \epsilon}{\partial m_v} \right)_{m_i} + \left( \frac{\partial \epsilon}{\partial m_i} \right)_{m_v} = 0 \quad (19.155a)$$

$$\left( \frac{\partial \epsilon}{\partial m_v} \right)_{m_i} - \mu_v = 0 \quad (19.155b)$$

$$\left( \frac{\partial \epsilon}{\partial m_v} \right)_{m_i} + \mu_i = 0 \quad (19.155c)$$

Because we have required equilibrium between the two types of point defects in the bulk solid (i.e.,  $\mu_i = -\mu_v$ ), Eqs. 19.155b and 19.155c are equivalent. Thus there are two independent relations, which serve to fix the equilibrium void radius  $R$  and the dislocation configuration (determined, for convenience, by the radius of curvature  $\mathcal{R}$ ).

The equilibrium void size is obtained from Eq. 19.155b, which can be written

$$\left( \frac{\partial \epsilon}{\partial m_v} \right)_{m_i} = \left( \frac{\partial \epsilon}{\partial R} \right)_{\mathcal{R}} \frac{dR}{dm_v} = \left( \frac{2\gamma}{R} \right) \Omega$$

The first term in the product of this formula is, according to Eq. 19.152, equal to  $8\pi R\gamma$ , and Eq. 19.153 shows that the second term is  $\Omega/4\pi R^2$ . The chemical potential of the vacancies is  $kT \ln(C_v/C_v^{eq})$ ; so Eq. 19.155b yields

$$C_v = C_v^{eq} \exp \left( \frac{2\gamma \Omega}{R kT} \right) \quad (19.156a)$$

and, using the restraint  $C_v C_i = C_v^{eq} C_i^{eq}$ ,

$$C_i = C_i^{eq} \exp \left( - \frac{2\gamma \Omega}{R kT} \right) \quad (19.156b)$$

Equation 19.156a can be recognized as the equilibrium concentration of vacancies at the surface of an isolated void in the solid (i.e., Eq. 19.95).

Combining Eqs. 19.155a and 19.155b yields

$$\left( \frac{\partial \epsilon}{\partial m_i} \right)_{m_v} + \mu_v = 0$$

The derivative in this formula is obtained from Eqs. 19.152 and 19.154:

$$\begin{aligned} \left( \frac{\partial \epsilon}{\partial m_i} \right)_{m_v} &= \tau_d \left( \frac{\partial \mathcal{L}}{\partial m_i} \right)_{m_v} \\ &= \tau_d \left( \frac{d\mathcal{A}}{dm_i} \right) \left( \frac{\partial \mathcal{L}}{\partial \mathcal{A}} \right)_R \\ &= \frac{\tau_d \Delta l}{b} \left( \frac{\partial \mathcal{L}}{\partial \mathcal{A}} \right)_R \end{aligned}$$

The partial derivative in the last line of this set of equalities (which is taken at constant  $R$  because  $m_v$  is held constant in the derivative on the left) is determined solely by the geometry of the curved dislocation in Fig. 19.21(b). In problem 19.16 at the end of this chapter,  $(\partial \mathcal{L} / \partial \mathcal{A})_R$  is found to be of the form

$$\left( \frac{\partial \mathcal{L}}{\partial \mathcal{A}} \right)_R = \frac{1}{\mathcal{R} f(R, \mathcal{R}, l)} \quad (19.157)$$

where the function  $f(R, \mathcal{R}, l)$  approaches unity as the void radius approaches zero. Combining the preceding three equations with the vacancy chemical potential yields

$$C_v = C_v^{eq} \exp \left( - \frac{\tau_d \Omega}{b \mathcal{R} f kT} \right) \quad (19.158a)$$

and, with the restriction  $C_v C_i = C_v^{eq} C_i^{eq}$ ,

$$C_i = C_i^{eq} \exp \left( \frac{\tau_d \Omega}{b \mathcal{R} f kT} \right) \quad (19.158b)$$

If either  $C_v$  or  $C_i$  is specified, Eqs. 19.156 and 19.158 determine the void size  $R$  and the dislocation line radius of curvature  $\mathcal{R}$  for a specified void spacing  $l$ , which is related to the size and density of voids in the solid by Eq. 18.25:

$$l = \frac{1}{(2RN)^{1/2}} \quad (19.159)$$

We now examine the case in which the vacancies and the interstitials are not in equilibrium (i.e.,  $C_i C_v \neq C_i^{eq} C_v^{eq}$ ). This situation cannot be treated by equilibrium methods;<sup>2,9,30</sup> so, instead of a thermodynamic analysis, we can only require that the system be in a stationary state. This means that the voids are not growing and the dislocations are not climbing and that the stationary configuration is affected by kinetic factors as well as equilibrium factors.

The existence of a stationary state requires that the net flux of point defects to the void and to the dislocation segment each be equal to zero. Following the argument applied to interstitial loops in the nonequilibrium solid, Eqs. 19.156a and 19.156b give the concentration of point defects at the surface of the void, and Eqs. 19.158a and 19.158b apply to the surface of the dislocation line segment between the voids. The concentrations  $C_i$  and  $C_v$  pertain to the bulk solid, far from the void and dislocation-line surfaces.

The fluxes of point defects to a unit area of void are

$$J_v^{void} = 4\pi R D_v (C_v - C_v^{void})$$

$$J_i^{void} = 4\pi R D_i (C_i - C_i^{void})$$

where  $C_v^{\text{void}}$  and  $C_i^{\text{void}}$  are now given by Eqs. 19.156a and 19.156b, respectively. Using these void surface concentrations and the zero net flux condition,

$$J_v^{\text{void}} = J_i^{\text{void}}$$

yields

$$D_v C_v - D_i C_i = D_v C_v^{\text{eq}} \exp\left(\frac{2\gamma}{R} \frac{\Omega}{kT}\right) - D_i C_i^{\text{eq}} \exp\left(-\frac{2\gamma}{R} \frac{\Omega}{kT}\right) \quad (19.160)$$

Similarly, the fluxes of point defects to a unit length of dislocation line are

$$J_v^d = Z_v D_v (C_v - C_v^d)$$

$$J_i^d = Z_i D_i (C_i - C_i^d)$$

where  $C_v^d$  and  $C_i^d$  are given by Eqs. 19.158a and 19.158b, respectively. Using these concentrations at the surface of the dislocation line and the zero net flux condition,

$$J_v^d = J_i^d$$

yields

$$Z_v D_v C_v - Z_i D_i C_i = Z_v D_v C_v^{\text{eq}} \exp\left(-\frac{\tau_d}{b\mathcal{R}} \frac{\Omega}{kT}\right) - Z_i D_i C_i^{\text{eq}} \exp\left(\frac{\tau_d}{b\mathcal{R}} \frac{\Omega}{kT}\right) \quad (19.161)$$

If  $C_i$  and  $C_v$  are specified,  $R$  and  $\mathcal{R}$  could be obtained directly from Eqs. 19.160 and 19.161.

The point-defect balances are used to determine the point-defect concentrations in the solid. At the stationary state that produces termination of void growth, each term in the vacancy balance of Eq. 19.134 is equal to the corresponding term in the interstitial balance of Eq. 19.135. In the saturated void-growth state, both network dislocations and loop dislocations are assumed to be interconnected to the voids, as shown in Fig. 19.21(b), so no distinction is made between them. The point-defect balances become

$$\begin{aligned} \nu \Sigma_s \Phi &= 4\pi R N D_v \left[ C_v - C_v^{\text{eq}} \exp\left(\frac{2\gamma}{R} \frac{\Omega}{kT}\right) \right] \\ &+ Z_v \rho_d D_v \left[ C_v - C_v^{\text{eq}} \exp\left(-\frac{\tau_d}{b\mathcal{R}} \frac{\Omega}{kT}\right) \right] \\ &+ 4\pi R_p N_p D_v C_v + k_{iv} C_i C_v \end{aligned} \quad (19.162)$$

$$\begin{aligned} \nu \Sigma_s \Phi &= 4\pi R N D_i \left[ C_i - C_i^{\text{eq}} \exp\left(-\frac{2\gamma}{R} \frac{\Omega}{kT}\right) \right] \\ &+ Z_i \rho_d D_i \left[ C_i - C_i^{\text{eq}} \exp\left(\frac{\tau_d}{b\mathcal{R}} \frac{\Omega}{kT}\right) \right] \\ &+ 4\pi R_p N_p D_v C_v + k_{iv} C_i C_v \end{aligned} \quad (19.163)$$

These equations differ from those which apply during void growth (Eqs. 19.136 and 19.137) in that the thermal emission terms from the dislocation have been altered to accommodate the picture of interconnected voids and dislocations in which the latter have ceased climbing. During growth, network dislocations are free to climb and dislocation loops are distinct from network dislocations. However, the two point-defect balances are not independent relations when saturation of void growth and dislocation climb occurs. Equation 19.163, for example, can be obtained by combining Eqs. 19.160 to 19.162. These three equations contain four unknowns,  $C_v$ ,  $C_i$ ,  $R$ , and  $\mathcal{R}$ . They can be solved for  $\mathcal{R}$  as a function of  $R$ ,  $N$ , and  $\rho_d$ . Prior to saturation, these three quantities increase by the void and loop growth and nucleation processes described earlier. When  $R$ ,  $N$ , and  $\rho_d$  attain values such that Eqs. 19.160 to 19.162 yield  $\mathcal{R} = 1/2$ , a stable interconnected network of voids and dislocations becomes possible, and void growth and dislocation climb cease provided that all voids and dislocations are linked together. If any dislocations are free to climb, however, growth does not terminate.

Bullough and coworkers<sup>24,31</sup> have proposed mechanisms for termination of void growth which are quite different from the saturation model just described. They calculate the force exerted on a circular dislocation loop by a nearby void. This force is determined by noting that the elastic stress field emanating from an isolated dislocation (e.g., Eq. 8.7 for a screw dislocation) cannot apply at the surface of the void, which must be free of all tractions. Willis and Bullough<sup>31</sup> add to the stress field of the dislocation an image or induced stress field whose magnitude and position dependence are determined by the requirement that the net stresses at the void surface vanish (the surface-tension force,  $2\gamma/R$ , appears to have been neglected). Once the field that performs the desired function at the void surface is found, the induced stress field away from the surface can be calculated. In particular, the value of the induced stress at the location of the dislocation loop enables the glide force and the climb force on the loop to be computed (by multiplication of the appropriate stress component by the Burgers vector of the loop). These forces are shown in Fig. 19.22. If the loop is unfaulted and of the interstitial type, the glide force is attractive. That is, if the critical glide stress (analogous to the critical resolved shear stress) is exceeded, the loop will glide directly into the void and be annihilated. When an interstitial dislocation loop is captured by a void, the latter shrinks by an amount equivalent to the number of interstitials contained in the loop. In addition to a glide force, the void-loop interaction induces a climb force on the loop which causes it to collapse. For this force to cause loop shrinkage, though, it would need to be greater than the climb force causing loop growth arising from interstitial supersaturation of the surrounding solid (Eq. 19.153). If the loop initially had a radius greater than that of the void and could not shrink by the induced climb force, it would be drawn toward the void and be trapped as a sort of Saturn ring around the periphery of the void.

In any case, the glide force is always effective in eliminating dislocation loops with radii smaller than that of

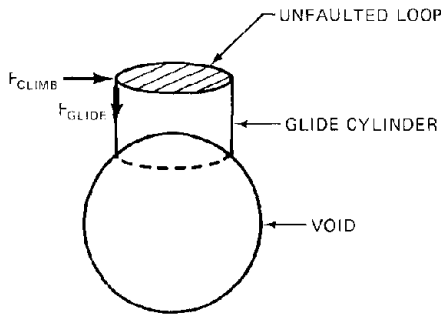


Fig. 19.22 Forces on a dislocation loop near a void. (After Ref. 31.)

the void provided that the loop lies within a capture volume around the void. The capture volume extends from the void surface to the radial position where the attractive stress field due to the void-loop interaction (i.e., the image field, which decreases rapidly with distance from the center of the void) is just equal to the critical glide stress. Loops farther out cannot be started off by the attractive glide force. For large voids (i.e.,  $R > 500 \text{ \AA}$ ), Willis and Bullough<sup>31</sup> calculate that the thickness of the spherical-shell capture volume is  $\sim 200 \text{ \AA}$ . Loss of dislocations from this entire volume around the voids results in cessation of void growth (because of the absence of the dislocations and their biasing effect) when the voids are sufficiently numerous that their capture volumes overlap.

According to the model just outlined, void-growth saturation should be accompanied by a drastic reduction in dislocation density. The expected reduction in dislocation density is observed in pure metals, such as nickel, after long irradiation, but it does not occur in stainless steel because of the greater difficulty in moving dislocations in such an impure alloy. However, even when the voids do not succeed in swallowing the dislocations, the induced stress field created by the necessity of maintaining the void surface stress-free persists. Voids then appear to contain image dislocations that preferentially absorb interstitials over vacancies just as real dislocations do. By this mechanism the neutrality of the void as a point-defect source is destroyed, and the void acquires a bias of its own for interstitials. The rates of point-defect absorption by voids which harbor image dislocations are given by multiplying Eqs. 19.95 and 19.96 by  $W_v$  and  $W_i$ , which are bias factors akin to  $Z_v$  and  $Z_i$  for dislocations and  $Y_v$  and  $Y_i$  for coherent precipitates. Using the modified void sink strengths in the point-defect balances and in the void growth law leads to replacement of  $Z_i - Z_v$  in Eq. 19.145 by  $Z_i - W_i Z_v / W_v$ . When this difference becomes zero, void growth ceases completely.

## 19.6 THE VOID CONTINUITY EQUATION AND VOID SWELLING

Section 19.3 described methods of calculating the rates at which small voids and dislocation loops reach the critical size for continued growth. In Sec. 19.4, overall conservation equations (the point-defect balances) were developed

for vacancies and interstitials to permit calculation of the instantaneous concentrations of point defects in the bulk of the solid. These balances require knowledge of the numbers and sizes of voids and dislocation loops in the material at the moment that the point-defect balances are applied. This information is obtained from void and loop conservation equations, which are derived in this section.

### 19.6.1 The Delta Function Distribution

Most theories of void growth place a great deal of emphasis on determination of the void-growth law,  $\dot{R}$ , but relatively little is said about what is to be done with this formula once it is obtained. Confrontation of the conservation equations governing the entire population of voids and loops in the solid is avoided by assuming simplified size distributions for these two types of defect clusters. Specifically, all voids are assumed to be of the same size at any given time, or the distribution is a delta function centered on the value of  $R(t)$  obtained by integration of the growth law. Similarly, the loop size distribution is assumed to be a delta function. This approach is valid provided that (1) nucleation and growth are distinct, sequential processes and (2) all void (or loop) nuclei are the same size.

If all voids and loops are nucleated at the same time and with the same size and processes that can change the size of a cluster in large chunks (i.e., coalescence or macroscopic resolution) are negligible, the void and loop distributions will remain delta functions throughout irradiation. That is, with time, all loops and voids simply grow uniformly but their number density remains constant. The void size at any time is determined by simultaneously integrating the void-growth law of Eq. 19.139 and the analogous growth laws for loops. Because of the complex dependence of  $\dot{R}$  on  $R$ , numerical integration is generally required.

The zero in time (or fluence) for growth is the end of the nucleation stage, which for stainless steel is taken to be the incubation fluence of  $10^{22}$  neutrons/cm<sup>2</sup> required before any voids are observed. It is assumed that the nucleation process provides  $N$  voids/cm<sup>3</sup> of starting size  $R_c$  (the radius of the critical nuclei) and  $N_l$  loops/cm<sup>3</sup> of initial size  $R_{lc}$ . By integration of the growth laws,  $R(t)$  and  $R_l(t)$  are determined, and the swelling at time  $t$  (or fluence  $\Phi t$ ) is calculated from Eq. 19.10. This approach is followed by Brailsford and Bullough.<sup>25</sup>

### 19.6.2 Eulerian Void Continuity Equation

When the nucleation and growth processes overlap in time, the void and loop conservation equations cannot be circumvented. In this instance, void and loop size distributions evolve during irradiation. The voids and loops present at a particular time arise from nuclei produced from the beginning of irradiation up to the time in question, and hence a distribution of sizes must be present. The continuity equation for voids was derived by Sears.<sup>32</sup> It is similar to the continuity equation for fission-gas bubbles in the fuel (Chap. 13).

The void distribution function  $N(R,t) dR$  is the number of voids per unit volume with radii between  $R$  and  $R + dR$  at time  $t$ . It is convenient to begin with a slightly different distribution function,  $N(m,t)$ , which is the number of voids

per unit volume containing  $m$  vacancies at time  $t$ . Inasmuch as  $R$  and  $m$  are related by

$$m = \frac{4\pi R^3}{3\Omega} \quad (19.164)$$

the two distribution functions satisfy

$$N(R,t) = \left( \frac{4\pi R^2}{\Omega} \right) N(m,t) \quad (19.165)$$

Let us define the current of voids in size space,  $I_m$ , as the number of voids passing from size  $m$  to size  $m+1$  per unit volume per second. Here  $I_m$  is similar to the nucleation rate considered in Sec. 19.3 except that it is defined for void sizes well beyond the critical void cluster size to which nucleation theory is restricted. The rate per unit volume at which voids enter the size  $m$  class is  $I_{m-1}$ . The rate at which voids leave this size class is  $I_m$ . Therefore, the void conservation statement is

$$\frac{\partial N}{\partial t} = I_{m-1} - I_m = - \frac{\partial I}{\partial m} \quad (19.166)$$

Because  $I_m$  varies slowly with  $m$ , the difference  $I_{m-1} - I_m$  can be approximated by the derivative indicated on the extreme right side of the above equation. Equation 19.166 applies only if the nucleation process does not produce voids of size  $m$  (i.e., if  $m > m_c$ ). The current  $I_m$  is given by Eq. 19.40, but for simplicity the thermal emission term is neglected in the present analysis (it can be easily reinstated). Thus

$$I_m = \beta_v(m) N(m,t) - \beta_i(m+1) N(m+1,t) \\ \simeq (\beta_v - \beta_i) N(m,t) \quad (19.167)$$

where the difference between  $\beta_i(m+1) N(m+1,t)$  and  $\beta_i(m) N(m,t)$  has been neglected. The arrival rate  $\beta_v$  is given by Eq. 19.37 in which the denominator is very near unity because the voids are large. The formula for  $\beta_i$  is the same as that for  $\beta_v$  if the subscripts are appropriately altered and  $I_m$  can be expressed in terms of the growth law by noting that Eq. 19.138 (without the thermal emission term) can be written as

$$\dot{R} = (\beta_v - \beta_i) \frac{\Omega}{4\pi R^2} \quad (19.168)$$

If Eq. 19.167 is inserted into Eq. 19.166, the size variable is changed from  $m$  to  $R$  by Eq. 19.164, the distribution function is changed from  $N(m,t)$  to  $N(R,t)$  by Eq. 19.165, and Eq. 19.168 is used, the void continuity equation is found to be

$$\frac{\partial N}{\partial t} = - \frac{\partial}{\partial R} (\dot{R}N) \quad (19.169)$$

which is valid for  $t > 0$  and  $R > R_c$ , the radius of the critical void nucleus.

In addition to the growth law  $\dot{R}$ , Eq. 19.169 requires an initial condition and a boundary condition (only one of each, since the equation is first order in each variable). The initial condition is

$$N(R,0) = 0 \quad (\text{for all } R) \quad (19.170)$$

which states that the metal contains no voids at the start of irradiation.

The boundary condition is related to the nucleation process, which proceeds simultaneously with growth. It is usually assumed that all void nuclei enter the solid as small clusters containing  $m_c$  atoms at a rate  $I_{nuc1} \text{ cm}^{-3} \text{ sec}^{-1}$ . The critical void size and the nucleation rate are prescribed by nucleation theory for the prevailing point-defect supersaturations (Sec. 19.3). The balance equation for voids of size  $m_c$  is

$$\frac{\partial N(m_c,t)}{\partial t} = I_{nuc1} - I_{m_c} \quad (19.171)$$

where  $I_{m_c}$  is the current of voids passing from size  $m_c$  to the next largest size. It is generally sufficient to apply a quasi-stationary approximation to Eq. 19.171 and equate  $I_{nuc1}$  to  $I_{m_c}$ . With the same manipulations used to obtain Eq. 19.169, the steady-state form of Eq. 19.171 provides the boundary condition

$$N(R_c,t) = \frac{I_{nuc1}(t)}{\dot{R}_c} \quad (\text{for all } t) \quad (19.172)$$

where  $\dot{R}_c$  is the growth rate of the critical size void nucleus.

Equations similar to Eqs. 19.169 and 19.172 are needed for dislocation loops as well as for voids. For loops, unfauling of sessile loops to form glissile loops would have to be added as a loss mechanism, and an additional conservation equation would be needed to describe the time rate of change of the network dislocations as well.

Determination of the void and loop distribution functions requires simultaneous solution of the conservation equations for these defect clusters together with their growth laws. Note that calculation of the evolution of the void and loop populations during irradiation is no longer simply a matter of integrating the growth laws. Rather, the growth laws must be integrated in the form that they appear in the void and loop conservation equations, where  $\dot{R}$  and  $\dot{R}_1$  are multiplied by  $N$  and  $N_1$  in a derivative. At any time  $t$ , the swelling is given by Eq. 19.9.

This unified approach to void swelling has been applied in the computer program developed by Li et al.,<sup>21</sup> a flow chart of which is shown in Fig. 19.23. They employed the conservation equation (Eq. 19.169) and the analogous partial differential equation for loops in terms of the  $m$  variable (for voids) rather than the  $R$  variable as was done here. A multigroup scheme was used to reduce the size of the  $m$  increments. A similar method was used by these authors in connection with bubble growth by coalescence (Eq. 13.201 is analogous to Eq. 19.169).

We do not present any results of either the delta function Brailsford-Bullough method of calculating void swelling or the Li-Harkness unified approach. The former is very good on the growth law but does not account for continued nucleation of new voids and loops during irradiation. The latter treats the void distribution function more realistically but incorporates inaccurate nucleation theory and does not contain the detail in the growth laws that the Brailsford-Bullough method provides. Despite these shortcomings of each method, there are enough unknown physical quantities in each model to provide a sufficient number of adjustable parameters to fit the

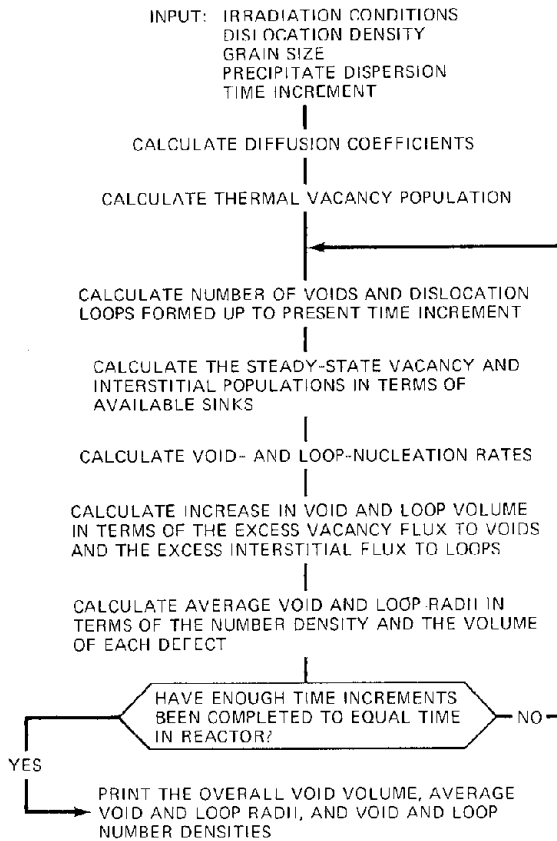


Fig. 19.23 Flow chart of a computer program for calculating void swelling. (After Ref. 21.)

experimentally observed void-swelling patterns discussed in Sec. 19.2. Neither model needs outlandish values of the adjustable parameters to qualitatively reproduce a wide variety of experimental results, which implies that the basic concepts of the models are sound. This sort of semiagreement between theory and experiment means that the model calculations are best used to extrapolate existing data rather than to determine absolute swelling from first principles. The theory is an aid to experiment but certainly cannot supplant the continued acquisition of data on void swelling by fast-neutron irradiation.

19.6.3 Lagrangian Void Continuity Equation

The method of accounting for the change in size and density of loops and voids during irradiation which was described above is Eulerian in nature because it follows flows of defects into and out of a fixed interval of cluster size. For some special cases a Lagrangian approach may be more useful. The void conservation equation can be succinctly derived by noting that all voids in the size range  $R$  to  $R + dR$  at time  $t$  arise from nuclei created (at size  $R_c$ ) in the time interval  $\tau$  to  $\tau + d\tau$ , or

$$N(R,t) dR = I_{nuc}(\tau) d\tau$$

which can be rearranged to give

$$N(R,t) = I_{nuc} [\tau(R,t)] \left( \frac{\partial \tau}{\partial R} \right)_t \quad (19.173)$$

The problem is to determine the relation between  $\tau$  and the variables  $t$  and  $R$  in order that the argument of  $I_{nuc}$  and the Jacobian  $(\partial \tau / \partial R)_t$  be expressed in terms of these quantities. This identification is accomplished by regarding the function  $R(t, \tau)$  as the radius at time  $t$  of a void nucleated at time  $\tau$ , which can be obtained by writing the growth law as

$$\frac{dR}{dt} = \dot{R} \quad (19.174)$$

Equation 19.174 can be integrated provided that  $\dot{R}$  is known explicitly as a function of  $R$  and  $t$ . That this is usually not the case is the reason that the Lagrangian approach is restricted to special situations. Sears<sup>32</sup> considers the artificial case in which  $C_v$  and  $C_i$  are independent of  $R$  (which, in general, is not true because the point-defect balances depend on the void average size). In this case Eqs. 19.174 and 19.138 can be combined and integrated to give

$$R^2(t, \tau) = R_c^2 + 2\Omega \int_{\tau}^t (D_v C_v - D_i C_i) dt' \quad (19.175)$$

If the integral on the right can be performed (i.e., if the time variations of  $C_v$  and  $C_i$  are known a priori), Eq. 19.175 can be solved for  $\tau$  as a function of  $R$  and  $t$ , and the right-hand side of Eq. 19.173 can be expressed entirely in terms of the last two variables.

A more realistic case in which a Lagrangian defect conservation equation is employed in the analysis of thermal annealing of depleted zones is discussed in Sec. 18.5.

19.7 IRRADIATION CREEP

Irradiation creep refers either to augmentation of thermal creep by irradiation or to development of creep under conditions in which thermal creep is absent. The former is termed *irradiation-enhanced creep*, and the latter is known as *irradiation-induced creep*. A sizeable number of thermal creep mechanisms have been identified (see Sec. 16.6), and an even greater number of irradiation creep theories have been proposed.<sup>33</sup> To be classed as irradiation creep, the applied stress must cause nonuniform deformation of the solid (not just swelling), and the deformation rate must change when the fast-neutron flux is altered.

Irradiation creep theories applicable to austenitic stainless steels can be divided into two broad categories, the distinction resting on whether or not irradiation-produced dislocation loops and voids are involved in the creep process. Inasmuch as the nucleation of these clusters is strongly temperature dependent, the two regimes are equivalent to low and high temperatures. The boundary occurs roughly at the minimum temperature for void formation (~350°C in stainless steel).

High-temperature irradiation creep is usually ascribed to (1) stress orientation of nucleating dislocation loops or (2) accelerated climb of dislocations followed by glide.

Two types of low-temperature irradiation creep have been identified. The first is a transient creep due to climb of pinned segments of the dislocation network in the solid, and the second is a steady-state form of creep arising from collapse of vacancy loops. Figure 19.24 demonstrates the simultaneous operation of transient and steady creep at low temperatures. After a long time of irradiation at a high stress, the load on the in-pile test specimen is reduced. The vertical line on the left of the graph represents immediate elastic strain recovery, following which an incubation period of  $\sim 2000$  hr is required before establishment of steady-state irradiation creep characteristic of the lower stress level. The strain offset between the end of the elastic recovery and the backward extrapolation of the new

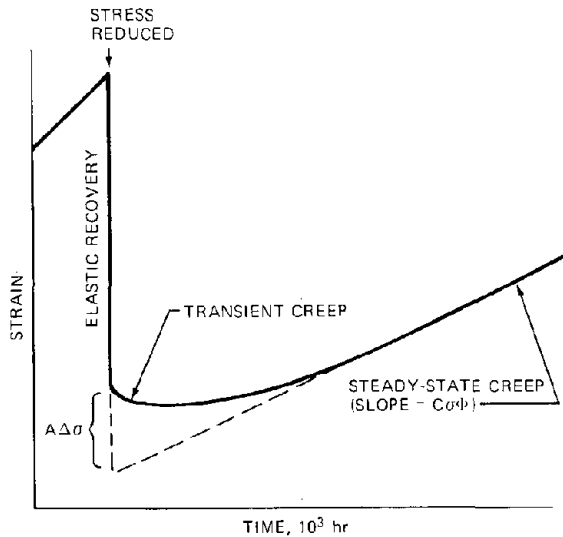


Fig. 19.24 Strain recovery in type 304 stainless steel irradiated at  $100^\circ\text{C}$  following a stress reduction in pile. (After E. R. Gilbert and L. D. Blackburn, in *Second International Conference on the Strength of Metals and Alloys*, p. 773, American Society for Metals, 1970.)

steady-state creep line represents the amplitude of the transient component of the low-temperature irradiation creep. The data in Fig. 19.24 can be represented by the formula:

$$\epsilon = A\sigma \left[ 1 - \exp\left(-\frac{\Phi t}{B}\right) \right] + C\sigma\Phi t \quad (19.176)$$

The first term on the right represents the recoverable transient strain. The steady-state creep rate is contained in the second term. Here, we explain the mechanisms by which these two forms of low-temperature irradiation creep occur and provide estimates of the constants A, B, and C in Eq. 19.176.

### 19.7.1 Transient Creep

Models of transient irradiation creep have been advanced by Hesketh<sup>34</sup> and by Lewthwaite and Proctor.<sup>35</sup> A

slightly modified form of Hesketh's analysis will be reviewed here.

Consider a metal in which the dislocation density is  $\rho_d$ . The dislocation network is modeled as a cubical grid of dislocation segments, with the distance between junctions where the segments of dislocation line are pinned (Sec. 13.12) given by

$$l = \left(\frac{3}{\rho_d}\right)^{1/2} \quad (19.177)$$

Since the theory is designed for temperatures well below the temperature of void formation, we will assume that the vacancies produced by the collision cascades are immobile. The vacancy and interstitial diffusion coefficients in stainless steel are approximately given by  $D_v \approx \exp(-e_v^*/kT)$  and  $D_i \approx \exp(-e_i^*/kT)$ , where the diffusivities are in square centimeters per second,  $e_v^* \approx 125$  kJ/mole, and  $e_i^* \approx 13$  kJ/mole. At  $100^\circ\text{C}$ ,  $D_v \approx 10^{-18}$   $\text{cm}^2/\text{sec}$  and  $D_i \approx 10^{-2}$   $\text{cm}^2/\text{sec}$ . The mean lifetime of a point defect can be estimated from Eq. 7.24 if the root-mean-square displacement of an atom at time  $t$  is identified with the size of the dislocation network. Taking  $r^2$  equal to  $l^2 \approx 10^{-10}$   $\text{cm}^2$  (for  $\rho_d = 10^{10}$   $\text{cm}^{-2}$ ) and the above values of the point-defect diffusivities, we find the average time for a vacancy to reach a dislocation is  $\sim 10^7$  sec, whereas an interstitial is absorbed in  $\sim 10^{-9}$  sec. Thus, it is a fair approximation to consider the vacancies as totally immobile and the interstitials as mobile enough to maintain quasi-steady-state concentrations of this defect at all times. The basic results of the analysis do not depend on this restriction, but the analysis is simpler than the case in which both species are mobile.

Consider a specimen that has been irradiated in a stress-free state for a time long enough to establish a steady-state microstructure (the irradiation-produced interstitials cause the pinned segments of the dislocation network to climb until the line tension of the curved dislocation balances the chemical stress due to the interstitial supersaturation). During the initial irradiation soaking, no creep occurs since no stress is applied. Figure 19.25 shows a representative cube of the dislocation network of the solid during irradiation. Each of the sides of the cube is assumed to consist of segments of edge dislocations of length  $l$ . The Burgers vectors of the segments are randomly oriented. Bowing of the dislocations under irradiation is depicted as the circular segments terminating at the pinning points (for clarity, only one-half of the bowed segments are shown in the drawing). The segments take on this configuration because of absorption of interstitial atoms from the irradiated solid; so the shaded circular segments represent extensions of the half-sheets of atoms of which the edge dislocations consist. The accumulation of excess interstitial atoms by the dislocation segments cause each of them to acquire a common radius of curvature  $R$ . The small irregular shapes within the cube in Fig. 19.25 are intended to represent the depleted zones which are formed in the collision cascade and which are stable against thermal annealing at low temperatures. The depleted zones are vacancy agglomerates.

Because irradiation creates equal numbers of vacancies and interstitials, a conservation condition relates the extent

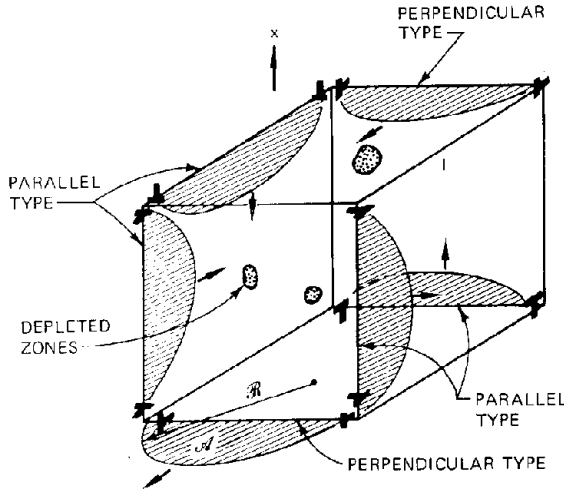


Fig. 19.25 Bowing of the segments of a dislocation network in an irradiation field. No stress is applied.

of climb of the dislocation segments, the number and size of the depleted zones, and the point-defect concentrations maintained by irradiation in the solid. The sum of the number of interstitials associated with the bowed dislocation lines and the bulk interstitial concentration  $C_i$  must be equal to the sum of the number of vacancies contained in the depleted zones and the bulk vacancy concentration  $C_v$ . This condition is independent of the point-defect balances, which equate the rates of production and destruction of each type of point defect.

The number of interstitial atoms associated with the bowed dislocation segments is obtained as follows. The cube shown in Fig. 19.25 contains 12 segments, but each of these is shared among four neighboring cubes; thus there are three segments associated with a volume  $l^3$  of solid. With Eq. 19.177, the number of segments per unit volume is  $\rho_d/l$ . If the areas of the shaded circular segments in Fig. 19.25 are called  $\mathcal{A}$ , the number of interstitial atoms contained in each is  $b\mathcal{A}/\Omega$ . The area  $\mathcal{A}$  is a function of the radius of curvature  $\mathcal{R}$  and the cube side  $l$ . The number of interstitials per unit volume contained in the bowed segments is  $b\mathcal{A}\rho_d/l\Omega$ .

At steady state, there will be a distribution  $N(R)$  of depleted zones, in which  $R$ , the zone radius, ranges from the maximum size created in the collision cascade,  $R_0$ , to zero size (see Sec. 18.5). A zone of radius  $R$  contains  $4\pi R^2/3\Omega$  vacancies. Thus, the balance on the total number of point defects can be written\*

\*A conservation statement analogous to Eq. 19.178 cannot be made during void growth because, in this instance, the dislocations are considered free to climb. Point defects can thus leave or enter a particular unit volume of solid by the motion of climbing dislocations. In the present situation, no point defects cross the surface of any unit volume in the solid, and correctly accounting for the fate of the nonrecombined point defects in this closed system leads to Eq. 19.178.

$$C_i + \frac{b\rho_d\mathcal{A}}{\Omega} = C_v + \frac{4\pi}{3\Omega} \int_0^{R_0} R^3 N(R) dR \quad (19.178)$$

The point-defect balances are

$$\nu_v \Sigma_s \Phi = k_{iv} C_i C_v \quad (19.179)$$

$$\begin{aligned} \nu_i \Sigma_s \Phi = Z_i \rho_d D_i (C_i - C_i^d) + k_{iv} C_i C_v \\ + 4\pi D_i C_i \int_0^{R_0} R N(R) dR \quad (19.180) \end{aligned}$$

Because of the assumption that the vacancies are immobile, they do not diffuse to dislocations or to depleted zones. Vacancies are removed from the solid only by recombination with migrating interstitials. The interstitial balance (Eq. 19.180) is the same as that employed in the analysis of depleted-zone annealing (Sec. 18.5) except for the concentration of interstitials at the dislocation surface. In the annealing study the dislocations were assumed free to climb, and  $C_i^d$  was equal to  $C_i^{eq} \approx 0$ . When the dislocations are pinned and climb is stopped by line tension, the interstitial concentration at the surface of the dislocation rises from  $C_i^{eq}$  for a straight dislocation free to climb to a value given by Eq. 19.158b when the line assumes a finite radius of curvature. When no voids are attached to the ends of the pinned segment, the factor  $f$  in Eq. 19.158b is unity, and  $C_i^d$  for the present analysis is given by

$$C_i^d = C_i^{eq} \exp \left[ \frac{\tau_d}{b\mathcal{R}} \frac{\Omega}{kT} \right] \quad (19.181)$$

Recalling the analysis of depleted-zone annealing in Sec. 18.5, the number of interstitials and free vacancies (i.e., vacancies not contained in nascent depleted zones) are related by

$$\nu_i = \nu_v + \frac{4\pi R_0^3}{3\Omega} \quad (19.182)$$

The distribution of depleted zones,  $N(R)$ , has been derived in the depleted-zone annealing analysis of Sec. 18.5. In the present application the vacancies are assumed to be immobile; thus Eq. 18.48 becomes

$$N(R) = \frac{\Sigma_s \Phi R}{D_i C_i \Omega} \quad (19.183)$$

If Eq. 19.179 is subtracted from Eq. 19.180, the difference  $\nu_i - \nu_v$  is taken from Eq. 19.182, and the distribution of Eq. 19.183 is used in the integral of Eq. 19.180, we find that the point-defect balances require that  $C_i = C_i^d$ , or, with Eq. 19.181,

$$\frac{\tau_d}{b\mathcal{R}} = \frac{kT}{\Omega} \ln \left( \frac{C_i}{C_i^{eq}} \right) \quad (19.184)$$

The left-hand side of this equation is the applied stress needed to bow a dislocation line to a radius of curvature  $\mathcal{R}$ . The right-hand side is the effective, or chemical, stress on the dislocation line due to the interstitial supersaturation.

Equation 19.178 provides an additional relationship between  $C_i$  and  $\mathcal{R}$ . The integral can be removed by use of Eq. 19.183, and  $C_v$  can be expressed in terms of  $C_i$  by Eq. 19.179, yielding

$$C_i + \frac{b\rho_d\mathcal{A}}{\Omega} = \frac{\nu_v \Sigma_s \Phi}{k_{iv} C_i} + \frac{4\pi \Sigma_s \Phi R_0^3}{15 \Omega^2 D_i C_i} \quad (19.185)$$

The radius  $\mathcal{R}$  is contained in Eq. 19.185 in the area  $\mathcal{A}$  (see problem 19.16 at the end of this chapter). Simultaneous solution of Eqs. 19.184 and 19.185 yields  $C_i$  and  $\mathcal{R}$ .

If the value of  $\mathcal{R}$  determined by this method is less than  $1/2$ , the configuration shown in Fig. 19.25 cannot be maintained. In Eq. 19.184

$$\frac{\tau_d}{b\mathcal{R}} \frac{\Omega}{kT} \simeq 10^{-4} \text{ cm}$$

for most metals at low temperatures ( $\sim 100^\circ\text{C}$ ). For a metal with a dislocation density of  $10^{10} \text{ cm}^{-2}$ , the minimum value of  $\mathcal{R}$  (equal to  $1/2$ ) is  $\sim 10^{-5} \text{ cm}$ . Therefore, Eq. 19.185 limits the allowable interstitial supersaturation for the maintenance of a stable configuration of bowed dislocation segments of  $C_i/C_i^{\text{eq}} < 10^4$ . If the dislocation density is  $10^{12} \text{ cm}^{-2}$ , however, the maximum permissible supersaturation of interstitials is  $10^4$ .

To approximately calculate  $C_i$  from Eq. 19.185, assume that the dislocation segments have bowed to nearly semicircular configurations ( $\mathcal{R} \simeq 1/2$ ), so

$$\mathcal{A} \simeq \frac{1}{2} \pi \mathcal{R}^2 = \frac{\pi l^2}{8}$$

Eliminating  $l$  in favor of  $\rho_d$  by using Eq. 19.177, Eq. 19.185 becomes

$$\Omega C_i + \left[ \frac{\pi 3^{1/2}}{8} b (\rho_d)^{1/2} \right] = \frac{b^2 \Omega \Sigma_s \Phi}{D_i} \times \left( \frac{\nu_v}{z_{iv}} + \frac{4\pi R_0^5}{15 \Omega b^2} \right) \frac{1}{\Omega C_i} \quad (19.186)$$

where the vacancy-interstitial recombination coefficient,  $k_{iv}$ , has been expressed by Eq. 13.42 with  $a_0 \simeq b$ . Using representative values of the constants in Eq. 19.186, we find that the second term on the left-hand side is very much larger than the coefficient of  $1/\Omega C_i$  on the right-hand side. Therefore, the solution of the quadratic equation is

$$C_i = \frac{8}{\pi 3^{1/2}} \frac{b}{(\rho_d)^{1/2} D_i} \left( \frac{\nu_v}{z_{iv}} + \frac{4\pi R_0^5}{15 \Omega b^2} \right) \Sigma_s \Phi \quad (19.187)$$

and  $\mathcal{R}$  is determined by substitution of Eq. 19.187 into Eq. 19.184.

For a flux of  $10^{13} \text{ neutrons cm}^{-2} \text{ sec}^{-1}$ ,  $R_0 \simeq 8 \text{ \AA}$ , and a dislocation density of  $10^{12} \text{ cm}^{-2}$ , Eq. 19.187 gives  $C_i \simeq 10^3 \text{ cm}^{-3}$ . The thermal equilibrium vacancy concentration at  $100^\circ\text{C}$  is about  $10^{-36} \text{ cm}^{-3}$ , so the vacancy supersaturation is  $\sim 10^{39}$ . This supersaturation is just a bit smaller than the value which, by Eq. 19.184, causes the dislocation segments to climb beyond the semicircular configuration ( $\mathcal{R} = 1/2$ ). Thus, the preceding analysis is limited to metals of high dislocation density and low fluxes. As the temperature is increased (which increases  $C_i^{\text{eq}}$ ), these restrictions are less stringent than they are at  $\sim 100^\circ\text{C}$ . Hesketh<sup>34</sup> discusses the consequences of interstitial supersaturations that are large enough to cause the dislocations to be pulled free of their pinning points by the chemical stress.

During the irradiation period preceding application of the stress to the specimen, all the dislocations climb by the same amount by absorption of excess interstitials. When

uniaxial tension in the vertical direction in Fig. 19.25 is applied, the edge dislocations whose extra half-layer of atoms is perpendicular to the direction of the applied stress (i.e., those with Burgers vectors parallel to the stress direction) are induced to climb because the stress reduces the concentration of interstitials at the dislocation core. These dislocations are identified as "perpendicular type" in Fig. 19.25. They constitute one-third of all the dislocation segments in the solid. The remaining two-thirds of the dislocation segments have their Burgers vectors at  $90^\circ$  to the stress axis, or the extra half-sheet of atoms is parallel to the stress direction. These segments, labeled "parallel type" in Fig. 19.25, are not directly affected by application of the stress.

At the final steady-state configuration achieved following application of the stress, the radius of curvature of the perpendicular-type dislocations changes from  $\mathcal{R}$  to  $\mathcal{R}_\perp$ , and that of the parallel-type segments changes from  $\mathcal{R}$  to  $\mathcal{R}_\parallel$ . The interstitial concentrations at the cores of these two dislocation types are altered from the stress-free value given by Eq. 19.181 to

$$(C_i^d)_\perp = C_i^{\text{eq}} \exp\left(\frac{\tau_d}{b\mathcal{R}_\perp} \frac{\Omega}{kT}\right) \exp\left(-\frac{\sigma\Omega}{kT}\right) \quad (19.188)$$

and

$$(C_i^d)_\parallel = C_i^{\text{eq}} \exp\left(\frac{\tau_d}{b\mathcal{R}_\parallel} \frac{\Omega}{kT}\right) \quad (19.189)$$

The point-defect balances become

$$\nu_v \Sigma_s \Phi = k_{iv} C_i' C_v' \quad (19.190a)$$

and

$$\begin{aligned} \nu_i \Sigma_s \Phi = & \frac{1}{3} Z_i \rho_d D_i [C_i' - (C_i^d)_\perp] \\ & + \frac{2}{3} Z_i \rho_d D_i [C_i' - (C_i^d)_\parallel] \\ & + k_{iv} C_i' C_v' + 4\pi D_i C_i' \int_0^{R_0} R N(R) dR \quad (19.190b) \end{aligned}$$

where  $C_i'$  and  $C_v'$  are the concentrations of point defects in the bulk solid after the system has come to equilibrium with the applied stress. The depleted-zone distribution is given by Eq. 19.183 with  $C_i$  replaced by  $C_i'$ . Following the procedure used in the stress-free condition, satisfaction of the point-defect balances requires that the bracketed terms in Eq. 19.190b both vanish, or Eq. 19.184 is replaced by two conditions:

$$\frac{\tau_d}{b\mathcal{R}_\perp} - \sigma = \frac{kT}{\Omega} \ln\left(\frac{C_i'}{C_i^{\text{eq}}}\right) \quad (19.191)$$

$$\frac{\tau_d}{b\mathcal{R}_\parallel} = \frac{kT}{\Omega} \ln\left(\frac{C_i'}{C_i^{\text{eq}}}\right) \quad (19.192)$$

The overall balance of point defects, which was expressed by Eq. 19.185 in the absence of stress, now becomes

$$C_i' + \frac{b\rho_d}{\Omega} \left( \frac{1}{3} \mathcal{A}_\perp + \frac{2}{3} \mathcal{A}_\parallel \right) = \frac{\nu_v \Sigma_s \Phi}{k_{iv} C_i'} + \frac{4\pi \Sigma_s \Phi R_0^5}{15 \Omega^2 D_i C_i'} \quad (19.193)$$

where  $\mathcal{A}_\perp$  and  $\mathcal{A}_\parallel$  are climb areas corresponding to the radii of curvature  $\mathcal{R}_\perp$  and  $\mathcal{R}_\parallel$ , respectively. The final

configuration of the dislocations in the stressed solid can be determined by solving Eqs. 19.191 to 19.193 for  $C'_i$ ,  $\mathcal{R}_\perp$ , and  $\mathcal{R}_\parallel$ . Inasmuch as the changes in the interstitial concentration and the radii of curvature of the two types of dislocations due to application of the stress are small compared to the values of these quantities established by prior irradiation, the new values can be expressed by

$$\mathcal{A}_\perp = \mathcal{A} + \left[ \frac{d\mathcal{A}}{d(1/\mathcal{R})} \right] \left( \frac{1}{\mathcal{R}_\perp} - \frac{1}{\mathcal{R}} \right) \quad (19.194)$$

$$\mathcal{A}_\parallel = \mathcal{A} + \left[ \frac{d\mathcal{A}}{d(1/\mathcal{R})} \right] \left( \frac{1}{\mathcal{R}_\parallel} - \frac{1}{\mathcal{R}} \right) \quad (19.195)$$

$$C'_i = C_i + \delta C_i \quad (19.196)$$

Solution of Eqs. 19.191 to 19.193 using the above forms with  $\delta C_i/C_i \ll 1$  is treated in problem 19.17 at the end of this chapter. To keep algebraic manipulations to a minimum, we make the even cruder approximation  $\delta C_i \approx 0$ , or  $C'_i \approx C_i$ , which permits the right side of Eq. 19.191 to be replaced by the left side of Eq. 19.184, or

$$\frac{\tau_d}{b} \left( \frac{1}{\mathcal{R}_\perp} - \frac{1}{\mathcal{R}} \right) = \sigma \quad (19.197)$$

Since the applied stress is positive (tension), Eq. 19.197 shows that  $\mathcal{R}_\perp < \mathcal{R}$ , or the perpendicular-type dislocations advance slightly upon application of the stress. This means that atoms are added to the bowed dislocation segments which lie at right angles to the stress axis. This transfer of matter results in deformation, or strain, in the direction of the applied stress, the magnitude of which may be determined as follows.

Figure 19.26 shows a block of the irradiated metal with initial dimensions X, Y, and Z. One internal plane containing a perpendicular-type dislocation segment and two planes with parallel-type segments are shown in the sketch. The shaded crescent shapes represent the area changes due to application of the stress. For the perpendicular-type dislocations, the change in area is  $\mathcal{A}_\perp - \mathcal{A}$ . The solid shown in the figure contains  $(\rho_d/l)XYZ$  dislocation segments of length  $l$ , one-third of which are of the perpendicular type. When these expand by  $\mathcal{A}_\perp - \mathcal{A}$ , a total of

$$\frac{1}{3} \frac{\rho_d}{l} (XYZ) \frac{b}{\Omega} (\mathcal{A}_\perp - \mathcal{A})$$

atoms are moved to planes perpendicular to the stress axis. Or the volume displaced in  $\Omega$  times the above expression, which is related to the deformation in the stress direction,  $\delta X$ , by

$$\delta X (YZ) = \text{atoms moved} \times \Omega$$

Combining the above two expressions yields the terminal creep strain:

$$\epsilon = \frac{\delta X}{X} = \frac{\rho_d b (\mathcal{A}_\perp - \mathcal{A})}{3l} \quad (19.198)$$

The area change  $\mathcal{A}_\perp - \mathcal{A}$  can be obtained from Eq. 19.194, in which the difference in the reciprocal radii of curvature is expressed by Eq. 19.197, and we have

$$\epsilon = \frac{\rho_d b^2 \sigma}{3l \tau_d} \left[ \frac{d\mathcal{A}}{d(1/\mathcal{R})} \right]$$

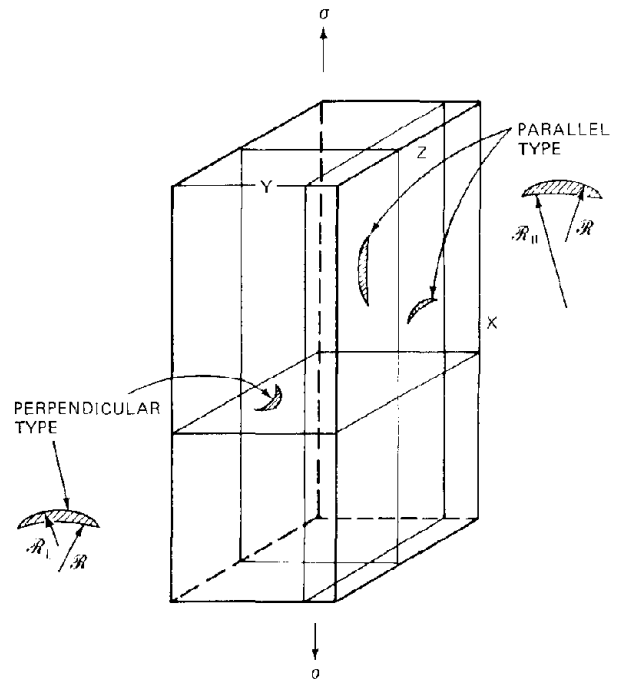


Fig. 19.26 Transient irradiation creep due to bowing of pinned dislocation segments.

In problem 19.16 at the end of this chapter, the bracketed term in the above formula is shown to be expressible in the form

$$\frac{d\mathcal{A}}{d(1/\mathcal{R})} = \frac{l^3}{12} F\left(\frac{1}{\mathcal{R}}\right) \quad (19.199)$$

where  $F$  approaches unity as  $1/\mathcal{R} \rightarrow 0$  but becomes large as the semicircular configuration ( $\mathcal{R} = l/2$ ) is approached. The dislocation-line tension is approximately equal to  $Gb^2$ , where  $G$  is the shear modulus; so the terminal creep becomes

$$\epsilon = \frac{\rho_d l^2 F(1/\mathcal{R})}{36G}$$

Noting that according to Eq. 19.177,  $\rho_d l^2 = 3$  and replacing the shear modulus  $G$  by Young's modulus  $E = 2(1 + \nu)G \approx 3G$ , we have

$$\epsilon = \frac{F(1/\mathcal{R})}{4} \left( \frac{\sigma}{E} \right) - \frac{F(1/\mathcal{R})}{4} \epsilon_{\text{elastic}} \quad (19.200)$$

If  $F(1/\mathcal{R}) \approx 1$ , Eq. 19.200 predicts that the amplitude of the transient strain should be one-fourth the elastic strain. This prediction is consistent with the experimental results shown in Fig. 19.24, in which the elastic recovery following stress reduction is several times larger than the magnitude of the transient strain recovery which follows. Lewthwaite and Proctor<sup>35</sup> report transient strains as large as three times the initial elastic deflection, which may be due to values of  $F(1/\mathcal{R})$  larger than unity, owing to bowing of the dislocation to a nearly semicircular shape.

Comparison of Eqs. 19.176 and 19.200 indicates that the theoretical value of the constant  $A$  is

$$\Lambda = \frac{F(1/\mathcal{R})}{4E} \quad (19.201)$$

The terminal creep strain attained when an irradiated specimen is stressed at low temperatures depends on the flux to which the specimen is exposed. The coefficient  $A$  given by Eq. 19.201 is proportional to the geometric factor  $F(1/\mathcal{R})$  given by Eq. 19.199, which increases as  $\mathcal{R}$  decreases. According to Eq. 19.184,  $\mathcal{R}$  becomes smaller as the interstitial concentration  $C_i$  becomes larger, and, by Eq. 19.187,  $C_i$  is directly proportional to the flux  $\Phi$ . This effect may be responsible for the larger values of the coefficient  $A$  observed by Lewthwaite and Proctor,<sup>3,5</sup> who irradiated their specimens in a fast reactor with a fast-neutron flux of  $\sim 2 \times 10^{14}$  neutrons  $\text{cm}^{-2} \text{sec}^{-1}$ , compared to the  $A$  values reported by Hesketh,<sup>3,4</sup> which were based on irradiations in a thermal reactor wherein the fission flux was  $\sim 4 \times 10^{13}$  neutrons  $\text{cm}^{-2} \text{sec}^{-1}$ .

However, the major irradiation dependence of the transient creep mechanism we are considering here lies in the exponential term in Eq. 19.176. This equation shows that in the absence of irradiation the expected terminal creep strain would take infinitely long to be attained. Rather than attempt to compute  $B$  directly from the theory, we follow the technique used by Hesketh<sup>3,4</sup> and by Lewthwaite and Proctor<sup>3,5</sup> of computing the strain rate at the moment that the stress is applied. This initial strain rate, denoted by  $\dot{\epsilon}_0$ , is related to the constant  $B$  by

$$B = \frac{A\sigma\Phi}{\dot{\epsilon}_0} \quad (19.202)$$

The exact time variation of the strain is more complex than the simple exponential form given in Eq. 19.176, but the estimate based on Eq. 19.202 at least gives the correct initial strain rate.

From Eq. 19.198 the initial strain rate is

$$\dot{\epsilon}_0 = \frac{\rho_d b}{3l} \left( \frac{d\mathcal{A}_1}{dt} \right)_{t=0}$$

where zero time is when the stress is applied to the specimen. If  $m_i$  is the number of atoms contained in the curved dislocation segment,

$$\frac{d\mathcal{A}_1}{dt} = \frac{\Omega}{b} \frac{dm_i}{dt}$$

where  $dm_i/dt$  is the rate of flow of interstitials to the dislocation segment,

$$\frac{dm_i}{dt} = J_1^d l$$

where  $l$  is approximately the length of dislocation line between pinning points and  $J_1^d$  is the flux of interstitials per unit length of perpendicular-type dislocation line. Prior to application of the stress, the flux of interstitials to the dislocation lines is zero because the system is at equilibrium. However, application of the stress reduces the interstitial concentration at the core of the perpendicular-type lines, thus inducing an interstitial flux of

$$J_1^d = Z_i D_i [C_i - (C_i^d)_{1,0}]$$

where  $(C_i^d)_{1,0}$  is the interstitial concentration at the core of the perpendicular-type dislocations at the moment that the stress is applied. Assembling the preceding four equations yields

$$\dot{\epsilon}_0 = \frac{1}{3} \rho_d \Omega Z_i D_i [C_i - (C_i^d)_{1,0}] \quad (19.203)$$

Just before the stress is applied, the concentration of interstitials at all dislocations in the solid is given by Eq. 19.181. After the specimen has been held at constant stress long enough for the new equilibrium configuration of the line segments to be attained, the interstitial concentration at the perpendicular-type dislocations is given by Eq. 19.188. However, at  $t = 0$ , the radius of curvature is still equal to the unstressed value  $\mathcal{R}$ , but the interstitial concentration at the dislocation core is instantaneously reduced by the second exponential term in Eq. 19.188. Therefore

$$(C_i^d)_{1,0} = C_i^{e,q} \exp\left(\frac{\tau_d}{b\mathcal{R}} \frac{\Omega}{kT}\right) \exp\left(-\frac{\sigma\Omega}{kT}\right) \quad (19.204)$$

If we expand the second exponential term in a Taylor series, the driving force in Eq. 19.203 becomes

$$C_i - (C_i^d)_{1,0} = C_i - C_i^{e,q} \exp\left(\frac{\tau_d}{b\mathcal{R}} \frac{\Omega}{kT}\right) + C_i^{e,q} \exp\left(\frac{\tau_d}{b\mathcal{R}} \frac{\Omega}{kT}\right) \left(\frac{\sigma\Omega}{kT}\right)$$

Now, according to Eq. 19.184, the first two terms on the right-hand side of this equation are equal to each other, and the coefficient of  $\sigma\Omega/kT$  in the last term is equal to  $C_i$ . Therefore, Eq. 19.203 becomes

$$\dot{\epsilon}_0 = \frac{1}{3} \rho_d \Omega Z_i D_i C_i \frac{\sigma\Omega}{kT}$$

Since  $C_i$  is not significantly changed at the instant of application of the stress,  $C_i$  in the above formula is given by Eq. 19.187, and the initial strain rate is

$$\dot{\epsilon}_0 = \frac{8}{3^{\frac{3}{2}}\pi} \frac{Z_i \Omega^2 \sigma b (\rho_d)^{\frac{1}{2}}}{kT} \left( \frac{\nu_v}{z_{iv}} + \frac{4\pi R_0^5}{15 \Omega b^2} \right) \Sigma_s \Phi \quad (19.205)$$

Substituting Eqs. 19.205 and 19.201 [the latter with  $F(1/\mathcal{R}) \simeq 1$ ] into Eq. 19.202 yields the coefficient  $B$ ,

$$B = \frac{3^{\frac{3}{2}} \pi}{32} \frac{kT}{\Sigma_s E Z_i \Omega^2 b (\rho_d)^{\frac{1}{2}} \left( \frac{\nu_v}{z_{iv}} + \frac{4\pi R_0^5}{15 \Omega b^2} \right)} \quad (19.206)$$

Evaluating Eq. 19.206 for  $\rho_d = 10^{12} \text{ cm}^{-2}$  yields  $B \simeq 10^{20} \text{ cm}^2$ , which is of the order of magnitude of the value of this parameter observed by Lewthwaite and Proctor.<sup>3,5</sup> Equation 19.205 indicates that the higher the dislocation density, the more rapidly is the terminal creep strain achieved. This prediction is also in accord with measurements of transient creep in cold-worked and annealed stainless steel.<sup>3,5</sup>

19.7.2 Steady-State Irradiation Creep  
by Vacancy Disk Collapse

Although dislocation loops formed by condensation of excess vacancies are not observed in the microstructure of metals irradiated above the low-temperature limit for void formation, vacancy loops are formed and persist during low-temperature irradiations. Vacancy loops are produced by collapse of platelets or disks of vacancies [Fig. 18.4(a)]. The latter are formed from the vacancies and small vacancy clusters in the depleted zone of a displacement spike. The mechanism by which the configuration shown in Fig. 17.27 transforms into a disk of vacancies is not known, but such platelets must be the intermediate step between the formless collection of vacancies in a displacement spike core and the regular configuration of a vacancy loop condensed on a close-packed plane. At the low temperatures where vacancy loops are observed, homogeneous nucleation of these defect clusters from the free vacancies in the matrix is virtually impossible because of the low value of the vacancy diffusion coefficient. Therefore, the vacancy platelets or vacancy loops must have originated from the complement of vacancies in the depleted zone created by the primary knock-on atom. Hesketh<sup>36</sup> has proposed a theory of irradiation creep based on the effect of stress on the propensity of vacancy disks to collapse into vacancy loops. This theory is reviewed here.

The process by which the depleted zone is transformed first into a vacancy platelet and then into a vacancy loop is depicted in Fig. 19.27. If the depleted zone contains  $m$  vacancies (either isolated or in small clusters), the radius of the vacancy platelet,  $R$ , formed from these vacancies is

$$m = \frac{\pi R^2}{a_0^2} \quad (19.207)$$

The disk is assumed to be 1 atom layer thick (i.e., a thickness equal approximately to a lattice constant  $a_0$ ). Figure 19.27(b) shows the platelet as a circular disk. However, computer simulation of the stability of shapes of this sort in metals shows that the disk will partially collapse near the center, in somewhat the same fashion that neighboring atoms relax into a single vacant lattice site. The relaxed or minimum-energy configuration is shown in Fig. 19.27(c). The computer studies also show that the distance separating the opposite faces of the platelet at the center,  $s$ , is given by

$$s = a_0 \left( 1 - \frac{R}{R_c} \right) \quad (19.208)$$

where  $R_c$  is the critical platelet radius beyond which total collapse into the loop of Fig. 19.27(d) is assured. The critical radius is related to the number of vacancies in the critical size disk by

$$m_c = \frac{\pi R_c^2}{a_0^2} \quad (19.209)$$

When  $R = R_c$  (or  $m = m_c$ ), the two faces of the disk just touch at the center, and this is the necessary condition for collapse of the entire platelet into a loop. Hesketh assumes that in small disks ( $m < m_c$ ) the platelets retain the

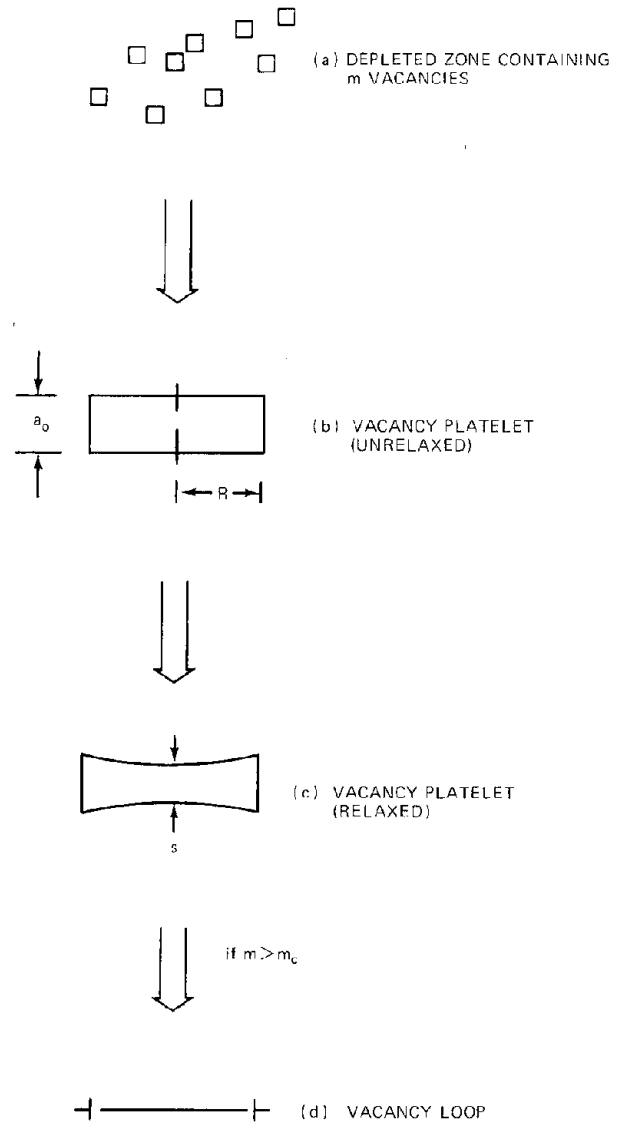


Fig. 19.27 Formation of vacancy disks and loops in an irradiated solid at low temperature.

configuration shown in Fig. 19.27(b) and that in disks larger than the critical size the platelets collapse to the loop configuration shown in Fig. 19.27(d).

We next determine how an applied stress perpendicular to the faces of the disk affects the critical size for collapse. Figure 19.28(a) shows that a compressive stress tends to reduce the central separation of the two faces. Conversely, tension would tend to bulge the two faces outward. The change in separation,  $s$ , due to the stress,  $\sigma$ , can be estimated by adapting the solution to a similar problem which has been treated by classical elasticity theory; this results in

$$s(\sigma) \simeq s(0) - \frac{4}{E} R\sigma \quad (19.210)$$

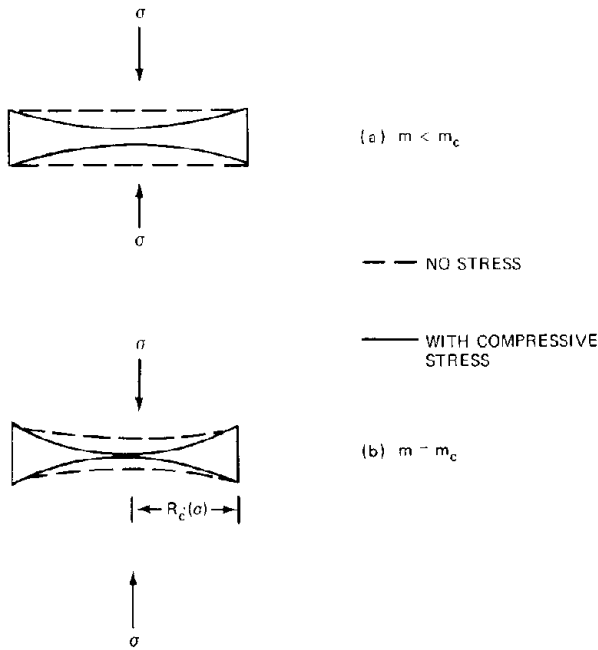


Fig. 19.28 Effect of stress on the shape of vacancy platelets.

where  $s(\sigma)$  is the separation of the faces at stress  $\sigma$  and  $E$  is Young's modulus.\* The stress effect suggested by Eq. 19.210 is plausible. Stress is more effective for large disks than for small ones and for weak solids (low  $E$ ) than for strong ones.

Figure 19.28(b) shows the disk that contains just the right number of vacancies to render  $s(\sigma) = 0$  (i.e., collapse occurs at this stress). The radius of such a disk,  $R_c(\sigma)$ , is less than the critical radius for collapse of a disk in a stress-free solid. The dashed lines show the configuration of a disk of the same radius when  $\sigma = 0$ . The interplanar separation  $s(0)$  can be obtained from Eq. 19.208 by setting  $R = R_c(\sigma)$  and  $R_c = R_c(0)$ :

$$s(0) = a_0 \frac{\Delta R_c}{R_c}$$

where  $\Delta R_c = R_c(0) - R_c(\sigma)$  and  $R_c(0)$  in the denominator has been denoted simply by  $R_c$ , since  $\Delta R_c$  is small compared to either  $R_c(\sigma)$  or  $R_c(0)$ .

Another expression for  $s(0)$  can be obtained by setting  $s(\sigma) = 0$  at  $R = R_c$  in Eq. 19.210, which gives

$$s(0) = \frac{4}{E} R_c \sigma$$

Equating the right-hand sides of the above two equations permits  $R_c$  to be written as

$$\Delta R_c = \frac{4 R_c^2}{E a_0} \sigma \tag{19.211}$$

The stress effect can be expressed in terms of the change in the number of vacancies in the critical-size disk by use of Eq. 19.209:

$$\Delta m_c = \left( \frac{dm_c}{dR_c} \right) \Delta R_c = \frac{2\pi R_c}{a_0^2} \Delta R_c \tag{19.212}$$

Substituting Eq. 19.211 into Eq. 19.212 and eliminating the ratio  $(R_c/a_0)^3$  by using Eq. 19.209 yields

$$\Delta m_c = \frac{8}{\pi^{3/2}} \frac{m_c^{3/2}}{E} \sigma \tag{19.213}$$

This formula gives the reduction in the critical size for disk collapse as a function of the applied compression. We next need the number of vacancy platelets formed in the solid which are affected by this alteration. Figure 19.29 shows a typical distribution of cluster sizes due to a single fast-neutron collision with a lattice atom. This distribution represents low-temperature irradiation, so the cluster distribution is not perturbed by vacancy or interstitial absorption from the matrix. Rather, Fig. 19.29 is supposed to represent the cluster distribution shown as the dashed histogram in Fig. 17.29(b). Hesketh takes the distribution to be of the form

$$N(m) = \frac{K}{m^2}$$

where  $K$  is a constant and  $N(m)$  is the number of depleted zones (or disks) formed from a single primary knock-on atom (PKA) which contain between  $m$  and  $m + dm$  vacancies.\* The distribution applies to depleted zones for

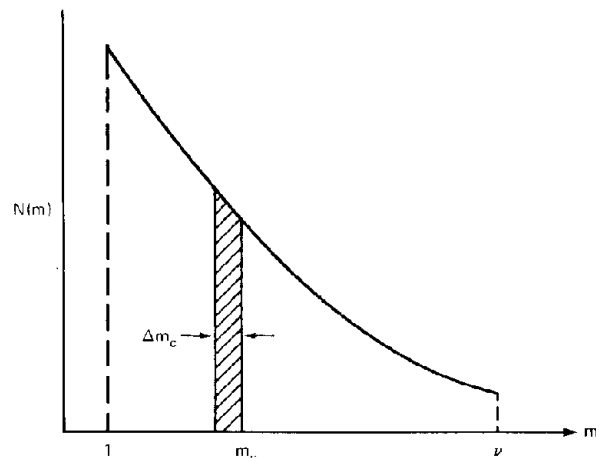


Fig. 19.29 Nascent cluster size distribution in an irradiated metal.

\*A factor  $1 - \nu^2$ , where  $\nu$  is Poisson's ratio, has been omitted from the second term on the right of Eq. 19.210 for simplicity. This factor is retained in Hesketh's analysis but is of no consequence numerically.

\*The cluster distribution shown in Fig. 19.29 is very different from that used in the analysis of depleted-zone annealing in Sec. 18.5. Here, the distribution consisted of two delta functions, one at  $m = 1$  and the other at the  $m$  value corresponding to a zone radius of  $R_0$ .

which  $1 < m \leq \nu$ , where  $\nu$  is the total number of Frenkel pairs created by a PKA (as calculated by isolated cascade theory, Sec. 17.7). For a typical fast-neutron spectrum,  $\nu \approx 500$  if annealing of the cascade is neglected. The constant  $K$  in the above distribution is determined by the requirement that the total number of vacancies contained in all clusters be equal to  $\nu$ , or

$$\nu = \int_1^{\nu} m N(m) dm$$

The preceding two equations yield  $K = \nu / \ln \nu$ , and the distribution is

$$N(m) = \left( \frac{\nu}{\ln \nu} \right) \frac{1}{m^2} \quad (19.214)$$

In an irradiated solid, vacancy platelets are formed with random orientations. Application of uniaxial stress does not change the randomness of the formation pattern. However, the vacancy disks that are perpendicular to the stress axis exhibit a different critical collapse size from the remaining platelets. Figure 19.30 shows a block of solid of dimensions  $x$ ,  $y$ , and  $z$  (perpendicular to the drawing) subject to compressive stress along the  $x$ -axis. Of the vacancy platelets formed by irradiation, one-third are of the perpendicular type, which are affected by the stress, and the remainder are not influenced by the stress.

The number of platelets created in the parallel orientation which collapse to vacancy loops is represented by the area under the distribution to the right of  $m_c$  in Fig. 19.29. Among the perpendicular-type platelets, all those to the right of the abscissa  $m_c - \Delta m_c$  are collapsed. The shaded area in Fig. 19.29, which is equal to  $N(m_c) \Delta m_c$ , represents the extra number of disks that are collapsed solely because the stress affects the perpendicular-type platelets but not the parallel-type disks. Because of the survival of a greater proportion of the parallel-type vacancy disks, the block of solid deforms more rapidly in the directions transverse to the stress axis than along it. The number of vacancies contained in the differential area in Fig. 19.29 is  $m_c N(m_c) \Delta m_c$ . The difference between the volume of empty space added per unit time to each of the two parallel-type disks (oriented perpendicular to the  $y$  and  $z$  axes) and that in the  $x$ -direction is

$$\begin{aligned} \frac{1}{3} \Sigma_s \Phi (XYZ) \Omega m_c N(m_c) \Delta m_c &= (XZ) \frac{dY}{dt} \\ &- (YZ) \frac{dX}{dt} = (XY) \frac{dZ}{dt} - (YZ) \frac{dX}{dt} \end{aligned}$$

Or, in terms of the strain rates in the principal directions,

$$\dot{\epsilon}_y - \dot{\epsilon}_x = \dot{\epsilon}_z - \dot{\epsilon}_x = \frac{1}{3} \Sigma_s \Phi \Omega m_c N(m_c) \Delta m_c \quad (19.215)$$

where

$$\dot{\epsilon}_x = \frac{1}{X} \frac{dX}{dt}$$

$$\dot{\epsilon}_y = \frac{1}{Y} \frac{dY}{dt}$$

$$\dot{\epsilon}_z = \frac{1}{Z} \frac{dZ}{dt}$$

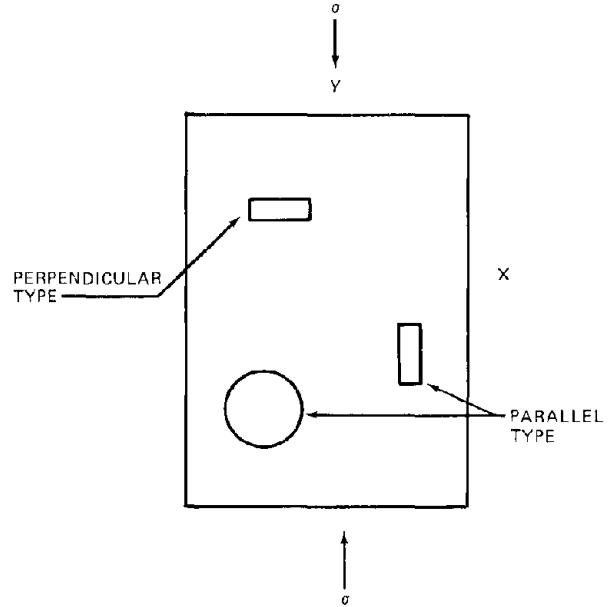


Fig. 19.30 Vacancy platelets in an irradiated solid.

Because uncollapsed platelets are present in disks of all orientations in the solid, continual buildup of disk volume occurs, and the solid undergoes volumetric swelling as well as creep (the latter is due to relative deformation in the three principal directions). The volume swelling rate is given by

$$\left( \frac{\Delta V}{V} \right) = 3\dot{\epsilon}_y = 3\dot{\epsilon}_z \quad (19.216)$$

The creep strain along the  $x$ -axis is the difference between the total strain rate in this direction and the component of volumetric swelling, or

$$(\dot{\epsilon}_x)_{\text{creep}} = \left| \dot{\epsilon}_x - \frac{1}{3} \left( \frac{\Delta V}{V} \right) \right| = \frac{1}{3} \Sigma_s \Phi \Omega m_c N(m_c) \Delta m_c$$

Using Eq. 19.214 for  $N(m_c)$  and Eq. 19.213 for  $\Delta m_c$ , we find the irradiation creep induced by the compressive stress to be

$$\begin{aligned} (\dot{\epsilon}_x)_{\text{creep}} &= \left[ \frac{8}{3\pi^{1/2}} \frac{1}{E} \left( \frac{\nu}{\ln \nu} \right) (m_c)^{1/2} \Omega \Sigma_s \right] \sigma \Phi \\ &= C \sigma \Phi \end{aligned} \quad (19.217)$$

Comparison of Eq. 19.217 with the second term on the right side of Eq. 19.176 shows that the coefficient  $C$  can be identified with the bracketed term in the above formula. Determining a numerical value from the parameters

$$\begin{aligned} E &= 2.1 \times 10^8 \text{ kN/m}^2 \\ \Omega &= 12 \text{ \AA}^3 \\ \Sigma_s &= 0.2 \text{ cm}^{-1} \\ \nu &= 500 \\ m_c &= 200 \end{aligned}$$

we find  $C$  to be  $20 \times 10^{-30} \text{ cm}^2 \text{ kN}^{-1} \text{ m}^{-2}$ . Experimental values of this coefficient obtained from in-pile creep tests

on steel are shown in Fig. 19.31. There is quite good agreement between the magnitude of the theoretical and observed creep-rate coefficients. However, the theory does not predict the pronounced decrease in  $C$  with temperature (this behavior is also contrary to thermal creep, which should increase rapidly with temperature). The absence of a temperature effect in the theory just presented arises from the implicit assumption that all the uncollapsed vacancy platelets formed in the collision cascade are stable indefinitely in the irradiated solid. That is, their number simply increases linearly with time (or fluence). Had the theory included destruction of the vacancy platelets by vacancy emission to the bulk of the solid or by absorption of the radiation-produced interstitials (which are mobile at the temperatures for which  $C$  has been measured), the number of surviving disks would have decreased drastically with increasing temperature. Thus, although the rapid drop of  $C$  with temperature is not explicitly included in Hesketh's analysis, this observation is at least consistent with his model.

The continuous (and linear) increase in the number of uncollapsed loops with time is responsible for the fact that the theoretical creep rate is constant (i.e., creep is steady state). However, as shown in problem 19.18 at the end of this chapter, lack of a mechanism for removal of vacancy platelets smaller than the critical size for collapse leads to predicted swellings which are far larger than have been observed in low-temperature irradiations (although low-temperature swelling due to accumulation of depleted zones and their progeny, vacancy disks, has been observed; see Fig. 16 of Ref. 33).

Contrary to the transient creep mechanism discussed earlier in this section, steady-state creep by stress-assisted vacancy disk collapse is irreversible. When the stress is removed, the extra  $N(m_c) \Delta m_c$  disks that were collapsed because of the stress do not spontaneously pop back into

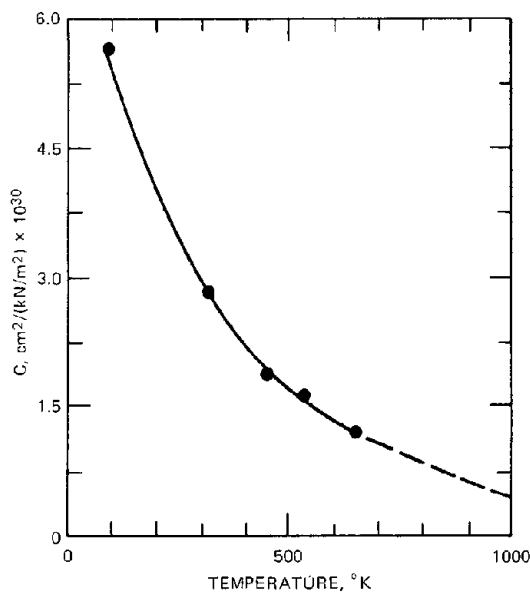


Fig. 19.31 Temperature dependence of the irradiation creep coefficient  $C$  (Ref. 33).

platelets. Thus, the creep strain persists. However, a difficulty arises if the theory is applied to creep induced by tension rather than compression. In the former case,  $N(m_c) \Delta m_c$  represents extra platelets perpendicular to the stress which have not collapsed because stress aids in their survival by causing the disk faces to bulge outward. When this stress is removed, one would expect that platelets larger than the stress-free critical size would no longer be stable and that collapse would occur, thereby removing the creep deformation established during the time that the tensile stress was applied.

### 19.7.3 Steady-State Creep Due to Stress-Oriented Nucleation of Interstitial Loops

At temperatures roughly bracketed by the onset of observable void formation and peak swelling (about 350 to 500°C in stainless steel), irradiation creep can be produced by preferential nucleation of interstitial loops on suitably oriented planes by the prevailing stress state. This mechanism was first proposed by Hesketh<sup>37</sup> and has subsequently been applied to stainless steel by Lewthwaite,<sup>38</sup> Wolfer et al.,<sup>39</sup> and Brailsford and Bullough.<sup>40</sup>

During irradiation interstitials nucleate into loops on a particular set of planes in the solid (e.g., the  $\{111\}$  planes in the fcc lattice). Loop nuclei formed on planes favorably oriented with respect to the applied stress have a greater chance of surviving than those created on planes where the nucleation process is unaffected by the stress. Although there are many sets of equivalent  $\{111\}$  planes in the fcc lattice, for simplicity we consider only the planes perpendicular to the applied stress (called perpendicular type) and those lying along the stress axis (parallel type). There are twice as many of the latter as of the former. The situation can be visualized by regarding the objects in the block shown in Fig. 19.30 as interstitial dislocation loops and considering the case of an applied tension rather than compression (although this is not an important choice).

Because stress favors the nucleation of perpendicular-type loops, there will be a slightly higher concentration of these clusters than of either of the two parallel-type loops on the planes lying along the stress direction. In addition to preferential loop nucleation on planes perpendicular to the tensile axis, the growth of the perpendicular-type loops is somewhat more rapid than that of the parallel-type loops. However, this effect has been shown to be of secondary importance<sup>40</sup> and will be neglected here.

Preferential nucleation of the perpendicular-type loops occurs because this orientation allows the applied stress to do work on the circular dislocation line as it grows. The energy of formation is lowered by the amount of external work communicated to the system in this manner. Consider generation of a loop from zero size to the critical nucleation radius  $R_{1c}$ . The stress has no bearing on the formation process for parallel-type loops, and the energy of the critical-size loop (assuming that the loop can be regarded as a macroscopic dislocation line with a line tension  $\tau_d$ ) is

$$E_{\parallel} = 2\pi R_{1c} \tau_d \quad (19.218)$$

However, a tensile stress  $\sigma$  exerts a force  $\sigma b$  per unit length in the outward radial direction of growing perpendicular-type loops [see Fig. 8.10(b)]. As the loop expands from radius  $R_1$  to  $R_1 + dR_1$ , the change in energy is

$$dE_1 = 2\pi\tau_d dR_1 - 2\pi R_1 \sigma b dR_1$$

or, upon integrating from  $R_1 = 0$  to  $R_1 = R_{1c}$ ,

$$E_1 = 2\pi R_{1c} \tau_d - \pi R_{1c}^2 \sigma b \quad (19.219)$$

Assuming that the probability of nucleating a loop in a particular orientation is proportional to a Boltzmann factor involving the energy of formation, the relative nucleation rates of the perpendicular and parallel-type loops are related by\*

$$\frac{P_{\perp}}{P_{\parallel}} = \frac{\exp(-E_1/kT)}{\exp(-E_{\parallel}/kT)} = \exp\left(\frac{\pi R_{1c}^2 \sigma b}{kT}\right) \quad (19.220)$$

The probabilities of nucleating loops on either of the two types of orthogonal planes must sum to unity:

$$P_{\perp} + 2P_{\parallel} = 1 \quad (19.221)$$

The area per atom on the (111) plane of the fcc structure is  $3^{1/2} a_0^2/4$  and the Burgers vector of the  $a_0/3$  (111) faulted dislocation loop is  $b = a_0/3^{1/2}$ . Therefore, the number of interstitials in a dislocation loop of radius  $R_1$  is

$$m_i = \frac{4\pi R_1^2}{3^{1/2} a_0^2} = \frac{\pi R_1^2 a_0}{3^{1/2} \Omega} = \frac{\pi R_1^2 b}{\Omega} \quad (19.222)$$

Where the relation between atomic volume and lattice constant for the fcc structure,  $\Omega = a_0^3/4$ , has been employed. Using Eq. 19.222 (with a subscript c attached to  $m_i$  and  $R_1$  to denote the critical-size loop) in Eq. 19.220 and combining the latter with Eq. 19.221 yields

$$P_{\perp} = \frac{\exp(m_{ic}\sigma\Omega/kT)}{2 + \exp(m_{ic}\sigma\Omega/kT)} \approx \frac{1}{3} \left(1 + \frac{2m_{ic}\sigma\Omega}{kT}\right) \quad (19.223)$$

where Taylor series expansions have been applied to the exponential terms. If the total density of interstitial loops is  $N_1$  (given, for example, by Eq. 19.18), the number density of perpendicular-type loops is  $P_{\perp}N_1$ , which is greater than the density of loops on either of the two sets of planes parallel to the stress axis. At some time during irradiation, the radii of all the loops will have grown from  $R_{1c}$  to  $R_1$ , but, because the effect of stress on growth subsequent to nucleation has been neglected,  $R_{1\perp} = R_{1\parallel} = R_1$ . The loop radius can be obtained from Eq. 19.16.

The number of interstitial atoms per unit volume contained in the perpendicular type loops is  $m_i N_1 P_{\perp}$ , where  $m_i$  is related to the loop radius by Eq. 19.222. If loop nucleation had occurred in the absence of stress, the number of interstitials per unit volume in loops of all orientations would have been  $m_i N_1/3$  (i.e.,  $P_{\perp} = 1/3$ ). Therefore, the additional number of interstitials present in the

perpendicular-type loops as a result of the slightly greater number of these clusters is

Extra atoms in perpendicular-type loops/cm<sup>3</sup>

$$= m_i N_1 \left(P_{\perp} - \frac{1}{3}\right)$$

Following the lines of the argument leading to Eq. 19.198, the creep strain due to these extra loops in planes perpendicular to the stress is

$$\frac{\delta X}{X} = \epsilon_x = m_i \Omega N_1 \left(P_{\perp} - \frac{1}{3}\right)$$

Or, using Eqs. 19.223 and 19.222,

$$\epsilon_x = \frac{2}{9} (\pi R_{1c}^2 N_1 b) \frac{m_{ic} \Omega \sigma}{kT} \quad (19.224)$$

If the critical loop nucleus is known ( $m_{ic}$  is probably about 3 but can be as large as 10) and experimental information on loop size and density during irradiation are known, Eq. 19.224 determines the creep rate. Alternatively, the fluence dependence of  $R_1$  and  $N_1$  can be obtained theoretically from the point-defect balances, the void and loop growth laws, and the nucleation rates of these two defect clusters (Secs. 19.4 and 19.5). This approach is used in Ref. 40. Consideration of all the equivalent set of {111} planes in the fcc lattice, rather than simply an orthogonal set of three, reduces the above creep rate expression by a constant factor of 2.5 (Ref. 38).

Attempts have been made to connect the creep strain to the void swelling. This is done by assuming that the number of interstitials contained in loops is equal to the number of vacancies in voids. A bit of consideration shows that the parenthetical term in Eq. 19.224 is equal to the fractional swelling of the solid due to the loops, and if this volume increase is equal to that due to the voids ( $\Delta V/V$ ), we have

$$\epsilon_x = \frac{2}{9} \left(\frac{\Delta V}{V}\right) \frac{m_{ic} \Omega \sigma}{kT} \quad (19.225)$$

There is no theoretical justification for the assignment of equal numbers of interstitials in loops and vacancies in voids. Excess interstitials can be absorbed by the network dislocations in the solid provided that the latter are free to climb. Interstitial loops disappear from the microstructure above about 500°C (Fig. 19.7), but the voids persist to above 600°C. Consequently, Eq. 19.224 is preferred to Eq. 19.225 if information on the fluence and temperature dependence of loop size and density is available. However, Eq. 19.225 can be modified by multiplication by the fraction of the total dislocation density contained in loops (i.e., one minus Eq. 19.15) and in this way be rendered a reasonably accurate predictor of the creep rate even when the loops and voids do not contain equal numbers of point defects.<sup>40</sup>

The model of irradiation creep just described is unique in that the stress affects only the nucleation process. Thus, if the specimen is unloaded after loop nucleation has occurred (and perturbed by the stress), the creep persists during stress-free growth. Conversely, application of the stress after nucleation has been completed should not produce this sort of irradiation creep.

\*The same result is obtained by proceeding through homogeneous nucleation theory with the formation energy of a loop reduced by the right term of Eq. 19.219. The exponential terms in Eqs. 19.77 and 19.78 would be increased by the term containing the stress.

### 19.7.4 Climb-Controlled Dislocation Glide

The effect of irradiation on creep controlled by diffusion of point defects to sinks in the solid was discussed in Sec. 16.10 in connection with the fuel. It was shown that radiation-produced point defects do not accelerate the normal creep rate when the sinks are grain boundaries. The same conclusion is reached when the sinks are dislocations and creep is entirely due to climb of the dislocations. However, the class of creep mechanisms constructed by Weertman (Refs. 24 and 25 in Chap. 16) are susceptible to enhancement by irradiation. It will be recalled from Sec. 16.8 that this type of creep involves climb of mobile dislocations either over obstacles in the glide plane or toward a dislocation of opposite sign in an adjacent parallel slip plane. Creep occurs in the first type when the mobile dislocation reaches the top of the barrier and quickly glides to the next obstacle, and, in the second type, when the pileup expands by glide to replenish one of its members that has been annihilated by an opposing dislocation from the adjacent slip plane. The separation of the rate controlling process (climb) from the strain controlling step (glide) in these mechanisms is essential to the existence of an irradiation effect on the creep rate.

The effect of irradiation on diffusional creep processes (which include the climb-controlled glide variant) has long been the subject of dispute (see Refs. 38 to 43 in Chap. 16). On the basis of recent investigations (Refs. 21, 39, and 41 to 44), irradiation enhancement of Weertman-type creep requires an imbalance in the rates at which dislocations absorb interstitials and vacancies produced by fast-neutron bombardment of the metal. In the sections on void swelling in this chapter, we showed that absorption of excess interstitials by the intrinsically biased dislocations can occur only if another sink that consumes excess vacancies is also present. At high temperatures the vacancy sinks fulfilling this role are undoubtedly the voids, but at low temperatures depleted zones can perform the same function.

Irradiation creep by the climb-controlled glide mechanism is due to the climb velocity  $(v_c)_{irr}$  with which the dislocation is endowed by virtue of capturing excess interstitials. For irradiation creep to be of significance,  $(v_c)_{irr}$  must be at least comparable to the climb velocity  $(v_c)_{th}$  induced in the blocked mobile dislocation by the stress arising from interaction with obstacles (Sec. 16.8). Irradiation simultaneously serves to reduce the creep rate because the obstacles that the mobile dislocation must climb over and glide between are either the voids and interstitial loops in the temperature range where swelling occurs or the depleted zones at low temperatures. The size and density of these clusters increase with fluence. These obstacles are responsible for the increased strength of irradiated metals (Secs. 18.5 to 18.7). They are also the cause of decreased creep rates in postirradiation tests, which should not be confused with in-pile irradiation creep. The former is a structural effect since the creep mechanisms are the same as in an irradiated metal, and only the nature and density of the obstacles to dislocation motion are affected by irradiation. In-pile, or irradiation, creep, which contains the additional element of enhanced climb by

absorption of point defects, is sometimes called dynamic creep to emphasize the importance of the neutron flux as well as the neutron fluence.

Creep due to climb-controlled glide of mobile dislocations in an irradiated solid can be analyzed by starting from the general formula relating strain rate and dislocation velocity (Eq. 8.21):

$$\dot{\epsilon} = \rho_m b v_d \quad (19.226)$$

where  $\rho_m$  is the density of mobile dislocations in the solid, which is generally less than the total dislocation density  $\rho_d$ . Part of  $\rho_d$  may consist of unfaulted interstitial loops that are sessile (i.e., not mobile), or are pinned by voids or enmeshed in dislocation tangles. The  $b$  is the Burgers vector of the mobile dislocation; and  $v_d$  is the average velocity of the moving dislocation, which is the ratio of the average distance that a mobile dislocation glides between obstacles and the time required for it to climb over the obstacle:

$$v_d = \frac{l}{(h/v_c)} \quad (19.227)$$

Here,  $l$  is the glide distance,  $h$  is the distance perpendicular to the glide plane which the mobile dislocation must climb in order to surmount the obstacle, and  $v_c$  is the climb velocity;  $h/v_c$  is the average time required for the dislocation to overcome the barrier by climb.

We imagine the obstacles to be arranged on the glide plane in a square array with the spacing given by Eq. 18.25:

$$l = \frac{1}{(2RN)^{1/2}} \quad (19.228)$$

where  $R$  and  $N$  are the radius and density, respectively, of the obstacles, which may be depleted zones, voids, or interstitial loops. The applied stress is assumed to be less than that at which the dislocation can pass through the array by cutting through the obstacles or by bowing around them and pinching off. In the present case the dislocation line must climb to a critical height perpendicular to the slip plane at which point the applied stress is sufficient to permit slip to continue. A two-dimensional view of the process is shown in Fig. 19.32. Rows of obstacles are viewed end-on. The separation of the spherical obstacles in the direction perpendicular to the drawing is the same as the distance between rows in the glide plane, namely  $l$ . If the obstacles in the real solid were arranged in the perfect square pattern used in the analysis, climb of a blocked dislocation over one row would be sufficient for the dislocation to slip past all the subsequent rows. However, this deficiency of the idealized model should not be taken too seriously since in an actual irradiated solid the random arrangement of obstacles ensures that a mobile dislocation will be stopped by obstacles after gliding from its previous pinning position a distance given, on the average, by Eq. 19.228.

Determination of the creep rate is reduced to calculating the obstacle height  $h$  and the climb velocity  $v_c$ .

We first consider the situation proposed by Harkness et al.<sup>43</sup> in which the obstacles to be overcome by climb are voids. Inasmuch as voids attract dislocation lines (Sec. 18.6), the first dislocation approaching the row of voids is trapped by them, in a sequence of events similar to

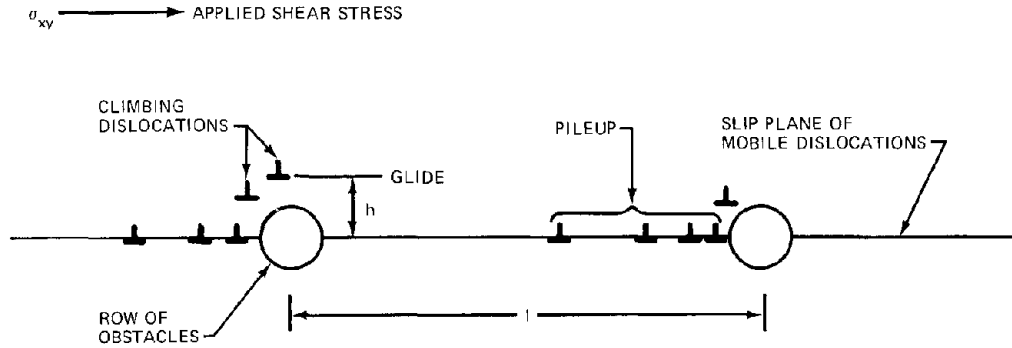


Fig. 19.32 Dislocation motion over irradiation-produced obstacles in the climb-controlled dislocation glide model of irradiation creep.

that shown in Fig. 18.22(b) except for the final pinching off (which does not occur here because the stress is less than the yield stress for this process). Succeeding mobile dislocations, however, are repelled by the first dislocation that has been sucked into the void row. They must climb over the trapped dislocation to continue on their way.

In the absence of irradiation, the climb process is identical to that analyzed in Sec. 16.7 (climb-to-escape model). The probability per unit time that a dislocation climbs over the pinned dislocation is given by Eq. 16.73, which can be used to define an average thermal climb velocity by

$$p = \frac{1}{C\tau_c} = \frac{(v_c)_{th}}{h} \quad (19.229)$$

where the barrier height  $h$  is given by Eq. 8.35 in which, to account for a dislocation pileup behind the trapped dislocation,  $\sigma_{xy}$  is multiplied by the intensification factor  $n$  of Eq. 8.39:

$$h = \frac{K}{4n\sigma_{xy}} = \frac{Gb}{8\pi(1-\nu)n\sigma_{xy}} \quad (19.230)$$

In Eq. 19.229  $C$  is a coefficient that arises from averaging the climb process over all impact parameters separating the slip planes of the trapped dislocation and the impinging mobile dislocation (Eq. 16.72), and  $\tau_c$  is a characteristic time for dislocation climb. When the climb velocity is based on the jog density of the line (i.e., Eq. 16.55),  $\tau_c$  is given by Eq. 16.67. If, on the other hand, the entire dislocation line maintains the equilibrium vacancy concentration appropriate to the stress acting on it, the climb velocity is given by Eq. 16.58, and  $\tau_c$  becomes

$$\tau_c = K \left[ \frac{\ln(\mathcal{R}/r_d)}{2\pi} \right] \frac{kTb}{D_{vo1}\Omega n^2 \sigma_{xy}^2} \quad (19.231)$$

Substituting Eqs. 19.230 and 19.231 into Eq. 19.229 and using Eq. 8.39 for  $n$  yields

$$(v_c)_{th} = \frac{\pi^2(1-\nu)}{2C \ln(\mathcal{R}/r_d)} \frac{D_{vo1}b\sigma_{xy}^2}{kTG} \quad (19.232)$$

where the length of the pileup in Eq. 8.39 has been taken as the spacing between obstacle rows.

Under neutron irradiation the velocity of dislocation climb is no longer governed by the thermal processes

inherent in the value given by Eq. 19.232. Instead, it is determined by the flow of interstitials and vacancies to the dislocations. Let  $J_i^d$  and  $J_v^d$  be the fluxes of interstitials and vacancies, respectively, to a unit length of dislocation line (Eq. 13.89). The net rate at which interstitials arrive at the line is  $J_i^d - J_v^d$ , and, since each interstitial contributes a volume  $\Omega$ , the rate at which the half-sheet of atoms comprising the edge dislocation gains volume is  $(J_i^d - J_v^d)\Omega$   $\text{cm}^3 \text{sec}^{-1} \text{cm}^{-1}$  of line. In  $\Delta t$  sec, each unit length of line gains a volume of  $(J_i^d - J_v^d)\Omega \Delta t$ , which is equal to the product of the width of the half-sheet of atoms,  $b$ , and the distance climbed in  $\Delta t$ , which is  $(v_c)_{irr} \Delta t$ . Thus, the climb velocity due to the net flow of irradiation-produced interstitials to the line is

$$(v_c)_{irr} = \frac{(J_i^d - J_v^d)\Omega}{b} \simeq (J_i^d - J_v^d) b^2 \quad (19.233)$$

Equation 19.233 demonstrates that the climb of dislocations caused by irradiation is due to precisely the same phenomenon that is responsible for void growth, namely, the bias of dislocation lines for interstitials.

The irradiation creep rate is obtained by combining Eqs. 19.226 and 19.227 and using Eq. 19.230 for  $h$  and Eq. 19.233 for  $v_c$ , which yields

$$\dot{\epsilon}_{irr} = \rho_m l \frac{8\pi(1-\nu)n\sigma_{xy}}{G} (J_i^d - J_v^d) b^2 \quad (19.234)$$

Now we note that the product of  $(J_i^d - J_v^d)$  and the total dislocation density of the solid,  $\rho_d$ , is the difference in the volumetric sink strengths of the dislocations for interstitials and vacancies, or

$$\rho_d(J_i^d - J_v^d) = Q_i^d - Q_v^d \quad (19.235)$$

where  $Q_i^d$  and  $Q_v^d$  are given by Eqs. 19.101 and 19.102, in which the notation  $N$  (representing the network dislocations) is replaced by  $d$  (representing all dislocations). For the present analysis the distinction between dislocation lines and dislocation loops is neglected. The irradiation creep rate can be related to void swelling by using the point-defect balances given by Eqs. 19.134 and 19.135. As before, we combine network dislocations and interstitial loops into the total dislocation density. Subtraction of one of the point-defect balances from the other shows that

$$Q_i^d - Q_v^d = Q_v^{void} - Q_i^{void} \quad (19.236)$$

which states that, in the absence of sinks other than voids and dislocations, the net flow of interstitials to dislocations is just equal to the net flow of vacancies to voids. Finally, the swelling rate is given by

$$\frac{d}{dt} \left( \frac{\Delta V}{V} \right) = \left( \frac{\Delta V}{V} \right) = (Q_v^{\text{void}} - Q_i^{\text{void}}) \Omega \quad (19.237)$$

Combining the preceding four equations and expressing the number of dislocations in the pileup by Eq. 8.39 yields the irradiation creep rate according to this model:

$$\dot{\epsilon}_{\text{irr}} = \left( \frac{\rho_m}{\rho_d} \right) \left[ \frac{8\pi^2(1-\nu)^2}{G^2} \right] \frac{l^2 b}{\Omega} \left( \frac{\Delta V}{V} \right) \sigma_{xy}^2 \quad (19.238)$$

which shows the direct connection between the swelling rate and the irradiation creep rate.

The creep rate under irradiation is less stress dependent than is the thermal creep rate. If Eq. 19.232 had been used in place of Eq. 19.233 in the foregoing derivation, the stress exponent would have been 4 instead of 2. If the mobile dislocation density is low or if the swelling rate is large, the mobile dislocations can climb over the dislocations trapped by the voids so quickly that pileups do not have time to develop. In this case we set  $n = 1$  wherever it appears, with the result that the irradiation and thermal creep rates are proportional to  $\sigma_{xy}$  and  $\sigma_{xy}^2$ , respectively. In any case the exponent of the stress is lower in irradiation creep than in thermal creep, and this prediction is confirmed by experiment.

The irradiation creep rate has a somewhat narrower temperature range than does the swelling rate. When the temperature is low, a substantial part of the total dislocation density is present as faulted loops, which cannot glide; so  $\rho_m/\rho_d$  is low. In addition,  $(\Delta V/V)$  is small at low temperatures, and the irradiation creep rate is reduced by both these factors. At the high-temperature extreme, irradiation creep by this mechanism ceases when the voids do not grow (i.e., when  $\Delta V/V \rightarrow 0$  at  $T \approx 600^\circ\text{C}$  in stainless steel). At sufficiently high temperature, the rapidly increasing thermal climb velocity given by Eq. 19.232 overtakes the irradiation-induced climb velocity, and normal Weertman thermal creep supplants irradiation creep as the principal deformation mechanism. Similarly, the  $\sigma_{xy}^2$  dependence of the thermal climb velocity implies that, at any temperature, thermal creep dominates irradiation creep if the applied stress is sufficiently high (but not high enough for the dislocations to cut through or bypass the voids by bowing and pinching off).

Equation 19.238 implies that the irradiation creep rate decreases with increasing fluence because the size and perhaps the density of voids increases during irradiation. According to Eq. 19.228, the obstacle separation is decreased accordingly.

The most difficult term in Eq. 19.238 to predict is the fraction of the total dislocation population which is mobile. Harkness et al.<sup>4,3</sup> identify the mobile dislocations with the line length of unfaulted loops in the microstructure. They assume that Frank loops unfault when  $R = 500 \text{ \AA}$  and consider that when the average loop radius exceeds this value,  $\rho_m/\rho_d = 1$ . When the average loop size is less than  $500 \text{ \AA}$ , they employ the approximation

$$\frac{\rho_m}{\rho_d} = \frac{R_1(\text{\AA})}{500}$$

where  $R_1$  is a function of fluence as determined by solution of the loop-growth law, which is obtained in the course of solving the void swelling (by the method shown in Fig. 19.23).

In addition to the voids, interstitial loops provide barriers to dislocation motion of strength comparable to that of the voids. Wolfer et al.<sup>3,9</sup> have formulated the climb-controlled glide model described above with loops instead of voids as obstacles. The loops directly repel mobile dislocations that approach them. The applied stress necessary to force a dislocation line past a row of loops of radius  $R_1$  separated by a distance  $l$  is given by combining Eqs. 18.54 and 18.58:

$$\sigma_{xy} = \frac{\alpha G b_1}{2(1-\nu)} \frac{R_1^2}{ly^2}$$

where  $y$  is the distance between the row of loops and the glide plane of the mobile dislocation. If the row of loops lies in the glide plane of the approaching dislocation and if the applied stress is too low for the line to penetrate the row (i.e., if  $\sigma_{xy} < \sigma_s$  of Eq. 18.61), the line has to climb by a height  $y$  in order to continue slip. Therefore,  $y$  can be written as the barrier height  $h$ . If we allow for dislocation pileup behind the row of loops by replacing  $\sigma_{xy}$  by  $n\sigma_{xy}$ , the above formula can be solved for the barrier height in terms of the applied stress:

$$h = \left[ \frac{\alpha G b_1}{2(1-\nu)} \frac{R_1^2}{nl\sigma_{xy}} \right]^{1/2} \quad (19.239)$$

If the previous derivation is repeated using Eq. 19.239 instead of Eq. 19.230 for  $h$ , the irradiation creep rate is found to be

$$\dot{\epsilon}_{\text{irr}} = \left( \frac{\rho_m}{\rho_d} \right) \left[ \frac{2\pi(1-\nu)}{\alpha G^2} \right]^{1/2} \frac{l^2}{R_1 b} \left( \frac{\Delta V}{V} \right) \sigma_{xy} \quad (19.240)$$

which, when compared with Eq. 19.238 for void obstacles, shows a lower stress dependence (linear instead of squared) and a greater penalty due to fluence because of the factor  $R_1$  in the denominator.

As a final example of climb-controlled glide models of irradiation creep, Duffin and Nichols<sup>4,4</sup> have advanced a mechanism in which the obstacles are depleted zones. In this model the swelling rate does not appear because depleted zones and voids do not coexist in an irradiated metal.

## 19.8 NOMENCLATURE

- $a_0$  = lattice constant
- $\mathcal{A}$  = area swept out by bowing of pinned dislocation segment
- A, B, C = constants in creep formula, Eq. 19.176
- $b$  = length of Burgers vector
- B = binding energy of a diinterstitial
- C = point-defect concentration (particles per unit volume); constant given by the right side of Eq. 16.72

$C^*$  = point-defect concentration at the surface of a coherent precipitate  
 $D$  = point-defect diffusion coefficient  
 $D_{vol}$  = volume self-diffusion coefficient  
 $E_{loop}$  = energy of a loop  
 $E_{void}$  = energy of a void  
 $f(R, \mathcal{R}, l)$  = function defined by Eq. 19.157  
 $F$  = force on a dislocation  
 $F(1/\mathcal{R})$  = function defined by Eq. 19.199  
 $F(\eta)$  = function defined by Eq. 19.142  
 $g$  = gibbs free energy of a cluster  
 $G$  = shear modulus; total Gibbs free energy  
 $h$  = climb height for a dislocation to overcome a barrier; enthalpy of a cluster  
 $h(m)$  = function defined by Eq. 19.43  
 $H$  = coefficient of  $M$  in Eq. 19.56  
 $I$  = nucleation current or void current  
 $j$  = gas atoms in a cluster  
 $J$  = flux of point defects to a cluster  
 $J^d$  = flux of point defects to a unit length of dislocation  
 $k$  = Boltzmann's constant; rate constant  
 $k_{iv}$  = vacancy-interstitial recombination rate constant  
 $K$  = coefficient of  $m^{1/2}$  in Eq. 19.6; given by Eq. 8.30  
 $l$  = distance between dislocation pinning points  
 $\mathcal{L}$  = length of a bowed dislocation segment  
 $m$  = vacancies per void or per vacancy loop; interstitials per interstitial loop  
 $M$  = total helium concentration in metal  
 $M_j$  = density of helium atom clusters containing  $j$  helium atoms  
 $n$  = number of dislocations in a pileup; number of point defects in a region of solid  
 $N$  = total number of voids per unit volume  
 $N(R)$  = void distribution function  
 $N_1$  = number of faulted dislocation loops per unit volume  
 $N_p$  = number of precipitate particles per unit volume  
 $N_s$  = number of lattice sites per unit volume  
 $p$  = helium pressure  
 $P$  = probability of nucleating a loop of a particular orientation  
 $Q_k^j$  = rate of absorption of a point defect of type  $k$  by all the defect clusters of type  $j$  in a unit volume of solid  
 $r_d$  = radius of a dislocation core  
 $R$  = rate of reaction; radius of a void  
 $\dot{R}$  = void growth rate  
 $\dot{R}_e$  = negative of void-shrinkage rate due to vacancy emission  
 $\dot{R}_0$  = void-growth rate in the absence of recombination and thermal emission of vacancies  
 $R_0$  = size of defect clusters created by collision cascade  
 $R_1$  = radius of a faulted dislocation loop  
 $\mathcal{R}$  = radial extent of the stress field around a dislocation; radius of curvature of a bowed dislocation line  
 $s$  = entropy of a cluster; distance between opposite faces of a vacancy platelet

$S$  = supersaturation of point defect  
 $t$  = time  
 $T$  = temperature, °K  
 $v_c$  = climb velocity of a dislocation  
 $v_d$  = glide velocity of a dislocation  
 $V$  = volume  
 $\Delta V$  = volume increase  
 $w$  = jump frequency  
 $W$  = combinatorial number  
 $x$  = defined by Eq. 19.146  
 $X, Y, Z$  = dimensions of a crystal  
 $Y$  = defined by Eqs. 19.129 and 19.130  
 $z$  = combinatorial number  
 $Z$  = combinatorial number for dislocations, Eqs. 19.99 and 19.100

#### Greek Letters

$\alpha$  = point-defect emission rate from a cluster  
 $\beta$  = point-defect arrival rate at a cluster  
 $\epsilon$  = creep strain; energy of formation  
 $\dot{\epsilon}$  = creep rate  
 $\epsilon_g$  = heat of solution of helium in metal  
 $\epsilon^*$  = energy of migration of a point defect  
 $\eta$  = dimensionless parameter, Eq. 19.143a  
 $\gamma$  = surface tension  
 $\gamma_{sf}$  = stacking-fault energy  
 $\gamma^*$  = defined by Eq. 19.122  
 $\mu$  = chemical potential  
 $\nu$  = vibration frequency; point defects produced per PKA  
 $\Omega$  = atomic value  
 $\Phi$  = total fast-neutron flux  
 $\rho_d$  = total dislocation density  
 $\rho_l$  = dislocation density as faulted loops  
 $\rho_m$  = density of mobile dislocations  
 $\rho_N$  = dislocation density due to perfect loops and the network dislocations  
 $\sigma$  = hydrostatic stress (positive in tension)  
 $\sigma_{xy}$  = shear stress  
 $\Sigma_s$  = macroscopic neutron-scattering cross section  
 $\tau$  = time  
 $\tau_d$  = line tension of a dislocation  
 $\theta$  = fraction of sites on trapping interface occupied by point defects;  $T=623$ , °K  
 $\xi$  = defined by Eq. 19.34

#### Subscripts and Superscripts

$c$  = in critical embryo or critical-size vacancy platelet  
 $eq$  = equilibrium  
 $f$  = forward reaction  
 $homo$  = homogeneous nucleation  
 $i$  = interstitial  
 $irr$  = due to irradiation  
 $m$  = containing  $m$  point defects  
 $nucl$  = nucleation  
 $p$  = precipitate particles  
 $r$  = reverse reaction  
 $th$  = due to thermal process  
 $v$  = vacancy

⊥ = edge dislocation with extra half-sheet of atoms perpendicular to applied stress; loop perpendicular to stress

∥ = edge dislocation with extra half-sheet of atoms parallel to the applied stress; loop parallel to the stress

## 19.9 REFERENCES

- C. Cawthorne and E. Fulton, *Nature*, 216: 576 (1967).
- D. J. Mazey, J. A. Hudson, and R. S. Nelson, *J. Nucl. Mater.*, 41: 257 (1971).
- F. S. Ham, *J. Appl. Phys.*, 30: 915 (1959).
- A. L. Bement, *Advan. Nucl. Sci. Technol.*, 7: 1 (1973).
- D. I. R. Norris, *Radiat. Eff.*, 14: 1 (1972); 15: 1 (1972).
- J. W. Corbett and L. C. Ianniello (Eds.), *Radiation Induced Voids in Metals*, Albany, N. Y., June 9–11, 1971, AEC Symposium Series, No. 26 (CONF-710601), 1972.
- Voids Formed by Irradiation of Reactor Materials*, Conference Proceedings, British Nuclear Energy Society, Reading, England, 1971.
- J. I. Bramman et al., Void Formation in Cladding and Structural Materials Irradiated in DFR, in *Radiation-Induced Voids in Metals*, Albany, N. Y., June 9–11, 1971, J. W. Corbett and L. C. Ianniello (Eds.), AEC Symposium Series, No. 26 (CONF-710601), p. 125, 1972.
- P. Murray, *Reactor Technol.*, 15: 16 (1972).
- H. R. Brager and J. L. Straalsund, *J. Nucl. Mater.*, 46: 134 (1973).
- E. E. Bloom, Nucleation and Growth of Voids in Stainless Steels During Fast-Neutron Irradiation, in *Radiation-Induced Voids in Metals*, Albany, N. Y., June 9–11, 1971, J. W. Corbett and L. C. Ianniello (Eds.), AEC Symposium Series, No. 26 (CONF-710601), p. 1, 1972.
- J. O. Stiegler, Void Formation in Neutron-Irradiated Metals, in *Radiation-Induced Voids in Metals*, Albany, N. Y., June 9–11, 1971, J. W. Corbett and L. C. Ianniello (Eds.), AEC Symposium Series, No. 26 (CONF-710601), p. 292, 1972.
- D. W. Keefer and A. C. Pard, *J. Nucl. Mater.*, 45: 55 (1972/1973).
- J. L. Katz and H. Wiedersich, *J. Chem. Phys.*, 55: 1414 (1971); a somewhat shorter version of this analysis appears in Ref. 6, p. 825.
- K. C. Russell, *Acta Met.*, 19: 753 (1971); calculations based on the theory are reported in *Radiat. Eff.*, 12: 127 (1972).
- J. L. Katz and H. Wiedersich, *J. Nucl. Mater.*, 46: 41 (1973); also in *Defects and Defect Clusters in bcc Metals and Their Alloys*, R. J. Arsenault (Ed.), p. 530, National Bureau of Standards, Washington, 1973.
- K. C. Russell, *Acta Met.*, 20: 899 (1972); also in *Defects and Defect Clusters in BCC Metals and Their Alloys*, R. J. Arsenault (Ed.), p. 545, National Bureau of Standards, Washington, 1973.
- K. C. Russell and R. W. Powell, *Acta Met.*, 21: 187 (1973).
- G. J. Dienes and A. C. Damask, *Point Defects in Metals*, Gordon and Breach, Science Publishers, Inc., New York, 1963.
- M. R. Hayns, *J. Nucl. Mater.*, 56: 267 (1975).
- S. D. Harkness, J. A. Tesk, and Che-Yu Li, *Nucl. Appl. Technol.*, 9: 24 (1970); also, *Met. Trans.*, 2: 1457 (1971).
- H. Wiedersich, *Radiat. Eff.*, 12: 111 (1972).
- A. D. Brailsford and R. Bullough, *J. Nucl. Mater.*, 44: 121 (1972).
- A. D. Brailsford and R. Bullough, British Report AERE-TP-538, 1973.
- A. D. Brailsford and R. Bullough, *J. Nucl. Mater.*, 48: 87 (1973).
- J. L. Straalsund and G. L. Gulhrrie, *Nucl. Technol.*, 16: 36 (1972).
- F. A. Garner et al., The Effect of Stress on Radiation-Induced Void Growth, in *Radiation-Induced Voids in Metals*, Albany, N. Y., June 9–11, 1971, J. W. Corbett and L. C. Ianniello (Eds.), AEC Symposium Series, No. 26 (CONF-710601), p. 841, 1972.
- S. D. Harkness and Che-Yu Li, Theoretical Study of the Swelling of Fast-Neutron-Irradiated Materials, in *Radiation-Induced Voids in Metals*, Albany, N. Y., June 9–11, 1971, J. W. Corbett and L. C. Ianniello (Eds.), AEC Symposium Series, No. 26 (CONF-710601), p. 798, 1972.
- J. L. Straalsund, *Scr. Met.*, 4: 459 (1970).
- H. Wiedersich and K. Herschbach, *Scr. Met.*, 6: 453 (1972).
- J. R. Willis and R. Bullough, in *Voids Formed by Irradiation of Reactor Materials*, Conference Proceedings, British Nuclear Energy Society, Reading, England, 1971, p. 133.
- V. F. Sears, *J. Nucl. Mater.*, 39: 18 (1971).
- E. R. Gilbert, *Reactor Technol.*, 14: 258 (1971).
- R. V. Hesketh, *Phil. Mag.*, 8: 1321 (1963).
- G. W. Lewthwaite and K. J. Proctor, *J. Nucl. Mater.*, 46: 9 (1973).
- R. V. Hesketh, in Proceedings of the International Conference on Solid State Research and Accelerators, A. N. Goland (Ed.), USAEC Report BNL-50083, pp. 389-401, 1967.
- R. V. Hesketh, *Phil. Mag.*, 7: 1417 (1962).
- B. W. Lewthwaite, *J. Nucl. Mater.*, 46: 324 (1973).
- W. G. Wolfer, J. P. Foster, and F. A. Garner, *Nucl. Technol.*, 16: 55 (1972); W. G. Wolfer and A. Boltax, in Conference on Irradiation Embrittlement and Creep in Fuel Cladding and Core Components, London, 1972, British Nuclear Energy Society, 1973.
- A. D. Brailsford and R. Bullough, *Phil. Mag.*, 27: 49 (1973); British Report AERE-TP-512, 1972.
- G. W. Lewthwaite, *J. Nucl. Mater.*, 38: 118 (1971).
- G. Martin and J. P. Poirier, *J. Nucl. Mater.*, 39: 93 (1971).
- S. D. Harkness, R. Grappel, and S. G. McDonald, *Nucl. Technol.*, 16: 25 (1972).
- W. J. Duffin and F. A. Nichols, *J. Nucl. Mater.*, 45: 302 (1972/1973).

## 19.10 PROBLEMS

19.1 Using Fig. 19.4, estimate the fraction of the vacancies created in an irradiation of fluence  $5 \times 10^{22}$  neutrons/cm<sup>2</sup> which is in voids.

19.2 Prove that Eq. 19.44 is the solution to Eq. 19.43 by using the fact that the logarithm of a product of terms is

the sum of the logarithms of each term and by carefully examining the behavior of  $h(m)$  and  $N^{eq}(m)$  as  $m \rightarrow 0$ .

**19.3** Determine the critical cluster size and the nucleation rate in classical nucleation theory (i.e., when  $\beta_i/\beta_v = 0$ ).

**19.4** Derive the void distribution function  $N(m)$  for the nonequilibrium case with steady-state nucleation.

**19.5** At the beginning of irradiation of stainless steel at  $500^\circ\text{C}$  with a flux of  $10^{14}$  neutrons  $\text{cm}^{-2} \text{sec}^{-1}$ , use the point-defect balances to compute:

(a) The vacancy and interstitial supersaturations  $S_v$  and  $S_i$ .

(b) The arrival-rate ratios  $(\beta_v/\beta_i)_{\text{disl}}$  and  $(\beta_i/\beta_v)_{\text{void}}$ .

(c) The void and loop nucleation rates. For void nucleation, make a rough estimate from Fig. 19.10.

Take point-defect migration and formation energies from problem 19.11. Use a dislocation density of  $10^9 \text{ cm}^{-2}$ . The steel contains no precipitates and is unstressed. Assume that the combinatorial number for vacancy interstitial recombination is 100. For dislocations, assume  $Z_i/Z_v = 1.02$ .

(d) How are the results of (b) and (c) changed when the steel contains  $4 \times 10^{12}$  incoherent precipitate particles/ $\text{cm}^3$  of radius equal to  $100 \text{ \AA}$ ?

**19.6** Apply homogeneous nucleation theory (as developed in Sec. 13.8 for fission gases in the fuel) to predict the nucleation time (or fluence) for helium bubbles in the cladding. The nucleation time is defined as the time at which the concentration of di-atoms passes through a maximum. Use the simplified method described in Sec. 13.8 (i.e., invoking Eq. 13.137). The fast-neutron flux is monoenergetic ( $E_n = 0.5 \text{ MeV}$ ) and is equal to  $10^{15}$  neutrons/ $\text{cm}^2 \text{sec}^{-1}$ . Assume a re-solution parameter of  $10^{-6} \text{ sec}^{-1}$  (problem 17.14) and make reasonable estimates of the other parameters needed in the calculation. Assume that the diffusion coefficient of helium in stainless steel is  $\sim 10^{-16} \text{ cm}^2/\text{sec}$ . Compare the fluence  $\Phi t_c$  for helium-bubble nucleation with the observed incubation fluence of  $\sim 10^{22}$  neutrons/ $\text{cm}^2$  needed for void formation in stainless steel.

**19.7** Incorporate re-solution into the theory of loop nucleation by chemical-reaction-rate theory. Use the microscopic picture of re-solution, in which the probability per second of any atom in an interstitial loop being redissolved by radiation is  $b$ . Include re-solution as a term of the form  $nbN_n$  in the balance on clusters of  $n$  interstitials. Assume that the combinatorial numbers  $z_{ni}$  and  $z_{nv}$  are equal to  $10n$ .

**19.8** We wish to determine the equilibrium vacancy concentration  $C_v$  in a solid in which a void of radius  $R$  and internal gas pressure  $p$  is embedded. The system (solid plus void) is subject to hydrostatic (compressive) stress  $\sigma$ . To determine  $C_v$ , we use the technique applied to obtain the equilibrium vacancy concentration at a dislocation loop (Sec. 19.5). The Gibbs free energy of a system containing

the void and the solid with vacancy concentration  $C_v$  and interstitial concentration  $C_i$  ( $C_v C_i = C_v^{eq} C_i^{eq}$ ) is given by

$$G = G_0 + g(m_v) + n_v \mu_v + n_i \mu_i$$

where  $G_0$  is the free energy of the stress-free solid without the void;  $g(m_v)$  is the reversible work required to create a void containing  $m_v$  vacancies against the external pressure (stress)  $\sigma$  with constant internal gas pressure  $p$  in the cavity;  $n_v$  and  $n_i$  are the number of vacancies and of interstitials, respectively, in the matrix of the block; and  $\mu_v$  and  $\mu_i$  are the chemical potentials of the point defects when the solid is under stress.

The value of  $\mu_v$  is equal to  $kT \ln(C_v/C_v^{eq})$  where  $C_v^{eq}$  is the equilibrium vacancy concentration in the stressed solid:

$$C_v^{eq} = (C_v^{eq})_0 \exp\left(-\frac{\sigma v}{kT}\right)$$

where  $(C_v^{eq})_0$  is the equilibrium vacancy concentration in the stress-free solid, and  $v$  is the volume change that occurs when one atom is moved from the interior of the matrix to the surface. In the text,  $v$  has been identified with the atomic volume  $\Omega$ , but this neglects the contraction of the lattice around the vacant lattice site. If the volume contraction around the vacant lattice site is  $\psi_v$ , then  $v$  is  $\Omega - \psi_v$ .

Determine  $C_v$ , the vacancy concentration for which the system described above is in thermodynamic equilibrium. In nonequilibrium situations (such as stress-induced void growth), this concentration is assumed to apply at the surface of the void.

**19.9** Removal of point defects by grain boundaries in the solid adds a term (assuming  $C_v^{eq}$  is small)

$$Q_v^{gb} = k_{gb}^2 D_v C_v \quad (1)$$

to the vacancy balance of Eq. 19.134 and a similar term to the interstitial balance. The value of  $k_{gb}^2$  is computed by the following method. The solid far from the grain boundary is assumed to be a homogeneous medium wherein the vacancy-balance equation, Eq. 19.136, applies. For simplicity, recombination is taken into account by defining an effective vacancy-production rate:

$$G' = \nu \Sigma_s \Phi - k_{iv} C_i C_v \quad (2)$$

Terms involving  $C_v^{eq}$  are neglected, and Eq. 19.136 is written as

$$G' = k^2 D_v C_v \quad (3)$$

where

$$k^2 = Z_v \rho_d + 4\pi R N + 4\pi R_p N_p \quad (4)$$

Because the grain boundary acts to maintain the equilibrium point-defect concentrations ( $C_v^{eq} \approx 0$  in this calculation), Eq. 3 is not valid close to the grain boundary. Here, the vacancy balance must contain a term representing diffusion of vacancies toward the grain boundary.

(a) Assuming that the concentration drop occurs very close to the grain boundary, the vacancy-diffusion equation in this region can be written for a semiinfinite medium in Cartesian coordinates. By solving this diffusion equation, determine the vacancy concentration profile in the vicinity

of the grain boundary and the vacancy flux to the grain boundary.

(b) Now consider the grain as a sphere of diameter  $d$ . Compute the total rate of removal of vacancies by the grain boundary from the flux computed in (a). From this result, determine  $Q_v^{gb}$  and hence  $k_{gb}^2$ .

19.10 Calculate and plot the relative void-growth rate  $R/R_0$  for molybdenum (melting point  $T_m = 2900^\circ\text{K}$ ) as a function of  $T/T_m$ . Use the following parameters:

$$\begin{aligned} \epsilon_v &= 190 \text{ kJ/mole} \\ \epsilon_v^* &= 190 \text{ kJ/mole} \\ \rho_d &= 10^{10} \text{ cm}^{-2} \\ \Sigma_s &= 0.3 \text{ cm}^{-1} \\ \Phi &= 10^{14} \text{ neutrons cm}^{-2} \text{ sec}^{-1} \\ \nu &= 100 \\ z_{iv} &= 30 \\ Z_i &= 1.02 \\ Z_v &= 1.0 \end{aligned}$$

Neglect voids as sinks ( $N \approx 0$ ) and precipitates ( $N_p = 0$ ) and loops as sinks ( $\rho_l = 0$ ). Assume the vacancy diffusion coefficient (in  $\text{cm}^2/\text{sec}$ ) is given by  $D_v = 10^{13} a_0^2 \exp(-\epsilon_v^*/kT)$ . Assume that the voids are  $300 \text{ \AA}$  in radius.

Compare the plot for molybdenum with Fig. 19.18 for stainless steel, taking the melting point of steel as  $1750^\circ\text{K}$ .

Would replacement of stainless steel by molybdenum avoid void swelling at the peak cladding temperature of  $650^\circ\text{C}$ ?

19.11 Show that the recombination properties of coherent precipitates are virtually nil when this type of sink is introduced into a solid containing equilibrium concentrations of vacancies and interstitials (i.e.,  $C_v^{eq}$  and  $C_i^{eq}$ ). The migration and formation energies of interstitials and vacancies can be taken as

$$\begin{aligned} \epsilon_i^* &= 13 \text{ kJ/mole} \\ \epsilon_i &= 420 \text{ kJ/mole} \\ \epsilon_v^* &= 125 \text{ kJ/mole} \\ \epsilon_v &= 160 \text{ kJ/mole} \end{aligned}$$

The temperature is  $500^\circ\text{C}$ .

19.12 Because of image dislocations in the voids, Eqs. 19.95 and 19.96 are multiplied by  $W_v$  and  $W_i$ , respectively. What is the growth law in the absence of recombination and thermal emission (i.e., the analog of Eq. 19.140)? Neglect the terms representing absorption by coherent precipitates.

19.13 (a) In problem 18.1a, replace the condition that the vacancy concentration is maintained at a value  $C_v^{eq}$  in the bulk solid by the condition that the only sinks for vacancies in the solid are the dislocations; the dislocation density is  $\rho_d$  and the void concentration is  $N$ . Determine the void radius as a function of time if the initial radius of all voids was  $R_0$ .

(b) Repeat problem 18.1a as stated but with the proviso that each void initially contains  $j$  helium atoms.

19.14 (a) Derive a growth law for interstitial loops (analogous to Eq. 19.138 for voids).

(b) Derive the analog of Eq. 19.140 for loops. Assume  $N_p = 0$ .

(c) Convert the loop-growth law to the time rate of change of the dislocation density of the solid.

(d) Define a dimensionless void size by Eq. 19.146 in which the dislocation density is replaced by  $\rho_{d0}$ , the value at the start of the growth period ( $t_0$ ). By choosing appropriate dimensionless dislocation density and time, convert Eq. 19.140 to a totally dimensionless equation. Integrate this equation with the initial condition  $R(t_0) = R_c$ . The void and dislocation loop densities,  $N$  and  $N_l$ , can be assumed constant. For this integration, assume that the dislocation density remains constant at its initial value. Take  $Z_i = Z_v$  except where the difference in these two quantities appears.

(e) Convert the result of part c to the same dimensionless quantities used in part d. Numerically integrate the dimensionless void- and loop- (or dislocation density) growth laws starting with the initial conditions:

$$R_c = 10 \text{ \AA}$$

and the cluster densities:

$$\begin{aligned} N &= 10^{14} \text{ voids/cm}^3 \\ N_l &= 10^{15} \text{ loops/cm}^3 \\ \rho_{d0} &= 10^9 \text{ cm}^{-2} \end{aligned}$$

Choose the initial loop radius ( $R_{lc}$ ) such that the number of vacancies in the void nuclei at  $t_0$  is equal to the number of interstitials in the embryo loops.

(f) The incubation period corresponds to a fast-neutron fluence of  $10^{22}$  neutrons/ $\text{cm}^2$ . Plot the results of the integrations in parts d and e. Compute the swelling at a fluence of  $5 \times 10^{22}$  neutrons/ $\text{cm}^2$ . This solution is applicable near the peak swelling temperature where recombination has become insignificant and the shrinkage term has not yet become important.

19.15 At some time  $t_0$  during irradiation, nucleation of voids occurs. For  $t > t_0$ , growth of the voids continues. Assume the growth is diffusion-limited and that the concentrations of vacancies and interstitials at the void surface are zero.

Neglect the changing sink concentrations due to void and loop growth for  $t > t_0$ , and assume that the concentrations of vacancies and interstitials in the matrix are constant in time.

Calculate the swelling at some time  $t > t_0$ , neglecting swelling at  $t_0$ , for the following two void distributions at  $t_0$ .

(a) At  $t_0$  all voids are of the same size,  $R_0$ . The total void density is  $N$ .

(b) At  $t_0$ , the voids are distributed in size according to the function  $N_0(R_0)$ .

(c) Show that the result of part b reduces to that of part a when the initial void distribution is described by a delta function.

19.16 Consider a segment of a circle of radius  $R$  which has an arc length  $\mathcal{L}$  and a chord distance of  $l$ .

(a) Prove that  $d\mathcal{L}/d\mathcal{A} = 1/R$ , where  $\mathcal{A}$  is the area of the segment.

(b) Derive the equation for  $d\mathcal{A}/d(1/\mathcal{R})$ .

(c) Repeat part a when the ends of the chord are the centers of smaller circles of radius  $R$ .

19.17 Solve Eqs. 19.191 to 19.193 using the approximations of Eqs. 19.194 to 19.196.

19.18 In the Hesketh model of irradiation creep by stress-enhanced vacancy-loop collapse, depleted zones with less than  $m_c \simeq 200$  vacancies remain in the solid as vacancy platelets. For  $m < m_c$ , the volume per platelet of size  $m$  is  $m\Omega$ . Using the inverse-square distribution function for vacancy platelet (or depleted zone) sizes produced by a neutron collision, compute the swelling due to uncollapsed

platelets in the absence of applied stress at a fast fluence of  $10^{20}$  neutrons/cm<sup>2</sup>. Assume  $\Sigma_s = 0.2 \text{ cm}^{-1}$ ,  $\Omega = 12 \text{ \AA}^3$ , and  $\nu = 500$  Frenkel pairs per fast-neutron collision.

19.19 The Lagrangian formulation of the void continuity equation is to be applied to a case of simultaneous growth and nucleation of voids in an irradiated metal. It is assumed that the vacancy and interstitial constants and the void nucleation rate are time-independent.

(a) What is the void distribution function  $N(R,t)$  for this model?

(b) What is the swelling as a function of time for specified values of  $C_v$ ,  $C_i$ , and  $I_{\text{nucl}}$ ?

# Chapter 20

## Interaction of Sodium and Stainless Steel

### 20.1 INTRODUCTION

The primary function of the sodium coolant in a liquid-metal fast breeder reactor (LMFBR) is to remove the fission heat produced in the fuel elements. This particular liquid metal has been chosen, in preference to the water coolant employed in light-water reactors (LWRs), for the following reasons:

1. The vapor pressure of sodium at the maximum coolant temperature is modest; at 700°C, the vapor pressure is 0.14 atm. This means that a heavy-wall steel pressure vessel is not necessary in an LMFBR.

2. Sodium has an acceptably large heat capacity to absorb the heat released by the fuel without a large temperature increase in flowing through the core. According to Table 10.2, the inlet and average outlet temperatures of the sodium coolant are 470°C and 650°C, respectively. The heat capacity per unit volume of sodium is about one-third that of water, but it is far greater than that of a gaseous coolant.

3. The very high thermal conductivity of sodium produces a temperature difference between the bulk sodium and the outside of the cladding of only 10 or 20°C. This low temperature drop serves to minimize the fuel center-line temperature at a specified linear power.

4. The boiling point of sodium (880°C at 1 atm) is sufficiently high that power limitations due to boiling heat transfer are absent.

5. Sodium has a sufficiently high atomic weight that excessive neutron moderation, which is undesirable in a fast reactor, is avoided.

6. Because sodium is a monatomic liquid, it is completely impervious to radiation damage, which, in a water coolant, produces radiolytic hydrogen and oxygen.

7. Sodium is the cheapest of the alkali metals.

The major potential disadvantage of liquid sodium is its extreme chemical reactivity and the high level of induced radioactivity due to neutron absorption (which produces 15-hr  $^{24}\text{Na}$ ). LMFBRs are designed with two separate sodium-coolant loops (Fig. 20.1) to ensure that the induced radioactivity will be safely contained. The primary loop circulates sodium between the core and the intermediate

heat exchanger, where the primary sodium heats sodium in the secondary coolant loop. The heat sink in the secondary loop is the steam generator, where the hot secondary sodium boils water to make steam for driving a conventional turbine. Great care must be exercised to keep the leakage of water into the secondary sodium circuit (or vice versa) to a minimum because sodium and water can react aggressively when mixed. Water that leaks into the secondary sodium circuit must be removed because it causes the sodium to become highly corrosive to the steel components of the coolant loop.

The most significant technological problems associated with using sodium as a coolant arise from the chemical behavior of this element with its environment rather than its response to radiation. The chemical behavior of sodium–stainless-steel systems can be divided into the following parts:

1. *General Corrosion.* Flowing high-temperature sodium very slowly dissolves the major metallic components of stainless steel (iron, chromium, and nickel) from the hot section of the primary coolant loop. These species are transported in the liquid to cooler sections of the loop, where deposition occurs. Corrosive attack in the hot section is uniform and does not appear to be accompanied by deep penetration of sodium into the grain boundaries of the metal (in this respect sodium corrosion differs from the attack of the inner wall of the cladding by fuel and fission products). At a temperature of 700°C, the corrosion rate is several tens of micrometers per year. The effect of this type of attack on reactor performance is manifest as a reduction in the resistance of the fuel-element cladding to internal pressure generated by released fission gases and fuel–cladding contact. As the cladding wall becomes thinner, the tangential stresses generated by internal loading of the cladding increase, and consequently so does the creep rate. The time to rupture is correspondingly reduced. The cladding is the thinnest structural member in the core, and hence is most susceptible to *thinning* or *wastage* due to sodium corrosion. As in the water coolant of an LWR, the oxygen concentration in the sodium in an LMFBR must be maintained at a low level (<5 ppm by weight) to avoid excessive general corrosion.

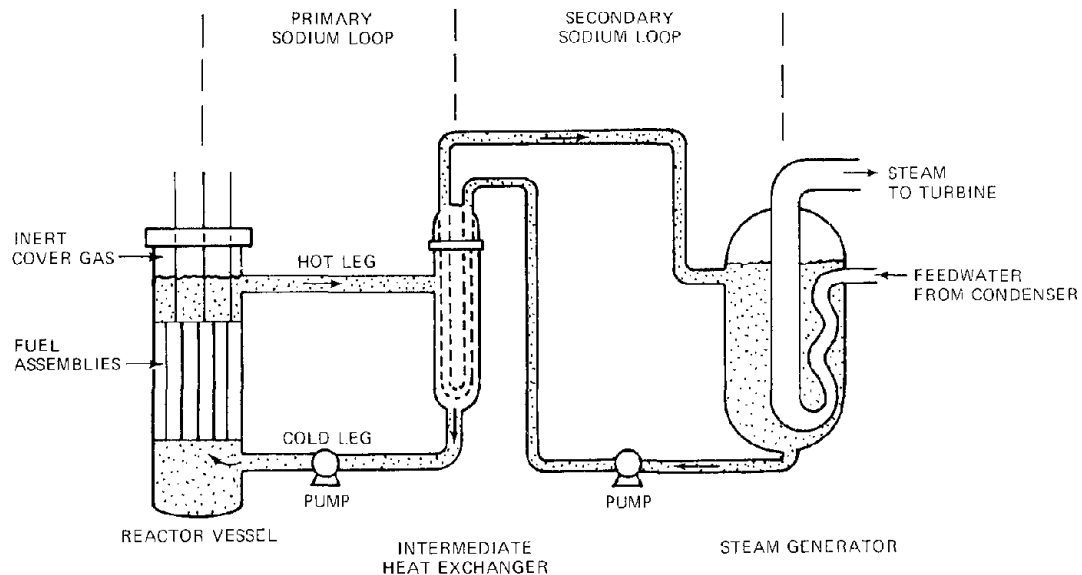


Fig. 20.1 Sodium coolant loops in an LMFBR.

2. *Selective Leaching.* Austenitic stainless steels consist of iron, chromium, and nickel in the approximate proportions 70:19:9 (Table 18.1). The dissolution rate of each of these components by sodium is different. Chromium and nickel appear to be removed at a more rapid rate than iron, which results in depletion of the two alloying elements in the surface layer of the steel adjacent to the flowing sodium. This selective leaching process alters the microstructure of the steel and can adversely affect its mechanical properties as well. The unequal removal rates for the three constituents of steel may be due to different solubilities of the elements in liquid sodium or, as is known to be the case for iron, to the acceleration of the corrosion rate of this species by oxygen dissolved in the sodium.

3. *Deposition.* The 200°C temperature difference between the core section of the primary coolant loop (the hot leg) and the intermediate heat exchanger (the cold leg) results in deposition of the metals that were removed in the core at the heat exchanger. The deposit may consist of elementary metals, but more likely it takes the form of loosely bound particles in which the metals are chemically combined with oxygen or carbon. Buildup of this type of deposit in the heat-exchanger tubes is deleterious to thermal performance because (1) the deposit has a higher resistance to heat transfer than the base metal and (2), if the deposit is thick enough, the cross-sectional area of the heat-exchanger tubes can be appreciably reduced, thereby requiring a greater pressure drop to drive the desired coolant flow.

4. *Transport of Radioactivity.* The major long-lived radioactive species produced by neutron irradiation of stainless steel are  $^{54}\text{Mn}$ ,  $^{58}\text{Co}$ , and  $^{60}\text{Co}$ . The first two of these nuclides are produced by (n,p) reactions on iron and nickel, respectively. The  $^{60}\text{Co}$  is generated from neutron capture in the small cobalt component of stainless steel. The cobalt content of type 316 stainless steel is ~0.3 wt.%, and it is all  $^{59}\text{Co}$ . The radioactivity induced in the steel in

the high-flux regions of the core is liberated from the metal by corrosion and migrates through the primary sodium loop. Much of the radioactive manganese and cobalt becomes immobilized in the corrosion-product scale deposited on the cooler surfaces of the loop, such as the intermediate heat exchanger. The level of radioactivity due to the deposits can be sufficiently high to seriously impair routine maintenance of components in the cold leg of the primary sodium loop.

5. *Carbon Transport.* In addition to transporting the major constituents of stainless steel around the coolant circuit, flowing sodium serves as a medium through which the minor elements in the steel can migrate about the loop. The element of principal concern is carbon, inasmuch as this species is largely responsible for the high-temperature strength of steel. Nitrogen transfer also occurs, but the concentration of this element is kept very low (<0.01%) to reduce helium production by the (n, $\alpha$ ) reaction. According to Table 18.3, the cross section for the nitrogen (n, $\alpha$ ) reaction is second only to that of boron among the components of steel. Carbon and nitrogen are termed interstitial components because of their location in interstitial sites in the bcc lattice of iron. It has been found that flowing sodium removes carbon from the high-temperature sections of the coolant circuit and releases carbon to the low-temperature components of the loop. Because of its high diffusivity in the solid (compared to the alloying metals), carbon is removed from, and penetrates to, appreciable depths beneath the surface. Owing to the significant effect of carbon on the mechanical properties of stainless steel, considerable effort has been expended to understand and predict the direction and extent of carbon transfer in LMFBR sodium-coolant loops. The removal and deposition processes are called *decarburization* and *carburization*, respectively.

6. *Sodium Chemistry.* The pressing need for oxygen monitoring of sodium arises from the influence of oxygen

on the corrosion of the steel. Carbon transfer is important because it affects the mechanical properties of the alloy. Hydrogen does not affect corrosion or mechanical properties, but its presence in the secondary coolant loop is a good indicator of the severity of water leakage into this circuit from the steam generator. In addition, it is essential from a safety standpoint to be able to quantitatively determine the tritium produced by the reactor and how much of this radioactive isotope of hydrogen escapes to the cover gas above the sodium in the core.

Because of the importance of the low-atomic-weight impurities oxygen, carbon, and hydrogen to the various processes that occur in the coolant circuits of an LMFBR, methods of quantitative detection of these elements in the parts-per-million (ppm) range in liquid sodium have been developed. The devices for performing these analyses are generally termed *meters* because they are intended to provide continuous on-line information on the sodium purity. Actually, they measure the chemical activity, rather than the concentration, of the impurity in the liquid metal. The principles of operation of these meters and the physical chemistry of the impurity species in sodium-stainless-steel systems require analysis of the thermodynamics and the kinetics of potential reactions in which these elements can partake. Hydrogen, oxygen, and carbon meters are discussed in Sec. 20.5.

**7. Sodium-Fuel Interactions.** In the event of a breach of the cladding, sodium contacts the mixed-oxide fuel. The liquid metal and the ceramic react to form the double oxide  $\text{Na}_3\text{MO}_4$ , where M is uranium or plutonium. Two potential consequences of this chemical reaction must be assessed. First, if the product of the sodium-fuel reaction is powdery and not as compact as the fuel, uranium, plutonium, and particulate matter bearing fission products can be swept into the primary coolant stream. Second, chemical combination of sodium and the fuel causes the fuel to swell, and what was a small leak in the cladding can become enlarged to a full rupture, a situation decidedly to be avoided.

Another aspect of the sodium-fuel interaction is thermal rather than chemical. In the event of a sizable overpower transient, the fuel can melt and be ejected in the molten state ( $T > 2800^\circ\text{C}$ ) into the liquid sodium, which is at a temperature less than  $700^\circ\text{C}$ . Some of the thermal energy contained in the liquefied fuel can be converted into mechanical energy by boiling of the sodium. As much as a few percent of the available thermal energy of the molten fuel can be converted to mechanical energy (i.e., kinetic energy of the sodium) in a few seconds.

## 20.2 GENERAL CORROSION

Current understanding of stainless-steel corrosion has been summarized in the comprehensive review by Weeks and Isaacs,<sup>1</sup> from which much of the discussion in this section has been drawn.

### 20.2.1 Experimental Corrosion Loops

Corrosion of stainless steel is studied in loops of the type shown in Fig. 20.2. Sodium circulates in the loop,

which is equipped with devices for flow measurement, oxygen control and measurement, and temperature measurement and control. Metal specimens in the form of small tabs are inserted in the various zones, which are held at temperatures and flow velocities expected in an LMFBR. The corrosion (or deposition) rates of these tabs are investigated as functions of the following variables:

1. Temperature ( $450^\circ$  to  $700^\circ\text{C}$ ).
2. Sodium velocity (1 to 10 m/sec).
3. Oxygen content of sodium (1 to 25 ppm by weight).
4. Downstream position of sample (to 700 pipe diameters).
5. Exposure time (to 10,000 hr).

Temperatures are controlled by the heater and coolers shown in Fig. 20.2. Sodium velocity is regulated by electromagnetic pumps. The oxygen content of the sodium is fixed by the temperature of a cold trap that contains solid  $\text{Na}_2\text{O}$ , the solubility of which is a known function of temperature. Downstream position refers to the location of the corrosion specimen measured from the point at which the sodium conditions (temperature or velocity) are changed. Downstream position is commonly expressed in terms of the pipe diameter, or as  $x/d$ .

### 20.2.2 Measured Corrosion Rates

Even though the test loop contains much less sodium than the coolant loops of an LMFBR (which hold  $\sim 1000$  tons of the liquid metal), Fig. 20.3 shows that steady-state corrosion at a particular location may not be attained for several thousand hours. This long transient is probably due to the need for the entire loop to come to a steady state. Because flowing sodium provides a means of communication between different sections of the circuit, a slow process in one part affects all parts of the loop. The adjustment of the surface composition of the metal in the hot leg (where selective leaching of nickel and chromium occurs) may be the principal sluggish process. This step involves solid-state diffusion of iron, nickel, and chromium in the surface layer of the metal, which is slow at the corrosion temperatures of interest.

Figure 20.3 shows that the corrosion rates increase with increasing temperature. Figure 20.4 shows the same effect on an Arrhenius plot. The activation energy for the corrosion process is  $> 125$  kJ/mole, although this figure can depend on the sodium velocity and the downstream position of the sample.

Figure 20.5 shows the effect of sodium velocity on stainless-steel corrosion at a fixed temperature and oxygen concentration for three downstream positions. The corrosion rate is seen to increase with velocity until a plateau is reached beyond which the rate is unaffected by further increases in velocity. The corrosion rate decreases downstream of the entrance to a zone (i.e., with increasing  $x/d$ ).

### 20.2.3 Corrosion Mechanisms of Pure Metals

There is no quantitative theory for predicting the corrosion rates shown in Figs. 20.3 to 20.5. Part of this theoretical deficiency is due to the lack of thermodynamic and morphological information concerning the composition

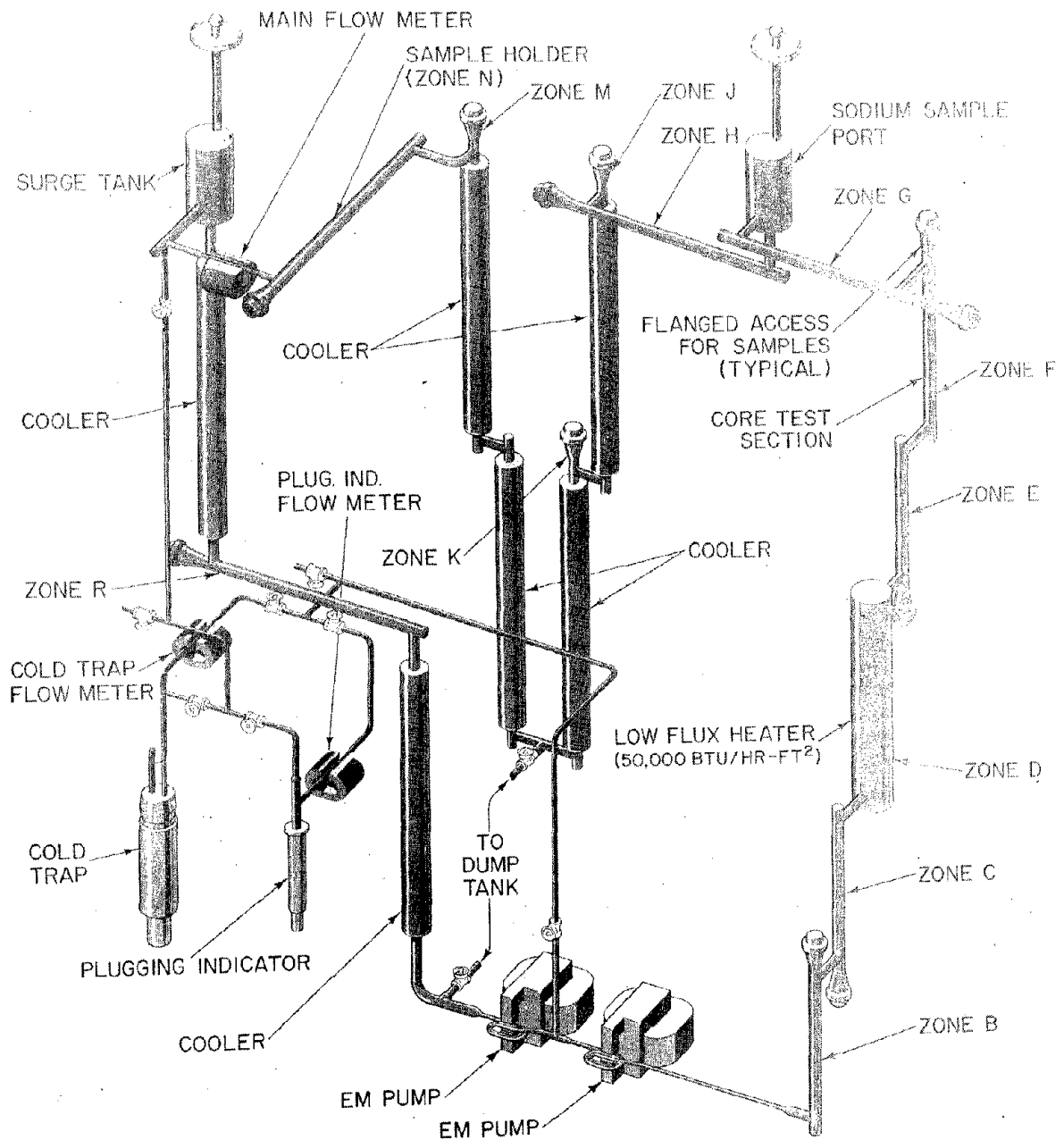


Fig. 20.2 Experimental sodium corrosion loop. (After Ref. 7.)

and stability of the corrosion products in liquid sodium and to our rudimentary understanding of the kinetics of processes by which atoms at the surface of the metal are released to the adjacent liquid sodium. However, a not inconsequential part of the inability of current models to predict or even correlate corrosion rates in the stainless-steel-sodium system is due to the peculiar nature of the loop experiments, which, although reflecting the geometry

of the coolant circuits in an LMFBR, produce data that are difficult to interpret in a fundamental manner. The main difficulty arises from the circulatory nature of the loop. The corrosion rate at any position depends on the concentration of the corrosion product in the bulk sodium at that location, which in turn is a function of the corrosion and deposition rates in all other parts of the loop. Consequently, determination (either experimentally or by

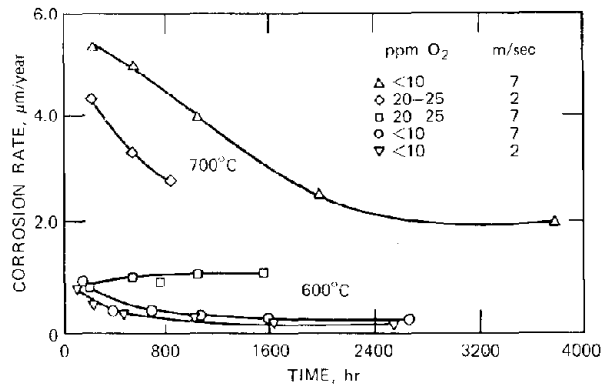


Fig. 20.3 Corrosion rates of type 316 stainless steel in flowing sodium. [After S. L. Schrock et al., in *Corrosion by Liquid Metals*, J. E. Draley and J. R. Weeks (Eds.), American Institute of Mining, Metallurgical and Petroleum Engineers, New York, 1970.]

calculation) of the point concentrations of corrosion products in the sodium is virtually impossible and, therefore, so is comparison of the corrosion data with theory. Nonetheless, there is general agreement on the main qualitative features of the effects of the various variables on the corrosion process. To illustrate the corrosion mechanism, we will first consider corrosion of the pure elements iron, nickel, and chromium rather than stainless steel. Inasmuch as iron is the primary constituent of this alloy, the rate of corrosion of steel must be controlled principally by the rate at which this element is dissolved by liquid sodium.

In the corrosion of a pure metal by sodium, the solid is dissolved in the liquid in elemental form at a rate that depends on the speed of two consecutive steps:

1. Release of metal atoms from the surface to the liquid sodium immediately adjacent to the solid (dissolution step).
2. Transport of the dissolved metal through the liquid boundary layer attached to the solid (convective-diffusion step).

Control of the corrosion rate by dissolution at the solid-liquid interface is characterized by a rather strong dependence on temperature and no dependence on fluid velocity. Rates subject to diffusion control are usually weakly temperature dependent and quite sensitive to fluid velocity. When both steps, which are in series, are of comparable magnitude, the rate is said to be in a regime of mixed control. [A similar division of controlling steps was used in the treatment of point-defect absorption by voids and dislocations (Secs. 13.4 and 13.5).]

Figure 20.6 shows (schematically) the concentration profile of dissolved metal in the vicinity of the surface. The equilibrium concentration in sodium (i.e., the solubility) is denoted by  $C_{sat}$ . When the rate of release from the solid to the liquid is slow compared to the rate of diffusional transport through the boundary layer, the actual concentration of the metal in the sodium next to the surface,  $C_{int}$ , is less than the saturation value. The rate of the dissolution step is assumed to be given by the product of a first-order

rate constant  $k_R$  and the departure from interfacial equilibrium, or by

$$\dot{m} = k_R (C_{sat} - C_{int}) \quad (20.1)$$

where  $\dot{m}$  is the corrosion rate expressed in grams of metal per square centimeter of surface per second. The units of the rate constant  $k_R$  are centimeters per second, and the concentrations are expressed in grams of metal per cubic centimeter of sodium.

The rate of mass transfer by convective diffusion in the boundary layer is given by

$$\dot{m} = k_d (C_{int} - C) \quad (20.2)$$

where  $C$  is the concentration of dissolved metal in the bulk sodium flowing past the point at which the corrosion rate is

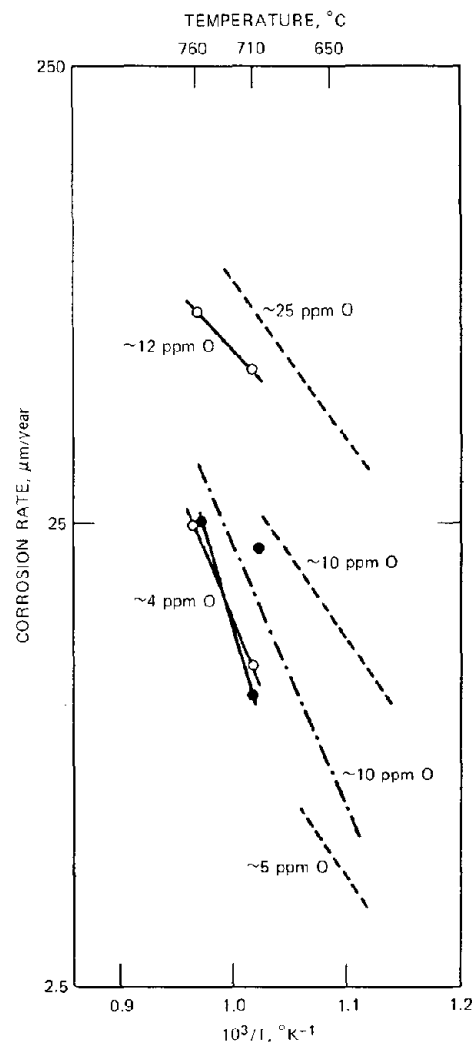


Fig. 20.4 Effect of temperature on the corrosion rates of various stainless steels.—, Romano and Klamut. ---, Thorley and Tyzack. —·—, GE equation. ●, 316 stainless steel. ○, 304 stainless steel. (After Ref. 1.)

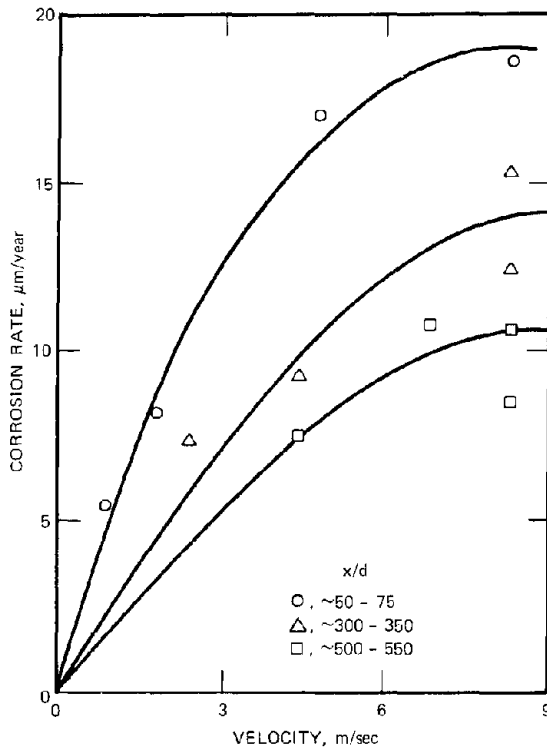


Fig. 20.5 Corrosion rate at 700°C as a function of sodium velocity at an oxygen level of less than 10 ppm. (After Ref. 7.)

measured. Eliminating  $C_{int}$  between Eqs. 20.1 and 20.2 yields

$$\dot{m} = \left( \frac{1}{k_R} + \frac{1}{k_d} \right)^{-1} (C_{sat} - C) \quad (20.3)$$

where  $k_d$  is the mass-transfer coefficient (centimeters per second), the magnitude of which can be estimated by analogy to the corresponding formulas for heat transfer. The mass-transfer coefficient is a function of the Reynolds and Schmidt numbers. For a pipe the former is defined by

$$Re = \frac{vd}{\nu} \quad (20.4a)$$

where  $v$  is the bulk sodium velocity,  $d$  is the pipe diameter, and  $\nu$  is the kinematic viscosity of sodium.

For a flat plate (which best represents the geometry of the test specimens inserted into the loop of Fig. 20.2), the Reynolds number is based on the distance from the leading edge:

$$Re_l = \frac{vl}{\nu} \quad (20.4b)$$

(Note that  $l$  is not equal to the distance downstream of the entrance to the test zone, which is denoted by  $x$ ).

The Schmidt number is:

$$Sc = \frac{\nu}{D} \quad (20.5)$$

where  $D$  is the diffusivity of the metal in liquid sodium.

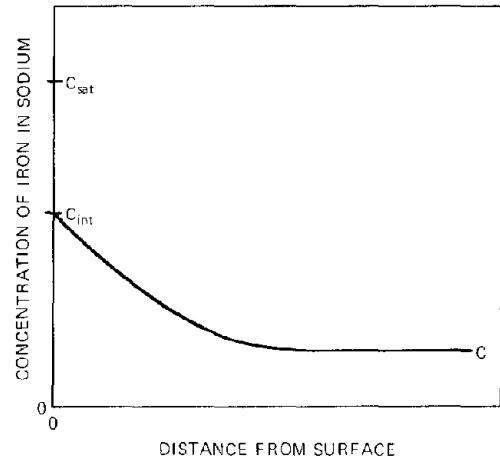


Fig. 20.6 Concentration distribution of iron in sodium near the surface.

The correlation between the mass-transfer coefficient and the dimensionless parameters depends on the magnitude of the Schmidt number (which replaces the Prandtl number in the mass-transfer analogs of heat-transfer correlations) and on whether the flow is laminar or turbulent. For the conditions typical of a sodium corrosion loop test,  $v = 500$  cm/sec,  $d = 2$  cm, and  $\nu = 1.5 \times 10^{-3}$  cm<sup>2</sup>/sec (at 700°C).

The diffusion coefficients of iron, nickel, and chromium in liquid sodium have not been measured but can be estimated by the method described in Ref. 2. For iron\*

$$D = 4.4 \times 10^{-4} \exp \left[ -\frac{18}{R(T/10^3)} \right] \quad (20.6)$$

At  $T = 700^\circ\text{C}$  the diffusion coefficient of iron in sodium is  $5 \times 10^{-5}$  cm<sup>2</sup>/sec. Using these figures, we find  $Sc \approx 30$  and  $Re \approx 6 \times 10^5$ . The flow is clearly in the turbulent regime (for pipes), and the Schmidt number is typical of ordinary liquid systems. A common empirical correlation that applies to both heat and mass transfer for these values of the dimensionless groups is<sup>3</sup>

$$\frac{k_d}{v} = Sc^{-\frac{2}{3}} j \quad (20.7)$$

where  $j$  is the Colburn  $j$ -factor for mass and heat transfer. For turbulent flow in pipes,

$$j = \frac{f}{2} = 0.023 Re^{-0.2}$$

where  $f$  is the friction factor. Combining the two preceding equations yields

$$\left( \frac{k_d}{v} \right)_{\text{pipes}} = 0.023 Sc^{-\frac{2}{3}} Re^{-0.2} \quad (20.8)$$

\*Activation energies are expressed in kJ/mole.

which is the familiar Chilton—Colburn equation. It is valid for  $0.5 \leq Sc \leq 120$ ,  $2300 \leq Re \leq 10^7$ , and  $x/d > 50$ . In the region  $x/d < 50$ , the turbulent flow and concentration fields in the pipe are developing, and the mass-transfer coefficient is larger than the values predicted by Eq. 20.8. Accelerated mass transfer in the upstream portion of a pipe is termed the entrance effect.

For turbulent flow over a flat plate,  $j$  can be expressed in terms of the skin-friction coefficient  $C_f$ :

$$j = \frac{C_f}{2} = 0.037 Re_1^{-0.2}$$

and Eq. 20.7 becomes

$$\left(\frac{k_d}{v}\right)_{\text{flat plate}} = 0.037 Sc^{-\frac{1}{3}} Re_1^{-0.2} \quad (20.9)$$

In this formula  $k_d$  is the average mass-transfer coefficient over the distance  $l$  from the leading edge. Since the length of the specimen tabs used in the sodium loop tests is comparable to the diameter of the pipe in which the sodium flows, Eqs. 20.8 and 20.9 show that the mass-transfer coefficients on the pipe wall and on the corrosion specimens are approximately equal. With the values of the Schmidt and Reynolds numbers previously calculated and a flow velocity of 5 m/sec, the predicted mass-transfer coefficients are on the order of  $k_d \approx 0.08$  cm/sec.

We compute the theoretical corrosion rate for complete diffusion control using iron as the dissolving metal. The solubility of iron in low-oxygen sodium (i.e., sodium with oxygen concentration less than  $\sim 10\%$  of the saturation value) is given by<sup>1</sup>

$$\ln C_{\text{sat(Fe)}} = 11.9 - \frac{82}{R(T/10^3)} \quad (20.10)$$

where  $C_{\text{sat(Fe)}}$  is in parts per million by weight. At  $700^\circ\text{C}$  the solubility of iron is  $\sim 6$  ppm, or  $5 \times 10^{-6}$  grams of iron per cubic centimeter of sodium. If the bulk concentration of iron in the flowing sodium is neglected ( $C = 0$ ) and the corrosion process is assumed to be completely diffusion controlled ( $k_d/k_R \ll 1$ ), Eq. 20.3 predicts a corrosion rate for iron of  $4 \times 10^{-7}$  g cm<sup>-2</sup> sec<sup>-1</sup>. The corrosion rate can also be expressed in terms of the velocity of recession of the surface by

$$u = \frac{\dot{m}}{\rho} \quad (20.11)$$

where  $\rho$  is the density of the solid (for iron,  $\rho = 7.9$  g/cm<sup>3</sup>). The predicted diffusion-controlled corrosion rate of iron in sodium that contains no dissolved iron is  $16,000$   $\mu\text{m}/\text{year}$ . This rate is more than two orders of magnitude greater than the rates shown on Figs. 20.3 to 20.5, and it must be said that the simple theory is rather dramatically wrong or at least has not been properly applied to the particular characteristics of the loop experiments.

In addition to failing to come even close to predicting the magnitude of the observed corrosion rates, the expected temperature dependence of the theoretical diffusion-controlled corrosion rate is in error. The activation energy for diffusion-controlled corrosion is the sum of the

enthalpy of solution of iron in sodium (which, from Eq. 20.10, is 82 kJ/mole) and the activation energy for diffusion of iron in liquid sodium ( $\sim 1.8$  kJ/mole), which is significantly less than the activation energies obtained from Fig. 20.4.

These comparisons of corrosion-rate magnitude and temperature dependence with observations suggest that the dissolution step characterized by the rate constant  $k_R$  is not rapid compared to boundary-layer convective diffusion and that the full rate constant in Eq. 20.3 should be employed in the theory. According to the simple model considered here, the velocity-independent plateaus of the curves in Fig. 20.5 correspond to complete control of the corrosion rate by the surface dissolution step (or  $C_{\text{int}} \approx C$ ). Using the corrosion rate on the plateau on the upper curve (20  $\mu\text{m}/\text{year}$ ), we conclude that  $k_d/k_R \approx 16,000/20 = 800$  for these corrosion conditions. If the sodium velocity is reduced from 9 m/sec characteristic of the level portion of the curves in Fig. 20.5 to 1 m/sec, Eqs. 20.8 and 20.9 indicate that the ratio  $k_d/k_R$  should be decreased to  $(800)/(9)^{0.8} = 140$ . Using Eq. 20.3, the ninefold reduction in flow velocity should have reduced the corrosion rate by the factor

$$\frac{(\dot{m})_1}{(\dot{m})_9} = \frac{1 + 1/800}{1 + 1/140} = 0.995$$

which is quite a bit different from the observed fourfold reductions in  $u$  due to decreasing the sodium velocity by a factor of nine.

## 20.2.4 Analysis of the Corrosion Loop

The error in the theoretical corrosion rate determined in the preceding section can be due to assuming no metal in the bulk sodium ( $C = 0$ ). The effect of sodium circulation in the loop can be incorporated into the simple corrosion mechanism used in the preceding discussion with the aid of Fig. 20.7. We consider a very simple loop, consisting of an isothermal hot leg maintained at temperature  $T_h$  and an isothermal cold leg at temperature  $T_c$ . Efficient heaters and coolers at the junctions between the two loops are assumed to feed appropriately preheated or precooled sodium in each leg of the loop. Sodium circulates through the loop in the direction of the arrows in the drawing. At all downstream locations  $0 \leq x \leq 2L$ , the corrosion rate is given by Eq. 20.3. The solubilities of the metal in sodium in the hot and cold legs are denoted by  $C_{\text{sat}}^h$  and  $C_{\text{sat}}^c$ , respectively. Since  $T_h > T_c$ ,  $C_{\text{sat}}^h$  is greater than  $C_{\text{sat}}^c$ , and metal is removed in the hot leg and deposited in the cold leg.

When steady state is established in the loop, the metal concentration distribution in the flowing sodium,  $C(x)$ , is less than  $C_{\text{sat}}^h$  in the hot leg but greater than  $C_{\text{sat}}^c$  in the cold leg. The downstream variation of the metal concentration can be calculated by a simple material balance on the flowing sodium into which Eq. 20.3 is incorporated as an exchange term with the surface. For a circular pipe the balance on metal in the sodium takes the form

$$\frac{dC}{dx} = \frac{4K_d}{vd} (C_{\text{sat}} - C) \quad (20.12)$$

where  $K_d$  is the overall mass-transfer coefficient in Eq. 20.3:

$$K_d = \left( \frac{1}{k_R} + \frac{1}{k_d} \right)^{-1} \quad (20.13)$$

Integration of Eq. 20.12 yields

$$\frac{C_{sat}^h - C(x)}{C_{sat}^h - C(0)} = \exp \left( - \frac{4K_{dh} x}{v d} \right) \quad (20.14a)$$

in the hot leg ( $0 \leq x \leq L$ ) and

$$\frac{C(x) - C_{sat}^c}{C(L) - C_{sat}^c} = \exp \left( - \frac{4K_{dc} x}{v d} \right) \quad (20.14b)$$

in the cold leg ( $L \leq x \leq 2L$ ). The terms  $K_{dh}$  and  $K_{dc}$  are the overall mass-transfer coefficients in the hot and cold legs, respectively and  $C(0)$  and  $C(L)$  are the concentrations of metal in the flowing sodium at the junctions between the two parts of the loop which are determined by appropriate matching conditions. A schematic of the concentration

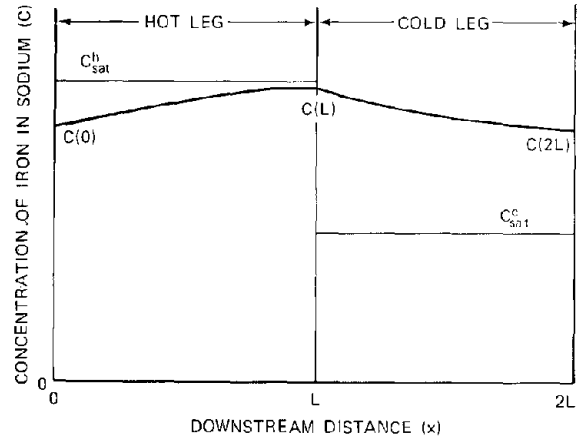


Fig. 20.8 Concentration of iron in sodium in a simple two-zone loop.

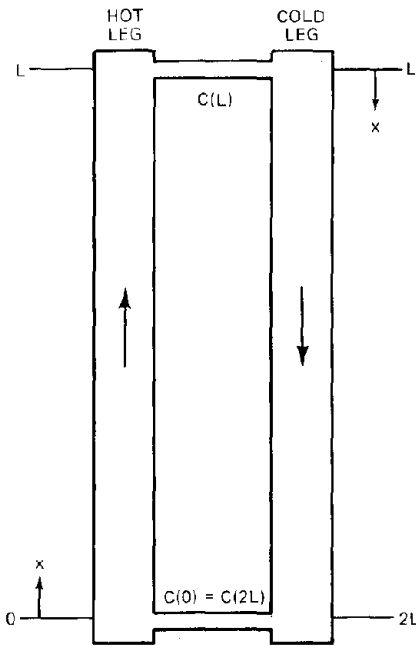


Fig. 20.7 A two-zone loop.

profiles along the loop is shown in Fig. 20.8 (see problem 20.1 for a detailed calculation). The sodium entering the hot leg is undersaturated with respect to the solubility at  $T_h$ , but  $C_{sat}^h$  is approached exponentially as the liquid flows up the hot leg. Similarly, the sodium entering the cold leg is supersaturated with respect to the solubility at the cold-leg temperature, and  $C(x)$  decreases exponentially toward  $C_{sat}^c$  during the return trip through the loop.

The driving force for corrosion in the hot leg is  $C_{sat}^h - C(x)$ , which from Fig. 20.8 is seen to decrease with

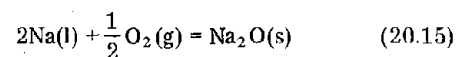
downstream  $x/d$ . This predicted downstream effect is qualitatively consistent with the data shown in Fig. 20.5.

The earlier calculation that yielded a two order-of-magnitude discrepancy between theoretical and experimental corrosion rates took as a driving force the full ordinate height  $C_{sat}^h$  in Figure 20.8. However, when the circulatory geometry of the loop is treated correctly, the driving force is reduced to the vertical distance between  $C_{sat}^h$  and  $C(x)$  in the figure. The driving force (and hence the corrosion rate) is reduced to zero as  $C_{sat}^h \rightarrow C_{sat}^c$  or when the temperature difference between the two legs vanishes. The corrosion rate also vanishes when the deposition rate constant of the cold leg,  $k_{R,c}$ , becomes very small. In this instance the cold leg is inefficient in removing metal from the sodium, and the entire loop becomes saturated with metal at the solubility value appropriate to the hot-leg temperature.

### 20.2.5 Effect of Oxygen on Iron Corrosion

The rate of corrosion of iron or stainless steel is found to increase with the concentration of oxygen dissolved in the sodium. The effect can be either thermodynamic or kinetic. If the dissolved oxygen can form an oxide of iron (perhaps combined with sodium as well), the corrosion analysis based on the assumption that iron dissolves as the element is incorrect. Even if the thermodynamic search for an oxygen effect proves fruitless, dissolved oxygen can accelerate one of the steps in the corrosion process, thereby rendering the phenomenon a kinetic one. We first examine the potential thermodynamic effect of oxygen on the iron-sodium system.

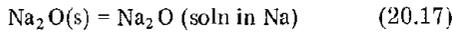
Oxygen probably dissolves in sodium as the monoxide  $Na_2O$ . However, it is not important for thermodynamic analysis whether the dissolved oxygen is chemically bound to two sodium atoms, exists as a free oxygen ion  $O^{-2}$ , or exists as an oxygen ion loosely solvated with two sodium ions. Assuming compound formation, we may commence by considering the reaction



the standard free energy of formation of  $\text{Na}_2\text{O}$  is<sup>1</sup>

$$\Delta G_{\text{fNa}_2\text{O}}^\circ = -397 + 118 \left( \frac{T}{10^3} \right) \quad \text{kJ/mole} \quad (20.16)$$

The other piece of thermodynamic information required to specify the equilibrium behavior of oxygen in sodium is the solubility, which represents the reaction



The solubility of pure solid  $\text{Na}_2\text{O}$  in liquid sodium is given by<sup>1</sup>

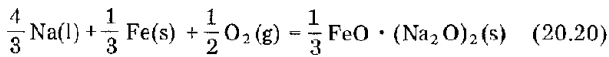
$$\ln C_{\text{sat(O)}} = 14.4 - \frac{46.5}{R(T/10^3)} \quad (20.18)$$

where  $C_{\text{sat(O)}}$  is in parts per million of oxygen by weight. This equation is plotted in Fig. 20.9. The accord between the various measurements suggests that the solubility of oxygen in sodium is established to within 10%. The oxygen content of sodium loops can be controlled by passing the flowing sodium over a bed of solid  $\text{Na}_2\text{O}$  held at a known temperature (which must be the lowest temperature in the loop). The oxygen concentration established at this point is determined by Eq. 20.18 and persists throughout the loop, provided that there are no strong sinks for oxygen in the circuit.

The thermodynamic effect of dissolved oxygen is expressed in terms of the *activity* of this species in sodium. By definition the activity of oxygen in sodium saturated with  $\text{Na}_2\text{O}$  is unity. In solution thermodynamics the activity of a dilute species is generally proportional to the concentration of this species. This rule is known as Henry's law. Since the activity of oxygen in oxygen-saturated sodium is unity, the oxygen activity for lower concentrations is given by

$$a_{\text{O}} = \frac{C_{\text{O}}}{C_{\text{sat(O)}}} \quad (20.19)$$

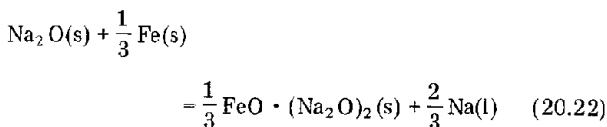
When sodium containing oxygen at a concentration greater than 10 to 20% of the saturation value is equilibrated with iron, an insoluble double oxide with the formula  $\text{FeO} \cdot (\text{Na}_2\text{O})_2$  precipitates out of solution. This compound is called sodium ferrite, and its standard free energy of formation from the elements according to the reaction



is<sup>1</sup>

$$\Delta G_{\text{fNaFerrite}}^\circ = -410 + 121 (T/10^3) \quad \text{kJ/mole} \quad (20.21)$$

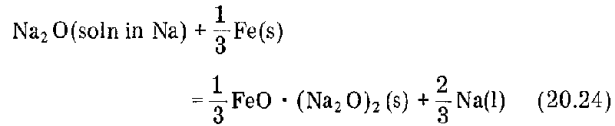
(Another double oxide,  $\text{NaFeO}_2$ , has been reported, but it is not as stable as sodium ferrite.) Subtracting reaction 20.15 from reaction 20.20 yields



for which

$$\Delta G^\circ = \Delta G_{\text{fNaFerrite}}^\circ - \Delta G_{\text{fNa}_2\text{O}}^\circ \quad (20.23)$$

The reaction of iron with oxygen dissolved in sodium at less than the saturation concentration is represented by the reaction



The oxygen activity,  $a_{\text{O}}^*$ , at which sodium ferrite just precipitates from sodium that is in contact with pure iron is determined by applying the law of mass action to the preceding reaction. Noting that all components are in their standard states (i.e., pure solids or liquids) except for  $\text{Na}_2\text{O}$ , there results

$$\frac{1}{a_{\text{O}}^*} = \exp \left( -\frac{\Delta G^\circ}{RT} \right)$$

Using Eqs. 20.16 and 20.23 yields

$$a_{\text{O}}^* = 1.43 \exp \left[ -\frac{1.56}{(T/10^3)} \right] \quad (20.25)$$

At 450°C this formula gives an oxygen activity of 0.17. The corresponding figure at 700°C is 0.29. Thus, pure iron and pure solid  $\text{Na}_2\text{O}$  cannot coexist in liquid sodium anywhere in this temperature range. With excess  $\text{Na}_2\text{O}$  all the iron would be converted to sodium ferrite, and with excess iron all the sodium monoxide would be consumed. Figure 20.9 and Eq. 20.19 show that at 450°C an oxygen activity of 0.17 corresponds to an oxygen concentration of (0.17) (776) = 132 ppm. At 700°C the critical oxygen concentration for sodium ferrite formation is 1650 ppm. When the oxygen concentration in sodium is less than the critical value, the double oxide  $\text{FeO} \cdot (\text{Na}_2\text{O})_2$  is unstable and decomposes into  $\text{Na}_2\text{O}$  and Fe, both dissolved in the sodium. Since most corrosion loops operate with oxygen concentrations in the tens of parts per million, we can conclude that dissolved oxygen should have no thermodynamic effect on the corrosion process. Iron should dissolve as the element and remain in this state throughout the loop.

It is a well established fact, however, that the rate of iron corrosion by sodium increases as the concentration of dissolved oxygen is raised. Since the preceding argument has revealed no thermodynamic basis for this effect, the accelerated corrosion rate must represent kinetic enhancement. The mass-transfer coefficient  $k_d$  should not be sensitive to dissolved oxygen, and the most likely source of the oxygen effect is the dissolution rate constant  $k_R$ . Weeks and Isaacs<sup>1</sup> have proposed a theory to explain this phenomenon.

They model the dissolution of iron into sodium after the accepted theory of desorption of an adsorbed gas from a solid surface. In this theory the adsorbed molecule is bound to a particular type of atomic site on the surface from which desorption is favored. The adsorbed molecule vibrates perpendicular to the surface, and every now and then a vibration possesses sufficient energy to permit the molecule to break the bond that holds it to the surface. The

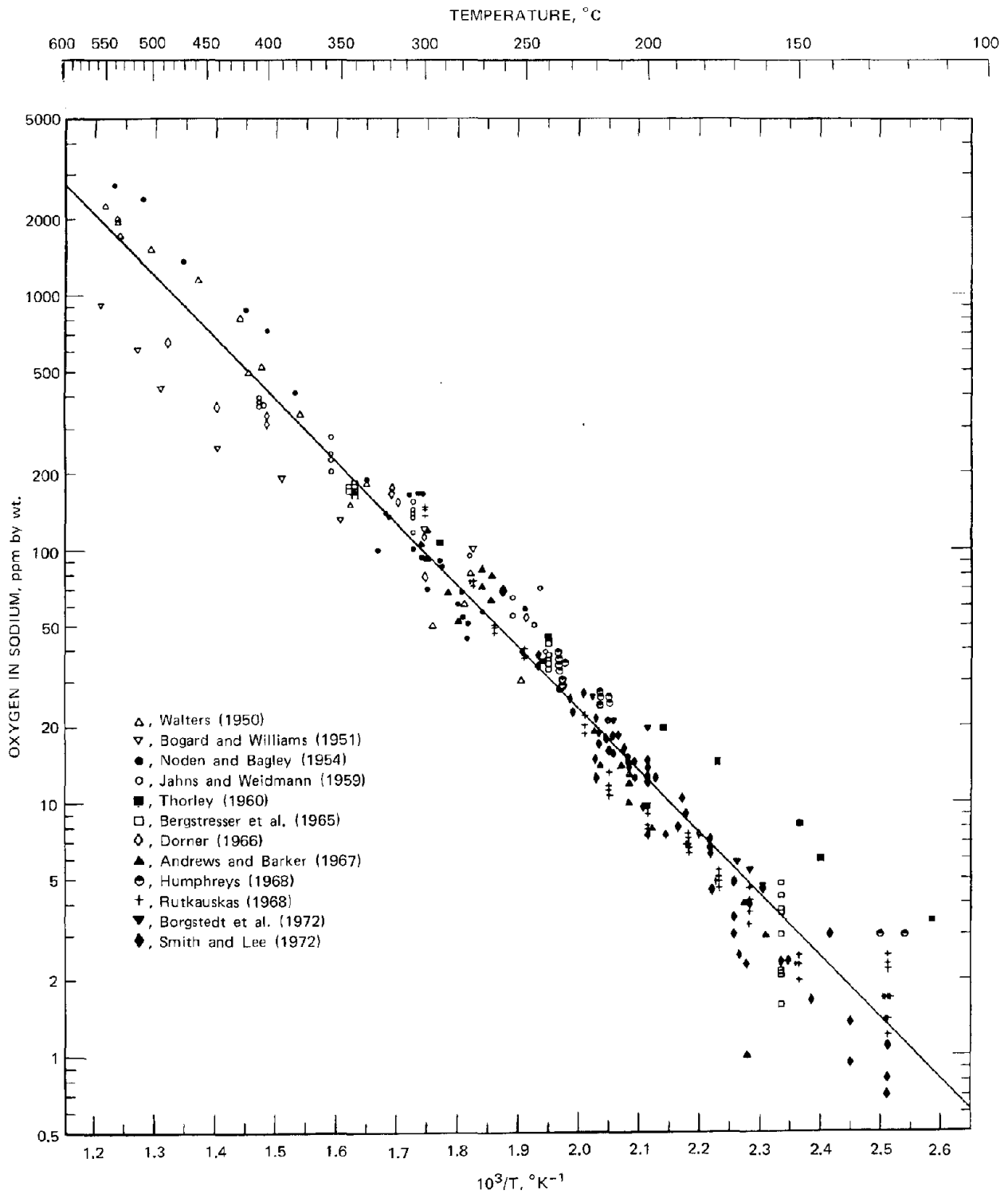


Fig. 20.9 Solubility of oxygen in liquid sodium; general equation from selected data. [After J. D. Noden, *J. Brit. Nucl. Energy Soc.*, 12: 329 (1973).]

rate of desorption is the product of a desorption rate constant and the density of molecules on active sites on the surface. Transferring this model to the iron-sodium system, Weeks and Isaacs propose that the iron surface contains a sparse population of active sites, each of which holds an adsorbed iron atom and that dissolution occurs from these sites. The rate of dissolution per unit area of surface is expressed by

$$R_{\text{dis}} = k_{\text{dis}}n \quad \text{atoms cm}^{-2} \text{ sec}^{-1} \quad (20.26)$$

where  $n$  is the density of active sites (sites/cm<sup>2</sup>) and  $k_{\text{dis}}$  is the dissolution rate constant. The latter is the probability per unit time that an adsorbed iron atom jumps from the active site into the adjacent liquid sodium.

In the event that the liquid sodium contains dissolved iron at a concentration  $C_{\text{int}}$ , the reverse step of condensation of iron on the surface also occurs. The rate of this step is given by

$$R_{\text{cond}} = k_{\text{cond}}C_{\text{int}} \quad (20.27)$$

The relationship between the rate constants  $k_{\text{dis}}$  and  $k_{\text{cond}}$  is determined by the requirement that at thermodynamic equilibrium (when  $C_{\text{int}} = C_{\text{sat}}$ ), the forward and reverse processes must be proceeding at equal rates, which requires that

$$k_{\text{dis}}n = k_{\text{cond}}C_{\text{sat}} \quad (20.28)$$

In the nonequilibrium situation represented by a corrosion experiment, the net rate for iron is

$$\dot{m} = \frac{M}{N_{\text{Av}}} (R_{\text{dis}} - R_{\text{cond}}) \quad \text{gFe cm}^{-2} \text{ sec}^{-1} \quad (20.29)$$

where  $M$  is the atomic weight of iron and  $N_{\text{Av}}$  is Avogadro's number. Substituting Eqs. 20.26 and 20.27 into Eq. 20.29 and eliminating  $k_{\text{cond}}$  by use of Eq. 20.28, we find that the corrosion rate is given by Eq. 20.1 in which the phenomenological rate constant  $k_{\text{R}}$  is related to the atomic rate constant  $k_{\text{dis}}$  by

$$k_{\text{R}} = \frac{Mk_{\text{dis}}n}{N_{\text{Av}}C_{\text{sat}}} \quad (20.30)$$

According to Weeks and Isaacs, oxygen in the sodium influences the atomic rate constant. In oxygen-free sodium  $k_{\text{dis}}$  assumes some value characteristic of a pure iron surface in contact with liquid sodium. However, even a small concentration of dissolved oxygen results in adsorption of sufficient oxygen on the surface so that each of the adsorbed iron atoms on the  $n$  active sites per square centimeter exists as the molecule FeO. Weeks and Isaacs speculate that the FeO species cannot dissolve unless it momentarily forms the double oxide FeO · (Na<sub>2</sub>O)<sub>2</sub>. This molecule is presumed to break up and release elemental iron to the solution as soon as the dissolution step is complete (because the double oxide is thermodynamically unstable). However, its transitory formation on the surface is essential to the removal of iron from the solid. Since the formation of a surface double-oxide molecule requires two Na<sub>2</sub>O molecules (the FeO is assumed to be on the surface

already), the dissolution rate constant should be proportional to the square of the oxygen concentration in the sodium. If we introduce the usual Boltzmann factor to allow for the temperature dependence of the dissolution step, the rate constant can be written

$$k_{\text{dis}} = A' C_{\text{O}}^2 \exp\left(-\frac{E_{\text{dis}}}{RT}\right) \quad (20.31)$$

where  $A'$  is a constant and  $E_{\text{dis}}$  is the activation energy for movement of an iron atom from an active site to the liquid adjacent to the surface. Combining Eqs. 20.30 and 20.31 yields

$$k_{\text{R}} = AC_{\text{O}}^2 n \exp\left(-\frac{E_{\text{dis}} - \Delta H_{\text{soln}}}{RT}\right) \quad (20.32)$$

where  $A$  is a collection of constants and  $\Delta H_{\text{soln}}$  is the enthalpy of solution of iron in sodium (from Eq. 20.10, equal to 82 kJ/mole). It arises from the term  $C_{\text{sat}}$  in the denominator of Eq. 20.30.

The theory of Weeks and Isaacs, although presented in atomic detail, does not provide a quantitative prediction of the corrosion rate. The constants  $A$  and  $E_{\text{dis}}$  in Eq. 20.32 are not given by the theory, and recourse to experimental data is required for their determination. However, the model does provide a physically plausible explanation of the effect of oxygen on the kinetics of iron corrosion. The only aspect of the model that can be tested against experiment is the predicted variation of the corrosion rate with the square of the oxygen concentration in systems in which convective diffusion is rapid and the bulk sodium is very undersaturated with respect to iron (so that Eq. 20.3 reduces to  $\dot{m} = k_{\text{R}}C_{\text{sat}}$ ). Available data for pure-iron corrosion in sodium confirm the second-power dependence predicted by the model; however, stainless-steel corrosion appears to vary with a power of the concentration of dissolved oxygen in the sodium somewhere between 1 and 1.5.

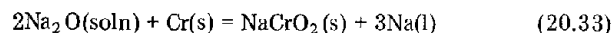
In addition to iron, stainless steel contains chromium and nickel, and these two elements are removed along with the primary component by liquid sodium. The solubilities of the three major constituents of stainless steel (in their elemental states) in liquid sodium are shown in Fig. 20.10.

### Nickel Corrosion

Contrary to iron, the solution of pure nickel is unaffected by the oxygen content of the liquid metal. Double oxides of nickel and sodium are thermodynamically unstable, and the dissolution rate of nickel does not appear to require catalysis by Na<sub>2</sub>O, as does the dissolution of iron. The corrosion rate of pure nickel should therefore be governed by liquid-phase convective diffusion, with the driving force equal to the difference between the solubility and the nickel concentration of the bulk sodium (i.e., by Eq. 20.3 with  $k_{\text{d}}/k_{\text{R}} \ll 1$ ).

### Chromium Corrosion

Chromium is a strong oxide former, and sodium chromite, NaCrO<sub>2</sub>, forms readily according to the reaction



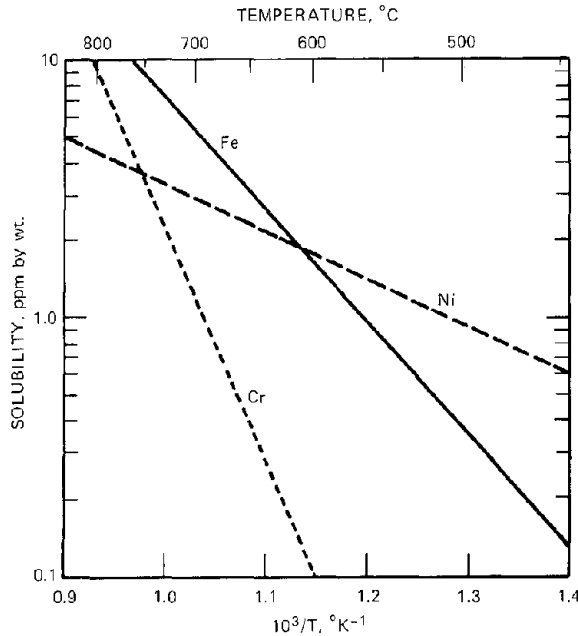


Fig. 20.10 Solubility of iron, nickel and chromium in oxygen-free sodium. (After Ref. 1.)

The reaction has been written for  $\text{Na}_2\text{O}$  in solution in sodium. The thermodynamics of the reaction gives the free-energy change when all participants are present in their pure (or standard) states. For the preceding reaction, the standard-state free-energy change can be obtained from the data of Wu and Chiotti<sup>4</sup> and Eq. 20.16:

$$\Delta G^\circ = 60 - 155 \left( \frac{T}{10^3} \right) \text{ kJ/mole} \quad (20.34)$$

The critical oxygen activity in sodium at which sodium chromite precipitation occurs can be determined by application of the law of mass action to reaction 20.33, which yields

$$\frac{1}{(a_{\text{O}}^*)^2} = \exp \left( -\frac{\Delta G^\circ}{RT} \right) \quad (20.35)$$

Using Eqs. 20.34 and 20.35, we can determine the oxygen activity for formation of  $\text{NaCrO}_2$  from oxygen in sodium that is in contact with pure chromium. The corresponding oxygen concentrations in the sodium are then found from Fig. 20.9 and Eq. 20.19. Proceeding in this manner, critical oxygen concentrations are found to be  $\sim 10$  ppm at  $450^\circ\text{C}$  and  $\sim 20$  ppm at  $700^\circ\text{C}$ . However, increasing the oxygen concentration in sodium loops beyond  $\sim 3$  ppm without adding large excesses of  $\text{Na}_2\text{O}$  is difficult. Presumably, the added oxygen first must consume all the exposed chromium metal surfaces (or coat them with a protective film of sodium chromite) before the oxygen level of the sodium can be raised above the critical concentration. The observation that chromium starts to react with oxygen at concentrations less than about 3 ppm instead of in the 10 to 20 ppm range calculated previously suggests that the free-

energy change of reaction 20.33 is  $\sim 10$  kJ/mole more negative than indicated by Eq. 20.34.

In any case, the critical oxygen concentrations for precipitation of sodium chromite are considerably smaller than those for formation of sodium ferrite, and formation and dissociation of  $\text{NaCrO}_2$  in various parts of a sodium loop can be an important feature of stainless-steel corrosion and solid deposition. To assess the effect of chromium on corrosion of stainless steel, we first develop models of corrosion of pure chromium metal in oxygenated sodium. In view of the substantial uncertainty in the thermochemistry of the sodium-chromium-oxygen system, two alternative models are analyzed.

We shall first consider the case in which the solubility of elemental chromium in sodium is represented by the dotted line in Fig. 20.10 but assume that the standard free-energy change of reaction 20.33 is very large and negative. The reaction between  $\text{Na}_2\text{O}$  and chromium is rapid and occurs in the sodium boundary layer adjacent to the surface in the manner depicted in Fig. 20.11. This mass-transfer-with-reaction process is analogous to the process of vaporization of oxide-forming metals in an oxidizing gas, which has been treated by Turkdogan, Grieveson, and Darken.<sup>5</sup> Because the free energy of formation of the oxide product ( $\text{NaCrO}_2$  in the present case) is assumed to be large and negative, dissolved oxygen (as  $\text{Na}_2\text{O}$ ) and dissolved chromium cannot coexist in the sodium boundary layer adjacent to the metal surface. Therefore, a zone free of  $\text{Na}_2\text{O}$  but containing a dissolved chromium concentration distribution exists next to the metal surface; the outer edge of the boundary layer contains a  $\text{Na}_2\text{O}$  concentration profile but is devoid of chromium. These two zones are separated by a reaction front wherein the concentrations of the two reactants vanish and the insoluble  $\text{NaCrO}_2$  product is formed. The concentration profiles of chromium and  $\text{Na}_2\text{O}$  are shown in Fig. 20.11. The oxide reaction product generated at the reaction front is assumed to be swept into the bulk sodium,

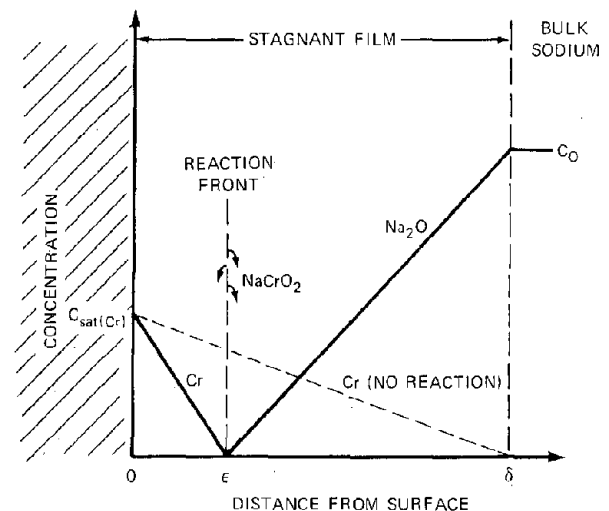


Fig. 20.11 Model of chromium corrosion based on rapid, irreversible reaction at a reaction front in the sodium film.

but, since it cannot dissociate (because the reaction is assumed to be irreversible), it has no effect on the corrosion rate.

If  $\text{NaCrO}_2$  were not produced in the corrosion process, chromium would dissolve in the same manner as nickel does, and the chromium distribution in the boundary layer would resemble the dashed line in Fig. 20.11. In this analysis we use the film theory of mass transfer, whereby the boundary layer is approximated by a stagnant film of sodium in which transport occurs by molecular diffusion. In the absence of reaction, the mass-transfer rate is given by

$$(\dot{m})_{\text{no reaction}} = k_d C_{\text{sat}}(\text{Cr}) = \frac{D_{\text{Cr}}}{\delta} C_{\text{sat}}(\text{Cr}) \quad (20.36)$$

Equation 20.36 determines the fictitious film thickness  $\delta$  as  $k_d/D_{\text{Cr}}$ , where  $D_{\text{Cr}}$  is the diffusion coefficient of chromium in liquid sodium and  $k_d$  is the mass-transfer coefficient (for pipe flow, given by Eq. 20.8). The figure shows that the irreversible reaction increases the chromium gradient near the wall and hence increases the corrosion rate. According to the film model, the latter is

$$\dot{m} = \frac{D_{\text{Cr}}}{\epsilon} C_{\text{sat}}(\text{Cr}) \quad (20.37)$$

The standoff distance of the reaction front,  $\epsilon$ , is determined by the requirement that the stoichiometry of reaction 20.33 be satisfied or that the atom flux of chromium to the reaction front from the surface be equal to one-half the molar flux of  $\text{Na}_2\text{O}$  to the reaction front from the bulk sodium. This condition leads to

$$\frac{D_{\text{Cr}} C_{\text{sat}}(\text{Cr})}{\epsilon M_{\text{Cr}}} = \frac{1}{2} \frac{D_{\text{Na}_2\text{O}} C_{\text{O}}}{\delta - \epsilon M_{\text{O}}} \quad (20.38)$$

where  $C_{\text{sat}}(\text{Cr})$  = solubility of elemental chromium in sodium in grams per cubic centimeter (obtained from Fig. 20.10 with the appropriate change in units)

$C_{\text{O}}$  = concentration of oxygen in the bulk sodium in grams of oxygen per cubic centimeter.

$M_{\text{Cr}}$  = atomic weight of chromium

$M_{\text{O}}$  = atomic weight of oxygen

Solving Eq. 20.38 for  $\epsilon$ , substituting the result into Eq. 20.37, and replacing  $D_{\text{Cr}}/\delta$  by the mass-transfer coefficient yields

$$\dot{m} = k_d C_{\text{sat}}(\text{Cr}) \left[ 1 + \frac{1}{2} \frac{D_{\text{Na}_2\text{O}} C_{\text{O}} M_{\text{Cr}}}{D_{\text{Cr}} C_{\text{sat}}(\text{Cr}) M_{\text{O}}} \right] \quad (20.39)$$

Comparison of Eqs. 20.36 and 20.39 shows that the bracketed term in Eq. 20.39 represents the enhancement of the corrosion rate by the irreversible reaction between chromium and sodium oxide. Assuming  $D_{\text{Na}_2\text{O}} \approx D_{\text{Cr}}$  and taking typical concentrations  $C_{\text{O}} \approx 10$  ppm and  $C_{\text{sat}}(\text{Cr}) \approx 1$  ppm (solubility at  $700^\circ\text{C}$ ), we find that Eq. 20.39 predicts a chromium removal rate that is  $\sim 20$  times greater than in the absence of  $\text{NaCrO}_2$  formation. At large oxygen concentrations, the rate of corrosion of chromium should be directly proportional to  $C_{\text{O}}$  and independent of the chromium solubility.

Equation 20.39 probably overestimates the effect of oxygen on chromium corrosion because it is based on the assumption that reaction 20.33 is irreversible (i.e., that  $\text{NaCrO}_2$  cannot dissociate). Another model of chromium corrosion in oxygenated sodium starts from the premise that reaction 20.33 occurs at the solid-liquid interface proper and is slow but reversible. The solubility of elemental chromium in sodium is neglected. If reaction 20.33 were rapid, the concentration of  $\text{Na}_2\text{O}$  at the solid-liquid interface would be determined by the thermodynamics of the reaction, which leads to an oxygen activity given by Eq. 20.35. The equilibrium oxygen concentration at the interface would be fixed by

$$C_{\text{O}}^* = C_{\text{sat}}(\text{O}) a_{\text{O}}^* \quad (20.40)$$

If reaction 20.33 is slow, however, the oxygen concentration at the interface will be larger than  $C_{\text{O}}^*$ , and the rate of production of  $\text{NaCrO}_2$  can be expressed in terms of the departure from equilibrium:

$$\dot{m} = k_{\text{R}} [C_{\text{int}}(\text{O}) - C_{\text{O}}^*] \quad (20.41)$$

where  $k_{\text{R}}$  is the rate constant for the forward step of reaction 20.33 and  $C_{\text{int}}(\text{O})$  is the concentration of  $\text{Na}_2\text{O}$  in the sodium immediately adjacent to the chromium surface. The  $\text{Na}_2\text{O}$  concentration distribution through the sodium boundary layer is shown schematically in Fig. 20.12, and the rate of transfer of oxygen to the surface by convective diffusion is given by

$$\dot{m} = k_d [C_{\text{O}} - C_{\text{int}}(\text{O})] \quad (20.42)$$

Combining the preceding two equations yields the corrosion rate

$$\dot{m} = \left( \frac{1}{k_{\text{R}}} + \frac{1}{k_d} \right)^{-1} (C_{\text{O}} - C_{\text{O}}^*) \quad (20.43)$$

This corrosion rate contains resistances due to both diffusion-convection and chemical reaction at the interface. The driving force is the difference between the bulk oxygen concentration and the maximum oxygen concentration permitted by the thermochemistry of reaction 20.33. The model also assumes that the  $\text{NaCrO}_2$  reaction product does not coat the metal and protect it from further attack; the oxide produced must be nonadherent and be easily sheared off the surface by flowing sodium for the model to be valid. If the  $\text{NaCrO}_2$  layer is adherent, oxygen from the sodium must dissolve in it and move by solid-state diffusion to the double-oxide-metal interface for reaction to occur. This is a very slow process, and, if diffusion through a protective film were controlling, the corrosion rate would be much smaller than that predicted by either of the preceding models (Eq. 20.39 or 20.43).

### 20.3 CORROSION AND SELECTIVE LEACHING OF STAINLESS STEEL

Having determined (in theory at least) the corrosion rate of the three principal metals in stainless steel, we are in

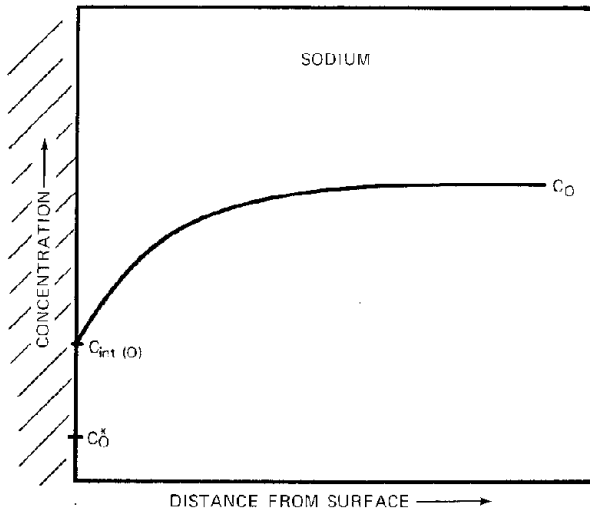


Fig. 20.12 Model of chromium corrosion based on slow reversible reaction at the sodium-chromium interface.

a position to estimate the corrosion rate of the ternary alloy and the effect of unequal component removal rates on the surface composition.<sup>5</sup>

Let  $\dot{m}_i^0$  be the rate of corrosion of pure metal  $i$  into sodium. The component corrosion rates are presumed to be known as functions of temperature, sodium velocity, and oxygen concentration of the sodium. Because  $\dot{m}_{Cr}^0$  and  $\dot{m}_{Ni}^0$  appear to be larger than  $\dot{m}_{Fe}^0$  for the same external conditions, nickel and chromium are removed more rapidly from the surface of the steel than iron, which imbalance results in depletion of nickel and chromium in the surface and enrichment in iron (selective leaching). Because of the changes in alloy composition, the original austenitic phase can change to ferrite near the surface. The alteration of the surface composition also sets up concentration gradients of iron, nickel, and chromium in the steel, and these elements will migrate by solid-state diffusion in the direction dictated by their concentration gradients. Eventually, however, a steady-state corrosion rate is achieved in which the removal rates of the three species at the interface and the concentration distributions in the adjacent solid become stationary. Figure 20.13 illustrates the steady-state situation.

The composition of the bulk steel is specified by the mass fractions  $\omega_i^0$  of the three major species. The composition of the alloy at the interface differs from the bulk composition. The interface concentrations are denoted by  $\omega_{int(i)}$ , also in mass fraction units. The removal rates of the three species by the liquid sodium,  $\dot{m}_i$ , are assumed to be less than the corresponding removal rates of the pure metals under the same sodium conditions by a factor equal to the mass fraction of the component in the metal exposed to the sodium, or

$$\dot{m}_i = \omega_{int(i)} \dot{m}_i^0 \quad (20.44)$$

The corrosion rate of the steel is the sum of the removal rates of the three components

$$\dot{m} = \dot{m}_{Fe} + \dot{m}_{Cr} + \dot{m}_{Ni} \quad (20.45)$$

We select a coordinate system moving with the corrosion velocity  $u = \dot{m}/\rho$ , where  $\rho$  is the density of steel. In this frame of reference, the interface is stationary, and the metal advances from left to right in Fig. 20.13 at a uniform velocity  $u$ . A material balance on the volume element between the plane labeled 1 in Fig. 20.13 and the interface

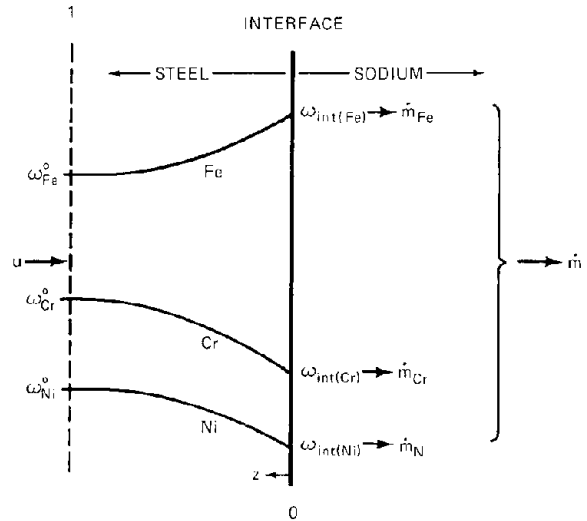


Fig. 20.13 Concentration distributions of iron, nickel, and chromium in stainless steel contacted with sodium.

requires that at steady state the rate at which each component enters plane 1 from the bulk of the steel be equal to the rate at which this species is removed from the interface by dissolution into the sodium, or

$$\dot{m}_i = \rho u \omega_i^0 = \dot{m} \omega_{int(i)}^0 \quad (20.46)$$

Equating the right-hand sides of Eqs. 20.44 and 20.46 yields

$$\omega_{int(i)} = \frac{\rho u \omega_i^0}{\dot{m}_i^0} \quad (20.47)$$

Inasmuch as the sum of the  $\omega_{int(i)}$  values is equal to unity, the corrosion rate is determined by the composition of the steel and the corrosion rates of the pure component metals under the same conditions according to

$$\rho u = \dot{m} = \left[ \sum \left( \frac{\omega_i^0}{\dot{m}_i^0} \right) \right]^{-1} \quad (20.48)$$

and the surface composition follows by using this result in Eq. 20.47:

$$\omega_{int(i)} = \frac{\omega_i^0 / \dot{m}_i^0}{\sum (\omega_i^0 / \dot{m}_i^0)} \quad (20.49)$$

The sums in Eqs. 20.48 and 20.49 include iron, nickel, and chromium.

The concentration distributions of the three metals near the surface, which are designated by  $\omega_i(z)$ , can be obtained by use of Fick's law of diffusion, which in this case must be supplemented by a convection term arising from the motion of the metal in the coordinate system fixed to the solid-liquid interface. The flux of species  $i$  at any point in the solid is

$$\dot{m}_i = \rho D_i \frac{d\omega_i}{dz} + \rho u \omega_i = \text{constant} \quad (20.50)$$

where  $z$  is measured from the interface into the metal ( $\dot{m}_i$  is, by choice, positive in the negative  $z$ -direction, so that the usual minus sign in front of the gradient in Fick's law is absent). Taking the derivative of Eq. 20.50 with respect to  $z$  gives the second-order differential equation

$$D_i \frac{d^2 \omega_i}{dz^2} + u \frac{d\omega_i}{dz} = 0 \quad (20.51)$$

which is subject to the boundary conditions

$$\begin{aligned} \omega_i(0) &= \omega_{int(i)} \\ \omega_i(\infty) &= \omega_i^0 \end{aligned} \quad (20.52)$$

The solution is

$$\frac{\omega_i - \omega_i^0}{\omega_{int(i)} - \omega_i^0} = \exp\left(-\frac{u}{D_i} z\right) \quad (20.53)$$

[A very similar situation is encountered in analysis of pore migration due to a temperature gradient in a mixed-oxide fuel. As discussed in Chap. 11, the plutonium distribution ahead of such a pore (Eq. 11.102) is of the same form as Eq. 20.53.]

The depth of the concentration perturbation can be estimated from the measured corrosion rate. For a 5% approach of the concentration to the bulk value in the steel, the argument of the exponential in Eq. 20.53 should be  $\sim 5$ . The diffusion coefficients in the iron-chromium-nickel system are  $\sim 3 \times 10^{-14}$  cm<sup>2</sup>/sec at 700°C. For a corrosion velocity of 25  $\mu\text{m}/\text{year}$ ,

$$\text{Depth of penetration} \simeq \frac{5D_i}{u} \sim 20 \mu\text{m}$$

Figure 20.14 shows typical data on selective removal of the constituents of stainless steel. The calculated penetration depth is in fair agreement with what is found experimentally. The surface of the specimens from which the data of Fig. 20.14 were obtained is 96% iron; thus, removal of this element by sodium controls the entire corrosion process. The ferritic layer that forms when the chromium and nickel concentrations become too small to sustain the austenitic phase is seen to range in size from one-fifth to one-half the depletion depth of the individual elements.

### 20.3.1 The Weeks-Isaacs Model

Weeks and Isaacs<sup>1</sup> have extended the model of corrosion of pure iron to apply to stainless steel. They note that, because of the selective leaching process described earlier in this section, iron is by far the dominant component on the

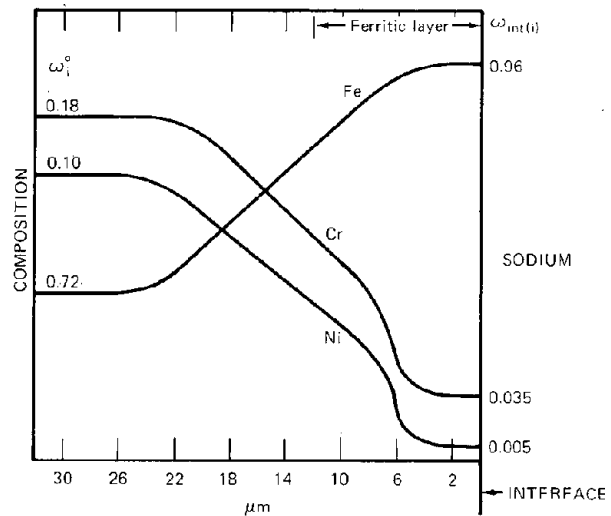


Fig. 20.14 Electron microprobe traces of a cross section of a stainless-steel specimen exposed to high-velocity sodium at 755°C for 2500 hr. (After A. J. Romano and C. J. Klamut, cited in Ref. 1.)

surface and therefore controls the dissolution rate of the alloy. The rate of corrosion of steel,  $\dot{m}$ , is related to the iron content of the steel by Eq. 20.46, in which  $\dot{m}_{Fe}$ , the corrosion rate of iron from the surface, is taken to be the same as that for pure iron,  $\dot{m}_{Fe}^0$ , because the surface is essentially all iron. The rate constant  $k_R$  for dissolution of pure iron (Eq. 20.32) is modified in two ways to account for chromium and nickel in the sodium. First, chromium and nickel are assumed to act as poisons to iron dissolution by occupying some of the active sites on the surface from which iron dissolves. Thus,  $n$  in Eq. 20.32 is replaced by  $n[1 - g(C_{Cr} + C_{Ni})]$ , where  $g$  is a constant and  $C_{Cr}$  and  $C_{Ni}$  are the bulk concentrations of chromium and nickel in the flowing sodium. Second, they replace the power 2 in  $C_O$  in Eq. 20.32 by  $2[1 - (\omega_{Cr}^0 + \omega_{Ni}^0)] = 2\omega_{Fe}^0$ , although the justification for this step is rather nebulous. They also assume that (1) the bulk sodium is undersaturated with respect to iron, so that  $C_{Fe} \ll C_{sat(Fe)}$ , and (2) the sodium velocity is sufficiently high to eliminate the boundary-layer mass-transfer resistance ( $k_d \gg k_R$ ).

Combining all the preceding modifications, the corrosion rate of stainless steel is expected to be of the form:

$$\dot{m} = \frac{k_R C_{sat(Fe)}}{\omega_{Fe}^0} = \frac{B}{\omega_{Fe}^0} (C_O)^2 \omega_{Fe}^0 \exp\left(-\frac{E_{dis}}{RT}\right) \times [1 - g(C_{Cr} + C_{Ni})] \quad (20.54)$$

where  $B$  is a constant. In all stainless steels of interest to LMFBR application,  $\omega_{Fe}^0$  is between 0.65 and 0.75. Using the lower figure as representative, we find the oxygen concentration dependence of the corrosion rate is governed by the term  $(C_O)^{1.3}$ . The poisoning effect of dissolved chromium and nickel on iron dissolution represented by the last term in the brackets of Eq. 20.54 is empirically related to the downstream position in a leg on the grounds that, as the sodium flows along such a section,  $C_{Cr}$  and  $C_{Ni}$

increase because the corrosion process releases these elements to the sodium. On the basis of comparison with the observed downstream effect,  $g(C_{Cr} + C_{Ni})$  is replaced by  $c(x/d)^2$ , where  $c$  is another constant. Evaluating the parameters  $B$ ,  $E_{dis}$ , and  $\epsilon$  from data, we find the corrosion rate equation to be

$$\dot{m} = 1.1 \times 10^8 (C_O)^{1.3} \exp \left[ -\frac{146}{R(T/10^3)} \right] \times \left[ 1 - 10^{-6} \left( \frac{x}{d} \right)^2 \right] \mu\text{m/year} \quad (20.55)$$

where  $C_O$  is in parts per million oxygen by weight.

Although Eq. 20.55 satisfactorily correlates stainless-steel corrosion data and reproduces the important effects of temperature, oxygen concentration, and downstream position, it is restricted to sodium velocities large enough to eliminate convection-diffusion as a major transport resistance. For the high sodium velocities expected in LMFBR sodium-coolant loops, Eq. 20.55 probably provides a good estimate of the steel corrosion rate. However, the Weeks-Isaacs formula does not correctly predict the transition from dissolution control to diffusion control. The mass-transfer coefficient in a pipe is rather accurately given by Eq. 20.8 (for  $x/d > 50$ , it is even conservative, since the entrance effect is not included). If a surface-dissolution rate constant were computed from Eq. 20.55 by dividing this equation by  $C_{sat(Fe)}$ ,  $k_R$  would be found to be very much smaller than  $k_d$  down to extremely small sodium velocities. Hence, the velocity effect shown in Fig. 20.5 is not at all predicted by the Weeks-Isaacs model when their surface-dissolution step is coupled to a diffusional transport resistance according to Eq. 20.3.

### 20.3.2 Microstructural Changes Due to Sodium Corrosion

Figure 20.15 shows the alterations in the morphology of the steel near the interface with flowing sodium to which the metal has been exposed. The small specks that appear after ~500 hr subsequently grow into distinguishable particles by 15,000 hr. These precipitates are the sigma phase of steel (an intermetallic compound of iron and ~45% chromium). The formation of this phase is ascribed to the loss of interstitial elements, principally carbon, from the steel. The last three panels of the montage reveal the growth of a layer of ferrite on the surface (dark gray). The appearance of this form of steel is due to the loss of the austenitic stabilizers nickel and chromium from the surface layer due to the selective leaching process described earlier in this section.

Figure 20.16 shows a scanning electron micrograph of the surface of sodium-exposed type 316 stainless steel. The surface is considerably roughened as a result of interaction with sodium, and small pits are visible. In titanium-stabilized grades of stainless steel (e.g., type 321), a substantial number of subsurface cavities are found. These voids are interlinked and extend to ~100  $\mu\text{m}$  below the surface. Types 304 and 316 stainless steel do not exhibit such extensive cavity formation.

## 20.4 DEPOSITION AND TRANSPORT OF INDUCED RADIOACTIVITY

The preceding two sections dealt with corrosion of stainless steel in the hot regions of a sodium loop. For the process to continue, the corrosion products must be removed in the cool portions of the circuit at the same rate

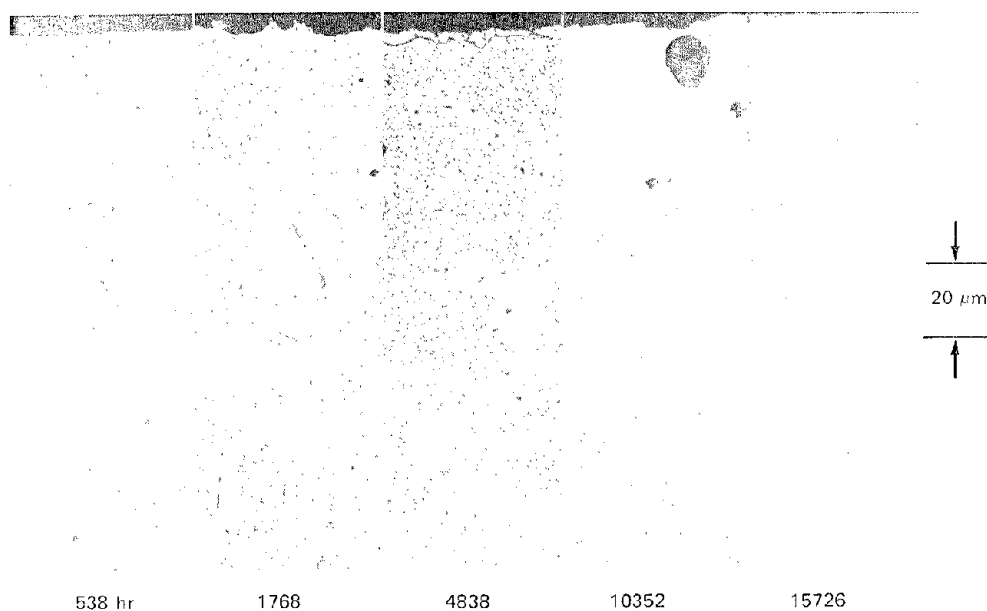


Fig. 20.15 Evolution of the near-surface microstructure of type 316 stainless steel exposed to sodium at 700°C for times up to 15,000 hr. [From D. W. Sandusky et al., *J. Nucl. Mater.*, 46: 225 (1973).]

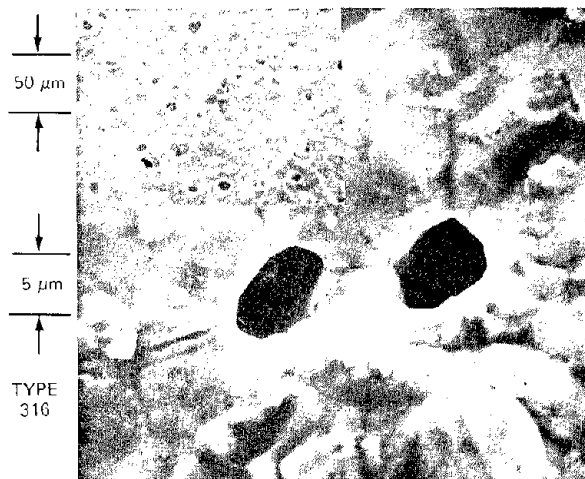


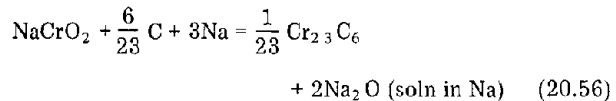
Fig. 20.16 Scanning electron micrograph of the surface of type 316 stainless steel exposed to sodium at 700°C for 15,000 hr. [From D. W. Sandusky et al., *J. Nucl. Mater.*, 46: 225 (1973).]

that dissolution proceeds in the hot region. In this manner, a steady transfer of mass from the high-temperature part of the circuit (core, hot leg) to the low-temperature parts (heat exchanger, cold leg) is established.<sup>7</sup> At the largest cold-leg deposition rates that have been observed in experimental loops, the transfer of several tons of structural metals via the flowing sodium could occur during the lifetime of the reactor.<sup>8</sup>

The deposition process is more complex than the corrosion process, and no quantitative theory of the former is available. Qualitatively, however, the deposition process is understood; the reduction of sodium temperature as the liquid metal flows through the heat exchanger reduces the solubility of the various species that were removed from the structural members in the hot zone. The supersaturation caused by the abrupt reduction in temperature is partially relieved by release of the dissolved metals from solution. Dissolved iron, nickel, chromium, and manganese can move to the cool surfaces as atomic species and condense, thereby reversing the corrosion process. Or, if the supersaturation is sufficiently high, the metals can precipitate out of solution by homogeneous nucleation. Much of the particulate matter suspended in flowing sodium is removed by stainless-steel or nickel mesh filters inserted into the cold-leg piping expressly for this purpose.

Deposition rates are high both at the beginning of a zone in which the sodium temperature first begins to decrease and in isothermal sections when turbulence is generated by a flow obstacle (e.g., an abrupt change in flow cross section or a fitting, such as a valve, elbow, or tee). Figure 20.17 shows the gross characteristics of the deposits in regions near a flow disruption. Figure 20.18(a) shows a scanning electron micrograph of a sodium-exposed surface in the cold leg of a test loop. The deposit is crystalline in nature and consists primarily of mixed carbides ( $\text{Cr}_{23}\text{C}_6$  and  $\text{Fe}_{23}\text{C}_6$ ),  $\text{NaCrO}_2$ , and a metallic austenite phase of

undetermined composition (although it contains iron, chromium, and nickel). As we shall discuss later, carbon is transferred in sodium loops in even greater quantities (relative to the amount in the original steel) than the major alloy constituents of the steel. The transferred carbon is responsible for the abundance of the  $\text{M}_{23}\text{C}_6$  carbides in the corrosion-product deposits. The proportion of the chromium in the carbide form depends on the oxygen content of the sodium according to the reaction



High oxygen concentrations (>15 ppm by weight) drive reaction 20.56 to the left, and the chromium precipitates primarily as the double oxide. Low oxygen concentrations favor carbide formation. As expected from the thermodynamic arguments presented earlier, neither nickel nor iron appears an oxide. Iron is contained in the austenitic phase and in the form of the  $\text{Fe}_{23}\text{C}_6$  carbide. The deposits in the lower temperature regions of the cold leg [Fig. 20.18(b)] do not exhibit the distinct crystalline structure characteristic of the high-temperature deposits. Here, iron appears as the alpha phase of the elemental metal ( $\alpha\text{-Fe}$ ).

The minor elements in the steel, silicon and manganese, are deposited as  $\text{Na}_2\text{SiO}_2$  and  $\alpha$ - or  $\beta$ -Mn, respectively. Much of the sodium found in the deposits is occluded with other particulate matter rather than chemically bound as double oxides.<sup>9</sup>

Deposition rates at a particular location can be as large as 3 to 4  $\text{mg cm}^{-2} \text{hr}^{-1}$  ( $\sim 100 \mu\text{m}/\text{year}$ ) and show the same dependence on sodium velocity (increasing with increasing  $v$ ) and downstream position (decreasing with increasing  $x/d$ ) as do corrosion rates. The chemical character of the deposits is illustrated by the data in Table 20.1. Chromium

Table 20.1 Analysis of Semiadherent Deposits from Cold Side of Primary Loop\*

Location (x/d)†	Temp., °C	Metallic elements, wt. %				
		Fe	Cr	Ni	Mn	Mo
940	650	1.3	95.2	3.7	0.08	0.01
1020	625	1.1	73.9	17.4	0.08	0.03
1080	600	1.0	52.8	31.6	10.00	0.01
1110	575	1.2	39.5	28.0	13.6	0.02

\*Data from Ref. 8.

†Pipe diameters downstream from pump exit.

is a major constituent at all temperatures and is the principal corrosion product attached to high-temperature surfaces in zones in which the temperature is decreasing with increasing downstream location. Large quantities of manganese are deposited on the cool end of the leg. The scarcity of iron in the deposits analyzed in Table 20.1 can be due to the suspension of fine particles of this element in the flowing sodium, removal from which occurs at flow disturbances or filters.

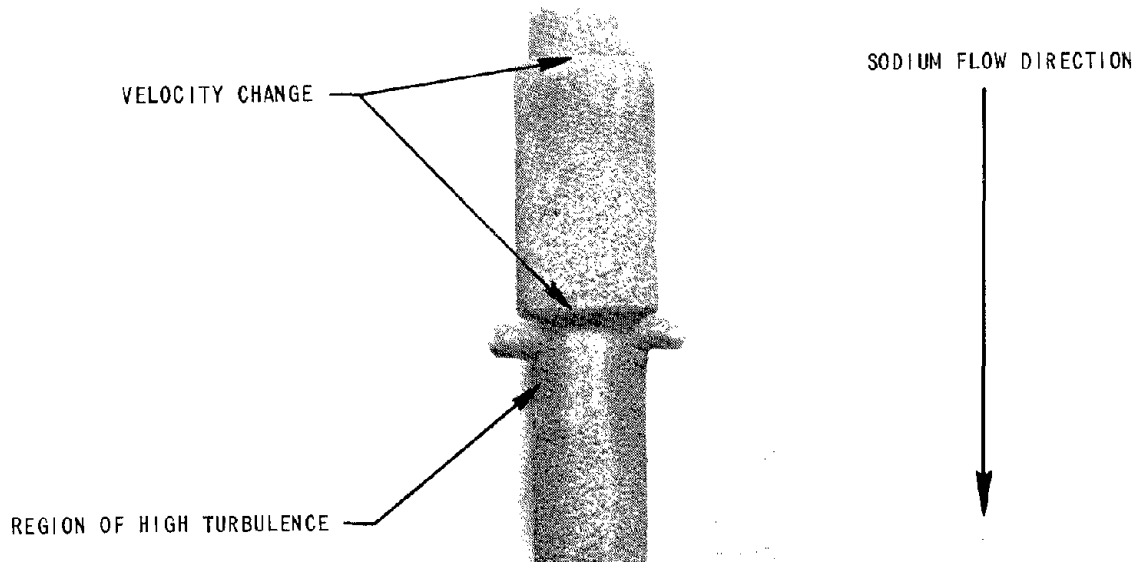


Fig. 20.17 Photograph illustrating enhancement of corrosion-product deposition near a flow discontinuity. [From W. E. Ray et al., *Nucl. Technol.*, 16: 249 (1972).]

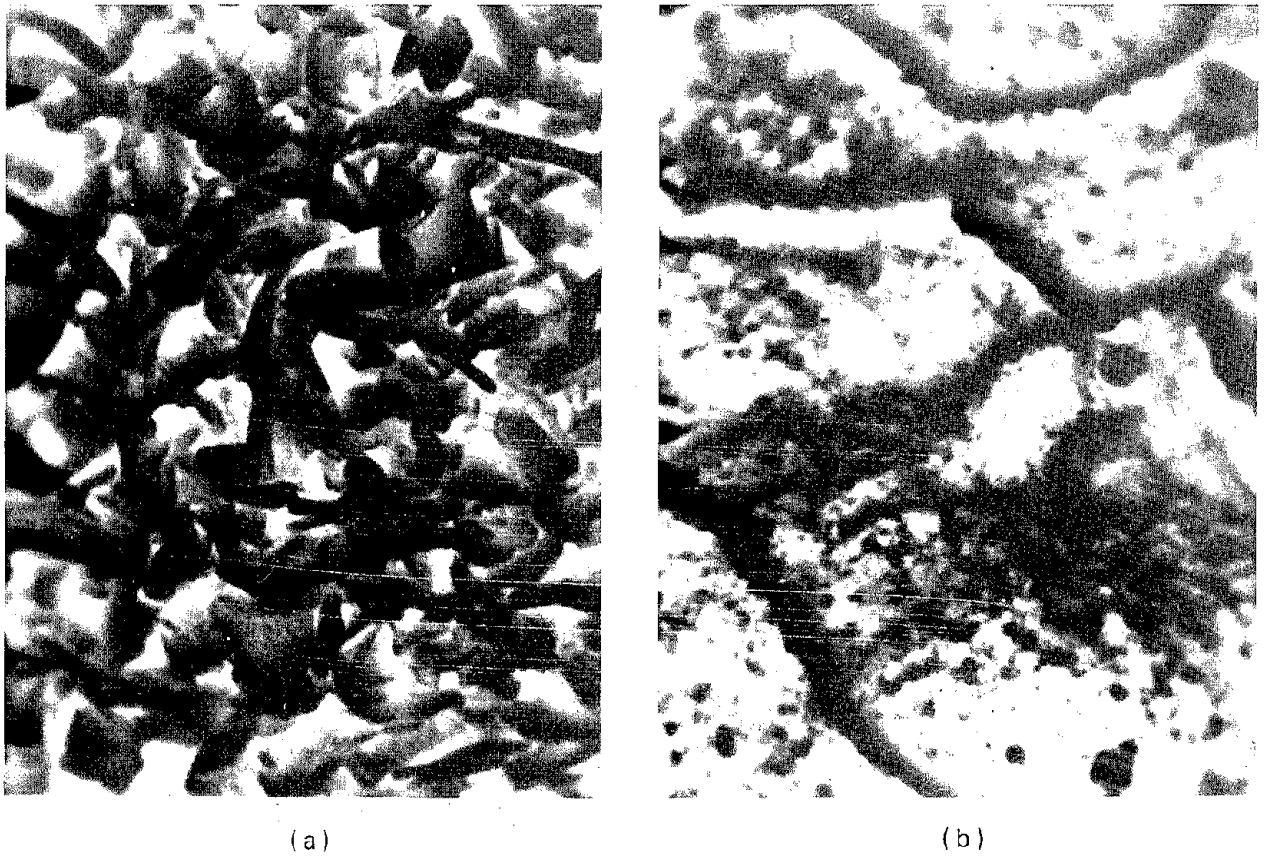


Fig. 20.18 Scanning electron micrographs of deposit on surface of type 316 stainless-steel surface after 3300 hr in flowing sodium. (a) 650°C. (b) 430°C. (From Ref. 7.)

Accumulation of deposits in the intermediate heat exchanger can adversely affect the hydraulic performance of this unit by reducing flow area. In addition, the heat-transfer resistance can increase owing to the inferior thermal conductivity of the scale compared to that of the base metal. An annual reduction of nearly 10% in the overall heat-transfer coefficient in the intermediate heat exchanger is estimated from sodium loop corrosion data.<sup>8</sup>

The initial deposits adhere tightly to the base-metal surface, but succeeding deposits tend to be less compact. Conceivably, an equilibrium deposit thickness could be attained when the scale thickness becomes limited by the shear force of the flowing sodium.

As indicated in the introduction to this chapter, the major radioactive species in the deposits are  $^{54}\text{Mn}$ ,  $^{58}\text{Co}$ , and  $^{60}\text{Co}$ . In agreement with observations of the deposition of nonradioactive manganese,  $^{54}\text{Mn}$  concentrates in the cold leg and in the cold trap of a sodium loop. The cobalt activity, however, appears to be more uniformly distributed about the loop and may even prefer to concentrate in the hot-leg piping.<sup>10</sup> As shown by Fig. 20.19, the rate of deposition of radioactivity is enhanced by flow disturbances, such as an area reduction.

The estimated external radiation level near the hot-leg piping of an LMFBR primary sodium loop is shown in Fig. 20.20. The burden of radioactivity decreases with decreasing sodium outlet temperature because the corrosion rate in the core is reduced as the temperature level is decreased. For high outlet sodium temperatures, the dose rate is too high for routine maintenance of the hot-leg parts. Consequently, components susceptible to substantial accumulation of radioactivity will have to be removed from the loop and decontaminated rather frequently. Scale removal by chelating agents (e.g., acetylacetone) is under investigation.<sup>11</sup> These chemicals (in aqueous solution) form complexes with the transition metals (particularly cobalt

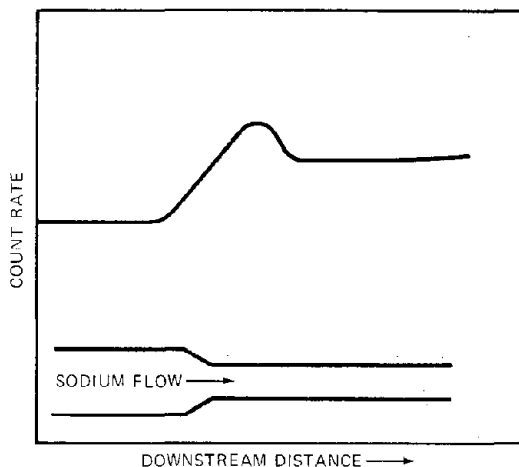


Fig. 20.19 Distribution of radioactivity in deposit near a flow perturbation caused by area reduction in the piping. [After W. F. Brehm et al., in *Corrosion by Liquid Metals*, J. E. Draley and J. R. Weeks (Eds.), p. 97, Plenum Publishing Corporation, New York, 1970.]

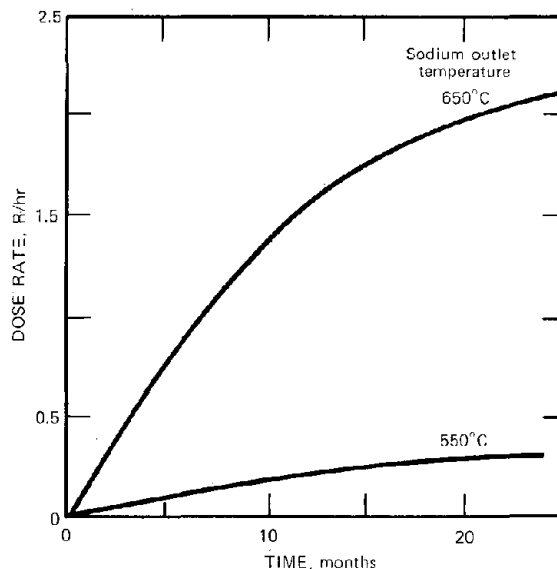


Fig. 20.20 Estimated dose rate 60 cm from the hot-leg piping in an LMFBR due to deposited  $^{54}\text{Mn}$  and  $^{58}\text{Co}$  for various sodium outlet temperatures. [After W. F. Brehm et al., in *Corrosion by Liquid Metals*, J. E. Draley and J. R. Weeks (Eds.), p. 97, Plenum Publishing Corporation, New York, 1970.]

and manganese) and can dissolve a 10- $\mu\text{m}$  thick scale in 100 hr. Carbides, however, are not dissolved by this treatment and will require a different decontamination procedure. Finally, some of the radioactivity diffuses into the base metal during deposition thereby requiring more-severe decontamination treatment than simply removing the scale.

## 20.5 SODIUM-IMPURITY CHEMISTRY AND MONITORING

Because of the detrimental effects of the impurity elements hydrogen, oxygen, and carbon on the reliable performance of the coolant loops in an LMFBR, a variety of meters have been developed to enable continuous on-line monitoring of the concentrations of these species in the flowing sodium. The meters are of three types:

1. Equilibrium meters in which the impurity concentration in the sodium is inferred from the amount of the species absorbed by a test metal specimen or by a suitable instrument placed in the coolant stream.

2. Electrochemical meters in which the concentration of dissolved impurity is determined by the voltage developed by a solid-state electrolytic cell immersed in the sodium stream.

3. Dynamic meters, the behavior of which cannot be determined solely from thermodynamic considerations but depends on kinetic factors as well.

The utility of absolute meters of types 1 and 2 depends on knowledge of the thermochemistry of the chemical

reactions that are responsible for the meter response. Because equilibrium is demanded of these meters, their response is more sluggish (in the sense that sufficient time must be allowed to make sure equilibrium is attained) than that of meters which operate in a dynamic nonequilibrium mode. Dynamic meters are usually calibrated against equilibrium meters.

The equilibrium and electrochemical meters measure the activity, not the concentration, of the selected impurity in the sodium. Additional thermodynamic data (in the form of solubilities of the element in question in liquid sodium) are required to determine solute concentrations. However, since most impurity interactions with the steel depend on the activity of the dissolved impurity rather than on its concentration, the direct activity readings are often sufficient.

Meters for hydrogen, oxygen, and carbon have been constructed and tested, but only the devices intended to monitor the first two of these elements are at a sufficiently advanced stage of development to permit incorporation as integral components of a sodium loop. The oxygen-hydrogen meter module developed by the Argonne National Laboratory is shown in Fig. 20.21. The module is a self-contained unit into which a small bleed stream from the main sodium flow is bypassed for analysis. The module

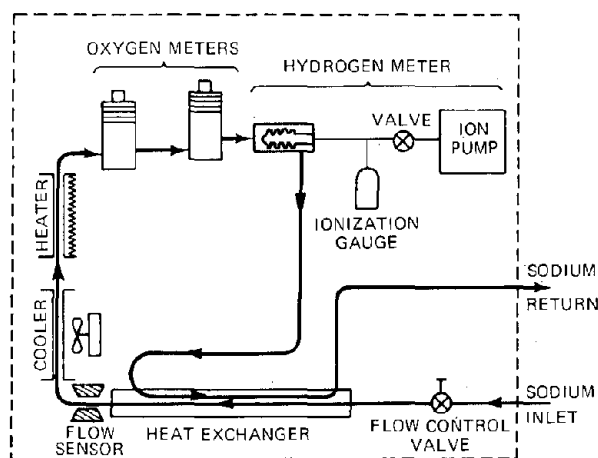


Fig. 20.21 Oxygen-hydrogen meter module. [After J. T. Holmes and G. O. Haroldsen, *Nucl. Technol.*, 21: 228 (1974).]

contains two electrochemical oxygen meters and a membrane hydrogen meter. Because meter efficiency peaks at  $\sim 480^\circ\text{C}$ , the module is equipped with a cooler and a heater to adjust the incoming sodium to this temperature. Following temperature adjustment, the sodium flows in series through the oxygen and hydrogen meters and then returns to the main coolant stream.

### 20.5.1 Hydrogen Meter

A sketch of the hydrogen meter<sup>1,2</sup> is shown in Fig. 20.22. The meter can be operated either in the

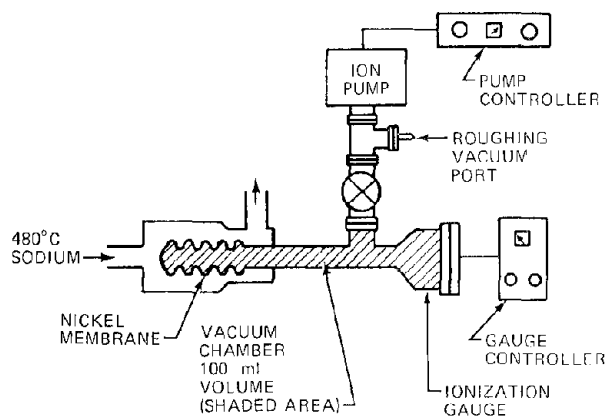


Fig. 20.22 The hydrogen meter. (After Ref. 12.)

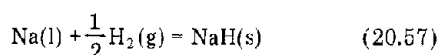
equilibrium or the dynamic mode. Hydrogen dissolved in the sodium (possibly as the hydride  $\text{NaH}$ ) equilibrates with the exposed surface of a nickel membrane that is 0.025 cm thick and presents a surface area of  $\sim 40\text{ cm}^2$  to the sodium. When a metal is exposed to gaseous hydrogen, the concentration of dissolved hydrogen at equilibrium depends on the pressure of hydrogen gas. When the hydrogen source is the liquid sodium, the equilibrium hydrogen concentration in the exposed face of the membrane depends on the hydrogen concentration in the sodium. When operated as an equilibrium device, the valve leading to the ion pump in the sketch is closed, and the pressure attained in the vacuum chamber is measured with an ionization gauge. In this case the nickel membrane has no effect on the meter reading; the gas in the vacuum chamber is in equilibrium with the hydrogen dissolved in the liquid sodium no matter what material is used as a membrane to separate the two phases (as a practical matter, the membrane must have a high enough permeability to permit attainment of equilibrium in a reasonable time). In the equilibrium mode the hydrogen meter provides a direct measure of the activity of the hydrogen dissolved in the sodium, namely, the equilibrium pressure of  $\text{H}_2$  above the solution.

When operated in the dynamic mode, the vacuum side of the membrane has a lower hydrogen concentration than the side exposed to the sodium, and a concentration gradient of atomic hydrogen is established between the sodium and vacuum sides of the nickel membrane. Hydrogen atoms diffuse down this gradient and escape to the vacuum on the inner side. The hydrogen permeating through the membrane is continuously removed by an ion pump. [An ion pump is a commercial item that removes gas molecules from a chamber by first ionizing them and then accelerating the ions through a potential of 5 kV. The high-energy ions strike a titanium surface and are (hopefully) irretrievably buried there.] Hence the hydrogen pressure in the vacuum chamber is lower than when the meter is operated in the equilibrium mode (i.e., when the ion pump is turned off). However, the relation between meter response and hydrogen concentration in the sodium depends on the speed of the ion pump and the characteristics of the nickel membrane. Meter performance in the

dynamic mode is difficult to specify theoretically (a calculation relevant to this process is the subject of problem 20.7). Consequently, the readings of the hydrogen meter when operated in the dynamic mode are calibrated against the absolute measurement of hydrogen activity obtainable when the meter operates as an equilibrium device.

Thermochemical analysis of the equilibrium mode of operation requires knowledge of the behavior of hydrogen in liquid sodium. Here we need the same sort of information as was required to assess the behavior of oxygen in sodium.

The standard free energy of formation of sodium hydride, which represents the reaction:



is (from the compilation in Ref. 7)

$$\Delta G_{f\text{NaH}}^\circ = -58 + 83\left(\frac{T}{10^3}\right) \text{ kJ/mole} \quad (20.58)$$

Application of the law of mass action to reaction 20.57 yields the pressure of hydrogen gas that is in equilibrium simultaneously with sodium saturated with hydrogen and pure solid sodium hydride:

$$\frac{1}{(p_{\text{H}_2})_{\text{sat}}^{1/2}} = \exp\left(-\frac{\Delta G_{f\text{NaH}}^\circ}{RT}\right) \quad (20.59)$$

If at a fixed temperature,  $p_{\text{H}_2} > (p_{\text{H}_2})_{\text{sat}}$ , all the sodium is consumed in forming NaH. If  $p_{\text{H}_2} < (p_{\text{H}_2})_{\text{sat}}$ , all the NaH dissolves in the liquid sodium and disappears as a distinct solid phase. The relationship between the concentration of dissolved hydrogen in sodium and hydrogen gas pressures less than saturation is depicted in Fig. 20.23. The square-root dependence of  $C_{\text{H}}$  on  $p_{\text{H}_2}$  is known as Sievert's law. This behavior is quite generally observed for all gas-metal

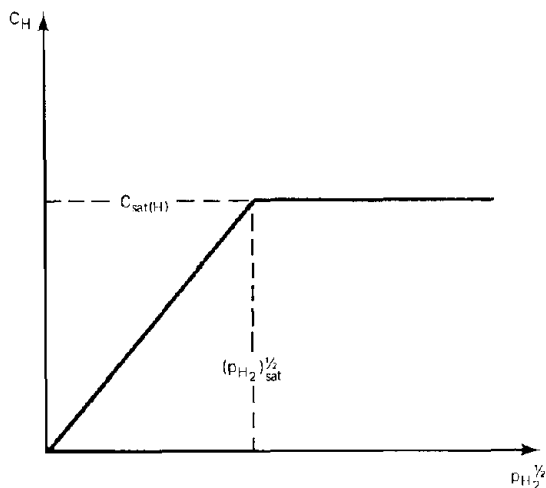
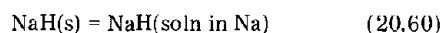


Fig. 20.23 Behavior of the concentration of hydrogen dissolved in liquid sodium as the hydrogen pressure is increased at constant temperature.

systems when the gas is di-atomic and dissolves in the metal as atoms (or as a compound containing a single gas atom). Sievert's law is the di-atomic analog of Henry's law, which governs the distribution of monatomic gases in condensed phases. For crystalline metals, the Sievert's law constant can be estimated from statistical mechanics (problem 5.9b), but in liquids no such estimate is possible.

The concentration of dissolved hydrogen when the hydrogen pressure is at the saturation value given by Eq. 20.59 is known as the solubility of hydrogen in sodium. Since at this point hydrogen gas is in equilibrium simultaneously with pure solid NaH and with hydrogen dissolved in the sodium phase (as NaH), the solubility can be represented by the reaction:



The solubility measured by the Argonne National Laboratory group with their hydrogen meter<sup>1,2</sup> is given by

$$\ln C_{\text{sat(H)}} = 14 - \frac{55}{R(T/10^3)} \quad (20.61)$$

where  $C_{\text{sat(H)}}$  is in parts per million of hydrogen by weight. Equation 20.61 is plotted as the solid line in Fig. 20.24. Other measurements of hydrogen solubility in sodium are also shown on the graph.

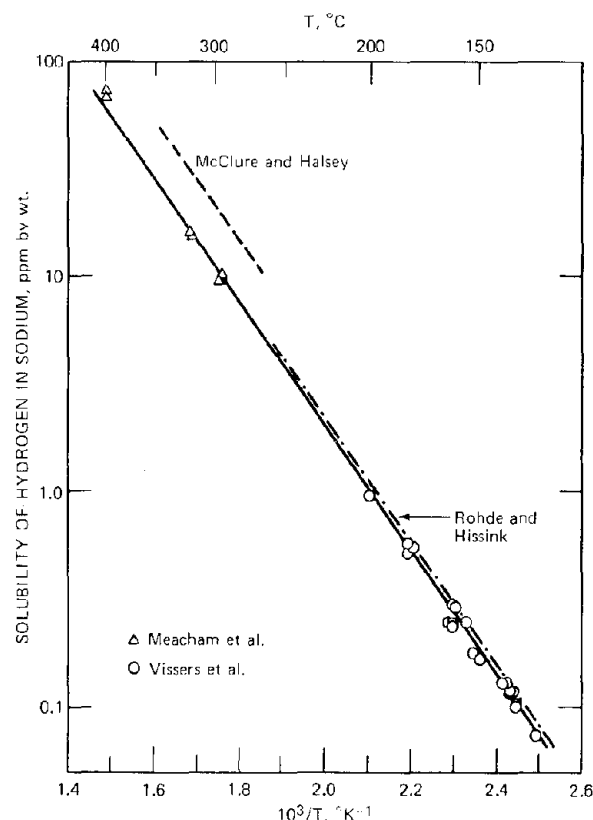


Fig. 20.24 Solubility of hydrogen in sodium. (After Ref. 12.)

The Sievert's law constant is defined by

$$K_H = \frac{C_H}{p_{H_2}^{1/2}} \quad (20.62)$$

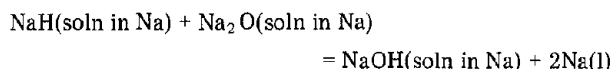
The units of  $K_H$  are parts per million of hydrogen by weight per atmosphere<sup>1/2</sup>. When the hydrogen meter of Fig. 20.22 is operated in the equilibrium mode, the  $H_2$  pressure inside the chamber is in equilibrium with the dissolved hydrogen in the sodium. Therefore, measurement of  $p_{H_2}$  gives  $C_H$  by Eq. 20.62.

Since this formula applies up to and including the saturation point (where solid NaH just begins to precipitate from the liquid sodium), we can write

$$K_H = \frac{C_{sat(H)}}{(p_{H_2})_{sat}^{1/2}} \quad (20.63)$$

The  $K_H$ ,  $C_{sat(H)}$ , and  $(p_{H_2})_{sat}$  are not independent thermodynamic quantities;  $K_H$  can be computed by substituting Eqs. 20.58, 20.59, and 20.61 into Eq. 20.63. The Argonne group, for example, measured  $C_{sat(H)}$  and  $K_H$  for various temperatures.<sup>1,2</sup> The standard free energy of formation of NaH calculated from their data (see problem 20.6) does not quite agree with that expressed by Eq. 20.58. Since this quantity appears to have been well established, either the solubility or the Sievert's law measurements obtained by the Argonne group are somewhat erroneous.

If oxygen and hydrogen are simultaneously present in liquid sodium, NaOH can be formed by the reaction:

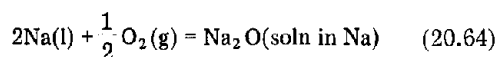


The thermodynamics of this reaction are not known. If oxygen is present in the sodium, the apparent solubility of hydrogen is larger than it is in pure sodium because some of the hydrogen is contained in the dissolved sodium hydroxide. For the same reason the apparent solubility of oxygen in sodium (Fig. 20.9) is enhanced by the presence of hydrogen in the system.

### 20.5.2 Electrochemical Oxygen Meter

The solid-state electrochemical cell developed by the Westinghouse Electric Corporation for the purpose of monitoring the activity of oxygen in liquid sodium is shown in Fig. 20.25. It consists of a steel housing through which sodium flows at  $\sim 480^\circ\text{C}$  and into which a crucible made of high-purity  $\text{ThO}_2$ -15 wt.%  $\text{Y}_2\text{O}_3$  is inserted. This ceramic acts as a solid electrolyte bridge for the cell. Oxygen ions can move through the ceramic, but electronic conduction is small (but unfortunately not negligible). The bridge is sealed to the inside of the housing by frozen sodium. The reference electrode on the inner surface is air, although the Sn/SnO<sub>2</sub> couple may be used in subsequent models because it improves cell performance.

The chemical reaction that occurs in the cell is



The oxygen gas in this reaction contacts the inner surface of the thoria-yttria crucible, and the Na<sub>2</sub>O dissolved in sodium contacts the outer surface. The cell voltage is measured between the inner and outer surfaces of the ceramic crucible. If the oxygen activity in the sodium (which is to be measured) is denoted by  $a_O$ , the oxygen gas pressure for which the preceding reaction would be in equilibrium is given by

$$\frac{a_O}{(p_{O_2})_{eq}^{1/2}} = \exp\left(-\frac{\Delta G_{fNa_2O}^\circ}{RT}\right) \quad (20.65)$$

where  $\Delta G_{fNa_2O}^\circ$  is the standard free energy of formation of Na<sub>2</sub>O, given by Eq. 20.16. If the oxygen pressure in the cell were equal to  $(p_{O_2})_{eq}$ , the cell voltage would be zero. When  $p_{O_2}$  in the reference gas is not equal to  $(p_{O_2})_{eq}$ , the cell voltage is given by (see also Eq. 11.13)

$$RT \ln p_{O_2} - RT \ln (p_{O_2})_{eq} = -4\mathcal{F}\Delta\epsilon \quad (20.66)$$

which, when combined with Eq. 20.65, gives the theoretical cell response:

$$\Delta\epsilon = \frac{RT}{4\mathcal{F}} \left( \ln p_{O_2} - 2 \ln a_O - 2 \frac{\Delta G_{fNa_2O}^\circ}{RT} \right) \quad (20.67)$$

In these equations,  $\mathcal{F}$  is the Faraday constant, equal to 96.48 kJ volt<sup>-1</sup> g<sup>-1</sup> equiv. The factor of 4 preceding  $\mathcal{F}$  arises because four electrons are transferred when one molecule of oxygen gas is converted to two molecules of Na<sub>2</sub>O.

When the oxygen activity in the sodium can be measured by other means, the observed and theoretical cell voltages do not quite agree; the discrepancy is caused by slight electronic conductance of the ceramic bridge. In addition, the cell voltage drifts with time as the solid electrolyte becomes degraded by exposure to sodium. Nevertheless, these two deficiencies can be overcome by periodic calibration of the electrolytic meter, and the advantages of the continuous, instantaneous monitoring of

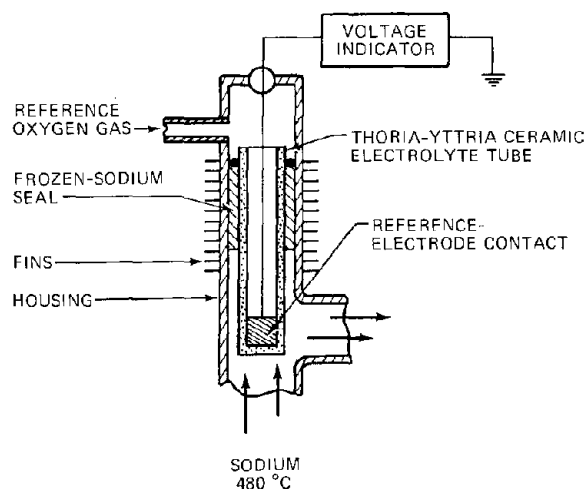


Fig. 20.25 Electrochemical oxygen meter. (After Ref. 12.)

oxygen activity in sodium by such cells are expected to be exploited in LMFBR coolant circuits.

### 20.5.3 Oxygen Analysis by the Vanadium-Wire Method

The partitioning of a solute between two immiscible (or partially miscible) solvents is an important unit operation in the chemical industry. Reprocessing of spent reactor fuels, for example, relies heavily on the widely differing distribution coefficients of uranium, plutonium, and fission products between aqueous nitric acid and an organic solvent containing tributyl phosphate. Oxygen distributes between liquid sodium and high-purity vanadium metal in a similar manner, and the equilibrium of this distribution forms the basis of a method of determining the activity of oxygen in sodium.<sup>1,3</sup>

Oxygen partitioning occurs between liquid sodium and any other second phase, the choice of which is determined by kinetic factors governing the time required to attain equilibrium and the ease of measuring the quantity of oxygen absorbed by the test material. Vanadium has proven to be a useful second phase for oxygen analysis. The concentration of oxygen in vanadium that has been equilibrated with sodium containing oxygen at the concentrations in typical sodium loops is quite large; at 750°C, for example, the oxygen content of vanadium metal equilibrated with sodium containing 1 ppm of oxygen is nearly 1 at.%, which can be accurately determined by conventional analytical techniques. The time required for equilibration of the test specimen depends on the diffusivity of oxygen in vanadium and the diameter of the wire [characteristic time for diffusion  $\approx$  (diameter)<sup>2</sup>/diffusivity], which can be made suitably small by use of fine wires and operation at high temperature.

To analyze the thermodynamics of the vanadium-wire equilibration method, we imagine vanadium and sodium samples to be in equilibrium with a reservoir of gas containing oxygen at a pressure  $p_{O_2}$ . The two metal phases are therefore in equilibrium with each other insofar as oxygen distribution is concerned. In reality, a separate gas phase need not be present to ensure equilibration of oxygen between the two metals, but the contrived system is useful for settling the thermodynamics. The oxygen pressure common to the vanadium and sodium specimens is presumed to be insufficient to cause separate oxide phases to precipitate from either metal. Further, we require that  $p_{O_2}$  be low enough to ensure the applicability of Sievert's law to oxygen dissolution in both sodium and vanadium. By analogy to the solution of hydrogen in sodium, we can write

$$K_O^V = \frac{C_O^V}{(p_{O_2})^{1/2}} \quad (20.68)$$

Assuming that Sievert's law applies to oxygen concentrations approaching the solubility limit,

$$K_O^V = \frac{C_{sat(O)}^V}{[(p_{O_2})_{sat}^V]^{1/2}} \quad (20.69)$$

From these two relations we can obtain the concentration of oxygen dissolved in vanadium metals:

$$C_O^V = C_{sat(O)}^V \left[ \frac{p_{O_2}}{(p_{O_2})_{sat}^V} \right]^{1/2} \quad (20.70)$$

Similarly, for sodium,

$$K_O^{Na} = \frac{C_O^{Na}}{(p_{O_2})^{1/2}} \quad (20.71)$$

and

$$K_O^{Na} = \frac{C_{sat(O)}^{Na}}{[(p_{O_2})_{sat}^{Na}]^{1/2}} \quad (20.72)$$

and

$$C_O^{Na} = C_{sat(O)}^{Na} \left[ \frac{p_{O_2}}{(p_{O_2})_{sat}^{Na}} \right]^{1/2} \quad (20.73)$$

where  $K_O^V$  = Sievert's law constant for oxygen in vanadium

$K_O^{Na}$  = Sievert's law constant for oxygen in sodium

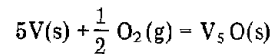
$C_{sat(O)}^{Na}$  = oxygen concentration in sodium when solid  $Na_2O$  first precipitates out

$(p_{O_2})_{sat}^{Na}$  = oxygen pressure that causes the appearance of the separate sodium oxide phase

The value of  $C_{sat(O)}^{Na}$  is given by Eq. 20.18, and  $(p_{O_2})_{sat}^{Na}$  is given by application of the law of mass action to Eq. 20.15:

$$\frac{1}{[(p_{O_2})_{sat}^{Na}]^{1/2}} = \exp\left(-\frac{\Delta G_{fNa_2O}^{\circ}}{RT}\right) \quad (20.74)$$

Similarly, the concentration of oxygen in vanadium cannot be increased indefinitely, because a separate oxide phase ( $V_5O$ ) forms at the concentration  $C_{sat(O)}^V$  known as the terminal solubility. The reaction that occurs is



The equilibrium oxygen pressure above coexisting solid vanadium (which is saturated with oxygen) and solid  $V_5O$  is given by the law of mass action as

$$\frac{1}{(p_{O_2})_{sat}^V} = \exp\left(-\frac{\Delta G_{fV_5O}^{\circ}}{RT}\right) \quad (20.75)$$

where  $\Delta G_{fV_5O}^{\circ}$  is the standard free energy of formation of  $V_5O$ .

The *distribution coefficient* of oxygen between vanadium and sodium is defined as the ratio  $C_O^V/C_O^{Na}$ , which can be obtained by dividing Eq. 20.70 by 20.73 and using Eqs. 20.74 and 20.75:

$$\frac{C_O^V}{C_O^{Na}} = \frac{C_{sat(O)}^V}{C_{sat(O)}^{Na}} \exp\left(\frac{\Delta G_{fNa_2O}^{\circ} - \Delta G_{fV_5O}^{\circ}}{RT}\right) \quad (20.76)$$

The distribution coefficient can be determined by measuring all four independent thermodynamic quantities

in Eq. 20.76 (i.e., the two terminal solubilities and the two free energies of formation). This method has been employed by Hooper and Trevillion.<sup>14</sup> However, it is simpler experimentally and more accurate to measure the distribution coefficient directly, as was done in the original study of the vanadium–oxygen–sodium system.<sup>13</sup> The results of the latter approach are shown in Fig. 20.26 in which the concentrations of oxygen in the two phases have been

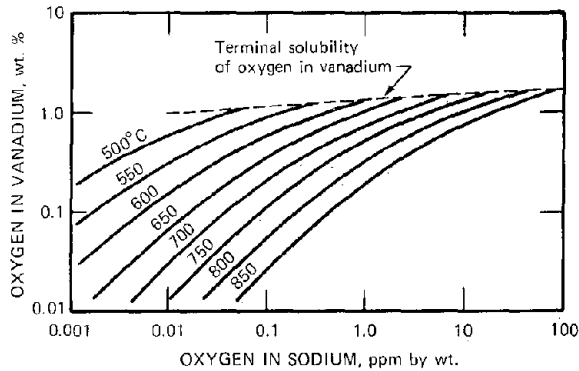


Fig. 20.26 Distribution of oxygen between sodium and vanadium. (After Ref. 13.)

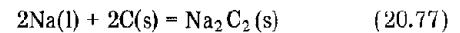
expressed in more convenient units than atom fractions. If the oxygen in vanadium obeyed Sievert's law (as does oxygen in sodium), the distribution coefficient would be independent of oxygen concentration, and the slopes of the curves at each temperature in Fig. 20.26 would have been unity. The curvature at high oxygen concentration in vanadium indicates that Sievert's law is not obeyed over most of the practical range of temperature and oxygen content. The distribution coefficient is a function of both concentration and temperature. The upper boundary line in Fig. 20.26 represents the termination of the curves at each temperature at the solubility of oxygen in vanadium. At each temperature, therefore, there is a maximum oxygen concentration in sodium beyond which the vanadium equilibration technique is no longer usable because of precipitation of  $V_5O$  in the wire. When the sodium contains more oxygen than this critical value, measurement of the gross oxygen content of the vanadium wire (which does not distinguish between  $V_5O$  and oxygen dissolved in vanadium metal) no longer has any useful relationship to the oxygen concentration in the sodium. It can be seen from Fig. 20.26 that vanadium wires must be operated at considerably higher temperatures than the  $480^\circ$  operating temperature of the electrochemical oxygen meter described earlier in order to be useful for analysis of oxygen concentrations in sodium of 1 to 10 ppm. If the range of the equilibration method is to be extended to 20 ppm, the operating temperature must be  $>750^\circ\text{C}$ .

The vanadium-wire equilibration method is, of course, neither continuous nor amenable to on-line readout of the oxygen concentration in a sodium loop. However, it is commonly employed to calibrate electrochemical oxygen

meters. The reliability of the method has been widely accepted, although there is some doubt that the distribution data shown in Fig. 20.26 represent true thermodynamic equilibrium.<sup>14</sup> However, the accuracy of the thermodynamic data on which this criticism was based has in turn been questioned.<sup>15</sup> Awaiting confirmatory experiments, the vanadium-wire equilibration method appears to be the most reliable technique for measuring the concentration of oxygen in the sodium of fast reactor coolant circuits.\*

#### 20.5.4 Carbon–Sodium Chemistry

Carbon is present in liquid sodium as a dimeric species, which can be either dissolved disodium acetylide,  $\text{Na}_2\text{C}_2$ , or the dicarbide ion,  $\text{C}_2^{2-}$ . Whichever form predominates, the thermodynamics of the sodium–carbon system can be described by the free energy of formation of the acetylide and the solubility of carbon in sodium. The formation of  $\text{Na}_2\text{C}_2$  from the elements is given by the reaction:



where  $\text{C}(s)$  represents graphite and  $\text{Na}_2\text{C}_2(s)$  is pure solid disodium acetylide. Between  $700$  and  $1100^\circ\text{K}$ , the free energy of formation of  $\text{Na}_2\text{C}_2(s)$  is approximately<sup>16</sup>

$$\Delta G_{f\text{Na}_2\text{C}_2}^\circ = 31 - 12 \left( \frac{T}{10^3} \right) \text{ kJ/mole} \quad (20.78)$$

The solubility of carbon in liquid sodium has been investigated by a number of laboratories. The results are summarized in Fig. 20.27. The results due to Ainsley et al.<sup>17</sup> are given by the relation

$$\ln C_{\text{sat}(\text{C})} = 17.6 - \frac{114}{R(T/10^3)} \quad (20.79)$$

where  $C_{\text{sat}(\text{C})}$  is in parts per million of carbon by weight. Figure 20.27 shows good accord on the enthalpy of solution of carbon in sodium (i.e., the slope of the solubility curves, or the  $114$  kJ/mole in Eq. 20.79), but the magnitudes of the solubilities measured by two of the four groups represented in the figure are four times larger than those measured by the other two laboratories.

The solubility means the weight of carbon (in the form of  $\text{Na}_2\text{C}_2$ ) in liquid sodium when liquid sodium is in contact with pure graphite. Because of the positive free energies of formation given by Eq. 20.78, solid disodium acetylide is not stable in the temperature range of sodium in LMFBRs (it decomposes to liquid sodium and graphite). It is, however, thermodynamically possible for solutions of  $\text{Na}_2\text{C}_2$  in sodium to exist provided that the activity of  $\text{Na}_2\text{C}_2$  is less than unity. When the carbon contained in the

\*Thermodynamic disputes such as this often rage for years, the classic example being the debate over the heat of sublimation of carbon, which was resolved only when mass-spectrometer experiments revealed that elemental carbon evaporates as polymers.

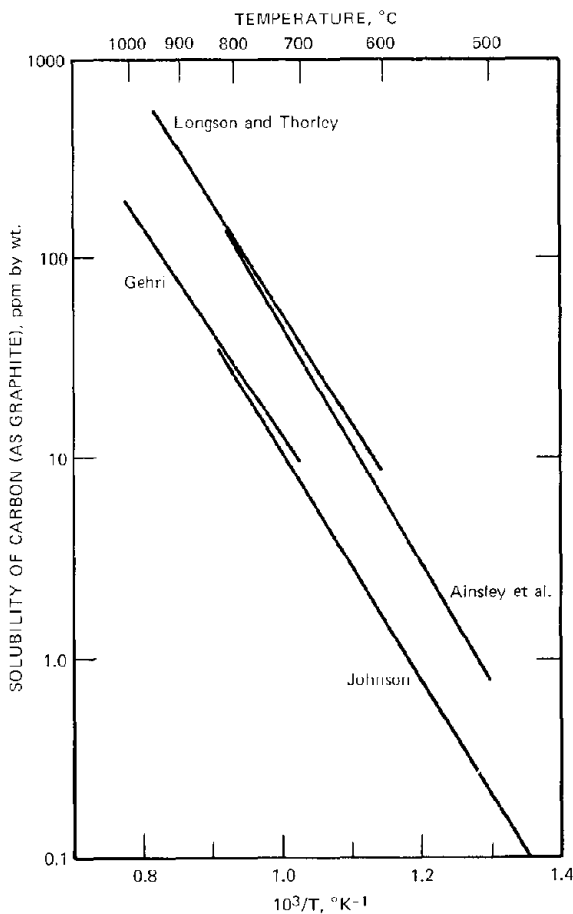


Fig. 20.27 Carbon solubility in liquid sodium. (After Ref. 17.)

sodium is also less than unit activity, the appropriate law of mass action for reaction 20.77 is

$$K_{\text{Na}_2\text{C}_2} = \exp\left(-\frac{\Delta G_{f\text{Na}_2\text{C}_2}^\circ}{RT}\right) = \frac{a_{\text{Na}_2\text{C}_2}}{a_{\text{C}}^2} \quad (20.80)$$

The sodium activity is unity since this component is in an essentially pure state. When the sodium is in contact with pure graphite ( $a_{\text{C}} = 1$ ), the mass-action expression reduces to

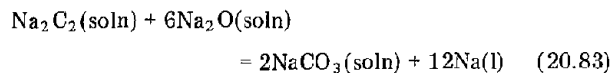
$$K_{\text{Na}_2\text{C}_2} = (a_{\text{Na}_2\text{C}_2})_{\text{sat}} \quad (20.81)$$

where  $(a_{\text{Na}_2\text{C}_2})_{\text{sat}}$  is the activity of  $\text{Na}_2\text{C}_2$  in sodium that is saturated with carbon. Since the solutions of carbon in sodium are quite dilute, Henry's law is obeyed by the dissolved disodium acetylide. Therefore,  $a_{\text{Na}_2\text{C}_2}$  is proportional to  $C_{\text{C}}$ , the concentration of carbon in sodium, and Eqs. 20.80 and 20.81 can be combined to give the following relation between the activity and the concentration of carbon in liquid sodium:

$$a_{\text{C}}^2 = \frac{a_{\text{Na}_2\text{C}_2}}{(a_{\text{Na}_2\text{C}_2})_{\text{sat}}} = \frac{C_{\text{C}}}{C_{\text{sat}}(C)} \quad (20.82)$$

This relationship differs from the analogous formula for oxygen in sodium (Eq. 20.19) in that the activity of the dissolved species is squared in Eq. 20.82 and raised to the first power in Eq. 20.19. The parabolic connection between concentration and activity of carbon in sodium is a consequence of the formation of the dimeric carbon species  $\text{Na}_2\text{C}_2$  in solution. Oxygen, on the other hand, does not associate with other oxygen atoms in solution.

The quantity of carbon present in one dissolved form or another in sodium can be increased by the presence of oxygen, which reacts with carbon according to



This reaction, which produces sodium carbonate, does not appear to appreciably increase carbon dissolution unless the oxygen content in the sodium is several hundred parts per million.<sup>17</sup>

### 20.5.5 Carbon Meters

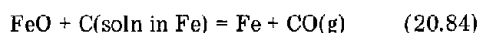
Four types of carbon-activity meters have been developed for liquid-sodium application.

#### UNC Meter

This meter is a dynamic diffusion membrane device named after the originator, the United Nuclear Corporation. A pure-iron membrane separates the sodium to be analyzed from a stream of gas flowing through the unit. Carbon in the sodium dissolves in the iron membrane and diffuses through it to the other face, where it is gasified to CO by reaction with water vapor in the gas stream. The CO is converted to methane in a catalytic bed, and the  $\text{CH}_4$  concentration is measured by a flame ionization detector. Basically, the UNC meter is analogous to the hydrogen meter operated in the dynamic (ion-pumped) mode. The reading of the UNC meter is determined by the carbon activity in the sodium, but calibration with an absolute carbon-activity meter is required to convert meter readings to carbon activity. Unfortunately the meter output is not proportional to carbon activity, and the limit of sensitivity is close to the expected carbon activity in LMFBR sodium circuits ( $a_{\text{C}} \approx 0.003$ ).

#### ANL Pressure Meter

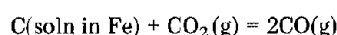
The pressure meter for determining carbon activity in sodium was developed at the Argonne National Laboratory<sup>18</sup> and resembles the UNC meter in that carbon diffuses from sodium through an iron membrane and is then oxidized to CO. It is also similar to the ANL hydrogen meter operated in the equilibrium mode because the quantitative determination of carbon activity in the sodium depends on measurement of the total gas pressure generated within the closed volume of the device. The inside of the tube (i.e., the face of the membrane not in contact with liquid sodium) is coated with a layer of FeO, which reacts with the carbon diffusing from the sodium side to produce CO and  $\text{CO}_2$ . The CO is produced by the reaction



At equilibrium the activity of carbon in the iron membrane is equal to the activity of carbon in the sodium, and the law of mass action for reaction 20.84 is

$$K_{\text{Fe}} = \frac{p_{\text{CO}}}{a_{\text{C}}} \quad (20.85)$$

where  $a_{\text{C}}$  is the carbon activity in sodium and  $K_{\text{Fe}}$  is the equilibrium constant of the reaction. A similar reaction can be written for the production of  $\text{CO}_2$  by reaction of dissolved carbon and  $\text{FeO}$ , but it is sufficient to establish the  $\text{CO}_2$  partial pressure by the equilibrium:



for which

$$K'_C = \frac{p_{\text{CO}}^2}{a_{\text{C}} p_{\text{CO}_2}} \quad (20.86)$$

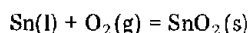
Combining Eqs. 20.85 and 20.86 gives the total pressure of carbon-bearing gases in the interior of the membrane volume:

$$p_{\text{CO}} + p_{\text{CO}_2} = K_{\text{Fe}} \left( 1 + \frac{K_{\text{Fe}}}{K'_C} \right) a_{\text{C}} \quad (20.87)$$

The coefficient of  $a_{\text{C}}$  in this formula is  $\sim 1$  atm at  $700^\circ\text{C}$ ; so the meter should have adequate sensitivity to carbon at activity levels well below unity. The meter is quite accurate but requires many days to attain equilibrium.

### Electrochemical Meter

The carbon electrochemical meter developed by Ruther et al.<sup>19</sup> is shown schematically in Fig. 20.28. A thin-walled iron tube into which is inserted a zirconia-calcia tube contacts the liquid sodium. The annular gap between the iron tube and the ceramic is filled with a mixture of  $\text{CO}$  and  $\text{CO}_2$  gas at a total pressure  $p_{\text{C}} = p_{\text{CO}} + p_{\text{CO}_2}$  which is externally fixed. The inside of the calcia-stabilized zirconia crucible contains a  $\text{Sn}/\text{SnO}_2$  reference electrode, which establishes the oxygen potential on one side of the cell according to the reaction



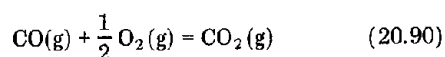
Since the standard free energy of this reaction,  $\Delta G_{\text{Sn}}^\circ$ , is accurately known, the oxygen potential of the reference half of the cell is

$$(\text{RT} \ln p_{\text{O}_2})_{\text{Sn}} = \Delta G_{\text{Sn}}^\circ \quad (20.88)$$

The oxygen potential at the outside of the ceramic tube is determined by the  $\text{CO}_2/\text{CO}$  gas-phase equilibrium of Eq. 11.5 according to the equilibrium constant

$$K_{\text{C}} = \frac{p_{\text{CO}_2}/p_{\text{CO}}}{(p_{\text{O}_2})^{1/2}} = \exp\left(-\frac{\Delta G_{\text{C}}^\circ}{\text{RT}}\right) \quad (20.89)$$

where  $K_{\text{C}}$  is the equilibrium constant for the reaction



and  $\Delta G_{\text{C}}^\circ$  is the standard free-energy change given by Eqs. 11.8 and 11.9. Finally, the  $\text{CO}$  and  $\text{CO}_2$  partial pressures are related to the activity of carbon in the sodium (or in the iron, since  $a_{\text{C}}^{\text{Na}} = a_{\text{C}}^{\text{Fe}}$  at equilibrium) by Eq. 20.86. If  $p_{\text{CO}}$  is expressed in terms of the total pressure of carbon oxides by

$$p_{\text{CO}} = p_{\text{C}} - p_{\text{CO}_2} = \frac{p_{\text{C}}}{1 + (p_{\text{CO}_2}/p_{\text{CO}})}$$

Eq. 20.86 can be written as

$$K'_C = \frac{p_{\text{C}}}{a_{\text{C}}} \left[ \left( 1 + \frac{p_{\text{CO}_2}}{p_{\text{CO}}} \right) \left( \frac{p_{\text{CO}_2}}{p_{\text{CO}}} \right) \right]^{-1} \quad (20.91)$$

The cell potential is (note similarity to Eq. 11.13 for the electrolytic cell developed for studying oxygen potentials of fuels)

$$\Delta G_{\text{Sn}}^\circ - \text{RT} \ln p_{\text{O}_2} = -4 \mathcal{F} \Delta \epsilon \quad (20.92)$$

The terms  $p_{\text{O}_2}$  and  $p_{\text{CO}_2}/p_{\text{CO}}$  can be eliminated from Eqs. 20.89, 20.91, and 20.92, and the theoretical cell potential can be expressed as a function of the specified total pressure of carbon oxides and the carbon activity in the sodium:

$$\Delta \epsilon = \frac{1}{4 \mathcal{F}} \left( 2\text{RT} \ln \left\{ \frac{1}{2} \left[ \left( 1 + \frac{4p_{\text{C}}}{K'_C a_{\text{C}}} \right) - 1 \right] \right\} + 2\Delta G_{\text{C}}^\circ - \Delta G_{\text{Sn}}^\circ \right) \quad (20.93)$$

The response of the meter is quite rapid (of the order of hours), and the cell potentials measured when the meter is contacted with sodium containing carbon at known activity are in good agreement with the values predicted by Eq. 20.93.

### Equilibration Tabs

There has been active experimental exploration of the equilibration methods for determining carbon activity in liquid sodium. This method is analogous to the vanadium-wire technique used for oxygen analysis of sodium. The tab material must meet the usual criteria for two-phase distribution devices. First, it must have a high enough equilibrium carbon concentration at low carbon activities in the sodium (down to  $a_{\text{C}} \approx 10^{-3}$ ) to permit reliable carbon analysis. Second, it must not form a precipitate phase at high carbon activities. Ideally, the tab material should retain carbon in solid solution up to a carbon activity of unity. Third, if the tab consists of more than one component, it must be stable against selective leaching of one of the constituents by exposure to sodium. The alloy consisting of 88 wt.% iron and 12 wt.% manganese appears to satisfy these requirements.<sup>18</sup>

When the tab is inserted into liquid sodium and equilibrium is established, the activity of carbon in the tab is equal to that in the sodium. The relation between carbon activity and carbon concentration in the Fe-12 wt.% Mn alloy can be established by passing a gas containing a known ratio of  $\text{CH}_4$  to  $\text{H}_2$  over the alloy. The  $\text{CH}_4/\text{H}_2$

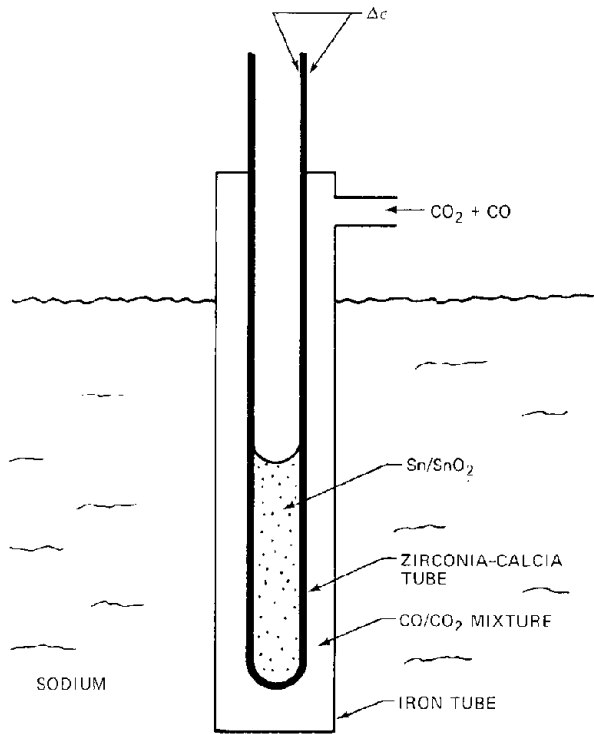


Fig. 20.28 The ANL electrochemical carbon meter. (After Ref. 19.)

mixture controls the "carbon potential" of the system (i.e.,  $RT \ln a_C$ ) in much the same manner that gases containing specified ratios of  $H_2O/H_2$  or  $CO_2/CO$  can be used to fix the oxygen potentials of oxide fuels (Sec. 11.4). The carbon activity is determined by the thermodynamics of the reaction



for which the equilibrium constant,

$$K_{CH_4} = \frac{p_{CH_4}}{p_{H_2}^2 a_C} \quad (20.95)$$

is well established. Controlling the  $p_{CH_4}/p_{H_2}$  ratio and the total pressure  $p_{CH_4} + p_{H_2}$  of the gas flowing over the metal specimen determines the carbon activity  $a_C$  in the specimen according to Eq. 20.95. With this method the activity-concentration relationship for the Fe-12 wt.% Mn alloy is found to be<sup>18</sup>

$$a_C = \frac{C_C^{tab}}{13,500 - 0.26C_C^{tab}} \quad (20.96)$$

where  $C_C^{tab}$  is the carbon concentration in the tab in parts per million by weight. A precipitate forms when the carbon concentration exceeds  $\sim 0.5$  wt.%; so this alloy is restricted to maximum carbon activities of  $\sim 0.4$ . This limitation is not a serious impediment to the application of the Fe-12 wt.% Mn tab as an equilibration meter in sodium

systems, however, inasmuch as the carbon activity in these systems is very much smaller than unity.

When  $a_C = 10^{-3}$ , Eq. 20.96 shows that the carbon content of the iron-manganese alloy equilibration tab is  $\sim 13$  ppm, which is approaching the limit of sensitivity for accurate measurement of carbon in metals. As an alternative to the binary alloy for carbon-activity measurements, Natesan and Kassner<sup>20</sup> have shown that the ternary alloy Fe-18 wt.% Cr-8 wt.% Ni (which is type 300 stainless steel without the impurities) is a reliable tab material for carbon-activity measurements by the equilibration technique. The carbon content of the ternary alloy at a given carbon activity is greater than that of the iron-manganese binary alloy. However, extensive carbide precipitation (primarily  $Cr_{23}C_6$ ) is responsible for the large carbon uptake. We shall demonstrate in the following section that an equilibrium carbon concentration in stainless steel is attained even when metal and carbide phases are present; so the iron-chromium-nickel alloy can function as an equilibrium tab monitor of carbon activity despite precipitation. The relationship between carbon activity and the chromium, nickel, and carbon concentrations of the tab has been determined by Natesan and Kassner (Eq. 20.113). The major disadvantage of the iron-chromium-nickel alloy as an equilibration tab is the long time required for attainment of equilibrium. The kinetics of carbon absorption by the tab are determined not only by the diffusion of carbon in the metal but by the rate of precipitation of the carbide phase as well.

The last three carbon meters described here measure the activity of carbon in liquid sodium. If desired, the concentration of carbon in the sodium can be obtained by use of Eqs. 20.82 and 20.79.

## 20.6 CARBURIZATION AND DECARBURIZATION OF STAINLESS STEEL

Carbon transport in sodium loops refers to the movement of carbon from one part of the loop to another. This migration is due to differences in the activity of carbon in components in various parts of the loop which arise principally from temperature differences. In a loop consisting entirely of austenitic stainless steel, for example, carbon is removed from the metal in the hot zones (decarburization) and absorbed by the metal in the cold region (carburization). In a loop containing both ferritic and austenitic steels, transport of carbon invariably occurs from the ferrite to the austenite, regardless of the temperature differences around the loop. The flowing liquid sodium is the agent for effecting carbon transfer. In this section we analyze the behavior of nonisothermal loops consisting only of austenitic stainless steel.

### 20.6.1 Carbon-Steel Thermodynamics

The direction and rate of carbon transfer in a sodium loop depends on the chemistry of both the carbon-sodium system and that of the carbon-stainless-steel system. The thermodynamics of carbon in sodium was reviewed in the

preceding section, and we begin this discussion with a summary of the available information on the interaction of carbon and austenitic stainless steels. There have been two investigations of this system: Tuma et al.<sup>21</sup> measured carbon activity and solubility in a stainless steel of the composition 18 wt.% Cr–9 wt.% Ni in the temperature range from 950 to 1200°C. Natesan and Kassner<sup>22</sup> have examined the thermodynamics of carbon in various alloys of nickel, chromium, and iron and have developed a carbon-activity–concentration relationship for alloys of the approximate composition of austenitic stainless steel.

The following thermodynamic information on the carbon–steel system is needed for carbon transport analysis:

1. The activity of carbon in solid solution in the gamma phase (or austenitic phase) of the alloy as a function of temperature and the concentrations of carbon, chromium, and nickel.

2. The carbon concentration in the austenitic phase at the phase boundary between the austenite and carbon phases as a function of temperature and the chromium and nickel content of the steel. This is the solubility of carbon in austenite.

3. The chromium–iron ratio in the  $M_{23}C_6$  carbide phase that forms when the carbon solubility is exceeded.

The solubility of carbon in the austenite phase of stainless steel is very low ( $\sim 50$  ppm by weight at 700°C), and carbon faithfully follows Henry's law. Thus, we can describe the carbon activity in the steel by

$$a_C = \omega_C \gamma_C (\omega_{Cr}, \omega_{Ni}, T) \quad (20.97)$$

where  $\omega_C$  is the weight fraction of carbon in the austenite phase (equal to  $10^{-5}$  times the concentration of this species in parts per million by weight) and  $\gamma_C(\omega_{Cr}, \omega_{Ni}, T)$  is the activity coefficient of carbon in the same alloy. The  $\omega_{Cr}$  and  $\omega_{Ni}$  are the mass fractions of chromium and nickel in the steel. The studies of Tuma et al.<sup>21</sup> give

$$\ln \gamma_C - \left( -0.5 + \frac{4.8}{T/10^3} \right) - \left( -6.9 + \frac{20.0}{T/10^3} \right) \omega_{Cr} + \left( 1.3 + \frac{3.4}{T/10^3} \right) \omega_{Ni} \quad (20.98)$$

which is valid for  $950 < T < 1200^\circ\text{C}$  and where  $\omega_{Cr}$  and  $\omega_{Ni}$  are not too different from 0.18 and 0.09, respectively.

This formula shows that the addition of chromium to the steel depresses the activity coefficient of carbon in steel (thereby rendering stainless steel a sink for carbon compared to low-chromium-content alloys). Nickel, on the other hand, increases the activity coefficient of carbon in the steel.

A schematic of a small part of the carbon–steel phase diagram at a fixed nickel concentration is shown in Fig. 20.29. The graph shows the carbon solubility vs. temperature relationship for two chromium contents of the steel. The area in the upper left-hand portion of the diagram is a single-phase austenite region wherein carbon is contained in solid solution in the alloy. The activity formulas given by

Eqs. 20.97 and 20.98 apply to this region. In the area to the lower right of the solubility line, austenite and the carbide phase coexist. The carbon concentration in the austenite in the two-phase mixture corresponds to the solubility limit, and the remainder of the carbon is bound in the carbide  $M_{23}C_6$ .

The solubility curves in Fig. 20.29 represent the maximum concentrations of carbon which can be held in

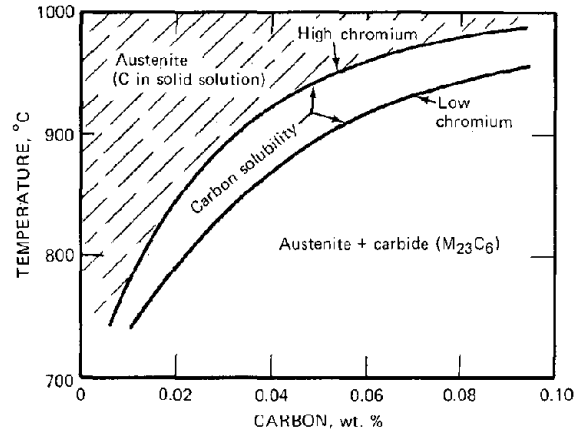


Fig. 20.29 Portion of the phase diagram for an austenitic steel containing 8 wt.% nickel (schematic).

solid solution in the austenite phase before precipitation of the  $M_{23}C_6$  carbide phase takes place. These lines represent the austenite–carbide phase boundary. For the 18 wt. % Cr–8 wt. % Ni steel, the carbon solubility limit is given by:<sup>21,22</sup>

$$\omega_{\text{sat}(C)} = 11 \exp \left( -\frac{11.9}{T/10^3} \right) \quad (20.99)$$

where  $\omega_{\text{sat}(C)}$  is the weight fraction of carbon in the austenite at the solubility limit. The carbon solubility is a function of the nickel and chromium content of the steel, and  $\omega_{\text{sat}(C)}$  can be expressed in the general form

$$\omega_{\text{sat}(C)} = G(\omega_{Cr}, \omega_{Ni}, T) \quad (20.100)$$

On the basis of very few data, Snyder, Natesan, and Kassner<sup>23</sup> propose an interim solubility relationship:

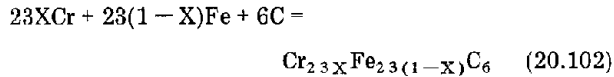
$$\omega_{\text{sat}(C)} = \exp [-B(T) - A(T) \omega_{Cr}] \quad (20.101)$$

where  $A$  and  $B$  are specified functions of temperature. Equation 20.101 is applicable only for  $\omega_{Ni} = 0.08$ .

To analyze carbon transport in a sodium–stainless-steel system, we need to develop a relation between carbon activity and the total carbon content of the steel. As suggested by Fig. 20.29, types 304 and 316 stainless steel, which contain  $\sim 0.05$  wt. % carbon, are supersaturated with carbon at temperatures of LMFBR operation. If precipitation of the carbide occurs, the total carbon content of the steel consists of contributions due to the carbon in solid solution in the austenite and the carbon contained in the

$M_{23}C_6$  carbide. Except for strongly decarburizing conditions in the hot leg of a sodium loop, carburization and decarburization occur in a two-phase mixture of austenite and carbide.

The carbide phase is formed by coprecipitation of the elements carbon, iron, and chromium from the austenite phase according to the reaction



where

$$X = \left( \frac{Cr}{Cr + Fe} \right)_{\text{carbide}}$$

defines the metal composition of the carbide phase. Because of the rudimentary state of the thermodynamics of the mixed carbide, the equilibrium of Eq. 20.102 cannot be accurately described. Hence, we shall consider  $X$  to be a fixed number (near unity) in the following analysis. We know that  $X$  increases as the carbon concentration in the steel decreases.<sup>21</sup> At low values of the carbon concentration,  $Cr_{23}C_6$  forms first because chromium is a stronger carbide former than is iron.

Consider a small specimen of stainless steel of initial composition  $\omega_{Cr}^0$  and  $\omega_{Ni}^0$  immersed in a large pool of liquid sodium in which the carbon activity is fixed at a value  $a_C$ . We assume that the carbon activity of the sodium is large enough to produce carbide precipitation (i.e.,  $\omega_C$  calculated using the specified values of  $a_C$ ,  $\omega_{Cr}^0$ , and  $\omega_{Ni}^0$  in Eq. 20.97 is larger than the saturation value given by Eq. 20.100 for the same chromium and nickel weight fractions). The  $M_{23}C_6$  carbide that precipitates is enriched in chromium ( $X > \omega_{Cr}^0$ ) with respect to the austenite phase, and, as carbide forms, the remaining metal becomes impoverished in chromium. Figure 20.29 demonstrates that, as the chromium content is reduced, the solubility of carbon in the austenite phase increases. When enough chromium-rich carbide has been formed and the austenite has been sufficiently depleted of chromium, the two-phase system achieves a unique composition at which Eqs. 20.97 and 20.100 are simultaneously satisfied.\* When equilibrium of the carbon in the sodium and that in the steel specimen is attained, let the fraction of the metal in the initial steel that is present bound to carbon in the  $M_{23}C_6$  carbide be

\*The formation of an equilibrium two-phase solid mixture when the solubility limit is exceeded requires that the solvent phase (i.e., the alloy of iron, chromium, and nickel) consist of more than one component and that the precipitate phase have a metal composition different from that of the original solvent. When the solvent consists of a single element, solute activities larger than the saturation value cause all the solvent to transform to the second phase. Thus, when the pressure of gaseous hydrogen in contact with sodium is larger than the saturation value given by Eq. 20.59, equilibrium is not attained, and all the sodium is converted to NaH. In this case  $P_{H_2}$  is the analog of  $a_C$ , and sodium and NaH are the counterparts of the austenite and carbide phases, respectively, in the carbon-stainless-steel system.

denoted by  $f$  and the chromium and nickel mass fractions in the remaining austenite be designated by  $\omega_{Cr}$  and  $\omega_{Ni}$ , respectively. Material balances on these two elements in the equilibrated steel require

$$\omega_{Cr}^0 = (1-f)\omega_{Cr} + fX \quad (20.103)$$

$$\omega_{Ni}^0 = (1-f)\omega_{Ni} \quad (20.104)$$

No nickel is present in the carbide phase.

Elimination of  $f$  from these two equations permits  $\omega_{Ni}$  to be expressed in terms of  $\omega_{Cr}$ :

$$\omega_{Ni} = \omega_{Ni}^0 \left( \frac{X - \omega_{Cr}^0}{X - \omega_{Cr}} \right) \quad (20.105)$$

Substituting Eq. 20.105 into the solubility equation, Eq. 20.100, and solving for  $\omega_{Cr}$  gives

$$\omega_{Cr} = H(\omega_C, \omega_{Cr}^0, \omega_{Ni}^0, X, T) \quad (20.106)$$

where, for clarity, the subscript "sat" has been removed from the symbol for the weight fraction of carbon in the austenite. The  $H$  in Eq. 20.106 describes the functional dependence of the chromium concentration of the austenite on the carbon concentration in this phase. The function  $H$  is specified (in principle) if the solubility function  $G$  is known (e.g., by Eq. 20.101). Equation 20.106 can then be used in Eq. 20.105 to obtain a similar formula relating  $\omega_{Ni}$  and  $\omega_C$ :

$$\omega_{Ni} = E(\omega_C, \omega_{Cr}^0, \omega_{Ni}^0, X, T) \quad (20.107)$$

The function  $E$  is also known if the function  $G$  is specified.

Equation 20.103 can be solved for the fraction of the original metal precipitated as carbide and  $\omega_{Cr}$  can be eliminated by use of Eq. 20.106:

$$f = \frac{\omega_{Cr}^0 - H(\omega_C, \omega_{Cr}^0, \omega_{Ni}^0, X, T)}{X - H(\omega_C, \omega_{Cr}^0, \omega_{Ni}^0, X, T)} \quad (20.108)$$

To simplify the mathematics, we assign a common atomic weight of 54 to all three metals in the steel; so the carbon content of the carbide phase is

$$\frac{\text{Wt. C in carbide}}{\text{Wt. (Fe + Cr) in carbide}} = \frac{12 \times 6}{54 \times 23} = 0.058$$

For small  $f$  and  $\omega_C$ , the mass fraction of total carbon in the equilibrated steel,  $\omega_C^T$ , is

$$\omega_C^T = \omega_C (1-f) + 0.058f \quad (20.109)$$

Inserting Eq. 20.108 into 20.109 yields the relation between the mass fraction of total carbon in the equilibrated steel and the mass fraction of carbon in the austenite phase:

$$\omega_C^T = S(\omega_C, \omega_{Cr}^0, \omega_{Ni}^0, T) \quad (20.110)$$

If the thermodynamics of the carbide phase were known, the chromium fraction in the carbide,  $X$ , would be

describable in terms of the concentrations  $\omega_C$ ,  $\omega_{Cr}^{\circ}$ , and  $\omega_{Ni}^{\circ}$ . Hence X is not an independent parameter, and we have accordingly deleted this variable from the list in the parentheses in Eq. 20.110.

Finally, Eq. 20.110 is solved for  $\omega_C$  and inserted into Eqs. 20.106 and 20.107, and the results of these substitutions and Eq. 20.110 are used in the activity equation, Eq. 20.97. We then have the desired relationship between the carbon activity in the steel (or in the sodium, which contains the same carbon activity as the steel) in terms of the temperature, the initial composition of the steel, and the total carbon concentration in the equilibrated specimen:

$$a_C = P(\omega_C^T, \omega_{Cr}^{\circ}, \omega_{Ni}^{\circ}, T) \quad (20.111)$$

The function P depends on the solubility expressing G and the activity coefficient in the austenite phase,  $\gamma_C$ .

Snyder, Natesan, and Kassner<sup>2,3</sup> have used their data and those of other investigators to correlate the carbon activity with the initial composition of the steel ( $\omega_{Cr}^{\circ}$  and  $\omega_{Ni}^{\circ}$ ) and the total mass fraction of carbon in the equilibrated specimen ( $\omega_C^T$ ). To good approximation, their results suggest that  $a_C$  is proportional to  $\omega_C^T$ , or that the two-phase mixture behaves as a single phase with a pseudo activity coefficient  $\gamma_C^*$  ( $\omega_{Cr}^{\circ}, \omega_{Ni}^{\circ}, T$ ):

$$a_C = \omega_C^T \gamma_C^* (\omega_{Cr}^{\circ}, \omega_{Ni}^{\circ}, T) \quad (20.112)$$

with

$$\begin{aligned} \ln \gamma_C^* = & \left( -0.3 + \frac{5.0}{T/10^3} \right) - \left( -24.8 + \frac{40.4}{T/10^3} \right) \omega_{Cr}^{\circ} \\ & - \left( 102 - \frac{94}{T/10^3} \right) (\omega_{Cr}^{\circ})^2 \\ & + \left( -2.1 + \frac{7.2}{T/10^3} \right) \omega_{Ni}^{\circ} \end{aligned} \quad (20.113)$$

These two equations are used in relating carbon activity and carbon concentration in the tab meter described at the end of the preceding section.

### 20.6.2 Carbon Transfer in Sodium Loops

Armed with the carbon activity—concentration relationships in both the sodium (Eq. 20.82) and the stainless steel (Eq. 20.112), we now seek to determine the conditions for carbon transfer between high-temperature and low-temperature components in an all-austenite steel loop in which sodium circulates. In order to illustrate the transport process in the simplest possible way, we consider the primitive loop depicted in Fig. 20.30. Two pots made of an inert metal (i.e., one that does not exchange carbon with sodium) each hold a small steel specimen of the same initial carbon content. The pot on the left is maintained at a higher temperature than the pot on the right, and sodium circulates between the two containers. We defer consideration of the kinetics of the carburization and decarburization processes until later and determine here the total

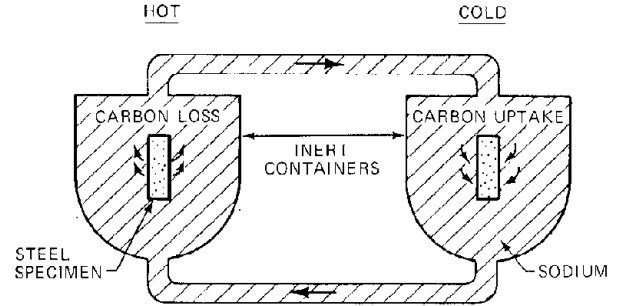


Fig. 20.30 A sodium loop for demonstrating carbon transport in a thermal gradient.

carbon concentrations of the two specimens when equilibrium in the entire loop is attained.

At equilibrium there is but a single activity of carbon in the hot pot which both the carbon in the steel and that in the sodium attain. Similarly, the activity of carbon in the sodium and that in the steel specimen in the cold pot reach a common value which, however, is different from the carbon activity in the hot pot (owing to the temperature difference between the two pots). Thus, the condition of chemical equilibrium in the two pots requires that

$$(a_C^{ss})_h = (a_C^{Na})_h \quad (20.114a)$$

$$(a_C^{ss})_c = (a_C^{Na})_c \quad (20.114b)$$

where ss = stainless steel

Na = sodium

h = the hot pot

c = the cold pot

If we use Eqs. 20.82 and 20.112 for  $a_C^{Na}$  and  $a_C^{ss}$ , the preceding conditions become

$$(\omega_C^T)_h (\gamma_C^*)_h = \frac{(C_C^{Na})_h}{[C_{sat(C)}^{Na}]_h} \quad (20.115a)$$

$$(\omega_C^T)_c (\gamma_C^*)_c = \frac{(C_C^{Na})_c}{[C_{sat(C)}^{Na}]_c} \quad (20.115b)$$

At equilibrium there is no net transfer of carbon between the flowing sodium and the steel specimens; so the carbon concentration in the sodium is the same throughout the loop  $[(C_C^{Na})_h = (C_C^{Na})_c]$ . Therefore, we can divide Eq. 20.115a by 20.115b to obtain the ratio of the carbon concentrations in the hot and cold steel specimens:

$$\frac{(\omega_C^T)_h}{(\omega_C^T)_c} = \frac{(\gamma_C^*)_c}{(\gamma_C^*)_h} \frac{[C_{sat(C)}^{Na}]_c^{1/2}}{[C_{sat(C)}^{Na}]_h^{1/2}} \quad (20.116)$$

If the steel specimen in the hot pot decarburizes and the cold sample picks up carbon, the ratio on the right-hand side of Eq. 20.116 must be less than unity. This equation demonstrates that the temperature dependence of both the

pseudo activity coefficient of carbon in steel and of the solubility of carbon in sodium determines the direction and extent of carbon transfer in this simple loop. The solubility of carbon in sodium decreases rapidly as the temperature drops (Fig. 20.27), and this behavior encourages carbon migration from the hot sample to the cold sample. The temperature dependence of  $\gamma_C^*$  (from Eq. 20.113) is more complex than that of  $C_{\text{sat}(C)}^{\text{Na}}$ , but, provided that  $\gamma_C^*$  increases with decreasing temperature no faster than the rate at which  $[C_{\text{sat}(C)}^{\text{Na}}]^{1/2}$  decreases with decreasing temperature, decarburization of the hot specimen and carburization of the cold specimen will occur. That the right-hand side of Eq. 20.116 is in fact less than unity is indicated by substitution of Eqs. 20.79 and 20.113 into Eq. 20.116 and the observation of decarburization of steel in the hot leg and of carburization of the same type of steel in the cold leg in sodium test loops.

This type of argument may also be applied to the transfer of carbon between ferritic steel and austenitic steel in an isothermal loop. In this instance the ratio of saturation carbon concentrations in the sodium appearing in Eq. 20.116 is unity, and we have

$$\frac{(\omega_C^T)_{\text{austenite}}}{(\omega_C^T)_{\text{ferrite}}} = \frac{(\gamma_C^*)_{\text{ferrite}}}{(\gamma_C^*)_{\text{austenite}}}$$

where  $(\gamma_C^*)_{\text{ferrite}}$  is the activity coefficient of carbon in the ferritic steel. Since the presence of chromium in the austenitic steel lowers the activity coefficient of carbon in this alloy, the ratio on the right-hand side of the preceding equation is larger than unity. Or the austenite absorbs carbon and the ferrite loses it.

### 20.6.3 The Kinetics of Carburization and Decarburization

The preceding analysis demonstrated the thermodynamic basis for carbon transport in nonisothermal sodium loops but provided no information on the kinetics of the transfer process. To analyze this aspect of the carburization/decarburization phenomenon, we need to examine in detail the processes by which carbon is removed from or added to steel exposed to sodium.

Sodium containing carbon at a fixed activity  $a_C$  contacts a plane surface of stainless steel. If the carbon activity in the sodium is greater than that of the steel (given by Eq. 20.112 with  $\omega_C^T$  equal to the initial carbon content of the fuel), carburization occurs. If the reverse is true, the steel is decarburized. We analyze the carbon uptake problem, although carbon loss to low-activity sodium can be treated in a similar manner.

Because the thickness of the steel specimen is usually quite large compared to the depth of carbon penetration, the metal is treated as a semi-infinite medium in which the carbon concentration in the steel far from the interface is unaffected by carbon diffusing into the surface layer from the sodium. We also neglect boundary-layer diffusion of carbon in the sodium and slow interfacial reactions between carbon in sodium and in the steel adjacent to the sodium. Inasmuch as the carbon concentration in commercial steels

(~0.05 wt.%) is in excess of the solubility limit for LMFBR operating temperatures, the steel is treated as a two-phase system during carburization. Under the strongly decarburizing conditions prevailing in the hot leg of a sodium loop, all the carbide phase may eventually be decomposed, and carbon diffusion occurs through a homogeneous austenite phase. The diffusion analysis must be modified when this situation occurs.

There are several levels of complexity in modeling steel carburization, and the various treatments reviewed in this section bear strong resemblances to analogous models of fission-gas release from irradiated fuels (Chap. 15).

#### Effective-Diffusion-Coefficient Method

The simplest model for treating the kinetics of steel carburization is to regard the metal as a homogeneous medium (despite the presence of two phases) in which carbon migration is characterized by an effective diffusion coefficient  $D_C^{\text{eff}}$ . The carbon penetration profile as a function of time is determined by solving the diffusion equation

$$\frac{\partial \omega_C^T}{\partial t} = D_C^{\text{eff}} \frac{\partial^2 \omega_C^T}{\partial z^2} \quad (20.117)$$

where  $t$  is the time of exposure and  $z$  is the distance from the sodium-steel interface. Equation 20.117 is subject to the following boundary condition at the sodium-steel interface:

$$\omega_C^T(0,t) = \frac{a_C}{\gamma_C^*(\omega_{C_r}^o, \omega_{N_i}^o)} \quad (20.118)$$

The designation of temperature in  $\gamma_C^*$  has been deleted since this parameter is held constant during the carburization process. Far from the interface, the boundary condition is

$$\omega_C^T(\infty,t) = (\omega_C^T)_o \quad (20.119)$$

where  $(\omega_C^T)_o$  is the total carbon mass fraction in the original steel. The initial condition is

$$\omega_C^T(z,0) = (\omega_C^T)_o \quad (20.120)$$

The solution to Eqs. 20.117 to 20.120 is

$$\frac{\omega_C^T(z,t) - (\omega_C^T)_o}{\omega_C^T(0,t) - (\omega_C^T)_o} = \text{erfc} \frac{z}{(4D_C^{\text{eff}}t)^{1/2}} \quad (20.121)$$

The effective diffusion coefficient of carbon in the steel has been determined by measuring the penetration of radioactive carbon into steel samples. The results of Agarwala et al.<sup>24</sup> are

$$(D_C^{\text{eff}})_{304} = 6.2 \exp\left[-\frac{187}{R(T/10^3)}\right] \quad (20.122a)$$

$$(D_C^{\text{eff}})_{316} = 0.4 \exp\left[-\frac{168}{R(T/10^3)}\right] \quad (20.122b)$$

for types 304 and 316 stainless steel, respectively. The units of the diffusion coefficients are square centimeters per second.

The effective-diffusion-coefficient method of predicting carburization or decarburization of steel is valid provided that the diffusion coefficient has been obtained for a steel with a composition similar to the alloy in question, and the carbon activity levels in the diffusion experiment are not too different from those in the system to be analyzed. The exposure time is another variable that should be similar in the experiment to determine  $D_C^{eff}$  and in the carburization calculation to which it is applied. However, the contact time of interest in LMFBR carburization/decarburization analyses is nearly four orders of magnitude larger than the diffusion time used to determine  $D_C^{eff}$ . Just as in the case of analysis of fission-gas release by the simple diffusion model (Sec. 15.5), use of apparent or effective diffusion coefficients predicated on an analysis ignores second-phase trapping centers in the medium. Applying the results to conditions other than those of the measurements is quite risky.

### Carbon Diffusion with Equilibrium Carbide Precipitation

One of the major deficiencies of the effective diffusion analysis can be removed by explicitly accounting for the presence of second-phase carbide precipitate in the metal. The diffusion analysis that removes this unrealistic assumption is analogous to the equilibrium trapping model of fission-gas diffusion in oxide fuels (Sec. 15.6). A computational scheme based on diffusion of carbon in austenite with local equilibrium between the metal and carbide phases has been developed by Snyder, Natesan, and Kassner.<sup>2,3</sup>

It is assumed that carbon diffuses only in the austenite and that the particles of the carbide phase are stationary. The metallic components of the austenite phase are immobile because the diffusion coefficients of iron, chromium, and nickel are much smaller than that of carbon in steel. The form of Fick's second law pertinent to this problem recognizes that the solid contains carbon in two phases but that diffusion occurs only in the austenite:

$$\frac{\partial \omega_C^T}{\partial t} - D_C \frac{\partial^2 \omega_C}{\partial z^2} \quad (20.123)$$

Here  $D_C$  is the true diffusion coefficient of carbon in the austenite phase of steel. This quantity has not been measured (because of the low solubility of carbon in high-chromium-content alloys), but the diffusivity of carbon in  $\gamma$ -Fe is given by<sup>2,5</sup>

$$D_C = 0.67 \exp \left[ \frac{157}{R(T/10^3)} \right] \text{ cm}^2/\text{sec} \quad (20.124)$$

The effect of nickel additions on the diffusion coefficient in  $\gamma$ -Fe-Ni alloys is small, but chromium appears to have an effect on  $D_C$ . Nevertheless, if Eq. 20.124 is accepted as a reasonable approximation to the diffusion coefficient of

carbon in the metallic phase of stainless steel, a diffusivity in the austenite phase approximately three times larger than the effective diffusion coefficient in type 304 stainless steel (Eq. 20.122a) is predicted at 700°C.

On the basis of the known relation between total carbon mass fraction in the two phase steel and that in the austenite phase, we can write Eq. 20.123

$$S'(\omega_C) \frac{\partial \omega_C}{\partial t} = D_C \frac{\partial^2 \omega_C}{\partial z^2} \quad (20.125)$$

where  $S'(\omega_C) = d\omega_C^T/d\omega_C$  is a function of  $\omega_C$  obtainable from Eq. 20.110.

The boundary and initial conditions for Eq. 20.125 pertain to the carbon content of the austenite phase, not to the total carbon mass fraction, as was the case in the effective diffusion coefficient model. At the sodium-steel interface, the carbon activity  $a_C$  is specified, and Eq. 20.112 determines  $\omega_C^T$  at this location. Equation 20.110 then fixes the carbon mass fraction in the austenite at the interface. This quantity is denoted by  $(\omega_C)_{int}$ , and the appropriate boundary condition is

$$\omega_C(0,t) = (\omega_C)_{int} \quad (20.126)$$

To determine the carbon concentration in the austenite far from the interface, we assume that, before exposure to the sodium, the steel has equilibrated internally. That is, the initial carbon supersaturation of the alloy has been relieved by precipitation of sufficient carbide phase so that the carbon mass fraction in the austenite,  $\omega_C^0$ , satisfies Eq. 20.110, or

$$(\omega_C^T)^0 = S(\omega_C^0, \omega_{Cr}^0, \omega_{Ni}^0)$$

which can be solved for  $\omega_C^0$ . The remaining boundary condition for Eq. 20.125 is

$$\omega_C(\infty,t) = \omega_C^0 \quad (20.127)$$

and the initial condition is

$$\omega_C(z,0) = \omega_C^0 \quad (20.128)$$

The nature of Eq. 20.125 and its associated boundary and initial conditions permits conversion of the partial differential equation to an ordinary differential equation by the variable transformation:

$$\eta = \frac{z}{(4D_C t)^{1/2}} \quad (20.129)$$

which, when inserted into Eq. 20.125, yields

$$\frac{d^2 \omega_C}{d^2 \eta} + 2\eta S'(\omega_C) \frac{d\omega_C}{d\eta} = 0 \quad (20.130)$$

With  $\omega_C$  now a function of the variable  $\eta$  only, Eq. 20.126 becomes

$$\omega_C(0) = (\omega_C)_{int} \quad (20.131)$$

and Eqs. 20.127 and 20.128 provide a single condition

$$\omega_C(\infty) = \omega_C^{\circ} \quad (20.132)$$

Equations 20.130 to 20.132 can be solved numerically to give  $\omega_C$  as a function of  $\eta$  or, according to Eq. 20.129, as a function of position and time. The total carbon concentration as a function of the same two variables is then obtained from Eq. 20.110.

### Effect of Carbide Precipitation Kinetics on the Rate of Steel Carburization

The preceding analysis of carbon penetration into stainless steel appears to be valid<sup>2,3</sup> for  $T > 600^{\circ}\text{C}$ . Below this temperature, the assumption of local equilibrium between the austenite phase and the carbide phase becomes progressively worse. Although Eq. 20.123 remains valid (it is merely a material balance), the relation between  $\omega_C^T$  and  $\omega_C$  given by Eq. 20.110 no longer applies to all the austenite. Instead, the austenite is permitted to be supersaturated with carbon during carburization and subsaturated during decarburization. The condition of thermodynamic equilibrium between the austenite and carbide phases applies only at the interface between these two phases (i.e., at the carbide particle surface). An additional kinetic step, namely, diffusion of iron, chromium, and carbon between the austenite-carbide interface and the bulk of the austenite phase, is added to the analysis. Thus, growth or dissolution of the carbide particles is assumed to be completely diffusion controlled. Diffusion controls the gross rate of migration of carbon from the sodium-steel interface to the interior of the steel and the small-scale transport of carbon and the metals from the interior of the austenite phase to the carbide particles in the vicinity. Possible kinetic restriction due to a slow reaction at the carbide-particle surface is not considered.

The treatment of precipitation kinetics in this model is identical to that used to describe diffusion-controlled growth of gas bubbles in the fuel or voids in the cladding. The metal contains a uniform distribution of spherical carbide particles of radius  $R$  ( $\approx 0.5 \mu\text{m}$ ). There are  $N$  carbide particles per cubic centimeter (assumed unchanged throughout the process). A capture volume of radius  $\mathcal{R}$  surrounding each carbide particle can be defined by the relation:

$$\left(\frac{4}{3}\pi\mathcal{R}^3\right)N = 1 \quad (20.133)$$

The radius  $\mathcal{R}$  is about 10 times larger than  $R$  (i.e.,  $\mathcal{R} \approx 5\mu\text{m}$ ).

Reaction 20.102 is assumed to be at equilibrium at the carbide-particle surface ( $r = R$ ). The mass fractions in the austenite far from the carbide particle are denoted by  $\omega_i$ , and at the particle surface the composition of the austenite is  $\omega_i^R$  (where  $i = \text{Fe, Cr, Ni, or C}$ ). According to the analysis of diffusion-controlled growth of spherical sinks in an infinite medium given in Sec. 13.5, the flux of species  $i$  from the austenite to the carbide particle is (see Eq. 13.70)

$$J_i = \frac{4\pi R D_i}{M_i} \rho_{ss}(\omega_i - \omega_i^R) \quad (20.134)$$

where  $D_i$  is the diffusion coefficient of species  $i$  in austenite,  $\rho_{ss}$  is the density of the austenite (assumed equal to the density of the steel), and  $M_i$  is the atomic weight of species  $i$ .

The stoichiometry of reaction 20.102 requires that

$$J_{Cr} = \frac{23X}{6} J_C \quad (20.135a)$$

$$J_{Cr} + J_{Fe} = \frac{23}{6} J_C \quad (20.135b)$$

When Eq. 20.134 is used in the first of these relations, we have

$$\frac{D_C}{D_M} \frac{X}{0.058} (\omega_C - \omega_C^R) = \omega_{Cr} - \omega_{Cr}^R \quad (20.136)$$

The atomic weight of the three metals has been taken as 54, and the diffusion coefficients of the three metals have been assumed to be equal to each other and denoted by  $D_M$ . Because thermodynamic equilibrium prevails at the carbide-austenite interface,  $\omega_{Cr}^R$  and  $\omega_C^R$  are related by Eq. 20.106. By the overall chromium balance on the steel,  $\omega_{Cr}$  is related to the initial chromium content by Eq. 20.103. Thus, Eq. 20.136 becomes

$$\frac{D_C}{D_M} \frac{X}{0.058} (\omega_C - \omega_C^R) = \frac{\omega_{Cr}^{\circ} - fX}{1 - f} - H(\omega_C^R, \omega_{Cr}^{\circ}, \omega_{Ni}^{\circ}, X) \quad (20.137)$$

where  $f$  remains to be determined.

Conservation of carbon in the austenite phase, including a Fick's law term for diffusion perpendicular to the sodium-steel interface, yields

$$\frac{\partial}{\partial t} [(1 - f) \omega_C] = D_C \frac{\partial^2 \omega_C}{\partial z^2} - 4\pi R D_C N (\omega_C - \omega_C^R) \quad (20.138)$$

We now relate  $f$  to the size and number density of carbide particles. Since  $f$  is the fraction of metal present as a carbide (locally),

$$\frac{\text{Grams metal in carbides}}{\text{Cm}^3 \text{ steel}} = f \rho_{ss}$$

Let  $\rho_C$  be the density of the carbide phase. The weight of metal per unit volume of carbide is  $\rho_C/1.058$ . The volume of carbide per unit of total steel volume is  $(R/\mathcal{R})^3$ ; so

$$\frac{\text{Grams metal in carbides}}{\text{Cm}^3 \text{ steel}} = \frac{\rho_C}{1.058} \left(\frac{R}{\mathcal{R}}\right)^3$$

and from these two equations,

$$f = \frac{\rho_C/\rho_{ss}}{1.058} \left(\frac{R}{\mathcal{R}}\right)^3 \quad (20.139)$$

To complete the analysis, we need the growth law for the carbide particles. This law is determined by the same

method used to obtain the void growth law in Sec. 19.5. The rate of change of the volume of a carbide particle is

$$\frac{d}{dt} \left( \frac{4}{3} \pi R^3 \right) = \frac{54(J_{Cr} + J_{Fe})}{(\rho_C/1.058)}$$

Or, expressing  $J_{Cr} + J_{Fe}$  by Eq. 20.135b, we find

$$\frac{dR}{dt} = \left( \frac{1.058}{0.058} \right) \left( \frac{\rho_{ss}}{\rho_C} \right) \frac{D_C}{R} (\omega_C - \omega_C^R) \quad (20.140)$$

Equations 20.138 and 20.140 must be solved (numerically) for  $\omega_C$  and  $R$  as functions of position and time. By Eq. 20.139  $f$  is a function of  $R$ , and solution of Eq. 20.137 gives  $\omega_C^R$  as a function of  $\omega_C$  and  $R$  ( $R$  enters via Eq. 20.139).

The boundary conditions for the present model are more difficult to assess than those applicable to the equilibrium model. At the steel-sodium interface, it is assumed that the carbon in the sodium is in equilibrium with the carbon in the austenite phase but that the carbide phase is not at equilibrium with the austenite (except at the carbide-austenite phase boundary). The mass fraction of carbon in the austenite depends on the extent of carbide precipitation at the sodium-steel interface; so  $(\omega_C)_{int}$  is a function of time. To obtain this boundary condition, we must solve the problem of carbide precipitation from an infinite medium of supersaturated austenite wherein the carbon activity is specified and constant.

At  $z = \infty$  the precipitation of carbide from an infinite medium of supersaturated austenite must also be treated, but in this case only the initial carbon content is specified. Determination of the boundary conditions at  $z = 0$  and  $z = \infty$  is set up in problem 20.10.

The initial carbon concentration in the austenite throughout the steel is equal to  $(\omega_C^T)^0$ , the total carbon mass fraction in the original steel.

Figure 20.31 shows the carbon distribution in steel at 700°C resulting from a 10,000-hr exposure to sodium with a carbon activity of  $4 \times 10^{-3}$ . The computation used the preceding equilibrium model. If the initial carbon concentration in the steel is greater than 0.04 wt.%, decarburization occurs. The carbon penetration depths shown in Fig. 20.31 are larger than typical cladding thicknesses, and appreciable carburization or decarburization is predicted at this temperature. (The semi-infinite medium approximation on which the calculated profiles are based does not apply when the thickness of the solid is small compared to the carbon penetration depth.) The penetration depths shown in Fig. 20.31 are much smaller than those computed by the effective-diffusion-model result (Eq. 20.121) with  $D_C^{eff}$  given by Eq. 20.122a. The large difference in the two calculations is not due to a large discrepancy between  $D_C^{eff}$  and  $D_C$  (indeed, in the calculation on which the curves of Fig. 20.31 are based,  $D_C$  is approximated by  $D_C^{eff}$ ). Rather, the smaller penetration in the equilibrium model compared to that in the effective diffusion model is due to correctly accounting for carbide precipitation during diffusion, which provides a powerful sink for migrating carbon and severely restricts penetration into the steel.

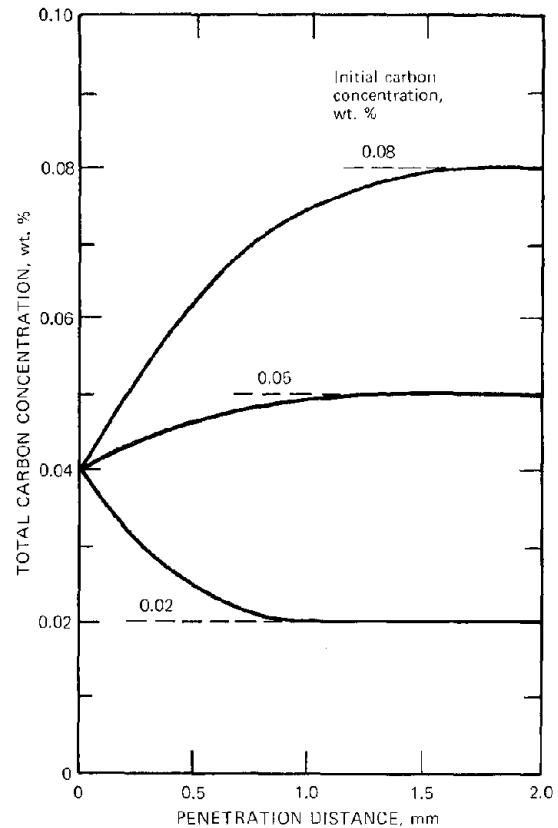


Fig. 20.31 Carbon diffusion profiles after a 10,000-hr exposure to sodium containing a carbon activity of  $4 \times 10^{-3}$  at 700°C. (Afler Ref. 23.)

Figure 20.32 shows a three-dimensional representation of carbon distributions at various temperatures between 400 and 800°C. In the calculation, the concentration of carbon in the sodium was fixed. Therefore, the activity of carbon in sodium, which determines the carbon activity of the steel at the interface, increases as temperature decreases. The calculations from which Fig. 20.32 resulted did not consider the dicarbide species in sodium; so the activity-concentration relation used was  $a_C = C_C^{Na} / C_{sat(C)}^{Na}$  instead of that given by Eq. 20.82. For  $660 < T < 800^\circ\text{C}$ , decarburization occurs because the solubility of carbon in sodium is high, and, for a fixed-carbon concentration in the sodium, Eq. 20.82 shows that  $a_C$  is low. The carbon activity in the sodium rises uniformly as the temperature is reduced, but for  $T < 530^\circ\text{C}$  carbide precipitation is so sluggish that very little carburization occurs.

Figure 20.33 shows the predicted effects of carbon transport along the length of fuel-pin cladding. Figure 20.33(a) shows the axial temperature profile, and Fig. 20.33(b) illustrates the variation of the average carbon content of the cladding at various axial positions after 5000 hr of contact with sodium of two different carbon concentrations. Maximum carburization occurs near the midplane of the core, but the upper half of the cladding (and presumably the remainder of the hot leg of the loop) is severely decarburized.

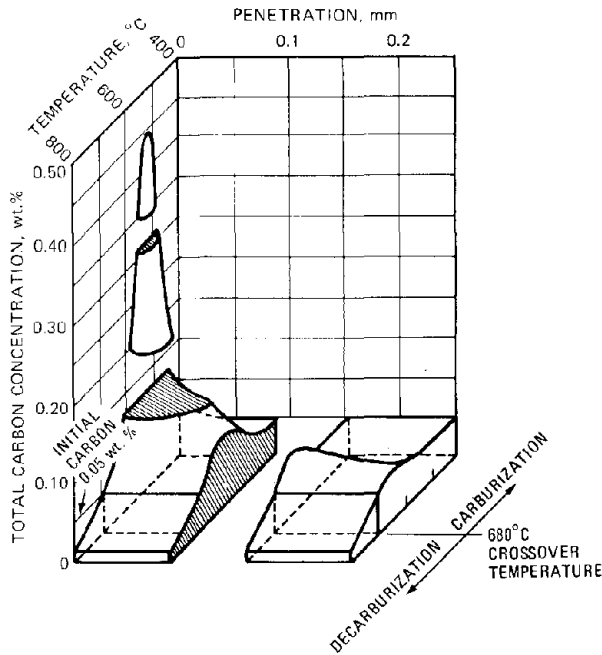


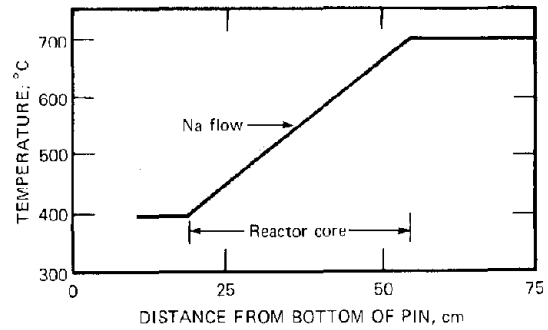
Fig. 20.32 Effect of temperature on the carburization/decarburization behavior of stainless steel (initial carbon content of 0.05 wt.%) due to 10,000-hr contact with sodium containing 0.13 ppm by weight carbon. (After Ref. 23.)

Figure 20.34 summarizes the results of computations of carbon penetration of the steel in the intermediate heat exchanger. Because of the low temperature, both carbon diffusion in the austenite and carbide precipitation are very slow; so carburization is restricted to the surface layers of the metal.

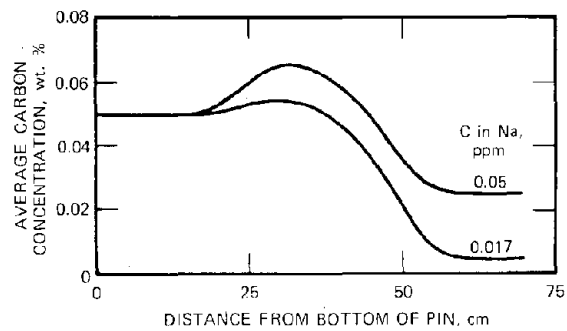
#### Carburization via the Grain Boundaries

In the preceding analysis of steel carburization, the morphology of the two-phase steel was assumed to consist of  $N$  spherical particles of radius  $R$  uniformly embedded in an austenite matrix. The particle density  $N$  was not predicted by the theory and would have to be determined by analysis of the homogeneous nucleation of carbide particles from a supersaturated austenite phase if the carburization problem were to be treated entirely from first principles. In practice, however,  $N$  is determined from microscopic examination of aged steels.<sup>2,3</sup>

It is known that carbides often precipitate along grain boundaries in the steel rather than in the bulk of the metal, which means that nucleation is heterogeneous rather than homogeneous. Grain boundaries are the preferred nucleation sites. It is very likely that carbide precipitates attached to grain boundaries are responsible for absorption of carbon from the sodium. In this case the most probable route by which carbon reaches the growing carbide-austenite interface is along grain boundaries rather than through the lattice. The controlling carburization mecha-



(a)



(b)

Fig. 20.33 Axial variation of the average carbon content of 0.37-mm wall stainless-steel cladding exposed to sodium containing 0.017 and 0.05 ppm by weight carbon for 5000 hr. (a) Axial temperature profile. (b) Variation of carbon content with position. (After Ref. 23.)

nism is then grain-boundary diffusion instead of volume diffusion in the lattice.

Nishio and Shimokawa<sup>2,6</sup> have attempted to explain their carburization data on the basis of classical grain-boundary diffusion theory.<sup>2,7</sup> However, this mathematical treatment does not account for simultaneous precipitation of the  $M_{23}C_6$  carbide in the grain boundaries during diffusion; so the results of this analysis are only somewhat more sophisticated effective diffusion coefficients than the one determined from the same type of data using the method discussed earlier. The volume diffusion coefficient of carbon in the austenite matrix obtained by Nishio and Shimokawa<sup>2,6</sup> is more than three orders of magnitude smaller than either  $D_C^{eff}$  or  $D_C$  given by Eqs. 20.122 or 20.124 at 700°C.

## 20.7 EFFECTS OF SODIUM EXPOSURE ON THE MECHANICAL PROPERTIES OF STAINLESS STEEL

The primary effects of sodium on the mechanical properties of the stainless-steel parts of the coolant loops in

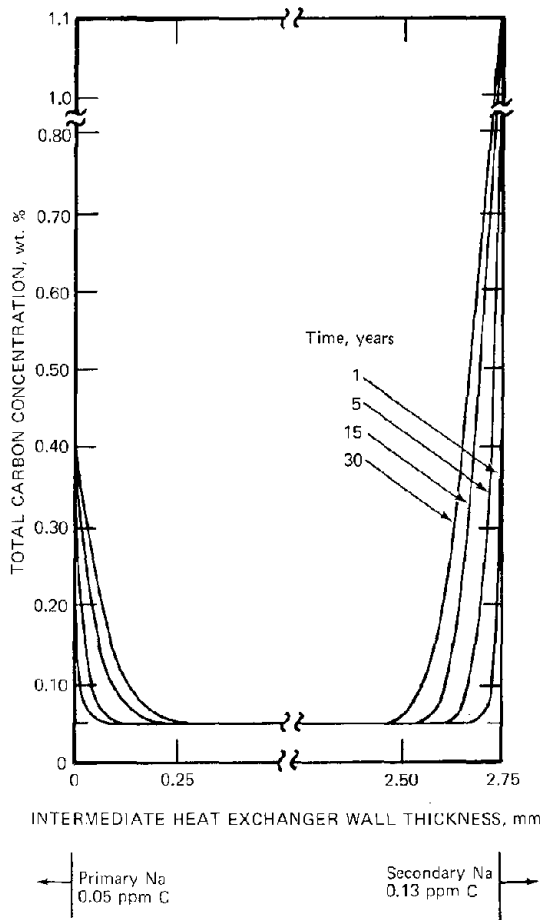


Fig. 20.34 Carbon concentration profiles across the stainless-steel intermediate-heat-exchanger piping after exposure to primary and secondary sodium containing 0.05 and 0.13 ppm carbon, respectively, for various times at 500°C. (After Ref. 23.)

an LMFBR arise directly from the loss or gain of carbon by the metal and indirectly from the change in the microstructure of the steel to the alteration of the carbon content. Selective leaching of the substitutional elements chromium and nickel has a negligible influence on mechanical properties, which are much the same for most alloys of iron, chromium, and nickel. Moreover, the metallic composition of the steel changes only in the surface layers of the exposed metal, and the base metal is unaffected.

The sodium per se does not affect mechanical properties since sodium is virtually insoluble in steel. Thus, any mechanical property change induced by contact of the steel with liquid sodium can equally well be reproduced by treatments not involving sodium provided that the composition and the microstructure of the steel following the two treatment routes are the same.

Table 20.2 summarizes the consequences of carburization and decarburization by sodium on the tensile and creep-rupture properties of stainless steel. The following discussion, which amplifies on the contents of the table, is

Table 20.2 Effect of Sodium Exposure on Properties of Steel

	Decarburization	Carburization
Tensile		
Yield stress	?	Increase
Ductility	?	Decrease
Creep		
rupture	Decrease	(Increase)?

drawn mainly from the review by Natesan, Kassner, and Li<sup>25</sup> and the paper by Spalaris and Zebroski.<sup>29</sup>

20.7.1 Tensile Properties

Figure 20.35 shows the distinct improvement in the 0.3% offset yield strength as the carbon content of the steel is increased. This behavior can be understood as an extension of the hardening function of carbon (hindering dislocation motion), which is the reason that this element is a desirable impurity in steel. One might expect that the strengthening would depend on the ratio of carbon in solid solution to that precipitated as carbides. Because of the strong temperature dependence of the carbide precipitation

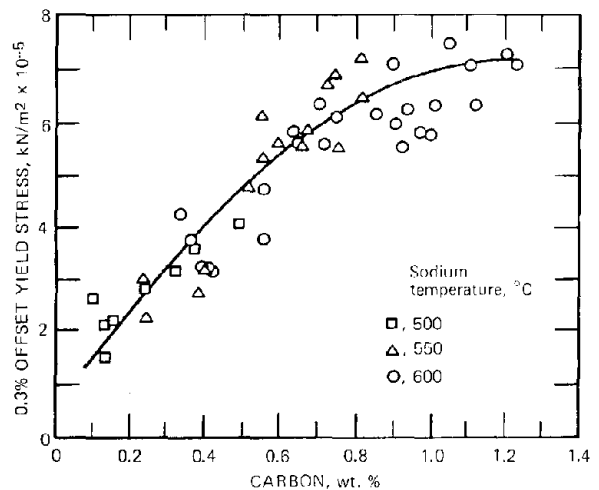


Fig. 20.35 Effect of carbon concentration on the yield strength of type 316 stainless steel carburized in sodium. (After Ref. 28.)

process in steel, carburization below  $T \approx 600^\circ\text{C}$  probably produces a higher proportion of carbon in the austenite compared to carbon as carbide than would carburization to the same total carbon concentration at higher temperatures. However, the data shown in Fig. 20.35 do not suggest such a variation.

Figure 20.36 shows tensile elongation (ductility) data on carburized steels. The curves provide an envelope for the rather scattered data that include both room-temperature and elevated-temperature mechanical test results and differ-

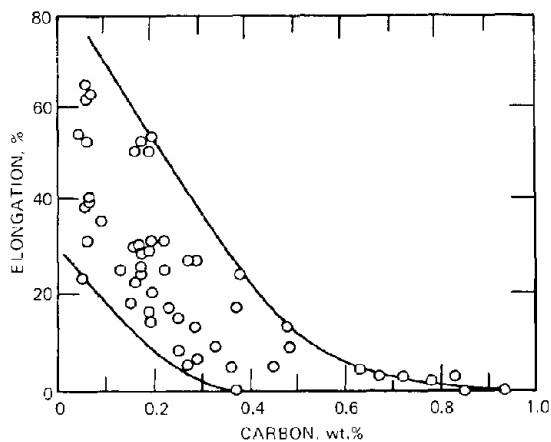


Fig. 20.36 Tensile elongation of type 304 stainless steel as a function of carbon content following exposure to various carburizing environments (sodium and  $\text{CH}_4/\text{H}_2$  gas mixtures). Data obtained at test temperatures from room temperature up to  $800^\circ\text{C}$ . (After Ref. 29.)

ent methods of carbon addition. Despite the scatter in the results, it is clear that steel that has experienced an increase in carbon content to greater than  $\sim 0.5$  wt. % (from the normal value of 0.05%) is essentially completely embrittled. For these specimens fracture occurs with no measurable elongation even at test temperatures as high as  $800^\circ\text{C}$ .

As was noted in the previous section, carburization is predicted in the cold zones of a sodium loop. The components in the cold leg, such as the intermediate heat exchanger, are constructed of thick steel parts (relative to the fuel-element cladding). Because the carbon penetration depths are small at low temperature and the affected parts are thick, complete carburization to carbon levels approaching 0.5 wt. % is not expected to occur (see Fig. 20.34). However, even the remote possibility of complete loss of ductility in a sodium loop component (e.g., carburization kinetics may not be well enough established to permit reliable extrapolation to 30-yr exposure times) is cause for concern and justification for seeking a remedy.

One solution is to eliminate the source of carbon from the reactor core by using stabilized grades of stainless steel, such as type 321 or type 347, for fuel-element cladding (types 304 and 316 are unstabilized). Addition of titanium or niobium to stainless steel very effectively immobilizes the carbon as the carbides of these two metallic species. The carbides of titanium and niobium are far more stable than the  $\text{M}_2\text{C}_6$  carbides formed from the major alloying elements of the steel (thermodynamic stability is measured by the solubility of carbon in the austenite phase contacting the metal carbide). Consequently, the rate of decomposition of the carbides of titanium and niobium is nil even under conditions that would severely decarburize an unstabilized steel. In fact, stabilized steels acquire carbon from sodium under these conditions.

The tensile properties of stainless steel that has been decarburized to low carbon concentrations [e.g., to the plateau values near the top of the fuel pin in Fig. 20.33(b)]

have not been determined. On the basis of a general understanding of the effect of carbon on steel tensile properties, reduced yield strength and improved ductility would be expected. However, loss of carbon in austenitic steels by sodium results in precipitation of the intermetallic compounds of iron and chromium of which the sigma phase is most prominent (see Fig. 20.15). This precipitate, which tends to embrittle steel, can cancel the potential gain in ductility due to removal of carbon from the austenite phase.

### 20.7.2 Creep-Rupture Properties

The creep strength of a metal can be expressed either by the time to rupture of a specimen at a specified initial stress or by the stress required to cause rupture in a fixed time (which is often called the stress-rupture strength of the metal). The elongation at rupture is a measure of the ductility in creep-rupture tests.

Pertinent data on the creep-rupture properties of austenitic steels carburized by sodium are not available (the studies intended to investigate this effect succeeded in carburizing only a small fraction of the total thickness of the specimens). However, the results of nonsodium studies of the effects of carbon and nitrogen addition on the rupture stress of steel are shown in Fig. 20.37. The higher than normal carbon contents were produced during fabrication. These data show that the stress-rupture strength, like the yield stress in tensile tests, increases with increasing carbon concentration.

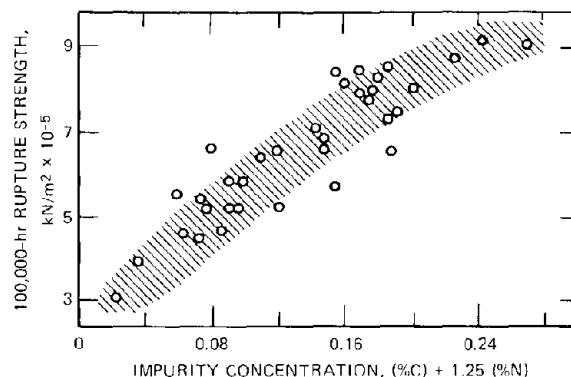


Fig. 20.37 Influence of carbon and nitrogen on the creep strength of type 304 stainless steel tested in air at  $650^\circ\text{C}$ . (After Ref. 28.)

Although the ductility (elongation to rupture) of the high-carbon-content steels decreases in a manner similar to that shown in Fig. 20.36, the creep rate is greatly reduced by the added carbon. Consequently, the rupture lifetime,  $t_R = \epsilon_F/\dot{\epsilon}$  is augmented despite the tendency of carbon to embrittle the metal. Carburization in flowing sodium which produces uniform increases in carbon concentration to the levels shown in the abscissa of Fig. 20.37 would be expected to improve the creep strength in a manner roughly equivalent to that shown on the graph.

Decarburization of austenitic steel by sodium, on the other hand, has been convincingly demonstrated to reduce the creep strength of the metal. Figure 20.38 shows the results of creep-rupture tests on stainless steel exposed to flowing sodium under conditions where carbon loss occurs. The data on sodium-exposed samples are compared with results for the exposure of specimens in an inert gas for the same period. Significant reduction in creep strength of the sodium-exposed steel compared with the inert-gas-exposed steel is observed. The elongation at fracture is also reduced by decarburizing sodium exposure.

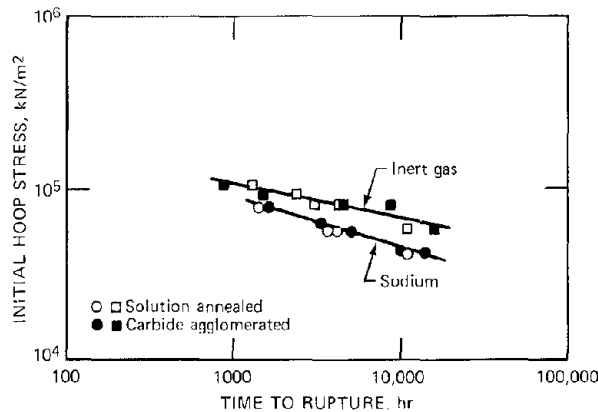


Fig. 20.38 Biaxial stress-rupture properties of type 316 stainless steel exposed to sodium or inert gas at 700°C for 5000 hr. (After Ref. 29.)

The extensive precipitation of sigma-phase particles observed in decarburized steel (Fig. 20.15) is believed to be responsible for the degradation of the creep-rupture properties. If the steel is fabricated with a low carbon concentration but without sigma-phase precipitation, its ductility is greater than, not less than, that of steel with a normal carbon content. The mechanism by which sigma-phase precipitates embrittle the metal and reduce its creep strength is not known. These particles can influence the size and number of helium bubbles in the metal, particularly if the particles are attached to grain boundaries. In this manner the long-term decarburization of steel in sodium reduces the resistance of the metal to helium embrittlement; the agent responsible for this undesirable effect is the sigma-phase precipitate.

Removal of carbon from stainless steel can impair the creep-rupture properties (both rupture stress and rupture ductility) to the same extent as exposure to a fast-neutron fluence of  $\sim 5 \times 10^{22}$  neutrons/cm<sup>2</sup>. It is clear that the effect of sodium on this particular mechanical property of steel needs to be accounted for in attempting to predict the performance of fuel elements whose lifetime is dictated by creep strain. What is not clear is whether sodium and fast-neutron exposure act independently or whether there is some as yet undiscovered synergistic effect when steel is subject to both environments simultaneously. Even if the processes due to sodium and fast neutrons act indepen-

dently of each other on an atomic scale, how are the macroscopic changes in mechanical properties to be added up? For example, if the ductility of a specimen decreases by, say, a factor of 5 after 1 year in a neutron flux without sodium and by a factor of 3 after the same time and temperature in sodium without neutrons, what should the ductility loss be when the sodium and the neutrons act together?

### 20.7.3 Other Material Properties

Adhesion (self-welding), wear, and friction between metal parts are affected by submersion in liquid sodium.

Self-welding is enhanced by surface cleanliness of the metals in contact. The solvent properties of liquid sodium act to remove protective layers normally found on metals (usually oxides) and thereby produce exceedingly clean surfaces that readily diffusion-bond together. Valve seats, cladding-wire wrap contact points, and the spacer pads on adjacent fuel subassemblies are subject to self-welding in high-temperature sodium.

The absence of a protective film on metals in sodium also increases the wear at sliding contacts. Sodium serves just the opposite function from lubricating oil between moving parts that are in contact. For this reason moving parts in contact under sodium are hardened surfaces (e.g., by nitriding) or else are fabricated of wear-resistant alloys, such as stellite.

Finally, higher coefficients of sliding friction between metals are observed in sodium environments than in gaseous atmospheres when tests are conducted at the same temperature.

## 20.8 SODIUM-FUEL INTERACTION

In this section we discuss the thermodynamic and kinetic bases from which the consequences of direct sodium contact with oxide fuel can be assessed. Such contact occurs when the fuel cladding is breached or when the fuel-cladding gap is filled intentionally with sodium during fabrication (sodium-bonded fuel elements). The reaction produces a solid of lower density than that of the fuel, and the resulting volume expansion can cause significant diametral strain of the fuel pin. Figure 20.39 shows the swelling observed in fuel that had been exposed to sodium either as sodium-bonded pins or as a result of a failed pin irradiated in a capsule containing stagnant sodium. The meaning of the abscissa will be explained later. The magnitude of the swelling shown in Fig. 20.39 justifies the concern about the sodium-fuel interaction and indicates the need for simple out-of-pile experiments to clarify the thermodynamics and kinetics of the swelling phenomenon. The in-pile experiments are complicated by the presence of the radial temperature gradient in the fuel, which results in oxygen redistribution. Isothermal out-of-pile experiments are easier to interpret in terms of basic mechanisms of the reaction.

Because of the precautions required when working with the mixed oxide (U,Pu)O<sub>2</sub>, many of the experiments designed to investigate sodium-fuel chemistry have used UO<sub>2</sub> as a substitute for the mixed oxide. The double oxides Na<sub>2</sub>U<sub>2</sub>O<sub>7</sub>, Na<sub>2</sub>UO<sub>4</sub>, Na<sub>4</sub>UO<sub>5</sub>, NaUO<sub>3</sub>, and Na<sub>3</sub>UO<sub>4</sub> have

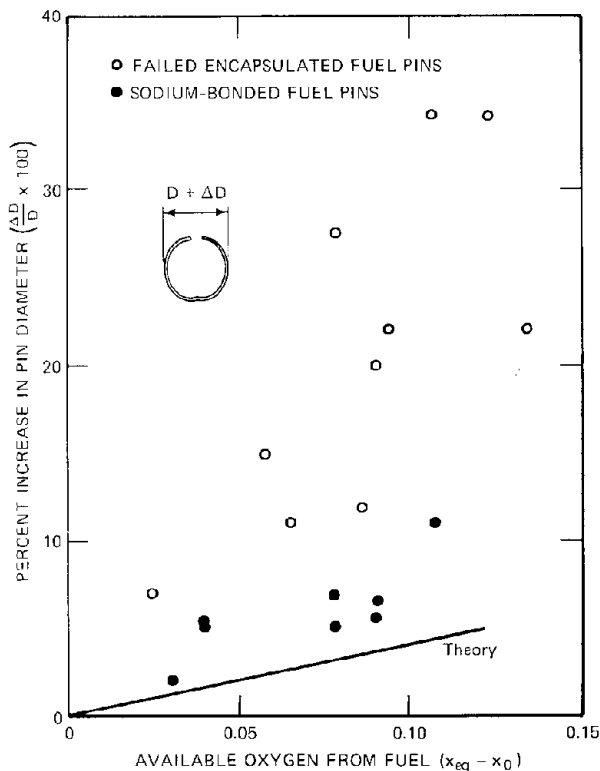


Fig. 20.39 Fuel-pin diametral strain due to sodium–fuel reaction. ○, failed encapsulated fuel pins. ●, sodium-bonded fuel pins. (After E. A. Aitken et al., in *Proceedings of the Conference on Fast Reactor Fuel Element Technology*, Apr. 13–15, 1971, New Orleans, La., p. 459, R. Farmakes (Ed.), American Nuclear Society, Hinsdale, Ill., 1971.)

all been observed in the sodium–uranium–oxygen system.<sup>30</sup> Under the conditions of temperature and oxygen potential characteristic of LMFBR sodium circuits, only  $\text{Na}_3\text{UO}_4$  is produced.

In mixed oxides the product of the sodium–fuel reaction is described by the generic formula  $\text{Na}_3\text{MO}_4$ , where M denotes a mixture of uranium and plutonium. It is commonly assumed that the uranium/plutonium ratio of the reaction product is the same as that of the fuel, which is denoted by  $\text{MO}_{2-x}$  (only hypostoichiometric fuels need be considered). This assumption has not received definitive experimental verification, but it has important implications on the kinetics of reaction product formation; if the uranium/plutonium ratio is the same in  $\text{MO}_{2-x}$  and  $\text{Na}_3\text{MO}_4$ , transport of the actinide metals from the fuel to the reaction zone is not necessary. Only sodium and oxygen need to move from the bulk of the reactant phases (sodium or fuel) to the interface where the chemical reaction occurs. Once there, sodium and oxygen can combine in the required proportions with the existing heavy-metal atoms. On the other hand, if the uranium/plutonium ratio in the reaction product were different from that of the fuel, one or the other of the heavy metals would have to migrate

from the interior of the fuel to the reaction zone. Since interdiffusion of uranium and plutonium in oxide crystals is very slow at the temperatures at which the sodium–fuel reaction occurs in a reactor ( $< 1000^\circ\text{C}$ ), the kinetics of the process would be correspondingly sluggish if transport of the heavy metals in the solid were a prerequisite to reaction.

The thermodynamics of the reaction product have been studied in the sodium–uranium–oxygen system.<sup>31</sup> It is assumed that the thermodynamics of  $\text{Na}_3\text{UO}_4$  are the same as those of  $\text{Na}_3\text{MO}_4$  or that partial substitution of uranium for plutonium does not affect the properties of the reaction product. However, the  $\text{U}/(\text{U} + \text{Pu})$  ratio is important in determining the thermodynamic behavior of the fuel  $\text{MO}_{2-x}$ .

### 20.8.1 Thermodynamics of the Two-Phase Sodium–Fuel System

The  $\text{Na}_3\text{MO}_4$  forms only when the oxygen potential of the sodium or of the fuel is greater than a threshold value. When the oxygen potential is lower than the threshold value (i.e., when the fuel is highly hypostoichiometric and the sodium is of low oxygen content), only two phases are present at equilibrium (the fuel  $\text{MO}_{2-x}$  and liquid sodium containing oxygen). When these two phases are equilibrated, the chemical potential of oxygen, or alternatively the oxygen potential,

$$\Delta\overline{G}_{\text{O}_2} = RT \ln p_{\text{O}_2} \quad (20.141)$$

must be the same in both phases. The term  $p_{\text{O}_2}$  is the oxygen pressure in equilibrium with the particular phase (sodium or fuel) at a specified temperature and oxygen content. Taken individually, the oxygen potential of each phase is a function of temperature and of the composition of the phase. The dependence of the fuel oxygen potential on the oxygen-to-metal ratio (or on the  $x$  in  $\text{MO}_{2-x}$ ), the  $\text{Pu}/\text{U} + \text{Pu}$  ratio  $q$ , and the temperature  $T$  was discussed in Chap. 11. At the high temperatures where the bulk of the fuel in a pin operates, the thermochemical models of Rand and Markin (Ref. 6 of Chap. 11) and Blackburn (Ref. 7 of Chap. 11) are reasonably accurate. If these models can be extrapolated to the lower temperature range where the fuel–sodium reaction is important (and this step is by no means sure), then the oxygen potential of the fuel can be considered to be known. We will use the Rand–Markin method in the following discussion because it can be expressed in rather simple analytical terms.

The oxygen potential of the fuel is given by

$$(\Delta\overline{G}_{\text{O}_2})_f - (\Delta\overline{H}_{\text{O}_2})_f - (\Delta\overline{S}_{\text{O}_2})_f \left( \frac{T}{10^3} \right) \quad (20.142)$$

where the subscript  $f$  denotes the fuel phase. Using Fig. 11.13, we approximate  $(\Delta\overline{S}_{\text{O}_2})_f$  by

$$(\Delta\overline{S}_{\text{O}_2})_f = -146 \text{ J mole}^{-1} \text{ } ^\circ\text{K}^{-1} \quad (20.143a)$$

and from Fig. 11.14:

$$(\Delta\overline{H}_{\text{O}_2})_f = -730 - 160(4 - V_{\text{Pu}}) \text{ kJ/mole} \quad (20.143b)$$

Equations 20.143a and b apply only to hypostoichiometric fuel not too close to exact stoichiometry. If the plutonium valence is expressed in terms of  $x$  and  $q$  by Eq. 11.15,  $V_{Pu}$  can be removed from Eq. 20.143b and the fuel oxygen potential written as

$$(\Delta\overline{G}_{O_2})_f = -A_f - B_f x \quad (20.144)$$

where

$$A_f = 730 - 146 \left( \frac{T}{10^3} \right) \quad (20.145)$$

$$B_f = \frac{320}{q}$$

The oxygen potential of the sodium phase is determined by the standard free energy of formation of  $Na_2O$  and the solubility of oxygen in sodium in the following manner. The law of mass action for reaction 20.64 is expressed by Eq. 20.65. Noting that Henry's law applies to  $Na_2O$  in liquid sodium, Eq. 20.19 relates the activity of oxygen in sodium to the concentration. Combining Eqs. 20.19 and 20.65 and expressing  $p_{O_2}$  in terms of the oxygen potential of the sodium defined by Eq. 20.141 yields

$$(\Delta\overline{G}_{O_2})_{Na} = 2R \left( \frac{T}{10^3} \right) \ln \left[ \frac{C_O}{C_{sat}(O)} \right] + 2\Delta G_{fNa_2O}^\circ \quad (20.146)$$

If we insert numerical values of the oxygen solubility from Eq. 20.18 and the free energy of formation of  $Na_2O$  from Eq. 20.16, the preceding equation becomes

$$(\Delta\overline{G}_{O_2})_{Na} = B_{Na} \ln C_O - A_{Na} \quad (20.147)$$

where

$$A_{Na} = 700 + 3 \left( \frac{T}{10^3} \right) \quad (20.148)$$

$$B_{Na} = 17 \left( \frac{T}{10^3} \right)$$

The oxygen concentration in the sodium,  $C_O$ , has the units of parts per million by weight.

At equilibrium between the fuel and sodium phases,

$$(\Delta\overline{G}_{O_2})_f = (\Delta\overline{G}_{O_2})_{Na} \quad (20.149)$$

Or, using Eqs. 20.144 and 20.147,

$$-A_f - B_f x = B_{Na} \ln C_O - A_{Na} \quad (20.150)$$

Note that the distribution of oxygen between the fuel and the sodium given by the preceding formula does not follow Henry's law, which would require a linear relation between  $x$  and  $C_O$ . Figure 20.40 is a plot of Eq. 20.150 for  $T = 1000^\circ K$  and  $q = 0.2$ . The left-hand ordinate of this graph gives the oxygen concentration of sodium that is in contact with the fuel  $(U_{0.8}Pu_{0.2})_{2-x}$  at  $1000^\circ K$ . The thick curve and the right-hand ordinate scale show the oxygen potential of the system (i.e., either that of the fuel or of the

sodium, since both are equal at equilibrium) as a function of oxygen composition. This line is a plot of Eq. 20.144.

The curve shown in Fig. 20.40 is theoretical in the sense that it was deduced without requiring data from experiments in which sodium and fuel are actually equilibrated.

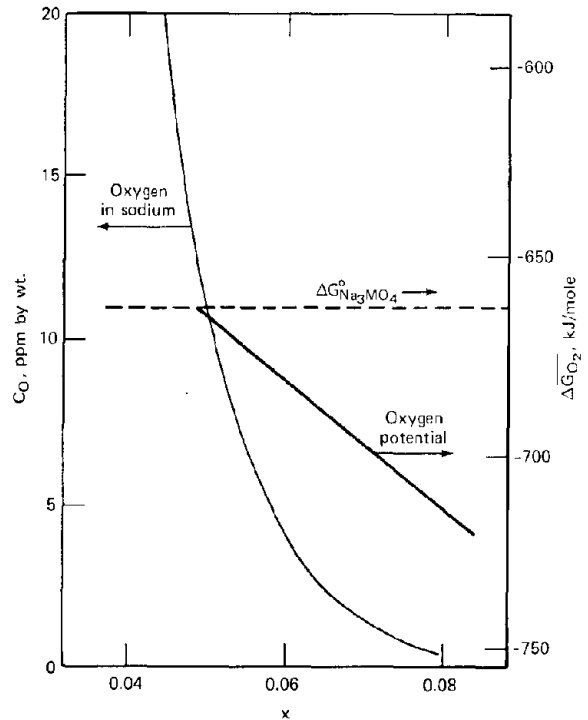


Fig. 20.40 Oxygen distribution between sodium and fuel phases at equilibrium and the oxygen potential of the system.  $T = 1000^\circ K$ .

Experiments of this sort have been performed<sup>32,33</sup> to test the results predicted by Eq. 20.150 (and similar equations using other models or data for the fuel oxygen potential than the Rand-Markin model we have employed here). The results of these experiments are in substantial disagreement with the predictions based on the supposedly known thermodynamics of oxygen in the fuel and in the sodium. The discrepancy between the data of Ref. 33 and Eq. 20.150, for example, is about three orders of magnitude. This spectacular lack of agreement between data and theory (or, more precisely, between equilibration data and other thermodynamic data manipulated by standard thermodynamic techniques to provide a prediction of oxygen distribution in sodium-fuel equilibration) is possibly due to the following:

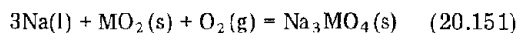
1. The equilibration data do not represent thermodynamic equilibrium, or the measurements are wrong.
2. Fuel oxygen potentials measured at temperatures above  $1000^\circ C$  cannot be accurately extrapolated to lower temperatures.
3. The free energy of formation of  $Na_2O$  and/or the solubility of oxygen in sodium are grossly in error.

Of these three possible reasons, only (3) is unlikely because the errors in  $\Delta G_{fNa_2O}^\circ$  or  $C_{sat(O)}$  would have to be very large to explain the observed  $C_O - x$  data in sodium-fuel equilibration experiments.

Despite the substantial roadblock caused by the failure of supposedly well established individual fuel and sodium thermochemistry to describe the two-phase fuel-sodium system, we shall continue the analysis of this system on the assumption that Eq. 20.150 adequately describes the oxygen concentrations in fuel and sodium in the two-phase equilibrium.

### 20.8.2 Thermodynamics of the Three-Phase Sodium-Fuel- $Na_3MO_4$ System

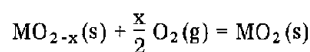
When the oxygen potential of the two-phase fuel-sodium system exceeds a threshold value, a third phase,  $Na_3MO_4$ , forms. According to the phase rule, one degree of freedom is lost because of the appearance of the additional solid phase; so the infinity of possible  $C_O - x$  values in the sodium-fuel distribution (Fig. 20.40) is now restricted to only one combination of  $C_O$  and  $x$  equilibrium in the system  $Na-MO_{2-x}-Na_3MO_4$ . Or, at a specified temperature, there is just one value of the oxygen potential for which the three phases can coexist. Based on careful measurement of the sodium-uranium-oxygen system, the standard free-energy change of the reaction



is<sup>31</sup>

$$\Delta G_{Na_3MO_4}^\circ = -923 + 262 \left( \frac{T}{10^3} \right) \quad \text{kJ/mole} \quad (20.152)$$

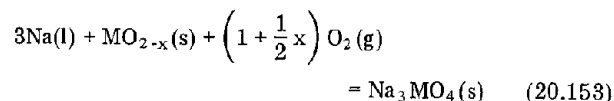
To obtain the standard free energy of the reaction in which  $MO_2$  in reaction 20.151 is replaced by  $MO_{2-x}$ , we use reaction B of Chap. 11:



for which the free-energy change is

$$\Delta G_B^\circ = -\frac{1}{2} \int_0^x (\Delta \overline{G}_{O_2})_f dx' \quad (11.43)$$

Addition of reactions 20.151 and B of Chap. 11 yields the desired reaction:



for which the standard free energy is the sum of Eqs. 20.152 and 11.43:

$$\Delta G^\circ = \Delta G_{Na_3MO_4}^\circ - \frac{1}{2} \int_0^x (\Delta \overline{G}_{O_2})_f dx' \quad (20.154)$$

Application of the law of mass action to reaction 20.153 yields

$$\exp\left(\frac{\Delta G^\circ}{RT}\right) = (p_{O_2})^{1+x/2} \quad (20.155)$$

If we take the logarithm of Eq. 20.155 and eliminate  $p_{O_2}$  in terms of the oxygen potential by using Eq. 20.141,  $\Delta \overline{G}_{O_2}$  is fixed as a function of temperature according to

$$\left(1 + \frac{1}{2}x\right) \Delta \overline{G}_{O_2} = \Delta G_{Na_3MO_4}^\circ - \frac{1}{2} \times \int_0^x (\Delta \overline{G}_{O_2})_f dx' \quad (20.156)$$

Because  $x$  is small compared to unity, the parenthetical term on the left can be approximated by unity and the integral on the right can be neglected. Thus the oxygen potential of the three-phase system is given by

$$(\Delta \overline{G}_{O_2})_f = (\Delta \overline{G}_{O_2})_{Na} = \Delta G_{Na_3MO_4}^\circ \quad (20.157)$$

Equation 20.157 consists of two relations which, when used in conjunction with Eqs. 20.144, 20.147, and 20.152, uniquely determines  $C_O$  and  $x$  for a fixed temperature. At 1000°K, for example, Eq. 20.152 gives  $\Delta G_{Na_3MO_4}^\circ = -661$  kJ/mole, which is equal to the oxygen potential of both the fuel and the sodium. Equations 20.144 and 20.145 yield  $x = 0.049$  and Eqs. 20.147 and 20.148 give  $C_O = 12$  ppm for this oxygen potential at 1000°K (this point is the intersection of the dashed line and the light curve in Fig. 20.40). Therefore, at this temperature the three-phase system should be in equilibrium when the fuel has the composition  $(U_{0.8}Pu_{0.2})O_{1.951}$  and the sodium contains 12 ppm by weight of oxygen. Table 20.3 gives the threshold fuel and sodium oxygen concentrations as functions of temperature. These results were obtained by a method essentially the same as the calculation described previously. The oxygen concentrations in the fuel and in the sodium must be maintained at values lower than those given in the table if formation of  $Na_3MO_4$  is to be thermodynamically impossible.

Comparison of the equilibration data from Ref. 33 with the thermodynamic predictions reveals poor agreement at all temperatures. Nonetheless, we will use the theoretical three-phase equilibrium defined by Eqs. 20.144 and 20.145, 20.147 and 20.148, and 20.152 and 20.157 as a basis for discussing the swelling experienced as a result of fuel-sodium contact and the kinetics of the swelling process.

Table 20.3 Calculated Oxygen Content\* of  $(U_{0.8}Pu_{0.2})O_{2-x}$  and of Sodium in Equilibrium with  $Na_3MO_4$

Temperature, °K	$-\Delta \overline{G}_{O_2}$ , kJ/mole	$2 - x$	$C_O$ , ppm by wt.
600	766	1.92	0.05
700	741	1.93	0.08
800	711	1.94	0.6
900	686	1.945	3
1000	661	1.95	11
1100	632	1.955	33
1200	607	1.96	77

\*Data from Ref. 31.

### 20.8.3 Maximum Swelling

The extent of fuel swelling due to  $\text{Na}_3\text{MO}_4$  formation depends not only on the thermodynamic properties described in the previous section but also on the supply of oxygen. The oxygen-to-heavy-metal ratio in the reaction product is about twice as large as it is in the original fuel. Therefore, both oxygen and sodium must be added to the fuel for the reaction to proceed. The sodium required for product formation obviously originates from the liquid-sodium reservoir with which the bare fuel material is in contact. The oxygen needed for the reaction, however, can be provided either by (1) the oxygen in the fuel or by (2) the oxygen in the sodium:

1. In experiments in which fuel pins are ruptured inside a capsule containing a few kilograms of sodium or in tests with sodium-bonded fuel pins, the amount of oxygen in the sodium (at concentrations of a few parts per million) is usually much smaller than the amount of oxygen bound in the fuel. In this case the fuel is the principal supplier of oxygen to the reaction. The reaction proceeds until the oxygen-to-metal ratio of the fuel is reduced from its initial value of  $2 - x_0$  to the value given by the third column of Table 20.3 at the appropriate temperature. In general, not all the fuel can be converted to  $\text{Na}_3\text{MO}_4$  because of this limitation on the oxygen supply.

2. When a fuel pin fails by cladding rupture in an LMFBR, however, the entire oxygen inventory of the primary sodium loop is potentially available for reaction. If the oxygen content of the flowing sodium is larger than the threshold value listed in the last column of Table 20.3, reaction proceeds until all the exposed fuel is converted to  $\text{Na}_3\text{MO}_4$ . If  $C_O$  in the sodium is less than the threshold value, no  $\text{Na}_3\text{MO}_4$  is formed, and oxygen is removed from (or added to) the fuel until the oxygen-to-metal ratio of the fuel and  $C_O$  satisfy the curve similar to that shown on Fig. 20.40 for the reaction temperature.

We consider here case 1 only, since fuel-sodium reactions in tests conducted in irradiation capsules and in out-of-pile capsules are limited in oxygen supply by the oxygen contained in the original fuel. Consider a closed system at temperature  $T$  which contains sodium whose oxygen content is negligible compared with that in the fuel piece, which weighs 270 g. The fuel contains 1 gram atom of heavy metals, and the initial oxygen-to-metal ratio of the fuel is  $2 - x_0$ . The equilibrium oxygen content of the fuel,  $x_{\text{eq}}$ , is obtained from the third column of Table 20.3, and it is assumed that  $x_0 < x_{\text{eq}}$ . When reaction 20.153 has come to equilibrium, let  $f$  be the fraction of the original heavy metal in the fuel which is contained in the reaction product  $\text{Na}_3\text{MO}_4$ . The remaining fraction  $(1 - f)$  of the fuel has the composition  $\text{MO}_{2-x_{\text{eq}}}$ . An oxygen balance on the system yields

$$2 - x_0 = (1 - f)(2 - x_{\text{eq}}) + 4f \quad (20.158)$$

The volume of fuel initially is

$$V_0 = \frac{270}{\rho_f}$$

where  $\rho_f = 10.9 \text{ g/cm}^3$  is the density of mixed-oxide fuel. The molecular weight of  $\text{Na}_3\text{MO}_4$  is  $\sim 371$ , and the density is  $\rho_p \approx 5.5 \text{ g/cm}^3$ . Therefore, the final volume of solid is

$$V = (1 - f) \frac{270}{\rho_f} + f \frac{371}{\rho_p}$$

The fractional volume increase is

$$\begin{aligned} \frac{\Delta V}{V} &= \frac{V - V_0}{V} \\ &= \left( \frac{371}{270} \frac{\rho_f}{\rho_p} - 1 \right) f \\ &= 1.7 \left( \frac{x_{\text{eq}} - x_0}{2 + x_{\text{eq}}} \right) \\ &\approx 0.8 (x_{\text{eq}} - x_0) \quad (20.159) \end{aligned}$$

where  $f$  has been eliminated by use of Eq. 20.158. If all swelling occurs in the radial direction (axial expansion of the fuel restricted by fuel-cladding friction), the diametral strain should be one-half the value given by the preceding formula. This line is plotted on Fig. 20.39. The observed swelling of all the fuel pins is much larger than that expected from Eq. 20.159, which suggests that

1. The method of measuring the diameter increase of the failed fuel pins (see insert of Fig. 20.39) is not representative of fuel swelling.

2. Other phenomena contribute to fuel swelling.

3. A larger fraction of the fuel is converted to  $\text{Na}_3\text{MO}_4$  than predicted by Eq. 20.158, which is predicated on oxygen supply by the fuel only. From the range of  $x_{\text{eq}} - x_0$  in the abscissa of Fig. 20.39,  $f < 7\%$ . If there were other sources of oxygen in the environment of the fuel pin (e.g., the sodium or impurities) to supplement the oxygen provided by the fuel proper,  $f$  could be larger.

4. The reaction product does not form at its theoretical (i.e., x ray) density of  $5.5 \text{ g/cm}^3$ . There is some evidence<sup>34</sup> that the density of the  $\text{Na}_3\text{MO}_4$  formed by the sodium-fuel reaction can be as low as  $1.6 \text{ g/cm}^3$ . When this value of  $\rho_p$  is used in Eq. 20.159 instead of the theoretical density, the slope of the line marked "theory" in Fig. 20.39 is five times as great as it is shown on the graph.

### 20.8.4 Kinetic Analysis

Although the preceding description of the sodium-fuel reaction illustrated significant uncertainties in either the theory or the corroborating experiments concerning the thermodynamics of the process, the state of understanding of the kinetics of the reaction is even more rudimentary. Indeed the kinetic analysis of this phenomenon is roughly comparable to the science of botany in the Middle Ages.

Consider the case of a bare cylindrical fuel rod (without cladding) of radius  $R$  exposed to flowing sodium. We stipulate that the oxygen potentials of both the fuel and the sodium are below the threshold for formation of  $\text{Na}_3\text{MO}_4$ ; therefore none of this phase appears at the sodium-fuel interface. If the initial oxygen potential of the fuel is greater than that of the sodium, oxygen will be removed from the fuel until a lower uniform oxygen

potential satisfying Eq. 20.149 is attained. We assume that the rate of removal of oxygen by the sodium is controlled by solid-state diffusion of oxygen in the fuel (wherein the oxygen diffusion coefficient is denoted by  $D_O^f$ ). The sodium velocity outside the solid is high enough to render boundary-layer resistance in the sodium film negligible. Quantitative kinetic analysis of this process is the subject of problem 20.13. Qualitatively, we see from the preceding formulation that the situation is analogous to heat conduction from a cylindrical solid in which the thermal diffusivity is replaced by the molecular diffusivity and the temperature is replaced by the concentration. In problems of this type, the time required for the average concentration (or temperature) in the solid to approach within 5% of its ultimate value occurs when the dimensionless time  $D_O^f t/R^2$  is approximately equal to unity. For  $R \approx 0.3$  cm and  $D_O^f \approx 4 \times 10^{-13}$  cm<sup>2</sup>/sec (which is the diffusivity of oxygen in stoichiometric  $UO_2$  at 1000°K), we find that 10,000 years is theoretically required for the average oxygen concentration in the fuel to have been changed from its initial value to within 5% of its equilibrium value. Experimentally observed equilibration times, however, are of the order of hundreds of hours.

One reason for the more rapid response of actual fuel-sodium equilibrations than is predicted by theory is that the oxygen does not have to diffuse through the entire specimen to reach a reaction zone. Rather, as shown in Fig. 20.41, sodium is apparently able to penetrate easily along grain boundaries and microcracks in the fuel so that the reaction appears to occur more or less uniformly within the fuel body. The characteristic distance over which oxygen must be transported is reduced from the diameter of the pellet to something of the order of the diameter of a grain. Thus, the distance  $R$  that enters into the estimation of the extent of the reaction is reduced from  $\sim 0.3$  cm to  $\sim 0.003$  cm (for a 30- $\mu$ m grain size), and the characteristic diffusion time is lowered from 10,000 years to 1 year. If the diffusivity of oxygen in the fuel were an order-of-magnitude higher than the values used in these estimates, the predicted and observed equilibration times would at least be of the same order of magnitude.\*

We analyze the kinetics of the fuel-sodium reaction (in which  $Na_3MO_4$  is produced) by the simple model illustrated in Fig. 20.42. Sodium access to the interior of the fuel specimen is assumed to be easy; so a plentiful supply of sodium surrounds each grain. The reaction occurs on the surface of the grains, and a reaction-product layer grows into the grain interior. The reaction front is at the fuel-product interface. The reaction-product layer is assumed to be sufficiently porous to permit entry of liquid sodium up to the reaction front. The rate of the reaction is assumed to be controlled by the diffusion of oxygen from

\*The diffusivity of oxygen in  $MO_{2-x}$  is probably larger than that in  $MO_{2.0}$  at the same temperature because oxygen migration occurs by a vacancy mechanism on the anion sublattice. Stoichiometric  $MO_2$  contains only the thermal concentration of anion vacancies, whereas the oxygen deficiency in  $MO_{2-x}$  is accompanied by creation of a site fraction  $x/2$  of vacancies on the anion sublattice (Sec. 11.3).



Fig. 20.41 Mixed-oxide fuel pellet ( $x_0 = 0.01$ ) after reaction with sodium for 40 days at 800°C.

the fuel in the interior of the grain to the reaction front, which moves radially inward as the reaction proceeds. At the product-fuel interface, the three phases of fuel, sodium, and reaction product are assumed to be in thermodynamic equilibrium. The oxygen-to-metal ratio in the fuel at this location, denoted by  $2 - x_{oq}$ , is that given by the third column of Table 20.3 for the reaction temperature.

If  $R_0$  denotes the original radius of the grain of fuel, the radius of the unreacted portion at time  $t$  is given by

$$R(t) = R_0 - \int_0^t v_f(t') dt' \quad (20.160)$$

where the inward velocity of the reaction front,  $v_f$ , remains to be determined.

Fick's second law for oxygen diffusion in the spherical fuel grain is given by

$$\frac{\partial x}{\partial t} = \frac{D_O^f}{r^2} \frac{\partial}{\partial r} \left( r^2 \frac{\partial x}{\partial r} \right) \quad \text{[for } 0 < r < R(t)] \quad (20.161)$$

The initial condition is

$$x(r,0) = x_0 \quad \text{[for } 0 < r < R_0] \quad (20.162)$$

and the boundary conditions are

$$x(0,t) = \text{bounded} \quad (20.163)$$

$$x[R(t), t] = x_{eq} \quad (20.164)$$

The velocity of the reaction front is determined by flux balances at the fuel-product interface. Consider a coordinate system moving radially inward at the reaction-front velocity. Heavy metals reach the interface at a flux equal to

$$(J_M)_{in} = \frac{\rho_f}{270} v_f$$

Because the density of the reaction product is less than that of the fuel, the velocity of the heavy metals leaving the interface, denoted by  $v_p$ , is larger than  $v_f$ , but the flux

$$(J_M)_{out} = \frac{\rho_p}{371} v_p$$

must be the same as  $(J_M)_{in}$ . Therefore, from the preceding equations,

$$v_p = \frac{371 \rho_f}{270 \rho_p} v_f \quad (20.165)$$

Because of the gradient in the oxygen concentration in the fuel near the interface, the flux of this species at the fuel side of the interface in the moving coordinate system is

$$(J_O)_{in} = -\frac{D_O^f \rho_f}{270} \left( \frac{\partial x}{\partial r} \right)_R + \frac{v_f \rho_f}{270} (2 - x_{eq})$$

Similarly, the flux of oxygen leaving the interface is

$$(J_O)_{out} = 4 \frac{\rho_p}{371} v_p$$

Equating  $(J_O)_{in}$  and  $(J_O)_{out}$  and eliminating  $v_p$  by Eq. 20.165 yields

$$v_f(t) = \frac{D_O^f}{2 + x_{eq}} \left( \frac{\partial x}{\partial r} \right)_R \quad (20.166)$$

A dimensionless concentration, time, and radial distance are defined by

$$\theta = \frac{x_{eq} - x}{x_{eq} - x_0} \quad (20.167)$$

$$\tau = D_O^f t / R_0^2 \quad (20.168)$$

$$\eta = \frac{r}{R_0}$$

The governing equations for the reaction become

$$\frac{\partial \theta}{\partial \tau} = \frac{1}{\eta^2} \frac{\partial}{\partial \eta} \left( \eta^2 \frac{\partial \theta}{\partial \eta} \right) \quad (20.169)$$

$$\theta(\eta, 0) = 1 \quad (20.170)$$

$$\theta(0, \tau) = \text{bounded} \quad (20.171)$$

$$\theta[\xi(\tau), \tau] = 0 \quad (20.172)$$

where, using Eq. 20.166 in Eq. 20.160,  $\xi = R/R_0$  is given by

$$\xi(\tau) = 1 + \left( \frac{x_{eq} - x_0}{2 + x_{eq}} \right) \int_0^\tau \left( \frac{\partial \theta}{\partial \eta} \right)_\xi d\tau' \quad (20.173)$$

Equations 20.169 to 20.173 have not been solved. However, Chambré<sup>35</sup> has treated the case in which the last term on the right of Eq. 20.173 is proportional to  $\tau$ . This situation occurs in the analysis of release of volatile fission products from an evaporating fuel sphere. His computations show that accounting for the inward movement of the sphere boundary can cause release rates to increase by orders of magnitude compared to the solution based on a stationary boundary. Thus, inward growth of the reaction product in the fuel-sodium reaction model can result in

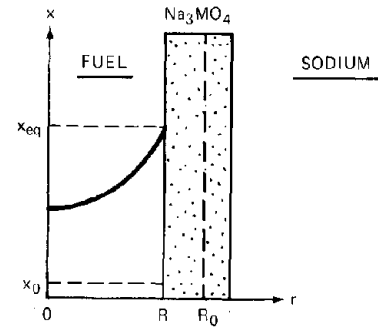
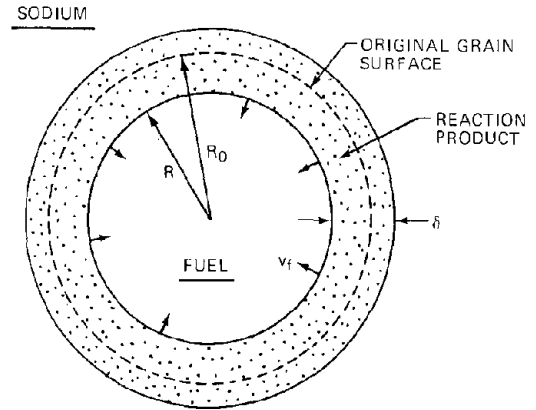


Fig. 20.42 Model of the sodium-fuel reaction in a grain surrounded by liquid sodium.

swelling rates significantly larger than those predicted by a simple diffusion model wherein the moving reaction front is not considered.

The preceding model neglected possible kinetic restrictions arising from the supply of sodium to the reaction front. If sodium does not penetrate readily through the grain boundaries and cracks in the solid and through the reaction-product layer on each grain, the rate will be slower than predicted by the model. In addition, all the oxygen for the reaction was assumed to come from the fuel inside the grain. If  $C_O$  in the sodium in which the sample is immersed is larger than that corresponding to  $x_{eq}$  (Table 20.3) and if oxygen migration from the bulk liquid along the same route followed by the sodium is easy, the overall rate of reaction could be accelerated. However, sodium need only flow through internal porosity in the fuel and reaction product, but oxygen must also diffuse in the liquid sodium that fills the interstices in the specimen. Since the oxygen content of the bulk sodium is low (parts per million range), the supply of oxygen from the sodium is probably quite meager. The initial sodium-fuel reaction can proceed rapidly by feeding only on the oxygen in the fuel and be augmented only much later by oxygen arriving slowly from the bulk sodium. On the other hand, if the oxygen concentration in the bulk sodium is less than that required for the three-phase equilibrium, the fuel can be partially reacted by using its own oxygen to produce the  $Na_3MO_4$ , and then much later the oxygen would be slowly drained away from the interior of the sample by diffusion through the sodium

filling the internal porosity. In this case the reaction product would first form in the grains and then be decomposed as the low oxygen potential of the external sodium slowly took effect.

The preceding model applies to an isothermal system in which the fuel specimen is immersed in a pool of sodium. In an actual cladding breach, however, the sodium contacts the surface of a fuel in which there is a strong temperature gradient. In hypostoichiometric fuel oxygen redistribution tends to maintain the oxygen-to-metal ratio at the fuel surface very close to 2.000 (Chap. 11) and appears to do so quite rapidly. Thus, oxygen consumed by the sodium–fuel reaction at the periphery can be replenished rapidly by whatever mechanisms are responsible for oxygen redistribution in the pin, thereby speeding up the sodium–fuel reaction by partially removing the oxygen-supply restriction at the surface. In addition, the oxygen released by burnup (Chap. 12) would be expected to be available to react and thus enhance the rate of the reaction of sodium with the fuel.

In a failed fuel pin, the sodium first enters through a small hole in the cladding, and, as the fuel in the vicinity of the defect swells, the hole is enlarged. The source of sodium is better represented by a point source on the surface of the fuel rather than as a uniform medium surrounding the entire fuel body. In this case ingress of sodium into the fuel and its subsequent reaction with the fuel may be dictated by the size of the opening in the cladding. The reaction product would grow inward in a manner reminiscent of a localized tumor (Fig. 20.43).

## 20.9 NOMENCLATURE

$a_i$  = thermodynamic activity of species  $i$   
 $C_i$  = concentration of species  $i$  in bulk sodium  
 $d$  = pipe diameter  
 $D$  = diffusion coefficient  
 $D^{\text{eff}}$  = effective diffusion coefficient  
 $E_{\text{dis}}$  = activation energy for dissolution in sodium  
 $f$  = fraction of the fuel that has reacted to form  $\text{Na}_3\text{MO}_4$ ; fraction of the metal in steel which is bound in a carbide; hydrodynamic friction factor  
 $\mathcal{F}$  = Faraday constant  
 $\Delta G^\circ$  = standard free-energy change of reaction  
 $\Delta G_{\text{fi}}^\circ$  = standard free energy of formation of compound  $i$   
 $\Delta \bar{G}_{\text{O}_2}$  = oxygen potential of fuel  
 $\Delta H_{\text{soln}}$  = enthalpy of solution in sodium  
 $j$  = Colburn  $j$ -factor  
 $J$  = flux  
 $k_d$  = mass-transfer coefficient  
 $k_R$  = reaction rate constant  
 $K_d$  = overall mass-transfer coefficient, Eq. 20.13  
 $K_1$  = equilibrium constant; Sievert's law constant for species  $i$   
 $l$  = distance from leading edge of flat plate  
 $L$  = length of isothermal leg in a loop  
 $\dot{m}$  = corrosion rate  
 $M$  = atomic weight  
 $n$  = density of active sites on a metal surface  
 $N$  = carbide particles per unit volume of steel; atom fraction of solute in solution

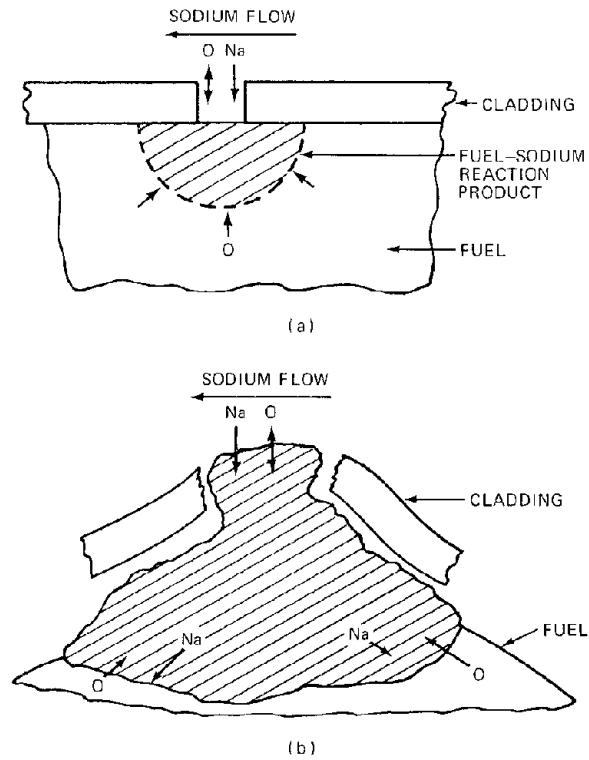


Fig. 20.43 Development of the fuel–sodium reaction product in a failed fuel element. (a) Short times. (b) After extensive reaction. [After E. A. Aitken et al., in *Proceedings of the Conference on Fast Reactor Fuel Element Technology*, Apr. 13–15, New Orleans, La., p. 459, R. Farmakes (Ed.), American Nuclear Society, Hinsdale, Ill., 1971.]

$N_{Av}$  = Avogadro's number  
 $p_i$  = partial pressure of species  $i$   
 $r$  = radial position  
 $\mathcal{R}$  = capture volume around a carbide particle  
 $R$  = rate of reaction; gas constant; radius of fuel grain  
 $Re$  = Reynolds number  
 $S' = d\omega_C^T/d\omega_C$   
 $Sc$  = Schmidt number ( $\nu/D$ )  
 $t$  = time  
 $T$  = temperature, °K  
 $u$  = recession velocity of steel surface  
 $v$  = sodium velocity  
 $v_f$  = velocity of sodium–fuel reaction front  
 $\Delta V/V$  = fuel swelling due to sodium–fuel reaction  
 $V_{Pu}$  = plutonium valence in fuel  
 $x$  = stoichiometry parameter in  $(U,Pu)\text{O}_{2 \pm x}$ ; downstream position in a sodium loop  
 $X$  = chromium-to-metal ratio in the carbide phase  
 $z$  = depth of penetration of carbon into steel

### Greek Letters

$\gamma$  = activity coefficient, Eq. 20.73  
 $\gamma_C^{\ddagger}$  = pseudo activity coefficient of carbon in steel, Eq. 20.112

$\delta$  = thickness of mass-transfer film  
 $\epsilon$  = thickness of reaction zone  
 $\Delta\epsilon$  = potential of electrochemical cell  
 $\eta$  = variable defined by Eq. 20.129 or 20.168  
 $\nu$  = kinematic viscosity  
 $\rho$  = solid density  
 $\omega$  = mass fraction  
 $\omega_{\text{int}}$  = mass fraction at sodium-steel interface  
 $\omega^{\text{R}}$  = mass fraction at carbide-austenite interface  
 $\omega^{\circ}$  = mass fraction in bulk steel

#### Subscripts and Superscripts

C = carbon  
 c = cold  
 cond = condensation  
 dis = dissolution  
 eq = at equilibrium  
 f = fuel  
 h = hot  
 int = interface  
 Na = sodium  
 O = oxygen  
 p = sodium-fuel reaction product ( $\text{Na}_3\text{MO}_4$ )  
 sat = at saturation  
 ss = stainless steel  
 \* = critical value for decomposition or precipitation;  
     equilibrium value  
 $\infty$  = in bulk steel, far from surface

## 20.10 REFERENCES

1. J. R. Weeks and H. S. Isaacs, *Adv. Corros. Sci. Technol.*, **3**: 1 (1973).
2. D. R. Olander and A. D. Pasternak, in *Nuclear Metallurgy*, Vol. 15, Symposium on Reprocessing of Nuclear Fuels (AIIME), p. 467, USAEC Report CONF-690801, Ames Laboratory, 1969. Correlation based on absolute rate theory using the sodium self-diffusion data of Meyer and Nachtrieb [*J. Chem. Phys.*, **23**: 1851 (1955)] and the iron viscosity data of Cavalier (The Physical Chemistry of Metallic Solutions and Intermetallic Compounds, Vol. 2, paper 4D, 1959).
3. W. M. Rohsenow and H. Choi, *Heat, Mass and Momentum Transfer*, Chap. 16, Prentice-Hall, Inc., Englewood Cliffs, N. J., 1961. This correlation does not apply to heat transfer to liquid metals in pipes because the Prandtl number is very small.
4. P. C. S. Wu and P. Chiotti, *Trans. Amer. Nucl. Soc.*, **17**: 161 (1973).
5. E. T. Turkdogan, P. Grieveson, and L. S. Darken, *J. Phys. Chem.*, **67**: 1647 (1963); see also D. E. Rosner, *Oxidation Metals*, **4**: 1 (1972).
6. E. G. Brush, *Trans. Amer. Nucl. Soc.*, **8**: 412 (1965).
7. General Electric Company, Effects of Sodium Exposure on the Corrosion and Strength of Stainless Steels, USAEC Report GEAP-10394, 1971.
8. W. E. Ray et al., *Nucl. Technol.*, **16**: 249 (1972).
9. E. Berkey, G. G. Sweeney, and W. M. Hickam, *Nucl. Technol.*, **16**: 263 (1972).
10. W. F. Brehm and G. L. Grandy, *Trans. Amer. Nucl. Soc.*, **17**: 161 (1973).
11. S. Weaver and E. Berkey, *Trans. Amer. Nucl. Soc.*, **16**: (1972).
12. D. R. Vissers et al., *Nucl. Technol.*, **21**: 235 (1974).
13. D. L. Smith, *Met. Trans.*, **2**: 579 (1971).
14. A. J. Hooper and E. A. Trevillion, *J. Nucl. Mater.*, **48**: 216 (1973).
15. D. L. Smith, *J. Nucl. Mater.*, **51**: 280 (1974).
16. G. K. Johnson et al., *J. Chem. Thermodyn.*, **5**: 57 (1973).
17. R. Ainsley et al., *J. Nucl. Mater.*, **52**: 255 (1974).
18. M. F. Roche et al., Determination of Carbon in Sodium by Tab Equilibrations and by Carbon Meters and the Carburization of Stainless Steels in Sodium Systems, USAEC Report ANL-8017, Argonne National Laboratory, 1973.
19. W. E. Ruther et al., *Nucl. Technol.*, **21**: 75 (1974).
20. K. Natesan and T. F. Kassner, *Nucl. Technol.*, **19**: 46 (1973).
21. H. Tuma et al., Carbon Activity and Solubility in a Stainless Chromium-Nickel Steel with About 18 Percent Cr and 9 Percent Ni, USAEC Report BNWL-tr-72, translated from *Arch. Eisenhuettenw.*, **40**(9): 727 (1969).
22. K. Natesan and T. Kassner, *Met. Trans.*, **4**: 2557 (1973).
23. R. B. Snyder, K. Natesan, and T. F. Kassner, *J. Nucl. Mater.*, **50**: 259 (1974).
24. R. P. Agarwala et al., *J. Nucl. Mater.*, **36**: 41 (1970).
25. R. P. Smith, *ASM (Amer. Soc. Metals), Trans. Quart.*, **230**: 476 (1964).
26. G. Nishio and J. Shimokawa, *J. Nucl. Mater.*, **47**: 87 (1973).
27. P. G. Shewmon, *Diffusion in Solids*, p. 166, McGraw-Hill Book Company, New York, 1963.
28. K. Natesan, T. F. Kassner, and Che-Yu Li, *Reactor Technol.*, **15**: 244 (1972/73).
29. C. N. Spalaris and E. L. Zebroski, in *Proceedings of the Conference on Fast Reactor Fuel Element Technology*, New Orleans, Apr. 13-15, 1971, American Nuclear Society, Inc., Hinsdale, Ill., 1971.
30. P. E. Blackburn et al., in *Proceedings of the Conference on Fast Reactor Fuel Element Technology*, p. 479, New Orleans, Apr. 13-15, 1971, American Nuclear Society, Inc., Hinsdale, Ill., 1971.
31. Papers by various Argonne National Laboratory workers, *J. Chem. Thermodyn.*, **4**: 401-439 (1972).
32. M. Chasanov et al., Chemical Engineering Division Fuels and Materials, Chemistry Semiannual Report, January-June 1973, USAEC Report ANL-8022, p. 5, Argonne National Laboratory, 1973.
33. D. L. Smith, *Nucl. Technol.*, **20**: 190 (1973).
34. D. E. Plumlee, *Trans. Amer. Nucl. Soc.*, **17**: 197 (1973).
35. P. L. Chambré, *J. Nucl. Mater.*, **18**: 187 (1966).

## 20.11 PROBLEMS

20.1 (a) Derive Eqs. 20.12 and 20.14.

(b) Determine the concentrations  $C(0)$  and  $C(L)$  at the junctions between the two legs of the loop in Fig. 20.7. Assume that  $4K_d L / r d$  is  $\ll 1$ .

(c) If deposition in the cold leg is inefficient (i.e.,  $K_{dc}$  is small) and  $C_{\text{sat}}^c \ll C_{\text{sat}}^h$ , show that the metal transport rate is independent of the temperature difference between the two legs.

20.2 The standard free energy of formation of sodium silicate ( $\text{Na}_2\text{SiO}_3$ ) is

$$\Delta G_{\text{fNa}_2\text{SiO}_3}^\circ = -511 + 95 \left( \frac{T}{10^3} \right) \text{ kJ/mole}$$

Calculate the critical oxygen activity in sodium at  $700^\circ\text{C}$  at which this double oxide precipitates out when the sodium contacts a type 316 stainless steel containing 0.3 wt.% Si. Assume that the silicon forms an ideal solid solution in steel.

20.3 Suppose the stability of the double oxide  $\text{FeO} \cdot (\text{Na}_2\text{O})_2$  is greater than expected (because  $\Delta G_{\text{fNa Ferrite}}^\circ$  is lower than the values given by Eq. 20.21) and that iron existed as the double oxide at all oxygen concentrations in a sodium loop. Derive the corrosion-rate equation comparable to Eq. 20.3 in which the concentration of dissolved oxygen appears explicitly and the rate constant  $k_R$  represents the reaction of  $\text{Na}_2\text{O}$  with the iron surface to produce sodium ferrite.

20.4 Use classical homogeneous nucleation theory (see problem 19.3) to calculate the nucleation rate of iron particles from liquid sodium. Assume the interfacial tension between liquid sodium and solid iron is 100 dynes/cm. Assume that the sodium temperature is instantaneously dropped from  $700$  to  $500^\circ\text{C}$  as the sodium enters the cold leg from the hot leg and that the sodium is saturated with iron at the hot-leg temperature.

20.5 Assume that a 1000-MW(e) fast reactor has 100,000 fuel pins of the dimensions shown in Table 10.2. Neglect radial variation of reactor power and assume that the axial power profile is a truncated cosine shape with a peak-to-minimum ratio of 1.8. The thermal efficiency of the plant is 40%. The sodium-film heat-transfer coefficient is  $12 \text{ W cm}^{-2} \text{ }^\circ\text{C}^{-1}$ ; the length of the axial blanket above and below the fueled section is 30 cm; and the oxygen content of the sodium is 5 ppm. Use the conversion-rate equation of Weeks and Isaacs, but neglect the downstream effect.

(a) What weight of metal is transferred from the core to the cold side of the sodium loop in 40 years? The load factor of the reactor is 75%.

(b) Estimate the  $^{54}\text{Mn}$  activity in the cold trap after 1 year of reactor operation. The total fast-neutron flux at the core midplane is  $7 \times 10^{15} \text{ neutrons cm}^{-2} \text{ sec}^{-1}$ , and the cross section for the  $^{54}\text{Fe}(n,p)^{54}\text{Mn}$  reaction, averaged over the neutron energy spectrum, is 16 mb. The half-life of  $^{54}\text{Mn}$  is 314 days.

20.6 The Sievert's law constant for hydrogen in sodium reported in Ref. 12 is

$$\ln K_H [\text{ppm}/(\text{atm})^{1/2}] = 5.29 - \frac{2.33}{R(T/10^3)}$$

Calculate the standard free energy of formation of  $\text{NaH}$  from this equation and Eq. 20.61, and compare the result with Eq. 20.58.

20.7 Derive the expression for the pressure in the vacuum chamber of Fig. 20.22 when the meter is operated in the dynamic mode. The speed of the ion pump is  $S$  liters/sec. Assume that the Sievert's law constant for distribution of hydrogen between nickel and gas-phase hydrogen,  $K_{\text{HNi}}$ , is known. The sole resistance to hydrogen transport from the sodium to the pump is the nickel membrane. The diffusion coefficient of hydrogen atoms in the nickel is  $D_{\text{HNi}}$ . The nickel membrane has a thickness  $\delta$  and a surface area  $A$ .

20.8 Calculate the theoretical electromotive force of the oxygen electrochemical meter for 5 ppm by weight of oxygen in sodium at  $370^\circ\text{C}$ . The oxygen reference gas is air.

20.9 The terminal solubility of oxygen in vanadium metal at  $750^\circ\text{C}$  has been measured as 2.3 wt.%. The equilibrium oxygen pressure over a solution of oxygen in vanadium is governed by a Sievert's law constant of  $2 \times 10^{16}$  in units of atom fraction/ $(\text{atm})^{1/2}$  at the same temperature. Deviation from Sievert's law is neglected.

(a) What is the distribution coefficient of oxygen between sodium and vanadium at  $750^\circ\text{C}$ ?

(b) What is the maximum concentration of oxygen in sodium (in parts per million by weight) at which the vanadium-wire equilibration method is applicable at this temperature?

(c) If  $\Delta G_{\text{fNa}_2\text{O}}^\circ$  is in error by 10 kJ/mole, by what factor does the result of question b change?

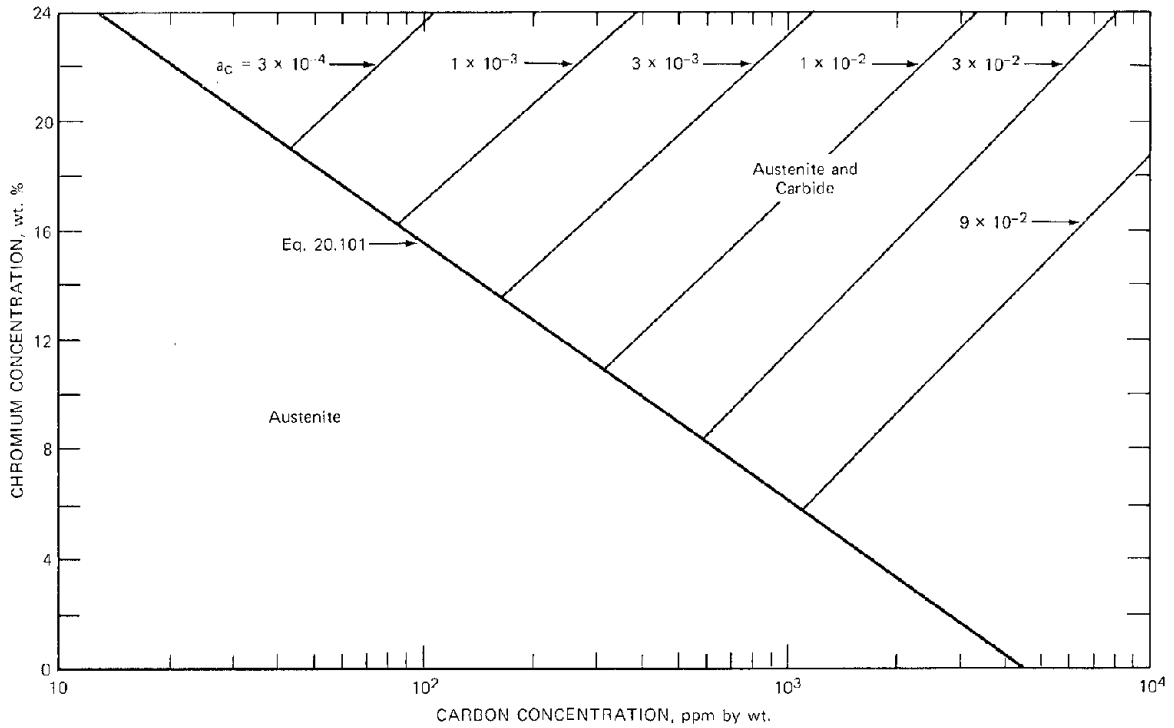
20.10 By considering diffusion-controlled growth of spherical carbide particles in an infinite medium, derive the appropriate boundary conditions at  $z = 0$  and  $z = \infty$  for use in conjunction with the precipitation-kinetics-controlled carburization process. The carbon activity of the sodium that contacts the steel at  $t = 0$  is  $a_C$ . The as-fabricated steel contains a concentration of total carbon  $(\omega_C^T)_{\text{fab}}$  all of which is contained in the austenite. Negligible carbide is present initially, but during carburization the concentration of carbide particles throughout the steel is constant at  $N$  particles/ $\text{cm}^3$ .

20.11 (a) Show that Eq. 20.138 is identical to Eq. 20.123.

(b) What conditions must be imposed in order that the precipitation-limited method of computing carburization kinetics [method (3)] reduces to the equilibrium method of calculation [method (2)]?

20.12 The accompanying graph shows the thermodynamics of stainless steel in graphical form. The carbon activity in the metal is fixed (e.g., by contact with sodium of specified carbon activity), and the temperature is specified. At a fixed nickel content of 8 wt.%, combination of Eqs. 20.112 and 20.113 yields a relation between  $\omega_{\text{Cr}}^\circ$  and  $\omega_{\text{C}}^T$  parametric in  $a_C$ . This family of isoactivity lines is shown on the drawing for a temperature of  $700^\circ\text{C}$ .

In a similar manner and at the same temperature, Eq. 20.101 has been plotted on the drawing. This solubility line relates  $\omega_{\text{sat}(\text{C})}$  and  $\omega_{\text{Cr}}$  in the austenite phase of the equilibrated steel.



(a) Suppose that stainless steel containing 18 wt.% Cr and 8 wt.% Ni is equilibrated with sodium in which the carbon activity is 0.01. What is the total carbon content in the steel at equilibrium?

(b) What are the chromium and carbon concentrations of the austenite phase in steel that has been equilibrated with sodium having a carbon activity of 0.01?

(c) Using the chromium and carbon balances derived in the text, determine the Cr/(Cr + Fe) ratio in the carbide phase (i.e., X).

(d) What are the implications of the result of question c?

20.13 Sodium flows past a bare cylinder of mixed-oxide fuel having an initial oxygen-to-metal ratio of  $2 - x_0$ . The oxygen concentration in the sodium stream is  $C_O$ . The oxygen potentials of the sodium ( $\Delta\bar{G}_{O_2}^{\text{Na}}$ ) and of the fuel ( $\Delta\bar{G}_{O_2}^{\text{f}}$ ) are both lower than the threshold necessary for formation of the  $\text{Na}_3\text{MO}_4$  phase. The oxygen potential of the fresh fuel is larger than that of the sodium; thus oxygen is removed from the fuel by the flowing sodium. Equilibrium at the fuel-sodium interface is maintained, and, to permit the kinetics to be solved, we linearize Eq. 20.150 to

$$C_O = 52 - 750x \quad (\text{for } T = 1000^\circ\text{K})$$

The oxygen dissolved from the fuel is transported into the flowing sodium by convective diffusion with a mass-transfer coefficient of  $k_d$ .

Solve the diffusion equation for the oxygen in the fuel with the appropriate conditions at the fuel-sodium interface reflecting chemical equilibrium and the transport resistance in the sodium film. How long an exposure of the fuel to sodium is required for the center line of the fuel to attain 50% of its equilibrium value?

$$\begin{aligned} D_0^f &= 4 \times 10^{-13} \text{ cm}^2/\text{sec} \\ R &= 0.3 \text{ cm} \\ k_d &= 0.75 \text{ cm/sec} \\ \rho_f/\rho_{\text{Na}} &= 2 \end{aligned}$$

Hint: Use results in *Conduction of Heat in Solids* by H. Carslaw and J. C. Jaeger, 2nd ed., Secs. 7.6 and 7.7, Oxford University Press, Inc., New York, 1959.

20.14 The maximum amount of mechanical work that can be released in the fuel-coolant interaction can be calculated thermodynamically. Suppose fuel powder at  $2500^\circ\text{K}$  contacts a large body of sodium at  $1000^\circ\text{K}$ . What fraction of the heat content of the fuel (above  $1000^\circ\text{K}$ ) can be converted to mechanical work in a reversible process?

# Chapter 21

## Modeling of the Structural Behavior of Fuel Elements and Assemblies

### 21.1 MATERIALS INPUT FUNCTIONS

From the microcosm of point defects, dislocations, and chemical reactions, we move into the domain of structural analysis, for this is the means by which atomistic theory is used to predict the macroscopic behavior of a reactor core during operation. The preceding chapters were devoted to preparing the scientific foundations necessary for rational analysis of the irradiation comportment of the principal components of the reactor, of which we shall select the fuel pin and the fuel assembly for detailed examination.

Superficially, a reactor fuel element is a simple object; its vital parts are cylindrical pellets of a fissile oxide encased in a metal tube. The ultimate purpose of the fuel-pin analysis may be simply stated: given the geometry of the fuel element (i.e., the fuel radius, the cladding thickness, and the size of the fuel-cladding gap), the initial chemical composition and porosity of the fuel, and the power history at which the pin is to operate, to calculate the length of time that the cladding performs its primary function of separating the coolant from the fuel. A fuel element is considered to have failed when the cladding is breached. The principal cause of cladding rupture is permanent strain (plastic flow and creep) due to internal loading by fission-gas pressure or fuel-cladding mechanical interaction. The apparent simplicity of the fuel pin is deceptive. Its mechanical behavior during irradiation depends on a great number of individual phenomena, only a few of which are adequately understood theoretically. These basic processes operate simultaneously within the fuel, and there is a large degree of interconnection between each of them. Figure 21.1 summarizes the complex relations between the physical, chemical, and mechanical processes (shown in ovals in Fig. 21.1) and the observable consequences on the fuel element (shown in rectangles in Fig. 21.1). Calculations based on Fig. 21.1 are so complicated that they can be performed only by high-speed computers. These computer analyses are called *fuel-modeling codes*; they attempt to follow the evolution of the important characteristics of the fuel and cladding as functions of irradiation time, beginning with the first application of power and terminating in failure by cladding rupture.

The circled items in Fig. 21.1 are the *materials input functions* for the code. These functions consist in part simply of a list of physical, chemical, or mechanical properties or they may represent calculations of the rates of particular processes (e.g., fission-gas swelling) by sub-routines nearly as large as the main fuel-modeling program. The materials input functions can either be based entirely on theory or be derived from observations. Often the theoretical framework of a basic process is used with sufficient adjustable parameters to force the model to agree with observed gross changes in the fuel-pin dimensions during irradiation. This procedure is known as calibrating or fine tuning the code.

The computer programs can either be restricted to the cladding or can consider the entire fuel element. Fuel and cladding are coupled via the thermal, mechanical, and chemical links listed in the central column of Fig. 21.1. Codes that treat the entire pin are called integral fuel-modeling codes for liquid-metal fast breeder reactor (LMFBR) analysis. The most important are LIFE (U. S. National Code)<sup>1,2</sup> and COMETHE/CRASH (Belgonucleaire).<sup>3,4</sup> Earlier fuel modeling codes developed in the United States<sup>5-8</sup> have been abandoned in favor of a concentrated development of the LIFE code. A review by Matthews<sup>9</sup> deals with the general problem of fuel-element modeling.

The sources of the materials input functions for the various calculations performed by the fuel-modeling code are described in the following sections.

#### 21.1.1 Temperature Distribution (Sec. 10.4)

Because of changes in the thermal conductivity, the porosity distribution, and the chemical distribution in the fuel during irradiation, the temperature distribution also changes slowly with time. A temperature distribution is determined at each time step by numerical solution of Eq. 10.49, using a thermal-conductivity expression that depends on fuel temperature, porosity, and oxygen-to-metal ratio and using a heat-source term that reflects the

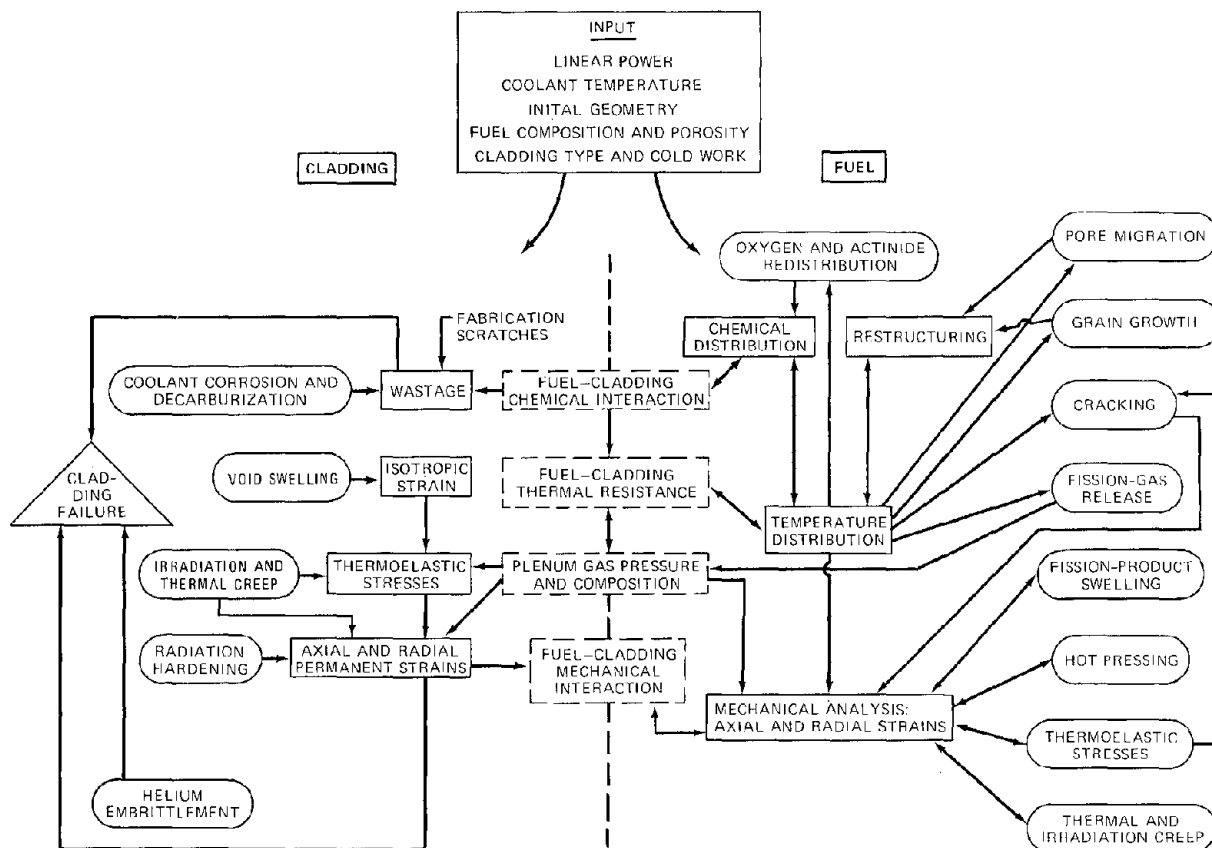


Fig. 21.1 Interrelation of mechanical, metallurgical, and chemical processes in fuel-element irradiation behavior.

radial nonuniformity introduced by actinide redistribution. Equations 10.47 and 10.48 are examples of the type of thermal-conductivity expressions used in thermal-analysis subroutines of fuel-modeling codes. The heat-source term in the conduction equation is given by Eq. 10.56. The temperature calculation also depends on the number and orientation of cracks in the fuel, on the size of the central void, and on the nature of the fuel-cladding gap. The temperature distribution depends sensitively on whether the gap is open or closed and whether it is filled with helium, fission gas, or liquid fission products.

### 21.1.2 Restructuring (Chap. 14)

The most important aspect of fuel restructuring in fast reactor fuel is the migration of the initial porosity of the fuel to the center by the process of vapor transport along the temperature gradient (Sec. 14.2). (Extensive fuel restructuring does not occur in light-water reactors, because the temperatures and temperature gradients are too small.) Equation 14.25 must be solved to describe the porosity redistribution phenomenon. The pore velocity is given by Eq. 14.11. The growth of equiaxed grains (Sec. 14.5) is important because grain size affects the creep strength of the fuel (Sec. 16.6). Other aspects of fuel restructuring are hot pressing (Sec. 16.11), which provides a means for

removing porosity in the equiaxed and unstructured zones of the fuel, and fuel cracking. Figure 21.2 shows schematically the structural evolution of an oxide fuel during irradiation.

### 21.1.3 Fuel Chemistry (Chaps. 11 and 12)

Oxygen redistribution along the temperature gradient is described in Sec. 11.6, and actinide redistribution is described in Sec. 11.7. The chemical and physical states of the fission products, their migration under the thermal gradient, and the swelling caused by solid fission products are reviewed in Chap. 12. Chemical attack of the cladding by the fuel (Sec. 12.6) is especially important to fuel-modeling calculations because it contributes to cladding wastage (i.e., thinning) and to removal of oxygen from the fuel (by immobilization as cladding corrosion product). Burnup increases the oxygen available for cladding attack. Figure 21.3 shows the chemical evolution of a fuel pin.

### 21.1.4 Fission-Gas Behavior (Chaps. 13 and 15)

Accurate fuel modeling requires knowledge of the fraction of the stable fission gases which have been produced up to a particular time and which have been released to the plenum. The remaining fission gas is





contained in the fuel, and it may be desirable to be able to predict the size distribution of the fission-gas bubbles as a function of radial position in the fuel during irradiation. Although codes such as BUBL and GRASS (Sec. 13.12) were designed to do just this, they have not yet been incorporated into integral fuel-modeling codes, all of which use the crudest of gas-release and swelling models.

### 21.1.5 Cladding Behavior (Chaps. 18 to 20)

The most important effects of radiation on the cladding are void swelling (Chap. 19), irradiation creep (Sec. 19.7), and reduction in ductility (Chap. 18). Corrosion of the outer surface of the cladding and uniform decarburization by sodium in LMFRs (Chap. 20) affect cladding strength and are included in the fuel-modeling codes. Radiation hardening (Secs. 18.4 to 18.8) can be important in determining the extent of plastic deformation of the cladding in regions of abnormally high stress.

### 21.1.6 Mechanical Properties

One of the most important mechanical properties of both fuel and cladding in the structural analysis is the thermal-expansion coefficient (Sec. 10.2). The creep properties of the fuel (thermal and irradiation) are reviewed in Chap. 16. Cladding thermal creep is governed by the same laws as thermal creep of the fuel, but with different numerical constants. The temperature variation of mechanical properties of the fuel (Secs. 16.2 and 16.3) is important because of the  $\sim 2000^\circ\text{C}$  temperature change across the fuel radius during operation. As the temperature increases, Young's modulus approaches zero and Poisson's ratio approaches  $1/2$ .

The output of a fuel-modeling calculation provides the detailed information as a function of irradiation time including:

1. The temperature and stress distribution in the fuel and cladding.
2. The extent of fuel cracking and fuel restructuring.
3. The fuel-cladding interfacial pressure.
4. The plenum gas pressure due to fission gases.
5. The net strain of the fuel and cladding, including the dilatational strain due to swelling and the radial and axial components of the permanent strains due to creep or plastic deformation.
6. The approach to fuel-pin failure, assessed, for instance, by the life-fraction rule (Sec. 18.11) or by a creep strain limit.

## 21.2 MECHANICAL MODELING OF FUEL-PIN BEHAVIOR (UNCRACKED FUEL)

In this section we review the stress-strain analysis, which, when combined with the materials input functions, determines the mechanical behavior of the fuel rod during irradiation. The fuel is assumed to remain free of cracks despite the fact that the thermal gradient induces stresses that exceed the fracture stress. The effect of fuel cracking on the analysis is considered in Sec. 21.3.

### 21.2.1 Gap Closure

One of the most important aspects of integral fuel-pin modeling is deciding whether or not the gap between the fuel and the cladding is closed or open. If the gap is open, only the plenum gas pressure loads the inside of the cladding and the outside of the fuel. If the gap is closed, the interaction force between the fuel and the cladding is due to contact of the two solids and is obtained only by mechanical analysis of the entire fuel pin.

The initial state of the pin is specified by the internal porosity of the fuel,  $P_0$ , and the thickness of the fuel-cladding gap in the as-fabricated element,  $t_{\text{gap}}^0$ .

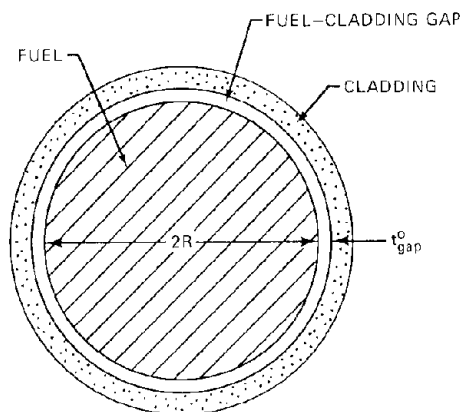


Fig. 21.4 Cross section of the fuel element before irradiation.

(Fig. 21.4). The smeared density of the fuel pin is related to the pore volume and the gap volume by

$$\text{Initial smeared density} = 1 - \frac{2\pi R t_{\text{gap}}^0 + \pi R^2 P_0}{\pi (R + t_{\text{gap}}^0)^2} \quad (21.1)$$

where  $R$  is the radius of the fuel.

When the fuel rod is first subject to neutrons and generates power, the temperature profile is approximately parabolic (Eq. 10.52), and the initial gap width changes because of thermal expansion of the fuel and the cladding. Although the thermal expansion coefficient of the cladding is larger than that of the fuel (see Figs. 10.8 and 10.9), the temperature rise of the fuel is considerably greater than that of the cladding. The net result is a reduction in the thickness of the gap upon startup.

The tangential strain of a cylindrical body is equal to the increase in radial position (i.e., radial displacement) divided by the initial radius (Eq. 21.5). According to the theory of thermoelasticity, the displacement of the outer surface of a solid cylinder is equal to  $\alpha \bar{T} R$ , where  $\alpha$  is an average linear coefficient of thermal expansion and  $\bar{T}$  is the average temperature of the solid, which is equal to  $(T_0 + T_g)/2$  for a parabolic temperature distribution. The temperature change across the cladding is small compared with its average temperature. The initial hot-gap thickness is given by

$$\frac{t_{\text{gap}}^{\circ}(\text{hot}) - t_{\text{gap}}^{\circ}(\text{cold})}{R} = \alpha_c T_c - \frac{1}{2} \alpha_f (T_0 + T_s) \quad (21.2)$$

where, for simplicity of notation,  $T_c$ ,  $T_0$ , and  $T_s$  refer to the temperature rises of the cladding, fuel center line, and fuel surface, respectively, above the temperature at which the cold gap is measured ( $\sim 25^\circ\text{C}$ ) and  $R_{\text{fuel}} \cong R_{\text{clad}} = R$ . Calculation of the initial hot-gap thickness (or equivalently, of the fuel center line and surface temperatures) is a trial-and-error affair because of the dependence of the gap conductance on the gap thickness (see problem 10.2). When fuel cracking is included in the analysis, the hot-gap thickness is smaller than the value obtained from Eq. 21.2 (see Sec. 21.3). The initial cold-gap thickness is chosen so that the gap still exists on the initial rise to power. As fuel swelling due to fission products increases with irradiation time, the gap gradually closes and the fuel and cladding interact mechanically. Much later in the life of the fuel element, the gap may reopen because of cladding swelling (which does not vary linearly with fluence).

### 21.2.2 Mechanical Analysis

The fuel-element geometry used in fuel-modeling codes is shown in Fig. 21.5. The fuel and cladding are divided into a number of axial regions and radial intervals; each elementary volume considered in the analysis is shown as the ring on the right of Fig. 21.5. The original LIFE code<sup>1,2</sup> divided the fuel into three radial zones, corresponding to the columnar grain, equiaxed grain, and unstructured regions shown in Fig. 10.23, and put the entire cladding cross section into one radial zone. Recent work, however, has shown that the radial mesh must be much finer than three fuel zones and one cladding zone to properly account for the very steep radial temperature gradient in the fuel pin.

Other restrictions placed upon the analysis are:

1. The system is axisymmetric (i.e., there is no tangential variation of any variable).
2. Although both the fuel and the cladding may move axially (and not necessarily at the same rate), planes perpendicular to the  $z$ -direction in each material remain plane during deformation. This is the *plane strain* assumption. Friction is allowed between the fuel and cladding.
3. The time dependence inherent in the analysis (due to the swelling and creep phenomena) is handled by treating the system as a succession of equilibrium states.
4. The central void communicates with the plenum; so the inner radius of the fuel and the top of the uppermost axial zone are loaded by the plenum gas pressure.
5. The outer radius of the fuel and the inner radius of the cladding are loaded by the plenum pressure if the fuel-cladding gap is open and by the fuel-cladding interfacial pressure if the gap is closed.
6. The outer radius of the cladding is subject to the coolant pressure.

As a result of restrictions 1 and 2, only the normal stresses along the three principal directions in the cylindrical coordinate system are nonzero; these are denoted by

$\sigma_r$ ,  $\sigma_\theta$ , and  $\sigma_z$  and are positive if in tension. There are no shear stresses.

The governing relations for the mechanical analysis are similar to those presented for elastic deformations in the Appendix, except that the elastic strains given by Eq. A.21 must be supplemented by terms representing thermal expansion, swelling, and permanent deformations due to creep or plastic flow.

The equilibrium conditions given by Eqs. A.29 to A.31 are simplified by eliminating shear stresses and axial and tangential derivatives, which leads to the single relation

$$\frac{d\sigma_r}{dr} + \frac{\sigma_r - \sigma_\theta}{r} = 0 \quad (21.3)$$

Letting  $\epsilon_r$ ,  $\epsilon_\theta$ , and  $\epsilon_z$  be the total strains in the three principal directions, the strain-displacement relations of Eq. A.32 become

$$\epsilon_r = \frac{du}{dr} \quad (21.4)$$

$$\epsilon_\theta = \frac{u}{r} \quad (21.5)$$

$$\epsilon_z = \text{constant with } r \text{ except for discontinuity at the fuel-cladding interface} \quad (21.6)$$

where  $u$  is the radial displacement. Equations 21.4 and 21.5 satisfy the compatibility conditions (shown for Cartesian coordinates in Sec. A-3 of the Appendix) which precludes treating cracking of the fuel.

The total strain in each direction is divided into the categories shown in Table 21.1.

The elastic strains are given by Eqs. A.22 of the Appendix, with appropriate change in the coordinate system. The *constitutive relations* used in fuel-modeling analyses become

$$\epsilon_r = \frac{1}{E} [\sigma_r - \nu(\sigma_\theta + \sigma_z)] + \alpha T + \epsilon^s + \epsilon_r^c \quad (21.7)$$

$$\epsilon_\theta = \frac{1}{E} [\sigma_\theta - \nu(\sigma_r + \sigma_z)] + \alpha T + \epsilon^s + \epsilon_\theta^c \quad (21.8)$$

$$\epsilon_z = \frac{1}{E} [\sigma_z - \nu(\sigma_r + \sigma_\theta)] + \alpha T + \epsilon^s + \epsilon_z^c \quad (21.9)$$

Equations 21.7 to 21.9 apply to both the fuel and the cladding provided the linear thermal-expansion coefficient  $\alpha$ , Young's modulus  $E$ , and Poisson's ratio  $\nu$  are chosen accordingly and appropriate material functions are used for the swelling and creep/plastic strains in each part of the fuel element.

In the fuel,  $\epsilon^s$  is given by

$$\epsilon_{\text{fuel}}^s = \frac{1}{3} \left[ \left( \frac{\Delta V}{V} \right)_{\text{solid fp}} + \left( \frac{\Delta V}{V} \right)_{\text{gaseous fp}} - \left( \frac{\Delta V}{V} \right)_{\text{hot pressing}} \right] \quad (21.10)$$

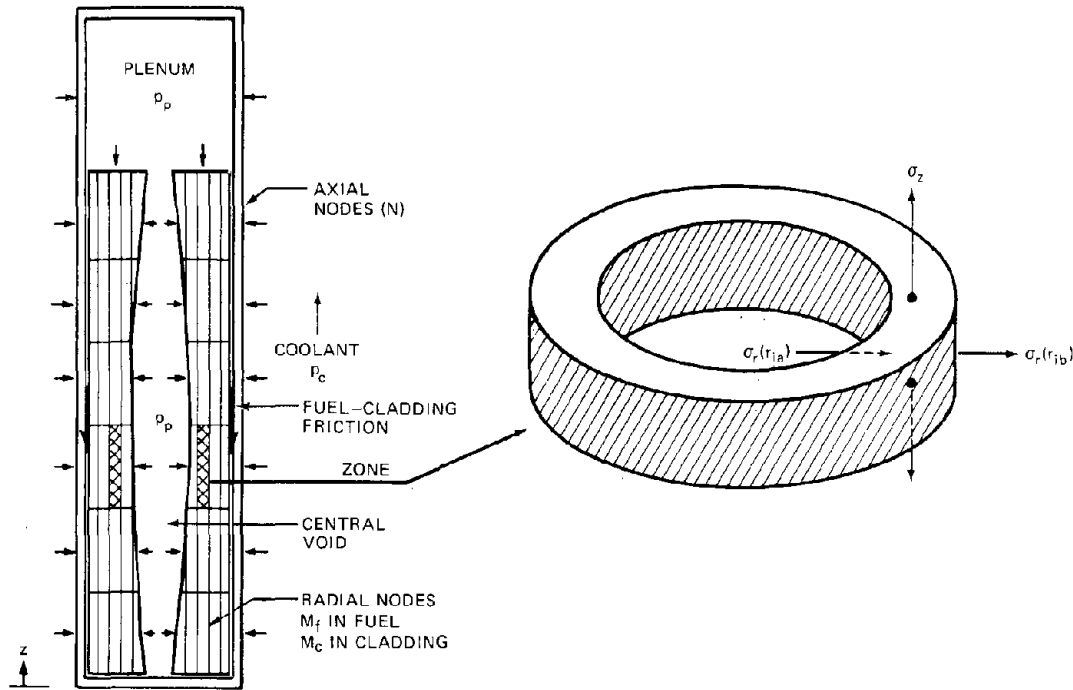


Fig. 21.5 Subdivision of a fuel element into radial and axial zones for mechanical analysis.

Table 21.1 Components of the Total Strain

Component	Symbol	Isotropic?	Permanent?
Elastic	None	No	No
Thermal	$\alpha T$	Yes	No
Swelling	$\epsilon^s$	Yes	Yes
Creep/plastic	$\epsilon_r^c, \epsilon_\theta^c, \epsilon_z^c$	No	Yes

Equation 12.43 shows that the swelling due to solid fission products is proportional to burnup (or the rate of this swelling component is constant); the coefficient of proportionality depends only on fission-product yields and the partial volumes of the fission products.

The gaseous-fission-product swelling term is related to the size and concentration of fission-gas bubbles by Eq. 13.19. A model for  $(\Delta V/V)_{\text{gaseous fp}}$  (either theoretical or empirical) must be supplied to the computation.

The hot-pressing contribution to fuel swelling is negative inasmuch as porosity is removed by this process. Typical hot-pressing kinetic formulas used in fuel-modeling analyses are given by Eqs. 16.177 and 16.190. The porosity  $P$  in these formulas must be interpreted as the cavity volume due to pores which do not contain fission gas rather than the total porosity.

In the cladding the swelling strain is due solely to void formation

$$\epsilon_{\text{clad}}^s = \frac{1}{3} \left( \frac{\Delta V}{V} \right)_{\text{void swelling}} \quad (21.11)$$

where  $(\Delta V/V)_{\text{void swelling}}$  can be determined from one of the theoretical models described in Sec. 19.6 or, more likely, by such empirical relations as Eq. 19.12.

The hydrostatic state of stress

$$\sigma_h = -\frac{1}{3} (\sigma_r + \sigma_\theta + \sigma_z) \quad (21.12)$$

affects all the swelling terms in Eqs. 21.10 and 21.11 except that due to solid fission products (which is termed "inexorable"). Because the stresses in the fuel and cladding vary with time, swelling rate expressions  $\dot{\epsilon}_{\text{fuel}}^s$  and  $\dot{\epsilon}_{\text{clad}}^s$  are used instead of integrated swelling strains. The swelling rates are integrated along with the creep rates as the fuel-modeling code traces the evolution of the fuel pin during irradiation.

The permanent strains labeled  $\epsilon_i^c$  ( $i = r, \theta, \text{ or } z$ ) in Eqs. 21.7 and 21.9 are composed of creep and plastic deformations

$$\epsilon_i^c = \epsilon_i^{\text{creep}} + \epsilon_i^{\text{plastic}} \quad (21.13)$$

Creep and plastic deformations occur at constant volume (unlike elastic deformation); so the components of  $\epsilon^c$  are related by the incompressibility condition

$$\epsilon_r^c + \epsilon_\theta^c + \epsilon_z^c = 0 \quad (21.14)$$

Formulation of the permanent strains based on the von Mises assumption that creep and plastic deformations occur only when the stress state deviates from pure hydrostatic

tension or compression (Sec. 18.3) leads to the stress-strain relations known as the Prandtl-Reuss flow laws or the Soderberg equations:

$$\epsilon_r^c = \left( \frac{\epsilon^*}{\sigma^*} \right) \left[ \sigma_r - \frac{1}{2} (\sigma_\theta + \sigma_z) \right] \quad (21.15)$$

$$\epsilon_\theta^c = \left( \frac{\epsilon^*}{\sigma^*} \right) \left[ \sigma_\theta - \frac{1}{2} (\sigma_r + \sigma_z) \right] \quad (21.16)$$

$$\epsilon_z^c = \left( \frac{\epsilon^*}{\sigma^*} \right) \left[ \sigma_z - \frac{1}{2} (\sigma_r + \sigma_\theta) \right] \quad (21.17)$$

where  $\sigma^*$  and  $\epsilon^*$  are the stress and strain deviators or the equivalent stress and equivalent strain, respectively, of the triaxial stress state

$$\sigma^* = \frac{1}{2^{1/2}} [(\sigma_r - \sigma_\theta)^2 + (\sigma_r - \sigma_z)^2 + (\sigma_\theta - \sigma_z)^2]^{1/2} \quad (21.18)$$

$$\epsilon^* = \frac{2^{1/2}}{3} [(\epsilon_r - \epsilon_\theta)^2 + (\epsilon_r - \epsilon_z)^2 + (\epsilon_\theta - \epsilon_z)^2]^{1/2} \quad (21.19)$$

Equations 21.15 to 21.17 and Eq. 21.19 can also be written in terms of the strain rates instead of the accumulated strains by placing dots over all the  $\epsilon$ 's. The creep/plastic stress-strain laws are of the same form as the elastic stress-strain relations (the first terms on the right-hand sides of Eqs. 21.7 to 21.9), but Young's modulus and Poisson's ratio in the stress-strain relations are replaced by  $\sigma^*/\epsilon^*$  and  $1/2$ , respectively. The ratio  $\sigma^*/\epsilon^*$  is called the creep or plasticity modulus of the material.

For deformation by creep,  $\sigma^*/\epsilon^*$  can be obtained from the creep laws determined in uniaxial tests by replacing the uniaxial stress and strain by the equivalent stress and the equivalent strain. Thus the creep formula corresponding to the Nabarro-Herring model (Eq. 16.27) is

$$(\dot{\epsilon}^*)^{\text{creep}} = \frac{B\sigma^*}{d^2} \exp\left(-\frac{E_d}{kT}\right) \quad (21.20a)$$

where  $B$  is a constant,  $E_d$  is the activation energy for this form of creep, and  $d$  is the grain diameter. The parameters  $B$  and  $E_d$  are the same as those obtained in uniaxial creep tests.

For thermal creep controlled by dislocation climb, Eq. 16.87 is transformed to

$$(\dot{\epsilon}^*)^{\text{creep}} = B'(\sigma^*)^{4.5} \exp\left(-\frac{E_d'}{kT}\right) \quad (21.20b)$$

where  $B'$  and  $E_d'$  are constants determined by uniaxial creep tests.

Equations 21.20a and 21.20b refer to secondary or steady-state creep. Primary creep can be included in the analysis by a creep law that explicitly includes the time

$$(\dot{\epsilon}^*)^{\text{creep}} = K(\sigma^*)^{n+t^m} \quad (21.21)$$

where  $K$ ,  $n$ , and  $m$  are empirical constants.

Except for diffusional creep (Eq. 21.20), the creep moduli are functions of the state of stress (i.e., of  $\sigma^*$ ).

Irradiation creep formulas (Eq. 16.132 for the fuel and Eqs. 19.176, 19.225, or 19.239 for the cladding) can be expressed in a similar fashion.

Plastic strain is expressed in analytical form suitable for programming by fitting the true stress-strain curves from tensile tests (e.g., the dashed curve in Fig. 18.11) by an equation of the form

$$(\epsilon^*)^{\text{plastic}} = a(\sigma^*)^b \quad (21.22)$$

where the constants  $a$  and  $b$  may be fixed by two points on the true stress-strain curve, e.g., the 0.2% offset yield point and the strain at the ultimate stress. For metals, the constants  $a$  and  $b$  depend on radiation hardening due to the fast-neutron flux. Plastic flow in the fuel is not currently considered in fuel modeling codes.

### 21.2.3 Solution for Radial Stresses and Displacements

The analysis up to this point is common to most fuel-modeling codes. If swelling and creep/plasticity were not considered, the problem would reduce to one of ordinary thermoelasticity for which analytical solutions are possible (see problems 21.1, 21.2, and 21.6 at the end of the chapter). However, the presence of time-dependent permanent strains and the sizeable variation of the mechanical properties of the fuel with position (mainly because of the radial temperature distribution) require numerical solution of the relevant equations. Moreover, the creep and swelling phenomena introduce time as a fundamental variable. The numerical solutions of the fuel-element structural behavior must not only deal with the spatial variation of the stresses and strains but with their time dependence as well. The various methods differ in the procedure for solving the set of equations, Eqs. 21.3 to 21.9. The technique described here is approximately that used in the LIFE code.<sup>1</sup>

The total strains  $\epsilon_r$  and  $\epsilon_\theta$  are eliminated by combining Eqs. 21.7 to 21.9 with Eqs. 21.4 and 21.5, and the stresses are expressed in terms of the radial displacement

$$\sigma_r = \frac{E}{1+\nu} \left[ \frac{du}{dr} + \frac{\nu}{1-2\nu} \left( \frac{du}{dr} + \frac{u}{r} + \epsilon_z - 3\alpha T - 3\epsilon^s \right) - (\alpha T + \epsilon^s + \epsilon_r^c) \right] \quad (21.23)$$

$$\sigma_\theta = \frac{E}{1+\nu} \left[ \frac{u}{r} + \frac{\nu}{1-2\nu} \left( \frac{du}{dr} + \frac{u}{r} + \epsilon_z - 3\alpha T - 3\epsilon^s \right) - (\alpha T + \epsilon^s + \epsilon_\theta^c) \right] \quad (21.24)$$

$$\sigma_z = \frac{E}{1+\nu} \left[ \epsilon_z + \frac{\nu}{1-2\nu} \left( \frac{du}{dr} + \frac{u}{r} + \epsilon_z - 3\alpha T - 3\epsilon^s \right) - (\alpha T + \epsilon^s - \epsilon_r^c - \epsilon_\theta^c) \right] \quad (21.25)$$

Equations 21.23 and 21.24 are substituted into the equilibrium condition, Eq. 21.3, and the following differential equation for the radial displacement is obtained:

$$\frac{d}{dr} \left[ \frac{1}{r} \frac{d(ru)}{dr} \right] = \left( \frac{1-2\nu}{1-\nu} \right) \left( \frac{d\epsilon_r^c}{dr} + \frac{\epsilon_r^c - \epsilon_\theta^c}{r} \right) + \left( \frac{1+\nu}{1-\nu} \right) \frac{d}{dr} (\alpha T + \epsilon^s) \quad (21.26)$$

The step leading to Eq. 21.26 requires that the elastic constants  $E$  and  $\nu$  be assumed independent of  $r$  (and hence of temperature). This approximation is valid only when the radial interval over which the resulting equation applies is small. The elastic constants and all other temperature- and porosity-dependent quantities in the creep and swelling terms are evaluated at the average conditions in the radial zone over which Eq. 21.26 is integrated.

Equation 21.26 is applied to each ring in the fuel element (shown on the right-hand side of Fig. 21.5). Each ring is characterized by subscripts  $i$  and  $j$ , representing the radial and axial positions in the pin, respectively. In the fuel, the first radial zones ( $i = 1$ ) form the boundary of the central void and the first axial zones ( $j = 1$ ) are at the bottom of the fuel pin. In the cladding the first radial zone starts at the inner surface of the cladding. The number of axial zones ( $N$ ) and radial zones ( $M_f$  in the fuel and  $M_c$  in the cladding) are chosen to balance speed of computing with accuracy. Equation 21.26 is integrated from the inner boundary of the  $i$ th radial zone ( $r_{ai}$ ) to radial position  $r$  within the ring. If the mesh is sufficiently fine, Poisson's ratio may be assumed to be constant within the ring, and the radial displacement is

$$u(r) = \frac{C_{1i}}{r} + C_{2i}r + \left( \frac{1+\nu}{1-\nu} \right) \frac{1}{r} \int_{r_{ai}}^r r' (\alpha T + \epsilon^s) dr' + \frac{1}{2} \left( \frac{1-2\nu}{1-\nu} \right) \left[ \frac{1}{r} \int_{r_{ai}}^r (\epsilon_r^c + \epsilon_\theta^c) r' dr' + r \int_{r_{ai}}^r (\epsilon_r^c - \epsilon_\theta^c) \frac{dr'}{r'} \right] \quad (21.27)$$

where  $C_{1i}$  and  $C_{2i}$  are constants of integration for the  $i$ th zone which remain to be determined. At this point the LIFE code assumes that the thermal, swelling, and permanent strains are constant within each ring,\* which reduces Eq. 21.27 to

$$u(r) = \frac{C_{1i}}{r} + C_{2i}r + \left( \frac{1+\nu}{1-\nu} \right) [(\alpha T)_i + (\epsilon^s)_i] \frac{r^2 - r_{ai}^2}{2r}$$

\*The assumption of constant strain within each ring results in discontinuous changes in the strain from one ring to the next. This unrealistic result becomes less important as the number of radial rings into which the fuel element is divided becomes larger, but, in the original LIFE code, only four radial zones are used ( $M_f = 3$ ,  $M_c = 1$ ). In this case, the step changes in strain between rings produces incorrect final results in some cases. Rather than eliminate this discrepancy by increasing the number of radial zones, the strain components may be arbitrarily assigned the  $r$ -dependence  $A + (B/r^2)$  within each ring, the constants  $A$  and  $B$  being determined by matching strains and strain gradients at ring boundaries.

$$+ \frac{1}{2} \left( \frac{1-2\nu}{1-\nu} \right) \left\{ [(\epsilon_r^c)_i + (\epsilon_\theta^c)_i] \frac{r^2 - r_{ai}^2}{2r} + [(\epsilon_r^c)_i - (\epsilon_\theta^c)_i] r \ln \frac{r}{r_{ai}} \right\} \quad (21.28)$$

where  $(x)_i$  denotes the constant values of the strain components in ring  $i$ . The strains are also dependent on the axial position of the ring (denoted by  $j$ ), but this description is omitted for clarity.

Since the radial boundary conditions needed to determine the integration constants apply to the radial stress component as well as to the displacement, Eq. 21.28 is substituted into Eq. 21.23, which leads to an equation for  $\sigma_r(r)$  as a function of  $C_{1i}$ ,  $C_{2i}$ , the strain components  $(\alpha T)_i$ ,  $(\epsilon^s)_i$ ,  $(\epsilon_r^c)_i$ , and  $(\epsilon_\theta^c)_i$ , the zone boundaries  $r_{ai}$ , and the axial strain  $\epsilon_z$ .

The boundary condition at the inside of the central void at  $r = r_0$  is

$$\sigma_r(r_0) = -p_p \quad (21.29)$$

where  $p_p$  is the plenum pressure. To ensure continuity of stress and displacement at the radial zone boundaries within the fuel, we have

$$\left. \begin{aligned} \sigma_r(r_{i-1,b}) &= \sigma_r(r_{ia}) \\ u(r_{i-1,b}) &= u(r_{ia}) \end{aligned} \right\} (1 < i \leq M_f) \quad (21.30)$$

The condition at the fuel-cladding interface depends on whether the gap is open or closed. For an open gap

$$\sigma_r(R) = -p_p \quad (21.31a)$$

For the outer fuel surface and the same condition for the inner surface at the cladding

$$\sigma_r(R) = -p_p \quad (21.31b)$$

If the gap is closed the conditions are

$$\sigma_r(R) = -p_{fc} \quad (21.32a)$$

in the fuel, and

$$\sigma_r(R) = -p_{fc} \quad (21.32b)$$

in the cladding. The fuel-cladding-interfacial pressure  $p_{fc}$  is yet to be determined.

The matching conditions within the cladding are expressed by

$$\left. \begin{aligned} \sigma_r(r_{i-1,b}) &= \sigma_r(r_{ia}) \\ u(r_{i-1,b}) &= u(r_{ia}) \end{aligned} \right\} (1 < i \leq M_c) \quad (21.33)$$

and at the outside of the cladding

$$\sigma_r(R + t_c) = -p_c \quad (21.34)$$

where  $p_c$  is the coolant pressure at the axial location where the radial integration is performed and  $t_c$  is the cladding thickness.

Since the boundary conditions were used to determine the integration constants  $C_{1i}$  and  $C_{2i}$  in each radial zone, the displacement distribution  $u(r)$  is now a function of:

1. The strain components  $(\alpha T)_i$ ,  $(\epsilon^s)_i$ ,  $(\epsilon_r^c)_i$ , and  $(\epsilon_\theta^c)_i$  in each ring.

2. The axial strain  $\epsilon_z$ , which may take on different values in the fuel and in the cladding.

3. The plenum pressure  $p_p$  and, if the fuel-cladding gap is closed, the interfacial pressure  $p_{fc}$ .

The dependence of  $u(r)$  on the axial strains of the fuel and cladding and on the interfacial pressure results from application of the boundary conditions. The radial displacements in the fuel and cladding may be written in the form

$$u_f [r, (\alpha T)_i, (\epsilon^s)_i, (\epsilon_r^c)_i, (\epsilon_\theta^c)_i, p_{fc}, \epsilon_{zf}] \quad (21.35a)$$

for  $r_0 \leq r \leq R$  and  $1 \leq i \leq M_f$ , and

$$u_c [r, (\alpha T)_i, (\epsilon^s)_i, (\epsilon_r^c)_i, (\epsilon_\theta^c)_i, p_{fc}, \epsilon_{zc}] \quad (21.35b)$$

for  $R \leq r \leq R + t_c$  and  $1 \leq i \leq M_c$ . At this juncture  $p_{fc}$  and the fuel and cladding axial strains  $\epsilon_{zf}$  and  $\epsilon_{zc}$  are unknown. Axial-force balances are needed for their computation.

### 21.2.4 Axial-Force Balances

Figure 21.6 shows that the axial forces acting on the stack of fuel between axial zone  $j$  and the upper surface of the fuel consist of the average axial stress, the plenum pressure, and the sum of the friction forces acting vertically on the outer surface of the fuel. These forces are positive if they restrict axial growth of the fuel and are zero if the fuel-cladding gap is open. The force balance on the hollow cylinder of fuel between the top of the stack and the dashed cross section in Fig. 21.6 is

$$-2\pi \int_{r_0}^R \sigma_z(r) r dr = \pi(R^2 - r_0^2) p_p + F + \sum_{k=j+1}^N F_k \quad (21.36)$$

The force balance on the cladding between the same axial location and the top of the fuel element is

$$-2\pi \int_R^{R+t_c} \sigma_z(r) r dr = \pi(R + t_c)^2 p_{c(top)} - \pi R^2 p_p - F - \sum_{k=j+1}^N F_k \quad (21.37)$$

where  $p_{c(top)}$  is the coolant pressure at the top of the fuel element.

The symbol  $F$  in the above equations is the axial friction force acting on the fuel-cladding interface at axial zone  $j$ . The subscript  $j$  has been omitted from the designation of the friction force, but the equations apply at each axial zone in the fuel element. The sums on the right-hand sides of Eqs. 21.36 and 21.37 are assumed to be

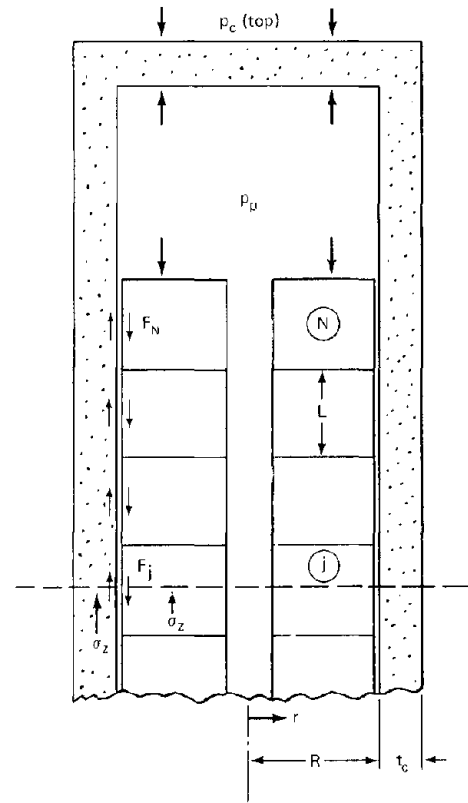


Fig. 21.6 Axial forces on the fuel and cladding.

known from previously completed computations on axial zones above zone  $j$ .

The axial stress distribution needed in the integrals in the force balances are given by inserting Eqs. 21.35 into Eq. 21.25. When the radial distribution of  $\sigma_z$  has been so used, Eqs. 21.36 and 21.37 can be solved for the axial strains in the fuel and cladding,  $\epsilon_{zf}$  and  $\epsilon_{zc}$ , in terms of

1. The radially averaged strain components  $\bar{\alpha T}$ ,  $\bar{\epsilon}^s$ ,  $\bar{\epsilon}_r^c$ , and  $\bar{\epsilon}_\theta^c$  in the fuel and in the cladding.\*
2. The fuel-cladding interfacial pressure  $p_{fc}$ .
3. The friction force  $F$ .

\*Radial averages of the strain components, which are assumed to be constant in each ring, are defined for the fuel by

$$\bar{x} = \frac{1}{\pi(R^2 - r_0^2)} \sum_{i=1}^{M_f} (x)_i \pi(r_{ib}^2 - r_{ia}^2)$$

where  $r_{ia}$  and  $r_{ib}$  are the inner and outer radial boundaries of ring  $i$  and  $R$  and  $r_0$  are the outer fuel and central void radii, respectively. In the cladding the radial average of a strain component is defined by

$$\bar{x} = \frac{1}{\pi[(R + t_c)^2 - R^2]} \sum_{i=1}^{M_c} (x)_i \pi(r_{ib}^2 - r_{ia}^2)$$

where  $t_c$  is the cladding thickness.

The axial force balances thus lead to equations for the axial strains in the fuel and in the cladding (see Ref. 1) which may be expressed in functional form by

$$\epsilon_{zf}[\bar{\alpha T}, \bar{\epsilon}^s, \bar{\epsilon}_r^c, \bar{\epsilon}_\theta^c, p_{fc}, F] \quad (21.38a)$$

where the strain components refer to the fuel, and

$$\epsilon_{zc}[\bar{\alpha T}, \bar{\epsilon}^s, \bar{\epsilon}_r^c, \bar{\epsilon}_\theta^c, p_{fc}, F] \quad (21.38b)$$

where the strain components refer to the cladding.

### 21.2.5 Time Stepping

Suppose the average stresses and the strain components due to creep/plasticity, swelling, and thermal expansion are known at a particular time  $t$  for the entire fuel element (i.e., for all rings at all heights). Calculation of the stresses and strains at  $t + \delta t$  is accomplished one axial zone at a time, beginning at the top of the fuel and moving downward.\* The computation at axial zone  $j$  is performed as follows.

The total strains  $\epsilon_r$ ,  $\epsilon_\theta$ , and  $\epsilon_z$  in each radial ring at  $t + \delta t$  are guessed. These estimates are used to generate average stress components  $\bar{\sigma}_r$ ,  $\bar{\sigma}_\theta$ , and  $\bar{\sigma}_z$  in each radial ring by manipulation of Eqs. 21.7 to 21.9 (see Ref. 1 for details). Since the creep and swelling rates are known functions of the stress, the component strains in each ring at  $t + \delta t$  [i.e.,  $(\alpha T)_i$ ,  $(\epsilon^s)_i$ ,  $(\epsilon_r^c)_i$ , and  $(\epsilon_\theta^c)_i$ ] can be calculated from the average stress components just determined. These strain components are then used in the radial displacement equation (Eqs. 21.35). Similarly, the same strain components are radially averaged and used in Eqs. 21.38 to obtain first estimates of the axial strains at  $t + \delta t$ .

The quantities of interest are the changes in  $\epsilon_{zf}$  and  $\epsilon_{zc}$  during the interval between  $t$  and  $t + \delta t$ . These differences are obtained by subtracting the known axial strains at time  $t$  from those calculated by the method described in the preceding paragraph:

$$\delta \epsilon_{zf}(p_{fc}, F) = \text{change in axial strain of fuel} \\ \text{in time } \delta t \quad (21.39)$$

$$\delta \epsilon_{zc}(p_{fc}, F) = \text{change in axial strain of cladding} \\ \text{in time } \delta t \quad (21.40)$$

Similarly the changes in the radial displacements of the fuel outer surface and the cladding inner surface during  $\delta t$  can be expressed in the following functional form:

$$\delta u_{Rf}(p_{fc}, \epsilon_{zf}) = \text{change in radial displacement of} \\ \text{fuel outer surface in time } \delta t \quad (21.41)$$

$$\delta u_{Rc}(p_{fc}, \epsilon_{zc}) = \text{change in radial displacement of} \\ \text{cladding inner surface in time } \delta t \quad (21.42)$$

Equations 21.39 to 21.42 are used to determine  $p_{fc}$  and  $F$  at  $t + \delta t$ . First, however, it must be ascertained whether the

gap opens up or remains closed in  $\delta t$ . It is assumed that the gap is closed at time  $t$ .

1. Assume the gap opens up in time  $\delta t$ : Set  $F = 0$ , replace  $p_{fc}$  by  $p_p$ , and determine the axial strain changes of the fuel and the cladding from Eqs. 21.39 and 21.40. Substitution of the axial strains at  $t + \delta t$  into Eqs. 21.41 and 21.42 determines the radial displacements of the fuel outer surface and of the cladding inner surface. If  $\delta u_{Rc} > \delta u_{Rf}$ , the original assumption is correct, and the gap has in fact opened in the time interval  $\delta t$ . If the calculated fuel displacement is greater than the calculated cladding displacement, the gap remains closed and procedure 2 is used.

2. The gap remains closed in time  $\delta t$ : If fuel-cladding contact is maintained, the radial displacement of the fuel outer surface must equal that of the cladding inner surface, or

$$\delta u_{Rf} = \delta u_{Rc} \quad (21.43)$$

To complete the problem, we must determine whether the fuel and the cladding are so tightly wedged together that they move in unison (axially) during the interval  $\delta t$  (the stick condition) or whether the frictional force is large enough to permit relative axial displacement (the slip condition).

(a) The stick condition: If the fuel and the cladding stick, then the change in fuel axial strain during  $\delta t$  is equal to the change in the cladding axial strain, or

$$\delta \epsilon_{zf} = \delta \epsilon_{zc} \quad (21.44)$$

Since the changes in strain in the fuel and cladding are functions of  $p_{fc}$  and  $F$  according to Eqs. 21.39 and 21.40, Eq. 21.44 is equivalent to a relation between  $p_{fc}$  and  $F$ . If a value of  $p_{fc}$  is selected,  $F$  is computed by the relation between these two variables implicit in Eq. 21.44, and then  $\delta \epsilon_{zf}$  and  $\delta \epsilon_{zc}$  are individually computed from Eqs. 21.39 and 21.40. Since the values of the fuel and cladding axial strains at the beginning of the interval are known, the axial strains at  $t + \delta t$  can be computed from the values of the  $\delta \epsilon_{zf}$  and  $\delta \epsilon_{zc}$  just determined. With  $\epsilon_{zf}$  and  $\epsilon_{zc}$  at  $t + \delta t$  known for the selected  $p_{fc}$ , the displacement changes  $\delta u_{Rf}$  and  $\delta u_{Rc}$  can be determined from Eqs. 21.41 and 21.42. The value of  $p_{fc}$  which causes Eq. 21.43 to be satisfied is the correct one. By this method,  $p_{fc}$  and  $F$  can both be determined if the fuel and cladding stick during the time interval  $\delta t$ .

To determine whether the  $p_{fc}$  and  $F$  values so calculated are compatible, we can also compute  $F$  from the definition of the coefficient of static friction,  $\mu_{sf}$ . Sticking occurs if

$$F < \mu_{sf}(2\pi RL) p_{fc} \quad (21.45)$$

where  $L$  is the height of an axial zone. The coefficient of static friction of  $UO_2$  and stainless steel is taken as  $\sim 0.8$ . If the value of  $F$  does not satisfy Eq. 21.45, the frictional force is so large that the fuel and cladding cannot stick together; instead, they slip.

\*In the LIFE code the calculation begins at the bottom of the fuel column.

(b) The slip condition: If the fuel and the cladding slip relative to each other in the time interval  $\delta t$ ,  $F$  and  $p_{fc}$  are taken to be related by the coefficient of sliding friction,  $\mu_{sl}$

$$F = \mu_{sl}(2\pi RL) p_{fc} \quad (21.46)$$

Using Eq. 21.46 in Eqs. 21.39 and 21.40, we can compute values of  $\delta\epsilon_{zf}$  and  $\delta\epsilon_{zc}$  (they are no longer equal) for each interfacial pressure selected. The value of  $p_{fc}$  and the associated values of  $\epsilon_{zf}$  and  $\epsilon_{zc}$  at  $t + \delta t$  are used in Eqs. 21.41 and 21.42 to give  $\delta u_{Rf}$  and  $\delta u_{Rc}$ . The  $p_{fc}$  value that satisfies Eq. 21.43 is the solution.

Whichever condition (open, stick, or slip) applies over the interval  $\delta t$ , the quantities  $p_{fc}$ ,  $F$ ,  $\epsilon_{zf}$ , and  $\epsilon_{zc}$  are determined at time  $t + \delta t$  for the particular axial zone under consideration by method 1, 2a, or 2b. Thus the radial displacement distributions given by Eqs. 21.35 are determined at  $t + \delta t$  because the strain components contained therein have been supplied by the initial guesses and  $p_{fc}$ ,  $\epsilon_{zf}$ , and  $\epsilon_{zc}$  have been determined in terms of these same guesses by the technique just outlined. To assess the accuracy of the guesses of the total strains which began the iteration, we compute the following radially averaged total-strain components:

$$\bar{\epsilon}_r = \frac{1}{\pi(R^2 - r_0^2)} \int_{r_0}^R \left( \frac{du}{dr} \right) 2\pi r dr \quad (21.47a)$$

and

$$\bar{\epsilon}_\theta = \frac{1}{\pi(R^2 - r_0^2)} \int_{r_0}^R \left( \frac{u}{r} \right) 2\pi r dr \quad (21.47b)$$

for the fuel and analogous integrals for the cladding.

The average total-strain components in the fuel and the cladding at the end of the time step given by Eqs. 21.47 are compared with the initial guesses. The computation is repeated using better initial guesses of the total strains until a consistent set of stresses and strains at  $t + \delta t$  are obtained.

After convergence at axial zone  $j$ , the code moves to the next axial region, and the entire radial iteration procedure is begun again. When the bottom of the fuel pin is reached, the time step is advanced, and the cycle is repeated.

The computation ceases when the desired irradiation history is completed or when the cumulative damage index of the cladding equals unity. A flow chart of the LIFE fuel-modeling code (which also includes cracking) is shown in Fig. 21.7.

### 21.3 FUEL CRACKING

Immediately upon startup and before swelling or creep has occurred to any appreciable extent, the fuel develops a network of cracks oriented either along radial planes passing through the fuel-pin axis (sometimes called  $\theta$  cracks because they are perpendicular to the  $\theta$  direction) or along horizontal planes perpendicular to the  $z$ -axis ( $z$  cracks). These cracks appear because the thermoelastic stress components exceed the fracture strength of the fuel in tension (Fig. 16.7). The parabolic temperature gradient in the fuel

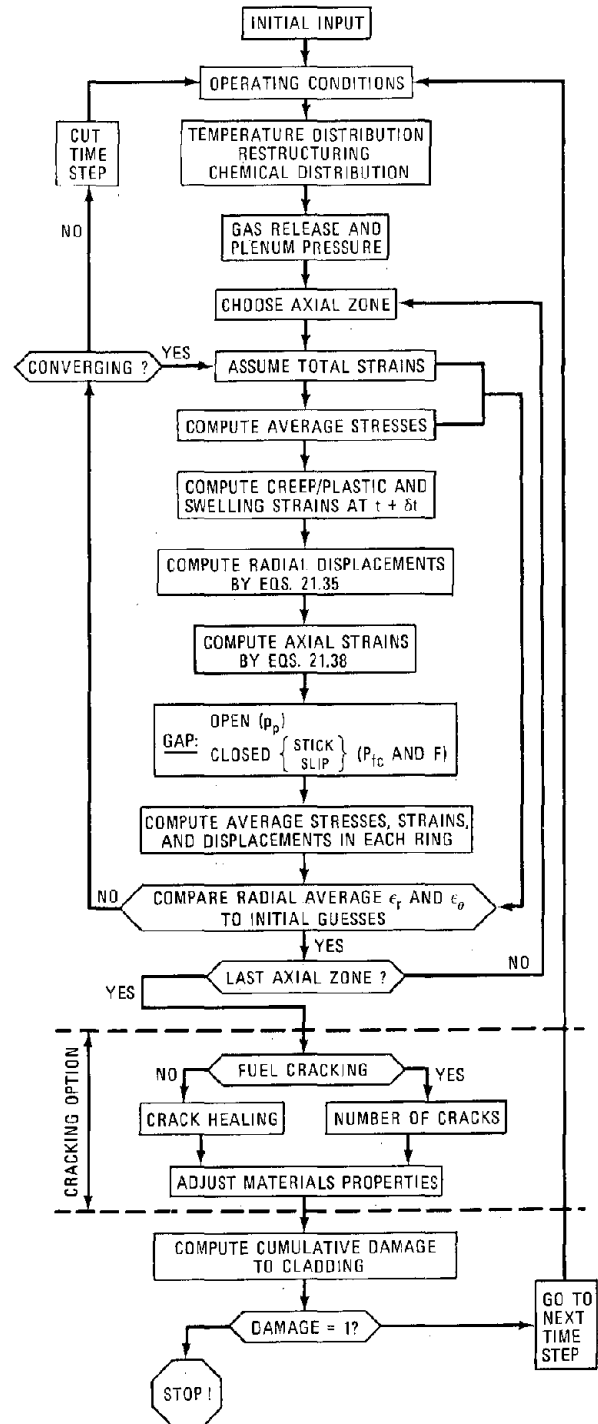


Fig. 21.7 Flow chart of the LIFE fuel-modeling code. (After Ref. 2.)

induces tensile stresses in the  $\theta$ - and  $z$ -directions in the outer region of the fuel where the fuel is brittle (because  $T < \sim 1400^\circ\text{C}$ ). In the inner core of the fuel, the thermal stresses are compressive, and, because the strength in compression is an order of magnitude greater than the tensile

strength, no cracking occurs in the interior. Moreover, the inside of the fuel is above the ductile-to-brittle transition temperature and therefore can sustain appreciable plastic deformation before fracture. Additional cracking occurs on each power change.

The thermal stress in the cladding due to the temperature drop through this component does not cause cladding cracking because the metal is ductile (initially at least). However, the thermal stresses can result in plastic flow at startup if the linear power is sufficiently large (see problem 21.2 at end of chapter) and continue to cause permanent deformation by creep through power operation of the fuel element.

The fuel-cracking phenomenon at startup may be analyzed with the aid of the equations developed in the previous section, which in the absence of swelling or creep strains can be treated by thermoelasticity theory.

Consider an infinitely long cylindrical fuel pin of radius  $R$  operated at linear power  $\mathcal{P}$  W/cm. If the thermal conductivity of the matrix is assumed independent of temperature, fission heat generation results in a parabolic temperature profile (Eq. 10.52). The temperature drop from the center line to the fuel surface is given by

$$T_0 - T_s = \frac{\mathcal{P}}{4\pi\bar{k}} \quad (21.48)$$

where  $\bar{k}$  is the average thermal conductivity of the fuel. Application of thermoelasticity theory to this situation (see problem 21.1 at end of the chapter) shows that the tangential or hoop stress in the fuel,  $\sigma_\theta$ , varies with fractional radius according to

$$\sigma_\theta = -\frac{\alpha E \mathcal{P}}{16\pi(1-\nu)\bar{k}} \left[ 1 - 3\left(\frac{r}{R}\right)^2 \right] \quad (21.49)$$

Stresses are positive if in tension. Equation 21.49 indicates compression of the fuel out to a fractional radius of  $1/3^{1/2}$  and tensile hoop stresses thereafter. The maximum stress, which occurs at the outer surface, is given by

$$(\sigma_\theta)_{\max} = \frac{\alpha E \mathcal{P}}{8\pi(1-\nu)\bar{k}} \quad (21.50)$$

The following properties are typical of  $\text{UO}_2$ :

$$\begin{aligned} \alpha &= 10^{-5} \text{ }^\circ\text{C}^{-1} \\ E &= 1.4 \times 10^8 \text{ kN/m}^2 \\ \nu &= 0.3 \\ \bar{k} &= 0.028 \text{ W cm}^{-1} \text{ }^\circ\text{C}^{-1} \end{aligned}$$

From Fig. 16.7 the fracture stress of  $\text{UO}_2$  is  $\sim 1.5 \times 10^5$  kN/m<sup>2</sup>. Application of Eq. 21.50 shows that the fracture stress is attained at the outer surface of the fuel pin when the linear power is  $\sim 50$  W/cm. Since this value is an order of magnitude lower than the normal linear power of an operating fuel pin (Table 10.2), it is evident that extensive cracking of the brittle outer portion of the fuel is unavoidable. The cracks due to the tangential stress occur on planes emanating in radial directions from the center and containing the fuel-pin axis. The cracks shown in Fig. 16.8 are of this variety. The radial cracks extend into the fuel to

a distance at which the tangential stress given by Eq. 21.49 becomes equal to the fracture stress, provided the temperature at this point is below the brittle-to-ductile transition. Because the maximum axial tensile stress is also given by Eq. 21.50, cracks on fuel cross sections perpendicular to the pin axis can also occur.

One of the most important functions of fuel cracking is to move void volume from the fuel-cladding gap to the interior of the fuel in the form of spaces between the cracked surfaces. Consider fissures along radial planes in the fuel (i.e.,  $\theta$  cracks). When the fuel cracks, the tangential stress at the crack location vanishes, and the two surfaces of the crack separate slightly because of the tensile hoop stresses in the interior of the wedges of solid which are separated by cracks. Since the solid is nearly incompressible, crack opening is accompanied by radially outward movement of the solid in the wedges. The temperature distribution remains parabolic throughout the fuel after cracking has occurred because heat does not flow in the  $\theta$  direction when the cylinder is intact, and radial gaps, to first approximation, do not perturb the heat flow lines. The thermoelastic stresses in the cracked fuel, however, are no longer axially symmetric;  $\sigma_\theta$  is zero at the crack surface but not in the interior of the cracked pieces. Consequently the formulas used in the preceding section are no longer applicable because they neglected tangential derivatives of the stresses and strains and did not consider shear stresses. Nevertheless, an approximate calculation of the tangential strain,  $\Delta R/R$ , which results from cracking in a parabolic temperature distribution is given below.

Suppose the radial cracks extend from the periphery of the fuel to radial position  $R_c$ . Since the tangential strain of the outer surface of a solid cylinder is  $\alpha\bar{T}$ , where  $\bar{T}$  is the average temperature, the tangential strain of the solid portion of the fuel pin between the center and  $R_c$  is

$$\frac{\Delta R_c}{R_c} = \frac{1}{2} \alpha (T_0 + T_c)$$

where  $T_0$  and  $T_c$  are the central temperature and the temperature at the root of the crack, respectively (both are measured above ambient temperature). The thickness in the radial direction of the wedges that result from cracking of the outside of the cylinder is  $L_c = R - R_c$ , where  $R$  is the radius of the fuel. We approximate the strain of these blocks of solid in the direction of the temperature gradient as the product of the linear coefficient of expansion and the average temperature of the wedges, or

$$\frac{\Delta L_c}{L_c} = \frac{1}{2} \alpha (T_c + T_s)$$

where  $T_s$  is the difference between the surface temperature of the fuel and ambient temperature. The total radial displacement,  $\Delta R = \Delta R_c + \Delta L_c$ , is given by the preceding two equations:

$$\begin{aligned} \Delta R &= \frac{1}{2} \alpha [R_c(T_0 + T_c) + L_c(T_c + T_s)] \\ &= \frac{1}{2} \alpha R \left[ \left(\frac{R_c}{R}\right) T_0 + T_c + \left(\frac{R - R_c}{R}\right) T_s \right] \end{aligned}$$

For a parabolic temperature distribution,  $T_c = T_0 - (T_0 - T_s)(R_c/R)^2$ , or the above formula can be written as

$$\frac{\Delta R}{R} = \frac{1}{2}\alpha[(1 + \eta_c - \eta_c^2)T_0 + (1 - \eta_c + \eta_c^2)T_s] \quad (21.51)$$

where  $\eta_c = R_c/R$  is the fractional radius at which the cracks begin. When no cracking occurs ( $\eta_c = 1$ ), Eq. 21.51 reduces to the strain formula used in determining the hot-gap thickness (Eq. 21.2). If the fuel fracture strength is zero, Eq. 21.49 shows that the crack roots start at  $\eta_c = 1/3^{1/2}$ . For  $T_0 = 2500 - 300 = 2200^\circ\text{K}$ ,  $T_s = 1000 - 300 = 700^\circ\text{K}$ , and  $\alpha = 1 \times 10^{-5} \text{ }^\circ\text{K}^{-1}$ , the fractional increases of the fuel radius due to thermal stresses in the cracked and uncracked portions of the fuel are

$$\left(\frac{\Delta R}{R}\right)_{\text{cracked}} = 5 \times 10^{-6} [(1.24)(2200) + (0.76)(700)] = 0.0163$$

and

$$\left(\frac{\Delta R}{R}\right)_{\text{uncracked}} = 5 \times 10^{-6} (2200 + 700) = 0.0145$$

This difference in tangential strain arises from the inability of the cracked outer annulus to contain the expansion of the hot fuel in the interior of the pellet. The larger expansion of cracked fuel compared to uncracked solid reduces the fuel-cladding gap at startup below the value computed from Eq. 21.2 (by about 10%).

The effect of cracking on the mechanical performance of the fuel cannot be exactly taken into account in the fuel-modeling codes described in the previous section. To do so would require (1) knowledge of the precise location and size of every crack in the fuel and (2) solution of the complete three-dimensional stress-strain problem in each of the blocks of intact solid without the aid of the major simplification afforded by the assumption of symmetry around the central axis which is used in the derivation of Sec. 21.2. Consequently the phenomenon is modeled by assuming that cracking occurs only on the principal planes (specifically only  $\theta$  and  $z$  cracks are considered). The effect of multiple cracking is treated in a manner that retains the cylindrical symmetry of the system in a macroscopic sense. Rather than treat a solid containing a population of discrete fissures, an equivalent continuous solid body with directionally dependent elastic constants is used in the stress analysis.<sup>2,10</sup> The properties of this nonisotropic but homogeneous medium are governed by the type and number of cracks in the real solid.

Suppose cracking occurs along radial planes ( $\theta$  cracks). It is intuitively expected that the fuel would be weakened in the  $\theta$ -direction but would retain essentially the solid-body strength in the other two principal directions. To reproduce this effect in the homogenized model of the cracked solid, we reduce Young's modulus in Eq. 21.8 from  $E$  to a lower value denoted by  $E'$ . At the same time, we decrease Poisson's ratio for all  $r\theta$  and  $z\theta$  contractions from

$\nu$  to  $\nu'$ . The constitutive equations in the cracked regions of the fuel assume the form

$$\sigma_r = \frac{1}{E'}(\sigma_r - \nu'\sigma_\theta - \nu'\sigma_z) + \alpha T + \epsilon^s + \epsilon_r^c \quad (21.52)$$

$$\sigma_\theta = \frac{1}{E'}(\sigma_\theta - \nu'\sigma_r - \nu'\sigma_z) + \alpha T + \epsilon^s + \epsilon_\theta^c \quad (21.53)$$

$$\sigma_z = \frac{1}{E'}(\sigma_z - \nu\sigma_r - \nu\sigma_\theta) + \alpha T + \epsilon^s + \epsilon_z^c \quad (21.54)$$

Using these constitutive relations in cracked portions of the fuel represents an attempt to compensate for the fact that the compatibility conditions (Eqs. 21.4 and 21.5) are not applicable in the real solid. However, analysis of the cracked fuel starting from Eqs. 21.52 to 21.54 retains the axial symmetry and freedom from shear stresses characteristic of the treatment of the intact solid. The result of using the modified constitutive relations along with the equilibrium and strain-displacement equations is a differential equation for the radial displacement similar to Eq. 21.26 but containing additional terms reflecting the difference in the primed and unprimed elastic constants in Eqs. 21.52 to 21.54.

A set of constitutive relations similar to Eqs. 21.52 to 21.54 for fuel with  $\theta$  cracks can be developed for horizontally cracked fuel or for simultaneous cracking perpendicular to both the  $\theta$ - and  $z$ -directions.

The new set of constitutive relations and the resulting displacement equation is applied to the cylindrical rings into which the fuel has been divided (Fig. 21.5) whenever the stresses  $\sigma_\theta$  or  $\sigma_z$  exceed the fracture stress in tension (Fig. 16.7). The LIFE code (Fig. 21.7) checks for cracking after each time step. Multiple cracking in a ring can occur if the linear power changes or simply from the constant power evolution of the stress distributions in the fuel. One crack is added to the ring each time the fracture stress is exceeded at a particular location. On the other hand, cracks may be removed by healing if the stress in the ring remains compressive for a sufficient duration of time. The fundamental study of crack healing is in its infancy; quantitatively expressible mechanisms of this process are not yet available, although some experiments designed to elucidate crack healing have been performed.<sup>11,12</sup> In the LIFE code<sup>2</sup> cracks are considered to have healed whenever the appropriate stress component in a ring with  $T > 1400^\circ\text{C}$  is compressive and is applied continuously for at least 1 hr.

Application of the nonisotropic but homogeneous model of a cracked region of the fuel requires input of the modified elastic constants  $E'$  and  $\nu'$ . In the LIFE calculation the reduction in elastic constants in the directions weakened by cracking is taken as

$$E' = \left(\frac{2}{3}\right)^N E \quad (21.55)$$

$$\nu' = \left(\frac{1}{2}\right)^N \nu \quad (21.56)$$

where  $N$  is the number of cracks in the particular direction. Although an attempt is made in Ref. 2 to justify these

formulas on theoretical grounds, the analysis, and in fact the entire treatment of cracking in fuel-modeling codes, is on a rather tenuous basis; the use of Eqs. 21.52 to 21.54 in conjunction with Eqs. 21.55 and 21.56 can only be justified by the success of the fuel-modeling code in reproducing computationally the observed structural changes in irradiated fuel.

## 21.4 FUEL-ELEMENT DEFORMATIONS DURING IRRADIATION

### 21.4.1 Cladding Strains

Although the fuel-modeling codes described in the preceding three sections of this chapter calculate the stress and strain patterns in both the fuel and the cladding in great detail, very few of these predictions are amenable to comparison with experimental measurements. Assessment of code accuracy and code calibration usually relies on comparison of the performance predictions with the following characteristics of a fuel element as determined by postirradiation examination of fuel rods in a hot cell:

1. Permanent diametral, or tangential, strain of the cladding as a function of axial position along the fuel rod. This measurement corresponds to the code prediction of  $\epsilon^s + \epsilon_b^c$  (the inelastic or irreversible strains) of the last radial ring in the cladding at the end of irradiation.

2. Cladding swelling due to void formation, which corresponds to  $3\epsilon^s$  in the code. Void swelling may be measured by the immersion method or by transmission electron microscopy (see Sec. 19.2), although the latter technique is too time-consuming for investigation of a large number of samples of irradiated cladding.

3. Postirradiation microscopic examination of cross sections of the irradiated fuel pin provides qualitative information on the extent of restructuring of the fuel and can indicate whether or not the fuel-cladding gap was open at the time of shutdown. The cracks observed in such examinations (e.g., Fig. 10.23), however, are cooling cracks and do not represent the cracks present in the fuel during irradiation.

Specially instrumented fuel elements can supply information on diametral strains as well as axial elongation of both the fuel and the cladding during operation. The diametral strains measured in-pile include elastic deformation and thermal expansion, both of which disappear when the power is turned off. In-pile structural measurements have been performed primarily in thermal facilities using light-water reactor fuel rods.<sup>13</sup>

The inelastic component  $\epsilon_b^c$  of the strain at the time of shutdown is determined by subtracting the measured swelling strain from the total strain. This inelastic-strain component is one of the indicators of cladding damage and approach to failure. Indeed, operating limits on LMFBR fuel pins may be given as a maximum allowable permanent diametral strain not including void swelling. The latter is not believed to affect the rupture lifetime of the cladding.

During normal operation the primary contribution to the inelastic strain  $\epsilon_b^c$  is due to creep and very little is due to plastic deformation. However,  $(\epsilon_b^c)^{creep}$  itself consists of

two components, thermal creep and irradiation creep. The irradiation creep may or may not be damaging to the cladding. Even though thermal-creep strain is probably the principal source of cladding damage and ultimately leads to failure, there is no way of dividing the measured cladding creep strain into thermal- and irradiation-induced components. This distinction, however, is easily made in the fuel-modeling code, although the accuracy of the prediction is difficult to gauge.

Figure 21.8 shows the LIFE code predictions of swelling and inelastic strain of a stainless-steel-clad mixed-oxide fuel rod that had been irradiated in a fast reactor.<sup>14</sup> The circle on the graph represents the measured diametral strain in the cladding at the axial location of peak linear power. The seemingly excellent agreement between the code prediction of  $\epsilon_b^c$  and the single datum is not to be construed as a measure of the reliability of the theoretical models embodied in LIFE. The code had previously been fine tuned on the basis of other cladding strain data because, when first applied to the fuel element represented by Fig. 21.8, the calculated cladding inelastic strain was a factor of 2 larger than the measurement. Therefore the code was recalibrated by adjusting the input materials constants (in this case, the fission-gas swelling rate, which was decreased by a factor of 4) to force agreement of the computation

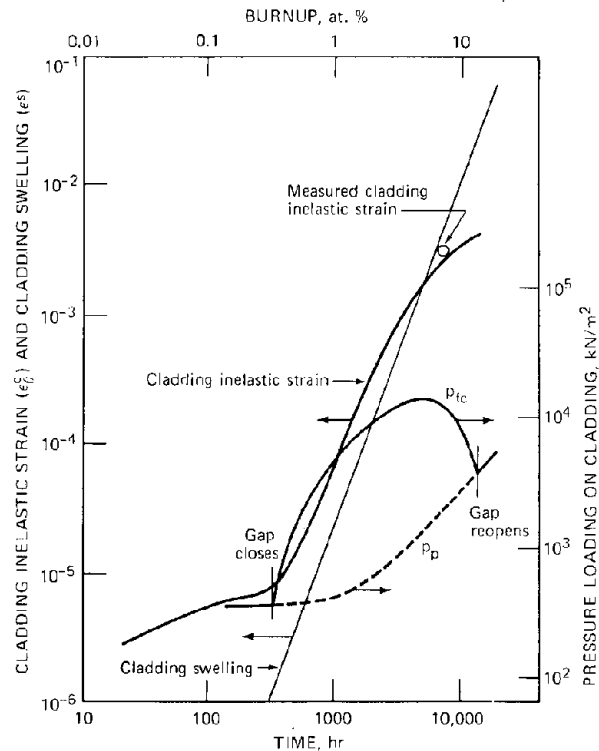


Fig. 21.8 Fuel-rod performance predicted by LIFE. Fuel density, 88.4% of theoretical density; fuel-cladding cold gap, 0.0066 cm; fuel-column length, 34 cm; fuel-pellet radius, 0.274 cm; cladding thickness, 0.038 cm; cladding temperature, 500°C; linear power, 440 W/cm; fast flux,  $1.7 \times 10^{15}$  neutrons  $\text{cm}^{-2} \text{sec}^{-1}$ . (After Ref. 14.)

with the single measurement. As a result of the recalibration, the predicted evolutions of strains and pressures with time shown in Fig. 21.8 are probably fairly reliable.

The inelastic strain in the cladding increases slowly from startup to  $\sim 400$  hr into irradiation as a result of creep induced by thermal stresses produced by the temperature drop through the cladding. During this period, the fuel-cladding gap is open and the plenum pressure, which adds to the thermal stresses in the cladding, is low because not much fission gas has been released yet. At 400 hr the fuel has swollen sufficiently to contact the cladding, and the cladding becomes loaded by the fuel-cladding interfacial pressure rather than by the plenum pressure due to released fission gas. The sharp rise in the interfacial pressure following fuel-cladding contact causes a correspondingly steep increase in cladding inelastic strain. The fuel-cladding interfacial pressure reaches a maximum of  $\sim 12,000$  kN/m<sup>2</sup> at  $\sim 5000$  hr and thereafter decreases until the gap reopens at  $\sim 11,000$  hr (although the actual fuel pin was not irradiated this long). Fuel-cladding contact is lost because cladding swelling [which increases as  $(\Phi t)^n$  with  $n > 1$ ] becomes more rapid than fuel swelling. The swelling curve for the cladding shown in Fig. 21.8 is one-third the volumetric void swelling and is similar in shape and magnitude to the swelling curve shown in Fig. 19.4. When the gap reopens, the cladding is once again loaded by the plenum-gas pressure, which has been increasing in an approximately linear fashion with time because of a roughly constant rate of fission-gas release from the fuel.

Figure 21.9 shows the computed effect of the initial fuel-cladding gap size,  $t_{\text{gap}}^0$ , on the inelastic cladding strain. The smaller the cold gap, the sooner the fuel makes contact with the cladding and the larger are the resulting cladding strains. In the computations for the curves in this plot, the smeared density was held constant; thus an increase of the initial gap size must be accompanied by a decrease in the porosity of the fabricated fuel pellets (Eq. 21.1).

Figure 21.10 shows the effect of cladding temperature on the cladding permanent strain. The cladding-temperature variation at constant linear power was achieved by adjusting the sodium coolant inlet temperature in the code. Cladding strain at  $375^\circ\text{C}$  is low because the thermal creep rate, which is highly temperature sensitive (see Eq. 21.20b), is small. For the same stress the creep rate at  $500^\circ\text{C}$  should be much larger than that at  $375^\circ\text{C}$ ; yet the curve for cladding strain at  $500^\circ\text{C}$  falls below that for  $375^\circ\text{C}$  cladding late in life. The explanation of this behavior is that  $500^\circ\text{C}$  is the peak swelling temperature for stainless steel (Fig. 19.3); so the cladding at this temperature literally runs away from the swelling fuel and prevents high interfacial pressure from developing. At temperatures above or below  $500^\circ\text{C}$ , the cladding does not possess this high recession velocity, and the strain due to fuel-cladding contact is more important than at  $500^\circ\text{C}$ . For cladding temperatures greater than  $500^\circ\text{C}$ , Fig. 21.10 shows that the cladding inelastic strains become large. At  $600$  and  $700^\circ\text{C}$  the creep strength of stainless steel is low, and the interfacial pressure is not relieved by cladding swelling, which virtually disappears at  $600^\circ\text{C}$  (Fig. 19.3). Consequently the combination of high temperature and high

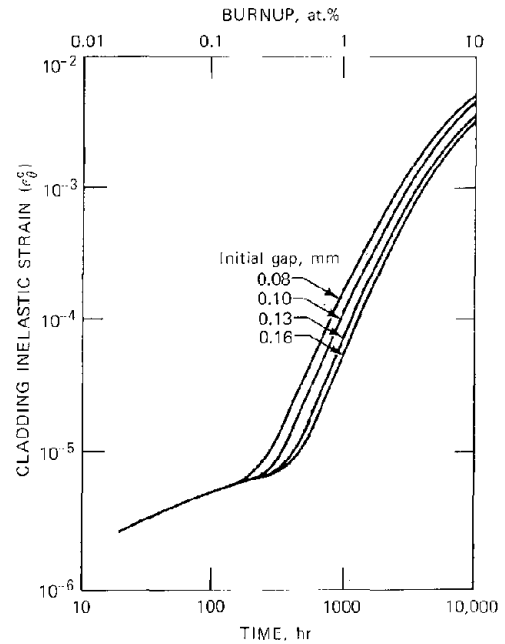


Fig. 21.9 Effect of fuel porosity and fuel-cladding gap size on fuel-element performance at constant smeared density. (After Ref. 14.)

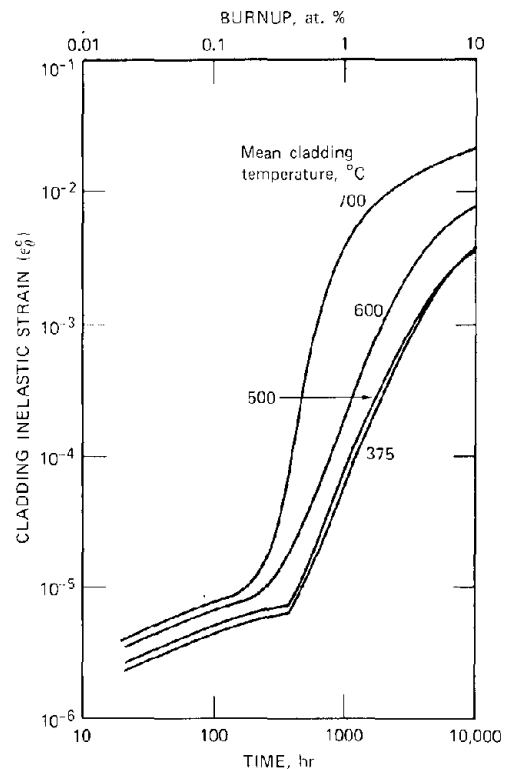


Fig. 21.10 Effect of cladding temperature on fuel-element performance for a fixed linear power of  $440$  W/cm. (After Ref. 14.)

stress in Eq. 21.20b generates large thermal-creep strains, which are manifest as the sizeable diametral strains predicted by the LIFE code.

Figure 21.10 predicts that the cladding deformation rate is drastically reduced at high burnups. This behavior is a direct consequence of the fission-gas swelling model used as a materials input function in the code. This model, although empirical, predicts saturation of swelling at all temperatures and more rapid attainment of saturation the higher the temperature. Such behavior is entirely consistent with such theoretical models of fission-gas swelling and release as BUBL and GRASS. In fact, the computation of fission-gas bubble distributions in Sec. 13.12 was performed for just such a saturated state of the fission gas in the fuel. When fuel swelling vanishes, the major reason for cladding deformation also disappears; the thermal stresses have been largely relieved by creep at high burnup, and the only remaining deformation process is that driven by the plenum pressure.

Figure 21.11 shows the axial distribution of the total cladding strain (i.e.,  $\epsilon_{\theta}^c + \epsilon^s$ ) and the swelling component alone for a set of irradiation parameters different from those used to prepare Figs. 21.8 to 21.10. However, it was

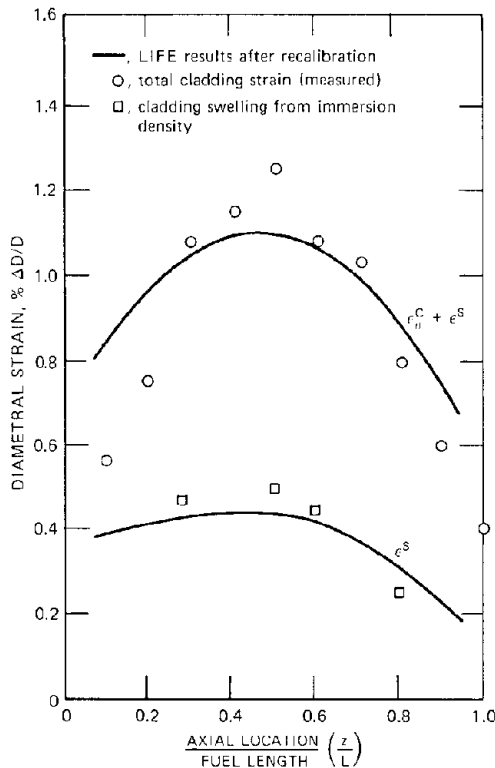


Fig. 21.11 Comparison of LIFE predictions and measurements of total permanent diametral strain and swelling strain. (From A. Boltax, W. E. Ray, and W. J. Rowan, Oxide Fuel Element Development Quarterly Progress Report of the Period Ending September 30, 1972, USAEC Report WARD-3045-T-3-9, Westinghouse Electric Corp., January 1973.)

again necessary to recalibrate LIFE by reducing fission-gas swelling to produce the agreement between code predictions and measurements shown in the graph. The relative importance of swelling strain,  $\epsilon^s$ , and creep strain,  $\epsilon_{\theta}^c$ , is satisfactorily predicted by the program. The observed axial distribution of the total strain is sharper than that predicted by the code, but the trends are similar; inelastic strain is greatest at the midplane, where the flux and hence the linear power are the largest. The high-power center portion of the fuel pin swells more than the fuel near the ends of the rod; therefore the cladding at the midplane experiences a greater interfacial pressure than it does at other axial locations. The cladding creeps largely in response to the interfacial pressure, and hence the diametral strain is largest at the rod midplane.

Because the coolant sodium flows upward through the core, the swelling strain is not symmetric about the core midplane. Cladding swelling due to void formation is greatest slightly above the midplane and decreases rapidly further up the core because the cladding temperature exceeds the maximum for swelling while the flux is decreasing. In the lower half of the core, however, the cladding temperature is generally closer to the 500°C maximum swelling temperature than it is in the top half of the core. Hence the swelling strain does not drop off as rapidly when moving from the midplane to the bottom of the fuel rod as it does when moving in the opposite direction (see problem 21.7 at end of the chapter).

#### 21.4.2 Axial Ratchetting

If the linear power of a fuel rod is subject to continuous off/on cycling and if fuel-cladding contact is made at a power less than the maximum, permanent axial deformation of the cladding may occur during each cycle. This mode of permanent strain of the cladding, which is fundamentally different from the steady deformations considered earlier in this chapter, is termed *axial ratchetting*. It has been studied analytically, but the phenomenon is difficult to observe because of the narrow range of conditions that permit its operation (Refs. 8, 10, 13, 15).

The process of axial ratchetting is shown schematically in Fig. 21.12. At zero power there is a fuel-cladding gap (Fig. 21.12a). As the rod power is raised, the fuel, which is hotter than the cladding, expands more than the cladding both axially and radially and fuel-cladding contact occurs before the maximum power in the cycle is achieved (Fig. 21.12b). The interaction forces between these two members place the cladding in tension both axially and tangentially, and the fuel experiences compression. Continued expansion of the nearly incompressible fuel further increases the tensile stresses in the cladding. When the yield point of the cladding is exceeded, immediate plastic flow occurs. If the maximum power is maintained long enough, the cladding creeps under the influence of the tensile stresses. For cladding deformation in the  $z$ -direction to occur, there must be significant friction between the fuel and the cladding; otherwise the fuel simply slips upward without taking the cladding along with it.

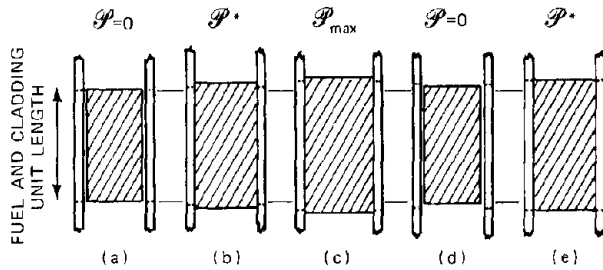


Fig. 21.12 Diagram of the axial ratchetting mechanism. The marks in the cladding provide reference points from which deformations can be measured. The lines between each drawing show the original position of the reference points. (After Ref. 8.)  $P^*$ , linear power at which fuel-cladding contact occurs;  $P_{max}$ , maximum linear power in cycle.

At the end of the maximum-power stage (Fig. 21.12c), permanent axial deformation of the cladding has occurred. When the power is reduced, the fuel returns to nearly its original size, but the cladding, having been deformed irreversibly, does not (Fig. 21.12d). Only the elastic strain of the cladding is recovered when contact with the fuel is lost. When the power cycle is repeated, fuel-cladding contact is again made, and the cladding receives another increment of permanent deformation (Fig. 21.12e). If the fuel piece returns to precisely the same shape and volume at the zero-power part of each cycle and thermally expands by exactly the same amount at each power increase, cladding deformation will cease after a number of cycles sufficient to extend the tube plastically to a size which either does not provide sufficient friction for the contact or which no longer results in creep or plastic flow during contact. However, two mechanisms are capable of continuing the axial ratchetting process indefinitely:

1. The fuel may consolidate during the power-reduction period in such a way that the fuel-cladding gap tends to fill up with fuel originating from the main body of the fuel stack. Fuel movement into the reopened gap may occur by gravity (i.e., by cracked pieces falling from the fuel and becoming lodged in the gap).

2. If the fuel is swelling at a constant rate during power cycling (e.g., by solid-fission-product swelling), the fuel volume at the end of each cycle continually increases. Fuel-cladding contact is thus made easier, and the fuel may be capable of pumping the cladding and of continuing indefinitely to deform the cladding during each cycle. Figure 21.13 shows the results of calculations with the cladding behavior code CRASH<sup>4</sup> for a situation in which both axial and radial ratchetting set in during uniform power cycling of a fuel rod.

### 21.4.3 Bamboosing

Another fuel-rod deformation problem that, to a first approximation, can be treated by linear thermoelasticity theory is the calculation of the strain in a finite cylinder (i.e., a fuel pellet) due to application of a radial temperature gradient. As a result of the absence of restraint at

the top and bottom of the pellet, the ends experience greater radial strain than the central cross section. The hourglass shape assumed by the pellets produces greater fuel-cladding interaction at the pellet-pellet interfaces than at axial positions corresponding to the middle of the pellets. The cladding deforms in response to this non-uniform interaction with the fuel by developing circumferential ridges. The phenomenon is known as *bamboosing* and is shown schematically in Fig. 21.14. The shapes of the pellets can be computed from thermoelasticity theory if the interaction of a pellet with its neighbors and with the cladding is neglected (i.e., if a single free pellet is considered). In this approximation the upper and lower faces of the pellet can be characterized by plane stress and the cross section through the middle by plane strain. The thermoelastic solution is discussed by Matthews.<sup>9</sup>

Bamboosing is possible only before the pellets have sintered together and formed a continuous fuel stack. The phenomenon is most likely to occur in fuel elements immersed in a coolant at sufficiently high pressure to collapse the cladding onto the fuel, which is the case in pressurized-water reactor fuels.

## 21.5 VOID SWELLING EFFECTS ON OTHER CORE COMPONENTS

The analysis in the first four sections of this chapter was directed at determining the longevity of a single fuel element in an LMFBR. Implicit in this discussion was the assumption that the lifetime of the reactor core was dictated by the time at which unacceptable numbers of cladding ruptures began to occur. However, fuel elements are bundled together and inserted into *wrappers* or *ducts*, which are packed together to form the core. Primarily because of void swelling, core lifetime may be limited by undesirable irradiation-induced deformations of the wrapper tube and not by the failure of fuel-element cladding. The consequences of void swelling in core

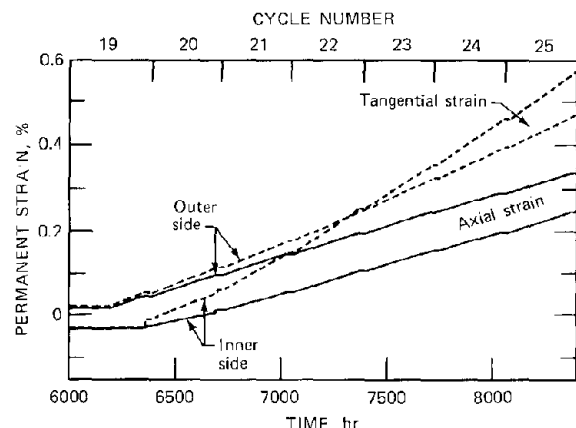


Fig. 21.13 Code predictions of axial and radial strains of cladding during ratchetting induced by power cycling. Fuel-cladding contact first occurs during the 19th cycle. (After Ref. 8.)

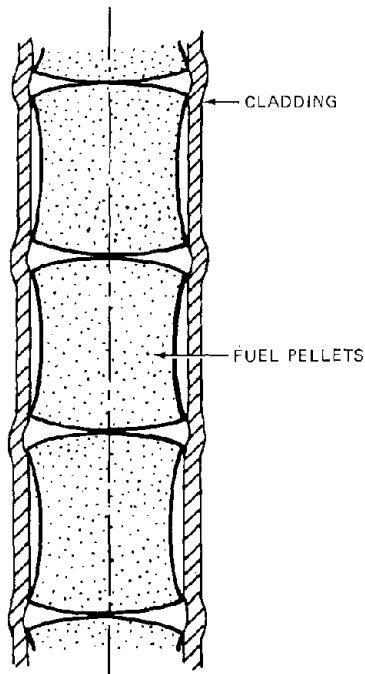


Fig. 21.14 Bambooning of fuel elements.

components other than fuel elements on LMFBR core performance have been reviewed by Huebotter and co-workers,<sup>1,6-18</sup> and much of the discussion in this section is based on their analyses.

Figure 21.15 shows longitudinal and cross-sectional views of an LMFBR fuel assembly. A cutaway rendering of the same component is shown in Fig. 10.4. There are 217 fuel elements placed inside the hexagonal-shaped wrapper in the triangular pattern shown in the cross-sectional view. Wires wrapped around each fuel element (Fig. 10.2) act as spacers and provide passageways for sodium flow past each element in the bundle. The wrapper is approximately 0.35 cm thick except for areas at the top and just above the core where the walls are thickened by  $\sim 0.06$  cm to form *spacer pads*. These are the zones where neighboring assemblies interact mechanically. Excessive void swelling at these contact points could cause stresses in the duct walls high enough to result in assembly failure, especially if the metal is embrittled by helium. The spacer pads are placed above the core region to escape the high flux that promotes both swelling and helium embrittlement of steel and thus avoid fracture at interassembly contact points.

A nozzle is attached to the bottom end of the wrapper. The nozzle is inserted into the permanent structure in the bottom of the reactor vessel and so supports the entire fuel assembly in cantilever fashion. Coolant sodium enters the assembly through slots in the nozzle and flows upward around the fuel bundle inside the wrapper.

Figure 21.16 shows two neighboring fuel assemblies supported by insertion of their nozzles in the upper and lower *grid plates*, which are fabricated from stainless steel. These plates are  $\sim 3$  m in diameter and  $\sim 10$  cm thick. The

holes in the upper and lower grid plates are accurately aligned so that the fuel assembly is plumb when seated in both plates. The *handling heads* on top of the wrapper tubes permit a refueling machine operating under the sodium pool in which the entire core is immersed to remove fuel assemblies after the allotted fuel burnup has been achieved. The fuel assemblies are approximately 4 m in length. They are packed together in the honeycomb fashion shown in Fig. 21.17 to form an approximately hexagonal-shaped core that contains about 400 fuel assemblies and is of the order of 3 m across the flats (for a 1000-MW reactor). Approximately one-tenth as many *guide tubes* for safety and control rods as there are fuel assemblies are interspersed among the fuel assemblies. Two rows of blanket assemblies (containing rods filled with  $^{238}\text{UO}_2$ ) comprise the periphery of the core.

The principal functions of the hexagonal wrapper around each fuel- or blanket-element bundle are:

1. To prevent the sodium coolant from bypassing the high-flow-resistance path alongside the fuel-pin bundle and flowing up the interassembly gap instead.

2. To provide structural support for the bundle of fuel elements or control rods contained in the wrapper.

3. To provide mechanical means (by the handling heads) for removal of spent fuel and replacement with fresh fuel.

4. To provide a barrier against propagation to the rest of the core of an accident that might be caused by rupture of one or more fuel pins in an assembly.

Other components of the core are:

1. Grid plates that support the assemblies.

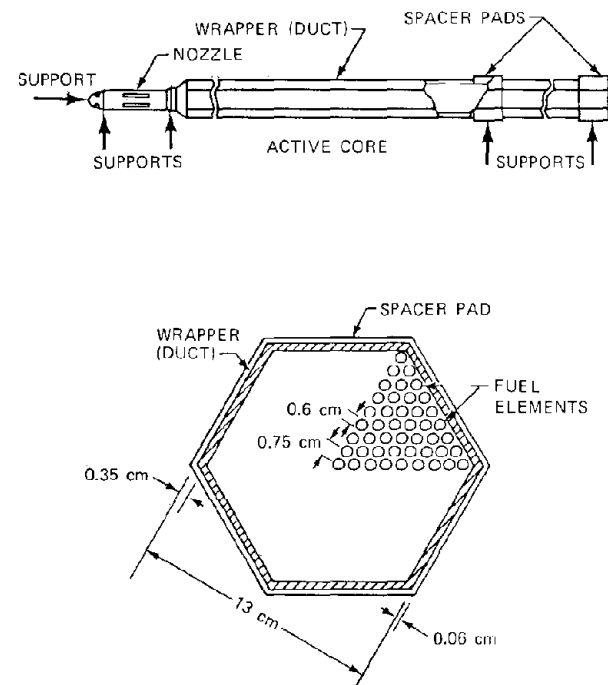


Fig. 21.15 Typical fuel assembly of an LMFBR. (After Refs. 16 to 18.)

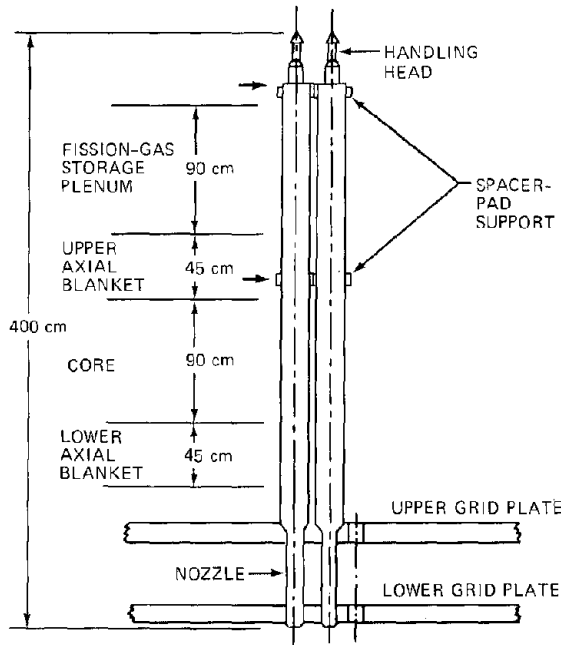


Fig. 21.16 Mounting of fuel assemblies on the grid plates. (After Ref. 17.)

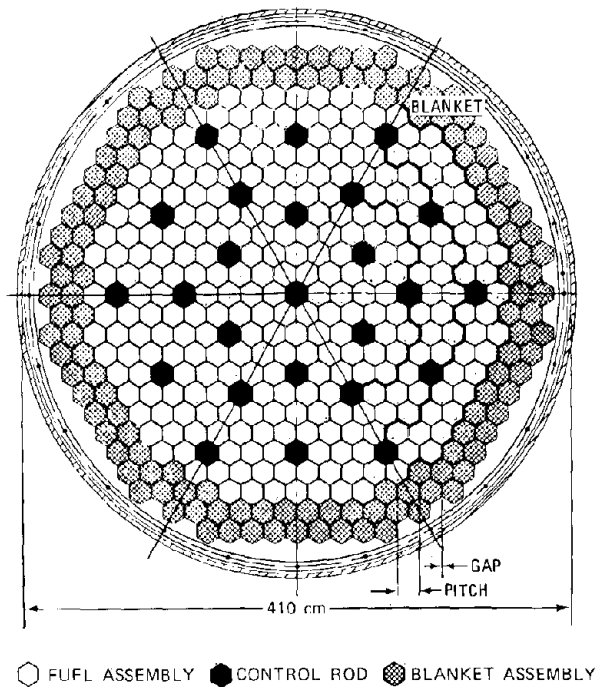


Fig. 21.17 Arrangement of assemblies in the reactor core. [From B. J. Goulding, 1000-MW(e) LMFBR Accident Analysis and Safety Design Study. Topical Report, Effect of Irradiation-Induced Metal Swelling on the Reference Design, USAEC Report BAW-1355, Babcock & Wilcox Co., November 1970.]

2. An instrument plate located above the core in the sodium pool. This component supports thermocouples and flowmeters for monitoring the sodium outlet conditions.

3. A core-restraint component that is designed to exert a lateral force on the array of assemblies to correct the disarray of the core due to bowing of the assemblies.

A prototype core-restraint device, a *core clamp*, is shown in Fig. 21.18. This component consists of six hydraulically operated yokes or rams that press inward on the six sides of the core which consist of the blanket assemblies (Fig. 21.17). The clamp acts at the elevation of the spacer pads on the assemblies. The object of the core clamp is:

1. To provide a calculable and reproducible structural response of the core which, if left unrestrained, would be substantially disarrayed by swelling and bowing of the wrappers.

2. To maintain the tops of the assemblies in position so that the handling heads can be located and grappled by the refueling machine, which operates under opaque sodium.

3. To provide adequate clearance and maintain sufficient duct straightness so that assemblies can be removed or inserted from the array without undue vertical friction forces due to rubbing against neighboring assemblies. The core clamp is released for refueling operations.

The hydraulically actuated core clamp shown in Fig. 21.18 is used only to test the mechanical performance of mock-up LMFBR cores; actual fast breeder reactors (in the United States at least) will use a passive restraint system in which core motion is restrained by a fairly rigid barrel-shaped structure enclosing it.

Concern with these aspects of overall core structural performance (and indeed, the reason for the decision to use core restraint) is a direct consequence of swelling of steel by voids generated under fast-neutron bombardment. The earlier sections of this chapter considered the effect of void swelling on the performance of individual fuel elements. In this instance it was found that metal swelling may be beneficial to fuel-element performance because it acts to relieve the fuel-cladding interfacial pressure built up by fuel swelling. When the other core components swell, however, there is no such redeeming feature; the consequences are uniformly undesirable. The problem is limited to the assembly wrapper tube because the other components of the core (grid plates, instrument plates, and core clamp) are in regions of sufficiently low flux that the effect of swelling on them is not significant even over the ~30-year lifetime of the reactor plant.

The effects of void swelling on the assembly may be divided into the uniform volume increase of metal (axial and radial) and the differential swelling caused by non-uniform temperature and flux between the side of an assembly closest to and the side furthest away from the core axis.

### 21.5.1 Elongation

Elongation refers to the permanent axial extension of an assembly due to void swelling. The axial-swelling strain may be computed by integrating one of the void-swelling

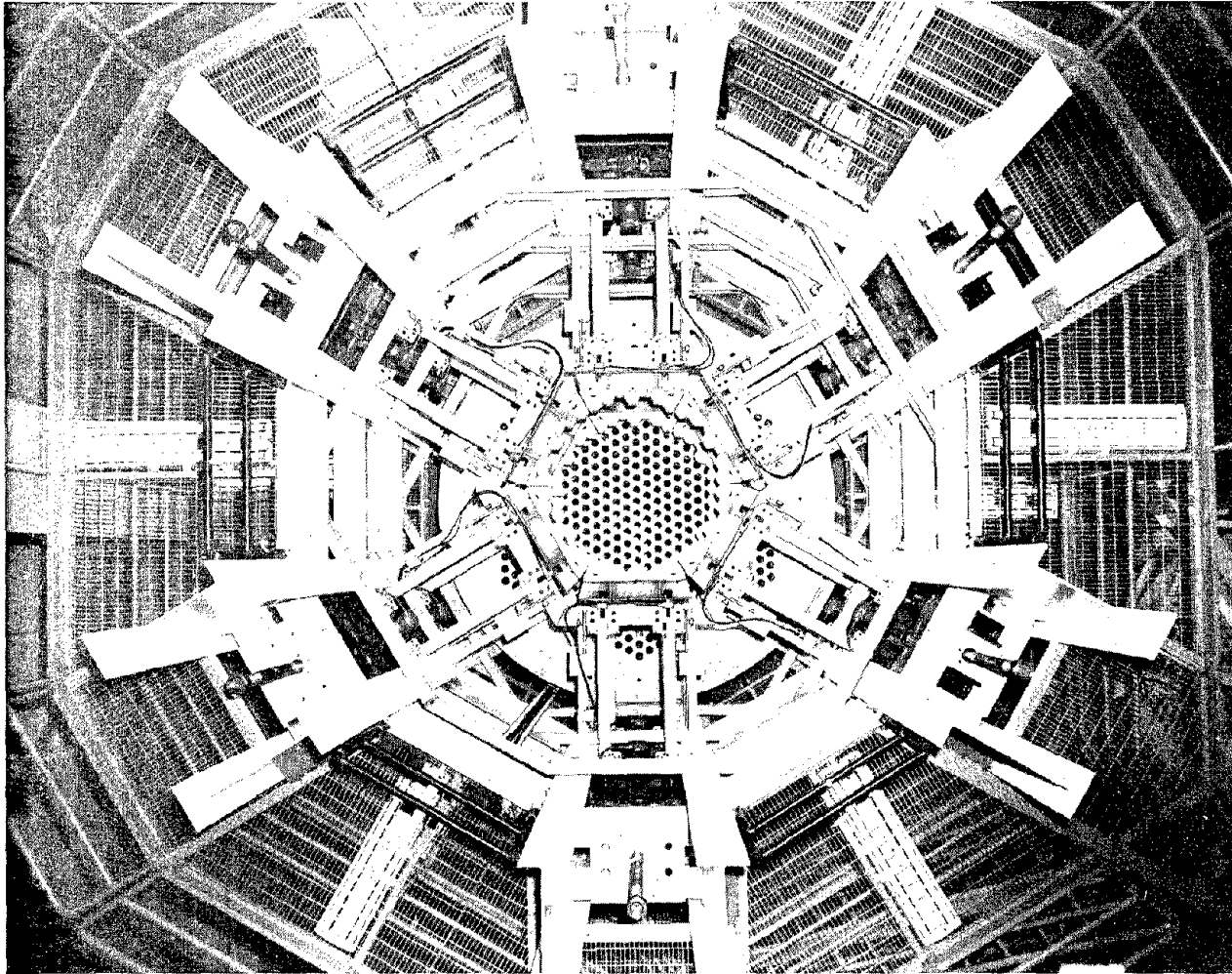


Fig. 21.18 A prototype core clamp. (From J. W. French, Core Restraint Developments, Quarterly Progress Report for Period Ending November 30, 1973, USAEC Report WARD-CR-3045-4, Westinghouse Electric Corp., 1973).

equations presented in Chap. 19 (e.g., Eq. 19.12b) over the length of the assembly, taking into account the axial variation of both the fast-neutron flux (which is approximately cosine in shape) and the coolant temperature (which increases monotonically from inlet to outlet). The axial strain or elongation is one-third the volume swelling so computed. Figure 21.19 shows the results of such a calculation for the rings of assemblies at different radial distances from the core axis. The walls of the duct closest to the core center elongate more than the opposite walls because of the radial flux and temperature gradients (these gradients are also responsible for bowing, which is discussed in the next section). The central fuel assembly elongates more than 4 cm, which corresponds to an axial swelling strain of about 1%. Elongation of the assemblies by this amount complicates the design of the machine for handling the assemblies, but this problem does not appear to be insurmountable.

Void swelling also causes the fuel elements proper to grow in length. The growth of the cladding is greater than

that of the duct walls because the cladding midwall temperature is 50 to 75°C higher than the average sodium temperature, which is the same as the temperature of the wrapper. A potential mechanical problem arises because the wires wrapped in helical fashion around the cladding to act as spacers (Fig. 10.2) are closer to the sodium temperature than to the cladding midwall temperature. This temperature difference means that the cladding swells axially more than does the wire around it (by ~0.2%). Excessive stress on the wire wrap near the end of life, which may cause breakage, can be avoided by allowing some initial slackness when the wire is wound around the cladding during fabrication.

The neutronics of the reactor are affected by core axial growth. The estimated reactivity decrease due to the elongation is \$2.\* This loss must be compensated for by increasing the mass of fissile plutonium in the fresh fuel,

\*A dollar (\$) is equal to a reactivity of one delayed-neutron fraction (~0.00023 for plutonium).

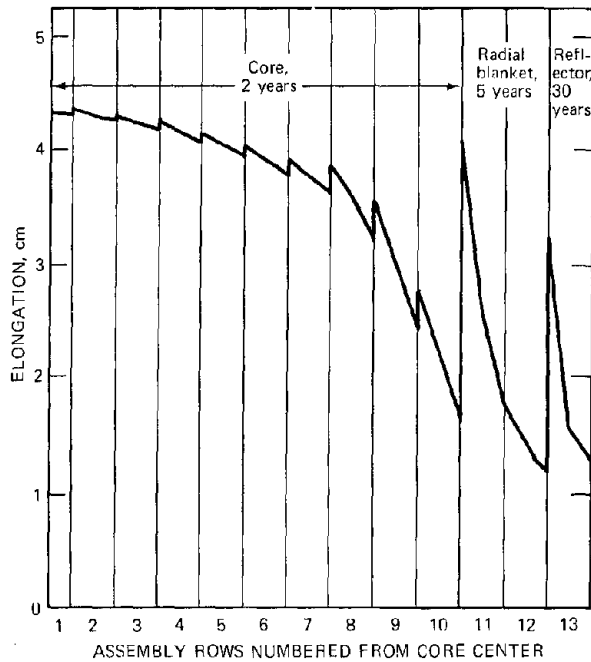


Fig. 21.19 Elongation of wrapper walls due to void swelling at the end of the nominal lifetime of each component. (After Ref. 18.)

which represents the first but by no means the worst adverse economic consequence of void swelling.

### 21.5.2 Dilation

Dilation refers to the uniform radial growth of the core due to swelling of each of its component assemblies. Radial dilation of these components is computed by the method described for calculating elongation. Figure 21.20 shows the radial dilation of the wrappers in various rings of the core after  $\sim 2$  years of operation. Maximum dilation occurs just above the core midplane because this location offers the combination of flux and temperature most propitious to void swelling (see problem 21.7 at end of chapter). At this position the diametral expansion of the central assembly is  $\sim 0.6$  cm. The consequence of radial dilation of the wrappers is the reduction in the clearance between assemblies. If swelling were absent, a gap between neighboring assemblies of  $\sim 1.3$  mm would be sufficient for assembly removal and insertion. However, as a result of void swelling, the central assembly must be separated from its six neighbors by gaps of  $\sim 7$  mm. The required clearance is reduced as the periphery of the core is approached. If initial clearances, ultimately to be filled by the swelling wrappers, were not provided, the core would push outward radially during irradiation and very quickly would cause unacceptable misalignment of control rods and their above-core extensions and handling heads and the refueling machine. The larger than normal gap size between the assemblies in the core introduces a significant economic penalty because the gap is filled with sodium, not fuel. The large clearances reduce the fuel-to-metal ratio of the core,

thereby increasing the critical mass and decreasing the breeding ratio.

The bundle of fuel rods inside the assembly swell radially more than the duct wall, and sufficient clearance must be provided during fabrication to accommodate differential swelling of fuel pins and wrapper. The  $\sim 1.5\%$  clearance needed for this purpose is more than the nominal clearance needed to load the bundle into the assembly. The loose fit of the fuel-pin bundle early in irradiation does not appear to cause operational problems.

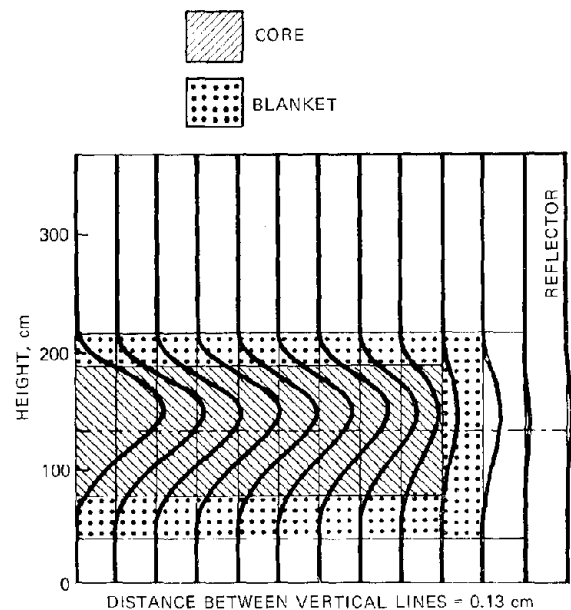


Fig. 21.20 Dilation of wrapper walls due to void swelling at end of life. (After Ref. 18.)

### 21.6 FUEL-ASSEMBLY BOWING

Bowing refers to the loss of duct straightness caused by differential temperatures and swelling strains on opposite faces of an assembly. This consequence of swelling is more severe than the effect of uniform expansion just discussed, which at least can be computed with reasonable accuracy. Bowing, on the other hand, involves a complex combination of thermal expansion, void swelling, irradiation creep, and mechanical interaction between neighboring assemblies which do not deform by equal amounts and which exert forces on each other at the spacer pads. Several computer programs are available for numerical analysis of the bowing problem. The codes CRASIB<sup>19</sup> and AXICRP<sup>20</sup> subdivide the fuel assembly into regions (similar to the method used in fuel-element modeling codes) and calculate the time-dependent loads, stresses, and shapes of the ducts due to nonuniform thermal expansion coupled with void swelling and irradiation creep. The fuel pins inside the wrapper are very compliant compared to the thick-walled duct and are not considered in the calculation. The fuel pins are assumed to follow the bowing of the duct. These codes, however, do

not allow for interassembly mechanical interaction. This aspect of bowing is treated in detail in the BOW-V code<sup>21</sup> which, unfortunately, is restricted only to thermal bowing. Complete structural analysis of the entire array of assemblies requires mating of CRASIB and BOW-V. We review here some of the elementary notions that underlie the computational methods used in these codes.

21.6.1 Elementary Beam Theory

Figure 21.21 shows a beam with its long dimension in the z-direction. The cross section may be any shape that is symmetric about the x- and y-axes, but a rectangle of dimensions 2h and b has been chosen for the present discussion. Bending occurs in the x-z plane because of (1) forces applied on the upper or lower faces of the beam in

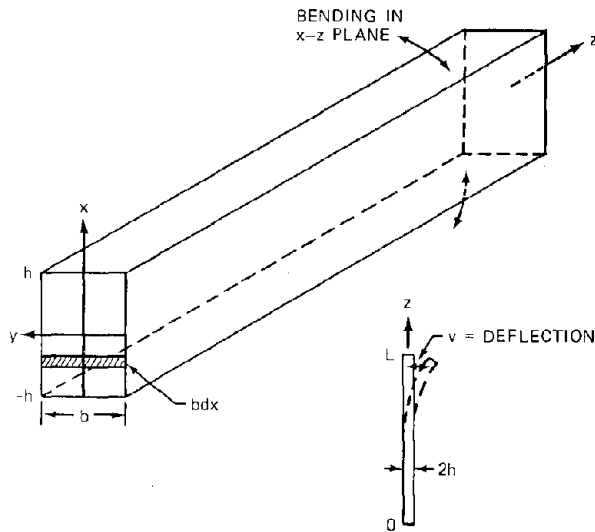


Fig. 21.21 Bending of a beam.

the x-direction and (2) volumetric thermal and swelling strains that depend on x. These strains are assumed to be symmetric about x = 0 and to vary linearly from x = -h to x = h.

The beam bends in the x-z plane as a result of one or a combination of these effects. To determine the stress distribution and the lateral displacement v(z) of the beam, we must satisfy three basic relations: (1) the strain-displacement equation, (2) the equilibrium equations, and (3) the constitutive equation. Solution of these equations requires specification of appropriate boundary conditions on the beam.

21.6.2 The Strain-Displacement Relation

The geometry of the curved beam at a particular z-position is shown in Fig. 21.22. The radius of curvature of the central plane (x = 0) is denoted by ρ. This plane is called the neutral fiber because it experiences zero strain compared to the neighboring fibers, and the length of a

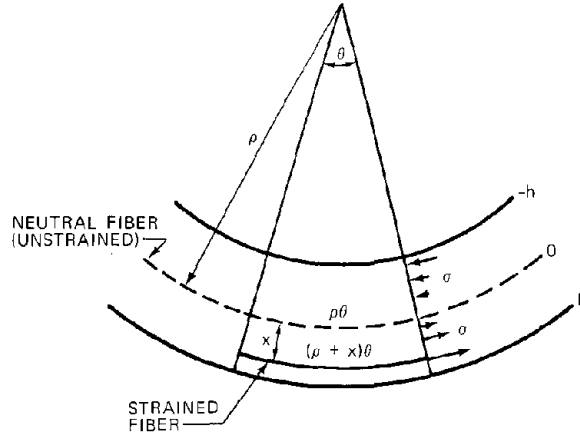


Fig. 21.22 Longitudinal section (x-z plane) of a bent beam.

segment on this plane remains constant as the beam is bent. However, the length of the fiber at ρ + x is (ρ + x)θ, which is greater than the length before bending by an amount xθ. Therefore the strain in the z-direction of the fiber at position x is

$$\epsilon_z = \frac{x\theta}{\rho\theta} = \frac{x}{\rho}$$

A theorem of plane geometry states that the reciprocal of the radius of curvature (provided that ρ is large) is equal to the second derivative of the curved segment. Denoting the deflection of the beam away from the z-axis in the x-z plane by v (see inset of Fig. 21.21), we have

$$\frac{1}{\rho} = \frac{d^2 v}{dz^2}$$

Combining the above two relations, we obtain the axial strain-displacement equation

$$\epsilon_z = x \frac{d^2 v}{dz^2} \tag{21.57}$$

21.6.3 Equilibrium Conditions

Figure 21.23 shows the forces and moments acting on a slice of beam of thickness Δz. The sides of the beam are

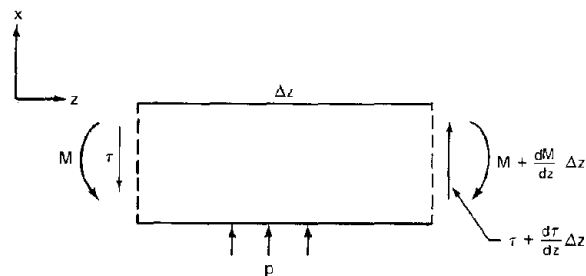


Fig. 21.23 Forces and moments on a section of a beam.

subject to an applied load (normal stress) distribution denoted by  $p(z)$ . The cross section perpendicular to the  $z$ -axis experiences a shear force denoted by  $\tau$  and a bending moment about the  $y$ -axis due to the distribution of normal stresses shown in Fig. 21.22. The moment acting on the differential area  $b dx$  is the product of the force  $o b dx$  and the lever arm  $x$ , or  $dM = x o b dx$ . Integrating over the entire cross section yields the moment due to the stress distribution

$$M = b \int_{-h}^h x \sigma dx \quad (21.58)$$

In order that the net force in the  $x$ -direction on the element in Fig. 21.23 be zero, we must have

$$\frac{d\tau}{dz} = -p \quad (21.59)$$

and, for the body to be in rotational equilibrium, the resultant torque must be zero

$$\frac{dM}{dz} = \tau \quad (21.60)$$

Eliminating  $\tau$  between the above two equations yields

$$\frac{d^2 M}{dz^2} + p = 0 \quad (21.61)$$

which is the desired equilibrium relation for the beam.

### 21.6.4 Constitutive Relation

The strain in the  $z$ -direction,  $\epsilon_z$ , is the sum of the elastic strain due to the internal stress distribution, thermal expansion, swelling, and creep. Neglecting creep (we will return to it later), the axial strain is

$$\epsilon_z = \frac{\sigma}{E} + \alpha T + \epsilon^s \quad (21.62)$$

where  $E$  is the Young's modulus, and  $\alpha$  is the linear coefficient of thermal expansion. The temperature  $T$  is measured with respect to the vertical ( $y$ - $z$ ) plane bisecting the beam, and  $\epsilon^s$  is one-third the volume swelling due to voids in the metal. Replacing the left-hand side of Eq. 21.62 by the strain-displacement relation (Eq. 21.57), multiplying the resulting equation by  $x b dx$ , and integrating over the  $x$ -dimension yields

$$\frac{d^2 v}{dz^2} b \int_{-h}^h x^2 dx = \frac{1}{E} b \int_{-h}^h x \sigma dx + \alpha b \int_{-h}^h T x dx + b \int_{-h}^h \epsilon^s x dx$$

We assume a linear variation of temperature across the beam (the  $x$ -axis corresponds to the negative of the radial direction from the core center line)

$$T = \frac{\Delta T}{2h} x \quad (21.63)$$

where  $\Delta T$  is the temperature difference between the hot and cold sides of the beam. Similarly the swelling strain is assumed to vary linearly in  $x$

$$\epsilon^s = \frac{\Delta \epsilon^s}{2h} x \quad (21.64)$$

where  $\Delta \epsilon^s$  is the difference in swelling strain between the flats of the assembly closest to and furthest from the core center line and is a function of the radial flux and the temperature distribution in the core. It also varies with time, whereas the temperature difference across the flats,  $\Delta T$ , does not.

The moment of inertia of the rectangular beam about the  $y$ -axis is defined by

$$I = b \int_{-h}^h x^2 dx \quad (21.65)$$

The moment of inertia is a geometrical property of the beam cross section. Equation 21.65 applies to the solid rectangular beam, but similar formulas may be obtained for other shapes, such as the hollow hexagonal configuration of the wrapper of a fuel assembly. Using Eqs. 21.63 to 21.65 and the definition of the moment, Eq. 21.58, the beam-deflection differential equation becomes

$$\frac{d^2 v}{dz^2} = \frac{M}{EI} + \frac{\alpha \Delta T}{2h} + \frac{\Delta \epsilon^s}{2h} \quad (21.66)$$

Determination of the deflection profile or camber of the beam requires specification of the moment  $M$  and integration of Eq. 21.66 with appropriate boundary conditions.

The total deflection  $v$  consists of contributions from the applied load (first term on the right-hand side) and from thermal and swelling expansions. Since the total deflection can be obtained by adding these three contributions, we examine each one separately.

1. Consider the assembly shown in Fig. 21.16 inserted into the grid plates by its nozzle. Let  $z = 0$  be the axial location of the upper grid plate, and suppose that a force  $F$  is applied laterally to the top spacer pad, which is a distance  $L$  from the upper grid plate. Since the applied load is zero except at  $x = L$ , Eq. 21.61 can be integrated to yield

$$M = az + b$$

where the constants  $a$  and  $b$  are determined by conditions applied at the free end. The applied force  $F$  is represented as a shear stress  $\tau$  on the end of the member. In addition, the moment  $M$  must vanish at the free end. The appropriate boundary conditions at  $z = L$  are

$$\begin{aligned} M &= 0 \\ \tau &= F \end{aligned}$$

Because the load  $p$  is zero along the length of the beam, Eq. 21.59 shows that  $\tau$  is constant along the length of the beam or that  $\tau = F$  for all  $z$ . Equation 21.60 requires that  $dM/dz = F$ , which specifies one of the integration constants as  $a = F$ . The second integration constant follows from the condition of zero moment at  $z = L$ ; the moment in the beam is thus

$$M = -F(L - z) \quad (21.67)$$

Since the assembly is cantilevered from the grid plate, we can write

$$v(0) = \left( \frac{dv}{dz} \right)_0 = 0 \quad (21.68)$$

Substituting Eq. 21.67 into 21.66 (neglecting the last two terms on the right-hand side), integrating, and using the boundary conditions at  $z = 0$  given by Eq. 21.68, we find the deflection

$$v = -\frac{Fz^2}{2EI} \left( L - \frac{z}{3} \right) \quad (21.69)$$

2. For a linear temperature distribution along the  $x$ -direction of the assembly wrapper, the temperature distribution through the beam is given by Eq. 21.63. In the absence of applied loads and void swelling, the deflection due to the nonuniform temperature across the assembly is obtained by solution of

$$\frac{d^2 v}{dz^2} = \frac{\alpha \Delta T}{2h} \quad (21.70)$$

The temperature difference across the flats,  $\Delta T$ , is a function of height  $z$  and is computed from thermal analysis of the fuel assembly. For the special (but unrealistic) case of  $\Delta T$  independent of  $z$ , integration of Eq. 21.70 with the boundary conditions of Eq. 21.68 yields

$$v = \frac{\alpha \Delta T}{4h} z^2 \quad (21.71)$$

3. For the transverse linear swelling profile, the deflection is obtained from

$$\frac{d^2 v}{dz^2} = \frac{\Delta \epsilon^s}{2h} \quad (21.72)$$

which requires specification of the axial variation of  $\Delta \epsilon^s$  and appropriate boundary conditions for integration.

In the absence of creep (either thermal or irradiation), unrestrained deflection of a fuel assembly with both temperature and swelling gradients is obtained by solving Eqs. 21.70 and 21.72 independently, each subject to Eq. 21.68. The total deflection profile is obtained by adding (superposing) the two component deflections. The result of such a calculation is shown in Fig. 21.24. The combined thermal and swelling deflections amount to 6 cm at the top of the fuel assembly. The thermal component of the bowing is recovered when the reactor is shut down for refueling, but the permanent camber due to swelling remains. This graph illustrates the potential difficulty of locating the handling heads of the assembly under sodium and the virtual certainty of mechanical interaction between assemblies in adjacent rows. Lateral forces, due either to the natural interaction of nearby assemblies or to the compacting action of the core restraint, are generally applied at the spacer-pad elevations. The deflections induced by these mechanical loads must be added to those arising from unrestrained bowing. The mechanical forces may be applied at more than one axial position, and the moment distribution is generally more complex than that given by Eq. 21.67. If the loads are due to interaction of adjacent assemblies at a single axial position, the force  $F$  in Eq. 21.67 is not known a priori but must be determined in the course of solving the deflection equation for all interacting assemblies (see problem 21.8 at the end of the chapter).

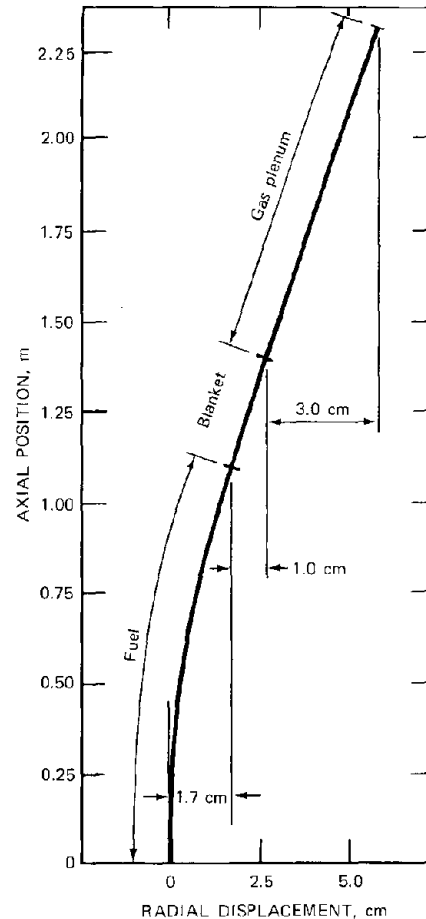


Fig. 21.24 Free bowing of a fuel assembly due to nonuniform thermal expansion and void swelling. (After Ref. 18.)

### 21.6.5 Effect of Irradiation Creep on Bowing

The major deficiency of the analysis just presented is the exclusion of creep, which acts to relieve the stresses established by the combined effects of the transverse temperature and swelling distributions and the mechanical interaction between assemblies. Because of the relatively low temperature of the duct walls ( $<650^\circ\text{C}$ ), thermal creep is not as important as irradiation creep. Irradiation creep is especially effective in the high-flux core region. To illustrate the effect of irradiation creep on bowing, we take the simple irradiation-creep expression (the steady-state creep component in Eq. 19.176)

$$\dot{\epsilon}^c = C\Phi\sigma \quad (21.73)$$

Relief of the bending stresses in the duct by irradiation creep is a form of stress relaxation. This phenomenon may be most clearly explained by considering a bar of solid loaded in tension in which creep takes place at a rate given by Eq. 21.73. Suppose the bar is subject to an initial tensile stress  $\sigma_0$  that causes an initial elastic strain equal to  $\sigma_0/E$ .

We now assume that the initial strain is held constant. The stress is reduced with time by creep of the material in a manner such that the total strain  $\sigma_0/E$  does not change. Thus the stress at any time during the test is given by

$$\frac{\sigma}{E} + \epsilon^c = \frac{\sigma_0}{E} \quad (21.74)$$

where  $\epsilon^c$  is the creep strain. Differentiating this equation with respect to time yields

$$\frac{1}{E} \frac{d\sigma}{dt} = -\dot{\epsilon}^c = -C\Phi\sigma \quad (21.75)$$

Integration gives the stress-relaxation formula for this simple case as

$$\sigma = \sigma_0 \exp(-C\Phi t) \quad (21.76)$$

The stress at constant strain is seen to decrease exponentially with time.

To introduce creep into the beam-deflection problem wherein applied forces, nonuniform thermal expansion, and nonuniform swelling are also present, we express the constitutive equation by

$$\epsilon_z = x \frac{d^2 v}{dz^2} = \frac{\sigma}{E} + \alpha T + \epsilon^s + \epsilon^c \quad (21.77)$$

which may be recognized as the constitutive equation for the metal (Eq. 21.9 for uniaxial tension or compression). The term  $\sigma/E$  on the right-hand side of Eq. 21.77 arises from the applied lateral load on the member. Multiplying Eq. 21.77 by  $bxdx$  and integrating from  $x = -h$  to  $x = h$  yields

$$I \frac{d^2 v}{dz^2} = \frac{M}{E} + b \int_{-h}^h (\alpha T + \epsilon^s) x dx + b \int_{-h}^h \epsilon^c x dx$$

where Eqs. 21.58 and 21.65 have been used. Assuming that the applied load creates a bending moment given by Eq. 21.67 and that the temperature and swelling gradients are constant (Eqs. 21.63 and 21.64), we find the above equation becomes

$$\frac{d^2 v}{dz^2} = -\frac{F(L-z)}{EI} + \frac{\alpha \Delta T}{2h} + \frac{\Delta \epsilon^s}{2h} + \frac{b}{I} \int_{-h}^h \epsilon^c x dx \quad (21.78)$$

According to Eq. 21.73, the creep strain is

$$\epsilon^c = C\Phi \int_0^t \sigma dt'$$

and the integral in Eq. 21.78 can be written as

$$\begin{aligned} \frac{b}{I} \int_{-h}^h \epsilon^c x dx &= \frac{bC\Phi}{I} \int_{-h}^h x dx \int_0^t \sigma dt' \\ &= \frac{C\Phi}{I} \int_0^t \left( b \int_{-h}^h x \sigma dx \right) dt' \end{aligned}$$

The second equality was obtained by interchanging the order of integration. Equation 21.58 shows that the quantity in parentheses is equal to the moment  $M$ , which is given by Eq. 21.67. Making the appropriate substitutions yields

$$\frac{b}{I} \int_{-h}^h \epsilon^c x dx = -\frac{C\Phi(L-z)}{I} \int_0^t F(t') dt'$$

and the deflection equation, Eq. 21.78, becomes

$$\frac{d^2 v}{dz^2} = -\frac{L-z}{EI} \left[ F(t) + C\Phi E \int_0^t F(t') dt' \right] + \frac{\alpha \Delta T}{2h} + \frac{\Delta \epsilon^s}{2h} \quad (21.79)$$

Because of creep,  $F$  is a function of time.

To illustrate the nature of the solution of Eq. 21.79, we take the simple case in which the boundary conditions are given by Eq. 21.68 and  $\Delta T$  and  $\Delta \epsilon^s$  are independent of  $z$ . Note that  $\Delta T$  is independent of time but that  $\Delta \epsilon^s$  contains the time dependence of the void-swelling law used. The quantity in the brackets of Eq. 21.79 is independent of  $z$ ; so the differential equation can be integrated analytically. The solution that satisfies Eq. 21.68 is

$$\begin{aligned} v(z,t) &= \frac{1}{2} \left( \frac{\alpha \Delta T}{2h} + \frac{\Delta \epsilon^s}{2h} \right) z^2 \\ &\quad - \frac{[F(t) + C\Phi E \int_0^t F(t') dt']}{2EI} \left( L - \frac{z}{3} \right) z^2 \end{aligned} \quad (21.80)$$

The nature of the mechanical loading of the assembly must be specified before the force  $F(t)$  can be determined. We suppose that the force  $F$  is that required to pin the top of the assembly in its original position so that

$$v(L) = 0 \quad (21.81)$$

Therefore the right-hand side of Eq. 21.80 is set equal to zero at  $z = L$ , and the following integral equation for  $F(t)$  results:

$$F(t) + C\Phi E \int_0^t F(t') dt' = \frac{3EI}{4hL} (\alpha \Delta T + \Delta \epsilon^s) \quad (21.82)$$

where the second term on the left-hand side represents the effects of creep. At  $t = 0$ , this term and the void-swelling contribution in the second term on the right-hand side both vanish, and the required restraining force is

$$F(0) = \frac{3EI}{4hL} \alpha \Delta T \quad (21.83)$$

To solve the integral equation for  $F(t)$ , we take the derivative of Eq. 21.82 with respect to time, noting that  $\alpha \Delta T$  is constant in time

$$\frac{dF}{dt} + C\Phi E F(t) = \frac{3EI}{4hL} \Delta \dot{\epsilon}^s \quad (21.84)$$

where  $\Delta \dot{\epsilon}^s$  is the difference in the swelling rates on either side of the wrapper tube. Solution of this first-order differential equation for  $F(t)$  leads to

$$F(t) = F(0) e^{-C\Phi E t} + \frac{3EI}{4hL} e^{-C\Phi E t} \int_0^t e^{C\Phi E t'} \Delta \dot{\epsilon}^s dt'$$

Or, using Eq. 21.83 for  $F(0)$  and integrating the last term by parts,

$$\begin{aligned} F(t) &= \frac{3EI}{4hL} \left( \alpha \Delta T e^{-C\Phi E t} + \Delta \epsilon^s \right) \\ &\quad - \frac{C\Phi E^2 I}{4hL} e^{-C\Phi E t} \int_0^t e^{C\Phi E t'} \Delta \epsilon^s dt' \end{aligned} \quad (21.85)$$

The exponential multiplying  $\alpha \Delta T$  in the first term on the right represents creep relaxation of the thermal stresses. The entire second term on the right results from creep relaxation of the stresses induced by nonuniform swelling across the duct.

The restraining force explicitly determined by Eq. 21.85 can be substituted into Eq. 21.80 to determine the complete time- and position-dependent deflection of the assembly. When the core restraint is removed and the power is shut off, the terms  $F(t)$  and  $\alpha \Delta T$  in the deflection equation vanish, and the unrestrained deflection is

$$v^*(z,t) = \frac{\Delta \epsilon^s}{4h} z^2 - \frac{C\Phi}{2I} \left( L - \frac{z}{3} \right) z^2 \int_0^t F(t') dt' \quad (21.86)$$

which includes the permanent set due to swelling (the first term on the right) and creep relaxation of the thermal and swelling strains (second term on the right). Note that creep reduces the extent of deflection in the unrestrained, cold core.

Figure 21.25 shows the results of deflection calculations using the CRASIB code.<sup>19</sup> The assembly deflection is forced to be zero at two upper axial locations that represent the action of core clamps at each of these elevations. Interaction between adjacent assemblies (except at the spacer pads) is not considered. Figure 21.25(a) (top) shows the thermal bowing of the restrained core. At shutdown all thermal bowing is removed. Deflection due to swelling is shown in Fig. 21.25(b). A permanent bow remains at shutdown and unclamping. The sum of the deflections in (a) and (b) yields those shown in Fig. 21.25(c). The top curve in (c) represents addition of the free bowing curve of Fig. 21.24 and the deflections due to mechanical loading at elevations shown by the arrows.

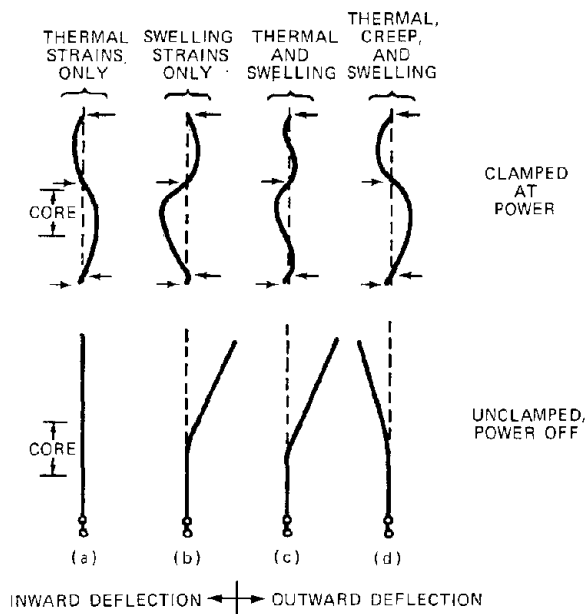


Fig. 21.25 Bowing of fuel assemblies with core clamps fixing the wrappers at the spacer-pad elevations. (After Ref. 18.)

Of particular note is the sharp curvature of the "clamped at power" duct in (c), which produces large bending stresses in the duct wall. These high-stress points are effectively relaxed by irradiation creep, as shown in Fig. 21.25(d). The dramatic effect of creep on bowing is shown in the "unclamped, power off" deflections represented in (c) and (d). When creep is neglected, the duct is predicted to bow outward, whereas inclusion of irradiation creep in the calculation produces a cold unrestrained inward bow. A similar reversal of bowing direction in the fueled region of the core appears when irradiation creep is included in the analysis. At-power bowing in the core is equivalent to core expansion (outward deflection) or compaction (inward deflection) and therefore is important in estimating the neutronic reactivity of the reactor. The magnitude of the deflections of assemblies is highly sensitive to the irradiation creep law used in the bowing analysis.

## 21.7 SOLUTIONS TO THE SWELLING PROBLEM

It is clear from the analyses presented in this chapter that the effects of void swelling in the fuel assemblies of an LMFBR are likely to be more difficult to cope with than the design of a sturdy fuel element. Huebotter et al.<sup>16</sup> have reviewed a number of methods of alleviating the metal-swelling problem. Wherever possible they have estimated the increased cost of electricity generated by LMFBRs attributable to the proposed modification. These estimates should be compared with the present  $\sim 15$  mills/kWh cost of nuclear power.

### 21.7.1 Mechanical

Two methods of accommodating swelling which form a part of the mechanical design of the core were discussed in the preceding section.

The interassembly gap must be large enough to allow for duct swelling without gross radial expansion of the core. The reduced breeding ratio and specific power that are unavoidable consequences of the lower fuel-to-metal ratio in the core will probably result in increased electric power costs as large as 0.1 mill/kWh. The larger reactor size will increase capital costs of LMFBRs, but the incremental cost has not been estimated.

Core restraint is needed to prevent extensive and possibly damaging mechanical interaction between assemblies. At least two in-core contacts, located at the spacer-pad elevations shown in Fig. 21.16, will be used. Accurate analytical prediction of the bowing of the fuel assemblies in a restrained-core design is imperative. If, as in the top drawing of Fig. 21.25(c), the deflections in the fueled zone are inward, the reactivity addition which this movement engenders must be accurately known for safety reasons. The prominent effect of irradiation creep on the magnitude and even the direction of in-core bowing implies that this form of creep needs to be thoroughly understood.

### 21.7.2 Neutronic

Inasmuch as swelling increases with fluence, an obvious method of reducing the swelling is to lower the maximum

burnup of the fuel. The burnup  $\beta$  and fluence  $\Phi t$  are related by Eq. 10.5:

$$\beta = q_0 \sigma_f \Phi t$$

where  $q_0$  is the initial enrichment of the fuel in plutonium and  $\sigma_f$  is the fission cross section. Metal swelling varies as  $(\Phi t)^n$  where  $n > 1$ ; so appreciable reduction in void formation can be achieved by discharging fuel at reduced burnup. However, if the burnup is decreased from the target value of 10% to 5%, the fuel-cycle cost is estimated to increase by about 0.3 mill/kWh. Much of this cost increase is incurred by the more frequent fuel replacement attendant on lower burnup, which increases the frequency of fabricating fuel elements.

Instead of reducing burnup, the fluence may be decreased by increasing the fuel enrichment  $q_0$ . The obvious disadvantage of this solution is the higher cost for fuel rich in plutonium.

### 21.7.3 Operational

Reduction of the sodium coolant temperature lowers the wrapper temperatures correspondingly and hence reduces swelling. However, the thermodynamic efficiency of the reactor plant is reduced because of the lower sodium outlet temperature. Lowering of the sodium outlet temperature from 600°C to 500°C increases the cost of electricity by about 0.3 mill/kWh, but this cost is offset by higher plant availability when the system is operated at a lower temperature level.

Periodic rotation of assemblies by 180° is a method of smoothing out nonuniform swelling that leads to bowing. Alternatively, assemblies may be removed from the core occasionally and straightened by annealing at temperatures high enough to eliminate voids from the metal (about 800°C). The former method reduces plant availability, and the latter requires a higher fuel inventory on site, both of which carry with them undesirable economic consequences.

### 21.7.4 Metallurgical

Maximum stainless-steel swelling occurs within the design temperature range of the sodium coolant in the core. Use of a refractory metal with a swelling temperature range above that of the sodium in the LMFBR would alleviate the swelling problem. Replacement of stainless steel in the entire core (or at least such components as the wrapper tubes in the high flux zones) by molybdenum, for example, would permit elimination of abnormally large interassembly gaps and obviate the need for core clamps. Even with these savings, the energy cost from LMFBRs with all-molybdenum cores would be ~0.1 mill/kWh higher than the cost of power from conventional designs. Molybdenum is more difficult to fabricate and has a higher absorption cross section for fast neutrons than does stainless steel.

The most desirable metallurgical solution to the swelling problem appears to be the modification of commercial alloys. We have seen that each of the various alloys has individual properties that are uniquely suited to fast reactor service; Nimonic PE16 is quite resistant to swelling because

its microstructure contains finely divided precipitate particles that act as recombination centers for vacancies and interstitials; titanium additions reduce the susceptibility of conventional stainless steels to helium embrittlement; types 321 and 347 stainless steels do not decarburize in sodium to the same extent as do types 316 and 304. If, by suitable metallurgical modification, a modest-cost alloy could be developed which would be more resistant to swelling than the present LMFBR core material (20% cold-worked type 316 stainless steel) yet retain the characteristic high-temperature strength and generally acceptable corrosion resistance to fuel and sodium of this alloy, the economic penalty of metal swelling would be substantially reduced.

The savings that could be realized by reducing swelling [i.e.,  $(\Delta V/V)_{\text{voids}}$ ] from 15% to 5% is estimated to be between 1 and 5 billion dollars for all LMFBRs constructed up to the year 2020. The incentive for seeking solutions to the void swelling problem is great.

## 21.8 NOMENCLATURE

- $b$  = beam thickness in the y-direction
- $C$  = constant in irradiation-creep formula
- $C_1, C_2$  = constants of integration of displacement differential equation
- $d$  = grain size
- $E$  = Young's modulus
- $E_d, E'_d$  = activation energies for creep
- $F$  = axial friction force at fuel-cladding interface; force on beam
- $h$  = beam thickness in the x-direction
- $I$  = moment of inertia of a beam
- $k$  = Boltzmann's constant
- $\bar{K}$  = average thermal conductivity of fuel
- $L$  = height of axial zone in fuel; length of beam
- $M$  = bending moment of beam
- $M_c, M_f$  = number of radial zones in cladding and fuel, respectively
- $N$  = number of axial zones; number of cracks in a region
- $p_o$  = coolant pressure
- $p_{fc}$  = fuel-cladding interfacial pressure
- $p_p$  = plenum pressure
- $\mathcal{P}$  = linear power
- $P_0$  = porosity of as-fabricated fuel
- $r$  = radial position in fuel element
- $r_{ai}$  = inner radial boundary of zone  $i$
- $r_{bi}$  = outer radial boundary of zone  $i$
- $r_o$  = radius of central void
- $R$  = fuel radius
- $R_c$  = radius of uncracked portion of fuel
- $t$  = time
- $t_c$  = cladding thickness
- $t_{gap}$  = gap thickness
- $t_{gap}^c$  = gap thickness in as-fabricated fuel element
- $T$  = temperature
- $T_c$  = temperature at root of crack in fuel; cladding temperature
- $T_0$  = fuel center-line temperature
- $T_s$  = fuel surface temperature

$u$  = radial displacement  
 $v$  = deflection of beam  
 $v^*$  = unrestrained deflection  
 $\Delta V/V$  = swelling  
 $x$  = direction along beam axis in the plane of bending  
 $y$  = direction along beam axis perpendicular to the plane of bending  
 $z$  = distance along the long axis of beam

#### Greek Letters

$\alpha$  = linear coefficient of thermal expansion  
 $\epsilon_i$  = strain component in principal direction  $i$   
 $\epsilon^*$  = equivalent strain  
 $\dot{\epsilon}$  = creep rate  
 $\theta$  = angle  
 $\mu_{sf}$  = coefficient of static friction  
 $\mu_{sl}$  = coefficient of sliding friction  
 $\nu$  = Poisson's ratio  
 $\rho$  = radius of curvature of a bent beam  
 $\sigma_i$  = stress component in principal direction  $i$   
 $\sigma^*$  = equivalent stress  
 $\sigma_0$  = initial stress  
 $\Phi$  = fast neutron flux

#### Subscripts and Superscripts

$c$  = creep/plastic deformation; cladding  
 $f$  = fuel  
 $h$  = hydrostatic  
 $i$  = radial position of zone in fuel pin  
 $j$  = axial position of zone in fuel pin  
 $r$  = radial  
 $s$  = swelling  
 $z$  = axial  
 $\theta$  = tangential  
 $'$  = values of fuel mechanical properties changed by cracking

## 21.9 REFERENCES

- V. Z. Jankus and R. W. Weeks, LIFE-I: A Fortran-IV Computer Code for the Prediction of Fast Reactor Fuel-Element Behavior, USAEC Report ANL-7736, Argonne National Laboratory, 1970.
- V. Z. Jankus and R. W. Weeks, *Nucl. Eng. Des.*, **18**: 83 (1972).
- R. Godesar, M. Guyette, and N. Hoppe, *Nucl. Appl. Technol.*, **9**: 205 (1970).
- M. Guyette, *Nucl. Eng. Des.*, **18**: 53 (1972).
- C. M. Friedrich and W. H. Guilinger, CYRGO-2: A Fortran-IV Computer Program for Stress Analysis of the Growth of Cylindrical Fuel Elements with Fission-Gas Bubbles, USAEC Report WAPD-TM-547, Bettis Atomic Power Laboratory, 1966.
- E. Duncombe, C. M. Friedrich, and W. H. Guilinger, *Nucl. Technol.*, **12**: 194 (1970).
- S. Oldberg, Jr., BEHAVE-2: Oxide Fuel Performance Code in Two Spatial Dimensions and Time, USAEC Report GEAP-13788, General Electric Company, 1972.
- F. J. Homan, W. J. Lackey, and C. M. Cox, FMODEL: A Fortran-IV Computer Code to Predict In-Reactors Behavior of LMFBR Fuel Pins, USAEC Report ORNL-4825, Oak Ridge National Laboratory, 1973.
- J. R. Matthews, *Advan. Nucl. Sci. Technol.*, **6**: 66 (1972).
- E. Duncombe and I. Goldberg, *Nucl. Appl. Technol.*, **9**: 47 (1970).
- J. T. A. Roberts and B. J. Wrona, *J. Amer. Ceram. Soc.*, **56**: 297 (1973).
- J. B. Ainscough and F. Rigby, *J. Nucl. Mater.*, **47**: 245 (1973).
- Aas Steiner, *Nucl. Eng. Des.*, **21**: 237 (1972).
- J. D. Stephen, R. E. Murata, S. Vaidyanathan, J. E. Turner, and W. G. Meinhardt, LIFE-II Fuel Performance Code: Evaluation of Predictions of Cladding Inelastic Strain, USAEC Report GEAP-13951-1, General Electric Company, 1973.
- D. P. Hines, S. Oldberg, and E. L. Zebroski, *Nucl. Appl. Technol.*, **9**: 338 (1970).
- P. R. Huebotter, T. R. Bump, W. T. Sha, D. T. Eggen, and P. J. Tulford, Design, Research, and Development Implications of Metal Swelling in Fast Reactors, USAEC Report ANL-7786, Argonne National Laboratory, 1971.
- P. R. Huebotter and T. R. Bump, Implications of Metal Swelling in Fast Reactor Design, in *Radiation-Induced Voids in Metals*, Albany, N. Y., June 9, 1971, AEC Symposium Series, No. 26 (CONF-710601), pp. 84-124, J. W. Corbett and L. C. Ianniello (Eds.), 1972.
- P. R. Huebotter, *Reactor Technol.*, **15**: 156 (1972).
- W. H. Sutherland and V. B. Watwood, Jr., Creep Analysis of Statistically Indeterminate Beams, USAEC Report BNWL-1362, Battelle-Northwest, 1970.
- W. H. Sutherland, *Nucl. Eng. Des.*, **11**: 269 (1970).
- D. A. Kurcera and D. Mohr, Report ANL/EBR-014, Argonne National Laboratory, 1970.

## 21.10 PROBLEMS

### 21.1

(a) Starting with Eqs. 21.23 to 21.25 and 21.27, derive the thermal-stress distribution in a solid fuel element of radius  $R$ . Neglect swelling, creep, and cracking. Assume the fuel stack is unrestrained axially. Express the tangential stress,  $\sigma_\theta$ , by Eq. 21.49.

(b) Derive the analog of Eq. 21.49 for fully restructured fuel with the same linear power. Assume that the initial density of the fuel was 85% and that the density after restructuring is 97% throughout the fuel.

(c) Apply the tangential-stress distributions determined in (a) and (b) to a fuel pin with a linear power of 500 W/cm. Plot the distributions and indicate the radial positions where the fracture stress is reached and where the brittle-ductile transition occurs.

### 21.2

(a) Using the same methods as in problem 21.1, show that the maximum tangential stress in a thin-walled cladding is given by

$$(\sigma_\theta)_{\max} = \frac{\alpha E}{2(1-\nu)} \Delta T_c$$

where  $\Delta T_c$  is the temperature drop across the cladding.

(b) Calculate the linear power  $\mathcal{P}$  at which  $(\sigma_\theta)_{\max}$  is equal to the yield stress of stainless steel. Use the following properties applicable to type 316 stainless steel at 1000°K:

$$\begin{aligned} E &= 1.4 \times 10^8 \text{ kN/m}^2 \\ \nu &= 0.32 \\ \alpha &= 1.2 \times 10^{-5} \text{ }^\circ\text{K}^{-1} \\ \sigma_Y &= 2.1 \times 10^5 \text{ kN/m}^2 \\ k &= 0.24 \text{ W cm}^{-1} \text{ }^\circ\text{C}^{-1} \\ R &= 0.32 \text{ cm} \\ t_c &= 0.038 \text{ cm} \end{aligned}$$

(c) What is the equivalent plenum pressure that would give the same maximum tangential stress as calculated in (b) if the cladding were isothermal? (See problem 18.6.)

(d) For a linear power one-half that determined in (b), calculate the expected lifetime of the fuel cladding. Use an appropriate plot of rupture time from Chap. 18 in the calculation.

(e) If the cladding is simultaneously subject to linear power  $\mathcal{P}$  and a plenum pressure  $p_p$ , what is the optimum cladding thickness based on thermoelasticity theory?

21.3 Consider a long thin-walled cylinder of inside radius  $R$  and wall thickness  $t_c$ . The tube is closed at both ends and contains a gas at pressure  $p_p$ . The system is isothermal. Assume that the tube deforms with a creep law

$$\dot{\epsilon}^* = E(\sigma^*)^n$$

Using the stress components appropriate to the thin-walled-tube situation, determine the tangential creep rate. Compare the diametral strain due to creep with that due to elastic deformation only.

21.4 At room temperature a fuel element has a fuel radius of  $R_0$  and a fuel-cladding gap of  $t_{\text{gap}}^0$ , which is much smaller than  $R_0$ . The coefficients of thermal expansion and compressibility of the fuel material are  $\alpha_f$  and  $\beta_f$ , respectively. (Note that the compressibility is the reciprocal of the bulk modulus.) The thermal-expansion coefficient of the cladding is  $\alpha_c$ . Assume  $\alpha_f > \alpha_c$ . The thermal expansion coefficients are here defined on a volume (not linear) basis. The fuel element is then heated externally so that the temperature rise is everywhere uniform (no temperature gradients).

(a) At what temperature  $T^*$  does the fuel-cladding gap close? At the same time that the fuel-cladding gap closes, the top and bottom of the fuel contact the ends of the cladding; thus, at  $T = T^*$  the fuel completely fills the cladding. As the temperature is increased above  $T^*$ , the fuel and cladding interact. The cladding may be assumed to be perfectly rigid and capable of thermal deformation only. The fuel is 100% dense but is completely plastic (i.e.,  $E = 0$  and  $\nu = 1/2$ ).†

(b) From thermodynamic considerations, what pressure is generated in the fuel element at  $T > T^*$ ?

21.5 A long solid cylindrical fuel element is heated uniformly (no temperature gradients) and contacts a totally

†Even though  $E = 0$  and  $\nu = 1/2$ , the bulk modulus, which is equal to  $E/3(1 - 2\nu)$ , is *not* zero.

rigid cladding at a temperature  $T^*$ . For  $T > T^*$  the expanding fuel is subjected to interfacial pressure  $p_{fc}$  from the cladding. The cladding is not permitted to expand either elastically or thermally; so the displacement of the outer radius of the fuel is always zero. Calculate the interfacial pressure for  $T > T^*$ , assuming that the fuel responds thermoelastically and in plane strain. Neglect creep. Consider two limiting cases:

1. Complete axial restraint of the fuel ( $\epsilon_z = 0$ ). Compare this result with that obtained in problem 21.4(b).

2. No axial restraint on the fuel. Assume that the fuel is free to slip axially relative to the rigid cladding.

21.6 A sphere of fuel (denoted by "1") of radius  $R$  is embedded in an infinite medium (denoted by "2"). The two materials are in contact with no stresses at temperature zero. In a neutron flux the fuel generates heat at a uniform volumetric rate  $H$ , and the fuel radius is  $R$ .

(a) What is the temperature distribution in each material? (Assume the fuel-cladding-gap resistance is negligible whether the gap is open or closed.)

(b) Derive the thermoelasticity equation for the radial stress distribution and solve the differential equations in both regions. Using appropriate boundary conditions, solve for the complete radial stress distribution. What is the criterion for the gap to be open? If the gap is closed, express the solution in terms of the interfacial pressure  $p_{fc}$ .

(c) For the closed-gap case, determine the interfacial pressure  $p_{fc}$ .

## 21.7

(a) Calculate the average axial temperature distribution in the cladding in a subassembly for the following conditions:

$$\begin{aligned} &\text{Sodium inlet temperature, } 470^\circ\text{C} \\ &\text{Sodium outlet temperature, } 650^\circ\text{C} \\ &\text{Sodium heat-transfer coefficient, } 12 \text{ W/cm}^{-2} \text{ }^\circ\text{C}^{-1} \\ &\text{Cladding thermal conductivity, } 0.22 \text{ W/cm}^{-1} \text{ }^\circ\text{C}^{-1} \\ &\text{Cladding thickness, } 0.038 \text{ cm} \\ &\text{Linear power, } 550 \cos(\pi z/2L), \text{ W/cm} \end{aligned}$$

(b) Calculate the axial fast flux profile assuming that the fuel contains 15% plutonium and has an average fission cross section of 2 barns.

(c) Calculate the void swelling profiles in the cladding using the empirical equation given in Chap. 19 for 20% cold-worked type 316 stainless steel.

21.8 Consider two adjacent fuel subassembly ducts with a clearance of  $\delta$  between them. The ducts have temperature gradients across them of  $\nabla T_1$  and  $\nabla T_2$ , respectively, where  $\nabla T_1 > \nabla T_2$ . They are supported at the grid plate in cantilever fashion [i.e.,  $v(0) = v'(0) = 0$ ]. The length of the ducts is  $L$ , and their moment of inertia is  $I$ .

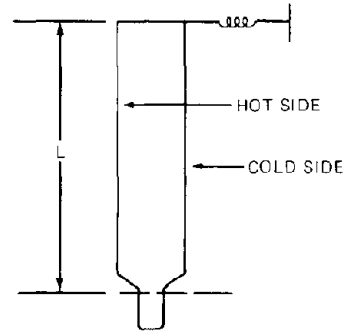
(a) What values of the difference  $(\nabla T_1 - \nabla T_2)$  cause the two ducts to just make contact at the top when the temperature gradients are applied?

(b) If the condition in (a) is exceeded, what are the deflections  $v_1(x)$  and  $v_2(x)$ ? What is the magnitude of the interaction force  $F$  between the two assemblies at the top? Neglect swelling and creep.

**21.9** A beam cantilevered at the bottom is restrained by a spring at height  $L$ . The restoring force exerted by the spring on the beam is proportional to the deflection at  $z = L$ . The spring constant is  $k$ . (See sketch.)

(a) Determine the deflection  $v(z,t)$  when the beam is subject to an axially uniform temperature difference  $\Delta T$  between opposite sides. Neglect swelling but include irradiation creep ( $\dot{\epsilon} = C\sigma\Phi$ ).

(b) What is the permanent deflection of the beam when the temperature difference, the neutron flux, and the spring loading are removed?



# Appendix—Elasticity Theory

## A.1 EQUILIBRIUM CONDITIONS

Figure A.1 shows an interior region of a solid bounded by the closed surface  $S$ . If the region contained in  $S$  is not accelerating, Newton's law of motion requires that the components of the forces on the region in each of the coordinate directions must be zero. If body forces such as gravity are neglected, the only forces acting on the region are those exerted on the surface  $S$  by the material outside  $S$ .

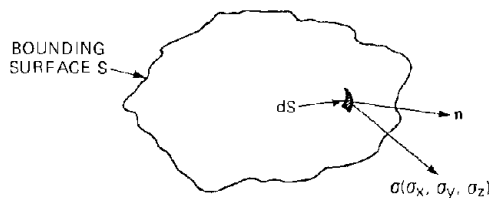


Fig. A.1 Region in a solid.

The forces on the surface  $S$  can be represented by a stress vector  $\sigma$ , which has components  $\sigma_x$ ,  $\sigma_y$ , and  $\sigma_z$  in the three directions of a Cartesian coordinate system. The magnitude and direction of the stress vector vary with position on the surface  $S$ . Figure A.1 shows a small element of area  $dS$  of the surface  $S$ . The outward normal to the surface at that point is denoted by  $n$ . The stress vector at the location of  $dS$  will in general have a component along the normal, which represents a normal stress, and components tangent to the surface element, which are shear stresses.

The  $x$ -component of the force on the element of surface  $dS$  is  $\sigma_x dS$ . The  $x$ -component of the net  $x$  force on the entire region enclosed by the surface  $S$  is the surface integral of  $\sigma_x dS$ . At equilibrium this integral and its counterparts in the  $y$ - and  $z$ -directions must be zero, or

$$\begin{aligned} \int_S \sigma_x dS &= 0 \\ \int_S \sigma_y dS &= 0 \\ \int_S \sigma_z dS &= 0 \end{aligned} \quad (\text{A.1})$$

To express  $\sigma_x$ ,  $\sigma_y$ , and  $\sigma_z$  in a more convenient manner, we consider the surface element  $dS$  in Fig. A.1 to be the oblique face of a very small tetrahedron, as shown in Fig. A.2. The three mutually perpendicular planes of the tetrahedron are each perpendicular to one of the coordinate axes. The components of  $\sigma$  can be expressed in terms of the unit normal  $n$  and the three stress vectors acting on the coordinate faces. The stress vectors on each coordinate plane are resolved into a normal stress component (e.g.,  $\sigma_{xx}$ ) and two shear components (e.g.,  $\sigma_{xy}$  and  $\sigma_{xz}$ ) that act tangentially to the coordinate plane.

The components of the stress vectors on the coordinate planes are written as  $\sigma_{ij}$ , where  $i$  refers to the coordinate plane in which the stress acts (e.g.,  $\sigma_{xx}$ ,  $\sigma_{xy}$ , and  $\sigma_{xz}$  all act on the plane perpendicular to the  $x$  axis) and  $j$  refers to the direction in which the stress component acts.

The area of each of the coordinate planes in Fig. A.2 is a projected area of the oblique face  $dS$ . The area over which  $\sigma_{xx}$ ,  $\sigma_{xy}$ , and  $\sigma_{xz}$  act is  $n \cdot i dS = n_x dS$ , where  $i$ ,  $j$ , and  $k$  are the unit vectors in the  $x$ ,  $y$ , and  $z$  directions, respectively. The direction cosines of the surface normal are  $n_x = n \cdot i$ ,  $n_y = n \cdot j$ , and  $n_z = n \cdot k$ .

The tetrahedron of Fig. A.2 is in mechanical equilibrium owing to the forces on its four faces, or the net force

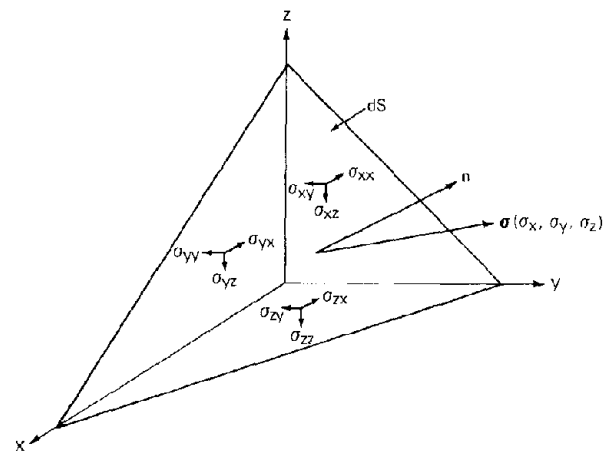


Fig. A.2 Diagram for relating surface forces to nine components of stress tensor.

in each coordinate direction is zero. According to the sign convention,\* force components on the coordinate faces are positive if pointing toward the negative coordinate axis under consideration. The x-direction force balance is

$$\sigma_x dS - \sigma_{xx} n_x dS - \sigma_{yx} n_y dS - \sigma_{zx} n_z dS = 0$$

If  $dS$  is canceled and the last three terms are written as the scalar product of  $\mathbf{n}$  and the vector whose components are  $\sigma_{xx}$ ,  $\sigma_{yx}$ , and  $\sigma_{zx}$ , the preceding formula becomes

$$\sigma_x = \mathbf{n} \cdot (\sigma_{xx}\mathbf{i} + \sigma_{yx}\mathbf{j} + \sigma_{zx}\mathbf{k})$$

Similarly,

$$\begin{aligned} \sigma_y &= \mathbf{n} \cdot (\sigma_{xy}\mathbf{i} + \sigma_{yy}\mathbf{j} + \sigma_{zy}\mathbf{k}) \\ \sigma_z &= \mathbf{n} \cdot (\sigma_{xz}\mathbf{i} + \sigma_{yz}\mathbf{j} + \sigma_{zz}\mathbf{k}) \end{aligned} \quad (\text{A.2})$$

Equation A.2 relates the components of the stress vector  $\sigma$  to the unit normal describing the orientation of the surface and the nine components of the stresses acting on the three coordinate planes, usually denoted collectively as the *stress tensor*:

$$\sigma_{ij} = \begin{pmatrix} \sigma_{xx} & \sigma_{xy} & \sigma_{xz} \\ \sigma_{yx} & \sigma_{yy} & \sigma_{yz} \\ \sigma_{zx} & \sigma_{zy} & \sigma_{zz} \end{pmatrix} \quad (\text{A.3})$$

An important relation between the off-diagonal elements of the tensor  $\sigma_{ij}$  can be obtained by applying the condition that the angular acceleration of any element of volume is zero. This restriction leads to the relations

$$\begin{aligned} \sigma_{xy} &= \sigma_{yx} \\ \sigma_{xz} &= \sigma_{zx} \\ \sigma_{zy} &= \sigma_{yz} \end{aligned} \quad (\text{A.4})$$

Or, of the nine components of the stress tensor of Eq. A.3, only six are independent; the tensor is symmetric.

\*The signs of the stress component  $\sigma_{ij}$  are determined by the following convention: consider a volume element bounded by planes perpendicular to the coordinate axes. If the outward normal of one of these plane surfaces is in the direction of a positive coordinate axis, the  $\sigma_{ij}$  are positive if the stress acts in the positive  $j$  direction. Thus a normal stress, such as  $\sigma_{xx}$ , is positive if in tension. Pressures that act inward in a volume element (compression) are considered as negative stresses. Conversely, if the outward normal of the plane is in the direction of a negative coordinate axis, the  $\sigma_{ij}$  are positive when the stress acts in the negative  $j$  direction. Again, the normal components are positive if they place the volume element in tension. The three coordinate planes of Fig. A.2 are surfaces with negative normals, and the  $\sigma_{ij}$  are positive as drawn on the figure. In a force balance on the element of Fig. A.2, therefore, the contribution to the total force in the positive x-direction due to the coordinate plane perpendicular to the x axis is  $-\sigma_{xx}$  times the area of the plane.

Substitution of Eq. A.2 into Eq. A.1 yields equilibrium relations in terms of the stress tensor  $\sigma_{ij}$ . For the x-direction, the result is

$$\int_S \mathbf{n} \cdot (\sigma_{xx}\mathbf{i} + \sigma_{yx}\mathbf{j} + \sigma_{zx}\mathbf{k}) dS = 0$$

Applying the divergence theorem\* to the surface integral in this equation yields the final form of the equilibrium relation:

$$\frac{\partial \sigma_{xx}}{\partial x} + \frac{\partial \sigma_{yx}}{\partial y} + \frac{\partial \sigma_{zx}}{\partial z} = 0 \quad (\text{A.5})$$

Similarly, for the y- and z-directions, the equilibrium conditions are

$$\frac{\partial \sigma_{xy}}{\partial x} + \frac{\partial \sigma_{yy}}{\partial y} + \frac{\partial \sigma_{zy}}{\partial z} = 0 \quad (\text{A.6})$$

$$\frac{\partial \sigma_{xz}}{\partial x} + \frac{\partial \sigma_{yz}}{\partial y} + \frac{\partial \sigma_{zz}}{\partial z} = 0 \quad (\text{A.7})$$

## A.2 DISPLACEMENTS

A body subjected to stress will become distorted or strained as a result. The state of strain is described by the displacement vector, which connects a point  $(x,y,z)$  in the unstrained body with the location to which this point has moved  $(x+u, y+v, z+w)$  in the strained condition. The lengths  $u$ ,  $v$ , and  $w$  are the components of the displacement vector; in general, they are functions of position in the solid.

The stress applied to the body is not related to the absolute values of the displacement components. The fact that a body is made to undergo translation or rotation because of an applied force, for example, has nothing to do with the material properties of the solid. The property that is uniquely determined by the applied stress is the relative displacement of points in the solid. The solid-line rectangle in Fig. A.3 represents a plane rectangular element of dimensions  $\delta x$  and  $\delta y$  in an unstressed body (for simplicity, only two dimensions are considered). After stress has been applied, the rectangle is distorted into the dashed four-sided figure. The arrows connecting the corners of the unstrained and strained figures are the displacement vectors for these four points. The displacement vector of the point  $(x,y)$  in the lower left-hand corner has components  $u$  and  $v$ . Since the relative motion of adjacent points is small, the displacement components at other locations can be approximated by Taylor series expansions about the values at the point  $(x,y)$ . Thus, the displacement components of the

\*For a vector  $\mathbf{F}$  defined over a region of volume  $V$  and surface  $S$ , the divergence theorem is

$$\int_S \mathbf{n} \cdot \mathbf{F} dS = \int_V \nabla \cdot \mathbf{F} dV$$

where, for Cartesian coordinates,

$$\nabla \cdot \mathbf{F} = \frac{\partial F_x}{\partial x} + \frac{\partial F_y}{\partial y} + \frac{\partial F_z}{\partial z}$$

lower right-hand corner  $(x + \delta x, y)$  are  $u + (\partial u/\partial x) \delta x$  and  $v + (\partial v/\partial x) \delta x$ .

The aspect of the displacement field which is directly related to the applied stress and the material properties is the collection of derivatives of the displacement,  $\partial u/\partial x$ ,  $\partial v/\partial x, \dots$ , not the displacements  $u$  and  $v$  proper. In three dimensions there are nine spatial derivatives of the displacement-vector components which can be expressed as the strain tensor:

$$S_{ij} = \begin{pmatrix} \frac{\partial u}{\partial x} & \frac{\partial u}{\partial y} & \frac{\partial u}{\partial z} \\ \frac{\partial v}{\partial x} & \frac{\partial v}{\partial y} & \frac{\partial v}{\partial z} \\ \frac{\partial w}{\partial x} & \frac{\partial w}{\partial y} & \frac{\partial w}{\partial z} \end{pmatrix} \quad (A.8)$$

The response of the solid to an applied force is governed by the law that relates the stress tensor of Eq. A.3 and the strain tensor of Eq. A.8. However, the stress tensor contains only six independent components, whereas the strain tensor of Eq. A.8 contains nine independent quantities. Thus, the symmetric stress tensor cannot be directly related to the strain components as given in Eq. A.8. To circumvent this difficulty, we can split the strain tensor  $S_{ij}$  into two parts:

$$S_{ij} = \epsilon_{ij} + \omega_{ij} \quad (A.9)$$

where  $\epsilon_{ij}$  is the symmetric deformation tensor:

$$\epsilon_{ij} = \frac{1}{2} \begin{bmatrix} \left( \frac{\partial u}{\partial x} + \frac{\partial u}{\partial x} \right) & \left( \frac{\partial u}{\partial y} + \frac{\partial v}{\partial x} \right) & \left( \frac{\partial u}{\partial z} + \frac{\partial w}{\partial x} \right) \\ \left( \frac{\partial v}{\partial x} + \frac{\partial u}{\partial y} \right) & \left( \frac{\partial v}{\partial y} + \frac{\partial v}{\partial y} \right) & \left( \frac{\partial v}{\partial z} + \frac{\partial w}{\partial y} \right) \\ \left( \frac{\partial w}{\partial x} + \frac{\partial u}{\partial z} \right) & \left( \frac{\partial w}{\partial y} + \frac{\partial v}{\partial z} \right) & \left( \frac{\partial w}{\partial z} + \frac{\partial w}{\partial z} \right) \end{bmatrix} \quad (A.10)$$

and  $\omega_{ij}$  is the skew-symmetric rotation tensor:

$$\omega_{ij} = \frac{1}{2} \begin{bmatrix} 0 & \left( \frac{\partial u}{\partial y} - \frac{\partial v}{\partial x} \right) & \left( \frac{\partial u}{\partial z} - \frac{\partial w}{\partial x} \right) \\ \left( \frac{\partial v}{\partial x} - \frac{\partial u}{\partial y} \right) & 0 & \left( \frac{\partial v}{\partial z} - \frac{\partial w}{\partial y} \right) \\ \left( \frac{\partial w}{\partial x} - \frac{\partial u}{\partial z} \right) & \left( \frac{\partial w}{\partial y} - \frac{\partial v}{\partial z} \right) & 0 \end{bmatrix} \quad (A.11)$$

The physical meaning of the components of  $\epsilon_{ij}$  and  $\omega_{ij}$  in terms of the type of motion experienced by the body can be seen from Fig. A.3.

Consider the bottom edge of the rectangle. Originally its length was  $\delta x$ ; under stress the corner  $(x, y)$  moves a distance  $u$  to the right, and the corner  $(x + \delta x, y)$  moves a distance  $u + (\partial u/\partial x) \delta x$  to the right. The strain is a fractional change in length, or

$$\frac{\text{Elongation in the } x\text{-direction}}{\text{Unit length}} = \frac{u + (\partial u/\partial x) \delta x - u}{\delta x} = \frac{\partial u}{\partial x}$$

This is the  $\epsilon_{xx}$  component of the deformation tensor. Thus, the diagonal elements of Eq. A.10 represent the *elongations* or *normal strains* in the three coordinate directions.

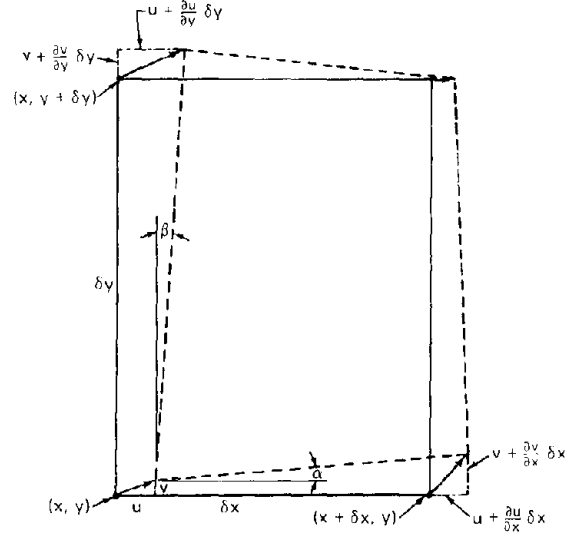


Fig. A.3 Deformation of a region of a solid (two-dimensional).

The angles  $\alpha$  and  $\beta$  in Fig. A.3 represent the departure of the four-sided figure from its original rectangular shape. Since the strains are small, these angles are given by

$$\alpha \approx \tan \alpha = \frac{v + (\partial v/\partial x) \delta x - v}{\delta x} = \frac{\partial v}{\partial x}$$

and

$$\beta \approx \tan \beta = \frac{u + (\partial u/\partial y) \delta y - u}{\delta y} = \frac{\partial u}{\partial y}$$

The sum  $\alpha + \beta$  represents the departure of the original angle from  $90^\circ$ , which is denoted as *shear strain*,

$$\text{Departure from } 90^\circ \text{ angle} = \alpha + \beta = \left( \frac{\partial u}{\partial y} + \frac{\partial v}{\partial x} \right)$$

This sum is twice the  $\epsilon_{xy}$  component of the deformation tensor. The other off-diagonal elements in Eq. A.10 represent the shear strains in the solid.

The angle of rotation of the plane figure in Fig. A.3 is the average of the angles  $\alpha$  and  $\beta$ , taking positive rotation in the clockwise sense, or

$$\begin{aligned} \text{Rotation as a solid body} &= \frac{1}{2} (\beta - \alpha) \\ &= \frac{1}{2} \left( \frac{\partial u}{\partial y} - \frac{\partial v}{\partial x} \right) \end{aligned}$$

Thus the tensor  $\omega_{ij}$  of Eq. A.11 represents pure rotation of the body.

Only the deformation tensor  $\epsilon_{ij}$  is determined by the stress tensor and material properties. Hooke's law is an example of such a relation for elastic deformations.

### A.3 COMPATIBILITY RELATIONS

Additional relationships between the deformation components  $\epsilon_{ij}$  reflect the requirement that the medium be a continuum, or that the solid has not been cracked and that there are no discontinuities in the displacements. Mathematically, these *compatibility conditions* require that certain rather obvious relations among the components of the deformation tensor exist. For example, if  $\epsilon_{xx}$  is differentiated twice with respect to  $y$ , the result is  $(\partial^3 u)/(\partial x \partial y^2)$ . Similarly, if  $\epsilon_{yy}$  is differentiated twice with respect to  $x$ , we obtain  $(\partial^3 v)/(\partial y \partial x^2)$ . Now if  $\epsilon_{xy}$  is differentiated with respect to  $x$  and  $y$ , the result is  $(1/2)[(\partial^3 u)/(\partial x \partial y^2) + (\partial^3 v)/(\partial x^2 \partial y)]$ , which is one-half the sum of  $\partial^2 \epsilon_{xx}/\partial y^2$  and  $\partial^2 \epsilon_{yy}/\partial x^2$ . In all, there are six compatibility equations relating the various components of  $\epsilon_{ij}$ . In Cartesian coordinates they are

$$\begin{aligned}\frac{\partial^2 \epsilon_{xy}}{\partial x \partial y} &= \frac{1}{2} \left( \frac{\partial^2 \epsilon_{xx}}{\partial y^2} + \frac{\partial^2 \epsilon_{yy}}{\partial x^2} \right) \\ \frac{\partial^2 \epsilon_{xx}}{\partial y \partial z} &= \frac{\partial}{\partial x} \left( -\frac{\partial \epsilon_{yz}}{\partial x} + \frac{\partial \epsilon_{xz}}{\partial y} + \frac{\partial \epsilon_{xy}}{\partial z} \right) \\ \frac{\partial^2 \epsilon_{xz}}{\partial x \partial z} &= \frac{1}{2} \left( \frac{\partial^2 \epsilon_{xx}}{\partial z^2} + \frac{\partial^2 \epsilon_{zz}}{\partial x^2} \right) \\ \frac{\partial^2 \epsilon_{yy}}{\partial x \partial z} &= \frac{\partial}{\partial y} \left( -\frac{\partial \epsilon_{xz}}{\partial y} + \frac{\partial \epsilon_{xy}}{\partial z} + \frac{\partial \epsilon_{yz}}{\partial x} \right) \\ \frac{\partial^2 \epsilon_{yz}}{\partial y \partial z} &= \frac{1}{2} \left( \frac{\partial^2 \epsilon_{yy}}{\partial z^2} + \frac{\partial^2 \epsilon_{zz}}{\partial y^2} \right) \\ \frac{\partial^2 \epsilon_{zz}}{\partial x \partial y} &= \frac{\partial}{\partial z} \left( -\frac{\partial \epsilon_{xy}}{\partial z} + \frac{\partial \epsilon_{yz}}{\partial x} + \frac{\partial \epsilon_{xz}}{\partial y} \right)\end{aligned}\quad (\text{A.12})$$

### A.4 STRESS-STRAIN RELATIONS

In the absence of plastic deformation, creep, or temperature changes, the stress-strain relation is given by the generalized form of Hooke's law. For the elastic solid, the six components of the stress tensor are related to the six components of the deformation tensor by the linear equations:

$$\begin{aligned}\sigma_{xx} &= c_{11} \epsilon_{xx} + c_{12} \epsilon_{yy} + c_{13} \epsilon_{zz} + c_{14} \epsilon_{yz} \\ &\quad + c_{15} \epsilon_{zx} + c_{16} \epsilon_{xy} \\ \sigma_{yy} &= c_{21} \epsilon_{xx} + c_{22} \epsilon_{yy} + c_{23} \epsilon_{zz} + c_{24} \epsilon_{yz} \\ &\quad + c_{25} \epsilon_{zx} + c_{26} \epsilon_{xy}\end{aligned}$$

$$\begin{aligned}\sigma_{zz} &= c_{31} \epsilon_{xx} + c_{32} \epsilon_{yy} + c_{33} \epsilon_{zz} + c_{34} \epsilon_{yz} \\ &\quad + c_{35} \epsilon_{zx} + c_{36} \epsilon_{xy} \\ \sigma_{yz} &= c_{41} \epsilon_{xx} + c_{42} \epsilon_{yy} + c_{43} \epsilon_{zz} + c_{44} \epsilon_{yz} \\ &\quad + c_{45} \epsilon_{zx} + c_{46} \epsilon_{xy} \\ \sigma_{zx} &= c_{51} \epsilon_{xx} + c_{52} \epsilon_{yy} + c_{53} \epsilon_{zz} + c_{54} \epsilon_{yz} \\ &\quad + c_{55} \epsilon_{zx} + c_{56} \epsilon_{xy} \\ \sigma_{xy} &= c_{61} \epsilon_{xx} + c_{62} \epsilon_{yy} + c_{63} \epsilon_{zz} + c_{64} \epsilon_{yz} \\ &\quad + c_{65} \epsilon_{zx} + c_{66} \epsilon_{xy}\end{aligned}\quad (\text{A.13})$$

The  $c_{ij}$  values are the *elastic moduli* of the medium. Not all 36 of the coefficients in Eq. A.13 are independent. Because the tensors  $\sigma_{ij}$  and  $\epsilon_{ij}$  are symmetric,  $c_{ij} = c_{ji}$ , which reduces the number of elastic constants to 21. This number is reduced still further according to the symmetry of the crystal structure of the solid; the greater the symmetry, the fewer the constants. For crystals of the cubic system, there are only three elastic constants. Finally, for materials that are macroscopically isotropic (either because the substance is noncrystalline or because the material is in polycrystalline form), only two constants remain. These two elastic constants are called *Lamé coefficients*  $\lambda$  and  $\mu$ . They determine the stress-strain relation by

$$\sigma_{ii} = 2\mu \epsilon_{ii} + \lambda \delta \quad (\text{A.14})$$

and

$$\sigma_{ij} = 2\mu \epsilon_{ij} \quad (i \neq j) \quad (\text{A.15})$$

Here  $\delta$  is the volume dilatation, or the fractional change in volume:

$$\delta = \epsilon_{xx} + \epsilon_{yy} + \epsilon_{zz} \quad (\text{A.16})$$

The elastic constants are usually expressed in terms of Young's modulus  $E$ , the shear modulus  $G$ , and Poisson's ratio  $\nu$ , instead of the Lamé coefficients. The relations between the conventional elastic moduli and the Lamé coefficients are

$$E = \frac{\mu(3\lambda + 2\mu)}{\lambda + \mu} \quad (\text{A.17})$$

$$G = \mu \quad (\text{A.18})$$

$$\nu = \frac{\lambda}{2(\lambda + \mu)} \quad (\text{A.19})$$

The values  $E$ ,  $G$ , and  $\nu$  are not independent but are related by

$$G = \frac{E}{2(1 + \nu)} \quad (\text{A.20})$$

Using Eqs. A.17 to A.19 in Eqs. A.14 and A.15 and solving for the strains yields

$$\begin{aligned}\epsilon_{xx} &= \frac{1}{E} [\sigma_{xx} - \nu(\sigma_{yy} + \sigma_{zz})] \\ \epsilon_{yy} &= \frac{1}{E} [\sigma_{yy} - \nu(\sigma_{xx} + \sigma_{zz})] \\ \epsilon_{zz} &= \frac{1}{E} [\sigma_{zz} - \nu(\sigma_{xx} + \sigma_{yy})]\end{aligned}\quad (\text{A.21})$$

$$\epsilon_{xy} = \frac{1}{2G} \sigma_{xy} \quad \epsilon_{xz} = \frac{1}{2G} \sigma_{xz} \quad \epsilon_{yz} = \frac{1}{2G} \sigma_{yz} \quad (\text{A.22})$$

In addition to the elongations caused by applied stresses, a change in temperature produces normal strains (but not shear strains) given by

$$(\epsilon_{ii})_{\text{thermal}} = \alpha \Delta T \quad (\text{A.23})$$

where  $\alpha$  is the coefficient of linear thermal expansion and  $\Delta T$  is the temperature rise with respect to a reference temperature. The thermal component given by Eq. A.23 is added to each of the normal strains given by Eq. A.21 to produce the total strain.

Effects other than applied stress or temperature change can contribute to the strain. In analyses of the performance of reactor fuel elements, for example, the elongations of Eq. A.21 are supplemented by contributions due to creep and fission-product swelling. Like the thermal component of the strain, these effects are accommodated into the stress-strain relations by adding appropriate terms to the right-hand sides of Eq. A.21. Relations such as Eqs. A.21 and A.22 to which other sources of displacement have been appended are known as *constitutive relations*.

## A.5 ELASTIC STRAIN ENERGY

The strain of a solid as a result of applied stresses means that work has been done on the material. This work is stored as internal energy, or *elastic strain energy*, in the medium.

The strain energy can best be illustrated by considering the one-dimensional analog of the solid, namely, the elastic string. If sufficient force is applied to a string to extend its length from  $x_0$  to  $x_f$ , the work done in the process is

$$W = k \int_{x_0}^{x_f} (x - x_0) dx = \frac{1}{2} k (x_f - x_0)^2$$

Here  $k$  is the Hooke's law constant of the string. The force on the string in the final state is

$$F = k(x_f - x_0)$$

The work done can also be written as

$$W = \frac{1}{2} F(x_f - x_0)$$

The elastic energy  $E_{el}$  stored in a unit length of string is  $W/x_0$ . The strain  $\epsilon$  of the string is  $(x_f - x_0)/x_0$ . Dividing the preceding formula by the initial length yields

$$E_{el} = \frac{1}{2} F\epsilon \quad (\text{A.24})$$

In a three-dimensional elastic medium, the single force  $F$  is replaced by the components of the stress tensor, and the strain is represented by the deformation tensor. The strain energy per unit volume is

$$\begin{aligned}E_{el} &= \frac{1}{2} (\sigma_{xx}\epsilon_{xx} + \sigma_{yy}\epsilon_{yy} + \sigma_{zz}\epsilon_{zz} + 2\sigma_{xy}\epsilon_{xy} \\ &\quad + 2\sigma_{xz}\epsilon_{xz} + 2\sigma_{yz}\epsilon_{yz})\end{aligned}\quad (\text{A.25})$$

The elastic-energy density can also be written in terms of the stresses alone by substituting Eq. A.21 into Eq. A.25:

$$\begin{aligned}E_{el} &= \frac{1}{2E} (\sigma_{xx}^2 + \sigma_{yy}^2 + \sigma_{zz}^2) - \frac{\nu}{E} (\sigma_{xx}\sigma_{yy} + \sigma_{xx}\sigma_{zz} \\ &\quad + \sigma_{yy}\sigma_{zz}) + \frac{1}{2G} (\sigma_{xy}^2 + \sigma_{xz}^2 + \sigma_{yz}^2)\end{aligned}\quad (\text{A.26})$$

For the case of a simple hydrostatic stress system ( $\sigma_{xx} = \sigma_{yy} = \sigma_{zz} = \sigma$  and  $\sigma_{xy} = \sigma_{xz} = \sigma_{yz} = 0$ ), Eq. A.26 reduces to

$$E_{el} = \frac{\sigma^2}{2K} \quad (\text{A.27})$$

where

$$K = \frac{E}{3(1 - 2\nu)} \quad (\text{A.28})$$

is the bulk modulus, which is the reciprocal of the coefficient of compressibility (see problem 1.5, Chap. 1).

## A.6 CYLINDRICAL COORDINATES

The behavior of a solid under applied stresses is determined by simultaneous application of the equilibrium conditions (Sec. A.1), the compatibility conditions (Sec. A.3), and a stress-strain relation (Sec. A.4). Strains and displacements are related by the components of the deformation tensor (Sec. A.2).

The analysis up to this point has been conducted in terms of Cartesian coordinates. However, many important problems (e.g., the stresses around a dislocation or in a reactor fuel element) are more conveniently treated in cylindrical coordinates. For this purpose the four relations listed in the preceding paragraph must be transformed from rectangular to cylindrical coordinates.

Transformation of the stress-strain relation requires only the replacement of  $x$ ,  $y$ , and  $z$  in Eqs. A.21 and A.22 by the radial, azimuthal, and axial coordinates  $r$ ,  $\theta$ , and  $z$ .

Since the number of relevant strain components is considerably reduced when simple shapes are treated, the compatibility relations for cylindrical coordinates are best determined from the set of strain components peculiar to the problem at hand. The method of generating compatibility relations for cylindrical coordinates is analogous to that used in Sec. A.3 for rectangular coordinates.

Transformation of the equilibrium relations and the components of the deformation tensor is straightforward but tedious. The results are

Equilibrium conditions:

$$\frac{1}{r} \frac{\partial}{\partial r} (r\sigma_{rr}) + \frac{1}{r} \frac{\partial \sigma_{r\theta}}{\partial \theta} - \frac{1}{r} \sigma_{\theta\theta} + \frac{\partial \sigma_{rz}}{\partial z} = 0 \quad (\text{A.29})$$

$$\frac{1}{r} \frac{\partial \sigma_{\theta\theta}}{\partial \theta} + \frac{\partial \sigma_{r\theta}}{\partial r} + \frac{2}{r} \sigma_{r\theta} + \frac{\partial \sigma_{\theta z}}{\partial z} = 0 \quad (\text{A.30})$$

$$\frac{1}{r} \frac{\partial}{\partial r} (r\sigma_{rz}) + \frac{1}{r} \frac{\partial \sigma_{\theta z}}{\partial \theta} + \frac{\partial \sigma_{zz}}{\partial z} = 0 \quad (\text{A.31})$$

Components of the deformation tensor:

$$\epsilon_{rr} = \frac{\partial u_r}{\partial r} \quad \epsilon_{\theta\theta} = \frac{u_r}{r} + \frac{1}{r} \frac{\partial u_\theta}{\partial \theta} \quad \epsilon_{zz} = \frac{\partial u_z}{\partial z} \quad (\text{A.32})$$

$$\epsilon_{r\theta} = \epsilon_{\theta r} = \frac{1}{2} \left( \frac{1}{r} \frac{\partial u_r}{\partial \theta} + \frac{\partial u_\theta}{\partial r} - \frac{u_\theta}{r} \right)$$

$$\epsilon_{rz} = \epsilon_{zr} = \frac{1}{2} \left( \frac{\partial u_r}{\partial z} + \frac{\partial u_z}{\partial r} \right) \quad (\text{A.33})$$

$$\epsilon_{z\theta} = \epsilon_{\theta z} = \frac{1}{2} \left( \frac{\partial u_\theta}{\partial z} + \frac{1}{r} \frac{\partial u_z}{\partial \theta} \right)$$

Stress components and displacements in cylindrical coordinates are shown in Fig. A.4. The  $\theta$ -direction is orthogonal to the radial and axial directions.

## A.7 NOMENCLATURE

- $c_{ij}$  = coefficients of generalized Hooke's law (elastic moduli)
- $E$  = Young's modulus
- $E_{el}$  = elastic strain energy per unit volume
- $F$  = force
- $G$  = shear modulus
- $i, j, k$  = unit vectors
- $K$  = bulk modulus
- $n$  = outward normal to surface
- $r, \theta, z$  = cylindrical coordinates

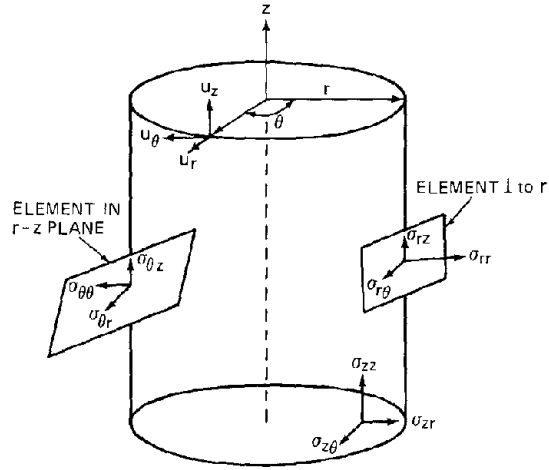


Fig. A.4 Stress components and displacements in the cylindrical coordinate system.

- $S_{ij}$  = strain tensor
- $T$  = temperature
- $u, v, w$  = components of displacement vector
- $W$  = work
- $x, y, z$  = Cartesian coordinates

### Greek Letters

- $\alpha$  = coefficient of linear thermal expansion
- $\delta$  = volume dilation
- $\epsilon_{ij}$  = symmetric deformation tensor (strain components)
- $\lambda, \mu$  = Lamé constants for an isotropic solid
- $\nu$  = Poisson's ratio
- $\sigma_{ij}$  = stress tensor (stress components)
- $\omega_{ij}$  = skew-symmetric rotation tensor

## A.8 ADDITIONAL READING

1. J. Weertman and J. R. Weertman, *Elementary Dislocation Theory*, Chap. 2, The Macmillan Company, New York, 1964.
2. Z. Zudans, T. C. Yen, and W. H. Steigelmann, *Thermal Stress Techniques in the Nuclear Industry*, Chap. 3, American Elsevier Publishing Company, Inc., New York, 1965.

# Index

- Absolute-rate theory of diffusion, 75-77
- Actinide redistribution  
 effect on temperature distribution, 143  
 in mixed-oxide fuel, 166-169
- Activation energy, of creep, 98  
 of diffusion, 72, 76-77, 81  
 of interstitial diffusion in a metal, 483  
 of plutonium diffusion in oxide fuels, 166  
 of surface diffusion, 79, 236
- Activity of carbon  
 in sodium, 542, 544  
 in steel, 544, 547, 551, 564-565
- Activity of molybdenum in metallic inclusions and in fuel, 182
- Activity of oxygen in sodium, 526, 539
- Activity coefficient of carbon in steel, 545, 547
- Alkaline earth oxide phase, 176, 178, 180, 185, 194, 197, 272
- Anion, 29, 146
- Annealing  
 of depleted zones, 435-437  
 of displacement spikes, 406-407  
 effect on microstructure of polycrystals, 96  
 of fuel assemblies, 593  
 postirradiation, 213-214, 233, 243, 287-288, 300-301, 307-311  
 of traps in  $UO_2$ , 311-312  
 of vacancies, 69
- Arrival-rate ratio, 474, 515
- Atomic disorder, 62
- Austenitic steel, 418-419, 545, 550
- Axial ratchetting, 582-583
- AXICRP code, 587
- Bambooning, 583
- Barium, 176, 180, 197
- Barriers  
 to diffusion, 72, 75  
 to dislocation motion, 90, 348, 431-432, 437-438, 510-512
- Beam  
 deflection of, 590, 596  
 theory of, 588
- Bethe's formula, 382, 415
- Biased migration, 200, 218, 237-238
- Biased sinks for point defects, 264, 484, 497, 511
- Biaxial stress state, 426-427, 460, 555
- Binary elastic collisions, 375-377
- Binding energy  
 of diinterstitials, 481, 483  
 of divacancy, 60  
 of oxygen atom-vacancy pair, 68  
 of vacancy-fission-gas atom complex, 66
- Blackburn's model, 154, 158
- Black-dot structure, 420-421
- Blanket in LMFBR, 114, 116, 584, 587
- Body-centered cubic lattice, 25  
 diffusion of impurities in, 74  
 interstitial sites in, 57
- Bohr radius, 380
- Boltzmann constant, 3
- Boltzmann law, 239
- Bond energy, 38, 384, 415
- Born-Haber cycle, 32, 35, 38
- Boron, 451
- Bose-Einstein statistics, 8-9
- Bowing  
 of dislocation line, 91, 432, 438, 500, 503  
 of fuel assembly, 587, 592
- Bravais lattice, 24
- Breakaway swelling and gas release, 263, 318-320
- Brittle fracture  
 of cladding, 419  
 in ferritic steels, 456-457  
 theory of, 338-341  
 in  $UO_2$ , 336-337
- Bubbles  
 coalescence of, 216-219, 243-249  
 critical size for detachment from defects, 250, 254  
 distribution function, 204, 233-235, 245, 254  
 forces on, 202  
 on grain boundaries, 314-320  
 growth of, 227-235, 243-249  
 helium (*see* Helium, bubbles)  
 migration in solids, 79, 235-243  
 nucleation of, 222-226
- number of gas atoms in, 203  
 pinning by dislocations and grain boundaries, 249-257  
 postirradiation annealing of, 213-214  
 re-solution of, 219-222  
*See also* Re-solution  
 sweeping by grain boundaries, 320-322  
 swelling due to, 204  
 as traps for migrating gas atoms, 312  
 in  $UO_2$ , 200  
 velocity in temperature gradient, 218, 256
- BUBL code, 251-260, 314, 322, 324, 431
- Bulk modulus, 242, 601
- Burgers vector, 83  
 of edge dislocation, 85  
 of screw dislocation, 86  
 in  $UO_2$ , 333-335
- Burnup, 114  
 effect on fission-gas release, 324  
 effect on heat-generation rate in fuel, 129  
 effect on melting point of fuel, 119  
 effect on oxygen potential of fuel, 180-184  
 effect on thermal conductivity, 124
- Capture radius of dislocations, 210, 214, 264, 465
- Capture volume  
 around carbide particles in steel, 550  
 around depleted zones, 435  
 around spherical sinks, 210-211  
 around voids, for dislocation loops, 497
- Carbides  
 in deposits of sodium corrosion process, 534  
 as precipitates, 422-423  
 in steel, 545-546, 549-552, 564
- Carbon  
 meters for, in liquid sodium, 542-544  
 in mixed-oxide fuel, 161, 163, 171  
 in sodium, 519, 541-542  
 solubility in austenite, 544

- in steel, 419, 422, 564-565  
transport in sodium, 547-548
- Carburization, 519, 544, 548-552
- Cascade  
computer simulation of, 402-403  
displacement, 373  
isolated, 373-374  
overlap, 407
- Cation, 29, 146
- Center-of-mass coordinates, 375
- Central void  
growth during restructuring, 133  
in irradiated fuel, 131, 274, 286  
temperature boundary condition at, 128, 134
- Cesium  
critical compressibility factor of, 103  
fission yield, 172-174  
in fuel-cladding gap, 188  
and fuel swelling, 195  
gaseous, ionization of, 54  
migration in fuel, 184  
*See also* specific compound
- Cesium chloride structure, 29, 41
- Channeling, 394-395, 402, 406, 416
- Charge of a moving ion, effective, 382
- Charpy V-notch test, 428-429
- Chemical potential  
in chemically reacting systems, 43-45  
in diffusion, 77-78  
of interstitials in solids, 484, 494  
in statistical mechanics, 1, 7  
of vacancies in solids, 69, 472, 485, 494  
of a void, 472, 477
- Chemical reaction-rate theory, 206, 480-483, 515
- Chemical stress, 233, 501-502
- Chromium  
composition in steel, 419  
corrosion by liquid sodium, 528-530  
effect on carbon activity in steel, 544  
solubility in liquid sodium, 529  
in stainless steel, chemical attack by fuel, 186-187, 198
- Cladding  
brittle fracture of, 419  
corrosion by fuel, 186-193  
irradiation effects in, 419  
in LWRs and LMFBRs, 118, 418  
strains during irradiation, 580-582
- Classical statistical mechanics, 101
- Clausius-Clapyron equation, 38
- Cleavage, 340
- Climb of dislocations, 86, 92-94  
effect of irradiation on, 510-511  
force causing, 88-89  
velocity of, 346-348, 372
- Close-packed planes  
in bcc crystals, 30, 83  
in fcc crystals, 28, 83
- Close-packed structures, 28-29
- CO<sub>2</sub>  
equilibrium constant of reaction  
 $\text{CO} + \frac{1}{2} \text{O}_2 = \text{CO}_2$ , 149-150  
role in oxygen redistribution, 161-163  
standard free energy of formation of, 163
- Coalescence  
of bubbles, on dislocation lines, 254  
in matrix, 216-219, 243-249  
of pores on a grain boundary, 281
- Coherent precipitates, 437-438, 484, 486-490
- Cohesive energy, 14, 29, 31
- Colburn j-factor, 523
- Cold work, 445  
effect on void swelling, 467, 491
- Collision  
relative kinetic energy of, 377  
relative speed of, 376
- Collision density, 378, 412
- Columnar grains, 131-132, 265, 267, 275  
growth rate of, 275-278
- Combinatorial factor (*see* Configurational partition function)
- Combinatorial numbers  
for divacancy formation, 207  
in Greenwood-Speight model, 244  
for interstitial clusters, 481  
for point-defect trapping on dislocations, 210  
for shallow traps in fuel, 312  
for a sphere, 216, 310  
for vacancy-interstitial recombination, 208  
for voids in metals, 473, 477  
for xenon atom interactions, 209, 223-224
- COMETHE/CRASH fuel-modeling code, 566, 583
- Compatibility relations, 600
- Compressibility, coefficient of, 13, 110, 119, 385, 601
- Compressibility factor, 102-103  
critical, for various fluids, 103  
xenon, 202
- Condensation coefficient, 272-273, 285
- Conductivity integral, 129-131
- Configurational entropy, 48, 473
- Configurational partition function, 47-49  
for divacancies in a crystal, 60  
for ionic solids, 63  
of liquids, 101
- Congruent melting of UO<sub>2</sub>, 116
- Congruent vaporization, 160
- Constitutive relations, 571, 579, 589-591, 600-601
- Contact pressure (interfacial pressure), 118, 138, 361, 574, 581-582, 595
- Continuity equation for void growth, 497-499
- Conversion ratio, 129, 143, 181
- Core clamp, 585
- Core of dislocation, 87, 264
- Corresponding states, principle of, 100-101
- Corrosion of steel  
by fuel, 186-193  
by liquid sodium, 518  
effect of mass-transfer resistance on, 522-525  
effect on mechanical properties of steel, 530-532  
effect of sodium velocity on, 523  
temperature dependence of, 522  
velocity of, 524, 531  
Weeks-Isaacs model of, 532-533
- Cottrell-Petch theory, 456-458
- Cracks  
and actinide redistribution, 169  
in brittle material (Griffith theory), 338-341  
in BUBL code, 259  
formation during power cycling, 326  
in fuel, 131-132, 287, 372, 577-579  
and oxygen redistribution, 160-163  
and pore generation, 266  
wedge-type, 446-449, 461
- CRASIB code, 587, 592
- Cr<sub>23</sub>C<sub>6</sub> (*see* Carbides)
- Creep, 97-98, 419  
diffusional, 341  
effect of radiation on, in oxides, 360-362  
in fuel elements, 572-573, 582  
irradiation (*see* Irradiation creep) modulus, 573  
in oxide fuels, 353-357  
power law, 353  
primary, 97, 573  
theories of, dislocation climb, 348-351, 573  
grain-boundary sliding, 351-353  
Nabarro-Herring model, 341-343, 573  
vacancy transport in grain boundaries (Coble model), 344-345, 461
- Creep rupture, 426, 428, 443, 554
- Critical constants, 102  
of UO<sub>2</sub>, 103, 106  
of xenon, 202
- Critical resolved shear stress, 83
- Critical size for bubble detachment from defects, 250, 254
- Critical stress  
for cracking, 447-448, 453, 456, 461  
for glide of dislocation loops, 496  
for unlimited void or bubble growth, 453, 493
- Cross section  
anisotropic scattering, 397  
Coulomb, 220  
definition, 377  
displacement, 396-399, 404  
elastic scattering in steel, 484  
for energy transfer, 380-382, 416  
for fission by fast and thermal neutrons, 114, 129

- hard sphere, 381  
 inelastic scattering, 397-398  
 of  $(n, \alpha)$  reactions, 452  
 Crowdion, dynamic, 392, 405  
 Crystal axis vectors, 24, 26  
 Crystal structure, basis of, 25  
 $\text{CsFeO}_2$ , 192  
 $\text{CsI}$ , 304  
 $\text{Cs}_2\text{MoO}_4$ , 163, 184, 190  
 $\text{Cs}_2\text{O}$ , 163, 179, 184, 190, 192  
 $\text{Cs}_2\text{UO}_4$ , 184
- Damage functions, 399-400  
 DBTT (*see* Ductile-to-brittle transition temperature)  
 Debye frequency, 19  
 Debye temperature, 19, 119, 121, 124  
 Decarburization, 519, 548  
 Deflection of beam, 590, 596  
 Densification, 113, 133, 265, 364, 366  
 Density  
   of gas in bubble, 203  
   of nuclear fuels, 30  
   of solids, theoretical, 127  
   of  $\text{UO}_2$ , 114  
 Density of states, 2  
   electrons, 33  
   ideal gas, 11  
 Depleted zones, 374, 404, 421, 432, 483, 501, 505  
   annealing of, 435-437  
 Deposition, 519, 533-536  
 Detailed balancing, principle of, 53  
   applied to vacancy emission from a dislocation, 347  
   applied to vaporization, 272  
   applied to void nucleation, 473  
 Diametral strain, 428, 580, 595  
 Diamond structure, 25  
 Diffusion  
   activation energy of, 72, 76-77, 81  
   atomic motions in, 71-72  
   of bubbles, 236-237  
   to dislocations, 214-215  
   Fick's laws of, 70-71  
   grain boundary, 344-345  
   mechanisms, interstitial diffusion in  
     bcc crystals, 74  
     self-diffusion in fcc crystals, 74-75  
   molecular, 70  
   radiation-enhanced, 206, 230, 263, 357, 360, 367  
   to spherical sinks, 211-214  
   surface, 79-80, 236  
   thermal, 77-79, 237  
   with trapping, 304-314  
   trapping length, 209-210, 306, 309-310  
 Diffusion coefficient  
   apparent, of Xe in fuel, 300, 308, 315  
   of bubbles, 217, 236-237  
   of carbon in steel, 548  
   definition of, 70  
   effect of radiation on, 206, 230, 263, 357, 360, 367  
   empirical, of Xe in fuel, 301, 313  
   formula for, Einstein, 74  
   grain boundary, 345, 352  
   of helium in stainless steel, 515  
   of iron in liquid sodium, 523  
   of iron, nickel, and chromium in steel, 532  
   measurement of, 81  
   of oxygen in  $\text{UO}_2$ , 560  
   of plutonium in oxide fuels, 166  
   surface, 19, 236  
   temperature dependence of, 77  
   of  $\text{U}^{4+}$  in  $\text{UO}_2$ , 241, 355-357  
   of  $\text{UO}_2$  vapor in helium and xenon, 270-271  
   vacancies and interstitials, 205, 483  
   volume, 240, 343, 355  
   of xenon in solid  $\text{UO}_2$ , 205-206, 313  
 Diffusional creep, 341  
 Diffusional release of fission products from fuel, 299-300  
 Diinterstitial, 481  
 Dilatation, 587  
 Dipole, 95, 334, 349  
 Dislocation  
   array, 95  
   attached to voids, equilibrium configuration, 494-495  
   bias towards interstitials, 263-264, 357, 465, 485, 491  
   bowing of, 91, 432, 438, 500, 503  
   bubble nucleation on, 226  
   capture radius, 210, 214, 264, 465  
   climb, 86, 88-89, 92-94, 346-348, 372, 510-512  
   core of, 87, 264  
   density of, in solid, 89  
   diffusion of point defects to, 214-215, 263-264  
   dipole, 95  
   edge, 84-85  
     *See also* Edge dislocation  
   forces on, 88-89  
   glide, 86, 90  
     *See also* Glide of dislocations  
   immobile, 93, 348, 512  
   interaction with impurities, 90, 456  
   line tension, 87-88  
     *See also* Line tension of a dislocation  
   loop, 86, 92, 99, 421-422  
   mobile, 348, 512  
   multiplication of, 90  
   network, 252, 431, 467, 469, 484, 500  
   pileup, 94-95, 99, 348, 430, 447, 456, 511  
   pinning, 90-91, 348  
   pinning of bubbles by, 249-250, 252-255  
   recovery, 469  
   screw, 85-86, 87, 88-89  
   in small-angle grain boundaries, 96  
   strain energy of, 86-87  
   trapping of point defects, 210, 306  
   in  $\text{UO}_2$ , 333-335  
   velocity, 92, 346-348, 510  
   Dislocation channeling, 442-443  
   Disodium acetylide (*see*  $\text{Na}_2\text{C}_2$ )  
   Dispersion relation, 18  
   Displaced atoms, number of  
     in a fast-neutron flux, 396-399, 484, 501, 507  
     with focusing or channeling, 396  
     with inverse power potential, 387  
     due to ion bombardment, 400-402  
     Kinchin-Pease model, 386-387  
     Lindhard's model, 389  
     in a thermal neutron flux, 396  
   Displacement (atomic)  
     cascade, 373  
     cross section, 396-399, 404  
     mean free path, 404  
     spike, 374, 404-406  
     threshold, 383-386, 415  
   Displacement (mechanical), 598  
   radial, in fuel elements, 571, 573-575  
     around a screw dislocation, 86  
     in single crystals, 83-84  
   Displacements per atom (dpa), 401-402, 416  
   Distance of closest approach, 377, 381, 392, 410  
   Distribution coefficient of oxygen  
     between sodium and vanadium, 540, 564  
   Distribution function  
     fission-gas bubbles in  $\text{UO}_2$ , 233-235, 254-258  
     helium bubbles in cladding, 479  
     vacancy clusters, 472-473, 506  
     voids in metals, 465-466, 473, 478, 497, 515  
   Divacancy, 56  
     equilibrium concentration, 60-61  
     formation rate, 206-208  
   Divergence theorem, 71, 598  
   Dollar of reactivity, 586  
   Doping, 63  
     of  $\text{UO}_2$ , effect on diffusion coefficient, 80, 205  
   Doppler coefficient, 100  
   Dorn theta parameter, 428  
   Duct (wrapper), 118, 583, 587, 589  
   Ductile fracture in  $\text{UO}_2$ , 338  
   Ductile-to-brittle transition temperature, 337, 341, 419, 429, 457  
   Ductility, 426, 454, 553  
   Dulong and Petit (law of), 20, 120  
   Dynamic crowdion, 392, 405
- Edge dislocation, 84-85  
   climb of, 346-348  
   in fcc and bcc structures, 98  
   forces on, 88-89  
   interaction with faulted loops, 439-440, 461  
   interactions between, 92-94  
   stress field around, 87, 98  
   in  $\text{UO}_2$ , 333-334

- Effective charge of a moving ion, 382
- Einstein  
 formula for diffusion coefficient, 74  
 formula for surface-diffusion coefficient, 79, 236  
 model of solid, 17, 47, 76  
 temperature, 17
- Elastic collision, 375
- Elastic energy density, 242, 340, 427, 438, 601
- Elastic moduli, 600
- Elastic waves in crystal, 17-19, 22
- Electrical neutrality in crystal, 63, 65, 179-180, 356
- Electrochemical cell  
 for measuring carbon activity in sodium, 543  
 for measuring oxygen activity in sodium, 539, 564  
 for measuring oxygen potential of fuel, 150-151
- Electron affinity, 34
- Electron microprobe, 175, 185, 188, 532
- Electron microscope, 419-420
- Electron radiation damage to solids, 416, 435
- Electronic disorder, 62
- Elongation, 599  
 at failure, 428, 443, 450  
 of fuel assemblies, 585-587
- Embrittlement, 419, 426, 451, 454, 462
- Empirical diffusion coefficient, 301-303, 313, 332
- Endothermic reaction, 46
- Energy  
 activation, of diffusion, 72, 76-77, 79, 81, 205, 355, 483, 500  
 for applicability of equivalent hard sphere model, 381  
 of bonds, 38, 384, 415  
 cohesive, 14, 31, 101  
 Coulomb, 32, 40  
 of dislocation loop, 464, 480, 485, 508  
 dissociation, 38  
 Fermi, 33, 382  
 of formation  
   Frenkel defect, 65, 80  
   interstitial, 61, 480, 483  
   Schottky defect, 64, 80  
   vacancy, 59-60, 472  
 of motion, 77, 79, 205, 355, 500  
 of neutralization of moving ion, 382  
 of reaction, 46  
 in statistical mechanics, 4  
 of sublimation, 32, 384  
 of transition from electronic stopping to atom-atom scattering, 381  
 of void surface, 464  
 zero point, 16
- Engineering stress and strain, 424
- Enrichment of fuel, 114-115, 181
- Ensemble  
 canonical, 1-2  
 definition, 1  
 grand canonical, 1, 17  
 microcanonical, 1-3
- Enthalpy  
 partial molar, of oxygen in fuel, 151, 171  
 of reaction, 51  
 in statistical mechanics, 6  
 of  $\text{UO}_2$ , 120  
 of vacancy formation, 231  
 of vaporization, 105
- Entropy  
 configurational, 48  
 excess, 53, 59, 61, 77  
 of mixing, 47-48, 51-52  
 of motion, 77, 205, 355  
 partial molar, of oxygen in fuel, 151, 171  
 of reaction, 51  
 in statistical mechanics, 5  
 of vaporization, 105
- Equation of state  
 caloric, 100  
 Debye, 21, 110  
 fundamental, 100  
 Grüneisen, 20, 110  
 microscopic basis, 100  
 reduced, 102-103  
 thermal, 100  
 universal, 102-103  
 of  $\text{UO}_2$ , 100, 106-112  
 xenon, 202
- Equiaxed grains, 131-132  
 growth kinetics, 278-282
- Equilibration tabs, 543-544
- Equilibrium  
 bubble, 233  
 in chemical systems, 44-45  
 divacancy concentration, 60-61  
 Frenkel defects, 64-65, 355  
 in ideal-gas mixture, 45-47  
 interstitial concentration, 61, 472  
 jog density on dislocations, 347  
 between phases, 44, 49  
 Schottky defects, 62-64, 355  
 in solids, 47  
 in statistical mechanics, 23, 45  
 vacancy concentration, 57-60, 75, 436, 472
- Equilibrium conditions in elasticity theory, 571, 588-589, 597-598, 602
- Equilibrium constant  
 in ideal-gas chemical reactions, 46-47, 49-51  
 in solid with defects, 48
- Equivalent sphere model of fuel, 199, 299, 313, 315
- Equivalent stress and strain, 368, 427, 573
- Eulerian continuity equation, 436, 497, 499
- Excitation energy for inelastic scattering, 397
- Exothermic reaction, 46
- Extensive property, 5
- Face-centered cubic lattice, 24  
 interstitial sites in, 57  
 self-diffusion in, 74-75
- Fast reactor (*see* LMFBR)
- Faulted dislocation loop, 421, 439, 464, 469-470
- $\text{Fe}_{23}\text{C}_6$  (*see* Carbides)
- $\text{FeO}(\text{Na}_2\text{O})_2$  (*see* Sodium ferrite)
- Fermi energy, 33, 382
- Fermi-Dirac statistics, 12-13  
 distribution function, 9  
 partition function for, 8
- Ferritic steel  
 composition of, 418-419  
 DBTT of, 458  
 decarburization of, 548  
 layer formed on stainless steel by liquid-sodium corrosion, 532-533
- Fick's laws of diffusion, 70-71
- FIMA (fissions per initial metal atom), 114
- Fission  
 cross section, 114  
 density, 114  
 rate per unit volume, 114  
 spike, 206
- Fission-enhanced and -induced creep, 360
- Fission fragments, 289, 291, 358-360, 407, 415
- Fission gases  
 bubbles in fuel, 200  
 density in fuel, 203  
 engineering release calculations, 324-328, 332  
 equation of state, 202  
 fuel swelling when solid-like, 198, 203  
 interaction between, 208  
 trapping by defects, 209  
 yields, 172-175, 202
- Fission products  
 chemical states of, 177-180  
 elemental yields of, 174, 181  
 gaseous, in fuel modeling codes, 567-568  
   knockout release, 294-299  
   recoil release, 293  
   release-to-birth rate ratio, 297  
 migration in fuel, 184-186  
 physical states, 175-177  
 solid, swelling due to, 193-195, 203
- Fission yields, 172-175, 202
- Flow stress, 425
- Fluence, 114, 399, 441, 466, 469
- Fluorite structure, 30, 62, 147, 193, 334
- Flux  
 definition, 378  
 of fission fragments in fuel, 408-409  
 neutron, axial profile in fuel element, 595  
 depression in LWR fuel pins, 129, 131  
 spectrum in reactors, 374, 398-399, 416  
 of recoil atoms in fuel, 410-413

- Focusing, 385, 390-392, 403, 415-416
- Force
- on atoms in a crystal, 403
  - balance on bubble surface, 202
  - on a bubble, 320
    - due to dislocations and grain boundaries, 250
    - due to stress gradients, 241-243
    - due to a temperature gradient, 238, 243, 281
  - on dislocations, 88-89, 93, 95, 348, 431, 439, 461
  - on grain boundaries, 278-279
- Force constants of potential functions
- He- $\text{UO}_2$  and Xe- $\text{UO}_2$ , 271
  - parabolic approximation, 384-385, 394
- Fourier's law of heat conduction, 78, 121
- Fowler-Smithells equation, 55
- Fractional release, 300-301
- Fracture
- stress, 339-341, 448, 456-457, 461
  - in  $\text{UO}_2$ , 337-338
- Frank dislocation loop, 421, 498, 512
- Frank-Read dislocation source, 90-91, 94-95, 348-350, 430, 455-456
- Free-electron model of metals, 32
- Free energy (*see* Gibbs free energy)
- Frenkel defects, 64-65
- in mixed-oxide fuels, 146
  - in  $\text{UO}_2$ , 68, 80-81, 120, 355
- Frenkel pairs, 69, 404
- yield due to fast neutrons, 484
- yield in fission, 204-205, 357, 408-410
- Frequency spectrum of solid, 16
- Debye, 19, 23
  - Einstein, 17, 23
- Friction, 555, 575-577, 582
- Friction factor, 523
- Friction hardening, 430-432, 456
- FTR (Fast Test Reactor), 115
- Fuel
- equivalent sphere model of, 199, 299, 313, 315
  - modeling codes for, 560
  - surface temperature of, 135, 277, 326
- Fuel assembly, 115, 117, 584
- Fuel-cladding chemical reaction, 186-193, 197, 567
- Fuel-cladding gap
- closure during startup, 570-571
  - conductance of, 136-139
  - in fuel modeling codes, 574, 576, 580-581
- Fuel element, 566
- limiting conditions on operation of, 115
  - LMFBR, 115-116, 118
  - LWR, 115, 118
  - mechanical modeling during irradiation, 571-577
  - operation with central melting, 130
  - temperature distribution in, 127-136, 143
  - thermal performance, 140-141
  - wire-wrapped, 116, 586
- Fusion, heat of, 13, 105-106, 112
- Gamma phase, 422
- Gap (*see* Fuel-cladding gap)
- Germanium, 60
- Gibbs free energy
- in chemical equilibrium, 44
  - of elemental solids, 52
  - of ideal-gas mixture, 49-50
  - in ionic solids, 63
  - of loop formation, 485
  - partial molar, of oxygen in fuel, 149, 151
  - in statistical mechanics, 6
  - of void formation, 478
  - of voids, 473, 477
  - of voids connected by dislocations, 494
- Gibbs phase rule, 145, 149
- Gibbs theorem, 52
- Glide of dislocations, 86
- during creep, 348, 350
  - force causing, 88-89
  - shear strain resulting from, 91-92
  - of unfaulked loops, 469, 496
- Gold, swelling of, 464
- Grain boundaries, 96-97
- accumulation of gas on, 314-318
  - corrosive attack by fuel, 188
  - diffusion in, 344-345
  - pinning of bubbles by, 250-251, 256-258
  - as sinks for point defects in metals, 484, 515
  - as sinks for vacancies in  $\text{UO}_2$ , 362
  - sliding, 351
  - and steel carburization, 552
  - tension in, 99, 249-250, 279
  - thickness of, 344, 352
  - as trapping centers, 306
  - triple point, 352, 446
  - vacancy diffusion in, 344, 352, 449-450
  - velocity of, 320-321
  - voids on, 363, 449
- Grain growth, 113, 132, 278-282, 285, 320-322, 362
- Grains in polycrystals, 96-97
- deformation by applied stress, 351
  - in  $\text{UO}_2$ , 252
- Graphite
- bonding in, 42
  - in HTGR, 144
  - specific heat of, 23
  - structure, 39
- GRASS code, 248, 251
- Greenwood-Speight swelling model, 243-244
- Grid plate, 584, 589
- Griffith energy criterion, 447
- Ground state, 4
- of components in an ideal-gas mixture, 46
- Growth of gas bubbles in solids, 227
- by coalescence, 243, 249
  - effect of stress on, 233
  - nonequilibrium, 230-233
  - with re-solution, 228-230
- Growth law
- of alkaline earth oxide, 197
  - for carbide precipitates in steel, 551
  - for depleted zones in a metal, 436
  - for dislocation loops, 516
  - for grain-boundary voids, 450, 461
  - for helium bubbles on grain boundaries, 452-453
  - for voids in metals, 490-492, 497, 516
- Gruber's method, 244-248
- Grüneisen parameter, 23, 42, 110
- Guide tube, 584
- Handling head, 584
- Hard-sphere scattering, 373
- equivalent hard-sphere radius, 381, 404, 410
- Hardness, Meyer, 138
- Heat capacity (*see* Specific heat)
- Heat-transfer coefficient
- fuel-cladding gap, 136-139
  - sodium in LMFBR, 135
- Heat of transport, 78, 239
- for oxygen migration in fuel, 164-165
  - for plutonium migration in fuel, 166
  - for surface diffusion, 80, 237
  - for vacancy diffusion, 241
- Helium
- bubbles, on grain boundaries, 452-454
    - in irradiated steel, 417, 423, 442
  - diffusion coefficient, in steel, 515
  - of  $\text{UO}_2$  in, 271
  - effect on void formation, 465, 471, 476-480, 492-494
  - embrittlement, 451, 455, 462
  - production rate in metals by fast neutrons, 451-452, 461
  - solubility in metals, 54, 477
- Helmholz free energy, 5
- Henry's law
- carbon in sodium, 542
  - $\text{Na}_2\text{O}$  in sodium, 526, 557
- Heterogeneous nucleation
- of fission-gas bubbles in  $\text{UO}_2$ , 222, 225-226
  - of voids in metals, 471, 477, 479-480
- Hexagonal close-packed structure, 25
- Homogeneous nucleation
- fission-gas bubbles in fuel, 222-225
  - helium bubbles in metal, 515
  - interstitial loops, 480-483
  - vacancy loops, 505
  - voids in metals, 471-480
- Hooke's law, 86, 336, 339, 425, 600
- Hot pressing, 265, 364, 367-369, 372, 572
- HTGR (high-temperature gas-cooled reactor), 143, 331
- Hydrogen
- diffusion in metals, 77, 81

- embrittlement of zircaloy, 79  
 meters in liquid sodium, 537-539  
 in oxide fuels, 150, 153, 161, 171  
 solubility, in metals, 55  
 in sodium, 538, 564
- Hyperstoichiometric oxide fuels, 113, 146, 153, 157
- Hypostoichiometric oxide fuels, 113, 146, 153, 155-157
- Ideal gas  
 in bubbles, 203  
 chemical equilibrium in, 45-47, 49-52  
 definition, 6, 103  
 entropy of, 13
- Ideal solution  
 of molybdenum in fuel and metallic inclusions, 182, 197  
 in oxide fuels, 146, 155
- IHX, 519, 553-554
- Image dislocations, 497, 516
- Impact test, 428-429
- Inclusions (metallic), 176, 180, 185, 194, 197, 238, 272, 285
- Incoherent precipitates, 438, 484, 515
- Incompressibility condition, 572
- Inconel, 467, 491
- Incubation period for void formation, 463, 466, 471, 497, 515
- Independent fission yield, 172
- Indistinguishability of particles, 6, 47
- Inelastic scattering, excitation energy for, 397
- Inelastic strain, 580-582
- In-pile creep, 360
- In-pile gas release, 288-289, 301-302, 311-313
- Intensive property, 5, 106
- Interfacial pressure, 118, 138, 361, 574, 581-582, 595
- Intergranular corrosion of cladding, 188
- Intergranular fracture, 337
- Intergranular gas bubbles, 260, 315
- Intermediate heat exchanger, 519, 553-554
- Interstitial, 56  
 absorption, by dislocations, 486  
 by voids, 484  
 composition of steel, 419  
 diffusion coefficient, 74, 205  
 dislocation loop, 421, 469-470, 480-483, 508-509  
 emission from loops, 480  
 equilibrium concentration in solid, 61, 472  
 formation energy, 61  
 impurities, 57, 519  
 migration energy, 483  
 on oxygen sublattice in  $UO_2$ , 147  
 sites for in crystal, 56-57  
*See also* Octahedral and Tetrahedral interstitial sites  
 split, 57, 67
- Intragranular gas bubbles, 260, 315
- Iodine  
 effect on stainless-steel corrosion, 190-191  
 fission product, 174, 180, 184  
 in fuel—cladding gap, 188
- Ion bombardment  
 displacements due to, 400-402  
 for implanting atoms in fuel, 288
- Ionic solid  
 bonding in, 34-38  
 crystal structure of, 29-30
- Ionization potential, 34
- Iron  
 corrosion by sodium, 525, 528  
 diffusion coefficient in sodium, 523  
 solubility in sodium, 524, 529  
 in stainless steel, chemical attack by fuel, 186-187, 190-193
- Irradiation creep  
 effect on bowing of fuel assemblies, 590-592, 596  
 in metals, 499-512  
 due to climb-controlled dislocation glide, 510-512  
 due to stress-oriented loop nucleation, 508-509  
 transient, 500-504  
 due to vacancy disk collapse, 505-508, 517, 590  
 in oxide fuels, 357-360
- Isotope effect on diffusion, 81
- Jellium model, 32
- Jog, 90, 210, 346-348
- Jump distance  
 of bubble, 236, 240  
 for diffusion, 72  
 for surface diffusion, 79, 236  
 of temperature in gas, 136, 144
- Jump frequency, 72, 75-77, 81  
 of bubble, 236, 239-240  
 during displacement-spike annealing, 407  
 for surface diffusion, 79, 236  
 in thermal spike, 359-360
- Junction, 431, 443
- Kinchin—Pease theory, 386-387, 406, 416, 435-436
- Kinetic theory of gases  
 diffusivity, 270-271  
 mean free path, 137  
 temperature jump distance, 136  
 thermal conductivity, 121
- Kink site on surface, 240
- Knock-on atoms, 205, 290-291, 316, 373
- Knockout, 287, 290, 293-299
- Knudsen cell, 158-159
- Krypton  
 release from  $UO_2$ , 296-298, 306  
 yields from fission, 202  
*See also* Fission gases
- Laboratory coordinates, 375
- Lagrangian continuity equation, 436, 499, 517
- Lamé coefficients, 600
- Laplace transform, 300-301, 308, 315-317
- Lattice constant, 25  
 of nuclear fuels, 30  
 in  $(U,Pu)O_2$ , 124
- Ledge  
 in creep models, 352  
 on surface, 273
- Legendre polynomials, 342, 344
- Lenticular pores, 265, 323
- Life fraction rule, 331, 454, 462, 570
- LIFE fuel modeling code, 361, 566, 571, 573, 577, 579-580
- Lindhard's energy partitioning theory, 387-389, 416
- Line tension of a dislocation, 87-88, 98, 249, 347, 438
- Linear power  
 definition, 128  
 effect on fission-gas release, 303-304, 324-325  
 effect on fuel cracking, 578, 594  
 in nuclear reactors, 118
- LMFBR (liquid-metal fast breeder reactor), 100, 113, 418, 463, 518-519, 585
- Loops (point defect), 421-422, 439, 464, 480-483, 485-486, 505, 508-509
- Loops (sodium), 521, 524-525, 563
- Luders strain, 425
- LWR (light-water reactor), 113, 331, 418
- Macrostate, 1
- Madelung constant, 26
- Markin—Rand—Roberts model, 161
- Mass action, law of  
 carbon reaction with  $FeO$ , 543  
 carbon in sodium, 542  
 chromium oxidation in stainless steel, 186  
 divacancy formation, 61  
 Frenkel defects, 64  
 in ideal gases, 46  
 molybdenum in fuel, 182  
 oxygen  
 in sodium, 540  
 in vanadium, 540  
 Schottky defects, 64  
 in semiconductors, 54  
 in solids with defects, 48
- Mass spectrometer, 158-159
- Mass transfer in liquid sodium, 522-525
- Materials input functions to fuel modeling codes, 566
- Matrix corrosion of cladding by fuel, 188
- Maxwell—Boltzmann distribution, 9  
 mean velocity of, in one dimension, 76

- Maxwell relation, 106
- Mean free path  
collision, 378  
displacement, 404  
in gas, 136  
of helium and xenon, 137  
neutrons, 129  
phonons, 121
- Meters for monitoring sodium purity, 520, 536-537
- Microstate, 1
- Microstructure  
of fuel in BUBL code, 253  
of irradiated steel, 419-423  
sinks for point defects, 484  
of steel exposed to liquid sodium, 533  
traps for fission-gas atoms in, 306  
of uranium carbide, 97
- Migration in solids  
brine cubes in salt, 285-286  
bubbles, biased, 237-238  
random, 236-237  
in a stress gradient, 241-243  
surface-diffusion mechanism, 236-238  
volume-diffusion mechanism, 239-241
- pores, migration velocity, 270-271, 276, 284  
redistribution in fuel pin, 273-275  
in UC, 270  
vacancies and interstitials, 204  
xenon, 205
- Miller indices, 26  
of Burgers vector, 83
- Mixed kinetic control of reaction  
point defects in solids, 210, 215-216, 474  
sodium corrosion of steel, 522
- Mixed-oxide fuel, 113  
melting point of, 117-118  
oxygen potential of, 148-155  
phase diagram, 147
- Mixture  
components of, 43  
ideal gas, partition function of, 45-46
- Mobility, 238  
of grain boundary, 279  
of pore, 280
- Molybdenum  
fission yield of, 174  
in fuel, 177, 180-182, 186, 195, 197  
void growth in, 516
- Moment, 589
- Moment of inertia, 589
- Momentum conservation in elastic  
collision, 375
- Monoclinic structure, 27
- MoO<sub>2</sub>, 163, 177, 185  
disproportionation, 198  
standard free energy of formation, 182  
standard free energy of vaporization, 198
- Mutual diffusion, 74
- MWD/MTU (megawatt days per metric ton of uranium), 114
- Nabarro-Herring creep, 341-343  
effect of radiation on, 358
- Na<sub>2</sub>C<sub>2</sub>, standard free energy of formation, 541
- Na<sub>2</sub>CO<sub>3</sub>, 542
- NaH, 537  
standard free energy of formation, 538, 564
- Na<sub>2</sub>O, 520, 534  
standard free energy of formation, 526, 564
- NaOH, 539
- Na<sub>2</sub>SiO<sub>3</sub>  
standard free energy of formation, 564
- Na<sub>3</sub>UO<sub>4</sub>, 520, 555  
density of, 559  
kinetics of formation in fuel, 559-562  
standard free energy of formation, 558
- NDT (*see* Nil ductility temperature)
- Nearest-neighbor atoms, 14, 60
- Nearest-neighbor sites, 72, 75, 79
- Necking, 338, 424
- Nernst-Einstein equation, 238, 264, 280
- Neutron  
diffusion, 71, 129  
energy spectrum in reactors, 114, 398  
fission spectrum of, 416  
fluence, 114, 115  
flux, 114, 115, 367, 374, 398-399, 416  
*See also* Flux, neutron
- Nickel  
composition in steel, 419  
corrosion by liquid sodium, 528  
effect on carbon activity in austenite, 544  
Ni-NiO equilibrium, 150  
reaction with thermal neutrons, 451  
solubility in liquid sodium, 529  
in stainless steel, chemical attack by fuel, 186-187
- Nil ductility temperature, 337, 419, 429, 458
- Normal coordinates, 15
- Normal stress, 597  
effect on dislocations, 88-89  
effect on vacancy concentration, 342, 346
- Nucleation  
in BUBL code, 252  
capillarity model, 473  
classical theory of, 471, 475, 480, 515  
current, 474, 479, 481, 483, 498-499  
density, 222, 224-225  
effect helium on, 476-480  
of gas bubbles in solids, 222-226, 263
- heterogeneous, 222, 225-226, 471, 477, 479-480  
homogeneous, 222-225, 471-483, 505, 515  
of interstitial loops in metals, 480-483, 508-509, 515  
of iron precipitates in liquid sodium, 564  
time, 222, 224-226  
Turnbull model, 234-235  
of voids in metals, 470-480, 515
- Occupation numbers, 6
- Octahedral interstitial site, 57, 61, 67, 81, 384
- Offset yield strength, 426
- Orowan stress, 438
- Orthorhombic structure, 27
- Oxygen  
balance in irradiated fuel, 182-183  
dissolved in metal as interstitial, 68  
interstitials in UO<sub>2</sub>, 80-81, 560  
meters, in liquid sodium, 539-540  
self-diffusion in UO<sub>2</sub>, 80-81, 560  
solubility in liquid sodium, 526-527
- Oxygen-to-metal ratio, 113  
during burnup, 181-183  
effect on creep in UO<sub>2</sub>, 354-355  
effect on fuel-cladding corrosion, 190  
effect on melting point of urania, 118  
effect on thermal conductivity, 122-123  
effect on thermal expansion coefficient of UO<sub>2</sub>, 119  
in oxide fuels, 145-146
- Oxygen potential  
definition of, 148-149  
effect of burnup on, 181  
measurement of, in oxide fuel, 149-151  
of mixed-oxide fuels, 152-155, 179  
in the Na-Na<sub>3</sub>UO<sub>4</sub>-UO<sub>2</sub> system, 556-558  
of urania, 151-152
- Oxygen redistribution, 160-166
- Pairwise additivity, 36, 101
- Partition function  
canonical, 16, 19  
of crystal, 16, 19  
definition, 4  
electronic, 10  
grand canonical, 7  
ideal gas, 10, 101  
single particle, 9, 46, 76-77  
translational, 11  
vibrational, 16
- Pauli exclusion principle, 6, 34-35, 379
- PE-16, 491, 593
- Phase diagrams  
mixed-oxide fuel, 147  
plutonia, 146  
uranium, 146, 149, 171
- Phase velocity, 17

- Phonons, 20  
density, 20, 121  
and thermal conductivity, 121
- Pileup of dislocations, 94-95, 99, 348, 430, 447, 456, 511
- Pinning of bubbles by dislocations and grain boundaries, 249-250, 252
- Pipe diffusion, 348
- PKA (*see* Primary knock-on atom)
- Planar barriers (*see* Barriers)
- Plane strain, 571, 583
- Plastic flow  
in fuel-element performance, 572-573  
and hot pressing, 368-369  
of  $UO_2$ , 336-338
- Plastic instability, 425, 442, 460
- Plenum, 116, 325, 332, 571, 574, 581, 595
- Plutonia phase diagram, 146
- Plutonium  
diffusion coefficient in mixed oxide, 166  
distribution ahead of a moving pore, 169  
fission yields from, 173  
ionic radius, 123  
in LMFBR fuel, 113, 115  
redistribution (*see* Actinide redistribution)  
valence states in mixed-oxide fuel, 146
- Plutonium dioxide, gaseous, specific heat of, 112
- Point-defect balances, 231, 436, 483-490, 496, 501-502, 515
- Point defects  
biased sinks for, 264, 484, 497, 511  
diffusion, to dislocations, 214-215  
to spherical sinks, 211-214  
interaction with dislocations, 209-210, 484-486  
production rates, 483-484  
recombination (*see* Recombination of vacancies and interstitials)  
sinks for, in metals, 484
- Poisson's ratio, 470-471, 473, 600  
effect of cracking on, 579-580  
of  $UO_2$ , 335
- Polygonalization, 96
- Pores  
in fuel, 265  
intersecting a plane, 144  
opening during power cycles, 326  
velocity in temperature gradient, 270-271  
*See also* Porosity
- Porosity  
and actinide redistribution, 169  
definition, 125  
effect on elastic constants of  $UO_2$ , 335  
effect on fracture strength of  $UO_2$ , 341  
effect on thermal conductivity of  $UO_2$ , 124-126  
of interconnected bubbles, 319  
and oxygen redistribution, 160-161  
redistribution in fuel pin, 273-275  
relation to density, 127  
removal, 363, 366, 368-369
- Postirradiation annealing, 213-214, 233, 243, 287-288, 300-301, 307-311
- Postulate of equal a priori probability, 3
- Potential function  
Born-Mayer, 35, 374, 379, 384, 391-392  
Coulomb, 35, 374, 379  
inverse power, 35, 380, 387, 410  
Lennard-Jones, 271  
Morse, 38  
parabolic approximation, 384-385, 394  
point center of repulsion, 35, 380, 387, 410  
screened Coulomb, 35, 380, 415  
universal, 101
- Prandtl number, 136
- Prandtl-Reuss flow laws, 573
- Precipitates, coherent, 437-438, 484, 486-490
- Pressure  
inside bubble, 265  
cohesive, 110  
deficit or excess in gas bubble, 203, 233  
in fuel element, 289, 325-326  
and partition function, 6, 101  
reduced, 102, 104  
saturation, 102  
standard state, 50  
at 0°K, 9, 110
- Pressure vessel, 458, 518
- Primary knock-on atom (PKA), 205, 373, 386, 404, 436, 483
- Probability distribution  
canonical, 4  
grand canonical, 8  
Maxwellian, 12  
in random walk, 74
- $PuO_2$ , 155
- Quasi-stationary approximation, 128, 212, 364, 483, 498
- Radiation anneal hardening, 455
- Radiation damage, 373  
due to electrons and gamma rays, 374, 416-417  
due to fast neutrons, 374, 396-399  
in multielement solids, 374, 407  
due to thermal neutrons, 396, 416
- Radiation hardening, 429, 573  
of austenitic stainless steel, 441  
by depleted zones, 432-435, 460  
of ferritic steel, 457-458  
by loops, 439-441  
by precipitates and voids, 437-439  
saturation of, 435-437
- Radioactivity, induced  
in sodium, 518  
in stainless steel, 519  
transport in sodium, 533-535, 564
- Rand-Markin model, 152-154, 557
- Random walk, 70, 72-73, 205, 218, 240
- Range  
of fission fragments and knock-ons  
in  $UO_2$ , 219, 291, 316, 409  
total and projected, 378-379
- Raoult's law, 155, 194
- Rare earths  
fission yields of, 174  
in  $UO_2$ , 179-180, 194, 205-206
- Reaction rates  
for bubble coalescence, 218  
of point defects, 206  
in sodium corrosion of steel, 522
- Reactors  
comparison of fast and thermal, 115, 141  
neutron energy spectrum in, 374, 398-399, 416  
*See also* LMFBR, LWR, and HTGR
- Recoil, 287, 289, 291, 293, 330
- Recoil atoms (*see* Knock-on atoms)
- Recombination of vacancies and interstitials  
by coherent precipitates, 486-490  
effect on Nabarro-Herring creep, 358  
effect on void growth in metals, 491  
in irradiation creep, 502  
rate constant for, 208, 484  
spontaneous, volume for, 406
- Rectilinear diameters, law of, 103-104
- Redistribution in fuel  
of oxygen, 160-166  
of plutonium, 166-169
- Reduced mass, 377
- Reference state, 4
- Relative kinetic energy of a collision, 377
- Relative speed of a collision, 376
- Relativistic kinematics, 416
- Relaxation of atoms  
around defects in germanium, 60  
around interstitial, 61  
around vacancies  
in metals, 60, 123, 515  
in  $UO_2$ , 123
- Release-to-birth rate ratio, 297, 302
- Replacement collision, 392-393, 403
- Reservoir, 3
- Re-solution  
of fission-gas bubbles, 219-222, 263-264, 410-413, 417  
of gas atoms from traps, 307, 309-310  
from grain-boundary bubbles, 314  
of helium atoms from bubbles, 417, 515  
of interstitials from loops, 515  
of vacancies from pores, 365, 372

- Restructuring of fuel, 131-132  
 effect on temperature distribution, 133-135, 144  
 in fuel modeling codes, 567  
 Reynolds number, 523  
 Richardson's equation, 54  
 Rupture time, 331, 428, 443, 450, 554  
 Rutherford scattering, 293, 381, 409, 415-416  
*See also* Cross section, Coulomb
- Saddle point, 75-77, 384, 415  
 Saha-Langmuir equation, 54  
 Saha's equation, 54  
 Saturation of void growth, 494-497  
 Scattering angle, 375-376  
 Schmidt number, 523  
 Schottky defect, 62-64  
 in  $\text{UO}_2$ , 80-81, 355  
 Screening radius, 380, 389, 410  
 Screw dislocation, 85-86  
 forces on, 88-89  
 stress, strain, and elastic energy around, 86-87  
 Selective leaching, 519, 531-532  
 Self-diffusion, 74-75  
 of  $\text{U}^{4+}$  in  $\text{UO}_2$ , 80, 241  
 Self-welding, 555  
 Sesquioxide, 179, 193, 205  
 Sessile dislocation (Frank dislocation loop), 421, 498, 512  
 Shear modulus, 84, 503, 600  
 of  $\text{UO}_2$ , 335-336  
 Shear strain, 599  
 in creep, 98  
 due to dislocation glide, 91  
 Shear stress, 597  
 critical resolved, 83-84  
 to decompose a dislocation array, 96  
 around a dislocation pileup, 95  
 effect on dislocations, 88-89  
 to operate a Frank-Read source, 91  
 Shockley dislocation, 421  
 Sievert's law  
 hydrogen in sodium, 538, 564  
 oxygen in sodium and in vanadium, 540-541  
 Sigma phase, 437, 533, 555  
 Simple cubic (sc) lattice, 24  
 Sintering, 113, 124, 171, 271, 362-364, 366  
 Skin-friction coefficient, 524  
 Slip in crystals, 82-84  
 direction, 83, 96  
 plane, 82-83, 85, 96  
 systems in  $\text{UO}_2$ , 333-334  
 Slowing-down density of recoils, 411  
 Smear density, 570, 581  
 Soderberg equations, 573  
 Sodium  
 boiling point, 518  
 coolant, 100, 518  
 heat-transfer coefficient, 135  
 temperature rise in LMFBR, 118, 135  
 corrosion of steel by, 518, 520  
 diffusion coefficient of iron in, 523  
 solubility  
 of carbon in, 541  
 of hydrogen in, 538, 564  
 of iron in, 524  
 of oxygen in, 527  
 Sodium-24, 518  
 Sodium-bonded fuel element, 330  
 Sodium chloride structure, 29, 62  
 Sodium chromite, 528, 534  
 Sodium ferrite, 526, 528, 564  
 Sodium-fuel interaction, 520, 555-562, 565  
 Solubility  
 of carbon in austenite, 544, 564-565  
 of carbon in sodium, 541-542  
 dynamic, 219  
 of gases in metals, helium, 54, 477  
 hydrogen, 54  
 of hydrogen in sodium, 538  
 of iron, nickel, and chromium in sodium (*see* listing under these metals)  
 of oxygen in sodium, 526, 527  
 Soret effect, 167  
 Sound, speed in crystal, 19, 23  
 Source hardening, 456, 530  
 Space lattice, 25  
 Spacer pad, 584, 589  
 Specific heat  
 Debye model, 20, 23  
 Einstein model, 17, 23  
 of  $\text{UO}_2$ , gaseous, 106-109  
 solid, 66, 119-121  
 Specific power of fuel, 116  
 Spike  
 displacement, 374, 404-406  
 fission, 206  
 thermal, 219  
 Split interstitial, 57, 61, 67  
 Stacking fault, 83, 421, 439, 464  
 Stainless steel (*see* Steel)  
 Standard-state for chemical reaction in gas, 50, 149  
 Standard-state free energy of reaction compilations, 51  
 $\text{CO} + \frac{1}{2} \text{O}_2 = \text{CO}_2$ , 149-150  
 of  $\text{CO}_2$  formation, 163  
 of fission-product oxides, 177, 179  
 of gaseous heavy-metal oxides, 157, 160  
 of  $\text{H}_2\text{O}$  formation, 171  
 in ideal-gas reactions, 50-51  
 of iodides of iron, nickel, and chromium, 193  
 of  $\text{MoO}_2$  vaporization and disproportionation, 198  
 of  $\text{Na}_2\text{C}_2$  formation, 541  
 of  $\text{NaH}$  formation, 538  
 of  $\text{Na}_2\text{O}$  formation, 526  
 of  $\text{Na}_2\text{SiO}_3$  formation, 564  
 of  $\text{Na}_3\text{UO}_4$  formation, 558  
 of  $\text{NiO}$  formation, 150  
 in nonstoichiometric mixed oxides, 156-157  
 of oxides of components of stainless steel, 186  
 of sodium chromite, 529  
 of sodium ferrite formation, 526  
 of  $\text{UO}_2$  formation, 152  
 of vaporization, of  $\text{PuO}_2$ , 157, 160  
 of  $\text{UO}_2$ , 155, 160
- Steel  
 composition, 419  
 corrosion by sodium (liquid), 518  
 diffusion coefficients of iron, nickel, and chromium in, 532  
 displacement cross section of, 399  
 effective diffusion coefficient of carbon in, 548  
 irradiation embrittlement of, 454-455, 462  
 radiation hardening of, 441-442  
 reaction with oxide fuel, 186  
 scattering cross section for fast neutrons, 484  
 stress-strain curves of, 425-426  
 surface tension of, 464  
 thermal conductivity of, 135  
 thermal expansion of, 119  
 void swelling of, 466-469  
 yield stress of, 595
- Stopping power, 375, 378, 382-383, 401, 409, 416  
 Strain deviator (equivalent stress and strain), 368, 427, 573  
 Strain-displacement relations, 571, 588, 599, 602  
 Strain energy (elastic energy density), 242, 340, 427, 438, 601  
 Strain hardening (work hardening), 90, 425, 430, 456, 460  
 Strain tensor, 599
- Stress  
 at bubble surface, 202-203  
 chemical, 233, 501-502  
 deviator (equivalent stress and strain), 368, 427, 573  
 effect on interstitial loop nucleation, 508-509  
 effect on swelling, 259  
 effect on vacancy concentration, 233, 342, 353, 492  
 effect on void growth, 492-494  
 hydrostatic, 242, 572  
 normal, 597  
 effect on dislocations, 88-89  
 effect on vacancy concentration, 342, 346  
 tensor, 598  
 unpinning or unlocking, 430
- Stress concentration factor, 339, 447  
 Stress gradient, bubble migration in, 241-243  
 Stress relaxation, 590-591  
 Stress rupture, 97, 419  
 Stress-strain diagrams, 425-426, 430, 573

- Stress-strain relations (constitutive relations), 571, 579, 589-591, 600-601
- Sublattice, 29, 146, 408
- Substitutional impurity, 54, 57, 63 in steel, 419
- Supersaturation  
of dissolved impurities in sodium, 534  
of point defects in solids, 232, 470, 472, 476, 483, 502, 515
- Surface diffusion, 79-80  
and bubble mobility, 236  
and coalescence, 243  
of  $\text{UO}_2$ , 236-237, 273
- Surface tension, 98  
in brittle-fracture theory, 339-340, 447  
of grain boundary, 249  
of solid, 202, 242  
of steel, 464  
of  $\text{UO}_2$ , 203
- Swelling  
due to fission gases, 204, 259, 263, 318, 372, 571  
due to sodium-fuel reaction, 559  
due to solid fission products, 193-195, 571  
due to voids in metals, 466-469, 498-499, 572, 580-582, 585, 589, 595
- System, thermodynamic, 1-2
- Tellurium, 188, 194
- Temperature  
columnar grain, 132-133, 277  
definition, 3  
equiaxed grain, 132-133, 282, 324  
reduced, 102
- Temperature distribution  
in cladding, 595  
in fuel, effect of porosity on, 274  
effect of restructuring on, 133-135, 144  
in fuel modeling codes, 566-567  
parabolic, 128, 303
- Temperature gradient  
in fuel, 113  
effect on bubble mobility, 237-238  
in lenticular pores, 268-269  
across fuel assembly duct, 589, 595
- Tensile test, 424
- Tetragonal structure, 27
- Tetrahedral interstitial site, 57, 61, 67
- Tetrahedra, 363, 461
- Thermal-accommodation coefficient, 136, 144
- Thermal conductivity  
elementary theory, 121-122  
of mixed-oxide fuel, effect of burn-up on, 124  
effect of O/M on, 122-123  
effect of plutonium content on, 123-124  
effect of porosity on, 124-126  
radiation contribution to, 122, 126  
of rare gases, 137  
of steel, 135
- Thermal creep (*see* Creep)
- Thermal diffusion, 77-79  
of  $\text{CeO}_2$  in  $\text{UO}_2$ , 184  
of oxygen in fuel, 165  
of plutonium in oxide fuel, 166-168
- Thermal expansion  
coefficient of, 13, 110  
of fuel and cladding during startup, 570-571, 595  
and fuel cracking, 578-579, 594  
linear, 118  
of stainless steel, 119  
strain due to, 601  
of  $\text{UO}_2$ , 119
- Thermal reactor (*see* LWR)
- Thermal spike, 137, 358-360
- Thermal stress  
in fuel, 577, 594  
in a solid rod, 578, 594  
in a thin-walled tube, 594-595
- Thermodynamics, irreversible, 77-78, 239
- Thinning, 145, 187, 518
- Third law of thermodynamics, 5
- $\text{ThO}_2$ - $\text{Y}_2\text{O}_3$  bridge, 539
- Thomas-Fermi model, 383, 389
- Titanium in steel, 554, 593
- Toughness, 428
- Tracer diffusion, 74-75
- Trails of moving pores, 265
- Transgranular fracture, 337, 340
- Transition state, 75
- Transition stress in creep, 353
- Trapping  
effect on diffusion, 304-314  
equilibrium, 229, 307-308, 315  
of fission gases by defects, 209-210
- Triclinic structure, 26
- Trigonal structure, 25
- Triple point (of grain boundary), 353, 461
- Ultimate tensile strength, 338, 419, 425
- Unfaulted dislocation loop (Frank dislocation loop), 421, 498, 512
- Uniform elongation, 425
- Unit cell  
of cavities on a grain boundary, 319, 321  
conventional, 24  
around a dislocation line, 372  
around a gas bubble, 211, 318  
of a porous body, 125, 368  
primitive, 24
- $\text{UO}$ , 155
- $\text{UO}_2$  (*see* Uranium dioxide)
- $\text{UO}_3$ , 155, 160, 168
- $\text{U}_4\text{O}_9$ , 145, 148
- Urania  
compounds of, 145  
oxygen potential of, 151-152  
phase diagram, 118, 146, 149
- Uranium  
crystal structure, 30  
fission yields from, 173  
ionic radius in  $\text{UO}_2$ , 123  
as reactor fuel, 114  
self-diffusion in  $\text{UO}_2$ , 80, 241  
valence states in mixed oxides, 146
- Uranium carbide  
bubble pinning in, 251  
crystal structure of, 29-30  
microstructure of, 97  
nucleation of gas bubbles in, 225  
pore migration in, 270  
as reactor fuel, 114
- Uranium dioxide  
bubble pinning in, 251  
critical constants, 103, 106  
crystal energy, 41  
crystal structure, 30  
Debye temperature, 119  
density, liquid, 104-105  
solid, 114  
elastic constants, 385-386  
equation of state, 100, 106-112  
fracture and flow characteristics, 337-339  
heat of fusion, 105-106  
heat of transport for surface diffusion, 238  
melting, congruent, 116  
melting point, 116-117  
point defects in, 68  
self-diffusion in, 80-81, 241  
slip systems in, 333-335  
specific heat of, gaseous, 107-108  
solid, 66, 119-121  
standard free energy of formation, 151-152  
surface diffusivity of, 236  
surface tension of, 203  
thermal conductivity of, 122-127  
thermal-expansion coefficient of, 104, 106, 118  
thermodynamics in two-phase region, 109, 112  
vapor pressure of, 105, 160, 270  
yields of Frenkel pairs due to fission in, 408-410
- Vacancy, 56  
absorption by voids and dislocations, 484-485  
anion and cation, 62  
diffusion coefficient, 74-75, 205  
dislocation loop, 421, 464, 471, 505  
emission from pores, 365  
emission from voids, 474, 483, 491  
equilibrium concentration of, 57-60, 436, 472  
effect of lattice contraction on, 515  
effect of stress on, 231, 342, 352  
formation energy, 59  
number of, per fission gas atom in equilibrium bubbles, 230  
in oxide fuels with fission products, 180  
re-solution of, 372  
on surface, 240

- Vacancy-fission-gas clusters, 66
- Valence of heavy metals in mixed-oxide fuel, 146, 153, 183
- Vanadium wire method, 540-541, 564
- Van der Waals constant, 221
- Van der Waals equation of state, 202
- Van der Waals forces, 39
- Vapor pressure (saturation pressure), 102  
 effect of total pressure on, 112  
 of sodium, 518  
 of  $\text{UO}_2$ , 105, 160, 270
- Vapor transport  
 in actinide redistribution, 168-169  
 mechanism of pore migration, 266-273
- Vaporization  
 congruent, 160  
 mechanism of gas release, 330  
 of  $\text{MoO}_2$ , 198  
 of oxide fuels, 155-157, 160
- Vibration of atoms in solid, 14, 79  
 anharmonic, 22  
 in diffusion, 76, 81, 355  
 around interstitial, 61, 67  
 partition function of, 15  
 relation to potential energy, 72  
 around vacancy, 59
- Voids in metals, 203, 422  
 absorption of point defects, 484  
 conditions for formation, 465  
 continuity equations, 497-499  
 critical nucleus of, 475  
 distribution function, 465-466  
 effect of stress on, 492-494  
 on grain boundaries, 449-451  
 growth and shrinkage, 460, 491  
 incubation period for formation, 463, 466, 471, 497, 515  
 nucleation of, 470-480  
 saturation of growth of, 494-497  
 surface energy of, 464  
 swelling due to, 466-469, 498-499, 572, 580-582, 585, 589, 595  
 temperature dependence of, 491-492
- Volume  
 reduced, 102  
 of solid fission products, 193-194
- Volume diffusion coefficient, 240, 355
- Volume diffusion mechanism of  
 bubble migration, 239-241
- Wastage, 145, 518
- Water  
 critical compressibility factor, 103  
 standard free energy of formation, 171  
 vapor, in fuel, 150, 153, 161
- Wave vector, 17
- Wavelength  
 de Broglie, 12  
 thermal, 12
- Weeks-Isaacs model, 532-533
- Wigner release, 69
- Work hardening, 90, 425, 430, 456, 460
- Wrapper, 118, 583, 587, 589
- Xenon  
 critical constants, 202  
 diffusivity in oxide fuels, 205  
 diffusivity of  $\text{UO}_2$  in, 271  
 equation of state, 202  
*See also* Fission gases
- Yield drop, 425, 455
- Yield strength, 425  
 of bcc metals, 456  
 of cladding, 419  
 of perfect crystals, 82-84, 90  
 of steel, effect of sodium on, 553  
 of  $\text{UO}_2$ , 337-338
- Yields  
 of fission products, 172-175, 202  
 of Frenkel pairs per fission, 205, 408-410  
 of knock-on ejection in  $\text{UO}_2$ , 293  
 of vacancies and interstitials due to fast neutrons, 205, 436
- Young's modulus, 503, 570-571, 573, 600  
 effect of cracking on, 579-580  
 of  $\text{UO}_2$ , 335-336
- Zeldovich factor, 475
- Zero-point energy, 16
- Zircaloy cladding for LWR, 118
- Zirconates, 176, 182, 193, 194
- Zirconium  
 fission yield, 174, 196  
 swelling of, 464  
 in  $\text{UO}_2$ , 175, 180
- $\text{ZrO}_2$ -CaO bridge, 151, 543

## NOTICE

This book was prepared as an account of work sponsored by the United States Government. Neither the United States nor the United States Energy Research and Development Administration, nor any of their employees, nor any of their contractors, subcontractors, or their employees, makes any warranty, express or implied, or assumes any legal liability or responsibility for the accuracy, completeness or usefulness of any information, apparatus, product or process disclosed, or represents that its use would not infringe privately owned rights.

## CURRENT AWARENESS PUBLICATIONS ON ENERGY

To provide complete coverage of literature related to major Department programs, announcement publications that are comprehensive in their coverage of certain energy fields are issued regularly. All information in these publications, plus additional backup information, is included in the Energy Data

Base of the Office of Scientific and Technical Information; all references are also available for machine searching via the on-line retrieval system, DOE/RECON, and the commercial on-line retrieval systems. Descriptions of these current awareness publications, which are supported either

directly or indirectly by the DOE, appear below. Department of Energy components may receive the listed publications free from the Office of Scientific and Technical Information, U. S. Department of Energy, P. O. Box 62, Oak Ridge, TN 37831. Telephone (615) 576 1301; FTS 626-1301.

### PUBLICATIONS OF THE OFFICE OF SCIENTIFIC AND TECHNICAL INFORMATION

#### *Energy Abstracts for Policy Analysis (EAPA)*

A monthly abstract journal devoted to the analysis of energy research, conservation, and policy. Scope and coverage are limited to substantive articles or reports and emphasize legislative, regulatory, and other legal aspects, as well as social, economic, and environmental impacts. *EAPA* is available from the Superintendent of Documents, U. S. Government Printing Office, Washington, D. C. 20402. The annual subscription price is \$72.00 for domestic (North America) or \$90.00 for foreign (outside North America) subscribers; a single issue is \$5.00 or \$6.25, respectively.

#### *Energy Research Abstracts (ERA)*

A comprehensive semimonthly abstract journal devoted to all areas of energy-related information

The following monthly update journals are available to the public on subscription from the National Technical Information Service, 5285 Port Royal Road, Springfield, VA 22161; use the identifying order number (PB- No.) when subscribing. The annual subscription price (12 issues plus cumulative index) is \$75.00 for domestic (North America) and \$150.00 for foreign (outside North America) subscribers; a single issue is \$7.00 and \$14.00, respectively.

#### *Current Energy Patents (CEP)*-PB85-902800

Devoted to international patent literature, including patent applications, on any aspect of energy production, conservation, and utilization.

#### *Energy and the Environment (EAE)*-PB85-914900

Devoted to information on the impacts of energy-related activities and radioactive and non-radioactive pollutants on the environment.

The following semimonthly bulletins are also available from the National Technical Information Service. The annual subscription rate for one volume (calendar) year (24 issues; no indexes) is \$40.00 for domestic (North America) and \$80.00 for foreign (outside North America) subscribers; use the identifying order number (PB- No.) when subscribing.

#### *Acid Precipitation (APC)*-PB85-901000

Covers all aspects of acid precipitation, including effects and possible control measures.

#### *Buildings Energy Conservation (BEC)*-PB85-900700

Covers worldwide information on the technology required for energy conservation in buildings of all types.

#### *Coal-Based Synfuels (CBS)*-PB85-901400

Covers all aspects of conversion of coal into gaseous or liquid fuels.

#### *Coal Preparation and Pollution Control (CPC)*-PB85-900800

Covers all aspects of coal preparation and cleaning and reducing pollution from its direct combustion.

#### *Direct Energy Conversion (DEC)*-PB85-946600

Covers the following areas: photovoltaics, magnetohydrodynamics, electrohydrodynamics, thermoelectrics, thermionics, and fuel cells.

produced by the Department of Energy, other U. S. government organizations, and foreign governments. *ERA* is available from the Superintendent of Documents, U. S. Government Printing Office, Washington, D. C. 20402. The annual subscription price for the 24 issues is \$146.00 for domestic (North America) subscribers or \$182.50 for foreign (outside North America) subscribers. A single issue is \$14.00 or \$17.50, respectively.

#### *DOE Patents Available for Licensing (PAL)*

DOE is prepared to grant exclusive or nonexclusive, revocable licenses under DOE-owned U. S. patents and patent applications; this semiannual publication provides abstracting and indexing coverage of this literature. *PAL* is available on subscription (use PB85-946800) from the National

Technical Information Service, 5285 Port Royal Road, Springfield, VA 22161. The annual subscription price is \$14.00 for domestic (North America) or \$28.00 for foreign (outside North America); a single issue is \$8.00 or \$16.00, respectively.

#### *Energy Meetings (EM)*

A monthly listing of conferences, symposia, workshops, etc., pertaining to DOE's programmatic interests. *EM* is available on subscription (use PB85-901500) from the National Technical Information Service, 5285 Port Royal Road, Springfield, VA 22161. The annual subscription price is \$40.00 for domestic subscribers and \$80.00 for subscribers outside the North American continent; a single issue is \$5.00 and \$10.00, respectively.

#### *Fossil Energy Update (FEU)*-PB85-914600

Devoted to information on the exploration, development, processing, and use of fossil fuels.

#### *Fusion Energy Update (FEU)*-PB85-915300

Devoted to information on controlled thermonuclear fusion, including plasma and fuel research and power plant engineering and conceptual design studies.

#### *Solar Energy Update (SEU)*-PB85-914500

Devoted to information on the utilization of solar energy, including biomass and tidal and wind power.

#### *Energy from Biomass (EFB)*-PB85-900600

Covers worldwide information on all aspects of biomass production, conversion, and utilization for energy.

#### *Geothermal Energy Technology (GET)*-PB85-914700

Covers information on the exploration, development, and utilization of geothermal resources.

#### *Heavy-Ion Reactions (HIR)*-PB85-900500

Covers all aspects of heavy-ion ( $A > 4$ ) reactions.

#### *Laser Research (LAR)*-PB85-901100

Covers all aspects of laser research and development, but excludes applications.

#### *Nuclear Fuel Cycle (NFC)*-PB85-913400

Covers all aspects of the nuclear fuel cycle, both front end and back end.

#### *Nuclear Reactor Safety (NRS)*-PB85-913500

Covers the safety aspects of accident analysis, safety systems, radiation protection, decommissioning and dismantling, and security measures.

#### *Radioactive Waste Management (RWM)*-PB85-902900

Covers the management aspects of transport and storage, waste processing, waste disposal, waste storage, radioactive effluents, and shipping containers.

#### *Solar Thermal Energy Technology (STT)*-PB85-901200

Covers research in materials, concentrators/receivers, salinity gradients, etc., for development of efficient and reliable solar thermal conversion systems.

#### *Unconventional Petroleum (UCP)*-PB85-901300

Covers all aspects of secondary and tertiary recovery of petroleum and of oil shales and tar sands.

## INTERNATIONAL ENERGY PUBLICATIONS

The Office of Scientific and Technical Information (OSTI) cooperates in the publication of international abstract journals with the following: (1) International Atomic Energy Agency, International Nuclear Information System, Vienna, Austria, for *Atomindex*; (2) International Energy Agency, Biomass Conversion Technical Information Service, Dublin, Ireland, for *Biomass Abstracts*; and (3) International Energy Agency, IEA Coal Research, London, England, for *Coal Abstracts*. In each case, the cognizant foreign agency provides the non-U. S. information to OSTI for inclusion in the Energy Data Base; in turn, OSTI provides the U. S. information for input into the respective journal.

#### *Atomindex*

A semimonthly abstract journal providing worldwide coverage of information on nuclear science and technology. *Atomindex* is available by subscription from UNIPUB, 345 Park Avenue South, New York, NY 10010. The cost of an annual subscription, 24 semimonthly issues and semiannual and annual cumulative indexes, is \$290.

#### *Biomass Abstracts*

A bimonthly abstract journal with comprehensive coverage of information in any step involved in the eventual conversion of biomass to energy. *Biomass Abstracts* is available free to Department of Energy components and contractors from OSTI. Non-DOE organizations may obtain *Biomass Abstracts* from Biomass Conversion Technical Information Service, Institute for Industrial Research and Standards, Ballymun Road, Dublin 9, Ireland, for 42 IR pounds per year. Make checks payable to the Institute.

#### *Coal Abstracts*

A monthly abstract journal providing comprehensive worldwide coverage of information in the field of coal science and technology. *Coal Abstracts* is available to Department of Energy components and contractors from OSTI. Non-DOE organizations may obtain *Coal Abstracts* from IEA Coal Research, Technical Information Service, 14-15 Lower Grosvenor Place, London SW1W 0EX, England, for 100 pounds sterling per year.

A quick and reliable reference for information on the status of nuclear facilities in the United States and U. S.-made reactors abroad.

## **Nuclear Reactors Built, Being Built, or Planned in the United States**

This publication compiles current information on U. S. nuclear facilities that are capable of sustaining a nuclear chain reaction, including reactors in the following classifications:

### **Civilian Reactors (Domestic)**

Power Reactors  
Experimental Power Reactor Systems  
Test, Research, and University Reactors

### **Military Reactors**

Defense Power Reactor Applications  
Developmental Power Reactors  
Test and Research Reactors

### **Production Reactors**

Materials Production Reactors  
Process Development Reactors

### **Reactors for Export**

Power Reactors  
Test, Research, and Teaching Reactors

### **Critical Assembly Facilities**

Civilian Reactors  
Military Reactors

Under the above headings are listed the location, type, principal contractor, power rating, docket number, startup, and, where applicable, the shutdown date. There is a statistical summary of all reactors listed for domestic and foreign use. Also, there is a map showing the location of the U. S. commercial nuclear power plants with a summary of their nuclear generating capacity.

The Technical Information Center, Office of Scientific and Technical Information, U. S. Department of Energy (DOE), gathers this information from relevant DOE groups both in Washington, D. C., and in the various operations offices across the country. Other sources of information are the U. S. Nuclear Regulatory Commission, the U. S. reactor manufacturers who are the principal nuclear contractors for foreign locations, and the U. S. embassies of about 30 foreign countries.

Published semiannually by DOE Office of Scientific and Technical Information, Technical Information Center. 48 pages, 8½ × 11 in., paper binding (DOE/TIC-8200-R48).

This issue is available as PB84-903001 from

National Technical Information Service  
U. S. Department of Commerce  
Springfield, Virginia 22161

Ongoing standing-order service at \$10.00 per copy is available through an NTIS Deposit Account (Order No. PB84-903000). If you already have such an account, send your account number with an order to NTIS, Attn: Subscription Section. To establish a new NTIS Deposit Account, send the minimum \$25.00 deposit to NTIS, Attn: Customer Accounts. For a single copy, send \$10.00 and request the latest revision by publication title.

